

Batteries

2022 Annual Progress Report

Vehicle Technologies Office

(This page intentionally left blank)

Disclaimer

This report was prepared as an account of work sponsored by an agency of the United States government. Neither the United States government nor any agency thereof, nor any of their employees, makes any warranty, express or implied, or assumes any legal liability or responsibility for the accuracy, completeness, or usefulness of any information, apparatus, product, or process disclosed or represents that its use would not infringe privately owned rights. Reference herein to any specific commercial product, process, or service by trade name, trademark, manufacturer, or otherwise does not necessarily constitute or imply its endorsement, recommendation, or favoring by the United States government or any agency thereof. The views and opinions of authors expressed herein do not necessarily state or reflect those of the United States government or any agency thereof.

Acknowledgements

The projects reported in this report were supported through various contracts funded by the U.S. Department of Energy, Vehicle Technologies Office. A list of contributing authors appears in the sections for specific projects in this report.

Acronyms

AIBN	(2,2'-Azobis(2-methylpropionitrile))
ABL	Active buffer layer
ABMR	Advanced Battery Materials Research
AC	Alternating current
ACPA	4,4'-Azobis(4-cyanopentanoic acid)
ACS	American Chemical Society
AEM	Advanced Electrolyte Model
AER	All-electric range
AFLB	"Anode-free" lithium battery
AFM	Atomic force microscopy
AFSE	Fluorinated saturated electrolyte (FSE) with 0.1% wt additive
AI	Artificial Intelligence
AIMD	Ab initio molecular dynamics
AIR	Areal interfacial resistance
ALD	Atomic layer deposition
ALS	Advanced Light Source
AMD	Applied Materials Division (at ANL)
AMO	Advanced Manufacturing Office
AMR	Annual Merit Review
ANL	Argonne National Laboratory
AOM	Amphiphathic organic molecules
APL	Applied Physics Laboratory
APR	Annual progress report
APS	Advanced Photon Source (laboratory)
AQ	Anthraquinone
AQC	Anthraquinone-2-carboxylic acid
AQT	Soluble-type 1,5-bis(2-(2-(2-methoxyethoxy) ethoxy) ethoxy) anthra-9,10-quinon
ARL	Army Research Laboratory
ASI	Area-specific impedance
ASLSB	All solid lithium-sulfur battery
ASR	Area-specific resistance
ASSB	All solid-state battery
ASSLB	All solid-state Li metal batteries
ASSLMB	All-solid-state Li metal battery
ATIR	Attenuated total reflectance (spectroscopy)
B500	Battery500 (Consortium)
BAM	Battery active materials
BCC	Body-centered cubic
BET	Brunauer, Emmett, and Teller (surface area analysis)
BEV	Battery electric vehicle
BIL	Bipartisan Infrastructure Law
BLI	Beyond Lithium-ion

BM	Black mass
BMF	Battery manufacturing facility
BMP	Black mass purification (at NREL)
BMR	(Advanced) Battery Materials Research (program)
BMS	Battery management system
BNL	Brookhaven National Laboratory
BOL	Beginning of life
BOM	Bill of materials
BTC	Battery Technology Center
BTFE	Bis(2,2,2-trifluoroethyl) ether
BTMS	Behind-the-Meter-Storage
CAD	Computer-aided design
CAFE	Corporate Average Fuel Economy
CAM	Cathode active materials
CAMP	Cell analysis, modeling, and prototyping (facility)
CB	Carbon black
CBD	Conductive binder domain
CBSE	Cluster-based solid electrolytes
CCA	Carbon conductive additive
CCC	Cell cooling coefficient
CC-CV	Constant current constant voltage (charging protocol)
CCD	Critical current density
CD	Current density
CE	Coulombic efficiency
CEI	Cathode electrolyte interfaces
CFM	Carbon-based framework materials
CLP	Cycle life projection
CM	Co-melting (synthesis method)
CMC	Carboxymethyl cellulose
CNEB	Climbing image nudged elastic band
CNM	Center for Nanoscale Materials (at ANL)
CNS	Carbon nano structures
CNT	Carbon nano-tubes
COA	Certificates of analysis
CP	Co-precipitation
CPE	Constant phase element
CPI	Composite polymer introduction (layer)
CSM	Continuous symmetry measure
CSTR	Continuous stirred tank reactor
CV	Cyclic voltammetry
CY	Calendar year
DAC	Dry aerosol calcination
DBU	Diazabicycloundecane
DCIR	Direct current inner resistance
DCM	Dichloromethane (solvent)

DCR	Direct current resistance
DCT	Diffraction contrast tomography
DEB	Double-end binding (sites)
DEGDME	Diethylene glycol dimethyl ether
DEMS	Differential electrochemical mass spectrometry
DEPP	Diethyl phenylphosphonite
DFEC	Bis(trifluoroethyl) carbonate (DFEC)
DFOB	(Lithium) difluoro(oxalate)borate
DFT	Density function theory
DL	Deep-learning (algorithm)
DLE	Direct lithium extraction
DLP	Double-layer pouch (cell)
DMC	Dimethyl carbonate
DME	Dimethyl ether
DMF	Dimethylformamide
DMSO	Dimethylsulfoxide
DOD	Depth-of-discharge
DOE	Department of Energy
DOL	Dioxolane
DOS	Density of state
DPA	Destructive physical analysis
DPDMS	Diphenyldimethoxysilane
DRS	Disordered rock-salt
DRT	Distribution of relaxation times (analysis)
DRX	Disordered (rocksalt) transition metal oxides
DS	Double-sided
DSC	Differential scanning calorimetry
DST	Dynamic stress test
DTG	Derivative Thermo-Gravimetric (technique)
EADL	Electrochemical Analysis and Diagnostic Laboratory (at ANL)
EB	Electron beam
EBSD	Electron back-scattering diffraction
EBSD/EDS	Electron backscatter diffraction - energy dispersive X-ray spectrometry
EC	Ethylene carbonate
EC/DEC	Ethylene carbonate/diethyl carbonate (electrolyte)
EC/DMC	Ethylene carbonate/dimethyl carbonate (electrolyte)
EC/EMC/DEC	Ethylene carbonate/ethyl methyl carbonate/diethyl carbonate (electrolyte)
EC-AFM	Electrochemical atomic force microscopy
EC-EMC	Ethylene carbonate –ethyl methyl carbonate electrolytes
ECMF	Electrocatalyst modified framework material
ECS	Electrochemical Society
EDS	Energy dispersive spectroscopy
EDTA	Electric Drive Transportation Association
EDV	Electric Drive Vehicle
EDX	Energy-dispersive x-ray (spectroscopy)

EEL	Electron Energy Loss (Spectroscopy)
EELS	Electron energy loss spectroscopy
EERE	Energy Efficiency and Renewable Energy (DOE Office)
EIA	Energy Information Administration
EIS	Electrochemical impedance spectroscopy
EMC	Ethylmethyl carbonate
EMN	Energy Materials Network
EMS	Energy management system
EMT	Effective medium theory (calculation)
EO	Ethylene oxide
EODV	Voltage at the end of discharge
EOL	End of life
EPA	Environmental Protection agency
EPD	Electrophoretic deposition
EPR	Electron Paramagnetic Resonance
ESS	Energy storage system
EV	Electric vehicle
EXAFS	Extended X-ray absorption fine structure
FAMU	Florida A&M University
FASP	Flame-assisted spray pyrolysis synthesis
FC	Fast-charge
FCC	Face-centered cubic (structure)
FCG	Full concentration-gradient
FDES	Fluorinated deep eutectic solvent
FEC	Fluoro ethylene carbonate
FEMC	Fluoroethyl methyl carbonate
FFT	Fast Fourier-transform
FIB	Focused ion beam
FMMB	Mono-methyl-2,2,3,3-tetrafluorobutandiol
FOA	Federal opportunity announcement
FRS	Filtered Rayleigh Scattering
FSE	Fluorinated saturated electrolyte
FSI	(Lithium) bis(trifluoromethanesulfonyl)imide
FSP	Flame spray pyrolysis
FSP-DP	Flame spray pyrolysis - droplet-to-particle mode
FSP-GP	Flame spray pyrolysis - gas-to-particle mode
FTC	Freeze tape casting (technique)
FTIR	Fourier transform infrared spectroscopy
FWHM	Full width at half maximum
FY	Fiscal year
GC	“generation/collection” (mode)
GCMA	Glycerol carbonate methacrylate
GDL	(Carbon paper) gas diffusion layer
GDOES	Glow discharge optical emission spectrometry
GED	Gravimetric energy density

GEIS	Galvanostatic electrochemical impedance spectroscopy
GEMT	(McLachlan) generalized effective medium theory
GGA	Generalized gradient approximation
GHG	Green-house gases
GITT	Galvanostatic intermittent titration
GIXRD	Grazing incidence X-ray diffraction
GMU	George Mason University
GN	Glutaronitrile
GOS	Grain orientation spread
GPA	Geometric phase analysis
GPC	Gel permeation chromatography
GREET	Greenhouse gas regulated energy and emissions and transpiration
GROD	Grain reference orientation deviation
GSAS	General structure analysis systems
GSE	Glassy solid electrolyte
HAADF	High-angle annular dark-field
HATN	Hexaazatrinaphthylene
HAWCS	Hybrid Alternative Wet-Chemical Synthesis
HAXPES	High energy x-ray photoelectron spectroscopy
HL	Homogeneous baseline (coating design)
HEV	Hybrid electric vehicle
HEXRD	High-energy XRD
HF	Hydrofluoric acid
HFB	Hexafluorobenzene
HFE	Hydrocarbon vs. fluoroether
HFTO	Hydrogen and Fuel Cell Technologies Office
HG	Hand-grinding (mixing strategy)
HOMO	Highest occupied molecular orbital (energy level)
HOMO/LUMO	Highest occupied molecular orbital/lowest unoccupied molecular orbital (energy level)
HP	Hot-pressed (sample)
HPC	Highly porous carbon
HPLC	High-performance liquid chromatography
HPPC	Hybrid pulse power characterization
HRTEM	High-resolution transmission electron microscopy
HV	High viscosity (slurry)
HVM	High volume manufacturing
IC	Incremental capacity
ICE	Internal combustion engine
ICP	Inductively coupled plasma
IEA	International Energy Agency
INL	Idaho National Laboratory
IOFM	Inorganic-organic framework materials
IPA	Isopropanol
IPF	Inverse pole figure
IR	Infra-red

IRCL	Irreversible capacity loss
IZ	Isoxazole
KIC	Plane strain fracture toughness
KMC	Kinetic Monte Carlo (simulations)
KPFM	Kelvin Probe Force Microscopy
LAADF	Low-angle annular dark-field
LAGP	$\text{Li}_{1.5}\text{Al}_{0.5}\text{Ge}_{1.5}(\text{PO}_4)_3$
LAM	Loss of active materials
LAMMPS	Large-scale atomic/molecular massively parallel simulator
LAMNE	Loss of active materials at the negative electrode
LAMPE	Loss of active materials at the positive electrode
LANL	Los Alamos National Laboratory
LATP	$\text{Li}_{1.17}\text{Al}_{0.17}\text{Ti}_{1.83}(\text{PO}_4)_3$
LBL	Lawrence Berkeley National Laboratory
LBS	Lithium thioborates
LCA	Life cycle analysis
LCE	Lithium-carbonate equivalent
LCFC	Low-cost fast charge (battery)
LCI	Life-cycle inventory
LCO	Lithium cobalt oxide
LCOE	Levelized cost of electricity
LCRC	Laboratory Computing Resource Center (at ANL)
LDV	Light-duty vehicles
LE	Liquid electrolyte
LEDC	Lithium ethylene dicarbonate
LFP	Li-iron phosphate
LGPS	$\text{Li}_{10}\text{GeP}_2\text{S}_{12}$
LHCE	Localized high concentration electrolyte
LHS	Left hand-side
LIBRA	Lithium Ion Battery Recycling Analysis
LIC	Lithium-ion conducting
LLI	Loss of lithium inventory
LLNL	Lawrence Livermore National Laboratory
LLS	Layered-layered spinel
LLZ	$\text{Li}_7\text{La}_3\text{Zr}_2\text{O}_{12}$
LLZO	Lithium lanthanum zirconate
LLZTO	$\text{Li}_{6.75}\text{La}_3\text{Zr}_{1.75}\text{Ta}_{0.25}\text{O}_{12}$
LMA	Lithium metal anode
LMB	Lithium metal battery
LMNOF	Li-Mn-Nb-O-F
LMO	Lithium manganese oxide
LMR	Lithium manganese rich (cathode)
LMSSB	Li metal solid-state battery
LMTO	$\text{Li}_{1.2}\text{Mn}_{0.4}\text{Ti}_{0.4}\text{O}_2$ (cathode)
LMTOF	Li-Mn-Ti-O-F

LNMO	$\text{LiNi}_{0.5}\text{Mn}_{0.5}\text{O}_2$
LNMT0	$\text{LiNi}_{0.5}\text{Mn}_{1.2}\text{TiO}_{0.3}\text{O}_4$
LNO	Lithium-nickel oxide
LNTMOF	$\text{Li}_{1.15}\text{Ni}_{0.45}\text{Ti}_{0.3}\text{Mo}_{0.1}\text{O}_{1.85}\text{F}_{0.15}$
LPBSI	$\text{Li}_7\text{P}_2\text{S}_8\text{Br}_{0.5}\text{I}_{0.5}$
LPC	Large particle cathodes
LPF	$\text{Li}/\text{LiFePO}_4$ (half-cell)
LPO	Li_3PO_4
LPS	Li_3PS_4
LPSBI	$\text{Li}_7\text{P}_2\text{S}_8\text{Br}_{0.5}\text{I}_{0.5}$
LPSIB	$\text{Li}_7\text{P}_2\text{S}_8\text{I}_{0.5}\text{Br}_{0.5}$
LPSX	$\text{Li}_{7-y}\text{PS}_{6-y}\text{X}_y$
LSCE	Locally-superconcentrated electrolyte
LSE	Localized saturated electrolyte
LSV	Linear scanning voltammetry
LT	Low-temperature
LTAP	$\text{Li}_{1.3}\text{Al}_{0.3}\text{Ti}_{1.7}(\text{PO}_4)_3$
LTMO	$\text{Li}_{1.2}\text{Mn}_{0.4}\text{Ti}_{0.4}\text{O}_2$
LTO	Lithium titanate, $\text{Li}_4\text{Ti}_5\text{O}_{12}$
LUMO	Lowest unoccupied molecular orbital (energy level)
LV	Low viscosity
LYB	Li_3YBr_6
LYC	Li_3YCl_6
MAS	Magic angle spinning
MC	Monte Carlo (method)
MCA	Multicomponent alloy
MCF	Methyl chloroformate
MERF	Materials Engineering Research Facility
MFA	Material flow analysis
MGF	Mixed glass former (glassy film)
MIC	Molecular ionic composites
ML	Machine learning
MLFF	Machine learning-based force field
MLMD	Machine learning-based molecular dynamic (simulation)
MLPC	Multi-layer pouch cell
MMB	Monomethyl butanediol
MOF	Metal Organic Framework
MOSN	Mixed oxy-sulfide-nitride (glass)
MP	Methyl propionate
MPFPC	Methyl (pentafluoropropyl)carbonate
MRS	Materials Research Society
MS	Mass spectroscopy
MSD	Mean square displacements
MSR	Material-stress reduction (protocol)
MTFPC	Methyl (tetrafluoropropyl)carbonate

NASICON	(Na) Super Ionic CONductor
NATM	Naturally abundant material
NBR	Nitrile butadiene rubber
NCA	$\text{LiNi}_{0.8}\text{Co}_{0.15}\text{Al}_{0.05}\text{O}_2$
NCM	$\text{Li}_{1+w}[\text{Ni}_x\text{Co}_y\text{Mn}_z]_{1-w}\text{O}_2$
NEB	Nudged elastic band (method)
NETL	National Energy Technology Laboratory
NEXAFS	Near-edge X-ray absorption fine structure (measurements)
NF	Nanoflakes
NG	Natural graphite (anode)
NHTSA	National Highway Transportation Safety Administration
NIB	Sodium (Na)-ion battery
NIR	Near-infrared (emission)
NKB	Nitrogen doped integrated Ketjen Black (particles)
NMA	$\text{LiNi}_{0.9}\text{Mn}_{0.05}\text{Al}_{0.05}\text{O}_2$
NMC	Nickel manganese cobalt (oxide)
NMCA	Nickel-manganese-cobalt-aluminium oxide (cathode)
NMFCN	NaMnFeCoNiO_2
NMP	N-methylpyrrolidone
NMR	Nuclear magnetic resonance
NP	Nanoparticles
NPDF	Neutron PDF
NR	Neutron reflectometry
NREL	National Renewable Energy Laboratory
NTO	(Lithium manganese) nickel titanium oxide
NVP	$\text{Na} \text{Na}_3\text{V}_2(\text{PO}_4)_3$ (cathode)
NVT	Canonical ensemble (N, V, T conditions)
OCV	Open circuit voltage
OEM	Original equipment manufacturer
OER	Oxygen evolution reactions
OES	Optical Emission Spectroscopy
OMSH	Ordered macroporous sulfur host
OPLS	Optimized potentials for liquid simulations
ORNL	Oak Ridge National Laboratory
ORR	Oxygen reduction reaction
OSE	Optical spectroscopic ellipsometry
OSU	Oregon State University
P&E	Processing Science & Engineering
P&ID	Piping and instrumentation diagram
PAA	Polyacrylic Acid
PAD	Polymer Assisted Deposition
PAN	Polyacrylonitrile
PAQ	9,10-phenanthrenequinone
PAW	Projected augmented wave
PBDT	Poly-2,2'-disulfonyl-4,4'-benzidine ter-ephthalamide

PBE	Perdew, Burke, and Ernzerhof (parameters)
PBLM	Parallel brick layer model
PC	Propylene carbonate
PCC	Project completion cell
PDF	Pair density function
PE	Polyethylene
PECVD	Plasma-enhanced chemical vapor deposition
PEEK	Polyetheretherketone
PEGDA	Poly(ethylene glycol) diacrylate
PEGDGE	Poly(ethylene glycol) diglycidyl ether
PEGDMA	Polyethylene glycol dimethacrylate
PEI	Polyethylenimine
PEM	Poly(ethylene malonate)
PEO	Polyethyleneoxide
PES	Prop-1-ene-1,3-sultone
PET	Polyethylene terephthalate
PEV	Plug-in electric vehicle
PEY	Partial electron yield
PFE	Pentafluoroethane
PFIB-SEM	Plasma focused ion beam scanning electron microscopy
PFM	Poly (9,9-dioctylfluorene-co-fluorenone-comethylbenzoic ester
PFPE	Perfluoropolyether
PFY	Partial fluorescence yield
PHEV	Plug-in hybrid electric vehicle
PHM	Poly(hexylene malonate)
PI	Principal investigator
PITT	Potentiostatic intermittent titration technique
PL	Photoluminescence
PLD	Pulsed laser deposition
PLIF	Planar Laser Induced Fluorescence
PMF	Poly(melamine-co-formaldehyde) methylated
PMS	Power management system
PMTH	Dipentamethylenethiuram hexasulfide
PNCM	Phosphate-affected NCM cathode
PNNL	Pacific Northwest National Laboratory
PPM	Poly(pentylene malonate)
PPO	Polyphenylene oxide
PSD	Particle size distribution
PSU	Pennsylvania State University
PTF	Post-Test Facility
PTFE	Poly(tetrafluoroethylene) (cathode)
PTM	Poly(trimethylene malonate)
PTO	Pyrene-4,5,9,10-tetraone
PTSI	p-toluenesulfonyl isocyanate
PVDF	Poly(vinylidene fluoride)

PVP	Poly(vinylpolypyrrolidone)
PXRD	Powder X-ray diffraction
QC	Quantum chemistry
R&D	Research and Development
RAFT	Reversible addition fragmentation chain-transfer
RAM	Resonant acoustic mixer
RCT	Rate capability test
RE	Reference electrode
RHS	Right hand-side
RIM	Reflection interference microscope
RIXS	Resonant inelastic x-ray scattering
RM	Redox mediator
RMD	Reactive molecular dynamics
RME	Relative molal enthalpy
RNGC	Realizing Next Generation Cathodes
RNMC	Reaction network-based Monte Carlo
ROI	Return on investment
RPM	Revolutions per minute
RPT	Reference performance test
RR	Reduced-repulsion (channel)
RRDE	Rotating ring disk electrode
RST	Reactive Spray Technology
RT	Room temperature
RTMS	Reciprocal ternary molten salts
SAED	Selected area electrode diffraction
SAXS	Small angle X-Ray scattering
SBC	Soluble base content
SBIR	Small Business Innovation Research
SCA	Supply chain analysis
SCN	Li ₆ PS ₅
SCP	Sulfur containing polymer
SDS	Safety data sheet
SE	Solid electrolyte
SECM	Scanning electrochemical microscope
SEI	Solid electrolyte interphase
SEM	Scanning electron microscopy
SLAC	Stanford acceleration laboratory
SNL	Sandia National Laboratories
SOA	State of the art
SOC	State of charge
SOW	Statement of work
SPAN	Sulfurized Polyacrylonitrile
SPC	Small particle cathodes
SPE	Solid polymer electrolyte
SPLE	Single-particle-layer electrode

SPM	Scanning probe microscopy
SRL	Synchrotron Radiation Lightsource
SRO	Short-range order
SSB	Solid-state battery
SSE	Solid-state electrolyte
SSE-A	Anode-side solid secondary electrolytes
SSLMB	Solid-state Li-metal battery
SSR	Supersaturation ratio
SSRL	Stanford Synchrotron Radiation Lightsource
SSS	Stainless steel spacers
STEM	Scanning transmission electron microscopy
STEM-	Scanning transmission electron microscopy- high-angle annular dark-field
STTR	Small Business Technology Transfer Program
SXRD	Surface X-ray diffraction
TAC	Technical Advisory Committee
TARDEC	(U.S. Army) Tank Automotive Research, Development and Engineering Center
TCP	Technology Collaboration Program
TEA	Technoeconomic analysis
TEGDME	Tetraethyleneglycoldimethyl
TEM	Transmission electron microscopy
TES	Tender-energy x-ray absorption spectroscopy
TEY	Total electron yield
TFE	Trifluoroethanol
TFP	Tris(2,2,2-trifluoroethyl) phosphate
TFSI	Bistriflimide (anion)
TGA	Thermal gravimetric analysis
TGC	Titration gas chromatography
THF	Tetrahydrofuran
TMA	Trimethylaluminum
TMB	Trimethylboroxine
TMDC	Transition metal dichalcogenide
TMO	Transition metal oxide
TMP	Trimethyl phosphate
TMPMA	Trimethylolpropane methacrylate
TOF-SIMS	Time-of-flight secondary ion mass spectrometry
TPP	Triphenylphosphate
TRL	Technology Readiness Level
TR-XAS	TR-XRD and absorption
TR-XRD	Time-resolved x-ray diffraction
TTE	Tetrafluoropropyl ether
TTT	Time-temperature-transition
TVR	Taylor Vortex Reactor
TXM	Transmission X-ray microscopy
UAH	University of Alabama at Huntsville
UCB	University of Valifornia, Berkeley

UCI	University of California, Irvine
UCSD	University of California, San Diego
UCV	Upper cutoff voltage
UF	Ultra-Fine (concentrator)
UHE	Ultra-high energy (cathode)
UHV	Ultrahigh vacuum (system)
UIC	University of Illinois at Chicago
UM	University of Michigan
UMD	University of Maryland
UNC	University of North Carolina
UNCC	University of North Carolina-Charlotte
URI	University of Rhode Island
USABC	United States Advanced Battery Consortium
USCAR	United States Council for Automotive Research
USDRIIVE	U.S. Driving Research and Innovation for Vehicle efficiency and Energy sustainability
USGS	United States Geological Survey
VC	Vinylene carbonate
VCU	Virginia Commonwealth University
VED	Volumetric energy density
VNCM	Virgin NCM cathode
VOC	Volatile organic compounds
VR	Voltage ramp
VSP	Voucher Service Provider
VTO	Vehicle Technologies Office
WAXS	Wide-angle X-ray scattering
WT-EXAFS	Wavelet-transformed EXAFS
XANES	X-ray absorption near edge structure
XAS	X-ray absorption spectroscopy
XCEL	EXtreme Fast Charge Cell Evaluation of Lithium-ion Batteries
XFC	Extreme fast charging
XPB	X-ray powder diffraction
XPEEM	X-ray photoemission electron microscopy
XPS	X-ray photoelectron spectroscopy
XRD	X-ray diffraction
XRF	X-ray fluorescence (microscopy)
XRR	X-ray reflectivity
XRS	X-ray Raman Spectroscopy
XSEDE	Extreme Science and Engineering Discovery Environment

Executive Summary

Introduction

The U.S. Department of Energy's (DOE) Vehicle Technologies Office (VTO) funds research, development, demonstration, and deployment of new, efficient, and clean mobility options that are affordable for all Americans. Technologies supported by VTO include electric drive components such as advanced energy storage devices (primarily batteries); power electronics and electric drive motors; advanced structural materials; energy efficient mobility systems; innovative powertrains to reduce greenhouse gas and criteria emissions from hard-to-decarbonize off-road, maritime, rail, and aviation sectors; and fuels. One of the major VTO objectives is to enable U.S. innovators to rapidly develop the next generation of technologies that achieve the cost, range, and charging infrastructure necessary for the widespread adoption of plug-in electric vehicles (PEVs). An important prerequisite for the electrification of the nation's light duty transportation sector is development of more cost-effective, longer lasting, and more abuse-tolerant PEV batteries. One of the ultimate goals of this research, consistent with the current vehicle electrification trend, is an EV which can provide the full driving performance, convenience, and price of an internal combustion engine (ICE) vehicle. To achieve this, VTO has established the following overarching goal (Source: FY2023 Congressional Budget Request¹):

... reducing electric vehicle (EV) battery cell cost by 50 percent to \$60/kWh by 2030 to achieve EV cost parity with internal combustion engine vehicles; eliminating dependence on critical materials such as cobalt, nickel, and graphite, reducing battery supply chain vulnerabilities by 2030; and establishing a lithium battery recycling ecosystem to recover 90 percent of spent lithium batteries and re-introducing 90 percent of key materials into the battery supply chain by 2030.

VTO works with key U.S. automakers through the United States Council for Automotive Research (USCAR) – an umbrella organization for collaborative research consisting of Stellantis N.V., the Ford Motor Company, and General Motors. Collaboration with automakers through the partnership known as U.S. Driving Research and Innovation for Vehicle Efficiency and Energy Sustainability (U.S. DRIVE) attempts to enhance the relevance and the success potential of its research portfolio. VTO competitively selects projects for funding through funding opportunity announcements (FOAs). Directly-funded work at the national laboratories are awarded competitively through a lab-call process. Stakeholders for VTO R&D include universities, national laboratories, other government agencies and industry (including automakers, battery manufacturers, material suppliers, component developers, private research firms, and small businesses).

This document summarizes the progress of VTO battery R&D projects supported during the fiscal year 2022 (FY 2022). In FY 2022, the DOE VTO battery R&D funding was approximately \$129 million. Its R&D focus was on the development of high-energy batteries for PEVs. The electrochemical energy storage roadmap (which can be found at the EERE Roadmap web page²) describes ongoing and planned efforts to develop electrochemical storage technologies for EVs. To advance battery technology, which can in turn improve market penetration of PEVs, the program investigates various battery chemistries to overcome specific technical barriers, e.g., battery cost, performance, life (both the calendar life and the cycle life), its tolerance to abusive conditions, and its recyclability/sustainability. VTO R&D has had considerable success, lowering the cost of EV battery packs to \$130/kWh in 2022, based on useable energy (representing a nearly 90% reduction since 2008) yet even further cost reduction is necessary for EVs to achieve head-to-head cost competitiveness with internal combustion engines (without Federal subsidies). In addition, today's batteries also need improvements in such areas as their ability to accept charging at a high rate, referred to as extreme fast charging (XFC) (15 minute charge) – to provide a “refueling” convenience similar to ICEs, and the ability to operate adequately at low

¹ <https://www.energy.gov/sites/default/files/2022-04/doe-fy2023-budget-volume-4.pdf>, FY 2023 Congressional Budget Request, Volume 4, Part 1, Page 9.

² <http://energy.gov/eere/vehicles/downloads/us-drive-electrochemical-energy-storage-technical-team-roadmap>.

temperatures. Research into “next-gen lithium-ion” batteries which would provide such functionalities is one of the R&D focus areas. VTO is funding research on both “next gen” chemistries (which employ an alloy anode and/or a high voltage cathode) and beyond lithium-ion (BLI) chemistries (which can, for example, employ a lithium metal anode). Current cycle and calendar lives of next gen and BLI chemistries are well short of goals set for EVs. To quantify the improvements needed to accelerate large-scale adoption of PEVs and HEVs, certain performance and cost targets have been established. Some sample performance and cost targets for EV batteries, both at cell level and at system (pack) level, are shown in Table ES- 1.

Table ES- 1: Subset of EV Requirements for Batteries and Cells

Energy Storage Goals (by characteristic)	Pack Level	Cell Level
Cost @ 100k units/year (kWh = useable energy)	\$100/kWh*	\$75/kWh*
Peak specific discharge power (30s)	470 W/kg	700 W/kg
Peak specific regen power (10s)	200 W/kg	300 W/kg
Useable specific energy (C/3)	235 Wh/kg*	350 Wh/kg*
Calendar life	15 years	15 years
Deep discharge cycle life	1000 cycles	1000 cycles
Low temperature performance	>70% useable energy @C/3 discharge at -20 °C	>70% useable energy @C/3 discharge at -20 °C
	*Current commercial cells and packs not meeting the goal	

The batteries R&D effort includes multiple activities, ranging from focused fundamental materials research to prototype battery cell development and testing. It includes, as mentioned above, R&D on “next-gen” and BLI materials and cell components, as well as on synthesis and design, recycling, and cost reduction. Those activities are organized into mainly two program elements:

- Advanced Battery and Cell R&D
- Advanced Materials R&D.

A short overview of each of those program elements is given below.

Advanced Battery and Cell R&D

The *Advanced Battery and Cell R&D* activity focuses on the development of robust battery cells and modules to significantly reduce battery cost, increase life, and improve performance. This work mainly spans the following general areas:

- United States Advanced Battery Consortium (USABC)-supported battery development & materials R&D (11 projects)
- Processing science and engineering (11 projects)
- Recycling and sustainability (five projects)
- Extreme fast-charging (multiple projects organized into three “thrust areas”)
- Beyond batteries (a single comprehensive project)
- Testing, Analysis, High-Performance Computing, Lab-I4 (eight projects)
- Small business innovative research (SBIR) (multiple Phase I and Phase II projects).

Chapters I through VII of this report describe projects under the *Advanced Battery and Cell R&D* activity. This effort involves close partnership with the automotive industry, through a USABC cooperative agreement. In FY 2022, VTO supported 11 USABC cost-shared contracts with developers to further the development of

advanced automotive batteries and battery components. The estimated DOE share of those USABC contracts (over the life of the contracts) is approximately \$39M. These include fast-charge and low-cost lithium ion batteries for electric vehicle applications (Zenlabs Energy), low-cost, high safety fast charge automotive cells (Microvast, Inc.), high energy and power density lithium-ion battery based on neocarbonixtm polymer binder-free electrode technology for EV applications (Nanoramic), evaluation of advanced Li-ion cell architectures for extreme fast charging (XFC) batteries for EVs (EnPower, Inc.), solvent-free electrode manufacturing for low cost/fast charging batteries (Worcester Polytechnic Institute), low-cost, fast-charge EV: system -Ni-rich NCM cathode, coated anode, fluorinated solvents (Farasis), pre-lithiation of silicon-containing anodes for high-performance EV batteries (Applied Materials), high performance electrolyte for LNMO/LTO batteries (Gotion), integrated, zero discharge process train, no tipping model (ABMC), silicon-based EV cells meeting cost, calendar life and power (Ionblox), and low cost, fast-charging silicon nanowire cell technology (Amprius).

In addition to the USABC projects listed above, VTO also supports eleven *processing science and engineering* projects at the national labs. Most strategies for increasing the performance (and reducing cost) of lithium-ion batteries focus on novel battery chemistries, material loading modifications, and increasing electrode thickness. The latter approach is generally considered useful for increasing energy density (and in turn, the overall cell capacity). However, practical thicknesses are constrained by ionic transport limitations (which limit cell power) and processing issues. Project participants in this area include ANL, BNL, LBNL, and ORNL. The estimated value of those advanced processing projects (over project lifetime) is approximately \$35M.

The *Recycling and Sustainability* activity involves studies of the full life-cycle impacts and costs of lithium-ion battery production/use; cost assessments and impacts of various recycling technologies; and the available material and cost impacts of recycling and secondary use. The participants include ANL, NREL, Farasis Energy, and Worcester Polytechnic Institute and the associated budget is approximately \$10M.

To become truly competitive with the internal combustion engine vehicle (ICEV) refueling experience, EV charging times must also be significantly shorter than at present. A research project to understand/enable extreme fast charging (XFC) in enhanced lithium-ion systems – charging an EV at power rates of up to 400 kW, began back in FY 2017. Projects on three “thrust areas”: anode & electrolyte thrust, electrode and cell design thrust, and electrochemical and thermal performance thrust. Team members include LBNL, INL, ANL, ORNL, NREL, and SLAC. In addition, a “behind the meter” storage project is taking place by a team which includes NREL, and SNL. This area focuses on novel battery technologies to facilitate the integration of high-rate EV charging, solar power generation technologies, and energy-efficient buildings while minimizing both cost and grid impacts.

The *battery testing, analysis, and high-performance computing* activity develops requirements and test procedures for batteries (to evaluate battery performance, battery life and abuse tolerance). Battery technologies are evaluated according to USABC-stipulated battery test procedures. The *battery testing* activity includes performance, life and safety testing, and thermal analysis and characterization. It currently includes four projects based at ANL, INL, SNL, and NREL. The testing activity also supports cell analysis, modeling, and prototyping (CAMP) projects at ANL, which include benchmarking and post-test analysis of lithium-ion battery materials at three labs (ANL, ORNL, and SNL). Projects include testing (for performance, life and abuse tolerance) of cells (for contract, laboratory-developed and university-developed cells), and benchmarking systems from industry; thermal analysis, thermal testing, and modeling; cost modeling; and other battery use and life studies. *Cost assessments and requirements analysis* includes an ANL project on developing the performance and cost model BatPaC. This rigorously peer-reviewed model developed at ANL is used to design automotive lithium-ion batteries to meet the specifications for a given vehicle, and estimate its cost of manufacture.

VTO also supports several *small business innovation research* (SBIR) contracts. These SBIR projects focus on development of new battery materials and components and provide a source of new ideas and concepts. The section on SBIR projects includes a short list of recent Phase I and Phase II projects awarded during FY 2022.

Advanced Materials R&D

The *Advanced materials research & development* activity (covered in Chapters VIII to Chapter XX of this report) addresses fundamental issues of materials and electrochemical interactions associated with rechargeable automotive batteries. It develops new/promising materials and makes use of advanced material models to discover them, utilizing scientific diagnostic tools and techniques to gain insight into their failure modes and processes. It is conducted by various national labs, universities, and industry partners. The work is divided into two general areas –“next gen” chemistries (which can, for example, employ an alloy anode and/or a high voltage cathode) and beyond lithium-ion (BLI) chemistries (which can, for example, employ a lithium metal anode). The projects are distributed as follows:

- Next generation (next-gen) lithium-ion battery technologies (24 projects)
 - Advanced anodes (17 projects)
 - Advanced cathodes (six projects)
 - Frontier science at interfaces (five projects)
 - No-cobalt/Low-cobalt cathodes (six projects)
 - Diagnostics (four projects)
 - Modeling of advanced material (four projects)
 - Low temperature electrolytes (three projects).
- Beyond lithium-ion battery technologies
 - Metallic lithium (four projects)
 - Solid-state batteries (32 projects)
 - Lithium sulfur (eight projects)
 - Lithium-air Batteries (three projects)
 - Sodium-ion batteries (four projects)
 - Battery500 Consortium (several keystone and seedling projects).

The *next generation lithium-ion battery* R&D area’s goal is to advance material performances, designs, and processes to significantly improve performance and reduce the cost of lithium-ion batteries using an alloy or intermetallic anode and/or high voltage cathode. Specific areas of investigation include high-energy anodes (e.g., those containing silicon or tin), high voltage cathodes, high voltage and non-flammable electrolytes, novel processing technologies, high-energy and low-cost electrode designs, and certain other areas. This work spans a range of U.S. DRIVE activities.

- Advanced anodes R&D includes 17 multi-lab collaborative projects – based in national laboratory consortiums (NREL, PNNL, ANL, ORNL, and LBNL), in industry (Applied Materials, Enovix, Group-14 Technology, Sila Nano, and Solid Power), and at universities (Stonybrook University, University of Delaware, and University of Maryland).
- Advanced cathodes R&D includes six projects based at five national labs (ANL, ORNL, LBNL, NREL, and PNNL) and a university (UC, Santa Barbara). In addition, there are six low-cobalt/no-cobalt cathode projects based at two industry partners (Cabot and Nexersis), one national lab (ORNL), and four universities (UCSD, UC Irvine, UTA, and PSU).
- Frontier science at interfaces R&D includes five projects, including those on molecular-level understanding of cathode-electrolyte interfaces (SLAC and NREL), interfacial studies of emerging cathode materials (LBNL), high-energy cathodes and their interfaces with electrolytes for next-generation Li-ion batteries (PNNL), fluorinated deep eutectic solvent (FDES)-based electrolytes (ANL), and *in situ* microscopies for the model cathode/electrolyte interface (NREL).

- Diagnostics R&D includes four projects ranging from interfacial processes to *in situ* diagnostic techniques and advanced microscopy, thermal diagnostics, and synthesis and characterization. The various researchers for these projects are based at LBNL, BNL, and PNNL.
- There are four modeling projects: electrode materials design and failure prediction (ANL), model-system synthesis and advanced characterization (LBNL), design of high-energy, high-voltage lithium batteries through first-principles modeling (LBNL), and characterization and modeling of Li-metal batteries: modeling and design of amorphous solid-state Li conductors (LBNL).
- There are three low-temperature electrolyte projects: ethylene carbonate-lean electrolytes (LBNL), fluorinated solvent-based electrolytes (ANL), and synthesis, screening and characterization of low temperature electrolyte (BNL).

R&D on *beyond lithium-ion battery technologies* includes solid-state technology, lithium metal systems, lithium sulfur, lithium air, and sodium-ion. The main areas of focus include new methods to understand/stabilize lithium metal anodes; lithium polysulfides to enable the use of sulfur cathodes; and developing electrolytes for lithium air and lithium sulfur cells. These systems offer further increases in energy and potentially reduced cost compared to the next-gen lithium-ion batteries. However, they also require additional breakthroughs in materials (often at a fundamental level) before commercial use. VTO is investigating the issues and potential solutions associated with cycling metal anodes. The main research topics include: coatings, novel oxide and sulfide-based glassy electrolytes, and *in situ* diagnostics approaches to characterize and understand Li metal behavior during electrochemical cycling.

- Metallic lithium R&D includes four projects based at three national laboratories (LLNL, PNNL, and SLAC).
- Solid state batteries R&D includes 32 projects. These are based at multiple national laboratories (ANL, PNNL, LBNL, NREL, LLNL, ORNL, BNL, SLAC), universities (University of California, University of Maryland, College Park, Iowa State University of Science and Technology, University of Michigan, Virginia Polytechnic Institute and State University, Penn State University Park, University of Wisconsin-Milwaukee, University of Houston, Virginia Commonwealth University, and University of Louisville), and industry members (Solid Power, Inc, and General Motors LLC).
- Lithium sulfur R&D includes eight projects – four of them based at national laboratories (ANL, LBNL, and PNNL) and the other four at universities (the University of Wisconsin Milwaukee, University of California, San Diego, University of Pittsburgh, and Penn State University).
- Additional beyond lithium-ion projects include three on Lithium-Air batteries (two at ANL and one at the University of Illinois) and four on Sodium-ion batteries (based at ANL, BNL, LBNL, and PNNL).

The *Battery500 Innovation Center* is a combined effort by a team of four national labs (PNNL, BNL, INL, and SLAC) and five universities (University of Texas-Austin, Stanford University, Binghamton University, University of Washington, and University of California, San Diego) with the goal to develop commercially viable lithium battery technologies with a cell level specific energy of 500 Wh/kg while simultaneously achieving 1,000 deep-discharge cycles. The consortium keystone projects focus on innovative electrode and cell designs that enable maximizing the capacity from advanced electrode materials. The consortium works closely with the R&D community, battery/materials manufacturers and end-users/OEMs to ensure that these technologies align well with industry needs and can be transitioned to production.

Recent Highlights

LiNiO₂ Enabled by Optimized Synthesis Conditions (ANL)

The LiNiO₂ (LNO) cathode has been of interest for many years because of its high energy and lack of expensive cobalt. However, it has never achieved commercial success due, in part, to cycling instabilities (presumed inherent to the material) at high states of charge. However, due to the sensitivity of LNO to

synthesis conditions such as precursor control, temperature, and atmosphere, virtually all LNO cathodes studied to date contain defects. Work at ANL has shown that near ideal, ‘defect-free’ LNO can be synthesized through better control of synthesis. ANL’s ‘defect-free’ LNO cycles at high capacities (>220 mAh/g) over many cycles without dopants, coatings, or electrolyte additives. Such high performance, including very low initial irreversible capacity (~96%), has never been reported for LNO. Key to achieving such results was precise control of synthesis parameters including novel precursor preparation, calcination conditions that facilitate minimum local defects ($\text{Li}^+/\text{Ni}^{2+}$ mixing, O_2 vacancies, stacking faults), optimized primary and secondary particle morphologies, and a higher resistance to secondary particle cracking. Surprisingly, synthesis of ‘defect-free’ LNO could be enabled within a wide range of O_2 partial pressures, even as low as 0.2 atm. Full-cell tests with graphite anodes and Gen 2 electrolyte (1.2 M LiPF_6 in EC:EMC (3:7 by weight)) showed performance on par with $\text{LiNi}_{0.9}\text{Mn}_{0.05}\text{Co}_{0.05}\text{O}_2$, when cycled over similar states of charge, Figure ES- 1. Note that three hour holds at the top of every charge were used to push stability limits.

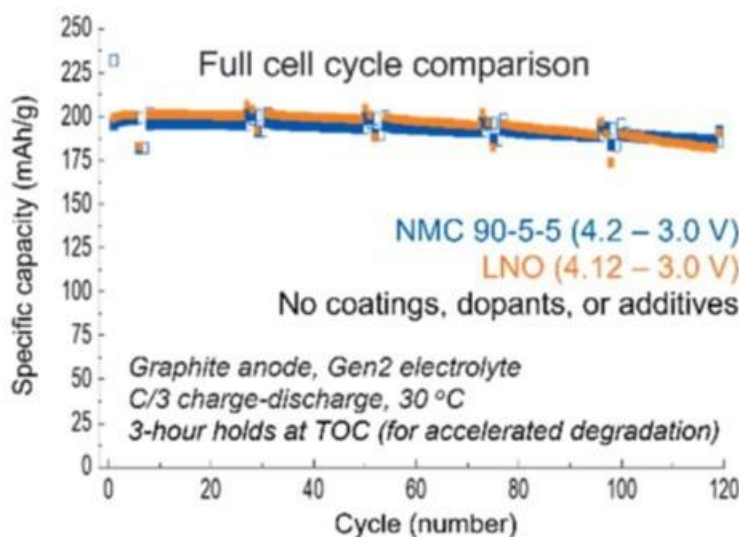


Figure ES- 1. Full cell performance comparison of optimized LNO vs. $\text{LiNi}_{0.9}\text{Mn}_{0.05}\text{Co}_{0.05}\text{O}_2$

Developing low-cost rechargeable lithium-sulfur batteries (Battery500 Consortium)

The Battery500 Consortium has advanced the performance of a lithium-sulfur (Li-S) battery through innovation in battery electrolytes and improved understanding of a polymer-derived sulfur cathode. A 2 Ah pouch cell with an energy density of 250Wh/kg (which is competitive with current lithium-ion EV cells) has been demonstrated.

Sulfurized PolyAcryloNitrile (SPAN) is a low-cost material containing no critical materials and is readily made by heating sulfur with PAN, an industrial product, at 300-500°C. Unlike elemental sulfur-based cathodes, SPAN appears to avoid the generation of soluble polysulfide species, which lead to capacity fade and is very sensitive to electrolyte amounts. To enable a long-life Li-SPAN battery, electrolytes need to be stable at both the Li anode and the SPAN cathode. The Consortium has developed a localized concentrated electrolyte consisting of 1.8 M lithium bis(fluorosulfonyl)imide (LiFSI) in diethyl ether (DEE) and Bis(2,2,2-trifluoroethyl) ether (BTFE). This electrolyte forms a protection layer on the SPAN surface that prevents loss of sulfur to the electrolyte. In addition, Li cycles stably due to the formation of a LiF-rich SEI. Both Li and SPAN show around 1000 stable cycles in coin cells using this new electrolyte.

To further improve the capacity and reversibility of SPAN, it is essential to understand its molecular structure and working mechanism. Using chemical analysis, electron microscopy, and surface analysis, we established that SPAN undergoes an irreversible transformation during the 1st cycle that reduces its residual hydrogen

content and produces a more extended conjugated molecular structure. As a result, its electronic conductivity increases by > 100x and raises the working potential. This structural feature will serve as a blueprint for design of next generation materials. Electrolyte innovation and electrode engineering have allowed the fabrication of a first generation 2 Ah Li-SPAN battery with an energy density of 250 Wh/kg, Figure ES- 2. Cycling ended when the Li metal anode caused an internal short. Work is in progress to further increase the capacity of SPAN and formulate new electrolytes that will extend the cycle life of Li-SPAN batteries. Team members are now scaling up SPAN cathode materials to enable more pouch cell manufacturing and testing.

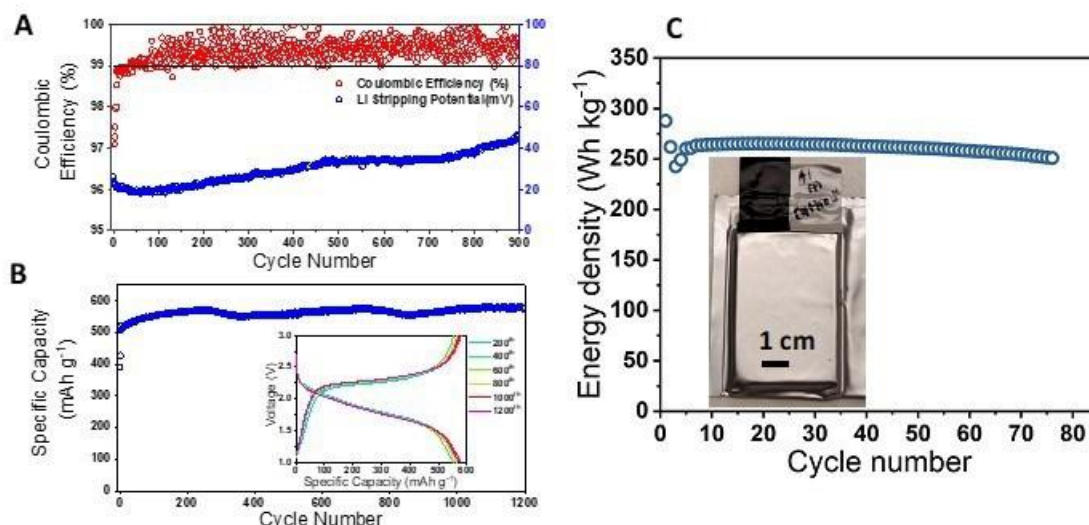


Figure ES- 2. Progress of developing a low-cost Li-S battery by the Battery500 Consortium. The sulfur cathode is sulfurized polyacrylonitrile (SPAN). (a) and (b), Stable cycling of Li and SPAN in a localized concentrated electrolyte, respectively. (c) Demonstration of a 1st Generation Li-SPAN pouch cell of 2 Ah with an energy density of 250 Wh/kg

High-Performance Low-Cobalt Cathode Materials for Li-ion Batteries - (Pennsylvania State University, Pacific Northwest National Laboratory, and Oak Ridge National Laboratory)

$\text{Li}[\text{Ni}_x\text{Co}_y\text{Mn}_{1-x-y}]\text{O}_2$ (NCM) cathode materials are a common choice for electric vehicles (EV) batteries due to their high energy density and good cycling. However, the increased price of cobalt (Co) over the past few years has increased the cost of the NMC. Therefore, developing cathode materials with low or no Co while still achieving high energy density and low cost is essential. Unfortunately, the cycling stability of many low-Co NMC cathodes is compromised by structural instability, non-uniform strain during cycling, and parasitic reactions between the cathode and electrolyte. The coating methods developed in this project are an effective strategy for alleviating these issues.

Specifically, we achieved a LiFePO_4 (LFP) coated NCM811 cathode (LFP/NCM811) via a dry coating approach, where the nanosized LFP is uniformly coated at the surface of NCM811 particles. Then, 2.5 Ah pouch cells were assembled using 10 wt% LFP coated NCM811 cathode and graphite anode. The cathode loading is 17.5 mg/cm^2 , the N/P ratio = 1.1, and the cell achieved 450 Wh/L and 200 Wh/kg. Figure ES- 3 demonstrates that the pouch cells can cycle stably at room temperature (RT), with capacity retention of 76.7% after 2413 cycles. Moreover, the cell could still achieve 67.3% capacity retention after 1609 cycles at 40°C .

In summary, LiFePO_4 coating significantly improves the cycling performance of pouch cells with low-Co layered structured cathode. The team continues to investigate more effective coating materials for $\text{Li}[\text{Ni}_x\text{Co}_y\text{Mn}_{1-x-y}]\text{O}_2$ cathode materials with a cobalt content ≤ 0.04 .

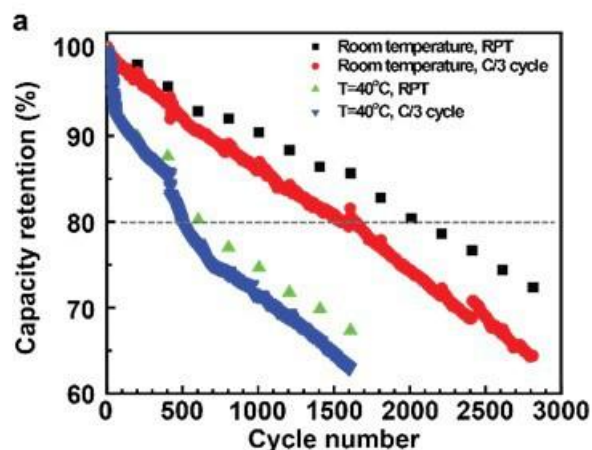


Figure ES- 3. Capacity retention pouch cells during C/3 cycling at RT and 40 °C

Rational electrolyte solvent molecule tuning for high-performance lithium metal and anode free batteries (Stanford University and SLAC National Accelerator Laboratory)

Lithium (Li) metal batteries offer improved energy density compared to current Li-ion batteries but are held back by relatively poor cycle life. Conventional electrolytes fall short when paired with Li metal anodes, let alone anode-free batteries. To enable practical Li metal and anode-free batteries, several requirements should be fulfilled: 1) high Coulombic efficiency (CE) including initial cycles, i.e. fast activation of Li anode; 2) anodic stability to avoid cathode corrosion; 3) practical conditions such as lean electrolyte and limited Li inventory; 4) high ionic conductivity for realistic cycling rates; 5) moderate Li salt concentration for low cost; 6) high boiling point and the absence of gassing to ensure processability and safety.

In 2022, researchers at Stanford University and SLAC investigated a family of fluorinated 1,2-diethoxyethanes (fluorinated-DEEs) as electrolyte solvents. Selected positions on DEEs are functionalized with various numbers of fluorine (F) atoms through iterative tuning, to reach a balance between CE, oxidative stability, and ionic conduction. Paired with 1.2 M LiFSI salt, we found that a partially fluorinated, locally polar $-\text{CHF}_2$ group results in higher ionic conduction than fully fluorinated $-\text{CF}_3$ while still maintaining excellent electrode stability. Specifically, the best-performing F4DEE and F5DEE both contain $-\text{CHF}_2$ group. In addition to high ionic conductivity and low and stable overpotential, they achieve roughly 99.9% Li CE with $\pm 0.1\%$ fluctuation (Figure ES- 4a) as well as fast activation, i.e. the CEs of the Li||Cu half cells reach $>99.3\%$ from the second cycle (Figure ES- 4b). Aluminum corrosion is also suppressed due to the oxidative stability that originates from fluorination. These features enable roughly 270 cycles in thin-Li||high-loading- $\text{LiNi}_{0.8}\text{Mn}_{0.1}\text{Co}_{0.1}\text{O}_2$ (NMC811) full batteries (Figure ES- 4c) and >140 cycles in fast-cycling anode-free Cu||LiFePO₄ (LFP) pouch cells (Figure ES- 4d), both of which are state-of-the-art performances.

The above solvents can be readily scaled up with low cost. Their high boiling point, high flash point, non-flammability and absence of gassing issue during battery cycling are desirable features.

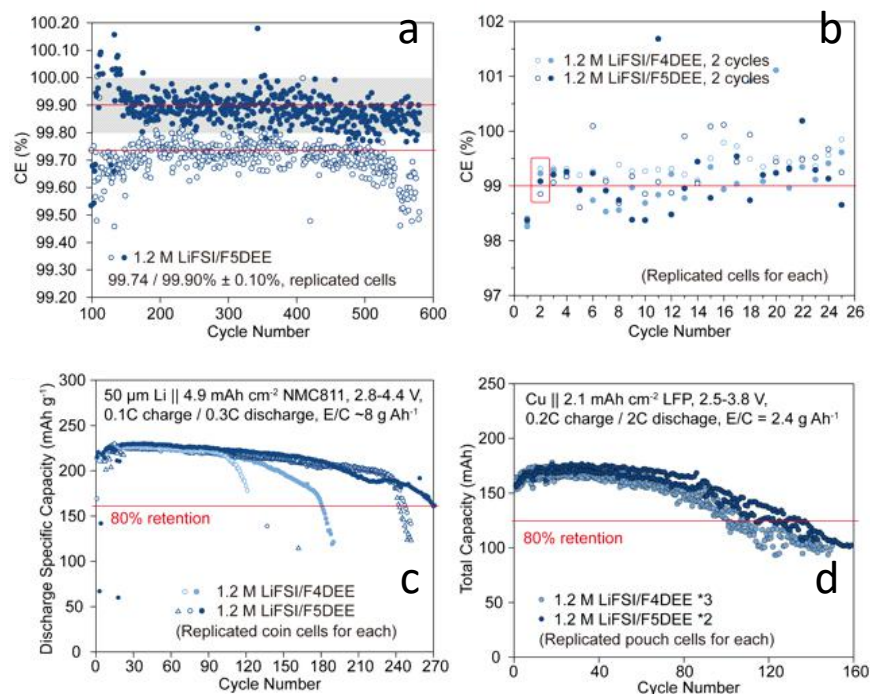


Figure ES- 4. Cycling performance of Li || Cu half cells, practical Li metal batteries and industrial anode-free pouch cells using NMC811 and LFP cathodes

Collaborative Activities

In addition to the above, VTO has in place extensive and comprehensive ongoing coordination efforts in energy storage R&D across all of DOE and with other government agencies. It coordinates efforts on energy storage R&D with both the Office of Science and the Office of Electricity. Coordination and collaboration efforts also include program reviews and technical meetings sponsored by other government agencies and inviting participation of representatives from other government agencies to contract and program reviews of DOE-sponsored efforts. DOE coordinates such activities with the Army's Advanced Vehicle Power Technology Alliance, the Department of Transportation/National Highway Traffic Safety Administration (DOT/NHTSA), the Environmental Protection Agency (EPA), and the United Nations Working Group on Battery Shipment Requirements. Additional international collaboration occurs through the International Energy Agency's (IEA's) Hybrid Electric Vehicles Technology Collaboration Program (HEV TCP); and bilateral agreements between the U.S. and China.

Organization of this Report

This report covers all the FY 2022 projects which are part of the advanced battery R&D program in VTO. We are pleased with the progress made during the year and look forward to continued cooperation with our industrial, government, and scientific partners to overcome the remaining challenges to delivering advanced energy storage systems for vehicle applications.



Brian Cunningham,
Program Manager, Batteries
Vehicle Technologies Office



Tien Q. Duong, Vehicle
Technologies Office



Haiyan Croft, Vehicle
Technologies Office



Simon Thompson, Vehicle
Technologies Office



Nicolas Eidson, Vehicle
Technologies Office



Tina Chen, Vehicle
Technologies Office



Thomas Do, Vehicle
Technologies Office



Jake Herb, Vehicle Technologies
Office

Table of Contents

Vehicle Technologies Office Overview	1
Annual Progress Report	1
Organization Chart.....	2
Batteries Program Overview.....	3
Introduction.....	3
Goals	3
State of the Art	3
Battery Technology Barriers	5
Program Organization Matrix	5
Battery Highlights from FY 2022	7
I USABC Battery Development & Materials R&D	21
I.1 Fast-Charge and Low-Cost Lithium Ion Batteries for Electric Vehicle Applications (Ionblox)	23
I.2 Low-Cost, High Safety Fast Charge Automotive Cells (Microvast, Inc.).....	31
I.3 Low-Cost and Fast-charging Lithium-ion Battery based on Neocarbonix™ NMP/PVDF- binder Free Electrode Processing for EV Applications (Nanoramic).....	35
I.4 Evaluation of Advanced Li-ion Cell Architectures for Extreme Fast Charging (XFC) Batteries for Electric Vehicles (EnPower, Inc.).....	74
I.5 Solvent-free Electrode Manufacturing for Low Cost/Fast Charging Batteries (Worcester Polytechnic Institute).....	78
I.6 Development of Advanced Low-Cost / Fast-Charge (LC/FC) Batteries for EV Applications (Farasis Energy USA).....	90
I.7 Pre-lithiation of Silicon-containing Anodes for High-Performance EV Batteries (Applied Materials, Inc.).....	96
I.8 Electrolyte Development: High Performance Electrolyte for High Voltage Batteries (Gotion)	102
I.9 Strategic Collaboration for the Development of a Self-Sustaining Model for the Recycling of Large-Format Lithium-Ion Batteries (American Battery Technology Company).....	109
I.10 Silicon-based EV Cells Meeting Cost, Calendar Life and Power (Ionblox, Inc.)	113
I.11 Low-cost, Fast-charging Silicon Nanowire Cell Technology (Amprius).....	119
II Processing Science & Engineering	127
II.1 Processing Next Generation Li-ion Battery Cathode Materials (ANL).....	129

II.2	Novel Processing Approaches for LLZO (ANL)	137
II.3	Supercritical Fluid Processing of Battery Cathode Materials (ANL).....	143
II.4	Process R&D and Scale-up of Critical Battery Materials (ANL).....	152
II.5	Structure-Activity Relationships in the Optimizing Electrode Processing Streams for LiBs (LBNL).....	164
II.6	Fabricate and Test Solid-state Ceramic Electrolytes and Electrolyte/Cathode Laminates (LBNL).....	167
II.7	Higher Energy Density via Inactive Components and Processing Conditions (LBNL).....	171
II.8	Minimizing Side Reactions in Next-Generation Lithium Ion Battery Cathodes Through Structure-Morphology Optimization (ANL)	177
II.9	<i>In Situ</i> Spectroscopies of Processing Next-Generation Cathode Materials (ANL, BNL)	191
II.10	Towards Solventless Processing of Thick Electron-Beam (EB) Cured LIB Cathodes (ORNL)	200
II.11	Performance Effects of Electrode Processing for High-Energy Lithium-Ion Batteries (ORNL)	206
III	Recycling and Sustainability	215
III.1	Battery and Critical Materials Life Cycle Analysis (ANL).....	216
III.2	Lithium-ion Battery Recycling Prize Support (NREL)	226
III.3	Battery ReCell Center (ANL).....	233
III.4	Development of Lithium Electrode Based Cell and Manufacturing for Automotive Traction Applications (Farasis Energy)	330
III.5	A Closed Loop Recycling Process for End-of-Life Electric Vehicle Li-ion Batteries-Phase III (Worcester Polytechnic Institute)	334
IV	Extreme Fast Charging (XFC)	346
IV.1	Extreme Fast Charge Cell Evaluation (XCEL) Thrust-1: Electrolytes for fast charging	348
IV.2	XCEL Thrust-2: Electrode & Cell Design for Fast Charging.....	354
IV.3	XCEL Thrust 3: Electrochemical and Thermal Performance.....	371
V	Beyond Batteries	381
V.1	Behind-the-Meter Storage (NREL, INL, ORNL, SNL, ANL)	382
VI	Testing, Analysis, High-Performance Computing, Lab-I4.....	393
VI.1	BatPaC Model Development (ANL)	394
VI.2	Battery Performance and Life Testing (ANL).....	405
VI.3	Battery Abuse Testing (SNL).....	408

VI.4	Battery Thermal Analysis and Characterization Activities (NREL)	411
VI.5	Cell Analysis, Modeling, and Prototyping (CAMP) Facility Research Activities (ANL).....	417
VI.6	Materials Benchmarking Activities for CAMP Facility (ANL)	425
VI.7	Electrochemical Performance Testing (INL).....	432
VI.8	Machine Learning for Accelerated Life Prediction and Cell Design (INL, NREL).....	436
VII	Small Business Innovation Research (SBIR).....	444
VIII	Next Generation Lithium-Ion Materials: Advanced Anodes R&D.....	447
VIII.1	Silicon Consortium Project (NREL, ANL, PNNL, SNL, ORNL, LBNL)	449
VIII.2	Si-Based Li Ion Batteries with Long Cycle Life and Calendar Life (PNNL).....	456
VIII.3	Silicon Anode Seedling Project (ANL)	462
VIII.4	Seedling Project: Two-Dimensional Silicon Nanostructures for Improved Silicon Anode Cycling Stability (Brookhaven National Laboratory, Stony Brook University)	466
VIII.5	Integrated Modeling and Machine Learning of Solid-Electrolyte Interface Reactions of the Si Anode (LBNL)	473
VIII.6	Advanced Anode Manufacturing through Ultra-Thin Li Deposition (Applied Materials, Inc.) 487	
VIII.7	Structurally and Electrochemically Stabilized Si-rich Anodes for EV Applications (Enovix Corporation)	496
VIII.8	Rationally Designed Lithium-Ion Batteries Towards Displacing Internal Combustion Engines (Group14 Technologies).....	505
VIII.9	Ultra-Low Volume Change Silicon-Dominant Nanocomposite Anodes for Long Calendar Life and Cycle Life (Sila Nanotechnologies)	511
VIII.10	Solid State Li Ion Batteries Using Si Composite Anodes (Solid Power Inc.)	514
VIII.11	Fully Fluorinated Local High Concentration Electrolytes Enabling High Energy Density Si Anodes (Stony Brook University)	517
VIII.12	Devising mechanically compliant and chemically stable synthetic solid-electrolyte interphases on silicon using ex situ electropolymerization for long cycling Si anodes (University of Delaware)	524
VIII.13	Rational Electrolyte Design for Li-ion Batteries with Micro-sized Si Anodes (University of Maryland, College Park).....	533
VIII.14	Silicon Consortium Project (SCP) (PNNL).....	541
VIII.15	Thin-film lithium metal manufacture by room temperature electrodeposition (Albemarle Corporation)	546
VIII.16	Pre-Lithiation of Silicon Anode for High Energy Li Ion Batteries (Stanford University)	552

VIII.17	Free-Energy Driven Approaches to Self-Forming and Self-Terminating SEIs on Si Anodes (LBNL).....	558
IX	Next-Gen Lithium-Ion: Advanced Cathodes R&D.....	566
IX.1	Design, Synthesis, & Characterization of Low-Cobalt Cathodes (ANL, ORNL, LBNL, NREL, PNNL).....	567
IX.2	Diagnostic Testing and Evaluation (ANL, ORNL, NREL, PNNL)	575
IX.3	Advanced Cathodes Theory and Modeling (ANL, LBNL, PNNL, NREL, ORNL).....	593
IX.4	Design and Synthesis of High Energy, Manganese Rich Oxides for Lithium-Ion Batteries (ANL)	605
IX.5	Disordered RockSalt Structured Cathode Materials: Electrochemistry and Synthesis (LBNL, ORNL, PNNL, UC Santa Barbara).....	612
IX.6	Disordered RockSalt Structured Cathode Materials: Characterization and Modeling (LBNL, ORNL, PNNL, UC Santa Barbara).....	622
X	Next-Gen Lithium-Ion Materials: Frontier Science at Interfaces	630
X.1	Molecular-level Understanding of Cathode-Electrolyte Interfaces (University of Colorado, NREL)	631
X.2	Interfacial Studies of Emerging Cathode Materials Lawrence Berkeley National Laboratory (LBNL).....	645
X.3	Understanding Modification of High-Energy Cathodes and Their Interfaces with Electrolytes for Next-Generation Li-ion Batteries (PNNL).....	655
X.4	Fluorinated Deep Eutectic Solvent (FDES)-Based Electrolytes (ANL).....	660
X.5	Developing In situ Microscopies for the Model Cathode/ Electrolyte Interface (NREL)	669
XI	Next Generation Lithium-Ion Materials: Low-Cobalt/No Cobalt Cathodes.....	677
XI.1	Aerosol Manufacturing Technology to Produce Low-Cobalt Li-ion Battery Cathodes (Cabot Corporation)	678
XI.2	Co-free Cathode Materials and their Novel Architectures (UCSD, UTA, LBNL).....	688
XI.3	Enhancing Oxygen Stability in Low-Cobalt Layered Oxide Cathode Materials by Three-Dimensional Targeted Doping (UC Irvine).....	697
XI.4	High-Nickel Cathode Materials for High-Energy, Long-Life, Low-Cost Lithium-Ion Batteries (UTA)	709
XI.5	Cobalt-Free Cathodes for Next Generation Li-Ion Batteries (Nexceris)	718
XI.6	High-Performance Low-Cobalt Cathode Materials for Li-ion Batteries (PSU)	723
XII	Next Generation Lithium-Ion Materials: Diagnostics	730
XII.1	Interfacial Processes (LBNL)	731
XII.2	Advanced in situ Diagnostic Techniques for Battery Materials (BNL).....	742

XII.3	Microscopy Investigation on the Fading Mechanism of Electrode Materials (PNNL)	749
XII.4	In-Operando Thermal Diagnostics of Electrochemical Cells (LBNL)	756
XIII	Next-Gen Lithium-Ion: Modeling Advanced Materials	762
XIII.1	Electrode Materials Design and Failure Prediction (ANL)	763
XIII.2	Characterization and Modeling of Li-Metal Batteries: Model-system Synthesis and Advanced Characterization (LBNL).....	771
XIII.3	Design of High-Energy, High-Voltage Lithium Batteries through First-Principles Modeling (LBNL).....	779
XIII.4	Modeling of Solid-State Conductors (Lawrence Berkeley National Laboratory) (LBNL) ...	787
XIV	Next-Gen Li-ion: Low Temperature Electrolytes	793
XIV.1	Ethylene Carbonate-Lean Electrolytes for Low Temperature, Safe Li-ion batteries (LBNL) 794	
XIV.2	Fluorinated Solvent-Based Electrolytes for Low Temperature Li-ion Battery (ANL).....	801
XIV.3	Synthesis, screening and characterization of novel low temperature electrolyte for lithium-ion batteries (BNL).....	808
XV	Beyond Li-ion R&D: Metallic Lithium	819
XV.1	Lithium Dendrite Prevention for Lithium Batteries (PNNL)	820
XV.2	Integrated Multiscale Model for Design of Robust 3-D Solid-state Lithium Batteries (LLNL)	828
XV.3	Advanced Polymer Materials for Li-ion (SLAC)	834
XV.4	Anode-Free Lithium Batteries (PNNL).....	843
XVI	Beyond Li-ion R&D: Solid-State Batteries	851
XVI.1	Lithium Dendrite-Free Solid Electrolytes for High Energy Lithium Batteries (University of Maryland, College Park).....	853
XVI.2	All Solid State Batteries Enabled by Multifunctional Electrolyte Materials (Solid Power Inc.) 858	
XVI.3	Development of Thin, Robust, Lithium-Impenetrable, High-Conductivity, Electrochemically Stable, Scalable, and Low-Cost Glassy Solid Electrolytes for Solid-State Lithium Batteries (Iowa State University).....	861
XVI.4	Physical and Mechano-Electrochemical Phenomena of Thin Film Lithium-Ceramic Electrolyte Constructs (University of Michigan).....	867
XVI.5	Low Impedance Cathode/Electrolyte Interfaces for High Energy Density Solid-State Batteries (University of Maryland, College Park)	873
XVI.6	Molecular Ionic Composites: A New Class of Polymer Electrolytes to Enable All Solid-State and High Voltage Lithium Batteries (Virginia Polytechnic Institute and State University)..	883

XVI.7	Hot Pressing of Reinforced All-solid-state Batteries with Sulfide Glass Electrolyte (General Motors LLC).....	894
XVI.8	Developing Materials for High-Energy-Density Solid State Lithium-Sulfur Batteries (Penn State University, University Park).....	904
XVI.9	Developing an In-situ Formed Dynamic Protection Layer to Mitigate Lithium Interface Shifting: Preventing Dendrite Formation on Metallic Lithium Surface to Facilitate Long Cycle Life of Lithium Solid State Batteries (University of Wisconsin-Milwaukee).....	912
XVI.10	Fundamental Understanding of Interfacial Phenomena in Solid-State Batteries (General Motors)	920
XVI.11	Multidimensional Diagnostics of the Interface Evolutions in Solid-State Lithium Batteries (University of Houston).....	931
XVI.12	First-Principles Modeling of Cluster-Based Solid Electrolytes (Virginia Commonwealth University).....	939
XVI.13	Predictive Engineering of Interfaces and Cathodes for High-Performance All Solid-State Lithium-Sulfur Batteries (University of Louisville).....	947
XVI.14	Design of Strain Free Cathode – Solid State Electrolyte Interfaces Using Chemistry-Informed Deep Learning (ANL)	958
XVI.15	Enabling continuous production of defect-free, ultrathin sulfide glass electrolytes for next generation solid state lithium metal batteries (ANL).....	969
XVI.16	Stable Solid-State Electrolyte and Interface for High-Energy All-Solid-State Lithium-Sulfur Battery (PNNL)	974
XVI.17	Scale-Up of Novel Li-Conducting Halide Solid State Battery Electrolyte (LBNL).....	983
XVI.18	Low-Pressure All Solid State Cells (NREL)	986
XVI.19	3D Printing of All-Solid-State Lithium Batteries (LLNL)	991
XVI.20	Substituted Argyrodite Solid Electrolytes and High-Capacity Conversion Cathodes for All-Solid-State Batteries (Oak Ridge National Laboratory).....	1002
XVI.21	Multifunctional Gradient Coatings for Scalable, High-Energy-Density Sulfide-Based Solid-State Batteries (ANL)	1009
XVI.22	Thick Selenium-Sulfur Cathode Supported Ultra-thin Sulfides Electrolytes for High-energy All-solid-state Lithium Metal Batteries (ANL)	1017
XVI.23	Synthesis of Composite Electrolytes with Integrated Interface Design (ANL).....	1027
XVI.24	Polymer Electrolytes for Stable Low Impedance Solid State Battery Interfaces (ORNL) ..	1035
XVI.25	Inorganic-Polymer-Composite Electrolyte with Architecture Design for Lithium Metal Solid State Batteries (BNL)	1047
XVI.26	Ion Conductive High Li ⁺ Transference Number Polymer Composites for Solid-State Batteries (LBNL).....	1052

XVI.27 Precision Control of the Li Surface for Solid-state Batteries (Oak Ridge National Laboratory)	1057
XVI.28 Lithium Halide-Based Superionic Solid Electrolytes and High Voltage Cathode Interfaces (ORNL)	1066
XVI.29 Polyester-Based Block Copolymer Electrolytes for Lithium-Metal Batteries (UCB).....	1073
XVI.30 Development of All Solid-State Battery using Anti-Perovskite Electrolytes (ANL)	1082
XVI.31 High-Conductivity and Electrochemically Stable Lithium Thioborate Solid-State Electrolytes for Practical All-Solid-State Batteries (Stanford University)	1090
XVI.32 Solid state batteries with long cycle life and high energy density through materials design and integration (LBNL).....	1094
XVII Beyond Li-Ion R&D: Lithium Sulfur Batteries	1110
XVII.1 A Novel Chemistry: Lithium-Selenium and Selenium-Sulfur Couple (ANL)	1111
XVII.2 Development of High Energy Lithium-Sulfur Batteries (PNNL).....	1122
XVII.3 Mechanistic Investigation for the Rechargeable Li-Sulfur Batteries (Brookhaven National Laboratory & University of Wisconsin-Milwaukee).....	1130
XVII.4 New electrolyte binder for Lithium sulfur battery (LBNL).....	1139
XVII.5 Strategies to Enable Lean Electrolytes for High Loading and Stable Lithium-Sulfur Batteries (UCSD).....	1146
XVII.6 New Engineering Concepts for High Energy Density Li-S Batteries (UPitt).....	1160
XVII.7 Development of Li-S Battery Cells with High Energy Density and Long Cycling Life (PSU)	1172
XVII.8 Nanostructured Design of Sulfur Cathodes for High Energy Lithium-Sulfur Batteries (Stanford University).....	1178
XVIII Beyond Li-ion R&D: Lithium-Air Batteries	1184
XVIII.1 Lithium-Air Batteries (ANL).....	1185
XVIII.2 Lithium Oxygen Battery Design and Predictions (ANL)	1194
XVIII.3 Development of a High-Rate Lithium-Air Battery Using a Gaseous CO ₂ Reactant (UIC).	1202
XIX Beyond Li-ion R&D: Sodium-Ion Batteries	1208
XIX.1 An Exploratory Studies of Novel Sodium-Ion Battery Systems (BNL).....	1209
XIX.2 Development of Advanced High-energy and Long-life Sodium-ion Battery (ANL).....	1215
XIX.3 Tailoring High Capacity, Reversible Anodes for Sodium-Ion Batteries (LBNL)	1230
XIX.4 Electrolytes and Interfaces for Stable High-Energy Sodium-ion Batteries (Pacific Northwest National Laboratory)	1239

XX Beyond Li-ion R&D: Battery500..... 1248

XX.1 Battery 500 phase 2 (PNNL) 1249

List of Figures

Figure ES- 1. Full cell performance comparison of optimized LNO vs. $\text{LiNi}_{0.9}\text{Mn}_{0.05}\text{Co}_{0.05}\text{O}_2$	xx
Figure ES- 2. Progress of developing a low-cost Li-S battery by the Battery500 Consortium. The sulfur cathode is sulfurized polyacrylonitrile (SPAN). (a) and (b), Stable cycling of Li and SPAN in a localized concentrated electrolyte, respectively. (c) Demonstration of a 1 st Generation Li-SPAN pouch cell of 2 Ah with an energy density of 250 Wh/kg	xxi
Figure ES- 3. Capacity retention pouch cells during C/3 cycling at RT and 40°C	xxii
Figure ES- 4. Cycling performance of Li Cu half cells, practical Li metal batteries and industrial anode-free pouch cells using NMC811 and LFP cathodes	xxiii
Figure 1. Chemistry classes, status, and R&D needs.....	4
Figure 2. Battery R&D Program Structure	6
Figure 3. Cycling performance of Li NMC811 cells using 1.2M LiPF_6 -FEC/DFEC/FEMC in different ratios..	8
Figure 4. Full cell performance comparison of optimized LNO vs. $\text{LiNi}_{0.9}\text{Mn}_{0.05}\text{Co}_{0.05}\text{O}_2$	8
Figure 5. Flow of synthetic–data-based DL modeling framework to classify and quantify the dominant aging modes.....	9
Figure 6. a-b) Voltage profiles of PC-NMC and SC-NMC ASSB cells, respectively. c-d) Discharge capacity and energy density retentions of the ASSB cells, respectively. e-f) Cross-sectional SEM images showing better mechanical stability of SC-NMC cathode composite upon cycling. All cells were cycled at room temperature at C/2 rate for 200 cycles followed by 3 cycles at C/5. This sequence was repeated throughout the testing. The performance fluctuation shown in c) and d) is due to room temperature variation in the laboratory, which ranged from 25±5°C during the test.....	10
Figure 7. Cross-section image of the separator/cathode structure. The separator is an oxide ceramic and the cathode is a solid composite of NMC active material, carbon, polymer catholyte, and trace residual solvent ..	11
Figure 8. Capacity retention of a cell with residual solvent cycled at 25°C and 20 hour full charge/discharge cycle. Right most figure shows the conductivity of the polymer/Li-salt composite with and without residual solvent.....	11
Figure 9. Calendar degradation of lithium-ion battery predicted by human-expert and ML models with 90% confidence intervals. ML models fit aging data with half of the error of human-expert models and have better confidence.....	12
Figure 10. Validation of ML lithium-ion battery life model on dynamic aging test with monthly variation of cycling and storage. Total degradation is the sum of three aging modes identified from accelerated aging test data and fit using ML.....	12
Figure 11. Development of Co-free cathode materials for next generation Li-ion batteries	13
Figure 12. Progress of developing a low-cost Li-S battery by the Battery500 Consortium. The sulfur cathode is sulfurized polyacrylonitrile (SPAN). (a) and (b), Stable cycling of Li and SPAN in a localized concentrated electrolyte, respectively. (c) Demonstration of a 1 st Generation Li-SPAN pouch cell of 2 Ah with an energy density of 250 Wh/kg.....	14
Figure 13. Capacity retention pouch cells during C/3 cycling at RT and 40°C	15
Figure 14. Cycling performance of Li Cu half cells, practical Li metal batteries and industrial anode-free pouch cells using NMC811 and LFP cathodes	16
Figure 15. Early prediction of LFP/graphite cycle life under extreme fast charging conditions using data from the 10 th and 100 th discharge cycle. Reproduced from Severson et al. Nature Energy 4, 383 (2019).....	17

Figure 16. The electrochemical and thermal stability performance of UCI's HE-N80 cathode. (a) DSC measurements of charged cathodes. (b) Comparison of HE-N80 and NMC-811. (c) Rate capability. (d) Cycle life in a single layer Li-ion pouch cell.	18
Figure 17. (A) Electrochemical performance of both low and high loading LNMO and the SEM cross-sections. (B) PFIB-SEM of dry-LNMO. Purple represents LNMO, green represent carbon and yellow represents porosity. (C) A three-component framework for the computational screening of electrolyte/cathode interface materials (D) Long-term cycling of LNMO full cell.	19
Figure 18. NMCAM-85 large-format pouch cells (2 Ah) achieve 1,000 cycles with greater than 80% capacity retention, cycled between 2.5 – 4.2 V.....	20
Figure 19. Tailored electrolyte stabilizes cathode performance, allowing cobalt-free NMA-90 to achieve 500 cycles with 88% capacity retention.....	20
Figure I.1.1 Projected & measured cell performance progression throughout the program CB#1, CB#2, & CB#3	25
Figure I.1.2 Footprints for 12 Ah and 50 Ah pouch cells that were prepared for CB#3.....	26
Figure I.1.3 Status of ongoing performance testing on baseline pouch cells.....	26
Figure I.1.4 Measurements (Capacity, Average Voltage, Thickness, Weight, Energy) on CB#3 cells after formation for 12 Ah cells.....	27
Figure I.1.5 Capacity and energy measurement versus voltage during charge and discharge for 12 Ah pouch cells.....	27
Figure I.1.6 Power and resistance measurement versus depth of discharge for 12 Ah pouch cells.....	27
Figure I.1.7 Measurements (Capacity, OCV, Resistance, Average Voltage, Weight, Thickness and Energy) after formation on 50 Ah footprint cells	28
Figure I.1.8 Cycling of two 12 Ah cells (CB#3) prepared with lithium metal powder at 1C/1C rate (left) and 4C/1C rate (right) at room temperature.	28
Figure I.1.9 Gap chart showing the USABC Targets versus data for CB#1, CB#2 & CB#3.	29
Figure I.2.1 Discharge capacity at RPT of year 1 deliverable cells undergoing DST cycling.....	32
Figure I.2.2 Discharge capacity at RPT of year 2 deliverable cells undergoing DST cycling.....	33
Figure I.3.1 SOW Plans for Budget Periods for 2022 and 2023	37
Figure I.3.2 Results for Neocarbonix (NX) Ni-Rich NMC/NCMA Electrode Development.....	38
Figure I.3.3 Results for Neocarbonix (NX) Ni-Rich NMC/NCMA Electrode Development (continued)	39
Figure I.3.4 Results for Neocarbonix (NX) Ni-Rich NMC/NCMA Electrode Development (continued)	40
Figure I.3.5 Results for Neocarbonix (NX) Ni-Rich NMC/NCMA Electrode Development (continued)	41
Figure I.3.6 Results for Neocarbonix (NX) Low-Cost Silicon Anode Electrode Development.....	42
Figure I.3.7 Results for Neocarbonix (NX) Low-Cost Silicon Anode Electrode Development (continued).....	43
Figure I.3.8 Results for Neocarbonix (NX) Low-Cost Silicon Anode Electrode Development (continued).....	44
Figure I.3.9 Results for Neocarbonix (NX) Low-Cost Silicon Anode Electrode Development (continued).....	45
Figure I.3.10 Results for Neocarbonix (NX) Low-Cost Silicon Anode Electrode Development (continued)....	45
Figure I.3.11 Results for Neocarbonix (NX) Low-Cost Silicon Anode Electrode Development (continued)....	46
Figure I.3.12 Results for Neocarbonix (NX) Low-Cost Silicon Anode Electrode Development (continued)....	46
Figure I.3.13 Results for Neocarbonix (NX) Low-Cost Silicon Anode Electrode Development (continued)....	47

Figure I.3.14 Results for Neocarbonix (NX) 14 Ah Battery Cell Development & Performance	47
Figure I.3.15 Results for Neocarbonix (NX) 14 Ah Battery Cell Development & Performance (continued)	48
Figure I.3.16 Results for Neocarbonix (NX) 14 Ah Battery Cell Development & Performance (continued)	49
Figure I.3.17 Results for Neocarbonix (NX) 14 Ah Battery Cell Development & Performance (continued)	50
Figure I.3.18 Results for Neocarbonix (NX) 14 Ah Battery Cell Development & Performance (continued)	51
Figure I.3.19 Results for Neocarbonix (NX) 14 Ah Battery Cell Development & Performance (continued)	52
Figure I.3.20 Results for NX Si-C ANODE ELECTRODE PRE-LITHIATION (40-50 wt.% Si Element Content)	52
Figure I.3.21 Results for NX Si-C ANODE ELECTRODE PRE-LITHIATION (40-50 wt.% Si Element Content) (continued)	53
Figure I.3.22 Results for NX Si-C ANODE ELECTRODE PRE-LITHIATION (40-50 wt.% Si Element Content) (continued)	54
Figure I.3.23 Results for NX Si-C ANODE ELECTRODE PRE-LITHIATION (40-50 wt.% Si Element Content) (continued)	55
Figure I.3.24 Results for NX Si-C ANODE ELECTRODE PRE-LITHIATION (40-50 wt.% Si Element Content) (continued)	56
Figure I.3.25 Results for NX Si-C ANODE ELECTRODE PRE-LITHIATION (40-50 wt.% Si Element Content) (continued)	57
Figure I.3.26 Results for NX Si-C ANODE ELECTRODE PRE-LITHIATION (40-50 wt.% Si Element Content) (continued)	57
Figure I.3.27 Results for NX Si-C ANODE ELECTRODE PRE-LITHIATION (40-50 wt.% Si Element Content) (continued)	58
Figure I.3.28 Results for Low-Cost Micro-Si Dominant Anode Electrode Development (Higher Si element wt.% \geq 80%)	58
Figure I.3.29 Results for Low-Cost Micro-Si Dominant Anode Electrode Development (Higher Si element wt.% \geq 80%) (continued)	59
Figure I.3.30 Results for Low-Cost Micro-Si Dominant Anode Electrode Development (Higher Si element wt.% \geq 80%) (continued)	60
Figure I.3.31 Results for Low-Cost Micro-Si Dominant Anode Electrode Development (Higher Si element wt.% \geq 80%) (continued)	61
Figure I.3.32 Results for Low-Cost Micro-Si Dominant Anode Electrode Development (Higher Si element wt.% \geq 80%) (continued)	62
Figure I.3.33 Results for Low-Cost Micro-Si Dominant Anode Electrode Development (Higher Si element wt.% \geq 80%) (continued)	62
Figure I.3.34 Results for Low-Cost Micro-Si Dominant Anode Electrode Development (Higher Si element wt.% \geq 80%) (continued)	63
Figure I.3.35 Results for Low-Cost Micro-Si Dominant Anode Electrode Development (Higher Si element wt.% \geq 80%) (continued)	64
Figure I.3.36 Results for Low-Cost Micro-Si Dominant Anode Electrode Development (Higher Si element wt.% \geq 80%) (continued)	65
Figure I.3.37 Results for Low-Cost Micro-Si Dominant Anode Electrode Development (Higher Si element wt.% \geq 80%) (continued)	65

Figure I.3.38 Results for Low-Cost Micro-Si Dominant Anode Electrode Development (Higher Si element wt.% \geq 80%) (continued).....	66
Figure I.3.39 Results for Low-Cost Micro-Si Dominant Anode Electrode Development (Higher Si element wt.% \geq 80%) (continued).....	66
Figure I.3.40 Results for Low-Cost Micro-Si Dominant Anode Electrode Development (Higher Si element wt.% \geq 80%) (continued).....	67
Figure I.3.41 Results for NX NCM91#1 NX Si-C#1 - 4.5 Ah Cells.....	67
Figure I.3.42 Results for NX NCM91#1 NX Si-C#1 - 4.5 Ah Cells (continued)	68
Figure I.3.43 Results for NX NCM91#1 NX Si-C#1 - 4.5 Ah Cells (continued)	68
Figure I.3.45 Results for NX NCM91#1 NX Si-C#1 - 4.5 Ah Cells (continued)	69
Figure I.3.46 Results for NX NCM91#1 NX Si-C#1 - 4.5 Ah Cells (continued)	69
Figure I.3.47 Results for NX NCM91#1 NX Si-C#1 - 4.5 Ah Cells (continued)	70
Figure I.3.48 Results for NX NCM91#1 NX Si-C#1 - 4.5 Ah Cells (continued)	70
Figure I.3.49 Slight gassing observed after the 200% SOC overcharge.....	71
Figure I.3.50 Results for NX NCM91#1 NX Si-C#1 - 4.5 Ah Cells (continued)	71
Figure I.3.51 Results for NX NCM91#1 NX Si-C#1 - 4.5 Ah Cells (continued)	72
Figure I.4.1 Comparison of the multilayer graphite anode / NMC811 cell's fast charge capability with that of a cell built with a homogeneous baseline anode comprised of the same graphite composition and density	75
Figure I.4.2 Hybrid Pulse Power Characterization (HPPC) for the EnPower multilayer anode / NMC811 cell 76	
Figure I.5.1 CC (solid lines) and CCCV (dashed lines) charging capacity of different types of NMC/graphite cells. Symbols: WC-WA – slurry-casted cathode and anode; DC_DA_DL – uniform dry NMC cathode and 2-layer dry graphite anode; DC_DL_DA_DL – 2-layer dry NMC cathode and 2-layer dry graphite anode. The tortuosity function $\tau(\epsilon)$ has the form of $1.5\epsilon\gamma$ in (a) and $\epsilon\gamma$ in (b).....	80
Figure I.5.2 (a) Rate performance of dry-printed (DE) NMC cathode half cells using EC:EMC=3:7 (w:w) vs EC:DMC 1:1 (w:w) predicted by battery simulation. (b) Measured rate capability of dry-printed (DE) and slurry-cast (MV) NMC cathode half cells using EC:EMC=3:7 (w:w) vs EC:DMC 1:1 (w:w) (LP57).....	80
Figure I.5.3 Comparison of the charging performance of the proposed 2-layer dry electrode designs against the uniform NMC/graphite full cells fabricated by the slurry-casting method (baseline) and dry-printing technique.	81
Figure I.5.4 3D structures of the dry (a) and slurry-cast (b) NMC cathodes reconstructed from nanotomography. Scale bar is 10 μ m. (c), (d) Mean square displacement of random walkers vs time in random walk simulations performed in the digitized dry (c) and slurry-cast (d) NMC cathode structures. Electrode tortuosity is proportional to the slope of the curve.	82
Figure I.5.5 2-side coated cathode with 30mg/cm ² on each side.	83
Figure I.5.6 5Ah cell electrode preparation for testing at WPI and Microvast.	83
Figure I.5.7 Relationship between bonding strength and porosity for anodes (15mg/cm ² loading, Gr:C65:PVDF = 96:2:2).....	84
Figure I.5.8 Cross-section SEM images and EDX mapping of (a) slurry cast cathode, (b) dry printed cathode, (c) slurry cast anode, (d) dry printed anode.	86
Figure I.5.9 High loading electrode rate performance (a) cathode electrodes, (b) anode electrodes.	87
Figure I.5.10 15 min-capped 3C charging ratio between wet and dry electrode	88

Figure I.6.1 Comparison in the cycling stability (a) capacity retention, (b) average discharge voltage and (c) cathode-specific energy density of single-layer pouch cells among with different types of lab-coated cathodes.	93
Figure I.6.2 Comparison in the cycling stability (a) capacity retention, (b) average discharge voltage and (c) cathode-specific energy density of pouch cells with Mn-rich (C2) cathodes among different coating (P-coated: pilot-line coated vs. L-coated: lab-coated), activation Vmax (ACT-4.5 V vs. ACT-4.4 V) and amount of A2 electrolyte additive (1 % vs. 2 %).	94
Figure I.6.3 Fast charge cycling behavior of a single-layer pouch cell with a graphite (A1) anode and a high-voltage (HV) NCM (C5) cathode	95
Figure I.6.4 Comparison in cycling stability of single-layer pouch cells with graphite (A1) anodes and blended cathodes (C5C2-blend 2) between 0 % (all regular C/2-rate) and 25 % fast charge (25 % fast charge + 75 % regular C/2-rate) cycling	95
Figure I.7.1 (a & b) Examples of silicon (SiOx) anode showing transfer of Li to anode. (C) Cell sizes and dimension for final BP-1 deliverable, and (d) Pouch cell assembly process - Cells in fixtures going through formation and cycling before shipment	99
Figure I.7.2 SpectraPower: Summary of cell voltage vs. Capacity data for (A) eight control and (B) seventeen pre-Li anode from formation cycle (first cycle charge/discharge), showing good consistency and reproducibility. These cells were delivered to INL for further cycling. C and D shows the summary of cell parameters Energy density and Coulombic efficiency improvements of pre-lithiated anode vs. control for the same set of cells	99
Figure I.7.3 Idaho National Lab summary of cell performance indicating (a) mass variation (b) open circuit voltage (c) AC impedance at 1 kHz and (d) Static capacity for all the final BP-1 cells delivered. All cells achieved target capacity and Impedance values are in the acceptable range for further DST cycle testing.	100
Figure I.7.4 Example image of Applied Materials pre-lithiated anodes generated in S2S tool as a part of the deliverable 1	100
Figure I.8.1 Gas generation measured in 2Ah MLPC containing HV-LNMO/C material after cycling for 120 cycles at 45°C under various procedures (P) that alter charging methods, upper cutoff voltage, and current rates. The data shared all has the same formulation showing the impact that procedure has on gas generation in addition to electrolyte formulation.....	104
Figure I.8.2 High temperature cycling performance in 2Ah MLPC containing HV-LNMO/C material showing additive packs improving retention over the baseline significantly at high temperatures. Formulation L6-4-C167 shows 8.4% retention improvement over the baseline.	105
Figure I.8.3 Gas generation after the cycling from Figure I.8.2 which went through high temperature cycling performance in 2Ah MLPC containing HV-LNMO/C material. Not only did these formulations greatly improve retention in high temperature cycling, but it also reduced gassing compared to the baseline.	105
Figure I.8.4 Photos of 2Ah MLPC containing HV-LNMO/C material after 120 cycles of 45°C cycling. The top photo shows the baseline gas generation while the bottom photo shows gas generation with L6-4-C167 optimized formulation and an optimized testing protocol. Significant improvement in swelling able to be seen.	106
Figure I.8.5 Photos of 2Ah MLPC containing HV-LNMO/C material after 120 cycles of 45°C cycling. The top photo shows the baseline gas generation while the bottom photo shows gas generation with L6-4-C167 optimized formulation and an optimized testing protocol. Significant improvement in swelling able to be seen.	107
Figure I.8.6 Photos of 2Ah MLPC containing HV-LNMO/C material after 120 cycles of 45°C cycling. The top photo shows the baseline gas generation while the bottom photo shows gas generation with L6-4-C167 optimized formulation and an optimized testing protocol. Significant improvement in swelling able to be seen.	107

Figure I.9.1 Demonstration of closed-loop North American lithium-ion battery supply chain	111
Figure I.10.1 Ionblox approach to reach the USABC calendar life and cell cost targets.....	114
Figure I.10.2 Ionblox electrolyte designs that were studied in 2022.	115
Figure I.10.3 Cathodes and their properties studied by Ionblox in 2022.....	115
Figure I.10.4 Ionblox cathode surface passivation test plan for Polymer #1.....	116
Figure I.10.5 Status of ongoing performance testing on baseline pouch cells.....	116
Figure I.10.6 Cell targets and gap chart of baseline pouch cells.....	117
Figure I.10.7 Measurements on baseline cells after formation.	117
Figure I.10.8 Capacity and energy measurement versus voltage during charge and discharge for baseline pouch cells.	118
Figure I.10.9 Power and resistance measurement versus depth of discharge for baseline pouch cells.....	118
Figure I.11.1 Single layer Si/NMC811 cell cycling at 1C//1C rates from 2.75-4.25V	122
Figure I.11.2 Peak specific discharge power in 3.7Ah Si/NMC811 cells with improved electrolyte formulations. Formulation #1045 is the baseline formulation at the start of the program.	123
Figure I.11.3 Peak specific discharge power at different discharge temperatures for baseline cell chemistry.	125
Figure I.11.4 Model predictors for cell capacity retention generated from the data from the DOE cells at end of life.	126
Figure II.1.1 Cycle life comparison of $\text{LiNi}_{0.95}\text{Mn}_{0.05}\text{O}_2$ obtained at different furnace applications. (Red spheres represent the tube furnace application. P1 and P2 stand for Prototype -1 and Prototype -2).....	131
Figure II.1.2 Cycle life comparison of LiNiO_2 cathode electrode: obtained from standard and modified calcination box furnaces at small scales (left) and reproducibility check using modified prototype- 2 at slightly larger scale (right) {Fixed calcination parameters: calcination temperature = 650°C; Dwell time = 12 h; under 100% O_2 gas flow}	131
Figure II.1.3 (Top row) Cross section SEMs of Co-free Mn-based cathode carbonate precursor particles showing a dense interior (left); bulk and cross-sectional morphologies of pretreated carbonate precursor (right) showing an onion peel-like structure. (Middle row) Morphologies of cathode active materials that are calcined directly at 900°C with varying Li/TM mol ratios (1.30 and 1.34 from left to right) showing rough surfaces with ranging levels of particle cracking particularly for the larger particles. (Bottom row) Morphologies of cathode active materials that are calcined at 900°C with prior 600°C hold with varying Li/TM mol ratios (1.30 and 1.34 from left to right) showing severe cracking.	132
Figure II.1.4 SEM images of particle morphologies formed in a continuous operation using 10L TVR (top two rows). Voltage profile (bottom row) comparison of materials obtained through fast and slow co-precipitation reaction (coin half cell: First formation cycle at C/20 (1C = 175 mA/g) between 2.0 V – 4.7 V at 30°C)	133
Figure II.1.5 Particle formation under high pH conditions in a fast-continuous operation displays flaky, platelets with $\leq 1\mu\text{m}$ platelet size having $\sim 100\text{nm}$ wall thickness (top rows). Voltage profile (bottom row) comparison of materials obtained through fast carbonate vs fast hydroxide co-precipitation reaction (coin half cell: First formation cycle at C/20 (1C = 175 mA/g) between 2.0 V – 4.7 V at 30°C).....	134
Figure II.2.1 Particle Production with Dry Aerosol Calcination Concept	139
Figure II.2.2 DAC trials using NCA green powder	140
Figure II.2.3 SP synthesis of AL- and Mg-doped LNO	140
Figure II.2.4 FSP configuration for 500 g/hour production.....	141
Figure II.3.1 Synthesis of polycrystalline and single-crystal NMC96-2-2 cathode materials	144

Figure II.3.2 Tap density increase by mixing polycrystalline and single-crystal NMC 96-2-2 cathodes	145
Figure II.3.3 Particle crack analysis by nano-indentation.....	145
Figure II.3.4 Cycling performance of polycrystalline and single-crystal NMC 96-2-2 cathodes	146
Figure II.3.5 Improved cyclability of single-crystal NMC 96-2-2 cathode by selected electrolytes).....	146
Figure II.3.6 Synthesis of Al-doped single-crystal NMC 96-2-2 cathode	147
Figure II.3.7 Surface protection of single-crystal NMC 96-2-2 cathode	147
Figure II.3.8 Synthesis of nano-sized carbon-layered single-crystal LFP cathode	148
Figure II.3.9 XRD of nano-sized carbon-layered single-crystal LFP cathode	148
Figure II.3.10 TGA/DSC of nano-sized carbon-layered single-crystal LFP cathode	149
Figure II.3.11 Physical properties of hydrothermal single-crystal LFP compared to solid-state LFP	149
Figure II.3.12 Electrochemical performance of hydrothermal single-crystal LFP and solid-state LFP	149
Figure II.3.13 BCDI analysis of single-crystal LFP	150
Figure II.3.14 Electrochemical performance of ALD Al ₂ O ₃ -coated granulated single-crystal LFP.....	150
Figure II.4.1 Reaction to form MTFPC	153
Figure II.4.2 Screening study GC results for synthesis of MPFPC.....	154
Figure II.4.3 ¹ H and ¹⁹ F NMR spectra of MTFPC.....	154
Figure II.4.4 Synthesis of MPFPC	154
Figure II.4.5 Select analytical spectra for MPFPC	155
Figure II.4.6 Analytical Data for FDMB	155
Figure II.4.7 Syrris ASIA flow chemistry system	157
Figure II.4.8 GC/MS spectra of the three component mixture from FMMB synthesis.	158
Figure II.4.9 NMR data for FMDFEB	159
Figure II.4.10 Flow chemistry reaction for Li-TCl.....	159
Figure II.4.11 Chemical structures for the synthesis of Li-TCl.....	160
Figure II.4.12 Current response to stepped voltage	161
Figure II.4.13 Current response to stepped voltage	161
Figure II.5.1 Example radiography image of electrode coating, taken in profile, with detected interfaces artificially highlighted in red. (LBNL)	166
Figure II.5.2 Example radiography image showing heating-driven stratification of electrode coating. (LBNL)	166
Figure II.6.1 Planar cell with NMC cathode and residual NMP. (a) Charge/discharge curves at -10°C with rate of 0.1 C; (b) Discharge capacity and coulombic efficiency versus cycle number at -10°C.....	168
Figure II.6.2 Planar cell with NMC cathode and various residual solvents. (a) Charge/discharge curves and (b) coulombic efficiency versus cycle number at 25°C with rate of 0.1 C.....	168
Figure II.6.3 Performance of cells with organic cathode including (a) comparison of capacity fade with liquid and solid LLZO separators, and (b) the impact of lower-voltage-cutoff with an upper-voltage-cutoff of 2.8V for a cell with LLZO separator and liquid catholyte.....	169

Figure II.6.4 Full ASSB cell. (left) Bilayer cell with cathode infiltrated into pores. (right) Charge/discharge curves at room temperature with a rate of 0.02 C for a LLZO bi-layer structure cell.	170
Figure II.7.1 Adhesion force per width of laminate from a 180° peel test for laminates consisting solely of different ratios of carbon and binder.	172
Figure II.7.2 Cohesion of films removed from the current collector at carbon to binder ratios from 0.2:0.8 to 0.8:0.2.	173
Figure II.7.3 Electronic conductivity of carbon/binder films with varying carbon to binder ratios.	173
Figure II.7.4 Open porosity of carbon/binder films with varying carbon to binder ratios.	173
Figure II.7.5 Confocal microscope images of active material and carbon mixed with a. sufficient carbon and b. insufficient carbon.	174
Figure II.7.6 Plot of total solvent amount versus total carbon surface area of several slurries. The slurries that resulted in good performing laminates are labeled with blue circles. A line of achieved through a regression analysis indicates a linear relationship between total solvent content and carbon black surface area in the slurry.	175
Figure II.7.7 Slurry viscosity <i>versus</i> active material content for	175
Figure II.8.1 Microstructure of LMR-NMC secondary cathode particles. (a)-(d) show the SEM images of cathode particles with increasing primary particle size as the sintering temperature increases from 925°C to 1000°C. The mean primary particles size is 100 nm, 200 nm, 400 nm, and 800 nm respectively from (a) to (d). The inset figures show magnified region to focus on the primary particles. (a1) to (d1) show the cross-section of a secondary particle with reference to particles seen in (a) to (d). The BET specific area decreases from 3.8 m ² /g to 1.0 m ² /g from (a) to (d) as the size of the primary particle increases from 100 nm to 800 nm. The average secondary particle size is same in (a) to (d). Two-dimensional computational microstructure is generated to match the average characteristics of experimental cathode particle, the primary particle size and shape and the specific interface area. (e) Ideal microstructure with open network of primary particles accessible to electrolyte. The specific interface area is larger than measured in experiments. (f) Microstructure with intra-agglomerate closed pores match the observed experimental specific interface area. The primary particle size is same in (e) and (f). (g) Computational domain for electrochemical model. The potential and concentration field are solved in the electrode and electrolyte. Electrode is shown in gray while electrolyte is shown in blue.	180
Figure II.8.2 (a) Change in surface energy of the transition metal carbonate precipitates as compared to their growth rate. MnCO ₃ demonstrates high reaction rate constants and extremely high supersaturation ratios, which results in very fast growth of the particles. On the other hand, Ni and Co containing NiCO ₃ , CoCO ₃ , and NMC111CO ₃ demonstrates slower reaction rate constant, which leads to slower growth of the primary particles through direct precipitation and the individual primary crystallites for these Ni and Co containing precursors is extremely small. Due to the smaller primary particle size of these Ni and Co containing precipitates, they demonstrate higher surface energies, which enhances their propensity to agglomerate during the formation of the secondary particles. (b) Demonstration of the two physical phenomena, namely “nucleation” and “growth”, that contributes to the formation of the cathode precursors. Growth of the transition metal carbonate precipitates can occur through three mechanisms, direct precipitation, surface nucleation, and agglomeration, all of which will be briefly studied as part of the present project.	181
Figure II.8.3 (a) Schematic representation of the two competing driving forces, the first one being tendency to precipitate, and the second one is minimization of surface energy, that contributes to the determination of the surface morphology of the TMCO ₃ precipitates. (b – d) High resolution transmission electron microscopy (HR-TEM) image of the aggregated primary particles for different transition metal carbonates. (b) Primary particles of CoCO ₃ (precipitated under CoSO ₄ ~ 4.5 mM and [NH ₄ ⁺]/[Co ²⁺] ~ 40). (c) Primary particle morphology of NiCO ₃ (precipitated under NiSO ₄ ~ 4.5 mM and [NH ₄ ⁺]/[Ni ²⁺] ~ 15). (d) Primary particle microstructures of NMC111CO ₃ (precipitated under (NiSO ₄ +MnSO ₄ +CoSO ₄) ~ 4.5 mM and [NH ₄ ⁺]/[Ni ²⁺ +Mn ²⁺ +Co ²⁺] ~ 40). (e – g) Simulated primary particle microstructures of CoCO ₃ , NiCO ₃ and	

NMC111CO ₃ using Monte Carlo based computational frameworks. Competition between the driving forces for precipitation and surface energy minimization are taken into consideration in this computational analysis.	183
Figure II.8.4 Stacked PXRD plots for the calcination process of high and low nickel content precursors show the evolution of phases (left). Snapshots of the in situ diffraction study highlighting the difference in the PXRD patterns for the two intermediate phases (top right) and the NMC layered phases (bottom right).	184
Figure II.8.5 Snapshots of NiO lithiation AIMD (1200 K) radial distribution function and schematic (ball and stick) representation of the simulation for a) t = 0 ps, b) t = 18 ps, c) t = 298 ps with 10 H ₂ O molecules taken off the cell, d) t = 1100 ps with all the water molecules taken off the cell. Red spheres represent O, silver spheres represent Ni, green spheres represent Li, and the small white spheres represent H.	185
Figure II.8.6 AIMD (1200 K) simulation cell snapshot showing the LiNiO ₂ layers gliding between perfect and defective layered structures.	186
Figure II.8.7 Ab initio molecular dynamic (1400K-1800K) simulation cell representing an interface between LiNiO ₂ and NiO. The arrows are pointing to blue spheres representing the initial and final position of the Ni vacancy in the NiO region.	186
Figure II.8.8 Computational simulation of the calcination of NMC111 and NMC811 cathode precursors with LiOH conducted at the mesoscale level using phase field based methodologies. (a) Initial microstructure of the NMC cathode precursors. (b) Computationally predicted particle microstructure of NMC111 after 2 hours of calcination. Particles appear to be less sintered than NMC811. (c) Computationally predicted microstructure of NMC811 after calcination for 2 hours. Particles are more sintered than NMC111. (d) Removal of water from the NMC111 and NMC811 at the beginning of the calcination process. (e) Increase in lithium concentration in the NMC111 and NMC811 cathodes during the calcination process. Due to the faster reaction with Li-salt, NMC111 demonstrates earlier lithiation than NMC811. (f) Evolution in primary particle size experienced by the NMC111 and NMC811 cathodes during calcination. Due to greater extent of lithiation, NMC111 demonstrates larger particle size than the NMC811.	187
Figure II.8.9 Performance of LMR-NMC cathode (a) Voltage discharge profile for three microstructures, (i) Ideal microstructure with primary particle size of 100 nm (ii) Microstructure with intra-agglomerate closed pores with primary particle size of 100 nm (iii) Ideal microstructure with primary particle size of 800 nm. The discharge capacity depends on the primary diffusion length as well as the agglomerate diffusion length. The inset figures show the contour of lithium concentration normalized with maximum lithium concentration for the three microstructures. The color scale ranges from 0.7 to 1. (b) Capacity described by primary diffusion length and ratio of agglomerate and primary diffusion length. The applied C-rate is 1.	188
Figure II.9.1 (a) Contour plots of in-situ temperature-resolved synchrotron X-ray diffraction (XRD) data, showing the phase progression during the calcination process in the synthesis of NMC811. (b) Normalized fraction of the major phases quantified by Rietveld refinement of the in-situ XRD.	193
Figure II.9.2 (a) In situ PDF analysis of the solid-state synthesis of NMC811 and LNO. (a) Representative PDF pattern solving the crystal nucleation and growth in LNO. (b) Comparison of the domain size of the crystals formed in LNO (blue) and NMC811 (red), obtained through the fitting to the PDF pattern.	194
Figure II.9.3 Phase progression during the solid-state synthesis of LiNiO ₂ (LNO). a, Contour plot showing multi-stage(labelled as I, II, III and IV) phase transformations, tracked in situ using temperature resolved synchrotron X-ray diffraction. b, Normalized fraction of the major phases quantified by the Rietveld refinement of in situ XRD patterns. c, Schematics illustrating the structure/atomic configuration of the involved phases and their correlations. A dual-phase composite of a stoichiometric LiNiO ₂ and a Li-containing disordered rock-salt forms at moderate temperatures from Li and Ni hydroxide precursors (P) and eventually transforms to a single phase layered LNO structure (L) with cation mixing at higher temperatures.	195
Figure II.9.4 Crystal growth during the calcination of NMC71515. (a) Morphology evolution of primary particles, shown by the SEM images taken from samples at different calcining statuses: pretreated at 500°C (10 h), calcined at 800°C (20 h), 850°C (10 h) and 900°C (10 h), from left to right. (b) Computationally simulated	

images of the particles at the corresponding calcining statuses. Both lithiation and sintering of the particles are considered in the simulations. (c) Comparison between the experimentally observed (symbols) and computationally predicted (solid lines) evolution in particle size at different temperatures, showing the lithiation-driven particle swelling and the growth of larger particles at the expense of smaller ones. 196

Figure II.9.5 (a) Synchrotron XRD patterns of 0, 0.7, 1.4 and 2.1% Nb-coated/substituted NMC 9055 heated at 725°C. (b–d) Enlarged view in 2θ (deg): (b) 4.5°–8.0°, \blacklozenge is Li_3NbO_4 ; (c) position shifts of the (003) and (104) peaks; (d) normalized (003) and (104) peaks, showing the variations of their intensity ratios. 197

Figure II.9.6 (a) In situ synchrotron XRD measurements (converted to Cu $K\alpha$) captured during the synthesis trial of $\text{Li}_{1.2}\text{Mn}_{0.4}\text{Ti}_{0.4}\text{O}_{1.6}\text{F}_{0.4}$ using precursors (MnF_2 , LiF , LiMnO_2 , Li_2TiO_3 , and C). (b) Refined mole fractions of all crystalline phases are plotted as a function of time, neglecting any molten or amorphous phases. (c) The out-of-plane LiMnO_2 lattice constant is refined as a function of temperature, showing a non-linear contraction associated with Li^+ extraction. (d) Heating profile used during the synthesis procedure. 198

Figure II.10.1 (a) FTIR spectra of green resin before and after EB curing. (b) CV of green resin coated Al foils after EB curing. Scanning speed is 0.1 mV/s within 2.0–4.5 V. (c) and (d) SEM images of NMC811 cathode after EB curing process. (e) EDX of NMC cathode. (f) cycling performance of NMC cathode with green resin. 202

Figure II.10.2 (a) Differential capacity curve of 15% Si containing graphite anode (inset are electrodes casted and EB cured). (b) cycling performance of Si-graphite electrode with two different resins (CPA and 2-CA respectively). 203

Figure II.10.3 Slurry formulation, coating, EB curing, coin cell configuration and cell performance of Li cells with NMC/PEO composite cathode. 204

Figure II.10.4 Polymer electrolyte Li cell shows significantly less T rise in nail penetration. 204

Figure II.10.5 Neutron diffraction patterns of NMC622 and graphite before and after EB radiation. 205

Figure II.11.1 Schematic illustration of the structured cathode electrodes using (FTC) techniques. 207

Figure II.11.2 The experimental setups that were used for the FTC cathodes. (a) benchtop configuration, (b–d) scale up configuration. 208

Figure II.11.3 Optical microscope images of FTC cathodes electrodes at several solid to water contents indicated on the figure. Solid to water weight ratio 1:1 (a,b), 2:1 (c,d), 4:1 (e,f), 10:1 (g,h). The freezing temperature was -9 °C. 208

Figure II.11.4 SEM images of the (a) unfilled FTC cathode and (b) filled with PEO and LiTFSI. 208

Figure II.11.5 Charge and discharge values of the single layer cathodes at several cycling rates. (a) 2 mAh/cm², (b) 3 mAh/cm², (c) 4 mAh/cm², (d) 6 mAh/cm². Significant capacity fading is shown at C-rates higher than 0.5 (green circle). 209

Figure II.11.6 Charge and discharge values at several cycling rates of a structured cathode with areal capacity 6 mAh/cm². 209

Figure II.11.7 Hybrid polymer electrolytes filled with platelet Al-LLZO. (a) electrolyte films, (b) cross-sectional SEM image, (c) schematic of the Li^+ dendrite suppression due to the platelet geometry of the Al-LLZO fillers, (d) SEM image of the Al-LLZO fillers, (e) XRD pattern of the Al-LLZO fillers. 210

Figure II.11.8 Summarized conductivity plot for the pristine and composite polymer electrolytes. 211

Figure II.11.9 Dielectric loss spectra analysis of the Li^+ ion conductivity mechanism at 60°C. 211

Figure II.11.10 (a) MD snapshots of the polymer electrolyte with LiTFSI and LiFSI. SAXS measurements and fitting analysis of the polymer electrolyte at 25 and 60°C. (b,c) PEO with LiFSI, (d,e) PEO with LiTFSI. 212

Figure II.11.11 Comparison plots of long-term stripping plating at 50 $\mu\text{A}/\text{cm}^2$ of (a) LiTFSI electrolyte versus composite Al-LLZO/LiTFSI electrolyte. (b) composite LiTFSI versus composite LiFSI electrolyte. 213

Figure III.1.1 The share of different nations in amount of Ni produced differs at the level of (a) mining (including beneficiation) and (b) processing (pyrometallurgy + refining) for its production from sulfide ores.	219
Figure III.1.2 GHG burden of Ni production from sulfide ores depends on ore grade, with mining and beneficiation playing a critical role at lower ore grades, while laterite ore-based Ni production causes higher GHG emissions than that from sulfide ores.	219
Figure III.1.3 SG anode production causes higher GHG burden than NG anode production.	221
Figure III.1.4 The share (%) of different nations in Ti supply depends on the Ti form produced.	222
Figure III.1.5 GHG emissions of Ti production.	222
Figure III.1.6 Projection of US cathode chemistry types courtesy of Circular Energy Storage, London.	223
Figure III.2.1 The Critical Materials Research Plan with three major research areas to address critical materials issues for Li-ion batteries and recovery of materials for re-introduction into the supply chain.	227
Figure III.2.2 Logo of the Lithium-Ion Battery Recycling Prize.	227
Figure III.2.3 The Lithium-ion Battery Recycling Prize consists of three progressive phases from concept through pilot validation for about three years.	228
Figure III.2.4 The Lithium-ion Battery Recycling Prize Phase III winner announcement.	230
Figure III.2.5 Graph illustrating the documented cost from each Phase III participating team.	230
Figure III.2.6 Map of the four Lithium-ion Battery Recycling Prize Phase III winning teams.	231
Figure III.3.1 Basic processing steps associated with direct recycling.	235
Figure III.3.2 a) Rate performance in half cells and b) cycle life in full cells of NMC 622 cathode recycled from an end-of-life cell via scalable processes versus a commercial NMC 622 baseline.	236
Figure III.3.3 Comparison of cycling of recycled NMC 622 depending on which steps were done in a rotary kiln.	237
Figure III.3.4 Half cell rate study and cycling for a) graphite recovered from manufacturing scrap and b) LiFePO ₄ from artificially created black mass (3 wt.% PVDF).	237
Figure III.3.5 Conventional Soxhlet extractor design.	238
Figure III.3.6 PVDF binder and cryovap solvent transfer apparatus.	240
Figure III.3.7 EDS mapping of NMC 811 electrode scrap.	241
Figure III.3.8 FTIR spectra of fresh DMF and recovered DMF from vacuum-assisted cryovap process. Inset digital photo shows recovered DMF.	241
Figure III.3.9 Froth flotation column set-up at Argonne National Laboratory.	243
Figure III.3.10 Schematic of optimized froth flotation process to separate NMC111 and LMO.	243
Figure III.3.11 Purity of NMC111 and LMO cathode materials achieved after a 2-step froth flotation process.	244
Figure III.3.12 Separation of binary cathode mixtures using Process A.	245
Figure III.3.13 Separation of double-side coated laminates by Process A.	246
Figure III.3.14 SEM-EDS of recovered cathode materials from cylindrical and pouch cell.	247
Figure III.3.15 Effects of PVDF removal processes on froth flotation recovery using two collectors (A and B).	247
Figure III.3.16 SEM images of froth and sink products after a NMC/LMO separation by froth flotation.	248

Figure III.3.17 XRD curve showing peak change in burnt cathode material.....	248
Figure III.3.18 Effect of surface treatment on different cathode chemistries	249
Figure III.3.19 a) a schematic drawing of a centrifugal ultrafine (UF) gravity separation concentrator.	250
Figure III.3.20 SEM image of (a) pristine NMC333, (b) delithiated NMC333, (c) 1-step relithiated NMC333, and (d) 2-step relithiated NMC333	252
Figure III.3.21 XRD of pristine NMC622, Solvent Y processed, and relithiated cathode powder	252
Figure III.3.22 Schematic illustration of ionothermal relithiation process.	254
Figure III.3.23 XRD patterns of relithiated products under different mass ratios of SolveY_ORNL to RTMS.	255
Figure III.3.24 Half-cell cycling performance (A) and the 100th half-cell charge capacities (B) of relithiated products under different mass ratios of SolveY_ORNL to RTMS.	255
Figure III.3.25 The first 4 charge-discharge curves(A) and cycling performance (B) of large scale ReLi_NMC 622 for half-cell tests.	256
Figure III.3.26 (A) Costs of cathode regeneration by different methods analyzed by EverBatt model and (B) XRD pattern and photo of recycled RTMS.	256
Figure III.3.27 Voltage profiles (a) and cycling stability (b) of the cycled NCM622, the pristine NCM622 and NCM622 regenerated at 220°C at 50g scale followed by annealing at 850°C in two batches (C-NCM622, T-NCM622, HS-NCM622-50g-Round 1, HS-NCM622-50g-Round 2).....	257
Figure III.3.28 Voltage profiles (a) and cycling stability (b) of samples treated by the mixture solution of 0.1M LiOH with 3.9M KOH, 1M LiOH with 3M KOH, 2M LiOH with 2M KOH, 3M LiOH with 1M KOH, and 4M LiOH as well as the control samples (C-NCM622 and T-NCM622).	258
Figure III.3.29 Voltage profiles (a) and cycling stability (b) of the pristine NCM111, the delithiated NCM111 regenerated at 220°C at 100g scale, use the ratio of 20ml, 40ml, 60ml, 80ml water respectively to wash 1g HT-NCM111, followed by annealing at 850°C (T-NCM111, HS-NCM111-100g-20ml/g wash, HS-NCM111-100g-40ml/g wash, HS-NCM111-100g-60ml/g wash, HS-NCM111-100g-80ml/g wash).....	258
Figure III.3.30 Voltage profiles (a) and cycling stability (b) of the pristine NCM111, the delithiated NCM111 regenerated at 220°C at 100g scale, use the ratio of 1.6ml water to wash 1g HT-NCM111, followed by annealing at 850°C, and the delithiated NCM111 regenerated at 220°C at 100g scale, use the ratio of 1.6ml water to wash 1g NCM111 after hydrothermal reaction, followed by annealing at 850°C, and then apply scavenge agent on the surface of NCM111 (T-NCM111, HS-NCM111-100g-1.6ml/g wash, HS-NCM111-100g-1.6ml/g wash + scavenge agent).....	259
Figure III.3.31 Redox mediator solubility in 1,2-dimethoxyethane (DME).	261
Figure III.3.32 Redox mediator screening (a) open circuit voltage, (b) charge and discharge capacity of the relithiated material	262
Figure III.3.33 (a) XRD patterns of pristine NMC622, solvent Y EOL NMC622, and relithiated NMC622 materials. (b) decomposition kinetics of redox mediator. (c) morphology images of pristine NMC622, solvent Y EOL NMC622, and relithiated NMC622.....	262
Figure III.3.34 Capacity for materials relithiated using the new and old redox mediators.....	263
Figure III.3.35 Exchange current density and diffusivity of cycled aged NMC111 and cycle aged commercial NMC 622 cathode materials with respect to lithium content.....	265
Figure III.3.36 a) Capacity restored to commercial NMC 622 and b) relithiation time for rapid relithiation protocol	265
Figure III.3.37 SEM imaging of EoL commercial NMC 622 prior to any rinsing or relithiation	266

Figure III.3.38 XPS analysis of surface species on treated and untreated EoL commercial NMC 622.....	266
Figure III.3.39 C/10 cycle performance of EoL commercial NMC 622 after additional rinsing step	267
Figure III.3.40 XRD analysis of structure of treated and untreated EoL commercial NMC 622	267
Figure III.3.41 XRD of an upcycling product before and after re-annealing to 850°C (left) and expanded view of higher angle peaks (right)	269
Figure III.3.42 SEM images of (a) upcycling products annealed at 720°C and (b) re-annealed at 850°C.	269
Figure III.3.43 Half-cell rate performance for re-annealed upcycling products	271
Figure III.3.44 Schematic illustration of ionothermal upcycling process.	272
Figure III.3.45 XRD patterns showing survey spectrum and zoom-in peaks of D-NMC111, Pristine NMC622, and Up-NMC622.	273
Figure III.3.46 Metal molar ratios of D-NMC 111, Pristine NMC622, and Up-NMC622 based on ICP results.	273
Figure III.3.47 (A) The first cycle charge/discharge curves of NMCs for half-cell tests. (B) The second cycle charge/discharge curves of NMCs for half-cell tests. (C) Cycle performance of NMCs for half-cell tests.....	274
Figure III.3.48 (a) SEM of upcycled D-NCM111 with Ni doped via hydrothermal and post annealing method (HS-upcycle-Ni doped). (b) Cycling stability of HS-upcycle-Ni doped, the pristine NCM111 and delithiated NCM111.	275
Figure III.3.49 (a) Cycling stability of upcycling NCM622 (Upcycling-NCM622) and pristine NCM622. (b) Rate performance of upcycling NCM811(Upcycling-NCM811) and pristine NCM811.....	275
Figure III.3.50 (a) Cycling stability of the cycled NCM622, regenerated NCM622 and regenerated NCM622 coated by B (HS-NCM622, HS-NCM622-B1 and HS-NCM622-B2) as well as the pristine NCM622. (b) FT-IR spectra of aged pristine NCM622, aged regenerated NCM622 samples, aged regenerated NCM622 coated by B (Aged T-NCM622, Aged HS-NCM622, Aged HS-NCM622-B coating).....	276
Figure III.3.51 (a) equipment for scale up experiment; (b) morphology of SC-NMC111-100g; (c) XRD pattern of SC-NMC111-100g.	277
Figure III.3.52 (a) rate performance comparison of SC-NMC111-100g and ANL-100g-Baseline; (b) cycle performance comparison between SC-NMC111-100g and ANL-100g-Baseline.....	277
Figure III.3.53 (a) Raman Spectra of Control811, SC811-5hrs, and SC811-25hrs; (b) XPS survey peaks of Etched-NMC811-25hrs, Etched-NMC811-2hrs, and Control811; (c) Mn2p spectra of Control811, Etched-NMC811-2hrs, and Etched-NMC811-25hrs.....	278
Figure III.3.54 Morphology and structure results for NMC111 etched in 0.5M H2SO4 and 1M H2SO4.	279
Figure III.3.55 SEM images of 0.2PNCM (a1, a2), 1PNCM (b1, b2) and 5PNCM (c1, c2) with precursors shown in row 1 and cathodes in row 2. (Insets: images at higher magnification).	280
Figure III.3.56 XRD patterns of (a) cathodes and (b) impurity phase region in cathodes. (c-f) Refinement results of VNCM, 0.2PNCM, 1PNCM, and 5PNCM cathodes.	281
Figure III.3.57 Electrochemical performance of as-prepared samples. (a) cycle at 0.33C, (b) cycle at 5C, (c) rate to 5C.....	281
Figure III.3.58 Custom built dual-shaft shredder with mailbox-style feed hopper, inert gas inlet, blades situated along two rotating shafts, and a sealed collection tank.....	284
Figure III.3.59 Comparison of ANL manufacturing scrap shreds vs. the same manufacturing scrap shredded by an industry partner using a similarly sized system.....	284
Figure III.3.60 An example of a process flow for shredding and separating components.....	285

Figure III.3.61 Set-up of an aspiration system used for liberating clumps and removing light from heavy materials.....	285
Figure III.3.62 Shredding cycled 18650 cylindrical cells under inert atmosphere at room temperature (top) and after freezing in liquid nitrogen (bottom)	286
Figure III.3.63 Shredding of a discharged pouch cell under inert atmosphere using two types of cameras to monitor thermal behavior.....	286
Figure III.3.64 Composition of sample types (e.g., blue and green) used for separation experiments	292
Figure III.3.65 Summary of separation results for three different types of feed materials which shows that separation is affected with increasing material complexity	292
Figure III.3.66 Results from a 2-step separation of 200 grams of a 1:1 mass ratio anode/cathode electrode mixture achieved >99% purity anode and cathode with >90% recovery.....	293
Figure III.3.67 Results from 2-step separation of commercial batteries shredded at Argonne National Laboratory.....	293
Figure III.3.68 (a) Half-cell and (b) full-cell performance of BMP-treated NMC-111 vs pristine NMC-111; shaded region reflects capacity variation between sample replicates.	295
Figure III.3.69 Selected XPS spectra for (a) O1s and (b) Ni2p3 showing surface modification of treated practical BM (yellow curves) as compared to as-received EoL material (orange curves) and pristine material (blue curves). Preliminary species assignments are overlaid at the respective binding energies for reference.	296
Figure III.3.70 SEM analysis of practical BM following BMP treatment, revealing the presence of flake-like crystallites which are confirmed by EDS to contain Al (likely as Al(OH) ₃) and K (likely as KOH).	296
Figure III.3.71 Evolution of full-cell differential capacity over 25 C/10 cycles following formation: (a) Pristine NMC-111; (b) NMC-111 after undergoing BMP + post-treatment rinse with deionized water; (c) Normalized differential discharge capacity for the condition shown in (b), with normalization calculated as the value from the treated cell minus the first-cycle value from a representative pristine cell. In (c), vertical dashed lines at 3.43 V and 3.8 V denote the low, middle, and high voltage regions of the plot, separating the expected graphite (~3.5 V) and NMC (~3.7 V) peaks from the side reactions occurring at low and high voltages. In all plots (a-c), line colors indicate the cycle number (increasing from dark to light tones) and a single representative cell replicate is shown; in (b), the first-cycle differential capacity behavior of the pristine cell is overlaid in black for reference.....	297
Figure III.3.72 (a) Full-cell performance and (b) impedance analysis of BMP-treated practical end-of-life material to evaluate the variable impacts of post-treatment solvent on subsequent performance. In (a), shaded region reflects capacity variation between sample replicates; in (b); curves with the same marker style and color reflect sample replicates.	298
Figure III.3.73 Full cell cycling for recycled NMC 622 with gen 2 (1.2 M LiPF ₆ in 3:7 EC:EMC) electrolyte and recycled electrolyte (1 M LiPF ₆ in 1:1 EC:DEC) along with a commercial NMC 622 with gen 2 electrolyte.	299
Figure III.3.74 NMC 111/graphite full cell cycling using electrolyte recycled using a rotary evaporator for the concentration step versus gen 2 baseline electrolyte.....	300
Figure III.3.75 Histograms generated for thickness and edge length from AFM images of the graphene prepared at 3krpm from a) and c) manufacturer A and b) and d) from manufacturer B.....	301
Figure III.3.76 Histograms generated for thickness from AFM images of the graphene from manufacturer A at different shear mixing stirring speeds.....	302
Figure III.3.77 EverBatt cost analysis of the recycling of graphite into graphene from graphite on copper foil. Cost is in \$/kg of graphite recycled.	303

Figure III.3.78 Cost and revenue comparison for hydro recycling (\$/kg cell recycled)	304
Figure III.3.79 LIBRA model top level modular structure	305
Figure III.3.80 Five projections of electric LDV sales in the United States in terms of the battery energy demanded each year.....	306
Figure III.3.81 Share of cobalt required for new LIB demand that can be met by cobalt recovered through recycled LIBs.....	307
Figure III.3.82 Share of nickel required for new LIB demand that can be met by nickel recovered through recycled LIBs.....	308
Figure III.3.83 Summary of the capacity retention for first generation (v1) and second generation (v2) relithiated NMC622 powders versus Baseline NMC622 powder evaluated in single-layer pouch cells with Gen2 electrolyte at 30°C.....	310
Figure III.3.84 Summary of upcycled single crystal NMC111 versus baseline NMC111 in single-layer pouch cells using Gen2 or Gen2+FEC electrolytes at 30°C.....	311
Figure III.3.85 XPS results of C1s, F1s and P2p regions from NMC622 after binder removal process using solvent Y.....	312
Figure III.3.86 CEI investigation using XPS.....	312
Figure III.3.87 SEI investigation using XPS.....	312
Figure III.3.88 Raman mapping analysis on the lithium plating.....	313
Figure III.3.89 FTIR analysis on aged graphite electrodes.....	313
Figure III.3.90 XRD and GIXRD analysis on the aged graphite anode.....	314
Figure III.3.91 Sampling locations for the point-scan EDS results presented in two prior tables. As shown, compositional analysis was conducted across the diameter of the secondary particle, facilitating analysis of secondary-particle-scale gradients in composition.	315
Figure III.3.92 Representative process for EBSD analysis and datatypes: Band Contrast (left); Inverse Pole Figure (IPF, middle); and Grain Reference Orientation Deviation (GROD, right). Sample shown is ORNL's upcycled material received in Q3, which shows improved structural homogeneity (lower average GROD and minimal evidence of primary-particle-scale core-shell gradients) relative to the sample received in Q1.	316
Figure III.3.93 EDS mapping results reveal a grain-scale gradient in composition for several elements. This is particularly evident for the transition metals, where primary particle edges appear to be enriched in Ni, relative to Co and Mn. This information will be used by the ORNL team to further improve upcycling process conditions.....	317
Figure III.3.94 Enlarged plot showing the characteristic temperature vs time curves of the cells penetrated at -120°C, -100°C, -80°C, and -60°C. Curves are offset on the x axis by 100s for visibility (x+100s for -100°C, x+200s for -80°C, x+300s for -60°C). Nail penetration did not initiate a continuous heat release at the three coldest temperatures, but is observed to do so in the -60°C sample.	318
Figure III.4.1 Coulombic efficiency at C/3 and C/5 in Li Cu coin cells as a function of cycle number (a) in E0 electrolyte and (b) in E1 electrolyte.....	332
Figure III.4.2 (a) Charge and discharge curves (Voltage vs. Capacity) and (b) Specific capacity and Coulombic efficiency vs. cycle number for 0.2Ah Li metal pouch cells.	333
Figure III.5.1 SEM images of recycled NMC622 precursors.	337
Figure III.5.2 The SEM images and XRD pattern for 0919NMC622-100g.	338
Figure III.5.3 SEM images, XRD pattern, and EDS mapping of 0919NMC622-100g-Al ₂ O ₃	338

Figure III.5.4 Electrochemical performance of 0919NMC622-100g-Al ₂ O ₃	339
Figure III.5.5 SEM images of (a) first batch of recycled precursor; (b) second batch of recycled precursor; (c) third batch of recycled precursor.	339
Figure III.5.6 Electrochemical performance comparison of recycled cathode materials made by three different batches of recycled precursors.	340
Figure III.5.7 XPS results of the control from A123.	341
Figure III.5.8 SEM images, XRD patter and EDS mapping of the control from Frarsis.	341
Figure III.5.9 Physical properties of 083122-PCAM3-W-C-Al.	342
Figure III.5.10 Physical properties of 090722-PCAM3--W-C-Zr/B.	342
Figure III.5.11 Physical properties of 090822-PCAM3-W-D-Zr/B (a), 091022-PMCA3-W-D-Zr-C-B (b), and 091222-PCAM3-W-D-B-C-Zr (c).	343
Figure III.5.12 Physical properties of Speed mixer-Zr/B-Doping.	344
Figure III.5.13 Electrochemical performance comparison between the control from Farasis and all coated/doped samples.	344
Figure IV.1 Energy delivered during a 15-minute fast charge and improvements seen with the incorporation of an improved binder, an improved separator, and an improved electrolyte.	347
Figure IV.1.1 Fluoroethylene carbonate additive effect on full-cell performance, and titration dead Li. a) Graphite NMC532 1C discharge capacity normalized to the initial (Cycle 1) value vs. cycle number, with cells undergoing two cycles of 6C CCCV to 4.2V charging to 80% SOC after five 1C cycles. The inset emphasizes capacity jumps between groups of 1C cycles due to the intermittent 6C cycles that induce Li plating. Error bars depict standard deviations across n cells. b) Titrated Li (Li ⁰ and Li _x C ₆) on extracted electrodes vs. the sum of the electrochemical capacity loss mechanisms for all cells tested in (a). The inset shows the fraction of the estimated loss accounted for by titrated Li, the position of each point relative to the dotted parity line.	349
Figure IV.1.2 LiDFOB additive's effect on charge acceptance in Gr NMC full cells. Total charge time for each cell to reach 80% SOC at 6C rate. Baseline is Gen. 2 with 3 wt% FEC.	350
Figure IV.1.3 Long-term cycling performance of cells employing LiFSI as a salt in a carbonate-based solvent cycled at 4C charging rate and discharge at 1C rate	350
Figure IV.1.4 (a) charge rate capability of HCE18 as a function of salt molality. Capacity broken down between constant current portion at stated rate and constant voltage hold at 4.1 V. (b) Comparison of salt diffusivity profiles across an XCEL cell during a 6C constant current charge. (c) HCE thermal conductivity predictions, and (d) relative molal enthalpy (RME) for selected HCEs using the AEM.	351
Figure IV.1.5 ESI-MS results on the model electrolyte system. (a) Concentration of lithium complexes vs. temperature for an electrolyte with 0.012M LiPF ₆ . (b) Calculation of equilibrium constant, K _{eq} for EC+Li(EC) ₂ ↔ Li(EC) ₃ in the electrolyte with salt concentration of 0.012M, 0.12M and 1.2M.	352
Figure IV.2.1 (Macro-homogeneous model predictions for graphite-NMC 811 cell with loading of 4.5 mAh/cm ² loading employing already demonstrated solutions during 15-minute charge. A.) Current and voltage of cell employing ramp protocol. B.) State of charge achieved and lithium plating potential.	356
Figure IV.2.2 (Left) BOL cell voltage and charge acceptance for pouch cells with different CBD loading (High CBD: 8wt%-10wt% and Low CBD: 4wt%-4wt% for anode-cathode). (Right) Custom-made 3-electrode cell EIS plot for cathode [2].	357
Figure IV.2.3 (Left) NREL macroscale 6C modeling with cell voltage and potential for lithium plating calculated for baseline round 2 and graded electrodes, considering porosity and particle size gradations. (Right) SEM cross section of a dual layer anode (dual coating) manufactured by ANL CAMP.	357

Figure IV.2.4 Charge and Discharge capacities of the low carbon/binder-high loading coin cells during the fast charge cycling protocol (2x-C/3, 150x-(6C CCCV Charge w-10 min limit, C/2 Discharge).....	358
Figure IV.2.5 Electrode composition and design parameters for Round 3-Batch 1. 45 meters of SLC1506T graphite anode (LN210035-101-2) and 55 meters of NMC811 cathode (LN210035-167-4) were coated.....	359
Figure IV.2.6 Discharge capacity for R3 and an \sim R2 loading (dual layer) vs. NMC811 in xx3450 pouch cells (left); and specific discharge capacities of R3 and \sim R2 cathodes being approximately the same (right table).	359
Figure IV.2.7 (a) Fast charge utilization of the single layer pouch cells with the various electrolytes. Solid and dashed lines show the two cells for each electrolyte; (b) change of impedance over the course of 1200 cycles. Solid lines shows the initial HPPC and dashed lines show the impedance after 1200 cycles. Arrows to the right indicate the average rise in impedance from cycling.	360
Figure IV.2.8 (a) μ -XRF maps corresponding to Ni, Co, and Mn at the cycled electrode with the 50 μ m focusing optics. (b) Three principle components 1, 2 and 3 from PCA multi-energy analysis across the Ni edge.	362
Figure IV.2.9 XANES spectra taken at 32 different points of a NMC811 cathode inside a pouch cell after 600 cycles under XFC conditions. Region of the cycled cell where XANES was taken, starting at the laser spot, and moving vertically downward in 50 μ m steps.	362
Figure IV.2.10 Current density in graphite electrodes at rest after fast charging. (a) The 3D tomogram of the electrode at the beginning of the rest period. (b) Current density in the plated lithium phase as a function of time. (c) Current density in the graphite phase at the same times. The range of the maps is reduced to avoid dominance by outliers.	364
Figure IV.2.11 (a) Average current density during rest after 6C charging for the graphite electrode. The turquoise diamonds represent the average lithium stripping ionic current density, $\langle i_L \rangle$. The gray squares represent the average lithiation current density into graphite, $\langle i_G \rangle$. (b-d) Violin plots showing the distribution, median, and interquartile range of i_L and i_G at (b) $t = 6.5$ min, (c) $t = 13.0$ min, and (d) $t = 19.5$ min. For the box plot within each violin plot, the white circle represents the median value, the bottom and top of each box represents the 25th and 75th percentile values, and the bottom and top whiskers (solid lines) represent the lower and upper adjacent values. The box has zero height at $t = 19.5$ min for i_L	365
Figure IV.2.12 XRD mapping comparison between Gen2 and B26 electrolytes using pouch cell configuration. Compositional characteristics are highlighted via 2D thermal maps respectively.	366
Figure IV.2.13 Focused beam X-ray diffraction measurements of graphite anode at the separator side (left) and the current collector end (right) during the fast charging process.	366
Figure IV.2.14 The configuration of operando SR-DPS apparatus: the stack containing two vibration-damping foam blocks, multilayer pouch cell, and 2D pressure sensor is clamped into a fixed constraint.	367
Figure IV.2.15 (left) Raw output from 2D pressure sensor of 1"×1" NMC811/graphite pouch cell with average initial gauge pressure of 80psi. (right) dP/dQ plot of aforementioned pouch cell at the first frame where the plating threshold is exceeded.	367
Figure IV.2.16 Video: Spatial temporal map of Li intercalation and plating during 3C charging and 0.5C discharging cycle. 90mAh pouch cell battery with NMC811/graphite electrodes and LP57 electrolyte. Positive dP/dQ value indicate lithiation or plating; negative dP/dQ value indicate de-lithiation or stripping.	368
Figure IV.2.17 Li-plating drastically reduced with improved cycling parameters. 80mAh pouch cell battery assembled with NMC532/graphite electrodes and LP57 electrolyte cycled at 3C charging 0.5C discharging for 3 cycles without SR-DPS adjustments (left) and after SR-DPS adjustments (right).	368
Figure IV.3.1 Charge acceptance for single layer pouch cells (R2) using different fast charge solutions including electrolytes, cathode material and charge protocol. The best performing solution combinations accepted over 2.7 mAh/cm ² of charge at the beginning of life.	372

Figure IV.3.2 Plot of experimental and synthetic data used to classify the failure modes for cells which underwent different XFC charging. The method shows distinction between the two electrolytes used for the evaluation.....	373
Figure IV.3.3 Macrohomogeneous model derived 10-minute voltage ramping protocols for graphite-NMC 811 R3 cells with loading of 3.1 mAh/cm ² loading A.) Current and voltage of cell employing ramp protocol. B.) State of charge achieved and lithium plating potential.	374
Figure IV.3.4 (Left) CCCs of a pouch cell with different external thermal designs and cooling. (Right) Temperature rise and temperature nonuniformities as a function of heat removal rates for baseline (CCC = 1.2 W/K) and optimized baseline (CCC = 8.2 W/K).	375
Figure IV.3.5 a) How cell voltage changes in an NMC532 cathode particle with radial or random grain orientations, with or without damage (dmg), and with or without electrolyte infiltration (EI). b) Lithium concentration distribution within a particle that has electrolyte infiltration after charging at 6C for 420 seconds.	376
Figure IV.3.6 a) Image quality of hundreds of SEM images were enhanced and cracks segmented using AI. (b) Average particle porosity, the 2D cracked area ratio of a particle, versus charge rate and number of cycles for multiple aged cells torn down at different cycle numbers. (c) Whisker/box plot showing average/min/max crack statistics from hundreds of SEM images.	376
Figure IV.3.7 Estimates of particle density as determined using micro-CT reconstruction. The results suggest that as cycling advances particle fragmentation as evidenced by increased bimodal distribution (Preefer et al 2022 accepted).	377
Figure V.1.1 Decrease in specific and volumetric energy density of ESS from the cell to the rack. Source: NREL.....	384
Figure V.1.2 Modular DC-coupled battery pack for BTMS. Source: NREL	385
Figure V.1.3 Overview of the BMS for a modular battery. Source: NREL.....	386
Figure V.1.4 Experimental setup for the three modular DAB converters. Source: NREL	386
Figure V.1.5 DAB converters following a reference current to verify the controller. Source: NREL	387
Figure V.1.6 Experimental results for SOC equalization. Source: NREL.....	387
Figure V.1.7 DAB converter current and voltage satisfying SOC equalization. Source: NREL.....	387
Figure V.1.8 Temperature contour and profiles of the maximum temperature in the failure cell, the impinged cell and neighbor cells predicted by the ejection model when SHR is 1000°C/min.....	389
Figure V.1.9 Flowchart of the multi-objective thermal design and optimization.	389
Figure V.1.10 Three different thermal control strategies were used for three 20 Ahr lithium iron phosphate cells connected in.....	390
Figure V.1.11 Nail penetration of the insulation only module.	391
Figure V.1.12 Average temperature of each cell (left, center, right) for the three thermal strategies during nail penetration.	391
Figure VI.1 Estimated costs of cells in automotive battery packs with different combination of electrodes. The packs are rated for 100 kWh _{Total} (85 kWh _{Useable}), 300 kW, 315 V, 168 cells, and produced at a plant volume of 100K packs/year	393
Figure VI.1.1 CAD drawings of the re-designed cell, module, and pack in BatPaC v5.0. Packs are made of multiple modules, each containing multiple cells.	396

Figure VI.1.2 ASI vs. Pulse time for a dataset with multiple variables. A) All simulations super-imposed on each other, with red being the highest C-rate. B) Subset of the database, a NMC532-G battery at fixed loading experiencing different C-rates.....	397
Figure VI.1.3 Comparison of the ASI from simulated pulses and the empirical correlation for three pulses from NMC532/graphite cells at different initial states of charge (SOC): 90% (red), 50% (blue), and 20% (black). The solid lines represent the simulated pulses, and the dashed lines represent the estimated values from the correlation.	398
Figure VI.1.4 The linearization of cathode (i.e., positive electrode) thickness with respect to charging time per Equation 2 for a NMC532-Graphite (Energy) couple at a fixed cell capacity.....	399
Figure VI.1.5 Parameter space for a) α and b) β as a function of cell geometry and maximum allowable temperature.	400
Figure VI.1.6 Absolute error in the predicted temperature at 120 seconds into a pulse a) assuming constant heat generation (I^2R) or b) using the new analytical expression. The error was determined by comparing the estimated temperature to the temperature predicted by a full, validated, thermal-electrochemical model. The constant heat generation used the corrected resistance at ten seconds.....	401
Figure VI.1.7 a) Total change in discharge energy per cycle during 100 cycles at a C/3 rate. b) Contribution to the energy change from changes in the ASI. c) Contributions to the energy change from changes in the capacity. d) Average coulombic efficiency of all C/3 cycles at all four cells, where the error bars represent the standard error. Data in a), b), and c) reflect the average of four cells and the error bars are the maximum and minimum values. Inset in b) is a zoom-in of the data. Inset in c) is the change in specific capacity of the cathode.....	402
Figure VI.1.8 Comparison of pack-level configurations and metrics with layout of layers in a module.	403
Figure VI.2.1 Relative capacity change (loss) averaged over several cells vs. cycle count for standard and XFC conditions.....	407
Figure VI.4.1 Efficiency summary of cells tested in NREL's calorimeters. Caption Credits/Source: NREL-Aron Saxon	413
Figure VI.4.2 Calorimeter normalized heat rate for graphite and graphite/Si NMC cells under C/10 charge and discharge. Caption Credits/Source: NREL-Aron Saxon.....	414
Figure VI.4.3 Heat response of cell under fast charge. The calorimeter test temperature was 30°C. Caption Credits/Source: NREL-Aron Saxon.....	415
Figure VI.4.4 Infrared image of lithium battery cell (graphite /high nickel content NMC) at the end of a fast charge. Caption Credits/Source: NREL- Aron Saxon.....	416
Figure VI.5.1 Images of the multifunctional coater installed in the CAMP Facility's dry room.	419
Figure VI.5.2 (a) Cross section radiograph of a coin cell with the electrode assembly sandwiched between the top and bottom spacers. The cell is placed on a motorized translation stage that is moved relative to a stationary X-ray beam. The green arrow shows the direction z of scanning.....	420
Figure VI.5.3 X-ray dilatometry showing movement of the electrode assembly during cycling of a NMC811/Li cell. Panel a shows hard edges of the NMC811 layer (filled circles) and the PE median of the separator (open circles). The spring-loaded spacer is at the top, with the Li foil pressed against the bottom of the coin cell through the bottom spacer (panel c). Upon cycling, the separator and NMC811 layer move as a single unit. In panel b, the constant drift (dashed lines) is subtracted to show reversibility of the periodic variation.	421
Figure VI.5.4 A Summary of the Formation, Capacity Check, and Rate Study Discharge Capacity Data from all eight cells that were cycled at 30°C and 4 psi per cell.....	422
Figure VI.5.5 C/3 Discharge capacity from the life cycle protocol at 30°C and 45°C of the four chosen xx6395 MLP cells. The C/20 data points (every 51 cycles) were omitted for ease of viewing C/3 capacity.....	423

Figure VI.6.1 Image of free-standing polymer electrolyte (left) and electrochemical impedance spectra of solid polymer electrolyte at various temperatures (right).....	427
Figure VI.6.2 Voltage profile (left) and cycle life (right) of Li/SPE/LFP cell.....	427
Figure VI.6.3 (A) Schematic of the full cell where a thin SE membrane is utilized. (B) SEM image of a cross-section of the full cell. EDX element mappings of (C) Ni, (D) S, and (E) Si in the cross section of the full cell. (F) The galvanostatic charge and discharge profile of the full cell with cathode mass loading of 10 mg cm^{-2} at first cycle at the rate of C/20, and (G) the corresponding dQ/dV profiles. (H) Rate performance and (I) long-term cycling performance of the full cell with cathode mass loadings of 10 and 20 mg cm^{-2}	428
Figure VI.6.4 Schematics of the established model including geometry, boundary condition, and defect area (left), (a) voltage response and detected phase-field variable ξ at the LCO/LLZO interface at 1C charging rate; (b) dendrite ξ growth evolution ($\xi = -1$ for dendrite/crack, $\xi = 1$ for intact solid electrolyte); (c) von Mises stress evolution σ_{Mises}	429
Figure VI.6.5 SEM images of CNS (left), Si electrodes with 1% CNS, and 10% LiPAA (middle) and electrochemical formation cycles of Si electrodes with carbon black, CNS, and polyimide (right).	430
Figure VI.8.1 Comparison of prediction capability using three different methods for three different battery packs. The combined analysis was across 2 cathode chemistries, 2 different cell designs and multiple charge protocols. Predictions were made using either 125 or 225 cycles (Kim et al., 2022).	438
Figure VI.8.2 Examples synthetic data used for deep learning models for classification and quantification of aging mode. Three different sets of chemistries and multiple cell designs have been considered using this tool over the last 2 years (Kim et al., 2022).	439
Figure VI.8.3 Example HF synthetic data for different charge and discharge rates as well as for the voltage response after a charge or discharge event. The information from the HF synthetic data can be used in several tools developed over the course of the project.....	440
Figure VI.8.4 Reduced-order predictive models fit to IC analysis of data produces a model that reproduces low-rate open-circuit voltage (OCV) for any arbitrary aging scenario.....	441
Figure VI.8.5 A combination of the aspects which researchers need to consider when developing a calendar or cycle life testing regime (Dufek, 2022).	442
Figure VIII.1.1 Performance of a silicon electrode with gravimetric capacity $>1,000 \text{ mAh/g}$ at C/3 in an 811 full cell.	450
Figure VIII.1.2 Capacity versus cycle number for milled silicon at various weight loadings.	452
Figure VIII.1.3 Variable RPT calendar life aging tests with 720, 1,440, and 2,160 hours of rest at open circuit between groups of three RPT cycles on graphite (A, B) and 80% silicon (C, D) versus NMC622 in coin cells.	453
Figure VIII.1.4 Variable RPT calendar life aging tests with 168, 336, and 672 hours of rest at open circuit between groups of three RPT cycles on graphite (A, B) and 80% silicon (C, D) versus NMC622 in coin cells.	454
Figure VIII.1.5 Graphite–NMC622 pouch cells compared to coin cells for A) calendar life tests with 336 hours of rest at open circuit between groups of three RPT cycles and B) constant 0.1C cycling.....	454
Figure VIII.2.1 (a). STEM images of (a and b) p-Si/C particle after calendar life test (120 days at 55°C), (c) pristine p-Si/C particle before testing and (d) p-Si/C particle after 450 cycles at 25°C	457
Figure VIII.2.2 EDS mapping of a p-Si/C particles after calendar life test (120 days at 55°C).	458
Figure VIII.2.3 STEM images of (a) NMC622 particle after calendar life test (120 days at 55°C), (b) pristine NMC622 particle before testing and (c) NMC622 particle after 450 cycles at 25°C	458

Figure VIII.2.4 Cycling stability and Columbic efficiency of p-Si/C NMC622 cells using different electrolytes at (a) room temperature and (b) 45°C.....	459
Figure VIII.2.5 Impedance evolution of NMC622 NMC622 symmetric cells consists of NMC622 cathodes charged to 100% SOC at different cut-off voltages in the baseline electrolyte (a) and E10 electrolyte (b) at 55°C.....	460
Figure VIII.2.6 Impedance evolution of symmetric Si Si cells consist of 100% SOC Si anodes retrieved from cycled Si NMC622 cells with different electrolytes at 55°C.....	460
Figure VIII.2.7 Impedance evolution of graphite graphite symmetric cells consist of 100% SOC graphite anodes retrieved from cycled graphite NMC622 cells with different electrolytes at 55°C.....	461
Figure VIII.3.1 A typical OCV aging data to define the capacity retention and the charge retention, showing a) the voltage profile of the tested cell before and after OCV aging, b) the charge/discharge capacity before the OCV aging, and c) the charge/discharge capacity after the OCV aging.....	464
Figure VIII.3.2 Relationship between the capacity retention and the charge retention for various cell chemistries.....	465
Figure VIII.4.1 (Left) Schematic representation of the topotactic synthesis and (right) scanning electron microscopy images of the 2D CaSi ₂ precursors and siloxene products before and after ultrasonication.....	467
Figure VIII.4.2 Characterization of as-received CaSi ₂ and siloxene nanosheets. XRD patterns for (A) as-received CaSi ₂ and (B) as-synthesized siloxene nanosheets. Raman spectrum of (C) CaSi ₂ and (D) siloxene. XPS analysis of the siloxene nanosheets showing the (E) Si 2p and (F) O 1s spectra.....	468
Figure VIII.4.3 (A) Cycling capacity of siloxene before and after sonication at a current density of 200 mA g ⁻¹ . (B) Rate capability test and (C) cycling capacity of siloxene in 1M LiPF ₆ electrolyte with and without FEC additives.....	469
Figure VIII.4.4 XPS fitting results of F 1s and P 2p spectra of cycle 3 discharged siloxene electrodes cycled in electrolyte with and without FEC.....	470
Figure VIII.4.5 Siloxene/NMC622 full-cell cycling. A) Specific capacity and coulombic efficiency versus cycle number and B) selected voltage profiles. Formation cycling was performed with three cycles at C/10 followed by three cycles at C/5. Subsequent extended cycling was then performed at C/2.....	471
Figure VIII.5.1 a) Illustration of change in molecular dynamics force-field when a chemical reaction happens based on templates of the reactants and products. b) Schematic representation of new MD algorithm combining “coarse grain” (rigid molecules) MD with reactions.....	475
Figure VIII.5.2 Illustrative overview of the contrastive self-supervised approach. Two augmentations of an input reaction are passed through the reaction encoder to get their reaction fingerprints h_i and h_j and then a projection head to get vector representations z_i and z_j , and the model maximizes the agreement between the two representations of the reaction.....	478
Figure VIII.5.3 Average fractions of SEI products (a, d) and gaseous byproducts (b, e) at the end of kMC simulations as a function of applied potential referenced to an Li/Li ⁺ electrode. Simulations were conducted under two conditions reflecting different regimes of SEI formation.....	478
Figure VIII.5.4 Reaction mechanism for the reaction of PF ₅ with Li ₂ CO ₃ . a) An energy diagram showing three pathways, leading either to LiPOF ₄ (black, pink) or POF ₃ (red). b) The same pathways, shown as 2D schematics.....	479
Figure VIII.5.5 Diffusion of rigid EC molecules in electrolyte compared to an all-atoms simulations using a higher temperature thermostat at 320K for EC.....	480
Figure VIII.5.6 Atomistic model of LiF microstructure. a) microstructure with atoms colored according to local ordering. Yellow color corresponds to locally disordered arrangement b) atoms colored by their displacement magnitudes over time of simulation. It is visually clear that largest displacements responsible for conductivity	

happen mostly at grain boundaries. c) numerical measurements of Li diffusion and conductivities in three different microstructures. Left column indicates the lateral length of the computational cells used in these simulations.....	480
Figure VIII.5.7 (a) Schematic of detailed SEI model with atomistic elementary reaction mechanism involving several solution and solid phase species. (b) Model prediction of varying electron diffusivity with voltage to match irreversible currents obtained from 180 hr voltage hold experiments on composite porous silicon anodes held at potentials from 100 mV to 250 mV. (c) Model prediction of SEI thickness variation with time for 180 hrs of voltage hold at varying Si anode potentials from 100 mV to 250 mV. (d) Comparison of leakage currents between model and experiments.....	482
Figure VIII.5.8 (a) List of reactions in intermediate SEI model. (b) Experimental SEI solid phase composition data in atom percentage obtained through XPS on thin film silicon held at 100 mV. (b-c) SEI model prediction of solid phase volume fraction and atomic percentage for thin film silicon held at 100 mV. (d) Experimental SEI solid phase composition data in atom percentage obtained through XPS on thin film silicon held at 350 mV. (e-f) SEI model prediction of solid phase volume fraction and atomic percentage for thin film silicon held at 350 mV.	483
Figure VIII.5.9 (a-b) Finite strain macrohomogeneous model predictions of (a) voltage and Si anode porosity evolution and (b) Si particle diameter and Si anode thickness evolution during slow charging (C/100) of a full Si NMC532 cell from 3.0 to 4.2 V with varying initial nominal porosities of 50% and 25%. (c-d) Generated virtual microstructure for (c) unlithiated and (d) lithiated Si anode consisting of active Si particles, carbon conductive additive, polyimide P84 binder, pore for tortuosity calculations. (e-f) Homogenization calculations based (e) porosity and (f) tortuosity values for Si anodes with initial nominal porosities 50% and 25%. Porosity and tortuosity values are shown with and without binder.....	484
Figure VIII.6.1 Cell manufacturing steps including pre-lithiation for silicon anodes	491
Figure VIII.6.2 (A) Examples of silicon (SiO _x) anode before and after pre-Lithiation and Pouch cell assembly process (Cell build was done by Ionblox).	491
Figure VIII.6.3 Ionblox (Zenlabs) Summary of electrochemical data from formation process for the cells showing good consistency and reproducibility (~14 μ m Pre-Li). Summary of cell parameters are shown with Energy density reaching 333 Wh/kg and 811 Wh/L.....	492
Figure VIII.6.4 SAFT America summary of cells with ~ 18 μ m Li per side: (A) Images of 7Ah pouch cells (B) Pouch cell in testing fixture (C) summarizes key parameters of cells delivered to INL for testing (x- axis represents the serial number of the cell).	492
Figure VIII.6.5 Update on the cycling Performance of 1.5 Ah (300Wh/kg) cells with NMC622 cathode and approx. 18 μ m Li Anode at PNNL	493
Figure VIII.6.6 Progress Summary for PFM binder selection (Lawrence Berkeley National Laboratory (LBNL): LBNL fabricated and evaluated high loading SiO _x anodes (~4.5 mAh/cm ²) for industrial prelithiation and demonstrated PFM binder with Applied Materials Pre-Li anodes delivering ~ 35 % capacity improvement in coin cell study.....	493
Figure VIII.6.7 Progress Summary BatPaC Cost Model (Argonne National Laboratory): Results of parametric sensitivity study for some key variables on the cost of cell manufacturing where each independent variables was changed by $\pm 10\%$	494
Figure VIII.6.8 Summary of Protection layer development (Applied Materials): Different types of protection layers were investigated (Type A, B and C), where type C shows best cycling of 160 cycles vs. control showing <120 cycles.....	494
Figure VIII.6.9 Applied Materials Process development (Li Deposition): 14 μ m Li deposition at different intervals (A-D) from beginning to end of the continuous R2R process run indicating stable process.	495
Figure VIII.7.1 Cycle life data of cells described in the adjacent three tables at 30°C.....	500

Figure VIII.7.2 Voltage curves at various cycles between cycle 60 and cycle 1500 for three different baseline loading, baseline pressure cells.....	500
Figure VIII.7.3 Calendar life data of the low loading, baseline pressure cells stored at 30°C (circle), 40°C (cross), and 50°C (square). More than 1 year of storage is shown at 4.2 V (blue), and more than 7 months of storage is shown at 4.1 V (orange).....	501
Figure VIII.7.4 Finite strain COMSOL model results for (a) voltage , (b) end of charge porosity and (c) anode thickness evolution during normal cycling for charge to 4.2 V. Open circuit potentials of NMC and SiO _x are obtained from slow current rate half cell data provided by Enovix. Good match is obtained for end of charge porosity and thickness between model and experiments showcasing accurate parametrization of the COMSOL model with experiments.....	503
Figure VIII.8.1 Calendar life update for baseline batteries comprising Group14 Si-C.	507
Figure VIII.8.2 Cycle stability for batteries comprising Group14 Si-C.....	508
Figure VIII.8.3 Schematic of interim batteries (pouch, ~ 0.4 Ah).....	508
Figure VIII.8.4 Interim build battery performance (Farasis cycling data).....	509
Figure VIII.8.5 Example of electrolyte optimization.....	510
Figure VIII.9.1 Mirror Cells testing indicates a VED projection of > 560 Wh/L at 1000x C/3 full discharge cycles.	512
Figure VIII.9.2 Mirror Cell testing indicates calendar life projection of 10+ years to 560 Wh/L	513
Figure VIII.10.1 A continuous Si anode coating	514
Figure VIII.10.2 Cycle life of the baseline and ultra-high energy (UHE) Si anodes in Li half cells (3 mAh/cm ² loading, C/5 – C/5, 0.05 – 1.0V): (left) Si anode capacity vs. cycle; (right) capacity retention vs. cycle. The UHE shows a reversible capacity of 2100 mAh/g and 90% capacity retention after 100 cycles.....	515
Figure VIII.10.3 Cycle life of a Si-NMC full pouch cell (3 mAh/cm ² loading, C/5–C/5, 100% DOD, 45°C). The cell retains 86% of initial capacity after 800 cycles.	516
Figure VIII.11.1 Viscosity measurements of Gen2 LHCEs and a control (1M LiPF ₆ in 3:7 v/v EC:DMC) electrolyte over a temperature range of 20°C -50°C. (a) Viscosity vs. temperature. (b) Arrhenius plot.	518
Figure VIII.11.2 (a) Contact angle measurements of Gen2 LHCEs and control (1M LiPF ₆ in 3:7 v/v EC:DMC) electrolyte on polyethylene separator over time.(b) Images of electrolyte droplets on polyethylene separator after 90 seconds of contact.....	519
Figure VIII.11.3 Conductivity measurements of Gen2 LHCEs and a control (1M LiPF ₆ in 3:7 v/v EC:DMC) electrolyte over a temperature range of 20°C -50°C. (a) Conductivity vs. temperature. (b) Arrhenius plot.	519
Figure VIII.11.4 Cyclic voltammograms of (a) control electrolyte (1 M LiPF ₆ 30:70 EC:DMC) and (b-f) Gen2 LHCEs in a 3-electrode cell configuration with Pt working electrode and Li reference and counter electrodes. Scan rate = 20 mV/s.....	520
Figure VIII.11.5 Galvanostatic cycling in half cell configuration for Si/graphite electrodes with 2.5 mg/cm ² loading cycled 50x at 0.3 A/g with Gen2 LHCE formulations: (a) Gravimetric capacity, (b) areal capacity, (c) capacity retention.....	520
Figure VIII.11.6 Galvanostatic cycling of single layer Si-graphite/NMC622 pouch cells at C/3 rate with Gen 2 LHCEs. Data is compared to cells cycled with control electrolyte (1M LiPF ₆ 3/7 EC/DMC). C/3 cycling rate between 3.0 – 4.3 V. (a) Specific capacity, (b) capacity retention, (c) coulombic efficiency. (d-f) Voltage profiles at (d) 100 cycles, (e) 50 cycles, (f) 100 cycles.....	521
Figure VIII.11.7 Galvanostatic cycling of duplicate single layer Si-graphite/NMC622 pouch cells at C/3 rate with Gen2 LHCE #1 and FEC containing carbonate electrolytes (1 M LiPF ₆ 30:70 EC:DMC + x wt % FEC, where x = 0, 2.5, 5.0, 10.0. (a) Gravimetric Capacity, (b) Areal Capacity, (c) Capacity Retention.	521

Figure VIII.11.8 X-ray photoelectron spectroscopy data in (a,b) C 1s , (c, d) F 1s and (e, f) Li 1s regions collected on Si-graphite electrodes recovered from 100x cycled full cells containing (a, c, e) control electrolyte (1M LiPF ₆ 3:7 EC:DMC) and (b, d, f) LHCE.	522
Figure VIII.12.1 Schematic description of the principles of electrophoretic deposition	525
Figure VIII.12.2 Demonstration of chitosan electrophoretic deposition on silicon thin film model surface....	527
Figure VIII.12.3 Cyclic voltammograms of uncoated silicon thin film (control), silicon thin film with chitosan EPD coating (Si/Chit), and silicon thin film with chitosan EPD coating in presence of 0.03 M Lithium acetate (Si/Chit+LiA).....	527
Figure VIII.12.4 EIS of uncoated silicon thin film (control), silicon thin film with chitosan EPD coating (Si/Chit), and silicon thin film with chitosan EPD coating in presence of 0.03 M Lithium acetate (Si/Chit+LiA). Solid line against the dotted data points in each of (b), (c), and (d) show the average of fits (over three cells for each Si sample type) compared to one representative EIS.	529
Figure VIII.12.5 Cycling performance: a) the average charge, and b) the average discharge capacity (μAh) vs cycle no. of the control, Si/Chit and Si/Chit-CH ₃ OO Li cells during long cycling. Each capacity profile is the average of 3 cells, all cells are cycled between 0.01 – 2 V vs. Li/Li ⁺ at the current rates of 2.5 μA (4 formation cycles), 8.33 μA (4 high-rate cycles), and 1.25 μA (4 RPT cycles).	530
Figure VIII.12.6 Comparison of cycling performance of p84 polyimide bound Si electrodes with and without chitosan synthetic SEI coating. Note that chitosan+CH ₃ COOLi remain under testing. SEM images are provided as visuals of the pristine porous electrode and after the EPD is performed.....	531
Figure VIII.13.1 Ionic conductivity and anodic stability of the 2S2 electrolyte. (A) Comparison of ionic conductivity of different electrolytes at room temperature. The ionic conductivities are referenced and calculated to the standard electrolyte. (B) Linear scanning voltammetry of mixed THF, all fluorinated 262 and 2S2 electrolytes using aluminum foil as working electrode, scan rate = 1 mV /sec. SEI chemical composition by XPS measurement on μSi electrodes after 50 cycles in μSi Li cells with 2S2 electrolyte. (C) C1s, O1s, F1s and S2P spectra are displayed in columns, which show the corresponding depth profiling results (from up to down, being 0S, 60S, 120S, 180S, 300S and 600S). All of the XPS results were fitted with CasaXPS software. The binding energy was calibrated with C1s at 284.8 eV; (D) the quantified atomic composition ratios for all elements of the formed SEI at different sputtering times for the proposed 2S2 electrolyte.	535
Figure VIII.13.2 (A) The cell performance of μSi(1-5 μm) NCA full cells in 2S2 electrolyte between 2.7 and 4.3V; (B) the initial, 2nd, 5th, 20th and 50th charge-discharge profiles of the proposed electrolyte in the μSi NCA full cells. The cycle rate is at 1/5 C, room temperature with the first formation cycle at C/20. (C) μSi full battery performance in large punch cell (areal capacity of ~4 mAh/cm ² for NCA and ~4.1 mAh/cm ² for μSi, with electrode size ~5 cm by 5 cm) at room temperature. Before cycling at C/5, two pre-cycles at C/20 were conducted. The average CE was calculated from the fifth to the final cycle. The dashed pink line indicates the capacity retention of 80% at 150 cycles; (D) The charge–discharge profiles of the μSi NCA full cells at the 1st, 5th, 50th, 100th and 150th cycle. The left inset figure illustrates the test conditions of the assembled punch cell under the normal pressure of 0.1 MPa, and the right inset shows the actual cell size of 5 cm by 5 cm.....	536
Figure VIII.13.3 (A) The charge/discharge curves and (B) The capacity retention of the 5.0 mAh/cm ² μSi 4.5 mAh/cm ² NMC811 full cell between 4.2 and 2.7 V in the IL electrolyte. (C) The evolution of the pristine and cycled micro-Si anode and the overall thickness of the electrode was measured with X-ray computed tomography.	537
Figure VIII.13.4 Schematic illustration of mechanism on the capacity loss (current leakage) during voltage hold.	538
Figure VIII.13.5 A,B Current decay versus time (A) and corresponding capacity loss versus time (B) during 180h voltage hold of silicon anode (micro-sized silicon and nano-sized silicon) in mixed THF electrolytes C-F. EIS results of Nano So Li cells (mixed THF electrolytes, after 20 cycles) before (C) and after (D) voltage hold, Micro Si Li cells (mixed THF electrolytes, after 20 cycles) before (E) and after (f) voltage hold. The resistance of SEI on silicon is marked with red color.....	539

Figure VIII.13.6 A,B, Current decay versus time (A) and corresponding capacity loss versus time (B) during 180h voltage hold of silicon anode in different electrolytes (mixTHF and carbonate electrolytes) and graphite in carbonate electrolytes. C-F, EIS results of Graphite||Li cells (carbonate electrolytes, after 20 cycles) before (C) and after (D) voltage hold, Micro Si||Li cells (carbonate electrolytes, after 20 cycles) before (E) and after (F) voltage hold. The resistance of SEI on silicon is marked with red color. 540

Figure VIII.14.1 Electron energy loss spectroscopy of the Si anodes during cycling. (a-b) HAADF images and EEL spectrums of the Si nanoparticles after 0 and 100 cycles. The EELS data shows the Si $L_{2,3}$ edge with background removed. The changes in the near edge fine structure shows that the Si has undergone a chemical transformation. (c-e) are reference EEL spectrums of the Si $L_{2,3}$ edge for Si, SiO_2 , and lithiated-Si standard samples. The reference spectrums for the standard samples are used to identify the EEL spectra for the cycled Si anodes. (f) shows an EELS model fit to quantify the various chemical compositions of Si present in the highlighted area of the spectral image (shown in the insert). 542

Figure VIII.14.2 STEM and EELS analysis of the Si-Gr anode after cycling in a carbonate-based electrolyte. (a-f) STEM images after 0, 1, 10, 20, 50, and 100 cycles. The roughness/porosity of the Si increases upon cycling. By measuring the Si $L_{2,3}$ edge of Si anodes after cycling and comparing the signals to the Si and SiO_2 references, it is possible to map the local valence state of Si with sub-nanometer resolution. (g-l) Si composition maps after 0, 1, 10, 20, 50, and 100 cycles. As the Si roughness and porosity increases with cycling, Si is gradually converted to SiO_2 . The oxidation of Si could play a major role in capacity loss for high cycled Si-based anodes. (m-r) Least-squares models for the quantification of Si and SiO_2 present in each spectral image. 543

Figure VIII.14.3 Scanning transmission electron micrographs (STEM) images and energy-dispersive x-ray spectroscopy (EDS) elemental maps Si-Gr anodes after increasing numbers of cycles. (a-f) shows STEM images, and (g-l) shows EDS mapping of Si particles after 0, 1, 10, 20, 50, and 100 cycles. The red areas marks Si counts, the blue represents element counts of the SEI components (oxygen, carbon, and fluorine), and green highlights areas of mixed Si and SEI counts (45 to 55% Si/SEI). The SEI penetrates into the center of the Si particle with cycling eventually leading to a Si/SEI composite structure. 544

Figure VIII.15.1 Single compartment electrodeposition cell setup with batch produced Li anode on Cu. Cross-sectional & front view of Li anode provided. 547

Figure VIII.15.2 Cell testing comparison of single electrodeposited Li anodes against commercial anode. .. 547

Figure VIII.15.3 Spray chamber to fabricate robust Gen 3B membrane 548

Figure VIII.15.4 Dual compartment electrodeposition cell setup with batch produced Li anode on Cu. 548

Figure VIII.15.5 Cell testing comparison of single & dual compartment electrodeposited Li anodes against commercial anode. 549

Figure VIII.15.6 Projected Li anode cost in $\$/m^2$ vs. Li anode thickness in μm 550

Figure VIII.16.1 Concept of *in situ* prelithiation. a, Schematic of *in situ* prelithiation process by applying a layer of the Li mesh on silicon anode in battery fabrication. b, The mechanism of *in situ* prelithiation reaction based on shorting mechanism. c, Digital photos of the Si anode before (upper) and after (bottom) 24-hour *in situ* prelithiation by lithium mesh. d, SEM images of the Si anode before (upper) and after (bottom) 24-hour *in situ* prelithiation by lithium mesh. 553

Figure VIII.16.2 Controllable prelithiation through Li mesh design. a, Digital photos of the designed prelithiation reagents with porosity of 80% and 70%, respectively, and their corresponding capacity. b, The initial Coulombic efficiency of Si anode with and without prelithiation. 554

Figure VIII.16.3 Uniformity of *in situ* prelithiation through Li mesh design. a, Cross-sectional SEM images of Li-mesh prelithiated Si anode of three locations, center (m-center), edge (m-edge), and beneath (m-beneath), shown in the inset schematics. b, Si 2p XPS spectra of Li-mesh prelithiated Si anode of three different zones, sputtering time = 0.5 minutes. 555

Figure VIII.16.4 Kinetics studies of the Li diffusion in the prelithiation process. a, The *in situ* optical cell used to visualize the Li diffusion process within Si electrodes. Left: schematic, right: a photo of the device. b, The optical microscopy image of the area of interest before shorting (time = 0 min) with labelled components and scales. c, *In situ* dark-field optical microscopy image displaying the prelithiation process within electrodes, scale bar = 100 μm 556

Figure VIII.17.1 Strategies in Year 1 and Year 2 of the Seedling project for electrolyte development for Si anode. Strategy 1: Locally super-concentrated electrolyte formulations comprising a lithium salt (i.e., anions), a solvent, and a fluorinated diluent in different molar ratios. Strategy 2: Fluorinated additives are introduced to the locally super-concentrated electrolyte to create chemomechanically stable interphase..... 560

Figure VIII.17.2 Year 1 Electrolyte Evaluation and Downselect for Year 2. (a) Electrolyte components where different anions (FSI-, ClO_4^- , DFOB-, TFSI-, BF_4^- , and OTf-), solvent (i.e., DME), and diluent (i.e., TTE). (b) Molar ratio for electrolyte formulation study where molar ratio of lithium salt is fixed as 1, while the ratio of solvent and diluent varies from 0 to 4 (1.2 to 4.0 in case of solvent due to the solubility limit of salts). (c) Capacity retention by anion variation while molar ratio of Li salt : DME : TTE is fixed to 1 : 2 : 2. (d) Capacity retention by DME concentration change while LiFSI and TTE ratios are fixed as 1 : 2. (e) Capacity retention by TTE concentration change while LiFSI and DME ratios are fixed as 1 : 2. (f) Voltage profiles and (g) cycling performance of nano SiO / LFP full cells with GenF (and LSCE. GenF here is 1.2 M LiPF₆ in EC:EMC (3:7 vol) LSCE here is LiFSI : DME : TTE = 1 : 2 : 2 All full cells were cycled at C/20 for the first 3 cycles as formation cycles. After that C/3 was applied for both charge and discharge rate.. 561

Figure VIII.17.3 Year 2 Additive Screen in Year 2. (a) Year 1 baseline electrolyte used for additive study and (b) the library of the fluorinated additives in Year 2. (c) Voltage profiles and (d) dQ/dV curves for the 1st charge of different additives with 3 wt% added on LSCE. The inset of (c) shows enlarged initial voltage profiles. (e-j) dQ/dV curves with different additive concentrations (1, 3, or 10 wt% in LSCE) with the additive of (e) SS, (f) PP, (g) PFS, (h) PS, (i) PF, and (j) PFF. 562

Figure VIII.17.4 Year 2 Additive Evaluation and Downselect for Year 2. (a) Summary of capacity retention at 50th, 100th and 200th cycle with different additives and concentrations. (b) Cycling performance of micro Si / LFP full cells with LSCE+PFS 1wt%, LSCE + SS 3wt% and LSCE. (c) Cycling performance of prelithiated nano Si / LFP full cells with LSCE + PFS 3wt%, LSCE, and GenF. 563

Figure VIII.17.5 Understanding the impact of SEI on capacity retention. Spectroscopic investigation of SEI layer on Si anode. (a-f) Areal capacity at 50th cycle of different 3 wt% additives vs. atomic % of each element in the SEI layer on the cycled Si anode from XPS measurement. The slope in the inset was calculated based on capacity change by atomic % variation from XPS data. (g) Atomic content of the SEI layer on the Si anode cycled by different electrolytes. (h) Summary of the slopes calculated from (a-f)..... 564

Figure VIII.17.6 Voltage stability window for LSCEs, passing the design criteria for stability > 4.5 V vs Li/Li⁺ 565

Figure IX.1.1 Cycling data of (a) LiNiO₂, (b) LiNi_{0.95}Co_{0.05}O₂, and (c) LiNi_{0.95}Mn_{0.05}O₂ after calcination at four different temperatures. Cells used Li metal anodes, 1.2 M LiPF₆ in EC:EMC (3:7, w/w), cycled between 4.3-2.8 V. The first three cycles were at C/10 (1C=200mA/g) and subsequent ageing cycles were C/10 charge, C/3 discharge. 568

Figure IX.1.2 Total heat generation ($\text{J/g}_{\text{oxide}}$) derived from DSC measurements as a function of state of charge for the three compositions shown in the figure above. 568

Figure IX.1.3 Chemical and structural characteristics of LiNiO₂ modified by ALD coatings of MgO, Al₂O₃, or TiO₂ followed by post-annealing at 600°C. The dopant concentration profile for (a) Mg, (d) Al and (g) Ti incorporated into LNO primary particles at the secondary particle surface as a function of distance from the surface to the particle interior, the presence of the dopants is evidenced by the STEM-EDS spectrum in the inset. The distribution of (b) Mg, (e) Al and (h) Ti incorporated into LNO primary particles residing inside the secondary particles as a function of distance from the surface to the particle interior, the presence of the dopants is also evidenced by the STEM-EDS spectrum in the inset. STEM-HAADF images of (c) MgO-LNO,

(f) Al_2O_3 -LNO and (i) TiO_2 -LNO taken at primary particle surfaces. HR-TEM images of cycled MgO-LNO and Al_2O_3 -LNO are also shown in the inset of (c) and (f), respectively. 569

Figure IX.1.4 (a) ^6Li NMR of LiNiO_2 , LiNiO_2 as-coated w/ Al_2O_3 , and Al_2O_3 -coated and annealed at 600°C . Included is a bulk-doped Al-containing LiNiO_2 for reference (green). Cells were cycled using Li metal anodes between 4.3-2.8 V, 3 formation cycles at C/10 (1C=200mA/g), ageing cycles at C/10 charge, C/3 discharge. 570

Figure IX.1.5 Scanning electron microscopy images of $\text{Mn}_{0.65}\text{Ni}_{0.35}(\text{OH})_2$ precursors synthesized by co-precipitation using a continuous stirred-tank reactor (CSTR), with varying parameters pH, temperature, and NH_3 :transition metal ratios in solution (NTR). 571

Figure IX.1.6 Fourier transform of the Sn K-edge EXAFS data for the parent phases of the Sn-doped materials: (a) Li_2SnO_3 ; (b) $\text{Li}_2[\text{Mn}_{0.99}\text{Sn}_{0.01}]\text{O}_3$; (c) $\text{Li}[\text{Mn}_{0.99}\text{Sn}_{0.01}]_{0.5}\text{Ni}_{0.5}\text{O}_2$; (d) $\text{Li}_2[\text{Mn}_{0.95}\text{Sn}_{0.05}]\text{O}_3$; and (e) $\text{Li}[\text{Mn}_{0.95}\text{Sn}_{0.05}]_{0.5}\text{Ni}_{0.5}\text{O}_2$, presented as k^3 -weighted. The circle, solid line, and dash line in each graph represent the raw data, fit, and range of fit respectively. 572

Figure IX.1.7 Fourier transform of the Sn K-edge EXAFS data for the Sn-doped cathode materials $(0.3\text{Li}_2[\text{Mn}_{1-x}\text{Sn}_x]\text{O}_3 \bullet 0.7\text{LiMn}_{0.5}\text{Ni}_{0.5}\text{O}_2)$: (a) $x = 0.01$ and (b) $x = 0.05$, presented as k^3 -weighted. The circle, solid line, and dash line in each graph represent the raw data, fit, and range of fit respectively. 572

Figure IX.2.1 Diagnostic tests are conducted at various stages of the oxide development process. 576

Figure IX.2.2 Molecular Structure of the additive compounds 577

Figure IX.2.3 a) LNMO/Li cells cycled between 3.5-4.95 V. 3x formation cycles at C/10 rate, followed by one cycle each at the discharge rate of C/20, C/10, C/5, C/2, 1C, 2C, and 3C, after C/10 charge. b) harvested cathode showing partial coating delamination. c) and d) SEM of pristine and cycled Al current collector foil. 578

Figure IX.2.4 a) ^1H NMR of Gen2 soaked in PE. b) ^{19}F NMR of Gen2 soaked in PE. c) ^1H NMR of Gen2 soaked in Glass. d) ^{19}F NMR of Gen2 soaked in Glass. All electrolytes were stored at 45°C for 3 months. 579

Figure IX.2.5 Broadening and shifts of ^1H NMR peaks, of electrolyte solutions that were used to soak various electrode laminates as indicated in the figure. 579

Figure IX.2.6 ^1H NMR profiles of the Gen2 electrolyte plus additive solutions, used to soak LNMO electrodes 580

Figure IX.2.7 Protocol for electrochemical testing of the 5V/Gr cells 581

Figure IX.2.8 Representative data from 5V/Gr cells. The left panel shows discharge capacity (left axis) and capacity fade (right axis). The right panel shows voltage profiles (C/25 rate) during the second and final cycle. 582

Figure IX.2.9 Impedance data from a 5V/Gr cell. The left panel shows Area Specific impedance (ASI) data as a function of cell voltage after the formation cycles, 100 cycles and 200 cycles from HPPC tests. The right panel contains EIS data after the initial cycles and after completion of the aging cycles. 582

Figure IX.2.10 Structural evolution of the $\text{LiNi}_{0.5}\text{Mn}_{1.5}\text{O}_4$ cathode upon battery cycling. STEM-HAADF images at the primary particle surface of (a) the pristine sample and (e) cycled sample illustrates evolution of the surface reconstruction region into a Li-deficient (Mn_3O_4 -like) phase. The STEM-EDS data at the primary particle surface of (b) the pristine and (f) cycled sample indicate the formation of P- and F-containing CEI species upon battery cycling. The STEM-HAADF images of the bulk lattice of (c) the pristine and (g) cycled sample show intra-granular cracking in the cycled sample. The low-magnification STEM-HAADF images of (d) the pristine and (h) cycled sample indicate increased void density upon battery cycling. 584

Figure IX.2.11 (a) Discharge capacity vs cycle number, (b) Coulombic efficiency vs. cycle number, (c) Voltage profiles vs. cycle number, and (d) ASI vs. HPPC number for LiNiO_2 /graphite cells. 587

Figure IX.2.12 Voltage profiles from LiNiO ₂ /Li half-cells measured at 2 mA/g. The cathode from the ‘Formed’ profile was cycled for 4 C/10 cycles against a graphite anode. The cathode from the ‘Aged’ profile was subjected to the full 119 cycle protocol before aging.	588
Figure IX.2.13 FTIR spectra changes, focusing on EC solvent molecule peak (1125-1350 cm ⁻¹) shift, by Mn complex formation in the (a) EC/EMC solvent mixture and (b) Gen 2 electrolyte.	589
Figure IX.2.14 FTIR spectra changes, focusing on PF ₆ ⁻ anion peak (800-900 cm ⁻¹) shift, by Mn complex formation in the Gen 2 electrolyte.	590
Figure IX.2.15 (a) Concentration of EC solvent determined from integrated FTIR peak absorption as a function of time during battery cycling (at C/10). (b) Gas chromatograms from GC-FID of headspace within a LNO/graphite cell at various points during first two cycles (at C/10). Various gas species, including ethylene, ethane, acetylene and propylene, are measured. (a) and (b) Increasing signal of ethylene gas evolved in the cell is correlated to the decreasing concentration of EC. Ethylene is a known product of EC reduction.	590
Figure IX.3.1 Form bottom to top: Configurational energy distribution and probability of occurrence of configuration in LiMn _{0.5} Ni _{0.5} O ₂	595
Figure IX.3.2 APb (A=Na, Li) schematic representation a) cubic structure, b) tetragonal structure. Lattice vector direction are shown for each structure and the unit cells are shown as black solid lines. (Na ions are represented by yellow spheres and Pb ions are represented by dark grey spheres. Translucent grey planes show polyhedron formed by Pb ₄ clusters.) Total density of states DOS for NaPb c) cubic phase, d) tetragonal phase and for LiPb e) cubic phase, f) tetragonal phase. The Energy of the Fermi level is indicated by a vertical dashed line	596
Figure IX.3.3 (a) – (e) Schematic representation of Li distribution in LiNiO ₂ layered with one Li/Ni exchange in the simulation cell. (f) energy change during Ni migration from the Li layer to the transition metal layer.	597
Figure IX.3.4 (a) Number of Li-M and M-M (M=Ni,Mn) pairs in the transition metal layer for each configuration. (b) LiMn _x (x=6,5,4,3,2,1) clusters in the transition metal layer for each configuration. All configurations are sorted by total energy and referred to the lowest energy.	598
Figure IX.3.5 (a) Energy domain distribution on 60%-MN5050/40%-Li ₂ MnO ₃ and probability of occurrence for each configuration, (b) schematic representation of species distribution for select configurations, purple, gray, and green circles represent Mn, Ni and Li atoms respectively.	599
Figure IX.3.6 XRD patterns of a) Li _{1.2} Ni _{0.2} Mn _{0.6} O _{2-x} F _x (x=0, 0.01, 0.025, 0.05 and 0.1) synthesized with LiF as F precursor and b) Li _{1.2} Ni _{0.2} Mn _{0.6} O _{2-x} F _x (x=0.025) synthesized with various salts as F precursors.	600
Figure IX.3.7 a) Laboratory and b) synchrotron XRD patterns of Li _{1.2} Ni _{0.2} Mn _{0.6} O _{2-x} F _x (x=0, 0.01, 0.025 and 0.05) synthesized with LiF-KF as F precursor, c-f) SEM images of as-synthesized Li _{1.2} Ni _{0.2} Mn _{0.6} O _{2-x} F _x samples, g) facet index of the octahedron particles (top) and atomic arrangement of the hexagonal layered structure (bottom).	601
Figure IX.3.8 STEM-HAADF images and the corresponding STEM-EDS maps of Ni and Mn of the Li _{1.2} Ni _{0.2} Mn _{0.6} O _{1.95} F _{0.05} single crystals at (a) the 003 facet and (b) the 102 facet, together with the corresponding element distribution profile as a function of the distance from the crystal surface (0 nm in distance) into the crystal bulk.	602
Figure IX.4.1 XRD patterns of FSP LT-LiNi _{1/3} Mn _{1/3} Co _{1/3} O ₂ samples before and after annealing at various temperatures.	607
Figure IX.4.2 STEM-HAADF images of a FSP LT-LiNi _{1/3} Mn _{1/3} Co _{1/3} O ₂ sample viewed down the [110] _{cubic} lithiated-spinel zone axis: (a) at room temperature, and (b) after annealing at 625 °C.	607
Figure IX.4.3 (a) First-cycle voltage profiles of Li/LT-LiNi _{1/3} Mn _{1/3} Co _{1/3} O ₂ cells with annealed electrodes, (b) capacity retention over 50 cycles, and (c) rate capability.	608
Figure IX.4.4 Normalized-capacity voltage profiles of Li/LT-LiNi _{1/3} Mn _{1/3} Co _{1/3} O ₂ cells showing smaller hysteresis when higher annealing temperatures are used.	609

Figure IX.4.5 (a) Ex-situ XRD patterns of a $\text{LT-LiNi}_{1/3}\text{Mn}_{1/3}\text{Co}_{1/3}\text{O}_2$ (625°C) electrode during the first charge/discharge cycle between 2.7 and 4.3 V, (b) points at which XRD data were collected on the voltage profile, and (c) variation of lattice parameter, a (top) and I_{311}/I_{400} ratio (bottom) during the first charge/discharge cycle.....	609
Figure IX.5.1 The left panel shows XRD patterns collected on a sample with a nominal composition of $\text{Li}_{1.2}\text{Mn}_{0.4}\text{Ti}_{0.4}\text{O}_{1.6}\text{F}_{0.4}$ synthesized with various temperatures and holding times. The right panel displays data from TGA/DSC measurements performed on the same sample during heat treatment to 1000°C	613
Figure IX.5.2 Schematics showing the three factors that limit fluorine solubility in DRX oxyfluorides synthesized using a solid-state route.....	614
Figure IX.5.3 Structural characterization of LMTO04 DRX samples annealed at 750°C , 900°C , and 1000°C for 1 hour under flowing Ar. At each temperature, the products are characterized by: (a) X-ray diffraction, (b) ^7Li solid-state nuclear magnetic resonance spectroscopy, and (c) selected area electron diffraction. Asterisks in panel (b) indicate spinning sidebands due to fast rotation of the sample during ssNMR data acquisition. Arrows in panel (c) are used to highlight diffuse scattering patterns that arise due to SRO in the cation sublattice.....	615
Figure IX.5.4 Electrochemical performance of LMTO04, LMTOF05, LMTOF06, and LMTOF07 DRX cathodes in half cells. (a-b) Galvanostatic voltage profiles during the (a) 1 st and (b) 20 th cycle. (c) Discharge capacity retention over 50 cycles. The cathodes were cycled between 1.5 V and 4.8 V vs. Li/Li^+ at a specific current of 10 mA g^{-1} for the first 5 cycles and 20 mA g^{-1} for subsequent cycles.....	616
Figure IX.5.5 Comparison of specific discharge energy density and roundtrip energy efficiency of cells using the DRX materials with three different duration of air exposure time: 0, 1, and 24 hr.	617
Figure IX.5.6 Specific discharge energy vs. cycle number for three cycling protocols: 4.7 V to OCV, 4.7 then constant voltage hold, and 4.8 V then OCV.	618
Figure IX.5.7 DRX cathode cycled with LiPF_6 electrolytes with either EMC or DMC as the solvent. A third cell contains DMC plus 3 wt.% of LiBOB	618
Figure IX.5.8 Nyquist plot obtained by subtracting the electrochemical impedance spectroscopy of the 65:34:10 cell from that of the 70:20:10 cell. While the cathode in the former cell only has ball milled carbon, the one in the latter cell has both ball milled carbon and a high surface area C65 conductive carbon additive.	619
Figure IX.5.9 The discharge energy and roundtrip energy efficiency of three cells with different types of conductive carbon additives: CB, GCNF, and CNT.	620
Figure IX.6.1 The left panel outlines a multi-step characterization methodology designed to determine the composition of DRX cathode materials and identify potential impurities. In the right panel, we show results from characterization of the F25 sample using a) synchrotron XRD, b) ^7Li , and c) ^{19}F solid-state nuclear magnetic resonance (NMR). While the XRD pattern shows a pure DRX phase with no LiF or Li_2O crystalline impurities (indexed with blue and purple reference lines, respectively), ^{19}F NMR analysis indicates the presence of LiF impurity and ^7Li NMR analysis shows LiF impurity as well as Li_2O and Li_2CO_3 impurities.	623
Figure IX.6.2 Scanning transmission electron microscopy - high-angle annular dark field (STEM-HAADF) images and corresponding EELS maps of Mn L_3 peak energy shifts, showing cycling-induced changes of Mn valence distributions in un-fluorinated (LMNOF_0 , left) and highly fluorinated ($\text{LMNOF}_{0.2}$, right) DRX cathode particles.	624
Figure IX.6.3 (a) Surface Mn state evolution of a $\text{LMNOF}_{0.05}$ electrode cycled with a standard binder/electrolyte system ($\text{PVDF}/\text{LiPF}_6$). The oxidation state of surface Mn is clearly lower than that of the bulk, but displays fairly reversible behavior upon cycling. Bulk Mn is evaluated by Mn-L mRIXS-iPFY analysis that is not shown here. (b) Surface O state evolution of $\text{LMNOF}_{0.05}$ in standard binder/electrolyte system. A typical pre-edge evolution is observed due to the TM state change, consistent with (a). (c) Surface O-K spectra reveal a strong carbonate cycling of LMNOF in F-free PE/LiClO_4 system over 20 cycles.	625

Figure IX.6.4 DEMS results for Li-Mn-Nb-O-F DRX cathodes cycled within various voltage windows. All cathodes were cycled at 0.1 Li h^{-1} (29.4 mA g^{-1}) using 1 M LiPF_6 in EC/EMC (3:7) as the electrolyte. 626

Figure IX.6.5 ^7Li solid-state NMR isotropic spectra collected on cathode samples obtained at various states of charge. (a) Discharge voltage profile obtained during the 30th cycle and plotted as a function of the depth of discharge (DoD). The recovered electrode samples were obtained at A (0% DoD, 4.8 V), A' (20%, 3.5 V), B (50%, 2.84 V), B' (65%, 2.7 V), C' (80%, 2.0 V), and C (100%, 1.5 V). (b) ^7Li fully isotropic pj-MATPASS spectrum collected on the pristine Li-Mn-Ti-O-F cathode sample (P), with a deconvolution of this spectrum using three Gaussian components (grey signals). A Lorentzian component was used to account for the Li-based diamagnetic impurities (dark blue signal). The grey line indicates a central chemical shift value of 290 ppm. (c) ^7Li fully isotropic pj-MATPASS spectra collected on ex situ cathode samples stopped at various stages of discharge during the 30th cycle as shown in (a). The blue and orange lines indicate chemical shift values of 580 ppm and 160 ppm, respectively. The sharp peak around 0 ppm is attributed to diamagnetic Li environments formed during electrode preparation and electrochemical cycling (e.g., due to residual Li-containing precursor phases or to electrolyte degradation)..... 627

Figure IX.6.6 STEM-HAADF images, EDS elemental maps showing carbon spatial distribution, and EELS analysis showing the electronic structure of the carbon coating on DRX particles. (a) Pristine LTMOF, (b) LTMOF carbon coated in the Ar environment, (c) LTMOF carbon coated in the Ar/H₂ environment. Scale bar is 500 nm. STEM-HAADF images of (d) LTMOF carbon coated in the Ar environment, (e) LTMOF carbon coated in the Ar/H₂ environment showing carbon on the surface and the points from where the EELS spectra were taken, and (f) EELS spectra taken at C-K edge for particle (d) (blue) and (e) (red). 627

Figure X.1.1 Structural evolution of cathode thin-film with/without carbonate-based electrolyte (A) XRR of 10 nm NMC532 films grown on SrTiO₃ substrates with 15 nm SrRuO₃ buffer layers; (B) Off-specular phi-scans of STO {001}, NMC {104}, and NMC {003} of the film; (C) SXRD of NMC532 films before and after exposure to EC-EMC solvent and LP57 electrolyte 633

Figure X.1.2 Transition metal-dependent degradation of NMC cathode in carbonate-based solvent and electrolyte. Total-reflection X-ray absorption near edge structure (XANES) of NMC thin-films before and after exposure to EC-EMC solvent and LP57 electrolyte at Ni, Co, and Mn K-edges 634

Figure X.1.3 Protonation reaction pathway between cathode and carbonate-based electrolyte. A) DFT calculation of EC and LiPF₆ salt decomposition reactions and their reaction activation energy on standard cathode Li_{0.5}NiO₂ surface; B) Illustration of the possible proton transfer pathways inside layered structure in cathode; C) Illustration of the interfacial degradation of NMC cathodes through surface protonation due to the deprotonation reaction of EC solvent on cathode surface..... 634

Figure X.1.4 Solvent effect on cathode degradation and stabilization. A) Ni L-edge XAS of NMC thin-film before and after exposure to carbonate electrolyte LP57, fluorinated electrolytes 1F and 3F; B) O K-edge XAS of NMC thin-films after exposure to carbonate electrolyte LP57 and fluorinated electrolytes 1F and 3F 635

Figure X.1.5 (A) Electrochemical stability window of carbonate-based LP57 electrolyte and fluorinated electrolytes. (B) Voltage drop of NMC thin-films after charging to 4.2 V in LP57 electrolyte; (C) The leakage current of the NMC532 thin-films during the potential hold at 4.2 V 636

Figure X.1.6 Preliminary TOF-SIMS (A) pristine NMC. (B) charged to 4.2 V and relaxed. (C) charged to 4.5 V and relaxed. (D) and (E) deuterium TOF-SIMS summary..... 637

Figure X.1.7 Structural evolution of LMO thin-film during fabrication (A) LMO films grown on 20 nm Pt substrates with 7 nm Cr adhesive layers ; (B) GI-XRD of As-doped Si substrate, Cr coated Si, Pt/Cr coated Si, and LMO thin film on Pt/Cr/Si, respectively. 637

Figure X.1.8 Electrochemistry Tests for PAD-LMO films. (A) Schematic of A Cone Cell for Thin Film Electrochemistry Tests (B) Cycle Voltammetry (CV) of PAD-LMO film of the 1st, 2nd, 5th and 10th cycles .. 639

Figure X.1.9 XPS Results for PAD-LMO films before and after CV The black curve stands for pristine LMO film and red curve for cycled LMO film..... 640

Figure X.1.10 NEXAFS Results for PAD-LMO films at pristine state (black curve), OCV (soaked in electrolyte, orange curve), cut-off at 4.3V (red curve) and after 1 full cycle (blue curve). (A) and (C): Manganese L ₂ and L ₃ edges, (B) and (D): Oxygen K-edge.	641
Figure X.2.1 XPS spectra on a Li ₄ Mn ₂ O ₅ electrode charged to 4.5V as a function of etching time. Longer etching times probe deeper into the sample.	647
Figure X.2.2 (Left) XRD patterns of the compounds synthesized for this study. (Middle) Mn K-edge XAS spectra, and (right) Mn L-edge spectra in TEY mode.	648
Figure X.2.3 First five cycles of cell containing the materials under study, cycled between 4.8-1.5V at C/20 rate. Upper right panel shows capacity retention as a function of cycle number for 22 cycles.	648
Figure X.2.4 Charge and discharge capacity as a function of cycle number between the indicated voltage limits for cells containing (upper left) 6.5 Li ₄ Mn ₂ O ₅ :3.5 LiMn ₂ O ₄ and (upper right) Li ₄ Mn ₂ O ₅ . Bottom panels show a comparison between capacity retention of cells containing 6.5 Li ₄ Mn ₂ O ₅ :3.5 LiMn ₂ O ₄ and Li ₄ Mn ₂ O ₅ cycled at 1C rate (lower left) or C/20 rate (lower right) between 4.8-2.0V.	649
Figure X.2.5 RIXS maps of pristine, charged, and discharged Li ₄ Mn ₂ O ₅ (a, b, c, d) and 6.5Li ₄ Mn ₂ O ₅ :3.5LiMn ₂ O ₄ electrodes (e, f,g). The prominent feature at an emission energy of 525 eV can be attributed to lattice oxygen. There is no signal at an emission energy of 523.8 eV and excitation energy of 531 eV, which would be characteristic of oxidized oxygen.	650
Figure X.2.6 DEMS results on cells containing 6.5Li ₄ Mn ₂ O ₅ :3.5LiMn ₂ O ₄ (left) and Li ₄ Mn ₂ O ₅ (right).	651
Figure X.2.7 Mn K-edge XAS data on (top left) pristine and 6.5Li ₄ Mn ₂ O ₅ :3.5LiMn ₂ O ₄ or (top right) Li ₄ Mn ₂ O ₅ electrodes charged to 4.8V and discharged to 2.5V. Bottom left (6.5Li ₄ Mn ₂ O ₅ :3.5LiMn ₂ O ₄) and right (Li ₄ Mn ₂ O ₅) show results for electrodes charged to 4.8V and discharged to 2.0V for the designated number of cycles. Note that the 6.5Li ₄ Mn ₂ O ₅ :3.5LiMn ₂ O ₄ electrode on the bottom left underwent 114 cycles while the Li ₄ Mn ₂ O ₅ one on the bottom right underwent only 25. All data obtained on electrodes in the fully discharged state.	652
Figure X.3.1 Validation of doped single crystal NMC76 in 1Ah pouch cell using graphite anode. a, The first charge-discharge curve of the graphite/NMC76 single crystal pouch cell at C/10 cycled between 2.6-4.2V (vs. Graphite). b, Cycling stability of 1Ah Li-ion pouch cells employing as-prepared NMC76 single crystal cathode that demonstrates 89% capacity retention for 400 cycles (cycling still in progress).	656
Figure X.3.2 Comparison of gas evolution from polycrystalline and single crystal NMC76 after different numbers of cycling. (a) and (c) display ,orphologies of pristine polycrystalline and single NMC76, respectively. (b) and (d) compare the evolution of CO ₂ , H ₂ , and O ₂ at different cycles of polycrystalline and single crystal NMC76 electrodes, respectively. The cells cycled in DEMS are tested between 2.7 and 4.5 V.657	
Figure X.3.3 a, Schemes for single layer pouch cell for gas collection and transfer. b,c) Quantified amounts of CO ₂ , O ₂ , and H ₂ in pouch cells after 200 cycles of polycrystalline NMC76 (b) and single crystal NMC76 (c).	658
Figure X.4.1 Synthesis and DFT calculations of fluorine substituted cation PMpyr ⁺ . (a) Comparison of HOMO/LUMO energy levels for PMpyr ⁺ and PMpyr ⁺ , (b) Synthesis route for PMpyrFSI, (c) PMpyr ⁺ and PMpyr ⁺ reduction pathway on Li metal, (d) PMpyr ⁺ and PMpyr ⁺ oxidation pathway on NMC622 cathode.662	
Figure X.4.2 MD simulation on electrolyte/electrode interaction. (a-c) Snapshot of electrolyte distribution on NMC622 and Li electrodes: cyan-IL cation+; white-H on the PMpyr ⁺ backbone highlight in adjacent figure; purple-F on the PMpyr ⁺ backbone; yellow-FSI; green-Li ⁺ . (d-f) Molecular number density profiles along the z axis normal to the surface of the NMC cathode (left panels) and lithium anode (right panels). The center of mass of each molecule is used to calculate molecule distribution: (a, d) (PMpyr) _{0.8} Li _{0.2} FSI electrolyte, (b, e) (PMpyr) _{0.8} Li _{0.2} FSI electrolyte and (c, f) (PMpyr) _{0.5} Li _{0.5} FSI electrolyte.	663
Figure X.4.3 XPS analysis of recovered electrodes. (a) Li metal anode and (b) NMC622 cathode harvested after formation using (PMpyr) _{0.8} Li _{0.2} FSI and (PMpyr) _{0.5} Li _{0.5} FSI electrolytes. (i) C 1s spectra, (ii) F 1s spectra, (iii) N 1s spectra and (iv) atomic concentration.	664

Figure X.4.4 Li/Cu and Li/Li symmetric cell performance. (a-c) Voltage profile of Aurbach test using (a) Gen 2, (b) (PMpyrf) _{0.8} Li _{0.2} FSI and (c) (PMpyrf) _{0.5} Li _{0.5} FSI. (d) Coulombic efficiency of Li/Cu cell cycled with current density of 0.1 mA/cm ² . (e) Voltage profile of Li/Li symmetric cell with current density of 0.5 mA/cm ²	665
Figure X.4.5 Li/Cu and Li/Li symmetric cell performance. (a-c) Voltage profile of Aurbach test using (a) Gen 2, (b) (PMpyrf) _{0.8} Li _{0.2} FSI and (c) (PMpyrf) _{0.5} Li _{0.5} FSI. (d) Coulombic efficiency of Li/Cu cell cycled with current density of 0.1 mA/cm ² . (e) Voltage profile of Li/Li symmetric cell with current density of 0.5 mA/cm ²	666
Figure X.5.1 Schematic of a typical scanning electrochemical microscopy / Al Hicks, NREL	670
Figure X.5.2 Cyclic voltammetric, AFM and XRD data for LNMO deposited using the PAD technique.....	671
Figure X.5.3 Cyclic voltammetry data for 1M LiClO ₄ in PC and ED at a 2mm Pt disk electrode.....	672
Figure X.5.4 Comparison of cyclic voltammetry data for LMO and LNMO with the “non-intercalating” Pt electrode.....	673
Figure X.5.5 G/C SECM data collected for a 10 μm Pt tip electrode placed ~ 2 μm above a 2 mm Pt substrate.	674
Figure X.5.6 G/C SECM tip linear sweep voltammetry (LSV) at varied substrate voltages.....	675
Figure XI.1.1 X-Ray diffraction plots for NCM9055 produced by RST (RST039) using improved calcination process HYO1.....	679
Figure XI.1.2 SEM images for different high nickel content NCMs (a) commercially available round NCM811; RST made cathode material (b) green powder, (c) NCM811, (d) NCM9055 and (e) improved NCM9055	680
Figure XI.1.3 X-ray diffraction patterns for NCM9055 made by RST (a) green powder, (b) interim material used in BP2 to make pouch cells, (c) improved material to be used for final cell deliverables.....	680
Figure XI.1.4 Electrochemical studies for NCM811 coated with different fumed alumina powders (FA-1, FA-2 and FA-3): (a) half coin cells and (b) full coin cells.	681
Figure XI.1.5 Full coin cell cycle life for cells made with NCM811 coated with FA-1 and with Li _x MyO ₂	681
Figure XI.1.6 Correlation of pH after 24h and fumed alumina contents of RST9055-039 coated samples	682
Figure XI.1.7 (a) 1st cycle efficiency and 1st C/10 capacity (4.2-2.8V) vs. fumed alumina contents of RST9055-039 coated samples. (b) 1C/1D, 45oC (4.2-2.8V) Capacity retention vs. cycles for RST9055-039 coated samples	682
Figure XI.1.8 (a) Initial discharge rate capability of CCA formulations with NCM811. (b) Ionic and electronic resistance extracted from hppc testing of CCA formulations with NCM811	683
Figure XI.1.9 From top to bottom: Capacity utilization, retention, and DC-IR during cycle-life testing of CCA formulations with NCM811	684
Figure XI.1.10 Full coin cells (4.3 mAh/cm ²) cycle life results for different coated cathodes at 45°C and 1C/1D charge/discharge rates.....	685
Figure XI.1.11 SEM images of FA-2 coated NCM9055 (a) secondary particle, (b) zoom-in view of the primary particles coated with fumed alumina	685
Figure XI.1.12 SAFT experiments: slurry and cathode layer made with alumina surface coated RST 9055... ..	686
Figure XI.1.13 Double layer pouch cell made with optimized surface coated NMC9055	686
Figure XI.2.1 (a) SEM cross-section of a 240 μm dry-coated LNMO electrode. (b) Voltage profiles of dry-coated LNMO with various loadings in half cells. (c) Full cell cycling performance between dry-LNMO and conventional slurry-based LNMO.	690

Figure XI.2.2 (a) Specific discharge capacity and (b) Coulombic efficiency (CE%) of high temperature (55°C) LNMO/graphite full cell cycling. 690

Figure XI.2.3 (a) Scanning electron microscope images of the pristine (baseline) and laser-treated (LT1 and LT2) Fe-LNMO cathode electrodes. (b) Scanning transmission electron microscope images of baseline and LT1 cathodes before electrochemical tests. (c) C1s, F1s, and O1s XPS data of baseline, LT1, and LT2 cathode electrodes before the electrochemical test. (d) Residual Li titration curve of Fe-LNMO cathode to determine the surface residual Li content. (e) Schematic illustration of a possible mechanism for the formation of surface LiF phase on the Fe-LNMO cathode. The scale bars in (a) and (b) are 5 μm and 5 nm, respectively..... 691

Figure XI.2.4 Electrochemical performance comparison of baseline, LT1, and LT2 cells. (a) First cycle charge-discharge curves, (b) rate capability test (based on Li||Fe-LNMO half cells), (c) cycle stability evaluation, (d) evolution of discharge curves, and (e) EIS plots of baseline, LT1, and LT2 full cells with graphite as the anode. The Li||Fe-LNMO and Gr||Fe-LNMO cells were operated at 3.5 V - 4.85 V and 3.3 V - 4.8 V, respectively. 1C equals 147 mA h g⁻¹..... 692

Figure XI.2.5 (a) C1s, O1s, and F1s XPS data of baseline, LT1, and LT2 cathode electrodes after 200 cycles in full cells with graphite as the anode. (b) XPS C, O, F, and P atomic concentrations of baseline, LT1, and LT2 cathode electrodes after 200 cycles in full cells..... 693

Figure XI.2.6 Normalized NMR ¹⁹F and ³¹P spectra of the retrieved electrolytes from baseline and LT1 full cells after 200 cycles..... 694

Figure XI.2.7 PCCs delivered to (A) INL and (B) TARDEC and ARL. First (C) formation and (D) C/3 cycle of each cell chemistry..... 695

Figure XI.2.8 LNMO-Graphite full cell areal loading and cycling performance comparison between project progress and recent literature. 695

Figure XI.3.1 (a) Representative SEM images showing the morphology of the secondary particles of UCI Gen2 cathode. The average diameter of the UCI Gen2 secondary particles is ~3 μm . (b) Coin-cell test of the UCI Gen2 cathode at C/10 within 2.5–4.4 V. (c) Rate capability test of UCI Gen2 cathode at 30 °C. 699

Figure XI.3.2 (a) Galvanostatic charge/discharge of UCI Gen2 cathode and NMC-811 at 50°C, C/10. (b) Cycling performance of UCI Gen2 cathode and NMC-811 at 50°C, C/2..... 700

Figure XI.3.3 (a) Wavelet-transformed Ni-K edge EXAFS of UCI Gen 2 and NMC-811 cathode after different cycles. (b) Detailed comparison of the Ni-O bonding in both cathodes. (c) Electrochemical impedance spectroscopy (EIS) of LNO, NMC-811, and UCI Gen2 cathodes under the same cell conditions..... 701

Figure XI.3.4 (a,b) HAADF-STEM images of delithiated NMC-811 and UCI Gen2 cathodes after at thermal abuse treatments at the same conditions. (c) Quantitative DSC result of charged (cut-off voltage 4.4V) NMC-811 and UCI Gen2 cathodes. (d) Atomic-resolution images showing the surface reconstruction of NMC-811 and UCI Gen2 cathodes after long-term cycling. 702

Figure XI.3.5 XRF result of Ni dissolution on Gr anodes (~250 cycles). Cycling condition: 2.5V-4.4V vs. Gr at 1C. Field of view: 0.25mm*0.25mm. 703

Figure XI.3.6 EDS elemental maps of UCI Gen2' cathode. The result shows similar element distribution as that in UCI Gen2 cathode. 704

Figure XI.3.7 Electrochemical performance of UCI Gen2' cathode. a, charge/discharge profile of UCI Gen2' cathode. b-c, dQ/dV profile of UCI Gen2' cathode and NMC-811. d, cycling performance in half-cell..... 704

Figure XI.3.8 (a) Charge/discharge curve of PC-811, QSC-811 and SC-811, respectively. (b) dQdV⁻¹ curves of initial cycle. (c) Relative Li ion diffusion constant of three cathodes, respectively. (d) Long-term cycling stability (2.5V-4.4V, C/3). (e) EIS curve of after long cycling. (f-h) dQdV⁻¹ evolution with cycling..... 705

Figure XI.3.9 TXM tomography of long-term cycled PC-811, QSC-811 and SC-811. scale bar, 2 μm 706

Figure XI.3.10 (a-c) HAADF-STEM images of cycled SC-811. (d-f) HAADF-STEM images of cycled QSC-811. (g-h) Super-resolution image corresponding to the (c) and (f) obtained by <i>AtomSegNet</i> . i, XRD of SC-811 and QSC-811 before and after cycling (Pristine: solid line; Cycled: dashed line).....	707
Figure XI.4.1 (a) First charge-discharge profiles of fluorine coated and uncoated samples in half-cell configuration, cycled at C/3 current rate at room temperature. The cycles were recorded after three formation cycles at C/10 current rate. (b) dQ/dV^{-1} curves corresponding to the first C/3 cycle. (c) Cycling performances of coated and uncoated samples in half cells at C/3 rate. (d) Rate capability of NMCAM and 1F-NMCAM. (e) Long-term cyclability of NMCAM and 1F-NMCAM in full cells cycled at C/3 charge and 1C discharge after three formation cycles. (f) Evolution of average charge and discharge voltages in full cells.....	711
Figure XI.4.2 (a, b) Charge-discharge cycles recorded at C/3 rate before and after long-term cyclability for NMCAM and their corresponding dQ/dV^{-1} plots. (c, d) Charge-discharge cycles recorded at C/3 rate before and after long-term cyclability for 1F-NMCAM and their corresponding dQ/dV^{-1} plots.....	712
Figure XI.4.3 HAADF-STEM images acquired at the surface of (a) NMCAM and (b) 1F-NMCAM particles after 500 cycles. (a-i, b-i) Fast Fourier transformations of the area shown in a and b. R and L, respectively, corresponds to rock-salt and layered structures. (a-ii, a-iii) The areas corresponding to rock-salt and layered structure on the surface of NMCAM particle highlighted, respectively, in red and green. The areas were obtained by carrying out inverse FFT. (b-ii, b-iii) The areas corresponding to rock salt and layered structure on the surface of the 1F-NMCAM particle highlighted, respectively, in red and green.....	713
Figure XI.4.4 Electrochemical performances of NMA-85 at various levels of Mg incorporation in coin half cells. (a) Initial voltage profile at C/3 rate. (b) Corresponding differential capacity plot of the initial voltage profile. (c) Cycling performance and capacity retention over 100 cycles at C/3 rate.....	714
Figure XI.4.5 (a) photographs of the $\text{Li}(\text{Ni}_{0.85}\text{Mn}_{0.10}\text{Al}_{0.05}\text{Mg}_{0.005})\text{O}_2$ (NMAM-85) powder delivered to Tesla Inc, (b) SEM image of NMAM-85 with particle size measurement, and (c) casted cathode electrode done by Tesla Inc.....	715
Figure XI.4.6 Voltage profiles of selected large-format pouch cells cycled between 2.5 and 4.2 V at C/3 rate, with cells maintained at 30°C. The average operating voltage on discharge is approximately 3.7 V.	716
Figure XI.5.1 Schematic of the technical approach for creating high-performance LNMTO Li-ion cathodes.....	719
Figure XI.5.2 Cycle performance of SLP-cells capacity comparing homogeneous LNMO core (and homogeneous LNMTO for Year 1) and LNMO/LNMTO core-shell cathodes for each of the project years...	720
Figure XI.5.3 SEM of LNMO and LNMO/LNMTO core/shell powder synthesized throughout the project...	720
Figure XI.5.4 Raman spectra (left) and interfacial (R_{sf}) and charge-transfer (R_{CT}) impedance measured by impedance spectroscopy of fresh and cycled LNMO and LNMO/LNMTO core/shell cathodes (left). $\text{LiNi}_{0.5}\text{Mn}_{1.35}\text{Ti}_{0.15}\text{O}_4$ (LNMTO-1), $\text{LiNi}_{0.5}\text{Mn}_{1.2}\text{Ti}_{0.3}\text{O}_4$ (LNMTO-2), and $\text{LiNi}_{0.5}\text{Mn}_{1.0}\text{Ti}_{0.5}\text{O}_4$ (LNMTO-3).	721
Figure XI.5.5 Initial cycling behavior of LNMO SLP-cells with different electrode (cathode/anode) porosities at 25 °C Electrolyte 1 M LiPF ₆ in 1:1 wt. EC/EMC (no additive). Cycling conditions: Cycle 1-2: C/10 then C/3.....	721
Figure XI.5.6 Rated capacity and energy of the fifteen 2-Ah PCCs with highest initial rated capacity.....	722
Figure XI.6.1 a) Capacity retention of the LFP-coated NCM/graphite cells during C/3 cycling at room temperature and 40°C. b) DCR of the LFP-coated NCM/Gr cells during C/3 cycling at room temperature and 40°C.	724
Figure XI.6.2 EIS over cycling at a) room temperature and b) 40°C of LFP-coated NCM811.....	725
Figure XI.6.3 STEM studies on the primary particle of the pristine 1%APO coated NCM92. a) Cross-sectional STEM-HAADF image captured at the edge of a primary particle along with b) the corresponding STEM-EDS Ni/Co/Mn mapping and c) the corresponding STEM-EDS P mapping in the same area with a) The scale bar in	

a) corresponds to 5 nm and applied to both b) and c). The STEM-EDS spectrum (d) is from the bottom part of a) inside the particle and the STEM-EDS spectrum e) is from the particle edge.....	725
Figure XI.6.4 The comparison in electrochemical performance of bare, PSU-1 and PSU-2 coated high-nickel cathodes.	726
Figure XI.6.5 SEM images on cross-sections of: a) before and b) after 50 cycles of bare NMC92 cathode; c) before and d) after 50 cycles of PSU-1 coated cathode.	726
Figure XI.6.6 Comparison in cycling performance of Ti-doped NMC92 cathodes synthesized by different calcination conditions.	727
Figure XI.6.7 The Ti-doped high-nickel cathode is fabricated into electrode and pouch cells	728
Figure XI.6.8 Cycling performance of pouch cell at C/3 and 1C rate	728
Figure XII.1.1 ATR-FTIR spectra of Li metal foil exposed to GEN 2 after various post-processing steps: (black) Li metal with dried electrolyte under vacuum (red) Li metal with electrolyte removed from the surface by a porous Celgard separator (blue) Li metal washed in DMC after the contact with GEN2 and (purple) fresh Li metal surface exposed to N ₂ atmosphere of ATR-FTIR.....	733
Figure XII.1.2 Topography and nano-FTIR spectra of Li metal surface after contact with GEN 2 electrolyte. The excess of electrolyte was removed by Celgard porous separator. Most of the Li metal surface is covered by thin iridescent film. a) topography of a patch of Li metal surface without a thin film b) topography of a thin film covering Li metal surface c) nano-FTIR spectra of different spots of the Li metal surface.....	734
Figure XII.1.3 Nano-FTIR study of Cu surface after a cycle of plating and stripping Li A) Near-field infrared amplitude image (2nd harmonic) recorded in white light position B) Nano-FTIR phase ϕ_3 spectra recorded from selected locations A-D	735
Figure XII.1.4 Nanoscale “white light” imaging of SEI layer on Lithium metal surface under various electrochemical conditions: a) Li metal electrode after oxidation under galvanostatic conditions b) Ni electrode after plating Li under galvanostatic conditions c) Li metal electrode after an oxidation-reduction cycle under galvanostatic conditions d) Ni electrode after a cycle of plating and stripping of Li	736
Figure XII.1.5 Nano-FTIR spectroscopy of SEI layer under various electrochemical conditions. Plated Li on Ni (red trace), oxidized Li surface (blue trace), plated and stripped Li "dead Li" (orange trace) and reduced Li surface after oxidation cycle (green trace). ATR-FTIR spectrum of dried GEN 2 electrolyte (grey trace).....	736
Figure XII.1.6 A schematic of experimental and device setup for graphene-liquid electrochemical in situ cell for infrared near-field imaging and nanospectroscopy, previously used in our group.....	737
Figure XII.1.7 Comparison of ATR-FTIR of 2M LiClO ₄ in PC (top green trace) and nano-FTIR spectra of the graphene / 2M LiClO ₄ in PC interface (bottom black trace). Light blue bars and black vertical lines highlight measured differences in IR absorption between the bulk and interface.....	737
Figure XII.1.8 a) Spatially-resolved Nano-FTIR spectra across the graphene / 2M LiClO ₄ in PC interface. Noted with the black lines are changes in shoulder of the peaks b) biased nano-FTIR data collected over single location	738
Figure XII.1.9 A.) Schematic of conceptualized in situ solid-state electrochemical cell to be prepared. B.) AFM topography data of a pristine LAGP surface. Colored diamonds indicate locations where nano-FTIR were collected. C.) Spatially dependent nano-FTIR absorption data which shows sub-diffraction-limit chemical heterogeneity across the LAGP surface; traces are color matched to the corresponding spatial locations shown in B.....	739
Figure XII.1.10 Surface-enhanced Raman spectroscopy (SERS) approach to investigate early SEI A) Schematic of in-situ SERS electrochemical cell. Thin translucent Cu thin film serves as working electrode and SERS substrate B) image of assembled 2-electrode electrochemical SERS cell.....	740

- Figure XII.1.11 Probing Li/GEN2 electrolyte interface via Surface-enhanced Raman spectroscopy a) Schematic of SERS experimental setup b) and c) Raman spectra of Cu-GEN2 interface collected during Li plating 740
- Figure XII.2.1 (a) Synchrotron XRD of #1. LPSIB (blue); #2. NMC811 charged to 4.5 V (red); #3. sample #2 mixed with LPSIB (black). (b) the short-range PDF data of LPSIB electrolyte with SP_4 and $\text{Li}(\text{S/I/Br})_4$ tetrahedra in the structure shown. (c) the short- and long-range PDF data of the samples #1, #2, and #3. 744
- Figure XII.2.2 (a) Cryo-HAADF-STEM of plated Li dendrite in baseline electrolyte without LiNO_3 additive; (b) Cryo-bright field-STEM of plated Li particles in electrolyte with LiNO_3 additive; (c) Cryo-TEM and selected area diffraction of the SEI formed in electrolyte with LiNO_3 additive. 745
- Figure XII.2.3 (a) computed tomography scan of cycled NMC811 electrode; (b) particles labelled based on their morphological damage extent; (c) to (e) details of representative particles having various degrees of damage; (f) XANES data of selected particles in (b); (g) ft-EXAFS data of selected particles in (b). 746
- Figure XII.2.4 Carbon K-edge XAS both in TEY (left panel) and PFY (right panel) of ex situ SPAN electrodes cycled in various electrolytes. 748
- Figure XII.3.1 Microstructure of Li deposits and solid electrolyte interphase (SEI) formed in the different electrolytes. (a-c) Cryo-TEM images of Li deposits formed in the carbonate-based electrolyte: (a) TEM image of Li deposits with whisker morphology. (b) High-resolution TEM images acquired from the stem region of the Li whisker. (c) High-resolution TEM images acquired from the tip region of the Li whisker. (d-f) Cryo-TEM images of Li deposits formed in the ether-based LHCE: (d) TEM image of Li deposits with whisker morphology. (e) High-resolution TEM images acquired from the stem region of the Li whisker. (f) High-resolution TEM images acquired from the tip region of the Li whisker. 750
- Figure XII.3.2 Structure and elemental composition of Li deposits and their SEIs formed in the carbonate-based electrolyte. (a) STEM-HAADF image showing the Li whisker. (b) EELS elemental mapping showing the elemental distribution of SEI. (c) EELS acquired from stem and tip region of the whisker. (d) EELS of Li. (e) EELS of P. (f) EELS of C. (g) EELS of O. (h) EELS of F. 751
- Figure XII.3.3 Microstructure of NMC811 and NMC811/LPS before and after charge. (a) pristine NMC811, (b) NMC811 charged to 4.2 V, (c) pristine NMC811/LPS, and (d) NMC811/LPS charged to 4.2 V. Insets are the selected area electron diffraction (SAED) patterns acquired from primary particle. High resolution TEM images of (e) pristine NMC811, (f) NMC811 charged to 4.2 V, (g) pristine NMC811/LPS, and (h) NMC811/LPS charged to 4.2 V. Insets are FFT patterns acquired from primary particle surface (orange color) and bulk region (blue color). 753
- Figure XII.3.4 Elemental composition of NMC811 and NMC811/LPS before and after charge to 4.2 V. (a-d) Overlapped energy dispersive x-ray spectroscopy (EDS) elemental maps, showing the element distribution across the secondary particle interior and surface. (e-h) Elemental maps acquired from NMC811 and NMC811/LPS. 754
- Figure XII.4.1 (a) Schematic of the rough lithium-LLZO contact with an expanded view of a single contact. The externally applied pressure leads to lithium deformation at the interface leading to an equilibrium distribution of lithium-LLZO contacts with average radius 'a' and number of contacts per unit area 'n'. (b) Schematic of the frequency dependent thermal waves for measuring sub-surface thermal properties including the lithium-LLZO thermal contact resistance. The high frequency waves have shorter penetration depth and probe the properties of layers close to the sensor while the low frequency waves penetrate deeper up to the electrolyte. The variation in the measurement frequency allows spatially resolved probing of sub-surface thermal properties and the isolation of the lithium-LLZO interface resistance. 757
- Figure XII.4.2 (a) Measured thermal interface resistance as a function of external stack pressure for anode-free (red) and symmetric (blue) cells. (b) EIS Nyquist plots for the symmetric (blue) and the anode-free (red) cells at atmospheric pressure (diamonds) and 1.25MPa (squares). There is no significant dependence of EIS spectra with pressure as the interface behavior is dominated by gold deposited on the electrolyte. Calculated mean contact radius (c) and number density of contacts (d) as a function of pressure for the symmetric (blue) and the

anode-free (red) cells. The shaded areas show the error bands in the theoretical estimates from the 3ω measurements..... 758

Figure XII.4.3 Measured mean contact radius (a) and number density of contacts (b) from thermal interface resistance (triangles) and profilometry (diamond) measurement. The results from thermal-contact resistance measurement agrees well with the results from profilometry and capture a general trend of interface degradation (decrease in contact density and increase in individual contact size) which is further verified by SEM images (c and d)..... 759

Figure XII.4.4 (a) The structure schematic of the assembled LAGP symmetric cell and insulation setup. (b) The temperature rises in 2 min under different frequency $\pm 2V$ sin wave. (c) The Example of fitting result between COMSOL simulation and experiments. 760

Figure XIII.1.1 (a) Schematic representation of the polymer/ceramic composite in contact with lithium metal. The brown domains are ceramics, and the green region is the polymer. (b) Zoomed in view at the electrode/electrolyte interface where both polymer and ceramic touch the lithium electrode. (c) Zoomed in view of the composite-electrolyte/lithium-metal interface where only polymer touches the electrode. (d) Current focusing within the polymer as a function of its elastic modulus. When both polymer and ceramic touch Li (red squares) major current focusing is observed in the ceramics. When only polymer touches Li (blue and cyan circles), current focusing is reduced substantially and occurs at the polymer domains..... 765

Figure XIII.1.2 In general only the polymer sees the Li electrode. (a) Phase map between polymer layer thickness and polymer/ceramic charge transfer resistance indicating domains of stable deposition (green) and regions with dendrite growth (yellow). (b) Current focusing at the polymer region for LLZO/PEO, LATP/PEO and $\text{Li}_6\text{PS}_5\text{Cl}/\text{PEO}$ composite electrolytes with different thickness of the polymer layer at electrode/electrolyte interface. 765

Figure XIII.1.3 Li ion transport mechanism study in PEO-LATP composite electrolyte at temperature 90°C . (a) Schematic representation of polymer and ceramic particles in composite electrolyte. Ceramic particles, polymer and interphase are represented in green, orange, and red respectively. Zoomed in view of ceramic particle depicts ceramic and polymer interface and interphase region near ceramic particle surface. (b) Effective conductivity of the composite electrolyte at a varying interface charge transfer resistance for different volume fractions of ceramics in polymer matrix. Solid lines represent case 1: $k_{\text{interphase}} = k_{\text{PEO}}$ and dotted lines represent case 2: $k_{\text{interphase}} = (1/2) k_{\text{PEO}}$. (c) Effective conductivity of the composite electrolyte at a varying volume fractions of ceramics in polymer matrix at different interface charge transfer resistance. Solid lines represent case 1: $k_{\text{interphase}} = k_{\text{PEO}}$ and dotted lines denote case 2: $k_{\text{interphase}} = (1/2) k_{\text{PEO}}$. (d) Transference number and Effective conductivity at low (solid line) and high (dotted line) interfacial charge transfer resistance. (e) Required ionic conductivity for the polymer electrolytes at different transference number for EV applications. Effective properties experienced by the composite electrolytes are represented by the blue oval patch. A yellow asterisk represents the current state of LATP-PEO system for $R_{\text{CT}} = 0.004 \Omega\text{m}^2$ 766

Figure XIII.1.4 During dendrite growth, change in stress induced electrochemical potential $\Delta\mu_e$ – depends on the lithium deposition induced increase in pressure within the electrode and electrolyte. Note that the change, or increase, in pressure is important, not the total pressure within the electrode and electrolyte. 767

Figure XIII.1.5 (a) Schematic diagram of the lithium electrolyte interface with a dendritic protrusion at the middle. Butler-Volmer reaction is assumed at the electrode/electrolyte interface. (b) During lithium deposition at $1 \text{ mA}/\text{cm}^2$, evolution of stress induced electrochemical potential at the tip of the protrusion as a function of electrolyte modulus. (c) Increase in height of the dendritic protrusion as a function of electrolyte modulus. Softer electrolytes cannot suppress the dendrites. Stiffer electrolytes can successfully prevent dendrite growth due to plastic deformation of lithium metal. 768

Figure XIII.1.6 (a) Lithium/solid-electrolyte mesh used in the present analysis. The grain interior and GBs are denoted by the blue and black regions respectively. Butler-Volmer reaction current is implemented at the lithium/solid-electrolyte interface. (b) Distribution of reaction current at the electrode/electrolyte interface (black line) after 1 s for GB conductivity and shear modulus being 50% and 10% of the grain interior,

respectively. (c) Increase in reaction current density at the GB region with time, which demonstrates an increasing trend. In (b) and (c), the blue dashed line indicates the applied current density..... 769

Figure XIII.1.7 (a) Current focusing at the grain boundary region after 1 s as a function of the shear modulus of the grain boundaries. Decreasing grain boundary modulus enhances the current focusing. (b) Phase map between conductivity and shear modulus of the grain boundaries indicating regions where current focusing should occur at the grain boundaries (yellow domain). Homogeneous distribution of reaction current can be achieved by adopting stiff grain boundary domains. 769

Figure XIII.2.1 SEM images of as-synthesized cathode particles: a) PC-NMC811 and (b) SC-NMC811. c, d) Cross-sectional SEM view of an assembled (SC-NMC811+LYC+C) | LYC | Li-In solid-state battery cell. An expanded view at the cathode side of the cell is shown in d). 773

Figure XIII.2.2 a, b) Voltage profiles collected on PC-NMC811 and SC-NMC811 cells cycled at 0.5C, respectively. LYC was used as electrolyte and Li-In alloy used as anode. c) Comparison of discharge capacity as a function of cycle number and d) rate capability comparison of the cells. 773

Figure XIII.2.3 SEM images (a, c, e, g) and cross-sectional FIB-SEM images (b, d, f, h) collected from as-prepared (a, b, e, f) and cycled (c, d, g, h) NMC811 composite cathodes. (a-d) collected from PC-NMC811 and (e-f) collected from SC-NMC811. The vertical lines in (b, d, f, h) are imaging artifacts from FIB processing. 774

Figure XIII.2.4 (a, b) Nyquist plots collected at 3.67 V during the 4th discharge of the ASSB cells with a PC-NMC811 (a) and SC-NMC811 CAM (b). The colored lines are shown to guide the placement of the various semi-circle components on the Nyquist plots. (c) The equivalent circuit model for fitting the EIS data. (d, e) Nyquist plots obtained at 3.67 V during the discharge of PC-NMC811 (d) and SC-NMC811 (e) ASSB cells at the indicated cycle number. (f) Resistance values obtained from fitting the corresponding Nyquist plots in (d) and (e). 775

Figure XIII.2.5 Post-mortem analysis of the interface between LYC and Li-In anode after 1000 cycles. a) Cross-sectional SEM image, b-d) EDX maps of In-L, Y-L and Cl-K, respectively, e) Y K-edge XAS spectra collected on Y metal, pristine LYC and the interface after cycling, and f) Y chemical map obtained from XRF imaging. 777

Figure XIII.3.1 [8] a) Schematic representation of the liquidus line (black) for a eutectic phase diagram. The line in purple shows the solubility, e.g. at a temperature T, the salt will not be soluble past the solubility line. b) Computed liquidus line based on activity coefficients calculated from the physical-chemical model developed. c) Sample structures of relevant species in solutions for the studied carbonate electrolyte, LiPF₆ in PC. These are the free Li⁺ and contact-ion pair (CIP). 780

Figure XIII.3.2 [8] a) Molecular dynamics “snapshot” of the solvation structure of a Li cation in the high concentration electrolyte (HCE) formulation, with the diluent in the second solvation shell. b) Molecular dynamics “snapshot” of the solvation structure of a Li cation in the HCE formulation with the diluent, in this case present in the first solvation shell. Atoms are shown in purple (Li), red (O), white (H), green (F), and orange (P). c) Radial distribution functions and coordination numbers for lithium coordinating with the diluent for different classical molecular dynamics force field charge parameters of the diluent. 781

Figure XIII.3.3 [9]. Li-Al-O phase diagrams. (a) The first phase-region (green triangle) formed by LiAl₅O₈, LiAlO₂ and Al for LiAl₅O₈ lithiation. (b) The first phase-region (green triangle) formed by LiAl₅O₈, Al₂O₃ and Al for Al₂O₃ lithiation. 783

Figure XIII.3.4 [9] (a) Distribution of the reduction and oxidation limits for each category that pass thermodynamic stability descriptor. (b) Distribution of the reaction energy with LiNiO₂, LiCoO₂, LiMn₂O₄ and LiFeOP₄ cathodes for each category that pass electrochemical stability descriptor. The horizontal dash lines represent the limits of the descriptors. The histograms in (a) and (b) illustrate the numbers of compounds for each category that pass the descriptors. 784

Figure XIII.3.5 [9] Distribution of the reaction energy ΔE_{rxt} with Li₃PS₄ (a) and HF (b) for each category that pass chemical stability with the cathodes descriptor. The horizontal dash lines represent the limits of the

descriptors. The histograms in (a) and (b) illustrate the numbers of compounds for each category that pass the descriptors.....	785
Figure XIII.4.1 Crystal structure of $\text{Li}_{6+1/4}\text{Si}_{1/4}\text{P}_{1-1/4}\text{O}_5\text{Br}$. Li-1 and Li-2 are the Li sites in the stoichiometric structure, and Li-3 is the site where additional Li is stuffed.....	788
Figure XIII.4.2 A Crystal structure of $\text{LiGa}(\text{SeO}_3)_2$. Green and pink polyhedrons represent the coordination environment of lithium and gallium respectively. b The iso-surface of Li-ion probability density from AIMD simulation at 1000 K.....	788
Figure XIII.4.3 Typical crystal structures of known superionic conductors with corner-sharing frameworks. (a) Structure $\text{Li}_{1+x}\text{Al}_x\text{Ti}_{2-x}(\text{PO}_4)_3$, (b) Structure of LiTa_2PO_8 , (c) structure of $\text{Li}_{1+x}\text{Ta}_{1-x}\text{Zr}_x\text{SiO}_5$	789
Figure XIII.4.4 Degree of distortion of octahedral Li environment in quaternary lithium oxide materials with (a) corner-sharing framework, and (b) non-corner-sharing frameworks.	789
Figure XIII.4.5 Structural features of CS-frameworks and their RR channels a Comparing the polyhedral packing ratio α , b site-ratio β and c dimensionality of RR channels of CS and non-CS frameworks. In d-f, the lithium probability densities from ab-initio molecular dynamics simulations are shown in red with isosurfaces P0/100, P0/1000, P0/1000 respectively. The occupied and unoccupied lithium sites are shown in green and white spheres respectively. The RR-channels are shown with black edges.....	790
Figure XIV.1.1 Orange Energy removed at C/3 at 30°C. Blue Energy removed at -20°C. Gen 2 is the baseline electrolyte. x1, x2, x3 are 0.5, 0.75 and 1 % of the additive, respectively. A1, A2, A3 are three different analogs of the selected additive.	795
Figure XIV.1.2 Specific discharge capacity with regard to the cathode (in blue) and the coulombic efficiency (in red) versus cycle number. The open points are for Gen 2 and the filled points are for Gen 2 plus 0.5% A1.	796
Figure XIV.1.3 Energy discharged from cells at different temperatures, one cell had the additive (green), that was fully charged at 30°C, normalized by the energy discharged at 30°C.	796
Figure XIV.1.4 Electrochemical impedance spectroscopy of two cells, one with and one without an additive, acquired at -20°C and -30°C. The filled data points are for the data taken at -30°C. The blue data points are for the cell without the additive.	797
Figure XIV.1.5 a. Electrochemical impedance spectroscopy of a cell without the additive after the 1st, 2nd, 3rd, and 20th formation cycles acquired at -20°C. b. 6 Electrochemical impedance spectroscopy of a cell with the additive after the 1 st , 2 nd , 3 rd , and 20 th formation cycles acquired at -20°C.	797
Figure XIV.1.6 (a) Total Resistance (b) SEI Resistance (c) Charge-transfer Resistance of Gr/NMC coin cell gathered at 50%SOC during a C/3 discharge at different temperatures in baseline electrolyte (1.0M LiPF_6 in 3:7 EC:EMC) with and without additive A.	798
Figure XIV.1.7 Hydrogen evolution measured using DEMS during the formation cycle of Gr/NMC622 cells in the presence of different wt% of additive A, performed at room temperature.	798
Figure XIV.1.8 Comparison of electrochemical techniques and electrophoretic NMR for (a) transference number and (b) thermodynamic factor. The thermodynamic factor is unity at $r = 0$, shown in blue, based on the thermodynamic requirement that all solutions are ideal in the limit of infinite dilution. Images are reprinted from Hickson et al.....	799
Figure XIV.2.1 (a) Binding energies of each solvent with Li ion. The dielectric constant for implicit solvation model was 6.02, and they were calibrated to $\text{EA} = 0$ eV. (b) ^{19}F - and (c) ^7Li -NMR spectra of different electrolytes. (d) Coordination number in Li solvation sheath of different electrolytes from MD simulation. (e) Ionic conductivities of different electrolytes at various temperatures, and (f) their calculated activation energies (E_a) from plots (e).	802

- Figure XIV.2.2 (a) dQ/dV profiles of graphite|NMC622 cells with different electrolytes during 1st charging. (b) Atomic ratio and XPS spectra of (c) C 1s, (d) F 1s, and (e) O 1s of cycled graphite anodes after three formation cycles with different electrolytes..... 804
- Figure XIV.2.3 Nyquist plots of graphite|NMC622 cells with (a) Gen 2, (b) 1M LiPF₆ in EA/FEC (9/1), (c) 1M LiPF₆ in EA-f/FEC (9/1), and (d) 0.9M LiPF₆ 0.1M LiDFOB in EA-f/FEC (9/1) electrolyte at various temperatures. Arrhenius plots of (e) R_{ct}-anode, and (f) R_{ct}-cathode fitted from (a-d). 805
- Figure XIV.2.4 (a) Voltage holding test of graphite|NMC622 cells with different electrolytes from 4.4 V to 4.9 V. C-rate capability with different electrolytes at (b) 25°C and (c) -20°C. Cyclability at (d) 2 C and (e) 6 C rate with different electrolytes at 25°C. (f) Cyclability at C/3 rate with different electrolytes at -20°C. 806
- Figure XIV.3.1 (a) ionic conductivity of LHCE-TTE3 and LHCE-TTE4.5. (b) Charge-discharge voltage profile of Li/SPAN cells at -20°C (dot line) and -30°C (solid line) using LHCE-TTE3 (blue) and LHCE-TTE4.5 (red). (c) Li-SPAN cycling stability at -30°C using LHCE-TTE3 (blue) and LHCE-TTE4.5 (red). (d) EIS results of Li/SPAN cells after 50 cycles at -30°C. 810
- Figure XIV.3.2 (a) Sulfur K-edge X-ray absorption spectroscopy (XAS) of Cu foil with deposited lithium in Li/Cu cells. X-ray fluorescence images of sulfur species on Cu foil collected at 2482 eV using (b) LHCE-TTE3 and (c) LHCE-TTE4.5. 811
- Figure XIV.3.3 Cycling performance of NMC 622 | graphite cells with (a) 1M LiPF₆ (b) 1M LiBF₄ (c) 1M LiDFOB as the salt at C/5 charge and C/3 discharge rate rates at -20°C. 811
- Figure XIV.3.4 FE-SEM (top) and SEM-EDX overlay images (center) and SEM-EDX elemental mapping (bottom, Blue- Carbon, Red- Oxygen, Green-Fluorine, light blue- Boron) of the SEI layer after 50 cycles at -20°C with each electrolyte formulation. 812
- Figure XIV.3.5 (a). Cycling performance of TTE based new electrolytes in NMC811 (2.5 mAh/cm²) || graphite full cells in comparison with baseline electrolyte at 0.5 C rate under 25°C (3.0-4.5 V). (b) Rate performance of F1 electrolytes in NMC811 (2.5 mAh/cm²) || graphite full cells at 25°C, and corresponding voltage profiles 813
- Figure XIV.3.6 (a). Long cycling performance of F1 electrolytes in NMC811 (2.5 mAh/cm²) || graphite full cells at 0.2 C rate at -30°C /-40°C. (b) Cycling performance at 0.1 C under different temperatures (60°C, 25°C, 0°C, -20°C, -30°C, -40°C, -50°C, -60°C), and voltage profiles using F1 electrolyte..... 814
- Figure XIV.3.7 Low temperature charge and discharge cycling performance of NMC811||graphite pouch cell under -30°C..... 814
- Figure XIV.3.8 (a) Temperature dependence of the conductivity of different electrolytes. For comparison, red stars represent conductivity values predicted with Molecular dynamics (MD). (b) Differential scanning calorimetry (DSC) cooling and heating curves of different electrolytes. Electrolytes were cooled to -90°C and then heated up to 90°C with 2°C/min, indicating wide temperature stability. (c) PDF data of F1 electrolyte, and single solvents. Greyline: experiment data; Redline: MD simulation predictions..... 815
- Figure XIV.3.9 MD simulation results: (a) a snapshot of the simulation box of F1 electrolyte. LiTFSI-F1 are highlighted by yellow isosurface, TTE and F4 by blue isosurface. (b) Walden plot for F1 electrolyte indicating strong ionic correlation. (c) Fraction of free Li⁺ and TFSI⁻ defined as the ions not coordinated to any counterion within 5.0 Å of Li-N(TFSI) from MD simulations of F1 electrolyte. Low fraction of free ions is consistent with Walden plot..... 816
- Figure XIV.3.10 Bulk structure and MD simulation results of the formulated electrolytes. **a–c**, Raman spectra of electrolytes at different LiFSI concentrations in Me₂O and the 1 M LiFSI-Me₂O-TFE-PFE mixture at 800–700 cm⁻¹ (the S–N–S bending vibration of FSI⁻) (**a**), 880–820 cm⁻¹ (the C–F stretching vibration of TFE and PFE molecules) (**b**) and 950–890 cm⁻¹ (the C–O–C stretching vibration of Me₂O) (**c**), **d–f**, Snapshots of the MD simulation cell containing the representative Li⁺ solvates (**d**), 1 M LiFSI-Me₂O (**e**) and 1 M LiFSI-Me₂O-TFE-PFE (**f**) at 273 K. In **e,f**, the blue isosurfaces highlight the locations of Li⁺ and FSI⁻. Colors: Li, purple; C,

grey; O, red; H, white; F, cyan; N, navy blue; S, yellow. **g.** Li^+ coordination numbers of Li–EO bonding and Li–O (from LiFSI) bonding at different temperatures. EO, ether oxygen. 817

Figure XV.1.1 Morphologies of (a) single layer PE separator (20 μm), (b) 3DOM PI and 7 μm PE and (c) electrospun PI and 7 μm PE; (d), (e), (f) Morphologies of Li deposited on Cu with separators (a), (b) and (c) respectively, in the electrolyte of DME-LHCE (i.e. LiFSI-1.2DME-3TTE) at the current density of 0.4 mA cm^{-2} for 10 h. 821

Figure XV.1.2 (a) Room temperature cycling performance of Li||NMC622 coin cells with three separators shown in the adjacent figure. (b) Room temperature cycling performance of Li||NMC622 coin cells with two dual separators. The cells contained 50 μm thick Li, 4.2 mAh cm^{-1} NMC622, 75 μL DME-LHCE (LiFSI-1.2DME-3TTE), and were cycled between 2.5–4.4 V with C/10 charge and C/5 discharge after three formation cycles at C/10, where 1C=4.2 mA cm^{-2} 822

Figure XV.1.3 Thermal stabilities of (a) 20 μm single layer PE, (b) electrospun PC and (c) electrospun PS separators; (d) Cycling performance of Li||NMC622 cells using 20 μm single layer PE, 7 μm PE+PC and 7 μm +PS dual separators with DME-LHCE electrolyte (LiFSI-1.2DME-3TTE). 822

Figure XV.1.4 DSC curves of Li||NMC622 cells using a single layer 20 μm PE separator and 7 μm PE+PI separator. (NMC622 was charged to 4.4 V). 823

Figure XV.1.5 (a, b) SEM images showing morphologies of (a) pristine PI fiber and (b) polymeric 3D current collector (Cu@PI membrane). (c) EDS images showing Cu distribution of Cu@PI membrane. 824

Figure XV.1.6 SEM images and EDS mapping images for Cu distribution on Cu@PI mat of (a) top-view and (b) their cross-sectional views. 824

Figure XV.1.7 SEM images of deposited Li morphologies on (a, c) bare Cu foil and (b, d) Cu@PI mat. 825

Figure XV.1.8 Room temperature cycling performance of Li||NMC622 coin cells using Cu@PI and bare Cu current collectors with DME-LHCE electrolyte (LiFSI-1.2DME-3TTE). 825

Figure XV.1.9 (a) Schematic diagram of using RIM to image the SEI formation dynamics. (b) Cyclic voltammetry (CV) curves of the first three cycles in 1 M LiPF_6/PC with 50 ppm H_2O as additive. (c) The optical reflection signal along with three CV cycles on Cu electrode in 1 M LiPF_6/PC with 50 ppm H_2O . (d) The corresponding current density (black curve and left axis) and voltage (red curve and right axis) in the first three cycles of CV scans. (e) The derivative of optical signals (the curve in c). 826

Figure XV.2.1 Temperature-dependent changes in (a) lattice parameters and (b) Li^+ diffusivity under hydrostatic pressure, computed from 1536-atom MLMD of LLZO. Adapted from Ref. [1]. 829

Figure XV.2.2 (a) $\Sigma 2(-1104)/[11-20]$ Model of a tilt grain boundary in LCO and (d) the histogram of diffusivities of individual Li^+ ions in the grain boundary region from MLMD. 830

Figure XV.2.3 (a) Calculated von Mises stress distribution within a generated 3D polycrystalline microstructure of LLZO. Half of the structure shows stress hotspots as isosurfaces exceeding a threshold of 1.0 GPa. (b) Volume fraction of stress hotspots as a function of applied longitudinal strain. 831

Figure XV.2.4 (a) Scanning electron microscopy of a polymer/LLZO/polymer system at the polymer/LLZO interface (top) and inside the porous bulk LLZO (bottom); scale bars are 10 μm . (b–d) Mesoscale modeling of (b) selected grain structures, (c) normalized electric current flux and density distributions, and (f) normalized von Mises stress distributions for two different representative microstructures (top: porous; bottom: dense). 832

Figure XV.3.1 Illustration of how a salt philic solvent phobic (SP^2) polymer coating on Li metal anode can induce the formation of desirable salt-derived solid electrolyte interphase (SEI). 835

Figure XV.3.2 Characterization of salt affinity and solvent phobicity: **A**, density functional theory (DFT) based calculation of Li^+ 's interaction energy with various polymer side chains; **B**, contact angle measurement of polymer coated Si wafer with ether (1M LiTFSI DME) or carbonate (1M LiPF_6 EC/DEC 10% FEC) electrolyte; **C**, comparison of salt affinity and solvent phobicity of various polymer side chain. SAEP is SP^2 837

Figure XV.3.3 Selectivity of PyTFSI and SASP polymer: **A**, experimental set-up for H-cell experiments; **B**, H-cell experiment with the polymer sandwiched in the middle, images taken after 3 hrs with the measured LiTFSI concentration labelled on the graph; rheological frequency sweep of the polymer after soaked in 1M LiTFSI DME electrolyte for 8 hrs, with the $\tan(\delta)$ at 10 rad s^{-1} marked; **C**, PyTFSI; **D**, SASP; **E**, conductivity (25°C) of the polymer before and after soaked in 1M LiTFSI DME for 8 hrs; **F**, Oxygen 1s XPS of SEI on the anode, and the signals attributed to either salt or solvent decomposition were separated with their relative percentage marked out. SASP is SP^2 839

Figure XV.3.4 Electrochemical characterization of SP^2 with different electrolytes: **A**, coulombic efficiency measured of coated Cu in Li|Cu geometry with 40 μL of ether (1M LiTFSI DOL/DME 1wt% LiNO_3), carbonate (1M LiPF_6 EC/DEC 10% FEC) or FDMB (1M LiFSI FDMB) electrolyte; **B**, EIS measurement overtime with either SP^2 coated Li|Li symmetric cell in electrolytes; **C**, calculated impedance increase (%) over 100 hours; **D**, voltage curve of Li|Li symmetric cell with and without SP^2 coating; **E**, SEM top view image of deposited Li on Cu electrode in carbonate electrolyte, scale bar 10 μm 840

Figure XV.3.5 Cycling of SP^2 coated Li anode in Li|NMC cells: **A**, rate capabilities; **B**, cycle life and capacity; **C**, coulombic efficiency of each cycle. **D**, comparison of cycle life (80% capacity retention) plotted against access lithium amount of the SP^2 coating with other coatings/ electrolyte strategies; The x axis locations of 4, 5, 7, 11, and 12 are 10 mAh cm^{-2} , and they are adjusted slightly to dodge..... 841

Figure XV.4.1 Schematic Li reservation on Cu (Li from cathode) by voltage optimization..... 845

Figure XV.4.2 Cu||NMC622 cell performance at different discharge cutoff- voltages. 845

Figure XV.4.3 (a) Cycling performances of Cu||NMC622 and Cu||NMC811 cells cycled between 3.5 – 4.5V. (b) Cycling performances and (c) Coulombic efficiencies of Cu||NMC811 cells cycled with different charge cut-off voltages. 846

Figure XV.4.4 (a)The schematic of Li deposition/stripping on Cu with and without PL_RX layer. (b) Digital photographs of the bare Cu, PLCu and PLCu_RX. (c) Li deposition/stripping voltage profiles of the bare Cu and PLCu_RX with an average CE value. (d) SEM images of the Cu surfaces after Li stripping from bare Cu substrate and (e) PL_Rx coated Cu substrate..... 847

Figure XV.4.5 (a) The voltage profiles and (b) Coulombic efficiency of the Li||Cu cells with different coating layers. (c) Discharge capacity and (d) Coulombic efficiency of the Cu||NMC811 with and without optimized coating layer..... 848

Figure XV.4.6 (a) Discharge capacity and (b) Coulombic efficiency of the 200 mAh Cu||NMC532 pouch cells with different types of LHCEs..... 848

Figure XV.4.7 (a) The Coulombic efficiency of the Li||Cu cells with additives. (b) Discharge capacity and (c) Coulombic efficiency and (d) energy of the Cu||NMC811 with the LHCE with additives. 849

Figure XV.4.8 (a) Voltage profile of Li||NMC811 baseline cell charged to 4.5V, (b) digital photograph of Cu electrode after the 1st Li deposition to 4.5V, (c) SEM images with EDX data (insets) for the top (left) and cross-sectional (right) views of the center (upper) and edge (lower) regions of the Cu electrode after the 1st Li deposition to 4.5V, (d) digital photographs displaying the non-uniform thickness of the SSS with a schematic illustration of the non-uniform Li deposition leading to a porous/brittle SEI layer by non-uniform pressure/current distribution on Cu electrode, and the cycling performance of Cu||NMC811 cell cycled between 3.5V – 4.4V with the commercial 2032 coin cell set..... 849

Figure XVI.1.1 (a) Digital image of the gel-like electrolyte. (b) Schematic of the solid-state full cell with the designed eLi anode. (c) Charge-discharge curves of the cell at rates of 0.1, 0.2, 0.5, and 1.0 C. (d) Cycling performance of eLi/LPSC/NMC622 solid cell at 0.2 C with an areal capacity of 1.0 mAh cm^{-2} , $1\text{C} = 160 \text{ mA g}^{-1}$. (e) Comparison of the cycling performance of NMC622 solid full cell with fresh Li and eLi anodes at 0.15C, the cathode has an areal capacity of 1.0 mAh cm^{-2} 854

Figure XVI.1.2 (a) Schematic of the proposed thin-film solid electrolyte. (b) EDS mapping of the full cell with the thin-film electrolyte of design 1. (c) charge-discharge curves of full cells with design 1 (dash line) and design 2 (solid line) in Table 1. (d) table of the proposed battery with a different structure.....	855
Figure XVI.1.3 (a) Critical current density of Li/LPSC/Li symmetric cell at fixed capacity of 4 mAh/cm ² under 80°C. (b) Cycling performance of the Li NMC811 cell. (c) Schematic of the proposed thick cathode solid-state battery. (d) Table of calculated energy density of the corresponding battery.....	855
Figure XVI.1.4 (a) Calculated energy density of three structural designs. (b) Structural parameters of three evaluated cell structure (c) Cycling performance of the Li NMC811 cell. (c,d) Cost evaluation for structure design 3. The prices of LPSC was adopted from commercial in c and from raw materials in d.	856
Figure XVI.2.1 The electrolyte development progress: Li ion conductivity and CCD at 70°C	859
Figure XVI.2.2 A solid-state-electrolyte separator coating on a slot-die coater.....	859
Figure XVI.2.3 Cycle life of an NMC/Li metal solid state pouch cell	860
Figure XVI.2.4 Storage test of an NMC/Li metal solid state pouch cell at 60°C	860
Figure XVI.3.1 A) Modeled TTT curves showing the 10% crystallization threshold for the pure SULFIDE, MOS, and MOSN glasses. B) Modeled viscosity curves for the three-glass series. Cutoffs for the curves are at the 15-hour mark of each glass on the TTT curve.	862
Figure XVI.3.2 A) An image of the ISU-6 preform following casting and annealing, approximately 10 cm x 25 cm x 0.5 cm. B) An image of thin film ISU-6 being drawn of around 200 μm in thickness. C) An image of a small piece of 60 μm thin film produced from the drawing process.....	863
Figure XVI.3.3 A) Arrhenius plot showing conductivity of various thin-film samples compared to the conductivity of a bulk glass piece. B) Expected ASR compared to experimental ASR showing that the thin films exhibit behavior close to what is expected.	864
Figure XVI.3.4 Specific capacity and coulombic efficiency of an LiFePO ₄ hybrid style cell cycled for 100 cycles.	865
Figure XVI.4.1 Our Perspective1 article accepted in Joule provides insight into the technological status of solid-state batteries and provides a guide for future challenges and opportunities to work with OEMs to advance the technology readiness level (TRL).	868
Figure XVI.4.2 Mechanical strain % vs time plot of Li-LLZO-Li cells consisting of thick (700 micron) and thin (100 micron) Li anodes. When Li was < 100 microns thick, negligible deformation occurred. This behavior suggests that Li-LLZO frictional or adhesion likely created hydrostatic stress in Li, thus limiting deformation when Li is thin (< 100 microns).	870
Figure XVI.4.3 Two distinct behaviors were observed when stripping in situ formed Li electrodes.....	871
Figure XVI.4.4 Cycling at 108 uA/cm ² at room temperature with carbon paper. A Li-LLZO-DOL/DME/S hybrid battery can be discharged to 1,300 mAh/g and be cycled 3 times with minimal capacity loss.	871
Figure XVI.5.1 TGA results of a) NMC811, b) NMC622, c) NMC111, and d) Al ₂ O ₃ coated NMC622 in both Ar and O ₂ atmospheres.	875
Figure XVI.5.2 XRD and Rietveld Refinement Analysis of a-b) NMC811, c-d) NMC622, and e-f) NMC111 co-sintered in a 1:1 wt ratio with LLZTO of varying amounts of excess Li in both Ar and O ₂ atmospheres ..	876
Figure XVI.5.3 Rietveld Refinement Results of XRD of Li ₂ SiO ₃ -NMC622 co-sintered in a 1:1 wt ratio with LLZTO onto LLZTO trilayers at 900°C in (a) Ar atmosphere and (b) O ₂ atmosphere. Similarly, Rietveld refinement results of XRD of Li ₄ SiO ₄ -NMC622 sintered in (c) Ar and (d) O ₂ atmosphere.	877
Figure XVI.5.4 Rietveld Refinement Results of XRD of LiAlO ₂ -NMC622 co-sintered in a 1:1 wt ratio with LLZTO onto LLZTO trilayers at 900°C in (a) Ar atmosphere and (b) O ₂ atmosphere. Similarly, rietveld refinement results of XRD of Li ₅ AlO ₄ -NMC622 sintered in (c) Ar and (d) O ₂ atmosphere.	877

- Figure XVI.5.5 Nyquist plots and Distribution of Relaxation Times Analysis of EIS of a) Li_2ZrO_3 -NMC622, b) LiAlO_2 -NMC622, and c) Li_2SiO_3 -NMC622 co-sintered in a 1:1 wt ratio with LLZTO onto LLZTO trilayers at 1000°C in O_2 879
- Figure XVI.5.6 Nyquist plots (inset) and Distribution of Relaxation Times Analysis of EIS of a) Li_5AlO_4 -NMC622, and b) Li_4SiO_4 -NMC622 co-sintered in a 1:1 wt ratio with LLZTO onto LLZTO trilayers at 1000°C in O_2 880
- Figure XVI.5.7 Nyquist of EIS of uncoated and Li_4SiO_4 coated NMC622 Li metal full cells co-sintered in a 1:1 wt ratio with LLZTO onto LLZTO trilayers at 1050°C in O_2 881
- Figure XVI.6.1 Temperature dependence of diffusion coefficients of Pyr_{13}^+ and FSI^- in MICs with 10 wt% PBDT and LiFSI or LiTFSI salt. (A) shows the effect of LiFSI wt% (10% or 20%) on the diffusion coefficients while (B) shows again the $\text{Pyr}_{13}\text{FSI}$ IL but with LiTFSI at 10 or 20 wt%. In both cases, the diffusion coefficients are a factor of 3 faster than when using $\text{Pyr}_{14}\text{TFSI}$ IL with these salts. There is also noticeably faster diffusion for the LiFSI salt system as compared to LiTFSI, and only a modest decrease in ion diffusion when using 20 wt% salt as opposed to 10 wt%. Battery cell testing is underway with these and related systems (see also the figure below). 884
- Figure XVI.6.2 Li/MIC/NMC622 cathode coin cell cycled at 60°C at C/3. The mass loading of the cathode material is 3.36mg/cm². (a) Galvanostatic charge/discharge profiles at C/3 for 50 cycles. (b) Charge/discharge profiles by different cycle numbers. (c) Coulombic efficiency (%) for 50 cycles. 885
- Figure XVI.6.3 Specific discharge capacity of LiFePO_4 electrodes prepared with 3% PBDT (red) and 3% PVDF (black) as binder over long-term cycling at 22°C. Performances of three cells are shown for each type of electrode. The cells are cycled at 0.2C for 5 cycles followed by 1000 cycles at 4C rate. Occasional pausing of the battery tester causes a few inconsistent data points in the plot. Electrodes with PBDT binder demonstrate better long-term cycling stability in spite of their slightly inferior capacity compared to their PVDF counterparts. The PBDT cells were run longer, up to 2000 cycles, with only minimal loss (10%) in specific capacity. 886
- Figure XVI.6.4 Images of the electrodes before and after tape peeling tests. The electrodes are pressed on an adhesive tape and then peeled off. The thin carbon coating layer on the aluminum substrate stays intact after the peeling test when using PVDF as the binder. However, when using PBDT as the binder, the majority of the carbon coating layer is peeled off along with the LiFePO_4 and carbon particles, exposing the metallic luster of the aluminum substrate. These tests strongly indicate that PBDT has higher binding strength than PVDF. ... 886
- Figure XVI.6.5 X-ray fluorescence imaging and X-ray absorption spectroscopy results of pristine and cycled molecular ionic composite (MIC) electrolytes. The cycled MIC sample displayed a heterogeneous distribution of sulfur species compared to the pristine sample. The evolution of decomposed sulfur species is revealed from distinct XANES. 887
- Figure XVI.6.6 Lithium symmetric cell performance with and without selected additives to aid in SEI formation. All plots are voltage profiles of symmetric cells cycled at 23°C with increasing steps of current density. The charge and discharge times are 0.5 h, respectively, and the current density is stepped every 10 cycles. (a) 5 wt% of fluoroethylene carbonate (FEC), (b) lithium difluoro(oxalate)borate (LiDFOB) salt, (c) lithium bis(oxalate)borate (LiBOB) salt, and (d) without additives. We observe significant gains (up to 2.3X) in limiting current for the FEC and LiDFOB additives. Future goals include exploration of a range of other additives, focusing on non-volatile compounds, spatial separation of additives near interfaces, and additives that can largely be consumed during dominant SEI formation. 888
- Figure XVI.6.7 (a) X-ray absorption near-edge spectroscopy and (b) extended X-ray absorption fine structure results of pristine and charged NMC811 cathodes in contact with MIC electrolytes; the transmission X-ray microscopy results of (c) pristine cathode, (d) 2nd charged cathode and (e) 35th charged cathode; The scale bars in c-e are all 5 μm . (f) the histogram of Ni K-edge energy distribution and (g) the depth-dependent Ni K-edge energy variation in the 2nd charged cathode. 889

Figure XVI.6.8 Proton (Pyr_{14}^+ cation) NMR signal attenuation curve (I/I_0 vs. NMR diffusometry parameter b) showing a diffusion coefficient $D = 2.0 \times 10^{-11} \text{ m}^2/\text{s}$ for a Li||Li cell charged/discharged for 100 cycles. Best fit to the data (black points) with a single diffusing component (red line) shows no significant heterogeneity introduced into the sample. The sample was sealed in glass under vacuum at room temperature after cell disassembly and cycling and measured on our 400 MHz NMR spectrometer. 890

Figure XVI.6.9 Temperature dependence of the cation (Pyr_{14}^+) and anion (TFSI^-) diffusion coefficients in cycled/charged MIC films. The solid data points represent the cation diffusion coefficients and the open data points represent the anion diffusion coefficients. The red triangles are the diffusion coefficients of the uncycled MIC film before assembly into a battery, and the diffusion coefficients agree with the uncycled MIC film reported in the Yu et al, *Advanced Energy Materials* 2021 paper (black squares). The blue circular data points are of the MIC film after charging to 4.4 V in a Li/MIC/NMC811 cell, and the green diamonds are of the MIC film after 20 cycles in a Li/MIC/LFP cell. Both MIC membranes collected after cell assembly and then charging, and/or cycling have similar diffusion coefficients, which are approximately half as high as the uncycled MIC material, possibly due to some mobile ions pushed into the porous cathode during cell assembly. These data provide critical information for further optimizing MIC composition, casting process, SEI/interface assessment and optimization, and cell assembly. 891

Figure XVI.6.10 Constant current charging step of Li/MIC/NMC811 cell, run at 60°C with a 0.1C charging rate and an upper cut off voltage of 4.4V. 891

Figure XVI.6.11 Charge/discharge profile of Li/MIC/ LiFePO_4 cell at room temperature. The cell was run at each constant current density for 5 cycles before increasing current density, for a total of 20 cycles..... 892

Figure XVI.6.12 Specific capacity of Li/MIC/NMC811 cells with (a) previous MIC composition and (b) modified MIC with mixed ion composition measured at 60°C when cycled between 2.5 V and 4.4 V..... 892

Figure XVI.7.1 a) Picture of reinforced SSE pellets after hot pressing at 240°C for 5 minutes. b) XRD profiles of hot-pressed SSE pellets. The binary sample devitrifies to $\text{Li}_7\text{P}_3\text{S}_{11}$ while the ternary sample remains a glass. c) Fractional extent of devitrification for binary and ternary samples as determined by the integration of a DSC exothermic feature. 895

Figure XVI.7.2 a) Picture of a 3-electrode test cell used in this study. b) Schematic of the 3-electrode test cell. The reference electrode is an annular Cu foil disc with Li metal coating held in place with a two-part sleeve. c) Voltage and current versus time for a 3-electrode cell with a Li metal counter electrode, an indium working electrode, and a Li reference electrode. 896

Figure XVI.7.3 a) SEM image of LLZO fibers obtained from a commercial vendor. b) XRD profile of the LLZO fibers indicate a significant Li_3TaO_7 impurity. 896

Figure XVI.7.4 a) A picture of the experimental setup used to expose sulfide SSE powders to a dry room environment. The setup includes a 300L volume tabletop glovebox, a cartridge-based desiccant system, a microcontroller system to control the moisture setpoint, a personal H_2S detector, and a fan to continuously mix the glovebox air. b) H_2S generation of different SSEs in a -40°C dew point dry room as a function of time. c) Reduction in ionic conductivity versus maximum H_2S reading for different sulfide SSEs. 897

Figure XVI.7.5 Ionic conductivity of LPSI sulfide SSE after exposure as a dry powder to different dry room environments for 30 minutes. The star marks the ionic conductivity of LPSI sulfide SSE after exposure to a -40°C dew point dry room for 30 minutes while immersed in anhydrous dodecane. 898

Figure XVI.7.6 a) Solubility times series for $(\text{Li}_2\text{S})_{60}(\text{SiS}_2)_x(\text{P}_2\text{S}_5)_{40-x}$ ($x = 0, 4, 20, 28, 40$) glasses soaked in 1:1 (v/v) DME:DOL. After 2 weeks the $x = 0, 4$ and 20 sample solutions show signs of discoloration, which is attributed to dissolution of the glass. The $x = 28$ and 40 sample solutions remain clear over the course of the experiment. b) Raman spectra of pristine DOL:DME solvent and solutions obtained by soaking $(\text{Li}_2\text{S})_{60}(\text{SiS}_2)_x(\text{P}_2\text{S}_5)_{40-x}$ ($x = 0, 4, 20, 28, 40$) glasses in DME:DOL. The location of structural unit vibrational modes are indicated with colored bars from left to right; namely, $\text{P}_2\text{S}_7^{4-}$ (pink), $\text{P}_2\text{S}_6^{4-}$ (blue), PS_4^{3-} (green), and S_8 (orange). Two vibrational modes of DME:DOL are also indicated (brown). c) Summary of dissolved species as a function of glass composition..... 899

Figure XVI.7.7 CCDs of symmetric Li/SSE/Li test cells with or without a liquid electrolyte interlayer and a different stack pressures at 25°C. The SSE separators are $(\text{Li}_2\text{S})_{60}(\text{SiS}_2)_{28}(\text{P}_2\text{S}_5)_{12}$ glass wafers of approximately 600 μm thickness. a) A test cell with direct Li/SSE contact and 3 MPa stack pressure experiences shorting failure at a CCD of 1,800 $\mu\text{A cm}^{-2}$. b) A hybrid test cell with liquid electrolyte Li/SSE interlayer and a 0.1 MPa stack pressure experiences shorting failure at a CCD of 3,000 $\mu\text{A cm}^{-2}$. Note: the test was paused for two days at 20 hours due to a planned facility power outage.....	899
Figure XVI.7.8 3 rd party validation of a 1 mm thick hot-pressed LiPSO sulfide glass pellet reinforced with Kevlar fiber pulp.....	900
Figure XVI.7.9 Ternary glass separator with 0.75 mS/cm ionic conductivity and 110 μm thickness.....	900
Figure XVI.7.10 a) Picture of the retrofitted glovebox. The glovebox is equipped with a custom system to maintain a dry room environment within a predetermined moisture setpoint range. b) Schematic of the glovebox moisture control system. It consists of a moisture probe, a microcontroller, a solid-state relay, and a cartridge-based desiccant system.	901
Figure XVI.7.11 a) Micro-CT image of a cold-pressed separator after a critical current density experiment. Red arrows point to Li metal deposit. b) Micro-CT image of a hot-pressed separator after a critical current density experiment. A red arrow points to a Li deposit that has expanded an incipient micro-crack. For both images the vertical direction corresponds to the thru plane, transverse direction of the separator. Large speckles in both images are attributed to the Kevlar [®] reinforcing fibers.	901
Figure XVI.7.12 a) $70\text{Li}_2\text{S} \cdot (30-x)\text{P}_2\text{S}_5 \cdot x\text{A}$ SSE solids mass loss after soaking in a variety of liquid electrolyte formulations. All SSEs soaked in $\text{Li}(\text{G}3)\text{TFSI}$ solvate ionic liquid are stable. b) UV-Vis molecular absorption spectroscopy results for $70\text{Li}_2\text{S} \cdot (30-x)\text{P}_2\text{S}_5 \cdot x\text{A}$ SSE samples soaked in $\text{Li}(\text{G}3)\text{TFSI}$ solvate ionic liquid electrolyte and c) $\text{Li}(\text{G}3)_4\text{TFSI}$ liquid electrolyte.	902
Figure XVI.8.1 (a) Arrhenius and Nyquist impedance plots for hot-pressed LPB SE pellet from 25 to 100°C. (b) Comparison of room-temperature ionic conductivity and synthesis temperature of LPB SSE and reported liquid-phase synthesized sulfide SSEs.....	905
Figure XVI.8.2 (a) Rate performance of different sulfur cathodes. (b) Cycling performance of the S-C-LPB cathode at 0.5 C under CCCV mode (cutoff current, 0.1 C; cutoff voltage, 2.5 V vs. Li-In/Li^+) between 0.8 and 2.5 V at 60°C.	906
Figure XVI.8.3 (a and e) SEM images of S-C-LPS (a) and S-C-LPB (e) cathode powders. (b and f) XRD of S-C-LPS (b) and S-C-LPB (f) cathode powders. (c and d) SEM and EDS mapping images of S-C-LPS cathode before (c) and after (d) lithiation. (g and h) SEM and EDS mapping images of S-C-LPB cathode before (g) and after (h) lithiation.	907
Figure XVI.8.4 Long-term cycling performance of the new sulfur cathode composite under 0.1 A g^{-1} (= 0.12 C) between 0.5 to 2.5 V at room temperature. The discharge capacity is based on the weight of sulfur.	908
Figure XVI.8.5 The 1 st -cycle galvanostatic charge-discharge curves of sulfur cathodes evaluated (a) with different areal sulfur loading of 2.5-6.0 mg cm^{-2} under 60°C and (b) with areal sulfur loading of $\sim 2.685 \text{ mg cm}^{-2}$ at room temperature. The current rate is 0.1 C.	908
Figure XVI.8.6 Rate performance of two developed sulfur cathodes, i.e., PSU-1 and PSU-2. The areal sulfur loading of the cathodes is 2-3 $\text{mg}_{\text{sulfur}} \text{cm}^{-2}$. Cells were tested at room temperature.....	909
Figure XVI.8.7 Cycling performance of the Li-S ASSBs using the new sulfur cathode at 0.1 C with high sulfur loading and content under room temperature.	909
Figure XVI.8.8 Cycling performance of the Li-S ASSBs using the as-synthesized alloy anodes. The cells were tested at 0.1 C under 60 °C, and the specific capacity is based on the weight of sulfur.	910
Figure XVI.8.9 XPS spectra of the S-C-LPB cathode (a) before and (b) after cycling at charged state.	910
Figure XVI.9.1 a) X-ray diffraction profiles. b) XPS spectra of the Si 2p region. c) SEM images of the pristine $\mu\text{-Si}$ and the as-synthesized $\mu\text{-Li}_x\text{Si}$. d) Electronic conductivity measurement of $\mu\text{-Li}_x\text{Si}$. e) DC polarization	

measurement of Li-In SSE μ -Li _x Si SSE Li-In symmetric cell. f) AC impedance measurement of Li-In SSE Li-In symmetric cell.	913
Figure XVI.9.2 a) The voltage profiles of μ -Li _x Si SSE LTO cell (up) along with correlated evolution of stress (middle) and stress change (bottom). b) Schematic of pressure-monitoring cell. c) Corresponding dQ/dV curves. d) Voltage and stress change plotted as a function of the molar amount of lithium extracted from or inserted into the μ -Li _x Si phase.	914
Figure XVI.9.3 a) Cycling and b-c) rate performance of Li-In SSE S full cell at 60°C. d) Cycling and e-f) rate performance of μ -Li _x Si SSE S full cell at 60°C. g) Cycling and e-f) rate performance of μ -Li _x Si SSE S full cell at 25°C.	915
Figure XVI.9.4 a) Flexibility test of the free-standing SSE membrane. b) Cross-sectional SEM images of SSE membrane b) before and c) after cold pressing. d) Ionic conductivity measurement of SSE membrane at 25°C. e) Galvanostatic voltage profiles and f) cycling performance of sheet-type Polyimide Li ₆ PS ₅ Cl LiIn cell at 60°C.	917
Figure XVI.9.5 All solid-state state sulfur Li ₆ PS ₅ Cl LiIn cell pouch cell (full cell, 2x3 inch), cell under test in a pressure fixture and first 3 cycles @60°C.	918
Figure XVI.10.1 (a) Photos of Li foil as it is cleaned and polished. (b) XPS at the K-edge of Li, O, and C, respectively, as its surface layer is slowly removed by the Ar-ion milling process.	921
Figure XVI.10.2 Thickness of the surface layer as a function of time after the sample is exposed to air. The solid and dashed lines are linear and parabolic functions for interface-controlled and diffusion-controlled processes, respectively.	922
Figure XVI.10.3 Predicted critical current density at different stack pressures for Li/Li ₂ O, Li/LiF and Li/LLZO interfaces considering Li hopping and creep induced Li flux.	924
Figure XVI.10.4 (a) Photo of the LLZTO lithium-rich cross-section. (b) SEM image of the lithium-rich cross-section highlighting the lithium microstructure. (c) Diagram depicting the mounted and polished lithium-rich cross-section with an overlay showing the indentation groupings. (d) Elastic modulus results for the lithium-rich cross-section grouped by area.	925
Figure XVI.10.5 The comparison of interfacial impedance of Li vs. LLZO with different interlayers.	926
Figure XVI.10.6 Structures after AIMD simulations. (a) DME molecule (b) TMP molecule, (c) LiNO ₃ molecule, and (d) DTL solution on the Li metal. Purple: Li, Brown: C, White: H, Red: O, Blue: N, Green: P. The colors for different elements are consistent in all the figures	926
Figure XVI.10.7 (a) EIS spectra taken on DTL-coated Li symmetric pouch cell. (b) Bare lithium symmetric pouch cell EIS data. The inset at the top right shows the spectra when the pouch cell is clamped. Note that the clamped cell interfacial impedance is too large to be shown on the plot in (b).	927
Figure XVI.10.8 Indentation modulus results on different thin films on Li-foil.	928
Figure XVI.10.9 Histogram of the moduli in previous figure.	928
Figure XVI.10.11 Forward and backward barriers for at different stack pressures for Li/Li ₂ O (a), Li/LiF (b) and Li/LLZO interfaces (c) for later KMC simulations. The red markers represent the vacancy formation energy and blue ones stand for the transition state energy. For the Li/LLZO interface, more NEB calculations will be performed to get all the necessary hopping barriers to perform the KMC simulations.	929
Figure XVI.11.1 Experimental setup of ToF-SIMS analysis. (a) Schematic illustration of the preparation of pristine LPS, (b) schematic illustration of the preparation of plated LPS.	932
Figure XVI.11.2 ToF-SISM analysis of plated and pristine LPS surface. (a-c) Mass spectra of pristine LPS and plated LPS in positive polarization mode. (d-f) The mass spectra of pristine LPS and plated LPS samples in negative polarization mode.	933

Figure XVI.11.3 Depth profile of Li_3O^+ , PS^+ and CsLi_3P^+ fragments in (a) pristine LPS and (b) plated LPS.	933
Figure XVI.11.4 Schematic illustration of an in situ ToF-SIMS stage and open-cell setup on the stage.	934
Figure XVI.11.5 Operando ToF-SIMS mapping of Li^+ and Ag^+ at the electrolyte–silver–carbon interface. The x- and y-axis represent the spatial coordinates in μm . The brightness in color represents the ion count. (Left column) Structure of the solid-state lithium metal cell used in the observation; the observation area is marked with a black square. (Top row) Mapping of Li^+ ; the strong Li^+ signal in the top region ($40 < y < 75$) originates from the solid electrolyte. (Bottom row) Mapping of Ag^+ ; Ag^+ signal is only present within the silver–carbon layer ($y < 40$).	935
Figure XVI.11.6 Evolution of the spatial distribution of Ag^+ and Li^+ during charging. Curves processed from ToF-SIMS spectra such as those displayed in adjacent figure.	935
Figure XVI.11.7 Spatially resolved chemical analysis of composite cathode. (a) Cross-section SEM image of the composite cathode pellet. (b) Zoomed-in mass spectra of pristine PTO, $\text{Li}_6\text{PS}_5\text{Cl}$ electrolyte and composite cathode (c) Secondary ion images of $\text{Li}_6\text{PS}_5\text{Cl}$ fragments, PO_x^- fragments, PTO fragments, and Li_2OH^+ fragments in composite cathode, respectively.	936
Figure XVI.11.8 Spatially resolved mechanical analysis of composite cathode. (a) Schematic illustration of in-SEM nanoindentation test on the identical region of interests for ToF-SIMS characterizations. (b and c) load-displacement curves of PTO and $\text{Li}_6\text{PS}_5\text{Cl}$ in composite cathode, respectively. (d) comparison of mechanical properties of pristine PTO, pristine $\text{Li}_6\text{PS}_5\text{Cl}$, PTO in composite cathode and $\text{Li}_6\text{PS}_5\text{Cl}$ in composite cathode.	937
Figure XVI.11.9 Correlating chemical and mechanical properties. (a) Young's modulus mapping results in the PTO domains of the composite cathode, scale bar 5 μm . (b) Hardness mapping results in the same PTO domains of the composite cathode, scale bar 5 μm . (c) Lithium distribution mapping in PTO domains overlapping with the indented area, the intensity is normalized by the total ion counts from ToF-SIMS analysis, scale bar 5 μm . (d) Mechanical properties of PTO domains with different lithium concentrations.	938
Figure XVI.12.1 (A) Interface model between a CBSE and Li-metal anode. Li atoms are in green, BH_4 units in light blue with H in pink, and PS_4 units in purple with S in yellow. (B) Evolution of P-S and B-H bonds vs. simulation time.	943
Figure XVI.12.2 Chemical/electrochemical stability and ion transport properties at the $\text{Li}_6\text{PS}_5(\text{BH}_4)$ -Li interface. (A) The charge transfer at the P and B sites for different terminal (t) groups (H_2 , B and LiS) at the interface. (B) Bond completeness for the clusters. (C) Calculated mean-square displacement of Li-ions as well as P and S along different directions, with the c-axis the direction perpendicular to the interfacial plane.	943
Figure XVI.12.3 (A) Li-uptake plot of Li_2S against the voltage. (B) Modeled structures at the $\text{Li}_6\text{PS}_5(\text{SCN})$ - Li_2S interface before and after the simulation run. (C) The analysis of the cluster completeness of the interfacial models with different terminal groups.	944
Figure XVI.12.4 (A) The built $\text{Li}_6\text{PS}_5(\text{SCN})$ - Li_3PO_4 interface model, where PS_4 clusters are in bigger tetrahedra, PO_4 cluster in smaller ones, SCN clusters in yellow-black-cyan, and Li in green. (B) The completeness analyses for PS_4 , PO_4 , and SCN clusters.	945
Figure XVI.13.1 Build-up of SEI at $\text{Li} (001) \parallel \text{Li}_7\text{PS}_6 (001)$ studied using reactive molecular dynamics simulations. Temporal evolution of the number of (a) $\text{P(e)} - \text{S(e)}$, (b) $\text{Li(a)} - \text{S(e)}$, and (c) $\text{Li(a)} - \text{P(e)}$ at the interface under no bias (blue) and applied electric field of $E = 0.5 \text{ eV/nm}$ normal to the interface (orange). (d) Time-evolution of the thickness of the as-formed SEI. Li(a) denotes lithium atoms belonging to anode, while S(e) and P(e) are sulfur and phosphorus atoms belonging to the electrolyte respectively.	949
Figure XVI.13.2 Composition of the SEI formed at interface formed between Li metal anode and Li_7PS_6 electrode obtained by RMD simulations. Evolution of the interface is studied (a-c) in absence of electric field ($E = 0$), and (d-f) under applied electric field $E = 0.5 \text{ eV/nm}$ along the positive z-direction (i.e., normal to the $\text{Li} (001) \parallel \text{Li}_7\text{PS}_6 (001)$ interface). Atomic snapshot of the $\text{Li} (001) \parallel \text{Li}_7\text{PS}_6 (001)$ interface after 1 ns are	

shown in panels (a) and (c) for $E = 0$ and $E = 0.5$ eV/nm respectively. The P atoms (panels (b, e)) and S (panels (c, f)) are colored by their charges..... 949

Figure XVI.13.3 Structural evolution of the interface between S_8 cathode and Li_7PS_6 electrode obtained by RMD simulations. (a) Initial configuration of the symmetric S_8 (001) || Li_7PS_6 (001) || S_8 (001) slab, and (b) distribution of charges in the sulfur atoms in the initial configuration. Evolution of the interface is studied (c,d) in absence of electric field ($E = 0$), and (e,f) under applied electric field $E = 0.5$ eV/nm along the positive z -direction (i.e., normal to the S_8 (001) || Li_7PS_6 (001) interface). Atomic snapshot of the S_8 (001) || Li_7PS_6 (001) interface after 0.4 ns are shown in panels (c) and (e) for $E = 0$ and $E = 0.5$ eV/nm respectively. Panels (b), (d), (f) show only the S atoms (colored by their charge) in the snapshots shown in (a), (c), and (e) respectively.. 950

Figure XVI.13.4 Solvent-based synthesis of iodine and fluorine doped argyrodite electrolytes. (a) XRD patterns for as-synthesized Li_6PS_5I , $Li_6PS_5F_{0.25}I_{0.75}$, $Li_6PS_5F_{0.5}I_{0.5}$ and $Li_6PS_5F_{0.75}I_{0.25}$ indicating high phase-purity of the argyrodites, (b) Arrhenius plots of solvent synthesized Li_6PS_5I after two different heating treatment temperatures (200°C, 290°C); TEM elemental mapping of synthesized Li_6PS_5I argyrodite after heating treatment at (c) 200°C and (d) 290°C. (S in Yellow, I in Red, O in Pink)..... 951

Figure XVI.13.5 Anion-disorder in dual-doped argyrodite SEs and its impact on Li-ion conduction. Atomic-scale structures of (a) Li_6PS_5I , and (b) $Li_6PS_5F_{0.25}I_{0.75}$ optimized by DFT. In each panel, the energy change associated with swapping a S atom at 4d site (cage-center) with a halogen (I in panel (a), and F in panel (b)) are indicated. The Li, P, S, F and I atoms are depicted as blue, purple, yellow, red, and green spheres, respectively. (c) Arrhenius plots (30-90°C) of Li_6PS_5I and hybrid-doped argyrodites obtained from EIS measurements..... 952

Figure XVI.13.6 Electrochemical stability of $Li_6PS_5F_{0.75}I_{0.25}$ SE against Li-metal obtained from cycling performance of Li-symmetric cell. (a) Voltage profiles of $Li_6PS_5F_{0.25}I_{0.25} \cdot 0.5LiF$ -based symmetric cell cycling up to 1,100 hours (0.05 mA cm⁻²). XPS spectra of cycled symmetric cell with $Li_6PS_5F_{0.25}I_{0.25} \cdot 0.5LiF$ SE: (b) I 3d, (c) S 2p, and (d) Li 1s. 953

Figure XVI.13.7 Effect of amount of functionalizing IL on the discharge profiles for batteries consisting of Li anode, SP-S cathode with 4.0 mg/cm² loading and 30% SE, and $Li_6PS_5F_{0.5}Cl_2$ electrolyte. Discharge profiles at selected cycles are shown for different amounts of functionalizing IL ($LiTFSI$ in $PYR:DOL(1:3)$ at 3M) at the cathode-SSE interface at 30°C, namely, (a) 40 μ L, (b) 10 μ L, and (c) 5 μ L. As the amount of IL decreases, the discharge profile changes from a two-plateau (at 40 μ L), indicative of a quasi-solid-state behavior to a single slope (at 5 μ L) akin to an all-solid-state Li-S battery..... 954

Figure XVI.13.8 Electrochemical cycling performance of batteries consisting of Li anode, SP-S cathode with 4.0 mg/cm² loading pressed with 25% SE, $Li_6PS_5F_{0.5}Cl_2$ SE with 5 μ L of ionic liquid ($LiTFSI$ in $PYR:DOL(1:3)$ at 3M) at the cathode-SSE interface. (a) Capacity variation, and Coulombic efficiency as a function of cycles at 60°C at C/20, (b) Discharge profiles at selected cycles..... 954

Figure XVI.13.9 Electrochemical cycling performance of batteries consisting of Li anode, SP-S cathode with 4.0 mg/cm² loading pressed with 25% SE, $Li_6PS_5F_{0.5}Cl_2$ SE with 5 μ L of ionic liquid ($LiTFSI$ in $PYR:DOL(1:3)$ at 3M) at the cathode-SSE interface under applied pressure. (a) A picture of the specialized cell being tested inside the glove box under applied pressure (b) Initial discharge curve at 0.05 C for batteries tested under 0, 5, 10, and 20 bar..... 955

Figure XVI.14.1 Zr doped (1/3 of Co sites) NMC811 energy distribution for several random cationic configurations. Insets show top view of three TM layers in the simulation cell for the lowest and highest energy configurations. Purple, blue grey, yellow and green tetrahedrons represent Mn, Co, Ni, Zr and Li sites. 960

Figure XVI.14.2 Side view schematic simulation cells comparing LNO and NMC811 lowest energy Li distribution (Li content: $x = 0.12$). Purple, blue grey, and green tetrahedrons represent Mn, Co, Ni and Li sites. Small red spheres represent oxygen ions. 961

Figure XVI.14.3 Probability of occurrence of a given configuration of Zr-doped $\text{LiNi}_{0.8}\text{Mn}_{0.1}\text{Co}_{0.1}\text{O}_2$ (a) one dopant per cell [3.7% of total transition metal content] (b) two dopants per cell [7.4% of total transition metal content].	961
Figure XVI.14.4 Parity plots of machine learning model energies for (a) Al doped NMC811 and (b) Mg doped NMC811	962
Figure XVI.14.5 Schematic representation of atomic arrangements for (a) NMC811, (b) Ca doped NMC811 and (c) La doped NMC811. Red, green, gray, purple, blue, light blue and orange spheres represent O, Li, Ni, Mn, Co, Ca and La respectively. Li slab space is also indicated.	962
Figure XVI.14.6 Energy of configurations, configurational density of states, Boltzmann factor and probability of occurrence of each tested configuration for (a) Ca and (b) La.	963
Figure XVI.14.7 The predicted ensemble mean and standard deviation total energies are plotted for each of 100,000 structures for the case where one Co atom is replaced by Mg in the transition metal layer. Structures with the best combination of low mean and high standard deviation total energy are plotted for all structure in red, and then in other colors corresponding to the most promising structures from selected subsets of structures.	964
Figure XVI.14.8 Comparison of a proton defect in O1-NiO ₂ and O3-NiO ₂ . O1-NiO ₂ is on the left. O3-NiO ₂ is on the right.	965
Figure XVI.14.9 A trajectory for proton motion in NiO ₂ .	966
Figure XVI.14.10 X-ray diffraction of La doped NMC811 material.	967
Figure XVI.15.1 Schematic of multimodal synchrotron analysis of sulfide glass samples.	970
Figure XVI.15.2 Schematic of an in-situ Raman and diffraction technique for multiple sample environments.	970
Figure XVI.15.3 Schematic of GDOES chemical composition depth profiling instrumentation.	971
Figure XVI.15.4 K-means clustering phase analysis of a Li-B-S glass with both phase heterogeneity due glass thickness and noncrystalline impurities.	971
Figure XVI.15.5 Phase analysis maps show the influence of different processing parameters on crystalline impurities. Note that synchrotron XRD can measure crystalline impurity levels to ~0.01%.	972
Figure XVI.15.6 The Raman spectra for two Li-B-S glasses, the first of which was intentionally crystallized.	972
Figure XVI.15.7 Changes in composition near-surface and in the bulk of Li-B-S electrolytes were evaluated using GDOES.	973
Figure XVI.16.1 (a) XRD patterns and (b) ionic conductivities of $\text{Li}_7\text{P}_2\text{S}_8\text{Br}_{1-x}\text{I}_x$ ($0 \leq x \leq 1$) at 20°C.	976
Figure XVI.16.2 a) Measurement of H ₂ S release, b) electrochemical impedance spectra (EIS), c) XRD patterns, and d) high-resolution C 1s spectra of $\text{Li}_7\text{P}_2\text{S}_8\text{Br}_{0.5}\text{I}_{0.5}$ powders with/without amphipathic organic molecules coating exposed to air with a relative humidity of 0.5% in a dry room.	977
Figure XVI.16.3 Adsorption of a) H ₂ O or b) 1BR on the stable surface of $\text{Li}_7\text{P}_2\text{S}_8\text{Br}_{0.5}\text{I}_{0.5}$ (LPSBI). The adsorption of 1BR on LPBSI with $E_{\text{ad}} = -0.9 \pm 0.7$ eV/adsorbate-atom is favorable compared to H ₂ O on LPSBI with $E_{\text{ad}} = -0.1 \pm 0.8$ eV/adsorbate-atom.	978
Figure XVI.16.4 Time-dependent EIS of Li/SSE/Li cells. a) Li/LPSBI/Li, b) Li/LPSBI-0.5%/Li, c) Li/LPSBI-Bromo/Li, and d) Li/LPSBI-Bromo-0.5%/Li.	979
Figure XVI.16.5 Nyquist plots of a) Li/Li ₇ P ₂ S ₈ Br/Li, b) Li/Li ₇ P ₂ S ₈ Br _{0.5} I _{0.5} /Li, and c) Li/Li ₇ P ₂ S ₈ I/Li cell with equivalent circuit fitting at 20°C. d) Evolution of areal interfacial resistance of each cell with time at 20°C.	980

Figure XVI.16.6 a-c) Long term cycling of a Li/Li ₇ P ₂ S ₈ Br _{0.5} I _{0.5} /Li cell at a) 0.5 mA cm ⁻² with a charge/discharge capacity of 0.25 mAh cm ⁻² at 20°C, b) 1 mA cm ⁻² with a charge/discharge capacity of 0.5 mAh cm ⁻² at 60°C, and c) 2 mA cm ⁻² with a charge/discharge capacity of 1 mAh cm ⁻² at 100°C.....	981
Figure XVI.17.1 Ionic conductivities of fresh and solvent-processed LYB powders at room temperature	984
Figure XVI.17.2 (Left) Free-standing LYB tape with binder; (Right) Ionic conductivity of LYB tape changes with time under pressure.....	985
Figure XVI.17.3 (Left) Galvanostatic cycling voltage profiles for a Li/SSE-A/halide/SSE-A/Li symmetric cell; (Right) Charge-discharge curves of the NMC811/halide/SSE-A/Li cell at room temperature with a rate of 0.1 C.....	985
Figure XVI.18.1 Cell testing hardware for SSE can be used to measure pressure in real time or to calibrate individual spring stacks (top).....	987
Figure XVI.18.2 Representative cell potential for small-area SSE graphite/LCO cell cycling at C/20 between 3.0 and 4.2V. The applied pressure is unknown but will be measured in coming months.	987
Figure XVI.18.3 A microstructured interface between the SSE and catholyte has many more less-tortuous pathways for ion conduction compared to a typical planar interface.....	988
Figure XVI.18.4 (a) NMC811/LPSCI catholyte sample in custom air-free holder with sapphire windows; (b) SEM image of a laser-ablated catholyte revealing the crosshatch channel pattern made using ultrafast laser ablation, as well as EDS of a region inside one of the channels.	988
Figure XVI.18.5 Diagram of the electrode and electrolyte stack	989
Figure XVI.18.6 Cycling data for the NMA vs. Si cell cycled at Room Temp and C/20. Erratic voltage profiles for the first charge/discharge can be caused by a loss of physical contact between active particles and the electrolyte.	990
Figure XVI.19.1 SEM images of a) pristine LLZTO film; b) SPE infilled LLZTO films, c) Backscattered electron image of the LLZTO/.....	993
Figure XVI.19.2 XPS survey scan of a) Pristine LLZTO film and acid treated LLZTO films, HCl and H ₃ PO ₄ ; b) High resolution Li 1s XPS spectra; c) High resolution C 1s XPS spectra; d) High resolution La 3d XPS spectra; e) High resolution P 2p XPS spectra; e) High resolution Cl 2p XPS spectra.	994
Figure XVI.19.3 a)-c) DC polarization curves for determining the Li ⁺ transference number under an applied voltage of 0.04 V at 60°C. a) Pristine LLZTO film; b) H ₃ PO ₄ treated films; c) HCl treated film. The inset shows the impedance taken just before and immediately after the DC polarization experiment. The curves were fitted with a decay function and the steady state at the end of the curve was extrapolated. d)-f) Voltage vs time plots of plating-stripping at different current densities. d) Pristine LLZTO film; e) H ₃ PO ₄ treated films; f) HCl treated film.....	994
Figure XVI.19.4 Voltage vs time plots at 60°C of the four model systems assembled to understand the conductivity differences: a) single SPE layer; b) SPE infilled porous LLZTO film (H ₃ PO ₄ treated); c) stacked SPE, densified LLZTO pellet (H ₃ PO ₄ treated) and SPE; d) stacked SPE and densified LLZTO pellet (H ₃ PO ₄ treated) bilayers with the polymer side initially connected to the positive electrode. Their corresponding cycling stability tests showing symmetric and asymmetric cycling behaviors.	995
Figure XVI.19.5 Young's modulus (E) and hardness (H) measured using spherical indentation.	996
Figure XVI.19.6 Conductivity of composite polymer electrolytes made from a) PEG/LLZTO and b) zPU/LLZTO recipes. c) Cycling tests of Li zPU/LLZTO LFP solid state batteries at 1C rate, room temperature.	997
Figure XVI.19.7 Direct ink writing printed single-crystal NMC811 cathode. Nozzle diameter is 200 μm, hatch spacing is 400 μm, and mass loading is ~ 10 mg/cm ²	997

- Figure XVI.19.8 Backscattered SEM cross-sections of composite cathodes coated on pre-sintered LLZTO pellets and co-sintered at 900°C for 2h in Ar (b-c). Optical image before sintering (a). d) Optical images of the back side of the LLZTO pellets after co-sintering at different temperatures and in different environments (air vs. Ar). Electrochemical measurements using Li as the anode: e) EIS comparison before cycling. f) Voltage profiles for the 1st charge/discharge cycle at C/20. 998
- Figure XVI.19.9 Representative voltage vs. capacity profiles for cathode materials sintered at 750°C and 900°C for 2h in Ar before electrode preparation. Half cells were cycled at C/10 charge/discharge using liquid electrolyte (1.2M LiPF₆ in 3:7 wt% EC/EMC) and Li as the anode. (a) LCO and (b) NMC 622. 999
- Figure XVI.19.10 75 wt% LCO / 25 wt% LLZTO pellets laser co-sintered at 26 W for 90 s using a laser diode array. a) Standard and backscattered SEM images of cross-sections after co-sintering. b) XRD comparison of laser and furnace co-sintered samples. 1000
- Figure XVI.20.1 (a) Temperature-dependent Li⁺ conductivity measurements for Li₆PS₅X (X = Cl, Br) prepared by HG and PM. (b) Raman spectra and (c) powder XRD patterns for Li₆PS₅X (X = Cl and Br) prepared by HG and PM methods. 1004
- Figure XVI.20.2 Electrochemical performance of SSBs containing NMC811 composite cathodes and Li_xIn anodes. (a,b) Schematics of the cell designs. Voltage profiles for cells containing (c) single layer Li₆PS₅Cl and (d) bilayer Li₆PS₅Cl/Li₃InCl₆ separators. (d) Discharge capacity over 40 cycles. Cells were cycled by polarizing the cathode between 2.6 – 4.3 V vs. Li/Li⁺ at a constant current of ±66 μA/cm² (cycle 1) and ±127 μA/cm² (cycles 2-40). Due to the use of Li_xIn anodes, potentials were referenced against Li/Li⁺ by adding 0.622V to the measured cell potential. 1005
- Figure XVI.20.3 (left) Photograph of an in-house developed Raman cell, (middle) schematic of the Raman mapping measurements to probe the NMC/SE interface, and (right) experimental setup for the *in-situ* Raman measurements. 1006
- Figure XVI.20.4 (a) Optical microscope image of the NMC/SE interface. (b) Raman spectrum taken from the bulk SE. (c) Raman map based on scaling single peak intensity of the P-S stretching mode centered at 425 cm⁻¹. 1006
- Figure XVI.20.5 (a) Raman mapping of the NMC/SE interface after K-means clustering analysis. (b) Comparison of the centroid spectra taken at the NMC/SE interface at different states of charge. (c) Magnified view of the P-S stretching mode in (b). 1007
- Figure XVI.21.1 (a) X-ray diffraction patterns for pristine Li₆PS₅Cl (LPSCl) from ANL, NEI, and Ampcera (the XRD pattern for the Kapton background is shown for comparison). (b) Arrhenius plots for the total Li⁺ conductivity of LPSCl from ANL, NEI and Ampcera in the temperature range of -20°C to 100°C. (c) Cycling stability of pristine LPSCl from ANL (black) and NEI (green) in Li||Li symmetric cells at 65°C. 1011
- Figure XVI.21.2 (a) S 2p, (b) P 2p, (c) Cl 2p and (d) O 1s XPS core level spectra for the Ampcera LPSCl SSE. 1012
- Figure XVI.21.3 Al 2p, O 1s, S 2p, P 2p, and Cl 2p core level spectra for Ampcera LPSCl SSE with varying numbers of ALD Al₂O₃ coating cycles. Intensities of the S 2p, P 2p and Cl 2p spectra are normalized for comparison. 1013
- Figure XVI.21.4 S 2p (left) and P 2p (right) core level spectra of uncoated LPSCl (top) and LPSCl coated with 10 ALD cycles (bottom) before and after Li metal deposition. 1014
- Figure XVI.21.5 Calculated densities of states for LPSCl SSE with varying concentration of oxygen. 1015
- Figure XVI.21.6 Calculated barriers for Li hopping in predicted reaction products of alumina with LPSCl – (a) Li₂S, (b) LiCl and (c) LiAlS₂ – indicate feasibility of Li ionic transport through the interfacial layers. 1016
- Figure XVI.22.1 Digital photos of all-solid-state sulfide lab at chemical sciences and engineering division of Argonne: (a) glovebox for synthesis, processing, and test of sulfides SSEs. (b) High-energy ball-milling with

gas-protected jars for the synthesis of sulfides SSEs. (c) in-house electrospinning for the fabrication of thin sulfides SSEs.	1018
Figure XVI.22.2 Design principle of Argyrodite sulfide electrolytes with multi dopants. M represents cations.	1019
Figure XVI.22.3 (a) A digital photo of in situ SXRD set up at Advanced Photon Source (APS) to probe the synthesis of sulfides SSEs. (b) A snapshot during in situ heating process.	1019
Figure XVI.22.4 (a) 2D Contour plot of in situ SXRD patterns during formation of $\text{Li}_6\text{PS}_5\text{Br}$. (b) Zoom-in view of 2θ range of $6.0\text{--}9.5^\circ$	1020
Figure XVI.22.5 Rietveld refinement of in situ SXRD pattern at 600°C during synthesis of $\text{Li}_6\text{PS}_5\text{Br}$	1020
Figure XVI.22.6 2D Contour plot of in situ SXRD patterns during formation of $\text{Li}_6\text{PS}_{4.8}\text{O}_{0.2}\text{Br}$: (a) heating from RT to 550°C ; (b) 550°C holding for 8 h followed by quenching ($30^\circ\text{C}/\text{min}$).	1020
Figure XVI.22.7 In situ SXRD patterns during (a) heating (25°C to 600°C) and (b) rapid cooling ($30^\circ\text{C}/\text{min}$) of a ball-milled mixture of $\text{Li}_2\text{S}/\text{P}_2\text{S}_5/\text{P}_2\text{O}_5/\text{LiBr}$ to form $\text{Li}_{5.5}\text{PS}_{4.3}\text{O}_{0.2}\text{Br}_{1.5}$	1022
Figure XVI.22.8 Contour plot of in situ SXRD pattern during synthesis of $\text{Li}_{5.5}\text{PS}_{4.5}\text{Br}_{1.5}$ from 25°C to 600°C . The heating rate is $5^\circ\text{C}/\text{min}$, and the time interval between two successive XRD patterns is 30 s. The color represent intensity, with blue and red represent low and high, respectively.	1022
Figure XVI.22.9 (Contour plot of in situ SXRD pattern during synthesis of $\text{Li}_{5.5}\text{PS}_{4.4}\text{O}_{0.1}\text{Br}_{1.5}$ from 25°C to 600°C . The heating rate is $5^\circ\text{C}/\text{min}$, and the time interval between two successive XRD patterns is 30 s. The color represent intensity, with blue and red represent low and high, respectively.	1023
Figure XVI.22.10 The effect of holding time on the crystal structures of final products during rapid cooling: (a) 0.5 h; (b) 12 h.	1023
Figure XVI.22.11 (a) Representative Rwp value of Rietveld refinement results and (b-f) selected refined in situ XRD patterns at different temperatures during synthesis of $\text{Li}_6\text{PS}_5\text{Br}$. Rwp represents the weighted profile residual, which is an indicator of refinement results.	1024
Figure XVI.22.12 (a) Lattice parameter a , (b) phase fraction of $\text{Li}_6\text{PS}_5\text{Br}$ and (c) percentage of site disorder as a function of temperature during synthesis of $\text{Li}_6\text{PS}_5\text{Br}$. Blue curves in (a-c) represent the temperature profile.	1025
Figure XVI.22.13 Crystal structure of $\text{Li}_6\text{PS}_5\text{Br}$ shown in S2-/Br- site disorder.	1025
Figure XVI.22.14 Comparison on the lattice parameter and percentage of site disorder of $\text{Li}_6\text{PS}_5\text{Br}$, $\text{Li}_6\text{PS}_{4.8}\text{O}_{0.2}\text{Br}$, $\text{Li}_{5.5}\text{PS}_{4.3}\text{Br}_{1.5}$ and $\text{Li}_{5.5}\text{PS}_{4.4}\text{O}_{0.1}\text{Br}_{1.5}$	1025
Figure XVI.23.1 <i>Electrolyte Membrane Synthesis and Optimization</i> . Schematics of cold pressing, drop casting and slot-die coating techniques with optical photographs of the resulting electrolyte membranes.	1028
Figure XVI.23.2 <i>Characterization of Composite Membranes</i> . Cross-section SEM of flexible LLZO fiber-PEO-LiTFSI CPEs prepared by (a) dropcasting and (b) slot-die coating. (c) Critical current density determination for drop-casted (red) and slot-die coated (blue) membranes in Cu-Li half-cell configuration (d) Arrhenius plot of bulk ionic conductivity for composite and polymer solid state electrolytes.	1029
Figure XVI.23.3 <i>Nanofibers at the Interface</i> . (a) Schematic of the composite electrolyte-lithium metal interface. (b) XPS survey scan of the composite, showing no LLZO and only PEO-LiTFSI at the surface. (c) XPS core level spectra of the composite before and after 10 nm of Li metal was vacuum deposited. Scans 1-5 represent ~ 1 hour of reaction time. (d) EIS data from Li-Li symmetric cells with 0 wt% and 50 wt% LLZO nanofiber composites over 20 hours. (e) Critical current densities for 0 and 50 wt% LLZO composite electrolytes with different working electrodes and Li counter electrodes. (f) Schematic of mesoscale model used to determine the dendrite growth velocity with poor and good quality SEIs, which shows that stronger, homogeneous SEIs slow dendrite growth more than heterogenous, thin, weak SEIs. (g) Addition to the model in (f) where LLZO nanofibers can physically block growing lithium dendrites, showing that dendrites can slow	

- dendrite growth and prolong cell shorting by up to an order of magnitude depending on the current density. 1030
- Figure XVI.23.4 *Nanofiber Percolation Threshold and Conductivity in CPEs*. (a) Schematic of percolating object aspect ratio and calculated percolation thresholds (volume and weight percent) for LLZO nanofibers in a PEO-LiTFSI matrix. (b) Ionic conductivity of composite polymer electrolytes with 0, 2, 5, 10, and 50 weight percent LLZO nanofibers. 50 wt% corresponds to 20 vol% of the LLZO filler in the polymer matrix. (b) Scanning electron micrograph of the as-prepared composite electrolyte, showing that nanofibers are coated with thin layers of polymer and are likely not in direct contact with each other. 1032
- Figure XVI.23.5 *Undoped, Al-Doped, and Ga-Doped LLZO Nanofibers*. (a) XRD of LLZO nanofibers without added dopants and with Al^{3+} and Ga^{3+} dopants, all showing cubic phase. STEM HAADF images and EDX elemental mapping of (b) Al-doped and (c) Ga-doped LLZO nanofibers showing uniform dopant distribution across multiple nanofibers. 1033
- Figure XVI.24.1 Synthesis of crosslinked PEO-PFPE copolymer membrane. (a) Synthesis scheme; (b, c) Scanning electron microscopy (SEM) images of 60w:40w PFPE:PEO membranes made using acetonitrile (ACN)/hexafluorobenzene (HFB) (a) and tetrahydrofuran (THF)/n-methyl-2-pyrrolidone (NMP) (b) mixed solvents. Inset of (b,c), digital pictures of the membranes. 1037
- Figure XVI.24.2 Structure, morphology and thermal properties of crosslinked PEO-PFPE copolymer membranes. (a, b) Small angle X-ray scattering (SAXS) (a) and wide angle X-ray scattering (WAXS) (b) profiles of PFPE, xPEO, 40 PFPE and 60 PFPE in the pristine form and with LiTFSI salt. SAXS and WAXS measurements were taken at room temperature. (c) A scanning probe microscopy (SPM) phase image showing the surface morphology 60 PFPE electrolyte membranes at the nanometer scale. (d-f) Differential scanning calorimetry (DSC) of dry xPEO/PFPE electrolytes. (d) DSC thermogram (2nd heating) of pristine xPEO, PFPE, 60PFPE and 40PFPE. (e) DSC thermogram (2nd heating) of xPEO, PFPE, 60PFPE and 40PFPE infused with LiTFSI salt. (f) Glass transition temperature (T_g) of the hydrocarbon and fluorocarbon phases of the membranes as a function of PFPE weight%. The values used in this plot are from samples without LiTFSI salt. 1038
- Figure XVI.24.3 Ionic conductivity and oxidative stability of crosslinked PEO-PFPE membranes. (a,b) Ionic conductivity of crosslinked PEO-PFPE in dry (a) and plasticized (b) states. (c-f) The potentiostat hold method to determine the electrochemical stability window of 60PFPE-LiTFSI and xPEO-LiTFSI. (c, e) Current vs time (left vertical axis) and potential vs time (right vertical axis). The hold time at each voltage step was 1 hr. (d, f) Current at 1 hr vs potential. 1040
- Figure XVI.24.4 (a) Schematic representation of the fabrication process of Trilayer with Porous LICGCTM Scaffold. (b-g) SEM images of surface of the as-cast green ceramic tape (b), cross-section of the sintered tape (c-d), cross-section of the sintered tape after filling with crosslinked-PEO+LiTFSI and spray coating the two surfaces with linear-PEO+LiTFSI ("Trilayer with Porous LICGCTM Scaffold") (e-g). 1042
- Figure XVI.24.5 (a) Ionic conductivity of the unfilled LICGCTM scaffolds as a function of volume % of their porosity. (b) Ionic conductivity of the scaffolds compared to effective medium theory (EMT) calculations. The measured conductivities of the scaffold fall nicely on the GEMT curve, which predicts the conductivity of randomly dispersed percolated particles. Conductivity of another morphology – vertically aligned percolated particles - is also modelled using PBLM model as a comparison. (c) Arrhenius plot of the ionic conductivity of the Trilayer with Porous LICGCTM Scaffold. 1043
- Figure XVI.24.6 (a) Current v. time obtained during the transference number measurement, comparing the steady state current obtained after 10h of polarization, for the Trilayer with Porous LICGCTM Scaffold and the pure crosslinked-PEO+LiTFSI electrolytes. Note, one of the plots is shifted by an hour on the x-axis for ease of viewing the initial current values. (b) Voltage profiles of symmetric cells made with Trilayer with Porous LICGCTM Scaffold and crosslinked-PEO+LiTFSI electrolytes, cycled at 0.2 mA/cm², 2.5 h each strip/plate, at 70 °C. (c) Long-term cycling of the two symmetric cells shown in (b). 1044
- Figure XVI.25.1 (a) Schematic illustration showing the UV-polymerization route to synthesize the single lithium ion conducting SPE from the anionic monomer, crosslinker, and plasticizer. (b) Li⁺ transference

number measured by the potentialstatic polarization method of SIC-SPE. (c) Voltage-time profile of the Li-Li symmetric cells when cycling at 0.2 mA/cm ² and 0.1 mAh/cm ² showing the concentration overpotential of SIC-SPE. (d) Li ⁺ transference number measured by the potentialstatic polarization method of MIC-SPE. (e) Voltage-time profile of the Li-Li symmetric cells when cycling at 0.2 mA/cm ² and 0.1 mAh/cm ² showing the concentration overpotential of MIC-SPE.....	1048
Figure XVI.25.2 (a) Powder XRD (a) and impedance (b) at room temperature of as-synthesized Li _{5.5} PS _{4.5} Cl _{1.5}	1049
Figure XVI.25.3 Li _{5.5} PS _{4.5} Cl _{1.5} (LPSCl _{1.5}) show a voltage stability to Li metal (a) and up to 6.0 V (b) in solid state batteries in cyclic voltammetry (CV) tests. Li/LPSCl _{1.5} /LPSCl _{1.5} -C (cathode composition 0.9:0.1-LPSCl _{1.5} :Carbon black (w/w)) were collected on a Solartron 1455A with a voltage sweeping rate of 0.1 mV s ⁻¹ from 0.1 to 6 V.....	1049
Figure XVI.25.4 sXAS and PDF characterization of the polymer electrolytes. (a) carbon (b) oxygen (c) fluorine K-edge sXAS of PVDF mixed with NMP and vacuum dried. (d) PDF results of polymer, salts and polymer electrolytes.....	1050
Figure XVI.26.1 Conversion and molecular weight data from a 20K PLiMTFSI synthesis.	1053
Figure XVI.26.2 XRD data showing characteristic amorphous peak for both the 60K (red) and 20K (blue) PLiMTFSI.....	1054
Figure XVI.26.3 Conductivity of prepared PLiMTFSI single-ion conducting polymer films as a function of temperature and plasticizer (TMP and GCMA) content.	1054
Figure XVI.26.4 NMR data for GCMA polymerization with AIBN in DMSO (top) and ACPA in acetonitrile (bottom). The peaks at 5.7 and 6.0 correspond to the monomer, while the double-humped peak from 0.6-1.0 represent the polymer.....	1055
Figure XVI.27.1 ATIR data of the 5 Li sources studied: Supplier #1, Supplier #2, Supplier #3, Supplier #4 and ORNL Evaporated Li from 400 cm ⁻¹ to 4000 cm ⁻¹	1058
Figure XVI.27.2 Initial XPS data of the 5 Li sources studies: Supplier #1, Supplier #2, Supplier #3, Supplier #4 and ORNL Evaporated Li, focused on the Li1s (a), the C1s (b), and the O1s (c) peaks.	1060
Figure XVI.27.3 Depth profiling XPS data of the 5 Li sources studies Supplier #1, Supplier #2, Supplier #3, Supplier #4 and ORNL Evaporated Li focused on the Li1s peaks with the different Li, C, and O species denoted as a function of etching time. The estimated etching rate based on a SiO ₂ standard was 12 nm/min for an estimated etch depth of ~200 nm per 1000s.....	1060
Figure XVI.27.4 Representative load-displacement curves obtained in metallic lithium from a) commercial supplier 1 and b) commercial supplier 2. The data were obtained using a diamond Berkovich indenter tip, a target strain rate 0.05 1/s, and a target depth of 800 nm.	1061
Figure XVI.27.5 a) The average elastic modulus of lithium obtained from the two commercial suppliers. (b) The average hardness of lithium obtained from the two commercial suppliers and an evaporated lithium deposited at ORNL (data from the ORNL specimen were published in 2018).	1062
Figure XVI.27.6 a) plating and stripping data for symmetric Li/liquid electrolyte/Li cells at a current density of 0.2 mA/cm ² for 2.5 hours per cycle. b) EIS data after 10 cycles.	1063
Figure XVI.27.7 Li/PEO-LiTFSI/Li symmetric cycling. All cells were cycled under the same conditions at 0.1 mA/cm ² for 10 hours at 70 °C. a) Commercial supplier #1, b) commercial supplier #2, c) commercial supplier #3, d) commercial supplier #4, and e) evaporated Li. f) A plot of the thickness of the estimated interface including the surface layer and distinct Li ₂ O layers (excluding the mixed Li ₂ O/Li metal layer) vs. the resistance determined from the plating overpotential.....	1064
Figure XVI.27.8 Li/LiPSCl Argyrodite (NEI)/Li test under 5MPa of pressure at room temperature at a current density of 0.1 mA/cm ² for 10 hours. Red – Commercial supplier #3, Purple – Evaporated Li.....	1065

Figure XVI.28.1 Results of the large scale Li_3InCl_6 synthesis with 10% excess InCl_3 from Ethanol solution. Top: XRD shows no impurities other than Al substrate. Bottom left: Nyquist plot shows electrolyte is highly conductivity with some grain boundaries present after pressing at 5 MPa. Bottom right: Arrhenius plot shows product is a superionic conductor with low activation energy.....	1068
Figure XVI.28.2 Arrhenius plot of overall conductivity of Li_3InCl_6 as a function of different synthesis methods and Li_3InCl_6 excess amounts.	1069
Figure XVI.28.3 Nyquist plot (left) and Bode plot (right) showing pressure induced effects of Li_3InCl_6 conductivity.	1070
Figure XVI.28.4 Optical micrographs of Dreamweaver Gold porous membranes before and after Li_3InCl_6 infiltration from ethanol solution precursor.	1070
Figure XVI.28.5 <i>In situ</i> neutron diffraction of Li_3InCl_6 being synthesized from ethanol solution.....	1071
Figure XVI.28.6 Scanning electron micrograph (SEM) cross-sections of a Li-In alloy/NMC85 full cell that uses ethanol-derived Li_3InCl_6 as the bulk solid electrolyte and the electrolyte within the cathode. After 50 cycles we see extensive delamination in both the cathode- Li_3InCl_6 composite and also the bulk Li_3InCl_6 itself.	1071
Figure XVI.29.1 Scheme 1. Synthetic scheme and nomenclature of polyesters made for this project.....	1074
Figure XVI.29.2 Effect of salt concentration (r) on the T_g of PPM/LiTFSI and PEO/LiTFSI electrolytes. ..	1075
Figure XVI.29.3 a) Structures of a series of poly(alkyl malonates) synthesized for this project. b) Ionic conductivity (κ) (blue squares) and glass transition temperature (T_g) (red circles) of polymer electrolytes comprising 40 wt% of LiTFSI salt at 90°C.....	1076
Figure XVI.29.4 The effect of salt concentration r on ionic conductivity, κ , of PPM/LiTFSI (blue circles) and PEO/LiTFSI (black squares) electrolytes at 90°C. Data for PEO/LiTFSI electrolytes were taken from previous work. ¹	1077
Figure XVI.29.5 a) Structures of a series of poly(alkyl malonates) synthesized for this project. b) current fraction of polymer electrolytes comprising 40 wt% of LiTFSI salt at 90°C. PEO stands for benchmark poly(ethylene oxide).	1078
Figure XVI.29.6 The effect of salt concentration r on a) current fraction, ρ +, b) electrolyte efficacy, $\kappa\rho$ +, of PPM/LiTFSI (blue circles) and PEO/LiTFSI (black squares) electrolytes at 90°C. Data for PEO/LiTFSI electrolytes were taken from previous work. ¹	1078
Figure XVI.29.7 The effect of salt concentration r on salt diffusion coefficient, D , of PPM/LiTFSI (blue circles) electrolytes at 90°C.....	1079
Figure XVI.29.8 Concentration cell open-circuit potential (U) as a function of natural log molality ($\ln[m]$) at 90°C. The fit is shown in dashed line. Three data points at each salt concentration represents reproducibility of the data.	1079
Figure XVI.29.9 Linear sweep voltammetry (3–6 V vs Li^+/Li) of PPM and PEO electrolytes at 90°C. The scanning rate is 1 mV/s.	1080
Figure XVI.29.10 Chronopotentiometry curve of a sodium/polymer/sodium symmetric cell with a PPM/NaTFSI electrolyte at $r = 0.06$, under a current density of 0.125 mA/cm ² at 80°C. The inset is the normalized Nyquist plot before and after polarization.	1081
Figure XVI.30.1 Evolution of HEXRD patterns during solid-state synthesis of Li_3OCl	1083
Figure XVI.30.2 a) HEXRD results of the anti-perovskite electrolytes with different Cl and Br ratios. Red arrows indicate the LiCl impurities in Li_2OHCl , and b) HEXRD spectra near (110) and (200) peaks.	1084
Figure XVI.30.3 DSC results of the anti-perovskite electrolytes with different Cl and Br ratios. Red arrow points to the endothermal peak from the orthorhombic to cubic phase transformation in Li_2OHCl	1085

Figure XVI.30.4 Measured Li^+ conductivity of protonated anti-perovskite electrolyte pellets prepared using cold press.	1086
Figure XVI.30.5 Scanning electron microscopy images of cold-pressed electrolyte pellets from a) Li_2HOCl , and b) $\text{Li}_2\text{HOCl}_{0.75}\text{Br}_{0.25}$, showing the presence of big voids in pellets that can significantly reduce the nominal lithium-ion conductivity of the electrolyte pellets.	1086
Figure XVI.30.6 Evolution of HEXRD patterns showing the interaction between metallic lithium and Li_3OCl electrolyte during heating, showing great chemical compatibility up to 220°C	1087
Figure XVI.30.7 Comparison of X-ray diffraction patterns of Li_3OBr before and after aging in the glovebox for 1 month, showing a slow degradation of Li_3OBr during storage.	1088
Figure XVI.30.8 (a) Illustration of a sample environment to study the moisture sensitivity of electrolyte samples; (b) image of the working sampler holder integrated in sector 17BM of Advanced Photon Sources; and (c) evolution of Li_3OBr and its decomposition product during the exposure to 40% humidity (~ 1070 Pa moisture partial pressure).	1088
Figure XVI.31.1 (a) Synthesis procedure and sintering profile for $\text{Li}_{10}\text{B}_{10}\text{S}_{20}$. (b-d) LBS powders optical images.	1091
Figure XVI.31.2 X-ray diffraction of $\text{Li}_{10}\text{B}_{10}\text{S}_{20}$ in blue, compared to calculated spectrum in red.	1091
Figure XVI.31.3 (a) Electrochemical impedance spectroscopy of 450-micron pellet of $\text{Li}_{10}\text{B}_{10}\text{S}_{20}$ using 360 MPa pressure, stainless steel electrodes. (b) voltage stability window of $\text{Li}_{10}\text{B}_{10}\text{S}_{20}$ using carbon-LBS composite cathode, Li metal anode.	1091
Figure XVI.31.4 (a) Electrochemical impedance spectroscopy over several days of 450-micron pellet of $\text{Li}_{10}\text{B}_{10}\text{S}_{20}$ using 35 MPa pressure, Li metal electrodes. (b) The ionic conductivity of this pellet over 15 days.	1092
Figure XVI.31.5 (a-c) XPS of $\text{Li}_{10}\text{B}_{10}\text{S}_{20}$ powder: (a) $\text{Li}1s$; (b) $\text{B}1s$; (c) $\text{S}2p$. (d-f) XPS of $\text{Li}_{10}\text{B}_{10}\text{S}_{20}$ powder after reaction with Li metal: (d) $\text{Li}1s$; (e) $\text{B}1s$; (f) $\text{S}2p$	1092
Figure XVI.31.6 Critical current density and constant current (0.3 mA cm^{-2} , 0.3 mAh cm^{-2}) testing of Li-LBS-Li cells at room temperature, 35 MPa pressure.	1093
Figure XVI.32.1 Image of final electrode coating.	1096
Figure XVI.32.2 (a) Computed DFT formation energy for ground-state structures predicted by cluster expansion in BCC (red triangle), FCC (green dot) and γ -brass (magenta cross) lattice types. The convex hull of formation energy is marked with dashed line, under which single-phase regions are shaded with light red (BCC), light green (FCC) and light magenta (γ). The composition range $0.4 < x_{\text{Li}} < 0.6$ is enlarged in the middle. Phonon energy and entropy contributions are not included. (b) Predicted ground-state structures as marked with arrows in (a).	1096
Figure XVI.32.3 Schematics of (a) amorphous carbon and (b) graphitic carbon electrodes. (c) Schematic of an asymmetric cell with ABL. (d) Discharging profile of the asymmetric cell. Optical microscopy images of (e) amorphous carbon and (f) graphitic carbon ABLs after Li plating.	1098
Figure XVI.32.4 Characterization of core-shell structures. TEM confirms the shell thickness can be tunable. (Scale bar: 250 nm).	1099
Figure XVI.32.5 Scanning electron microscope (SEM) images of (a-b) NMC and (c-d) NMC/graphene composite. (e) XRD of NMC and NMC/graphene composite. (f) TGA result of NMC/graphene composite.	1100
Figure XVI.32.6 (a, b, c) XRD patterns and (c, d, e) Nyquist plots of $\text{Li}_{3-x}\text{Y}_{1+x}\text{Cl}_6$ ($0 \leq x \leq 0.13$) samples prepared from solid-state (a, d), co-melting (b, e) and mechanochemical synthesis (c, f).	1101

- Figure XVI.32.7 Comparison of normalized unit cell volumes (a) and room-temperature ionic conductivities (b) of $\text{Li}_{3-x}\text{Y}_{1+x}\text{Cl}_6$ ($0 \leq x \leq 0.13$) samples prepared by different synthesis methods. ▲ indicates trigonal phase and □ indicates orthorhombic phase. 1102
- Figure XVI.32.8 Thin LLZO film fabrication process (left). Schematic illustration of lamination step and effect of lamination pressure on properties of fabricated LLZO film (right). 1102
- Figure XVI.32.9 Debinding time vs. green body weight. The inset pictures are fabricated LLZO film with different debinding times. The white area in the central area of the LLZO film has a relatively low density because of incomplete debinding. 1103
- Figure XVI.32.10 Schematic view of sintering condition (upper) and effect of dead weight on the flatness of the sintered thin LLZO film (below). 1103
- Figure XVI.32.11 Picture of sintered LLZO films that were sintered at different temperatures. 1104
- Figure XVI.32.12 Property testing of different mol% of LiTFSI in SN. (a) Nyquist plot. (b) DC Polarization. (c) LSV. 1105
- Figure XVI.32.13 (a) Comparison of three possible methods for preparing the solid electrolyte-polymer composites. Note that the solution-precipitation method has an advantage of a high mechanical strength owing to its smaller polymer-domain size and uniformly distributed microstructure. (b) Schematic showing the preparation process of the solution-precipitation method. 1105
- Figure XVI.32.14 Morphological and structural changes with dissolution time in EtOH. (a-c) SEM images of (a) pristine LPSCl powder, (b) LPSCl precipitate after dissolution in EtOH for 5 min, and (c) after dissolution for 30 min. Scale bars in SEM images are 10 μm . (d) XRD results of LPSCl with a different dissolution time in EtOH. As the time increases, the intensities of the representative LPSCl peaks (denoted as a triangle) decreases. Please note that the sharp peak at $\sim 13^\circ$ and the bump peak at $\sim 20^\circ$ were from a different airtight XRD holder used in yellow and red patterns. (e) Ionic conductivities of LPSCl with different dissolution times. Note that a shorter dissolution time of LPSCl is preferred to exhibit a higher conductivity. 1107
- Figure XVI.32.15 Scanning electron microscope (SEM) images of LPSCl-PEO composites with the polymer content of 2%w, 8%wt, and 12% wt (from left to right). 1108
- Figure XVI.32.16 Chemical and Mechanical evaluations of LPSCl-PEO composite. (a-b) Elemental mappings of (O, P, S Cl) in LPSCl-PEO composites with 2 wt.% polymer content. Note that the composites are prepared by two different methods: (a) dispersion mix and (b) solution-precipitation methods. (Scale bar: 1 μm) 1108
- Figure XVII.1.1 (a) Calculated specific energy versus areal S loading for Li/S pouch cells with different E/S ratios assuming that the specific capacity and the average discharge voltage are 1,000 mAh/g and 2.05 V, respectively. (b). Configuration of interdigitated type battery winding for the pouch cell stacking. 1113
- Figure XVII.1.2 (a) Charge/discharge curves of 1.2 g-sulfur pouch cell using sulfur/macroporous host with double-end binding cathode under different current density ranging from 41.67 mA/g to 166.67 mA/g. (b). Cycling performance of 1.2-g-sulfur pouch cell using sulfur/macroporous host with double-end binding cathode at 83.33 mA/g. 1113
- Figure XVII.1.3 Weight analysis pie chart of the 1.2-g-sulfur pouch cell through interdigitated type battery winding. 1113
- Figure XVII.1.4 Charge/discharge curve of the 3d-omsh/ZnS,Co-N-C/S cathode at 0.1 C and the corresponding in situ HEXRD patterns. Points A/D and B/C indicate the critical voltage point of the appearance/disappearance of Li_2S (marked by the black boxes in HEXRD) and Li_2S_2 (marked by the blue boxes in HEXRD), respectively. 1115
- Figure XVII.1.5 In situ UV-vis observations and the corresponding discharge curves of (a) KB/S and (b) 3d-omsh/ZnS,Co-N-C/S cathodes at 0.1 C. Inset of (a): digital photograph of the in situ cell of KB/S cathode after testing; inset of (b): digital photograph of the in situ cell of 3d-omsh/ZnS,Co-N-C/S cathode after testing. The

color bars indicate the derivative of reflectance, with pink color means positive number, blue color corresponds to negative number. 1116

Figure XVII.1.6 ToF-SIMS (a) depth profiles and (b) 3D rendering of S- secondary ions distribution of cycled (I) KB/S, (II) ANL-macroporous carbon/S, (III) Macroporous carbon/ZnS/S, (IV) Macroporous carbon/Co-N-C/S, and (V) Macroporous carbon/ZnS,Co-N-C/S cathodes after 100 cycles at 1 C. (c) ToF-SIMS S-element mappings on the surface of cycled Li metal anode of (I) Li-KB/S, (II) Li-Macroporous carbon/S, (III) Li-Macroporous carbon/ZnS/S, (IV) Li-Macroporous carbon/Co-N-C/S, and (V) Li-Macroporous carbon/ZnS,Co-N-C/S cells after 100 cycles at 1 C. The color bar in (b) and (c) represents the signal intensity, with yellow color represent high intensity and black color represent low intensity. The region outlined by red dash-line in (c) indicated the location of migrated sulfur species. 1116

Figure XVII.1.7 (a) The charge/discharge curve of the Li/S pouch cell using ANL double-end binding host with an E/S ratio of 2.5 $\mu\text{L}/\text{mg}$. (b) BatPaC simulation of the cell specific energy of our Li/S pouch cell based on various cell capacities. 1118

Figure XVII.1.8 Electrochemical characterization of Li/S cells at various E/S ratios. The 1st discharge voltage curves and EIS results of sulfur cathode with S loading of $14.3 \text{ mg}/\text{cm}^2$ at $167.5 \text{ mA}/\text{g}$ and E/S ratios of (a, d) $10 \mu\text{L}/\text{mg}$, (b, e) $4 \mu\text{L}/\text{mg}$, and (c, f) $2 \mu\text{L}/\text{mg}$. Inset in (d) shows the equivalent circuit. (g-i) shows the impedance evolution during discharge process at (g) $10 \mu\text{L}/\text{mg}$, (h) $4 \mu\text{L}/\text{mg}$, and (i) $2 \mu\text{L}/\text{mg}$. The red dotted circles in Figure a-c correspond to the ex situ point shown in Figure g-i. 1118

Figure XVII.1.9 Structure and composition analysis of cathode material. (a) SEM image of OMSH host material. (b, c) TEM and corresponding EDS chemical mapping of OMSH-Se/S (interesting elements are S, Zn, Se, and Co). High-resolution XPS spectra of (d) S 2p and (e) Se 3d of OMSH-SeS cathode material. (f) TGA curve of OMSH-SeS cathode material under argon atmosphere from room temperature to 450°C 1119

Figure XVII.1.10 Electrochemical characterizations of OMSH-Se/S cathode material. a) Cycling performance of OMSH-Se/S cathode in HFE-based electrolyte at 160 mA g^{-1} with a areal Se/S loading of $2 \text{ mg}/\text{cm}^2$. b) Cycling performance of OMSH-Se/S cathode with higher areal Se/S loading conditions ($3.0 \text{ mg}/\text{cm}^2$ and $5.8 \text{ mg}/\text{cm}^2$) in HFE-based electrolyte at $200 \text{ mA}/\text{g}$. c) Voltage profiles of various cycles of OMSH-Se/S cathode under high areal Se/S loading ($5.8 \text{ mg}/\text{cm}^2$) condition in HFE-based electrolyte. Voltage profiles of OMSH-Se/S cathode ($\sim 6.5 \text{ mg}/\text{cm}^2$) that rested for 1 week after 2 initial cycles in d) DME- and e) HFE-based electrolytes. f) Cycling performance of OMSH-Se/S cathode after resting for 1 week in HFE-based electrolyte. Hollow and solid symbols in (a, b, f) represent coulombic efficiency and discharge capacity, respectively. 1120

Figure XVII.2.1 3-D pore-scale models for SPC (a) and LPC (e); The electrolyte and air distribution along the electrode depth x for SPC (b) and LPC (f); Top and cross-sectional view of Micro-computed tomography (micro-CT) images of SPC (c) and LPC (g); Tortuosity and flow path of SPC (d) and LPC (h). 1124

Figure XVII.2.2 (a) Schematic of a single-particle-layer electrode with low tortuosity in vertical and planar direction. (b) SEM image of sulfur/carbon materials around $50 \mu\text{m}$. (c) Reconstructed micro-CT image of single-particle-layer electrode. (d) Discharge and charge curves of the single-particle-layer electrode during first cycle. (e) Cycling performance of single-particle-layer electrode at different porosity. (f) Cycling performance of single/multi-particle-layer electrodes. 1125

Figure XVII.2.3 Ex situ synchrotron XRD characterization of the LPC and SPC at different depths of discharge. Typical first cycle discharge/charge curves and the corresponding XRD patterns ($l = 0.19316$) for the LPC (a, b) and SPC (c, d). Successive diffraction patterns are vertically offset by 6,000 relative to that of the pristine cathode (point 0, no offset). 1126

Figure XVII.2.4 X-ray nano-computed tomography (X-ray nano-CT) images of sulfur concentration distribution in (a) NKB11, (b) NKB12 and (c) NKB15, respectively. The scale bar is $6 \mu\text{m}$. (d) Discharge/charge curves of different NKB/S electrodes in the first cycle. (e) Discharge/charge curves different NKB/S electrodes after 40 cycles. (f) Cycling performance of different NKB/S electrodes in 40 cycles at low E/S ratio. 1127

Figure XVII.2.5 (a) Discharge/Charge curves of 5mg/cm ² NKB11/S electrode at different cycles. (b) Cycling performance of the 5mg/cm ² NKB11/S electrode. (c) Discharge/Charge curves of NKB11/S-Polymer electrodes at different cycles. (d) Cycling performance of NKB11/S-Polymer cathodes.....	1128
Figure XVII.3.1 SEM images of the pristine a) PMTH and b) Li ₆ PS ₅ Cl. c) SEM image and EDS mapping of the ball-milled PMTH cathode composite. d) Comparison of ¹ H NMR spectra between the pristine PMTH and the ball-milled PMTH cathode composite.	1132
Figure XVII.3.2 a) Conversion reaction mechanism of PMTH molecule. b) CV profiles at 0.05 mV s ⁻¹ . c) Galvanostatic voltage profiles and corresponding dQ/dV curves. d) Cycling performance at 0.1 C and e) rate performance at 25°C. Cross-sectional SEM images of the cathode-SSE pellet f) before (inset is the thickness measurement) and g) after cycling. EDS mapping of cathode SSE interface h) before and i) after cycling. Top-view SEM images of cathode and SSE surface j) before and k) after cycling.....	1134
Figure XVII.3.3 a) Prolonged cycling performance at 60°C. b) Galvanostatic voltage profiles of high active mass loading PMTH cathode and c) its cycling performance at 0.05 C. d) Energy density comparison of the state-of-the-art organic cathodes reported in Li-organic ASSBs.	1135
Figure XVII.3.4 (a) Color changes of 5 mM Li ₂ S ₆ solution with different carbon samples of (1) baseline, (2) NC750, (3) NC800, (4) NC900, (5) NC950, and (6) SuperC65; (b) Corresponding HPLC chromatograms of the derivatized polysulfides mixtures; (c) HPLC chromatograms of the derivatized polysulfides (5 mM Li ₂ S ₆) mixtures with NC800 and PWA.	1136
Figure XVII.3.5 (a) Cycling performance and (b) Galvanostatic charge-discharge curves of S/NC800 pouch cell with the E/S ratio of 10 uL mg ⁻¹ ; (c) HPLC chromatograms of S/NC800 and S/Ketjenblack pouch cells after 3 cycles.	1138
Figure XVII.4.1 The synthesis scheme of 1,1,1,2,2,3,3,4,4-nonafluoro-6-(2-methoxyethoxy)hexane (F ₄ EO ₂).	1140
Figure XVII.4.2 Li-S cell cycling results as a function of cycle number at 0.1 C rate with different electrolyte compositions. (a) Sulfur specific gravimetric discharge capacities. (d) Coulombic efficiencies.	1142
Figure XVII.4.3 SEM surface images of the cycled Li-S battery electrode using different electrolyte solutions. (a-c) Li-anodes, and inset photo images are the surface of Li metal. (d-f) sulfur cathodes. (a,d) T5FDLiTFSI electrolyte. (b,e) T5FDLiTFSI-FSI electrolyte. (e,f) T5FDLiFSI electrolyte.....	1143
Figure XVII.4.4 High-resolution XPS spectra of the surface of cycled Li-anode after washing off the electrolyte. (a) fluorine 1s and (b) sulfur 2p.	1144
Figure XVII.5.1 (a and b) SEM images of the nanostructured C-S cathode, (c) Voltage profiles of C-S composite electrodes at different C-rates using 100 μm Li and E/S ratio of 10 μl mg _{sulfur} ⁻¹ and (d) the corresponding cycling stability.	1149
Figure XVII.5.2 (a) Photo of the C-S cathode from the disassembled cell after 200 cycles (Previous figure, d) and immersed in DOL/DME solvents and the schematic of protecting S samples for TGA Photo of Li metal from the disassembled cell after 200 cycles; (b and c) TGA curves and the data table of the above cycled C-S cathode; (d) The schematic of TGC quantification of Li metal loss including the sample of the cycled Li metal by polysulfide shuttle from the disassembled cell after 200 cycles (Previous figure, d); (e) The Li mass quantified by TGC.	1150
Figure XVII.5.3 (a) The schematic of the HPLC-UV methodology used to investigate the LiNO ₃ amount; (b) The cycling behavior of the nanostructured C-S and the bulk C-S cathode in baseline electrolyte with E/S ratio of 10 μl mg _{sulfur} ⁻¹ and 100 μm Li. The S loading of is 3.8 mg _{sulfur} cm ⁻² of the nano C-S and 2.52 mg _{sulfur} cm ⁻² of the bulk C-S; (c) HPLC-UV spectra of the fresh electrolyte, DOL/DME solvent, LiNO ₃ and LiTFSI in DOL/DME solvent, and the cycled electrolyte of the nano C-S cathode; (d) HPLC-UV spectra of the pristine electrolyte and cycled electrolyte for bulk C-S cathode; (e) The standard curve of LiNO ₃ concentration ranging from 0.5 mM to 1 mM.	1151

Figure XVII.5.4 (a) The roll-to-roll S electrode casting at GM; (b) The corona treatment by plasma to increase the adhesion to the Al current collector; (c) Electrochemical performance of 5.2 mg_{sulfur} cm⁻² sulfur cathode electrode, c) charge-discharge profiles and d) discharge-discharge capacities and CE vs. cycle number; (e and f) The schematic and the photos of the design of a Li-S pouch cell; (g) The voltage profiles of various cycles of the 1 Ah Li-S pouch cell delivering a super high energy density of 400 Wh kg⁻¹. 1152

Figure XVII.5.5 (a) The schematic of the synthesis of the HATN/CNT composite; (b) the SEM image of HATN/CNT, and the digital photo of the composite before and after polymerization (inset); (c) The voltage profile of HATN/CNT-S cathode without S melt infusion in baseline electrolyte of 1 M LiTFSI in a DOL/DME mixture (1:1, v/v) with 2wt.% LiNO₃, using 100 μm Li and E/S ratio of 6 μl mg_{sulfur}⁻¹; (d) The Cryo-FIB SEM image of the cross-section of the UCSD nano C-S cathode with highly porous structure; (e) The Cryo-FIB SEM image of the cross-section of the HATN/CNT-S cathode via electrochemical infusion, which is highlighted with a low average 2-D tortuosity (τ) of 1.22 and a bulky particle size of >10 μm; (f) The EDX spectrum of the selected area (red rectangle in 4e), showing the successful electrochemical S infusion. 1154

Figure XVII.5.6 (a) The top-view of SEM images of the pristine HATN/CNT-S cathode and after 1st discharge (b) with a similar S loading of ~5 mg cm⁻² under a small magnification; (c) Voltage profiles of the HATN/CNT-S cathode with ~6.30 mg_{sulfur} cm⁻², using 100 μm Li with an E/S ratio of 6 μl mg_{sulfur}⁻¹ and an E/C ratio of 5 g/Ah. The inset schematics illustrates the cell assembly; (d) The cycling behavior of the optimized HATN/CNT-S cathode at 0.1 C, 1 C = 1000 mA g⁻¹. 1155

Figure XVII.5.7 (a and b) The lab-scale trial of the HATN monomer synthesis at Ampcera; (c) The scaling-up synthesis of HATN monomer at Ampcera. 1156

Figure XVII.5.8 (a) The photo of Li chip immersed into NewEle for 2 days; (b) The cycling behavior of the UCSD Nano C-S cathode in baseline electrolyte of 1 M LiTFSI in a DOL/DME mixture (1:1, v/v) with 2wt.% LiNO₃ and in 10 mM this NewEle additive, using 100 μm Li and E/S ratio of 10 μl mg_{sulfur}⁻¹. Cycling behavior by S-specific capacity and areal capacity; (c) The schematic of Cryo-FIB-SEM used to characterize lithium and sulfur in this project; (d) Cryo-FIB images of the cycled Li in the NewEle system (cross-section), and (e) the EDX spectrum of the red dash zone of the cycled Li metal with quantitative elemental analysis. 1158

Figure XVII.6.1 Cycling performance of functional ECs embedded CFM-S (Li anode) cycled in coin cell configuration with S loading 2.8mg cm⁻² and electrolyte (E)/ sulfur (S); E/S = 4μl mg⁻¹ S. 1162

Figure XVII.6.2 Cycling performance of S infiltrated electronically conducting framework materials cycled in coin cell configuration with S loading 4.6 mg cm⁻² and electrolyte (E)/ sulfur (S); E/S = 4μl mg⁻¹ S. 1162

Figure XVII.6.3 Cycling performance of S infiltrated carbon coated electronically conducting framework materials cycled in coin cell configuration with S loading 4.2 mg cm⁻² and electrolyte (E)/ sulfur (S); E/S = 4μl mg⁻¹ S. 1163

Figure XVII.6.4 Electrochemical cycling performance and Coulombic efficiency of CFM-S containing FAM cycled between 1.7-2.8V. 1163

Figure XVII.6.5 Electrochemical cycling performance and Coulombic efficiency of IOFM-S cycled between 1.7-2.8V. 1164

Figure XVII.6.6 First principles theoretical calculations showing (a) phase stability of non-lithiated alloys; (b) lithiated alloy phase stability. 1165

Figure XVII.6.7 Electrochemical cycling performance and Coulombic efficiency of CFM-S electrode cycled between 1.8-2.8V at C/20 and 1.7-2.8V at C/10 current rates. 1166

Figure XVII.6.8 Electrochemical cycling performance and Coulombic efficiency of POFM1-S electrode cycled between 1.8-2.8V at C/20 and 1.7-2.8V at C/10 current rates. 1167

Figure XVII.6.9 Activation barriers for Li-vacancy hopping. 1168

- Figure XVII.6.10 Electrochemical cycling performance and areal discharge capacity of synthesized MCA4 electrode cycled at 1 mA current for 1 h for alloying and de-alloying, respectively for 30 cycles. 1169
- Figure XVII.7.1 (a) Reduced heating procedure (*i.e.*, decreased heating time upon SPAN synthesis) was used to increase the sulfur content in obtained SPAN powders so as the specific capacity. (b) XRD spectra of SPAN cathodes synthesized with varying heating time from 2 to 7.5 h. (c) Cycling performances of SPAN cathodes synthesized with varying heating time from 2 to 7.5 h. 1174
- Figure XVII.7.2 (a) Initial capacities of SPC-1a, SPC-1b, and SPC-1c cathodes. (b)-(d) Cycling performance of SPC-1a2 (b), SPC-1a6 (c), and SPC-1a10 (d) cathodes in carbonate electrolytes. The areal active material loading is around 2 mg/cm². The cells were activated at 0.05 A/g (based on composite weight) for the 1st cycle and then cycled at 0.1 A/g. 1175
- Figure XVII.7.3 (a) Cycling performances of optimized SPC-1 cathodes with reduced heating procedure of 4 h in carbonate electrolyte. (b) Optimized SPC-1 cathodes (blue) delivered enhanced specific capacities over 630 mAh/g compared with SPAN baseline (red) in carbonate electrolyte. 1175
- Figure XVII.7.4 (a) Cycling performances of optimized SPC and SPAN cathodes in carbonate electrolyte at current density of 100 mA/g. The SPC cathodes with show much improved specific capacity (initial specific capacity > 1000 mAh/g based on SPC weight, or > 800 mAh/g based on cathode weight) than that of routine SPAN cathode. (b) CV curves of SPC and SPAN cathode-based batteries at scan rate of 0.1 mV/s. 1176
- Figure XVII.7.5 (a) Charge-discharge curves of optimized SPC-2 cathode-based battery at current density of 100 mA/g in carbonate electrolyte. (b) Cycling performance and CE evolution of optimized SPC-2 cathode-based battery at current density of 100 mA/g in carbonate electrolyte. 1177
- Figure XVII.8.1 Designing redox mediators (RMs) for all-solid-state lithium-sulfur batteries (ASSLSBs). (a) The proposed reaction scheme of the RMs for ASSLSBs. Effective RMs solubilized in the solid polymer electrolytes (SPEs) shuttle electrons between current collectors and the surfaces of isolated Li₂S particles. During the charging process, RM_{ox} chemically oxidizes Li₂S to polysulfides while RM_{ox} is reduced to RM_{red} (step A, chemical reaction). RM_{red} diffuses toward the current collector and is oxidized to the initial state of RM_{ox} near the current collector surface (step B, electrochemical reaction). The light blue color indicates the SPEs. (b) Schematic first charge profiles of ASSLSBs with (orange line) and without RM (blue line). A high charging voltage (~ 4 V versus Li⁺/Li) is necessary to activate Li₂S in the first charge process. Li₂S is directly converted to elemental sulfur through a two-phase transformation. Grey: Li₂S particles; yellow: sulfur. (c-e) Cyclic voltammograms (CV) curves and chemical structure of (c) AQT, (d) AQC, and (e) LiI in PEO/LiTFSI solid polymer electrolytes (SPEs) at a scan rate of 0.1 mV s⁻¹. The dotted line is the equilibrium potential of Li₂S (~2.15 V versus Li⁺/Li). 1180
- Figure XVII.8.2 Operando XAS to understand RM chemistry in ASSLSBs. Operando S K-edge XAS spectra of (a) bare Li₂S cathodes and (d) Li₂S@AQT cathodes in polymer-based ASSLSBs for the first charge process. XAS spectra of Li₂S (2473.5 eV) and S (2472.7 eV) shown in the bottom are used as references. The pre-edge feature at 2470.7 eV is identified as the fingerprint of LiPSs from the terminal S. (b) Contents of Li₂S and S calculated from two-phase fitting of the XAS spectra in (a) as a function of test time. The corresponding charge curve shows a high energy barrier around 4 V for Li₂S activation. Schematics for proposed Li-S reaction mechanism in ASSLSBs, using Li₂S cathodes (c) without/(f) with AQT RM. (e) The average chain length of LiPSs as a function of the state of charge for Li₂S@AQT cathodes during the first charging. 1181
- Figure XVII.8.3 Electrochemical performance of Li₂S cathodes without/with AQT redox mediator (RM) in ASSLSBs. (a) Cycling performance and Coulombic efficiency of Li₂S cathodes without/with AQT at 0.1 C for 30 cycles. (b) Typical charge-discharge voltage profiles of Li₂S cathodes without/with AQT at the 5th cycle and the 20th cycle at 0.1 C. Nyquist plots of (c) the Li₂S-Li cell and (d) the Li₂S@AQT-Li cell before and after different cycles. Inset in the first figure shows the zoom-in Nyquist plot for the Li₂S@AQT-Li cell. 1182
- Figure XVII.8.4 Electrochemical performance of Li₂S cathodes with AQT RM in ASSLSBs. (a) Voltage profile at the 2nd cycle of the Li₂S@AQT cell with a high mass-loading (3.7 mg cm⁻²) at a current density of 0.25 mA cm⁻². (b) Cycling performance of the high loading cell. (c) Specific capacity of Li₂S@AQT cathodes cycled from 0.06 to 0.48 C. All cells are operated at 60°C. 1182

Figure XVIII.1.1 A) Open circuit potential of SEI vs Li metal (reference electrode) when exposed to O ₂ gas. B) Cycling profile of the SEI vs Li metal cell in Ar atmosphere <i>after</i> forming exposing the SEI to O ₂ . Cyclic voltammograms of the pristine SEI and SEI exposed to O ₂ gas C) 1 st scan and D) 2 nd scan, indicating the relatively reversible CV current peak at ~3.0 V vs Li ⁺ /Li.	1186
Figure XVIII.1.2 A) Schematic of interlayer-based electrochemical cell we developed for studying the catalyst B) Constant current charging profile of the bare SEI-based cathode. Deposited Li ₂ O ₂ over the surface on a carbon paper gas diffusion layer (GDL), C) high and D) low magnification. SEM of the carbon paper GDL after charging in an interlayer position (no electrical contact to circuit at E) high and F) low magnification.	1187
Figure XVIII.1.3 Attenuated total reflectance-Fourier transform infrared spectroscopy of A) as formed solid electrolyte interphase (SEI) catalytic layer, B) SEI exposed to oxygen for 6 hours, C) SEI deposited with Li ₂ O ₂ , D) SEI with Li ₂ O ₂ delithiated, and E) the separator used in the cell in D.	1188
Figure XVIII.1.4 X-ray photoelectron spectroscopy of the SEI-coated cathode before and after exposure to O ₂ at A) C 1s and B) O 1s.	1189
Figure XVIII.1.5 A) Deep discharge of Li-O ₂ using carbon paper and using SEI-coated carbon paper at 50 uA cm ⁻² until 3 mAh cm ⁻² or until voltage cutoff of 2 V vs Li ⁺ /Li is reached. Potentiostatic hold of Li-O ₂ battery at 2.5 V vs Li ⁺ /Li. B) The cumulative capacity by integrating the current response. C) The current response of the carbon paper and the SEI-coated carbon paper. D) Expanded view of the current response showing details of the current peak, indicating passivation.	1190
Figure XVIII.1.6 Microscopy of discharge product. SEM of SEI-carbon paper A) before and B) after discharge. SEM of carbon paper C) before and D) after discharge. E) Cryogenic TEM of discharge product clearly indicating the Li ₂ O ₂ spatially sits over the SEI-layer rather than inside. F) SAED of the discharge product indicating it is mostly Li ₂ O ₂	1190
Figure XVIII.1.7 (a) The first five cycles of a Li-O ₂ cell with rGO/GDL cathode with a current density 0.05 mA/cm ² , (b) The first five cycles of a Li-O ₂ cell with Ir ₃ Li-rGO/GDL cathode (c) Deep discharge of Ir ₃ Li-rGO cathode in a Li-O ₂ cell, (d) Raman spectra of deep discharged Ir ₃ Li-rGO cathode in a Li-O ₂ cell showing strong LiO ₂ peaks at different areas.	1192
Figure XVIII.2.1 (a) Galvanostatic cycling results of Li-air cell with SnS/rGO and MoS ₂ cathodes at the current density of 0.3mAcm ⁻² . No redox mediator was used for both batteries. The dashed black line represents the charge potential of MoS ₂ at the 1 st cycle. (b) Cycle numbers vs charge/discharge potential for the fresh (blue) and replaced (red) Li anode after 50 cycles of operation of the SN catalyst. (c-d) Linear sweep voltammetry results of SnS/rGO NFs, MoS ₂ NFs, Au NPs and Pt NPs electrodes under ORR and OER with a sweeping rate of 10mV/s.	1196
Figure XVIII.2.2 DFT calculations for (top) six O ₂ adsorption on SnS considered in DFT calculations (an example of O ₂ adsorption structure is given for C1) and (bottom) O ₂ adsorption energies for the six sites. .	1197
Figure XVIII.2.3 G4MP2 free energies for LiO ₂ disproportionation to Li ₂ O ₂ in DMSO solvent.	1197
Figure XVIII.2.4 Characterization results of the anode in Li-air battery with RM of SnI ₂ . The results include (a) XPS of Sn 3d region after 5 cycles. (b) HAADF and inserted bright field image of the Sn protected anode. (c) EDS mapping of the anode surface. The area taken was from the rectangular box marked in figure b. All scale bars represent a length of 100nm, (d) EELS results from the same region of the Sn protected anode surface. (e) Anode EIS results. The dots represent the experimental data, and the lines represent the fitted data. Symmetrical study of electrolyte with the cell consists of two Li metal electrodes for (f) attenuation test under different current densities and (g) long-time durability test of electrolyte at a constant current density of 0.5mAcm ⁻²	1199
Figure XVIII.2.5 DFT calculations for (a) initial and final structure of SnI ₂ reacting on a Li metal (100) surface, (b) initial and final structure of SnI ₂ reacting on a SnS surface.	1200

Figure XVIII.3.1 **LSV and EIS results.** (A-B) Linear sweep voltammetry results of (NbTa)_{0.5}BiS₃ NFs, Au and Pt nanoparticles (NPs) coated cathode electrodes under: (A) CO₂RR and (B) CO₂ER. (C-D) EIS measurements for (NbTa)_{0.5}BiS₃ NFs coated cathode catalyst at different applied overpotentials during: (C) CO₂RR and (D) CO₂ER. Insets show control experiments in DMSO electrolyte (without IL). (E-F) EIS measurements of different catalysts tested during: (E) CO₂RR and (F) CO₂ER with the overpotential of 150 mV. 1204

Figure XVIII.3.2 **Electrochemical performance of Li-CO₂ battery.** Discharge/charge curves at the current density and capacity of: (A) 0.5 mA/cm² and 0.2 mAh/cm² (2000 mAh/g), (B) 0.5 mA/cm² and 0.5 mA/cm² (5000 mAh/g), and (C) 0.3 mA/cm² and 0.3 mA/cm² (3000 mAh/g). (D) Rate capability results of (NbTa)_{0.5}BiS₃. (E) Cycling results for (NbTa)_{0.5}BiS₃ with ZnI₂, only (NbTa)_{0.5}BiS₃, (NbTa)_{0.5}BiS₃ with LiI. (F) Comparison of gravimetric current density vs capacity of the Li-CO₂ battery for our work (black stars) with other works. 1205

Figure XVIII.3.3 **DFT calculations.** (A-B) Surface energies with/without spin polarized surface. Note that due to the very small energy, the Nb terminated (110) surface energy does not show in (A). (C) The top and side views of (i) Ta-terminated, (ii) Nb-terminated, (iii) Bi-terminated (NbTa)_{0.5}BiS₃ (110) surfaces. The black lines are the periodic boundaries of the supercells. (D) The potential-dependent mechanistic analysis of Li₂CO₃ and C formations on a Nb-terminated (NbTa)_{0.5}BiS₃ (110) surface. The adsorption configurations are present in the bottom panels. The Nb, Ta, Bi, S, C and O atoms are in green, blue, purple, yellow, brown, and red, respectively. 1206

Figure XIX.1.1 Structure characterization. (a) XRD of pristine NaMnFeCoNiO₂; (b) HAAD-STEM image of pristine NaMnFeCoNiO₂; (c) HAAD-STEM image of NaMnFeCoNiO₂ after 1st charge; (d) schematic illustration of phase transformation during 1st charge..... 1211

Figure XIX.1.2 In situ XRD with up cut-off voltage of 4.1 V..... 1212

Figure XIX.1.3 (a) In situ XANES and (b) in situ Fourier transformed EXAFS for copper and manganese during the 1st charge-discharge process. (c) evolution of bond lengths for fitted short copper-oxygen (top panel), long copper-oxygen (middle panel), and manganese-oxygen (bottom panel) during charge-discharge. The error bar for copper-oxygen bond length is very small and cannot be seen in the figure. 1213

Figure XIX.1.4 Cu L₃ edge (left panel) and O K-edge (right panel) for P3-NaCuMnO at pristine state, charged to 3.66 V, and charged to 4.10 V. The vertical dotted lines indicate the position of main peak, and the upward arrows indicate the rising of shoulder peaks and their positions. 1214

Figure XIX.2.1 (a) Cycling performance of strained O3 NaNi_{0.4}Mn_{0.4}Co_{0.2}O₂ cathode within 2.0–3.8 V (vs. Na/Na⁺) at 0.08C (1C=180 mA g⁻¹). (b) Normalized capacity retention of O3 NaNi_{0.4}Mn_{0.4}Co_{0.2}O₂ cathode at different cycling conditions. The capacity loss rate in (b) is the slope of the linear fitting curve of the capacity. 1216

Figure XIX.2.2 In situ synchrotron characterization during charge/discharge. In situ Ni K-edge XANES of strained O3 NaNi_{0.4}Mn_{0.4}Co_{0.2}O₂ within 2.0–4.4V: (a) during charge, (b) during discharge and (c) 2D contour plot during charge/discharge. Voltage profiles and the corresponding 2D contour plot of in situ SXRD patterns during charge/discharge of O3 NaNi_{0.4}Mn_{0.4}Co_{0.2}O₂ cathode within (d) 2.0–4.4 V and (e) 2.0–3.8 V. The colour in (c-e) represent the intensity, with red for highest and blue for lowest..... 1217

Figure XIX.2.3 (a) Ni, (b) Co and (c) Mn K-edge XANES of strained O3 NaNi_{0.4}Mn_{0.4}Co_{0.2}O₂ cathode at different charge/discharge states..... 1218

Figure XIX.2.4 (a) Low and (b) high magnification, (c) high-resolution bright-field TEM image, (d) SAED pattern, (e) GPA analysis and (f) atomic structural model of the strained O3 NaNi_{0.4}Mn_{0.4}Co_{0.2}O₂. Inset in (c) is the zoomed-in view of the region marked by white square. The color in (c) represent the intensity, with red for highest and blue for lowest. θ is the angle between layered direction and strain direction. The yellow, red, blue, grey and purple spheres in (f) represents Na, O, Ni, Co and Mn atoms, respectively. 1219

Figure XIX.2.5 TEM characterization on cycled O3 $\text{NaNi}_{0.4}\text{Mn}_{0.4}\text{Co}_{0.2}\text{O}_2$ cathode particle (2.0–4.4 V for 100 cycles). (a) Low and (b) high magnification TEM image. (c) Zoomed-in view of the dashed square area in (b). (d–e) Zoomed-in views of the dashed rectangle area in (a). (f) Zoomed-in view of dot-circle area in (a). 1220

Figure XIX.2.6 Strain relaxation under different condition. Low and high magnification TEM images of O3 $\text{NaNi}_{0.4}\text{Mn}_{0.4}\text{Co}_{0.2}\text{O}_2$ cathode after 100 cycles within 2.0–4.4 V at different condition: (a–b) 0.08 C under room temperature; (c–d) 0.2 C under 55°C, and (e–f) 1 C under room temperature. 1221

Figure XIX.2.7 In situ HEXRD characterization in coin cell configuration at 25°C. (a) The waterfall plot and (b) contour plot of in situ HEXRD patterns for CuMgTi-571 within 2.0–4.3 V. (c) Evolution of cell parameters and cell volume during the charge/discharge process. 1222

Figure XIX.2.8 The 2D contour XRD plots of de-sodiated (a) CuMgTi-571 and (b) NaMnO_2 during the heating from 30°C to 450°C at 5°C min⁻¹, the tested samples during heating are de-sodiated cathode powder scraped from 4.2 V-charged cathodes. 1223

Figure XIX.2.9 XRD pattern (a, b), voltage profile (c, d), and cycle performance (e, f) of NMF111 (a, c, e) and NMF112 (b, d, f); ($i = 10$ mA/g for the first three cycles and 30 mA/g for the next cycles). 1224

Figure XIX.2.10 XRD pattern (a, b), voltage profile (c, d), and cycle performance (e, f) of NMF111 (a, c, e) and NMF112 (b, d, f); ($i = 10$ mA/g for the first three cycles and 30 mA/g for the next cycles). 1225

Figure XIX.2.11 (a–c) Powder XRD patterns of $\text{Na}[(\text{Ni}_{0.5}\text{Mn}_{0.5})_{1-x}\text{Fe}_x]\text{O}_2$ ($x = 0, 1/3$, and $2/3$), and (d) changes in the c/a lattice parameter ratio before and after air-exposure. 1226

Figure XIX.2.12 SEM particle morphologies of $\text{Na}[(\text{Ni}_{0.5}\text{Mn}_{0.5})_{1-x}\text{Fe}_x]\text{O}_2$ ($x = 0, 1/3, 1/2, 2/3$, and 0.8) before and after air-exposure for five days. 1226

Figure XIX.2.13 **X-ray photoelectron spectroscopy (XPS)** Ni2p spectra of the pristine and air-exposed (a) $\text{Na}[(\text{Ni}_{0.5}\text{Mn}_{0.5})_{1-x}\text{Fe}_x]\text{O}_2$, (b) $\text{Na}[(\text{Ni}_{0.25}\text{Mn}_{0.25}\text{Fe}_{0.5})_{1-x}\text{Fe}_x]\text{O}_2$, and (c) $\text{Na}[(\text{Ni}_{0.1}\text{Mn}_{0.1}\text{Fe}_{0.8})_{1-x}\text{Fe}_x]\text{O}_2$; (d) open-circuit voltages profiles of $\text{Na}[(\text{Ni}_{0.5}\text{Mn}_{0.5})_{1-x}\text{Fe}_x]\text{O}_2$ 1227

Figure XIX.3.1 (top left) Two-dimensional contour plot and (top right) selected *in situ* high-temperature synchrotron XRD patterns of NTO collected from room temperature to 775 °C during the heating process in air. Note that the x -axes have been converted to 2θ $\text{CuK}\alpha$ values. Le Bail fitting of XRD patterns collected at (bottom left) room temperature using the *Immm* space group and (bottom right) 200°C using the *Cmcm* space group. The crystal structures of NTOs heated at room temperature and 200°C visualized with VESTA are also shown. Gold spheres represent Na atoms and blue spheres represent Ti in octahedral sites. Modified from reference 6. 1232

Figure XIX.3.2 (a) Raman spectra and (b) laboratory XRD patterns of NTOs heated *ex situ* in air at temperatures ranging from 60°C to 800°C. Taken from reference 6. 1233

Figure XIX.3.3 Galvanostatic discharge-charge voltage profiles of sodium half cells containing 500 °C-heated NTO cycled between 0.1 and 2.0 V vs. Na^+/Na (a) without and (b) with an initial ‘activation’ cycle between 0.05 and 2.0 V vs. Na^+/Na . The inset in (a) shows the discharge capacity as a function of cycle number. (c) The second cycle galvanostatic discharge-charge voltage profiles between 0.1 and 2.0 V vs. Na^+/Na of NTOs heated to the indicated temperatures (d) the corresponding dQ/dV plots, and (e) capacity retention over 50 cycles. For the initial cycle, a cycling voltage window of 0.1 – 2.0 V vs. Na^+/Na is used for 60 °C- and 100°C-heated NTOs, while 0.05 – 2.0 V vs. Na^+/Na was used for 350 °C-, 500 °C-, and 800 °C heated NTOs. (f) Galvanostatic intermittent titration technique (GITT) voltage profile of 500 °C-heated NTO, the inset shows the evolution of electrochemical impedance spectroscopy (EIS) spectra as a function of discharge potentials. All the cells were cycled at a current rate of 8 mA g⁻¹ (0.008 mA cm⁻²) using a sodium metal anode and a solution of 0.5 M NaBPh₄ in DEGDME as the electrolyte. Taken from reference 6. 1234

Figure XIX.3.4 Capacity retention of sodium half-cells containing NTO-60°C or NTO-500°C as a function of cycle number in the 0.1–1.0V region (left) and the 1.0–2.0V region (right). Taken from reference 6. 1235

Figure XIX.3.5 *Ex situ* synchrotron XRD patterns of electrodes containing NTO-500°C (a) and NTO-60°C (b) discharged and charged to the indicated potentials. Taken from reference 6. 1235

Figure XIX.3.6 *Ex situ* HRTEM images of individual 500 °C-heated NTO particles in the (a) pristine state, and after initial discharge to (b) 0.1 and (c) 0.05 V vs. Na⁺/Na. Their corresponding fast Fourier transform (FFT) patterns of the local regions highlighted by the red squares are shown in (d-f). Taken from reference 6. 1236

Figure XIX.3.7 *Ex situ* Ti K-edge XAS spectra of pristine, discharged and charged NTO-60°C (a) and NTO-500°C (c) electrodes. Pre-edge regions are shown in (b) and (d). 1237

Figure XIX.4.1 (a) Cycling performance of mixed electrolytes based on tetraglyme- fluorinated solvent (VC, FEC, BTFE or TTE) in 90:10 (%vol.) with 1M NaBF₄ in Na||NaNMC half-cell at C/10 rate, mass loading: 3.0 – 4.0 mg/cm²; at voltage range of 2 – 4.2 V. (b-c) Cycling performance of rational electrolytes of NaFSI: co-solvent: TFP = 1: 1.5: 2 in mol. used for full cell of HC||NaNMC (mass loading 1.5 mAh cm⁻²), 3 formation cycles at 0.05 C and cycling at 0.2 C rate (1C = 200 mA/g), voltage range of 1.2 – 4.2 V. 1241

Figure XIX.4.2 Electrochemical performance of HC||NaNMC full cells. **a**, cycling performance of HC||NaNMC full cells using different electrolytes cycled at 0.2 C after three formation cycles at 0.1 C. The cathode loading is 1.5 mAh cm⁻². **b–d**, Voltage curves as a function of cycle number of HC||NaNMC full cells using NaPF₆/EC:EMC (**b**), NaFSI/TFP (**c**) and NaFSI/DMC:TFP (**d**) electrolytes. **e–f**, Rate performance of HC||NaNMC full cells at different charge C-rates with a constant discharge rate at 0.33 C (**e**) and different discharge C-rates with a constant charge rate of 0.33 C (**f**) after three formation cycles at 0.1 C. 1242

Figure XIX.4.3 XPS characterization to identity SEI dissolution. **a,d**: The absolute value of difference of quantified SEI atomic composition ratios between the cycled and cycled-soaked hard carbon anodes as a function of the sputtering thickness. **b, c, e, f**: XPS spectra of C 1s (**b, e**), P 2p (**c**), and N 1s (**f**) of the hard carbon anodes (signal depth = 0 nm). The cycled hard carbon anodes were cycled in NaPF₆/EC:EMC (**a**, upper of **b** and **c**), NaFSI/TFP (**d**, upper of **e** and **f**) electrolytes for 100 cycles. The cycled-soaked hard carbon anodes were soaking cycled hard carbon electrodes with EC: EMC (**a**, bottom of **b** and **c**) and TFP (**d**, bottom of **e** and **f**) solvents for 50 h. 1243

Figure XIX.4.4 Voltage vs time and CE calculated using the reported protocol of cycling in three different electrolytes. 1244

Figure XIX.4.5 Capacity retention of Na||NVP half-cell in DEGDME and TEGDME based electrolytes for 100 cycles 1245

Figure XIX.4.6 (a) Sodium stripping/plating efficiency in two different electrolytes (testing condition: plating 4 mAh cm⁻² and fully stripping to 1 V and cycling for 10 cycles at 0.5 mA cm⁻²). (b) Cycling performance of half-cell Na||NVP cathode in 10 cycles at 0.2C. 1245

Figure XIX.4.7 (a) Initial charge-discharge profile of Cu||NVP cell in two electrolyte; (b) Cycling performance of the anode-free sodium batteries for 50 cycles (formation cycle: 1st cycle: 0.1 C, charge CV, cycling: 2nd – 7th cycle: 0.2 C, charge CV, 8th cycle: 0.3 C, discharge 0.2 C, charge CV; NVP loading mass: 3-4 mg/cm²) 1246

Figure XX.1.1 Electrochemical performances of NC, NMC, and NATM cathodes in coin cells with Li-metal anode and in pouch cells with graphite anode. (a) Charge and discharge curves and (b) dQ dV⁻¹ curves of the 3rd C/10 formation cycle. (c) Rate performance tests with a constant C/5 charge rate. Cyclability evaluation in (d) coin cells for 100 cycles at a C/3 rate between 2.8 and 4.4 V and in (e) pouch cells for 800 cycles at a C/2 rate between 2.5 and 4.25 V. (f) Normalized peak areas of the raw TOF-SIMS data of the interphasial fragments on the cathodes after 800 cycles. Each sample is sputtered three times on three different locations to yield normalized average peak areas. (g) SEM images of pristine and cycled cathodes after 800 cycles. The scale bars in (g) are 20 μm. 1251

Figure XX.1.2 (a) Schematic illustrations of the LP57 electrolyte and LSE. (b) Raman spectra of the three electrolytes in the range of 600 to 1000 cm⁻¹. (c) ⁷Li NMR spectra of different electrolytes to study Li⁺ coordination. (d) SEM images of LiNiO₂ microspheres with an average diameter of 12 μm (secondary particles). The inset zooms into the surface of a secondary particle to show the primary particles. (e) Self-

discharge performance of LiNiO_2 cathodes tested at 45 °C. (f) Cycling performances of LiNiO_2 with the LP57 electrolyte (300 cycles), LiFSI-based LHCE (M47, 300 cycles), LSE(EC/EMC) (500 cycles), and LSE(FEC/EMC) (600 cycles) at room temperature with 2 mA h cm^{-2} loading. The charge rate was C/2 and the discharge rate was 1C in the voltage range of 2.8 – 4.4 V. STEM images at the surface of a cycled LiNiO_2 particle with (g) the LP57 electrolyte and (h) the LSE. (i) Coulombic efficiency (CE) of the developed LSE measured with a Li || Cu coin cell. The test current and capacity were, respectively, 0.5 mA cm^{-2} and 1 mAh cm^{-2} 1252

Figure XX.1.3 (a) Molecular design from DME to DEE. (b) MD simulations for 1 M LiFSI/DME, 1 M LiFSI/DEE, 4 M LiFSI/DME and 4 M LiFSI/DEE. (c) Aurbach method to determine the average Li metal CE using different electrolytes. (d) Cycling performance of thin-Li | high-loading NMC811 full cells under limited electrolyte and practical cycling conditions. 1253

Figure XX.1.4 Chemical species changes during XPS measurement. (a) Atomic ratio as a function of three SEI preparation methods. (b) SEI atomic ratio as a function of sampling region. (c) SEI atomic ratio as a function of duration of SEI inactivity under ultrahigh vacuum. (d) Atomic concentration of model SEI (Li_2CO_3 + LiF mixture) for different Ar^+ sputtering times. 1254

Figure XX.1.5 *Operando* DSC measurements (dotted curves for electrochemical test and solid curves for the measured heat flux) of novel ether-based M47, ED2, T3, Stanford (1M LiFSI in FDMB) electrolytes and traditional carbonate electrolyte (1M LiPF_6 in EC/DMC (1:1)) for TARGRAY NMC 811 that were charged and held at 4.5 V, while ramp heating and isothermally holding at 30 °C, 45 °C and 60 °C for 20h, **a)** Al-coated MTI coin cell parts **b)** Al-coated Hohsen coin cell with Al foil added on cathode side. 1255

Figure XX.1.6 (a) XPS study of coin cell components. (b) Heat evolved for NMC 811 with the M47 electrolyte using the aluminum protected Hohsen and MTI cells. (c, d) Studies of X4 (PNNL) and FDMB (Stanford) electrolytes. Ex-situ DSC profiles of electrolyte alone, electrolyte + Targray NMC811 charged to 4.8 V, and electrolyte + Li metal anode after charge. (e, f) Cycling and Heat evolution of coin cells cycled between 4.4 and 2.8 V at C/10 current rate. 1256

Figure XX.1.7 (a) The 10th charge/discharge curves and (b) Coulombic efficiency of Li/Cu batteries in HCE, LHCE, and F5DEE electrolytes (at 1 mA cm^{-2} current density and 1 mAh cm^{-2} areal capacity) 1257

Figure XX.1.8 (a) Nyquist plots of the bare PE and LATP-coated PE separators. (b) cycling performance of the Li||NMC811 batteries with bare PE or ultra-thin LATP-coated PE separator. 1258

Figure XX.1.9 (a) Aurbach coulombic efficiency of Li||Cu cell in different electrolytes, (b) charge curves of different electrolytes with various resting time, (c) electrochemical performance of the NMC811||Li coin cells tested in different electrolytes, and (d) wettability of the electrolytes on Celgard separators and Li metals after 1st charge. 1259

Figure XX.1.10 Morphology of Li-metal anode after 10 cycles: (a-c) top-view SEM images and (d-f) cross-view images of Li anodes in different electrolytes. 1260

Figure XX.1.11 11 Charge-discharge curves of Li||SPAN half cells in (a) 4 M LiFSI in DME, (b) the nitrate-reinforced electrolyte; and (c) long-term cycling performance in both electrolytes. 1261

Figure XX.1.12 (a) Li plating/stripping efficiency and (b) cycling performance of Li||SPAN full cell in nitrate-reinforced electrolyte 1261

Figure XX.1.13 Capacity retentions and voltage profiles of high areal capacity (> 6 mAh cm^{-2}) Li||SPAN cells in different electrolytes. (a) Charge/discharge areal capacity retention of Li||SPAN cells with different electrolytes. (b) Voltage profiles of Li||SPAN cells with different electrolytes. Cycle numbers versus Sand's capacity of cells with different electrolytes based on data measured (c) without and (d) with separator. Cells were cycled under C/20 for 2 cycles, and then followed by C/5 cycling. 1263

Figure XX.1.14 The XPS depth profiling of deposited Li metal. Chemical evolution of F 1s, O 1s, C 1s, and Li 1s of (a) Bisalt electrolyte and (b) Gen 2 electrolyte before and after 3 weeks of resting in its corresponding electrolyte. 1264

- Figure XX.1.15 (a) Average CEs of Li||Cu cells with HCEs using six solvating solvents. (b) Average CEs of Li||Cu with SS4-based LHCEs and E-baseline. (c) Li deposition morphologies on Cu electrodes at a current density of 0.5 mA cm^{-2} for a capacity of 1 mAh cm^{-2} 1265
- Figure XX.1.16 Charging/discharging profiles of Li||SPAN cells at a current density of C/20 with (a) E-baseline, (b) SS4-LHCE-1, and (c) SS4-LHCE-2. (d) Performances of Li||SPAN cells with studied electrolytes at a current density of C/5 in the voltage range of 1 – 3 V. 1266
- Figure XX.1.17 (a) Ionic conductivities at different temperatures. (b) Charge-rate capability of Li||SPAN cells with the studied electrolytes at a constant discharging current density of C/5 in the voltage range of 1 – 3 V. 1266
- Figure XX.1.18 Sulfurized Pyridine Polymer for Battery (A) Structure of three polymers before and after sulfurization (B) IR for SPAN and SP4VP ; (C) Charge/Discharge curves for SPAN, SP2VP and SP4VP in liquid battery. (Cathode Weight Ratio: Active Material: Carbon Black: Binder 8:1:1, with LFP EC/DMC Electrolyte, Charge/Discharge rate 0.2C) 1268
- Figure XX.1.19 a) The cycling performance and the voltage profiles of SPAN synthesized at three different temperatures: b) 300°C (300SPAN), c) 450°C (450SPAN) and d) 550°C (550SPAN). 1269
- Figure XX.1.20 Functional groups and structure of SPAN. (A) XPS spectra for SPAN synthesized at different temperature; (B) Compositional ratio in SPAN derived from XPS results shown in (A); and (C) molecular structure of SPAN. 1270
- Figure XX.1.21 Characterizations of thin film SPAN. (a) photo of thin film SPAN synthesized on-top of Ti substrate. (b) FIB-SEM image of the cross-section of thin film SPAN on Ti substrate. Top-view SEM images for the (c) precursor (polyacrylonitrile) thin film and (d) SPAN thin film. (e) STEM-EDX mapping of thin film SPAN and (f) FTIR spectra of the powder and thin film SPAN. (g) Schematic and (h) results of the electrical conductivity test for SPAN thin film before and after the 1st cycle. 1271
- Figure XX.1.22 The effect of morphology control on limiting the corrosion of Li in liquid electrolyte. a) Schematics of stacking pressure control set up. b) Trend of Li^0 mass retention (%) of Li plated under 2 different stacking pressure (coin cell pressure and 350 kPa pressure) in Gen 2 electrolyte. c) The comparison between Li^0 mass retentions (%) of Li plated in Gen 2 electrolyte with 350 kPa and in Bisalt electrolyte in coin cell. d-k) The top-view and cross-sectional SEM images of the deposited Li metal in Gen 2 electrolyte: under coin cell pressure after d, h) freshly deposited, e, i) after 7 days of resting and under 350 kPa pressure after f, j) freshly deposited, g, k) after 7 days of resting. 1272
- Figure XX.1.23 (a) Electrochemical performance of Li/Cu cells at 1 mA cm^{-2} . (b) Coulombic efficiency of Li/Cu cells at 1 mA cm^{-2} and 1 mAh cm^{-2} for 400 cycles. (c) Galvanostatic Li plating/stripping profile of Li/Cu cells at 1 mA cm^{-2} and 2 mAh cm^{-2} . (d) Long-term cycling of Li/Li symmetric cell with the additive $\text{Mg}(\text{ClO}_4)_2$. (e) Rate performance of symmetrical cell. SEM top-view/cross-section images of cycled Li-metal anodes (100 cycles) obtained from LHCE (f, g) without and (h, i) with the additive..... 1273
- Figure XX.1.24 Electrochemical characterizations of the Li/NCM811 cells. (A) Charge and discharge curves of Li/NCM811 cells with LHCE with and without $\text{Mg}(\text{ClO}_4)_2$ additive at C/10 rate for 100 cycles. (B) Charge and discharge profiles of LHCE with additive under various rates. (C) Rate performance, long term cycling performance, and Coulombic efficiency of the Li/NCM811 cells with LHCE with and without $\text{Mg}(\text{ClO}_4)_2$ additive 1274
- Figure XX.1.25 (a, b) Selected galvanotactic charge and discharge curves and CE versus cycle number of Li||Cu coin cell using LTO@PE separator. The electrolyte is the 1.49 M lithium bis(fluorosulfonyl)imide (LiFSI) in a mixture of DME and 1,1,2,2-tetrafluoroethyl-2,2,3,3-tetrafluoropropyl ether (TTE), with DME and TTE a molar ratio of 1.2:3. The deposition capacity is 1 mAh cm^{-2} at a current density of 1 mA cm^{-2} with a volume of $60 \mu\text{L}$ for each coin cell. In this testing procedure, a given amount of Li metal is plated on a Cu foil and then stripped off with a cutoff voltage of 1 V vs Li/Li^+ 1275
- Figure XX.1.26 (a, b) Selected galvanotactic charge and discharge curves of $50 \mu\text{m}$ Li||NMC622 (4 mAh cm^{-2}) full cell using PE and LTO@PE separators. (c) Capacity versus cycle number of $50 \mu\text{m}$ Li||NMC622 full cell.

All cells were charged and discharged at C/10 for the first formation cycle and then cycled at a C/3 charge and discharge in the voltage window of 2.7–4.4 V. The electrolyte was LHCE, with a volume of 60 μ L for each coin cell.....	1275
Figure XX.1.27 Initial data showing no significant impact to the specific capacity as a function of cathode thickness.	1276
Figure XX.1.28 Top-view (left) and cross-sectional view (right) of electrochemically deposited Li metal on Cu foam in LHCE.....	1276
Figure XX.1.29 (a) The initial discharge/charge profiles of Li SPAN cells with different electrolytes at C/10 rate. Sampling points (I, II, III and IV) for XPS characterizations are marked with dots and numbers. (b) One SPAN structure used in AIMD simulation. (c, d) S 2p and F 1s XPS spectra collected on the surfaces of SPAN cathodes at different discharge states (points I, II and III) and charge state (point IV) in (c) LPF-carbonate and (d) LFSI-ether electrolytes, respectively. (e, f) N 1s XPS spectra at signal depth of 0 nm for SPAN (e) at point I in LPF-carbonate and (f) at point IV in LFSI-ether. (g, h) S 2p, F 1s and N 1s XPS spectra collected on the surfaces of (g) pristine SPAN and (h) SPAN after 5 cycles in LFSI-ether. (Signal depth = 10 nm).	1277
Figure XX.1.30 Crystal structure of Li_7NbN_4 as the typical LIC with Li-ion channels in [100] and [110] directions. Green arrows denote the hopping of Li-ions/vacancies for the different Li-hopping pathways. ..	1279
Figure XX.1.31 Potential energy profiles for Li-mobility in [100] (red) and [110] (blue) directions.	1279
Figure XX.1.32 XPS depth profiles for (top) HCE and (bottom) LHCE electrolyte cells at (a, d) 10°C, (b, e) 25°C, and (c, f) 45°C during formation cycles.	1280
Figure XX.1.33 Comparison of different results developed using the eCAD method. A) using coin cell data at C/20 and C/10, b) with different cathode formulations, cell configurations and electrolytes, c) comparison to galvanostatic intermittent titration (GITT) results and d) comparison of eCAD derived state-of-charge (SOC) and XRD determined SOC.....	1282
Figure XX.1.34 Analysis of the formation cycle of a Li-NMC622 cell using the eCAD technique. (a) The charge and discharge voltage profiles and the associated $V_{\text{IR-free}}$ profiles. Also presented is the pseudo-OCV vs. SOC curve, which is obtained from a validated Li-NMC622 cell during an initial RPT at C/20. (b) The reconciled charge and discharge $V_{\text{IR-free}}$ vs. SOC profiles in correspondence with the Li content in NMC622.	1284
Figure XX.1.35 (a) Charge capacity retention curve of the Li-NMC622 cell in the cycle aging test. (b) Projections of useful life based on charge capacity retention as a function of cycle number. (c) Projections of useful life based on the Li inventory retention and CAM utilization as a function of cycling rate	1285
Figure XX.1.36 a) SPAN powders with over 10 g per batch. b) XRD pattern of SPAN powders after vulcanization and removal of elemental sulfur. c) Discharge curves of SPAN prepared at different sealing states. d) Cycling performances of Li-SPAN cells with different SPAN mass loadings.	1286
Figure XX.1.37 (a) Optimization of slurries for doctor-blade casting reproducible and high-quality SPAN electrodes. (b) Discharge curves of a typical SPAN electrode and (c) discharge capacities vs. cycling number for 6 batches SPAN electrodes based on Gen 2 recipe.	1287
Figure XX.1.38 Electrochemical performance of sulfur cathodes with areal sulfur loading of (a,b) 3.75 mgS/cm^2 and (c,d) 5.2 mgS/cm^2	1288
Figure XX.1.39 Photo of Testing cell within oil bath during testing.....	1288
Figure XX.1.40 Ultrasonic transmission image of the fresh cell and end of life (EOL) cell.....	1289
Figure XX.1.41 Operando atomic force microscopy of lithium plating in three stages. (a) SEI growth on copper at +30 mV vs. Li/Li^+ potential prior to the lithium plating. Measurement over 25 hours reveals dual microstructure (grain + particles) which roughens with time. (b) Lithium nucleation showing a broad distribution of nuclei sizes. (c) Later-stage lithium growth showing faceted grain structure. The amount of charge passed is indicated in the figure.	1290

- Figure XX.1.42 Operando electrochemical atomic force microscope images of lithium metal deposited in LiFSI-1.2DME-3TTE electrolyte: (a) before indentation and (b) after indentation to measure the soft SEI thickness (c) over 6 hours. 1291
- Figure XX.1.43 μ -XRF maps for Ni, Co, and Mn of a pristine NMC811 electrode using 1 μ m focusing optics. 1292
- Figure XX.1.44 (a) Photograph of the three Li-S pouch cells used in operando synchrotron diffraction experiments with points being probed marked with red squares. (b) Voltage profile for the three cells. Blue: GM-1 (high loading, longest calendar aging). Red: GM-2 (high loading). Green: GM-3 (low loading). Cells were evaluated with a CC-CV-rest protocol. 1292
- Figure XX.1.45 (a) Points exhibiting a typical response during cycling. (b) Points with low activity. 1293
- Figure XX.1.46 Characterization of the electrolyte structure. (a) X-ray PDF data for low (1M) and high (5M) concentration LiFSI electrolytes with PC, DMC, or DME as the solvent. (b) Molecular structure of the three solvents and the FSI anion. Carbon atoms are shown in black, hydrogen in dark blue, oxygen in red, nitrogen in green, and sulfur in purple. (c) Comparison of measured and calculated (using the electrolyte structure determined by MD simulation) PDF patterns for HCE and LCE DME electrolytes, and of (d) partial PDFs calculated from MD simulations for pairs of Li-anion oxygen (blue) and Li-solvent oxygen (orange). 1294
- Figure XX.1.47 PDF results comparing SPAN structural changes during cycling in the UCSD electrolyte (left) and the DOL/DME electrolyte (right), with the peak corresponding to the C-S bond distance highlighted. . 1295
- Figure XX.1.48 Electrochemical performance of Li||NMC76 cells using different electrolytes. Charge-discharge profiles from selected cycles within 2.8V-4.8V. The baseline electrolyte is 1M LiPF₆ in EC||EMC (3:7) and the ‘with additive’ electrolyte is the baseline electrolyte with 1% LiDFP (by weight) or 2% LiDFP (by weight) added. (b) Electrochemical impedance spectroscopy (EIS) results of Li||NMC76 after 200 cycles using different electrolytes. (c) Equivalent circuit for EIS modeling (R_b : contact resistance, R_{sf} : surface film resistance, R_{ct} : charge transfer resistance). (d) EIS fitting results for Li||NMC76 cells after 200 cycles with different electrolytes. 1296
- Figure XX.1.49 (a) HPLC-UV chromatograms of five different standards of elemental S in DME: 0.0151mM, 0.0756mM, 0.378 mM, 0.7556mM and 0.9445mM. (b) Calibration curve obtained by plotting the area under the S peak in HPL-UV chromatogram against the S concentration. (c) HPLC-UV chromatogram of derivatized polysulfides using methyl triflate as a derivatization agent. (d) Plot of logarithm of retention time of a particular derivatized polysulfide against the number of S atoms in it. 1297
- Figure XX.1.50 3D reconstruction of deposited Li metal plated under different stacking pressures resulting in different Li porosities: (a) 50 kPa and 43.57% porosity; (b) 150 kPa and 36.90% porosity; (c) 250 kPa and 8.61% porosity and (d) 350 kPa and 0.51% porosity. (e) Li metal corrosion rate and its correlation with the porosity of the freshly deposited Li. All Li is plated in Gen 2 electrolyte. A total amount of 0.318 mAh of Li is plated at a rate of 0.5 mA/cm² for each sample. 1298
- Figure XX.1.51 Schematic of methodology to quantify and track inventory losses in Li-S battery 1299
- Figure XX.1.52 (a) Chromatograms of different Elemental Sulfur Concentrations, and (b) the calibration curve for Elemental Sulfur. 1300
- Figure XX.1.53 Near the anode surface, solvated Li⁺ in LCE electrolyte complex (top) diffuses through the electrolyte guided by the anion high electron affinity. In HCE (bottom left) Li⁺ gets trapped in a thick 3D network that is broken only through anion reduction and thick SEI formation. In LHCE, the presence of the diluent in the 2nd solvation shell disrupts the strong cation-anion interaction and allows Li⁺ migration with barriers comparable to LCE. 1301
- Figure XX.1.54 Evolution of SEI morphology at the Li metal surface in a 5M LiFSI in DMC solution from AIMD/classical MD simulations. Left: Well defined regions of amorphous Li oxide connected by less dense regions of LiF_x and LiS_xN_y structures. Right: Blue and gray are outer and inner surfaces enclosing Li oxide volumes. 1302

List of Tables

Table ES- 1: Subset of EV Requirements for Batteries and Cells	xvi
Table 1: Subset of Requirements for Advanced High-Performance EV Batteries and Cells. (Cost and Low Temperature Performance are Critical Requirements).	3
Table I.2.1 Percent change in cell values between year 1 and year 2 deliverable cells	33
Table I.3.1 LCFC-EV Neocarbonix Battery Parameters	36
Table I.5.1 Comparison of Our Technology to Current Slurry Casting Technology.....	79
Table I.5.2 Proposed 2-layer Electrode Design for High Loading Cells	81
Table I.5.3 Comparison of Dry vs Slurry-cast NMC Cathode Tortuosity Calculated from Nanotomography and Electrochemical Measurement.....	82
Table I.5.4 Summary of Electrodes Fabricated (Batch 1-14).	85
Table I.5.5 Summary of Electrodes Fabricated (Batch 15-23).	86
Table I.5.6 Average Porosity and Tortuosity of the High-loading Dry Printed and Slurry Cast Electrodes.	87
Table I.6.1 A comparison in first-cycle efficiency, C/20 and C/3 capacities among different cathode materials using half coin cells	92
Table I.6.2 A comparison in C/3 capacity, DCR, discharge rate capability, fast charge capability and initial cathode-specific energy density of single-layer pouch cells among different cathodes	93
Table I.7.1 Budget period 1 summary and status updates of key performance deliverables	97
Table I.7.2 Below captures all the proposed milestone and corresponding status updates All Budget Period-1 milestones were completed and preparations started towards meeting Budget Period-2 objectives, as summarized below:	98
Table I.11.1 End of Program Cell Performance Objectives.....	120
Table I.11.2 Baseline cell technology gap analysis table.....	124
Table II.4.1 Summary of FDMB- based materials.....	156
Table II.4.2 DoE variables used to determine optimized monoalkylation reaction conditions	157
Table II.4.3 New materials based on monomethyl-tetrafluorobutanediol	158
Table III.1.1 Major details on Li-based brines in the U.S. and North America.....	220
Table III.1.2 Mine production and reserves of phosphates across different supply sources..... (USGS Phosphate Rock Data [1000 metric tons]. Contained phosphorous is about 10 times lower.)	223
Table III.2.1 Total Impact of Proposed Solutions.....	231
Table III.3.1 Comparison of different Soxhlet extractors.	239
Table III.3.2 XRD data showing details of phase change in recycled cathode material.....	249
Table III.3.3 Elemental composition for relithiated NMCs	253
Table III.3.4 Half-cell data for relithiated cathodes from solvent Y process.....	253
Table III.3.5 Redox mediator cost and capacities	260
Table III.3.6 Capacities for materials relithiated using new and old redox mediators.....	263

Table III.3.7 Elemental composition for re-annealed upcycled products measured using GDOES and EDS (values in parentheses).....	270
Table III.3.8 Half-cell data for upcycled products.....	270
Table III.3.9 ICP-MS results of SC-NMC111-100g.....	277
Table III.3.10 ICP-MS results for etched solution and etched powder.....	279
Table III.3.11 Rietveld refinement results of the prepared NCM622 cathodes	281
Table III.3.12 EverBatt Modeling of ReCell Processes in FY22.....	304
Table III.3.13 Spatially resolved compositional data for ORNL upcycled sample received in Q1. Site locations refer to positions indicated in Figure I.1.90a. Compositions are reported as a relative atomic percent, such that the sum (Ni + Mn + Co) = 1.	316
Table III.3.14 Spatially resolved compositional data for ORNL upcycled sample received in Q3, showing significant improvement in homogeneity as compared to the sample received in Q1 (prior table). Site locations refer to positions indicated in Figure I.1.90b. Compositions are reported as a relative atomic percent, such that the sum (Ni + Mn + Co) = 1.	316
Table III.3.15 Temperatures of interest from the nail penetration experiments.....	319
Table III.3.16 Developed and optimized solvent-based processes	322
Table III.4.1 Average Coulombic Efficiency at C/3 and C/5 with Cycling in E1 Electrolyte.....	332
Table III.5.1 ICP results of recycled NMC622 cathode materials	337
Table III.5.2 SBC results of the control sample and recycled NMC622.	338
Table III.5.3 ICP results of the control from Farasis.	342
Table IV.2.1 Anode microstructure ionic transport coefficients, experimentally measured with electrochemical impedance spectroscopy (EIS), fitted in a macroscale P2D model, and calculated from microstructure analysis.	356
Table IV.2.2 Single-layer pouch cells fabricated at the CAMP facility and distributed to teams.	360
Table V.1.1 Design standards certifications to be used for the rack design. Source: NREL	383
Table V.1.2 Important design parameters for the advanced rack design. Source:NREL.....	384
Table VI.2.1 Status of cell testing deliverables in FY2022	406
Table VI.3.1 2022 USABC Battery Abuse Testing Changes	409
Table VI.5.1 Summary of Electrode Library Distributions	423
Table VI.6.1 PEGDA polymer electrolyte compositions.....	427
Table VI.6.2 Si Electrodes Compositions.....	430
Table VI.7.1 Articles Tested for USABC	434
Table VI.7.2 Articles Tested for Benchmark.....	434
Table VI.7.3 Articles Tested for Low Cobalt	435
Table VIII.1.1 Batch-to-Batch Reproducibility of PC-Milled Silicon for SCP Baseline	451
Table VIII.2.1 Electrolyte composition	459
Table VIII.6.1 Cell Performance data summary for Pre-lithiated Anodes.....	488
Table VIII.6.2 Cell Performance data summary for Lithium Metal Anodes	488

Table VIII.6.3 Li Deposition system manufacturing performance	488
Table VIII.6.4 Proposed milestone and corresponding status updates	490
Table VIII.7.1 Summary of measured quantities and their standard deviation from key Budget Period 1 300 mAh-class cell builds using a 3.6 mAh/cm ² NMC622 cathode with 3.2 g/cc electrode density.	498
Table VIII.7.2 Summary of measured quantities and their standard deviation from key Budget Period 2 300 mAh-class cell builds using a 5.1 mAh/cm ² NMC 622 cathode with 3.3 g/cc electrode density.	498
Table VIII.7.3 Summary of modeled energy density values for key cell builds from Budget Period 1 and Budget Period 2. An updated model was used to improve the accuracy of the modeled GED value.....	499
Table VIII.7.4 Summary of modeled energy density values for the high loading, high pressure case, showing a projection to 3 Ah and 100 Ah size. Approximately 800 Wh/L and 270 Wh/kg are modeled in the 100 Ah cell size.	499
Table VIII.7.5 Summary of modeled energy density values for the high loading, high pressure case, where the NMC 622 cathode is directly substituted with input parameters taken from coin cell data, tested using high nickel NMC 811-type material, but otherwise uses the same design parameters.	502
Table VIII.7.6 Summary of modeled energy density values for a possible future cell design with a pathway to hitting the program gravimetric energy density target.....	502
Table VIII.8.1 Electrochemical Objectives for DOE Project – EE0009187.....	505
Table VIII.9.1 Target cell performance	511
Table VIII.10.1 Capacity and Cycle Life of the Si Anodes	515
Table VIII.11.1 Description of Gen2 LHCEs including molarity of each electrolyte component – LiFSI is lithium bis (trifluoromethanesulfonyl) imide salt, VI and II are solvents and IV and V are diluents.....	518
Table VIII.12.1 Summary of program objectives	525
Table VIII.17.1 Ionic Conductivity of LSCEs.....	564
Table IX.1.1 Summary of the EXAFS fitting parameters on the Sn-doped materials. The error in the last digit(s) is given in parentheses. CN = coordination number; R = correlation distance; σ^2 = disorder.....	573
Table IX.2.1 Soak test results for LNMO electrodes in Gen2 electrolyte solutions with various additives.....	580
Table IX.2.2 Results based on the mass spectra of the liquid products	586
Table X.2.1 Compositions synthesized for this study.....	647
Table X.2.2 Gases detected during the first and second cycles of DEMS cells shown in adjacent figure	651
Table XI.1.1 Project performance targets for cathode active material and cell made with this material.....	678
Table XI.1.2 Conductive carbon additives formulation tested using commercial NCM811 (a< 1wt%)	683
Table XI.1.3 Summary table showing initial cathode energy densities	686
Table XI.4.1 Performance Targets.....	710
Table XI.4.2 Preliminary cycling metrics for the 2 Ah large-format pouch cells produced by Tesla Inc. using UT Austin’s Co-free NMAM-85. The listed values are averages from the 16 individual cells.....	715
Table XIII.4.1 Summary of Properties of 10 Screened Superionic Conductors with a CS Framework. The pristine and target composition extrapolated Li-ion conductivity of the target composition at 300 K ($\sigma_{300\text{ K}}$), the activation energy of the target composition (E_a), pristine and target energy above the hull (E_{hull}), and dopant incorporation energy (E_d) are listed. The pristine and target compositions are the same if no dopants are introduced. bounds (error bar) are included.....	791
Table XV.4.1 Summarized performance of Cu NMC622 cells at different discharge cutoff-voltages.....	846

Table XVI.5.1 Stability of LLZO–NMC 111 Under Varying Li Chemical Potential.	878
Table XVI.5.2 Stability of LLZO–NMC 111 Interface Under Varying O ₂ Chemical Potential.....	878
Table XVI.5.3 Comparison on EIS Reduction with Respect to Various Coating Material	880
Table XVI.7.1 Summary of Raman spectroscopic data of sulfide and oxysulfide glass SSEs before and after exposure to a dry room environment. Fractional peak areas are assigned to the vibrational modes of different glass structural units.....	898
Table XVI.14.1 NiO ₂ Cell parameter and energies for different oxygen stacking sequences and DFT functionals.....	965
Table XVI.15.1 Processing parameters to reduce or remove crystalline impurities	972
Table XVI.19.1 Ionic conductivity (σ_{Li}) at RT and 60°C, activation energy (E_a) at 60°C, transference number (t_{Li+}) at 60°C, and critical current density (CCD) at 60°C of the polymer SE and hybrid system (LLZTO/ Polymer) with different acid treatments conducted on LLZTO films.	993
Table XVI.24.1 Sample description and SAXS/WAXS/DSC results.....	1038
Table XVI.24.2 Li ion transference number of xPEO-LiTFSI and 60PFPE-LiTFSI	1041
Table XVI.26.1 Lithium Carbonate content of various LLZO samples	1056
Table XVI.27.1 Surface Composition from XPS (at.%) Before Etching	1059
Table XVI.27.2 Surface Composition from XPS (at.%) Before Etching	1061
Table XVI.29.1 Structural characterization of polyesters made for the current project	1074
Table XVII.4.1 Structural characterization of polyesters made for the current project.....	1141
Table XVII.6.1 ΔH interface for $c_{Li} = 5$ at. % for the different MCAs considered.	1170
Table XIX.3.1 Structural parameters of NTOs heated to indicated temperatures during the in situ XRD experiment	1232
Table XIX.4.1 Coulombic efficiency of stripping/plating process in half-cell Na different current collectors	1244
Table XIX.4.2 The values indicating the performance of anode-free sodium batteries in two electrolytes ...	1246
Table XX.1.1 Cohesive energies and band gaps of the considered LIC systems	1278
Table XX.1.2 XPS depth profile atomic ratios of fluorine, sulfur, and nitrogen to carbon, average over the range of the SEI for each electrolyte and temperature (a cut-off of 20 minutes sputtering was used for depth profiles with linear trends).....	1281

Vehicle Technologies Office Overview

Vehicles move our national economy. Annually, vehicles transport 18 billion tons of freight—about \$55 billion worth of goods each day³—and move people more than 3 trillion vehicle-miles.⁴ Growing our economy requires transportation, and transportation requires energy. The transportation sector accounts for approximately 30% of total U.S. energy needs⁵ and the average U.S. household spends over 15% of its total family expenditures on transportation,⁶ making it, as a percentage of spending, the most costly personal expenditure after housing. Transportation is critical to the overall economy, from the movement of goods to providing access to jobs, education, and healthcare.

The transportation sector has historically relied heavily on petroleum, which supports over 90% of the sector's energy needs today,⁷ and, as a result, surpassed electricity generation to become the largest source of CO₂ emissions in the country.⁸ The Vehicle Technologies Office (VTO) will play a leading role to decarbonize the transportation sector and address the climate crisis by driving innovation within and deployment of clean transportation technologies.

VTO funds research, development, demonstration, and deployment (RDD&D) of new, efficient, and clean mobility options that are affordable for all Americans. VTO leverages the unique capabilities and world-class expertise of the National Laboratory system to develop new innovations in vehicle technologies, including: advanced battery technologies; advanced materials for lighter-weight vehicle structures and better powertrains; energy-efficient mobility technologies and systems (including automated and connected vehicles as well as innovations in connected infrastructure for significant systems-level energy efficiency improvement); combustion engines to reduce greenhouse gas and criteria emissions; and technology integration that helps demonstrate and deploy new technology at the community level. Across these technology areas and in partnership with industry, VTO has established aggressive technology targets to focus RDD&D efforts and ensure there are pathways for technology transfer of federally supported innovations into commercial applications.

VTO is uniquely positioned to accelerate sustainable transportation technologies due to strategic public-private research partnerships with industry (e.g., U.S. DRIVE, 21st Century Truck Partnership) that leverage relevant expertise. These partnerships prevent duplication of effort, focus DOE research on critical RDD&D barriers, and accelerate progress. VTO advances technologies that assure affordable, reliable mobility solutions for people and goods across all economic and social groups; enable and support competitiveness for industry and the economy/workforce; and address local air quality and use of water, land, and domestic resources.

Annual Progress Report

As shown in the organization chart (below), VTO is organized by technology area: Batteries R&D; Electrification R&D; Materials Technology R&D; Decarbonization of Offroad, Rail, Marine, and Aviation; Energy Efficient Mobility Systems; and Technology Integration. Each year, VTO's technology areas prepare an Annual Progress Report (APR) that details progress and accomplishments during the fiscal year. VTO is pleased to submit this APR for Fiscal Year (FY) 2022. The APR presents descriptions of each active project in FY 2022, including funding, objectives, approach, results, and conclusions.

³ Bureau of Transportation Statistics, DOT, Transportation Statistics Annual Report 2020, Table 4-1, <https://www.bts.gov/tsar>.

⁴ Davis, Stacy C., and Robert G. Boundy. Transportation Energy Data Book: Edition 39. Oak Ridge National Laboratory, 2021, <https://doi.org/10.2172/1767864>. Table 3.8 Shares of Highway Vehicle-Miles Traveled by Vehicle Type, 1970-2018.

⁵ [Ibid. Table 2.2 U.S. Consumption of Total Energy by End-use Sector, 1950-2018.](#)

⁶ [Ibid. Table 11.1 Average Annual Expenditures of Households by Income, 2019.](#)

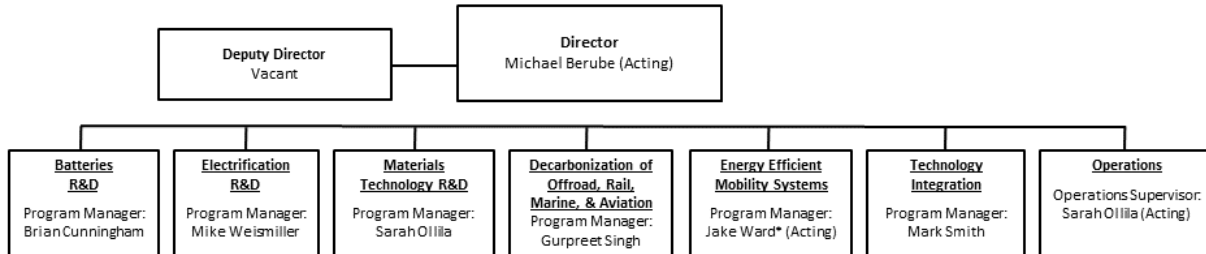
⁷ [Ibid. Table 2.3 Distribution of Energy Consumption by Source and Sector, 1973 and 2019.](#)

⁸ Environmental Protection Agency, Draft U.S. Inventory of Greenhouse Gas Emissions and Sinks, 1990-2019, Table 2-11. Electric Power-Related Greenhouse Gas Emissions and Table 2-13. Transportation-Related Greenhouse Gas Emissions.

Organization Chart

Vehicle Technologies Office Federal Staff

September 2022



**based at NETL-Pittsburgh*

Batteries Program Overview

Introduction

During the fiscal year 2022 (FY 2022), the Vehicle Technologies Office (VTO) battery program continued research and development (R&D) support of battery technologies for plug-in electric vehicles (PEVs), e.g., plug-in hybrids, extended range electric vehicles, and all-electric vehicles. One objective of this support is to enable U.S. innovators to rapidly develop next generation of technologies that achieve the cost, range, and charging infrastructure necessary for the widespread adoption of PEVs. Stakeholders involved in VTO R&D activities include universities, national laboratories, other government agencies and industry partners – including automakers, battery manufacturers, material suppliers, component developers, private research firms, and small businesses. VTO works with key U.S. automakers through the United States Council for Automotive Research (USCAR) – an umbrella organization for collaborative research consisting of Stellantis N.V., the Ford Motor Company, and the General Motors Company. Collaboration with automakers through the U.S. DRIVE (Driving Research and Innovation for Vehicle Efficiency and Energy Sustainability) partnership enhances the relevance and the success potential of the research platform. An important prerequisite for the electrification of the nation’s light duty transportation sector is the development of more cost-effective, longer lasting, and more abuse-tolerant PEV batteries and accordingly, VTO battery R&D is focused on the development of high-energy batteries for PEVs.

Goals

The goal of this research is to address barriers to EVs reaching the full driving performance, convenience, and price of an internal combustion engine (ICE) vehicle. EVs have the advantage of a very high efficiency compared to other vehicle types, a simplified drivetrain, and a flexible primary energy source (i.e., the electricity needed to charge an EV can come from coal, natural gas, wind turbines, hydroelectric, solar energy, nuclear, or any other resource). Another current focus is the 12V start/stop (S/S) micro-hybrid architecture, in which the engine is shut down whenever a vehicle stops. Vehicles with the S/S functionality are being deployed worldwide. Table 1 shows a subset of the targets for high-performance EVs set by U.S. DRIVE⁹.

Table 1: Subset of Requirements for Advanced High-Performance EV Batteries and Cells
(Cost and Low Temperature Performance are Critical Requirements)

Energy Storage Goals (by characteristic)	System Level	Cell Level
Cost @ 100k units/year (kWh = useable energy)	\$125/kWh*	\$100/kWh
Peak specific discharge power (30s)	470 W/kg	700 W/kg
Peak specific regen power (10s)	200 W/kg	300 W/kg
Useable specific energy (C/3)	235 Wh/kg*	350 Wh/kg
Calendar life	15 years	15 years
Deep discharge cycle life	1000 cycles	1000 cycles
Low temperature performance	>70% useable energy @C/3 discharge at -20 °C	>70% useable energy @C/3 discharge at -20 °C

State of the Art

Battery R&D attempts to advance battery technology to help improve the market penetration of PEVs by overcoming the current barriers. To accomplish this, it focuses on: (1) a significantly reduced battery cost, (2) increased battery performance, e.g., extreme fast charge (XFC) and low temperature performance for enhanced

⁹ <https://uscar.org/download/246/energy-storage-system-goals/12837/goals-for-advanced-high-performance-batteries-for-electric-vehicle-ev-applications.pdf>

lithium-ion, (3) improved life advanced chemistry cells, (4) increased tolerance to abusive conditions; and (5) more cost-effective recycling and sustainability.

The current status of the broad battery chemistry types (current lithium-ion, next gen, and BLI) is summarized in Figure 1. Battery R&D spans mainly three areas:

- **Current technology (enhanced lithium-ion):** including cells with current materials (graphite anode/transition metal oxide cathode) and features like XFC compatibility, low temperature performance and improved abuse tolerance.
- **Next-gen lithium-ion:** Cells containing an alloy anode, usually silicon-based, and/or a high voltage (>4.5 V) cathode.
- **Beyond lithium-ion (BLI):** Cells containing Li metal anodes.

Over the past 12 years, PEVs have become more commercially viable, with battery costs dropping almost 90% since 2010. Further cost reductions in high-energy batteries for PEVs are always desirable. In addition, although today's batteries approach very attractive cost numbers, they still need the ability to accept extreme fast charging (XFC) and to perform better in low-temperature operations to compete with ICEs in all-weather performance and "refueling" convenience. Research into "enhanced lithium-ion" batteries (which would providing these functionalities) is one of the R&D focus areas. For further gains in energy density and cost reduction, research is needed in both "next gen" chemistries (which employ an alloy anode and/or a high voltage cathode) and BLI chemistries (see Figure 1). Cycle and calendar lives of next-gen and BLI chemistries fall well short of EV goals. Most cells employing a significant amount of silicon provide around 1,000 deep-discharge cycles but with less than five years of calendar life; BLI cells typically provide much less of a cycle life (400 cycles or less). In addition, the requisite low temperature performance and extreme fast charge capability are lacking in all chemistries.

Current Technology Lithium-ion (Graphite/NMC)		Next Generation Lithium-ion (Silicon Composite/High -voltage NMC)		Longer-term Battery Technology (Lithium Metal)	
Battery Pack Cost		Battery Pack Cost		Battery Pack Cost	
<ul style="list-style-type: none"> Current: \$235/kWh Potential: \$100-\$160/kWh 		<ul style="list-style-type: none"> Current: \$256/kWh Potential: \$90-\$125/kWh 		<ul style="list-style-type: none"> Current: ~\$320/kWh Potential: \$70-\$120/kWh 	
Large-format EV cells	20-60 Ah	Large-format EV cells	20-60 Ah	Large-format EV cells	TBD (Today)
Current cycle life	1,000 -5,000	Current cycle life	500 -700	Current cycle life	400
Calendar life	10-15 years	Calendar life	Low	Calendar life	TBD
Mature manufacturing		Mature manufacturing		Mature manufacturing	
Fast-charge		Fast-charge		Fast-charge	
R&D Needs		R&D Needs		R&D Needs	
<ul style="list-style-type: none"> High-voltage cathode/electrolyte Lower-cost electrode processing Extreme fast-charging 		<ul style="list-style-type: none"> High-voltage cathode/electrolyte Lower-cost electrode processing Durable silicon anode with increased silicon content 		<ul style="list-style-type: none"> High-voltage cathode Lithium protection Highly-conductive solid electrolyte 	

Figure 1. Chemistry classes, status, and R&D needs

Because of the large variation in different battery technologies, battery research also includes multiple activities focused to address remaining high cost areas within the entire battery supply chain.

Battery Technology Barriers

The major remaining challenges to commercializing batteries for PEVs are as follows:

A. Cost. The current cost of high-energy lithium-ion batteries is approximately \$150 – \$200/kWh (on usable energy basis), a factor of two-three times too high from where it needs to be. The main cost drivers are the high cost of raw materials, costs associated with materials processing, the cell and module packaging, and manufacturing.

B. Performance. Historically, a higher energy density was needed to reduce the weight and volume of PEV batteries, but those weight and volume issues have been to a large degree been addressed. The use of higher energy materials is still an effective way to reduce costs further and extend driving range, but cell chemistries that provide higher energy have life and performance issues. Also, existing chemistries (e.g., graphite anodes paired with transition metal oxide cathodes) need improvement in XFC and low temperature performance to compete favorably with gas-powered vehicles in the areas of performance and customer convenience.

C. Life. The life issue for mature lithium-ion technologies has mainly been mostly addressed. However, both next-gen and BLI cell technologies still suffer major cycle and calendar life issues.

D. Abuse Tolerance. Many lithium-ion batteries are not intrinsically tolerant to abusive conditions; however, full packs have been engineered by automotive OEMs to mitigate much of the risk. The reactivity of high nickel cathodes and flammability of current lithium-ion electrolytes are areas for possible improvement. The characteristics of next-gen and BLI chemistries to abusive conditions are not well-understood. However, silicon anode cells show very high temperatures during thermal runaway and lithium metal-based batteries have a long history of problematic dendrite growth which can lead to internal shorts and thermal runaway. Thus, research into enhanced abuse tolerance strategies will continue.

E. Recycling and Sustainability. Currently, automotive OEMs pay a relatively large cost (5-15% of the battery cost) to recycle end of life PEV batteries. The various chemistries used in lithium-ion cells results in variable backend value. Alternatively, unless they get recycled, lithium-ion batteries could lead to a shortage of key materials (lithium, cobalt, and nickel) vital to the technology. Finding ways to decrease the cost of recycling could thus significantly reduce the life cycle cost of PEV batteries, avoid material shortages, lessen the environmental impact of new material production, and potentially provide low-cost active materials for new PEV battery manufacturing.

Program Organization Matrix

VTO's energy storage effort includes multiple activities, ranging from focused fundamental materials research to prototype battery cell development and testing. The R&D activities can involve either shorter-term pre-competitive research by commercial developers or exploratory materials research generally spearheaded by national laboratories and universities. The program elements are organized as shown in Figure 2. Battery R&D activities are organized into the following program elements: Advanced Batteries and Cells R&D, Battery Materials R&D, and the current focus.

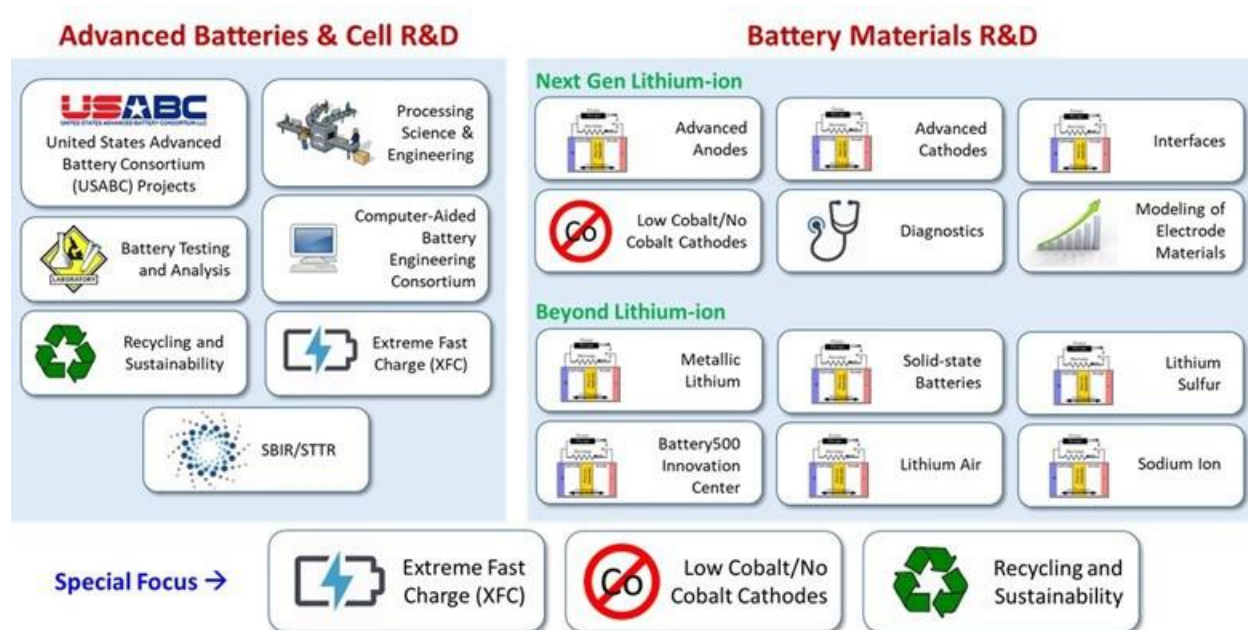


Figure 2. Battery R&D Program Structure

Advanced Cell and Battery Research and Development activity. This activity focuses on the development of robust battery cells to significantly reduce battery cost, increase life, and improve performance. Part of this effort takes place in close partnership with the automotive industry, through a cooperative agreement with the *United States Advanced Battery Consortium* (USABC). In FY 2022, the USABC supported eleven cost-shared contracts with developers to further the development of batteries and battery components for PEVs. In addition to the USABC projects, DOE supports battery and material suppliers via contracts administered by the National Energy Technology Laboratory (NETL). Other projects in this area include performance, life and abuse testing of contract deliverables, laboratory- and university-developed cells, and benchmarking new technologies from industry; thermal analysis, thermal testing and modeling; cost modeling; secondary usage and life studies; and recycling studies for core materials. The *processing science & engineering* activity supports the development and scale-up of manufacturing technologies needed to enable market entry of next-generation battery materials and cell components – emphasizing disruptive materials and electrode production technologies that could significantly reduce cost and environmental impact while increasing yield and process control relative to existing production technologies. Several *small business innovation research* (SBIR) projects, also supported by VTO, are focused on the development of new battery materials/components and are the source of new ideas and concepts and are covered in that chapter.

Advanced Materials Research activity. This activity addresses fundamental issues of materials and electrochemical interactions associated with rechargeable automotive batteries. It develops new/promising materials and uses advanced material models to discover them and their failure modes, as well as scientific diagnostic tools and techniques to gain insight into why they fail. This work is carried out by researchers at national labs, at universities, and at commercial facilities. It includes the *next generation lithium-ion* research activity focused on the optimization of next generation, high-energy lithium-ion electro-chemistries that incorporate new battery materials. It emphasizes identifying, diagnosing, and mitigating issues that impact the performance and lifetime of cells constituted of advanced materials. Research continues in the six areas of advanced anodes, advanced cathodes, advanced electrolytes, electrode issues, interfaces, diagnostics, and modeling. The *beyond lithium-ion* (BLI) Technology activity addresses fundamental issues associated with lithium metal batteries, develops new/promising materials and uses advanced material models to discover such materials using scientific diagnostic tools/techniques. It includes solid-state battery technologies, lithium

metal, lithium sulfur, lithium air, and sodium-ion systems. The VTO *Battery500* projects are also managed in conjunction with this program element.

Special Focus. The current focus targets three areas of battery research. The first area is concerned with enabling *extreme fast charging* (XFC) in enhanced lithium-ion systems. It started with a 2017 research project to understand XFC, followed by a set of XFC awards (listed in the last year's report). In the second area, recognizing the issues of price volatility and supply reliability with cobalt, DOE started several projects to develop and optimize low cobalt cathode materials. The third area consists of a set of *recycling and sustainability* projects, which involve studies of full life-cycle impacts and costs of battery production and use; cost assessments and impacts of various battery recycling technologies; and the material availability for recycling and secondary usage and their cost impacts.

As a further resource, the Electrochemical Energy Storage Roadmap describes ongoing and planned efforts to develop battery technologies for PEVs and can be found at the EERE Roadmap page <http://energy.gov/eere/vehicles/downloads/us-drive-electrochemical-energy-storage-technical-team-roadmap>. VTO also has extensive ongoing *collaboration* efforts in batteries R&D across the DOE and with other government agencies. It coordinates efforts on energy storage with the DOE Office of Science, and the DOE Office of Electricity. Coordination and collaboration efforts include membership and participation in program reviews and technical meetings by other government agencies, and the participation of representatives from other government agencies in the contract and program reviews of DOE-sponsored efforts. DOE also coordinates with the Department of Army's Advanced Vehicle Power Technology Alliance, the Department of Transportation/National Highway Traffic Safety Administration (DOT/NHTSA), the Environmental Protection Agency (EPA), and the United Nations Working Group on Battery Shipment Requirements. Additional international collaboration occurs through a variety of programs and initiatives. These include: the International Energy Agency's (IEA's) Hybrid Electric Vehicles Technology Collaboration Program (HEV TCP); and the G8 Energy Ministerial's Electric Vehicle Initiative (EVI); as well as bilateral agreements between the U.S. and China.

Battery Highlights from FY 2022

The following are some of the highlights associated with battery R&D funded by VTO (including highlights related to market developments, R&D breakthroughs, and commercial applications).

Electrolytes for Li-metal Anodes via Solvation-Protection Strategy (ANL)

The development of a stable electrolyte system is crucial to the use of Li metal batteries (LMBs). Researchers at ANL have developed a new "solvation-protection" strategy to stabilize Li metal anodes. Fluoroethylene carbonate (FEC) was introduced into the difluoroethylene carbonate/fluoroethyl methyl carbonate (DFEC/FEMC) electrolyte system to serve as a solvation protection agent. Although DFEC enables stable cycling of a Li metal anode, a Li||NMC811 cell with DFEC/FEMC electrolyte (and no FEC) displays inferior cycling performance because of Li complexes solvated solely by FEMC. Owing to the relatively high solvating power of FEC, the solution structures of Li complexes can be altered. The FEC/DFEC/FEMC electrolyte not only maintains the beneficial effect of DFEC in forming a robust SEI on the Li, but also confers outstanding anodic stability provided by FEMC, evidenced by the stable cycling of Li||NMC cells (Figure 3).

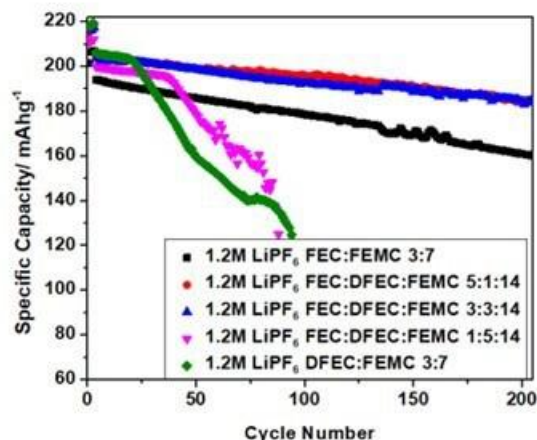


Figure 3. Cycling performance of Li | NMC811 cells using 1.2M LiPF₆-FEC/DFEC/FEMC in different ratios.

LiNiO₂ Enabled by Optimized Synthesis Conditions (ANL)

The LiNiO₂ (LNO) cathode has been of interest for many years because of its high energy and lack of expensive cobalt. However, it has never achieved commercial success due, in part, to cycling instabilities (presumed inherent to the material) at high states of charge. However, due to the sensitivity of LNO to synthesis conditions such as precursor control, temperature, and atmosphere, virtually all LNO cathodes studied to date contain defects. Work at ANL has shown that near ideal, ‘defect-free’ LNO can be synthesized through better control of synthesis. ANL’s ‘defect-free’ LNO cycles at high capacities (>220 mAh/g) over many cycles without dopants, coatings, or electrolyte additives. Such high performance, including very low initial irreversible capacity (~96%), has never been reported for LNO. Key to achieving such results was precise control of synthesis parameters including novel precursor preparation, calcination conditions that facilitate minimum local defects (Li⁺/Ni²⁺ mixing, O₂ vacancies, stacking faults), optimized primary and secondary particle morphologies, and a higher resistance to secondary particle cracking. Surprisingly, synthesis of ‘defect-free’ LNO could be enabled within a wide range of O₂ partial pressures, even as low as 0.2 atm. Full-cell tests with graphite anodes and Gen 2 electrolyte (1.2 M LiPF₆ in EC:EMC (3:7 by weight)) showed performance on par with LiNi_{0.9}Mn_{0.05}Co_{0.05}O₂, when cycled over similar states of charge, Figure 4. Note that three hour holds at the top of every charge were used to push stability limits.

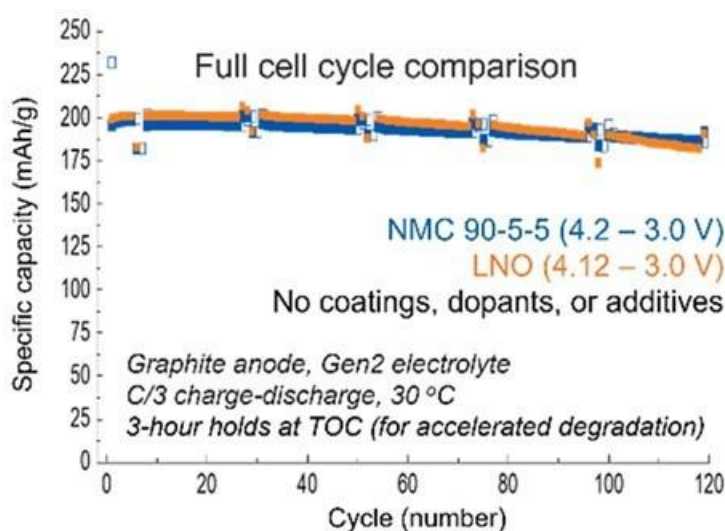


Figure 4. Full cell performance comparison of optimized LNO vs. LiNi_{0.9}Mn_{0.05}Co_{0.05}O₂

Use of synthetic data and deep learning enable rapid identification of failure modes (INL)

Early identification of battery aging modes/mechanisms can enable accurate forecasting of battery life and possibly shorten the research and development cycle for new battery designs. An INL team developed a deep-learning (DL) algorithm for rapidly classifying and quantifying battery aging modes. The DL framework classifies and quantifies the dominant aging modes upon training with synthetic data and was used to classify the dominant aging modes in less than 100 fast charge cycles of graphite/ $\text{LiNi}_{0.5}\text{Mn}_{0.3}\text{Co}_{0.2}\text{O}_2$ (NMC532) cells. Upon classification, the framework tracked the evolution of the aging modes through 600 cycles at different charging rates (1C–9C) (Figure 5). The method has been used for NMC532, NMC811 and $\text{Li}_4\text{Ti}_5\text{O}_{12}/\text{LiMn}_2\text{O}_4$ cells to show its applicability.

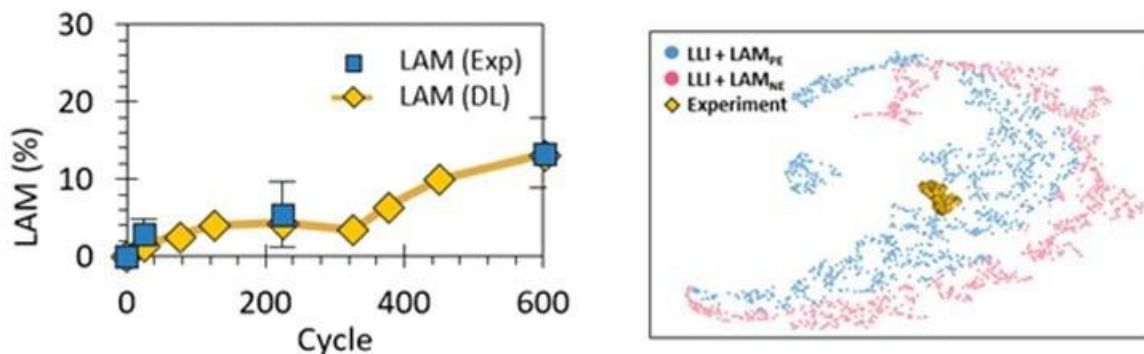


Figure 5. Flow of synthetic-data-based DL modeling framework to classify and quantify the dominant aging modes

Cyclable All-Solid-State Cell Chemistries with High Energy Densities (LBNL)

All-solid-state batteries (ASSBs) with Li metal anodes are capable of delivering higher energy densities and better abuse tolerance than current Li ion cells. The development of practical ASSBs, however, has met challenges such as Li dendrites, cathode instabilities due to oxidative degradation of the solid electrolyte (SE), and loss of mechanical integrity. In this work, we report novel solutions with the following features: 1) conductive halide SEs with high oxidative stability to enable use of 4 V CAM and 2) single-crystal CAM particles to eliminate intergranular cracking associated with volume changes. Results obtained on ASSB cells with a single-crystal $\text{LiNi}_{0.8}\text{Mn}_{0.1}\text{Co}_{0.1}\text{O}_2$ (SC-NMC) CAM with 9.04 mg/cm^2 loading, a 300 μm thick Li_3YCl_6 (LYC) SE, and a Li-In alloy anode are shown in Figure 6, along with data for an equivalent ASSB cells with a commercial polycrystalline NMC811 (PC-NMC). Much improved cycling performance was obtained in the SC-NMC cell. At C/2 rate, the discharge capacity decreased from ~ 105 to 80 mAh/g after 830 cycles in the PC-NMC cell and ~ 140 to 125 mAh/g after 1000 cycles in the SC-NMC cell, a capacity retention of $\sim 76\%$ and 89% , respectively. Post-mortem analysis reveals superior mechanical stability of the SC-NMC cathode whereas large morphological changes were observed on the cycled PC-NMC counterparts, including cracking within the NMC particles and disconnections between the LYC and NMC. The design principle described here is general and it can be expanded to ASSB cells with other types of halide SEs and CAM materials.

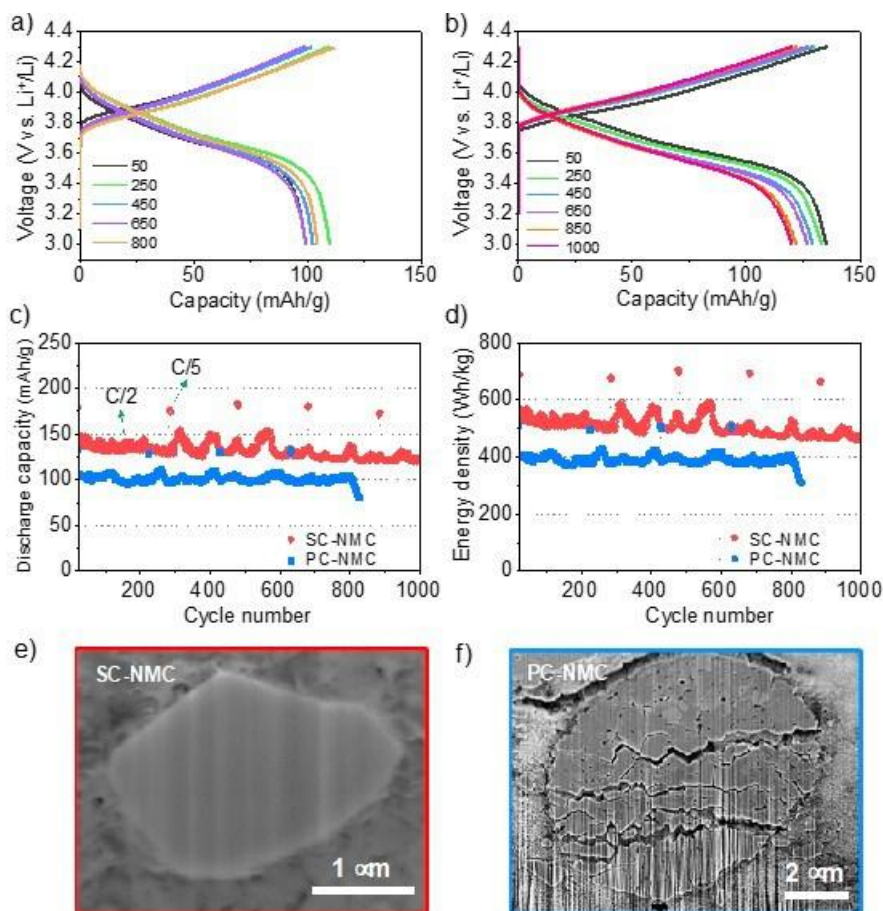


Figure 6. a-b) Voltage profiles of PC-NMC and SC-NMC ASSB cells, respectively. c-d) Discharge capacity and energy density retentions of the ASSB cells, respectively. e-f) Cross-sectional SEM images showing better mechanical stability of SC-NMC cathode composite upon cycling. All cells were cycled at room temperature at C/2 rate for 200 cycles followed by 3 cycles at C/5. This sequence was repeated throughout the testing. The performance fluctuation shown in c) and d) is due to room temperature variation in the laboratory, which ranged from $25 \pm 5^\circ\text{C}$ during the test

Polymer catholyte for solid state batteries enhanced with residual solvent (LBNL)

All-solid state batteries (ASSB) promise high energy density via the use of a Li metal anode, and improved safety due to the absence of a flammable liquid electrolyte. Favorable cathode performance and durability are challenging to achieve, however, when restricting the choice of electrolyte materials to only solids. Here, we show that retained residual solvent improves the performance of a cathode containing solid polymer binder. The very small amount of solvent retained in the polymer/Li-salt composite plasticizes the polymer, increasing Li-ion conductivity. The cathode was combined with a solid sintered ceramic separator and Li metal anode (Figure 7), demonstrating a pathway to a viable ASSB. Drying the cathode to different extents greatly impacts conductivity of the composite and therefore total cathode performance (Figure 8). By optimizing the amount of residual solvent and polymer/Li-salt ratio, promising performance and capacity retention was achieved (Figure 8). The positive effect of residual solvent was observed over a very wide temperature range from -10°C to 60°C . Multiple solvents produced a similar effect, providing flexibility to select the solvent based on cost, safety, reactivity, and manufacturing considerations. The cycling data were obtained using a $\text{LiNi}_{1/3}\text{Mn}_{1/3}\text{Co}_{1/3}\text{O}_2$ cathode ($2\text{mg}/\text{cm}^2$ loading), Li metal anode, and a 300-micron thick $\text{Li}_{6.25}\text{Al}_{0.25}\text{La}_3\text{Zr}_2\text{O}_{12}$ electrolyte. It was found that, without the residual solvent, the cell impedance was too high to cycle the cell.

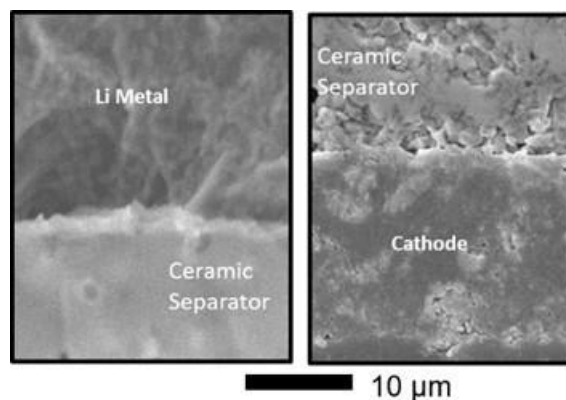


Figure 7. Cross-section image of the separator/cathode structure. The separator is an oxide ceramic and the cathode is a solid composite of NMC active material, carbon, polymer catholyte, and trace residual solvent

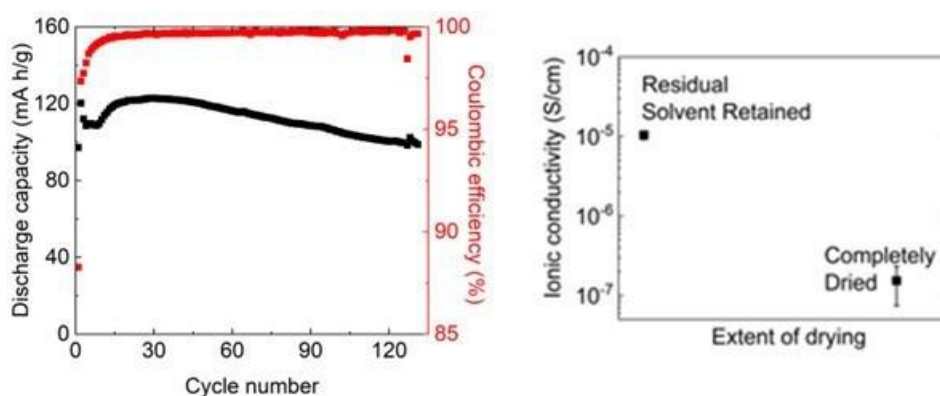


Figure 8. Capacity retention of a cell with residual solvent cycled at 25 °C and 20 hour full charge/discharge cycle. Right most figure shows the conductivity of the polymer/Li-salt composite with and without residual solvent

Machine Learning Enhances Battery Life Prediction (NREL)

Accurate lifetime predictions are crucial for optimizing battery system design and use. Examples include maximizing battery revenue, extending battery life, establishing fast-charge control policies, and maintenance. But identifying accurate battery lifetime models is challenging because degradation rates are sensitive to many factors including temperature, state-of-charge, depth-of-discharge, and dis/charging current rates. Thus battery life-predictive models may require six to nine months of test data. NREL researchers developed the ‘Autonomous Identification of Battery Lifetime Models’ toolkit, AI-Batt, which uses machine-learning (ML) to autonomously identify high-performing models from tens of millions of possibilities, resulting in models that have roughly twice the accuracy of models identified by humans (Figure 9) (Gasper et al, 2021, J. Echem. Soc. 168 020502). After training life models to fit accelerated aging data, lifetime predictions can then be made for real-world applications with dynamic loads or varying use (Figure 10) (Gasper et al, 2022, J. Echem. Soc. 169 080518). Battery life models identified via ML are used for a variety of applications, such as electric-vehicle battery life prediction (Smith et al, 2021, J. Echem. Soc. 168 100530), health prediction (Gasper et al, 2022, Cell Rpts. Phys. Sci., 101184), and for stationary energy storage optimization. NREL has incorporated battery lifetime models into several open-source technoeconomic energy system simulation tools, such as REOpt[®] and System Advisor Model. Presently, NREL is merging ML-based lifetime prediction with physics-based electrochemical models. This physics/ML hybrid method promises to improve accuracy across a wide variety of use cases, such as during extreme fast charge. It also enables early life prediction by requiring less test data, as well as provides transferrable learnings across cell designs and chemistries.

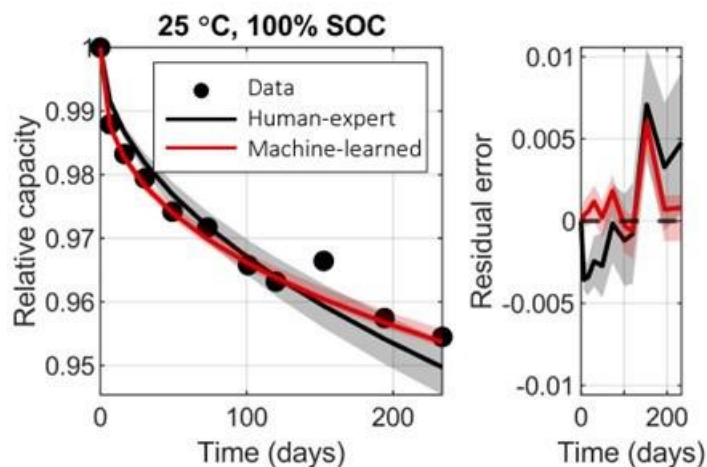


Figure 9. Calendar degradation of lithium-ion battery predicted by human-expert and ML models with 90% confidence intervals. ML models fit aging data with half of the error of human-expert models and have better confidence

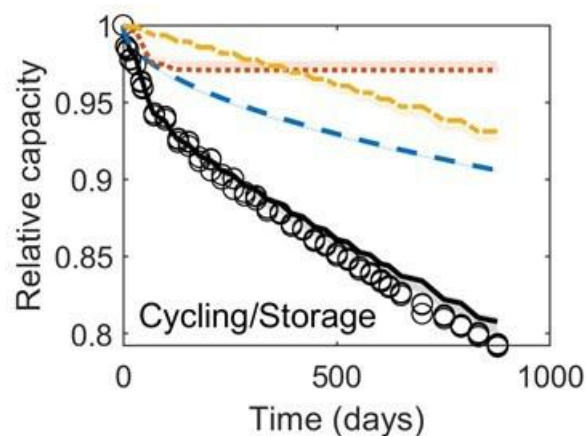


Figure 10. Validation of ML lithium-ion battery life model on dynamic aging test with monthly variation of cycling and storage. Total degradation is the sum of three aging modes identified from accelerated aging test data and fit using ML

A New Hydrothermal Manufacturing Process for Lithium-Ion Cathodes (ORNL)

As demand for electric cars increases, so does the need for sustainable production of battery components, including cathodes. But a variety of problems are associated with traditional cathodes and the methods of processing them. The first obstacle is a reliance on cobalt, a rare metal mined and refined abroad, which poses risks to American manufacturing supply chains. The balance of other metals common in cathodes can also make the manufacturing process longer and more hazardous. For example, high nickel concentration has led to the widespread use of a chemical mixing method for cathode production that requires large quantities of ammonia for corrosive reactions. Using the toxic chemical increases costs, heightens health and environmental concerns, and wastes large amounts of water to reduce acidity.

Researchers at ORNL recently developed a new, ammonia free, hydrothermal synthesis process for producing Li-ion cathodes, including a cobalt-free cathode material, $\text{LiNi}_{0.9}\text{Mn}_{0.05}\text{Al}_{0.05}\text{O}_2$, termed NMA9055 (Figure 11a). This novel process offers the key advantage of moving the cathode industry to cleaner and more cost-competitive production while putting less burden on our environment. The developed material has properties like the conventional Co-based cathodes and thus can be seamlessly manufactured and integrated into current industrial scale manufacturing techniques.

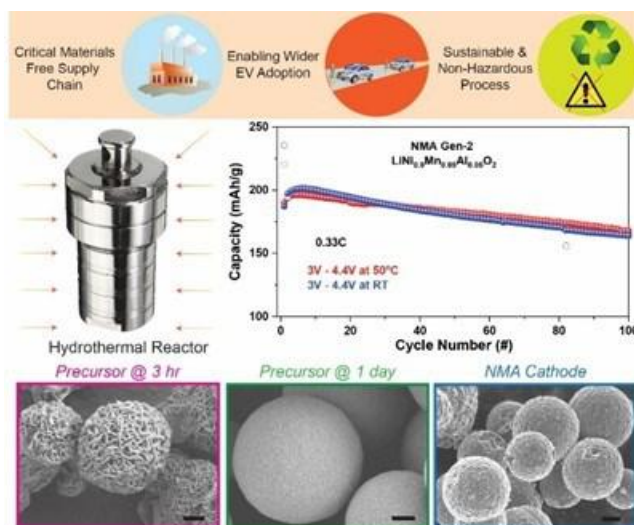


Figure 11. Development of Co-free cathode materials for next generation Li-ion batteries

Developing low-cost rechargeable lithium-sulfur batteries (Battery500 Consortium)

The Battery500 Consortium has advanced the performance of a lithium-sulfur (Li-S) battery through innovation in battery electrolytes and improved understanding of a polymer-derived sulfur cathode. A 2 Ah pouch cell with an energy density of 250Wh/kg (which is competitive with current lithium-ion EV cells) has been demonstrated.

Sulfurized PolyAcryloNitrile (SPAN) is a low-cost material containing no critical materials and is readily made by heating sulfur with PAN, an industrial product, at 300-500°C. Unlike elemental sulfur-based cathodes, SPAN appears to avoid the generation of soluble polysulfide species, which lead to capacity fade and is very sensitive to electrolyte amounts. To enable a long-life Li-SPAN battery, electrolytes need to be stable at both the Li anode and the SPAN cathode. The Consortium has developed a localized concentrated electrolyte consisting of 1.8 M lithium bis(fluorosulfonyl)imide (LiFSI) in diethyl ether (DEE) and Bis(2,2,2-trifluoroethyl) ether (BTFE). This electrolyte forms a protection layer on the SPAN surface that prevents loss of sulfur to the electrolyte. In addition, Li cycles stably due to the formation of a LiF-rich SEI. Both Li and SPAN show around 1000 stable cycles in coin cells using this new electrolyte.

To further improve the capacity and reversibility of SPAN, it is essential to understand its molecular structure and working mechanism. Using chemical analysis, electron microscopy, and surface analysis, we established that SPAN undergoes an irreversible transformation during the 1st cycle that reduces its residual hydrogen content and produces a more extended conjugated molecular structure. As a result, its electronic conductivity increases by > 100x and raises the working potential. This structural feature will serve as a blueprint for design of next generation materials. Electrolyte innovation and electrode engineering have allowed the fabrication of a first generation 2 Ah Li-SPAN battery with an energy density of 250 Wh/kg, Figure 12. Cycling ended when the Li metal anode caused an internal short. Work is in progress to further increase the capacity of SPAN and formulate new electrolytes that will extend the cycle life of Li-SPAN batteries. Team members are now scaling up SPAN cathode materials to enable more pouch cell manufacturing and testing.

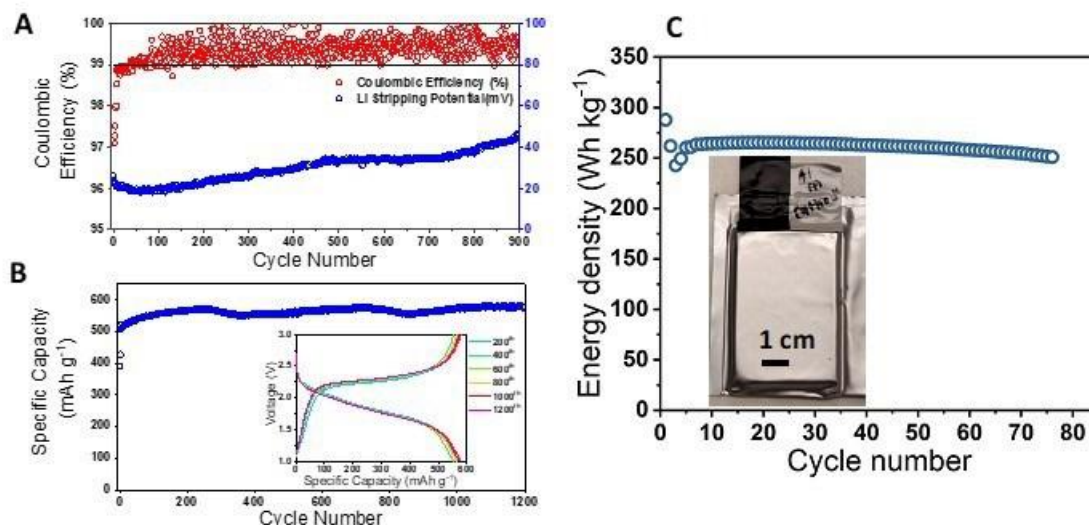


Figure 12. Progress of developing a low-cost Li-S battery by the Battery500 Consortium. The sulfur cathode is sulfurized polyacrylonitrile (SPAN). (a) and (b), Stable cycling of Li and SPAN in a localized concentrated electrolyte, respectively. (c) Demonstration of a 1st Generation Li-SPAN pouch cell of 2 Ah with an energy density of 250 Wh/kg

High-Performance Low-Cobalt Cathode Materials for Li-ion Batteries (Pennsylvania State University, Pacific Northwest National Laboratory, and Oak Ridge National Laboratory)

$\text{Li}[\text{Ni}_x\text{Co}_y\text{Mn}_{1-x-y}]\text{O}_2$ (NCM) cathode materials are a common choice for electric vehicles (EV) batteries due to their high energy density and good cycling. However, the increased price of cobalt (Co) over the past few years has increased the cost of the NMC. Therefore, developing cathode materials with low or no Co while still achieving high energy density and low cost is essential. Unfortunately, the cycling stability of many low-Co NMC cathodes is compromised by structural instability, non-uniform strain during cycling, and parasitic reactions between the cathode and electrolyte. The coating methods developed in this project are an effective strategy for alleviating these issues.

Specifically, we achieved a LiFePO_4 (LFP) coated NCM811 cathode (LFP/NCM811) via a dry coating approach, where the nanosized LFP is uniformly coated at the surface of NCM811 particles. Then, 2.5 Ah pouch cells were assembled using 10 wt% LFP coated NCM811 cathode and graphite anode. The cathode loading is 17.5 mg/cm^2 , the N/P ratio = 1.1, and the cell achieved 450 Wh/L and 200 Wh/kg. Figure 13 demonstrates that the pouch cells can cycle stably at room temperature (RT), with capacity retention of 76.7% after 2413 cycles. Moreover, the cell could still achieve 67.3% capacity retention after 1609 cycles at 40°C.

In summary, LiFePO_4 coating significantly improves the cycling performance of pouch cells with low-Co layered structured cathode. The team continues to investigate more effective coating materials for $\text{Li}[\text{Ni}_x\text{Co}_y\text{Mn}_{1-x-y}]\text{O}_2$ cathode materials with a cobalt content ≤ 0.04 .

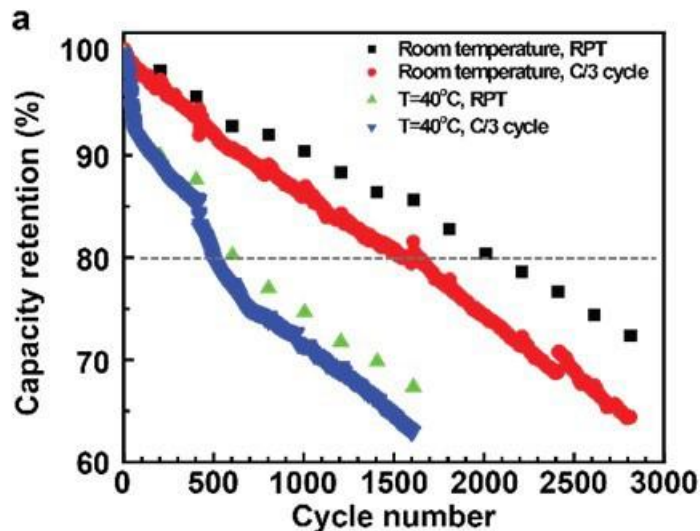


Figure 13. Capacity retention pouch cells during C/3 cycling at RT and 40 °C

Rational electrolyte solvent molecule tuning for high-performance lithium metal and anode free batteries (Stanford University and SLAC National Accelerator Laboratory)

Lithium (Li) metal batteries offer improved energy density compared to current Li-ion batteries but are held back by relatively poor cycle life. Conventional electrolytes fall short when paired with Li metal anodes, let alone anode-free batteries. To enable practical Li metal and anode-free batteries, several requirements should be fulfilled: 1) high Coulombic efficiency (CE) including initial cycles, i.e. fast activation of Li anode; 2) anodic stability to avoid cathode corrosion; 3) practical conditions such as lean electrolyte and limited Li inventory; 4) high ionic conductivity for realistic cycling rates; 5) moderate Li salt concentration for low cost; 6) high boiling point and the absence of gassing to ensure processability and safety.

In 2022, researchers at Stanford University and SLAC investigated a family of fluorinated 1,2-diethoxyethanes (fluorinated-DEEs) as electrolyte solvents. Selected positions on DEEs are functionalized with various numbers of fluorine (F) atoms through iterative tuning, to reach a balance between CE, oxidative stability, and ionic conduction. Paired with 1.2 M LiFSI salt, we found that a partially fluorinated, locally polar $-\text{CHF}_2$ group results in higher ionic conduction than fully fluorinated $-\text{CF}_3$ while still maintaining excellent electrode stability. Specifically, the best-performing F4DEE and F5DEE both contain $-\text{CHF}_2$ group. In addition to high ionic conductivity and low and stable overpotential, they achieve roughly 99.9% Li CE with $\pm 0.1\%$ fluctuation (Figure 14a) as well as fast activation, i.e. the CEs of the Li||Cu half cells reach $>99.3\%$ from the second cycle (Figure 14b). Aluminum corrosion is also suppressed due to the oxidative stability that originates from fluorination. These features enable roughly 270 cycles in thin-Li||high-loading- $\text{LiNi}_{0.8}\text{Mn}_{0.1}\text{Co}_{0.1}\text{O}_2$ (NMC811) full batteries (Figure 14c) and >140 cycles in fast-cycling anode-free Cu||LiFePO₄ (LFP) pouch cells (Figure 14d), both of which are state-of-the-art performances.

The above solvents can be readily scaled up with low cost. Their high boiling point, high flash point, non-flammability and absence of gassing issue during battery cycling are desirable features.

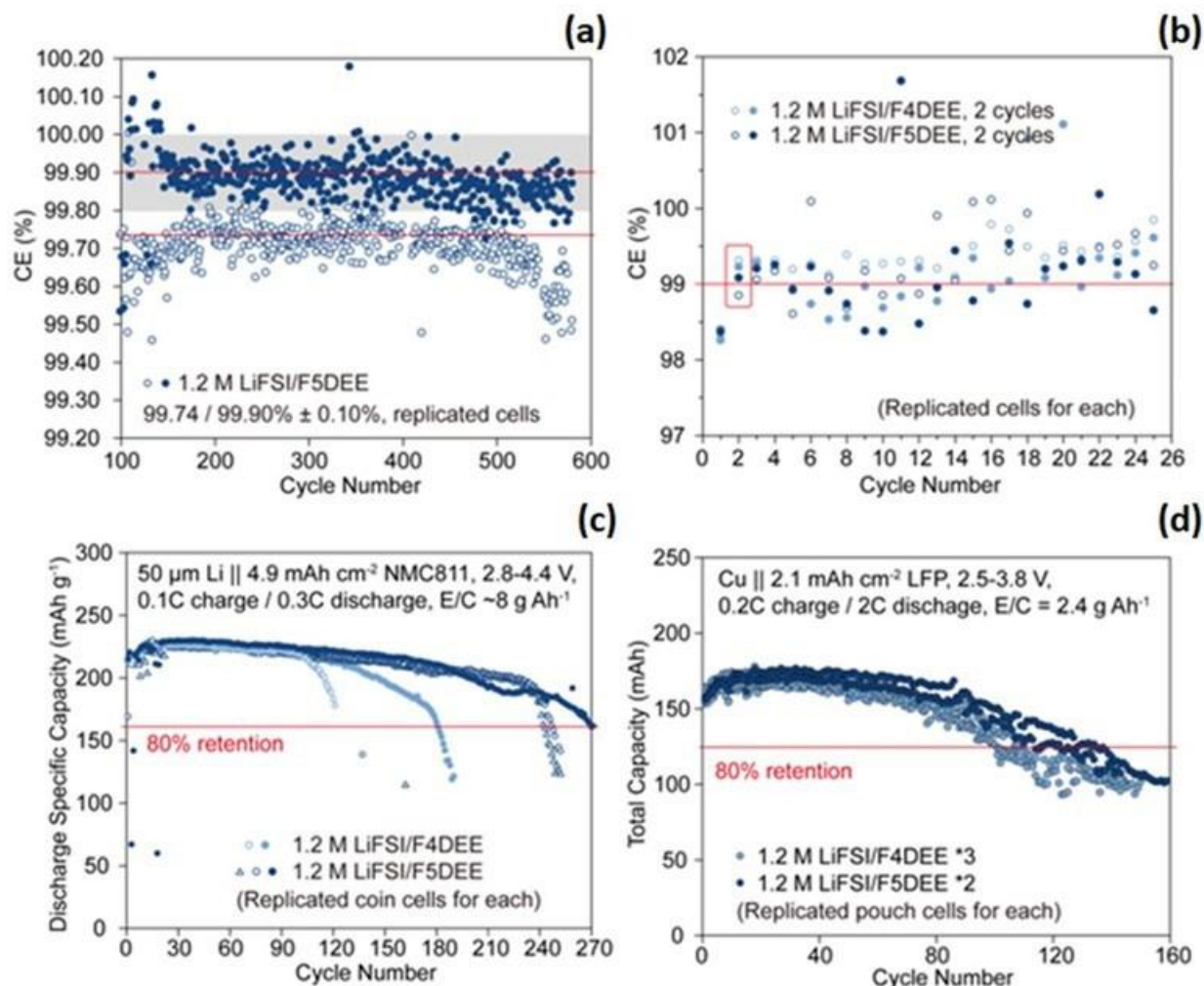


Figure 14. Cycling performance of Li||Cu half cells, practical Li metal batteries and industrial anode-free pouch cells using NMC811 and LFP cathodes

Explainable machine-learning model for battery aging and lifetime prediction (SLAC National Accelerator Laboratory & Stanford University)

The long lifetime and diverse operating conditions of EV Li-ion batteries is a key bottleneck in the R&D cycle. Even under accelerated testing conditions, hundreds to thousands of batteries must be aged for one or more years to fully assess the performance and degradation modes, even for just one battery chemistry/cell design. As such, accelerating battery testing represents a substantial opportunity to speed up the adoption of new battery chemistry and cell design. SLAC National Accelerator Laboratory and Stanford University have established the Battery Informatics Lab to harness the power of artificial intelligence and machine learning to predict battery performance using minimal experimental data. The goal of this work is three-fold: (1) use early aging data to predict battery performance such as cycle life, calendar aging, resistance growth and probability of lithium plating; (2) estimate and identify battery degradation modes across a diverse set of operating conditions, including real vehicle driving cycles; (3) predict battery aging modes to accelerate materials and cell design via rational and actionable feedback.

We have experimentally demonstrated early prediction of cycle life on both lithium iron phosphate/graphite and nickel-cobalt-aluminum/Silicon-graphite cylindrical cells, generating a dataset totaling more than 600 cells cycled over four years. The cycling conditions included extreme fast charging conditions (10 minutes to 80%

state-of-charge). Using the first 5 to 100 cycles, we successfully predict the cycle life of cells spanning hundreds to thousands of cycles, Figure 15. Beyond cycle life, our machine learning model also predicts resistance/power fade and other cell characteristics relevant to EVs. Beyond performance predictions, our machine learning models are also interpretable, mapping the aging behavior to both cycling conditions (such as charging and discharging rates, depth of discharge, and cutoff voltages) to internal cell conditions (such as anode and cathode state-of-lithiation). We expect this artificial intelligence/machine learning approach for predicting battery aging and lifetime to dramatically shorten the R&D cycle, from years to month, enabling more rapid materials and cell design innovations.

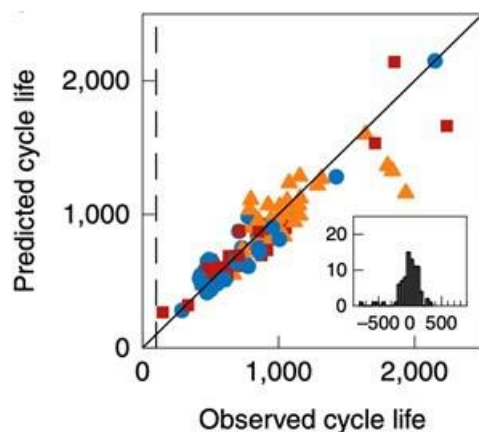


Figure 15. Early prediction of LFP/graphite cycle life under extreme fast charging conditions using data from the 10th and 100th discharge cycle. Reproduced from Severson et al. *Nature Energy* 4, 383 (2019)

Zero-cobalt, zero-strain, high-rate cathodes with improved thermal stability (University of California, Irvine)

Cobalt (Co) is considered the highest material supply chain risk for electric vehicle (EV) batteries. However, eliminating Co from $\text{LiNi}_x\text{Mn}_y\text{Co}_z\text{O}_2$ (NMC) cathodes can exacerbate thermal and chemomechanical instabilities due to high-nickel (Ni) concentrations sometimes used, particularly at the material surface where it is exposed to reactive electrolyte. In addition, the volume change in high-Ni cathode materials can cause both structural degradations and mechanical failures. Another drawback is that nearly all high-Ni cathodes, irrespective of Co-level, suffer from intrinsically poor thermal tolerance in the charged (delithiated) state, owing to the combination of the strong oxidizability of Ni^{4+} and oxygen release. Although high-Ni cathodes enable higher capacities, it inevitably results poorer stability and abuse tolerance particularly at elevated voltages.

To address these issues, the team at UC Irvine has developed a new class of concentration-complex stoichiometric layered oxides^{3,4} that have 1) zero cobalt content, 2) zero strain (<1% relative volume change) between 2.5V – 4.3V window, and 3) high thermal stability. At the same time, they can deliver equal or higher capacity, energy density, and rate capability as their NMC counterparts with the same Ni content. They have demonstrated two zero-cobalt chemistries. The first has high Ni content (Ni content = 80%, HE-N80) targeting high-power and long-range EV applications aiming to displace NMC-811. Differential scanning calorimetry (DSC), capacity, rate capability, and cycling data for HE-N80 is shown in Figure 16 and demonstrates the advantage of this material compared to NMC811. A second cathode with lower Ni content (Ni content = 50%, HE-N50), targeting medium-range EV applications, is comparable in energy to NMC-532. Both cathodes have excellent cycle life due to the combined effect of zero strain, high oxygen retention, suppressed phase transformation and reduced transition metal (TM) dissolution. The manufacturing process of these cathodes are the same as NMC-811 and NMC-532 respectively allowing them to be quickly scaled up in domestic manufacturing facilities.

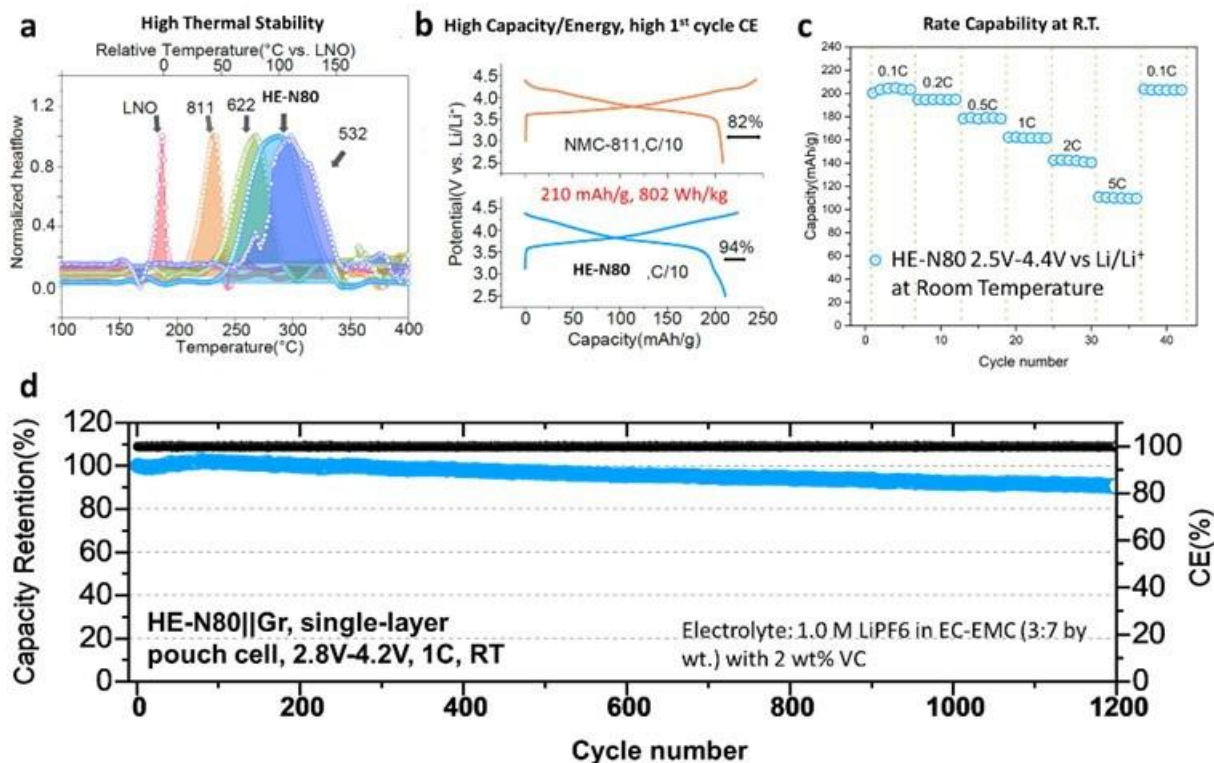


Figure 16. The electrochemical and thermal stability performance of UCI's HE-N80 cathode. (a) DSC measurements of charged cathodes. (b) Comparison of HE-N80 and NMC-811. (c) Rate capability. (d) Cycle life in a single layer Li-ion pouch cell.

Enabling Long Cycle Life in High Voltage Co-Free Spinel Oxide Cathode (University of California San Diego)

$\text{LiNi}_{0.5}\text{Mn}_{1.5}\text{O}_4$ (LNMO) is a promising cathode for next generation lithium ion batteries due to its high operation voltage ($\sim 4.7\text{V}$) and cobalt-free nature. However, it is still facing challenges such as poor cycling stability and low electronic conductivity. In this work, researchers at UCSD developed a dry electrode fabrication method to enable high areal loading LNMO (up to 9.5 mAh/cm^2 , over two times that of current electric vehicle battery cells) as shown in Figure 17A. Compared to 3 mAh/cm^2 loading, the cell performance at this high loading is unaffected. This fabrication method is also a solvent-free process, rendering this method environmentally benign. Researchers also used plasma focused ion beam scanning electron microscopy (PFIB-SEM) to investigate phase uniformity. The results (Figure 17B) show that active materials and conductive carbon are uniformly distributed, which allows fast electron transport.

Assisted with computation at different facets of the material, researchers found that fluoroethylene carbonate (FEC) molecules have the highest energy barrier which allows stronger oxidation stability at high voltage (Figure 17C). Together with novel all-fluorinated electrolyte, the cycling stability the LNMO/graphite full cell is also significantly enhanced (Figure 17D). This developed dry electrode methodology can be applied to other cathode materials operating with voltages higher than 4.5 V .

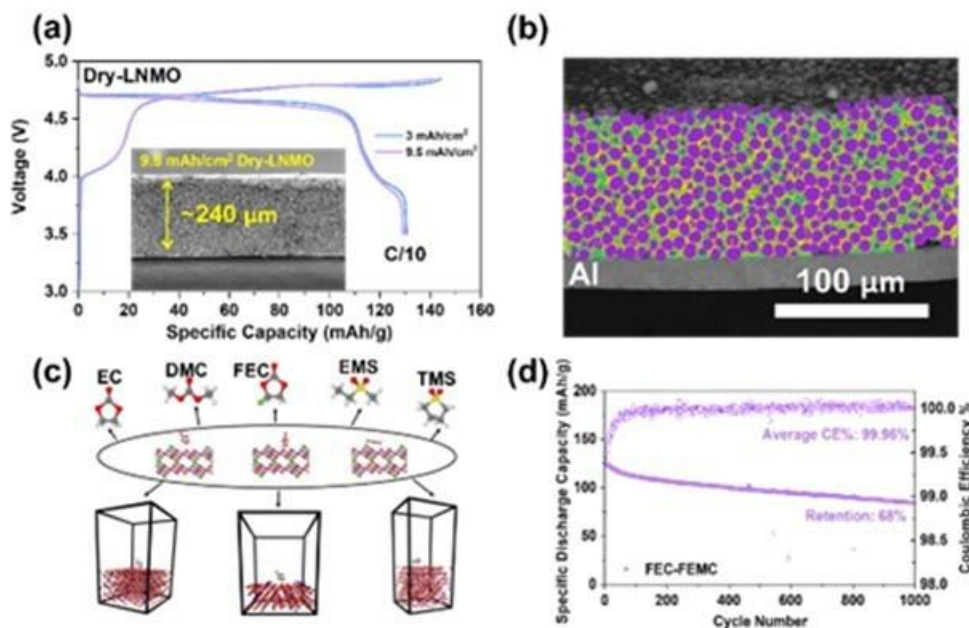


Figure 17. (A) Electrochemical performance of both low and high loading LNMO and the SEM cross-sections. (B) PFIB-SEM of dry-LNMO. Purple represents LNMO, green represent carbon and yellow represents porosity. (C) A three-component framework for the computational screening of electrolyte/cathode interface materials (D) Long-term cycling of LNMO full cell.

Low and no cobalt containing high energy cathodes, (University of Texas at Austin)

Despite the success of lithium (Li)-ion technology, energy and cost requirements remain extremely stringent, especially for electric vehicles (EV). University of Texas at Austin researchers are working to advance Li-ion cathodes with no- and low-cobalt high-nickel cathodes produced using industrially scalable methods. The team developed a cathode with 85% nickel-content and only 5% cobalt ($\text{LiNi}_{0.85}\text{Co}_{0.05}\text{Mn}_{0.075}\text{Al}_{0.02}\text{Mg}_{0.005}\text{O}_2$, NMCAM-85). The cathode achieved over 1,000 cycles in 2Ah pouch cells (1M LiPF_6 in EC/EMC (3:7 wt.) + 2% VC electrolyte), with cathode-level energy densities above 650 Wh/kg (Figure 18).

Recently, they developed a completely cobalt-free cathode ($\text{LiNi}_{0.90}\text{Mn}_{0.05}\text{Al}_{0.05}\text{O}_2$, NMA-90) which delivers performance similar to the cobalt-containing NMCAM-85. NMA-90 achieves 500 cycles with 88% capacity retention in 200 mAh pouch full cells using the same electrolyte as in the NCAM-85 cells (Figure 19).

In addition, the team has worked to scale-up cathode synthesis. Cathode production in kilogram quantities introduces additional challenges typically overlooked at lab scale. Of critical importance are homogeneous dispersion of lithium sources and oxygen diffusion within the precursor bed. The team found that calcination crucibles have a critical packing depth, above which the material receives insufficient oxygen. Furthermore, heavy crucible loadings caused lithium congregation at the bottom of the crucible. These problems may be circumvented by stacking multiple half-filled crucibles inside the furnace, and by remixing the reagents after a brief initial heating to redistribute lithium. In doing so, the team produced multiple kilograms of high-performance cathode material for large-format pouch cells.

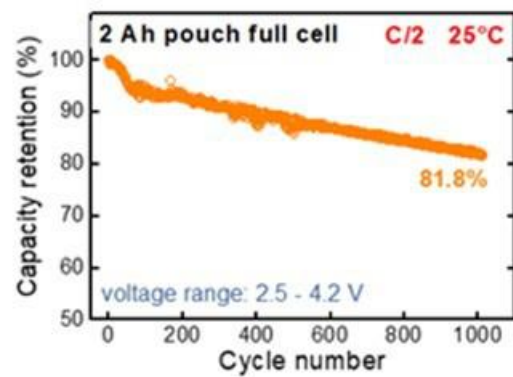


Figure 18. NMCAM-85 large-format pouch cells (2 Ah) achieve 1,000 cycles with greater than 80% capacity retention, cycled between 2.5 – 4.2 V

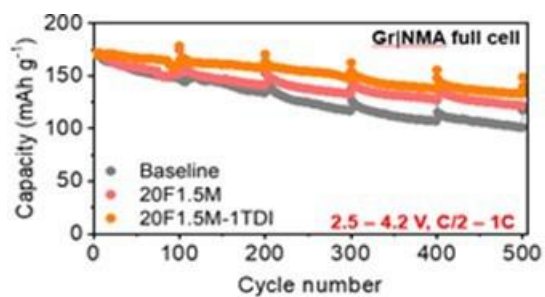


Figure 19. Tailored electrolyte stabilizes cathode performance, allowing cobalt-free NMA-90 to achieve 500 cycles with 88% capacity retention

I USABC Battery Development & Materials R&D

The United States Advanced Battery Consortium (USABC) is a subsidiary of USCAR and a cooperative agreement with the DOE. The USABC mission is to develop electrochemical energy storage technologies that advance commercialization of next generation EV applications through funding precompetitive development contracts. The consortium, comprised of General Motors, Ford, and Stellantis, competitively awards battery and material development contracts, for which the recipient contributes a 50% cost share. USABC issues requests for proposal information, evaluates submitted proposals, and manages the resulting development contracts. The USABC working structure consists of a technical advisory committee (TAC) which makes technical recommendations to the USABC management committee (MC).

USABC has developed mid- and long-term battery goals for EV applications, plug-in hybrid vehicle applications, separators, 12V start-stop batteries, and other vehicular applications. In addition, it developed standard test procedures to evaluate performance of batteries and progress towards goals. The goals and test procedures can be found at <https://uscar.org/usabc/>. Table I.0.1 and Table I.0.2 show some of the goals.

In 2022, the USABC continued to fund and manage multiple contracts in the areas of low cost and fast charge EV batteries, beyond Li-ion batteries (i.e. cells using a Li metal anode), high voltage electrolytes, novel recycling technology, and prelithiation technology.

Table I.1 USABC Goals for low-cost/fast-charge advanced batteries for EVs (CY 2023)

End of Life Parameter	Units	Value
Peak Discharge Power Density, 30 s	W/l	1400
Peak Specific Discharge Power, 30 s	W/kg	700
Usable Energy Density	Wh/l	550
Specific Usable Energy (defined at power target)	Wh/lg	275
Calendar Life	Years	10
Cycle Life (25% FC)	Cycles	1000
Cost (@ 250k annual volume)	\$/kWh	75
Normal Recharge Time	Hours	<7
Fast Rate Charge Minutes 8	Minutes	80% UE in 15 minutes

Table I.2 USABC Goals for non fast-charge batteries for EVs (CY 2023)

End of Life Parameter	Units	Value
Peak Discharge Power Density, 30 s	W/l	1500
Peak Specific Discharge Power, 30 s	W/kg	700
Usable Energy Density	Wh/l	750
Specific Usable Energy (defined at power target)	Wh/lg	350
Calendar Life	Years	15
Cycle Life (25% FC)	Cycles	1000
Cost (@ 250k annual volume)	\$/kWh	100
Normal Recharge Time	Hours	<7

The rest of this chapter contains detailed reports on the status of the following individual projects.

- Fast-Charge and Low-Cost Lithium Ion Batteries for Electric Vehicle Applications (Ionblox)
- Low-Cost, High Safety Fast Charge Automotive Cells (Microvast, Inc.)
- Low-Cost and Fast-charging Lithium-ion Battery based on Neocarbonix™ NMP/PVDF-binder Free Electrode Processing for EV Applications (Nanoramic)
- Evaluation of Advanced Li-ion Cell Architectures for Extreme Fast Charging (XFC) Batteries for Electric Vehicles (EnPower, Inc.)
- Solvent-free Electrode Manufacturing for Low Cost/Fast Charging Batteries (Worcester Polytechnic Institute)
- Development of Advanced Low-Cost / Fast-Charge (LC/FC) Batteries for EV Applications (Farasis Energy USA)
- Pre-lithiation of Silicon-containing Anodes for High-Performance EV Batteries (Applied Materials, Inc.)
- Electrolyte Development: High Performance Electrolyte for High Voltage Batteries (Gotion)
- Strategic Collaboration for the Development of a Self-Sustaining Model for the Recycling of Large-Format Lithium-Ion Batteries (American Battery Technology Company)
- Silicon-based EV Cells Meeting Cost, Calendar Life and Power (Ionblox, Inc.)
- Low-cost, Fast-charging Silicon Nanowire Cell Technology (Amprius).

I.1 Fast-Charge and Low-Cost Lithium Ion Batteries for Electric Vehicle Applications (Ionblox)

Herman Lopez, Principal Investigator

Ionblox Inc.
3390 Gateway Blvd.
Fremont, CA 94538
E-mail: herman@ionblox.com

Brian Cunningham, DOE Technology Development Manager

U.S. Department of Energy
E-mail: brian.cunningham@ee.doe.gov

Start Date: February 1, 2019
Project Funding: \$1,245,738

End Date: June 30, 2022
DOE share: \$622,869

Non-DOE share: \$622,869

Project Introduction

To reduce our dependence on fossil fuels and decrease greenhouse gas emissions, electric vehicles (EVs) have received intense attention as a possible solution. Electrification of automobiles is gaining momentum with the main barrier preventing widespread adoption being the lack of available low cost, high energy, fast-charging and safe energy storage solutions. Lithium-ion batteries (LIBs) are presently the best energy storage solution used in current and upcoming EVs. Further improvements to the performance of LIBs by integrating high-capacity active materials, novel passive components and unique cell designs will be critical for the success and mass adoption of EVs.

This project has been based on developing novel electrolyte formulations, optimized cell designs and a scalable pre-lithiation solution that enables the use of high-capacity silicon oxide anodes that would result in lithium-ion batteries capable of meeting the Low-Cost and Fast-Charge (LC/FC) USABC goals for advanced EV batteries in CY 2023. High specific capacity anodes containing high amounts of active silicon (>50%), Nickel-rich Ni-Co-Mn (NCM) cathodes and uniquely tailored electrolyte formulations have been integrated in large capacity (10-50 Ah) pouch cells targeting Fast-Charge and Low-Cost energy solutions. During this program, Ionblox has demonstrated Fast-Charge and Low-Cost LIBs maintaining other performance requirements of EV cells, including energy, power, cycle life, calendar life, and safety.

Objectives

The key objectives in this program are:

- Develop unique electrolyte formulations integrating commercially available organic solvents, salts and additives that will improve performance with Silicon anodes and Ni-rich NCM cathodes.
- Evaluate and support the development of a pre-lithiation solution for high capacity and high percent active silicon anodes addressing manufacturability, reproducibility, cost, and safety.
- Develop optimized cell designs to build and deliver cells that will meet the USABC EV battery goals for commercialization in calendar year 2023.
- Evaluate and integrate cost effective and high performing active and passive materials, processing steps and cell designs to meet the Low-Cost and Fast-Charge targets.
- Build, deliver and test large format (10 Ah - 50 Ah capacity) pouch cells integrating optimized high-capacity silicon-based anode, NCM cathode, electrolyte, separator and pre-lithiation to meet the USABC EV goals of fast-charge, low cost, energy, power, cycle life, calendar life, safety, and temperature.

Approach

Ionblox has utilized a system-level approach to screen, develop and optimize the critical cell components (cathode, anode, electrolyte, separator), pre-lithiation process (process, dose), cell design (N/P ratio, electrode design) and cell formation and testing protocols that would enable meeting the USABC EV cell level goals for the year 2023. The development was based on integrating pre-lithiated silicon-based high-capacity anodes, high-capacity Ni-rich NCM cathodes, high voltage electrolytes and composite separators into large capacity (10-50 Ah) pouch cells. The developed cells were optimized to meet the Low-Cost and Fast-Charge targets along with high energy density and power, good cycle life and calendar life, safety, and low and high temperature performance. During the program, Ionblox used three cell build iterations to meet the program targets and deliver cells to the National Laboratories for independent testing. Cells have been tested both at Ionblox and independently by three National Laboratories: Idaho National Laboratory (INL), Sandia National Laboratory (SNL) and National Renewable Energy Laboratory (NREL).

During the program, Ionblox leveraged its material, processing and cell design and development expertise to screen, engineer and optimize various electrolyte formulations, pre-lithiation approaches and cell design solutions addressing the challenges associated with meeting the USABC Low-Cost and Fast-Charge cell targets. Ionblox identified development areas that have been addressed and improved during the program. Significant material and cell development in the areas of electrolyte engineering, pre-lithiation development and cell design engineering have been implemented. Material and cell development typically started at the coin-cell level where initial screening, testing and optimization took place. Ionblox has extensive experience working with coin-cells ensuring that identical electrode formulations, specifications, cell designs, components, formation, etc. are identical to what is used in the pouch cell designs and therefore ensuring similar results are obtained. Once the critical parameters were optimized at the coin-cell level, results were validated and fine-tuned at the pouch cell level typically in 12 Ah capacity pouch cells.

Ionblox has shown a path for their silicon-dominant cell technology to meet the USABC program EV cell cost target of 75 \$/kWh. The path to reach the target cell cost is achieved by several approaches. First, the high energy density of the cells increases the kWh of a given system, which reduce the \$/kWh ratio and cost target gap. In addition, by utilizing a high-capacity silicon-based anode, the quantity of active material reduced, and cost decreased. While the current costs for silicon oxide and pre-lithiation are higher compared to graphite-based cells, Ionblox continues to evaluate and qualify cost effective options and believes that the cost of these important components and processes will continue to decrease significantly as existing suppliers scale production and additional suppliers come online. Ionblox has identified and qualified cost-effective silicon suppliers that are projecting similar costs to graphite once manufacturing production levels continue to scale. Ionblox has also partnered with a cell manufacturing partner and equipment vendors to build pre-lithiation equipment capable of meeting the Low-Cost and manufacturing program targets.

During the duration of this program, Ionblox met the majority of the USABC Low-Cost and Fast-Charge cell specifications by integrating silicon-dominant anodes, unique electrolyte formulations and cell designs that have improved fast charging, cycle life and calendar life. The final cell build of the program is anticipated to further improve the calendar life and cost of the cells by integrating an optimized electrolyte formulation and a lower cost pre-lithiation solution, respectively.

The program consists of 3 cell builds that include a baseline cell build at the beginning of the program (CB#1), a second cell build (CB#2) midpoint in the program and a final cell build (CB#3) at the conclusion of the program. The cell builds were structured in a way that as the program progressed, the cell targets increased with respect to specific energy, energy density, and cycle life and lowered with respect to cell cost.

Figure I.1.1 shows the projected usable BOL (beginning of life) and EOL (end of life) cycle life (a), cell cost (b), specific energy (c) and energy density (d) for the three cell builds. The measured cell parameters and calculated cost for the baseline cells (CB#1), CB#2 and final CB#3 cells are shown in the figure. Cycle life at 100% fast charge (4C rate - 15-minute) from CB#1 is already nearing the target 1,000 cycles and Zenlabs

anticipates CB#2 and CB#3 to exceed the cycle life target. Cell cost for CB#2 is identical to CB#1 and higher than anticipated because CB#2 continued to use the costlier pre-lithiation process. CB#3 was intended to use a cost effective pre-lithiation solution that would greatly reduce the cell cost. There are two cost calculations for CB#3, the first uses a costlier lithium metal powder Pre-Li process and the second uses a more cost-effective Li-doped SiO_x material that eliminates the need for Pre-Li. CB#1, CB#2 and CB#3 are on track with the anticipated specific energy, energy density and cost targets.

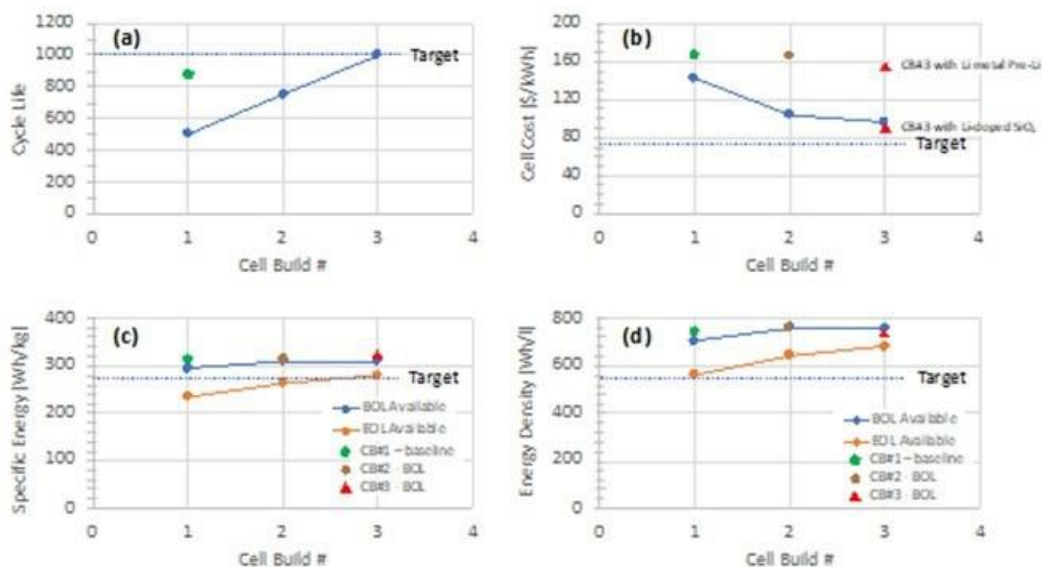


Figure I.1.1 Projected & measured cell performance progression throughout the program CB#1, CB#2, & CB#3

Results

Development during 2022 focused on delivery and testing of the final program Cell Build #3 (CB#3) cells both at Ionblox and at the National Labs (INL, NREL, SNL). This USABC program was completed on June 30, 2022, with the successful completion of the final cell deliverable (CB#3) to the National Labs and submission of the final USABC program report.

For the final CB#3 cell deliverable of the program, cathode #19 and electrolyte #50 were down-selected based on capacity retention, resistance growth, cycle life, gassing, and fast charge rate performance. CB#3 used two different approaches to compensate for the high irreversible capacity loss (IRCL) of the SiO_x anodes. The first approach used lithium metal powder as the pre-lithiation source and the second used Li-doped SiO_x anode with low IRCL. As shown in Figure I.1.2, two different cell formats were prepared and delivered to the National Labs as the final CB#3 cell deliverable. 39 cells of 12 Ah capacity footprint and 5 cells of 50 Ah capacity footprint lithiated by lithium metal powder were delivered to the National Labs for independent testing. 6 additional cells of 12 Ah capacity footprint prepared by Li-doped SiO_x were also delivered to Idaho National Laboratory.

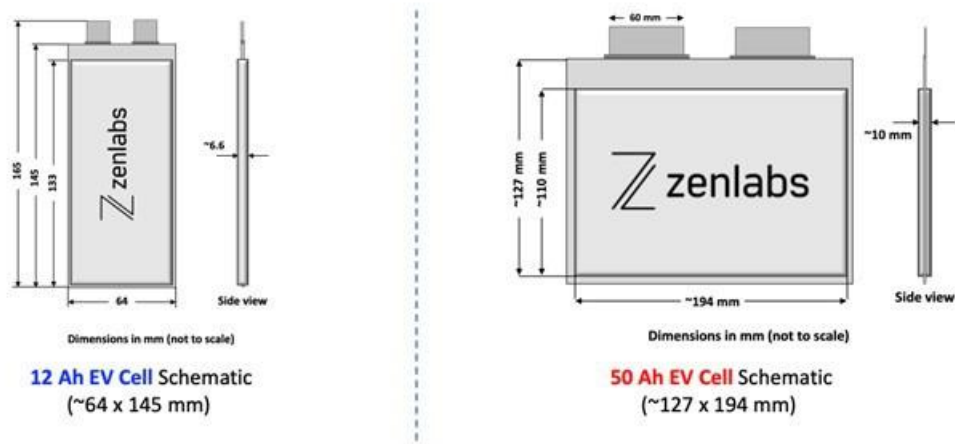


Figure I.1.2 Footprints for 12 Ah and 50 Ah pouch cells that were prepared for CB#3

CB#3 Pouch Cells Performance Measurements at Ionblox

Cell performance measurements are ongoing at Ionblox in parallel with the testing at the National Labs. The testing status of the CB#3 cells at Ionblox is ongoing and are summarized in Figure I.1.3. Testing results will continue to be presented in future USABC reports as part of the new USABC program.

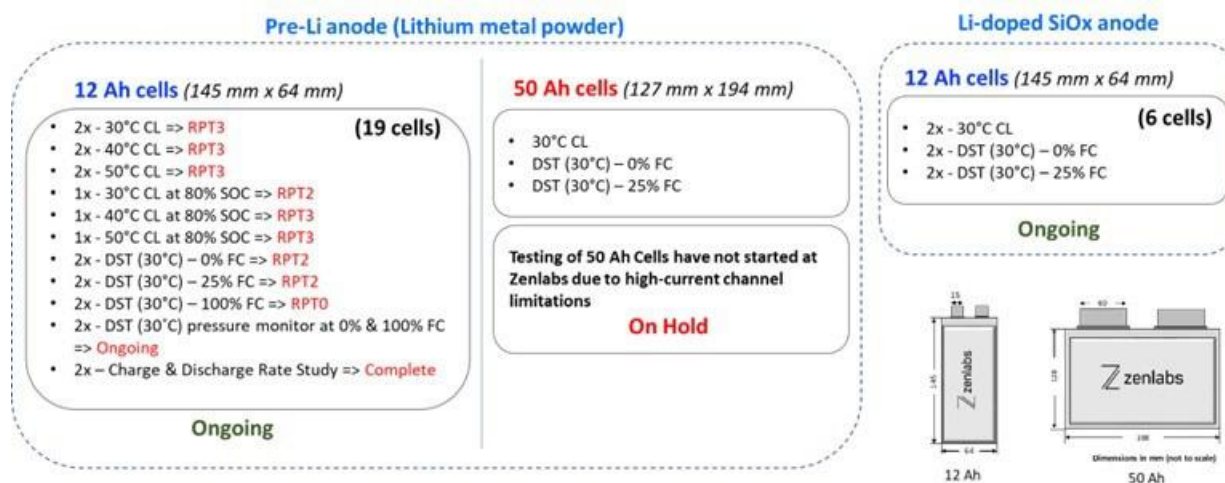


Figure I.1.3 Status of ongoing performance testing on baseline pouch cells

CB#3 Pouch Cells- 12 Ah Footprint

The 70 cells that were built as part of CB#3 showed consistent capacity, energy, OCV, weight and thickness. The summary of these measurements is shown in Figure I.1.4. The cell results are consistent across the cells with standard deviations < +/- 1% across the measured capacity, average voltage, thickness, and energy.

The capacity and energy measurement during charge and discharge on eight 12 Ah cells are shown in Figure I.1.5. The identical measurements confirm consistent charge and discharge curves for both energy and capacity.

The power and resistance measurements in Figure I.1.6 show that the CB#3 cells at RPT-0 are meeting the discharge and Regen power requirements of the USABC program. Additionally, these measurements confirm consistent power and resistance results for eight cells.

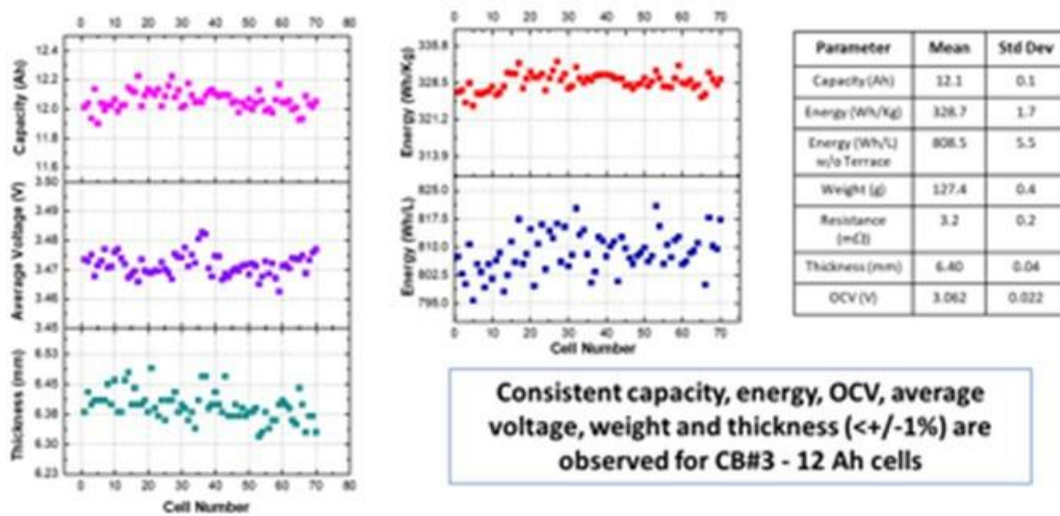


Figure I.1.4 Measurements (Capacity, Average Voltage, Thickness, Weight, Energy) on CB#3 cells after formation for 12 Ah cells.

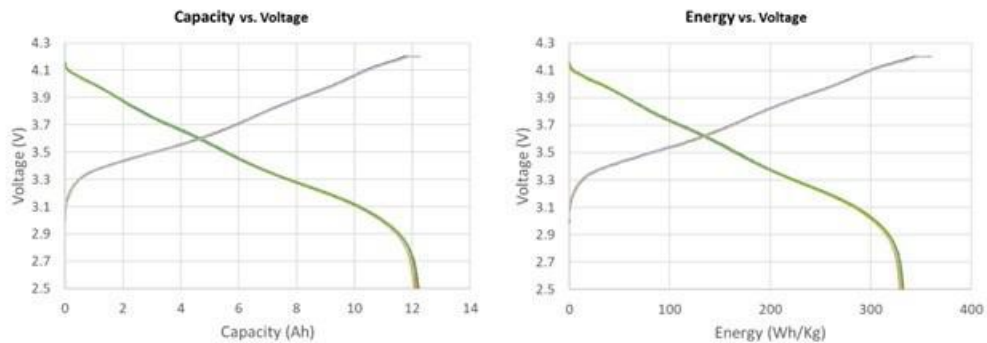


Figure I.1.5 Capacity and energy measurement versus voltage during charge and discharge for 12 Ah pouch cells.

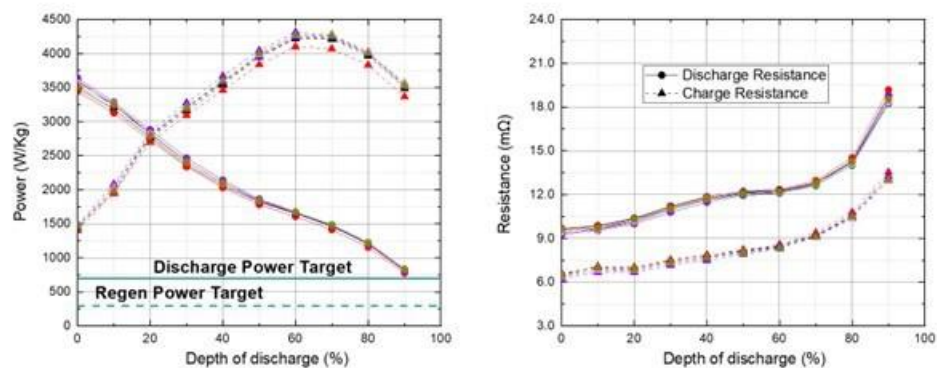


Figure I.1.6 Power and resistance measurement versus depth of discharge for 12 Ah pouch cells

CB#3 Pouch Cells- 50 Ah Footprint

The capacity, OCV, resistance, average voltage, weight, thickness and energy measurements from 50 Ah footprint cells are summarized in Figure I.1.7. The measurements confirmed the consistency in cell production standard deviations of $< \pm 1\%$.

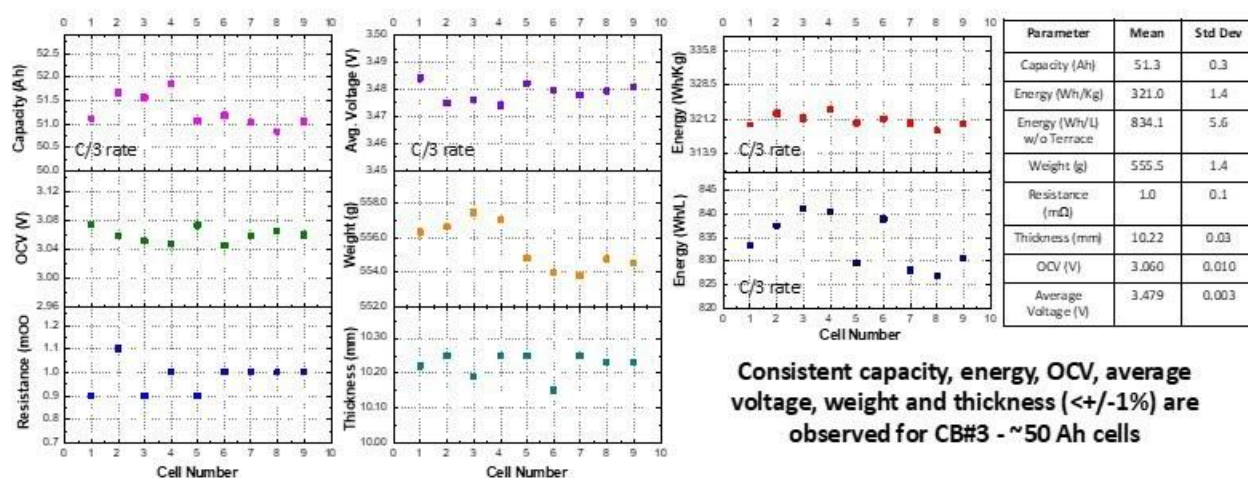


Figure I.1.7 Measurements (Capacity, OCV, Resistance, Average Voltage, Weight, Thickness and Energy) after formation on 50 Ah footprint cells

CB#3 Pouch Cells- Cycling Data

During 2022, the CC-CV cycling tests of two CB#3 cells completed. The CC-CV cycling results at standard 1C/1C rate and fast charge (4C/1C rate) are shown in Figure I.1.8. The measurements show the cycling data of ~850 cycles before the cells reach 80% capacity retention cycled at room temperature under a 1C/1C charge and discharge rate at the voltage window of 4.2V to 2.5V. The cycle life results under a 4C/1C rate CC-CV cycling protocol (4.2V to 2.5V) show ~450 cycle before reaching 80% capacity retention.

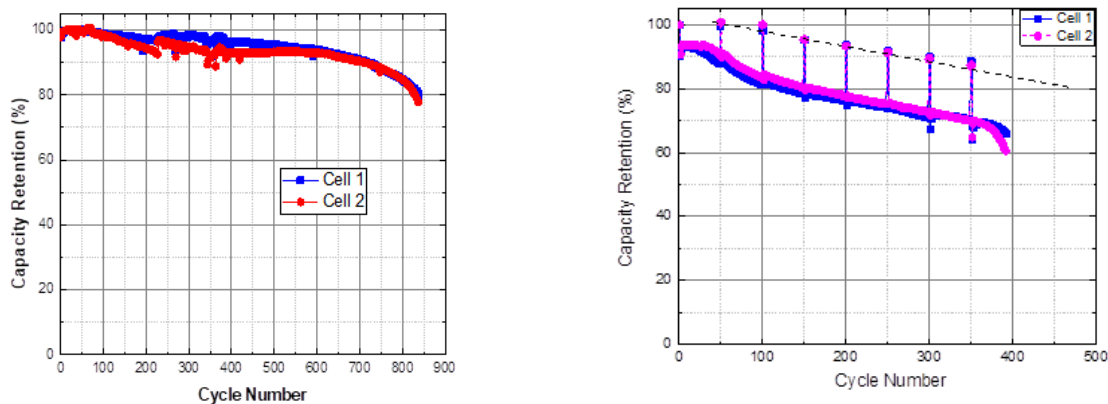


Figure I.1.8 Cycling of two 12 Ah cells (CB#3) prepared with lithium metal powder at 1C/1C rate (left) and 4C/1C rate (right) at room temperature.

The summary of the measured performance vs USABC requirements and the Gap Chart of the CB#1, CB#2, and CB#3 cells are shown in Figure I.1.9. The table shows the data for CB#1 (DST cycling at 0% fast charge, DST cycling under 100% fast charge, and Calendar life at 30°C), CB#2 and CB3 BOL and estimated EOL. The EOL values for CB2 & CB3 are estimated because the testing is ongoing. As the program progressed, the goals for the different cell builds increased with respect to cycle life, specific energy, energy density, and decreased for cell cost. The cell cost for CB#2 did not decrease as anticipated. Reduction in cell cost (\$/kWh) for the final cell build of the program took place by integrating a lower cost lithiation method using Li-doped SiOx. CB#3 consists of two types of cells integrating lithium metal powder pre-lithiation and Li-doped SiOx. The cost for CB#3 cells using lithium doped SiOx is lower because there is no additional pre-lithiation cost that is required. Ionblox leveraged its learning from previous USABC programs and focused on all aspects of the cell to enhance the fast-charge capability and decrease cost while meeting the various USABC cell performance metrics (capacity, energy, power, cycle life, calendar life, safety, and high and low temperature performance). The cell specifications for CB#1 exceeded the cycle life and energy goals at the beginning of the program with cell cost being above the target. Energy specifications for CB#2 and CB#3 at the beginning of life also meet the anticipated program targets. Cycle life and calendar life testing for CB#2 and CB#3 are ongoing at INL and at Ionblox.

#	End of Life (EOL) Characteristics at 30°C	Units	USABC EOL Cell Level Targets	CB#1 (#1) - DST 0% FC		CB#1 (#7) - DST 100% FC	
				BOL (RPT0)	EOL (RPT 15)	BOL (RPT0)	EOL (RPT8)
1	Peak Discharge Power Density, 30 s Pulse	W/L	1400	3979*	1050*	3808*	1792*
2	Peak Specific Discharge Power, 30 s Pulse	W/kg	700	1618*	427*	1548*	731*
3	Peak Specific Regen Power, 10 s Pulse	W/kg	300	2598*	1669*	2225*	1708*
4	Available Energy Density @ C/3 Discharge Rate	Wh/L	550	846*	556*	825*	596*
5	Available Specific Energy @ C/3 Discharge Rate	Wh/kg	275	344*	226*	335*	242*
6	Available Energy @ C/3 Discharge Rate	kWh	50	>50	>50	>50	>50
7	Calendar Life	Years	10				
8	DST Cycle life	Cycles	1000		1680		896
9	Cost	\$/kWh	75	169		169	
10	Normal Recharge Time	Hours	< 7 Hours, J1772	< 7hr		< 7hr	
11	Fast High Rate Charge	Minutes	80% ΔSOC in 15 min	>80		>80	
12	Minimum Operating Voltage	V	>0.55 Vmax	0.58 Vmax	0.58 Vmax	0.58 Vmax	0.58 Vmax
13	Unassisted Operating at Low Temperature	%	> 70% E _{usable} @ C/3 Discharge rate at -20°C	79		79	
14	Survival Temperature Range, 24 Hr	°C	-40 to + 66	passed		passed	
15	Maximum Self-discharge	%/month	< 1	0.82		0.82	
16	Battery scaling factor (BSF)	# of cells	288 (96s, 3p)	1536 (96s, 16p)	1536 (96s, 16p)	1536 (96s, 16p)	1536 (96s, 16p)
17	Battery capacity	Ah	>40	12	12	12	12

#	End of Life (EOL) Characteristics at 30°C	Units	USABC EOL Cell Level Targets	CB#1 (#15) - C.L. at 30°C		CB#2		CB#3 (Final)	
				BOL (RPT0)	EOL (RPT 16)	BOL (RPT0)	EOL (estimated)**	BOL (RPT0)	EOL (estimated)**
1	Peak Discharge Power Density, 30 s Pulse	W/L	1400	3393*	2459*	3060	2448	2986	2400
2	Peak Specific Discharge Power, 30 s Pulse	W/kg	700	1380*	1000*	1272	1018	1210	1000
3	Peak Specific Regen Power, 10 s Pulse	W/kg	300	2605*	1643*	2538	2030	2801	2000
4	Available Energy Density @ C/3 Discharge Rate	Wh/L	550	742*	670*	757	606	792	640
5	Available Specific Energy @ C/3 Discharge Rate	Wh/kg	275	302*	273*	315	252	336	276
6	Available Energy @ C/3 Discharge Rate	kWh	50	>50	>50	>50	>50	>50	>50
7	Calendar Life	Years	10		2.4		>2.4		>12.4
8	DST Cycle life	Cycles	1000				> 1000		> 1000
9	Cost	\$/kWh	75	169		169		169 / 90	
10	Normal Recharge Time	Hours	< 7 Hours, J1772	< 7hr		< 7hr		< 7hr	
11	Fast High Rate Charge	Minutes	80% ΔSOC in 15 min	>80		>80		>80	
12	Minimum Operating Voltage	V	>0.55 Vmax	0.58 Vmax	0.58 Vmax	0.58 Vmax	0.58 Vmax	0.60 Vmax	0.60 Vmax
13	Unassisted Operating at Low Temperature	%	> 70% E _{usable} @ C/3 Discharge rate at -20°C	79		79			
14	Survival Temperature Range, 24 Hr	°C	-40 to + 66	passed		passed			
15	Maximum Self-discharge	%/month	< 1	0.82		<1%			
16	Battery scaling factor (BSF)	# of cells	288 (96s, 3p)	1536 (96s, 16p)	1536 (96s, 16p)	1536 (96s, 16p)	1536 (96s, 16p)	1536 (96s, 16p)	1536 (96s, 16p)
17	Battery capacity	Ah	>40	12	12	12	12	12	12

* data collected by INL

** values are estimated

Figure I.1.9 Gap chart showing the USABC Targets versus data for CB#1, CB#2 & CB#3.

Conclusions

The program focused on meeting the USABC low-cost and fast-charge USABC EV cell targets by developing novel electrolyte formulations, a scalable pre-lithiation solution that enabled the use of high-capacity silicon oxide anodes, and optimized cell designs. In addition to the low-cost and fast-charge specifications, the cells also needed to meet the energy, power, rate, temperature, and safety metrics associated with the USABC EV cell targets. At the conclusion of the program, the extensive materials, processing, and design development culminated in multiple cells builds (CB#1, CB#2, & CB#3) that were delivered to the National Labs for independent validation of performance. From the data collected from CB#1 by the National Labs, the cells showed high energy density (>320 Wh/kg), high specific energy (>800 Wh/L), high discharge and Regen power (>1500 W/kg), fast charging capabilities (80% of the C/3 capacity in a 10-minute charge), long cycle life at a 3hr charge (1456 DST cycles), long cycle life at a 15-minute charge (920 DST cycles), long calendar life at 30°C storage (> 2 years with $>90\%$ capacity retention) and low cost (projected $< \$100/\text{kWh}$). Cell testing of CB#2 and CB#3 continue, and results will be updated in future reports.

Testing results from both CB#2 and CB#3 will continue to be updated during the new Ionblox Fast-Charge and Low-Cost USABC program. The new USABC program continues to focus on meeting all USABC EV cell specifications with special attention to meeting Calendar life, minimizing impedance growth and meeting the cell cost targets.

Key Publications

1. “Fast-Charge and Low-Cost Lithium Ion Batteries for Electric Vehicles”, ES247_Lopez_2021_p, US DOE Vehicle Technologies Program Annual Merit Review, AMR, 2021.
2. “Fast-Charge and Low-Cost Lithium Ion Batteries for Electric Vehicles”, ES247_Lopez_2020_p, US DOE Vehicle Technologies Program Annual Merit Review, AMR, 2020.

Acknowledgements

Oliver Gross from Stellantis (oliver.gross@stellantis.com) served as the USABC Program Manager for this project. This work was performed under the guidance and support from the USABC technical work group: Oliver Gross (program manager), Meng Jiang, Minghong Liu, Jack Deppe, Brian Cunningham, Lee Walker, Aron Saxon, Joshua Lamb, and Loraine Torres-Castro.

I.2 Low-Cost, High Safety Fast Charge Automotive Cells (Microvast, Inc.)

Wenjuan Mattis, PhD

Microvast, Inc.
3259 Progress Dr. #121
Orlando, FL 32826
E-mail: wenjuanmattis@microvast.com

Brian Cunningham, DOE Technology Development Manager

U.S. Department of Energy
E-mail: brian.cunningham@ee.doe.gov

Start Date: January 15, 2020

End Date: January 15, 2023

Project Funding: \$4,500,000

DOE share: \$2,250,000

Non-DOE share: \$2,250,000

Project Introduction

Automakers worldwide have announced plans to begin transitioning from gasoline powered vehicles to ones driven via electricity. To make these bold adoption plans a reality the lithium-ion battery must continue to improve so electric drive trains can become competitive in cost and convenience to a traditional gasoline powered vehicle.

Making the battery cost less is quite challenging, specifically for higher energy or higher power cells, as raw materials make up a significant portion of the batteries cost; meaning the most significant cost benefits must arise from lowering the material prices. Metals such as Li, Cu, Co, Ni, and Al are heavily used in today's battery cells with cobalt being the most expensive and least sustainable, historically. Therefore, one of the most immediate challenges facing the Li-ion battery community today is how to eliminate the use of cobalt while still having a high-performance material, especially if cost parity to internal combustion engine vehicles is to be achieved.

Fast charge creates additional technical complications that must be overcome, mostly in high energy cells. It is well-documented that Li plating and dendrite formation can occur, potentially leading to performance or safety issues as the cells continue to age.

Objectives

This project is designed to develop low-cost (i.e., approaching 75 \$/kWh when manufactured at significant scale), high energy (> 310 Wh/kg), fast charge (< 15-minutes) Li-ion battery cells for use in electric vehicles. These three terms have historically not been possible in one cell system, so careful engineering is necessary to prepare a cell capable of meeting the power, energy and cost goals. In addition, the designed cell must consider effects from temperature (hot and cold conditions), as well as safety, for the technologies under development to be practically applied in a mainstream product.

Approach

In order to develop a high energy, low-cost, fast charging, and safe battery cell for automotive applications, every aspect of the cell's components must be considered. A Li-ion cell is a complex system, and, as such, each component within the cell can influence the cell's eventual specifications.

One of the most important aspects of this project is to lower the cobalt content in the cathode while simultaneously providing high capacity and durability. Eliminating cobalt is a significant technical challenge, primarily because its use in the cathode does provide positive impact to material performance on matters such as capacity, stability and rate. So, to reduce cobalt without sacrificing performance, the project will employ full concentration gradient (FCG) cathode technology. FCG, as a designer cathode, will allow cobalt to be

minimized and selectively delivered spatially within the cathode material to maximize its utility within the powder particle.

Another unique material approach being explored in this project is the use of a fast charge electrolyte additive that provides dual passivation to the SEI and CEI. A stable interface is important to slow resistance growth; however, it hinders fast charge. The project will develop a new synthesis process for this compound which is intended to lower the cost of production.

The project cell will also integrate a graphite/silicon composite based anode blend to help provide energy density for the cell. In addition, it will incorporate Microvast's specialty aramid separator that aids in cell safety, as it is significantly more stable thermally than traditional polymer or polymer ceramic coated materials used in automotive cells today. Through the combination of these advanced materials, the project goals for a low-cost, fast charge cell will be attained.

Results

To evaluate the cell performance, USABC requested three testing conditions be considered: 0% fast charge cycles, 25% fast charge cycles or 100% fast charge cycles with a dynamic stress test (DST) discharge in all cases. The cells delivered at the end of year 1 (260 Wh/kg, graphite anode) were removed from testing after 2,000 cycles this past year to clear channel space. One interesting trial was the impact of using a C/3 charge after fast charge to return the battery to 100% state of charge (SOC) before the DST occurs (Figure I.2.1). By topping off the SOC before the energy metered DST, the cycle life more than doubled on a battery undergoing only fast charging under the prescribed test conditions.

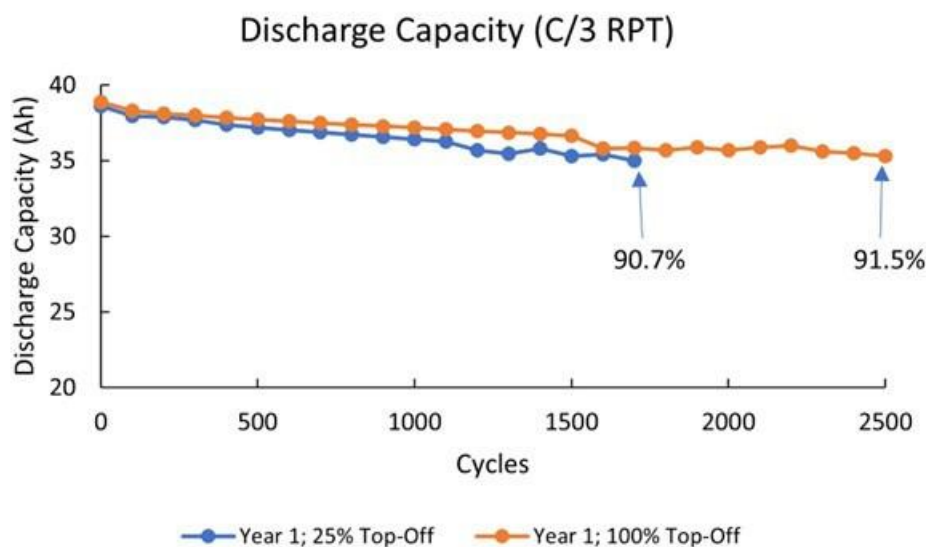


Figure I.2.1 Discharge capacity at RPT of year 1 deliverable cells undergoing DST cycling

The main effort in the past year has been to increase the energy density of the project batteries in order to reach the goal while still maintaining fast charge performance. A set of cells with ~300 Wh/kg was delivered to USABC for testing validation. The performance is still under test, but some progress is shown in Figure I.2.2. These higher energy cells do show lower cycle life under 100% fast charge testing, but the 25% fast charge retention shows good promise. These cells can reach high energy density because the cathode is higher in Ni content, and the anode charge storage was improved by more than 25%. The cell, despite being near 300 Wh/kg, shows very little thermal change during the 3C fast charge with recorded temperature rise never going beyond 10 °C at the anode tab when multiple cells were evaluated at beginning of life.

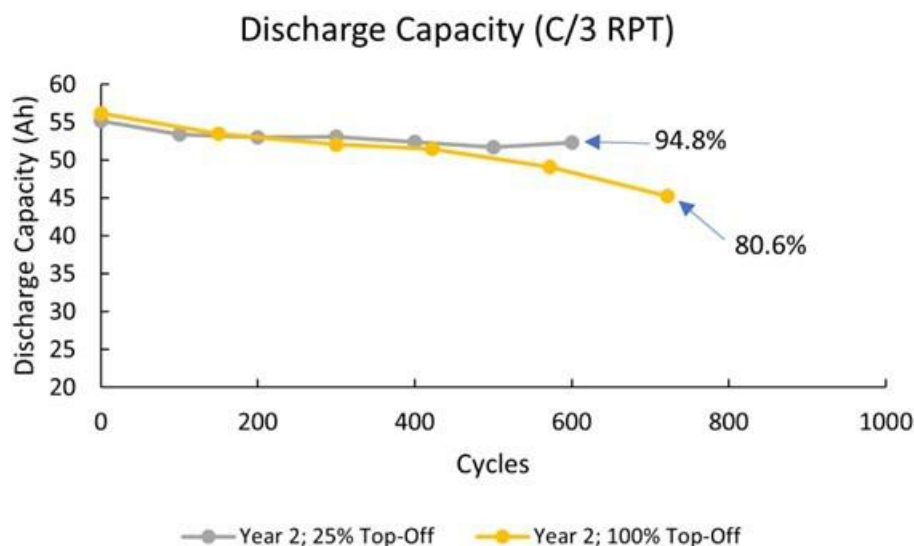


Figure I.2.2 Discharge capacity at RPT of year 2 deliverable cells undergoing DST cycling

The cells delivered were also tested at Microvast for some basic safety performance (overcharge, short circuit, thermal stability and crush). Using an international standard as the testing condition, all cells were found to pass the safety testing. Developing a battery that is safe is of key importance. The fact that our cell is showing tolerance to abuse testing is very encouraging. The changes in value from year 1 to year 2 are presented in Table I.2.1.

Table I.2.1 Percent change in cell values between year 1 and year 2 deliverable cells

Characteristics at 30°C (BOL)	Units	Improvement
Available Energy Density	Wh/L	19%
Specific Available Energy	Wh/kg	17%
Usable Energy Density	Wh/L	20%
Specific Usable Energy (defined at power target)	Wh/kg	15%
Fast Charge DST Depth	Minutes	33%
Fast Charge Rate	C	36%
30s Discharge Power @ UET	W/kg	-17%
10s Regen Power @ 20%DOD	W/kg	-24%

In the past year a prototype cell has also reached the > 310 Wh/kg energy density goal that the project set for fast charge cells. The 55 Ah cells show very similar performance to date compared to cells built > 290 Wh/kg, which saw many cells able to cycle over 900 times under the 100%FC conditions. The prototypes meeting the energy density require further evaluation and improvement to meet all the USABC project objectives, but it is

encouraging that the energy density and fast charge cycle life are on track to meet project goals by the project end.

Conclusions

The project is showing good progress in developing a 310 Wh/kg fast charge Li-ion battery. After year one's focus on materials (cathode & electrolyte additive), this year centered on developing the cell to reach the target energy density goals while still providing fast charge. There is some power loss as the cell grows in energy density, but overall, most performance metrics are increased from year 1 to year 2. In addition, it appears very feasible to reach > 1,000 cycles with our cell designs when cycling against the USABC protocols.

Acknowledgements

Microvast would like to thank Vijay Saharan, our USABC program manager, and all the members of the USABC work group for their advice and support during the project.

I.3 Low-Cost and Fast-charging Lithium-ion Battery based on Neocarbonix™ NMP/PVDF-binder Free Electrode Processing for EV Applications (Nanoramic)

Dr. Ben Cao, Principal Investigator

Nanoramic Laboratories
7 Audubon Rd Suite 100
Wakefield, MA 01880
E-mail: ben.cao@nanoramic.com

Brian Cunningham, DOE Technology Development Manager

U.S. Department of Energy
E-mail: Brian.Cunningham@ee.doe.gov

Start Date: October 1, 2021
Project Funding: \$3,600,000

End Date: April 30, 2024
DOE share: \$1,800,000

Non-DOE share: \$1,800,000

Project Introduction

Nanoramic has re-invented the way electrodes are manufactured by completely removing high molecular weight polymers such as PVDF and the toxic NMP solvent from the active material layer. This dramatically improves LiB performance while decreasing the cost of manufacturing and the capital expenditures related to mixing, coating, and drying, NMP solvent recovery, and calendaring. In the Neocarbonix™ (NX) electrodes, a 3D nanoscopic carbon matrix works as a mechanical scaffold for the electrode active material and mimics the polymer chain entanglement. Chemical bonds are also present between the surface of the carbon, the active materials, and the current collector promoting adhesion and cohesion. As opposed to polymers, however, the 3D nanoscopic carbon matrix is very electrically conductive, which enables very high power (high C-rates). This scaffold structure is also more suitable for producing thick electrode active material, which is a powerful way to increase the energy density of LiB cells.

Objectives

- Nanoramic aims to advance the Li-ion battery energy storage devices ("pouch cells") by combining Ni-rich NMC/NCMA (or other new types) Neocarbonix cathodes and Si-dominant (Si element weight% $\geq 50\%$) Neocarbonix anodes.
- The R&D objectives of this LCFC EV battery project include (see Table I.3.1):
 1. LCFC-EV battery cell capacity ≥ 9 -10 Ah at BOL (with some 65 Ah large cells).
 2. LCFC-EV battery energy density: ≥ 330 Wh/kg, ≥ 850 Wh/L at BOL.
 3. LCFC-EV battery fast-charging: 80%SOC in 15 mins.
 4. LCFC-EV battery DST cycle life with C/3 charge at 30°C: 1000 cycles with C/3 capacity retention $\geq 80\%$.
 5. LCFC-EV battery DST cycle life with $\geq 3.5C$ 15 mins fast-charge (25%FC) at 30°C: 1000 cycles with C/3 capacity retention $\geq 80\%$.
 6. LCFC-EV battery cost $\leq \$79$ /kWh at BOL.
- Timeframe: 30 months
- Budget and Cost Share: Total project budget $\sim \$3.6M$, 50% cost share.
- PI: Dr. Ben Cao (Program Manager and Technical Lead)
- Co-PI: Dr. Ji Chen (Electrode Engineering Lead).

Table I.3.1 LCFC-EV Neocarbonix Battery Parameters

LCFC-EV Neocarbonix Battery Parameters at BOL		Descriptions
Cell Capacity		≥65 Ah
Specific Energy		≥330 Wh/kg
Energy Density		≥850 Wh/L
Fast-charging 15 mins		≥80%SOC
DST Cycle Life with C/3 Charge at 30°C		≥1000 cycles with 80% capacity retention
DST Cycle Life with ≥3.5C 15 mins Fast-Charging (25%FC) at 30°C		≥1000 cycles with 80% capacity retention
Cost		≤ \$79/kWh

Approach

Nanoramic has accomplished several sub-tasks proposed in the Statement of Work (SOW). The milestones are shown below.

- Neocarbonix (NX) Ni-Rich NMC/NCMA Electrode Development
- Neocarbonix (NX) Low-Cost Silicon Anode Electrode Development
- Neocarbonix (NX) 14 Ah Battery Cell Development & Performance
- Neocarbonix (NX) Si-C Anode Electrode Pre-Lithiation (40-50 wt.% Si Element Content)
- Low-Cost Micro-Si Dominant Anode Electrode Development (Higher Si element wt.%≥80%)
Progress
- Neocarbonix (NX) Si Anode Electrolyte Development (Higher Si Element wt.%≥80%)
- Neocarbonix (NX) NCM91||Si 4.5Ah Battery Prototype Cell Development (Based on current USABC developed NX electrodes)
- Neocarbonix (NX) Ni-Rich NCM||Si ~4Ah Battery Prototype Cell Safety Test Performance (3rd Party Validation Results).

Figure I.3.1 shows the SOW plans for budget periods in 2022 and 2023.

SOW PLAN FOR BUDGET PERIOD#1 2022

For Recipient Use Only
Protected Information

SOW PLAN FOR BUDGET PERIOD#1 2023

For Recipient Use Only
Protected Information

Figure I.3.1 SOW Plans for Budget Periods for 2022 and 2023

Results

Neocarbonix (NX) Ni-Rich NMC/NCMA Electrode Development

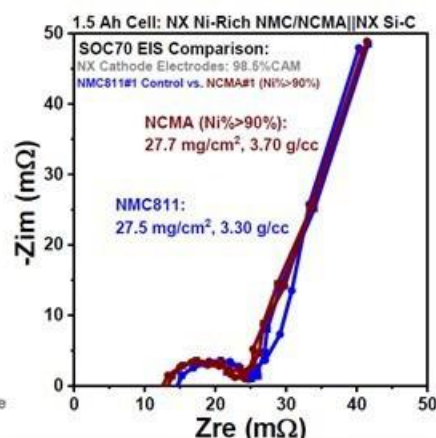
In this quarter, next generation Ni-rich NMC/NCMA (Ni% \geq 90%), high specific capacity, low-cost cathode active material (CAM) has been evaluated to decide which CAM will be utilized in the final LCFC-EV battery design. The decision of which CAM to be used is still pending to wait for more evaluation results from cell testing. Results for this task are shown in the figures below (Figure I.3.2 to Figure I.3.5).

- 1.1: High-capacity Ni-rich NMC/NCMA cathode active material selections and evaluations
 - To begin work at the beginning of Q1 2022 and completed at the end of Q3 2022
- 1.2: Neocarbonix cathode electrode formulation optimizations
 - To begin work at the beginning of Q1 2022 and completed at the end of Q4 2022
- 1.3: High loading ≥ 5.6 mAh/cm² NX cathode electrode manufacturing process optimizations
 - To begin work at the beginning of Q1 2022 and completed at the end of Q1 2023

- NCMA#1 (>90%Ni) CAM based cathode electrodes: ~ 27.7 mg/cm² with 98.5%CAM, press density ~ 3.7 g/cc.
- NMC811#1 CAM control (same as TAP cathode): ~ 27.5 mg/cm² with 98.5%CAM, press density ~ 3.3 g/cc.
- NX 1.5Ah R&D standard battery cells assembled using NX Si-C#1 anode (same as TAP).

NX 1.5Ah Battery Test Cell Name (4.2-2.5V)	Cathode Type	Initial Discharge Capacity C/10 (mAh)	Discharge Capacity C/3 (mAh)	Thickness w/ package (mm) SOC 30	Energy Density w/o package (Wh/L) (4.2-2.5V) 0.1 C-Rate
NMC811#1 Control	~ 27.5 mg/cm ² , ~ 3.3 g/cc, 98.5%CAM	1618	1545	3.26	882
NCMA#1	NCMA#1 (>90%Ni), ~ 27.7 mg/cm ² , ~ 3.7 g/cc, 98.5%CAM	1896	1821	3.32	1021

- Energy Density Wh/L calculation was only based on stacked core: electrodes (after Si anode expansion) + separators (measured) w/o packages
- Intent here is to compare the CAM NCMA#1 vs. NMC811#1 influence to the initial 0.1C-Rate energy density Wh/L
- NCMA#1 CAM is much easier to calender into higher press density 3.7-3.8 g/cc to achieve much higher energy density in Wh/L



- NX 1.5Ah R&D cells 25%fast-charging (FC) cycling performance comparison: NMC811#1 control vs. NCMA#1
- NCMA#1 shows **slightly worse FC capability** compared with NMC811#1 NX electrodes

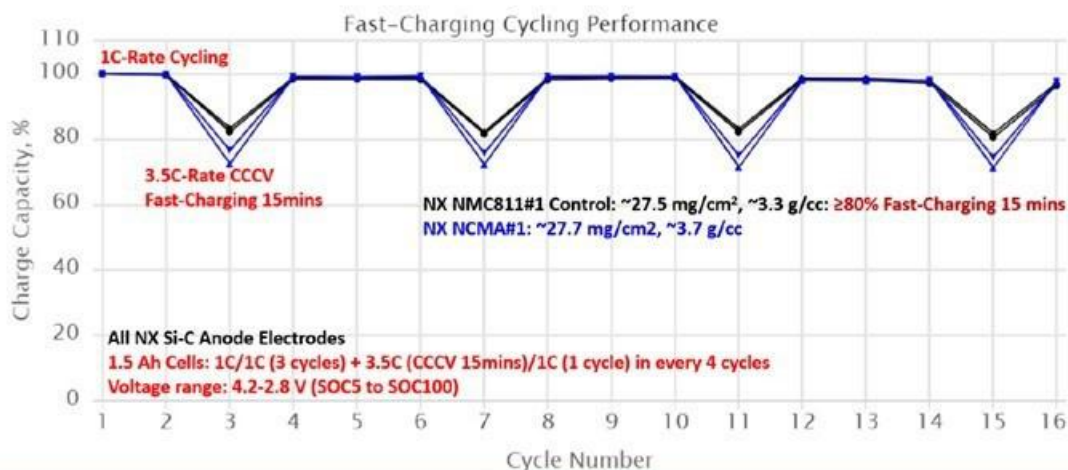
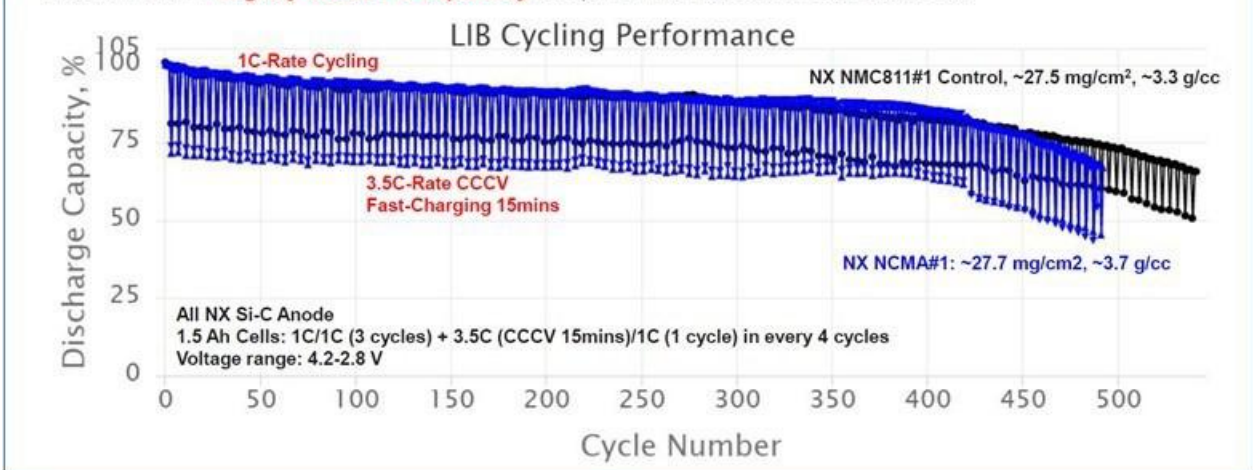


Figure I.3.2 Results for Neocarbonix (NX) Ni-Rich NMC/NCMA Electrode Development

- NX 1.5Ah R&D cells 25% fast-charging (FC) cycling performance comparison: **NMC811#1 control vs. NCMA#1**
- NCMA#1 shows **slightly worse FC capability** compared with NMC811#1 NX electrodes



- NX 1.5Ah R&D cells 1C1C cycling performance comparison: **NMC811#1 control vs. NCMA#1**
- NCMA#1 shows **slightly worse 1C1C cycling capability** compared with NMC811#1 NX electrodes

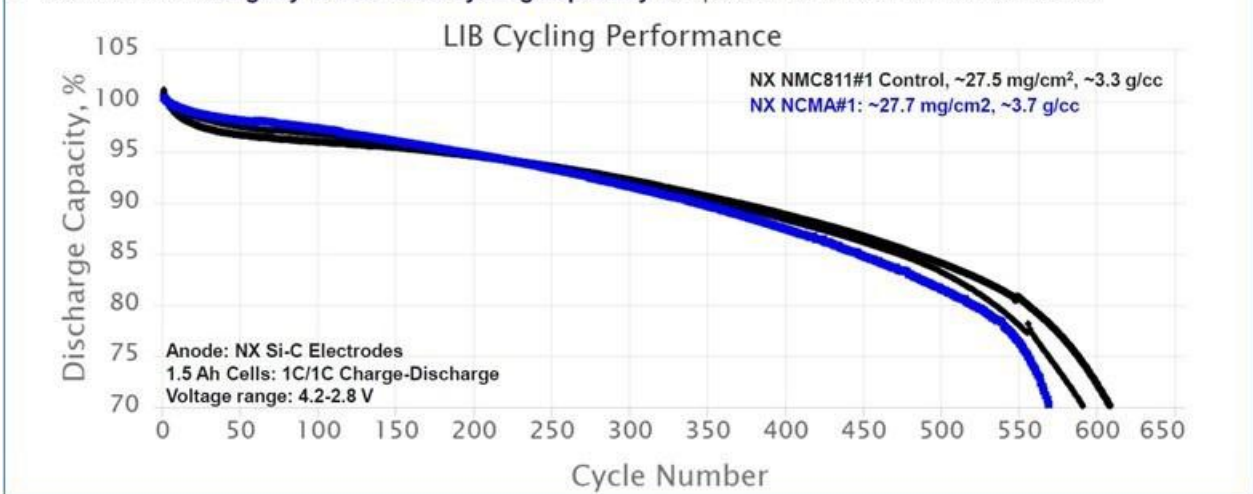


Figure I.3.3 Results for Neocarbonix (NX) Ni-Rich NMC/NCMA Electrode Development (continued)

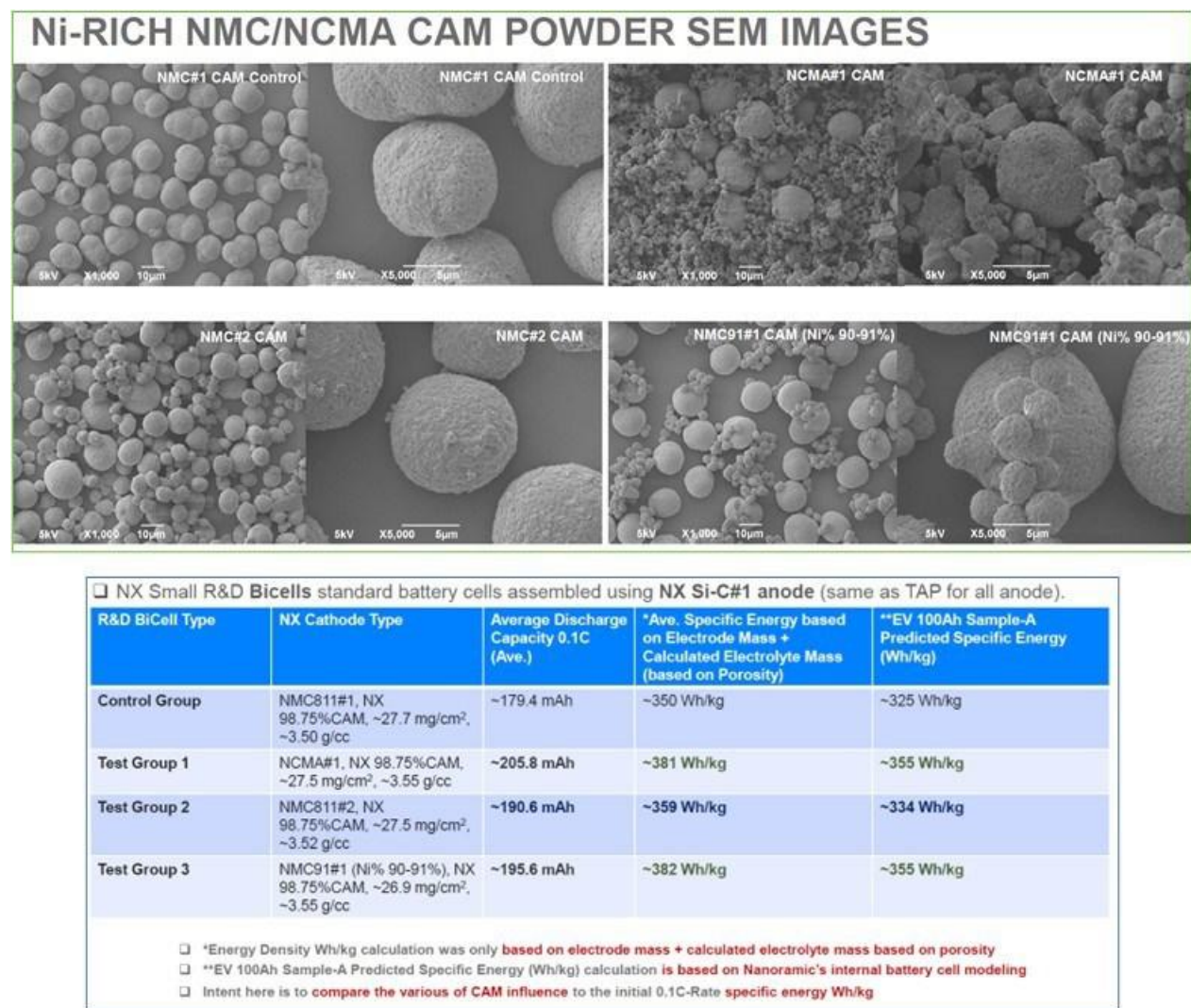


Figure I.3.4 Results for Neocarbonix (NX) Ni-Rich NMC/NCMA Electrode Development (continued)

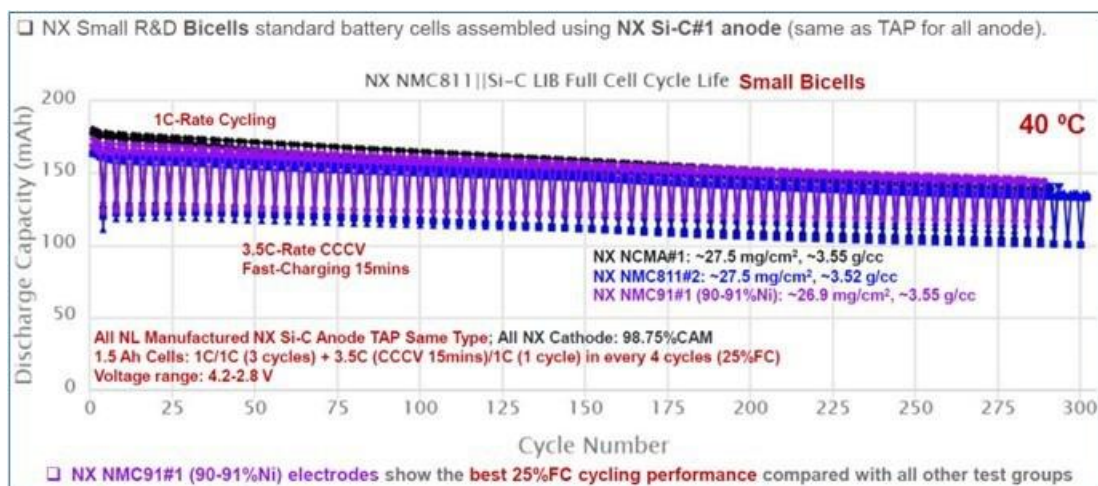


Figure I.3.5 Results for Neocarbonix (NX) Ni-Rich NMC/NCMA Electrode Development (continued)

Nanoramic has demonstrated >3x faster coating speed (60m/min) in R2R coating during the manufacturing process of the NX NCM91#1 Cathode Electrode compared to the conventional NMP method (~12-15 m/min) using the same oven size (18m).

Neocarbonix (NX) Low-Cost Silicon Anode Electrode Development

In this quarter, Nanoramic has developed NX Si-dominant anode electrode with lower-cost micro-size Si-C anode active material (AAM). Results for this task are shown in the figures below (Figure I.3.6 to Figure I.3.13).

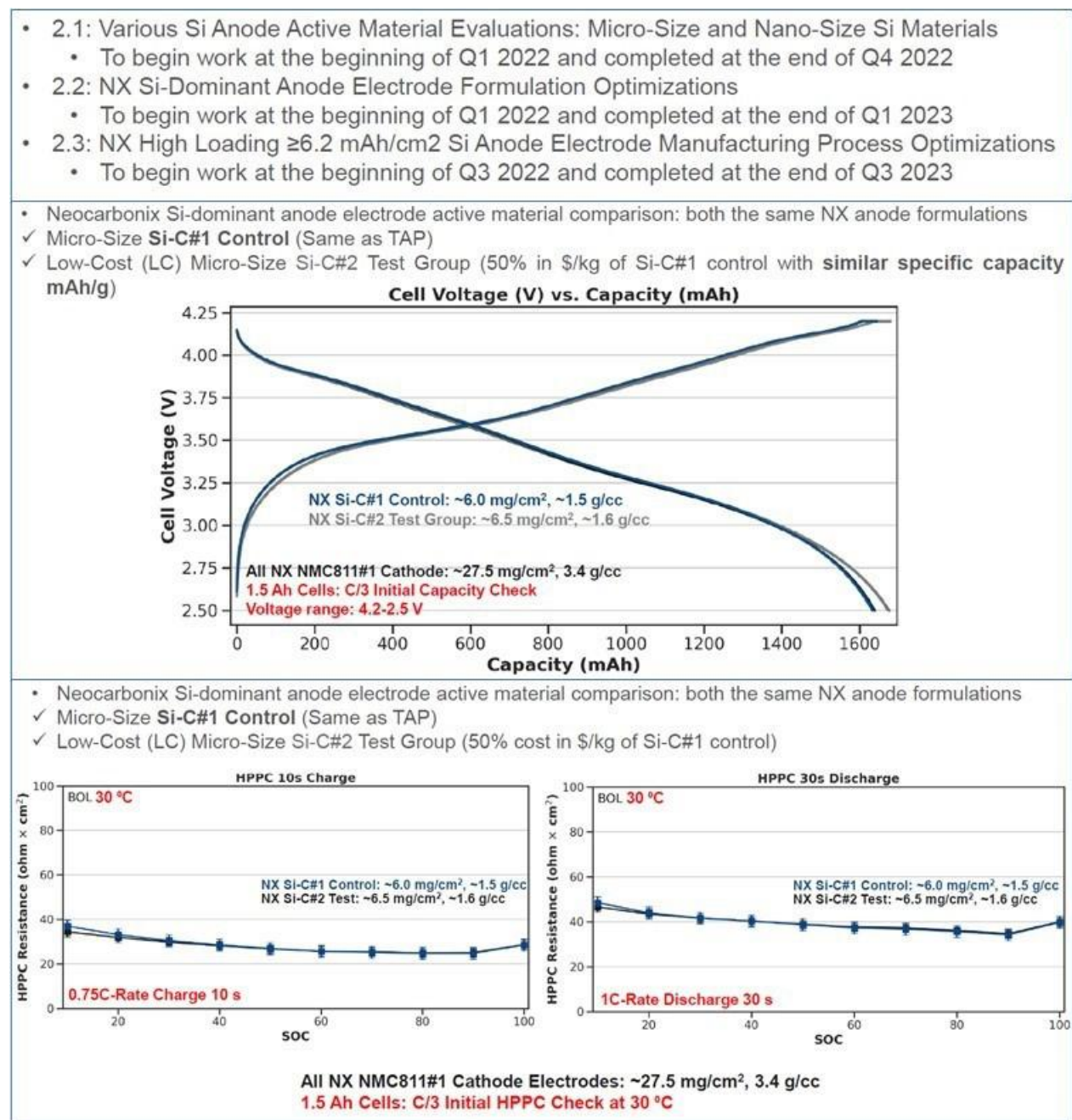
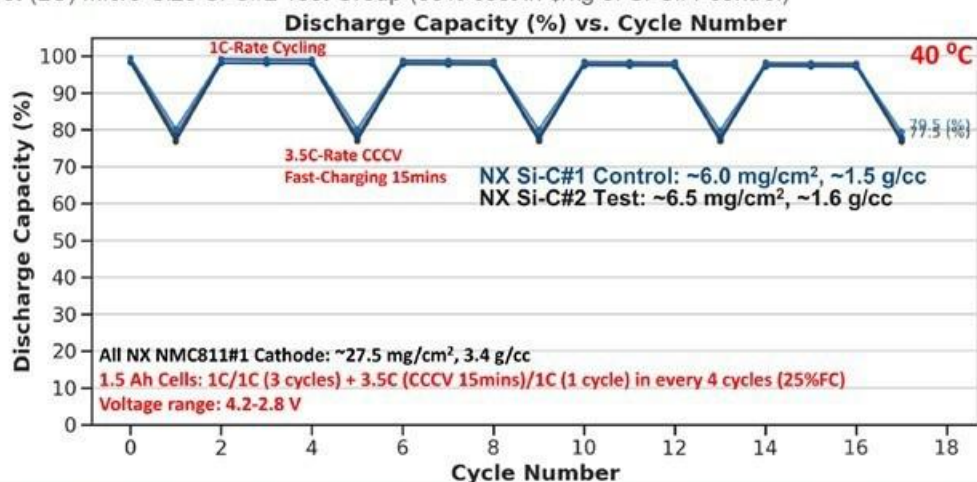


Figure I.3.6 Results for Neocarbonix (NX) Low-Cost Silicon Anode Electrode Development

- Neocarbonix Si-dominant anode electrode active material comparison: both the same NX anode formulations
- ✓ Micro-Size **Si-C#1 Control** (Same as TAP)
- ✓ Low-Cost (LC) Micro-Size Si-C#2 Test Group (50% cost in \$/kg of Si-C#1 control)



- Neocarbonix Si-dominant anode electrode active material comparison: both the same NX anode formulations
- ✓ Micro-Size **Si-C#1 Control** (Same as TAP)
- ✓ Low-Cost (LC) Micro-Size Si-C#2 Test Group (50% cost in \$/kg of Si-C#1 control)

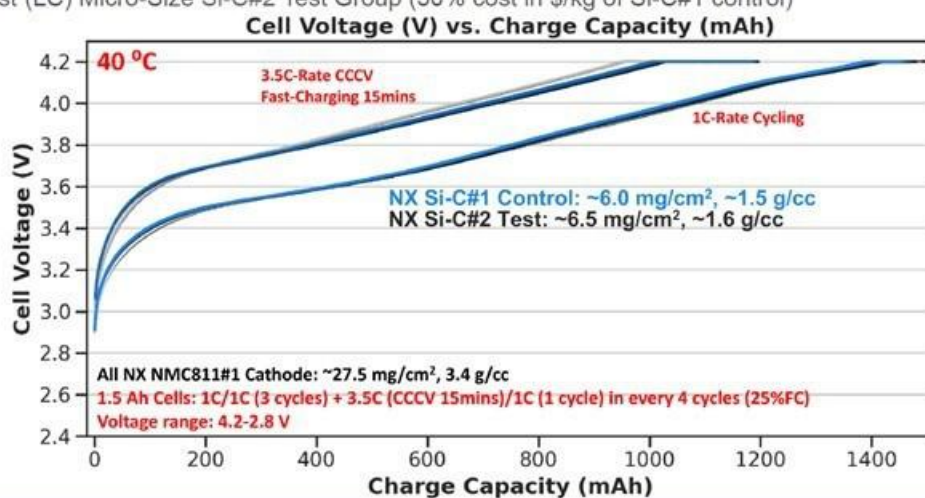


Figure I.3.7 Results for Neocarbonix (NX) Low-Cost Silicon Anode Electrode Development (continued)

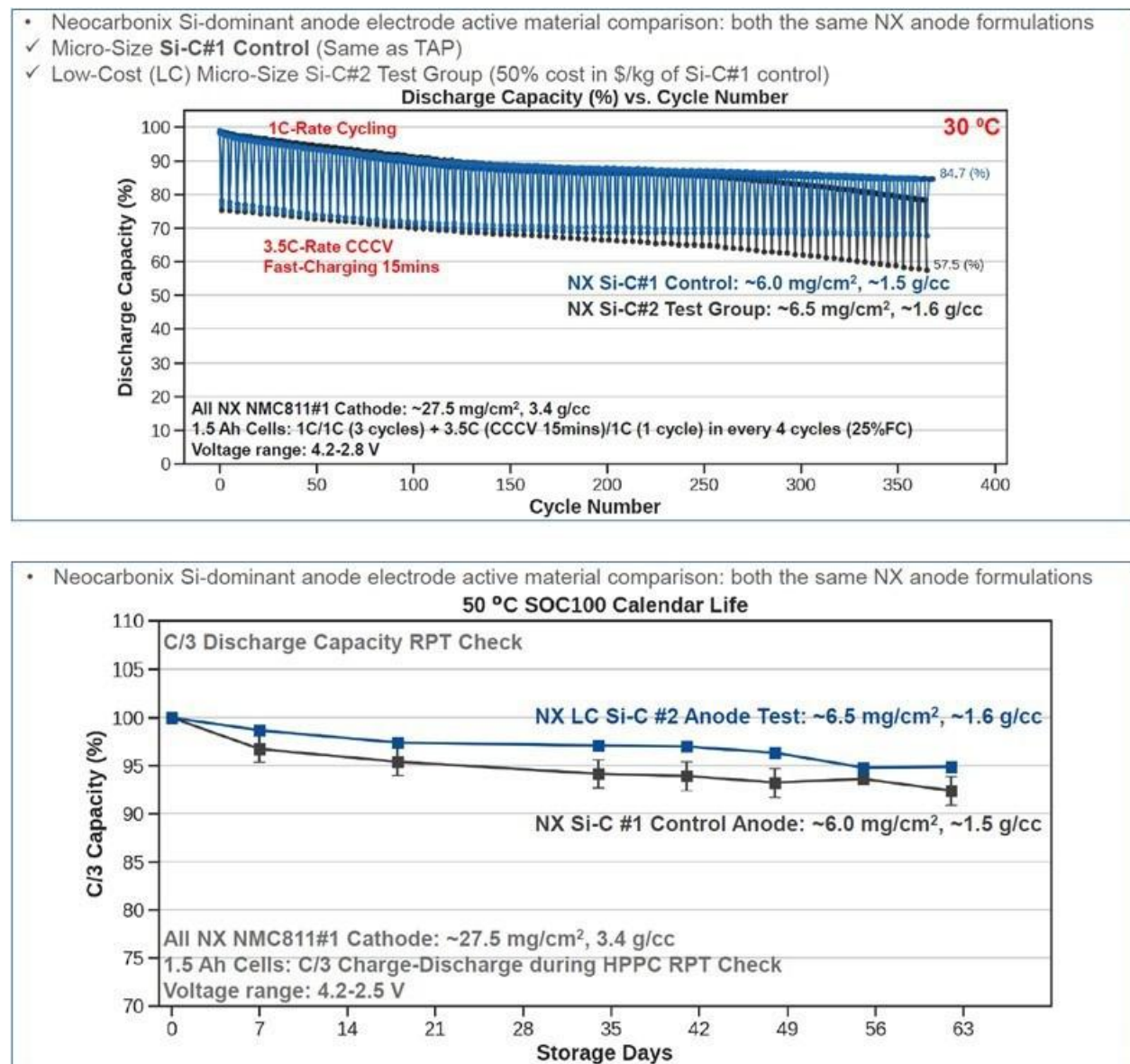


Figure I.3.8 Results for Neocarbonix (NX) Low-Cost Silicon Anode Electrode Development (continued)

- Neocarbonix **LC Si-C#2** anode material based NX various formulations.
 - Micro-Size **Si-C#1 Control** (Same as TAP)
 - Low-Cost (LC) Micro-Size Si-C#2 Test Group (50% cost in \$/kg of Si-C#1 control): **LC Si-C#2**
 - NX NCM91 cathode loading: ~5.8 mAh/cm² with 3.65 g/cm³ press density
- Initial HPPC DCIR check shows that LC Si-C#2 best formula-1 still has higher resistance compared with NX Si-C#1 control old formulas.

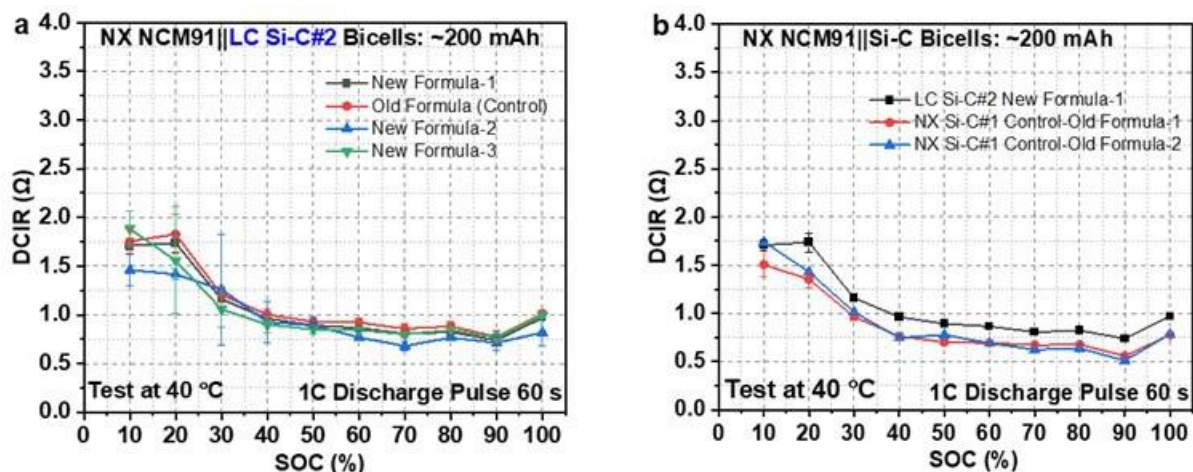


Figure I.3.9 Results for Neocarbonix (NX) Low-Cost Silicon Anode Electrode Development (continued)

- For NX LC Si-C#2 AAM with various new NX formulations, the New Formula-1 performs the best on Crate discharge tests in average. (See adjacent figure.)
- Comparing the NX LC Si-C#2 new formula-1 with NX Si-C#1 control two old formulas; it achieves similar Crate performance as the control-old-formula-1 but still show worse performance compared with control-old-formula-2 in average.

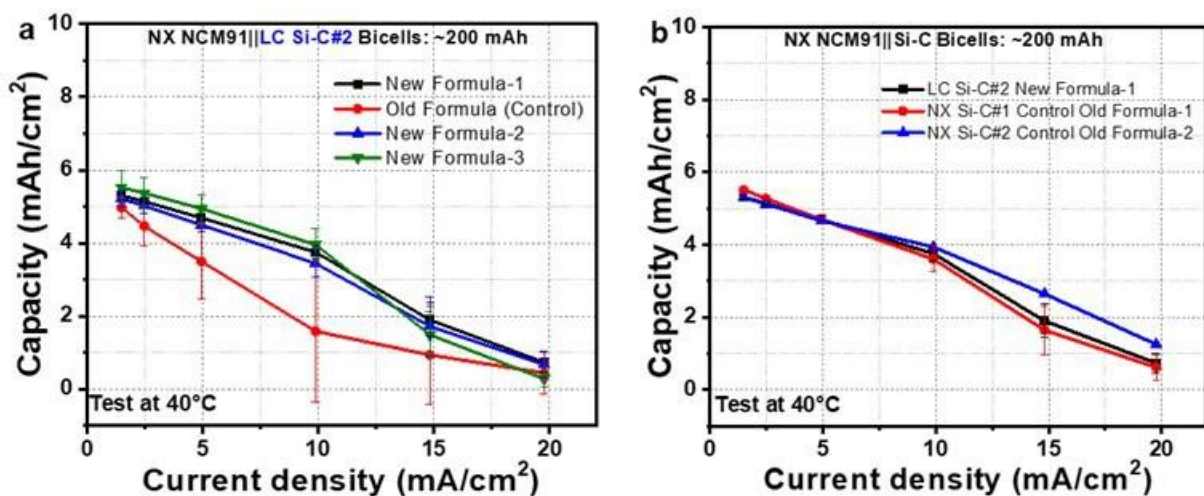


Figure I.3.10 Results for Neocarbonix (NX) Low-Cost Silicon Anode Electrode Development (continued)

- When the C/3 capacity retention % is compared before and after Crate discharge cycling, after 30 cycles, the New Formula-3 shows the highest retention % (~94.1%) which is ~0.4% higher than New Formula-1 (best Crate mAh/cm² performance formula) (~93.7%). (See the adjacent figure.)

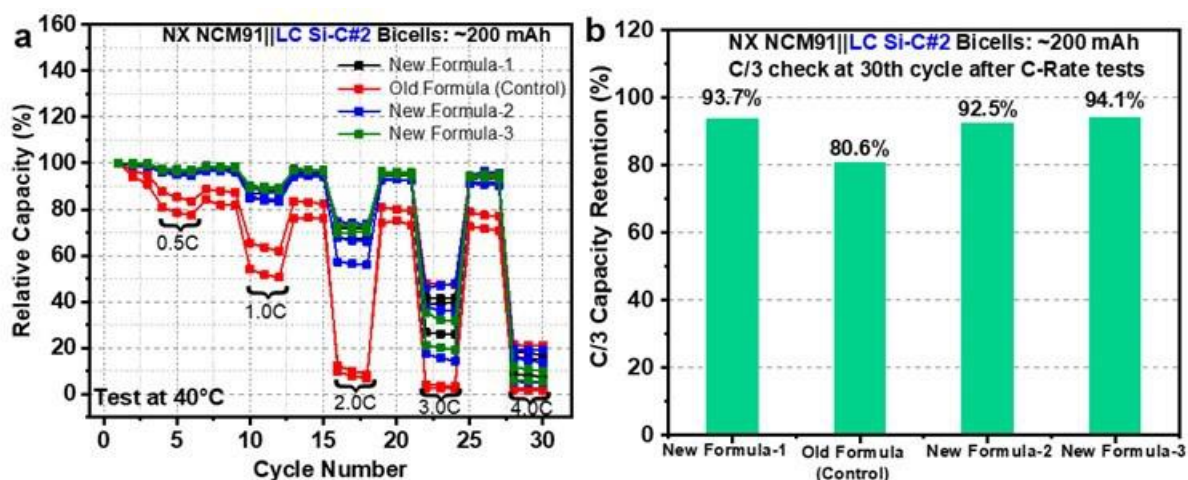


Figure I.3.11 Results for Neocarbonix (NX) Low-Cost Silicon Anode Electrode Development (continued)

- After 30 cycles various C-rate tests, NX LC Si-C#2 New Formula-1 shows the highest C/3 capacity retention % (~93.7%) compared with the control groups. (See the adjacent figure.)

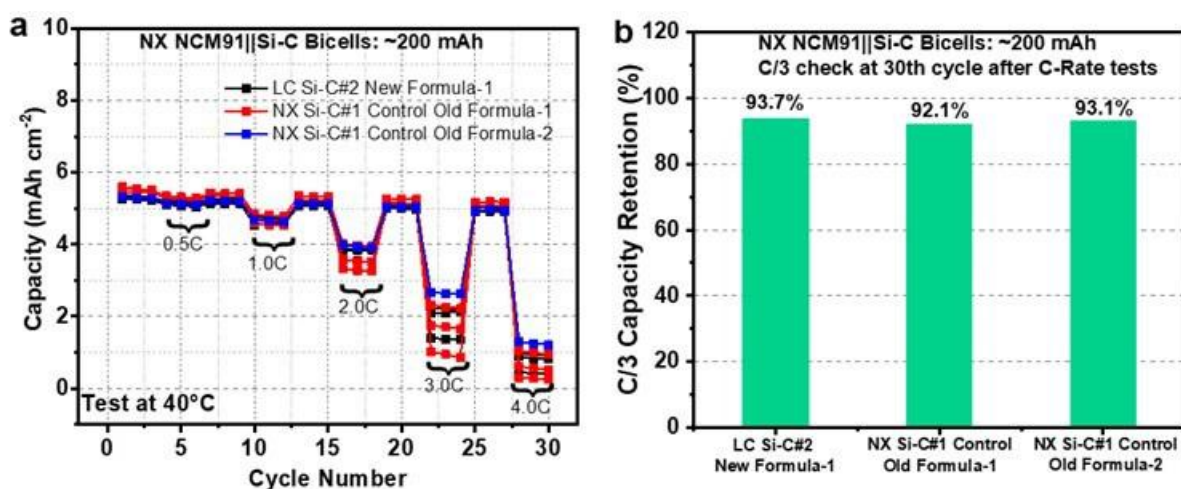


Figure I.3.12 Results for Neocarbonix (NX) Low-Cost Silicon Anode Electrode Development (continued)

- After 250 cycles of 1C1C cycling, NX LC Si-C#2 New Formula-1 shows the highest capacity retention % ~88.0% and a Delta V increase of 13.50% compared with the control groups of ~84.6% Capacity Retention and 23.13% increase in Delta V. (See the adjacent figure.)

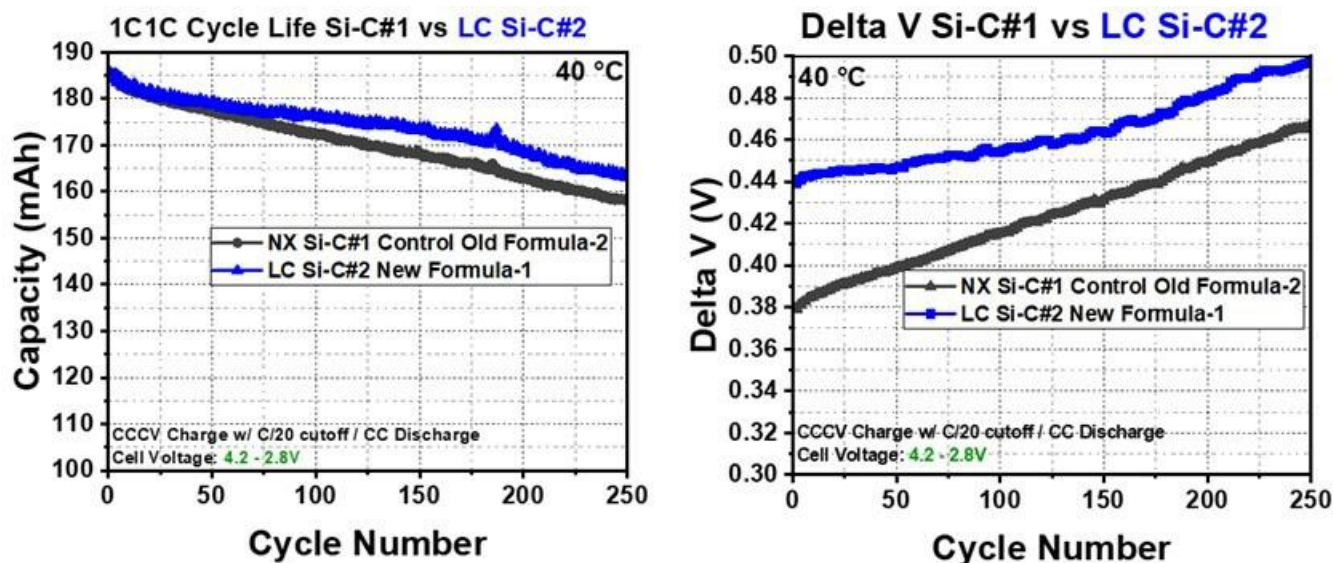


Figure I.3.13 Results for Neocarbonix (NX) Low-Cost Silicon Anode Electrode Development (continued)

Neocarbonix (NX) 14 Ah Battery Cell Development & Performance

The results for Neocarbonix (NX) 14 Ah Battery Cell Development & Performance are summarized in the figures below. Results are shown in the figures below (Figure I.3.14 to Figure I.3.19).

NX 14Ah Cell Series#	Measured Volume (mL)	Measured Weight (g)	C/10 Discharge Capacity (30 °C)	C/10 Discharge Energy (30 °C)	C/3 Discharge Capacity (40 °C)	C/3 Discharge Energy (40 °C)	C/10 Specific Energy (30 °C)	C/10 Energy Density (30 °C)	C/3 Specific Energy (40 °C)	C/3 Energy Density (40 °C)
20211216B01 C04K08120	63.6 mL	170.8 g	14.8 Ah	50.7 Wh	14.8 Ah	50.9 Wh	297 Wh/kg	796 Wh/L	298 Wh/kg	799 Wh/L
20211216B01 C08K08120	62.7 mL	169.3 g	14.9 Ah	51.1 Wh	15.0 Ah	51.3 Wh	302 Wh/kg	814 Wh/L	303 Wh/kg	817 Wh/L
20211216B01 C09K08120	61.9 mL	169.8 g	15.1 Ah	51.7 Wh	15.1 Ah	51.8 Wh	304 Wh/kg	834 Wh/L	305 Wh/kg	836 Wh/L
20211216B01 C10K08120	62.9 mL	166.6 g	15.2 Ah	52.1 Wh	15.3 Ah	52.2 Wh	313 Wh/kg	828 Wh/L	313 Wh/kg	829 Wh/L
20211216B01 C11K08120	64.3 mL	172.0 g	15.5 Ah	53.0 Wh	15.5 Ah	53.1 Wh	308 Wh/kg	824 Wh/L	309 Wh/kg	826 Wh/L

- NX 14Ah cell energy density: 303 to 313 Wh/kg, 817 to 836 Wh/L
- NX NMC811 cathode: PVDF/NMP free (Alcohol solvent) processing with ~5.5 mAh/cm² high areal capacity
- NX Si-C anode: water/alcohol based solution processing with >40-50% Si element content in anode with >1100 mAh/g based on anode active layer

Figure I.3.14 Results for Neocarbonix (NX) 14 Ah Battery Cell Development & Performance

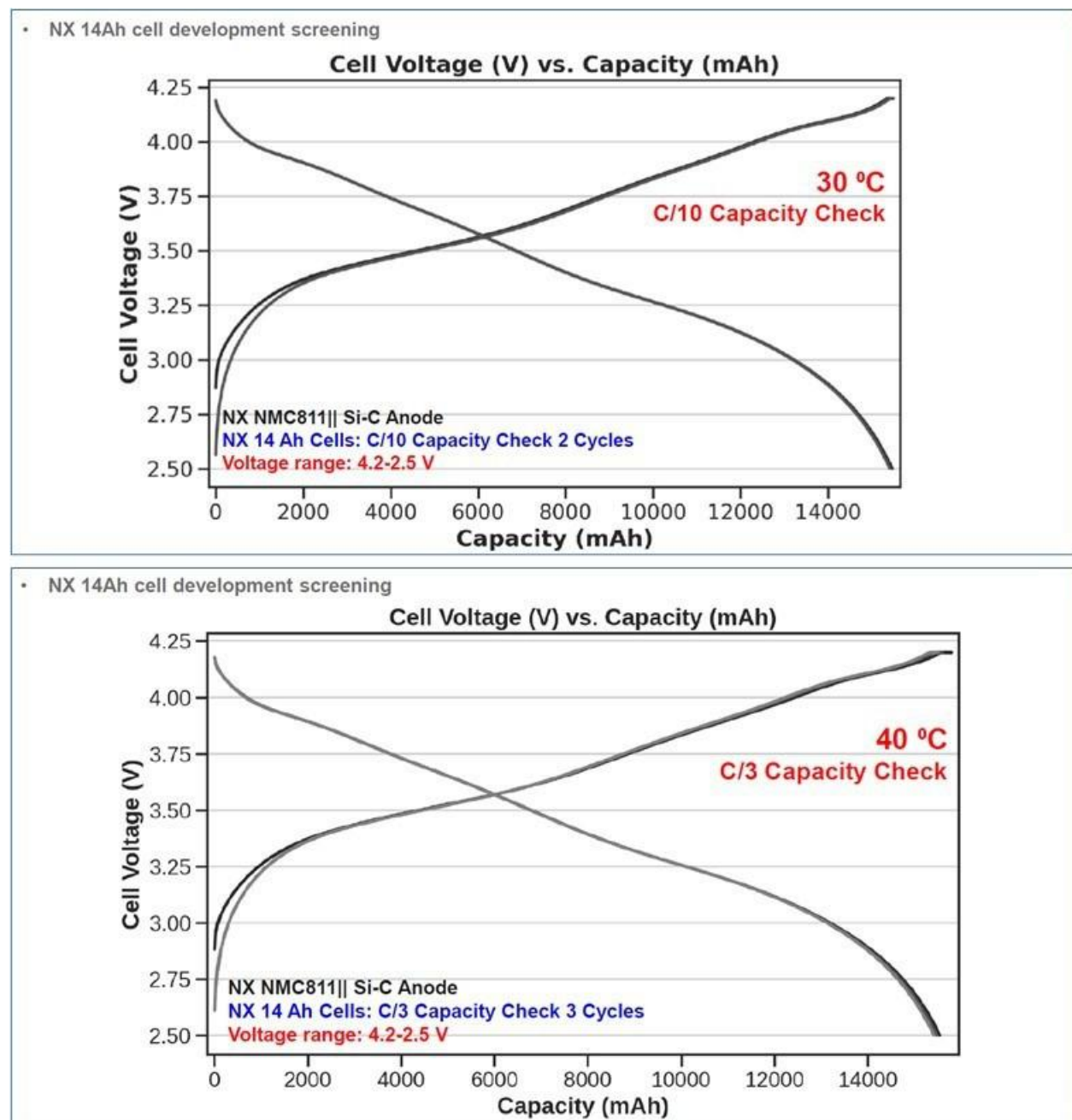


Figure I.3.15 Results for Neocarbonix (NX) 14 Ah Battery Cell Development & Performance (continued)

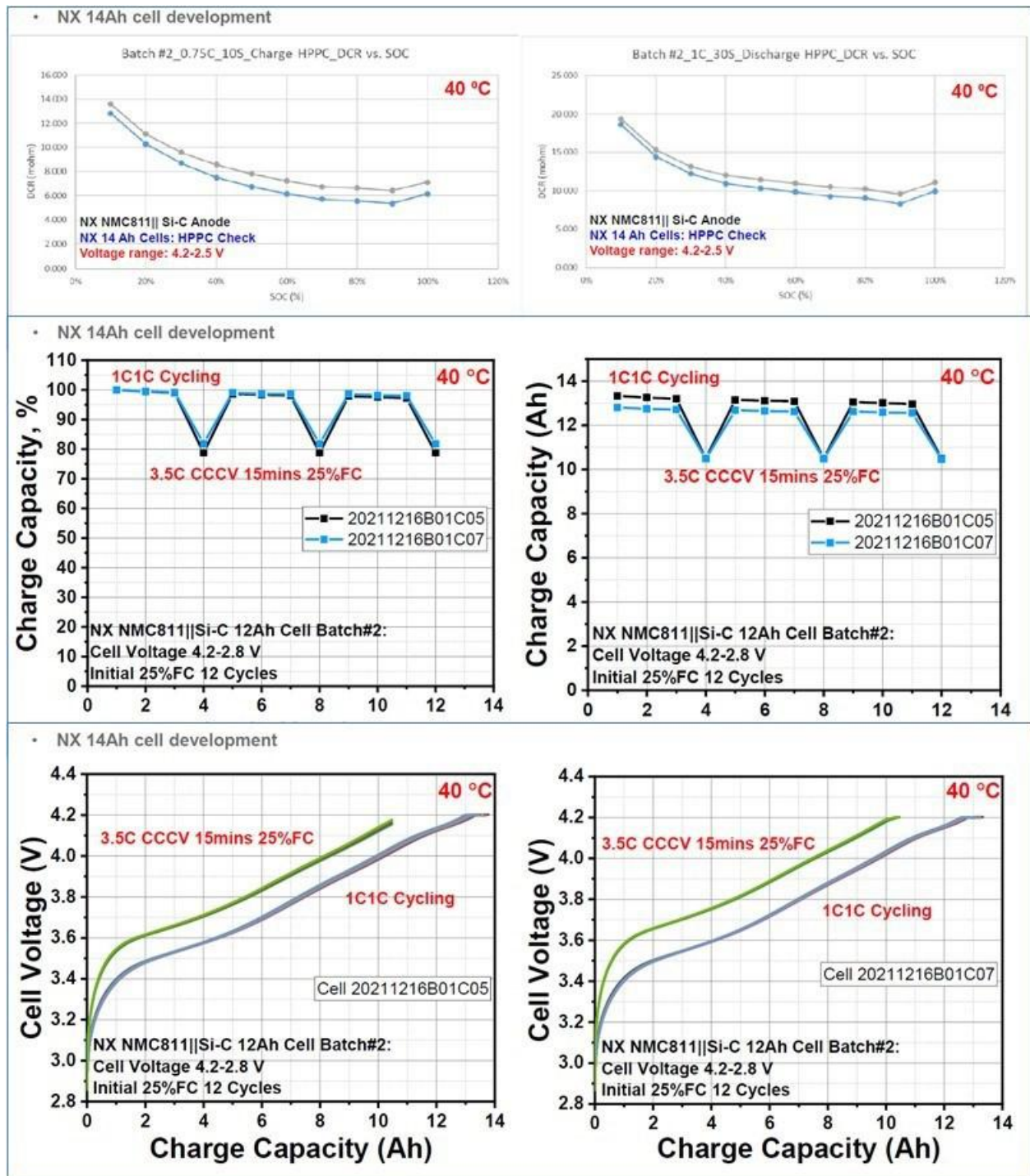
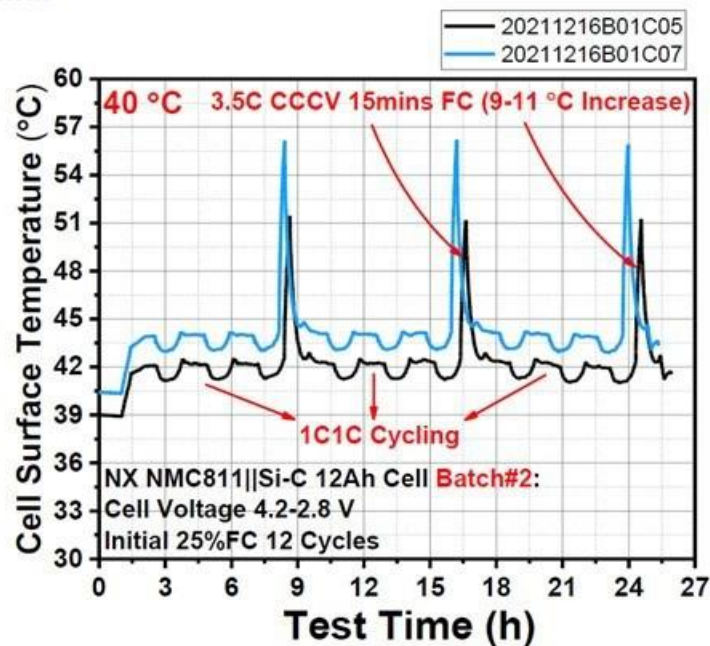


Figure I.3.16 Results for Neocarbonix (NX) 14 Ah Battery Cell Development & Performance (continued)

- NX 14Ah cell development



- NX 14Ah cell development

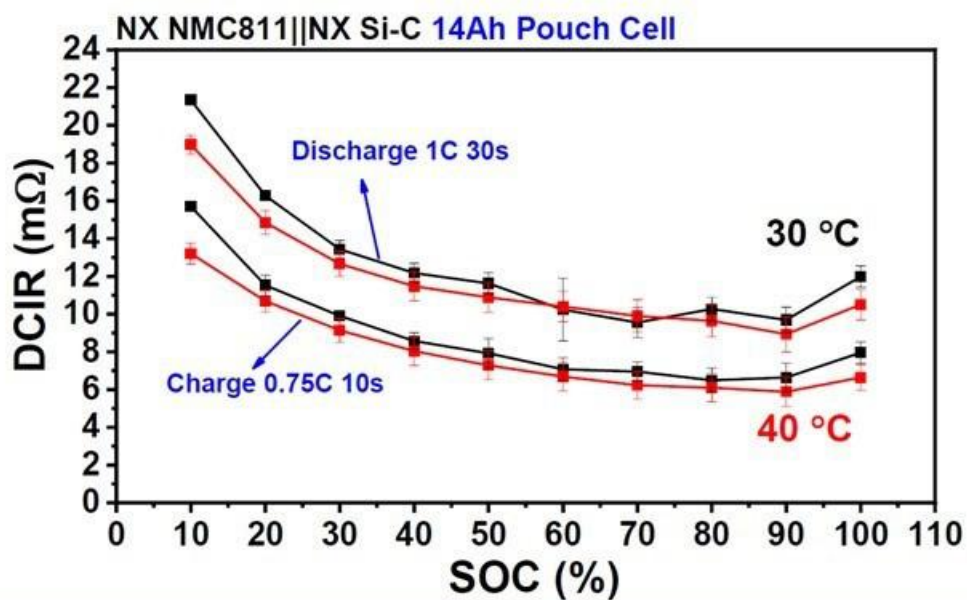


Figure I.3.17 Results for Neocarbonix (NX) 14 Ah Battery Cell Development & Performance (continued)

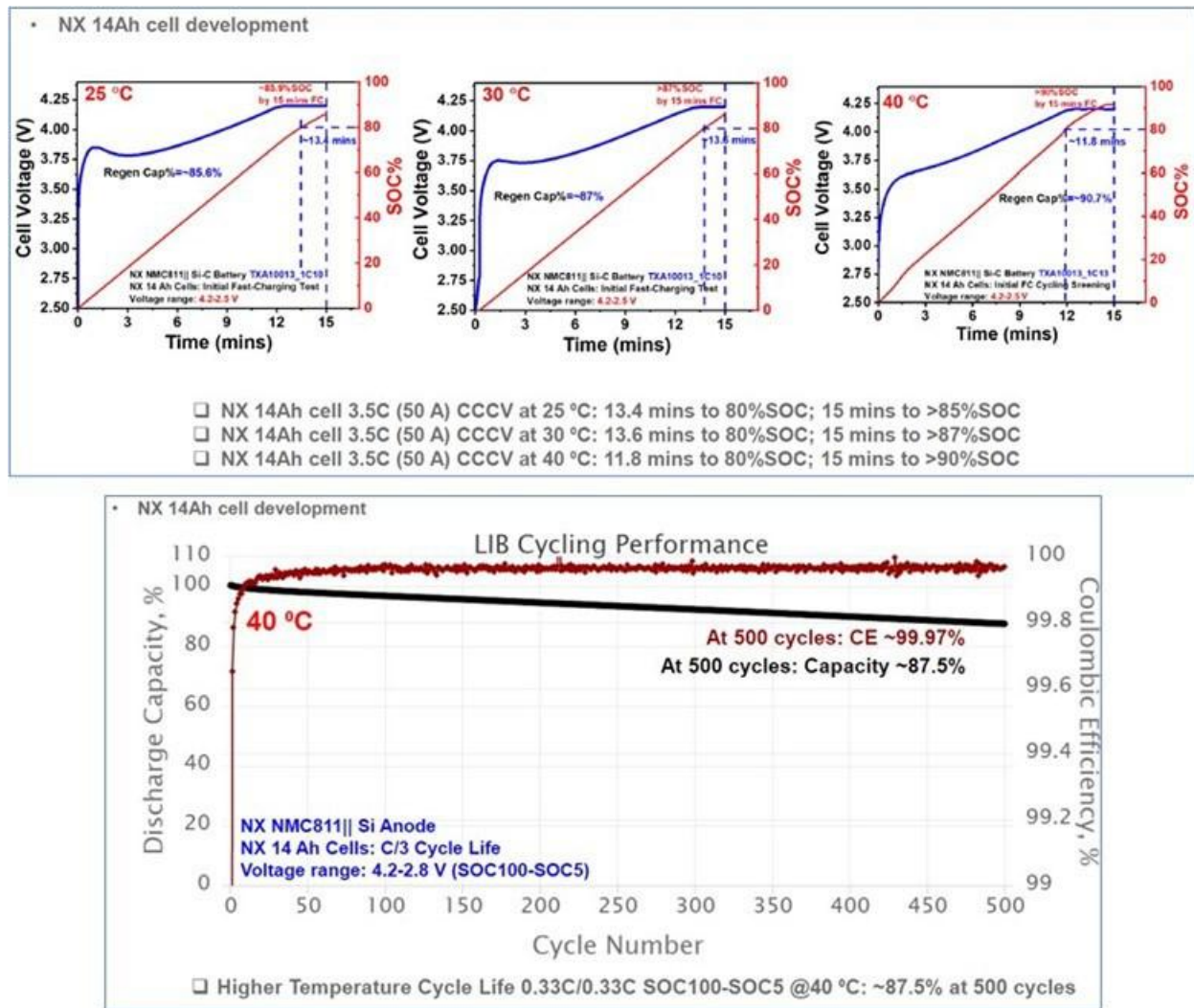


Figure I.3.18 Results for Neocarbonix (NX) 14 Ah Battery Cell Development & Performance (continued)

UPDATE NOTE: Previous data for LIB Cycling performance shown was for 300 cycles with a ~92.3% Capacity retention.

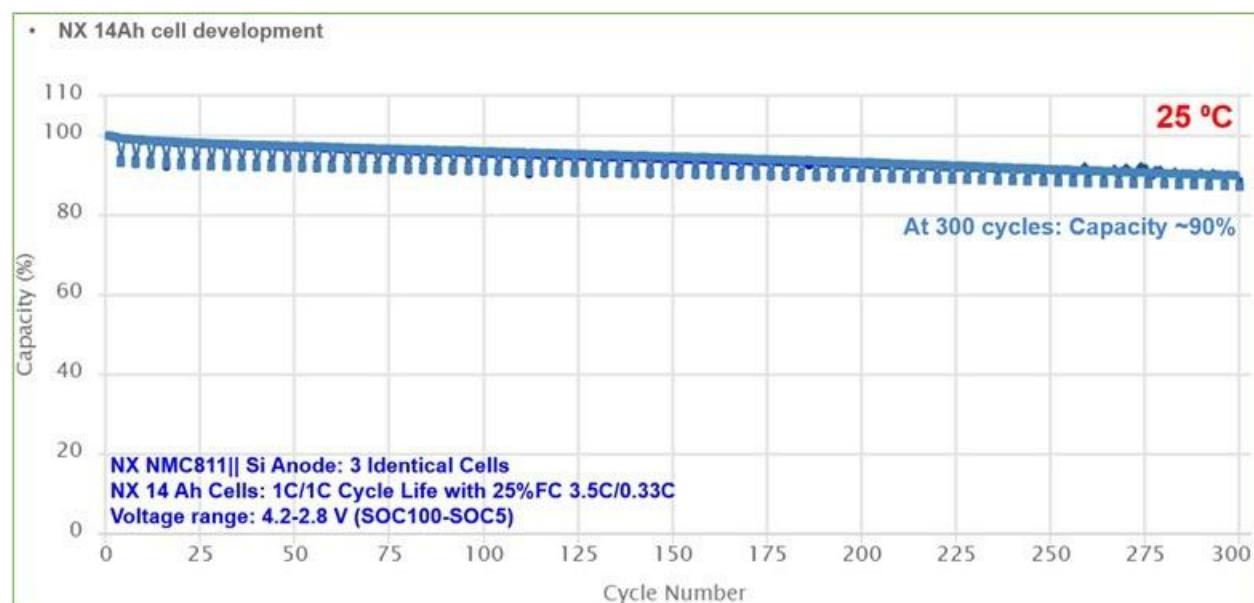


Figure I.3.19 Results for Neocarbonix (NX) 14 Ah Battery Cell Development & Performance (continued)

UPDATE NOTE: Previous data for LIB Cycling performance shown was for 98 cycles with a ~96.2% Capacity retention.

Nx si-c anode electrode pre-lithiation (40-50 wt.% si element content)

The results for NX Si-C ANODE ELECTRODE PRE-LITHIATION (40-50 wt.% Si Element Content) are shown below. Results for this task are shown in the figures below (Figure I.3.20 to Figure I.3.27).

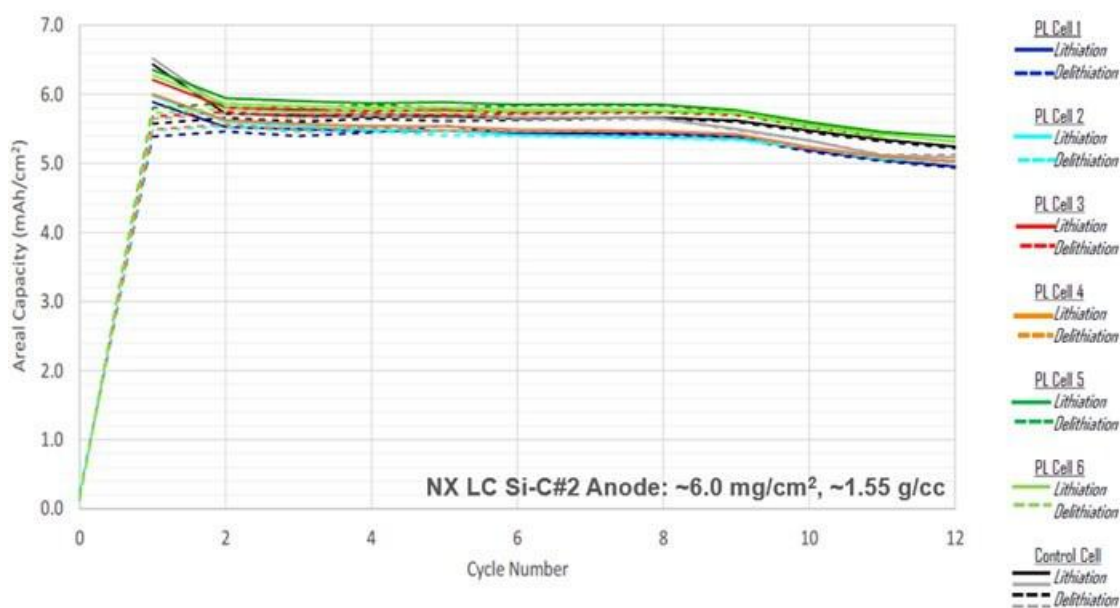


Figure I.3.20 Results for NX Si-C ANODE ELECTRODE PRE-LITHIATION (40-50 wt.% Si Element Content)

Various prelithiated NX Si-C#2 anodic half cells were tested with 0.2-0.7 mAh/cm² of prelithiation.

Test Protocol (Control and Prelithiated Anodic Half-Cell)

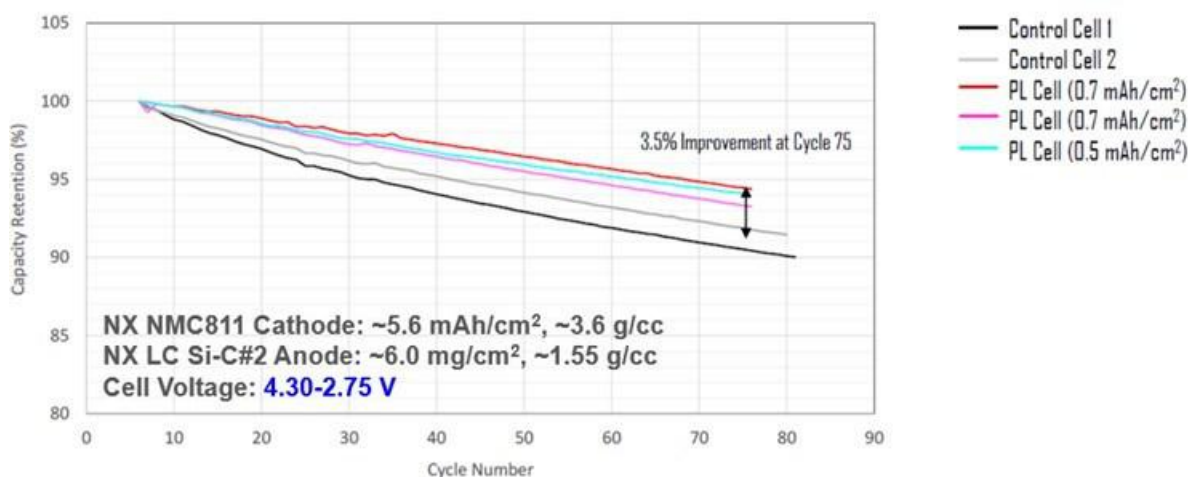
- Formation (2x)
 - CC Charge (C/10) to 5 mV + CV at 5 mV to C/20
 - CC Discharge (C/10) to 1.0V.
- Cycling
 - C/5 (2x)
 - C/3 (20x)
 - C/2 (20x).

Physical observations of electrode post lithiation:

- Electrode remains flat with no curling
- No discoloration
- No edge delamination.

Full Cell Formation and Cycling

Prelithiated bicell capacity retention at 75 cycles improved by ~3.5% under 4.3-2.75 V higher voltage cutoff C/3 cycling test. (See adjacent figure.)



*% Improvement based on PL Cell Capacity Retention relative to average Control Cell Capacity Retention at Cycle 75

Figure I.3.21 Results for NX Si-C ANODE ELECTRODE PRE-LITHIATION (40-50 wt.% Si Element Content) (continued)

Test Protocol (Control and Prelithiated Full Cell: 2-layers cathode +1-layer anode bicells)

1. **Conditions 24 hr. soak at 45°C:**
 - Formation and Cycling at 26.5°C
 - Clamp pressure: 60 psi.
2. **Formation (2x):**
 - CC Charge (C/10) to 4.3V + CV at 4.3V to C/20
 - CC Discharge (C/10) to 2.75V.
3. **Cycling:**
 - C/5 (x2)
 - C/3 (ongoing cycles).

Prelithiated bicell shows higher average CE% during cycling under 4.3-2.75 V higher voltage cutoff C/3 charge-discharge test. (See adjacent figure.)

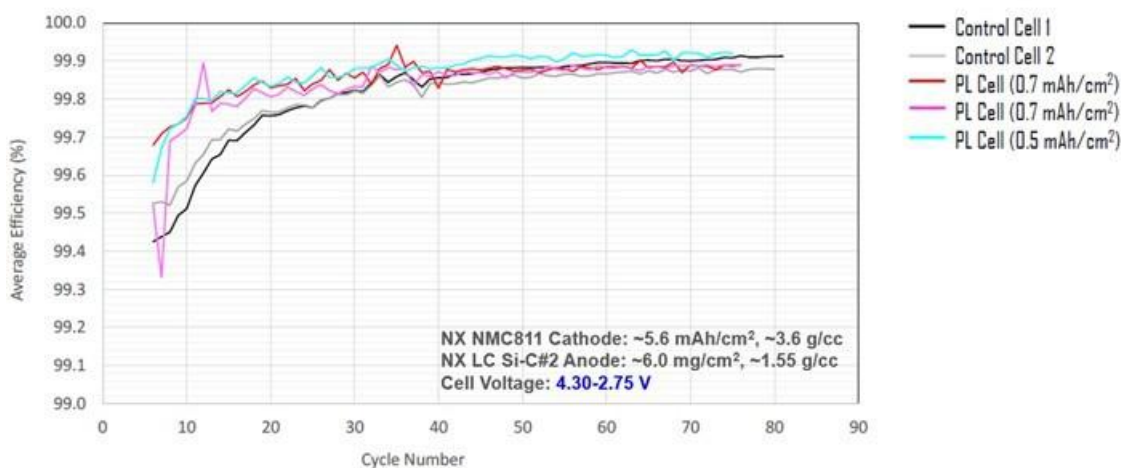


Figure I.3.22 Results for NX Si-C ANODE ELECTRODE PRE-LITHIATION (40-50 wt.% Si Element Content) (continued)

Prelithiated bicell shows ~9% improvement in specific energy at cycle#75 during cycling under 4.3-2.75 V higher voltage cutoff C/3 charge-discharge test.

The specific energy density was calculated based on active electrode weight (cathode + anode electrode weight) for both Control cells and Prelithiated (PL) cells.

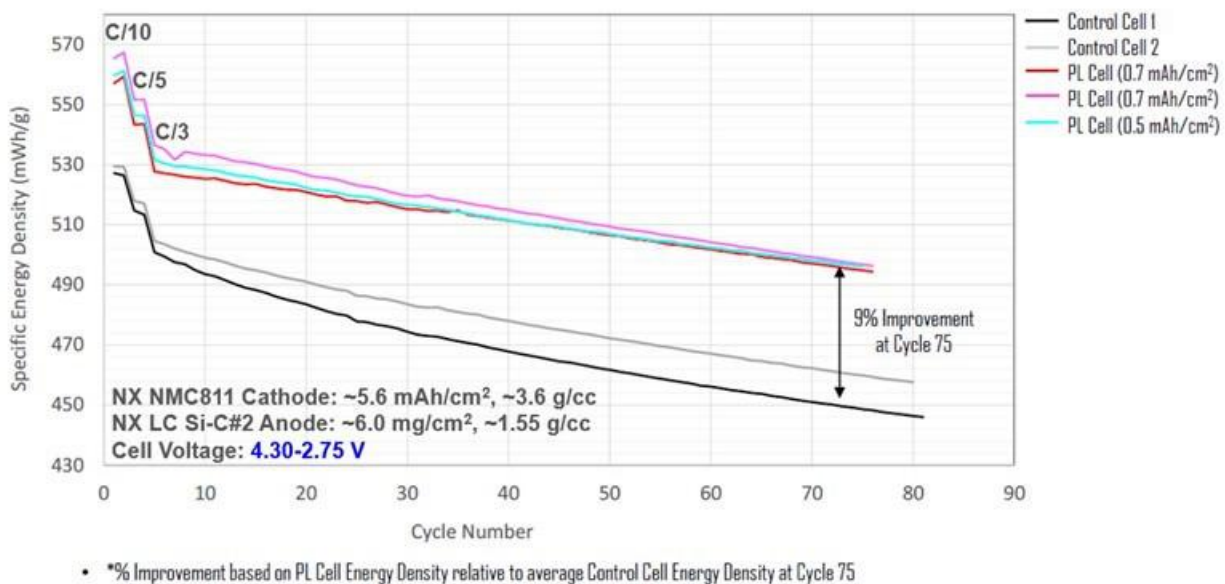


Figure I.3.23 Results for NX Si-C ANODE ELECTRODE PRE-LITHIATION (40-50 wt.% Si Element Content) (continued)

Nx Si-C Anode Electrode Pre-Lithiation (40-50 wt.% Si Element Content) Conclusions

By cycle 75 under 4.30-2.75 V C/3 cycling, prelithiated full cells demonstrate the following gains relative to controls:

- >3.5% Improvement in Capacity Retention
- Obvious Improvement of Coulombic Efficiency (CE) % during C/3 Cycling
- ~9% Increase in Specific Energy based on Active Electrode Total Weight.

Next steps: pre-lithiation cost model analysis will be conducted to see the impact on \$/kWh while it improves the energy density (Wh/kg) and cycling performance.

Prelithiation Mass Production Cost-Benefit Model

Cost-benefit model incorporates energy, capacity, and cycle life benefits of prelithiation to any specific cell design, as well as including primary prelithiation operating costs, formation, and related costs savings.

The cost model is based extensive preliminary engineering such as raw materials, labor, preliminary estimate of capital depreciation, and US energy, labor, and water rates. (See adjacent figure.)

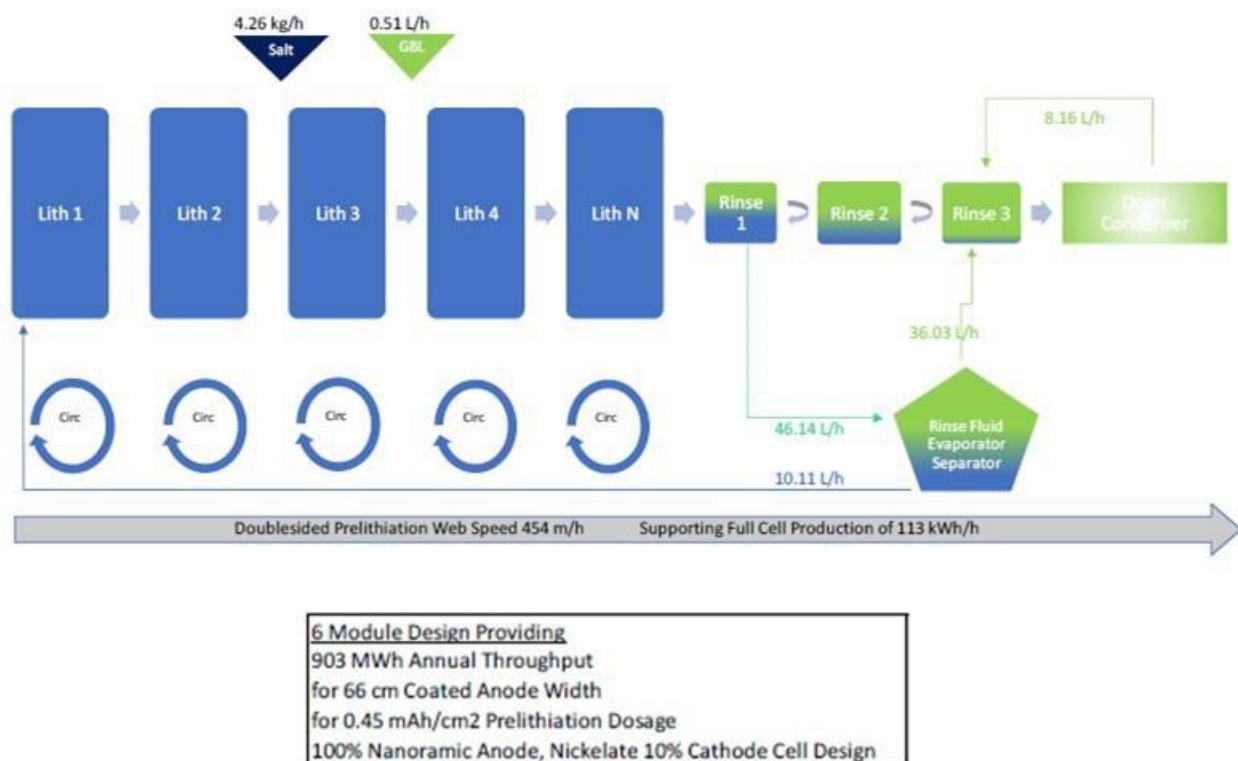
Example Prelithiation Design Line:

Figure I.3.24 Results for NX Si-C ANODE ELECTRODE PRE-LITHIATION (40-50 wt.% Si Element Content) (continued)

- 700mm anode
- Planned 7x24 operations
- Modular design – scalable production.
- Example Throughput:
 - 6 modules: annual throughput of 0.9 GWh/line for 0.45 mAh/cm² dosage
 - Single pass design – simultaneous prelithiation across both sides.
- Environmentally beneficial
 - Benign process
 - Output – prelithiated cells have lower carbon footprint.

Summary of Benefits of Prelithiation Coating Line

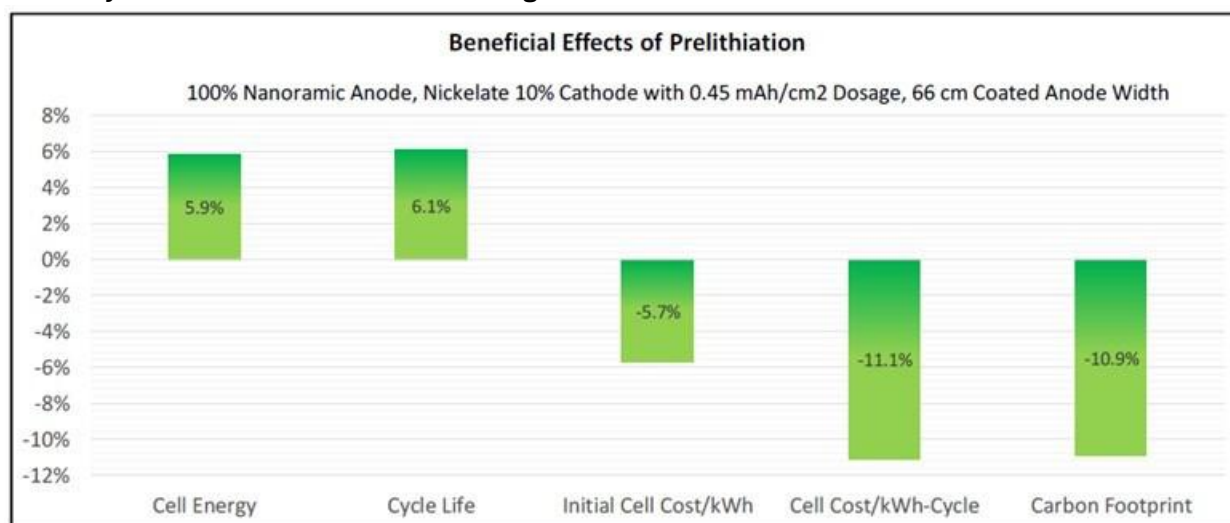


Figure I.3.25 Results for NX Si-C ANODE ELECTRODE PRE-LITHIATION (40-50 wt.% Si Element Content) (continued)

- Prelithiated cell is compared to a conventional cell with the same materials.
- Energy and cycle life improvements are taken directly from cell balance calculations.
- Cell Cost/kWh-cycle considers the initial cell cost reduction/kWh and the cycle life improvement.
- Carbon footprint impact is underestimated - it considers the energy and cycle life improvements, but not the formation energy savings.

Conventional vs Prelithiated Cell Cost Comparison

Conventional cell cost @ \$100/kWh -- note that value is not critical; this is just used to calculate the comparison. Anode costs account for the higher N:P of a prelithiated cell versus a conventional cell, assuming anode powder = \$50.00/kg. Furthermore, a summary of key cost assumptions for other various components of the model are summarized below:

Prelithiation Cost			Key Cost Assumptions*		
6 Module Design Providing 903 MWh Annual Throughput for 100% Nanoramic Anode, Nickelate 10% Cathode with 0.45 mAh/cm ² Dosage, 66 cm Coated Anode Width			Salt	\$14.00	per kg
Cost Component	Per Ah of Prelithiation Dosage	Per Full Cell kWh	Solvent	\$5.60	per L
			CO ₂	\$1.30	per kg
Salt	\$ 0.022	\$ 0.53	Other Chemicals	\$0.74	per dry kg
Solvent	\$ 0.001	\$ 0.02	Energy		
CO ₂	\$ 0.001	\$ 0.03	Electricity	\$0.06	\$/kWh
Other Chemicals	\$ 0.001	\$ 0.03	Heating	\$0.06	\$/kWh
Other	\$ 0.003	\$ 0.08	Cooling	\$0.06	\$/kWh
Energy	\$ 0.007	\$ 0.16	Dry Air	\$0.06	\$/kWh
Labor	\$ 0.006	\$ 0.14	Water		
Subtotal Operating Costs	\$ 0.041	\$ 0.99	Purchase	\$0.0026	\$/L
Depreciation	\$ 0.052	\$ 1.25	Disposal	\$0.0013	\$/L
Total	\$ 0.094	\$ 2.24	Labor	\$30.00	\$/h

Figure I.3.26 Results for NX Si-C ANODE ELECTRODE PRE-LITHIATION (40-50 wt.% Si Element Content) (continued)

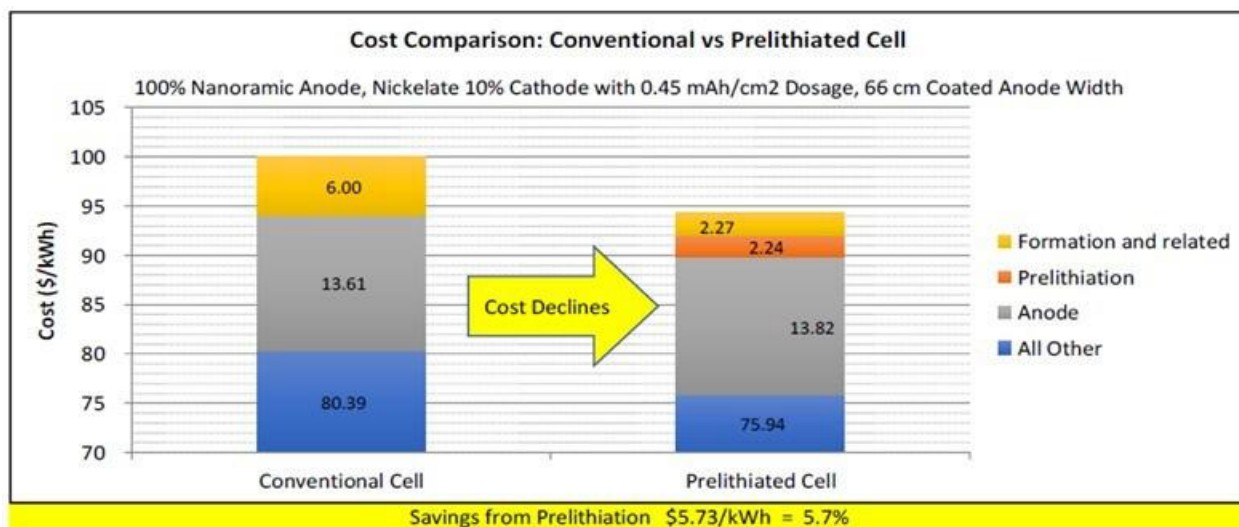


Figure I.3.27 Results for NX Si-C ANODE ELECTRODE PRE-LITHIATION (40-50 wt.% Si Element Content) (continued)

- Capacity gain of 5.9% from prelithiation is taken directly from the cell balance calculations, which also show 6.1% cycle life improvement.
- Estimated formation savings of 60%.

The results for prelithiation show great performance and cost savings, however, Nanoramic decides to not use pre-lithiation for now to achieve the good performance battery cells during this project for the final battery cell delivery; Nanoramic wants to focus on Neocarbonix electrode technology.

Low-Cost Micro-Si Dominant Anode Electrode Development (Higher Si element wt.% ≥ 80%)

Results for this task are shown in the figures below (Figure I.3.28 to Figure I.3.31).

Low-Cost Micro-Si (Msi) Aam Powder Sem Images

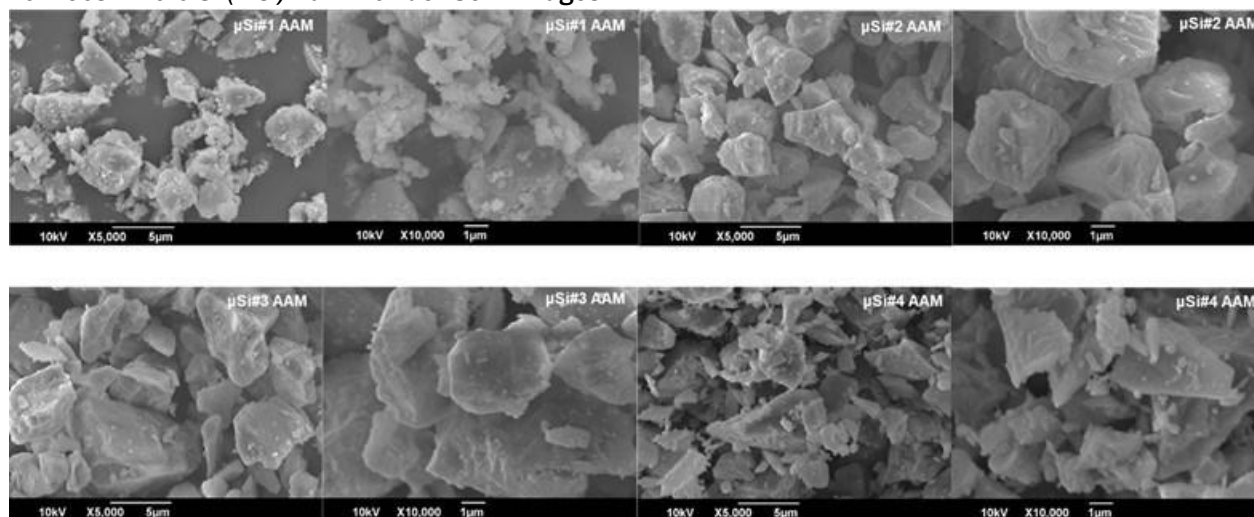


Figure I.3.28 Results for Low-Cost Micro-Si Dominant Anode Electrode Development (Higher Si element wt.% ≥ 80%)

Small 3-electrode bicells 1c/1c cycling tests Low-cost micro-si (μSi) $\geq 80\%$ Si Element Electrode Development

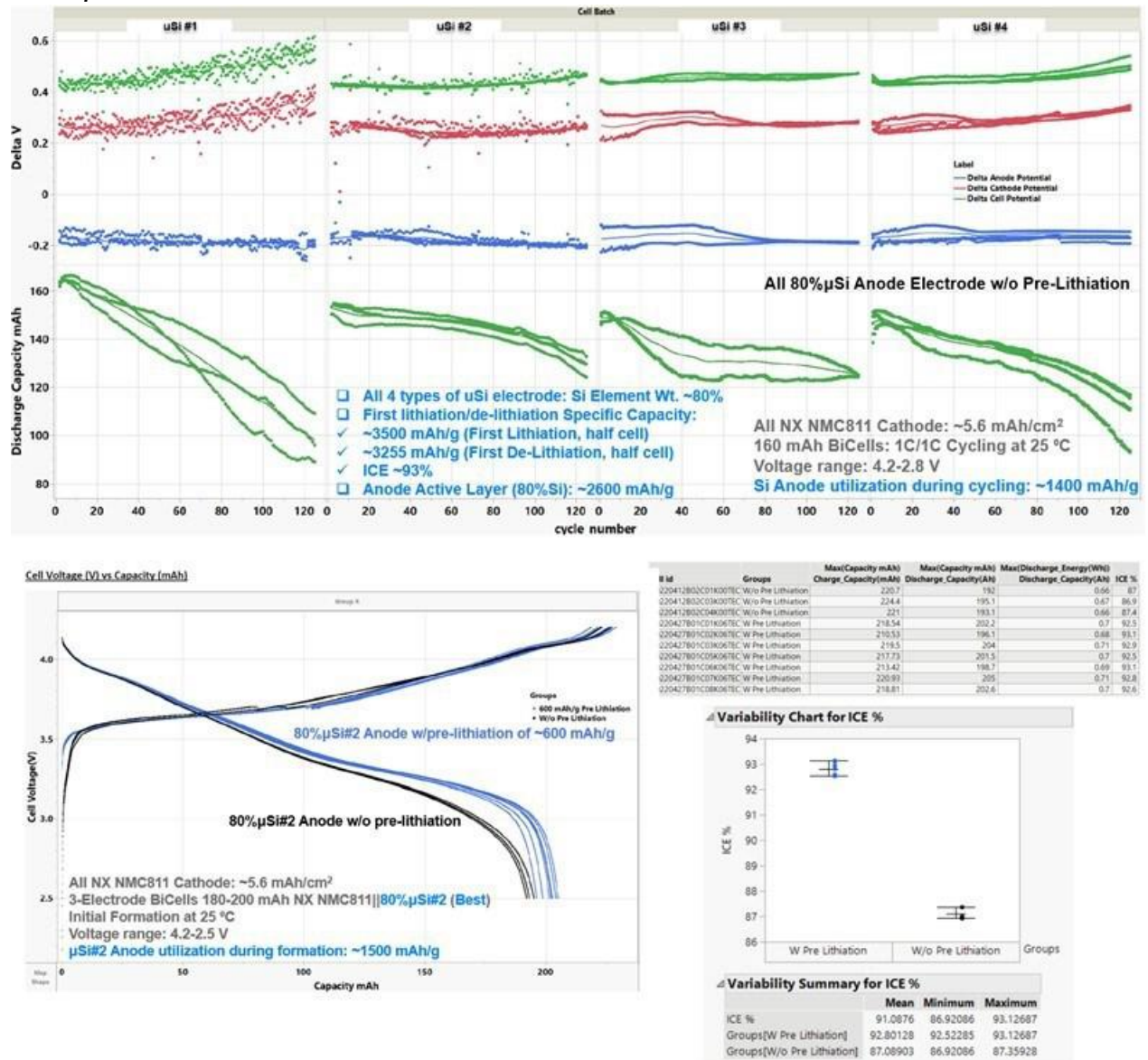


Figure I.3.29 Results for Low-Cost Micro-Si Dominant Anode Electrode Development (Higher Si element wt.% $\geq 80\%$) (continued)

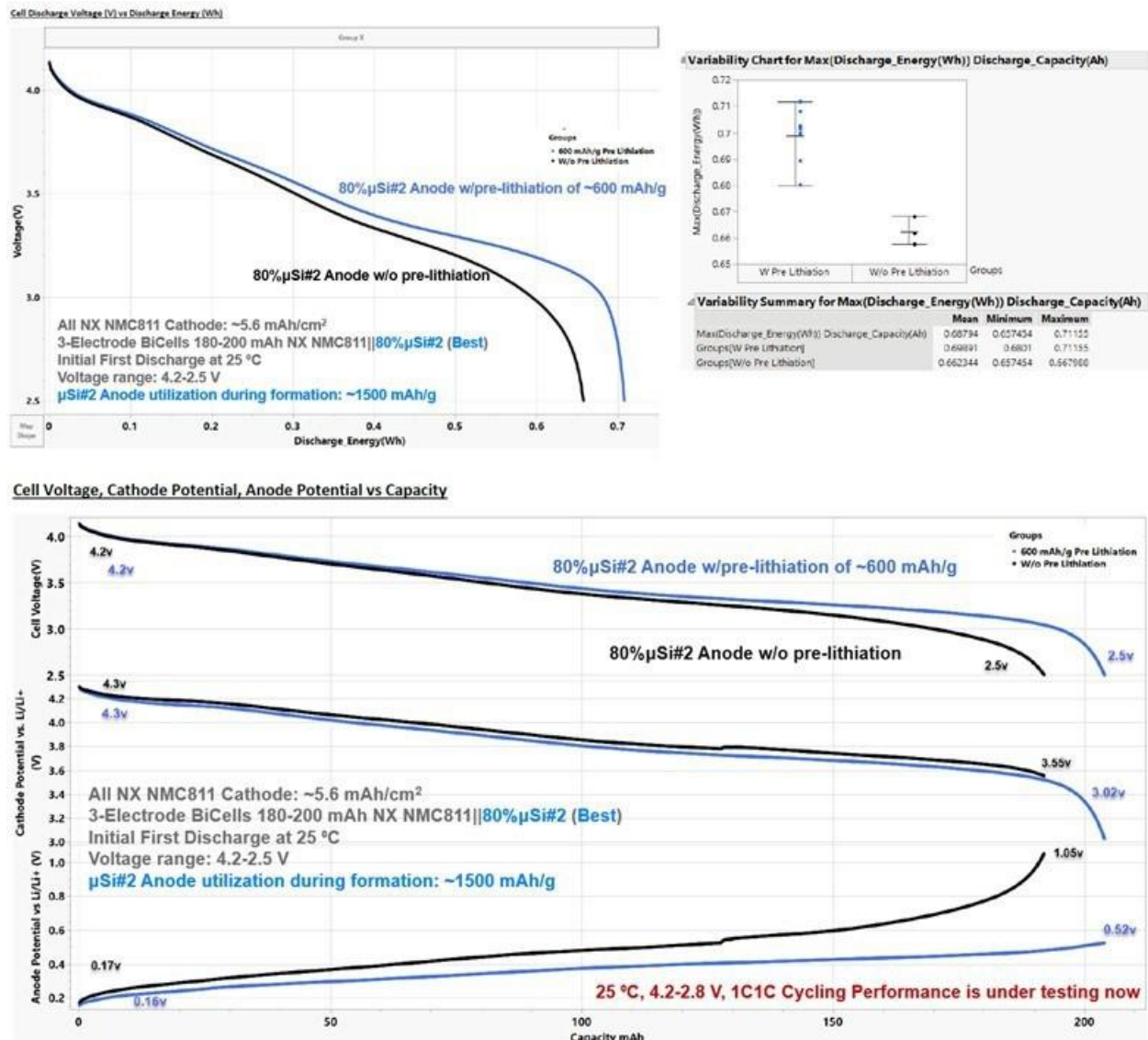
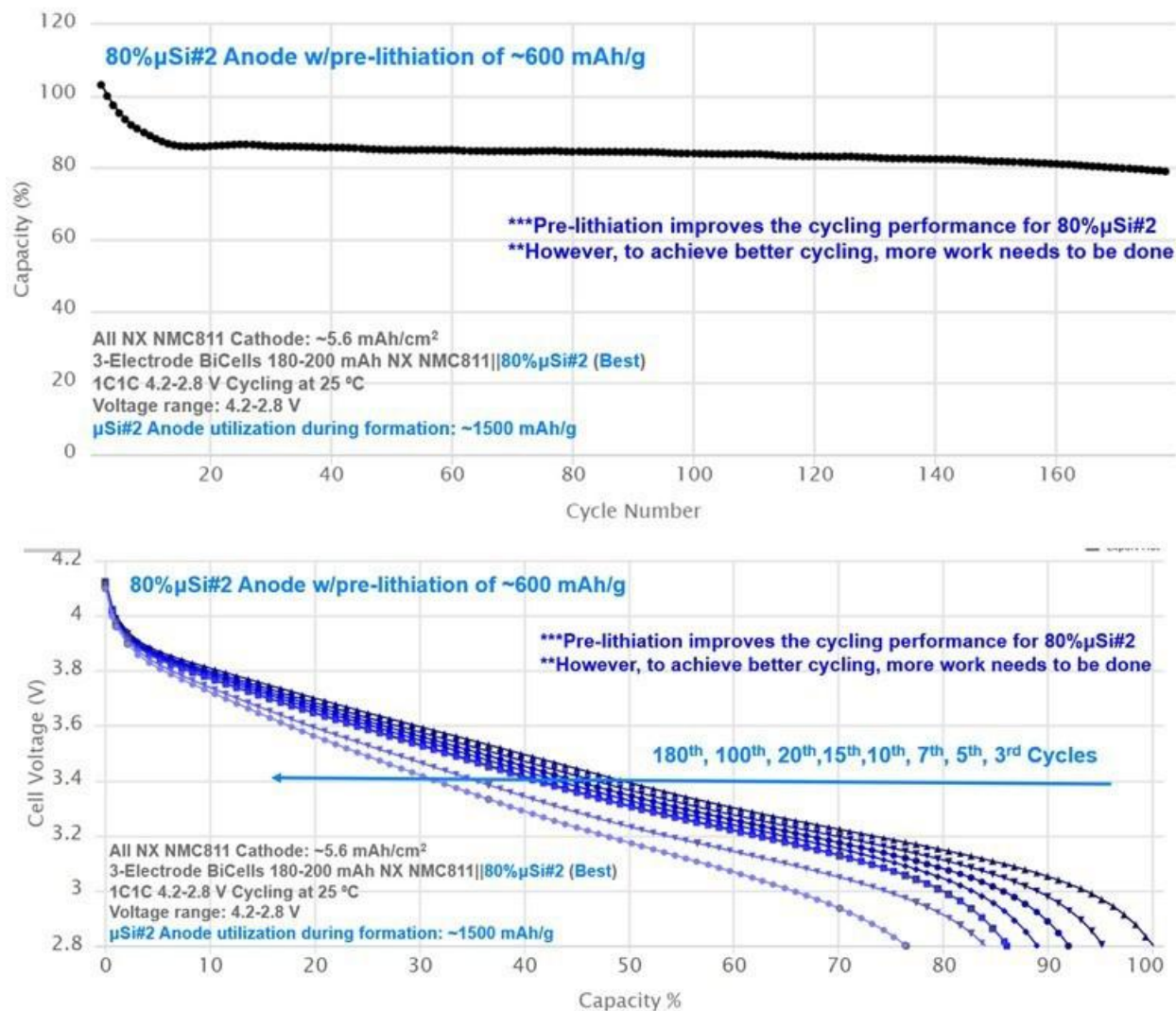


Figure I.3.30 Results for Low-Cost Micro-Si Dominant Anode Electrode Development (Higher Si element wt.%≥80%) (continued)

Figure I.3.31 Results for Low-Cost Micro-Si Dominant Anode Electrode Development (Higher Si element wt.% \geq 80%) (continued)

Low-cost micro-si dominant anode electrode development (higher si element wt.% \geq 80%) progress conclusions

- μ Si#2 is the best performance without pre-lithiation
- Pre-lithiation ~600 mAh/g can improve the cycling performance to 180 cycles
- However, we need to do more development work to further improve the cycle life of 80%micro-Si anode electrodes.

Nx Si Anode Electrolyte Development (Higher Si Element wt.% \geq 80%)

Results for this task are shown in the figures below (Figure I.3.32 to Figure I.3.36).

For the Si anode electrolyte development, 10 electrolytes were compared using the following cell build:

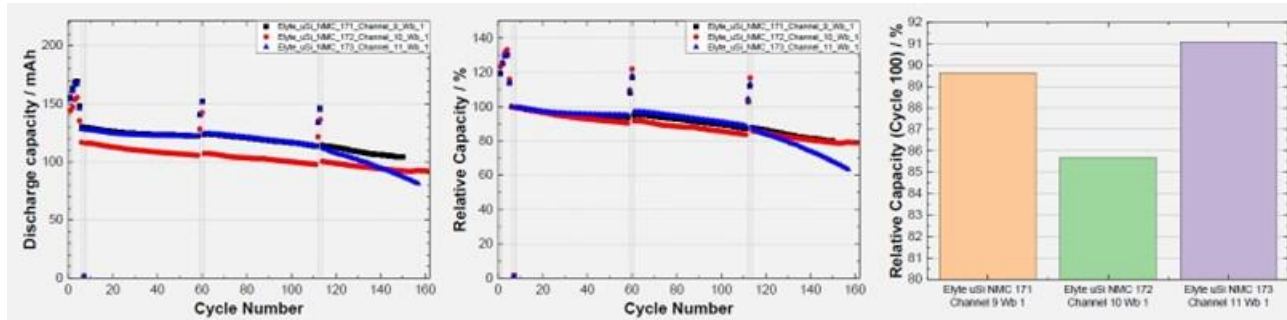
- NX Ni-Rich NMC811 || NX μ Si (~80%Si) Small Bicells Build: one cathode + two anode layers
- NX Cathode NMC811: 26-27 mg/cm², ~3.65 g/cc, ~5.5 mAh/cm² loading.

- NX Anode μSi ($\sim 80\%\text{Si}$): $3.8\text{--}4.0\text{ mg/cm}^2$
- Electrolyte Amount: 5 mL/Ah
- Nominal Capacity: $150\text{--}160\text{ mAh}$, 1C1C cycle life from $4.2\text{--}2.8\text{ V}$ at 25°C .

Electrolyte	ID	Li Salt Blend	Solvent Blend	Additive
1 (baseline)	22-224_1	1.2M LIFS/LIPF6	tenery carbonate co-solvent combination partially substituted with FEC	VC
2	22-224_2	1.2M LIFS/LIPF6	tenery carbonate co-solvent combination partially substituted with FEC	VC and organosilicon-1
3	22-224_3	1.2M LIFS/LIPF6	tenery carbonate co-solvent combination partially substituted with FEC	VC and phosphite
4	22-224_4	1.2M LIFS/LIPF6	tenery carbonate co-solvent combination partially substituted with FEC	VC and carbonitrile
5	22-224_5	1.2M LIFS/LIPF6	tenery carbonate co-solvent combination partially substituted with FEC	VC and phophazine
6	22-224_6	1.2M LIFS/LIPF6	tenery carbonate co-solvent combination partially substituted with FEC	VC and higher amount of organosilicon-2
7	22-224_7	1.2M LIFS/LIPF6	tenery carbonate co-solvent combination partially substituted with FEC	VC and cyclic sulfate-1
8	22-224_8	1.2M LIFS/LIPF6	tenery carbonate co-solvent combination partially substituted with FEC	VC and cyclic sulfate-2
9	22-224_9	1.2M LIFS/LIPF6	tenery carbonate co-solvent combination partially substituted with FEC	VC and lower amount of organosilicon-2
10	22-224_10	1.2M LIFS/LIPF6	various cyclic and linear carbonate solvent combinations	nitrile- and phosphate-based

Figure I.3.32 Results for Low-Cost Micro-Si Dominant Anode Electrode Development (Higher Si element wt.% $\geq 80\%$) (continued)
The C/3 RPT capacity check at every 50 cycles was measured to understand cell SOH degradation.

Elyte#1: Baseline



Elyte#2: Organosilicon-1 additive

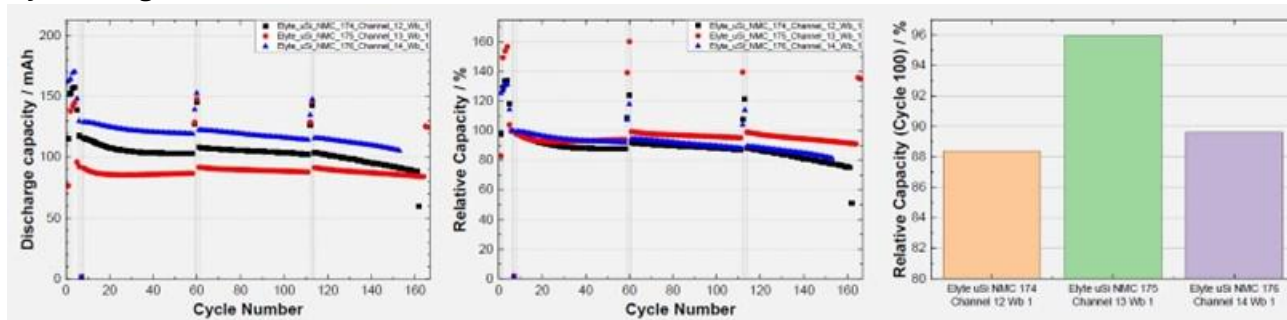


Figure I.3.33 Results for Low-Cost Micro-Si Dominant Anode Electrode Development (Higher Si element wt.% $\geq 80\%$) (continued)

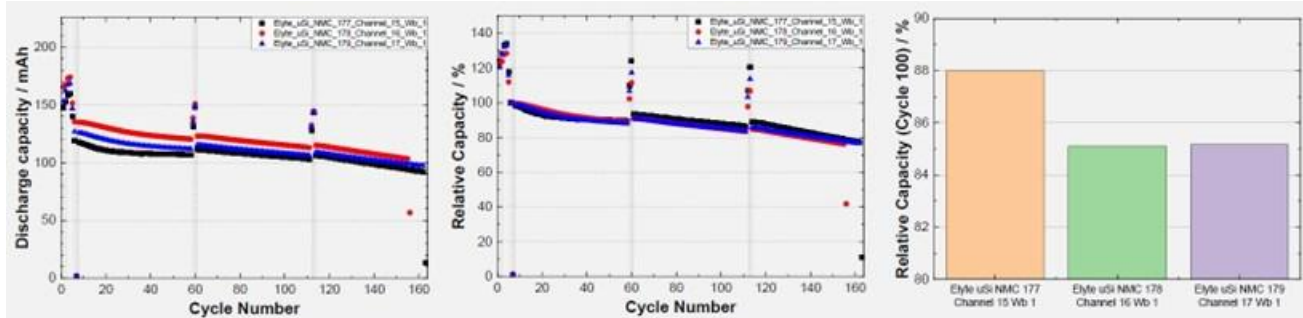
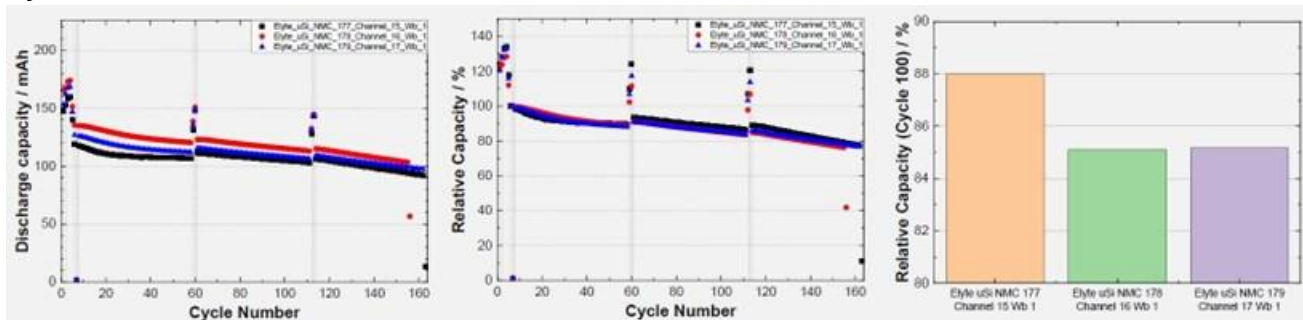
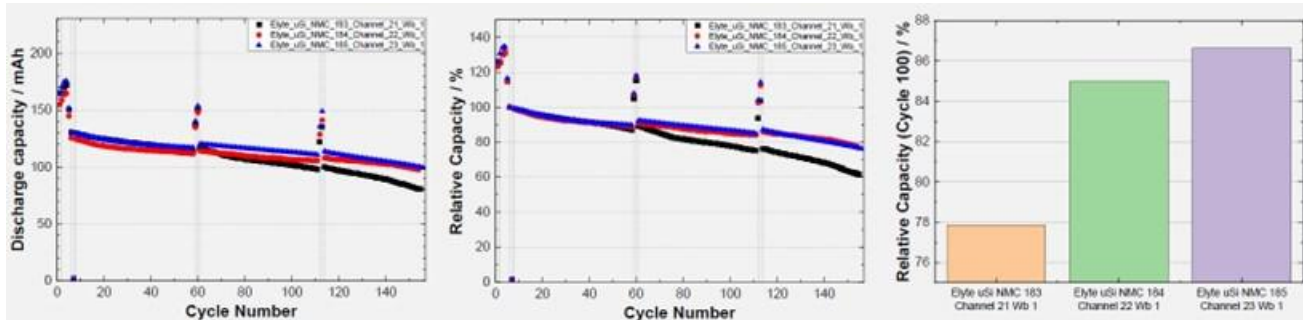
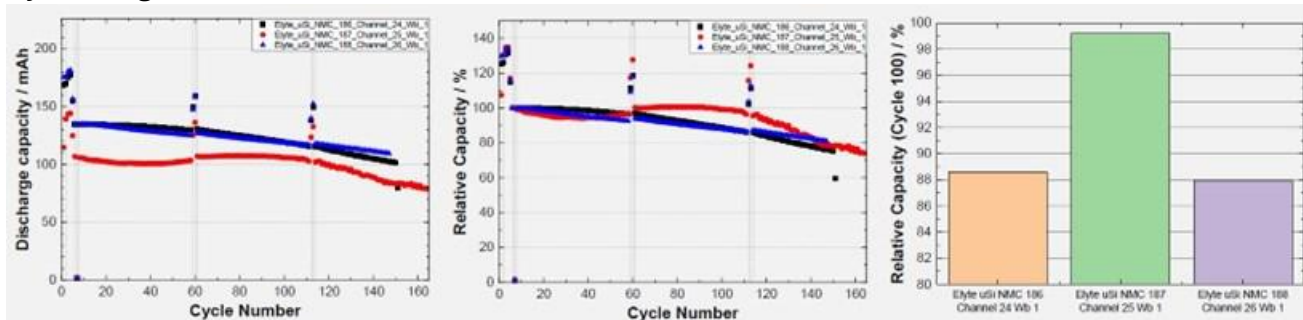
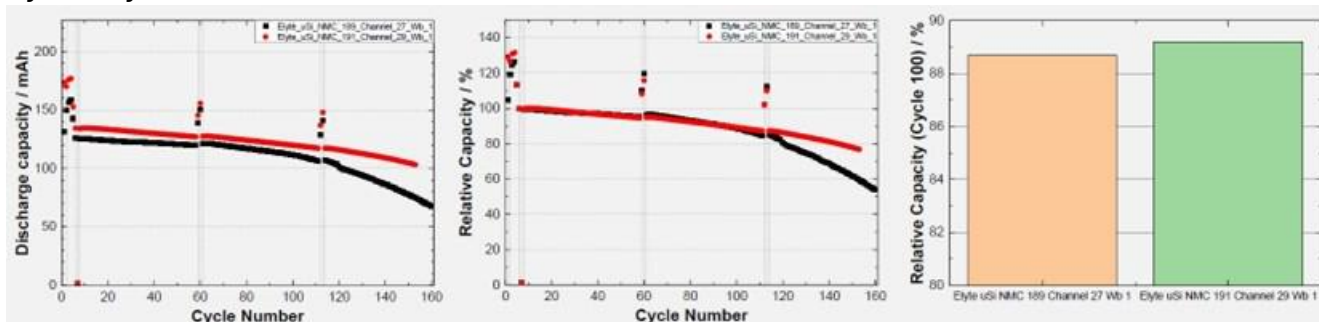
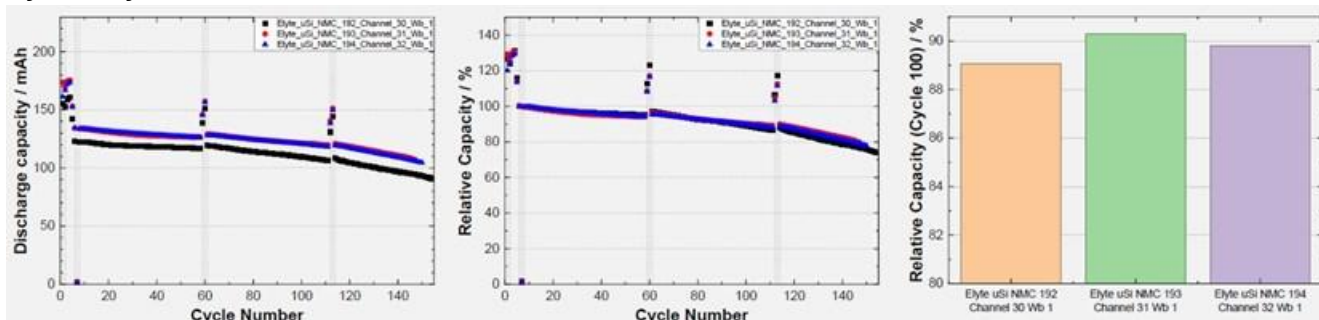
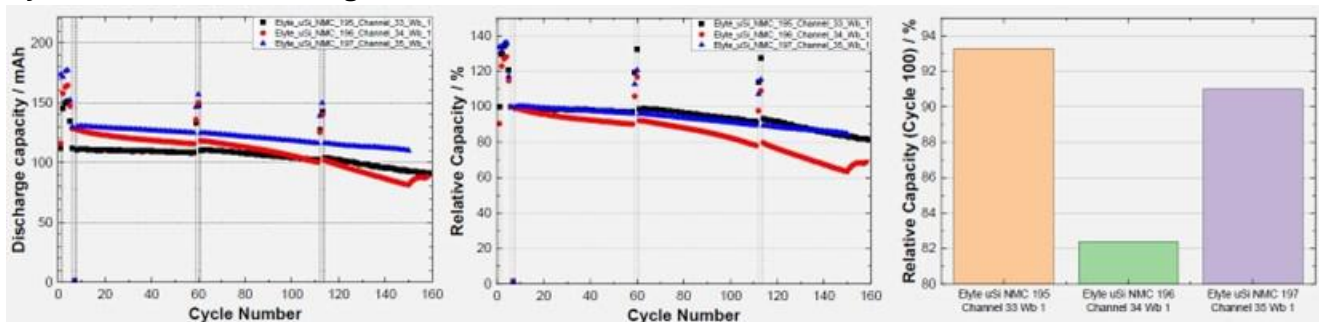
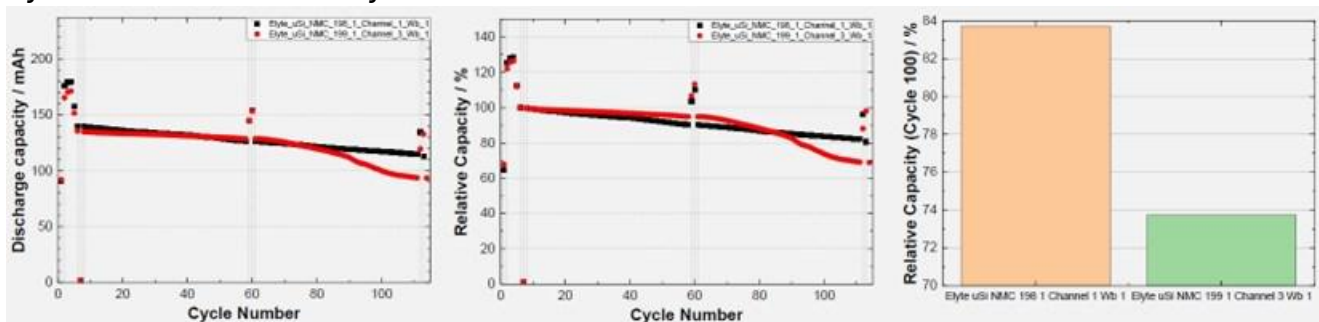
Elyte#3: Phosphite-based additive**Elyte#4: Carbonitrile-based additive****Elyte#5: Phosphazine-based additive****Elyte#6: Organosilicon-2 additive**

Figure I.3.34 Results for Low-Cost Micro-Si Dominant Anode Electrode Development (Higher Si element wt.%≥80%) (continued)

Elyte#7: Cyclic Sulfate-1 additive**Elyte#8: Cyclic Sulfate-2 additive****Elyte#9: Lower amount of organosilicon-2 additive****Elyte#10: Commercial electrolyte**Figure I.3.35 Results for Low-Cost Micro-Si Dominant Anode Electrode Development (Higher Si element wt.% \geq 80%) (continued)

The absolute and relative discharge capacities of Electrolyte 8 (cyclic sulfate-2 additive) was one of the highest, together with Electrolyte 6 (with organosilicon-based additive).

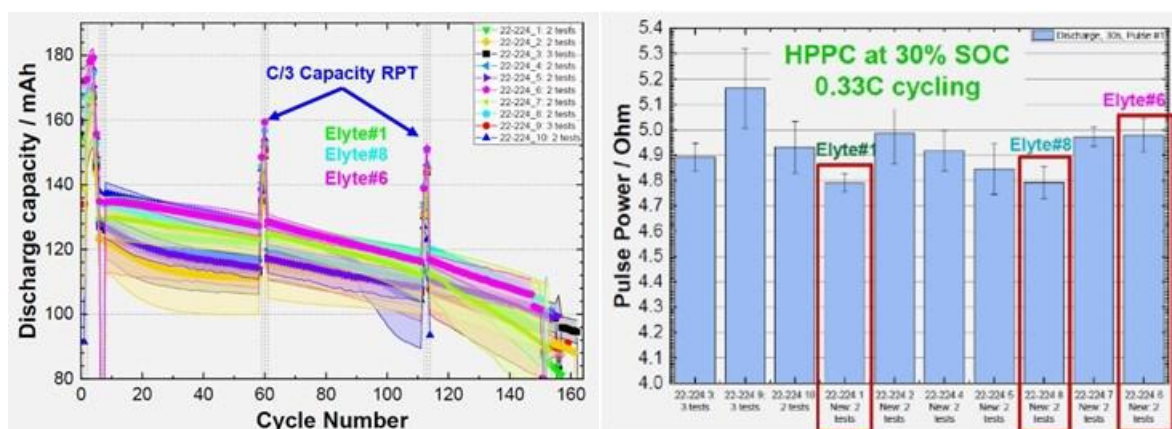


Figure I.3.36 Results for Low-Cost Micro-Si Dominant Anode Electrode Development (Higher Si element wt.% \geq 80%) (continued)

Elyte#6 and #8 cells were able to retain a SOH of 90% after 100 cycles and overcoming the baseline Elyte#1. These above results can also be applied to NX Si-C (40-50%Si) anode cell system, not only Micro-Si (\sim 80%Si). Next step will be that both above two best Elyte#6 & #8 will be tested in multi-layer cells with NX Si-C (40-50%Si) anode electrodes.

NX NCM91 || Si 4.5Ah Battery Prototype Cell Development (Based On Current Usabc Developed Nx Electrodes)

Results for this task are shown in the figures below (Figure I.3.37 to Figure I.3.40).

Cell Specifications (25 °C)	NX NCM91#1 NX Si-C#1	NX NCM91#1 NX LC Si-C#2
NX NCM91#1 Electrode Loading	\sim 5.8 mAh/cm ²	
Core D (mm)	44.38	44.64
Core C (mm)	61.41	61.01
Thickness (\sim 3 atm) T1 [mm]	6.43	6.91
Core Volume (mL)	17.53	18.81
Total Volume (mL) (pouch edges)	17.96	19.23
Measured Weight (g)	48.73	48.54
Voltage range (V)	4.2 - 2.5	4.2 - 2.5
C/3 Core Energy Density (Wh/L) (25°C)	908.73	839.45
C/3 Total Energy Density (Wh/L) (25°C)	886.97	821.11
C/3 Total Specific Energy (Wh/kg) (25°C)	326.90	325.30

Figure I.3.37 Results for Low-Cost Micro-Si Dominant Anode Electrode Development (Higher Si element wt.% \geq 80%) (continued)

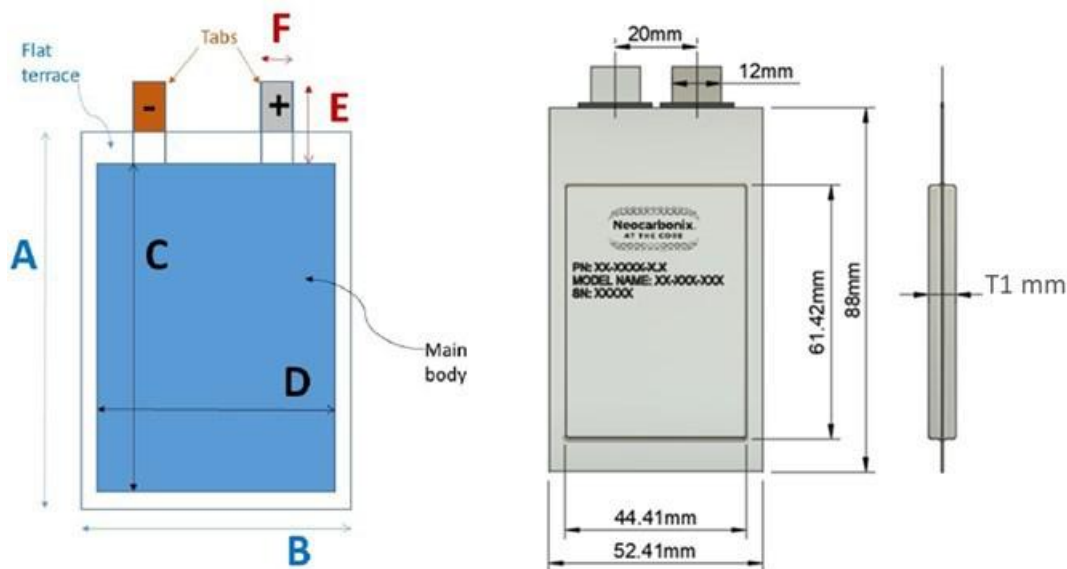


Figure I.3.38 Results for Low-Cost Micro-Si Dominant Anode Electrode Development (Higher Si element wt.% \geq 80%) (continued)

- Combined developed NX NCM91#1 cathode electrodes with NX Si-C#1 anode electrodes vs. NX LC Si-C#2 anode electrodes
- Both NX NCM91#1 cathode electrode loading: ~ 5.8 mAh/cm² with press density of ~ 3.6 g/cm³, NCM91 CAM%: 98.75% in electrode active layers
- Same other cell components for both cell designs

Cell Parameters (25 °C)	NX NCM91#1 NX Si-C#1	NX NCM91#1 NX LC Si-C#2
C/3 Energy (Wh) (25°C)	15.93	15.79
C/3 Capacity (Ah) (25°C)	4.643	4.622
1C SOC50 30s @ 25°C (mΩ)	38.9	41.7

Figure I.3.39 Results for Low-Cost Micro-Si Dominant Anode Electrode Development (Higher Si element wt.% \geq 80%) (continued)

- Initial charge-discharge curves show very typical Ni-rich NMC cathode combined with high Si% anode electrodes.

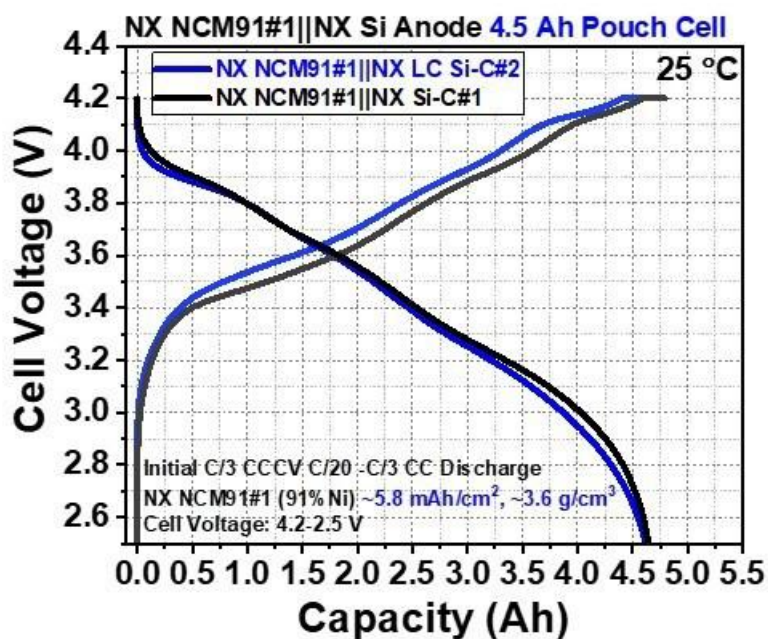


Figure I.3.40 Results for Low-Cost Micro-Si Dominant Anode Electrode Development (Higher Si element wt.%≥80%) (continued)

NX NCM91#1 || NX Si-C#1 - 4.5 Ah Cells

Results for this task are shown in the figures below (Figure I.3.41 to Figure I.3.51).

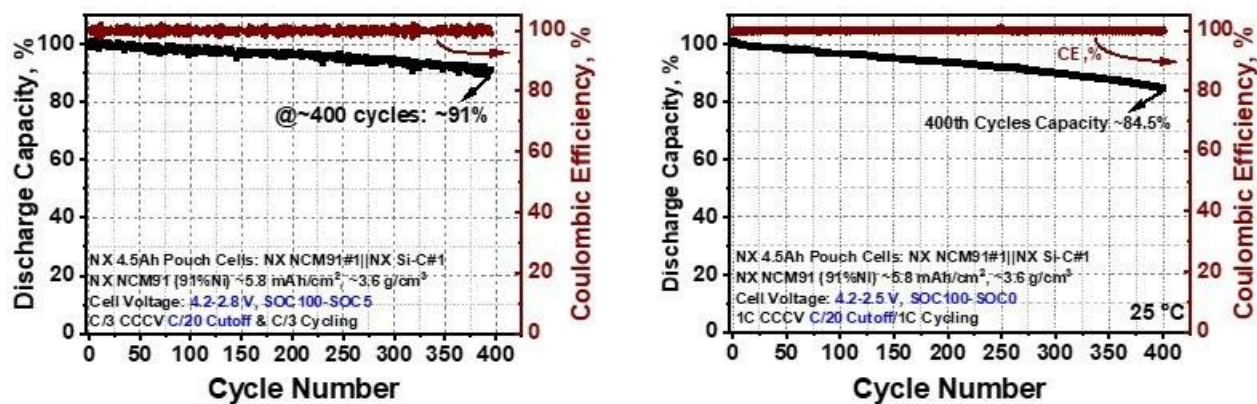


Figure I.3.41 Results for NX NCM91#1 || NX Si-C#1 - 4.5 Ah Cells

- Cycle Life C/3 (left) from 4.2-2.8 V (SOC100-SOC5) achieves 400 cycles with ~91% capacity retention
- Cycle Life 1.0C/1.0C (right) from 4.2-2.5 V (SOC100-SOC0) achieves 400 cycles with ~84.5% capacity retention

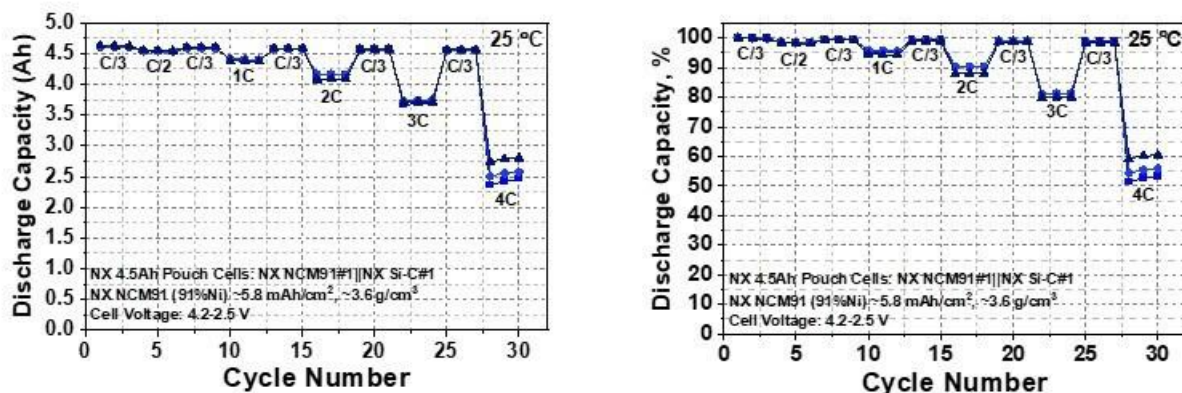


Figure I.3.42 Results for NX NCM91#1 || NX Si-C#1 - 4.5 Ah Cells (continued)

- Discharge C-rate cycling test shows stable trends for all the C/3, C/2, 1C, 2C, 3C, and 4C
- Discharge 4C-rate capacity and retention to first 3 cycles of C/3 discharge is ~60% even with high loading electrodes $\geq 5.8 \text{ mAh/cm}^2$.

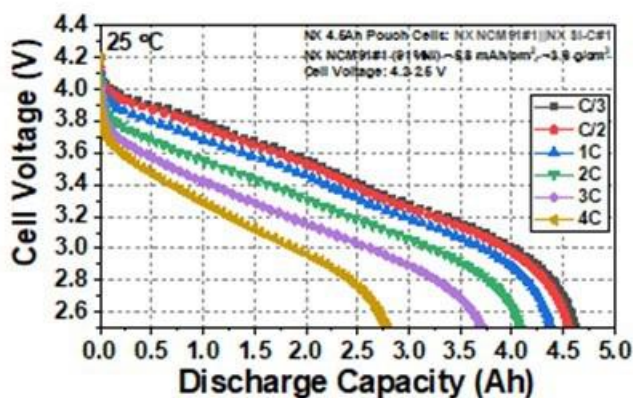


Figure I.3.43 Results for NX NCM91#1 || NX Si-C#1 - 4.5 Ah Cells (continued)

Figure I.3.44 Results for NX NCM91#1 || NX Si-C#1 - 4.5 Ah Cells (continued)

- Charge C-rate cycling test shows stable trends for all the C/3, C/2, 1C, 2C, 3C, and 3.5C CC-region capacity.

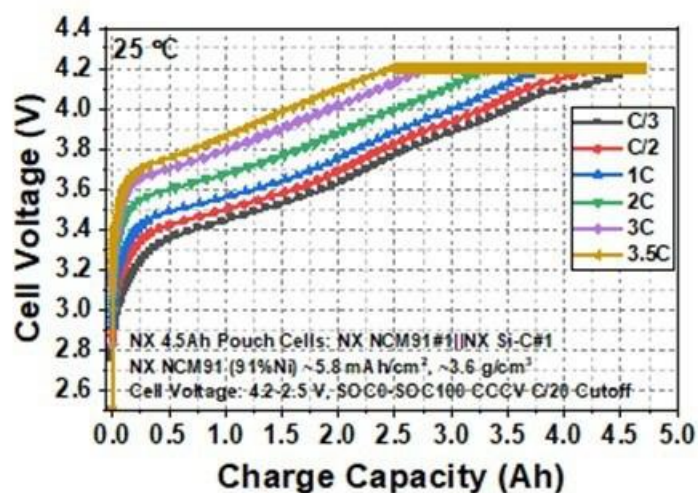


Figure I.3.45 Results for NX NCM91#1 || NX Si-C#1 - 4.5 Ah Cells (continued)

- C-rate charge curves show stable trends for all the C/3, C/2, 1C, 2C, 3C, and 3.5C: CC-region Charge 3.5C-rate capacity and retention to first 3 cycles of C/3 discharge is ~56%.

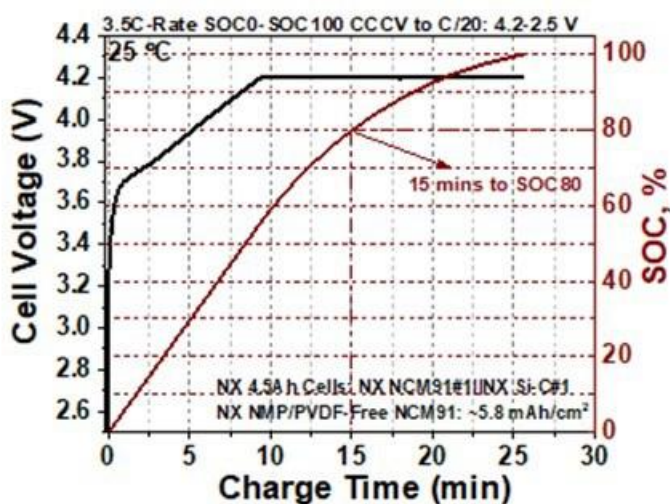


Figure I.3.46 Results for NX NCM91#1 || NX Si-C#1 - 4.5 Ah Cells (continued)

- Under 3.5C-Rate fast-charge, SOC80 can be achieved at ~15 mins even with such high loading NX battery electrodes ≥ 5.8 mAh/cm².
- All NX NCM91#1||LC Si-C#2 cells' electrochemical tests are in progress
- Will share more data when tests completed.

Nx Ni-Rich Ncm | Si ~4ah Battery Prototype Cell Safety Test Performance (3rd Party Validation Results)

Third Party testing was completed at a reputable testing facility using the NX 4.5 Ah pouch cells from section g. The following test were performed:

Safety Test Category	Safety Test Protocol (SOC100)
Over Charge	1C Charge from SOC100 to SOC200
Short Circuit 1mΩ	External short circuit under 1 mΩ
Short Circuit 10mΩ	External short circuit under 10 mΩ
Thermal Ramp	5 °C/min hold at 130 °C, 150 °C, 170 °C and 200 °C for 30 mins

Figure I.3.47 Results for NX NCM91#1 || NX Si-C#1 - 4.5 Ah Cells (continued)

Overcharge to SOC200

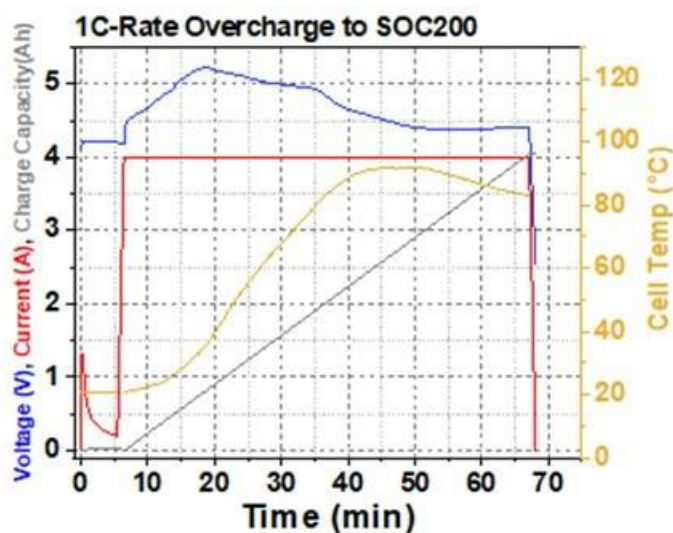


Figure I.3.48 Results for NX NCM91#1 || NX Si-C#1 - 4.5 Ah Cells (continued)

- No thermal runaway observed
- Cell Peak Temp: ~91°C.



Figure I.3.49 Slight gassing observed after the 200% SOC overcharge.

Short Circuit 1 m Ω & 10 m Ω

The 1 m Ω & 10 m Ω short circuit tests were both performed with a calibrated 0.1039m Ω shunt with different length test leads.

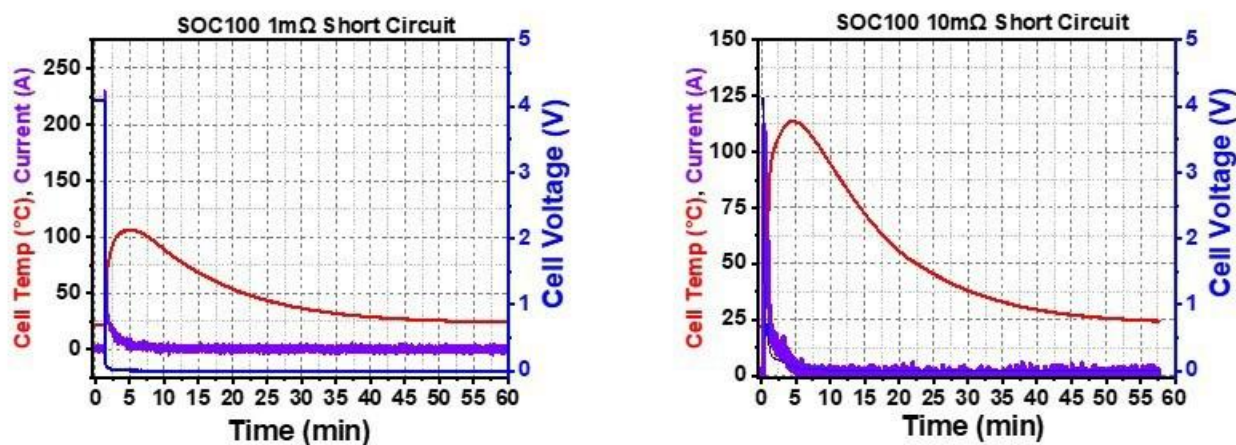


Figure I.3.50 Results for NX NCM91#1 || NX Si-C#1 - 4.5 Ah Cells (continued)

- No thermal runaway
- Cell Peak Temp 1 m Ω -SC: ~106°C
- Cell Peak Temp 10 m Ω -SC: ~113°C.

Thermal Ramp

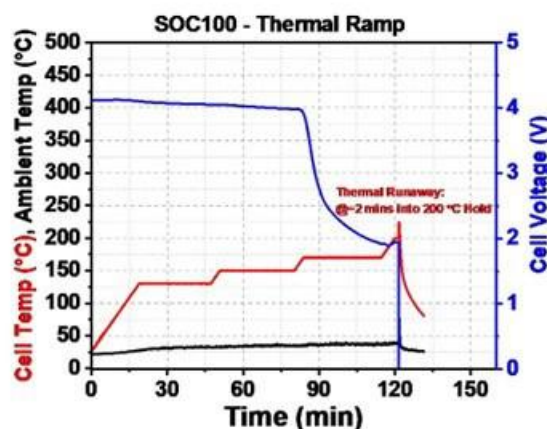


Figure I.3.51 Results for NX NCM91#1 || NX Si-C#1 - 4.5 Ah Cells (continued)

- No thermal runaway at 130°C-170°C hold
- Most conventional battery cells will have thermal runaway between 150°C-170°C hold.
- Thermal runaway at ~2 mins into 200°C hold.

Conclusions

The widespread applications of lithium-ion batteries have prompted significant investment in research of electrode and cell designs and further optimization for scale-up manufacturing of the said designs. Drastic improvement in both the battery performance and manufacturing processing would enable greater use of lithium-ion batteries in sustainable applications, particularly in electric vehicles, while at the same time reducing the economic and environment impacts of the use of such energy storage systems.

The technology, Neocarbonix, as described in this project would enable such aforementioned improvements. Significantly higher gravimetric and volumetric energy density as well as high power density can be achieved through increase in mass loading of electrochemically active materials on an electrode-level. Concurrently, lower production costs in terms of \$/kWh can be achieved using scalable and industrially proven aqueous and/or other low boiling point based solution processing methods and elimination of toxic solvent from manufacturing.

Successful demonstration and optimization of the described technology concepts in this project would achieve the following:

1. Develop further *NX battery electrodes for both cathode and anode based on various types of CAMs & AAMs* to achieve higher performance LCFC EV battery cells.
2. Achieve *cell-level higher volumetric energy density* (25%-30% improvement in energy density in Wh/L)—thereby significantly increasing projected range of electrical vehicles using such battery designs.
3. Pre-lithiation: C/3 Cycling improvements in Capacity retention (>3.5%), CE%, and Increase in Specific Energy based on Active Electrode Total Weight (~9%)
 - a. Prelithiation mass production cost-benefit model demonstrates:
 - Cost savings of large scale, modular designed prelithiation lines with example throughputs shows improvements with a **reduced cell cost/kWh-cycle of 11.1% and -10.91% in carbon footprint.**
 - **Capacity gain of 5.9% from prelithiation and 6.1% cycle life improvements** with assumption of **current cell cost at \$100/kWh and \$50.00/kg for anode powder**

- **60% cost savings** in formation.
- 4. Generate **14 Ah** battery cell electrochemical performance results and more life test performance are updated.
- 5. Demonstrated >3X NX NCM91#1 R2R coating speeds compared to conventional NMP electrodes: **60 m/min vs ~12-15 m/min in an 18m oven**
- 6. **Elyte #6 (VC w/ organosilicon-based additive) & #8 (VC w/ cyclic sulfate-2 additive) both retained 90% SOH after 100 cycles** compared to the baseline **Elyte #1 (VC w/ no additive)** in NX Si Anode development.
- 7. NX NCM91#1 || NX Si-C#1 - 4.5 Ah Cells
 - a. C/3 & 1C Cycle Life achieves ~91/84.5% capacity retention, respectively, after 400 cycles
 - b. Discharge C-rate stability up to the tested 4C rate with ~60% capacity retention
 - c. Charge C-rate stability up to the tested 3.5C rate with ~56% CC capacity retention
 - d. 3.5C-Rate fast-charge, SOC80 can be achieved at ~15 mins even with such high loading NX battery electrodes ≥ 5.8 mAh/cm².
- 8. NX NCM91#1 || NX Si-C#2 - 4.5 Ah Cells and full comparison study with NX NCM91#1 || NX Si-C#1 - 4.5 Ah Cells
 - a. Initial HPPC DCIR check shows that LC Si-C#2 best formula-1 still has higher resistance compared with NX Si-C#1 control old formulas.
 - b. For NX LC Si-C#2 AAM with various new NX formulations, the New Formula-1 performs the best on Crate discharge tests in average.
 - c. Comparing the NX LC Si-C#2 new formula-1 with NX Si-C#1 control two old formulas; it achieves similar Crate performance as the control-old-formula-1 but still show worse performance compared with control-old-formula-2 in average.
 - d. When the C/3 capacity retention % is compared before and after Crate discharge cycling, after 30 cycles, the New Formula-3 shows the highest retention % (~94.1%) which is ~0.4% higher than **New Formula-1 (best Crate mAh/cm² performance formula)** (~93.7%).
 - e. After 30 cycles various Crate tests, NX LC Si-C#2 New Formula-1 shows the highest C/3 capacity retention % (~93.7%) compared with the control groups
 - f. After 250 cycles of 1C1C cycling, **NX LC Si-C#2 New Formula-1** shows the highest capacity retention % **~88.0% and a Delta V increase of 13.50%** compared with the control groups of **~84.6% Capacity Retention and 23.13% increase in Delta V**.
- 9. Safety Testing
 - a. No thermal runaway after 200% SOC Overcharge
 - b. No thermal runaway after 1m Ω and 10 m Ω Short Circuit
 - c. No thermal runaway between 130°C -170°C Thermal Ramp; thermal runaway at 200°C.

Future Work

1. Continue work with coating speeds in NX Si Anode
2. Test Elyte#6 & #8 in multi-layer cells with NX Si-C (40-50%Si) anode electrodes.
3. NX NCMA (~90%Ni) new CAM based electrode R2R process development and performance tests: still waiting for the new CAM to be delivered.
4. NX low-Cost SiGr anode electrode formulation optimizations for longer cycle life and tested in multi-layer ~4.5 Ah & ≥ 10 Ah pouch cells.
5. NX Si anode new additive-based electrolyte formulation tests in multi-layer pouch cells: ~4.5Ah cells.
6. Start the NX battery cell ~50Ah Ni-Rich||SiGr A-sample cell design and modeling work.

I.4 Evaluation of Advanced Li-ion Cell Architectures for Extreme Fast Charging (XFC) Batteries for Electric Vehicles (EnPower, Inc.)

Adrian Yao, Principal Investigator

EnPower, Inc.
8740 Hague Rd
Indianapolis IN 46256
E-mail: adrian@enpowerinc.com

Brian Cunningham, DOE Technology Development Manager

U.S. Department of Energy
E-mail: brian.cunningham@ee.doe.gov

Start Date: February 22, 2021

End Date: May 22, 2022

Project Funding: \$367,799

DOE share: \$183,899

Non-DOE share: \$183,899

Project Introduction

As Battery Electric Vehicle (BEV) adoption increases to serve the needs of mainstream consumers, it is ever more critical for battery cell technology to be low-cost with fast-charging capability, all while maintaining a minimum required vehicular range to be practical. However, an inherent tradeoff between energy (range) and power (fast-charge) exists for all Li-ion cells, and current battery cell technology is unable to satisfy both requirements. EnPower addresses this fundamental energy-power tradeoff with its unique and proprietary multilayer electrode architectures that increase the rate capability of thick, high energy density electrodes. By using simultaneous multilayer slot-die coating, EnPower is also able to keep costs low with no detriment to throughput and yield. In this Technology Assessment Program (TAP), EnPower will iterate through multiple designs of multilayer graphite anodes and multilayer NMC811 cathodes to arrive at a semi-optimized cell design. 4.2 Ah Pouch cells incorporating both multilayer anodes and cathodes will be shipped to Idaho National Laboratory (INL) for final testing upon completion of the TAP.

Objectives

The objective of the project is to demonstrate the feasibility of EnPower's multilayer electrode technology in commercially relevant pouch cell form factors. Cell performance targets include:

- ≥ 250 Wh/kg (in 4.2Ah pouch cell form factor)
- 80% Δ SOC fast-charge in < 20-mins

Approach

In this TAP, EnPower first iterated through approximately (6) multilayer graphite anode designs all paired with an identical NMC622 cathode pair to downselect a best-performing design. Subsequently, EnPower iterated through approximately (6) multilayer NMC811 cathode designs all paired with the previously downselected multilayer anode, again identifying a best-performing architecture. Using this semi-optimized multilayer anode-cathode pair, EnPower also iterated through several electrolyte formulations tailored for fast-charging capability while keeping component costs in mind. Internal testing compared cells with multilayer electrode architectures against cells having "homogeneous baseline" electrodes that are chemically- and dimensionally identical references of their multilayer counterparts. These homogeneous baseline electrodes represent state-of-art conventional electrode architectures. Once a cell stack design (anode, cathode, electrolyte) was selected, final 4.2 Ah pouch cells were shipped to INL for third-party testing and validation.

Results

During the first half of this project, the work progressed well, showing improvements as previously reported (see the 2021 APR). EnPower developed using testing at 40°C. When tested at 30°C, the cells showed noticeably lower rate performance.

Work begun on electrolyte formulation improvements provided some means to enhance the rate capability at this lower temperature, at the expense of some other performance metrics. The long-term cycling with the best rate capability electrolyte formulation turned out to yield lower capacity retention than with EnPower's standard electrolyte formulation comprised of typical solvents, salt concentration, and additive. Therefore, the standard formulation was used in the final deliverable build.

Also, upon reaching the time of building the cells to be delivered to INL, EnPower encountered a production issue surrounding the making of the multilayer cathode. The single crystal NMC811 material was in poor condition (causing slurries to gel up) that was not caught during receipt months prior. For expediency, because replacement material was not procurable in a short time frame, a typical polycrystalline single layer cathode was substituted in the cell design.

Successful and encouraging results were found in the comparison between the multilayer (ML) design and the homogeneous baseline (HBL) coating design. The HBL is the comparison by which EnPower demonstrates the benefit of multilayer over the conventional single layer-coated electrode comprised of the same materials, composition, loading, and calender density. Figure I.4.1 shows the improved fast charge time by arranging the same materials in the HBL electrode into the ML architecture. For these two cells, faster charging times led to lithium plating as evidenced by characteristics in the voltage profiles, which are confirmed by selected cell openings.

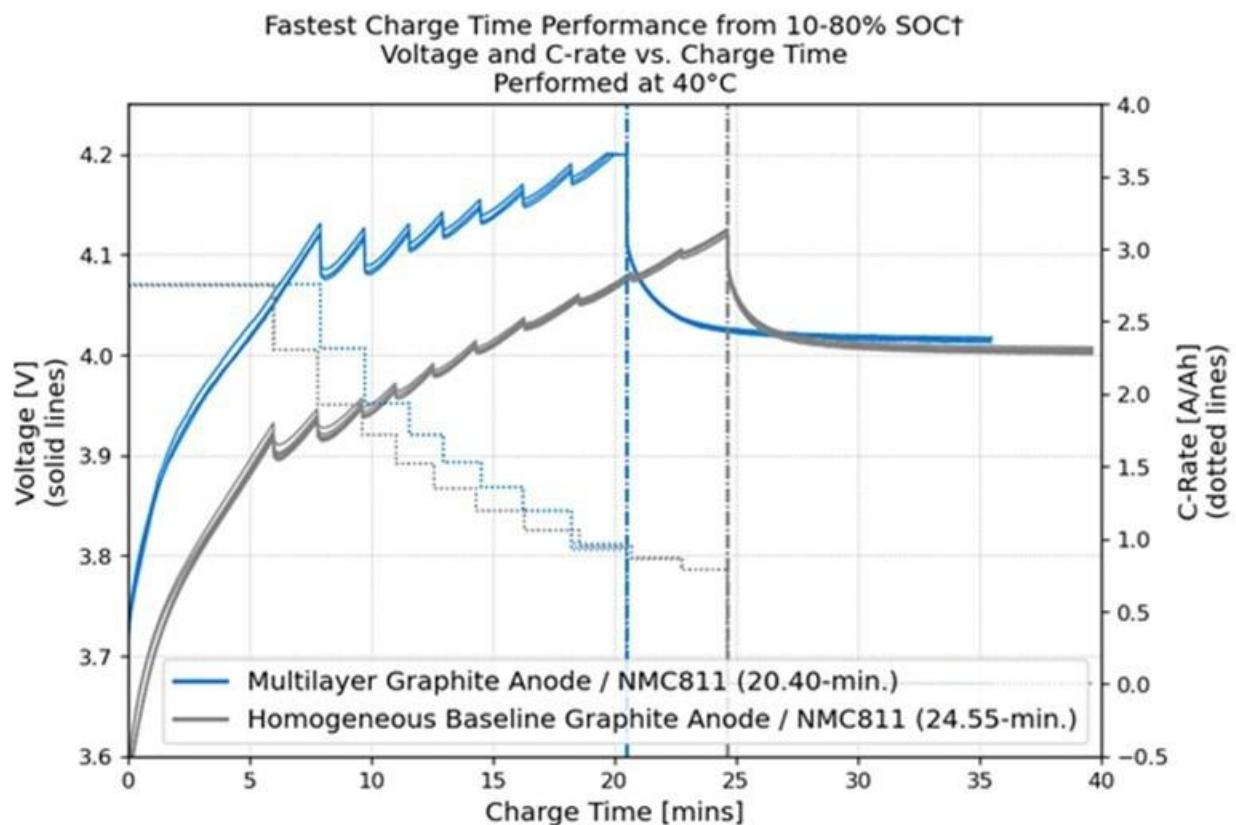


Figure I.4.1 Comparison of the multilayer graphite anode / NMC811 cell's fast charge capability with that of a cell built with a homogeneous baseline anode comprised of the same graphite composition and density

The final cell deliverable exhibited lower fast charge capability. Initial results from the INL testing demonstrated the final cell design's failure to meet the <20 min. fast charge and for cycling at either the 25% or 100% FC condition. Contributing factors include the testing by EnPower to ~80% SOC and discharging the capacity to low SOC instead of charging to the maximum operating voltage and discharging only 80% of the usable energy, thereby starting the fast charging protocol at a higher SOC condition than that used in development.

Otherwise, the cell performs well on all other metrics, including peak discharge power density, and was of consistent manufacturing quality. Figure I.4.2 shows results from the Hybrid Pulse Power Characterization (HPPC) test results of the deliverable cell. The specific energy as determined using the development pouch cell format employed by EnPower (4.2 Ah) scaled to a ≥ 13 Ah cell size meets the ≥ 250 Wh/kg objective.

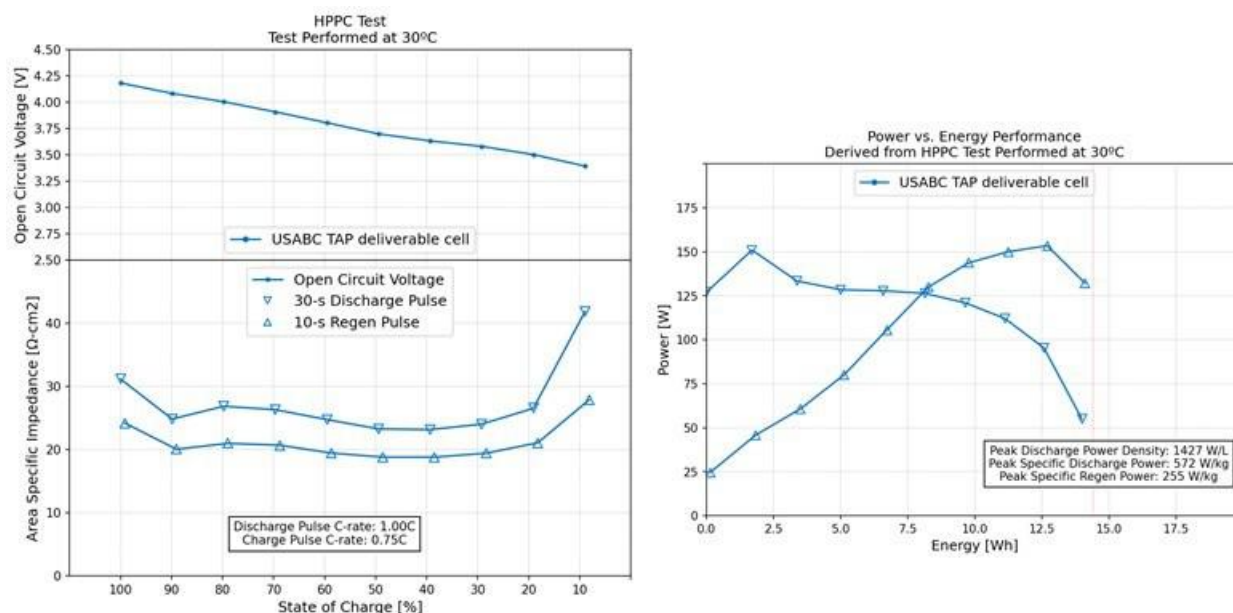


Figure I.4.2 Hybrid Pulse Power Characterization (HPPC) for the EnPower multilayer anode / NMC811 cell

Ways in which EnPower is addressing these multiple production and development challenges include qualifying new suppliers, expanding incoming quality control procedures, and committing more testing time to verify long-term performance in addition to the quick screening tests for assessing improvements and short-term performance metrics. Primarily, the predominant factor leading to the ultimate poor FC cycling performance in the INL testing is the different testing conditions during development – test temperature and SOC range. EnPower is focusing development testing toward the higher SOC conditions to address the more aggressive charging conditions.

Conclusions

EnPower has successfully validated the feasibility of the multilayer electrode technology, demonstrating its ability to significantly enhance cell performance at $>30^{\circ}\text{C}$, especially with respect to fast-charge cycling. EnPower is now focused on tuning its technology to perform at lower temperatures and under higher states of charge conditions for which the USABC/INL testing emphasizes.

Using only graphite-based anode active materials in this drop-in technology enables a low-cost cell based on both the materials and scalability in existing manufacturing infrastructure. The combined performance and cost benefits favor an accelerated adoption in mass-market BEVs.

Acknowledgements

EnPower thanks the United States Advanced Battery Consortium (USABC), a subsidiary of the United States Council for Automotive research (USCAR), for support on this project.

I.5 Solvent-free Electrode Manufacturing for Low Cost/Fast Charging Batteries (Worcester Polytechnic Institute)

Yan Wang, Principal Investigator

Worcester Polytechnic Institute
100 Institute Road
Worcester, MA 01609
E-mail: yanwang@wpi.edu

Brian Cunningham, DOE Technology Development Manager

U.S. Department of Energy
E-mail: brian.cunningham@ee.doe.gov

Start Date: November 19, 2019	End Date: September 15, 2023	
Project Funding (FY22): \$935,160	DOE share: \$446,685	Non-DOE share: \$488,475

Project Introduction

In conventional lithium ion batteries, a slurry made of active materials, conductive additive and polymeric binder is cast onto the current collector. The coated electrodes are subsequently dried and calendared. In the slurry casting method, organic solvent (NMP) is used to make the slurry, which contributes significantly to the total cost of lithium ion battery manufacturing (the solvent itself, solvent drying and recovery). In efforts to lower the battery cost associated with the NMP solvent, different approaches have been investigated. Finding a less expensive solvent to replace NMP has been the subject of much research. Water based approaches have been studied and found to compare favorably to organic solvent based approaches [1-3]. This approach has achieved significant success on the anode side of Li-ion batteries, and aqueous slurries using Styrene Butadiene Rubber (SBR) as the binder have already been commercialized for graphitic anodes. However, the costly time-consuming and energy-intensive drying step following coating remains part of the fabrication process. In addition, NMP is still being used to dissolve PVDF binder on the cathode side, since binders dissolved in aqueous systems are not chemically or electrochemically stable at the high voltages seen at the positive electrode.

Complete elimination of the solvent is a promising approach to lower both the cost and manufacturing time of Li-ion batteries. Michael Wixom (previously at A123 Systems) at Navitas Systems, who collaborate with Maxwell Technologies, has proposed and developed a solvent-free electrode manufacturing process [4]. Telsa acquired Maxwell to commercialize the technology in 2019. In the manufacturing process, the active material, conductive carbon and Polytetrafluoroethylene (PTFE) binder were pressed onto current collector directly to fabricate the electrode, as a viable approach to fabricate supercapacitors. However, to make Li-ion battery electrodes, the following additional challenges have been identified: (1) PTFE is not electrochemically stable in a lithium battery anode; (2) it is difficult to fabricate thin electrodes, which are essential to provide sufficient power for Li-ion batteries; (3) the electrode is stiff, which complicates or precludes winding for cylindrical cells/prismatic wound cell formats.

Structured electrodes have been demonstrated to improve battery charging rates. For example, experiments [5, 6] reveal that electrolytic transport becomes a major source of cell polarization at conditions of high current and/or large electrode thicknesses, both of which are the case for high rate charging of EV batteries. To enable fast charge, different structured electrodes have been developed [7, 8]. However, previous methods often utilize complex manufacturing processes and are difficult to scale up.

Objectives

The project's objective is to develop low cost batteries capable of fast charging for EV applications according to the USABC targets. In order to achieve the goal, the team will further develop a solvent-free manufacturing method for hetero-structured electrodes in order to achieve fast charging capability and low cost batteries. The hetero-structure enables fast charging and solvent-free manufacturing allows low cost. It is inherently challenging to fabricate hetero-structured electrodes using the traditional slurry casting method due to the complicated solvent drying process. In this project, the team will fabricate advanced electrodes with NMC622 and graphite as the cathode and anode materials, respectively.

Approach

Our proposed solvent-free manufacturing could potentially achieve low cost and fast charge concurrently. In this project, solvent-free manufacturing is used to fabricate electrodes with layered structures, whereby layers have varying porosities strategically tuned to enable fast charge batteries. During electrode fabrication, dry mixed powder is directly sprayed onto the current collector. Subsequent hot rolling results in melting of the binder and formation of a strong bond between particles and current collector. In order to enable high rate, electrodes with a multi-porosity hetero-structure will be fabricated. Compared to other methods, such as co-extrusion, to fabricate multi-porosity hetero-structured electrodes, the proposed method does not involve any solvent or complicated hardware and can be easily scaled up. Due to the elimination of solvent, the solvent-free manufactured layered electrodes allow for fast charge (structured electrode), low cost (no solvent and drying), and fast production (no drying step) when compared to the conventional wet processed electrodes.

Table I.5.1 is a comparison of our technology to current slurry casting technology to fabricate battery electrodes.

Table I.5.1 Comparison of Our Technology to Current Slurry Casting Technology

	Current technology	Our proposed technology
Material mixing	Wet mixing with solvent	Dry mixing without solvent
Coating	Slurry casting	Dry printing
Dry	Dry step needs	No drying
Solvent recovery	Organic solvent needs to be recovered	No recovery step
Electrode	Uniform porosity electrode	Porosity graded electrode (proposed work)

Results

Modeling

We re-calibrated the model by using the new tortuosity data measured by WPI. The new model was used to compare the CCCV charging capacities of high-loading slurry-casted electrodes and dry-printed 2-layer electrode configurations (NMC: 30 mg/cm², graphite: 20 mg/cm²). For nC CCCV charging, the CC charging step stops when cell voltage reaches 4.2 V and the duration of the CV step is set to keep the total charging time at 60/n minutes. The followings are observed from the calculations (see Figure I.5.1):

- The 2-layer dry electrodes outperform the slurry-casted electrodes during both CC and CV charging steps.
- The charging capacity in the CV step accounts for the majority of the charging capacity (>60%) at 4C.
- Using 2-layer NMC cathode does not bring notable increase to the charging capacity compared to uniform NMC cathode. A combination of 2-layer graphite anode and uniform NMC cathode should be the targeted configuration for manufacturing.

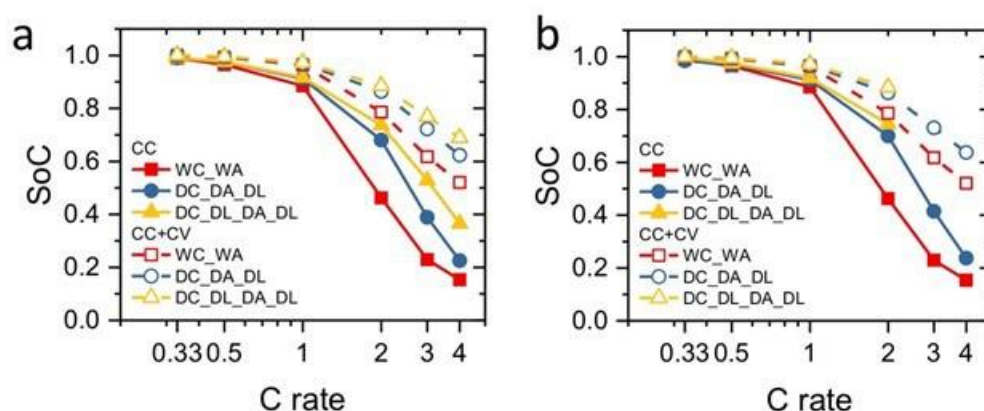


Figure I.5.1 CC (solid lines) and CCCV (dashed lines) charging capacity of different types of NMC/graphite cells. Symbols: WC-WA – slurry-casted cathode and anode; DC_DA_DL – uniform dry NMC cathode and 2-layer dry graphite anode; DC_DL_DA_DL – 2-layer dry NMC cathode and 2-layer dry graphite anode. The tortuosity function $\tau(\epsilon)$ has the form of $1.5\epsilon^Y$ in (a) and ϵ^Y in (b).

The effect of changing electrolyte from 1M LiPF₆ in EC:EMC:DEC = 26:52:22 (w:w:w) to 1M LiPF₆ in EC:DMC 1:1 (w:w) on the charging rate performance was evaluated by modeling. As shown in Figure I.5.2, EC:DMC 1:1 (w:w) is predicted to deliver 10% higher charging capacity at 3C than EC:EMC = 3:7 (w:w) in dry-printed NMC half cells. Guided by the prediction, similar comparison was also performed experimentally and an even larger improvement was observed, see Figure I.5.2b. It indicates that DMC-based electrolytes may have good wetting properties with dry-printed electrodes, which also contributes to the better charging performance.

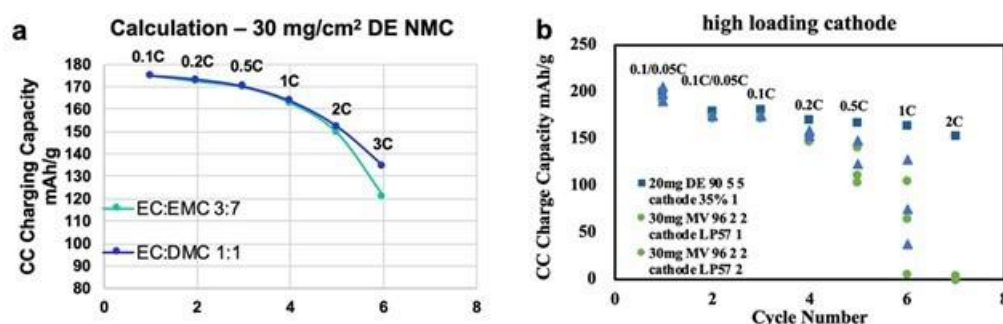


Figure I.5.2 (a) Rate performance of dry-printed (DE) NMC cathode half cells using EC:EMC=3:7 (w:w) vs EC:DMC 1:1 (w:w) predicted by battery simulation. (b) Measured rate capability of dry-printed (DE) and slurry-cast (MV) NMC cathode half cells using EC:EMC=3:7 (w:w) vs EC:DMC 1:1 (w:w) (LP57).

We employed the refined model to optimize the 2-layer electrode designs for the dry-printing process. As shown in Table I.5.2, the suggested designs pair a 2-layer graphite anode with either a uniform or 2-layer NMC cathode. For both anode and cathode, the two layers have an equal loading. The layer next to the separator has a high porosity of 45% and the layer next to the current collector has a low porosity of 25%, which leads to an average porosity of 36%. The reason for proposing two different designs is that the (2-layer cathode + 2 layer anode) configuration offers modestly higher charging performance, but the (uniform cathode + 2 layer anode) configuration is more convenient to manufacture.

Table I.5.2 Proposed 2-layer Electrode Design for High Loading Cells

Design Type	Cathode				Anode			
	Porosity (%)		Loading (mg/cm ²)		Porosity (%)		Loading (mg/cm ²)	
	Layer 1*	Layer 2*	Layer 1	Layer 2	Layer 1	Layer 2	Layer 1	Layer 2
2-layer cathode + 2-layer anode	25	45	15	15	25	45	7.5	7.5
uniform cathode + 2-layer anode	36		30		25	45	7.5	7.5

Figure I.5.3 compares the charging performance of the proposed 2-layer dry-printed electrode designs vs. the baseline (slurry-cast uniform electrodes) by model predictions. 4C CCCV charging with an overall charging time of 15 minute was considered. Using EC:EMC 3:7 or EC:DMC 1:1 electrolyte, the (uniform cathode+2 layer anode) design delivers 20-21% higher capacity than the baseline. Part of the improvement comes from the lower tortuosity of the dry-printed electrode structure than the slurry-cast counterpart, and part is due to the enhanced electrolyte transport facilitated by the 2-layer electrode configuration. Replacing the uniform NMC cathode with the 2-layer configuration of the same average porosity further increases the CCCV charging capacity by ~5%. Our study also shows that EC:DMC electrolyte is more advantageous than the EC:EMC electrolyte for high-rate charging/discharging applications because the former has c.a. 10% high ionic conductivity at 1M LPF₆. For 15 min CCCV charging, EC:DMC enables 7 – 8.5% higher capacity in the suggested electrode designs.

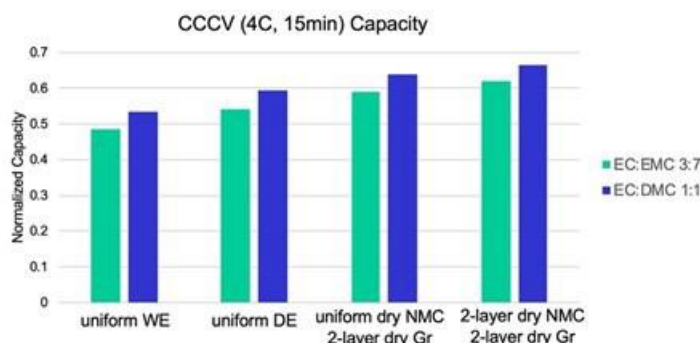


Figure I.5.3 Comparison of the charging performance of the proposed 2-layer dry electrode designs against the uniform NMC/graphite full cells fabricated by the slurry-casting method (baseline) and dry-printing technique.

Electrochemical measurements at WPI reveal that the dry-printed cathodes and anodes have lower tortuosity than the slurry-cast counterparts, which is especially pronounced at the cathode side. To understand the structure origin of such difference, we performed nanotomography measurement of dry-printed and slurry-cast NMC cathodes to reconstruct the electrode structure digitally. The reconstructed 3D electrode structures are shown in Figure I.5.4a and b. Tortuosity of the two types of cathodes were calculated from the digitized electrode structures through random walk simulation, Figure I.5.4c and d. Because carbon and PVDF are transparent to the X-ray energy (8.4 keV) used in tomography characterization, only NMC particles are visualized in the tomographic images, and the computed tortuosity does not include the blocking effect of carbon and PVDF binder. The tortuosity in the electrode depth direction is 1.325 and 1.48 for the dry and slurry-cast cathodes, respectively. These values are much lower than the electrochemical impedance measurements and do not exhibit large difference between each other. Notably, the calculated tortuosity values are in very good agreement with estimates based on the Bruggeman relation $\tau = \epsilon^{-0.5}$, where ϵ is porosity (Table I.5.3). Combined with the SEM characterization of the cross sections of the dry and slurry-cast cathode samples, we conclude that the carbon and binder domain (CBD) in the electrodes significantly increases the electrode tortuosity and causes it to deviate from the Bruggeman behavior. The lower tortuosity of the dry

cathode originates from the more preferential distribution of the carbon and binder domain in its pore space, which retains a larger portion of open pores and facilitates the ionic transport across the electrode. This is reasonable because the organic solvent used in the slurry casting process causes the binder polymer chains to swell and occupy a larger volume of the pore space than in the solvent-free dry printing process.

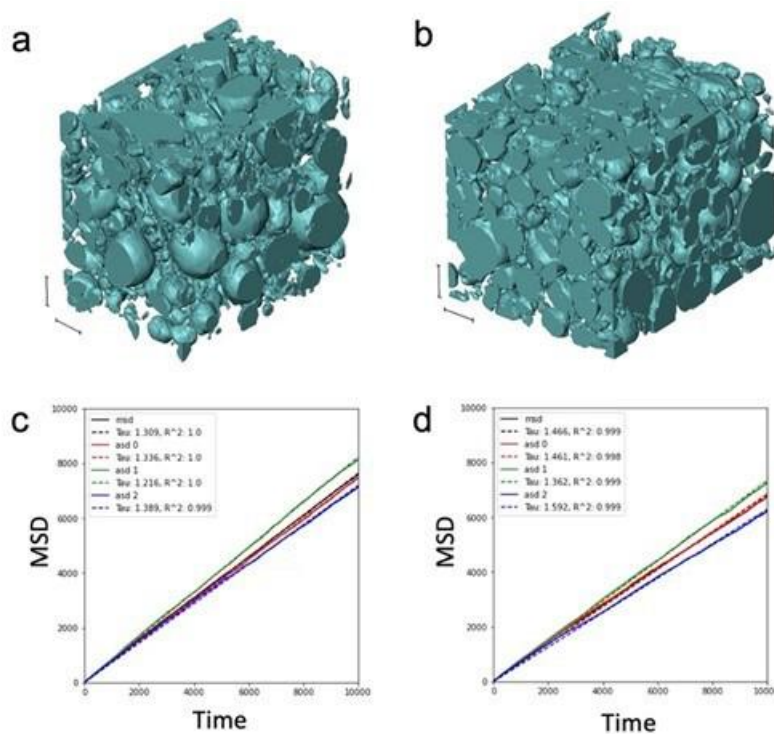


Figure I.5.4 3D structures of the dry (a) and slurry-cast (b) NMC cathodes reconstructed from nanotomography. Scale bar is 10 μm. (c), (d) Mean square displacement of random walkers vs time in random walk simulations performed in the digitized dry (c) and slurry-cast (d) NMC cathode structures. Electrode tortuosity is proportional to the slope of the curve.

Table I.5.3 Comparison of Dry vs Slurry-cast NMC Cathode Tortuosity Calculated from Nanotomography and Electrochemical Measurement

Cathode	Tomography Calculation		Electrochemical Measurement	
	Dry	Slurry	Dry	Slurry
Porosity	57.1% (including CBD)	46.5% (including CBD)	35%	35%
Tortuosity	1.332	1.479	1.9	3.4
Bruggeman relation $\tau = \epsilon^{-0.5}$	1.32	1.47	1.69	1.69

Electrode fabrication

Firstly, the mixing has been scaled-up and 2-sided coating has been demonstrated. The mixing process was scaled-up to ~1kg per batch. The active material was also increased from 90% to >95%. The mixing parameters were selected such that the carbon and binders are distributed on the surface of active material particles. The powder mixing is optimal as indicated by >200kPa bonding strength measured by pulling test. A roll-to-roll system to achieve 2-sided coating electrodes was developed. Briefly, current collector was fed through the coating system two times to coat on the two sides followed by thermal annealing at 200°C for ~10 seconds. Next, Cathode layer of 30mg/cm² was sprayed on top of the PVDF followed by heating (250°C for 10mins), rolling to ~40% porosity and winding step. The foil roll was connected back to the unwinder to spray the backside with 30mg/cm² Cathode materials and rolling to ~40% porosity. Lastly, the sample undergoes final rolling to ~35% porosity (Figure I.5.5).

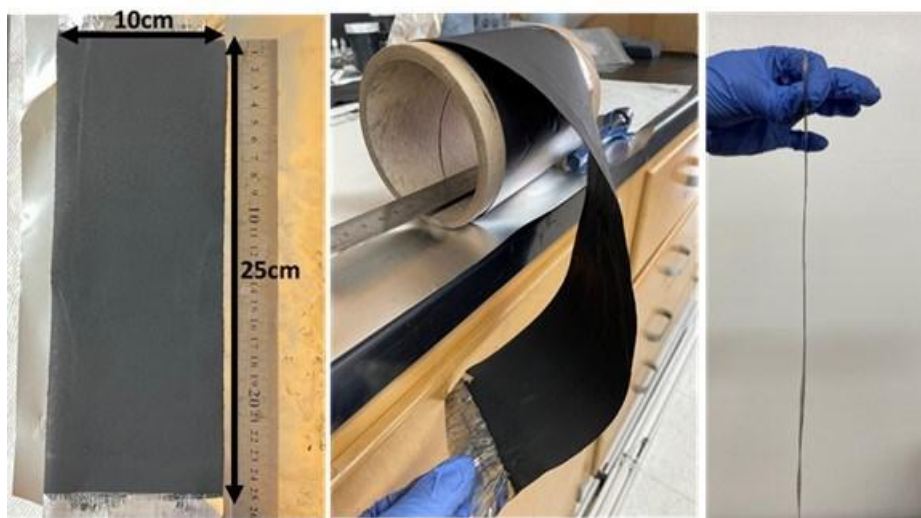


Figure I.5.5 2-side coated cathode with 30mg/cm² on each side.

Secondly, large electrode with uniformity of material loading ~5% have been demonstrated. Single sided coin cell electrodes were punched from the large electrode and used to evaluate uniformity (Figure I.5.6). The coin cell electrodes have also been sent to WPI for testing.



Figure I.5.6 5Ah cell electrode preparation for testing at WPI and Microvast.

Thirdly, processes were then optimized to manufacture cathodes and anodes. Dry cathodes were manufactured for optimization of high loading (30mg/cm² and 35% porosity) 96:2:2 composition. To control the quality and

consistency of the manufactured cathodes, bonding strength and electrical resistance measurements were done for different types of carbon black and tested at WPI/Microvast for electrochemical performance. First, Acetylene Carbon (NMC: PVDF: Acetylene Carbon as 96:2:2) was used to premix dry powder at different mixing speeds and manufacture cathodes for comparison. The electrical resistance measurements of these electrodes show large variation in measured resistances for each mixing speed. Replacing the Acetylene Carbon with C65 gives more consistent measurements and lower resistance values. Additionally, it was observed that lower porosity (~28%) of dry cathodes gives higher bonding strength than ~35% porosity dry cathodes. By this comparison study, it was concluded that dry cathodes manufactured with C65 give consistent electrical conductivity and using this finding, certain mixing parameters were finalized for optimum bonding strength and conductivity for 30mg/cm² loading and 35% porosity cathodes. For the high-loading dry manufactured anode of 15 mg/cm² and 96:2:2 composition, the bonding strength has been optimized by changing the dry mixing and calendaring processes. Various relationships between bonding strength and porosity were obtained (Figure I.5.7). Each relationship between bonding strength and porosity was obtained by one set of mixing and calendaring parameters. Two sets of parameters were selected to fabricate anodes with mechanical strength ~150 kPa at porosity of ~40%, and mechanical strength ~150kPa at porosity of 35%. The electrical conductivities have been measured for both dry and slurry manufactured anodes, the conductivity for dry anode (105 mS/cm) is comparable with that of Microvast casted anode (91 mS/cm).

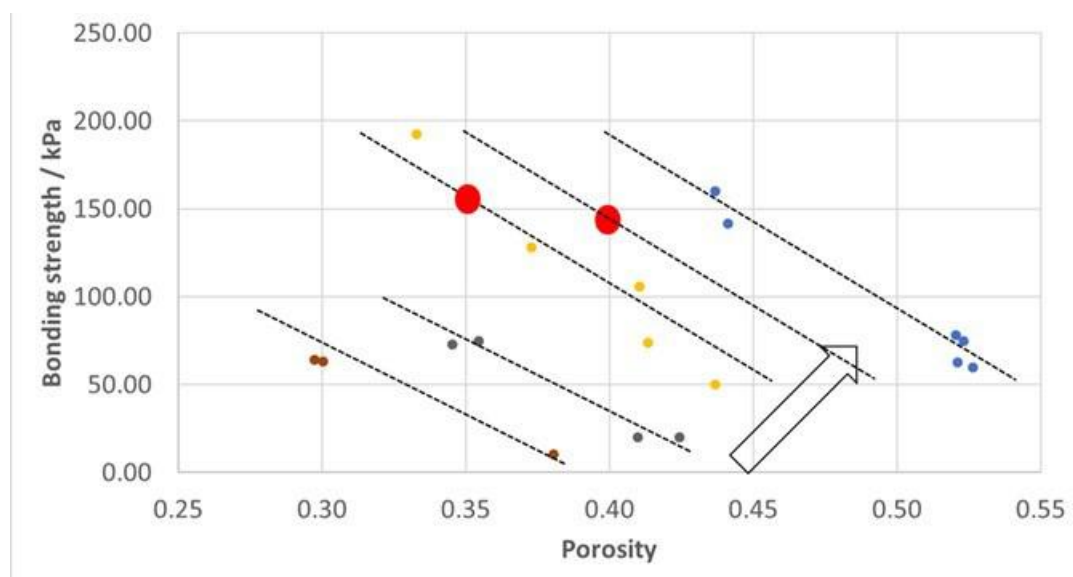


Figure I.5.7 Relationship between bonding strength and porosity for anodes (15mg/cm² loading, Gr:C65:PVDF = 96:2:2).

Finally, various designs (total of 23 batches) of electrodes were manufactured for testing to determine the optimal manufacturing parameter and design for deliverables (Table I.5.4 and Table I.5.5). The composition is NMC:PVDF:C (96:2:2) for cathode and graphite:PVDF:C (96:2:2) for anode. Cathode is fixed at single layer (35% porosity) for all the designs and only the design of anode is varied. In each batch, four pairs of cathode and anode were fabricated. In Batch 1-3, single-layer anode (35% porosity) is fabricated to establish the baseline of single-layer electrodes. It was found C65 (Batch 3) shows much less variation in electrode conductivity compared with acetylene carbon black. Therefore, C65 is selected as the conductive carbon for the rest of the batches and Batch 3 is the baseline for single-layer electrodes. In Batch 4, anode higher porosity (41%) was fabricated with hot rolling (roller temperature 110°C). In Batch 5, two-layer anode with top porosity at 50% and bottom porosity at 30% was fabricated. PVDF layer is necessary to ensure bonding between the two layers. Batch 6 and 7 have the same design parameters as Batch 4 and 5 except that the rolling was performed at room temperature. Batch 8 and 9 are two-layer anodes with less porosity difference between the two layers. Due to the less porosity difference, PVDF layer can be removed. Batch 10 has slightly larger porosity difference as compared with Batch 8 and 9. The above electrodes (Batch 4-10) have been tested at

Microvast. However, significantly variation was observed within each batch and from batch to batch for these electrodes. It was determined the glove box used to handle the materials was contaminated during the period of preparing these electrodes. The glove box was cleaned thoroughly and contaminants were completely removed. Batch 11 (replicate of Batch 9) was then fabricated and normal condition was resumed. Batch 13 and 14 were fabricated with greater difference in porosity between the two layers. The design for the deliverable is likely to be selected from Batch 11, 13 and 14. In addition, Batch 12 with single layer design was fabricated to test the cycling performance.

Table I.5.4 Summary of Electrodes Fabricated (Batch 1-14).

Batch	Shipping date	Anode					Cathode				Note
		Layer		Porosity	Cold/Hot Roll	Carbon	Layer	Porosity	Cold/Hot Roll	Carbon	
1	2/25/2022	1		35%	Cold	MTI C65	1	35%	Cold	AMB CB	
2	3/22/2022	1		35%	Cold	MTI C65	1	35%	Cold	AMB CB	
3	4/2/2022	1		35%	Cold	MTI C65	1	35%	Cold	MTI C65	
4	4/7/2022	1		41%	Hot	MTI C65	1	35%	Cold	MTI C65	
5	4/29/2022	2	PVDF	bottom 30% top 50%	Hot	MTI C65	1	35%	Cold	MTI C65	
6	5/7/2022	1		41%	Cold	MTI C65	1	35%	Cold	MTI C65	
7	5/10/2022	2	PVDF	bottom 30% top 50%	Cold	MTI C65	1	35%	Cold	MTI C65	
8	5/14/2022	2	No PVDF	bottom 35% top 40%	Cold	MTI C65	1	35%	Cold	MTI C65	
9	5/19/2022	2	No PVDF	bottom 35% top 45%	Cold	MTI C65	1	35%	Cold	MTI C65	
10	5/19/2022	2	PVDF	bottom 30% top 40%	Cold	MTI C65	1	35%	Cold	MTI C65	
11	6/9/2022	2	No PVDF	bottom 35% top 40%	Cold	MTI C65	1	35%	Cold	MTI C65	
12	6/16/2022	1		35%	Cold	MTI C65	1	35%	Cold	MTI C65	Trace solvent treated
13	6/23/2022	2	Less PVDF	bottom 27-28% top 42-43%	Cold	MTI C65	1	35%	Cold	MTI C65	Trace solvent treated
14	6/29/2022	2	PVDF	bottom 27-28% top 42-43%	Cold	MTI C65	1	35%	Cold	MTI C65	

Batch 15-23 were manufactured for testing to determine the optimal mixing parameters and design to improve the cycling performance by increasing the bonding strength of cathodes and anodes. The baseline composition is NMC:PVDF:C (96:2:2) for cathode and graphite:PVDF:C (96:2:2) for anode. The optimization in this quarter involves mixing sequence optimization and composition optimization. Batch 15 was the design from the previous quarter which needs to be improved in terms of cycling performance. To improve cathode of Batch 15, a sequential mixing recipe was developed and implemented in batch 16-17 and 18-1. In the sequential mixing, PVDF was introduced to the mixer and mixed for 10 mins before carbon was introduced and mixed for 10 mins. The sequential mixing improves bonding strength without affecting the electrical conductivity of cathode. A revised sequential mixing recipe (sequential mixing-1) was developed by introducing carbon earlier to the mixing process (batch 20-1). It was found both bonding strength and electrical conductivity were improved. In addition, attempts were made to improve the bonding strength of cathodes by increasing the binder content (increase PVDF to 3% from 2%, batch 20-2). Although bonding strength was improved, increase in resistance is noticeable. Similarly, bonding strength of anodes were also improved by adjusting the binder and carbon content (batch 21-1, 21-2). By increasing binder and reducing carbon contents, significant improvement in bonding strength was obtained. However, resistance was found to increase noticeably. Batch 21-2 design was chosen for deliverables.

Table I.5.5 Summary of Electrodes Fabricated (Batch 15-23).

Batch no	Shipping date	No. of Pairs shipped	Anode info	Cathode info
15	6/29/2022	3	2-layer	1-layer; all-together mixing
16	7/9/2022	6	1-layer	1-layer; sequential mixing
17	7/23/2022	4	2-layer	1-layer; sequential mixing
18-1	8/2/2022	4	2-layer	1-layer; sequential mixing
18-2	8/2/2022	2	2-layer; solvent treatment	1-layer; sequential mixing, solvent treatment
18-3	8/2/2022	2	2-layer	1-layer; sequential mixing
19	8/6/2022	4	1-layer	1-layer; sequential mixing
20-1	8/13/2022	4	2-layer	1-layer; sequential mixing-1
20-2	8/13/2022	4	2-layer	1-layer; sequential mixing (95 3 2)
21-1	8/20/2022	4	1-layer; 95:4:1	1-layer; sequential mixing (95 3 2)
21-2	8/20/2022	4	1-layer; 96:4:0	1-layer; sequential mixing (95 3 2)
22	8/27/2022	4	1-layer	1-layer; all-together mixing
23	9/19/2022	4	1-layer	1-layer; all-together mixing

Electrode testing

The 20mg/cm² (10mg/cm² for the anode) 90:5:5 electrode cross-section was prepared by ion-polishing. The slurry cast cathode cross-section in Figure I.5.8a shows that the CBD (carbon binder domain) phase fills in most of the space between the AM (active materials) particles with few open pores, which is also proved by the carbon mapping. In the dry-printed electrode (Figure I.5.8b), The C65 and PVDF form clusters, which can bridge the AM particles and leave more open pores to benefit the electrolyte diffusion. Similar microstructure differences could be observed from the ion-polished anode cross-section SEM images in Figure I.5.8c and Figure I.5.8d. More open pores could be observed between the graphite particles in the dry-printed anode than in the slurry-cast anode.

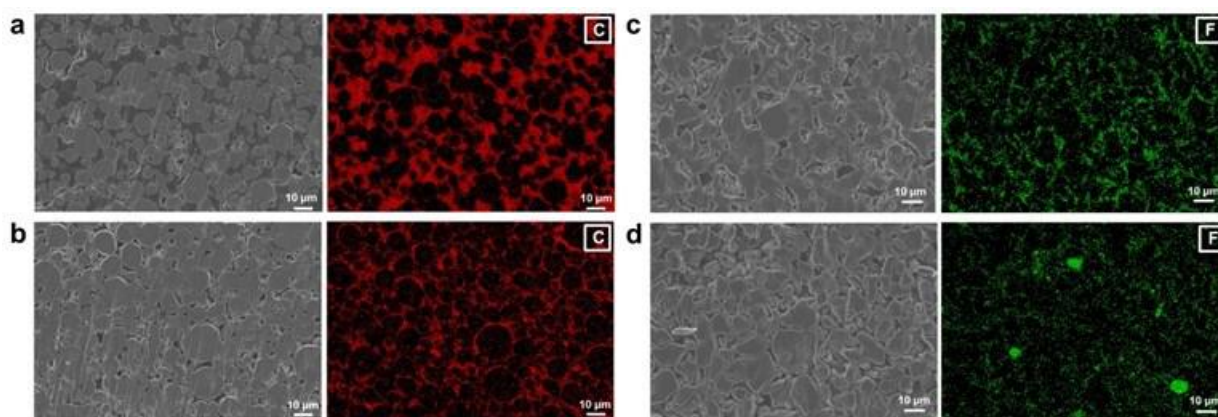


Figure I.5.8 Cross-section SEM images and EDX mapping of (a) slurry cast cathode, (b) dry printed cathode, (c) slurry cast anode, (d) dry printed anode.

To further improve the electrode's energy density, the ratio of the active material has been increased to 96% (2% C65 and 2% PVDF). Higher loading is achieved with 30mg/cm² for the cathode and 15mg/cm² for the anode. The preliminary coin cells have been tested for rate performance comparison. The WPI and Microvast slurry-cast high-loading electrodes were selected as the control group for rate performance testing. Figure I.5.9a shows that the DE cathodes slightly outperform the slurry cast electrodes at 0.5C. In Figure I.1.9b, the DE anodes exhibit higher capacity at 0.2 and 0.5 C than the control group.

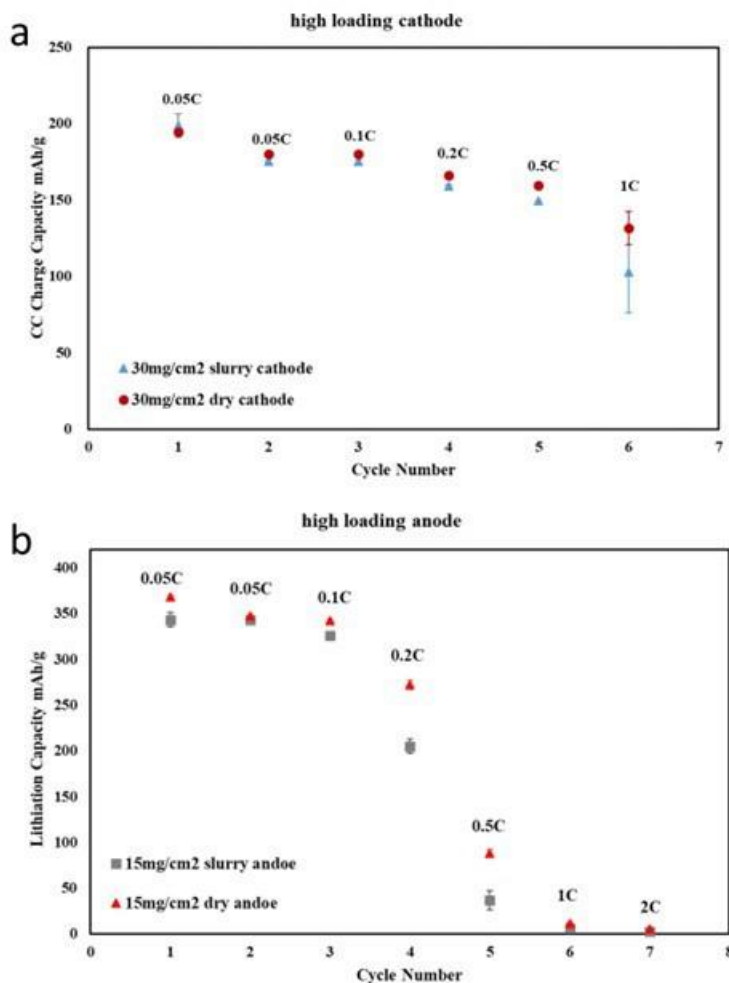


Figure I.5.9 High loading electrode rate performance (a) cathode electrodes, (b) anode electrodes.

Table I.5.6 shows the tortuosity of the 30mg/cm² (15mg/cm² anode) 96:2:2 electrodes. Both dry-printed cathode and anode have significantly lower tortuosity values than the Microvast slurry cast electrodes. The tortuosity of all 96:2:2 ratio electrodes decreases compared to the 90:5:5 electrodes. The reason is the porous CBD phase has much higher tortuosity than the bulk AM matrix. Reducing the CBD ratio could lead to a significant tortuosity drop.

Table I.5.6 Average Porosity and Tortuosity of the High-loading Dry Printed and Slurry Cast Electrodes.

Cathode		Dry Printed Electrode	Slurry Cast Electrode
Average Porosity		31.86%	33.70%
τ		1.94	3.42
Anode		Dry Printed Electrode	Slurry Cast Electrode
Average Porosity		30.95%	37.70%
τ		1.96	2.68

Cell fabrication and testing

To evaluate the dry electrodes single layer pouch cells are made and compared to single layer pouch cells using traditional wet coating electrodes. This year the electrode loading for anode and cathode was increased, resulting in ~55% higher areal capacity. The electrodes were also adjusted to have more active material, less carbon and binder compared to 1st year where 90:5:5 was used. Not surprisingly, initially the wet casted electrode - done on a pilot scale equipment line – showed much better performance to 3C fast charging at this new loading & electrode consistency when compared to the cells made from dry electrodes. Since wet electrode manufacture is a mature technology, this is not surprising. As the team worked to optimize the dry electrode, manufacture the fast charge capacity ratio and consistency of electrode batch steadily improved, as seen in Figure I.5.10. The dry electrode now is comparable to wet electrode manufacture under this new, higher loading.

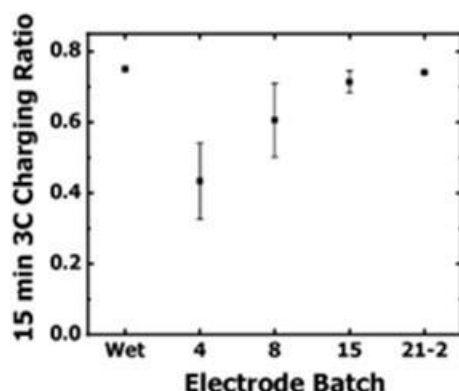


Figure I.5.10 15 min-capped 3C charging ratio between wet and dry electrode

Interestingly, fast discharge is much improved in the dry electrode system compared to the wet cast electrode. The present hypothesis is the cathode electrode when prepared thru dry manufacturing has more open pore structure, which allows better diffusion of incoming Li-ions to the active material. Also, it should be noted that the discharge 3C test is just a constant current procedure, while for fast charge a CCCV protocol that ends after 15-minutes of total charge time is used. This procedure difference is one reason it appears there is asymmetric performance on charge vs discharge capacity retention.

Conclusions

In summary, thick electrodes with high loading have been modeled, designed and fabricated. Different batches of electrodes were fabricated in order to improve the rate performance. The fast charging of dry electrode now is comparable to wet electrode manufacture under this new, higher loading. Interesting, fast discharge is much improved in the dry electrode system compared to the wet cast electrode.

References

1. Bitsch, B., J. Dittmann, M. Schmitt, P. Schaffer, W. Schabel, and N. Willenbacher. 2014. "A novel slurry concept for the fabrication of lithium-ion battery electrodes with beneficial properties." *Journal of Power Sources* no. 265:81-90. doi: 10.1016/j.jpowsour.2014.04.115.
2. Ruffo, R., C. Wessells, R. A. Huggins, and Y. Cui. 2009. "Electrochemical behavior of LiCoO₂ as aqueous lithium-ion battery electrodes." *Electrochemistry Communications* no. 11 (2):247-249. doi: 10.1016/j.elecom.2008.11.015.
3. Doberdo, I., N. Löffler, N. Laszczynski, D. Cericola, N. Penazzi, S. Bodoardo, G. T. Kim, and S. Passerini. 2014. "Enabling aqueous binders for lithium battery cathodes - Carbon coating of aluminum current collector." *Journal of Power Sources* no. 248:1000-1006. doi: 10.1016/j.jpowsour.2013.10.039.

4. Wixom, Michael. 2013. *Dry Process Electrode Fabrication* 2013 [cited 13 May 2013]. Available from http://energy.gov/sites/prod/files/2014/03/f13/es134_wixom_2013_p.pdf.
5. Zheng, Honghe, Jing Li, Xiangyun Song, Gao Liu, and Vincent S. Battaglia. 2012. "A comprehensive understanding of electrode thickness effects on the electrochemical performances of Li-ion battery cathodes." *Electrochimica Acta* no. 71:258-265. doi: 10.1016/j.electacta.2012.03.161.
6. Gallagher, K. G., S. E. Trask, C. Bauer, T. Woehrle, S. F. Lux, M. Tschech, P. Lamp, B. J. Polzin, S. Ha, B. Long, Q. L. Wu, W. Q. Lu, D. W. Dees, and A. N. Jansen. 2016. "Optimizing Areal Capacities through Understanding the Limitations of Lithium-Ion Electrodes." *Journal of the Electrochemical Society* no. 163 (2):A138-A149.
7. Bae, C. J., C. K. Erdonmez, J. W. Halloran, and Y. M. Chiang. 2013. "Design of battery electrodes with dual-scale porosity to minimize tortuosity and maximize performance." *Advanced Materials* no. 25 (9):1254-8. doi: 10.1002/adma.201204055.
8. Sander, J. S., R. M. Erb, L. Li, A. Gurijala, and Y. M. Chiang. 2016. "High-performance battery electrodes via magnetic templating." *Nature Energy* no. 1.

Acknowledgements

The development team (WPI/TAMU/Rice/Microvast) would like to thank the following for all of the help, advice, support and suggestions: USABC program manager Lamuel David (Stellantis, email lamuel.david@stellantis.com) and USABC work group members Zoe Zhou (Ford), Meng Jiang (GM), Brian Cunningham and Bryant Polzin (DOE), and Brian Ingram (ANL).

I.6 Development of Advanced Low-Cost / Fast-Charge (LC/FC) Batteries for EV Applications (Farasis Energy USA)

Madhuri Thakur, Principal Investigator

Farasis Energy USA
21363 Cabot Blvd
Hayward, CA 94545
E-mail: mthakur@farasis.com

Brian Cunningham, DOE Technology Development Manager

U.S. Department of Energy
E-mail: Brian.Cunningham@ee.doe.gov

Start Date: February 1, 2021
Project Funding: \$4,060,000

End Date: February 28, 2024
DOE share: \$2,030,000

Non-DOE share: \$2,030,000

Project Introduction

The goal of this project is to develop a low cost/ fast charge lithium-ion cell technology that meets the USABC goals for Advanced Low-Cost/Fast-Charge (LC/FC) batteries for EV's applications. Farasis headed the development effort which will bring together technical contributions from many leaders in the Li-ion technology industry including Umicore, BASF, Talga, Imerys, Celgard, Zeon and Solvay, etc. The 36-month development effort will be iterative, with an intermediate Go/No Go Milestone based on cell performance goals and progress tracked against the USABC goals for Advanced Low-Cost/Fast-Charge (LC/FC) Batteries. The major objective of this project is to develop cell technology capable of providing 275 Wh/kg after 1000 cycles at a cost target of \$75/kWh and with having charge time of 15 min for the 80 % of the capacity. Key technologies that be developed and integrated into cells include a low-cost cathode, high surface area anode, and electrolyte additives, etc. As a large volume battery manufacturer, a major goal of the project will be to help accelerate production and enable the commercialization of several novel cell component technologies (including low cobalt NCM, Mn-rich NCM, electrolytes, coated graphite as well as high surface area natural graphite) by supporting scale-up and providing a commercialization path. Deliverables will include large pouch cells produced at our manufacturing facility in China/Europe/US with parallel performance and safety testing done at Farasis, cost models associated with the deliverable technology, and a production roadmap to commercialization comprising all components of the cell. The project's total budget will be ~ \$4.06 M with Farasis covering 50 % of the cost.

The key barriers for this project include fast charging without Li plating, low cost, and energy density. Fast charging is a crucial enabler of the mainstream adoption of electric vehicles (EVs) to make them competitive to the IC engine cars. None of today's EVs can withstand fast charging due to the risk of lithium plating. Efforts to enable fast charging hampered by the trade-off nature of a lithium-ion battery. The implementation of the fast charge can lead to sacrificing cell durability. Compromise is required between fast charge capability and cell durability, especially for energy-dense cells. To achieve the target of energy density of the cells, high-voltage and high-capacity cathodes are desired. However, the selection of such cathodes will be limited by the cost target.

Objectives

- Develop an EV cell technology of providing 275 Wh/kg after 1000 cycles at a cost target of \$0.075/Wh.
- Develop a fast charge cell having charge time of 15 min for the 80 % of the capacity.
- Develop low-cost, high-capacity cathodes such as Mn-rich, Ni-rich cathodes or their blended composite cathode.
- Develop high surface area graphite anodes with fast charge capability.

- Develop and optimize electrolytes and conductive additives to stabilize Mn-rich / Ni-rich cathodes and improve the safety.
- Optimize the negative/positive electrode formulation for maximum energy density and cycle life, and fast charging capability.

Approach

Phase I of the project, which lasted for approximately 15 months, will be focused on the development and characterization of materials and the development of negative/positive electrode technology. Initial sets of single-layer pouch (SLP) or double-layer pouch (DLP) cells (ca. 0.1-0.5 Ah) were used to evaluate different positive/negative electrode composites and material combinations in an iterative manner. The specific plan includes: (1) to evaluate the capacity and first-cycle efficiency of different low-cost cathode materials using coin cell builds, (2) to identify a graphite candidate with excellent fast charge capability as the anode material, and (3) to down-select low-cost, high-capacity cathodes while having good cycling stability. Several types of graphite materials with different size, surface area and morphology were evaluated using SLP or DLP cell builds. Three criteria including cell resistance, discharge rate capability and fast charge capability were used for the screening of graphite anode materials. The cathode materials were down-selected using SLP or DLP cell builds among a wide range of materials including Ni-rich NCM, stabilized Mn-rich cathode materials, zero-Co cathode materials, and their blended composites. Three criteria including cell resistance, discharge rate capability and cycling stability were also used for the screening of low-cost high-capacity cathode materials. A second iteration leads to narrow down the range of electrode designs, introduce materials improvements. The electrolyte development effort was conducted in parallel with the cell optimization work. The electrolyte work will focus on evaluating and optimizing electrolyte formula with additives to meet the requirement of the graphite anodes and the down-selected low-cost, high-capacity cathodes. A combination of device-level testing and fundamental electrochemical measurements will be used to guide the development of large form factor cells for Phase II of the project. In the middle of Phase I, baseline cells with a capacity of ca. 73 Ah using Farasis “next-generation” cell chemistry have been built and delivered to national labs for evaluation and testing.

Phase II of the project is scheduled for approximately 17 months and shifts to manufacturing and testing of larger format pouch cells using a refined subset of cell chemistries developed in Phase I. Some ongoing chemistry developments will continue at this stage to address specific issues identified in Phase I builds and to pursue further optimization of cell-level performance. To achieve the targeted energy density of 300 Wh/kg we need to evaluate the Mn-rich and the Ni-rich cathode with a capacity between 210-240 mAh/g. Other cell components such as foil, separators, electrolyte, conductive additives, and pouch materials is also get evaluated for fast charge cell development. This will occur in two iterations starting with ca. 75 Ah form factor cells (Gen1 cells) for the intermediate evaluation and progressing to the final deliverable cells (Gen 2 cells) based on a larger pouch cell form factor, which will be ca. 87 Ah using the optimized high-energy cell chemistry with achieving a cost target of \$0.075/Wh and a charge time of 15 min for the 80 % of the capacity. Phase II of the program will also include testing to guide system development in future applications; these tests will characterize cells in small groups to efficiently evaluate their behavior on a large scale where thermal management, cycling-induced gradients, and failure isolation become important.

Results

Cathode materials evaluation: Farasis has evaluated the capacity, first-cycle efficiency and cycling stability of 2 Mn-rich, 3 Ni-rich, 1 high-voltage NCM (HV-NCM) cathode materials and 3 blended cathode materials consisting of Mn-rich and Ni-rich cathode materials with different compositions. Based on compromising the C/3 capacity, cost and cycling stability of the cathode materials evaluated, the cathode materials have been down selected. 1 stabilized Mn-rich (C2), 1 high-voltage NCM (HV-NCM) (C5) and their blended cathode materials (C5C2) have been selected as candidates for further optimization for the project. Table I.6.1 shows a comparison in first-cycle efficiency, C/20 and C/3 capacities among several cathode materials using half coin cell builds. We found pilot-line coated (P-coated) C2 Mn-rich cathode materials show slightly higher C/20, and significantly higher C/3 capacity than lab-coated (L-coated) ones, showing that improving coating quality

can significantly improve rate performance of C2 Mn-rich cathodes. P-coated C5 HV-NCM cathode materials also show slightly higher C/20, and higher C/3 capacity than L-coated ones. Moreover, C/3 capacity of C2 Mn-rich cathode materials at charge cut-off voltage (V_{\max}) of 4.5 V strongly depends on the activation V_{\max} (4.5-4.7 V) during the first formation cycle. In addition, at the same V_{\max} (for example, 4.5 V), P-coated C2 Mn-rich cathode materials show slightly higher C/20 and C/3 capacity than P-coated C5 HV-NCM.

Table I.6.1 A comparison in first-cycle efficiency, C/20 and C/3 capacities among different cathode materials using half coin cells

Cathode Materials	Loading (mg/cm ²)	First-cycle efficiency (%)	C/20 capacity (1 st cycle) (mAh/g)	C/3 capacity (3 rd cycle) (mAh/g)
Mn-rich (C2) Lab-coated	13.0	89.9	261 (2.0-4.7 V)	207 (2.0-4.5 V)
High-voltage NCM (C5) Lab-coated	13.0	89.6	198 (2.75-4.5 V)	183 (2.75-4.5 V)
Mn-rich (C2) Pilot-line coated	14.5	95.1	203 (2.0-4.5 V)	194 (2.0-4.5 V)
		94.5	258 (2.0-4.6 V)	222 (2.0-4.5 V)
		93.6	270 (2.0-4.7 V)	225 (2.0-4.5 V)
High-voltage NCM (C5) Pilot-line coated	18.0	90.9	200 (2.75-4.5 V)	186 (2.75-4.5 V)

Positive electrode development

A set of single-layer pouch (SLP) cells have been built and evaluated with a fixed L-coated graphite anode and different L-coated cathodes. The cathode materials vary with different phase structures and compositions. Several criteria were used to narrow the cathode materials for future cell builds: C/3 capacity, initial cathode-specific energy density, DCR, and cycling stability. Table I.6.2 shows a comparison in C/3 capacity, DCR, discharge rate capability, fast charge capability, and initial cathode-specific energy density of SLP cells among different cathodes. The cells with C3 Ni-rich cathodes show high initial cathode-specific capacity, relatively low DCR, good discharge rate performance, and excellent fast charge capability, but their high materials cost due to high Ni and Co amount limit their use in this project. Although C6 Ni-rich cathode materials have very low materials cost, their use is excluded for further optimization in this project due to low C3 capacity, low initial cathode-specific energy density, and high DCR of the cells with C6 Ni-rich cathodes. Therefore, C2 Mn-rich, C5 HV-NCM, and their blended composites (C5C2-blend 1 and C5C2-blend 2) will be selected for cathode materials used for further optimization and future low-cost, fast-charge cell development.

Besides the cathode-specific energy density and materials cost, cycling stability is another important factor for screening cathode materials and cathode development in this project. Figure I.6.1 shows a comparison of the cycling stability of SLP cells among different types of L-coated cathodes. Among these cathodes, the cell with L-coated C2 Mn-rich cathodes shows poor cycling stability, low average discharge voltage, and high voltage fade. However, due to the extremely low materials cost and potentially high specific capacity (depending on activation V_{\max} and operating V_{\max}) of Mn-rich cathode materials, it is worthy to further optimize and develop the Mn-rich cathodes for low-cost, fast charge cell development in this project. The cells with C3 Ni-rich cathodes show long cycle life, stable average discharge voltage with cycling, and high initial cathode-specific energy density, but the high material cost of C3 Ni-rich cathode restricts their use for low-cost, fast-charge cell development. The cells with low-cost C6 Ni-rich cathodes show long cycle life, and stable average discharge voltage with cycling, but low initial cathode-specific energy density, which limit their use in this project. The cells with relatively low-cost C5 HV-NCM cathodes show good cycle life, stable average discharge voltage with cycling, and high initial cathode-specific energy density. Therefore, C5 HV-NCM cathode material is considered one of the good candidates for low-cost, fast-charge cell development. To reduce the materials cost of C5 HV-NCM cathode while maintaining high cathode-specific energy density and good cycling stability, a blended cathode consisting of C5 HV-NCM and C2 Mn-rich is also considered as another candidate. We found that the cells with blended C5C2 cathodes show a comparable cycle life with the

cells with C5 HV-NCM cathodes, much less voltage fade than the cells with C2 Mn-rich cathodes, and relatively high cathode-specific energy density.

Table I.6.2 A comparison in C/3 capacity, DCR, discharge rate capability, fast charge capability and initial cathode-specific energy density of single-layer pouch cells among different cathodes

Cathode	C/20 capacity @ 1 st cycle (mAh/g)	C/3 capacity @ 4.4 V (mAh/g)	DCR_discharge @ 50% DoD (ohm)	Rate_discharge (ratio of 3C to C/5)	Fast charge capability (max SoC**)	Initial cathode-specific energy density (Wh/kg)
C3: Ni-rich NCM	188 (@ 4.3 V)	182* (@ 4.3 V)	0.576-0.710	84.7-89.0 % (ave. 87.4 %)	> 80.0 %	~ 679
C2: Mn-rich	199 (activated @ 4.5 V)	180	0.610-0.674	71.1-76.0 %	N/A	~ 619-666
	171 (activated @ 4.4 V)	165	0.769-0.807	77.7-80.9 %	N/A	~ 617
C5: HV-NCM	191 (@ 4.4 V)	183	0.585-0.594	77.0-81.2 % (ave. 78.3 %)	> 75.6 %	~ 676
C5C2 Blended: Blend 1	190 (activated @ 4.5 V)	186	0.534-0.563	84.2-87.1 % (ave. 85.8 %)		~ 682
	181 (activated @ 4.4 V)	180			> 74.6 %	~ 673
C5C2 Blended: Blend 2	185 (activated @ 4.5 V)	181	0.566-0.613	78.3-81.8 % (ave. 79.6 %)		~ 659-678
	174 (activated @ 4.4 V)	171	0.596-0.608	79.1-86.3 % (ave. 82.9 %)	> 78.8 %	~ 636-651
C6: Ni Rich	182 (@ 4.4 V)	173	0.640-0.698	73.0-79.0 % (ave. 75.3 %)	> 75.6 %	~ 642-649

* For C3 cathode, C/3 capacity is measured at 4.3 V; for other cathodes, C/3 capacity is measured at 4.4 V.

** Maximum SoC for being charged to at 3C rate while there is no Li plating during fast charge.

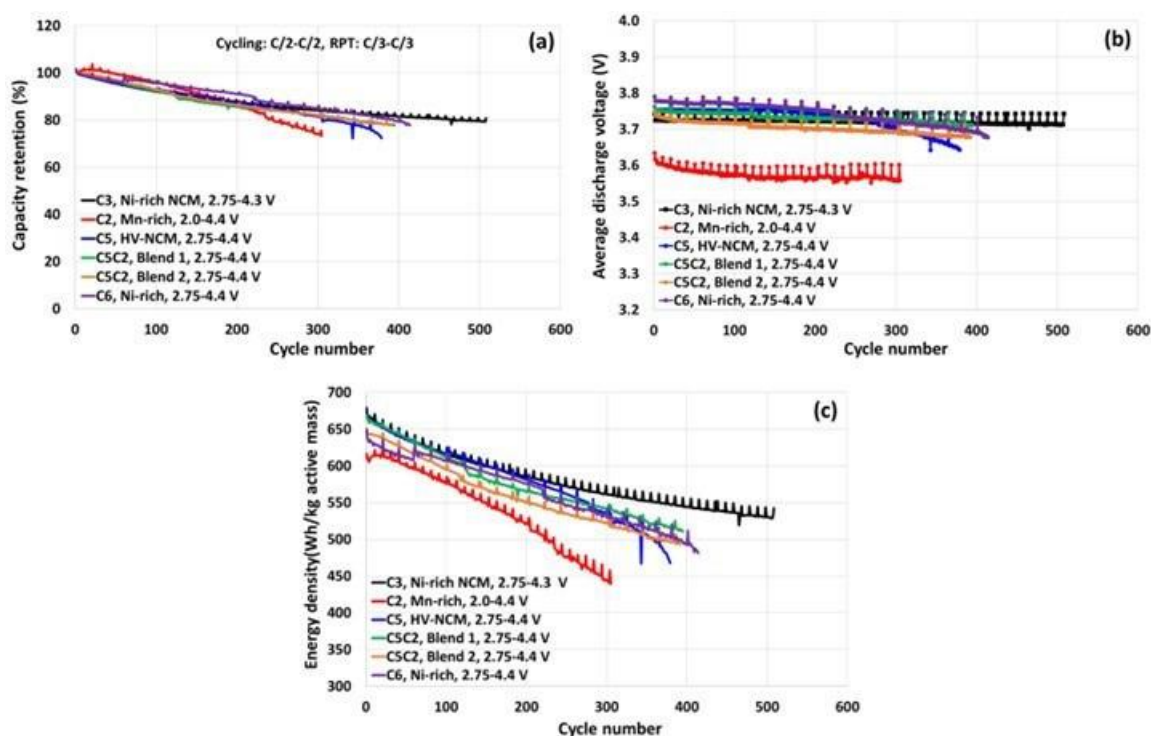


Figure I.6.1 Comparison in the cycling stability (a) capacity retention, (b) average discharge voltage and (c) cathode-specific energy density of single-layer pouch cells among with different types of lab-coated cathodes.

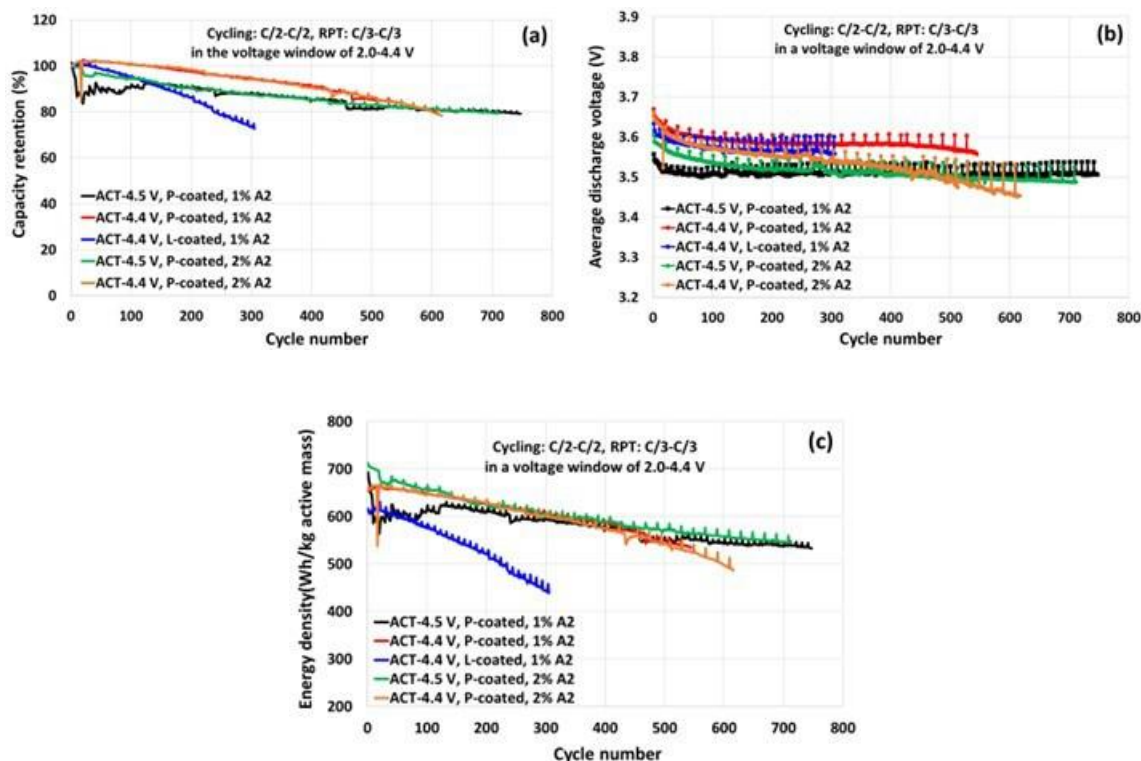


Figure I.6.2 Comparison in the cycling stability (a) capacity retention, (b) average discharge voltage and (c) cathode-specific energy density of pouch cells with Mn-rich (C2) cathodes among different coating (P-coated: pilot-line coated vs. L-coated: lab-coated), activation Vmax (ACT-4.5 V vs. ACT-4.4 V) and amount of A2 electrolyte additive (1 % vs. 2 %).

Figure I.6.2 shows a comparison in the cycling stability of single/double-layer pouch cells with Mn-rich (C2) cathodes among different coating, activation Vmax and amount of A2 electrolyte additive. Compared with the cells with L-coated Mn-rich cathodes, the cells with P-coated C2 Mn-rich cathodes show about 2.6 times improvement in cycle life at a capacity retention of 80 % in the case of being both activated and operated at 4.4 V. The cells with P-coated C2 cathodes can achieve > 600 and > 700 cycles at a capacity retention of 80 % in the case of being activated and operated at 4.4 V for the cells with low anode loading anodes, and in the case of being activated at 4.5 V and operated at 4.4 V for the cells with a little bit high anode loading anodes, respectively. Moreover, activation at high Vmax (such as 4.5 V) can increase the specific capacity of Mn-rich cathode materials and thus initial cathode-specific energy density, while leads to low average discharge voltage and severe voltage fade. We also found that increasing the amount of A2 electrolyte additive from 1 % to 2 % doesn't improve the cycling stability of the cells with C2 Mn-rich cathodes, as well as doesn't suppress the voltage fade. To improve the cycling stability and suppress voltage fade of Mn-rich cathodes, new electrolyte additives need to be explored in the future.

Fast charge cell development

Figure I.6.3 shows fast charge (15 min charge to 80 % SoC) cycling behavior of a single-layer pouch (SLP) cell with a graphite (A1) anode and a high-voltage (HV) NCM (C5) cathode. Please note that 80 % SoC is based on the actual cell capacity of aged cells. The cell with C5 HV-NCM cathode can achieve ~100 fast charge cycles at a capacity retention of 83.5 %. Figure I.6.4 shows a comparison in cycling stability of SLP cells with graphite (A1) anodes and blended (C5C2-blend 2) cathodes between 0 % (all regular C/2-rate) and 25 % fast charge (25 % fast charge + 75 % regular C/2-rate) cycling. In the initial and medium stages, there is a similar decay rate in the capacity retention for the cells with C5C2 blended cathodes between 0 % and 25 % of total cycles as fast charge, showing that fast charge doesn't cause Li plating or cause little Li plating. However, in the final stage, due to possible Li plating, the cell being cycled in the case of 25 % of total cycles

as fast charge shows a higher decay rate in the capacity retention than that in the case of all regular C/2-rate cycling. Farasis will continue fast charge cell development and improve fast charge cycling performance of single/double-layer pouch cells with optimal low-cost and high-capacity cathodes.

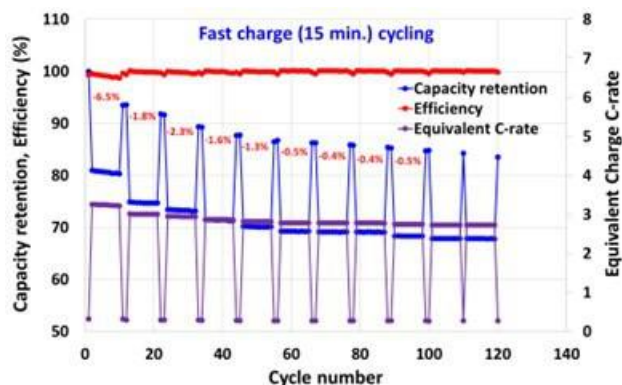


Figure I.6.3 Fast charge cycling behavior of a single-layer pouch cell with a graphite (A1) anode and a high-voltage (HV) NCM (C5) cathode

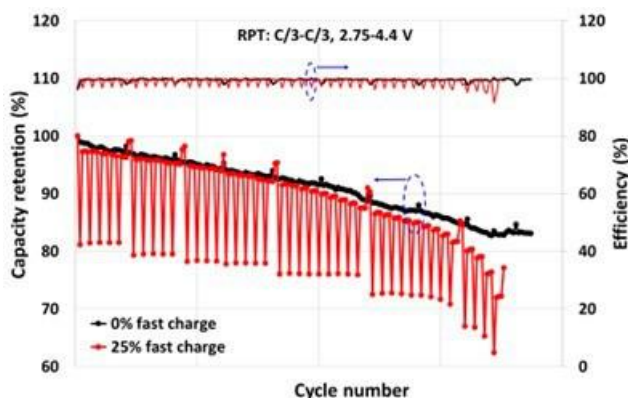


Figure I.6.4 Comparison in cycling stability of single-layer pouch cells with graphite (A1) anodes and blended cathodes (C5C2-blend 2) between 0 % (all regular C/2-rate) and 25 % fast charge (25 % fast charge + 75 % regular C/2-rate) cycling

Conclusions

Farasis has shown > 600 and ~700 cycles in a double-layer pouch cell with a lab-coated graphite anode and a pilot-line coated Mn-rich cathode before reaching 80 % capacity retention. Farasis has identified 2-3 candidates with excellent cycling stability as low cost and high-capacity cathode materials from several types of cathode materials. Farasis has built ~ 75 Ah capacity Gen 1 cells with optimized chemistry with an energy density of ~270 Wh/kg and a charge time of 18 min for the 80 % of the capacity. The Gen 1 cells have been delivered to national labs for related performance evaluation and tests. Next year, Farasis will finalize graphite anode material with excellent fast charge capability and low-cost cathode material with good cycling stability as optimized chemistry for Gen 2 cells. Farasis will build ~ 87 Ah capacity Gen 2 cells with optimized chemistry with an energy density of ~300 Wh/kg and a charge time of 15 min for the 80 % of the capacity. The Gen 2 cells will be also delivered to national labs for related performance evaluation and tests.

I.7 Pre-lithiation of Silicon-containing Anodes for High-Performance EV Batteries (Applied Materials, Inc.)

Subra Herle, Ph.D., Principal Investigator

Applied Materials, Inc.
3225 Oakmead Village Dr
Santa Clara, CA 95054
E-mail: Subra_Herle@amat.com

Brian Cunningham, DOE Technology Development Manager

U.S. Department of Energy
E-mail: Brian.Cunningham@ee.goe.gov

Start Date: April 5, 2021

End Date: July 31, 2022

Project Funding: \$2,922,239

DOE share: \$1,426,053

Non-DOE share: \$1,496,186

Project Introduction

The increasing energy density (Wh/kg and Wh/L) of the Li-ion cell is needed to improve EV cell performance and decrease the cost (\$/kWh). In the last decade, significant attention has been focused on enabling high-capacity cathode materials and thinner, better separators to increase cell capacity from the cathode side. More recently, Cell Manufacturers are also exploring improved anode performance with the use of silicon-blended graphite anodes. Si/SiO_x blended with graphite can significantly improve the anode capacity and enables fast-charge EV cells. These gains, however, are offset by a first-cycle irreversible loss of lithium which can degrade performance by 30% or more. Additionally, only some of the lithium that enters the Si/SiO_x-Gr anode is active. Some of the lithium is consumed during the solid electrolyte interface (SEI) cell formation cycle. The continual buildup of SEI layers upon subsequent cell cycling further decreases energy density causing gradual cell degradation. Cell manufacturers are “pre-lithiating” the Si/SiO_x-Gr anode to counter the first-cycle irreversible lithium loss. Pre-lithiation provides additional lithium to the anode to compensate for the loss during the first cycle and SEI formation, and therefore, increases energy density by >10-30% over equivalent graphite-based cells. Applied Materials high volume manufacturing (HVM) tools and technology innovation can provide benefits that none of the existing approaches for prelithiation can meet, including ease of integration with existing Li-ion battery process flows, uniform, defect-free lithium films, scalable thickness, and to industry-standard widths, all at low cost/performance, in a safe environment.

Objectives

The objective of this program is to develop and validate a prelithiation process for high volume manufacturing specifically targeted for the requirements of an EV battery and battery manufacturing and demonstrate that silicon-graphite anode-based cells can meet USABC’s EV CY2020 goals for specific energy and other performance, cost targets. The key end of program goals are listed in Table I.7.1.

Approach

With funding support from USABC and working closely with partners, we will use a production-proven platform combined with a PVD deposition source to pre-lithiate Si/SiO_x graphite anode and specifically address 1st cycle irreversible loss of such anodes. Si-based anodes are necessary to increase cell energy density and fast charge capability to meet USABC goals. Cells will be made with varying weight fractions of silicon/silicon suboxide with graphite blended in the anode formulation and different thicknesses of lithium deposited on the silicon anodes to bridge the 1st cycle irreversible loss.

In Budget Period-1 (BP-1), Applied Materials engaged with SpectraPower (subcontractor) and Farasis Energy (subcontractor, manufacturing partner) extensively to review and provide guidance in alignment with the project scope of work (SoW) to provide pre-lithiated anode samples and testing in R&D type coin and pouch cells in the first phase of the program. SpectraPower will initially focus on screening for high silicon content

SiOx-C materials coupled with NMC532 and NMC 811 cathodes. These studies will allowed us to identify optimal anode compositions and understand the required processing conditions and baseline for the 2Ah multilayer pouch cells, while giving us visibility into potential integration issues to help devise solutions (2Ah cells vs. baseline). Learnings from this work will lead to the final delivery of 2 Ah cell pre-lithiated cells and corresponding control baseline cells to Idaho National laboratory for independent testing and evaluation. In Budget Period 1, Applied Materials prelithiation task used a Sheet-to-Sheet (S2S) deposition tool before switching to the Roll-to-Toll (R2R) lithium deposition system based on Applied's production-proven SmartWeb™ platform. Li-coated anodes were shared with project partners for integration into cells for testing and characterization. The Li deposition and cell fabrication processes will be optimized towards volume manufacturing performance targets while meeting the battery performance targets, as validated by the project collaborators.

Table I.7.1 Budget period 1 summary and status updates of key performance deliverables

Program Cell Performance Goals		
Parameter	Pouch Cells (Pre-lithiated Silicon Anodes), 2Ah Year-1	Pouch Cells (Pre-lithiated Silicon Anodes), >29 Ah Year-2 (End of Program)
Gravimetric Energy Density	≥200 Wh/kg	≥349 Wh/kg
Cycle Life (DST)	500 Cycles	≥1000 Cycles
Calendar Life	N/A	≥ 3 Years (Est.)
Peak Power Performance	N/A	>Current Li-ion Baseline
Fast Charge	>Current Li-ion Baseline	>Current Li-ion Baseline
Status update (BP1)	Completed BP1 deliverables 1. SpectraPower Completed 2 Ah Cell build (~205 Wh/kg) 2. 17 cells of 2 Ah capacity pre-lithiated & 8 cells of 2 Ah control cells delivered to INL; Testing in progress	Ongoing

Results

Results are summarized in Figure I.7.1 to Figure I.7.4. Based on prior experiments and testing BTR NCM811 was selected as the cathode material and 25% BTR SiOx for the anode material. In addition, the experiments with different levels of lithiation indicated that ~6μm of Li is the optimal for prelithiation of the baseline anode. The multilayer cell builds (with and without pre-lithiation) have been completed. It has been shown that the full multilayer pre-lithiated cell build versions improve performance in capacity, coulombic efficiency, and cycle life over non-prelithiated baseline cells as shown in Figure I.7.3. Throughout Year 1, the areal capacities have been increased, starting with ~3-3.5 mAh/cm², with the final cell build ending at the project goal of 4.5 mAh/cm².

Table I.7.2 Below captures all the proposed milestone and corresponding status updates All Budget Period-1 milestones were completed and preparations started towards meeting Budget Period-2 objectives, as summarized below:

M.S.	Milestone Description	Status as of 10/14/2022
	Budget Period - 1	Completed
1	Confirm Cell Baseline Cathode Loading NMC 532 and 811 cathode loading: detailed studies conducted	NMC 811 chosen over NMC 532 for baseline cells
2	Anode Loading and Lithium Thickness: Several anode manufacturers tested and optimized. This was followed by optimum pre-Li thickness for performance	BTR Silicon Oxide (25 %) selected Optimum Pre-Li loading studies completed Pre-Li thickness of 6 um was down selected for SiO _x - Gr anode
3	Pre-treatment and post-treatment (Passivation) CO ₂ passivation analysis	Pretreatment: Optimized drying conditions -Completed Particle removal- Not required Post treatment: Optimized CO ₂ surface passivation- Packaging & Shipping Pre-Li Anode Protocol- Completed
4	2Ah Cell Performance Verification Go/No-Go condition: 2Ah pre-lithiated cells show improvement over non-pre- lithiated baseline.	Demonstrated 2 Ah cell with prelithiation →10 % improvement in capacity vs. baseline cells →>10 % Coulombic Efficiency Improvement
5	Delivery of 2Ah Cell to INL for Verification Delivery of 17 prelithiated cells along with 8 baseline cells	Data package for Go/No go decision End of July → Completed 2 Ah Cell Delivered to INL for testing →Testing in progress
	Budget Period - 2	In Progress

During the first part of the BP1, a Sheet-to-sheet (S2S) pre-lithiation tool was utilized to generate samples. The sample size for pre-lithiation was 180 mm x 210 mm. Several batches of pre-lithiated anode were generated using SpectraPower provided anode. The anode sheets were pre-dried before process development. The pre-lithiated anodes were vacuum sealed in Aluminum pouch and shipped to SpectraPower for further cell building and testing.

SpectraPower built coin cells and single layer pouch cells to screening of cathode and anode materials. Based on this study NMC 811 cathode powder and 25wt% SiO_x anode were chosen for the program. The binder, carbon additive and electrolyte formulations were recommended by Applied Materials in alignment with Farasis Energy.

The electrode slurry composition and target electrode loading were also provided. SpectraPower did initial electrochemical characterization to determine appropriate pre-Li dosage. Based on these studies 2 Ah budget period 1 deliverable specifications were determined. SpectraPower completed building and shipping of 2 Ah capacity cells to INL. Table I.7.2 summarizes the status of BP1 deliverables.



Figure I.7.1 (a & b) Examples of silicon (SiOx) anode showing transfer of Li to anode. (c) Cell sizes and dimension for final BP-1 deliverable, and (d) Pouch cell assembly process - Cells in fixtures going through formation and cycling before shipment

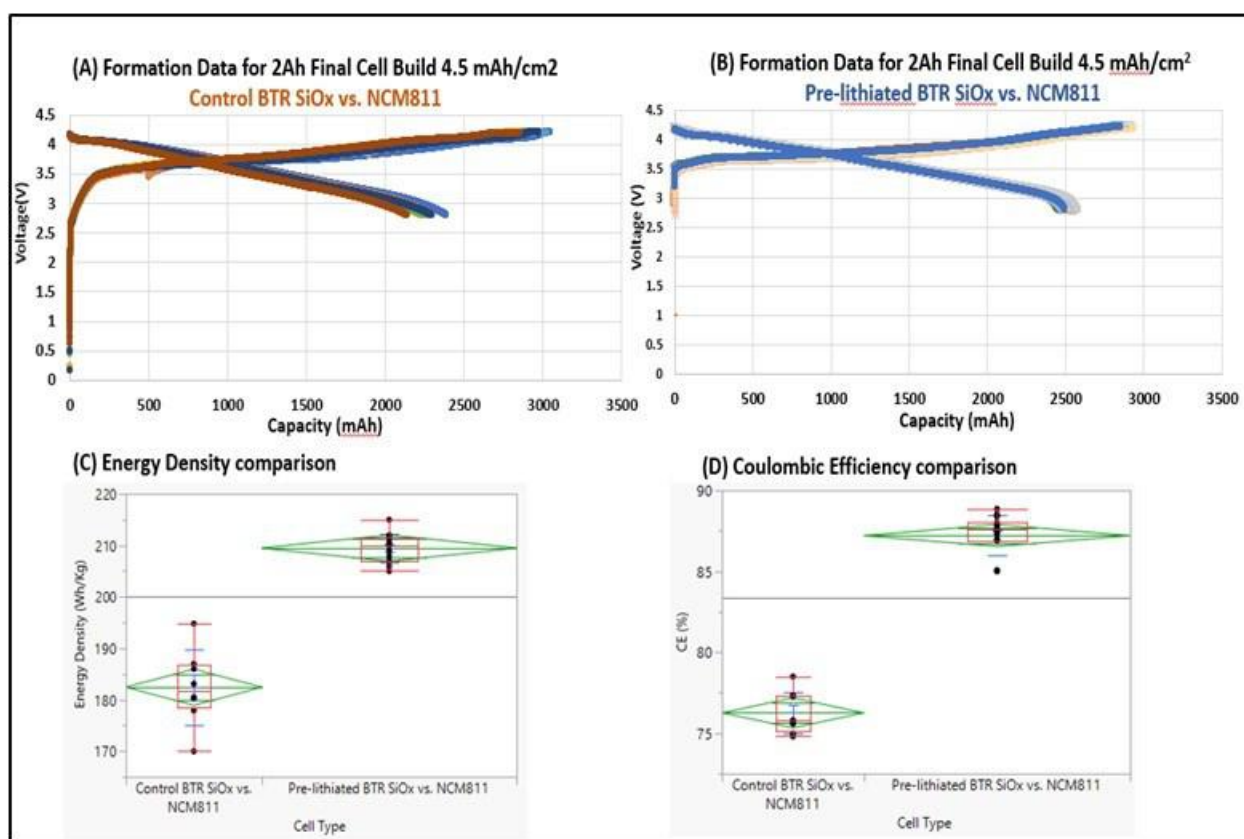


Figure I.7.2 SpectraPower: Summary of cell voltage vs. Capacity data for (A) eight control and (B) seventeen pre-Li anode from formation cycle (first cycle charge/discharge), showing good consistency and reproducibility. These cells were delivered to INL for further cycling. C and D shows the summary of cell parameters Energy density and Coulombic efficiency improvements of pre-lithiated anode vs. control for the same set of cells

Idaho National Laboratory (INL) provided the initial status updates for budget period 1 (Interim Cells) as a part of year 1 deliverables. 2 Ah pre-Lithiated Cells (17) and 2 Ah non- prelithiated control cells (8) shipped to INL. Initial results are summarized below. All the 2 Ah cells delivered met the initial specifications needed for further testing and characterization. Further, beginning of life (BOL) Specific Energy 207Wh/kg, Energy Density 380 Wh/L for the Pre-Li cells meets the 2 Ah target specifications.

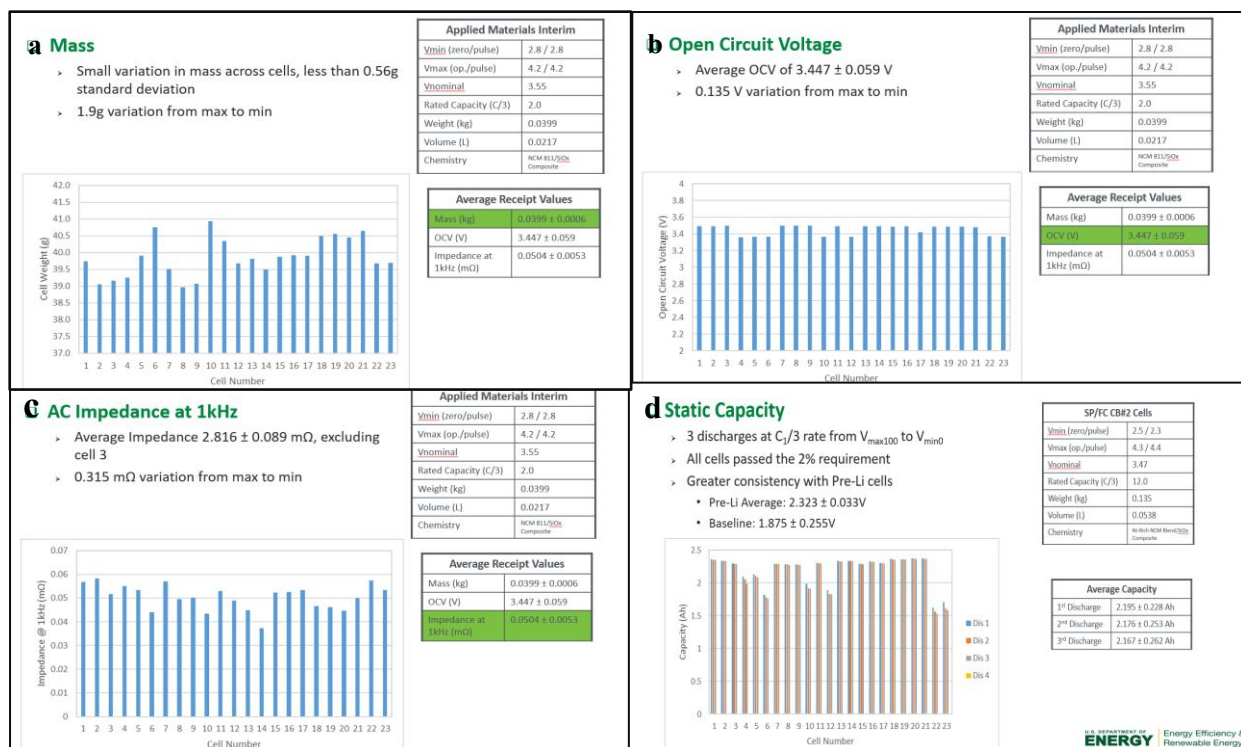


Figure I.7.3 Idaho National Lab summary of cell performance indicating (a) mass variation (b) open circuit voltage (c) AC impedance at 1 kHz and (d) Static capacity for all the final BP-1 cells delivered. All cells achieved target capacity and Impedance values are in the acceptable range for further DST cycle testing.

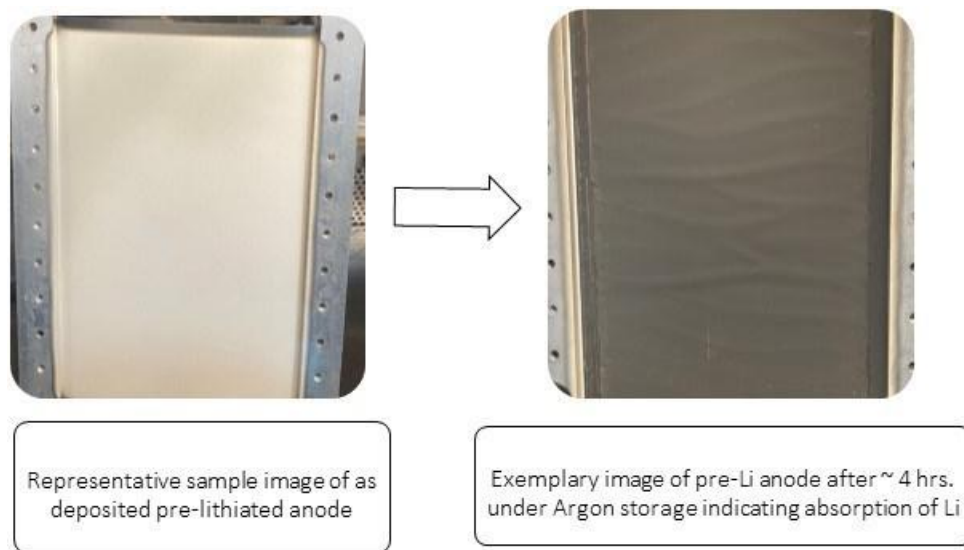


Figure I.7.4 Example image of Applied Materials pre-lithiated anodes generated in S2S tool as a part of the deliverable 1.

Program (schedule) Update

A four month extension to BP1 was requested and approved by USABC. Delays were a result of supply chain logistics issues caused by Covid pandemic. The cascading effect of the shift in timeline will be reflected in the year 2 program status and deliverables. We continue to work with SpectraPower and Farasis Energy to meet the program deliverables.

Conclusions

In 2022, the Applied Materials-led team consisting of SpectraPower and Farasis completed all Year-1 milestones and deliverables and started work towards Year-2 objectives.

Acknowledgements

Ajeay M. Joshi (Ajeay_M_Joshi@amat.com) served as the Program Director for this project at Applied Materials, Inc. The Applied Materials-led team would like to sincerely thank our partners (SpectraPower and Farasis Energy) for their contributions and consistent efforts in supporting us to enable this technology and Dr. Lee Walker at INL for the cell testing results (Baseline Cells).

We would also like to thank USABC, DOE program managers and reviewers for their constant encouragement and providing guidance throughout. We also acknowledge significant contributions from our Applied Materials engineering and process team for their support.

I.8 Electrolyte Development: High Performance Electrolyte for High Voltage Batteries (Gotion)

Dr. Jennifer Hoffmann, Principal Investigator

Gotion Inc.

8001 E. Pleasant Valley Rd.

Independence, OH 44131

E-mail: j.hoffmann@gotion.com

Brian Cunningham, DOE Technology Development Manager

U.S. Department of Energy

E-mail: Brian.Cunningham@ee.doe.gov

Start Date: March 20, 2019

End Date: October 31, 2022

Project Funding: \$2,628,200

DOE share: \$1,267,844

Non-DOE share: \$1,360,356

Project Introduction

As the automotive industry continues to expand into electromobility with electric vehicles to meet emission requirements and driving performance, the need for advanced materials to meet standards for safety, energy density, and cost demand technical advances in battery systems and materials. High voltage spinel ($\text{LiNi}_{0.5}\text{Mn}_{1.5}\text{O}_4$ or LNMO or HVS) cathode electrode material has the potential to meet or even exceed these targets given the large voltage range, carbon anode pairing, and cobalt free structure. The factors impeding its commercialization high temperature gas generating reactions and incompatible electrolyte at the 4.8-5.0V upper cutoff potential. By resolving the gas generation issues of the material and developing electrolyte formulations utilizing novel additives and solvent systems, the advances in electromobility commercialization can be realized at a cost that is significant over other advanced materials currently on the market.

Objectives

The primary objective of this project is to develop electrolyte formulations and novel electrolyte additives to reduce the gas generation, transition metal dissolution, and improve the performance of the LNMO cathode system while being stable at high voltage. The electrolytes and additives developed for these electrode materials are targeted to have minimal gas generation, high cycle life, high power charge/discharge capabilities, wide operating temperature, and competitive cost. In addition to this primary objective, the analysis of the interactions of the electrolyte with these materials leading to the understanding of gassing and failure mechanisms is also being targeted.

Approach

The approach to this project has been updated this past year and can be classified into 4 task categories that are defined as follows:

- Focus Area 1: Novel additive design, synthesis, screening, and scale up.
- Focus Area 2: Development and optimization in 2 Ah HV-LNMO v. Carbon Anode pouch cells.
- Focus Area 3: Scale up to 10 Ah HV-LNMO v. carbon anode pouch cell with continued evaluation and optimization.
- Focus Area 4: Supplier evaluation and selection of HV-LNMO cathode material.

Focus area 1 works to develop novel additives that are targeted for solid electrolyte interface (SEI) formation, cathode electrolyte interface (CEI) formation, and manganese dissolution prevention. Additives are synthesized and screened in coin cells before testing small batches of the best candidates in pouch cells in subsequent focus areas. In addition, surface analyses that aid in development and understanding of additives with the electrode materials are also conducted. The impact the additives have on the electrolyte properties

such as vapor pressure, flashpoint, conductivity, electrochemical stability, and other important areas are also investigated to track any notable trends that could be useful in further development. Most promising candidates are then scaled up for large batch production and selected for patent protection.

Focus area 2 utilizes the additives developed during work in focus area 1 along with other unique but commercially available additives, uncommon and/or novel solvent and lithium salt formulations, and adjustments to testing protocols to maximize the functionality of the electrolyte in 2 Ah multi-layer pouch cell (MLPC) test vehicles using HV-LNMO as the cathode paired with a carbon anode. Testing includes but is not limited to cycling at various temperatures, storage testing, electrochemical stability testing, impedance growth evaluation, and gas analysis. Surface analysis or further electrolyte property measurements that give information toward failure mechanisms, gas generation mechanisms, or additive and electrolyte mechanisms can also be carried out. While focus area 1 is aimed at compound development, focus area 2 aims to put those compounds to use to improve performance and reduce gas generation. Focus area 3 continues the work of focus area 2 but in a larger test vehicle that is a more accurate representation of a commercial product.

Focus area 4 is conducted in tandem with the previous focus areas. Developing a successful high voltage electrolyte for HV-LNMO cathode material and creating a MLPC requires material that is of good quality, appropriate pricing, and good stability. During the launch of this project, a consistent supplier was more difficult to come by than originally projected so alternates were evaluated comparing particle size, morphology, reactivity, composition, and stability. It is important to note that this focus area is designed to evaluate materials that are the best fit for this project specifically and does not claim to identify the best material(s) on the market for commercial applications.

Results

This project initially underwent some delays result from the COVID-19 pandemic and the impact on the supply chain; however, in the past year, the largest impact has been indirect, residual influence on the supply chain. The progress of the program has been forward moving, but with limitations in raw materials for novel compounds, it has been a slower recovery than anticipated.

The 12 novel additives that were developed for this program were narrowed down to five for scale up with two selected for patent application. The five selected compounds were synthesized in larger quantities, but due to the slow patent process further development stopped. Patents for two of the compounds have been submitted and are moving through the patent process. Improvements to impedance and cycling were monitored and noted, but improvements to gas generation specifically with two of the compounds focused on in the project was the desired outcome. In addition to the 12 synthesized compounds, 5 novel compounds were evaluated with excellent results for not only gas reduction, but also high temperature performance. The final formulation that was delivered included 3 novel additives and two commercially accepted compounds. The publication of the other novel compounds identified is being reviewed as part of the closing of the project.

The majority of the work done resided focus area 2 in order to manage supply chain. By delaying scale up, quantities could be better controlled and therefore more data generated. In order to meet targets, the novel compounds HV-P, HV-02, HV-09 were considered the main additive pack. HV-P provides CEI and SEI formation, HV-02 significantly reduces gassing, and HV-09 improves capacity and long-term performance. This additive pack in the baseline, which is referred to as D2, was used to evaluate the formation and testing procedures in order to ensure best SEI formation and stability. The areas of focuses included upper cut-off voltage evaluations, rate of testing evaluations, and charging procedures variances. The findings showed that the procedure greatly impacts the gas generation in a cell. While capacity and cycling retention showed some benefits to certain procedures, the impact on gas generation was far greater. Procedure 1 (P1) and procedure 4 (P4) showed excessive gassing to the point volume data could not be gathered. In contrast, procedure 2 (P2) showed some of the lowest gas generation measured during cycling up to this point. The gas generation comparison can be seen in Figure I.8.1.

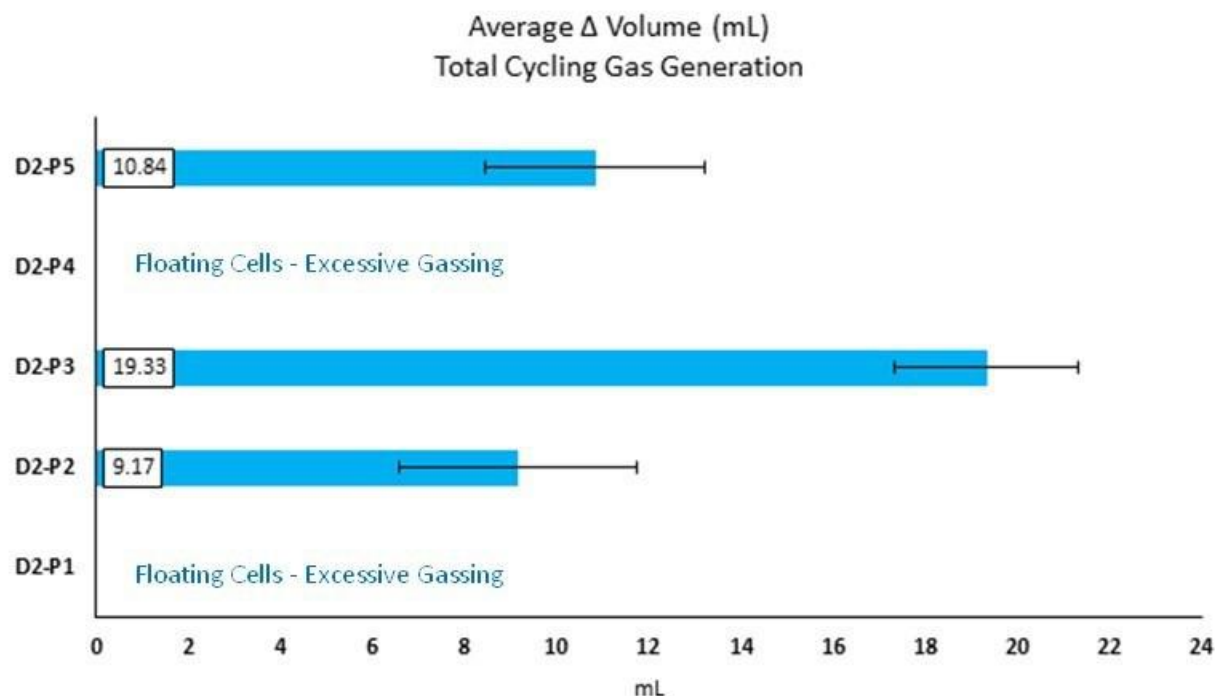


Figure I.8.1 Gas generation measured in 2Ah MLPC containing HV-LNMO/C material after cycling for 120 cycles at 45 °C under various procedures (P) that alter charging methods, upper cutoff voltage, and current rates. The data shared all has the same formulation showing the impact that procedure has on gas generation in addition to electrolyte formulation.

In addition to understand the impact of different testing procedures and identifying procedures that effectively limit gas generation and maintain or improve performance, additional formulations were evaluated. Other additives investigated were common additives such as fluoroethylene carbonate (FEC) and succinic anhydride. Fluorinated compounds and acid scavengers were screened extensively as part of this final stage of optimization, but careful attention to synergistic combinations allowed for improvement in high temperature cycling and high temperature storage. In Figure I.8.2 and Figure I.8.3, the impact of some of the additive combinations is apparent with improvements in retention over the black baseline, L6-4. Not only is retention performance improved, but the gas generation was also greatly improved over the excessive gassing of the baseline. Figure I.8.4 shows images of the improvements in gas generation compared to the baseline. Photos are taken after cycling to be able to still evaluate impact on gas generation and swelling when volume measurements are not possible. With the additive pack added to the L6-4 baseline in formulation L6-4-167, we were able to greatly improve the capacity retention while keeping the gas generation very low.

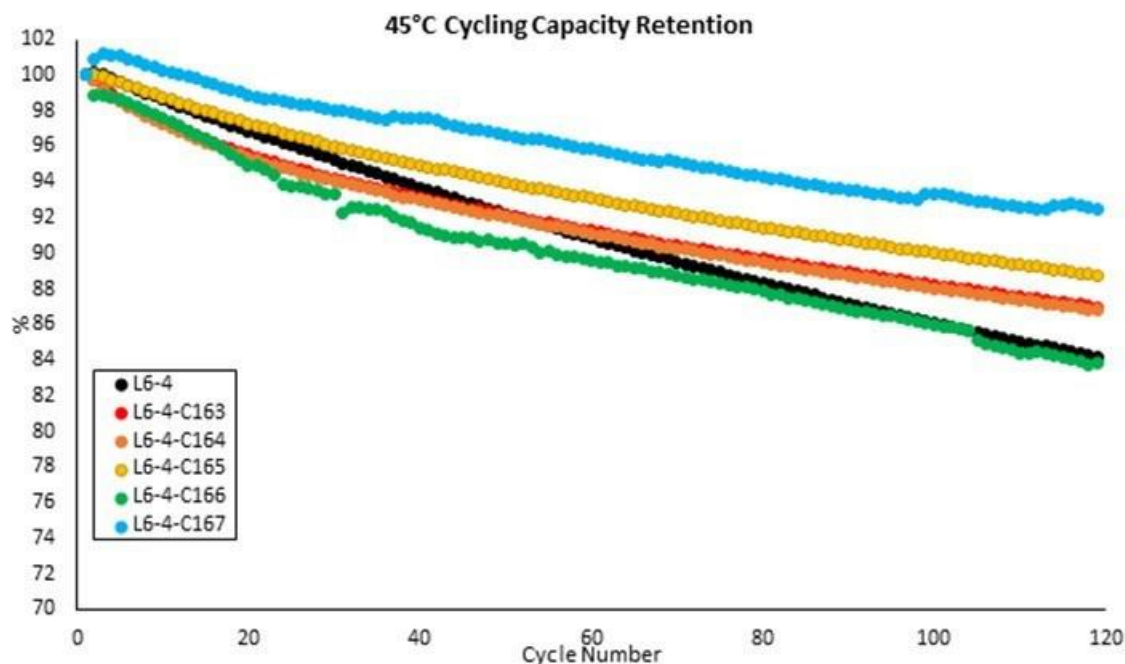


Figure I.8.2 High temperature cycling performance in 2Ah MLPC containing HV-LNMO/C material showing additive packs improving retention over the baseline significantly at high temperatures. Formulation L6-4-C167 shows 8.4% retention improvement over the baseline.

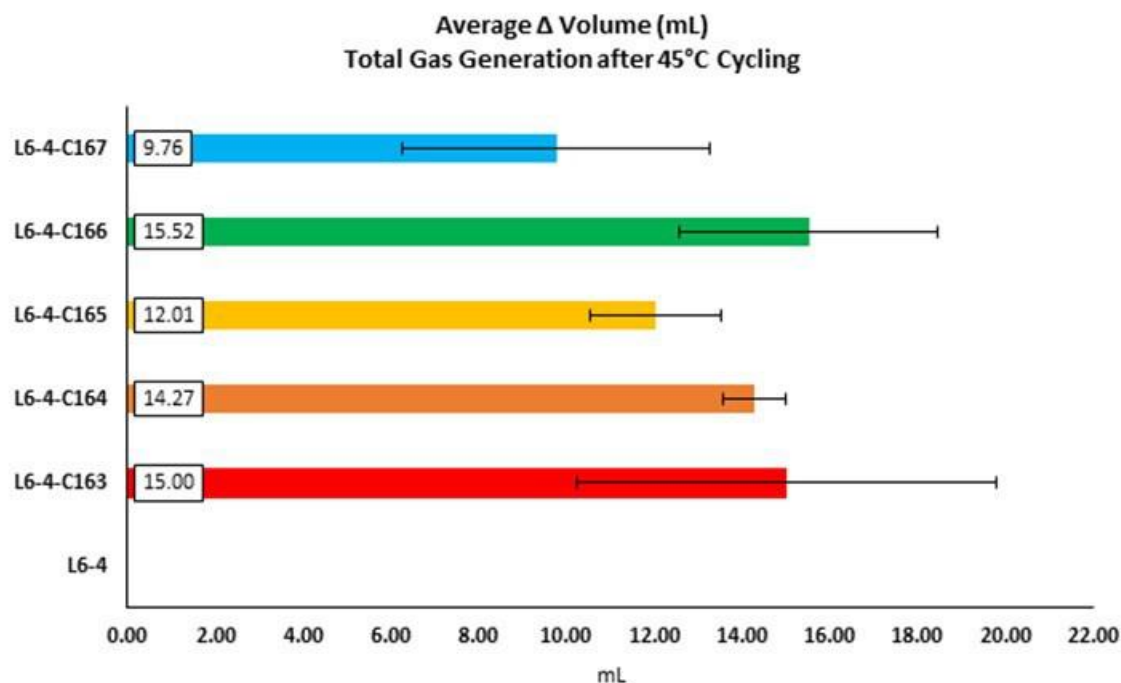


Figure I.8.3 Gas generation after the cycling from Figure I.8.2 which went through high temperature cycling performance in 2Ah MLPC containing HV-LNMO/C material. Not only did these formulations greatly improve retention in high temperature cycling, but it also reduced gassing compared to the baseline.

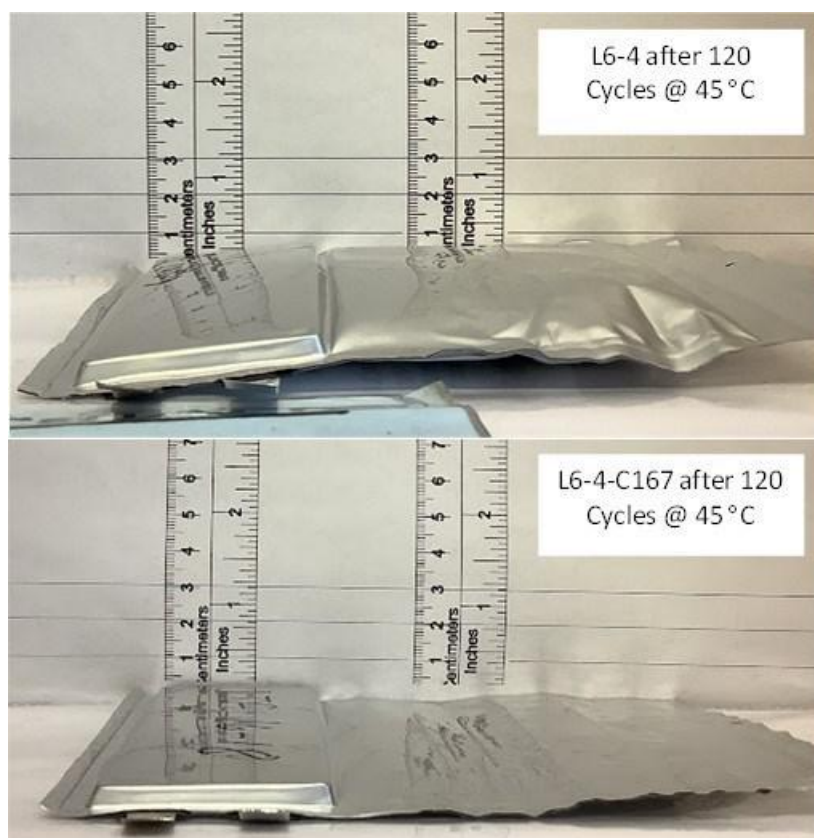


Figure I.8.4 Photos of 2Ah MLPC containing HV-LNMO/C material after 120 cycles of 45°C cycling. The top photo shows the baseline gas generation while the bottom photo shows gas generation with L6-4-C167 optimized formulation and an optimized testing protocol. Significant improvement in swelling able to be seen.

In the final quarter of the year, scale up from the 2Ah MLPC optimization work into 10Ah MLPC cells was completed. Many of the additive packs had to have concentration adjustments and the procedures were also evaluated to ensure optimized testing. Even with the scale up, our additives showed strong performance. Figure I.8.5 shows the 1-week, 45°C, 100% state of charge (SOC) results which show improved remaining and recovered capacity over the baseline. In addition to stabilized storage performance, Figure I.8.6 shows the improvement to gas generation. The additive pack utilizing HV-P, HV-02, and HV-09 showed a 92% reduction in gas generated during storage testing in 10 Ah MLPC. Scale up was not able to be completed to the extent originally planned, but progress was able to be made to further move this material towards commercial viability in high energy density lithium batteries at low cost.

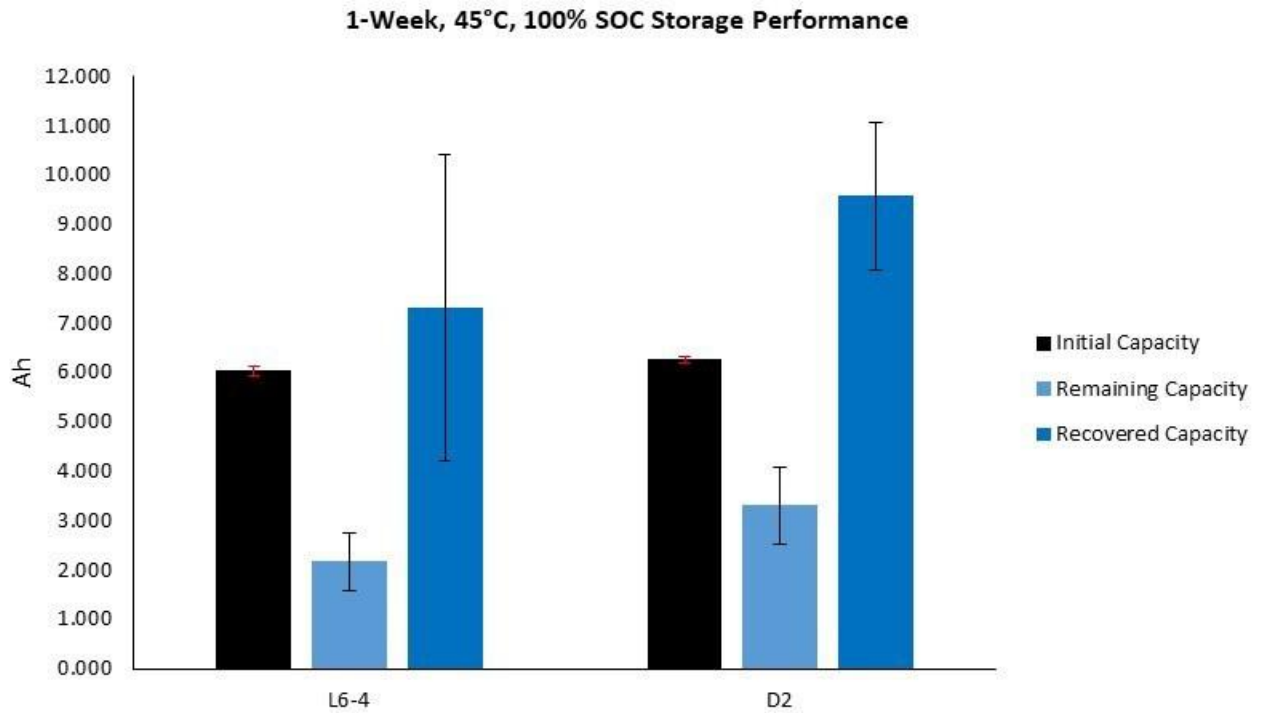


Figure I.8.5 Photos of 2Ah MLPC containing HV-LNMO/C material after 120 cycles of 45 °C cycling. The top photo shows the baseline gas generation while the bottom photo shows gas generation with L6-4-C167 optimized formulation and an optimized testing protocol. Significant improvement in swelling able to be seen.

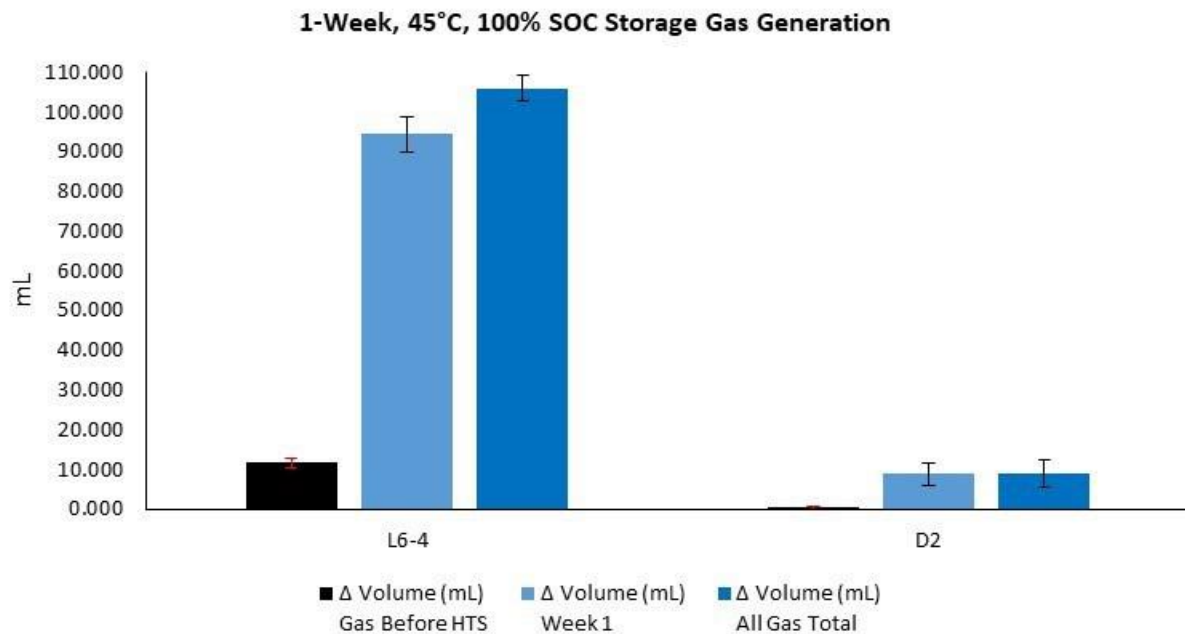


Figure I.8.6 Photos of 2Ah MLPC containing HV-LNMO/C material after 120 cycles of 45 °C cycling. The top photo shows the baseline gas generation while the bottom photo shows gas generation with L6-4-C167 optimized formulation and an optimized testing protocol. Significant improvement in swelling able to be seen.

Conclusions

The project concluded with understanding the impact of optimizing procedures on reducing the gas generation, identifying novel additives that work synergistically to improve performance and reduce gassing, and then taking those findings to scale up in a more commercial adjacent test vehicle. While much of the publication work is still pending, deliverables for the project were met and are undergoing further testing as well. This project has now concluded.

Key Publications

1. Jongjung Kim, Venkata A. K. Adiraju, Nuwanthi Rodrigo, Jennifer Hoffmann, Martin Payne, and Brett L. Lucht *ACS Applied Materials & Interfaces* **2021** 13 (19), 22351-22360
2. Jongjung Kim *et al* 2021 *J. Electrochem. Soc.* **168** 080538

Acknowledgements

It is important to acknowledge Dr. Brett Lucht of the University of Rhode Island and his technical group as they have been integral in the design, development, and synthesis of the novel additives in this project. Dr. Lucht and his group have carried out extensive surface analysis of the materials and been of huge assistance with the LNMO supplier comparison.

The PI of this project would also like to acknowledge Dr. Martin Payne for all his assistance in meeting project requirements and finances. His participation and support of this project has made the extensive work being carried out possible.

I.9 Strategic Collaboration for the Development of a Self-Sustaining Model for the Recycling of Large-Format Lithium-Ion Batteries (American Battery Technology Company)

Ryan M Melsert, Principal Investigator

American Battery Technology Company
100 Washington St, Suite 100
Reno, NV, 89503
E-mail: RMelsert@batterymetals.com

Brian Cunningham, DOE Technology Development Manager

U.S. Department of Energy
E-mail: Brian.Cunningham@ee.goe.gov

Start Date: October 1, 2021

End Date: March 31, 2024

Project Funding: \$2,000,000

DOE share: \$500,000

Non-DOE share: \$1,500,000

Project Introduction

As vehicle-related research and development in advanced battery technology continues to progress, the market competitiveness and penetration of EVs, PHEVs, and HEVs have been steadily increasing. However, the total life cycle costs of the associated large format batteries still present an obstacle to further adoption, and a major potential avenue to decrease these costs is to increase the residual value of these batteries at their end of lives. Unfortunately, many currently available operations for the recycling of large format lithium-ion batteries require a tipping-fee to be paid in order for these batteries to be processed, actually further increasing their life cycle costs. This recycling business model is unsustainable, as it prohibitively adds life cycle costs and discourages end users from returning their batteries to the market at end-of-life.

This project team has developed an integrated processing train for the recycling of large format lithium-ion batteries that substantially reduces both upfront capital and operating costs, while refining the battery metals to the specialty chemical specifications defined by leading cathode manufacturers in order to extract additional revenue and establish a true closed-loop circular economy. Through these enhancements, this integrated process is able to operate economically while providing high residual value to end-of-life material owners, which provides an economic incentive for current holders and stockpilers of feedstock to return their materials to the market to enable the closed-loop supply chain to operate.

Objectives

The objective of this project is to demonstrate that the existing business model of the lithium-ion battery recycling industry can be challenged, and that a sustainable recycling system can be operated that can result in the manufacturing of cells from recycled battery metals that have equal performance to otherwise identical cells from virgin-sourced material, while also being produced at lower cost, with lower environmental footprint, and from domestic US-based resources.

The primary USABC targets addressed in this program are those of cell cost, maximum percentage of active cathode manufactured from recycled materials, and the percentage of battery metals that are sourced from the domestic US. In addition to these metrics, it is critical to demonstrate that both active cathode powders and full multilayer test cells that are manufactured from these recycled metals can achieve the same performance as otherwise identical components that are manufactured from virgin metals. As a result, the performance metrics of standalone active cathode powder and of full multilayer pouch test cells need to be achieved in order for the above USABC performance targets to be validated. The active cathode powder and cell level test procedures for this project will follow the guidelines set forth in the “United States Advanced Battery Consortium Battery Test Manual for Electric Vehicles” as detailed by the US DOE VTO.

Approach

In order to validate the commercial performance of these recycled battery metal products, an approach has been established that consists of three major tasks spread across two budget periods.

- **Budget Period 1 (10/1/21 - 9/30/22):**
 - **Task 1**
 - Bench scale recovery and purification of battery metals from recycled sources, analytical characterization of recycled metals to ensure all product specifications are being achieved
 - Synthesizing of high-energy density active cathode material from control group virgin-sourced battery metals, in order to prepare material for test cell development
 - Cell development and balancing of half-cell, single-layer pouch cells, and multi-layer pouch cells using control group virgin-sourced battery metals
 - Performance testing of multi-layer pouch cells from control group virgin-sourced active cathode material to establish benchmarks
- **Budget Period 2 (10/1/22 - 3/31/24):**
 - **Task 2**
 - Large scale recycling of large format automotive cells, recovery and purification of battery metals, and analytical characterization of products
 - Synthesis of high energy density active cathode material from various blends of recycled and virgin sourced battery metals
 - Fabrication of multi-layer pouch cells from each blend of recycled and virgin sourced battery metals active cathode material
 - Performance testing of test cells, and comparison of cell performance against control group cells
 - **Task 3**
 - Analysis of life cycle operations with cost, performance, and environmental impact metrics

In order to ensure that industry relevant high energy density active cathode materials are utilized in this evaluation, ABTC has formed a strategic collaboration for this project team with BASF, one of the largest manufacturers of high-energy density automotive cathode material in North America. Through this strategic collaboration, during this project BASF is receiving recycled battery cathode grade metal feedstocks (Nickel, Cobalt, and Manganese Sulfates, as well as Lithium Hydroxide) from ABTC's battery recycling processes, and is using these metal feedstocks to synthesize its high energy density active cathode material. Multiple batches of this active cathode material are being manufactured using various blends of virgin-sourced and recycled-sourced battery metal feedstocks, and BASF will characterize the performance of these active cathode material batches in order to quantify the impact on performance of virgin versus recycled battery metal feedstocks.

In addition to synthesizing active cathode material from recycled battery metals, this project is taken a step further and an additional strategic collaboration has been formed with C4V. C4V is a battery R&D and manufacturing company that operates out of the Northeast Center for Chemical Energy Storage (NECCES), a US DOE Center of Excellence Energy Frontier Research Center, at Binghamton University. This center has world class facilities for the fabrication and testing of all types of form factors and chemistries of high energy density lithium-ion batteries. During this project, C4V is receiving the batches of virgin-sourced and recycled-sourced active cathode material from BASF and is fabricating large format automotive test cells in order to quantify the performance of these various batches of active cathode material at the cell level. These cells will be tested through individual characterizations, cycle life, and calendar life procedures and the impact on virgin vs recycled battery metal feedstocks for each batch will be quantified.

These strategic collaborations between battery recyclers, cathode manufacturers, and cell manufacturers in North America will enable the demonstration of the full closed-loop circular manufacturing supply chain of

large format lithium-ion battery cells. The program includes battery module and cell recycling, battery metal recovery and purification, active cathode synthesis, large format cell manufacturing, and rigorous testing of these cells side-by-side with otherwise identical cells manufactured from virgin sourced battery metals. (See Figure I.9.1.)

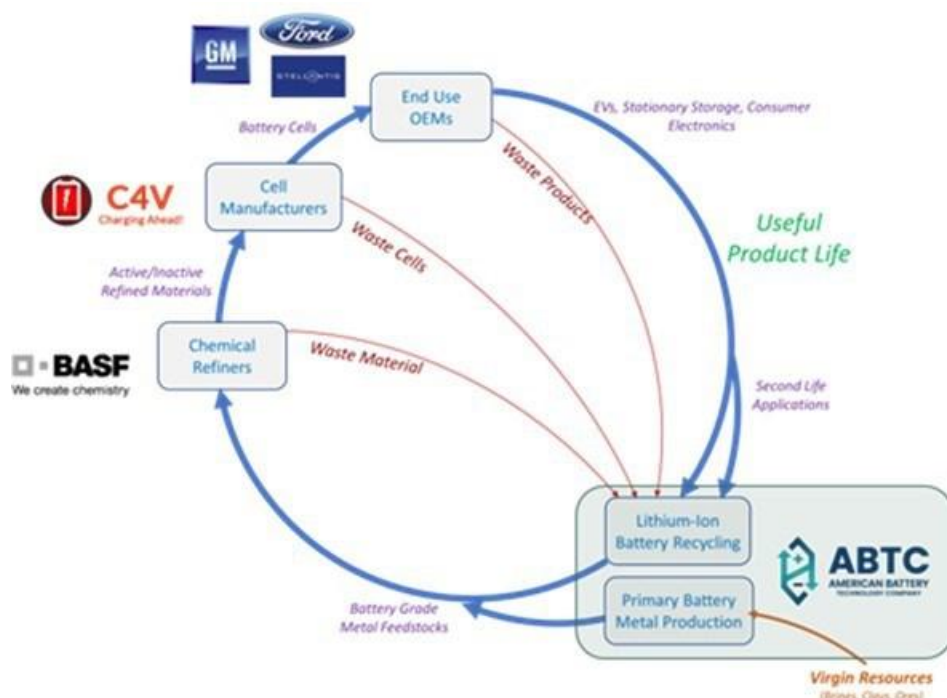


Figure I.9.1 Demonstration of closed-loop North American lithium-ion battery supply chain

Results

The project team has completed all activities within Budget Period 1, including the generation of bench scale samples of recycled lithium hydroxide and transition metal sulfates, the characterization of these products by both ABTC and BASF to confirm they meet all required product specifications, the synthesis of control group active cathode material from virgin sourced metals, the cell development and fabrication of cells from this control group active cathode material, and the performance testing of these control group cells.

The testing and performance benchmarking of the control group cells were performed throughout Q3 and Q4 2022, and the initial results were presented to the USABC team. The data to date demonstrates that the performance of the tested cells are aligned with industry metrics, and that these control group cells will serve as successful baselines for the sensitivity studies to be performed during the second year of this project. Further details around results are outlined below;

- 1) All 4 bench scale battery metal samples (nickel sulfate, cobalt sulfate, manganese sulfate, and crystallized lithium hydroxide monohydrate powders) have been generated, and have undergone analytical characterization and have had certificates of analysis (COA) issued by ABTC
- 2) The purities of these battery metal samples were evaluated by BASF, and were confirmed to achieve all required specifications to be manufactured into high energy density cathode precursor and active cathode material
- 3) The initial production batch of cathode precursor material was synthesized and converted into active cathode material by BASF, and delivered to the C4V team for initial cell development
- 4) All non-cathode materials have been procured for fabrication of control group pouch cells by C4V

- 5) Initial coin cells were fabricated from control group active cathode material for initial cell development
- 6) Single and multi-layer control group cells have been fabricated and tested, and final cell balancing was performed to finalize the cell-level design specifications
- 7) Multi-layer pouch cells were fabricated and have undergone initial performance testing to set baseline metrics for subsequent sensitivity studies

The project team is now in the process of recycling batches of large format automotive lithium-ion batteries, recovering and purifying the elemental battery metals, and generating large batches of battery metal products in order to enable the large scale synthesis of blended batches of active cathode materials.

Conclusions

In conclusion, the industry for the recycling of large-format automotive lithium-ion batteries is still nascent, with no commercial scale operations within North America and only a handful of pilot and demonstration facilities currently operating. These initial facilities generally operate in a manner that allow for end-of-life batteries to be processed into non-hazardous materials, however the current paradigm does not allow for extracted battery metals to be manufactured at significantly lower costs or environmental impact than comparable virgin-sourced battery metals from mining operations. Furthermore, these recycled battery metals are generally blended with virgin-sourced battery metals in the manufacturing of new large-format automotive battery cells, and the industry requests the demonstration and validation that cells made from a substantial quantity of recycled metals can achieve the same performance as cells made from virgin-sourced battery metals.

In order to demonstrate this wide breadth of operations within the battery manufacturing supply chain, a strategic collaboration has been formed to bring together each of the necessary skillsets and facilities to address this scope of work. Through this combined effort, an integrated recycling system is being demonstrated that processes commercial quantities of battery feedstock, the constituent battery metals are being extracted and purified to battery grade specifications, active cathode material is being manufactured from these recycled battery metals, large-format battery cells are being fabricated from these recycled materials, and then these automotive cells will be tested against otherwise identical cells manufactured with virgin-sourced battery metals.

At the end of this demonstration process, the recorded operational data will be used to calculate the total cost of production of these recycled battery metals versus comparable virgin-sourced battery metals, the relative environmental impact of these operations compared to baseline processes, and the performance of these battery cells versus stated USABC project goals.

Acknowledgements

ABTC would like to acknowledge the diligence and hard work performed by its collaborators, BASF and C4V, throughout the undertaking of this program. Without their efforts, this project development and demonstration of a self-sustaining business model for the recycling of large format lithium-ion batteries within North America wouldn't be possible.

ABTC would also like to thank the USABC team for providing an opportunity to showcase an integrated network for closing the domestic battery manufacturing supply chain. We are grateful for the group's dedication to decarbonizing transportation and look forward to continuing to build long-lasting and mutually beneficial collaborations.

I.10 Silicon-based EV Cells Meeting Cost, Calendar Life and Power (Ionblox, Inc.)

Masoud Rahman, Principal Investigator

Ionblox, Inc.

3390 Gateway Blvd.

Fremont, CA 94538

E-mail: Masoud@ionblox.com

Brian Cunningham, DOE Technology Development Manager

U.S. Department of Energy

E-mail: Brian.Cunningham@ee.doe.gov

Start Date: April 5, 2022

End Date: June 30, 2024

Project Funding: \$1,285,886

DOE share: \$642,943

Non-DOE share: \$642,943

Project Introduction

It is well known that silicon-based anodes suffer from continuous growth of the solid electrolyte interphase (SEI) which increases the cell resistance, consumes lithium, and decreases the capacity, power, and energy of the cell. The continuous growth of the SEI is driven by the large volume expansion of the silicon anodes combined with an unstable SEI that promotes electrolyte decomposition.

Ionblox has been able to achieve several USABC cell targets such as power, energy, fast charge, and cycle life. This project will continue the research and development that started during the first USABC LC/FC1 project and focuses on meeting the calendar life, resistance, and cell cost targets. This program will focus on electrolyte and active material development to properly passivate and form stable protective layers on the anode (SEI) and cathode (cathode electrolyte interphase - CEI) surfaces.

Objectives

The key goals of this project are: 1) reaching the USABC calendar life and resistance cell targets via surface passivation, anode and cathode material development and electrolyte engineering; and 2) meeting the USABC cell cost target by optimizing the lithiation process of the silicon anode.

Approach

A unique aspect of the current LC/FC2 program is that it will continue building on the success of the previous LC/FC1 program. The LC/FC2 program will start on solid footing with cells already performing well with respect to cycle life, energy, fast charge, rate capability, and safety. Ionblox understands the last remaining challenges needing development to qualify and commercialize the technology and therefore will primarily focus on improving the calendar life, reducing resistance growth (as a function of storage and cycling) and meeting the cell cost targets. Additional cell specifications with respect to fast charging, high energy, high power, low temperature performance, safety and manufacturability will also be met during this program.

The proposed program will focus on electrolyte and active material development to properly passivate and form stable protective layers on the active anode (SEI) and cathode (CEI) surfaces. Novel electrolyte formulations will minimize unwanted surface electrolyte reactions, while maintaining low temperature performance, high-rate capability, long cycle life, low cost, and ability to pass the safety requirements for EVs. Active material development will focus on surface passivation to minimize unwanted side reactions and improve calendar life. Regarding the USABC cost target, Ionblox key approach will be based on Li-doped SiO_x material/process development to reduce cost and improve the overall performance of the cells. Tradeoffs in cell cost and performance between pre-lithiation of the anode and Li-doped SiO_x will be made. The summary of Ionblox approach in this program is shown in Figure I.10.1.

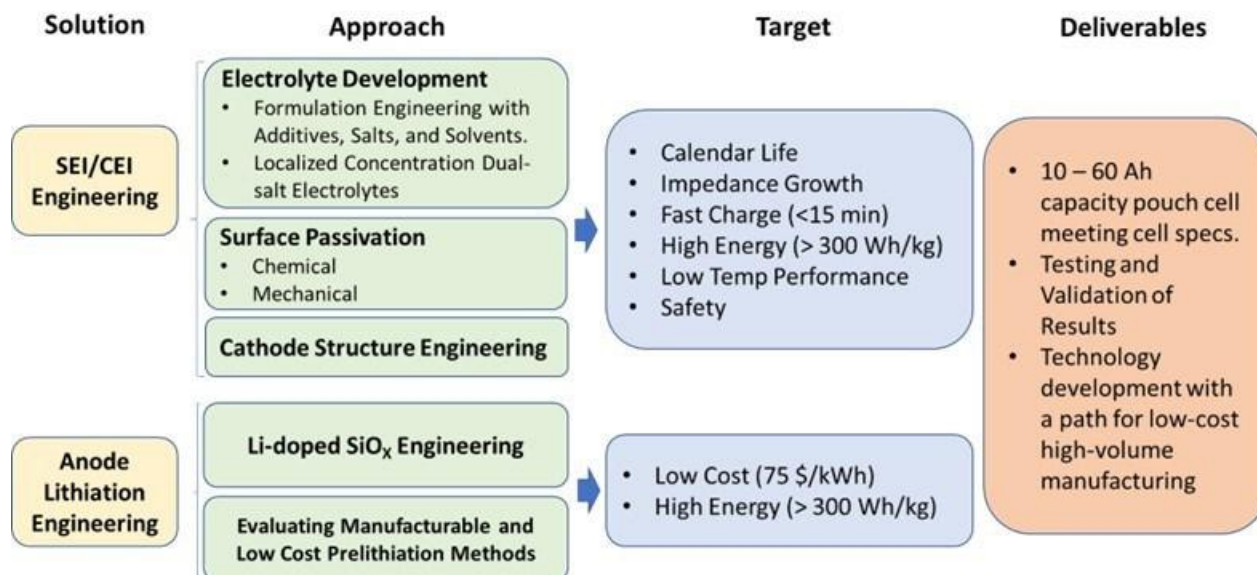


Figure I.10.1 Ionblox approach to reach the USABC calendar life and cell cost targets

Results

In this section the progress on electrolyte development, cathode structure engineering, and surface passivation has been presented.

Electrolyte Development:

During 2022, eight electrolyte formulations (summarized in Figure I.10.2) were designed to evaluate the effect of additives, solvents, salts, and localized high concentration approaches on calendar life (CL) and resistance growth (RG). The electrolytes were designed with the objectives of SEI/CEI stabilization, anti-gassing, thermal stability, and HF-scavenging. The evaluations started on coin cells with identical anodes and cathodes. The charge rate performance tests showed that all electrolytes either matched or exceeded the baseline rate performance within a margin of error. The cycle life study (1C/1C) on coin cells showed that the majority of the electrolytes were in-line or exceeded the baseline. The resistance growth during cycling (measured via HPPC pulses every 100 cycles) showed that dual salt formulations (E5, E6) exhibited faster resistance growth while E2 and E4 have lower overall resistances. The calendar life measurements started for E0, E1, and E2. During RPT0, the electrolyte formulations showed very similar performance. The CL testing of E0, E1, and E2 will continue in Q3. Additionally, the CL testing of promising formulations (E3 to E6) will begin.

The localized high concentration electrolyte (LHCE) cells showed poor rate capability performance. L1 formulation was not able to perform beyond 1C/1C. Ionblox will continue to explore other LHCE formulations, however, any further testing on L1 and L2 will not continue.

Electrolyte Code	Description
E0	Baseline formulation
E1	Anti-gassing additive
E2	Solvent modification
E3	Solvent modification
E4	Salt concentration modification
E5	Dual salt modification
E6	Dual salt modification
L3	LMCE formulation
L2	LMCE formulation

Figure I.10.2 Ionblox electrolyte designs that were studied in 2022.

Active Material: Cathode Structure Engineering

The cathode chemistry, crystallinity, morphology, and surface properties can affect the stability of the CEI and SEI layers. During 2022, the coin cell evaluation of eight NCM-based cathodes or their mixtures (summarized in Figure I.10.3) was started. Charge rate studies showed higher specific capacities for cathodes with increasing Ni content. Additionally, both single crystal (SC) and poly crystalline (PC) cathodes showed similar rate performances. High temperature (45°C) cycling measurements showed that Cathodes #2, #3, #7, and #8 showed similar performance. Additional cycling measurements will continue in 2023. The CL studies started with RPT-0 completed. The CL measurement will continue in 2023. While continuing the evaluation of Cathodes #1 to #8, Ionblox is planning to start the evaluation of Cathode #9 (in-house mixture of cathode #3 and #5).

Cathode #	Crystallinity	NCM	Voltage range (V)
1	SC	811	2.5-4.2
2	PC	811	2.5-4.2
3	PC	811	2.5-4.2
4	SC	811	2.5-4.2
5	SC	811	2.5-4.2
6*	Bi-modal	811	2.5-4.2
7	SC	622	2.5-4.3
8	PC	~90% Ni	2.5-4.2

Figure I.10.3 Cathodes and their properties studied by Ionblox in 2022.

Active Material: Surface Passivation/Engineering

One of the key approaches to increase the calendar life and control the resistance growth is the surface passivation via polymeric coatings. During 2022, Ionblox started the coating process optimization for Polymer #1 to passivate the cathode and evaluate the CEI stabilization. The results are summarized in Figure I.10.4. The high and medium concentration of Polymer #1 resulted in thick surface coatings which resulted in failing of the coin cell performance during rate studies. Ionblox will continue optimizing the coating process parameters with a focus on coating thickness which is controlled by coating time. Additionally, the coating process optimization of Polymer #2 (conducting polymer) has started and will be reported in future reports.

Coating #	Polymer 1 (non-conducting polymer)	Coating Time	
CO-1	High Concentration	Long	Failed during rate-study
CO-2	Medium Concentration	Long	Failed during rate-study
CO-3	Low Concentration	Long	Capacity lower than the baseline
CO-4	Low Concentration	Medium	Ongoing

Figure I.10.4 Ionblox cathode surface passivation test plan for Polymer #1.

Baseline Pouch Cells Performance Measurement

The last cell-build from the previous program (LC/FC1-CB#3) will be used as a baseline for this program. The cell performance measurements are ongoing at Ionblox in parallel with similar testing at the National Labs. The tests and status of ongoing measurements on pouch cells are summarized in Figure I.10.5.

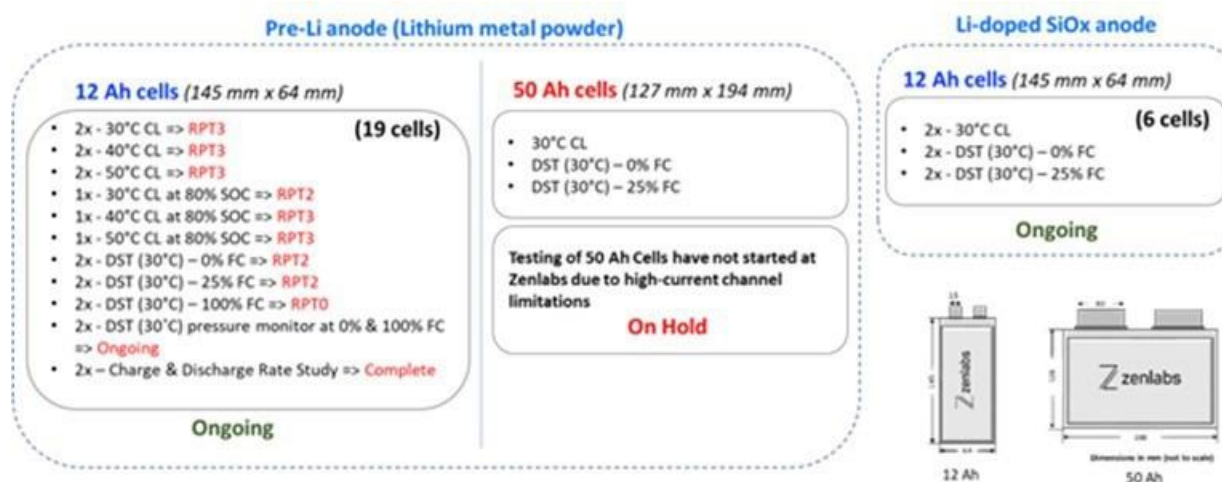


Figure I.10.5 Status of ongoing performance testing on baseline pouch cells

The summary of the measured performance vs USABC requirements and the Gap Chart of the baseline pouch cells is shown in Figure I.10.6. While the tests are still ongoing, up to this point the data show that the baseline cells are meeting the USABC cell target except for the cost. The cost will be one of the key objectives of the LC/FC2 program and Ionblox is targeting the USABC goal of \$75 per kWh for Final-Build cells (deliverable on Q8 of this program).

End of Life Characteristics at 30 degC	Units	USABC EOL Cell Target	CL at 30°C 100% SOC		DST 0% FC		DST 25% FC		DST 100% FC	
			BOL	EOL	BOL	EOL	BOL	EOL	BOL	EOL
			RPT 0	RPT 3	RPT 0	RPT 1	RPT 0	RPT 1	RPT 0	RPT 1
Peak Discharge Power Density, 30 s Pulse	W/L	1400	3248	3110	3407	3475	3319	3231	3350	
Peak Specific Discharge Power, 30 s Pulse	W/kg	700	1314	1258	1378	1406	1343	1307	1355	
Peak Specific Regen Power, 10 s Pulse	W/kg	300	2122	1915	2296	2061	2318	1885	2298	
Usable Energy Density	Wh/L	550	779	787	797	805	804	808	809	
Specific Usable Energy (Defined at Power Target)	Wh/kg	275	315	318	322	326	325	327	327	
Calendar Life	Years	10		0.27						
Cycle Life (DST 25% FC)	Cycles	1000						100		
Cost (@ 250k annual volume)	\$/kWh	75								
Normal Recharge Time	Hours	< 7 Hr, J1772	<7		<7		<7		<7	
Fast Rate Charge	Minutes	80% U.E. Target in 15mins	>80		>80		>80		>80	
Minimum Operating Voltage	V	>0.55 Vmax	0.60	0.60	0.60	0.60	0.60	0.60	0.60	0.60
Unassisted Operating Temperature Range	Wh/kg	70% Specific Usable Energy at 20 30°C								
Survival Temperature Range, 24 Hr	30°C	-40 to 66								
Maximum Self-Discharge	%/month	<1								

Figure I.10.6 Cell targets and gap chart of baseline pouch cells

Additionally, the pouch cells that were built as the baseline for this program showed consistent capacity, energy, OCV, weight and thickness. The summary of the measurements on the 70 baseline cells is shown in Figure I.10.7. The capacity and energy measurement versus voltage for the baseline pouch cells is shown in Figure I.10.8. The measurement on eight cells showed consistent charge and discharge curves as well as energy and capacity.

The power and resistance measurements in Figure I.10.9 show that the baseline cells at RPT-0 are meeting the discharge and regen power requirements of the USABC program. Additionally, consistent results were obtained for eight cells.

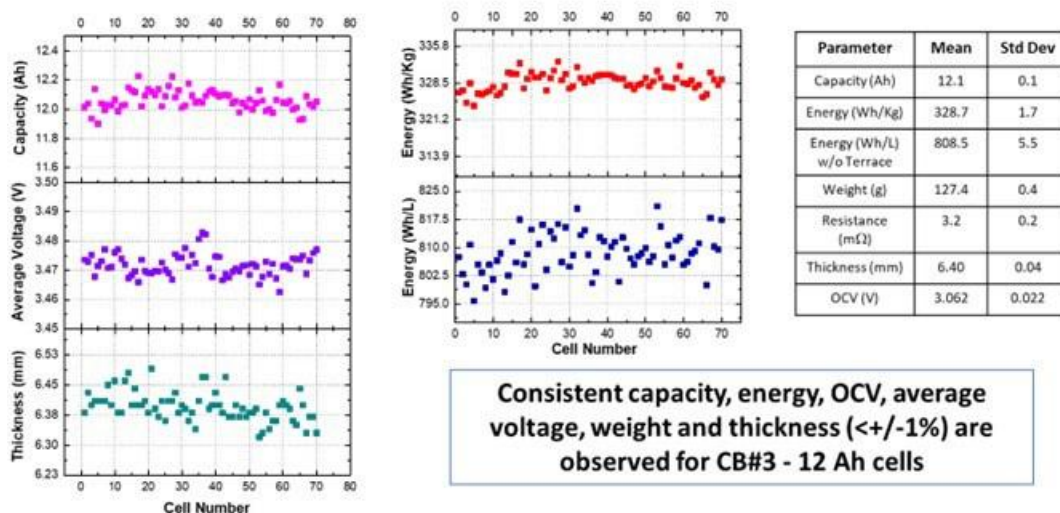


Figure I.10.7 Measurements on baseline cells after formation.

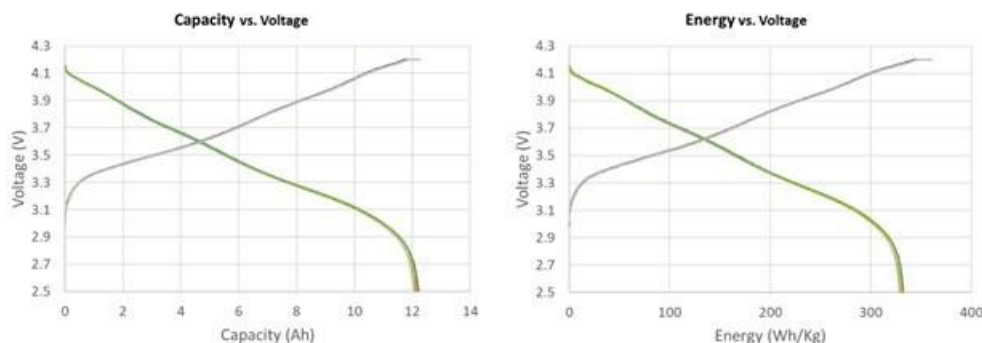


Figure I.10.8 Capacity and energy measurement versus voltage during charge and discharge for baseline pouch cells.

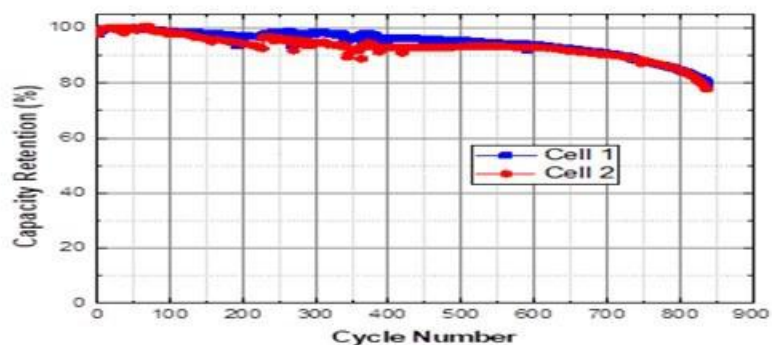


Figure I.10.9 Power and resistance measurement versus depth of discharge for baseline pouch cells.

Conclusions

During 2022, the testing of baseline pouch cells started at Ionblox and the National Labs. The measurements will continue in 2023. The measurements show that Ionblox baseline cells are meeting the majority of the USABC target cell requirements. The cell cost and calendar life will be key areas of focus for this program. The electrolyte design, cathode selection, surface passivation approaches to improve the calendar life and resistance growth has started, and the measurements are ongoing. More information on the impact of each of these approaches will become available in 2023.

Acknowledgements

This work is being performed under the guidance and support from the USABC technical work group: Lamuel David (Lamuel.David@stellantis.com) served as the USABC program manager. Oliver Gross, Meng Jiang, Brian Robert, Jack Deppe, Brian Cunningham, Lee Walker, Aron Saxon and Loraine Torres-Castro are the additional team members.

I.11 Low-cost, Fast-charging Silicon Nanowire Cell Technology (Amprius)

Ionel Stefan, Principal Investigator

Amprius, Inc.
1180 Page Ave.,
Fremont, CA 94538
E-mail: ionel@amprius.com

Brian Cunningham, DOE Technology Development Manager

U.S. Department of Energy
E-mail: Brian.Cunningham@ee.goe.gov

Start Date: March 1, 2022

End Date: August 31, 2024

Project Funding (FY22): \$608,984

DOE share: \$304,492

Non-DOE share: \$304,492

Project Introduction

Amprius' differentiating technology – an anode made of silicon nanowires – is potentially capable of meeting the USABC performance and commercialization criteria. Silicon offers significantly higher energy capacity than graphite but expands during lithiation. As a result, conventional approaches to silicon anodes have not enabled the long cycle life required for electric vehicle applications. Amprius grows pure silicon nanowires directly on the current collector, without binders or conductive additives. Nanowires do not rely on particle-to-particle contact and thus enable longer cycle life than particle-based approaches as well as higher rate and power.

In a previous USABC contract that ended in 2018, Amprius cells with silicon nanowire anode and NMC721 cathode met or exceeded most USABC 2020 goals for EV applications and has reduced the gap in Cycle and Calendar Life. Silicon anodes have much lower thickness than graphite anodes and a voltage that is at least 100 mV higher, which enables fast charging and prevents lithium plating. Amprius cells can charge to 80% SOC in 15 minutes. Test results were confirmed by tests at Idaho National Laboratory in both 3 Ah and 10 Ah cell form factors.

The main gaps remaining toward commercialization are the cost of production for the silicon nanowire anode, as well as cycle and calendar life performance. The silicon nanowire anode is a direct replacement for graphite anode, and the rest of the cell components and assembly process are largely similar or identical to those used in graphite cells. Due to the importance of scale-up and cost reduction direction for Amprius' business, activities related to scale-up have already started with Amprius funding and will not be sought here. However, a description of these activities and timely updates of the results and cost model will be proposed instead. Most of the work proposed here for funding will address the other two main remaining gaps, cycle and calendar life, with additional tasks on cell development for EV applications.

Amprius proposes a program with a 2.5 years duration, to develop and demonstrate EV cell technology that, at the minimum, meets all USABC goals for fast charge cells. Silicon composition and surface modifications, based on latest insights into material changes during cycling, coupled with electrolyte development, should close the performance gap in cycle and calendar life. Cell design activities for larger form factors will seek to preserve and enhance the intrinsic fast charge capabilities of smaller cells with size silicon nanowire anodes. At program's end, Amprius will deliver cells with energy densities greater than 1,000 Wh/L and specific energy of 400 Wh/kg, capable to reach at least 80% SOC during 15 minutes of fast charging.

Objectives

The objective of the two and a half-year program is to develop a material structure and composition for the silicon nanowire anode which, based on preliminary results, will significantly strengthen the material and, thereby, extend cycle life and calendar life. The material change relies on dopants introduced in the silicon structure during fabrication, which reduce silicon domain sizes and, thus, stress induced cracking. Coupled with electrolyte development, material changes should reduce and eliminate the performance gap in cycle and calendar life. A parallel effort will include a plasma deposition technology development that targets increases in silane utilization during anode fabrication, a key performance parameter for reducing the cost of the fabricated anode, to meet USABC targets. At the end of the program, Amprius expects to meet all end of life requirements in the EV Gap Chart, while exceeding the requirements by more than 20% at the beginning of life for most parameters (see Table I.11.1).

Table I.11.1 End of Program Cell Performance Objectives.

End of Life Characteristics at 30 °C	Units	Cell Level Goals	Amprius Targets for program at BOL, 30 °C
Peak Discharge Power Density, 30 s Pulse	W/L	1400	3000
Peak Specific Discharge Power, 30 s Pulse	W/kg	700	1200
Peak Specific Regen Power, 10 s Pulse	W/kg	300	400
Usable Energy Density	Wh/L	550	1000
Specific Usable Energy (defined at power target)	Wh/kg	275	400
Calendar Life	Years	10	>10
Cycle Life (25% FC)	Cycles	1000	>1000
Cost (@ 250k annual value)	\$/kWh	75	<75
Normal Recharge Time	Hours	< 7 Hours, J1772	<7
Fast Rate Charge	Minutes	80% U.E. Target in 15 min	>80% U.E. in 10 min
Minimum Operating Voltage	V	>0.55 Vmax	>0.55 Vmax
Unassisted Operating Temperature Range	Wh/kg	70% Specific Useable Energy at -20 °C	70% Specific Useable Energy at -20 °C
Survival Temperature Range, 24 h	°C	-40 to +66	-40 to +66
Maximum Self-discharge	%/month	<1	<0.5

Approach

Amprius' silicon nanowire anode cells already meet most of the criteria, as discussed in the previous section. The most significant performance gaps are in cycle life and calendar life, and cost is a major gap related to the scale-up of the technology toward large volume manufacturing. Calendar life was significantly improved in the previous USABC project by electrolyte development by improving SEI and CEI formation, and the work proposed here will continue and build upon that experience. The cycle life gap mitigation is the major focus of the project and preliminary experiments suggest that the material modification direction is the most constructive toward that goal.

The project tasks have objectives that target the USABC goals. In particular, the silicon material and electrolyte properties will be optimized toward the USABC goals. A short list of the main objectives is described below:

1. Find Si doping or alloying compositions that improve targeted metrics
2. Find material density and electrode loading levels that improve targeted metrics
3. Optimize electrolyte composition to improve targeted metrics
4. Optimize cell design and anode/electrolyte/cathode matching to improve targeted metrics
5. Deliver cells for external evaluation and verification of progress.

The main tasks cover four main work directions, with relatively independent task objectives, although targeting the same goals.

The first three tasks cover the bulk of the research and, although they mainly address the same barriers (cycle life and calendar life barriers), they do it by relatively independent approaches. The first task addresses the intrinsic problem of silicon surface cracking by modifications in silicon density and composition (doping and alloying), in the nanowire volume and at the surface. This task is scheduled to last 18 months, and will test at least three dopant elements (nitrogen, oxygen and carbon).

The second task addresses the same barriers by changes to the electrolyte composition development. This task is scheduled to last 24 months, developing electrolyte formulation for different anode compositions, as well as for different cathode types (Ni-content, coatings).

The third task includes the development of a larger form factor cell for EV applications and improves performance by optimization to cycling parameters (voltage, N/P ratio), which directly affect or interact with the anode material. Results from this task use optimized anode and electrolyte materials from Tasks 1 and 2 and give feedback to the respective development by evaluating the cells in USABC matrix of tests. This task is scheduled to last for 27 months, with three rounds of cell evaluation starting at 9 months intervals.

The last two tasks have testing, verification and reporting as objectives. Three sets of 30 cells are scheduled to be delivered, including the baseline cell (~3Ah, 4.5x50x56mm small form factor) at 6 months into the program, interim cell (~10Ah, 9x54x66mm) at 18 months, and the optimized cell (target 80Ah, 8x99x300mm) at the end of the project.

Results

Dopant type 1 reduced impedance increase during cycling, with small overall effect on cycle life

In FY2022, Amprius evaluated the first dopant element of the three proposed for evaluation during the project. The dopant was introduced in the silicon material during the silicon deposition process by mixing dopant gas with the silane precursor gas. Single and multi-layer cells were assembled with the anodes produced for evaluation of the electrochemical properties, and on cycle life in particular. Although a strong effect on stabilizing the impedance increase was observed, the increase in cycle life was relatively modest. A comparison of cycling data is shown in Figure I.11.1. The dopant level corresponds to increasing flow level of dopant gas, with 1 being the reference level (no dopant gas).

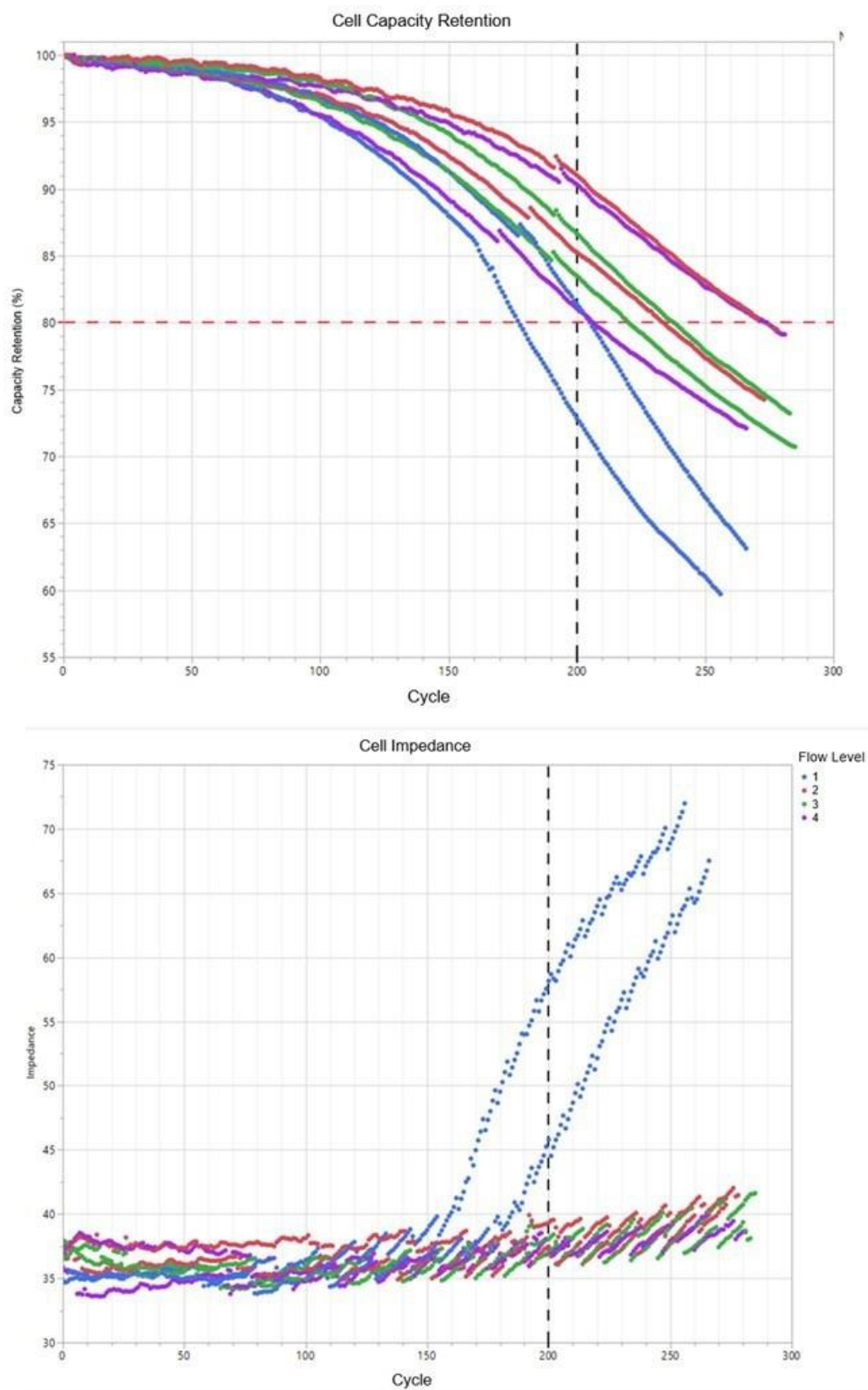


Figure I.11.1 Single layer Si/NMC811 cell cycling at 1C//1C rates from 2.75-4.25V

Tests are continuing with the other two proposed dopant materials in FY2023.

Amprius reduced the main gap in performance, cycle life, by identifying electrolyte additives that improve Solid Electrolyte Interphase (SEI) stability.

The electrolyte solution formulation was optimized with new solvents, additives and salts, as well as with new formulation strategies, such as super-concentrated electrolytes, localized high concentration electrolytes, and gel electrolyte forming additives. The formulation development used materials compatible with pure silicon anodes that were available at the start of the project.

Both new solvents and additive sets have resulted in improved calendar life, the most consequential result expected from electrolyte development. For example, in Figure I.11.2., the new electrolyte formulation 1179 results in no power degradation after 2 months of storage at 45°C. Power degradation is usually the most deleterious effect observed at high temperature and the first few month results are very promising. Tests are continuing in FY2023.

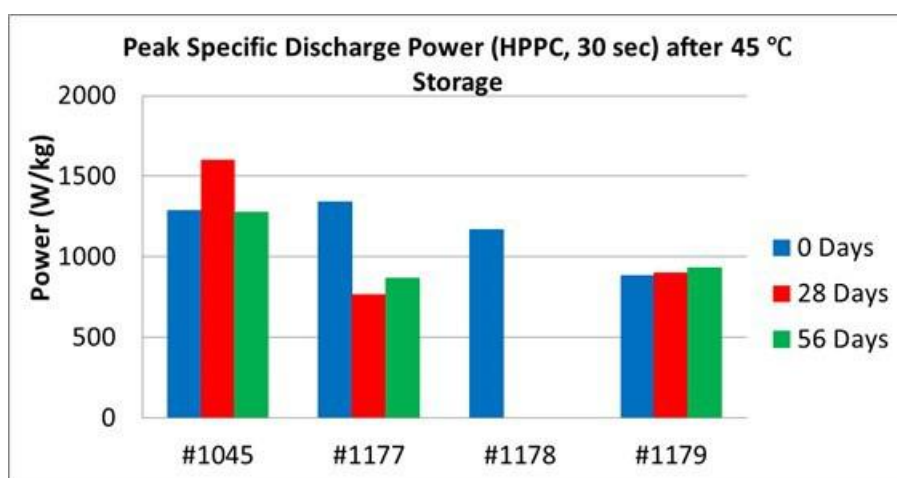


Figure I.11.2 Peak specific discharge power in 3.7Ah Si/NMC811 cells with improved electrolyte formulations. Formulation #1045 is the baseline formulation at the start of the program.

Amprius performed the baseline evaluation of the silicon nanowire technology at the start of the program

Preliminary round of testing on baseline battery cells shows promising results. The cells meet the targets for capacity, available energy, power, and thermal performance.

Below are the cell and test parameters used during the preliminary round of testing:

- Target cell's capacity at beginning of life = 3.7 Ah
- Target cell's energy at beginning of life = 13.0 Wh
- Available energy at end of life = 10.4 Wh
- $V_{\max,100} = V_{\max,op} = 4.25$ V
- $V_{\min,0} = 2.50$ V
- $V_{\min,op} = 3.2$ V
- $V_{\min,pulse} = 2.25$ V
- $V_{\max,pulse} = 4.35$ V
- $I_{MAX} = 2C$.

The baseline test results are summarized in Table I.11.2. The DST cycle life and calendar life tests are continuing in FY2023.

Table I.11.2 Baseline cell technology gap analysis table

End of Life Characteristics at 30°C	Units	Cell Level Goals	Baseline Q3
Peak Discharge Power Density, 30 s Pulse	W/L	1400	>2800
Peak Specific Discharge Power, 30 s Pulse	W/kg	700	>1300
Peak Specific Regen Power, 10 s Pulse	W/kg	300	>810
Usable Energy Density	Wh/L	550	>900
Specific Usable Energy (defined at power target)	Wh/kg	275	>400
Calendar Life	Years	10	TBD
Cycle Life (25% FC)	Cycles	1000	>200
Cost (@ 250k annual value)	\$/kWh	75	TBD
Normal Recharge Time	Hours	< 7 Hours, J1772	<7
Fast Rate Charge	Minutes	80% U.E. Target in 15mins	~90%
Minimum Operating Voltage	V	>0.55 Vmax	0.59 Vmax
Unassisted Operating Temperature Range	Wh/kg	70% Specific Useable Energy at -20°C	82% Specific Useable Energy at -20°C
Survival Temperature Range, 24 Hr	°C	-40 to +66	-40 to +66
Maximum Self-discharge	%/month	<1	<0.5

The Si/NMC811 baseline cells exceed power and energy goals by more than 50%, as expected based on the performance at the start of the program. The rest of the performance metrics, measured for the first time for this chemistry, also indicated very good performance. Highlights of the baseline performance evaluation include a fast charge of 90% of usable energy in 15 minutes, a loss of less than 20% of usable energy at -20°C, and a self-discharge rate of <0.5% per month. As shown in Figure I.11.3, the baseline cells met the 30°C peak discharge power target of 700 W/kg even at -10°C.

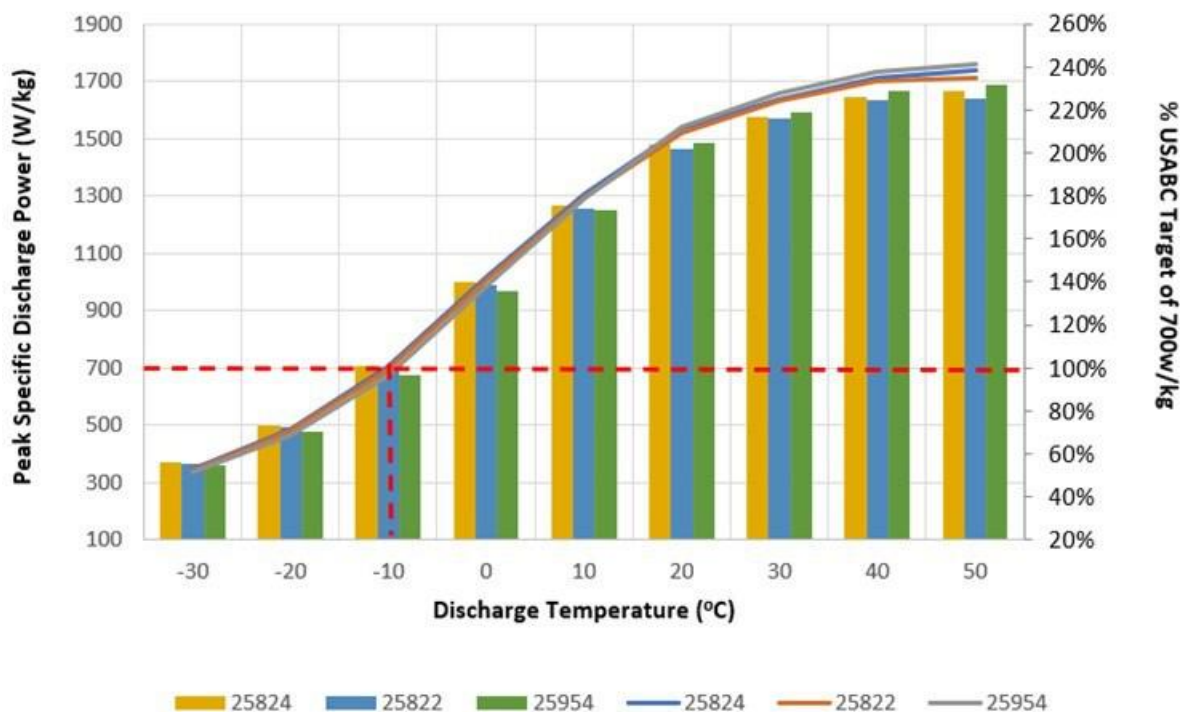


Figure I.11.3 Peak specific discharge power at different discharge temperatures for baseline cell chemistry

Amprius performed cell parameter optimization using design-of-experiment methodology

For performance optimization, a design-of-experiment which included 5 input factors with 3 levels each resulted in a reduction of tests from 120 combinations to 18 combinations, using 5 replicates for each. The five factors optimized simultaneously included anode loading, cathode loading, upper cutoff voltage, lower cutoff voltage, and anode prelithiation capacity. The primary response variable metric was the number of cycles to 80% retained capacity.

The resulting model was used to create profiler charts, one of which is presented below in Figure I.11.4. Such a factor response profile can be used to evaluate the impact of changing the value of any of the input factors. The analysis of the main factor analysis indicate that cutoff voltages have the largest effect on cycle life, with the lower cutoff voltage having the highest impact. These findings are applied to future test protocols. Further optimization using the same methodology will address a wider window of factor levels.

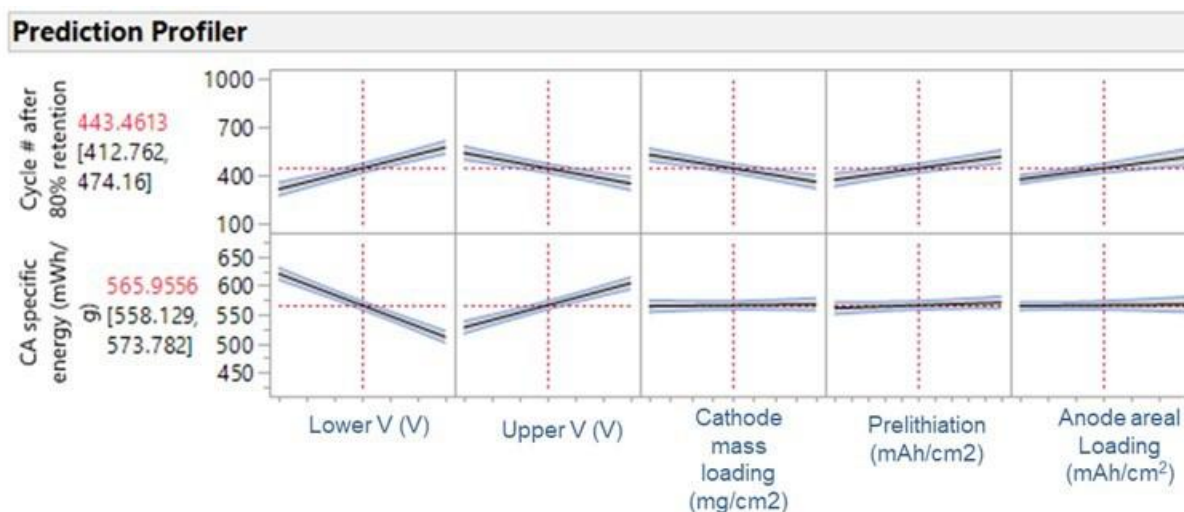


Figure I.11.4 Model predictors for cell capacity retention generated from the data from the DOE cells at end of life.

Conclusions

During the project's first year, Amprius started the task work to reduce the gaps in cycle life and calendar life. These tasks included silicon nanowire anode material structure, loading, and composition optimization, electrolyte development, and cell parameters optimization. Silicon doping showed relatively small effects with the first dopant element, but anode structure and loading, as well as cycling parameters increased cycle life more than 500 cycles in single layer cells.

The baseline cell chemistry (Si/NMC811) was evaluated using USABC test protocols in the first year. The 3.7Ah cells exceed energy and power goal targets by at least 50%, and the chemistry showed very good low temperature performance, power density and storage loss. Calendar and cycle life tests are continuing in FY2023. During FY2022, Amprius built and delivered 21 baseline cells with a capacity of 3.7Ah to Idaho National Laboratory for baseline performance evaluation.

During FY2023, Amprius will continue to increase cycle life and calendar by optimizing anode structure and exploring advanced components, extend cell cycle life by tuning anode structure and testing new electrolyte formulations, and finish the design and assembly of the interim cells with capacities ≥ 10 Ah.

II Processing Science & Engineering

The processing science & engineering activity supports the development and scale-up of manufacturing technologies needed to enable market entry of next-generation battery materials and cell components that could significantly reduce cost and environmental impact while increasing yield and process control relative to existing production technologies. The research portfolio spans material discovery, scale-scale up, slurry formulation, electrode engineering, and cell prototyping.

Material discovery scale-up address several related barriers to manufacturing cost and material performance for novel battery materials. These seek to develop new advanced manufacturing processes that reduce cost and provide advanced new materials for evaluation. The industry-relevant continuous processes are developed for scalable production of cathode materials, precursors and electrolytes, such as continuous flow, co-precipitation, supercritical fluid synthesis and flame spray pyrolysis. In situ experimentation and multiscale modeling are applied to designing new processes for improving battery performance and reducing processing cost.

Slurry formulation

LBNL investigated the effect of the ratio between carbon black and binder on slurry properties (i.e., viscosity) and electrode properties (i.e., adhesion and cohesion strength). There appears to be an ideal solvent content with regard to mixing and casting that correlates linearly with the surface area of carbon additives. LBNL also built and tested early iterations of a miniature automated coating/drying line, which can observe electrode coating production process.

Material screening and prototyping

ANL screened two electrolytes, free-standing polymer electrolyte and sulfide based (Li₆PS₅Cl) electrolyte, for all solid-state batteries. Promising results have been demonstrated. Particularly, the sulfide based all-solid-state batteries with NMC811 and silicon electrodes demonstrated 70% capacity retention after 1000 cycles. Additionally, ANL installed a multifunctional coater which provides many new capabilities to the CAMP Facility including interchangeable coating heads, corona treatment and an IR drying zone. Volume evolution during lithium plating and stripping was also evaluated using operando energy dispersive X-ray diffraction (EDXRD).

Electrode engineering and prototyping

ORNL has developed a two-layer electrode architecture with a denser energy layer at bottom and a more porous power layer on top, which showed improved capacity with high areal capacity (6 mAh/cm²) compared to the conventional structure and can be applied for fast charging application. In addition, Li⁺ dynamics in hybrid polymer electrolytes based on PEO electrolyte, Al-LLZO filler and LiTFSI or LiFSI salt were evaluated via experiment and simulation. ORNL also continues developing an electron beam curing process for electrode manufacturing, which could enable solventless processing high throughput (i.e., >300 m/min line speed) and significant processing energy saving. A new green radiation curable resin from domestic supplier was evaluated and is compatible with both NMC and graphite and graphite/silicon materials. This technology was licensed to Ateios Systems and won an R&D 100 Award and a 2022 FLC Technology Transfer Award in 2022.

The rest of this chapter contains detailed reports on the status of the following individual projects.

- Processing Next Generation Li-ion Battery Cathode Materials (ANL)
- Novel Processing Approaches for LLZO (ANL)
- Supercritical Fluid Processing of Battery Cathode Materials (ANL)
- Process R&D and Scale-up of Critical Battery Materials (ANL)
- Structure-Activity Relationships in the Optimizing Electrode Processing Streams for LiBs (LBNL)
- Fabricate and Test Solid-state Ceramic Electrolytes and Electrolyte/Cathode Laminates (LBNL)

- Higher Energy Density via Inactive Components and Processing Conditions (LBNL)
- Minimizing Side Reactions in Next-Generation Lithium-Ion Battery Cathodes Through Structure-Morphology Optimization (ANL)
- In Situ Spectroscopies of Processing Next-Generation Cathode Materials (ANL, BNL)
- Towards Solventless Processing of Thick Electron-Beam (EB) Cured LIB Cathodes (ORNL)
- Performance Effects of Electrode Processing for High-Energy Lithium-Ion Batteries (ORNL).

II.1 Processing Next Generation Li-ion Battery Cathode Materials (ANL)

Ozge Kahvecioglu, Principal Investigator

Argonne National Laboratory
9700 South Cass Avenue
Lemont, IL 60439
E-mail: okahvecioglu@anl.gov

Haiyan Croft, DOE Technology Development Manager

U.S. Department of Energy
E-mail: haiyan.croft@ee.doe.gov

Start Date: October 1, 2021

End Date: September 30, 2022

Project Funding: \$800,000

DOE share: \$800,000

Non-DOE share: \$0

Project Introduction

The multifaceted objective of the program is to provide the research community with materials that they design and want to investigate and therefore ascertain the key missing link between discovery of advanced active battery materials, evaluation of these materials, and ultimately high-volume manufacturing of the selected targets to reduce the risk associated with their commercialization. We perform systematic process and material engineering research to develop cost-effective customized synthesis and to produce sufficient quantities of high-quality target materials by optimizing process parameters tailored to specific material compositions, evaluating material purity profiles, and applying emerging manufacturing technologies to address challenges associated with manufacturing of advanced materials. The technical targets of this program are the development of customized synthesis processes for each material selected, scaling up to multi-kilogram quantities with reproducibility under rigorous quality control, and evaluation of emerging manufacturing technologies to assist fundamental research and to reduce the commercialization risk of newly invented active battery materials.

Objectives

The multifaceted objective of the program is to provide the research community with materials that they design and want to investigate and therefore ascertain the key missing link between discovery of advanced active battery materials, evaluation of these materials, and ultimately high-volume manufacturing of the selected targets to reduce the risk associated with their commercialization. We perform systematic process and material engineering research to develop cost-effective customized synthesis and to produce sufficient quantities of high-quality target materials by optimizing process parameters tailored to specific material compositions, evaluating material purity profiles, and applying emerging manufacturing technologies to address challenges associated with manufacturing of advanced materials. The technical targets of this program are the development of customized synthesis processes for each material selected, scaling up to multi-kilogram quantities with reproducibility under rigorous quality control, and evaluation of emerging manufacturing technologies to assist fundamental research and to reduce the commercialization risk of newly invented active battery materials.

Approach

Over the past four years, the advantages of utilizing an emerging synthesis technology, the Taylor Vortex Reactor (TVR), for the production of cathode precursors for lithium-ion batteries, were demonstrated. This innovative reactor has a cylindrical rotor and tremendous Taylor vortices in the annulus. It produces homogenous micro-mixing with high mass and heat transfer, enabling a high degree of uniform supersaturation thus eliminating local concentration and temperature gradient. This results in faster kinetics and denser particles with minimal optimization. The TVR continuously produces spherical precursor particles with

a narrow particle size distribution, which is critical to achieve high-quality battery materials, and is now the preferred platform for rapid production of new chemistries that are not commercially available. Within the scope of the project, the calcination scale-up challenges were studied through the comparison of commercial box furnaces (up to ~70 g/batch) and benchtop tube furnaces (5-25g/batch). Differences in both heating system were identified; such as, heating homogeneity and temperature gradient, gas flow pattern, partial pressure, surface-to-volume changes as the load goes up, and etc. These findings led to new designs/prototypes for efficient gas flow inside the commercial box furnaces, which resulted in similar calcination efficiency with benchtop tube furnaces. The project team continued supporting the researchers across the Nation by providing a wide-range of different commercially non-available chemistries, morphologies and/or particle sizes.

Results

Low/No Cobalt Nickel-based Cathode Materials

The project team continued studying on fundamental understanding of calcination challenges for the LNO-based materials. Previous studies showed that lithium kinetics are strongly dependent on the hydroxide precursor's physical properties (e.g.; porosity, particle size & distribution, density, morphology) for the same composition within. One of MERF's responsibilities is to consistently provide high quality, hydroxide precursors with a wide range of chemistries while keeping all physical properties similar as the composition changes. This would allow the basic R&D scientists to compare the materials solely based on ranging Ni, Mn, and Co ratios. For fair comparison of the calcined oxide cathode materials, each Ni-rich hydroxide chemistry was synthesized at larger quantities (up to 2.0 kg) to eliminate the batch-to-batch variability. These materials were then calcined using the same calcination conditions using two different heating system: to compare both small scale vs large scale calcinations, as well as scalable box furnaces vs lab-type tube furnaces.

Comparison of calcination furnaces and scales: Ni-based cathode materials

Ni-based compositions are sensitive to synthesis and powder-handling conditions, so large quantities of high quality materials are critical for apple-to-apple comparison. The project team studied the optimization of $\text{Ni}_{0.95}\text{Mn}_{0.05}(\text{OH})_2$ material that was previously introduced into the low/no cobalt Deep-Dive program in FY21. In FY22, the team designed two prototypes for efficient O_2 gas flow inside the scalable commercial box furnaces to enable larger calcination quantities (up to 120g) without compromising the performance quality that was achieved at <10g scale calcinations in benchtop tube furnaces. The calcination parameters were applied at the same conditions, except the scale, for both furnace types where the optimal calcination temperature applied was 740°C under pure oxygen gas flow. Figure I.11.4 displays comparable performances for the cathode materials synthesized using different furnace types, even when the scale is larger for commercial box furnaces. All cathode electrodes showed similar capacity-increasing trend during the first 3-formation cycles, where the cathodes obtained from tube furnace application showed > 5mAh/g capacity or more on the formation cycles. This was immediately tapered out to the same levels or lower compared to commercial furnace product for the following cycles. The small scale tube furnace calcination product achieved 85.8% capacity retention over 50 cycles compared to 87.0% for large scale commercial box furnace calcination product.

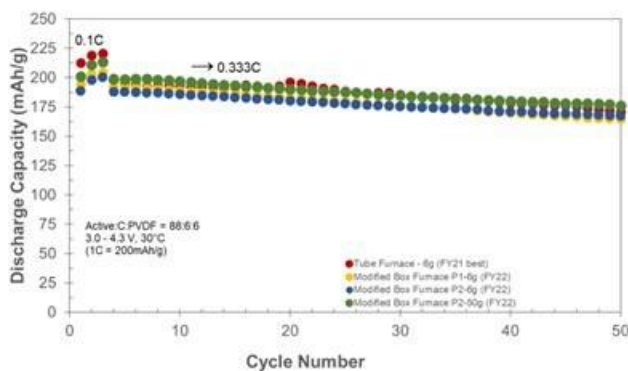


Figure II.1.1 Cycle life comparison of $\text{LiNi}_{0.95}\text{Mn}_{0.05}\text{O}_2$ obtained at different furnace applications. (Red spheres represent the tube furnace application. P1 and P2 stand for Prototype -1 and Prototype -2)

With the insights gained through the applications of different calcination furnace types, the project team further studied the calcination scale up of LNO material in modified commercial box furnaces using two prototypes (P1 and P2). Initially, the electrochemical performances of cathodes synthesized in a standard unmodified box furnace was compared to the modified versions of the same furnace at the same calcination scale (see Figure II.1.2). Later in the study, a new and improved prototype design was developed and tested, showing a higher capacity retention (89% over 100 cycles) when the interior gas flow pattern was improved in the box furnaces. These modifications were also tested at ~65 g scale calcinations in different batches for reproducibility check, where the cathode electrodes achieved more than 85% capacity retention over 100 cycles as displayed in Figure II.1.2 (left). Also, each cathode material from different batches showed ≥ 240 mAh/g discharge capacity in the first 3 formation cycles. The capacity values for larger scale were slightly higher than that of smaller scale calcinations which was mainly due to increased O_2 gas flow. The box furnace with prototype-2 modification (multi direction gas flow attachment) allowed better controlled O_2 gas distribution thus enabling greater surface area coverage of each batch during calcination which is critical for the lithiation of the Ni-rich cathodes.

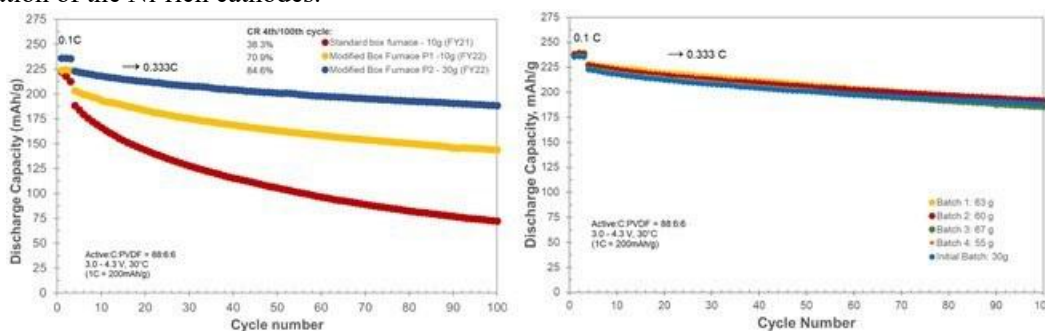


Figure II.1.2 Cycle life comparison of LiNiO_2 cathode electrode: obtained from standard and modified calcination box furnaces at small scales (left) and reproducibility check using modified prototype- 2 at slightly larger scale (right) (Fixed calcination parameters: calcination temperature = 650°C ; Dwell time = 12 h; under 100% O_2 gas flow)

No Cobalt Low Nickel, Manganese-based Cathode Materials

Majority of our activities were concentrated around the new cobalt free and manganese rich composition. We apply a carbonate based co-precipitation route to synthesize $\text{Mn}_{0.65}\text{Ni}_{0.35}\text{CO}_3$, via continuous operation using Taylor Vortex Reactors. We adopted a small batch type synthesis route from our collaborators and converted it to a continuous co-precipitation route using TVRs. Figure II.1.3 (a-c) shows general morphologies obtained from the preliminary studies of co-precipitated, pretreated and calcined products, where the particle size distribution is bi-modal leading the larger particle to crack during pretreatment and calcination processes. Regardless of the calcination process conditions, the tap densities were increased while the surface area decreased. However, the particles went through severe cracking which was more obvious when the lithium to transition mol ratio also increased. This was initially attributed to the unstable particle construction in the co-

precipitation process which may have led to cracking in calcination process. Extensive co-precipitation studies were done, including lowering reactant molarities, decreasing residence time (τ), temperature (T), TM/ NH_3 mol ratios, varying co-precipitating agents (Na_2CO_3 , Li_2CO_3), varying pH, different pH probe-types, P&ID control vs manual operations, and etc. These operations all showed that continuous carbonate co-precipitation process had inherent process flaws where the steady-state conditions are diminished after some certain time passes ($2 \times$ and $4 \times$ residence times, τ , for slow and fast reactions, respectively). Further optimization studies will be done with an engineering control by applying equivalent flow rates for both transition metal solution and sodium carbonate solution and bypassing P&ID control to eliminate false feedback occurring between the pH controller and pH pump during the continuous operation. We also started the continuous hydroxide co-precipitation process for this material to compare the efficiency of both synthetic route.

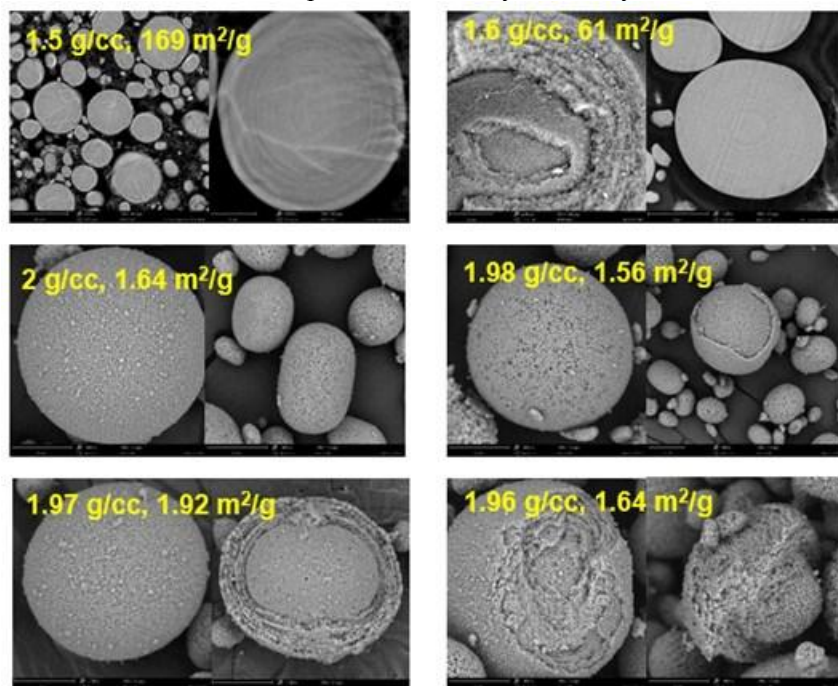


Figure II.1.3 (Top row) Cross section SEMs of Co-free Mn-based cathode carbonate precursor particles showing a dense interior (left); bulk and cross-sectional morphologies of pretreated carbonate precursor (right) showing an onion peel-like structure. (Middle row) Morphologies of cathode active materials that are calcined directly at 900°C with varying Li/TM mol ratios (1.30 and 1.34 from left to right) showing rough surfaces with ranging levels of particle cracking particularly for the larger particles. (Bottom row) Morphologies of cathode active materials that are calcined at 900°C with prior 600°C hold with varying Li/TM mol ratios (1.30 and 1.34 from left to right) showing severe cracking.

Fast Reaction: Reducing Residence Time (τ) in Continuous Co-precipitation

Over the past year, during the carbonate co-precipitation optimization studies, we also investigated the particle formation in a continuous operation via reducing residence time using a 10L TVR. Figure II.1.4 shows the morphologies of the particles sampled from the initial hours towards the end of the reaction. This particular experiment was done using a 10L TVR applying a very short residence time (1 hour) when considering the scale of the reactor. To compare, the typical residence time for CSTRs at 4L scale ranges from 8-12 h. Also note that, as a common practice; in continuous operations, the steady state conditions are typically achieved after $4\text{--}6 \times$ the residence time. Also as mentioned above, the carbonate route intrinsically had process flaws which the steady state conditions were disturbed after $4 \times$ the residence time for fast reaction as in this case, which could be easily seen via the particle shape/size differences. Initially, the particles formed nodular structures as early as within the 30th minute of the operation (the SEM image is not shown) which then became more spherical after the 4th residence time. This observation encouraged the team that fast reactions can be applicable with the TVRs even if the scale is relatively larger than that of CSTRs. Advantages of using a large

scale TVR with substantially reduced residence time resulted in a production rate of 200g/h starting from the 4th hour of the continuous operation. Yet, due to the pH fluctuation after 4th hour (also the 4th residence time), this process required a detailed optimization studies for a successful operation. Electrochemical performance comparisons were made for these non-optimal materials produced at fast ($\tau = 1$ h) and slow ($\tau = 4$ h) co-precipitation reactions followed by high temperature calcination, displayed promising feature for fast reaction product (Figure II.1.4, bottom row). However, these materials weren't optimized and therefore until an optimal/target particle specification is achieved, the true performance of these materials are subject to change.

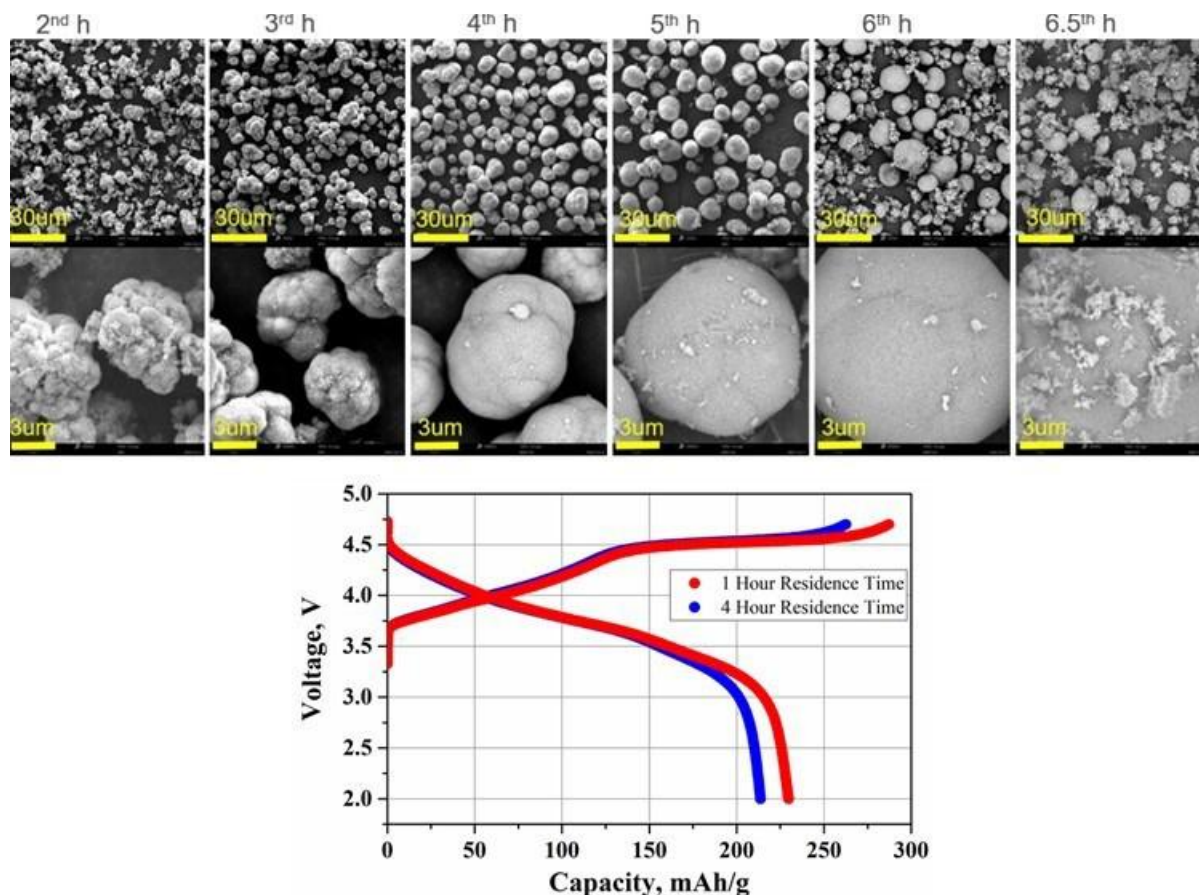


Figure II.1.4 SEM images of particle morphologies formed in a continuous operation using 10L TVR (top two rows). Voltage profile (bottom row) comparison of materials obtained through fast and slow co-precipitation reaction (coin half cell: First formation cycle at C/20 (1C = 175 mA/g) between 2.0 V – 4.7 V at 30 °C)

Preliminary Hydroxide Co-precipitation Synthesis for $\text{Mn}_{0.65}\text{Ni}_{0.35}(\text{OH})_2$

Achieving and preserving steady state condition in a continuous co-precipitation operation is a complex process, involving strict engineering controls to eliminate overseen events to ensure the process operates properly and continuously [1]. The project team developed an expertise on successfully synthesizing high quality NMC-based hydroxide precursors in continuous mode over the past 7 years using the TVRs. Adopting this knowledge and translating it for the synthesis of Mn-based hydroxide precursors is the logical route for the quick observation of particle formation; yet it is a non-trivial task. Initial hydroxide co-precipitation route was applied for this composition in a high pH environment (pH = 11.6) using the similar continuous co-precipitation conditions for Ni-based hydroxides (e.g.; mol ratio of TM: $\text{NH}_3 = 1$; pH control with P&ID; T = $50 \pm 0.2^\circ\text{C}$; 800rpm), except with reduced residence time ($\tau = 1$ h). Application of higher pH condition resulted dispersed particle formation showing $\sim 1\mu\text{m}$ size platelets with $\sim 100\text{nm}$ wall thicknesses, as seen in Figure II.1.5. The particles remained consistent in size and morphology throughout the whole operation. Based on the preliminary synthesis results, optimization studies will be done screening lower pH conditions along with

varying mol ratios of both TM:NH₃ and NaOH:NH₃ in the continuous operation. This particular synthesis produced ~240 g/h of consistent product till the end of the reaction. The preliminary product was calcined into final cathode oxide material and the first cycle profiles of both fast carbonate vs hydroxide synthesis reaction product were compared. The materials from both synthesis routes weren't optimized. However, the product calcined from hydroxide co-precipitation route delivered ≥ 250 mAh/g first discharge capacity (see Figure II.1.5, bottom row), which was comparable to an optimal benchtop carbonate-based product (not shown here).

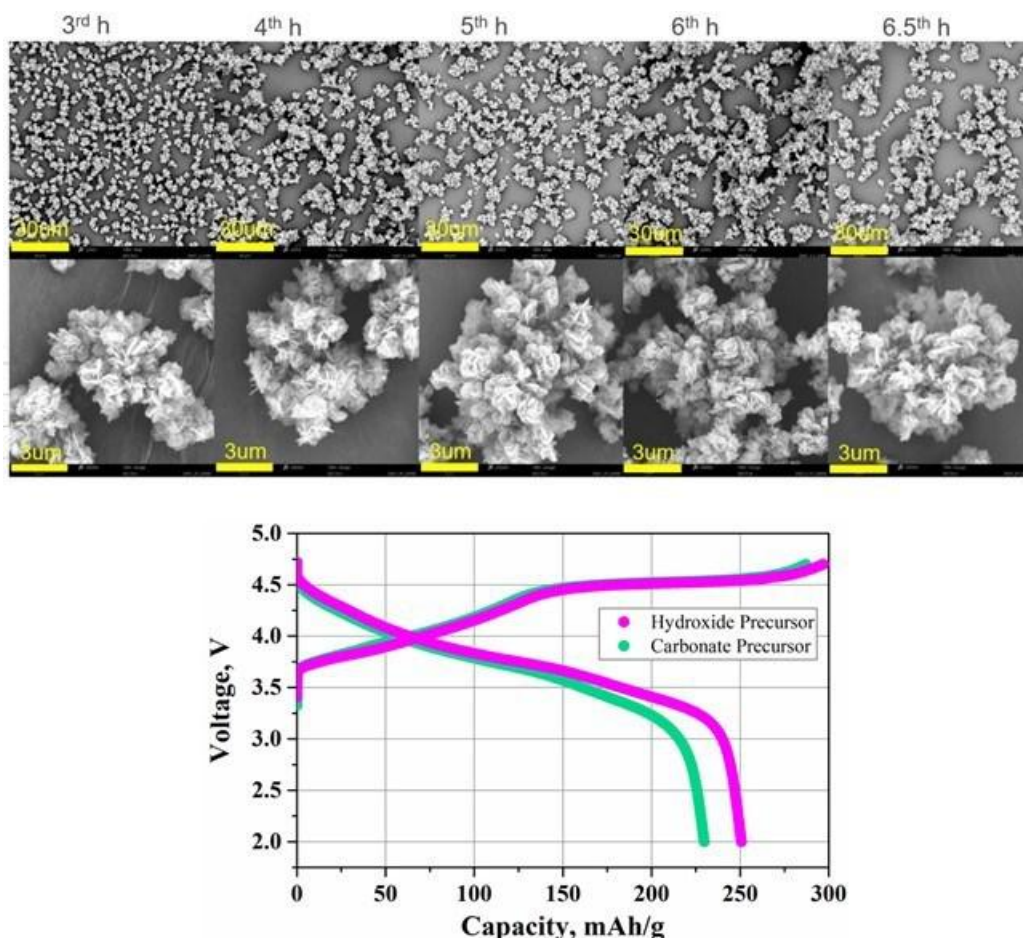


Figure II.1.5 Particle formation under high pH conditions in a fast-continuous operation displays flaky, platelets with $\leq 1\mu\text{m}$ platelet size having $\sim 100\text{nm}$ wall thickness (top rows). Voltage profile (bottom row) comparison of materials obtained through fast carbonate vs fast hydroxide co-precipitation reaction (coin half cell: First formation cycle at C/20 ($1C = 175\text{ mA/g}$) between 2.0 V – 4.7 V at 30°C)

Materials in Support of Battery R&D Community

In FY22, we continued supporting researchers at the Northwestern University by providing Ni-rich chemistries for the research of enabling ambient storage of LNO materials via carbon-based coatings. Over the past year, MERF also provided $\text{LiNi}_{0.6}\text{Co}_{0.2}\text{Mn}_{0.2}\text{O}_2$ batches with a larger D50 and more controlled particle distribution for AMO project DE-EE00009112. This project is developing an acoustic additive manufacturing process for fabricating thick, fine feature 3D Lithium-ion battery electrodes. Preliminary testing with MERF NMC-622 shows promise for improving the quality of 3D electrodes fabricated relative to commercially available NMC. MERF have continued collaborating with Brookhaven National Laboratory (BNL) under the Process Science and Engineering Program focusing on “synthesis by design” (BAT183). In the past year, MERF has provided new materials as needed, such as Ni-based hydroxides (Ni = 90% or more) with the collaborators at BNL for the structural and morphological evolution studies during the sintering process for both chemistries. Last year, MERF also initiated a collaboration with Prof. Feng Lin in Virginia Tech and provided 13 different cathode

precursors at a total of 1.1 kg scale (Low/No cobalt, Ni-rich hydroxide; Cobalt free manganese based carbonates and etc.). This work will use MERF-made precursors to synthesize layered cathodes with different grain sizes and orientations in secondary particles, which will then become platform materials to investigate how the charge propagations are regulated by grain properties under operating conditions. MERF also provided Ni(OH)₂ materials for the ReCell program participants for upcycling the spent battery cathode materials. This work required more than 400 g material which was made available to the collaborators.

Conclusions

MERF's experimental active cathode materials process R&D and scale-up program assists the battery research community, allows for a comprehensive evaluation of new materials by industrial laboratories, and supports basic research. In fiscal year 2022 the program provided several new and/or reproduced, not commercially available materials. Samples of uniform, high-quality materials were distributed for further evaluation and research. Different cathode active material compositions have been synthesized using 1L TVR, and some of the material with higher quantity demand were scaled up in 10L TVR. Scalability of TVR technology was also studied for faster reaction with substantially reduced residence time. All the materials produced at MERF were shared with the collaborators either in the form of precursor or active cathode material, ranging from 100 to 1,000 g per sample.

Key Publications

1. Gregory Krundick, Kris Pupek, Ozgenur Kahvecioglu, Trevor Dzwiniel, Youngho Shin, and Joseph Libera, "Accelerating Complex Battery Materials to Market: Leveraging Science to De-risk Technology Scale-up and Accelerate Commercialization." Poster Presentation presented at the 13th International Conference on Advanced Lithium Batteries for Automobile Applications, Ben Guerir, Morocco, October 17, 2022.
2. Feng Wang, Pallab Barai, Ozge Kahvecioglu, Krzysztof Z. Pupek, Jianming Bai, and Venkat Srinivasan, "Process Design for Calcination of Nickel-Based Cathode Materials by In Situ Characterization and Multiscale Modelling", *Journal of Materials Research* 37, (2022): 3197-3215.
3. Mark Wolfman, Xiaoping Wang, Juan C. Garcia, Pallab Barai, Joanne E. Stubbs, Peter J. Eng, Ozge Kahvecioglu, Tiffany L. Kinnibrugh, Kenneth E. Madsen, Hakim Iddir, Venkat Srinivasan, and Tim T. Fister, "The Importance of Surface Oxygen for Lithiation and Morphology Evolution during Calcination of High-Nickel NMC Cathodes", *Advanced Energy Materials* 12, Issue 16 (2022): 2102951.
4. Daniel P. Abraham, Marco-Tulio F. Rodrigues, Jihyeon Gim, Adam Tornheim, Ozgenur Kahvecioglu, Mei Luo, Andressa Y. R. Prado, Stephen E. Trask, and Jason Croy, "Concealed Cathode Degradation in Lithium-Ion Cells with a Ni-Rich Oxide", *Journal of The Electrochemical Society* 169, no. 4 (2022): 040539.
5. Kyu-Young Park, Yizhou Zhu, Carlos, Carlos G. Torres-Castanedo, Hee Joon Jung, Norman S. Luu, Ozge Kahvecioglu, Yisuel Yoo, Jung-Woo T. Seo, Julia R. Downing, Hee-Dae Lim, Michael Bedzyk, Chris Wolverton, and Mark C. Hersam, "Elucidating and Mitigating High-Voltage Degradation Cascades in Cobalt-Free LiNiO₂ Lithium-Ion Battery Cathodes", *Advanced Materials* 34, Issue 3 (2022): 2106402.
6. Ozge Kahvecioglu, Carrie Siu*, "Current and Future Trends in Materials for Advanced Lithium Batteries" Invited Talk presented at the 48th International Conference on Metallurgical Coatings and Thin Films, San Diego, CA, May 25, 2022 (*presenter).

References

1. Feng Wang, Pallab Barai, Ozge Kahvecioglu, Krzysztof Z. Pupek, Jianming Bai, and Venkat Srinivasan, "Process Design for Calcination of Nickel-Based Cathode Materials by In Situ Characterization and Multiscale Modelling", *Journal of Materials Research* 37, (2022): 3197-3215.

Acknowledgements

Dr. Carrie Siu, Dr. Mateusz Zuba, Francis Kim, Gerald Jeka, Andrew Turczynski, and Dr. Kris Pupek are greatly acknowledged for their assistance in the synthesis and characterization studies. Participants of Low/No Cobalt Deep-Dive program and all our collaborators funded by VTO and AMO that are using MERF-made materials are acknowledged for their continuous feedback on the TVR-made materials.

II.2 Novel Processing Approaches for LLZO (ANL)

Joseph Libera, Principal Investigator

Argonne National Laboratory
9700 South Cass Avenue
Lemont, IL 60439
E-mail: jlibera@anl.gov

Haiyan Croft, DOE Technology Development Manager

U.S. Department of Energy
E-mail: haiyan.croft@ee.doe.gov

Start Date: October 1, 2021
Project Funding: \$400,000

End Date: September 30, 2022
DOE share: \$400,000

Non-DOE share: \$0

Project Introduction

Aerosol manufacturing technology holds the potential of commodity scale production of energy storage materials in powder form. Reduced liquid chemical waste and suitability for continuous operation are advantages of aerosol processing has competing liquid based synthesis. Aerosol synthesis of powders falls broadly into several categories: (a) spray drying, (b) spray pyrolysis, (c) flame spray pyrolysis and (d) gas combustion synthesis where (a)-(c) are droplet based and (d) is gas phase entirely. At the Argonne's MERF aerosol synthesis facility modalities (a)-(c) are pursued for materials research into energy storage materials.

Flame spray pyrolysis (FSP) is a materials synthesis technique that uses solutions of organic and/or inorganic metal salts in flammable liquids. In the gas-to-particle mode (FSP-GP), the liquid solution is atomized using oxygen and combusted to atomic species from which particles condense and are collected in the exhaust filters. If the available combustion enthalpy is insufficient, particle formation follows the droplet-to-particle modality (FSP-DP) and the produced solids retain some history of the spray droplets.

Spray pyrolysis (SP) starts as in FSP by producing liquid droplets of metal salt solutions but not using combustible solvents. Droplet solvent is removed by evaporation in a tube furnace followed by solid-state reaction of the dried particle to produce the desired solid materials. Optional addition of enthalpic components such as ethylene glycol or organic acids allows for exothermic support of the solid-state reactions.

In Spray Drying (SD) the drying of the droplets and subsequent solid-state reactions that characterize Spray Pyrolysis are decoupled and only the dried particles are collected to be separately solid state reacted in calcination furnaces. This technique allows for the exclusion of the spray solvent and/or combustion gases in the calcination steep and enable controlled atmosphere calcination such as inert gas or pure oxygen.

At Argonne's MERF facility, we use these three modalities synergistically to produce the same target material and thus gain greater understanding of the material apart from the process. In, general FSP-GP produces nano-sized powder, while FSP-DP produces micron-sized agglomerates of nano-sized primary particles. SP produces micron sized secondary particles consisting of sub-micron primary particles. SD produces micron particles of the constituent metal salts which following a separate calcination retain their particle characteristics. For the FSP and SP techniques, we seek to optimize the process to produce ready to use particles in the proper phase purity. However, the gaseous environment in the processing reactors requiring separate calcination and or powder refinement can thermodynamically prohibit this. In the industrial setting even these additional steps are amenable to continuous processing following continuous aerosol powder production.

Objectives

Develop Aerosol Manufacturing Technology as a manufacturing option for Li-ion battery active cathode phase and for solid electrolyte powder for use in conventional and solid-state Li-ion batteries for the automotive sector. Obtain economically competitive protocols and recipes using the lowest cost precursor and solvent

options. Produce optimized LLZO for separator and catholyte applications. Leverage the advantages of the atomically mixed nano-powder produced by FSP to access otherwise difficult to produce materials.

Approach

Solid-state electrolyte (a) garnets such as aluminum doped lithium lanthanum zirconium oxide Al-LLZO and energy storage materials (b) high Ni cathode active phases are the focus of development using multiple aerosol technologies. Aerosol synthesis is co-optimized with downstream calcination, powder refinement, and validation in battery test cells. The research focuses on the lowest cost precursors available in commodity scales, typically nitrates salts of the metals. Advanced concepts are explored that utilize unique powder morphology and phases accessible only by aerosol processing.

The ANL MERF FSP reactor has features that allow for convenient and high throughput sample production. A glovebox design filter box allows for collection of nanomaterials and restoration of the filter media within 15 minutes of a run completion allowing for up to 6 generated and collected samples per workday. Material that deposits on the walls of the reactor does not significantly cross-contaminate from sample to sample. On a day to day basis, a clean-in-place brushing fixture allows for the combustion tube to be cleaned of wall deposits for changeover to new material systems further assuring no cross contamination between runs. This year, a scale up by 10x was facilitated by the addition of a baghouse to enable a nominal production rate of 500 g/hour.

The ANL FSP facility has been designed to produce powder materials in an industrially relevant way using liquid spray (droplet) combustion, which can produce materials at the highest possible rate compared to ultrasonic atomization or gas-fed precursor introduction. In order to best navigate the complexities of spray combustion, the ANL FSP facility has a suite of in-situ advanced diagnostics. These include (a) laser diagnostic system for Filtered Rayleigh Scattering (FRS) and Planar Laser Induced Fluorescence (PLIF) imaging of temperature and species distribution respectively, (b) Optical Emission Spectroscopy (OES) of the flame zone, (c) In-situ Raman spectroscopy and (d) particle size analysis using Scanning Mobility Particle Sizing (SMPS). Ex-situ diagnostics are also applied including (a) XRD and temperature programmed XRD, (b) BET-SA, (c) DSC-IR/MS, (d) electrochemical testing and electron microscopy (SEM and TEM).

Several years of research at ANL has exposed two major challenges in producing some Li-containing metal oxides directly in one-step. (a) While the obtained green powders can be successfully calcined into the target layered phase, as the formulations tend toward high-Ni, sintering behavior becomes predominant and complete loss of green powder particle morphology occurs necessitating post-processing, erasing much of the advantage of aerosol synthesis. (b) Direct conversion to the target phase is in competition with the impurity phases Li_2CO_3 and LiOH , which readily occur in SP or FSP, but become greater challenges in high-Ni target formulations. In order overcome these challenges, a new overall processing scheme is proposed where some or all of the calcination is performed in the aerosol phase while retaining the principle advantages of continuous processing and short overall processing time. The scheme is shown schematically in Figure II.2.1. Baghouse separation is an inexpensive and in mature industrial technology. In the first baghouse, we are essentially performing a gas/solid separation where the solid is fed continuously to the next step of dry aerosol calcination with a new gas stream more amenable to the target phase formation. This process of gas/solid separation can be repeated gain if necessary depending on the sensitivity of the phase formation to the activities of the outgas products such as H_2O and/or CO_2 .

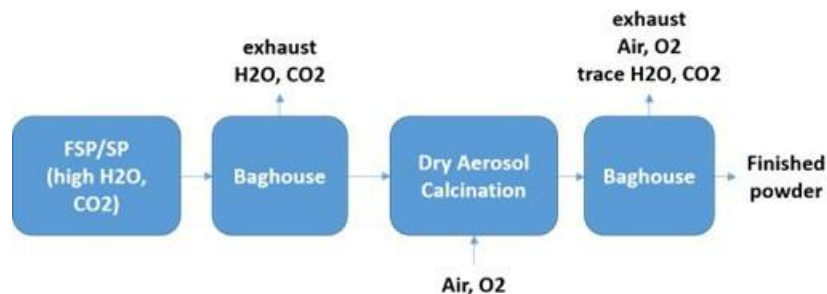


Figure II.2.1 Particle Production with Dry Aerosol Calcination Concept

Results

Identifying the need for DAC

There appears to be direct relationship between the lithium ion conductivity of a target Li-metal oxide and the sensitivity to hydroxide/carbonate competition with the target phase. Thus, the materials LLZO and NCM9055 are not obtained in a single step using either SP or FSP given the high H₂O or CO₂ in the synthesis environment. However, both of these materials readily form the target phases in post-calcination operations where the activity of H₂O and CO₂ are kept low in the calcination environment. However, both of these materials also exhibit extensive sintering that seems to be related the fluxing by unreacted lithium carbonate when T > 700 deg C. This sintering necessitates milling and sieving to produce powders meeting application specifications. With both LLZO and NCM9055, milling operations produce a large fraction of undesirable fines and an overall surface area > 2 m²/g. For both of these materials, their very high moisture sensitivity makes this very problematic. However, for NCM9055, we found that very long calcination times including a slow ramp from 525 to 725 deg. C avoided sintering altogether and preserved the starting particle morphology. It is worth noting that the reason for needing very high temperature for NCM9055 is the relatively high amount of rock salt structure in green powders formed in SP and FSP processing. Conversion of rock salt to layered-phase is kinetically difficult so higher temperatures or longer time is required. So in order to avoid long calcination times it is important to react the majority of carbonate in a contact-less sintering environment such as provided by dry aerosol calcination.

Dry Aerosol Calcination

Dry aerosol calcination (DAC) requires powder to be entrained/fluidized in a carrier gas and transported through a calcination furnace. While many technologies exist at large scale, a convenient research unit in the form a venturi-type entrainment aerosolizer was deployed in the ANL FSP system. The TOPAS SAG410 unit was adapted to the FSP by substituting for the burner assembly and otherwise maintaining the closed system gas control and furnace arrangement. The unit is capable processing 2-325 g powder/m³ of gas. In general, DAC is able to process ~10x more powder mass/unit gas volume than either the SP or FSP synthesis steps so that the calcination DAC equipment required in a production setting will be able to service multiple synthesis units. For evaluating the feasibility, DAC at the ANL facility is performed by batch-wise processing of previously generated powder by SP or FSP. An example of DAC performance is shown in Figure II.2.2. Green powder with an NCA target composition generated in the SP system was used to compare DAC with typical muffle furnace calcination protocol. The muffle furnace calcination consisted of 12 hours calcination at 650 deg C. Surface area measurements were performed to reveal the degree of sintering where the green powder surface area was SA = 6.3 m²/g. From Figure II.2.3 we see that one pass of the powder using DAC at 850 or 950 deg C reduced the surface area of the powder to less than 12 hours at 650 deg. C in the muffle furnace. This example demonstrates the equivalence of very short time DAC calcination with long duration muffle furnace treatment. Importantly, the green powder particle morphology is preserved using DAC even at 950 deg C whereas in the muffle furnace, heavy sintering occurs for T > 700 C.

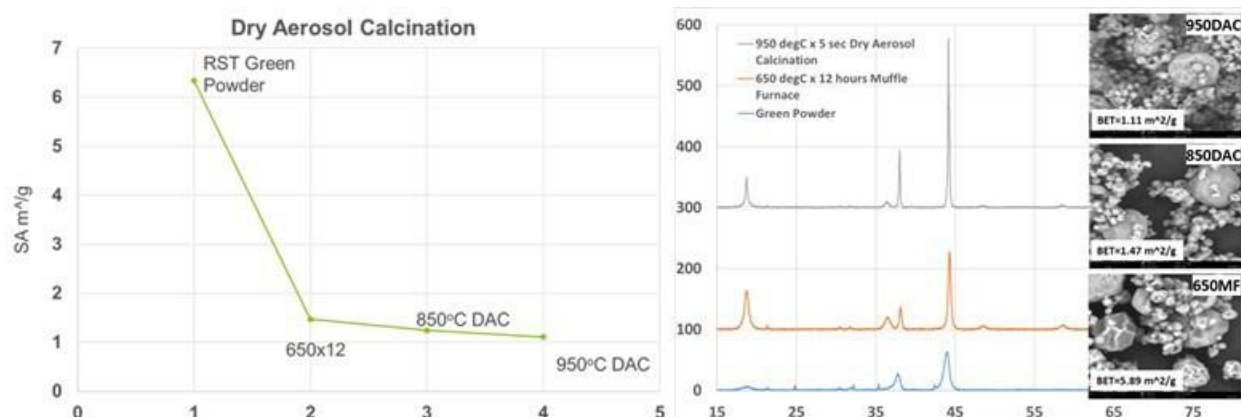


Figure II.2.2 DAC trials using NCA green powder

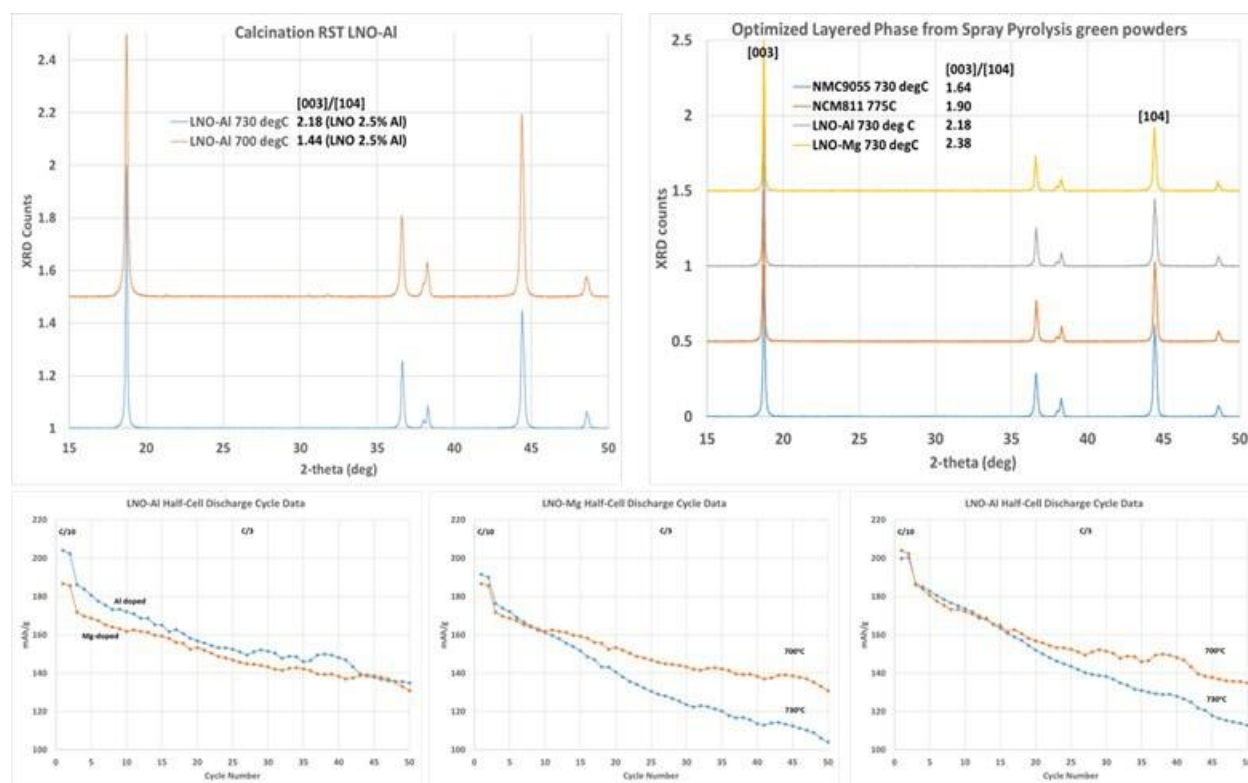


Figure II.2.3 SP synthesis of AL- and Mg-doped LNO

LNO Synthesis using Spray Pyrolysis

Mg- and AL-doped LNO was synthesized by SP using aqueous nitrate solutions. All atoms Li, Al or Mg and Ni were present in the starting spray solution so that the green powder was obtained in one simple step. Calcination followed the protocol described above for NCM9055, which preserves the starting particle morphology. The quality of the layered phase was evaluated using the ratio of the [003] and [104] XRD reflections. This ratio was optimized at 730 deg C calcination temperature. Samples of Al- and Mg-doped LNO calcined at 700 or 730 deg C were used to make half-cells for electrochemical evaluation. Although the 730 samples provided a better ratio, the 700 deg C samples showed better initial capacity and retention than the 730 deg C samples.

Scale-Up of Flame Spray Pyrolysis

The original design of the ANL FSP unit was for a 1x production rate of nominally 50g/hour which is limited by the collection rate capability and exhaust handling blower. However, the current burner can accommodate a 10x production rate and collection at 10x can be accomplished by the addition of a baghouse. A unit was purchased and installed into a support frame that includes engineering control enclosures for the maintenance of the unit and collection of the generated nanopowders. It was desired to maintain the lower 1x original production rate while allowing for configurability to accommodate 10x production for short periods when larger samples are requested and to test the sensitivity of material properties to production rate. In order to allow for both scenarios, a rework of the exhaust handling strategies for the two configurations was made that allows for switching between the two in 1-2 days. Figure II.2.4 shows the configuration for 10x production.



Figure II.2.4 FSP configuration for 500 g/hour production

COVID-19 Impact

Impact of the covid-19 pandemic was limited to delivery of the baghouse unit which was delayed by 6 months by backorders following emergence from covid-19 restrictions by the manufacturer. Commissioning of the scaled FSP system was planned for FY22 but has been delayed to FY23.

Conclusions

A limitation of Spray Pyrolysis and Flame Spray Pyrolysis that prevents direct synthesis of certain important Li-containing phases was identified. A potential solution to this limitation is Dry Aerosol Calcination that can be used as a continuous post-synthesis processing step, which preserves the important feature of continuous production in aerosol technology. A aerosolizer unit was purchased and retrofitted to the existing FSP processing unit that allows for the evaluation of the DAC concept for materials produced in either the SP or FSP synthesis units. These evaluation data will determine the feasibility of continuous powder production with the desired target phase properties. The concept was demonstrated for NCA and showed that despite the very short residence time, an equivalent outcome to that of long duration muffle furnace calcination is possible. Mg- and Al-doped Lithium nickel oxide cathode was synthesized by Spray Pyrolysis. FSP production at 500 g/hour was enabled by the addition of a baghouse to the ANL FSP facility.

Key Publications

1. Formation of lithium-metal-oxygen layer and removal of lithium carbonate on solid state electrolytes, K Donghyeon, JW Elam, JA Libera, Y Liang, KIM HackSung, AU Mane, US Patent App. 17/207,445.
2. Solvent-free processing of lithium lanthanum zirconium oxide coated-cathodes, JL Durham, JA Libera, AL Lipson, Y Liang, US Patent App. 16/938,037.
3. Cathode materials for use in lithium cells and batteries, MM Thackeray, E Lee, JA Libera, KU Kyojin, US Patent App. 17/351,944
4. Understanding the constant-voltage fast-charging process using a high-rate Ni-rich cathode material for lithium-ion batteries, K Ku, SB Son, J Gim, J Park, Y Liang, A Stark, E Lee, J Libera, Journal of Materials Chemistry A 10 (1), 288-295.

5. Investigating the Calcination and Sintering of $\text{Li}_7\text{La}_3\text{Zr}_2\text{O}_{12}$ (LLZO) Solid Electrolytes Using Operando Synchrotron X-ray Characterization and Mesoscale Modeling, P Barai, T Fister, Y Liang, J Libera, M Wolfman, X Wang, J Garcia, Hakim Iddir, and Venkat Srinivasan, *Chemistry of Materials* 33 (12), 4337-4352.

Acknowledgements

We greatly acknowledge the long-term support and vision provided by Peter Faguy. The authors greatly acknowledge the continuing collaboration and advice from Toivo Kudas and Cabot Corporation. We also acknowledge the contributions to this research by E.J. Lee. We greatly acknowledge the expertise of Hack-Sung Kim in the development of the custom Raman spectrometer. We also acknowledge the Manufacturing Science and Engineering Initiative at ANL for providing support for the advanced diagnostics for the FSP unit.

II.3 Supercritical Fluid Processing of Battery Cathode Materials (ANL)

Youngho Shin, Principal Investigator

Argonne National Laboratory
9700 South Cass Avenue
Lemont, IL 60439
E-mail: yshin@anl.gov

Haiyan Croft, DOE Technology Development Manager

U.S. Department of Energy
E-mail: haiyan.croft@ee.doe.gov

Start Date: October 1, 2021

End Date: September 30, 2022

Project Funding: \$600,000

DOE share: \$600,000

Non-DOE share: \$0

Project Introduction

The development of advanced, rapid, reproducible manufacturing processes for cathode materials is essential for improving performance, increasing lifespan, ensuring safety, and reducing prices of lithium-ion batteries. Polycrystalline cathode particles currently used in lithium-ion batteries, produced via conventional co-precipitation process, are intrinsically vulnerable to grain-boundary fracture (by the anisotropic volume change during lithium extraction/insertion) inside particles that lead to rapid impedance growth and capacity decay. An emerging supercritical fluids technology, under process development and scale-up as one of the main goals of this program, can provide advanced materials with high electrode density due to a robust single crystal particle structure without internal void fraction, improved rate capability due to submicron particle size, cycling stability due to suppressed particle crack and resistance layer, and facet-controlled particle morphology, thus enabling consequent mass production of high-performance battery cathode materials. These material properties are the result of a higher degree of supersaturation and the instant formation of mono-crystalline oxide particles because of the dramatically reduced solubility of metal ions under supercritical hydrothermal reaction condition. The supercritical hydrothermal reaction is a practical and scalable synthesis process for the production of mono-crystalline cathode materials mitigating the intrinsic and structural problems of conventional polycrystalline cathode materials.

Objectives

The aim of the project is to establish a flexible R&D capability of supercritical fluid reaction as an emerging manufacturing process for active battery materials. This process is one of the emerging manufacturing technologies with the goal of reducing the risks associated with the discovery of advanced active battery materials, market evaluation of these materials, and their commercialization with mass production. The production and delivery of advanced mono-crystalline battery materials with the desired particle size, composition distribution, and shape are also essential roles of this program to support fundamental research groups. We perform systematic engineering research to develop a cost-effective supercritical fluids process and to produce sufficient quantities of target materials with high quality by optimizing the synthesis parameters and material composition. These advanced battery materials, which are not yet commercially available and not achievable by traditional co-precipitation techniques, are produced and distributed to research groups and industrial partners to get their feedback to further optimize the synthesis process. Our effort deepens fundamental understandings of the structure-property relationship of battery cathode materials and ultimately can contribute to selecting the customized material composition before the material would be deemed suitable and desirable for large scale manufacturing.

Approach

Single-crystal cathode particles mitigating rapid impedance growth and capacity decay (these are typical drawbacks of current polycrystalline cathode particles due to the intergranular fracture during cycling) are developed and produced. The morphology of single-crystal cathode particles can be customized by changing reactants, solvents, reaction pressure, and reaction temperature of the hydrothermal process. The advanced single-crystal active battery materials with tunable particle size, morphology, and composition distribution are synthesized by the installed batch supercritical hydrothermal reaction system. The synthesis condition is optimized and then customized material is produced in quantities suitable for distribution for a comprehensive investigation. The mechanical and electrochemical characterization of the produced cathode materials is carried out in collaboration with research groups and industrial partners. The battery cathode materials selected for FY22 are single-crystal nickel-rich NMC and LFP cathode materials. In collaboration with various research groups, material characterization such as Bragg coherent X-ray diffraction imaging, nano-indentation, HRTEM, XPS, XRD, and electrochemical performance of the synthesized cathode materials is performed to support fundamental research and to improve the synthesis process based on feedback. To further improve the electrochemical performance of produced materials, collaboration research such as ALD surface treatment and customized electrolyte selection for single-crystal composition is conducted.

Results

The characteristics of Ni-rich single-crystal cathode material produced using the installed batch hydrothermal reactor system were compared with the polycrystalline cathode material produced via the conventional co-precipitation process (Figure II.3.1). This single-crystal cathode materials have many advantages and potential in terms of robust material structure, improved electrochemical performance, high electrode density without internal void fractions, reduced surface area mitigating side reactions, facet-controlled morphology for faster Li transport, improved surface coating effects, and so on. Through various comparative evaluations, the advantages of single-crystal cathodes were confirmed, and based on these results, the demand for the process development and scale-up of a continuous-flow supercritical hydrothermal process toward mass production has been grounded.

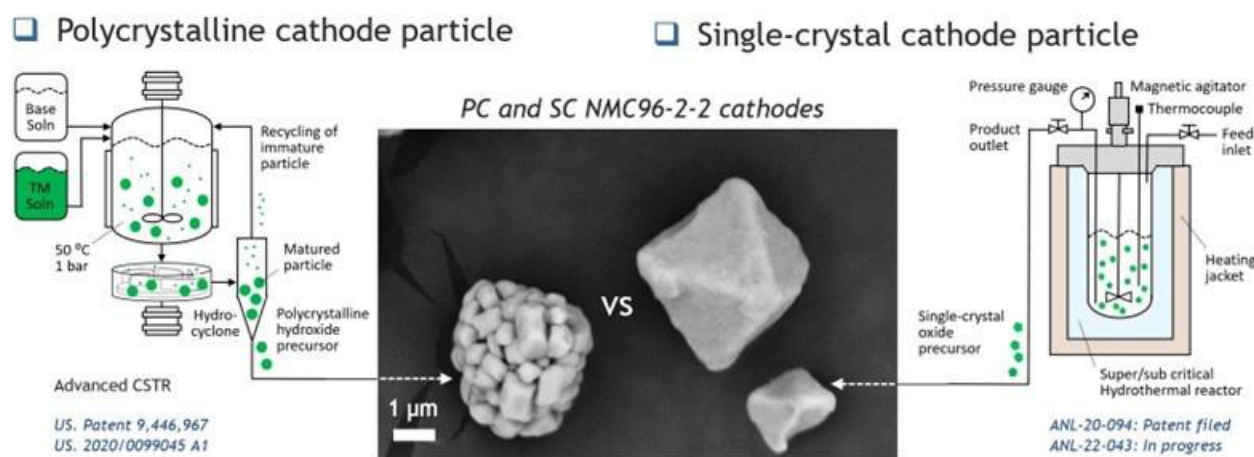


Figure II.3.1 Synthesis of polycrystalline and single-crystal NMC96-2-2 cathode materials

Figure II.3.2 shows the result of tap density increase by mixing polycrystalline and single-crystal cathode powders. By mixing 11 μm -sized polycrystalline cathode with 3 μm -sized single-crystal cathode at a ratio of 0.74:0.26, a 22% tap density increase was obtained. This 22% tap density increase improves the cathode loading of the electrode, resulting in an increase of the volumetric energy density of the battery.

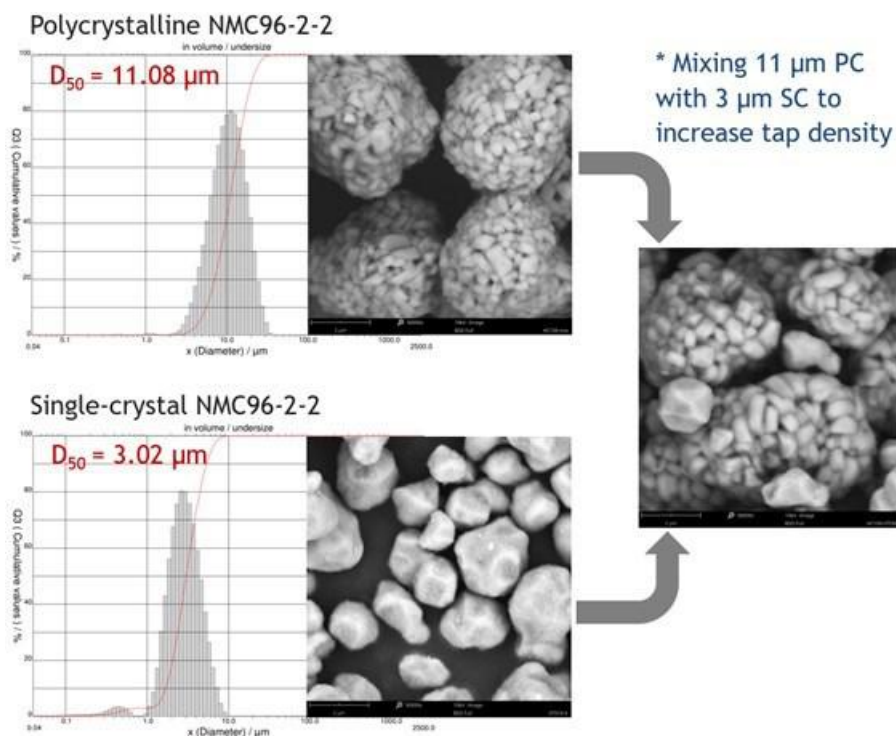


Figure II.3.2 Tap density increase by mixing polycrystalline and single-crystal NMC 96-2-2 cathodes

By nano-indentation study to investigate the particle breaking force (Figure II.3.3), single-crystal particle exhibits five times the particle strength of polycrystalline particle. This demonstrates that the single-crystal material synthesized by the hydrothermal method has significantly better mechanical strength than the polycrystalline material synthesized by the coprecipitation method.

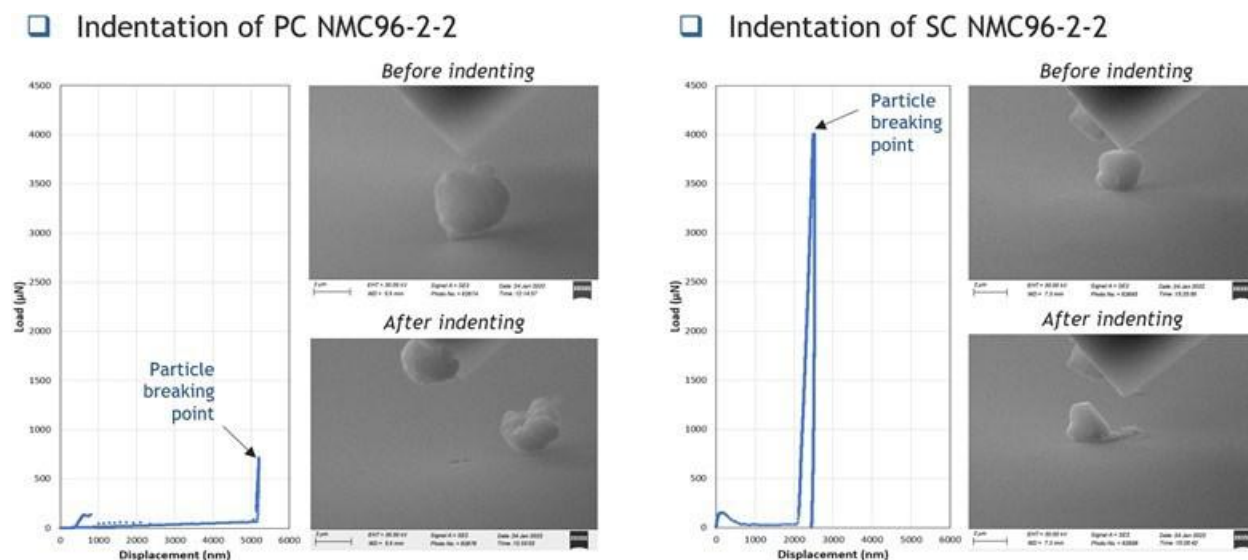


Figure II.3.3 Particle crack analysis by nano-indentation

Due to these material properties, the capacity retention of single-crystal material is remarkably improved compared to polycrystalline material. The capacity retention of single-crystal NMC 96-2-2 is ~72% after 100 cycles and ~60% after 200 cycles, which is remarkably improved compared to that of polycrystal NMC 96-2-2 (Figure II.3.4).

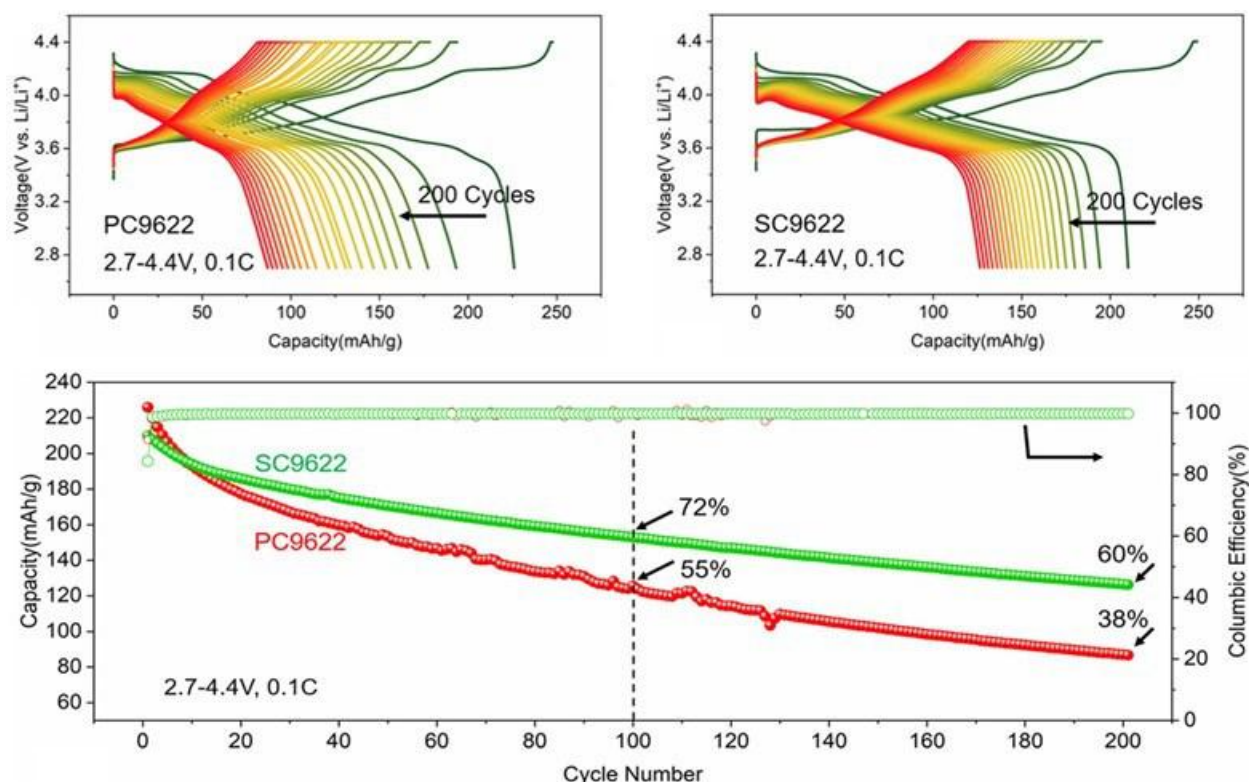


Figure II.3.4 Cycling performance of polycrystalline and single-crystal NMC 96-2-2 cathodes

The capacity retention and high-voltage stability of single-crystal material are significantly improved compared to polycrystalline materials when new types of electrolytes are used such as DMC-based LHCE and TMP-based LHCE (Figure II.3.5). TMP-based LHCE behaves better because TMP (a phosphate solvent) may form a good passivation on cathode surface to prevent further O₂ release. More characterizations are planned to find the detail mechanism of this improvement.

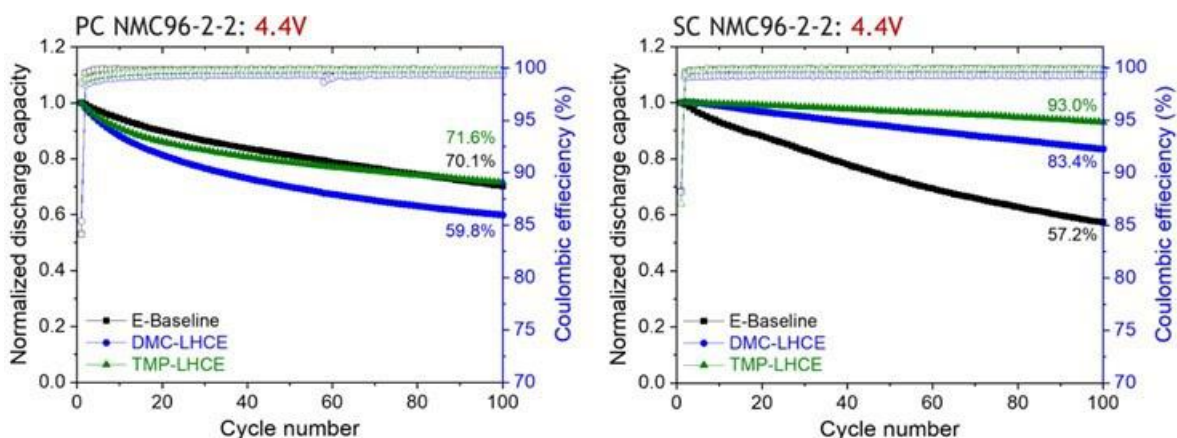


Figure II.3.5 Improved cyclability of single-crystal NMC 96-2-2 cathode by selected electrolytes

To further improve the performance of Ni-rich single-crystal material, 0.1%, 0.2%, 0.3%, and 0.4% Al-doped single-crystal particles were prepared and evaluated (Figure II.3.6) and thus Al-doped single-crystal material shows more improved rate performance.

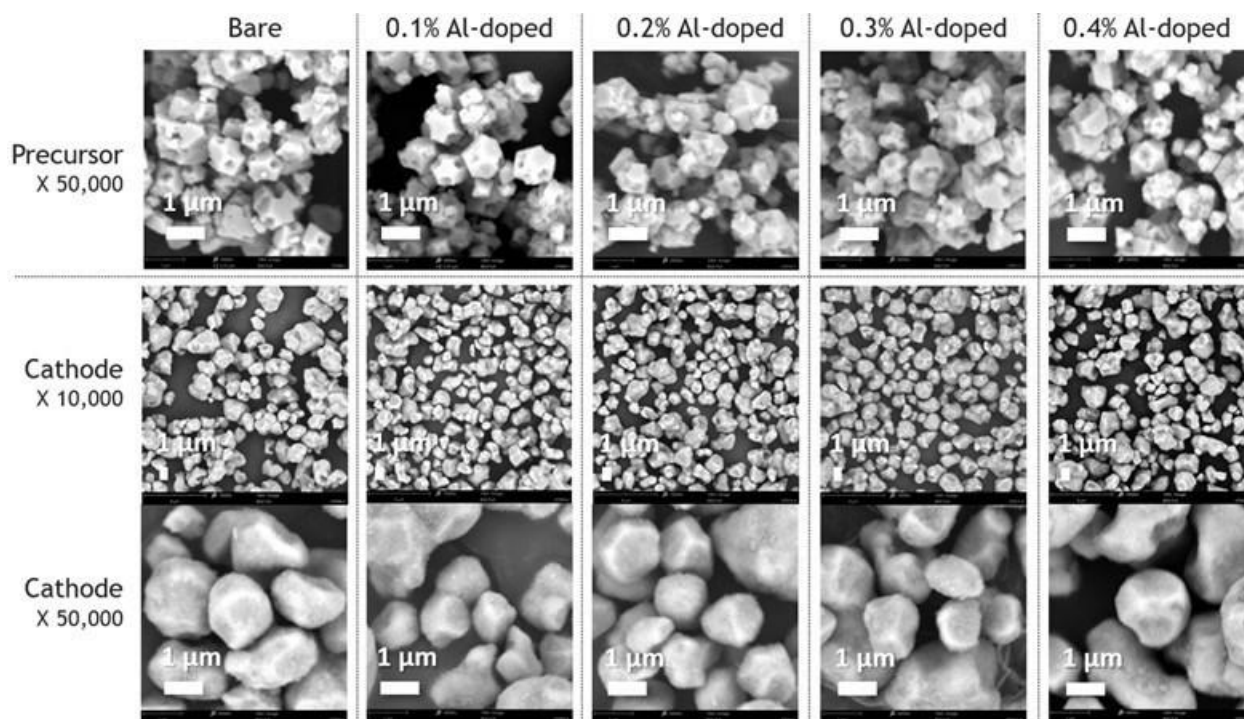


Figure II.3.6 Synthesis of Al-doped single-crystal NMC 96-2-2 cathode

Additional carbon-coating to protect the surface of Al-doped SC NMC96-2-2 was applied. By XPS analysis, it was revealed that peak intensity for carbonate in C1s region is lower with carbon-coated and 0.4% Al-doped/carbon-coated single-crystal NMC 96-2-2 after air storage for 5 days (Figure II.3.7).

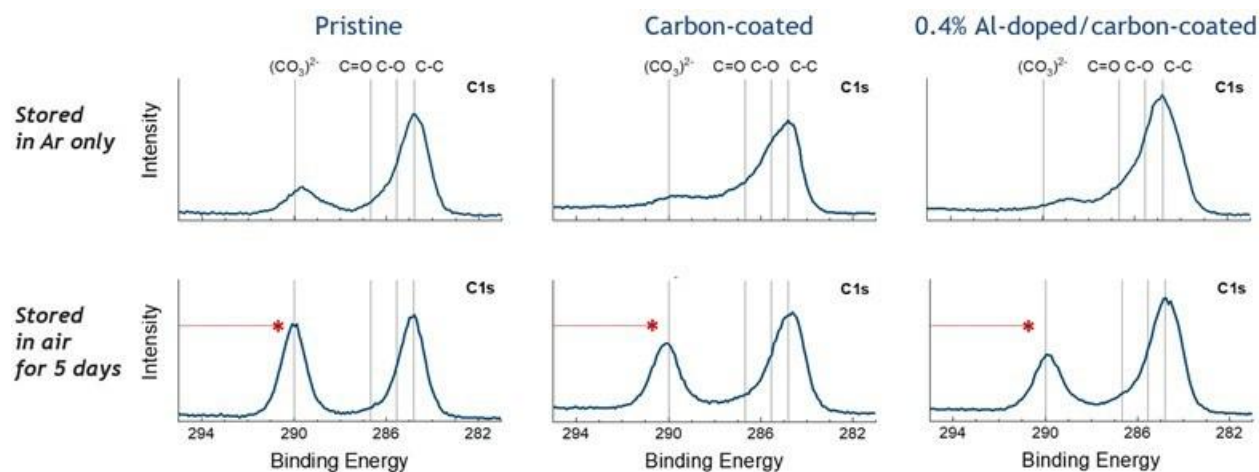


Figure II.3.7 Surface protection of single-crystal NMC 96-2-2 cathode

The recent price increase of cobalt and nickel is causing concern about the application of lithium-ion batteries. For this reason, we synthesized lithium iron phosphate by the installed hydrothermal process. The target is to maximize the fast-charge capability of LFP material. To approach this goal, 200 nm-sized and carbon-layered single-crystal LFP was produced and evaluated (Figure II.3.8).

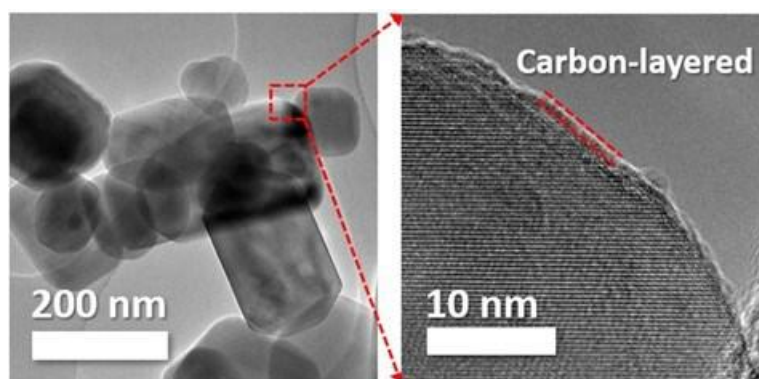


Figure II.3.8 Synthesis of nano-sized carbon-layered single-crystal LFP cathode

Figure II.3.9 shows XRD results of carbon-layered grain-free single-crystal LFP material before annealing and after annealing. TGA/DSC analysis indicates the existence of carbon together with single-crystal LFP particles (Figure II.3.10). The single-crystal LFP particles synthesized by hydrothermal reaction are 12 times smaller and 42% less surface area than solid-state LFP particles (Figure II.3.11) which results in improved rate performance and longer life. Due to the high crystallinity, smaller particle size, and lower surface area of single-crystal LFP, high C-rate performance and C/10 cyclability are improved (Figure II.3.12).

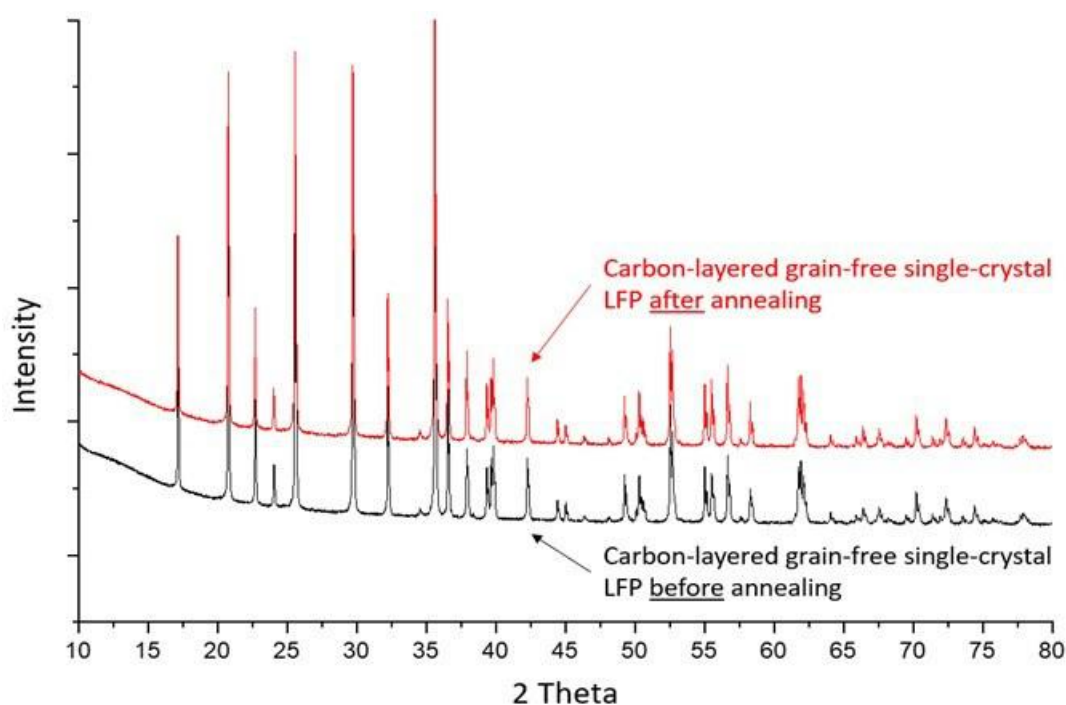


Figure II.3.9 XRD of nano-sized carbon-layered single-crystal LFP cathode

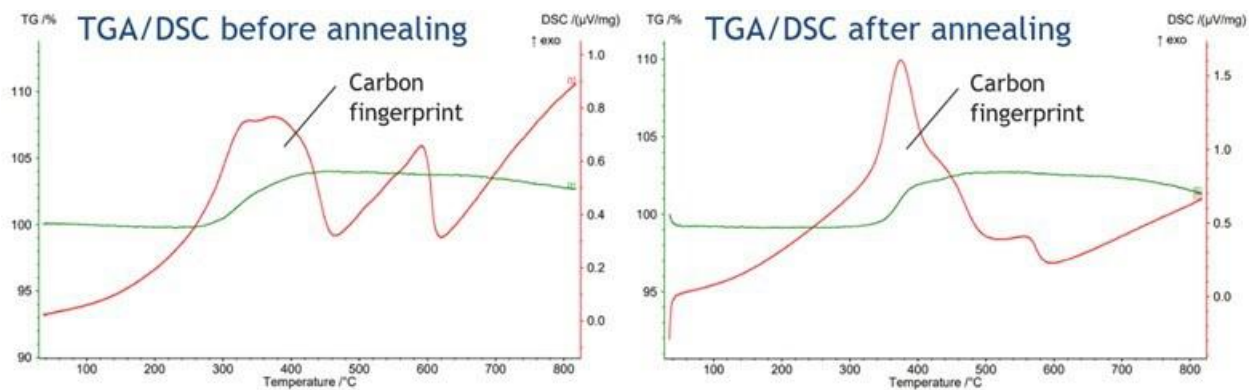


Figure II.3.10 TGA/DSC of nano-sized carbon-layered single-crystal LFP cathode

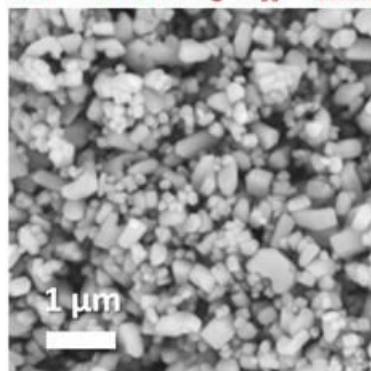
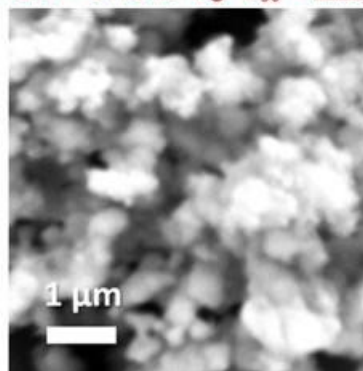
Hydrothermal SC LFP**BET = 4.15 m²/g D₅₀ = 210 nm****Solid-state LFP****BET = 7.15 m²/g D₅₀ = 2.50 μm**

Figure II.3.11 Physical properties of hydrothermal single-crystal LFP compared to solid-state LFP

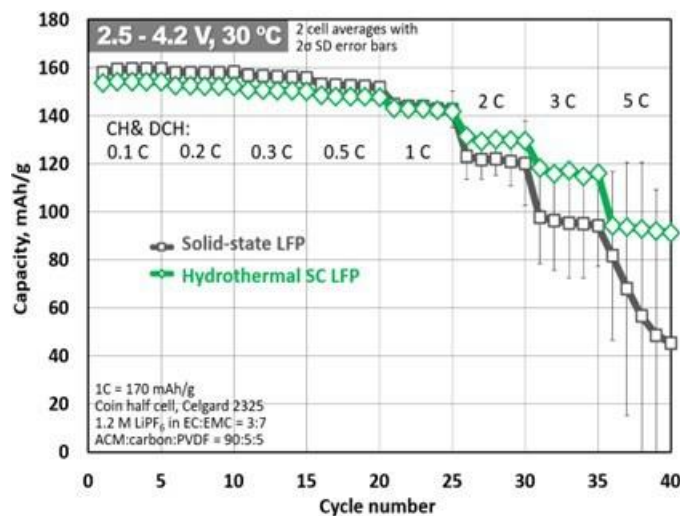


Figure II.3.12 Electrochemical performance of hydrothermal single-crystal LFP and solid-state LFP

The prepared single-crystal LFP particles by hydrothermal reaction do not have void fraction, grain, and defect inside particles. BCDI demonstrates relatively unstrained simple coherent x-ray diffraction patterns of single-crystal LFP particle (Figure II.3.13). We will study further the correlation between the strain of single-crystal cathode and its performance.

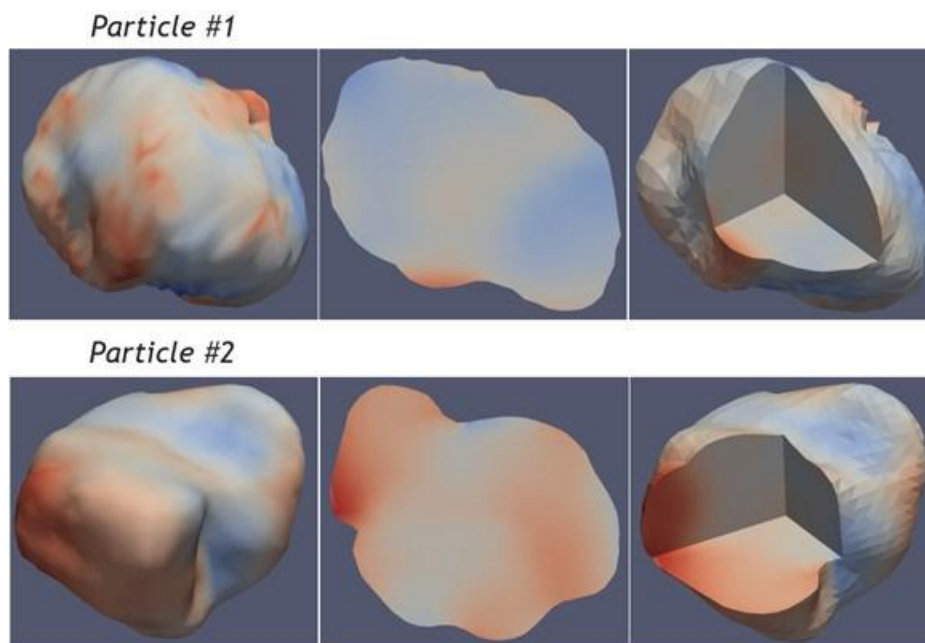
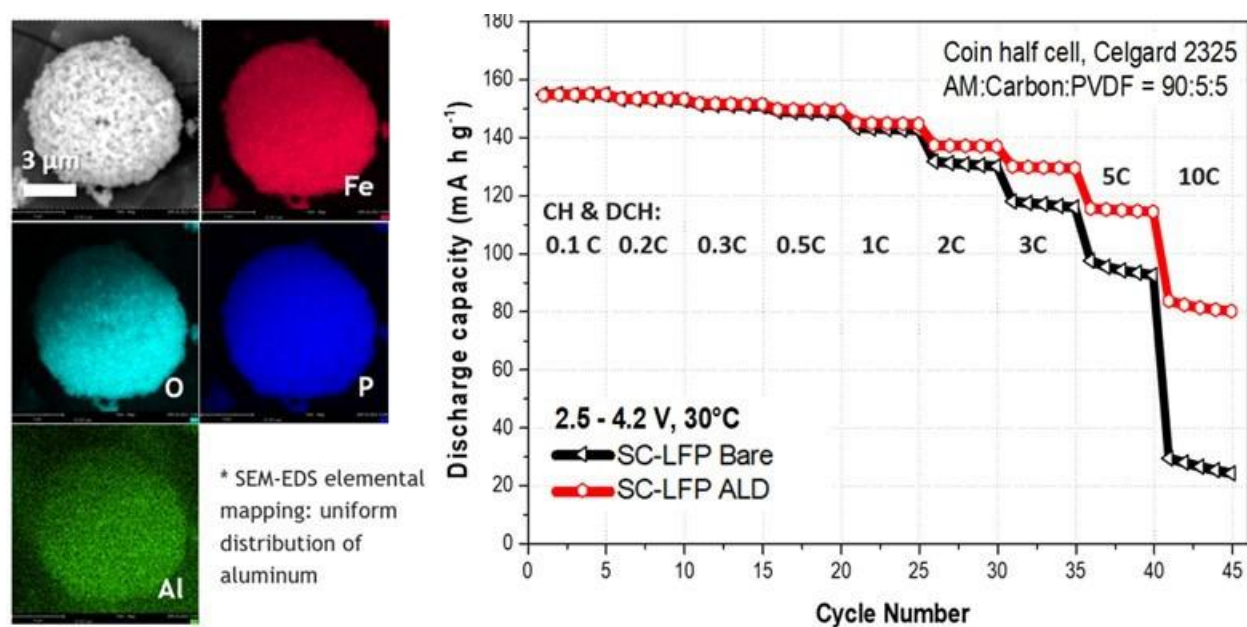


Figure II.3.13 BCDI analysis of single-crystal LFP

We further investigated ALD Al_2O_3 -coating on the granulated secondary LFP particles and this improve the rate capability and cycle life significantly (Figure II.3.14).

Figure II.3.14 Electrochemical performance of ALD Al_2O_3 -coated granulated single-crystal LFP

Conclusions

The supercritical fluid system is a material synthesis platform that is able to produce single-crystal cathode materials with a solid structure and unique mechanical/electrochemical properties. This supercritical hydrothermal process is a powerful manufacturing technology for advanced single-crystal battery materials with the desired particle size, composition distribution, and morphology which are not commercially available and difficult to produce using other conventional technologies. Various advantages and potentials of single-

crystal cathode compared to polycrystalline cathode were revealed through various analyses and evaluations. Based on these relatively superior physical and electrochemical properties of the single-crystal cathode, the need for the process development and scale-up of a continuous-flow supercritical hydrothermal process toward mass production of single-crystal cathode materials is generated. We will conduct the development of an advanced continuous-flow supercritical hydrothermal process, process scale-up, and production of high-performance single-crystal battery materials to support fundamental research groups and industry partners.

Key Publications

1. Chemo-mechanically stable ultrahigh-Ni single-crystalline cathodes with improved oxygen retention and delayed phase degradations, Chunyang Wang, Rui Zhang, Carrie Siu, Mingyuan Ge, Kim Kisslinger, Youngho Shin*, Huolin L. Xin*, Nano Lett. 2021, 21, 22, 9797–9804
2. Scalable Synthesis of Pt/SrTiO₃ Hydrogenolysis Catalysts in Pursuit of Manufacturing-Relevant Waste Plastic Solutions, Ian L. Peczak, Robert M. Kennedy, Ryan A. Hackler, Rongyue Wang, Youngho Shin, Massimiliano Delferro*, and Kenneth R. Poeppelmeier*, ACS Appl. Mater. Interfaces 2021, 13, 49, 58691–58700
3. Resolution-enhanced X-ray Fluorescence Microscopy via Deep Residual Networks, Longlong Wu, Seongmin Bak, Youngho Shin, Yong. S Chu, Shinjae Yoo, Ian K. Robinson, and Xiaojing Huang, npj computational materials, submitted.

Patent and Invention Disclosures

1. Invention disclosure ANL-IN-22-043: METHOD FOR CARBON-LAYERED GRAIN-FREE SINGLE-CRYSTAL CATHODE PARTICLE AND PARTICLE PREPARED BY THE SAME.

Acknowledgements

We gratefully acknowledge the collaboration with Dr. Seongmin Bak (BNL), Dr. Feng Wang (BNL), Dr. Seoung-Bum Son (Argonne Post-Test Facility), Dr. Wu Xu (Pacific Northwest National Laboratory), Dr. Donghyeon Kang (Argonne AMD), and Dr. Wonsuk Cha (Argonne APS), Prof. Huolin Xin (UCI), and Prof. Sangkee Min (University of Wisconsin-Madison).

II.4 Process R&D and Scale-up of Critical Battery Materials (ANL)

Krzysztof Pupek, Principal Investigator

Argonne National Laboratory
9700 South Cass Avenue
Lemont, IL 60439
E-mail: kpupek@anl.gov

Haiyan Croft, DOE Technology Development Manager

U.S. Department of Energy
E-mail: haiyan.croft@ee.doe.gov

Start Date: October 1, 2021
Project Funding: \$800,000

End Date: September 30, 2022
DOE share: \$800,000

Non-DOE share: \$0

Project Introduction

New experimental materials are constantly invented to improve the safety, energy density, cycle life, and calendar life of lithium ion batteries for EV. These materials are typically synthesized in discovery laboratories in small batches providing amounts sufficient only for limited basic evaluation but not in quantities required for full scale validation and prototyping. In addition, bench-scale processes are often un-optimized, not validated, and generate materials with inconsistent purity and yield. This project aims to assist the advanced battery research community by enabling access to larger quantities of high quality innovative materials.

New electrolyte formulations and new electrolyte materials will be required for recently emphasized cathode materials based on earth abundant elements (Mn-rich layered oxides and disordered rock salts). We are using continuous flow reaction technology to speed up process optimization and lower production cost that allows for faster production and easier scale up.

Objectives

The objective of this project is to conduct research toward scaling up production of advanced materials for Li-ion batteries originally created in small quantities by discovery scientists at various research organizations. Scaling up the original route used by discovery scientists often requires an extensive modification of the bench-scale chemistry and systematic, science-based process research and development to allow for 1) safe and cost effective production, 2) development of an engineering flow diagram, 3) design of a mini-scale system layout, 4) construction of the experimental system, and 5) validation of the optimized process, all of which are needed for full industrial implementation. The experimental system will be assembled and the materials will be manufactured in quantities sufficient for full scale industrial evaluation and to support further research. The materials produced by the program will be fully characterized to confirm chemical identity and purity. Analytical methods will be developed for quality control. The electrochemical performance of the materials will be validated to confirm that these properties match the original data generated by the discovery scientist. Sample of the materials produced by the project will be available to the advanced lithium ion battery research community to support basic development and large scale performance validation.

Approach

New materials for experimental electrolyte formulations often have complex molecular structure that translates frequently into increased synthesis difficulties and cost. Argonne's Applied Materials Division's Process R&D group, operated in the newly expanded Materials Engineering Research Facility (MERF) is evaluating emerging production technologies to address the challenges. A comprehensive, systematic approach to scale-up of advanced battery materials has been defined. This approach starts with analyzing of the original route the new material was first made in the discovery lab and initial electrochemical evaluation. This determines if the material is to be added to the inventory database, ranked, prioritized and selected for scale up. The Applied

Materials Division's Process R&D group at Argonne consults with the DOE technology manager to prioritize new materials based on level of interest, validated performance and scale up feasibility. The new candidate materials for scale up are discussed with DOE for final approval. The Process R&D group evaluates several approaches, including non-standard manufacturing technologies, to determine the best route to scale up of each particular material. One such technology is a Continuous Flow Chemical Reactor that enables the continuous synthesis of materials from discovery through process development and production scale. Continuous flow reactor technology can be used for rapid screening of reaction conditions to better understand the fundamentals of process kinetics and thermodynamics. The technology offers a cost-effective and safer alternative to traditional batch processes by improving material and energy usage and minimizing the environmental impact of the manufacturing operation. At this point, the scale-up process begins with a feasibility study, followed by proof of concept testing, first stage scale-up and, as needed, further scale-up cycles. Several Go/No Go decisions are made after feasibility determination and electrochemical validation testing. For each material, we will develop a scalable manufacturing process, analytical methods and quality control procedures. We also prepare a "technology transfer package" which includes detailed procedures of the revised process for material synthesis, materials balance, analytical methods and results (Specification Sheet) and the SDS for the material. The detailed process description allows for preliminary estimates of production cost, an important factor for decision making in industry. We apply the newly developed process to manufacture kilogram quantities of the material. We fully chemically characterize each material and make samples available for industrial evaluation and to the research community. We also provide feedback to discovery chemists helping to guide future research.

Results

Last year, we reported on the synthesis of methyl (tetrafluoropropyl)carbonate (MTFPC) scaled up to the 100g level (Figure II.4.1), made by the reaction of methyl chloroformate with 2,2,3,3-tetrafluoropropan-1-ol, with an emphasis on flow-chemistry amenable conditions. The optimization work for this initially determined that acetonitrile and diazabicycloundecane (DBU) were the preferred solvent and base. A second more detailed optimization showed that 1.2eq of methyl chloroformate (MCF) was the optimal amount of reagent (Figure II.4.2), and that the amount of DBU had to be at least 1.1 molar equivalents. The amount of acetonitrile solvent did not have a large effect on the reaction. Simple distillation after an aqueous work-up provided clean material by NMR (Figure II.4.3).



Figure II.4.1 Reaction to form MTFPC

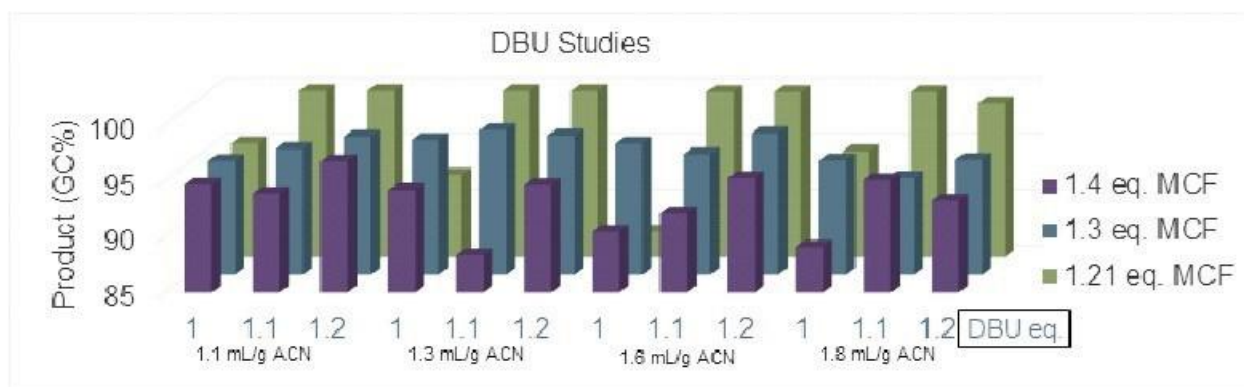
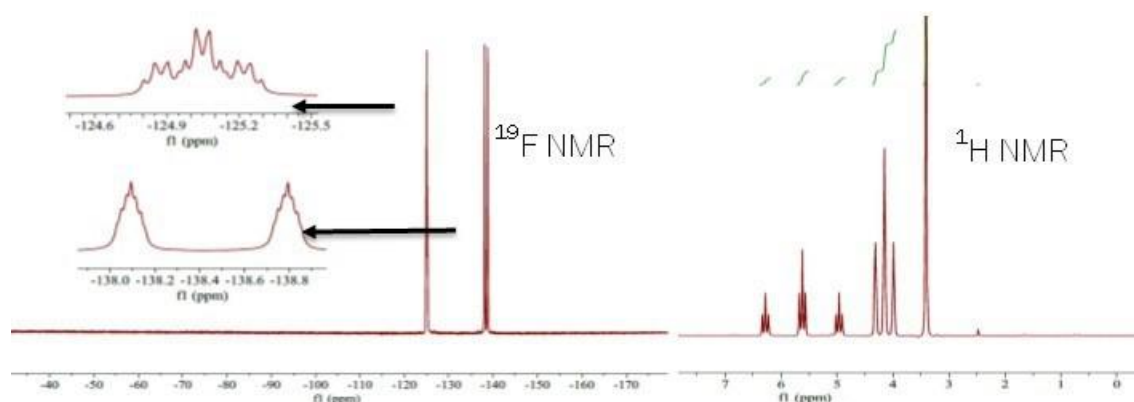


Figure II.4.2 Screening study GC results for synthesis of MPFPC

Figure II.4.3 ^1H and ^{19}F NMR spectra of MTFPC

Additional work to extend this reaction procedure to the analogous methyl (pentafluoropropyl)carbonate (MPFPC, Figure II.4.4) initially succeeded. However, the workup for this reaction was far more difficult. MPFPC, unlike the tetrafluoro analog, co-distills with both water and DBU, making an aqueous workup unfeasible. Several attempts were made to dry the distillate using molecular sieves, resins, and additional azeotropic distillations. These did not succeed in reducing the water level of the product.

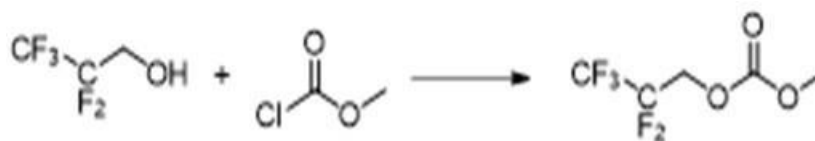


Figure II.4.4 Synthesis of MPFPC

New reaction conditions were required for this material to overcome the separation and purification challenges posed by the unexpected water affinity. Although not amenable to flow synthesis, anhydrous inorganic bases were examined, with the intent that the base and byproducts could be removed with a simple filtration and thus avoid any aqueous workup. Using 1.1 equivalents of MCF, 1.0 equivalents of K_2CO_3 , and acetone as a reaction solvent lead to good conversion in the reaction. After filtration, simple distillations gave material in 60% yield, with a relatively low water content by Karl Fischer (KF) water titration. The NMR spectra for this material show no impurities, and GC/MS analysis shows high purity (99.6%). (See Figure II.4.5.)

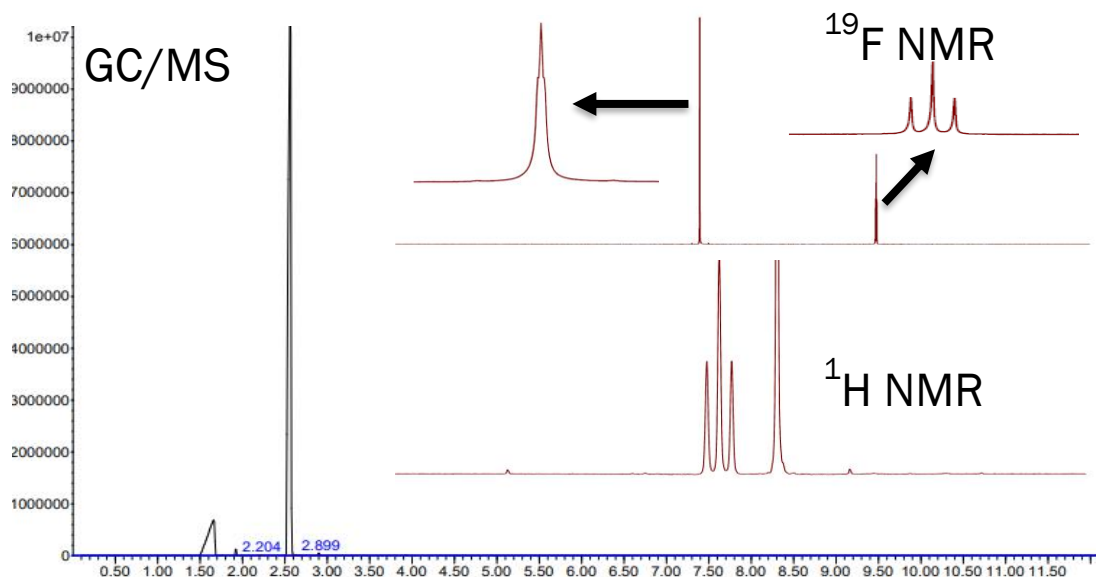


Figure II.4.5 Select analytical spectra for MPFPC

Based on a recent paper, we began to explore the chemistry and electrochemistry of 2,2,3,3-tetrafluorobutanediol ethers¹⁻³. These authors report that 2,2,3,3-tetrafluorobutanediol, dimethyl ether (FDMB) is an effective battery solvent with lithium bis(fluorosulfonylimide) (Li-FSI) as a salt, exhibiting high voltage stability and compatibility with lithium metal anodes. This system is also reported to form a very thin (6nm) SEI layer.

We initially repeated the synthesis of FDMB to run different electrochemistry experiments on a small scale; however, the reported use of sodium hydride (NaH) as the deprotonation reagent was deemed to be hazardous. We developed safer reaction conditions based on a mixed phase system of sodium hydroxide in water and tetrahydrofuran with a phase transfer reagent: tetrabutylammonium bromide. These conditions replicated the reported experimental results and matched the reported NMR spectra. Our analysis by GC/MS indicated >99.5% purity. (See Figure II.4.6.)

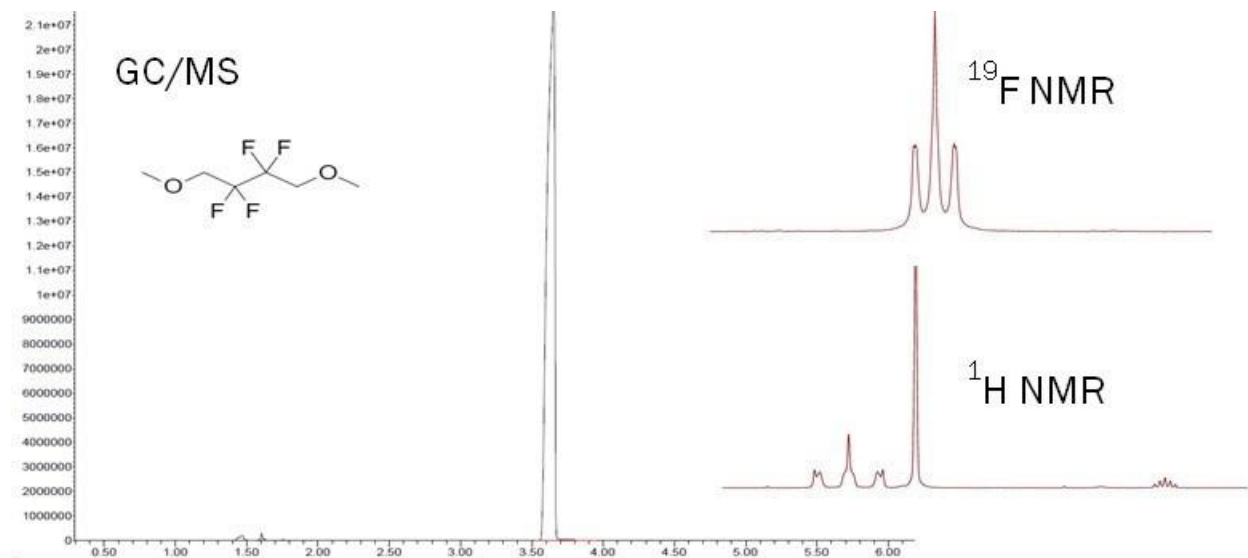


Figure II.4.6 Analytical Data for FDMB

We have noted one discrepancy with the literature reporting. One of the claims is that LiFSI forms a complex with the FDMB to form a dark solution. In our initial tests, LiFSI dissolved cleanly to a clear colorless solution that appears stable over time. This was repeated with several batches- only one showed a darkening upon LiFSI dissolution. Careful examination of that particular batch suggested that it was a slight impurity that was responsible for the color.

Our major focus was to develop new materials based on the FDMB molecule. Many different solvents based off of butanediol ethers were synthesized (Table II.4.1), and are all fully characterized by ^1H NMR, ^{13}C NMR, and ^{19}F NMR in addition to GC/MS. These are currently or planned to be under evaluation in coin cell tests with LiFSI.

Table II.4.1 Summary of FDMB- based materials.

Compound	Linear formula	GC/MS purity
FDMB	$\text{CH}_3\text{-O-CH}_2\text{-CF}_2\text{-CF}_2\text{-CH}_2\text{-O-CH}_3$	>99.5
DMB	$\text{CH}_3\text{-O-CH}_2\text{-CH}_2\text{-CH}_2\text{-CH}_2\text{-O-CH}_3$	>99.5
F-DTEB	$\text{CF}_3\text{-CH}_2\text{-O-CH}_2\text{-CF}_2\text{-CF}_2\text{-CH}_2\text{-O-CH}_2\text{-CF}_3$	99.52
F-DAB	$\text{CH}_2=\text{CH-CH}_2\text{-O-CH}_2\text{-CF}_2\text{-CF}_2\text{-CH}_2\text{-O-CH}_2\text{-CH=CH}_2$	99.53
DTEB	$\text{CF}_3\text{-CH}_2\text{-O-CH}_2\text{-CH}_2\text{-CH}_2\text{-CH}_2\text{-O-CH}_2\text{-CF}_3$	99.77
TFEG	$\text{CH}_3\text{-O-CH}_2\text{-CH}_2\text{-O-CH}_2\text{-CF}_2\text{-CF}_2\text{-CH}_2\text{-O-CH}_2\text{-CH}_2\text{-O-CH}_3$	99.63
FDNBC	$\text{CH}_3\text{-O-C(O)-O-CH}_2\text{-CF}_2\text{-CF}_2\text{-CH}_2\text{-O-C(O)-O-CH}_3$	99.46
DMBC	$\text{CH}_3\text{-O-C(O)-O-CH}_2\text{-CH}_2\text{-CH}_2\text{-CH}_2\text{-O-C(O)-O-CH}_3$	99.11

However, several of these compounds showed limited solubility of lithium salts. Making a comparison to the fluorinate alkyl carbonates, where non-symmetric structures showed better solubilizing properties, we turned to the synthesis of non-symmetric fluorinated butanediol ethers.

To accomplish this, we first wanted to synthesize mono-methyl-2,2,3,3-tetrafluorobutandiol (FMFB, $\text{CH}_3\text{-O-CH}_2\text{-CF}_2\text{-CF}_2\text{-CH}_2\text{-OH}$). The planned synthesis was to use the same reaction, but limit reagents to 1 equivalent each of base and methyl iodide. It proved very difficult to control the selectivity between mono- and di-methylated materials and gave a very low yield (21%) of desired product, in part due to the difficulty in separating the two products. This led to development of a flow chemistry process for the material, where much better selectivity could be expected. A quick design of experiments (DoE) study was run using the Syrris Asia flow reactor system to look at optimization of the selectivity and conversion by variation of the concentrations, time and temperature (Figure II.4.7). Due to the longer reaction time needed, a flow coil of 16ml volume was set up and used. The DoE parameters and results are shown in Table II.4.2.



Figure II.4.7 Syrris ASIA flow chemistry system

Table II.4.2 DoE variables used to determine optimized monoalkylation reaction conditions

[Mel] in THF	Equiv TFBD/NaOH	Equiv Mel	Time (hrs)	Selectivity (%)	Conversion (%)	Equiv Mel
1	0.3	1	1	97.42	89.01	1
0.5	0.3	1	2	94.95	94.03	1
1	1	0.3	1	99.99	24.86	0.3
1	1	1	2	99.99	65.58	1
0.5	1	0.3	2	99.99	28.83	0.3
0.5	1	1	1	99.99	72.64	1
Model 0.75	0.69	1.14	1.5	>99.99	76.46	0.69

The data were used to develop a model. The model conditions were then run (blue entry in Table II.4.2), resulting in good conversion and excellent selectivity. This was designed to facilitate isolation of pure mono-methyl product. As seen by the GC data (Figure II.4.8), the mono- and di-methyl materials are very similar in boiling point, as determined by close GC peak retention times. The starting diol is readily separated from both, as seen by the noticeably longer retention time from both methylated materials. Thus, selectivity is more important to the process than conversion in product purification and isolation.

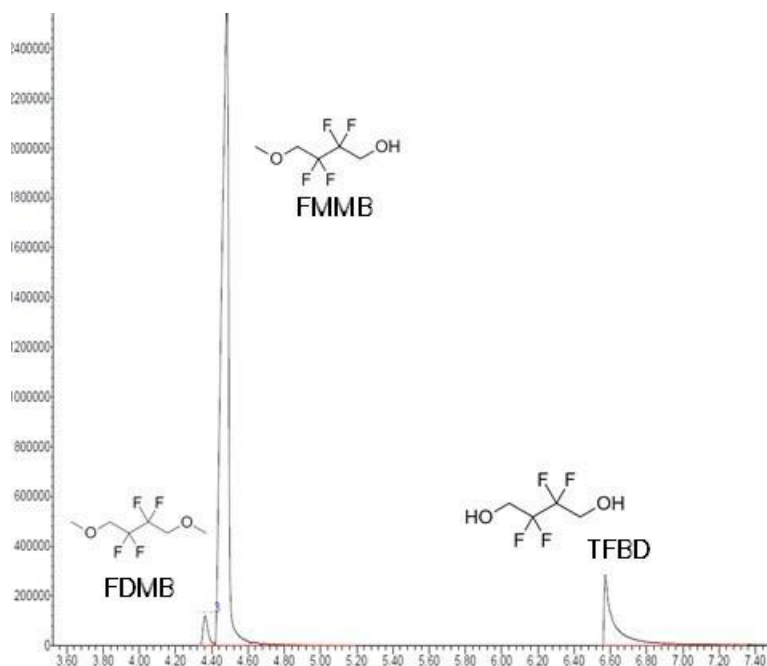


Figure II.4.8 GC/MS spectra of the three component mixture from FMMB synthesis.

With a ready supply of monomethyl 2,2,3,3-butanediol (FMMB), a new set of derivatives was synthesized. A select few materials have also been synthesized from commercial monomethyl butanediol (MMB). These new materials (Table II.4.3) are under investigation in coin cells.

Table II.4.3 New materials based on monomethyl-tetrafluorobutanediol

Compound	Linear formula	GC/MS purity
FMMB	$\text{CH}_3\text{-O-CH}_2\text{-CF}_2\text{-CF}_2\text{-CH}_2\text{-O-H}$	>99.5
F-DMBEE	$\text{CH}_3\text{-O-CH}_2\text{-CF}_2\text{-CF}_2\text{-CH}_2\text{-O-CH}_2\text{-CH}_2\text{-O-CH}_3$	>99.7
FMMB-Tos	$\text{CH}_3\text{-O-CH}_2\text{-CF}_2\text{-CF}_2\text{-CH}_2\text{-O-SO}_2\text{-C}_6\text{H}_4\text{-CH}_3$	99.92
FMDFEB	$\text{CH}_3\text{-O-CH}_2\text{-CF}_2\text{-CF}_2\text{-CH}_2\text{-O-CH}_2\text{-CHF}_2$	>99.5
FMDFTB	$\text{CH}_3\text{-O-CH}_2\text{-CF}_2\text{-CF}_2\text{-CH}_2\text{-O-CH}_2\text{-CF}_2\text{-CHF}_2$	>99.5
FMBMC	$\text{CH}_3\text{-O-CH}_2\text{-CF}_2\text{-CF}_2\text{-CH}_2\text{-O-C(O)-O-CH}_3$	>99.5
DMBEE	$\text{CH}_3\text{-O-CH}_2\text{-CH}_2\text{-CH}_2\text{-CH}_2\text{-O-CH}_2\text{-CH}_2\text{-O-CH}_3$	>99.5
TMMB	$\text{CH}_3\text{-O-CH}_2\text{-CH}_2\text{-CH}_2\text{-CH}_2\text{-O-CH}_2\text{-CF}_3$	99.86
MBMC	$\text{CH}_3\text{-O-CH}_2\text{-CH}_2\text{-CH}_2\text{-CH}_2\text{-O-C(O)-O-CH}_3$	99.47

An example analysis is shown below in Figure II.4.9 for the compound FMDFEB (formula in Table II.4.3). Due to the unsymmetric structure, each CF_2 group has a separate signal in the ^{19}F spectrum. The middle CF_2 groups each appear as triplets due to proton coupling. The terminal CHF_2 group appears as a large doublet ($^1J_{\text{CF}}$) split into a smaller triplet ($^3J_{\text{CF}}$). In the ^1H spectrum, the CHF_2 signal is easily seen as a triplet of triplets pattern centered at about 6 ppm. The remaining CH_2 protons overlap significantly at this field strength (80MHz).

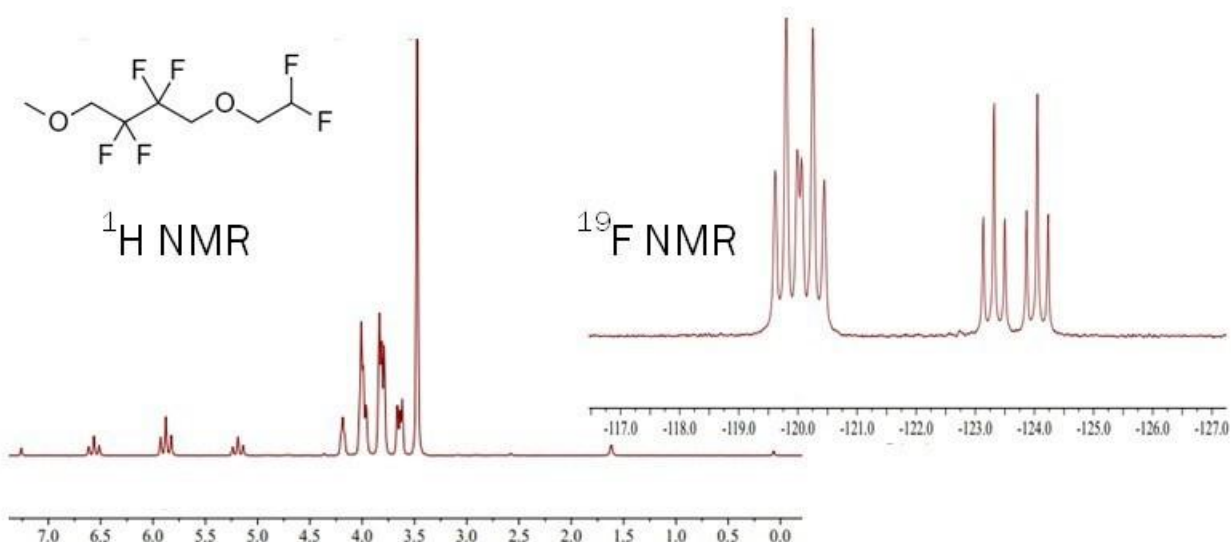


Figure II.4.9 NMR data for FMDFEB

We have continued to develop lithium tricyanoimidazole (Li-TCI) synthesis procedures, this year developing a full flow synthesis and separation. This year we moved to using HPLC pumps for continuous delivery of solutions to the flow reactor (Figure II.4.10). In addition, a membrane separator was added post-reaction to separate the aqueous stream from the product-containing organic phase.

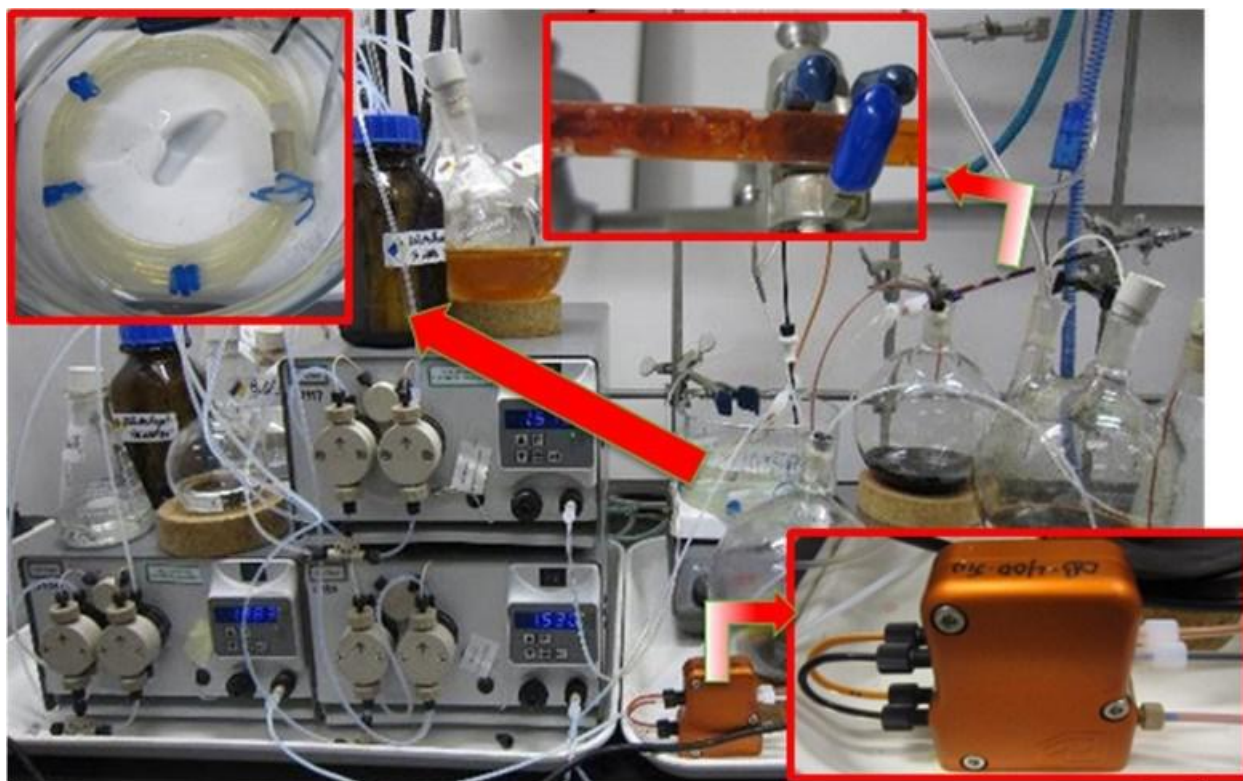


Figure II.4.10 Flow chemistry reaction for Li-TCI.

2-Amino-4,5-dicyanoimidazole is reacted with tert-butyl nitrite to form a diazonium intermediate in the flow reactor coil (Figure II.4.10, Figure II.4.11). As this material is explosive, flow chemistry is the only technology available to produce even medium scale amounts of this material. The chemical inventory of the system is kept very low, as the material is quenched in the tube reactor immediately upon exiting the flow reactor coil. In Figure II.4.10, this is seen in the expanded views. The light yellow coil reactor (left expanded box) allows sufficient time for the starting 2-amino-4,5-dicyanoimidazole to fully react with tert-butyl nitrite in a mixed acetonitrile/dimethyl sulfoxide/water system containing the 2-amino-4,5-dicyanoimidazole; tert-butyl nitrite is dissolved in butyl acetate. At this point, the reaction is homogenous. As this exits the coil, it is mixed with an aqueous solution of potassium cyanide, copper (I) cyanide, and potassium carbonate. This immediately forms an orange triphasic (gas, aqueous, organic layers) solution (top expanded box) and generates nitrogen gas bubbles. The gas evolution caused extensive problems in previous reactor designs. The bubbles caused plug flow and/or made for variable retention times. Here, the reactor tube design allows the bubbles to form and exit the tube reactor without interfering with the liquid flow rate. Upon exiting the tube reactor, the reaction eluent is collected into a flask. This allows the gas/liquid separation. The aqueous and organic layers are then separated with a continuous membrane separator (lower expanded box), with the darker aqueous (copper byproducts) being rejected by the membrane, and the product-containing orange organic phase permeating through the membrane.

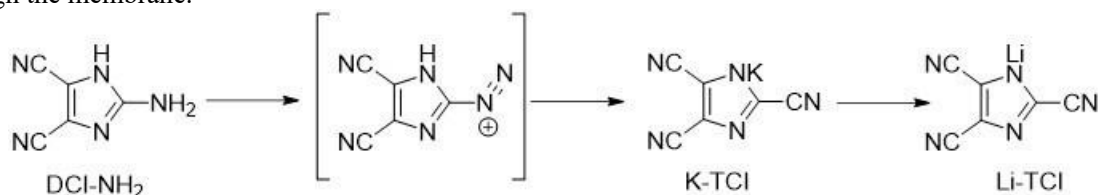


Figure II.4.11 Chemical structures for the synthesis of Li-TCl

Finally, we have initiated corrosion suppression studies to mitigate the effect of LiFSI on the aluminum current collector at high voltages (Figure II.4.12 and Figure II.4.13). We use “Cathode-free” CR2032 coin cells with an aluminum-clad stainless steel coin cells casing assembled as follows: “Al-clad cap – Al foil – separator – separator – Li metal – spacer – spacer – spring – s. s. cap”. Cells were charged from 3.5 V to 5.0 V in 0.05 V steps and held 1 h at each step to monitor for any current increase. Al-clad case is essential to prevent stainless steel corrosion by LiFSI-bearing electrolyte. Figure II.4.12 clearly shows the “corrosion current” generated in a simple Li-FSI (lithium bis(fluorosulfonyl)imide) solutions. Added salts have a positive, but limited effect.

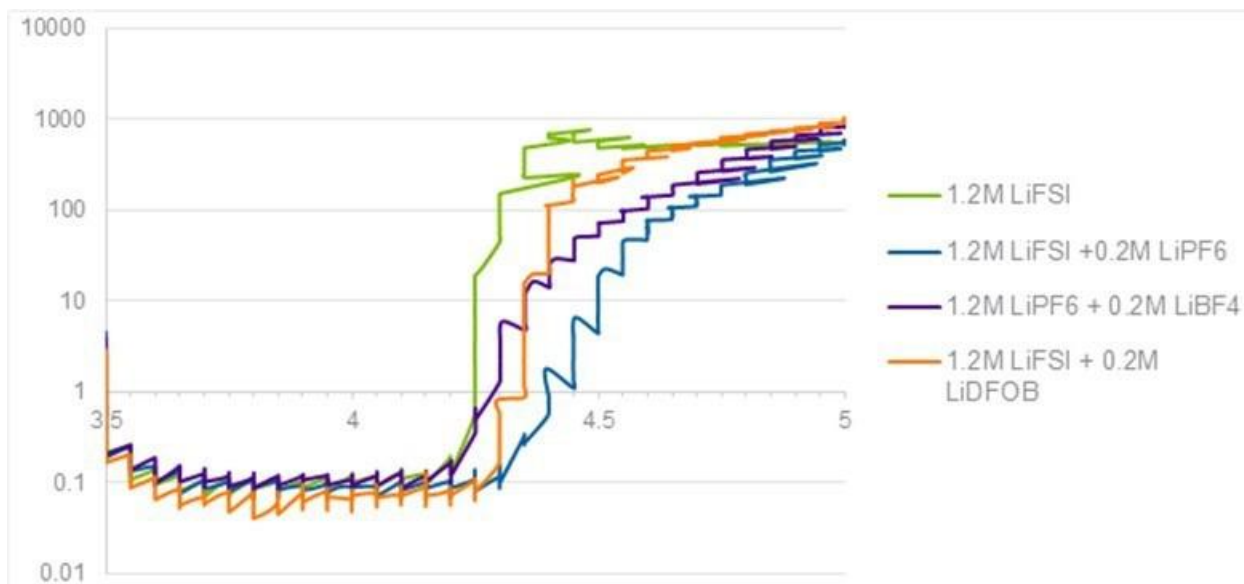


Figure II.4.12 Current response to stepped voltage

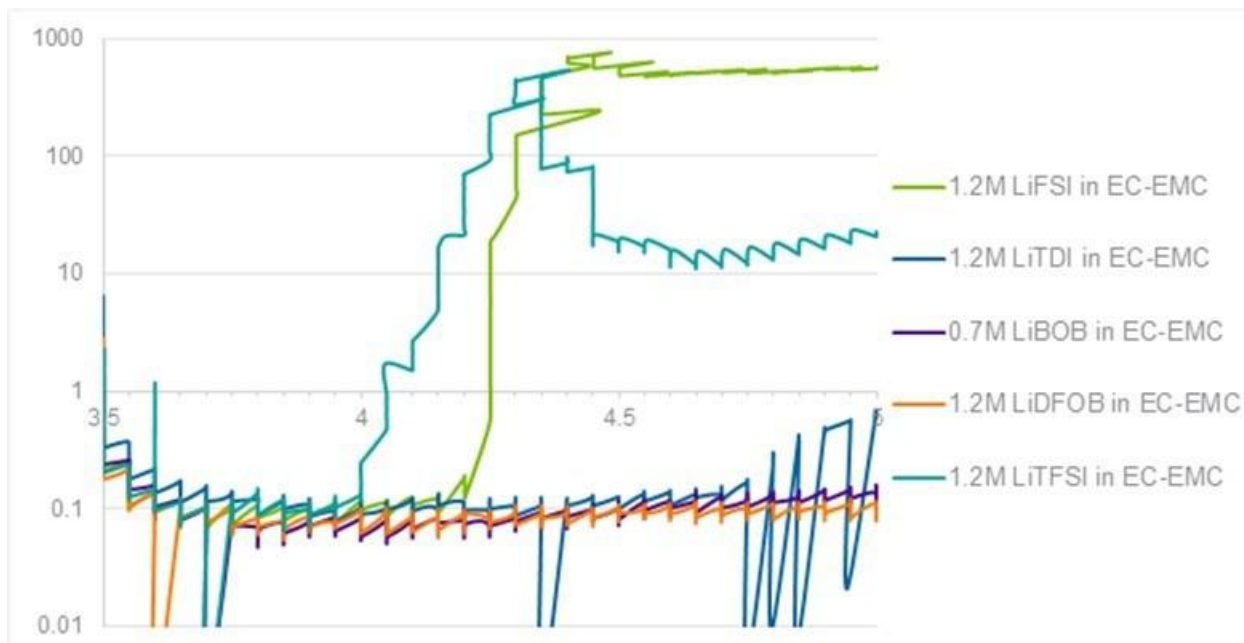


Figure II.4.13 Current response to stepped voltage

Figure II.4.13 shows the current suppression effect by three electrolyte formulations: 0.7M LiBOB in EC-EMC, 1.2M LiDFOB in EC-EMC, and 1.2M Li-TDI in EC-EMC. [LiBOB = lithium bis(oxalatoborate); EC= ethylene carbonate, EMC = ethyl methyl carbonate, LiDFOB = lithium difluoro(oxalate)borate, Li-TDI = lithium 2-trifluoromethyl, 4-5-dicyanoimidazole].

These results from these two figures are encouraging, but more work needs to be done. Clearly Li-FSI and to some extent Li-TFSI are not stable to aluminum at the higher voltages (ca. 4.05 for FSI and 4.25 for TFSI), that are needed for high energy cells. Li-FSI is the most likely replacement for LiPF₆, as Li-FSI is significantly more stable to heat and hydrolysis. What is still needed is a methodology to use this material (Li-FSI) at a higher voltage- possibly by using blended salt mixtures or additives to help prevent electrochemical reaction of

the aluminum components. In initial screening tests, we have demonstrated that other materials (LiBOB, LiDFOB, Li-TDI) are stable at these voltages and do not show any current “leakage” in these tests.

We continue to test these and other additives and design new materials to act as “corrosion inhibitors” in LiFSI cells.

The project has been affected by the COVID-19 pandemic, mostly this has been expressed as delays in procurement of lab supplies, chemicals and equipment. In particular, component parts for existing equipment has taken a long time to procure. Certain vendors have either gone out of business or offer limited supplier—this has delayed the coin cell testing whilst we find and evaluate new vendors for aluminum-clad coin cell components needed for the corrosion testing. Common stainless steel parts cannot be used in this test.

Conclusions

The Process group’s experimental materials scale-up program assists the battery research community and allows for a comprehensive evaluation of new materials by industrial laboratories as well as supports basic research. In FY22 the program provided several new, not commercially available materials. Samples of high, uniform quality materials were distributed for further evaluation and research. Over 250 samples, ranging from grams to hundreds of grams of experimental battery materials have been provided to researchers since the program inception.

Evaluation of emerging manufacturing technologies such as continuous flow reactors, microwave assisted reactions, acoustic mixing or reactive distillations to improve product quality while lowering manufacturing costs are all under consideration. We utilize our recently acquired, customized Syrris ASIA320 and Corning Advanced-Flow™ continuous flow chemical reactors to develop expedient manufacturing processes for new electrolyte solvents, salts and additives by improving safety, minimize waste stream and lower material and energy costs.

The large emphasis placed on new cathode materials, especially disordered rock salts and manganese-rich layered oxides, will require new electrolytes to fully meet the potential of these novel materials. New classes of electrolyte solvents (fluorinated butandiol ethers) have started to be developed. New imidazole-based structures have been synthesized and will be investigated for aluminum passivation for use in high voltage LiFSI-based cells. Flow chemistry and flow reactions have proven invaluable in these projects – there is no other practical route to manufacture these materials.

New materials are initially available only in small amounts, if at all. Because manufacturers minimally require kilo amounts for validation and advanced development, this drastically slows the development of the technology. This program is uniquely positioned to deliver experimental materials in sufficient quantity to enable thorough investigation and validation by the broad, independent research community.

Key Publications

Patents and Patent Applications

1. Dzwiniel, Trevor; Pupek, Krzysztof; “Continuous method for preparing carbonate esters.” U.S. Patent 11,028,065, June 8, 2021.
2. Liao, Chen; Dzwiniel, Trevor L.; Liu, Kewei; “Borate salts, polymers and composites.” U.S. Patent Application US20210071000 A1 March 3, 2021.

Papers

1. Liu, Kewei; Xie, Yingying; Yang, Zhenzhen; Kim, Hong-Keun; Dzwiniel, Trevor L.; Yang, Jianzhong; Xiong, Hui; Liao, Chen; “Design of a single-ion conducting polymer electrolyte for sodium-ion batteries.” *Journal of the Electrochemical Society* (2021), 168(12), 120543.

2. Liu, Kewei; Li, Xiang; Cai, Jiyu; Yang, Zhenzhen; Chen, Zonghai ; Key, Baris ; Zhang, Zhengcheng; Dzwiniel, Trevor L.; Liao, Chen; “Design of High-Voltage Stable Hybrid Electrolyte with an Ultrahigh Li Transference Number.” *ACS Energy Letters* (2021), 6(4), 1315-1323.
3. Yang, Jianzhong ; Liu, Qian; Pupek, Krzysztof Z.; Dzwiniel, Trevor L.; Dietz Rago, Nancy L.; Cao, Jiayu; Dandu, Naveen; Curtiss, Larry; Liu, Kewei; Liao, Chen; Zhang, Zhengcheng; “Molecular Engineering to Enable High-Voltage Lithium-Ion Battery: From Propylene Carbonate to Trifluoropropylene Carbonate.” *ACS Energy Letters* (2021), 6(2), 371-378.

References

1. Yu, Z., Wang, H., Kong, X. et al.; Molecular design for electrolyte solvents enabling energy-dense and long-cycling lithium metal batteries; *Nat Energy* **5**, 526–533 (2020).
2. Peiyuan Ma, Priyadarshini Mirmira, and Chibueze V. Amanchukwu; Effect of Building Block Connectivity and Ion Solvation on Electrochemical Stability and Ionic Conductivity in Novel Fluoroether Electrolytes; *ACS Central Science* **2021** 7 (7), 1232-1244.
3. Sang Cheol Kim, Xian Kong, Rafael A. Vilá, William Huang, Yuelang Chen, David T. Boyle, Zhiao Yu, Hansen Wang, Zhenan Bao, Jian Qin, and Yi Cui; Potentiometric Measurement to Probe Solvation Energy and Its Correlation to Lithium Battery Cyclability; *Journal of the American Chemical Society* **2021** 143 (27), 10301-10308.

Acknowledgements

MERF Critical Battery Materials Team: Trevor Dzwiniel, Thomas Do, Amber Tabaka and Argonne's Collaborators: John Zhang, Daniel Abraham, Qian Liu, Wenquan Lu, Bryant Polzin, Steven Trask.

II.5 Structure-Activity Relationships in the Optimizing Electrode Processing Streams for LiBs (LBNL)

Vince Battaglia, Principal Investigator

Lawrence Berkeley National Laboratory
1 Cyclotron Road, MS 70R0108B
Berkeley, CA 94720
E-mail: vsbattaglia@lbl.gov

Haiyan Croft, DOE Technology Development Manager

U.S. Department of Energy
E-mail: haiyan.croft@ee.doe.gov

Start Date: October 1, 2021

End Date: September 30, 2022

Project Funding: \$500,000

DOE share: \$500,000

Non-DOE share: \$0

Project Introduction

Conventional porous electrodes for Li-ion and other batteries are produced by mixing slurries containing solvents, active material, conductive additive, and binder, and casting these onto foil current collectors on which the coatings dry and consolidate. It is well-known that final product performance can be highly dependent on the fabrication processes, in which each step involves a wide range of potential design decisions. For instance, with a single simple IR heater, one might vary the construction of the heater, heater position, heating power, and exposure time, all of which might be characterized by continuous variables, making the process design space extremely large even in this simple case. Unfortunately, it is difficult to understand connections among process choices and outcomes due to the difficulty of observing these processes, particularly in industrially-relevant settings, making it difficult to construct accurate models. For this reason, it is typical to optimize processes through trial-and-error, which tends to be time-consuming and costly. Our interest in this project is in reducing these costs as processes are moved from the lab scale to industrial scale.

Objectives

Our objectives in this project are to understand the mechanisms by which process choices influence product outcomes for battery electrodes and to make this information useful to electrode manufacturers and researchers.

Approach

Our initial approach in this project is to make industrially-relevant electrode fabrication processes more observable. We are creating experimental setups that will mimic industrially-relevant conditions, and are using these setups in combination with various instruments in order to probe fabrication processes. As our understanding of these processes grows, we will summarize our findings as mathematical models implemented as open-source software, facilitating use by electrode manufacturers and researchers.

Results

Our initial approach in this project is to make industrially-relevant electrode fabrication processes more observable. We are creating experimental setups that will mimic industrially-relevant conditions, and are using these setups in combination with various instruments in order to probe fabrication processes. As our understanding of these processes grows, we will summarize our findings as mathematical models implemented as open-source software, facilitating use by electrode manufacturers and researchers.

Conclusions

Jointly with Advanced Manufacturing Office (AMO) and Hydrogen and Fuel Cell Technologies Office (HFTO) funding, we completed the first iteration of our custom automated miniature coating/drying line with infrared (IR) heating capability. We designed this apparatus to interoperate with both a confocal microscope

system in our laboratory, as well as with the hard X-ray microtomography beamline at the Advanced Light Source (ALS). We have also begun constructing a custom convective heating unit which we will integrate for later studies.

To enable convenient remote control of the miniature coating/drying line in closed beamline hutches, we additionally developed a general-purpose networked control platform, initially based on an inexpensive, commercially-available single-board computer. This platform uses open protocols and can be readily customized for new applications, and developers can choose from a wide range of programming languages when implementing new controllers. The platform was designed with security as a priority: network communications are encrypted, and safety limits are enforced when responding to instructions. Our platform will be considered for later open-source release.

We additionally developed “just-in-time” slurry production procedures, with the goal of being able to continuously supply consistent samples for immediate use in multi-day X-ray beamline experiments. Switching from a high-shear mixer to a planetary ball mill was key to rapidly producing well-mixed samples with minimal trapped air bubbles, as determined from a series of trial coating experiments. Samples consisted of silica active material, carbon black, and polyacrylic acid (PAA) [unmodified or with Li or Cs substitutions], suspended in a mixture of water and isopropyl alcohol, as well as nickel manganese cobalt oxide (NMC), polyvinylidene fluoride (PVDF), and carbon black in N-methyl-2-pyrrolidone (NMP).

We secured beamtime allotments at the hard X-ray tomography beamline (beamline 8.3.2) at the ALS. Over two sessions, we developed procedures for quickly installing and aligning the miniature automated coating/drying line robot in the 8.3.2 beamline hutch and performing microradiography experiments, with approximately two days of beamline experiments in total. Radiography images were collected every 5 seconds during experiments, the longest of which lasted for over an hour. We varied sample composition and IR heating power. Most of our experiments involved the water/alcohol-based slurries, although we also examined the more conventional NMP-based slurries in several experiments.

After the first beamtime session, which was severely shortened due to ALS maintenance, we modified the apparatus to simplify and hasten the process of aligning the sample platform with the X-ray beam. Previously, this required adjustment of all four feet of the apparatus, and with the modification, only adjustment of a single micrometer head is needed.

We developed an automated image analysis pipeline to rapidly and consistently process the image sequences collected in the radiography experiments. The electrode coatings in these images were distinguishable from the surrounding material, and density variations within the coatings were observable (for an example, see the labeled radiography profile sample in Figure II.5.1). The image analysis pipeline automatically detects interfaces, corrects for platform tilt in the casting direction, and aligns images (as we observed significant vertical platform movement throughout these experiments, largely attributable to thermal expansion). From these analyses, we first detected that sample alignment with the X-ray beam worsens prior to or early in each experiment, presumably due to flow of lubricant in the complicated tilt-correction joint, which complicates image analysis and which we will address later through additional upgrades to the miniature coating/drying line.

Despite these complications, we were able to observe some surprising phenomena that we have sought to explain qualitatively, including heating-driven coating stratification (see Figure II.5.2) and prolonged fluid flow for coatings produced from less viscous slurry samples. Based on our explanations, some of these phenomena are likely to be specific to manually-intensive lab-scale fabrication, and some are more general. Our findings should be immediately relevant to anyone preparing electrodes at the laboratory scale and seeking a better understanding of relationships to industrial electrode production. We will investigate these phenomena further in future experiments using these and other tools, and we are presently documenting our findings in a manuscript that will be submitted for review shortly.

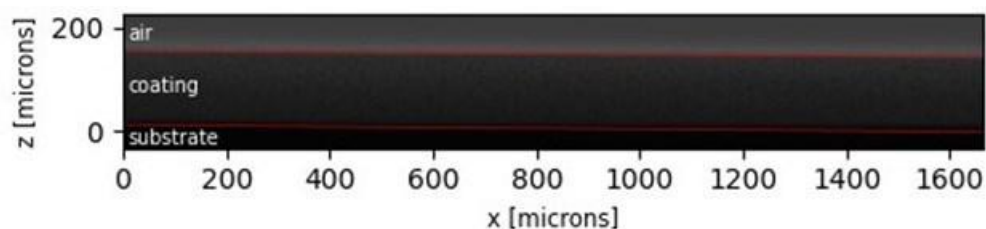


Figure II.5.1 Example radiography image of electrode coating, taken in profile, with detected interfaces artificially highlighted in red. (LBNL)

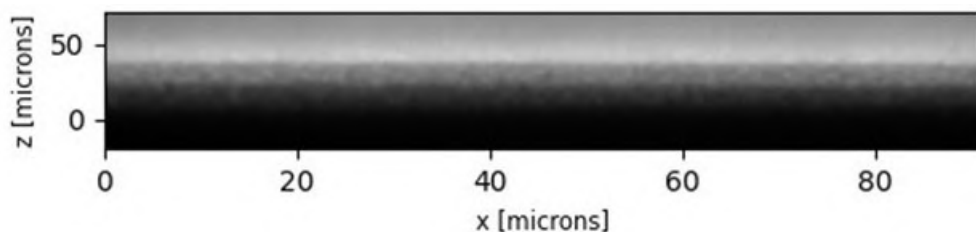


Figure II.5.2 Example radiography image showing heating-driven stratification of electrode coating. (LBNL)

Key Publications

1. Zhang, B., Fan, B., Huang, Z., Higa, K., Battaglia, V. S., and Prasher, R. S. (October 3, 2022). "A Review of Dispersion Film Drying Research." ASME. *J. Electrochem. En. Conv. Stor.* August 2023; 20(3): 030801. <https://doi.org/10.1115/1.4055392>

Acknowledgements

Kenneth Higa, Buyi Zhang, Dilni Kaveendi Chandrasiri, Denny Tan, Daniel Collins-Wildman, Patricius Bloemhard, Eric Lizotte, Gabriela Martin-Nyenhuis, Yanbao Fu, Dula Parkinson, and Ravi Prasher also contributed to this project as LBNL employees or affiliates.

II.6 Fabricate and Test Solid-state Ceramic Electrolytes and Electrolyte/Cathode Laminates (LBNL)

Mike Tucker, Principal Investigator

Lawrence Berkeley National Laboratory
1 Cyclotron Rd
Berkeley, CA 94720
E-mail: MCTucker@LBL.gov

Simon Thompson, DOE Technology Development Manager

U.S. Department of Energy
E-mail: Simon.Thompson@ee.doe.gov

Start Date: October 1, 2021

End Date: September 30, 2022

Project Funding: \$200,000

DOE share: \$200,000

Non-DOE share: \$0

Project Introduction

Ceramic solid state battery technology is limited by processing constraints such as Li loss during sintering, reaction between active materials and electrolyte during processing, and non-ideal microstructure and electrochemical/mechanical properties of layers fabricated via conventional processing routes. This project addresses these limitations by elucidating behavior of the key materials during processing, including sintering behavior, reactivity, and phase stability. Of particular importance is the fabrication of thin, completely dense electrolyte and thick, highly porous cathode scaffold layers using high-volume, low-cost fabrication processes. The project focuses on $\text{Li}_{6.25}\text{Al}_{0.25}\text{La}_3\text{Zr}_2\text{O}_{12}$ (LLZO).

Objectives

The project objectives are: to determine processing methods and conditions that enable high-volume, low-cost production of solid state battery ceramic electrolyte, electrolyte-cathode bilayer structures, and solid state batteries based on these structures; and, demonstrate improved electrochemical and mechanical performance for these structures.

Approach

The impact of processing conditions and precursor properties on layer structure, electrochemical performance, and mechanical properties will be determined. Commercially-available LLZO and cathode powders are used for all experiments to eliminate batch variations and ensure experimentally observed processing improvements are not due to variation of powder properties. Phased development efforts focus independently on LLZO sintering, porous scaffold and bilayer fabrication, and cathode materials and deposition. The results are used to inform the holistic fabrication of a complete cell.

Results

Creating and maintaining good interfacial contact between LLZO and cathode material is expected to be one of the more difficult challenges to producing practical solid-state batteries. In order to overcome this issue an ionically conductive polymer is used as part of a composite cathode to act as a flexible, high-contact-area interfacial catholyte material between the LLZO and cathode active material. The viability of the composite cathode strategy was assessed by assembling planar model cells with LLZO pellets or the tape cast LLZO sheets developed in the previous reporting period. It was demonstrated that residual N-Methylpyrrolidone (NMP) solvent remaining in a PVDF/LiTFSI solid polymer catholyte after incomplete drying can dramatically lower the interfacial resistance between LLZO electrolyte and $\text{LiNi}_{1/3}\text{Mn}_{1/3}\text{Co}_{1/3}\text{O}_2$ (NMC111) cathode active material. All-solid-state batteries were assembled with LLZO dense/porous bi-layer structures. The cathode slurry, composed of 80% coated single crystal $\text{LiNi}_{0.8}\text{Mn}_{0.1}\text{Co}_{0.1}\text{O}_2$ (NMC811), 10% carbon black and 10% PVDF, was infiltrated into the porous structures under vacuum. An alternative organic cathode (OC) was also

explored, and LLZO electrolyte dramatically improves initial capacity and capacity retention compared to a cell with Celgard separator and liquid electrolyte by preventing crossover of the organic cathode to the anode.

NMC111 Battery Cells

Dense and stable LLZO electrolyte pellets were prepared by sintering in Ar atmosphere, followed by removal of the Li-deficient surface layer by polishing. No dendrite growth was detected for a Li/LLZO/Li symmetric cell cycled at 0.35 mA cm^{-2} over 100 cycles. ASSB cells were prepared with Li metal anode and NMC cathode with PVDF/LiTFSI catholyte. It was found that residual NMP in the cathode has a large impact on cell performance, and incomplete drying therefore reduces the interfacial impedance initially. The amount of residual NMP solvent in the cathode was optimized and the smallest interfacial resistance was obtained with 8.6% NMP. A model study of free-standing PVDF-LiTFSI film suggests that the primary effect of residual NMP is on the catholyte conductivity via solvent absorption and plasticizing the PVDF. Also, LiTFSI content was optimized to 8.5%. Full cells were cycled at 60°C , 25°C and -10°C and the highest retention was obtained at -10°C , showing the temperature-dependence of the capacity fade. A typical charge-discharge curve at -10°C with a rate of 0.1 C is shown in Figure II.6.1 with a discharge capacity of 117 mAh/g. The cell shows no degradation in the first 50 cycles but starts degrading after that. The total capacity retention is more than 70% after 100 cycles, a lower fade rate than at 25°C .

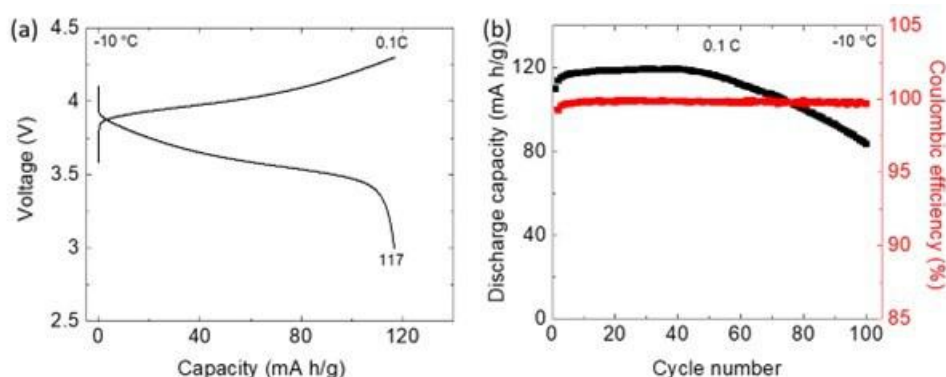


Figure II.6.1 Planar cell with NMC cathode and residual NMP. (a) Charge/discharge curves at -10°C with rate of 0.1 C; (b) Discharge capacity and coulombic efficiency versus cycle number at -10°C .

The solvent residue in the polymer catholyte plays a critical role on the cell performance and cells with DMSO residue in the cathode show better performance. The cell with DMSO as the solvent has improved capacity retention and coulombic efficiency, compared to the cells with NMP or DMF as the solvent. (Figure II.6.2)

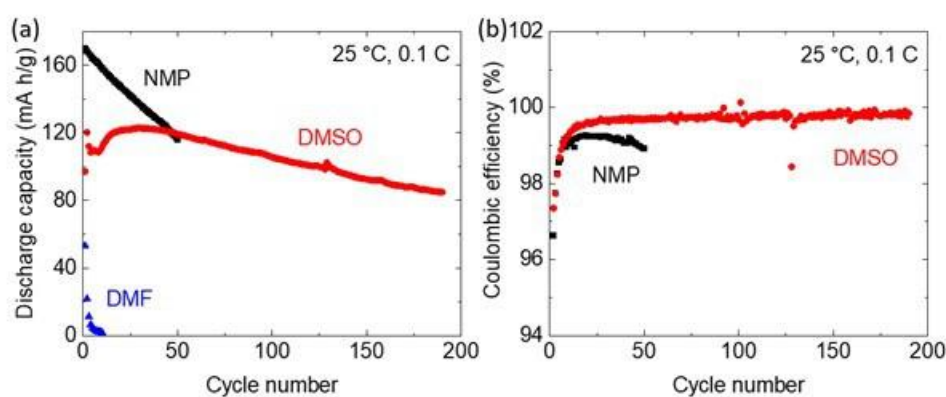


Figure II.6.2 Planar cell with NMC cathode and various residual solvents. (a) Charge/discharge curves and (b) coulombic efficiency versus cycle number at 25°C with rate of 0.1 C.

Organic Cathode

Solid state organic cathode (OC) cells were fabricated with LLZO electrolyte separator and liquid catholyte. LLZO can serve as an enabling material for production of lithium batteries with high capacity small molecule organic cathode materials. The OC used here has a theoretical capacity of 307 mAh/g. By preventing crossover of the organic cathode to the anode, the solid separator dramatically improves initial capacity and capacity retention relative to a cell with Celgard separator and liquid electrolyte (Figure II.6.3a). With the liquid electrolyte, visible discoloration and reaction products are apparent on the Li-alloy anode after cycling. Consumption of cathode material via crossover was not observed with the LLZO separator, but relatively rapid capacity fade still occurred. Multiple cells with LLZO separator were cycled with various upper and lower voltage cutoffs to determine if the capacity fade was associated with an oxidative or reductive side reaction. Increasing the lower voltage cutoff from 1.6V to 2.0V or higher dramatically increased capacity retention (Figure II.6.3b). This result suggests that a reduction side reaction at low cell voltage consumes cathode active material. Increasing the lower cutoff voltage mitigates capacity fade, but reduces the total available capacity. Further work should focus on identifying the side reaction mechanism and products. If the entire capacity of the organic cathode can be utilized, then the energy density can be competitive despite the relatively low average discharge voltage.

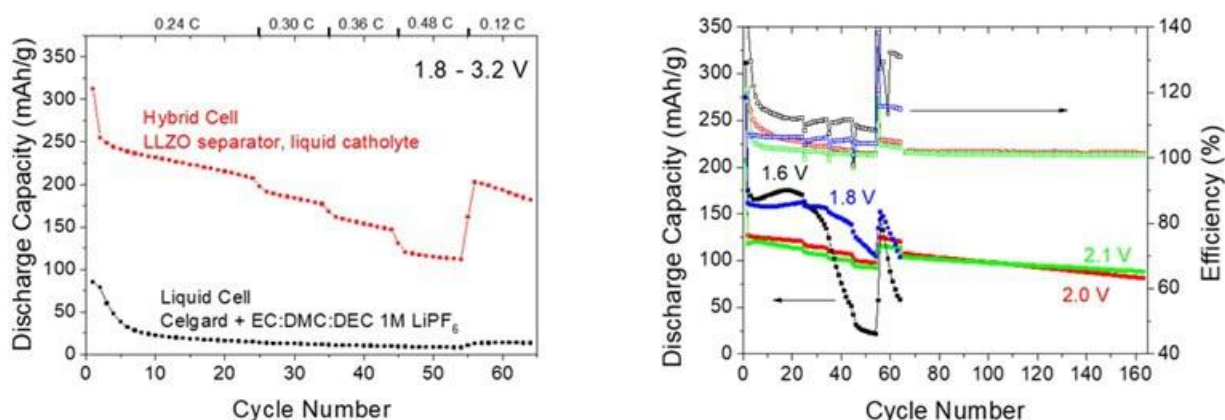


Figure II.6.3 Performance of cells with organic cathode including (a) comparison of capacity fade with liquid and solid LLZO separators, and (b) the impact of lower-voltage-cutoff with an upper-voltage-cutoff of 2.8V for a cell with LLZO separator and liquid catholyte.

Porous Scaffold and Bilayer Structure Processing

LLZO bi-layer structures were prepared with the recipe developed in the previous reporting period. The dense layer is ~50 μm and the porous layer is ~150 μm with a porosity of ~70%. Cathode suspension was infiltrated into the porous structure after Li anode was prepared. The cell was dried at 100°C overnight. The all-solid-state battery was tested in a Ar-filled glove box without sealing at room temperature with a rate of 0.02 C. The discharge capacity is a little over 30 mAh/g and is stable for 4 cycles (cycling ongoing) (Figure II.6.4). This is a first proof of concept, and future work will focus on improving cathode loading in the porous substrate and utilization of the cathode active material.

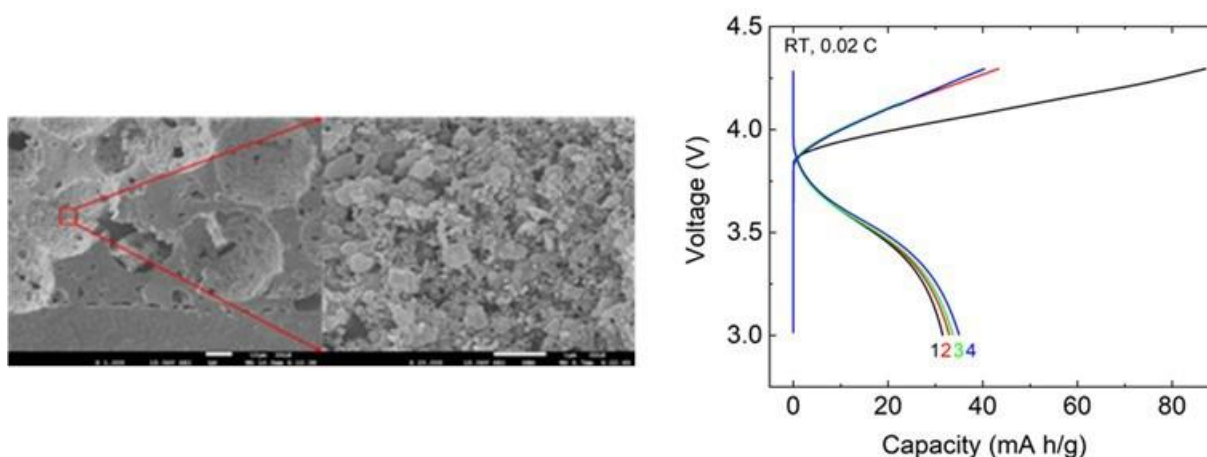


Figure II.6.4 Full ASSB cell. (left) Bilayer cell with cathode infiltrated into pores. (right) Charge/discharge curves at room temperature with a rate of 0.02 C for a LLZO bi-layer structure cell.

Conclusions

This project aims to prepare LLZO-based electrolyte and electrolyte/cathode scaffold structures using scalable processing techniques such as tape casting and furnace sintering. Work in this project period focused on planar structures for NMC111 and organic cathodes and bi-layer structures for single crystal NMC811. A catholyte, consisting of PVDF, LiTFSI and a small amount of solvent residue which can mitigate the interfacial resistance between cathode with LLZO electrolytes, is developed. LLZO thin separators dramatically improve initial capacity and capacity retention with an organic cathode. In addition, all-solid-state batteries are assembled with LLZO dense/porous bi-layer structures, although the discharge capacity is still low.

Key Publications

1. Shen, Fengyu, Robert Jonson, and Michael C. Tucker. 2022. "The impact of residual solvent on catholyte performance in solid-state batteries" *J. Materials Chem. A*, <https://doi.org/10.1039/D2TA04847G>
2. Shen, Fengyu, Robert Jonson, Dilworth Parkinson, and Michael C. Tucker. 2022. "Preparing Li-garnet electrodes with engineered structures by phase inversion and high shear compaction processes" *J. American Ceramic Soc.*, 105: 90-98. <https://doi.org/10.1111/jace.18037>

Acknowledgements

All data presented in this report was generated by Fengyu Shen and Robert Jonson.

II.7 Higher Energy Density via Inactive Components and Processing Conditions (LBNL)

Vincent Battaglia, Principal Investigator

Lawrence Berkeley National Laboratory
1 Cyclotron Rd
Berkeley, CA 94720
E-mail: vsbattaglia@lbl.gov

Haiyan Croft, DOE Technology Development Manager

U.S. Department of Energy
E-mail: Haiyan.Croft@ee.doe.gov

Start Date: October 1, 2021

End Date: September 30, 2022

Project Funding (FY22): \$290,000

DOE share: \$290,000

Non-DOE share: \$0

Project Introduction

The problems in electrode fabrication we are addressing in this project are two-fold 1) that high loading electrodes can be made much thinner if the conductive additive and polymer binder fractions can be minimized, but there is no guidance on what properties of the active material, carbon, and binder dictate how low can we reduce the inactives before there is an impact on power or cycle life, and 2) what is the correct amount of solvent to use for mixing and casting the slurry.

Objectives

For the problem of understanding what properties dictate the lower limits of binder and carbon content, we will figure out how little binder is needed to make a cohesive laminate and how little carbon is needed to make the electrode electronically conductive, while investigating several forms of conductive additive. We will also investigate if the additives support each other or work against each other when all three components are combined. For the problem of getting the solvent composition correct, we will bring understanding to the role the solvent is playing in mixing and drying and how one optimizes between the two.

Approach

Our general approach to addressing these problems is to break the problem down into fewer components. To determine the minimum amounts of additives required to provide cohesion and conductivity, we studied the properties of two component systems to provide insights in constructing the three-component system. For example, we investigate the properties of laminates consisting of simply carbon and binder. By properties, we mean we measure adhesion, cohesion, porosity, and electronic conductivity to identify ratios of carbon and binder that lead to an overall optimum. We will investigate different combinations of mixtures of carbon and active material to determine the minimum carbon content required to achieve percolation and transform the powder mixture from a semi-conductor or insulator to a conductor. We will also investigate the properties of a cast layer of active material and binder to determine the laminates properties, like cohesion and adhesion, as a function of the ratio of the two. From these basics, we will start investigating the impact of a third component starting from a low level and working our way up. Ultimately, our goal is to be able to determine, *a priori*, the best combination of materials by measuring the properties of each individual component and pairwise combination of components, how much is needed of each to fabricate an electrode of minimum carbon and binder that results in an electrode of high energy density and good enough power density to meet the USABC pulse discharge and charge metrics.

The amount of solvent clearly impacts the viscosity. The viscosity plays several roles: it needs to be high enough to transmit energy throughout the mixture for good mixing, low enough to allow for intimate mixing of the two components, high enough to keep the slurry from running off the substrate and low enough to prevent

rippling of the cast slurry. We plan multiple rheological experiments at several concentrations and temperatures to fully understand how to arrive at the optimum concentration and drying conditions.

Results

The effort this year focused on understanding how the ratio of the binder and carbon and how the total amount of solvent in the initial slurry impact key mechanical and performance metrics of a cathode.

Carbon to binder ratio

In an effort to reduce the overall carbon and binder content of the electrode, we wanted to understand the impact of varying the two relative each other. Therefore, we made a series of laminates of different ratios of carbon and binder, specifically carbon fractions of 20, 30, 35, 40, 45, 50, 55, 70, and 80 % were cast and evaluated.

One measurement we made of the laminate was the force needed to peel the laminate from the current collector at an angle of 180 ° (essentially pulling it back over itself.) As the data shows in Figure II.7.1, there is a peak in the adhesion between 35 and 50% carbon. Surprisingly, at least initially, was that films with carbon contents of 35% or lower showed very little adhesive properties. It is also not worthy that films of carbon content of 50% or greater also showed poor adhesion.

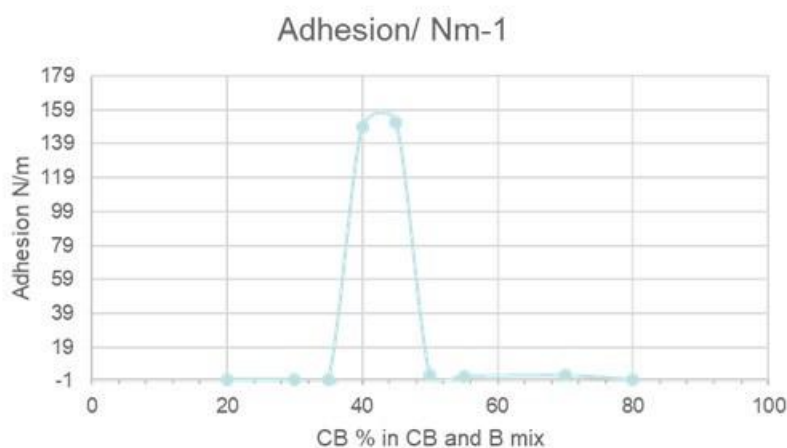


Figure II.7.1 Adhesion force per width of laminate from a 180° peel test for laminates consisting solely of different ratios of carbon and binder.

For the same laminates, we also measured the degree of cohesion using the same instrument. Here (Figure II.7.2) we find that the cohesion drops precipitously with increase in carbon content falling to around half of its initial value (measured at a carbon fraction of 20 %) at a carbon fraction of 40%. We also measured the electronic conductivity of the films as a function of carbon content, that data is provided in Figure II.7.3. Here we see that the electronic conductivity with carbon content starts to climb at 35% carbon and peaks around 45% carbon.

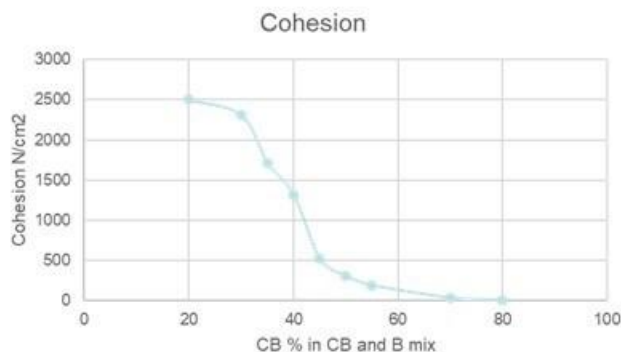


Figure II.7.2 Cohesion of films removed from the current collector at carbon to binder ratios from 0.2:0.8 to 0.8:0.2.

Finally, we measure the open porosity of the films as a function of carbon content. We see in Figure II.7.4 that the porosity starts to increase at 35% which is also where the adhesion and the conductivity start to increase. The porosity continues to climb as successively more carbon is added and begins to level off near 70% carbon.

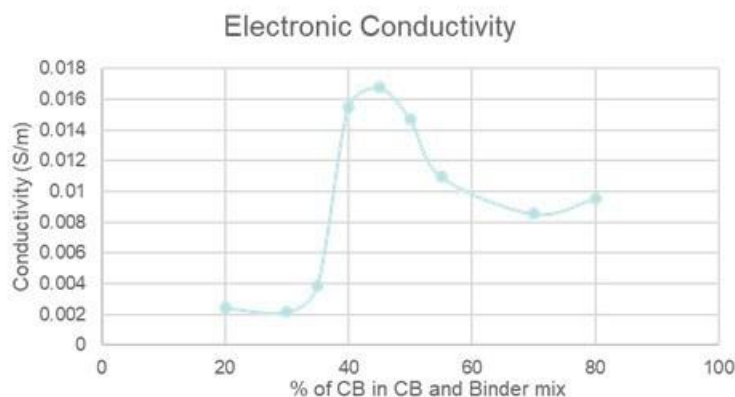


Figure II.7.3 Electronic conductivity of carbon/binder films with varying carbon to binder ratios.

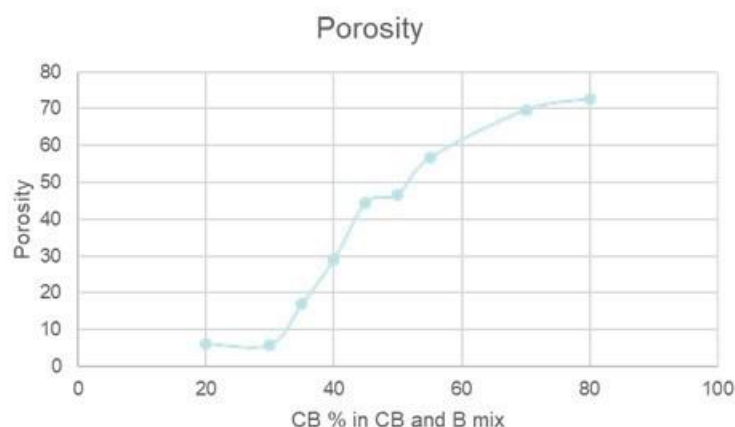


Figure II.7.4 Open porosity of carbon/binder films with varying carbon to binder ratios.

We assume that the porosity is playing a significant role in what is happening to the other properties. At low carbon content, the porosity is low and remains low with the addition of carbon. This indicates that as the solvent leaves the cast slurry, the polymer is collapsing and shrinking to maintain a compact formation with

little porosity. The shrinking of the film during drying implies that the polymer is changing from an extended formation when dissolved in the solvent to a contracted form as the solvent leaves. During this time of polymer contraction the polymer loses contact points with the current collector foil. By the end of the drying, the polymer is fully collapsed and the dry film literally falls off of the foil. At around 35% carbon content we start to measure void porosity in the dried film which we believe means that there is enough carbon in the film to provide structure to the film and limit polymer contraction. The more carbon is added, the less contraction there is, and the greater is the porosity, adhesion, and conductivity. The cohesion appears to be inversely related to the porosity. As the porosity continues to increase, the cohesion continuously decreases as there is just less polymer per cross section which makes the film weaker. We also see that the adhesion and the conductivity reach a maximum value before falling. We believe this is because an increase in carbon brings an increase in surface area to be covered by the polymer, and that too much surface area overwhelms the polymer and the polymer can no longer form a continuous coating. This leads to an incoherent film that is a poor electronic conductor and with few connections to the foil that severely reduces adhesion. The upshot of this is that one should prepare laminates with this polymer and carbon black at a ratio between 2:3 and 9:11. This will need to be adjusted down when considering the additional surface area contributed by the active material.

We also investigated mixing in solvent, combinations of active material and carbon at ratios of 92.8:3.2, 94.6:2.4, 98:0.88, and 99:0.44. Here we measured the particle size distribution at the end of mixing and found that for mixtures with less than 0.88 % binder, the maximum particle size began to decrease after just twenty minutes of mixing. This was supported by confocal microscope imagery provided in Figure II.7.5.a and Figure II.7.5.b. where one can see that the active material powder with significant carbon was larger than the powder with a deficient level of carbon.

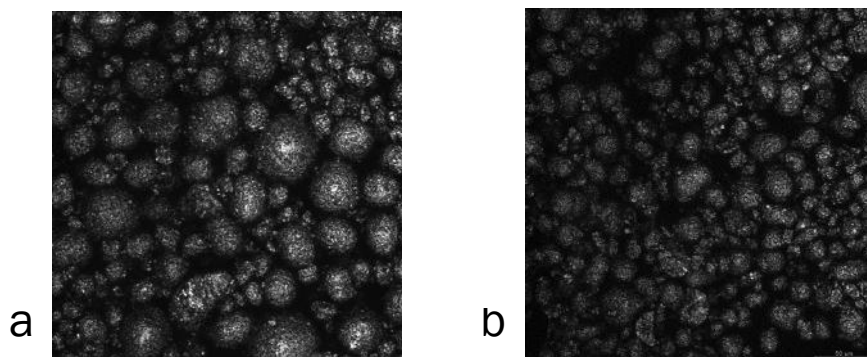


Figure II.7.5 Confocal microscope images of active material and carbon mixed with a. sufficient carbon and b. insufficient carbon.

Solvent content

Finally, we investigated the amount of solvent that is added to the slurry during the mixing steps and compared it to the quality of the coating and the cycling performance. The results of this experiment are reflected in the graph of Figure II.7.6 where the results of good performing electrodes are plotted in blue and the poor performing electrodes are filled in as red. A fit of the blue data suggests a linear relationship between liquid added to the slurry and total carbon black surface area.

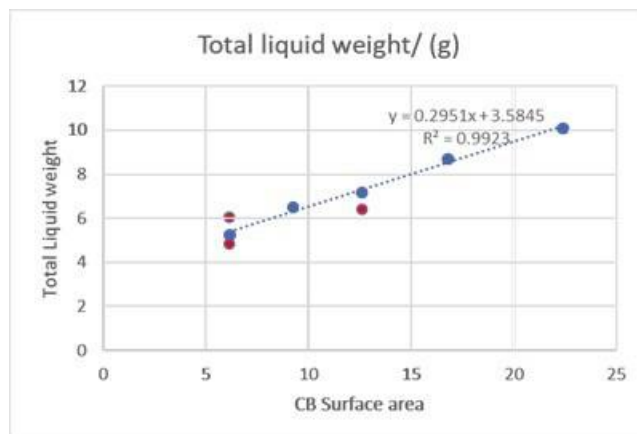


Figure II.7.6 Plot of total solvent amount versus total carbon surface area of several slurries. The slurries that resulted in good performing laminates are labeled with blue circles. A line of achieved through a regression analysis indicates a linear relationship between total solvent content and carbon black surface area in the slurry.

We initially assumed that the correct amount of solvent to add to a slurry was such that the viscosity at a low shear rate was constant. A plot of viscosity of the slurry *versus* active material content of the solid components is provided in Figure II.7.7 for the laminates that performed well. We see here that the viscosity of the best electrodes is not constant but declines as the amount of active material increases (amount of carbon additive decreases.) Thus, the viscosity of the slurry is not as important as the ratio of solvent to carbon. Apparently, controlling the slurry to carbon content, which to a large extent controls the viscosity is more important than holding it to a single value.

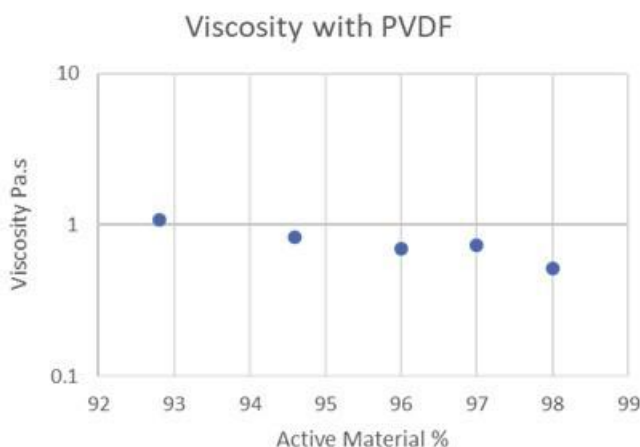


Figure II.7.7 Slurry viscosity *versus* active material content for

Conclusions

From this year's work we arrived at the following conclusions. The carbon additive does more than provide conductivity to the laminate, it is also responsible for the open porosity of the laminate. The porosity limits the contraction of the binder which promotes adherence to the current collector. The carbon structure also leads to long range conductivity in the laminate. The increase in carbon does reduce the cohesiveness of the laminate but as long as the ratio to binder is less than 55:45, there should be enough cohesiveness to keep the laminate together. Overall, for Denka Black (an acetylene black) the carbon to binder ratio should be somewhere between 2:3 and 11:9 when not considering the active material. The addition of active material will likely reduce this range. It appears for NMC 333 that carbon should first be mixed with this, at least at a ratio of 98:0.8 to prevent particle breakdown during mixing. There appears to be an ideal solvent content with regard to mixing and casting that correlates linearly with the surface area of carbon additive.

Acknowledgements

Dilni Wellalage performed the bulk of this research as a postdoc in the group.

II.8 Minimizing Side Reactions in Next-Generation Lithium Ion Battery Cathodes Through Structure-Morphology Optimization (ANL)

Venkat Srinivasan, Principal Investigator

Argonne National Laboratory
9700 South Cass Avenue
Lemont, IL 60439
E-mail: vsrinivasan@anl.gov

Haiyan Croft, DOE Technology Development Manager

U.S. Department of Energy
E-mail: haiyan.croft@hq.doe.gov

Start Date: October 1, 2021

End Date: September 30, 2022

Project Funding (FY22): \$500,000

DOE share: \$500,000

Non-DOE share: \$0

Project Introduction

Lithium ion batteries are finding application in almost all the sectors, starting from electronics and electric vehicles, which extends towards the marine as well as aviation industries. However, such widespread adoption of lithium ion based energy storage technologies calls for further enhancement in the performance metrics demonstrated by the present day battery chemistries, such as, increase in energy density, enhanced cycle life, etc. In order to satisfy the ever increasing demand of the market, new lithium ion chemistries need to be discovered, and synthesized at scale, for successful implementation in the commercially available lithium ion batteries. It is evident that along with finding better battery materials, it is necessary to understand how those materials are made. It does not add much value to discover an excellent material with superior performance if it cannot be synthesized in a cost effective fashion and at large scales. Accordingly, it is necessary to study the “science behind the synthesis” of conventional, as well as novel, materials with potential application in lithium ion batteries. A thorough understanding of the synthesis mechanism can eventually help to devise strategies for making the same material in a cheaper fashion, or can possibly enable the fabrication using easily scalable routes.

In the present research, synthesis of cathode materials used in lithium ion battery is being investigated, while some effort is also being devoted to understanding their performance. Conventional cathode synthesis routes involve two steps, where at first the transition metal hydroxide ($\text{TM}(\text{OH})_2$) or transition metal carbonate (TMCO_3) based cathode precursors are coprecipitated in water based reactors. In the second step, these precursor powders are calcined at high temperatures with lithium salt to oxidize and lithiate them, which finally leads to the formation of the cathode active particles. Note that further surface treatment on top of the as-calcined cathode particles may be needed before incorporation into a real battery electrode, which is not being studied as part of the present effort. It is worth noting that the final cathode particles are obtained after the calcination process where both oxidation and lithiation of the cathode particles occur, which leads to substantial changes in its lattice structure as well as particle morphology. However, elucidating only the calcination step is not sufficient for deciphering the science behind the cathode synthesis. To understand and successfully control the final structure (lattice structure) and morphology (particle size, size distribution, porosity, tap density) of the cathodes, it is necessary to properly elucidate both the coprecipitation and calcination steps of the cathode synthesis process.

Conventional lithium ion battery cathodes demonstrate layered lattice structure where the lithium and transition metals exist in different layers. Majority of the cathode precursors as well as final calcined particles are several microns in diameter, and possess a spherical shape. Each of these secondary particles consist of multiple smaller primary particles, for which the size can range from several tens to hundreds of nanometers.

Size of these primary particles differ substantially between the precursors and the final cathodes. Even though the final cathode particles are determined by the calcination process conducted at an elevated temperature ($\sim 700^{\circ}\text{C}$ to 1000°C), the coprecipitation step substantially influences various attributes of these cathode particles. For example, size of the secondary particles obtained from the coprecipitation step does not change significantly even after calcination, rate of the oxidation and lithiation reaction that occur during calcination depends heavily on the size of the primary particles achieved after coprecipitation, distribution of the transition metals within the cathode particles (for example, gradient cathodes) is again defined by how the coprecipitation is conducted.

Competition between different thermodynamic and kinetic aspects, that impacts the formation of the final cathode particles, will be investigated in the present study. During coprecipitation, competition between the rate of precipitation, minimization of surface energy, and transport of mass through the reacting solution dictates the growth mechanism as well as the morphology, along with surface roughness, of the final precipitates. Similarly, during calcination, interplay between the reaction rate constant, mass transport, and sintering of particles dictate the quality and microstructure of the final cathodes. Competition between these driving forces will be elucidated using appropriate experimental characterization and multiscale computational schemes.

Regarding estimation of cathode performance, this research work explores the link between morphology and performance of lithium manganese rich NMC (LMR-NMC) cathodes. The LMR-NMC material exhibits low diffusion, particularly at low state of charge and performs poorly at high C-rates. Adapting the morphology to obtain smaller diffusion lengths would improve the performance. The LMR-NMC cathode particle (referred to as secondary particle) is agglomeration of nano sized primary particles. There are two different diffusion characteristics associated with the porous secondary particle, first, the size of the primary particle, and second, the nature of agglomeration. Presence of clustering, formation of chains of primary particles or intra-agglomeration closed pores will increase the agglomerate diffusion length. Smaller primary and agglomerate diffusion length is desirable for improved performance. Tailoring the morphology to achieve desired diffusion characteristics is a promising avenue for better performance.

Objectives

In the present effort, three major aspects are investigated: i) Coprecipitation of transition metal carbonate cathode precursors, ii) Calcination of Ni-rich cathodes, and iii) Performance estimation of LMR-NMC cathode particles. Regarding coprecipitation, impact of different transition metals on the morphology of the precipitated carbonate based cathode precursors will be investigated. Changing the transition metal type can modify the supersaturation ratio, which provides the driving force for the precipitation process. Understanding the competition between the reaction rate constant and mass transport processes, that helps in determining the final morphology of the precipitated cathode precursors, is one major objective of this project. Calcination of the Ni-rich NMC cathodes has always been a challenge due to the difficulties associated with oxidizing Ni^{2+} to Ni^{3+} state. Importance of the presence of oxygen in oxidizing Ni, and successfully reacting with the lithium salt, will be elucidated here. Along the same direction, understanding the intermediate phase adopted by the Ni-rich cathode precursors during the calcination process is also an objective of the present research. The final goal of the project is to connect the synthesis conditions to the overall performance of the cathode particles. Accordingly, estimation of voltage vs. capacity performance experienced by the cathode particles must be conducted. Deciphering the influence of the structure and morphology of the cathode particles on the overall capacity is another major objective of the present effort.

Approach

For proper elucidation of the synthesis of cathode particles and estimating their performance, both experimental and computational approaches are adopted as part of this project. Coprecipitation experiments are conducted in batch mode and the precipitated particles are characterized using scanning electron microscopy (SEM), transmission electron microscopy (TEM) and energy dispersive X-ray (EDX) mapping techniques. Regarding calcination, cathode precursors are reacted with lithium salt under elevated temperatures, which is

characterized *in situ* using X-ray diffraction (XRD) techniques. On the computational side, density functional theory (DFT) and ab-initio molecular dynamics (AIMD) based calculations are conducted to understand the variation in lattice structure occurring at the atomic scale. At the mesoscale level, interaction between different particles is captured using the Monte Carlo and phase field based computational methodologies. Some detailed of each of the procedures will be briefly discussed below.

For proper elucidation of the coprecipitation step, various transition metal carbonates (MnCO_3 , NiCO_3 , CoCO_3 and NMC111CO_3) are precipitated in a batch reactor, and the morphology as well as chemical composition of the final precipitates are investigated using appropriate characterization techniques. Concentration of the transition metal sulfates (TMSO_4) are maintained at around 4.5 mM, while the concentration of the precipitating agent, ammonium bicarbonate (NH_4HCO_3) in the present case, is estimated to maximize the supersaturation ratio of the transition metal carbonates (TMCO_3) within the reacting solution. Morphology of the precipitates are characterized using the SEM and TEM imaging techniques, where SEM provides information regarding the secondary particle morphology (length scale $\sim 10\ \mu\text{m}$) and TEM provides information regarding the morphology of the primary particles (length scale $\sim 100\ \text{nm}$). Impact of different transition metals on the size of the primary and secondary particles, along with their surface roughness, are characterized using these imaging schemes.

Regarding calcination, NMC111(OH)_2 and NMC811(OH)_2 are calcined with LiOH under a temperature ramp of $5^\circ\text{C}/\text{min}$ from room temperature to a maximum temperature of 800°C , and the evolution of different phases are visualized *in situ* using the XRD technique. Depending on the amount of Ni present within the cathode precursor, different intermediate phases are observed, which substantially controls the reaction of lithium with the cathode precursors, and finally impacts the evolution of the desired layered phase.

The atomistic calculations are carried out using spin-polarized Density Functional Theory (DFT) as implemented in the Vienna Ab Initio Simulation Package (VASP). The exchange-correlation potentials are treated by the generalized gradient approximation (GGA) and the interaction between valence electrons and ion cores is described by the projected augmented wave (PAW) method. Moreover, the GGA+U scheme is used for applying the on-site correlation effects among 3d electrons of the transition metal.

At the mesoscale level, fundamental mass balance relations are satisfied for determining the equilibrium concentration of different cations and anions within the batch reactor. Various equilibrium relations available in the literature are adopted for conducting the analysis. A Monte Carlo based approach is adopted to capture the evolution of the particle morphology, which considers the competition between the rate of reaction and transport of reactants within the solution while determining the final morphology of the cathode precursors. A phase field based methodology is developed for understanding the calcination of NMC cathodes, which involves the chemical reactions and mass transport processes associated with the removal of water, incorporation of oxygen within the lattice structure, addition of lithium within the cathode through reaction with lithium salt, and surface diffusion mediated sintering of the cathode primary particles. Interplay between the different reaction mechanisms observed in NMC811 and NMC111 in lithiating the cathode precursors, will be explored in the subsequent sections.

Finally, regarding the computational estimation of the performance of the cathode particles, there are two parts to the overall methodology, the first being generating and characterizing computational microstructure, and the second one is electrochemical modeling to solve for concentration and potential fields in electrode and electrolyte particle.

Computational microstructure

The aim of the computationally generated microstructure is to mimic the key features of cathode particles seen in experiments, the spherical shape of primary and secondary particles, the size of primary particles and the BET specific area as seen in Figure II.8.1(a) to Figure II.8.1(d). An important requirement of microstructure is maintaining connectivity of electrode and electrolyte phases. Two distinct microstructures are realized, ideal

microstructure and microstructure with intra-agglomerate closed pores shown in Figure II.8.1(e) and Figure II.8.1(f). The ideal microstructure has open arrangement of primary particles and has largest interface area for a given primary particle size. Introduction of intra-agglomerate closed pores in computational microstructure reduces the interface area and correlates well with experimental values. It also increases the agglomerate diffusion length. To obtain the diffusion characteristics, the distribution of length of line segments inside the solid electrode (the origin and termination of line segments is the electrode/electrolyte interface) is generated. To distinguish between the diffusion corresponding to primary particle and the effect of agglomeration, this distribution in diffusion length is divided in two domains, corresponding to primary particle length scale (\overline{L}_p) and the agglomeration length scale (\overline{L}_A). Microstructures generated using same primary particles have similar values of \overline{L}_p but different values of \overline{L}_A , reflecting the manner of agglomeration. The closed pores that are evenly distributed throughout the secondary particle have smaller value of \overline{L}_A , while larger closed pores or adjoining closed pores result in large values of \overline{L}_A .

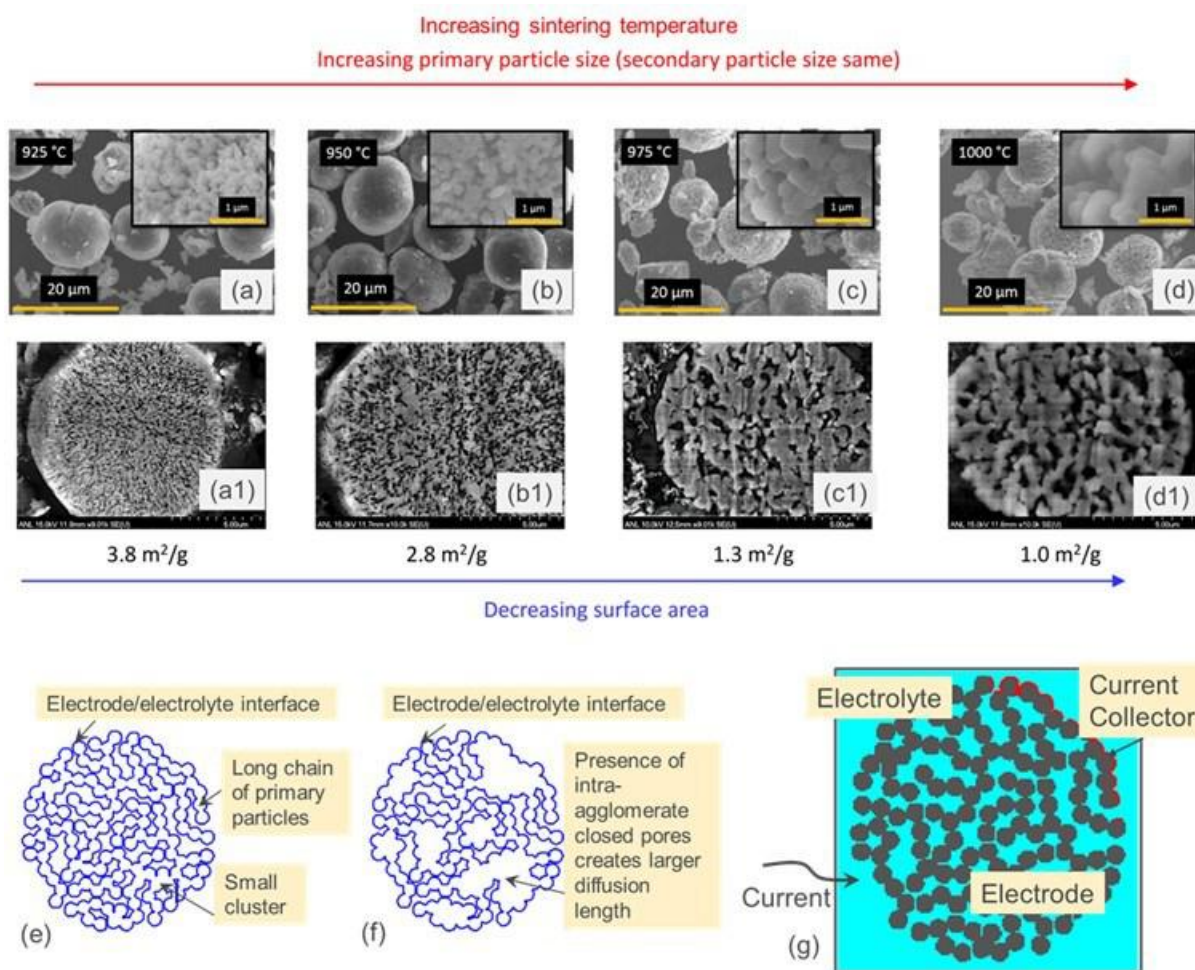


Figure II.8.1 Microstructure of LMR-NMC secondary cathode particles. (a)-(d) show the SEM images of cathode particles with increasing primary particle size as the sintering temperature increases from 925°C to 1000°C. The mean primary particles size is 100 nm, 200 nm, 400 nm, and 800 nm respectively from (a) to (d). The inset figures show magnified region to focus on the primary particles. (a1) to (d1) show the cross-section of a secondary particle with reference to particles seen in (a) to (d). The BET specific area decreases from 3.8 m²/g to 1.0 m²/g from (a) to (d) as the size of the primary particle increases from 100 nm to 800 nm. The average secondary particle size is same in (a) to (d). Two-dimensional computational microstructure is generated to match the average characteristics of experimental cathode particle, the primary particle size and shape and the specific interface area. (e) Ideal microstructure with open network of primary particles accessible to electrolyte. The specific interface area is larger than measured in experiments. (f) Microstructure with intra-agglomerate closed pores match the observed experimental specific interface area. The primary particle size is same in (e) and (f). (g) Computational domain for electrochemical model. The potential and concentration field are solved in the electrode and electrolyte. Electrode is shown in gray while electrolyte is shown in blue.

Electrochemical model

The partial differential equations for mass and charge conservation in electrode and electrolyte is solved using finite volume method in MATLAB. The electrochemical reaction at the interface is modeled using Butler-Volmer kinetics. The computational domain is shown in Figure II.8.1(g) featuring a single secondary particle. The ionic flux enters at the left domain boundary while the electronic flux enters at the current collector boundary shown in red.

Results

Since the present project has three major objectives, the results section will also be divided into three parts, where the first one will cover the results associated with the coprecipitation process, the second section will discuss about the calcination mechanism, and finally the third section will delve into analyzing the performance of the cathode particles.

Coprecipitation of TMCO_3 cathode precursors

The working principle of the coprecipitation process is to create an extremely high driving force for precipitating the desired compound, which demonstrates negligible solubility in water, by using other salts that is heavily water soluble. In the present case TMCO_3 (with low solubility in water) is precipitated by mixing water soluble TMSO_4 and NH_4HCO_3 . Dissociation of the bicarbonates (HCO_3^-) to carbonates (CO_3^{2-}) provides the anions necessary for the coprecipitation to occur. Equilibrium concentration of the various ions within the reacting solution is estimated using the mass balance relations, while taking into consideration the possibility of metal ammonia complex formation. The major driving force for the precipitation process is provided by the supersaturation ratio (SSR), which is defined as the ratio between concentration of the reactants (TM^{2+} , CO_3^{2-}) over the solubility product of the transition metal carbonate being investigated ($K_{\text{SP,TMCO}_3}$). Depending on the concentration of the reactants and the type of the transition metal carbonate being precipitated, it is possible to have SSR in the range of $10^4 - 10^6$ (for example, MnCO_3), where others might demonstrate SSR values around 10 (for example, NiCO_3). This variation in SSR can substantially affect their rate of precipitation, which will be investigated in the subsequent paragraphs.

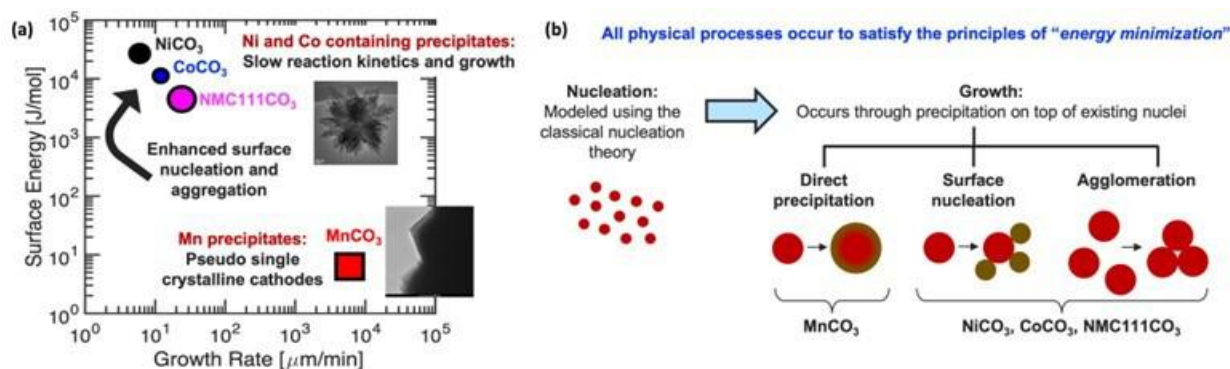


Figure II.8.2 (a) Change in surface energy of the transition metal carbonate precipitates as compared to their growth rate. MnCO_3 demonstrates high reaction rate constants and extremely high supersaturation ratios, which results in very fast growth of the particles. On the other hand, Ni and Co containing NiCO_3 , CoCO_3 , and NMC111CO_3 demonstrates slower reaction rate constant, which leads to slower growth of the primary particles through direct precipitation and the individual primary crystallites for these Ni and Co containing precursors is extremely small. Due to the smaller primary particle size of these Ni and Co containing precipitates, they demonstrate higher surface energies, which enhances their propensity to agglomerate during the formation of the secondary particles. (b) Demonstration of the two physical phenomena, namely "nucleation" and "growth", that contributes to the formation of the cathode precursors. Growth of the transition metal carbonate precipitates can occur through three mechanisms, direct precipitation, surface nucleation, and agglomeration, all of which will be briefly studied as part of the present project.

Precipitation of the transition metal carbonate (TMCO_3) from the reacting solution is favorable because it leads to a decrease in the overall Gibbs free energy of the solution. As already mentioned earlier, supersaturation ratio (SSR) dictates the driving force for the precipitation reaction to occur. Rate of reaction depends on the reaction rate constant (k_{reac}) as well as the SSR of the compound being precipitated. Tendency of the

precipitates to agglomerate with others depends on their surface energy, which is inversely proportional to the size of the precipitating particles. The surface energy and growth rate experiences by the different TMCO_3 precipitates are demonstrated in Figure II.8.2(a). Due to its higher reaction rate constant and larger magnitudes of SSR, precipitation of MnCO_3 occurs extremely quickly, which leads to larger size of the single crystalline particles, and very small surface energies that discourages the aggregation phenomena. On the other hand, Ni and Co containing precipitates demonstrate smaller magnitudes of reaction rate constant, which leads to slower growth of the particles. Smaller particle sizes higher surface energy and encourages growth of the particles through surface nucleation and/or agglomeration mechanism. Note that the SSR of NiCO_3 is small, in the range of 10. However, the SSR for CoCO_3 and NMC111CO_3 is in the same range as that of MnCO_3 . This combination of smaller reaction rate constant with higher SSR influences the roughness of the precipitated particles, which will be discussed later.

At this point it is worth revisiting the precipitation mechanisms at play during the coprecipitation process. It is schematically demonstrated in Figure II.8.2(b) that precipitation of TMCO_3 involve two major steps; the first one being nucleation, where multiple small nanometer sized nuclei of the precipitates are formed from the heavily supersaturated solution, and in the second step growth of these nuclei occurs to minimize the free energy of the reacting solution. Depending on the reaction rate constant (k_{reac}) and supersaturation ratio, growth of these nuclei can occur through different routes, for example, direct precipitation, surface nucleation and growth, and agglomeration of multiple small sized particles. All these mechanisms are possible during this precipitation of the TMCO_3 , where a wide range of k_{reac} and SSR are possible.

It is evident from Figure II.8.2 that due to the smaller reaction rate constant for the Ni and Co containing carbonate precipitates, they demonstrate extremely small sized primary particles, which grow through a heterogeneous nucleation mediated surface growth mechanism and/or agglomeration process. However, even for the surface growth mechanism, precipitation of these transition metal carbonate precursors are governed by two different driving forces; (i) Driving force for precipitation, which is dictated by the extent of supersaturation ratio, and (ii) Driving force for surface energy minimization, which most probably occurs through diffusion in the reacting solution (see Figure II.8.3(a)). Morphology of the experimentally precipitated Ni and Co containing transition metal carbonates are characterized using the high resolution TEM technique. Morphology of the CoCO_3 precipitates is shown in Figure II.8.3(b), which demonstrated higher magnitudes of SSR and resulted in a rough surface. High resolution images of NiCO_3 precipitates are depicted in Figure II.8.3(c), where the SSR during reaction is maintained at a lower level and the final particles demonstrate smooth surface. Finally, morphology of the NMC111CO_3 precipitates, as extracted using high resolution imaging techniques, are shown in Figure II.8.3(d), surface of which appear to be extremely rough in nature. As shown in Figure II.8.3(e) and II.10.3(g), CoCO_3 and NMC111CO_3 demonstrates higher supersaturation ratios ($\text{SSR} \sim 10^4$), which leads to larger driving force of precipitation without much room for the surface energy minimization mechanism to kick in. This results in a rougher precipitate morphology for CoCO_3 and NMC111CO_3 . On the contrary, as shown in Figure II.8.3(f), precipitation of NiCO_3 occurs under much lower supersaturation ratios ($\text{SSR} \sim 10$), which minimizes the driving force for precipitation, and allows for diffusion to play a role in minimizing the surface energies. Hence, experimentally observed (see Figure II.8.3(c)) and computationally predicted (see Figure II.8.3(f)) precipitates of NiCO_3 demonstrate smooth surface. Thus, competition between various mass transport and reaction rates help to understand the morphology of the precipitated TMCO_3 .

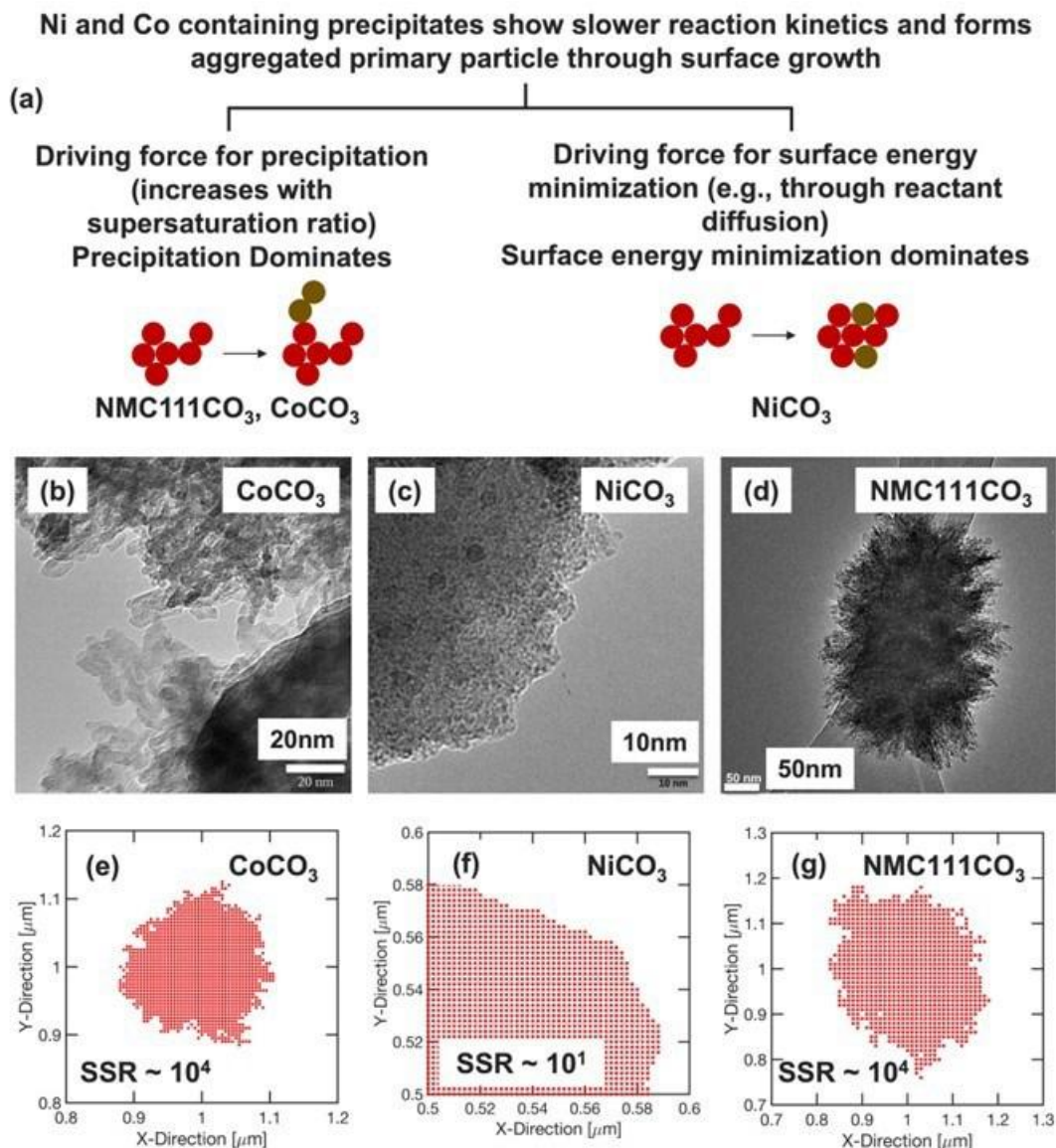


Figure II.8.3 (a) Schematic representation of the two competing driving forces, the first one being tendency to precipitate, and the second one is minimization of surface energy, that contributes to the determination of the surface morphology of the TMCO₃ precipitates. (b – d) High resolution transmission electron microscopy (HR-TEM) image of the aggregated primary particles for different transition metal carbonates. (b) Primary particles of CoCO₃ (precipitated under CoSO₄ ~ 4.5 mM and [NH₄⁺]/[Co²⁺] ~ 40). (c) Primary particle morphology of NiCO₃ (precipitated under NiSO₄ ~ 4.5 mM and [NH₄⁺]/[Ni²⁺] ~ 15). (d) Primary particle microstructures of NMC111CO₃ (precipitated under (NiSO₄+MnSO₄+CoSO₄) ~ 4.5 mM and [NH₄⁺]/[Ni²⁺+Mn²⁺+Co²⁺] ~ 40). (e – g) Simulated primary particle microstructures of CoCO₃, NiCO₃ and NMC111CO₃ using Monte Carlo based computational frameworks. Competition between the driving forces for precipitation and surface energy minimization are taken into consideration in this computational analysis.

Calcination of Ni-rich NMC cathodes

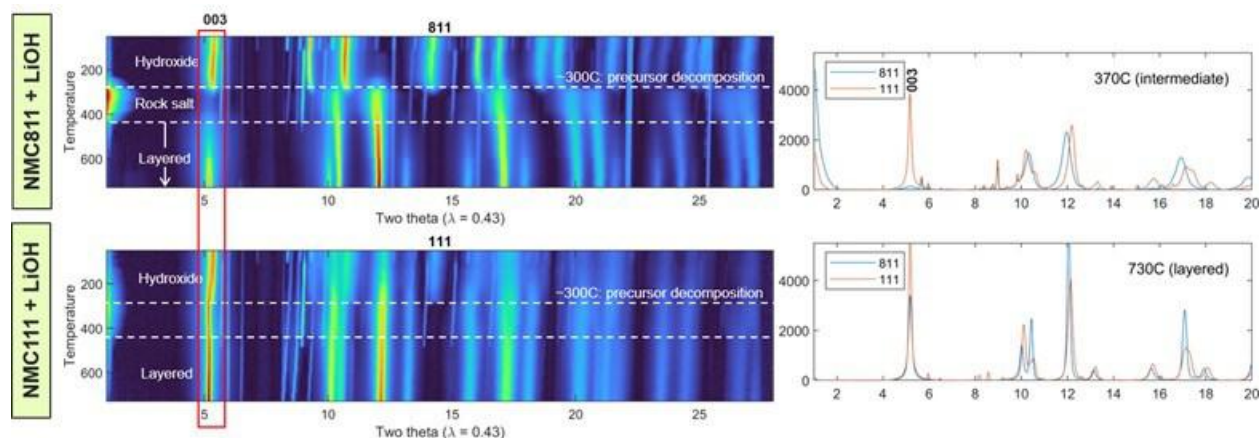


Figure II.8.4 Stacked PXRD plots for the calcination process of high and low nickel content precursors show the evolution of phases (left). Snapshots of the in situ diffraction study highlighting the difference in the PXRD patterns for the two intermediate phases (top right) and the NMC layered phases (bottom right).

The influence of transition metal ratios on the NMC calcination process and rate of lithiation are being explored using in situ powder diffraction (see Figure II.8.4). The diffraction analysis shows that different intermediates form during calcination using LiOH. For high nickel content precursors (NMC811), a rocksalt intermediate is observed with the loss of the 003 peak typical for a spinel or layered material. A spinel intermediate forms for the low nickel content precursors. Lithiation of the two intermediates is predicted to differ with a faster reaction with the lithium salt for low nickel content precursors (spinel) thus enhancing formation of the layered phase in NMC111 than NMC811.

To better understand the effect of pre-treatment on the lithiation of the rocksalt intermediate and to understand how the close-packed rocksalt lattice transforms to the layered cathode, Ab-initio molecular dynamic (AIMD) simulations were used on a model NiO lattice in contact with molten LiOH simulated at $T = 1200$ K to accelerate the reaction. Figure II.8.5 shows the evolution of the radial distribution functions (RDFs) and the corresponding ball and stick models with time. Initially, there is a narrow distribution of Ni–O nearest neighbor distances at 2 \AA , with some larger bonds associated with surface sites (see Figure II.8.5(a)). Critically, when oxygen is adsorbed at the surface of the NiO slab, lithiation begins within 18 ps from the start of the simulation (see Figure II.8.5(b)), whereas simulations without oxygen termination result in no reaction over 30 ps at the NiO/LiOH interface.

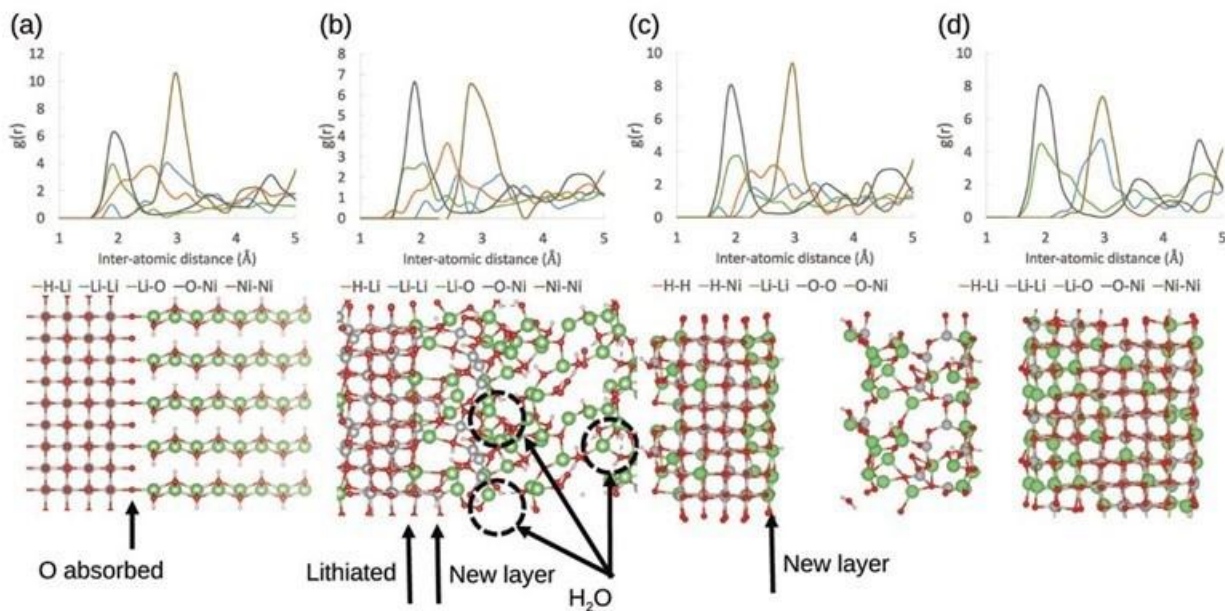


Figure II.8.5 Snapshots of NiO lithiation AIMD (1200 K) radial distribution function and schematic (ball and stick) representation of the simulation for a) $t = 0$ ps, b) $t = 18$ ps, c) $t = 298$ ps with 10 H_2O molecules taken off the cell, d) $t = 1100$ ps with all the water molecules taken off the cell. Red spheres represent O, silver spheres represent Ni, green spheres represent Li, and the small white spheres represent H.

Surface oxygen leads to Ni^{3+} sites in the next layer and a broadening of the 3 Å Ni-Ni peak in the RDF. As seen in Figure II.8.5(b), metal vacancies within the polar surface of the NiO are quickly filled by the Ni^{3+} surface migration and adsorption of Li^+ from the hydroxide melt. Subsequent oxygen sorption and further Ni surface migration leads to bulk metal vacancies that are readily filled by lithium, leading to a disordered lithiated rocksalt structure. The accumulation of water molecules in the simulation box impedes further conversion. In a real system, water would evaporate and move away from the interface, maintaining a favorable driving force for the completion of the overall lithiation reaction. To mimic a real system, water molecules were removed from the system once formed, as shown in Figure II.8.5(c) and Figure II.8.5(d). The system is hence equilibrated at a new chemical potential and the reaction cycle continues.

The next step is the formation of the final layered structure from the disordered $\text{Li}_x\text{Ni}_{1-x}\text{O}_2$. After lithiation of NiO, the AIMD simulation was continued for a cumulative total of several nanoseconds. At this point, signs of layered ordering begin to manifest, particularly in the surface layers. However, despite the complete layering of LiNiO_2 being thermodynamically favorable, the simulation did not reach this stage within a reasonable time (several months of elapsed real time). The time scale needed to reach a fully layered material is therefore not suitable for AIMD, since it may be on the order of tens of nanoseconds or more, and a cooling procedure would be required to reduce entropy contributions.

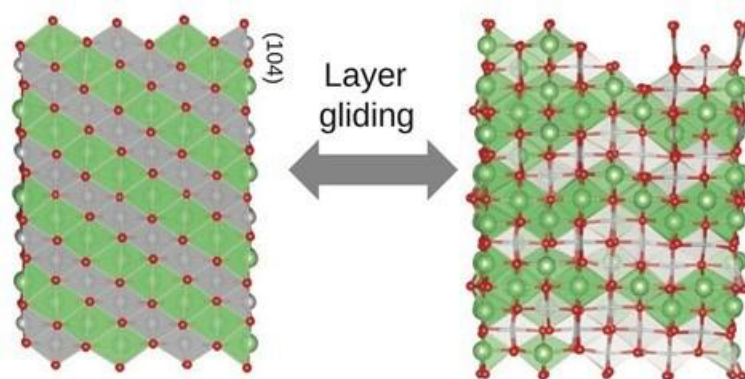


Figure II.8.6 AIMD (1200 K) simulation cell snapshot showing the LiNiO_2 layers gliding between perfect and defective layered structures.

To better understand the connection between layered and disordered rock salt structures, a new simulation was conducted at 1200 K starting with the ideal layered material with a surface 104 facet to match the 100-oriented rocksalt lattice discussed above. At the beginning of the simulation, adjacent layers within the LiNiO_2 break and glide into a new equivalent equilibrium position. Each layer is stoichiometric, and the surface is non-polar, making each layer intrinsically stable. The layered phase initially forms in several small domains, eventually merging to form larger corrugated domains with respect to the 104 surface. The final structure contains layers oriented in two different crystallographic directions, producing extended defects (Figure II.8.6). This configuration is similar to the configuration obtained after lithiation of NiO (AIMD Figure II.8.5, right panel). This result shows that the AIMD lithiation of NiO at 1200 K has reached a stable configuration and a complete layering would not be possible even if the simulation were allowed to run indefinitely. The formation of different orientations of the layers is a consequence of fluctuations and symmetry, combined with a low defect formation energy at the boundary between the two layered domains.

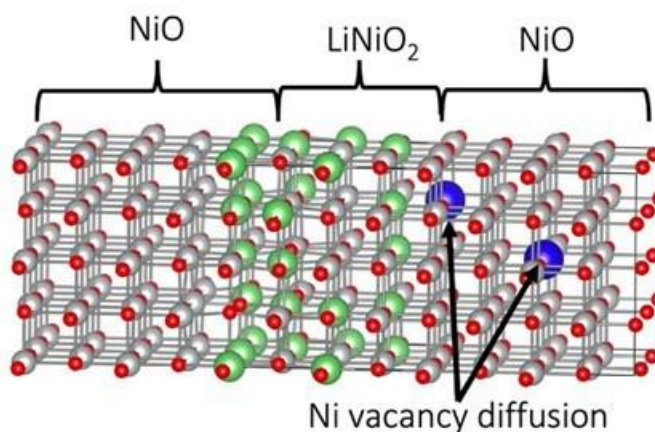


Figure II.8.7 Ab initio molecular dynamic (1400K-1800K) simulation cell representing an interface between LiNiO_2 and NiO . The arrows are pointing to blue spheres representing the initial and final position of the Ni vacancy in the NiO region.

A final simulation cell was set up to understand the Li diffusion from a Li-rich region (lithiated surface layers) into a NiO region with a Ni vacancy near the interface (Figure II.8.7). The cell depicts the $\text{LiNiO}_2/\text{Ni}_{1-\epsilon}\text{O}$ interface, where ϵ represents the concentration of Ni vacancies. The cell was set up with one Ni atom vacancy for every 64 Ni sites in the NiO region, equivalent to 1.6% (mole/mole). The vacancy was set close to the interface and next to one Li ion in the LiNiO_2 region. Contrary to expectations, Li ions do not immediately fill the Ni vacancy. Instead, the vacancy diffuses to the center of the NiO region, four-layers away from the

interface. The Ni ions in the NiO region around the vacancy fill the vacancy faster than Li can hop into it. When the Ni vacancy forms, two Ni ions oxidize to Ni^{3+} , compared to all Ni^{2+} in a perfect NiO lattice. However, there are still four Ni^{2+} ions surrounding the vacancy. One of these surrounding Ni^{2+} moves to the vacant site, leaving a vacancy behind. The process repeats until the vacancy reaches the center of the NiO region. In contrast, all the Ni ions in the LiNiO_2 region are Ni^{3+} and do not change sites during the simulation, nor do the Li ions in LiNiO_2 . Hence, whenever the degree of lithiation in a disordered NiO rocksalt region reaches the full LiNiO_2 stoichiometry, the diffusion of Li into the material's core region (NiO) slows down or stops entirely. Consequently, the extent of lithiation of a NiO particle is size dependent and there may be a critical size where the lithiation becomes very slow.

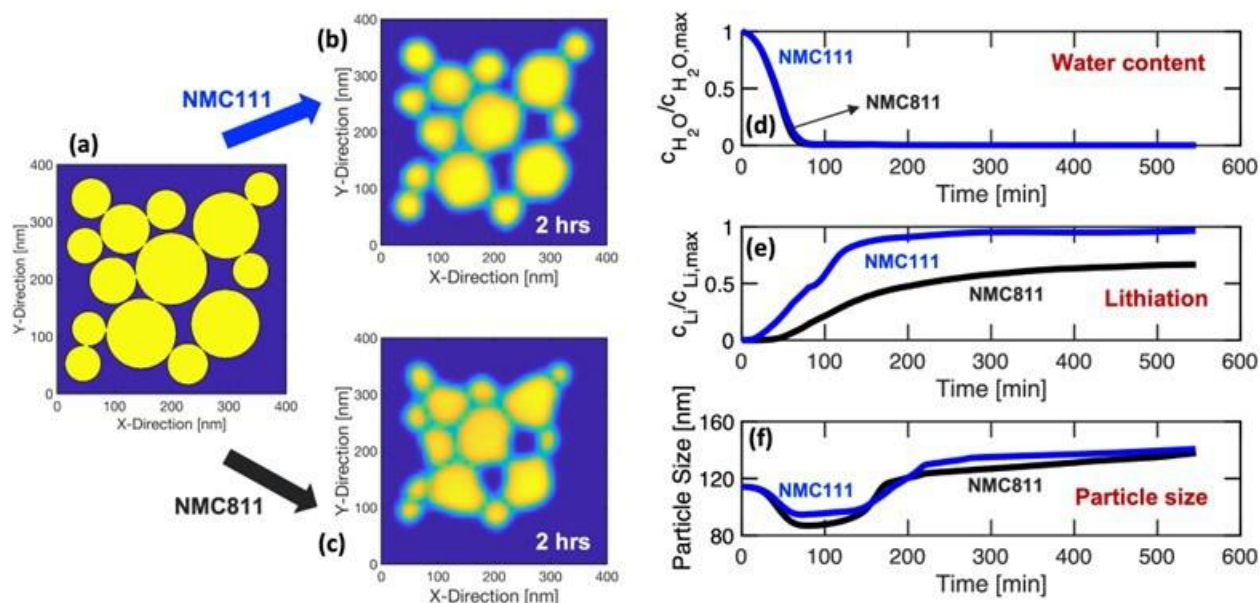


Figure II.8.8 Computational simulation of the calcination of NMC111 and NMC811 cathode precursors with LiOH conducted at the mesoscale level using phase field based methodologies. (a) Initial microstructure of the NMC cathode precursors. (b) Computationally predicted particle microstructure of NMC111 after 2 hours of calcination. Particles appear to be less sintered than NMC811. (c) Computationally predicted microstructure of NMC811 after calcination for 2 hours. Particles are more sintered than NMC111. (d) Removal of water from the NMC111 and NMC811 at the beginning of the calcination process. (e) Increase in lithium concentration in the NMC111 and NMC811 cathodes during the calcination process. Due to the faster reaction with Li-salt, NMC111 demonstrates earlier lithiation than NMC811. (f) Evolution in primary particle size experienced by the NMC111 and NMC811 cathodes during calcination. Due to greater extent of lithiation, NMC111 demonstrates larger particle size than the NMC811.

Following the experimental investigation of the calcination of NMC111 and NMC811 cathodes (as shown in Figure II.8.4), computational simulation of the calcination process is conducted at the mesoscale level for similar NMC based cathode precursors with LiOH as the source of lithium. The initial microstructure of the cathode precursors is shown in Figure II.8.8(a). The LiOH particles are not simulated separately, rather it is assumed that they exist around the cathode particles, and any open surface of the precursor can react with the lithium salt. Microstructure of the NMC111 and NMC811 cathode precursors after calcining for 2 hours is demonstrated in Figure II.8.8(b) and II.10.8(c), respectively. NMC111 appears to be less sintered than NMC811. According to the observations in the calcination experiments (see Figure II.8.4), NMC111 goes through a spinel intermediate, which experiences faster lithiation with LiOH. On the other hand, NMC811 experiences a rocksalt intermediate during the calcination process, which tends to lithiate slowly and experiences faster sintering of the rocksalt intermediate. At the beginning to the calcination process, both the NMC111 and NMC811 hydroxide based precursors release water before converting to the intermediate step. Figure II.8.8(d) captures the removal of water for the two types of precursors, which almost overlaps on top of each other. Due to the ease of oxidation and lithiation experienced by the spinel intermediates, lithium enters the NMC111 structure more quickly than NMC811, which exists in an intermediate rocksalt phase (see Figure

II.8.8(e)). In general, Ni^{2+} existing in a rocksalt phase is more difficult to oxidize as well as lithiate, and would require special surface treatments to enhance the oxygen concentration that can help to make the reaction with lithium salt faster (see Figure II.8.5). Finally, the evolution in particle size during calcination experienced by the NMC111 and NMC811 cathodes are shown in Figure II.8.8(f). Despite the enhanced sintering experienced by the NMC811 particles, the overall particle size is not much different from NMC111. Also, the final particle size at the end of calcination is larger for NMC111 than NMC811. Note that NMC111 experiences enhanced lithiation than NMC811 (see Figure II.8.8(e)), which leads to larger amount of lithiation induced particle growth for the former. Overall, the developed computational methodology at the mesoscale level is successful in capturing the differences associated with the calcination of different cathode precursors.

Performance estimation of Li-Mn-rich NMC cathode particles

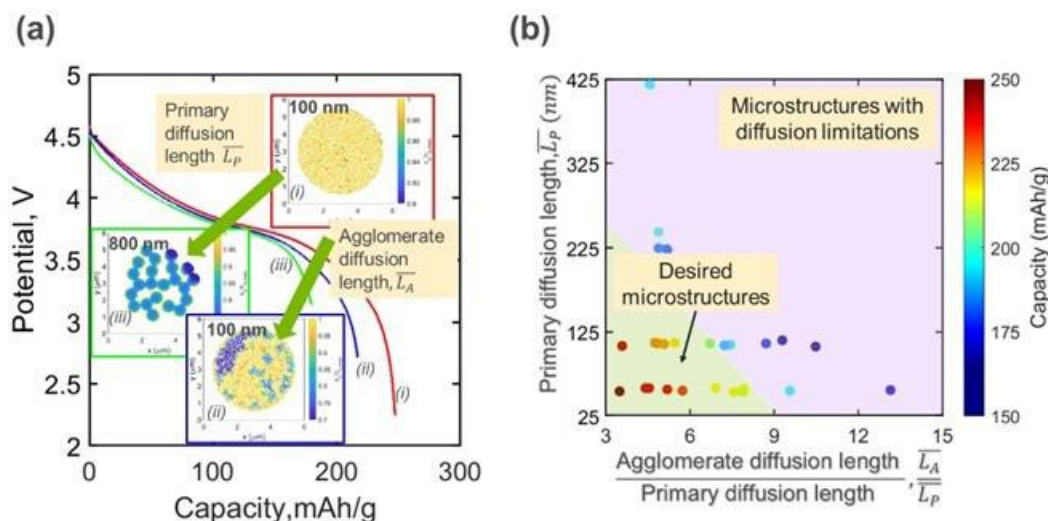


Figure II.8.9 Performance of LMR-NMC cathode (a) Voltage discharge profile for three microstructures, (i) Ideal microstructure with primary particle size of 100 nm (ii) Microstructure with intra-agglomerate closed pores with primary particle size of 100 nm (iii) Ideal microstructure with primary particle size of 800 nm. The discharge capacity depends on the primary diffusion length as well as the agglomerate diffusion length. The inset figures show the contour of lithium concentration normalized with maximum lithium concentration for the three microstructures. The color scale ranges from 0.7 to 1. (b) Capacity described by primary diffusion length and ratio of agglomerate and primary diffusion length. The applied C-rate is 1.

Figure II.8.9 captures the performance of cathode particle with different morphology and diffusion characteristics. Figure II.10.9(a) shows the discharge profile for three different microstructure which differ in primary particle size (microstructure (i) and (iii)) or agglomerate diffusion length (microstructure (i) and (ii)). The largest capacity is obtained for ideal microstructure with 100 nm primary particle size while smallest capacity is for microstructure with 800 nm primary particle. Even though, (i) and (ii) have same \bar{L}_P , microstructure (ii) with larger \bar{L}_A has smaller capacity. The contours of normalized lithium concentration show uniform distribution for microstructure (i), regions of low lithium concentration for microstructure (ii) and sharp gradient at the interface and low lithium concentration for microstructure (iii). This figure points to the relevance of the two diffusion lengths in predicting the capacity. Diffusion limitation is observed if either primary, \bar{L}_P , or agglomerate diffusion length, \bar{L}_A , becomes large.

Figure II.8.9(b) summarizes the interplay between primary and ratio of agglomerate and primary diffusion length on capacity. Microstructures with larger values of \bar{L}_P or \bar{L}_A/\bar{L}_P have smaller capacity due to diffusion limitation. The desired microstructures have small \bar{L}_P and \bar{L}_A/\bar{L}_P ratio corresponding to the lower triangle as seen in Figure II.8.9(b).

Conclusions

Detailed experimental and computational analysis of the cathode synthesis process is conducted at different length and time scales using appropriate techniques. Transition metal carbonate cathode precursors are

coprecipitated in batch reactors, and their chemical composition as well as particle morphologies are characterized using various high resolution imaging techniques (SEM, TM, EDX). Computational methodologies are developed that is capable of deciphering the competition between the rate of precipitation and mass transport mechanisms that leads to certain morphologies of the cathode precursors. It is concluded that transition metals with high supersaturation ratio, but smaller reaction rate constants, lead to the formation of extremely small sized primary particles. An aggregate of this small primaries provides the secondary particles, which is observed for every Ni and Co containing cathode precursors. Presence of these smaller primary particles should impact their calcination mechanism in some fashion.

Calcination of NMC111 and NMC811 hydroxide cathode precursors are conducted with LiOH. It is observed experimentally that NMC111 calcines through a spinel intermediate, whereas the NMC811 demonstrates a rocksalt intermediate, which has large influence on the overall lithiation and layering mechanism. Atomistic simulations reveal that presence of oxygen is a necessity for successfully lithiating the Ni-rich cathode precursors, which prefers to form the rocksalt intermediate. Even, diffusion of lithium within the rocksalt intermediate phase can be a challenge, which further worsens the extent of lithiation possible within Ni-rich cathodes. Continuum analysis at the mesoscale level reveals that the different intermediates (spinel for NMC111 vs rocksalt for NMC811) not only experience different amount of lithiation, but also their sintering behavior differ from each other, which results in a difference in the primary particle sizes within the final calcined cathodes.

Finally, computational analysis of the electrochemical response of the sintered cathode particles provides information regarding the modifications needed in the cathode morphology that can successfully enhance cathode capacity. The performance of diffusion limited LMR-NMC cathode can be improved by tailoring the morphology of secondary particles. Two diffusion lengths, primary and agglomerate diffusion lengths, are required to characterize the secondary particle. Improvement in capacity is seen with smaller values of $\overline{L_p}$ and $\overline{L_p}/\overline{L_A}$. For a diffusion limited material, using smaller primary particles to get better performance is intuitive, but introducing closed pores and relating the two diffusion lengths to performance, points in a new direction for optimization of the morphology.

Key Publications

1. M. Wolfman, X. Wang, J. C. Garcia, P. Barai, J. E. Stubbs, P. J. Eng, O. Kahvecioglu, T. L. Kinnibrugh, K. E. Madsen, H. Iddir, V. Srinivasan, and T. T. Fister. The Importance of Surface Oxygen for Lithiation and Morphology Evolution during Calcination of High-Nickel NMC Cathodes. *Advanced Energy Materials* 12 16 2102951 (2022).
2. F. Wang, P. Barai, O. Kahvecioglu, K. Z. Pupek, J. Bai, and V. Srinivasan. Process Design for Calcination of Nickel-based Cathode Materials by *In Situ* Characterization and Multiscale Modeling. *Journal of Materials Research* 1 – 19 (2022).
3. D. Tewari, A. Gutierrez, J. R. Croy, and V. Srinivasan. Designing Cathode Morphology for Materials with Solid Transport Limitation. In: *The Electrochemical Society Fall Meeting* October 2022.

Acknowledgements

The authors acknowledge the computing resources provided by the Laboratory Computing Resource Center (LCRC) at Argonne National Laboratory. Portions of this work were performed at GeoSoilEnviroCARS (The University of Chicago, Sector 13), Advanced Photon Source (APS), Argonne National Laboratory. GeoSoilEnviroCARS is supported by the National Science Foundation – Earth Sciences (EAR – 1634415) and Department of Energy- GeoSciences (DE-FG02-94ER14466). This research used resources of the Advanced Photon Source, a U.S. Department of Energy (DOE) Office of Science User Facility operated for the DOE Office of Science by Argonne National Laboratory under Contract No. DE-AC02-06CH11357. Regarding the computational and experimental research, the atomistic computations were conducted by Juan Garcia and Hakim Iddir, and the mesoscale level computational modeling and subsequent analysis was carried out by Pallab Barai and Venkat Srinivasan. All the experimental research was conducted by Timothy Fister, Mark

Wolfman and Xiaoping Wang. Also, Venkat Srinivasan managed the entire project, and made sure that the project follows the correct direction without deviating much from its primary goal.

II.9 *In Situ* Spectroscopies of Processing Next-Generation Cathode Materials (ANL, BNL)

Feng Wang, Principal Investigator

Argonne National Laboratory
Applied Materials Division
9700 S. Cass Avenue
Lemont, IL 60439
E-mail: fengwang@anl.gov

Jianming Bai, Co-Principal Investigator

Brookhaven National Laboratory
National Synchrotron Light Source II
Upton, NY 11973
E-mail: jmbai@bnl.gov

Haiyan Croft, DOE Technology Development Manager

U.S. Department of Energy
E-mail: haiyan.croft@ee.doe.gov

Start Date: October 1, 2021

End Date: September 30, 2022

Project Funding (FY22): \$350,000

DOE share: \$350,000

Non-DOE share: \$0

Project Introduction

Lithium-ion battery technology provides critical energy-storage needs for society, ranging from everyday electronics to electrified transportation and power grids. The demand for lighter devices and longer-duration storage continues to fuel the need for energy-denser batteries. This need, in turn, requires designing new battery materials, understanding how they function and, ultimately, making them through scalable synthesis and processing – namely, manufacturing at scale. Technical advances in characterization and computation in the past decade have greatly facilitated the discovery and design of battery materials, but how to make them with the required capacity, power, lifespan, and safety is another layer of complexity and may become the real hurdle to their practical use – very often we know what we want, but don't know how to make them. The difficulty largely lies in the knowledge gap in understanding the processes of materials synthesis and processing, wherein reactions often proceed via kinetic pathways under non-equilibrium conditions, so making it hard to be predicted by theories or computations. As there are a variety of processing parameters (precursor concentration, temperature, pressure, pH value, reaction time, ...), materials processing for optimal performance mostly relies on trial and error.

Under this project, *in situ* spectroscopic techniques are developed deliberately for studying the synthesis and processing of next-generation commercially viable cathode active materials (CAMs), enabling synthesis and processing by design. This project involves broad collaborations across national laboratories, universities and industries. A long-term synergistic collaboration was established between Argonne National Laboratory (ANL) and Brookhaven National Lab (BNL) under the *Processing Science & Engineering* (P&E) program. The team has been working closely to develop fundamental processing science and processing technologies by leveraging the unique capabilities and expertise at ANL and BNL, particularly in *in situ* characterization, precursor development, multiscale modeling and scale-up. The tools and techniques under this project are also used to support other projects funded under the P&E and other programs by the Vehicle Technology Office (VTO), such as Battery 500 program (in collaboration with Binghamton University) and *deep-dive* programs (in collaboration with Lawrence Berkeley National Lab (LBNL) and ANL).

The material focus of this project is on nickel (Ni)-based low cobalt (Co) layered oxides, currently the most intensely pursued CAMs owing to their high capacity and low cost. To enable commercial application of high-Ni cathodes, strategies are needed to manage the competing factors of high Ni loading. High output capacity requires high Ni content; but as Ni content increases, Ni sitting at octahedra tends to go to Li sites in the crystal lattice, resulting in reduced electrochemical activity. Cathodes are generally charged to high voltages (above 4.2 V) to achieve high energy density, meanwhile introducing a number of mechanical issues such as cracking due to lattice collapse, gas release, structural reconstruction (or surface densification). Such undesired phenomena may happen concomitantly and, consequently, lead to poor cyclability and voltage decay, which has been a main obstacle to the realization of high-Ni CAMs with true commercial potential. Eventually, addressing such issues relies on synthesis and processing, in obtaining the materials with controlled structure morphology and surface properties.

Objectives

This project is part of the P&E program, aiming at developing processing science and technologies for scaling up production of next-generation CAMs, with a current focus on Ni-based low-Co cathodes. Specifically:

- Developing a fundamental understanding of calcination and other scalable processes for processing Ni-based cathode materials.
- Designing scalable processes for surface-stabilization of Ni-based cathodes.

Approach

One unique approach taken in this project is to develop mechanistic understanding of materials processing through in situ studies using the world-leading facilities at Brookhaven, Argonne and other national laboratories. Synchrotron X-ray based in situ techniques are developed for real-time probing of the intermediate phases and their structural evolution as the materials are being synthesized/processed. This allows access to the details of the processes, elucidating how the processing parameters affect the kinetic reaction pathways and, consequently, the target material phases and their properties. Such studies, with the insights into the reaction process and the involved intermediates under real conditions, provide a basis for materials synthesis/processing by design – rationally selecting synthesis/processing parameters to improve performance and reduce cost.

Since most of battery materials are in the polycrystalline form, powder diffraction is commonly employed for monitoring the structural evolution during synthesis/processing. Among various scattering and spectroscopy techniques, X-ray diffraction (XRD) is arguably the most powerful tool for in situ characterization of synthesis and processing reactions. Advanced synchrotron facilities provide powerful powder diffraction capability that allows following the reactions and processes with high precision and in short time. Over the years, various in situ techniques have been developed for studying synthesis/processing reactions. With the special design of sample configuration and environment, one same sample may be loaded into different beamlines/facilities for complementary characterization using multiple in situ techniques, such as x-ray fluorescence imaging, X-ray absorption spectroscopy (XAS), XRD, and X-ray total scattering coupled with pair distribution function (PDF) analysis. This capability enables both bulk measurements with a large volume of materials being sampled and local probing of structural/chemical evolution in heterogeneous materials and at surfaces/interfaces. By coupling with electrochemical characterization of the final products, such studies shed light on the processing-structure-property relationship, thereby providing a science basis for designing scalable processes suited to commercial production of next-generation cathode materials.

Results

In FY22, this project focused on in situ spectroscopies of the calcination processing of Ni-based low-Co CAMs. Unique spectroscopic techniques were developed for studies of lithiation-driven structural and morphological changes in Ni-based CAMs, including correlated in situ XRD/PDF for probing crystallization, X-ray spectromicroscopy for probing local structural and chemical evolution and in situ scanning calorimetry analysis (DSC) performed simultaneously with XRD on the correlation between crystallographic and thermal changes during calcination of CAMs. Through in situ studies using those unique techniques, new insights into

the processes and reactions in calcination of Ni-based CAMs were obtained, including the kinetic and thermodynamic limits to the lithiation-driven crystallization of LiNiO_2 (LNO) and $\text{LiNi}_{0.8}\text{Mn}_{0.1}\text{Co}_{0.1}\text{O}_2$ (NMC811), impact of Mn on structural ordering and crystallization and impact of the Nb coating both to the surface and bulk. Those insights were further applied to developing protocols for stabilizing Ni-based CAMs, such as controlling the constituent components and their phase morphology, lithium stoichiometry control. In addition, efforts were made on studying surface coating of high-Ni CAMs in collaboration with Binghamton University and fluorination of disordered rocksalts (DRX) in collaboration with LBNL.

Lithiation-driven crystallization during calcination of Ni-based CAMs

Ni-based CAMs, with 80% or higher Ni concentration, are among the most promising low-cost, high-energy-density cathodes for next-generation LIBs. They are generally synthesized through a two-step process, namely, Co-precipitation to obtain the transition metals hydroxides and then calcination, with the mixture of transition metal and lithium hydroxides. Control of the calcination conditions has been found crucial to obtaining high-performance CAMs, wherein structural ordering and morphology of the final products needs to be finely tuned to maximize capacity while minimizing surface areas exposed to the electrolyte. However, the calcination process is complicated, involving phase transformation accompanied with non-equilibrium crystallization of intermediates prior to forming the layered oxides, posing challenges to making desired phases and properties.

In this work, a collaborative study was made on the calcination of $\text{LiNi}_{0.8}\text{Mn}_{0.1}\text{Co}_{0.1}\text{O}_2$ (NMC811) and the archetypal LiNiO_2 (LNO), involving joint efforts of in situ characterization (under this project), precursor fabrication (under the BAT #167) and multiscale modeling (under BAT # 402). The hydroxide precursors of $\text{Ni}(\text{OH})_2$ and $\text{Ni}_{0.8}\text{Mn}_{0.1}\text{Co}_{0.1}(\text{OH})_2$ were synthesized via a modified co-precipitation method in a continuously stirred tank reactor (CSTR). Correlated *in situ* synchrotron X-ray diffraction (XRD) and pair distribution function (PDF) was applied to tracking the calcination process. The typical contour plot of the in situ XRD obtained during calcination of NMC811 is given in Figure II.9.1 (a), showing the overall trend of the phase transformation. Through quantitative Rietveld refinement, the phase fractions of all the involved phases and their evolution as a function of temperature were obtained (Figure II.9.1(b)).

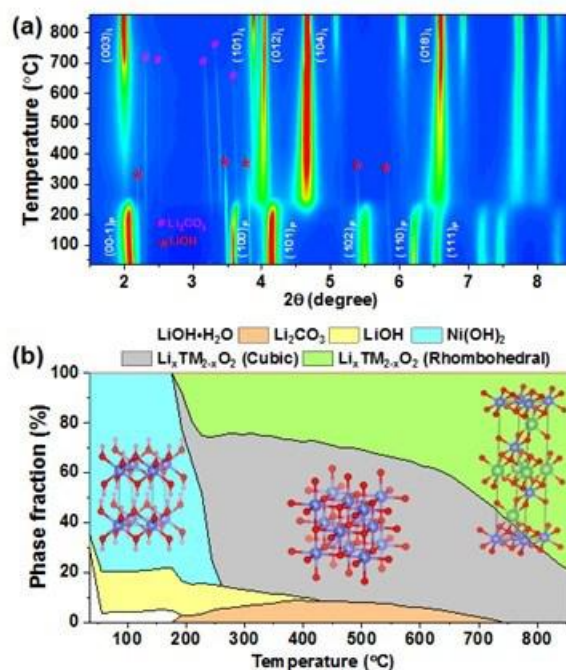


Figure II.9.1 (a) Contour plots of in-situ temperature-resolved synchrotron X-ray diffraction (XRD) data, showing the phase progression during the calcination process in the synthesis of NMC811. (b) Normalized fraction of the major phases quantified by Rietveld refinement of the in-situ XRD.

To better understand the nucleation and growth mechanisms of the layered phase, correlated in situ PDF measurements were conducted simultaneously with in situ XRD for a complete picture of the structural information including both crystalline and amorphous phases. Using XRD alone, the disordered phases and those at interfaces cannot be accounted for due to the nature of short-range ordering, especially in the early stage of phase nucleation and growth. Therefore, the local synchrotron X-ray probing technique, total scattering coupled with PDF analysis, was applied here to gain details about local structural evolution. Figure II.9.2 (a) shows the typical contour plot of the in situ PDF pattern obtained from the Fourier transform of the total scattering data, with which, the length of the local structure ordering in each stage is visualized. Quantitative analysis of the domain sizes of the layered phase both in NMC811 and LNO was obtained by fitting to the PDF patterns, with the main results presented in Figure II.9.2 (b). The two systems exhibit an overall similar process, but there is subtle difference. Particularly, NMC811 exhibits continuous crystal growth while LNO shows 3 distinct stages of the crystallization, starting with the early nucleation, followed with slow, quasi-static growth and then fast growth at high temperatures. Results from the correlated in situ XRD/PDF studies indicates that the phase transformation and crystallization processes are overall similar in the two systems (NMC811 and LNO), both going via intermediate rocksalt and the final layered phases. However, slower kinetics of the transformation to the low-Li-containing rocksalt and distorted layered phases was observed in LNO compared to the Mn/Co containing NMC811. On the other hand, the crystal growth in NMC811 is surprisingly slower than that in LNO, indicating the high energy barrier of TM ion migration in the presence of Mn and Co. The role of Mn/Co in hindering particle growth was further studied through correlated multiscale modeling under the BAT # 402). The obtained into the crystallization thermodynamics and kinetics from this study may guide the design of calcination of Ni-based cathode materials, i.e., intentionally controlling their structure and morphology for improved electrochemical performance.

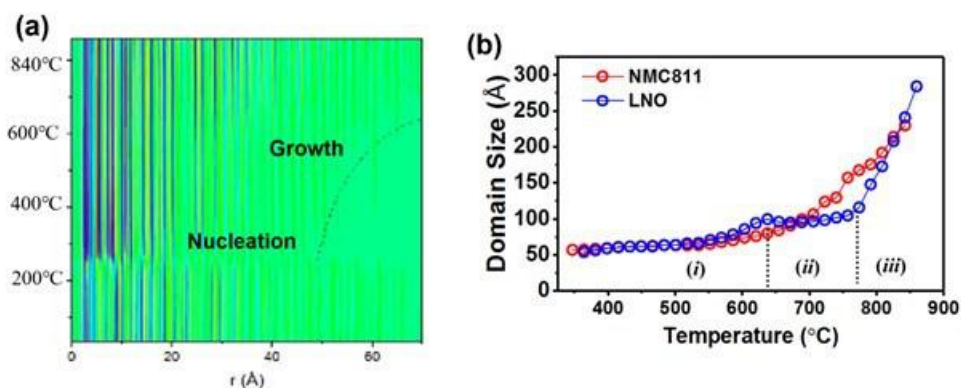


Figure II.9.2 (a) In situ PDF analysis of the solid-state synthesis of NMC811 and LNO. (a) Representative PDF pattern solving the crystal nucleation and growth in LNO. (b) Comparison of the domain size of the crystals formed in LNO (blue) and NMC811 (red), obtained through the fitting to the PDF pattern.

Synthesis of composite cathodes for high-voltage operation

Guided by in situ synchrotron XRD studies and quantitative analysis, a new type of lithium nickel oxide was synthesized for use as CAM for Li-ion batteries. This compound is a composition of two crystallographic components: a major stoichiometric layer-structured phase (LNO) and a minor Li-containing disordered rock-salt (DRS) phase embedded in the same cubic close-packed oxygen lattice. The contour plot of the in situ XRD data was provided in Figure II.9.3 (a), showing the overall phase transformation process, which can be differentiated into four stages: I (room temperature to 176°C), II (176°C -329°C), III (329°C -654°C) and IV (above 654°C). As illustrated in the phase evolution diagram (Figure II.9.3(b)), the structure of the precursors, i.e., Ni and Li hydroxides, is maintained in stage A drastic phase transformation occurs in stage II, featuring the fast growth of a Li-containing DRS phase under the consumption of the hydroxides. In stage III, the two nickel-containing phases, namely the DRS and the layered LNO, coexist, with the latter gradually catching up with the former. Finally, in stage IV, the fast-growing layered phase becomes dominant. From stages II to IV,

residual lithium carbonate and hydroxide occur as minor components. The composite cathodes, containing layered and Li-containing disordered rock-salt phases (as illustrated in Figure II.9.3(c)), exhibited high cycling stability, of 85.5% after 300 cycles at 2 C when charged up to 4.8 V (not shown here). The exceptional cycling capability is attributed to a synergistic effect on suppressing the abrupt H2-H3 phase transition. The findings provide a guideline for developing high-energy-density cobalt-free Ni-based cathodes.

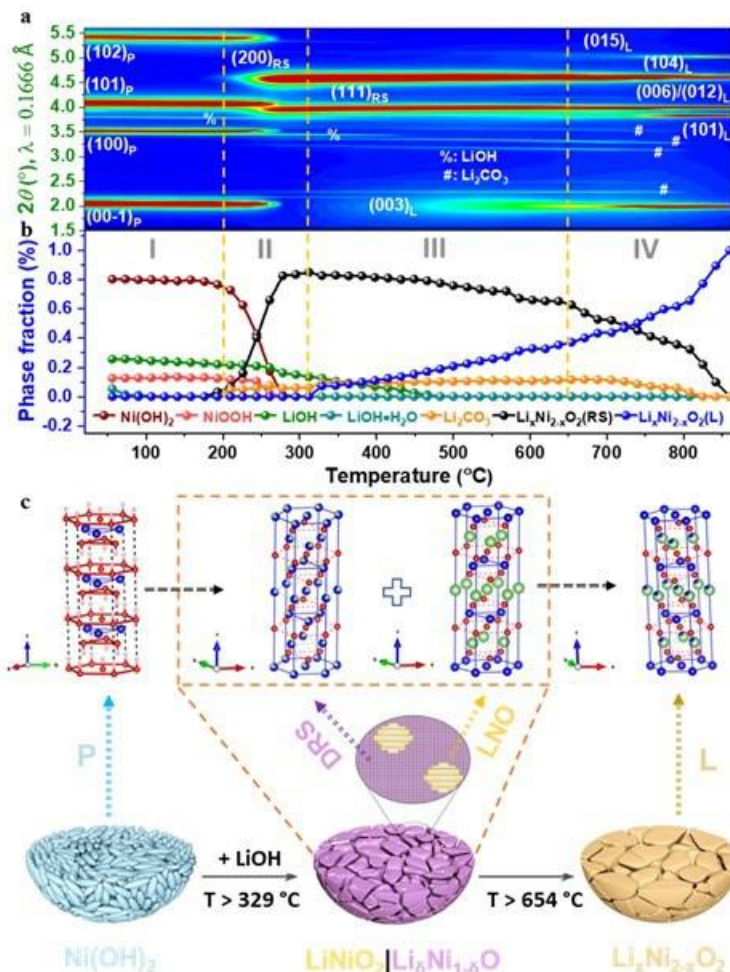


Figure II.9.3 Phase progression during the solid-state synthesis of LiNiO_2 (LNO). a, Contour plot showing multi-stage (labelled as I, II, III and IV) phase transformations, tracked in situ using temperature resolved synchrotron X-ray diffraction. b, Normalized fraction of the major phases quantified by the Rietveld refinement of in situ XRD patterns. c, Schematics illustrating the structure/atomic configuration of the involved phases and their correlations. A dual-phase composite of a stoichiometric LiNiO_2 and a Li-containing disordered rock-salt forms at moderate temperatures from Li and Ni hydroxide precursors (P) and eventually transforms to a single phase layered LNO structure (L) with cation mixing at higher temperatures.

Lithiation-driven morphology evolution through correlated characterization and modeling

Besides the structural evolution, significant changes in particle morphology occur during calcination of high-Ni layered oxides from the hydroxide counterparts, which was studied through correlated characterization and modeling with NMC71515 as a model system. As shown by the scanning electron microscopy (SEM) images (in Figure II.9.4 (a)), the primary particles initially exhibited a platelet-like morphology in precursors, and after heat treatment at 500°C (typically done as the first step of calcination), the platelet-like look was largely lost, and particles became smaller as a result of the phase transformation from the initial hydroxides to the intermediate rocksalt with reduced long-range ordering. In contrast to the abundance of open space (or voids) between primary particles in precursors and intermediates, the particles in the final product became densely

packed, with limited open space being seen. The primary particles grew significantly, from the thin platelet particles to large spherical particles (up to a few hundred nanometers), indicating that crystal growth mostly occurred at high temperatures. In order to understand the particle growth process, simulations at the mesoscale level were conducted (in collaboration under BAT # 402), showing that an increase in primary particle size is possible due to lithiation-induced volume expansion as well as sintering-induced growth of the larger particles at the expense of the smaller ones (Figure II.9.4 (b)).

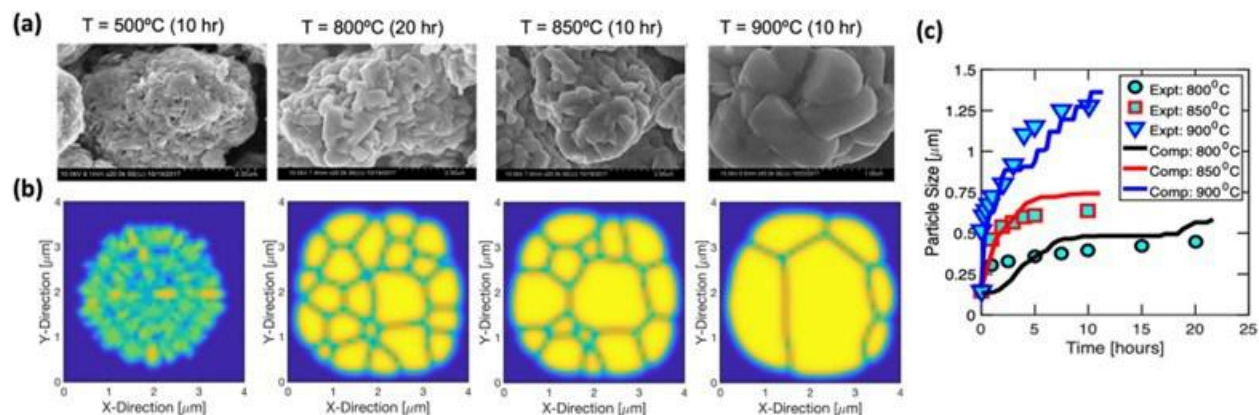


Figure II.9.4 Crystal growth during the calcination of NMC71515. (a) Morphology evolution of primary particles, shown by the SEM images taken from samples at different calcining statuses: pretreated at 500°C (10 h), calcined at 800°C (20 h), 850°C (10 h) and 900°C (10 h), from left to right. (b) Computationally simulated images of the particles at the corresponding calcining statuses.

Both lithiation and sintering of the particles are considered in the simulations. (c) Comparison between the experimentally observed (symbols) and computationally predicted (solid lines) evolution in particle size at different temperatures, showing the lithiation-driven particle swelling and the growth of larger particles at the expense of smaller ones.

A comparison between the experimentally observed and computationally predicted cathode primary particle size during the high temperature calcination process is shown in Figure II.9.4 (c), where the computational predictions are denoted by the solid lines and the experimental observations are shown by the symbols. It is evident from Figure II.9.4 (b, c) that increasing the calcination temperature results in larger primary particles, which is consistent with experimental observations on other high-Ni cathodes. It is also interesting to note that calcining cathodes at lower temperatures should ensure smaller primary particles irrespective of the calcination time, which can be beneficial from the standpoint of performance as well as long term cycle life. Development of such comprehensive computational schemes for predicting the calcination of cathode particles can substantially accelerate the optimization of cathode microstructures required for the development of high-Ni cathodes for next-generation applications.

Structural and morphological tuning of Ni-based Co-free CAMs

Eliminating Co from Ni-based cathodes is desirable for the practical battery applications, but synthetic optimization of the structural/morphological properties and the electrochemical performance has yet to be realized. In this work, we investigated how Li stoichiometry plays the role in tuning the structure and morphology for optimization of $\text{Li}_x\text{Ni}_{0.95}\text{Mn}_{0.05}\text{O}_2$ (NM9505). Precursor powder of $\text{Ni}_{0.95}\text{Mn}_{0.05}(\text{OH})_2$ was synthesized via co-precipitation method using a Taylor Vortex Reactor (under BAT #167). By varying Li content in a wide range ($0.85 \leq x \leq 1.1$) during calcination, layered-structured particles were obtained at Li-excess conditions and nanostructured while the composites consisting of layered and rocksalt phases were obtained at Li deficient condition. High performance was demonstrated in the Li-deficient NM9505 composites, offering 90% 1st-cycle efficiency, close-to-zero voltage fade, and 90% capacity retention for 100 deep cycles up to 4.4 V against Li metal – over-performing those Li-excess and near-stoichiometric counterparts.

Further studies were made on the calcination process through correlated structural analysis and multiscale modeling (in collaboration under BAT # 402). Li-stoichiometry was shown to play a crucial role in determining the kinetic pathways of structural ordering and crystal growth. During the calcination process, the liquid-phase sintering occurs with the presence of excess Li, leading to large-sized stoichiometric CAMs as commonly reported in the literature. With deficient Li, small-sized particles consisting of intergrown rocksalt and layered phases are formed. These findings demonstrate the efficient route to structural and morphological tuning via Li stoichiometry for stabilizing Ni-based Co-free cathodes in practical applications.

Synchrotron XRD analysis on the role of Nb substitution in $\text{Li}_x\text{Ni}_{0.90}\text{Mn}_{0.05}\text{Co}_{0.05}\text{O}_2$ (NMC9055)

This is a collaboration with Binghamton University (with Whittingham Group). Ex situ XRD studies were made on the synthesized Nb-substituted NMC9055, showing that all of diffraction peaks can be indexed by a hexagonal $\alpha\text{-NaFeO}_2$ structure (R-3m space group; Figure II.9.5). With the increasing of Nb concentration, some extra peaks appeared (Figure II.9.5 (b)), and they belong to the Li_3NbO_4 phase. The enlarged XRD patterns in Figure II.9.5(c, d)) shows the diffraction peaks gradually and slightly shifted toward lower angles. The slightly expanded lattice parameters indicated that Nb has been successfully participated into NMC 9055 hexagonal structure by considering the larger radius of Nb^{5+} than Ni^{3+} , Co^{3+} , and Mn^{4+} . The results helped to explain the role of Nb in stabilizing NMC9055 during long cycling. Further studies through in situ XRD on the Nb-coated NMC9055(OH)₂ precursors were carried out for better understanding the role of Nb on tuning the structure and morphology of NMC9055 during the calcination. The results will be reported in the future.

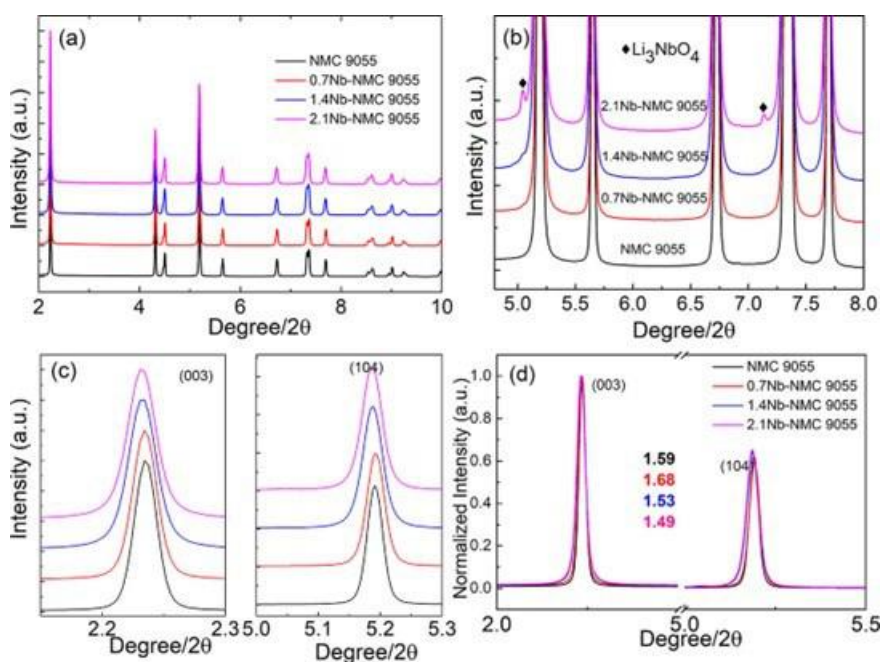


Figure II.9.5 (a) Synchrotron XRD patterns of 0, 0.7, 1.4 and 2.1% Nb-coated/substituted NMC 9055 heated at 725 °C. (b–d) Enlarged view in 2θ (deg): (b) 4.5°–8.0°, \blacklozenge is Li_3NbO_4 ; (c) position shifts of the (003) and (104) peaks; (d) normalized (003) and (104) peaks, showing the variations of their intensity ratios.

In situ XRD on the fluorination in disordered rocksalt cathodes

This is a collaboration with LBNL (with Ceder group under the DRX deep dive project), in evaluating synthesis routes targeting $\text{Li}_{1.2}\text{Mn}_{0.4}\text{Ti}_{0.4}\text{O}_{1.6}\text{F}_{0.4}$ and in the process clarify the specific reaction pathways that make high F uptake so challenging. In situ XRD was applied to monitoring the structural evolution of the intermediate during synthesis. Figure II.9.6 (a) showed the in situ XRD patterns measured during the synthesis trial based on 2LiMnO_2 , $3\text{Li}_2\text{TiO}_3$, LiF, MnF_2 , and C. Synchrotron XRD was used to monitor this route in situ, allowing many patterns to be captured with fine temperature resolution. The heatmap with high (low)

diffraction intensities being represented by bright (dark) coloring was used to pinpoint reaction temperatures and estimate the relative amounts of all intermediate phases. In Figure II.9.6 (b), the corresponding mole fractions are plotted as a function of time, and Figure II.9.6 (d) illustrates the relationship between time and temperature by showing the heating profile used during the synthesis. From refinement, the non-linear lattice contraction in LiMnO_2 was obtained as shown in Figure II.9.6 (c), which was further correlated with the evolution in MnF_2 and LiF for tracking the lithiation and fluorination process. In particular, the $\text{LiMnO}_2|\text{MnF}_2$ reaction mechanism was clarified, suggesting that all F ions were trapped in LiF , therefore limiting the fluorination in the final DRX product.

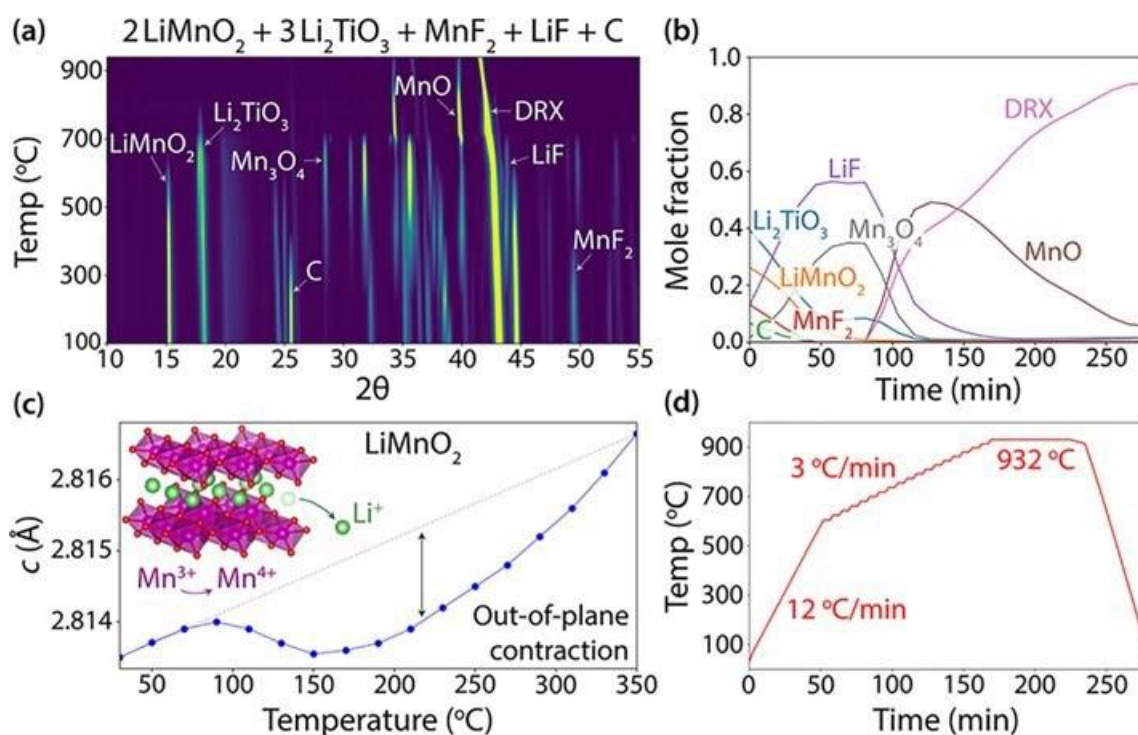


Figure II.9.6 (a) In situ synchrotron XRD measurements (converted to Cu $K\alpha$) captured during the synthesis trial of $\text{Li}_{1.2}\text{Mn}_{0.4}\text{Ti}_{0.4}\text{O}_{1.6}\text{F}_{0.4}$ using precursors (MnF_2 , LiF , LiMnO_2 , Li_2TiO_3 , and C). (b) Refined mole fractions of all crystalline phases are plotted as a function of time, neglecting any molten or amorphous phases. (c) The out-of-plane LiMnO_2 lattice constant is refined as a function of temperature, showing a non-linear contraction associated with Li^+ extraction. (d) Heating profile used during the synthesis procedure.

Conclusions

In FY22, progress was made in the development and application of *in situ* spectroscopic techniques for fundamental understanding and rational process design for calcination processing of Ni-based low-Co cathode materials, as briefly summarized here.

- *In situ* spectroscopy techniques and processing reactors were developed and applied to studies of processing Ni-based CAMs and other types of low Co cathode materials.
- New insights into the processes and reactions in calcination of Ni-based CAMs were obtained, including: i) Kinetic and thermodynamic limits to the lithiation-driven crystallization; ii) Impact of Mn on structural ordering and crystallization; iii) Impact of the Nb coating both to the surface and bulk
- With insights from *in situ* studies, protocols were developed for stabilizing Ni-based CAMs: i) Controlling the constituent components and their phase morphology; ii) Li-stoichiometry control.
- Additional efforts were made on understanding of the limitations to the fluorination in DRX cathode materials.

In FY23, this project will continue the efforts on processing Ni-based and other types of low Co/Co-free CAMs. New research activities have already been initiated, including studies of the impacts of lithium stoichiometry, surface coating/doping on particle morphology during processing of Ni-based Co-free CAMs, and the process design for surface-conditioning of Ni-based cathode materials. Such studies may also be extended to other low-Co/Co-free cathodes, such as Mn-based earth-abundant layered oxides and disordered rocksalts.

Key Publications

1. F. Wang, P. Barai, O. Kahvecioglu, J. Bai, and V. Srinivasan, “Rational Design of Calcination of Nickel-based Cathode Materials by in situ Characterization and Multiscale Modeling”, *J. Mater. Res.* 37, 3197–3215, 2022 (invited).
2. J. Yao, J. Qi, Q. Dong, Y. Shen, L. Chen, S. Liu, Y. Wang, L. Li, Q. Mao, S. Yang, L. Gao, K. Zhang, K. Xu, F. Wang, J. Zhao, J. Bai, “A New Lithium Nickel Oxide Cathode Material with a Composite Structure for High-Performance Li-ion Batteries”, Online: DOI: 10.21203/rs.3.rs-1450650/v1.
3. F. Xin, A. Goel, X. Chen, H. Zhou, J. Bai, S. Liu, F. Wang, G. Zhou, M.S. Whittingham. “Electrochemical Characterization and Microstructure Evolution of Ni-rich Layered Cathode Materials by Niobium Coating/Substitution”, *Chem. Mater.* 34, 7858–7866, 2022.
4. N. Szymanski, Y. Zeng, T. Bennett, S. Patil, J. Keum, E. Self, J. Bai, Z. Cai, R. Giovine, B. Ouyang, F. Wang, C. Bartel, R. Clément, W. Tong, J. Nanda, G. Ceder, “Understanding the fluorination of disordered rocksalt cathodes through rational exploration of synthesis pathways”, *Chem. Mater.* 34, 7015–7028, 2022.
5. F. Wang, J. Bai, “Synthesis and Processing of High-Nickel Cathode Materials by Design”, *Batteries & Supercaps*, 5, e202100174, 2022 (invited).
6. S. Liu, K. Chen, O. Kahvecioglu, J. Bai and F. Wang, “Lithiation-Driven Crystallization of Ni-Based Cathode Materials during Calcination”, 241st ECS Meeting (May 29-June 2, 2022).
7. K. Chen, S. Liu, C. Cao, A.M. Kiss, J. Bai, and F. Wang, “Impact of Transition Metal Dissolution to the Interfacial Stability of Lithium Metal Batteries”, 241st ECS Meeting (May 29-June 2, 2022).

Acknowledgements

We thank the contribution by the team members, Ke Chen, Sizhan Liu, Yusuf Celebi and by collaborators, Lu Ma, Steve Ehrlich, Mingyuan Ge, Andy Kiss, Wah-Keat Lee, Juergen Thieme (BNL), Pallab Barai, Ozge Kahvecioglu, Krzysztof Pupek, YoungHo Shin, Venkat Srinivasan (ANL), Gerbrand Ceder (LBNL), Fengxia Xin, Hui Zhou, Stan Whittingham (Binghamton University).

II.10 Towards Solventless Processing of Thick Electron-Beam (EB) Cured LIB Cathodes (ORNL)

Zhijia Du, Principal Investigator

Oak Ridge National Laboratory
One Bethel Valley Rd
Oak Ridge, TN 37831
E-mail: duz1@ornl.gov

Jianlin Li, Co-Principal Investigator

Oak Ridge National Laboratory
One Bethel Valley Rd
Oak Ridge, TN 37831
E-mail: lij4@ornl.gov

Haiyan Croft, DOE Technology Development Manager

U.S. Department of Energy
E-mail: haiyan.croft@ee.doe.gov

Start Date: October 1, 2021

End Date: September 30, 2022

Project Funding (FY22): \$300,000

DOE share: \$300,000

Non-DOE share: \$0

Project Introduction

There are a variety of technical attributes to electron beam (EB) curing of LIB binders. EB curing uses solvent-free compositions that have low emissions (VOCs, etc.) and are recognized by federal, state and local governments as being a more desirable technology. Solvent or water-based processing requires high drying energy and results in significant CO₂ emissions. EB curing offers significant process energy savings, is ultra-high speed, and utilizes much more compact equipment than conventional drying ovens (much less plant floor space required). Furthermore, it is compatible with heat-sensitive substrates. Conventional thermal drying of LIB electrodes is typically conducted using multiple temperature stages; however, EB can be conducted in a single step. Solvent-free electrode compositions are rated as non-flammable, which translates into lower insurance costs, less stringent storage requirements and, a reduction in handling hazards.

EB treatment is a fast, robust materials processing technology that commonly delivers low cost and excellent performance for high-volume materials production. Based on decades of development and commercial deployment, self-shielded machines routinely operate with high reliability and low maintenance in industrial roll-to-roll production environments. ORNL is developing, demonstrating, and transitioning technology for high-speed roll-to-roll EB processing of LIB electrodes (i.e. coating formation and binder curing). Further specific advantages of this processing route for LIBs are:

Unmatched throughput – We estimate ≥ 600 m²/min throughput can be achieved based on ≥ 300 m/min line speed for roll widths up to 2 m (\$1.5-2.0M installed with machine footprint ~ 10 m²).

Thicker electrodes (synergy with Task 1) – Up to 150 microns can be achieved at the throughput rate mentioned above. Coatings of several hundred microns could be processed at higher capital cost per unit throughput, modest reduction in energy efficiency, and larger equipment footprint.

Excellent energy efficiency – Electrical efficiencies $\geq 60\%$ are possible, including voltage transformer losses (i.e., $\geq 60\%$ of electrical line energy is converted to productive EB energy).

Environmentally friendly – EB processing requires no solvent and no initiator and has low emissions.

Objectives

- Significant process energy savings
- Ultra-high electrode processing speed
- Utilize much more compact equipment than conventional drying ovens.

Approach

ORNL is working on a multiphase approach to develop, demonstrate, and transition EB processing of roll-to-roll battery materials.

- Phase 1 – Demonstrate key differentiating attributes of high throughput and thick layer processing.
- Phase 2 – Address the key challenges of EB curing parameters and resulting material performance; develop coating methods requiring little or no solvent.
- Phase 3 – Demonstrate an optimized curing system in conjunction with a high-speed coating line together with a key equipment partner and battery manufacturer.

Results

To evaluate some new emerging green resins (such as BPA free), the cross-linking has been confirmed by FTIR before curing and after curing at a dose of 120 kGy as shown in Figure II.10.1a. The characteristic absorption peak for the C=C bond in the acrylate group from the resin is around 810 cm^{-1} and its intensity corresponds to the concentration of unreacted acrylate groups. The decrease in absorption intensity after curing indicates that most of the acrylated groups have been cross-linked.

The samples have been evaluated in the cyclic voltammetry (CV) to test the stability after EB curing in Li half cells as shown in Figure II.10.1b. The resin was coated onto Al foil and cured under EB. The consecutive nature of the CV curve is quite stable within the scanning voltage window and the faradaic current response is rather low (at $\mu\text{A}/\text{cm}^2$ level) implying that EB cured polymers are electrochemically inert at the potentials for cathode materials intercalation/de-intercalation. Figure II.10.1c and d show the morphology of the electrodes after EB curing process. NMC particles used in this study were composed of tiny primary particles ($0.2\text{--}1\text{ }\mu\text{m}$) agglomerated into larger secondary particles ($3\text{--}8\text{ }\mu\text{m}$). The NMC particles and carbon black are uniformly dispersed in both electrodes without any appreciable defects such as agglomeration or cracks. EDX in Figure II.10.1e shows the distribution of elements across the electrode with C from carbon black and Ni/Mn/Co/O from NMC. The NMC particles are well distributed throughout the carbon network. Figure II.10.1f shows the cycling performance for EB cured NMC electrodes with green resin. The NMC electrodes shows excellent cycling stability with 150 mAh/g capacity maintained after 55 cycles. This demonstrates that using the EB-cured green resin as the binder can achieve good cycling life.

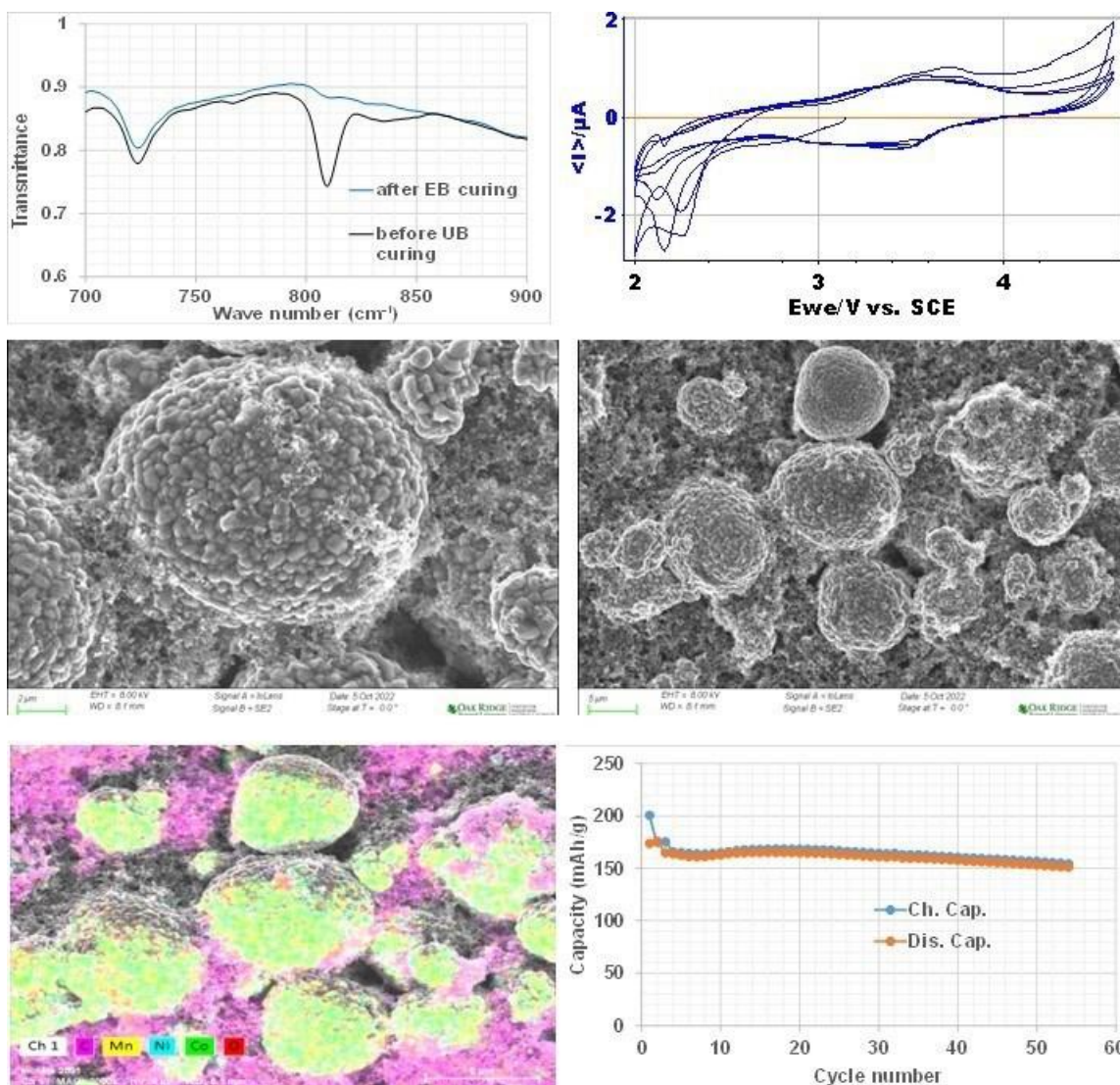


Figure II.10.1 (a) FTIR spectra of green resin before and after EB curing. (b) CV of green resin coated Al foils after EB curing. Scanning speed is 0.1 mV/s within 2.0–4.5 V. (c) and (d) SEM images of NMC811 cathode after EB curing process. (e) EDX of NMC cathode. (f) cycling performance of NMC cathode with green resin.

To explore the possible processing of radiation curing for Si containing graphite anodes, two different resins (denoted here as CPA and 2-CA) were used in the slurry formulation. 15% of amorphous Si was used with graphite as the active materials. Both formulations resulted in electrodes with good quality as shown in the Figure II.10.2. Li half coin cells were assembled and cycled under C/3 between 5 mV and 1.0 V. Differential capacity curve shows the features of broad peaks from amorphous Si and sharp peaks from graphite, corresponding to the alloying reaction of $x\text{Li} + a\text{-Si} \leftrightarrow a\text{-Li}_x\text{Si}$ and intercalation reaction of $\text{Li} + \text{C}_6 \leftrightarrow \text{LiC}_6$. Different cycling performance is shown in the figure. The formulation with 2-CA shows a rapid capacity fade at the very first few cycles. The formulation with CPA shows better cycling performance with 50% capacity retention after 100 cycles. Further study will be conducted to optimize the formulation of Si-graphite electrode for ebeam curing process.

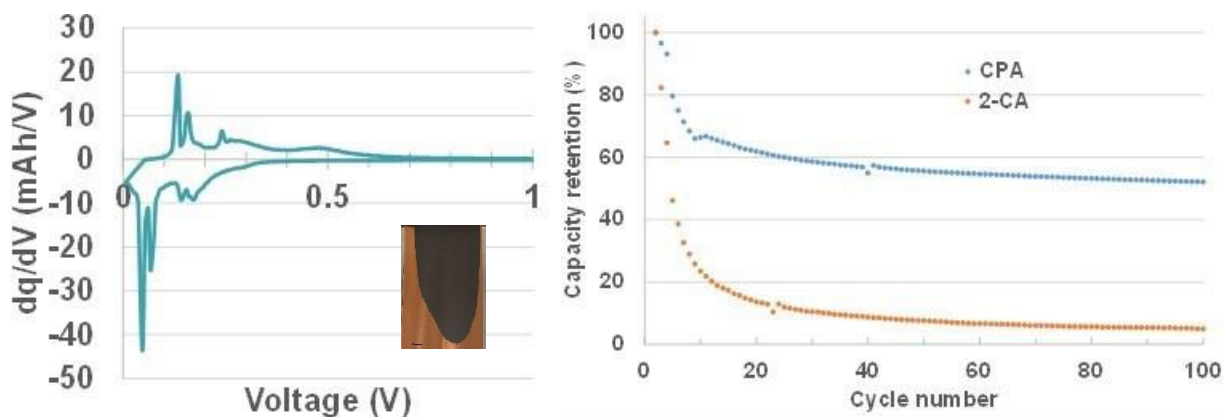


Figure II.10.2 (a) Differential capacity curve of 15% Si containing graphite anode (inset are electrodes casted and EB cured). (b) cycling performance of Si-graphite electrode with two different resins (CPA and 2-CA respectively).

To explore the possibility of EB curing in the manufacturing of cathode composite in Li metal battery, Li ion conducting polymer was formulated with NMC particles, carbon black into slurry, casted and EB cured as shown in Figure II.10.3. The Li ion conducting polymer precursor is formulated with acrylated polymer and LiTFSI as the salt. The curing of the acrylated polymer electrolyte in cathode is performed at 90 kGy. A similar polymer electrolyte membrane was prepared with similar precursor formulation and cured under UV light with photoinitiator. Then full cells were assembled with composite cathode, polymer electrolyte membrane and Li metal electrode. Figure II.10.3 also shows the voltage profiles of the cells. The curve shows sloping charging/discharging characteristics which is typical for NMC cathode materials. The cell also shows good cycling performance in the first 9 cycles (300+ hours). Then the voltage shows some failure mechanism at high voltage.

Figure II.10.4 shows the comparison of the result from nail penetration of an NMC/graphite Li-ion cell with Gen2 liquid electrolyte and the a NMC/Li metal cell with the same setup in Figure II.10.3 but in a pouch cell. Both cells have similar capacity and were charged to 90% state of charge. In the Li-ion cell, the temperature on the nail tip can rise as high as 20°C while the Li metal polymer cell shows only minimal temperature rise. This might be due to the safety feature of the polymer electrolyte or the huge internal resistance of the Li metal polymer cell.

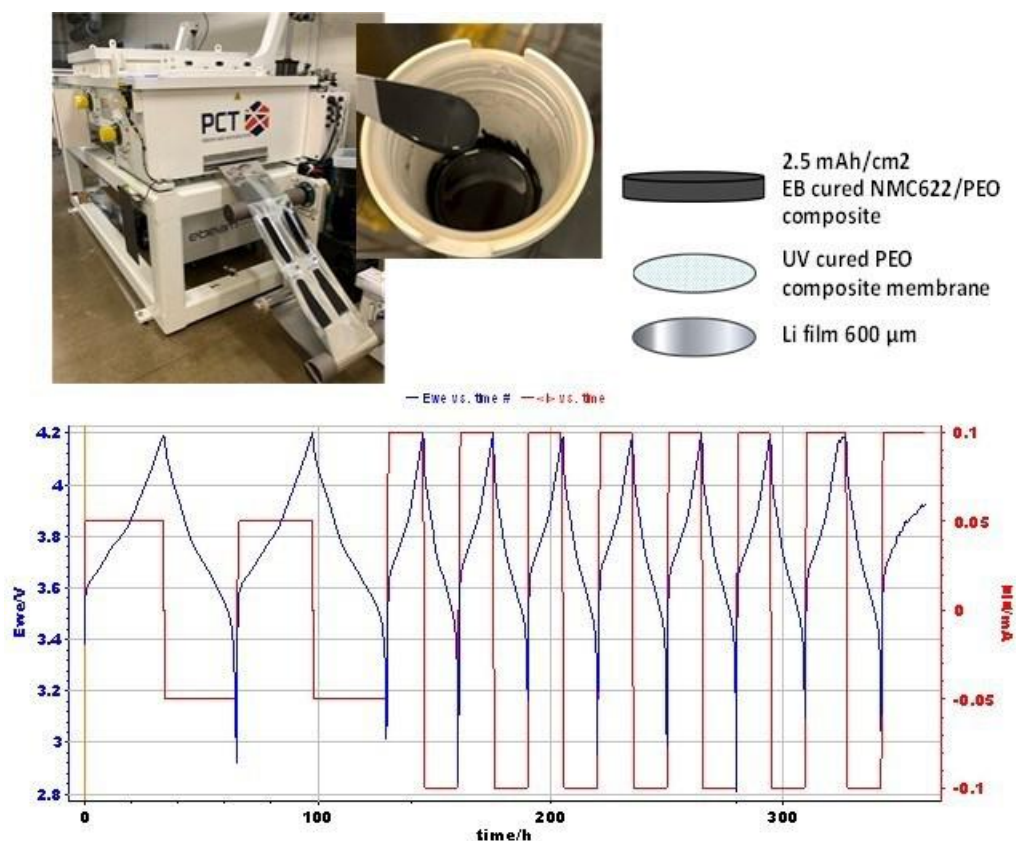


Figure II.10.3 Slurry formulation, coating, EB curing, coin cell configuration and cell performance of Li cells with NMC/PEO composite cathode.

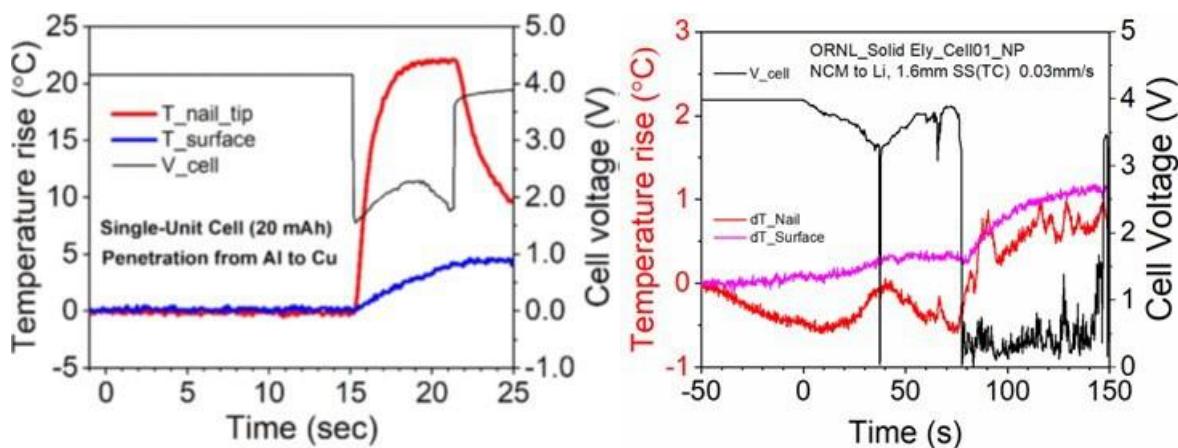


Figure II.10.4 Polymer electrolyte Li cell shows significantly less T rise in nail penetration.

To better understand if the ebeam irradiation has effect on the microstructures of materials, neutron diffraction was conducted on NMC622 and graphite powders before and after EB radiation as shown in Figure II.10.5. Unlike the experiments conducted previously on electrode with carbon black and binder, only neat active materials powders were placed under EB curing. Both lithium transition metal oxide cathode and graphite show no change before and after EB. Therefore, EB curing process can be used without interfering the crystal structure of active materials.

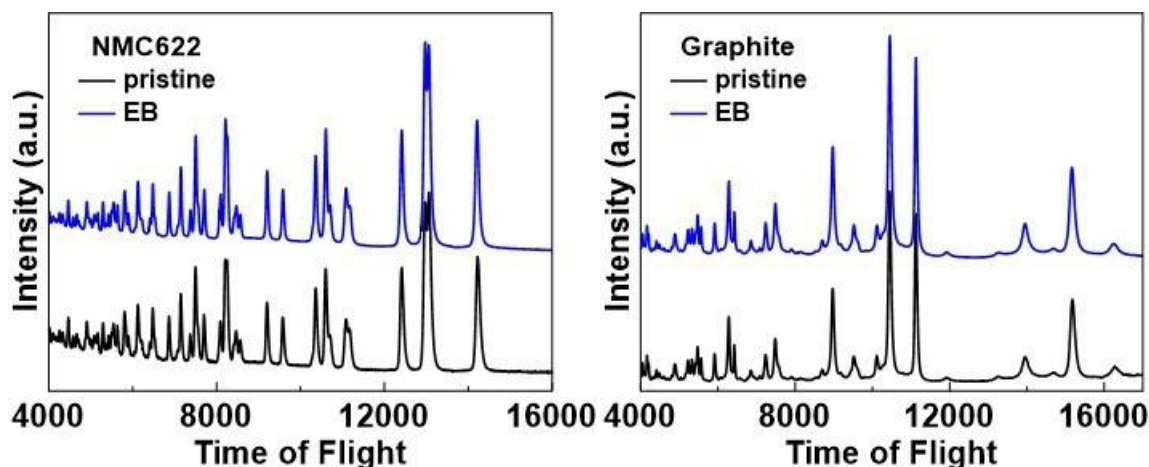


Figure II.10.5 Neutron diffraction patterns of NMC622 and graphite before and after EB radiation.

Conclusions

- A new green radiation curable resin from US supplier was evaluated and is compatible with EB process for Li ion electrode.
- EB radiation has no effect on both cathode and anode active material microstructures.
- More R&D work is needed for the EB curing process and its application for graphite and Si/graphite electrodes.
- Initial evaluation of EB process and application in Li metal polymer cells were carried out and will be tested in LFP for better voltage compatibility.

Key Publications

1. Toward Solventless Processing of Thick Electron-Beam (EB) Cured Lithium-Ion Battery Cathodes, Zhijia Du, Christopher James Janke, David L Wood III, Jianlin Li, VTO AMR 2022.

Acknowledgements

We would like to acknowledge the collaboration from Prof Guangsheng Zhang at UAH and Dr Jue Liu at SNS at ORNL.

II.11 Performance Effects of Electrode Processing for High-Energy Lithium-Ion Batteries (ORNL)

Jianlin Li, Principal Investigator

Oak Ridge National Laboratory
Energy & Transportation Science Division
2370 Cherahala Blvd., GRID Center, MS-6479
Knoxville, TN 37932
E-mail: lij4@ornl.gov

Haiyan Croft, DOE Technology Development Manager

U.S. Department of Energy
E-mail: haiyan.croft@ee.doe.gov

Start Date: October 1, 2021

End Date: September 30, 2022

Project Funding (FY22): \$500,000

DOE share: \$500,000

Non-DOE share: \$0

Project Introduction

This project at the DOE Battery Manufacturing R&D Facility (BMF) at ORNL builds on past research successes in the areas of battery electrode process development and optimization, cost reduction, cell energy density improvements, and manufacturability advancements, which support the Vehicle Technologies Office (VTO) and Electrochemical Energy Storage Tech Team ultimate targets of \$60/kWh system cost, 500 Wh/kg cell energy density, 800 W/kg cell power density, and 10-15 min extreme fast charging times. Our goal is to perform the science needed to reduce high-risk, high-payoff technologies to lower risk levels, such that U.S. industry will consider their integration in future products. Once a new material, process, or concept has demonstrated feasibility for integration and scaling, the BMF will work to make it a viable processing methodology (preferably with industry partners) with validated performance in a full pouch cell design. While doing so, the BMF will leverage a large array of complimentary projects and sponsors that will provide additional experience and a fast, efficient methodology for solving problems faced by the domestic lithium-ion battery (LIB) industry.

Objectives

To improve cell energy and power density and reduce battery pack cost by manufacturing thick electrodes with tailored electrode architecture via advanced processing and high-energy, high-voltage cathode materials:

- Fabricate thick (6-8 mAh/cm²) and crack-free cathodes via aqueous processing
- Evaluate compatibility of high Ni-NMC with aqueous processing
- Develop bilayer electrodes via freeze tape casting for improved rate performance
- Develop polymer electrolyte for solid-state batteries
- Understand the conduction mechanism in polymer electrolyte and optimize the formulation
- Demonstrate a solid-state battery with an energy density ≥ 300 Wh/kg (cell level).

Approach

- Fabricate crack-free NMC622 cathodes with high areal loading (4-8 mAh/cm²) via aqueous processing.
- Develop bilayer electrode architecture via freeze tape casting
- Develop composite polymer electrolyte
- Characterize the electrochemical performance of the composite electrolytes
- Investigate the electrolyte-cathode interface
- Evaluate rate performance and long term cyclability.

Results

Develop tailored electrode architecture via freeze tape cast.

Freeze tape casting (FTC) techniques were employed to tailor the architecture of structured cathode electrodes. The structured electrodes were based on a double-layer configuration. A bottom dense layer was utilized to enhance the energy density whereas a top porous layer with vertically aligned walls was utilized to enhance the power density. The porous structure of the power layer was achieved by ice templating this layer on top of the densified energy layer of the cathode. The aim of this configuration is to address challenges that are associated with the manufacturing of thick and crack-free electrodes and address mass transport limitations in thick electrodes by enabling low-tortuosity and speed up the Li^+ ion dynamics in the aligned cathode architectures.

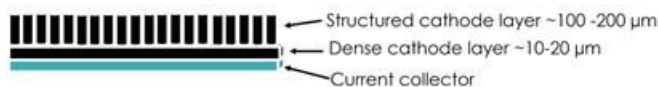


Figure II.11.1 Schematic illustration of the structured cathode electrodes using (FTC) techniques.

Crack-free electrodes with high areal loading ($4\text{--}8\text{ mAh/cm}^2$) were fabricated, their microstructure was characterized, and their performance was evaluated. A schematic illustration of the developed structures is shown in Figure II.11.1. Three processing variables were optimized to tailor the architecture of the cathodes. The solid to water content in the slurry formulation determines the thickness and the density of the structured cathode walls; the freezing temperature or freezing temperature sequence is associated with the size of water crystals and controls the wall distance as well; and the wet gap thickness of the slot-die applicator determines the thickness and therefore the active material loading of the cathode. To optimize the processing parameters of the FTC cathodes two experimental setups were used, a small-scale benchtop configuration and an industrial-scale roll-to-roll configuration. Both experimental setups are shown in Figure II.11.2. The benchtop setup was used for the initial coating configurations whereas, the large-scale configuration provided a more precise control of the FTC parameters (i.e., temperature). The freeze bed temperature can be varied to -50°C . A slot-die applicator and a two-zone freeze bed are available (Figure II.11.2c, d). Aqueous slurry formulations based on standard Ni-rich layer oxides (NMC 622), carbon black (CB) and cellulose binder (90, 5, 5 wt%, respectively) were used. To lower the pH of the slurry and mitigate the corrosion of the aluminum current collector, phosphoric acid (1.5 wt% with respect to the solid content) was added in the slurry according to our previous studies [1]. Optical microscope images of the FTC cathode electrodes at several solid to water contents are shown in Figure II.11.3. The optimal freezing temperature was -9°C . All coatings are structured, and the density of the coating features is increasing when the solid content is increasing. Electrode architectures like those shown in Figure II.11.3a and b can be infiltrated with solid electrolytes and be utilized in solid state battery applications. A representative scanning microscope image of an infiltrated cathode with polyethylene oxide and lithium bis(trifluoromethanesulfonyl)imide (LiTFSI) salt is shown in Figure II.11.4. The architecture of the pristine cathode (unfilled) is like that shown in Figure II.11.3a and b. The filled with polymer electrolyte cathode is shown in Figure II.11.4b. Such structures can be utilized in cathodes for solid state batteries. These FTC cathodes have shown significant advantages in the electrochemical cycling and interfacial resistance of solid-state cathodes compared to the non-structured cathodes according to our recent work [2]. The performance improvements were found to be associated with the low-tortuosity and speed up of the Li ion transport mechanism due to the formation of aligned conductive paths and the better utilization of the electrolyte/active material interface.

Denser electrode structures like those in Figure II.11.3g and h were utilized in conventional Li^+ ion batteries. The denser scaffold configuration resulted in robust electrode structures that do not need to be infiltrated with a solid phase in order to retain their structure.

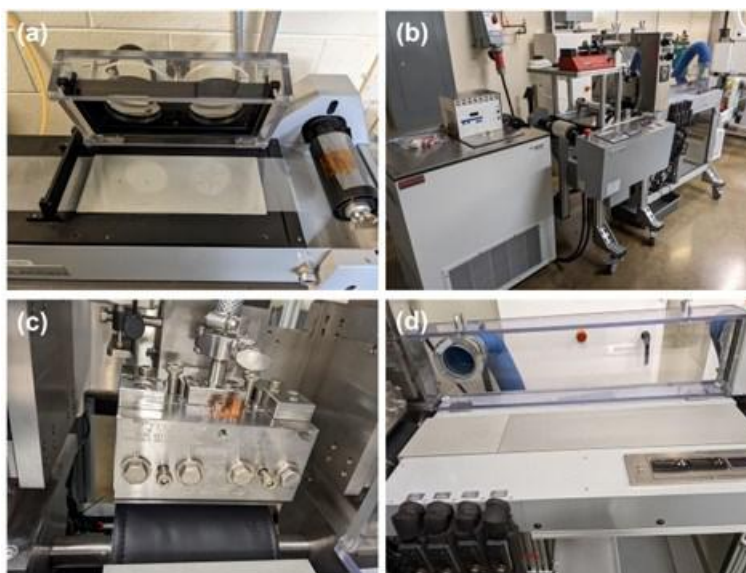


Figure II.11.2 The experimental setups that were used for the FTC cathodes. (a) benchtop configuration, (b-d) scale up configuration.

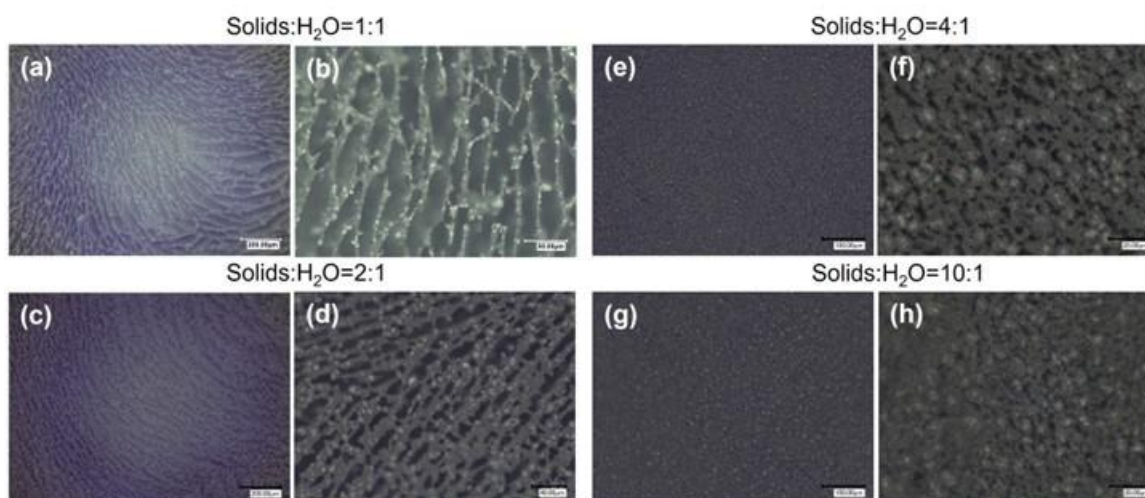


Figure II.11.3 Optical microscope images of FTC cathodes electrodes at several solid to water contents indicated on the figure. Solid to water weight ratio 1:1 (a,b), 2:1 (c,d), 4:1 (e,f), 10:1 (g,h). The freezing temperature was -9°C .

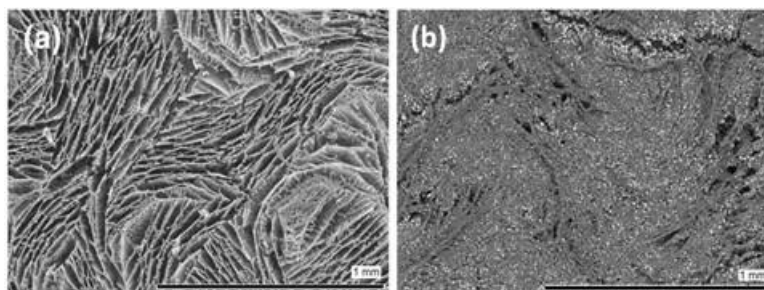


Figure II.11.4 SEM images of the (a) unfilled FTC cathode and (b) filled with PEO and LiTFSI.

We investigated two-layer electrode configurations. A bottom dense layer was utilized to enhance the energy density whereas a top porous layer with vertically aligned walls was utilized to enhance the power density. This configuration is anticipated to enhance the performance of the Li^+ ion batteries at high active material

loadings and high cycling rates due to the limitation of the Li^+ ion diffusion in the bulk structure of the thick cathode. Initially, conventional single layer cathodes at several areal capacities (mAh/cm^2) were tested to obtain baseline values and evaluate the performance degradation at high capacity and cycling rates. The cathodes were based on standard formulations (90 wt.% NMC622, 5 wt.% carbon black, 5 wt.% binder) and cells were assembled using Li metal for the anode. The charge and discharge values at several C-rates are shown in Figure II.11.5 for 2, 3, 4, and 6 mAh/cm^2 . A noticeable degradation in the FTC cathodes with capacity values comparable to those in Figure II.11.5 were also cycled using the same testing capacity of the cells is shown in Figure II.11.5d for the 6 mAh/cm^2 at charge and discharge rate higher than 0.5C. protocols. For areal capacity values 4 mAh/cm^2 or lower, the structured and non-structured cathodes showed comparable charge and discharge values. The cycling of the structured cathode at 6 mAh/cm^2 is shown in Figure II.11.6. At 0.5C rate and higher rates the capacity values start to become higher compared to the non-structured cathode. The cycled cathode was based on a 4 mAh/cm^2 bottom dense layer and a 2 mAh/cm^2 top structured layer. This is an ongoing study. Cathodes with higher than 6 mAh/cm^2 as well as different areal capacity ratios for the bottom and top structured layer are under investigation to optimize the FTC cathodes and maximize the cycling improvement against the conventional single layer cathode architecture.

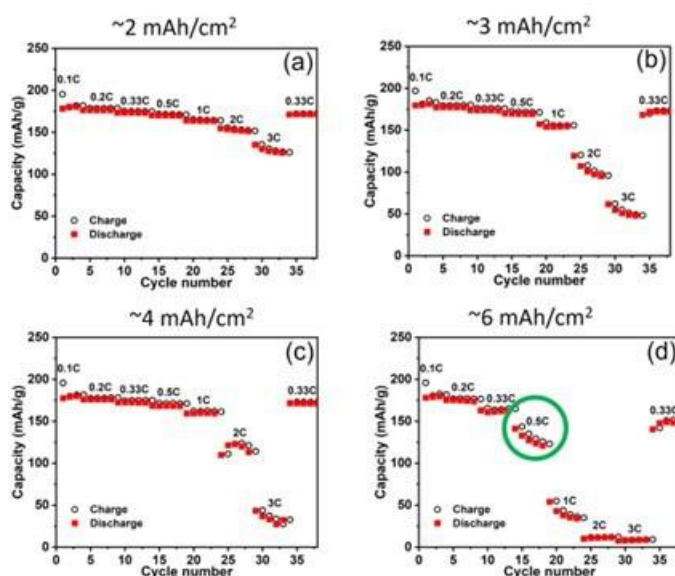


Figure II.11.5 Charge and discharge values of the single layer cathodes at several cycling rates. (a) 2 mAh/cm^2 , (b) 3 mAh/cm^2 , (c) 4 mAh/cm^2 , (d) 6 mAh/cm^2 . Significant capacity fading is shown at C-rates higher than 0.5 (green circle).

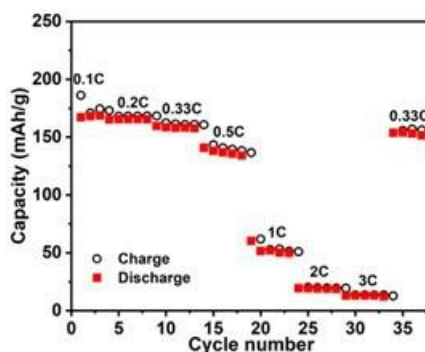


Figure II.11.6 Charge and discharge values at several cycling rates of a structured cathode with areal capacity 6 mAh/cm^2 .

Development of polymer electrolytes for FTC cathodes

The Li^+ ion conductivity mechanism was investigated in hybrid polymer electrolytes filled with scaffold structures of electrospun aluminum-substituted lithium lanthanum zirconate $\text{Li}_7\text{La}_3\text{Zr}_2\text{O}_{12}$ (Al-LLZO). Such

composite electrolytes can be utilized as separators and/or catholytes in composite structured cathodes like those shown in Figure II.11.3. The objectives of this study are:

- i) Delineate the Li^+ ion conductivity mechanism at the Al-LLZO interface and in the polymer matrix.
- ii) Correlate the conductivity mechanism with the dendrite formation and the electrochemical performance.
- iii) Determine the electrochemical stability of the two most commonly used Li salts: lithium bis(trifluoromethanesulfonyl)imide (LiTFSI) and lithium bis(fluorosulfonyl)imide.

Polyethylene oxide (PEO) was used for the polymer matrix. The structure of the composite electrolyte films is shown in Figure II.11.7. The platelet Al-LLZO fillers were synthesized using electrospinning techniques [3]. The planar geometry of the fillers results in a good adsorption of the polymer electrolyte and therefore to a more robust polymer-filler interface. The planar geometry of the fillers is anticipated to provide better screening against dendrite formation (Figure II.11.7c). X-ray diffraction patterns (XRD) confirmed that the synthesized Al-LLZO is in the cubic phase (Figure II.11.7e) that is more conductive.

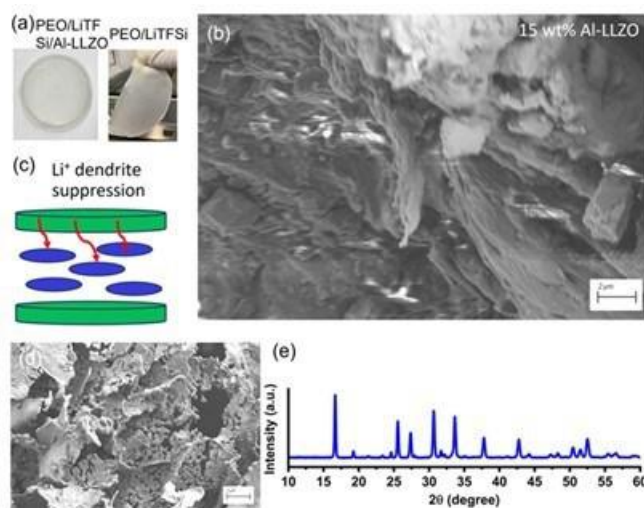


Figure II.11.7 Hybrid polymer electrolytes filled with platelet Al-LLZO. (a) electrolyte films, (b) cross-sectional SEM image, (c) schematic of the Li^+ dendrite suppression due to the platelet geometry of the Al-LLZO fillers, (d) SEM image of the Al-LLZO fillers, (e) XRD pattern of the Al-LLZO fillers.

Dielectric relaxation spectroscopy was employed to measure the conductivity and relaxation mechanisms of the composites over broad temperature (25 to 120°C) and frequency (10^{-2} to 10^7 Hz) ranges. The summarized plot for the conductivity of the pristine and composite electrolytes with LiTFSI and LiFSI salts is shown in Figure II.11.8. The composite electrolytes are more conductive than the pristine electrolytes. In both systems (LiTFSI and LiFSI) the 7wt% composite is more conductive and the LiFSI electrolytes are more conductive compared to the respective LiTFSI electrolytes. The correlation between the Al-LLZO fillers and the Li^+ ion diffusion in the electrolyte was investigated by analyzing the dielectric losses spectra associated with the Li^+ ion polarization peaks. The spectra analysis for the LiTFSI composites at 60°C is shown in Figure II.11.9. A bimodal relaxation associated with the LiTFSI coordination sites is present only in the PEO/LiTFSI electrolyte. The low frequency relaxation corresponds to strongly bound ions whereas, the high frequency relaxation to more mobile ions.

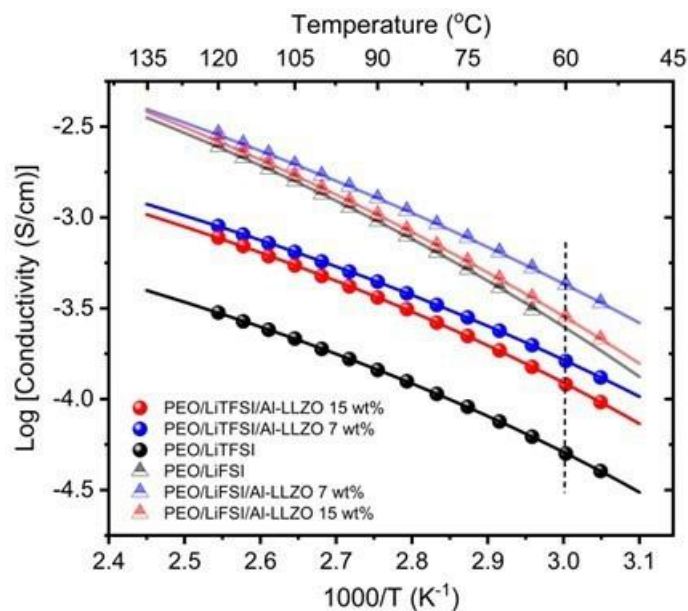


Figure II.11.8 Summarized conductivity plot for the pristine and composite polymer electrolytes.

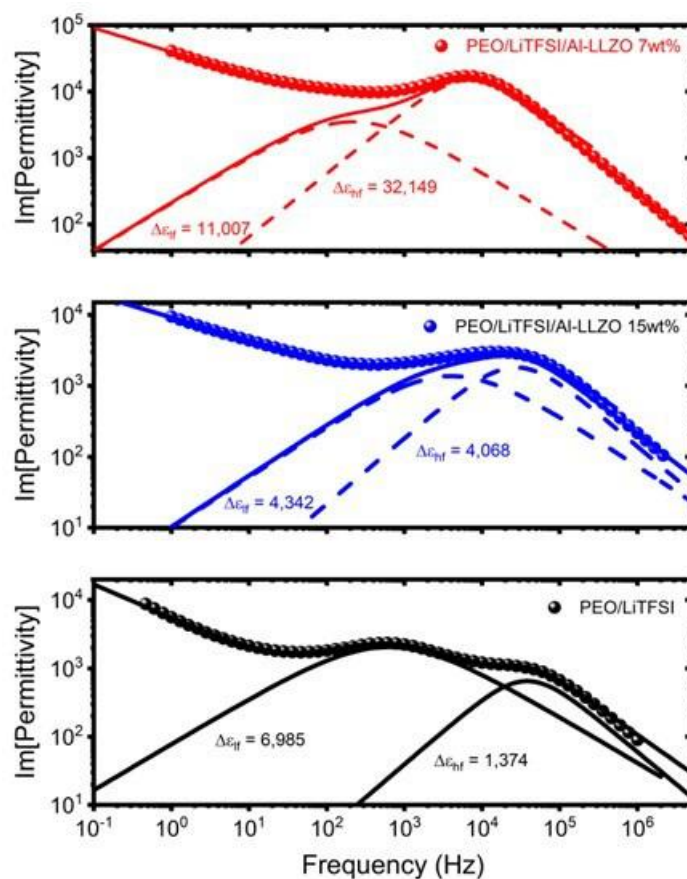


Figure II.11.9 Dielectric loss spectra analysis of the Li^+ ion conductivity mechanism at 60°C.

The Al-LLZO speeds-up the Li ion dynamics due to a possible conduction mechanism through the Al-LLZO/PEO interface. The ratio of the dielectric strengths ($\Delta\epsilon$) of the mechanisms is correlated to the

improvements in the conductivity values. The polymer-filler interface can enhance the Li^+ ion transport mechanism in the polymer matrix. Molecular dynamics (MD) computer simulation studies were performed to better understand this interfacial process. Moreover, according to the fitting analysis results in Figure II.11.8, the conductivity mechanism in the LiTFSI and LiFSI based electrolytes is different. To better understand the dependence of the Li^+ ion conduction on the chemical structure of the Li salts, MD simulations and small angle x-ray (SAXS) measurements were carried out. Representative snapshot images and scattering spectra analysis are shown in Figure II.11.10. According to the MD simulation results in the LiFSI electrolytes the Li^+ ions are more decorrelated from the PEO matrix; whereas, in the LiTFSI electrolytes are characterized by more coupled dynamics. Plots of the radial distribution function showed larger number of Li^+ ion clusters in the LiFSI electrolytes. The SAXS measurements are in excellent agreement with the MD results. The LiFSI electrolytes are characterized by more pronounced ionic clusters compared to the LiTFSI electrolytes. In the LiTFSI electrolytes the Li^+ ions are more uniformly distributed the polymer phase (Figure II.11.10b-e). In the LiFSI electrolytes the Li^+ ion conduction process occurs predominantly through ionic clusters and therefore the conductivity values are higher; however, the cluster formation of the Li^+ ions has detrimental effects on the electrochemical performance of the electrolyte. Long-term galvanostatic cycling measurements at current density $50 \mu\text{A}/\text{cm}^2$ are shown in Figure II.11.11. The composite electrolyte has lower overpotential than the pristine electrolyte due to the dendrite suppression of the platelet fillers. The planar geometry of the Al-LLZO filler resulted in improvements that are comparable to those in composite electrolytes with 50-70 wt% ceramic electrolyte. The LiTFSI based composite electrolyte has significantly longer life than the respective LiFSI electrolyte due to the more uniform Li^+ ion distribution.

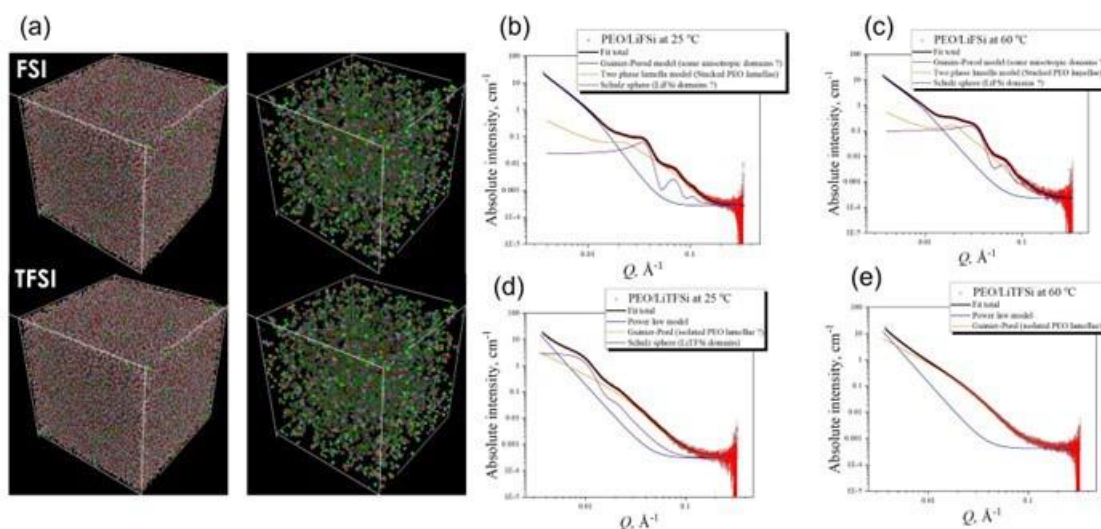


Figure II.11.10 (a) MD snapshots of the polymer electrolyte with LiTFSI and LiFSI. SAXS measurements and fitting analysis of the polymer electrolyte at 25 and 60 °C. (b,c) PEO with LiFSI, (d,e) PEO with LiTFSI.

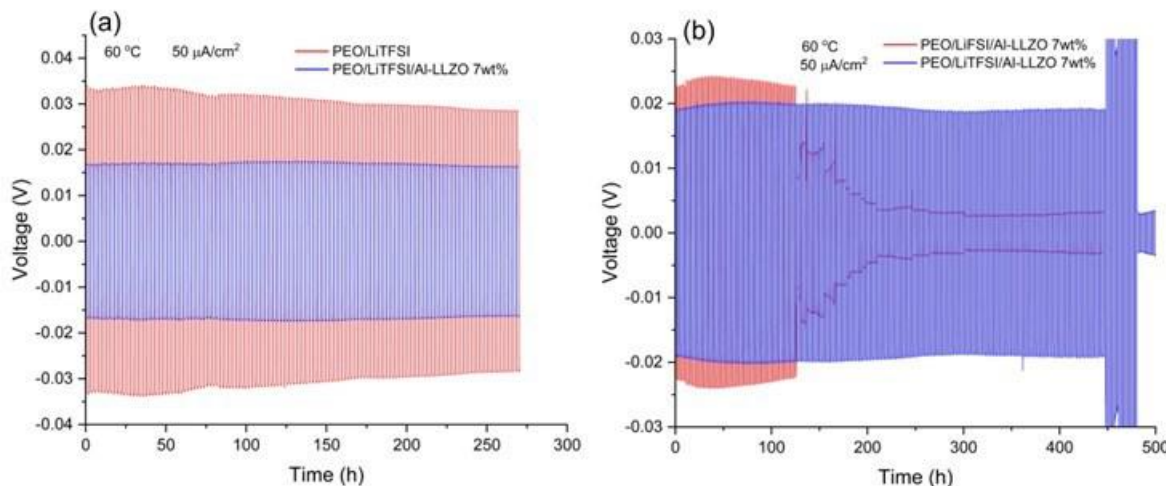


Figure II.11.11 Comparison plots of long-term stripping plating at $50 \mu\text{A}/\text{cm}^2$ of (a) LiTFSI electrolyte versus composite Al-LLZO/LiTFSI electrolyte. (b) composite LiTFSI versus composite LiFSI electrolyte.

Conclusions

The drying conditions of the freeze tape cast coatings were optimized to avoid collapse of the structures, and formation of defects and cracks. Thick and crack-free NMC622 cathodes were synthesized. Dense structures were achieved by reducing the water content of the slurry to Solids: H_2O = 10:1. The optimal bed freeze temperature was -9°C . The resulted structures were characterized by more robust interface between the bottom and the structured layer. Two-layer FTC and single layer conventional cathodes with several areal capacities were cycled. For areal capacity values $4 \text{ mAh}/\text{cm}^2$ or lower, the structured and non-structured cathodes showed comparable charge and discharge values. The cycling of the structured cathode at $6 \text{ mAh}/\text{cm}^2$ at 0.5C or higher rates showed improved capacity values compared to the non-structured cathode.

Hybrid polymer electrolytes based on Al-LLZO platelet fillers and LiTFSI or LiFSI salt were investigated. The platelet geometry of the Al-LZO fillers resulted in substantial improvement of the stripping/plating performance. The composite electrolytes are more conductive than the pristine electrolytes (with the 7wt% composite having the highest conductivity). The Li^+ ion dynamics in the PEO/LiTFSI electrolyte were characterized by a bimodal mechanism due to strongly and loosely coordinated ions. The Al-LLZO fillers significantly change the conductivity mechanism. The Li^+ ion dynamics become faster, and the conductivity increases due to a possible interfacial conductivity mechanism. The LiFSI based electrolytes are more conductive than the LiTFSI based electrolytes. However, the more uniform Li^+ ion distribution in the LiTFSI electrolytes resulted in improved long-term galvanostatic cycling performance. Tailoring the first principles that govern the conductivity mechanism in hybrid polymer electrolytes will provide the tools for the predictive design of advanced electrolytes and cathodes that will be used in FTC cathodes.

Key Publications

1. J. Li, A. Kukay, "Polymer electrolytes via freeze tape casting for solid-state batteries", Invention disclosure ID 202205109.
2. J. Li, D. Parikh, "Hybrid electrode architectures for lithium-ion battery electrodes", Invention disclosure ID 202205081.
3. D. Parikh, J. Li, "Dual layer hybrid freeze tape casting of graphite anode for extreme fast charging applications", *Carbon*, 196 (2022) 525-531.
4. J. Sharma, G. Polizos, C. Jafta, D. Wood, and J. Li, "Review—electrospun inorganic solid-state electrolyte fibers for battery applications", *Journal of The Electrochemical Society*, 169 (2022) 050527-050541

5. R. Sahore, M. Wood, A. Kukay, Z. Du, K. Livingston, D. Wood, J. Li, “Performance of different water-based binder formulations for Ni-rich cathodes evaluated in $\text{LiNi}_{0.8}\text{Mn}_{0.1}\text{Co}_{0.1}\text{O}_2$ /graphite pouch cells”, *Journal of The Electrochemical Society*, 169 (2022) 040567.
6. A. Shodiev, F. Zanotto, J. Yu, M. Chouchane, J. Li, and A. Franco, “Designing Electrode Architectures to Facilitate Electrolyte Infiltration for Lithium-Ion Batteries”, *Energy Storage Materials*, 49 (2022) 268-277.
7. J. Li, J. Fleetwood, B. Hawley, W. Kays, “From materials to cell: state-of-the-art and prospective technologies for lithium-ion battery electrode processing”, *Chemical Reviews*, 122 (2022) 903-956
8. G. Polizos, R. Tao, J. Li. “Structured cathodes enabled by freeze tape casting for high energy density/high power Li-ion batteries. Oral Presentation, 242nd ECS Meeting, Atlanta 10/10/2022.

References

1. A. Kukay, R. Sahore, A. Parejiya, W. Blake Hawley, J. Li, D. L. Wood. Aqueous Ni-rich-cathode dispersions processed with phosphoric acid for lithium-ion batteries with ultra-thick electrodes, *J. Colloid Interface Sci.* 581 (2021) 635–643.
2. G. Polizos, S. Kalnaus, X.C. Chen, M. Dixit, M. Balasubramanian, J. Sharma¹, R. Tao, J. Li. Two-layer cathode architecture for high-energy density and high-power density solid state batteries (under review).
3. G. Polizos, J. Sharma, C.J. Jafta, N. Muralidharan, G.M. Veith, J.K. Keum, A. Kukay, R. Sahore, D.L. Wood III. Nanostructured ligament and fiber Al-doped $\text{Li}_7\text{La}_3\text{Zr}_2\text{O}_{12}$ scaffolds to mediate cathode-electrolyte interface chemistry, *J. Power Sources* 513 (2021) 230551.

Acknowledgements

The PI is grateful to ORNL team members Georgios Polyzos, Dhruvad Parikh, Ronnie Tao, Alexander Kukay, Blake Hawley, Anand Parejiya, Yangyang Wang, Zhijia Du, Kelsey Livingston and Ilias Belharouak, for valuable data collection and analysis, and external collaborators Congrui Jin, Alejandro Franco and Abbas Shodiev for contributing on electrolyte wetting investigation. We also thank Dr. Ozge Kahvecioglu at the Materials Engineering Research Facility (MERF), Argonne National Laboratory, for providing the NMC811 powder with smaller particle size, which is through project I.2.F “Process R&D for Next Generation Cathode Materials (BAT167)”.

III Recycling and Sustainability

Lithium-ion batteries are used for a range of applications – from smartphones and laptops to electric vehicles and other applications. Recycling techniques for these batteries exist, but it is necessary to ensure their cost effectiveness before large-scale adoption. Improving this cost-effectiveness will help users turn them in for recycling instead of discarding them. This will lead to lower raw material costs and make batteries more affordable. In addition, it will also reduce the consumption of substantial amounts of critical materials (e.g., cobalt) which are both expensive and often dependent on foreign sources.

To address the currently limited infrastructure for collection, storing, and transporting discarded lithium ion batteries for eventual recycling, a Battery Recycling Prize was established by the Vehicle Technologies Office (VTO) to be directed and administered by the National Renewable Energy Laboratory (NREL). This effort is complements early-stage laboratory, university, and industry research to develop low-cobalt (or no cobalt) active cathode materials for next-generation Li-ion batteries and the Lithium Battery R&D Recycling Center with the aim of developing closed-loop cost-effective recycling processes to recover critical lithium battery materials. Researchers are using less energy-intensive processing methods and capturing more valuable forms of materials for “direct recycling”— the recovery, regeneration, and reuse of battery components directly without breaking down the chemical structure. ReCell is mainly based at Argonne, but on the whole the center is a collaboration between the lab, the National Renewable Energy Laboratory, Oak Ridge National Laboratory, Michigan Technological University, the University of California at San Diego, and Worcester Polytechnic Institute.

The rest of this chapter contains detailed reports on the status of the following individual projects.

- Battery and Critical Materials Life Cycle Analysis (ANL)
- Lithium-ion Battery Recycling Prize Support (NREL)
- Battery ReCell Center (ANL)
- Development of Lithium Electrode Based Cell and Manufacturing for Automotive Traction Applications (Farasis Energy).

III.1 Battery and Critical Materials Life Cycle Analysis (ANL)

Jarod Kelly, Principal Investigator

Argonne National Laboratory
9700 South Cass Avenue
Lemont, IL 60439
E-mail: jkelly@anl.gov

Linda Gaines, Co-Principal Investigator

Argonne National Laboratory
9700 South Cass Avenue
Lemont, IL 60439
E-mail: lgaines@anl.gov

Michael Wang, Co-Principal Investigator

Argonne National Laboratory
9700 South Cass Avenue
Lemont, IL 60439
E-mail: mqwang@anl.gov

Brian Cunningham, DOE Technology Development Manager

U.S. Department of Energy
E-mail: Brian.Cunningham@ee.doe.gov

Start Date: October 1, 2021

End Date: September 30, 2022

Project Funding (FY22): \$270,000

DOE share: \$270,000

Non-DOE share: \$0

Project Introduction

This project examines automotive batteries and the critical materials used in them, spanning raw material extraction, their processing into usable chemical forms and/or battery components, their subsequent assembly into batteries, and end-of-life. This is accomplished using multiple analytical techniques, including life-cycle analysis (LCA), material flow analysis (MFA), and supply chain analysis (SCA). These techniques enable the identification of hot spots along the supply chains of critical materials and batteries for energy use, greenhouse gas (GHG) emissions, and other environmental burdens. We consider battery materials produced for current batteries, along with battery assembly and use in battery electric vehicles (BEVs).

Understanding material production using LCA is essential to determine the energy and environmental burdens of battery production, as embodied emissions of battery materials comprise a significant share of their life-cycle burdens. Additionally, regional aspects of material extraction and processing can influence the environmental effects of battery production. Such aspects include the ore types used to extract materials, technologies used for material extraction and processing (energy and material inputs), transportation distances and modes used, and local energy input parameters. We study multiple battery materials for their energy and environmental burdens, based on their respective supply chain in the U.S. battery mix.

This project updated Argonne's Greenhouse gases, Regulated Emissions and Energy use in Technologies (GREET®) model with: (a) Important material and energy input data (life-cycle inventory or LCI data) for the production of battery materials (lithium from brine and ore, nickel from sulfide ores with varying ore grades, cobalt, and titanium); and (b) Material composition and energy/power density of automotive batteries (lithium-ion batteries or LIBs) for light-, medium-, and heavy-duty vehicles across hybrid, plug-in hybrid, electric, and fuel-cell powertrains. We also investigated ongoing initiatives for commercial-scale domestic production of battery-grade lithium (Li) chemicals (lithium carbonate/Li₂CO₃ and lithium hydroxide/LiOH) from geothermal

and chemical brines, and their likely environmental burdens via a preliminary LCA. These updates serve as vital resources to the LCA community and to researchers interested in understanding the environmental burdens of current supply chains and comparing them with the burdens of alternative supply chain routes. We also conducted studies to understand existing supply chains of titanium and phosphates for the U.S. and the likely prospects of domestic phosphate production in the future. This project also facilitates engagement within the International Energy Agency (IEA) Hybrid and Electric Vehicle (HEV) Technology Collaboration Programme (TCP) Task 40 and Task 46 projects, which are associated respectively with critical raw materials for electric vehicles, and the electrification of two-wheelers, and medium-duty and heavy-duty vehicles.

Objectives

- Battery Life Cycle Analysis with Expanded GREET Model
 - Battery LCA Expansion and Update
 - Characterize, update, and release the lithium-ion battery (LIB) bill-of-material (BOM) and energy/power density of all vehicles in Argonne's GREET LCA model to provide up-to-date information for computing LIB energy and environmental burdens
 - Characterize, update, and release state-of-knowledge on nickel (Ni) production within the GREET model to provide up-to-date information on its environmental burden for various ore grades
 - Identify potential, horizon battery technologies as substitutes to automotive LIBs
 - Investigate the prospects for domestic production of battery-grade Li-chemicals from brines and advance understanding of the likely processes used and resultant environmental impacts
 - Characterize, implement/update, and release state-of-knowledge on LIB anode production (graphite – natural and synthetic; silicon) within the GREET model to provide up-to-date information for LCA
 - IEA HEV TCP Task 46 support for the study of medium- and heavy-duty vehicle LCA.
- Battery Critical Materials Assessment
 - Characterize, implement, and release state-of-knowledge data on titanium (Ti) production and supply chain within the GREET model to provide up-to-date information on its environmental burden
 - Characterize, implement, and release state-of-knowledge data on titanium on phosphorous and phosphates through literature review and material flow analysis.
 - IEA HEV TCP Task 40 support for the study of critical materials.

Approach

Argonne has developed and updated the GREET LCA module for battery materials and batteries, based on industrial insights, relevant supply chains (for U.S. battery use), and market changes. In FY22, we made research efforts to collect LCI data related to batteries and critical materials. Argonne updated the LCI for the production of nickel (Ni), titanium (Ti), and LIB anodes, accounting for their corresponding supply chains (domestic production and imports) in meeting the U.S. demand for these materials. For Ni, we focused on the variation in material and energy inputs for its production from sulfide ores as a function of ore grade. For Ti, we leveraged production inventory information in literature for its sponge metal, ingot, and powder forms. For LIB anodes, we updated the inventory for synthetic graphite (SG) and silicon (Si) anodes and provided a new inventory for natural graphite (NG) anodes. Argonne also investigated the current efforts aimed at the domestic production of battery-grade Li-chemicals and provided a preliminary LCI for their domestic production from geothermal brines. We also explore next-generation batteries that could be important alternatives to LIBs for automotive applications (and others), as well as study the sources and supply of phosphorous for LIBs. Additionally, Argonne updated the BOM and energy/power density of LIBs for light-, medium-, and heavy-duty vehicles in the GREET model across hybrid, plug-in hybrid, electric, and fuel-cell powertrains.

We have maintained close interactions with stakeholders for technological developments associated with LIB production and performance, and to maintain Argonne's position as the world's leader in battery and critical

materials LCA. During FY22, Argonne staff: 1) gave invited talks and presentations to government, industry, and academia; 2) interacted with international groups such as the IEA to coordinate research; 3) improved the understanding of environmental impacts of battery materials production; and 4) responded to numerous requests for information.

Results

In FY22, Argonne updated its life-cycle inventory (LCI) within GREET for nickel, titanium, and LIB anodes, as well as BOM and energy/power density of LIBs for all vehicles spanning different powertrains. For Ni, we developed a detailed production pathway for Class I Ni metal production from sulfide ores and updated its LCI as a function of ore grade (with a default ore grade related to global production). For Ti, we introduced a new pathway for its production in sponge metal and powder forms and provided their respective LCI. For two LIB anodes (silicon and synthetic graphite), we updated their respective LCI to consider their recent industrial-scale production. Additionally, we introduced a new pathway for the production of natural graphite anode (a substitute for synthetic graphite anode in LIBs) and developed its LCI. All LCIs consider the supply chain of these materials for meeting their respective demand in the United States (both production and imports). Further, we used the latest version of Argonne's Battery Performance and Cost (BatPaC) model (BatPaC 5.0) to update the LIB BOM and energy/power density of light-duty, medium-duty, and heavy-duty vehicles with hybrid, plug-in hybrid, battery electric, and fuel-cell powertrains. Also, we have provided a tentative LCI of lithium (Li)-chemical production (meant for battery production) from geothermal brines, as an addition to our investigation of commercial initiatives for this production within the US and North America. All these efforts (including the aforementioned LCIs) are documented in publicly available technical reports. We have additionally investigated phosphorous as a potentially important battery material given the expansion of the LFP (lithium iron phosphate) cathode chemistry.

Nickel (Ni), a vital constituent of key LIB cathode chemistries like NMC and NCA, is produced from sulfide and laterite ores that are located in different countries and show a wide variation in ore grade. Previously, Argonne provided a single LCI for Ni production, averaged across these various ore locations, ore types, and ore grades. The continued mining of sulfidic Ni ores – the dominant Ni source – to meet the metal's ever-increasing demand, including the rapidly growing LIB demand, has caused a major temporal decline in ore grade, and thereby, an increase in environmental burdens from Ni production [1], [2]. This decline has also increased Ni production from laterite ores, despite its relatively lower ore grade and higher energy- and GHG-intensity of Ni production over sulfide ores [1], [3].

In FY22, Argonne provided separate, independent production pathways and corresponding LCIs for sulfide and laterite ore-based Ni production. Seven ore grades were chosen for sulfide ores (0.5% to 3.0% in steps of 0.5%, plus a default ore grade of 2.05% per literature), while a single ore grade (1.6%) was used for laterite ores due to limited data. The U.S. is near-entirely dependent on imports to meet its Ni demand, with data also showing significant differences in shares of various nations for Ni mining versus for its subsequent processing of sulfide ores (Figure III.1.1), reflecting the globalized nature of the metal's supply chain. For sulfide ores, ore grade influences material and energy inputs for only the mining and beneficiation steps, but not the other stages (pyrometallurgical treatment and refining). We only updated energy inputs to vary with ore grade due to a lack of similar variation data on material inputs. Even with this limitation, the change in ore grade (3.0% to 0.5%) causes over a 100% increase in the GHG burden of sulfidic Ni production, with the combined share of mining and beneficiation steps increasing from 31% to 70% of total Ni GHG emissions (Figure III.1.2). Lateritic Ni production is more energy intense, as expected. Its GHG burden is found to be more than twice that of sulfidic Ni at 0.5% ore grade (Figure III.1.2). The findings reinforce the need for alternative, less energy-intensive technologies for Ni production, judicious management of Ni reserves (especially sulfide ores) to prolong their lifetime, and large-scale adoption of appropriate techniques for Ni recycling.

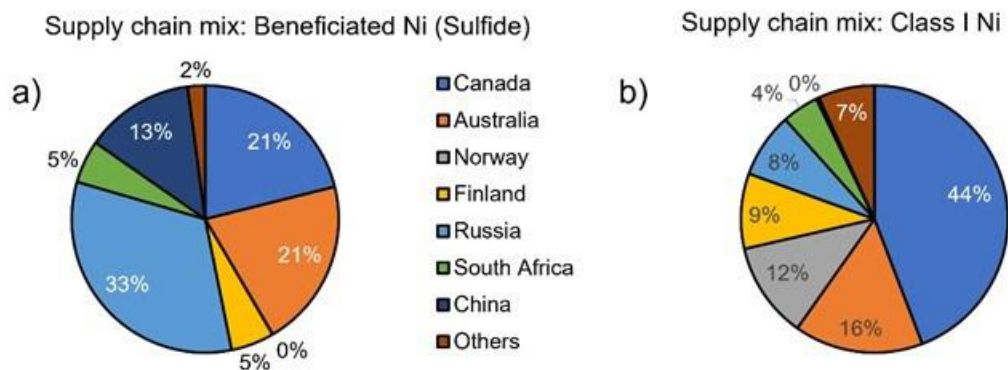


Figure III.1.1 The share of different nations in amount of Ni produced differs at the level of (a) mining (including beneficiation) and (b) processing (pyrometallurgy + refining) for its production from sulfide ores.

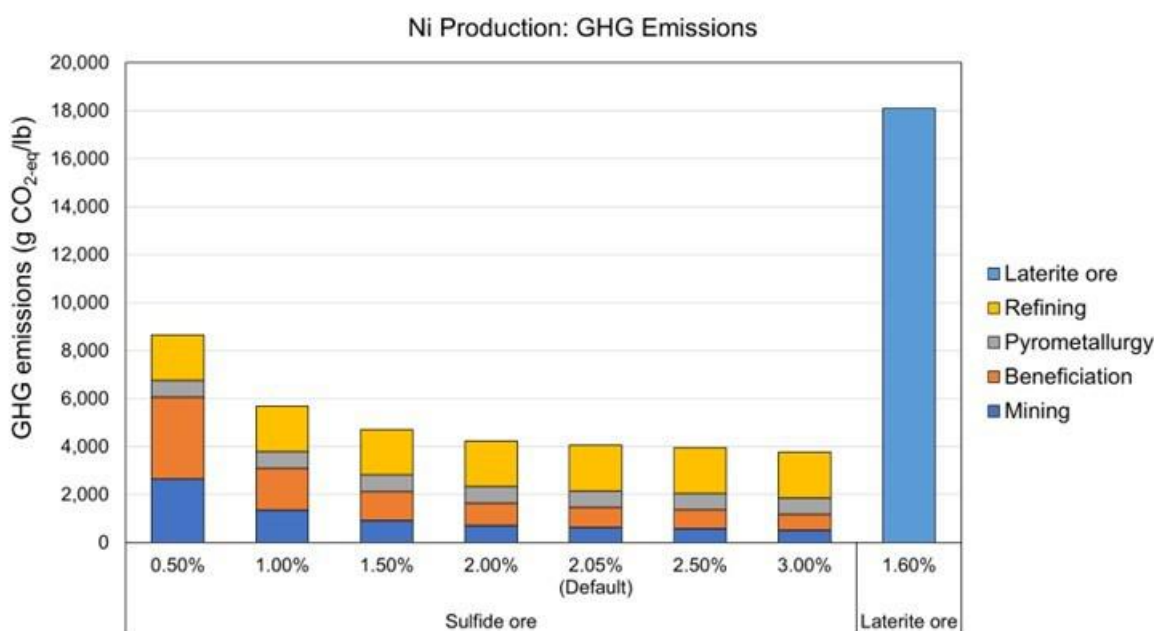


Figure III.1.2 GHG burden of Ni production from sulfide ores depends on ore grade, with mining and beneficiation playing a critical role at lower ore grades, while laterite ore-based Ni production causes higher GHG emissions than that from sulfide ores.

In FY20 and FY21, Argonne updated the LCI for producing battery-grade Li-chemicals (Li_2CO_3 and LiOH) from Chile's Salar brines and Australia's spodumene reserves. The lack of these reserves makes the U.S. import-dependent for its demand for these chemicals. To address this gap, the federal government has promoted multiple ongoing efforts to domestically produce Li-chemicals from existing chemical and geothermal brines. These brines are treated using direct lithium extraction (DLE) – a group of technologies that selectively remove Li from brines, leaving behind the residual brine for other purposes (e.g., electricity generation in the case of geothermal brines). In FY22, we investigated these ongoing initiatives for domestic Li-chemical production. Our findings are reported in a technical report [4], detailing the prominent DLE technologies and major brines of focus (Table III.1.1). Successful completion of all projects in Table III.1.1 will result in 0.5 million metric tons of annual Li_2CO_3 production. This can transform the U.S. into the global leader in the more sustainable production of these chemicals, given that global demand is expected to be 3-4 million metric tons of Li_2CO_3 by 2030. DLE-based production is also touted as more environmentally friendly than Salar brine-based Li-chemical production on several counts, including lower land use, suitability for co-production of brines with lower Li-content, and residual brine transfer to reserve (which avoids issues related

to brine evaporation in Salar brines). Since this merits a comparison of environmental burdens from DLE and other modes of Li-chemical production, we also provided a preliminary LCI of domestic Li-chemical production from geothermal brines in the Salton Sea, based on an existing study [5]. Our results, albeit tentative, indicate lower GHG burdens for DLE-based production over that from all sources except for Li_2CO_3 production from Chilean Salar brines. However, the production pathway provided in GREET is preliminary, and more work is needed to develop these DLE pathways and the associated LCIs to understand the corresponding environmental burdens for Li-chemical production for comparison with existing pathways.

Table III.1.1 Major details on Li-based brines in the U.S. and North America

Company	Location	Brine type	Resource potential (LCE, in million metric tons)	Projected annual production (LCE, kilo metric tons)
EnergySource Minerals	Imperial, CA (Salton Sea)	G		13
Controlled Thermal Resources		G	15	300
BHE Renewables		G		90
Compass Minerals	Ogden, UT (Great Salt Lake)	I	2.4	20-25
US Magnesium		I		10
Standard Lithium	El Dorado, AK (LANXESS plant, Smackover Arkansas)	I (O earlier)	3.14	21
	25 miles of Smackover (Lafayette County, AK)	O	1.195	19.5
	San Bernardino, CA (Bristol Lake)	I		
E3 Metals Corporation	Alberta, Canada	O	7	13
Schlumberger	Clayton Valley, NV	N.A.		65.3 metric tons
^a Brine types: G - Geothermal; I - Industrial; O - Oil; LCE: Lithium-carbonate equivalent				

Apart from cathodes, anodes are also critical for optimal LIB performance. While graphite (natural and synthetic forms) is the conventional anode choice, alternatives like silicon (Si) and Li anodes are being evaluated to benefit from their higher battery energy capacity [6]. Previous GREET versions provided LCIs for synthetic graphite (SG), Si, and Li anodes, but no LCI for natural graphite (NG) anodes that are good substitutes for SG due to their lower cost and higher capacity. Other limitations include using energy inputs for the SG LCI from thermodynamics-related calculations and the variation in supply chains of anodes used in these versions with those per USGS data (e.g., China-based SG instead of domestic SG). In FY22, Argonne (a) updated the production pathway and LCI for SG and Si anodes, and (b) incorporated a new production pathway and LCI for NG anode production. Our supply chain data considers complete import dependence of NG and Si anodes from China while considering SG production to be entirely domestic – as data indicated in [7]. Our modified SG production pathway considers calcination (conversion of green coke to needle coke), which shows its significant influence on SG's GHG burden due to substantial methane process emissions (Figure III.1.3). The results also confirm that NG anodes have a lower GHG burden than their SG counterpart, despite the production of NG anodes in an electric grid dominated by coal (China: Figure III.1.3). This GHG gap between NG and SG is expected to only widen upon including material and energy inputs for spheronization, purification, and coating steps for SG production when data is available.

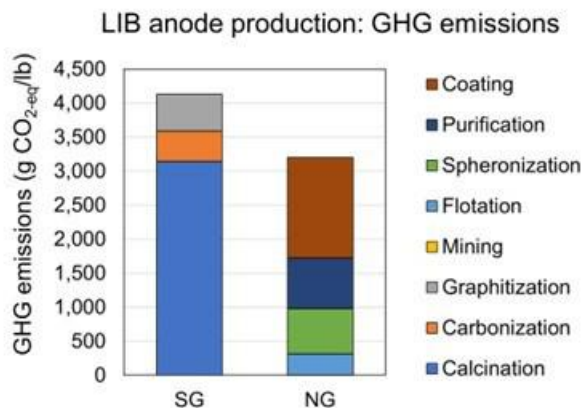


Figure III.1.3 SG anode production causes higher GHG burden than NG anode production.

Apart from LIB anodes, we investigated the state-of-literature on alternative batteries that can replace LIBs in automotive applications in the near-future. We identified three potential candidates: lithium-sulfur (Li-S), lithium-air (Li-A), and solid-state batteries (SSBs). Both Li-S and Li-A batteries require Li anodes, while SSBs can use similar cathodes as LIBs, making them the most attractive among the three alternatives. SSBs also offer higher safety, longer cycle life, higher energy density (solid electrolyte reduces empty space between cells), and fewer requirements for packaging and state-of-charge monitoring. Li-S batteries also exhibit high energy density, low cost, low toxicity, and flexibility for use in diverse applications. However, they are also known for several limitations, including performance deterioration over time due to component degradation, active material loss that increases internal battery resistance, and cathode corrosion caused by the diffusion of shorter polysulfides from sulfur anodes. Li-A batteries are known for long storage life, high operating voltage and specific energy, and recyclable components. However, challenges like the need for cathode protection from water and CO₂, Li anode corrosion due to moisture, and dendrite formation hinder the commercialization prospects of Li-A batteries. More details are provided in our technical report [8].

Titanium (Ti) is an important material for several existing and upcoming applications due to its high-temperature stability and excellent corrosion resistance. These qualities are especially relevant for DLE-based Li-chemical production, where the equipment needs protection from the corrosive nature of geothermal and industrial brines. Similar to Li-chemicals and Ni, the U.S. is highly dependent on imports to meet its Ti demand of sponge metal and for subsequent production of other Ti forms (ingot, forged ingot, and powders) (Figure III.1.4). Also, Ti's environmental burdens are not well understood, with only a handful of studies available on this subject [9], [10]. In FY22, Argonne leveraged literature [9] to incorporate a detailed production pathway and associated LCI for Ti production in all four forms within GREET, coupling it with supply-chain related information (Figure III.1.4). Multiple stages account for significant contributions to GHG burdens of Ti production in different forms due to its considerable use of material and energy inputs (Figure III.1.5), making the GHG burdens comparable to that from platinum in GREET (57,386 g CO₂-eq/lb). This highlights the need for either suitably modifying Kroll's process to lower its energy intensity and enable replacing fossil fuels with renewable-based electricity, or developing alternative technologies that can achieve these objectives to lower environmental burdens of Ti production.

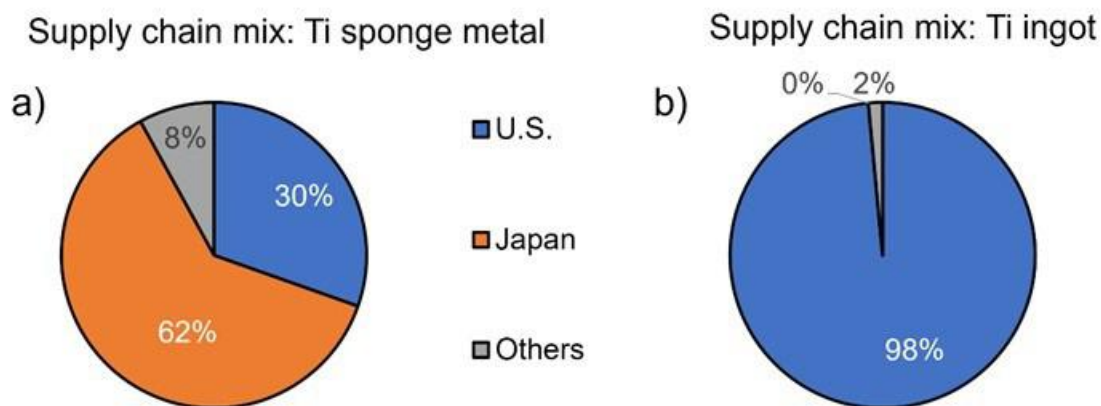


Figure III.1.4 The share (%) of different nations in Ti supply depends on the Ti form produced.

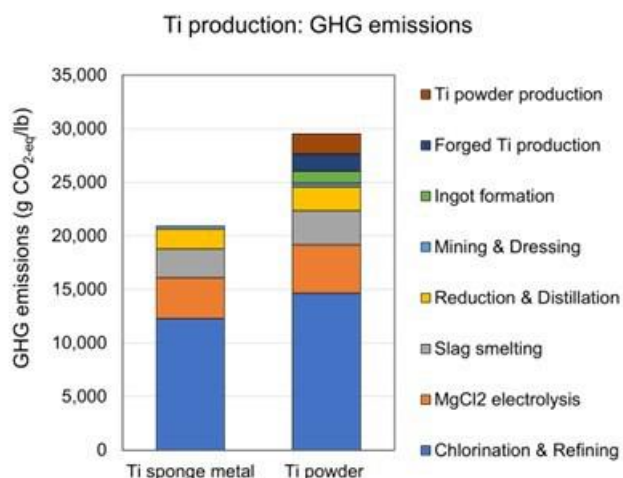


Figure III.1.5 GHG emissions of Ti production.

Embodied emissions from battery materials have a significant influence on the environmental burdens of batteries. This use is a function of battery material composition (or BOM) and its energy/ power density. In FY22, Argonne updated both these parameters for LIBs used in various powertrains of all vehicles (light/medium/heavy-duty) in the GREET model, based on Argonne's Battery Performance and Cost (BatPaC 5.0) model. The prominent change vis-à-vis previous GREET versions was on the choice of steel for battery module and pack enclosures – shifting from the earlier practice of using aluminum for these enclosures in previous GREET versions. Further, BatPaC 5.0 model also fine-tunes the operational parameters of LIBs to reflect their actual performance for various vehicles, further modifying their respective energy/power densities for the concerned automotive application. These changes are also considered in computing energy use and environmental burdens of LIBs for different vehicles and powertrains in the GREET model.

Among the alternatives to replace or supplement cobalt and nickel for cathode production, phosphates (e.g., lithium iron phosphate or LFP) have several advantages. Although current LFP designs result in lower energy density, solid-state batteries or designs similar to the BYD Blade could enable a battery with an LFP cathode to have sufficient energy density for mass-market electric cars. In addition, LFP may find wide use in medium- and heavy-duty vehicles. It is already making rapid inroads in US market (see Figure III.1.6). Also, LFP could be recycled economically by direct recycling, and PNE's commercial plant has just been funded, so there will be recycling capacity available when these batteries go out of service. A key consideration is that LFP could

actually be made via an entirely domestic supply chain. Therefore, it is appropriate to verify sufficient phosphorus availability for battery production. The domestic supply chain for iron has not been examined yet, but is believed to be quite sufficient.

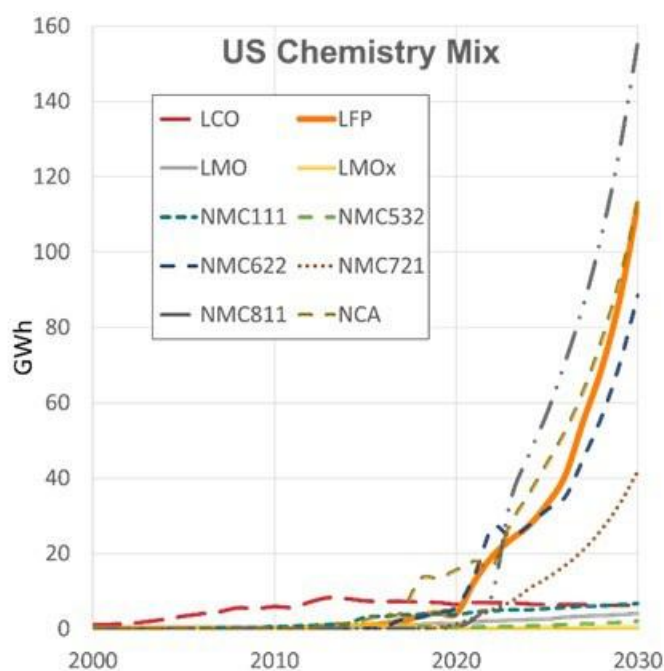


Figure III.1.6 Projection of US cathode chemistry types courtesy of Circular Energy Storage, London.

The U.S. has significant resources and is a major player in the world phosphorus market (see Table III.1.2), with most of the product going to agriculture as fertilizer. There is also a smaller market for higher-value agricultural chemicals like herbicides and pesticides, via established U.S. production of phosphoric acid, which is an intermediate in production of LFP. Battery demand could utilize existing capacity, eventually becoming a major competitor. Globally by 2050, LFP batteries could require >3 Mt/y of phosphorous, compared to the current industrial market of about 1 Mt/y.

Table III.1.2 Mine production and reserves of phosphates across different supply sources (USGS Phosphate Rock Data [1000 metric tons]. Contained phosphorous is about 10 times lower.)

Country	Mine Production (2021)	Reserves
United States	22,000	1,000,000
China	85,000	3,200,000
Morocco	38,000	50,000,000
Russia	14,000	600,000
Total	220,000	71,000,000

There is LFP production capacity being developed in North America (Quebec) by First Phosphate. In addition, the US has reserves of vivianite, a crystalline form of iron phosphate that could serve as a ready-made precursor for LFP.

Phosphorus is unusual among industrial chemicals because so much of it is lost to the environment. There is significant potential for both increasing supply of phosphorus and abating a major water pollution problem by recovery and treatment of agricultural runoff and human waste streams. Many of these streams are not usable back to agriculture because they contain iron; this should not be an issue for reuse in LFP production.

Finally, related to IEA activities, the IEA HEV TCP Task 46 for medium- and heavy-duty vehicle LCA kicked off in 2022 with several organizational meetings to finalize membership, plan for specific work tasks, and to layout the plan for future meetings and expert workshops. In October 2022, Task 46 hosted its first expert workshop which engaged numerous LCA practitioners, and medium- and heavy-duty vehicle stakeholders in discussion related to LCA of those vehicles. Discussion further helped provided cohesion for the desired outcomes of the Task 46 activities. In the near term, Task 46 will conduct several LCAs of medium- and heavy-duty vehicles subject to specific global conditions with harmonization of components to the extent that they are representative of the operating vehicles in those locales.

The IEA HEV TCP Task 40, Critical Materials for Electric Vehicles, has been completed. Its main results were summaries of projected global critical material requirements, without consideration of material origins or processing locations. The group also considered alternatives. The main US contribution was putting the potential contribution to supply from recycling into perspective. Although recycling will be crucial in an eventual circular economy, rapid growth and long product lifetimes mean that large quantities of virgin material will still be required for several decades. These results will be summarized at the December 2022 Critical Minerals Coordination Group meeting. Excessive material needs imply the necessity to consider options with lower material demands. One example is battery swapping, which has significant potential to reduce material demand under certain limited conditions. Therefore, Argonne plans to continue IEA effort under the new Task 48, Battery Swapping.

Conclusions

Amidst the continuing advancements in battery technologies and shifts in the supply chain of critical materials, Argonne continues to examine their respective environmental burdens. With research of extensive literature review and active engagement with researchers and industry, Argonne has improved its modeling capabilities for both batteries and battery-related critical materials. Argonne has also studied the potential for domestic Li production from brine reserves of varying nature and presented a preliminary analysis of its resultant environmental burden. The U.S. has been a player in this arena, and with growing need for Li in the future, it has the potential to become a global champion in the Li metal industry and control its entire Li chemical (and even possibly Li metal) supply chain. Argonne has also updated the material composition and performance characteristics of automotive LIBs to better reflect their modern-day functioning and resultant environmental burdens.

Key Publications

1. Christian Bauer, Simon Burkhardt, Neil P. Dasgupta, Linda Ager-Wick Ellingsen, Linda L. Gaines, Han Hao, Roland Hischer, Liangbing Hu, Yunhui Huang, Jürgen Janek, Chengdu Liang, Hong Li, Ju Li, Yangxing Li, Yi-Chun Lu, Wei Luo, Linda F. Nazar, Elsa A. Olivetti, Jens F. Peters, Jennifer L. M. Rupp, Marcel Weil, Jay F. Whitacre and Shengming Xu. “Charging sustainable batteries”, *Nature Sustainability* | VOL 5 | March 2022 | 176–178. <https://doi.org/10.1038/s41893-022-00864-1>.
2. Iyer, R.K., Kelly, J.C., 2022a. Updated Production Inventory for Lithium-Ion Battery Anodes for the GREET® Model, and Review of Advanced Battery Chemistries (No. ANL-22/74). Argonne, IL (United States). <https://doi.org/10.2172/1891640>.
3. Iyer, R.K., Kelly, J.C., 2022b. Lithium Production from North American Brines (No. ANL-22/73). Argonne, IL (United States). <https://doi.org/10.2172/1891626>.
4. Iyer, R.K., Kelly, J.C., 2022c. Updates to Vehicle-Cycle Inventory for Select Components of Light-Duty, Medium-Duty, and Heavy-Duty Vehicles. Argonne.
5. Iyer, R.K., Kelly, J.C., 2022d. Life-Cycle Inventory of Critical Materials: Nickel, Copper, Titanium, and Rare-Earth Elements. Argonne.
6. Competition for Phosphorus from the Battery Industry, Sustainable Phosphorus Summit, November 2022.
7. Lithium-Ion Battery Material Supply and Recycling Issues, IEA/HEV Task 40 CRM4EV, April 2022.

References

1. G. M. Mudd, “Global trends and environmental issues in nickel mining: Sulfides versus laterites,” *Ore Geol. Rev.*, vol. 38, no. 1–2, pp. 9–26, Oct. 2010, doi: 10.1016/J.OREGEOREV.2010.05.003.
2. S. Northey, S. Mohr, G. M. Mudd, Z. Weng, and D. Giurco, “Modelling future copper ore grade decline based on a detailed assessment of copper resources and mining,” *Resour. Conserv. Recycl.*, vol. 83, pp. 190–201, Feb. 2014, doi: 10.1016/J.RESCONREC.2013.10.005.
3. G. M. Mudd and S. M. Jowitt, “A Detailed Assessment of Global Nickel Resource Trends and Endowments,” *Econ. Geol.*, vol. 109, no. 7, pp. 1813–1841, Nov. 2014, doi: 10.2113/ECONGEO.109.7.1813.
4. R. K. Iyer and J. C. Kelly, “Lithium Production from North American Brines,” Argonne, IL (United States), ANL-22/73, Oct. 2022. doi: 10.2172/1891626.
5. T. Y. Huang, J. R. Pérez-Cardona, F. Zhao, J. W. Sutherland, and M. P. Paranthaman, “Life Cycle Assessment and Techno-Economic Assessment of Lithium Recovery from Geothermal Brine,” *ACS Sustain. Chem. Eng.*, vol. 9, no. 19, pp. 6551–6560, May 2021, doi: 10.1021/ACSSUSCHEMENG.0C08733/SUPPL_FILE/SC0C08733_SI_001.PDF.
6. I. Hasa and S. Passerini, “Silicon anode systems for lithium-ion batteries,” in *Silicon Anode Systems for Lithium-Ion Batteries*, P. N. Kumta, A. F. Hepp, M. K. Datta, and O. I. Velikokhatnyi, Eds. Elsevier, 2022, pp. 3–46.
7. USGS, “USGS.gov | Science for a changing world,” *U.S. Department of the Interior*, 2022. <https://www.usgs.gov/> (accessed Mar. 03, 2022).
8. R. K. Iyer and J. C. Kelly, “Updated Production Inventory for Lithium-Ion Battery Anodes for the GREET® Model, and Review of Advanced Battery Chemistries,” Argonne, IL (United States), ANL-22/74, Oct. 2022. doi: 10.2172/1891640.
9. F. Gao *et al.*, “Environmental impacts analysis of titanium sponge production using Kroll process in China,” *J. Clean. Prod.*, vol. 174, pp. 771–779, Feb. 2018, doi: 10.1016/J.JCLEPRO.2017.09.240.
10. Y. Xia, H. D. Lefler, Z. Z. Fang, Y. Zhang, and P. Sun, “Energy consumption of the Kroll and HAMR processes for titanium production,” in *Extractive Metallurgy of Titanium: Conventional and Recent Advances in Extraction and Production of Titanium Metal*, Z. Z. Fang, F. H. Froes, and Y. Zhang, Eds. Elsevier, 2020, pp. 389–410.

III.2 Lithium-ion Battery Recycling Prize Support (NREL)

Lauren Lynch, Principal Investigator

National Renewable Energy Laboratory
15013 Denver West Pkwy
Golden, CO 80401
E-mail: lauren.lynch@nrel.gov

Sandra Loi, Co-Principal Investigator

National Renewable Energy Laboratory
15013 Denver West Pkwy
Golden, CO 80401
E-mail: sandra.loi@nrel.gov

Brian Cunningham, DOE Technology Development Manager

U.S. Department of Energy
E-mail: brian.cunningham@ee.doe.gov

Start Date: October 1, 2017
Project Funding: \$9,805,223

End Date: September 30, 2023
DOE share: \$9,805,223

Non-DOE share: \$0

Project Introduction

Lithium-ion (Li-ion) batteries have become the primary choice for portable electronics (smartphones, tablets, and laptops), power tools, and electric vehicles (EV) for personal, commercial, industrial, and military applications. The demand for Li-ion batteries for EVs is expected to grow as manufacturing and materials costs are reduced while performance improves. The U.S. Energy Information Administration (EIA) projects that U.S. light-duty battery EV sales will reach 1.3 million by 2025, and others project even higher sales growth. Global EV sales are expected to reach 30 million by 2030, up from 1.1 million in 2017. This growth in EV sales and increased demand for consumer and stationary uses are expected to double the demand for Li-ion batteries by 2025 and quadruple the demand by 2030.

Demand for the global production of battery materials, such as lithium, cobalt, manganese, nickel, and graphite, will grow at similar rates depending on the future changes in the composition. The growth in demand for Li-ion batteries for EVs is expected to establish EVs as the largest end-user of cobalt and lithium, and could create a particularly high supply risk for cobalt as it could be expensive, and its availability depends on foreign sources for production. To address this potential risk, the DOE Vehicle Technologies Office (VTO), within the Office of Energy Efficiency and Renewable Energy (EERE), developed a Research Plan to Reduce, Recycle, and Recover Critical Materials in Li-ion Batteries. A goal identified in the Plan is to reduce the cost of electric vehicle battery packs to less than \$150/kWh with technologies that significantly reduce or eliminate the dependency on critical materials (such as cobalt) and utilize recycled material feedstocks. However, Li-ion batteries are only recycled at a rate of about 5% currently. Analysis has shown that recycled material could potentially provide one-third of United States cathode material needs for Li-ion batteries by 2030. The current recycling supply chain for collecting, sorting, safe storing, and transporting Li-ion batteries and recovering valuable materials is limited, particularly for larger batteries used in EVs and industrial applications. Preventing the Li-ion batteries from ending up at landfills, particularly consumer electronics (as some have caused fires), is important not for the recovery of key materials but for the economy and the environment.

To achieve the above goal and address potential critical materials issues, VTO initiated three key areas of R&D (Figure III.2.1):

1. supporting laboratory, university, and industry research to develop low-cobalt (or no cobalt) active cathode materials for next-generation Li-ion batteries,
2. establishing the ReCell Lithium Battery Recycling R&D Center focused on cost-effective recycling processes to recover lithium battery critical materials, and
3. launching the Lithium-Ion Battery Recycling Prize to incentivize American entrepreneurs to find innovative solutions to solve current challenges associated with **collecting, sorting, storing, and transporting** discarded Li-ion batteries safely and economically for the eventual recovery of valuable materials for re-introduction to the battery production supply chain.



Figure III.2.1 The Critical Materials Research Plan with three major research areas to address critical materials issues for Li-ion batteries and recovery of materials for re-introduction into the supply chain.

While the first two initiatives focus on creating next-generation cobalt-free Li-ion batteries and conduct research into the recovery of critical materials and re-introduction of these materials in recycled batteries, the \$5.5-million Lithium-Ion Battery Recycling Prize (whose logo is shown in Figure III.2.2) leverages innovative ideas from American entrepreneurs to develop and demonstrate a supply chain that safely transitions spent batteries to specialized battery recycling facilities. The prize is a collaboration between VTO and DOE's Advanced Manufacturing Office (AMO) with \$4.5M funding support from VTO and \$1M from AMO.



Figure III.2.2 Logo of the Lithium-Ion Battery Recycling Prize.

The \$5.5-million prize was designed to be implemented in three progressive phases for approximately four years to bring ideas from concept, to prototype and partnering, through pilot validation. In each phase, expert reviewers will evaluate submissions and a federal consensus panel for recommendation to the DOE selection officials. DOE assigned the administration and execution of the Lithium-Ion Battery Recycling Prize to National Renewable Energy Laboratory (NREL) to use an already-established framework for American-Made Challenges. Figure III.2.3 provides an overview of the three phases of the contest, the amount awarded, and the number of awards available in each phase.



Figure III.2.3 The Lithium-ion Battery Recycling Prize consists of three progressive phases from concept through pilot validation for about three years.

On November 15, 2021, President Joseph R. Biden, Jr. signed the Infrastructure Investment and Jobs Act, also commonly known as the Bipartisan Infrastructure Law (BIL). The BIL is a once-in-a-generation investment in infrastructure, designed to modernize and upgrade American infrastructure to enhance U.S. competitiveness, drive the creation of good-paying union jobs, tackle the climate crisis, and ensure stronger access to economic, environmental, and other benefits for disadvantaged communities. As part of this effort, the BIL authorizes appropriations of \$200 million for the research, development, and deployment of technologies to collect, transport, sort, and process (recycle) end-of-life LIBs and for the potential use of LIBs in second use application. There is an additional \$135M appropriated to cover battery end-of-life (EOL) areas to accelerate and increase battery recycling rates. Section 40207(e) of the BIL titled Lithium-Ion Battery Recycling Prize defines the continuation of the Lithium-Ion Battery Recycling Prize for additional rounds after completion of Phase III.

This progress report provides a summary of activities of the prize for the fourth year and Phase III “Pilot Validation,” which awarded a \$2M cash prize distributed equally among the Phase III winners.

Objectives

The purpose of the Lithium-Ion Battery Recycling Prize is to incentivize American entrepreneurs to develop and demonstrate processes that, when scaled, have the potential to capture 90% of ALL spent or discarded lithium-based battery technologies in the U.S.— including consumer electronics, stationary, and transportation applications— for eventual recycling and materials recovery. This 90% recycling rate of lithium-based batteries would be a significant achievement compared to the 5% recycling rate demonstrated at the beginning of the prize. It is the goal of this prize to find innovative solutions to current challenges in safe and economic collecting, sorting, storing, and transporting discarded (or end-of-life) Li-ion batteries.

In Phase III of the prize, participants were asked to substantially advance their end-to-end solutions from proof-of-prototype to a refined pilot of the technology. The Phase III Final Submissions included

demonstration and analysis to validate a small-scale pilot prototype focusing on solutions under real-world applications and scenarios for one or multiple applications (consumer electronics, electric vehicles, and stationary storage). The participating teams also demonstrated their ability to recover Li-ion batteries and verify the commercial feasibility of achieving the end-to-end solution's projected impact when fully scaled. The proposed solutions may or may not include an intermediate step for secondary use.

Approach

In FY22, NREL Prize Administrators successfully guided the DOE Lithium-Ion Battery Recycling Prize to the conclusion of Phase III. Six finalist teams participated in Phase III of the prize, which focused on pilot validation of their proposed concept solutions.

Continued Outreach and Support in Phase III

Throughout Phase III, the NREL Prize Administrator provided ongoing support and resources for the participating teams in the ongoing pilot validation of their concept solutions. To prepare the teams for success in their final submission, the administrator coordinated a voluntary networking event with the Suppliers Partnership for the Environment Responsible Battery Work Group on December 7, 2021. Five teams joined this virtual event to present their concept solutions and receive feedback from industry experts. In addition, the NREL Prize Administrator partnered with NAATBatt International to support the NAATBatt Annual Conference on February 7-10, 2022. This collaboration covered registration fees for two team members to present and share a poster during a prize-focused session at the event.

In addition to cash prizes, winners of the Phase II contest received vouchers to consult expertise outside of their own organization. Phase III participants worked alongside pre-approved Voucher Service Providers (VSPs) within the American-Made Network to support the validation of their concept solution. Throughout Phase III, the NREL Prize Administrators oversaw the voucher work progress, voucher payment process, and necessary support to successfully facilitate this collaboration. In total, Phase III participating teams spent \$667,000 in voucher funds at five different VSP facilities.

Virtual Site Visits for Phase III Participating Teams

On March 8–11, 2022, the NREL Prize Administrator organized and hosted virtual “site visits” for the six Phase III participating teams. These visits allowed teams to demonstrate their proposed solution on location, while reviewing aspects of their pilot validation approach. The NREL Prize Administrator developed detailed site visit expectations and a draft agenda to guide teams through introductions, progress updates, voucher work, and the live site tour. These site visits included up to two hours of multimedia presentations and discussions between teams, supporting partners, and prize judges from NREL, DOE, the Department of Transportation, and the Environmental Protection Agency.

Phase III Final Submission, Presentations, and Judging

Phase III submissions to the prize were due on April 8, 2022. The NREL Prize Administrator provided ongoing communication, submission templates, and technical support to participating teams leading up to the final submission. Following the final submission, teams were required to attend Phase III virtual Participants Day to demonstrate how their proposal meets the goals of the prize on April 27–28, 2022. This event included 30-minute presentations from participating teams, followed by a Q&A session with Phase III prize judges from NREL, DOE, the Department of Transportation, and the Environmental Protection Agency. After each presentation, the NREL Prize Administrators met with judges to review feedback and take notes to inform the final scoring.

After the conclusion of Phase III, NREL Prize Administrators combined this feedback, alongside key information metrics and results from the participating teams to present winner recommendations to VTO. This summarized information was used to determine the Phase III winning teams.

Phase III Winner Announcement

Once the four Phase III winning teams were identified, NREL Prize Administrators developed the promotion plan to announce the winners publicly. The winner announcement (Figure III.2.4) included a press release and e-blast from VTO, an update on the HeroX website, graphic design, and social media. This announcement took place June 21, 2022. In addition to this announcement, NREL Prize Administrators developed a media kit and recommended guidance to help teams celebrate their wins. After the conclusion of the prize, NREL continued to support with ongoing opportunity announcements for future funding.



Figure III.2.4 The Lithium-ion Battery Recycling Prize Phase III winner announcement.

Results

As part of the Lithium-Ion Battery Recycling Prize, Phase III participating teams reported investing \$4,300,371 in the development of their proposed recycling solutions (Figure III.2.5). In addition, Phase III participating teams spent \$667,000 in voucher funds at five different VSP facilities. As a result of their Phase III pilot validation, these teams successfully delivered over 87,000 of battery cells and modules to recyclers (see Table III.2.1). Multiple teams also included solutions for second-use applications as part of their Phase III final submission.

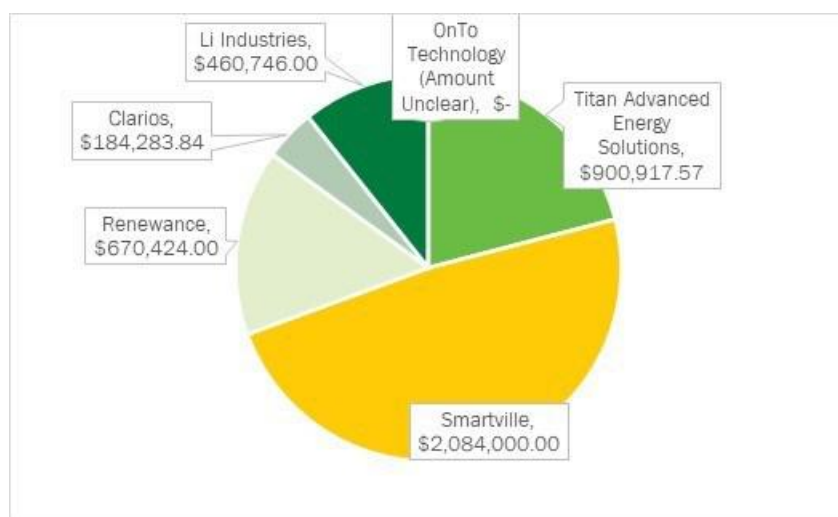


Figure III.2.5 Graph illustrating the documented cost from each Phase III participating team.

Table III.2.1 Total Impact of Proposed Solutions

Battery Use	Number of batteries projected to be delivered to recyclers by your pilot validation project as defined in Phase II	Actual number of batteries delivered to recyclers as result of pilot validation in Phase III
Consumer Electronics	75,500	46,181
Electric Vehicles	2,500	811
Stationary storage and/or other large industrial uses	27,102	41,683

Phase III Winning Teams

Of the six participating teams, four winners (Li Industries, Renewance, Smartville, and Titan Advanced Energy Solutions) were selected to share the \$2 million cash prize evenly (Figure III.2.6). These winners included:

- **Li Industries:** Li Industries developed a machine learning-based, automated Smart Battery Sorting System capable of accurately and efficiently sorting and separating batteries by several characteristics, including chemical composition, size, weight, and packaging type.
- **Renewance:** The Renewance Connect digital platform tracks and manages Li-ion batteries throughout their full life cycle by improving access to and utilizing existing infrastructure for decommissioning, collection, warehousing, sorting, transportation, and recycling services.
- **Smartville:** Smartville deployed distributed heterogeneous unifying battery (HUB) facilities to fully balance conditions and certify Li-ion batteries to reduce costs and create value in the reverse logistics supply chain.
- **Titan Advanced Energy Solutions:** Battago is Titan's Battery Market Intelligence platform built to generate, aggregate, and connect battery data to create a transparent marketplace and bridge the gap between battery owners, integrators, and end of life recyclers.



Figure III.2.6 Map of the four Lithium-ion Battery Recycling Prize Phase III winning teams.

References

1. “Department of Energy Announces Battery Recycling Prize Phase III Winners.” Energy.gov. June 21, 2022. <https://www.energy.gov/eere/articles/doe-announces-battery-recycling-prize-phase-iii-winners>
2. “Laboratory Partnerships Bolster Battery Recycling Prize Solutions.” NREL.gov. May 11, 2022. <https://www.nrel.gov/news/program/2022/laboratory-partnerships-bolster-battery-recycling-prize-solutions.html>
3. “Call2Recycle Partners with Li Industries to Innovate Battery Sorting and Recycling.” Globe Newswire. April 26, 2022. <https://www.globenewswire.com/news-release/2022/04/26/2429229/0/en/Call2Recycle-Partners-with-Li-Industries-to-Innovate-Battery-Sorting-and-Recycling.html>
4. “Titan Advanced Energy Solutions Wins the U.S. Department of Energy's Battery Recycling Prize.” Titan Advanced Energy Solutions. June 23, 2022. <https://www.titanaes.com/post/titan-wins-doe-battery-recycling-prize>
5. “DOE Announces Battery Recycling Prize Phase III Winners.” Electric Energy Online. June 22, 2022. <https://electricenergyonline.com/article/energy/category/ev-storage/143/968231/u-s-department-of-energy-doe-announces-battery-recycling-prize-phase-iii-winners.html>
6. “Establishing closed-loop EV battery recycling.” SAE.org. March 31, 2022. <https://www.sae.org/news/2022/03/establishing-closed-loop-ev-battery-recycling>
7. “Li Industries Wins Department of Energy Battery Recycling Prize Phase III.” Li Industries. June 21, 2022. <https://www.li-ind.com/posts/doe-announces-battery-recycling-prize-phase-iii-winners>

Acknowledgements

The DOE Battery Recycling Prize Team included Connie Bezanson, Samuel Gillard, Helena Khazdozian. The NREL Battery Recycling Prize Team included Nicholas Langle, Lauren Lynch, Sandra Loi, Rebecca Martineau, and Julie Sodano.

III.3 Battery ReCell Center (ANL)

Jeff Spangenberg, Principal Investigator

Argonne National Laboratory
9700 South Cass Avenue
Lemont, IL 60439
E-mail: jspangenberg@anl.gov

Brian Cunningham, DOE Technology Development Manager

U.S. Department of Energy
E-mail: Brian.Cunningham@ee.doe.gov

Start Date: October 1, 2021	End Date: September 30, 2022	
Project Funding (FY22): \$6,900,000	DOE share: \$6,900,000	Non-DOE share: \$0

Project Introduction

The use of lithium-ion batteries has steeply risen in recent years, starting with electronics and expanding into many applications, including the growing electric vehicle (EV) and grid storage industries. But the technologies to optimize recycling of these batteries have not kept pace.

The ReCell Center, U.S. Department of Energy's (DOE) first advanced battery recycling center, will help the United States grow a globally-competitive recycling industry and reduce our reliance on foreign sources of battery materials.

Objectives

DOE sees an opportunity to economically recycle lithium-ion and future batteries and accelerate the growth of a profitable recycling market for spent EV, electronics, and stationary storage batteries. This can be done by developing novel recycling techniques to make lithium-ion recycling cost-effective by using less energy-intensive processing methods and capturing more metals and other high-value materials in forms that make reuse easier.

A profit-driven battery recycling infrastructure will help meet the Vehicle Technology Office's goal of lowering the cost of new batteries and increasing the use of domestic recycled battery materials.

Approach

ReCell is a collaboration of researchers from academia and national laboratories that are working together with industry to develop new recycling processes and battery designs that will enable greater material recovery at end of life. The most promising processes and designs will be demonstrated at pilot scale at the ReCell laboratory facilities based at Argonne. Validated processes and designs will be licensed to industry for commercialization.

Toward the end of this year BIL FOA awards were determined and the ReCell team is excited to help many of the recipients. The vision of the national labs helping industry succeed and continue to improve the recycling industry is front and center.

Direct recycling has been a major focus area for ReCell with the hope that enough barriers are removed or better understood through the team's work that industry would start looking closer at it and eventually start to take the lead in further development and ultimately commercialization. We are happy to learn the industry has really stepped up their interest in the technology and similarly, more companies both start-up and established are working in their own capacity to explore this technology. This is a rewarding feeling for the ReCell team and hope to help continue the momentum.

Relithiation is a key step in the direct recycling process, and ReCell currently has five potential techniques under investigation: solid state, hydrothermal, ionothermal, electrochemical, and redox mediated. Each technique was provided an identical sample to process, and the products are being compared to determine the optimum path forward for the relithiation work. We have completed a comparison of the effectiveness of each of these techniques to process end-of-life cathode materials. This report is being assembled now and will be available shortly.

Work has been underway to demonstrate the feasibility of recycling manufacturing scrap using direct recycling. This represents an early point-of-entry for the technology. The benefits of recycling can be realized with fewer steps than needed for end-of-life material recycling. The ReCell team has collected manufacturing scraps and subject it to the processes required to feed the recycled material back into the cell fabrication process. Successful deployment of this concept could enable significant savings on the production of new cells. This year's work in this area has been focused on creating a robust process that can effectively delaminate the active material from the foils. There will be continued work on this task and we are hopeful that a pilot system will be completed for demonstration.

FY22 included more funding for ReCell over the previous years. This funding was focused on procuring equipment for the pilot plant. In addition, Argonne is preparing an additional 12,000 square feet of high bay research space that the pilot plant will be installed in along with other battery recycling equipment for research. This new space is expected to be complete in January of 2024.

As we enter FY23 the scope of ReCell expands. Figure III.3.1 shows the slightly revised focus areas. The main changes result in the move of all direct recycling related projects moving into the Direct Recycling of Materials focus area. Advance Resource Recovery represents projects that work to recover materials that may not be directly recycled. This focus area also allows the ReCell team to work on hydro and pyro based issues. This let's us work with industry on challenges that are more closely related to where they are focused. The focus of Modeling and Analysis has not changed much, but we will be working on second life projects in our Design for Sustainability focus area. Below are quick descriptions of our updated focus areas.

- Direct Recycling of Materials: *Recycling materials back to their original purpose without destroying their chemical structure*
- Advanced Resource Recovery: *Recapturing materials for reuse in batteries or other applications through chemical conversion*
- Design for Sustainability: *Working toward more sustainable batteries by improving material choice, battery design, and second life opportunities*
- Modeling and Analysis: *Developing tools to provide a deep materials/process understanding, and evaluate economic and environmental impacts*

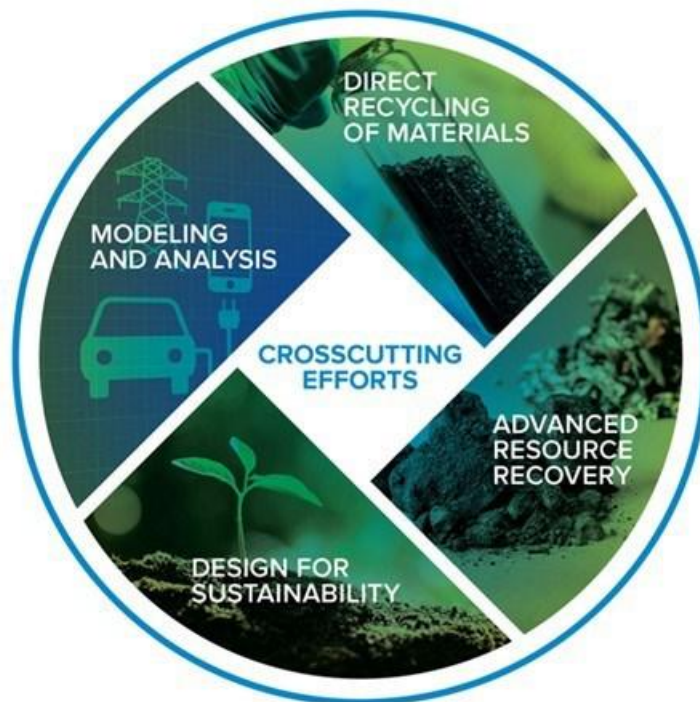


Figure III.3.1 Basic processing steps associated with direct recycling

Results

Direct Recycling Projects

Thermal Binder Removal

Once cathode materials are separated to be recycled, the poly(vinylidene difluoride) (PVDF) binder needs to be removed to allow for further processing. This can be done using a large quantity of n-methyl-2-pyrrolidone (NMP) or other solvents, but this may not be cost effective for battery recycling. As an alternative to solvent based methods, thermal decomposition can be used to eliminate the binder. This has the advantage of no liquid waste, and can be performed at temperatures as low as 500 °C. We have previously shown that this can lead to performance similar to the pristine materials if any lithium loss is compensated for by the addition of lithium. We had found that these processes work best with good air contact and that a thick bed depth will lead to worse performance. This led us to using a rotary kiln for this process due to the improved air contact over fixed bed furnaces and the scalability with continuous operation that a rotary kiln provides. In testing this process showed improved performance of the cathode material as compared to using a muffle furnace. This year, this process was incorporated into a complete recycling process going from shredded batteries to new cells.

The goal of the project is to remove the PVDF binder from various materials without effecting their electrochemical performance. This process can be used to delaminate the electrode materials from the current collectors. It also can be used on powdered materials such as black mass just to remove the PVDF and carbon black. Once a method is found, we plan to scale this process up to kilogram and higher scales to fully demonstrate that the process can work in a commercial operation.

The initial approach was to determine what needed to be done to maintain the performance of NMC cathodes during the thermal binder removal process. This included adding various additives to act as fluorine getters. After determining that LiOH was an effective additive we worked to scale that process up to find if there were issues with the scale up process. These issues led to a design of a scaled-up process. Once we determined the binder removal process, we integrated this process into a recycling process to see if it can be used to

successfully recycle cathode materials. In addition, we will then explore thermal binder removal options for other materials including graphite and LiFePO_4 .

This year we integrated the rotary kiln process into a complete recycling process to demonstrate the viability of the process. In particular, an end-of-life commercial 63 Ah pouch cell was shredded to a size suitable for separations. These shreds were then rinsed to remove electrolyte and dried. Then a combination of separation processes were utilized to get a relatively pure fraction of cathode material on the aluminum current collector. These electrode pieces were then fed into the rotary kiln at 500°C with a residence time of approximately 1 hr. This removed the PVDF and carbon black from the cathode material allowing it to simply be sieved from the aluminum foil. This cathode material had a composition of $\text{Li}_{0.92}\text{Ni}_{0.608}\text{Co}_{0.196}\text{Mn}_{0.196}\text{O}_2$ based on inductively coupled plasma mass spectrometry (ICP-MS) results. Based on this composition ground LiOH was added to the material to both compensate for the Li deficiency and to compensate for the lithium loss due to formation of LiF on the surface. This material was then heat treated in a muffle furnace at 750°C followed by a rinsing step to remove excess Li from the surfaces and a reanneal. The resulting material was tested in both half cells and full cells to determine the electrochemical performance as shown in Figure III.3.2. The rate performance of the material was very similar to a pristine NMC 622. In full cells the recycled NMC 622 performed just slightly worse as compared to the commercial material (cycling for the pristine is still ongoing).

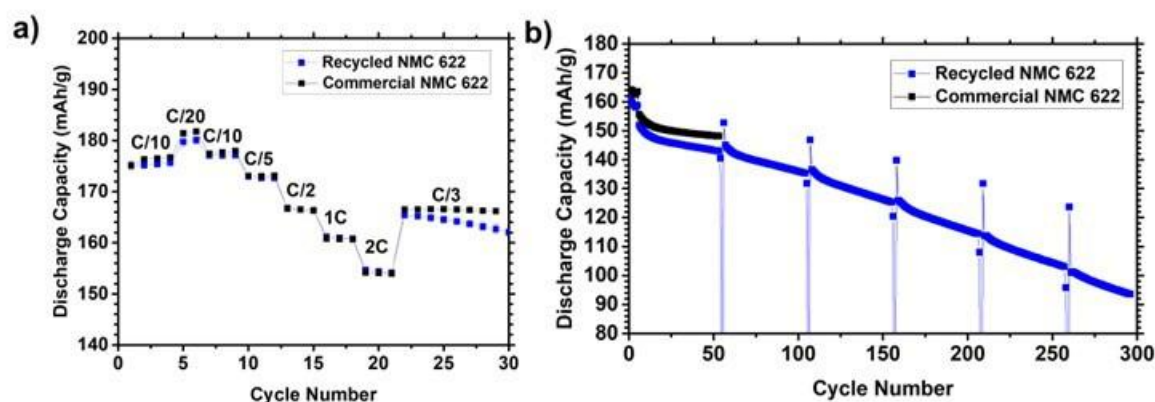


Figure III.3.2 a) Rate performance in half cells and b) cycle life in full cells of NMC 622 cathode recycled from an end-of-life cell via scalable processes versus a commercial NMC 622 baseline.

For both scalability and the potential to improve the cyclability we are attempting to shift processing steps from muffle furnaces to a rotary kiln process. The resulting cycling is shown in Figure III.3.3, which shows that as we move to the rotary kiln the capacity seems to be reduced, but cyclability improves. We believe that with further optimization that similar initial capacity can be achieved and more work on this front will be ongoing.

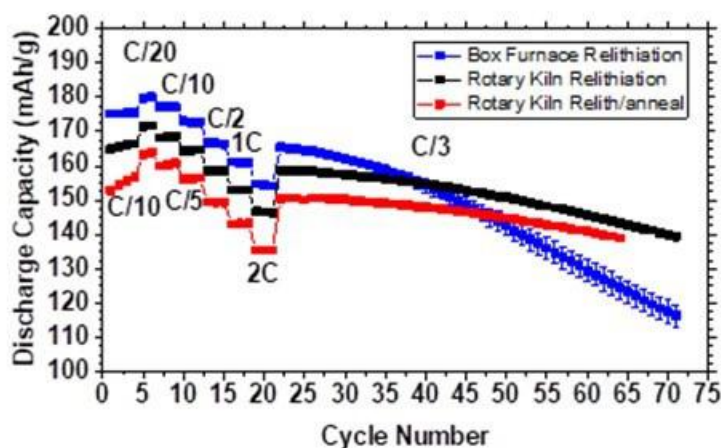


Figure III.3.3 Comparison of cycling of recycled NMC 622 depending on which steps were done in a rotary kiln.

In addition to the work on NMC cathodes we are also extending this work to other cathode and anode materials including graphite and LiFePO_4 . Electrochemical cycling data for the recovered electrodes after thermal treatment are shown in Figure III.3.4. The cycling is reasonably comparable to pristine materials indicating that this could be a good method for delamination and binder removal. We are still working on determining the remaining binder quantity and what happens during the thermal process.

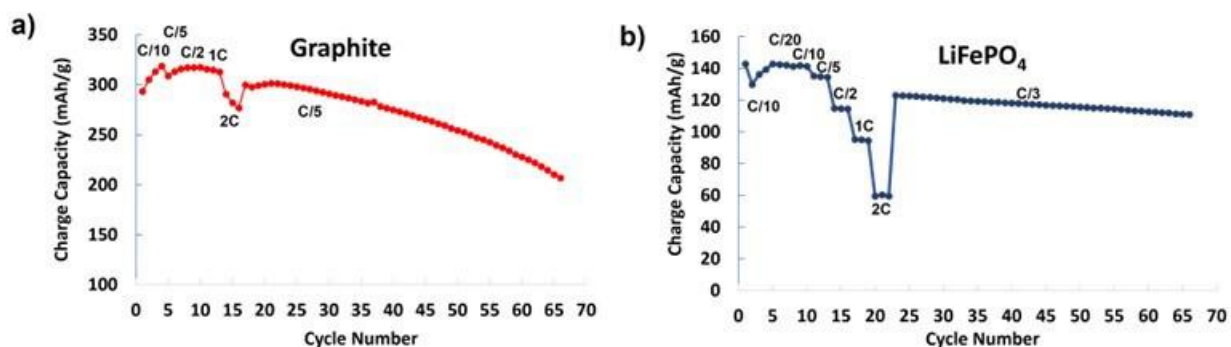


Figure III.3.4 Half cell rate study and cycling for a) graphite recovered from manufacturing scrap and b) LiFePO_4 from artificially created black mass (3 wt.% PVDF).

Binder Removal via Soxhlet Extraction

In the recycling process of end-of-life (EOL) LIBs, most recent research focuses on the cathode materials. Remaining components, such as anodes and poly(vinylidene difluoride (PVDF) binder can be removed by thermal treatment at the high temperature. However, harmful gases generated from the combustion are a threat to the environment safety. Considering the potentially huge amount of EOL battery cell (10,000 MT/yr) waste, the actual amount of PVDF is not negligible. The scope of this project is to develop the Soxhlet extraction method to remove the polymer binder (e.g. PVDF) from End-of-Life (EoL) battery cathodes and to recover PVDF. The electrodes in Li-ion batteries have polymer binders to hold active materials and conductive carbon additives. However, when it comes to recycle EoL battery cathode, it is necessary to remove and/or separate the polymer binder from the electrode to recycle cathode materials such as LCO and NMC. In the ReCell center, thermal decomposition of PVDF has been studied as an option, but a solution method hasn't been investigated. It is mainly because the previous method to dissolve PVDF involves a large amount of toxic and high-boiling-point solvents (e.g. NMP). Toxic waste production is inevitable, and it cannot be considered

as a feasible way to remove PVDF. It is necessary to minimize the use of organic solvent and environmental impact. In the Soxhlet method, samples are repeatedly extracted with solvent regenerated by distillation through a periodic siphoning process. Therefore, a minimal amount of solvent is required, and fresh solvent is fed via distillation into the sample container every time. It can be also scaled up to a manufacturing scale. In FY21, the aim of this project is to develop and demonstrate the Soxhlet extraction method for PVDF removal and recovery.

The project ended in the Q3 period. This report mainly summarizes the main activities in this project.

Soxhlet Extraction Process Design



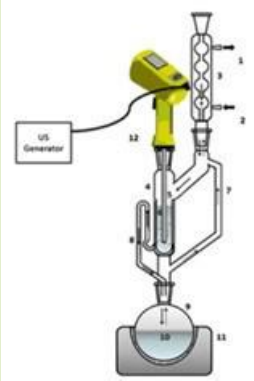
The conventional Soxhlet extractor contains three main components: a percolator, a thimble and a siphon mechanism (Figure III.3.5). The percolator is used to circulate the solvent. A distillation flask with solvent is placed on the bottom and heated by a heater and a reflux condenser filled with condensed solvent is on the top of main chamber of the Soxhlet extractor. A thimble made of filter paper is placed into the main chamber and used to hold the material which is needed to be extracted (here it is cathode material of A-C021). Through the siphon mechanism, the thimble can be emptied in a cyclic fashion.



Figure III.3.5 Conventional Soxhlet extractor design

Prior to designing a real Sono-Soxhlet extractor, we made a batch-scale simulated Sono-Soxhlet extractor to evaluate the feasibility of introducing sonication to the Soxhlet process. The ultrasonic source was a handheld ultrasonic homogenizer (Type: UP200Ht from Hielscher Ultrasound Technology). 10 ml solvent with several pieces of cathodes was placed into 30 ml glass vial. With the success of this batch-scale model, a Sono-Soxhlet imitation reactor was designed and custom glassware was ordered so we could combine Soxhlet extraction with sonication to facilitate material release from the current collector as well as more rapid reaction times. Table III.3.1 is summary of the comparison between different Soxhlet extraction designs that were utilized during the course of this project.

Table III.3.1 Comparison of different Soxhlet extractors.

Reactor #	Reactor Description	Reactor Photo	Pros	Cons
1	Conventional Soxhlet Extractor		Minimal solvent needed	Slow reaction time, difficult to remove recycled cathode material from paper filter
2	Sono-Soxhlet Extractor (Batch Scale)		Useful for evaluating the feasibility of Sono-soxhlet imitation extraction	Disabled the solvent reuse functionality
3	Sono-Soxhlet imitation extractor		High efficiency, short reaction time, minimal solvent	Required custom glassware

We also developed and tested a cryovap solvent transfer method to recover PVDF and solvent from a PVDF binder solution. We examined a conventional rotovap technique to evaporate solvent Y from ORNL, but its high boiling point (b.p.) made it difficult to recover the solvent from the solution. To address this issue, we chose a lower b.p. solvent for PVDF. Dimethylformamide (DMF) is a good PVDF solvent and has a b.p. of 152~154°C. Other well-known PVDF solvents are NMP and DMSO, and their b.p.s are 202~204 and 189°C, respectively. Therefore, there is a clear advantage to use DMF for the solvent recovery process. Figure III.3.6



Figure III.3.6 PVDF binder and cryovap solvent transfer apparatus

shows a cryovap solvent transfer apparatus. A flask filled with PVDF solution was placed in a water bath and connected to a solvent transfer manifold. The manifold was connected to a liquid nitrogen solvent trap to collect solvent and also connected to a Schlenk line to evacuate the whole apparatus. The starting solution in the flask had 5 wt.% PVDF in it. We could use either static or dynamic vacuum for the solvent transfer, and we used a dynamic vacuum by leaving the vacuum valve open to minimize the total process time. First, we started the reaction at room temperature, but it took a long time to notice any changes in the solution level. Therefore, we increased the water bath temperature gradually. After it reached $\sim 50^\circ\text{C}$, the solvent transfer rate was notably increased, and the transfer reaction was finished within 1 hour. The volume of the recovered DMF solvent was measured and the apparent volume recovery is $\sim 93\%$.

Once we addressed rapid reaction time through sonication and chose the optimal solvent recovery process with the cryovap solvent transfer apparatus, the last hurdle was finding the optimal thimble, or mesh filter, to collect the NMC particles. Previously, we had tested two types of thimbles for Soxhlet process: (1) cellulose thimble and (2) porous polypropylene thimble. However, neither of them was promising because of pore-clogging and slow solvent draining problems. Thus, we tested a new custom-made thimble in order to address these problems made of a stainless-steel mesh filters with smooth surface, mono-layer structure and small pore size (Average pore size of $43\mu\text{m}$, $15\mu\text{m}$ and $5\mu\text{m}$). Prior to applying the filters to the Soxhlet experiment, we performed filtering tests using those stainless-steel mesh screens. Based on filtering tests we conducted with DMF solvent and NMC 111 particles, the $5\mu\text{m}$ stainless-steel mesh filter was chosen and used as thimble in the following Soxhlet process.

Results and Characterization

Once we completed the work above to design the optimal Soxhlet extraction process, we tested the sono-Soxhlet extraction successfully using stainless-steel mesh filters. We characterized recovered NMC 811 powder from ‘vacuum-assisted sono-Soxhlet extraction’ and recovered solvent from the ‘vacuum-assisted cryovap process’. XRD patterns and SEM images of both electrode scrap and recovered powder were taken to confirm that the Soxhlet process had no effect on the crystal structure and morphology of recovered cathode material. After vacuum-assisted sono-Soxhlet process, NMC811 secondary particles are exposed well and no distinct carbon black/PVDF are detected. A large amount of carbon and fluorine are revealed in the electrode scrap (Figure III.3.7), while the signal of fluorine in the recovered NMC811 powder reduces significantly. Even though fluorine was

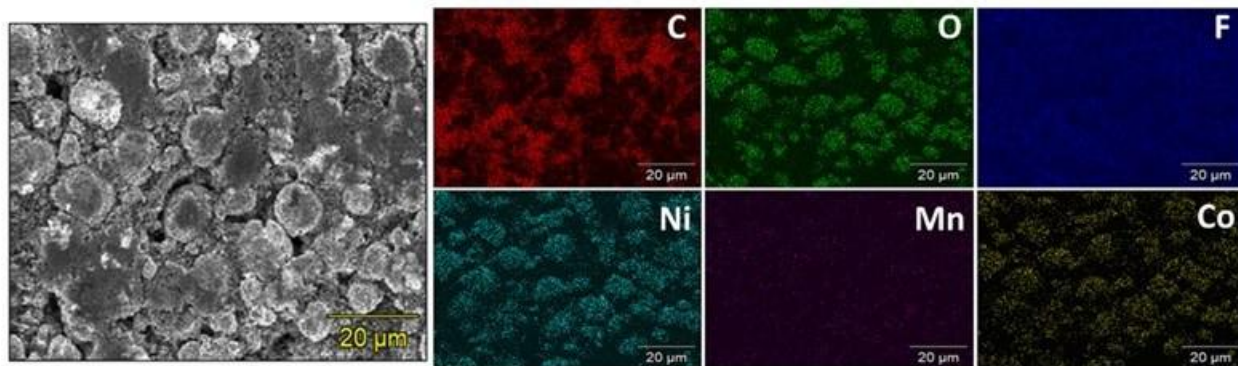


Figure III.3.7 EDS mapping of NMC 811 electrode scrap

not removed completely, the obvious decrease of the fluorine content confirmed the efficient removal of PVDF through the vacuum-assisted sono-Soxhlet extraction process. To minimize solvent usage, the vacuum-assisted cryovap process was introduced to recover and recycle DMF which was used in the sono-Soxhlet process. The recovered DMF was examined by FTIR and compared with fresh DMF, as shown in Figure III.3.8. All peaks

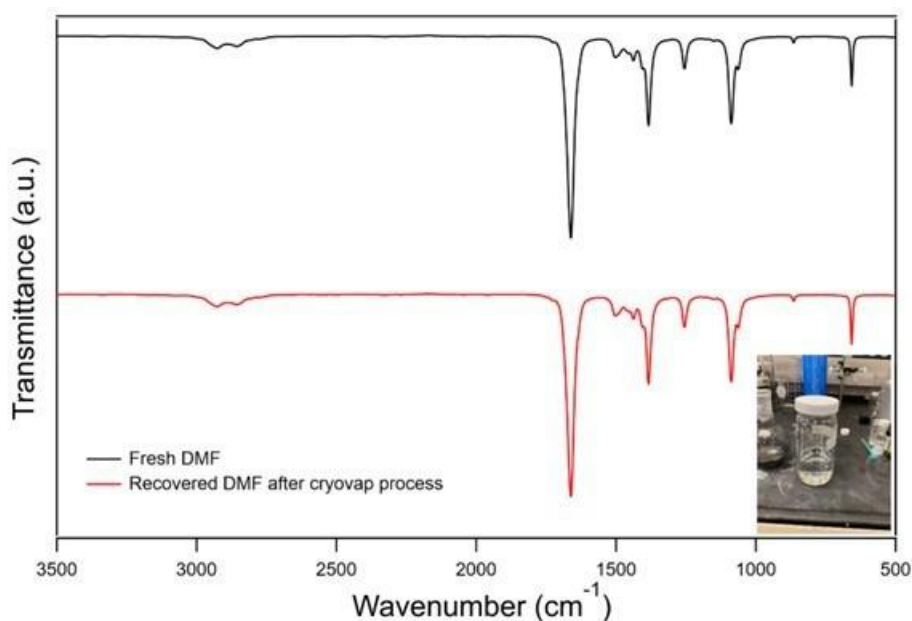


Figure III.3.8 FTIR spectra of fresh DMF and recovered DMF from vacuum-assisted cryovap process. Inset digital photo shows recovered DMF.

of the recovered DMF were indexed to those of the fresh DMF without any impurities. The recovery yield of DMF in the lab-scale experiment was 90.7%, which should be higher in any future scaled-up experiments. The inset photo in Figure III.3.8 shows the recovered DMF was transparent and visibly the same as fresh DMF solvent. Recovered DMF potentially could be reused as fresh extractant in the continuous sono-Soxhlet extraction to reduce the cost and relieve environmental burden.

Cathode/Cathode Separation

Most direct recycle operations will involve the collection of “black mass” which is a mixture of anode and cathode powders recovered from size reduced cells. Even if cells are presorted before processing, it is still highly likely that some mismatch of battery types, and ultimately cathode materials, will occur. Additionally

some manufacturers utilize a mixture of different chemistries for the cathode, such as lithium manganese oxide (LMO) and lithium nickel manganese cobalt oxide (NMC). While the LMO is less likely to be reused, the NMC could be used in a modern cell. Direct recycling of lithium-ion batteries will require the ability to effectively separate different cathode chemistries. Recovering and separating complex mixtures of cycled cathode powders will make recycled material more usable in the battery market. This work focuses on scale-up of proven techniques as well as the separation and recovery of complex mixtures of cycled cathode powders.

In FY22, cathode/cathode separation was accomplished by froth flotation and a mechanical separation process, referred to as “Process A” and detailed in previous anode/cathode separation quarterly reports (FY21 Q2, Q3, and Q4). Froth flotation was used to separate mixtures of cathode powders while different cathode electrodes were separated using Process A. The objective is to achieve high separation efficiency using each process where cathode fractions with purities $\geq 95\%$ can be generated.

Laboratory-scale Denver cell experiments at Michigan Technological University demonstrated efficient separation of NMC111 and LMO by froth flotation. Argonne translated the process to a froth column and scaled the process to achieve good separation. A 10 L froth flotation column was used to separate pristine NMC111 (Toda) and LMO (Targray). Argonne The feed was prepared as a 14 L slurry (2.5 wt.% solids) to provide sufficient material for 2nd stage NMC111 and LMO purification. Four different 2-stage froth flotation experiments were conducted. Tests 1 – 3 were conducted without tailings solution recirculation and used DI water as the froth washing solution. Additional frother was added to the feed to compensate for the dilution of frother in the column. Test 4 was conducted with tailings solution recirculation. Solution from the tailings outlet was pumped back into the column through the wash water supply line. The frother concentration in the column was controlled to be consistent during operation. Operation conditions were similar to the “Base test” applied for the 1st stage. Operation conditions were optimized for 2nd stage NMC111 and LMO purification where the effect of frother/collector concentration and wash water flow rate were investigated. Detailed operation conditions are described in the FY22 Q1 Milestone report.

The milestone for FY22 Q1 was to optimize the pilot froth flotation process to achieve $\geq 95\%$ purity LMO and NMC cathode fractions after multi-stage separation. Froth flotation of pristine LMO and NMC111 in the 10 L pilot-scale froth column was conducted at Argonne (Figure III.3.9). From our experimental results in FY21, it was determined that a multi-stage froth flotation operation would be necessary to achieve $\geq 95\%$ purity LMO and NMC111. 2-stage froth flotation was imitated by conducting series of batch column operations. The froth and tailings from the first batch operation (first-stage), whose main components are NMC111 and LMO, respectively, were sent to another batch operation (second-stage) separately to further improve NMC111 and LMO grades (Figure III.3.10). 2-stage froth flotation experiments achieved above 95% NMC111 in the recovered froth. However, the LMO grade of the recovered tailings reached approximately 92% after three different 2-stage flotation experiments. Using these conditions, it was determined that a third stage would be necessary to achieve $> 95\%$ LMO (Figure III.3.11). We conducted smaller scale Denver cell tests (3rd stage of purification) on the 2nd stage froth and tailings from Test 4 which improved NMC111 and LMO grades to 97.6% and 98.7%, respectively, which allowed us to achieve our FY22 Q1 milestone.

In Q2, we began cathode/cathode separation experiments using Process A. First, preliminary experiments by Process A were conducted to examine how to adjust operating parameters to separate different cathode chemistries. Single-side coated cathode laminates of NMC532, NCA, LFP, LCO and LMO cut into 1-1.5cm pieces were used for experiments. The preliminary experiments suggested that these cathode chemistries could be separated by adjusting operating parameters of Process A. Based on the results, cathode/cathode separation were capable for a binary mixtures including LCO/NCA, NCA/NMC532 and NMC532/LFP.



Figure III.3.9 Froth flotation column set-up at Argonne National Laboratory

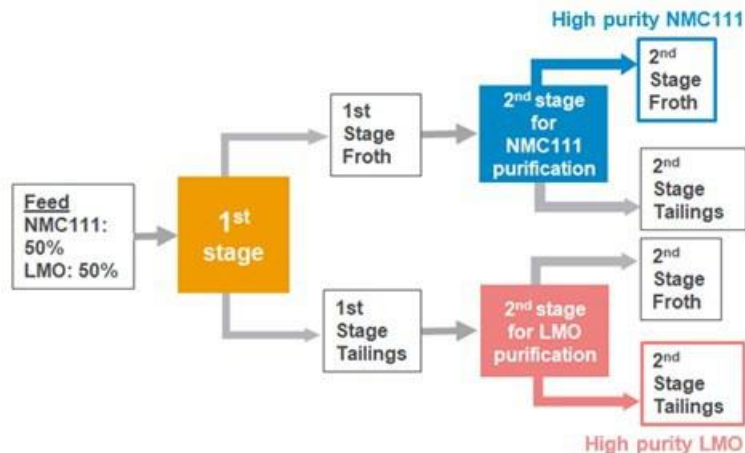


Figure III.3.10 Schematic of optimized froth flotation process to separate NMC111 and LMO

We investigated multi-step operation of Process A using 20 grams of 1:1 mass ratio binary mixtures (NMC532/NCA, LFP/NMC532, NCA/LCO) to achieve $\geq 95\%$ purity for recovered cathode materials (Figure III.3.12). Cathode pieces used for these experiments were single-side coated electrodes with pristine active materials with sizes ranging between 0.5-1.5 cm. Materials were continuously fed to Process A using a relatively slow feed rate to prevent material build up. In order to improve purity, collected fractions were fed through Process A several times. A NMC532/NCA mixture was fed through Process A four times to achieve 94% purity NMC532 (43% recovery) and 96% purity NCA (30% recovery). A LFP/NMC532 mixture required 3 steps to achieve 96% purity LFP (47% recovery) and 95% purity NMC532 (61% recovery) while a NCA/LCO mixture required only 2 steps to achieve 94% NCA purity (88% recovery) and 99% purity LCO (86% purity). These results demonstrate that different cathode chemistries can be purified to near 95% after multi-step operation of Process A.

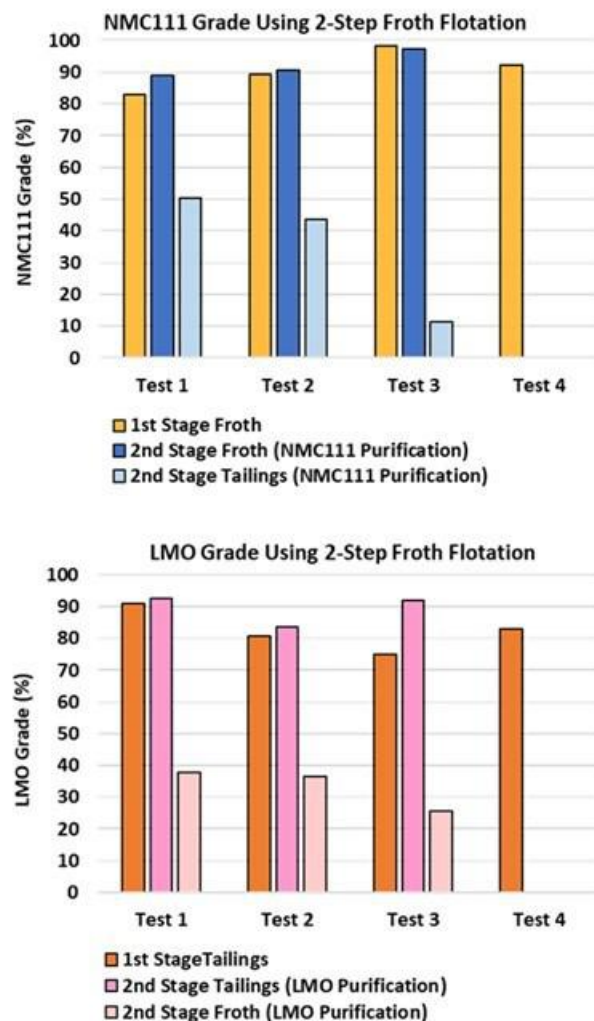


Figure III.3.11 Purity of NMC111 and LMO cathode materials achieved after a 2-step froth flotation process

In Q4, we focused on the separation of LFP and NMC111 electrodes with pristine active materials coated on both sides of the aluminum current collector foil. Pristine cathode electrodes coated on both sides of the current collector (i.e., double-side coated) are representative of cathode electrodes obtained from commercial cells and the Process A separation performance was expected to be similar between them. The main goal was to see if increased loadings of active material influenced material separation.

Before conducting cathode/cathode separation from a mixture, differences in Process A performance between single-side and double-side coated pristine LFP electrodes was investigated using the same operating conditions. LFP electrodes were continuously fed to Process A at a relatively slow feed rate that would prevent materials build-up. After a 1-step operation, the recovery of LFP electrodes collected was measured. When compared at the same operating condition, the recovery of double-side coated LFP was higher than that of single-side coated LFP, indicating that the loading of active cathode materials on foil affects Process A performance.

We conducted Process A experiments with unmixed LFP or NMC111 electrodes to verify the operating condition at which the highest percentage of LFP and NMC111 would be collected in the opposite fractions. This condition was used for the separation of binary mixture of double-side coated pristine LFP and NMC111 in a 1:1 mass ratio. Collected fractions from Process A were fed through multiple times (i.e., in a series of

steps) to improve the purities of LFP and NMC111 (Figure III.3.13). The same process conditions were used for separation steps 1-4. After the 3rd separation step, NMC111 purity reached 98% with 45% recovery from the original feed, while LFP purity was 85% with 73% recovery. After the 4th and final separation step, purities of both cathode materials were reduced. These results suggested that other operating conditions would be required to improve the LFP purity to above 90% without compromising recovery.

Results of cathode/cathode separation from binary mixtures using Process A

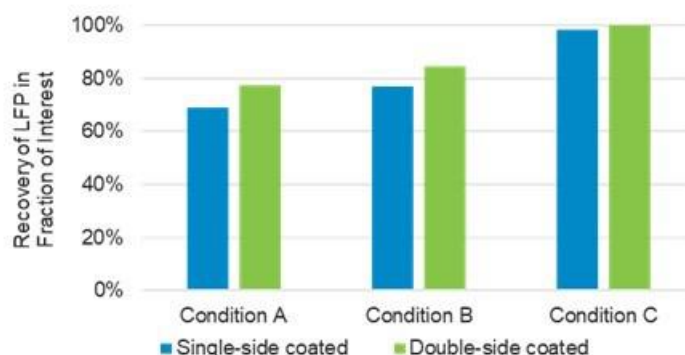
	NMC532 Fraction % LFP Purity (% LFP Recovery)	NCA Fraction % NMC532 Purity (% NMC532 Recovery)
1 st step	69% (76%)	73% (65%)
2 nd step	74% (67%)	87% (55%)
3 rd step	90% (49%)	94% (34%)
4 th step	94% (43%)	96% (30%)

	LFP Fraction % LFP Purity (% LFP Recovery)	NMC532 Fraction % NMC532 Purity (% NMC532 Recovery)
1 st step	76% (82%)	80% (74%)
2 nd step	88% (72%)	93% (58%)
3 rd step	96% (47%)	95% (61%)

	NCA Fraction % NCA Purity (% NCA Recovery)	LCO Fraction % LCO Purity (% LCO Recovery)
1 st step	87% (92%)	92% (87%)
2 nd step	94% (88%)	99% (86%)

Figure III.3.12 Separation of binary cathode mixtures using Process A

Comparison of separation performance of single-side and double-side coated LFP laminates by Process A



LFP and NMC111 separation from a double-side coated LFP/NMC111 mixture by multi-step Process A operation

	<u>LFP Fraction</u> % LFP Purity (% LFP Recovery*)	<u>NMC111 Fraction</u> % NMC111 Purity (% NMC111 Recovery*)
1 st step	71% (88%)	83% (64%)
2 nd step	77% (76%)	95% (55%)
3 rd step	85% (73%)	98% (45%)
4 th step	76% (65%)	84% (39%)

* (Mass of collected cathode)/(Mass of cathode in the 1st step feed)

Figure III.3.13 Separation of double-side coated laminates by Process A

Cathode/Cathode Separation via Froth Flotation

The overall objective of this project is to separate mixed cathode compositions using froth flotation process for direct recycling of the recycled cathode active materials. Separation of mixed pristine NMC111/LMO and NCA/LMO materials by froth flotation process has been demonstrated. Prior results demonstrated that froth flotation process achieved a good separation without any significant impacts on functional integrity of the recycled materials during the recycling process. A demonstration of cathode/cathode separation from spent Li-ion batteries has not been accomplished yet.

The objective of this project for FY22 is to investigate the performance of froth flotation in separating mixed cathode compositions from spent battery materials, scrap battery materials, and commercial black mass. Various new collectors and surface treatment methods have also been examined.

Multiple sources of Li-ion batteries were used including spent Li-ion battery pouch cells, spent cylindrical cells from consumer electronics, as well as black mass samples from commercial vendors. In Q1, separation performance with various flotation collector chemicals were used for spent cathode materials. In Q2, the focus was to evaluate the impact of various PVDF removal processes on the froth flotation performance of mixed cathode materials. In Q3 and Q4, froth flotation separation process was employed to separate mixed cathode active materials recovered from both wet and dry EV cells.

Separation of electrode active materials from spent Li-ion batteries was first investigated. In the first set of experiments, commercial black mass samples were received from ANL, and they were supplied from a commercial recycler. Two samples were used. The first one is the black mass as received; the second sample is the black mass after a thermal pyrolysis treatment. The thermal treatment removes carbonaceous materials

including carbon additives and PVDF binders. Bench-scale froth flotation experiments were performed with Denver cells using various flotation chemicals. Results showed that with a thermal pyrolysis treatment, the flotation performance was inferior compared to the pristine materials, suggesting that a certain degree of surface modification occurred during the thermal treatment process.

The effect of PVDF removal methods on froth flotation separation of mixed cathode materials was investigated. Two methods were investigated including a thermal treatment and a mechanical de-agglomeration method. Two collectors were evaluated. Flotation studies with single material showed that the recovery of cathode materials after a thermal treatment at 500 °C was significantly reduced compared to that without the thermal treatment. In addition, collector A was found to be stronger than the other two collectors surveyed. The recovery of NMC materials dropped from 80% using collector A to less than 50% after a thermal treatment process. The results confirmed that the pyrolysis treatment changed the surface chemistry of recycled cathode active materials, which in turn impact the cathode/cathode separation *via* froth flotation process. (See Figure III.3.14 and Figure III.3.15.)

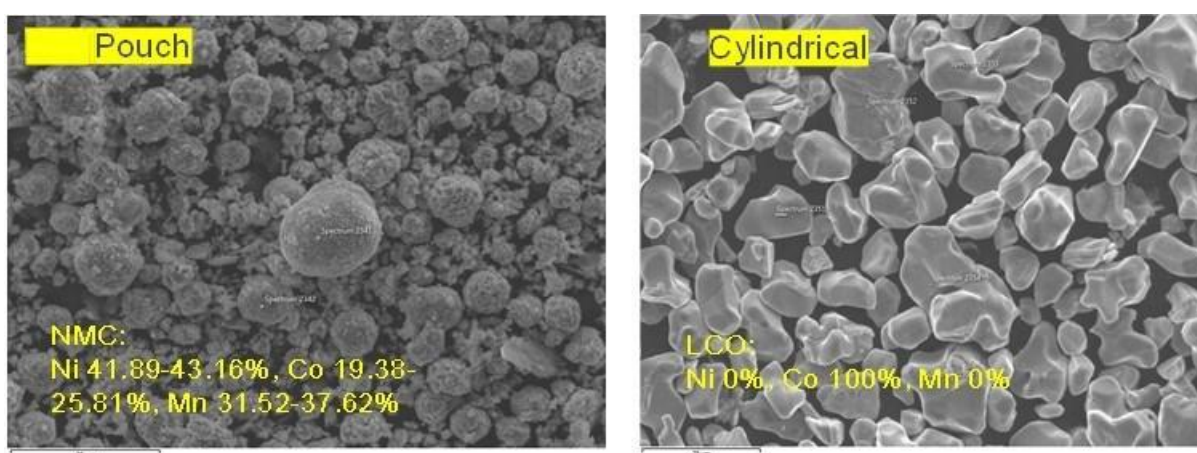


Figure III.3.14 SEM-EDS of recovered cathode materials from cylindrical and pouch cell.

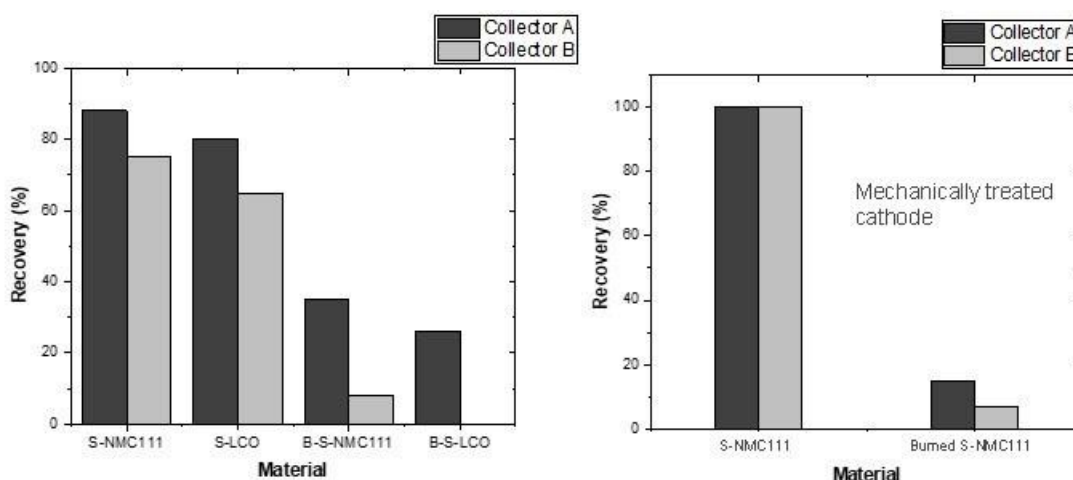


Figure III.3.15 Effects of PVDF removal processes on froth flotation recovery using two collectors (A and B).

Separation of spent NMC111 and pristine LMO by froth flotation method was performed. The goal was to determine if the recycled cathode active materials had similar flotation performance as the pristine materials. The recycled NMC materials were recovered from an EV battery cell, while the pristine LMO materials were used. A mechanical delamination and separation process was applied to obtain individual recycled NMC

materials from spent Li-ion batteries. The results showed that the froth flotation process was able to separate NMC111 from a mixture of cathode materials. The percentage of NMC in the froth product reached 95%+, and the percentage of LMO in the sink product reached 99%. This result confirmed that the froth flotation process can be applied to separate mixed cathode materials from battery scraps and spent battery cathode. Further experiments are needed with spent LMO materials.

To further investigate the changes in both bulk and surface properties of recycled cathode materials after a thermal treatment, XRD analysis was performed with both thermally treated and mechanically recovered cathode materials. The XRD results indicated that the pyrolysis of the recycled cathode active materials caused a phase change, and a $\text{Co}_{2.25}\text{Ni}_{0.75}\text{O}_4$ phase was formed after a thermal treatment. This phase change was likely associated with the decomposition of PVDF at a temperature of 400 °C and a possible thermal reduction of cathode active materials. (See Figure III.3.16, Figure III.3.17, and Table III.3.2.)

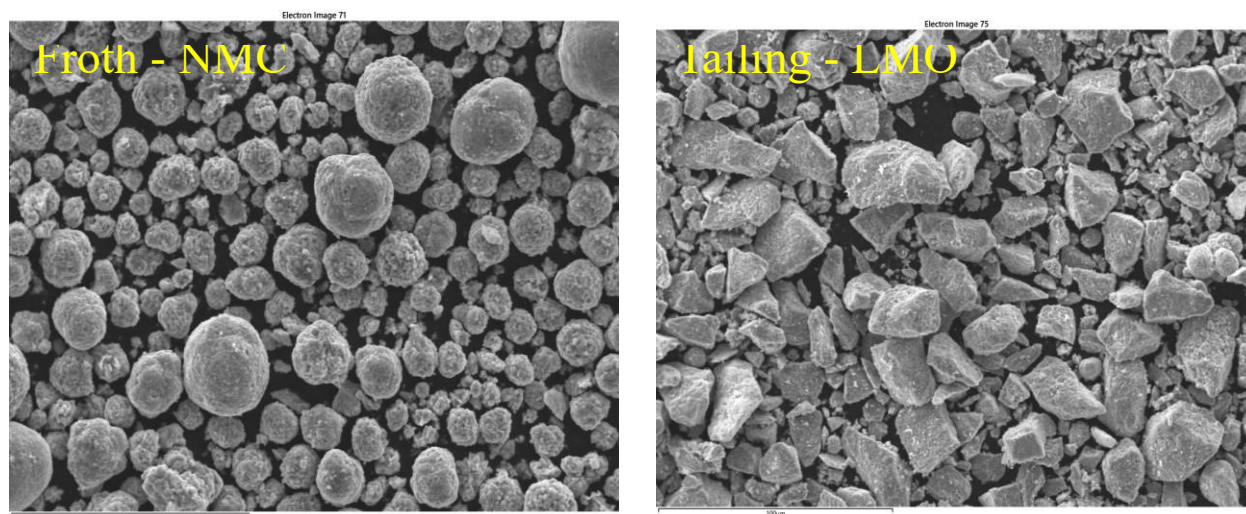


Figure III.3.16 SEM images of froth and sink products after a NMC/LMO separation by froth flotation.

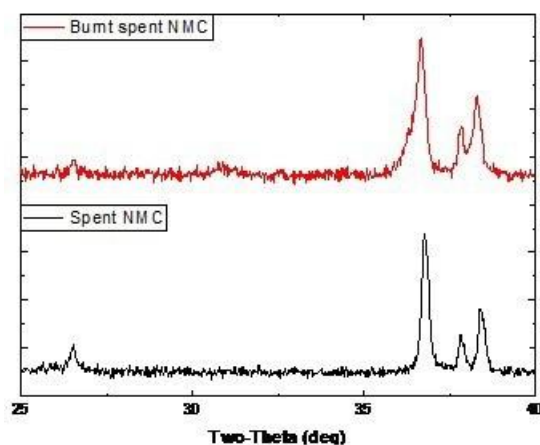


Figure III.3.17 XRD curve showing peak change in burnt cathode material

Table III.3.2 XRD data showing details of phase change in recycled cathode material.

Phases	Recycled NMC	Burnt NMC
*NMC111(Li_x)	95.4	91.2
Co_{2.25}Ni_{0.75}O₄	0.0	7.1
C (Graphite)	4.6	1.8

To increase the separation efficiency of other cathode mixtures, such as LCO/LMO mixture, we investigated various surface treatment methods to improve the froth flotation performance. Results obtained with a new pre-treatment method showed that the recovery rate of NMC622 after a surface treatment was improved from 12% to 90% with 922 collectors. Likewise, the recovery rate of NMC811 was increased from 21% to 60% after the surface treatment. The present result demonstrates that this new pre-treatment method improves the separation performance of cathode mixture. Detailed mechanism on surface adsorption and particle characterization will be performed in the next quarter to better understand the adsorption mechanism. (See Figure III.3.18.)

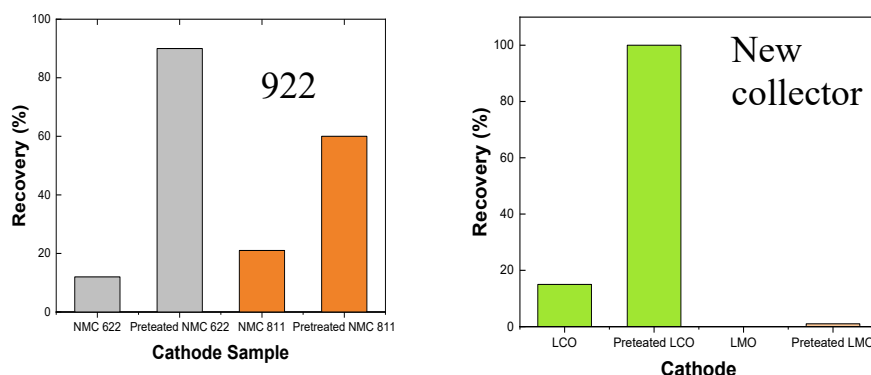


Figure III.3.18 Effect of surface treatment on different cathode chemistries

Solvent-Based Gravity Separation

Direct recycling involves recycling of cathode active materials from Li-ion batteries in the solid phase and reuse in new battery manufacturing after functional repairs as necessary. It is necessary that the recycling process concentrates, purifies, and yields 99% purity of electrode active materials from Li-ion batteries. Froth flotation process was the only method to separate anode and cathode materials from the black mass. Prior to the froth flotation separation experiments, a removal of PVDF binder from both the cathode and anode composite materials is needed. Both the water chemistry in separation processes and the pre-treatment process impact the electrochemistry of recycled anode and cathode materials from Li-ion batteries.

The aim of this project is to develop a recycling process that separates anode and cathode active materials while preserving their functional integrity. This separation process is based on centrifugal gravity separation process and can potentially be operated in non-aqueous liquid that preserves the functional integrity of electrode active materials. For FY22, the objective of this project focuses on separation of electrode active materials from Li-ion batteries and developing strategies to increase both the recovery and grade of cathode active materials in the concentrate product.

The NMC111 powders have density of ~4.8 g/cm³, while graphite powders have density of ~2.266 g/cm³. Separation between the two materials can be achieved due to the difference in specific densities in a liquid medium. In this study, separation of mixed fine powders was conducted using a Falcon L40 enhanced gravity

concentrator with an Ultra-Fine (UF) concentrator. Figure III.3.19 shows a schematic drawing of the UF concentrator. Black mass was mixed with DI water or other liquids to prepare a slurry. An overhead agitator (Caframo) was used to stir the slurry for a few minutes to ensure the slurry was properly mixed. In each trial, the slurry was slowly fed into a central tube of the Falcon L40 concentrator at a flow rate of approximately 2 L/min. The concentrator bowl rotated at a speed of 1,000 – 3,000 RPM, at which particles in the slurry within the rotating bowl were subject to a centrifugal force of up to 50-300 G. The UF concentrator consists of two sections including 1) a migration zone and 2) a retention zone. At the migration zone, under the centrifugal force, particles preferentially concentrate along the wall of the rotating bowl, creating strong interlayer shears. Due to the difference in particle settling velocities enhanced by centrifugal force, fine heavy particles arrive at the wall prior to coarse light ones. As the slurry continues to feed into the bowl, more particles compact along the wall of the rotating bowl. Smaller, denser particles move across the interlayers, then into its inner wall, pushing coarser and lighter particles out of the bed. These lighter and coarser particles are flushed with the overflow stream. Particle beds within the concentrator bowl are collected manually in a laboratory setting or by flushing with water in commercial operations.

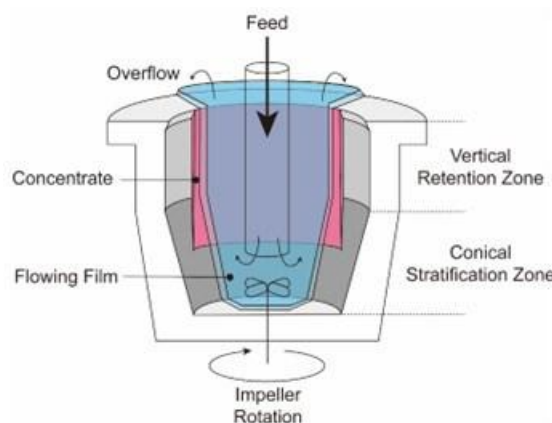


Figure III.3.19 a) a schematic drawing of a centrifugal ultrafine (UF) gravity separation concentrator.

A direct recycling route for spent Li-ion batteries was developed. Li-ion batteries are first dismantled, shredded, and crushed. In this study, large-format Li-ion battery pouch cells were used. They were discharged to 2.7 V at a C/5 rate and held at 2.7 V for at least 48 hours prior to its opening in the fume hood. The electrode sheets were manually recovered, soaked in isopropanol alcohol (IPA) to remove remaining electrolyte, and dried under the fume hood. The active materials from electrode sheets were delaminated from current collectors by a mechanical delamination process in water. The delaminated anode active materials contained graphite and 3-6% of binders, while cathode active materials contained 5-10% of PVDF binders and carbon additives. The mixture of delaminated anode active materials and cathode active materials were processed in a muffle furnace (Thermolyne, Thermo Fisher) at temperatures of 200-500 °C for two hours in the open environment. The black mass after a pyrolysis treatment at 400-500 °C was free of PVDF binders and carbon additives. Separation experiments of PVDF-free anode and cathode materials were performed.

Chemical Relithiation

Among the first steps of a recycling effort focused on end of life lithium-ion cells is the need to ascertain the lithium content of the recovered materials and develop the process to restore that active lithium content. This loss of lithium over time, seen as gradual cycle-to-cycle loss of active lithium is caused by the lithium ion trapping outside the circuit in a variety of irreversible processes (SEI formation, corrosion, and electronic isolation of particles). At approximately 20% loss, various issues including electrode cell balancing, voltage drift, and impedance changes, make the cathodes performance more difficult to predict and the user observes loss of performance. The recovered material's structure is a lithium-deficient version of the starting materials, with further observable structural changes related to the temperature of operation, initial stoichiometry, or

processing conditions. Typical structural changes include site mixing of lithium and nickel, surface oxygen loss, and surface structure degradation (crossover, metal dissolution). The relithiation section focuses on a variety of methods to achieve and evaluate relithiation including performance, ease of use, costs, and waste generated to achieve a stoichiometric material. For the solid-state methods, we have focused this past year on reducing costs and waste materials by going to a significantly decreasing the amount of carrier solvent (to solvent-free) method in association with calculations completed by the EverBatt team led by Qiang Dai (ANL). The lowest cost method used a dry coating of the lithium source (hydroxide) followed by a short duration RAM mixing to homogenize the sample. The best process was a two-tier anneal stage that allowed the lithium precursor to decompose to active lithia in a temperature window before the temperature ramp decomposed the lattice by oxygen loss. Annealing under an oxygen atmosphere was found to be beneficial to the electrochemical performance of the final product. A review of the processes for NMC622 relithiation, led by the NREL team, has been undertaken.

The objective is to develop a near solvent-free to solvent free, low cost relithiation process for lithium-deficient NMC622 (supplied by ORNL) based on a two-stage thermal relithiation process.

During FY22, the solid-state relithiation effort focused on completing a test run of the scale up process in association with CAMP and MERF. Determining the role of multi-stage annealing, establishing needed protocol steps for washing the scaled up samples, and establishing the new protocols for NMC622.

During FY22, the NMC333 solid-state relithiation effort focused on completing a test run of the scale up process in association with CAMP and MERF. While initial scaling indicated recovered performance, most of the experimental methods use a high temperature anneal. This step created issues with particle growth and sintering that effected the electrode creation process. Subsequent runs sieving the powders did not change performance but resulted in better electrode loadings (see Figure III.3.20).

Once the NMC relithiation section completed our efforts on the more thermally stable NMC333 baseline materials (MERF/ANL) that reflected the common cathodes in use from approximately 8y ago. To reflect more currently used cathode systems, the section moved to evaluate these processes for NMC622, a Ni-rich cathode that is more commercially used for the past 5y. Samples were provided to the re-lithiation teams by ORNL after a program wide relithiation benchmarking exercise that indicated the best electrochemical performance (from powder isolated from the electrode) was from materials supplied by the ORNL solvent Y process. The properties (XRD, TGA) of the scaled-up Solvent Y batch were verified to be consistent with the previous results.

The solid-state relithiation process developed for NMC333 process was utilized for the subsequent NMC622 materials. Overall minor modifications were evaluated to the annealing temperatures to reflect the lower thermal stability of delithiated NMC622. The new materials were tested by mixing the delithiated cathode with LiOH with or without an ethanol carrier solution and using the resonant acoustic mixer (RAM). The mixed powder was then annealed at 720°C. Figure III.3.21 shows an overlay of XRD data for a relithiated product with the pristine and solvent Y process powder. The peaks for the relithiated product align with those of the pristine NMC, exhibiting a decreased separation between the 108 and 110 peaks observed in the solvent Y processed sample.

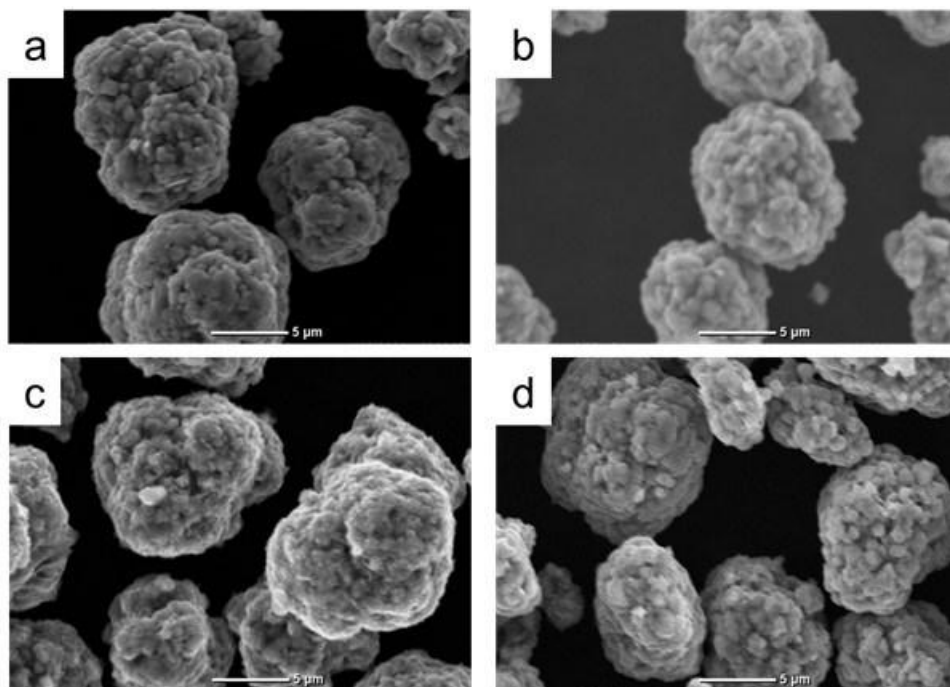


Figure III.3.20 SEM image of (a) pristine NMC333, (b) delithiated NMC333, (c) 1-step relithiated NMC333, and (d) 2-step relithiated NMC333

GDOES compositional analysis of the relithiated NMCs are shown in Table III.3.3. The Li contents recovered for the ethanol and RAM mixed products were consistent with each other. The amount of LiOH used in the 50 g scale-up was increased slightly and was reflected in the final Li content of the product being near 1.05.

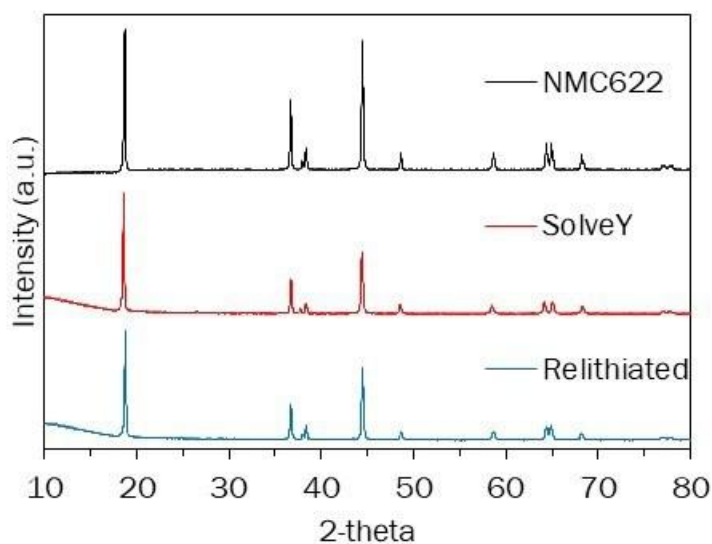


Figure III.3.21 XRD of pristine NMC622, Solvent Y processed, and relithiated cathode powder

Table III.3.3 Elemental composition for relithiated NMCs

	[Li]	[Ni]	[Mn]	[Co]
Ethanol mix	0.992	0.657	0.190	0.153
RAM mix	0.992	0.647	0.202	0.151
RAM mix (50 g)	1.053	0.660	0.187	0.153

Table III.3.4 Half-cell data for relithiated cathodes from solvent Y process

	Ethanol mix	RAM mix	RAM mix (50 g)
1 st Cycle Charge (mAh/g)	201.2	202.5	197.8
1 st Cycle Discharge (mAh/g)	167.1	169.8	163.1
4 th Cycle Charge (mAh/g)	168.2	170.2	167.5
4 th Cycle Discharge (mAh/g)	167.0	170.0	165.2

Half-cell testing data for the relithiated cathode powders are shown in Table III.3.4. The capacity values for the relithiated cathode using RAM mixing were slightly higher than those from the ethanol mixing. Because of this, RAM mixing was used for the scale-up relithiation. These changes to the relithiation process have been updated into the EverBatt model and should result in lower costs associated with the solid-state process.

For these studies, it was noted during processing that a small difference in performance was seen for most of the samples relithiated samples. Initial analysis by XRD indicated no bulk sample impurities; however a more detailed analysis indicated that the surface contained LiF, probably from electrolyte salt decomposition. Addition of washing step was found to restore the anticipated capacities. Some possible evidence for proton insertion on air exposure washing due to ion exchange was noted, we have initiated a collaborative study with Fulya Dogan and Sohyun Park to use MAS-NMR, a tool that can be specific to lattice protons, as a methods to evaluate any proton concentration. Protons carried thru the process can interact and decompose the electrolyte salts in the reconstructed cells making HF and/or water.

Ionothermal Relithiation

Lithium-ion batteries (LIBs) with high energy density make a significant contribution to solving energy storage issues but simultaneously cause serious environmental issues due to their hazardous materials, such as carcinogenic heavy metals and toxic electrolytes.[1] With the rapidly increasing use of LIBs in our highly electrified society, proper handling of end-of-life (EOL) LIBs has become an urgent and promising task, in which the regeneration of highly valuable cathode materials such as lithium metal oxides is the primary and motivated objective at present.[2] The objective of this project is to develop a cost-effective ionothermal lithiation process that entails ionic liquids (ILs) or reciprocal ternary molten salts (RTMS) to relithiate and/or upgrade spent cathodes at ambient pressure and low temperature. ILs are a family of non-conventional molten salts that offer many advantages, such as negligible vapor pressures, negligible flammability, wide liquidus

ranges, good thermal stability, and much synthesis flexibility. The unique solvation environment of these ILs and RTMS provides new reaction or reactive flux media for controlling the formation of solid-state materials with a minimum perturbation of morphologies. In addition, ILs and RTMS can be readily recycled and reused after the ionothermal lithiation. During first 3 years of this project, ionothermal relithiation of chemically delithiated NMC111(D-NMC111) was extensively investigated under different reaction conditions. The effect of lithium precursor, the type of ionic liquid, different temperatures, and reaction time were studied. The recovered materials were analyzed by various characterization techniques including TGA, XRD, SEM, and ICP-OES, which demonstrate that our ionothermal approaches towards restoring Li into D-NMC111 for direct regeneration of cathode materials are promising and feasible.[3] Large scale lithiation experiments (50 g) have been successfully performed. Preliminary results show no significant difference in thermal stability, morphology, and electrochemical performance for the restored NMC111 in small or large scale ionothermal relithiations using either fresh IL and spent IL. During the project's year 4, the ionothermal relithiation of spent NMC622 (SolveY_ORNL) in RTMS has been investigated at different experiment conditions providing promising and interesting results. The technoeconomic analysis has been performed using EverBatt model for the ionothermal relithiation process based on RTMS for spent NMC622 (SolveY_ORNL). EverBatt model indicates that this process for spent NMC622 (SolveY_ORNL) is around \$19.21/kg, which is lower than those of conventional hydro recycling technologies (\$25.22/kg), pyro recycling technologies (\$30.11/kg), and virgin powder (\$29.25/kg).

The objective is to develop a flux relithiation method based on ionic liquids (ILs) or molten salts (MS) fluxes to relithiate the EOL LIBs cathode materials such as spent NMC 622 (SolveY_ORNL).

During FY22, the ionothermal relithiation of spent NMC622 (SolveY_ORNL) in RTMS has been further investigated and scaled up. RTMS systems (LiCl/NaNO₃) have been formulated with low eutectic point and moderate oxidation activity in order to relithiate spent NMC 622 (SolveY_ORNL). The ratio of molten salts to spent NMC 622 has been optimized to achieve large scale relithiation. The reuse of RTMS has been investigated to lower the cost of the ionothermal relithiation process.

A high-temperature flux relithiation method based on reciprocal ternary molten salts (RTMS) fluxes to relithiate spent NMC622 (SolveY_ORNL) has been optimized (Figure III.3.22). The ratios of SolveY_ORNL to RTMS from 1:1 to 1:4 have been investigated. The XRD patterns of relithiated samples exhibited narrower peak splitting around 65°C compared to that of SolveY_ORNL, which is identical to that of pristine NMC 622. No changes in XRD patterns of relithiated samples were observed by varying mass ratio of SolveY_ORNL to RTMS (Figure III.3.23).

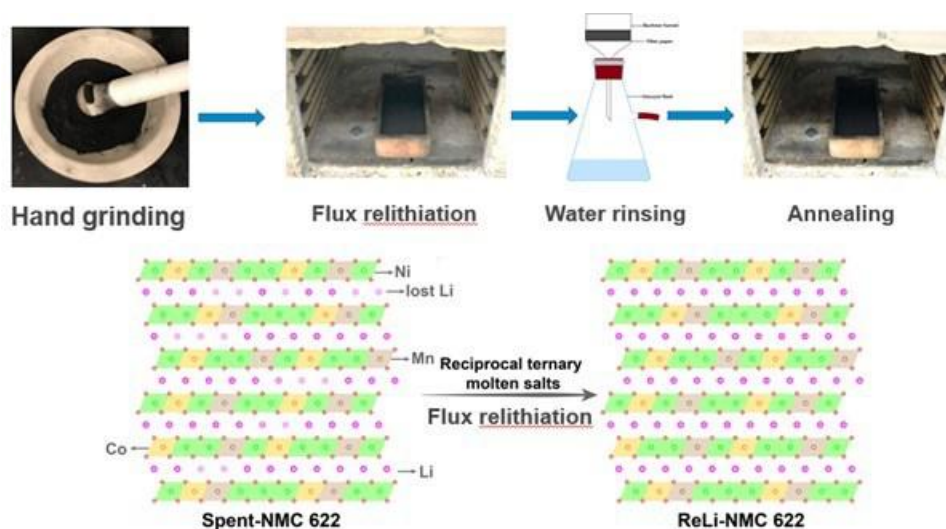


Figure III.3.22 Schematic illustration of ionothermal relithiation process.

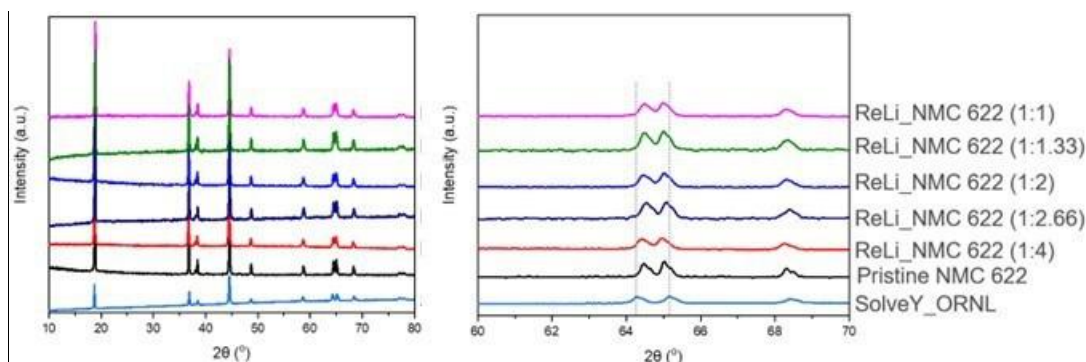


Figure III.3.23 XRD patterns of relithiated products under different mass ratios of SolveY_ORNL to RTMS.

All the relithiated samples were used as active materials in cathodes, and paired with Li foil to evaluate their half-cell electrochemical performance. As shown in Figure III.3.24A, all the relithiated samples exhibited much higher capacities than that of SolveY_ORNL. Among relithiated samples, ReLi_NMC 622 (1:2) exhibited the highest capacities at 0.1 C for the first 4 cycles, which were identical to those of pristine NMC 622. Except for ReLi_NMC 622 (1:1) all other relithiated samples exhibited better cycling performance than pristine NMC 622, because of their higher charge capacities at the 100th cycle (Figure I.1.24B). Best cycling performance was obtained at the mass ratio of SolveY_ORNL to RTMS 1:2.

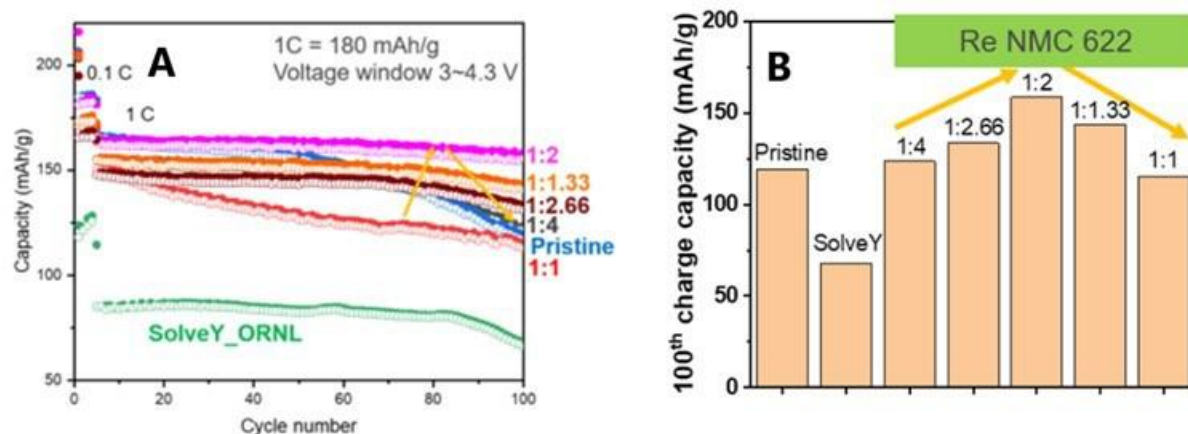


Figure III.3.24 Half-cell cycling performance (A) and the 100th half-cell charge capacities (B) of relithiated products under different mass ratios of SolveY_ORNL to RTMS.

The ionothermal relithiation of SolveY_ORNL was scaled up to 50 g. Two batches of 50 g have been sent to ANL_CAMP for the full cell performance tests. For scale up synthesis, the mass ratio of SolveY_ORNL to RTMS is 1:2. The half-cell tests for ReLi-NMC 622 were performed before shipping out to ANL. As shown in Figure III.3.25A, ReLi-NMC 622 exhibited a high first charge capacity of 207 mAh/g at 0.1 C. The reversible charge and discharge capacities at 0.1 C were 170 and 169 mAh/g. During 120 charge/discharge cycles at 1 C, ReLi-NMC 622 exhibited better cycling performance than pristine NMC 622 (Figure III.3.25B). According to the feedback from CAMP, the relithiated samples through ionothermal process shows the best stability performance among different direct recycling methods. The assembled pouch cells are cycled at C/2 for 500 cycles, which show comparable capacities with the pristine NMC 622.

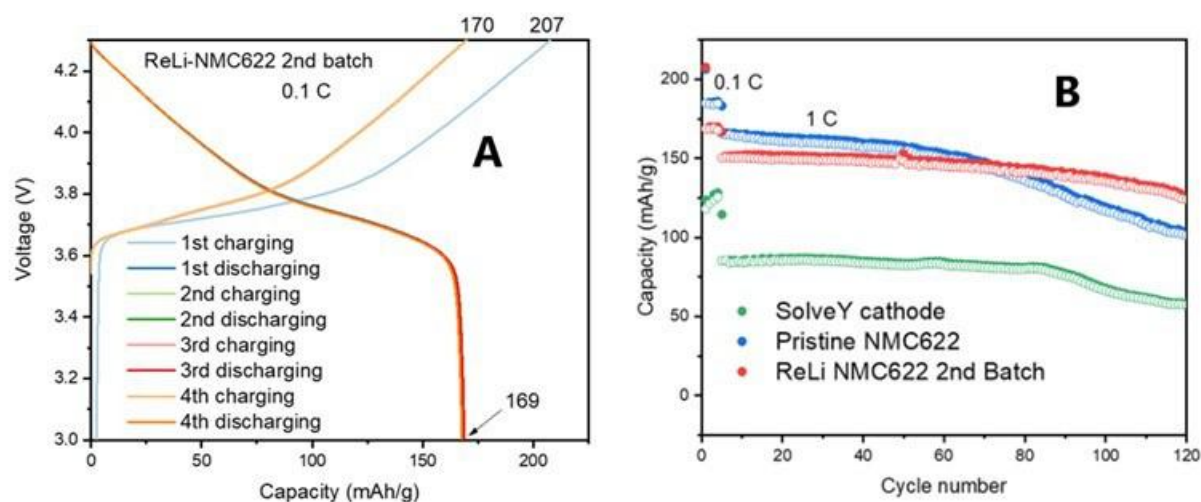


Figure III.3.25 The first 4 charge-discharge curves(A) and cycling performance (B) of large scale ReLi_NMC 622 for half-cell tests.

The technoeconomic analysis of ionothermal relithiation based on RTMS was performed by EverBatt model. As shown in Figure III.3.26A, the cathode regeneration cost by ionothermal relithiation is around \$19.21/kg, which is lower than those of conventional hydro recycling technologies (\$25.22/kg), pyro recycling technologies (\$30.11/kg), and virgin powder (\$29.25/kg). To further reduce cathode regeneration cost, the RTMS was collected after relithiation process. By optimizing the heating process, up to 90% of RTMS can be recovered for the second round of ionothermal relithiation. The XRD pattern reveals sharp peaks corresponding to NaCl, NaNO₃, and LiNO₃, which are consistent with the composition of fresh RTMS (Figure III.3.26B). The photo of recycled salts shows white powder, suggesting the absence of transition metal ions. By reusing 90% of RTMS for once, the cathode regeneration cost decreases from \$19.21/kg to \$14.88/kg, which is much lower than those of conventional recycling technologies.

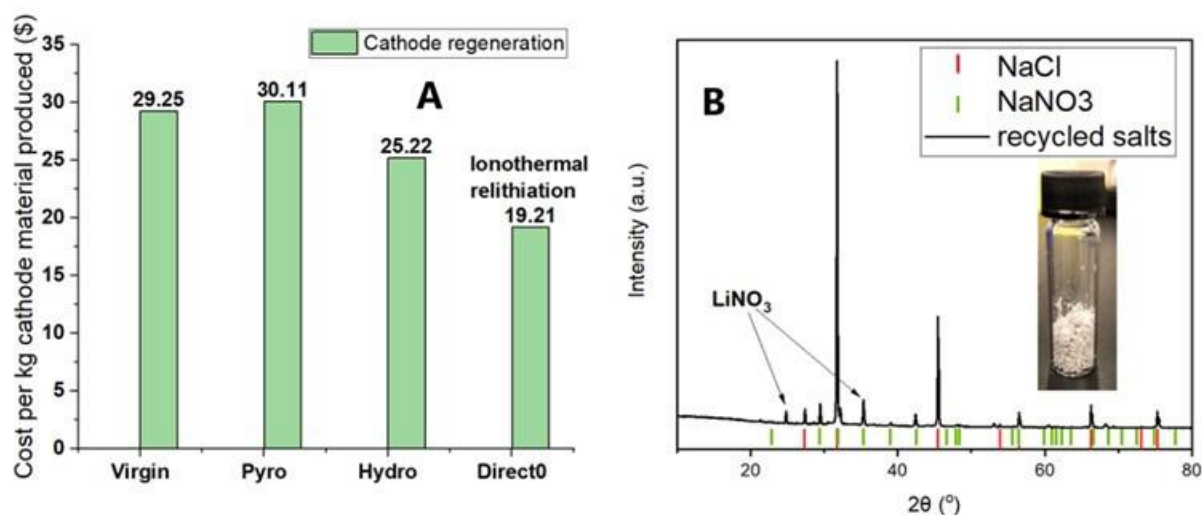


Figure III.3.26 (A) Costs of cathode regeneration by different methods analyzed by EverBatt model and (B) XRD pattern and photo of recycled RTMS.

Hydrothermal Relithiation

The direct regeneration method based on hydrothermal relithiation with a subsequent short annealing step developed by UCSD team can successfully resolve the compositional and structural defects of chemically delithiated NCM111 (D-NCM111). It also recovers the electrochemical performance to the same level as the pristine Toda NCM111 (T-NCM111).^{1,2} The process parameters involved in the hydrothermal and annealing steps, such as temperature, time and the Li-bearing precursor composition, have been extensively explored and optimized. The life cycle analysis indicates the optimized direct recycling method is significantly advantageous in terms of operation cost, greenhouse gas emissions, and energy consumption compared with currently commercialized pyrometallurgical and hydrometallurgical recycling routes. Moreover, the underlying relithiation mechanism has been thoroughly studied with advanced characterizations and density functional theory calculation, which is favorable for designing rational routes to directly recycle a diverse range of cathode materials, such as NCM622. In order to validate the process for practical adoption, the possibility of achieving a larger-scale regeneration should be also explored. Extensive characterization and electrochemical testing have been performed to demonstrate the scalability of the hydrothermal relithiation process.

This project is to validate the hydrothermal relithiation process for spent NCM cathode materials such as NCM111 and NCM622, the process parameters involved in the hydrothermal relithiation, washing and annealing steps have been explored, including the possibility of achieving a reasonably large-scale (e.g., > 100g per batch) regeneration for NCM111 and NCM622 in a more economical way.

The feasibility and scalability of hydrothermal relithiation for spent, delithiated NCM111 and NCM622 will be evaluated through extensive characterization, electrochemical testing as well as the life cycle analysis.

In the past four quarters, we validated our direct regeneration process for high Ni materials (cycled NCM622 or C-NCM622) through coin cell test with 4 M LiOH at 220°C followed by annealing at 850°C and scaled up the process from 1 g to 50 g with two different batches (HS-NCM622-50g-Round 1 and HS-NCM622-50g-Round 2). Both of them show capacity retention of ~92% at C/3 after 50 cycles in half cell, achieving same level of the capacity of pristine NCM622 (T-NCM622) as shown in Figure III.3.27. This indicates the cycled NCM622 can be recovered effectively at scale of 50g using our hydrothermal treatment method.

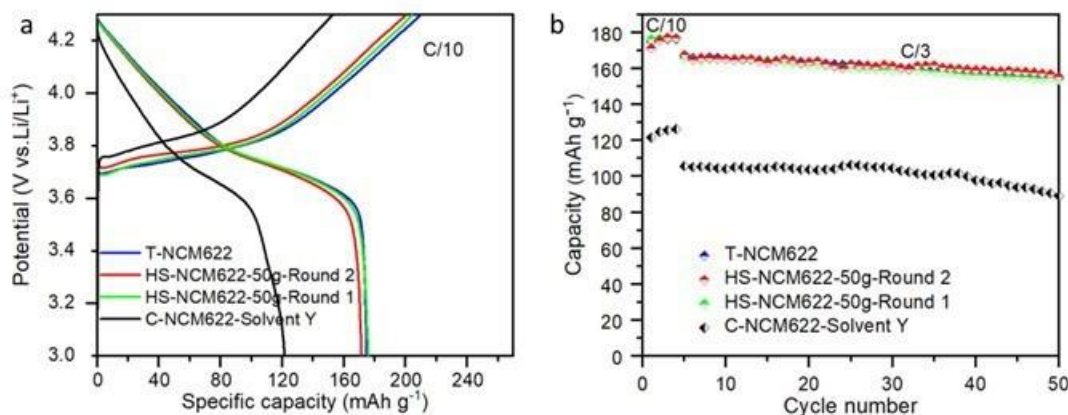


Figure III.3.27 Voltage profiles (a) and cycling stability (b) of the cycled NCM622, the pristine NCM622 and NCM622 regenerated at 220°C at 50g scale followed by annealing at 850 °C in two batches (C-NCM622, T-NCM622, HS-NCM622-50g-Round 1, HS-NCM622-50g-Round 2).

We also validated that in our direct regeneration process for C-NCM622, the 4M LiOH solution can be replaced by 2M LiOH with 2M KOH (HS-NCM622-2M LiOH&2M KOH) or 3M LiOH with 1M KOH (HS-NCM622-3M LiOH&1M KOH) mixture solutions while maintaining the same effectiveness of relithiation (capacity retention of ~92% at C/3 after 50 cycles in half cell), which can effectively reduce the overall regeneration costs³ as shown in Figure III.3.28.

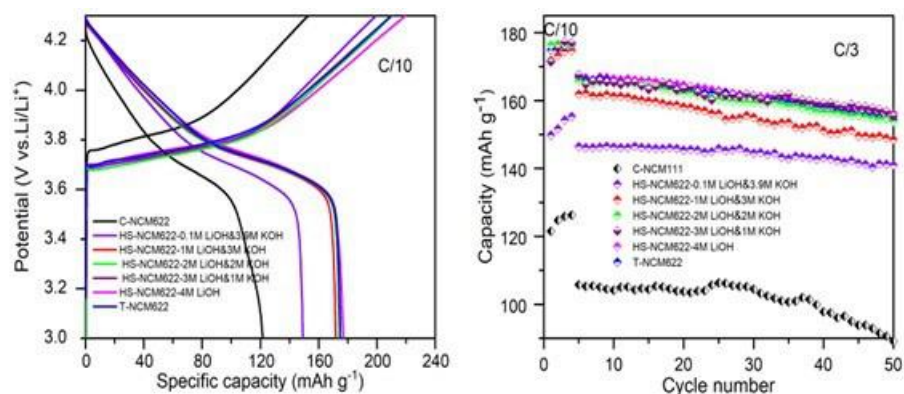


Figure III.3.28 Voltage profiles (a) and cycling stability (b) of samples treated by the mixture solution of 0.1M LiOH with 3.9M KOH, 1M LiOH with 3M KOH, 2M LiOH with 2M KOH, 3M LiOH with 1M KOH, and 4M LiOH as well as the control samples (C-NCM622 and T-NCM622).

We also worked on further scaling up the regeneration process from 50 g to 100 g for D-NCM111 with two approaches: optimizing washing steps or applying a scavenge agent to remove alkaline residues on the surface of NCM111 after hydrothermal reaction. After optimizing washing steps, these results indicate that the ratio of around 40ml water (HS-NCM111-100g-40ml/g wash) among the test range to wash 1g HT-NCM111 can be effectively to regenerate D-NCM111 at scale of 100g using our hydrothermal treatment method. Inadequate washing (HS-NCM111-100g-20ml/g wash) will cause relative lower capacity retention which may be caused by the increased charge transfer resistance at the electrode/electrolyte interface from excessive alkaline residues on the NCM111 surface. On the other hand, the relative lower capacity retention could also be caused by proton exchange from excessive washing, ratio of 60ml (HS-NCM111-100g-60ml/g wash) or 80ml (HS-NCM111-100g-80ml/g wash) water. However, requiring 40ml of washing water per gram of cathode material would mean that, 40L (10.5669 gallons) of water is needed to recycle 1kg spent NCM111 in washing steps only, which is not promising for further scale up process. (See Figure III.3.29.)

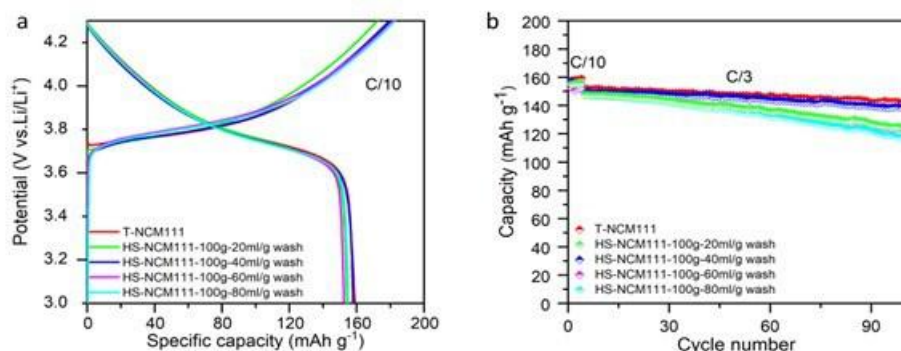


Figure III.3.29 Voltage profiles (a) and cycling stability (b) of the pristine NCM111, the delithiated NCM111 regenerated at 220°C at 100g scale, use the ratio of 20ml, 40ml, 60ml, 80ml water respectively to wash 1g HT-NCM111, followed by annealing at 850 °C (T-NCM111, HS-NCM111-100g-20ml/g wash, HS-NCM111-100g-40ml/g wash, HS-NCM111-100g-60ml/g wash, HS-NCM111-100g-80ml/g wash).

To mitigate these washing issues, we also tried removing lithium residues via a scavenge agent. The relithiated NCM111 was washed using the ratio of 1.6ml water, followed by annealing at 850 °C (denoted as 'HS-NCM111-100g-1.6ml/g wash'). After the scavenging agent was applied (denoted as 'HS-NCM111-100g-1.6ml/g wash + scavenge agent'), the initial capacity was up to 153.9 mAh/g at C/3, and it could achieve the capacity retention of 93.2%, achieving the same level of capacity retention as the T-NCM111 (93.2%). This indicates the effectiveness of using a scavenging agent to remove alkaline residues on the surface of

regenerated NCM111 that can be recovered effectively at scale of 100g using our hydrothermal treatment method. (See Figure III.3.30)

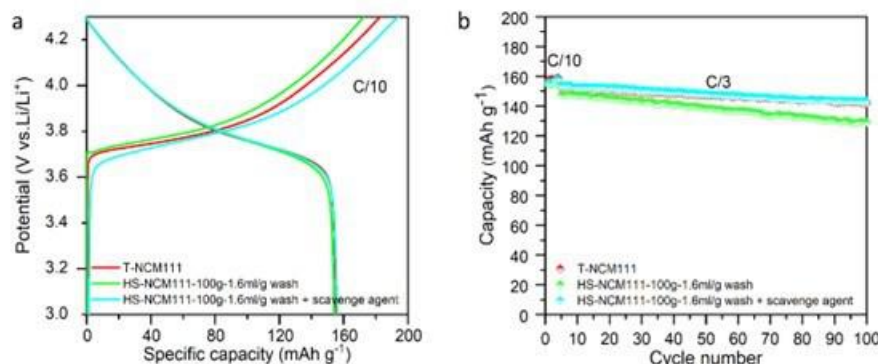


Figure III.3.30 Voltage profiles (a) and cycling stability (b) of the pristine NCM111, the delithiated NCM111 regenerated at 220°C at 100g scale, use the ratio of 1.6ml water to wash 1g HT-NCM111, followed by annealing at 850 °C, and the delithiated NCM111 regenerated at 220°C at 100g scale, use the ratio of 1.6ml water to wash 1g NCM111 after hydrothermal reaction, followed by annealing at 850 °C, and then apply scavenger agent on the surface of NCM111 (T-NCM111, HS-NCM111-100g-1.6ml/g wash, HS-NCM111-100g-1.6ml/g wash + scavenger agent).

Relithiation via Redox Chemistry

Direct recycling of lithium-ion battery (LIB) material is gaining momentum to keep up with the electric vehicles (EVs) consumer demand.¹ Recycling of LIBs is motivated by environmental regulation² and material constraints.³ The speed, cost, and scale of direct recycling of LIBs will determine how quickly it gets adopted widely.^{2,3,4} Under ReCell Center led by Argonne National Laboratory (ANL), relithiation of spent cathode materials are explored using hydrothermal, ionothermal, solid state, and relithiation via redox mediators.⁵

Relithiation via redox mediators uses quinones (redox mediators) to restore lithium content in recovered spent cathode material.^{5,6} The project uses redox mediators to directly recycle End-of-Life (EOL) cathode material using redox mediator chemistry approach. The redox mediators shuttle charges between EOL cathode material and a lithium source such as Li metal or lithium salts (i.e., LiOH, LiCl, Li₂CO₃, etc.).⁶ The process inserts lithium ions into the EOL material without damaging the structure. The project demonstrates a path to scale up process for directly recycling cathode materials. The developed approach is rapid, cheap, operates at relatively low temperature, and the degree of lithium deficiency of the starting EOL cathode is not required to design the redox relithiation reaction.⁶

In FY20 and FY21, this relithiation process was successfully used in direct recycling of chemically delithiated NCM111.⁶ Seven redox mediators were first screened to determine which one had the most compatible reduction potential against lithium and the fastest charge shuttling kinetics. DTBQ redox mediator was selected to carry out relithiation reaction of delithiated NCM111.⁶ Materials were successfully relithiated to a first charge capacity of 182.5 mAh/g, which is comparable to the first charge capacity of the pristine cathode material (184 mAh/g).⁶

In FY22, the redox relithiation approach was used to explore the relithiation of commercial EOL NMC622. However, due to the high cost of the DTBQ redox mediator and the high temperature required to remove it during annealing, an alternative redox mediator was required to optimize the relithiation reaction and reduce cost. The new redox mediator needs to be cheap to reduce the cost of the process, soluble in DME to form lithium rich solvent, and stable during relithiation of EOL NMC622 material.

The initial objective for FY22 was focused on optimizing the redox reaction and reducing cost of the process by introducing a new redox mediator. Different quinones were obtained and screened. A cheap, soluble in DME, and stable redox mediator was selected. This new redox mediator was used to address the next objective which was to transition from relithiating chemically delithiated materials to relithiating commercial EOL

NMC622 materials that had been cycled to 20% capacity loss. Additionally, we were given the objective of scaling up relithiation of EOL materials to 50g batches. The relithiated EOL NMC622 materials were characterized using XRD, ICP, and SEM. The performance was characterized using electrochemical analysis.

In FY22, six new redox mediators were screened to obtain the replacement for DTBQ redox mediator. The new redox mediator was used to relithiate solvent Y EOL NMC622 material provided by Oak Ridge National Laboratory (ORNL) and ANL. The solvent Y EOL NMC622 and the relithiated solvent Y EOL materials were characterized using XRD to study the structure, SEM to study the morphology, and ICP-OES to determine the lithium content. The redox mediator is dissolved in DME to make 0.5M concentration of redox mediator solvent. The redox mediator solvent is reduced when lithium metal is added into the solvent and stirred overnight. Then at 60°C the oxidation reaction takes place when EOL NMC622 is added into the lithium-rich solvent, and the solution is stirred for 2hrs during the reaction. This new redox mediator is unique because it does not need additional lithium source. In the previous work, lithium chip enclosed in a Celgard separator was used during the reaction, however, this is not required for the new process. The relithiated material is filtered and rinsed 3 times with fresh DME before annealing at 720°C for 4hrs. In FY22, both the relithiation reaction and cost of the process were optimized.

In FY21, the redox mediator was determined to be the most expensive component of direct recycling through relithiation via redox mediators by cost modelling using EverBatt. Therefore, cost optimization was explored in FY22. Seven different redox mediators with different chemistries were explored to optimize the redox chemistry relithiation reaction are listed in Table III.3.5.

Table III.3.5 Redox mediator cost and capacities

Redox Mediators	Redox mediator symbol	Cost (\$) Based on Concentrations		Capacity (mAh/g)	
		0.5M	1M	charge	discharge
1,4-Naphthoquinone	NQ	0.73	1.13	173.83	99.44
anthraquinone	AQ	0.83	1.13	175.09	123.59
2,5-di-tert-butylhydroquinone	DTBHQ	1.21	1.50	170.85	130.55
9,10-phenanthrenequinone	PAQ	7.44	7.55	-	-
2-tert-butyl-1,4-benzoquinone	TBBQ	8.55	8.94	129.40	127.75
2,6-di-tert-butyl-1,4-benzoquinone	DTBBQ	13.81	14.10	135.31	99.14
3,5-di-tert-butyl-o-benzoquinone	DTBQ	15.49	15.78	-	-

The factors considered during the selection process were cost, solubility, and redox reaction potential and kinetics for each redox mediator. First, the cost of the redox mediator was determined using their purchase cost from Sigma Aldrich and were compared based on 0.5M and 1M concentrations of the redox mediator. The new redox mediator needed to be cheaper than DTBQ. The calculated cost for 0.5M and 1M concentrations is shown in Table III.3.5. The redox mediators have varying costs with 3,5-di-tert-butyl-o-benzoquinone (DTBQ) being the most expensive and 1,4-Naphthoquinone being the cheapest. Since all the new redox mediators were lower in cost than DTBQ, they all made it through to the next stage of the selection process.

The next step of the selection process was verifying that each redox mediator was soluble in DME which is required to make the lithium rich solvent to carry out relithiation. To test the solubility of each redox mediator, 0.5M and 1M concentrations of the different redox mediators were prepared using 8mL DME and calculated masses. The redox mediators were added into 8mL DME and stirred overnight. As shown in Figure III.3.31, all

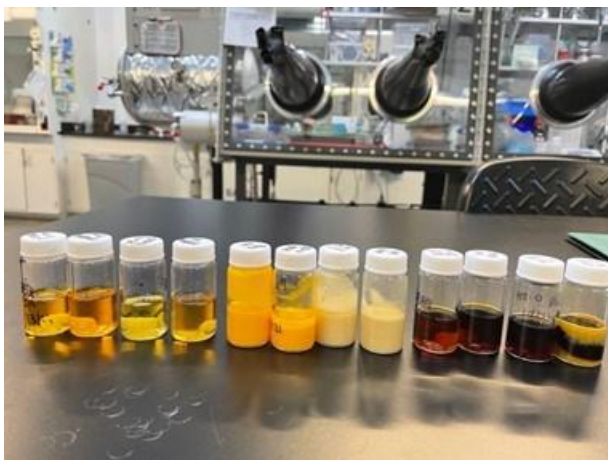


Figure III.3.31 Redox mediator solubility in 1,2-dimethoxyethane (DME).

the redox mediators dissolved in DME except 9,10-phenanthrenequinone (PAQ) and anthraquinone had a partial solubility. Even though anthraquinone is among the cheapest quinone on the list, due to insolubility, it was eliminated along with PAQ.

Finally, the remaining redox mediators were evaluated based on their redox potential against lithium and rapid reaction kinetics while fully relithiating EOL NMC622 material. To determine the most compatible redox mediator with EOL NMC622 material, the 0.5M and 1M concentration redox mediators in DME were used as electrolyte in half type-coin cells. The solvent Y EOL NMC622 was used as a cathode and the lithium metal was used as an anode. Then the coin cells sat at open circuit voltage for 4000 minutes without applied current and the potential of the cell was monitored. All redox mediators had completed the lithiation reaction at 1500 minutes except 9,10-phenanthrenequinone as shown by the potential drops in Figure III.3.32a. Then the coin cells were disassembled. The cathodes were rinsed using fresh DME and then reassembled using 1.2M LiPF_6 EMC:EC 50:50 (v/v) (Gen 2) electrolyte. The reassembled coin cells were then cycled at C/10. Then the capacities were compared. DTBHQ showed the highest discharge capacity of 130.55 mAh/g as shown in Table III.3.5 and Figure III.3.32b, so it was chosen as the new redox mediator for the rest of the results shown for this fiscal year. The structure and morphology of pristine, EOL NMC 622 and relithiated EOL NMC622 material using DTBHQ was compared to evaluate the success of the new redox mediator. The XRD patterns showed no extra peaks for impurities and shifting of the c-axis indicative of lithium reinsertion as shown in Figure III.3.33a. The redox mediator burnt off at 350°C as shown in Figure III.3.33b. Thermogravimetric Analysis (TGA) and Derivative Thermo-Gravimetric (DTG) techniques were used to determine the kinetic parameters of the redox mediator. At around 350°C there is an 89.8% weight loss change in the redox mediator and the rate of change of weight of the redox mediator occurs at 10.2%. Therefore, the heat treatment at 720°C to anneal the relithiated NMC 622 should remove all the redox mediator in the relithiated NMC622 material. The SEM morphology shows similar structure with all the material as shown in Figure III.3.33c. The material structure is well-preserved after relithiation, and no damage is observed after annealing.

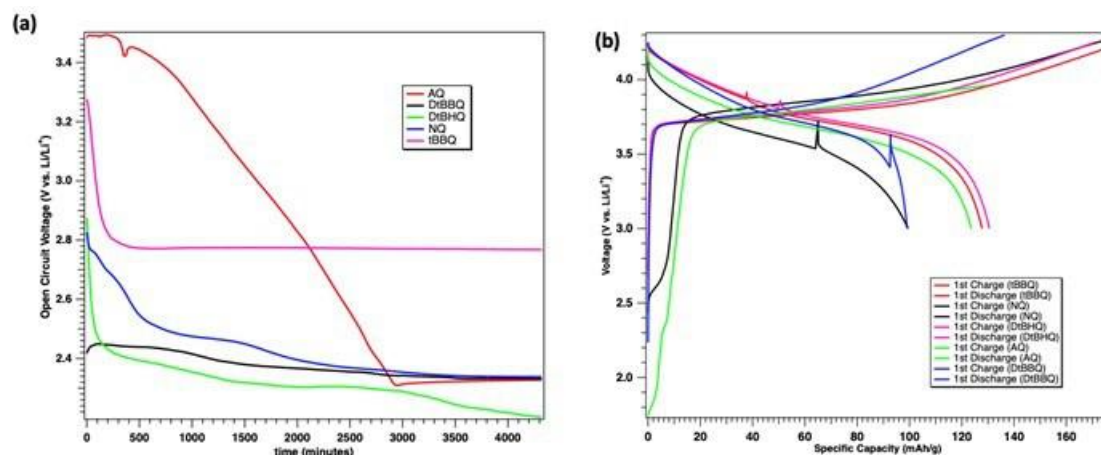


Figure III.3.32 Redox mediator screening (a) open circuit voltage, (b) charge and discharge capacity of the relithiated material

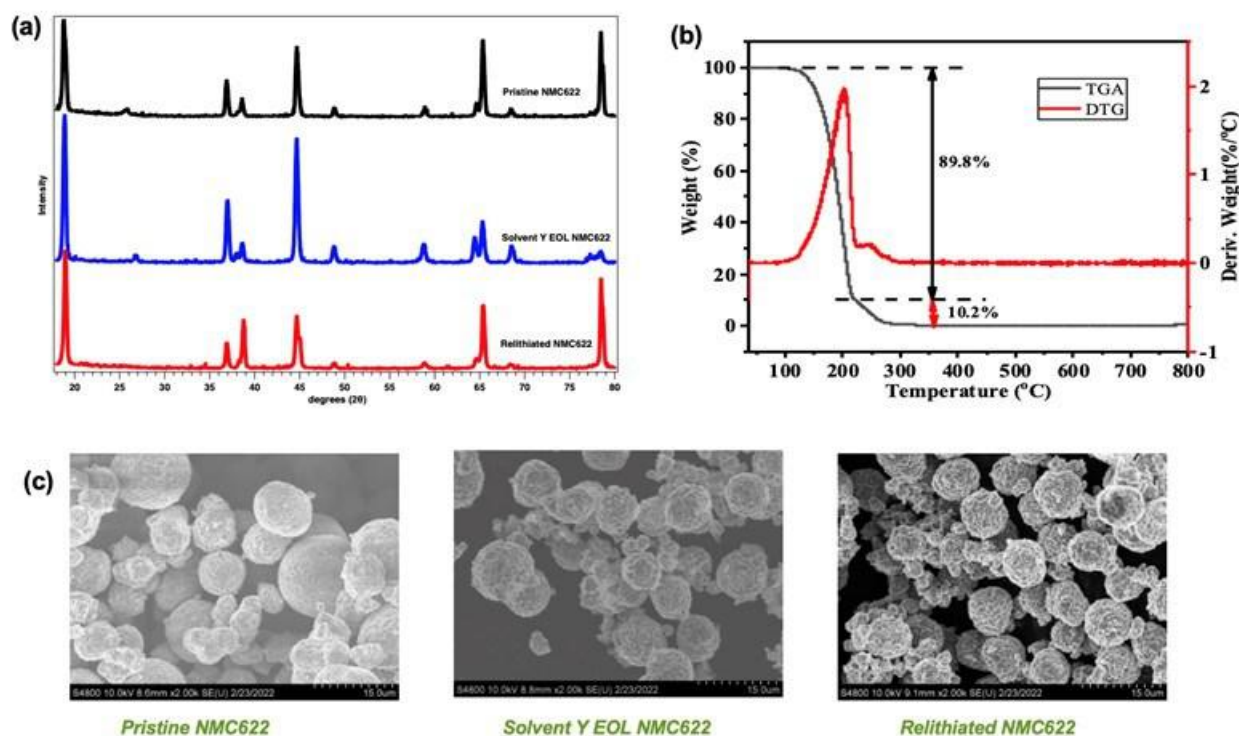


Figure III.3.33 (a) XRD patterns of pristine NMC622, solvent Y EOL NMC622, and relithiated NMC622 materials. (b) decomposition kinetics of redox mediator. (c) morphology images of pristine NMC622, solvent Y EOL NMC622, and relithiated NMC622.

The performance of the relithiated material from redox mediators DTBQ and DTBHQ were also compared. The relithiation of 5g of EOL cathode material using 0.5M concentration of lithium rich DTBHQ and DTBQ redox mediators was carried out. The materials from relithiation using DTBHQ redox mediator showed better C/10 cycling performance compared to materials from relithiation using DTBQ redox mediator from previous work as shown in Figure III.3.34 and Table III.3.6.

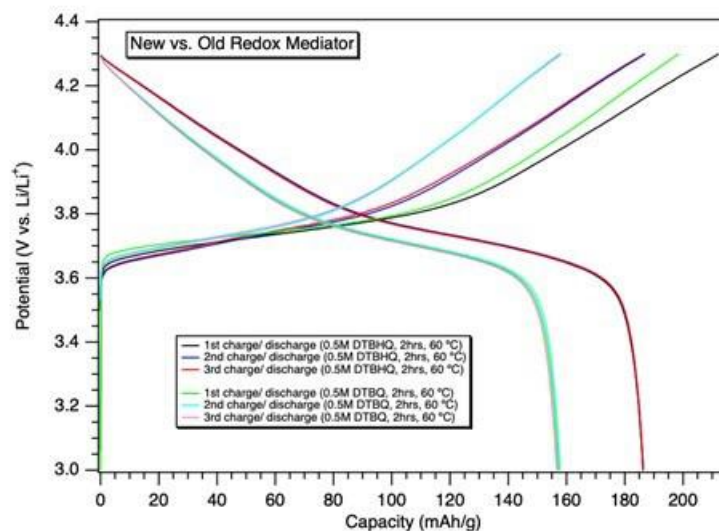


Figure III.3.34 Capacity for materials relithiated using the new and old redox mediators.

Table III.3.6 Capacities for materials relithiated using new and old redox mediators.

Cycle	New Redox Mediator (DTBHQ)		Old Redox Mediator (DTBQ)	
	Charge (mAh/g)	Discharge (mAh/g)	Charge (mAh/g)	Discharge (mAh/g)
1	212.30	186.36	198.61	157.79
2	186.58	186.24	158.26	157.21
3	187.03	186.30	157.70	156.60

ICP-OES data was used to determine the lithium content in the powder after relithiation. The lithium ratio is restored from 0.844 to 1.094 for solvent Y EOL NMC622. The restored lithium content is close to the lithium ratio 1.055 of Targray pristine NMC622. To demonstrate the scalability of this process, 50g of EOL NMC 622 material was relithiated using a 1M DTBHQ solution. The relithiated NMC622 material from the scale up process had lower reversible capacities of around 130 mAh/g compared to the 5g batches shown above. The cause of this drop in capacity for the 50g scale up relithiated NMC622 material is a focus for ongoing research in this project and we are optimistic it can be addressed in the next fiscal year. Potential factors that could be leading to this drop in capacity could include annealing temperature, redox mediator concentration, EOL NMC622 material mass to redox mediator solution ratio or changes in pH of the redox mediator solution at higher volumes.

Electrochemical Relithiation

The scope of this project was to develop a direct recycling method that utilizes electrochemical relithiation for EoL (End of Life) battery cathodes. The electrochemical relithiation protocol developed by this project was optimized for application to large scale direct recycling such as roll to roll processes. This means that the electrochemical relithiation was optimized for rapid relithiation to reduce cost by minimizing the amount of time the EoL cathodes must be in an electrochemical bath during lithiation. Scanning voltage discharge protocols at elevated temperatures have been identified as promising candidates for rapid relithiation of EoL NMC 111 cathodes that were electrochemically aged in coin cells.

In FY22, the aim of this project was to continue to optimize electrochemical relithiation protocols by incorporating model-driven process parameters and applying them a wider range of commercial cathode compositions cycle aged in large format cells. In Q2, this project had a milestone to develop a rapid electrochemical relithiation protocol for end-of-life NMC 622 cathode materials that achieves >95% capacity recovery compared to virgin NMC 622 cathode materials.

Over the course of this project, a novel model-driven technique was developed to design optimal rapid electrochemical relithiation protocols. The EoL material that needed to be relithiated would first be analyzed to determine overall lithium loss and to determine if any surface degradation had occurred that would lead to increased impedance to relithiation. Once the material had been characterized, a novel continuum scale model was utilized for rapid screening of relithiation protocols including multi-step constant current (CC), constant voltage (CV) and scanning voltage options. The model was validated to replicate initial experimental data followed by full parametric variation including varying current rates, scanning voltage step thresholds, scan rates and temperature. Utilizing this model-driven approach was an efficient and reliable way to reduce the time taken to find the optimal relithiation protocol for a given material.

For the FY22 Q2 milestone, a commercial cycled NMC 622 cathode material was provided to test the electrochemical relithiation technique. The available NMC 622 material was cycled at higher temperatures and to a greater degree of capacity loss than our previous NMC 111 materials that were used to validate our electrochemical relithiation technique. The key differences between these two materials affecting the performance of our electrochemical relithiation technique are shown by comparing the exchange current density and diffusivity of the two materials in Figure III.3.35. Both diffusivity and exchange current density of the cycle aged commercial NMC 622 cathode are much lower compared to the NMC 111 material. From this we can conclude that the NMC 622 material has a much higher impedance to relithiation. The previous relithiation protocol developed for the cycled NMC 111 material was used for the EoL NMC 622 material. The protocol involved a high constant current of 2.5C until the voltage reached 3.3V followed by a scanning voltage step to 2.8V. Figure III.3.36a and b show that the high impedance to relithiation causes the potential to drop almost immediately to 3.3V followed by less than 10 mAh/g of capacity restored during the scanning voltage step. After continued model validation of the new commercial NMC 622 material parameters, the new suggested protocol was determined to be a constant current step to 2.8V at C/25 followed by a scanning voltage step from 2.8V to 2.5V at 0.1 mV/s at 60°C. This protocol took about 3 hours which was the minimum time the model predicted for relithiating the commercial NMC 622 material without resorting to higher temperatures requiring more thermally tolerant electrolyte. Reducing the relithiation rate and increasing the temperature for electrochemical relithiation allowed us to restore the first charge capacity of the material to 183 mAh/g at a C/10 rate followed by a reversible charge and discharge capacity of 145 mAh/g. These values show that the electrochemical relithiation technique does not sufficiently restore the material to 95% of the pristine NMC 622 performance.

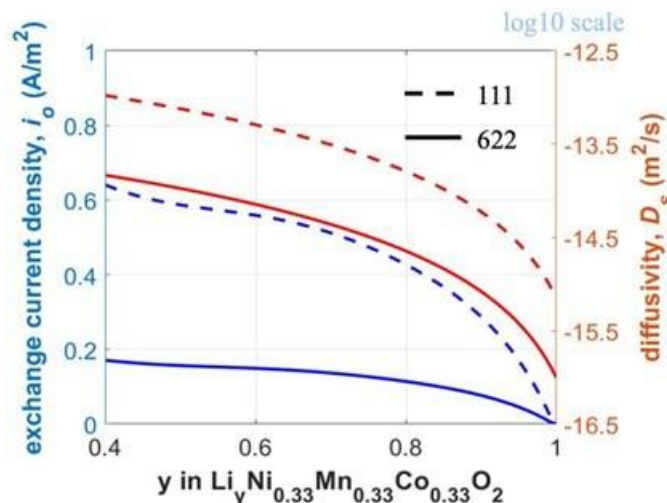


Figure III.3.35 Exchange current density and diffusivity of cycled aged NMC111 and cycle aged commercial NMC 622 cathode materials with respect to lithium content

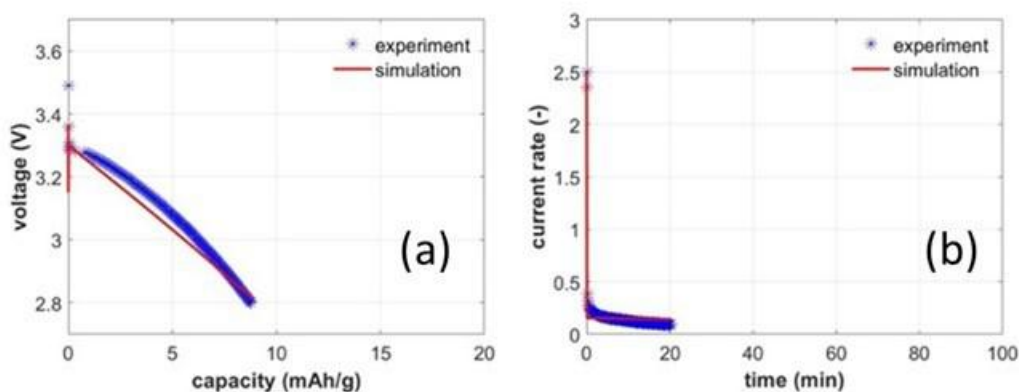


Figure III.3.36 a) Capacity restored to commercial NMC 622 and b) relithiation time for rapid relithiation protocol

Since the electrochemical relithiation method was successful for the cycle degraded NMC 111, but not as successful at restoring the performance of the cycle degraded commercial NMC 622, it was important to understand what the determining factors are for electrochemical relithiation to be successfully applied to an end of life (EoL) cathode material. We chose to characterize the degradation characteristics of the commercial NMC 622 and to apply some potential mitigation techniques to help understand the limitations for the electrochemical relithiation technique when material degradation occurs. Possible sources of degradation in this EoL NMC cathode materials are lithium loss through SEI formation, mechanical degradation, impedance from surface impurities and surface deconstruction. The first degradation mode that we investigated was mechanical degradation of the NMC 622 particles themselves. We checked specifically for excessive interparticle cracking within the primary particles of the NMC 622 using SEM imaging as shown in Figure III.3.37.

significant effect on the cycling performance. These results indicate that the underlying issue preventing electrochemical relithiation from successfully fully relithiating these EoL commercial NMC 622 material is not addressed with the usual solvent rinsing steps we attempted here.

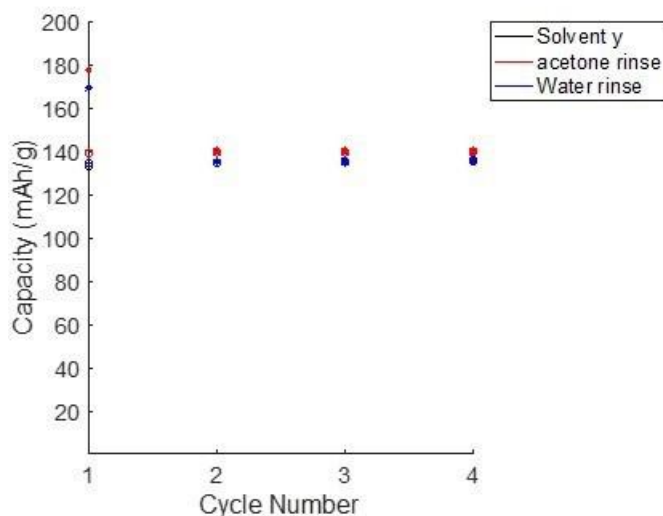


Figure III.3.39 C/10 cycle performance of EoL commercial NMC 622 after additional rinsing step

XRD data was also taken for the EoL electrode material before and after the delamination step and with the previously listed rinsing steps attempted at NREL in order to analyze bulk structural changes. Figure III.3.40 shows the bulk structure of the EoL commercial NMC 622 is not drastically altered after delamination or after any rinsing step other than c-axis shifting inherent in delithiated material. While no rietveld refinement has been done on this set of data at NREL, work from ReCell consortium partners has shown evidence of possible cation exchange in the structure of the NMC 622 material.

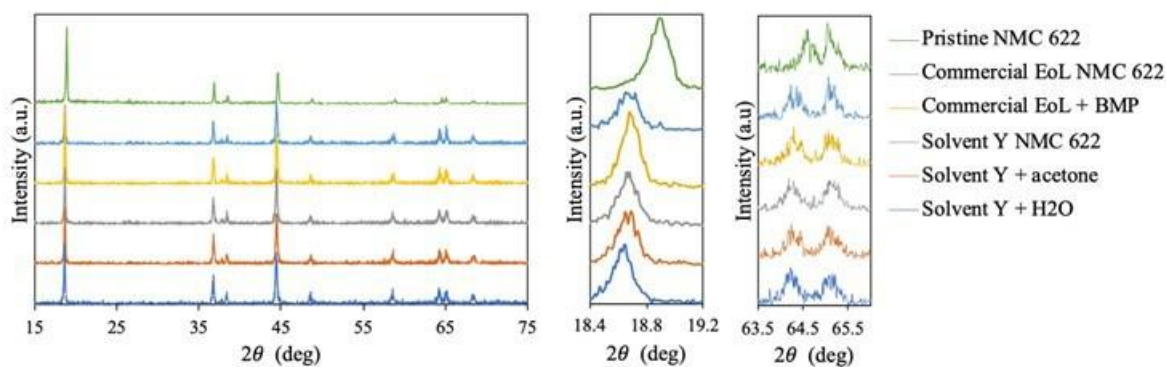


Figure III.3.40 XRD analysis of structure of treated and untreated EoL commercial NMC 622

Solid State Cathode Upcycling

Battery upcycling is a process used to recover materials from previous generations of energy storage materials, reverse the effects of degradation and impurity build-up, and alter the stoichiometry to supply new materials to the market and lower the overall costs of energy storage. A significant issue in this growing market is that batteries supplied to recyclers reflect chemistries from 5-10 years ago, while current cathodes have moved to more nickel-rich, incorporated new dopants, and added coatings to achieve higher energy density and longer-lived materials compositions. As these changes in chemistry and cell design continue to evolve, the materials recovered for recycling are less likely to match with those needed in the current marketplace. In addition to the available materials stream, materials from non-transportation sectors may also play a role in adding anomalous

materials to the waste stream, for instance LiCoO_2 from consumer electronics. We are designing and evaluating methods to upcycle the metal ratios of recovered cathode materials to convert them to more current cathode formulations that are more relevant to the marketplace. Our focus is upcycling our baseline cathode NMC333 ($\text{LiNi}_{0.33}\text{Mn}_{0.33}\text{Co}_{0.33}\text{O}_2$) system to NMC622 and NMC811. Moving towards NMC811 is more than a stoichiometric extension from NMC622 due to small differences in cation ordering and electronic structure that make NMC811 more similar to a stabilized LiNiO_2 type cathode. For upcycling, additional details related to the NMC811 cation diffusion and oxide stability will be investigated. We are working with cross-cutting teams led by Fulya Dogan and Tim Fister to employ additional characterization methods that probe the structural changes in the upcycled material.

The objective is to develop a thermally driven coating-based method that utilizes methods similar to initial CSTR-type synthesis methods to upcycle the stoichiometries of NMC333 to NMC622 and eventually NMC811.

Utilizing a CAMP-supplied NMC333, we have been investigating the role of materials coatings and methods in the upcycling to NMC622. In our previous work we have examined the role of metal salts (nickel, manganese, cobalt, or lithium) deposition in creating a viable stoichiometric coating method, atmosphere, oxidation state of the nickel, complex hydroxide formation, annealing protocols, and the role of time at temperature to produce a quality NMC622 product. In this past year we have improved our material cycling performance significantly by improving the coating and annealing process, and achieving a homogenous cation distribution (by XAS-based and EBSD data) however we have not achieved full expected NMC622 performance. Efforts with the new characterization resources available to the teams are being utilized to investigate non-bulk sources of impedance, interfacial phases, and small level impurities.

The work this past year focused on re-evaluating the 1) annealing processes with a goal to improve performance, 2) investigating various routes to control samples particle size, and 3) work with Tim Fister at APS to examine the role of cation diffusion at temperatures and the metastable nature of the initial surface phases formed.

Several products that were originally prepared from 690°C - 820°C were mixed with additional LiOH and re-annealed to 850°C under oxygen atmosphere. Figure III.3.41 shows the XRD data for a sample originally prepared at 700°C and the 850°C re-anneal. In the XRD, notable differences appear at higher angles, where the re-annealed product shows improved separation between the 108 and 110 peaks, with elimination of an intermediate peak seen in this region. Similar changes were also observed for the other re-annealed products. The morphology changes upon re-annealing were evaluated using SEM (Figure III.3.42). Following annealing, the primary particles at the surface appeared to be better defined and are larger in size. Compared to the overall particle growth from the starting NMC, there was not further overall particle growth as a result of the second annealing step.

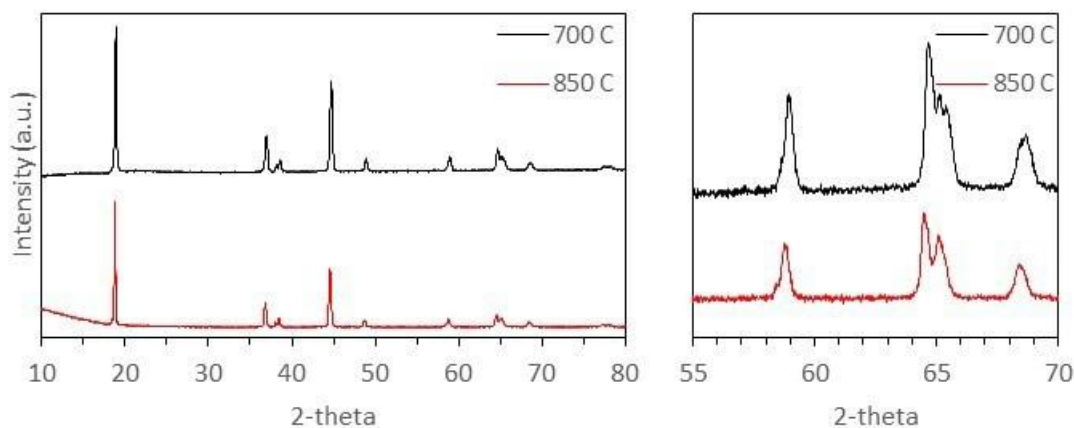


Figure III.3.41 XRD of an upcycling product before and after re-annealing to 850 °C (left) and expanded view of higher angle peaks (right)

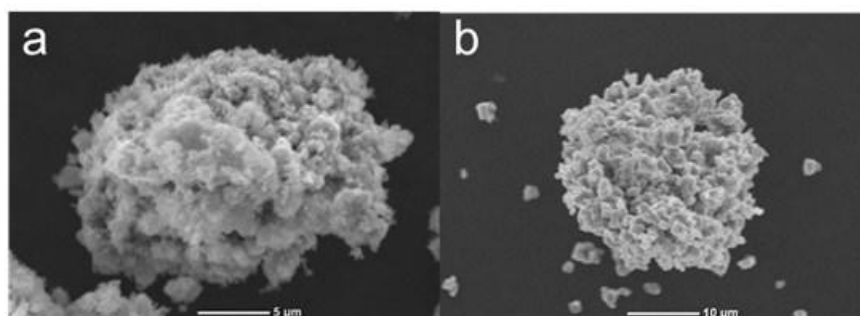


Figure III.3.42 SEM images of (a) upcycling products annealed at 720 °C and (b) re-annealed at 850 °C.

Elemental composition for upcycling products was evaluated using GDOES and EDS (Table III.3.7). The GDOES compositions show lithium contents slightly higher than target values. The amount of lithium added during the re-anneal can be reduced in order to maintain the target content. The transition metal composition remained consistent with the high nickel content from the original annealing. Compared to previous results, there is better agreement in the transition metal contents measure from GDOES and EDS. This may indicate a more uniform elemental distribution than was observed previously. Half cell testing data for the re-annealed upcycling products are shown in Table III.3.8 and Figure III.3.43. The re-anneal of the product originally prepared at 710 °C in air had the highest capacity out of these samples.

Table III.3.7 Elemental composition for re-annealed upcycled products measured using GDOES and EDS (values in parentheses)

Original Temperature	[Li]	[Ni]	[Mn]	[Co]
690°C	1.134	0.622 (0.630)	0.176 (0.185)	0.201 (0.186)
690°C	1.051	0.597 (0.624)	0.211 (0.193)	0.192 (0.184)
710°C	1.130	0.623 (0.625)	0.174 (0.179)	0.203 (0.196)
710°C	1.123	0.597 (0.597)	0.205 (0.219)	0.199 (0.184)
715°C	1.098	0.539 (0.613)	0.236 (0.198)	0.225 (0.189)
820°C	1.146	0.617 (0.632)	0.184 (0.188)	0.199 (0.180)

Table III.3.8 Half-cell data for upcycled products

Original Temperature	690 C air	690 C O ₂	700 C air	700 C O ₂	710 C air	800 C O ₂	820 C air
1 st Cycle Charge (mAh/g)	173.30	163.84	168.22	177.36	179.39	153.58	165.19
1 st Cycle Discharge (mAh/g)	141.38	129.20	129.25	139.55	149.88	121.16	137.06
4 th Cycle Charge (mAh/g)	139.30	122.70	110.23	136.99	146.84	121.65	137.29
4 th Cycle Discharge (mAh/g)	138.33	121.27	108.48	133.91	145.44	120.91	136.35

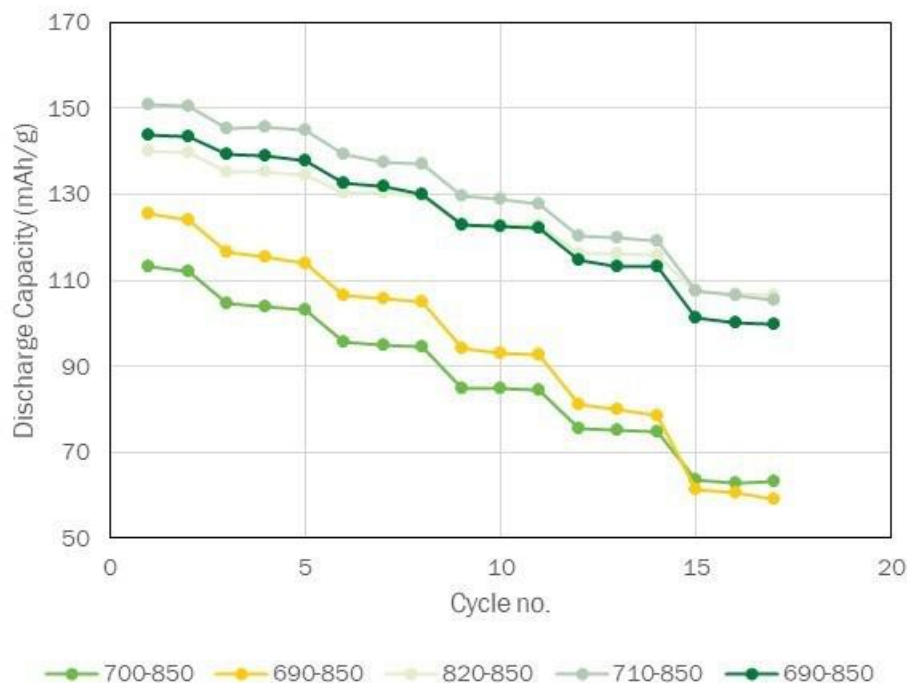


Figure III.3.43 Half-cell rate performance for re-annealed upcycling products

In addition to controlling the stoichiometry of these new samples, we continue to be aware that that possible end-users are typically concerned with the average particle size of the products purchased. In previous years we were able to show that the upcycling of NMC333 to NMC622 using these thermally driven coating methods typically resulted in an average particle size increase from 12-15 μm to 16-18 μm . In response to previous comments, we initiated a particle size reduction study of these materials and evaluated mainly methods to controllably dissolve the surface, once the particles have achieved a homogenous stoichiometry.

Specifically we have used common mineral acids to control the particle size, taking advantage of a relatively straightforward dissolution process. In these studies the performance of the materials was found to have been damaged by the process. Based on TGA data we were able to infer some ion exchange occurs, as expected with acid exposure, and re-lithiation is required. To better understand this particle reduction process we have enlisted Fulya Dogan (CSE/ANL) as our local-environment MAS-NMR expert to evaluate the role of ion-exchange. These tools are useful to ascertain the amount, depth, and environment of inserted protons and will give us a new tool to identify pathways to a less surface destructive process if particle size reduction is deemed an essential component of the ReCell effort.

In support of our upcycling effort, we have initiated a new APS collaboration with Tim Fister to investigate the role of reaction kinetics in forming a viable Li-Ni-O coating on the surface of the NMC333 to drive the product to NMC622. Initial studies indicate that a critical but poorly crystalline phase forms at the interface over a narrow temperature window and that acts to nucleate the desired NMC phase. In addition, related to the coating synthesis, we have seen that the best process appears to limit the amount of excess lithium with sulfate salts as coating precursors. Early data shows that while high temperature XRD shows clean patterns, on cooling residual surface sulfate appears to combine with available lithium to form crystalline Li_2SO_4 . In a situation similar the results seen in the relithiation studies, the materials synthesis and processing needs to be modified to add a wash step to clean the surface to slightly improve the electrochemical performance.

Ionothermal Upcycling

The direct recycling can hardly sustain the fast development of cathode materials because the recycling of End-of-Life lithium batteries (EOL LIBs) generally happen years later after production.^[1] Beyond the direct recycling, the direct upcycling is to upcycle spent cathodes to the next-generation cathodes, which is of great significance to maximize the value of spent materials and to sustain the fast development of LIBs.^[1] The key process of upcycling technology is to heal the compositional and structural defects of degraded Li-deficient cathode particles, which can retain the highly added value of cathode particles to the maximum extent. Unlike the slight weight change during the relithiation process,^[2] a significant weight change of NMC will happen during the upcycling process because of the insertion of Li, Ni, and O, which requires a high temperature to construct layered structure. Besides, the sufficient oxidation of inserted Ni^{2+} to Ni^{3+} is required to minimize lattice oxygen vacancies and Li/Ni antisite defects in Ni-rich NMC. Reciprocal ternary molten salts (RTMS) are those molten salts containing two cation species and two anion species that offer many advantages, such as negligible vapor pressures, negligible flammability, wide liquidus ranges, good thermal stability, and much synthesis flexibility.^[3] The objective of this project is to develop a cost-effective ionothermal process to upcycle chemically delithiated NMC111(D-NMC111) to NMC 622 in reciprocal ternary molten salts (RTMS) at ambient pressure.

The objective is to develop an ionothermal flux method based on reciprocal ternary molten salts (RTMS) to upcycle D-NMC 111 to Ni-rich NMCs (e.g. NMC622 and NMC811).

In FY22, ionothermal upcycling experiments of D-NMC111 to NMC622 has been extensively investigated under different reaction conditions. The effect of lithium and nickel precursors in RTMS, different temperatures, and reaction time have been studied. The upcycled materials have been analyzed by various characterization techniques including TGA, XRD, SEM, and ICP-OES, which validated our feasible ionothermal approaches for not only restoring Li into D-NMC111 but also upcycling D-NMC111 to NMC622. Systematic lab-scale experiments have been performed and investigated. The scale-up experiments (50 g) have been performed for the full cell tests at ANL_CAMP. The ionothermal upcycling of D-NMC 111 to NMC 811 has been initially investigated.

A high-temperature flux method based on reciprocal ternary molten salts (RTMS) fluxes for upcycling D-NMC111 to NMC622 (Up-NMC622) has been optimized (Figure III.3.44).

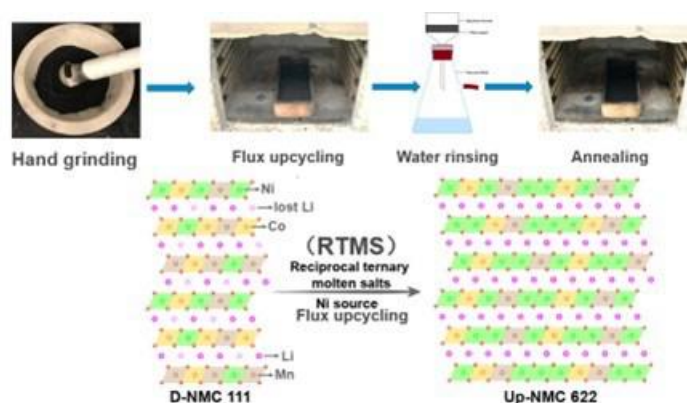


Figure III.3.44 Schematic illustration of ionothermal upcycling process.

Compared to D-NMC111, NMC622 has a narrower peak splitting between (108) and (110) in XRD pattern due to its higher Ni content (Figure III.3.45). The XRD patterns of Up-NMC622 and Pristine NMC622 reveal same features that the split between (108) and (110) in XRD pattern of Up-NMC622 is similar to that of P-NMC622 (0.56° vs 0.55°). D-NMC 111 had a chemical composition of $\text{Li}_{0.93}\text{Ni}_{0.33}\text{Co}_{0.33}\text{Mn}_{0.33}\text{O}_2$ calculated from inductively coupled-plasma optical emission spectroscopy (ICP-OES) results. The chemical composition

of Up-NMC622 is $\text{Li}_{1.08}\text{Ni}_{0.63}\text{Co}_{0.19}\text{Mn}_{0.18}\text{O}_2$, almost coincides with that of Pristine NMC622 ($\text{Li}_{1.05}\text{Ni}_{0.62}\text{Co}_{0.19}\text{Mn}_{0.20}\text{O}_2$), suggesting the successful upcycling in chemical composition (Figure III.3.46).

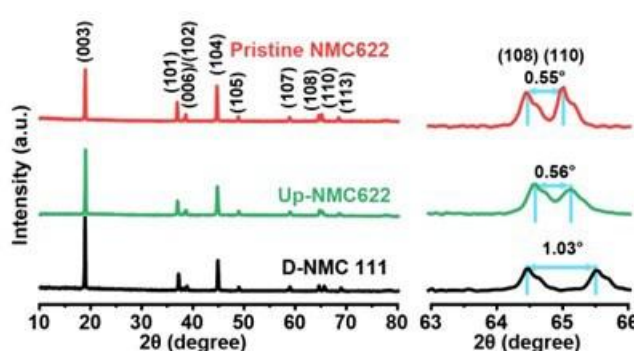


Figure III.3.45 XRD patterns showing survey spectrum and zoom-in peaks of D-NMC111, Pristine NMC622, and Up-NMC622.

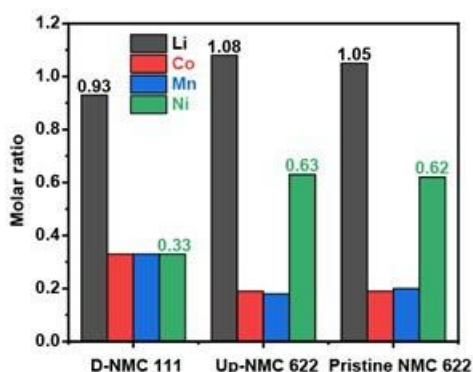


Figure III.3.46 Metal molar ratios of D-NMC 111, Pristine NMC622, and Up-NMC622 based on ICP results.

All the NMC samples were used as active materials in cathodes and paired with Li foil to evaluate their half-cell electrochemical performance. As shown in Figure III.3.47A, the first charge capacity of Up-NMC622 is 195.4 mAh/g, close to that of pristine NMC622 (197.3 mAh/g), much higher than that of D-NMC 111 (140.5 mAh/g). In addition, the charge-discharge capacities of Up-NMC622 are close to those of Pristine NMC622 (Figure III.3.47C), and much larger than that of D-NMC111 during 100 cycles, validate the sustainable superior performance of Up-NMC622 in half-cell tests. In full cell tests, Up-NMC 622 exhibited similar capacities to pristine NMC622, and higher capacities than D-NMC 111 over 100 cycles at a higher specific current of 200 mA/g. Therefore, the RTMS flux method is effective for the upcycling of D-NMC111 to Up-NMC622. The ionothermal upcycling was scaled up to 50 g. 50 g of Up-NMC622 has been sent to ANL_CAMP for full pouch cell tests.

The upcycling of D-NMC111 to Up-NMC811 was also investigated by RTMS flux method. After upcycling, the chemical composition of Up-NMC811 is $\text{Li}_{1.08}\text{Ni}_{0.79}\text{Co}_{0.11}\text{Mn}_{0.10}\text{O}_2$, which coincides with that of P-NMC 811 ($\text{Li}_{1.07}\text{Ni}_{0.76}\text{Co}_{0.12}\text{Mn}_{0.12}\text{O}_2$), suggesting the successful upcycling of chemical composition. The XRD patterns of Up-NMC811 and Pristine NMC811 reveal same features that the split between (108) and (110) in XRD pattern of Up-NMC811 is similar to that of P-NMC811 (0.40° vs 0.46°). In half-cell tests, the first charge capacity of Up-NMC811 is almost the same as that of Pristine NMC811 (215.2 vs 216.2 mAh/g). However, the coulombic efficiency of Up-NMC811 is lower than that of Pristine NMC811, resulting in a low discharge capacity (153.7 mAh/g). Though Up-NMC811 is not as good as Pristine NMC811 in battery performance, Up-NMC811 still has upgraded charge-discharge capacities compared to D-NMC111. Further optimization of upcycling conditions for NMC811 will be done in the next year.

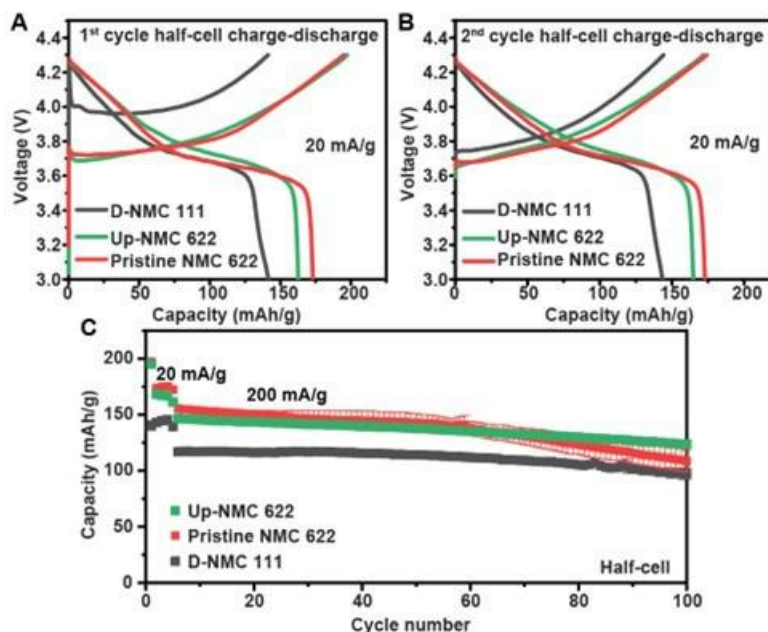


Figure III.3.47 (A) The first cycle charge/discharge curves of NMCs for half-cell tests. (B) The second cycle charge/discharge curves of NMCs for half-cell tests. (C) Cycle performance of NMCs for half-cell tests.

Hydrothermal Upcycling

Battery industry is advancing to new cell chemistries to improve the energy density and reduce the cell cost. Therefore, the last generation of cells which used NCM111 (or other low-Ni chemistry) as the cathode material may not be utilized in large scales in future batteries. Therefore, it is crucial to develop upcycling technology that can convert NCM111 (or low-Ni) cathodes into other materials such as high-Ni cathodes to provide comparable performance and cost to the most advanced cathode materials. The direct regeneration method combining hydrothermal relithiation with subsequent short annealing developed by UCSD team can successfully resolve the compositional and structural defects of chemically delithiated NCM111 (D-NCM111). It also recovers the electrochemical performance to the same level as pristine Toda NCM111 (T-NCM111).^{1,2} Besides direct recycling of degraded NCM111, this material will be exploited as a feedstock to produce other cathodes with high Ni content (e.g., NCM433, NCM622, NCM811), for upcycling, which can potentially deliver much higher energy density and are more relevant to today's market. This effort will focus on establishing effective direct upcycling method of D-NCM111 into NCM433 or other high-performance cathodes via hydrothermal method. In addition, for high-nickel NCM-based materials, several shortcomings such as poor thermal stability, unstable surface structure, too high surface alkali content, and fast degradation during storage in air have been identified in previous reports.^{3,4} Therefore, further improving the performance of polycrystal NCM-based materials, for upcycling, which delivers higher energy density and superior stability is also necessary.

Degraded NCM111 was utilized as a feedstock to produce other cathodes with high Ni content (e.g., NCM433, NCM622, NCM811) to upgrade capacity or to further improve the performance of polycrystal NCM-based materials, for upcycling, which can deliver higher energy density and superior stability and can meet the dramatic expansion of requirements in today's market.

Two approaches were focused on: 1) exploring new processing steps to convert polycrystalline particles to single crystalline particles by increasing Ni content and tuning morphology and 2) exploring surface coating to suppress the side reactions between the cathode and electrolyte as well as enhancing the structural stability of the particles in order to improve the performance of regenerated high-Ni NCM-based materials.

In the past FY, we upcycled D-NCM111 and doped with Ni via hydrothermal (HT-upcycle-Ni doped) and post annealing method (HS-upcycle-Ni doped). As for the SEM of upcycled D-NCM111 doped with Ni shown in Figure III.3.48, there are some small particle aggregates on the surface of upcycled NCM111. These small particle depositions may be caused by the small amount of doped Ni that only grew on the NCM111 surface, will increase the charge transfer resistance at the electrode/electrolyte interface. From cycling stability data, we can also observe that upcycled NCM111 with Ni doped via hydrothermal method reveals superior electrochemical performance compared with delithiated NCM111, but still shows worse discharge capacity than that of pristine NCM111 due to some small particles aggregates on the surface of the upcycled NCM111. Considering these and previous results, phase separation issues remain a major concern with hydrothermal upcycling process. We believe a more “aggressive” process is needed for upcycling, since it is difficult for the oxidation reaction to occur in aqueous solution for D-NCM111, but easier to proceed during sintering process.

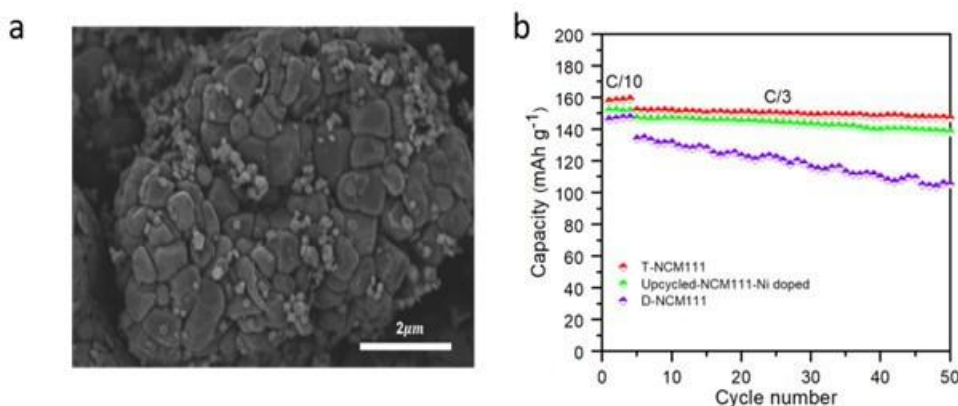


Figure III.3.48 (a) SEM of upcycled D-NCM111 with Ni doped via hydrothermal and post annealing method (HS-upcycle-Ni doped). (b) Cycling stability of HS-upcycle-Ni doped, the pristine NCM111 and delithiated NCM111.

In a parallel effort, we successfully upgraded polycrystalline delithiated NCM111 (D-NCM111) into single crystalline NCM433, NCM 622 and NCM811. As shown in Figure III.3.49, the upcycling single crystal NCM622 (Upcycling-NCM622) has the better cycling retention under C/3 long cycling due to its integrity of single crystal. In addition, the upcycling NCM811 (Upcycling-NCM811) has the similar discharge capacity, on par with the pristine NCM811 at 0.1C. As the result of the micro-sized single crystal particles obtained during the upcycling process, the rate performance of high nickel cathodes is significantly improved.

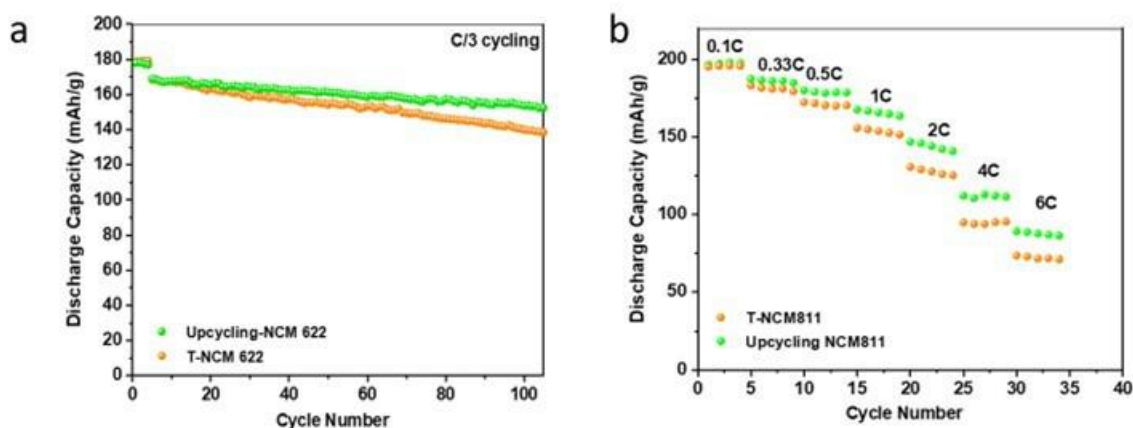


Figure III.3.49 (a) Cycling stability of upcycling NCM622 (Upcycling-NCM622) and pristine NCM622. (b) Rate performance of upcycling NCM811 (Upcycling-NCM811) and pristine NCM811.

To improve the performance of high-nickel NCM-based materials, in the past quarters, we have also been working on using coating materials to suppress the side reactions between the cathode and electrolyte as well as enhancing the structural stability of the particles. We demonstrated a facile, dry-coating strategy to apply B coating on the hydrothermal regenerated high-Ni NCM-based material (NCM622). The cycling performance of the regenerated NCM622 with different amount of B coating applied (HS-NCM622-B1 and HS-NCM622-B2) was enhanced compared with the uncoated regenerated NCM622 sample (HS-NCM622). The regenerated NCM622 sample with B coating also shows enhanced air stability compared with the uncoated pristine sample via half-cell test. The existence of surface impurities (Li_2CO_3) can be obviously observed on the surface of aged pristine NCM622 (Aged T-NCM622) and aged regenerated NCM622 (Aged HS-NCM622) samples after they were stored in the moist air for 7 days. The FT-IR spectra shown in Figure III.3.50 display the absorption peaks at 1496, 1425, and 861 cm^{-1} that correspond to the vibration of the CO_3^{2-} group.⁴ This further confirms the existence of surface impurities on the stored materials. However, with B coating, even after being stored in moist air for 7 days, no obvious peaks corresponding to Li_2CO_3 or LiOH for the aged, regenerated NCM622 coated by B (Aged HS-NCM622-B coating) can be observed. This may be due to B coating behaving as an inert layer to suppress undesired side reactions.

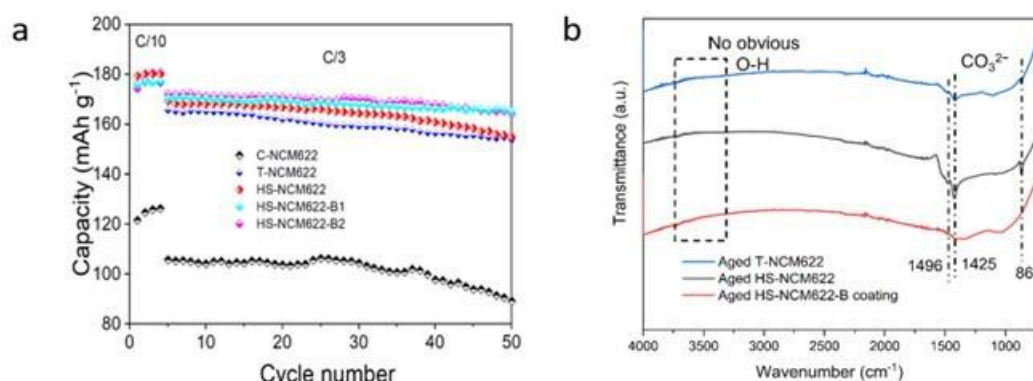


Figure III.3.50 (a) Cycling stability of the cycled NCM622, regenerated NCM622 and regenerated NCM622 coated by B (HS-NCM622, HS-NCM622-B1 and HS-NCM622-B2) as well as the pristine NCM622. (b) FT-IR spectra of aged pristine NCM622, aged regenerated NCM622 samples, aged regenerated NCM622 coated by B (Aged T-NCM622, Aged HS-NCM622, Aged HS-NCM622-B coating).

Single Crystal Cathode Production

Lithium-ion batteries, especially cathode materials, are very dynamic. The cathode materials in spent lithium-ion batteries may not find a market even if high quality materials can be recovered. For example, NMC111 is one of the common cathode materials for EV batteries, however, the industry is moving to high-nickel NMC to increase the energy density and lower the cost. Single-crystal cathode materials hold the promise of better performance in terms of cycle life and rate performance. Conventional cathode materials are secondary particles that include numerous primary particles, which can be potential single-crystal particles. In this project, the team will develop methods to upgrade NMC polycrystal materials to single crystal NMC particles.

We have successfully upcycled polycrystalline $\text{LiNi}_{1/3}\text{Mn}_{1/3}\text{Co}_{1/3}\text{O}_2$ (NMC111) and $\text{LiNi}_{0.6}\text{Mn}_{0.2}\text{Co}_{0.2}\text{O}_2$ (NMC622) into single crystal structure on a bench scale. Both upcycled single crystal NMC111 and NMC622 (SC-NMC111, SC-NMC622) showed comparable or better rate and cycle performance than polycrystalline NMC111 and NMC622. However, in the scaled-up experiment of NMC111, upcycled SC-NMC111 exhibited a worse cycle performance. Furthermore, we found it had a different phenomenon when applied to $\text{LiNi}_{0.8}\text{Mn}_{0.1}\text{Co}_{0.1}\text{O}_2$ (NMC811). Therefore, in FY22, we will improve the cycle performance of SC-NMC111 in the scaled-up experiment and further understand the mechanism of the different phenomenon in NMC811 to produce SC-NMC811 with promised performance.

In FY22, we etched another batch of NMC111 for scale up experiment. More Li salt was added to ensure enough Li in the single crystal cathode powder. The morphology, structure and composition were confirmed by SEM, XRD and ICP-MS. Then, the electrochemical performance of scaled up SC-NMC111 was tested by coin cells. To understand the different phenomenon in NMC811, XRD is applied to understand the structure change. And XPS and Raman are used to investigate the surface composition and chemical state change. In addition, the overview composition change is monitored by ICP-MS. At last, the electrochemical performance of SC-NMC811 is evaluated by coin cells.

To scale up the process, we enlarged the equipment as Figure III.3.51a shows. We etched 100g commercial NMC111 and successfully converted it to single crystal morphology with good layered structure (Figure III.3.51b and c). In Table III.3.9, the content of transition metals kept the ratio of 1:1:1. And the Li content was restored to 1.10 after sintering.

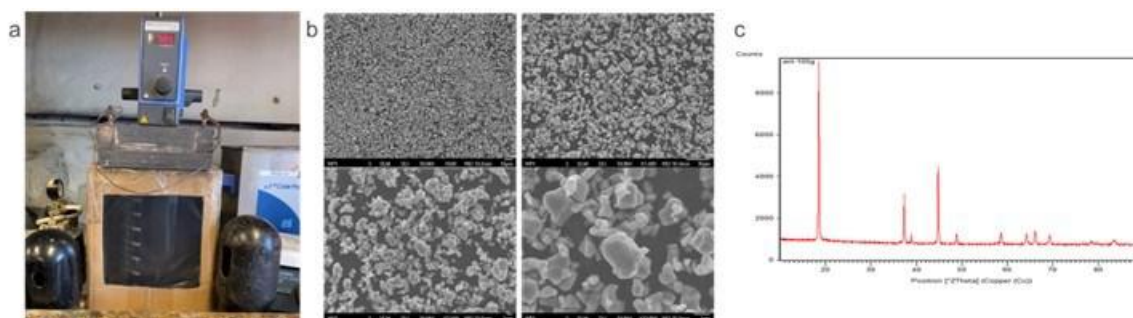


Figure III.3.51 (a) equipment for scale up experiment; (b) morphology of SC-NMC111-100g; (c) XRD pattern of SC-NMC111-100g.

Table III.3.9 ICP-MS results of SC-NMC111-100g.

ICP	Li	Ni	Mn	Co
SC-NMC111-100g	1.10	0.34	0.33	0.34

Then, the SC-NMC111-100g was used to build coin cells to confirm the electrochemical performance. In Figure III.3.52a and b show the rate and cycle performance comparison of SC-NMC111-100g and ANL-100g-Baseline. The discharge capacity of SC-NMC111-100g is slightly higher than ANL-100g-Baseline under most current density. And after 100 cycles, the capacity retention of SC-NMC111-100g is also better than ANL-100g-Baseline.

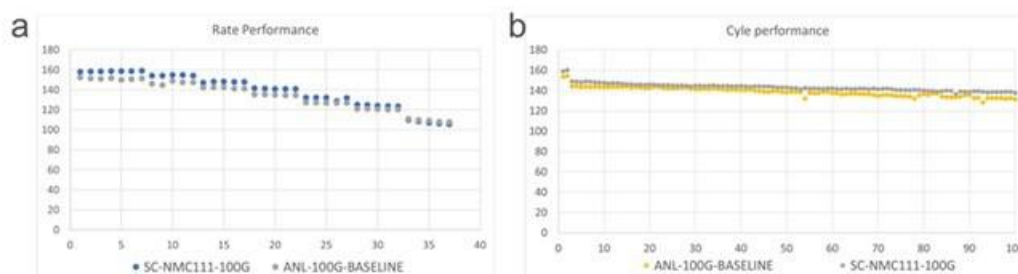


Figure III.3.52 (a) rate performance comparison of SC-NMC111-100g and ANL-100g-Baseline; (b) cycle performance comparison between SC-NMC111-100g and ANL-100g-Baseline.

Then, the upcycling process was applied to NMC811. We noticed that there is a different phenomenon for NMC811 during etching. The dissolving percentage of lithium and transition metals were recorded by ICP-MS. At first 5 hours, the content of Li and NMC dissolved in the sulfuric acid increased with time. However,

after 5 hours, the dissolving percentage of Mn decreased with time, indicating the precipitation of Mn during the etching process.¹

To investigate surface conditions, Raman and XPS were employed. Figure III.3.53a shows the Raman spectra. SC811-25hrs sample shows two different types of peaks, which means that the precipitation of Mn may be not uniform. All main peaks shift to 600 cm^{-1} , indicating the increasing Mn content and decreasing Ni content.² XPS survey peaks are shown in Figure III.3.53b. The overall intensity of Etched-NMC811-25hrs is lower than the other two samples, due to the formation of manganese oxide covered on the surface of particles. All transition metal peaks of Etched-NMC811-2hrs are the strongest, indicating that more transition metals are exposed by etching process. Figure III.3.53c exhibits the Mn 2p spectra of all samples and the composition of Mn^{3+} and Mn^{4+} is calculated.³ The Etched-NMC811-25HRS has a strong Mn 2p spectra compared to Control811 and Etched-NMC811-2hrs indicating the possibility of manganese-rich on the particle surface. And for 2 hours etching, Mn reduces to lower valance state because of O oxidation and Li^+/H^+ exchange. Then, prolonging the etching time, the higher valance state of Mn presents. This may be attributed to the formation of Mn-rich oxide coating on the surface. To compensate for the charge differences, the overall valance state increase on the surface. Due to the increase amount of Mn^{4+} and combined with Raman data, the small quantity of spinel phase possibly presented is MnO_2 .

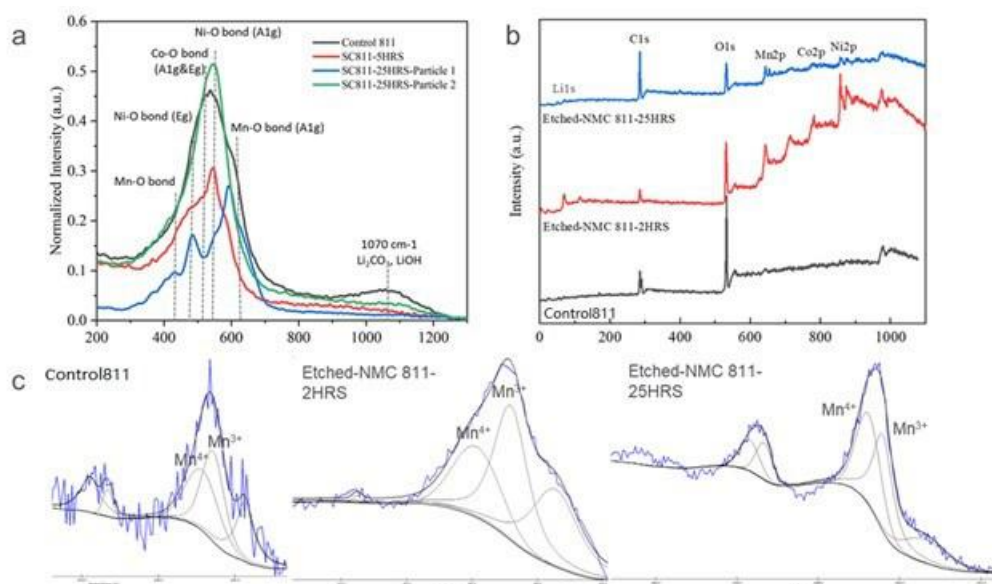
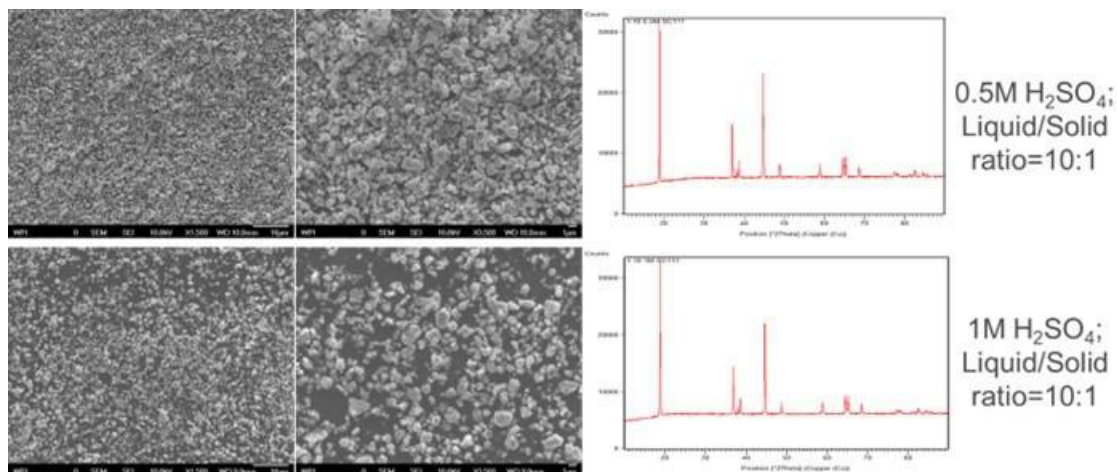


Figure III.3.53 (a) Raman Spectra of Control811, SC811-5hrs, and SC811-25hrs; (b) XPS survey peaks of Etched-NMC811-25hrs, Etched-NMC811-2hrs, and Control811; (c) Mn2p spectra of Control811, Etched-NMC811-2hrs, and Etched-NMC811-25hrs.

To further reduce the cost of the upcycling process, we tried to reduce the amount of sulfuric acid. Two different concentrations of H_2SO_4 were used in the etching process. One is 0.5M, which keeps the same concentration as previous experiments. Another is 1M, which keeps the same concentration of H^+ as in previous experiments. In Figure III.3.54, polycrystal NMC111 was successfully converted to single crystal NMC111 in both sulfuric acids with good layered structure. Then, the elements composition in the solution and powder was studied by ICP-MS in Table III.3.10. In both etching solutions, the amount of dissolved elements is significantly decreased, resulting in a higher yield. Besides, in 0.5M H_2SO_4 etched powder, the Li content is close to 1, leading to fewer Li sources required for restoring it back to 1. However, in the 1M H_2SO_4 etched powder, the Li content is similar to previous experiments, because of the same concentration of H^+ .

Table III.3.10 ICP-MS results for etched solution and etched powder.

	Li	Ni	Mn	Co
0.5M EC solution (%)	9.3	3.6	3.7	3.5
0.5M EC powder (molar ratio)	0.98	0.33	0.33	0.34
1M EC solution (%)	17.2	7.0	7.2	7.6
1M EC powder (molar ratio)	0.62	0.33	0.33	0.34

Figure III.3.54 Morphology and structure results for NMC111 etched in 0.5M H₂SO₄ and 1M H₂SO₄.

Role of Impurities in Recycled Cathodes

The hydrometallurgical method has become a major approach in lithium-ion battery recycling industry, due to its high productivity, low cost, wide applicability as well as ideal recovery efficiency.¹ In order to improve its design and control over manufacturing process to enable a stable and high-quality output, a lot of resources have been invested in related research fields. The most important step within hydrometallurgy recycling stream is to synthesize precursor materials via chemical co-precipitation reaction. Specifically, metal sulfate solution is pumped into a continuous stirred-tank reactor (CSTR) to precipitate out $M(OH)_2$ (M = transition metal complex) in alkaline environment. Precursor $M(OH)_2$ is then sintered with lithium source to obtain final $LiMO_2$ cathode.

In real practice, spent lithium-ion batteries (LIBs) are firstly shredded, followed by a series of separation, acid leaching and purification procedures. The resulting solution, MSO_4 , contains all key elements in NCM cathodes (Ni, Co and Mn) that are intended to be recovered. However, a variety of impurities could be introduced into the metal sulfate solution during the process which may impact on properties of the final cathode product. The main challenge for hydro recycling is to ensure the properties of recovered materials are as good as those of virgin ones. Therefore, to understand the impacts on recovered NCM cathodes from different impurities is essential for hydrometallurgy recycling.

The project objective is to determine the impacts of different impurities on the recovered NCM622 precursor and cathode materials via hydrometallurgy method. The possible impurities in metal sulfate solution can be categorized into three groups: cations, insoluble particles, and anions. It is expected that different types of impurities may affect the material properties in different ways. To have a thorough understanding of the possible impacts brought by different impurities on the recovered materials can offer a guidance for hydrometallurgy recycling in real industrial practice. In this case, we could avoid the adverse outcomes and select the favorable ones. More importantly, the hydro recycling process can be altered in advance to optimize the output and to reduce the unnecessary losses.

To fully understand the impacts of impurity on recovered materials in hydrometallurgy recycling, we started this contamination study to investigate the possible changes between virgin materials and impurity-affected materials that were synthesized via hydrometallurgy method with relevant impurity involved during process. Metal sulfate solution ($\text{Ni}:\text{Co}:\text{Mn} = 6:2:2$) was used in co-precipitation reaction to get virgin precursor then followed by sintering with Li_2CO_3 to obtain virgin NCM622 cathode as the baseline. Then the impurity-affected materials were obtained by adding relevant impurity substances into the metal sulfate solution. After the same production process, both virgin and impurity-affected materials were carefully analyzed and compared against each other to reveal the differences then discover the reasons behind it. In the year of 2022, we have studied the phosphate impurity (PO_4^{3-}) under this project. The anion impurity PO_4^{3-} usually comes from the hydrolysis of lithium salt (LiPF_6) or the acid dissolution of LiFePO_4 cathode.² The virgin cathode (VNCM) and phosphate-affected cathode (PNCM) were successfully synthesized via co-precipitation. And the subsequent characterization and analysis were completed.

According to the SEM data shown in Figure III.3.55, both as-prepared precursor and cathode particles quickly lose spherical shape and shrink rapidly with the impurity concentration rises. In particular, the particle morphology becomes quite irregular and derives from the spherical appearance under 5 at% phosphate level. It indicates that PO_4^{3-} ions have a negative impact on the nucleation and growth process of the $\text{M}(\text{OH})_2$ during co-precipitation, with the effecting being concentration dependent.

The XRD patterns in Figure III.3.56a show that all cathode materials have a good crystallinity up to 5 at% phosphate impurity. However, three additional peaks are detected in the range of 21 deg to 35 deg in 5PNCM, which are associated with Li_3PO_4 (LPO) extra phase. The existence of the impurity phase LPO in PNCM cathode materials is further confirmed by the technique XPS and TEM. It is found that PO_4^{3-} ions are embedded in precursor after co-precipitation synthesis. They react with Li^+ ions during sintering to form segregated LPO impurity phases, which eventually remain distributed throughout the cathode particles.

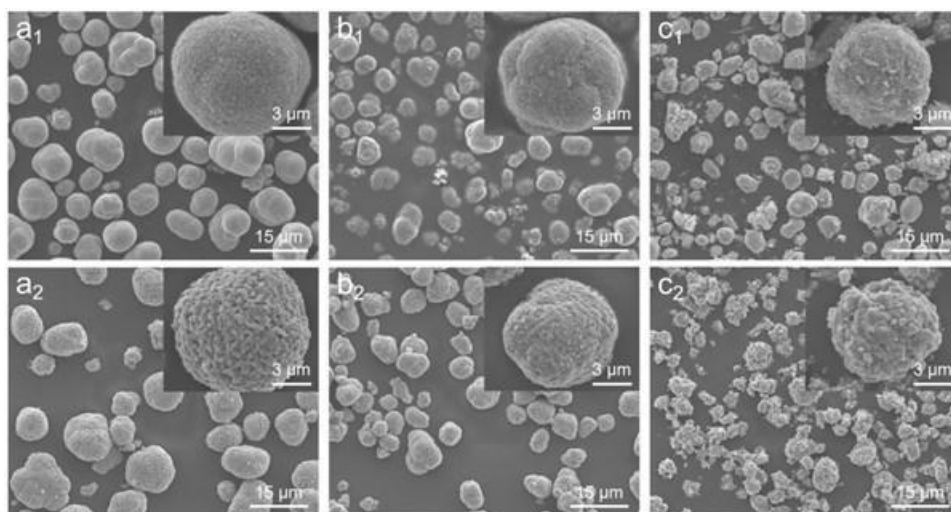


Figure III.3.55 SEM images of 0.2PNCM (a1, a2), 1PNCM (b1, b2) and 5PNCM (c1, c2) with precursors shown in row 1 and cathodes in row 2. (Insets: images at higher magnification).

The detailed crystallographic parameters are calculated by Rietveld refinement given in Table III.3.11. Both a and c axis are intended to expand under the influence of phosphate impurity. The most obvious change is the increase of the cation mixing degree from VNCM to 5PNCM. In particular, 5PNCM exhibits a cation mixing degree of 8.2%, more than double of the VNCM. The abnormal increase in cation mixing may result from incomplete lithiation of the Ni-rich component of the cathode. It is hypothesized that some lithium reacts preferentially with the phosphate ions to form the Li_3PO_4 impurity phase. This would result in a slight lithium

deficiency in cathode lattice, which could increase the degree of cation mixing during sintering and finally deteriorate the material properties.

According to the electrochemical testing results as illustrated in Figure III.3.56, it is found that the discharge capacity goes down rapidly with the increase of impurity involved for all cases. In 1/3C test, the virgin cathode delivers the best capacity of 157 mAh/g after 100 cycles.

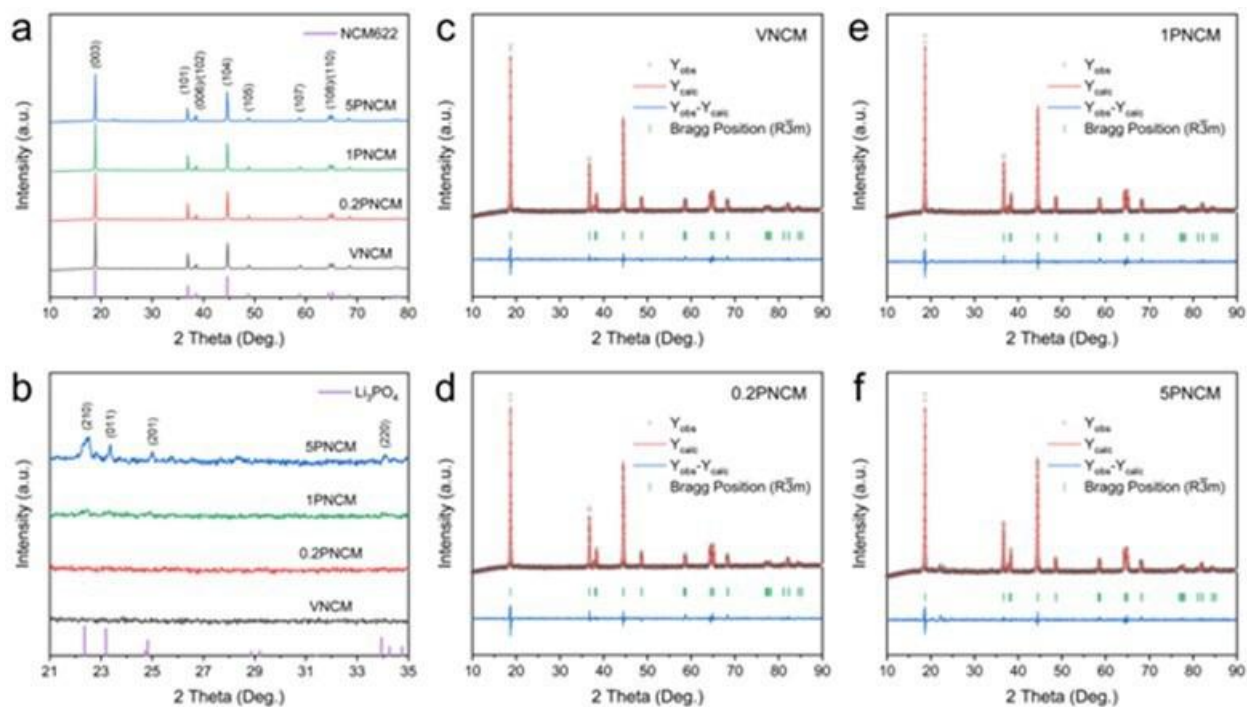


Figure III.3.56 XRD patterns of (a) cathodes and (b) impurity phase region in cathodes. (c-f) Refinement results of VNCM, 0.2PNCM, 1PNCM, and 5PNCM cathodes.

Table III.3.11 Rietveld refinement results of the prepared NCM622 cathodes

Sample	a (Å)	c (Å)	V (Å ³)	NiLi (%)	Chi ²
VNCM	2.867	14.222	101.23	3.52	2.92
0.2PNCM	2.867	14.226	101.30	4.32	2.99
1PNCM	2.868	14.229	101.35	4.92	2.84
5PNCM	2.873	14.231	101.72	8.22	2.67

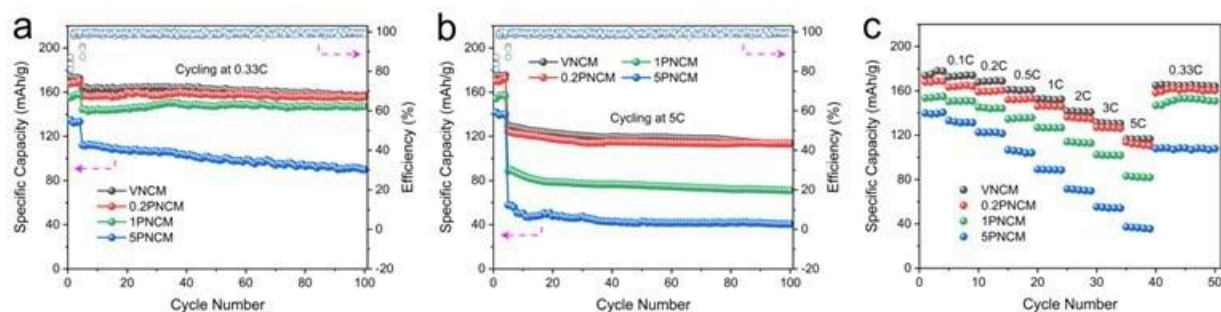


Figure III.3.57 Electrochemical performance of as-prepared samples. (a) cycle at 0.33C, (b) cycle at 5C, (c) rate to 5C.

And the discharge capacity drops to 147 mAh/g for 1PNCM, then it further declines to 91 mAh/g for 5PNCM. A same phenomenon is also observed in 5C cycling test as shown in Figure III.3.57b. For the rate performance, it is clear that all impurity-based samples have worse results compared to the virgin counterpart. Besides, the specific discharge capacity degrades fast as the impurity level increases.

Hence, it is evident that the electrochemical properties of the recovered cathodes could be seriously damaged by the presence of phosphate impurity. The deterioration of particle morphology, the increase of cation mixing, and the presence of secondary phases are believed to be responsible for the observed performance degradation.

Recovery of Other Materials

Cell Preprocessing

Pre-processing cells is a critical step in ReCell's direct recycling model. The configuration of battery packs, modules, and cells varies between different electric vehicle models and presents significant challenges for disassembly and material liberation. As a consequence, current commercial methods for battery size reduction used by recyclers have been determined to create a large amount of contamination. This type of contamination is an issue of great importance when direct recycling is the preferred route of recycling. A clean black mass needs to be generated for recycling to be economically and technically viable. In addition, pre-processing techniques must not adversely affect separation processes further down the line (e.g., we may not want to shred with water because it will cause problems for the recovery of electrolyte salts).

The Cell Pre-Processing project in ReCell aims to determine scalable technologies that can safely and cost effectively size reduce batteries or manufacturing scrap. The overarching goal is to produce contaminant-free black mass or electrodes that can be used as feedstock for the ReCell Center's direct recycling processes. In addition, after a battery is broken down via shredding/crushing/milling, the casing (pouch/can) material, separator, current collector foils, etc. must be separated. Technologies to separate some of the battery components are also being evaluated under Cell Pre-Processing.

In FY22, a custom built dual-shaft shredder was installed at Argonne National Laboratory. The system is sealed to allow for shredding batteries under an atmosphere of inert, flowing gas and also gives us the capability to shred batteries under liquid (Figure III.3.58). The performance of the shredder was first demonstrated with manufacturing scrap (i.e., dry pouch cells with no electrolyte). We then determined safe conditions for shredding discharged end-of-life (EOL) pouch cells from a commercial vendor. For safety during shredding, EOL cells were discharged to 2.8-3.0 V (commercial 40 Ah pouch cells containing NMC cathode), the shredding system was flooded with inert purge gas, and one cell was fed at a time. Various methods have been used for liberation of materials and component separation and are discussed in the results section.

In the beginning of FY22 Q1, a custom-built, inert-atmosphere shredder was safety approved at Argonne to shred manufacturing scrap and discharged, end-of-life (EOL) cells (Figure III.3.58). During FY22 Q2, dry manufacturing scrap pouch cells were shredded to produce ~2.5 kg of material. This material was processed to compare to our previous results where the same pouch cells were shredded by our industry partner in a similar commercial system. The shredder at Argonne produced shreds with 95% of material measuring > 2.8 mm. These results are similar to shreds provided from our industry partner where ~94% of material was > 2.8 mm in size. The fines (material < 500 μ m) produced were about 1.5% and 2.2% for the Argonne and commercial shredders, respectively. Overall, these results show that the dual shaft shredder at Argonne performs similarly to the commercial unit that we tested previously (Figure III.3.59). During FY22 Q1, discharged end-of-life pouch cells were also shredded under flowing Argon gas. The end-of-life shredded battery material was used for liberation experiments in diethyl carbonate and put into other direct recycling processes established at Argonne. See Figure III.3.60 for an example of a process flow we use to process and separate materials after shredding.

To address the clumps (i.e., layers of pouch cell battery stuck together after shredding) generated after shredding, we have been investigating ways to liberate these clumps and make material more accessible for downstream recycling processes. Liberation experiments of EOL shredded material was conducted in FY22 Q1 using diethyl carbonate. The amount of clumps observed from EOL cells was about 30% lower than what was observed in shredded manufacturing scrap. We achieved 80.5% liberation of a clump fraction after 3 min. stirring at 1800 RPM. We have previously used aspiration for removing separator and other light materials from shreds as a post-processing technique and recently found that it is also effective for liberating clumps. In FY22 Q2, we investigated aspiration as a dry, simple method for liberating clumps and were able to liberate about 20% of clump material. Aspiration is a dry, simple process that separates light from heavy material using controlled air flow (Figure III.3.61). A sample of shreds (> 5.6 mm) was fed through aspirator and we found that approximately 65% of the sample was made up of thin or thick layers of clumps (heavy fraction) while the remaining 35% was made up of plastics and electrodes (light fraction). By taking the heavy fraction (i.e., clumps) and feeding it through the aspirator 5 times, we were able to liberate nearly 20% more material. The remaining clumps are tightly bound and require more aggressive methods to be liberated. In Q3, a rotor beater mill and a mandoline slicer were evaluated for clump liberation. The rotor beater mill liberated all the clumps, however, generate a significant amount of powder during operation ($\sim 35\%$ of material was < 500 μm after processing). The mandoline slicer liberated 39% clumps by weight, but led to single layer pieces being squashed/compacted and collected with remaining clumps after aspiration.

After installing the shredding in Q1, pouch cells were the only type of battery shredded in the system. During Q2, cycled 18650 cylindrical cells were obtained as another cell format to test. The cells were received in the discharged state and shredded under inert atmosphere. The 18650 cylindrical cells were shredded under two conditions: at room temperature or were frozen in liquid nitrogen immediately prior to shredding. Freezing in liquid nitrogen can be an effective method for mitigating thermal runaway in cycled cells – please refer to NREL’s low temperature work conducted as part of ReCell. Overall, good liberation of material from the steel cell casing of the cylindrical cells was observed and few clumps were identified in the shredded material (Figure III.3.62). Cells frozen in liquid nitrogen appeared to be more brittle during shredding, the separator was torn to a greater extent, and more cathode material fell off of the current collector. The shreds from both room temperature and liquid nitrogen frozen 18650 cells have been washed and are being further analyzed outside of the glovebox.

In Q4, we installed a thermal imaging camera on the shredder to monitor the thermal behavior of discharged cells while they are being shredded. We discharged a 40 Ah pouch cell to 3.0 V and monitored the thermal activity of the cell as it went through the blades of the shredder under inert atmosphere. The cell showed no significant activity when fully discharged. See Figure III.3.63 for a snapshot of the cell going through the blades, the temperature stayed below 30°C during the shredding process.

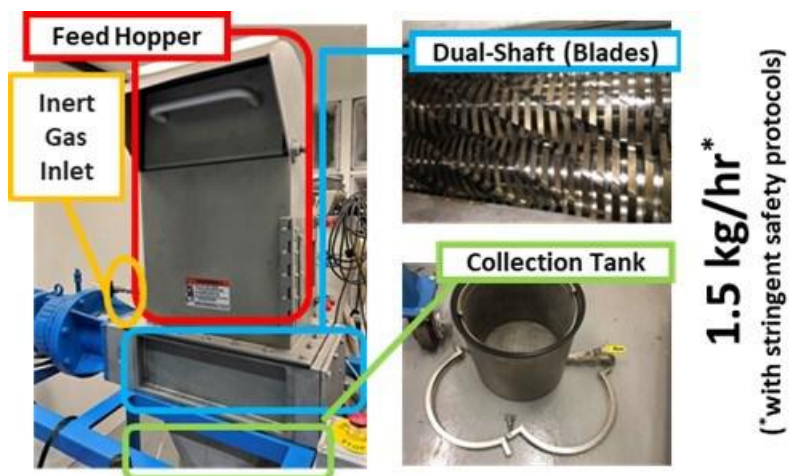


Figure III.3.58 Custom built dual-shaft shredder with mailbox-style feed hopper, inert gas inlet, blades situated along two rotating shafts, and a sealed collection tank

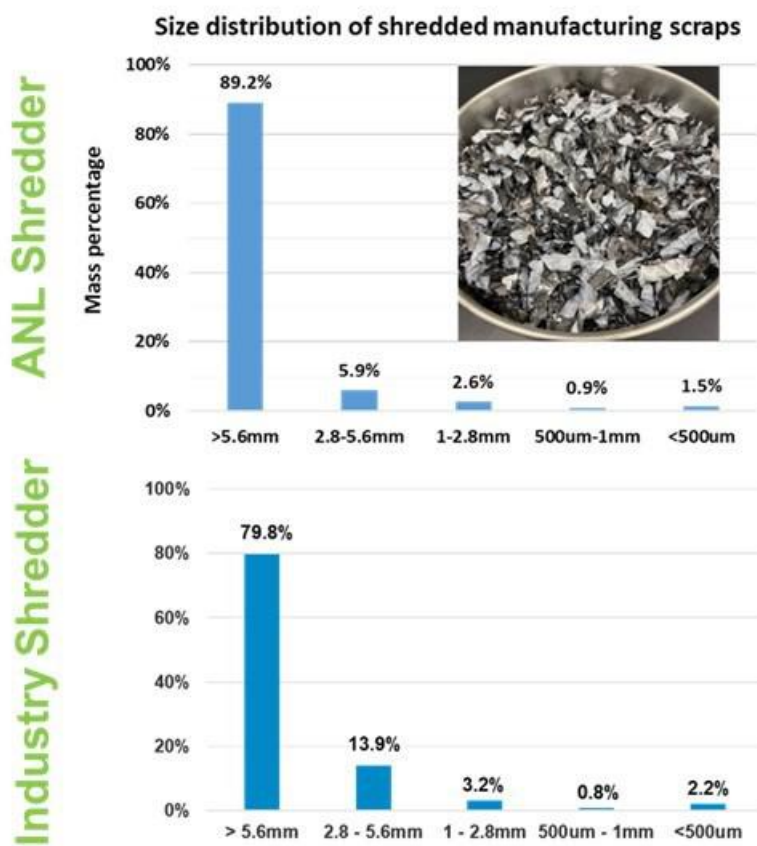


Figure III.3.59 Comparison of ANL manufacturing scrap shreds vs. the same manufacturing scrap shredded by an industry partner using a similarly sized system

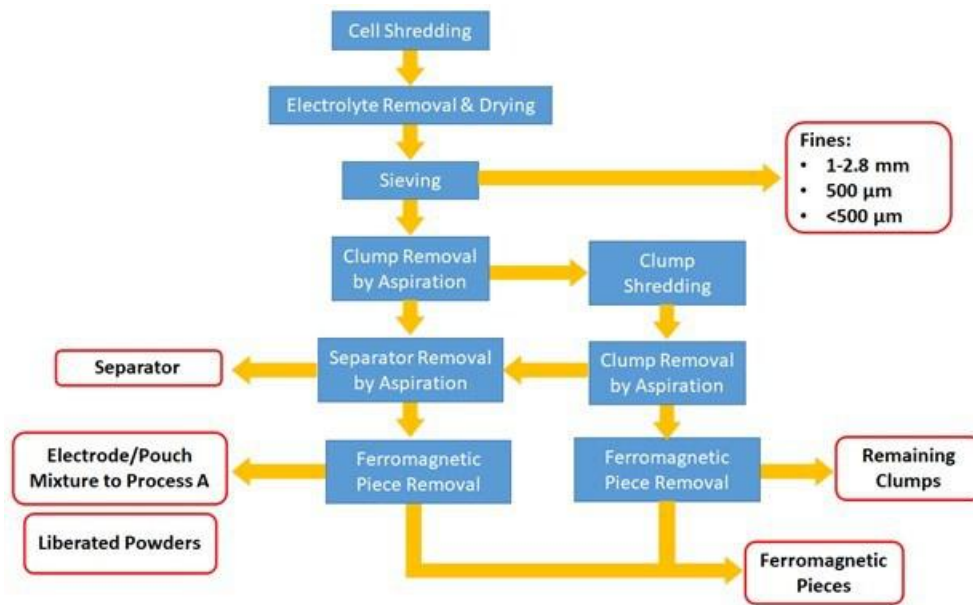


Figure III.3.60 An example of a process flow for shredding and separating components

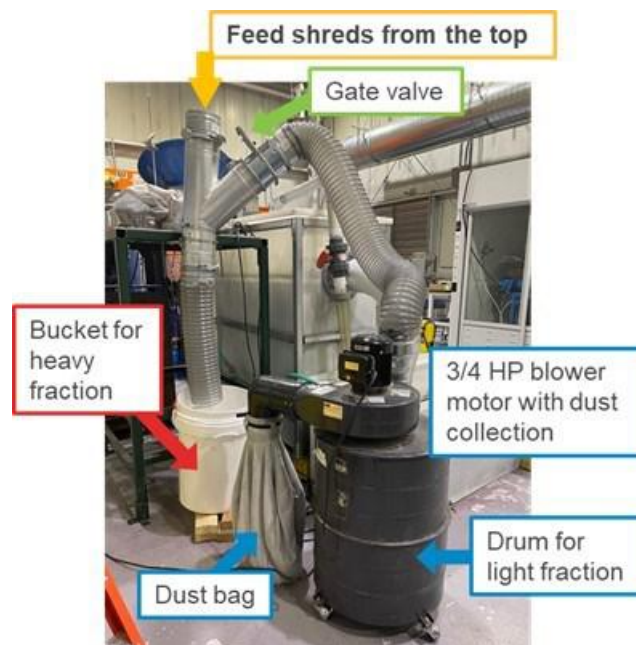


Figure III.3.61 Set-up of an aspiration system used for liberating clumps and removing light from heavy materials



Figure III.3.62 Shredding cycled 18650 cylindrical cells under inert atmosphere at room temperature (top) and after freezing in liquid nitrogen (bottom)

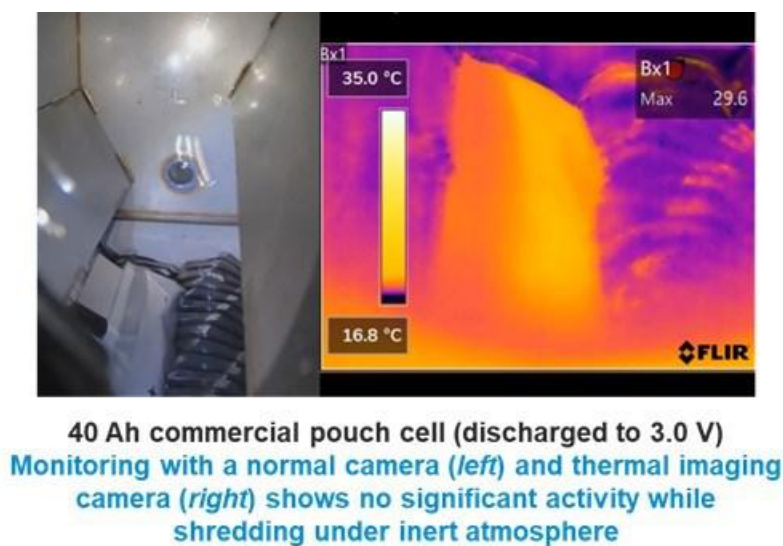


Figure III.3.63 Shredding of a discharged pouch cell under inert atmosphere using two types of cameras to monitor thermal behavior

Solvent-based Electrode Recovery

Electrode materials are tightly bonded to their respective metal current collectors through polymeric binders. To recover electrode materials, especially cathode materials that represent the most recoverable value, an

efficient and damage-free separation process needs to be developed to isolate electrode materials from metal foils like aluminum (the cathode current collector) and copper (the anode current collector). Both hydrometallurgical and direct recycling strategies require the separation of active electrode material from metal foil, which is an enabling yet challenging task in the pre-processing step. Traditional separation processes involve the use of highly toxic solvents like NMP and DMF, which severely limit their industrial applications. In the present project, the team will utilize several green solvents to recover both electrode materials and metal foils from spent electrodes as well as from manufacturing scraps.

The objective of this project is to develop efficient recovery processes for the separation of black mass from current collectors. The separation processes involve the use of green solvents that are inexpensive, nontoxic and do not cause water and/or air pollution, and do not incur a penalty in terms of damages to active materials and current collectors. The recovery of cathodes and anodes also have high peeling-off efficiency and are cost effective, scalable, energy efficient and environmentally friendly. The work plan is based on a wet-chemical recovery approach for separating the black mass from metal foils by either solvating the PVDF binder or weakening its binding with laminates. Three types of green solvents-based separation processes have been developed to efficiently recover both electrode materials and metal foils. In FY22, this project will continue to optimize the SolveX and Y processes to further reduce the cost. It will also determine separation conditions, evaluate full cell electrochemical performance, and provide cost analysis for the direct recycling and remanufacturing of PVDF-based anode scraps via SolveZ process.

In FY22, the SolveX process was optimized to recover commercial NMC cathode scraps by tuning reaction temperature and time. The SolveY process was used to recover a large quantity of spent cathode powder for the relithiation teams. In addition to the existing SolveX and SolveY processes that were developed in FY20 and FY21, we demonstrated a new solvent-based process (SolveZ) to separate anode materials from copper foils to directly recycle anode scraps and remanufacture into new anode.

In FY22, the SolveX process was optimized for the separation and reprocessing of industrial NMC cathode scraps. Different reaction temperatures (198°C, 160°C, and 120°C) with or without the addition of LiOH or KOH were investigated. The recovered cathode films were characterized by XRD, XPS, and ICP-OES. In addition, the electrochemical performance of those reprocessed NMC cathode were also studied. It is found that adding LiOH reduced the delamination temperature from 198°C to 120°C with similar reaction time. Also, adding LiOH could help maintain both the crystal structure and the electrochemical performance of the reprocessed cathode.

The SolveY process was used to recover spent cathode powder (>800 g) from commercial spent cathode. Those reclaimed spent cathode powder was distributed to the relithiation team members for regeneration studies. Furthermore, we demonstrated that increasing the solid/solvent ratio from 1/5 to 1/4 could help reduce the cost by ~16% without reducing the recovering efficiency.

Anode scrap that comprises critical materials such as graphite and valuable Cu should be recycled and reintegrated into the battery supply chain. In FY22, we demonstrated a simple yet efficient water-based recovery process (SolveZ) for delaminating anode films from Cu foils through the intercalation of water between the hydrophilic Cu foil and hydrophobic anode coating. By simply immersing the anode coatings in only water, the anode films were completely delaminated from Cu foils without damaging any components, which was confirmed by XRD, XPS, and SEM. Thus, the anode films consisting of graphite, carbon black, and PVDF binder were separated and recovered without changing their composition because none of the components dissolve in water. Because of the absence of harsh chemicals, the recovered anode films and Cu foils are battery grade and free of damage in terms of physical and chemical properties. Those anode films were reprocessed into slurry by simply adding NMP solvent to dissolve the PVDF binder. A new anode was then fabricated by recasting the slurry onto Cu foil and then dried and calendered. The electrochemical performance of the recoated anode was evaluated in both half coin cells and full coin cells and compared with that of the baseline anode under galvanostatic cycling. The reversible discharge capacities at C/10 are 353

mAh/g for the recoated anode and 357 mAh/g for the baseline anode, suggesting that the water-based separation process has no apparent effect on the electrochemical performance of the recycled graphite anode. Additionally, no capacity fading is observed for both recoated and baseline anodes after 50 cycles at C/3 charge/discharge rates, further emphasizing the damage-free characteristic of the water-based recovery process.

The cost and revenue of the SolveZ process were analyzed by the EverBatt model. The total cost to process 1 kg of anode scraps was estimated to be only \$0.81, most of which arises from capital investments, and the operating cost, including the costs for labor (\$0.05), materials (i.e., DI water, \$0.11), and utilities (\$0.03), accounts for 23.5% of the total cost. Because the recovered graphite and copper are battery grade, this water-based process can generate a high revenue of \$8.75/kg of anode scraps processed. This environmentally friendly and cost-effective separation technique allows battery manufacturers to directly recycle and reuse their electrode scraps safely and effectively on-site.

Solvent-based Dual Process

Within the loop of Direct Recycling, separation and subsequent direct regeneration of active cathode materials are of great importance as cathode represents one of the most valuable components in a lithium-ion cell. Cathode materials are tightly bonded to Al foil through the organic PVDF binder, making them challenge to be separated. In addition, the separated cathode materials are lithium deficient, further requiring a relithiation process to convert those delithiated cathode particles to a stoichiometric material. Current strategy involves several isolated separation and regeneration processes that make recycling complicated and expensive. It is thus desirable to develop a process with dual functionality that can separate and simultaneously restore lithium in the same solvent system. In this project, the team will develop a solvent-based dual process to separate as well as regenerate the cathode active materials.

The objective of this project is to accomplish both separation and regeneration of cathode materials through a one-pot solvent-based dual process. This process utilizes a greener solvent that will not only delaminate the spent cathode films from aluminum foils but also restore the lithium back to stoichiometry. This process avoids complicated processes, making recycling scalable and more profitable. Furthermore, the process is completed in a greener solvent at a relatively low temperature and ambient pressure, which will both reduce energy consumption and alleviate environmental impact.

In FY22, this project will further the optimization of relithiation conditions (e.g., lithium precursor concentration, temperature, and time) for both separating and relithiating spent NMC cathode from the industrial cells. It will also identify the optimal annealing conditions to regenerate cathode materials with desirable electrochemical performance. The process will be scaled up to produce 25 to 50 g of regenerated cathode powder.

Direct regeneration of chemically delithiated NMC111 was successfully demonstrated in FY21. In FY22, we focused on the relithiation of real spent NMC cathode from industrial cells. Spent cathode powder was obtained by removing the PVDF binder using the SolveY process. In contrast to chemically delithiated NMC111, the regeneration of real spent cathode required different relithiation conditions such as reaction temperature, reaction time, and LiOH concentration. We were able to successfully regenerate the industrial spent cathode powder, which was confirmed by characterizations like XRD and ICP-OES. Both half-cell and full-cell tests for the regenerated NMC cathode showed similar capacities and cycle performance as the baseline cathode.

Techno-economic analysis using EverBatt modeling was performed to evaluate both cost and environmental impact of this relithiation process. It was found that the cost of regenerated NMC111 is 20% less than the virgin NMC111, while the GHG emission is much lower than both virgin material production and other recycling methods. To reduce the processing cost, we increased the LiOH concentration so that less polyol solvent would be required. More optimizations are under work.

Aqueous Sequential Separation

In a typical recycling process, the spent cells are discharged and shredded, followed by electrolyte recovery and component separation to remove/reclaim components like plastics, pouch material, and steel casing. As a result, a feedstock of anode and cathode on their current collectors is generated. This feedstock contains the most valuable components in a lithium-ion cell, including black mass (e.g., active cathode materials and graphite), Cu foils, and Al foils. To reclaim active cathode materials with high purity for direct regeneration, separation of electrode materials and their current collector as well as of anodes and cathodes is required. Current techniques require a complex set of separation processes to produce clean streams of material, resulting in lower recovery rates and higher costs. It is thus extremely important to develop a simple and cost-effective separation process to efficiently recover high-purity cathode materials as well as other materials so that different concentrated feedstocks are provided for further direct regeneration and recovery processes. In this project, the team will investigate an aqueous process to recover both electrode materials and current collectors using buffer solutions and surfactant additives in a single pot.

The objective of this project is to develop an aqueous separation process to sequentially separate anode/cathode and electrode/current collectors to recover cathode films, anode films and metal foils. This process utilizes a buffer solution to first peel off anode films from copper foils, followed by adding a surfactant to facilitate the delamination of cathode films. The designed water solution does not damage the active cathode materials nor corrode the metal foils. In addition, this process enables room temperature separation in a low-priced water solution, reducing energy consumption and processing costs.

In FY22, this project will provide cost analysis, yield, and efficiency for both anode/cathode and cathode/Al separation via the sequential separation process. This process will also be explored to separate and recover materials from industrial spent cells.

In FY22, the process was scaled up to separate and recover materials from a 2 Ah pouch cell made of NMC622/graphite. A nearly 100% peeling-off efficiency has been observed for both delamination of anode films from copper foil and cathode films from aluminum foils. The separated materials were characterized by XRD and ICP-OES. Furthermore, the lithium in the spent anode was dissolved in water and recovered in the form of Li_2CO_3 by heating up the solution and adding Na_2CO_3 . In addition to the separation of lab-made pouch cells, two types of industrial cathodes were investigated for delamination in the surfactant/buffer solution under various separation conditions. One of them was delaminated easily to produce cathode films and aluminum foils, while the other one was hard to be delaminated under separation conditions like sonication and heating.

Besides the separation process, we also removed the PVDF binder in the recovered anode films after delamination in the buffer solution via the SolveY process. Characterizations such as XRD, TGA, and XPS were used to analyze the SolveY recovered graphite. For example, the TGA results indicate the removal of binder when compared with the delaminated anode films. The SolveY recovered graphite showed high reversible capacities with 335 mAh/g at C/10. It also exhibited good cycle performance, where it maintained 317 mAh/g at C/3 after 50 cycles.

Cost analysis for this process was evaluated by EverBatt model. According to preliminary modeling results, it took \$2.49 to process 1 kg spent battery. Since the process is to be combined with other processes for complete materials recovery, we did not assign a value for recovered cathode/anode films. It is worth to mention that cost of materials (e.g., surfactant, buffer salts) account for ~50% of the total cost, indicating the necessity of process optimization to reduce cost.

Anode/Cathode Separation and Purification

After battery shredding, electrolyte recovery, and component separation (i.e. plastics, cell casing, magnetic ferrous-based metals) we are left with electrode fragments that include anode/copper foil and cathode/aluminum foil. Separation of the anode and cathode is a critical step in the direct recycling process to

purify black mass. Being able to efficiently produce multiple clean streams of material (cathode, anode, and Al/Cu foil) will make direct battery recycling more profitable. The separation of anode, cathode, and metals can be achieved in a couple different ways. First, delamination and binder removal (i.e., via thermal binder removal or a solvent-based delamination and binder removal process) must be performed on the anode/cathode mixture to yield two product streams consisting of mixed Al/Cu foils sieved from combined anode/cathode powders. The mixed anode/cathode powders and metals would each have to undergo separation processes. The second method will produce more clean streams of product by separating the electrode laminates while attached to foils prior to delamination and binder removal. At this point, you would have one batch that contains cathode and Al foil while the other is anode and Cu foil. Binder removal would be performed on the two batches to produce separate streams of Al foil, Cu foil, anode powder, and cathode powder. The presence of four separate product streams after a simple anode/cathode separation would reduce black mass complexity and significantly streamline subsequent steps in the direct recycling process.

The ReCell Center has successfully established several anode/cathode separation processes that yield high purity materials. These processes include froth flotation and gravity separation. Argonne National Lab has been working toward developing a mechanical separation process, referred to as “Process A”, since FY21. Process A has been used to separate anode and cathode while active materials are still attached to foils (i.e., electrodes). Experiments in FY21 demonstrated that Process A could effectively separate manufacturing scrap, which is made up of a mixture of anode and cathode electrodes. In FY22, Process A is being investigated to separate anode and cathode electrodes from a mixture of shredded battery materials. The objective is to optimize various operating parameters of Process A to effectively separate anode and cathode in shredded battery materials. This fiscal year we are initially targeting $\geq 95\%$ purity for recovered anode and cathode fractions. The end goal of this project is to fully optimize Process A to separate shredded battery materials (i.e., from dry manufacturing scrap cells or end-of-life cells) to achieve battery grade anode and cathode materials with purities above 99%.

In FY22 Q1, the custom built dual-shaft shredder installed at Argonne National Laboratory was used to shred dry, pouch cells. The shreds were processed in a couple of different ways to determine the impact of impurities (e.g., clumps, separator, pouch materials) on separation efficiency and purity of separated products. The goal was to start with a simple mixture and progressively add in different components (e.g., clumps, separator, and pouch material) to increase the complexity of material being separated. See Figure III.3.64 for a list of the different compositions that were created for separation by Process A.

In FY22 Q1, equipment for Process A was received. We had to build and install guarding to comply with Argonne’s safety standards and make the equipment safe for use in the laboratory. The guarded system was fully safety approved and used for anode/cathode separation experiments. Samples were prepared (see Approach section) for separation experiments. Anode/cathode separation by Process A was conducted on shredded battery materials from dry manufacturing scrap pouch cells. Experimental results indicated that plastic separator present in the feed reduced the separation efficiency of anode and cathode electrodes. During Q2, the impact of impurities in the feed (i.e., component layer clumps from shredding, separator, and pouch material) on anode/cathode separation and purity of recovered products was investigated.

Experiments were conducted on shredded manufacturing scrap pouch cells at a lower feed rate compared to previous experiments. At a lower feed rate, anode and cathode were separated effectively by a single-step operation of Process A – see Figure III.3.65 for a summary of the results. While a majority of the anode from the feed (~99%) was collected in the anode fraction, thick (> 3 mm) clumps, most of the separator, and a majority of the pouch material was also collected in this fraction leading to an anode fraction with significantly reduced purity. These experiments also showed that thinner clumps (i.e., layers of pouch cell battery stuck together after shredding) were collected in both anode and cathode fractions. It was determined that adjusting the parameters of Process A can be effective for selectively removing clumps, with different thickness and bound components, from the anode and cathode electrodes of interest. For comparison, shredded feed material without clumps was prepared two ways: with separator and pouch material or only containing pouch material.

The purity of single-layer cathode electrode pieces in the cathode fraction achieved $\geq 98\%$ (99% recovery) using a single-step operation regardless of whether the feed contained separator and/or pouch material. However, plastics were still collected in the anode fraction during these Process A separation experiments. This led to anode electrode purities of 88% with separator and pouch present (99% recovery) and 92% with pouch present (99% recovery). As a result, the anode fraction requires further processing or passes through Process A to remove plastics and obtain high purity material.

In Q3 and Q4, we worked toward increasing the feed rate of materials and optimizing the conditions to achieve good separation. Samples used for these experiments included a 1:1 mixture of anode and cathode, shredded manufacturing scrap, and material from an end-of-life battery. During a 2-step separation experiment, a feed rate of > 6 kg/hr was used for the 1st step and > 3 kg/hr feed rate was used for the second purification step. First, the operating conditions were optimized for a 2-step Process A operation to separate anode and cathode electrodes from 200 grams of representative anode/cathode mixture (i.e., mixture of anode and cathode electrodes manually collected from the manufacturing scrap shreds). Collected fractions from the first step were fed again to Process A to improve anode and cathode purities in both fractions. Different operating conditions were applied for the first and second steps to optimize the separation efficiency. Operating at a feed rate of 6.9 kg/hr in the first step and 3.4-3.8 kg/hr in the second step, $>99\%$ purities of both anode and cathode electrodes with $>90\%$ recovery was achieved. (See Figure III.3.66.)

The operating conditions applied to the separation of representative anode/cathode mixture were applied to the separation of manufacturing scrap shreds. The majority of separators and clumps in the manufacturing scrap shreds were removed by aspiration prior to the 2-step Process A operation. The feed rates of the manufacturing scrap shreds were similar to the anode/cathode mixture (i.e., 7 kg/hr in the first step and 3.2-3.9 kg/hr for the second step). Due to the small quantities of impurities (i.e., separators, pouch materials and thin clumps), the purities of single-layer cathode and anode electrodes after the 2-step Process A operation were 90% and 93%, respectively. However, recoveries of single-layer cathode and anode electrodes were $>90\%$, and majority of separator-attached cathode electrodes were collected in the cathode fraction. (See Figure III.3.67.)

In addition to manufacturing scrap, we have also applied this separation technique to end-of-life (EOL) battery shreds to separate anode and cathode electrodes. A single operation of Process A was conducted for the shreds of EOL battery cells that were manufactured by the same vendor as the manufacturing scrap used in previous experiments. EOL battery shreds were after a majority of the separator was removed by aspiration, while clumps were still left in the shreds. Due to their high density, clumps contained in the shreds slightly increased the feed rate to 7.4 kg/hr. Although the recovery of single-layer cathode and anode electrodes were $>90\%$ after the single operation, remaining clumps significantly reduced the purities of both fractions (i.e., 68% and 46% purity of single-layer cathode and anode electrodes, respectively). Similar to the previous results, the majority of thick clumps were collected in the anode fraction while thin clumps were collected in both fractions. Optimized operating condition are required to concentrate impurities in the anode fraction and improve the purity of cathode fraction.

Feed samples tested with Process A		Experiment		
		1	2	3
Clumps	Clumps (> 1cm)	25%		
	Clumps (3mm – 1cm)	29%		
	Thin clumps (<3mm)	24%		
Single Layer	Cathode	11%	50%	52%
	Anode	9.6%	44%	45%
	Separator	0.7%	3%	
	Pouch	0.7%	3%	3%

Figure III.3.64 Composition of sample types (e.g., blue and green) used for separation experiments

Results from a 1-Step Operation of Process A				
Experiment	Cathode Fraction		Anode Fraction	
	Cathode purity*	Cathode recovery**	Anode purity*	Anode recovery**
1: with clumps, separator, pouch materials	54%	99%	13%	99%
2: with separator, pouch materials	98%	99%	88%	99%
3: with pouch materials	99%	99%	92%	99%

* Purity of single-layer cathode and anode in the fraction and doesn't include anode and cathode in clumps

** Single-layer cathode or anode collected in the fraction divided by single-layer cathode or anode in the feed

Figure III.3.65 Summary of separation results for three different types of feed materials which shows that separation is affected with increasing material complexity

	Cathode Fraction % Cathode Purity (% Cathode Recovery*)	Anode Fraction % Anode Purity (% Anode Recovery*)
1st step	93% (97%)	97% (93%)
2nd step	>99% (94%)	>99% (92%)

* (Mass of collected anode or cathode)/(Mass of anode or cathode in the 1st step feed)

Figure III.3.66 Results from a 2-step separation of 200 grams of a 1:1 mass ratio anode/cathode electrode mixture achieved >99% purity anode and cathode with >90% recovery

Separation of commercial battery cell shreds by Process A:

Manufacturing scrap after 2-step separation (left) and End-of-life cell after 1-step separation (right)

	Cathode Fraction % Purity (% Recovery*)	Anode Fraction % Purity (% Recovery*)		Cathode Fraction % Purity (% Recovery*)	Anode Fraction % Purity (% Recovery*)
Cathode	90% (91%)	0.5% (0.4%)	Cathode	68% (97%)	3% (3%)
Anode	0.7% (0.7%)	93% (90%)	Anode	3% (8%)	46% (92%)
Cathode with separator	8% (73%)	0.2% (2%)	Cathode with separator	4% (98%)	0.1% (2%)
Pouch	0.7% (8%)	6% (61%)	Pouch	4% (45%)	6% (55%)
Separator	0.4% (36%)	0.3% (28%)	Separator	0.3% (38%)	0.6% (62%)
Thin clumps	0.7% (31%)	0.4% (18%)	Thin clumps	19% (58%)	16% (42%)
			Thick clumps	0.7% (3%)	28% (97%)

* (Mass of collected material)/(Mass of material in the 1st step feed)

Figure III.3.67 Results from 2-step separation of commercial batteries shredded at Argonne National Laboratory

Purification of Black Mass

Successful implementation of direct recycling at scale is contingent on the ability to produce high-purity material outputs. The presence of metallic impurities within recycled cathode materials both reduces purity metrics – a critical factor to industrial acceptance of the recycled product – and adversely impacts cell performance. In particular, mechanical shredding (the predominant preprocessing technique utilized in direct recycling) introduces trace levels of Al and Cu from the electrode current collector. These contaminants are particularly challenging to remove from the fine shredded fraction, where the contaminants are on the same order of size magnitude as the target cathode particles and traditional separation approaches (optical sorting, magnetic separation, froth floatation, etc.) are unviable. Without appropriate purification, this fine fraction cannot be directly recycled.

To date, few strategies exist to selectively remove metallic impurities from mixtures of shredded end-of-life material (black mass; BM) while concurrently achieving the target goal of direct recycling: i.e., recovering the active material in maximally intact form. Hydrometallurgical purification strategies typically employ conditions under which all metals (including target cathode active materials such as Li, Ni, Co, and Mn) are converted to ionic form via chemical leaching. These leaching techniques – typically acidic solution-based processes – are highly effective to ionize impurity metals, but also promote the breakdown of the cathode's physicochemical structure. Thus, existing hydrometallurgical approaches are problematic in the context of direct recycling, and new methods are warranted to enable the selective ionization of contaminants while retaining the active material intact. Alkaline aqueous conditions are reported to be nondestructive to metal oxides, and also enable effective ionization of Al₂O₃ and CuO. However, matrix and process parameters must be

optimized to enable rapid and complete ionization of these metals without inducing damage to the cathode active material.

Thus, in the present work, we are optimizing an aqueous dissolution process to ionize solid Al and Cu so that the target cathode active material can be recovered in the solid phase via physical filtration. This “black mass purification” (BMP) approach will ultimately operate in conjunction with a reversible and tunable adsorbent filter to recover ionized metals from solution. The BMP process enables effective purification of trace-level contaminants from shredded BM, and improves the circularity of the overall process line by (1) enabling direct recycling of an otherwise-unusable BM feedstock; (2) enhancing overall component recovery by enabling the selective recapture of metallic contaminants in purified form.

The primary objective for the BMP task in FY22 was continued development of optimized methods for Al and Cu corrosion. Success is measured by the ability to fully and rapidly ionize the target metals while avoiding structural, chemical, and electrochemical damage to the cathode active material (NMC). This FY, emphasis was placed on applying the BMP process to practical samples of shredded black mass, which represent a considerably more complex matrix than the idealized systems tested in FY21. Scale-up from bench scale (1g) to pilot scale (≥ 50 g) was initially targeted for this FY, but supply chain delays in reactor acquisition resulted in a greater emphasis being placed on continued process development at smaller scale. In particular, project goals were adjusted to focus on tuning process and post-process conditions to improve the full-cell behavior of the recovered cathode material from practical shredded BM. The final objective for this task – synthesis and optimization of a functionalized adsorbent material to selectively bind ionized Al and Cu for high-purity recovery – is complementary to the primary objective, and work on this task will continue to be pursued at a lower priority level in FY23.

Parameter optimization for BMP treatment and post-treatment conditions was evaluated through a rational experimental framework. We have applied the matrix conditions iteratively developed in FY21 for the rapid solubilization of Al and Cu to samples of both simulated BM (i.e. pristine NMC powder spiked with known concentrations of contaminants) and practical shredded end-of-life material, obtained from the CAMP facility (both before and after thermal treatment) and directly from industrial suppliers. We have also evaluated the impact of BMP treatment on graphite. All testing this FY was conducted using the bench-scale CSTR-type reactor with sonication developed in FY21. We have evaluated the efficacy of purification by quantifying residual contamination in these samples, and have evaluated impacts on NMC by structural (XRD), chemical (ICP, SEM/EDS), and electrochemical analysis.

A critical focus of this FY has been identifying matrix and process condition improvements to enhance the practical full-cell behavior of material following BMP treatment. To accomplish this, robust electrochemical analysis was first conducted to identify the source and root cause of capacity loss in full cells prepared with treated material. The results of this analysis informed iterative process improvements associated with the filtration step and post-treatment rinse step, with optimization of the latter still ongoing. Experimental validation of process improvements was conducted using electrochemical analysis coupled with XPS and SEM/EDS.

Efforts towards scale-up have been initiated via the purchase of a custom-designed 1L reactor (Pope Inc.) and associated balance-of-plant supplies. With delays associated with component supply chain constraints, the reactor is scheduled for delivery by the end of Q1 FY23. Additionally, a framework for technoeconomic analysis (TEA) has been developed through collaboration with the EverBatt team at Argonne National Laboratory (ANL). Specifically, the TEA was tailored to more accurately represent the value provided by the BMP process, which includes the ability to directly recycle an input stream that would otherwise be unusable.

This FY, effort was also made to increase visibility of this research. This included presenting at an international conference (US/UK Workshop Series in Electrochemical Energy Storage Research – London, UK, July 2022); engaging in discussions with several industry representatives; and preparing and submitting a manuscript highlighting the accomplishments of the project to date.

In FY22, the idealized conditions identified in FY21 for the rapid ionization of Al and Cu in alkaline solution were further refined to improve at-scale processability and practical viability. This initially involved identifying the minimum solvent volume /maximum contaminant concentration required to achieve full corrosion of Cu, the limiting contaminant species (~ 0.75 g-Cu/L-solution under the present bench-scale design). This parameter was used to inform the design of the pilot-scale reactor, which has been specified to process ~ 50 g of black mass with an expected total contaminant concentration of 1-2%. Further, diffusion limitations were identified as a constraint for the extent of Cu corrosion, prompting the inclusion of baffling and an axial impeller in the pilot-scale reactor to ensure optimal mixing and avoid the presence of “dead zones”.

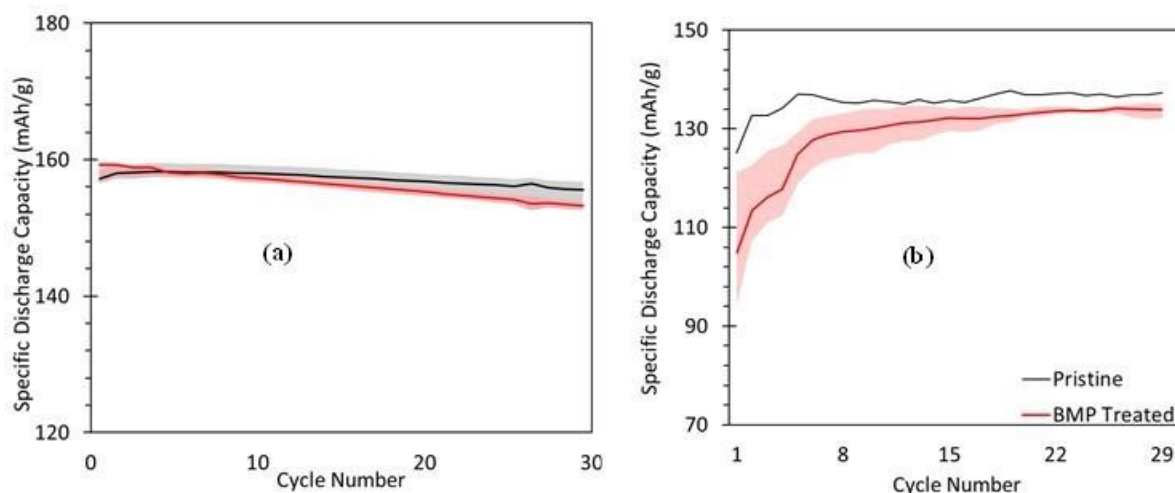


Figure III.3.68 (a) Half-cell and (b) full-cell performance of BMP-treated NMC-111 vs pristine NMC-111; shaded region reflects capacity variation between sample replicates.

As discussed in the Background section above, optimal conditions for the purification of black mass must simultaneously maximize the corrosion rate/extent of the undesired contaminants (Al₂O₃, Cu₂O) while avoiding adverse impacts to the properties and performance of the cathode active material. The BMP process does not adversely impact the bulk structural properties of NMC (see FY21 reporting), and half-cell performance of treated NMC-111 is equivalent to that of pristine NMC-111 (FY21 reporting and Figure III.3.68a). However, early-FY22 tests of the treated material in practical full cells (NMC vs graphite) revealed evidence of electrochemical variability and more substantial capacity loss (Figure III.3.68b). It should be emphasized that, in the context of practical implementation in a direct recycling line, the “no-treatment” condition is objectively the worst outcome: as noted previously, the fine fraction of the black mass is unviable for direct recycling when even low levels of Al₂O₃ and Cu₂O contamination are present. But given that the ultimate target for a successful BMP process is to induce no measurable effect on the active NMC, and it is imperative to identify, report on, and improve on any disparities between pristine and treated material such that iterative adjustments can be made and the highest quality material produced.

With this end goal in mind, comprehensive electrochemical analysis and several complementary analytical techniques (XPS, SEM, EDS) were employed across two sample types (pristine NMC and practical BM) to fully probe the origin of this behavior and drive associated process improvements. These analyses revealed both an incomplete removal of ionized contaminant species (in the case of practical BM) and changes to the surface properties of the treated NMC. Both of these behaviors can be directly tied to our post-treatment filtration and rinsing steps, rather than the treatment process itself.

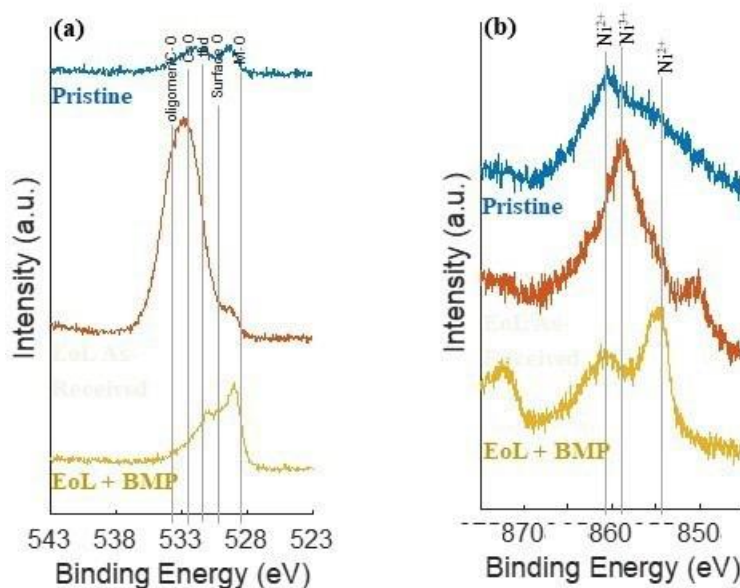


Figure III.3.69 Selected XPS spectra for (a) O1s and (b) Ni2p3 showing surface modification of treated practical BM (yellow curves) as compared to as-received EoL material (orange curves) and pristine material (blue curves). Preliminary species assignments are overlaid at the respective binding energies for reference.

In FY21 and early FY22, our post-treatment protocol involved centrifugation of the treatment solution at room temperature, decanting the supernatant solution (containing ionized contaminants and residual solvent), and subsequently briefly (~10 sec) rinsing with deionized water to remove residual KOH. XPS analysis – conducted this FY on practical end-of-life BM through a collaboration with the Electrochemical Relithiation task – suggested that the [BMP + post-treatment] process may be inducing elevated Ni reduction ($\text{Ni}^{3+} \rightarrow \text{Ni}^{2+}$) and higher surface oxygen content (Figure III.3.69); further, EDS (Figure III.3.70) reveals the presence of dispersed Al and K contamination, which appear as flake-like crystallites in treated samples. Impedance analysis reveals a higher resistance in treated materials relative to pristine, and differential capacity analysis shows substantial reactivity outside the voltage range of “standard” reversible NMC electrochemistry (Figure III.3.71). Taken together, these findings imply both that the ionized contaminants (e.g., Al) and the treatment solvent (KOH) has not been sufficiently removed during the post-treatment step, and may be intercalating into the graphite counter-electrode in full cells. These analyses further suggest an adverse role of the water-rinsing step in inducing Li/ H^+ exchange, which could drive the observed $\text{Ni}^{3+}/\text{Ni}^{2+}$ reduction and result in near-surface structural rearrangement (spinel, rock salt)¹ as well as the evolution of surface-resistive species such as LiOH, Li_2CO_3 , LiHCO_3 , etc.²

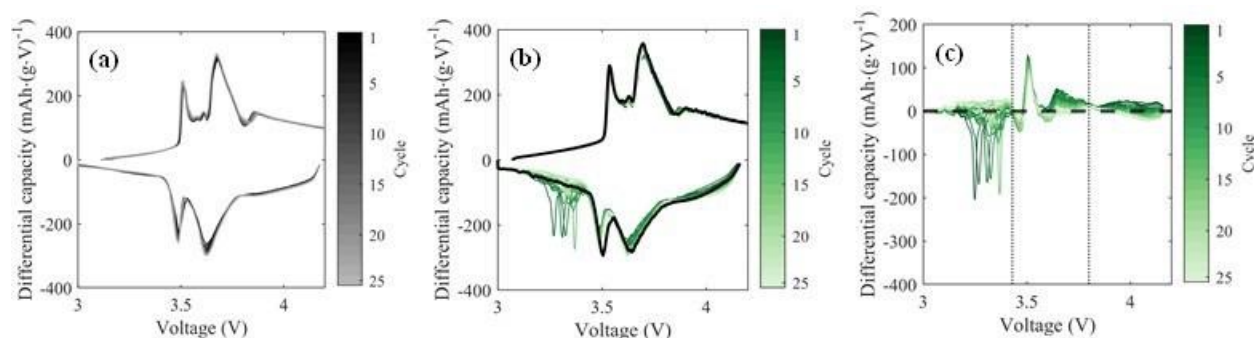


Figure III.3.70 SEM analysis of practical BM following BMP treatment, revealing the presence of flake-like crystallites which are confirmed by EDS to contain Al (likely as $\text{Al}(\text{OH})_3$) and K (likely as KOH).

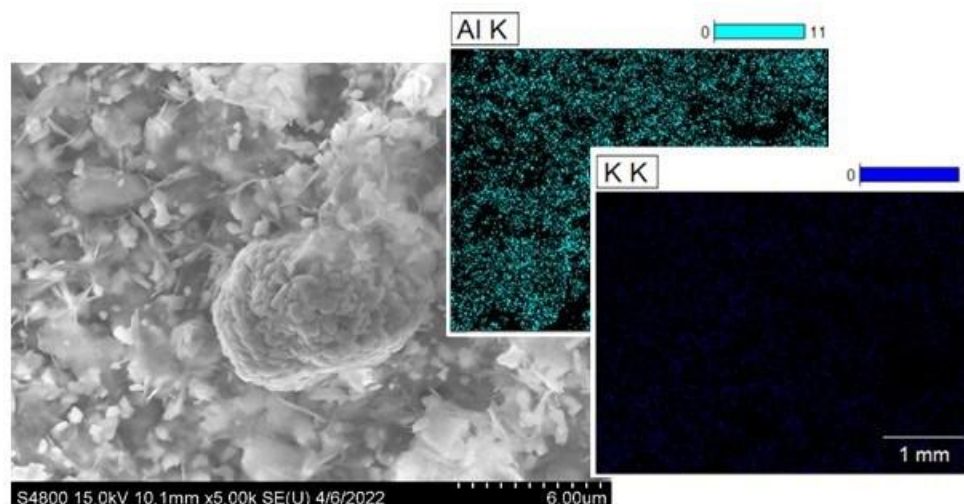


Figure III.3.71 Evolution of full-cell differential capacity over 25 C/10 cycles following formation: (a) Pristine NMC-111; (b) NMC-111 after undergoing BMP + post-treatment rinse with deionized water; (c) Normalized differential discharge capacity for the condition shown in (b), with normalization calculated as the value from the treated cell minus the first-cycle value from a representative pristine cell. In (c), vertical dashed lines at 3.43 V and 3.8 V denote the low, middle, and high voltage regions of the plot, separating the expected graphite (~3.5 V) and NMC (~3.7 V) peaks from the side reactions occurring at low and high voltages. In all plots (a-c), line colors indicate the cycle number (increasing from dark to light tones) and a single representative cell replicate is shown; in (b), the first-cycle differential capacity behavior of the pristine cell is overlaid in black for reference.

A series of studies was conducted in FY22 to identify promising candidates for post-treatment solvents and determine whether changes to the post-treatment protocol could result in improved full-cell performance of BMP-treated material. For these studies, a sample of practical BM was processed using the optimized BMP treatment parameters (i.e., sonication and stirring at 60°C for 2.5 hr under ambient atmospheric oxygen); to reduce the possibility of solubility-driven reprecipitation of $\text{Al}(\text{OH})_3$, samples were vacuum-filtered immediately after treatment (while the solution was still hot). Following room-temperature vacuum-drying, all samples were then rinsed with a supplemental aliquot (75 mL) of 0.1 M KOH. After another round of room-temperature vacuum drying, samples were manually shaken for a 30-second period with 40 mL of one of four organic solvents. Samples were then vacuum-dried again at room temperature prior to electrode fabrication. The solvents utilized were selected based on ability to solvate $\text{Al}(\text{OH})_3$ and K^+ ; further, these solvents reflected a range of dielectric constants and steric hindrance. Room-temperature vacuum-drying was employed to avoid surface reconstruction to M_3O_4 (spinel)- or MO (rock salt)-type structures, which has been reported for high-Ni NMCs following higher-temperature drying.¹ SEM/EDS conducted on the post-treated samples confirmed elimination of the flake-like crystallites observed in (Figure III.3.70), and full-cell electrochemical cycling data (Figure III.3.72) suggests that treatment with any of the solvents studied is superior in terms of both performance and cell resistance to the baseline condition (i.e., a single rinse with KOH). For this sample set, a direct comparison with the original post-treatment protocol (deionized water) was not conducted, but the impact of changing the post-treatment solvent identity is clearly evident. It is anticipated that optimizing the post-treatment conditions will eliminate the surface irregularities previously observed in treated material, creating a truly “purified” BM that is optimized for downstream direct recycling processes (e.g., relithiation). Finalizing an optimized post-treatment protocol is the focus of early FY23 efforts, and will be the final bench-scale tuning required to fully define the BMP process for scale-up.

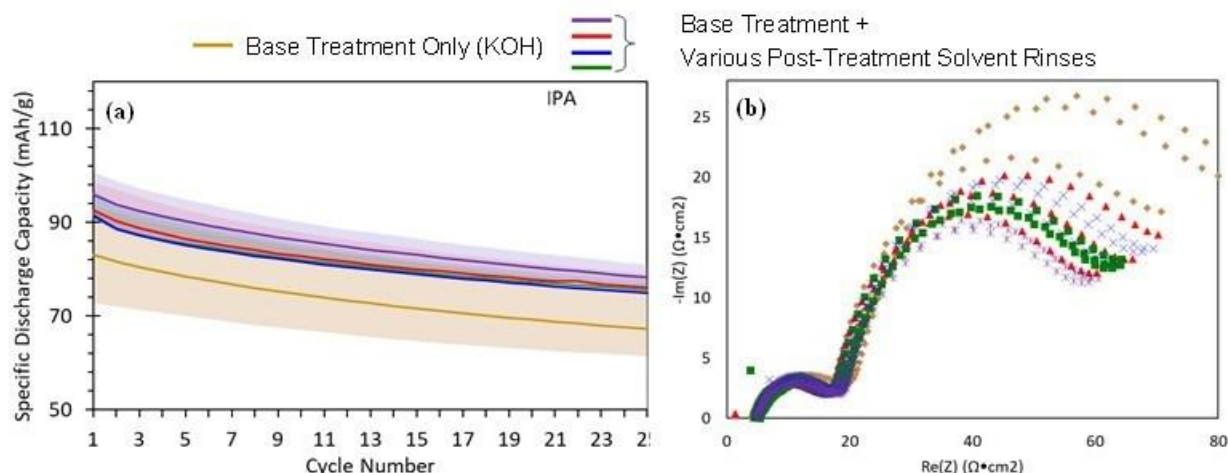


Figure III.3.72 (a) Full-cell performance and (b) impedance analysis of BMP-treated practical end-of-life material to evaluate the variable impacts of post-treatment solvent on subsequent performance. In (a), shaded region reflects capacity variation between sample replicates; in (b); curves with the same marker style and color reflect sample replicates.

The TEA framework established in collaboration with the EverBatt team in FY22 is being iteratively employed with efforts to identify an optimal post-treatment rinse solvent. Without conclusively knowing the nature of this solvent and its ability to be reused, it is difficult to accurately quantify the value offered by the BMP process; however, the EverBatt model will continue to be refined as the BMP method parameters are finalized in early FY23.

Finally, a custom-designed 1L pilot-scale reactor and all associated balance-of-plant supplies have been purchased. Initial safety reviews have been initiated, and installation is planned for Q2 FY23. This will enable the optimized BMP process parameters (both treatment and post-treatment steps) reported herein to be applied to larger batches of industrial BM, in line with overall scale-up goals outlined by the ReCell consortium.

Electrolyte Component Removal and Recovery

During the battery recycling process, electrolyte needs to be removed from the materials to allow for further processing to recover other materials. This can be done in several ways, including supercritical CO_2 , thermal drying, water washing and solvent extraction. Of these, only supercritical CO_2 with added co-solvent or solvent extraction can recover the LiPF_6 , which is the most valuable component of the electrolyte. We have demonstrated that the electrolyte can be extracted by diethyl carbonate (DEC), and then reconstituted with better cycling than 1.2 M LiPF_6 in 3:7 ethylene carbonate to ethyl methyl carbonate (EC:EMC) electrolyte. This process was demonstrated at 0.5 L scale and the materials washed are being utilized for many other projects across ReCell. We previously have tried different methods for purification, but none of the purification methods really provide sufficient benefit. During this year we are working on the scale up of the process and purchasing equipment to wash at large scales.

The objective of this project is primarily to remove the electrolyte from electrode shreds to prevent downstream contamination. In addition, we want to determine if the electrolyte can be reused in batteries to prevent it from becoming waste. These goals need to be demonstrated at scale for both production of materials for the rest of the ReCell center as well as to demonstrate the potential effectiveness in commercial applications.

In this project, we initially explored a wide range of solvents and other techniques for removing electrolyte. After this initial exploration, using carbonate solvents to recover the salt was chosen as the main option as it can provide very clean cathode material for direct recycling. This type of process produces a dilute rinsate that needs to be recycled. This project has approached this by using vacuum distillation to concentrate the LiPF_6 . This concentrate is then reconstituted into a new electrolyte that can work well in full cells.

This year, the focus of this project was on scaling the rinsing and concentration process. In particular, we started to look at whether electrolytes can survive short air exposure going from the shredder to the glovebox. Then further onto utilizing a rotary evaporator to concentrate the electrolytes, which in the current apparatus requires an additional air exposure. We utilized diethyl carbonate (DEC) to extract electrolytes from end-of-life cells shredded in inert atmosphere. This requires air exposure as the materials are collected from the shredder and transported to a glovebox for rinsing. The rinsate was then concentrated in a vacuum oven at 80°C to provide a concentrate. After this process there was not any significant degradation of the LiPF_6 as determined by NMR. After concentration, the composition was determined by NMR and this allows for the correct additions to make 1 M LiPF_6 in 1:1 EC:DEC. Then this electrolyte was used to make recycled NMC 622/graphite full cells. The resulting cycling is shown in Figure III.3.73. The recycled electrolyte performs similarly to the pristine gen 2 electrolyte. There is a slightly reduced initial capacity, but improved cyclability.

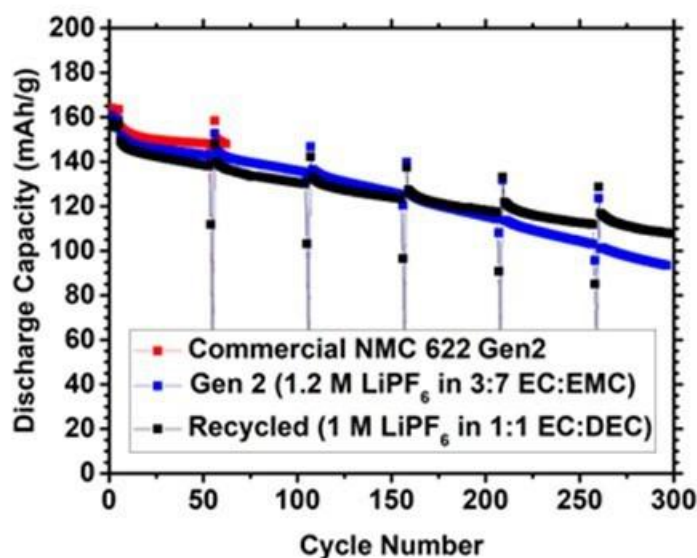


Figure III.3.73 Full cell cycling for recycled NMC 622 with gen 2 (1.2 M LiPF_6 in 3:7 EC:EMC) electrolyte and recycled electrolyte (1 M LiPF_6 in 1:1 EC:DEC) along with a commercial NMC 622 with gen 2 electrolyte.

We then worked to scale up the concentration process using a rotary evaporator. In our current set up this requires additional air exposure, which leads to questions over whether we can still reuse such an electrolyte. In order to make a successful electrolyte, the solvent needs to be very clean and the entire process needs to occur in a relatively short period of time. The initial full cell coin cell cycling data for such a recycled electrolyte is shown in Figure III.3.74. In this case the recycled electrolyte very slightly outperforms the gen 2 baseline electrolyte.

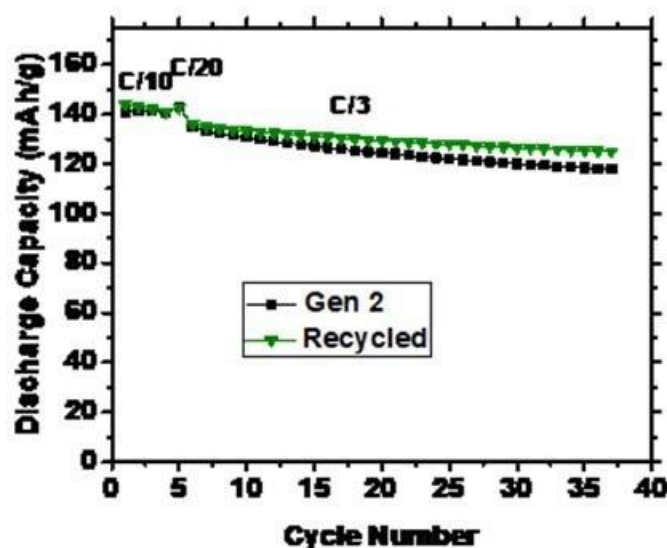


Figure III.3.74 NMC 111/graphite full cell cycling using electrolyte recycled using a rotary evaporator for the concentration step versus gen 2 baseline electrolyte.

Graphite to Graphene

Maximizing the generated revenue from recycling all components of Li-ion batteries can greatly improve the profitability of Li-ion battery recycling. Currently it is a challenge to recycle the graphite anode because the product doesn't have enough value. It has been previously published that cycled anode graphite can be more easily exfoliated into graphene than other graphite sources. If this process can be scaled the graphene produced would have a much higher selling price than graphite, resulting in substantial revenue gains. The challenge in scaling this process has two parts. The first is finding a process to simply create the needed graphite feedstocks for this process. The second is finding the best exfoliation method, additives, and conditioning steps to improve yield and throughput. We will be testing traditional and innovative processes to determine the optimal conditions and then determine the costs and environmental impacts for these processes using the EverBatt model.

The objective of this project is to find a process that can recover graphite and exfoliate it into graphene in a scalable way at minimal cost. Then to further demonstrate this process by producing sufficient graphene for evaluation in various applications by commercial partners.

The first step in this process is to harvest graphite from spent cells. It was previously determined that graphite can be removed from copper by simply placing the electrode in water. Other projects have demonstrated techniques that can recover graphite on copper foil from a spent cell. For this project, graphite has been mostly obtained from hand sorted electrodes to minimize the amount of material that needs to be processed. We then looked at a couple of possible methods to exfoliate graphene and chose high shear mixing due to its low cost and scalability. With the method chosen we are determining the best possible exfoliation process using a combination of additives and shear mixing conditions. In addition, we have explored differences in the manufacturer on the quality of the graphene produced.

During this year we attempted to gain a better understanding of the effects of materials type and processing conditions on the quality of graphene produced. In particular, we analyzed the effect of manufacturer and stirring speed on the quality of the graphene. This was done in conjunction with Xiaodong Li's group at the University of Virginia who performed extensive atomic force microscopy (AFM) analysis of the samples. The resulting histograms for the thickness and edge length are shown in Figure III.3.75. It is clear from this data that graphites from different manufacturers have very different exfoliation behavior. This is likely due to

differences in crystallite size and degree of ordering in the graphite. This implies that commercially some manufacturers of cells will be more amenable to be turned into graphene than others.

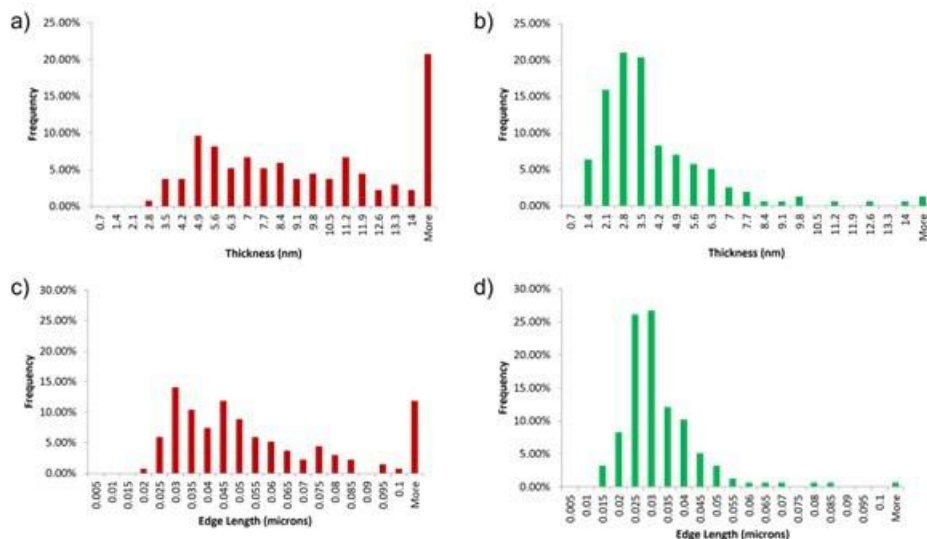


Figure III.3.75 Histograms generated for thickness and edge length from AFM images of the graphene prepared at 3krpm from a) and c) manufacturer A and b) and d) from manufacturer B.

In addition, we explored how the stirring speed will affect the graphene production. Using manufacturer A material we tested three speeds to look how the exfoliated graphene changes. The results in Figure III.3.76 show that at higher stirring speed the thickness is reduced as anticipated. For this material, it requires at least 7 krpm to achieve even few layer graphene and higher shear would be needed to generate single layer graphene. This type of understanding is needed to correctly optimize the exfoliation process and determine its energy usage.

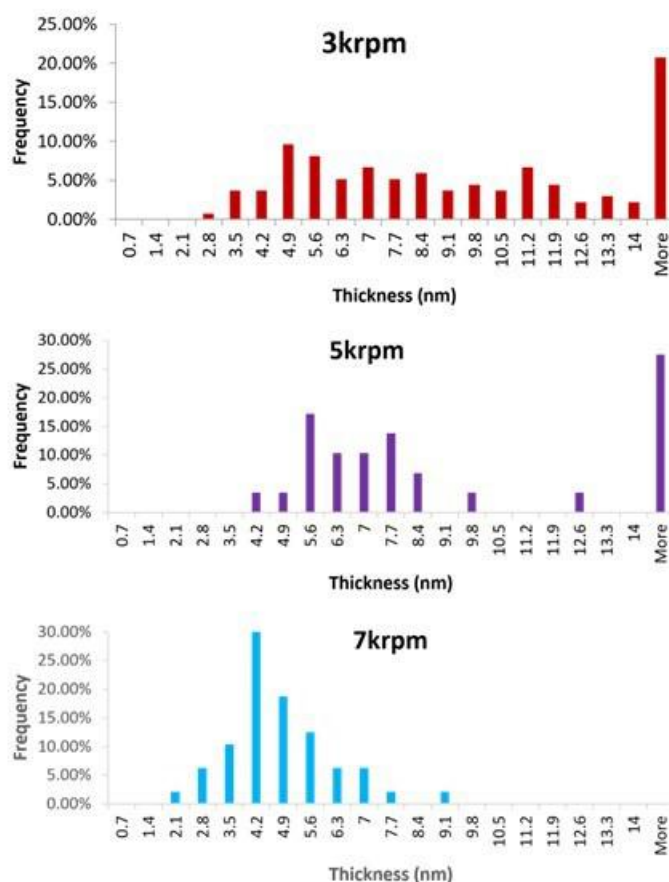


Figure III.3.76 Histograms generated for thickness from AFM images of the graphene from manufacturer A at different shear mixing stirring speeds.

To further understand the potential commercial possibilities of this process we worked to generate a model for commercial production of graphene in EverBatt. This model assumes a 10% yield for graphene production and all of the graphite from a 10,000 ton per year battery recycling plant goes through this process. The total cost came to \$2.63/kg of graphite processed, or equivalently \$26.30/kg of graphene produced. The remaining graphite could also be potentially sold to another application further increasing the potential revenue. An analysis of the cost breakdown indicates that electricity is likely the greatest expense for the graphene production. This may be somewhat reduced in commercial applications due to higher efficiency mixing system, but in this model we assumed the same electrical usage per kg graphene production at the small scale. In any case, if this model prediction is correct, this would still be a major reduction in the cost of graphene, which could enable new high volume applications such as composite materials to be produced. (See Figure III.3.77.)



Figure III.3.77 EverBatt cost analysis of the recycling of graphite into graphene from graphite on copper foil. Cost is in \$/kg of graphite recycled.

Modeling and Analysis

EverBatt

Recycling has the potential to reduce the cost and environmental footprint of lithium-ion batteries (LIBs). Argonne has developed the EverBatt model to estimate the cost and environmental impacts associated with closed-loop recycling of LIBs, and we have been using the model to help inform and direct R&D efforts at the ReCell Center. Specifically, in FY22 we have been expanding EverBatt to include unit processes proposed for direct cathode recycling and recovery of other battery components; updating existing unit processes in EverBatt based on new process information; and evaluating promising configurations of direct recycling processes in EverBatt to identify cost/environmental hotspots and barriers to commercialization.

The objective of the project is to enhance the understanding of the cost and environmental impacts of different battery recycling technologies, particularly direct recycling, and to inform battery recycling R&D.

To model ReCell unit processes in EverBatt, we meet with individual PIs to collect information on the equipment used and reagents consumed, together with the emissions generated and materials recovered for their process. We then build the process in EverBatt based on collected information, adding new materials and/or equipment to the model as needed. Since most of the ReCell processes are under-development and will continue to evolve, we also set up key experimental parameters as inputs in the EverBatt model for each ReCell process, so that the PIs can easily run scenario analyses or update the results as they explore new process designs. If possible, we also combine the unit process of interest with appropriate upstream and downstream processes to form a complete direct recycling design.

Once we have a working EverBatt model for the unit process of interest, we will meet with the PIs again to demonstrate how to modify the model inputs and how to interpret the model results, and we will continue to update the model as new information becomes available. With an EverBatt model for their process, the PIs can pinpoint cost and environmental hotspots and thus identify opportunities for improvement.

In FY22, we added 5 processes to EverBatt, and updated the modeling of 4 processes based on new information, as summarized in Table III.3.12.

Table III.3.12 EverBatt Modeling of ReCell Processes in FY22

	Q1	Q2	Q3	Q4
Added Processes	Solvent-based dual process	Aqueous sequential separation; RE roll	Graphite to graphene; Balck mass purification	N/A
Updated Processes	Solid state relithiation	Ionothermal relithiation	Redox relithiation	RE roll

Analyses of these processes show that materials separation does not incur substantial costs, while achieving good yields and product purity levels are key to the success of direct recycling. For most of the processes we have analyzed in FY22, materials consumption is a significant cost contributor. Recycle and reuse leftover reagents and solvents therefore represent an opportunity for cost reduction and should be explored in process optimization and scale-up. For processes that use water and/or other solvents, the quantities and compositions of the waste streams are still not well understood and should be further investigated to enable the modeling of waste treatment. In addition, for processes that use deionized (DI) water, we plan to examine the economics of on-site DI water production, since its use can be a notable cost contributor.

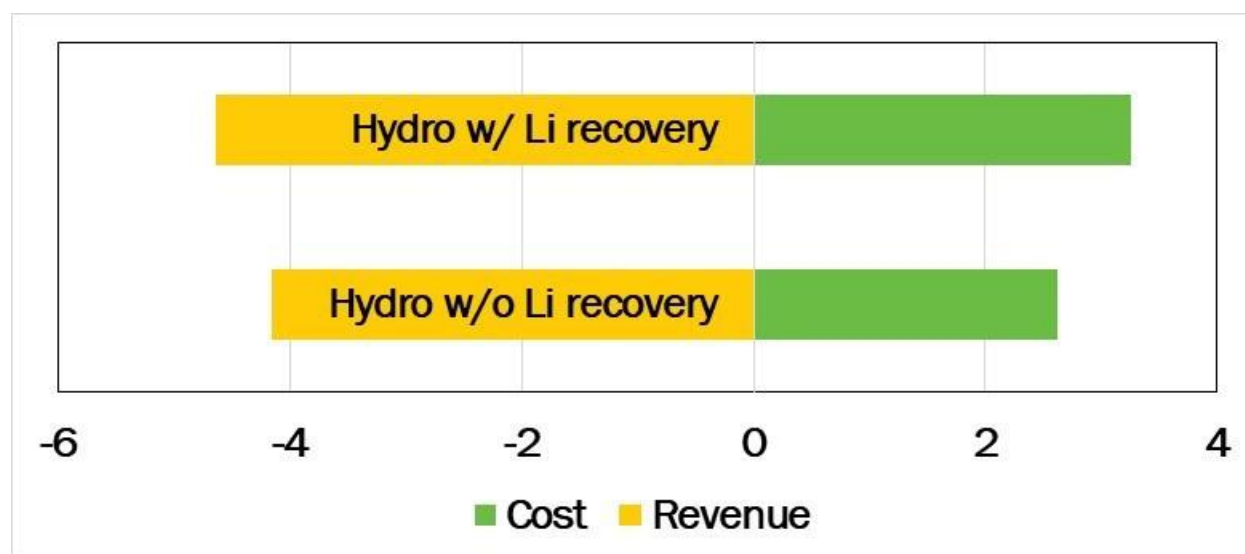


Figure III.3.78 Cost and revenue comparison for hydro recycling (\$/kg cell recycled)

To inform R&D at ReCell, we also examine the prospect of lithium recycling from end-of-life (EOL) batteries and manufacturing scrap. We show that the Li content in EOL cells is comparable to that in concentrated spodumene ore (3-4 wt%), while the Li content in manufacturing scrap is comparable to that in concentrated Li brine (~6 wt%). Both therefore can be valuable Li resources. Since among all Li materials, metallic Li is the most valuable on per kg Li content basis, we conclude that Li recovery as metallic Li looks promising, although research on feasible technologies is still needed. Lastly, we refine our cost modeling for Li recovery from EOL batteries via hydrometallurgical (hydro) recycling, to provide a baseline for future Li recovery technologies. The results are shown in Figure III.3.78.

LIBRA

NREL is analyzing the material and component supply chain for lithium-ion battery (LIB) manufacturing and recycling to determine the dynamic factors driving the economic viability of this nascent industry. Material availability, supply shocks, and technology adoption all impact the continued operation of this supply chain, which in turn enables the rapid electrification of the transportation sector that has been identified as a

cornerstone of the global strategy to mitigate greenhouse gas emissions. NREL conducts many types of analyses for the LIB supply chain, including trade flow analyses, global resource assessments and projections of regional industry growth patterns. For this report, we will focus on NREL's systems dynamics model, Lithium-ion Battery Resources Assessment (LIBRA). The LIBRA Model identifies and explores the critical factors for the successful buildout of LIB manufacturing and recycling capacity both domestically and globally. LIBRA tracks the flows and stocks of battery materials, financing, and industrial maturity leading to more efficient plant operations through 2050 under varying policy scenarios and LIB demand conditions. The model has been used to evaluate the material circularity of the LIB industry with a particular focus on how that can lead to the achievement of established climate goals and benchmark projections. The various modules included in LIBRA are shown in Figure III.3.79.

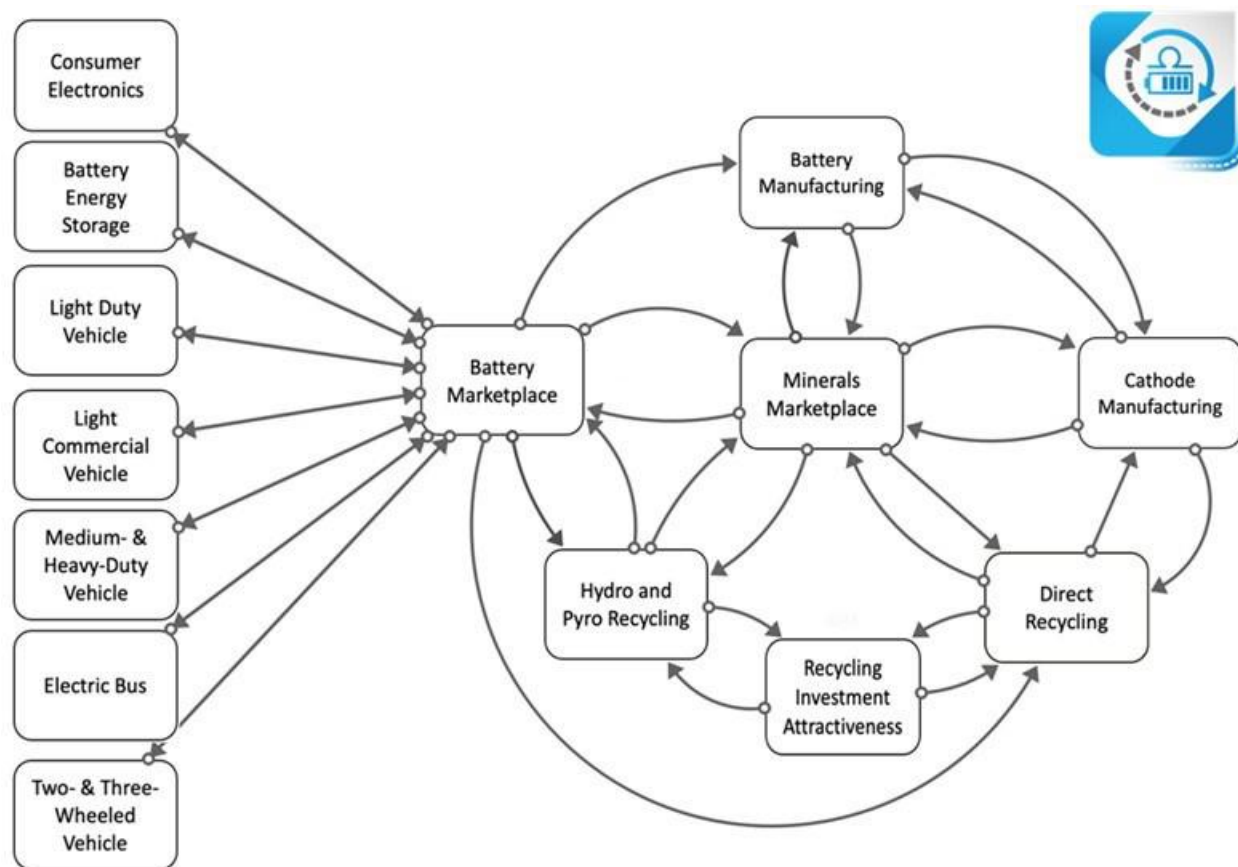


Figure III.3.79 LIBRA model top level modular structure

The objectives of this project are to evaluate the most impactful barriers and drivers of the LIB supply chain in the United States and globally. More specifically, these modeling efforts are designed to answer questions similar to those below. While the questions below are illustrative of the types of questions LIBRA can be used to answer, they are not exhaustive.

Sample key questions

- To what extent can LIB recycling contribute to the domestic battery industry development?
- What are the top hurdles for economic development of the domestic battery manufacturing and recycling industries?
- How can we work with partner countries to enhance the domestic supply chain?
- What aspect of the supply chain exerts the most leverage on the development of the domestic industry's development?

- What impact would investment and external market shocks have on the growth of the industry?
- How might evolving chemistries impact recycling and the evolution of the recycling industry?
- How do variations in demand for LIBs impact the development of battery manufacturing and recycling capacities in the United States and globally?
- How do various factors such as policy decisions, plant financing, material constraints, or market shifts impact the potential circularity of the LIB supply chain?

The LIBRA team uses sensitivity analysis and informative scenarios to evaluate ranges of outcomes under different conditions over time with projections extending to 2050. An example sensitivity analysis is shown below where we ran five projections of electric light-duty vehicle adoption from different sources to see how they impact results. With projections extending out multiple decades, uncertainty in the inputs can be high and lead to significant variation in modeled outcomes. Sensitivity analysis is useful for evaluating the range and extent of these variations and determining which inputs are the most important.

NREL relies upon a number of sources for predictions of how battery demand will change over time with adoption of EVs and electrification of the grid. Sources we've found to be adequately documented and regularly updated include Bloomberg New Energy Finance (BNEF) (BNEF 2022), Wood-Mackenzie (Wood Mackenzie 2021), and the International Energy Agency (IEA) (IEA 2022). Most of our runs as defined from our “base case” are derived from the BNEF projection because of the specificity in its projections which delineate between a wider variety of vehicle types. Variations among these three sources provide a bounded set that allows us to assess the impact of deployment on the development of the domestic battery manufacturing and recycling industries. These projections (Figure III.3.80) range from the IEA STEPS scenario which continues existing EV adoption policies with a comparatively conservative level of EV adoption up to the BNEF Net Zero scenario showing the resulting EV adoption from policies targeting a net-zero emission fleet by 2050.

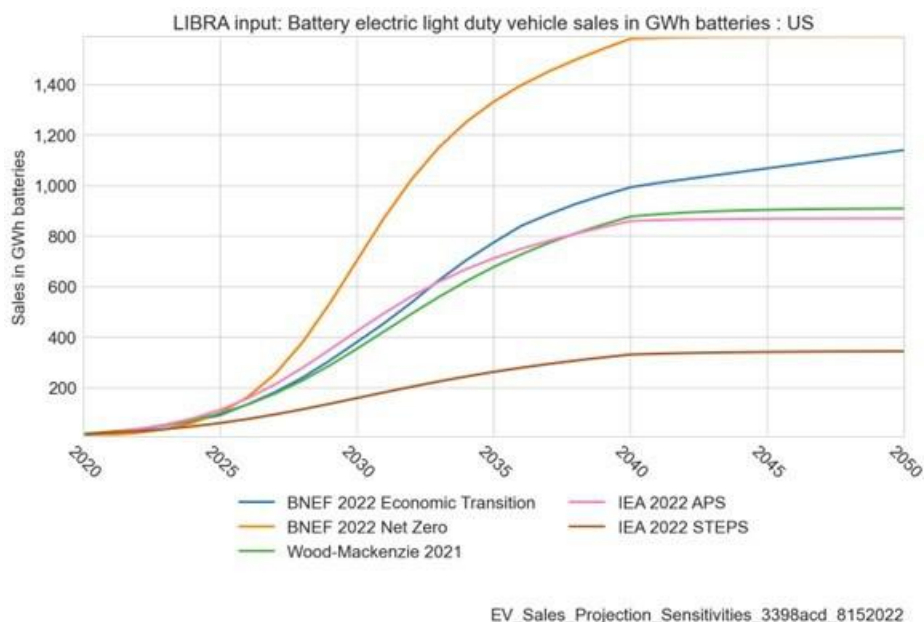


Figure III.3.80 Five projections of electric LDV sales in the United States in terms of the battery energy demanded each year

The key metrics shown below (and others like them) are used to evaluate system-level questions including those described in the objectives section that can help inform large-scale decision-making and planning. These metrics can be used as indicators of the viability of these new industries that are integral to the maintenance of the LIB supply chain. The metrics used to evaluate these outcomes are characterized by significant feedback in the model and sensitivity to a wide range of inputs.

Sample Key Metrics

- *Share of mineral demand for new batteries manufactured in the U.S. for the U.S. market that can be met by recycling*
 - Metric = Recycled Minerals Recovered / Minerals Demanded for Domestic Manufacturing
- *Tonnes of batteries recycled per year*
- *MWh of cathodes/batteries manufactured per year to meet exogenous domestic demand projection*

The impact of materials recovered from recycling depends on numerous factors, including earlier sales of batteries (shown in Figure III.3.80), battery chemistries at the end-of-life, recycling economics, virgin material prices, collection rates, and battery sorting. The domestic share of demand for cobalt and nickel that can be met by recycling given the various EV deployment projections, are shown in Figure III.3.81 and Figure III.3.82, respectively. It is again important to note that these results reflect a particular scenario for the other input parameters. Other scenarios can be run in LIBRA that vary different subsets of inputs using parametric sensitivity analysis or broader multivariate analyses.

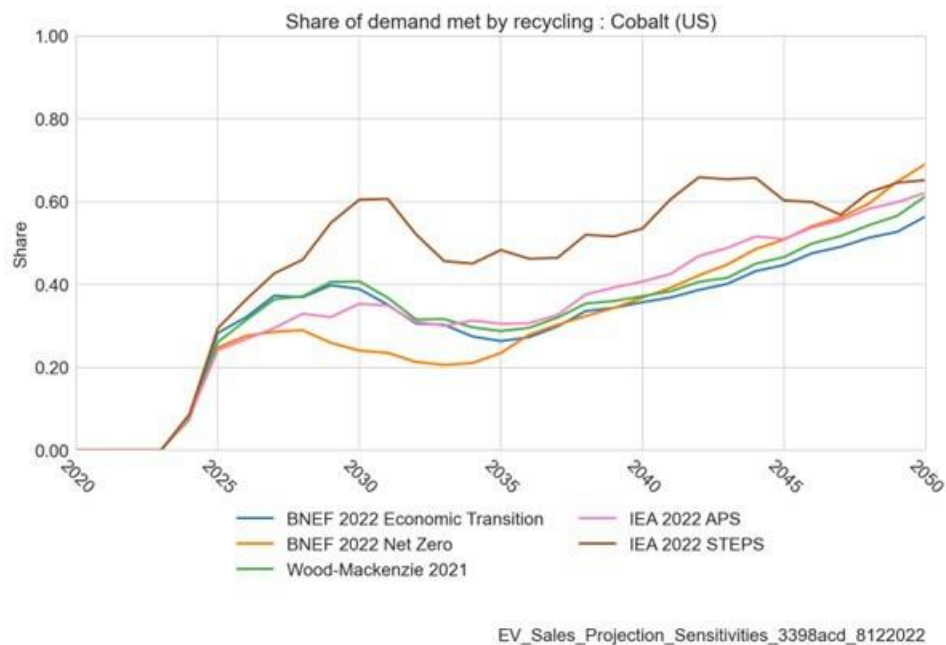


Figure III.3.81 Share of cobalt required for new LIB demand that can be met by cobalt recovered through recycled LIBs

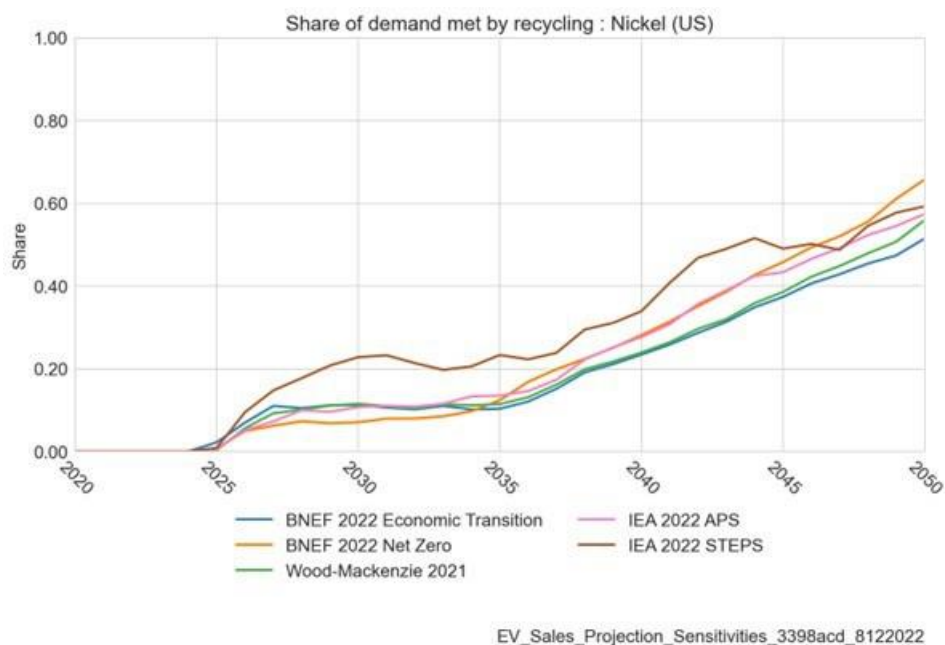


Figure III.3.82 Share of nickel required for new LIB demand that can be met by nickel recovered through recycled LIBs

The Net Zero BNEF scenario has the most rapid escalation of EV adoption among the five cases shown but also has one of the lowest shares of cobalt and nickel recovered. While there may be more resources available to be recycled with higher EV adoption in the long run, the demand for new batteries increases much faster than those recycled resources become available. In contrast, the IEA STEPS scenario has the lowest level of EV adoption, and a higher share of new battery demand can be met. With a shorter battery lifetime, recycled consumer electronics materials are able to meet a higher share of new demand with a lower rate of EV adoption- the demand for electronics and stationary storage do not vary across these five scenarios. The relative order of the five scenarios is similar for both cobalt and nickel.

The share of demand met by recycling before 2035 does not change significantly for either metal as both the availability of recycled materials (the denominator of the metric shown in Figure III.3.81 and Figure III.3.82) and the demand for those materials for new batteries (the numerator of the metric) are increasing over time. However, the rate of increase in EV sales slows after 2035, resulting in a general upward trend to 2050. The shape of these figures is driven by many parameters, but one significant impact is related to the transition in battery chemistries used over time, moving away from cobalt-rich chemistries and toward nickel-rich chemistries.

Modeling and Analysis

CAMP Support

Numerous recycled battery materials are created in the ReCell Center that need to be validated in prototype electrodes and pouch cells. Validating the electrochemical performance of recycled battery materials is critical to establishing their market viability. The Cell Analysis, Modeling, and Prototyping (CAMP) Facility at Argonne validates these materials (active cathode powders, graphite, electrolytes, etc.) in prototype electrodes and pouch cells and compares their electrochemical performance to baseline electrodes (and electrolyte). Two areas of particular interest this year were in relithiation of harvested spent NMC622 cathode powder and upcycling of baseline NMC111 polycrystalline powder to single-crystal powder.

The objective of this crosscutting activity is to validate the electrochemical performance of the candidate recycled cathode powders in commercial quality electrodes and single-layer pouch cells.

The CAMP Facility uses pristine NMC111 or NMC622 cathode materials and SLC1520P graphite as the baseline materials in capacity-matched electrodes and cells. All recycled or upcycled cathode or graphite materials are compared against these baseline materials in terms of electrochemical performance data. Other recycled battery materials, such as electrolyte or binder, are also evaluated in electrodes and cells and compared against their pristine version. All electrodes are first tested in coin cells for initial validation and then tested in single-layer pouch cells for rate performance, HPPC impedance, and cycle life, if warranted. Results from the coin or pouch cell studies are provided to the relithiation teams to aid them in their optimization efforts. Fully-optimized materials that do not perform as well as the baseline material have little market viability. Recycled materials that do perform as well as the baseline have to pass the next hurdle of cost competitiveness.

Relithiation of harvested spent NMC622 cathode powder

The CAMP Facility received four relithiated NMC622 powders from four relithiation teams (Hydrothermal, Ionothermal, Solid State, and Redox) near the end of FY21. The initial NMC622 powder was recovered by ORNL's Solvent Y process applied to electrodes harvested from industrial End-of-Life (EOL) cells from an industrial collaborator. All four relithiated powders were coated, but the coating quality was marginal, yet still useable. The poor quality of the electrodes was attributed to the higher pH of the powders caused by the relithiation processing and to the presence of large hard agglomerates (that may have formed during sintering). A fifth relithiation process was also validated in which a portion of the Solvent Y recovered NMC622 was retained by the CAMP Facility and made into an electrode and then sent to NREL for electrochemical relithiation of the electrode (eChem). Both the pristine NMC622 powder and Solvent Y recovered NMC622 powder blended well in the slurry process and yielded good quality electrodes. All six NMC622 powders were coated by the CAMP Facility to match an anode (A005B, SLC1520P graphite) from the Electrode Library. Electrodes were punched from these electrodes and made into single layer pouch cells in the xx3450 format with at least four duplicate cells per electrode set. These cells are referred to as "Baseline" for the pristine NMC622 and "first generation" for the five relithiated NMC622 powders in Figure III.3.83.

The coating observations and initial results of the first generation cells were relayed back to the relithiation teams. They decided to further optimize their process to provide a second generation of harvested and relithiated NMC622 powder, except for the eChem team, which did not affect the electrode quality. The second generation of powders were received from the hydrothermal, solid-state, ionothermal, and redox process teams near the middle of Q2. These powders were coated using the same composition, slurry process, and drying conditions as the first generation. The quality of all four electrodes were much better than the first generation of powders. Single-layer pouch cells using these four NMC622 electrodes were made like the first generation cells and put on formation and then life cycle protocol testing at 30°C.

In the third quarter, the first generation of pouch cells finished the 2nd life cycle protocol with a total of 517 cycles, at which time only the ionothermal and baseline pouch cells were restarted – these cells went on to complete 1026 life cycles with 85% and 83% capacity retention – end of test. The second generation of pouch cells have all completed 517 cycles. Only the ionothermal pouch cells were restarted after 517 cycles, which were at 710 life cycles with 86% capacity retention at the end of FY22. Results summarized in Figure III.3.83.

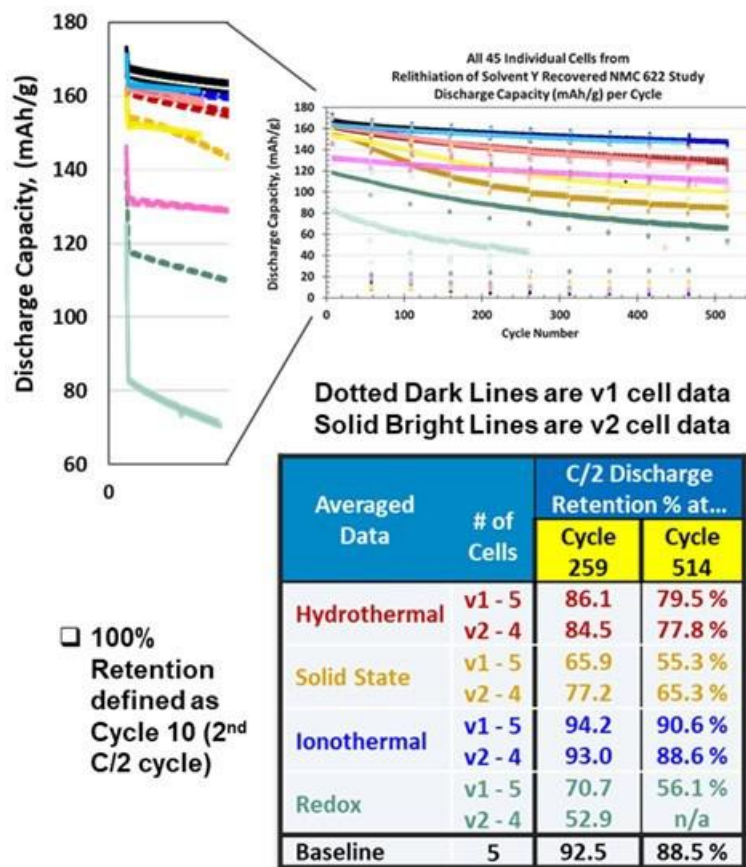


Figure III.3.83 Summary of the capacity retention for first generation (v1) and second generation (v2) relithiated NMC622 powders versus Baseline NMC622 powder evaluated in single-layer pouch cells with Gen2 electrolyte at 30 °C.

Upcycling of pristine NMC111 to single-crystal cathode powder

In the third quarter, the CAMP Facility received 50 grams of up-cycled single-crystal NMC111 from WPI. It was then coated to match the SLC1520P graphite electrode in the Electrode Library and then tested in half-cells to determine capacity, voltage profile and rate capability. The half-cell data looked promising, so single-layer pouch cells were made and are undergoing testing at the end of FY22. Preliminary results were sent to WPI for their Q4 milestone see Figure III.3.84.

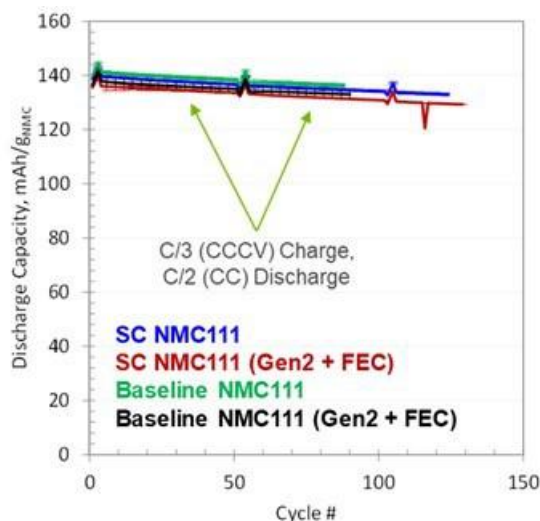


Figure III.3.84 Summary of upcycled single crystal NMC111 versus baseline NMC111 in single-layer pouch cells using Gen2 or Gen2+FEC electrolytes at 30 °C.

Post Test Support

The Post Test Facility (PTF) at Argonne National Laboratory provides expert materials characterization in support of the ReCell Program. We process recycled materials, powders, electrodes, and cells. The facility combines microscopy, spectroscopy and chromatography within a controlled-atmosphere glove box to gain a deep understanding of component interactions as well as chemical and structural changes during battery operation. We provide characterization data that helps elucidate differences between baseline and recycled samples. These results will help us identify issues in the recycled materials, such as how well does a given recycling process separate an initial mixture of cathode, anode, supporting foils and casing materials?

The objective of the PTF is to provide expert analyses of physical, spectroscopic, metallographic and electrochemical evaluation of materials for all facets of the ReCell Program. These analyses lead to a better utilization, upcycling, and recycling of materials investigated in the project.

The PTF is unique in that all its work, from dismantling the cell to harvesting and analyzing its components, can be performed in a glove box. This keeps the air-sensitive battery materials pristine and intact, yielding more information about what's really going on with recycled battery materials in the lithium-ion batteries (LIBs). The techniques at PTF are used in a systematic fashion enabling comprehensive determinations on functionalities of recycled materials in the LIBs.

Impurities detection of the recycled materials.

Any possible impurities remained on the powder materials after binder removal process was investigated. Figure III.3.85 shows the X-ray photoelectron spectroscopy (XPS) results of $\text{Li}(\text{Ni}_{0.6}\text{Mn}_{0.2}\text{Co}_{0.2})\text{O}_2$ (NMC622) after binder removal process using solvent Y. Two different types of solvent Y were used and labeled as new and original. As PVDF $((\text{CF}_2\text{CH}_2)_n)$ binder shows characteristic XPS peaks (CF_2) in C1s (at ~292 eV) and F1s (at ~688 eV) regions, those regions were mainly observed. First of all, no PVDF related peaks were observed from XPS spectra in C1s and F1s regions meaning that PVDF binder were well removed with solvent Y. However, there are still XPS peaks observed in F1s and P2p regions. Those peaks were regarded as some remaining impurities on the surface after binder removal process. Possible compositions for those impurities are LiF and $\text{Li}_x\text{P}_y\text{F}_z$, which are assumed to be originated from cathode electrolyte interface (CEI) layer.

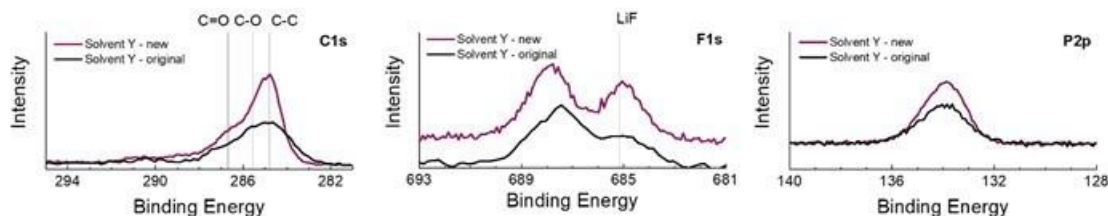


Figure III.3.85 XPS results of C1s, F1s and P2p regions from NMC622 after binder removal process using solvent Y.

Recycled electrolyte.

Aged electrolyte was collected by research group in Argonne (Albert Limpson) and re-used to for the battery testing. After cycle tests, the cathode electrolyte interface (CEI)/ solid electrolyte interface (SEI) of NMC/graphite cells cycled with fresh electrolyte and recycled electrolyte were investigated to consider the reliability of the recycled electrolyte. The cell with recycled electrolyte showed lower cycle retention than the cell with fresh electrolyte. Cells were transferred to the PTF for further analysis to understand the reason of lower cycle retention. First, XPS analysis was performed on the graphite surface (SEI) and NMC surface (CEI) of both samples. As shown in Figure III.3.86 and Figure III.3.87, XPS analysis did not reveal noticeable differences of surface chemistries in SEI and CEI.

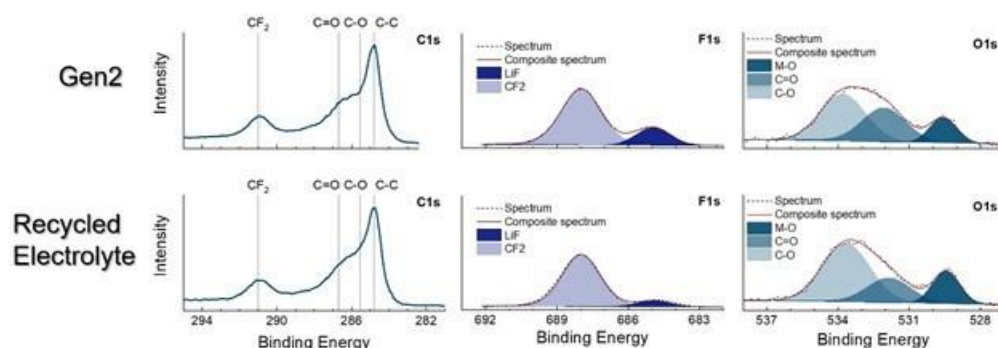


Figure III.3.86 CEI investigation using XPS.

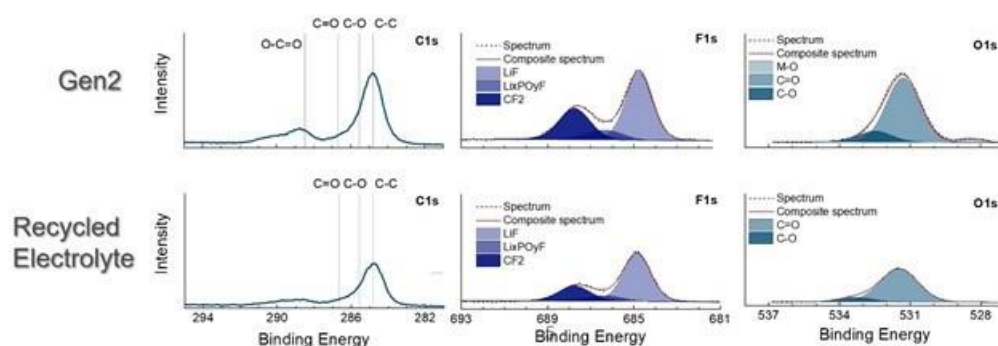


Figure III.3.87 SEI investigation using XPS.

However, metal plating on the graphite anode was only observed from the cell cycled with recycled electrolyte. Raman mapping analysis was further performed and confirmed this is lithium metal plating. (Figure III.3.88) It was assumed that the lithium metal plating occurred because of lower ionic conductivity of recycled electrolyte. The electrolyte with low conductivity could result in lithium-ion reduction to metal on the surface instead of lithium intercalation into the graphite. As the lithium plating is known to be irreversible, this

could be the reason for lower capacity retention of the cell with the recycled electrolyte. This study suggests conducting the conductivity test prior to battery test to reduce the time for evaluation of recycled electrolyte.

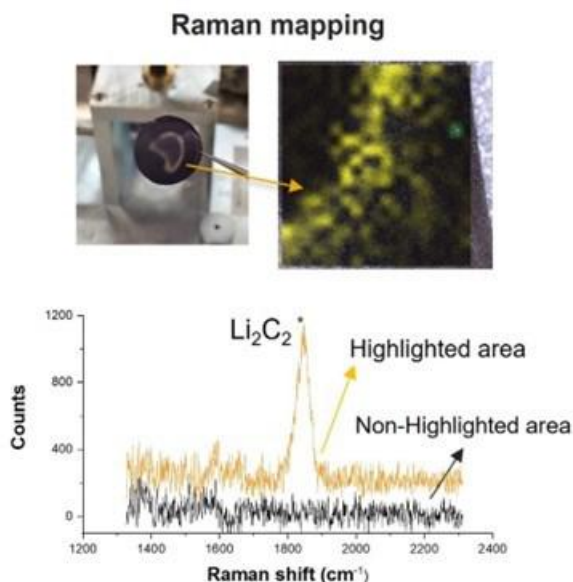


Figure III.3.88 Raman mapping analysis on the lithium plating.

SEI investigation.

It has been well known that how SEI on the graphite forms in the aged cells, but its relationships to the recycling process have not been systemically explored yet. In this regard, two aged graphite anodes (received from NREL) were investigated first with Fourier transform infrared (FTIR) and results are shown in Figure III.3.89. There is no known information such as electrochemical performances or cycle history of these two samples. The results show that lithium carbonate, polyethylene carbonate, LEDC and lithium oxide are main components of SEI layer. In FTIR analysis, the most difference between samples can be found in intensity for Li-O stretch peak observed in $\sim 550\text{ cm}^{-1}$. This could be from either ROLi or Li_2O . Stronger Li-O peak intensity from sample B could be related to the white residues observed in optical images.

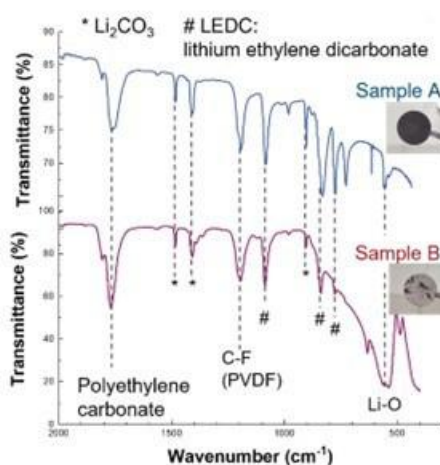


Figure III.3.89 FTIR analysis on aged graphite electrodes.

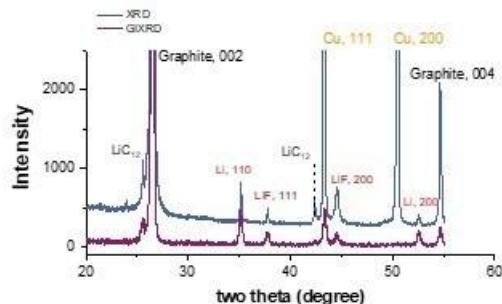


Figure III.3.90 XRD and GIXRD analysis on the aged graphite anode.

In addition, Grazing Incidence X-ray Diffraction (GIXRD) was applied on the sample B to achieve crystalline structure information on the surface of graphite anodes. A GIXRD has the same operating principles as XRD, but it can manipulate X-ray incident angle to lower angle to focus more on the crystal structure of surface film instead of bulk. The results revealed that ratio of peaks intensity from SEI components over graphite was highly increased. However, Li-O related peaks were not detected. This could be either quantity of Li-O component is not sufficient to be detected via XRD or Li-O forms amorphous phase on the graphite anode surface. (See Figure III.3.90.)

More aged graphite anodes are planned to be investigated by using the same experimental scheme and the team at NREL is planning to investigate the relationship between SEI properties and recycling process in coming fiscal year.

Diagnostics of Aged Materials

Over the past several years, we have developed and optimized a streamlined advanced characterization method coupling electron backscatter diffraction (EBSD) with electron dispersive spectroscopy (EDS). The combination of EBSD and EDS is particularly powerful, as it yields simultaneous structural (EBSD) and chemical (EDS) signatures. Our EBSD and associated data processing methods enable statistical quantification of both grain size and intra-grain misorientation, which serves as a proxy for material strain. High data quality and spatial resolution across multiple length scales – from sub-grain to electrode – has been achieved. As a crosscutting technique, this analysis method may be utilized both to analyze degraded material and to assess particle-scale changes resulting from a diverse set of recycling methods. EBSD/EDS data collected at a statistical scale can inform metrics enabling batteries from different life histories to be distinguished in a mixed recycling stream. This technique may also be applied to materials undergoing novel recycling processes (separation, purification, upcycling, etc.) to track impacts to NMC chemistry and structure. Data from new samples analyzed via EBSD/EDS may be compared to our growing database of material parameters.

The EBSD/EDS diagnostic techniques developed and optimized in FY19 and FY20 have been employed in support of multiple subtasks. The objective of this task is to provide on-demand collaboration with the various ReCell subtasks, tailoring analysis approach and data collection to productively inform improvements to the subtask processing methods.

To date, the majority of collaborations have involved the relithiation and upcycling subtasks, with our analytical approach uniquely tailored to the individual subtask needs. In all cases, electrodes are obtained from subtask collaborators and are prepared (mounted, cross-sectioned, ion milled) at NREL prior to analysis. At least 10 distinct particles are analyzed per sample to ensure a representative dataset. Typical analysis may include: 1) Evaluating median grain reference orientation deviation (GROD) and grain orientation spread (GOS; both parameters extracted from EBSD) to assess lattice misorientation; 2) Tracking these parameters (GOS, GROD) at the primary and/or secondary particle scale to identify structural core-shell gradients resulting from materials processing; 3) Pairing this EBSD analysis with spatially resolved EDS (line scan or selective point scan) to identify compositional gradients across primary or secondary particles.

In FY22, the following samples were analyzed using tailored EBSD/EDS methods to address specific material questions or concerns for each sample:

- 1) A polycrystalline upcycled NMC-622 material from UCSD was analyzed using EBSD to track trends in misorientation at both the primary particle and secondary particle scale;
- 2) An upcycled NMC-622 sample from ORNL was analyzed with both EBSD and line-scan EDS across the diameter of the secondary particle to analyze core-shell gradients arising from upcycling conditions;
- 3) An upcycled sample from ANL was also analyzed with both EBSD and line-scan EDS across the diameter of the secondary particle to analyze core-shell gradients, with the specific aim of evaluating processing condition impacts on Ni distribution.
- 4) An additional polycrystalline upcycled NMC-622 sample from ORNL was analyzed via EBSD and line-scan + point-scan EDS to track improvements made in processing methods, as compared to the previous material analyzed. Data has been shared with the individual sub-tasks and details will be incorporated into the individual sub-task reporting.

A highlighted result is the improvement in materials processing parameters achieved by the ORNL upcycling team, informed and measured by the present methods. The sample received from ORNL in Q1 showed significant compositional gradient across the diameter of the secondary particle; structural heterogeneity was also observed at the primary particle scale, with higher lattice misorientation near the primary particle edges. As shown in Figure III.3.91 and Table III.3.13 and Table III.3.14, adjustments to ORNL's methods resulted in significant improvements in compositional homogeneity at the secondary particle scale. These improvements were also manifest as a more homogeneous distribution of lattice misorientation (and lower average misorientation) in the improved material (Figure III.3.92), suggesting greater structural homogeneity and reduced strain.

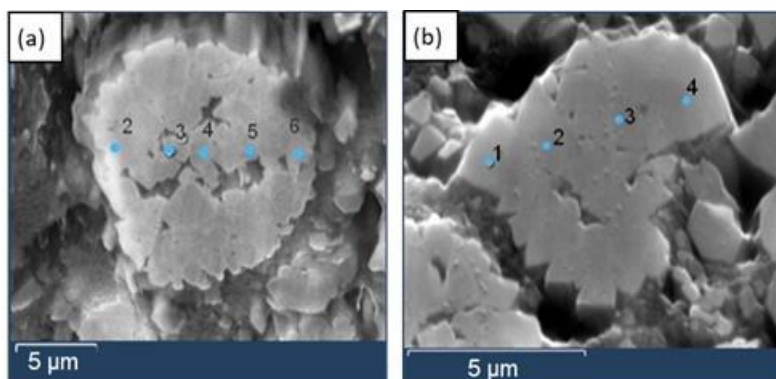


Figure III.3.91 Sampling locations for the point-scan EDS results presented in two prior tables. As shown, compositional analysis was conducted across the diameter of the secondary particle, facilitating analysis of secondary-particle-scale gradients in composition.

Table III.3.13 Spatially resolved compositional data for ORNL upcycled sample received in Q1. Site locations refer to positions indicated in Figure I.1.90a. Compositions are reported as a relative atomic percent, such that the sum (Ni + Mn + Co) = 1.

Scan Location, Q1 Particle (a)	Ni (rel. at. %)	Mn (rel. at. %)	Co (rel. at %)
Site 2	54.2	19.8	26.1
Site 3	58.3	18.9	22.9
Site 4	58.2	19.5	22.3
Site 5	57.7	19.4	23.0
Site 6	66.6	15.1	18.3

Table III.3.14 Spatially resolved compositional data for ORNL upcycled sample received in Q3, showing significant improvement in homogeneity as compared to the sample received in Q1 (prior table). Site locations refer to positions indicated in Figure I.1.90b. Compositions are reported as a relative atomic percent, such that the sum (Ni + Mn + Co) = 1.

Scan Location, Q1 Particle (a)	Ni (rel. at. %)	Mn (rel. at. %)	Co (rel. at %)
Site 1	74.3	14.3	11.4
Site 2	52.2	24.0	23.8
Site 3	48.2	25.9	25.9
Site 4	62.9	18.8	18.3

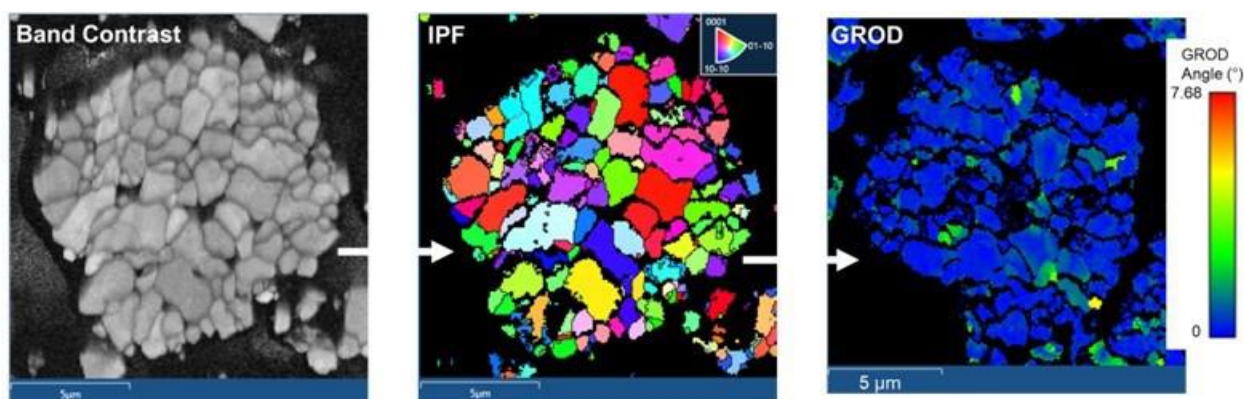


Figure III.3.92 Representative process for EBSD analysis and datatypes: Band Contrast (left); Inverse Pole Figure (IPF, middle); and Grain Reference Orientation Deviation (GROD, right). Sample shown is ORNL's upcycled material received in Q3, which shows improved structural homogeneity (lower average GROD and minimal evidence of primary-particle-scale core-shell gradients) relative to the sample received in Q1.

Finally, our coupled EBSD/EDS methods continue to support further improvements in ORNL's processes. The sample received in Q3 showed evidence of a primary-particle-scale Ni gradient (Figure III.3.93), suggesting that upcycling may not be uniformly upgrading the primary particle composition and may instead be inducing a core-shell compositional gradient. This insight has been shared with the ORNL team and will be incorporated into their ongoing method development efforts.

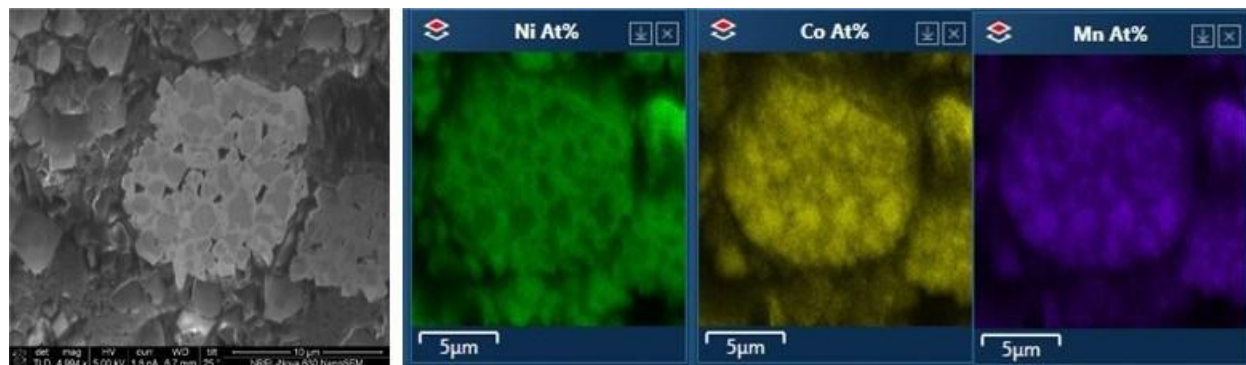


Figure III.3.93 EDS mapping results reveal a grain-scale gradient in composition for several elements. This is particularly evident for the transition metals, where primary particle edges appear to be enriched in Ni, relative to Co and Mn. This information will be used by the ORNL team to further improve upcycling process conditions.

Low Temperature Cell Processing Analysis

Cost models predict that transportation of end-of-life (EOL) battery packs will be an expensive component of any recycling process, with estimates generally ranging from 35 to 50% of total recycling costs.^{1,2} As a class 9 hazardous material, lithium-ion batteries (LIBs) must be transported in accordance with various requirements that inflate these costs. For instance, cells must be separated within a package, their terminals must be individually taped, and the total mass of cells and their container cannot exceed 30kg.^{3,4} Although designed in the interest of safety, these requirements are difficult to achieve in a cost-effective manner for a hypothetical recycling process, as they would necessitate a great deal of individual handling and packaging for the cells entering the recycling stream.

Freezing batteries in liquid nitrogen is known to passivate them, and is currently being employed as a safety measure prior to cell shredding in existing recycling plants. While it can be demonstrated in practice that the cells are rendered inert at cryogenic temperatures, there exists little quantifiable information about the phenomenon. The aim of this project is to better quantify the effects of freezing batteries, and to assess its applicability to EOL transportation. If cells could be maintained in an inert state during transportation, it may enable the alleviation of packaging requirements and consequently a large cost savings in the overall recycling process.

In FY21, freezing experiments were conducted to evaluate the inherent effects of freezing batteries. Given the thin plastic, metal, and ceramic layers within the cell, each with a differing coefficient of thermal expansion, such results as delamination/cracking of active materials, or even tearing of the separator leading to a short, seemed plausible. However, the results of the freezing experiments suggested that cryogenic freezing is a relatively low-risk process for LIBs, imparting no observable damage to any components. These results were confirmed in both fresh cells (100% state of health (SOH)) and aged cells (75% SOH) in both fully charged and fully discharged states. The focus of the work in FY22 was the evaluation of the abuse response of frozen batteries.

The goal of the low-temperature cell analysis project was to determine the viability of an EOL battery transportation process. Having demonstrated in FY21 that freezing cells appears to be a reversible process that imparts no observable damage to the cell components, the work in FY22 transitioned to evaluating the safety factor afforded at cryogenic temperatures. This was accomplished by inducing cell failure (nail penetration) at varying temperatures and monitoring the cell's temperature and voltage responses. The initial tests were

conducted without active cooling, meaning that the cells were thawing via natural convection throughout the experiments. Constant-temperature tests were planned for this FY, but were delayed due to lab maintenance issues and will instead commence in FY23.

The experiments conducted in FY22 were accomplished using a custom-built nail penetration apparatus. Cells (NMC811/AG pouch cells, 5Ah, 100% SOC) were placed into a pan, equipped with voltage and temperature sensors. The pan rested beneath a nail, driven by a linear actuator. The pan was filled with enough liquid nitrogen to freeze the cell and ensure a homogeneous temperature throughout. After the nitrogen boiled off and the cell thawed to a given setpoint temperature, the linear actuator drove the nail into the cell, where it remained for the rest of the experiment. The setpoints tested were: -120°C , -100°C , -80°C , -60°C , -20°C , and 20°C . Two pristine cells (one cell per experiment, two repeats) were tested at each temperature, and aged cells ($\approx 75\%$ SOH) were tested at -100°C and -20°C (one cell at each temperature). Since active cooling was not employed, both the initial response to nail penetration and the progression of thermal runaway as the cell thawed were evaluated in these experiments. The constant temperature tests, which will proceed in FY23, will enable a more refined measurement of the cells' release of energy, as the contribution of natural convection to cell heating will be eliminated.

The cells that were penetrated at 20°C and -20°C entered into thermal runaway immediately upon nail penetration. The cells penetrated at -60°C began to produce heat immediately, but the initial heat release rate was slow, leading to a delay in the onset of thermal runaway. The cells penetrated at colder temperatures (-80°C and below) did not show any initial response to the nail penetration aside from a brief, miniscule temperature increase attributed to conduction from the nail. After this temperature increase, the cells resumed thawing via natural convection until achieving an average temperature of approximately -73°C , at which point they began to measurably generate heat. They then continued self-heating until the initiation of thermal runaway. For this study, the onset of thermal runaway was defined as the temperature at which the heating rate of the cell exceeded 1°C/s . (See Figure III.3.94, Table III.3.15.)

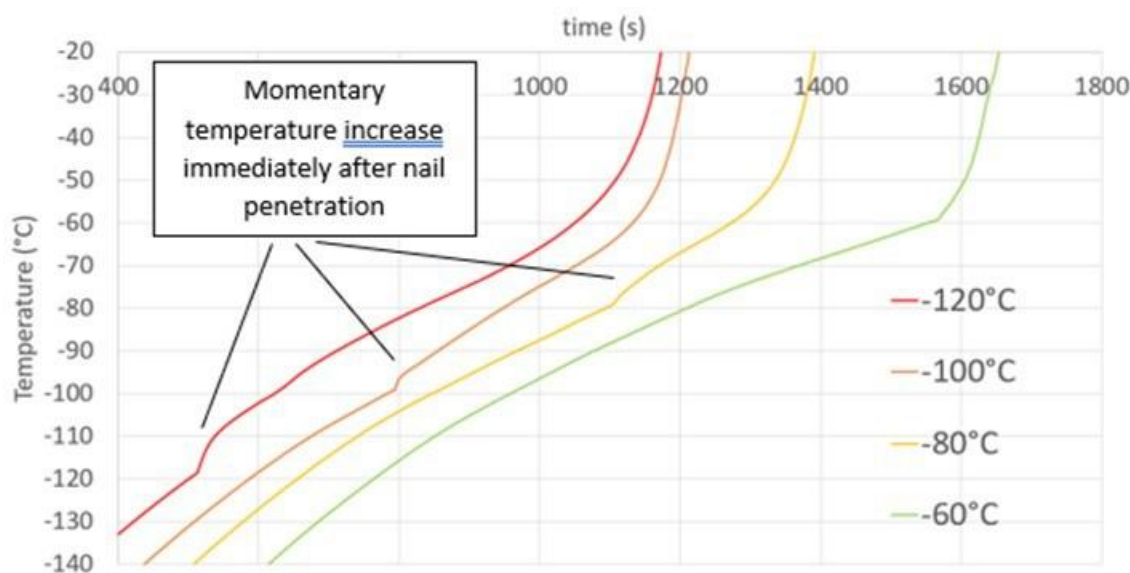


Figure III.3.94 Enlarged plot showing the characteristic temperature vs time curves of the cells penetrated at -120°C , -100°C , -80°C , and -60°C . Curves are offset on the x axis by 100s for -100°C , $x+200\text{s}$ for -80°C , $x+300\text{s}$ for -60°C . Nail penetration did not initiate a continuous heat release at the three coldest temperatures, but is observed to do so in the -60°C sample.

Table III.3.15 Temperatures of interest from the nail penetration experiments.

Nail Penetration Temperature (°C)	Onset of self-heating (°C)		Onset of thermal runaway (°C)		Peak temperature (°C)	
-120	-73.94	-73.8	-21.71	-24.15	523	651
-100	-72.97	-73.28	-24.53	-20.94	575	531
-100 aged	-75.24		8.53		475	
-80	-72.27	-71.32	-22.95	-24.86	539	508
-60	-60	-60	-29.64	-24.63	547	531
-20	-20	-20	-20	-20	517	632
-20 aged	-20		-20		660	
20	20	20	20	20	685	653

The peak temperatures of the cells after thermal runaway did not appear to be greatly influenced by the cell temperature at the moment of nail penetration. The baseline cells achieve the highest temperatures, however, the variation in peak temperatures between experiments is too great to conclude a dependency between nail penetration temperature and severity of thermal runaway. The temperature variation is presumed to result from the expansion of the cells as they enter into thermal runaway; cells may expand differently, which will influence the temperature measured by the thermocouples depending upon how far removed they are from “hot spots” within the cell. However, prior to the onset of thermal runaway, the heating rates within the cells was much more consistent. For the samples penetrated at -60°C and below, the onset of thermal runaway occurred in a fairly tight grouping, ranging mostly between -20°C and -25°C. One outlier to this trend was a cell penetrated at -60°C, which crossed the 1°C/s threshold slightly earlier, at -29.64°C. While the cause of this deviation is unknown, it is arguably unremarkable given its small magnitude. The other deviation from the trend is the aged cell penetrated at -100°C, which heated very slowly and did not enter thermal runaway until it had reached 8.5°C.

The most probable explanation for the findings of these experiments is that ionic current governed the heating rates within the cells. It is well-established in literature that the conductivity of LIB electrolyte increases exponentially with temperature. Additionally, it is suggested in literature that for the specific conditions in which the cells were prepared for these experiments, the electrolyte freezing point was just under -80°C.^{5,6} It is reasonable to conclude that kinetic constraints began to relax within the cells following the melting point of electrolyte, enabling a modicum of ionic current to pass within the cells after further thawing. This current became detectable as heat between -71°C and -75°C, and continued to heat the cell, and thus accelerate in a positive feedback loop until the onset of thermal runaway. In the case of the aged cell penetrated at -100°C, the buildup of SEI over the cell’s cycle life presumably increased the internal resistance within the cell, further constraining ionic current and the release of heat.

Conclusions

Thermal Binder Removal

Thermal binder removal provides a solvent free approach to both delamination and binder removal. On NMC cathodes this process was successfully integrated into a complete recycling. The cycling performance is comparable to pristine commercial NMC with perhaps somewhat worse cyclability. Work is ongoing to try to improve these processes and scale them up using the rotary kiln. We have also demonstrated the potential to use thermal processes to delaminate and potentially remove PVDF from graphite anodes and LiFePO₄ cathode via some process modifications.

Binder Removal via Soxhlet Extraction

During the course of this work we identified an optimal solvent, introduced a vacuum-assisted cryovap process and evaluated various Soxhlet designs for low temperature scalable binder removal from end of life NMC

cathodes. However, NMC particle yield even after introducing steel mesh was still relatively low and the process does not control against fluorine contamination of the recovered NMC materials. We are wrapping up this task and no extensive experimental work is planned. Should this work ever continue, future activities would include attempting to prevent fluorination of the NMC surface and designing a more efficient thimble for NMC recovery.

Cathode/Cathode Separation

Two processes, froth flotation and Process A, were evaluated in FY22 to separate different cathode chemistries. Both processes were capable of producing cathode materials with purities $\geq 95\%$ purity. Further optimization must be conducted to further improve purities and recoveries of both fractions of materials.

Cathode/Cathode Separation via Froth Flotation

In FY22, cathode/cathode separation using froth flotation was applied on commercial black mass, scrap battery cathode, and spent batteries. The present result demonstrated that froth flotation process with spent cathode and black mass after a thermal treatment was inferior to that of pristine materials. For instance, recovery of NMC111 from a binary NMC/LMO mixture reached 95% with 95% grade in the froth product. The separation performance was significantly reduced after the cathode materials were thermally treated. Result obtained with XRD analysis confirmed that a heat treatment caused a phase change in the crystal structure as well as a change in surface chemistry of the cathode materials. New surface treatment method was investigated. Result showed that the new collector exhibited a stronger collecting capacity, but the separation efficiency was deteriorated. FY23 will be focusing on scaling up the cathode/cathode separation process for spent batteries and understanding the mechanism involved in surfactant adsorption as well as the impact of binder removal processes on cathode/cathode separation.

Solvent-Based Gravity Separation

Centrifugal gravity separation has been studied to separate anode and cathode materials from spent Li-ion batteries. Black mass with and without the PVDF were used as the feed materials for gravity separation experiments. Two PVDF removal processes were used including 1) a thermal pyrolysis process and 2) a solvent wash process. Results showed that, for untreated black mass, the grade of cathode active materials in the final concentrate product after rougher and cleaner circuits reached over 97%, but the recovery was 40–50%. The presence of PVDF binder lowers the effective density of cathode materials. As a result, the cathode agglomerate materials are reported to the tailing stream. Both the thermal pyrolysis method and solvent wash method have been studied for binder removal. Treated black masses were fed for gravity separation circuits. Final concentrate product has a 99.2% grade of cathode active material at an 85% recovery. Small cathode active particles were lost in final tailing product. In addition, the NMP was found to be more effective in dissolving PVDF binders compared to DMSO solvents. Follow-up separation result shows a 95% pure of cathode active materials were recovered in the concentrate product. However, the recovery was only 32% to 50%. The low recovery rate is attributed to an incomplete dissolution of PVDF and an incomplete segmentation between PVDF and individual electrode active materials.

Chemical Relithiation

Relithiation of the cycled commercial cathode powder focused on material recovered using the solvent Y process. Lithium salts addition, with and without ethanol coating, combined with resonant acoustic mixing were both used as methods for mixing LiOH with the cathode prior to annealing. Characterization results and electrochemical performance appeared consistent between the two methods. Using the RAM allows easier scalability and reduces waste associated with the relithiation process. Some issues with surface impurities on scale-up were noted and subsequent washing steps appear to have corrected the problem.

Ionothermal Relithiation

An ionothermal relithiation method based on RTMS flux has been successfully developed to relithiate spent NMC622 (SolveY_ORNL). The ionothermal relithiation of spent NMC 622 has been scaled up to 50 g per batch. The relithiated NMC 622 exhibited comparable capacity to pristine NMC 622 in both half-cell and full

cell tests. Up to 90% of RTMS can be reused to lower the recycling cost. By reusing 90% of RTMS for once, the cathode regeneration cost is \$14.88/kg, much lower than those of conventional recycling technologies (\$25.22~30.11/kg).

Hydrothermal Relithiation

In summary, for the past year, the hydrothermal relithiation process has been successfully scaled up to 50g to relithiate cycled NCM622 and 100g to relithiate delithiated NCM111 in one pot. After process optimization for the hydrothermal relithiation process, 4 M LiOH solution can be replaced by 2 M LiOH with 2 M KOH to reduce the regeneration costs for C-NCM622 regeneration. Besides, alkaline impurity removal after hydrothermal reaction has shown to affect the regeneration effectiveness especially on large scale regeneration. Two approaches (optimize washing steps and use scavenge agents) were used to optimize the scaling up process of the hydrothermal direct regeneration process to remove alkaline residue.

Relithiation via Redox Chemistry

Solvent Y EOL NMC622 powder that was cycled to 20% capacity loss was used to carry out relithiation in FY22. In FY20 and FY21 DTBQ redox mediator was used successfully to relithiated NMC111 to match pristine NMC111, however, it is the most expensive component of the redox relithiation process at \$15.49 and \$15.78 for 0.5M and 1M concentration respectively in a volume of 8mL. Therefore, additional redox mediator screening to find a cheaper redox mediator was necessary. The screening process comprised of cost, solubility, and the ability to relithiate EOL NMC622 material. The redox mediator DTBHQ met all the screening criteria, it was cheaper at \$1.21 and \$1.50 for 0.5M and 1M concentration respectively at 8mL volume. The relithiated EOL NMC622 material using DTBHQ performed better than the EOL NMC622 material relithiated using DTBQ. The redox chemistry relithiation recovered the lithium content in the EOL cathode powder from 0.844 to 1.094 that is comparable to lithium ratio of targray pristine NMC622. The relithiated powder had restored capacity during C/10 formation that was close to that of pristine NMC622 material. Ongoing work to facilitate scale up of this process includes relithiation of EOL NMC622 at different DTBHQ redox mediator concentrations and temperatures. Additionally, improving capacity of the 50g scaled up material and reusing the recovered DTBHQ solvent will be explored in FY23.

Electrochemical Relithiation

The limiting factor for success of this milestone and electrochemical relithiation as a technique is the level of surface reconstruction and potentially blocking surface impurity species which are linked to the degree of degradation during cycling for any EoL NMC material. This technique would likely need to be paired with a sophisticated State-of-Health (SoH) screening to be applied to valid materials that would need to be without the aforementioned significant surface defects. Another option for successfully applying the electrochemical relithiation technique would be to design it to be in addition to a high temperature annealing step that would help mitigate surface deconstruction and possibly help remove surface impurities.

Solid State Cathode Upcycling

Previous upcycled cathode samples were re-annealed to higher temperature with the goal of improving morphology and homogeneity. Bulk, EBSD, and surface elemental analysis indicates that the composition is more uniform after re-annealing than previous samples were. The increase in lithium content indicates that less additional LiOH is needed to compensate for potential lithium loss at the high temperature re-anneal. Additional efforts have been established with characterization teams to account for the data that shows the samples are homogeneous NMC622 but the electrochemical data shows a lower than expected performance.

Ionothermal Upcycling

The successful upcycling of D-NMC111 to Ni-rich NMC cathodes has been achieved under ambient pressure and air atmosphere via an RTMS flux upcycling strategy. The ionothermal upcycling of D-NMC111 to Up-NMC622 has been scaled up to 50 g per batch. The upcycling D-NMC 111 to Up-NMC 811 has also been investigated, further optimization on upcycling conditions will be done during next year to achieve better battery performance.

Hydrothermal Upcycling

Two major directions were explored in the upcycling effort: 1) Successfully upgraded Delithiated-NCM111 into single crystal NCM 811 which demonstrates the comparable discharge capacity at 0.1C as the pristine polycrystal NCM 811 and superior rate performance compared with pristine NCM811; 2) After apply a surface coating to stabilize the high-Ni cathode, the regenerated NCM622 sample with B coating shows enhanced cycling performance and air stability in air compared with the uncoated pristine sample.

Single Crystal Cathode Production

In FY22, we successfully improved the electrochemical performance of SC-NMC111 obtained in scale up experiment. Both rate and cycle performance of single crystal NMC111 are comparable or even better than that of polycrystal NMC111. In the study of upcycling NMC811, the polycrystal NMC811 was successfully converted to single crystal NMC811. However, the discharge capacity of single crystal NMC811 is lower than polycrystal NMC811, which is possible because of reduced Ni content. And the cycling performance was significantly improved by single crystal NMC811. Thus, next, we will focus on how to improve the discharge capacity of single crystal NMC811. Finally, in the experiments of reducing the amount of acid, polycrystal NMC111 was upcycled to single crystal NMC111 with good morphology, structure, and electrochemical performance. Reducing sulfuric acid results in fewer loss of transition metals in the solution and higher yield, leading to cost decreasing of upcycling process.

Role of Impurities in Recycled Cathodes

This work demonstrates the significant harmful effects of phosphate impurity in regard to hydrometallurgy recycling processes for NCM cathodes. Any procedures that may introduce phosphate should be of concern, as it is crucial to remove this impurity prior to the recovery process in order to achieve a suitable cathode product.

Cell Preprocessing

During FY22, a custom built dual shaft shredder was installed at Argonne National Lab and two different styles of cells were shredded (e.g., pouch cells and 18650 cylindrical cells). The shredder was effective at shredding both cell designs and shredding discharged cells under inert atmosphere was determined to be a safe method for size reducing end-of-life batteries. Different methods have been investigated for separating components and liberating clumps generated after shredding.

Solvent-Based Electrode Recovery

Table III.3.16 summarizes those three solvent-based processes that have been developed and optimized. Depending on the types of the electrodes, one can choose the right solvents to recycle and reuse the active electrode materials. In addition, all three processes can be used to directly recycle and reprocess electrode scraps. In FY22, the SolveZ process has been mainly studied to determine separation conditions, evaluate half and full cell electrochemical performance, and provide cost analysis for the direct recycling and remanufacturing of PVDF-based anode scraps.

Table III.3.16 Developed and optimized solvent-based processes

Process	Electrode types	Form of recovered materials	Temperature	Remanufacturing electrode scraps?
SolveX	Spent cathode Spent anode Cathode scraps Anode scraps	Electrode films (with binder)	RT to 195 °C	Yes
SolveY	Spent cathode Cathode scraps	Cathode powder (w/o binder)	100 to 150 °C	Yes
SolveZ	Spent anode Anode scraps	Anode films (with binder)	RT to 100 °C	Yes

Solvent-Based Dual Process

In summary, spent cathode from industrial cells has been successfully regenerated using polyol-based relithiation process. Cost analysis has also been performed via EverBatt, which was also used to guide the optimization of relithiation conditions to further reduce cost.

Aqueous Sequential Separation

In summary, an aqueous sequential separation process has been successfully demonstrated to recover anode films, cathode films and metal current collectors. Lithium in the spent anode has been recovered in the form of lithium carbonate. In addition, cost analysis calculated by EverBatt model showed a processing cost of \$2.49 to recycle 1 kg of spent battery. The importance of this project has been highlighted by 2021 U.S. DRIVE Highlight.

Anode/Cathode Separation and Purification

During FY22, we have worked toward optimizing Process A conditions for separating shredded battery materials. We have been successful in separating a simple mixture of anode and cathode materials with greater than 99% purity and more than 90% recovery at high feed rates (> 3 kg/hr). When increasing the complexity of the feed material and conducting using similar parameters, we are able to achieve $\geq 90\%$ purity of anode and cathode with $\geq 90\%$ recovery. More optimization is required to separate materials directly from the shredder and improve purities/recovery.

Purification of Black Mass

Significant progress has been made in FY22 towards the practical implementation of an optimized black mass purification process. In particular, the optimized treatment parameters identified in FY21 have been applied to both simulated (i.e., lab-prepared) and industry-supplied samples of black mass. This FY, evaluation of treated material in a practical full-cell configuration revealed electrochemical performance disparities that had not been evident solely through half-cell analysis; this prompted a more thorough characterization of the treated material from a structural, chemical, and electrochemical perspective. We determined that, although the treatment process itself does not appear to impact the NMC, there is evidence that our choice of post-treatment solvent (originally deionized water) and our methods for filtration of the ionized contaminants had been inducing poor surface properties that led to adverse reactivity and high surface resistance. Iterative improvements to the post-treatment process, initiated in Q3 and still ongoing, suggest a promising pathway to eliminate these surface-level effects and produce a truly “purified” BM that can be further processed in downstream direct recycling methods. Additional accomplishments this FY included the design and acquisition of a pilot-scale reactor; completing a framework for TEA in collaboration with the EverBatt team to more accurately account for the value that the BMP process brings to a direct recycling line; presentation at an international conference; and the preparation and submission of a manuscript to disseminate the project results to date.

Electrolyte Component Removal and Recovery

We have demonstrated electrolyte recycling using cycled commercial cells. In addition, we have determined that the electrolyte can still be viable if exposed to air briefly. This includes transporting the shreds from the shredder to an inert atmosphere glovebox and processing the rinsate in a rotary evaporator. The performance of the recycled electrolyte is similar to that of baseline electrolyte. Work is ongoing to purchase equipment to scale the rinsing and drying process. The concentration process will be scaled using existing equipment available at the Materials Engineering Research Facility.

Graphite to Graphene

Graphene production from end-of-life anode materials seems to be a viable option that could significantly increase revenue for battery recycling. This is particularly true for anode materials that seem to be more amenable to the exfoliation process. The cost is predicted to be \$26.30/kg, which would enable new applications and greater usage for graphene. Currently we are working on scaling this process up to process 500 g of graphite per batch. This will generate more material that can be used by commercial partners to make

composites. In the meantime, we have also been working with other partners to prove out applications including coating carbon fiber to improve carbon fiber reinforced plastics, graphene/polymer composites, and printed electronics.

EverBatt

A better understanding of the costs for both individual processes and direct recycling will help identify possible barriers to scale-up. We will continue to model the cost for ReCell unit processes once data become available, and will focus on providing cost estimates for promising configurations of direct recycling for EOL batteries and manufacturing scrap, respectively. We will also start tracking waste streams generated through various recycling processes and refine the modeling of waste treatment/disposal in EverBatt.

LIBRA

NREL has developed the LIBRA system dynamics model to create a robust and data-based analysis platform to better understand the U.S. and global lithium-ion battery supply chain with a particular focus on the buildout of battery manufacturing and recycling capacity. The primary objective of LIBRA is to ask and answer questions about the future trajectory of the supply chain under varying circumstances using sensitivity and scenario analysis. Areas of analysis from this past year include variations in EV deployment, the future distribution of battery chemistries used in LIB applications, the impact of battery sorting, and the value of manufacturing scrap to the industry. These systems are dynamic and interconnected- our system dynamics framework is designed to capture the feedback between these systems, especially as it develops and evolves over time.

CAMP Support

Results from life cycle testing of the first and second generation of relithiated NMC622 in single-layer pouch cells were summarized in a comparison plot. It was observed that the ionothermal relithiated cathode performs very similar to the baseline cathode. These two pouch cell builds reached 1,027 cycles with 85% and 83% capacity retention, respectively. Upcycled single-crystal NMC111 is still undergoing life cycle testing. Preliminary results indicate that it has similar capacity and capacity retention as the pristine polycrystalline NMC111.

The CAMP Facility actively supports the efforts of the ReCell Center by providing baseline materials, fabricating trial electrodes and baseline electrodes, fabricating and testing coin cells, and fabricating single-layer pouch cells. It should be noted that several of the planned tasks for FY21 were modified or delayed because of reduced laboratory time due to the COVID19 pandemic.

Post Test Support

The PTF will continue to provide expert materials characterization in support of the ReCell Program. The planned, future work includes characterizing recycled materials that were produced as part of this project. As the recycling processes mature, cells will be constructed from the materials. The PTF will continue to be an important source of materials characterization for fabricated cells based on materials produced in the ReCell Program.

Diagnostics of Aged Materials

Optimized EBSD/EDS diagnostic techniques continue to be available in support of all ReCell sub-tasks. These diagnostic tools can inform improvements in materials processing to produce high-quality (re/up)cycled outputs. The coupled EBSD/EDS techniques developed in FY19/FY20, along with advanced data processing techniques, can reveal trends in chemistry and morphology at the primary and secondary particle scales. Tailored analysis methods are employed to track chemical uniformity (EDS) and lattice misorientation (proxy for strain; EBSD), both of which can inform process improvements and can serve as indicators of material quality. To date, this task has been employed for collaborative work with UCSD, ANL, and ORNL.

Low Temperature Cell Processing Analysis

First, the findings of the nail penetration experiments suggest that the heat release from a LIB can be tempered by the cell's internal resistance. This would suggest that if maintained at a sufficiently low temperature, the release of energy from a cell could be a slow and benign process that would not lead to thermal runaway. Secondly, the initial responses (or lack thereof) of the cells penetrated at or below -80°C suggest that a LIB is completely inert while the electrolyte remains frozen. The constant-temperature tests planned for FY23 will help to verify this conclusion. Either of these findings could aid in the establishment of parameters governing cryogenic LIB transportation.

Key Publications

Thermal Binder Removal

1. Bradley Ross, Michael LeResche, Donghao Liu, Jessica Durham, Erik Dahl, and Albert Lipson, "Mitigating the Impact of Thermal Binder Removal for Direct Li-ion Battery Recycling," *ACS Sustainable Chemistry and Engineering* 8, no. 33 (July 2020): 12511-12515.

Solvent-based Gravity Separation

1. Zhan, Ruiting, and Lei Pan. "A cycling-insensitive recycling method for producing lithium transition metal oxide from Li-ion batteries using centrifugal gravity separation." *Sustainable Materials and Technologies* 32 (2022): e00399.

Solid State Relithiation

1. Anthony T. Montoya, Zhenzhen Yang, Erik U. Dahl, Krzysztof Z. Pupek, Bryant Polzin, Alison Dunlop, J. T. Vaughey "Direct Recycling of Lithium-Ion Battery Cathodes: A Multi-Stage Annealing Process to Recover Pristine Structure and Performance" *ACS Sustainable Chemistry and Engineering*, 2022.

Ionothermal Relithiation

1. Sheng Dai, Huimin Luo, Tao Wang, Yaocai Bai, Jianlin Li, and Ilias Belharouak "DIRECT REGENERATION OF LITHIUM ION CATHODES BY IONOTHERMAL RELITHIATION" *patent application*, filed on May 4, 2022, 63/184,270

Hydrothermal Relithiation:

1. Gao, Hongpeng, Duc Tran, and Zheng Chen. "Seeking direct cathode regeneration for more efficient lithium-ion battery recycling." *Current Opinion in Electrochemistry* 31 (2022): 100875.
2. Yu, Xiaolu, Sicen Yu, Zhenzhen Yang, Hongpeng Gao, Panpan Xu, Guorui Cai, Satchit Rose, Christopher Brooks, Ping Liu, and Zheng Chen. "Achieving low-temperature hydrothermal relithiation by redox mediation for direct recycling of spent lithium-ion battery cathodes." *Energy Storage Materials* 51 (2022): 54-62.
3. Yu, Xiaolu, Weikang Li, Varun Gupta, Hongpeng Gao, Duc Tran, Shatila Sarwar, and Zheng Chen. "Current Challenges in Efficient Lithium-Ion Batteries' Recycling: A Perspective." *Global Challenges* (2022): 2200099.

Relithiation via Redox Chemistry

1. Wu, Xiaoxue, Jun Ma, Junxiong Wang, Xuan Zhang, Guangmin Zhou, and Zheng Liang. "Progress, Key Issues, and Future Prospects for Li-Ion Battery Recycling." *Global Challenges* (2022): 2200067.
2. Bird, Robert, Zachary J. Baum, Xiang Yu, and Jia Ma. "The regulatory environment for lithium-ion battery recycling." (2022): 736-740.
3. Makwarimba, Chengetai Portia, Minghui Tang, Yaqi Peng, Shengyong Lu, Lingxia Zheng, Zhefei Zhao, and Ai-gang Zhen. "Assessment of recycling methods and processes for lithium-ion batteries." *Iscience* (2022): 104321.
4. Dunn, Jessica, Alissa Kendall, and Margaret Slattery. "Electric vehicle lithium-ion battery recycled content standards for the US—targets, costs, and environmental impacts." *Resources, Conservation and Recycling* 185 (2022): 106488.
5. <https://recellcenter.org/research> (accessed: December 2022).

- Park, Kyusung, Jiuling Yu, Jaclyn Coyle, Qiang Dai, Sarah Frisco, Meng Zhou, and Anthony Burrell. "Direct Cathode Recycling of End-Of-Life Li-Ion Batteries Enabled by Redox Mediation." *ACS Sustainable Chemistry & Engineering* 9, no. 24 (2021): 8214-8221.

Ionothermal Upcycling

- Tao Wang, Huimin Luo, Juntian Fan, Bishnu P. Thapaliya, Yaocai Bai, Ilias Belharouak, and Sheng Dai, Flux upcycling of spent NMC 111 to nickel-rich NMC cathodes in reciprocal ternary molten salts. *iScience*, 2022, 25, 103801.

Hydrothermal Upcycling

- Gao, Hongpeng, Duc Tran, and Zheng Chen. "Seeking direct cathode regeneration for more efficient lithium-ion battery recycling." *Current Opinion in Electrochemistry* 31 (2022): 100875.
- Yu, Xiaolu, Weikang Li, Varun Gupta, Hongpeng Gao, Duc Tran, Shatila Sarwar, and Zheng Chen. "Current Challenges in Efficient Lithium-Ion Batteries' Recycling: A Perspective." *Global Challenges* (2022): 2200099.

Single Crystal Cathode Production

- Ma, X., Vanaphuti, P., Fu, J., Hou, J., Liu, Y., Zhang, R., Bong, S., Yao, Z., Yang, Z. and Wang, Y., 2021. A universal etching method for synthesizing high-performance single crystal cathode materials. *Nano Energy*, 87, p.106194.

Role of Impurities in Recycled Cathode

- Zheng, Y.; Azhari, L.; Meng, Z.; Gao, G.; Han, Y.; Yang, Z.; Wang, Y. The Effects of Phosphate Impurity on Recovered $\text{LiNi}_{0.6}\text{Co}_{0.2}\text{Mn}_{0.2}\text{O}_2$ Cathode Material via a Hydrometallurgy Method. *ACS Appl. Mater. Interfaces* **2022**.

Solvent-based Electrode Recovery

- Belharouak, I.; Bai, Y.; Essehli, R., (Invited) Toward Solvent-Based Direct Recycling of Lithium-Ion Batteries. ECS Meeting Abstracts 2022, MA2022-01 (5), 608-608.
- Belharouak, I.; Bai, Y.; Essehli, R., Recovery of materials from electrode scraps and spent lithium-ion batteries via a green solvent-based separation process. 17/551,636, US Patent App.
- Belharouak, I.; Bai, Y.; Essehli, R., Recovery of materials from spent batteries using a green solvent. 17/551,395, US Patent App.
- Bai, Y.; Li, M.; Jafta, C. J.; Dai, Q.; Essehli, R. Polzin, B. J.; Belharouak, I., Direct recycling and remanufacturing of anode scraps. *Under review*

Solvent-based Dual Process

- Yaocai Bai, Ilias Belharouak, Jianlin Li, Rachid Essehli. Relithiation process for direct regeneration of cathode materials from spent lithium-ion batteries. 17/363,272, US Patent App.

Aqueous Sequential Separation

- Aqueous Sequential Separation of Electrodes from Used Lithium-Ion Batteries. U.S. DRIVE Highlight, 2021, Page 34
- Belharouak, I.; Bai, Y.; Method of recycling materials from lithium-ion batteries. 17/706,981, US Patent App.

Purification of Black Mass

- K. Fink, P. Gasper, R. Brow, J. Major, A. Colclasure, M. Keyser, "Optimized purification methods for metallic contaminant removal from directly recycled Li-ion battery cathodes" (*submitted*)

EverBatt

- Nguyen-Tien, V., Dai, Q., Harper, G.D.J., Anderson, P.A., Elliott, R.J.R., 2022. Optimising the geospatial configuration of a future lithium ion battery recycling industry in the transition to electric vehicles and a circular economy. *Applied Energy* 321, 119230.
<https://doi.org/10.1016/j.apenergy.2022.119230>

Post Test Support

1. Ma, X.; Chen, M.; Zheng, Z.; Bullen, D.; Wang, J.; Harrison, C.; Gratz, E.; Lin, Y.; Yang, Z.; Zhang, Y.; Wang, F.; Robertson, D.; Son, S.-B.; Bloom, I.; Wen, J.; Ge, M.; Xiao, X.; Lee, W.-K.; Tang, M.; Wang, Q.; Fu, J.; Zhang, Y.; Sousa, B. C.; Arsenault, R.; Karlson, P.; Simon, N.; Wang, Y. Recycled cathode materials enabled superior performance for lithium-ion batteries. *Joule* 2021, 5, 2955–2970, DOI: 10.1016/j.joule.2021.09.005

Diagnostics of Ages Materials

1. Fink, Kae and Pereira, Drew, Helio Moutinho, Patrick Walker, Joshua Major, Mowafak M. Al-Jassim, and Shriram Santhanagopalan, "Application of Electron Backscatter Diffraction Techniques to Quantify Effects of Aging on Sub-Grain and Spatial Heterogeneity in NMC Cathodes," *Energy Storage Materials* 44 (2022): 342-352.

Low Temperature Cell Processing Analysis

1. N. Sunderlin, A. Colclasure, C. Yang, J. Major, K. Fink, A. Saxon, M. Keyser. "Effects of cryogenic freezing upon lithium-ion battery safety and component integrity" (submitted)

References**Ionothermal Relithiation**

1. P. Meister, H. Jia, J. Li, R. Kloeppsch, M. Winter and T. Placke, *Chem. Mater.*, **2016**, 28, 7203.
2. M. Chen, X. Ma, B. Chen, R. Arsenault, P. Karlson, N. Simon and Y. Wang, *Joule*, **2019**, 3, 2622.
3. Tao Wang, Huimin Luo, Yaocai Bai, Jianlin Li, Ilias Belharouak, and Sheng Dai, Direct recycling of spent NCM cathodes through ionothermal lithiation. *Advanced Energy Materials*, 2020, 10(30): 2001204.

Hydrothermal Relithiation

1. Shi, Yang, Gen Chen, and Zheng Chen. "Effective regeneration of LiCoO₂ from spent lithium-ion batteries: a direct approach towards high-performance active particles." *Green chemistry* 20, no. 4 (2018): 851-862.
2. Shi, Yang, Gen Chen, Fang Liu, Xiujun Yue, and Zheng Chen. "Resolving the compositional and structural defects of degraded LiNi_xCo_yMn_zO₂ particles to directly regenerate high-performance lithium-ion battery cathodes." *ACS Energy Letters* 3, no. 7 (2018): 1683-1692.
4. Xu, Panpan, Zhenzhen Yang, Xiaolu Yu, John Holoubek, Hongpeng Gao, Mingqian Li, Guorui Cai et al. "Design and optimization of the direct recycling of spent Li-ion battery cathode materials." *ACS Sustainable Chemistry & Engineering* 9, no. 12 (2021): 4543-4553.

Ionothermal Upcycling

1. Alexandre Beaudet, François Larouche, Kamyab Amouzegar, Patrick Bouchard, and Karim Zaghib, Key challenges and opportunities for recycling electric vehicle battery materials. *Sustainability*, 2020, 12, 5837.
2. Tao Wang, Huimin Luo, Yaocai Bai, Jianlin Li, Ilias Belharouak, and Sheng Dai, Direct recycling of spent NCM cathodes through ionothermal lithiation. *Advanced Energy Materials*, 2020, 10(30): 2001204.
3. Tao Wang, Huimin Luo, Juntian Fan, Bishnu P. Thapaliya, Yaocai Bai, Ilias Belharouak, and Sheng Dai, Flux upcycling of spent NMC 111 to nickel-rich NMC cathodes in reciprocal ternary molten salts. *iScience*, 2022, 25, 103801.

Hydrothermal Upcycling

1. Shi, Yang, Gen Chen, and Zheng Chen. "Effective regeneration of LiCoO₂ from spent lithium-ion batteries: a direct approach towards high-performance active particles." *Green Chemistry* 20, no. 4 (2018): 851-862.

- Shi, Yang, Gen Chen, Fang Liu, Xiujun Yue, and Zheng Chen. "Resolving the compositional and structural defects of degraded $\text{LiNi}_x\text{Co}_y\text{Mn}_z\text{O}_2$ particles to directly regenerate high-performance lithium-ion battery cathodes." *ACS Energy Letters* 3, no. 7 (2018): 1683-1692.
- Noh, Hyung-Joo, Sungjune Youn, Chong Seung Yoon, and Yang-Kook Sun. "Comparison of the structural and electrochemical properties of layered $\text{LiNi}_x\text{Co}_y\text{Mn}_z\text{O}_2$ ($x = 1/3, 0.5, 0.6, 0.7, 0.8$ and 0.85) cathode material for lithium-ion batteries." *Journal of Power Sources* 233 (2013): 121-130.
- Li, Jiyang, Xin Wang, Xiangbang Kong, Huiya Yang, Jing Zeng, and Jinbao Zhao. "Insight into the Kinetic Degradation of Stored Nickel-Rich Layered Cathode Materials for Lithium-Ion Batteries." *ACS Sustainable Chemistry & Engineering* 9, no. 31 (2021): 10547-10556.

Single Crystal Cathode Production

- Billy, E., Joulié, M., Laucournet, R., Boulineau, A., De Vito, E. and Meyer, D., 2018. Dissolution mechanisms of $\text{LiNi}_{1/3}\text{Mn}_{1/3}\text{Co}_{1/3}\text{O}_2$ positive electrode material from lithium-ion batteries in acid solution. *ACS applied materials & interfaces*, 10(19), pp.16424-16435.
- Ruther, R.E., Callender, A.F., Zhou, H., Martha, S.K. and Nanda, J., 2014. Raman microscopy of lithium-manganese-rich transition metal oxide cathodes. *Journal of The Electrochemical Society*, 162(1), p.A98.
- Liu, H., He, B., Xiang, W., Li, Y.C., Bai, C., Liu, Y.P., Zhou, W., Chen, X., Liu, Y., Gao, S. and Guo, X., 2020. Synergistic effect of uniform lattice cation/anion doping to improve structural and electrochemical performance stability for Li-rich cathode materials. *Nanotechnology*, 31(45), p.455704.

Role of Impurities in Recycled Cathode:

- Chen, M. Y.; Ma, X. T.; Chen, B.; Arsenault, R.; Karlson, P.; Simon, N.; Wang, Y. Recycling End-of-Life Electric Vehicle Lithium-Ion Batteries. *Joule* **2019**, 3, 2622-2646.
- Liu, Y.; Mu, D.; Li, R.; Ma, Q.; Zheng, R.; Dai, C. Purification and Characterization of Reclaimed Electrolytes from Spent Lithium-Ion Batteries. *The Journal of Physical Chemistry C* **2017**, 121, 4181-4187.

Purification of Black Mass:

- Pritzl, Daniel, Tobias Teufl, Anna T. S. Freiberg, Benjamin Strehle, Johannes Sicklinger, Heino Sommer, Pascal Hartmann, and Hubert A. Gasteiger, "Washing of Nickel-Rich Cathode Materials for Lithium-Ion Batteries: Towards a Mechanistic Understanding," *Journal of the Electrochemical Society* 166 (2019): A4056-A4066.
- Wood, Marissa, Jianlin Li, Rose E. Ruther, Zhijia Du, Ethan C. Self, Harry M. Meyer, Claus Daniel, Ilias Belharouak, and David L. Wood, "Chemical Stability and Long-Term Cell Performance of Low-Cobalt, Ni-Rich Cathodes Prepared by Aqueous Processing for High-Energy Li-Ion Batteries," *Energy Storage Materials* 24 (2020): 188–197.

LIBRA

- BNEF. 2022. "Electric Vehicle Outlook Report 2022." Bloomberg New Energy Finance (BNEF). <https://about.bnef.com/electric-vehicle-outlook/>.
- IEA. 2022. "Global EV Outlook 2022." IEA. 2022. <https://www.iea.org/reports/global-ev-outlook-2022>.
- Wood Mackenzie. 2021. "Battery Raw Materials Service – 2021 Update to 2040." Wood Mackenzie. <https://www.woodmac.com/industry/metals-and-mining/battery-and-raw-materials/>.

Low Temperature Cell Processing Analysis

- Margaret Slattery, Jessica Dunn, Alissa Kendall. "Transportation of electric vehicle lithium-ion batteries at end-of-life: A literature review." *Resources, Conservation and Recycling*. 174 (2021)
- Qiang Dai, Jarod Kelly, Linda Gaines, Michael Wang. Life Cycle Analysis of Lithium-Ion Batteries for Automotive Applications. *Batteries*. 5 (2019)

3. Haibo Huo, Yinjiao Xing, Michael Pecht, Benno Züger, Neeta Khare, Andrea Vezzini. "Safety requirements for Transportation of Lithium Batteries. *Energies*, 2017
4. Stefan Windisch-Kern, Eva Gerold, Thomas Nigl, Aleksander Jandric, Michael Altendorfer, Bettina Rutrecht, Silvia Scherhauser, Harald Raupenstrauch, Roland Pomberger, Helmut Antrekowitsch, Florian Part. "Recycling chains for lithium-ion batteries: A critical examination of current challenges, opportunities and process dependencies." *Waste Management*. 138 (2022)
5. R. P. Day, J. Xia, R. Petibon, J. Rucska, H. Wang, A. T. B. Wright, J. R. Dahn. "Differential Thermal Analysis of Li-Ion Cells as an Effective Probe of Liquid Electrolyte Evolution during Aging." *Journal of The Electrochemical Society*. 162 (2015)
6. R. Petibon, L. Rotermund, K. J. Nelson, A. S. Gozdz, J. Xia, J. R. Dahn. "Study of Electrolyte Components in Li Ion Cells Using Liquid-Liquid Extraction and Gas Chromatography Coupled with Mass Spectrometry." *Journal of The Electrochemical Society*. 161 (2014)

Acknowledgements

The following individuals worked as individual task leaders/members for the tasks described in this project and ReCell in general: Eva Allen (Argonne), Yaocai Bai (ORNL), Ilias Belharouak (ORNL), Tom Bethel (NREL), Ramesh Bhawe (ORNL), Zheng Chen (UCSD), Andrew Colclasure, (NREL), Jaclyn Coyle (NREL), Qiang Dai (Argonne), Sheng Dai (ORNL), Shailesh Dangwal (ORNL), Fulya Dogan (Argonne), Alison Dunlop (Argonne), Trevor Dzwiniel (Argonne), Rachid Essehli (ORNL), Donal Finegan (NREL), Kae Fink (NREL), Tim Fister (Argonne), Tinu Folayan (MTU), Paul Gasper (NREL), Johathan Harter (ORNL), Golam AHM Hyder (Argonne), Brian Ingram (Argonne), Allison Irion-Bennett (Argonne), Syed Islam (ORNL), Andy Jansen (Argonne), Ozge Kahvecioglu (Argonne), Yana Karslyan (Argonne), Matt Keyser (NREL), Cyrus Kibichi (NREL), Tiffany Kinnibrugh (Argonne), Jayanthi Kumar (ORNL), Mengya Li (ORNL), Tim Lichtenstein (Argonne), Albert Lipson (Argonne), Eric Lopato (Argonne), Huimin Luo (ORNL), Beihai Ma (Argonne), Xiaotu Ma (WPI), Jessica Durham Macholz (Argonne), Margaret Mann (NREL), Colin Moore (Argonne), Helio Moutinho (NREL), Lei Pan (MTU), Parans Paranthaman (ORNL), Sohyun Park (Argonne), Jasmine Pattany (NREL), Candido Pereira (Argonne), Saurab Prakash Pethe (ORNL), Haruka Pinegar (Argonne), Bryant Polzin (Argonne), Melissa Popeil (NREL), Juliane Preimesberger (NREL), Kris Pupek (Argonne), Vicky Putsche (NREL), Matt Riddle (Argonne), Brian Rowden (ORNL), Aron Saxon (NREL), Andrew Schiek (NREL), Carrie Siu (Argonne), Braeton Smith (Argonne), Kandler Smith (NREL), Seoung-Bum Son (Argonne), Venkat Srinivasan (Argonne), Xiao-Guang Sun (ORNL), Nate Sunderlin (NREL), Bishnu Thapaliya (ORNL), Steve Trask (Argonne), John Vaughey (Argonne), Ankit Verma (NREL), Patrick Walker (NREL), Tao Wang (ORNL), Yan Wang (WPI), Dustin Weigl (NREL), Nevi Winofa (NREL), Eliot Woods (Argonne), Lu Yu (ORNL), Xiaolu Yu (UCSD), John Zhang (Argonne), Yadong Zheng (WPI), and Mateusz Zuba (Argonne)

III.4 Development of Lithium Electrode Based Cell and Manufacturing for Automotive Traction Applications (Farasis Energy)

Madhuri Thakur, Principal Investigator

Farasis Energy USA, Inc.
21363 Cabot Blvd
Hayward, CA 94545
E-mail: mthakur@farasis.com

Brian Cunningham, DOE Technology Development Manager

U.S. Department of Energy
E-mail: Brian.Cunningham@ee.doe.gov

Start Date: August 1, 2022
Project Funding: \$2,610,000

End Date: August 31, 2024
DOE share: \$1,305,000

Non-DOE share: \$1,305,000

Project Introduction

This project is to develop lithium (Li) electrode-based cell and manufacturing for automotive traction applications. To increase the energy density of the lithium-ion battery beyond 350 Wh/Kg and 850 Wh/L we need to use high energy density cathode material with pre-lithiated silicon anode or Li metal anode. Li metal is an ideal electrode for rechargeable batteries due to its extremely high theoretical specific capacity $\sim 3860 \text{ mAh g}^{-1}$, low density (0.534 g cm^{-3}) and the lowest negative electrochemical potential (-3.040 V vs. the standard hydrogen electrode). Unfortunately, uncontrollable dendritic Li growth and limited Coulombic efficiency during Li plating/stripping inherent in these batteries have prevented their practical applications over the past 40 years. With the emergence of post-Li-ion batteries, safe and efficient operation of Li metal anodes has become an enabling technology which may determine the fate of several promising candidates for the next generation energy storage systems, including rechargeable Li–air batteries, Li–S batteries, and Li metal batteries which utilize intercalation compounds as cathodes. To implement the Li metal batteries in the electric vehicles (EVs) application needs to see the scalability of these technologies. Farasis will work on all the cell components of the Li metal batteries such as cathode materials (Ni rich, high voltage NCM or Mn-rich), separator, electrolyte, and Li anode (pure Li foil, Li alloy foils etc.). Farasis will optimize the cell design as well as selection of the materials. The 24-months of development effort will be iterative, with an intermediate Milestone based on cell performance goals and progress tracked against the USABC goals for lithium electrode-based cell and manufacturing for the automotive application. Key technologies that are developed and integrated into cells include a cathode material (NCM), Li metal anode in a liquid, salt-concentrated electrolyte with different additives as well as a coated separator. As a large volume battery manufacturer, a major goal of the project will be to accelerate production and enable the commercialization of several novel cell component technologies (including Li metal anode) by supporting scale-up and providing a commercialization path. Deliverables will include small single- or double-layer or multi-layer pouch cells to validate the production capability of this electrode. The project's total budget will be $\sim \$2.61 \text{ M}$ with Farasis covering 50% of the cost.

Objectives

- Develop a Li metal cell technology of providing Beginning-of-Life (BOL) energy density of $\sim 400\text{--}450 \text{ Wh/kg}$, End-of-Life (EOL) energy density of 375 Wh/kg after 500 cycles at a cost target of $\sim \$50\text{--}60/\text{kWh}$ based on the Li metal price.
- Develop Lithium anode with Li metal foils, Li alloy foils, Li-X composite and surface coating.
- Develop electrolyte technology using new solvent, salt components and additives to improve Li Coulombic efficiency and SEI formation on the Li metal surface.
- Develop coated separators to suppress Li dendrite formation/growth and internal shorting.

Optimize cell design with integration of advanced Li anode, electrolyte, separators and high energy density cathode, and deliver 0.4Ah (Phase 1) and 2Ah (Phase 2) Li metal pouch cells.

Approach

- Phase I of the project will last ~12 months, and the focus will be development and characterization of different Li anodes with high energy density cathode materials and down-selection of the materials targeting the energy density of ~375 Wh/kg in the big cells. Initial evaluation will be done on the coin cells for different Li metal anodes, cathodes, electrolyte and separator studies. We will use different thickness Li foils/Li alloy foils coated on Cu foils as the anodes, and Ni-rich NCM electrodes with a loading of ~20 mg/cm² as the cathodes. The electrolyte used is diluted salt-concentrated electrolytes with some additives to stabilize Li metal anodes and NCM cathodes. The cells can achieve a specific capacity of 200-220 mAh/g NCM, and a cycle life of 200-250 cycles at C/3 charge and discharge rate. Based on the technology demonstrated by coin cells, the large-format pouch cells are expected to achieve an energy density of ~350 Wh/kg and a cycle life of 200-250 cycles. At the end of month 12 we will deliver 0.4 Ah pouch cells to the National Labs for performance evaluation tests.
- Phase II of the project is scheduled for 12 months, where the focus will be to achieve high energy density with good cycle life. We will focus on the optimization of electrolyte and separator and see the impact of different N/P ratios on the cycle life. We will also optimize the manufacturing process of pouch cells. The final deliverable will be 2 Ah pouch cells with target energy density of ~400-450 Wh/kg and a cycle life of 500 cycles.

Results

Li metal electrode technology development: Li Coulombic efficiency has been tested in Li/Cu coin cells to evaluate the stability of Li metal anode with electrolyte. Figure III.4.1 shows that Li Coulombic efficiency at C/3 and C/5 in Li/Cu coin cells as a function of cycle number. Li Coulombic efficiency in conventional Li-ion battery electrolyte 1.2M LiPF₆ (E0) is low (<85% before violent fluctuation after 30 cycles) and fluctuates heavily with cycling, which implies unstable Cu/Li/electrolyte interface. Comparatively, Li Coulombic efficiency in our Li metal battery baseline electrolyte (E1) fluctuates slightly (<2% spread), suggesting stable Li metal surface with E1 electrolyte. Li Coulombic efficiency at C/3 is average 98.93% for cycles 6 to 50 and increases to average 99.25% after 50 cycles so far. Li Coulombic efficiency at C/5 is average 99.03% for cycles 6 to 50 and 99.24% after 50 cycles (Table III.4.1). Lower C-rate (C/5 vs C/3) does not obviously increase the Li Coulombic efficiency as expected. From this Li Coulombic efficiency of 99.25% we have achieved, Li metal pouch cells with 40µm thick Li metal anode can achieve ~300 cycles of cycle life. We will improve moisture control in the electrolyte and cell fabrication process, and optimize Li metal anode, separator and electrolyte so as to increase Li Coulombic efficiency and enhance the cycle life of Li metal cells.

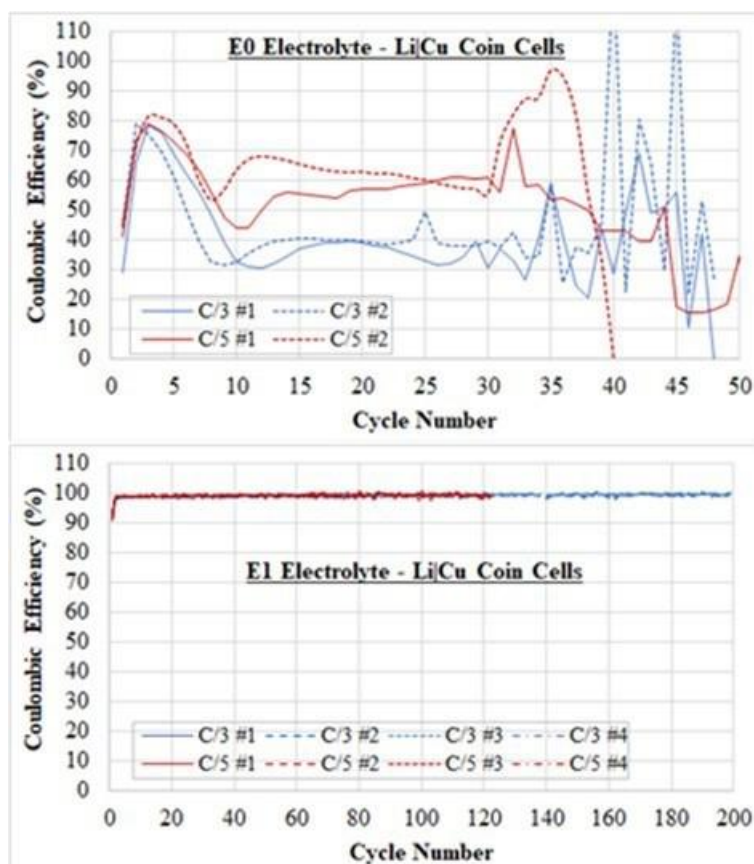


Figure III.4.1 Coulombic efficiency at C/3 and C/5 in Li|Cu coin cells as a function of cycle number (a) in E0 electrolyte and (b) in E1 electrolyte.

Table III.4.1 Average Coulombic Efficiency at C/3 and C/5 with Cycling in E1 Electrolyte

Cell#	C/3		C/5	
	Cycles 6-50	Cycles 51-199	Cycles 6-50	Cycles 51-122
1	98.92%	99.21%	98.95%	99.18%
2	98.95%	99.24%	99.09%	99.20%
3	98.91%	99.26%	99.05%	99.32%
4	98.93%	99.29%	99.02%	99.24%
Average	98.93%	99.25%	99.03%	99.24%

Li metal cell development: We have fabricated 0.2Ah Li metal pouch cells in the dry room. The pouch cells used a double-sided NCM cathode ($\sim 4\text{mAh/cm}^2$) and 2 layers of single-sided $18\mu\text{m}$ thick Li foil on Cu foil as anode. Two initial formation cycles were C/10 charge and discharge between 2.75V and 4.3V. The subsequent cycles were running at C/10 charge and C/3 discharge between 2.75V and 4.3V. Figure III.4.2(a) presents the charge and discharge curves (Voltage vs. Capacity) with cycling. Charge curves (@C/10) and discharge curves (@C/3) after cycle 4 are overlapped with cycling, indicating little capacity fade with cycling. Figure III.4.2(b) shows specific capacity and Coulombic efficiency vs. cycle number. Cycles 1 and 2 are formation cycles; cycles 22 and 42 are capacity check @C/10; their specific capacity is $\sim 230\text{mAh/g}$, higher than 225mAh/g - 222mAh/g for the other cycles @C/3 discharge. Capacity retention is $>98.9\%$ after 57 cycles. Coulombic efficiency is stable at $\sim 102\%$ @C/3 discharge, but is $\sim 100\%$ for cycles 2, 22 and 42 @C/10 discharge.

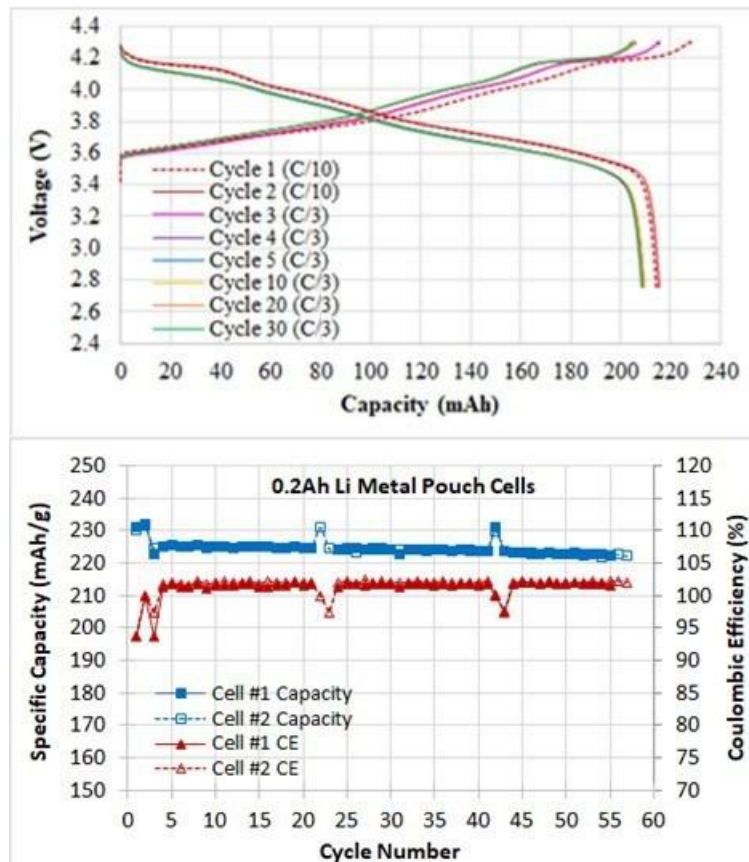


Figure III.4.2 (a) Charge and discharge curves (Voltage vs. Capacity) and (b) Specific capacity and Coulombic efficiency vs. cycle number for 0.2Ah Li metal pouch cells.

Conclusions

Farasis has tested 57 cycles so far in 0.2Ah Li metal pouch cells with 18 μ m thick Li foil on Cu foil and NCM cathode and capacity retention is >98.9%. Li Coulombic efficiency of 99.25% at C/3 in Li/Cu coin cells has been achieved, and in this case Li metal pouch cells with 40 μ m thick Li metal anode can achieve ~300 cycles of cycle life. Farasis will improve moisture control in the electrolyte and cell fabrication process, and optimize Li metal anode, separator and electrolyte so as to increase Li Coulombic efficiency and enhance the cycle life of Li metal pouch cells. Farasis will build 0.4 Ah Phase 1 pouch cells with optimized chemistry, which will be delivered to national labs for performance evaluation tests.

III.5 A Closed Loop Recycling Process for End-of-Life Electric Vehicle Li-ion Batteries-Phase III (Worcester Polytechnic Institute)

Yan Wang, Principal Investigator

Worcester Polytechnic Institute

100 Institute Road

Worcester, MA 01609

E-mail: yanwang@wpi.edu

Brian Cunningham, DOE Technology Development Manager

U.S. Department of Energy

E-mail: Brian.Cunningham@ee.goe.gov

Start Date: October 1, 2020

End Date: September 30, 2021

Project Funding: \$800,000

DOE share: \$800,000

Non-DOE share: \$0

Project Introduction

The U.S. Department of Energy (DOE) has established aggressive goals to lower the cost of lithium ion batteries for EVs. Therefore, in the Phase III program, the team will target lowering the cathode cost by 30% (relative to commercial equivalent) by significantly increasing the amount of recycled materials (>80%) in the synthesized cathode materials. In the WPI/BRs recycling process, virgin materials (CoSO_4 , NiSO_4 and MnSO_4) must be added to the leaching solution in order to reach the target ratio of Ni, Mn and Co. Earlier generation spent EV batteries use mostly NMC111 or mixed NMC111 and LMO or NMC622 as the cathode materials, and the leaching solution has more Mn than Co and Ni. However, in order to increase the energy density and lower the cost, high nickel cathode materials (for example NMC622 or above) are preferred by the EV industry. Therefore, in order to transform the Mn-rich leaching solution into a Ni-rich metal sulfate solution, supplemental virgin materials CoSO_4 and NiSO_4 are needed. In the BRs' cost model, the virgin materials currently account for 45% of the bill of materials (BOM) cost, since 0.36 kg of virgin materials are added to the leaching solution per kg of NMC622 cathode output. Therefore, in order to further reduce the cathode cost by 30%, which will help reach the DOE cost target (less than \$100/kWh, ultimately \$80/kWh) [1], the team will increase the use of recycled materials to >80%.

In addition, the lithium ion battery (LIB) industry is a dynamic field with ongoing innovations and continually evolving materials delivering ever improving performance. It is critical that recycling technologies keep pace with state of the art LIB technologies. $\text{LiNi}_x\text{Mn}_y\text{Co}_z\text{Al}_a\text{O}_2$ ($x \geq 0.8$) has the potential to be used in the next generation of lithium ion batteries [2]. The specific capacity of $\text{LiNi}_x\text{Mn}_y\text{Co}_z\text{Al}_a\text{O}_2$ is >200mAh/g. Al can be introduced as dopant and/or coating to stabilize the materials. Therefore, it is critical to be able to synthesize such high nickel cathode materials from spent lithium ion batteries in order to remain competitive in the cathode supplier space.

Finally, the team will further improve the performance of recovered NMC622 from spent lithium ion batteries. Compared to A123 control NMC622, the recycled materials have inferior cycle performance and elevated gas generation. The reduced cycle life is likely because the stabilizing alumina coating developed rapidly in Phase II cannot fully protect the NMC622. The gas generation is likely because the soluble base content on recovered NMC622 is higher than that of control powder. It is expected that the process improvement from this task will equally benefit the higher nickel work streams.

During this 3 year program, ≥ 300 coin cells, 40 1Ah cells and 20 10Ah large format cells will be produced from recycled automotive lithium ion batteries and 20 1Ah cells and 20 10Ah large format cells from control materials will be produced. 36 1Ah cells and 24 10Ah cells will be delivered to Argonne National Laboratory

for testing using EV application USABC test methods. The cost of the proposed program is \$1,996,180, which includes a 50% cost share by WPI, A123 and Battery Resources. At the end of program, the team expects to be able to lower the cathode cost by 30%, produce high quality NMCA and solve the cycle life and gas generation issues observed with the recycled NMC622. Achieving these targets is challenging, but necessary in order to offer a product with low cost, high quality and high energy, and to remain aligned with market trends.

Objectives

The overall objective of phase III program is: 1) to lower the cathode cost by >30% relative to commercial equivalent material through increasing the recycled content of the metal sulfate solution to >80% (<20% virgin materials); 2) to develop $\text{LiNi}_x\text{Mn}_y\text{Co}_z\text{Al}_a\text{O}_2$ ($x \geq 0.8$) and other possible doping or coating strategies for Ni-rich cathode materials from the spent EV batteries; 3) to improve the performance of the recovered NMC622 (solve the gas generation and improve the cycle life) in order to be comparable with commercial material.

Approach

High-quality NMC111&NMC622 have been successfully synthesized using WPI's closed loop recycling process for end-of-life xEV Li-ion batteries. Although much knowledge has been gained from this experience, technical challenges remain in obtaining additional Ni and Mn from other recycling streams in order to further lower the cathode cost, synthesizing NMCA precursor and cathode powder by co-precipitation and solid state reaction. In addition, the recovered NMC622 has worse cycle life and gas generation compared to control powder, which also need to be addressed.

Recovering Ni from Ni/MH will be studied in order to reduce the amount of the virgin metal sulfate and lower the cost of the recovered cathode materials. In typical Ni/MH batteries, Ni accounts for 17.9wt% [3]. According to Inside EVs [4], ~60,000 tons Ni/MH batteries (Toyota Prius HEVs) were sold in 2013. Assuming that HEVs with Ni/MH batteries have 8~10 years life, there are 60,000 tons of spent Ni/MH batteries in U.S, which have over 10,000 tons of Nickel. In Ni/MH batteries, the cathode is $\text{Ni}(\text{OH})_2$ coated on Nickel foam. The anode is hydrogen absorbing alloys coated on steel. Although there is a high content of Ni in Ni/MH batteries, obtaining high concentration of pure Ni solution can be challenging. Impurities will significantly degrade the performance of recovered cathode materials. If the concentration of obtained solution is not high enough, a high amount of virgin chemicals will still need to be added in order to reach target concentrations. In addition to Ni/MH batteries, the team will also investigate other recycling streams for Ni that can be readily incorporated into the existing process.

High Nickel $\text{LiNi}_x\text{Mn}_y\text{Co}_z\text{Al}_a\text{O}_2$ ($x \geq 0.8$) has the advantages of high capacity and safety and is considered a promising next generation cathode material for lithium ion batteries which could enable a driving range of 300 miles. However, the ultra-high nickel amount will also increase issues related to capacity fade. Therefore, we would expect technical challenges related to the precursor synthesis and cathode sintering steps. Although our previous research on NMC111 and NMC622 should provide good guidance, the optimum synthesis conditions for NMCA precursor need to be determined. It will thus be necessary to thoroughly investigate the effects of various factors on the key properties (eg. morphology, tap density etc.) of resultant precursor, and experimentally determine the ideal combination of pH, temperature, reactant concentrations and flowrates, residence time, stirring speed, etc.

The high Ni content also has implications on the preparation of NMCA by high temperature calcination of precursor and the Li source. For good electrochemical performances of NMCA, the calcination needs to occur in an oxygen environment, unlike static (closed reactor) air atmosphere for NMC111, and flowing air for NMC622. This seems to be attributed to the difficulty of oxidizing Ni^{2+} . Therefore, it is essential to examine effects of oxygen partial pressure on resultant cathode properties. Moreover, compared to the calcination temperature and calcination time required for NMC111 and NMC622, the temperature and calcination time for NMCA are expected to be lower and shorter in order to minimize undesired cation mixing. It is thus critical to optimize the calcination temperature and furnace residence time in order to produce high quality NMCA cathode powder.

Aluminum incorporation in the NMCA needs to be carefully studied. There are the following three possible ways to add Al in NMCA. We will study these different approaches separately and a combination of these approaches to determine how to improve the cycle life.

- 1) During precursor synthesis. $\text{Al}_2(\text{SO}_4)_3$ can be added into metal sulfate solution. Then Al^{3+} will be co-precipitated with Ni^{2+} , Mn^{2+} and Co^{2+} as $\text{NiMnCoAl}(\text{OH})_2$ precursor.
- 2) During sintering. $\text{Al}(\text{OH})_3$ is mixed with $\text{NiMnCo}(\text{OH})_2$ precursor and Li source (LiOH) for sintering.
- 3) After sintering. Al_2O_3 can be coated onto LiNiMnCoO_2 surface by dry or wet methods.

Therefore, a detailed study needs to be conducted to determine the best way to dope or coat Al. In addition, the amount of Al doping or coating needs to be determined.

Another technical challenge is to improve the cycle life and reduce the gas generation of recovered NMC622 developed in the Phase II program. It is expected that improvement strategies found to be effective for this will also enhance and inform results for Phase III chemistry.

Results

NMC622

To solve the cycling and gas generation problems in Phase II, WPI re-ran the co-precipitation reaction for recycled NMC622 to reduce the SBC. A twelve days reaction was operated in this quarter. And Figure III.5.1 shows the morphology and tap density of precursors. Except for the 24 hours precursor, all precursors are spherical with a tap density of 2.17g/cc, which is comparable to the previous experiment of recycled NMC622. Then, the overflow powder was around 9kg, which was washed, resulting in low SBC after the cathode sintering process.

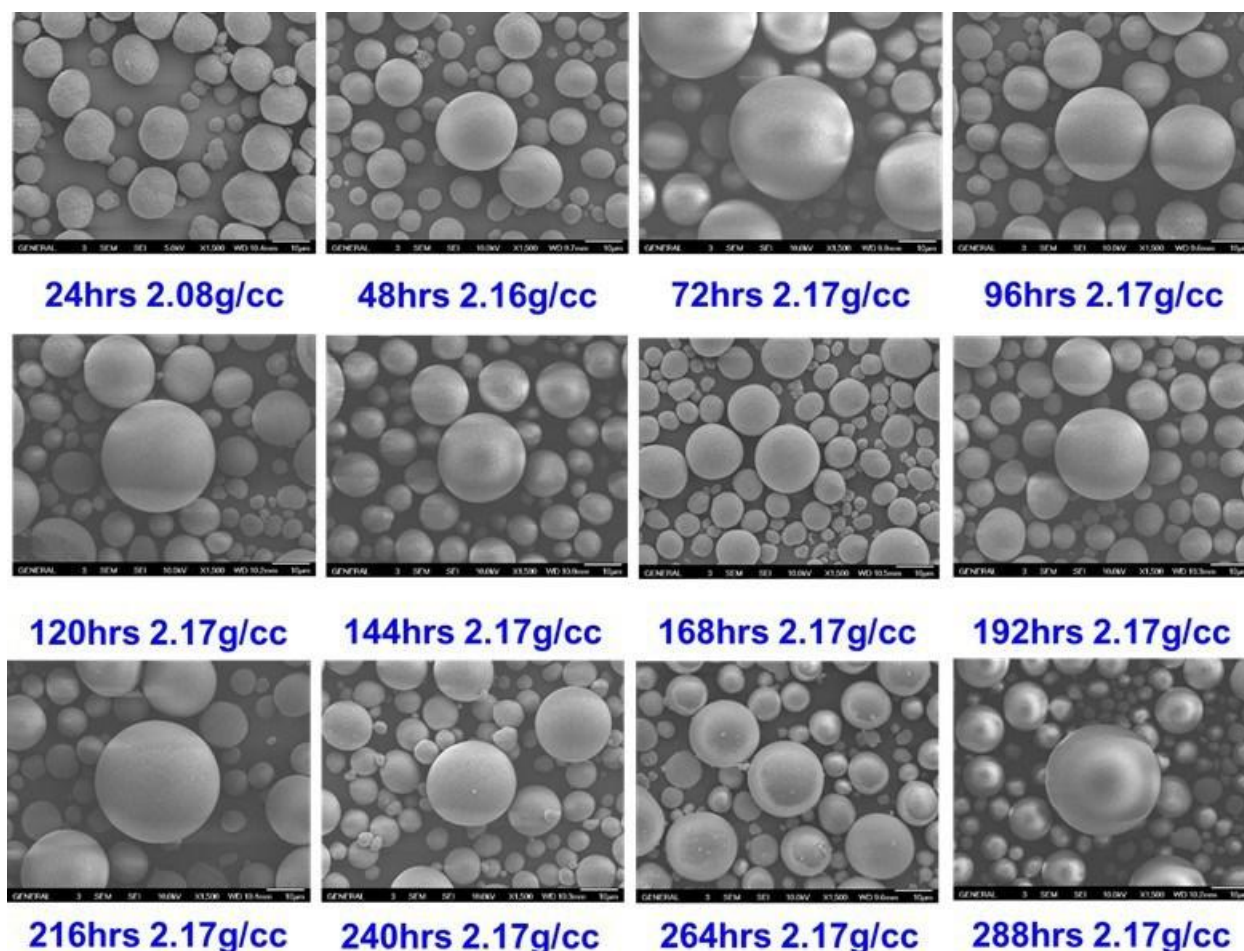


Figure III.5.1 SEM images of recycled NMC622 precursors.

After washing, 100g of the precursor was mixed with Li_2CO_3 and sintered. Figure III.5.2 shows the spherical shape and layered structure of 0919NMC622-100g. Then, 0919NMC622-100g was coated with Al_2O_3 , which was labeled as 0919NMC622-100g- Al_2O_3 . After coating, the morphology and structure were well kept from 0919NMC622-100g in Fig. 3. Furthermore, the EDS mapping results in Figure III.5.3 showed the uniform Al coating on the surface of the cathode. The content of transition metals, lithium, and Al was tested by ICP-MS. As shown in Table III.5.1, all content is consistent with our design.

Table III.5.1 ICP results of recycled NMC622 cathode materials

mol/L	Ni	Mn	Co	Li	Al
0919NMC622-100g	0.60	0.20	0.20	1.05	-
0919NMC622-100g- Al_2O_3	0.60	0.20	0.20	1.05	0.351 wt. %

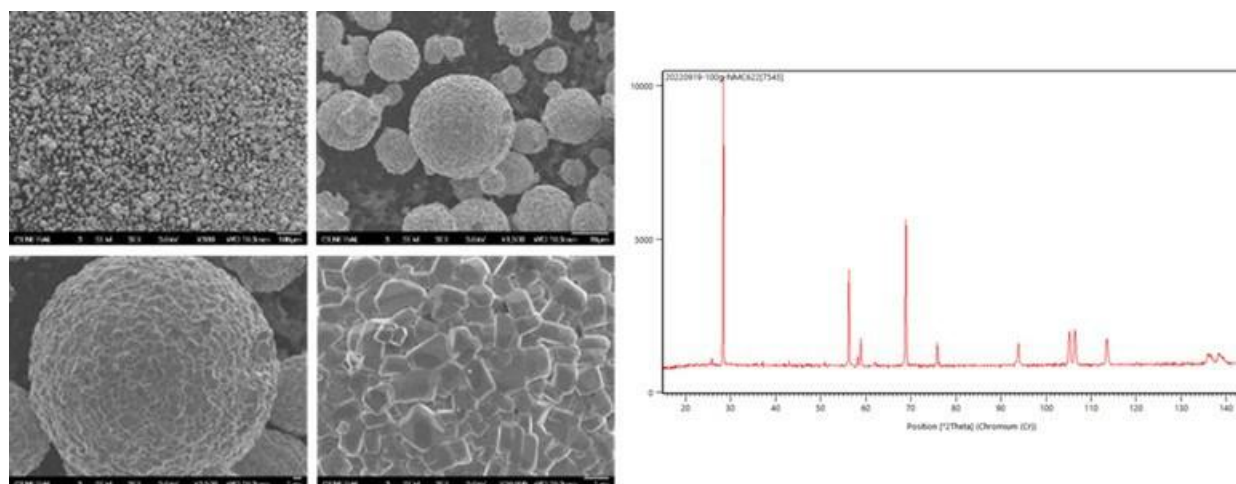
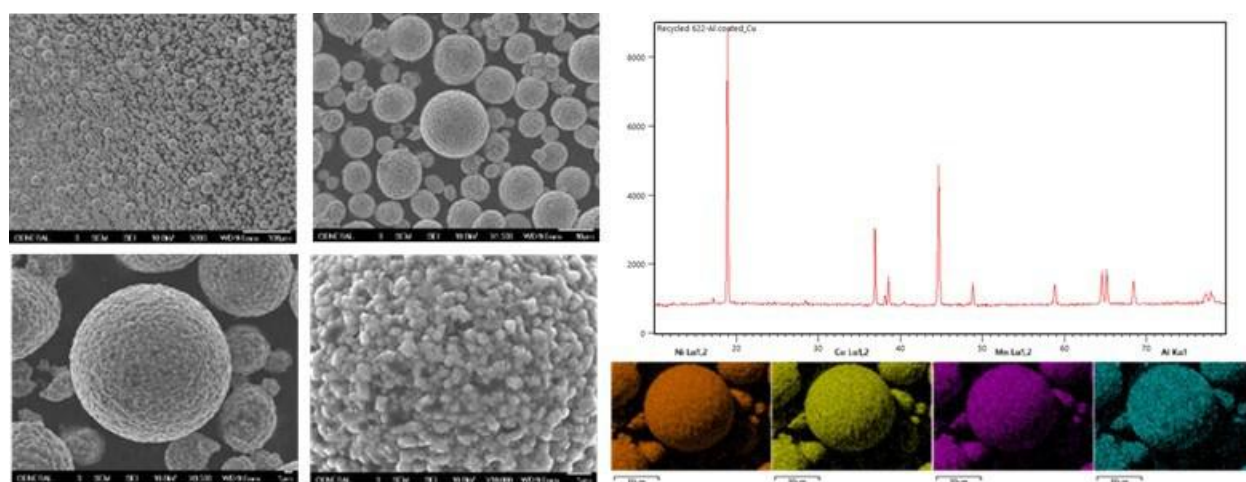


Figure III.5.2 The SEM images and XRD pattern for 0919NMC622-100g.

Figure III.5.3 SEM images, XRD pattern, and EDS mapping of 0919NMC622-100g-Al₂O₃.

Then, the SBC was tested before and after coating and compared to the control. In Table III.5.2, the SBC of 0919NMC622-100g and 0919NMC622-100g-Al₂O₃ is close to the control. The free lithium content is only 0.125wt.% and 0.137wt.% before and after coating. The electrochemical performance of 0919NMC622-100g-Al₂O₃ was shown in Figure III.5.4. At C/20, the discharge capacity is 176.8mAh/g and the average initial coulombic efficiency is 89.39%, which is comparable to the precious results of control NMC622.

Table III.5.2 SBC results of the control sample and recycled NMC622.

Sample Name	Residual Lithium			Free Lithium (ppm)	Free Lithium (wt.%)
	Li ₂ CO ₃ (ppm)	LiOH (ppm)	Total (ppm)		
Control (Test by WPI)	3284.04	2128.89	5414.93	1233.78	0.123
Control (Tested by A123)	3511.263	2179.029	5690.292	1291.228	0.129
0919NMC622-100g	2298.831	2834.083	5132.914	1253.056	0.125
0919NMC622-100g-Al ₂ O ₃	1409.402	3800.954	5210.356	1366.152	0.137

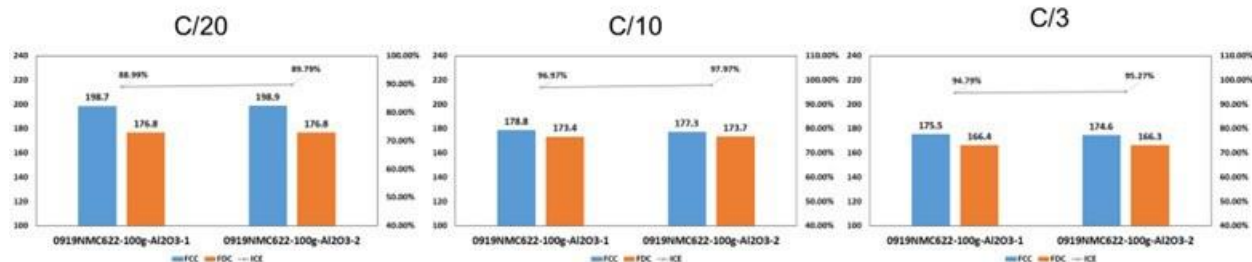


Figure III.5.4 Electrochemical performance of 0919NMC622-100g-Al2O3.

High Nickel NMC (83% Ni)

Last year, we determined the parameters of co-precipitation experiments through experiments with virgin materials. This year, WPI synthesized three batches of recycled Ni-rich precursor with recycled solution based on the parameters of co-precipitation reactions with virgin materials. The first batch of recycled precursor (Figure III.5.5a) was obtained under a wider pH range because the pH controller was not perfect after a long time using. Then, we prepared the second batch of recycled precursors with a new pH controller and the pH was perfectly controlled at 11. However, cracks were observed on the surface of the precursor (Figure III.5.5b). Therefore, to remove the cracks, we reduced the pH from 11 to 10.97, and no cracks were observed in the third batch of recycled precursor (Figure III.5.5c).

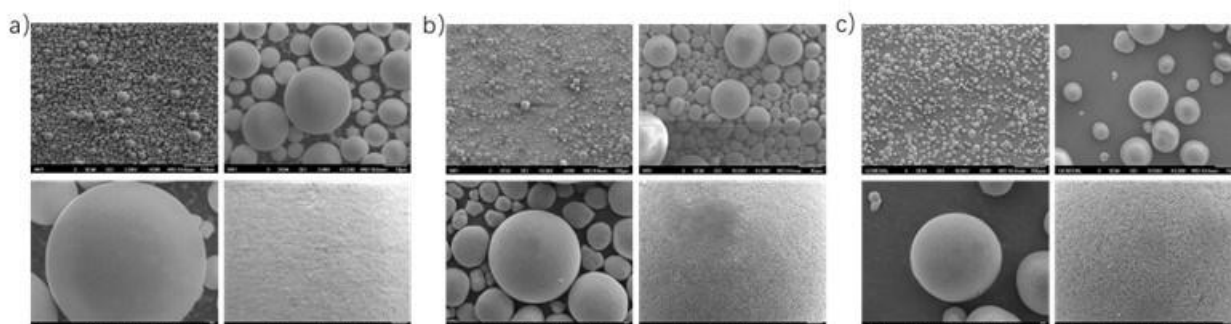


Figure III.5.5 SEM images of (a) first batch of recycled precursor; (b) second batch of recycled precursor; (c) third batch of recycled precursor.

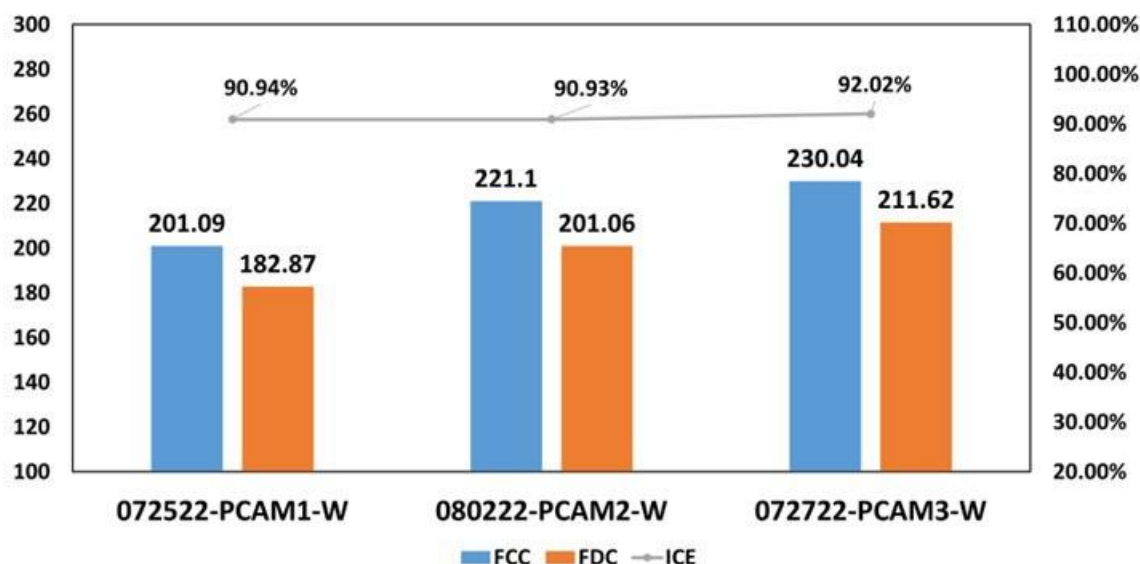
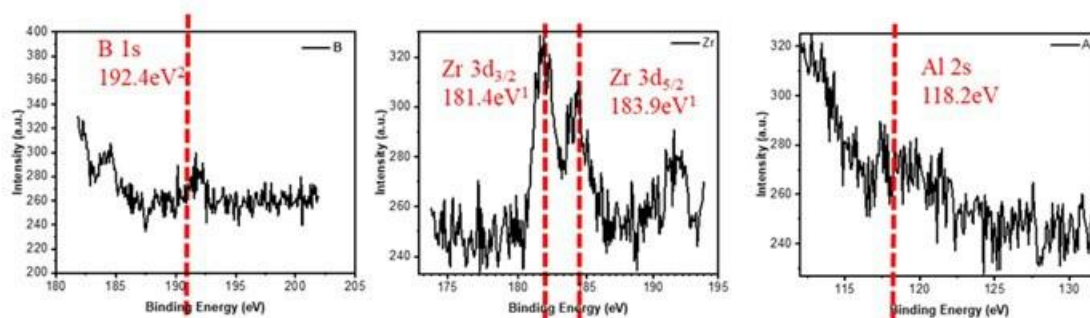


Figure III.5.6 Electrochemical performance comparison of recycled cathode materials made by three different batches of recycled precursors.

Then, all three batches of recycled precursors were sintered with LiOH in an oxygen atmosphere to obtain cathode materials. In Figure III.5.6, all recycled cathode materials show a spherical shape with a perfect layered structure. And the tap density is similar and consistent. Then, the powders were delivered to Farasis for electrochemical performance tests. Figure III.5.7 shows the electrochemical performance comparison of all three batches of cathode materials. The third batch exhibits the best electrochemical performance. Thus, we would use the third batch of recycled precursor to further investigate the coating or doping strategies of Ni-rich recycled materials.

To determine the coating or doping strategies, XPS was employed to investigate the type and position of coating or doping elements in the control sample from A123. Figure III.5.7 shows the XPS results of B, Zr, and Al at the surface and depth for the control sample from A123. There is no obvious peak for Al, which is consistent with our ICP results, indicating no Al coating or doping in the control from A123. The peaks of B and Zr at the surface are stronger than that at depth, which means that most B and Zr are distributed at the surface of the control from A123. Thus, B and Zr should be coated at the surface of the control from A123.

Control-Surface



Control-Depth profile

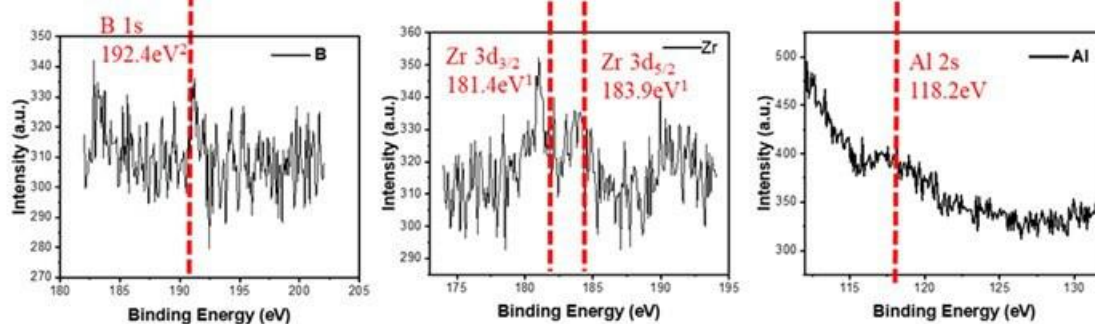


Figure III.5.7 XPS results of the control from A123.

Figure III.5.8 shows the morphology, structure, and EDS mapping results of the control from Farasis. Compared to the control from A123, the control from Farasis is more spherical, but there are some cracks on the large particles. Both control samples have a great layered structure. The main difference is that the control from Farasis detected Sr and Zr from EDS mapping, which means that the control from Farasis has a different coating strategy. To confirm the coating and doping strategy of the control from Farasis, ICP-MS was used to study what elements were applied to coating or doping in Table III.5.3. The content of Ni and Co is slightly different from the control from A123. The coating/doping elements of the control from Farasis include Zr, B, Sr, and Mg. Other elements are less than the coating or doping amount.

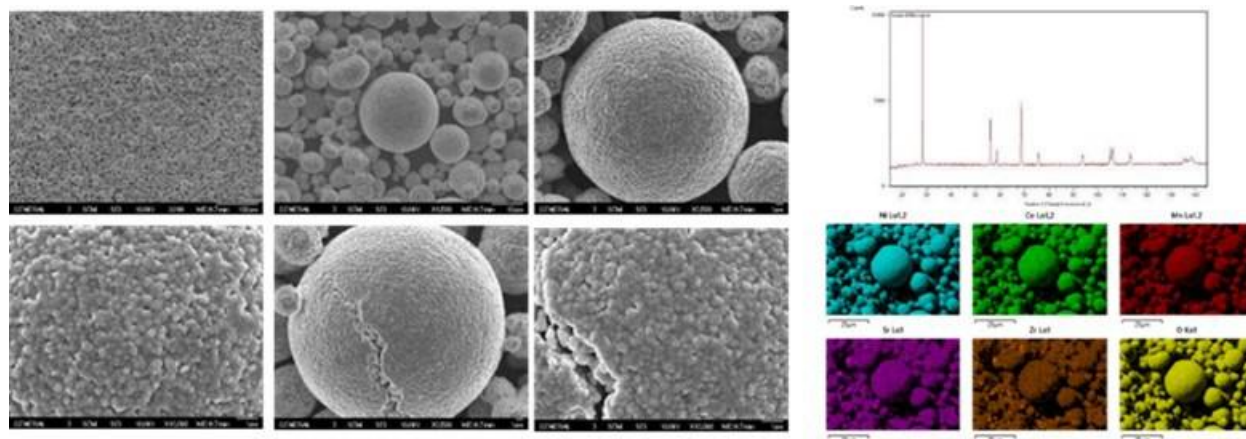


Figure III.5.8 SEM images, XRD pattern and EDS mapping of the control from Farasis.

Table III.5.3 ICP results of the control from Farasis.

	Li	Ni	Mn	Co	Zr	B	Sr	Mg	Ti	W	La
Control	1.01	0.82	0.06	0.12	0.19 mol.%	1.41 mol.%	0.19 mol.%	0.49 mol.%	0.005 mol.%	0.002 mol.%	0.03 mol.%

Then, because the recycled cathode made by the third batch of precursors exhibits the best electrochemical performance, we applied different coating and doping strategies to the third batch of recycled precursors. First of all, Al_2O_3 coating was first investigated. The Al_2O_3 -coated recycled 83Ni was named as 083122-PCAM3-W-C-Al. Figure III.5.9 shows the morphology, structure, tap density, and composition. The Al_2O_3 coating didn't change the morphology and structure and the tap density is comparable to the uncoated cathode materials. Besides, based on the ICP-MS results, the composition was the same as our expectation.

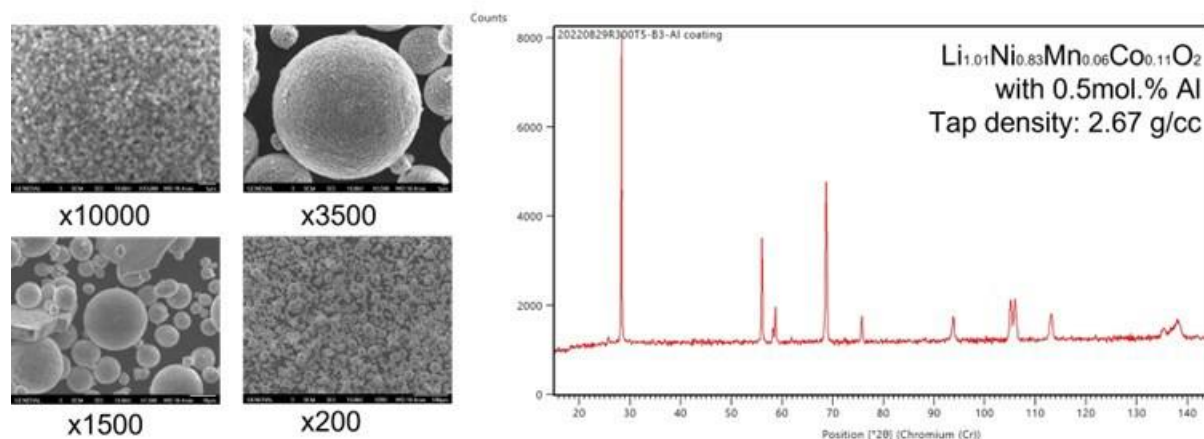


Figure III.5.9 Physical properties of 083122-PCAM3-W-C-Al.

Then, 0.2mol.% Zr and 1mol.% B co-coated cathode materials were prepared. The Zr and B co-coated recycled 83Ni cathode was labeled as 090722-PCAM3-W-C-Zr/B. In Figure III.5.10, 090722-PCAM3-W-C-Zr/B shows a spherical shape with a good layered structure. The tap density is 2.68g/c, which is comparable to the uncoated cathode materials. However, from the ICP-MS results, the Zr and B content is lower than the design, because ZrO_2 and B_2O_5 will form large particles during the heat treatment and the large particles will be sieved out.

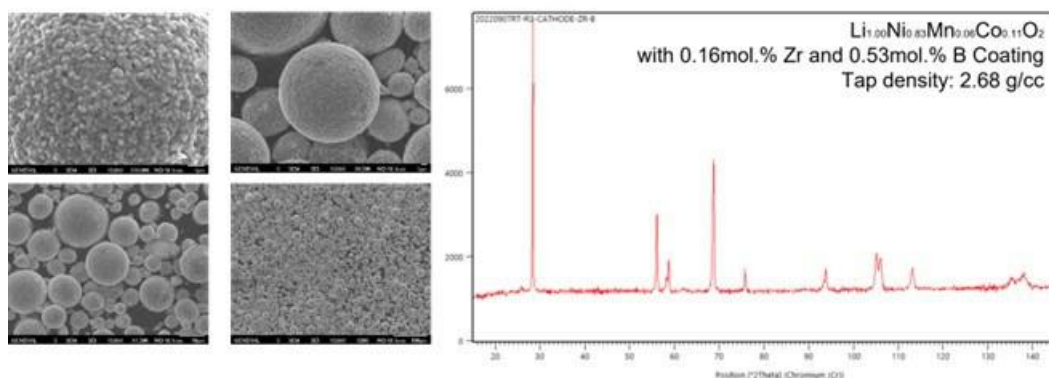


Figure III.5.10 Physical properties of 090722-PCAM3-W-C-Zr/B.

After that, different doping and coating strategies were studied. Zr and B co-doping, Zr doping with B coating, and B doping with Zr coating are named 090822-PCAM3-W-D-Zr/B (Figure III.5.11a), 091022-PMCA3-W-D-Zr-C-B (Figure III.5.11b), and 091222-PCAM3-W-D-B-C-Zr (Figure III.5.11c). All coating or doping materials have similar morphology, layered structure, and tap density. In addition, all coating or doping elements didn't reach the designed number. The 091222-PCAM3-W-D-B-C-Zr has the closest number to the design amount of Zr and B.

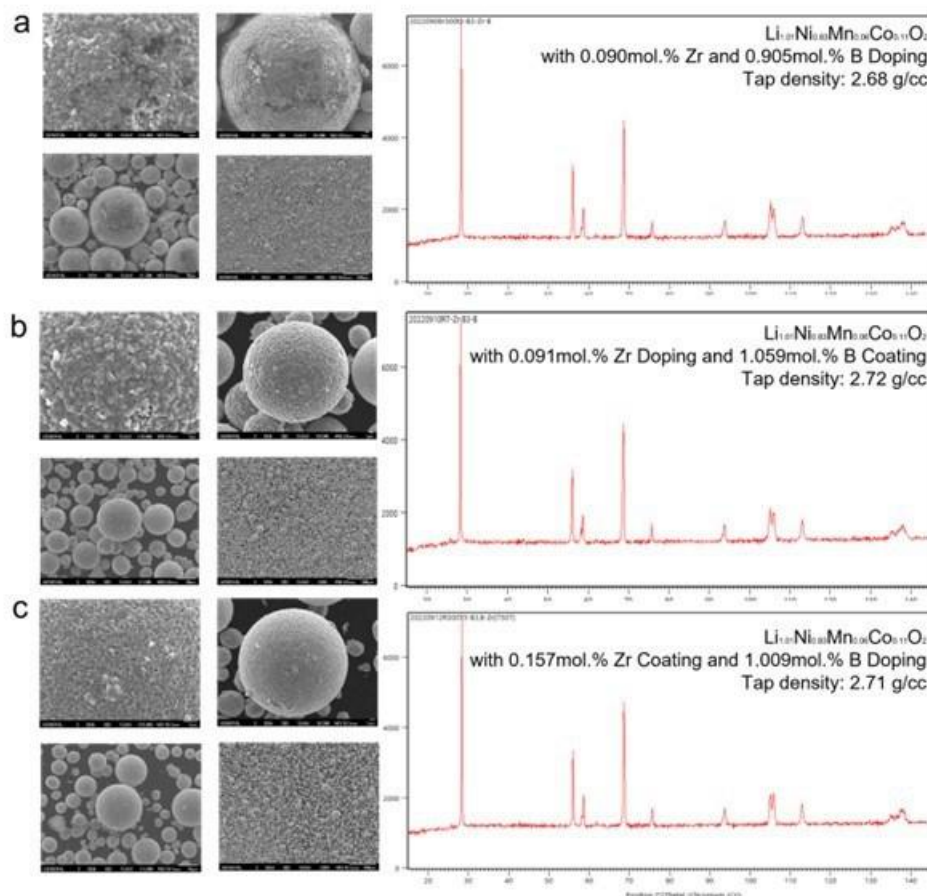


Figure III.5.11 Physical properties of 090822-PCAM3-W-D-Zr/B (a), 091022-PMCA3-W-D-Zr-C-B (b), and 091222-PCAM3-W-D-B-C-Zr (c).

We also investigated the different effects of mixing methods on electrochemical performance. We used a speed mixer to mix the precursors with dopants and LiOH and obtained Speed mixer-Zr/B-Doping cathode materials. In Figure III.5.12, the morphology and layered structure are comparable to other samples. And the content of the dopants is the highest in all coating and doping samples. The tap density was not tested because the obtained Speed mixer-Zr/B-Doping cathode materials were not enough due to the lab-scale speed mixer.

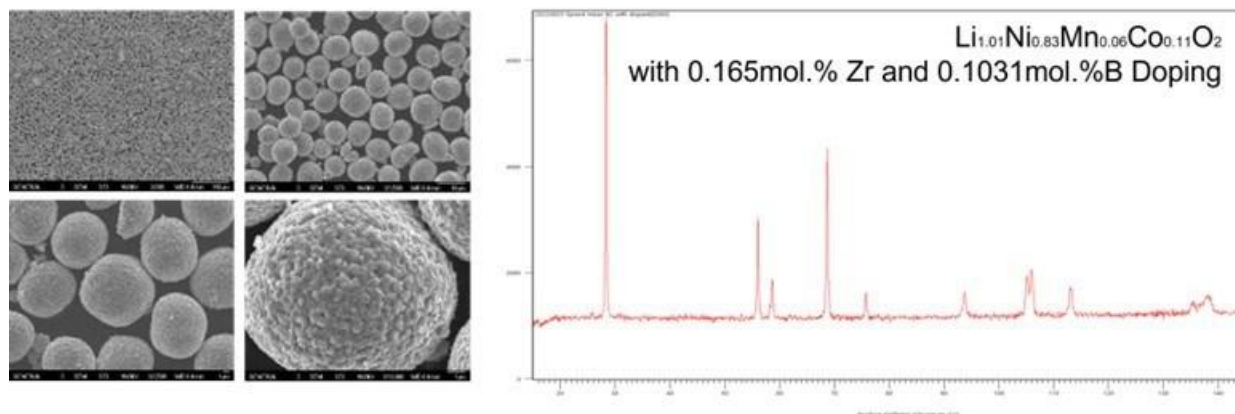


Figure III.5.12 Physical properties of Speed mixer-Zr/B-Doping.

Finally, the electrochemical performance of cathode materials with different coating and doping was tested in Figure III.5.13. In summary, all coated and doped samples have a lower discharge capacity and initial coulombic efficiency compared to the control sample from Farasis. Among all coated and doped samples, the Al_2O_3 coated sample has the best electrochemical performance. In addition, the Zr/B co-doped sample using a speed mixer has the best performance among Zr/B coated/doped samples, indicating that the mixing method has a significant effect on the performance of coated/doped samples.

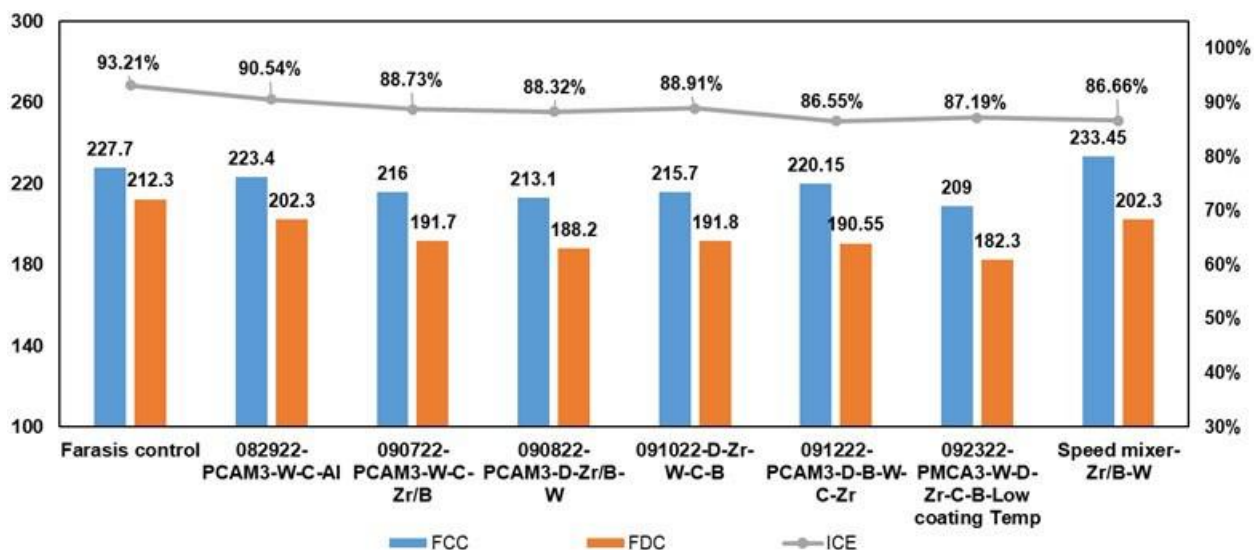


Figure III.5.13 Electrochemical performance comparison between the control from Farasis and all coated/doped samples.

Conclusions

In this USABC Phase III project, the team has successfully lowered SBC of NMC622 powder through washing method and the powder has been delivered to Farasis for single layer pouch cell tests. In addition, the parameters of co-precipitation have been optimized for recycling materials. Then, the recycled precursors with optimized parameters are used to prepare cathode materials and investigate different coating and doping strategies.

References

1. Offices, E. g. <https://www.energy.gov/eere/vehicles/batteries>.
2. Kim, U.-H.; Kuo, L.-Y.; Kaghazchi, P.; Yoon, C. S.; Sun, Y.-K., Quaternary Layered Ni-Rich NCMA Cathode for Lithium-Ion Batteries. *ACS Energy Letters* **2019**, 4 (2), 576-582.
3. Lin, S.-L.; Huang, K.-L.; Wang, I.-C.; Chou, I.-C.; Kuo, Y.-M.; Hung, C.-H.; Lin, C., Characterization of spent nickel–metal hydride batteries and a preliminary economic evaluation of the recovery processes. *Journal of the Air & Waste Management Association* **2016**, 66 (3), 296-306.
4. Insideevs <https://insideevs.com>.

Acknowledgements

Renata Arsenault, Ford Motor Co. (rarsena4@ford.com) served as the USABC Program Manager for this project. The development team (WPI/AE/Farasis) would like to thank the following for all of the help, advice, support and suggestions: USABC program manager Renata Arsenault (Ford) and USABC work group members Nakia Simon (Stellantis), Kely Markley (GM), Brian Cunningham (DOE), Bryant Polzin (DOE), and Brian Ingram (ANL).

IV Extreme Fast Charging (XFC)

Over the last ten years, lithium-ion batteries for plug-in electric vehicle applications have reached near high volume production levels and, as a result, costs have decreased significantly. Reduced battery costs have allowed EV manufacturers to offer a wide variety of vehicles with driving ranges comparable to traditional ICE vehicles. The Tesla Model 3 and S, Chevy Bolt, Ford Mustang Mach E, and many others, offer well over 200 miles of range per charge, and most offer over 300 miles per charge with battery upgrades.

However, the time needed to recharge these EVs remains a challenge. Gas powered cars can be refueled in minutes, whereby a 100kWh EV battery takes anywhere from 30 minutes to overnight to fully recharge which limits even broader consumer acceptance of electric vehicles.

Charging infrastructure is a challenge being addressed through large investments enabled by the Bipartisan Infrastructure Law (BIL). However, today's high energy cells use relatively thick (for high energy density) and porous graphite anodes and transition metal cathodes. These thick electrodes lead to relatively high polarization impedance (which makes charging at high rates inherently difficult), and they result in large salt concentration gradients which can lead to lithium plating on the anode surface. Lithium plating can cause rapid capacity fade and internal shorts leading to potentially catastrophic thermal runaway.

The “eXtreme fast Charge cell Evaluation of Lithium-ion batteries” (XCEL) program was formed to address this fast charge issue. Specifically, it is working to both identify the issues with and improve the fast charge acceptance of graphite/NMC based cells. Silicon containing cells often enable fast charging due to the much thinner silicon anode electrode. However, silicon exhibits poor calendar life which has inhibited its use in automotive batteries. Thus, this fast charge program is focused exclusively on graphite anode cells.

The program is led by Argonne National Laboratory, with significant support from Idaho National Laboratory, Lawrence Berkeley National Laboratory, National Renewable Energy Laboratory, SLAC National Accelerator Laboratory, and several universities.

The focus areas of the program are electrode and cell design, electrolyte development, electrochemical and thermal performance evaluation, and modeling and diagnostics. One of the main conclusions of the XCEL program has been that an “all solutions” approach may be required to enable fast charge (10-15 minutes) in high energy graphite anode cells. Early results showed the ability of a combination of improved binder, use of a more porous separator, and an enhanced electrolyte, worked collaboratively to greatly improve fast charge capability, Figure IV.1.

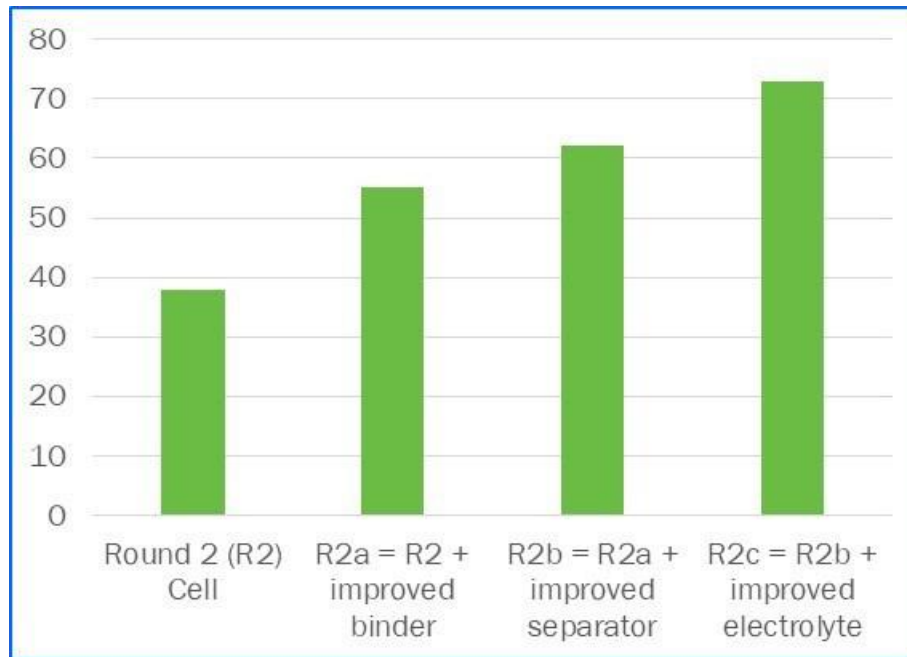


Figure IV.1 Energy delivered during a 15-minute fast charge and improvements seen with the incorporation of an improved binder, an improved separator, and an improved electrolyte.

The rest of this chapter contains detailed reports on the status of the following individual projects.

- Extreme Fast Charge Cell Evaluation (XCEL) Thrust-1: Electrolytes for fast-charging.
- XCEL Thrust-2: Electrode & Cell Design for Fast Charging.
- XCEL Thrust 3: Electrochemical and Thermal Performance.

IV.1 Extreme Fast Charge Cell Evaluation (XCEL) Thrust-1: Electrolytes for fast charging

Venkat Srinivasan, Principal Investigator

Argonne National Laboratory
9700 South Cass Avenue
Lemont, IL 60439
E-mail: vsrinivasan@anl.gov

Bryan D. McCloskey, Co-Principal Investigator

Lawrence Berkeley National Laboratory and University of California, Berkeley
201-D Gilman Hall
Berkeley, CA 94720
E-mail: bmcclosk@berkeley.edu

Brian Cunningham, DOE Technology Development Manager

U.S. Department of Energy
E-mail: brian.cunningham@ee.doe.gov

Start Date: October 1, 2021	End Date: September 30, 2024	
Project Funding (FY22): \$1,480,000	DOE share: \$1,480,000	Non-DOE share: \$0

Project Introduction

Rapid charging of lithium-ion batteries is a crucial step towards electrifying our transportation system and reducing harmful greenhouse gas emissions. Electric vehicle (EV) fast charging is primarily limited by the deposition of metallic lithium on graphite anodes, or ‘Li plating’, which can cause capacity fade and catastrophic cell shorting. It has now been established that the electrolyte serves an important role in controlling battery rate capabilities and battery lifetime, particularly when operating repeatedly under extreme conditions (e.g., fast charging rates and low or high temperatures). The aim of this thrust in the Extreme Fast Charging Program (XCEL) is to understand how to design more effective electrolytes that eliminate bottlenecks to allow Li-ion batteries to be charged in 10 minutes or less to 80% capacity. As discussed below, three different classes of electrolytes are being pursued, each of which could potentially improve upon current state-of-art compositions by improving ion transport or interfacial properties that control charge transfer kinetics and longterm stability. Furthermore, this thrust interfaces with modelling and characterization teams in XCEL that allow us to understand thermal and mass transport and interfacial properties of our electrolyte systems, which then help guide further development.

Objectives

- Discovery of new fast-charge electrolytes that enable high charge acceptance at a 6C charge rate ($\geq 80\%$ of the 1C capacity basis), demonstrate excellent cycle-life ($\leq 20\%$ capacity loss per 1000 cycles in CAMP pouch cells), and that exhibit good performance and survivability from 10°C to 45°C .
- Develop electrolyte formulations with high Li ion transference number and high ionic conductivity, which will significantly increase the Li ion mass transport from cathode to anode during fast charging.
- Experimentally determine the concentration of lithium-ion complexes in the electrolyte and calculate equilibrium constants for Li^+ desolvation.

Approach

- Examine electrolyte formulations with multiple solvent systems to suppress Li plating during fast charging.
- Explore additives to optimize electrode/electrolyte interface for better long term fast charging cycling.

- Electrospray-ionization mass spectrometry (ESI-MS) is used to quantify Li-ion complex concentration in electrolytes to understand thermodynamics of ion desolvation.

Results

Fluoroethylene carbonate (FEC) additives

Figure IV.1.1a shows the effect of increasing fluoroethylene carbonate (FEC) content in a standard carbonate-based electrolyte on capacity fade during fast charging. The FEC weight percent (X) is varied in 1.2 M LiPF₆ electrolyte, resulting in FEC:EC: EMC wt% ratios of X:(30-X):70. To compare lithium plating behavior across electrolyte compositions, a Graphite|LiNi_{0.5}Mn_{0.3}Co_{0.2}O₂ (NMC532) cell was cycled 140 times, alternating 5 moderate 1C CCCV charging cycles to 4.2V, holding until C/5 current, with 2 6C CCCV fast charging cycles to 4.2V, holding until 80% capacity. Figure IV.1.1a shows that the 5-15% FEC full-cells outperform the FEC-free electrolyte, undergoing on average only about 30% of the capacity fade over the 100 1C cycles, with similar 6C CCCV charge times compared to 0% FEC. The 2% FEC electrolyte, included for the common use of FEC as an additive, performed only slightly worse than the higher concentrations. From our Li reversibility analysis, the lack of a clear concentration effect on performance may indicate small amounts of plating occurring mostly beneath the FEC-derived SEI. Figure IV.1.1b shows significantly less Li titrated during electrode water exposure for the FEC electrolyte cells compared to the 0% FEC cells, as anticipated from the electrochemical measurements in (a). There is also a strong correlation between the sum of the 6C cycle losses calculated from capacity data and titrated Li. For the 0% FEC electrolyte, the fraction of the loss accounted for by titrated Li is about 81%, whereas only 20-40% for the lower FEC concentrations (inset).

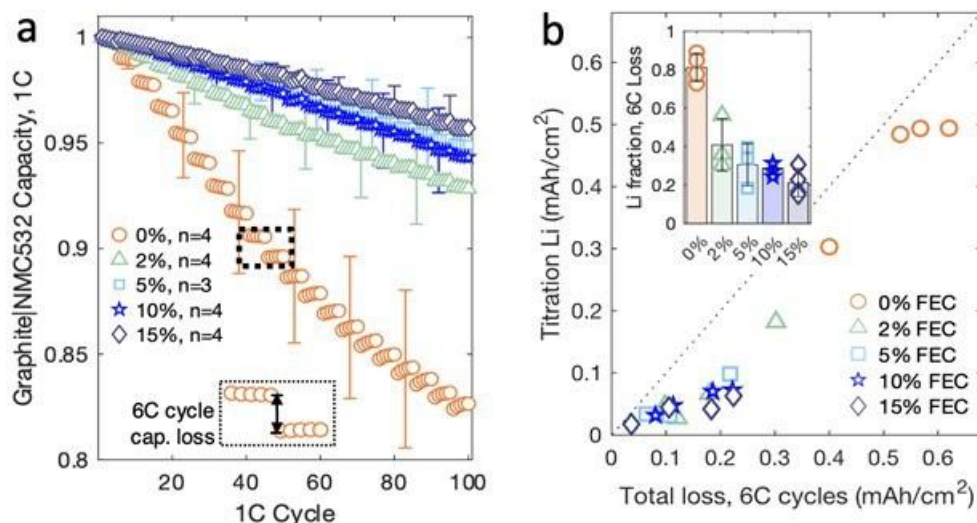


Figure IV.1.1 Fluoroethylene carbonate additive effect on full-cell performance, and titration dead Li. **a)** Graphite|NMC532 1C discharge capacity normalized to the initial (Cycle 1) value vs. cycle number, with cells undergoing two cycles of 6C CCCV to 4.2V charging to 80% SOC after five 1C cycles. The inset emphasizes capacity jumps between groups of 1C cycles due to the intermittent 6C cycles that induce Li plating. Error bars depict standard deviations across *n* cells. **b)** Titrated Li (Li⁰ and Li_xC₆) on extracted electrodes vs. the sum of the electrochemical capacity loss mechanisms for all cells tested in (a). The inset shows the fraction of the estimated loss accounted for by titrated Li, the position of each point relative to the dotted parity line.

Dual salt compositions

Based on prior literature [1], we hypothesized that dual salt electrolytes containing Li difluoro(oxalato)borate (LiDFOB) as one of the salts can serve to reduce Li plating irreversibility at graphite anodes. We found that a 0.1 M (1 wt%) LiDFOB and 1.2 M LiPF₆ electrolyte in 3:7 EC:EMC (3 wt% FEC additive) improves charge acceptance during 6C fast charging compared to a similar electrolyte without LiDFOB (Figure IV.1.2). Specifically, the baseline cells shown in green reach the 4.6 V upper cutoff voltage earlier during charging and, as a result, take longer to be charged to the same SOC.

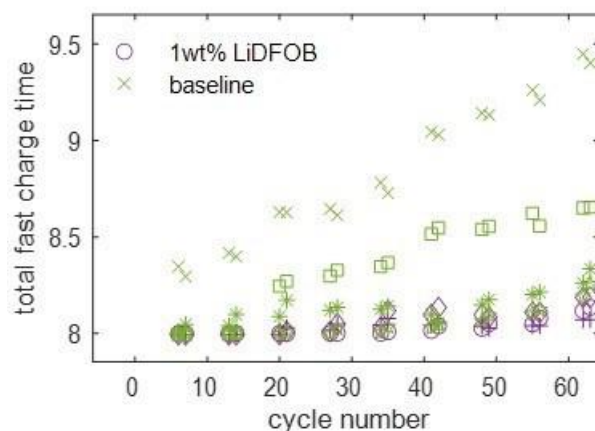


Figure IV.1.2 LiDFOB additive's effect on charge acceptance in Gr|NMC full cells. Total charge time for each cell to reach 80% SOC at 6C rate. Baseline is Gen. 2 with 3 wt% FEC.

LiFSI as a salt

Figure IV.1.3 shows the long-term cycling performance of pouch cells (NMC622/graphite) with different LiFSI concentration in the electrolyte at a charging rate of 4C. The cell with 0.75 M electrolyte shows high capacity fade with less than 70% capacity attainable after 200 cycles. The cycling performance is gradually improved with the increase of electrolyte concentration. The poor cycling performance associated with low electrolyte concentration is probably related to the polarization and Li ion depletion during fast charging. The Li ion depletion can lead to metallic Li plating and thus more capacity fading from increased side reactions. The cell with 1.50 M electrolyte shows the best performance with the highest attainable capacity and stability in 200 cycles. The 1.50 M LiFSI electrolyte also had the best conductivity of all electrolytes studied (10.4 mS/cm). The cycling performance for 1.75 M and 2.00 M electrolyte are satisfactory except the attainable capacity through 200 cycles are lower than observed for the 1.50 M electrolyte. This is likely due to the lower ion conductivity and high viscosity observed at high concentrations. The gradual increase of the capacity with cycling number for 2.00 M electrolyte might be ascribed to the slow wetting of the cell from the high viscosity of the electrolyte. We have also verified that this electrolyte is compatible with NMC811 electrodes from Argonne's CAMP facility. In particular, a prepared NMC811/graphite full cell had 80% capacity retention after 500 6C charging cycles.

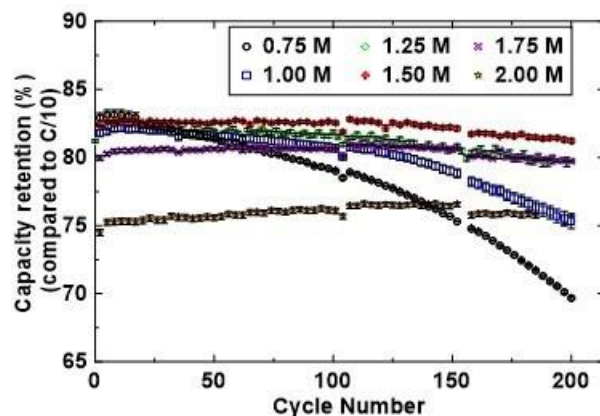


Figure IV.1.3 Long-term cycling performance of cells employing LiFSI as a salt in a carbonate-based solvent cycled at 4C charging rate and discharge at 1C rate

Highly concentrated electrolyte systems

Our foundation consists of advanced electrolyte property modeling that identifies and prescreens electrolyte candidates (Advanced Electrolyte Model, AEM), laboratory testing of candidates using coin and pouch cells, and a key collaboration that provides simulation of cell performance using our electrolytes (NREL, Andrew

Colclosure). FY22 focused on moving to highly-concentrated electrolytes (HCE), looking for candidates that possess competitive transport properties (conductivity, diffusivity, etc.), while having lowered lithium desolvation energies during the charge steps (Figure IV.1.4b). We have been successful, identifying several candidates that have salt concentrations ranging from 2.8 to 3.6 molal salt (Figure IV.1.4a). A sample of our 'HCE16' was sent to CAMP to incorporate into pouch cells that will be further tested for charge-rate and cycle-life capabilities. On the modeling side, a chemical physics approach was added that predicts the important property of electrolyte thermal conductivity, which is obtained through AEM over salt concentration and temperature (Figure IV.1.4c). This complements other thermophysical terms such as relative enthalpy and excess heat capacity that are already obtained through AEM (Figure IV.1.4d). Through this we can determine transport and thermal bottlenecks that occur in a cell during XFC and have identified the cathode side as an area of particular concern, but that can be mitigated with improved electrolytes.

Electrolyte speciation

Electrolytes with various lithium salt concentrations (0.012 M, 0.12 M and 1.2 M) were directly injected into a electrospray ionization mass spectrometry (ESI-MS) nebulizer at 30°C, 50°C, 100°C and 150°C. The concentrations of complexes formed in these electrolytes were determined from mass spectrometry (MS) ion currents. Common complexes observed were lithium ethyl carbonate (LiEC), lithium ethyl methyl carbonate (LiEMC), $\text{Li}(\text{EC})_2$, $\text{Li}(\text{EC})(\text{EMC})$, $\text{Li}(\text{EMC})_2$ and $\text{Li}(\text{EC})_3$. An example of MS data is shown in Figure IV.1.5a for an electrolyte with 0.012 M LiPF_6 . The concentrations of each complex in the electrolyte change with carrier gas temperature suggesting those solvation structures in the electrolyte evolve with temperature. The equilibrium constant, $\ln(K_{eq})$ for various de-solvation reactions was calculated from the experimentally quantified species concentrations. Figure IV.1.4b shows an example of $\ln(K_{eq})$ calculation results for the reaction, $(\text{EC}) + \text{Li}(\text{EC})_2 \leftrightarrow \text{Li}(\text{EC})_3$ from each electrolyte samples. The enthalpy (ΔH) and entropy (ΔS) can be estimated from the data in Figure IV.1.1b using a van't Hoff equation, $\ln(K_{eq}) = -\Delta H/RT + \Delta S/R$.

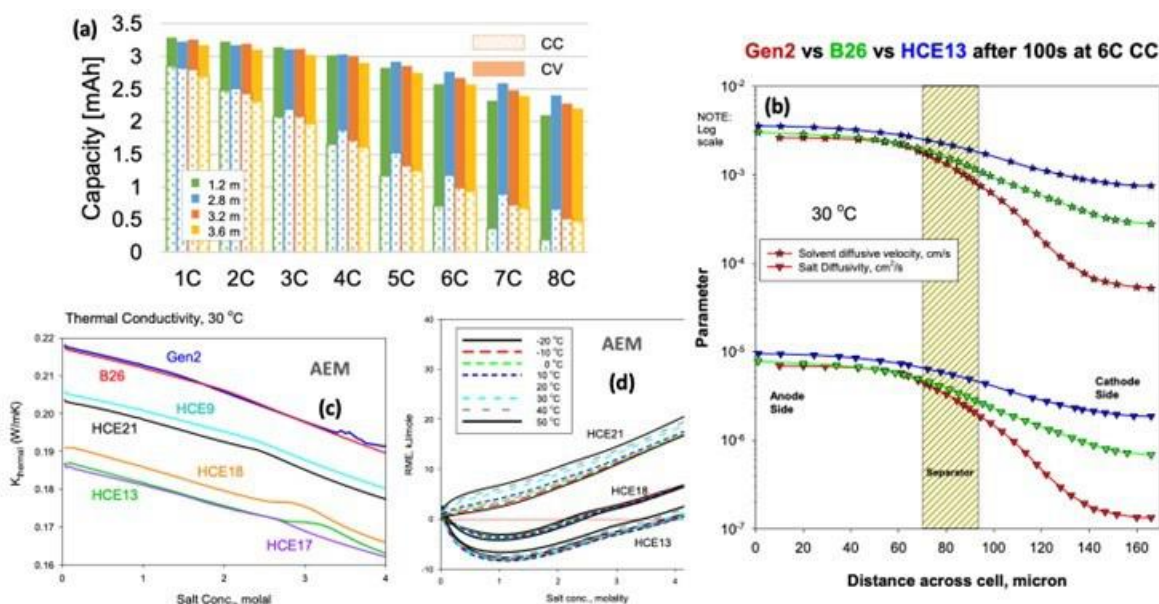


Figure IV.1.4 (a) charge rate capability of HCE18 as a function of salt molality. Capacity broken down between constant current portion at stated rate and constant voltage hold at 4.1 V. (b) Comparison of salt diffusivity profiles across an XCEL cell during a 6C constant current charge. (c) HCE thermal conductivity predictions, and (d) relative molal enthalpy (RME) for selected HCEs using the AEM.

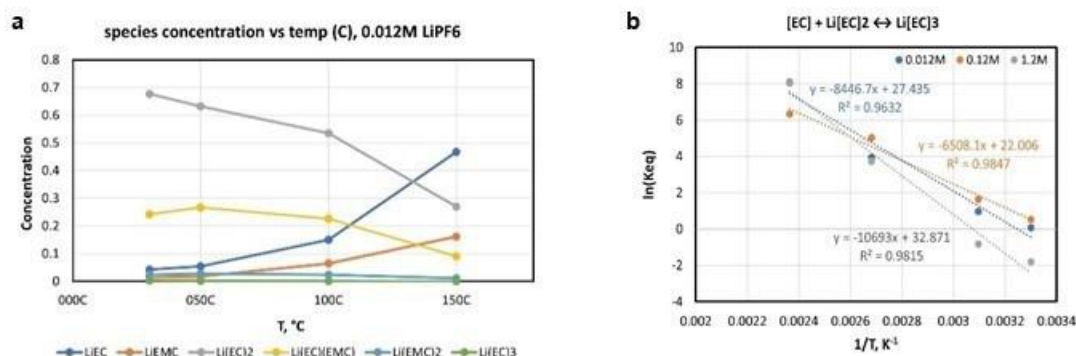


Figure IV.1.5 ESI-MS results on the model electrolyte system. (a) Concentration of lithium complexes vs. temperature for an electrolyte with 0.012M LiPF₆. (b) Calculation of equilibrium constant, K_{eq} for $EC + Li(EC)_2 \leftrightarrow Li(EC)_3$ in the electrolyte with salt concentration of 0.012M, 0.12M and 1.2M.

Conclusions

We have shown that FEC is a promising electrolyte additive that boosts Li plating reversibility and improves fast charging performance. Secondary Li salts, such as LiDFOB, could further facilitate better charge acceptance at high C rates. We also found that LiFSI concentration affect fast charging performance and needs to be optimized (in the first electrolyte solvent version, 1.5 M LiFSI was found to be optimal). The LiFSI-based electrolytes were also found to be compatible with NMC811/graphite cells. Highly concentrated electrolytes have now been identified that provide superior transport properties to conventional carbonate-based electrolytes, thereby resulting in promising fast charging performance in NMC811/graphite cells. ESI-MS was found to be an effective method to quantify Li-ion solvation as a function of concentration in LiPF₆ electrolytes. Equilibrium constants for Li desolvation were calculated from these data, and future work will focus on comparisons of desolvation energetics among the various electrolyte classes being studied within the XCEL program.

Key Publications

1. Xianyang Wu, Lin Ma, Jue Liu, Kejie Zhao, David L. Wood III, and Zhijia Du. "Understanding the effect of salt concentrations on fast charging performance of Li-ion cells." *Journal of Power Sources* (2022) 545, 231863.
2. Gao, N.; Kim, S.; Chinnam, P.; Dufek, E. J.; Colclasure, A. M.; Jansen, A.; Son, S.-B.; Bloom, I.; Dunlop, A.; Trask, S., Methodologies for Design, Characterization and Testing of Electrolytes that Enable Extreme Fast Charging of Lithium-ion Cells. *Energy Storage Materials* (2022) 44, 296-312.
3. Son, S.-B.; Trask, S.; Tsai, Y.; Lopykinski, S.; Kim, M.; Bloom, I., Across-Depth Heterogeneity and Irreversibility of Fast-Charge-Driven Lithium Plating. *Journal of The Electrochemical Society* (2022) 169 (6), 060506
4. McShane, E. J.; Bergstrom, H. K.; Weddle, P. J.; Brown, D. E.; Colclasure, A. M.; McCloskey, B. D. "Quantifying graphite solid-electrolyte interphase chemistry and its impact on fast charging." *ACS Energy Letters* (2022) 7, 2734-2744.
5. Vikrant, K. S. N.; McShane, E.; Colclasure, A. M.; McCloskey, B. D.; Allu, S. "Quantification of dead lithium on graphite anode under fast charging conditions." *Journal of the Electrochemical Society* (2022) 169(4), 040520.
6. Brown, D. E.; McShane, E. J.; Konz, Z. M.; Knudsen, K. B.; McCloskey, B. D. "Detecting the onset of Li plating during fast charging of Li-ion batteries using operando electrochemical impedance spectroscopy." *Cell Reports Physical Science* (2021) 2(10), 100589.

References

1. Weber, Rochelle, Matthew Genovese, A. J. Louli, Samuel Hames, Cameron Martin, Ian G. Hill, and J. R. Dahn. 2019. "Long Cycle Life and Dendrite-Free Lithium Morphology in Anode-Free Lithium

Pouch Cells Enabled by a Dual-Salt Liquid Electrolyte.” *Nature Energy* 4 (8): 683–89.
<https://doi.org/10.1038/s41560-019-0428-9>.

Acknowledgements

This section was coauthored by co-PIs Kevin Gering (INL), Seoung Bum Son (ANL), and Zhijia Du (ORNL), as well as Zachary Konz (LBNL) and Ning Guo (LBNL). We also thank Stephen Trask, Andrew Jansen, Alison Dunlop, and their CAMP Facility colleagues for providing pouch cells and the graphite and NMC electrodes used in our studies.

IV.2 XCEL Thrust-2: Electrode & Cell Design for Fast Charging

Venkat Srinivasan, Principal Investigator

Argonne National Laboratory
9700 South Cass Avenue
Lemont, IL 60439
E-mail: vsrinivasan@anl.gov

Andrew Jansen, Co-Principal Investigator

Argonne National Laboratory
9700 South Cass Avenue
Lemont, IL 60439
E-mail: jansen@anl.gov

Yi Cui, Co-Principal Investigator

Stanford University
Department of Materials Science and Engineering, Stanford University
Stanford, CA 94305
E-mail: yicui@stanford.edu

Brian Cunningham, DOE Technology Development Manager

U.S. Department of Energy
E-mail: brian.cunningham@ee.doe.gov

Start Date: October 1, 2021	End Date: September 30, 2024	
Project Funding (FY22): \$1,480,000	DOE share: \$1,480,000	Non-DOE share: \$0

Project Introduction

The XCEL Program in FY 2018-2021 (Phase I) centered on the influence of areal capacity loading on lithium plating during extreme fast charging (XFC). Two sets of capacity-matched electrodes were designed and fabricated with identical compositions – only the capacity loading was changed. The low loading electrode set (Round 1) utilized a 2 mAh/cm² graphite loading and the higher loading set utilized a 3 mAh/cm² graphite loading. Numerous pouch cells were fabricated and delivered to the national laboratory and university teams. These two cell builds were the early baselines for the XCEL Program. It became clear after extensive testing that lithium plating is rare on the Round 1 anodes, but is abundant on the Round 2 anodes during 6C charging. In FY 2020, a multi-thrust approach was formed to solve the problems related to XFC, the chief of which is lithium plating. One of these thrusts, the XCEL-Electrode & Electrolyte Thrust was directed to determine impact of carbon and binder domains in the positive and negative electrodes, and the impact of improved electrolyte compositions. The XCEL Program began Phase II at the start of FY 2022 with three main thrusts with the singular goal of achieving fast charge cycles (6C rate) with >4 mAh/cm² loading on the anode. This report summarizes the activities of one of the thrusts, the Electrode & Cell Design Thrust.

Objectives

The goal of the XCEL Electrode & Cell Design Thrust in FY 2022 was to develop higher Ni-content NMC (e.g. NMC811) cathodes with low carbon and binder content, new electrode architectures (e.g., dual layer), and improved electrolyte compositions. It is anticipated that these combined tasks will result in a cell system with over 4 mAh/cm² loading (anode) that can achieve >600 cycles at 6C charge with no lithium-plating.

Approach

The Electrode & Cell Design Thrust enlists a multi-prong approach with coordinated efforts between several national labs:

- NREL's modeling tools are used to investigate strategies to reduce electrode level limitations to extreme fast charging. Novel microstructure tools are used to study the effect of changing carbon binder content on both ionic and electronic conductivity. P2D models are used to investigate the effect of dual layer electrodes on fast charge acceptance/lithium plating. The models are used to project how far electrode loadings can be increased while maintaining high fast charge acceptance/avoiding lithium plating with solutions already demonstrated by XCEL team.
- Electrodes and cells are fabricated by the CAMP Facility (Argonne) that best approximate the electrode architectures predicted by modeling effort. Cells will be made with graphite vs. NMC811 electrodes with anode loadings near 4 mAh/cm². Latest advanced electrolytes from the Electrolyte Thrust teams will be utilized in a final cell build each year and compared to baseline.
- Post-Test Facility (Argonne) conducts post-mortem analysis of cells for presence of lithium plating and provides analysis of electrode architecture via SEM, etc. during electrode development.
- Operando x-ray characterization are conducted to detect lithium plating/stripping during cycling, and degradation of cathode material.

Results

Model Prediction of Ideal Electrode Architecture (NREL Focus)

NREL's macro-homogeneous modeling was used to investigate strategies to enable extreme fast charging of cells with EV relevant electrode loadings of 4-5 mAh/cm². Modeling has shown that no single solutions/improvement is likely to enable XFC of high loading cells. Instead, multiple improvements should be combined to enhance lithium-ion diffusion/kinetics to enable more uniform intercalation/de-intercalation throughout entire electrode thickness. The XCEL consortia has already demonstrated the following solutions for improving fast charge acceptance/mitigating lithium plating:

- Separators with higher porosity/lower tortuosity (Celgard 2500 over 2320)
- Lowering the amount of carbon/binder domain in cathode
- Cathodes with higher specific capacity (NMC 811 vs. 532)
- Dual layer anodes
- Electrolytes with enhanced ion transport
- Advanced voltage ramping charge protocol.

The predicted fast charge performance of a graphite-NMC 811 cell having a loading of 4.5 mAh/cm² (anode of 5.1 mAh/cm²) and employing previously demonstrated improvements is shown in Figure IV.2.1. Models predict almost 80% charge acceptance can be achieved in 15 minutes without plating. Note, simulations are run for small format single layer cells operating iso-thermally at 30°C. Large format cells will rapidly warm to elevated temperatures of 45°C -50°C during fast charging and likely reducing the amount of required charge time.

Battery performance is strongly correlated with electrode microstructure and weight loading of the electrode components. Among them are the carbon-black and binder additives (CBD) that enhance effective electronic conductivity and provide mechanical integrity. However, these both reduce effective ionic transport in the electrolyte phase and reduce energy density. Therefore, an optimal additive loading is required to maximize performance, especially for fast charging where ionic transport is essential. Such optimization analysis is however challenging due to the nanoscale imaging limitations that prevent characterizing this additive phase and thus quantifying its impact on performance. Herein, an additive-phase generation algorithm has been developed [1] to remedy this limitation and identify a percolation threshold used to define a minimal additive loading [2]. Improved ionic transport coefficients from reducing additive loading has been quantified through homogenization calculation, macroscale model fitting, and experimentally taking electrochemical impedance spectroscopy of blocking symmetric cells, with good agreement between the methods (cf. Table IV.2.1). Rate capability test demonstrates capacity improvement at fast charge at the beginning of life (BOL) during 6C CC charging, in agreement with macroscale model, and attributed to a combination of lower cathode impedance, reduced electrode tortuosity and cathode thickness (cf. Figure IV.2.2).

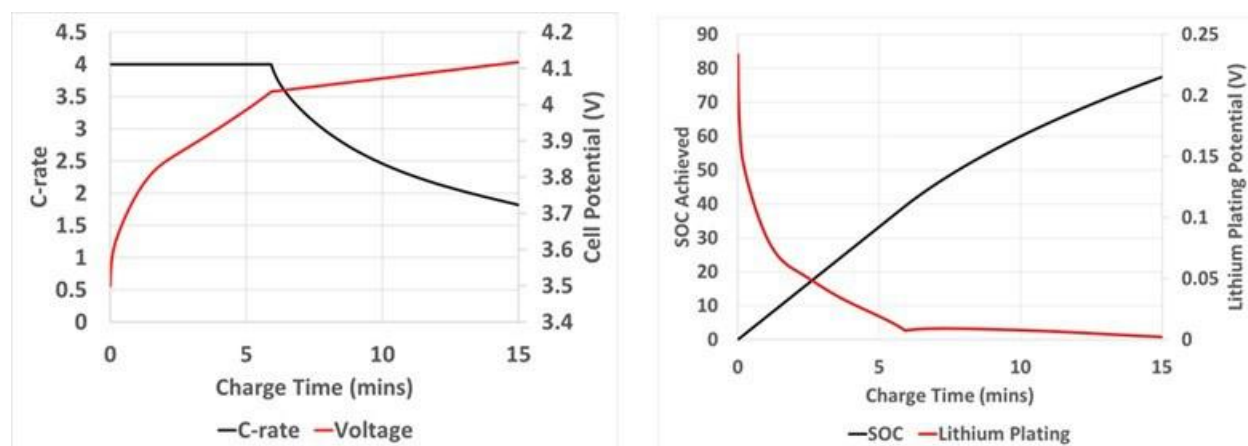


Figure IV.2.1 (Macro-homogeneous model predictions for graphite-NMC 811 cell with loading of 4.5 mAh/cm² loading employing already demonstrated solutions during 15-minute charge. A.) Current and voltage of cell employing ramp protocol. B.) State of charge achieved and lithium plating potential.

CBD impacts negatively ionic effective diffusion, more than active material for the same volume. Therefore, rebalancing loading in favor of the latter proved to be advantageous for fast charge applications. Lower over-polarization has been achieved for C-rate above 1, and single-layer pouch cell at 6C CC-CV demonstrated capacity improvement, from 37% (80%) to 55% (86%), end of CC (CC-CV 10min), from high to low CBD content. However, cycling experiments revealed delamination at the anode side; therefore, recommendation is to lower additive loading for the cathode (4wt%) but to keep it moderate for the graphite (8wt%). To improve anode effective transport properties, other solutions are to be pursued such as dual layer architecture as discussed below and/or laser ablated microstructure [3].

Table IV.2.1 Anode microstructure ionic transport coefficients, experimentally measured with electrochemical impedance spectroscopy (EIS), fitted in a macroscale P2D model, and calculated from microstructure analysis.

	EIS		P2D fit		Microstructure analysis	
	High CBD	Low CBD	High CBD	Low CBD	High CBD	Low CBD
Porosity	0.382	0.374	0.33	0.374	0.345	0.375
Tortuosity factor	4.10–4.12	2.98–3.10	4.23	2.674	4.42	2.932
Bruggeman exponent	2.466–2.471	2.108–2.150	2.3	2.0	2.39	2.097
MacMullin number	10.73–10.79	7.97–8.29	12.81	7.150	12.81	7.82

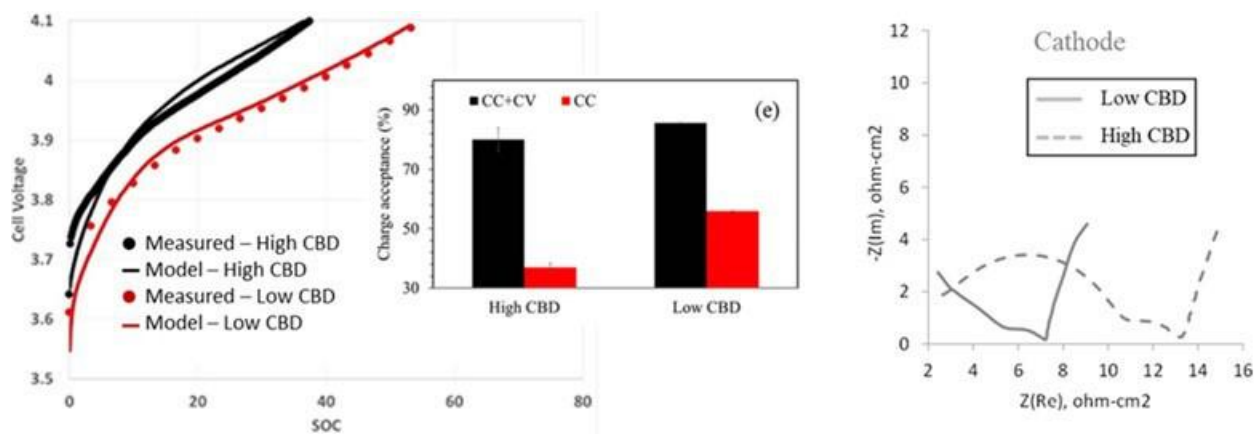


Figure IV.2.2 (Left) BOL cell voltage and charge acceptance for pouch cells with different CBD loading (High CBD: 8wt%-10wt% and Low CBD: 4wt%-4wt% for anode-cathode). (Right) Custom-made 3-electrode cell EIS plot for cathode [2].

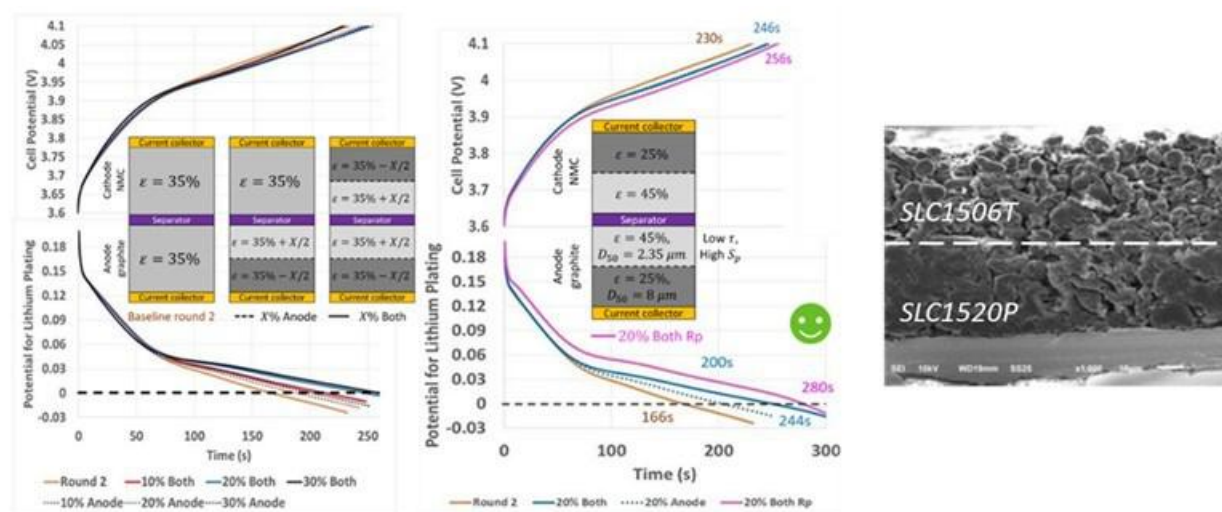


Figure IV.2.3 (Left) NREL macroscale 6C modeling with cell voltage and potential for lithium plating calculated for baseline round 2 and graded electrodes, considering porosity and particle size gradations. (Right) SEM cross section of a dual layer anode (dual coating) manufactured by ANL CAMP.

Graded electrode can relax the significant electrolyte concentration gradients induced during fast charging operation. These results in non-uniform material utilization and aggravated capacity fade induced by material degradation such as lithium plating and excessive cathode cracking. Most significant contributions in the literature are from Shodiev [4] and Wood [5], respectively to investigate the impact of porosity and particle size gradation on performance. A practical application of the graded electrode concept is a dual layer manufactured through dual coating with each layer being functionalized: a power layer (high porosity) near the separator and an energy layer (low porosity) near the current collector (cf. Figure IV.2.3 right). Macroscale modeling indicates most gains are achieved with a 20% porosity offset between the two layers for both electrodes (cf. Figure IV.2.3 left). Combining both graded porosity and particle size provides further improvement. A power layer composed of high porosity and small particles results in a reduction in locally tortuosity and increased specific surface area improving uniformity of electrode utilization during fast charge (cf. Figure IV.2.3 middle).

High Loading, Low Carbon/Binder Scoping Study

Industry focuses on high-energy density/ high-loading electrodes for cost effectiveness in EVs. To help align with industry standards, higher loadings than our previous two standards (R1 and R2) were explored in a

scoping study using 96% Superior Graphite SLC1506T and 97% NMC811 in coin cells (active material content was increased for both anodes and cathodes with aim to further increase energy density). Three sets of electrodes with loadings higher than the R2 loading were created and compared to the R2 loading, all of which had lower carbon/binder content. The cells were formed, put on rate study, an initial HPPC, and then cycled through a fast 6C cycle life protocol (Figure IV.2.4).

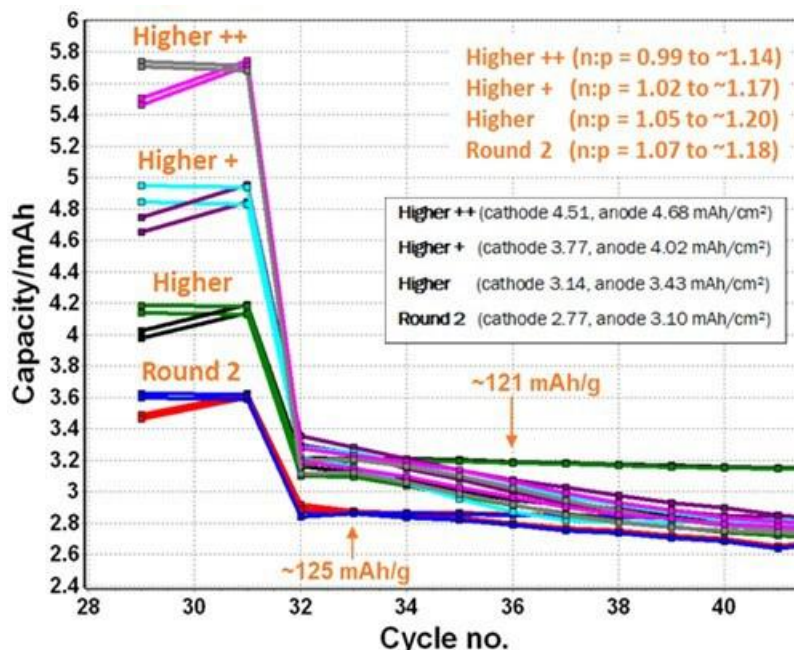


Figure IV.2.4 Charge and Discharge capacities of the low carbon/binder-high loading coin cells during the fast charge cycling protocol (2x-C/3, 150x-(6C CCCV Charge w-10 min limit, C/2 Discharge).

Based on an analysis of the data and general observations, it was determined that the NMC811 content should be lowered to 96 wt%, and that the anode should have more binder to improve adhesion. It was decided to go back to the original formulation of the anode (92 wt% binder).

Milestone: Produce and Distribute Baseline Anodes (>30m) and Cathodes (>30m) to XCEL Teams

The CAMP Facility produced 55 meters of NMC811 and 45 meters of SLC1506T graphite monolayer at >3.2 mAh/cm² as its first quarter milestone. Based on the previous scoping studies, the new R3 baseline electrodes were designed to have 96 wt% NMC 811 and the CAMP's standard 91.83 wt% SLC1506T formulation capacity matched at a higher R3 loading (3.6 mAh/cm² anode). Cathode was designed to be capacity matched to the anode with an n:p ratio range between 1.1 and 1.2 (when considering 1st cycle, reversible cycle, 1C, and C/10) for a 3-4.1V range (see Figure IV.2.5). These electrodes were then distributed to the various XCEL teams.

Anode: LN210035-101-2 (single-sided) 91.83 wt% Superior Graphite SLC1506T 2 wt% Timcal C45 carbon 6 wt% Kureha 9300 PVDF Binder 0.17 wt% Oxalic Acid <small>XCEL FY22 Q1, Round 3; SLC1506T, Lot#: 16066-1001, received Oct. 2018</small> <small>"SS" = single sided -> CALENDERED</small> Cu Foil Thickness: 10 μm Total Electrode Thickness: 95 μm SS Coating Thickness: 85 μm Porosity: 35.4 % Total SS Coating Loading: 11.91 mg/cm² Total SS Coating Density: 1.40 g/cm³ Expected SS Areal Capacity: 3.62 mAh/cm² <small>[Based on rev. C/10 of ~335 mAh/g for 0.005 to 1.5 V vs. Li]</small> Made by CAMP Facility	Cathode: LN210035-167-4 (single-sided) 96 wt% Targray NMC811 2 wt% Timcal C-45 2 wt% Solvay 5130 PVDF Binder <small>XCEL FY22 Q1, Round 3; Prod: SNMC03006 (NMC811 "unwashed"), Lot#: LT-200280164, MFG. Date: 2020.02.04</small> <small>"SS" = single sided -> CALENDERED</small> Al Foil Thickness: 20 μm Total Electrode Thickness: 78 μm SS Coating Thickness: 58 μm Porosity: 33.7 % Total SS Coating Loading: 17.19 mg/cm² Total SS Coating Density: 2.96 g/cm³ Expected C/10 Areal Capacity: 3.07 mAh/cm² <small>[Reversible C/10 of 187 mAh/g for 3.0 to 4.2 V vs. LiLi⁺]</small> Made by CAMP Facility
--	--

Figure IV.2.5 Electrode composition and design parameters for Round 3-Batch 1. 45 meters of SLC1506T graphite anode (LN210035-101-2) and 55 meters of NMC811 cathode (LN210035-167-4) were coated.

Single layer pouch cells were made using these R3 loading electrodes (NMC811, 14.1 cm², SLC1506T, 14.9 cm²). The cells had a reversible C/10 discharge capacity of 170 mAh/g (~40 mAh) and a reversible C/2 discharge capacity ~160 mAh/g (~37.5 mAh). The specific discharge capacities agree with the expected values based on cells near R2 loadings, as can be seen in Figure IV.2.6.

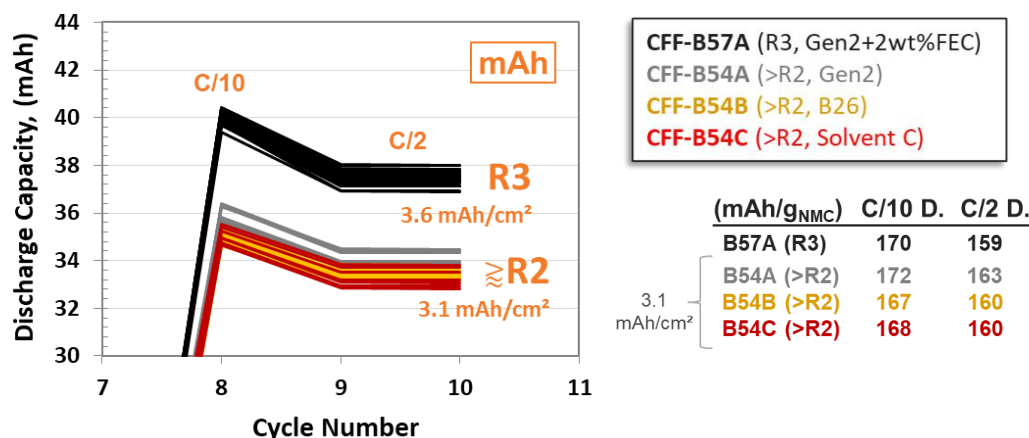


Figure IV.2.6 Discharge capacity for R3 and an ~>R2 loading (dual layer) vs. NMC811 in xx3450 pouch cells (left); and specific discharge capacities of R3 and ~>R2 cathodes being approximately the same (right table).

New Baseline Electrolyte Scoping Study (Argonne Focus)

It is generally assumed that commercial cells have electrolyte additives to improve SEI layer formation. The CAMP Facility performed a brief additive study using two additives commonly used: FEC and VC (2 wt% each added to Gen2 electrolyte). XCEL-II Baseline Round 3 loading electrodes were assembled into six single layer pouch cells with two cells each using the previous baseline (Gen2) electrolyte, Gen2 + 2 wt% FEC, and Gen2 + 2 wt% VC. These cells were formed, degassed, and cycled with 6C fast charge cycles and periodic HPPC pulses at 30°C. The cells containing the FEC additive showed an increase in capacity utilization, as well as a decrease in impedance rise (Figure IV.2.7). It was decided to make Gen2 + 2wt% FEC the new baseline electrolyte.

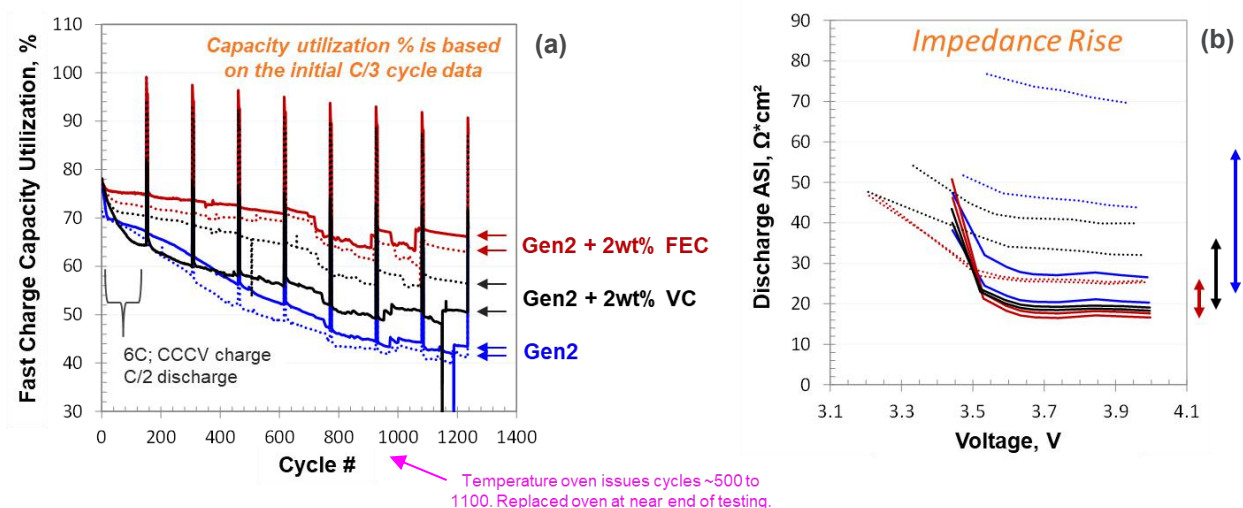


Figure IV.2.7 (a) Fast charge utilization of the single layer pouch cells with the various electrolytes. Solid and dashed lines show the two cells for each electrolyte; (b) change of impedance over the course of 1200 cycles. Solid lines show the initial HPPC and dashed lines show the impedance after 1200 cycles. Arrows to the right indicate the average rise in impedance from cycling.

Milestone: Fabrication of Final Pouch Cell Build Using R3 Loading Using New Baseline Electrolyte & Electrolyte Thrust's Top 3 Electrolytes (ORNL, INL, UC-Berkeley, Argonne-CAMP)

CAMP assembled 84 single-layer pouch cells using the capacity-matched R3 baseline electrodes and Celgard 2500 separator. Some cells were sent dry (no electrolyte) to electrolyte development teams; while others were filled, formed, degassed, impedance tested at 1 kHz, capacity checked, and then shipped for further electrochemical testing. See Table IV.2.2 for R3-loading cell distributions.

Table IV.2.2 Single-layer pouch cells fabricated at the CAMP facility and distributed to teams.

R3 Loading Cells Made & Distributed in FY22	# of cells	Build Name	Electrolyte
INL - Dry Cells (to INL)	15	CFF-B57	No Electrolyte
ORNL - Dry Cells (to ORNL)	5	CFF-B57	No Electrolyte
INL - Formed Baseline Cells (to INL)	30	CFF-B57A	Gen2 + 2wt% FEC
Ford - Formed Baseline Cells (to FORD)	10	CFF-B57A	Gen2 + 2wt% FEC
ORNL Electrolyte Thrust Team – Formed (to INL, Deliverable)	8	CFF-B57B	ORNL V2
INL Electrolyte Thrust Team – Formed (to INL, Deliverable)	8	CFF-B57C	INL HCE16
UC-Berkeley Electrolyte Thrust Team – Formed (to INL, Deliverable)	8	CFF-B57D	UCB Dual Salt

The Electrolyte Thrust teams from INL, ORNL, and UC-Berkeley each chose their best electrolyte formulations they developed during Q1 to Q3 of FY2022 (INL “HCE16”, ORNL “V2”, & UCB “Dual Salt”). They each sent the CAMP Facility their electrolyte components with mixing instructions. The CAMP Facility assembled R3-loading single-layer pouch cells (electrodes described in Figure IV.2.5) with the freshly mixed electrolyte from the electrolyte thrust teams, as well as the new baseline electrolyte (Gen2 + 2 wt% FEC). These cells were formed, degassed, impedance tested @ 1 kHz, capacity checked, and then shipped to INL for electrochemical testing.

Single-Walled Carbon Nanotubes Scoping Study (Argonne-CAMP)

Single-walled carbon nanotubes (SWCNT) were developed in industry to improve electrode impedance. The CAMP Facility is exploring its impact on fast charge in a small scoping study with NMC811. Two different trial cathodes were coated: one with 96 wt% NMC811 and one with 0.05 wt% SWCNT added to NMC811. Each cathode chemistry combination was coated for ~R2 and ~R3 loadings. The electrodes were assembled into four different single layer pouch cell sets (14.1 cm² cathodes, 14.9 cm² anodes, Celgard 2500, and Gen2 + 2 wt% FEC). These cells were tested, formed, tested for impedance at 1 kHz, and cycled from 3-4.1V with a 6C fast charge cycle that contained periodic HPPC pulses. Impedance measurements at 1 kHz taken after formation showed that the cells containing SWCNT resulted in impedance values that were half of the baseline cells. HPPC impedance was also reduced by 40%. These cells are still under test.

Mapping the Degradation of NMC Cathodes Cycled Under XFC Conditions (SLAC-Weker Focus)

The SLAC team studied the degradation of NMC811 cathode under extreme fast charging (XFC, ≤10–15 min charging) conditions in a full single-layer graphite pouch cell with NMC811 cathodes. Micro X-ray fluorescence (μ-XRF) and micro X-ray absorption near edge structure (μ-XANES) on the full pouch cells are being used to elucidate the effects of XFC on the cathode state-of-charge (SOC). μ-XRF provides elemental maps of the different transition metals in the batteries. μ-XANES yields information about the oxidation states of the transition metals, and therefore can be used to distinguish differences in SOC in regions of interest within the cathode.

Using the SSRL beamline 2-3, preliminary measurements were performed *in situ* on an XFC cycled cell after 600 cycles and *ex situ* on a cathode sheet. The samples were mapped using X-ray micro fluorescence (μ-XRF) with an adjustable X-ray beam size of 10 and 50 μm. Figure IV.2.8a shows elemental maps corresponding to Ni, Mn and Co taken simultaneously from the NMC cathode inside the XFC cycled cell with a 50-μm focused X-ray beam. Additionally, μ-XANES maps were collected at five different energies across the Ni K-edge (8343, 8347, 8351.5, 8354, and 8355 eV). Using principle component analysis, we find three principal components (C1, C2 and C3; Figure IV.2.8b), which show no change in the state of charge within the imaged region.

For higher energy resolution XANES, μ-XANES was measured with 295 energy points at 32 positions in a line along the cycled pouch cell (see Figure IV.2.9). There are no apparent differences between the spectra, which agrees with the PCA results and suggests we need to cover a larger portion of the sample to observe the expected heterogeneity. These preliminary data demonstrate feasibility of the technique on full cells and highlight the need for a larger X-ray beam and larger imaging region. The remainder of the study will be conducted on beamline 7-2 at SSRL, another μ-XRF beamline suited for larger samples. The focusing optics on beamline 7-2 allow for a larger spot size and therefore increased depth of focus, which will be important for imaging the electrode through the aluminized pouch material *in situ*. Additionally, imaging will be guided by full cell maps using XRD previously collected by the Argonne team to identify our regions of interest for each technique described. These maps were not available at the time the preliminary data were collected.

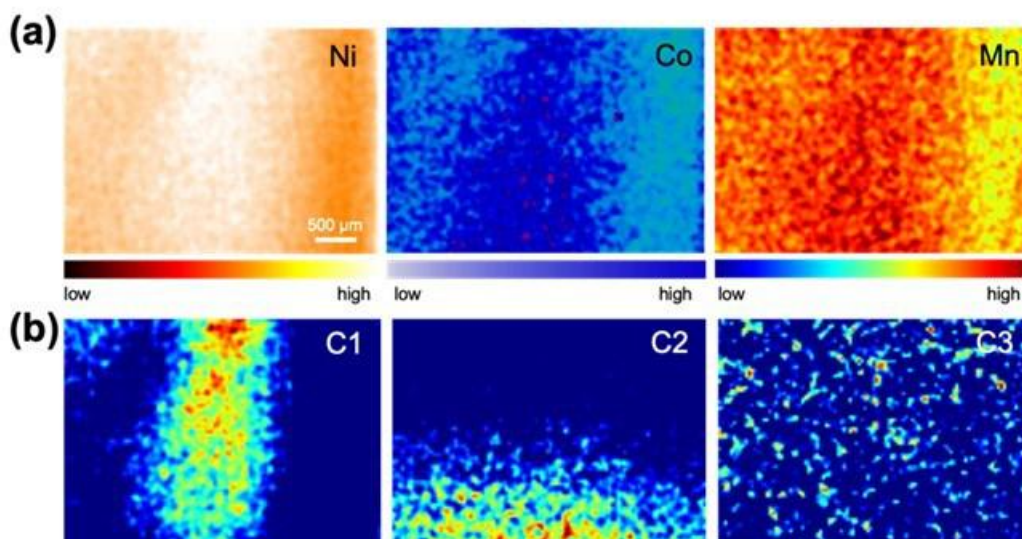


Figure IV.2.8 (a) μ -XRF maps corresponding to Ni, Co, and Mn at the cycled electrode with the 50 μ m focusing optics. (b) Three principle components 1, 2 and 3 from PCA multi-energy analysis across the Ni edge.

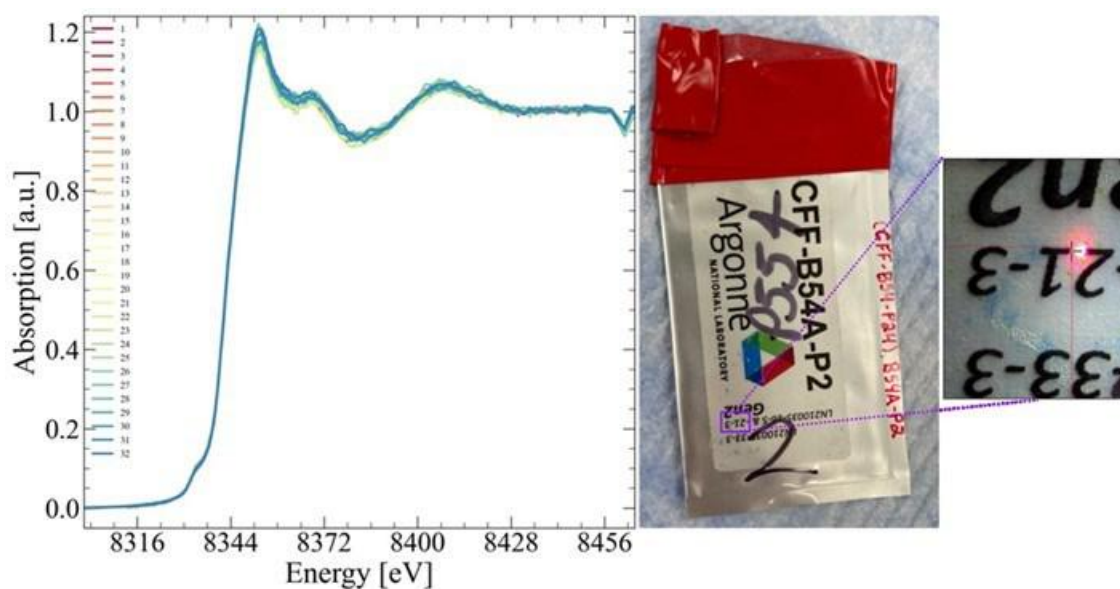


Figure IV.2.9 XANES spectra taken at 32 different points of a NMC811 cathode inside a pouch cell after 600 cycles under XFC conditions. Region of the cycled cell where XANES was taken, starting at the laser spot, and moving vertically downward in 50 μ m steps.

Current Density Measurements in Batteries at Rest Using Micro-tomography (LBNL Focus)

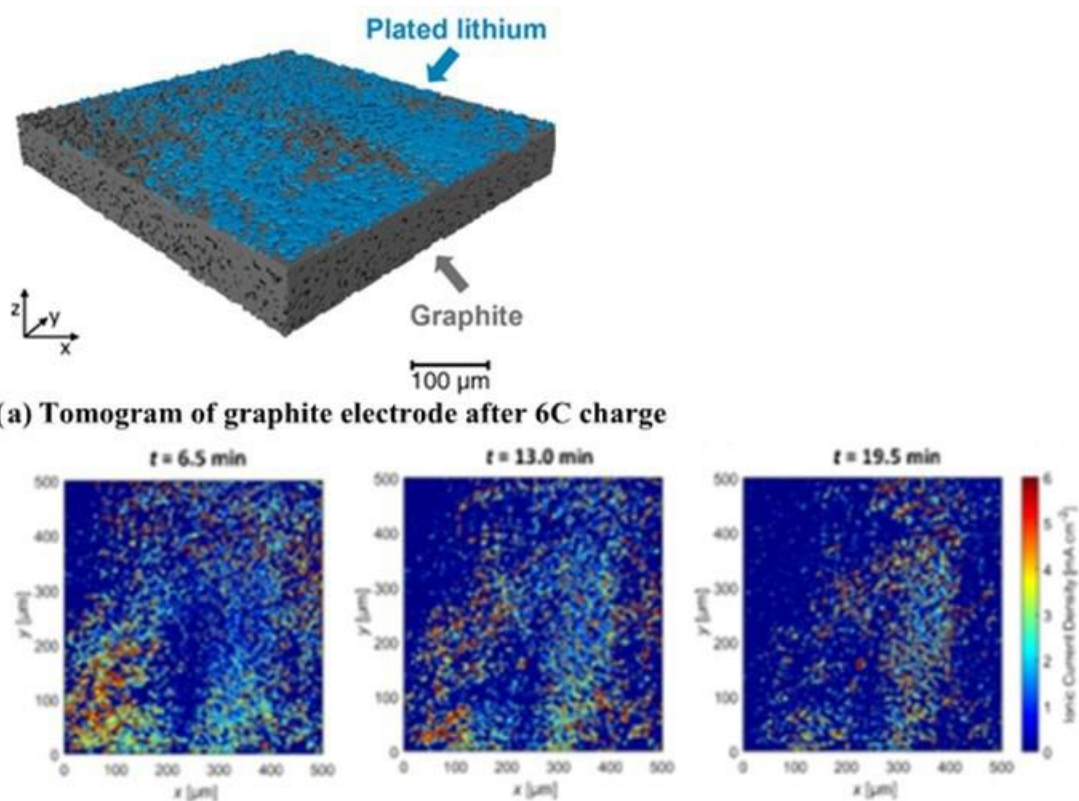
X-ray micro-tomography is a non-invasive technique that can yield spatial information about materials and systems in three dimensions (3D). Cells in different states-of-charge are placed between the source and the detector. Experiments use a monochromatic beam as the source with energies in the 20 keV range. Cells are rotated through 180 degrees and about 1000 projection images are collected and magnified. The exposure time for each image is in the 100-200 ms range. 3D reconstruction algorithms are used to synthesize the projection images to produce the morphology of the cell with a resolution of 1-5 μ m. If the same cell is imaged at difference states-of-charge, then it is possible to determine local currents by quantifying morphological differences between successive tomograms. Digital volume correlation has emerged as a standard tool for quantifying these differences.

A graphite electrode was studied in a half-cell at rest after 6C fast charging using time-resolved X-ray microtomography [6]. The fast charging step results in plated lithium near the electrode-separator interface (Figure IV.2.10a). When the cell is set to open circuit, a significant fraction of the plated lithium “disappears” from the tomograms, while the graphite particles underneath the plated lithium swell. The time-resolved tomograms enable quantifying spatially and temporally current densities at both lithium and graphite phases – the stripping current density at the lithium plate and the intercalation current density in the graphite (Figure IV.2.10b and c). The average current densities at the two phases are within 15%, and they decrease from about 1.5 to 0.5 mA cm² during the first 20 minutes of the resting period (Figure IV.2.11a). The median current density at the graphite electrode is 0, suggesting that most of the internal current has ceased by the end of the experiment. Surprisingly, the range of stripping current density was independent of time, with outliers above 20 mA cm² (Figure IV.2.11d). The persistence of outliers provides a clue as to the origin of catastrophic failure in batteries at rest.

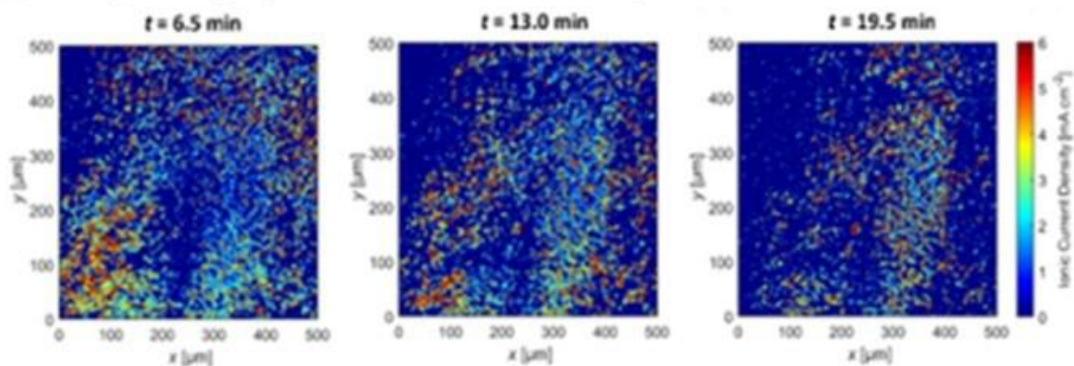
In-situ and Operando Investigation of NMC811-based Cells Subjected to Fast Charge (Argonne-APS Focus)

Enabling the fast charge capabilities in layered oxide-based batteries require deep understanding of relationships between active battery components, additives and electrolytes. It was demonstrated previously that high-rate-induced anode heterogeneity may lead to uneven material degradation resulting in higher cell-to-cell variability and potentially leading to lithium plating. Engineered solutions that promote homogenous performance were evaluated and tested. Periodical mapping of the equivalent battery cells utilizing different electrolytes showed that cell performance and degradation, including lithium plating probability, can be altered through modifications to battery components that influence Li transport and/or diffusivity. For example, high loading (97%) nickel-rich LiNi_{0.8}Mn_{0.1}Co_{0.1}O₂ (NMC811) batteries cycled in the presence of Gen2 electrolyte (1M LiPF₆ in 3:7 wt% EC:EMC) indicated future plating probability as early as 100 cycles with clear presence of lithium metal deposited on the anode within 400 cycles. In contrast, batteries utilizing B26 electrolyte (LiPF₆ in EC:DMC:DEX:EP:PN (20:40:10:15:15) with 3% VC & 3% FEC) did not show any presence of heterogeneity within the anode and no clear evidence of lithium metal was found at the end of the experiment ~1300 cycles. (Figure IV.2.12).

Among the proposed strategies that could mitigate electrode heterogeneities both in plane and through plane is to design electrode architectures incorporating microstructural heterogeneity, such as, for example, engineered porosity through laser ablation. This could mitigate transport limitations that give rise to the depth-dependent heterogeneity, reduce overcharging of the material close to the separator and utilize material close to the current collector better and therefore decrease the probability of lithium plating. *Operando* measurements during fast charge conditions however, are often challenging as many techniques require battery containers modifications that often hinder performance. Recently enabled high energy X-ray (105 keV) beam focusing at 11-ID-C station at APS allows studying reaction front *operando* in unmodified coin-cells with fast charge relevant data point density. Currently, the effects of the various electrolytes and laser ablation on the reaction front development are being evaluated. Figure IV.2.13. shows the difference in graphite behavior during fast charge period between materials close to the separator (left), and current collector (right).



(b) Current density maps in the plated lithium phase



(c) Current density maps in the graphite phase

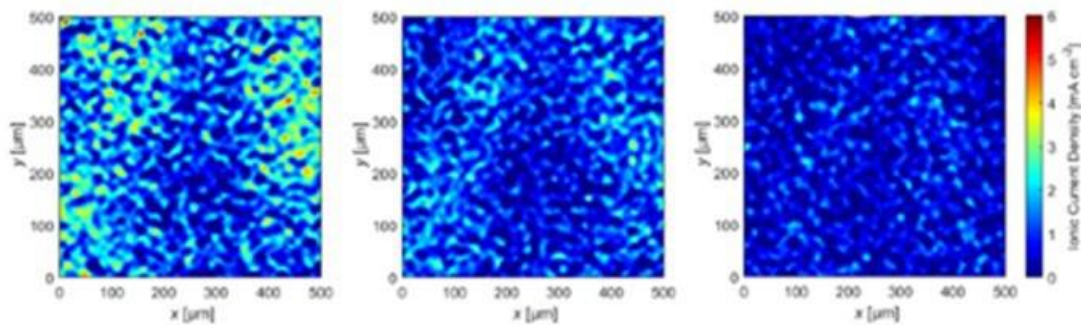


Figure IV.2.10 Current density in graphite electrodes at rest after fast charging. (a) The 3D tomogram of the electrode at the beginning of the rest period. (b) Current density in the plated lithium phase as a function of time. (c) Current density in the graphite phase at the same times. The range of the maps is reduced to avoid dominance by outliers.

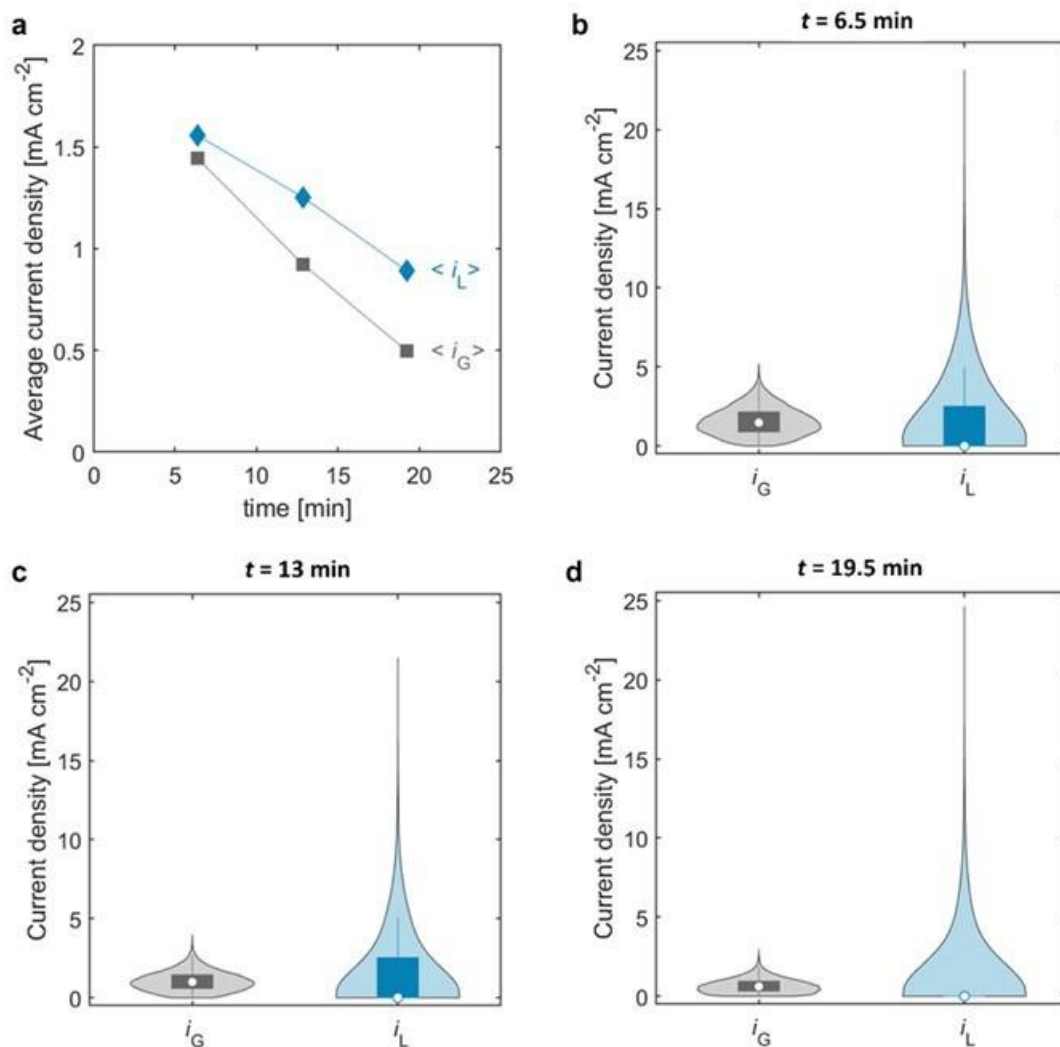


Figure IV.2.11 (a) Average current density during rest after 6C charging for the graphite electrode. The turquoise diamonds represent the average lithium stripping ionic current density, $\langle i_L \rangle$. The gray squares represent the average lithiation current density into graphite, $\langle i_G \rangle$. (b-d) Violin plots showing the distribution, median, and interquartile range of i_L and i_G at (b) $t = 6.5$ min, (c) $t = 13.0$ min, and (d) $t = 19.5$ min. For the box plot within each violin plot, the white circle represents the median value, the bottom and top of each box represents the 25th and 75th percentile values, and the bottom and top whiskers (solid lines) represent the lower and upper adjacent values. The box has zero height at $t = 19.5$ min for i_L .

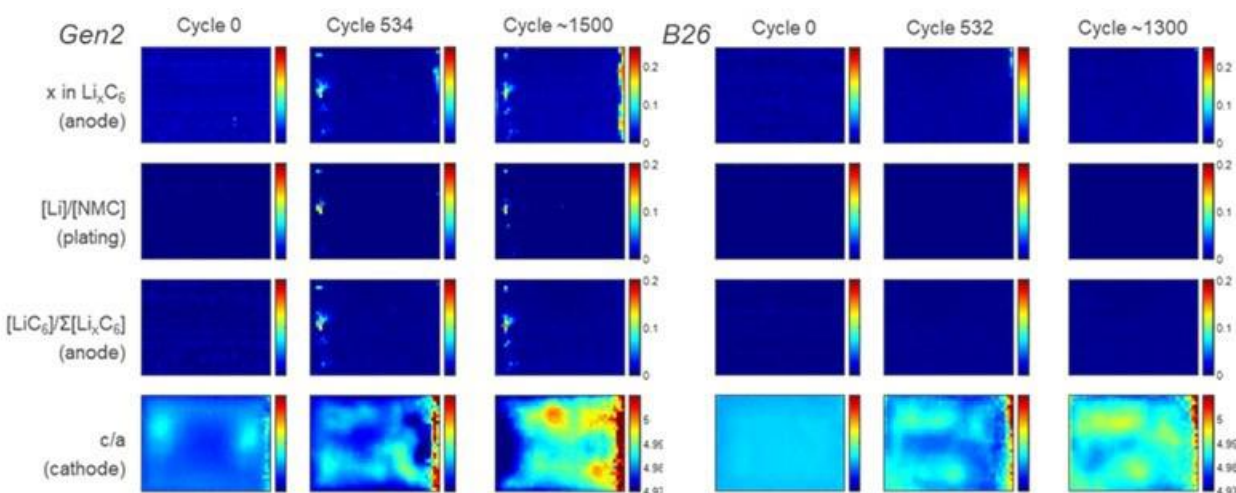


Figure IV.2.12 XRD mapping comparison between Gen2 and B26 electrolytes using pouch cell configuration. Compositional characteristics are highlighted via 2D thermal maps respectively.

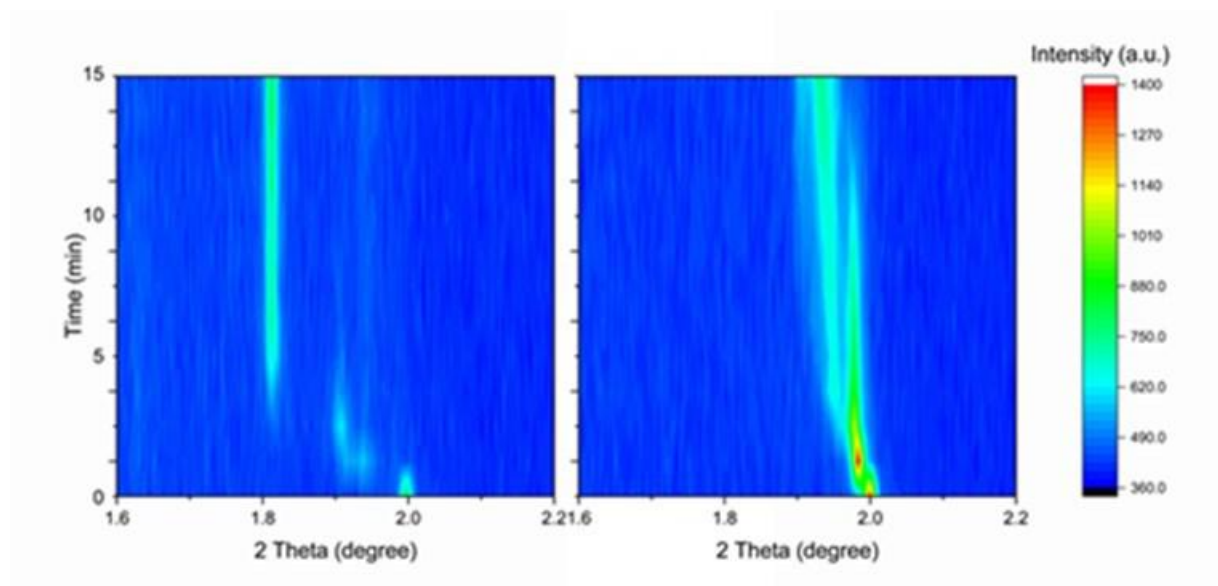


Figure IV.2.13 Focused beam X-ray diffraction measurements of graphite anode at the separator side (left) and the current collector end (right) during the fast charging process.

Localized Li Detection with Spatially Resolved Differential Pressure Sensing (SR-DPS) (SLAC/Stanford Focus)

The Cui group at Stanford developed an operando Li-plating detection technique that allows identification of localized Li-plating behaviors. This project is a continuation of the previous global Li detection project based on the differential pressure sensing techniques (DPS). DPS measures the change of cell pressure per unit of charge, which has been proven to be an effective and non-intrusive approach to detect Li-plating operando. Instead of the DPS technique measuring the global pressure change per unit charge, we introduce a spatially resolved differential pressure sensing (SR-DPS), which integrates a 2D pressure sensor map into the stacking battery. This SR-DPS sensor can provide spatially resolved pressure data at a refresh rate of up to 500Hz. Currently, we have successfully observed localized Li-plating and its growth patterns. We have also explored the compatibility of the application program interface (API) of the pressure sensor with that of the battery tester. APIs are built-in environments that allow customers to construct custom programs to interface one

software with other software. We have confidence in developing an automated battery management system (BMS) using DPS measurements.

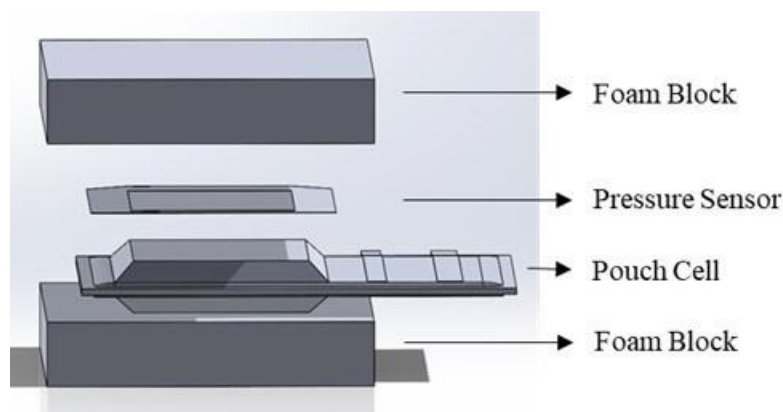


Figure IV.2.14 The configuration of operando SR-DPS apparatus: the stack containing two vibration-damping foam blocks, multilayer pouch cell, and 2D pressure sensor is clamped into a fixed constraint.

The configuration of the spatially resolved operando DPS system is shown in Figure IV.2.14: the stack containing multilayer pouch cell, 2D pressure sensor, and vibration-damping foam blocks are clamped into a fixed constraint. The setup can provide a real-time 2D map of the pressures across the pouch cell in a 44x44 matrix with a spatial resolution of 600 microns (Figure IV.2.15a). Using similar methods as that outlined in previous reports, we can obtain the local dP/dQ values and capture the associated plating behaviors by comparing the dP/dQ data of each pixel with the established dP/dQ plating threshold surface at low C-rates (Figure IV.2.15b). Furthermore, we are able to study the spatial evolution of Li plating.

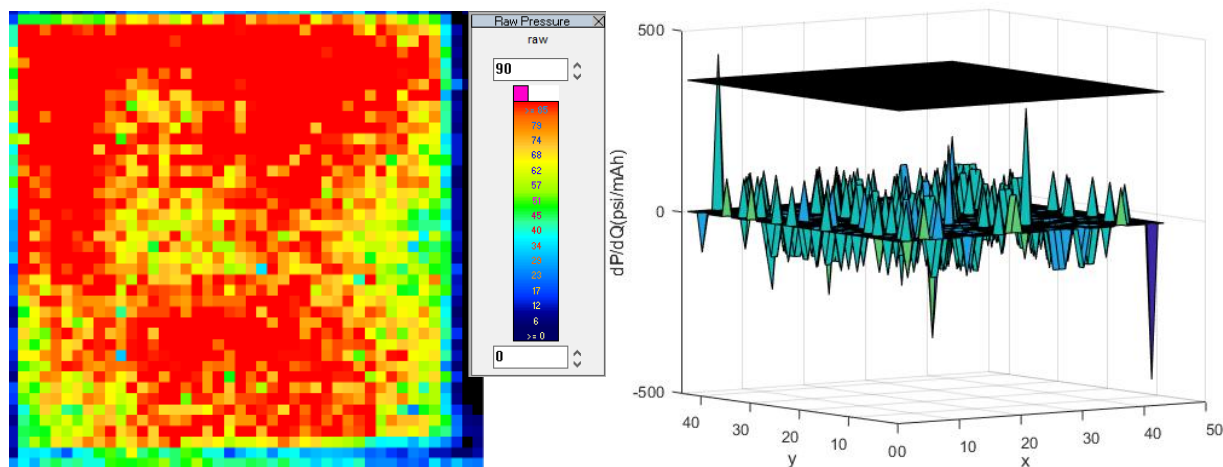


Figure IV.2.15 (left) Raw output from 2D pressure sensor of 1"×1" NMC811/graphite pouch cell with average initial gauge pressure of 80psi. (right) dP/dQ plot of aforementioned pouch cell at the first frame where the plating threshold is exceeded.

Using SR-DPS, we were able to generate videos of the DPS data and analyze the spatial-temporal evolution of Li plating at high C-rates (Figure IV.2.16, Video Link). Interestingly, it was observed that Li preferentially plates along high-pressure gradients. The drastic drop in pressure along the edges of the electrode causes the ionic conductivity to differ greatly, which encourages Li plating. The symmetrical dP/dQ curve during charging and discharging observed in the previous DPS experiments are also confirmed in our SR-DPS experiments.

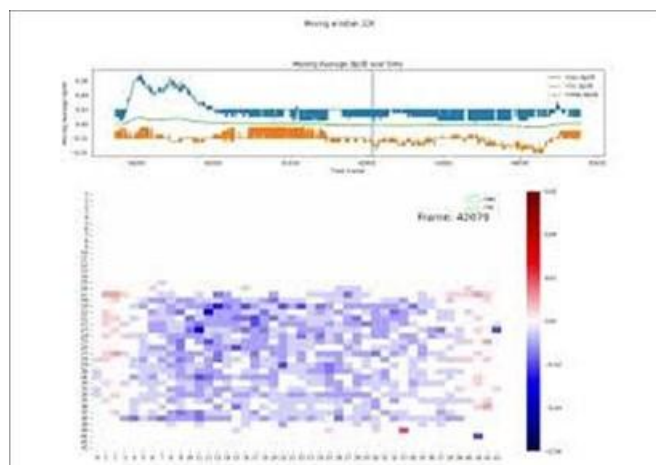


Figure IV.2.16 Video: Spatial temporal map of Li intercalation and plating during 3C charging and 0.5C discharging cycle. 90mAh pouch cell battery with NMC811/graphite electrodes and LP57 electrolyte. Positive dP/dQ value indicate lithiation or plating; negative dP/dQ value indicate de-lithiation or stripping.

By obtaining the maximum dP/dQ value per frame of the generated video during post analysis, we were successful in adjusting the charging protocol to drastically reduce the amount of plated lithium and reducing the charging time (Figure IV.2.17). Through post analysis, we determined the optimal cutoff current for the constant voltage step for different C-rates. However, since this is not a dynamic process, we still see minor plating occurring after adjustments.

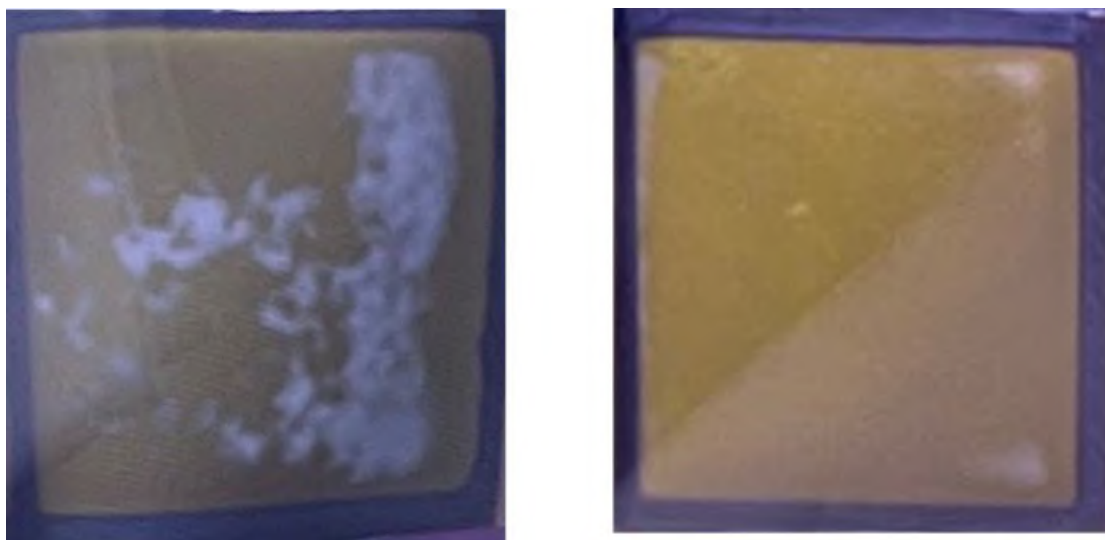


Figure IV.2.17 Li-plating drastically reduced with improved cycling parameters. 80mAh pouch cell battery assembled with NMC532/graphite electrodes and LP57 electrolyte cycled at 3C charging 0.5C discharging for 3 cycles without SR-DPS adjustments (left) and after SR-DPS adjustments (right).

Conclusions

The Electrode & Cell Design Thrust of the XCEL Phase II Program successfully coordinated its efforts to develop the ideal structured electrode to enable fast charging with minimal lithium plating. In particular:

- Using already demonstrated XFC solutions, models predict cells with EV relevant loadings can be re-charged in 15 minutes without lithium plating. Reducing the amount of carbon/binder content in the cathode from 10% to 4% significantly improves fast charge performance due to enhanced ionic transport. A dual layer anode significantly delays lithium plating onset due to reduced local tortuosity near separator.

- A third single-layer pouch cell benchmark was developed with a higher loading (R3 loading) and higher active material (NMC811) content in the cathode than the previous two benchmarks to better match industrial needs for an EV lithium-ion battery. A new baseline electrolyte was selected to be “Gen2” + 2 wt% FEC.
- Single-layer pouch cells were fabricated with the new baseline electrodes and electrolyte, in addition to cell builds with three candidate electrolytes from the Electrolyte Thrust teams to meet the FY22 deliverable.
- Scoping studies based on utilizing single-walled carbon nanotubes (SWCNT) in the cathode to lower the impedance look promising.
- Degradation of NMC811 cathode under XFC conditions in full single-layer pouch cells were studied using micro X-ray fluorescence (μ -XRF) and micro X-ray absorption near edge structure (μ -XANES).
- X-ray micro-tomography was used to quantify spatially and temporally current densities at both lithium and graphite phases.
- Focused beam X-ray diffraction measurements were made of the graphite anode at the separator side and the current collector end during the fast charging process.

Key Publications

1. F. Usseglio-Viretta, P. Patel, E. Bernhardt, A. Mistry, P. P. Mukherjee, J. Allen, S. J. Cooper, J. Laurencin, and K. Smith, *MATBOX: An Open-source Microstructure Analysis Toolbox for microstructure generation, segmentation, characterization, visualization, correlation, and meshing*, SoftwareX, 17, 100915, 2022
2. F. Usseglio-Viretta, A. M. Colclasure, A. R. Dunlop, S. E. Trask, A. N. Jansen, D. P. Abraham, M.-T. F. Rodrigues, E. J. Dufek, T. R. Tanim, P. R. Chinnam, Y. Ha, and K. Smith, *Carbon-binder weight loading optimization for improved lithium-ion battery rate capability*, J. Electrochem. Soc., 169, 070519, 2022
3. Sangwook Kim, Tanvir R Tanim, Eric J Dufek, Don Scofield, Timothy D Pennington, Kevin L Gering, Andrew M Colclasure, Weijie Mai, Andrew Meintz, Jesse Bennett. “Projecting Recent Advancements in Battery Technology to Next-Generation Electric Vehicles” *Energy Technology* **10**, 2200303 (2022).
4. Nathan Dunlap, Dana B Sulas-Kern, Peter J Weddle, Francois Usseglio-Viretta, Patrick Walker, Paul Todd, David Boone, Andrew M Colclasure, Kandler Smith, Bertrand J Tremolet de Villers, Donal P Finegan. “Laser ablation of Li-ion electrodes for fast charging: Material properties, rate capability, Li plating, and wetting” *Journal of Power Sources* **537**, 231464 (2022).
5. Eric J McShane, Helen K Bergstrom, Peter J Weddle, David E Brown, Andrew M Colclasure, Bryan D McCloskey. “Quantifying Graphite Solid-Electrolyte Interphase Chemistry and its Impact on Fast Charging” *ACS Energy Letters* **7**, 2734-2744 (2022).
6. Tanvir R Tanim, Zhenzhen Yang, Donal P Finegan, Parameswara R Chinnam, Yulin Lin, Peter J Weddle, Ira Bloom, Andrew M Colclasure, Eric J Dufek, Jianguo Wen, Yifen Tsai, Michael C Evans, Kandler Smith, Jeffery M Allen, Charles C Dickerson, Alexander H Quinn, Alison R Dunlop, Stephen E Trask, Andrew N Jansen. “A Comprehensive Understanding of the Aging Effects of Extreme Fast Charging on High Ni NMC Cathode” *Advanced Energy Materials* **12**, 2103712 (2022).
7. KSN Vikrant, Eric McShane, Andrew M Colclasure, Bryan D McCloskey, Srikanth Allu. “Quantification of Dead Lithium on Graphite Anode under Fast Charging Conditions” *Journal of the Electrochemical Society* **169**, 040520 (2022).
8. Eric J Dufek, Daniel P Abraham, Ira Bloom, Bor-Rong Chen, Parameswara R Chinnam, Andrew M Colclasure, Kevin L Gering, Matthew Keyser, Sangwook Kim, Weijie Mai, David C Robertson, Marco-Tulio F Rodrigues, Kandler Smith, Tanvir R Tanim, Francois LE Usseglio-Viretta, Peter J Weddle. “Developing extreme fast charge battery protocols—A review spanning materials to systems” *Journal of Power Sources*, 231129 (2022).
9. Ningshengjie Gao, Sangwook Kim, Parameswara Chinnam, Eric J Dufek, Andrew M Colclasure, Andrew Jansen, Seoung-Bum Son, Ira Bloom, Alison Dunlop, Stephen Trask, Kevin L Gering.

“Methodologies for Design, Characterization and Testing of Electrolytes that Enable Extreme Fast Charging of Lithium-ion Cells” *Energy Storage Materials* **44**, 296-312 (2022).

Key Publications

1. F. Usseglio-Viretta, P. Patel, E. Bernhardt, A. Mistry, P. P. Mukherjee, J. Allen, S. J. Cooper, J. Laurencin, and K. Smith, *MATBOX: An Open-source Microstructure Analysis Toolbox for microstructure generation, segmentation, characterization, visualization, correlation, and meshing*, SoftwareX, 17, 100915, 2022
2. F. Usseglio-Viretta, A. M. Colclasure, A. R. Dunlop, S. E. Trask, A. N. Jansen, D. P. Abraham, M.-T. F. Rodrigues, E. J. Dufek, T. R. Tanim, P. R. Chinnam, Y. Ha, and K. Smith, *Carbon-binder weight loading optimization for improved lithium-ion battery rate capability*, J. Electrochem. Soc., 169, 070519, 2022
3. Nathan Dunlap, Dana B Sulas-Kern, Peter J Weddle, Francois Usseglio-Viretta, Patrick Walker, Paul Todd, David Boone, Andrew M Colclasure, Kandler Smith, Bertrand J Tremolet de Villers, Donal P Finegan. “Laser ablation of Li-ion electrodes for fast charging: Material properties, rate capability, Li plating, and wetting” *Journal of Power Sources* **537**, 231464 (2022).
4. A. Shodiev, M. Chouchane, M. Gaberscek, O. Arcelus, J. Xu, H. Oularbi, J. Yu, J. Li, M. Morcrette, and A. Franco, *Deconvoluting the benefits of porosity distribution in layered electrodes on the electrochemical performance of Li-ion batteries*, Energy Storage Materials, 47, 462-471, 2022
5. M. Wood, J. Li, Z. Du, C. Daniel, A. R. Dunlop, B. J. Polzin, A. N. Jansen, G. K. Krumdick, D. L. Wood III, *Impact of secondary particle size and two-layer architectures on the high-rate performance of thick electrodes in lithium-ion battery pouch cells*, J. Power Sources, 515, 230429, 2021
6. Ho, A.S., Parkinson, D.Y., Trask, S.E., Jansen, A.N., and Balsara, N.P. (2022). Manuscript under review.

Acknowledgements

Key contributors (alphabetical order per Lab) to the XCEL Electrode & Cell Design Thrust work include: Daniel Abraham, Shabbir Ahmed, Pavan Badami, Harry Charalambous, Alison Dunlop, LeRoy Flores, Brian Ingram, Tianyi Li, Marco Rodrigues, Eli Shkrob, Seoung-Bum Son, Steve Trask, Kamila Wiaderek, Zhenzhen Yang (Argonne); Nitash Balsara, Guoying Chen, Alec Ho (LBNL); Andrew Colclasure, Donal Finegan, Kandler Smith, Francois Usseglio-Viretta (NREL); and Yi Cui, Tony Li, Fang Liu, Johanna Weker Nelson, Molleigh Preefer, Erick Espinosa Villatoro (Stanford/SLAC)

IV.3 XCEL Thrust 3: Electrochemical and Thermal Performance

Eric Dufek, Principal Investigator

Idaho National Laboratory
2525 Fremont Ave
Idaho Falls, ID 83415
E-mail: eric.dufek@inl.gov

Brian Cunningham, DOE Technology Development Manager

U.S. Department of Energy
E-mail: brian.cunningham@ee.doe.gov

Start Date: October 1, 2021	End Date: September 30, 2024	
Project Funding (FY22): \$1,480,000	DOE share: \$1,480,000	Non-DOE share: \$0

Project Introduction

Extreme fast charging (XFC) of Li-ion batteries can create life and safety issues (Ahmed et al. 2017). With respect to performance loss one of the key complications is plating of Li metal on the negative electrode during fast charging. When this occurs, there is a pronounced loss of Li inventory and subsequent enhanced electrolyte degradation due to the reaction of electrolyte molecules with Li metal. Additional degradation modes including cathode aging can complicate analysis as new charging protocols are developed. As part of this thrust a team consisting of researchers at Idaho National Laboratory (INL), the National Renewable Energy Laboratory (NREL), Ford, the Stanford Linear Accelerator (SLAC) and Argonne National Laboratory (Argonne) is developing methods to both more clearly understand life and failure mode analysis for cells undergoing fast charge and to use understanding of cell design to develop new fast charge protocols. Using a combination of experimental and physics-based models, which incorporate both electrochemical and thermal performance, the team was able to develop methods to achieve a 25% increase in charge acceptance in a 10 min charge and a three-fold improvement in charge acceptance for charging segments that did not include a constant voltage component.

Objectives

Key objectives during FY22 were to continue to increase knowledge on the limitations of fast charge using graphite-based Li-ion batteries and to use that knowledge to improve performance. Overall objectives were to increase charge acceptance in cells with a fixed charge time of 10 minutes, identify failure modes and develop means to facilitate early identification of failure modes using electrochemical signatures. The team also investigated different modes of improving charge acceptance including the use of different temperatures and cell design aspects. This thrust also evaluated the performance of solutions developed in the other XCEL thrusts including electrolyte and electrode design solutions.

Approach

Using existing and expanding knowledge the team developed advanced charging algorithms using both experimental work and physics-based models. Both 3-electrode and pseudo-2D (P2D) model outputs provided understanding on when issues with Li metal plating or non-uniform thermal distribution could emerge in cells undergoing fast charge. Using this knowledge specific protocols were developed that limited Li plating. Improved performance was validated using single layer pouch cells. Key failure modes were validated using post-test characterization including analysis of the electrolyte, optical imaging and advanced characterization using different scientific user facilities.

Results

Within the Electrochemical and Thermal Performance Thrust in FY22 several activities were performed spanning the development of protocols, development of methods to understand the thermal impacts of fast charging, validation of performance and verification of failure modes.

Charge Protocol Development

Electrochemical P2D models were used to predict how different protocols impact the probability of Li plating. Different protocols were then developed which used either multiple current steps (material stress reduction, MSR) or a constant current to a fixed voltage after which point a voltage ramp (VR) was applied for the remainder of the 10 minute charge (Mai, Colclasure, and Smith 2020 and Kim et al 2022). These protocols, in addition to improvements in electrolyte, electrode/cell design and active material, have shown the ability to increase charge acceptance. An example of these modifications are shown in Figure IV.3.1 where the combination of a shift to NMC811, the use of a new electrolyte and the use of advanced charge protocols enabled over 90% charge acceptance during a 10-minute charge. This equates to a charge acceptance of 2.7 mAh/cm² for the Round 2 (R2) cells. In addition to having high charge acceptance the protocols also minimized the time in a constant voltage (CV) portion of the protocol. For the VR during early cycling the charge acceptance prior to the CV was 89% while the MSR had a charge acceptance of over 79% prior to reaching the CV. Both show considerable improvement from prior work. In addition to high charge acceptance the best performing cells had only about 10% capacity fade through the first 600 cycles.

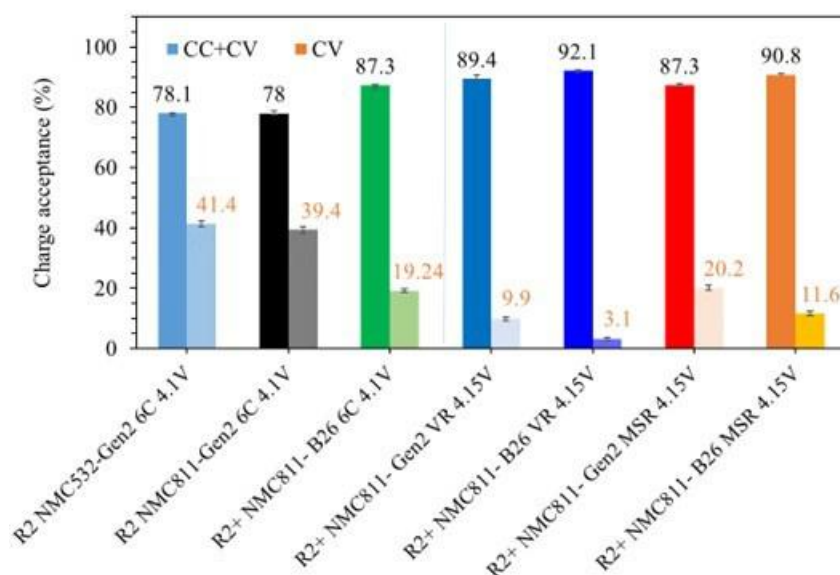


Figure IV.3.1 Charge acceptance for single layer pouch cells (R2) using different fast charge solutions including electrolytes, cathode material and charge protocol. The best performing solution combinations accepted over 2.7 mAh/cm² of charge at the beginning of life.

Using methods developed in other programs (Chen et al 2021 and Kim et al 2022) the failure modes of the cells were classified. The work shows that in the highest charge acceptance protocols there was no distinct evidence of Li plating and there was only minor difference in the extent of loss of lithium inventory for each of the different protocols. Indeed, most of the R2 cells exhibited ~10% loss of lithium inventory through 600 fast charge cycles. The methods also shows that the aging patterns of the cells did have some correlation to the different electrolytes used as evidenced by the different groupings shown in Figure IV.3.2.

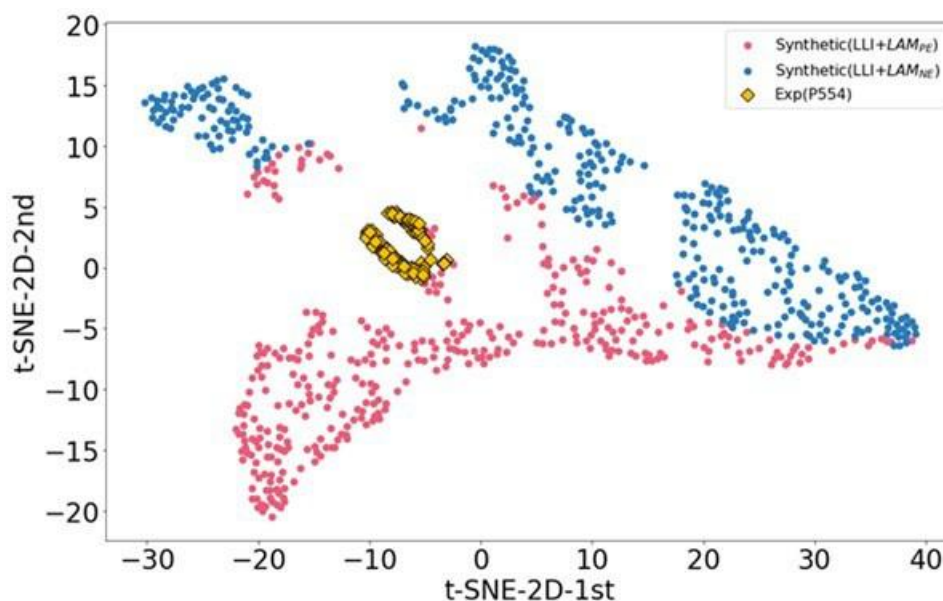


Figure IV.3.2 Plot of experimental and synthetic data used to classify the failure modes for cells which underwent different XFC charging. The method shows distinction between the two electrolytes used for the evaluation.

During the second half of the fiscal year work transitioned to Round 3 (R3) cells. NREL's macro-homogeneous modeling was used to develop voltage ramping protocols for R3 cell builds having a cathode loading of 3.1 mAh/cm². Compared to R2 cells, these cells use cathodes with low carbon binder content and a lower resistance separator. However, the cells employ a traditional Gen2 electrolyte. Instead of the traditional constant-current constant-voltage protocol, NREL has developed an advanced voltage ramping protocol that maximizes fast charge acceptable while avoiding lithium plating (Mai et al., 2020). Instead of constant voltage step, the voltage is ramped at a set rate to keep the anode potential slightly above the onset of lithium plating. NREL model predictions for standard CC-CV protocols matched well with experimental measurements performed at INL. NREL then used their models to develop a 10- and 15-minute ramp protocol. The 10-minute protocol is shown in Figure IV.3.3 and is predicted to achieve 68% capacity in 10 minutes while avoiding lithium plating. The protocol consists of an initial current of 6.5C up to 4.08V and then voltage ramping occurs at 0.08 mV/s to a max cutoff of 4.13V. A traditional 6C CC-CV protocol is predicted to achieve a similar capacity, but with significant amounts of plating. A 15-minute ramping protocol was also developed using a 5C initial current and predicted to achieve 83% capacity without plating. These suggested ramping protocols were shared with INL and have been implemented in electrochemical testing of R3 cell build.

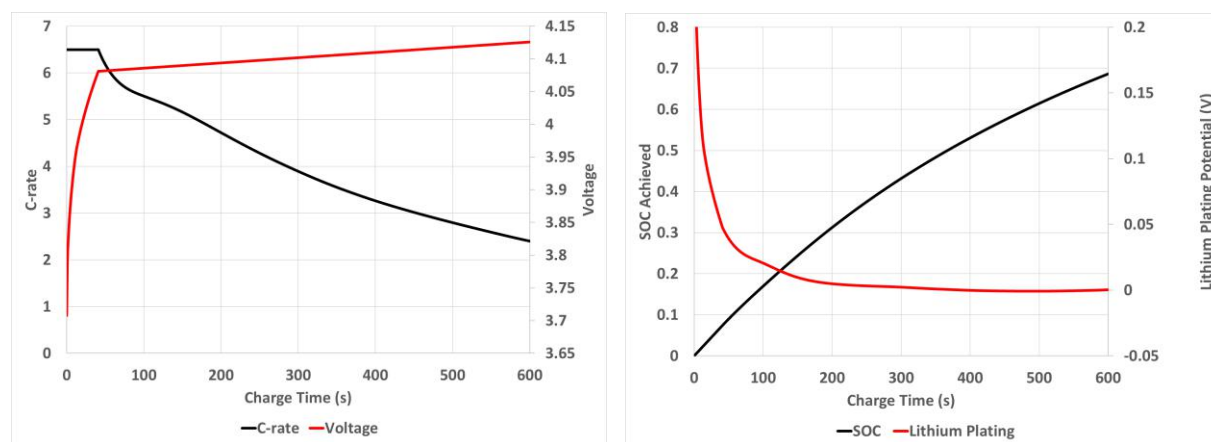


Figure IV.3.3 Macrohomogeneous model derived 10-minute voltage ramping protocols for graphite-NMC 811 R3 cells with loading of 3.1 mAh/cm² loading A.) Current and voltage of cell employing ramp protocol. B.) State of charge achieved and lithium plating potential.

Heating/Cooling System Design to Achieve Cost/Life Requirements: Life and cost of battery systems under extreme fast charging conditions are strongly impacted by temperature. The cell cooling coefficient (CCC) is an effective metric to compare cooling strategies for fast charge applications. Cell and cooling designs with higher CCCs offer better fast charging thermal performance, leading to effective temperature control, reduced temperature and associated electrochemical heterogeneities. CCCs can be enhanced by improving cell thermal properties and optimizing cell shapes and thermal packaging. Compared to experimental evaluation, 3D thermal modeling is more efficient to quantify CCCs. Modeling results suggest prismatic cells with aluminum cans have considerably higher CCCs than pouch cells. For typical cold plate and fin cooling, cooling performance can be improved by reducing the thermal resistances between cells and cold plates. Significant enhancement can be achieved by double-sided cooling, as shown in Figure IV.3.3. As illustrated in Figure IV.3.4, higher CCC cell can reduce temperature nonuniformity from ~15°C to 3°C at a heat removal rate of ~50%. For a cell with sufficient high CCCs, cooling capacity is then determined by the desired charge range and maximum allowable temperature, instead of limiting by cell temperature non-uniformity.

In FY22, the team initiated a review of XFC technologies and their documented benefits. Technologies include

- Advanced electrolytes
- Active material architectures
- Electrode architectures
- Heat transport enhancements
- Cell heating
- Cooling systems
- Charge protocols
- Combined strategies.

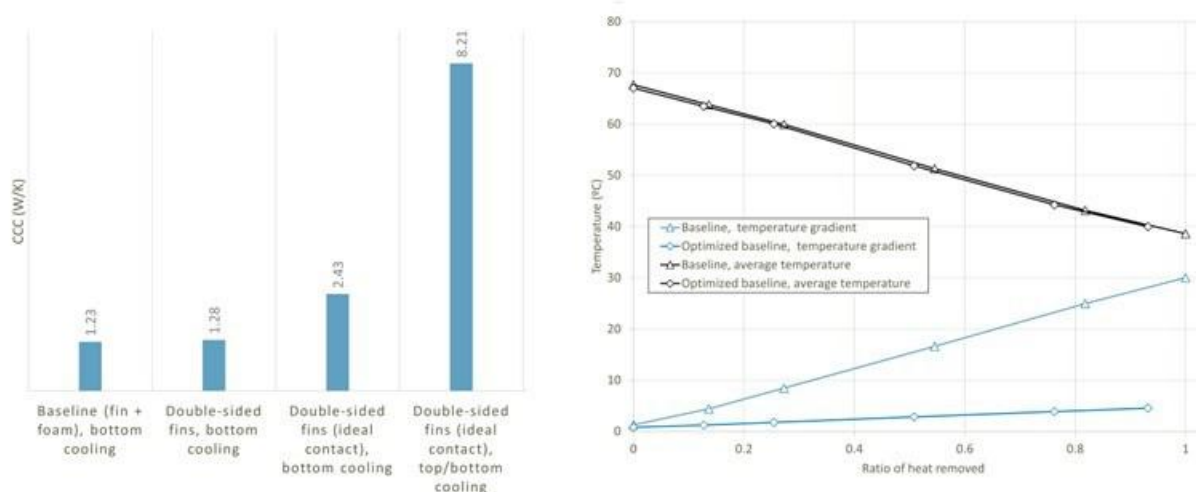


Figure IV.3.4 (Left) CCCs of a pouch cell with different external thermal designs and cooling. (Right) Temperature rise and temperature nonuniformities as a function of heat removal rates for baseline (CCC = 1.2 W/K) and optimized baseline (CCC = 8.2 W/K).

No complete apples-to-apples comparison can yet be made as several gaps in literature and XCEL team data were found that the team is now looking to fill with models and additional experiments. However some preliminary conclusions are that XFC technologies should use – or enable the use of – thick electrodes, which bring the lowest possible system cost together with the highest possible energy density. Achieving fast charge together with long life requires combining multiple strategies, employing advanced electrolytes for fast ion transport, cell-internal heating or pre-heating of the cell prior to fast charge, employing advanced electrochemical charge protocols such as voltage-ramp, and lowering the tortuosity of electrodes such as through laser ablation or dual-layer coatings. Technologies requiring further study include single-crystal cathode materials and optimization of cooling systems (expected to be ~7-kW liquid cooling for 90-kWh pack) while avoiding exotic thermal solutions (e.g. immersion cooling, or oversized ~20-kW cooling systems).

Enhanced Scientific Understanding of Degradation: The electrochemical and thermal performance thrust is also interested in methods to increase the scientific understanding of cell failure and performance degradation. As identified earlier in the XCEL project, during fast charge, cathode materials can undergo mechanical stress which can result in fracturing of the secondary particle and subsequently lead to increased impedance and reduced charge acceptance. To capture performance and degradation for arbitrary cathode materials (e.g. NMC532, NMC 811), a 3D polycrystalline model of cathode primary/secondary particle architecture was created (Allen et al., 2021). The model accepts material transport/mechanical properties for any cathode material, as well as their anisotropic grain architecture mapped using FIB-SEM with electron backscattering (EBSD). (See Figure IV.3.5.)

Past simulations investigated how particle geometry affect capacity loss, which found that smaller secondary particles with fewer (or single) primary particles had better capacity retention. FY22 focused on adding a model for electrolyte infiltration (EI). As the secondary particle cracks along grain boundaries, cracks that are connected to the surface are assumed to fill with electrolyte and those surfaces become electrochemically active. When EI is enabled, overall damage and the internal resistances of the particle are reduced.

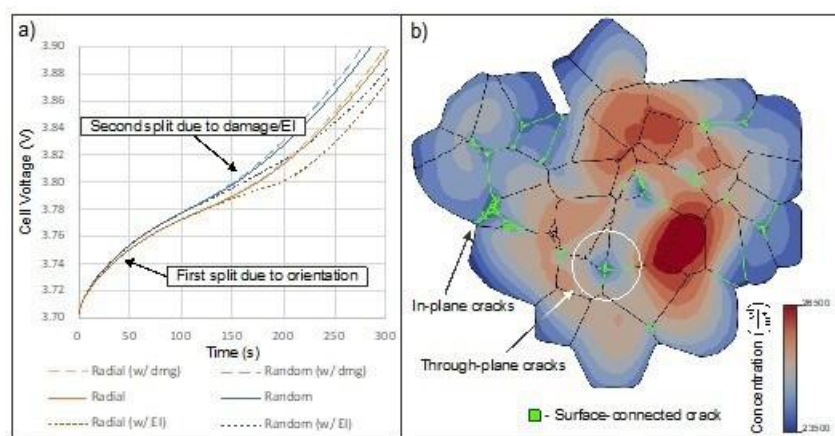


Figure IV.3.5 a) How cell voltage changes in an NMC532 cathode particle with radial or random grain orientations, with or without damage (dmg), and with or without electrolyte infiltration (EI). b) Lithium concentration distribution within a particle that has electrolyte infiltration after charging at 6C for 420 seconds.

The initial 3D polycrystalline cathode damage model was validated versus capacity fade observed for the NMC532 cells aged at varying charge rates, with loss of cathode active material inferred from incremental capacity analysis as well as directly measured from half-cells built from full cell teardowns at different cycle numbers. Deeper validation is needed to resolve the interaction of cracking with material/capacity loss for multiple cathode architectures and NMC blends. In two papers, the XCEL team and University of Ulm developed an artificial intelligence (AI) method to segment/quantify cracking observed in SEM images (Furat et al., 2021) and applied this automated method to hundreds of SEM images from the XCEL program (Furat et al., 2022). Shown in Figure IV.3.6 below, the study found that particle porosity (2D crack area) increases monotonically with cycles and C-rate. Electrode-thickness grows roughly proportional to particle porosity. Crack magnitude depends on C-rate for first 25 cycles (cracks widen), then cycling throughput thereafter (size and length increase). The initial break-in process of the first 25 cycles is well described by the 3D polycrystalline model. Additional investigation in FY23, adding physics of electrolyte infiltration and material electrical isolation, seeks to capture the slower fatigue processes.

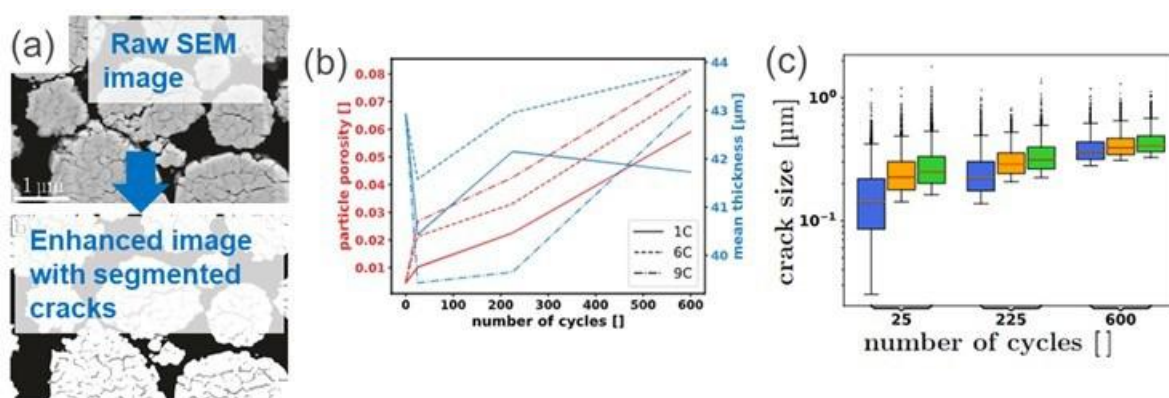


Figure IV.3.6 a) Image quality of hundreds of SEM images were enhanced and cracks segmented using AI. (b) Average particle porosity, the 2D cracked area ratio of a particle, versus charge rate and number of cycles for multiple aged cells torn down at different cycle numbers. (c) Whisker/box plot showing average/min/max crack statistics from hundreds of SEM images.

The second effort to look at impacts to aging induced by particle fracture used nano and micro- X-ray computed tomography (CT) to understand how the shape and size distribution of particles changed as cells went through different levels of cycling. This study identified that, as cells aged the distribution of particle

volume shifted to a bimodal distribution suggesting that particles were fracturing over time and that as cycle count increased the number of fractured particles also increased. This occurred irrespective of cycling rate though there was a more distinct fracturing trend for cells cycled at 9C for early cycling. However, as cycling increased, slower charged cells exhibited more distinct fracturing likely due to higher charge throughput for these cells. This result of inversion in aging mirrors electrochemical data showing more distinct aging for cells cycled at 1C (Tanim et al. 2022). The work extended analysis to also look at the sphericity of particles. This is a general indicator of the degree of particle fracture and if the fractured components are more similar to individual or small groups of primary particles vs larger and non-uniformly shaped aggregates of primary particles. (See Figure IV.3.7.)

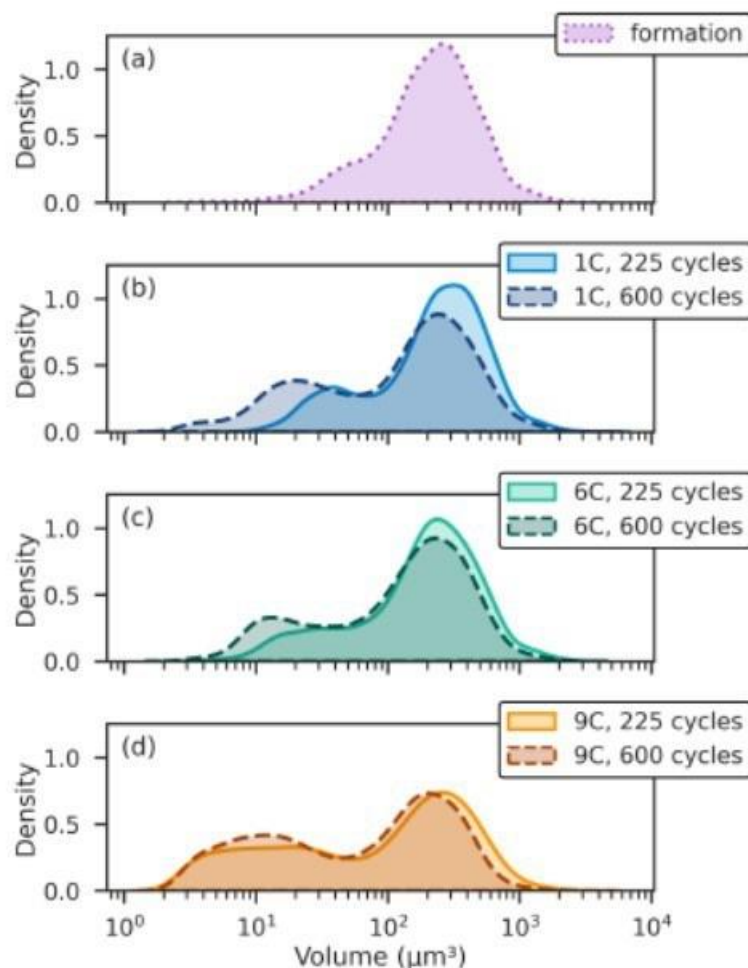


Figure IV.3.7 Estimates of particle density as determined using micro-CT reconstruction. The results suggest that as cycling advances particle fragmentation as evidenced by increased bimodal distribution (Preefer et al 2022 accepted).

Conclusions

Supporting optimization of electrochemical/thermal solutions for XFC, the team has conducted experiments, and is developing electrochemical/thermal models, to identify major degradation processes in graphite/NMC cells under XFC. Models, experiments, and prototype builds are employed in a feedback loop to achieve a fundamental understanding and advance fast charge design. With advanced design and protocols, models show 15-minute charging is possible for high energy density batteries. This model guidance will be followed up with additional prototype cell builds and tests in FY23.

NREL developed advanced voltage ramping protocols for R3 cell builds for charge times of 10 and 15 minutes that have been implemented in electrochemical testing by INL. INL also characterized and performed charge protocol optimization on R2 cells and used advanced analysis methods to classify and quantify the extents of aging for the cells. As more data is captured, the charge profiles will be scaled to understand possible impacts to electric vehicle charging infrastructure.

Degradation processes span many length scales in Li-ion batteries, from materials to 3D large format systems. The team is working to integrate relevant physics into a single model framework capable of exploring the complete materials-to-systems design space, weighing the cost and benefits of each XFC technology. In FY23, the team will develop a prototype of this complete model, expand its XFC technologies scorecard, and draft a review article comparing fast-charge technologies.

The 3D polycrystalline cathode cracking model will be further enhanced with electrical isolation and validated versus experiments. Through homogenization, a reduced-order version of this cathode active material loss model will be integrated into a pseudo-2D electrochemical model together with previously integrated SEI growth and Li plating mechanisms. Electrolyte wetting and dry-out processes are also under investigation. These studies complement CT studies performed by SLAC which have provided additional information on particle fracture and align with electrochemical analysis.

A 3D system-level model showed that cell cooling coefficient (CCC) is an effective metric to design thermal management for battery fast charging. Cell and cooling designs with higher CCCs offer better fast charging thermal performance and allow large heat removal rates without producing unacceptable temperature heterogeneities. After CCC optimization, active cooling can be delayed to both control cell maximum temperature and reduce energy consumption by the cooling system.

Key Publications

1. J. M. Allen, P. J. Weddle, A. Verma, A. Mallarapu, F. L. E. Usseglio-Viretta, D. Finegan, A. Colclasure, W. Mai, O. Schmidt, V. Furat, D. Diercks, T. Tanim, and K. Smith. *Quantifying the influence of charge rate and cathode-particle architectures on degradation of Li-ion cells through 3D continuum-level damage models*. Journal of Power Source (published, Sep. 2021)
2. Furat, D.P. Finegan, Z. Yang, T. Kirstein, K. Smith, V. Schmidt, "Super-resolving microscopy images of Li-ion electrodes for fine-feature quantification using generative adversarial networks," *Nature Computational Materials* (2022) 8:68.
3. Furat, D.P. Finegan, Z. Yang, T. Tanim, K. Smith, V. Schmidt, "Quantifying the Impact of Charge Rate and Number of Cycles on Structural Degeneration of Li-ion Battery Electrodes," *J. Echem. Society* 169 (2022) 100541.
4. C. Yang, K. Kandler, A. M. Colclasure, M. Keyser, *Mitigating Heterogeneities in Lithium-Ion Battery Modules Under Fast Charging*, ECS Meeting Abstracts MA2022-02(5):563.
5. Sangwook Kim, Tanvir R Tanim, Eric J Dufek, Don Scofield, Timothy D Pennington, Kevin L Gering, Andrew M Colclasure, Weijie Mai, Andrew Meintz, Jesse Bennett. "Projecting Recent Advancements in Battery Technology to Next-Generation Electric Vehicles" *Energy Technology* **10**, 2200303 (2022).
6. Nathan Dunlap, Dana B Sulas-Kern, Peter J Weddle, Francois Usseglio-Viretta, Patrick Walker, Paul Todd, David Boone, Andrew M Colclasure, Kandler Smith, Bertrand J Tremolet de Villers, Donal P Finegan. "Laser ablation of Li-ion electrodes for fast charging: Material properties, rate capability, Li plating, and wetting" *Journal of Power Sources* **537**, 231464 (2022).
7. Eric J McShane, Helen K Bergstrom, Peter J Weddle, David E Brown, Andrew M Colclasure, Bryan D McCloskey. "Quantifying Graphite Solid-Electrolyte Interphase Chemistry and its Impact on Fast Charging" *ACS Energy Letters* **7**, 2734-2744 (2022).
8. Tanvir R Tanim, Zhenzhen Yang, Donal P Finegan, Parameswara R Chinnam, Yulin Lin, Peter J Weddle, Ira Bloom, Andrew M Colclasure, Eric J Dufek, Jianguo Wen, Yifen Tsai, Michael C Evans, Kandler Smith, Jeffery M Allen, Charles C Dickerson, Alexander H Quinn, Alison R Dunlop, Stephen

- E Trask, Andrew N Jansen. “A Comprehensive Understanding of the Aging Effects of Extreme Fast Charging on High Ni NMC Cathode” *Advanced Energy Materials* **12**, 2103712 (2022).
9. KSN Vikrant, Eric McShane, Andrew M Colclasure, Bryan D McCloskey, Srikanth Allu. “Quantification of Dead Lithium on Graphite Anode under Fast Charging Conditions” *Journal of the Electrochemical Society* **169**, 040520 (2022).
 10. Eric J Dufek, Daniel P Abraham, Ira Bloom, Bor-Rong Chen, Parameswara R Chinnam, Andrew M Colclasure, Kevin L Gering, Matthew Keyser, Sangwook Kim, Weijie Mai, David C Robertson, Marco-Tulio F Rodrigues, Kandler Smith, Tanvir R Tanim, Francois LE Usseglio-Viretta, Peter J Weddle. “Developing extreme fast charge battery protocols—A review spanning materials to systems” *Journal of Power Sources*, 231129 (2022).
 11. Ningshengjie Gao, Sangwook Kim, Parameswara Chinnam, Eric J Dufek, Andrew M Colclasure, Andrew Jansen, Seoung-Bum Son, Ira Bloom, Alison Dunlop, Stephen Trask, Kevin L Gering. “Methodologies for Design, Characterization and Testing of Electrolytes that Enable Extreme Fast Charging of Lithium-ion Cells” *Energy Storage Materials* **44**, 296-312 (2022).
 12. Chuntian Cao, Hans-Georg Steinruck, Partha P. Paul, Alison R. Dunlop, Stephen E. Trask, Andrew N. Nelson, Robert M. Kasse, Vivek Thampy, Maha Yusuf, Johanna Nelson Weker. “Conformal Pressure and Fast-Charging Li-ion Batteries” *Journal of the Electrochemical Society*, 040540 (2022).
 13. Parameswara R. Chinnam, Tanvir R. Tanim, Eric J. Dufek, Charles C. Dickerson, Meng Li. “Sensitivity and reliability of key electrochemical markers for detecting lithium plating during extreme fast charging” *Journal of Energy Storage*, 103782 (2022)

References

1. Ahmed, S., I. Bloom, A.N. Jansen, T. Tanim, E.J. Dufek, A. Pesaran, A. Burnham, et al. (2017) Enabling Fast Charging – A Battery Technology Gap Assessment. *Journal of Power Sources* 367.
2. Mai, Weijie, Andrew M. Colclasure, and Kandler Smith. 2020. “Model-Instructed Design of Novel Charging Protocols for the Extreme Fast Charging of Lithium-Ion Batteries Without Lithium Plating.” *Journal of The Electrochemical Society* 167 (8): 080517
3. Kim, S., T.R.Tanim, E.J. Dufek, D. Scofield, T.D. Pennington, K.L. Gering, A.M. Colclasure, W. Mai, A. Meintz, J.Bennett (2022) Projecting recent advancements in battery technology to next-generation electric vehicles. *Energy Technology* 10(8).
4. J. M. Allen, P. J. Weddle, A.Verma, A.Mallarapu, F.L.E.Usseglio- Viretta, D. Finegan, A. Colclasure, W. Mai, O. Schmidt, V. Furat, D. Diercks, T. Tanim, and K. Smith. *Quantifying the influence of charge rate and cathode-particle architectures on degradation of Li-ion cells through 3D continuum-level damage models*. *Journal of Power Source* (published, Sep. 2021)
5. Furat, D.P. Finegan, Z. Yang, T. Kirstein, K. Smith, V. Schmidt, “Super-resolving microscopy images of Li-ion electrodes for fine-feature quantification using generative adversarial networks,” *Nature Computational Materials* (2022) 8:68.
6. Furat, D.P. Finegan, Z. Yang, T. Tanim, K. Smith, V. Schmidt, “Quantifying the Impact of Charge Rate and Number of Cycles on Structural Degeneration of Li-ion Battery Elelectrodes,” *J. Echem. Society* 169 (2022) 100541.
7. Preefer, M.B., T.R. Tanim, S.S. Welborn, D.N. Agyeman-Budu, A.R. Dunlop, S.E. Trask, E.J. Dufek, A.N. Jansen, J. Nelson Weker (accepted) The evolution of LiNi0.5Mn0.3Co0.2O2 particle damage from fast charging in optimized, full Li-ion Cells.

Acknowledgements

The activities described were a collaborative effort utilizing the capabilities of many researchers. Key contributors across the different national laboratories include Daniel P. Abraham, Ira Bloom, Bor-Rong Chen, Parameswara R. Chinnam, Andrew M. Colclasure, Kevin L. Gering, Matthew Keyser, Sangwook Kim, David Robertson, Marco-Tulio F. Rodrigues, Kandler Smith, Tanvir R. Tanim, Francois L. E. Usseglio-Viretta, Peter Weddle, Molleigh B. Preefer, Johanna Nelson Weker, Alison R. Dunlop, Stephen E. Trask, Andrew N. Jansen, David N. Agyeman-Budu, Chuanbo Zhang, Yeyoung Ha, Maha Yusuf, Partha P. Paul, Chuntian Cao, Bryant J.

Polzin, Michael F. Toney, and Vivek Thampy. Donal P. Finegan, Eric J. McShane, Bryan D. McCloskey, Seong-bum Son, Zhenzhen Yang and Michael Evans.

V Beyond Batteries

The “Beyond Batteries” initiative, also referred to as the Behind-the-Meter Storage (BTMS), focuses on novel critical-materials-free battery technologies to facilitate the integration of EV charging, solar power-generation technologies, and energy-efficient buildings while minimizing both costs and grid impacts. For extreme fast charging at levels of 650 kW (or higher), novel approaches are required to avoid significant negative cost and resiliency impacts. However, it is reasonable to assume that BTMS solutions would be applicable to other intermittent renewable energy generation sources or short-duration, high-power-demand electric loads.

BTMS research is targeted at developing innovative energy-storage technology specifically optimized for stationary applications below 10 MWh that will minimize the need for significant grid upgrades. Additionally, avoiding excessive high-power draws will eliminate excess demand charges incurred during 350-kW fast charging using current technologies. The key to achieving this is to leverage battery-storage solutions that can discharge at high power but then recharge at standard lower-power rates, acting as a power reservoir to bridge to the grid and other on-site energy-generation technologies such as solar photovoltaics (PV), thereby minimizing costs and grid impacts. To succeed, new and innovative integration treatments must be developed for seamless interaction between stationary storage, PV generation, building systems, and the electric grid.

Key components of BTMS address early-stage research into new energy-generation and building-integration concepts, critical-materials-free battery energy-storage chemistries, and energy-storage designs with a focus on new stationary energy-storage strategies that will balance performance and costs for expanded fast-charging networks while minimizing the need for grid improvements. BTMS systems are envisioned to improve grid stability and levelized cost of electricity (LCOE) for fast charging of light-, medium-, and heavy-duty EVs as they are expected to penetrate the market requiring various levels of charging infrastructure (350 kW to 1+MW).

The rest of this chapter contains a single comprehensive report on the status of the BTMS project.

V.1 Behind-the-Meter Storage (NREL, INL, ORNL, SNL, ANL)

Anthony Burrell, Principal Investigator

National Renewable Energy Laboratory
15013 Denver West Parkway
Golden, CO, 80401
E-mail: anthony.burrell@nrel.gov

Brian Cunningham, DOE Technology Development Manager

U.S. Department of Energy
E-mail: Brian.Cunningham@ee.doe.gov

Start Date: October 1, 2018
Project Funding: \$2,400,000

End Date: September 30, 2023
DOE share: \$2,400,000

Non-DOE share: \$0

Project Introduction

Behind the meter storage (BTMS) systems are envisioned to improve grid stability and levelized cost of electricity (LCOE) for fast charging of light-, medium-, and heavy-duty EVs as they are expected to penetrate the market requiring various levels of charging infrastructure (350 kW to 1+MW). With rapid growth in research and design of efficient and high-performance chemistries for novel battery cells such as those made from lithium ion, battery systems could prove to be the solution that can minimize stability challenges posed by high penetration of EVs in the market. However, we need to address the hazards associated with lithium-ion batteries used in stationary applications for BTMS to become a reality.

Objectives

The main objective is to develop a strategy to enable a fail-safe rack design over a three-year period. “Fail-safe” is defined as preventing cell to cell propagation in a best-case scenario and preventing rack to rack propagation in a worst-case scenario.

Approach

In 2017, Bloomberg estimated that 94MWh of grid storage were affected by lithium-ion battery fires in South Korea. After a thorough review, the Korean Ministry of Trade, Industry and Energy (MOTIE) determined that the four primary causes of the fires were:

- 1) **Insufficient battery protection systems against electric shock** - systems were not able to properly protect against electrical hazards due to ground faults or short circuits. Existing fusing for the energy storage system (ESS) was not able to interrupt large electrical surges which led to catastrophic failure of the contactors. The short circuit current allowed the failures to cascade to the bus bar which resulted in fires inside the ESS.
- 2) **Inadequate management of operating environment** - Of the 23 fire incidents that occurred, 18 were installed in harsh conditions - the mountains or coastal areas. It was concluded that these environments resulted in conditions including large temperature swings, high humidity and elevated levels of dust and particulates which ultimately led to failure modes resulting in fires.
- 3) **Faulty Installations** - Human error during installations led to system faults resulting in ESS fires.
- 4) **ESS System Integration** - The integrated protection and management systems were found to be insufficient with the ESS installation. The committee indicated that there were gaps in the energy management system (EMS), integration of the battery management system (BMS), and power management system (PMS) leading to the potential for fires.

More recently, South Korea experienced five ESS fires in 2019 and MOTIE determined that the fires originated due to internal defects within the batteries in combination with high charging rates at high states of charge. The committee attributed the defects to foreign matter in the cathode and lithium plating on the

separator and anode after performing a physical analysis of the batteries. Due to similar concerns associated with lithium-ion ESS, the BTMS program is assuming that existing and future quality control measures at battery manufacturing facilities will not eliminate all single cell thermal runaway events and that improvements are needed to the EMS, BMS, and PMS systems. Thus, BTMS formed a team, Enabling Technologies for Advanced Rack Design, that has developed a four-pronged approach to mitigate the hazards associated with BTMS systems:

- **Advanced Cell, Module, and Rack Thermal Design:** Battery thermal management techniques will be investigated to regulate battery systems under normal temperature ranges to minimize temperature differences and achieve optimum performance and life. These thermal management strategies will further be optimized to mitigate/prevent thermal runaway propagation that might occur in a battery system.
- **Advanced Battery Management Systems (BMS):** Develop advanced BMS systems capable of cell balancing, state of health estimation, regulating temperature gradients between cells, and monitoring the health of individual cells and the pack.
- **Advanced Sensors and Controls:** Advances in battery management sensing and controls will be investigated in the interest of maximizing life, performance, and safety of large battery systems.
- **System Safety:** Reduce, isolate or eliminate the combustible products/potential within the cell and system design.

As expected, there are several standards and certification guidelines available and the Team will be using them to inform the “fail-safe” design. The following specifications in Table V.1.1 will help guide the development of technologies engineered under this task. Even though this is not a comprehensive list, the specifications outlined below are commonly used within the grid storage industry.

Table V.1.1 Design standards certifications to be used for the rack design. Source: NREL

Safety	Description
UL 9540	Safety for energy storage systems and equipment.
UL 1973	Batteries for use in light electric rail applications and stationary applications. ¹
NFPA 70E	Standard for electrical safety in the workplace.
UL 1642	Standard for lithium batteries. ²
IEC 61508	Functional safety of electrical/electronic/programmable electronic safety-related systems. ³

¹ Applicable to battery modules and racks only.

² Applicable to battery cells only.

³ Evaluation of battery management system only, in support of UL 1973, UL 9540, and IEC 62619 certification.

The technologies contributing to a safe rack design involve a very complicated design space. To limit the number of design considerations, we will only be considering three cathode/anode combinations: lithium manganese oxide (LMO)/lithium titanate oxide (LTO), lithium iron phosphate (LFP)/lithium titanate oxide, and lithium iron phosphate/graphite. The chemistries were chosen due to their lack of critical materials and excellent safety record. It is understood that the specific and volumetric energy densities of these battery systems is lower than those used for transportation and consumer electronics, but we are assuming that weight and space restrictions will not be as severe for behind-the-meter-storage applications. Furthermore, our focus will be to develop a system primarily focused on the volumetric energy density as this is considered a more critical/important parameter. Figure V.1.1 shows graphically how the specific and volumetric energy densities will be affected from the cell to rack level – our target will be developing a rack system with 36% of the cell’s specific energy density and 30% of the cell’s volumetric energy density.

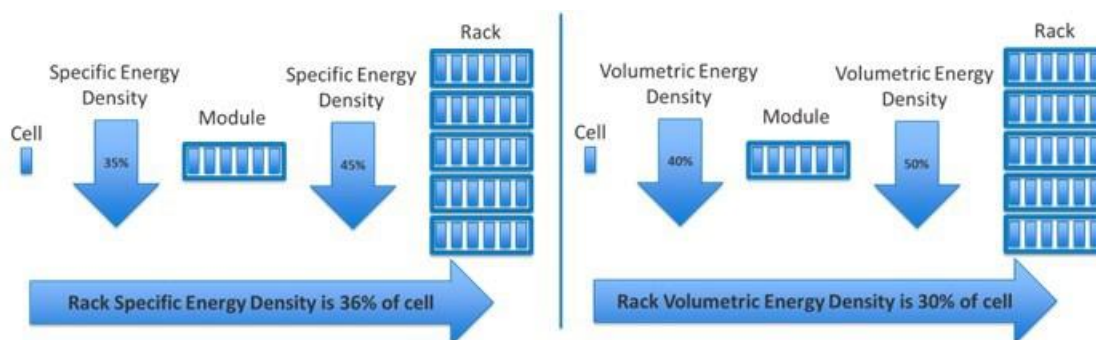


Figure V.1.1 Decrease in specific and volumetric energy density of ESS from the cell to the rack. Source: NREL

Another important aspect of the study will be to limit the battery discharge capacities to 10 Ah, 50 Ah, and 100 Ah. Even though some existing grid storage systems are using cells greater than 250 Ah, cell-to-cell propagation is difficult to limit or prevent in larger cells if a cell enters thermal runaway. As such, part of the study will investigate the positives/negatives of various series and parallel connected systems to achieve the appropriate fail-safe design and overall energy metrics for the system. Finally, temperature is critical to the lifetime and safety of the system. Initial, design specifications will be to limit the temperature of the batteries to between 20°C and 45°C and limit the temperature spread across the cells in the rack to 3°C. Table V.1.2 summarizes the important design parameters for our study. However, it should be noted each of the four efforts under this task will have additional design variables such as overvoltage, undervoltage, overcurrent, balancing requirements, etc... and these will be covered in the subsequent sections of this report.

Table V.1.2 Important design parameters for the advanced rack design. Source:NREL

Design Parameter	Units	
Rack Specific Energy Density	Wh/kg	> 36% of Cell Specific Energy Density
Rack Volumetric Energy Density	Wh/liter	> 30% of Cell Volumetric Energy Density
Rack Power Density	W/kg	> 40% of Cell Power Density
Rack Design Cost – (Cells, Modules, Racks, and BMS)	\$/kWh	210
Power Conversion Cost (Inverter, Electrical BOS)	\$/kW	240
Maximum Temperature ¹	°C	45
Minimum Temperature ¹	°C	20
Temperature Delta across Rack	°C	3

¹ TBD by cell development team.

As previously indicated, we envision this effort to occur over the next three years. A generic timeline of the activities is given below.

- Year 1: Simulation and Design – the first year's effort will focus on modeling and designing the
- Year 2: Bench scale prototypes/verification
- Year 3: System integration and characterization

Results

Advanced Battery Management System (BMS)

Battery management systems (BMS) are essential for the safe operation and longevity of a battery pack. In FY22, we developed an active balancing method-based BMS for different cell chemistry structures to be used

in behind-the-meter storage (BTMS) applications. The proposed structure utilizes modular isolated dual active bridge (DAB) DC/DC converters to actively balance the battery pack through a low voltage (LV) bus. No communication is required among the modular DAB converters. Instead, a supervisory controller monitors all the cell voltage, current, and state of charge (SOC) values. Detailed modeling and the control approach of the modular DAB converters are accomplished in FY22. Moreover, the control strategy of the supervisory control is also analyzed. The proposed method and structure can be extended to any combination of the number of cells to design the battery pack. Simulation results are provided for a system consisting of three cells in parallel to form a cell block and 14 cell blocks in series to form the battery module. Experimental results are provided for three modular DAB converters operating with a LiFeMnPO_4 prismatic cell with 3.2V, 20Ah rating.

BMS Design Progress

In FY21, modular isolated DAB converters are selected to be used for cell balancing and connecting the strings to the high voltage DC bus because of advantages such as bidirectionality and galvanic isolation. Supervisory control monitors the SOC of individual cell groups and generate reference currents for these cell groups to actively balance their SOC by transferring charge through a low voltage (LV) bus. The inner or primary control of the cell groups is designed to follow the reference current and simultaneously maintain the LV bus voltage. In FY22, simulation and initial experimental results are provided to validate the proposed method.

Overview of the modular battery pack design including the associated BMS is shown in Figure V.1.2. In this modular battery pack, each module is constructed by connecting several cells in parallel first and in series afterwards. The configuration has a low power DAB converter connected across each cell group in series through an LV bus. These converters enable power to transfer between the series-connected cell blocks to minimize SOC imbalance. Multiple modules are connected in series to increase the power and energy rating, and the string is finally connected to a high voltage (HV) DC bus through another DAB. Since the modular strings are decoupled from the HV bus, this allows for strings of different battery chemistries to be integrated within the pack. Figure V.1.3 shows the communication structure for the BMS system composed of three modular DAB converters.

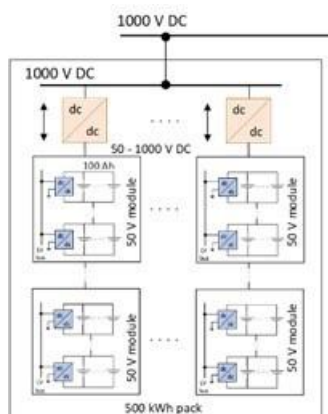


Figure V.1.2 Modular DC-coupled battery pack for BTMS. Source: NREL

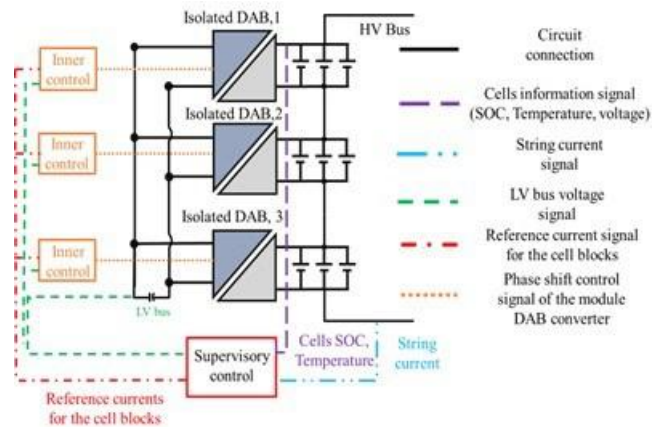


Figure V.1.3 Overview of the BMS for a modular battery. Source: NREL

The experimental setup of the three modular 50W DAB converters integrated on a single 3.2V, 20 Ah, LiFeMnPO₄ prismatic cell along with the supervisory control is shown in Figure V.1.4. The output of the DAB converters is connected to the LV DC bus through a capacitor. The supervisory control is implemented in the dSPACE MicroAutobox. To validate the performance of the single DAB converter, it is operated at a 50W discharge mode. Two different experimental test procedures are followed to validate the performance of the proposed topology and control approaches. First, fixed reference currents are given as input for the DAB converters without implementing supervisory control approach. While providing the reference currents, one of the converters is kept in discharging mode while the other two are in charging mode. As shown in Figure V.1.5, during the transient period, the LV bus voltage is regulated as 12V while following the reference currents for the DAB converters. As the voltage loop control gains are higher, it prioritizes the LV bus voltage regulation while still maintaining the reference current. This validates the performance of the proposed controller. Then, a supervisory controller is included in the system to validate the overall performance of the system. The trajectory of the SOC_s for different cell blocks is shown in Figure V.1.6, where the SOC_s are slowly converging towards a steady-state value which is the average value of the SOC_s, and they are becoming balanced. The reference currents for the cell blocks, along with the LV bus voltage regulation, are shown in Figure V.1.7, where the balancing currents slowly become zero after the SOC_s are balanced. While the SOC_s are getting balanced, and the balancing currents are becoming zero, the LV bus voltage is maintained at 12V, which further validates the performance of the proposed structure and the control methodology through experimental results.

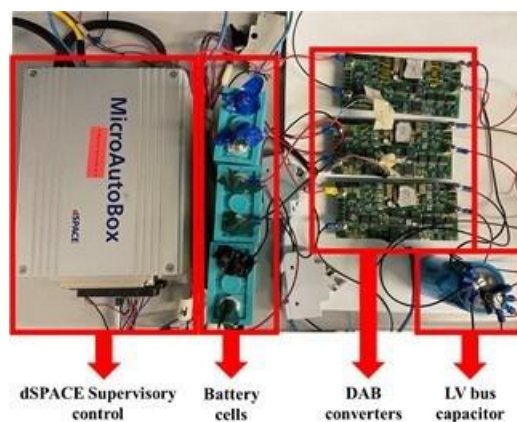


Figure V.1.4 Experimental setup for the three modular DAB converters. Source: NREL

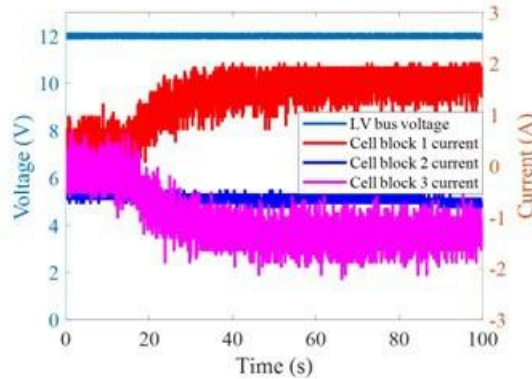


Figure V.1.5 DAB converters following a reference current to verify the controller. Source: NREL

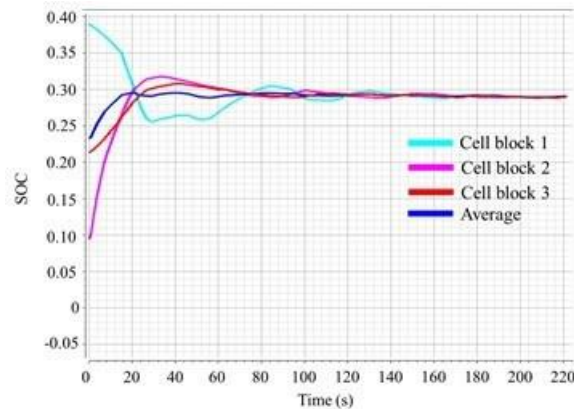


Figure V.1.6 Experimental results for SOC equalization. Source: NREL

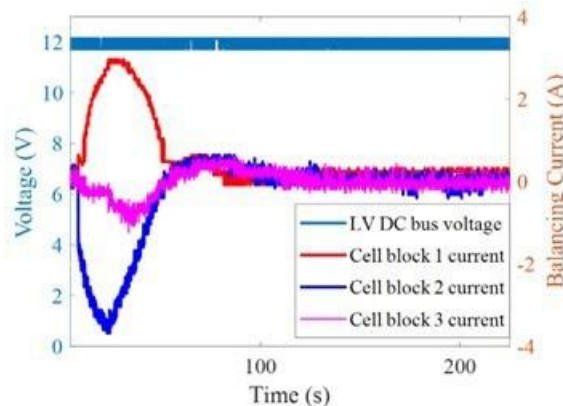


Figure V.1.7 DAB converter current and voltage satisfying SOC equalization. Source: NREL

Advanced Cell, Module, and Rack Thermal Design

Advanced thermal design aims to maintain desired temperature for battery rack operating at target temperature ranges, and to prevent cell-to-cell thermal runaway propagation. In FY 22, additional thermal runaway propagation modes and mitigation solutions were investigated with 3D thermal model, including heat conduction by busbars and mass ejection. Based on modeling analysis and experimental study, silicone-based fire-retardant foams were incorporated in the 60 Ah module used for nail penetration testing at Sandia National Laboratory (SNL). Additionally, Energy dissipation of neighboring cells/modules to prevent thermal runaway propagation was proposed. A multi-objective optimization tool is being developed, which is based on a trade-

off analysis between passive thermal insulation and dissipation considering both nominal operating and fail-safe conditions.

Thermal Design Progress

Cells at less than 50% SOC produce significantly less amount of thermal runaway heat. As such, thermal runaway propagation can be stopped if energy within the neighboring cells can be rapidly dissipated to lower their SOC. The key is the energy dissipation time should be less than thermal runaway propagation intervals. LFP and LTO cells can be discharged at high C-rates. For example, 50% DOD can be achieved at 6C in five minutes. Recent thermal runaway experiments show propagation interval is about two minutes for NMC/Gr prismatic cells. Abuse testing in FY23 will verify whether propagation between LFP/LTO prismatic cells take longer time. Preliminary analysis shows this approach may work better to prevent module-to-module thermal runaway propagation. This approach is an active approach and compatible with modular battery racking systems.

In FY21, cell-to-cell thermal runaway propagation caused by prismatic cell surface thermal contact was studied. In FY22, thermal runaway heat dissipation from the failed cell to neighboring cells through busbar heat transfer was investigated using a 3D thermal model. The model estimates busbar heat transfer does not likely lead to thermal runaway propagation between LFP cells if cells are only thermally connected with busbars. Compared to heat transfer through busbar, surface thermal contact was predicted to be a higher risk. Heat transfer through busbar and tab took a significantly longer time to reach a quasi-steady state between the failing cell and its neighboring cells. There was no thermal shock produced in neighboring cells. The dissipated heat was gradually absorbed by neighboring cells' active material without large temperature gradients.

Additionally, an ejection model was developed to address potential propagation due to thermal runaway mass ejection. Self-heating rate (SHR) is employed to quantify ejection hazards. SHR can be used to distinguish thermal runaway hazards for different cell chemistries, SoCs, and abuse trigger conditions. Ejecta temperature is identical to instant average temperature of the thermal runaway cell. As shown in Figure V.1.8, the 3D model capture temperature distributions within the failure cell, neighboring cells, and the impinged cell. Neighboring cells contacting the failed cell may have a higher risk due to direct heat conduction. The model was used to compare the difference between slow and fast thermal runaway. In the simulations, the amount of thermal runaway heat releases by the failed cell was constant but SHRs were varied from 1°C/min to 1000°C/min. The model predicted higher SHR led to hotter ejecta, increasing risk of thermal runaway propagation caused by cell ejection. For LFP cells, temperatures of the impinged cell were below the onset temperature of rapid thermal runaway (i.e., 150°C).

To balance thermal designs for cell nominal operations and thermal runaway mitigation, multi-objective optimization is required. The multi-objective optimization being developed is illustrated in Figure V.1.9. In FY21 and FY22, single-objective optimizations for nominal condition and fail-safe design have been completed. Multi-objective optimization is based on a trade-off analysis between passive thermal insulation and dissipation considering both nominal and abusive conditions.

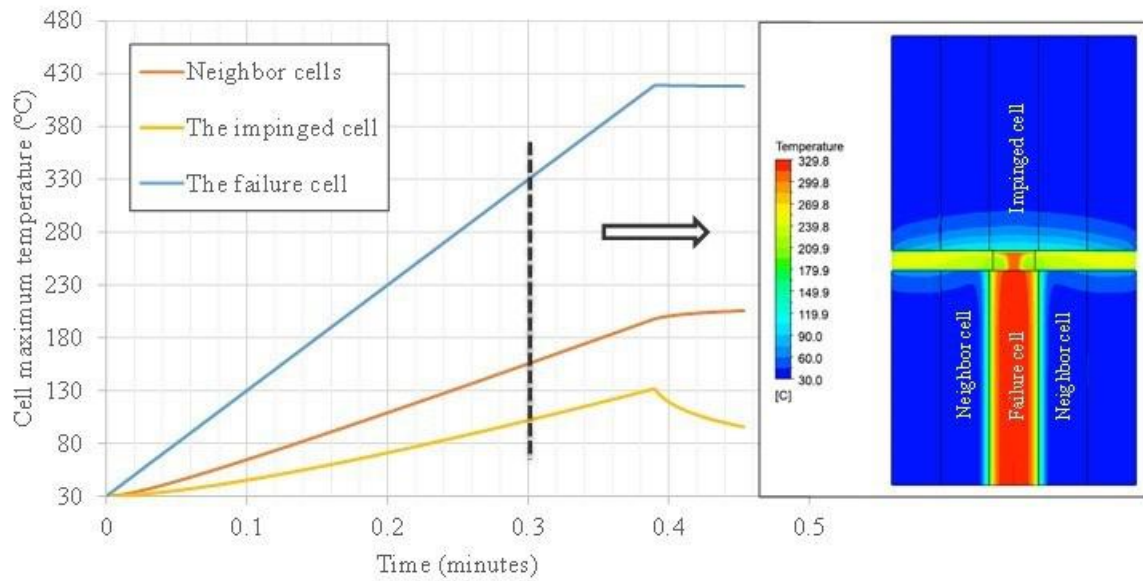


Figure V.1.8 Temperature contour and profiles of the maximum temperature in the failure cell, the impinged cell and neighbor cells predicted by the ejection model when SHR is 1000 °C/min.

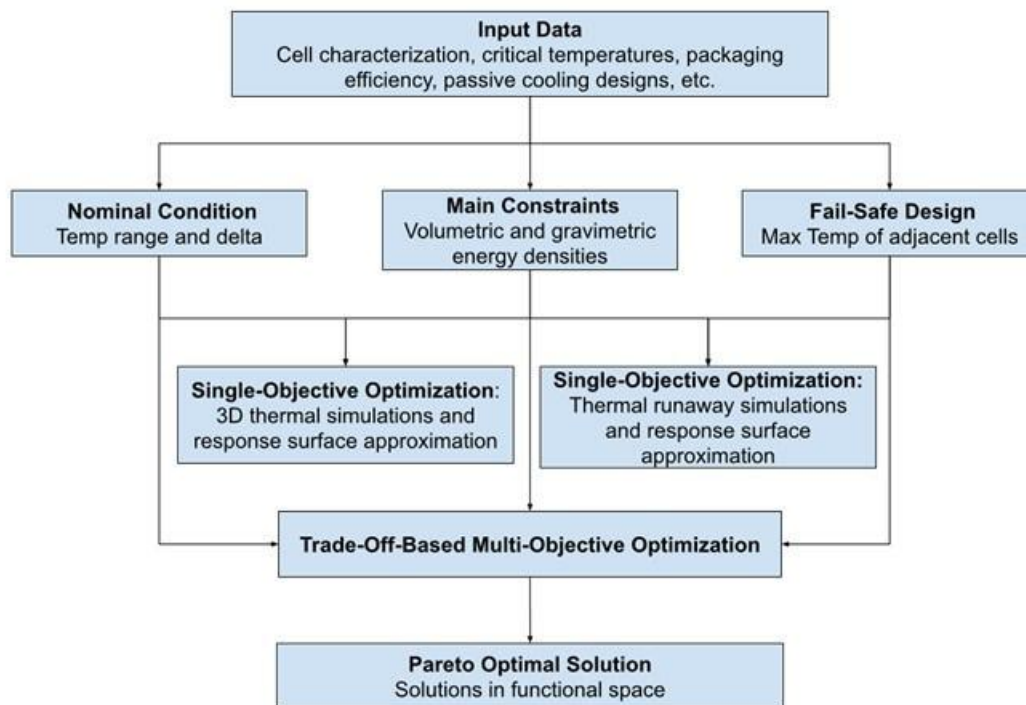


Figure V.1.9 Flowchart of the multi-objective thermal design and optimization.

System Safety Progress

The BTMS program is currently performing a scoping exercise where a fail-safe rack design will be realized in three years. The program is assuming the risk that a single cell thermal runaway event is unavoidable and to limit cell to cell propagation the heat generated from a cell runaway event must be managed. The results discussed herein will outline the abuse testing performed on a representation of a multicell BTMS module.

To prevent cell to cell propagation in a module the management of the heat generated from a cell thermal runaway must be managed. Different strategies on how to effectively do this have been reported on previously. The series of tests were intended to probe how to best mitigate the thermal runaway heat source as well as the cell discharge heat source in a parallel rack design. In these tests graphite lithium iron phosphate (LFP) cells were chosen because they were determined to be the most exothermic of the low energy density chemistries as determined by accelerating rate calorimetry. As shown in Figure V.1.10, three test cases were assembled to probe various thermal management strategies under a 1S3P configuration of 20Ahr LFP cells.



Figure V.1.10 Three different thermal control strategies were used for three 20 Ahr lithium iron phosphate cells connected in parallel.

The Control case contained no thermal mitigations and was used to demonstrate a worst case scenario. The Insulation test case contained a sheet of 2.85" x 6.10" pad of Rogers Corporation PCL-350 3mm foam between each cell. The intent of this foam was to isolate the heat generated from a runaway event from propagating to adjacent cells. The final test case incorporated insulation along with fuses between the individual cells. This test case contained the foam sheets described above as well as AA72AB0 thermal fuse that will open the circuit at 72°C and/or 60A (rated for 35A continuous). The intent of this test case was to not only isolate the heat generated from a runaway event, but additionally eliminate the other parallel cells from contributing to the heat generation via discharge. Each test case is designed to determine impact of each heat source and the contributions of each heat source was evaluated via thermocouples and thermal imaging.

Before testing could commence a discussion was held to determine the most appropriate thermal runaway initiation method. Two options were considered utilizing a heating element or nail penetration. While both methods were viable, nail penetration was chosen as it is more representative of an internal short circuit defect. The center cell of the module was penetrated with a nail to represent worst case for heat propagation and due to the cell construction, the penetration location on the cell was adjusted to the inner quarter on the long side. A short time lapse of an abuse case is shown in Figure V.1.11.

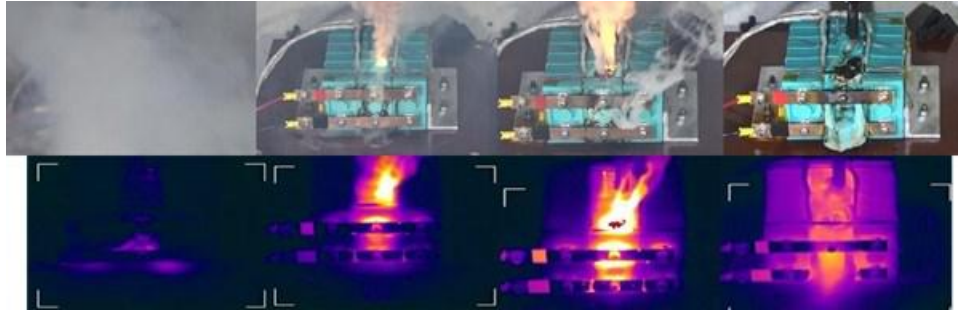


Figure V.1.11 Nail penetration of the insulation only module.

The eight images show the video and the corresponding thermal image at the same point in time. From left to right the image steps through initiation of thermal runaway (~2 min), approximately half way through the runaway event (~8 min), the highest temperature reached during the event (~12 min), and the final thermal equilibrium when the event had finished (~60 min). The data shown above was further augmented with thermocouples. Each cell had a total of 10 thermocouples to probe the heat flux across the cell. Results from the thermocouples from each test is depicted in Figure V.1.12.

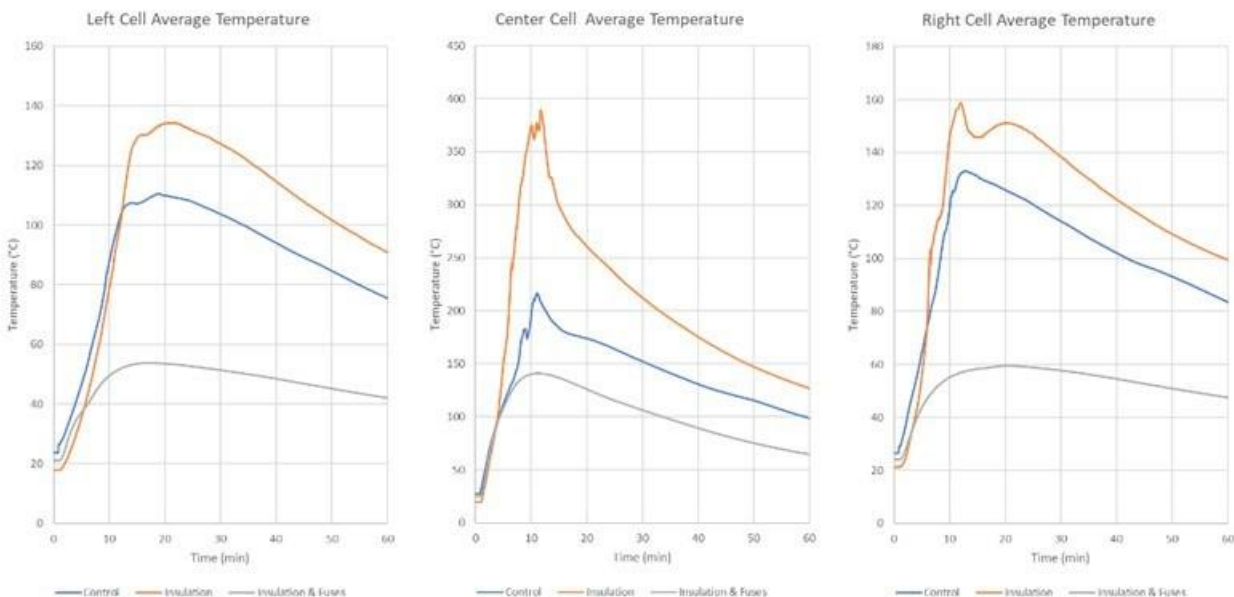


Figure V.1.12 Average temperature of each cell (left, center, right) for the three thermal strategies during nail penetration.

Results show that in the three tests the insulation test case demonstrated the highest temperatures, while the insulation and fuses produced the lowest temperatures. These results suggest that insulation may not be an appropriate strategy for a parallel design. This is because the heat from both the runaway and the cell discharge are sequestered in the center cell and the heat eventually transfers to the adjacent cell. While the adjacent cells did not vent, their temperatures exceeded +140°C. This further suggest that a heat conduction strategy may prove more effective in this use case. However, when the insulation is paired with fusible links the isolation strategy is very effective as the cell discharge heat source has been eliminated. While the center cell reached ~140°C the adjacent cells did not go above 60°C, well within their operational temperature. It is currently unknown what the temperature of the cells would be when only fusible links are used will be a future test case. Results from the rack test show that with the proper controls in place cell to cell propagation can be prevented in a rack design. By understanding the sources of heat present in thermal runaway and rack design and placing proper controls in the design a fail-safe design can be achieved.

Conclusions

In FY22, we developed passive thermal management strategies that prevented cell-to-cell propagation within a 1S3P module. In FY23, the thermal management strategies will be optimized and applied to a 5 kWh module.

Acknowledgements

We would also like to acknowledge the co-authors of this report – Matthew Keyser (NREL), John Kisacikoglu (NREL), Chuanbo Yang (NREL), and Brian Perdue (SNL).

VI Testing, Analysis, High-Performance Computing, Lab-I4

The *battery testing, analysis, high-performance computing, and Lab-I4* activity develops requirements and test procedures for batteries (to evaluate battery performance, battery life and abuse tolerance). Battery technologies are evaluated according to USABC-stipulated battery test procedures. Benchmark testing of an emerging technology is performed to remain abreast of the latest industry developments. The *battery testing* activity includes performance, life and safety testing, and thermal analysis and characterization. The testing activity also supports cell analysis, modeling, and prototyping (CAMP) projects at ANL, which include benchmarking and post-test analysis of lithium-ion battery materials at three labs (ANL, ORNL, and SNL). Projects include testing (for performance, life and abuse tolerance) of cells (for contract, laboratory-developed and university-developed cells), and benchmarking systems from industry; thermal analysis, thermal testing, and modeling; cost modeling; and other battery use and life studies. *Cost assessments and requirements analysis* includes the ANL project on developing the performance and cost model BatPaC. This rigorously peer-reviewed model developed at ANL is used to design automotive lithium-ion batteries to meet the specifications for a given vehicle and estimate its cost of manufacture. An analysis using BatPaC compared the estimated costs of cells and packs for different electrode chemistries (Figure VI.1).

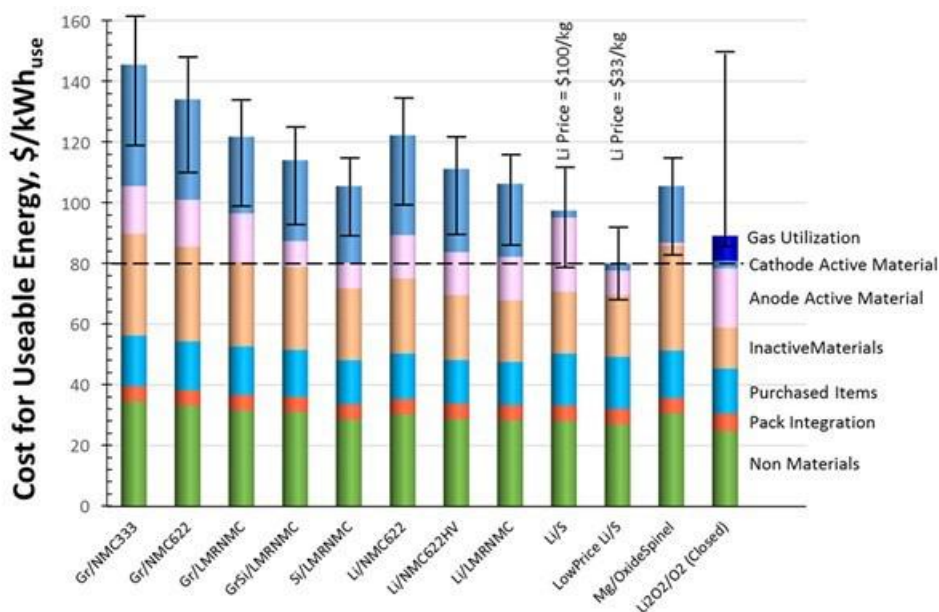


Figure VI.1 Estimated costs of cells in automotive battery packs with different combination of electrodes. The packs are rated for 100 kWh_{Total} (85 kWh_{Useable}), 300 kW, 315 V, 168 cells, and produced at a plant volume of 100K packs/year

The rest of this chapter contains detailed reports on the status of the following individual projects.

- BatPaC Model Development (ANL)
- Battery Performance and Life Testing (ANL)
- Battery Abuse Testing (SNL)
- Battery Thermal Analysis and Characterization Activities (NREL)
- Cell Analysis, Modeling, and Prototyping (CAMP) Facility Research Activities (ANL)
- Materials Benchmarking Activities for CAMP Facility (ANL)
- Electrochemical Performance Testing (INL)
- Machine Learning for Accelerated Life Prediction and Cell Design (INL, NREL).

VI.1 BatPaC Model Development (ANL)

Shabbir Ahmed, Principal Investigator

Argonne National Laboratory
9700 South Cass Avenue
Lemont, IL 60439
E-mail: Shabbir.Ahmed@anl.gov

Brian Cunningham, DOE Technology Development Manager

U.S. Department of Energy
E-mail: brian.cunningham@ee.doe.gov

Start Date: October 1, 2020	End Date: September 30, 2024	
Project Funding (FY22): \$900,000	DOE share: \$900,000	Non-DOE share: \$0

Project Introduction

A performance and cost model (Knehr et al. 2022) was developed at Argonne to design automotive Li-ion batteries that can meet the specification of a given vehicle, and then to estimate the cost of manufacturing such batteries. It is the product of long-term research and development at Argonne through sponsorship by the U.S. Department of Energy.

Over a decade, Argonne has developed methods to design Li-ion batteries for electric-drive vehicles based on modeling with Microsoft® Office Excel spreadsheets. These design models provided all the data needed to estimate the annual materials requirements for manufacturing the batteries being designed. This facilitated the next step, which was to include the manufacturing costs of the batteries.

The BatPaC model has been peer reviewed and is available on the web (<https://www.anl.gov/cse/batpac-model-software>). It captures the interplay between design and cost of Li-ion batteries for transportation applications. BatPaC helps estimate the impact of R&D advances on the mass, volume, and cost of lithium-ion cells and battery packs. Moreover, BatPaC is the basis for the quantification of battery costs in U.S. EPA and NHTSA 2017-2025 Light-Duty Vehicle Technical Assessment. This assessment is used to guide the mileage (i.e., CAFE) and CO₂ emission standards.

Objectives

To develop and utilize efficient simulation and design tools for lithium-ion batteries

- designed to meet energy storage capacity, pulse power, and fast charge specifications
- to predict mass, dimensions, and volume
- to estimate the cost and performance characteristics when manufactured in large volume
 - Specific Energy (Wh/kg), Energy Density (Wh/L)
 - Inventory of key materials needed for manufacturing the battery and that available in the final product
 - Breakdown of cost contributors.

Approach

The battery pack design and cost calculated in BatPaC represent projections for a specified level of annual battery production (50 GWH plant capacity). As the goal is to predict the near future (less than 7 years) cost of manufacturing batteries, a mature manufacturing process is assumed. The model designs a manufacturing plant with the sole purpose of producing the battery being modeled. The assumed battery design and manufacturing facility are based on common practice today but also assume some problems have been solved to result in a more efficient production process and a more energy dense battery. The proposed solutions do not have to be

the same methods used in the future by industry. It is assumed the leading battery manufacturers, those having successful operations in the near future, will reach these ends by some means.

For a selected battery chemistry, BatPaC solves the governing equations to determine the size of each layer, cell, and module that make up the battery pack that can meet the desired requirements for power and energy. This allows the calculation of the mass of each material, the volume of the components, and the heat removal needed during discharge. The cost of the pack is then estimated based on a predefined manufacturing process.

Current effort is directed at

- Improving the design capability by including correlations derived from continuum modeling and updating the default material properties to reflect recent experimental and industrial performance data
- Reducing the uncertainty of model predictions by setting up independent models of the manufacturing processes
- Validating the results through discussions with manufacturers and component developers
- Updating the default price of materials used in BatPaC calculations.

Results

Key Accomplishments

- Released BatPaC v5 with a manual describing the methods and assumptions
- Developed a correlation for estimating the electrode thickness limits associated with fast charging
- Developed a correlation for estimating the area specific impedance (ASI) for extended power pulse times
- Developed an analytical expression for estimating the temperature rise in Li-ion batteries during adiabatic operation of long-duration power pulses
- Studied the influence of temperature on ASI increase and capacity fade during initial cycling
- Developed baseline pack designs for cylindrical cell.

Release of BatPaC v5.0

BatPaC v5.0 was released in February 2022 and was followed by the release of a fully re-written manual in July 2022. The new version of BatPaC contains several new features that are presented in the following list:

Improvements to Calculations

- 1) The cell, module, and pack were redesigned to better reflect industry practices (see Figure VI.1.1).
- 2) The BatPaC simulated plant was redesigned based on a comprehensive study of a manufacturing plant.
- 3) A new algorithm for sizing the battery, based on charging requirements of an all-electric vehicle, was developed.
- 4) The battery management system calculation was updated to better reflect industry practice.

Additions to User Functionality

- 1) An algorithm for designing packs based on non-standard power requirements was included.
- 2) The ability to include additive materials in the cells was added.
- 3) The operating temperature was included as an input, which modifies the area specific impedance.
- 4) The percent utilization of the manufacturing plant capacity was added to evaluate scenarios where the production capacity is less than the design capacity.
- 5) Scenarios were provided for calculating the pack cost – *i.e.*, all manufacturing done in-house or purchasing some components from third parties. The option to calculate pack cost with or without profits and warranty was also included.

Improvements to Inputs

- 1) Energy- and power-type cells were created for all default chemistry couples. This expanded the number of default options from 9 to 17 and provided defaults for high and low-power applications.
- 2) A tool (worksheet) was added to enable new chemistry couples with self-consistent parameters.
- 3) Two new worksheets were included for defining alternate pack configurations.
- 4) The costs of raw materials and purchased items were updated.

Enhancements of User Interface and Results

- 1) The ‘Recycle’ worksheet was expanded to track recoverable scrap from the manufacturing floor.
- 2) An “Errors and Warnings” section was provided in the ‘Dashboard’ worksheet to guide the user away from common pitfalls in battery design.
- 3) All worksheets were reformatted and reorganized to make it easier to follow the calculations.

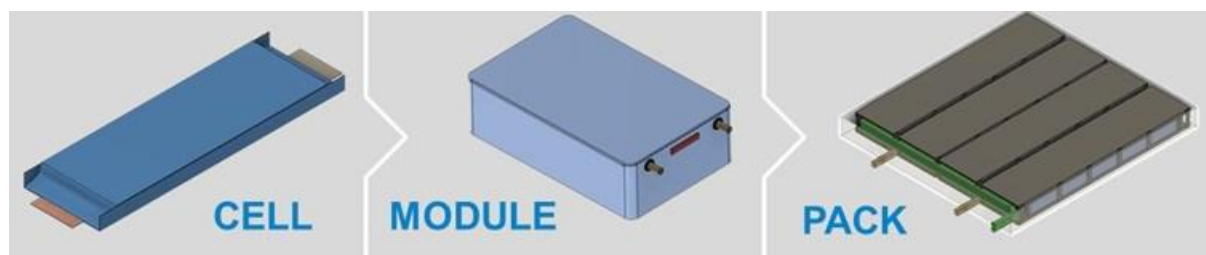


Figure VI.1.1 CAD drawings of the re-designed cell, module, and pack in BatPaC v5.0. Packs are made of multiple modules, each containing multiple cells.

Correlations for high pulse power as a function of SOC, duration, and chemistry

As different vehicles and applications of lithium-ion battery packs are being explored, the use cases change *e.g.*, trucks during extended climbs/descents, eVTOL, *etc.* One major difference between different vehicles is the SOC at which the vehicle needs to draw peak power and the duration of that pulse. For BatPaC to handle these applications, a correlation was developed using a simulated dataset of a Li-ion cell that was discharged under adiabatic conditions across a wide range of operating and design parameters. Initial SOC's ranged from 20% to 90%. C-rates ranged from 1 to 12C. Electrode loadings ranged from 1 to 4 mAh cm⁻². To increase the diversity of the dataset, simulations were conducted for fast and sluggish kinetics, representing that of power and energy cells respectively. In addition, three lithium-ion chemistry couples were simulated (NMC532-graphite, LFP-graphite, and LFP-LTO). These chemistry couples varied in their electrode porosities, particle sizes, kinetic properties, electrode conductivities, and thermodynamic behavior. (See Figure VI.1.2.)

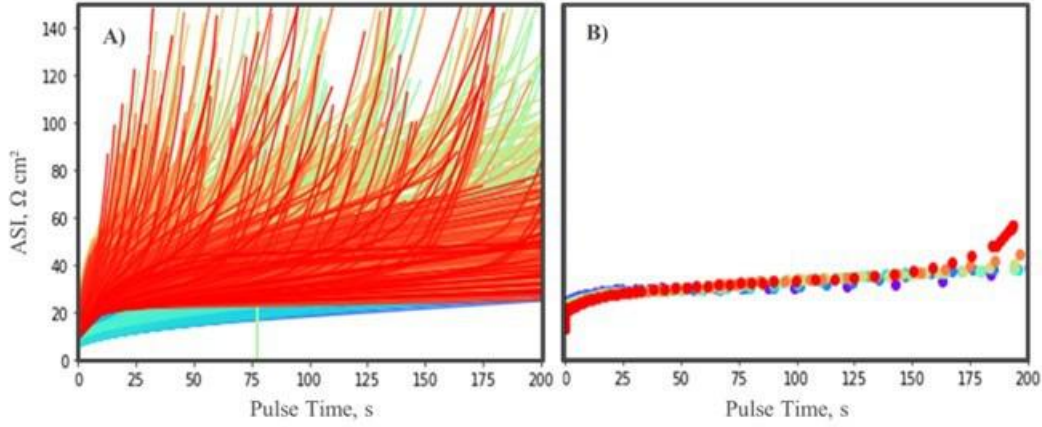


Figure VI.1.2 ASI vs. Pulse time for a dataset with multiple variables. A) All simulations super-imposed on each other, with red being the highest C-rate. B) Subset of the database, a NMC532-G battery at fixed loading experiencing different C-rates.

The dataset was used to develop a correlation for predicting the default electrochemical ASI ($ASI_{echem,0}$) as a function of SOC and pulse duration for the adiabatic set of pulses (isothermal pulse equation not shown). It is given as follows:

$$ASI_{echem,0} = ASI_{2s,SOC} - \left(1 - \frac{1}{2\sqrt{2}}\right) ASI_{intf,0} + \frac{4(A SI_{10s,SOC} - ASI_{2s,SOC} + ASI_{intf,0})}{10\sqrt{10}} \sqrt{t} + ASI_{10s,SOCe} - ASI_{10s,SOC} \quad (1)$$

where $ASI_{2s,SOC}$ and $ASI_{10s,SOC}$ refer to the default two- and ten-second ASIs, respectively, at the SOC at the start of the pulse. $ASI_{intf,0}$ is the combined interfacial resistances of the positive ($ASI_{intf,pos,0}$) and negative ($ASI_{intf,neg,0}$) electrodes at the default case. The following figure (Figure VI.1.3) shows how the simulations compare to the correlation in BatPaC, showing larger deviations at the longer pulse durations.

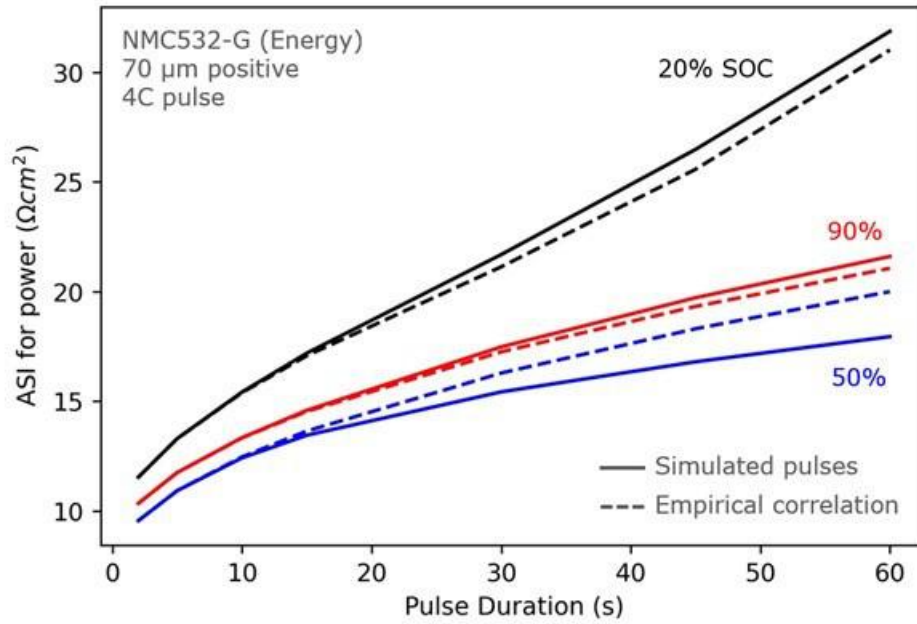


Figure VI.1.3 Comparison of the ASI from simulated pulses and the empirical correlation for three pulses from NMC532/graphite cells at different initial states of charge (SOC): 90% (red), 50% (blue), and 20% (black). The solid lines represent the simulated pulses, and the dashed lines represent the estimated values from the correlation.

Correlations for electrode thickness required to achieve fast charging

The growing importance of fast charge necessitated a more rigorous simulation of the fast charge module (relative to that in BatPaC 4.0). Using a continuum model previously developed, a dataset was generated by exercising the model for the default electrode couples and the range of maximum allowable temperatures (Song et al. 2021). This dataset was diverse and included power and energy couples; lithium titanate and graphite negative electrodes; and layered oxide and spinel positive electrodes. An analysis of the dataset found that the following expression linearized the charge time with respect to the positive electrode (*i.e.*, cathode) thickness:

$$\delta_{pos} = \frac{\alpha \ln^2(t_{chg}) + \beta}{Q\rho_{act/etode}} \quad (2)$$

where the slope (α) and intercept (β) are functions of the design parameters and need to be fit, and t_{chg} is the desired charge time (minutes). The linearization of the data with this expression is demonstrated in Figure VI.1.4.

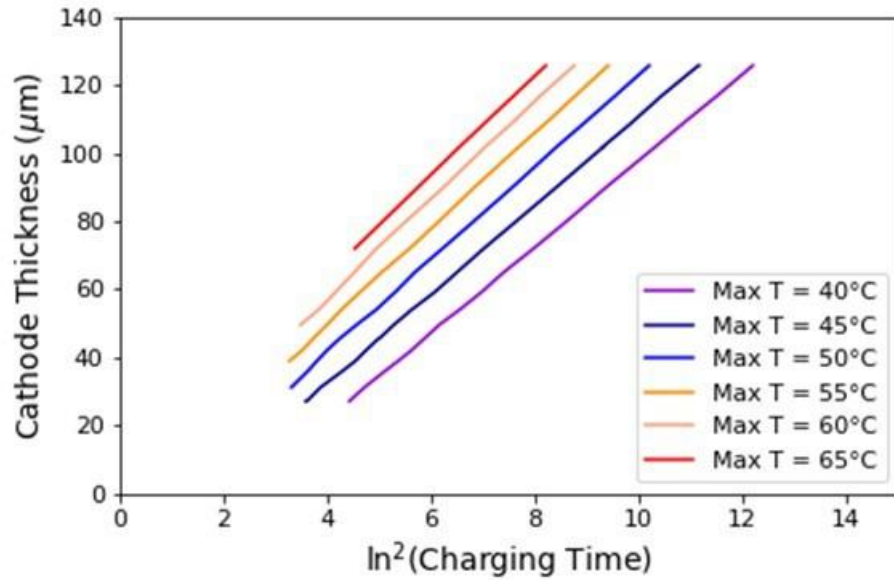


Figure VI.1.4 The linearization of cathode (i.e., positive electrode) thickness with respect to charging time per Equation 2 for a NMC532-Graphite (Energy) couple at a fixed cell capacity.

A series of Pearson and Kendall correlations were used to determine the dominant inputs that affect the slope (α) and intercept (β) parameters. The functional forms of α and β were determined using data from the NMC532-G (energy) couple. Figure VI.1.5 provides an illustration of how the values of α and β depend on the cell geometry and maximum allowable temperature. From this analysis, the functional form of the expression was found to be:

$$\alpha = \alpha_1 L + \alpha_2 L^2 + \alpha_3 T_{max} \quad (3)$$

$$\beta = (\beta_1 L + \beta_2 T_{max} L + \beta_3 T_{max} + \beta_4 T_{max}^2) \frac{ASI_{10s,50\%}}{12.5} \quad (4)$$

Equations 3 and 4 highlight that the slope (α) is not a function of chemistry dependent parameters and is mainly dictated by operation. However, the intercept (β) does have a dependency on the reference 10s ASI value at 50% SOC.

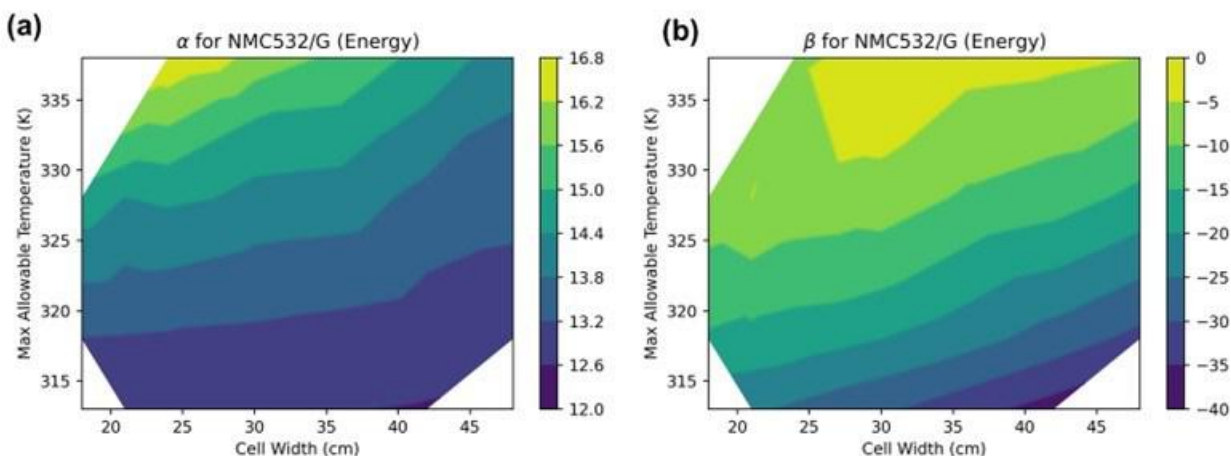


Figure VI.1.5 Parameter space for a) α and b) β as a function of cell geometry and maximum allowable temperature.

Estimating adiabatic temperature rise

The current version of BatPaC (v5.0) has a feature in the thermal worksheet that calculates the maximum adiabatic temperature during the high-power battery pulse resulting from vehicle acceleration. This calculation is part of a check done by BatPaC to make sure the pack design does not lead to excessive temperatures. The current calculation uses the resistance calculated by BatPaC to determine the rate of heat generation based on Joule heating (I^2R , where I is the applied current and R is the resistance). Joule heating provides a reasonable estimate at short times and low currents, but it is unable to capture the heat generation over long pulses at higher rates (see Figure VI.1.6a). These types of pulses are becoming more common as BatPaC is adapted to study electric trucks and aerial electric vehicles, where vehicles can experience sustained pulses $> 6C$ for >120 seconds.

To address this issue, a thermal-electrochemical modeling study led to a new analytical expression that can be used to quickly estimate the temperature rise during a high-power, long-duration pulse. The study produced an analytical expression that relies on several cell parameters that are already available in BatPaC: *i*) the thicknesses and porosities of the positive electrodes, negative electrodes, and separator and *ii*) the resistances at two and ten seconds into the power pulse. The expression also relies on two fitted parameters whose values were determined in the study: *i*) a diffusion-like parameter whose value is close to the lithium salt's diffusion coefficient in the electrolyte and *ii*) an apparent activation energy.

The accuracy of the new analytical expression is significantly better than the Joule heating equation. Figure VI.1.6 compares the two methods for estimating the temperature against a full, validated, thermal-electrochemical model. Similar results were obtained when comparing the two expressions against experimental data in the literature. The new analytical expression greatly reduced the underprediction of the temperature. This is important since underprediction can lead to false conclusions about the safety of the pack. A manuscript detailing the new expression was recently submitted as a journal publication. The expression will be incorporated into the next version of BatPaC.

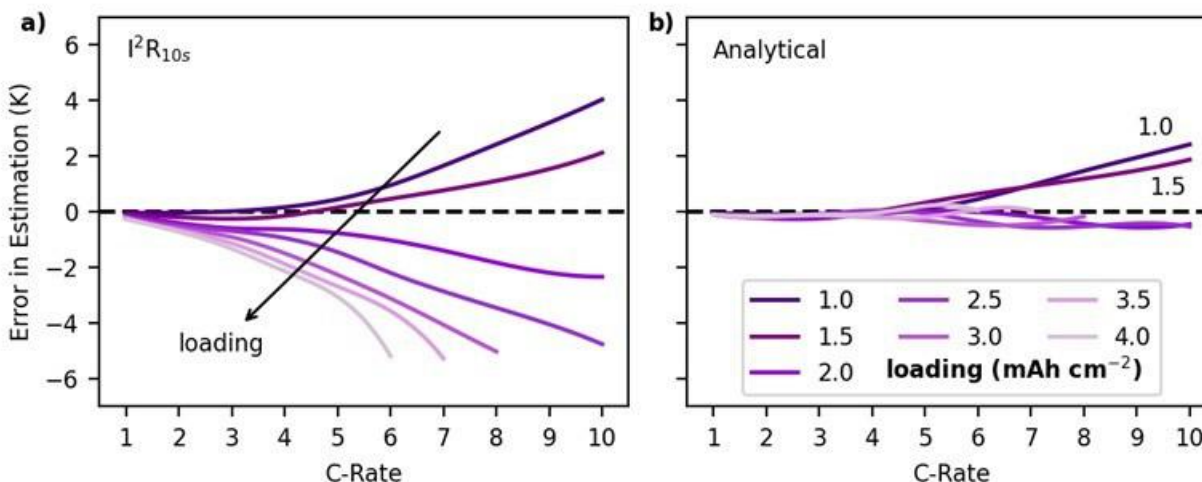


Figure VI.1.6 Absolute error in the predicted temperature at 120 seconds into a pulse a) assuming constant heat generation (I^2R) or b) using the new analytical expression. The error was determined by comparing the estimated temperature to the temperature predicted by a full, validated, thermal-electrochemical model. The constant heat generation used the corrected resistance at ten seconds.

Influence of temperature on initial cycling

To understand how best to implement cycle lifetime into BatPaC, it is necessary to understand the effect that temperature has on the performance of different electrode couples. Our previous study looked at how temperature impacts the ASI, with higher temperatures yielding lower resistances during mild cycling (Kubal et al. 2022). Figure VI.1.7 summarizes the impact of temperature on energy loss during the mild cycling test conducted at a $C/3$ -rate. According to the results, energy decay increases with increasing temperature and is most prevalent for the cells with NMC811 cathodes. The capacity loss also shows a slight dependence on cathode composition at 40°C with losses of $\text{NMC811} \gg \text{NCA} > \text{NMC622} > \text{NMC532} > \text{NMC111}$. This agrees with observations in the literature, whereby increasing nickel content is known to decrease cycling stability.

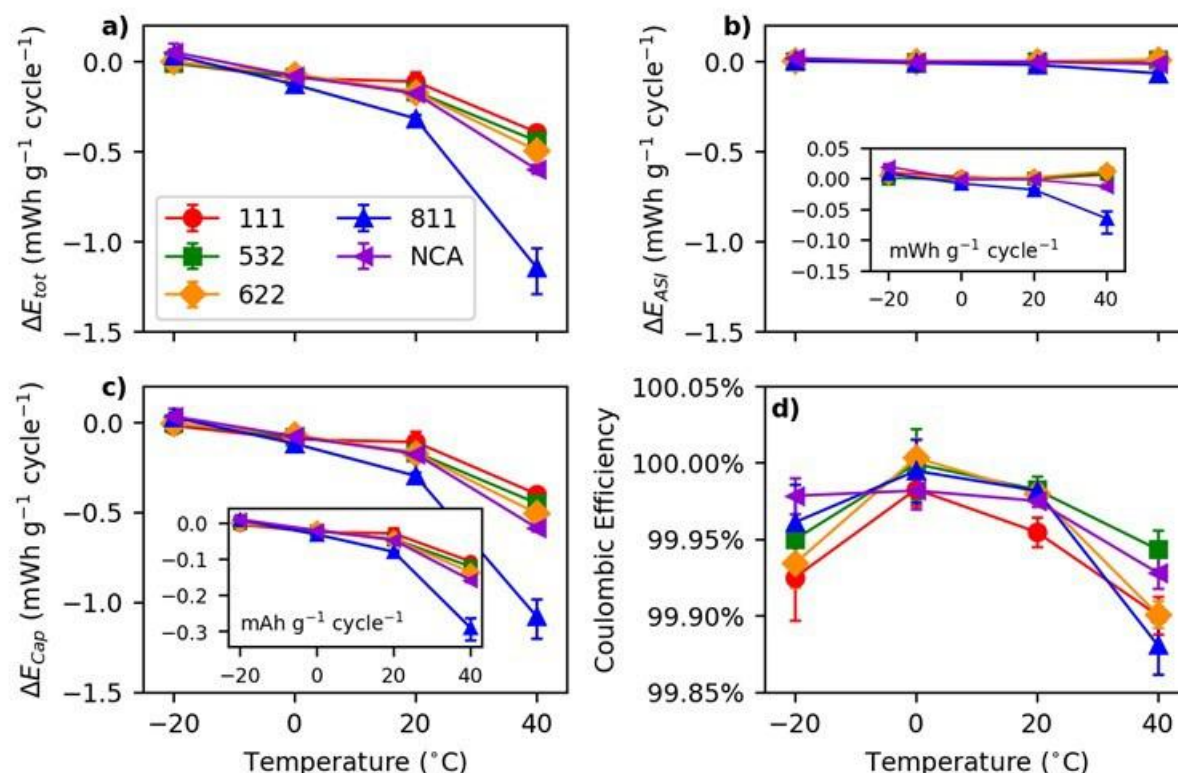


Figure VI.1.7 a) Total change in discharge energy per cycle during 100 cycles at a C/3 rate. b) Contribution to the energy change from changes in the ASI. c) Contributions to the energy change from changes in the capacity. d) Average coulombic efficiency of all C/3 cycles at all four cells, where the error bars represent the standard error. Data in a), b), and c) reflect the average of four cells and the error bars are the maximum and minimum values. Inset in b) is a zoom-in of the data. Inset in c) is the change in specific capacity of the cathode.

Pack design for cylindrical cells

Up until now BatPaC calculations represent stiff pouch cells. To enable valid comparisons with packs incorporating cylindrical cells that are being used by several manufacturers, a sister version of BatPaC is being adapted to represent these packs. Creating a comparable pack design between the cylindrical and pouch cells will allow valid comparisons. The following commonalities have been incorporated to ensure the designs are comparable:

- The use of laminated busbars, comparable to the interconnect panels in the current version
- Same material used for module and pack housing
- Cell terminals are on opposite ends of the cells
- Cooling panel(s) running along the top and bottom of the pack
- Inclusion of modules

There are also several differences in the initialization of the pack. In the pouch cell design, the cell sizes are adjusted to obtain a fixed, input energy. However, with cylindrical cells, the volume of these cells is fixed, meaning the cell capacity/energy is unknown a-priori, as it is a function of the electrode couple. Thus, the target pack voltage must be given for the new design, which is then used to calculate the number of cells required to meet the target specifications. Figure VI.1.8 shows a schematic of the pack with cylindrical cells and a table comparing the stiff pouch design to the cylindrical cell design.

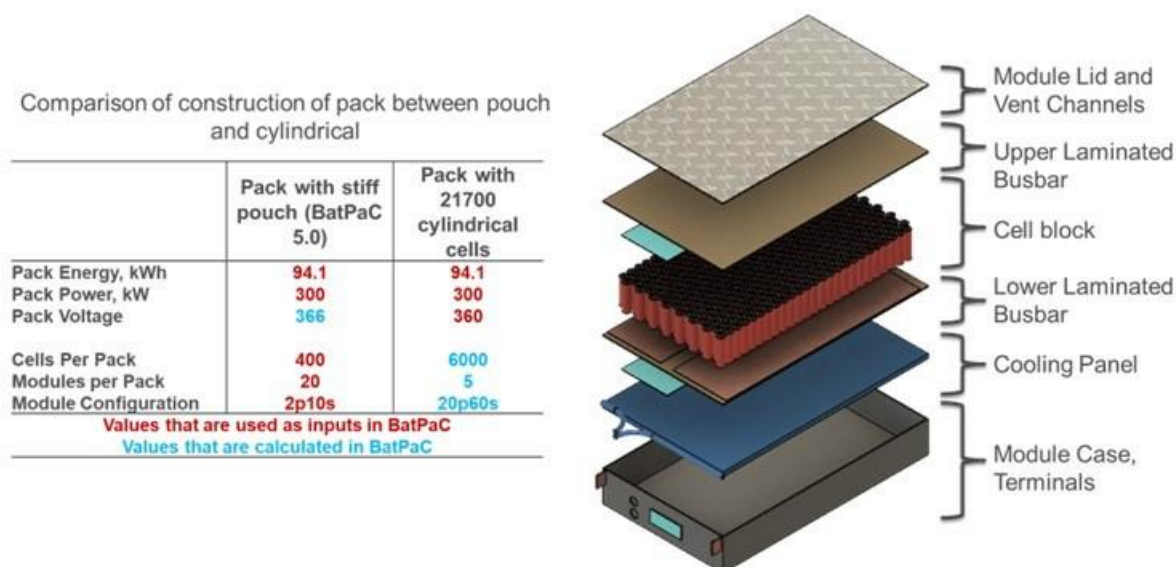


Figure VI.1.8 Comparison of pack-level configurations and metrics with layout of layers in a module.

Conclusions

- A new version of BatPaC (BatPaC v5.0) was released with improvements to the calculations, additions to the user functionality, improvements to the inputs, and enhancements to the user interface.
- A new correlation was developed and implemented into BatPaC for estimating the area specific resistance based on state of charge and length of the power pulse. The correlation expands BatPaC's ability to design packs for new vehicle types with minimal changes to the formulation.
- A new correlation was developed and implemented into BatPaC for determining the electrode thickness which achieves fast charging criteria. The correlation determines the electrode thickness that achieves the desired charge time while maintaining the cell temperature below a maximum value.
- A new analytical expression was developed for accurately estimating the temperature rise during adiabatic, high-power, long-duration, power pulses. The expression will improve the accuracy of temperature calculations within BatPaC.
- The influence of temperature and electrode material on cell degradation was studied. It provided benchmark information showing that increasing nickel content and temperature increase degradation.
- A new pack design and initialization strategy were developed for cylindrical cells. These are the first steps in the development of a new version of BatPaC for cylindrical cells.

Key Publications

1. Juhyun Song, Zhe Liu, Kevin W. Knehr, Joseph J. Kubal, Hong-Keun Kim, Dennis W. Dees, Paul A. Nelson, Shabbir Ahmed, "Pathways towards managing cost and degradation risk of fast charging cells with electrical and thermal controls," *Energy & Environmental Science*, 2021, 14, 6564-6573. [\[https://doi.org/10.1039/D1EE02286E\]](https://doi.org/10.1039/D1EE02286E)
2. Joseph J. Kubal, Kevin W. Knehr, Naresh Susarla, Adam Tornheim, Alison R. Dunlop, Dennis D. Dees, Andrew N. Jansen, Shabbir Ahmed, "The influence of temperature on area-specific impedance and capacity of Li-ion cells with nickel-containing positive electrodes," *Journal of Power Sources*, 2022, 543, 231864. [\[https://doi.org/10.1016/j.jpowsour.2022.231864\]](https://doi.org/10.1016/j.jpowsour.2022.231864)
3. Kevin W. Knehr, Joseph J. Kubal, Paul A. Nelson, and Shabbir Ahmed, "Battery Performance and Cost Modeling for Electric-Drive Vehicles: A Manual for BatPaC v5.0", ANL/CSE-22/1, July 2022. [\[https://doi.org/10.2172/1877590\]](https://doi.org/10.2172/1877590)

References

1. Knehr, Kevin W., Joseph J. Kubal, Paul A. Nelson, and Shabbir Ahmed. 2022. “Battery Performance and Cost Modeling for Electric-Drive Vehicles: A Manual for BatPaC v5.0.” ANL/CSE-22/1. Argonne National Lab. (ANL), Argonne, IL (United States). <https://www.osti.gov/servlets/purl/1877590>.
2. Kubal, Joseph J., Kevin W. Knehr, Naresh Susarla, Adam Tornheim, Alison R. Dunlop, Dennis D. Dees, Andrew N. Jansen, and Shabbir Ahmed. 2022. “The Influence of Temperature on Area-Specific Impedance and Capacity of Li-Ion Cells with Nickel-Containing Positive Electrodes.” *Journal of Power Sources* 543 (September): 231864.
3. Song, Juhyun, Zhe Liu, Kevin W. Knehr, Joseph J. Kubal, Hong-Keun Kim, Dennis W. Dees, Paul A. Nelson, and Shabbir Ahmed. 2021. “Pathways towards Managing Cost and Degradation Risk of Fast Charging Cells with Electrical and Thermal Controls.” *Energy & Environmental Science* 14 (12): 6564–73.

Acknowledgements

K. Knehr, J. Kubal, P. Nelson, D. Dees, A. Deva, Cell Analysis Modeling and Prototyping Facility (CAMP), D. Robertson, E. Islam, G. Henriksen.

VI.2 Battery Performance and Life Testing (ANL)

Brian J. Ingram, Principal Investigator

Argonne National Laboratory
9700 South Cass Avenue
Lemont, IL 60439
E-mail: ingram@anl.gov

Haiyan Croft, DOE Technology Development Manager

U.S. Department of Energy
E-mail: haiyan.croft@ee.doe.gov

Start Date: October 1, 2021

End Date: September 30, 2022

Project Funding (FY22): \$850,000

DOE share: \$850,000

Non-DOE share: \$0

Project Introduction

The development and commercialization of new battery technology for a diverse set of applications is important for transportation, communications, and infrastructure advancements. In particular, the Vehicle Technologies Office (VTO) supports low cost, secure, and clean energy technologies to transport people and goods throughout the United States. Electrified transportation drives research into high energy battery chemistries and high power systems (i.e., fast charge). An independent evaluation and assessment of performance and lifetime is critical to meaningful establish meaningful technology and scientific breakthroughs. The Electrochemical Analysis and Diagnostics Laboratory (EADL) at Argonne National Laboratory provides a vast set of capabilities and knowledge to evaluate batteries using standard tests and protocols, based on those developed by the U.S. Advanced Battery Consortium (USABC). [1-4] The EADL supports VTO and USABC supported battery development projects to guide R&D priorities and an independent technology evaluation.

Objectives

- Provide DOE, USABC, and battery developers with reliable, independent, and unbiased performance and life evaluations of cells, modules, and battery packs.
- Benchmark battery technologies that were not developed with DOE/USABC funding to ascertain their level of maturity.

Approach

The EADL is committed to collecting accurate, reproducible, and reliable data sets. The EADL has over 200 test channels with a range of available sizes from (10 V, 2 A) to (60 V, 250 A) which are routinely calibrated for accuracy. All testing is conducted in environmental chambers, which enables evaluation at thermal conditions consistent to typical battery usage conditions (i.e., -70°C to 180°C) controlled within $\pm 1^\circ\text{C}$.

The EADL evaluates batteries using standardized and unbiased protocols, allowing a direct comparison of performance within a technology, between developers, and across technologies. Additionally, since the test plans and conditions based on these protocols are inputted into a programmable test equipment, the EADL provides flexibility to partners interesting in simulate a wide range of operation conditions. For those tested using the USABC methods, the performance of small cells can be compared to that of larger cells and full-sized pack by means of a battery scaling factor [1-2]

Results

Batteries, which were fabricated during programs with developers, are sent to Argonne for evaluation. Cells tested at the EADL under the USABC benchmarking programs were aged and tested against the appropriate application target (LCFC-EV, HP-EV, etc) or specific targets developed for battery chemistries under

development. Here, the purpose of evaluation is two-fold: to provide confirmation of other test information and to provide an independent assessment of the state of the given battery technology, that is, how does it compare to the USABC [1-4] and/or project goals. In addition evaluation of cells received from developers, several VTO programs are supported by the EADL: Next-Gen Lithium-Ion, Extreme Fast Charging, and Behind-the-Meter Storage were supported in FY22. A list of program deliverables associated with Argonne during fiscal year 2022 is given in Table VI.2.1, along with their status.

Table VI.2.1 Status of cell testing deliverables in FY2022

Developer	Sponsor	Application	Quantity (nominal cell size)	Status at year end
WPI	USABC	Recycle / EV	24 (1 Ah)	Complete
WPI	USABC	Recycle / EV	24 (10 Ah)	On-going
WPI / Microvast	USABC	LCFC / EV	18 (0.45 Ah)	On-going
24M	USABC	LCFC / EV	18 (52 Ah)	On-going
Nanograf	USABC	Silicon / EV	24 (1 Ah)	Complete
Univ. Michigan	DOE	XFC / EV	18 (2.9 Ah)	Complete
Stonybrook	DOE	XFC / EV	9 (2.1 Ah)	Complete
Group 14	DOE	Silicon / EV	15 (0.4 Ah)	On-going
Enovix	DOE	Silicon / EV	15 (0.266 Ah)	On-going
Sila Power	DOE	Silicon / EV	12 (1 Ah)	On-going
Solid Power	DOE	Silicon / EV	12 (0.25 Ah)	On-going
Next-Gen Lithium-Ion	DOE	EV	various	On-going
Extreme Fast Charging	DOE	XFC / EV	18 (0.03 Ah)	On-going
Behind-the-Meter Storage	DOE	BTMS	8 (2 Ah)	On-going

The EADL supported numerous applications in development in FY2022. For instance, the technological goal of achieving very high charge rates represents a significant scientific and technical challenges. Here, not only does the technology have to avoid lithium deposition at the high charge rate, but the technology must also avoid life-shortening degradation caused by i^2R heating from the high current/power. Solving this challenge is critical to increase consumer's interest in electric vehicles by enabling reduced time to charge a battery to meet driver's expectations relative to refueling at the pump. There are, in principle, many ways to do this, including increasing the pack voltage so that the current at high power is relatively low. This is an engineering solution. Perhaps, a better way to overcome these issues is to develop or adapt lithium-ion technology to tolerate or avoid the problems.

One such investigation is highlighted in Figure VI.2.1 which compares results for the relative capacity change (loss) vs. cycle count for standard and XFC conditions. At 500 cycles, the cell operated under the XFC protocol maintained >20% BOL capacity. These results indicate that solutions to the XFC are possible and that project goals can be met. Furthermore, the observed decreasing rate of capacity fade with cycling provides some insight into the potential mechanisms contributing to the fade, which can be used to guide future R&D effort.

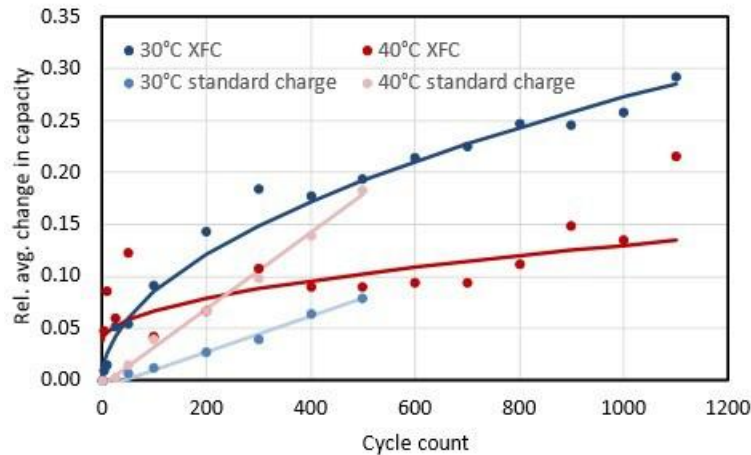


Figure VI.2.1 Relative capacity change (loss) averaged over several cells vs. cycle count for standard and XFC conditions.

Conclusions

We will continue to support DOE's and the USABC's cell development efforts by providing unbiased evaluation of cell performance. In the case cited above, there appears to be successful efforts to address the general fast-charging problem and commensurate understanding of the underlying mechanisms.

Key Publications

1. FreedomCAR Battery Test Manual for Power-Assist Hybrid Electric Vehicles, DOE/ID-11069, October 2003.
2. FreedomCAR Battery Test Manual for Plug-In Hybrid Electric Vehicles, June 2010.
3. Electric Vehicle Battery Test Procedures Manual, Revision 3.1, October 2020.
4. Battery Test Manual for 12 Volt Start/Stop Vehicles, Rev. 1, May 2015, INL/EXT-12026503.

Acknowledgements

The following EADL staff contributed and supported this program: David Robertson and LeRoy Flores. In addition, the former group leader and principal investigator, Ira Bloom, managed and led the program through majority of FY2022. His on-going contributions and commitment to providing an efficient and meaningful hand-off of knowledge is greatly appreciated.

VI.3 Battery Abuse Testing (SNL)

Loraine Torres-Castro, Principal Investigator

Sandia National Laboratories
1515 Eubank Dr. SE, M/S 0613
Albuquerque, NM, 87185
E-mail: ltorre@sandia.gov

Haiyan Croft, DOE Technology Development Manager

U.S. Department of Energy
E-mail: haiyan.croft@ee.doe.gov

Start Date: October 1, 2021

End Date: September 30, 2022

Project Funding (FY22): \$350,000

DOE share: \$350,000

Non-DOE share: \$0

Project Introduction

Abuse tests are designed with the intention of bounding safe operating limits of EV energy storage devices by realizing a worst-case scenario. From these abuse tests, quantitative data on cell/module/pack response is obtained, allowing for determination of failure modes and providing guidance to developers toward improved materials and designs. Standard abuse tests with defined start and end conditions are performed to provide comparison between technologies. Due to the ever-evolving nature of energy storage research and implementation, new tests and protocols are developed and evaluated to best simulate real-world failure conditions.

In scaling from the cell to battery level, it is important that safety performance analysis includes a detailed understanding of cell interactions. Single point failures from a single cell or group of cells can be initiated by several triggers including internal defects, internal short circuit, misuse, abuse, or a component failure at the battery or system level. Propagation of that single failure event (regardless of the initiation trigger) through an entire battery system or vehicle is an unacceptable outcome to ensure EV safety. As these batteries are scaled up in size from Wh to kWh, safety issues are of increasing importance and, by extension, it is necessary to reevaluate testing methods to ensure all relevant data is collected. As a result, Sandia National Laboratories reviewed and published an updated version of the United States Advanced Battery Consortium (USABC) Battery Abuse Testing Manual for Electric and Hybrid Vehicle Applications.

Abuse testing of advanced high energy materials has also revealed the limits of existing test hardware, particularly regarding the maximum temperature observed during thermal runaway. Continuous development of capabilities is necessary to ensure necessary data is collected. This development has included the stand up of high temperature thermocouples that are able to detect these extreme temperatures and pressure sensors to understand the pressure build up prior to, and during battery failure.

Objectives

- Provide independent abuse testing support for DOE and USABC
- Complete abuse testing of all deliverables in accordance with USABC testing procedures
- Provide battery safety testing support for DOE VTO programs.

Approach

Abuse tolerance tests evaluate the response to anticipated abuse conditions. The goals of safety testing include a) testing of energy storage devices to failure and documentation of the conditions that resulted in failure, b) systematic evaluation of failure modes and abuse conditions using destructive physical analysis (DPA), c) provide quantitative measurements of cell/module response, d) document improvements in abuse response, and e) develop new abuse test procedures that more accurately determine cell performance under the most probable abuse conditions. Electrical (overcharge/overvoltage, short circuit, over discharge/voltage reversal, and partial

short circuit), mechanical (controlled crush, penetration, blunt rod, drop, water immersion, laser induced short circuit, and mechanical shock and vibration) and thermal abuse (thermal stability, simulated fuel fire, elevated temperature storage, rapid charge/discharge, and thermal shock cycling) cover the main categories of possible conditions evaluated. These techniques are applied to USABC deliverables, and the results reported to DOE and USABC.

Results

Accomplishments

- Completed testing of USABC deliverables and reported results to the USABC Technical Assessment Committee (TAC)
- Provided support to the Behind the Meter Storage Program using tools developed as part of this testing program.
- Provided testing support for the Lithium-ion recycling prize through the DOE voucher program.
- Published a revised version of the United States Advanced Battery Consortium (USABC) Battery Abuse Testing Manual for Electric and Hybrid Vehicle Applications.
- USCAR 2021 Team Award: USABC Abuse Test Group.

Testing was performed for USABC development programs, including testing deliverables from Farasis, Microvast, Gotion, and Zenlabs. Test results have been reported to the USABC TAC. Sandia continues to make functional improvements to battery testing to enable the testing of new high energy materials. Sandia also participated in a working group to prepare a revised test manual for USABC battery abuse testing. The test procedures used in the new manual were developed by the USABC Abuse test working group and prepared at Sandia. The revised manual was published in January 2022. The main changes to the manual are listed in Table VI.3.1.

Table VI.3.1 2022 USABC Battery Abuse Testing Changes

Test	Previous Version	2022 Version
Nail Penetration	Heated blunt nail (50 °C)	Sharp nail at ambient temperatures
Mechanical Crush		Two stage crush; crush to 15% deformation, then to 50% deformation
Thermal Ramp	Heating rate: 5 °C/min	Heating rate: 2 °C/min
Overcharge	Maximum state of charge: 250%	Maximum state of charge: 200%
External Short Circuit	Short circuit resistance: 1mOhm, and 10mOhm.	Short circuit resistance: 10mOhm (1mOhm as secondary option but not required)

The development and maintenance of Battery Safety and Abuse Testing at Sandia has also allowed support for other DOE VTO programs. This has included support of the Behind the Meter Storage (BTMS) program performing testing of cells of interest for the program and support of the Lithium-Ion Battery Recycling Prize voucher program.

Conclusions

Development and testing of higher energy, larger format cells and modules continues for USABC developers in hopes to meet the VTO goals. We provide a means to field the most inherently safe chemistries and designs to help address the challenges in scaling up lithium-ion technologies of interest. This has required careful control and monitoring of tests with the potential of high energy release, as well as standing up a larger facility at SNL to support module level testing. Testing performed at SNL has provided critical information to cell developers to aid in the development of increasingly abuse tolerant cell chemistries and module designs.

Independent testing is necessary to perform objective evaluations of ever changing cell designs and chemistries by the DOE and US automobile manufacturers.

SNL continues to provide necessary safety testing support to DOE programs. The capabilities developed as part of this battery safety testing program currently support work done as part of the Behind the Meter Storage program and the Lithium-ion Recycling program.

Key Publications

1. Y. Chen, L. Torres-Castro, K-H Chen, D. Panley, J. Lamb, M. Karulkar, N. Dasgupta “Operando detection of Li plating during fast charging of Li-ion batteries using incremental capacity analysis” J. Power Sources, Volume 539, 2022, 231601, DOI: [10.1016/j.jpowsour.2022.231601](https://doi.org/10.1016/j.jpowsour.2022.231601)
2. Y Preger, L Torres-Castro, T Rauhala, J Jeevarajan “Perspective—On the Safety of Aged Lithium-Ion Batteries” J. Electrochem. Soc., Volume 169, 2022, 030507, DOI: [10.1149/1945-7111/ac53cc](https://doi.org/10.1149/1945-7111/ac53cc)
3. K. P. Hand et. al “Science Goals and Mission Architecture of the Europa Lander Mission Concept” Planet. Sci. J, Volume 3, 2022, 22, DOI: [10.3847/PSJ/ac4493](https://doi.org/10.3847/PSJ/ac4493)
4. A. Bates, Y. Preger, L. Torres-Castro, K. Harrison, S.Harris, J. Hewson al “Are solid-state batteries safer than lithium-ion batteries?” Joule, Volume 6, 2022, 742, DOI: [10.1016/j.joule.2022.02.007](https://doi.org/10.1016/j.joule.2022.02.007)

Acknowledgements

Sandia Contributors

Joshua Lamb, Lucas Gray, Genaro Quintana, Alex Bates, Kyle Fenton

National Lab and Industry Partners

USABC TAC Team. Sandia National Laboratories is a multi-mission laboratory managed and operated by National Technology and Engineering Solutions of Sandia, LLC., a wholly owned subsidiary of Honeywell International, Inc., for the U.S. Department of Energy’s National Nuclear Security Administration under contract DE-NA0003525.

VI.4 Battery Thermal Analysis and Characterization Activities (NREL)

Matthew Keyser, Principal Investigator

National Renewable Energy Laboratory
15013 Denver West Parkway
Golden, CO 80401
E-mail: Matthew.Keyser@nrel.gov

Haiyan Croft, DOE Technology Development Manager

U.S. Department of Energy
E-mail: Haiyan.Croft@ee.doe.gov

Start Date: October 1, 2021

End Date: September 30, 2024

Project Funding (FY22): \$500,000

DOE share: \$500,000

Non-DOE share: \$0

Project Introduction

While EDVs promise to curb America's need for imported oil, designing high-performance, cost-effective, safe, and affordable energy-storage systems for these cars can present challenges, especially in the critical area of battery thermal control. As manufacturers strive to make batteries more compact and powerful, knowing how and where heat is generated becomes even more essential to the design of effective thermal-management systems. NREL's thermal characterization activities provide developers, manufacturers, and OEMs with the knowledge necessary to assure that batteries are designed to perform strongly, last a long time, and operate at maximum efficiency.

The Vehicle Technologies Office has a goal to reduce the cost of electric vehicle battery packs to less than \$100/kWh for graphite/NMC (short term), \$75/kWh for silicon/NMC (next-gen lithium ion), and \$50/kWh for Li metal/NMC or Sulfur (long term target) with technologies that significantly reduce or eliminate the dependency on critical materials (such as cobalt) and utilize recycled material feedstocks [1]. To meet these metrics, the battery packs will need to have higher energy densities resulting in a very compact system. Even if the energy efficiency of the next generation of batteries increases, because of the compactness of these batteries more heat is being generated per unit volume with less heat transfer area. Thus, more advanced heat rejection systems are needed to keep the battery temperatures in the "goldilocks" zone that prevents acceleration of the aging mechanisms within the battery.

The chemistries of advanced energy-storage devices—such as lithium-based batteries—are very sensitive to operating temperature. High temperatures degrade batteries faster while low temperatures decrease their power and capacity, affecting vehicle range, performance, and cost. Understanding heat generation in battery systems—from the individual cells within a module, to the inter-connects between the cells, and across the entire battery system—is imperative for designing effective thermal-management systems and battery packs.

Inadequate or inaccurate knowledge of the thermal characteristics of batteries makes it difficult to design effective thermal-control systems. This can negatively affect lifespan, safety, and cost, ultimately resulting in negative consumer perception and reduced marketability. In 2012, Nissan had to address problems with the battery for its Leaf fully electric vehicle (EV) losing capacity in the hot Arizona climate. Many attributed this issue to inadequate battery-thermal management.

Accurately measuring battery thermal performance under various electrical loads and boundary conditions makes it possible for battery-system engineers to design effective thermal-management systems. NREL, with the funding from DOE VTO, has developed unique capabilities to measure the thermal properties of cells and evaluate thermal performance of active, air, and liquid cooled battery packs. Researchers also use electro-

thermal finite element models to analyze the thermal performance of battery systems in order to aid battery developers with improved thermal designs. In addition, our lumped capacitance multi-node battery-vehicle-ambient model can predict the temporal temperature of batteries as a function drive cycle, ambient temperature, and solar radiation. These one-of-a-kind tools allow NREL to work with the battery manufacturers and OEMs to meet stringent EDV life, performance, cost, and safety goals.

Objectives

- Thermally characterize battery cells and evaluate thermal performance of battery packs provided by USABC developers.
- Provide technical assistance and modeling support to U.S. DRIVE/USABC and developers to improve thermal design and performance of energy storage systems.
- Evaluate extreme fast charging effects on battery thermal performance.
- Quantify the impact of temperature and duty-cycle on energy storage system life and cost.
- Address high energy storage cost due to battery packaging and integration costs
- Reduce the cost, size, complexity, and energy consumption of thermal management systems
- Optimize the design of passive/active thermal management systems—explore new cooling strategies to extend the life of the battery pack.

Approach

NREL has measured the thermal properties of the cells and batteries with many different chemistries (lead acid, NiMH, and many versions of lithium cells) through heat generation, heat capacity, and infrared thermal imaging; conducted performance thermal testing of battery and ultracapacitor modules and packs; analyzed the thermal performance of cells and modules; and developed thermal models. Researchers perform thermal testing, analysis, and modeling (1) to assist DOE/USABC battery developers in designing cells/modules/packs for improved thermal performance, and (2) to evaluate and validate the thermal performance of cell/module/pack deliverables from DOE/USABC battery developers and suppliers.

NREL's equipment can benchmark how changing the design of the cell using a different cathode, anode, current collector, electrolyte, additive, or separator affects the overall performance of the cell. The information garnered from these tests helps battery and advanced vehicle manufacturers improve their designs, while providing critical data for the development of thermal management systems that will reduce the life-cycle cost of battery systems. Using NREL's unique R&D 100 Award-winning calorimeters and infrared thermal imaging equipment, we obtain thermal characteristics of batteries and ultracapacitors developed by USABC battery developers and other industry partners. NREL supports the Energy Storage Technical Team by participating in various work groups such as the Zenlabs, Farasis, and USABC Electric Vehicle Cell Development and Beyond Lithium Ion Working Groups.

Results

Calorimeter Testing

Figure VI.4.1 shows the efficiency of cells tested in FY22 and prior to FY22 at NREL at a calorimeter temperature of 30°C. The lithium-ion cells were fully discharged from 100% SOC to 0% SOC under a C/2, C/1, and 2C currents. The cells in this figure have been developed under the LCFC programs within USABC. These cells are designed for mainly high energy applications (the LCFC program maintains aggressive energy level targets). It should be noted that as the specific energy of these graphite systems increases, the efficiency decreases. This is primarily due to the impact of thicker electrodes have on the thermal performance. In contrast, the efficiency of the silicon blend cells is increasing due to chemistry optimization. Silicon containing cells can maintain high energy content with lower electrode thickness due to the much greater material energy density when compared to graphite. The general trend shows that silicon containing systems still need improvements to reach the heat efficiency of graphite cells with similar electrode thickness. DOE and USABC are investigating both graphite and silicon to improve energy density, power density, cycle life and/or cost benefits. NREL's calorimeters provide the fundamental understanding of whether the inefficiencies shown below are due to chemistry or cell design.

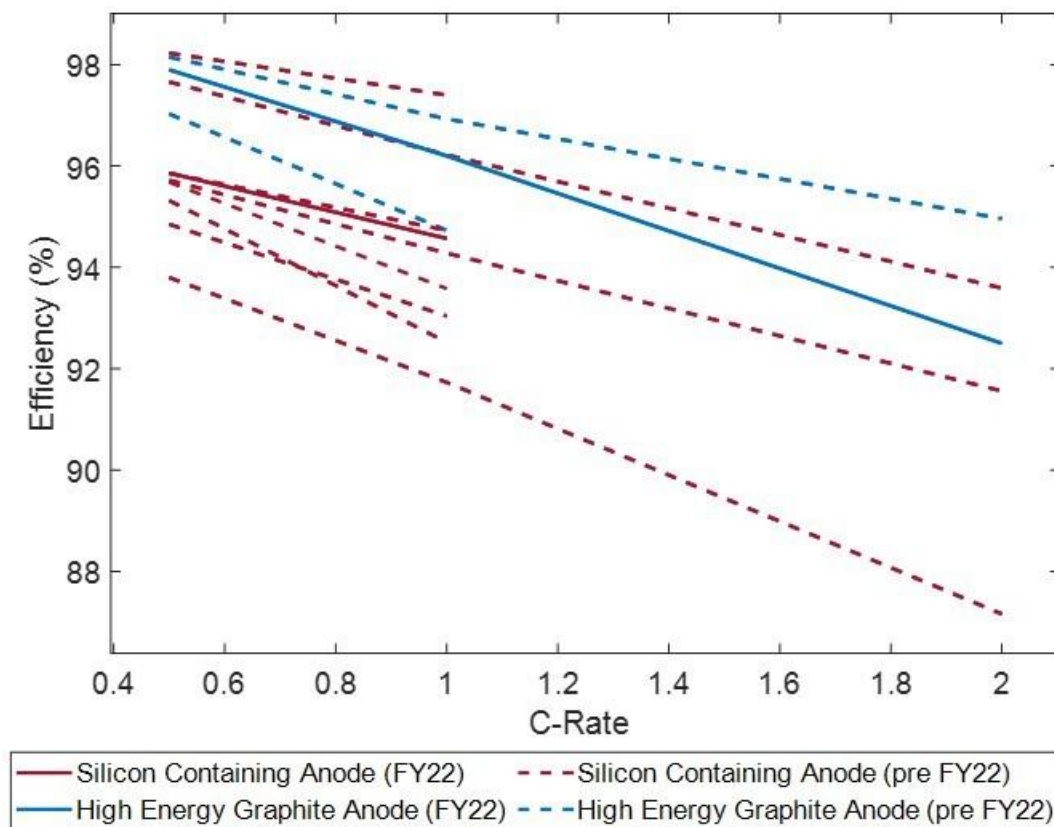


Figure VI.4.1 Efficiency summary of cells tested in NREL's calorimeters. Caption Credits/Source: NREL-Aron Saxon

NREL's calorimeters were designed to be accurate enough to measure the electrochemical response from batteries under test – this capability allows NREL to understand benefits associated with design and chemistry changes to the cell. Figure VI.4.2 shows the entropic heat generation rates normalized to the Ah capacity of two cells – one cell has a graphite anode and the other has a graphite/Si anode – under a C/10 charge and discharge at 30°C. The cells in this figure were cycled over their entire state-of-charge range – minimizing the current decreases the joule heating of the cell and allows for the entropic heat signature to be assessed. From the figure, we can observe how the entropic response changes with introducing increasing amounts of Si. The response flattens out and the magnitude of peaks and valleys prevalent in graphite due to its phase changes are reduced. The entropic response in cells has been a historic indicator of understanding material processes without deconstructing the full cell and how these processes impact cell performance.

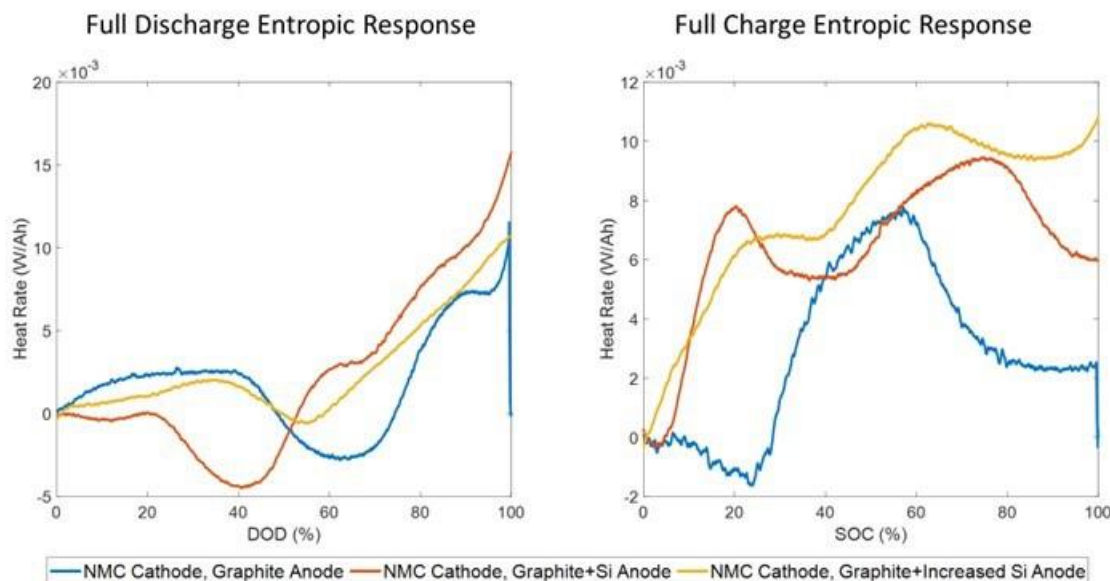


Figure VI.4.2 Calorimeter normalized heat rate for graphite and graphite/Si NMC cells under C/10 charge and discharge. Caption Credits/Source: NREL-Aron Saxon

NREL has also been involved with testing cells under fast charge conditions. The USABC test procedure consists of a fifteen-minute fast charge with a goal of returning 80% of the cell's usable capacity into the cell. If the maximum operational voltage is reached during the charge, then the current is tapered to complete the charge. Figure VI.4.3 illustrates the heat generation results of a cell that was tested at NREL under this condition under three different charge rates – (X-n)C, (X)C, and (X+n)C. The results indicate that both the XC and (X+n)C cases returned the same amount of usable capacity into the cell. The XC rate however, produced the least amount of heat per energy inserted. This case provides evidence that charge algorithm optimization is needed in addition to chemistry optimization to provide the most return for fast charge cases. NREL is continuing research into charge algorithm optimization and novel thermal management strategies to lessen the burden of fast charging on the cells lifetime while minimizing the thermal management system.

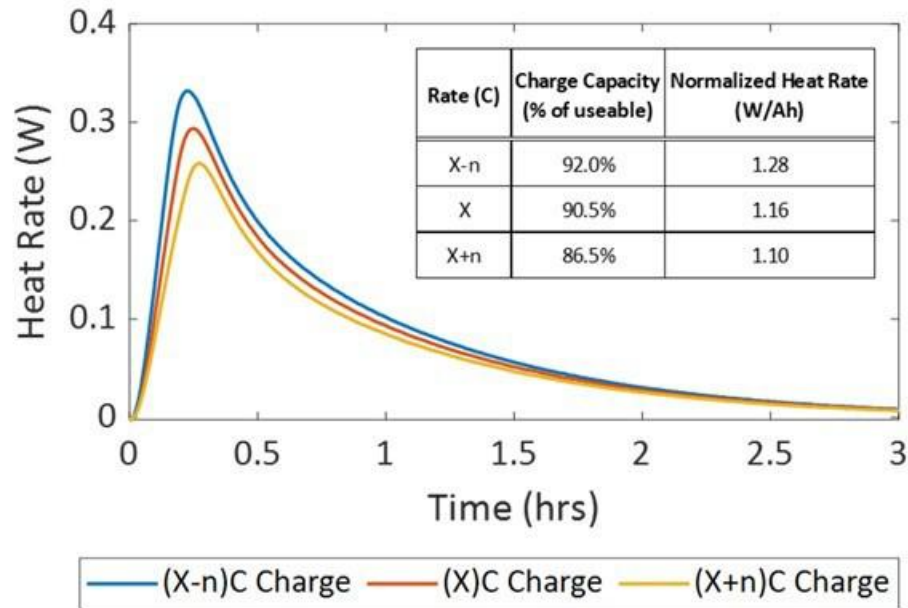


Figure VI.4.3 Heat response of cell under fast charge. The calorimeter test temperature was 30 °C. Caption Credits/Source: NREL-Aron Saxon

Infrared Imaging of Cells

NREL performs infrared (IR) thermal imaging of battery manufacturer's cells to determine areas of thermal concern. We conduct IR thermal imaging under a set of prescribed procedures and environments to minimize the error from different sources such as reflective cell surfaces, radiation from surrounding surfaces, and cooling from the power cables attached to the cell. NREL combines the IR imaging equipment with a battery cycler to place the cells under various drive cycles, such as a US06 charge depleting cycle for a PHEV, to understand the temperature differences within the cell. We then make recommendations to the battery manufacturers and USABC on how to improve the thermal design of the cell to increase its cycle life and safety.

Figure VI.4.4 shows a lithium battery (High Nickel Content NMC/Graphite) at the end of a high-rate charge. Each IR image has a temperature spread associated with it – by decreasing the temperature spread a visual reference can be used to determine where the heat is preferentially being generated within the cell. For this cell, the heat generation is uniform across the surface of the battery. The cell's highest temperature point is in the center of the cell. This indicates that there is not a bias towards either the positive or negative tab. When the cell temperature is not uniform and consistent or symmetrical, individual cells within modules and packs age differently affecting the cycle life of the module. NREL is working with battery developers to understand how temperature non-uniformities affect the efficiency and cost of the cell over its life.

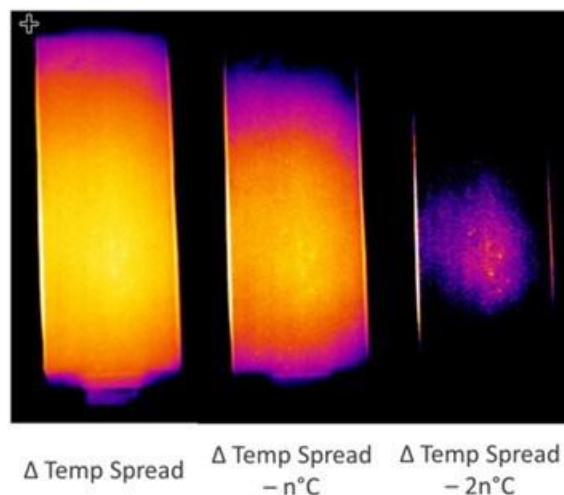


Figure VI.4.4 Infrared image of lithium battery cell (graphite /high nickel content NMC) at the end of a fast charge. Caption Credits/Source: NREL- Aron Saxon

Conclusions

NREL has thermally tested cells and modules from Zenlabs and Farasis during FY22 across multiple USABC programs. We have provided critical data to the battery manufacturers and OEMs that can be used to improve the thermal design of the cell, module, pack, and their respective thermal management systems. The data included heat generation of cells under typical profiles for HEV, PHEV, and EV applications, which is essential for designing the appropriately sized battery thermal management system. In FY23, NREL will continue to thermally characterize cells and modules for USABC, DOE, and USDRIVE but the focus will shift to fast charging applications and the heat generation for battery chemistries beyond lithium ion.

Key Publications

1. Steven Boyd, Batteries Overview, Annual Merit Review, Washington DC, 2022.

Acknowledgements

We would like to acknowledge Aron Saxon-the co-author of this report as well as Andrew Schiek and Tom Bethel for program support.

VI.5 Cell Analysis, Modeling, and Prototyping (CAMP) Facility Research Activities (ANL)

Andrew N. Jansen, Principal Investigator

Argonne National Laboratory
9700 South Cass Avenue
Lemont, IL 60439
E-mail: Jansen@anl.gov

Stephen E. Trask, Co-Principal Investigator

Argonne National Laboratory
9700 South Cass Avenue
Lemont, IL 60439
E-mail: STrask@anl.gov

Haiyan Croft, DOE Technology Development Manager

U.S. Department of Energy
E-mail: Haiyan.Croft@ee.doe.gov

Start Date: October 1, 2018

End Date: September 30, 2023

Project Funding (FY22): \$800,000

DOE share: \$800,000

Non-DOE share: \$0

Project Introduction

The “valley of death” is a phrase often used to describe the path a new discovery must traverse to become a commercial product. This is especially true for novel battery materials invented in research laboratories around the world. Often researchers are resource limited and are only able to make gram quantities of their new material. The CAMP Facility is appropriately sized to enable the design, fabrication, and characterization of high-quality prototype cells using just a few hundred grams of the latest discoveries involving high energy battery materials. Prototype cells made in the CAMP Facility generally have 400-mAh capacity, which straddles the gap between coin cells and industrially-sized cells nicely – two orders of magnitude from each end point. Thus, a realistic and consistent evaluation of candidate chemistries is enabled in a time-effective manner with practical quantities of novel materials in cell formats commonly used in industry.

The CAMP Facility is an integrated team effort designed to support the production of prototype electrodes and cells, and includes activities in materials validation (benchmarking), modeling, and diagnostics. It is not the aim of this facility to become a small battery manufacturer, but instead to be a laboratory research facility with cell production capabilities that adequately evaluate the merits and limitations of new lithium-ion chemistries in a close-to-realistic industrial format. The source of these materials (anodes, cathodes, electrolytes, additives, separators, and binders) may originate from DOE Battery Programs, as well as from other R&D organizations such as universities, national labs, and industrial vendors. Electrochemical couples with high energy density based on earth-abundant elements are given extra priority.

The CAMP Facility has the capability to make two prototype cell formats in their 150 m² dry room: pouch cells (xx3450 format, with capacity around 0.5 Ah; and xx6395, with capacity around 2 Ah). Pouch cells are generally easier to assemble and are a useful indicator of gassing problems in a cell during cell aging and cycling. Central to this effort is a pilot-scale coating machine that operates with slurry sizes that range from 20 mL to 2 L. These key features of the CAMP Facility enable a professional evaluation of both novel materials (typically limited quantities) and commercial materials for benchmarking. In addition, the Materials Engineering Research Facility (MERF) is available for scaling up materials for these prototype cell builds.

Objectives

The objective of this core-funded effort is to design, fabricate, and characterize high-quality prototype electrodes and cells that are based on the latest discoveries involving high-energy anode and cathode battery materials. Using this multi-disciplined facility, analytical diagnostic results can be correlated with the electrochemical performance of advanced lithium-ion battery technologies for electric vehicle (EV) applications.

- Link experimental efforts through electrochemical modeling studies.
- Identify performance limitations and aging mechanisms.
- Support lithium-ion battery projects within the DOE-EERE-VTO.

In FY22, the CAMP Facility milestone objectives were to:

- Develop methods to coat electrodes with novel solid-state electrolyte materials that are being developed in literature. (efforts described in Section VI.6)
 - Produce 5 meter of cathode electrode with solid-state electrolyte.
- Develop X-ray methodologies to quantify electrode expansion in NMC/Li cells.
 - Determine expansion-contraction between charged and discharged states for at least one high-Ni NMC cathode.
- Maintain supply of advanced prototype electrodes in Electrode Library.
 - Fabricate >100 meters of needed anode and cathode electrodes to support DOE battery programs.
- Finish installation and training related to multifunctional coater at Argonne.
 - Coater needs to be able to coat 3 mAh/cm² electrode loadings uniformly at 0.5 m/min.

Approach

The general approach used in this effort is to start small and grow large in terms of cell size and amount of resources devoted to each novel battery material. At various points in the development process, decisions are made to either advance, modify, or terminate studies to maximize utilization of available resources. Coin cells (2032 size) are used for materials validation purposes with initial studies performed at 30°C. After formation cycles, the coin cells go through rate capability testing, HPPC testing, and limited cycle life testing. Additional temperatures and test conditions are employed, if warranted.

Using the results obtained by the materials validation of promising materials (also refer to Section VI.6), single-sided electrodes are fabricated on the larger dry-room coater for diagnostic study. The new cell chemistries are studied in detail using advanced electrochemical and analytical techniques, including the employment of micro-reference electrode cells. Factors are identified that determine cell performance and performance degradation (capacity fade, impedance rise) on storage and on extensive deep-discharge cycling. The results of these tests are used to formulate data-driven recommendations to improve the electrochemical performance/life of materials and electrodes that will be incorporated in the prototype cells that are later fabricated in the dry room. This information also lays the foundation for electrochemical modeling focused on correlating the electrochemical and analytical studies, in order to identify performance limitations and aging mechanisms.

If the results from diagnostics and modeling still look promising, full cell builds are conducted using double-sided electrodes. The electrodes are then punched and assembled into full cells in the dry room using semi-automated cell assembly equipment. Formation procedures are conducted on the cells to encourage electrolyte wetting and uniform solid-electrolyte-interface (SEI) formation. These cells undergo rigorous electrochemical evaluation and aging studies under the combined effort of the CAMP Facility team and Argonne's Electrochemical Analysis and Diagnostic Laboratory (EADL). After testing, select cells are destructively examined by the Post-Test Facility to elucidate failure mechanisms. This information is then used to further improve the new chemistry, as well as future electrode and cell builds.

Results

The CAMP Facility is designed to work closely with materials researchers across the many electrochemical energy storage programs throughout the DOE-EERE-VTO. In addition to its own yearly R&D tasks, it actively coordinates its efforts to provide support to other national lab team programs such as: Realizing Next Generation Cathodes (RNGC), Silicon Consortium Project (SCP), ReCell Advanced Battery Recycling Center, eXtreme Fast Charge Cell Evaluation of Lithium-Ion Batteries (XCEL), and Behind-the-Meter-Storage (BTMS), and Liquid Electrolyte Projects. The Materials Benchmarking Activities (Section VI.6) is a segment of the CAMP Facility. The CAMP Facility also complements the capabilities of other DOE support facilities such as: Materials Engineering Research Facility (MERF - Argonne), Post-Test Facility (PTF - Argonne), Battery Abuse Testing Lab (BATLab - SNL), and Battery Manufacturing Facility (BMF - ORNL). More information about these programs can be found in the relevant chapters and sections of this annual report. The remainder of this CAMP Facility section will discuss the results of the CAMP Facility deliverables and related topics for FY22.

Multifunctional Coater Specifications Confirmed during Factory Acceptance Test

The new multifunctional roll-to-roll coater from Frontier was successfully installed in Argonne's CAMP Facility dry room (Figure VI.5.1). Completion of the ventilation system to remove the ozone generated by the corona treater is underway. Once the ventilation system is operational, full training will be provided by Frontier to Argonne staff. This coater provides many new capabilities to the CAMP Facility: interchangeable coating heads, gravure coating, single-slot die coating, the progressive cavity pump, corona treatment of substrates, and an IR drying zone.



Figure VI.5.1 Images of the multifunctional coater installed in the CAMP Facility's dry room.

Visualizing Electrode Assembly Movement in Lithium Batteries using operando X-ray Diffraction

Rechargeable lithium-metal battery cells have returned to the forefront of energy storage because of their potential to deliver high specific energy densities. These cells contain a Li metal anode, which has a specific capacity of 3,860 mAh/g, more than 10x that of graphite anode. However, there are well-known disadvantages for Li-metal cells that have prevented their widespread use in commercial applications. Organic (e.g., carbonate) electrolytes are easily reduced on lithium; this reaction causes formation of ionic deposits known as the solid electrolyte interphase (SEI) that eventually depletes the electrolyte, increases anode impedance, and causes premature cell failure. Other concerns include the large volume changes that result from expansion and contraction of the lithium anode during electrochemical cycling. The successful implementation of Li-metal batteries depends on addressing these concerns that requires identifying the causes for the detrimental behaviors.

In this study, electrode assembly displacements in Li-metal cells were examined that occur during lithium plating and stripping using *operando* energy dispersive X-ray diffraction (EDXRD). These experiments were conducted on 2032-format coin cells with a $\text{LiNi}_{0.8}\text{Mn}_{0.1}\text{Co}_{0.1}\text{O}_2$ (NMC811) oxide cathode, Li-metal anode, a trilayer Celgard 2320 separator and a LiPF_6 -bearing carbonate electrolyte. A cross section radiograph of the coin cell shows a spring-loaded electrode assembly, with the cathode, separator, and Li metal sandwiched between stainless steel spacers (Figure VI.5.2). By tracking relative displacements of the Al current collector, NMC811 edges and polyethylene (PE) separator during electrochemical cycling we determine the reversible and irreversible movements of the cathode/separator assembly.

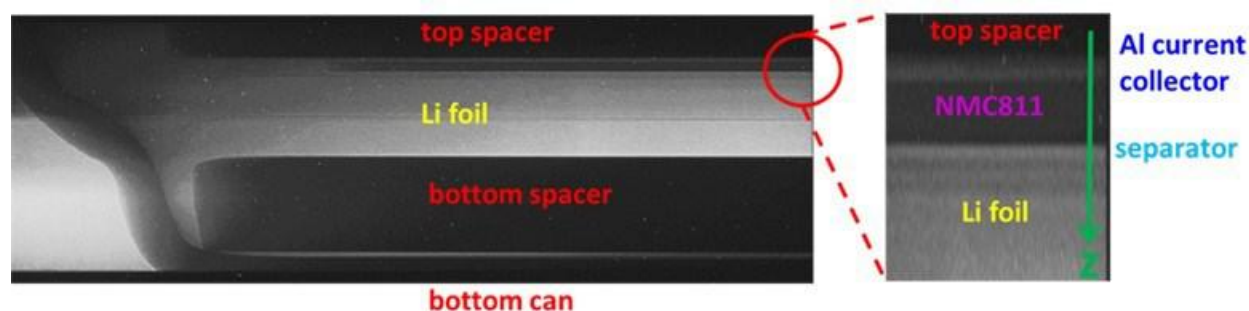


Figure VI.5.2 (a) Cross section radiograph of a coin cell with the electrode assembly sandwiched between the top and bottom spacers. The cell is placed on a motorized translation stage that is moved relative to a stationary X-ray beam. The green arrow shows the direction z of scanning.

The movements of the cathode and PE median in the separator are summarized in Figure VI.5.3, which show data for three consecutive charge/discharge cycles on a NMC811/Li cell. Each cycle consists of a constant current (CC), $C/2$ rate, capacity-limited charge to 190 mAh/g and discharge at a $C/2$ rate to 2.5 V followed by a constant voltage (CV) hold. During charge, Li^+ ions extracted from the cathode traverse through the separator and deposit on the Li-metal; the resulting increase of the anode thickness causes the separator and cathode to move towards the top spacer (Figure VI.5.3c). On discharge as Li^+ ions are stripped from the foil and inserted into the cathode, the separator and cathode move in the reverse direction, but they do not return to their original locations, indicating an irreversible change in the cell (Figure VI.5.3a). This irreversibility progressively increases with continued cycling. The reversible movement of the PE and NMC811 edges, quantified in Figure VI.5.3b, is $16\text{ }\mu\text{m}$ for a 4.4 mAh capacity exchange (or $3.6\text{ }\mu\text{m}/\text{mAh}$). This value is larger than that estimated from a uniform Li plating ($2.85\text{ }\mu\text{m}/\text{mAh}$); the difference is due to the non-uniformity of lithium plating and stripping, and to the SEI-forming side reactions that increase material volume in the anode. These parasitic reactions and associated SEI build-up on the *mossy* lithium cause an irreversible drift of the cathode/separator assembly, which is $11.3\text{ }\mu\text{m}/\text{cycle}$! Note that the relative positions of the NMC811 and PE separator layer remain constant during the cycling (Figure VI.5.3b) indicating that the separator is not compressed and that there is efficient transduction of the load through the separator.

In summary, an *operando* X-ray technique was developed to visualize electrode assembly movement during Li plating and stripping in 2032-type coin cells. During charge and discharge, deposition and removal of Li^+ ions cause expansion or contraction of the Li foil thickness, respectively. The oxide cathode and separator move in sync, indicating that there is no separator compression (and pore closures therein) during this process. In this cell, this periodic movement is $\sim 3.6\text{ }\mu\text{m}$ per mAh of capacity transferred between the electrodes. The accumulation of SEI products during this cycling transforms the lithium morphology from planar to mossy during each cycle. For a carbonate-based electrolyte, the irreversible expansion is $\sim 11.3\text{ }\mu\text{m}$ per cycle. This significant expansion points to the need for electrolytes that have better stability against lithium metal.

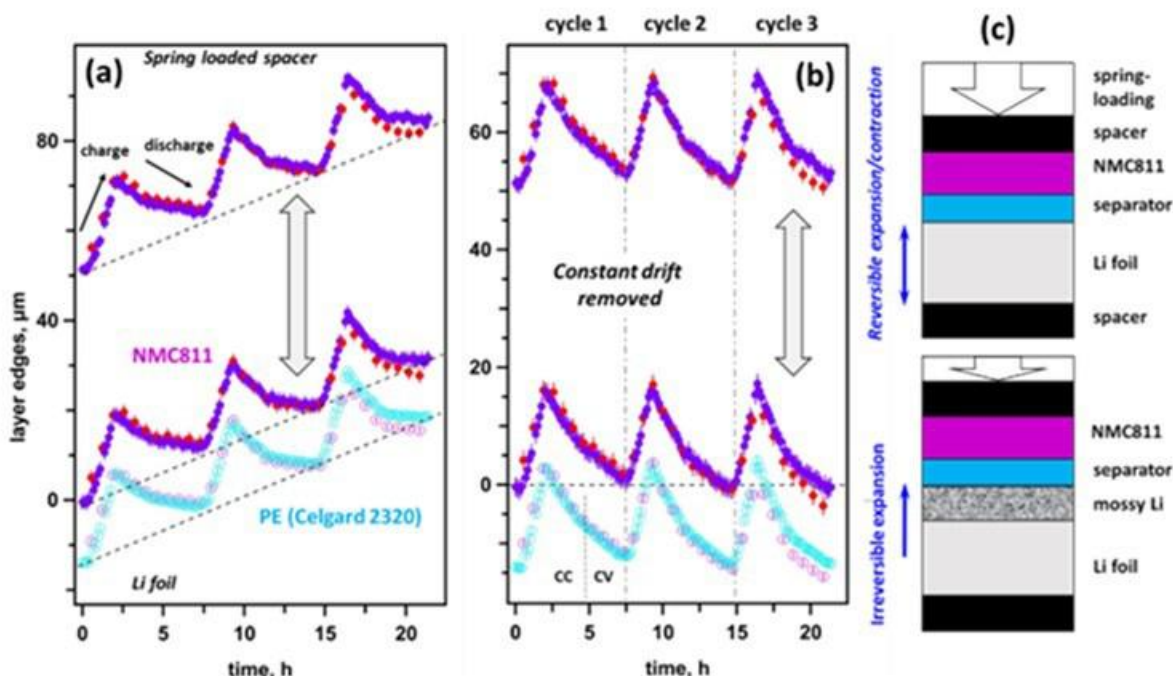


Figure VI.5.3 X-ray dilatometry showing movement of the electrode assembly during cycling of a NMC811/Li cell. Panel a shows hard edges of the NMC811 layer (filled circles) and the PE median of the separator (open circles). The spring-loaded spacer is at the top, with the Li foil pressed against the bottom of the coin cell through the bottom spacer (panel c). Upon cycling, the separator and NMC811 layer move as a single unit. In panel b, the constant drift (dashed lines) is subtracted to show reversibility of the periodic variation.

Support of Activities in MERF

Argonne's MERF scaled LFP cathode material using a new synthesis route and provided a batch of this earth-abundant cathode for validation in pouch cells. MERF also provided a commercial LFP powder to use as the baseline. The CAMP Facility coated the powders in electrodes that were capacity matched (~ 2.6 mAh/cm²) to existing Superior Graphite SLC1506T graphite baseline anode, which has a loading near 2.8 mAh/cm². These electrodes (cathode area 14.1 cm²) were assembled into 2 sets of xx3450 sized single layer (SL) pouch cells with Celgard 2500 separator, ~ 610 μ L of Gen 2 electrolyte; 4 cells per cathode.

Two tap charges and six formation cycles (3x-C/10, 3x-C/2, from 3.5-3.0V) were carried out on the cells. They were then degassed, put onto a capacity check protocol (1.5x-C/10, 2x-C/2, from 3.5-3.0V), and then subjected to a rate study. The rate study used 3.5V UCV for the slower rates, and then a 3.6 V UCV for the last two faster rates (2x-C/20, 3x-C/10, 3x-C/2, 3x-1C, 3x-2C, 3x-5C; all symmetric charge and discharge rates). These results are summarized in Figure VI.5.4.

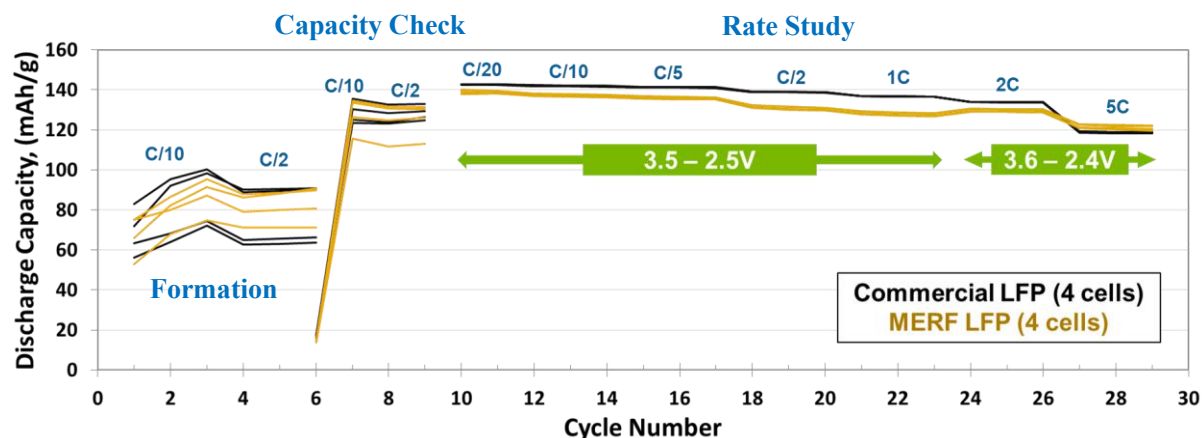


Figure VI.5.4 A Summary of the Formation, Capacity Check, and Rate Study Discharge Capacity Data from all eight cells that were cycled at 30°C and 4 psi per cell

As expected, the deviation starts out large, but then after the formation, degassing, and capacity check, the cell-to-cell deviations are significantly reduced. The MERF-made LFP has a little less capacity utilization in the slower cycles, but seems to have near same performance at the faster rates. All 8 cells were placed on a cycle life protocol that consisted of 1C symmetric charge and discharge rates with a C/20 cycle and HPPC test every 100 cycles. These pouch cells finished testing in FY22 with 500 cycles where it was observed that the commercial baseline cells had better capacity retention, which was not unexpected since the commercial LFP is fully optimized.

Support of Realizing Next Generation Cathodes (RNGC)

In FY21 the RNGC team provided the CAMP Facility with 200 grams of a promising material, $\text{Ni}_{0.9}\text{Mn}_{0.05}\text{Co}_{0.05}$, to fabricate electrodes and assemble >1.5 Ah pouch cells for further demonstration. Learned approaches of controlling the slurry temperature were applied and resulted in minimal/no gelation. The absence of the gelation resulted in the ability to achieve a uniform coating. Cell assembly and testing of these electrodes were done in FY22: xx6396 sized (49.1 cm² per side of a graphite anode, 46.3 cm² per side of an cathode) multilayer pouch cells (2 SS anodes, 6 DS anodes, and 7 DS cathodes). The electrodes were capacity matched for n:p ratio range of 1.10-1.26 (covering 1st cycle, reversible cycle, C/10, and 1C data), with Celgard 2500 separator, 9.005 mL of 1.0 M LiPF_6 + 0.05 M LiDFP in EC/EMC (1/9) electrolyte solution. All six cells were formed the same way at 30°C, resulting in a reversible C/10 capacity of 1.58 Ah.

The cells were degassed, performed a capacity check at 30°C, and had the best four cells chosen to continue with testing. The four remaining cells were split into two sets of 2 cells. One set of cells were placed in a 45°C oven to do life cycle testing on, and the remaining set at 30°C to also do life cycle testing (Figure VI.5.5). The life cycle testing protocol included a slow high-resolution cycle of C/25 for dV/dQ analysis, an 18 pulse high resolution HPPC protocol (10 sec each pulse), and then 50 cycles from 4.2-3.0 V of C/3 charge & discharge. This was looped four times per protocol, and the protocol was restarted until the C/3 discharge retention was less than 80%, then an ending slow cycle and HPPC pulses. The 45°C cells had finished their testing in FY22, while the 30°C cells will finish their testing in FY23, at which point a full analysis will be done on the cells.

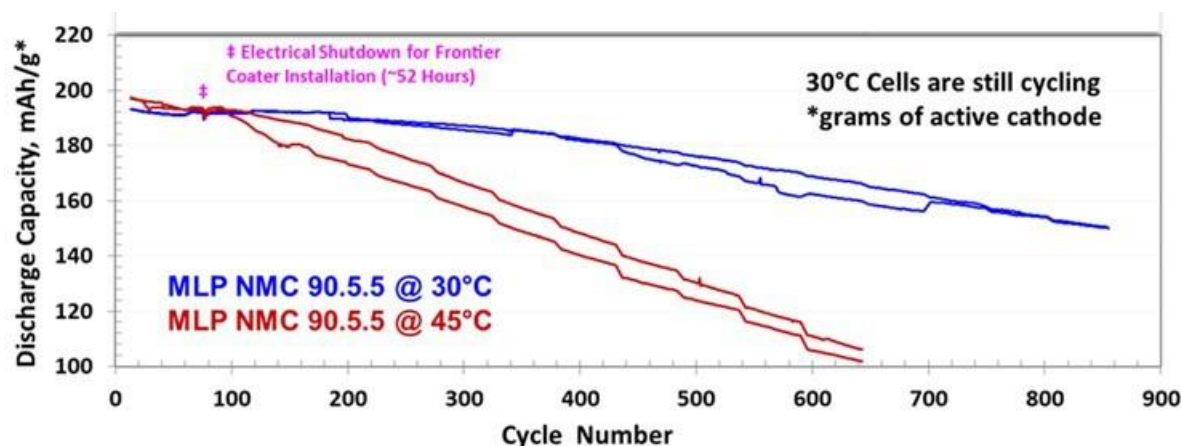


Figure VI.5.5 C/3 Discharge capacity from the life cycle protocol at 30°C and 45°C of the four chosen xx6395 MLP cells. The C/20 data points (every 51 cycles) were omitted for ease of viewing C/3 capacity.

Summary of Electrode Library Activities

Table VI.5.1 highlights the distribution of electrodes from the Electrode Library, which is maintained by the CAMP Facility. The Electrode Library serves as a supply of standard electrode samples that are designed to be interchangeable with one another (capacity matched). Electrodes can be made with as little as 20 g of experimental material and can be made to match an existing counter electrode. From October 1, 2021 to September 30, 2022, 1756 sheets of electrode were fabricated and distributed by the CAMP Facility, which is >42 square meters of electrodes. These electrodes were supplied by the CAMP Facility in support of DOE's numerous activities in advanced battery R&D (11 labs, 27 universities, and 14 companies). In addition to these electrodes, the CAMP Facility fabricated ~310 pouch cells for DOE projects (consisting of many unique combinations of electrodes, electrolytes, and separators).

Table VI.5.1 Summary of Electrode Library Distributions

Electrodes Delivered	FY19		FY20		FY21		FY22	
Argonne	160	15 %	245	25 %	302	17 %	704	40 %
Other National Labs	224	21 %	299	30 %	354	20 %	253	14 %
Universities	296	28 %	333	33 %	426	23 %	243	14 %
Industry	388	36 %	121	12 %	725	40 %	556	32 %
Total:	1068		998		1807		1756	

Conclusions

The new multi-functional coating system from Frontier was installed in Argonne's dry room, but still awaiting installation of ventilation system for ozone. This multi-functional coating system provides two new coating methods to the CAMP Facility (i.e., gravure and single-slot die). It also has an IR heating zone and corona treatment. It will be fully operational in early FY23.

An *operando* X-ray technique was developed to visualize electrode assembly movement during Li plating and stripping, where it was observed that the oxide cathode and separator move in sync, indicating that there is no separator compression during this process.

The CAMP Facility continued its support of numerous DOE programs, much of which was performed through the CAMP Facility's Electrode Library. Numerous prototype electrodes (>100 meters) and pouch cells were fabricated and delivered to DOE-EERE programs.

Several of the planned tasks for FY22 were modified because of reduced laboratory time due to the COVID19 pandemic. These restrictions were lifted in March of 2022.

Key Publications

1. I.A. Shkrob, P. Badami, J.S. Okasinski, M.-T.F. Rodrigues, S.E. Trask, D.P. Abraham, "Visualizing electrode assembly movement and lithiation heterogeneity in lithium-metal batteries using *operando* energy dispersive X-ray diffraction" *Journal of Power Sources* 553 (2023) 232273.
2. Additional publications related to the CAMP Facility are listed in section VI.6 and in numerous other projects across the DOE and many universities.

Acknowledgements

Key contributors to this work: Daniel Abraham, Shabbir Ahmed, Caleb Calvary, Alison Dunlop, Jihyeon Gim, Ozge Kahvecioglu, Hyun-Woo Kim, Jae-Jin Kim, Chen Liao, Wenquan Lu, Bryant Polzin, Yan Qin, Marco-Tulio Fonseca Rodrigues, Devashish Salpekar, YoungHo Shin, Steve Trask, Jack Vaughey, Zhenzhen Yang.

VI.6 Materials Benchmarking Activities for CAMP Facility (ANL)

Wenquan Lu, Principal Investigator

Argonne National Laboratory
9700 South Cass Avenue
Lemont, IL 60439
E-mail: LuW@anl.gov

Andrew N. Jansen, Co-Principal Investigator

Argonne National Laboratory
9700 South Cass Avenue
Lemont, IL 60439
E-mail: Jansen@anl.gov

Haiyan Croft, DOE Technology Development Manager

U.S. Department of Energy
E-mail: Haiyan.Croft@ee.doe.gov

Start Date: October 1, 2018

End Date: September 30, 2023

Project Funding (FY22): \$400,000

DOE share: \$400,000

Non-DOE share: \$0

Project Introduction

High energy density electrode materials are required to achieve the requirements for electric vehicle (EV) application within the weight and volume constraints established by DOE and the USABC. One would need a combination of anode and cathode materials that provide 420 mAh/g and 220 mAh/g, respectively, as predicted by Argonne's battery design model (BatPac), if one uses a 20% margin for energy fade over the life of the battery assuming an average cell voltage of 3.6 volts. Therefore, the search for new high energy density materials for lithium-ion batteries (LIB) is the focus of this material benchmarking project. In addition to electrode materials, other cell components, such as separators, binders, current collectors, etc., are evaluated to establish their impact on electrochemical performance, thermal abuse, and cost.

This benchmarking effort is conducted as part of the Cell Analysis, Modeling, and Prototyping (CAMP) Facility (Refer to Chapter VI.5) to identify and support promising new materials and components across the "valley of death", which happens when pushing a new discovery towards a commercial product. The CAMP Facility is appropriately sized to enable the design, fabrication, and characterization of high-quality prototype cells, which can enable a realistic and consistent evaluation of candidate chemistries in a time-effective manner. However, the CAMP Facility is more than an arrangement of equipment, it is an integrated team effort designed to support the production of prototypes electrodes and cells. In order to utilize the facility more efficiently and economically, cell chemistries are validated internally using coin type cells to determine if they warrant further consideration. In addition, the bench marking will advance the fundamental understanding of cell materials and facilitate advance the technology development.

Objectives

- The primary objective is to identify and evaluate low-cost materials and cell chemistries that can simultaneously meet the life, performance, and abuse tolerance goals for batteries used in EV applications.
- The secondary objective is to enhance the understanding of the impact of advanced cell components and their processing on the electrochemical performance and safety of lithium-ion batteries.
- This project also provides the support to the CAMP Facility for prototyping cell and electrode library development, and the MERF facility for material scale up.

Approach

Though there are an overwhelming number of materials being marketed by vendors for lithium-ion batteries, there are no commercially available high-energy materials that can meet all the requirements for all-electric-range (AER) vehicle within the weight, volume, cost, and safety constraints established for EVs by DOE and the USABC. Identification of new high-energy electrode materials is one of the challenges for this project.

Under materials benchmarking activities, we constantly reach out to, or are approached by, material developers to seek opportunities to test their advanced or newly released products. By leveraging Argonne's expertise in electrode design and cell testing, we can provide not only a subjective third opinion to material suppliers, but also deeper understanding on their materials, which can aid their material development. This deep understanding becomes even more important when the material developers are small companies or new players, who often overlook overall requirements of battery materials.

In addition to industrial partners, we also work closely with scientists from various research institutes, such as universities and research laboratories. They often come up with novel materials with advanced electrochemical performance, but small quantities, which is only enough for validation purpose. These test results help us to determine how much effort should be expanded to explore the material potential.

In general, we will validate any potential cell material, which has impact on the cell performance, mainly in terms of electrochemical performance, electrode optimization, and thermal stability. The electrochemical performance is the centerpiece of the materials benchmarking activities, which will be tested using 2032-sized coin-type cells under test protocols derived from USABC PHEV 40 requirements [Battery Test Manual For Plug-In Hybrid Electric Vehicles, Idaho National Laboratory]. The freshly made coin cells will undergo three formation cycles at a C/10 rate. The cells are then tested for the rate performance. For the rate test, the charging rate is typically set at C/5, while the discharge rate varies from C/5, C/3, C/2, 1C to 2C. Three cycles are performed for each discharge rate. After the rate test, the cells then undergo cycling test at C/3 rate. During the cycling test, we change the current rate to C/10 every 10th cycle to check the rate effect. Also, Hybrid Pulse Power Characterization (HPPC) is conducted every 10th cycle, which will be used to calculate the Area Specific Impedance (ASI).

This fiscal year, we have investigated various battery materials, such as cathode, anode, conductive additives, and solid-state electrolyte. In this report, we will report the progress on solid-state electrolyte, such as (solid polymer electrolyte and $\text{Li}_6\text{PS}_5\text{Cl}$). Lithium dendrite formation growth with all solid-state batteries (ASSB) was also investigated. The report also includes electrode optimization using carbon nanostructures provided by Cabot.

Results

Organic Solid State Electrolyte Processing Development

Poly (ethylene glycol) diacrylate (PEGDA) has been used as a cross-linking agent to copolymerize with other monomers in the application of solid polymer electrolytes (SPE). Instead of UV curing, PEGDA based SPE were prepared through an in-situ thermal polymerization method of a blended precursor solution in liquid electrolyte.

Two approaches were attempted to process SPE thin film, stand-alone thin film (Figure VI.6.1 (left)) and direct-casting SPE on electrode fabrication. The polymer electrolyte consists of PEGDA, LiTFSi , Glutaronitrile (GN) and 2,2-Azobis(2-methylpropionitrile (AIBN). The detailed composition is listed in Table VI.6.1. The impedance of stand-alone polymer electrolyte was tested using electrochemical impedance spectroscopy (EIS) at various temperature and the test results are shown in Figure VI.6.1 (right). The room temperature ionic conductivity is determined to be 0.14 mS/cm.

Table VI.6.1 PEGDA polymer electrolyte compositions

Components	PEGDA	LiTFSI	GN	AIBN
Weight %	40	30	30	0.1

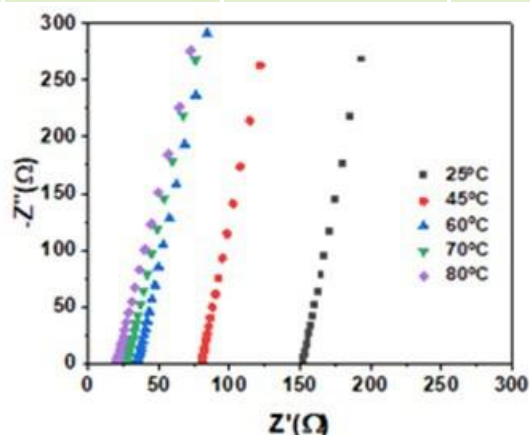


Figure VI.6.1 Image of free-standing polymer electrolyte (left) and electrochemical impedance spectra of solid polymer electrolyte at various temperatures (right)

The electrochemical performance of the polymer electrolyte was tested using Li/LiFePO₄ (LFP) half-cell. Both lithium anode and LFP cathode were coated with solid polymer electrolyte. The ASSB was cycled between 2V - 4V at 45°C. As shown in Figure VI.6.2, very typical voltage profile and specific capacity were obtained for LFP electrode during formation cycle with C/20 rate. The cell capacity retention is about 86% after 50 cycles.

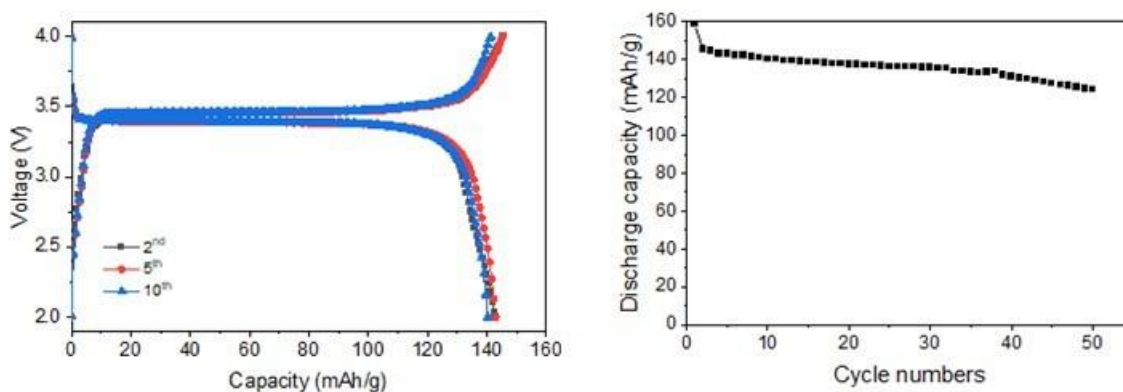


Figure VI.6.2 Voltage profile (left) and cycle life (right) of Li/SPE/LFP cell

Sulfide Based Solid State Electrolyte

Li₆PS₅Cl was studied by collaborating with Northeastern University [1]. ASSB using Si as anode and LiNi_{0.8}Co_{0.1}Mn_{0.1}O₂ (NMC811) as cathode was fabricated and tested. Figure VI.6.3A illustrates the architecture of Si/SSE/NMC811 full cell. Figure VI.6.3B-E present the SEM image and EDX mapping of a cross-section of the full cell with cathode mass loading of 10 mg/cm². The thickness of the cathode, SE, and anode layer are 62, 50, and 32 μm, respectively. Figure VI.6.3F-G presents the voltage profiles and differential capacity plot of the full cell at the first two cycles at the rate of C/20. Typical electrochemical characteristics of Si and NMC811 was obtained. Figure VI.6.3H shows the rate performance of the full cells with two different loadings (10 and 20 mg/cm²). Although the mass loading was doubled, the full cell with higher loading shows negligible overpotential increase at high rates. Figure VI.6.3I displays the long-term cycling. Both full cells with different loading have similar capacity retention – about 70% after 1000 cycles.

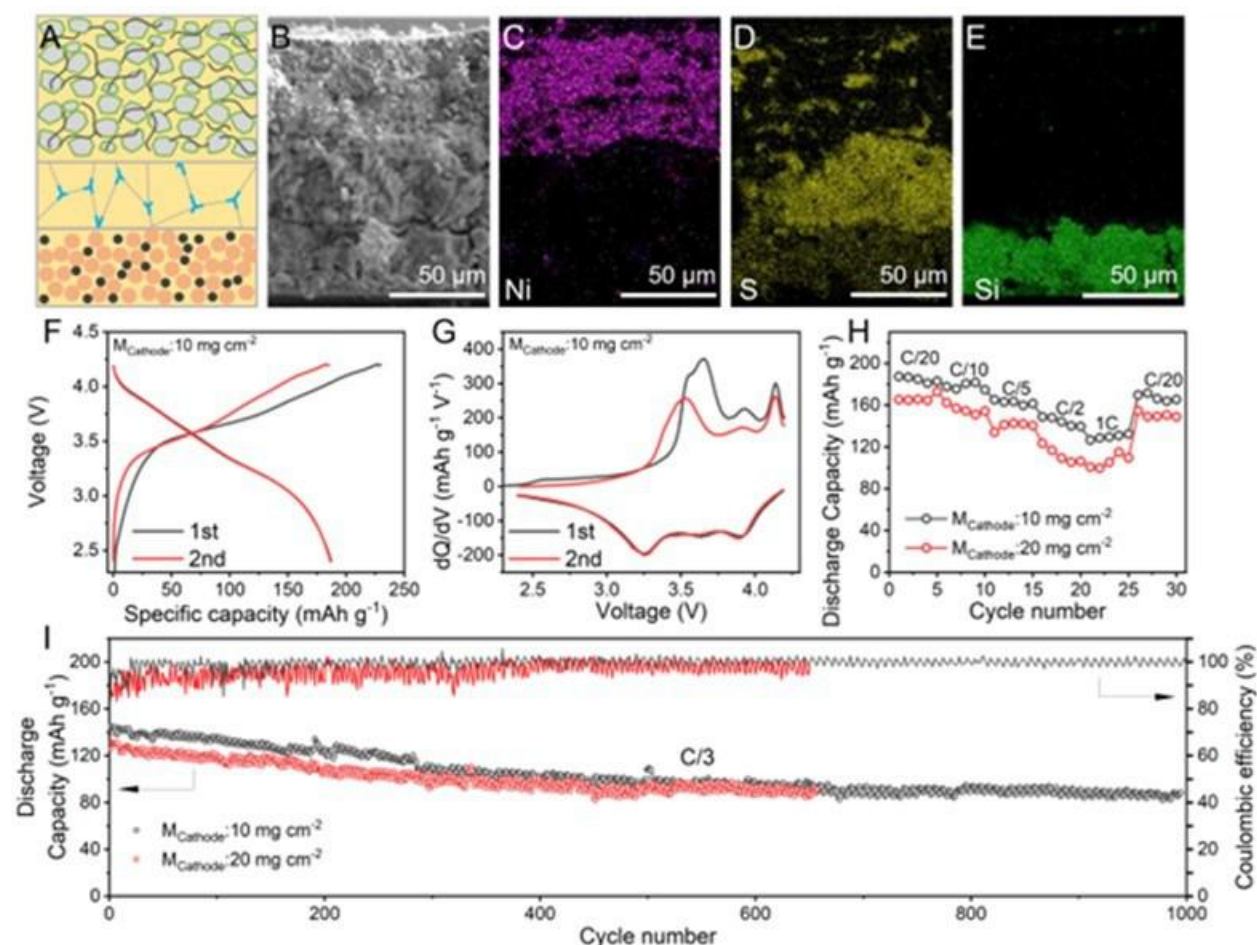


Figure VI.6.3 (A) Schematic of the full cell where a thin SE membrane is utilized. (B) SEM image of a cross-section of the full cell. EDX element mappings of (C) Ni, (D) S, and (E) Si in the cross section of the full cell. (F) The galvanostatic charge and discharge profile of the full cell with cathode mass loading of 10 mg cm^{-2} at first cycle at the rate of C/20, and (G) the corresponding dQ/dV profiles. (H) Rate performance and (I) long-term cycling performance of the full cell with cathode mass loadings of 10 and 20 mg cm^{-2} .

Lithium Dendrites and Cracks in Solid State Electrolyte

Lithium dendrites and cracks are the two main challenges for ASSB development. Working with University of North Carolina-Charlotte (UNCC), we studied these two issues using an electrochemical-mechanical model to directly couple dendrite growth and crack propagation from a physics-based perspective at the cell level [2]. The promising inorganic solid electrolyte LLZO is selected in this study. To generalize the model and describe crack propagation/dendrite growth from the cell level, the SE is modeled as a homogenized domain (Figure VI.6.4 left). Li metal and LiCoO_2 (LCO) are used as the anode and cathode, respectively. We designate the pre-defect at the Li/SE interface to represent the unavoidable interfacial defects, such as voids, impurities, and cracks (pre-defects in different dimensions cause similar crack propagation behavior).

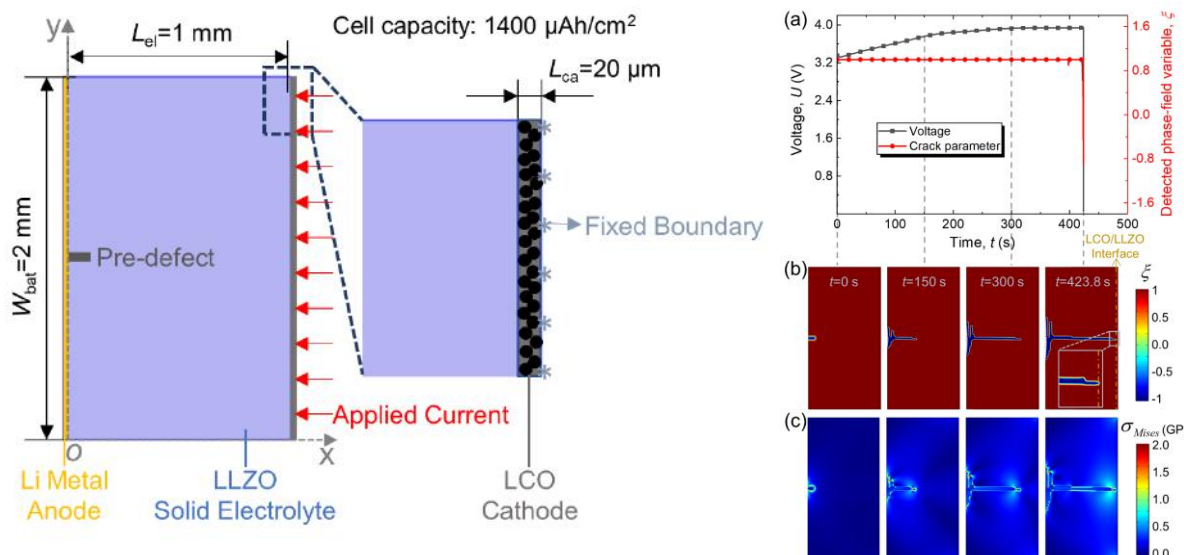


Figure VI.6.4 Schematics of the established model including geometry, boundary condition, and defect area (left), (a) voltage response and detected phase-field variable ξ at the LCO/LLZO interface at 1C charging rate; (b) dendrite ξ growth evolution ($\xi = 1$ for dendrite/crack, $\xi = 1$ for intact solid electrolyte); (c) von Mises stress evolution σ_{Mises} .

With the pre-existing defect and under a 1C charging rate, the Li dendrite grows around the defect from the beginning of charge until the short circuit. Figure VI.6.4 summarizes the dendrite growth process using the battery model, mechanical model, phase-field model, and short-circuit model. According to the battery model, the battery voltage increases during the charging process until 423.8 s, at which point the dendrite leads to the short circuit and the voltage drops (Figure VI.6.4a). The phase-field model solves the evolution of crack propagation and feeds the phase-field variable ξ ($\xi = 1$ for intact/no crack SE, $\xi = -1$ for crack/dendrite) to other models to affect the effective electrolyte conductivity in the battery model. The cracks initially become large in random directions, then transverse mainly in the direction from the anode side towards the cathode side (Figure VI.6.4b) (battery model to mechanical model). The cracks provide space for Li dendrite growth (mechanical model to phase-field model). In return, the Li dendrite affects the von Mises stress σ_{Mises} and crack propagation (phase-field model to mechanical model). The strong correlation between the mechanical model and the phase-field model leads to a similar von Mises stress and phase-field distribution within the SE, as shown in Figure VI.6.4c.

Novel Carbon Nano Structures (CNS)

CNS has been developed by Cabot Corp. It is well accepted that carbon nanotubes (CNT) can provide much better electronic conductivity due to its one-dimensional structure, which forms three-dimensional conductive networks in electrode. In addition to its superior conductivity, CNT can also improve the mechanical strength of battery electrodes, which is very critical to Si electrode to mitigate its volume expansion during cycling. The current challenge to apply CNT for battery is its high cost and uniform mixing.

CNS, a branched CNT from Cabot, was used as received. SEM image in Figure VI.6.5 (left) shows its nanotube morphology. 1% CNS was blended with Paraclete Si powder and LiPAA binder to make Si electrode. As shown in Figure VI.6.5 (middle), very uniform CNS distribution was obtained. In addition, nano size Si particles were observed to be embedded in 3-dimensional network. In order to investigate the effect of CNS, total three Si electrodes were prepared, including carbon black as baseline. In addition, we also studied the binder effort on Si electrode using polyimide (PI). The compositions of three electrodes are listed in Table VI.6.2. Electrochemical performance of all three electrodes is shown in Figure VI.6.5 (right). It can be seen from 3rd formation cycle that Si electrode with only 1% CNS has higher specific capacity compared to Si

electrode with 10% C45 using same LiPAA binder. Even higher specific capacity was obtained for Si electrode using 1% CNS and 20% PI binder, which can be attributed to the better binding capability of PI binder.

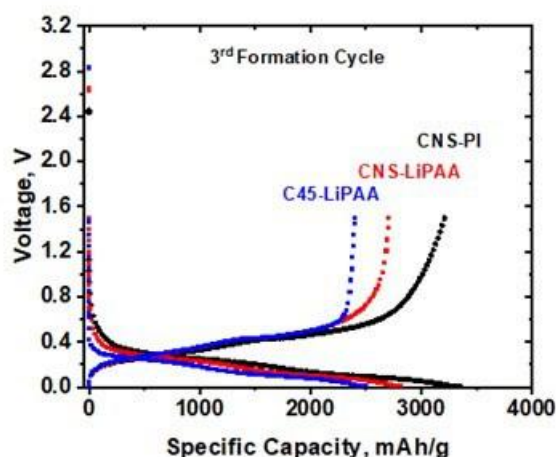


Figure VI.6.5 SEM images of CNS (left), Si electrodes with 1% CNS, and 10% LiPAA (middle) and electrochemical formation cycles of Si electrodes with carbon black, CNS, and polyimide (right).

Table VI.6.2 Si Electrodes Compositions

Si electrode composition	Si/C45/LiPAA	Si/CNS/LiPAA	Si/CNS/Polyimide
Ratio of each component	70/10/20	79/1/20	79/1/20

Conclusions

We continued the development of all solid-state batteries (ASSB) at the CAMP Facility, focusing on process development of electrolyte separator preparation, electrode making, and ASSB fabrication.

- We successfully fabricated the stand-alone polymer electrolyte film, which was tested in Li/LFP half-cell.
- Working with Northeastern University, we fabricated sulfide based ASSB and obtained good cycle life.
- Working with University of North Carolina-Charlotte, we established an electrochemical-mechanical model directly coupling dendrite growth and crack propagation from a physics-based perspective at the cell level.
- Carbon nanostructure (CNS) developed at Cabot was used as conductive additive. The CNS has potential to improve the electrochemical performance of Si electrode and energy density of lithium ion batteries.

Key Publications

1. High Performance and Scalable Sulfide-based All-solid-state Batteries Enabled by Electrochemo-Mechanically Stable Electrodes: Daxian Cao, Xiao Sun, Yejing Li, Alexander Anderson, Wenquan Lu, Hongli Zhu, Adv. Mater., 2022, 2200401
2. Unlocking the Electrochemical-Mechanical Coupling Behaviors of Dendrite Growth and Crack Propagation in All-Solid-State Batteries, Chunhao Yuan, Wenquan Lu, Jun Xu, Advanced Energy Materials. 2021, 2101807.
3. Approaching Theoretical Specific Capacity of Iron-Rich Lithium Iron Silicate Using Graphene-incorporation and Fluorine-doping, Tianwei Liu; Yadong Liu; Yikang Yu; Yang Ren; Chengjun Sun; Yuzi Liu; Jiayi Xu; Cong Liu; Zhenzhen Yang; Wenquan Lu; Paulo Ferreira; Zisheng Chao; Jian Xie, J. Mater. Chem. A, 2022, 10, 4006-4014.

4. Editorial for focus on nanophase materials for next-generation lithium-ion batteries and beyond, *Nanotechnology*, Xiangbo Meng, Zonghai Chen, Jianlin Li, Katharine L. Harrison, Wenquan Lu, and Xueliang (Andy) Sun, *Nanotechnology*, 33 (2022), 410201.
5. Electrode Prototyping Activities in ANL's Cell Analysis, Modeling and Prototyping (CAMP) Facility, Steve Trask, Andrew Jansen, Daniel Abraham, Shabbir Ahmed, Eva Allen, Pavan Badami, Caleb Calvary, Michael Caple, Kanchan Chavan, Zonghai Chen, Andrew Chuang, Abhas Deva, Alison Dunlop, James Gilbert, Hyun Woo Kim, Kevin Knehr, Joseph Kubal, Yejing Li, Chen Liao, Kewei Liu, Wenquan Lu, Mei Luo, John Okasinski, Saran Pidaparthi, Bryant Polzin, Andressa Prado, Yan Qin, Marco Rodrigues, Devashish Salpekar, Ilya Shkrob, Sanpei Zhang, 2022 DOE Vehicle Technology Office Annual Merit Review and Peer Evaluation Meeting, Washington D.C., 06/21/2022
6. Materials Benchmarking Activities For Cell Analysis, Modeling, and Prototyping (CAMP) Facility, Wenquan Lu, Hyun-Woo Kim, Yan Qin, Caleb Calvary, Yejing Li, Jae Jin Kim, Devashish Salpekar, Steve Trask, Alison Dunlop, Bryant Polzin, Chen Liao, and Andrew Jansen, 2022 DOE Vehicle Technology Office Annual Merit Review and Peer Evaluation Meeting, Washington D.C., 06/21/2022

Acknowledgements

Contributions from Hyun-Woo Kim, Yan Qin, Caleb Calvary, Yejing Li, Jae Jin Kim, Devashish Salpekar, Steve Trask, Alison Dunlop, Bryant Polzin, and Chen Liao are gratefully acknowledged. We would also like to acknowledge the contribution from Northeastern University and University of North Carolina-Charlotte. At last, we want to thank Cabot Corp. for providing the carbon nanostructure materials.

VI.7 Electrochemical Performance Testing (INL)

Lee Walker, Principal Investigator

Idaho National Laboratory

2525 Fremont Ave

Idaho Falls, ID 83402

E-mail: lee.walker@inl.gov

Haiyan Croft, DOE Technology Development Manager

U.S. Department of Energy

E-mail: Haiyan.Croft@ee.doe.gov

Start Date: October 1, 2021

End Date: September 30, 2022

Project Funding (FY22): \$3,200,000

DOE share: \$3,200,000

Non-DOE share: \$0

Project Introduction

The advancement of battery technologies that can meet the emerging demands for vehicle electrification requires in-depth understanding of the performance of early-stage pre-commercial batteries, state-of-the-art commercial cells and the ability to adapt evaluation methods as mobility needs change. The Battery Test Center (BTC) at Idaho National Laboratory (INL) has been supporting the evolution of electrified transportation through high-quality, independent testing of electrical energy storage systems for more than 30 years. Independent testing provides data for quantitative assessment of the fundamental technology gaps that exist in early-stage battery development. Test methods and techniques are continuously improved to offer data on relevant metrics as vehicle applications evolve and as new core gaps are identified. Advancing electrified powertrain transportation including understanding both high-energy battery chemistries and high power, extreme fast charging needs, is a top priority in advancing how people and goods are transported in the United States. As a designated core capability and lead test facility for the Vehicle Technologies Office (VTO), the BTC at INL directly supports the US Advanced Battery Consortium (USABC) and other VTO programs by providing discrete information on failure modes, mechanisms, and shortfalls in emerging technologies. Gaps in performance relative to targets are used as a metric to guide future R&D priorities.

The development and deployment of batteries in new, diverse applications requires both that the batteries function in the necessary environment as well as a deep understanding of their performance, life and expected failure mechanisms. In the past the primary means to advance knowledge on performance and life was to test batteries for extended periods of time under a range of different scenarios. Testing of batteries in this manner can take upwards of a year to make reasonable estimations of life and to clearly identify failure modes and rates. The need to shorten the design and testing cycle is critical to bringing new battery chemistries and cell designs into emerging applications such as in stationary energy storage to support electric vehicle charging stations capable of extreme fast charging.

Objectives

The activities at the INL BTC are focused on providing high fidelity, science-based performance and life testing, analysis, modeling, and reporting. To ensure the alignment with future industry and government needs, it is a key objective to update test and analysis procedures as new concepts and design space become achievable. Refined procedures help identify promising future research paths and identify key fundamental gaps that need to be addressed.

Approach

With 20,000 square feet of laboratory space, the INL BTC is equipped with over 800 test channels for advanced energy storage testing at the cell-level (e.g., up to 7V, 300A), module-level (e.g., up to 65V, 1200A), and pack-level (e.g., 500-1000V, 500A). Test equipment is programmed to perform distinct test profiles while

simultaneously monitoring for compliance with operating limits such as voltage, current and temperature. The output from such tests enables principles-based analysis to be performed that can aid in identification of key technology gaps.

To ensure high quality, repeatable and dependable data is used for analysis, batteries and other energy storage devices are typically subjected to specific test sequences while housed inside precision thermal chambers. To enhance performance testing across a wide range of thermal conditions, driven by automotive usage scenarios, the thermal chambers can be operated across a broad temperature range (e.g., -70°C to 200°C). This temperature range enables key information to be extracted by modifying the chemical kinetic degradation rates within the evaluated items and enables accelerated aging analysis.

Successful performance testing and accurate life modeling are highly dependent on the fidelity of the acquired test data. The INL BTC has developed advanced calibration verification and uncertainty analysis methodologies to ensure that voltage, current, and temperature measurements are within the tolerance specified by the test equipment manufacturer (e.g., 0.02% of the full scale). These measured test parameters are subsequently used in various mathematical combinations to determine performance capability (e.g., resistance, energy, power, etc.). INL has also quantified the error associated with these derived parameters using the accuracy and precision of the relevant measured parameter (e.g., voltage) to ensure high-quality and repeatable results and meaningful presentation.

The INL BTC is also equipped with facilities that enable the characterization of batteries in aggressive use cases. One such use case is vibration that mimics what would be seen over the life of a battery in a typical automotive setting. Analysis of vibration on batteries at INL utilizes a high-capacity vibration table to perform non-destructive tests to understand reliability and safety of new cell topologies to mechanical vibration and shock. Emerging cell designs that vary from current state of the art cell designs are the focus of mechanical vibration and shock testing at INL.

Adjacent to the vibration table are two fire-rated isolation rooms that can be used for tests that push the known limits of battery operation. These aggressive use cases include extreme fast charging, subtle over- or under-charging, high-temperature thermal characterization for under-hood systems, among many others. The isolation rooms allow for safe testing of emerging cell technologies at or near the design limits and help characterize future use cases. The rooms also enable identification of key changes in performance fade that may emerge in aggressive use cases that can directly inform future rounds of early-stage material and cell development activities. These complimentary non-destructive evaluation capabilities comprise INL's Non-Destructive Battery Evaluation Laboratory.

Results

The INL BTC continues to test articles of various sizes and configurations using standardized test protocols developed by INL with industry partnerships for different electric drive vehicle application. Table VI.7.1, Table VI.7.2, and Table VI.7.3 summarize the testing activities under the USABC, Benchmarking programs and Low Cobalt FOA, respectively, for FY-22. Technologies developed through USABC contracts are aged and tested against the appropriate application target (HP-EV, LC/FC-EV, HEV, PHEV, 12V S/S, 48V HEV) and, where applicable, they are compared to previous generations of test articles from the same developer. 362 articles were tested for USABC in FY-22, including 2 modules and 360 cells. The purpose of the Benchmark program is to evaluate device technologies that are of interest to VTO but are not deliverables developed under a contract. In some cases, Benchmark devices are used to validate newly developed test procedures and analysis methodologies. Benchmark activities also are used to understand which gaps need to be fundamentally addressed to improve cell performance. 28 cells were tested for the Benchmark program in FY-22. A new testing program was started in FY-20 to evaluate deliverables from the VTO Low Cobalt FOA programs. Testing of the first round of deliverable cells was continued into FY-22, end of program deliverables were started in FY22 and are expected to continue into FY23. The purpose of the program is to find Li-Ion battery chemistries that have little to no cobalt content. 84 cells were tested for the Low Cobalt program in FY-22.

Analysis was performed for all articles tested, and results were presented regularly at quarterly review meetings and USABC Technical Advisory Committee (TAC) meetings to USABC representatives from different automotive manufacturers, DOE VTO representatives, developers, and national laboratory staff. INL worked with the USABC test methods committee to develop the methodology and update the manual for testing EV batteries.

Table VI.7.1 Articles Tested for USABC

Developer	Application	System	Number of Articles Tested	Status at Year End
Farasis	LC/FC-EV	Cell	12	Completed
Applied Materials	HP-EV	Cell	25	Ongoing
Benchmark	LC/FC-EV	Cell	30	Ongoing
Enpower	LC/FC-EV	Cell	24	Ongoing
Farasis	HP-EV	Cell	15	Ongoing
Farasis	Recycle	Cell	12	Ongoing
Farasis	Recycle	Cell	12	Ongoing
Farasis	Recycle	Cell	12	Ongoing
Gotion	HP-EV	Cell	17	Ongoing
Microvast	LC/FC-EV	Cell	24	Ongoing
Microvast	LC/FC-EV	Cell	21	Ongoing
Microvast	HP-EV	Cell	36	Ongoing
Microvast	HP-EV	Module	2	Ongoing
Nanoramic	HP-EV	Cell	18	Ongoing
Saft	HEV	Cell	13	Ongoing
Zenlabs	LC/FC-EV	Cell	23	Ongoing
Zenlabs	LC/FC-EV	Cell	27	Ongoing
Zenlabs	LC/FC-EV	Cell	28	Ongoing
Zenlabs	LC/FC-EV	Cell	5	Ongoing
Zenlabs	LC/FC-EV	Cell	6	Ongoing

Table VI.7.2 Articles Tested for Benchmark

Developer	Application	System	Number of Articles Tested	Status at Year End
Applied Materials	EV	Cell	4	Ongoing
Daikin	EV	Cell	24	Ongoing

Table VI.7.3 Articles Tested for Low Cobalt

Developer	Application	System	Number of Articles Tested	Status at Year End
Cabot	Low Cobalt	Cell	12	Completed
Nextech-Nexceris	Low Cobalt	Cell	12	Completed
ORNL	Low Cobalt	Cell	12	Completed
UT – Austin	Low Cobalt	Cell	12	Completed
Penn State	Low Cobalt	Cell	12	Ongoing
Penn State	Low Cobalt	Cell	12	Ongoing
UC - Irvine	Low Cobalt	Cell	12	Ongoing

Collaborative work continued in FY-22 between the 21st Century Truck Partnership (21CTP) and INL. This work has focused on developing battery specifications for commercial trucks with electric drives. Targets were finalized for class-8 line-haul battery electric trucks, class-6 battery electric box truck, and class-4 battery electric step vans. 21CTP consists of OEM companies across the commercial vehicle market, DOE-VTO, and National Labs.

Conclusions

The ability to perform discrete performance and life evaluation of emerging technologies in an independent, reliable manner is a direct aid to the identification of key technology gaps. Over the course of FY-22, the INL BTC was able to directly support many different endeavors within VTO with a keen focus on advancing battery technologies for emerging trends in electrified transportation. As a core capability in performance and life analysis for VTO, INL has identified key performance fade modes that exist in cells and has advanced the understanding of performance and evaluation protocols for multiple programs funded by VTO and USABC. A total of 474 devices were tested in FY-22. The work also continues to develop the update of the USABC EV test manual and the submission/acceptance of 2 peer reviewed manuscripts. In FY-23, INL plans to continue this level of support for multiple programs with broad support for the USABC and Benchmark programs. INL will also continue developing and refining standard test protocols and analysis procedures in collaboration with USABC and on providing information on core fundamental performance gaps that need to be addressed across VTO programs. Also, in FY-23, INL will continue to work with the 21st Century Truck Partnership to build battery targets for next generation electric commercial vehicles and publication of their electrification roadmap for commercial vehicles.

Acknowledgements

The following staff at INL supported this work Matthew Shirk, Tanvir Tanim, Sergiy Sazhin, Eric Dufek, Randy Bewley, Charles Dickerson, Chinh Ho, Jordan Todd, Kevin Meudt, Michael Evans.

VI.8 Machine Learning for Accelerated Life Prediction and Cell Design (INL, NREL)

Eric Dufek, Principal Investigator

Idaho National Laboratory
2525 Fremont Ave
Idaho Falls, ID 83415
E-mail: eric.dufek@inl.gov

Kandler Smith, Co-Principal Investigator

National Renewable Energy Laboratory
15013 Denver West Pkwy
Golden, CO 80401
E-mail: kandler.smith@nrel.gov

Simon Thompson, DOE Technology Development Manager

U.S. Department of Energy
E-mail: Simon.Thompson@ee.doe.gov

Start Date: October 1, 2019

End Date: September 30, 2024

Project Funding (FY22): \$1,250,000

DOE share: \$1,250,000

Non-DOE share: \$0

Project Introduction

The development and deployment of batteries in new, diverse applications requires both that the batteries function in the necessary environment as well as a deep understanding of their performance, life and expected failure mechanisms. In the past the primary means to advance knowledge on performance and life was to test batteries for extended periods of time under a range of different scenarios. Testing of batteries in this manner can take upwards of a year to make reasonable estimations of life and to clearly identify failure modes and rates. The need to shorten the design and testing cycle is critical to bringing new battery chemistries and cell designs into emerging applications such as in stationary energy storage to support electric vehicle charging stations capable of extreme fast charging and the use of batteries in an assortment of different emerging areas of mobility. Connection of physics-based life models and machine learning (ML) provides the opportunity to enable more robust assessment of battery aging, failure mechanism identification and understanding as new use case scenarios are proposed. The current project is focused on means to apply ML to enhance the estimation of life while also identifying key failure pathways, building knowledge and algorithms transferrable to future designs and chemistries. During the first portion of the project existing data sets will be used for both training and validation of ML approaches to better characterize expected battery life. The work also looks to link ML with existing physics-based life models at INL and NREL.

Work in this project is focused on clearly aligning physics-based models with experimental data, synthetic data as generated from different electrochemical models and advanced data analysis methods. As a combined set of efforts, it is envisioned that the time needed for validation of both performance and key failure modes will be significantly reduced. The project also aims to develop tools that will help in the design space to more quickly align different materials and design considerations with application-specific needs. The combined set of tools are targeting a robust experimental-modeling-analysis framework which will provide more discrete information to stakeholders and battery developers to enable technology innovation with rapid turn-around.

Key contributions from this work during FY22 included the ability to expand deep learning and synthetic data generation tools to new chemistries, implementation of a protected battery datahub and a comparison of different life and failure mode prediction methods. The team also expanded synthetic data generation to

include the use of high-fidelity synthetic data which can inform on the condition of a battery on a cycle-by-cycle basis.

Objectives

Key objectives during FY22 were aligned with expanded development of the tool architecture, demonstration of the ability to not just predict and validate performance at a fixed point in aging, but also the prediction of failure mode and failure mode extent and initiating the creation of a centralized datahub. These outcomes and objectives were achieved through the direct linkage of physics-based life models with electrochemical models and targeted experimental characterization. The use of statistical, machine learning and deep learning methods complemented the other activities.

Approach

To achieve the project objectives the team has taken an approach that blends the use of physical data acquisition, synthetic data generation using electrochemical models and battery life models. The bulk of activities focused on the use of single layer pouch cells with a graphite/NMC532 or a graphite/NMC811 chemistry that had undergone different types of fast-charging characterization. Additional analysis on LTO/LMO cells was performed. Cells were characterized across different rates with post-test analysis for targeted confirmation of failure modes and extent of failure modes. Synthetic data was generated using a combination of incremental capacity (IC) models and electrochemical models based on a pseudo-2D (p2D) framework. Both sets of models incorporate key elements of the cell design including chemistry and electrode details and also aspects of failure modes including loss of lithium inventory (LLI), loss of active materials at the positive (LAM_{PE}) and negative (LAM_{NE}) electrodes. The p2D model further included changes in transport and kinetic properties with aging for diagnosis of high-rate data.

Advanced analysis used a combination of techniques including a suite of machine and deep learning frameworks, algebraic life models and targeted data extraction were used to analyze critical data for predictions. To maintain the link with physicality, analysis focused on using key electrochemical and environmental data points that inform both on how and why a cell is performing in a specific manner. For more complete details on each of the different tools used please refer to citations (Chen et al., 2021; Gasper et al., 2021; Kim et al., 2022; Kunz et al., 2021).

Results

During FY22 and in previous years several efforts have been underway to predict life and also develop rapid methods which can classify and quantify failure modes. These efforts are seen as being critical for advancing the validation of new technologies or to implement existing batteries into new applications. Critical to the work has been the advancement of methods to better understand loss of lithium inventory (LLI) and loss of active material (LAM). One specific set of tools used during FY22 was a combined approach to evaluate the efficacy of different methods to predict both life and failure mode for cells used in different uses and with different cell designs. This effort used a combination of sigmoidal rate expressions (SREs), synthetic data generation and different machine learning (ML) or deep learning (DL) techniques. As shown in Figure VI.8.1 the combined methods are effective at predicting capacity for different use cases (in this case different fast charge protocols) and across different cell designs and builds. The methods also effectively classified LLI with both capacity and LLI predictions having error of less than 2% absolute error with overall error typically below 3%. For each of the methods predictions were performed using less than three weeks of data. (Kim et al, 2022).

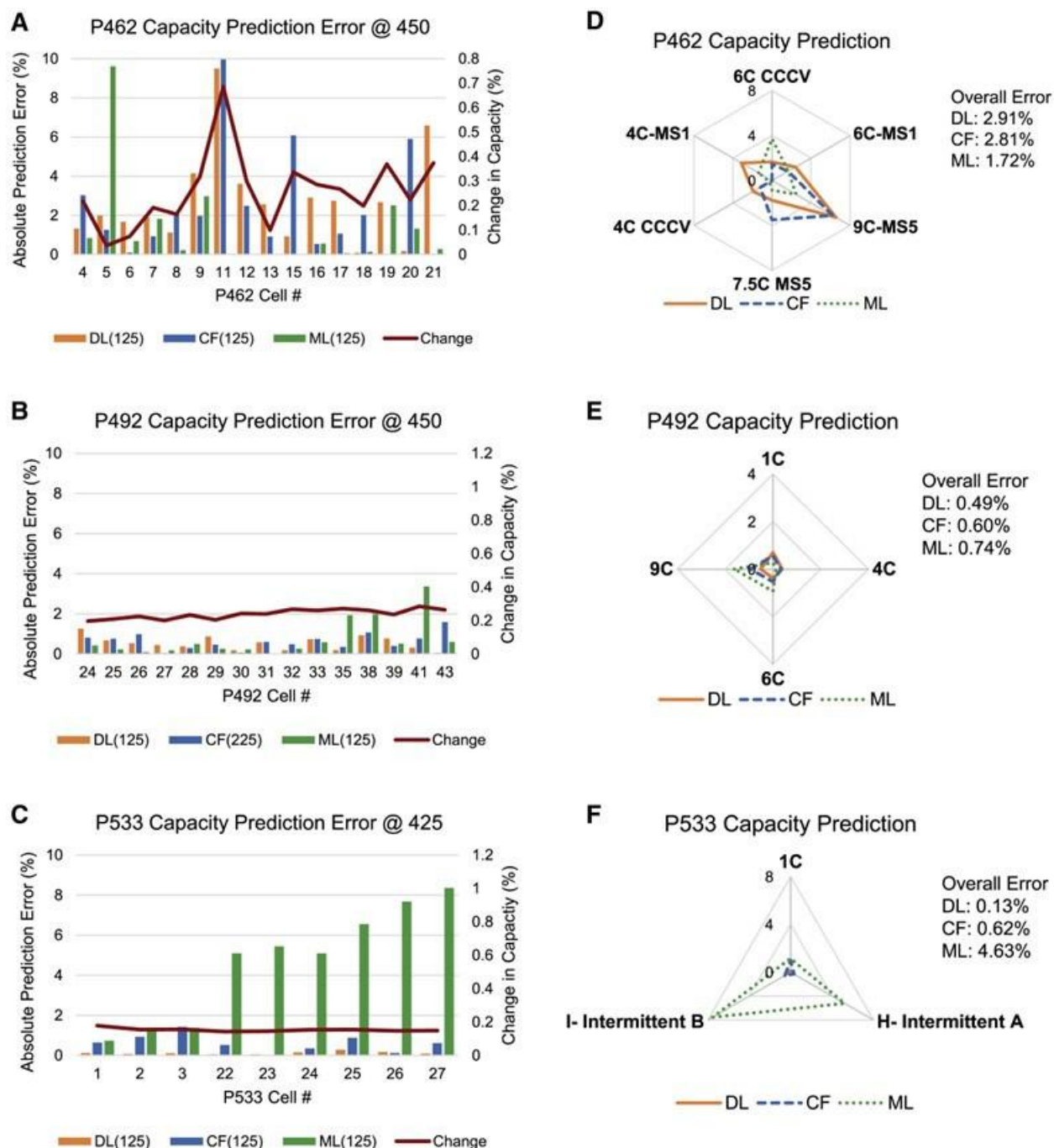


Figure VI.8.1 Comparison of prediction capability using three different methods for three different battery packs. The combined analysis was across 2 cathode chemistries, 2 different cell designs and multiple charge protocols. Predictions were made using either 125 or 225 cycles (Kim et al., 2022).

Building on classification the team next focused on quantifying both performance predictions and failure modes. This required a slight shift in approach due to the sparse experimental data. To account for this limitation the team utilized an incremental capacity (IC) model which was used to generate extensive synthetic data sets (26,000). Using these and a deep learning approach it was possible to quantify failure mode (LLI and LAM) and predict capacity fade across several different conditions and use cases (Figure VI.8.1). This use of synthetic data significantly reduced the number of experimental resources needed and allowed both

rapid prediction and quantification of failure modes (Kim et al., 2021). Extensions of this work were able to additionally predict and quantify failure mode at 400+ cycles using as little as 100 cycles.

The DL methods and synthetic data generation using incremental capacity (IC) models was also significantly expanded in FY22. During FY21 early work had generated data for a single graphite/NMC chemistry (Kim et al, 2021). This type of analysis uses models to generate more than 20,000 data sets which can be used to aid in the classification of failure modes using limited data. In addition to classification the tool can be used to predict and quantify failure using limited numbers of experimental reference performance tests (RPTs). An example of the expansion to other chemistries is included in Figure VI.8.2 where synthetic and experimental data for two different graphite/NMC cell types are shown in addition to LTO/LMO. Of distinct interest for the NMC811 and LTO/LMO data sets is that the DL methods were able to identify different aging pathways and groupings of cells based either on electrolyte content or variation in use case. The expansion to new battery active materials was to ensure continued support for DOE's Behind the meter storage (BTMS) and eXtreme Fast Charge and Cell Evaluation of Li-ion Batteries (XCEL) projects.

Different Battery Chemistries

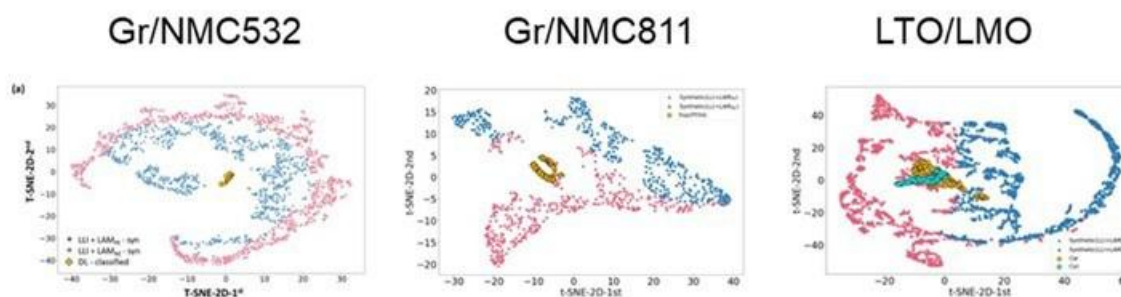


Figure VI.8.2 Examples synthetic data used for deep learning models for classification and quantification of aging mode. Three different sets of chemistries and multiple cell designs have been considered using this tool over the last 2 years (Kim et al., 2022).

The IC-based tools are useful for tracking LLI and LAM, however this quasi-thermodynamic analysis can only be applied to low-rate capacity data ($\sim C/20$) that is infrequently measured such as the data acquired during RPTs. The requirement for low-rate data necessitates that other methods which can apply to higher rate cycling or to cycle-by-cycle conditions be developed. To address this need in FY22 pseudo 2-dimensional (p2D) battery models were modified and used to generate synthetic data. Expanding on work in late FY21, the p2D model incorporated five aging parameters identified from experiments: LAM_{PE} , LLI , $\tau_{DS\ PE}$, R_{ct} , and R_{Ω} . LAM_{PE} and LLI were obtained from afore-mentioned incremental capacity analysis. Changes in positive electrode diffusivity, attributed to NMC particle fracture, were obtained by fitting an exponential-relaxation model—with time constant $\tau_{DS\ PE}$ —to cycle-by-cycle end-of-discharge voltage (EODV) data. Charge-transfer and ohmic resistance changes, respectively ΔR_{ct} , and ΔR_{Ω} , were obtained from EIS measurements. The resulting p2D model compares favorably to voltage response and relaxation for all charge/discharge aging cycles throughout life as validated using experimental data.

The high-fidelity (HF) synthetic data can show dramatic impacts at different charge and discharge rates and can predict the voltage response after a charge or discharge when the cell is sitting at rest. This information is critical to have as it can be incorporated into different analysis methods including the decision tree frameworks developed in FY21 to classify LLI from SEI growth or Li plating. (See Figure VI.8.3.)

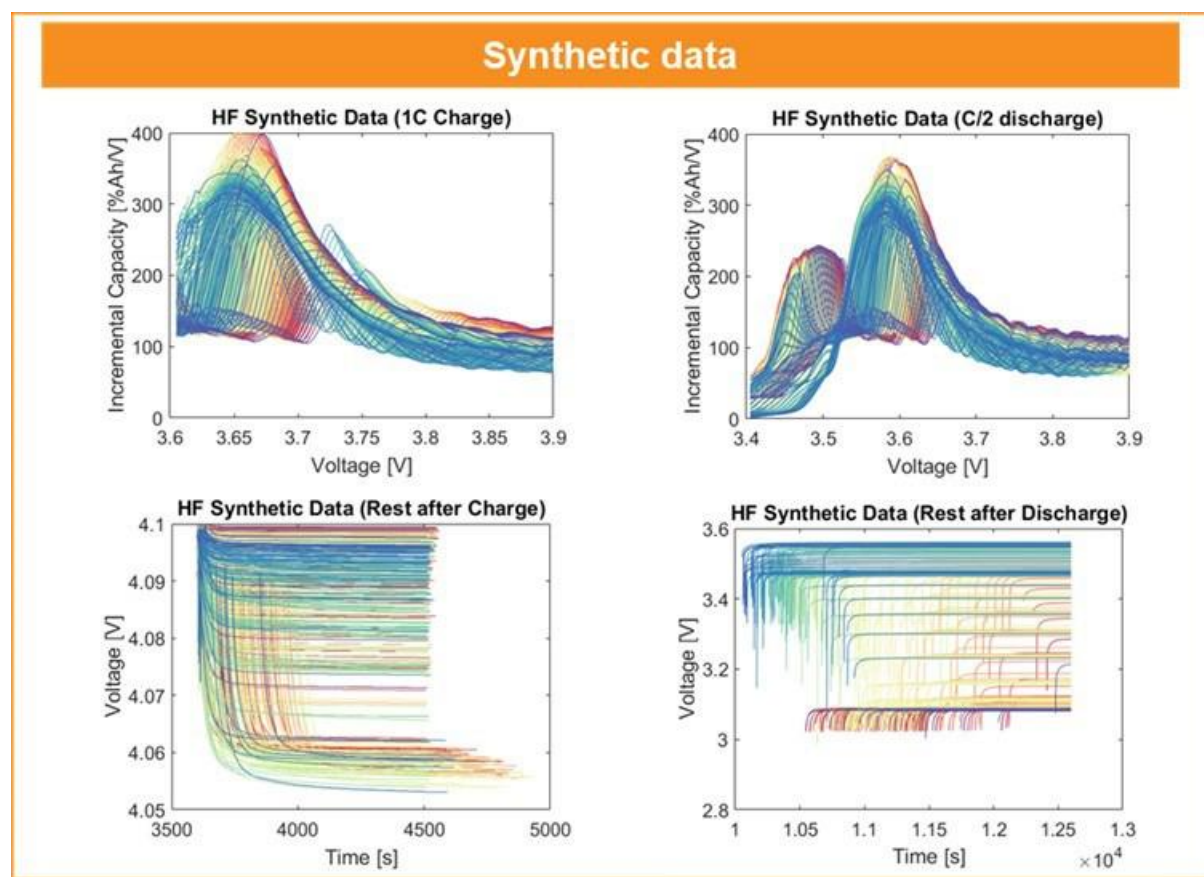


Figure VI.8.3 Example HF synthetic data for different charge and discharge rates as well as for the voltage response after a charge or discharge event. The information from the HF synthetic data can be used in several tools developed over the course of the project.

In FY22, the team continued to support development of predictive battery lifetime models and their integration into technoeconomic tools. These reduced-order models forecast battery capacity/power fade for arbitrary environments and charge/discharge use profiles. (See Figure VI.8.4.)

- Using the team's LFP, NMC, and LTO models, the BTMS-program simulated stationary battery lifetimes when employed at corner electric-vehicle fast-charging stations to minimize electric-utility demand charges for commercial facilities in several geographic markets (Guittet et al., 2022).
- Simplified versions of lifetime models were integrated into the [ReOpt](#) open-source energy planning platform, a mixed-integer linear program that optimizes renewable energy system component sizes and dispatch at microgrid sites.
- A publication documented extension of the AI-Batt lifetime model identification toolset to capture cycling fade in a commercial graphite/LFP battery and quantified lifetime uncertainty for several simulated use scenarios (Gasper et al., 2022).
- Based on IC analysis of LTO/LMO aging data, the team developed reduced-order models tracking physical degradation mechanisms LAM and LLI. The resulting model predicts open-circuit potential and capacity changes for the LTO battery for any arbitrary aging condition. Future work will add resistance/polarization growth mechanisms to produce a performance-predictive aging model capable of reproducing current/voltage response throughout lifetime, including accelerated capacity fade caused by “knee” effects such as shifting electrode stoichiometries and resistance growth.

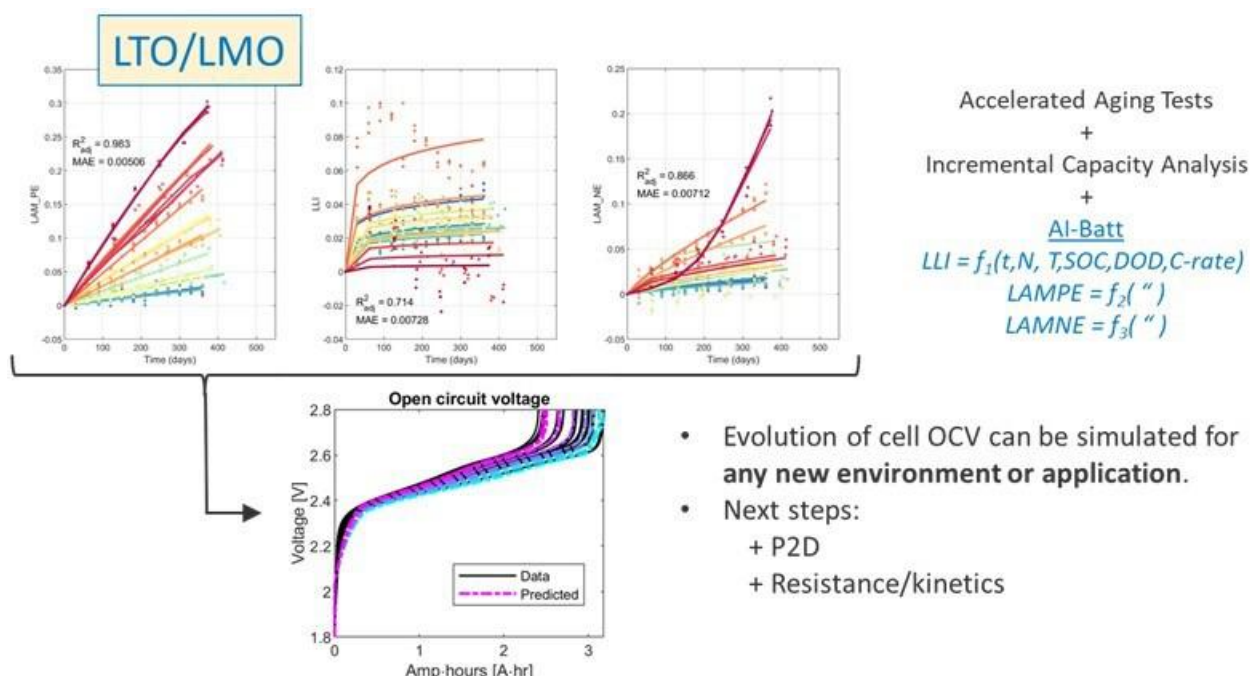


Figure VI.8.4 Reduced-order predictive models fit to IC analysis of data produces a model that reproduces low-rate open-circuit voltage (OCV) for any arbitrary aging scenario

Enhancing the types of experimental data available to researchers for tool development has and will continue to be a focal point for research within this project. In FY22 there were several efforts to expand knowledge to the entire community on data tools. Several members of the team from both NREL and INL participated in a training course put on by the Materials Research Society (MRS) in the spring of 2022. The team also contributed to other efforts including a commentary on how to appropriately structure calendar life data to better enable machine learning tools (Dufek et al, 2022). The importance of considering data structuring was critical as the team further refined the vision for a research-focused data hub which has flexible access and ability to protect information across projects. Team members collaborated with an international team to outline approaches and standards for data sharing, define challenge problems, and create a roadmap for further collaboration on open-data and AI tools that can accelerate battery research, development, and deployment (Ward et al., 2022). (See Figure VI.8.5.)

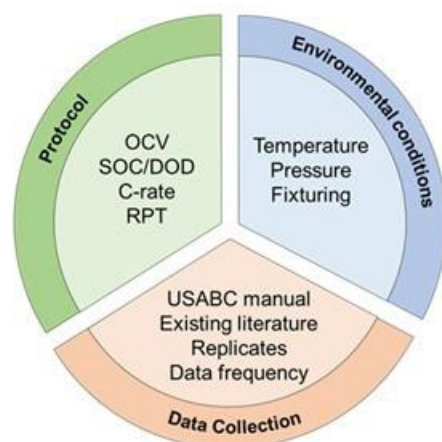


Figure VI.8.5 A combination of the aspects which researchers need to consider when developing a calendar or cycle life testing regime (Dufek, 2022).

Building on early activity in FY21 the team was able to create a pre-production data hub capable of hosting DOE battery R&D data and enabling sharing of datasets amongst DOE researchers and, for selected published datasets, the general public. The datahub leverages existing and approved infrastructure currently utilized throughout other DOE Energy Materials Network (EMN) and non-EMN data hubs. Importantly, the hub supports secure authentication and access mechanisms for users which will protect project-specific information and allow users to use tools developed as part of this project. In FY23 some of these tools will be incorporated into the data hub at <https://batterydata.energy.gov> and portions of the datahub will be accessible to an identified group of individuals beyond the contributors to this project.

Conclusions

Leveraging methods developed earlier in this project the ability to make performance, failure mode and life predictions using significantly less data has been demonstrated. Multiple methods have shown the ability to predict both performance and failure modes using limited data. Each of the methods demonstrated the ability to predict error to less than 3% across different cell chemistries and for different charge protocols. This is critical in adapting different ML techniques for emerging use cases.

The team also expanded capability for synthetic data generation focusing both on high-fidelity synthetic data which opens opportunities for cycle-by-cycle analysis and expanding the use of IC-based tools for RPT-based analysis with new cell chemistries. The combination of these two advances positions the team to look at emerging chemistries and cell designs and to consider how to more rapidly move through performance validation and influence cell design.

The datahub at [Batterydata.energy.gov](https://batterydata.energy.gov) was prepared for internal use and should be in full production during fiscal year 2023.

Key Publications

1. Kim, S., Yi, Z., Kunz M.R., Dufek, E.J., Tanim, T.R., Chen, B.R., Gering, K.L. (2022) Accelerated battery life predictions through synergistic combination of physics-based models and machine learning. *Cell Reports Physical Science*, 3(9). <https://doi.org/10.1016/j.xcrp.2022.101023>
2. Dufek, E.J., Tanim, T.R., Chen B.R., Kim, S. (2022) Battery Calendar aging and machine learning. *Joule*, 6(7). <https://doi.org/10.1016/j.joule.2022.06.007>
3. Kim, S., Yi, Z., Chen, B.R., Tanim, T.R., Dufek, E.J. (2022) Rapid failure mode classification and quantification in batteries: A deep learning modeling framework. *Energy Storage Materials*, 45, <https://doi.org/10.1016/j.ensm.2021.07.016>

4. P. Gasper, N. Collath, H.C. Hesse, A. Jossen, K. Smith, “Machine-learning assisted identification of accurate battery lifetime models with uncertainty,” *J. Electrochem. Society* 169 (2022) 080518. <https://doi.org/10.1149/1945-7111/ac86a8>
5. L. Ward, S. Babinec, E.J. Dufek, D.A. Howey, V. Viswanathan, M. Aykol, D.A.C. Beck, B. Blaiszik, B.-R. Chen, G. Crabtree, S. Clark, V. de Angelis, P. Dechent, M. Dubarry, E.E. Eggleton, D.P. Finegan, I. Foster, C. Gopal, P. Herring, V.W. Hu, N.H. Paulson, Y. Preger, D.U. Sauer, K. Smith, S. Snyder, S. Sripad, T.R. Tanim, L. Tao, “Principles of the Battery Data Genome,” *Joule* 6 (2022) 2253.

References

1. Kim, S., Yi, Z., Kunz M.R., Dufek, E.J., Tanim, T.R., Chen, B.R., Gering, K.L. (2022) Accelerated battery life predictions through synergistic combination of physics-based models and machine learning. *Cell Reports Physical Science*, 3(9). <https://doi.org/10.1016/j.xcrp.2022.101023>
2. Dufek, E.J., Tanim, T.R., Chen B.R., Kim, S. (2022) Battery Calendar aging and machine learning. *Joule*, 6(7). <https://doi.org/10.1016/j.joule.2022.06.007>
3. Kim, S., Yi, Z., Chen, B.R., Tanim, T.R., Dufek, E.J. (2022) Rapid failure mode classification and quantification in batteries: A deep learning modeling framework. *Energy Storage Materials*, 45, <https://doi.org/10.1016/j.ensm.2021.07.016>
4. Chen, B. R., Kunz, M. R., Tanim, T. R., & Dufek, E. J. (2021). A machine learning framework for early detection of lithium plating combining multiple physics-based electrochemical signatures. *Cell Reports Physical Science*, 2(3). <https://doi.org/10.1016/j.xcrp.2021.100352>
5. Gasper, P., Gering, K., Dufek, E., & Smith, K. (2021). Challenging Practices of Algebraic Battery Life Models through Statistical Validation and Model Identification via Machine-Learning. *Journal of the Electrochemical Society*, 168(2). <https://doi.org/10.1149/1945-7111/abddel>
6. D. Guittet, M. Mitchel, M. Gilleran, E. Bonnema, P. Gasper, M. Shirk, K. Smith, P. Mishra, M. Mann, A. Burrell, “Levelized Cost of Charging for Extreme Fast Charging with Stationary LMO/LTO Batteries,” *submitted*.

Acknowledgements

The activities described were a collaborative effort utilizing the capabilities of many researchers. Key contributors across the different national laboratories include Bor-Rong Chen, Parameswara R. Chinnam, Andrew M. Colclasure, Paul Gasper, Kevin L. Gering, Rachel Hurst, Ross Kunz, Sangwook Kim, Tanvir R. Tanim, Cody Walker, Malik Hassanaly, Peter Weddle and Zonggen Yi. This work was also aided by collaboration with the XCEL and BTMS programs run by Venkat Srinivasan and Anthony Burrell.

VII Small Business Innovation Research (SBIR)

Simon Thompson, DOE Technology Development Manager

U.S. Department of Energy

E-mail: Simon.Thompson@ee.doe.gov

Project Introduction

The Batteries R&D program at the Vehicle Technologies Office supports small businesses through the Small Business Innovation Research (SBIR) and Small Business Technology Transfer (STTR) programs. Both were established by law and are administered (for all of DOE) by the Small Business Administration Research (SBIR) office within the DOE Office of Science. Grants under these programs are funded by set-aside resources from all Extramural R&D budgets; 3.0% of these budgets are allocated for SBIR programs while 0.45% for STTR grants. Grants under these programs are awarded in two phases: a 6-9 month Phase I with a maximum award of \$200,000 and a 2 year Phase II with a maximum award of \$1.1M. Both Phase I and Phase II awards are made through a competitive solicitation and review process.

Objectives

Use resources available through the Small Business Innovation Research (SBIR) and Small Business Technology Transfer (STTR) programs to conduct research and development of benefit to the advanced batteries program within the Vehicle Technologies Office.

Approach

The advanced batteries team participates in this process by writing a topic which is released as part of the general DOE solicitation. Starting in FY12, the advanced batteries team decided to broaden its applicant pool by removing specific subtopics and allowing businesses to apply if their technology could help advance the state of the art by improving specific electric drive vehicle platform goals developed by the DOE with close collaboration with the United States Advanced Battery Consortium.

Results

Phase II Awards Made in FY 2022

Under the SBIR/STTR process, companies with Phase I awards made in FY 2021 were eligible to apply for a Phase II award in FY 2022. The following three Phase II grants were awarded:

Real-time Electromagnetic Characterization of Thermal Runaway Conditions in Li-ion Modules (Parthian Energy LLC, Pasadena, CA)

A real-time module screening detection technology to reduce increase safety and reduce cost Parthian Energy is developing a rapid battery diagnosis product, PES, which can detect internal short circuits in a few minutes, either during manufacturing or during use.

Domestic Halloysite-Derived Silicon as a Low-Cost High-Performance Anode Material for Li-Ion Batteries (Applied Minerals Inc, Eureka, UT)

To enable the widespread adoption of electric vehicles, the cost of lithium-ion battery electrode materials must be reduced. This project will enable commercial production of high-performance, low-cost battery electrode material through an innovative process derived from a unique domestic mineral resource found in Utah. The technology provides a large cost savings on the production of silicon anode material compared to current methods for lithium-based batteries providing enhanced range in the transportation sector.

Optimizing the Silicon anode interfacial stability to achieve high energy, fast charge Li-ion EV batteries at scale (Graphenix Development Inc, Rochester, NY)

Graphenix Development Inc (GDI) is developing coatings and optimizing battery electrolyte composition to protect the surface of a 100% Si anode, which offers very high energy density while avoiding issues of Si-graphite composite anodes. Their technology also aims to reduce the pressure required for optimal performance in order to meet limitations set by electric vehicle producing companies.

Phase I Awards Made in FY 2022

Six Phase I grants were awarded in the summer of FY 2022.

Next Generation of High Energy Density Batteries at Low Cost (NanoHydroChem, LLC, Amherst, NY)

This project led by NanoHydroChem, LLC advances the state of the art in less-expensive, longer-range lithium-based batteries for transportation based on validation and scale-up of novel silicon anode materials. The silicon active material will be integrated into up to 80% Si anode content. Silicon (Si) is considered as one of the promising candidates for anode materials to replace graphite in the focused effort to increase the energy density of batteries in the transportation sector. This project led by NanoHydroChem, LLC addresses this effort through the development of an innovative anode design with up to 80% Si content. By utilizing silicon waste from the solar and semiconductor industry, this technology aims to reduce industry waste and to be drop-in compatible with current battery manufacturing production lines.

Robust In Situ-Formed Polymer Electrolytes for Stabilizing High-Silicon Content Anodes (Anthro Energy, Inc., San Jose, CA)

This project led by Anthro Energy, Inc. pushes the limits of state-of-the-art lithium-ion batteries through the incorporation of a polymer electrolyte with a silicon-graphite composite anode demonstrating extreme mechanical and electrochemical performance. This technology facilitates increased battery competitiveness in the transportation sector through cost reduction and longer-range of lithium-based batteries.

Reliable Fabrication of All-Solid-State Lithium Batteries with High Cell-Level Specific Energy (LiBeyond, LLC, Pearland, TX)

This project led by LiBeyond, LLC advances the state of the art in less-expensive, longer-range lithium-based batteries for transportation. manufacturing process for thin, durable electrolyte layers is a step towards improved solid-state batteries that will hasten the decarbonization of the transportation sector. Fast charge and long-range capabilities are necessary for facilitating the wide-spread adoption of electric vehicles. To address this, LiBeyond, LLC is utilizing advanced quantitative analysis techniques to develop improved and thinner solid-state electrolytes for lithium metal batteries. Cheaper and more robust solid-state batteries will hasten the transportation sector's push to reduce greenhouse gas emissions.

High-Energy, High-Power Solid-State Li-ion Battery (SSLiB) Cells Based on High-Voltage 5V Electrode for Electric Drive Vehicle Applications (BioEnno Tech, LLC, Santa Ana, CA)

BioEnno Tech, LLC has developed a novel class of all-solid-state lithium-ion batteries utilizing a composite solid-state electrolyte, high voltage cathode, and high-capacity lithium metal anode. The combination of these materials is a significant step towards the decarbonization of the transportation sector by addressing major concerns in electric vehicles of battery safety, increased range, and operation in extreme temperature.

Ultrafast Calcination of Lithium Ion Battery Cathode Materials (Vuronyx Technologies, Arlington, MA)

One of the major hurdles for the adoption of electric vehicles is the increased cost due to high battery prices. Much of this cost is due to a single component of batteries, the cathode. This technology developed by Vuronyx Technologies addresses the high cathode cost through a new processing method for cathode active materials (CAMs). They utilize a NMC chemistry-agnostic flame-assisted spray pyrolysis synthesis (FASP) method to reduce the energy use, water use, emissions, and time of traditional CAM manufacturing methods. In particular, this method can reduce the processing time from 10-20 hours to 20-40 minutes.

Novel High-Capacity Composite Anodes for the Upcycling of Spent Graphite from End-of-Life Lithium-Ion Batteries (Semplastics EHC, LLC, Oviedo, FL)

This project led by Semplastics EHC, LLC advances the state of the art in lithium-based battery recycling through novel process development. Demonstration of graphite anode upcycling with improved energy density will ensure that less used battery materials end up in landfills and decreases the carbon footprint of the battery supply chain. Reduction of industry reliance on foreign sources for battery-grade materials is supported through recycling/upcycling efforts. The project will accomplish graphite upcycling through transforming impure graphite material into a new polymer-derived ceramic anode materials for the next generation of lithium-based batteries.

VIII Next Generation Lithium-Ion Materials: Advanced Anodes R&D

The growing need to decarbonize the transportation sector with lower cost PEV batteries has led to the search for higher energy and lower cost materials. Silicon is an earth-abundant element that provides much higher capacity (approximately 10 times that of currently used graphite) and results in cells that are easily fast charged. However, silicon anodes undergo significant volume change (as much as 300% change per cycle), which can lead to stress buildup and particle cracking. In addition, the interface between lithiated silicon and most electrolytes appears to be unstable, leading to relatively poor calendar life.

DOE has funded both applied and fundamental research into silicon anodes for many years and the performance of those anodes have improved significantly. Just a decade ago, moderate energy density cells with majority silicon anodes achieved only 100-200 cycles. Today, some automotive sized cells (10-50 amp-hours) achieve well over 1000 cycles and over 300Wh/kg, significantly higher than most graphite-based cells. Developers and researchers are testing anodes with 100% silicon (such as Amprius and Evonix), and various blends of silicon, silicon oxide, or silicon carbide, with graphite (such as Ionblox, Farasis Energy, Nanograft). With the higher capacity of silicon, the anode thickness in silicon containing cells is much thinner than that in graphite cells of the same energy, leading to improved fast charge performance. While the cycle life of silicon has now improved to meet and even exceed EV targets, the calendar life remains a significant concern, driven by the lack of a stable anode/electrolyte interface.

Improving this unstable solid electrolyte interphase (SEI), is the focus of the SEISTa (Silicon Electrolyte Interface Stabilization) program. This consortium is led by researchers from the National Renewable Energy Laboratory, with participation of researchers from Argonne National Laboratory, Lawrence Berkeley National Laboratory, Oak Ridge National Laboratory, Sandia National Laboratories, and several universities.

The work in SEISTa is organized into several thrusts that are investigating: novel silicon materials; electrolyte solvents, salts, and additives; novel electrode designs; new and improved binders; advanced diagnostics and modeling; and mechanical and thermal analyses. The focus of each group and activity is to understand the root cause of the poor calendar life of Si anode containing cells and to improve it significantly.

The rest of this chapter contains detailed reports on the status of the following individual projects.

- Silicon Consortium Project (NREL, ANL, PNNL, SNL, ORNL, LBNL)
- Si-Based Li Ion Batteries with Long Cycle Life and Calendar Life (PNNL)
- Silicon Anode Seedling Project (ANL)
- Seedling Project: Two-Dimensional Silicon Nanostructures for Improved Silicon Anode Cycling Stability (Brookhaven National Laboratory, Stony Brook University)
- Integrated Modeling and Machine Learning of Solid-Electrolyte Interface Reactions of the Si Anode (LBNL)
- Advanced Anode Manufacturing through Ultra-Thin Li Deposition (Applied Materials, Inc.)
- Structurally and Electrochemically Stabilized Si-rich Anodes for EV Applications (Enovix Corporation)
- Rationally Designed Lithium-Ion Batteries Towards Displacing Internal Combustion Engines (Group14 Technologies)
- Ultra-Low Volume Change Silicon-Dominant Nanocomposite Anodes for Long Calendar Life and Cycle Life (Sila Nanotechnologies)
- Solid State Li Ion Batteries Using Si Composite Anodes (Solid Power Inc.)
- Fully Fluorinated Local High Concentration Electrolytes Enabling High Energy Density Si Anodes (Stony Brook University)

- Devising mechanically compliant and chemically stable synthetic solid-electrolyte interphases on silicon using ex situ electropolymerization for long cycling Si anodes (University of Delaware)
- Rational Electrolyte Design for Li-ion Batteries with Micro-sized Si Anodes (University of Maryland, College Park)
- Silicon Consortium Project (SCP) (PNNL)
- Thin-film lithium metal manufacture by room temperature electrodeposition (Albemarle Corporation)
- Pre-Lithiation of Silicon Anode for High Energy Li Ion Batteries (Stanford University)
- Free-Energy Driven Approaches to Self-Forming and Self-Terminating SEIs on Si Anodes (LBNL).

VIII.1 Silicon Consortium Project (NREL, ANL, PNNL, SNL, ORNL, LBNL)

Anthony K. Burrell, Principal Investigator

National Renewable Energy Laboratory
15013 Denver West Parkway
Golden, CO, 80401
E-mail: Anthony.Burrell@nrel.gov

Brian Cunningham, DOE Technology Development Manager

U.S. Department of Energy
E-mail: Brian.Cunningham@ee.doe.gov

Start Date: October 1, 2020	End Date: September 30, 2025	
Project Funding (FY22): \$7,500,000	DOE share: \$7,500,000	Non-DOE share: \$0

Project Introduction

The current energy storage roadmap for transportation has identified next-generation anodes as key components leading to the development of electric vehicle battery packs costing less than \$100/kWh by 2028. While the cycle life of silicon (Si)-based cells and the overall capacity have improved significantly, calendar life achieves only ~10% of the target. Historically, Si anode research has focused on the large crystallographic expansion (~320%) that Si experiences upon lithiation to form Li_xSi . However, it has become clear that other failure mechanisms are also present. Specifically, the limited calendar life of Si cells demonstrates that a passivating solid-electrolyte interphase (SEI) does not form on the Si anode. This program will remove the barriers associated with the development of advanced lithium-ion negative electrodes based upon Si as the active material, with a specific focus on understanding the formation and evolution of the SEI on Si to solve the calendar life challenge.

Objectives

The targets for this project detailed in the lab call require the delivery of >2-Ah full cells, with Si-based anodes, that deliver 1,000 cycles at C/3, have useable energy >375 Wh/kg, energy density >750 Wh/L, and a calendar life >10 years. Meeting all these requirements in a single cell will require a comprehensive program to understand the limits of Si SEI stability and cell design.

For FY22 the milestones were:

- Q1: Have established single-layer pouch cell build protocols for the Silicon Consortium Project (SCP).
- Q2: Identify a silicon baseline material source and route to reproducibly scale its production or purchase commercially to 600 g for the Q4 build.
- Q3: Determine whether mechanical perturbation of the SEI impacts calendar life.
- Q4: Identify active cell components and cell designs to achieve stable calendar life electrode performance with a cell build capable of completing 1,000 cycles with <20% capacity fade and >3-year calendar life, using an NMC 811 cathode. Cells will be on test by the end of Q4, and testing will be complete in FY23.

Approach

Understanding the Relationship Between Calendar Life and Mechanical Properties of Silicon Electrodes

Silicon has over 10 times the theoretical capacity of graphite anodes. Problems with large volume change and short cycle life have been greatly improved through the use of nanomaterials. Poor calendar life remains a hinderance toward the commercialization of high-silicon-loading lithium-ion batteries. An unstable SEI is

thought to be at least partially responsible for the rapid decline in cell performance with time. The SEI is potentially degraded by both mechanical perturbation during cycling and chemical degradation during calendar aging. Standard calendar aging tests include periodic cycling to evaluate the extent of calendar aging. Therefore, cycling during calendar aging tests may contribute to calendar aging due to mechanical perturbation of the SEI with these cycles. Previous work by the consortium, including microcalorimetry and the comparison of calendar aging when Si is cycled on rigid/flexible substrates, provided evidence that SEI passivation may “reset” due to mechanical SEI degradation every time it is cycled between rest periods in the calendar aging test protocol. Cycles in calendar aging tests are called reference performance tests (RPTs). The work for this milestone built off these initial findings to understand if calendar life is affected by both chemical and mechanical SEI degradation, or if it is dominated by chemical degradation.

Isothermal microcalorimetry was used to show that RPT cycles during calendar aging tests cause a spike in heat generation that is likely associated with mechanical perturbation of the SEI during cycling. Then, calendar aging tests were performed in which the RPT frequency was varied during calendar aging rest periods, but the total number of cycles and total time were kept constant, to identify whether RPTs degraded calendar life.

Results

Demonstration of Long-Cycle-Life Silicon Anodes in 811 Full Cells

The SCP is focused on the mitigation of calendar life, but it also has targets that relate to cycle life and energy density. In the past year, we have demonstrated multiple silicon materials in full cells that meet the cycling requirements in full cells. An example is shown Figure VIII.1.1 using boron-doped silicon prepared using plasma-enhanced chemical vapor deposition.

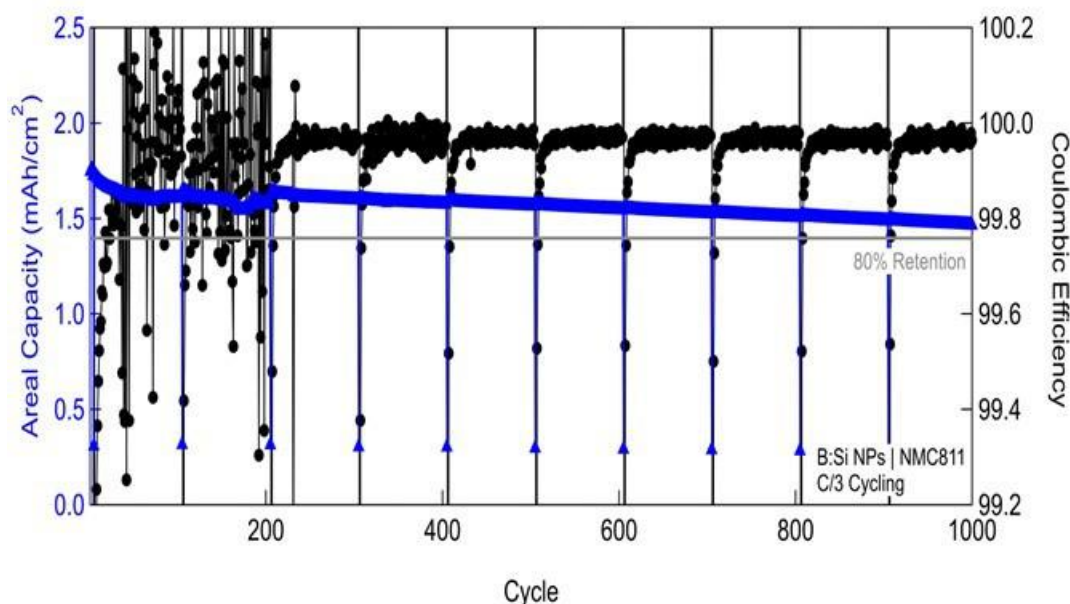


Figure VIII.1.1 Performance of a silicon electrode with gravimetric capacity >1,000 mAh/g at C/3 in an 811 full cell.

Identification of the Silicon Source and Route to Scale for the 2-Ah Full Cell Build

One of the challenges the SCP has had to overcome is the utilization of a baseline silicon material. Previous efforts have demonstrated commercial suppliers of silicon produced materials that exhibited significant batch-to-batch reproducibility issues as evident by variations in particle sizes, particle homogeneity, and surface chemistry as measured through zeta potential measurements. These batch-to-batch irregularities impacted cycling performance through a change in surface chemistry that directly impacted electrode processing and the resulting electrode homogeneity. Further, these variations in particle sizes negatively impacted the electrode performance by shifting electrochemical diffusion process time domains (longer in larger particles), as well as changes in SEI chemistry due to large variations in particle surface areas.

For these reasons, the SCP undertook a major effort to synthesize (1) reproducible (particle size, zeta potential) and (2) scalable (>500 grams) silicon for the entire consortium to use. The consortium prepared a baseline silicon powder through a mechanical milling processes. This material was distributed to the entire consortium for use in their studies, as well as to Argonne National Laboratory's Cell Analysis, Modeling, and Prototyping (CAMP) facility for the build of the Q4 cells. Further, material is available to researchers interested in baselining their material's performance by reaching out to Gabriel Veith at Oak Ridge National Laboratory at no cost. Finally, while the material used in the Q4 build is considered the SCP baseline material, this baseline will shift up as improvements in materials chemistry are implemented.

For the Q2 milestone, boules of silicon were cleaned in a multistep process involving hot acetone, methanol, hot ammonia hydroxide/hydrogen peroxide (3:1), and finally an HF dip (5%) followed by rinsing in 18-MW deionized water. The materials were pulverized into powders <18 mesh and then high-energy-milled through a combination of planetary and attrition milling. Sacrificial solvents were employed to prevent refusing of particles during the energetic milling process. For the Q2 milestone, it was determined that a sacrificial additive of PC produced a highly reproducible product. One thousand grams of material were produced and shipped to CAMP for the Q4 build.

Table VIII.1.1 shows representative particle size data as measured by light scattering from several batches of materials along with surface zeta potential. Each batch was milled with PC following a preset procedure with 8 minutes of milling and 20 minutes of rest (repeat 6 times). Note that the reaction is highly exothermic, and care should be taken to start with small quantities. The samples were exposed to air and allowed to passivate prior to removal and separation. The resulting particle size is about 223 nm with a tight particle size distribution. The particles have a zeta potential greater than 35 mV, indicating their stability in solution during electrode formation. Other solvents were investigated (NMP, DME, VC, DMC, hexane), but PC was determined to form the most reproducible particles. The current hypothesis is the high boiling point of the PC (242°C) with the high dielectric strength yields an ideal protective coating on the surface. From X-ray spectroscopy, the amount of residual carbon/PC appears to be quite small (<<<1 wt%).

Table VIII.1.1 Batch-to-Batch Reproducibility of PC-Milled Silicon for SCP Baseline

Batch	Diameter (nm)	Diameter Error (nm)	Zeta Potential (mV)
1	233	9	
2	213	15	-49
3	219	8	-41
4	240	18	-45
5	242	27	
6	266	55	
7	228	32	
8	213	11	-42
9	226	10	-46

Figure VIII.1.2 shows representative cycling data measured at C/10 and C/2 for the milled silicon mixed with 10 wt % C45 carbon black and 10 wt % P84 polyimide binder. One can see excellent cycling performance consistent with metallic-like silicon. This baseline material was used for the Q4 sample build and is available to the consortium team members. Further, the milling team continues to make improvements to the surface chemistry of the silicon material, which will become the next generation of baseline material.

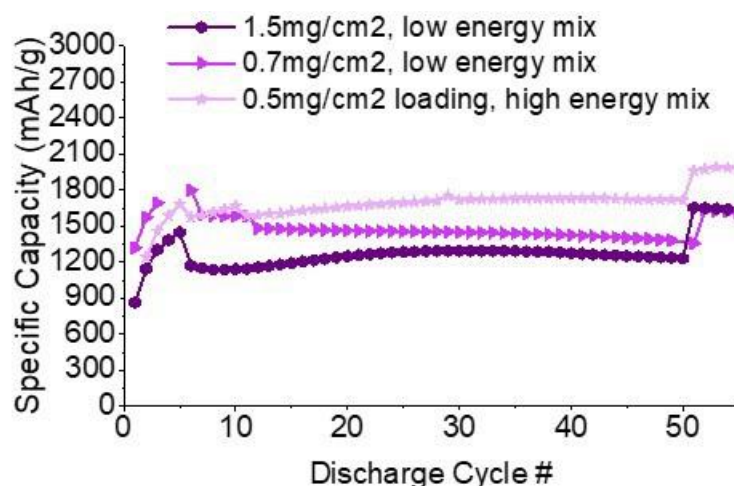


Figure VIII.1.2 Capacity versus cycle number for milled silicon at various weight loadings.

Understanding the Relationship Between Calendar Life and Mechanical Properties of Silicon Electrodes

Isothermal microcalorimetry was performed on 80% silicon–LiFePO₄ coin cells after formation, after ~3 weeks of rest, and after three RPT cycles. A heat increase was observed after the RPTs, implying there is an increase in instability and poorer passivation of the SEI after cycling. There are other possible sources of heat generation, such as lithium diffusion and subsequent relaxation within the silicon; however, due to the sustaining increase in heat generation (measured for several days after cycling completed), it seemed more likely to result from increased reactivity due to a decrease in SEI passivation. This is corroborated by modeling of the current decay during repeated voltage holds performed on similar silicon–LiFePO₄ cells. The irreversible current for a voltage hold extrapolated from the previous voltage hold was less than the actual irreversible current. This could indicate increased parasitic reactions due to SEI perturbation during the cycles between voltage holds and contributed to the motivation for calendar life testing with varied RPT frequency.

To further understand the extent to which mechanical SEI perturbation during RPTs contributes to calendar aging, calendar aging tests with varied RPT cycling frequency were performed. The goal of these tests was to separate the impact of RPT cycling from calendar aging time. Coin cells containing 80% silicon–NMC622 and graphite–NMC622 were fabricated and tested with 1-week, 2-week, 1-month, 2-month, and 3-month rest periods between RPTs over a 6-month period. After 6 months, the cells were cycled continuously until all cells had approximately the same time since assembly and the same total number of cycles. Figure VIII.1.3 and Figure VIII.1.4 show little variation in the capacity fade with varied RPT frequency, which implies that the time since assembly is the dominant factor in determining capacity fade. Contrastingly, plots of these same data versus cycle number show a much greater variation with capacity fade until the end of the test when the number of cycles (and also time) were the same for all data sets. This result implies that the cycle number is not the dominant factor in determining capacity fade during calendar aging tests, and the time since assembly instead correlates most strongly with capacity fade. Figure VIII.1.4 shows shorter rest times between RPTs than Figure VIII.1.3. RPT frequency has more impact on capacity fade during calendar aging when the aging times are shorter. This implies that as rest time increases, SEI perturbation resulting from RPTs impacts calendar life less. For shorter rest periods, the interruption of the SEI with cycling is more likely to impact calendar life estimates. Despite this trend, time since assembly still correlates more strongly with capacity fade than cycle number.

Surprisingly, graphite–NMC622 cells showed significant capacity fade during calendar aging tests. Graphite–NMC622 pouch cells were tested as a comparison. Figure VIII.1.5 shows that pouch cells exhibit better cycle and calendar life behavior than coin cells, suggesting that pouch cells should be used for calendar aging tests.

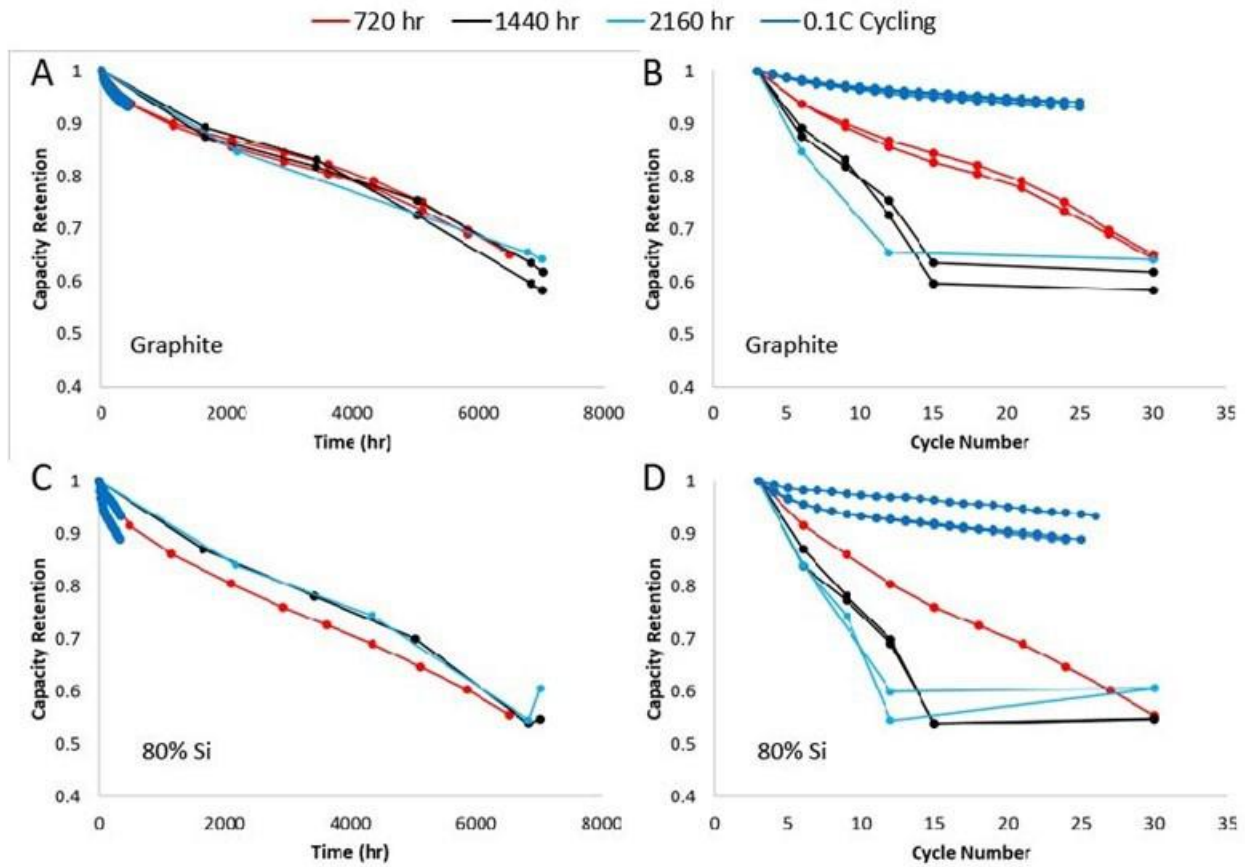


Figure VIII.1.3 Variable RPT calendar life aging tests with 720, 1,440, and 2,160 hours of rest at open circuit between groups of three RPT cycles on graphite (A, B) and 80% silicon (C, D) versus NMC622 in coin cells.

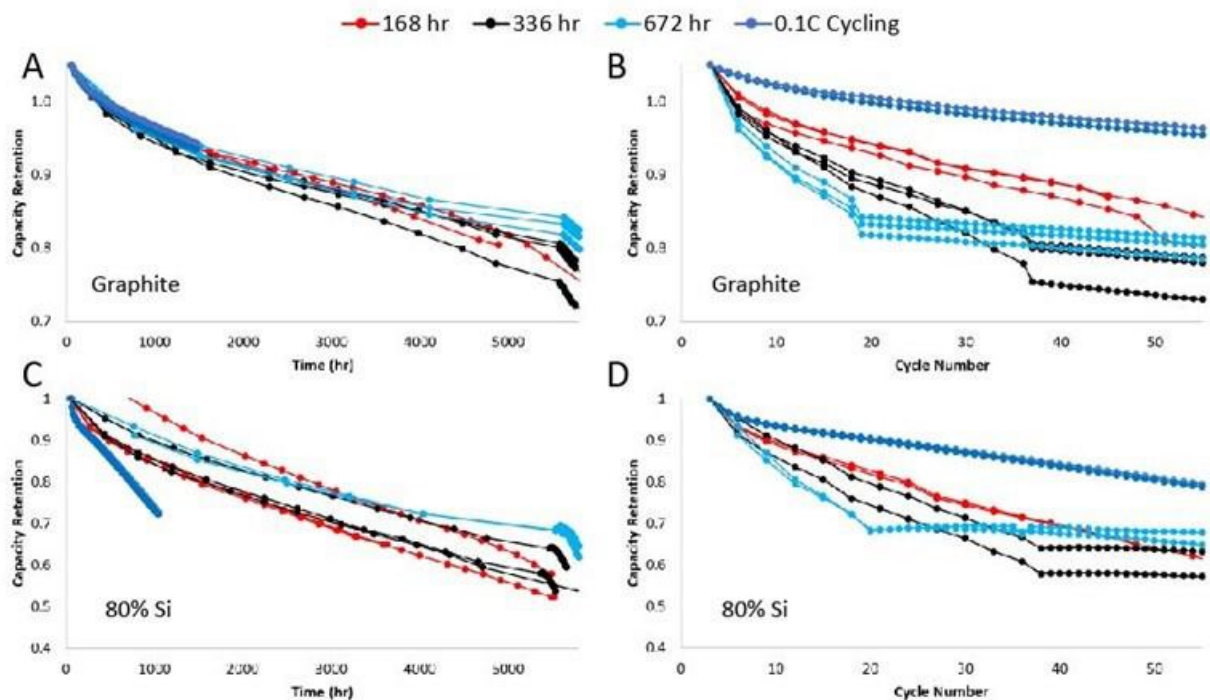


Figure VIII.1.4 Variable RPT calendar life aging tests with 168, 336, and 672 hours of rest at open circuit between groups of three RPT cycles on graphite (A, B) and 80% silicon (C, D) versus NMC622 in coin cells.

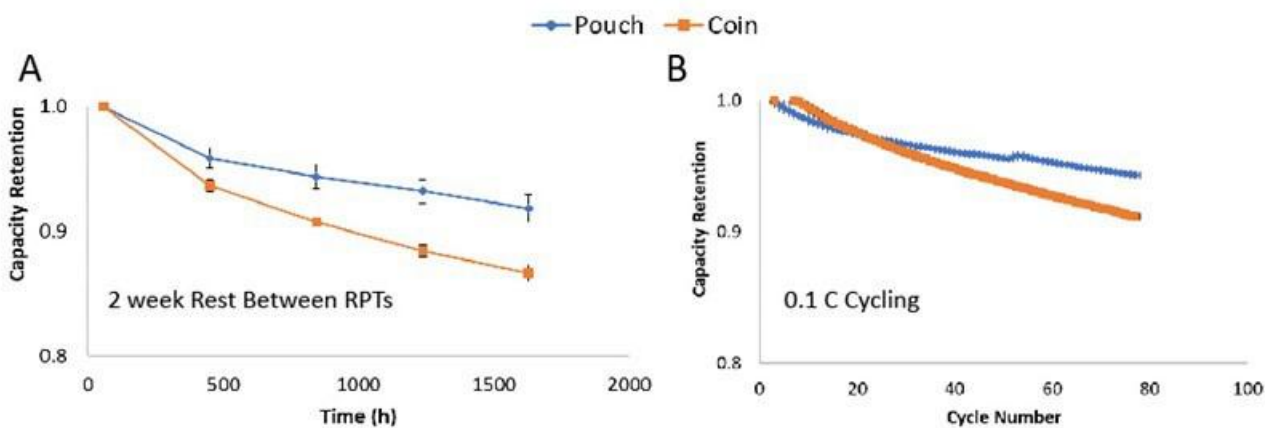


Figure VIII.1.5 Graphite-NMC622 pouch cells compared to coin cells for A) calendar life tests with 336 hours of rest at open circuit between groups of three RPT cycles and B) constant 0.1C cycling.

Conclusions

Demonstration of Long-Cycle-Life Silicon Anodes in 811 Full Cells

The SCP has demonstrated silicon anodes that can cycle for >1,000 cycles at C/3 against a high-nickel cathode. Anodes with this performance will be used to target and mitigate calendar life issues.

Identification of the Silicon Source and Route to Scale for the 2-Ah Full Cell Build

The Q2 milestone was accomplished through mechanochemical milling of silicon boules in sacrificial propylene carbonate solvent. Particles were approximately 223 nm in diameter with a high zeta potential and could be made at scales in excess of 1 kg. The reproducibility was evaluated over 30 times.

Understanding the Relationship Between Calendar Life and Mechanical Properties of Silicon Electrodes

Mechanical perturbation of the SEI does likely impact calendar life, but the impact is shown to be minimal in comparison to chemical degradation. Therefore, understanding and mitigating chemical degradation pathways should be prioritized.

VIII.2 Si-Based Li Ion Batteries with Long Cycle Life and Calendar Life (PNNL)

Ji-Guang Zhang, Principal Investigator

Pacific Northwest National Laboratory
902 Battelle Boulevard
Richland, WA 99354
E-mail: jiguang.zhang@pnnl.gov

Ran Yi, Co-Principal Investigator

Pacific Northwest National Laboratory
902 Battelle Boulevard
Richland, WA 99354
E-mail: ran.yi@pnnl.gov

Brian Cunningham, DOE Technology Development Manager

U.S. Department of Energy
E-mail: Brian.Cunningham@ee.doe.gov

Start Date: October 1, 2020

End Date: September 30, 2023

Project Funding (FY22): \$400,000

DOE share: \$400,000

Non-DOE share: \$0

Project Introduction

Silicon (Si) has been regarded as one of the most promising anode materials for next generation lithium-ion batteries (LIBs) because it has 10 times higher theoretical specific capacity (4200 mAh/g) than that of graphite. However, severe volume change (~300%) of Si during lithiation and delithiation hinders the practical application of Si anode. In the last decade, significant progresses have been made on the specific energy and cycle life of Si based LIBs. However, calendar-life of these batteries is still less than two years which is far less than 10-year target required by DOE.

Objectives

In this project, we will investigate the mechanisms of short calendar life of Si based LIBs and extend their cycle life using porous Si materials and localized high concentration electrolytes (LHCEs) tailored to improve the stability of SEI layer on the surface of Si particles. The scalability of the production process of the porous Si materials will also be studied in order to reach the goals required by DOE's EV program.

Approach

- Investigate the mechanisms of short calendar life of Si based LIBs through post-mortem analysis of the cathode, Si-based anode, and electrolyte after storage to identify the main factors affecting calendar life of Si based LIBs. Detailed characterizations will be carried out to study the structure and composition evolution of both cathode and anode after calendar life test, especially the properties of SEI/CEI layers.
- Study crosstalk effect on calendar life in Si based LIBs by storing cathode and anode separately.
- Tailor localized high concentration electrolytes (LHCEs) to improve the stability of SEI layer on the surface of Si particles. SEI layers formed in LHCEs is rich in inorganic components such as LiF and Li₂O. These SEIs have a much better mechanical stability and can tolerate large volume expansion of Si particle without break down and expose Si directly to electrolyte, therefore largely minimize the continuous growth of high impedance SEI layers.

Results

1. Investigate the mechanisms of short calendar life of Si based LIBs

We investigated the failure mechanism responsible for limited calendar life of single layer pouch (SLP) cells (~64 mAh, p-Si/C||NMC622) using the USABC calendar life test protocol. Micron sized porous Si with nanopores (named p-Si/C) developed in PNNL was used in this work. Electrolyte used in this work is a LHCE consists of LiFSI-2DMC-0.1EC-0.1FEC-3TTE (by mol.). Both anode and cathode have been evaluated at 55°C after 120 days. Pristine electrodes were also evaluated as a reference. Figure VIII.2.1a and b show the STEM images of the P-Si/C particles retrieved from the pouch cell after 120 days storage at 55°C.

A thick SEI layer is found on the outside of the p-Si/C particle (Figure VIII.2.1a). The p-Si/C particle is wrapped by a broken shell which is attributed to the SEI layer. The thickness of the SEI layer is estimated to be about 100 nm. Figure VIII.2.1b shows the cross-section of a particle. Other than a rough SEI layer on outside, inside of the p-Si/C particle after storage test has similar feature to the pristine p-Si/C (Figure VIII.2.1c). These results indicate that the p-Si/C anode did not undergo significant particle level structural change during storage and the main change to the p-Si/C particle is the formation of SEI layer on the surface of particles. During the calendar life test, the anode is mainly stored at 100% SOC in expanded state without repeated volume expansion/shrinkage, which induced little structure degradation inside of particles. This is in sharp contrast to a similar p-Si/C particle after 450 cycles (cycling time is also about 120 days) coupled with the same NMC622 cathode at 25 °C as shown in Figure VIII.2.1d. The p-Si/C particle after long term cycling shows an etched surface caused by repeated volume change.

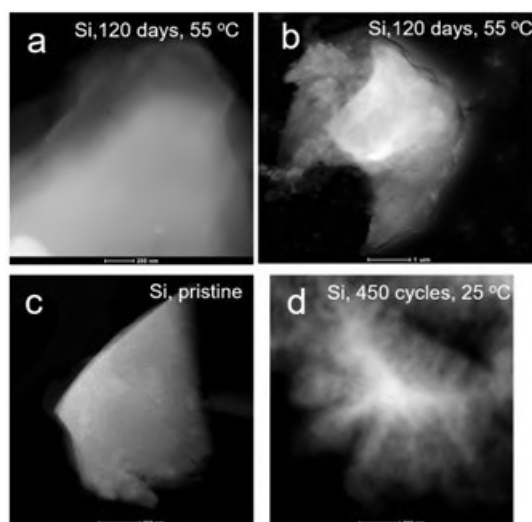


Figure VIII.2.1 (a). STEM images of (a and b) p-Si/C particle after calendar life test (120 days at 55 °C), (c) pristine p-Si/C particle before testing and (d) p-Si/C particle after 450 cycles at 25 °C.

The composition of the anode has also been studied by EDS. Figure VIII.2.2 shows the EDS mapping of a p-Si/C particle. O, C, S and F are from the electrolyte used in this study which contains LiFSI as salt and oxygen-containing solvent. The contour of Si signals is smaller than those of O, C, S and F, which indicates the formation of SEI layer on p-Si/C particle surface. In addition, the Si contour is smooth, showing that bulk of Si particle experienced much less structure change as those observed in cycled p-Si/C particles.

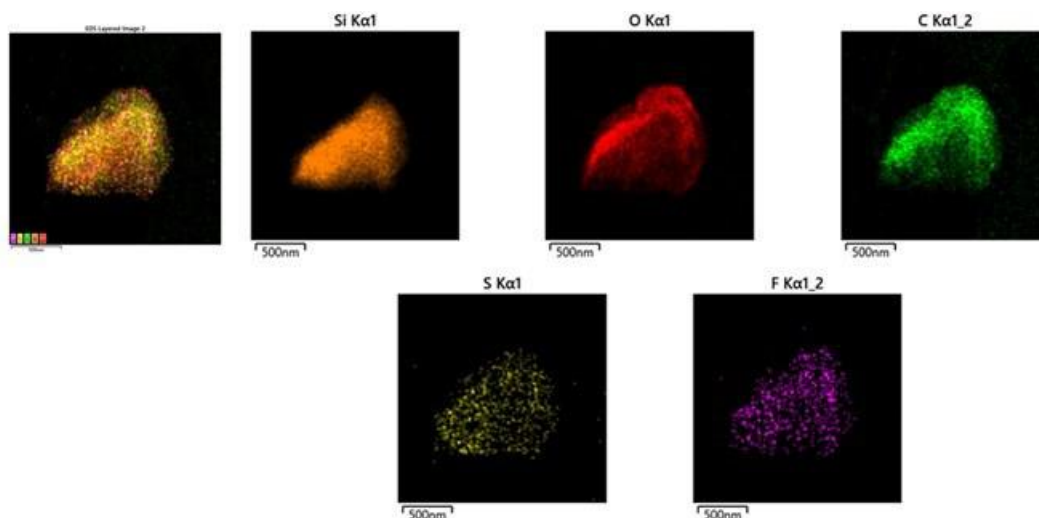


Figure VIII.2.2 EDS mapping of a p-Si/C particles after calendar life test (120 days at 55 °C).

Figure VIII.2.3 shows the STEM images of the NMC622 particle after 120 days storage at 55 °C. Compared to pure layered structure of the pristine NMC622 particle (Figure VIII.2.3b), a CEI layer of 2.5-5.5 nm thick and a disordered rock salt layer of 5.5-7.5 nm thick are clearly observed on top of layered structure of NMC622 particle. This structure evolution is similar to those observed on the NMC622 particle after 450 cycles at 25 °C as shown in Figure VIII.2.3c (cycling time is also about 120 days). NMC622 particle after long-term cycling also exhibits a 5 nm thick rock salt layer (Figure VIII.2.3c). It is well known that the rock salt layer in NMC622 particle can lead to large impedance increase on cathode. This is consistent with our previous finding that EOL cathode retrieved from p-Si/C||NMC622 cell after storage test plays a dominate role on the overall impedance increase of EOL cells.

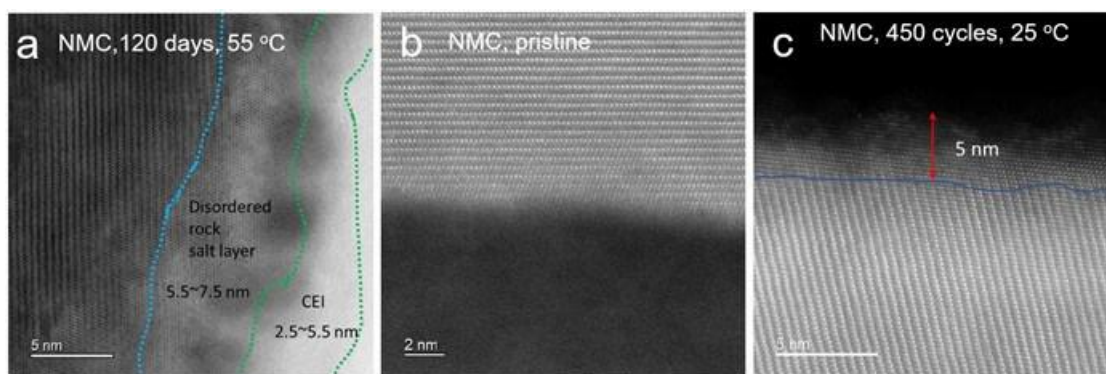


Figure VIII.2.3 STEM images of (a) NMC622 particle after calendar life test (120 days at 55 °C), (b) pristine NMC622 particle before testing and (c) NMC622 particle after 450 cycles at 25 °C.

2. Develop new electrolytes to improve the calendar life of Si-based LIBs

Based on the data above, the impedance growth largely originates from both SEI layer on the Si-based anode and CET layer on the NMC cathode. In order to improve the calendar life during high temperature storage, the improvement on the interphase stability of both anode and cathode is required. Toward this goal, new electrolytes have been explored. These new electrolytes need to be stable at a wide temperature range required by USABC's testing protocol. Table VIII.2.1 shows the composition of the new electrolytes used to improve the high temperature performance of Si-based LIBs. Full cells consisting of PNNL's micron sized nano Si/C composite anode and NMC622 cathode (3.3 mAh/cm²) were tested in the new localized high concentration

electrolytes with LiFSI salt, two different solvents, and two different additives. LiPF₆ in EC-PC-EMC (1:3:6 by wt) + 1 wt% VC + 7 wt% FEC was used as a baseline. The full cells were cycled at both room temperature (25°C) and 45°C for initial evaluation. The voltage range of full cells is 2V - 4.2V with 0.7C charge rate and 0.5C discharge rate. The cells were tested as prepared without prelithiation or other pretreatments.

Table VIII.2.1 Electrolyte composition

Si-baseline	1.2M LiPF ₆ in EC-PC-EMC (1:3:6 by wt) + 1 wt% VC + 7 wt% FEC
E1	LiFSI-2DMC-0.2EC-3TTE+1 wt% LiPF ₆
E7	LiFSI-2.8DMC-0.2EC-2TTE+1 wt% LiPF ₆
E8	LiFSI-2.8DMC-0.2EC-2TTE+1 wt% LiPO ₂ F ₂
E9	LiFSI-2.8EP-0.2EC-1TTE+1 wt% LiPF ₆
E10	LiFSI-2.8EP-0.2EC-1TTE+1 wt% LiPO ₂ F ₂

Figure VIII.2.4 show cycling stability and coulombic efficiency of Si||NMC622 cells at room temperature (25°C) and 45°C, respectively. The cells with newly developed E9 and E10 electrolytes demonstrate significantly better cycling stability at 45°C. The capacity retention of E9 and E10 is almost 100% after 120 cycles while a capacity retention of about 70% was obtained using E1. E10 also shows the highest cycling coulombic efficiency at 45°C. In addition to improved performance at 45°C, cells with E9 and E10 also show better cycling stability than those with E1 at room temperature (25°C). The variation in cycling stability can be attributed to the variation in the cell fabrication process.

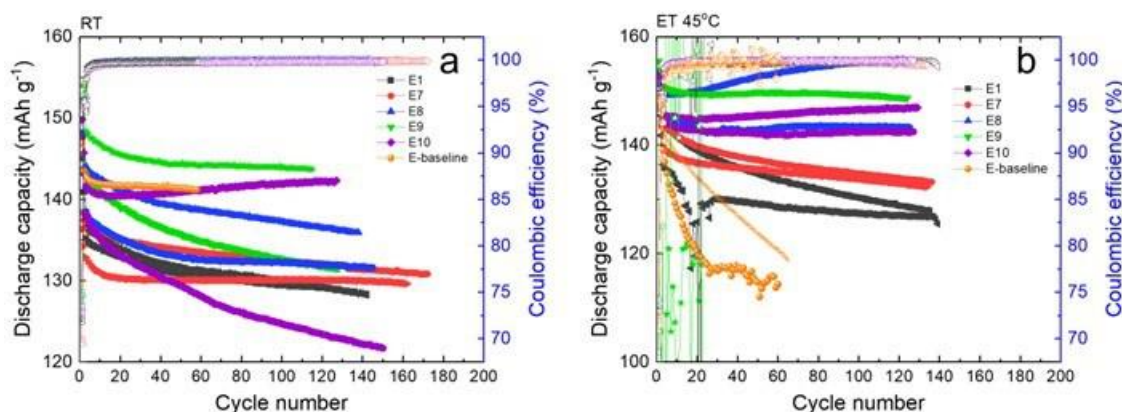


Figure VIII.2.4 Cycling stability and Coulombic efficiency of p-Si/C || NMC622 cells using different electrolytes at (a) room temperature and (b) 45°C.

After evaluation on the high temperature cycling stability of cells with different electrolytes, one of the best electrolytes (E10) developed has been used to evaluate its effect on the calendar life of Si||NMC622 cells compared to baseline electrolyte. Fresh Si anodes (PNNL's micron sized p-Si/C composite anode) and fresh cathodes were firstly cycled in half cells against Li metal for 10 cycles in different electrolytes using different upper voltages. Then the anodes and cathodes were charged to 100% SOC. The cycled electrodes were harvested and then re-assembled in symmetric cells (NMC622||NMC622 and Si||Si) which were stored at 55°C for 8 days. The use of symmetric cells can mitigate the uncertainty related to Li metal anode typically observed in Li||Si half cells, especially at elevated temperature. Impedances of these cells were measured and tracked during the storage period.

As shown in Figure VIII.2.5 when Si-baseline electrolyte was used, upper voltages used during cycling of Si||NMC622 cells have a significant impact on the impedance growth of NMC622 during storage. For the cell

charged to 4.2V, no clear increase in the impedance was observed during eight-day storage. However, for the cells charged to 4.4 V, rapid increase in the impedance of NMC622||NMC622 symmetric cell were observed. In contrast, when E10 (LHCE) electrolyte was used, no significant increases in impedances were observed in NMC622||NMC622 symmetric cells no matter whether the cathode was pre-cycled to an upper voltage of 4.2 or 4.4 V (Figure VIII.2.5b). This finding clearly revealed that 1) NMC622 cathode is very sensitive to the cycling voltage when the baseline electrolyte was used, especially at elevated temperature (55°C), and 2) E10 electrolyte can form a stable CEI at 4.4V even at elevated temperature (55°C).

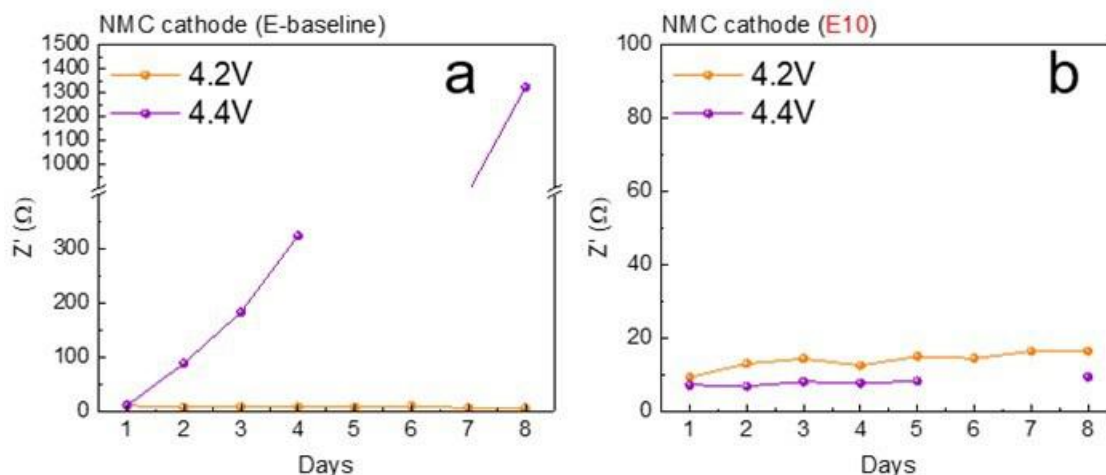


Figure VIII.2.5 Impedance evolution of NMC622 || NMC622 symmetric cells consists of NMC622 cathodes charged to 100% SOC at different cut-off voltages in the baseline electrolyte (a) and E10 electrolyte (b) at 55°C.

Figure VIII.2.6 shows the impedance evolution of fully lithiated Si anodes measured in Si||Si symmetric cells. The Si anode with the baseline electrolyte exhibits three times impedance growth after 8 days compared to the first day while the Si anode with E10 electrolyte shows almost no impedance growth under the same conditions.

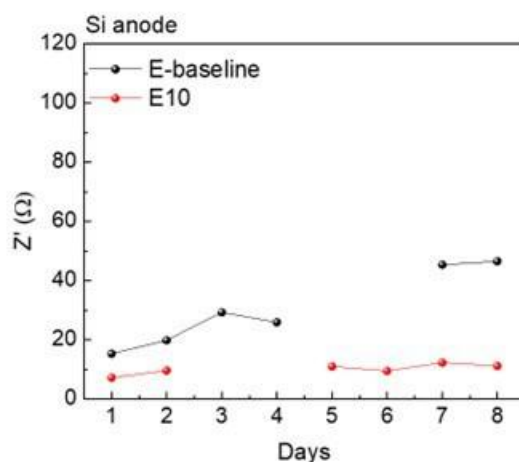


Figure VIII.2.6 Impedance evolution of symmetric Si || Si cells consist of 100% SOC Si anodes retrieved from cycled Si || NMC622 cells with different electrolytes at 55°C.

It is well known that 1) FEC can decompose at high temperatures, which may lead to shorter calendar life of batteries and 2) Unlike in the case of Si based LIB, graphite-based LIBs have no serious calendar life issues when FEC-free electrolyte was used. To understand if FEC is the main factor that triggers the impedance growth, the graphite anode (from Argonne National Laboratory CAMP facility) was used to study the

influence of the Si-baseline electrolyte and FEC-free baseline electrolyte (which is the typical electrolyte used in graphite-based LIBs). In the case of FEC-free electrolyte, no impedance growth of the graphite anode was observed. However, with the Si-baseline electrolyte that contains FEC, even the graphite anode shows a drastic increase of impedance as shown in Figure VIII.2.7. This result provides solid evidence that FEC is the main factor that leads to rapid increase of anode impedance at elevated temperature. It also justifies the efforts on development of FEC-free electrolytes such as E10 and new additives that can suppress the detrimental effects of FEC at elevated temperature.

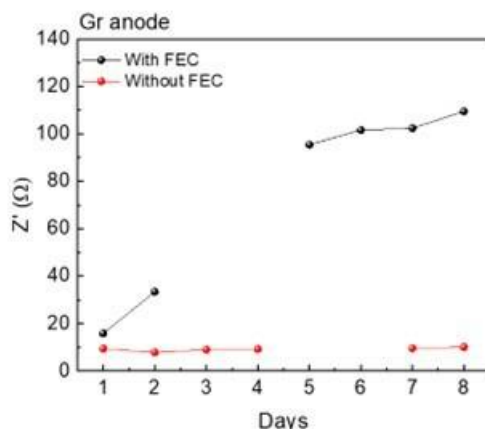


Figure VIII.2.7 Impedance evolution of graphite | graphite symmetric cells consist of 100% SOC graphite anodes retrieved from cycled graphite | NMC622 cells with different electrolytes at 55 °C.

Conclusions

- The postmortem analysis has been carried out on PNNL's carbon coated porous Si anode (p-Si/C) and NCM622 cathode after calendar life test (120 days at 55°C). It has been found that 1) Si anode underwent minimal structural degradation at the particle level except formation of a SEI layer on outer surface of particles; 2) cathode suffered both CEI formation and structural degradation as a thick (5-7 nm) disordered rock salt layer was formed.
- New electrolytes have been developed to stabilize Si-based LIBs at both room temperature (25°C) and elevated temperature (45°C). Compared to the cells with baseline electrolyte, the cells with newly developed E9 and E10 electrolytes not only exhibit better cycling stability at room temperature, but also demonstrate much better cycling stability at elevated temperature (45°C) with almost 100% capacity retention in 120 cycles.
- It has been found that 1) the increase in the impedance of NMC622 cathode highly depends on its voltage (NMC622 cycled at 4.2V shows no impedance growth at 55°C for 8 days, while severe impedance growth were observed when cycled at 4.4V; 2) even graphite anodes stored in FEC-containing carbonate electrolytes show severe impedance growth 55°C while no impedance growth in FEC-free carbonate electrolytes; 3) compared to the cells with baseline electrolyte, E10 alleviates the impedance growth of both Si anode and NMC622 cathode during high temperature storage. A detailed mechanism of FEC decomposition at high temperature and its effects on SEI of anodes will be further investigated and the crosstalk between anodes and cathodes will also be investigated.

Key Publications

1. Qiuyan Li, Ran Yi, Yaobin Xu, Xia Cao, Wu Xu, Ji-Guang Zhang, Failure analysis and design principles of silicon-based lithium-ion batteries using micron-sized porous silicon/carbon composite, *Journal of Power Sources* 2022, 548, 232063.

Acknowledgements

Key contributors include Ju-myung Kim, Xia Cao, Qiuyan Li, Yaobin Xu and Chongmin Wang.

VIII.3 Silicon Anode Seedling Project (ANL)

Zonghai Chen, Principal Investigator

Argonne National Laboratory
9700 South Cass Avenue
Lemont, IL 60439
E-mail: Zonghai.chen@anl.gov

Brian Cunningham, DOE Technology Development Manager

U.S. Department of Energy
E-mail: Brian.Cunningham@ee.doe.gov

Start Date: October 1, 2020	End Date: September 30, 2023	
Project Funding (FY22): \$150,000	DOE share: \$150,000	Non-DOE share: \$0

Project Introduction

Silicon anode has recently attracted substantial attention primarily due to its high specific capacity, 10 times higher than the graphitic counterpart. However, the deployment of Silicon anode has been hindered by its insufficient calendar life. Major progress has been made to mitigate the detrimental impact of volumetric changes during charge/discharge cycles by size and morphology control. However, aggressive parasitic reactions between lithiated silicon and the non-aqueous electrolytes limits the calendar life of batteries using silicon anode. Stabilizing the silicon/electrolyte interface has been one of the top challenges to enable its application in high energy density electric vehicle batteries. Here, we propose to develop an accurate calendar life model, based on the high precision leakage current measurement, in order to predict the calendar life of silicon-based batteries. High precision leakage current measurement provides an accurate determination of the Si SEI stability for a charged cell hold, and the associated physical characteristics occurring in the battery.

Objectives

The objective of this project is two-fold. The first objective is to establish an accurate model to predict the calendar life of electric vehicle batteries using silicon anode from leakage current measurements. The second objective is to collaborate with the Si consortium team to support determination of chemical/electrochemical phenomena occurring in the Si anode and provide a decoupling mechanism between Li inventory issues versus active material electrical isolation. The resulting model will be used to accelerate the down selection of Si anodes, surface coating technologies, and electrolyte additives for long calendar life silicon-based automobile batteries.

Approach

The fundamental assumption of this project is that the parasitic reaction at the silicone/electrolyte interface is the root of the performance loss of the silicone anode, and that the precise measurement of the rate of parasitic reaction can provide the fundamental basis for predicting the calendar life of silicon anode containing cells. Following are details of the approaches adopted for this project.

1. Precise measurement of parasitic current
The quality of the calendar predicting model heavily depends on the availability of high quality parasitic current data that mimics the parasitic reactions during the storage of the batteries at high state of the charge (SOC). In this project, a home-developed high precision leakage current (HpLC) measurement system is deployed for accurately measuring the evolution of leakage current as a function of storage time.
2. Mathematic modeling the parasitic reactions

Mathematic descriptors of parasitic reactions will be developed based on physical model of solid/electrolyte interphase (SEI) growing model. The descriptors are then parameterized using the high-quality parasitic current data collected using HpLC system.

3. Assisting development of high-performance silicon-based chemistries

The ultimate goal of this project is to utilize the knowledge obtained from the calendar life prediction to assist the develop of the advanced silicon anode chemistry with extended life. It is also our goal to investigate the impact of surface chemistry, binder, as well as electrolyte composition on the parasitic current and the life of the silicon anode, and to accelerate the development of long-life silicone-based lithium-ion chemistry.

Results

In the previous year, the home-built high precision leakage current (HpLC) measurement was utilized to precisely measure the rate of parasitic reactions between the lithiated anode materials and the electrolyte. Two physical models, a voids filling model and a continuous SEI growth model, were implemented to describe the rate of parasitic reactions. Using graphite and SiO as model anode materials, consistent predictions were obtained using both models. It was predicted that the fully lithiated graphite would lose 20% of hosted charged in about 4 months while fully lithiated SiO anode would lose 20% of the charge in about 2 months. The predicted number is far below the commonly expected calendar life of both graphite and SiO anodes. The focus of this year is to fundamentally understand the intrinsic connection between the desired calendar life prediction and the voltage hold measuring protocol.

Figure VIII.3.1 shows a typical data collected for an open-circuit-voltage (OCV) storage experiment, routinely used for the calendar life measurement. In this exercise, multiple electrode materials and multiple cell configurations were used. To be consistent from sample to sample, a charging process is referred to the removal of lithium from the cathode and/or insertion of lithium into the anode, while discharging represents the reverse process. In a typical OCV experiment, a cell, either a full cell or a half cell, is initially cycled with a constant current of C/10 for 5 cycles so that a stable SEI or cathode electrolyte interphase (CEI) is formed (see Figure VIII.3.1a). Then, the cell is fully charged to 100% state of charge (SOC) using a C/10 rate before OCV aging. After aging, the cell is then cycled for another 4 cycles at C/10 rate to evaluate its electrochemical performance after the OCV aging (see Figure VIII.3.1b and Figure VIII.3.1c for representative capacity before and after OCV aging). Figure VIII.3.1a also schematically shows 4 measured numbers that are of particular interest in this exercise. Q1 is referring to the initial reversible capacity measured during the last discharging process; Q2 is referring to the hosted charge before the OCV aging; Q3 is the remaining charge hosted in the electrode material after the OCV aging, and Q4 is the reversible capacity of the electrode material after the OCV aging. Then, both *capacity retention* and *charge retention* after the OCV aging can be defined as following equations.

$$\text{Capacity retention} = Q_4/Q_1 * 100\% \quad (\text{VIII.3.1})$$

$$\text{Charge retention} = Q_3/Q_2 * 100\% \quad (\text{VIII.3.2})$$

In above equations, *capacity retention* is the actual physical measurement to define the calendar life of the cell while *charge retention* is the parameter being modelled in our effort. The physical discrepancy between the *capacity retention* and the *charge retention* can be the root for under-predicting the calendar life as reported in the previous year.

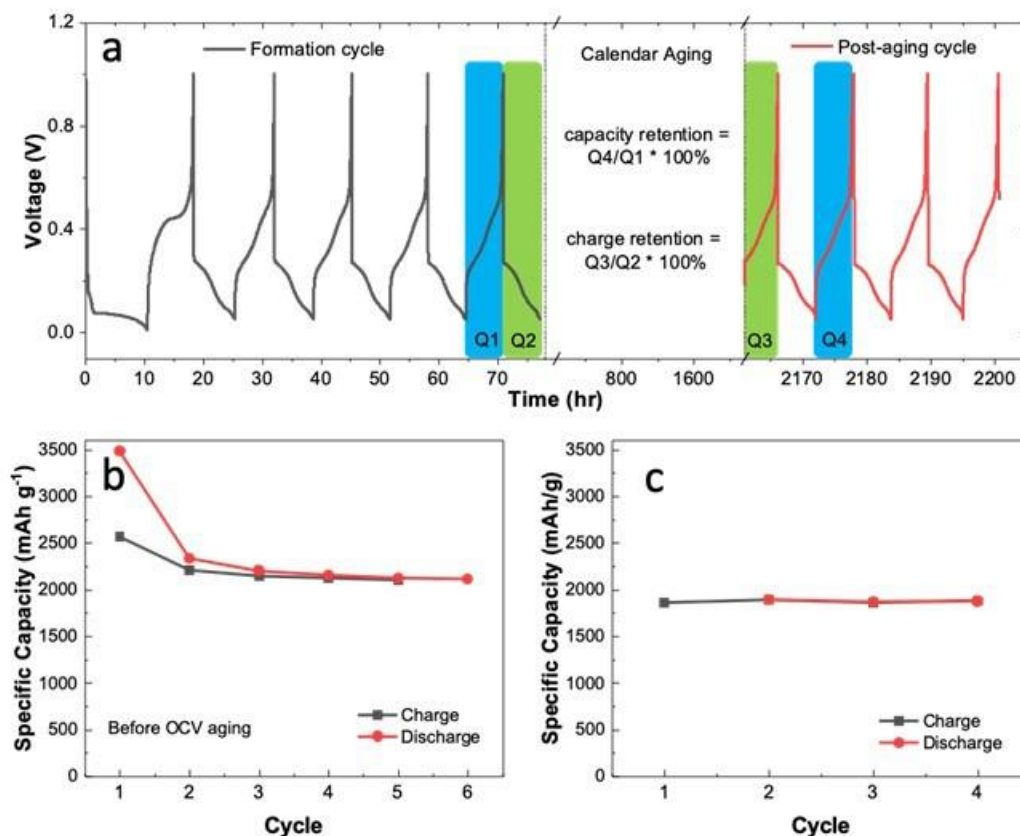


Figure VIII.3.1 A typical OCV aging data to define the capacity retention and the charge retention, showing a) the voltage profile of the tested cell before and after OCV aging, b) the charge/discharge capacity before the OCV aging, and c) the charge/discharge capacity after the OCV aging.

To obtain the relationship between the capacity retention and the charge retention, the OCV storage experiment up to 4 months was conducted for many cell chemistries, including two cathode materials LiFePO_4 (LFP) and $\text{LiNi}_{0.5}\text{Mn}_{0.3}\text{Co}_{0.2}\text{O}_2$ (NMC), two anode materials, graphite (Gr) and Si anode provided by Oak Ridge National Laboratory (Si), and two electrolytes, 1.2 M LiPF_6 in ethylene carbonate (EC)/ethyl methyl carbonate (EMC) (3:7 by weight) with and without 4 wt% fluorinated ethylene carbonate (FEC) as the electrolyte additive. Figure VIII.3.2 shows a clear linear relationship between the capacity retention and the charge retention for all cell chemistries investigated. It confirms that it is feasible to predict the calendar life of batteries by modelling their charge retention behavior. Figure VIII.3.2 also reveals a critical parameter, the slope (ρ) between the capacity retention and the charge retention. As shown in Figure VIII.3.2, the slope (ρ) varies greatly from 0.21 to 1.0 depending on the active material used in the cells. Using Gr/Li cell as an extreme example, if the Gr/Li cell was given long enough time to fully age, the parasitic reactions consumed all the lithium stored in graphite to reach 0% SOC, the parasitic reactions will theoretically self-terminated since no more charge is available to participate into the parasitic reactions. Figure VIII.3.2 theoretically predicts that this fully aged Gr/Li cell could be properly charged again and deliver 79% of its initial reversible capacity ($\rho=0.21$) after one full OCV age. In other words, this Gr/Li can barely meet the 80% reversible capacity retention target after a very long calendar life aging. On the other extreme, the Si/Li cell has a slope (ρ) close to 0.89, meaning that the charge consumed during calendar life aging has a stronger contribution to the capacity loss after the aging. Making it worse, the rate of parasitic reaction occurring on the surface of lithiated Si is much faster than that for lithiated graphite, leading to much shorter calendar life for batteries using Si-based anodes. This also echos the results in open literature that graphite/Si blend can have a better calendar life than Si since its slope (ρ) can be expected within these two extremes ($\rho=0.89$ for Si, and $\rho=0.21$ for graphite). The second learning from Figure VIII.3.2 is that the performance loss of full cells after calendar

aging is not a simple summation between the cathode and the anode. In this exercise, we investigated three different set of cell chemistries, Gr/NMC, Si/NMC, and Si/LFP. The experimental data consistently show that the slope of the full cells is larger than their corresponding half cells, implying that the charge balance during the aging is also crucial for cell design to improve its calendar life.

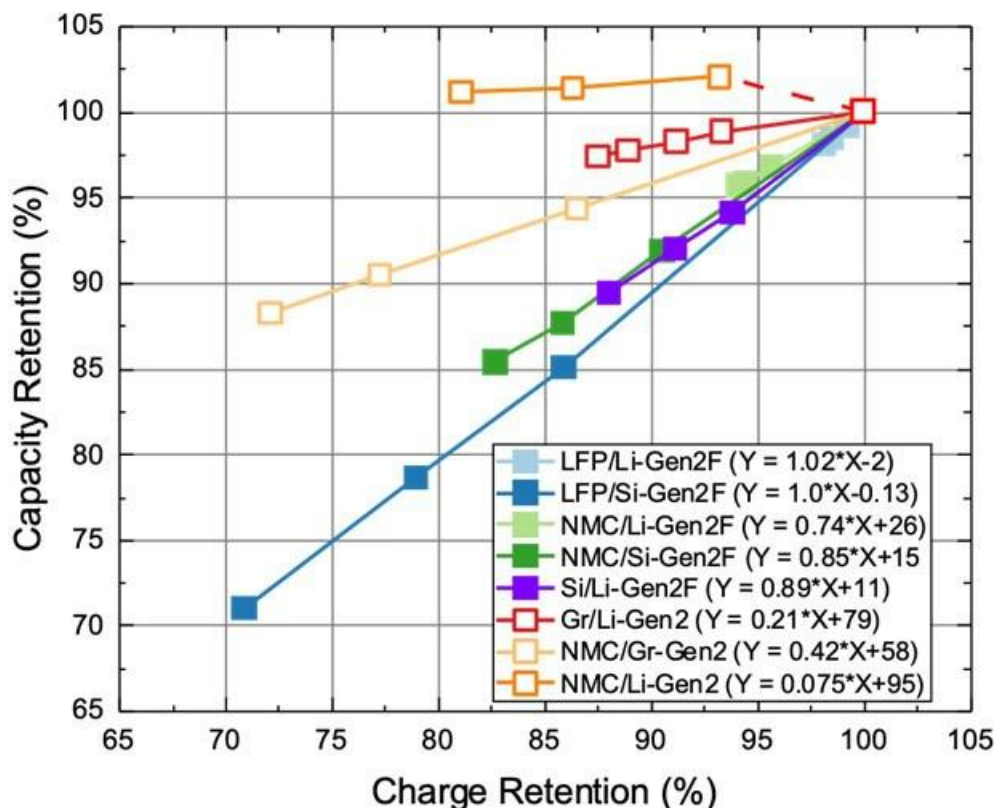


Figure VIII.3.2 Relationship between the capacity retention and the charge retention for various cell chemistries.

Conclusions

The parasitic reactions between the charged electrode materials and the electrolyte are the fundamental root for the performance loss of lithium-ion batteries during calendar life aging. Simple modeling of the rate of parasitic reactions and predicting the amount of charge consumed by these parasitic reactions generally severely under-predicts the calendar life. The accuracy of calendar life prediction can be significantly improved by incorporating the slope (ρ) between the capacity retention and the charge retention obtained from relatively short term OCV aging.

Acknowledgements

This report is coauthored by Dr. Jiyu Cai, and Dr. Guiliang Xu. We also wish to thank Steve Trask and Marco Rodrigues of ANL-CAMP facility in providing standardized Si electrode, graphite electrode and electrolyte for this project. We also thank Dr. Gabriel Veith of Oak Ridge National Laboratory for providing high quality Si anode material. We also thank Zhenzhen Yang of post-testing facility at ANL for assist in surface characterization using XPS. Dr. Yuzi Liu and Dr. Xinwei Zhou are also acknowledged for help in electron microscopy characterization. We also sincerely acknowledge the consortium calendar life team for routinely update and discussion.

VIII.4 Seedling Project: Two-Dimensional Silicon Nanostructures for Improved Silicon Anode Cycling Stability (Brookhaven National Laboratory, Stony Brook University)

Amy C. Marschilok, Principal Investigator

Brookhaven National Laboratory
Interdisciplinary Science Department
Upton, NY, 11973
E-mail: amarschilok@bnl.gov

Lei Wang, Co-Principal Investigator

Brookhaven National Laboratory
Interdisciplinary Science Department
Upton, NY, 11973
E-mail: lwang@bnl.gov

Kenneth J. Takeuchi, Co-Principal Investigator

Stony Brook University
100 Nicolls Road, 667 Chemistry
Stony Brook, NY, 11790
E-mail: kenneth.takeuchi.1@stonybrook.edu

Brian Cunningham, DOE Technology Development Manager

U.S. Department of Energy
E-mail: Brian.Cunningham@ee.doe.gov

Start Date: October 1, 2020

End Date: September 30, 2023

Project Funding (FY22): \$600,000

DOE share: \$600,000

Non-DOE share: \$0

Project Introduction

The progress of next generation portable electronics and widespread adoption of electric vehicles hinges on the development of batteries with greater energy density. For this purpose, Si has been the subject of substantial research due to its potential as a replacement for graphite as the negative electrode in Li-ion batteries. The high capacity (3580 mAh g⁻¹), moderate working potential (~0.4 V vs Li/Li⁺), low cost, and environmental abundance make Si a material of interest. However, large volume expansion during lithiation causes particle fracturing and continuous solid electrolyte interphase (SEI) growth. The mechanical degradation experienced by Si electrodes during Li (de)alloying reactions require tremendous efforts in material design to mitigate the parasitic effects.

Objectives

The objective of the project is to design 2-dimensional (2D) silicon-based anode materials that exhibit favorable mechanical properties and are capable of buffering the volume change associated with (de)lithiation.

Approach

In this work, 2D siloxene nanosheets with controllable size and surface oxidation were synthesized by using a facile topotactic reaction followed by ultrasonication as an exfoliation step. Detailed structural and chemical characterization via electron microscopy, x-ray photoelectron spectroscopy and Raman spectroscopy was conducted to study the morphology, composition, and structure of the siloxene materials and further correlate

them with the resulting electrochemistry. The obtained siloxene nanosheets were tested in Li-ion based half cells and full cells.

Results

1. Successful preparation of 2D siloxene nanosheets with controllable thickness

The 2D siloxene sheets were synthesized by topochemical reactions[1] under N_2 using bulk $CaSi_2$ in HCl where Ca was deintercalated from the Si sheet with H_2 gas generation. A slow color change from black to yellow/green was observed (Figure VIII.4.1 left). The 2D siloxene nanosheets were further exfoliated via ultrasonication in ethanol for 1 h. The morphology evolution was characterized by scanning electron microscopy (SEM), as shown in Figure VIII.4.1 right. The bulk $CaSi_2$ has a major particle size in the range of tens of micrometers and a compact layering stacking structure (Figure VIII.4.1 right A-C). After reaction with concentrated HCl, the material transformed to smaller particles with a loose sheet stacking structure and a size distribution of $11.0 \pm 4.6 \mu m$ (Figure VIII.4.1 D-F). After 1 h ultrasonication, smaller individual sheets with size a distribution of $6.6 \pm 2.4 \mu m$ were obtained (Figure VIII.4.1 G-I). The thickness of the siloxene nanosheets was measured by atomic force microscopy (AFM). There are some very thin layers with a thickness of 3-4 nm corresponding to ~5-7 layers of siloxene, however, the majority of the nanosheets have thicknesses ~13 nm, and some show thickness of ~70 nm.

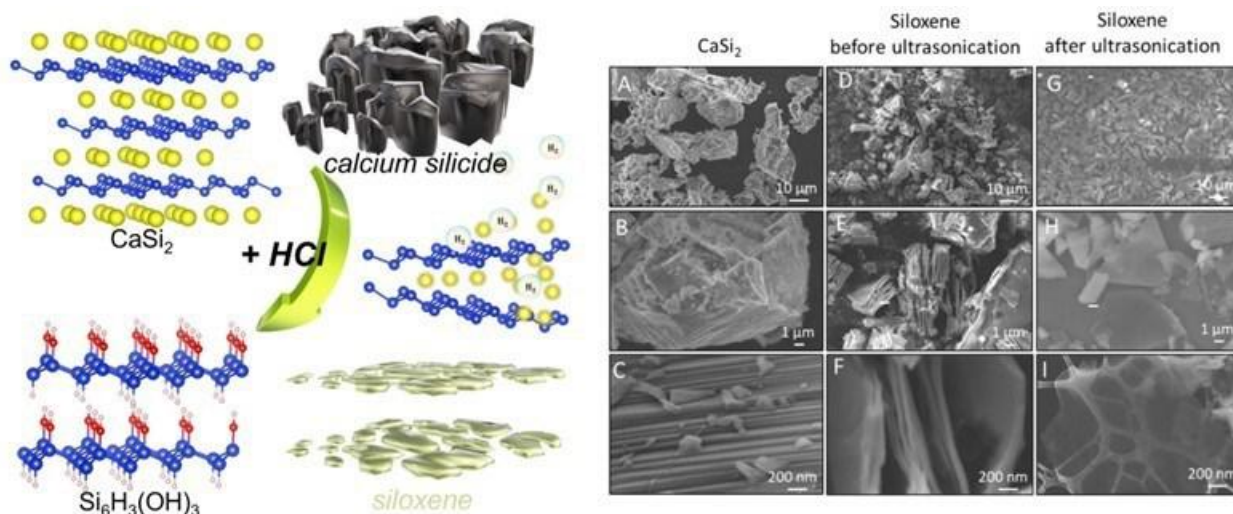


Figure VIII.4.1 (Left) Schematic representation of the topochemical synthesis and (right) scanning electron microscopy images of the 2D $CaSi_2$ precursors and siloxene products before and after ultrasonication.

2. Phase purity and surface oxidation of 2D siloxene nanosheets

The diffraction pattern for $CaSi_2$ is shown in Figure VIII.4.2A. Two noticeable (3R and 6R) reflection patterns for $CaSi_2$ are present with the 6R stacking sequence being dominant (70 wt.%). The diffraction peaks of $FeSi_2$ (7 wt.%) and bulk Si (16 wt.%) impurities appear in the as-received $CaSi_2$ powder. The diffraction pattern of the synthesized siloxene nanosheets is shown in Figure VIII.4.2B. The peaks corresponding to $CaSi_2$ mostly disappear after the reaction and $FeSi_2$ /bulk Si diffraction peaks are present with reduced intensity. Two broad peaks at 13.3° and 27.2° correspond to the (001) and (100) planes of the 2D siloxene nanosheets with a hexagonal unit cell. The in-plane hexagonal lattice constant coincides with that of $CaSi_2$, indicating that the reaction is topochemical and the two-dimensional Si network of $CaSi_2$ is preserved. The synthesized material diffraction pattern was refined using trigonal $Si_6H_6O_3$ with P3 space group. The interlayer layer spacing for the siloxene phase before and after sonication was identified as 6.12 Å and 6.24 Å, respectively. Besides siloxene, crystalline Si, $CaSi_2$, and $FeSi_2$, small amounts of other impurities were also present. Post sonication, the weight percentage of siloxene in the material increased to ca. 56 wt.%, with ca. 26 wt.%, 9 wt.%, and 9 wt.% of bulk Si, $CaSi_2$, and $FeSi_2$, respectively.

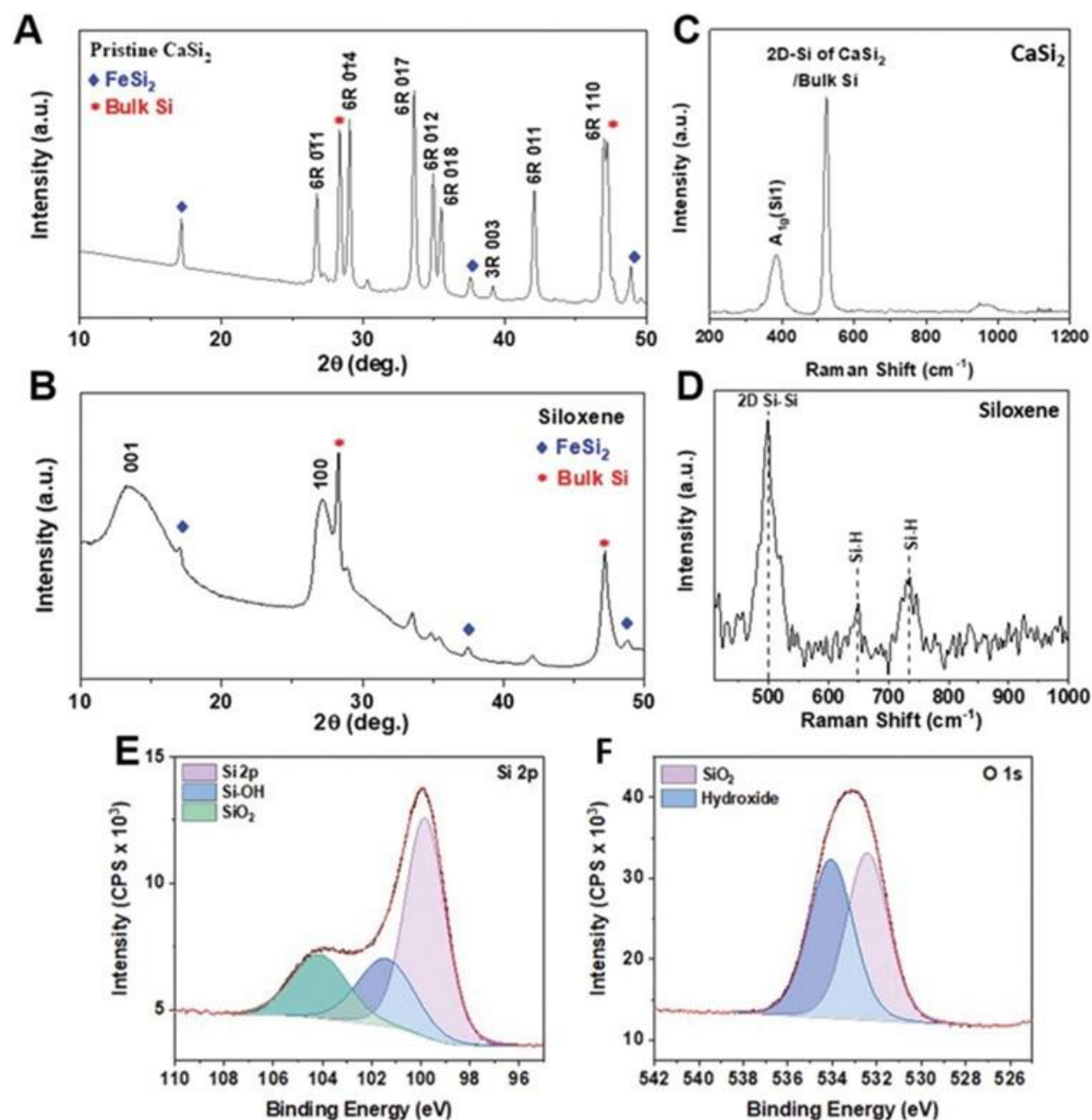


Figure VIII.4.2 Characterization of as-received CaSi_2 and siloxene nanosheets. XRD patterns for (A) as-received CaSi_2 and (B) as-synthesized siloxene nanosheets. Raman spectrum of (C) CaSi_2 and (D) siloxene. XPS analysis of the siloxene nanosheets showing the (E) Si 2p and (F) O 1s spectra.

The Raman spectrum of CaSi_2 is shown in Figure VIII.4.2C with an intense band at 519 cm^{-1} , which is assigned to the 2D-Si network of CaSi_2 or bulk Si. The band at 385 cm^{-1} is attributed to 6R- CaSi_2 . The Raman spectrum of the siloxene is shown in Figure VIII.4.2D. The Raman band at 380 cm^{-1} is assigned to the 2D-Si plane for siloxene. The first-order transverse optical phonon of a 2D Si-based material appears at $\sim 500\text{ cm}^{-1}$ (E_{2g} symmetry). The bands at 649 and 735 cm^{-1} correspond to the Si-H vibrations after Ca deintercalation. The Si 2p and O 1s X-ray photoelectron spectroscopy (XPS) spectra are depicted in Figure VIII.4.2E and F. The quantitative ratio of Si-Si and Si-oxide is 85:15, showing much less oxidation than other reports of siloxene made by topochemical reactions (Si-Si:Si-oxide = 20:80)[1-3] and commercial nano Si (Si-Si:Si-oxide = 30:70)[4]. The O 1s signal shows significant peaks at 532.4 and 534.0 eV in the deconvoluted spectrum, which correspond to the $\text{Si}(\text{OH})_x$ and Si-O bonds of the 2D Si network, respectively Figure VIII.4.2F. The O/Si ratio

in the siloxene is found to be 0.69 from the XPS analysis, which is much lower than previously reported siloxene work with O/Si ratios of 1.55[3] or 1.39 [1].

3. Impact of ultrasonication and electrolyte additives on electrochemistry

The ultrasonication process serves as an effective exfoliation step to decrease the thickness of siloxene sheets prepared by the topotactic reaction. The thinner and more dispersed nanosheets prepared after sonication delivered higher capacities when cycled at a current density of 200 mA g^{-1} using a 1 M LiPF_6 in EC:DMC (3:7, v/v) electrolyte (Figure VIII.4.3A). The rate capability testing (Figure VIII.4.3B) shows similar performance for cells with and without 10% fluoroethylene carbonate (FEC) at discharge rates of 400, 800, 1600, 3200 mA g^{-1} and back to 400 mA g^{-1} with a constant charge rate at 400 mA g^{-1} . A high capacity of 935 mAh g^{-1} at 3200 mA g^{-1} was obtained as well as high reversibility when the discharge rate was returned to 400 mA g^{-1} . Due to the strong rate performance, the cycling stability was tested at 1000 mA g^{-1} for cells with both electrolytes. For these high-rate tests, the siloxene was first cycled three times at 200 mA g^{-1} as a formation step. After 200 cycles, the siloxene delivers a capacity of 750 mAh g^{-1} and capacity retention of 77% with 10% FEC versus a capacity of 200 mAh g^{-1} and capacity retention of 13% without FEC (Figure VIII.4.3C).

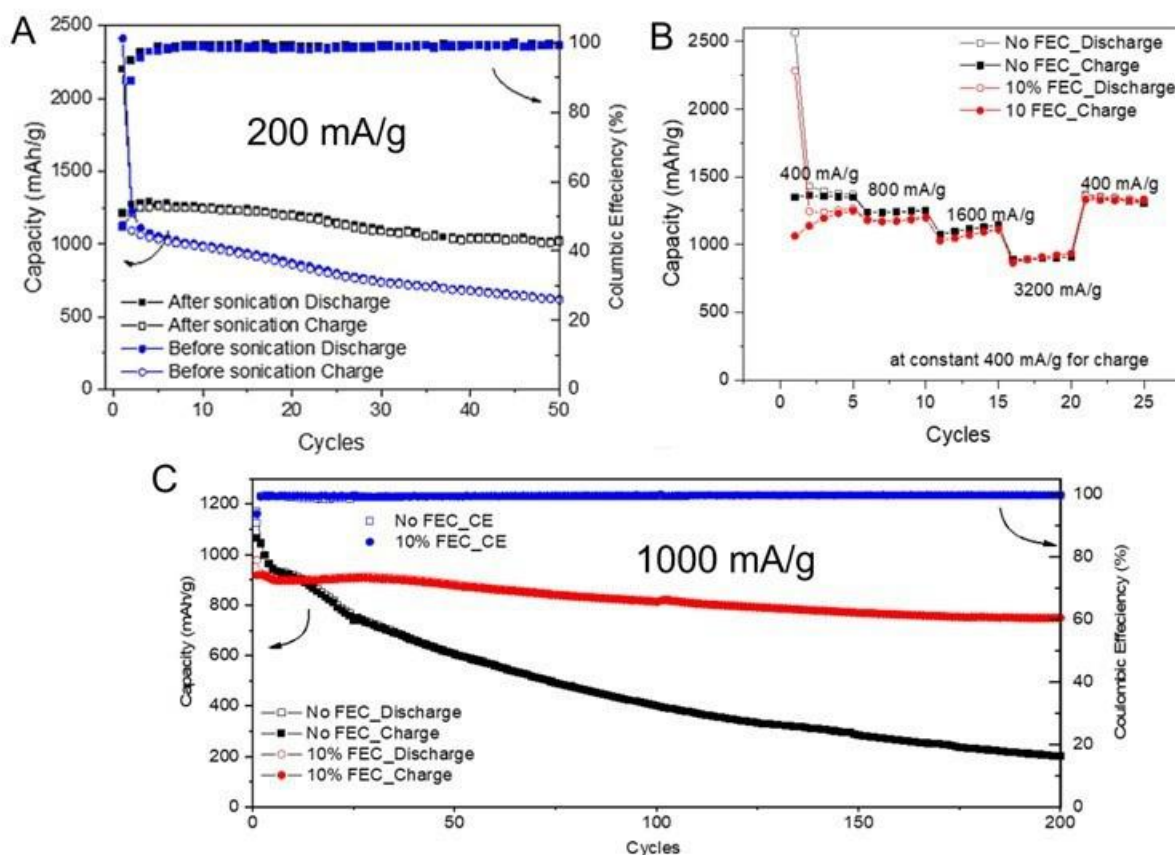


Figure VIII.4.3 (A) Cycling capacity of siloxene before and after sonication at a current density of 200 mA g^{-1} . (B) Rate capability test and (C) cycling capacity of siloxene in 1 M LiPF_6 electrolyte with and without FEC additives.

XPS was also performed on cycled siloxene electrodes in the discharged state tested in electrolyte with and without FEC to investigate differences in SEI composition (Figure VIII.4.4). The F 1s spectra for both electrodes after discharge show two peaks, one corresponding to LiF at 685 eV and another corresponding to fluorophosphates ($\text{Li}_x\text{PO}_y\text{F}_z$, Li_xPF_y) at $\sim 687 \text{ eV}$. The latter is associated with the decomposition of LiPF_6 as well as residual LiPF_6 salt left behind after washing. LiF is perceived as an SEI stabilizing component, especially for Si-based anodes for enhanced cycling stability. Notably, in electrolyte with FEC the discharged electrode had a higher concentration of LiF (83.6%) compared to the non-FEC electrolyte (28.7%). The P 2p

spectra were evaluated to further confirm the presence of the corresponding fluorophosphate peaks assigned to $\text{Li}_x\text{PO}_y\text{F}_z$ (≈ 134 eV) and Li_xPF_y (136.5 eV). In the electrolyte with FEC, the discharged electrode contained a higher percentage of $\text{Li}_x\text{PO}_y\text{F}_z$ (68.1%) compared to the non-FEC electrolyte (47.6%). Coupling with the F 1s spectra, this shows electrodes cycled with FEC electrolyte have a higher concentration of LiF and that $\text{Li}_x\text{PO}_y\text{F}_z$ was formed in situ on the surface of the electrodes. The formed LiF/ $\text{Li}_x\text{PO}_y\text{F}_z$ SEI layer was previously reported to enhance cycling stability [5].

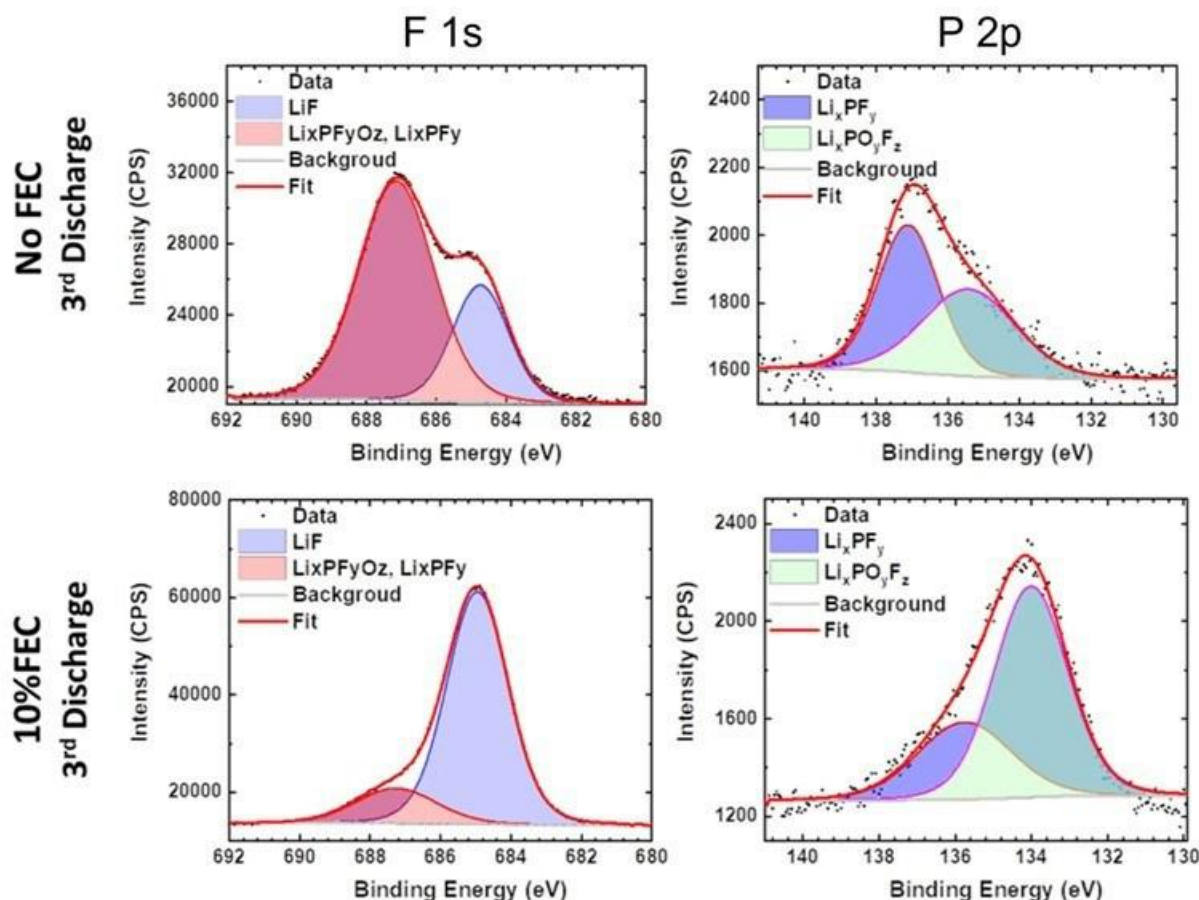


Figure VIII.4.4 XPS fitting results of F 1s and P 2p spectra of cycle 3 discharged siloxene electrodes cycled in electrolyte with and without FEC.

4. Siloxene/NMC622 Full-Cell Testing

One of the potential issues with half-cell testing is that the Li electrode provides a practically infinite amount of Li^+ ions for the working electrode. This is in contrast to the practical limitations of full cells, which have a finite amount of Li^+ . Therefore, to test siloxene in a more practical context, we assembled siloxene/NMC622 full cells with FEC electrolyte. Formation cycles were performed at C/10 and C/5 followed by long-term cycling at C/2. The discharge capacity and voltage profiles for one cell is shown in Figure VIII.4.5. Over 100 cycles, the cell delivered an average discharge capacity of 100 mAh g^{-1} . These results show that siloxene is stable in a full-cell configuration.

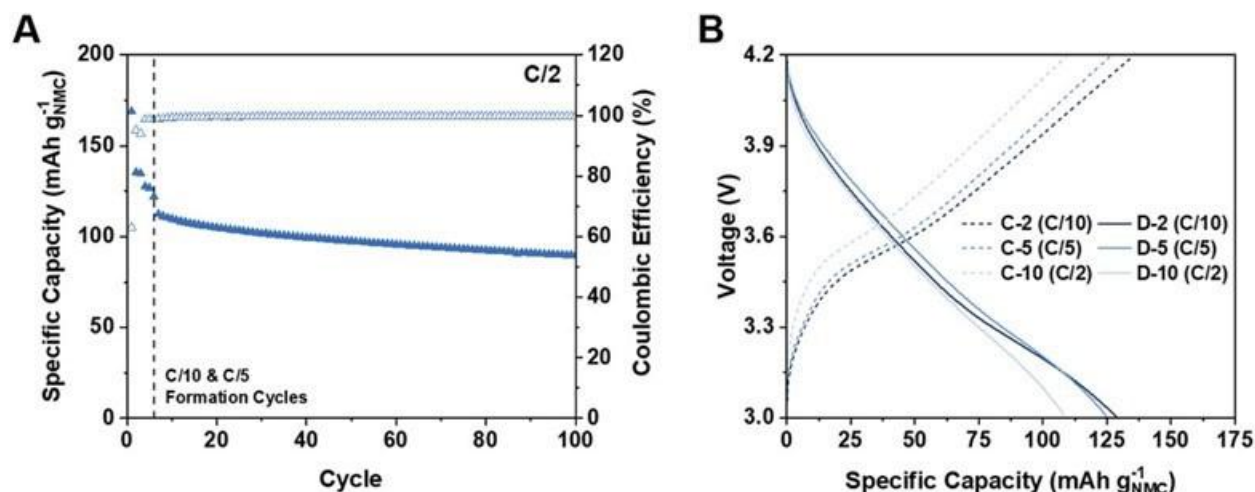


Figure VIII.4.5 Siloxene/NMC622 full-cell cycling. A) Specific capacity and coulombic efficiency versus cycle number and B) selected voltage profiles. Formation cycling was performed with three cycles at C/10 followed by three cycles at C/5. Subsequent extended cycling was then performed at C/2.

Conclusions

Siloxene was synthesized by a topochemical reaction between concentrated HCl and CaSi₂ followed by ultrasonication as an exfoliation step. SEM images showed that the exfoliation step effectively separated the loosely bonded nanosheets and AFM was used to measure the nanosheet thickness. The 2D siloxene nanosheets showed low oxidation with only 15% Si-oxide by XPS. The siloxene nanosheets were tested for reversible lithium storage in half cells with a focus on the effects of FEC as an electrode additive. The cells exhibited good rate capability with a lithiation capacity of 935 mAh g⁻¹ at 3200 mA g⁻¹ and high coulombic efficiency. We found that the addition of 10 wt% FEC to the electrolyte greatly increased the capacity retention for the siloxene sheets, especially at a high rate of 1000 mA g⁻¹. Cells with FEC containing electrolyte delivered 750 mAh g⁻¹ at cycle 200 with 77% capacity retention compared to 200 mAh g⁻¹ and 13% capacity retention for cells without FEC. Full cells were constructed with NMC622 cathodes where 100 cycles at ≈100 mAh g⁻¹ confirmed the stability of the siloxene electrodes. These results compare favorably with previous reports of 2D Si-based materials, in many cases displaying superior capacity and capacity retention despite the greatly increased simplicity of our method. Ex situ XPS and Raman of the electrodes from cells with FEC showed a high concentration of LiF/Li_xPO_yF_z in the SEI layer, which likely contributed to the enhanced cycling. Future work will further investigate the effects of nanosheet morphology and seek to fully understand the (de)lithiation mechanism.

Key Publications

1. Arnot, D.J., W. Li, D.C. Bock, C.A. Stackhouse, X. Tong, A.R. Head, E.S. Takeuchi, K.J. Takeuchi, S. Yan, L. Wang, and A.C. Marschilok, Low-Oxidized Siloxene Nanosheets with High Capacity, Capacity Retention, and Rate Capability in Lithium-Based Batteries. *Advanced Materials Interfaces*, 2022. 9(17): p. 2102238.

References

1. Krishnamoorthy, K., P. Pazhamalai, and S.-J. Kim, Two-dimensional siloxene nanosheets: novel high-performance supercapacitor electrode materials. *Energy & Environmental Science*, 2018. 11(6): p. 1595-1602.
2. Ramachandran, R., X. Leng, C. Zhao, Z.-X. Xu, and F. Wang, 2D siloxene sheets: A novel electrochemical sensor for selective dopamine detection. *Applied materials today*, 2020. 18: p. 100477.

3. Li, S., H. Wang, D. Li, X. Zhang, Y. Wang, J. Xie, J. Wang, Y. Tian, W. Ni, and Y. Xie, Siloxene nanosheets: a metal-free semiconductor for water splitting. *Journal of Materials Chemistry A*, 2016. 4(41): p. 15841-15844.
4. Housel, L.M., W. Li, C.D. Quilty, M.N. Vila, L. Wang, C.R. Tang, D.C. Bock, Q. Wu, X. Tong, and A.R. Head, Insights into reactivity of silicon negative electrodes: Analysis using isothermal microcalorimetry. *ACS applied materials & interfaces*, 2019. 11(41): p. 37567-37577.
5. Fu, C., J. Wang, J. Wang, L. Meng, W. Zhang, X. Li, and L. Li, A LiPF₆-electrolyte-solvothermal route for the synthesis of LiF/LixPFyO_z-coated Li-rich cathode materials with enhanced cycling stability. *Journal of Materials Chemistry A*, 2019. 7(40): p. 23149-23161.

Acknowledgements

The co-PIs for this project include Esther S. Takeuchi (Stony Brook University and Brookhaven National Laboratory), and Shan Yan (Brookhaven National Laboratory).

VIII.5 Integrated Modeling and Machine Learning of Solid-Electrolyte Interface Reactions of the Si Anode (LBNL)

Kristin A. Persson, Principal Investigator

Lawrence Berkeley National Laboratory
1 Cyclotron Rd
Berkeley, CA 94720
E-mail: kapersson@lbl.gov

Jean-Luc Fattebert, Co-Principal Investigator

Computational Sciences and Engineering Department
Oak Ridge National Laboratory
One Bethel Valley Rd
Oak Ridge, TN 37831
E-mail: fattebertj@ornl.gov

Andrew Colclasure, Co-Principal Investigator

National Renewable Energy Laboratory
Center for Integrated Mobility Sciences
Golden, CO 80401
E-mail: andrew.colclasure@nrel.gov

Brian Cunningham, DOE Technology Development Manager

U.S. Department of Energy
E-mail: Brian.Cunningham@ee.doe.gov

Start Date: October 1, 2019

End Date: September 30, 2022

Project Funding: \$4,500,000

DOE share: \$4,500,000

Non-DOE share: \$0

Project Introduction

Lithium-ion batteries (LIB) with silicon (Si) anodes hold great promise for energy storage applications. Given the high theoretical capacity of Si electrodes (3500 mAh/g), these batteries are expected to meet the energy storage demands of the future. Significant scientific challenges need to be overcome before the widespread use of Si-anode LIB. One of the outstanding challenges is understanding the solid electrolyte interphase (SEI), which is a critical but poorly understood component of Si-anode LIB. The SEI has been shown to crack due to volume changes during battery operation, reducing more electrolytes in the process. This report discusses our efforts to model the SEI using a multi-scale approach. We utilize DOE high-performance computing (HPC) facilities to perform density functional theory calculations and classical molecular dynamics simulations and develop continuum models and predictive machine learning models. The insights generated by our models illustrate how the SEI forms on the anode during cycling. The resulting electrolyte stability insights, SEI phase evolution, and microstructure analysis will provide valuable data for feedback and close integration with the existing DOE Si Consortium program to ultimately advance our understanding of the Si anode reactivity and the development of novel Si electrolytes.

Objectives

The overall objective is to understand SEI formation and instability on Si-anodes and improve battery cycling times. The three teams (LBNL, ORNL and NREL) use a multi-scale modelling approach to focus on different length and time scales, using complementary modelling approaches.

The LBNL team seeks to use a first-principles data-driven approach, leveraging high-throughput workflows and machine learning models to construct and analyze massive chemical reaction networks. The reaction

networks include thousands of species and millions of reactions that may participate in the SEI formation cascade. We aim to identify the most likely reaction paths to form key SEI species with minimal imposed bias. The thermodynamics and kinetics of the identified pathways are provided to the ORNL and NREL teams.

The ORNL team seeks to simulate atomistically the SEI and its growth on a Si anode. By supplementing classical molecular dynamics (MD) simulations with the most important reactions identified by the LBNL team or via experimental feedback, ORNL aims to capture approximate *ab initio* reactivity on much longer timescales than are tractable for fully *ab initio* MD while accounting for atomistic interphase growth, SEI spatial composition and molecular diffusion to obtain novel atomistic insight into SEI properties. State-of-the-art techniques are used and developed to extend the explored timescale as much as possible.

The NREL team develops continuum-level models to assist in 1) optimizing electrode microstructure to effectively utilize the Si nano-particles during nominal cycling, 2) providing electrode-design guidelines for accommodating extreme solid-electrolyte interface (SEI) growth during calendar-life studies, 3) and upscale fundamental (electro-)chemical reaction mechanisms, developed from atomistic-scale models, to length- and time-scales relevant for studying battery degradation during cycling and calendar aging. Three continuum-level models are developed to meet project goals. Two continuum-level models are developed to explain SEI formation and reactivity during calendar-life studies. The atomistically informed, chemically complex continuum-level model upscales competing decomposition pathways predicted from the atomistic team (LBNL) to length- (order nm) and time- (order hours/months) scales relevant for understanding calendar-life issues. The “intermediate” mechanism continuum-level model provides key insights into how voltage-hold irreversible currents are extremely sensitive to the potential-dependent composite SEI electrical conductivity. Aside from chemically complex modeling, a finite-strain electrode-level model is developed to determine optimal electrode designs considering both maximum stresses (that can result in current-collector shredding or electrode delamination) and pore-closure effects from Si-particle expansion.

Approach

LBNL

To construct massive chemical reaction networks that include all possible species and reactions that may participate in the SEI formation cascade, we have developed two foundational tools: (1) a reaction network-based Monte Carlo (RNMC) model to handle a massive number of reactions, and (2) a graph neural network machine learning model to leverage unlabeled chemical reaction data for the prediction of reaction kinetics.

Our RNMC approach uses extensible filters, rather than prescriptive templates, to eliminate reactions based on physical or practical criteria without relying heavily on human chemical intuition. By filtering, the massive set of all stoichiometrically valid reactions in a chemical space is reduced to a still huge but computationally tractable set of chemically reasonable - though potentially unintuitive - reactions. To overcome the scaling limitations of graph-based pathfinding, we use a Monte Carlo-based approach, where the reactive space is sampled using reaction thermodynamics.

The RNMC approach is based solely on thermodynamics. To get a complete picture, we need to incorporate kinetics (determined by the reaction activation barrier). Due to the size of the reaction space, we cannot afford to compute them all via density functional theory. Thus, we aim to build a machine learning model for fast estimation of activation barriers and remove pathways that robustly exhibit large activation barriers. Recently, we developed the BonDNet graph neural network model (Wen M. , Blau, Spotte-Smith, & Persson, 2021) to predict bond dissociation energy which we will adapt to allow changing the training target from bond dissociation energies to activation barriers. We note that generating a large enough training set of activation barriers is challenging. Thus, we have elected to develop a transfer learning approach for graph neural networks instead. We first pre-train the model on several unlabeled reactions without activation barriers using self-supervised contrastive learning, then fine-tune the model with a limited supply of labels. This pretraining will distill general knowledge of chemical reactions into the model to help it improve on the target task, i.e., activation energy prediction.

ORNL

To model the SEI formation at the atomistic level and properly bridge the timescale from femtoseconds (to capture atom vibrations in MD simulations) to nano/microseconds (for the SEI growth), we simulate chemical reactions in classical molecular dynamics based on a traditional force-field approach. While classical MD simulations do not account for reactive events such as bond breaking or bond formation, it is possible to modify the atomic potential of each atom in a reactant molecule with the atomic potential of the product by identifying if two molecules are in a likely configuration for a pre-defined chemical reaction to occur. To do that, each reaction requires the specification of a reactant and product template describing the geometry, atomic charges and atomical potential parameters (see illustration in Figure VIII.5.1a). This capability exists as *bond/react* (Gissinger, Jensen, & Wise., 2017) in the open-source molecular dynamics code LAMMPS (<https://lammps.sandia.gov>) used for our simulations. Other parameters to control the reaction such as the probability can be tuned in our simulations to favor one reaction over another. In our simulations, we choose these reactions rates close to 1, thus much higher than the actual rates, which leads to an accelerate simulation of the chemistry happening in the system. In addition, in FY22, we looked at combining this approach with a coarse grain model of molecular movements in between reactions to further speedup MD and reach longer time-scales. Speculating a fully formed SEI made of LiF only, we also looked at the conductivity of an SEI model microstructure.

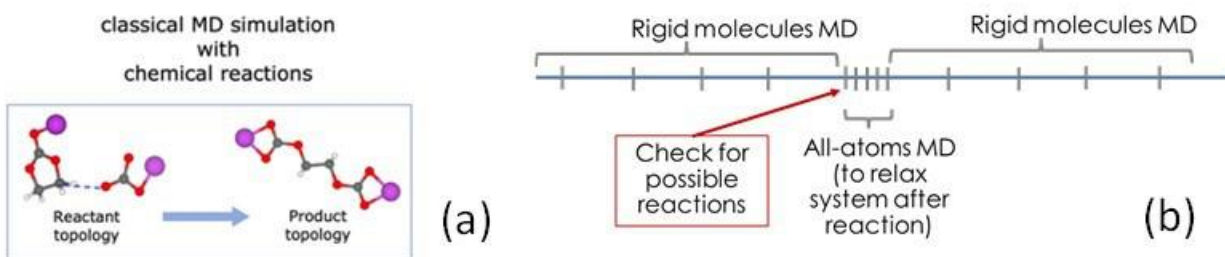


Figure VIII.5.1 a) Illustration of change in molecular dynamics force-field when a chemical reaction happens based on templates of the reactants and products. b) Schematic representation of new MD algorithm combining “coarse grain” (rigid molecules) MD with reactions.

The SEI formation was studied using the above framework in an EC/LiPF₆ electrolyte in an all-atom simulation. We included a set of reactions and first-principles data for the EC decomposition provided by the LBNL team, combined with a PF₆⁻ decomposition reaction found in the literature. All the atomic potential parameters (bonded and nonbonded) were obtained from the commonly used optimized potentials for liquid simulations (OPLS) force field. Our simulations can model the formation of SEI components by specifying the reaction topologies for all the reactions happening near the Si anode. Even though the technique developed during the first two years of this project allows the observation of many reactions in the early stage of SEI growth, we realized that further acceleration was needed to get to a fully formed SEI. Towards that goal, we have been optimizing the algorithm we use as well as the reaction set with the following changes to reduce the computational cost: (i) we reduced the frequency check for reaction templates, (ii) we eliminated reactions that never happen in practice (iii) we do not consider some coordination as explicit reactions anymore. With these optimizations, we now reduced the reaction sets for EC decomposition from eight reactions down to five. We also develop a strategy where we “freeze” the geometry of molecules in between reactions to enable longer MD steps (4X longer). After each reaction, an all-atoms MD needs to be run for some time to let reaction products “relax” their geometry (see Figure VIII.5.1b).

NREL

NREL developed three continuum-level models to explain/study failure modes in Si anodes. These models can be separated into two categories: chemically complex particle-level models and chemo-mechanic models. The chemically complex models capture SEI formation dynamics at different voltage-holds and during cycling.

The chemo-mechanic models capture stress/strain dynamics induced by the large Si particle expansion/contraction on cycling.

SEI modeling

Two models are developed to simulate Si SEI formation and electrolyte decomposition. The “intermediate” mechanism model simulates approximately 10 irreversible global reactions informed from literature (Single, Horstmann, & Latz, *Revealing SEI Morphology: In-Depth Analysis of a Modeling Approach.*, 2017) (Single, Horstmann, & Latz, *Dynamics and morphology of solid electrolyte interphase (SEI).*, 2016). The intermediate mechanism captures SEI dynamics from electrolyte decomposition of ethylene carbonate (EC) and fluoroethylene carbonate (FEC). The mechanism also includes solid-solid reactions that produce the expected inorganic/organic layered structure. The intermediate mechanism model is calibrated to the voltage-hold irreversible current response (Tier 1 protocol for the Si consortium on estimating calendar-life). The intermediate mechanism is used to 1) determine an equivalent SEI electrical conductivity that is required to produce such side-reaction currents, and 2) predict the SEI thickness dynamics as a function of hours/days for each Si material considered in the consortium.

Alongside the “intermediate” mechanism model, an “atomistically informed” mechanism model is also developed. The atomistically informed reaction mechanism model considers complex (electro-)chemical reaction mechanisms produced from atomistic calculations (LBNL). The atomistically informed reaction mechanism includes predominant decomposition pathways for EC and FEC. The more complex reaction model has order 60 electrolyte species, 10 SEI solid-phase species, and 7 gas-phase species. The complex reaction mechanism includes order 50 (potentially competing) reactions. The goal for the atomistically informed model is to introduce a bridge between fundamental reaction insights (order fs to ps) into models that are more apt to calendar-life predictions. In this way, intuition on beneficial additives will ideally move from empirically added, to mathematically determined and optimized.

Both SEI continuum-level models solve conservation equations that resolve heterogeneous electrochemical reactions, ion and solvent transport, electronic resistance, and moving-boundary domains. The reaction mechanisms (both intermediate and atomistically informed) are introduced using CANTERA. By writing the models in a chemical-agnostic way, the reaction network can be easily extended to include additive species and subsequent decomposition pathways. The insights developed on SEI formation will help inform the Si consortium on deleterious electrolyte reduction reactions and provide possible mitigation strategies to reduce continual SEI formation during calendar aging.

Chemo-mechanics modeling

Electrode-level finite-strain chemo-mechanics models are developed to explore Si stress/strain dynamics from extreme particle-level expansion/contraction on lithiation/delithiation during cycling. This model was derived in previous years under this program (Mai, Colclasure, & Kandler, 2019), and is now being used to provide guidance to electrode-level design parameters. For example, the model can be used to understand the relative resistances (e.g., kinetic vs. transport) within the Si-containing cell. These cell-level resistances dynamically change during cycling. For example, as the Si particles lithiate, they expand, which reduces the electrolyte pore-volume and increases the electrolyte tortuosity. This constriction on Li-ion transport in the electrolyte can be a significant resistance that dramatically reduces the cell’s cycling capacity.

The electrode-level chemo-mechanics model is expanded to include 1) electrode-designs for at least three types of Si considered in the consortium (i.e., NREL PECVD Si, Oakridge milled Si, and paraclete), 2) incorporation of SEI growth dynamics, and 3) pressure effects. A major outcome from this model is suggestions on the initial porosity and expected stress effects that lead to pouch-level rippling. The electrode-level chemo-mechanics model is expected to accelerate high-loading electrode development by considering not only electrochemical and transport overpotentials, but also the strongly coupled influences of chemo-mechanics.

Validation

There are several opportunities for experimental validation within the Si consortium. For the finite-strain chemo-mechanical model, there are renewed efforts to resolve mechanics issues (pouch-cell rippling of Cu current-collector). In the consortium, there is an effort to progress from coin-cell performance evaluation to pouch-cells. Unfortunately, the Si expansion/contraction stresses seem to have a significant influence on electrode delamination and Cu rippling in pouch cells. These mechanics issues seem to be present for electrode designs that showed little to no deformation in coin-cells. The intent for the mechanics modeling is to determine stress-relieving designs that alleviate these issues so calendar-life can be studied independently from cycling issues. The mechanics model requires experimentally determined physical parameters and validation from stress-relieving designs (i.e., does the Cu fail or not fail under different length-scale cells).

For the chemically complex models, significant effort has been given to validating based on the voltage-hold (Tier 1 protocol) irreversible currents. Additional (chemically sensitive) experiments are also pursued such as X-ray Photoelectron Spectroscopy (XPS), Neutron Reflectometry (NR), and gas-phase detection tests. These experiments provide solid-phase, liquid-phase, and gas-phase validation, respectively. In the last year, XPS was used to validate the intermediate model predictions. It was found that the model predicted some of the relative species trends measured, but did not capture the heterogeneity inherent to the XPS experiment. In the coming year, significant effort will be put forth to validate the atomistically informed reaction model to gas-phase detection studies under several voltage-hold conditions for the Oakridge milled Si.

In summary, in FY22, NREL developed two different types of continuum-level models to assist the Si consortium on developing a long-lasting, energy-dense Si anode. The continuum-level models include chemo-mechanical models that assist in understanding optimal electrode loadings, thicknesses, porosity, and chemically complex SEI models that interpret voltage-hold leakage currents, and predict electrode/electrolyte decomposition reactions that ultimately result in reduced calendar-life for Si-containing cells. The chemomechanical model will be extended in the next fiscal year to help determine and optimize stress-relieving strategies that improve pouch-cell cyclability (i.e., more than a few cycles after formation). The SEI models will be extended to include more decomposition pathways (e.g., FEC) and include predominant gas-phase species measured in these cells.

Results

LBNL

Machine learning activation barriers

We have been developing machine learning models for the estimation of activation barriers. It is still excessively computationally expensive to generate a large enough dataset from first principles to train a machine learning model to predict activation barriers accurately. As a result, we seek to develop new techniques to train machine learning models with a limited supply of labelled data (i.e., data with computed activation barriers).

To minimize the number of required DFT-computed activation barriers, we have developed a transfer learning approach based on self-supervised contrastive learning (Wen M. , Blau, Xie, Dwaraknath, & Persson, 2022). Our approach involves training the model in two stages. First, we pre-train the model on unlabeled reaction data using unsupervised contrastive learning. Second, we fine-tune the model's parameters on a small number of labelled reactions. The contrastive pretraining model learns by making the representations of two augmented versions of a reaction which are like each other but distinct from other reactions (see Figure VIII.5.2 for a schematic of the implemented self-supervised approach). We tested this on a proof-of-concept problem, classifying reactions into separate families and found that this pretraining approach can significantly improve model performance for small datasets.

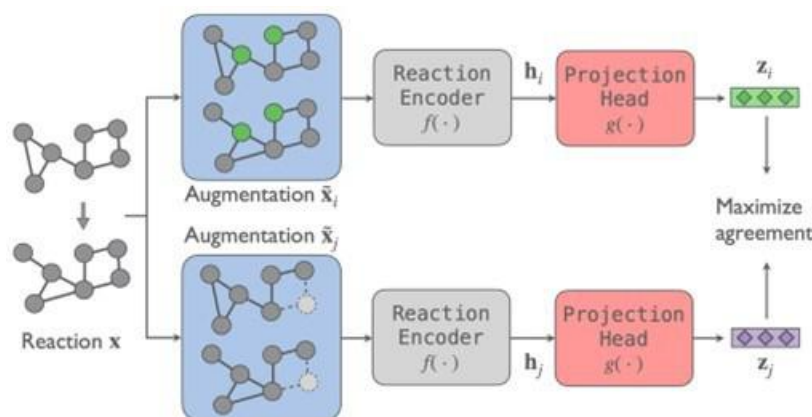


Figure VIII.5.2 Illustrative overview of the contrastive self-supervised approach. Two augmentations of an input reaction are passed through the reaction encoder to get their reaction fingerprints h_i and h_j and then a projection head to get vector representations z_i and z_j , and the model maximizes the agreement between the two representations of the reaction.

Micro-kinetic models of the SEI through chemical reaction networks

We then applied the developed machine learning and reaction network models to study the SEI. We have built a massive electrochemical reaction network to capture all possible elementary reactions (Spotte-Smith, et al., 2022). We have expanded this methodology and created a new method, called reaction network Monte Carlo (RNMC), that enables us to analyze a (chemical reaction network) CRN containing over 80 million reactions between over 5,000 species to automatically identify reaction pathways to a range of crucial SEI products and gaseous byproducts. With rate constants derived from high-throughput transition-state calculations and Marcus theory, we perform kinetic Monte Carlo (kMC) simulations to study SEI formation under varying chemical and electrochemical conditions. We perform kMC simulations under representative chemical and electrochemical conditions to understand how competition between various reaction pathways could change over the course of SEI formation cycling (as shown in Figure VIII.5.3). The results of our simulation recover the Peled-like separation of the SEI into inorganic and organic domains resulting from rich reactive competition. We have also confirmed previously postulated SEI decomposition routes, indicating possible opportunities for SEI engineering.

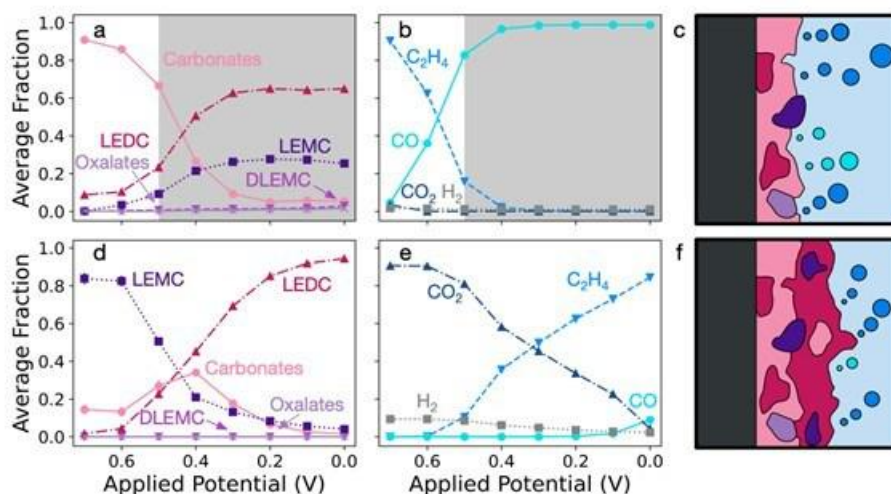


Figure VIII.5.3 Average fractions of SEI products (a, d) and gaseous byproducts (b, e) at the end of kMC simulations as a function of applied potential referenced to an Li/Li⁺ electrode. Simulations were conducted under two conditions reflecting different regimes of SEI formation.

Mechanistic pathways to understand the electrolyte decomposition

Finally, we identify elementary reaction mechanisms for LiPF_6 decomposition using DFT calculations. We focused primarily on hydrolysis (which, despite the rigorous drying performed on Li-ion battery electrolytes, is widely reported to be a significant driver of LiPF_6 decomposition to form HF, LiF, and other species (Sloop, Pugh, Wang, Kerr, & Kinoshita, 2001)) and reactions with additional major electrolyte and interphase species (e.g. ethylene carbonate or EC, Li_2CO_3). In line with previous theoretical studies (Okamoto, 2013), we find that the proposed hydrolysis mechanism suffers from high energy barriers. Moreover, every step in the mechanism is thermodynamically unfavorable ($\Delta G > 0$). While hydrolysis could be potential in proximity to the positive electrode at high potentials or elevated temperatures, it should not meaningfully participate in early SEI formation.

We propose another mechanism to explain the decomposition of LiPF_6 . Following an initial elimination step to form LiF, PF_5 could react rapidly with Li_2CO_3 (mechanism shown in Figure VIII.5.4). Reactions between LiPF_6 and inorganic carbonates have been suggested before, but such proposed pathways have been largely ignored in the literature. Further, no elementary mechanism for this reaction has yet been reported. In addition to having lower barriers than any previously reported LiPF_6 decomposition mechanism, the proposed mechanism is notable for being entirely chemical in nature. This means that LiPF_6 decomposition during early SEI formation should have no explicit dependence on applied potential; however, because Li_2CO_3 forms as a result of the electrochemical reduction of EC, an implicit dependence should be expected.

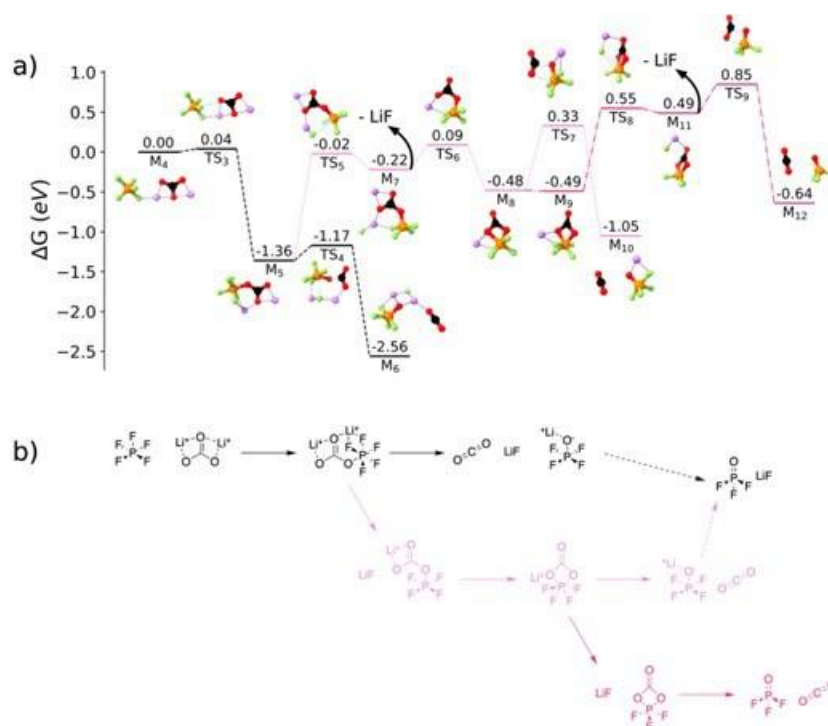


Figure VIII.5.4 Reaction mechanism for the reaction of PF_5 with Li_2CO_3 . a) An energy diagram showing three pathways, leading either to LiPOF_4 (black, pink) or PO_2F_3 (red). b) The same pathways, shown as 2D schematics.

ORNL

Using our new optimized algorithm, we find that with rigid molecules, the new set of reactions, leads to a 6X speedup (time-to-solution) compared to the original scheme. We have been validating this approach by comparing with all-atoms MD, and running very long simulations to demonstrate effectiveness of technique and SEI formation on longer time-scales. Figure VIII.5.5 shows the diffusion of EC using the all-atoms MD versus a rigid molecule approach with a higher temperature T for the thermostat of the EC molecules. A very good agreement was reached for $T = 320$ K. We expect to demonstrate the effectiveness of this new approach

in the near future with longer SEI formation studies. The initial attempt to do that was paused while a software bug is being address in LAMMPS to enable these simulations to run smoothly for very long times.

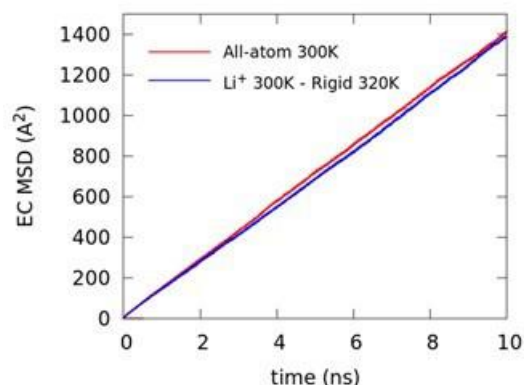


Figure VIII.5.5 Diffusion of rigid EC molecules in electrolyte compared to an all-atoms simulations using a higher temperature thermostat at 320K for EC.

Jumping to a fully formed microstructure, we “created” a fully formed SEI made of a few polycrystals of LiF as a surrogate model for the whole SEI, and measure Li diffusivity and conductivity in these polycrystals. Initial structure was created with the software AtomsK (<https://atomsk.univ-lille.fr>). After removing spurious atoms too close to each other, the system was annealed at 500 K for 250 ps to remove dependencies on initial configuration. Self-diffusion data for Li were measured over 20 ns of simulation run, for three different systems (see Figure VIII.5.6). Results are consistent with other studies focused on smaller subsystems, and show conductivities that (i) happen mostly along the grain boundaries (ii) are much smaller than in the electrolyte.

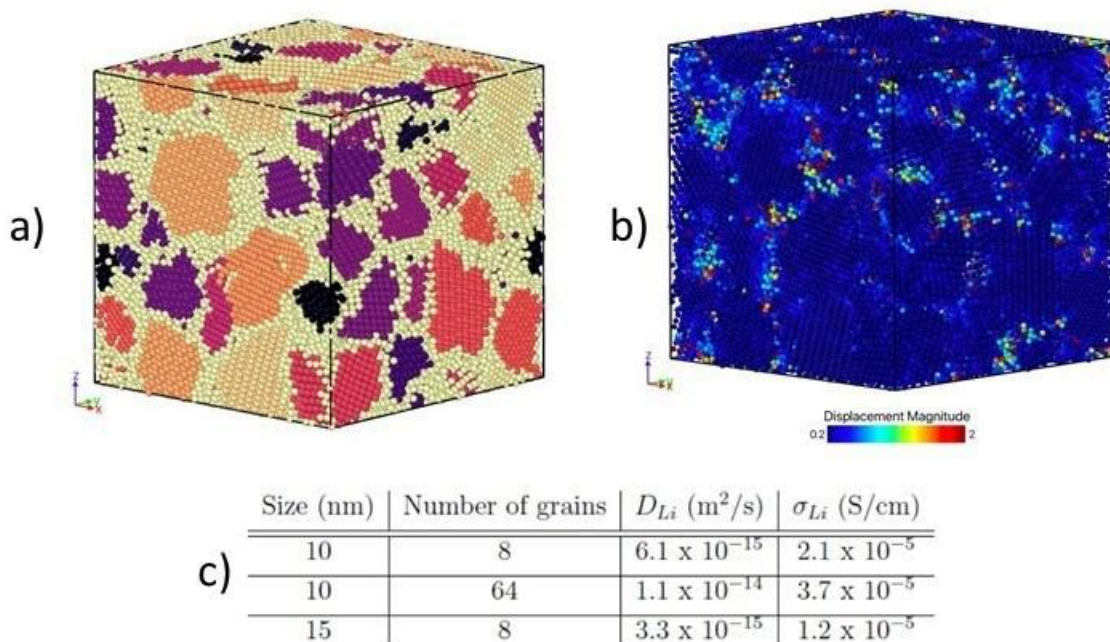


Figure VIII.5.6 Atomistic model of LiF microstructure. a) microstructure with atoms colored according to local ordering. Yellow color corresponds to locally disordered arrangement b) atoms colored by their displacement magnitudes over time of simulation. It is visually clear that largest displacements responsible for conductivity happen mostly at grain boundaries. c) numerical measurements of Li diffusion and conductivities in three different microstructures. Left column indicates the lateral length of the computational cells used in these simulations.

NREL

Figure VIII.5.7(a-d) shows the schematic of the detailed SEI model domain with reaction pathways upscaled from atomistic to the continuum realm and some salient results on model validation with electrochemical data (current, capacity) from composite silicon anode voltage hold experiments. The reaction mechanism consists of heterogeneous reduction reactions and homogeneous pathways to LEDC and Li_2CO_3 formation with SEI growth occurring through LEDC deposition from the electrolyte phase. The continuum-level physics includes complex reaction mechanism implemented via CANTERA, species transport, charge, and lattice site conservation. To validate the model, we compare it to experimentally measured leakage current from 180 hr voltage hold experiments on composite Si anodes in the half cell configuration. The model captures SEI solid phase electron diffusion limited growth and requires potential dependent SEI electronic diffusivity to match the leakage current data (see Figure VIII.5.7b and Figure VIII.5.7d). An order of magnitude drop in electron diffusivity magnitudes is observed from 100 mV to 250 mV hold. Different salt/solvent decompositions are activated at varying potentials resulting in SEI compositional variability with voltage. Consequently, the composite SEI electron diffusivity is a function of individual species diffusivity present in the SEI and is likely to be the cause of why a potential dependent conductivity in the model is required to match the experimental leakage currents. The trend matches electron conduction limited growth with intermediate SEI mechanism also showcasing a large solid phase potential gradient across the SEI. Figure VIII.5.7c showcases film thickness evolution with time and it follows the square root of time behavior generally observed in literature. Low Si voltage hold (100mV) or higher lithiation state of the silicon leads to a stronger driving force for electrolyte decomposition producing SEI products at a rapid rate. Consequently, a thicker SEI is observed after the 180 hr hold at 100 mV (~9 nm) as compared to the 250 mV hold (~2 nm). During cyclic aging, the Si anode generally experiences potentials varying from 100 to 750 mV; adaptive charging protocols lowering the time spent at high states of charge can provide a pathway towards stabilizing Si SEI growth.

Figure VIII.5.8 illustrates comparison of the SEI solid phase composition between intermediate SEI model and experiments. The NREL team performed V-hold experiments at different potentials (10, 100, 350 mV) on Si thin film anodes to analyze electrochemical and composition data related to irreversible SEI growth and compare with model. Analysis of electrochemical data through capacity deconvolution model reveals insights into SEI growth on Si; high SEI parasitic capacity is observed at low voltage (high SOC) for thin film silicon as well. Furthermore, X-ray photoelectron spectroscopy (XPS) on EMC rinsed samples provides solid-phase composition data (see Figure VIII.5.8b and Figure VIII.5.8d). Measured SEI layer is extremely thin (~5 to 10 nm), indicating possible exfoliation of organic SEI due to solvent rinse, or rest at delithiated state of 900 mV in the last reference performance test cycle causing dissolution of the organic SEI. The compositional profiles do not show abrupt interfaces, presumably due to sample roughness and/or lateral inhomogeneities. SEI component peaks for compounds like LiF, Li_2CO_3 are only visible in the first few sputters indicating thin SEI layers. Lithium fluorophosphates $\text{Li}_x\text{PF}_y\text{O}_z$ are also formed in the SEI. There is significantly more Li 1s signal associated with the 350 mV voltage hold likely associated with Li_2O while more LiF is observed for the 100 mV case. Thus, inorganic SEI is rich in LiF and Li_2O with more Li_2O at high voltage (350 mV) vs more LiF at low voltage (100 mV). Figure VIII.5.8(c,d) and Figure VIII.5.8(e,f) showcase the intermediate SEI model predictions for solid phase volume fraction and subsequent conversion to elemental atom percentage in the SEI at 100 mV and 350 mV respectively. For 100 mV, a bilayer SEI structure is predicted with inorganic rich inner SEI. Higher Li percentage in inorganic SEI is seen from model with large contribution coming from Li_2O , Li_2CO_3 , LiF. The outer layer comprises majorly of organic LEDC with LiF as a minor contributor. At 350 mV, model predicts that the SEI layer loses its dual-layer nature with uniform composition across the SEI. The model matches experimental trend of LiF concentration increase from 350 mV to 100 mV but requires new decomposition reaction pathways occurring at higher potentials to see Li_2O depletion from 350 mV to 100 mV.

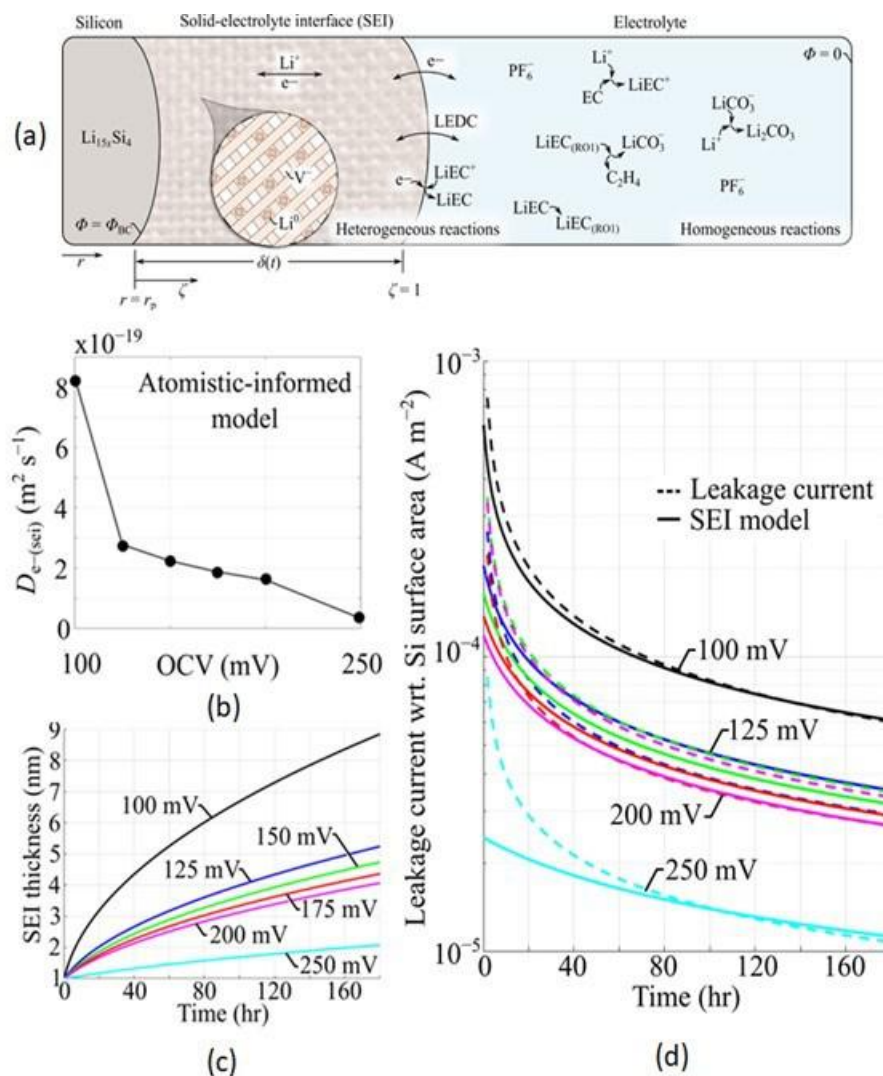


Figure VIII.5.7 (a) Schematic of detailed SEI model with atomistic elementary reaction mechanism involving several solution and solid phase species. (b) Model prediction of varying electron diffusivity with voltage to match irreversible currents obtained from 180 hr voltage hold experiments on composite porous silicon anodes held at potentials from 100 mV to 250 mV. (c) Model prediction of SEI thickness variation with time for 180 hrs of voltage hold at varying Si anode potentials from 100 mV to 250 mV. (d) Comparison of leakage currents between model and experiments.

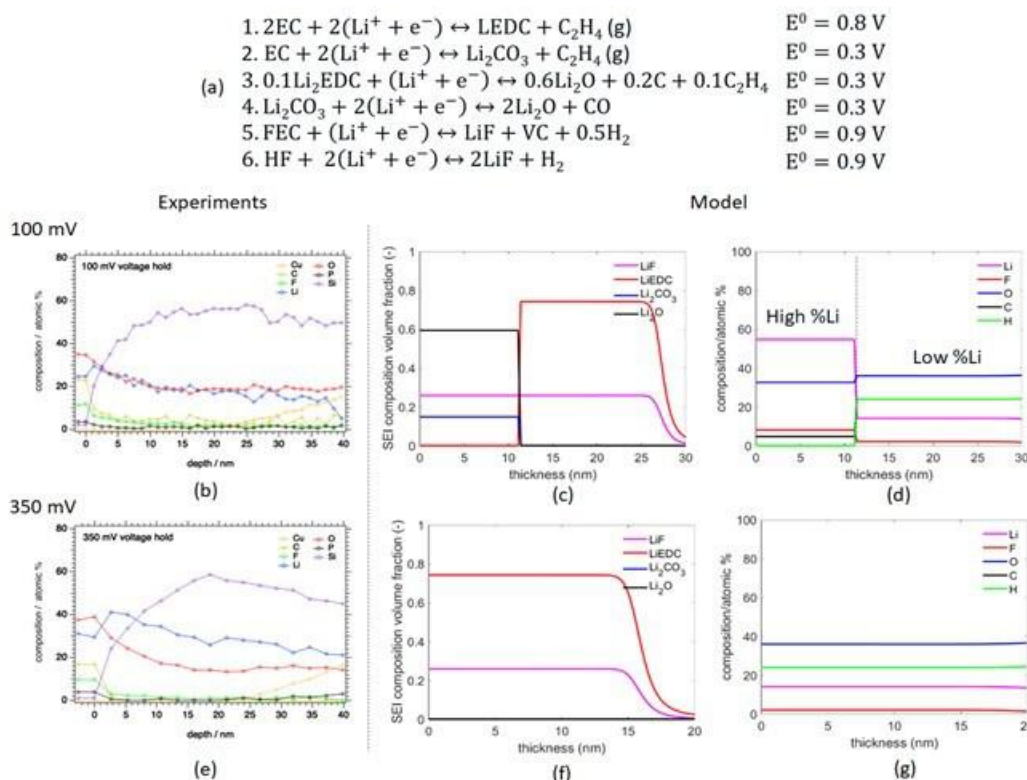


Figure VIII.5.8 (a) List of reactions in intermediate SEI model. (b) Experimental SEI solid phase composition data in atom percentage obtained through XPS on thin film silicon held at 100 mV. (b-c) SEI model prediction of solid phase volume fraction and atomic percentage for thin film silicon held at 100 mV. (d) Experimental SEI solid phase composition data in atom percentage obtained through XPS on thin film silicon held at 350 mV. (e-f) SEI model prediction of solid phase volume fraction and atomic percentage for thin film silicon held at 350 mV.

Finally, a finite strain chemo-mechanics Si lithiation model is combined with virtual microstructure generation and transport homogenization calculations to understand the role of electrolyte transport limitations and its variation with Si state of charge. The chemo-mechanics model is used to determine Si particle expansion, porosity reduction and anode thickness increase at different states of charge during slow charging (C/100) of a 5 mAh/cm² full Si|NMC532 cell from 3.0 to 4.2 V with varying initial nominal porosities of 50% and 25% (see Figure VIII.5.9(a,b)). For initial porosities of 50% and 25%, Si anode reaches porosities of 40% and 10% at top of charge respectively showcasing large porosity reduction due to Si expansion. Si particle diameter increases from 100 nm to 130 nm while anode thickness shows substantial increase as well. These parameters are utilized as inputs for artificial microstructure generation of (un)lithiated Si anodes with conductive additive and binder (see Figure VIII.5.9c and Figure VIII.5.9d). Figure VIII.5.9e showcases that the (un)lithiated artificial microstructures porosity match with the macrohomogeneous model predictions (shown in Figure VIII.5.9a) indicating accurate electrode architectural representation. Tortuosity computations on Si microstructures with initial porosity 50% reveal that the tortuosity increases from 1.7 to 1.9 showcasing miniscule transport limitations. Hence, an initial porosity ~50% is desirable. Tortuosity computations on Si microstructures with initial porosity 25% reveal that the tortuosity increases from 6.1 to 259 showcasing exacerbated transport limitations due to minimal porosity and limited percolation pathways. The conductive binder domain induces a significant degradation of ionic transport in the system.

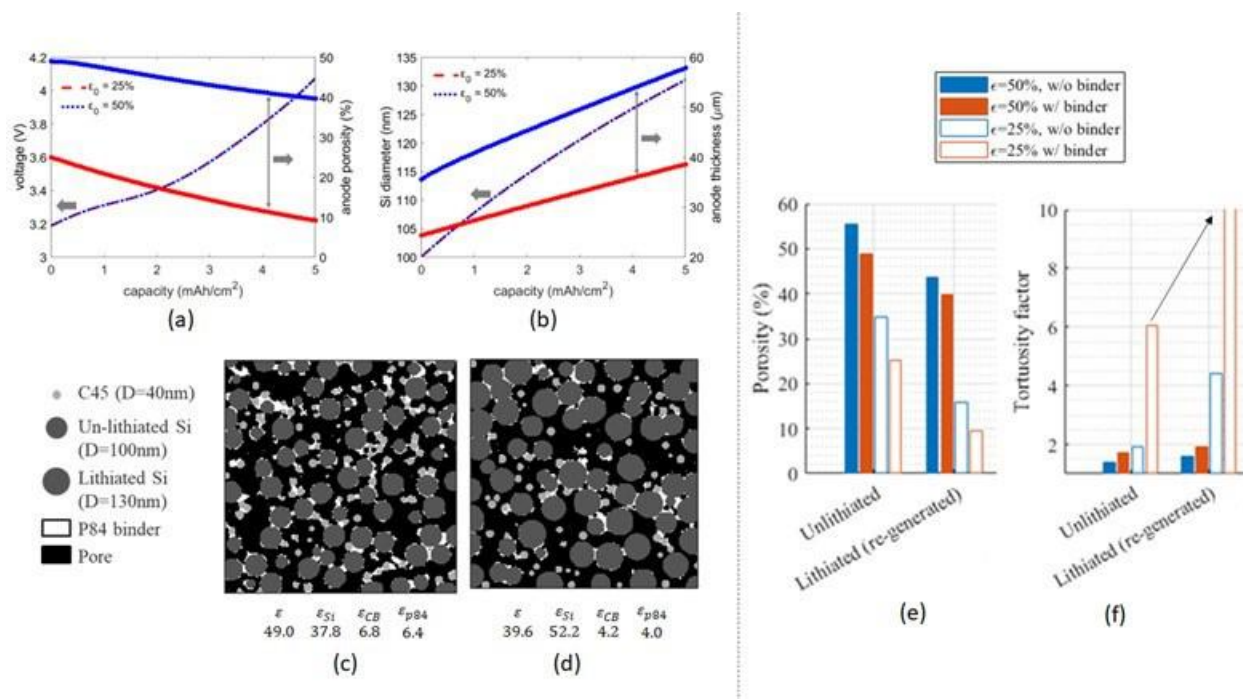


Figure VIII.5.9 (a-b) Finite strain macrohomogeneous model predictions of (a) voltage and Si anode porosity evolution and (b) Si particle diameter and Si anode thickness evolution during slow charging (C/100) of a full Si|NMC532 cell from 3.0 to 4.2 V with varying initial nominal porosities of 50% and 25%. (c-d) Generated virtual microstructure for (c) un lithiated and (d) lithiated Si anode consisting of active Si particles, carbon conductive additive, polyimide P84 binder, pore for tortuosity calculations. (e-f) Homogenization calculations based (e) porosity and (f) tortuosity values for Si anodes with initial nominal porosities 50% and 25%. Porosity and tortuosity values are shown with and without binder.

Conclusions

LBNL

- We have developed a transfer learning approach based on self-supervised contrastive learning to predict activation barriers. We applied this model to a few prototype examples and found that we can significantly improve model performance for small datasets.
- We have built a massive electrochemical reaction network based on graph theory in order to develop a micro-kinetic model to understand the SEI.
- We have performed density functional theory calculations to find a low-barrier mechanism for the decomposition of LiPF_6 through the chemical reaction of PF_5 with Li_2CO_3 .

ORNL

- We assembled reactive molecular dynamics simulations of the Si anode and electrolyte, including reactions that describe EC and PF_6^- decomposition. We continue working with LBNL to add more reactive complexity and make our simulations more quantitative kinetics using reaction energy barriers.
- A rigid molecules MD strategy was developed to further speed up time-to-solution in between reactions, using timesteps 4X larger than before. After adjusting temperature thermostats for the various groups of atoms, diffusion properties were shown to match very well all-atoms simulations. Long simulations of SEI growth with rigid molecules are currently on hold due to a software issue.
- A model microstructure of SEI made of LiF only was build for various grain sizes and enabled the computation of microstructure conductivity. The model showed a clear dominance of atomic motions through grain boundaries versus bulk in determining overall conductivity.

NREL:

- Developed atomistic, intermediate SEI model and validated with electrochemical and composition data from voltage hold experiments to provide strategies for stable SEI growth e.g. hold voltage.
- In the next fiscal year, the chemically complex SEI models will be further validated with gas-phase composition data from gas chromatography–mass spectrometry (GC-MS) experiments on voltage hold Si pouch cells. The finite strain model will be used to delineate strategies for alleviating stress-based deformation and transport limitations for the Si anode.
- Developed finite strain models coupled to virtual microstructure generation and homogenization calculations to understand electrolyte transport limitations during Si lithiation and provide anode design metrics e.g. optimal porosity.
- In the next fiscal year, the finite strain models will be extended to consider “stress-relief” designs (such as laser patterning) to improve pouch cyclability.

Key Publications

1. Wen, Mingjian, Samuel M. Blau, Xiaowei Xie, Shyam Dwaraknath, and Kristin A. Persson. “Improving machine learning performance on small chemical reaction data with unsupervised contrastive pretraining.” *Chemical Science* 13.5 (2022): 1446-1458
2. Spotte-Smith, E. W. C., Kam, R. L., Barter, D., Xie, X., Hou, T., Dwaraknath, S., S. M. Blau & Persson, K. A. (2022). Towards a Mechanistic Model of Solid-Electrolyte Interphase Formation and Evolution in Lithium-ion Batteries, *ACS Energy Letters*, 7, 1446-1453.
3. Spotte-Smith, Evan, et al. "Elementary Decomposition Mechanisms of Lithium Hexafluorophosphate in Battery Electrolytes and Interphases." (2022).
4. Alzate-Vargas, Lorena, Samuel M. Blau, Evan Walter Clark Spotte-Smith, Srikanth Allu, Kristin A. Persson, and Jean-Luc Fattebert. “Insight into SEI growth in Li-ion batteries using molecular dynamics and accelerated chemical reactions.” *J. Phys. Chem. C* 125 (2021): 18588–18596.
5. Alzate-Vargas, Lorena and Vikrant, K. S. N. and Allu, Srikanth and Fattebert, Jean-Luc, “Atomistic modeling of LiF microstructure ionic conductivity and its influence on nucleation and plating”, *Phys. Rev. Materials* 6 (9), 095402, (2022), 10.1103/PhysRevMaterials.6.095402
6. Maxwell C. Schulze, Marco-Tulio F. Rodrigues, Josefine D. McBrayer, Daniel P. Abraham, Christopher A. Apblett, Ira Bloom, Zonghai Chen, Andrew M. Colclasure, Alison R. Dunlop, Chen Fang, Katharine L. Harrison, Gao Liu, Shelley D. Minter, Nathan R. Neale, David Robertson, Adam P. Tornheim, Stephen E. Trask, Gabriel M. Veith, Ankit Verma, Zhenzhen Yang and Christopher Johnson (2022). “Critical Evaluation of Potentiostatic Holds as Accelerated Predictors of Capacity Fade during Calendar Aging”. *J. Electrochem. Soc.*, 169 no. 5 (2022): 050531.

References

1. M. Wen, S. M. Blau, E. W. C. S. Spotte-Smith and K. A. Persson, "BonDNet: a graph neural network for the prediction of bond dissociation energies for charged molecules.," *Chemical Science*, pp. 1858-1868, 2021.
2. J. R. Gissinger, B. D. Jensen and K. E. Wise., "Modeling chemical reactions in classical molecular dynamics simulations," *Polymer*, vol. 128, pp. 211-217, 2017.
3. F. Single, B. Horstmann and A. Latz, "Revealing SEI Morphology: In-Depth Analysis of a Modeling Approach.," *J. Electrochem. Soc.*, vol. 164, no. 11, p. E3132, 2017.
4. F. Single, B. Horstmann and A. Latz, "Dynamics and morphology of solid electrolyte interphase (SEI).," *Phys. Chem. Chem. Phys.*, vol. 18, no. 27, pp. 17810-17814., 2016.
5. W. Mai, A. Colclasure and S. Kandler, "A Reformulation of the Pseudo2D Battery Model Coupling Large Electrochemical-Mechanical Deformations at Particle and Electrode Levels," *J. Electrochem. Soc.*, vol. 166, no. 8, p. A1330, 2019.
6. M. Wen, S. M. Blau, X. Xie, S. Dwaraknath and K. A. Persson, "Improving machine learning performance on small chemical reaction data with unsupervised contrastive pretraining.," *Chemical science*, vol. 13, no. 5, pp. 1446-1458, 2022.

7. E. W. C. Spotte-Smith, R. L. Kam, D. Barter, X. Xie, T. Hou, S. Dwaraknath, B. S. Xiaowei Xie and K. A. Persson, "Toward a Mechanistic Model of Solid–Electrolyte Interphase Formation and Evolution in Lithium-Ion Batteries.," *ACS Energy Letters*, vol. 7, no. 4, pp. 1446-1453, 2022.
8. S. E. Sloop, J. K. Pugh, S. Wang, J. B. Kerr and K. Kinoshita, "Chemical reactivity of PF₅ and LiPF₆ in ethylene carbonate/dimethyl carbonate solutions.," *Electrochemical and Solid-State Letters*, vol. 4, no. 4, p. A42, 2001.
9. Y. Okamoto, "Ab initio calculations of thermal decomposition mechanism of LiPF₆-based electrolytes for lithium-ion batteries.," *Journal of The Electrochemical Society*, vol. 160, no. 2, p. A404, 2013.

Acknowledgements

ORNL: Lorena Alzate Varga (moved to LANL in September 2022)

LBNL: Mingjian Wen, Hetal D. Patel, Evan Walter Clark Spotte Smith, Xiaowei Xie

NREL: Ankit Verma, Peter Weddle, Francois Usseglio-Viretta, Andrew Colclasure, Kandler Smith.

VIII.6 Advanced Anode Manufacturing through Ultra-Thin Li Deposition (Applied Materials, Inc.)

Subra Herle, Ph.D., Principal Investigator

Applied Materials, Inc.
3225 Oakmead Village Dr
Santa Clara, CA 95054
E-mail: Subra_Herle@amat.com

Brian Cunningham, DOE Technology Development Manager

U.S. Department of Energy
E-mail: Brian.Cunningham@ee.doe.gov

Start Date: May 25, 2021
Project Funding: \$6,528,338

End Date: September 30, 2022
DOE share: \$2,820,373

Non-DOE share: \$3,707,965

Project Introduction

Much of the doubling in Li-ion battery energy density over the past 30 years has been achieved through cathode material improvement. Improvements in anode energy density have languished, partly due to integration and manufacturing challenges, including the lack of an effective, scalable solution for incorporating minimal amounts of lithium for pre-lithiation of Si/SiO_x-C and producing ultra-thin lithium metal anodes (1-20µm) cost-effectively in high volume.

None of the existing approaches meet high volume manufacturing (HVM) requirements for lithiation and prelithiation. In this respect, Applied Materials' current strategy is unique, considering and including ease of integration with existing Li-ion battery process flows and production of defect-free lithium films scalable in thickness and to industry-standard widths, at a low cost, in a safe environment.

Objectives

The project aims to develop and validate a cost-effective ultra-thin Li deposition system for advanced anode high-volume manufacturing (HVM) and demonstrate the following.:

- **Objective 1:** Advanced batteries with pre-lithiated SiO_x-C anodes with energy density >337Wh/kg from TRL 5 to TRL 7 (See Table VIII.6.1.)
- **Objective 2:** Advanced batteries with Li-metal anode with energy density >375Wh/kg from TRL 4 to TRL 6 (See Table VIII.6.2.)
- **Objective 3:** Develop a Li deposition system to meet high volume mfg. (HVM) requirements TRL 4 to TRL 8 (See Table VIII.6.3.)

Samples generated from Applied Materials ultra-thin Li deposition system are validated for Pre-Lithiation and Lithium metal anode: Current updates on cell performance data are summarised below (see Status description later in this section).

Table VIII.6.1 Cell Performance data summary for Pre-lithiated Anodes

Partners: Ionblox & Applied Materials	Cell Performance for Pre-lithiated Anodes (Minimum Manufacturing Goals)		
Parameter	Pouch Cells (Pre-lithiated Si-Anodes) (>2 Ah) BP-1	Pouch Cells (Pre-lithiated Si-Anodes) (>10 Ah) BP-2	Pouch Cells (Pre-lithiated Si-Anodes) (>10 Ah) BP-3
Energy Density	≥300 Wh/kg	≥319 Wh/kg	≥337 Wh/kg
Cycle Life	600 Cycles	1000 Cycles	1100 Cycles
Fast Charge	N/A	80% in ≤15 minutes	80% in ≤15 minutes
Status	Completed (305 Wh/Kg & 700 cycles)	Cells delivered to INL for testing (333 Wh/Kg)	Ongoing

Table VIII.6.2 Cell Performance data summary for Lithium Metal Anodes

Partners: SAFT America, PNNL & Applied Materials	Cell Performance for Lithium Metal Anodes (Minimum Manufacturing Goals)		
Parameter	Pouch Cells (Lithium Metal Anodes) (5-10 Ah) BP-1	Pouch Cells (Li Metal Anodes) (~10 Ah) BP-2	Pouch Cells (Pre-lithiated Si-Anodes) (>10 Ah) BP-3
Energy Density	≥300 Wh/kg	≥337 Wh/kg	≥337 Wh/kg
Cycle Life	200 Cycles	300 Cycles	1100 Cycles
Fast Charge	N/A	N/A	80% in ≤15 minutes
Status	Completed (300 Wh/Kg & 200 cycles PNNL)	Completed: Cells delivered to INL for testing (SAFT, 300 Wh/Kg & 300 cycles PNNL)	Ongoing

Table VIII.6.3 Li Deposition system manufacturing performance

Li Deposition System Manufacturing Target Performance (Measured with respect to established Baseline)		
Parameter	Measure (Minimum Manufacturing Goals)	End of Program Performance Goals (10 μm Li deposition)
Mechanical System Throughput, Web Speed Increase	≥100%	>20m/min
Substrate Width Increase	≥100%	800 mm
Uniformity Increase	≥50%	+/- 7.5%
Uptime Increase	≥50%	Roll-to-Roll Baseline TBD
Status	Line speed & uniformity requirements met for 400 mm wide substrate	

Approach

With funding support from DoE and working closely with leading U.S. battery makers Ionblox (formerly Zenlabs Energy: pre-lithiated SiOx-C anode) and Saft America (Li metal anode) and leveraging advanced battery research capabilities of key National Laboratories (PNNL, LBNL, ANL), Applied Materials is accelerating the time to market of a high productivity lithiation solution based on physical vapor deposition for both SiOx-C anodes and Li-metal anodes. Applied Materials is accelerating the development of its current R&D roll-to-roll (R2R) lithium deposition system based on Applied's production-proven SmartWeb™

platform. Li-coated anodes are being fabricated and shared with project partners for integration into cells and characterization. As validated by the project collaborators, the deposition equipment and processes will be optimized to achieve volume manufacturing performance targets while meeting battery performance and cost targets. Ionblox is focusing on high silicon content SiOx-C based batteries and Saft & Pacific Northwest National Lab (PNNL) on high energy density Li-metal batteries. Lawrence Berkeley National Laboratory (LBNL) will be responsible for investigating prelithiated SiOx-C and lithium metal surface and interface properties, stabilization, and providing metrology services for the program. The partners will work with Argonne National Laboratory (ANL) to update the techno-economic BatPaC models to incorporate battery architectures that use prelithiated Si/SiOx-C and Li metal anode-based batteries.

Budget Period 1 (BP-1)

Hardware and Process Baseline and Pathfinding (Completed)

In Budget Period 1 of the project, the team designed, procured and operationalized hardware for Li deposition and surface protection. Hardware and Process baselines were established and deposited samples generated for pathfinding and initial cell testing.

Budget Period 2 (BP-2)

Roll-to-Roll (R2R) HVM Test Preparations (Completed)

In Budget Period 2, the team completed scale up design for the Li deposition and protection equipment, procured and operationalized scaled up components and continued to optimize hardware and process. Cell testing was moved to large format cells to meet or exceed interim performance goals towards high volume manufacturing (HVM).

Budget Period 3 (BP-3)

R2R HVM Validation (In Progress)

In Budget Period 3, the team will focus on validating the Li deposition and protection hardware and process to meet the equipment and cell performance goals for high volume manufacturing (HVM). The team will also establish a cell and pack level technoeconomic model incorporating these advanced anodes.

Results

The project has reached the end of budget period 2 (BP2). In BP2, we completed the scale-up and design for the Li deposition and protection equipment. We further made significant efforts to scale up components to enhance the performance and continue optimizing hardware and process development for the two deposition tools at our facility in Sunnyvale, CA. Cell testing and characterization were carried out for BP2 deliverables for both the Silicon anodes and Lithium metal anodes: Studies were directed toward large capacity pouch cell formats to meet interim performance goals towards high volume manufacturing (HVM).

The key outcomes for budget period 2 involved Lithium deposition hardware development in significantly improving the deposition rate (3X times). Furthermore, several samples with new chemistries were generated using the protection layer equipment to study the surface properties of Lithium. The highlight of this BP2 was delivering to Idaho National Laboratory (INL) 1) **twenty-three 7 Ah** multilayer Lithium metal pouch cells (*Applied Materials-SAFT-America*) 2) and **six cells using prelithiated SiOx anode 10 Ah** (*Applied Materials-Ionblox*). These cells will be further evaluated for performance at INL. Budget Period 3 continuation has been authorized.

Additional Updates

Applied Materials will pursue in the current phase of the program Substrate Independent Deposition and Transfer (SIDT) process. This approach will help us speed up the activities for deliverables. Each Si/SiOx anode substrate has many variations in chemistry, coating width, and patterns, variation in anode thickness non-uniformity, degree of degassing in our R2R system, web handling characteristics, etc. However, we needed an independent approach to characterize our hardware and utilize this opportunity for faster alternate pre-lithiation with our partners. Apart from the direct line-of-sight process for the prelithiation of anodes, we

have also started working on an alternate strategy for prelithiation. Polyethylene terephthalate (PET) has been known as a substrate in the industry for extruded films of Li. We decided to explore PET as a substrate of choice considering its stability at higher temperatures, cost-effectiveness and ready availability in the market in wide roll formats at various thicknesses and widths. This new Li-transfer approach and learning can significantly improve the throughput based on substrate width scalability. Applied Materials R2R platforms can handle more than 1-meter-wide PET substrates.

Table VIII.6.4 below captures all the proposed milestone and corresponding status updates. All Budget Period-1 and 2 milestones were completed, and preparations started towards meeting Budget Period-3 objectives, as summarized below.

Table VIII.6.4 Proposed milestone and corresponding status updates

Milestone	Type	Status as of 10/30/2022
Complete Gen. 2 source testing on test stand.	Technical	Met in PQ-5. Gen 2 was installed, tested, and characterized in S2S tool. Further testing is in progress on R2R tool.
Addition of Second Process Chamber	Technical	Modular design completed and second process chamber installed.
Protection layer material for scale up to R2R processing Selected	Technical	Met in PQ-5. In-situ R2R CO ₂ passivation hardware was installed, and baseline validated on Li on Cu rolls.
Design of protection layer hardware for R2R testing Completed	Technical	In-situ CO ₂ passivation capability designed, incorporated, and experimentally validated in the R2R tool.
Polymer selected	Technical	LBNL selected poly (9,9-dioctylfluorene-co-fluorenone-comethylbenzoic ester (PFM) binder for further performance evaluation.
Go/No Go Decision: Complete Gen. 2 source testing on test stand. Addition of Second Process Chamber	Go/No Go	Li Metal based cells (SAFT) Delivered to Idaho National Lab (INL) BP-2 deliverable completed → Cell testing in progress. Pre-Li SiO _x -C anode Delivered to INL BP-2 deliverable completed → Cell testing in progress. R2R system: Gen 2 source on R2R demonstrated double sided Li deposition
	Technical	Met in PQ-5. Gen 2 was installed, tested, and characterized in S2S tool. Further testing is in progress on R2R tool
	Technical	Modular design to enable DS coating configuration concept completed. One of the modular chambers is being currently installed in the lab.

In the rest of this section, we capture the program's key highlights and learnings, including data from Applied Materials and our partners (see Figure VIII.6.1 to Figure VIII.6.9).

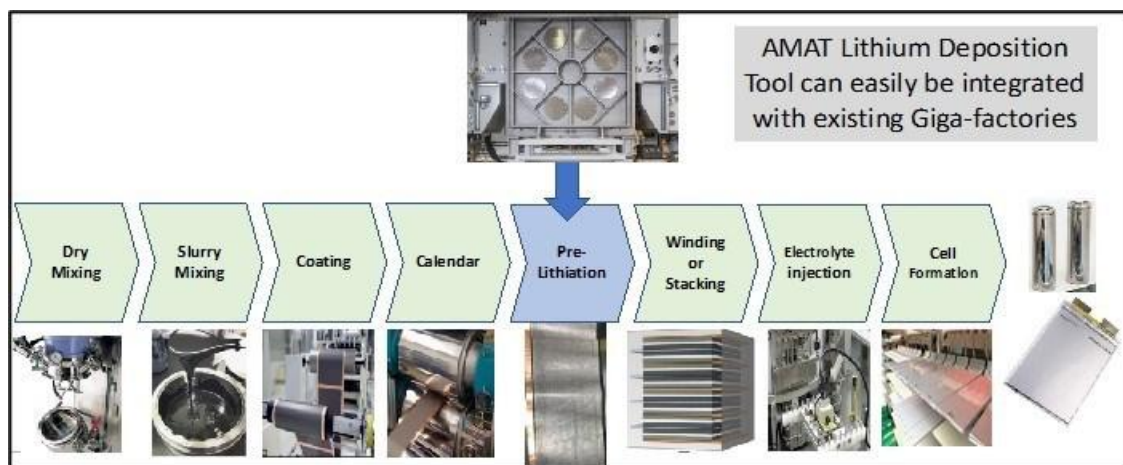
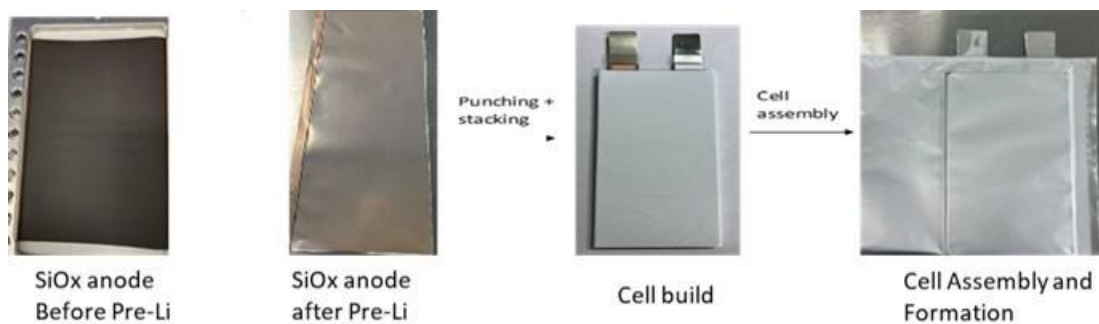


Figure VIII.6.1 Cell manufacturing steps including pre-lithiation for silicon anodes

Figure VIII.6.2 (A) Examples of silicon (SiOx) anode before and after pre-Lithiation and Pouch cell assembly process (Cell build was done by **lonblox**).

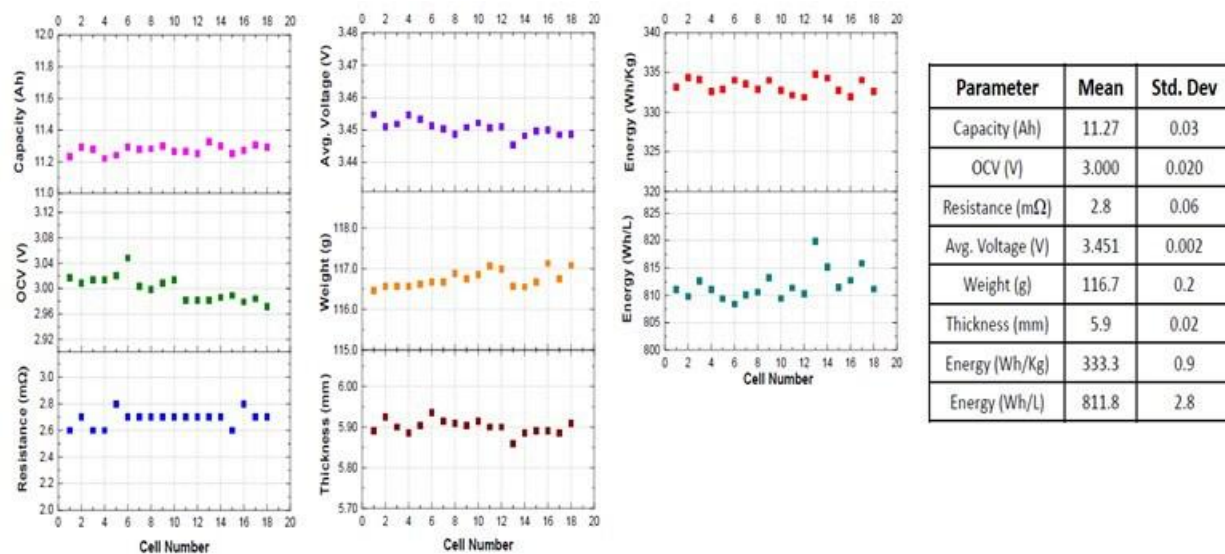


Figure VIII.6.3 Ionblox (Zenlabs) Summary of electrochemical data from formation process for the cells showing good consistency and reproducibility (~14 μm Pre-Li). Summary of cell parameters are shown with Energy density reaching 333 Wh/kg and 811 Wh/L.

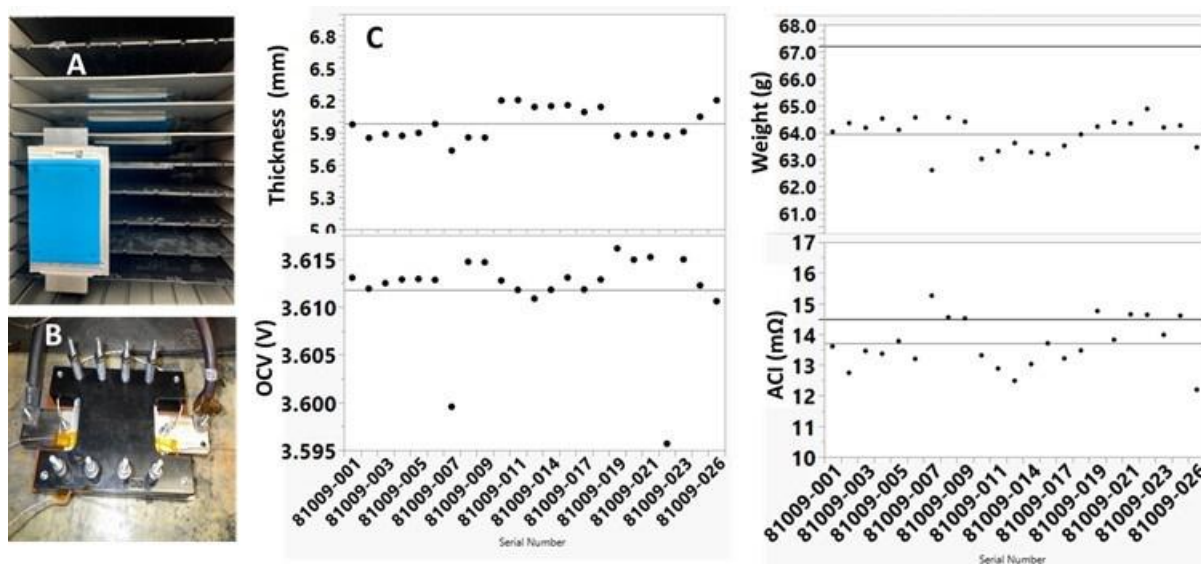


Figure VIII.6.4 SAFT America summary of cells with ~18 μm Li per side: (A) Images of 7Ah pouch cells (B) Pouch cell in testing fixture (C) summarizes key parameters of cells delivered to INL for testing (x-axis represents the serial number of the cell).

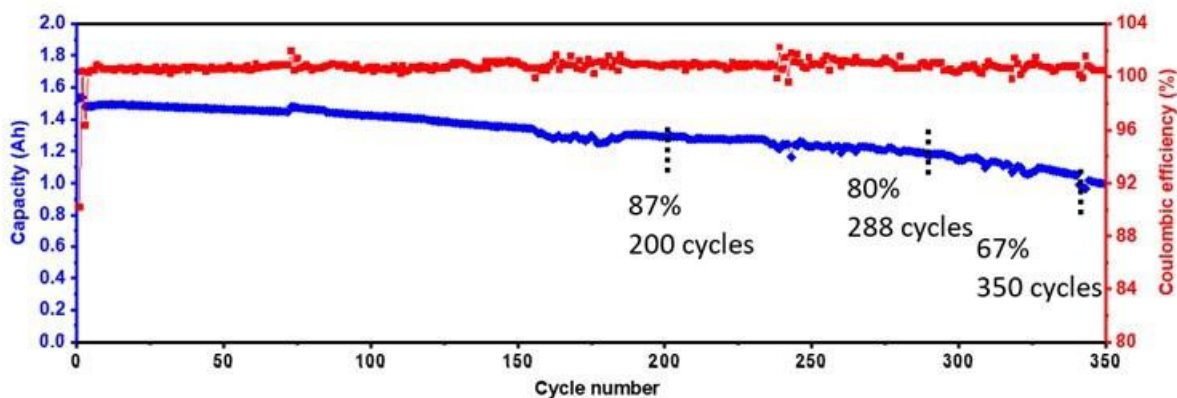


Figure VIII.6.5 Update on the cycling Performance of 1.5 Ah (300Wh/kg) cells with NMC622 cathode and approx. 18 μm Li Anode at PNNL

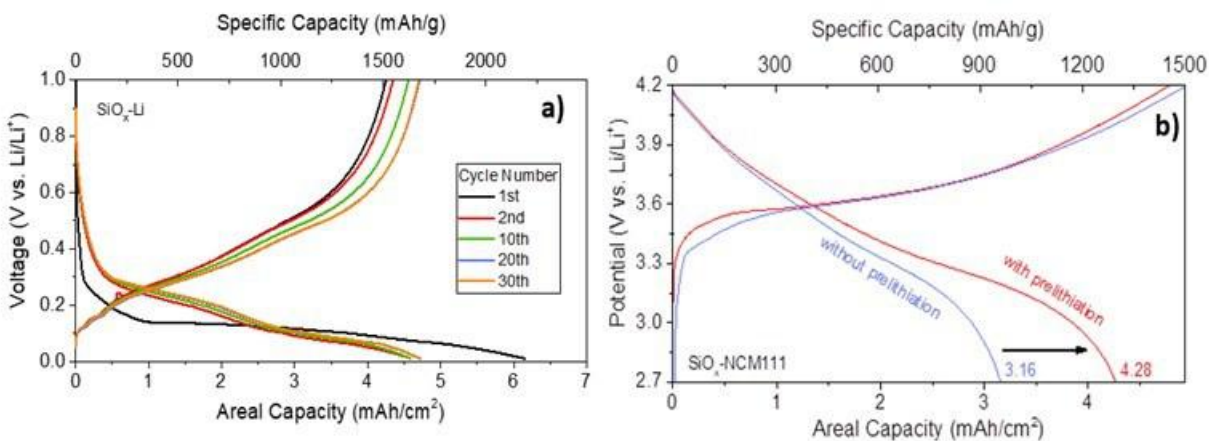


Figure VIII.6.6 Progress Summary for PFM binder selection (Lawrence Berkeley National Laboratory (LBNL): LBNL fabricated and evaluated high loading SiO_x anodes ($\sim 4.5 \text{ mAh/cm}^2$) for industrial prelithiation and demonstrated PFM binder with Applied Materials Pre-Li anodes delivering $\sim 35\%$ capacity improvement in coin cell study.

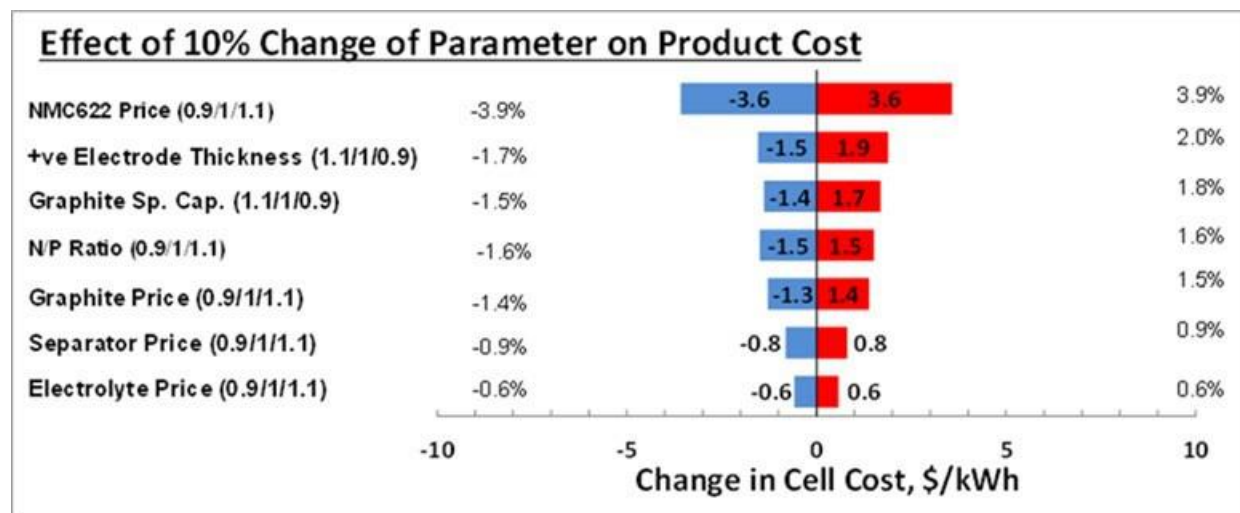


Figure VIII.6.7 Progress Summary BatPaC Cost Model (Argonne National Laboratory): Results of parametric sensitivity study for some key variables on the cost of cell manufacturing where each independent variables was changed by $\pm 10\%$.

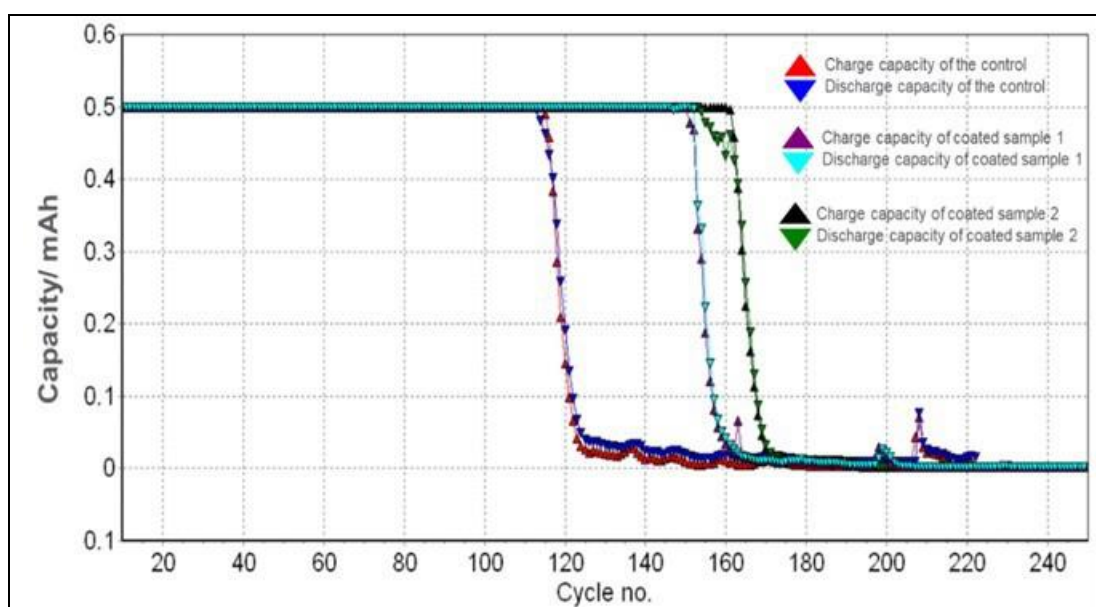


Figure VIII.6.8 Summary of Protection layer development (Applied Materials): Different types of protection layers were investigated (Type A, B and C), where type C shows best cycling of 160 cycles vs. control showing <120 cycles.

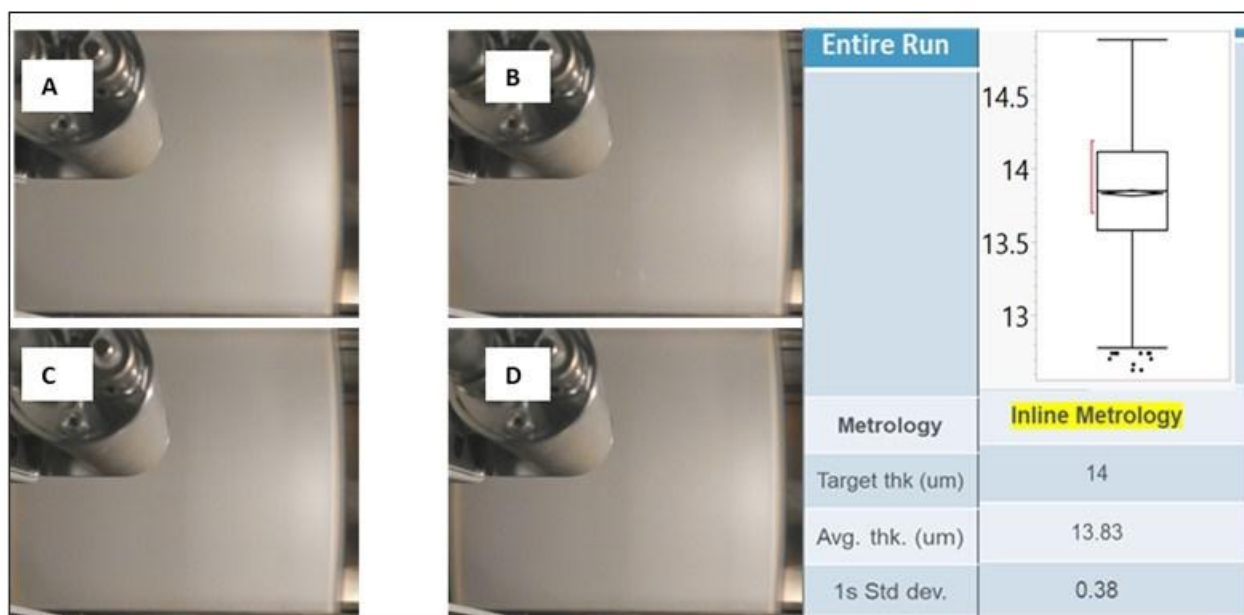


Figure VIII.6.9 Applied Materials Process development (Li Deposition): 14 μm Li deposition at different intervals (A-D) from beginning to end of the continuous R2R process run indicating stable process.

Conclusions

In 2022, the Applied Materials-led team consisting of Ionblox, Saft America, LBNL and PNNL and ANL completed all Year-1 and Year-2 milestones and deliverables and started work towards Year-3 objectives.

Key Publications

1. Poster summarizing Year-1 results, presented at the 2021 EERE VTO Annual Merit Review, June 2021 Vehicle Technologies Annual Merit Review, Project ID: BAT 495.

Acknowledgements

Ajey M. Joshi, Ph.D. (Ajey_M_Joshi@amat.com) served as the Program Director for this project. The Applied Materials team would like to sincerely acknowledge our key partners (Ionblox, Saft America, LBNL, PNNL, and ANL) for their expert contributions and consistent efforts in supporting us to enable this technology. We also acknowledge significant contributions from our Applied Materials engineering and process team, who have worked tirelessly to make significant progress towards the overall program goals.

VIII.7 Structurally and Electrochemically Stabilized Si-rich Anodes for EV Applications (Enovix Corporation)

John Thorne, Principal Investigator

Enovix Corporation
3501 W. Warren Avenue
Fremont, CA, 94538
E-mail: jthorne@enovix.com

Andrew Colclasure, Co-Principal Investigator

National Renewable Energy Laboratory
Center for Integrated Mobility Sciences
Golden, CO 80401
E-mail: andrew.colclasure@nrel.gov

Brian Cunningham, DOE Technology Development Manager

U.S. Department of Energy
E-mail: Brian.Cunningham@ee.doe.gov

Start Date: October 1, 2020	End Date: September 30, 2023	
Project Funding (FY22): \$3,156,600	DOE share: \$1,548,878	Non-DOE share: \$1,607,722

Project Introduction

Silicon has long been heralded as the next important anode material in lithium-ion batteries. Silicon anodes can theoretically store more than twice as much lithium than the graphite anode used in nearly all lithium-ion batteries today (1800mAh/cm³ vs. 800mAh/cm³). However, to successfully commercialize a practical high energy silicon anode lithium-ion battery, four significant technical problems need to be solved:

- Formation expansion: When fully charged, a silicon anode can more than double in thickness, resulting in significant swelling that can physically damage the battery, causing failure.
- Formation efficiency: When first charged, a silicon anode can absorb and permanently trap as much as 50%-60% of the original lithium in the battery, reducing the battery's capacity by 50%-60% unless a pre-lithiation solution is implemented
- Cycle swelling. A silicon anode will swell and shrink when the battery is charged and discharged, respectively, causing damage to both the package and the silicon particles in the anode, which can crack, and further trap lithium on the fresh silicon surfaces exposed by the cracks.
- Cycle and calendar life. Silicon particles can become electrically disconnected from the electrode when the silicon anode is in its shrunken state and can crack when the silicon anode is swollen, both of which can lower cycle life. In addition, when silicon particles become disconnected from the electrode, they are no longer able to accept lithium and neighboring particles must absorb the excess, causing over charging and further opportunities for physical damage. Electrolyte continuously reacts with Si surface and unlike graphite does not form a well passivating surface.

These four problems have limited the practical application of silicon anodes in conventional lithium-ion battery cells. Enovix has developed a 3D cell architecture and manufacturing process that uniquely solves these four technical problems to enable 100% active silicon anodes. While Enovix technology has been well vetted and proven in the consumer space, its significant potential to improve the state of the art in electric vehicle (EV) batteries remains largely unexplored. This project is intended to study the effect of Enovix's unique cell architecture against the automotive performance requirements of high energy density (achieved by using a silicon anode) coupled with high cycle and calendar life.

Objectives

The objective of this project is to build and deliver cells using the Enovix architecture with an optimized silicon anode, automotive class cathode, and electrolyte formulation that can achieve the following performance and long-term stability targets required for EV applications:

- 750 Wh/L energy density,
- 350 Wh/kg specific energy,
- <20% energy fade after 1000 C/3 cycles, and
- 10-year calendar life.

Approach

Enovix

We continue to work toward accomplishing the above targets by utilizing the cell design and manufacturing capabilities of Enovix, the modeling and fundamental understanding of expertise of National Renewable Energy Laboratory (NREL) and the electrolyte development know-how of Mitsubishi Chemical Corporation (MCC). Baseline cells with automotive cathode were built in Year 1 to demonstrate the current 100% active silicon anode capability and performance. Using an iterative approach, several cell designs continue to be implemented with various electrode designs, porosities, materials, internal pressures, test protocols, and electrolytes to increase volumetric and gravimetric energy density while maintaining the stated cell stability requirements. Cells with the best anode material-electrolyte combinations were determined in Year 2, and optimized anode-electrolyte-stack pressure will be built and performance tested in Year 3. Cells designs that project to > 750 Wh/L packaged energy density, < 20% energy fade after 1000 C/3 cycles, and 10-year calendar life were built in Year 2 using NMC 622. Additional cell designs will be introduced in Year 3, including new cathode electrodes with higher loadings, new cathode material(s), and higher press densities. They will be used as a primary driver to step up the core gravimetric energy density. The best performing cell design will be implemented in a ~3 Ah format.

NREL

NREL is developing continuum-level models to aid electrolyte and electrode design for silicon-based (Si and SiO_x) anode formulations. A detailed multiphase-multispecies solid electrolyte interphase (SEI) model implements $\cong 5$ electrolyte decomposition/ deposition irreversible global reactions informed by the literature and provides fundamental insights into associated capacity fade and SEI composition [1,2]. The model captures bi-layer (inorganic-organic) SEI features, electronic conduction limited growth and can be leveraged to aid electrolyte design. Furthermore, chemo-mechanic models incorporating Si particle expansion, SEI growth are developed which capture pore closure and expansion at the electrode level and can provide electrode design inputs for optimal transport and stress [3]. These design requirements can include initial electrode porosities, particle size, stack pressure, current protocol limits etc. This model will accelerate high-loading electrode development by considering not only electrochemical and transport overpotentials, but also the strongly coupled influences of chemo-mechanics.

Results

Table VIII.7.1 and Table VIII.7.2 show measured values of key cell builds from Budget Period 1 and Budget Period 2 in the 300 mAh-class cell format. Corresponding modeled values are shown in Table VIII.7.3. Measured values of the Volumetric Energy Density (VED) generally match modeled values to within 1%. Measured values of the Gravimetric Energy Density (GED) generally match modeled values to within 2%.

Table VIII.7.1 Summary of measured quantities and their standard deviation from key Budget Period 1 300 mAh-class cell builds using a 3.6 mAh/cm² NMC622 cathode with 3.2 g/cc electrode density.

Quantity	Unit	Low loading Low pressure		Low loading Baseline pressure		Low loading High pressure	
		Value	St.dev.	Value	St.dev.	Value	St.dev.
x length	mm	29.71	±0.21	29.76	±0.24	29.17	±0.40
y length	mm	16.90	±0.12	17.07	±0.06	17.20	±0.14
z length	mm	3.52	±0.06	3.45	±0.06	3.46	±0.11
Cell weight	g	4.37	±0.04	4.43	±0.09	4.45	±0.05
Capacity	mAh	252.0	±0.4	265.3	±0.2	274.6	±1.6
Energy	Wh	0.878	±0.012	0.920	±0.007	0.950	±0.004
Core VED	Wh/L	850	±9	887	±8	921	±7
Packaged VED	Wh/L	495	±3	524	±12	544	±21
Packaged GED	Wh/kg	201	±6	207	±6	213	±2

Table VIII.7.2 Summary of measured quantities and their standard deviation from key Budget Period 2 300 mAh-class cell builds using a 5.1 mAh/cm² NMC 622 cathode with 3.3 g/cc electrode density.

Quantity	Unit	<i>High loading</i> Baseline pressure		High loading High pressure	
		Measured value	St.dev.	Measured value	St.dev.
x length	mm	29.83	±0.16	29.77	±0.11
y length	mm	17.08	±0.12	17.10	±0.04
z length	mm	3.49	±0.05	3.44	±0.06
Cell weight	g	4.48	±0.06	4.58	±0.03
Capacity	mAh	0.293	±0.002	0.304	±0.001
Energy	Wh	1.013	±0.008	1.050	±0.002
Core VED	Wh/L	974	±8	1012	±6
Packaged VED	Wh/L	567	±10	598	±11
Packaged GED	Wh/kg	226	±3	230	±2

Inputted values for capacities, cell voltages, active material areas, tend to overestimate the core energy by 1-4%, which is partly due to reference capacities and energies measured at 25°C in the full cells, compared to cycle life measurements and modeled values which target 30°C, and accounts for ~1-2% of the capacity and energy. Capacity and energy are also observed to increase by ~2-4% in the first 30-60 cycles in all cell designs, and show similar values to modeled values of capacity and energy at C/3 in this cycle range at 30°C. Measurement of the packaged VED after 30 cycles demonstrates similar values to measured cycle 1 packaged VED despite this increase in the capacity and energy. The methods used to model packaged energy density have proven to be an excellent predictor of measured packaged energy density in at least five different NMC-SiO_x cell designs.

Table VIII.7.3 Summary of modeled energy density values for key cell builds from Budget Period 1 and Budget Period 2. An updated model was used to improve the accuracy of the modeled GED value.

Quantity	Unit	Low loading Low pressure	Low loading Baseline pressure	Low loading High pressure	High loading Baseline pressure	High Loading High pressure
Modeled Core VED	Wh/L	878	916	946	983	1024
Modeled VED	Wh/L	510	528	547	568	594
Modeled GED	Wh/kg	197	204	209	222	230

Table VIII.7.4 Summary of modeled energy density values for the high loading, high pressure case, showing a projection to 3 Ah and 100 Ah size. Approximately 800 Wh/L and 270 Wh/kg are modeled in the 100 Ah cell size.

High Loading, High Pressure: projection to larger size for conservative 5.1 mAh/cm ² NMC622/SiO _x cell				
Parameter	Unit	300 mAh cell	3 Ah cell	100 Ah cell
Cell dimensions (x*y*z)	mm	30*17*3.4	70*38*5.1	325*125*11.5
Cathode active material	-	NMC 622	NMC 622	NMC 622
Anode active material	-	SiO _x	SiO _x	SiO _x
Cathode loading	mAh/cm ²	5.1	5.1	5.1
Cathode specific capacity	mAh/g	177	177	177
Cathode density	g/cc	3.3	3.3	3.3
Voltage range	V	2.5-4.2	2.5-4.2	2.5-4.2
Cell capacity	Ah	0.293	2.899	109.0
Volumetric energy density	Wh/L	594	722	798
Gravimetric energy density	Wh/kg	230	254	270

Table VIII.7.4 shows a projection to larger sizes for the highest energy design. Based on existing data from key cell builds, the highest energy design is expected to meet 3 of 4 program objectives, i.e. > 1000 cycles, > 10 years calendar life, and > 750 Wh/L. Figure VIII.7.1 shows the cycle life performance of Enovix 3D cells with NMC622 described above. The discharge capacity in units of Ah, and the corresponding normalized energy and normalized capacity are shown. The low loading, baseline pressure cells from Budget Period 1 exceeded 1500 cycles to 80% energy. All cell designs had overlapping capacity and energy fade trajectories, despite core energy densities ranging from 850 Wh/L to > 1000 Wh/L. Figure VIII.7.2 shows voltage curves at various cycles for three cells in the baseline design.

Figure VIII.7.3 shows the calendar life data stored at the 4.2 V upper cutoff voltage used for cycle life data shown in Figure VIII.7.1 for the low loading, baseline pressure design. Recovered capacity exceeds 99% at 40°C and 30°C after approximately 12 months. Recovered capacity is about 96% after > 11 months at 50°C. This data suggests cells exceed 10 years of calendar life at room temperature using 100% active silicon anodes. When the top of charge storage voltage is reduced to 4.1 V at each temperature, a significant improvement is observed in 50°C, suggesting calendar life can be extended significantly if the top of charge storage voltage is reduced.

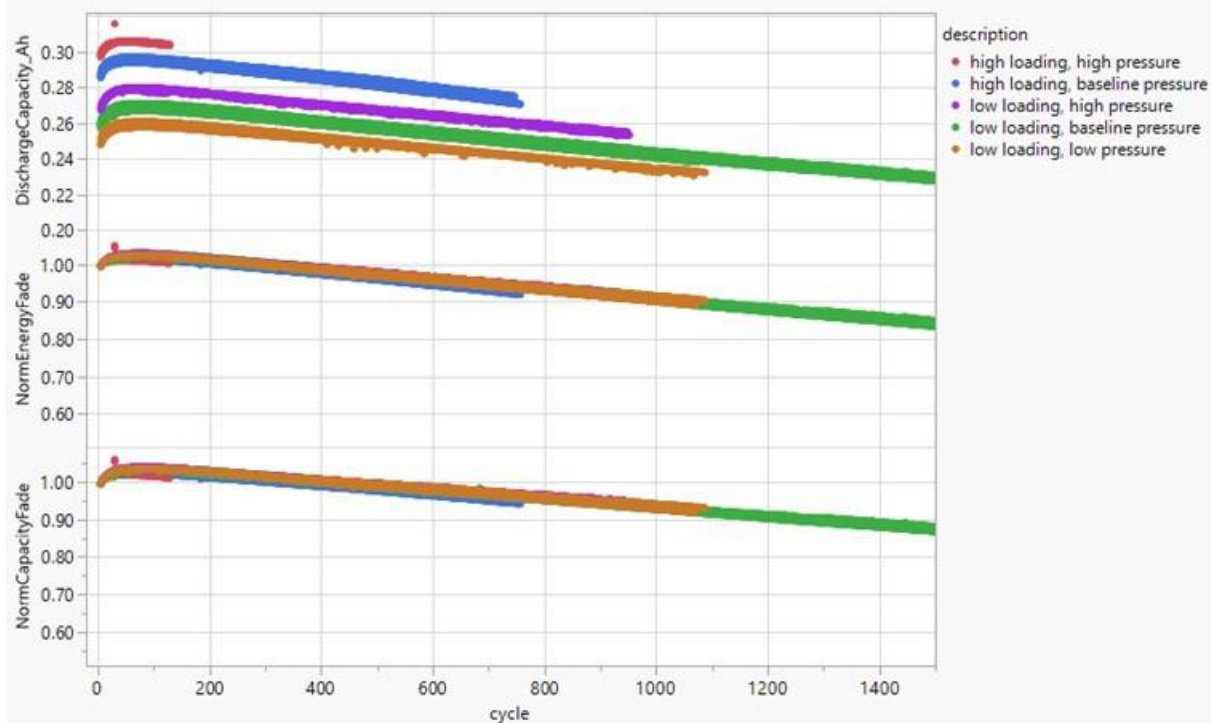


Figure VIII.7.1 Cycle life data of cells described in the adjacent three tables at 30 °C.

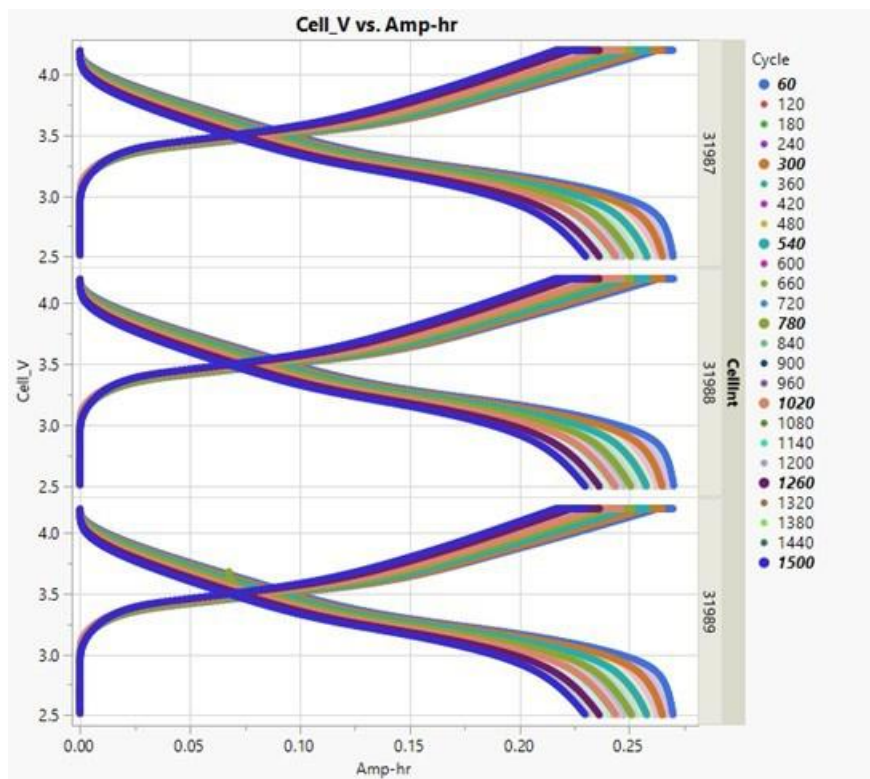


Figure VIII.7.2 Voltage curves at various cycles between cycle 60 and cycle 1500 for three different baseline loading, baseline pressure cells.

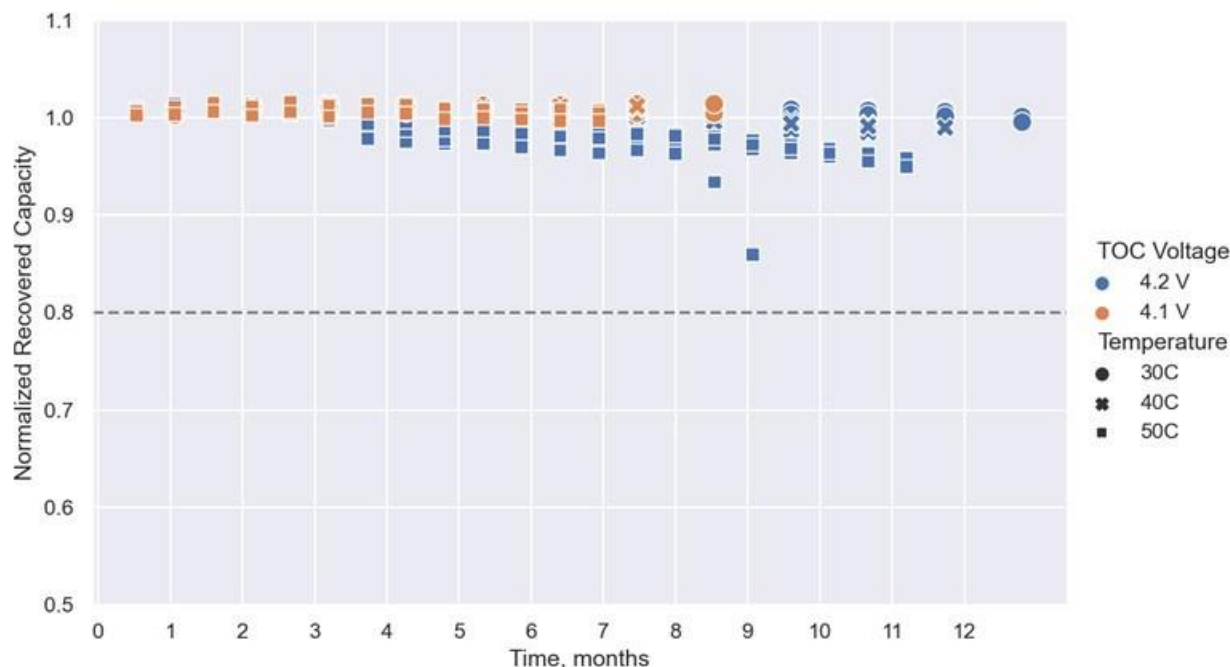


Figure VIII.7.3 Calendar life data of the low loading, baseline pressure cells stored at 30°C (circle), 40°C (cross), and 50°C (square). More than 1 year of storage is shown at 4.2 V (blue), and more than 7 months of storage is shown at 4.1 V (orange).

Table VIII.7.5 shows modeling outputs for a cell identical in design to the high loading, high pressure case that was built in Budget Period 2, except the cathode is substituted with an NMC 811-type material that was tested in-house. This material had measured 220 mAh/g, with 88% first cycle efficiency. This is a marked increase in capacity compared to the NMC 622 material currently in use which has approximately 177 mAh/g and 90% first cycle efficiency. For the same cathode areal capacity of 5.12 mAh/cm², and increased press density of 3.55 g/cc (achieved in-house and as advertised by the material vendor), the single-sided cathode coating thickness excluding the current collector decreases from 91.5 µm to 68.2 µm in the cell design model. This enables more electrodes to be incorporated into Enovix fixed volume cells. The prelithiation capacity must be adjusted accordingly to maintain the same anode to cathode ratio. Otherwise, all design parameters are identical. Volumetric and gravimetric energy density reach 918 Wh/L and 316 Wh/kg respectively in the 100 Ah cell format, or a > 15% increase purely due to a drop-in higher energy cathode electrode.

A future cell design is described in Table VIII.7.6 which represents one possible route to achieving the volumetric and gravimetric energy density goals defined by the program. This cell design is based on that described in Table VIII.7.5, with the following changes: 1. Cathode loading is increased from 5.12 mAh/cm² to 6.38 mAh/cm², which corresponds to 30 mg/cm². This loading was tested and characterized in the lab with the baseline inactive formulation, using experimentally obtained specific capacity obtained for the NMC 811-type material. 2. A new generation SiO_x material was modeled based on numbers extracted from coin cell data measured in the lab in preliminary studies, and has significantly higher capacity, which enables reduced anode mass loading. 3. Target unlithiated excess anode material was reduced. Measured excess anode is always higher than target excess anode by several percentage points in all the experimental cell designs presented. 4. Aluminum foil thickness was changed from 15 µm to 12 µm. 5. The prelithiation was not increased proportionally to the cathode areal capacity as was done in previous builds where the loading was increased, which reduces the anode to cathode ratio. The described changes increase the GED from ~320 Wh/kg to ~350 Wh/kg, and VED is in excess of 1000 Wh/L.

Table VIII.7.5 Summary of modeled energy density values for the high loading, high pressure case, where the NMC 622 cathode is directly substituted with input parameters taken from coin cell data, tested using high nickel NMC 811-type material, but otherwise uses the same design parameters.

High Loading, High Pressure: projection to larger size for conservative 5.1 mAh/cm ² NMC811-type/SiO _x cell				
Parameter	Unit	300 mAh cell	3 Ah cell	100 Ah cell
Cell dimensions (x*y*z)	mm	30*17*3.4	70*38*5.1	325*125*11.5
Cathode active material	-	NMC 811-type	NMC 811-type	NMC 811-type
Anode active material	-	SiO _x	SiO _x	SiO _x
Cathode loading	mAh/cm ²	5.12	5.12	5.12
Cathode specific capacity	mAh/g	220	220	220
Cathode density	g/cc	3.55	3.55	3.55
Voltage range	V	2.5-4.2	2.5-4.2	2.5-4.2
Cell capacity	Ah	0.332	3.349	125.7
Volumetric energy density	Wh/L	673	835	918
Gravimetric energy density	Wh/kg	267	298	316

Table VIII.7.6 Summary of modeled energy density values for a possible future cell design with a pathway to hitting the program gravimetric energy density target.

Aggressive 6.38 mAh/cm ² NMC811-type/SiO _x cell				
Parameter	Unit	300 mAh cell	3 Ah cell	100 Ah cell
Cell dimensions (x*y*z)	mm	30*17*3.4	70*38*5.1	325*125*11.5
Cathode active material	-	NMC 811-type	NMC 811-type	NMC 811-type
Anode active material	-	SiO _x	SiO _x	SiO _x
Cathode loading	mAh/cm ²	6.38	6.38	6.38
Cathode specific capacity	mAh/g	220	220	220
Cathode density	g/cc	3.55	3.55	3.55
Voltage range	V	2.5-4.2	2.5-4.2	2.5-4.2
Cell capacity	Ah	0.373	3.746	141.1
Volumetric energy density	Wh/L	755	933	1033
Gravimetric energy density	Wh/kg	294	326	346

Based on these results, cell designs for Budget Period 3 will target higher loading, higher density, and/or higher capacity cathodes. They will be implemented using the anode parameters similar or slightly higher to those established in the above summarized cells, and are expected to achieve the stability targets. The corresponding volumetric energy density target increases beyond 900 Wh/L in the 100 Ah design based on the current experimentally validated anode design, prelithiation, and anode to cathode ratio, and measured values are expected to exceed 750 Wh/L in a ~3 Ah cell format, which will be built in Budget Period 3. Future cell designs will also target the 350 Wh/kg objective with additional design parameter adjustments. A newer iteration of SiO_x is currently being tested at Enovix which can contribute to the needed increase the gravimetric energy density. Cycle life currently exceeds program targets by significant margin. Therefore, additional adjustments include a reduction in prelithiation and reduced anode to cathode ratio, which are necessary to achieve the target.

NREL built and parametrized the finite strain COMSOL model for cycling based on Enovix's thickness and porosity evolution data for its cell configurations. First charge data with formation and prelithiation is available. Validation is ensured through matching of the final anode thickness and porosity outputted by the model with the experimental numbers obtained from Enovix preliminary calculations. Figure VIII.7.4(a) shows the simulated voltage profiles during charging of the cell during normal cycling. For the high-pressure case, Enovix preliminary calculations suggest that the final SiO_x end of charge thickness and porosity are 40.2 microns and 19.1% respectively. The COMSOL model is initialized and charged to 4.2 V such that the model matches this final thickness and porosity (see Figure VIII.7.4 (b,c)). At C/10, we see that the anode is lithiated throughout its thickness indicating a uniform porosity throughout the anode. The physical properties of interest for this match are the Li molar volume in host SiO_x and the SEI volume fraction present in the system after the formation. A molar volume of $8\text{e-}6 \text{ m}^3/\text{mol}$ indicating a final to initial volume ratio of 2.45 for $\text{Li}_{3.75}\text{SiO}$ vs Li_0SiO and an SEI volume fraction of 3% after formation provides a good match across the four different Enovix cell configurations. It is notable that sufficient end porosity is observed even for the high-pressure case which can alleviate transport limitations in this system.

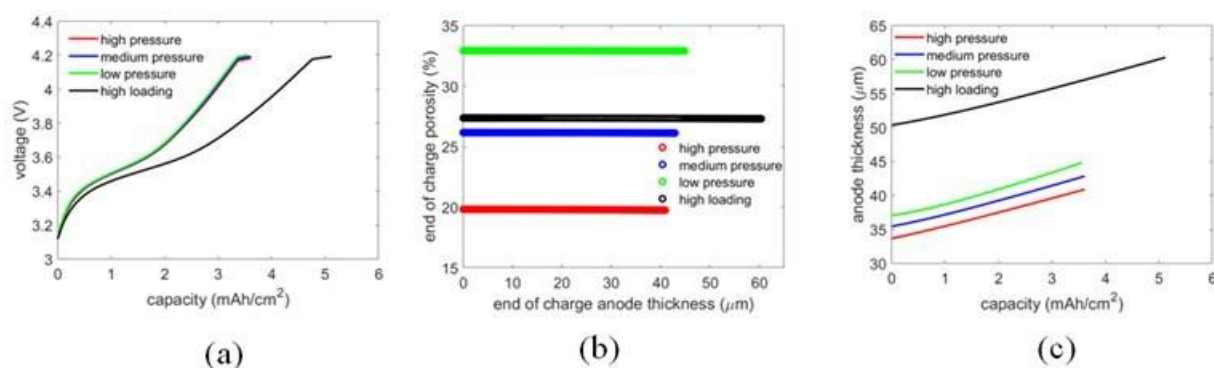


Figure VIII.7.4 Finite strain COMSOL model results for (a) voltage, (b) end of charge porosity and (c) anode thickness evolution during normal cycling for charge to 4.2 V. Open circuit potentials of NMC and SiO_x are obtained from slow current rate half cell data provided by Enovix. Good match is obtained for end of charge porosity and thickness between model and experiments showcasing accurate parametrization of the COMSOL model with experiments.

Conclusions

300 mAh-class cells have been built with NMC 622 cathodes and 100% active Si anodes, and are in cycling, calendar life testing. These cells have achieved the designed volumetric and gravimetric energy densities. Baseline cells from budget period 1 have achieved > 1500 cycles to 80% energy after more than one year of cycling at 30°C, and achieved approximately 96% capacity after nearly one year of storage at top of charge (4.2 V) in a 50°C test chamber. These results indicate viability of using 100% active silicon anodes, projecting to > 10 years of calendar life, and exceed the target energy retention and calendar life objectives. NREL has provided input and verification of cell designs with cell parameters provided by Enovix. Additional cell designs were implemented where measured packaged energy densities range from ~500 Wh/L to ~600 Wh/L in the 300 mAh-class format, with modeled gravimetric and volumetric energy density values generally within 1-2% of measured values, and show similar cycle life stability. The highest energy cell design projects to 800 Wh/L and 270 Wh/kg in a 100 Ah cell format, and this cell design is expected to achieve 3 of 4 of the program objectives. When an NMC 811-type material is substituted in place of the NMC 622 in the highest energy cells currently in test, with otherwise identical cell design parameters (i.e. anode loading, anode to cathode ratio), cell energy projects to 920 Wh/L and 317 Wh/kg in the 100 Ah cell format. Future cell designs in year 3 will increase both volumetric and gravimetric energy densities in attempt to reach the 4th program objective of 350 Wh/kg.

References

1. Single, Fabian, Birger Horstmann, and Arnulf Latz. "Revealing SEI Morphology: In-Depth Analysis of a Modeling Approach." *J. Electrochem. Soc.* 164 no. 11 (2017): E3132.

2. Single, Fabian, Birger Horstmann, and Arnulf Latz. “Dynamics and morphology of solid electrolyte interphase (SEI).” *Phys. Chem. Chem. Phys.* 18 no. 27 (2016): 17810-17814.
3. Mai, Weijie, Andrew Colclasure, and Kandler Smith. “A Reformulation of the Pseudo2D Battery Model Coupling Large Electrochemical-Mechanical Deformations at Particle and Electrode Levels” *J. Electrochem. Soc.* 166 no. 8 (2019): A1330.

Acknowledgements

Enovix: Kang Yao, Murali Ramasubramanian, Ashok Lahiri, James Wilcox, Chaojun Shi, Manuel Schnabel

NREL: Ankit Verma, Shriram Santhanagopalan, Ahmad Pesaran

VIII.8 Rationally Designed Lithium-Ion Batteries Towards Displacing Internal Combustion Engines (Group14 Technologies)

Henry R. Costantino, Principal Investigator

Group14 Technologies, Inc.
8502 Maltby Road
Woodinville WA 98072
E-mail: rcostantino@group14.technology

Brian Cunningham, DOE Technology Development Manager

U.S. Department of Energy
E-mail: Brian.Cunningham@ee.doe.gov

Start Date: January 1, 2022 End Date: December 31, 2022
Project Funding (FY22): \$1,631,597 DOE share: \$1,278,495 Non-DOE share: \$353,102

Project Introduction

Group14 Technologies is leading a world-class team composed of Cabot Corporation, Silatronix, Arkema, Pacific Northwest National Laboratory, and Farasis Energy to research, fabricate, test and demonstrate lithium ion batteries (LIB) implementing ~30% silicon-carbon (Si-C) composite anodes achieving aggressive next generation automotive energy targets. The project's centerpiece technology is Group14's high performing Si-C composite anode material already proven to provide 35% increased energy density at 12% composite blended with graphite, >1000 cycle stability, and a projected cell cost of <\$125/kWh in conventional LIBs under a prior DOE VTO award (DE-EE0001201). This project advances this baseline by taking a holistic approach to increase silicon content for higher energy density and to improve calendar and cycle life through the optimization and incorporation of carbon additives, surface coatings and binders for the anode along with high performance co-solvent electrolyte additives. These anode improvements are being paired with high-nickel, low-cobalt, commercially available cathode to achieve the project's performance targets.

Objectives

This three year project will culminate in a ~0.4Ah pouch cell which demonstrates targets of >350 Wh/kg, >750 Wh/L, >1000 cycle stability, and >10 year calendar life. This target will be achieved incrementally each year of the project with a LIB build achieving the baseline, interim and final cell targets listed in Table VIII.8.1 below:

Table VIII.8.1 Electrochemical Objectives for DOE Project – EE0009187

Objective	Metric	Baseline	Interim	Final
Useable Specific Energy at 30°C and C/3	Wh/kg	>340	>350	>350
Useable Energy Density at 30°C and C/3	Wh/L	>750	>750	>750
Calendar Life	Years to 20% fade	>3	>5	>10
Cycle Life (C/3 deep discharge to 350 Wh/kg)	Cycles to 20% fade	~300	~600	~1000

Approach

Our approach is to leverage Group14 Technologies' carbon and Si-C composite expertise in conjunction with our partnering organizations' expertise to holistically improve the performance of a LIB as measured by our yearly electrochemical targets. Within this collaboration, each of our partners contribute a unique approach toward improving the battery:

- **Group14 Technologies:** Our core technology is to create a composite material that accounts for and overcomes the failings of traditional silicon based anode material solutions. The basis for Group14 Si-C's superior performance is its rationally designed structure. At its foundation is an amorphous carbon scaffold, with its porosity fine-tuned for promoting intra-particle growth of the desired type and size of silicon. The resulting Si-C composite includes internal void space to buffer expansion, nano-silicon to prevent particle fracture with cycling, and a carbon scaffold to enhance conductivity and particle integrity while minimizing exposed silicon surface area. Our approach for this project is to further optimize both the carbon scaffold and to modify the resulting Si-C in order to protect the surface from adverse interactions that may negatively impact cell performance.
- **Cabot Corporation:** Global leader in nanoengineered conductive carbon additives for LIBs. Their role in the project is: (1) to assist Group14 in characterization of carbon and resulting Si-C and (2) to optimize the carbon additive type and loading to maximize performance.
- **Silatronix:** Producers of organosilicon co-solvent additives that improve LIB cycle and calendar stability. Silatronix pioneered industrial relevant analytical methods for investigating silicon-electrolyte interactions, including quantitative gassing analysis and identification of degradation mechanisms. Leveraging their expertise, they will produce an optimized electrolyte formulation that will synergize with Group14 Si-C to extend battery life by controlling degradation mechanisms.
- **Arkema:** A specialty chemicals and advanced materials developer and supplier that successfully commercialized several electrode binders and separators coating resins, especially for high-energy, high-voltage LIBs. Their role in the project is to develop an optimized binder solution to maximize cohesion of Group14's Si-C composite with other anode components and to promote the long term cycling and calendar performance of the battery.
- **Farasis Energy:** A leading U.S. developer and supplier of LIBs for EVs. Farasis has designed and built its own Li-ion cell and battery system manufacturing plant and has been in high volume production since 2010 with fully automated production capability of 4 GWh/y. By leveraging Farasis' battery production research and experience the best design and form factor of LIB will be utilized to promote high energy density and increase cycle life.
- **Pacific Northwest National Lab (PNNL):** World-renowned experts in energy storage research. PNNL lead in mechanistic investigations regarding LIB materials and assure the guidance to the project towards success. PNNL provides critical advanced materials characterization support toward synergizing the team's optimization efforts.

Results

The primary project objectives for FY22 were: (1) to deliver devices and data for interim LIBs, (2) perform screening and down-selection of critical battery components, and (3) deliver optimized carbon scaffold to support the final LIB build. As discussed with the Department of Energy (DoE) during the regular quarterly project meetings, these objectives have been satisfactorily completed. The project's current focus is final screening of down-selected critical battery components in 0.4Ah pouch cells in order to demonstrate performance targets in support of the final battery build.

In the last annual progress report, we discussed the cycle life data for the baseline build. For the current reporting period, we now have data available for the calendar life. These data are shown in Figure VIII.8.1. For this test, the cells were stored at 30°C and 45°C with 100% state of charge (SoC) for 30 days increments. Battery performance was then measured after each 30 day interval at a C/3 rate followed by an HPPC test at C/10 rate (1C pulse) and charge-discharge at C/3 to calculate the capacity. As can be seen, there was relatively low degradation in performance observed, for example, the capacity loss after 9 months was 4% and 11% at 30°C and 45°C, respectively.

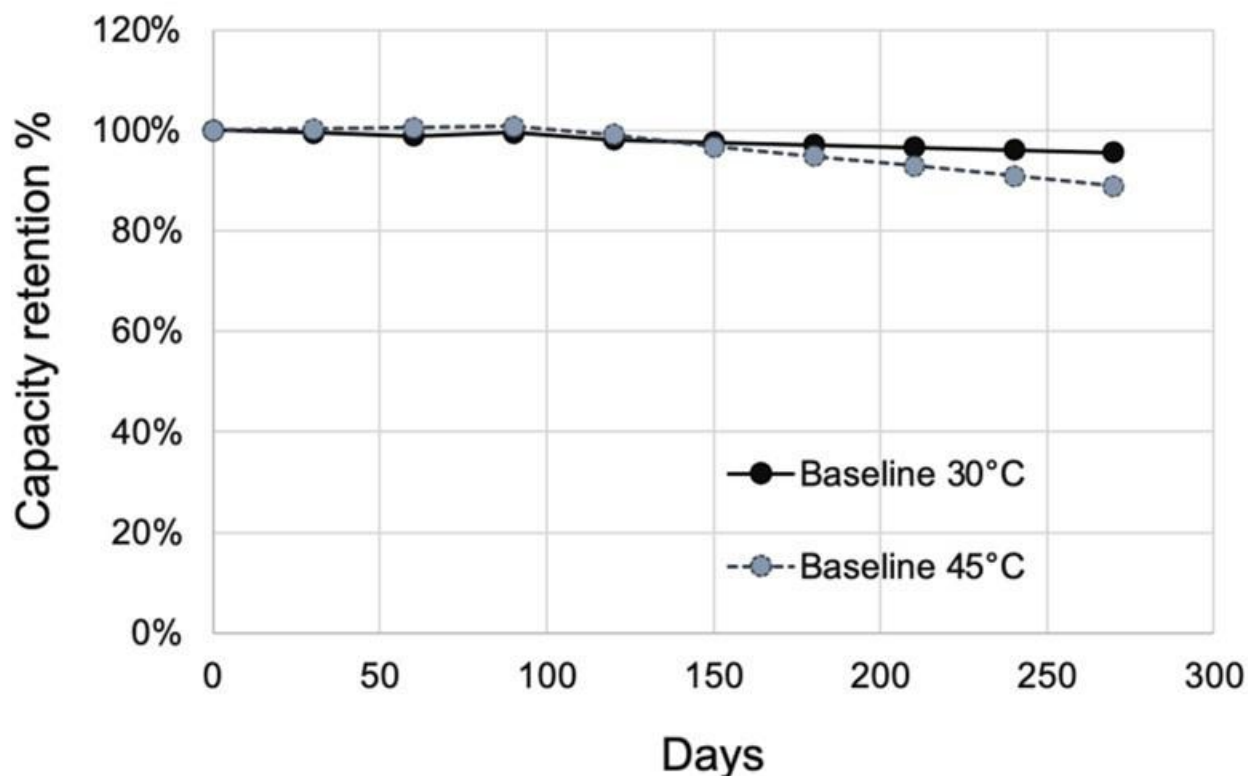


Figure VIII.8.1 Calendar life update for baseline batteries comprising Group14 Si-C.

The first key milestone and deliverable in FY22 was the design, development, production and delivery of interim LIB devices and data. Data are shown in Figure VIII.8.2 for the baseline batteries (gray curve) compared to sequential iterations (yellow curve) leading to the interim build battery configuration (blue curve), as well as demonstrating the effect of addition of 1% OS3 additives (green curve). As can be seen, the projected cycle stability of the batteries representing the interim build demonstrate >600 cycles, a substantial progress from the cycle stability of the baseline batteries. Furthermore, the data show an encouraging trend for further cycle stability improvement with the addition of 1% Silatronix OS3 additive in the electrolyte.

Farasis initiated production of 15 x 0.5Ah cells, Figure VIII.8.3, with the following components: modified Si-C from Group14 (down-selected from a pool of 13 samples tested by Farasis), baseline electrolyte with OS3 additive from Silatronix, commercial graphite, commercial binder, commercial carbon additive, and commercial cathode. These cells are being tested at both Farasis and Argonne National Lab to serve as a benchmark for component screening and the final build. The intent of the interim build was to combine Group14's modified Si-C (SCC55™) and down-selected battery components to achieve key interim build metrics: >340 projected Wh/kg and >600 cycle life stability.

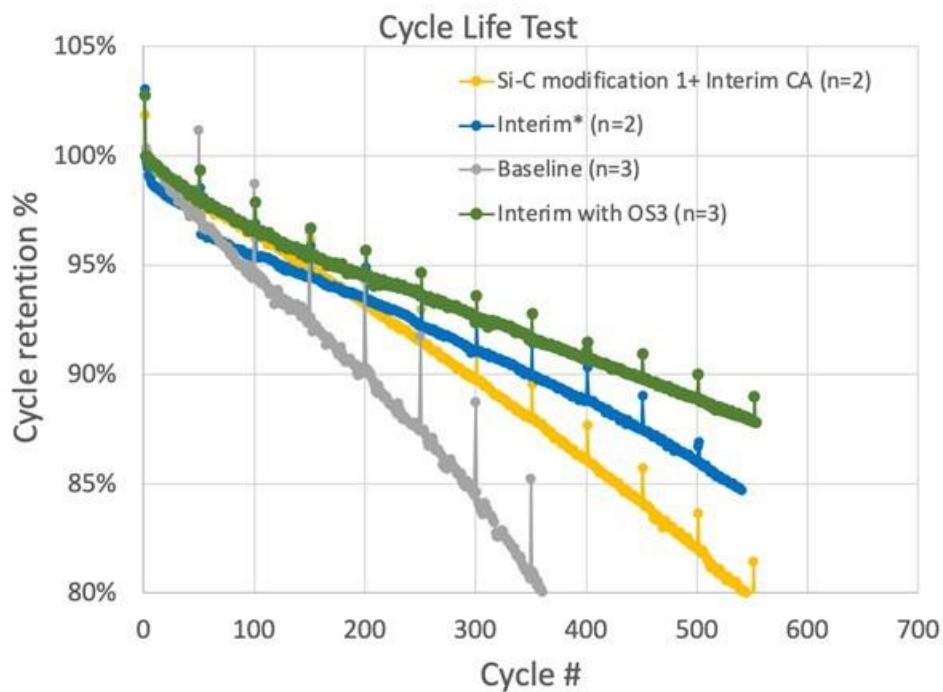


Figure VIII.8.2 Cycle stability for batteries comprising Group14 Si-C

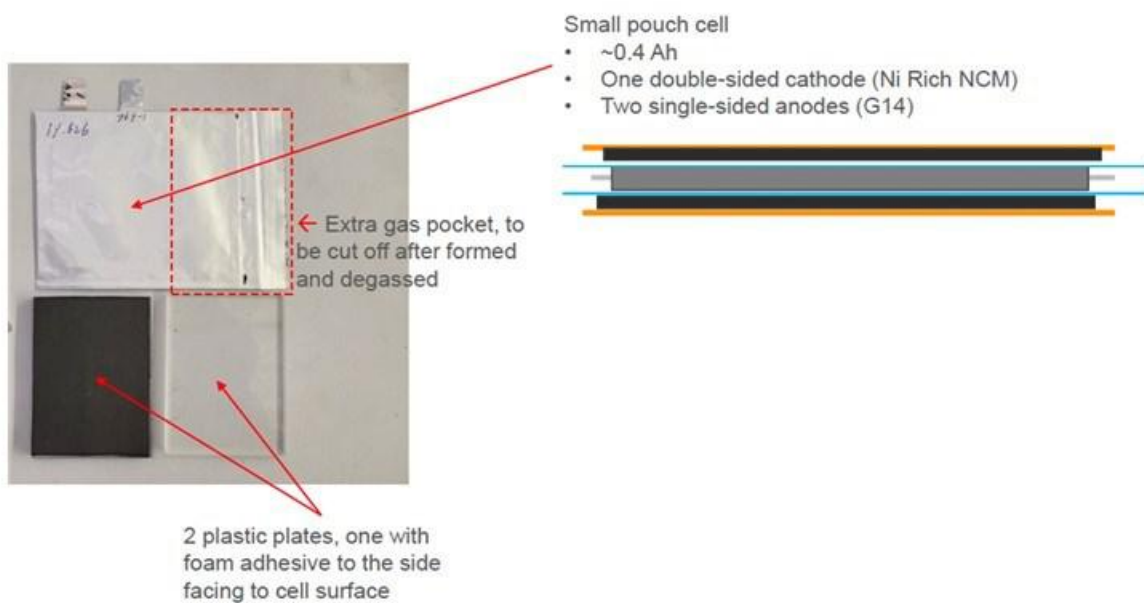


Figure VIII.8.3 Schematic of interim batteries (pouch, ~ 0.4 Ah)

The cycling data for the interim cells produced at Farasis are shown in Figure VIII.8.4. The cycling of the cells, the data collection, and data analysis were all conducted at Farasis. These data confirm the marked improvement in the interim build cell performance compared to the baseline cell performance. Specifically, the current data for the interim cells demonstrate >600 cycle stability, exceeding the minimum target.

This improved performance reflects the co-optimization of the anode active material with other battery components, according to the project plan. To this end, as discussed in the annual report, the interim cells comprise the scaled-up carbon scaffold for the interim build, and the type and level of binder, conductive additive, and electrolyte down-selected and produced for the interim build.

Notably, as shown in Figure VIII.8.4, the performance of interim build strategy (Si-C, binder, carbon additive, and electrolyte additive) in 0.4 Ah pouch cells has exceeded 800 cycles to <20% energy fade.

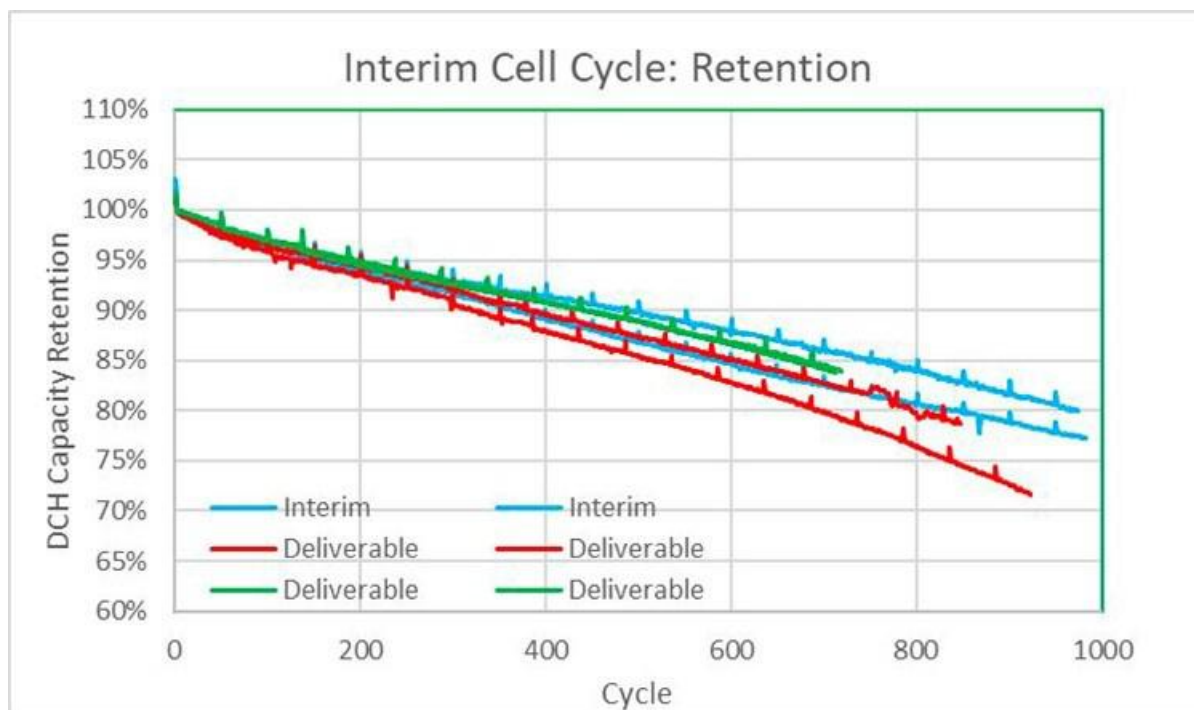


Figure VIII.8.4 Interim build battery performance (Farasis cycling data)

Beyond the annual progress demonstrating the performance improvement from baseline to interim build, the key activities and objectives over the last year focused on preparation for the final cell build. To this end, there were three key objectives. The first objective was to select and produce carbon scaffold to support the final build. This objective was met, and we currently have substantial inventory and ability to produce commercial-scale (far exceeding the current project requirement) carbon scaffold with the desired properties at our Woodinville, WA Battery Active Materials (BAM) plant. The second objective was to select and produce silicon-carbon composite to support the final build. This objective was met, and we currently have substantial inventory and ability to produce commercial-scale (far exceeding the current project requirement) of silicon-carbon composite with the desired properties at our Woodinville BAM plant.

The third objective was continued screening of the other key battery components (binder, conductive additive, electrolyte) in FY22 towards down-selection for the final cell build employed for FY23's final deliverable. For the conductive additive, Cabot demonstrated an improvement in recovered capacity through the use of new, optimized carbon nano-structures. For the electrolyte, Silatronix evaluated and optimized various organosilicon compounds to increase the longevity of LIB devices. To this end, Silatronix screened various electrolyte compositions for their ability to minimize gas generation in the presence of the anode at high temperature (data

shown in Figure VIII.8.5). For this test, pouches containing anode and the electrolyte combinations were held at 45 C for four weeks, and gassing was determined by volume change. The base electrolyte composition was 1.2M LiPF₆ in EC/EMC/DEC (1/1/1 v/v/v)+1v% VC. As can be seen, there was a dramatic gas reduction for cells with OS3®-containing electrolyte. The benefit of OS3® was observed in presence of both 3% and 10% fluoroethylene carbonate (FEC)

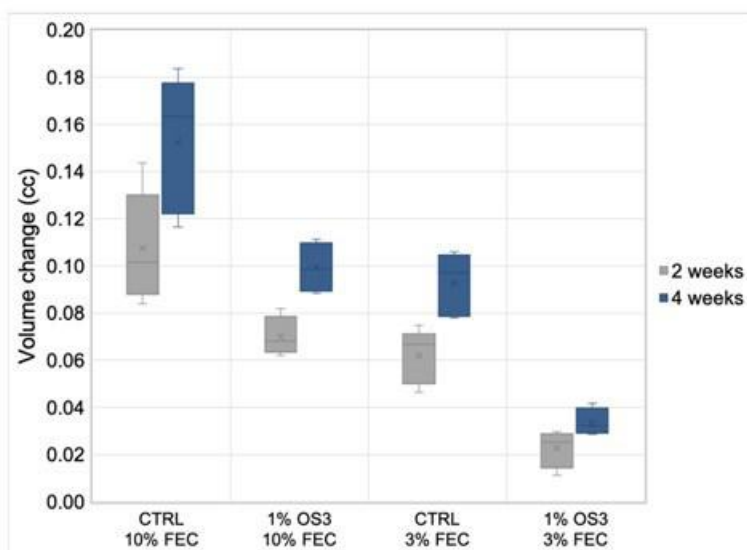


Figure VIII.8.5 Example of electrolyte optimization.

Conclusions

Three primary project goals have been accomplished in FY22: (1) deliver devices and data for interim LIBs, (2) perform screening and down-selection of critical battery components, and (3) deliver optimized carbon scaffold to support the final LIB build. The interim build cells exceed project targets, for example achieving >800 cycles to <20% energy fade. Over the course of FY22, Group14, Cabot, Farasis, Arkema, Silatronix and PNNL have collaborated towards significant optimization of each of the functional materials that comprise the anode. Based on our collaboration, we have down-selected anode active and other battery components towards the final cell build.

Acknowledgements

The PI thanks John Van Citters and Dan Casioppo for managing the project and Avery Sakshaug, Dr. Abirami Dhanabalan, Dr. Nate Phillip and Dr. Rajan Patel (Group14 Technologies) for their critical contributions to the project. The PI would also like to thank Cabot, Arkema, Farasis and Silatronix for their guidance on the project using their excellent domain expertise. Finally, the PI would like to thank Dr. Chongmin Wang of PNNL for his many contributions to the characterization of key materials throughout the project.

VIII.9 Ultra-Low Volume Change Silicon-Dominant Nanocomposite Anodes for Long Calendar Life and Cycle Life (Sila Nanotechnologies)

Naoki Nitta, Principal Investigator

Sila Nanotechnologies
2470 Mariner Square Loop
Alameda, CA 94501
E-mail: nnitta@silanano.com

John Tannaci, Co-Principal Investigator

Sila Nanotechnologies
2470 Mariner Square Loop
Alameda, CA 94501
E-mail: jtannaci@silanano.com

Brian Cunningham, DOE Technology Development Manager

U.S. Department of Energy
E-mail: Brian.Cunningham@ee.doe.gov

Start Date: October 1, 2020 End Date: December 31, 2023
Project Funding (FY22): \$4,600,000 DOE share: \$3,600,000 Non-DOE share: \$1,000,000

Project Introduction

Today's state-of-the-art Li-ion battery cells use a small fraction of silicon in the anode to boost cell energy density. Anode silicon content is kept low because higher amounts would cause massive volume change, resulting in undesirable electrolyte reactions which have detrimental effects on both calendar and cycle life. Batteries for automotive applications have particularly stringent calendar and cycle life requirements, posing a challenging problem for high energy density cell development. However, higher energy density cells are able to deliver more energy storage per cell and therefore open a path to achieving lower cost.

Sila's silicon-dominant anode material technology is manufactured with scalable processes and inputs, and has ultra-low volume change, enabling high-capacity anodes to achieve both long calendar and cycle life. Sila Nanotechnologies has already begun commercial sales of its silicon anode material for consumer applications, starting with wearable electronics, and is scaling up production to enter larger battery markets. This project applies Sila's anode technology to research, develop, fabricate, and validate high energy density silicon-dominant Li-ion battery cells meeting automotive cycle life and calendar life requirements.

Objectives

The objective is to research, fabricate, and test lithium battery cells that implement $\geq 30\%$ silicon content electrodes with commercially available cathode technology and achieve cell performance identified in Table VIII.9.1 below.

Table VIII.9.1 Target cell performance

Beginning of Life Characteristics at 25 °C	Cell Level
Usable Specific Energy @ C/3	>350Wh/kg
Usable Energy Density @ C/3	>750Wh/L
Calendar Life @ C/3	>10 Years
Cycle Life (C/3 deep discharge to 350Wh/kg, <20% energy fade)	>1,500

Approach

Sila's nano-engineered particles enable ultra-low volume change silicon-dominant anodes and are the most promising candidate for silicon-based electric vehicle Li-ion batteries. This project utilizes Sila's proprietary particles and know-how for its application in standard Li-ion battery manufacturing processes. Both the bulk and surface properties of the particle are engineered for improved performance, and the electrode construction process is optimized around the adjustments made to the particle, as are electrolyte formulations. Sila's state of the art analysis techniques are also employed, and new methods are developed to understand how material and process changes impact cell performance.

In addition, Sila has partnered with ARL to simulate electrolyte reaction mechanisms and reveal the causes of cell performance differences between formulations with different electrolyte components. Sila has also partnered with PNNL to develop Localized High Concentration Electrolytes for higher automotive commercial readiness and achieve even better performance with Sila's anode material.

Results

Various improvements were made to Sila's silicon Li-ion battery chemistry and production process at the particle, electrode, and electrolyte levels. Some improvements from early in the grant were incorporated into a prototype production line to produce larger format pouch cells for demonstration purposes. 1Ah prototype stacked pouch cells were built utilizing Sila's nano-engineered silicon anode particles (no graphite or other non-Si active material present) and a placeholder NCM811 cathode, and were tested for cycle life (Figure VIII.9.1) and calendar life (Figure VIII.9.2). Calendar life data in particular far exceeded expectations, although the 10+ year projection is based on what data points are available from several months of testing.

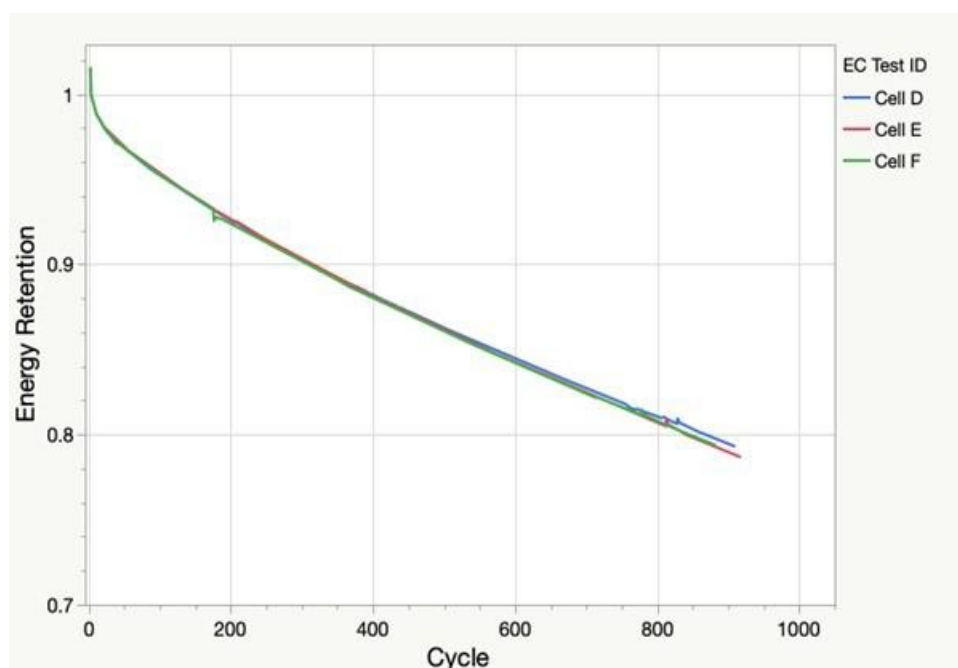


Figure VIII.9.1 Mirror Cells testing indicates a VED projection of > 560 Wh/L at 1000x C/3 full discharge cycles.

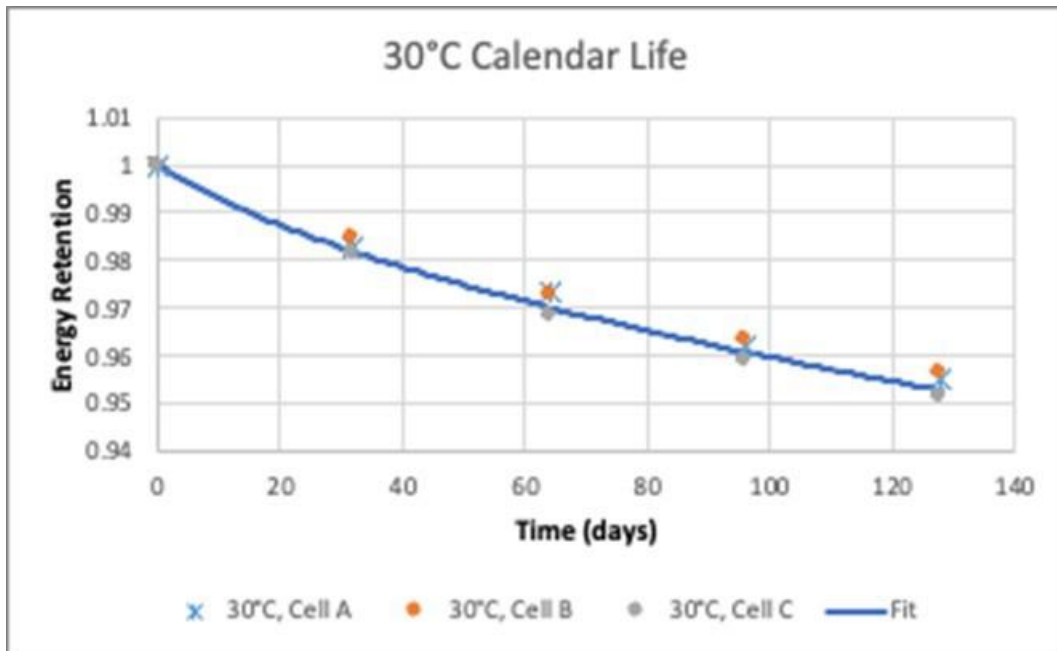


Figure VIII.9.2 Mirror Cell testing indicates calendar life projection of 10+ years to 560 Wh/L

Conclusions

Sila has achieved all go/no-go milestones for 2022, with mirror cells identical to those sent for validation projected to meet > 560 Wh/L at 1000 cycles (25°C) and 10+ years of calendar life at 30°C.

VIII.10 Solid State Li Ion Batteries Using Si Composite Anodes (Solid Power Inc.)

Pu Zhang, Principal Investigator

Solid Power Inc.
486 S Pierce Ave, Suite E
Louisville, CO 80027
E-mail: pu.zhang@solidpowerbattery.com

Brian Cunningham, DOE Technology Development Manager

U.S. Department of Energy
E-mail: Brian.Cunningham@ee.doe.gov

Start Date: October 1, 2020	End Date: September 30, 2023	
Project Funding (FY22): \$1,512,342	DOE share: \$1,177,874	Non-DOE share: \$334,468

Project Introduction

Solid Power is teaming with Argonne National Laboratory (Dr. Wenquan Lu) to develop an all-solid-state lithium-ion battery (ASSB) that will achieve high energy, long cycle life, and long calendar life. It is based on a high-capacity solid-state Si composite anode. The project will enable scalable production of large format all-solid-state batteries required by the vehicle market.

Objectives

The project objective is to develop all-solid-state Li ion batteries that implement high energy silicon anodes for EV application. The all solid state battery (ASSB) cell will be able to deliver > 350 Wh/kg specific energy, > 750 Wh/L energy density, > 1000 cycle life, and > 10 years calendar life.

Approach

The project will develop a solid state electrolyte (SSE) for Si anode and synthesize a Si-SSE composite anode. The solid state electrolyte system addresses the calendar life challenge of the Si anode batteries by forming highly stable SEI. A high-Ni content NMC cathode will be selected to match the Si anode. The all-solid-state cell will be assembled by scalable roll-to-roll processes developed by Solid Power.

Results

1. Si composite anode development

The Si composite was synthesized by integrating a Si powder and a Solid Power's sulfide solid state electrolyte (SSE). The Si-SSE composite material was mixed with a binder, a conductive carbon additive and a solvent to form an anode slurry. The slurry was then coated to Cu foil to form an electrode. A roll-to-roll process has been developed to coat the Si anode. Figure VIII.10.1 shows a Si anode coated by a slot-die coater.



Figure VIII.10.1 A continuous Si anode coating

A high energy Si composite anode has been successfully developed with a reversible capacity of 1500 mAh/g at electrode level as a baseline. To further improve the cell specific energy to 350 Wh/kg, an ultra-high energy Si anode (with Si content up to 70%) is being developed in this year.

To verify the new ultra-high energy (UHE) anode capacity, Si-Li coin half cells were built and tested at C/5 – C/5, 0.05 – 1.0V and 70°C. Both the baseline anode and the UHE anode were coated at a loading of 3 mAh/cm². The UHE Si anode achieves a capacity of 2100 mAh/g at electrode level, 40% higher than the baseline. After 100 cycles, the UHE anode cell retains 90% of the initial capacity after 100 cycles while the baseline retains 95%. The anode performance results are summarized in Table VIII.10.1 and Figure VIII.10.2. The current UHE anode still shows slightly lower cycling stability than the baseline. The UHE anode will be further developed with improved cycling stability.

Table VIII.10.1 Capacity and Cycle Life of the Si Anodes

Property	Baseline Si anode in BP1	New Si anode in BP2
Reversible Capacity (at Electrode Level)	1500 mAh/g	2100 mAh/g
Capacity Retention at Cycle 100	95%	90%

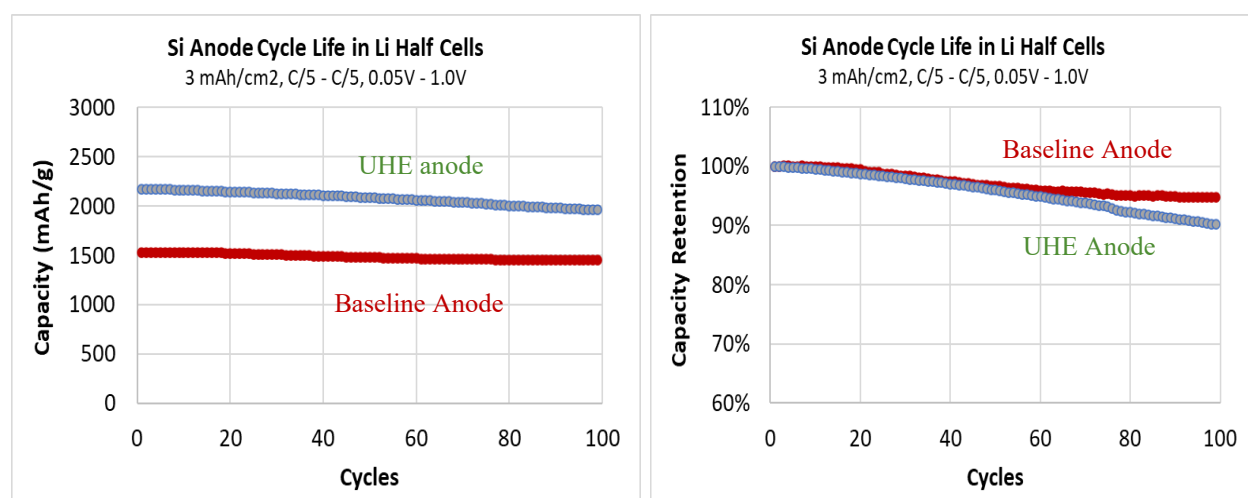


Figure VIII.10.2 Cycle life of the baseline and ultra-high energy (UHE) Si anodes in Li half cells (3 mAh/cm² loading, C/5 – C/5, 0.05 – 1.0V): (left) Si anode capacity vs. cycle; (right) capacity retention vs. cycle. The UHE shows a reversible capacity of 2100 mAh/g and 90% capacity retention after 100 cycles.

2. Full cell demonstration

An NMC622 cathode was selected to match the anode to form a full pouch cell. The solid state pouch cell was assembled with the NMC cathode, an SSE separator, and the Si composite anode (at 1500 mAh/g). When cycled at C/5 – C/5, 100% DOD, and 45°C, the cell shows 90% first cycle efficiency and retains 86% capacity after 800 cycles (Figure VIII.10.3).

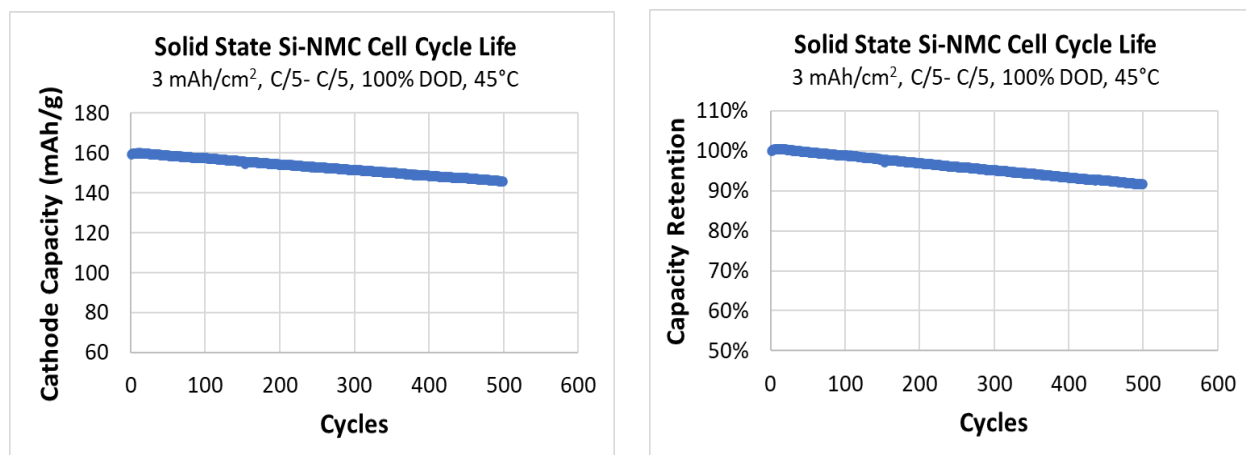


Figure VIII.10.3 Cycle life of a Si-NMC full pouch cell (3 mAh/cm² loading, C/5–C/5, 100% DOD, 45 °C). The cell retains 86% of initial capacity after 800 cycles.

Conclusions

Si-SSE composite materials have been developed with a specific capacity up to 2100 mAh/g (at electrode level). A Si anode with the loading of 3 mAh/cm² was coated by using a roll-to-roll process. All-solid-state NMC-Si pouch cells have been assembled and tested. The cycle life of > 800 at 100% DOD has been demonstrated in all-solid-state Si-NMC pouch cells.

VIII.11 Fully Fluorinated Local High Concentration Electrolytes Enabling High Energy Density Si Anodes (Stony Brook University)

Amy Marschilok, Principal Investigator

Stony Brook University
100 Nicolls Road, 675 Chemistry
Stony Brook, NY 11790-3400
E-mail: amy.marschilok@stonybrook.edu

Brian Cunningham, DOE Technology Development Manager

U.S. Department of Energy
E-mail: Brian.Cunningham@ee.doe.gov

Start Date: October 1, 2020
Project Funding: \$350,000

End Date: September 30, 2023
DOE share: \$350,000

Non-DOE share: \$0

Project Introduction

Silicon (Si) is highly desirable as an anode material for next-generation automotive battery cells due to its low operating potential and >3500 mAh/g specific capacity, ~10x graphite. However, during electrochemical cycling using conventional Li-ion electrolyte systems, the solid electrolyte interphase (SEI) which forms on Si is not stable, consuming electrolyte in each cycle and limiting cycle life.¹ The dynamic growth of the SEI is further aggravated by the large silicon volume change (>300%) in each (de)lithiation cycle. Thus, a critical need to enable practical Si-based anodes for high energy density is the development of novel electrolytes that result in mechanically and chemically stable SEI.

Objectives

The objective is to research, fabricate, and test lithium battery cells that implement $\geq 30\%$ silicon content electrodes with commercially available cathode technology and have the potential to achieve the potential to achieve 1000 cycles with >350 Wh/kg, >750 Wh/L, and <20% energy fade.

Approach

The technological approach is to use fluorinated localized high concentration electrolytes (LHCEs), where each component of the electrolyte contains at least one fluorine in its structure, to construct a functional SEI on Si based anodes. The approach combines the SEI modification strategies of fluorinated carbonate solvents and local high concentration electrolytes. The resulting synergy of anion and fluorinated solvent decomposition will form a mechanically robust, fluorinated SEI that enables extended cycling with high capacity retention. Diluting the LiFSI/fluorinated carbonate concentrated electrolyte with inert hydrofluoroethers will reduce viscosity and increase wettability while preserving the coordination environment of the concentrated electrolyte. The strong electron withdrawing fluorine substituents on the solvents will enable high oxidative stability, permitting the Si-based anode to be paired with NMC811 cathodes.

Results

1. Characterization of LHCE Transport and Stability Properties of Gen2 LHCEs

Work in this fiscal year was focused on the characterization and testing of Generation 2 (Gen2) LHCEs having varied diluent type and concentration. Gen2 LHCEs were prepared with a 1:2 ratio of fluorinated solvents VI: II, at concentrations of 3.0, 3.5 and 4.0 M. The HCEs were then diluted with new fluorinated hydrofluoroether diluents IV and V using solvent:diluent ratios of 1:1, 2:1, and 4:1. For several formulations, significant solution instability occurred where either salt precipitation or solvent immiscibility was observed. Five stable formulations were identified and their compositional details are listed in in Table VIII.11.1.

Table VIII.11.1 Description of Gen2 LHCEs including molarity of each electrolyte component – LiFSI is lithium bis (trifluoromethanesulfonyl) imide salt, VI and II are solvents and IV and V are diluents.

LHCE ID	LiFSI molarity in HCE (M)	Solvent:diluent molar ratio	Molarity in LHCE (M)				
			LiFSI	VI	II	IV	V
Gen2 #1	3.0	2:1	2.04	1.64	3.28	2.46	-
Gen2 #2	3.0	4:1	2.43	1.95	3.90	1.46	-
Gen2 #3	3.5	4:1	2.86	1.87	3.73	1.40	-
Gen2 #4	3.0	4:1	2.38	1.91	3.84	-	1.44
Gen2 #5	3.5	4:1	2.82	1.84	3.67	-	1.38

Viscosity measurements of the electrolytes and a control carbonate – based electrolyte (1M LiPF₆ 30:70 ethylene carbonate : dimethyl carbonate) were measured as a function of temperature (20°C – 50°C) using a microviscometer (Figure VIII.11.1). At 20°C, the control electrolyte viscosity was 2.8 mPa s, in good agreement with prior literature.¹ The viscosity (η) can be correlated with temperature according to an Arrhenius type relationship. Figure VIII.11.1b depicts the Arrhenius plots of the log of the viscosity ($\log \eta$) versus the inverse of temperature for the control electrolyte and FLHCEs. All samples follow a nearly linear relationship ($R^2 \geq 0.99$), where viscosity decreases as temperature increases. At 25°C, viscosities of the FLHCEs ranged from 7.6 – 35 mPa s. The viscosity of the electrolytes was strongly influenced by the final molarity of the LiFSI and the diluent type. Formulations with higher salt concentration had greater viscosity. Furthermore, electrolytes utilizing diluent V had greater viscosity than electrolytes utilizing diluent IV at similar salt concentrations.

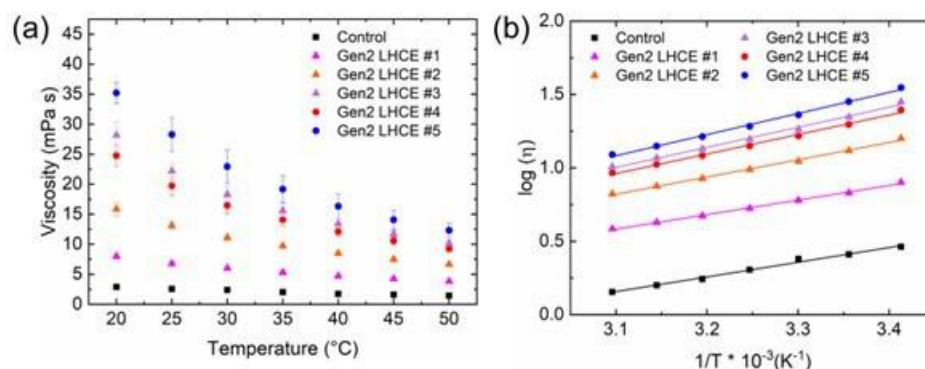


Figure VIII.11.1 Viscosity measurements of Gen2 LHCEs and a control (1M LiPF₆ in 3:7 v/v EC:DMC) electrolyte over a temperature range of 20 °C -50 °C. (a) Viscosity vs. temperature. (b) Arrhenius plot.

Contact angle measurements of the Gen2 LHCEs were characterized to understand the wettability on a polymeric separator. The measurements are performed by contacting a drop of electrolyte liquid on a needle with the polymer substrate. The contact angle is defined as the angle between the substrate surface and the tangent line at the point of contact between the droplet and the substrate. The measurements were collected as a function of time to account for the time needed for equilibration of the droplet on the substrate, and are plotted in Figure VIII.11.2. The LHCEs all had similar contact angle values after 90 s that ranged between 33° - 40° and exhibited a slight improvement in wettability compared to the control, which had a contact angle of 47°.

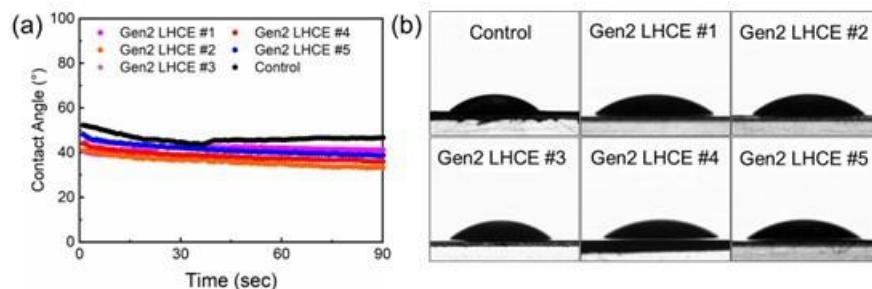


Figure VIII.11.2 (a) Contact angle measurements of Gen2 LHCEs and control (1M LiPF₆ in 3:7 v/v EC:DMC) electrolyte on polyethylene separator over time. (b) Images of electrolyte droplets on polyethylene separator after 90 seconds of contact.

The electrochemical properties (conductivity, voltage stability) of the Gen2 electrolytes were also characterized. Conductivity measurements of the Gen2 LHCEs, and a control carbonate – based electrolyte (1M LiPF₆ 30:70 ethylene carbonate : dimethyl carbonate) were measured as a function of temperature (20°C – 50°C) using electrochemical impedance spectroscopy (EIS). EIS was used to obtain the ohmic resistance of each electrolyte, which was then used to calculate conductivity.^{3,4,5} The results are plotted in Figure VIII.11.3. At 20°C, the control electrolyte conductivity was 10.7 mS/cm, in good agreement with the prior literature.⁶ Figure VIII.11.3b depicts the Arrhenius plots of the log of the conductivity (log σ) versus the inverse of temperature for the control electrolyte and FLHCEs. All samples follow a nearly linear relationship ($R^2 \geq 0.99$), where viscosity decreases as temperature increases. At 20°C, viscosities of the FLHCEs ranged from 2.2 – 2.9 mS/cm. These values are within the same range as the Gen1 electrolytes tested previously in Y1 (2.0 – 3.0 mS/cm), suggesting that the diluent type does not have a strong effect on the electrolyte conductivity.

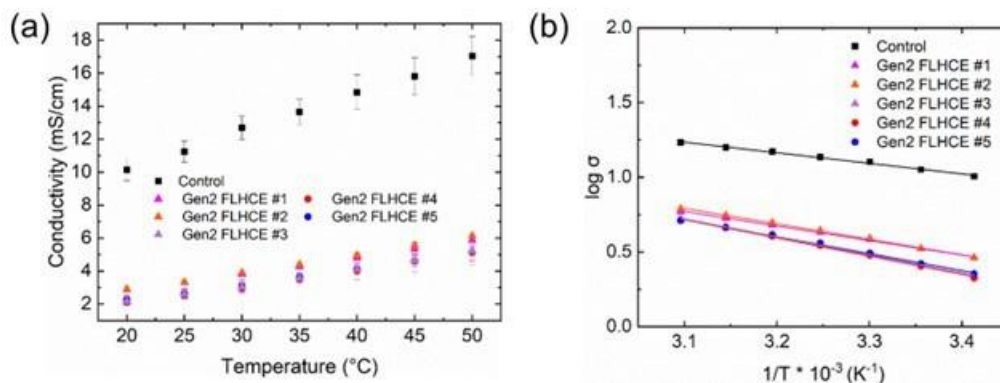


Figure VIII.11.3 Conductivity measurements of Gen2 LHCEs and a control (1M LiPF₆ in 3:7 v/v EC:DMC) electrolyte over a temperature range of 20°C -50°C. (a) Conductivity vs. temperature. (b) Arrhenius plot.

The upper voltage stability of the Gen2 LHCEs was assessed in a 3-electrode cell configuration with Pt working electrode and Li reference and counter electrodes. Scans were completed at 20 mV/s starting at 3.0 – 4.0 V, with the voltage incrementally increased until the current density reached 1×10^{-4} A/cm². The limiting current of 1×10^{-4} A/cm² is a conventional value cited in other reports to determine electrochemical stability.^{7,8} The cyclic voltammograms for all the Gen2 LHCEs and the control electrolyte are plotted in Figure VIII.11.4. Notably, all electrolytes exhibited high stability, with upper voltage limits above 4.9 V in this test. It was found that electrolytes utilizing diluent IV (Gen2 LHCEs 1-3) had slightly higher voltage stability (5.1 – 5.3 V) compared to electrolytes utilizing diluent V (4.9 V). It is noted that these values are comparable to the Gen1 LHCEs, which had voltage stability limits between 4.9 – 5.0 V.

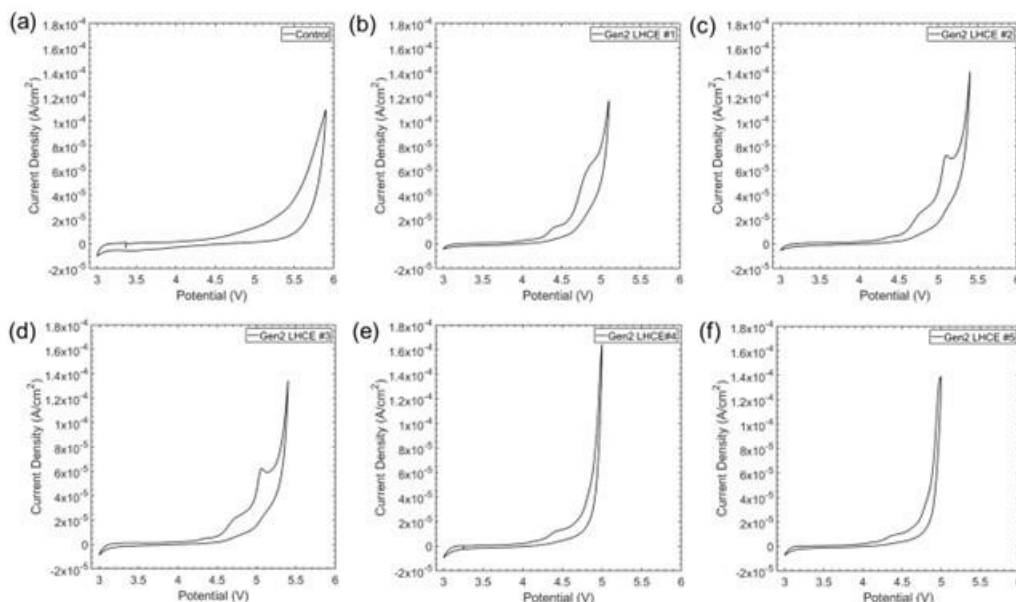


Figure VIII.11.4 Cyclic voltammograms of (a) control electrolyte (1 M LiPF₆ 30:70 EC:DMC) and (b-f) Gen2 LHCEs in a 3-electrode cell configuration with Pt working electrode and Li reference and counter electrodes. Scan rate = 20 mV/s.

2. Characterization of Electrochemical Behavior of Gen2 LHCEs

The Gen2 FLHCEs with compositions specified in Table I.1.1 were subjected to galvanostatic cycling in a half cell configuration, at a rate of 0.3 A/g between voltage limits of 0.005 – 1.2 V for 50 cycles (Figure VIII.11.5). Data for the Gen1 LHCE with the highest capacity retention (Gen 1 LHCE #2) is included in the plots as a comparison. All electrolytes exhibited a capacity retention > 60%, which was significantly above the retention of the control electrolyte at 37%. Notably, Gen2 LHCE #1 exhibited an increase in capacity after 100 cycles compared to the Gen1 electrolyte (780 mAh/g vs. 720 mAh/g).

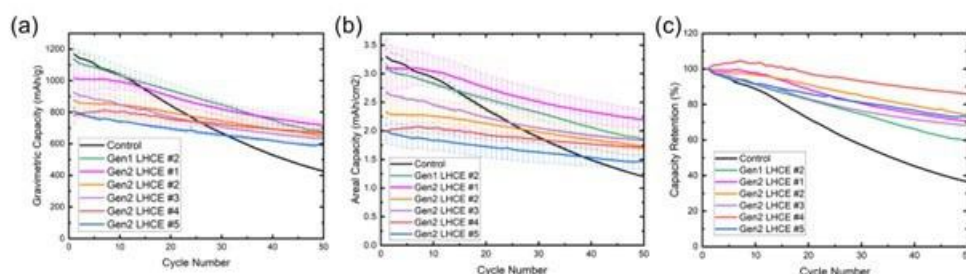


Figure VIII.11.5 Galvanostatic cycling in half cell configuration for Si/graphite electrodes with 2.5 mg/cm² loading cycled 50x at 0.3 A/g with Gen2 LHCE formulations: (a) Gravimetric capacity, (b) areal capacity, (c) capacity retention.

Further electrochemical characterization of the cells in Si-graphite/NMC622 full cells using a single layer pouch cell configuration (20 cm² cathode area), where active material loading of the Si-graphite and NMC622 electrodes were 2.5 mg/cm² and 18.5 mg/cm² respectively. Cycling was performed at C/3 rate between 3.0 – 4.3 V for 100 cycles (Figure VIII.11.6). All FLHCEs tested exhibited capacity retention values between 60 – 68%, compared to 20% for the control electrolyte. Gen2 LHCE #1 exhibited the highest delivered capacity after 100 cycles (91 ± 3 mAh/g), which represents a small improvement over the Gen1 LHCE with the highest capacity retention (Gen1 LHCE #2, 87 ± 2 mAh/g).

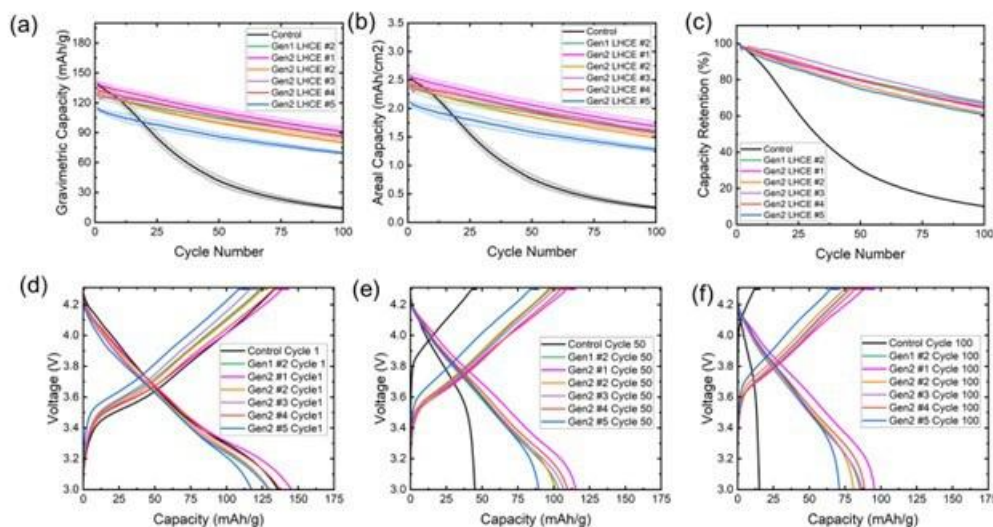


Figure VIII.11.6 Galvanostatic cycling of single layer Si-graphite/NMC622 pouch cells at C/3 rate with Gen 2 LHCEs. Data is compared to cells cycled with control electrolyte (1M LiPF₆ 3/7 EC/DMC). C/3 cycling rate between 3.0 – 4.3 V. (a) Specific capacity, (b) capacity retention, (c) coulombic efficiency. (d-f) Voltage profiles at (d) 100 cycles, (e) 50 cycles, (f) 100 cycles.

The electrochemical cycling behavior of Gen2 LHCE #1 was further assessed against fluoroethylene carbonate (FEC) containing carbonate electrolytes (1 M LiPF₆ 30:70 EC:DMC + x wt % FEC, where x = 2.5, 5.0, 10.0) in Figure VIII.11.7. The LHCE exhibits similar initial capacity (140 ± 2 mAh/g) as the carbonate based control electrolytes but reduced capacity fade over 100 cycles. The Go/No-go milestone for the Y2 budget period was the demonstration of full cells using Gen2 LHCE capable of 100 cycles at C/3 rate with 20% improvement in capacity retention compared to cells with control electrolyte. The Gen2 LHCE demonstrates $\geq 20\%$ improvement in capacity retention compared to all control compositions tested (1M LiPF₆ EC/DMC, 1M LiPF₆ EC/DMC + 2.5% FEC, 1M LiPF₆ EC/DMC + 5.0% FEC, 1M LiPF₆ EC/DMC + 5.0% FEC, 1M LiPF₆ EC/DMC + 10.0% FEC), satisfying the Go/No-go requirement.

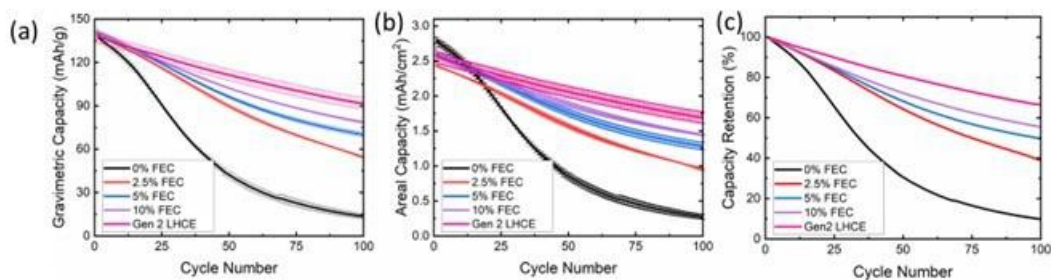


Figure VIII.11.7 Galvanostatic cycling of duplicate single layer Si-graphite/NMC622 pouch cells at C/3 rate with Gen2 LHCE #1 and FEC containing carbonate electrolytes (1 M LiPF₆ 30:70 EC:DMC + x wt % FEC, where x = 0, 2.5, 5.0, 10.0). (a) Gravimetric Capacity, (b) Areal Capacity, (c) Capacity Retention.

3. X-ray Photoelectron Spectroscopy Characterization of SEI Layer

Post cycling characterization of cycled Si-graphite electrodes from full cells using X-ray photoelectron spectroscopy (XPS) to interrogate the composition of the solid electrolyte interphase (SEI) layer. Spectral regions including C 1s, F 1s, Si 2p, F 1s, Li 1s, and P 2p were investigated. Figure VIII.11.8 shows selected spectra for electrodes cycled in control (1M LiPF₆ 3:7 EC:DMC) electrolyte and LHCE. For both electrolyte types, the C 1s spectra (Figure VIII.11.8 a, b) are comprised of five distinct peaks, assigned to the following

bond types: C-C and C-H (~ 284.7 eV), C-O (~ 286 eV), O-C-O, C=O, and O-C=O (288-289 eV), CO_3 species (~ 290 eV), and C-Li (283.5 eV).⁹ The anode cycled with control electrolyte had the higher relative atomic concentration of carbonate species as compared to electrodes cycled with the LHCE, indicating a more organic rich SEI layer. F 1s spectra (Figure VIII.11.8 c, d) for both control and LHCE cycled electrodes show peaks corresponding to salt complexes (~ 687 - 688 eV)¹⁰ and LiF (~ 685 eV)¹¹ before and after sputtering. The presence of LiF indicates that the fluorinated components (salt, solvent, and diluent) formed an inorganic phase. Electrodes cycled with the LHCE had significantly greater concentrations of LiF in the SEI compared to the control electrolyte.

Significant differences between the control-cycled and LHCE-cycled electrodes were also observed in the Li 1s spectra (Figure VIII.11.8 e, f). In both sample types, convolution of LiF and LiCO_3 contributions is observed at ~ 55 eV. However, for the LHCE-cycled electrode, additional signal at ~ 53 eV - 54 eV is observed, assigned to Li_2O .¹² The concentration of this species increases significantly after sputtering, indicating that the inner region of the SEI on Si is rich in Li_2O . The LHCE-cycled electrodes also exhibited signal in the S 2p region, directly indicating the presence of the FSI⁻ anion and its decomposition products in the SEI layer.¹³

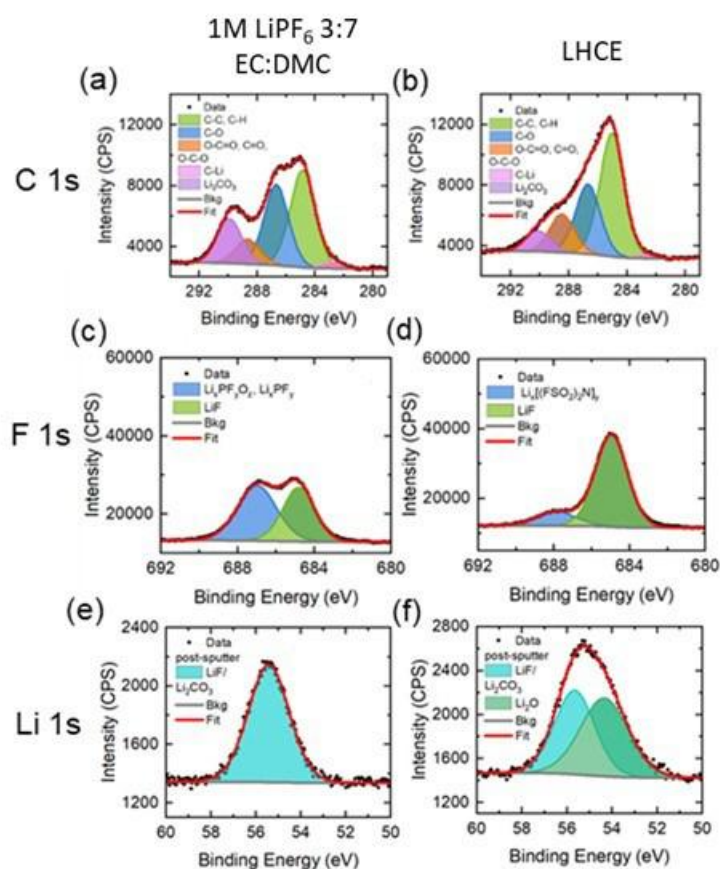


Figure VIII.11.8 X-ray photoelectron spectroscopy data in (a,b) C 1s, (c, d) F 1s and (e, f) Li 1s regions collected on Si-graphite electrodes recovered from 100x cycled full cells containing (a, c, e) control electrolyte (1M LiPF_6 3:7 EC:DMC) and (b, d, f) LHCE.

Conclusions

Gen2 fluorinated local high concentration electrolytes were prepared function of hydrofluoroether chemistry and concentration and the physical properties (viscosity, wettability) and electrochemical properties (conductivity, viscosity) of the electrolyte were fully characterized. Electrochemical behavior was evaluated in half cell and full cell configurations. The Gen2 LHCEs exhibited $\geq 20\%$ improvement in capacity retention compared to all control compositions tested (1M LiPF_6 EC/DMC, 1M LiPF_6 EC/DMC + 2.5% FEC, 1M LiPF_6

EC/DMC + 5.0% FEC, 1M LiPF₆ EC/DMC + 5.0% FEC, 1M LiPF₆ EC/DMC + 10.0% FEC). XPS analysis indicated that the LHCE-derived SEI has higher Li content, including LiF and Li₂O species, as well as sulfur species associated with decomposition of the FSI⁻ anion. The modified SEI enables improved capacity retention of the Si-graphite electrode over extended cycling.

Key Publications

1. Lutz, D. M.; McCarthy, A. H.; King, S. T.; Singh, G.; Stackhouse, C. A.; Wang, L.; Quilty, C. D.; Bernardez, E. M.; Tallman, K. R.; Tong, X.; Bai, J.; Zhong, H.; Takeuchi, K. J.; Takeuchi, E. S.; Marschilok, A. C.; Bock, D. C., Progress Towards Extended Cycle Life Si-based Anodes: Investigation of Fluorinated Local High Concentration Electrolytes. *Journal of The Electrochemical Society* 2022, 169 (9), 090501.

References

1. Veith, G. M.; Doucet, M.; Sacci, R. L.; Vacaliuc, B.; Baldwin, J. K.; Browning, J. F., Determination of the Solid Electrolyte Interphase Structure Grown on a Silicon Electrode Using a Fluoroethylene Carbonate Additive. *Scientific Reports* 2017, 7 (1), 6326.
2. Logan, E. R.; Tonita, E. M.; Gering, K. L.; Li, J.; Ma, X.; Beaulieu, L. Y.; Dahn, J. R., A Study of the Physical Properties of Li-Ion Battery Electrolytes Containing Esters. *Journal of The Electrochemical Society* 2018, 165 (2), A21-A30.
3. Liu, Q.; Dzwiniel, T. L.; Pupek, K. Z.; Zhang, Z., Corrosion/Passivation Behavior of Concentrated Ionic Liquid Electrolytes and Its Impact on the Li-Ion Battery Performance. *Journal of The Electrochemical Society* 2019, 166 (16), A3959-A3964.
4. Nilsson, V.; Bernin, D.; Brandell, D.; Edström, K.; Johansson, P., Interactions and Transport in Highly Concentrated LiTFSI-based Electrolytes. *ChemPhysChem* 2020, 21 (11), 1166-1176.
5. Nilsson, V.; Kotronia, A.; Lacey, M.; Edström, K.; Johansson, P., Highly Concentrated LiTFSI-EC Electrolytes for Lithium Metal Batteries. *ACS Applied Energy Materials* 2020, 3 (1), 200-207.
6. Xu, K., Nonaqueous Liquid Electrolytes for Lithium-Based Rechargeable Batteries. *Chemical Reviews* 2004, 104 (10)4303-4417.
7. Yim, T.; Choi, C. Y.; Mun, J.; Oh, S. M.; Kim, Y. G., Synthesis and Properties of Acyclic Ammonium-based Ionic Liquids with Allyl Substituents as Electrolytes. *Molecules* 2009, 14 (5), 1840-1851.
8. Di Leo, R. A.; Marschilok, A. C.; Takeuchi, K. J.; Takeuchi, E. S., Battery electrolytes based on saturated ring ionic liquids: Physical and electrochemical properties. *Electrochimica Acta* 2013, 109, 27-32.
9. Briggs, D.; Beamson, G., Primary and secondary oxygen-induced C1s binding energy shifts in x-ray photoelectron spectroscopy of polymers. *Analytical Chemistry* 1992, 64 (15), 1729-1736.
10. Kang, S.-J.; Park, K.; Park, S.-H.; Lee, H., Unraveling the role of LiFSI electrolyte in the superior performance of graphite anodes for Li-ion batteries. *Electrochimica Acta* 2018, 259, 949-954.
11. Hennessy, J.; Nikzad, S., Atomic Layer Deposition of Lithium Fluoride Optical Coatings for the Ultraviolet. *Inorganics* 2018, 6 (2), 46.
12. Eijima, S.; Sonoki, H.; Matsumoto, M.; Taminato, S.; Mori, D.; Imanishi, N., Solid Electrolyte Interphase Film on Lithium Metal Anode in Mixed-Salt System. *Journal of The Electrochemical Society* 2019, 166 (3), A5421-A5429.
13. Chen, H.; Pei, A.; Lin, D.; Xie, J.; Yang, A.; Xu, J.; Lin, K.; Wang, J.; Wang, H.; Shi, F.; Boyle, D.; Cui, Y., Uniform High Ionic Conducting Lithium Sulfide Protection Layer for Stable Lithium Metal Anode. *Advanced Energy Materials* 2019, 9 (22), 1900858.

Acknowledgements

The co-PIs for this project include Kenneth J. Takeuchi (Stony Brook University and Brookhaven National Laboratory), Amy C. Marschilok (Stony Brook University and Brookhaven National Laboratory), David C. Bock (Brookhaven National Laboratory) and Lei Wang (Brookhaven National Laboratory).

VIII.12 Devising mechanically compliant and chemically stable synthetic solid-electrolyte interphases on silicon using ex situ electropolymerization for long cycling Si anodes (University of Delaware)

Koffi Pierre Yao, Principal Investigator

University of Delaware
210 South College Ave.
Newark, DE, 19716
E-mail: claver@udel.edu

Ajay K. Prasad, Co-Principal Investigator

University of Delaware
210 South College Ave.
Newark, DE, 19716
E-mail: prasad@udel.edu

Thomas Epps, Co-Principal Investigator

University of Delaware
210 South College Ave.
Newark, DE, 19716
E-mail: thepps@udel.edu

Daniel Abraham, Co-Principal Investigator

Argonne National Laboratory
9700 S Cass Ave.
Lemont, IL, 60439
E-mail: abraham@anl.gov

Brian Cunningham, DOE Technology Development Manager

U.S. Department of Energy
E-mail: Brian.Cunningham@ee.doe.gov

Start Date: January 1, 2022
Project Funding: \$1,000,000

End Date: December 31, 2022
DOE share: \$1,000,000

Non-DOE share: \$0

Project Introduction

Silicon (Si) is capable of $\sim 3500 \text{ mAh}\cdot\text{g}^{-1}$ and operates near the lithium potential making it a potential replacement for graphite anodes ($\sim 372 \text{ mAh}\cdot\text{g}^{-1}$) with a tenfold increase in capacity. Nonetheless, the reactive surface of silicon and lithium-silicide products combined with the 350% expansion of particles during cycling results in instability of the native solid electrolyte interphase (SEI) required to halt cyclical reductive degradation of battery electrolytes. Consequently, during operation, loss of lithium inventory, densification of the electrode, and loss of electrical contact curtail the cell cycling and calendar life. Cells with silicon anodes are typically unable to achieve the DOE target of $350 \text{ Wh}\cdot\text{kg}^{-1}$ and $750 \text{ Wh}\cdot\text{L}^{-1}$ beyond 1000 cycles and 10 years calendar life. To solve the cycling and calendar life shortcomings of silicon as an anode, an SEI which is (i) resistant to chemical attack from the silicon surface and (ii) mechanically stable over repeated straining is needed to retain its function of protecting the electrolyte over extended cycling and/or storage.

Objectives

The program aims to produce cells based on Si anodes paired with existing transition metal oxide cathodes capable of achieving greater than $350 \text{ Wh}\cdot\text{kg}^{-1}$, $750 \text{ Wh}\cdot\text{L}^{-1}$ at the cell level with a target calendar life of 10 years and cycle life of 1000 cycles (Table VIII.12.1).

Table VIII.12.1 Summary of program objectives

Beginning of Life Characteristics at 30 °C	Cell Level
Useable Specific Energy @ C/3	>350 Wh/kg
Useable Energy Density @ C/3	>750 Wh/L
Calendar Life (<20% energy fade)	>10 Years
Cycle Life (C/3 deep discharge to 350Wh/kg, <20% energy fade)	>1,000

As described in the introduction, a key to enabling long cycling and long calendar life silicon anodes is to devise a stable SEI to protect the electrolyte and lithium inventory against cyclical consumption in degradation processes. Our project objective is to remedy the continuous electrolyte decomposition on Si surfaces by devising a chemically stable polymer synthetic SEI capable of withstanding the expansion of Si particles with minimal damage. We aim to achieve this solution using electrodeposition methods to apply a thin elastomeric polymer film to function as a synthetic SEI.

Approach

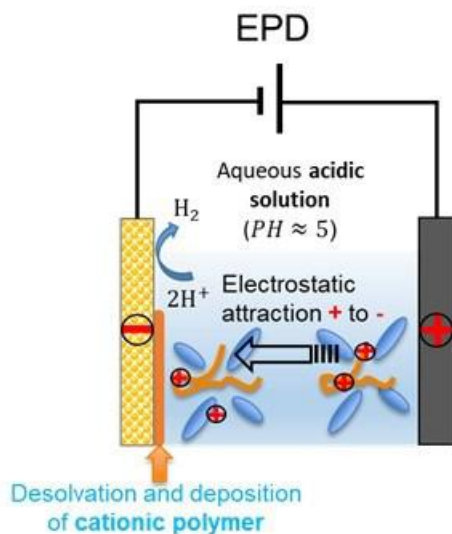


Figure VIII.12.1 Schematic description of the principles of electrophoretic deposition

Electrophoretic deposition (EPD) is employed as an electrochemical tool to apply the elastomeric polymer as synthetic SEI on silicon electrodes. (See Figure VIII.12.1.) The process consists of dissolving a charged polymer to deposit in a precursor electrolyte. Subsequent application of an electric field between parallel working (silicon) and counter electrodes drives the charged polymer to coat the working electrode. As the deposition is controlled by the electric field, control of the deposition quantity can be achieved through control of the electric charge. Externalization of the SEI application process from an operating battery environment enables the use of a wider range of precursors to achieve a synthetic SEI with the requisite strain resistance to withstand the ~350% expansion/contraction of silicon during electrochemical cycling. Furthermore, as EPD is a priori a physical deposition process, the chemistry of electrodeposited polymer is minimally changed. The

approach therefore offers the ability to select the chemistry, chain length, conductivity, and stability of the synthetic SEI components by choice of the polymer to electrodeposit. Herein, we describe progress achieved through EPD of polymeric and ionically conductive chitosan on silicon thin films (for simplified characterization) and on porous silicon electrodes (for electrochemical cycling in coin cells).

Our approach to controlling the chemistry and compounds in the SEI is novel; therefore, we begin with electrodeposition of chitosan on silicon thin films followed by characterization by AFM, IR spectroscopy, XPS, EIS, and electrochemical cycling. We later translated the EPD procedure as validated on Si thin films to pre-apply chitosan as a synthetic SEI onto silicon electrodes.

The workflow is as follows:

- 1) Utilize silicon thin film as model surfaces for polymer EPD procedure tuning.
- 2) Spectroscopically characterize and optimize the film growth, quality, chemistry, stability, and electrochemical properties.
- 3) Translate the validated electrocoating methods to coat elastomeric and ionically conductive SEIs on Si-anodes with over 30% Si loading.
- 4) Validate the long-term stable cycling and calendar life of cells equipped with our electrocoated Si.

Results

Chitosan is a derivative of chitin, the most abundant naturally occurring aminopolysaccharide found in crustaceans, insects, and fungi¹. Chitosan has found numerous applications in biomedicine and is therefore easily sourced commercially. In aqueous solutions at pH less than 6, chitosan dissolves and develops cationic charges at the primary amine groups of the chain². The cationic nature of chitosan after partial protonation in water allows its cathodic electrophoretic deposition onto silicon surface as demonstrated in Figure VIII.12.2. Silicon thin film was produced by sputter deposition onto a copper foil (Figure VIII.12.2a). EPD was performed in a precursor solution of hydrochloric acid in distilled water wherein chitosan is dissolved. The precursor solution pH is balanced to 5 using NaOH. The silicon thin film working electrode is connected to the negative terminal of a potentiostat while an aluminum foil connected to positive terminal is the counter electrode. A reference electrode of Ag/AgCl is used to set the potential at the silicon film electrode. For visually inspectable demonstration, chitosan is deposited onto a silicon thin film at -20 V between working and counter to obtain a micrometer-thick polymer film (Figure VIII.12.2a, white film at bottom). A microscope image of the deposition in Figure VIII.12.2b shows a mostly conformal polymer film; cracks in the film arise upon drying at 80 °C in a vacuum oven prior to imaging and AFM. AFM on a 10 x 10 μm^2 area in Figure VIII.12.2c confirms the conformal polymer film electrodeposition on the silicon surface. Nano-FTIR taken at various locations on the film in Figure VIII.12.2d (color-mapped to locations in Figure VIII.12.2c) ascertain the chemistry of the film to be the intended chitosan polymer. After successfully demonstrating the EPD of chitosan, the deposition potential is lowered to -3.2 V versus Ag/AgCl in the production of silicon thin films pre-coated with a chitosan synthetic SEI for electrochemical cycling investigation. Chitosan deposition was again ascertained at the lowered voltage using the investigation pipeline shown in Figure VIII.12.2.

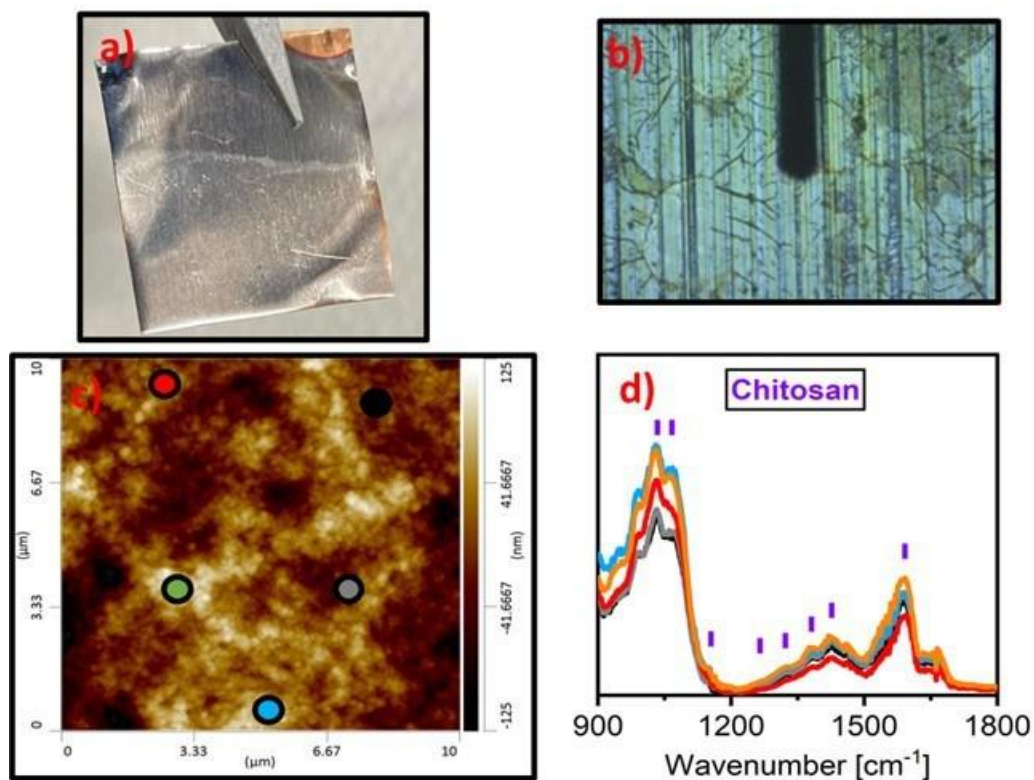


Figure VIII.12.2 Demonstration of chitosan electrophoretic deposition on silicon thin film model surface

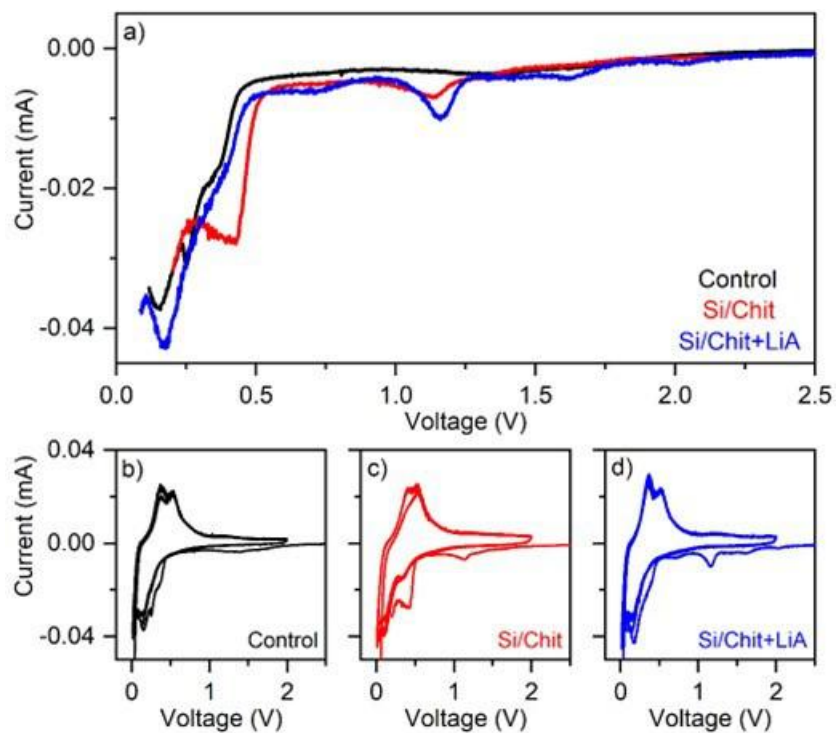


Figure VIII.12.3 Cyclic voltammograms of uncoated silicon thin film (control), silicon thin film with chitosan EPD coating (Si/Chit), and silicon thin film with chitosan EPD coating in presence of 0.03 M Lithium acetate (Si/Chit+LiA).

Two precursor solutions of chitosan were prepared for EPD coating of silicon thin films to be investigated electrochemically. One precursor contains chitosan-only and the other contains chitosan + 0.03M of lithium acetate (CH_3COOLi). The impetus for the addition of CH_3COOLi was to cap the amine end-groups of Chitosan through an amidation reaction with the Carboxyl group of the acetate and thereby mitigate reaction with similar carboxyl groups on the activated EC in the battery electrolyte after reductive ring-opening. The effect of the two types of chitosan synthetic SEIs were investigated by performing the EPD using the chitosan and the chitosan + CH_3COOLi solutions separately on the silicon thin film at -3.2 V vs Ag/AgCl for 5 minutes. The washed and dried chitosan-coated silicon thin films were used to make half-cells against lithium with the EC:EMC (1M LiPF_6) as electrolyte (no FEC additive added). Control cells with the bare silicon thin film are assembled in a similar manner to use as reference.

Electrochemical characteristics of the cells are first examined by Cyclic Voltammetry (CV) between 0.01 and 2 V vs. Li/Li^+ with scanning rate of 2 mV/s (Figure VIII.12.3). The first cycles of each CV are plotted separately in Figure VIII.12.3a to assess the difference in redoxes among those the three samples. The redox peak at potential ~ 1.12 V, which is only observed in the chitosan-only and the chitosan+ CH_3COOLi samples in the first cycle, is assigned to the initial lithiation of the pre-applied synthetic chitosan SEIs. Moreover, an intense reduction peak at ~ 375 mV appears when the Si thin film is coated with a chitosan-only layer during the first cycle. But this reduction peak is suppressed when with the addition of lithium acetate in the precursor solution. This peak at ~ 375 mV is associated with the EC reduction to form the natural SEIs; its suppression when CH_3COOLi is added to the precursor (compared to without) is an indication of a change in the molecular structure of the EPD coated chitosan in presence of CH_3COOLi . This chemical modification is revealed by XPS (not shown herein for brevity). XPS data indicates successful grafting of carboxyl end groups to the amine groups of chitosan in presence of CH_3COOLi at EPD which likely did not favor interactions with carboxyl-like products from the electrochemical reduction of EC in a battery environment. The cyclic voltammograms of the first four cycles for the bare control Si thin film, Si thin film with chitosan, and Si thin films with chitosan+ CH_3COOLi additive are shown in Figure VIII.12.3b, c, and d, respectively. Beyond the first reduction sweep, the CVs of the control, silicon/chitosan, and silicon/chitosan+ CH_3COOLi become nominally similar. The lithiation and delithiation of the underlying silicon is the main redox in the range of 0-1.5 V characterized by two clear reduction peaks on the down-sweep and two oxidation peaks on the up-sweep.

Next, the electrochemical impedance (EIS) of films was probed to gauge the potential increase (or decrease) in interface resistance to be expected from the chitosan synthetic SEI electrodeposition on the silicon surface. A custom fitting algorithm was developed in Python to explore both the space of possible model circuits as well as the space of solutions to those models against the data. Several common battery EIS models were tested for consistency and minimization of fit residuals. The model which consistently and reasonably (low residuals) fitted cells of all three samples (control, Si/Chit, and Si/Chit+ CH_3COOLi) is shown in Figure VIII.12.4a. The circuit as described from left to right is devised to capture the anticipated impedance behaviors of the Li foil counter electrode ($R_{\text{ct_Li}}$, $W_{\text{d_Li|Et}}$, and $C_{\text{Li|Et}}$), the electrolyte (R_{Et}), the natural and/or synthetic SEI on Si ($\text{CPE}_{\text{Et|SEI}}$), and finally the Si thin film electrode ($R_{\text{ct_Si}}$, $\text{CPE}_{\text{SEI|Si}}$). “R” indicates a pure resistor, “C” a pure capacitor, and “W” a purely diffusive medium in the form of a Warburg element. Constant phase elements (CPE) are flexible in capturing the spectrum of capacitive to diffusive behavior and are chosen to model the interfaces electrolyte|SEI and SEI|Si because a mix of capacitive and diffusive behavior is expected from those interfaces.

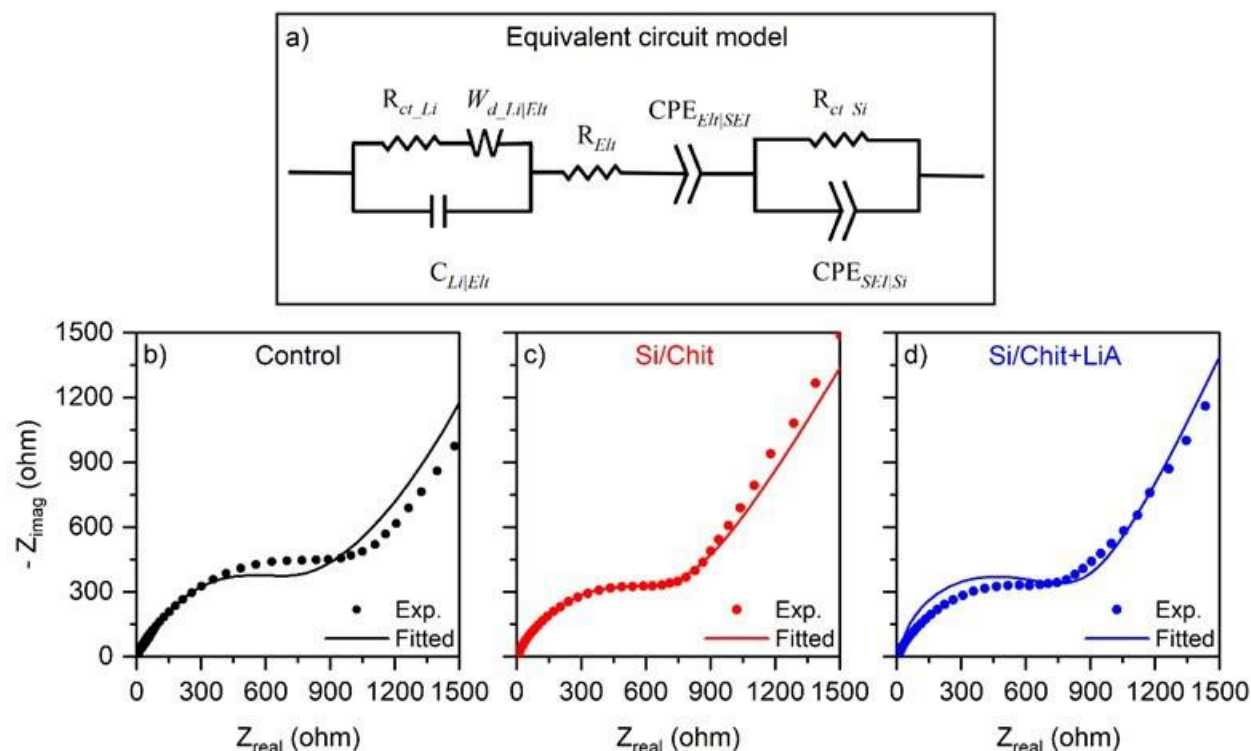


Figure VIII.12.4 EIS of uncoated silicon thin film (control), silicon thin film with chitosan EPD coating (Si/Chit), and silicon thin film with chitosan EPD coating in presence of 0.03 M Lithium acetate (Si/Chit+LiA). Solid line against the dotted data points in each of (b), (c), and (d) show the average of fits (over three cells for each Si sample type) compared to one representative EIS.

The EIS Nyquist plots of the control, Si/Chit, and Si/Chit+CH₃COOLi half-cells obtained after the formation cycles along with the fitted profiles (average of three per Si samples) are shown in Figure VIII.12.4b, c, d. All spectra show depressed semi-circles that signal the presence of complex mixed electrochemical processes at the electrodes other than pure resistance, capacitance, and diffusion phenomena.

Fitting and averaging across three cells per sample type (a sample type being either Figure VIII.12.4a or b or c) shows consistency in the impedance of the Li electrode and the electrolyte among the three kinds of cells as ought to be expected. The average values of charge transfer resistance $R_{ct, Li}$ at the lithium electrode were 343, 302, and 364 $\Omega \cdot \text{cm}^2$ while the electrolyte resistance R_{Elt} were 4.15, 5.33, 5.39 $\Omega \cdot \text{cm}^2$ for the control, Si/Chit, and Si/Chit+CH₃COOLi half-cells, respectively. The double-layer region at the Elt|SEI interface is found to be mostly capacitive in all the three cases with the phase angle $\sim 73^\circ$ ($\alpha_{CPE} \approx 0.80$). The impedances diverge most at the interfaces of Si thin films without and with the synthetic chitosan SEI. Without chitosan SEI, the control Si electrode shows a higher charge transfer resistance ($R_{ct, Si}$) of 1016 $\Omega \cdot \text{cm}^2$, and the SEI|Si interface appears diffusive as the $CPE_{SEI|Si}$ has a phase angle of $\sim 39.6^\circ$ ($\alpha_{CPE} \approx 0.44$). On the other hand, cells containing Si with a chitosan SEI have 5 times lower $R_{ct, Si}$ value than the control cell. The chitosan coated Si electrode exhibits the lowest average resistance of 228 $\Omega \cdot \text{cm}^2$. A slightly higher resistance of the chitosan+CH₃COOLi coated Si electrode (276 $\Omega \cdot \text{cm}^2$) is likely due to higher deposition of the artificial SEI as seen from higher current during EPD. In presence of the chitosan layer, the SEI|Si interfaces are found to be more capacitive in nature ($CPE_{SEI|Si}$ phase angle $\sim 70.2^\circ - 65.7^\circ$, $\alpha_{CPE} \approx 0.78 - 0.73$) in contrast to the control electrode ($CPE_{SEI|Si}$ phase angle $\sim 39.6^\circ$, $\alpha_{CPE} \approx 0.44$). *The detailed EIS analysis concludes that the EPD coating of Li⁺ conductive chitosan on Si thin film electrodes reduces the charge transfer resistance by a factor of 5 in agreement with previous literature examination of chitosan in electrochemical cells³.*

The cycling performance of the three sets of cells (control, Si/Chi, Si/Chit+CH₃COOLi) are shown in Figure VIII.12.5a (charge capacity) and Figure VIII.12.5b (discharge capacity). Error bars are obtained from

averaging over three repetitions of each type of Si electrodes. Early in the cycling, the capacity output of Si electrodes with and without chitosan synthetic SEI are indistinguishable. Divergence in capacity retention is most clearly seen past 50 cycles. Beyond 50 cycles, the cycling capacity of the control cell (black line: control) continues a steep drop while the rate of decay slows measurably for cells with Si films precoated with chitosan synthetic SEIs. After 112 high-rate cycles, cells with chitosan+CH₃COOLi SEIs show the highest average retained capacity of ~ 8.3 μAh , twice as much as the ~ 4.3 μAh of control cells, and 1.4 times greater than the ~ 6.1 μAh of Si films with chitosan-only synthetic SEIs. The terminal reference performance test (RPT) at the end of cycling shows recovery of capacity from all three types of Si thin films with and without chitosan SEIs; however, the trend in capacity retention is maintained. We conclude that chitosan synthetic SEIs achieved by EPD not only reduce the charge transfer resistance at the silicon thin film surface but also boosts the capacity retention on extended cycling. *Furthermore, the improved retention after extended cycling suggests that the conformal polymer synthetic SEI devised in this project is promising in achieving the intended objective of protecting the electrolyte against continued cyclic reduction, thereby reducing loss of lithium inventory and electrolyte in the cell.*

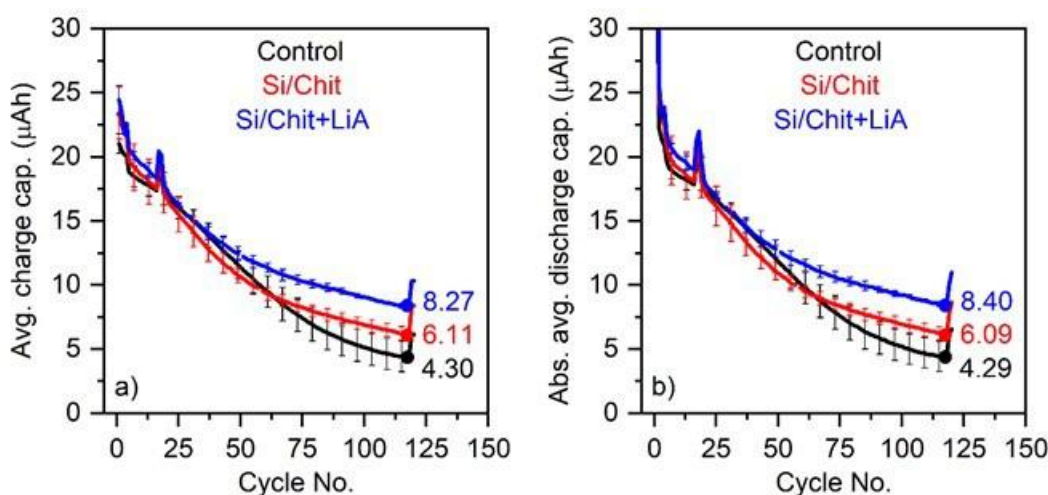


Figure VIII.12.5 Cycling performance: a) the average charge, and b) the average discharge capacity (μAh) vs cycle no. of the control, Si/Chit and Si/Chit-CH₃COOLi cells during long cycling. Each capacity profile is the average of 3 cells, all cells are cycled between 0.01 – 2 V vs. Li/Li⁺ at the current rates of 2.5 μA (4 formation cycles), 8.33 μA (4 high-rate cycles), and 1.25 μA (4 RPT cycles).

The established EPD procedure for applying a synthetic SEI onto silicon surfaces is translated to coating practical porous Si electrodes for cell cycling. In Figure VIII.12.6, the capacity retention at C/3 for porous electrodes obtained from Argonne National Laboratory Cell Analysis, Modeling, and Prototyping (CAMP) Facility are shown with and without chitosan EPD. Half-cells were used for this performance comparison. The CAMP silicon electrodes contain 80 wt% silicon, 10 wt% carbon, and 10 wt% polyimide cured at 350 °C. Electrodes of untreated Si (p84 Si control) and Si subject to the EPD electrocoating conditions without chitosan present (p84 silicon w/o polymer) serve as controls against which the performance gains of electrodes with EPD-applied chitosan SEIs (p84 Si w/ chitosan) are compared. As is common for silicon electrodes, rapid loss of initial capacity is seen in the first 10 cycles. Cycling capacity settled at a higher value of ~ 750 $\text{mAh}\cdot\text{g}^{-1}$ compared to ~ 570 $\text{mAh}\cdot\text{g}^{-1}$ in the controls. Over 100 cycles, capacity decay is observed for all three electrode types. Terminal capacities after 100 C/3 cycles were 154, 73, and 289 $\text{mAh}\cdot\text{g}^{-1}$ for the porous control, control subject to blank EPD conditions, and chitosan EPD coated electrodes, respectively. *In agreement with results obtained from Si thin film cycling in Figure VIII.12.5, the capacity retention of electrodes with EPD-deposited chitosan SEI is ~ 1.88 times greater than that of the control without a synthetic SEI. The approach pursued herein to pre-apply a synthetic polymer SEI on the surface of Si electrodes by electrophoretic deposition appears effective at boosting the capacity retention over extended cycling of silicon electrodes.*

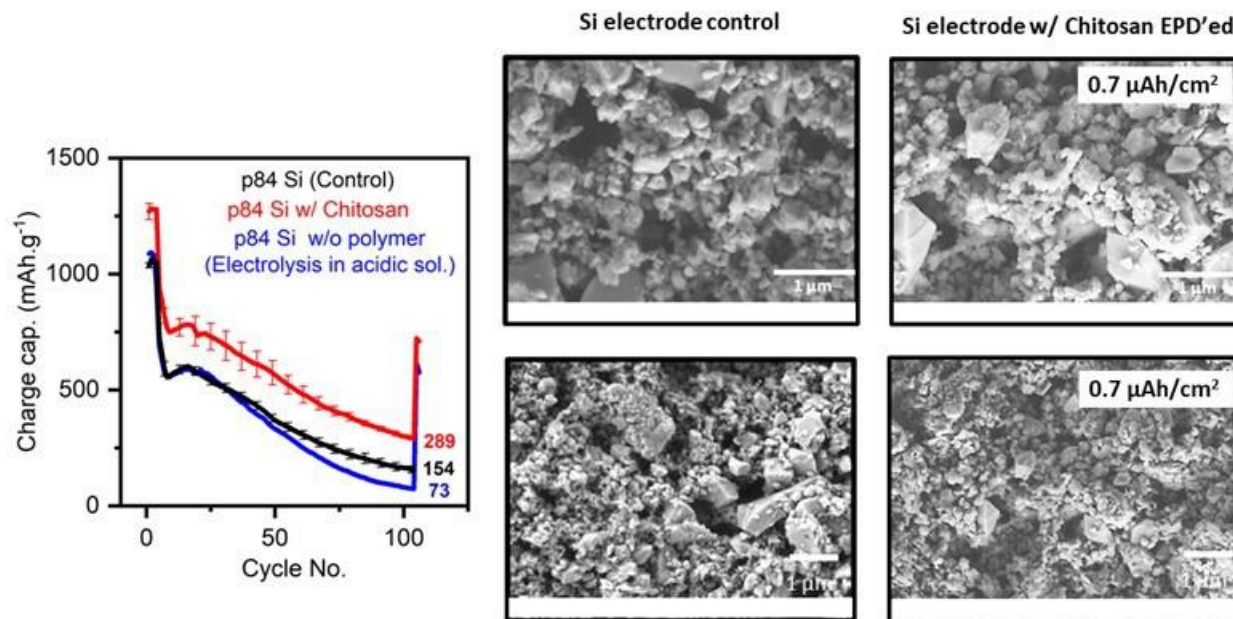


Figure VIII.12.6 Comparison of cycling performance of p84 polyimide bound Si electrodes with and without chitosan synthetic SEI coating. Note that chitosan+CH₃COOLi remain under testing. SEM images are provided as visuals of the pristine porous electrode and after the EPD is performed.

Conclusions

Major strides have been made to achieving our goal of controlling the chemistry, morphology, and mechanical properties of the SEI on silicon electrodes to protect the battery electrolyte against cyclical reductive degradation due to the silicon surface reactivity and expansion on cycling. The following achievements signal promise for the approach to achieve the project objectives in the long term:

- 1) Electrophoretic deposition (EPD) of cationic polymers such as chitosan has been demonstrated on silicon surfaces both as thin films and practical porous electrodes. A well-chosen cationic polymer such as chitosan is ion-conductive to act as a synthetic SEI which is more mechanically compliant than the short chain molecular fragments found in the battery operando-generated SEI.
- 2) Electrochemical impedance studies suggest a fivefold reduction in the charge transfer resistance at the silicon surface in presence of a chitosan synthetic SEI.
- 3) The synthetic SEI and its deposition pattern can be modified by judicious choice of secondary additives such as CH₃COOLi in the EPD precursor, providing more degrees of freedom to create a designer SEI.
- 4) Silicon thin films as well as practical porous electrodes with electrodeposited chitosan synthetic SEI already achieve twofold the capacity retention of control electrodes without pre-applied SEIs and without FEC in the electrolyte.

Future effort will focus on quantifying gains in capacity retention in full cells and demonstrating enhanced calendar life of silicon electrodes in presence of our artificial SEI achieved through electrodeposition.

Key Publications

1. Rownak J. Mou, Sattajit Barua, Ajay K. Prasad, Thomas Epps III, Koffi P.C. Yao; Taking control of the chemistry and morphology the SEI on silicon electrodes; Manuscript drafted for submission.
2. Rownak J. Mou, Sattajit Barua, Koffi P.C. Yao; The morphology and chemistry of the SEI formed by FEC additive on silicon anodes; Manuscript drafted and under editing.

3. Rownak J. Mou, Sattajit Barua, Ajay K. Prasad, Thomas Epps III, Koffi P.C. Yao; Chitosan as an artificial SEI on high-loading silicon electrodes; Manuscript planned for 2023 using results and further investigation of Figure VIII.13.6.

References

1. Elieh-Ali-Komi, D. & Hamblin, M. R. Chitin and Chitosan: Production and Application of Versatile Biomedical Nanomaterials. *Int. J. Adv. Res.* **4**, 411–427 (2016).
2. Sogias, I. A., Khutoryanskiy, V. V. & Williams, A. C. Exploring the Factors Affecting the Solubility of Chitosan in Water. *Macromol. Chem. Phys.* **211**, 426–433 (2010).
3. Prasanna, K., Subburaj, T., Jo, Y. N., Lee, W. J. & Lee, C. W. Environment-Friendly Cathodes Using Biopolymer Chitosan with Enhanced Electrochemical Behavior for Use in Lithium Ion Batteries. *ACS Appl. Mater. Interfaces* **7**, 7884–7890 (2015).

Acknowledgements

The P.Is acknowledge the research efforts of graduate student researchers Rownak Jahan Mou, Sattajit Barua, and Mengying Yang. The P.Is also thank Brian Cunningham and Adrienne Riggi for productive technical discussions and invaluable assistance in the management on the project. The P.Is recognize the contribution and support of Argonne National Laboratory CAMP Facility personnel including Steve Trask and Marco-Tulio Fonseca Rodrigues for providing the program electrodes.

VIII.13 Rational Electrolyte Design for Li-ion Batteries with Micro-sized Si Anodes (University of Maryland, College Park)

Professor Chunsheng Wang, Principal Investigator

Department of Chemical & Biomolecular Engineering
University of Maryland
College Park, MD 20742
E-mail: cswang@umd.edu

Oleg Borodin, Co-Principal Investigator

U.S. Army Combat Capabilities Development Command
Army Research Laboratory
Adelphi, MD 20783
E-mail: oleg.a.borodin.civ@mail.mil

Brian Cunningham, DOE Technology Development Manager

U.S. Department of Energy
E-mail: Brian.Cunningham@ee.doe.gov

Start Date: October 1, 2019

End Date: September 30, 2022

Project Funding (FY22): \$200,000

DOE share: \$200,000

Non-DOE share: \$0

Project Introduction

The success of micro-sized graphite (10 μm) anodes in carbonate electrolyte for Li-ion batteries is attributed to the formation of organic-inorganic solid electrolyte interphase (SEI) through simultaneous reduction of LiPF_6 salt and carbonate solvents at $\sim 0.8\text{V}$ (vs. Li/Li^+). The organic-inorganic SEI can accommodate the small volume change of graphite during lithiation/delithiation without cracking, ensuring a high Coulombic efficiency (CE) of $>99.98\%$ and a cycle life of >1000 . Si anodes are the most promising anode materials for next-generation Li-ion batteries (LIBs) due to favorable average potentials (0.3 V vs Li^+/Li) and 10 times higher capacities than graphite anodes. However, since both Si particles and the SEI undergo larger volume changes during cycling, the SEI is more prone to be damaged and cannot effectively prevent the side reactions between Si and the electrolyte, resulting in SEI thickening and pulverization of the Si particles. Thus, Si-based Li-ion batteries usually demonstrate rapid capacity decay and low coulombic efficiency (CE). Extensive efforts have been devoted to suppressing the Si and SEI cracking during charge/discharge cycling, and the battery community has reached a consensus that the carbon-coated nano-sized Si and fluoroethylene carbonate (FEC)-contained electrolytes is the best combination to enable high-capacity Si anodes. However, the technique still suffers from high cost, low $i\text{CE}$ and low volumetric energy density, which limits the practical applications.

Objectives

Large ($>10\ \mu\text{m}$) Si microparticles (μSi) are especially attractive due to their low production cost. The objectives of this project are to research, fabricate and test lithium-ion batteries that implement $\geq 30\%$ silicon content electrodes with commercially available cathode and have the potential to achieve cell level energy density of $>350\ \text{Wh/Kg}$ (C/3) for 1000 cycle life with $< 20\%$ energy fade. The main objective is to screen, select and investigate the solvation structures and properties of a variety of electrolytes for the μSi anode. The tasks for the first budget period are: (1) screen and select inorganic salts solvents to promote LiF SEI formation on Si and LiF CEI on NCA and NCM cathodes; (2) theoretically and experimentally investigate the solvation structures and properties of the developed electrolytes.

Approach

Large ($>10\ \mu\text{m}$) Si microparticles (μSi) are especially attractive due to their low production cost. The objectives of this project are to research, fabricate and test lithium-ion batteries that implement $\geq 30\%$ silicon content electrodes with commercially available cathode and have the potential to achieve cell level energy density of $>350\ \text{Wh/Kg}$ (C/3) for 1000 cycle life with $< 20\%$ energy fade. The main objective is to screen, select and investigate the solvation structures and properties of a variety of electrolytes for the μSi anode. The tasks for the first budget period are: (1) screen and select inorganic salts solvents to promote LiF SEI formation on Si and LiF CEI on NCA and NCM cathodes; (2) theoretically and experimentally investigate the solvation structures and properties of the developed electrolytes.

Results

1. Electrochemical Performance of μSi || Li Cells with Modified All fluorinated Electrolytes

We screened and modified all fluorinated electrolytes (1.0 M LiPF_6 in FEC, FEMC, and HFE by a volume ratio of 2:6:2) by replacing the carbonate in the original formula with sulfone (SL-based 262) to accommodate the large volume change in the micro-silicon (μSi) anode. The proposed sulfone-based electrolyte was proved to have high ionic conductivity of $3.93\ \text{mS/cm}$ at room temperature (Figure VIII.13.1A), and the anodic stability was further pushed to $5.3\ \text{V}$ versus Li^+/Li , a value high enough to run high voltage layered oxide cathodes, like NMC 811 or NCA (Figure VIII.13.1B). We postulated a unique protective SEI layer could be responsible for the excellent cycle performance. The SEI composition is examined via X-ray photoelectron spectroscopy (XPS) to validate our hypothesis about the formed SEI layer. The XPS with an Ar^+ sputtering depth profiling (0S, 60S, 120S, 180S, 300S and 600S) was conducted for μSi electrodes after 50 cycles. The selected XPS spectra (C, O, F and S) and element ratio on the μSi electrodes after 50 plating/stripping cycles in the 2S2 electrolyte was shown in Figure VIII.13.1C and D. The organic species (C content) aggressively decreased to negligible amount ($\sim 5.2\%$) along with the O species increasing to a high ratio of 35% after 300 S sputtering, manifesting that more Li_2O will be noticed in the inner layer of the SEI. In addition, the F-content is still abundant throughout the etching process, which confirms that a highly inorganic-rich ($\text{Li}_2\text{O}/\text{LiF}$) bilayer SEI layer on SiMPs is obtained for electrodes cycled in the designed electrolyte.

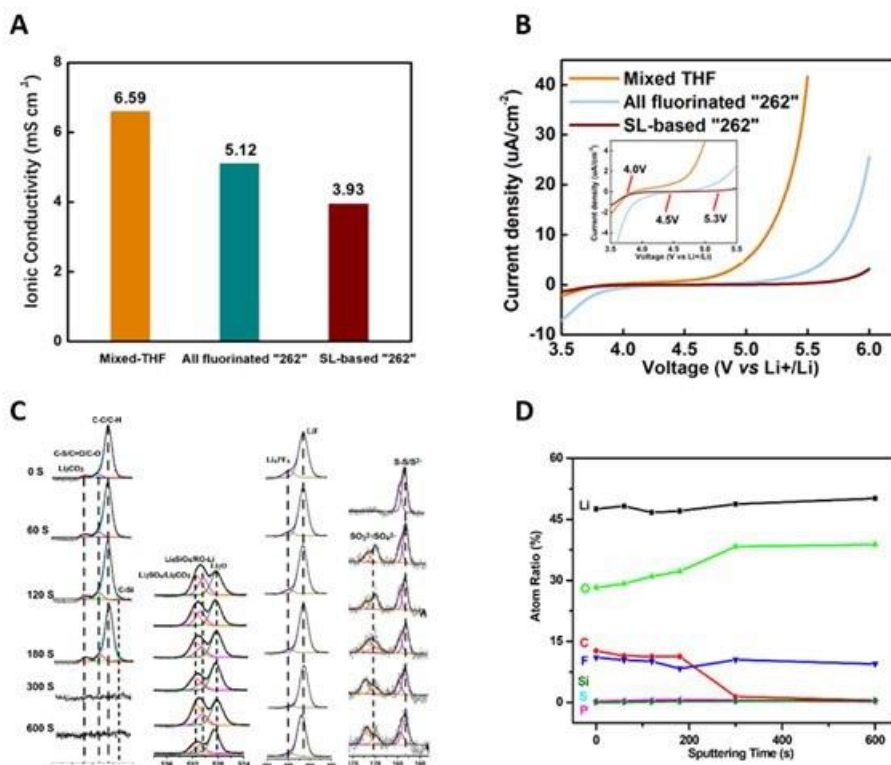


Figure VIII.13.1 Ionic conductivity and anodic stability of the 2S2 electrolyte. (A) Comparison of ionic conductivity of different electrolytes at room temperature. The ionic conductivities are referenced and calculated to the standard electrolyte. (B) Linear scanning voltammetry of mixed THF, all fluorinated 262 and 2S2 electrolytes using aluminum foil as working electrode, scan rate = 1 mV/sec. SEI chemical composition by XPS measurement on μ Si electrodes after 50 cycles in μ Si || Li cells with 2S2 electrolyte. (C) C1s, O1s, F1s and S2P spectra are displayed in columns, which show the corresponding depth profiling results (from up to down, being 0S, 60S, 120S, 180S, 300S and 600S). All of the XPS results were fitted with CasaXPS software. The binding energy was calibrated with C1s at 284.8 eV; (D) the quantified atomic composition ratios for all elements of the formed SEI at different sputtering times for the proposed 2S2 electrolyte.

The unique Li₂O/LiF thin SEI film formed in the μ Si electrodes enables us to construct a practical full-cell battery with high loading and improved cycling performance (Figure VIII.13.2). In a full cell (coin cell) of μ Si (~4.1 mAh/cm²) || NCA (4 mAh/cm²), without any pre-cycling nor pre-lithiation, our designed electrolyte enables a stable cycling (200 cycles, 81% capacity retention) and a high CE (approaches 99.9% after the 10th cycle) at practical values of high areal capacity loading and N/P ratio (~1.1) (Figure VIII.13.2A). Under the full charge/discharge conditions between 2.7-4.3V, the full cell showed an initial CE (*i*CE) of 80.1%, (Figure VIII.13.2B). Besides, the practical 100 mAh punch cell exhibit stable cycling with high *i*CE of 81.3% and an excellent cycle CE (which approaches 99.9% after the fifth cycle) at practical critical parameters such as current density (0.2C), cell pressure (0.1MPa), temperature (ambient, uncontrolled ~25°C) and N/P ratio (1.1). (Figure VIII.13.2C-D) The practical μ Si||NCA punch full cell retained 83% of its capacity after 150 cycles in the designed electrolyte, demonstrating its superior cycle stability in the LIBs with SiMPs as the anode.

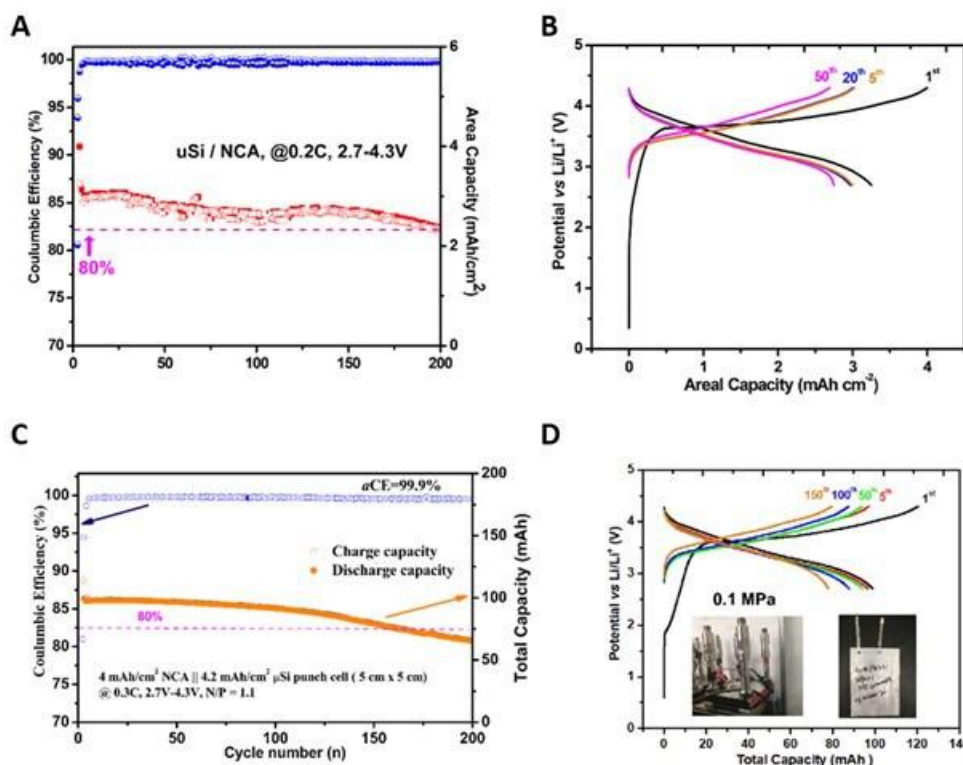


Figure VIII.13.2 (A) The cell performance of $\mu\text{Si}(1\text{-}5\text{ }\mu\text{m}) || \text{NCA}$ full cells in 2S2 electrolyte between 2.7 and 4.3V; (B) the initial, 2nd, 5th, 20th and 50th charge-discharge profiles of the proposed electrolyte in the $\mu\text{Si} || \text{NCA}$ full cells. The cycle rate is at 1/5 C, room temperature with the first formation cycle at C/20. (C) μSi full battery performance in large punch cell (areal capacity of $\sim 4\text{ mAh/cm}^2$ for NCA and $\sim 4.1\text{ mAh/cm}^2$ for μSi , with electrode size $\sim 5\text{ cm}$ by 5 cm) at room temperature. Before cycling at C/5, two pre-cycles at C/20 were conducted. The average CE was calculated from the fifth to the final cycle. The dashed pink line indicates the capacity retention of 80% at 150 cycles; (D) The charge-discharge profiles of the $\mu\text{Si} || \text{NCA}$ full cells at the 1st, 5th, 50th, 100th and 150th cycle. The left inset figure illustrates the test conditions of the assembled punch cell under the normal pressure of 0.1 MPa, and the right inset shows the actual cell size of 5 cm by 5 cm.

2. Solvent-free ionic liquid electrolyte

Another strategy to improve the anodic stability of the electrolyte is to avoid using the reductive THF as an electrolyte solvent. We developed an ionic liquid (IL) electrolyte that efficiently forms dense and ceramic-based SEI on lithium metal. The IL electrolyte demonstrates an ionic conductivity of 4.07 mS/cm , and anodic stability of 4.5 V vs. Li^+/Li reported last year. The full cell ($\mu\text{Si} || \text{NMC811}$) using this IL cycled at 0.1 C did not demonstrate a noticeable variation of overpotentials (Figure VIII.13.3A). It showed around 88% of capacity retention at the 100th cycle (Figure VIII.13.3B, the capacity retention was calculated by normalizing to the highest capacity at 0.1 C), corresponding to over 2000 mAh/g Si utilization for the μSi anode. Such, the compatibility of the developed electrolyte towards μSi anode and NMC811 cathode was confirmed by the stability of full cell under the low C-rate cycling. Further, the structural evolution of the μSi particles was monitored using x-ray computed tomography. (Figure VIII.13.3C). The Si electrodes only expand in the first few cycles and then become stable in 300 cycles as evidenced by the particle boundaries and electrode thickness. This suggests that the LiF-SEI effectively protects the electrolyte penetration into cracked Si particles making the volume change reversible. Therefore, the total thickness of the Si anode only experiences negligible changes during charge/discharge in 20-300 cycles.

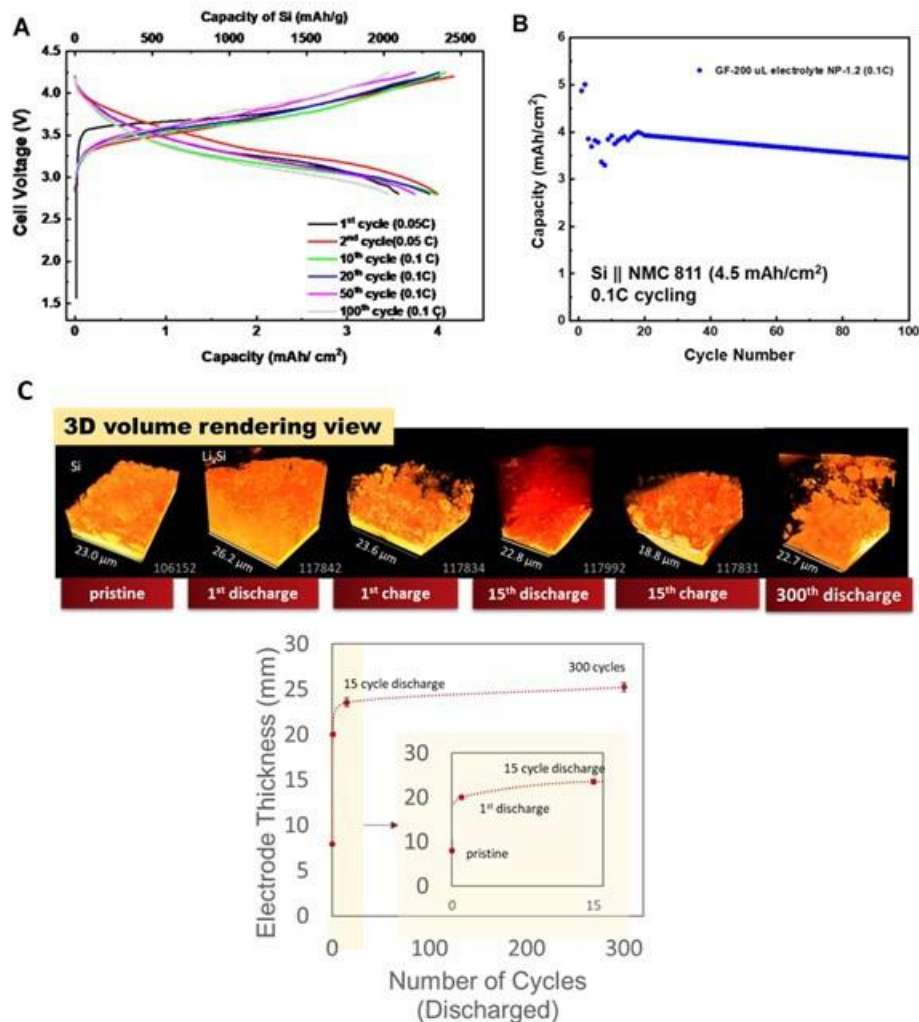


Figure VIII.13.3 (A) The charge/discharge curves and (B) The capacity retention of the 5.0 mAh/cm² μ Si || 4.5 mAh/cm² NMC811 full cell between 4.2 and 2.7 V in the IL electrolyte. (C) The evolution of the pristine and cycled micro-Si anode and the overall thickness of the electrode was measured with X-ray computed tomography.

3. Calendar life of micro-sized Si anode with LiF-rich SEI

We summarized the relationship between calendar life with silicon particle sizes and SEI growth (SEI stability), and further explored the mechanism behind it. We summarized the 180h of voltage hold for silicon anodes with different particle sizes in different electrolytes. The results show that micro-silicon has comparative calendar life with graphite. Because there is no volume expansion during voltage hold, any capacity loss (current leakage) during storage is quantified by the Li consumption in SEI (growth and dissolution). Therefore, the key to improving calendar life is to reduce the SEI growth rate, reduce the SEI dissolution and reduce the contact between the active Si surface and electrolyte. The mechanism was detailed and illustrated in Figure VIII.13.4. The calendar life is mostly influenced by Si particle size (surface area contact), SEI growth rate, and SEI dissolution. Among them, the SEI growth rate and the SEI dissolution determine the SEI stability which is directly related to the Columbia efficiency (CE). Therefore, an anode with higher CE could always show a better calendar life when the particle size is at the same level, as is reported last year.

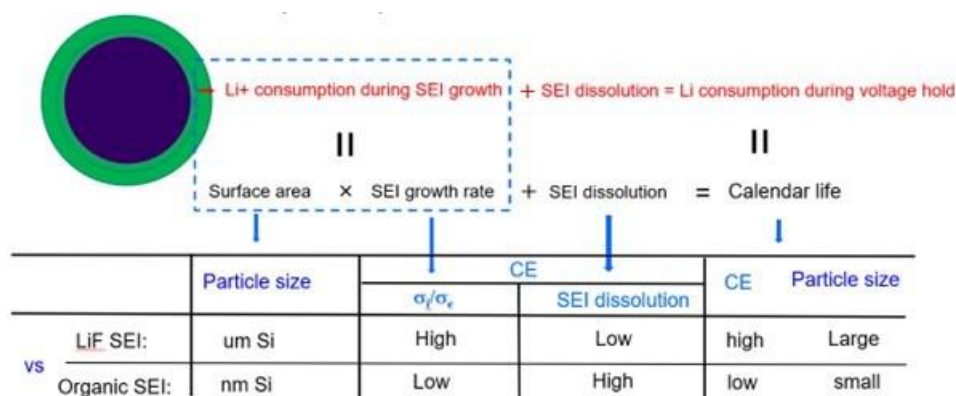


Figure VIII.13.4 Schematic illustration of mechanism on the capacity loss (current leakage) during voltage hold.

Increasing the particle size could reduce the surface area of Si particles, which explains the huge differences in calendar life between nano-silicon anode (0.304 mA/Ah@180h) and micro-silicon anode (0.081 mA/Ah @180h) with the same mixTHF electrolyte (Figure VIII.13.5A). The same electrolytes resulted in similar SEI components with similar SEI growth rates, but a large surface area largely increases the Li^+ consumption during SEI growth rate. As is shown in Figure VIII.13.5B, the irreversible capacity loss is about three times higher in nano-Si than in micro-Si. This is a more serious problem in the full cells test due to the limited Li resources. EIS spectra of Li||Si cells with different sizes of silicon are shown in Figure VIII.13.5C-F. The R1 represents electrode and electrolyte resistances, CPE stands for the double-layer capacitance of the electrolyte/electrode interface, R2 and R3 stand for the SEI on lithium and silicon (SEI on silicon is marked with red color), R4 stands for the charge transfer resistance. The resistance increases from 3.191 Ω to 4.622 Ω (1.45 times increase) in nano-Si, demonstrating that a large amount Li^+ was consumed in SEI growth. In sharp contrast, there is no obvious resistance increase in the resistance of micro-Si (an increase from 4.428 to 4.699).

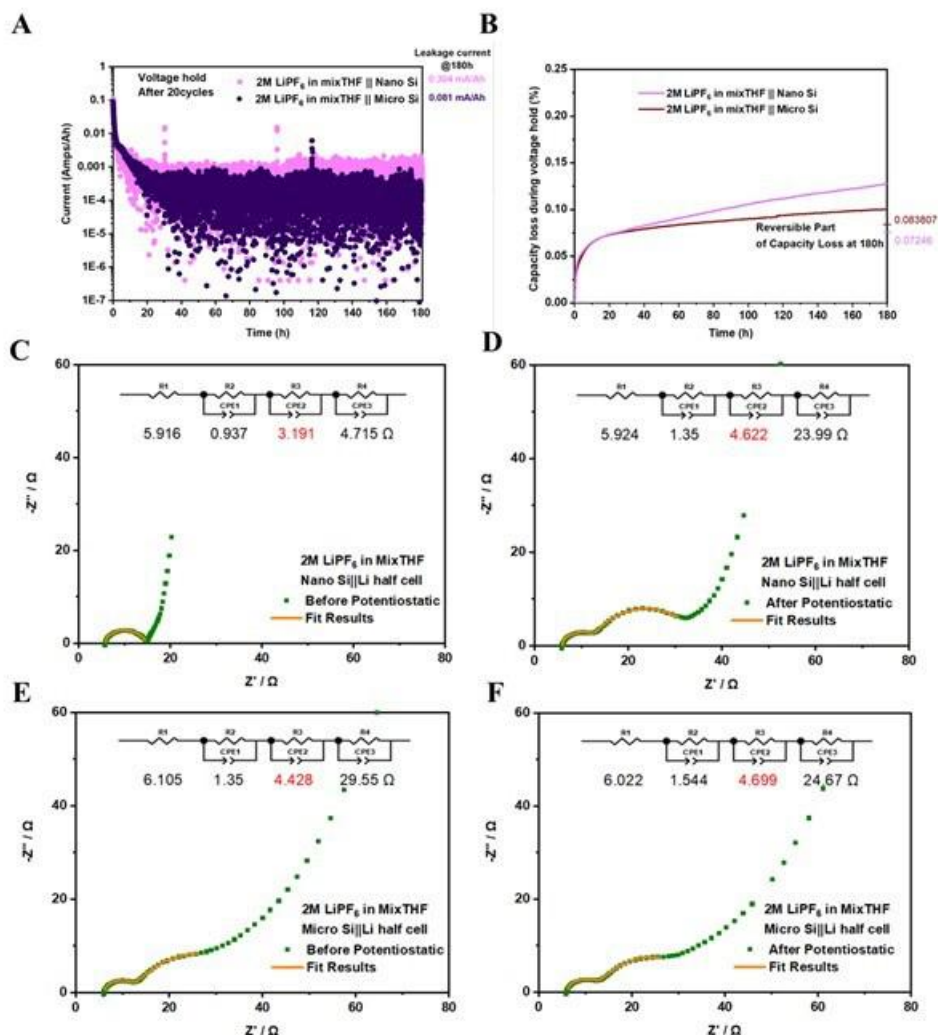


Figure VIII.13.5 A,B Current decay versus time (A) and corresponding capacity loss versus time (B) during 180h voltage hold of silicon anode (micro-sized silicon and nano-sized silicon) in mixed THF electrolytes C-F. EIS results of Nano Si | Li cells (mixed THF electrolytes, after 20 cycles) before (C) and after (D) voltage hold, Micro Si | Li cells (mixed THF electrolytes, after 20 cycles) before (E) and after (F) voltage hold. The resistance of SEI on silicon is marked with red color.

For the Si anode with the same size, the electrolyte composition determines the SEI components which determine the SEI growth rate. We compared two different electrolytes, mixTHF electrolyte, and EC/DEC+10wt%FEC electrolyte. The former could form LiF-rich SEI with better passivation ability (lower SEI growth rate), while the carbonate electrolyte always results in organic-rich SEI with a higher SEI growth rate. As a result, the mixTHF electrolyte shows a lower leakage current than that of carbonate-based electrolytes (0.203 mA/Ah @180h) (Figure VIII.13.6A). In the meantime, the irreversible capacity loss is also much higher in the carbonate-based electrolyte (Figure VIII.13.6B). For Si and graphite with similar particle sizes, the lithiated Si has higher volume changes than that of lithiated graphite, which requires SEI with the least bonding to lithiated Si. The organic-rich SEI formed by carbonate electrolyte strongly bonds to silicon, reducing the calendar life of Si. However, the organic-rich SEI that is strongly bonded to graphite anode can perfectly accommodate small volume changes of graphite. EIS spectra also suggest the same conclusions with no obvious resistance increase on graphite after voltage holding (Figure VIII.13.6C and Figure VIII.13.6D), which corresponds to the small leakage current and irreversible capacity loss. However, the resistance of organic-rich SEI on Si increase from 4.259 Ω to 5.348 Ω (Figure VIII.13.6E and Figure VIII.13.6F), indicating that the organic SEI cannot effectively passivate the highly reactive lithiated Si, and the SEI grows tremendously.

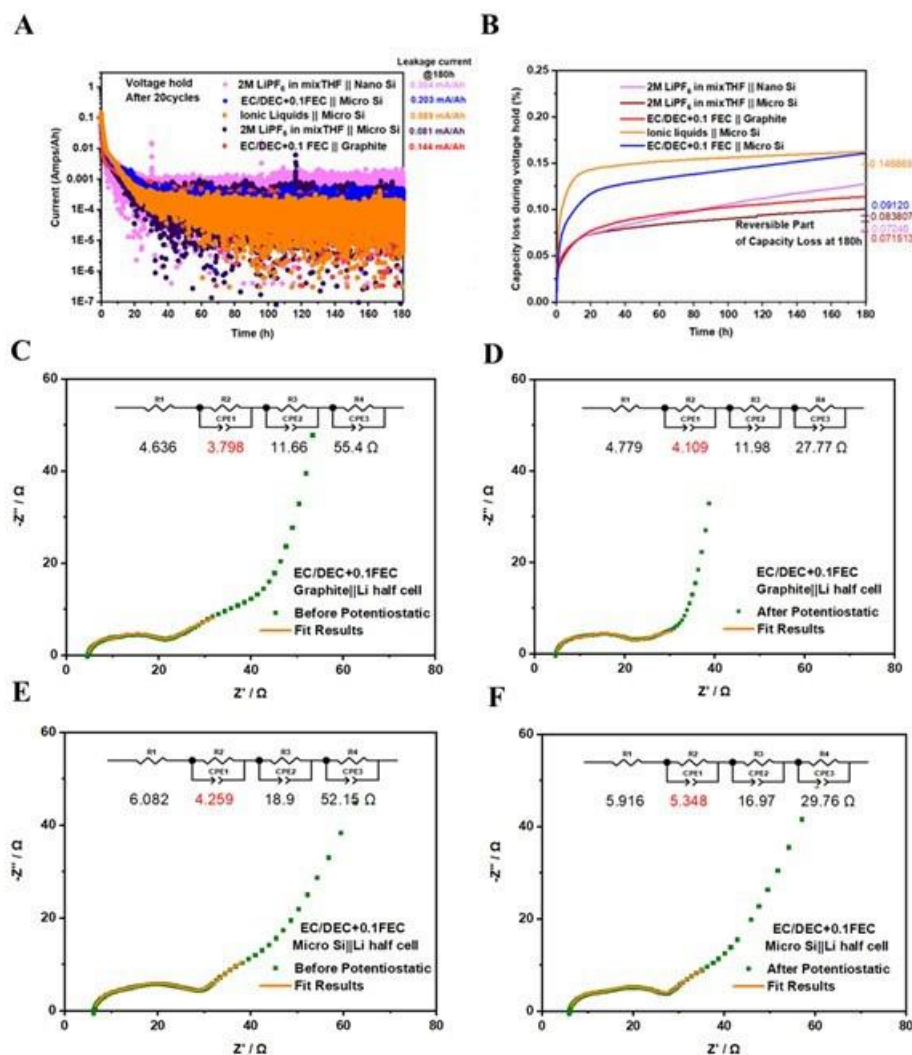


Figure VIII.13.6 A,B, Current decay versus time (A) and corresponding capacity loss versus time (B) during 180h voltage hold of silicon anode in different electrolytes (mixTHF and carbonate electrolytes) and graphite in carbonate electrolytes. C-F, EIS results of Graphite || Li cells (carbonate electrolytes, after 20 cycles) before (C) and after (D) voltage hold, Micro Si || Li cells (carbonate electrolytes, after 20 cycles) before (E) and after (F) voltage hold. The resistance of SEI on silicon is marked with red color.

Conclusions

In summary, to make a stable Si-NMC 811 cell, we developed electrolytes with high electrochemical windows, which can form LiF-rich SEI based on our study on the mixTHF electrolytes. We designed a high voltage-stable 2S2 electrolyte (SL-based 262) to form inorganic-rich (Li₂O/LiF) bilayer SEI layer on SiMPs, which enable a μ Si || NCA stable cycling (200 cycles, 81% capacity retention). The practical μ Si||NCA punch full cell retained 83% of its capacity after 150 cycles in the designed electrolyte, demonstrating the practicability of this electrolyte. In the meantime, we have demonstrated through using solvent-free IL electrolytes to form inorganic-SEI, 88% capacity retention at 100th cycle in μ Si|| NMC811 full cells can be achieved. Further optimization of the electrolytes and cell configuration will be performed in the next fiscal year, targeting high cycling life as well as high energy density for the μ Si-NMC full cell. Calendar aging of the Si anodes was also investigated through leakage current, our result shows that larger particle size and low SEI growth rate could significantly enhance the calendar life problem of silicon anodes. The solubility of SEI will be investigated to refine our proposed mechanism.

VIII.14 Silicon Consortium Project (SCP) (PNNL)

Jie Xiao, Principal Investigator

Pacific Northwest National Laboratory
902 Battelle Blvd
Richland, WA, 99352
E-mail: jie.xiao@pnnl.gov

Brian Cunningham, DOE Technology Development Manager

U.S. Department of Energy
E-mail: Brian.Cunningham@ee.doe.gov

Start Date: October 1, 2021

End Date: September 30, 2022

Project Funding (FY22): \$400,000

DOE share: \$400,000

Non-DOE share: \$0

Project Introduction

While the cycle life of silicon (Si)-based cells has improved in the past years, calendar life of Li-ion batteries containing Si-dominant anode is still not satisfactory. Historically, Si anode research has focused on the crystallographic expansion (~320%) that Si experiences upon lithiation with valuable knowledge gathered. 1-4 To be deployed on a broad scale for EVs, calendar life is another critical parameter that needs to be evaluated. Specifically, the limited calendar life of Si cells suggests that a “protective” solid electrolyte interphase (SEI) does not form on the Si anode. The understanding and mitigation of calendar life will remove the barriers associated with the large-scale deployment of advanced lithium-ion batteries utilizing anode with >50% Si. Therefore, research is needed with a specific focus on understanding the formation and evolution of the SEI on Si to solve the calendar life challenge.

Objectives

The ultimate goal of this project is to establish the correlation of the structural and chemical evolution of both Si and the SEI layer with battery performance in terms of cycling stability and calendar life. The work will attempt to answer the following scientific questions:

- 1) How do the passive and active Si electrode components evolve structurally and chemically during electrochemical cycling and calendar life aging?
- 2) What is the critical factor that controls the calendar life of Si?
- 3) What is the correlation between cycling stability and calendar life for anode dominated by Si?

Approach

- *In-situ*, *ex-situ* and Cryo- Transmission Electron Microscope (TEM) will be utilized to understand the structural and chemical evolution of Si (active and passive), and to gain insight into the SEI layer's chemical reactivity, at different scales, at the relevant interfaces and interphases.
- Energy dispersive X-ray spectroscopy (EDS) captured during the *in-situ* TEM and *ex-situ* TEM will give direct visualization of spatial distribution and evolution of element with progression of the cycling of battery.
- Electron energy loss spectroscopy captured during *in-situ* TEM and *ex-situ* TEM will give electronic structural information, which can be correlated to spatial evolution between SEI and Si.

Results

Chemical Transformation of Si during Cycling

Combination of cryo-STEM and Electron Energy Loss Spectroscopy (EELS) provides a method to characterize the morphological and chemical changes of Si anodes during cycling. Cryo-EELS characterization of the Si anode in Si-Gr/NMC622 full cells was performed after 0, 1, 10, 20, 50, and 100 cycles. The changes in the chemistry of the Si materials at various cycles can be correlated with the capacity retention of the electrochemistry data to provide insight into the mechanisms of capacity loss during cycling. High angle annular dark field (HAADF) images (shown in the inserts of Figure VIII.14.1a and b) show the structural evolution of the Si nanoparticles during cycling. In comparison to the fresh particles (Figure VIII.14.1a), there is a clear increase in roughness/porosity for samples after 100 cycles (Figure VIII.14.1b).

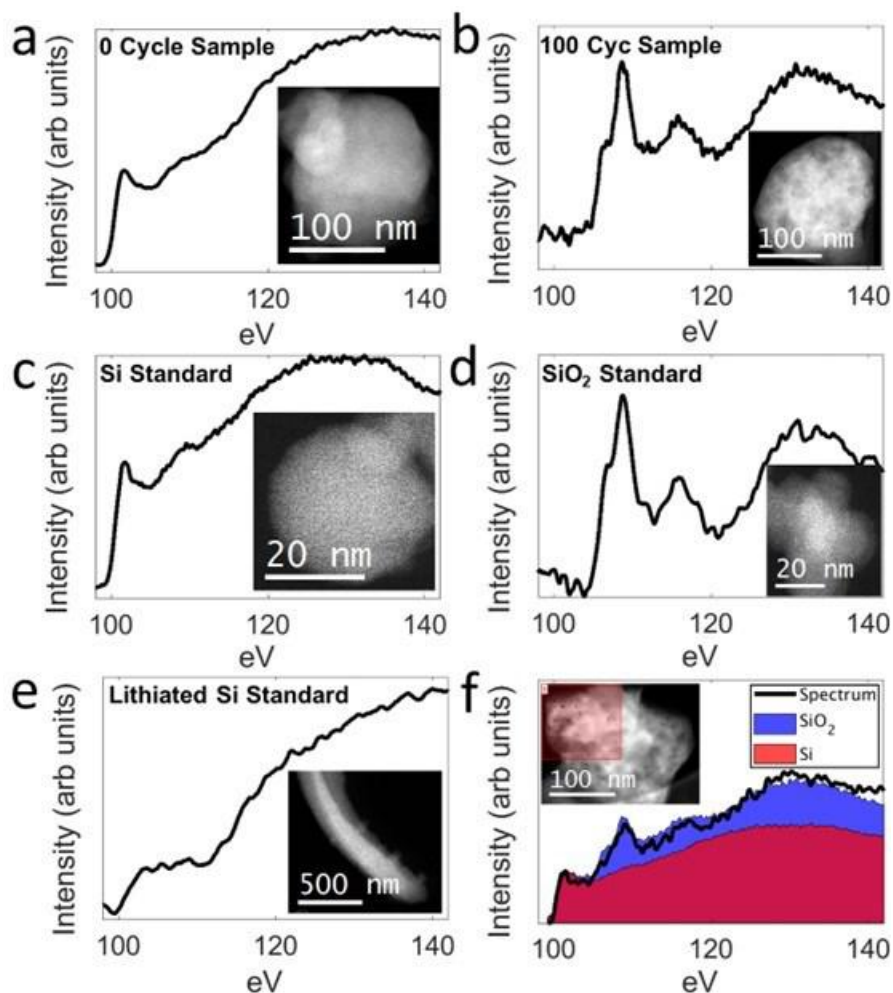


Figure VIII.14.1 Electron energy loss spectroscopy of the Si anodes during cycling. (a-b) HAADF images and EEL spectrums of the Si nanoparticles after 0 and 100 cycles. The EELS data shows the Si $L_{2,3}$ edge with background removed. The changes in the near edge fine structure shows that the Si has undergone a chemical transformation. (c-e) are reference EEL spectrums of the Si $L_{2,3}$ edge for Si, SiO_2 , and lithiated-Si standard samples. The reference spectrums for the standard samples are used to identify the EEL spectra for the cycled Si anodes. (f) shows an EELS model fit to quantify the various chemical compositions of Si present in the highlighted area of the spectral image (shown in the insert).

The morphological changes in Si could be caused by nanoparticle cracking, pulverization, and void formation due to the volume expansion and contraction that occur during cycling. Another potential cause for the Si structural evolution is changes in the Si chemical composition. Figure VIII.14.1a-b shows the EELS of a Si- $L_{2,3}$ edge for samples after 0 and 100 cycles. The dramatic change in the EELS corresponds to a change in the

Si chemical composition. To identify the EELS of the fresh and highly cycled Si, reference samples were used to identify the primary chemical composition. A reference spectrum for Si, SiO₂, and lithiated-Si are shown in Figure VIII.14.1c-e. These reference spectra are consistent with previous studies. Evidently, the EELS data for the pristine (0 cycle sample) corresponds to Si, and the spectrum for the 100-cycle sample corresponds to SiO₂.

The fraction of the Si oxidized to SiO₂ shows dependence on the cycle number, featuring increased oxidation with increased cycling. To quantify the spatial distribution of Si and SiO₂, a least squares model fit was developed for a spectral image of the sample (where EELS is measured at every point throughout an area of the sample). The model uses a linear combination of the Si and SiO₂ reference spectra to determine the local chemical compositions present throughout an EEL spectral image. An example of this model is shown for a 20-cycle sample in Figure VIII.14.1f. By determining the local chemical composition of the Si throughout the sample, the model can be used to generate maps of the Si valence state distribution in each of the cycled samples. STEM images, EELS Si composition maps, and model fits are shown in Figure VIII.14.2a-r. Before cycling, the Si has a thin native oxide on the particle surface. During the cycling process, the Si shows increased oxidation from the nanoparticle surface towards the center. The silicon oxidation also appears to be correlated with the increase in roughness and porosity for the highly cycled samples.

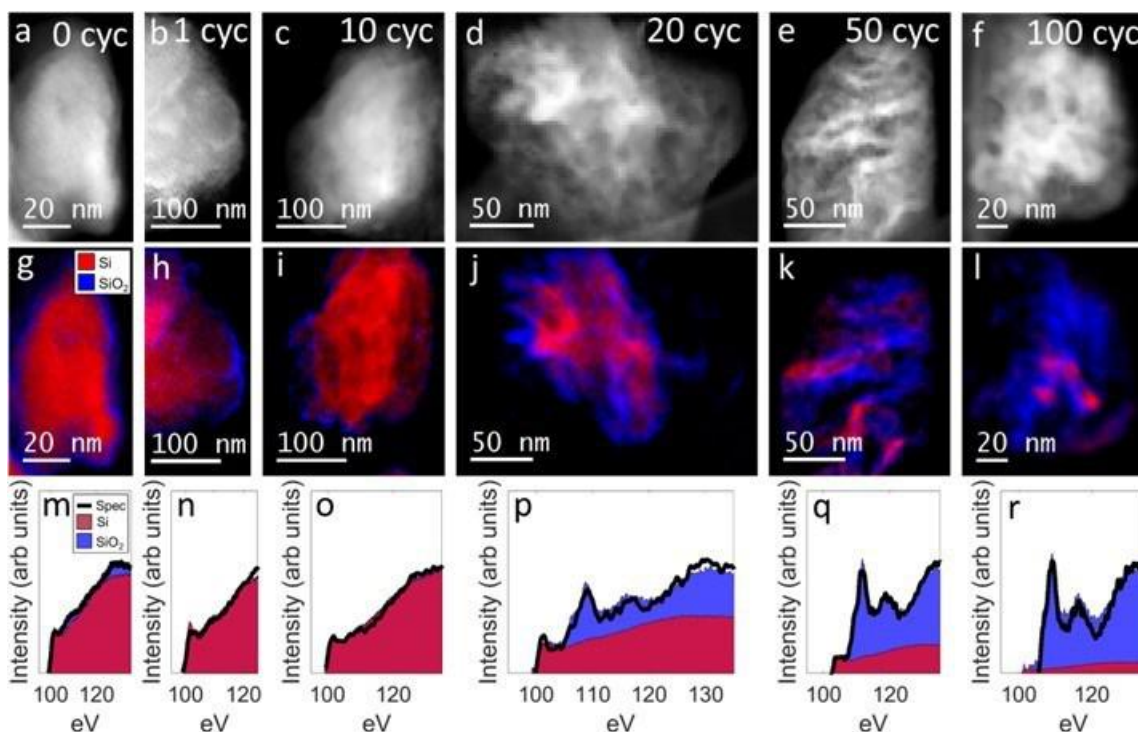


Figure VIII.14.2 STEM and EELS analysis of the Si-Gr anode after cycling in a carbonate-based electrolyte. (a-f) STEM images after 0, 1, 10, 20, 50, and 100 cycles. The roughness/porosity of the Si increases upon cycling. By measuring the Si L_{2,3} edge of Si anodes after cycling and comparing the signals to the Si and SiO₂ references, it is possible to map the local valence state of Si with sub-nanometer resolution. (g-l) Si composition maps after 0, 1, 10, 20, 50, and 100 cycles. As the Si roughness and porosity increases with cycling, Si is gradually converted to SiO₂. The oxidation of Si could play a major role in capacity loss for high cycled Si-based anodes. (m-r) Least-squares models for the quantification of Si and SiO₂ present in each spectral image.

SEI Structural and Chemical Development during Cycling

Cryo-EDS characterization of the particles is a useful tool to determine the elemental distribution of the system, which can be employed to investigate the formation and evolution of the SEI. EDS elemental mapping showed that the primary components of the SEI consisted of carbon and oxygen, with small amounts of fluorine and phosphorus. Figure VIII.14.3 shows the STEM images and their corresponding EDS maps for the sample following 0-100 cycles. Areas with majority Si counts are shown in red, SEI components (C, O, F, and P) are shown in blue, and areas with mixed Si/SEI counts are highlighted in green. By comparing the spatial

distribution of the Si and the combined SEI components, these maps can be used to show how the Si and SEI evolve during the cycling process. From this characterization, several observations can be made: (1) the outer SEI layer forms after the first lithiation to create a core shell structure (Figure VIII.14.3g), (2) during successive cycling the SEI penetrates the Si rather than growing on the surface (Figure VIII.14.3h-j), and (3) extensive cycling creates a Si/SEI composite structure (Figure VIII.14.3k and l). The formation of a Si/SEI composite structure at high cycles could cause a loss in specific capacity of the Si or cause a decrease in conductivity. These could be additional mechanisms for capacity loss⁵⁻⁷, increased electrode resistances and therefore, worsened calendar life in Si-based cells.

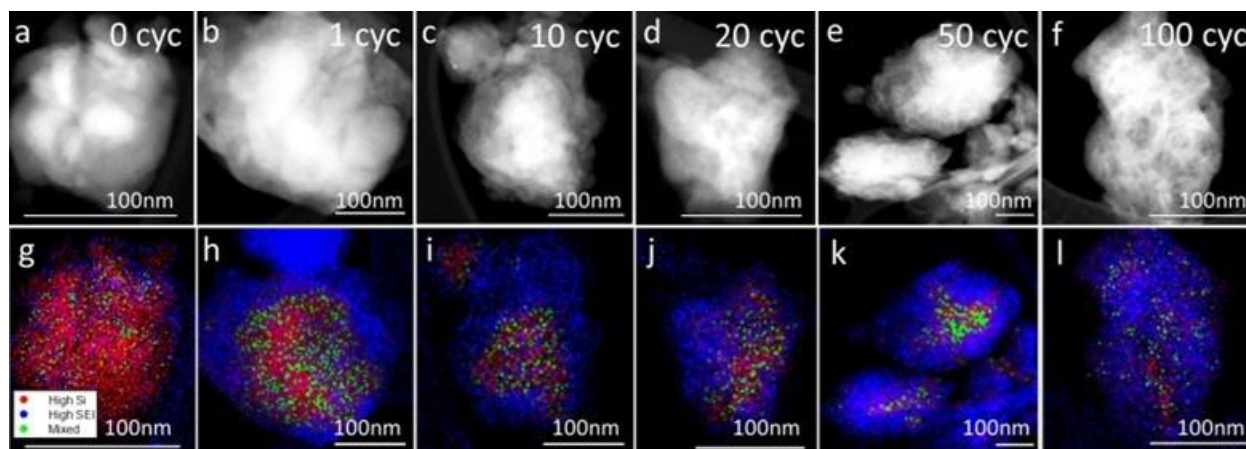


Figure VIII.14.3 Scanning transmission electron micrographs (STEM) images and energy-dispersive x-ray spectroscopy (EDS) elemental maps Si-Gr anodes after increasing numbers of cycles. (a-f) shows STEM images, and (g-l) shows EDS mapping of Si particles after 0, 1, 10, 20, 50, and 100 cycles. The red areas marks Si counts, the blue represents element counts of the SEI components (oxygen, carbon, and fluorine), and green highlights areas of mixed Si and SEI counts (45 to 55% Si/SEI). The SEI penetrates into the center of the Si particle with cycling eventually leading to a Si/SEI composite structure.

Conclusions

The integration of cryo-STEM, EELS, and EDS characterization of silicon anodes provides key insights into the chemo-mechanical evolution of Si anodes, which is critical for the design of Si-based anodes with enhanced performance and stability during storage. EELS was used to determine the chemical composition of Si with sub-nanometer resolution, which unexpectedly shows that cycling causes Si to oxidize from the outer surface towards the center. Several mechanisms of Si oxidation are identified and the subject of future work. EDS also shows that cycling causes the SEI to penetrate the particle, eventually making a Si/SEI composite structure. The gradual oxidation of Si and SEI layer penetration as revealed by EELS and EDS collectively contribute to the capacity loss and resistance increase of extensively cycled Si electrodes. It is apparent that separation of Si from liquid electrolyte is a critical step for the stable cycling and long-time storage of Si. To reach this goal, the formation of a stable SEI layer will be vital, which is now under further investigation and modification.

Key Publications

1. Joseph Quinn, Bingbin Wu, Yaobin Xu, Jie Xiao, Chongmin Wang, Tracking the oxidation of silicon anodes using cryo-EELS upon battery cycling *ACS Nano*, under revision.

References

1. J.Y. Huang, L. Zhong, C.M. Wang, J. P. Sullivan, W. Xu, L.Q. Zhang, S. X. Mao, N.S. Hudak, X.H. Liu, A. Subramanian, H.Y. Fan, L. Qi, A. Kushia, J. Li, In situ observation of the electrochemical lithiation of a single SnO₂ nanowire electrode. *Science*, 2010, 330, 1515.
2. M. Gu, L.R. Parent, B.L. Mehdi, R.R. Unocic, M.T. McDowell, R.L. Sacci, W. Xu, J.G. Connell, P.H. Xu, P. Abellan, X.L. Chen, Y.H. Zhang, D.E. Perea, J.E. Evans, L.J. Lauhon, J.G. Zhang, J. Liu, N.D. Browning, Y. Cui, I. Arslan, C.M. Wang, Demonstration of an electrochemical liquid cell for

- operando transmission electron microscopy observation of the lithiation/delithiation behavior of Si nanowire battery anodes. *Nano Lett.* 2013, 13, 6106.
3. Zihua Zhu, Yufan Zhou, Pengfei Yan, Rama Sesha Vemuri, Wu Xu, Rui Zhao, Xuelin Wang, Suntharampillai Thevuthasan, Donald R. Baer, and Chong-Min Wang, In Situ Mass Spectrometric Determination of Molecular Structural Evolution at the Solid Electrolyte Interphase in Lithium-Ion Batteries, *Nano Lett.* 2015, 15, 6170–6176
 4. Y. He, D.M. Piper, M. Gu, J.J. Travis, S.M. George, S.-H. Lee, A. Genc, L. Pullan, J. Liu, S.X. Mao, J.G. Zhang, C.M. Ban, C.M. Wang, In situ transmission electron microscopy probing of native oxide and artificial layers on silicon nanoparticles for lithium ion batteries. *ACS Nano* 2014, 8, 11816.
 5. Wetjen, M.; Solchenbach, S.; Pritzl, D.; Hou, J.; Tileli, V.; Gasteiger, H. A. Morphological Changes of Silicon Nanoparticles and the Influence of Cutoff Potentials in Silicon-Graphite Electrodes. *J. Electrochem. Soc.* **2018**, 165 (7), A1503–A1514.
 6. Zhang, X.; Weng, S.; Yang, G.; Li, Y.; Li, H.; Su, D.; Gu, L.; Wang, Z.; Wang, X.; Chen, L. Interplay between Solid-Electrolyte Interphase and (in)Active LixSi in Silicon Anode. *Cell Rep. Phys. Sci.* **2021**, 2 (12), 100668.
 7. He, Y.; Jiang, L.; Chen, T.; Xu, Y.; Jia, H.; Yi, R.; Xue, D.; Song, M.; Genc, A.; Bouchet-Marquis, C.; Pullan, L.; Tessner, T.; Yoo, J.; Li, X.; Zhang, J.-G.; Zhang, S.; Wang, C. Progressive Growth of the Solid–Electrolyte Interphase towards the Si Anode Interior Causes Capacity Fading. *Nat. Nanotechnol.* **2021**, 16 (10), 1113–1120.

Acknowledgements

We thank Drs. Joseph Quinn, Bingbin Wu, Yaobin Xu, and Chongmin Wang at PNNL for their contributions.

VIII.15 Thin-film lithium metal manufacture by room temperature electrodeposition (Albemarle Corporation)

Prayag Biswal, Principal Investigator

Albemarle Corporation
4250 Congress Street, Suite 900
Charlotte, NC, 28209
E-mail: prayag.biswal@albemarle.com

Haiyan Croft, DOE Technology Development Manager

U.S. Department of Energy
E-mail: Haiyan.Croft@ee.doe.gov

Start Date: May 12, 2020

End Date: April 11, 2024

Project Funding: \$5,391,760

DOE share: \$4,310,960

Non-DOE share: \$1,080,800

Project Introduction

Albemarle Corporation with its partners, Argonne National Laboratory and Solid Power, will develop and prototype pilot-scale production of room-temperature electrodeposited lithium (Li) metal films to accelerate the adoption of next generation re-chargeable lithium metal batteries. The proposed electrodeposition technology has the potential to significantly improve the efficiency and cost of manufacturing ultra-thin lithium metal anodes thereby opening up a new pathway to cost-effective lithium metal batteries. This program will demonstrate that electrodeposition can be a commercially viable path to low-cost lithium metal anodes. Success will motivate further scale-up of U.S.-based lithium metal anode production and encourage the growth of a domestic battery industry based on this enabling technology.

Objectives

The objective of the project is to research, develop, and establish an economically feasible roll-to-roll electrodeposition method to produce ultra-thin ($\leq 20 \mu\text{m}$) high-quality lithium (Li) metal anodes from low-cost aqueous lithium salts at room temperature.

Approach

The approach for the project is as follows:

1. Optimization of single compartment cell (May 2020 – February 2022)
This includes selection of the electrolyte (catholyte) chemistry, batch production of lithium anodes at high deposition rates ($\sim \mu\text{m}/\text{min}$), and validation of produced lithium anodes through coin & pouch cell testing.
2. Optimization of dual compartment cell (May 2020 – February 2022)
This includes development of water impermeable lithium-ion conductive membrane, development of engineering controls to mitigate stray crossover water, batch production of lithium anodes at high deposition rates ($\sim \mu\text{m}/\text{min}$), and validation of lithium anodes through coin and pouch cell testing.
3. Process scale up and validation in prototype system (August 2020 – April 2024)
4. Development of electrodeposition cost model (November 2020 – April 2024).

Results

Deposited high-quality Li metal from proprietary electrolyte in single compartment cell

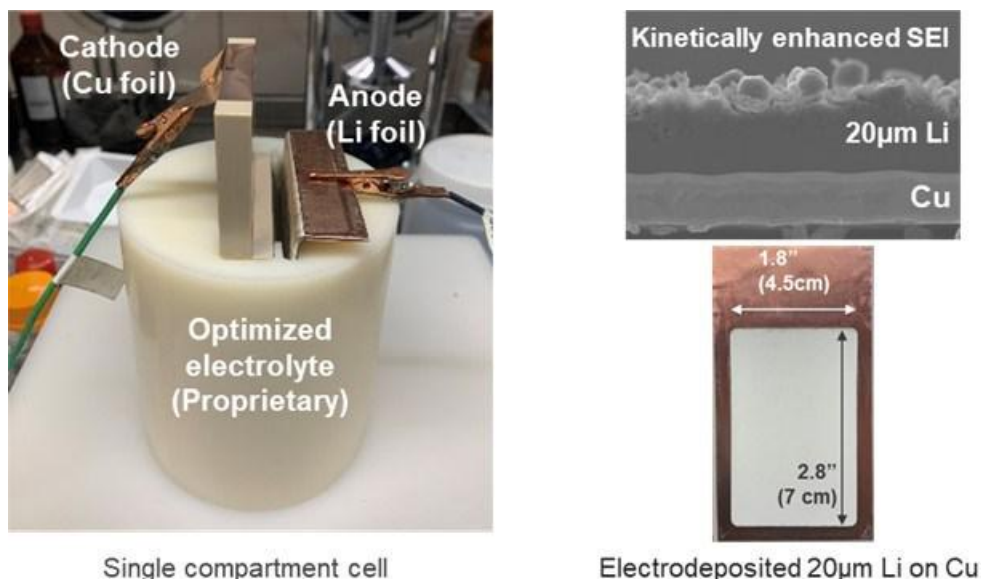


Figure VIII.15.1 Single compartment electrodeposition cell setup with batch produced Li anode on Cu. Cross-sectional & front view of Li anode provided.

We fabricated a single compartment cell that consists of a lithium electrolyte chamber with platinum (Pt) anode and copper (Cu) cathode. (See Figure VIII.15.1.) We performed multiple electrodeposition runs to down-select the electrolyte (catholyte) chemistry that enables uniform Li deposits at high current densities. (See Figure VIII.15.2.) Having selected the best electrolyte (catholyte) chemistry, we batch produced 20 μm Li anodes on Cu of size 4.5 cm x 7 cm. Cross-sectional imaging of the anodes shows a kinetically enhanced SEI that is known to promote faster charge transfer of lithium ions at the anode interface, thereby stabilizing lithium deposition.

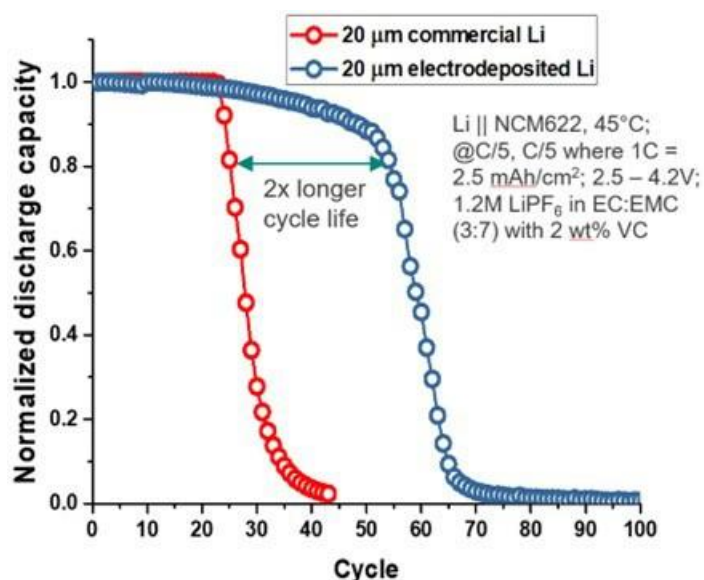


Figure VIII.15.2 Cell testing comparison of single electrodeposited Li anodes against commercial anode.

Independent cell testing performed at Argonne National Lab Cell Analysis, Modeling, and Prototyping (CAMP) Facility shows that single compartment electrodeposited Li anode achieves 2 times longer cycle life than the commercial anode of same thickness. We attribute this longer cycle life to kinetically enhanced SEI of the electrodeposited anode.

Developed new Li-ion selective membrane with proprietary engineering controls to enable dual compartment electrodeposition

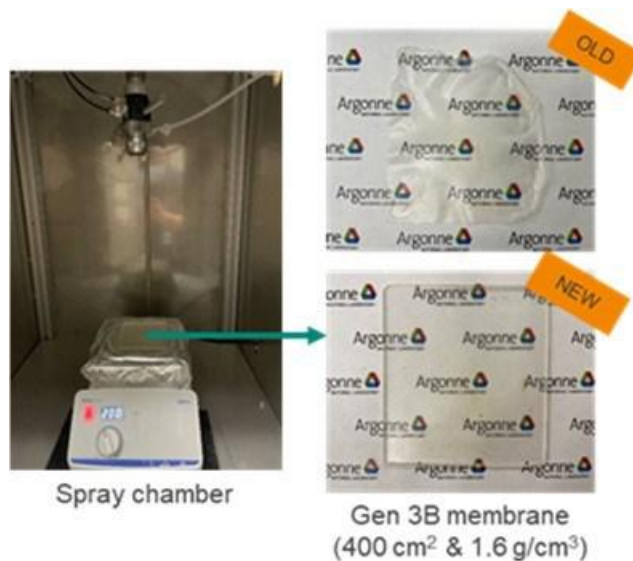


Figure VIII.15.3 Spray chamber to fabricate robust Gen 3B membrane

We developed three different generations of membrane chemistries & architectures to reduce water crossover into catholyte. The third generation (3B) membrane of 300 μm thickness shows nearly fifteen-fold reduction in water crossover compared to earlier generations. We also developed proprietary engineering controls that can eliminate crossover water. We were able to limit water crossover to below 300 ppm by combining action of the Gen 3B membrane with engineering controls. This water crossover limit enables high-quality deposition of Li metal. (See Figure VIII.15.3.)

Deposited high-quality Li metal from aqueous salt in dual compartment cell

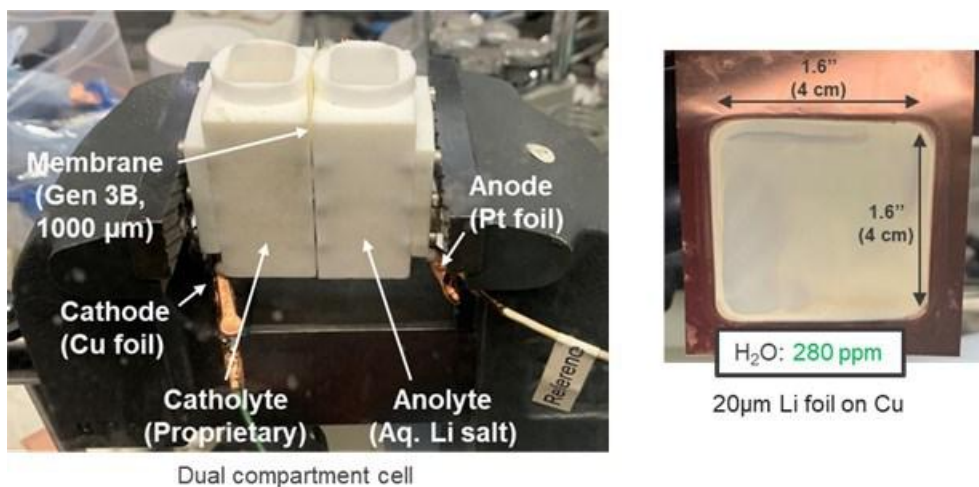


Figure VIII.15.4 Dual compartment electrodeposition cell setup with batch produced Li anode on Cu

We fabricated a dual compartment cell that consists of anolyte chamber with Pt anode, a Gen 3B membrane, & catholyte chamber with Cu cathode. Proprietary engineering controls were added to the cell to mitigate water crossover. Next, we deposited 20 μm Li anode on Cu of size 4 cm x 4 cm with water crossover below 300 ppm. (See Figure VIII.15.4, and Figure VIII.15.5)

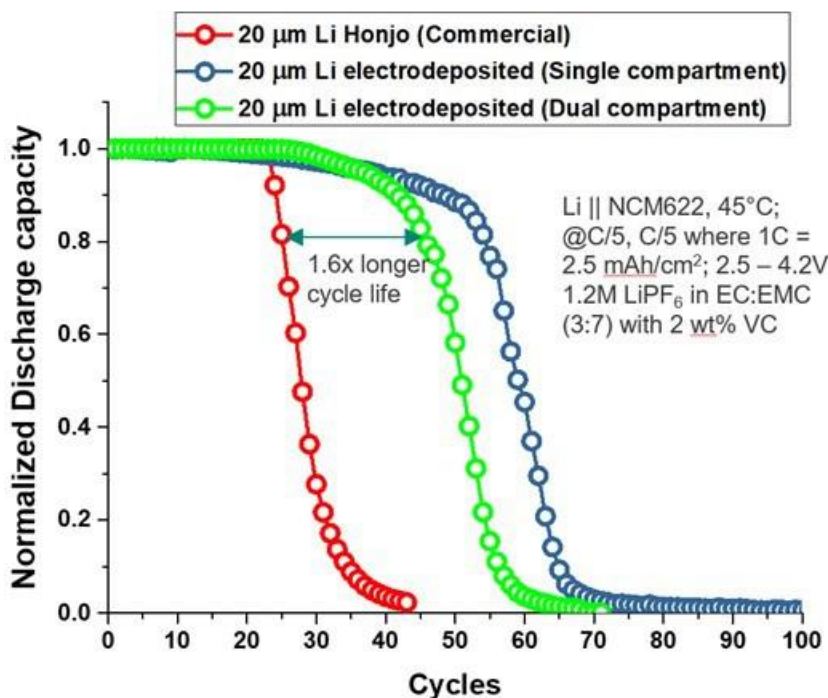


Figure VIII.15.5 Cell testing comparison of single & dual compartment electrodeposited Li anodes against commercial anode.

Independent cell testing performed at the Argonne National Lab CAMP facility shows that dual compartment electrodeposited Li anode achieves 1.6 times longer cycle life than the commercial anode of same thickness.

Ongoing fabrication of prototype unit to demonstrate roll-to-roll manufacturing of electrodeposited Li

We evaluated 5 electrodeposition equipment manufacturers and selected a vendor for the design and construction of the prototype unit. Next, we performed preliminary process, mechanical, and electrical design of the unit. This was followed by a detailed hazard identification and mitigation study that addressed the issue of Li as a potential ignition source. We addressed the recommendations and finalized design of the unit. The prototype shall be installed in Argonne National Lab by February 2023 followed by validation by September 2023.

Techno-economic analysis shows electrodeposition route of manufacturing Li anodes has potential to be cost effective at GWh scale for thicknesses < 8 μm

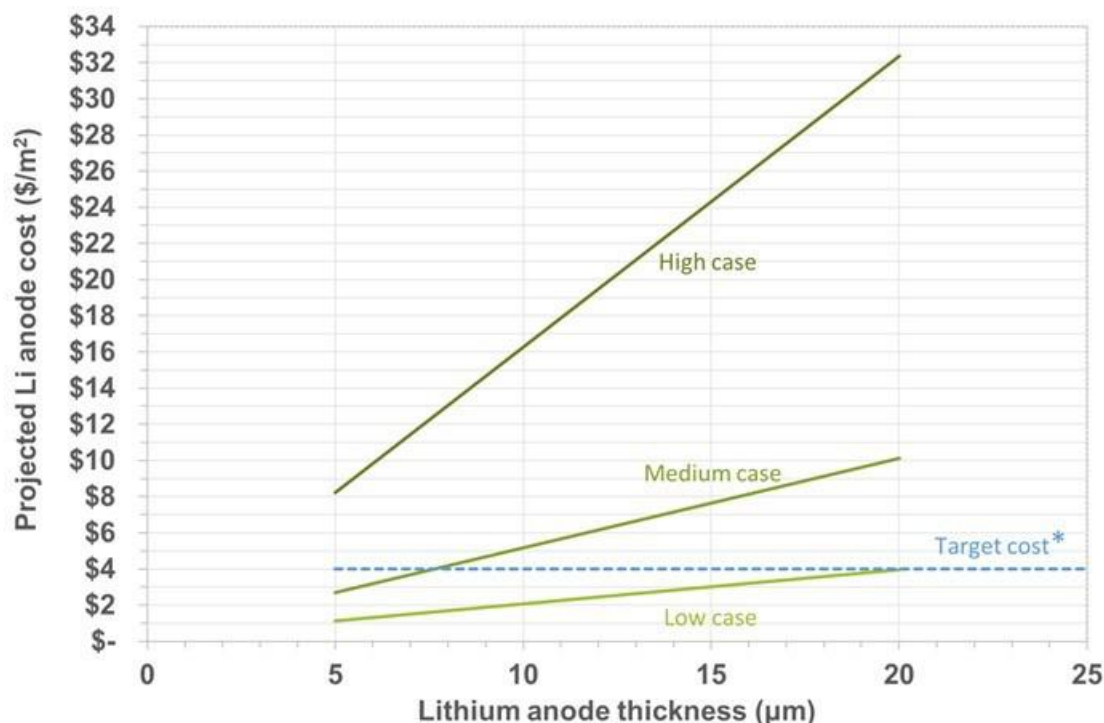


Figure VIII.15.6 Projected Li anode cost in \$/m² vs. Li anode thickness in μm

A preliminary techno-economic analysis (TEA) was performed by considering that the lithium anodes produced will supply a 25 GWh cell facility producing 18650 cells. The TEA accounts for process, engineering, material, and labor costs. The target cost was set from the work of Albertus et al.1 (See Figure VIII.15.6.)

Note: The techno-economic model is not final and is ongoing revisions as we continue prototype scale up.

Conclusions

In conclusion, we deposited high-quality lithium metal from aqueous lithium salt in dual compartment cell. We achieved this through development of proprietary electrolyte (catholyte) that enables uniform deposition of lithium metal and a new generation Li-ion conductive membrane with engineering controls that mitigates water crossover. We also made significant progress in fabrication of the prototype unit that will enable us to demonstrate roll-to-roll manufacturing of electrodeposited lithium in FY2023. Finally, we performed techno-economic analysis to estimate that electrodeposition route of manufacturing lithium anodes has potential to be cost effective at GWh scale for thicknesses < 8 μm .

Key Publications

1. A poster summarizing key achievements was presented at the 2022 EERE VTO Annual Merit Review in June.

References

1. Albertus, et al. "Status and challenges in enabling the lithium metal electrode for high-energy and low-cost rechargeable batteries." *Nature Energy* 3.1 (2018): 16-21.

Acknowledgements

We would like to thank (VTO) Haiyan Croft, Ahmad Pesaran, Jack Deppe for providing technical guidance and valuable insights during the monthly review meetings, (NETL) Aaron Yocum and Jacquelyn Wilson for helping navigate the contracting aspects, (Argonne National Laboratory) John Hryn, Edward Barry, Donghyeon Kang, Zachary Hood, Matthew Earlam, & Michael Dziekan for phenomenal lab scale research work and process scale-up activities. CAMP facility for cell testing, (Solid Power Inc.) Brian Francisco and Adam Jansons for cell testing., and (Albemarle Corporation) Kristina Butler, Subramanian Venkatachalam, & Job Rijssenbeek for project oversight..

VIII.16 Pre-Lithiation of Silicon Anode for High Energy Li Ion Batteries (Stanford University)

Yi Cui, Principal Investigator

Stanford University

Department of Materials Science and Engineering, Stanford University
Stanford, CA 94305

E-mail: yicui@stanford.edu

Tien Duong, DOE Technology Development Manager

U.S. Department of Energy

E-mail: Tien.Duong@ee.doe.gov

Start Date: October 1, 2021

End Date: September 30, 2022

Project Funding (FY22): \$500,000

DOE share: \$500,000

Non-DOE share: \$0

Project Introduction

Lithium-ion Batteries (LIBs) offer superior performance among all rechargeable battery technologies, and are the main power sources for portable electronic devices and electric vehicles. Silicon is a high-performance anode material for next generation lithium ion batteries, with an order of magnitude higher capacity than traditional graphite anode. In our lab, challenges of Si anode materials associated with large volume change (>300%) during lithium insertion and extraction are largely addressed by well-designed nanostructures[1]. However, the common issue associated with these anode materials is the increased solid electrolyte interphase (SEI) formation on high-surface-area nanostructures during the first cycle. The process consumes an appreciable amount of lithium, resulting in irreversible loss of capacity and low 1st CE (50-80%)[2], while a value of at least 90% is needed for real applications. Such capacity loss is usually compensated by additional loading of cathode materials in commercial lithium ion batteries. However, the lithium metal oxide cathodes have much lower specific capacity than the anodes. The excessive loading of cathode material causes appreciable reduction of battery energy density. It is therefore highly desirable to suppress such loss and consequently increase the 1st CE through prelithiation. In addition, pre-storing lithium inside anodes enable the opportunity to pair with Li-free cathodes such as sulfur and oxygen cathodes. This project's success will make high-energy-density Li ion batteries for EVs.

Objectives

Prelithiation of high-capacity electrode materials is an important means to enable those materials in high-energy batteries. This study pursues three main directions: (1) developing facile and practical methods to increase 1st cycle CE of anodes, (2) synthesizing fully lithiated anode to pair with high-capacity Li free cathode materials, and (3) prelithiation from the cathode side. The challenge associated with the anode prelithiation is the high chemical reactivity of prelithiation materials, which are hard to survive multiple processing steps (exposure to air and solvent, slurry mixing, coating and baking) during battery electrode fabrication. A protective coating is therefore needed. Different passivation coatings have been used to increase the dry-air and solvent stability of prelithiation reagents. At the end of battery assembly, the coatings are activated to ensure quick lithium ions diffusion for prelithiation. The passivation coatings can improve the dry-air stability of prelithiation materials to a certain extent, but much study is still needed to improve solvent stability to better compatible with practical battery fabrication. We plan to explore a new solvent-free dry method for anode prelithiation through *in situ* prelithiation. Prelithiation reagents are added to the battery in the assembly step, to avoid the concern of solvent compatibility. We also plan to design prelithiation reagents for this solvent-free method, and accurately control the prelithiation amount of anode materials to pair with different-capacities cathode materials.

Approach

Three main approaches have been developed for prelithiation: 1) Synthesizing lithium alloying Li_xM particles as novel prelithiation reagents to provide a low-cost and general strategy for prelithiation. The synthesized Li-rich compounds should be able to mix with various anode or cathode materials during slurry process and serve as prelithiation reagents. 2) Developing new prelithiation process based-on pressure-induced prelithiation. By direct contact with Li and Si under pressure, heat-free and solvent-free prelithiation can be achieved without the concern of solvent compatibility. Also, prelithiation amount is controllable through contact time and pressure. 3) Developing new *in situ* prelithiation process based on shorting-mechanism. A layer of thin lithium is inserted above Si anode in cell fabrication to achieve *in situ* prelithiation during battery resting period. Prelithiation reagents need to be carefully designed for this approach to control prelithiation amount and avoid excessive Li. Besides prelithiation step, a series of morphological and chemical composition characterizations including SEM, TEM, XPS, Raman spectroscopy, XRD, etc. and electrochemical testing are conducted for performance characterization.

Results

Here, we present an *in situ* prelithiation method with high efficiency, high compatibility and precise control. This prelithiation process takes one step to apply the additive Li onto the Si anode in fabrication, which requires no further cell disassembling and reduces electrolyte waste. With the electrolyte addition, prelithiation takes place spontaneously between contacted Si and Li during the battery resting period based on shorting mechanism. Due to no extraction of lithium out of the cell after prelithiation, the inserted Li amount requires to be carefully controlled to match the desired prelithiation amount. We design a series of lithium mesh with varied porosity as prelithiation reagent. Prelithiation capacity is tuned by Li mesh porosity to precisely control the prelithiation degree. This *in situ* prelithiation demonstrates a dry one-step prelithiation strategy as a promising prelithiation design towards practical applications.

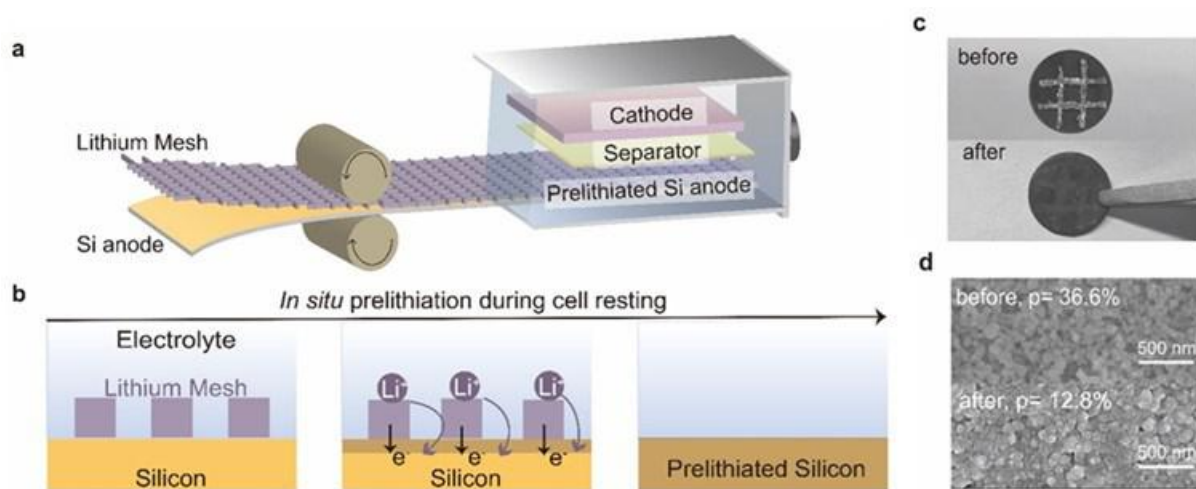


Figure VIII.16.1 Concept of *in situ* prelithiation. a, Schematic of *in situ* prelithiation process by applying a layer of the Li mesh on silicon anode in battery fabrication. b, The mechanism of *in situ* prelithiation reaction based on shorting mechanism. c, Digital photos of the Si anode before (upper) and after (bottom) 24-hour *in situ* prelithiation by lithium mesh. d, SEM images of the Si anode before (upper) and after (bottom) 24-hour *in situ* prelithiation by lithium mesh.

The *in situ* prelithiation is achieved by applying a layer of the Li mesh on the Si anode in battery fabrication (Figure VIII.16.1a). After assembly, the Li mesh in direct contact with the Si anode is surrounded by electrolyte, which creates conditions for shorting reaction between the Si anode and the Li mesh. As illustrated in Figure VIII.16.1b, electrons can transport from the Li mesh directly to the Si anode by the Si-Li contact points while Li^+ ions can flow from Li to Si through electrolyte. Considering that batteries congenitally

require a resting period after assembly for electrolyte wetting, our prelithiation approach utilizes this resting period to achieve *in situ* prelithiation during battery resting. The highlight of *in situ* prelithiation is no need to extract the inserted Li foil after prelithiation, and thus it prevents cell reassembly and reduces electrolyte waste. However, this strength also requires to insert right amount of Li in cell assembly. Commercially available 25- μm thick Li foils provide 5 mAh cm^{-2} capacity, much beyond the desired prelithiation amount. Therefore, we use patterned Li mesh here to provide desired prelithiation amount. Shown in Figure VIII.16.1c, lithium mesh inserted is fully consumed after *in situ* prelithiation, illustrating prelithiation completes after a 24-hour simultaneous resting and prelithiation period. Scanning electron microscopy (SEM) characterizations display Si particles expand and sinter into each other after 24-hour resting, with the porosity of Si electrode decreasing from 36.6% to 12.8% (Figure VIII.16.1d). These phenomena indicate silicon lithium alloying and demonstrate successful prelithiation.

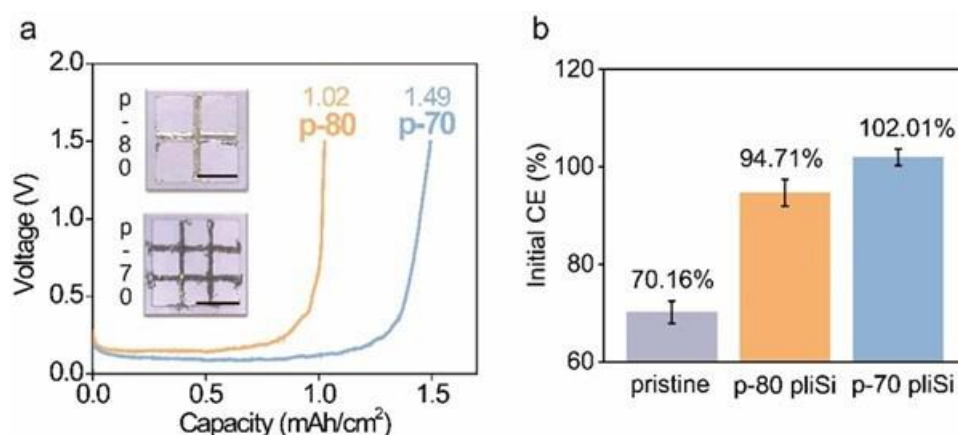


Figure VIII.16.2 Controllable prelithiation through Li mesh design. a, Digital photos of the designed prelithiation reagents with porosity of 80% and 70%, respectively, and their corresponding capacity. b, The initial Coulombic efficiency of Si anode with and without prelithiation.

Along with simplicity, our *in situ* prelithiation approach also exhibits precise control of prelithiation degree. Due to no extraction of lithium out of the cell after *in situ* prelithiation, the inserted Li amount requires to be carefully controlled to match the desired prelithiation amount. However, the presently commercialized Li foils have thickness over 25 micron, providing capacities higher than 5 mAh cm^{-2} . This capacity is much higher than the initial capacity loss in common battery systems. To avoid excessive Li, we design porous Li meshes as prelithiation reagents for *in situ* prelithiation. As shown in Figure VIII.16.2a, lithium mesh of porosity of 80% (p-80) and 70% (p-70) are designed and produced. 25 micron Li foils are used to fabricate lithium mesh. p-80 and p-70 have capacity around 1 mAh cm^{-2} and 1.5 mAh cm^{-2} , respectively. We use these two Li meshes to prelithiate Si anodes through *in situ* prelithiation method. Si anodes of capacity around 5 mAh cm^{-2} are used here. Figure VIII.16.2b shows that Si anodes without prelithiation have low initial CE of around 70.16%, indicating the initial capacity loss is around 1.5 mAh cm^{-2} . Through prelithiation with p-80 Li meshes ($\sim 1\text{ mAh cm}^{-2}$), the initial capacity loss is partially compensated, and the initial CE is improved to around 94.71%. Meanwhile, prelithiation with p-70 Li meshes (1.5 mAh cm^{-2}) fully compensate the initial capacity loss and improves the initial CE to nearly ideal 100%. These results suggest through tuning the porosity of Li meshes, we are able to achieve controllable prelithiation capacity. By further matching the Li mesh capacity with the desired prelithiation capacity of anode materials, we are able to fully compensate the initial capacity loss and achieve nearly ideal 100% initial CE.

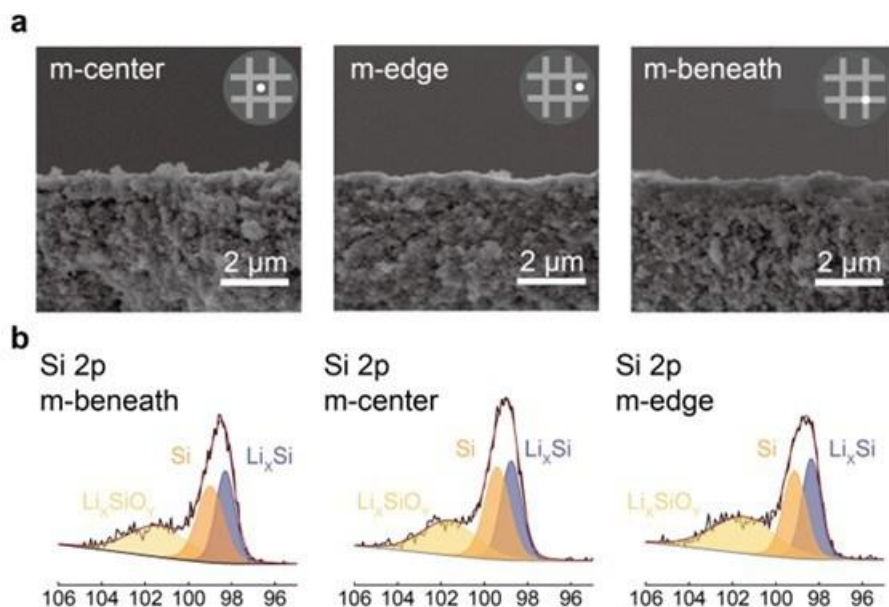


Figure VIII.16.3 Uniformity of *in situ* prelithiation through Li mesh design. a, Cross-sectional SEM images of Li-mesh prelithiated Si anode of three locations, center (m-center), edge (m-edge), and beneath (m-beneath), shown in the inset schematics. b, Si 2p XPS spectra of Li-mesh prelithiated Si anode of three different zones, sputtering time = 0.5 minutes.

Our *in situ* prelithiation method achieves reasonable uniformity through Li mesh patterning. Uneven prelithiation is not ideal because the accompanied irregular volume expansion is likely to cause high local stress and thus produce suboptimal electrode performance. To investigate uniformity of our prelithiation method, patterned p-70 Li mesh was used as an example prelithiation reagent whose grid structure divided the Si anode into 9 zones, among which, one center (m-center), one edge (m-edge) were chosen for SEM and XPS characterizations. As shown in Figure VIII.16.3a, the cross-sectional SEM images of Li-mesh prelithiated Si anode in three different zones show similar features, indicating morphological homogeneity. Moreover, XPS study is conducted to study the chemical uniformity. The high resolution spectra of Si 2p peak in three zones of Li-mesh prelithiation were acquired (Figure VIII.16.3b). The Si 2p peak was deconvoluted into three components: Li_xSi at 98.2 eV, Si at 99.2 eV, and Li_xSiO_y at 102 eV. As shown in Figure VIII.16.3b, Li-mesh prelithiated Si anode display similar chemical compositions in the studied three zones. Particularly, the similar Si/ Li_xSi ratio indicates Si anodes are prelithiated to similar degree in these three zones, supporting we achieve chemically uniform prelithiation through Li mesh design. These studies demonstrate homogeneity at different locations in the prelithiated electrodes. The uniformity along the thickness of the electrodes will need further studying.

Li diffusion kinetics within the electrodes is an important yet unanswered question in the prelithiation process. Here, we design an *in situ* optical cell to reveal the Li diffusion process based on the gray-scale of the electrodes (Figure VIII.16.4a). We choose a thin Si anode with a thickness of $\sim 3\ \mu\text{m}$ to laterally visualize the bulk Li^+ diffusion. All the components were placed between a glass substrate and a transparent cover glass slide and sealed with epoxy to enable *in situ* optical observation. An outer circuit with a switch controls shorting precisely. Figure VIII.16.4b shows the interfacial Si electrode before shorting with labelled components and scales. The snapshots are taken at different shorting time to reveal a gradual color change from yellow to black with prelithiation process (Figure VIII.16.4c). This color changes of the electrodes towards darker colors after prelithiation have been widely observed and reported, indicating the transformation from Si to Li_xSi . At electrode/electrolyte interface, the color changes happen faster compared to locations further away from the interface, revealing a gradual Li diffusion from electrode surface to the bulk. In practical, this distance from the interface indicates the thickness of the electrodes. This optical cell study provide an insight of Li diffusion process along the thickness of Si electrodes.

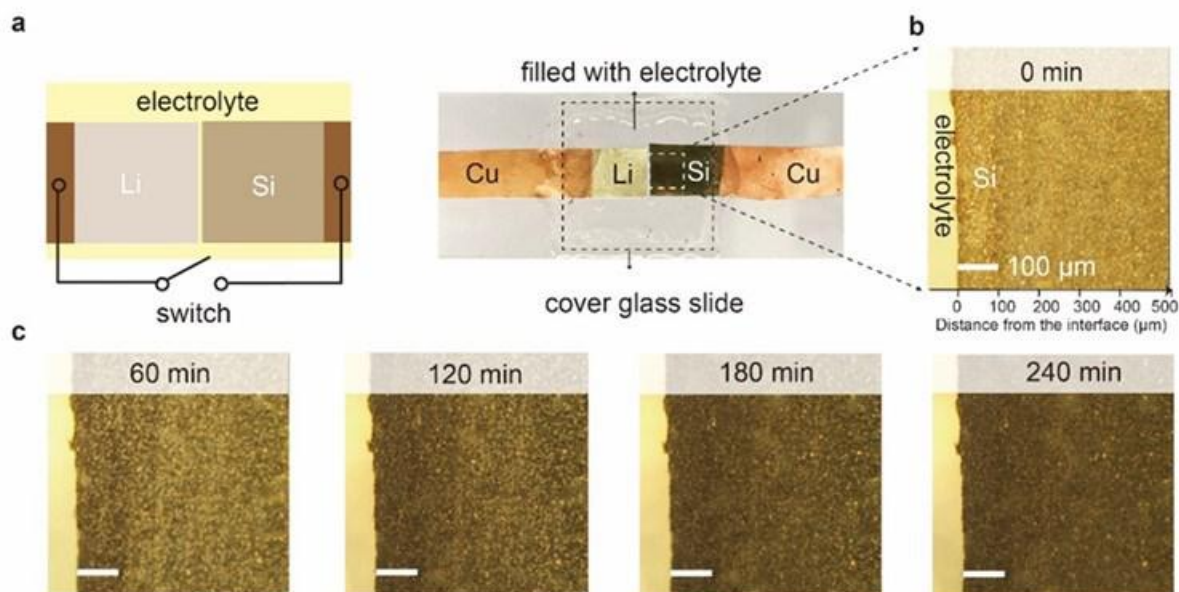


Figure VIII.16.4 Kinetics studies of the Li diffusion in the prelithiation process. a, The *in situ* optical cell used to visualize the Li diffusion process within Si electrodes. Left: schematic, right: a photo of the device. b, The optical microscopy image of the area of interest before shorting (time = 0 min) with labelled components and scales. c, *In situ* dark-field optical microscopy image displaying the prelithiation process within electrodes, scale bar = 100 μm .

Conclusions

In the past year, we have developed an *in situ* prelithiation approach as a new dry prelithiation approach for facile and controllable prelithiation. It takes one step to apply a layer of Li mesh onto the Si anode in battery fabrication, and prelithiation spontaneously happens in the battery resting period by shorting mechanism. The Li mesh design precisely controls prelithiation capacity through porosity tuning. Li mesh with 70% and 80% porosity were fabricated, providing prelithiation capacity of 1.5 mAh cm⁻² and 1 mAh cm⁻², respectively. These capacity amounts can appropriately compensate the irreversible capacity loss in the first cycle of various anode materials. By matching the Li mesh capacity with the initial capacity loss, we precisely improve the initial CE of Si anodes from ~70% to ~100%. We further study the uniformity of *in situ* prelithiation. SEM characterizations of three different zones of the prelithiated Si anode show the morphological uniformity. Further XPS studies show similar Si/Li_xSi ratio in these three zones, indicating Si anodes are prelithiated to similar degree across the electrodes. These results support we achieve both morphologically and chemically uniform prelithiation through Li mesh design. In addition, we design optical cell studies that reveal a gradual Li diffusion from electrode surface to the bulk, providing an insight of Li diffusion process within Si electrodes. In sum, this work provides new insights for studying and designing prelithiation strategies towards applicable high-energy-density Si anodes.

Key Publications

1. Zhao, Jie, Zhenda Lu, Nian Liu, Hyun-Wook Lee, Matthew T. McDowell, and Yi Cui. "Dry-air-stable lithium silicide–lithium oxide core–shell nanoparticles as high-capacity prelithiation reagents." *Nature communications* 5, no. 1 (2014): 1-8.
2. Zhao, Jie, Zhenda Lu, Haotian Wang, Wei Liu, Hyun-Wook Lee, Kai Yan, Denys Zhuo, Dingchang Lin, Nian Liu, and Yi Cui. "Artificial solid electrolyte interphase-protected Li_xSi nanoparticles: an efficient and stable prelithiation reagent for lithium-ion batteries." *Journal of the American Chemical Society* 137, no. 26 (2015): 8372-8375.

3. Zhao, Jie, Hyun-Wook Lee, Jie Sun, Kai Yan, Yayuan Liu, Wei Liu, Zhenda Lu, Dingchang Lin, Guangmin Zhou, and Yi Cui. "Metallurgically lithiated SiO_x anode with high capacity and ambient air compatibility." *Proceedings of the National Academy of Sciences* 113, no. 27 (2016): 7408-7413.
4. Sun, Yongming, Hyun-Wook Lee, Zhi Wei Seh, Nian Liu, Jie Sun, Yuzhang Li, and Yi Cui. "High-capacity battery cathode prelithiation to offset initial lithium loss." *Nature Energy* 1, no. 1 (2016): 1-7.
5. Sun, Yongming, Hyun-Wook Lee, Guangyuan Zheng, Zhi Wei Seh, Jie Sun, Yanbin Li, and Yi Cui. "In situ chemical synthesis of lithium fluoride/metal nanocomposite for high capacity prelithiation of cathodes." *Nano letters* 16, no. 2 (2016): 1497-1501.
6. Sun, Yongming, Hyun-Wook Lee, Zhi Wei Seh, Guangyuan Zheng, Jie Sun, Yanbin Li, and Yi Cui. "Lithium Sulfide/Metal Nanocomposite as a High-Capacity Cathode Prelithiation Material." *Advanced Energy Materials* 6, no. 12 (2016): 1600154.
7. Sun, Yongming, Yanbin Li, Jie Sun, Yuzhang Li, Allen Pei, and Yi Cui. "Stabilized Li_3N for efficient battery cathode prelithiation." *Energy Storage Materials* 6 (2017): 119-124.
8. Zhao, Jie, Jie Sun, Allen Pei, Guangmin Zhou, Kai Yan, Yayuan Liu, Dingchang Lin, and Yi Cui. "A general prelithiation approach for group IV elements and corresponding oxides." *Energy Storage Materials* 10 (2018): 275-281.
9. Chen, Hao, Yufei Yang, David T. Boyle, You Kyeong Jeong, Rong Xu, Luize Scalco de Vasconcelos, Zhuojun Huang et al. "Free-standing ultrathin lithium metal-graphene oxide host foils with controllable thickness for lithium batteries." *Nature Energy* (2021): 1-9.

References

1. Liu, Yayuan, Guangmin Zhou, Kai Liu, and Yi Cui. "Design of complex nanomaterials for energy storage: past success and future opportunity." *Accounts of chemical research* 50, no. 12 (2017): 2895-2905.
2. Zhao, Jie, Zhenda Lu, Nian Liu, Hyun-Wook Lee, Matthew T. McDowell, and Yi Cui. "Dry-air-stable lithium silicide-lithium oxide core-shell nanoparticles as high-capacity prelithiation reagents." *Nature communications* 5, no. 1 (2014): 1-8.

VIII.17 Free-Energy Driven Approaches to Self-Forming and Self-Terminating SEIs on Si Anodes (LBNL)

Brett Helms, Principal Investigator

Lawrence Berkeley National Lab
1 Cyclotron Road
Berkeley, CA, 94720
E-mail: bahelms@lbl.gov

Brian Cunningham, DOE Technology Development Manager

U.S. Department of Energy
E-mail: Brian.Cunningham@ee.doe.gov

Start Date: December 1, 2020	End Date: November 30, 2023	
Project Funding (FY22): \$225,000	DOE share: \$225,000	Non-DOE share: \$0

Project Introduction

Unlike most anodes used in next-generation high energy density batteries, lithiated Si does not form a long-lasting passivating solid-electrolyte interphase (SEI) during formation or on charge due to SEI delamination, reconstruction, or dissolution depending on the electrolyte used. As a result, electrolyte degradation is continuous when the battery is charged and results in permanent loss of the Li inventory and shortens the battery's useful life [1–12]. Advanced electrolytes could play an important role in the creation of more stable, resilient, and self-terminating SEI, mitigating initial capacity loss on charge and thereafter slowing the fade rate. If realized, the pairing of such electrolytes with silicon anodes would further the development of EV batteries with useable energy >350 Wh/kg, energy density >700 Wh/L, and a calendar life >10 years.

Concept

To address this outstanding problem, we propose to design and develop a new class of localized super-concentrated fluorinated electrolytes embodied with geminal surfactants (i.e., surfactants with two head-groups) that spontaneously assemble at the anode–electrolyte interface and in doing so promote the formation of an adherent organo–LiF composite SEI that is compliant to volume changes and resistant to dissolution. These geminal surfactants are prepared at scale from readily available starting materials and provide access to a broad range of property sets to direct their assembly to the interface as well as tailor the chemomechanical properties of the composite SEI that is generated during formation; they are also electrochemically stable up to 4.5 V vs. Li/Li⁺ and therefore compatible with a broad range of cathode chemistries, such as LFP and NMC.

Objectives

In the current reporting period, our seedling project pursued four research objectives, which are listed in turn. We aligned these research objectives to be parallel with related efforts in the Silicon Anode Research Consortium to enable direct transfer of our findings to that team.

- Objective 1: Evaluate full cell cycling performance with electrolytes down-selected in Year 1. Cathode areal capacity > 1.5 mAh/cm². Rate = C/3. Temperature = 25 °C. Identify at least one electrolyte enabling capacity retention >80% after 100 cycles. Develop design space for a second round of electrolyte formulation and screens, varying lithium salt, solvent, fluorinated diluent, and LiF-generating additive.
- Objective 2: Benchmark accuracy and reproducibility of liquid handling robot to formulate electrolytes in high-throughput; automate analytical capabilities for quantifying electrolyte conductivity and voltage stability. Synthesize at least 4 mono and divalent LiF-generating additives.
- Objective 3: Execute 2nd round of electrolyte screens. Implement the automated screening capabilities to downselect at least 10 electrolytes. Using the downselected electrolytes in 3-electrode full cells,

galvanostatically lithiate Si to 0.2 V and then drive further lithiation potentiostatically at 0.1 V and monitor the leakage current over at least 24 h. For at least three top performing electrolyte formulations, quantify the amount of current leakage over at least 120 h.

- Objective 4: Evaluate full cell cycling performance for at least 200 cycles with downselected electrolytes. Cathode areal capacity > 1.5 mAh/cm². Rate = C/3. Temperature = 25 °C. Downselect at least three electrolytes for testing in Si anode full cells in Year 3 that satisfy the following criteria: conductivity > 6 mS/cm at 25 °C; voltage stability at least 4.5 V vs. Li/Li⁺ by LSV; < 0.05 mAh/cm² capacity lost to electrolyte degradation during formation over the last 4 h of observation, showing < 20% loss of the total Li inventory during formation; shows capacity retention >80% of the maximum discharge capacity after 200 cycles in full cells.

Approach

To meet the above objectives, we acquired from ORNL, CAMP, and NREL or fabricated electrodes with the following specifications.

Anodes:

CAMP-Paraclete nSiO: 1.74 mAh/cm²

NREL Si: 1.20 mAh/cm²

LBNL Si microparticles (SiMP): 0.88 mg/cm²

CAMP-ORNL Si: 2.00 mAh/cm²

Cathodes:

CAMP-LFP125: 1.25 mAh/cm²

CAMP-LFP181: 1.81 mAh/cm²

These electrodes were assembled into a variety of formats, including Si|Li and Si|LFP 2032 coin cells, for testing our electrolytes (30 µL per coin cell) as described above. As reference electrolytes, we used Gen2 and GenF electrolytes developed by the Silicon Anode Research Consortium.

To test our hypotheses for SEI, we prepared locally super-concentrated electrolytes comprising various lithium salts such as LiPF₆, LiBF₄, LiTFSI, LiDFOB, LiClO₄, LiFSI, and LiOTF alongside DME as the solvent and TTE as the fluorinated diluent. As interphase-stabilizing additives, we prepared a library of difunctional organic LiF-generating compounds with diverse compositions and end-group structures such as sulfonyl fluorides and trifluorovinyl ethers. Using liquid handling robots, we prepared libraries of electrolytes varying in composition on the basis of the molar ratios of salt, solvent, diluent, and additive. We evaluated their transport properties and performance in silicon anode cells to monitor and track progress toward our objectives for this reporting period. These results are discussed below in detail.

Results

Electrolytes from Year 1 were prepared according to the strategy defined as Strategy 1 in Figure VIII.17.1. Electrolytes from Year 2, the current reporting period introduce interphase-stabilizing additives according to the strategy defined as Strategy 2 in Figure VIII.17.1. Use of liquid handling robots aid in the precise formulation across a broad spectrum of chemical space, satisfying Objective 2.

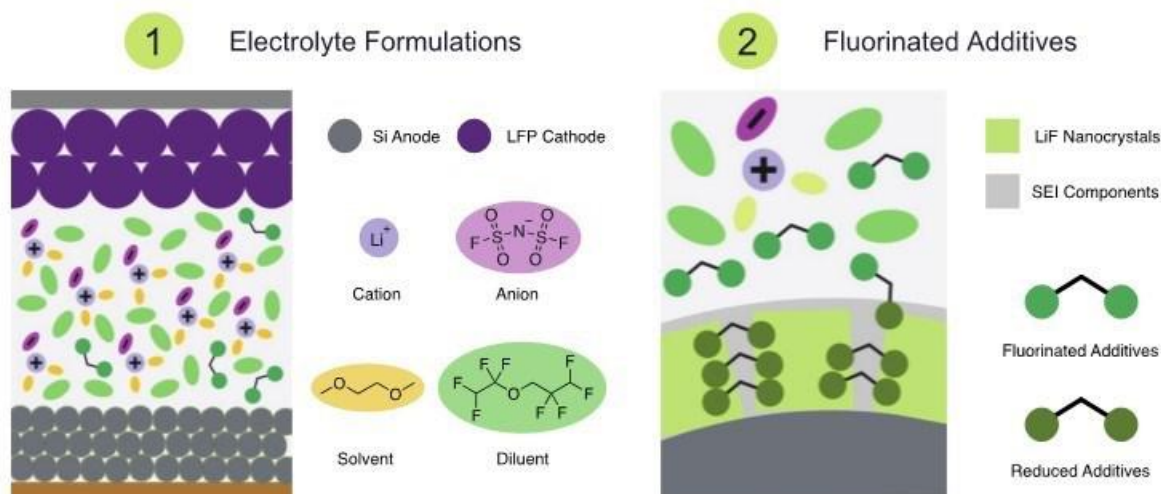


Figure VIII.17.1 Strategies in Year 1 and Year 2 of the Seedling project for electrolyte development for Si anode. Strategy 1: Locally super-concentrated electrolyte formulations comprising a lithium salt (i.e., anions), a solvent, and a fluorinated diluent in different molar ratios. Strategy 2: Fluorinated additives are introduced to the locally super-concentrated electrolyte to create chemomechanically stable interphase.

We evaluated full cell cycling performance with electrolytes down-selected in Year 1 (Figure VIII.17.2a–b) using CAMP Paraclete nano SiO anode and the CAMP LFP181 cathode with areal capacity of 1.74 mAh/cm^2 ; as prescribed, cells were cycled at $C/3$ rate at $T = 25^\circ\text{C}$. We found that the initial capacity lost on the first cycle and the rate of capacity fade thereafter was most highly dependent on the choice of lithium salt in the locally-superconcentrated electrolyte (LSCE). Triflate and tetrafluoroborate anions in particular showed precipitous losses on both figures of merit for silicon anode full cells, whereas electrolytes featuring LiFSI, LiClO_4 , and LiDFOB were demonstrably superior (Figure VIII.17.2c). Optimized solvent ratios relative to the salt were 2:1 (Figure VIII.17.2d). The ratio of solvate electrolyte to diluent was not impactful on capacity loss and fade rate (Figure VIII.17.2e). Based on these data, we downselected LSCE where $\text{LiFSI} : \text{DME} : \text{TTE} = 1 : 2 : 2$, as it satisfied Objective 1; specifically, with this electrolyte in the relevant cell format tested under the requisite cycling protocols, we observed 82% capacity retention after 200 cycles (Figure VIII.17.2f–g). We further demonstrated that this electrolyte is superior to the GenF electrolyte standard electrolyte of the consortium, validating part of our initial hypothesis that LSCEs have the potential to offer superior performance traits to Si anode cells implementing them.

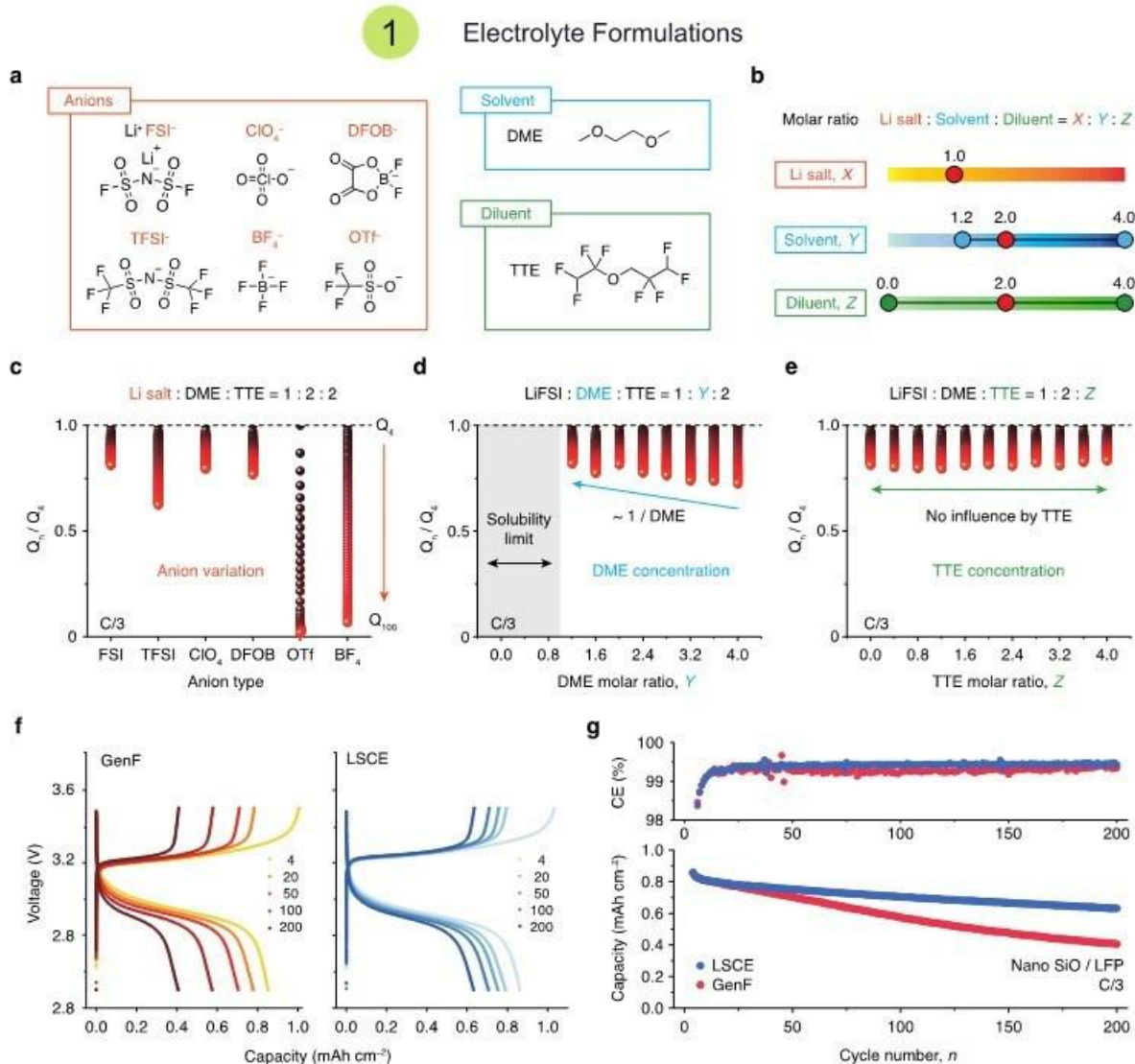


Figure VIII.17.2 Year 1 Electrolyte Evaluation and Downselect for Year 2. (a) Electrolyte components where different anions (FSI-, ClO_4^- , DFOB-, TFSI-, BF_4^- , and OTf-), solvent (i.e., DME), and diluent (i.e., TTE). (b) Molar ratio for electrolyte formulation study where molar ratio of lithium salt is fixed as 1, while the ratio of solvent and diluent varies from 0 to 4 (1.2 to 4.0 in case of solvent due to the solubility limit of salts). (c) Capacity retention by anion variation while molar ratio of Li salt : DME : TTE is fixed to 1 : 2 : 2. (d) Capacity retention by DME concentration change while LiFSI and TTE ratios are fixed as 1 : 2. (e) Capacity retention by TTE concentration change while LiFSI and DME ratios are fixed as 1 : 2. (f) Voltage profiles and (g) cycling performance of nano SiO / LFP full cells with GenF (and LSCE). GenF here is 1.2 M LiPF₆ in EC:EMC (3:7 vol) LSCE here is LiFSI : DME : TTE = 1 : 2 : 2 All full cells were cycled at C/20 for the first 3 cycles as formation cycles. After that C/3 was applied for both charge and discharge rate..

We next turned our attention to the design and screening of difunctional additives with the potential to electrochemically transform into a hybrid interphase rich with LiF, a known beneficial SEI component for Si anode cells. For these, we considered sulfonyl fluorides and trifluorovinyl ether functionality as preferentially reactive over other components in the LSCE (Figure VIII.17.3a–b). To test this hypothesis, we screened the additives, with respect to dQ/dV to monitor and track the reactivity of the additives (Figure VIII.17.3c–d). We also tracked the influence of additive loading in the electrolyte on the extent of reactivity at the Si anode (Figure VIII.17.3e–j). Additives SS and PFS and to a lesser extent PS exhibited the most reactivity, indicating the sulfonyl fluoride group is preferentially reactive, with onsets ~ 2.2 V vs. Li/Li⁺.

2

Fluorinated Additives

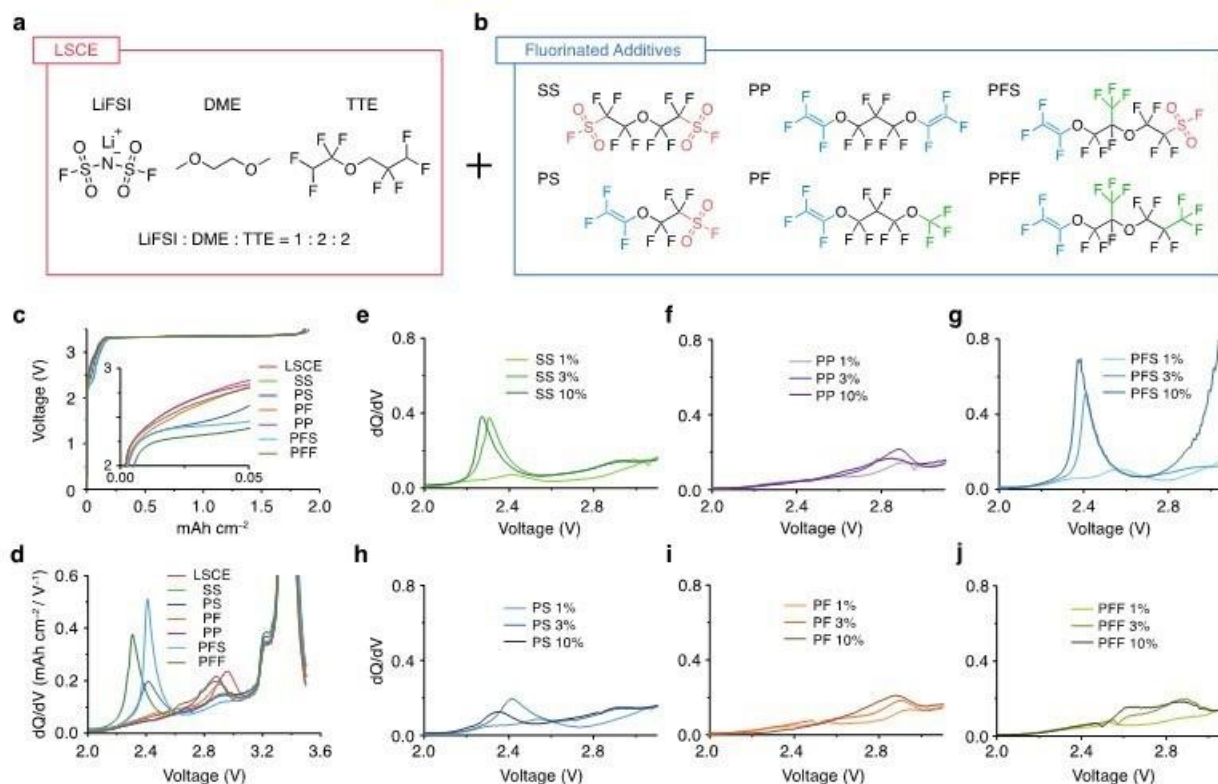


Figure VIII.17.3 Year 2 Additive Screen in Year 2. (a) Year 1 baseline electrolyte used for additive study and (b) the library of the fluorinated additives in Year 2. (c) Voltage profiles and (d) dQ/dV curves for the 1st charge of different additives with 3 wt% added on LSCE. The inset of (c) shows enlarged initial voltage profiles. (e-j) dQ/dV curves with different additive concentrations (1, 3, or 10 wt% in LSCE) with the additive of (e) SS, (f) PP, (g) PFS, (h) PS, (i) PF, and (j) PFF.

We were advised to discontinue use of the CAMP Paraclete SiO electrodes to stay aligned with the Si anode consortium. Therefore, in our further evaluations of the new additives, we carried out tests in full cells assembled with either LBNL's Si microparticle anodes alongside pre-lithiated nano Si anode cast at NREL using Si nanoparticles prepared by Nate Neale; we continued to use the CAMP LFP181 cathode with areal capacity of 1.74 mAh/cm²; as prescribed, cells were cycled at C/3 rate at $T = 25^\circ\text{C}$. We observed that for SS, PFS, and PS additives, all of which show higher initial rates of incorporation in to the SEI, performance advantages over the baseline LSCE were readily evident; however, in each case, the optimum loading of a specific additive was with a defined range unrelated to the behaviors of the other additives (Figure VIII.17.4)a. For example, SS provided maximum benefits at 3% loading that diminished at both lower and higher loadings. However, for PFS, performance gains were seen at low concentrations of additive; and still, for PS, performance gains were seen at high concentrations of additive. Despite the complexity of the chemical space explored here, we find our screening protocols enabling the additive downselect process for the electrolytes.

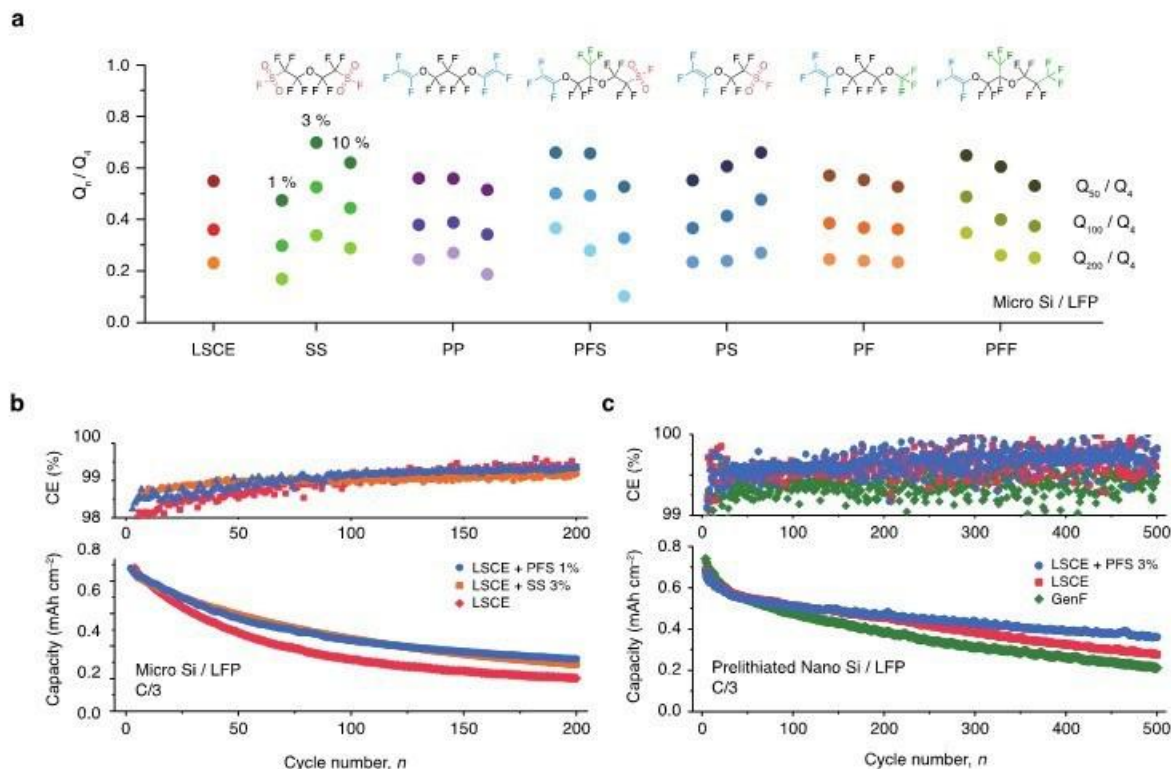


Figure VIII.17.4 Year 2 Additive Evaluation and Downselect for Year 2. (a) Summary of capacity retention at 50th, 100th and 200th cycle with different additives and concentrations. (b) Cycling performance of micro Si / LFP full cells with LSCE+PFS 1wt%, LSCE + SS 3wt% and LSCE. (c) Cycling performance of prelithiated nano Si / LFP full cells with LSCE + PFS 3wt%, LSCE, and GenF.

We further find that the Si anodes from different partners within the Silicon Anode Research Consortium will have different preferences for which of the electrolyte additives are most beneficial (Figure VIII.17.4b–c). For example, we observed that LBNL Si anodes comprising Si microparticles benefit from both SS and PFS additives, whereas pre-lithiated Si nanoparticles from NREL prefer PFS. We note that PFS-containing additives outperform the controls, including the LSCE without additive and GenF.

To clarify the origins of the beneficial characteristics of our LSCEs and additives, we extracted the electrolyte after formation and at different stages in cycling to understand interphase composition and evolution (Figure VIII.17.5). We find that the highest capacity accessed and retained are for cells incorporating additives that both enrich the SEI with LiF, but also with flexible fluoroethers tethered to those materials through sulfur bonds. In this way, we have validated our program's central hypothesis, that the creation of the hybrid interphase is beneficial to cell performance.

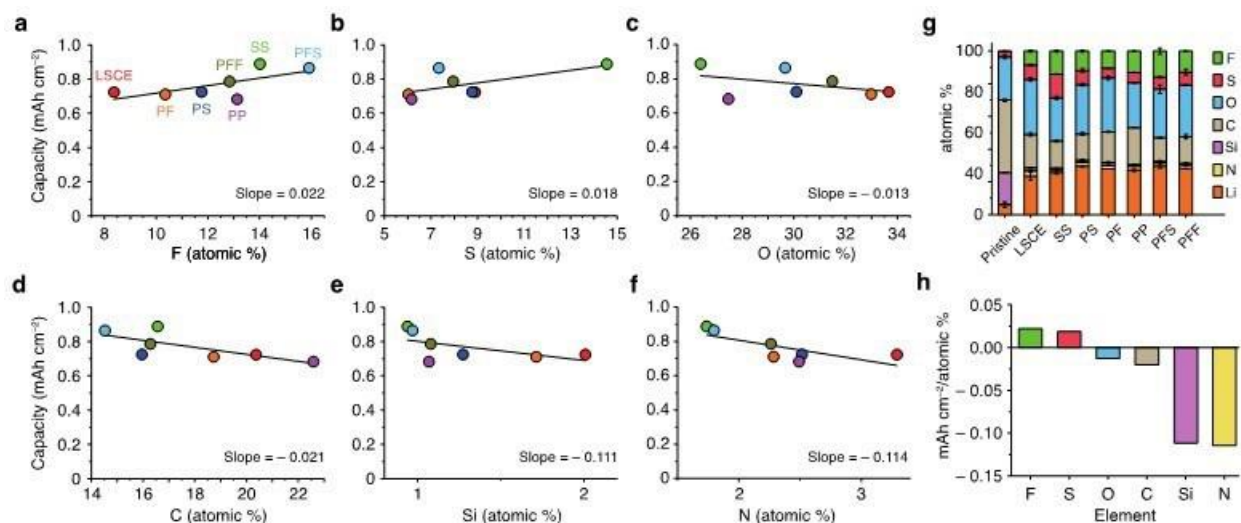


Figure VIII.17.5 Understanding the impact of SEI on capacity retention. Spectroscopic investigation of SEI layer on Si anode. (a-f) Areal capacity at 50th cycle of different 3 wt% additives vs. atomic % of each element in the SEI layer on the cycled Si anode from XPS measurement. The slope in the inset was calculated based on capacity change by atomic % variation from XPS data. (g) Atomic content of the SEI layer on the Si anode cycled by different electrolytes. (h) Summary of the slopes calculated from (a-f).

Completing Objective 4, we provide below a full description of the electrolyte transport properties (Table VIII.17.1 Ionic Conductivity of LSCEs) and voltage stability (Figure VIII.17.6).

Table VIII.17.1 Ionic Conductivity of LSCEs

Formulation (LiFSI : DME : TTE)	Conductivity (mS/cm)	Temperature (Celsius)
1.0 : 2.0 : 0.0	7.166	24.9
1.0 : 2.0 : 0.4	7.253	25.6
1.0 : 2.0 : 0.8	7.840	25.5
1.0 : 2.0 : 1.2	7.231	25.5
1.0 : 2.0 : 1.6	6.996	25.4
1.0 : 2.0 : 2.0	6.798	25.4
1.0 : 2.0 : 2.4	6.476	25.4
1.0 : 2.0 : 2.8	6.379	25.5
1.0 : 2.0 : 3.2	5.938	25.4
1.0 : 2.0 : 0.0	5.592	25.4

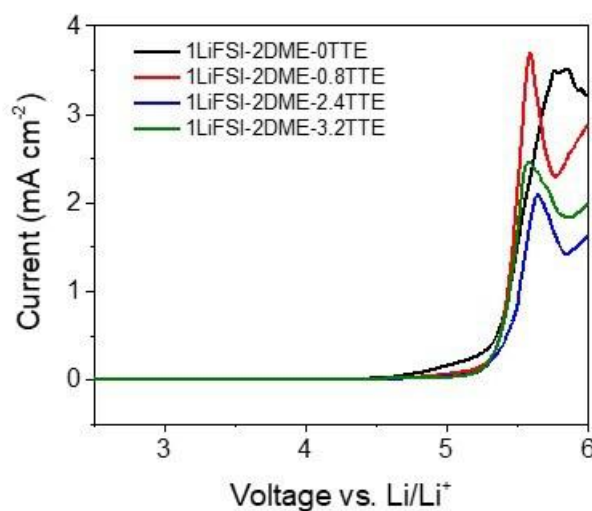


Figure VIII.17.6 Voltage stability window for LSCs, passing the design criteria for stability > 4.5 V vs Li/Li⁺

Conclusions

For our Year 3 downselect, we will move forward with LSCs containing SS, PFS, PS, and PFF additives, recognizing that while we have met our Year 2 targets for keeping initial capacity loss to ~20%, we have only satisfied the capacity retention challenge after 200 cycles with the CAMP Paraclete Si anodes and not yet others under development in the Si Anode Research Consortium. Notably, our electrolytes remain superior than those standards and ours likewise avoid gas generation across the cycle life in pouch cells. We will scale the electrolyte in Year 3 and provide it to performers in that program for validation in the larger pouch cell formats.

References

1. Yin, Y. *et al. ACS Appl. Mater. Interfaces* **12**, 26593 (2020)
2. Steinrück, H.-G. *et al. J. Chem. Phys.* **152**, 084702 (2020)
3. Li, Z. *et al. Adv. Energy Mater.* **10**, 1903110 (2020)
4. Huang, G. *et al. ACS Nano* **14**, 4374 (2020)
5. Coyle, J. E. *et al. J. Phys. Chem. C* **124**, 8153 (2020)
6. Schneier, D. *et al. J. Electrochem. Soc.* **166**, A4020 (2019)
7. Hu, Z. *et al. Adv. Funct. Mater.* **29**, 1906548 (2019)
8. Chen, J. *et al. Nat. Energy* **5**, 386 (2020)
9. Xie, H. *et al. ACS Appl. Energy Mater.* **3**, 1609 (2020)
10. Jin, Y. *et al. J. Am. Chem. Soc.* **140**, 9854 (2018)
11. Park, S.-J. *et al. J. Am. Chem. Soc.* **137**, 2565 (2015)
12. Lee, M. *et al. ACS Appl. Energy Mater.* **3**, 1899 (2020).

Acknowledgements

Postdoctoral researchers, Jiwoong Bae and Youngmin Ko performed the experiments. Liana Klivansky assisted with the XPS. Anthony Burrell, Nathan Neale, Marco Rodrigues, and Gabriel Veith are thanked for their helpful discussions, electrodes, and collaboration.

IX Next-Gen Lithium-Ion: Advanced Cathodes R&D

As a sustainable and promising store of renewable energy, lithium-ion batteries have replaced other types of batteries for many small-scale consumer devices. However, it has become clear that design and fabrication of electrode materials is necessary to meet the growing global demand for energy and the power densities needed to make electric vehicles fully commercially viable. To dramatically enhance battery performance, further advances in materials chemistry are essential, especially in novel nanomaterials chemistry. The construction of nanostructured cathode materials by reducing particle size can boost electrochemical performance.

- Design, Synthesis, & Characterization of Low-Cobalt Cathodes (ANL, ORNL, LBNL, NREL, PNNL)
- Diagnostic Testing and Evaluation (ANL, ORNL, NREL, PNNL)
- Advanced Cathodes Theory and Modeling (ANL, LBNL, PNNL, NREL, ORNL)
- Design and Synthesis of High Energy, Manganese Rich Oxides for Lithium-Ion Batteries (ANL)
- Disordered RockSalt Structured Cathode Materials: Electrochemistry and Synthesis (LBNL, ORNL, PNNL, UC Santa Barbara)
- Disordered RockSalt Structured Cathode Materials: Characterization and Modeling (LBNL, ORNL, PNNL, UC Santa Barbara).

IX.1 Design, Synthesis, & Characterization of Low-Cobalt Cathodes (ANL, ORNL, LBNL, NREL, PNNL)

Jason R. Croy, Principal Investigator

Argonne National Laboratory
9700 South Cass Avenue
Lemont, IL 60439
E-mail: croy@anl.gov

Tien Duong, DOE Technology Development Manager

U.S. Department of Energy
E-mail: Tien.Duong@ee.doe.gov

Start Date: October 1, 2018 End Date: September 30, 2022
Project Funding (FY22): \$3,500,000 DOE share: \$3,500,000 Non-DOE share: \$0

Project Introduction

State-of-the-art Li-ion batteries (LIBs) for transportation applications contain transition metal (TM) oxide cathodes consisting of $\text{Li}_{1+x}\text{Ni}_a\text{Co}_b\text{Al}_c\text{O}_2$ (NCA) or $\text{Li}_{1+x}\text{Ni}_a\text{Mn}_b\text{Co}_c\text{O}_2$ (NMC-abc) oxides, where $x = \sim 0\text{--}0.05$ and $a+b+c = 1$. Both oxide chemistries contain Co, which has been recognized over many years of research as an important component in terms of structure, stability, and electrochemical performance. Currently, however, geopolitical concerns associated with Co mining, availability, and cost have caused the LIB community to pursue the development of low- to no-cobalt layered oxides as next-generation cathodes. The goal of this work is to show progress towards the realization of low/no-cobalt oxides having acceptable performance (energy/power densities), safety, and cycle/calendar life by way of new insights into cathode design and synthesis as they pertain to the critical roles of Co in layered oxides.

Objectives

- Understanding of local ordering as a function of Co and dopant/substitution content.
- Synthesis of new, low- to no-cobalt cathodes showing promise with respect to an NMC-622 baseline.
- Synthesis and understanding of LiNiO_2 -based oxides with low- to no-cobalt compositions.
- Atomic-scale characterization, understanding, design, and synthesis of NiMn-based cathodes.

Approach

- Advanced characterization of Ni-rich, low- and no-cobalt cathodes including synchrotron techniques, solid-state NMR, electron microscopy, and theory/modeling.
- Advanced characterization of MnNi-based, low- and no-cobalt cathodes including synchrotron techniques, solid-state NMR, electron microscopy, and theory/modeling.
- Development of novel surface modifications for low/no-cobalt oxides
- Large batch co-precipitation synthesis of model and new compositions for practical evaluation.
- Synthesis of standardized materials for distribution and study across multiple teams.

Results

Previous reports from this program have shown that pure LiNiO_2 can cycle at high capacities (>220 mAh/g) over many charge/discharge cycles without dopants, coatings, or electrolyte additives. Key to achieving such performance was an understanding of the correlated effects of synthesis conditions such as temperature, moisture, and the mechanisms of $\text{LiOH}/\text{Li}_2\text{CO}_3$ formation and decomposition, on the final cathode primary and secondary particles. Such high performance has never been reported for LiNiO_2 and the fact that this material cycles as well or better (e.g., higher capacity with long cycle life) than most reports of doped LiNiO_2 , calls into question the necessity, or true effect, of modifying compositions. Following a strategy similar to the

optimization of LiNiO_2 (previously reported), follow up studies were conducted on $\text{LiNi}_{0.95}\text{Co}_{0.05}\text{O}_2$ and $\text{LiNi}_{0.95}\text{Mn}_{0.05}\text{O}_2$ to assess the effects of Co and Mn.

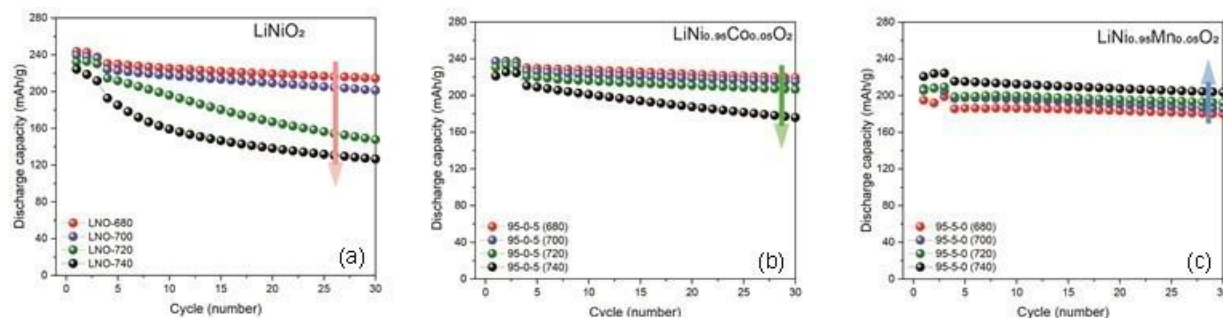


Figure IX.1.1 Cycling data of (a) LiNiO_2 , (b) $\text{LiNi}_{0.95}\text{Co}_{0.05}\text{O}_2$, and (c) $\text{LiNi}_{0.95}\text{Mn}_{0.05}\text{O}_2$ after calcination at four different temperatures. Cells used Li metal anodes, 1.2 M LiPF_6 in EC:EMC (3:7, w/w), cycled between 4.3–2.8 V. The first three cycles were at C/10 ($1\text{C}=200\text{mA/g}$) and subsequent ageing cycles were C/10 charge, C/3 discharge.

Figure IX.1.1 shows the most critical results of the study comparing initial cycling performance. Figure IX.1.1(a) shows the extreme sensitivity of pure LiNiO_2 to calcination temperature. Here it can be seen that capacity retention quickly drops when the calcination temperature increases above 700°C from an initial starting temperature of just 680°C , revealing a very narrow range for optimized performance. In contrast to this trend, the addition of 5% Co, Figure IX.1.1(b), results in consistent performance over a range of $\sim 40^\circ\text{C}$, roughly double that of the pure LiNiO_2 . For the $\text{LiNi}_{0.95}\text{Mn}_{0.05}\text{O}_2$ oxides shown in Figure IX.1.1 (c), an interesting trend appears where increasing the calcination temperature from 680°C to 740°C also increases the capacity. However, all of the 5% Mn samples cycle in a stable manner spanning a calcination range of 60°C . High-resolution microscopy images revealed slight differences in primary particle growth/coarsening suggesting that small amounts of Mn and/or Co may inhibit particle growth during calcination. While the details of these observations are still under investigation, it is clear that the addition of Co and Mn mitigates the sensitivity of LiNiO_2 to calcination temperature, suggesting that Co/Mn containing samples are easier to prepare, revealing one of the major benefits of including them, especially for larger scale calcinations.

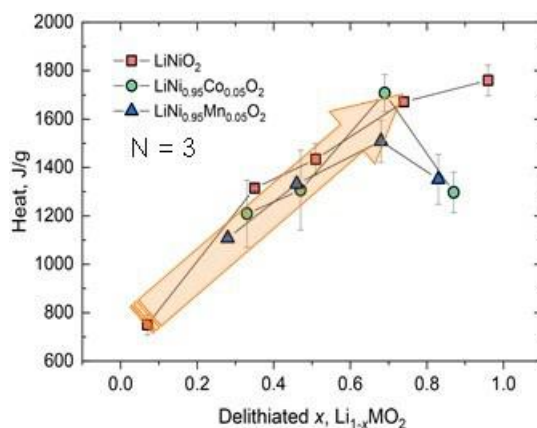


Figure IX.1.2 Total heat generation ($\text{J/g}_{\text{oxide}}$) derived from DSC measurements as a function of state of charge for the three compositions shown in the figure above.

A commonly reported shortcoming of pure LiNiO_2 is its thermal instability and Co/Mn containing compositions may improve this characteristic to some degree. The optimized samples of Figure IX.1.2 above were probed via differential scanning calorimetry at various states of charge (SOCs). 2032 coin-cells were disassembled at desired voltages (3.0, 3.7, 3.85, 4.1, and 4.3 V) after 3 formation cycles between 4.3–2.8 V. Electrodes consisted of 88% active materials, 6% C-45, and 6% PVDF binder and three cells were measured at each data point for reproducibility. At all SOC's up to $\sim 70\%$ delithiation, all compositions showed the same

total heat generation. However, above ~70% SOC, both Co and Mn substitution reduced heat generation compared to the pure LiNiO₂. Therefore, in addition to enabling more controllable synthesis of final cathode products, substitution with Co and Mn does influence thermal stability in a positive way.

In addition to Co and Mn, other dopants are now being explored to study their effects on the high-performing, baseline LiNiO₂ of this project. For example, Ti, Mg, and Al are commonly reported to enhance the stability of LiNiO₂, however, as this program has shown, pure LiNiO₂ can cycle just as well, or better, than LiNiO₂ using these dopants. Furthermore, previous reports from this program have shown that the method used for doping elements can have an influence on cathode performance. In particular, atomic layer deposition (ALD) as a method of doping precursor hydroxides, before calcination/lithiation, was found to be highly effective in achieving uniform distribution of Al dopants in Ni-rich compositions. Recently, ALD was used to coat MgO, Al₂O₃, and TiO₂ on LiNiO₂ at a thickness of ~1 nm. Subsequently, the coated LiNiO₂ powders were heat treated at 600°C for 5 hours under oxygen to study elemental diffusion into the surface of the oxide.

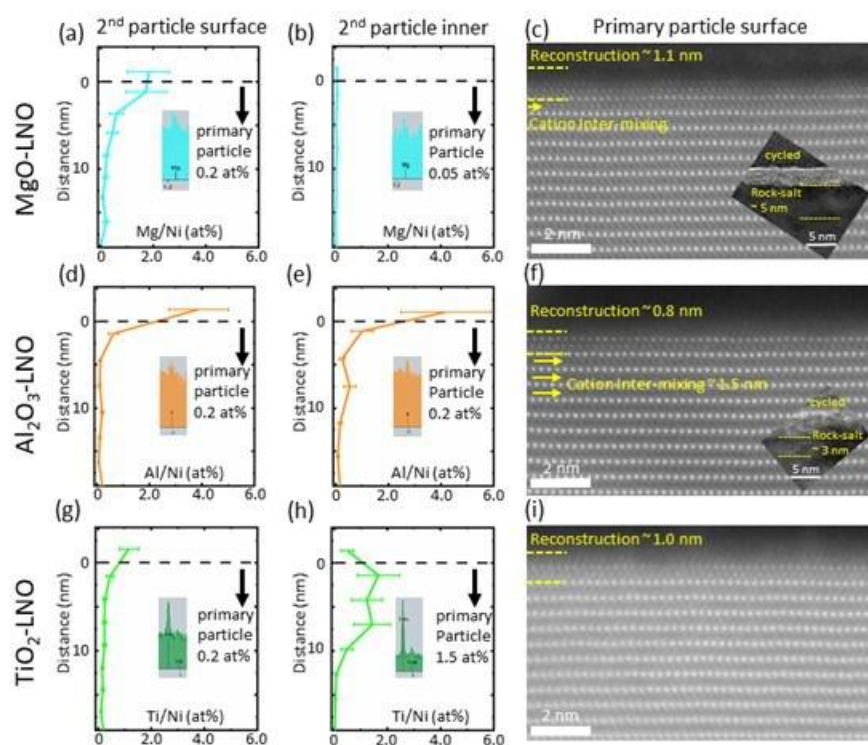


Figure IX.1.3 Chemical and structural characteristics of LiNiO₂ modified by ALD coatings of MgO, Al₂O₃, or TiO₂ followed by post-annealing at 600°C. The dopant concentration profile for (a) Mg, (d) Al and (g) Ti incorporated into LNO primary particles at the secondary particle surface as a function of distance from the surface to the particle interior, the presence of the dopants is evidenced by the STEM-EDS spectrum in the inset. The distribution of (b) Mg, (e) Al and (h) Ti incorporated into LNO primary particles residing inside the secondary particles as a function of distance from the surface to the particle interior, the presence of the dopants is also evidenced by the STEM-EDS spectrum in the inset. STEM-HAADF images of (c) MgO-LNO, (f) Al₂O₃-LNO and (i) TiO₂-LNO taken at primary particle surfaces. HR-TEM images of cycled MgO-LNO and Al₂O₃-LNO are also shown in the inset of (c) and (f), respectively.

Figure IX.1.3 (a), (d), and (g), show the distribution of Mg, Al, and Ti, respectively, found at surfaces of primary particles that make up the secondary particle surface. Figure IX.1.3(b), (e), and (h), show the corresponding distributions measured at surfaces of primary particles that were found within the secondary particle. These preliminary results show that Al is the most uniformly distributed of the metals while Mg has the lowest amount of bulk incorporation. ²⁷Al nuclear magnetic resonance (NMR) spectroscopy showed that upon 600°C annealing of the Al₂O₃ film, Al begins to diffuse into the structure and form some Al environments similar to Al environments in bulk-doped samples. ⁶Li NMR showed signatures in agreement

with this finding, Figure IX.1.4(a), suggesting only limited bulk Al incorporation, preserving core Li environments within the LiNiO_2 . Electrochemical cycling of the Al_2O_3 -coated oxides, as deposited and after 600°C annealing, is shown in Figure IX.1.4(b). While the pristine LiNiO_2 cycles remarkably well, the Al_2O_3 treatments had the effect of moderately increasing first cycle charge capacities. Furthermore, the first-cycle efficiency was increased slightly from $\sim 97\%$ for the uncoated and as-coated sample to $\sim 98\%$ for the $\text{Al}_2\text{O}_3/600^\circ\text{C}$ sample resulting overall in more cycling capacity for the coated samples, with the $\text{Al}_2\text{O}_3/600^\circ\text{C}$ having a slight advantage. In addition, although the rates of capacity fade appear similar across the samples, the Al_2O_3 -treated cathodes may have a long-term advantage with respect to stability. The 600°C treated electrode delivers ~ 220 mAh/g, $\sim 91\%$ capacity retention relative to the first C/3 discharge, after 100 cycles. Testing and characterization for this sample set is ongoing.

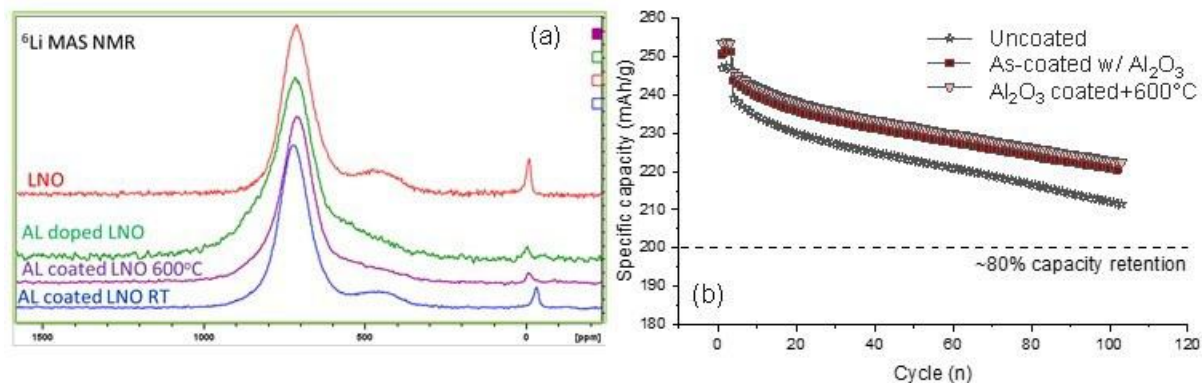


Figure IX.1.4 (a) ^6Li NMR of LiNiO_2 , LiNiO_2 as-coated w/ Al_2O_3 , and Al_2O_3 -coated and annealed at 600°C . Included is a bulk-doped Al-containing LiNiO_2 for reference (green). Cells were cycled using Li metal anodes between 4.3–2.8 V, 3 formation cycles at C/10 ($1\text{C}=200\text{mA/g}$), ageing cycles at C/10 charge, C/3 discharge.

As alternatives to Ni-rich cathodes, this program has also been pursuing lower Ni content cathodes that contain more Mn and zero Co. Previous reports have shown that NMC-622 performance can be obtained with layered cathodes utilizing just 5% or less Co, $\sim 35\%$ Mn, and $\sim 60\%$ Ni.¹ In an effort to eliminate Co and further reduce Ni content, a baseline Li- and Mn-rich (LMR) $0.3\text{Li}_2\text{MnO}_3 \cdot 0.7\text{LiMn}_{0.5}\text{Ni}_{0.5}\text{O}_2$ composite cathode was adopted for study. As a first step, an understanding of how to realize good particle morphologies and tap densities using hydroxide precursors was initiated. Hydroxides and carbonates are common precursors for cathode active materials where hydroxides are often favored. However, a clear understanding of the advantages, disadvantages, and control of reaction parameters, for hydroxides vs carbonates, that influence final particles architectures is lacking for Mn-rich chemistries. Gaining a deeper understanding of these parameters is critical in that primary and secondary particle morphologies can have significant effects on particle and electrode-level performance, especially for LMRs.^{2,3}

Studies have been initiated on hydroxide production through synthesis of $\text{Mn}_{0.65}\text{Ni}_{0.35}(\text{OH})_2$ precursors by co-precipitation using a continuous stirred-tank reactor (CSTR). Various parameters are being studied such as pH, ammonia content, and temperature, among others. Figure IX.1.5 shows images of precursors under different reaction conditions. Calcination/lithiation studies showed that high tap densities (~ 2.3 g/cc) could be obtained. Interestingly, while charge capacities were as expected (~ 280 mAh/g, 4.6 V vs. Li/Li^+ , 30°C), discharge capacities were low (~ 225 mAh/g). This is in contrast to what was observed for the same Mn-rich particles made from carbonate precursors (not shown, see ref. 3). A detailed study is now ongoing to model and characterize fundamental differences in hydroxide vs carbonate co-precipitation of Mn-rich compositions and the influence on electrode-level performance. Such detailed understanding will be essential to controlling not only morphologies, but also compositions as reaction conditions change (e.g., dopant profiles).

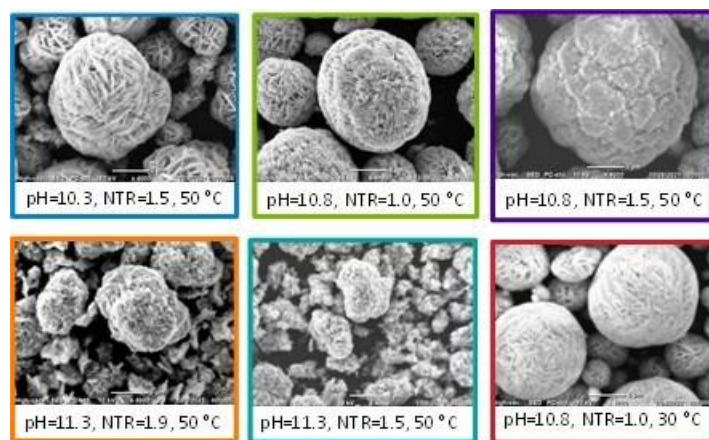


Figure IX.1.5 Scanning electron microscopy images of $\text{Mn}_{0.65}\text{Ni}_{0.35}(\text{OH})_2$ precursors synthesized by co-precipitation using a continuous stirred-tank reactor (CSTR), with varying parameters pH, temperature, and NH_3 :transition metal ratios in solution (NTR).

Related to synthetic control of Mn-rich cathodes is the ability to control, and subsequently understand, the effects of dopants placed at specific sites on important properties. For example, Mn sites in the Li/Mn rich, Li_2MnO_3 component of LMRs may play a particularly important role in dopant design. One critical and unique property of LMRs that is governed by Li/Mn rich domains is the low-SOC impedance.³ The low SOC impedance as well as electronic conductivity are being systematically evaluated as a function of dopant selection and site occupancy in the baseline composition noted above. Understanding the dopant local atomic and electronic structure is of paramount importance to help develop robust structure-property-function relationships.

As the first system of study, Sn-doped cathode materials with the chemical formula of $0.3\text{Li}_2[\text{Mn}_{1-x}\text{Sn}_x]\text{O}_3 \bullet 0.7\text{LiMn}_{0.5}\text{Ni}_{0.5}\text{O}_2$ (in composite notation), with $x = 0.01$ and 0.05 have been prepared and are currently being investigated within the consortium. Taking advantage of the element specificity as well as the sensitivity of X-ray Absorption Spectroscopy (XAS) to dilute elements, we have investigated the local environment of Sn-doped materials. We seek to understand the local structure of Sn dopants in LMRs materials and compare it with that seen in the Sn-doped parent phases ($\text{Li}_2[\text{Mn}_{1-x}\text{Sn}_x]\text{O}_3$ and $\text{Li}[\text{Mn}_{1-x}\text{Sn}_x]_{0.5}\text{Ni}_{0.5}\text{O}_2$).

Sn K-edge XAS measurements for the doped materials were carried out using fluorescence mode, and the standard Li_2SnO_3 was measured in transmission mode. Figure IX.1.6 shows the Fourier transform (FT) of the EXAFS data and the corresponding fits to the data of Sn in Li_2SnO_3 , Sn-doped Li_2MnO_3 , and Sn-doped $\text{LiMn}_{0.5}\text{Ni}_{0.5}\text{O}_2$ materials. The fits performed account for the structural information encoded in the first two peaks of the FT, corresponding to the Sn-O and the Sn-metal environment. Structural parameters extracted from the fits are summarized in Table IX.1. The local structure of Sn in Li_2SnO_3 (monoclinic, C2/c space group) consists of 6 Sn-O correlations at ~ 2.07 Å in the first shell and 3 Sn-Sn correlations at ~ 3.06 Å in the second shell. The 3 Sn-Li correlations also present in the second shell of the honeycomb layer are not perceptible to EXAFS due to the very weak back-scattering amplitude of lithium. To within the accuracy of the EXAFS data, all the Sn-doped materials are octahedrally coordinated to oxygen at a correlation distance of ~ 2.05 Å. This distance is comparable to the $\text{Sn}^{4+}\text{-O}$ bond distance seen in the Li_2SnO_3 standard. The Sn-TM (TM: Mn, Ni) correlation distance in the second shell is longer by ~ 0.10 Å when compared to the TM-TM correlation distance found in the host lattices. For instance, the Mn-Mn correlation distance in Li_2MnO_3 is ~ 2.85 Å; however, a significantly expanded Sn-TM correlation distance of ~ 2.94 Å is seen in the Sn doped Li_2MnO_3 . Similarly, the TM-TM distance in $\text{LiMn}_{0.5}\text{Ni}_{0.5}\text{O}_2$ is ~ 2.89 Å, whilst the corresponding Sn-TM correlation distance is expanded to ~ 2.99 Å in the Sn-doped $\text{Li}[\text{Mn}_{1-x}\text{Sn}_x]_{0.5}\text{Ni}_{0.5}\text{O}_2$ material.

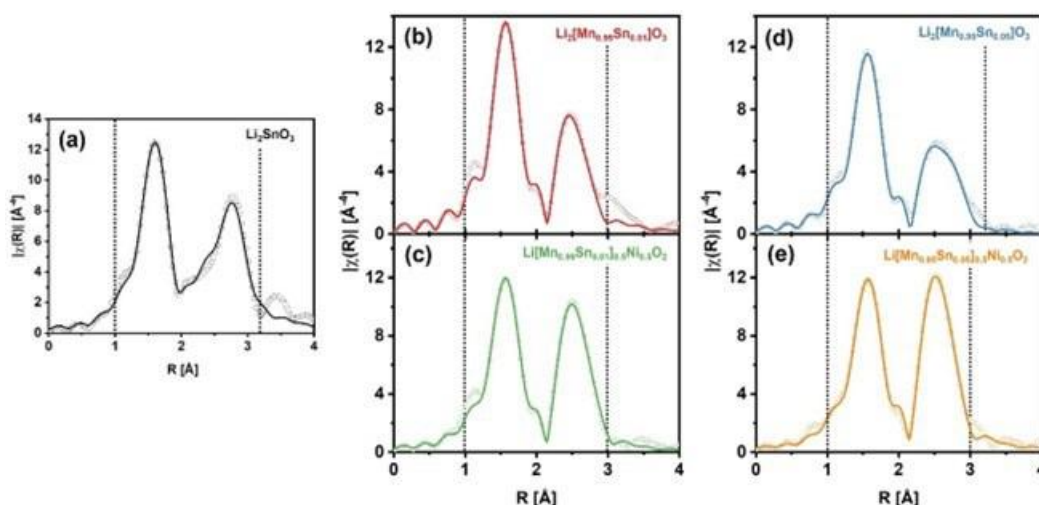


Figure IX.1.6 Fourier transform of the Sn K-edge EXAFS data for the parent phases of the Sn-doped materials: (a) Li_2SnO_3 ; (b) $\text{Li}_2[\text{Mn}_{0.99}\text{Sn}_{0.01}]\text{O}_3$; (c) $\text{Li}[\text{Mn}_{0.99}\text{Sn}_{0.01}]_{0.5}\text{Ni}_{0.5}\text{O}_2$; (d) $\text{Li}_2[\text{Mn}_{0.95}\text{Sn}_{0.05}]\text{O}_3$; and (e) $\text{Li}[\text{Mn}_{0.95}\text{Sn}_{0.05}]_{0.5}\text{Ni}_{0.5}\text{O}_2$, presented as k^3 -weighted. The circle, solid line, and dash line in each graph represent the raw data, fit, and range of fit respectively.

Interestingly, inclusion of Sn-O and Sn-TM scattering paths was found to be sufficient to adequately fit the EXAFS of the 1% Sn-doped Li_2MnO_3 material within R-range of 1 – 3 Å. The presence of ~2.6 Sn-Mn correlations is consistent with Sn randomly substituting for manganese. However, that was not the case for the corresponding 5% counterpart for which the inclusion of an additional Sn-Sn correlation was deemed essential. This revised model accurately describes the data of the 5% Sn-doped Li_2MnO_3 sample, with Sn-Mn and Sn-Sn correlations contributing in a 2:1 ratio at 2.93 Å and 3.08 Å, respectively. This finding reveals that when the dopant level is increased from 1 to 5%, the Sn doesn't randomly distribute in manganese sites. There is a clear tendency for the formation of Sn-Sn correlations upon increase in the dopant level. We note also that the Sn-Sn correlation distance is comparable to that seen in Li_2SnO_3 . In strong contrast to the 5% Sn-doped Li_2MnO_3 sample, the Sn EXAFS of the $\text{Li}[\text{Mn}_{1-x}\text{Sn}_x]_{0.5}\text{Ni}_{0.5}\text{O}_2$ can be modeled with just Sn-TM correlations, for both $x=0.01$ and 0.05. This shows that the $\text{LiMn}_{0.5}\text{Ni}_{0.5}\text{O}_2$ material can accommodate Sn dopants up to $x=0.05$, without any detectable Sn-Sn local correlations.

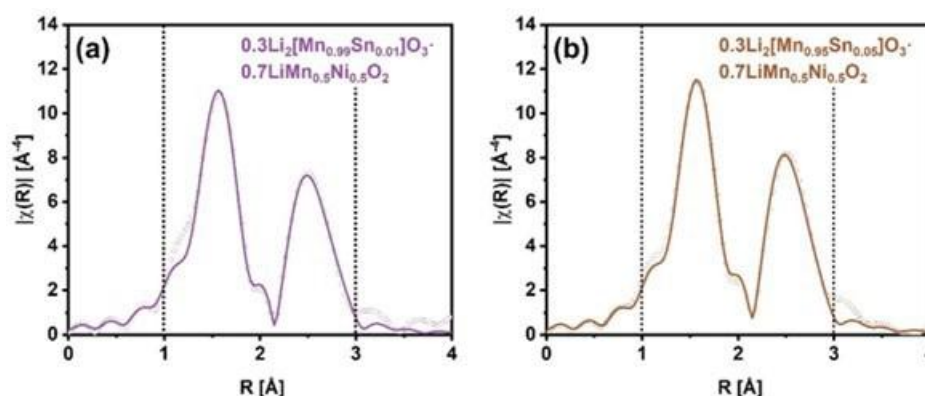


Figure IX.1.7 Fourier transform of the Sn K-edge EXAFS data for the Sn-doped cathode materials ($0.3\text{Li}_2[\text{Mn}_{1-x}\text{Sn}_x]\text{O}_3 \bullet 0.7\text{LiMn}_{0.5}\text{Ni}_{0.5}\text{O}_2$): (a) $x = 0.01$ and (b) $x = 0.05$, presented as k^3 -weighted. The circle, solid line, and dash line in each graph represent the raw data, fit, and range of fit respectively.

Figure IX.1.7 shows the FT of the EXAFS data and the corresponding fits to the data of Sn-doped LMR cathode materials. The Sn local environment in the $0.3\text{Li}_2[\text{Mn}_{1-x}\text{Sn}_x]\text{O}_3 \cdot 0.7\text{LiMn}_{0.5}\text{Ni}_{0.5}\text{O}_2$ ($x=0.01$ and $x=0.05$) samples are similar to that of the $\text{Li}[\text{Mn}_{1-x}\text{Sn}_x]_{0.5}\text{Ni}_{0.5}\text{O}_2$ materials – in particular, the second-shell Sn-TM correlation distance of $\sim 2.98 \text{ \AA}$ is similar (Table IX.1.1). Although this value may seem reasonable, a coordination number of $\sim 3.5 \pm 1$ for the Sn-TM is not, especially as the Sn-TM coordination number of the layered parent materials were fitted to $\sim 5 \pm 1$. We attribute the much-lowered coordination number observed to excess Li^+ ions (available in LMR) to clustering around Sn^{4+} .

Table IX.1.1 Summary of the EXAFS fitting parameters on the Sn-doped materials. The error in the last digit(s) is given in parentheses. CN = coordination number; R = correlation distance; σ^2 = disorder

Sample	Correlation	CN	R [\AA]	σ^2 [10^{-4} \AA^2]
Li_2SnO_3	Sn-O	6 (set)	2.07 (1)	29 (7)
	Sn-Sn	3 (set)	3.06 (1)	26 (5)
$\text{Li}_2[\text{Mn}_{0.99}\text{Sn}_{0.01}]\text{O}_3$	Sn-O	5.7 (5)	2.04 (1)	18 (10)
	Sn-Mn	2.6 (10)	2.94 (1)	24 (26)
$\text{Li}_2[\text{Mn}_{0.95}\text{Sn}_{0.05}]\text{O}_3$	Sn-O	6 (set)	2.05 (1)	29 (8)
	Sn-Mn	2.0 (4)	2.93 (2)	30 (16)
	Sn-Sn	1.0	3.08 (3)	30 (16)
$\text{Li}[\text{Mn}_{0.99}\text{Sn}_{0.01}]_{0.5}\text{Ni}_{0.5}\text{O}_2$	Sn-O	5.5 (5)	2.05 (1)	26 (11)
	Sn-Mn/Ni	4.8 (10)	2.99 (1)	42 (15)
$\text{Li}[\text{Mn}_{0.95}\text{Sn}_{0.05}]_{0.5}\text{Ni}_{0.5}\text{O}_2$	Sn-O	5.8 (4)	2.05 (1)	27 (9)
	Sn-Mn/Ni	5.2 (8)	2.99 (1)	34 (11)
$0.3\text{Li}_2[\text{Mn}_{0.99}\text{Sn}_{0.01}]\text{O}_3 \cdot 0.7\text{LiMn}_{0.5}\text{Ni}_{0.5}\text{O}_2$	Sn-O	5.6 (4)	2.05 (1)	33 (11)
	Sn-Mn/Ni	3.5 (10)	2.99 (1)	46 (21)
$0.3\text{Li}_2[\text{Mn}_{0.95}\text{Sn}_{0.05}]\text{O}_3 \cdot 0.7\text{LiMn}_{0.5}\text{Ni}_{0.5}\text{O}_2$	Sn-O	5.3 (4)	2.04 (1)	26 (9)
	Sn-Mn/Ni	3.4 (8)	2.98 (1)	35 (17)

Conclusions

Enabled by detailed studies and understanding of synthesis parameters, this program has realized extremely high-performing LiNiO_2 cathodes. These oxides can deliver over $\sim 220 \text{ mAh/g}$ for many cycles and perform better than most doped/modified LiNiO_2 reported in the literature. As a result, questions around the necessity of dopants, and what their true effects may be, have arisen. An initial study was conducted by incorporating 5% Co ($\text{LiNi}_{0.95}\text{Co}_{0.05}\text{O}_2$) and 5% Mn ($\text{LiNi}_{0.95}\text{Mn}_{0.05}\text{O}_2$) into a high-performing LiNiO_2 baseline. The most dramatic effect of both Co and Mn was to alleviate the extreme sensitivity of pure LiNiO_2 synthesis on temperature. Co roughly doubled the temperature range that effective calcination could be carried out while Mn allowed better performance at the highest temperatures. However, the addition of Co and Mn did not result in noticeably enhanced performance over pure LiNiO_2 under the electrochemical cycling conditions tested. These results imply that reports of enhanced performance of Co/Mn doped LiNiO_2 stem, at least in part, to the more facile synthesis (less control required) offered by incorporating these elements. Other elements of interest (e.g., Al, Ti, Mg) are also being studied with respect to both dopant and coating applications.

In addition to Ni-rich cathodes, this program has also studied ‘low Ni’, Co-free oxides with higher Mn contents as more sustainable alternatives. These cathodes rely on a high degree of synthetic control and a deep understanding of synthesis-property relationships for optimized performance. As such, detailed studies aimed at gaining new insights into co-precipitation reaction parameters and their influence on final cathode product properties have been initiated and are ongoing.

Likewise, understanding dopant control (i.e., site selectivity) and the associated influence on performance is key to advancing Mn-rich cathodes. Synchrotron spectroscopy studies, utilizing element-specific X-ray absorption, have revealed that Sn dopants can be incorporated into the lattice sites of Li- and Mn-rich materials, with a strong tendency for some of the excess lithium to be clustered around Sn. Additional spectroscopic characterization, as well as electrochemical studies, are ongoing to elucidate the influence of Sn in these compositions.

Key Publications

1. Lianfeng Zou, Peiyuan Gao, Haiping Jia, Xia Cao, Haiping Wu, Hui Wang, Wengao Zhao, Bethany E. Matthews, Zhijie Xu, Xiaolin Li, Ji-Guang Zhang, Wu Xu, and Chongmin Wang, “Non-sacrificial Additive for Tuning the Cathode-Electrolyte Interphase of Lithium-Ion Batteries” *ACS Appl. Mater. Interfaces*, 14 (2022), 4111–4118.
2. Jason R. Croy, “U.S. DOE-VTO Focus on Transition-Metal Oxide Cathodes for Transportation Applications” US UK Workshop on Energy Storage Research Collaboration: Cathode Materials and Recycling, Royal Institution, London, July 27, 2022 – *Invited*
3. Mahalingam Balasubramanian, “Advanced Spectroscopy Studies of Battery Materials” US-UK Workshop on Energy Storage Research Collaboration: Cathode Materials and Recycling, Royal Institution, London, July 27, 2022 – *Invited*
4. Jason R. Croy, “Enabling Sustainable Materials for Next-Gen Cathodes: R&D At Argonne National Laboratory” International Battery Seminar and Exhibit, Orlando, FL, March 30, 2022 – *Invited*
5. Eungje Lee, Jihyeon Gim, Jinhyup Han, Ozgenur Kahvecioglu, Shankar Aryal, Chongmin Wang, Lianfeng Zhou, Fulya Dogan, Boyu Shi, Juan Garcia, Hakim Iddir and Jason R. Croy “High-Performance LiNiO₂: A New Baseline for State-of-the-Art Ni-Rich Cathodes” The 242nd Electrochemical Society Meeting, October 9, 2022 - October 13, 2022. – *Invited*
6. Eungje Lee, Jihyeon Gim, Jinhyup Han, Ozgenur Kahvecioglu, Chong-Min Wang, Peng Zuo, Fulya Dogan, Juan Garcia, Hakim Iddir and Jason R. Croy "Synthesis of high-performance LiNiO₂ and derivatives" 21st International Meeting on Lithium Batteries (IMLB 2022), Sydney AU, June 26, 2022 - July 1, 2022.
7. Jihyeon Gim, Jinhyup Han, Peng Zuo, Chongmin Wang, Fulya Dogan, Anil U. Mane, Seoung-Bum Son, Jeffrey W. Elam, Eungje Lee, Khalil Amine and Jason R. Croy, “Optimization of High Ni ($\geq 95\%$) Cathode Materials: Synthesis, Calcination & Modification” 21st International Meeting on Lithium Batteries (IMLB 2022), Sydney AU, June 26, 2022 - July 1, 2022.
8. Jihyeon Gim, Jinhyup Han, Ozgenur Kahvecioglu, Peng Zuo, Lianfeng Zou, Fulya Dogan, Anil U. Mane, Pragathi Darapaneni, Chongmin Wang, Jeffrey W. Elam, Eungje Lee, Khalil Amine, and Jason R. Croy “Performance optimization of high Ni ($\geq 90\%$) cathode materials: Synthesis & Modification” The 242nd Electrochemical Society Meeting, October 9, 2022 - October 13, 2022.

References

1. J.R. Croy, B.R. Long, M. Balasubramanian, *J. Power Sources*, 440 (2019) 227113.
2. Gutierrez, J.T. Kirner, M. Tamadoni Saray, M. Avdeev, L. Geng, R. Shahbazian Yassar, W. Lu, J.R. Croy, *J. Electrochem. Soc.*, 169 (2022) 020574.
3. J. Chen, A. Gutierrez, M. Tamadoni Saray, R. Shahbazian Yassar, M. Balasubramanian, Y. Wang, J.R. Croy, *J. Electrochem. Soc.*, 168 (2021) 080506.

Acknowledgements

Contributions from the following individuals are acknowledged: Jihyeon Gim, Eungje Lee, Jinhyup Han, Rajesh Pathak, Anil U. Mane, Jeffrey W. Elam, Peng Zuo, Chongmin Wang, Yan Qin, Wenquan Lu, Fulya Dogan, Anh Vu, Ozge Kahvecioglu, Chun Yuen Kwok, Mahalingam Balasubramanian, Subhadip Mallick, Arturo Gutierrez, and Jason R. Croy.

IX.2 Diagnostic Testing and Evaluation (ANL, ORNL, NREL, PNNL)

Daniel P. Abraham, Principal Investigator

Argonne National Laboratory
9700 South Cass Avenue
Lemont, IL 60439
E-mail: abraham@anl.gov

Tien Duong, DOE Technology Development Manager

U.S. Department of Energy
E-mail: Tien.Duong@ee.doe.gov

Start Date: October 1, 2018	End Date: September 30, 2022	
Project Funding (FY22): \$3,500,000	DOE share: \$3,500,000	Non-DOE share: \$0

Project Introduction

State-of-the-art lithium-ion batteries (LIBs) being developed for transportation applications contain a transition metal (TM) oxide cathode and a graphite anode; both serve as host-matrices to house lithium ions during battery operation. The cathode typically contains $\text{Li}_{1+x}\text{Ni}_a\text{Co}_b\text{Al}_c\text{O}_2$ (NCA) or $\text{Li}_{1+x}\text{Ni}_a\text{Mn}_b\text{Co}_c\text{O}_2$ (NMC) oxides, where $x \sim 0-0.05$ and $a+b+c = 1$. Both oxide chemistries contain Co, which is known to preserve the layered structure during lithium extraction/insertion reactions. However, the possibility of a global Co shortage and soaring costs has galvanized the LIB community to seek explore layered oxides with lower Co contents and eventually develop Co-free cathodes, while maintaining cell performance (energy/power densities), safety and cycle/calendar life. In past years, we have focused our efforts on nickel-dominant oxides based on LiNiO_2 , with minimal or zero cobalt content. In FY22, however, because of the high-price and volatility of nickel, we started examining oxide compositions that have more manganese and less nickel. These oxides include $\text{LiNi}_{0.5}\text{Mn}_{1.5}\text{O}_4$, the high-voltage spinel, which has the potential for delivering reasonably high-energy densities, while having a relatively low nickel content and zero cobalt content.

The goal of the diagnostic testing and evaluation team is to identify constituents and mechanisms responsible for cell performance, performance degradation and safety. Various diagnostic tools (electrochemical, physicochemical, mechanical, etc.) are used to characterize the behavior of materials (both active and inactive) contained in the electrodes and cells; this characterization may be conducted before, during, and after electrochemical cycling. Understanding the fundamental mechanisms allows the development of rational solutions to minimize performance degradation and thermal instability in the materials and electrodes, leading to safer and long-life and battery cells.

Objectives

- Explore causes of coating delamination observed in 5V spinel electrode and determine mitigation methods
- Examine capacity fade and impedance rise behavior of 5V spinel electrodes during aging in full cells
- Using analytical electron microscopy, correlate microstructural evolution in the 5V spinel material with the electrochemical changes observed during electrochemical cycling in full cells
- Identify electrolyte decomposition species associated with the transition metal dissolution in lithium-ion cells containing various layered oxide, spinel oxide and iron phosphate cathodes
- Determine sources of performance loss in LiNiO_2 /graphite cells cycled using a 4.2 V Upper Cutoff Voltage
- Investigate the cathode-electrolyte interfacial region formed during electrochemical cycling of LiNiO_2 and $\text{LiNi}_{0.9}\text{Mn}_{0.5}\text{Co}_{0.5}\text{O}_2$ materials with a Spectro-electrochemical cell designed and built for in-situ collection of ATR-FTIR spectra.

- Correlate (electro)chemical degradation of the electrolyte with gas evolution in lithium-ion cells using a combination of in-situ gas chromatography with flame ionization detection and in-situ ATR-FTIR.

Approach

The approach pursued to meet the above objectives is summarized in Figure IX.2.1. Promising oxides synthesized and evaluated by the cathode team are scaled-up (i.e. produced in larger quantities) at Argonne's MERF. Then oxide electrodes, fabricated at Argonne's CAMP, are tested in half (vs. Li) and full cell (vs. Graphite) configurations using standardized test protocols. Post-test characterization is conducted on electrodes harvested from the cycled cells in order to determine the mechanisms that degrade cell performance.

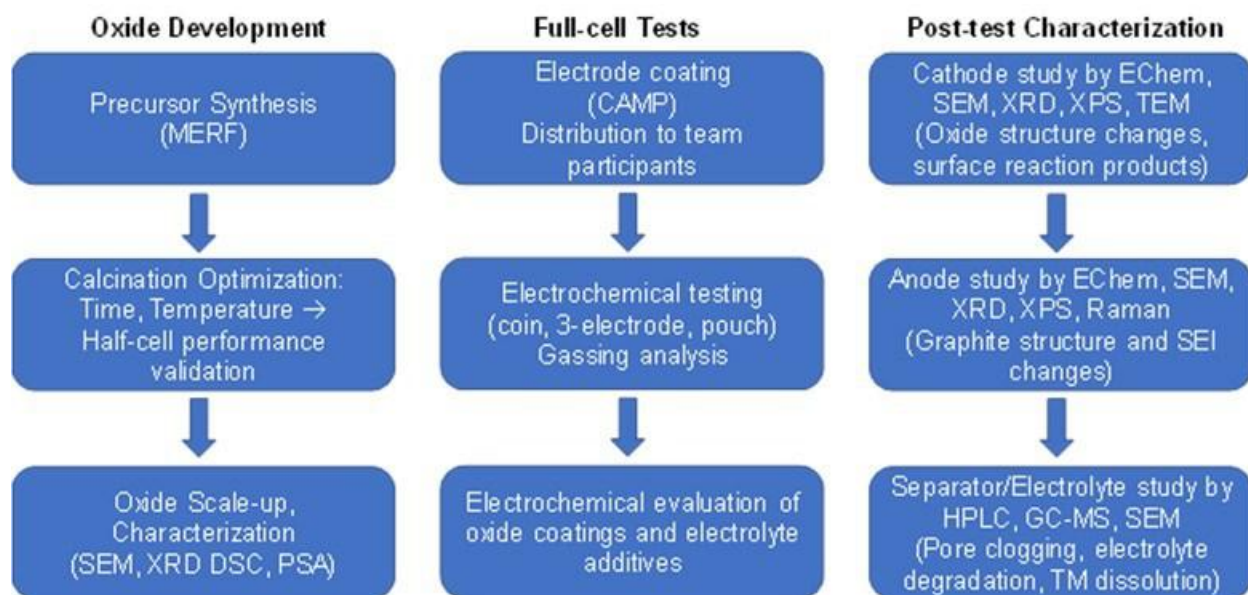


Figure IX.2.1 Diagnostic tests are conducted at various stages of the oxide development process

Results

Examining coating delamination issues of the high voltage spinel electrodes: Chen Liao et al. ANL

The high voltage spinel cathode, $\text{LiNi}_{0.5}\text{Mn}_{1.5}\text{O}_4$ (LNMO), has an average working voltage of 4.7 V, high-rate performance, faster diffusion properties, and is viewed as a promising cathode material for high-energy lithium-ion batteries. The absence of Co in these materials is also an advantage because of the controversies and geopolitical tensions associated with Co mining. However, the high working voltage of LNMO exceeds the stability of conventional electrolytes. The redox center in LNMO is Ni, which changes valence from Ni^{2+} to Ni^{4+} , while Mn remains in the 4+ state. Acid leaching at high voltages can cause Mn dissolution from the material; the degradation of LNMO//Gr is associated with transition metal dissolution, which cross over to the graphite anode and accelerate Li inventory loss. For example, decomposition of ethylene carbonate can lead to formation of glycolic acid and difluorophosphoric acid (HPO_2F_2), which can cause the coating delamination observed during cycling of cells with LNMO cathodes.

To explore the causes of delamination and determine mitigation methods, we conducted soak tests on various transition metal oxide (TMO) electrodes. These electrodes include LNMO, $\text{LiNi}_{0.4}\text{Mn}_{0.2}\text{Co}_{0.2}\text{O}_2$ (NMC422), $\text{LiNi}_{0.8}\text{Mn}_{0.1}\text{Co}_{0.1}\text{O}_2$ (NMC811) and $0.3\text{Li}_2\text{MnO}_3 \cdot 0.7\text{LiNi}_{0.5}\text{Mn}_{0.5}\text{O}_2$ (LMR-NM); the soak tests were conducted in Gen2 electrolyte (1.2 M LiPF_6 in ethylene carbonate (EC)/ethyl methyl carbonate (EMC), 3/7 w/w). The characterizations methods, NMR and SEM, were used to explore the stability of electrolytes, electrodes, and interfaces. Additionally, electrolytes formulated with different categories of additives were used in the soaking test to test their ability to hinder coating delamination. The molecular structures of these electrolyte additives are shown in Figure IX.2.2. The acronyms used are as follows: vinylboronic anhydride pyridine complex

(tVCBO), tris(trimethylsilyl) phosphite (TMSPi), lithium difluorooxalato borate (LiDFOB), prop-1-ene-1,3-sultone (PES), p-toluenesulfonyl isocyanate (PTSI), diethyl phenylphosphonite (DEPP), diphenyldimethoxysilane (DPDMS), succinic anhydride (SA), triphenylphosphate (TPP), and trimethylboroxine (TMB).

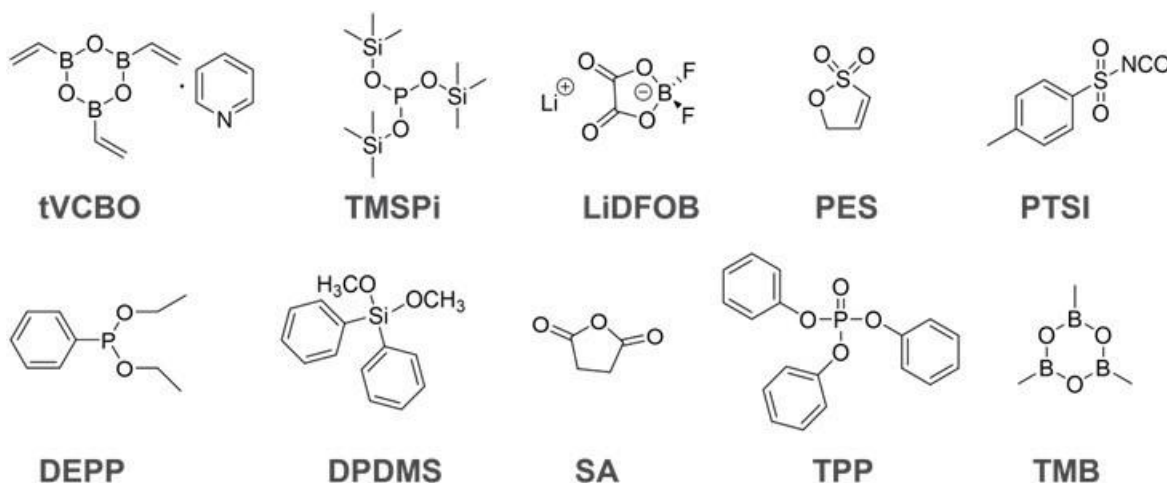
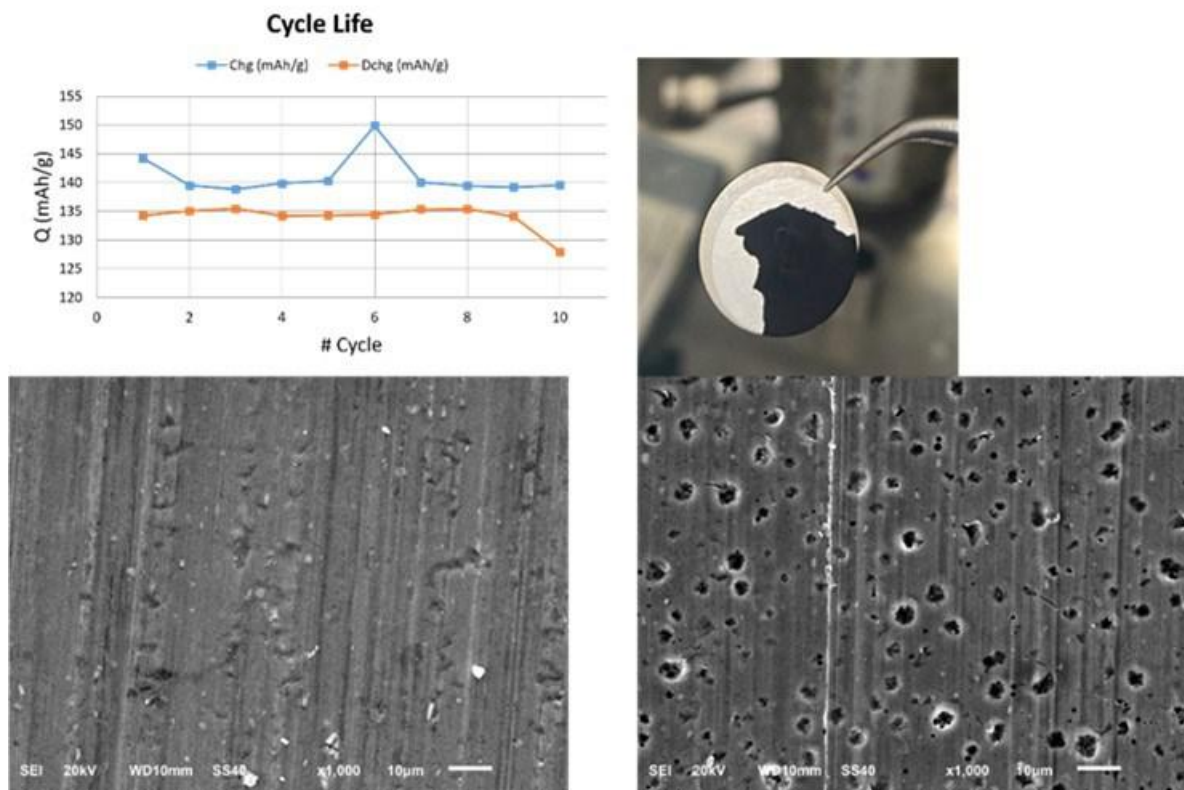


Figure IX.2.2 Molecular Structure of the additive compounds

A typical soaking experiment procedure, using Gen2 and LNMO as examples, was as follows: two LNMO electrodes (each 14 mm dia.) were added to vials with 2 ml Gen2 electrolyte. Two types of vials, glass and polyethylene (PE) were used for the electrolyte soaking. To prevent oxygen and moisture contamination, the electrolyte samples were prepared in glovebox filled with Ar and kept in sealed mason jars and stored in a 45°C oven for 3 months. Control experiments were carried out with Gen2 electrolyte in glass and polyethylene (PE) vials, in the absence of LNMO electrodes, to determine reactivity of the containers with the electrolyte. To prepare the additive-containing electrolytes, 3 wt% of the compounds was added to the Gen2 electrolyte and used immediately for the soaking experiments.

Observation of delamination

When the LNMO electrode is cycled with an upper cut-off voltage of 4.95 V vs Li using a commercial carbonate-based electrolyte, coating delamination issues are observed (Figure IX.2.3). Further examination of the delaminated electrode with SEM showed obvious etching dents on the aluminum foil, which were absent on the pristine electrode. These dents indicate corrosion of the aluminum current collector foil.



Mechanisms of electrolyte decomposition

The coating delamination apparently results from the formation of acidic electrolyte decomposition products that etch the Al current collector. To test this hypothesis, experiments were carried out with only the Gen 2 electrolyte, TMO electrodes soaked in Gen2 electrolyte, and LNMO electrodes soaked in Gen 2 electrolyte containing various additives. Results from the tests are as follows:

Gen 2 electrolyte stored in glass and polyethylene vials: Previous research has shown that the conventional carbonate electrolytes are not stable in glass vials; specifically, in addition to PF_6^- hydrolysis products (OPF_3 , $\text{OPF}_2\text{O}(\text{H})$, $\text{OPF}(\text{OH})_2$), secondary products formed through reactions with the carbonate solvents (OPF_2OMe , $\text{OPF}(\text{OMe})_2$, OPFOMeOH , and $\text{OPF}_2(\text{OCH}_2\text{CH}_2\text{OMe})$), are observed. The secondary products appear late, in severely decomposed electrolytes. Using two different vials (glass and PE), we demonstrated that the Gen2 electrolyte stored in PE mainly decomposes into $\text{OPF}_2(\text{OH})$ (Figure IX.2.4 a,b). When Gen2 is stored in a glass vial, the electrolyte decomposition products, $\text{OPF}_2(\text{OCH}_2\text{CH}_2\text{OMe})$ and OPF_2OMe , are dominant (Figure IX.2.4 c,d). In addition, fluoroborate species also appear in the glass vials. Clearly, more side reactions and decomposition happens when the electrolyte is stored in glass vials, which is caused by the accelerated decomposition in the presence of borosilicate. The ^{19}F NMR peaks at ~ -150 ppm and -155 ppm, assigned to $\text{OPF}_2(\text{OH})\text{-BF}_3$, and BF_4^- , confirm the participation of borosilicate glass in the side reactions.

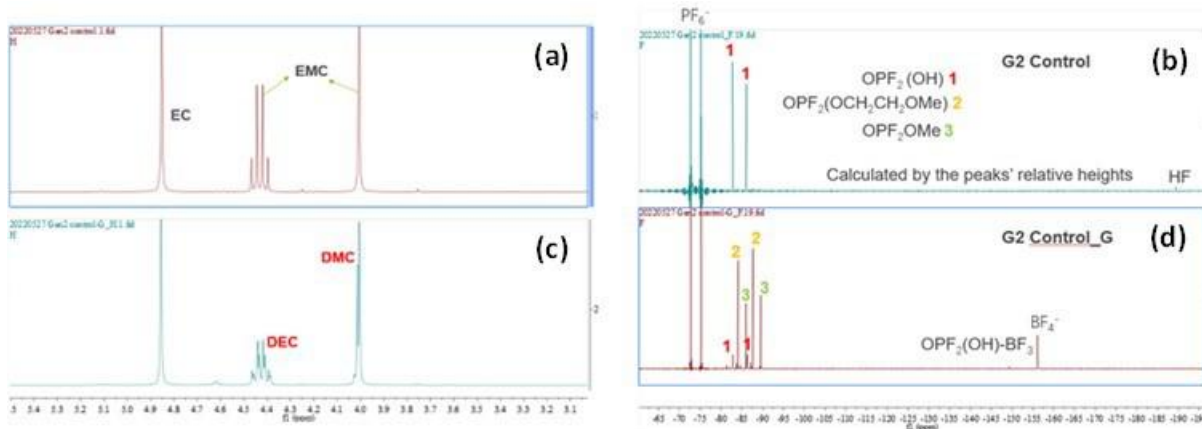


Figure IX.2.4 a) ^1H NMR of Gen2 soaked in PE. b) ^{19}F NMR of Gen2 soaked in PE. c) ^1H NMR of Gen2 soaked in Glass. d) ^{19}F NMR of Gen2 soaked in Glass. All electrolytes were stored at 45°C for 3 months.

Transition metal oxide electrodes soaked in Gen 2 electrolyte: Various transition metal oxide (TMO) electrodes were soaked in Gen2 electrolyte and the resulting solutions were examined at the end of test period. The ^1H NMR chemical shift was used as a qualitative measure of the Mn^{2+} in solution (Figure IX.2.5, green line): Mn^{2+} presence causes significant downfield shift (towards higher ppm) and broadened peak width. In the absence of Mn^{2+} , a mixture of EC/EMC has the following ^1H NMR pattern in the 1.4-5 ppm region: 4 peaks around 4.52 (s, 4H, $-\text{CH}_2$ from EC), 4.2 (q, 2H, $-\text{CH}_2-$ from EMC), 3.8 (s, 3H, $-\text{CH}_3$ from EMC), and 1.5 (s, 3H, $-\text{CH}_3$ from EMC). After the soaking experiment, dissolved diamagnetic Mn^{2+} causes loss of the coupling features, significant line broadening, and a downfield shift for all the peaks. For example, in the LMO soaked solution (Figure IX.2.5, green line), chemical shifts of the EC/EMC solvent shifted to the region between 2 and 7 ppm, with the same 4 peaks now broadened. Figure IX.2.5 provides a measure of electrode stability in Gen2 electrolyte. The ranking from least stable to the most stable is as follows: LMO > LNMO > NMC442 \approx LMR \approx NMC811.

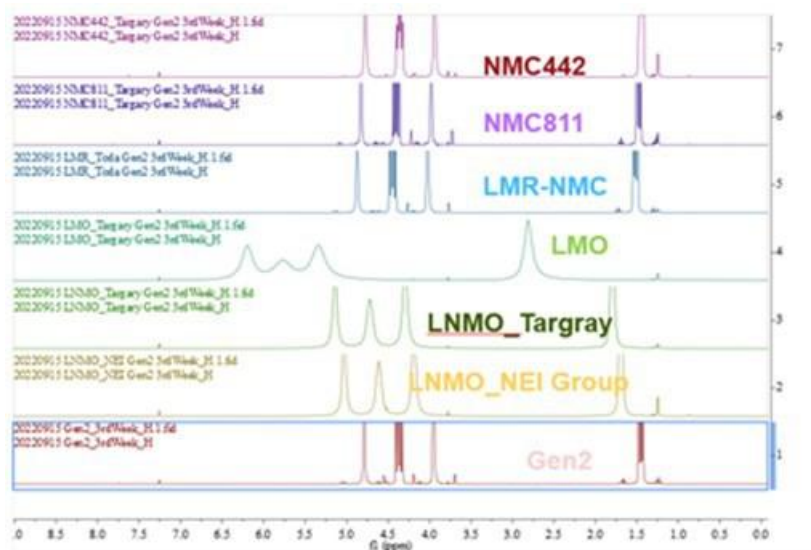


Figure IX.2.5 Broadening and shifts of ^1H NMR peaks, of electrolyte solutions that were used to soak various electrode laminates as indicated in the figure.

LNMO electrodes soaked in Gen 2 electrolyte containing various additives: Under the soaking conditions described above, LNMO coating delamination, as well as the electrolyte color change are shown in Table IX.2.1. Of the 10 additives tested shown in Figure IX.2.2, 7 prevented coating delamination during the soaking

of LNMO electrodes. Furthermore, as described earlier, we used the ^1H NMR shift to qualitatively monitor Mn dissolution amount. Both LiDFOB and PTSI appear promising for preventing LNMO delamination issues, especially LiDFOB. As shown in Figure IX.2.6, LiDFOB showed the least peak shift and broadening, with no transesterification or $\text{OPF}_2(\text{OH})$ presence. The PTSI electrolyte also showed minimal peak shifts/broadening, which corroborates with the observation of no color change compared to baseline. In contrast, for electrolytes containing dissolved Mn^{2+} , for example the TMB (# 10, top line) electrolyte, the ^1H NMR spectrum still features 4 peaks in the region of 4-7 ppm, but with loss of the coupling feature, significant broadness, and a downfield shift of ~ 3 ppm for all the peaks. Figure IX.2.6 shows that, other than LiDFOB and PTSI, all remaining 8 additives showed significant peak broadening and downfield chemical shifts. The following is in the order of increasing dissolved Mn^{2+} : 3# LiDFOB < 5# PTSI < 1# tVCBO < 10# TMB < 2# TMSPI < 8# SA \approx #7 DPDMS < #4 PES < #9 TPP < #6 DEPP. That is, Mn^{2+} dissolution is lowest in solutions with LiDFOB and highest in solutions with the DEPP additive.

Table IX.2.1 Soak test results for LNMO electrodes in Gen2 electrolyte solutions with various additives

Entry	Additives	Delamination	Color
1	tVCBO	Y	light brown
2	TMSPI	N	light yellow
3	LiDFOB	N	clear
4	PES	Y	brown
5	PTSI	N	clear
6	DEPP	N	dark brown
7	DPDMS	N	Brown
8	SA	N	purple
9	TPP	N	dark brown
10	TMB	Y	brown

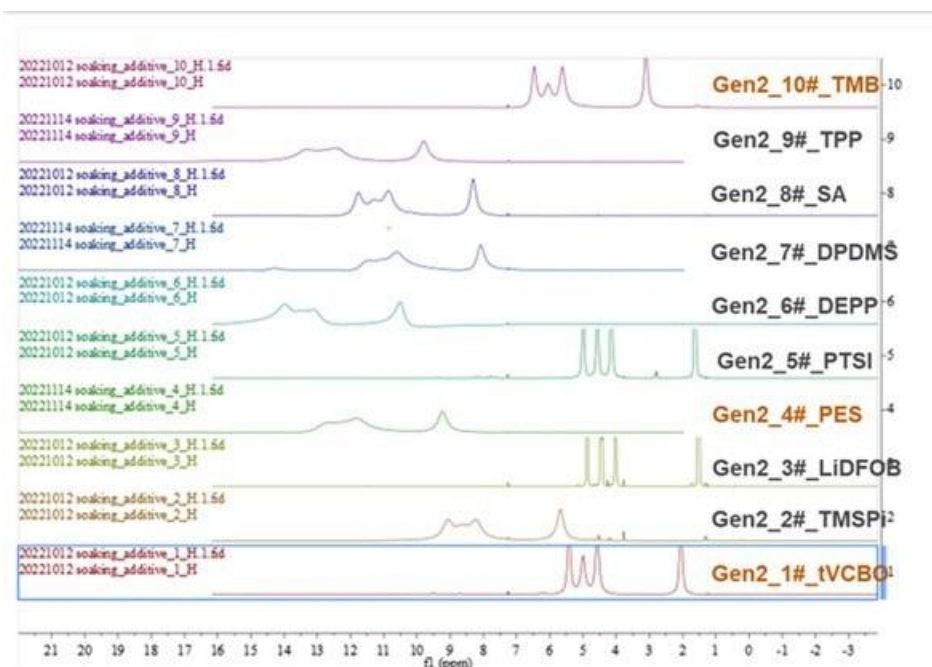


Figure IX.2.6 ^1H NMR profiles of the Gen2 electrolyte plus additive solutions, used to soak LNMO electrodes

Electrochemical characteristics of full cells with 5V spinel electrodes P. Badami et al., ANL

The 5V spinel oxide ($\text{LiMn}_{1.5}\text{Ni}_{0.5}\text{O}_4$) is a promising positive electrode (cathode) material for lithium-ion cells because it can deliver an energy density of ~ 650 Wh/kg and has the potential for superior rate capability because the spinel structure has 3-D ionic channels for Li^+ ion diffusion. Furthermore, it is reported to have better thermal stability and it is considered more sustainable than the typical NMC oxides because it does not contain cobalt. Hence, this spinel oxide was examined, as a Co-free alternative cathode, in a full configuration with a graphite negative electrode (anode).

In our cells, the positive electrode had a 66 μm thick coating, containing 90 wt% $\text{LiMn}_{1.5}\text{Ni}_{0.5}\text{O}_4$, 5.7 wt% conductive carbon, 0.05 wt% single walled carbon nanotubes (SWCNT) and 4.25 wt% PVdF binder, on a 20 mm thick Al current collector; the electrode had 40.9% porosity and a spinel loading of 13.7 mg/cm^2 . The negative electrode had a 47 μm thick coating, containing ~ 92 wt% graphite, 2 wt% conductive carbon and 6 wt% PVdF binder, on a 10 μm thick Cu current collector; the electrode had 37.5% porosity and a graphite loading of 5.9 mg/cm^2 . The electrodes were dried at 120°C before the coin cell assembly which was conducted in an Argon atmosphere glovebox. In addition to the electrodes, the cells contain Celgard 2320 separator and the 5V spinel baseline electrolyte (SVS-BL) which is 1.0 M lithium hexafluorophosphate salt (LiPF_6) in a 1:9 v/v solvent mixture of ethylene carbonate (EC) and ethyl methyl carbonate (EMC).

Cell testing was conducted with a Maccor cycler, with the cells placed in a constant temperature chamber at 30°C. The tests were conducted using a standard test protocol (see Figure IX.2.7) in the 3.8 – 4.7 V range. The protocol included five C/10 initial (formation) cycles followed by a series of C/3 aging cycles that included a 1h hold at the UCV (4.7 V) to accelerate aging. Reference performance tests were conducted after the formation cycles and periodically during cell aging; these tests included C/25 cycles to determine cell capacity and hybrid pulse power characterization (HPPC) tests to determine cell impedance. Electrochemical impedance spectroscopy (EIS) measurements were also conducted after the formation cycles and after the final aging cycle to obtain additional information on cell impedance.

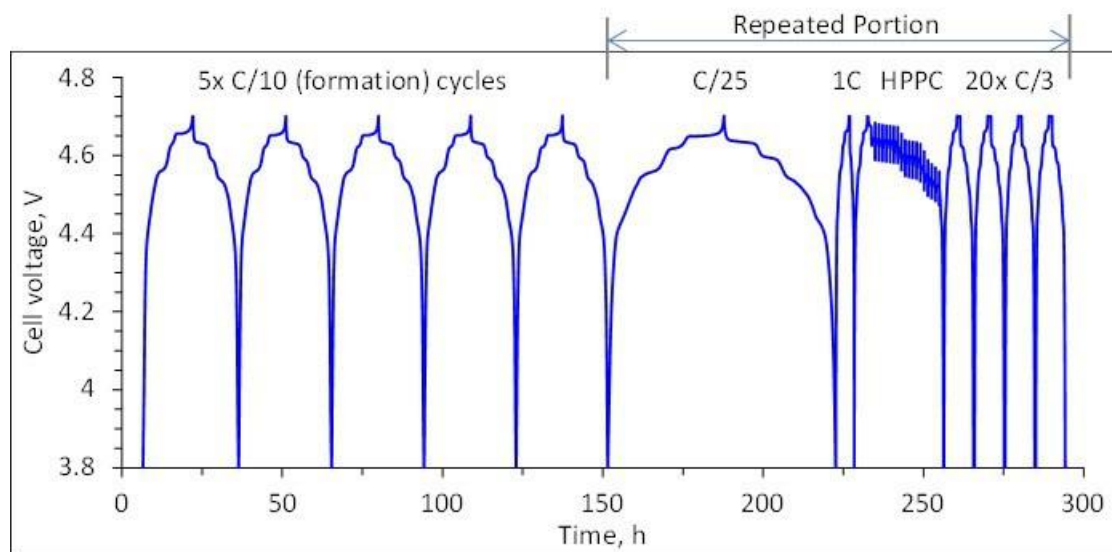


Figure IX.2.7 Protocol for electrochemical testing of the 5V/Gr cells

Representative discharge capacity data and voltage profiles from the 5V/Gr cells are shown in Figure IX.2.8. Cell capacity decreased during cycling, from ~ 118 mAh/g (C/25 rate) after the initial cycles to ~ 75 mAh/g after ~ 200 cycles, which is a capacity fade of $\sim 36\%$ (when measured at C/25 rate). Note that the capacities measured at C/25 and C/3 rates are similar, whereas the C/1 capacities are lower, especially after the accelerated aging, which points to impedance increase in the cell. The cell voltage profiles indicate that the

length of the upper plateau (at ~ 4.65 V) decreases after the accelerated aging; this decrease results from the electrode voltage shifts (slippage) that are a consequence of lithium inventory loss during aging.

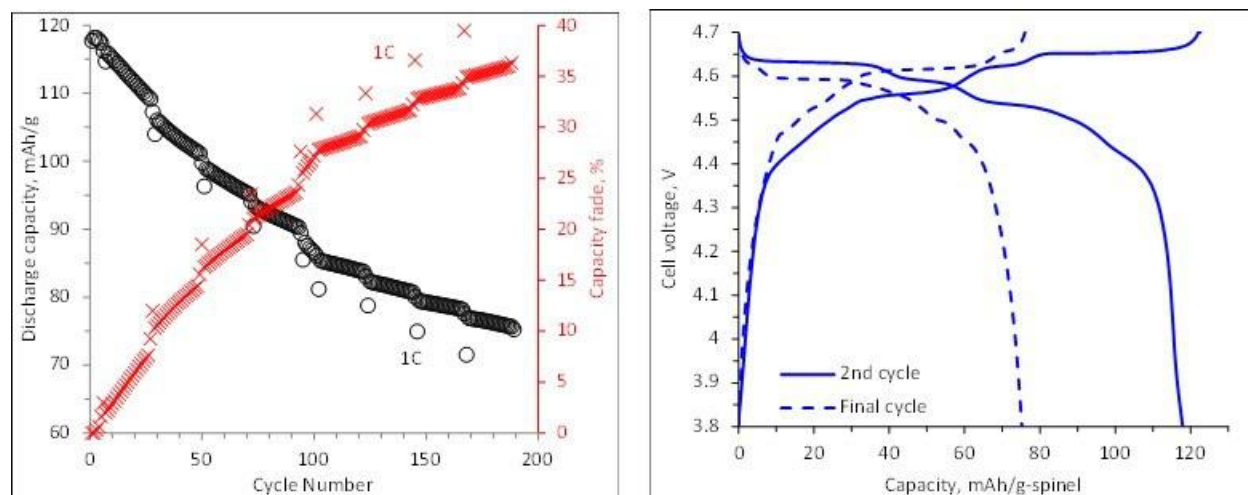


Figure IX.2.8 Representative data from 5V/Gr cells. The left panel shows discharge capacity (left axis) and capacity fade (right axis). The right panel shows voltage profiles (C/25 rate) during the second and final cycle.

The cell impedance increase that occurs during aging is shown in Figure IX.2.9: the left panel contains data from HPPC tests and the right panel contains data from EIS measurements. The HPPC data shows that the cell ASI at ~ 4.6 V increases from ~ 23 ohm-cm² to ~ 50 ohm-cm². The EIS data (right panel) indicates increases in both the mid- and high-frequency arcs. The mid-frequency arc likely arises from processes at both the positive electrode-electrolyte, and negative electrode-electrolyte interfaces. The high-frequency arc increase likely arises at the coating current collector interface of the positive electrode, as we noticed coating delamination during cell disassembly. Other experiments have indicated that this coating delamination is the result of Al current collector corrosion at the high-operating voltages.

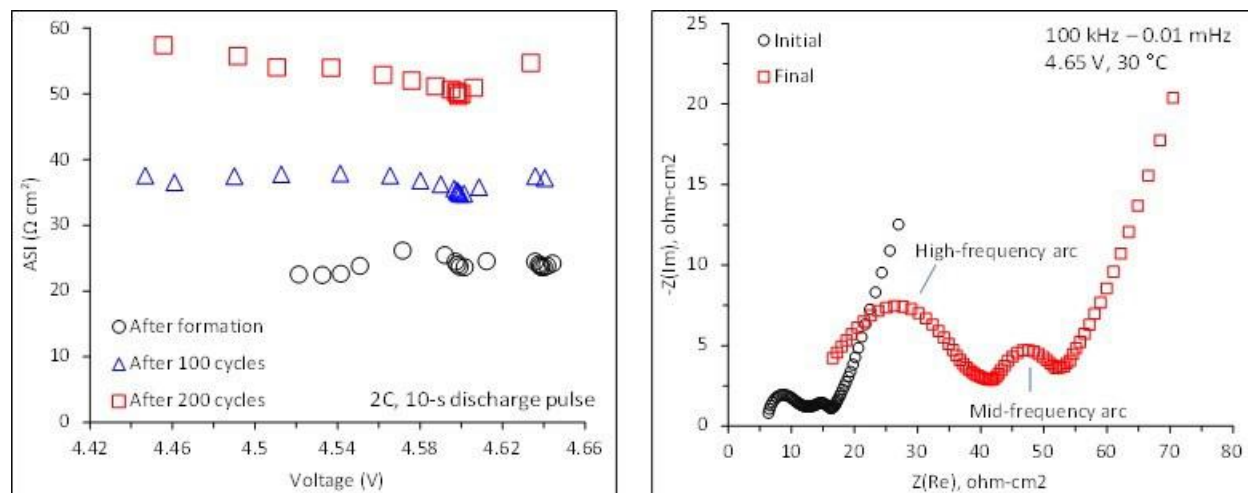


Figure IX.2.9 Impedance data from a 5V/Gr cell. The left panel shows Area Specific impedance (ASI) data as a function of cell voltage after the formation cycles, 100 cycles and 200 cycles from HPPC tests. The right panel contains EIS data after the initial cycles and after completion of the aging cycles.

Experiments are underway to delineate the mechanisms of cell performance degradation. These include experiments in 3-electrode cells to determine the relative contributions of the electrodes to cell impedance rise. We are also conducting detailed analysis of the harvested electrodes to determine the sources of the mid-frequency impedance rise. The cause of this rise could include the structural changes observed in the positive

electrode as shown in this report. We are also examining alternative current collectors to solve the “coating-delamination” problem. Results from these experiments will be detailed in subsequent reports.

Structural evolution of the 5V spinel after accelerated aging: Chongmin Wang and Peng Zuo, PNNL

Microstructural evolution in the cathode during electrochemical cycling, such as the formation of electrochemically inactive phases or active material loss, directly contributes to capacity loss of the cathode. The spinel phase $\text{LiNi}_{0.5}\text{Mn}_{1.5}\text{O}_4$, which is compositionally dominated by the earth abundant element Mn, is emerging as a promising cathode used in Li-ion batteries for high-voltage applications. However, the capacity fading mechanisms for this cathode is less understood. In order to correlate the microstructural evolution of the material with electrochemical cycling, scanning transmission electron microscopy- high-angle annular dark-field (STEM-HAADF) imaging as well as the affiliated spectroscopy techniques of STEM-X-ray energy dispersive spectroscopy (STEM-EDS) were employed to investigate structure changes down to the atomic level.

Upon battery cycling, various microstructural changes have been identified in the cycled $\text{LiNi}_{0.5}\text{Mn}_{1.5}\text{O}_4$, including phase transformations at the primary crystal surface, cathode-electrolyte interphase (CEI) formation, intra-granular cracking of primary particles, and void formation. These structural evolutions are illustrated in Figure IX.2.10, wherein we compare the microstructure of samples in the pristine (uncycled) state and after 100-cycles. The pristine sample (Figure IX.2.10a) features a well-formed spinel structure in the bulk, with a surface reconstruction region (~1.1 nm thick) showing either a Mn_3O_4 -like or rock-salt-like structure. The STEM-HAADF image clearly indicates that the octahedral sites are occupied by the heavy element Ni/Mn, while the tetrahedral sites are occupied by Li. The atomic arrangement matches well with the target phase $\text{LiNi}_{0.5}\text{Mn}_{1.5}\text{O}_4$.

After 100 cycles, the surface is reconstructed to a rock-salt structure of 1.4 nm in thickness and a Mn_3O_4 -like phase of 4.9 nm in thickness, followed by a region of cation inter-mixing with a thickness of 2.0 nm as illustrated in Figure IX.2.10e. The STEM-HAADF image intensity arises from the spinel tetrahedra sites and is associated with the replacement of Li by Ni/Mn in the Mn_3O_4 -like structure. It is apparent that the development of a thick surface reconstruction layer upon cycling correlates with the capacity fade displayed by the cell. A cathode electrolyte interface (CEI) layer containing fluorine and phosphorus, is observed on top of the cycled primary particles as shown in Figure IX.2.10f; the CEI is absent for the sample in the pristine state (Figure IX.2.10b).

Another significant structural feature of the cathode upon cycling is the intra-granular cracking as illustrated in Figure IX.2.10g, which does not exist in the pristine bulk lattice (Figure IX.2.10c); the true structural nature of the intra-granular cracks is not clear at this time. Based on elemental mapping, we notice that the crack tip is filled with signature elements of the electrolyte, indicating that during battery cycling, the electrolyte penetrates along the crack path. Often, the intra-granular cracking is attributed to mechanical effects, but the true origin of such cracking features remains unknown. It is apparent that the intra-granular cracking leads to material loss and exposes more surfaces to the electrolyte, both of which could result in capacity loss of the spinel cathode.

Void formation is another feature of the spinel structure as illustrated by the STEM-HAADF images in Figure IX.2.10d,h. Although pre-existing voids are observed in the pristine material, upon electrochemical cycling the density of voids increases. For the layered-oxide cathode, it has been reported that void formation is related to vacancy condensation, wherein the vacancies are introduced during material synthesis. Similarly, we postulate that the increased void density in the cycled spinel could also originate from vacancy condensation, where the vacancy is introduced during the material fabrication. In general, pre-existing vacancies and their condensation to form voids will not affect the materials capacity; however, formation of voids through vacancy condensation will change Li ion transport characteristics, thereby affecting electrochemical properties of the cathode.

Our multiscale microscopic study, down to the atomic-scales, reveals general characteristics of the structural and chemical evolution of the high-voltage spinel $\text{LiNi}_{0.5}\text{Mn}_{1.5}\text{O}_4$ during electrochemical cycling. These characteristics include surface reconstruction, CEI formation, intra-granular cracking and void formation, all of which directly correlate with electrochemical properties of the cathode. Detailed work is needed to understand the true origin of these observed structural and chemical features.

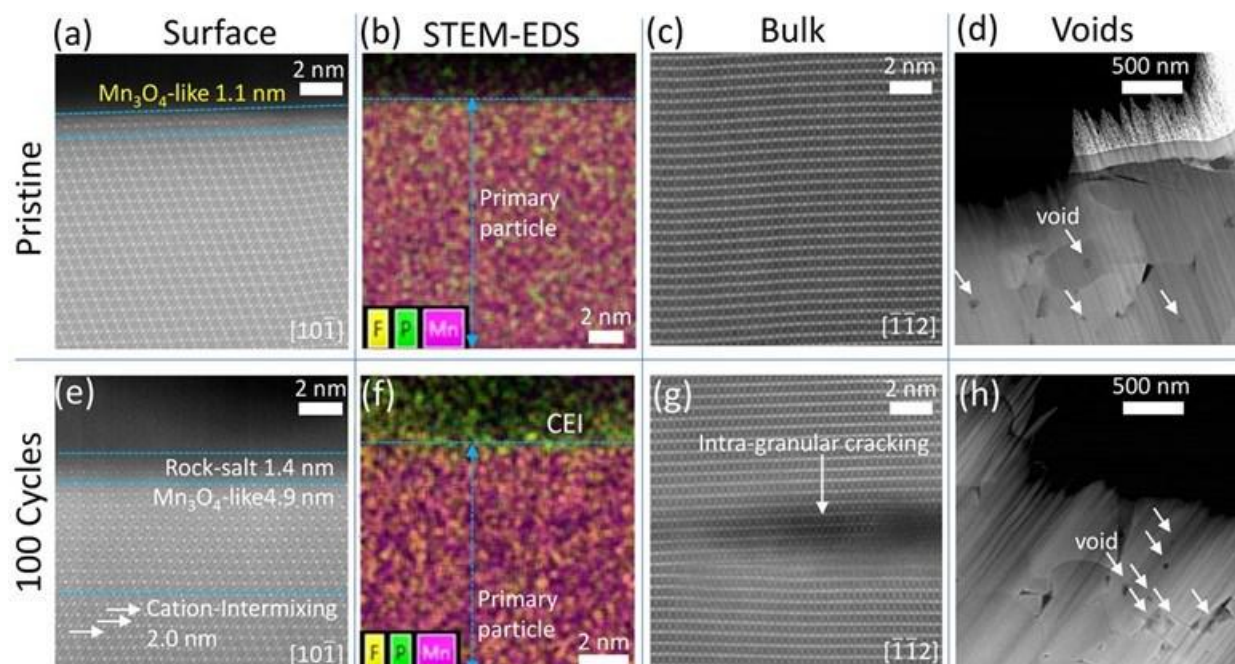


Figure IX.2.10 Structural evolution of the $\text{LiNi}_{0.5}\text{Mn}_{1.5}\text{O}_4$ cathode upon battery cycling. STEM-HAADF images at the primary particle surface of (a) the pristine sample and (e) cycled sample illustrates evolution of the surface reconstruction region into a Li-deficient (Mn_3O_4 -like) phase. The STEM-EDS data at the primary particle surface of (b) the pristine and (f) cycled sample indicate the formation of P- and F-containing CEI species upon battery cycling. The STEM-HAADF images of the bulk lattice of (c) the pristine and (g) cycled sample show intra-granular cracking in the cycled sample. The low-magnification STEM-HAADF images of (d) the pristine and (h) cycled sample indicate increased void density upon battery cycling.

Identifying transition metal containing ion species in the electrolyte: Seoung-Bum Son et al., ANL

Lithium-ion batteries make use of a variety of cathode materials depending on the application, each with their distinct pros and cons. For example, a LiFePO_4 cathode is suited for high-power uses due to their low operating voltage and fast discharge kinetics, whereas $\text{LiNi}_x\text{Mn}_y\text{Co}_z\text{O}_2$ cathodes are better suited for energy intensive applications. Commonly, cathode materials all are susceptible to transition metal dissolution (or leaching), resulting in degraded battery performance and life due to deposition of these elements on the negative electrode. Although there have been numerous studies to identify the underlying leaching mechanisms, the precise chemistry of the species resulting in metal leaching remains elusive. The main objective of the study is to identify electrolyte decomposition species associated with the transition metal dissolution in the lithium-ion battery system and contribute to developing advanced lithium-ion battery systems.

We studied the reaction of various delithiated cathode materials in pure solvent systems (as a static, model system), in order to isolate the underlying chemistry relative to LiPF_6 and its decomposition products. Our cathodes comprised LiFePO_4 (LFP), LiCoO_2 (LCO), LiMn_2O_4 (LMO), $\text{LiNi}_{0.8}\text{Mn}_{0.1}\text{Co}_{0.1}\text{O}_2$ (NMC811) and LiNiO_2 (LNO); these were investigated in contact with ethylene carbonate (EC)/ethyl methyl carbonate (EMC) solvent using Electrospray Ionization-Mass spectroscopy (ESI-MS) and elemental analysis to elucidate the dissolved species present in the solution.

The cathode materials were chemically delithiated by reaction with NO_2BF_4 in dry acetonitrile at room temperature and under argon (Ar) gas. The post-delithiation elemental composition of the materials was

determined by inductively coupled plasma mass spectrometer (ICP-MS). The LFP material was oxidized to FePO_4 , equivalent to 100% state of charge (SOC), whereas the other materials retained 40-50% lithium content, representing 90-100% SOC, in a charged cell vs. graphite at 4.1 V. The LNO material was over-delithiated compared to what it would be in a practical cell. 100-120 mg of each delithiated material was placed in contact with 2 ml of EC/EMC (3:7, weight ratio) solvent at 50°C for 1 week. The process yielded about 1.5 mL of a pale colored liquid which was collected for ESI-MS analysis.

Our findings from the ESI-MS experiment are summarized in Table IX.2.2. Species such as $\text{Li}(\text{EC})^+$ can easily be rationalized as the result of a lithium leaching reaction and its subsequent coordination with a molecule of EC. The apparent concentration of these species varies with positive electrode material, from $\text{Li}(\text{EC})^+$ as the major constituent (as with LNO), to electrolyte degradation products as the major positively charged product (as with LFP). For some species, more than one proposed formula was found to meet the carbon stoichiometry and formula weight restrictions. These are included in Table IX.2.2 for the sake of completeness and to show the type of compounds that are possible. Furthermore, in Table IX.2.2, if the number of carbons was calculated from more than one observation, the standard deviation; if not, the standard deviation in the number of carbon atoms was assumed to be 10% of the reported value. Fewer species were found in the negatively charged ions, usually, only two or three. In general, the proposed formulae were solvated forms of simple or complex anions. All contained electrolyte compounds or fragments as one would expect from electrolyte degradation, such as ethoxy, methoxy, hydroxyl groups, and water.

Many differences are seen when we compare our results with those in the research literature. The primary source of this difference is the leachant used. Most reports in the literature use LiPF_6 or some other active material as part of the leachant, which can introduce additional reaction pathways, the products of which may dominate the ones seen here. The method used for mass spectrometry can affect the observations, as well. In publications where liquid chromatography and mass spectrometry were used, the mobile phase can be acidic and change the nature of the compounds observed. For example, if something as simple as $\text{LiOCH}_2\text{CH}_3$ were present in the analyte, the acidic mobile phase would change it to ethanol or to protonated ethanol ($\text{H}^+[\text{HOCH}_2\text{CH}_3]$). The unprotonated species would not be seen. The protonated species, in theory, would; its apparent mass is 47 Da. However, the lower mass limit of the mass spectrometer was set to 50 Da; hence the signal due to the species would not be observed. If formic acid were used in the mobile phase, the other reaction product, LiO_2CH ($m/e = 52$ Da), would be at the lower end of the mass region of interest. This peak may be lost in the other peaks present due to column bleed. In the present work, we used direct injection into the nebulizer of the mass spectrometer, eliminating the above artifacts.

The principles of hydrometallurgy usually include a corrosive agent, such as H^+ and OH^- , to explain the loss of metals from a corroding surface. The reaction system studied in this work did not contain an overt source of H^+ or OH^- . Examining the chemical species associated with the metals shows that water, hydroxy, and carbonate groups are present, presumably from the oxidation of the organic solvent. Since these species are present, it is not too hard to conceive of protons being present in the reaction mixture. These nascent protons and hydroxide groups are the likely active agents causing leaching of metals from the oxides. No other source of leaching agents would be needed. Interestingly, we noted that all transition metal-containing species were negatively charged. Given the expected electrolyte oxidation products and the coordinating ability of the metals, this was, in part, expected. However, with the evidence on hand, it is impossible to know which positive ion is associated with which negative ion. Also, it is not known if all transition metal-containing species were identified in the experiment. The mass spectrometer would detect only charged compounds, not neutral ones.

Table IX.2.2 Results based on the mass spectra of the liquid products

Observed m/e, Da	Number of Carbons	Empirical Formula	Calculated FW	Relative Amount Based on Peak Area*					Proposed Linear Formula
				LFP	LCO	LMO	LNO	NMC 811	
Positive ions									
95.0	3.0±0.6	[LiC ₃ H ₄ O ₃] ⁺	95.04	0.33	0.42	0.40	0.58	0.31	[Li(EC)] ⁺
111.1	3.6±0.9	[LiC ₄ H ₈ O ₃] ⁺	111.10	0.04	0.34	0.47	0.42	0.22	[Li(EMC)] ⁺
141.1	7.7	[LiC ₆ H ₁₄ O ₃] ⁺	141.16	0.08					[LiCH ₃ O(CH ₂ CH ₂ O) ₂ CH ₃] ⁺
183.1	4.6	[LiC ₆ H ₈ O ₆] ⁺	183.01		0.08	0.09			[Li(EC) ₂] ⁺
185.1	7.8±0.7	[LiC ₆ H ₁₀ O ₆] ⁺	185.08	0.55				0.43	[LiCH ₃ OC(=O)OCH ₂ CH ₂ OC(=O)OCH ₃] ⁺
		[LiC ₇ H ₁₄ O ₅] ⁺	185.13						[LiCH ₃ OC(=O)OCH ₂ CH 2OCH ₂ CH ₂ OCH ₃] ⁺
		[LiC ₈ H ₁₈ O ₄] ⁺	185.17						[LiCH ₃ O (CH ₂ CH ₂ O) ₃ CH ₃] ⁺
199.1	6.6±1.3	[LiC ₇ H ₁₂ O ₆] ⁺	199.20		0.07	0.07			[Li(EC)(EMC)] ⁺
215.1	4.0±3.2	[LiC ₈ H ₁₆ O ₆] ⁺	215.20		0.04			0.02	[Li(EMC) ₂] ⁺
288.3	10.1	[LiC ₉ H ₁₄ O ₁₀] ⁺	289.14		0.06				?
Negative ions									
180	2.3	[LiC ₂ H ₁₀ O ₅ Co] ⁻	179.97		0.79				[(C ₂ H ₅ O)Li(H ₂ O) (OH)3Co(II)] ⁻
279.8/2 80	4.0±0.8	[C ₅ H ₂₇ O ₁₂] ⁻	279.26	0.74		0.84		0.67	[(CH ₃ O)(EMC)(H ₂ O) ₈] ⁻
		[LiC ₄ H ₁₀ O ₁₀ Mn] ⁻	279.99						[MnLi(CO ₃)(EC)(H ₂ O) (OH) ₂] ⁻
		[LiC ₄ H ₂₂ O ₉ Ni] ⁻	279.85						[NiLi(CH ₃ O) ₄ (H ₂ O) ₅] ⁻
		[LiC ₄ H ₂₂ O ₉ Ni] ⁻	279.85						[NiLi(C ₂ H ₅ O) ₂ (H ₂ O) ₅ (OH) ₂] ⁻
566.2- 566.9	9.4±1.5	[LiNiC ₁₂ H ₅₂ O ₁₉] ⁻	566.18	0.26	0.21	0.16	0.19	0.29	[Ni(II)Li(C ₂ H ₅ O) ₄ (EMC) (H ₂ O) ₁₂] ⁻
		[LiMnC ₁₀ H ₃₉ O ₁₅] ⁻	566.40						[MnLi(C ₂ H ₅ O) ₃ (EMC) ₂ (H ₂ O) ₈ (OH)] ⁻
		[C ₁₂ H ₃₉ O ₂₄] ⁻	567.42						[(EMC) ₄ (H ₂ O) ₁₁ (OH)] ⁻
		[LiCoC ₁₀ H ₄₂ O ₂₁] ⁻	566.30						[CoLi(CH ₃ O) ₃ (EC)(EMC) (H ₂ O) ₁₁ (OH)] ⁻
863.7	21.9	[NiC ₂₄ H ₆₈ O ₂₈] ⁻	863.47					0.04	[Ni(III)(OCH ₃)(OCH ₂ CH ₃)(EC)(EMC) ₄ (H ₂ O) ₉] ⁻

Determining performance loss in LiNiO₂/Graphite Full cells: Adam Tornheim et al., ANL

The objective of this work was to evaluate the source of performance loss in LiNiO₂/graphite cells cycled using a 4.2 V Upper Cutoff Voltage (UCV). The LiNiO₂ cathode comprised 90 wt% LiNiO₂, 5 wt% C45 carbons, and 5 wt% PVdF binder. Initial discharge capacities were ~220 mAh/g; this value is limited by the loss of lithium inventory to the graphite electrode during the SEI formation process. Figure IX.2.11a shows that the cell capacity decreases continuously during cycling. After two of our 119-cycle accelerated-aging protocols, the C/10 capacity decreases by ~60 mAh/g and the “minimum” impedance (as measured by HPPC tests) increases by a factor of four, from ~24 Ωcm² to ~105 Ωcm² (Figure IX.2.11d); note that the coulombic efficiency (CE) remains relatively high (~99.8) during the cycling (Figure IX.2.11b).

Following one 119 cycle protocol, a cell was disassembled, and the harvested-cathode was combined with a fresh lithium anode and fresh electrolyte; this cell was cycled at a low (C/100) rate to evaluate the cathode capacity and voltage profile with minimal contributions from impedance. This ‘aged’ cathode voltage profile is compared to that of a cathode taken from a formed (~4 cycles) cell to evaluate the effect of aging on cathode capacities (Figure IX.2.12). While the aged cathode shows the same general profile as the formed cathode, the

gravimetric capacity has decreased from 249 mAh/g to 222 mAh/g. This loss of cathode capacity makes up roughly 2/3 of the capacity lost by the full cell during the test.

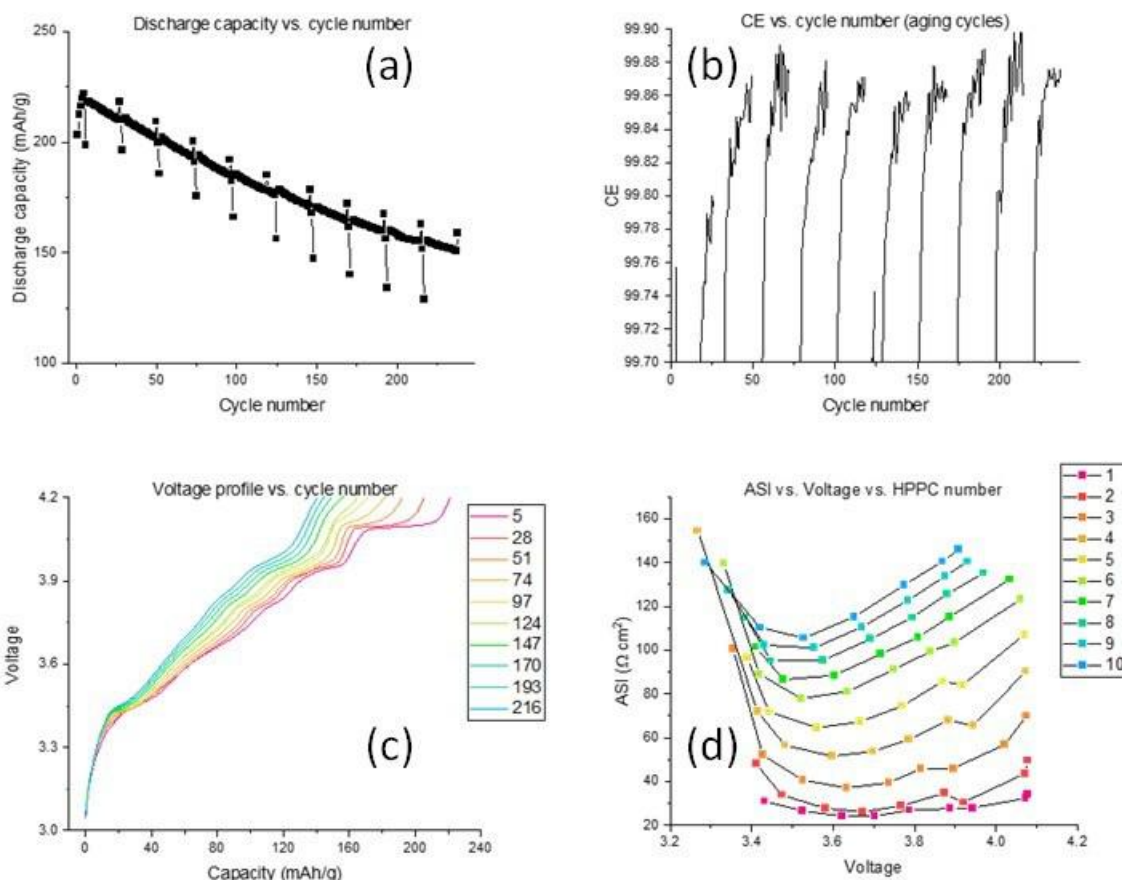


Figure IX.2.11 (a) Discharge capacity vs cycle number, (b) Coulombic efficiency vs. cycle number, (c) Voltage profiles vs. cycle number, and (d) ASI vs. HPPC number for $\text{LiNiO}_2/\text{graphite}$ cells.

In addition to the cathode gravimetric capacity, the harvested cathodes can provide information on the lithium inventory of the cell. As cells are cycled, electrolyte reduction reactions at the anode (such as those during the initial SEI formation) cause a loss in cyclable lithium inventory, which is one component of a full cell's lost capacity. The net loss of cyclable lithium inventory can be determined from the initial discharge of the extracted cathodes, as these cathode sites are available to be lithiated because the anode lacked sufficient lithium inventory to do so during the full cell discharge.

The initial discharge capacities of the formed and aged cathodes indicated net inventory losses of 16 and 26 mAh/g, respectively. These data indicate that for the $\text{LiNiO}_2/\text{Graphite}$ cell, the main source of capacity loss is active material loss; this conclusion is different from that of many other NMC/Gr cells for which electrolyte reduction, and subsequent lithium inventory losses to the SEI, are the major source of capacity loss. The stability of the graphite/electrolyte interface with LiNiO_2 cathodes is further supported by the high coulombic efficiency, which nears 99.87%, even for the C/3 cycles with holds at top-of-charge.

One additional observation is that our specific protocol used C/3 cycling with 3 h holds at top-of-charge, with the CCCV step allowing further delithiation than traditional galvanostatic cycling. From Figure IX.2.12 we can see that the voltage profile of the aged cathode is relatively unchanged, yet the C/10 full cell voltage profiles in Figure IX.2.11c show substantial shortening of the $\text{H2} \rightarrow \text{H3}$ plateau. Eventually, the increase in overpotential

during charge will cause the full-cell voltage to reach the UCV (4.2 V) before this transition is reached, which would cause loss in charging capacity. For cells cycled galvanostatically, the capacity retention would likely be worse because of the continuing impedance rise of the cell.

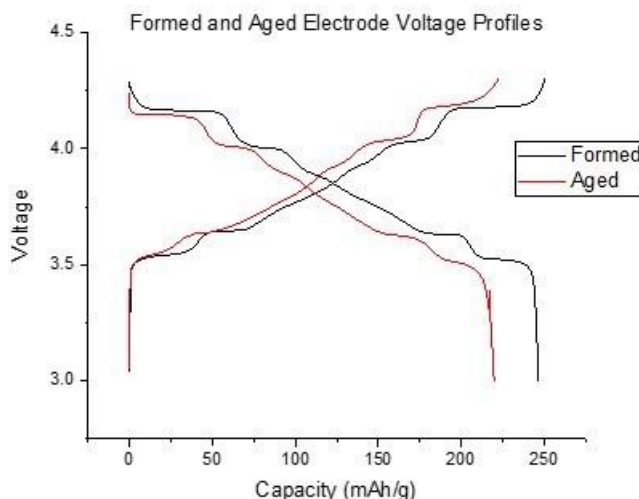


Figure IX.2.12 Voltage profiles from LiNiO_2/Li half-cells measured at 2 mA/g. The cathode from the 'Formed' profile was cycled for 4 C/10 cycles against a graphite anode. The cathode from the 'Aged' profile was subjected to the full 119 cycle protocol before aging.

In-situ multi-modal characterizations of low/no cobalt cathodes: Sang-Don Han et al., NREL

In prior reports, we have shown how in-situ ATR-FTIR can be used to investigate the cathode-electrolyte interfacial region during electrochemical cycling of a $\text{LiNi}_{0.6}\text{Mn}_{0.2}\text{Co}_{0.2}\text{O}_2$ (NMC622) and $\text{LiNi}_{0.9}\text{Mn}_{0.5}\text{Co}_{0.5}\text{O}_2$ (NMC9055) cathodes. We have now extended our studies to understand how the upper cutoff voltage (UCV) and the state of charge (SoC) and depth of discharge (DoD) during cycling affects electrode and electrolyte aging behaviors in/on the high-Ni cathodes, including LiNiO_2 (LNO as a reference) and NMC9055, to better understand how the transition metal redox chemistry and corresponding structure changes (e.g., local and long-range order) and the surface chemistry (e.g., electrode/electrolyte reactivity and transition metal dissolution and crosstalk) dictate the electrochemical performance. For these studies, a custom Spectro-electrochemical full cell was designed and built for in-situ collection of ATR-FTIR spectra while enabling reliable electrochemical battery cycling. In addition, using a combination of in-situ gas chromatography with flame ionization detection (GC-FID) and in-situ ATR-FTIR, (electro)chemical degradation of the electrolyte is correlated with gas evolution in the battery.

FTIR peak assignment library – transition metal complex formation

Increasing the cell operating voltage is one of the realistic strategies to extend the energy density, specifically for critical material free cathode materials including manganese (Mn)-rich oxides, but it is inevitably accompanied by a plethora of electrode degradation mechanisms that lead to rapid performance loss. Specifically, transition metal dissolution and crosstalk are detrimental factors causing capacity fade and battery failure, but their fundamental mechanisms were not well understood. We, thus, have explored transition metal complex formation on the anode and its effect on solid-electrolyte interphase (SEI) formation and evolution. We built upon initial measurements to refine FTIR peak assignment library with a systematic approach using simplified model systems. For example, Mn-based salts (e.g., manganese (ii) hexafluorophosphate and manganese (ii or iii) 2,4-pentanedionate (Mn(ii or iii)-PD)) in the solvent mixtures of ethylene carbonate (EC) and ethyl methyl carbonate (EMC) or a standard Gen 2 electrolyte [1.2 M lithium hexafluorophosphate (LiPF_6) in EC:EMC (3:7 wt.%)] were analyzed to deconvolute the complicated transition metal complex system. Focusing on the EC solvent molecule peak ($1125\text{--}1350\text{ cm}^{-1}$) shift based on Mn complex formation in the

EC/EMC solvent mixture (Figure IX.2.13a), there is not much difference between EC/EMC and 0.001 Mn(iii)-PD due to measurement challenges at small volumes. Both 0.001 Mn(ii)-PD and 0.005 Mn(ii)-PD shows almost the same peak position, whereas there is an apparent blue shift for 0.005 Mn(iii)-PD due to stretching of bond distances that bring about decrease of vibrational frequencies (i.e., lower frequency \rightarrow high wavenumber). Mn complex formation in the Gen 2 electrolyte and corresponding FTIR spectra change is similar to that of EC/EMC solvent mixture (Figure IX.2.13b).

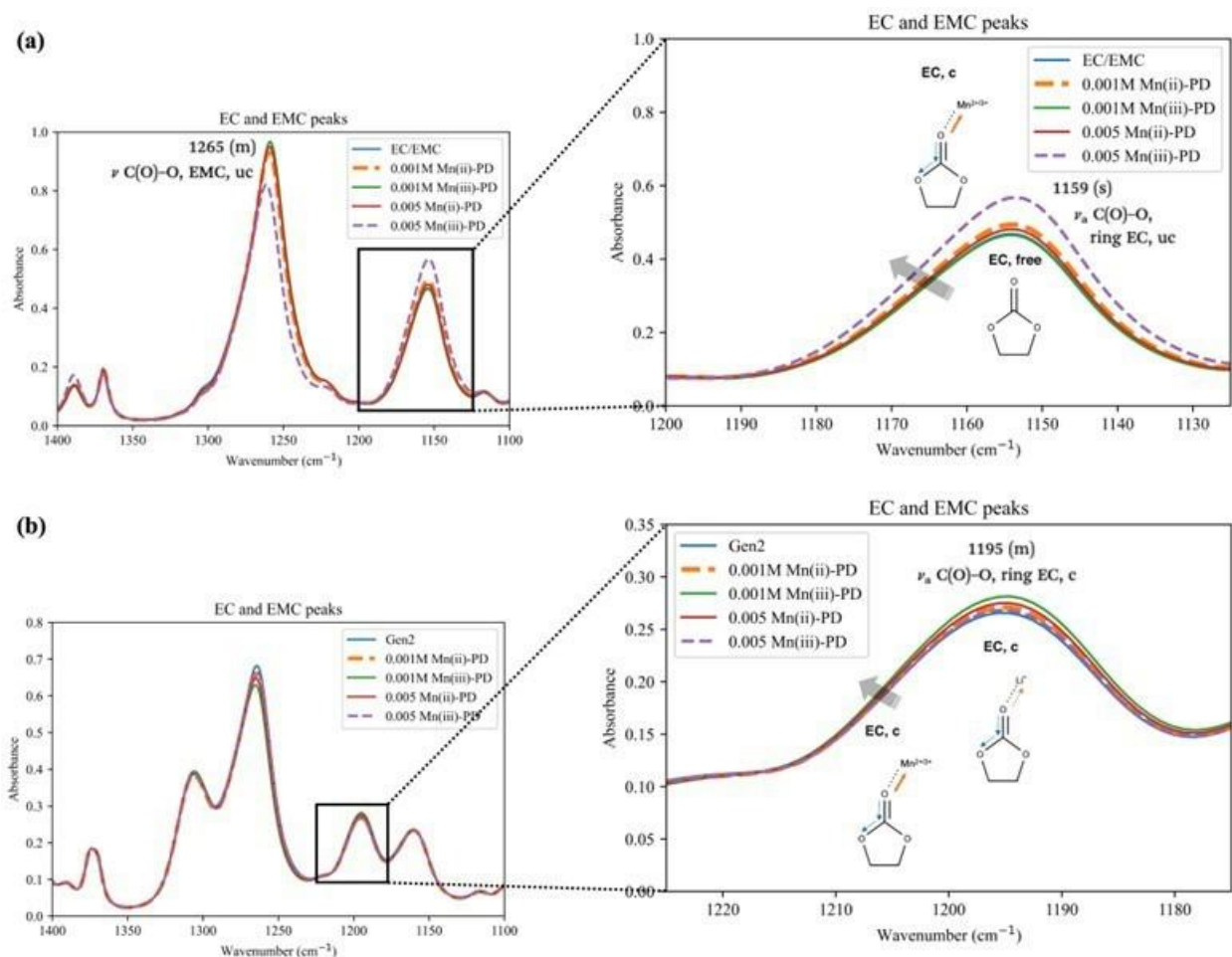


Figure IX.2.13 FTIR spectra changes, focusing on EC solvent molecule peak (1125-1350 cm^{-1}) shift, by Mn complex formation in the (a) EC/EMC solvent mixture and (b) Gen 2 electrolyte.

In the case of Gen 2 electrolyte, we analyzed PF_6^- anion peak (800-900 cm^{-1}) as well (Figure IX.2.14). Similar to the change of EC solvent molecule peak, we observed almost the same peak position for 0.001 and 0.005 Mn(ii)-PD, but there is a red shift for 0.001 Mn(iii)-PD due to shortening of bond distance that bring about increase of vibrational frequencies (i.e., higher frequency \rightarrow lower wavenumber).

Overall, it is challenging to observe peak shift differences based on Mn salt concentration due to limited solubility of Mn salts in both EC/EMC solvent mixture and Gen 2 electrolyte. Apparent peak shifts for the mixtures with Mn(iii)-PD may indicate Mn(III) is a preferable oxidation state to form Mn complex in both EC/EMC mixture and Gen2 electrolyte. Computational simulation as a complimentary study will be conducted to assign FTIR peak corresponding to a specific coordination of transition metal complexes.

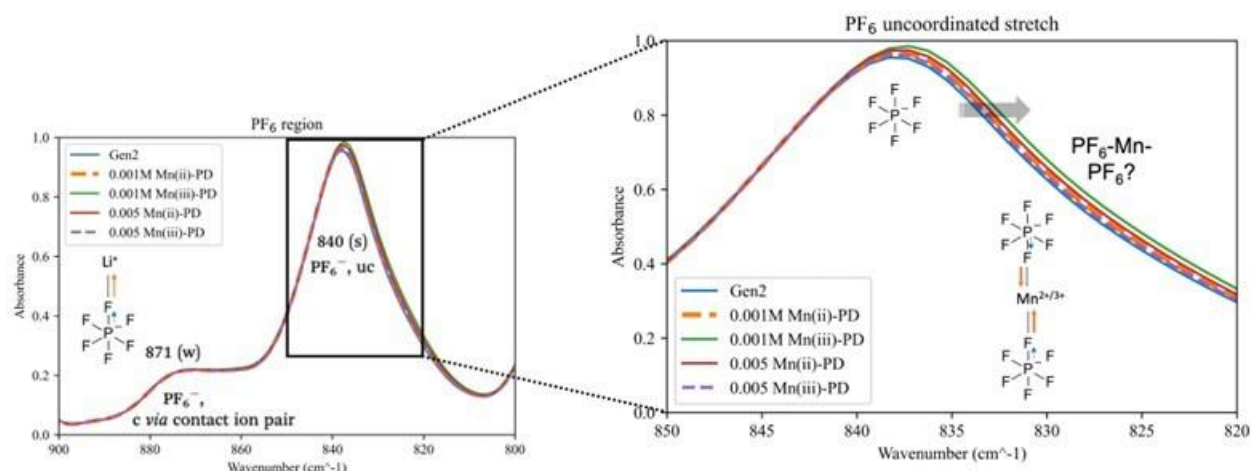


Figure IX.2.14 FTIR spectra changes, focusing on PF_6^- anion peak ($800\text{--}900\text{ cm}^{-1}$) shift, by Mn complex formation in the Gen 2 electrolyte.

Multi-phase Spectro-electrochemical study of battery electrolyte degradation

During battery operation, particularly in the first few cycles, electrolyte components react electrochemically and form solid products on the surfaces of the electrodes as well as gaseous species that accumulate in the cell. Using a combination of in-situ GC-FID and in-situ FTIR, electrochemical degradation of the electrolyte solvent is correlated with gas evolution in the cell (LNO/graphite). In-situ FTIR shows decreasing concentration of ethylene carbonate (EC) solvent, as calculated from the integrated FTIR intensity of EC vibrational absorption (Figure IX.2.15a). Ethylene gas is a known by-product of EC electrochemical reduction and is produced during SEI formation. Concurrently, the headspace of an in-situ gas cell was extracted and the gas composition analyzed using chromatography. GC-FID measured increasing amounts of ethylene gas until the end the first charging cycle (Figure IX.2.15b). Quantifying both multiphase reactions occurring during battery operation is critical to understanding and mitigating battery degradation pathways.

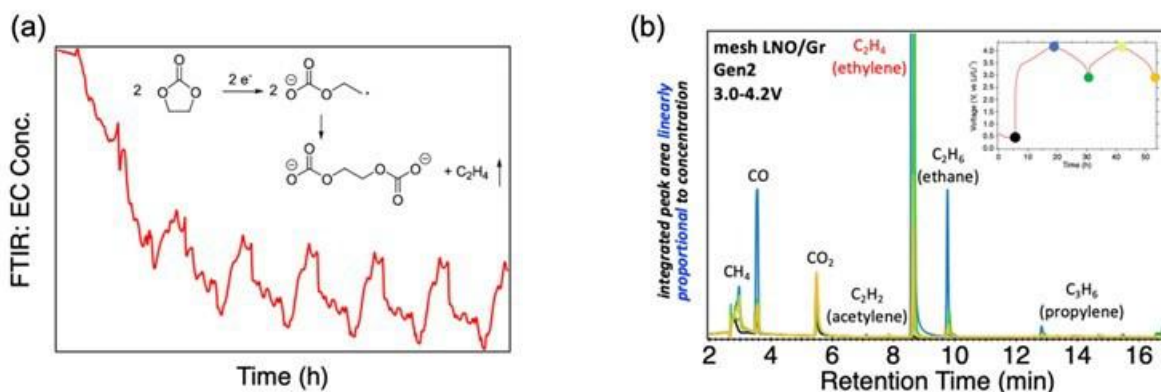


Figure IX.2.15 (a) Concentration of EC solvent determined from integrated FTIR peak absorption as a function of time during battery cycling (at C/10). (b) Gas chromatograms from GC-FID of headspace within a LNO/graphite cell at various points during first two cycles (at C/10). Various gas species, including ethylene, ethane, acetylene and propylene, are measured. (a) and (b) Increasing signal of ethylene gas evolved in the cell is correlated to the decreasing concentration of EC. Ethylene is a known product of EC reduction.

Conclusions

- Coating delamination was observed for 5V spinel electrodes cycled in cells with a upper cutoff voltage of 4.7 V. Such delamination was also seen for electrodes soaked (not cycled) in the electrolyte and stored in glass vials at 45°C. The delamination is believed to be the result of electrolyte decomposition into acidic side products that subsequently etch and pit the aluminum current collector.

Various electrolyte additives were examined for their ability to prevent the 5V spinel coating delamination during the soak test. The additives, LiDFOB and PTSL, were observed to mitigate such delamination.

- Full cells containing 5V spinel positive electrode and graphite negative electrode show capacity fade and impedance rise on accelerated aging. The capacity fade has contributions from lithium inventory losses to the graphite SEI. The major contributions to impedance rise include the coating delamination at the spinel-current collector interface, and hindered interfacial processes at the electrode-electrolyte interfaces of both electrodes.
- Analytical electron microscopy studies on the 5V spinel material show the following after aging in full cells: retention of the bulk spinel structure; reconstruction at particle surfaces resulting in the presence of Mn_3O_4 -like and rock-salt like phases; increase in void density in the particles, which could result from vacancy-condensation during cycling; absence of intergranular cracks; and development of intragranular cracks that could be the result of lithium and transition metal loss during cycling.
- Electrolyte decomposition species associated with the transition metals dissolved from the cathodes are seen in the Electrospray Ionization-Mass spectroscopy (ESI-MS) data; all the transition metal-containing complexes are seen as negatively-charged species.
- For LiNiO_2 /Graphite cells, the main source of capacity loss is active material loss in the LiNiO_2 electrode; lithium inventory loss to the graphite SEI is a smaller contributor.
- Multi-modal approaches using various techniques, including in-situ ATR-FTIR and GC-FID, were applied to examine to aging behavior of various cells containing layered oxide (low Co or no Co) cathodes. Spectral changes, resulting from Mn complex formation at the cathode-electrolyte interfaces, were observed. We are refining the FTIR peak assignments with a systematic approach, i.e., manganese salts in solvent mixtures, to deconvolute the complicated transition metal complex system and will complement these data using information gained from computational simulations.

Key Publications

1. M.-T.F. Rodrigues, J. Gim, A. Tornheim, O. Kahvecioglu, M. Luo, A.Y.R. Prado, S.E. Trask, J. Croy, D.P. Abraham, "Concealed cathode degradation in lithium-ion cells with a Ni-rich oxide", J. Electrochem. Soc. 2022, 169, 040539.
2. J. Yang, M.-T.F. Rodrigues, Z. Yu, S.-B. Son, K. Liu, N. L. Dietz-Rago, L. Chen, Z. Zhang, D.P. Abraham, C. Liao, "Design of a Scavenging Pyrrole Additive for High Voltage Lithium-Ion Batteries" J. Electrochem. Soc. 169, 040507 (2022).
3. J. Yang, M.-T.F. Rodrigues, S.-B. Son, J.C. Garcia, K. Liu, J. Gim, H. Iddir, D.P. Abraham, Z. Zhang, C. Liao, "Dual-Salt Electrolytes to Effectively Reduce Impedance Rise of High-Nickel Lithium-Ion Batteries", ACS Appl. Mater. Interfaces 13, 40502 (2021).
4. A. Tornheim and D. O'Hanlon, "What do Coulombic Efficiency and Capacity Retention Truly Measure? A Deep Dive into Cyclable Lithium Inventory, Limitation Type, and Redox Side Reactions", J. Electrochem. Soc 2020, 167, 110520.
5. B. J. Tremolet de Villers and S.-D. Han, "Batteries: Materials Principles and Characterization Methods; Chapter 4. Vibrational Spectroscopy for Batteries," IOP Publishing Ltd. 2021.
6. J. Yang, S. Park, S. Lee, J. Kim, D. Huang, J. Gim, E. Lee, G. Kim, K. Park, Y.-M. Kang, E. Paek, and S.-D. Han, "High-Voltage Deprotonation of Layered-Type Materials as Newly Identified Cause of Electrode Degradation," 2022, under revision.
7. Y. Zhang, G. Teeter, N. S. Dutta, S. Frisco, and S.-D. Han, "Mechanistic Understanding of Aging Behaviors of Critical-Material-Free $\text{Li}_4\text{Ti}_5\text{O}_{12}/\text{LiNi}_{0.9}\text{Mn}_{0.1}\text{O}_2$ Cells with Fluorinated Carbonate-Based Electrolytes for Safe Energy Storage with Ultra-Long Life Span," 2022, under revision.
8. S.-D. Han, "In Situ Spectroscopic Characterization of the Electrode-Electrolyte Interphase." Oral presentation, 2022 TMS Annual Meeting & Exhibition, Anaheim, CA.
9. B. J. Tremolet de Villers, J. Yang, J. Gim, and S.-D. Han, "In Situ Infrared Spectroscopy for High-Nickel Lithium-Ion Battery Cathodes: Elucidating the Relationships Between Vibrational Signatures

and Cathode-Electrolyte Interphase Phenomena,” Oral presentation, 2022 MRS Spring Meeting, Honolulu, HI.

Acknowledgements

We acknowledge contributions from the following individuals: P. Badami, S.-M. Bak, M. Balasubramanian, I. Belharouak, I. Bloom, A. Dunlop, F. Dogan, C. Engtrakul, S.-D. Han, D. Huang, A.N. Jansen, J. Kim, S. Lee, C. Liao, W. Lu, H. Luo, D.W. Mulder, S. Nanayakkara, E. Paek, S. Park, B.J. Polzin, M.-T.F. Rodrigues, J. Sharma, S.-B. Son, R.C. Tenent, A. Tornheim, S.E. Trask, Y. Tsai, B.J. Tremolet de Villers, B. Wang, C. Wang, J. Yang, Z. Yang, M. Zhou, L. Zou, P. Zou.

IX.3 Advanced Cathodes Theory and Modeling (ANL, LBNL, PNNL, NREL, ORNL)

Hakim Iddir, Principal Investigator

Argonne National Laboratory
9700 South Cass Avenue
Lemont, IL 60439
E-mail: Iddir@anl.gov

Guoying Chen, Co-Principal Investigator

Lawrence Berkeley National Laboratory
1 Cyclotron Road
Berkeley, CA, 94720
E-mail: gchen@lbl.gov

Tien Duong, DOE Technology Development Manager

U.S. Department of Energy
E-mail: Tien.Duong@ee.doe.gov

Start Date: October 1, 2018	End Date: September 30, 2022	
Project Funding (FY22): \$3,500,000	DOE share: \$3,500,000	Non-DOE share: \$0

Project Introduction

Geopolitical concerns over critical resources, and in particular cobalt, as well as market demand have instigated new efforts to improve the sustainability of lithium-ion cathode technologies. This project will use first-principles modeling applied to prototypical cobalt free cathode oxides including LiNiO_2 (LNO), $\text{LiNi}_{0.5}\text{Mn}_{0.5}\text{O}_2$, and newly developed derivatives thereof in order to advance cathode design in accord with DOE targets for cost, performance, and sustainability.

Objectives

- Identify promising surface and bulk dopant elements and provide a fundamental understanding of their efficacy in modifying the properties of low/no cobalt oxides with respect to cobalt as a counterpart.
- Improve cathode design by understanding and elucidating the mechanisms and tendencies of facet-dependent degradation, stability, and dopant segregation.
- Narrow the gap in understanding between structure-property relationships by elucidating the effects that local phenomena (e.g., cation ordering) have on measured, physical and electrochemical data.

Approach

The calculations required to accomplish the project goals were performed within the spin polarized density functional theory (DFT) methodology as implemented in the Vienna Ab Initio Simulation Package (VASP) [1], [2]. The generalized gradient approximation (GGA) is used to model the exchange-correlation potentials as developed by Perdew, Burke, and Ernzerhof (PBE) [3]. The interaction between valence electrons and ion cores is described by the projected augmented wave (PAW) method [4]. Furthermore, the GGA+U scheme is used for applying the on-site correlation effects among 3d electrons of the transition metals, where the parameter of (U-J) is set to 5.96, 5.00, and 4.84 eV for Ni, Co, and Mn, respectively [5]. The magnetization was used to assign the oxidation state of the ions. Therefore, in order to get a better representation of the electronic structure, a single point calculation with a screened hybrid functional (HSE06) is performed after each geometry optimization [6]. Total energy and hyperfine shift calculations were accomplished using the Vienna Ab initio Simulation Package (VASP) under the projector augmented wave (PAW) pseudopotentials with the generalized gradient approximation (GGA) of the Perdew-Burke-Ernzerhof (PBE) exchange-correlation function.

The distribution of transition metal dopants in layered materials plays a major role in the structural characteristics and electrochemical performance of the cathode. We have explored hundreds of configurations of several dopant candidates in low Co and Co-free materials. To understand the effect of temperature we have calculated the configurational density of states that accounts for the configurational entropy of the system and the probability of occurrence, which is equivalent to the mole fraction of a configuration in the material.

Combining single-crystal model systems with controlled physical properties (composition, size, morphology, surface orientation etc.) and single-particle-based diagnostic techniques to enable better understanding of composition-structure-property-performance correlations at the intrinsic material's level.

Results

Understanding lithium local environments in $\text{LiMn}_{0.5}\text{Ni}_{0.5}\text{O}_2$ cathodes: a DFT-supported ^6Li solid-state NMR study

This year we completed and published our study on local environments in $\text{LiMn}_{0.5}\text{Ni}_{0.5}\text{O}_2$. In this study an in-depth analysis of DFT calculations is used to understand and interpret experimental structural characterization data and its correlation to materials synthesis conditions to focus on characterization assisted material development. We combined ^6Li NMR with DFT calculations to elucidate the spectral difference observed from the 15 hours and 1-week annealed samples. Considering the previously reported TM ordering, including zigzag, flower, and row configurations, we generated the NMR spectrum of each configuration to inspect and breakdown the experimental NMR spectrum into possible major contributions. These special configurations have each unique contribution to the overall NMR spectrum. Inclusion of Ni-Mn disorder and Li/Ni exchange into these configurations produces a plethora of configurations all within a very small energy range centered around the main peak of the normal distribution. This shows why in general the prepared samples must contain a large number of different configurations that will all contribute to the overall broadening of the NMR spectra, and we further demonstrated that the Li/Ni mixing is the primary cause of the broadening. We have also showed for the first time that NMR shifts near 1400 ppm do not necessarily emanate from Li in the transition metal layer but could result from configurations of Li in the Li layer that are well within the accessible majority distribution.

Lastly, we combined the spectrum of each conformation to generate the overall computed spectra, where the longer annealed sample exhibits reduced amount of zigzag and flower primarily due to the enough driving force supported by the high temperature and long annealing time. We believe DFT-supported experimental characterization studies are crucial to understand the effect of synthesis conditions and improve material properties. Beyond our previous analysis we computed the effect of temperature in the configuration distribution. The top panel in Figure IX.3.1 shows the probability distribution of configurations at different temperatures. The high entropy configurations are favored at higher temperatures whereas the lowest total energy configurations are favored at room temperature. Hence, synthesis conditions are crucial to fine tune the configurational disorder of the material.

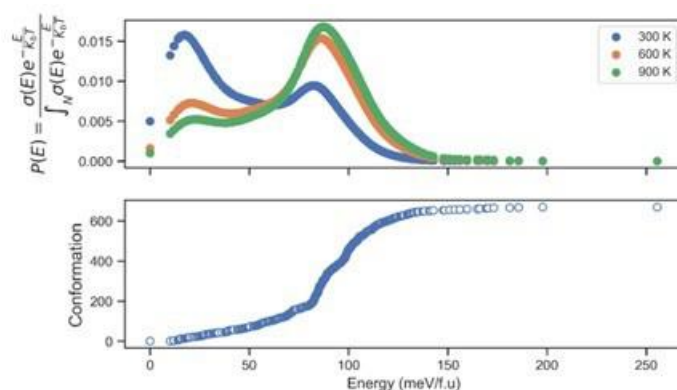


Figure IX.3.1 From bottom to top: Configurational energy distribution and probability of occurrence of configuration in $\text{LiMn}_{0.5}\text{Ni}_{0.5}\text{O}_2$.

Pb-based nanocomposite anode for sodium-ion batteries: comparison of electrochemical reaction kinetics with Na and Li

The Zintl phase as an intermediate during the alloying reaction is a unique property of the Na storage reaction of Pb/PbO-C nanocomposite, and it can affect the phase transition and electrochemical performance. The Zintl phase typically has high electrical resistivity based on its highly ionic character. This phenomenon was influenced by the formation of a NaPb phase, which can be classified as a Zintl phase. The NaPb has polyanions of tetrahedral Pb_4^{4-} clusters, created by transferring electrons from Na atoms like an ionic compound, reducing the electronic conductivity of the NaPb Zintl phase relative to other Na_xPb alloys. We suggest that the formation of Zintl phase in the NaPb intermediate on the surface of Pb/PbO nanoparticles negates deeper sodiation reactions as a high resistive barrier. This phenomenon lowers the reversible capacity by limiting the depth of reaction and contributing capacity loss in SIBs. Meanwhile, most Li-Pb alloys cannot follow the Zintl-Klemm rules, except $\text{Li}_{17}\text{Pb}_4$, which is classified as an extended Zintl-like phase with Li-Pb clustering.

The electronic properties of the cubic and tetrahedral intermediate phases for NaPb and LiPb were evaluated by DFT calculations. DFT calculations predict a difference in energy of 0.17 eV/f.u. between the cubic and the tetragonal phase for LiPb and -0.10 eV/f.u. for NaPb. Hence, LiPb prefers to be in the cubic phase, whereas NaPb prefers the tetrahedral phase with Pb_4 cluster formation. Essentially, the Li atom has a smaller ionic size than the Na atom and prefers the cubic phase of LiPb, which is more thermodynamically favored than the tetrahedral Zintl phase. Figure IX.3.2 shows the Density of States (DOS) of the cubic and tetragonal phases for LiPb and NaPb. The cubic phases for both LiPb and NaPb present a metallic character (Figure IX.3.2c and d) with a large number of electronic states at the Fermi level available to transport current. Nevertheless, the tetragonal phases for both LiPb and NaPb show a semiconductor character (Figure IX.3.2d and f) with a small band gap and the Fermi level close to the band edge. Since the thermodynamically favored phase of NaPb is tetragonal, NaPb has a smaller conductivity compared to LiPb (cubic phase). The Bader analysis for NaPb cubic phase assigns 0.74 “excess electrons” to the Pb ions indicating a formal oxidation state of -1 for Pb and +1 for Na. The NaPb tetragonal phase present an almost identical electron count per Pb ion (0.75). However, the Na ions Bader volume in the cubic phase is 10.53 \AA^3 , whereas in the tetragonal phase the average volume is 13.03 \AA^3 . Therefore, the volume of the Pb ions in the tetragonal phase is smaller than in the cubic phase. Although the charge per ion is the same for both phases, there is more charge separation in the tetragonal phase. Furthermore, the clustered Pb ions in the tetragonal phase exacerbates the separation of the charge in the system, hence reducing the electronic conductivity.

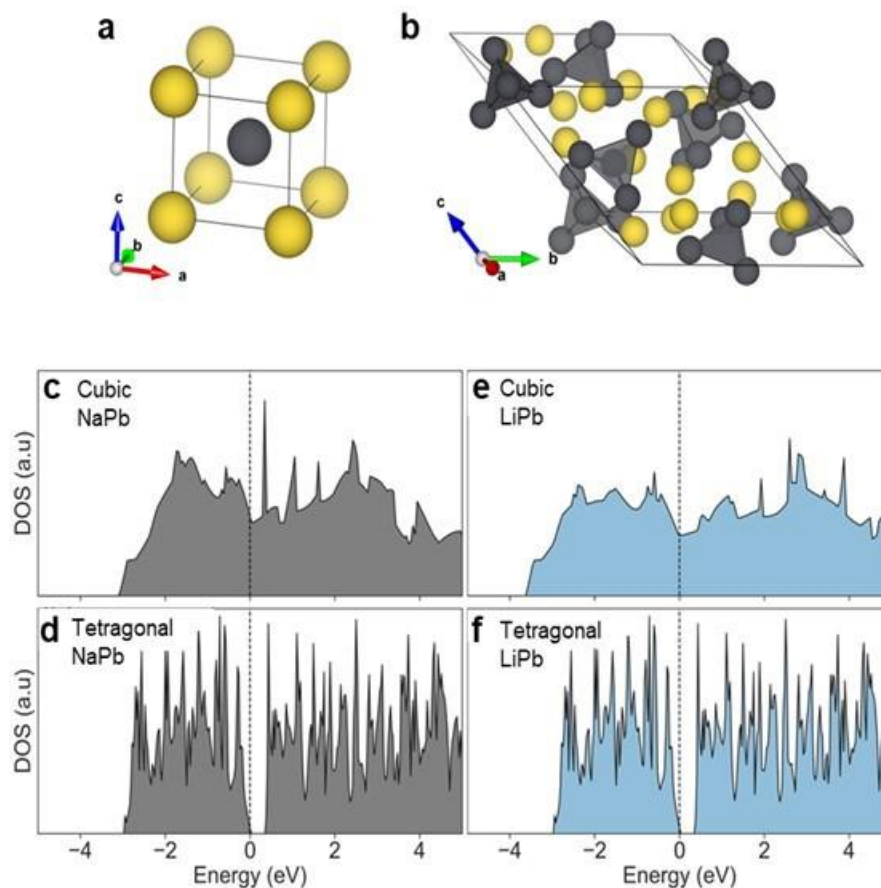


Figure IX.3.2 APb (A=Na, Li) schematic representation a) cubic structure, b) tetragonal structure. Lattice vector direction are shown for each structure and the unit cells are shown as black solid lines. (Na ions are represented by yellow spheres and Pb ions are represented by dark grey spheres. Translucent grey planes show polyhedron formed by Pb_4 clusters.) Total density of states DOS for NaPb c) cubic phase, d) tetragonal phase and for LiPb e) cubic phase, f) tetragonal phase. The Energy of the Fermi level is indicated by a vertical dashed line

Ni migration across layers at high state of charge in Ni-rich materials

It has been found that the capacity loss of $LiNiO_2$ is reduced when cycled at voltages higher than 4.3V. A possible explanation is the migration of Ni in the Li layer (from defects) back into the transition metal layer, hence, “cleaning” the migration path for Li diffusion. Nudge elastic band DFT calculations were performed to test the hypothesis. Figure IX.3.3f shows the energy barriers and driving force for migration at different states of charge (SOC). The driving force is larger (thermodynamics) and the activation energy is smaller (kinetics) with increase in SOC. Higher states of charge (SOC) promote Ni migration to the TM layer. Once Ni is back in the TM layer, the Li/Ni exchange defect formation has a positive energy, confirming the irreversibility of the process at high SOC.

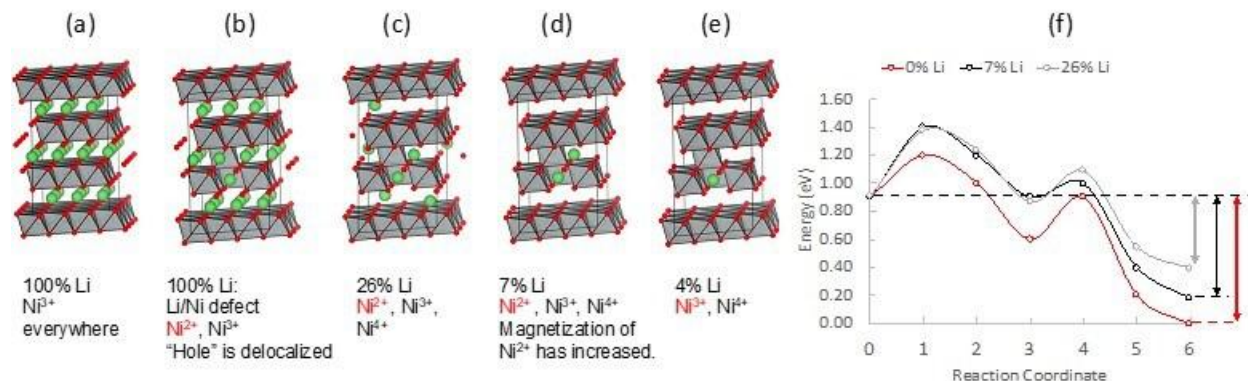


Figure IX.3.3 (a) – (e) Schematic representation of Li distribution in LiNiO₂ layered with one Li/Ni exchange in the simulation cell. (f) energy change during Ni migration from the Li layer to the transition metal layer.

Earth abundant elements distribution and domain structure in Li-rich Mn-rich based cathode materials

Elemental distribution in lithium manganese rich materials may create distinct domains. Their distribution impacts the cathode electrochemical properties. The excess Li and Mn form Li₂MnO₃-like regions. These domains have LiMn₆ clusters in the transition metal layer. Those clusters, and their three-dimensional arrangement are characteristic of pure Li₂MnO₃. They carry the same drawbacks as the original material. However, the composite system accommodates other clusters at the domain interfaces, such as LiMn₅, LiMn₄, LiMn₃. Any extra disorder forms other clusters, such as LiMn₂ and LiMn. The arrangement of transition metals in the LiMn_{0.5}Ni_{0.5}O₂ domains also influences the total energy. An understanding of the ion distribution is essential to explain the electrochemical properties and the effect of synthesis conditions in the performance of the material.

Figure IX.3.4a shows the number of Li-metal pairs and metal-metal pairs in the transition metal layers for each tested configuration as a function of the total energy. The composite “ordered” ribbon model, the lowest energy configuration is composed of Li-Mn pairs within the Li₂MnO₃ region and Mn-Ni pairs in the LiMn_{0.5}Ni_{0.5}O₂ region. Next in the energy scale are configurations with a few ions swapped between domains. The number of Li-Mn and Mn-Ni pairs decreases at the expense of increasing number of Mn-Mn, Ni-Ni, Li-Li and Li-Ni pairs. Figure IX.3.4b shows the distribution of LiMn_x (x=6,5,4,3,2,1) clusters for each configuration. The ordered composite configuration has a larger amount of LiMn₆ and LiMn₅ clusters. The decrease in the number of LiMn₆ and LiMn₅ clusters correlates with the increase in energy. For the more disordered structures, there is no correlation with the cluster content. Honeycomb and zigzag-like regions are evident when Li-Mn and Ni-Mn are dominant. Contrary to the high energy range, in the low energy range, the tridimensional structure of Li₂MnO₃ regions is distinguishable.

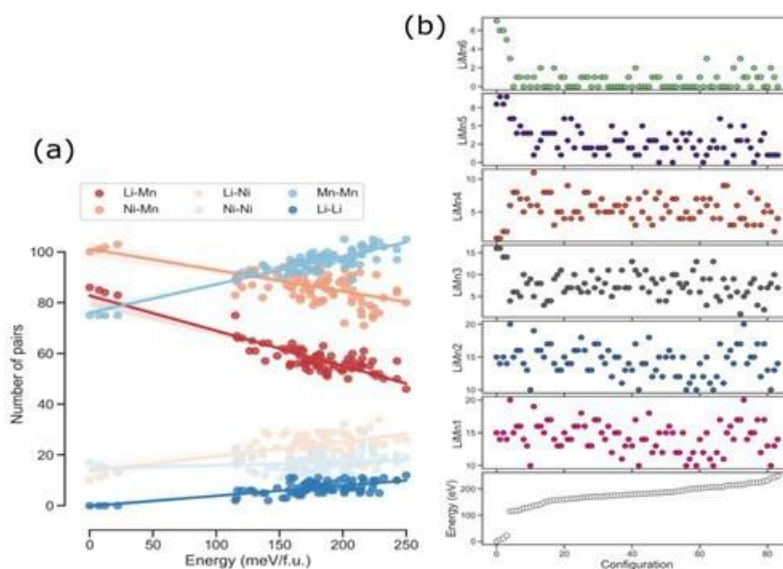


Figure IX.3.4 (a) Number of Li-M and M-M (M=Ni,Mn) pairs in the transition metal layer for each configuration. (b) LiMn_x (x=6,5,4,3,2,1) clusters in the transition metal layer for each configuration. All configurations are sorted by total energy and referred to the lowest energy.

The DFT predicted low energy configurations are the ground state at 0K. Ground state configurations may be good estimations of finite temperature states. However, in multicomponent systems the configurational entropy promotes different atomic arrangements at higher temperatures. Figure IX.3.5 shows the total energy for several random configurations, where Li, Mn, and Ni are shuffled within the transition metal layer. The energies are sorted with respect to the lowest energy structure we have found so far—the composite ribbon model. The spread in energy for all these configurations is about 250 meV/f.u. This widespread in energy indicates the sensitivity to the atomic local ordering. Any departure from the perfect ribbon model incurs a minimum energy cost, while configurations where the ribbon feature is absent tends to have similar energies. Most of the “random” configurations have an energy in a band centered around 200 meV/f.u. relative to the ordered configuration energy. To account for finite temperature effects, a probability of occurrence for each tested configuration is calculated (Figure IX.3.5a). The probability of occurrence assists in understanding the effect of synthesis temperature on the potential local orderings of the TMs that can be achieved.

Usually, high temperatures are used during synthesis, low-energy equilibrium configurations, predicted by DFT (at 0K), might not be thermodynamically reachable, a mix of configurations is expected. For example: at 600K the probability of occurrence increases for configurations around 200 meV higher than the ground state, at the expense of the “ordered” configurations (see orange circles in Figure IX.3.5a). Hence, a mix of ordered regions and disordered regions would be present in the material at 600K. At 900K the disordered structures have a higher probability of occurrence than the ordered. Therefore, the whole material would be mostly disordered with no defined Li₂MnO₃ regions. In practice, during the cooling process some of these high energy configurations might be trapped within the structure and a composite with mixed local configurations and ordering will be formed.

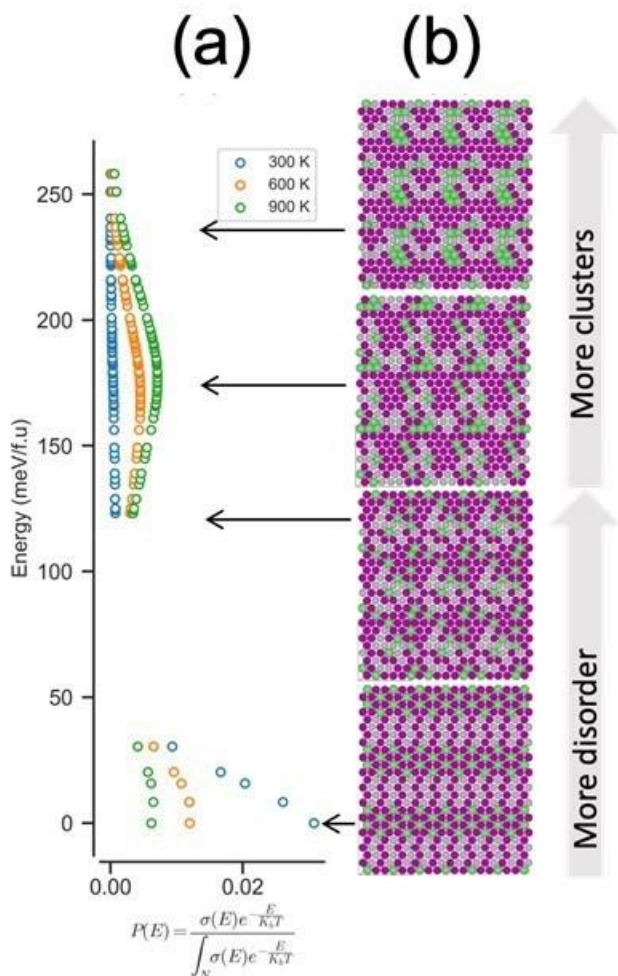


Figure IX.3.5 (a) Energy domain distribution on 60%-MN5050/40%-Li₂MnO₃ and probability of occurrence for each configuration, (b) schematic representation of species distribution for select configurations, purple, gray, and green circles represent Mn, Ni and Li atoms respectively.

Fluorination of Li-rich layered oxide single crystals

Fluorine has played an important role in the development of lithium-ion battery cathodes. It is often introduced into the bulk lattice through anion substitution or onto cathode particle surface through specific modifications or coatings. Previous studies have shown significant impact on interfacial chemistry when F-containing species are present on the surface. [7] In recent studies, partial F substitution into the oxygen sublattice of a new class of cathode materials, cation-disordered Li-excess rocksalts, was found to reduce oxygen loss and impedance rise, leading to improved cycling stability. [8-10] Unfortunately, current fluorination methods are largely inadequate, and quantitative characterization of F content and its distribution (e.g. in the bulk *vs.* on the surface of cathode particles) face significant challenges. In FY22, we explored alternative fluorination methods and synthesis conditions to prepare fluorinated Li-rich layered oxides. Single-crystal model systems were used in order to perform better-controlled studies.

Most fluorination methods use solid-state reactions with LiF as the F source. [11,12] As LiF is thermodynamically very stable and F anions are known to prefer environments surrounded by Li instead of transition-metals (TM), the method often leads to the segregation of LiF secondary phase during synthesis. This is clearly shown in the fluorination of a Li- and Mn-rich oxide, Li_{1.2}Ni_{0.2}Mn_{0.6}O₂ (referred to as LNMO hereafter). Upon increasing the F level (x) from 0.01 to 0.1 in Li_{1.2}Ni_{0.2}Mn_{0.6}O_{2-x}F_x (referred to as F-LNMO

hereafter), LiF impurity content increases continuously (Figure IX.3.6a). The results suggest limited F incorporation in the layered crystal structure, even in the presence of excessive F source. Here we adopted a modified molten-salt synthesis method to prepare F-LNMO single crystals. *In situ* fluorination was carried out by mixing a selected fluoride salt with the stoichiometric amounts of Li, Ni and Mn precursors in a KCl flux. The mixture was annealed at 450°C followed by 900°C for 12 hours. It was found that the chemical nature, particularly the fluoroacidity of the F salt, plays a critical role in the phase purity of synthesized F-LNMO compounds. Figure IX.3.6b shows the X-ray diffraction (XRD) patterns collected on a $\text{Li}_{1.2}\text{Ni}_{0.2}\text{Mn}_{0.6}\text{O}_{2-x}\text{F}_x$ sample ($x=0.025$, denoted as LNMO-F2.5) synthesized with various F-salts. The phase purity follows the following order: $\text{LiF-KF} > \text{NaF-MgF}_2 > \text{NaF-CaF}_2 > \text{LiF-NaF} > \text{LiF} > \text{LiF-CaF}_2$, which is the exact opposite of fluoroacidity of the F salts in the molten state. [13] Note that fluoroacidity defines the ability of a salt in giving out F^- , with the basic form being F^- givers and the acidic form being F^- acceptors. Following a similar procedure, a series of $\text{Li}_{1.2}\text{Ni}_{0.2}\text{Mn}_{0.6}\text{O}_{2-x}\text{F}_x$ with $x=0.01$ (denoted as LNMO-F1), 0.025 and 0.05 (denoted as LNMO-F5) were prepared using LiF-KF as the F precursor. The laboratory XRD patterns (Figure IX.3.7a) show well-defined peaks with high crystallinity and the absence of LiF impurities in all samples. Synchrotron XRD patterns collected at BL 11-3 at Stanford Synchrotron Radiation Lightsource (SSRL) are shown in Figure IX.3.7b, along with the reference patterns of spinel LiMn_2O_4 and LiF. Aside from the detection of a small amount of LiF impurity in all F-LNMO samples, the presence of a LiMn_2O_4 -type spinel phase is also shown, especially in LNMO-F5, suggesting that increasing F content promotes the formation of a spinel secondary phase. Our study highlights the challenges in detecting LiF impurities using the laboratory XRD technique.

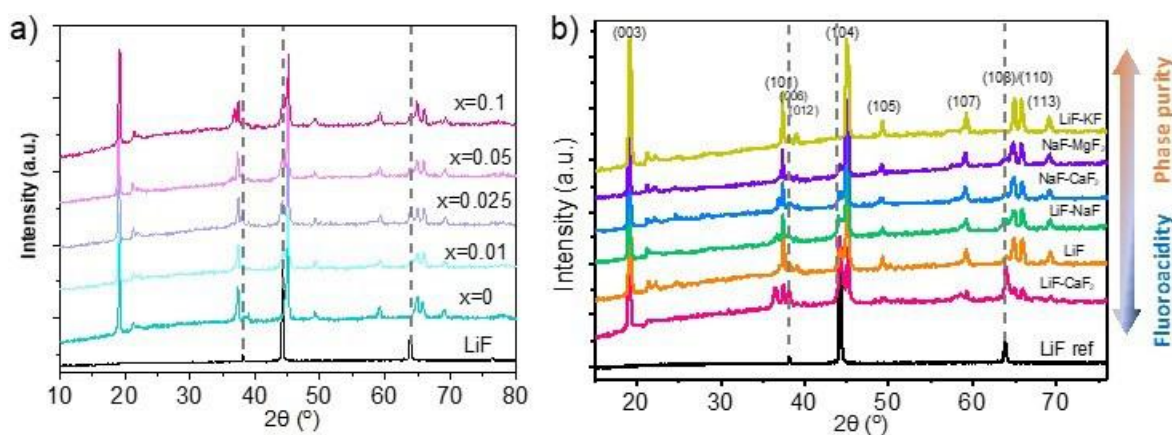


Figure IX.3.6 XRD patterns of a) $\text{Li}_{1.2}\text{Ni}_{0.2}\text{Mn}_{0.6}\text{O}_{2-x}\text{F}_x$ ($x=0, 0.01, 0.025, 0.05$ and 0.1) synthesized with LiF as F precursor and b) $\text{Li}_{1.2}\text{Ni}_{0.2}\text{Mn}_{0.6}\text{O}_{2-x}\text{F}_x$ ($x=0.025$) synthesized with various salts as F precursors.

Figure IX.3.7c-f show the scanning electron microscopy (SEM) images of the $\text{Li}_{1.2}\text{Ni}_{0.2}\text{Mn}_{0.6}\text{O}_{2-x}\text{F}_x$ series. All particles adopted the same octahedron shape with an average size of $\sim 1\ \mu\text{m}$. Focused ion beam (FIB) lithography combined with STEM were used to analyze the orientation of the surface facets, which were determined to be predominantly $\{012\}$ -family planes of the layered structure (Figure IX.3.7g top). A small percentage of (003) planes are also present. The determined angle between (003) and (012) planes for LNMO and LNMO-F5 particles are approximately 73° and 72° , respectively, consistent with the theoretical value of 71° based on the hexagonal lattice of the space group $R\bar{3}m$ (Figure IX.3.7g bottom).

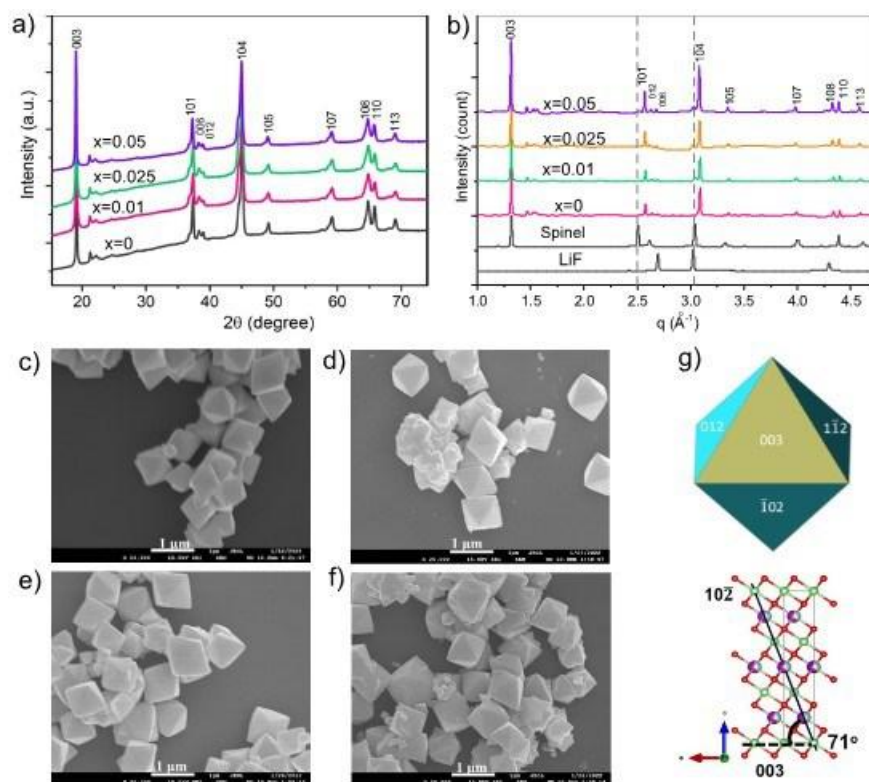


Figure IX.3.7 a) Laboratory and b) synchrotron XRD patterns of $\text{Li}_{1.2}\text{Ni}_{0.2}\text{Mn}_{0.6}\text{O}_{2-x}\text{F}_x$ ($x=0, 0.01, 0.025$ and 0.05) synthesized with LiF-KF as F precursor, c-f) SEM images of as-synthesized $\text{Li}_{1.2}\text{Ni}_{0.2}\text{Mn}_{0.6}\text{O}_{2-x}\text{F}_x$ samples, g) facet index of the octahedron particles (top) and atomic arrangement of the hexagonal layered structure (bottom).

Crystal-facet dependent Ni surface segregation in $\text{Li}_{1.2}\text{Ni}_{0.2}\text{Mn}_{0.6}\text{O}_2$ and $\text{Li}_{1.2}\text{Ni}_{0.2}\text{Mn}_{0.6}\text{O}_{1.95}\text{F}_{0.05}$

Element segregation is an important factor in determining the final phase formation and eventually affects the electrochemical properties for cathode materials. A detailed understanding on the element segregation and the resulted phase formation is very important for properly assessing the cathode electrochemical performance. However, element segregation has been far less explored for the emerging micron-size single crystals of high-capacity $\text{Li}_{1.2}\text{Ni}_{0.2}\text{Mn}_{0.6}\text{O}_2$ compared to nanoparticles of the same composition. Scanning transmission electron microscopy (STEM), X-ray energy dispersive spectroscopy (STEM-EDS) and electron energy loss spectroscopy (STEM-EELS) were employed to investigate the element distribution in the micron-size single crystals of both $\text{Li}_{1.2}\text{Ni}_{0.2}\text{Mn}_{0.6}\text{O}_2$ and $\text{Li}_{1.2}\text{Ni}_{0.2}\text{Mn}_{0.6}\text{O}_{1.95}\text{F}_{0.05}$.

Strong Ni segregation was found at the 102 facets but not at the 003 facets, as a result the bulk composition was deviated to a Ni-deficient one from the nominal composition. As shown in the STEM-HAADF image of Figure IX.3.8, the 102 facet has a significantly higher intensity compared to the bulk lattice, while the 003 surface only shows a slightly higher intensity. Since the intensity in the STEM-HAADF imaging is composition-related, roughly proportional to Z^2 (Z is the atomic number), this observation suggests that more heavier ions are accumulated at the 102 facets. In order to understand the STEM-HAADF image intensity variation in the crystal, the local composition was investigated by STEM-EDS. A strong Ni segregation at the 102 facet is revealed by the STEM-EDS Ni-map in Figure IX.3.8(b), in contrast, no such Ni segregation is observed at the 003 facet in Figure IX.3.8(a). At the same time, no Mn surface segregation is observed for both facets. In comparison to the Ni to Mn ratio of 1:3.2 measured by SEM-EDS on the average level, the composition quantification shows that the Ni-segregated 102 facet has a Ni to Mn ratio of 1:0.8. As a result of the Ni segregation, the bulk composition is deviated to a Ni-deficient one with Ni:Mn = 1:8.5 while the 003 facet formed a composition with slightly more Ni of Ni:Mn = 1:5.9. All the elements are quite uniformly distributed in the bulk lattice as indicated by the element profiles in Figure IX.3.8. Further compositional

inspections on the non-fluorinated sample also shows a Ni-segregation at the 102 facets with a similar Ni to Mn ratio of 1:0.7, indicating the Ni-segregation is only facet-dependent but independent on fluorination for the micron-size $\text{Li}_{1.2}\text{Ni}_{0.2}\text{Mn}_{0.6}\text{O}_2$ single crystals.

Facet-dependent Ni surface segregation is observed in the micron-size single crystals of $\text{Li}_{1.2}\text{Ni}_{0.2}\text{Mn}_{0.6}\text{O}_2$ and $\text{Li}_{1.2}\text{Ni}_{0.2}\text{Mn}_{0.6}\text{O}_{1.95}\text{F}_{0.05}$, resulting in a composition modification to the bulk lattice. Such segregation is only observed at the crystal facet terminated by a mix of cations and anions such as the 102 facet, but not in those surfaces terminated only by the transition metal layer, such as the 003 atomic plane. The formation of Li-Ni anti-site defects and the Ni diffusion from the bulk to the surface along the Li slab could be the key factors in forming the Ni-rich surface.

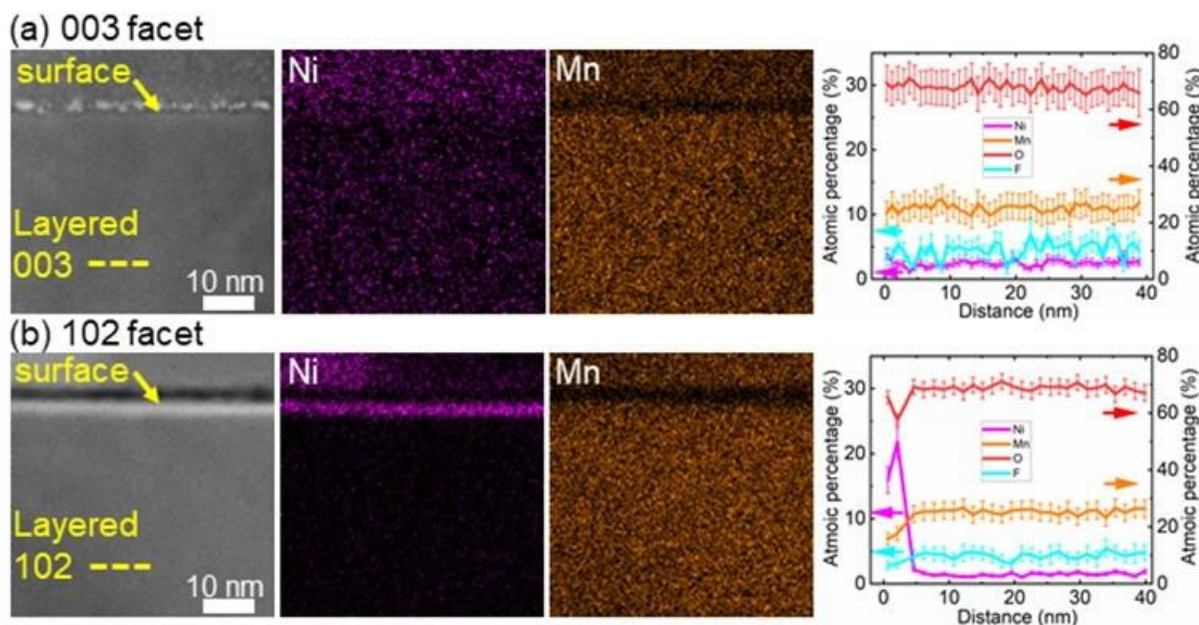


Figure IX.3.8 STEM-HAADF images and the corresponding STEM-EDS maps of Ni and Mn of the $\text{Li}_{1.2}\text{Ni}_{0.2}\text{Mn}_{0.6}\text{O}_{1.95}\text{F}_{0.05}$ single crystals at (a) the 003 facet and (b) the 102 facet, together with the corresponding element distribution profile as a function of the distance from the crystal surface (0 nm in distance) into the crystal bulk.

Conclusions

- The analysis based on a combination of the calculated-NMR and the experimental spectra of $\text{LiMn}_{0.5}\text{Ni}_{0.5}\text{O}_2$ cathodes suggests that most configurations contributing to the experimental spectra are in fact composed of a blend of configurations higher in energy than the classical well-ordered ground state structures.
- The extended annealing of $\text{LiMn}_{0.5}\text{Ni}_{0.5}\text{O}_2$ slightly enhances Ni/Mn and Li/Mn orderings while reducing the Li/Ni mixing ratio.
- NMR shifts near 1400 ppm, for $\text{LiMn}_{0.5}\text{Ni}_{0.5}\text{O}_2$ cathodes, do not necessarily emanate from Li in the transition metal layer but could result from configurations of Li in the Li layer that are well within the accessible majority distribution.
- LiPb prefers to be in the cubic phase, whereas NaPb prefers the tetrahedral phase with Pb_4 cluster formation
- The distribution of elements in $\text{MN5050-Li}_2\text{MnO}_3$ materials is temperature dependent, with more clusters and disorder promoted at higher temperatures.
- Facet-dependent Ni surface segregation is observed in the micron-size single crystals of $\text{Li}_{1.2}\text{Ni}_{0.2}\text{Mn}_{0.6}\text{O}_2$ and $\text{Li}_{1.2}\text{Ni}_{0.2}\text{Mn}_{0.6}\text{O}_{1.95}\text{F}_{0.05}$, resulting in a composition modification to the bulk lattice.

- Alternative synthesis methods were developed to fluorinate the single crystals of a Li-rich layered oxide, LNMO. Fluoroacidity, which defines the ability of a salt in giving out F^- , with the basic form being F^- givers and the acidic form being F^- acceptors, was found to play a critical role in the phase purity of the synthesized F-LNMO compounds.
- Using the more basic LiF-KF as the F precursor, a series of F-LNMO samples with the octahedron particle morphology were prepared. The particles were predominantly enclosed by {012}-family planes, along with a small percentage of (003) planes. Facet-dependent behavior was clearly demonstrated on the crystal samples, with Ni preferentially segregates to the spinel-like SRL on (012) surface, whereas on the (003) surface, a rocksalt-type SRL forms without elemental enrichment. Our study highlights the importance of surface engineering in materials properties and behavior.

Key Publications

Peer-review publications:

1. Shin, W.; Garcia, J. C.; Vu, A.; Ji, X.; Iddir, H.; Dogan, F. Understanding Lithium Local Environments in $LiMn_{0.5}Ni_{0.5}O_2$ Cathodes: A DFT-Supported 6Li Solid-State NMR Study. *J. Phys. Chem. C* **2022**, 126 (9), 4276–4285.
2. Lianfeng Zou, Peiyuan Gao, Haiping Jia, Xia Cao, Haiping Wu, Hui Wang, Wengao Zhao, Bethany E. Matthews, Zhijie Xu, Xiaolin Li, Ji-Guang Zhang, Wu Xu, and Chongmin Wang, “Non-sacrificial Additive for Tuning the Cathode-Electrolyte Interphase of Lithium-Ion Batteries”, *ACS Appl. Mater. Interfaces*, 14, **2022**, 4111–4118
3. Linze Li, Jiangtao Hu, Jie Xiao, and Chongmin Wang, “Origin, Nature, and the Dynamic Behavior of Nanoscale Vacancy Clusters in Ni-Rich Layered Oxide Cathodes”, *ACS Appl. Mater. Interfaces*, 13, **2021**, 18849–18855.
4. M. Kim, L. Zou, S.-B. Son, I. D. Bloom, C. Wang and G. Chen, “Improving $LiNiO_2$ Cathode through Particle Design and Optimization,” *J. Mater. Chem. A* 10, 12890 (2022). DOI: 10.1039/d2ta02492f
5. Y. Lu, T. Zhu, E. McShane, B. D. McCloskey and G. Chen, “Single-Crystal $Li_{1-x}Ni_xMn_{1-y}Co_yO_2$ Cathodes for Extreme Fast Charging,” *Small* (2022). DOI: 10.1002/sml.202105833

Patents and Invention Disclosures:

1. U.S. Patent Application No. 17/834,076 titled “Methods of Synthesizing Single-Crystal $Li_{1-x}Ni_xMn_{1-y}Co_yO_2$ Cathode Materials,” Y. Lu and G. Chen, June 2022

Conference presentations:

1. Garcia, Juan, Javier Bareno, Guoying Chen, Jason Croy and Hakim Iddir. "Strain-driven surface reconstruction and cation segregation in layered $Li(Ni_{1-x}Mn_xCo_y)O_2$ (NMC) cathode materials ." Abstract of presentation at the 2022 Materials Research Society Spring Meeting and Exhibit, , May 8, 2022 - May 25, 2022.
2. Lee, Eungje, Jihyeon Gim, Jinhyup Han, Ozgenur Kahvecioglu, Chong-Min Wang, Peng Zou, Fulya Dogan, et al. "Synthesis of high-performance $LiNiO_2$ and derivatives." Abstract of presentation at the 21st International Meeting on Lithium Batteries (IMLB 2022), Sydney AU, June 26, 2022 - July 1, 2022.
3. Park, Jehce, Jinhyup Han, Jihyeon Gim, Seong-Min Bak, Shabbir Ahmed, Hakim Iddir, Juan Garcia, et al. "Insights into the Na-alloying mechanism and Zintl phase transition of lead-based anodes." Abstract of presentation at the 242nd Electrochemical Society Meeting. October 9, 2022 - October 13, 2022.

References

1. G. Kresse and J. Furthmüller, “Efficiency of ab-initio total energy calculations for metals and semiconductors using a plane-wave basis set,” *Comput. Mater. Sci.*, vol. 6, no. 1, pp. 15–50, Jul. 1996, doi: 10.1016/0927-0256(96)00008-0.

2. G. Kresse and J. Hafner, “Ab Initio molecular dynamics for liquid metals,” *Phys. Rev. B*, vol. 47, no. 1, pp. 558–561, Jan. 1993, doi: 10.1103/PhysRevB.47.558.
3. J. P. Perdew, K. Burke, and M. Ernzerhof, “Generalized Gradient Approximation Made Simple,” *Phys. Rev. Lett.*, vol. 77, no. 18, pp. 3865–3868, Oct. 1996, doi: 10.1103/PhysRevLett.77.3865.
4. P. E. Blöchl, “Projector augmented-wave method,” *Phys. Rev. B*, vol. 50, no. 24, pp. 17953–17979, Dec. 1994, doi: 10.1103/PhysRevB.50.17953.
5. J. C. Garcia *et al.*, “Surface Structure, Morphology, and Stability of Li(Ni_{1/3}Mn_{1/3}Co_{1/3})O₂ Cathode Material,” *J. Phys. Chem. C*, vol. 121, no. 15, pp. 8290–8299, Apr. 2017, doi: 10.1021/acs.jpcc.7b00896.
6. A. V. Krukau, O. A. Vydrov, A. F. Izmaylov, and G. E. Scuseria, “Influence of the exchange screening parameter on the performance of screened hybrid functionals,” *J. Chem. Phys.*, vol. 125, no. 22, p. 224106, Dec. 2006, doi: 10.1063/1.2404663.
7. U. Breddemann, E. M. Erickson, V. Davis, F. Schipper, M. Ellwanger, M. Daub, A. Hoffmann, C. Erk, B. Markovsky, D. Aurbach, I. Krossing, Fluorination of Li-Rich Lithium-Ion-Battery Cathode Materials by Fluorine Gas: Chemistry, Characterization, and Electrochemical Performance in Half Cells, *ChemElectroChem*, 6, 2019, 3337–3349.
8. Z. Lun, B. Ouyang, D. A. Kitchaev, R. J. Clément, J. K. Papp, M. Balasubramanian, Y. Tian, T. Lei, T. Shi, B. D. McCloskey, J. Lee, G. Ceder, Improved Cycling Performance of Li-Excess Cation-Disordered Cathode Materials upon Fluorine Substitution, *Adv. Energy Mater.* 9, 2019, 1802959.
9. J. Lee, J. K. Papp, R. J. Clément, S. Sallis, D.-H. Kwon, T. Shi, W. Yang, B. D. McCloskey, G. Ceder, Mitigating Oxygen Loss to Improve the Cycling Performance of High Capacity Cation-Disordered Cathode Materials, *Nat. Commun.* 8, 2017, 981.
10. N. Takeda, S. Hoshino, L. Xie, S. Chen, I. Ikeuchi, R. Natsui, K. Nakura, N. Yabuuchi, Reversible Li Storage for Nanosize Cation/Anion-Disordered Rocksalt-Type Oxyfluorides: LiMoO₂ – x LiF (0 ≤ x ≤ 2) Binary System, *J. Power Sources* 367, 2017, 122–129.
11. R. A. House, L. Jin, U. Maitra, K. Tsuruta, J. W. Somerville, D. P. Förstermann, F. Massel, L. Duda, M. R. Roberts, P. G. Bruce, Lithium Manganese Oxyfluoride as a New Cathode Materials Exhibiting Oxygen Redox, *Energy Environ. Sci.* 11, 2018, 926–932.
12. J. Lee, D. A. Kitchaev, D.-H. Kwon, C.-W. Lee, J. K. Papp, Y.-S. Liu, Z. Lun, R. J. Clément, T. Shi, B. D. McCloskey, J. Guo, M. Balasubramanian, G. Ceder, Reversible Mn²⁺/Mn⁴⁺ Double Redox in Lithium-Excess Cathode Materials. *Nature* 556, 2018, 185–190.
13. Bieber, A. L et al. Fluoroacidity evaluation in molten salts. *Electrochim. Acta* 56, 5022–5027 (2011).

Acknowledgements

Contributions from the following individuals are acknowledged: Jason Croy, Mali Balasubramanian, Jehee Park, Eungje Lee, Fulya Dogan, Anh Vu, Woonchul Shin, Faxing Wang, Peng Zuo and Chongmin Wang.

IX.4 Design and Synthesis of High Energy, Manganese Rich Oxides for Lithium-Ion Batteries (ANL)

Jason R. Croy, Principal Investigator

Argonne National Laboratory
9700 South Cass Avenue
Lemont, IL 60439
E-mail: croy@anl.gov

Tien Duong, DOE Technology Development Manager

U.S. Department of Energy
E-mail: Tien.Duong@ee.doe.gov

Start Date: October 1, 2018

End Date: September 30, 2022

Project Funding (FY22): \$600,000

DOE share: \$600,000

Non-DOE share: \$0

Project Introduction

Recent concerns over the growing dependence of energy storage technologies on critical materials such as cobalt has led to significant efforts in the development of low-cobalt, high-nickel cathode oxides for lithium-ion batteries, notably for electric vehicle applications. And, while these efforts are proving successful, similar concerns are being raised over growing dependence on Ni and the related issues of supply and demand as well as sustainability. This project seeks to expand the available portfolio of cathode oxides by utilizing earth-abundant manganese as the majority component. Successful development of earth-abundant cathodes would help to simultaneously address issues related to cost, supply, and sustainability while alleviating the burden future markets will likely place on other battery-critical materials such as cobalt and nickel.

Objectives

- Develop low-cost, Co-free, Mn-oxide-based cathodes for electric vehicle applications
- Improve the design, composition, and performance of advanced electrodes with stable architectures and surfaces, facilitated by an atomic-scale understanding of electrochemical/degradation processes
- Research and development of new synthesis and processing methods that can enable a higher degree of control over the physiochemical properties of Mn-based oxide cathodes
- Development of new and novel Mn-rich oxides as lithium-ion cathodes and integrated components.

Approach

1. A bottom-up approach to fabricate Mn-rich cathodes with ~50% or more Mn is taken whereby
 - The extent of Li/Mn ordering is limited (i.e., $x < 0.30$) and, therefore, the damaging effects of the electrochemical activation process and subsequent cycling
 - Introducing novel spinel-type domains (especially at surfaces) to help improve rate capability, stability, and cyclable capacities
 - Detailed exploration of synthesis-structure-property relationships to enable high performance
2. Explore novel spinel-based materials with unique local structures as a new class of cathodes and as stabilizing components of LLS electrode materials – *focus for FY22*
3. Explore new materials and processes for stabilization of Mn-rich cathode surfaces under extended electrochemical cycling with verification in graphite cells under standardized electrochemical protocols.

Results

Stoichiometric manganese-based spinel electrodes such as LiMn_2O_4 , $\text{LiMn}_{1.5}\text{Ni}_{0.5}\text{O}_4$ and substituted derivatives thereof offer one-half of their theoretical capacity (~140 mAh/g) when charged and discharged above 4 V over the compositional range ($0 < x < 1$). The other one-half of capacity is delivered at ~3 V but is

unusable in commercial cells because of crystallographic (Jahn-Teller) distortions that occur in the lithiated spinel structure, which limit the reversibility of this reaction. Furthermore, fully-lithiated spinel $\text{Li}_2\text{Mn}_2\text{O}_4$ and $\text{Li}_2\text{Mn}_{1.5}\text{Ni}_{0.5}\text{O}_4$ spinel materials are unstable in air and are difficult to synthesize in practice, which also limits their viability as cathodes for Li-ion cells. Following the early discovery that lithiated cobalt and nickel spinels, $\text{LT-Li}_2\text{M}_2\text{O}_4$ ($\text{M}=\text{Co}, \text{Ni}$) could be prepared in air at a relatively low temperature (LT, 400 °C)¹, recent research at Argonne has exposed a variety of cathode structures with lithiated spinel character such as $\text{LT-Li}_2\text{Co}_{2-x}\text{Al}_x\text{O}_4$ ($0 < x \leq 0.3$)² and $\text{LT-Li}_2\text{MnNiO}_4$ ³ that have attractive electrochemical properties. These lithiated-spinel materials are under investigation as cathodes in their own right, as well as stabilizers for high-capacity (>250 mAh/g), lithium- and manganese-rich $x\text{Li}_2\text{MnO}_3 \bullet (1-x)\text{LiMO}_2$ ($\text{M}=\text{Mn}, \text{Ni}, \text{Co}$) cathodes that suffer from voltage fade and impedance rise effects. In this respect, the goal is to design more cost-effective and thermally-stable cathode materials to compete with today's Ni-rich, layered NMC systems.

In collaboration with Kyojin Ku and Joe Libera of the Applied Materials Division at Argonne National Laboratory, a novel composite $\text{LT-LiNi}_{1/3}\text{Mn}_{1/3}\text{Co}_{1/3}\text{O}_2$ electrode structure has been synthesized by flame spray pyrolysis (FSP) and subsequent annealing between 400 and 650 °C. In the FSP method, a solution containing lithium and transition metal precursors is sprayed into a flame where the vaporized precursors undergo nucleation and growth to yield a homogeneously-distributed lithium-metal-oxide product. This technique has a potential advantage over conventional solid-state synthesis and ball-milling techniques during which decomposition of the precursor materials and long-distance atomic diffusion require significant thermal energy and time for the product to reach equilibrium. Attempts to prepare comparable, cubic $\text{LT-LiNi}_{1/3}\text{Mn}_{1/3}\text{Co}_{1/3}\text{O}_2$ products without impurities by other techniques, for example, high energy ball milling, have not yet been successful.

In this study, the rationale for attempting to synthesize a lithiated-spinel $\text{LiNi}_{1/3}\text{Mn}_{1/3}\text{Co}_{1/3}\text{O}_2$ structure was influenced by three main factors: (1) the cobalt component might aid the formation of a lithiated-spinel configuration as it does in LT-LiCoO_2 ;¹ (2) the nickel component might suppress layered formation as it does in $\text{LT-LiCo}_{1-x}\text{Ni}_x\text{O}_2$ samples ($0 < x \leq 0.2$);⁴ and (3) in both LT- and high-temperature (HT) $\text{LiNi}_{1/3}\text{Mn}_{1/3}\text{Co}_{1/3}\text{O}_2$ structures, the nickel ions are typically divalent, while the manganese ions are tetravalent and would therefore act as electrochemically-inactive spectator ions as trivalent aluminum ions do in $\text{LiCo}_{1-x}\text{Al}_x\text{O}_2$ electrodes, thereby significantly enhancing electrochemical and structural stability.² The lattice parameter, a , of the cubic lithiated spinel phases varies markedly with decreasing cobalt from 8.000 Å in LT-LiCoO_2 and $\text{LT-LiCo}_{0.85}\text{Al}_{0.15}\text{O}_2$ to 8.109 Å in $\text{LT-LiNi}_{1/3}\text{Mn}_{1/3}\text{Co}_{1/3}\text{O}_2$ and to 8.217 Å in $\text{LT-Li}_2\text{MnNiO}_4$. These variations are attributed to differences in (i) composition, (ii) the ionic radii of the transition metal ions, (iii) the degree of disorder and (iv) the consequent binding energy within the lithium-rich and transition-metal-rich layers, (iii) and (iv) being dependent on the annealing temperature. Thus far, the cobalt-free composition $\text{LT-Li}_2\text{MnNiO}_4$, described in our previous annual report, has shown the best electrochemical performance.³

Figure IX.4.1 shows the XRD patterns of the flame-sprayed $\text{LT-LiNi}_{1/3}\text{Mn}_{1/3}\text{Co}_{1/3}\text{O}_2$ product when cooled to room temperature and thereafter annealed in air at 400, 500, 600, 625 and 650 °C. Apart from a slight sharpening of the 111 peak at $\sim 18^\circ 2\theta$ and a slight change in the relative height of the (311) and (222) peaks between 36 and $39^\circ 2\theta$, there is little change to the XRD patterns of samples when annealed below 600 °C. At 625 °C and above, a slight broadening of the (440) peak at $\sim 65^\circ 2\theta$ indicates the onset of a doublet peak and a transformation of the structure towards the more ordered, layered configuration of the high temperature analogue, $\text{HT-LiNi}_{1/3}\text{Mn}_{1/3}\text{Co}_{1/3}\text{O}_2$, which has trigonal ($R\text{-}3m$) symmetry ($c/a = 4.97$)⁵ and deviates significantly from ideal cubic-close-packing ($c/a = 4.90$).

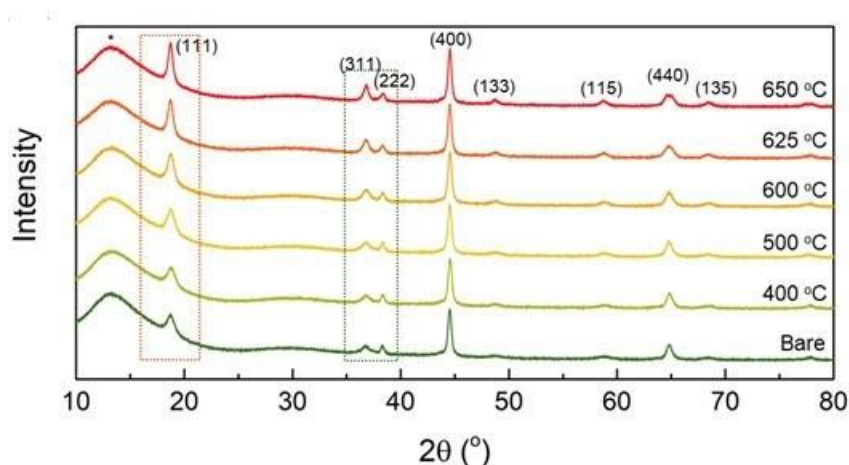


Figure IX.4.1 XRD patterns of FSP LT-LiNi_{1/3}Mn_{1/3}Co_{1/3}O₂ samples before and after annealing at various temperatures.

Scanning-transmission-electron-microscopy (STEM) and high-angle-annular-dark-field (HAADF) imaging techniques were used to probe the structural features of the as-prepared FSP powder at room temperature (Figure IX.4.2a), and after annealing at 625 °C (Figure IX.4.2b). The images clearly confirm that both products are not a single phase but rather an intergrowth of lithiated-spinel- and layered-like components that dominate the LT-LiNi_{1/3}Mn_{1/3}Co_{1/3}O₂ structure with interspersed regions of more randomly disordered rock salt configurations, particularly in the room-temperature product (Figure IX.4.2a).

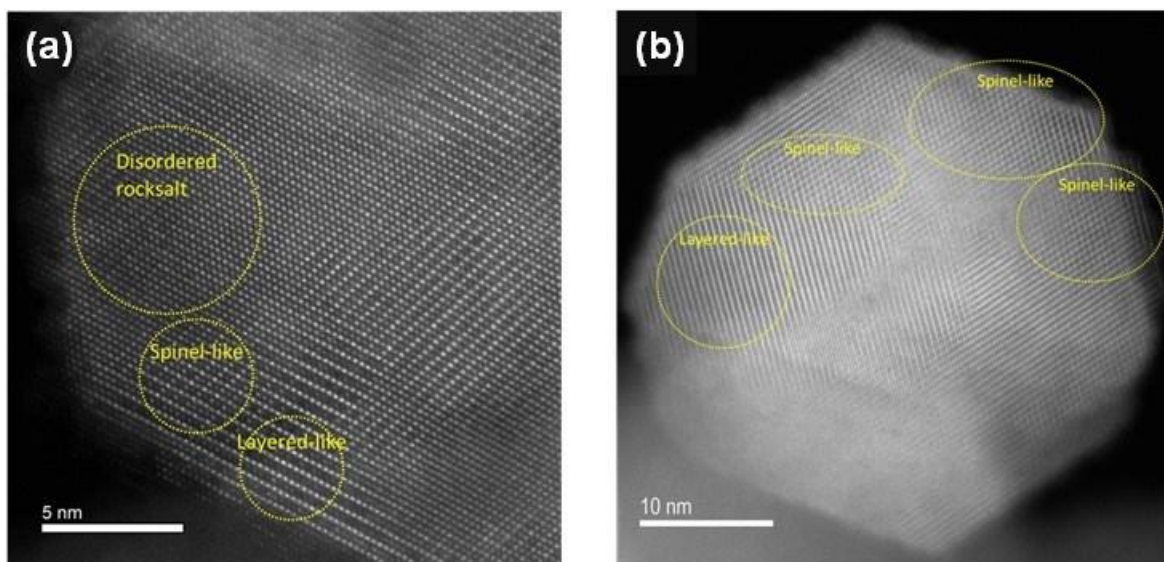


Figure IX.4.2 STEM-HAADF images of a FSP LT-LiNi_{1/3}Mn_{1/3}Co_{1/3}O₂ sample viewed down the [110]_{cubic} lithiated-spinel zone axis: (a) at room temperature, and (b) after annealing at 625 °C.

The electrochemical charge-discharge profiles of Li/LT-LiNi_{1/3}Mn_{1/3}Co_{1/3}O₂ cells annealed at 400, 500 and 625 °C are shown in Figure IX.4.3a. Cells were cycled between 4.3 and 2.7 V to monitor the cycling stability of the electrodes without the complications of possible oxygen participation in the reactions, whether electrochemically at higher potentials (>4.5 V) or with the electrolyte, both of which can lead to capacity loss. X-ray absorption spectroscopy (XAS) showed that the redox reactions occur predominantly on the cobalt and nickel ions, i.e., Co³⁺ ↔ Co⁴⁺ and Ni²⁺ ↔ Ni³⁺, while the tetravalent manganese ions, Mn⁴⁺, act mainly as spectator ions as they do in layered HT-LiNi_{1/3}Mn_{1/3}Co_{1/3}O₂ and spinel HT-LiMn_{1.5}Ni_{0.5}O₄ electrodes. The electrochemical signature of cells with LT-LiNi_{1/3}Mn_{1/3}Co_{1/3}O₂ electrodes is characteristic of a typical single-

phase reaction adopted by layered and disordered rock salt systems, consistent with the composite character of the electrode. Such two-phase to single-phase reaction transitions have also been observed in other spinel-related cathode materials, e.g., slightly disordered $\text{LT-LiCo}_{1-x}\text{Al}_x\text{O}_2$ ($0 < x < 0.3$).²

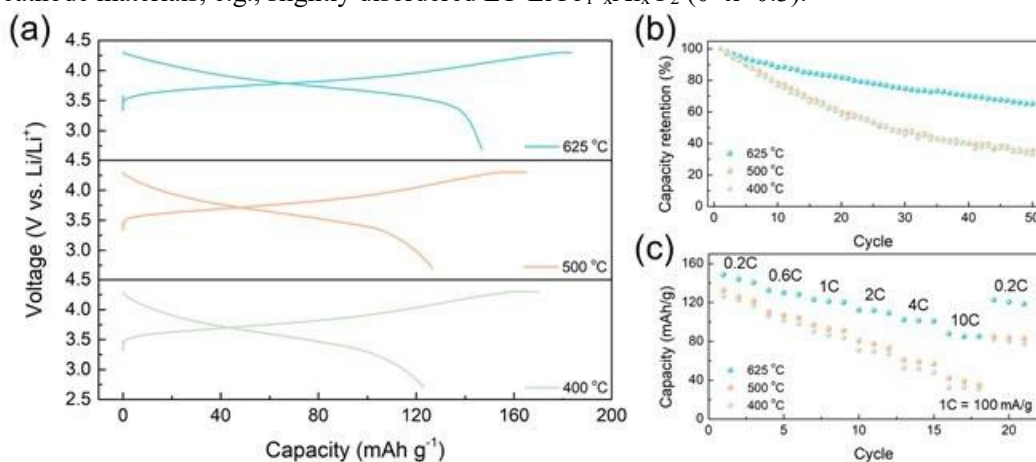


Figure IX.4.3 (a) First-cycle voltage profiles of Li/LT- $\text{LiNi}_{1/3}\text{Mn}_{1/3}\text{Co}_{1/3}\text{O}_2$ cells with annealed electrodes, (b) capacity retention over 50 cycles, and (c) rate capability.

A conventional layered HT- $\text{LiNi}_{1/3}\text{Co}_{1/3}\text{Mn}_{1/3}\text{O}_2$ electrode is typically synthesized at 850-900 °C; it has a theoretical capacity of 278 mAh/g for the complete extraction and reinsertion of lithium. LT- $\text{LiNi}_{1/3}\text{Co}_{1/3}\text{Mn}_{1/3}\text{O}_2$ electrodes annealed at 400 and 500 °C provide only ~45% of this capacity on the initial discharge from 4.3 V (123 and 126 mAh/g , respectively) at a 0.2C rate (Figure IX.4.3a), which fades rapidly on cycling (Figure IX.4.3b). On the other hand, a LT- $\text{LiNi}_{1/3}\text{Co}_{1/3}\text{Mn}_{1/3}\text{O}_2$ electrode, annealed at 625 °C, provides a higher capacity (148 mAh/g , 53% utilization), which approaches the value reported for layered HT- $\text{LiNi}_{1/3}\text{Co}_{1/3}\text{Mn}_{1/3}\text{O}_2$ electrodes in lithium cells (~165 mAh/g , ~60% utilization, C/10 rate, 4.3-3.0 V)⁵ and improved cycling stability (Figure IX.4.3b). Of particular significance is that ~60 % of the capacity supplied by the annealed (625 °C) LT- $\text{LiNi}_{1/3}\text{Co}_{1/3}\text{Mn}_{1/3}\text{O}_2$ electrode at a 0.2 C rate was delivered at 10 C (Figure IX.4.3c). This notable rate capability for such a complex, disordered, and composite electrode structure is tentatively attributed to the remarkable structural compatibility between the lithiated-spinel and layered components that share an almost perfectly-matched cubic-close-packed oxygen array with interlinked 3-dimensional and 2-dimensional pathways for Li^+ -ion transport.

The normalized voltage profiles in Figure IX.4.4 clearly show that an LT- $\text{LiNi}_{1/3}\text{Co}_{1/3}\text{Mn}_{1/3}\text{O}_2$ electrode, annealed at 625 °C substantially reduces the voltage hysteresis during electrochemical cycling. This enhancement in performance is attributed to the conversion of the disordered rock salt component to lithiated-spinel and layered configurations as the annealing temperature is increased.

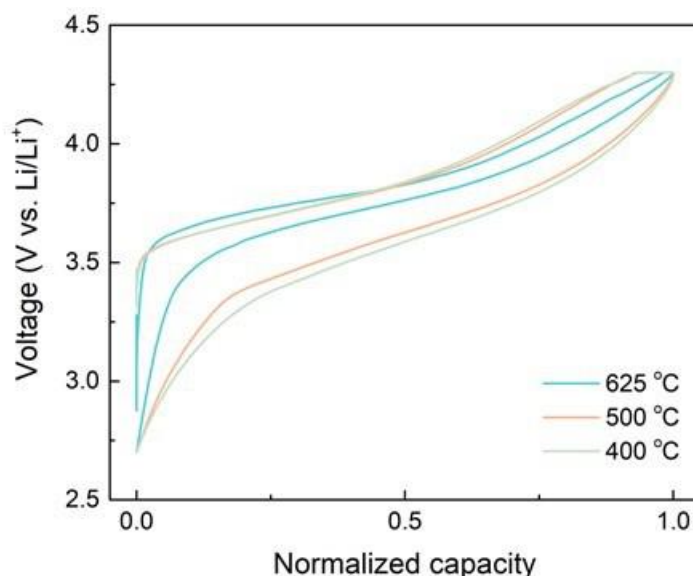


Figure IX.4.4 Normalized-capacity voltage profiles of Li/LT-LiNi_{1/3}Mn_{1/3}Co_{1/3}O₂ cells showing smaller hysteresis when higher annealing temperatures are used.

Ex-situ XRD patterns of a LT-LiNi_{1/3}Co_{1/3}Mn_{1/3}O₂ cathode that had been annealed at 625 °C, were collected at various points between 2.7 and 4.3 V on the initial electrochemical cycle of a Li/LT-LiNi_{1/3}Co_{1/3}Mn_{1/3}O₂ cell (Figure IX.4.5a, b). The reversible variations in the lattice parameter, a of the cubic unit cell and the I_{311}/I_{400} peak intensity ratio are plotted, as a function of the state of charge and discharge during the first cycle, in Figure IX.4.5c. The lattice parameter, $a = 8.107$ Å decreases isotropically by 1.0% to 8.036 Å during lithium extraction; the corresponding isotropic volume change of the cubic LT-LiNi_{1/3}Co_{1/3}Mn_{1/3}O₂ structure is an attractive 2.6%.

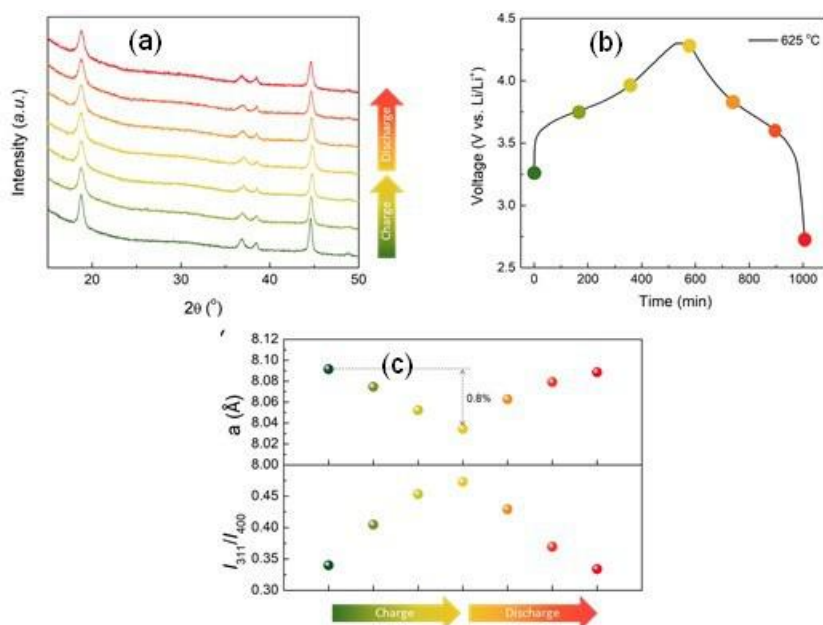


Figure IX.4.5 (a) Ex-situ XRD patterns of a LT-LiNi_{1/3}Mn_{1/3}Co_{1/3}O₂ (625 °C) electrode during the first charge/discharge cycle between 2.7 and 4.3 V, (b) points at which XRD data were collected on the voltage profile, and (c) variation of lattice parameter, a (top) and I_{311}/I_{400} ratio (bottom) during the first charge/discharge cycle.

Conclusions

This research project has exposed a new approach to tailor the compositional design of electrode structures and the cation distribution therein to optimize electrochemical performance and stability.

The compositional versatility of lithiated spinel electrode structures, $\text{Li}_2\text{M}_2\text{O}_4$ ($\text{M}=\text{Mn}, \text{Ni}, \text{Co}$) when synthesized at a relatively low temperature (400 – 650 °C) has been demonstrated. For cobalt-rich systems, single-phase lithiated spinel materials can be made, whereas the relatively low-cost, manganese-based systems yield structurally-compatible intergrowths of disordered rock salt, lithiated spinel and layered components that transform at higher temperatures into a predominant layered configuration. These materials are of interest not only as electrode materials for Li-ion batteries in their own right, but also as stabilizing agents for layered, high-capacity, manganese-rich electrode structures.

This project is a work in progress.

Key Publications

1. Thackeray, M. M.; Lee, E.; Shi, B.; Croy, J. R. Review – From LiMn_2O_4 to Partially-Disordered $\text{Li}_2\text{MnNiO}_4$: The Evolution of Lithiated-Spinel Cathodes for Li-Ion Batteries, *J. Electrochem. Soc.*, **169**, (2022) 020535.
2. Gutierrez, A.; Kirner, J. T.; Tamadoni Saray M.; Avdeev, M.; Geng, L.; Shahbazian Yassar, R.; Lu, W.; Croy, J. R., Critical Barriers to Successful Implementation of Earth-Abundant, Mn-Rich Cathodes for Vehicle Applications and Beyond: The Effect of Particle Morphology, *J. Electrochem. Soc.* **169**, 0205474 (2022).
3. Gutierrez, A.; Chen, J.; Vu, A.; Lin, Y.; Wen, J.; Dogan, F.; Balasubramanian, M.; Croy, J.R. *Development of Earth-Abundant Cathodes for Vehicle Applications and Beyond*, 242nd ECS Meeting, Atlanta, GA (October 10, 2022).
4. Gutierrez, A.; Chen, J.; Saray, M.T.; Yassar, Y.S.; Balasubramanian, M.; Wang, Y.; Croy, J.R. *Probing the Impedance at Low States-of-Charge of Li- and Mn-rich Cathodes*, 14th AIChE Midwest Regional Conference (March 2, 2022).
5. Croy, J.R. *Sustainable Cathodes for Li-Ion applications*, American Chemical Society, Fall 2022, Chicago, IL, August 22, 2022) – **Invited**
6. Croy, J.R. *Sustainable Cathodes for Li-Ion applications*, 21st International Meeting on Lithium Batteries, Sydney, (June 7, 2022) – **Invited**
7. Croy, J.R. *Development of Manganese-Rich Cathode Materials for Lithium-Ion Batteries: Promise, Progress, and Critical Barriers* International Manganese Institute, 46th Annual Conference, Cape Town, (June 1, 2022) – **Invited**
8. Croy, J.R. *Development of Manganese-Rich Cathode Materials for Lithium-Ion Batteries: Promise, Progress, and Critical Barriers*, International Manganese Institute, 46th Annual Conference, Cape Town, (June 1, 2022) – **Invited**
9. Thackeray, M.M. *The Pros and Cons of Cathode Chemistries for Li-Ion Batteries*, International Manganese Institute, 46th Annual Conference, Cape Town, (June 1, 2022) – **Invited**
10. Thackeray, M. M. *Lithium-ion Batteries: The Need for Clean Energy Storage – From Scientific Discovery to Technological Application*, New Fellows' Seminar, Royal Society, London, UK, (July 12, 2022) – **Invited**
11. Thackeray, M. M. *Oxford University 1982/82 – A Defining Moment*, 100th Birthday Celebration in Honor of John B. Goodenough, University of Texas, Austin, TX, (July 22, 2022) – **Invited**

References

1. Gummow, R. J.; Thackeray, M. M.; Lithium-Cobalt-Nickel-Oxide Cathode Materials Prepared at 400 °C for Rechargeable Lithium Batteries, *Solid State Ionics*, **53-56**, (1992) 681.
2. Lee, E.; Kwon, B. J.; Dogan, F.; Ren, Y.; Croy, J. R.; Thackeray, M. M., Lithiated Spinel $\text{LiCo}_{1-x}\text{Al}_x\text{O}_2$ as a Stable Zero-Strain Cathode, *ACS Applied Energy Materials* **2** (9), (2019) 6170.

3. Shi, B.; Gim, J.; Li, L.; Wang, C.; Vu, A.; Croy, J.R.; Thackeray, M.M.; Lee, E. LT-LiMn_{0.5}Ni_{0.5}O₂: A Unique Co-Free Cathode for High Energy Li-Ion Cells, *Chem. Comm.* **57**, (2021) 11009.
4. Lee, E.; Blauwkamp, J.; Castro, F. C.; Wu, J.; Dravid, V. P.; Yan, P.; Wang, C.; Kim, S.; Wolverton, C.; Benedek, R.; Dogan, F.; Park, J. S.; Croy, J. R.; Thackeray, M. M. Exploring Lithium-Cobalt-Nickel Oxide Spinel Electrodes for ≥ 3.5 V Li-Ion Cells. *ACS Appl. Mater. Inter.* **8**, (2016) 27720.
5. Zhu, J.; Chen, G. Single-Crystal Based Studies for Correlating the Properties and High-Voltage Performance of Li[Ni_xMn_yCo_{1-x-y}]O₂ Cathodes. *J. Mater. Chem. A*, **7**, (2019) 5463.

Acknowledgements

Contributions from the following individuals are acknowledged: Boyu Shi, Eungje Lee, Michael M. Thackeray, Arturo Gutierrez, Jiajun Chen, Kyojin Ku, Jinhyup Han, Linze Li, Jihyeon Gim, Anthony Stark, Joseph Libera, Chongmin Wang, Linze Li, Yujia Liang, and Jason R. Croy.

IX.5 Disordered RockSalt Structured Cathode Materials: Electrochemistry and Synthesis (LBNL, ORNL, PNNL, UC Santa Barbara)

Guoying Chen, Principal Investigator

Lawrence Berkeley National Laboratory
1 Cyclotron Road
Berkeley, CA 94720
E-mail: GChen@lbl.gov

Tien Duong, DOE Technology Development Manager

U.S. Department of Energy
E-mail: Tien.Duong@ee.doe.gov

Start Date: October 1, 2018
Project Funding: \$1,940,000

End Date: September 30, 2022
DOE share: \$1,940,000

Non-DOE share: \$0

Project Introduction

The projected growth of Li-ion battery (LIB) production towards multiple TWh/year will require several million tons of Co/Ni combined, which constitutes a very sizeable fraction of the annual production of these metals. The recent development of Li-excess cation-disordered rocksalts (DRX) provides an alternative to develop high energy density LIB cathodes that use more abundant and less expensive elements, and can respond to the industry need for lower cost, less resource intensive cathode materials. DRX materials have been shown to deliver energy densities over 1000 Wh/kg, and its cation disordered nature allowing for a wide range of chemistry free of Co and/or Ni. The ability to substitute some of the oxygen by fluorine in locally Li-rich environments provides an extra handle to optimize performance through increasing transition-metal (TM) redox capacity. As this class of cathodes are relatively new, further materials design and development are needed in order to properly evaluate their promises and challenges towards eventual commercialization. To do so, fundamental understanding of what controls DRX performance characteristics, particularly rate capability, cycling stability and voltage slope, is critical. This project has assembled necessary research expertise in modeling, synthesis, electrochemistry and characterization to tackle these challenges. The current chapter reports on the Synthesis and Electrochemistry components of the project and it has a companion report on Modeling and Characterization of the materials.

Objectives

The goals of this project are as follows:

- Understand the factors that control DRX cycling stability, particularly to what extent cycle life is controlled by impedance growth on the surface and by bulk changes in the material
- Understand what controls the rate capability of DRX materials, particularly rate limitation posed by bulk transport and surface processes
- Investigate the root of voltage profile slope in DRX
- Develop Co-free high energy density DRX cathodes.

Approach

This project originally focused on three representative baseline systems and their analogues: 1) Mn-redox based $\text{Li}_{1.2}\text{Mn}_{0.625}\text{Nb}_{0.175}\text{O}_{1.95}\text{F}_{0.05}$ (LMNOF), 2) Ni-redox based $\text{Li}_{1.15}\text{Ni}_{0.45}\text{Ti}_{0.3}\text{Mo}_{0.1}\text{O}_{1.85}\text{F}_{0.15}$ (LNTMOF), and 3) a high F-content $\text{Li}_2\text{Mn}_{1/2}\text{Ti}_{1/2}\text{O}_2\text{F}$ (LMTOF-II) that utilizes the $2e^- \text{Mn}^{2+}/\text{Mn}^{4+}$ redox couple. The team operates in six thrust areas representing the challenges and opportunities in DRX materials:

1. Characterization of the local and global structures of the bulk material before, during and after cycling, including detailed characterization of TM and O redox processes in the bulk and on the surface.
2. Characterization and manipulation of short-range cation ordering (SRO) to enhance rate capability.
3. Characterization and modeling of the DRX surface chemistry and processes during cycling to high voltages
4. Electrolyte/cathode interface issues and impedance growth due to surface processes
5. Fluorine solubility limits and synthesis of highly fluorinated compounds with scalable methods
6. Electrochemistry and testing in coin and pouch cells.

The current report focuses on items (5-6) whereas items (1-4) are discussed in the report for the next section..

Results

Fluorination of DRX materials

Partial fluorine substitution for oxygen has been shown to raise the capacity and improve the cyclability of DRX oxide cathodes. Yet, their synthesis remains challenging due to the limited solubility of fluoride precursors (*e.g.*, LiF) and Li metal oxides. While high-energy ball milling can be used to increase fluorine uptake, it requires high energy input and affords poor control over the particle morphology. Therefore, to better understand whether traditional solid-state synthesis can be used to prepare DRX oxyfluorides with high fluorination levels, we evaluated several different precursor sets targeting a composition of $\text{Li}_{1.2}\text{Mn}_{0.4}\text{Ti}_{0.4}\text{O}_{1.6}\text{F}_{0.4}$. Characterization was performed *in situ* to monitor the reaction pathway associated with each precursor set. The study revealed that high fluorine content ($\sim 25\%$) is achievable in DRX materials, excluding later transition metals such as Mn. For example, $\text{Li}_3\text{TiO}_3\text{F}$ was successfully prepared; however, incorporation of Mn into the DRX phase led to loss of fluorine from it. The tradeoff between Mn and F contents is illustrated in the observed reaction pathways when heating a precursor mixture of Li_2CO_3 , MnO, TiO_2 , and LiF (Figure IX.5.1). In the left panel, the XRD patterns of the corresponding products synthesized at various high temperatures are shown. A highly fluorinated DRX phase was formed at 700°C , as evidenced by the absence of LiF impurity, but prominent MnO peaks remained. Upon heating the sample to 1000°C , the MnO peaks were reduced while new LiF peaks appeared. These changes were coupled with expansion of the DRX lattice constant, suggesting the uptake of larger Mn^{2+} ions. Interestingly, after holding the sample at 1000°C for 12 hours, the LiF peaks disappeared completely. Although one may assume that this indicates fluorination of the DRX phase, what we found was the evaporation of LiF instead. This is shown in the TGA/DSC measurements (right panel in Figure IX.5.1), which reveals a clear endothermic peak associated with LiF melting at 848°C , followed by a rapid mass loss as the molten phase evaporated under the Ar flow.

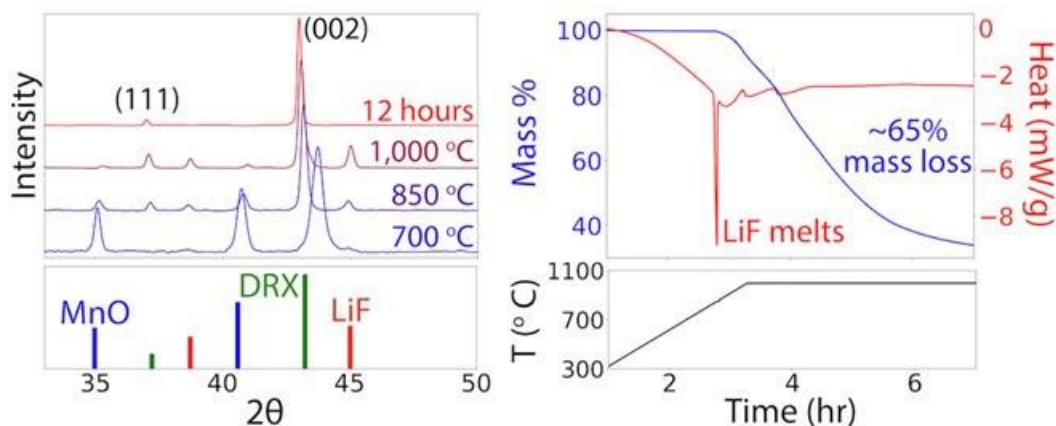


Figure IX.5.1 The left panel shows XRD patterns collected on a sample with a nominal composition of $\text{Li}_{1.2}\text{Mn}_{0.4}\text{Ti}_{0.4}\text{O}_{1.6}\text{F}_{0.4}$ synthesized with various temperatures and holding times. The right panel displays data from TGA/DSC measurements performed on the same sample during heat treatment to 1000°C .

To determine whether alternative fluoride precursors could be used for the synthesis of DRX oxyfluorides with higher F contents, we performed first principles calculations aiming to identifying precursor sets with a high fluorine chemical potential and a large thermodynamic driving force to form the target, $\text{Li}_{1.2}\text{Mn}_{0.4}\text{Ti}_{0.4}\text{O}_{1.6}\text{F}_{0.4}$. Three of these sets were experimentally evaluated, with each containing MnF_2 as a novel fluorinating agent. By using *in situ* XRD, we found that MnF_2 consistently reacted with the Li-containing precursor at a low temperature ($\leq 400^\circ\text{C}$), well before the DRX phase could form ($\geq 700^\circ\text{C}$). Therefore, although each sample started from a high fluorine chemical potential that favored the target phase, early formation of LiF lowered the chemical potential and precluded the formation of a highly fluorinated DRX phase. Based on these findings, we identified three principal factors that limit fluorine solubility in DRX materials during solid-state synthesis. These factors are summarized in Figure IX.5.2.

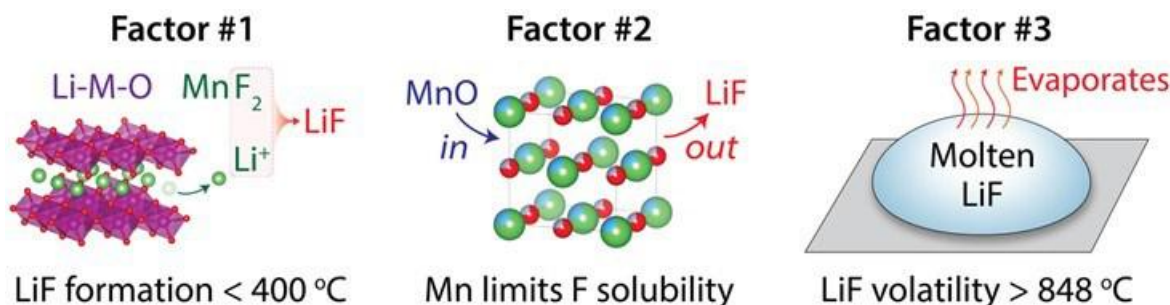


Figure IX.5.2 Schemics showing the three factors that limit fluorine solubility in DRX oxyfluorides synthesized using a solid-state route.

Alternative DRX synthesis methods

Considering the challenges in synthesizing highly fluorinated DRX oxyfluorides using the solid-state route, we developed an alternative sol-gel process to prepare such materials. Compared to traditional solid-state and mechanochemical routes, the sol-gel approach enables atomic-scale mixing of the precursors, which can lead to lower energy reaction pathways and facilitate formation of the desired phase during annealing. Sol-gel processes can also produce powders with controlled morphology at relatively low temperatures. A total of four targeted materials with the nominal compositions of $\text{Li}_{1.2}\text{Mn}_{0.4}\text{Ti}_{0.4}\text{O}_2$ (LMTO04), $\text{Li}_{1.2}\text{Mn}_{0.5}\text{Ti}_{0.3}\text{O}_{1.9}\text{F}_{0.1}$ (LMTOF05), $\text{Li}_{1.2}\text{Mn}_{0.6}\text{Ti}_{0.2}\text{O}_{1.8}\text{F}_{0.2}$ (LMTOF06), and $\text{Li}_{1.2}\text{Mn}_{0.7}\text{Ti}_{0.1}\text{O}_{1.7}\text{F}_{0.3}$ (LMTOF07) were synthesized. LMTO04 oxide powders were prepared using a two-step synthesis involving: (i) pyrolysis of a sol-gel precursor at 400°C in air followed by (ii) high-temperature annealing under flowing Ar. *Ex-situ* characterization of samples annealed at 750 – 1000°C was performed to evaluate the synthesis pathway and formation of the intermediate phase(s). As shown by the powder XRD patterns (Figure IX.5.3a), a mixture of spinel phase(s) [obtained from step (i)] fully reacted to form phase-pure DRX after heating at 1000°C for 1 h. ^7Li solid-state nuclear magnetic resonance (ssNMR) measurements confirmed the presence of a disordered cation sublattice in the 1000°C sample, as evidenced by the broad ^7Li line shape (Figure IX.5.3b). Notably, the materials exhibited short-range cation ordering (SRO) as determined by selected area electron diffraction (SAED, Figure IX.5.3c) and neutron total scattering. We note that SRO has a dramatic impact on the material's electrochemical properties, and identifying these structure/function correlations is an ongoing activity within the program.

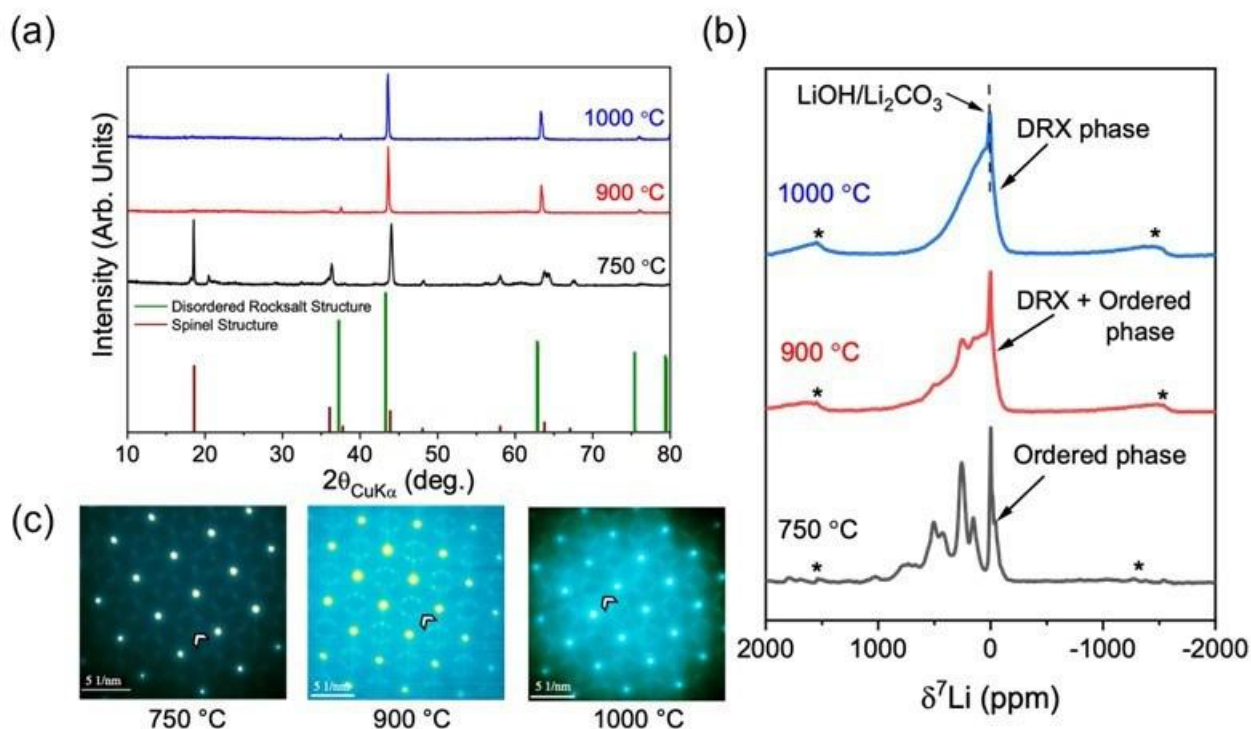


Figure IX.5.3 Structural characterization of LMT004 DRX samples annealed at 750 °C, 900 °C, and 1000 °C for 1 hour under flowing Ar. At each temperature, the products are characterized by: (a) X-ray diffraction, (b) ^7Li solid-state nuclear magnetic resonance spectroscopy, and (c) selected area electron diffraction. Asterisks in panel (b) indicate spinning sidebands due to fast rotation of the sample during ssNMR data acquisition. Arrows in panel (c) are used to highlight diffuse scattering patterns that arise due to SRO in the cation sublattice.

The electrochemical performance of LMT0 and LMT0F cathodes was evaluated in half cells containing Li metal anodes and a standard Li-ion liquid electrolyte (1.2M LiPF_6 in EC/EMC). As shown in Figure IX.5.4a, all cells exhibited a sloping voltage profile during the first cycle with high reversible capacities of 200 – 250 mAh/g. After 20 cycles, the Mn-rich materials (LMT0F06 and LMT0F07) developed distinct voltage plateaus and higher capacities up to 275 mAh/g (Figure IX.5.4b), owing to a cycling-induced phase transformations. Similar structural rearrangements have been reported for Mn-Ti DRX cathodes prepared through the solid-state and mechanochemical routes. Overall, the materials exhibited good cycling stability with minimal/no capacity fade over 50 cycles (Figure IX.5.4c). These results provide proof of concept for high-performing Mn-rich DRX cathodes prepared through a novel sol-gel route.

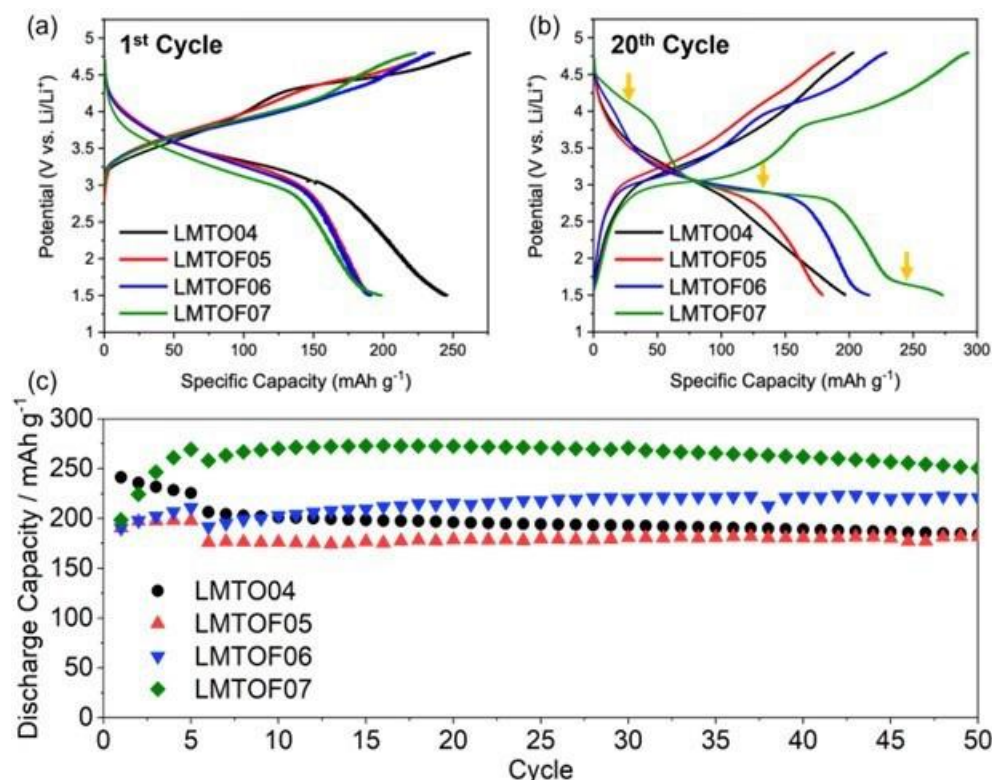


Figure IX.5.4 Electrochemical performance of LMT004, LMT0F05, LMT0F06, and LMT0F07 DRX cathodes in half cells. (a-b) Galvanostatic voltage profiles during the (a) 1st and (b) 20th cycle. (c) Discharge capacity retention over 50 cycles. The cathodes were cycled between 1.5 V and 4.8 V vs. Li/Li⁺ at a specific current of 10 mA g⁻¹ for the first 5 cycles and 20 mA g⁻¹ for subsequent cycles.

The sol-gel method was also extended to prepare a range of Mn-rich and F-doped DRX powders (LMT0F05, 06, and 07) by reacting the sol-gel oxide precursor with LiF at high temperatures. Notably, such an approach yielded lower-than-expected fluorine content. When the dried gel was mixed with LiF and subjected to annealing at 1000°C, minimal fluorine uptake was observed. We attribute this result to the volatility of LiF, which was not prevented by the use of a gel precursor. Even though the metal and oxygen atoms are mixed intimately within the dried gel, they are not mixed as well with the LiF precursor, thus slowing their reaction and allowing evaporation of LiF to occur. Although the approach appears to be largely ineffective in synthesizing highly fluorinated compositions, it can be extended to other Co-free DRX cathodes that cover a vast compositional landscape.

Electrode formulation, cell fabrication and cycling protocols

To prepare DRX electrodes, the active material is often ball milled with a carbon additive in the first step. The mixture is then made into a slurry by adding binder (such as PVDF) and additional carbon. During cell cycling, using a high charging voltage can increase energy output but it also accelerates electrolyte degradation and induces irreversible reactions in DRX itself. Over-lithiation upon discharge to low voltages, on the other hand, results in a gradual loss of capacity over time. Optimization of electrode and cell fabrication, as well as establishing proper voltage limits and cycling protocols, are therefore critical tasks in achieving DRX capacity and cycle life balance. In FY22, we carried out systematic evaluation on a number of parameters influencing electrode quality and cyclability. Below we discuss the impact of the following five aspects on the LMT0F06 DRX cathode material synthesized by a solid-state route: 1) air exposure time, 2) upper cutoff voltage, 3) electrolyte composition, 4) additional carbon, and 5) carbon additive type.

Air exposure time:

Li-rich DRX materials have been shown to be sensitive to air exposure which requires careful handling of the material throughout each of the processing steps, including slurry preparation, slurry mixing, slurry casting, laminate drying, electrode punching, electrode calendaring, tab welding, and pouch cell preparation. Since many of these steps involve tools that are way too large to fit in a glovebox, allowing some air exposure time would therefore greatly simplify cell making efforts. For this reason, we prepared cathodes using DRX powders that were exposed to air for 0, 1, and 24 hours, respectively. After the designated time of air exposure, all remaining processing steps in electrode and cell fabrication were conducted in a similar fashion. The first sign of the problem with air exposure is often shown during the slurry preparation and mixing steps as the binder is sensitive to water content in the solvent. Here we found that the level of DRX air exposure had negligible impact on the slurry properties. Once electrodes were prepared, they were tested in pouch-cell half-cells. Figure IX.5.5 compares discharge energy and roundtrip energy efficiency as a function of cycle number. The results are very similar for all three samples but the one exposed to air for 24 hours had a slightly lower roundtrip energy efficiency. Careful examine of the coulombic and voltage efficiency indicates that the difference is a result of slightly worse coulombic efficiency of that sample. The study suggests that an hour or even up to 24 hours of air exposure does not lead to significant damage to electrochemical performance, allowing some relaxation in DRX handling.

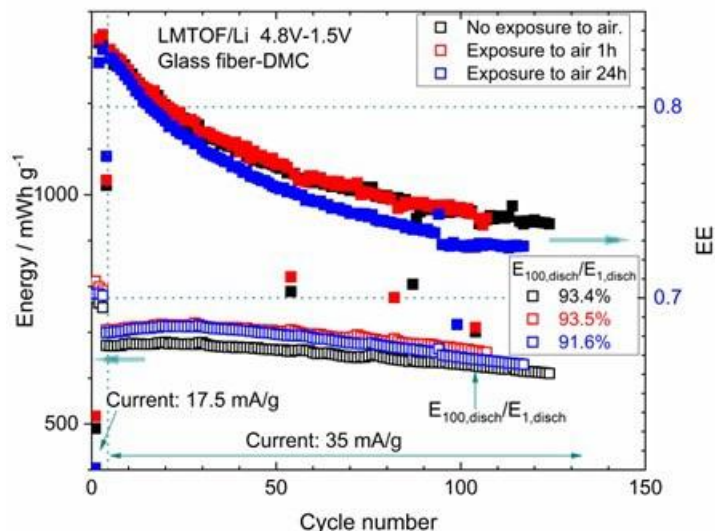


Figure IX.5.5 Comparison of specific discharge energy density and roundtrip energy efficiency of cells using the DRX materials with three different duration of air exposure time: 0, 1, and 24 hr.

Charging time above 4.7 V:

To evaluate the effect of time spent above 4.7 V during the charging process, we investigated three different charging protocols: 1) charge to 4.7 V and then go to open circuit voltage (OCV), 2) charge to 4.7 and then hold the voltage there until the current dropped to $C/50$, and 3) charge to 4.8 V and then switch to OCV. The lower cutoff voltage was kept the same at 1.5 V. Figure IX.5.6 shows the relationship between specific discharge energy (based on cathode active material) vs. cycle number. The capacity was the highest for the cell held at 4.7 V, surpassing that of the cell charged to 4.8 V. This suggests that the time spent at 4.7 at constant voltage results in more charge storage than that from the constant current charging from 4.7 to 4.8 V. In addition, the cell that was held at 4.8 V shows the fastest energy fade, indicating that a voltage hold at 4.7 V is better for cell life than charging the cell to 4.8 V. The cell that was only charged to 4.7 V and put to OCV started with less capacity than the cell with a voltage hold at 4.7 V. However, after 100 cycles, the former cell delivered more energy than the latter. Although further work is needed in order to optimize DRX cycling protocols, our study clearly shows that limiting upper charging voltage to below 4.8 V is beneficial to cell performance.

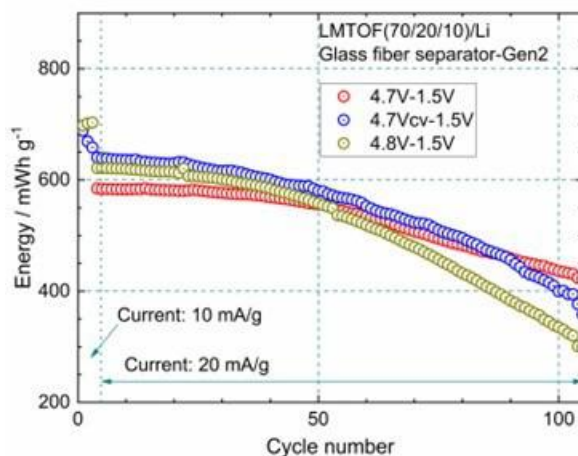


Figure IX.5.6 Specific discharge energy vs. cycle number for three cycling protocols: 4.7 V to OCV, 4.7 then constant voltage hold, and 4.8 V then OCV.

Electrolyte composition:

The dependence of cell performance as a function of the electrolyte composition was also investigated. Specifically, we evaluated DMC as a replacement for EMC and also investigated the effect of LiBOB additive by using the following three compositions: 1) 1.2 M LiPF_6 -EC/EMC (1/2 wt., referred to as Gen2); 2) 1.0 M LiPF_6 -EC/DMC (1/2 wt., referred to as DMC); and 3) 1.0 M LiPF_6 -EC/DMC (1/2 wt.) + 3 wt.% LiBOB (referred to as LiBOB). Figure IX.5.7 compares the capacity retention of the cells. The DMC cell has approximately the same initial discharge capacity as that of the Gen 2 cell, however, after 70 cycles, the capacities are at 215 mAh/g and 160 mAh/g for the DMC and Gen2 cells, respectively. The LiBOB cell has a slight improvement over the DMC cell initially, but it falls below the DMC cell at the 45th cycle and stays below from there. We believe that the superior performance of the DMC cell is partly due to the improved coulombic efficiency early on in the cycle life. The study suggests that DMC based electrolytes are better suited for cells equipped with a DRX cathode.

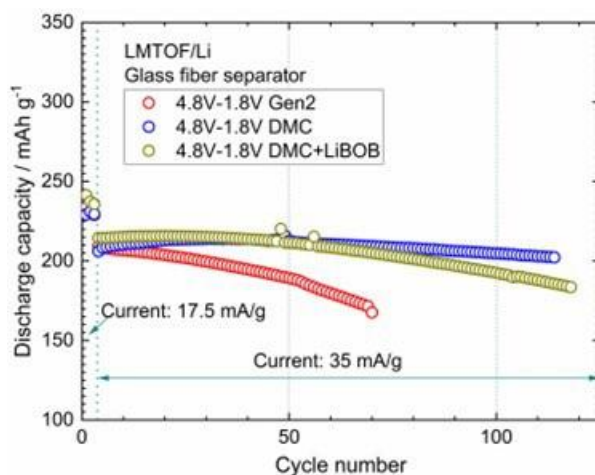


Figure IX.5.7 DRX cathode cycled with LiPF_6 electrolytes with either EMC or DMC as the solvent. A third cell contains DMC plus 3 wt.% of LiBOB.

Additional carbon:

Due to the low electronic conductivity of DRX, the active material is typically mixed with carbon black prior to fabricating composite electrodes. This produces a mass of active material particles with an electronically conductive coating, resulting in electrodes with an overall higher carbon content than that in an NMC-based

electrode where the active material to carbon ratio is often kept around 94:3. To understand the impact of the additional carbon, we fabricated electrodes with carbon-coated DRX in two formulations: 70:20:10 and 65:34:10 (active material: carbon: binder). Half cells were made and electrochemical impedance spectroscopy (EIS) was performed. Figure IX.5.8 shows the Nyquist plot by subtracting the EIS data of the 65:34:10 cell from the 70:20:10 cell, leaving two main semi-circles. The frequency of the peaks of the semi-circles coincide with the impedance due to charge transfer and electrolyte transport. The increase in these two sources increases the impedance in this frequency range by 33%, 30% attributed to the increase in charge transfer. We believe that the C65 carbon added during slurry making is a high surface area carbon that provides pore structure to the electrode. The porosity created by this type of carbon improves electrolyte transport, not only increasing electrolyte diffusion through the electrode but also facilitating ionic transport to the surface. The carbon coating introduced during the initial ball milling step, on the other hand, is not providing these functions. Further examine of the coulombic capacity, coulombic efficiency, the energy on discharge and the roundtrip energy efficiency reveals that there is more capacity and energy delivered with the additional carbon, that the coulombic efficiency is not changed but the energy efficiency is improved with the additional carbon. Again, this indicates that the additional carbon mainly has the effect of reducing impedance in the cell, which we attribute to improved electrolyte transport as a result of higher porosity.

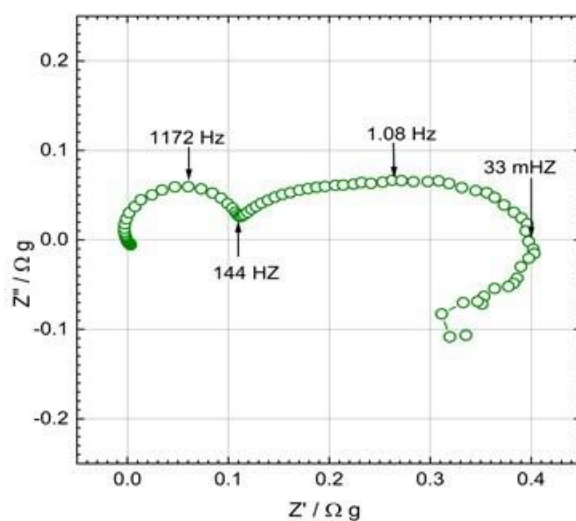


Figure IX.5.8 Nyquist plot obtained by subtracting the electrochemical impedance spectroscopy of the 65:34:10 cell from that of the 70:20:10 cell. While the cathode in the former cell only has ball milled carbon, the one in the latter cell has both ball milled carbon and a high surface area C65 conductive carbon additive.

Type of carbon additive:

With a goal of reducing the carbon content in the DRX electrodes, we compared three different carbon additives, C65 carbon black from Timcal (CB), graphitized carbon nano-fibers (GNCF), and carbon nano-tubes (CNT). All additives were introduced during slurry preparation, along with the electrode active material that was previously ball milled with carbon black. The amount of each carbon added was held constant at 6.4%. A plot of the discharge energy and roundtrip energy efficiency vs. cycle number for the three electrodes is provided in Figure IX.5.9. Although the electrode with CNT has slightly less coulombic efficiency than the other two, the energy vs. cycle life as well as the round-trip energy efficiency are identical for all three types of carbons. Results from the hybrid pulse power characterization, not shown here, are also identical for the three types of carbons. Further evaluation on cells with reduced total carbon content (currently 25% total carbon content by weight is used) is under way, although our preliminary results clearly indicate the limited role of carbon type, especially when the variations in surface area are considered as well.

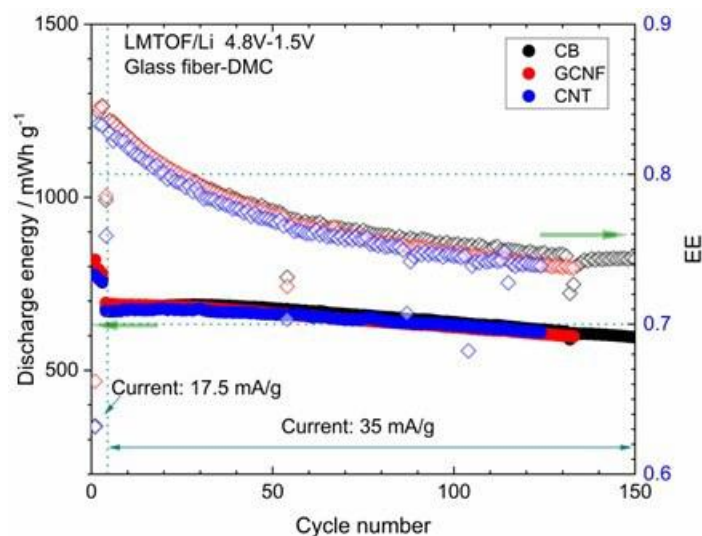


Figure IX.5.9 The discharge energy and roundtrip energy efficiency of three cells with different types of conductive carbon additives: CB, GCNF, and CNT.

Conclusions

In FY22, the Synthesis and Electrochemistry part of the “DRX deep-dive” program focused on increasing fluorination levels in DRX, developing alternative synthesis techniques, and determining performance-controlling factors in electrode formulation, cell fabrication and cycling protocols. Three principal factors were found to limit fluorine solubility in DRX materials during solid-state synthesis. An alternative sol-gel process was developed to prepare DRX materials. The method produced DRX materials with good cycling stability and provided proof-of-concept for its use in synthesizing high-performing Mn-rich DRX cathodes. From the electrode fabrication efforts, we found that DRX materials can be exposed to air for at least an hour and probably longer without a significant impact on cell performance. Cycle life performance is improved by charging to an upper cutoff voltage of 4.7 V instead of 4.8 V, and alternative electrolytes that mainly consist of DMC instead of EMC are more compatible for stable DRX cycling. The addition of conductive carbon improves the overall electrode performance, likely a result of providing an open porous structure to the laminate. Our preliminary results show limited impact from the type of carbon introduced during the slurry making process.

Key Publications

1. S. Patil, D. Darbar, E. C. Self, T. Malkowski, V. C. Wu, R. Giovine, N. J. Szymanski, R. D. McAuliffe, B. Jiang, J. K. Keum, K. P. Koirala, B. Ouyang, K. Page, C. Wang, G. Ceder, R. J. Clément, J. Nanda, “Alternate Synthesis Method for High-Performance Manganese Rich Cation Disordered Rocksalt Cathodes”, *Adv. Energy Mater.* **2022**
2. J. Ahn, R. Giovine, V. C. Wu, K. P. Koirala, C. Wang, R. J. Clément and G. Chen, “Ultrahigh-Capacity Rocksalt Cathodes Enabled by Cycling-Activated Structural Changes”, submitted
3. N. J. Szymanski, Y. Zeng, T. Bennett, S. Patil, J. K. Keum, E. C. Self, J. Bai, Z. Cai, R. Giovine, B. Ouyang, F. Wang, C. J. Bartel, R. J. Clément, W. Tong, J. Nanda, G. Ceder “Understanding the Fluorination of Disordered Rocksalt Cathodes through Rational Exploration of Synthesis Pathways”, *Chem. Mater.* **2022**, 34, 7015
4. D. Darbar, T. Malkowski, E. C. Self, I. Bhattacharya, M. V. V. Reddy, J. Nanda “An overview of cobalt-free, nickel-containing cathodes for Li-ion batteries”, *Mater. Today Energy* **2022**, 30, 101173.
5. N. Muralidharan, E. C. Self, M. Dixit, Z. Du, R. Esshli, R. Amin, J. Nanda, I. Belharouak, “Next-Generation Cobalt-Free Cathodes – A Prospective Solution to the Battery Industry’s Cobalt Problem”, *Adv. Energy Mater.* **2022**, 12, 2103050

Acknowledgements

Juhyeon Ahn, Oxana Andriuc, Vincent Battaglia, Tyler Bennet, Jordan Burns, Zijian Cai, Dongchang Chen, Guoying Chen, Jianli Cheng, Raphaelle Juliette Clement, Matthew Crafton, Emily Foley, Yanbao Fu, Raynald Giovine, Yang Ha, Kenny Higa, Mathew Horton, Tzu-Yang Huang, Huiwen Ji, Robert Kostecki, Linze Li, Zhengyan Lun, Bryan McCloskey, Jagjit Nanda, Bin Ouyang, Kristin Persson, Rohit Satish, Ethan C. Self, Martin Siron, Wei Tong, Chongmin Wang, Ruoxi Yang, Wanli Yang, Yuan Yue, Yiman Zhang, Peichen Zhong

IX.6 Disordered RockSalt Structured Cathode Materials: Characterization and Modeling (LBNL, ORNL, PNNL, UC Santa Barbara)

Gerbrand Ceder, Principal Investigator

Lawrence Berkeley National Laboratory
1 Cyclotron Road
Berkeley, CA 94720
E-mail: gceder@berkeley.edu

Tien Duong, DOE Technology Development Manager

U.S. Department of Energy
E-mail: Tien.Duong@ee.doe.gov

Start Date: October 1, 2018
Project Funding: \$4,810,000

End Date: September 30, 2022
DOE share: \$4,810,000

Non-DOE share: \$0

Project Introduction

The projected growth of Li-ion battery (LIB) production towards multiple TWh/year will require several million tons of Co/Ni combined, which constitutes a very sizeable fraction of the annual production of these metals. The recent development of Li-excess cation-disordered rocksalts (DRX) provides an alternative to develop high energy density LIB cathodes that use more abundant and less expensive elements, and can respond to the industry need for lower cost, less resource intensive cathode materials. DRX materials have been shown to deliver energy densities over 1000 Wh/kg, and its cation disordered nature allowing for a wide range of chemistry free of Co and/or Ni. The ability to substitute some of the oxygen by fluorine in locally Li-rich environments provides an extra handle to optimize performance through increasing transition-metal (TM) redox capacity. As this class of cathodes are relatively new, further materials design and development are needed in order to properly evaluate their promises and challenges towards eventual commercialization. To do so, fundamental understanding of what controls DRX performance characteristics, particularly rate capability, cycling stability and voltage slope, is critical. This project has assembled necessary research expertise in modeling, synthesis, electrochemistry and characterization to tackle these challenges. The current chapter reports on the Modeling and Characterization components of the project and it has a companion report on Synthesis and Electrochemistry of the materials.

Objectives

The goals of this project are as follows:

- Understand the factors that control DRX cycling stability, particularly to what extent cycle life is controlled by impedance growth on the surface and by bulk changes in the material
- Understand what controls the rate capability of DRX materials, particularly rate limitation posed by bulk transport and surface processes
- Investigate the root of voltage profile slope in DRX
- Develop Co-free high energy density DRX cathodes.

Approach

This project originally focused on three representative baseline systems and their analogues: 1) Mn-redox based $\text{Li}_{1.2}\text{Mn}_{0.625}\text{Nb}_{0.175}\text{O}_{1.95}\text{F}_{0.05}$ (LMNOF), 2) Ni-redox based $\text{Li}_{1.15}\text{Ni}_{0.45}\text{Ti}_{0.3}\text{Mo}_{0.1}\text{O}_{1.85}\text{F}_{0.15}$ (LNTMOF), and 3) a high F-content $\text{Li}_2\text{Mn}_{1/2}\text{Ti}_{1/2}\text{O}_2\text{F}$ (LMTOF-II) that utilizes the $2e^- \text{Mn}^{2+}/\text{Mn}^{4+}$ redox couple. The team operates in six thrust areas representing the challenges and opportunities in DRX materials:

1. Characterization of the local and global structures of the bulk material before, during and after cycling, including detailed characterization of TM and O redox processes in the bulk and on the surface.

2. Characterization and manipulation of short-range cation ordering (SRO) to enhance rate capability.
3. Characterization and modeling of the DRX surface chemistry and processes during cycling to high voltages
4. Electrolyte/cathode interface issues and impedance growth due to surface processes
5. Fluorine solubility limits and synthesis of highly fluorinated compounds with scalable methods
6. Electrochemistry and testing in coin and pouch cells.

The current report focuses on items (1-4) whereas items (5-6) are discussed in the report for the prior section..

Results

1) Methodology for quantifying fluorine solubility

Our findings from the solid-state synthesis experiments targeting highly fluorinated DRX compounds revealed that X-ray diffraction (XRD) analysis alone is insufficient to prove (or disprove) the presence of fluorine in reaction products. The formation and potential evaporation of LiF, in addition to the possible appearance of minor impurities including Li_2O and Li_2CO_3 , are difficult to characterize in a quantitative fashion using conventional techniques such as XRD. The presence of such phases can have a significant impact on the electrochemical performance of DRX cathodes, and therefore it is critical to develop new methodologies for their identification. Accordingly, we have outlined and validated a systematic experimental workflow as shown in Figure IX.6.1. This procedure is designed to accurately determine the composition of DRX cathode materials. It also includes a straightforward water-based washing procedure to remove possible Li-containing surface impurities from DRX samples. The new methodology has been applied to various cathode chemistries, including Li-Mn²⁺-Ti⁴⁺-O-F-based DRX materials obtained *via* solid-state: $\text{Li}_{1.25}\text{Mn}_{0.25}\text{Ti}_{0.50}\text{O}_{1.75}\text{F}_{0.25}$ (F25) and $\text{Li}_{1.25}\text{Mn}_{0.20}\text{Ti}_{0.55}\text{O}_{1.85}\text{F}_{0.15}$ (F15), as well as those from high-energy ball-milling such as $\text{Li}_{1.33}\text{Mn}_{0.33}\text{Ti}_{0.33}\text{O}_{1.33}\text{F}_{0.66}$ (F66). We have also applied the approach to several Li-Mn³⁺-Nb⁵⁺-O-F-based DRX compositions synthesized by solid-state methods, including $\text{Li}_{1.2}\text{Mn}_{0.6+x/2}\text{Nb}_{0.2-x/2}\text{O}_{2-x}\text{F}_x$ with $x = \{0.1, 0.2, 0.3\}$ (denoted as NF10, NF20, and NF30, respectively). With this method, F25 and F66 were found to be $\text{Li}_{1.21}\text{Mn}_{0.267}\text{Ti}_{0.525}\text{O}_{1.88}\text{F}_{0.12}$ and $\text{Li}_{1.32}\text{Mn}_{0.34}\text{Ti}_{0.33}\text{O}_{1.45}\text{F}_{0.55}$, respectively. On the other hand, F15 had a stoichiometry of $\text{Li}_{1.18}\text{Mn}_{0.21}\text{Ti}_{0.55}\text{O}_{1.88}\text{F}_{0.12}$ which is close to its target value. After washing, the stoichiometry of F25 was $\text{Li}_{1.21}\text{Mn}_{0.265}\text{Ti}_{0.525}\text{O}_{1.88}\text{F}_{0.12}$. A significant reduction of Li-based impurities was observed, concurrent with a 14% increase in discharge capacity (from 159 to 182 mAh/g) after 20 cycles. These results highlight a significant discrepancy between the target composition and the actual stoichiometry obtained in DRX materials synthesized by conventional solid-state methods, which can be attributed to both LiF volatility during the high temperature sintering and the limited solubility of fluorine in DRX materials.

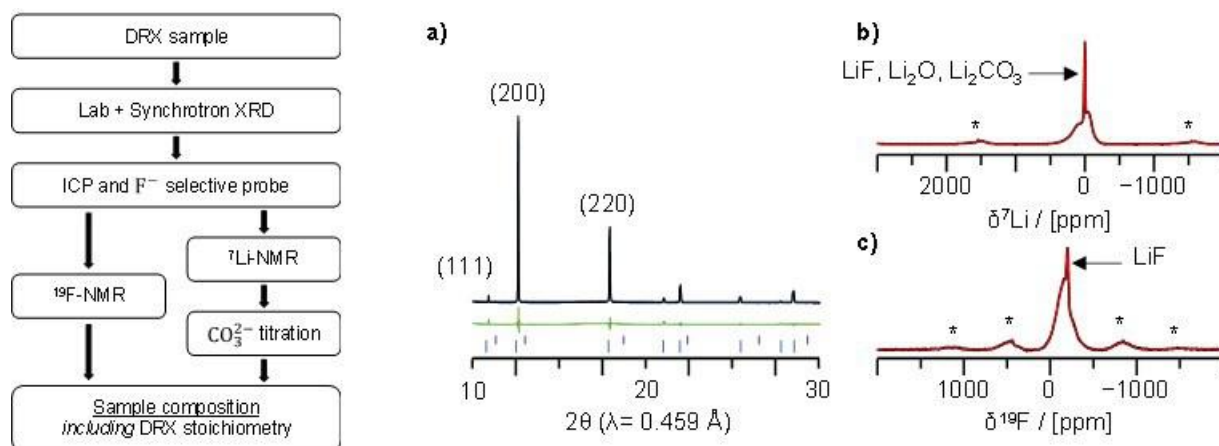


Figure IX.6.1 The left panel outlines a multi-step characterization methodology designed to determine the composition of DRX cathode materials and identify potential impurities. In the right panel, we show results from characterization of the F25 sample using a) synchrotron XRD, b) ^7Li , and c) ^{19}F solid-state nuclear magnetic resonance (NMR). While the XRD pattern shows a pure DRX phase with no LiF or Li_2O crystalline impurities (indexed with blue and purple reference lines, respectively), ^{19}F NMR analysis indicates the presence of LiF impurity and ^7Li NMR analysis shows LiF impurity as well as Li_2O and Li_2CO_3 impurities.

2) Effect of fluorine substitution level

The impact of fluorination level on surface redox processes was investigated on a series of $\text{Li}_{1.2}\text{Mn}_{(0.6+x)/2}\text{Nb}_{(0.2-x)/2}\text{O}_{2-x}\text{F}_x$ (LMNOF_x, $x = 0, 0.05$, and 0.2) samples, using both scanning transmission electron microscopy (STEM) and electron energy loss spectroscopy (EELS) analyses. In pristine LMNOF₀, the average Mn oxidation state was found to be trivalent in the particle bulk, but a distinct energy shift of the Mn L_3 peaks is observed within a thin surface layer (~ 5 nm), indicating that the reduction of Mn valence is present at the surface due to oxygen deficiency. On the other hand, in the cycled LMNOF₀ particles (Figure IX.6.2), there is a much stronger gradient distribution for the energy shifts of the Mn L_3 peaks from the bulk to the surface, indicating that the Mn valence reduction penetrates much deeper (up to 35 nm into the bulk). Since the Mn valence reduction can compensate for oxygen loss, such observed cycling-induced changes of the Mn valence distribution indeed suggest oxygen loss during cycling.

Increasing the F concentration to a high level ($x = 0.2$) in the DRX composition can improve the structural stability drastically, which is confirmed by our characterizations of the LMNOF_{0.2} cathode particles (Figure IX.6.2). The maps of the Mn L_3 peak energy shifts show that in both the pristine and cycled LMNOF_{0.2} particles, the Mn valence reduction mostly occurs within ~ 5 nm of the surface, corresponding to the local oxygen loss only at the very surface. These findings clearly demonstrate the critical role of high-level fluorination in the DRX cathode for greatly enhanced structural stability during cycling.

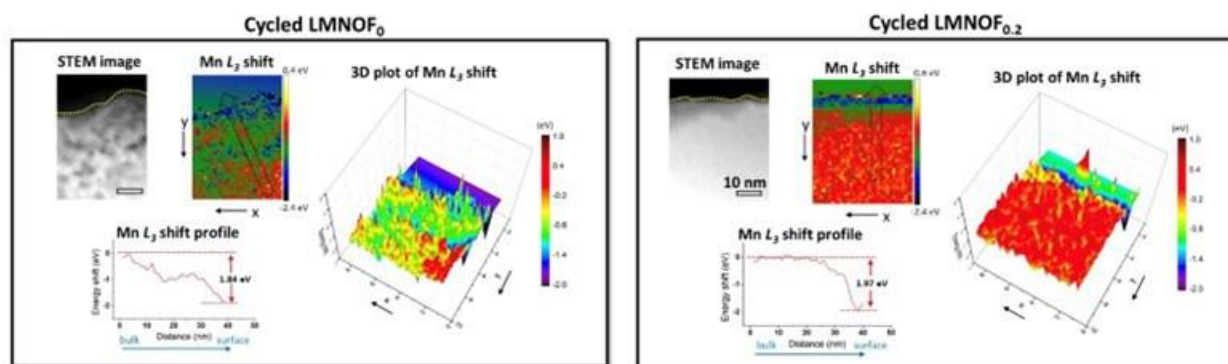


Figure IX.6.2 Scanning transmission electron microscopy - high-angle annular dark field (STEM-HAADF) images and corresponding EELS maps of Mn L_3 peak energy shifts, showing cycling-induced changes of Mn valence distributions in un-fluorinated (LMNOF₀, left) and highly fluorinated (LMNOF_{0.2}, right) DRX cathode particles.

Results from the soft X-ray absorption (sXAS) analysis further validate these observations. Figure IX.6.3 displays the surface Mn and O sXAS spectral evolution upon electrochemical cycling of LMNOF_{0.05} cycled in the standard PVDF/LiPF₆ binder/salt system, in comparison with F-free binder/electrolyte PE/LiClO₄ systems. The surface Mn state shows a very reversible redox in standard electrolyte, although the overall oxidation states are lower compared with the corresponding bulk state (Figure IX.6.3a). Such behavior is in sharp contrast with other Li-rich system with no fluorination based on similar sXAS measurements. This is generally consistent with the suppressed oxygen activities in fluorinated electrode materials, indicating a surface stabilization effect through fluorination.

Figure IX.6.3b-c are surface O-K sXAS evolutions during the 1st and 20th cycles. While the spectral variations of the standard binder/electrolyte system are dominated by the expected TM changes in the pre-edge range (528-533 eV) of the O-K sXAS, F-free system shows a strong cycling of carbonate species on the surface across extended cycles, indicating the occurrence of substantial electrolyte degradation.

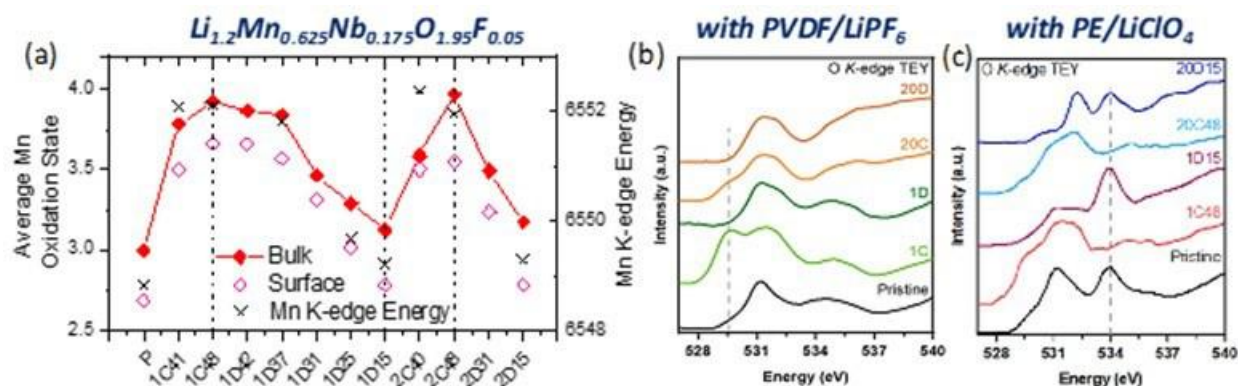


Figure IX.6.3 (a) Surface Mn state evolution of a LMNOF_{0.05} electrode cycled with a standard binder/electrolyte system (PVDF/LiPF₆). The oxidation state of surface Mn is clearly lower than that of the bulk, but displays fairly reversible behavior upon cycling. Bulk Mn is evaluated by Mn-L mRIXS-iPFY analysis that is not shown here. (b) Surface O state evolution of LMNOF_{0.05} in standard binder/electrolyte system. A typical pre-edge evolution is observed due to the TM state change, consistent with (a). (c) Surface O-K spectra reveal a strong carbonate cycling of LMNOF in F-free PE/LiClO₄ system over 20 cycles.

The above results suggest that either increasing fluorination in DRX bulk material or using an alternative electrolyte system are effective in stabilizing DRX electrode surface under high-voltage operations. Mitigating the finite amount of F loss in the near surface region and optimizing the binder/electrolyte system, however, are not trivial tasks. We are currently investigating chemical oxidation reactions taking place at the cathode of Li-ion batteries. By studying the feasibility of these reactions, we will elucidate which decomposition products are formed in the cathode-electrolyte interphase of DRX electrodes and the mechanisms responsible for their formation. Our approach builds upon the framework recently developed for the solid-electrolyte interphase at the anode [1]. We determine likely intermediates by fragmenting initial solvent molecules, such as ethylene carbonate (EC) and LiPF₆ along with likely gaseous reactants, such as O₂ into smaller molecules and atoms. These fragments are then recombined to generate potential reaction intermediates. The feasibility of a reaction to pass through any given intermediate is determined by constructing chemical reaction networks parameterized by free energies from density functional theory (DFT) computations. We have started by investigating the oxidation of EC. Through the process of fragmentation and recombination, we determined ~3000 new reaction intermediates whose free energies are being computed. We have also included proton transfer reactions, which have been suggested [2] to cause reactions to occur at less oxidative potentials. We will study different electrolytes and salts and compare predicted gaseous products with available experiments. We will expand recent work [3] by our group, which describes a mechanism for the decomposition of LiPF₆ through reactions with Li₂CO₃ to form reaction products such as POF₃ and F₂PO₂H and investigate the possibility of this reaction occurring at the cathode.

To further understand electrolyte degradation, we turn to outgassing measurements in various operating voltage windows of the LMNOF_{0.05}. Noting that residual Li₂CO₃ can contribute to CO₂ outgassing, along with electrolyte degradation processes, we first use solid-state NMR to understand the phase purity of the LMNOF materials. Our ⁷Li and ¹⁹F solid-state NMR results indicated that the as-prepared DRX cathodes are phase pure and that F is well incorporated into the bulk DRX framework. Specifically, no Li-containing diamagnetic impurity phase was observed in the ⁷Li solid-state NMR data, and no residual LiF precursor was observed even for highly fluorinated (x=0.6) active materials. The ⁷Li solid-state NMR results are consistent with the low amount of surface carbonate species measured by acid titration.

To mitigate CO₂ outgassing without substantially lowering Mn-DRX cathodes' capacities, we fine-tuned the discharge cut-off voltage between 1.5-2.25 V for cycling LMNOF_{0.05} in a conventional electrolyte, 1 M LiPF₆ in EC/EMC (3:7 v/v), as shown in Figure IX.6.4. Our DEMS results indicate that uplifting discharge cut-off voltage can suppress low-voltage CO₂ evolution in the following charge, and we identified 1.85 V as the optimal discharge cut-off voltage for LMNOF cathodes. In summary, our DEMS technique identified

electrolyte degradation as the dominant source of CO₂ evolution, which can be effectively suppressed by fine-tuning operating voltage windows for Mn-based DRX cathodes.

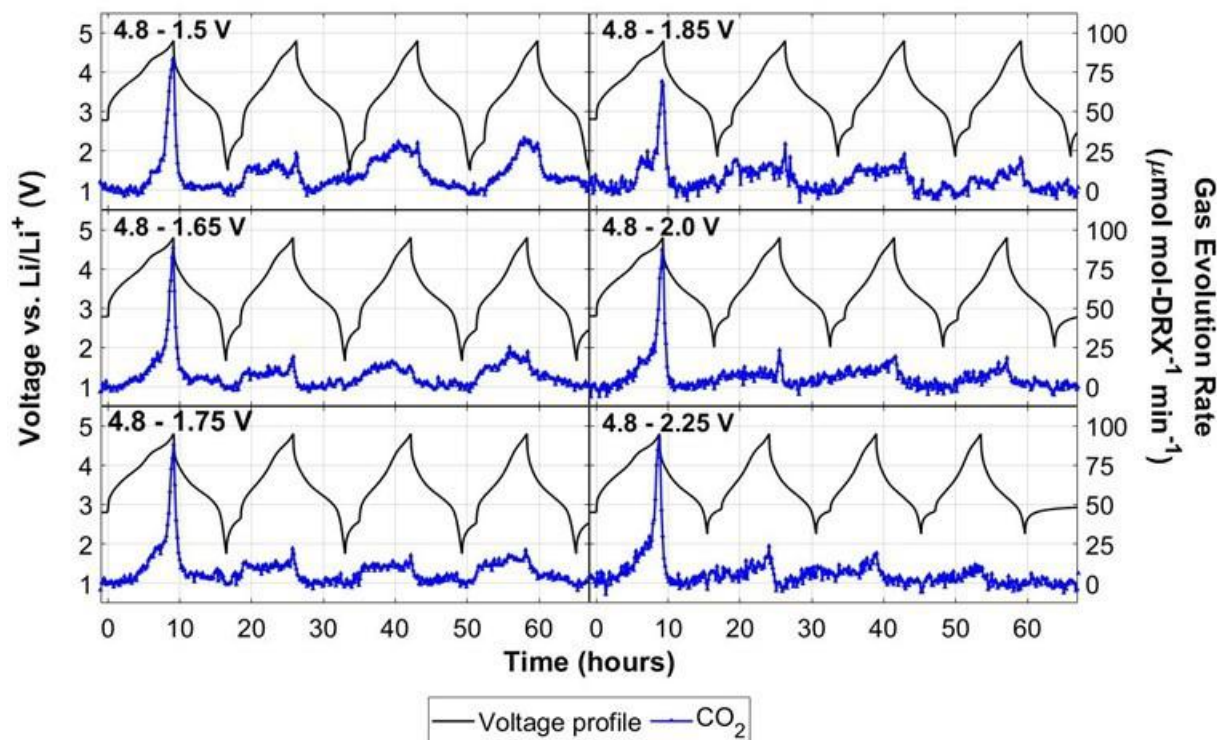


Figure IX.6.4 DEMS results for Li-Mn-Nb-O-F DRX cathodes cycled within various voltage windows. All cathodes were cycled at 0.1 Li h⁻¹ (29.4 mA g⁻¹) using 1M LiPF₆ in EC/EMC (3:7) as the electrolyte.

F substitution into the O anionic sublattice lowers the overall anionic valence and enables a higher amount of Mn to be incorporated into the DRX material. Following our team's recently-published study of the Mn-rich and F-rich Li_{1.2}Mn_{0.7}Nb_{0.1}O_{1.8}F_{0.2} cation-disordered rocksalt cathode, revealing bulk structural rearrangements during cycling leading to a 125% increase in reversible capacity after 30 cycles, we explored a Mn- and Ti-based DRX material with a higher Mn content of 0.8. This material also shows bulk changes upon extended cycling, as is clearly observed from the changes in the distribution of Li local environments as studied by ⁷Li solid-state NMR (Figure IX.6.5). For example, the ⁷Li spectrum collected on a discharge sample (sample C) after 30 cycles features a broad signal characteristic of Li in the bulk disordered rocksalt cathode, but the average resonance frequency of this signal (orange line at 160 ppm in Figure IX.6.6c) is a lot lower than that observed for the pristine cathode (grey line at 290 ppm in Figure IX.6.6b). Those bulk structure changes are accompanied by a significant evolution of the electrochemical curve, with the development of plateau-like features at ~4 V and ~3V, reminiscent of bulk structural changes reported in ordered (layered) Mn-rich oxide cathodes. Yet, unlike layered oxide cathodes, the bulk changes occurring in the disordered rocksalt cathode of interest are beneficial rather than deleterious, and lead to a very high and stable reversible capacity of ~320 mAh/g after 30 cycles. Those promising results provide new materials design rules for ultrahigh capacity, Mn-based Li-ion cathodes.

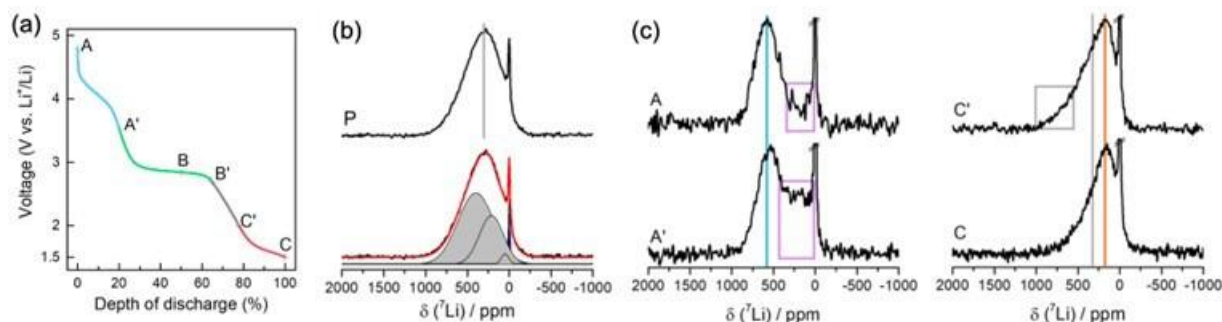


Figure IX.6.5 ^7Li solid-state NMR isotropic spectra collected on cathode samples obtained at various states of charge. (a) Discharge voltage profile obtained during the 30th cycle and plotted as a function of the depth of discharge (DoD). The recovered electrode samples were obtained at A (0% DoD, 4.8 V), A' (20%, 3.5 V), B (50%, 2.84 V), B' (65%, 2.7 V), C' (80%, 2.0 V), and C (100%, 1.5 V). (b) ^7Li fully isotropic pj-MATPASS spectrum collected on the pristine Li-Mn-Ti-O-F cathode sample (P), with a deconvolution of this spectrum using three Gaussian components (grey signals). A Lorentzian component was used to account for the Li-based diamagnetic impurities (dark blue signal). The grey line indicates a central chemical shift value of 290 ppm. (c) ^7Li fully isotropic pj-MATPASS spectra collected on ex situ cathode samples stopped at various stages of discharge during the 30th cycle as shown in (a). The blue and orange lines indicate chemical shift values of 580 ppm and 160 ppm, respectively. The sharp peak around 0 ppm is attributed to diamagnetic Li environments formed during electrode preparation and electrochemical cycling (e.g., due to residual Li-containing precursor phases or to electrolyte degradation).

3) Carbon coating and characterization

Carbon coating of cathode particles can effectively increase the electrical conductivity while preventing them from direct exposure to electrolyte. To reveal the morphology and structure of carbon coating on DRX cathodes, HAADF imaging, energy dispersive spectroscopy (EDS) and EELS was performed on particles that were carbon coated using the chemical vapor deposition method. Specifically, $\text{Li}_{1.2}\text{Mn}_{0.4}\text{Ti}_{0.4}\text{O}_2$ (LTMO) DRX cathode particles were carbon coated at 600°C in Ar and Ar/ H_2 environments and C_2H_2 was used as a carbon source. Figure IX.6.6 shows STEM-HAADF images and EDS mapping of cathode particles in pristine and carbon coated states. As evident from the Figure IX.6.6a, Ti, Mn and O elements are uniformly distributed in LTMO particle in the pristine state. Figure IX.6.6b is the HAADF and EDS images of LTMO particle carbon coated in the Ar environment, which reveals the non-uniform (30–60 nm) thickness of the carbon coating. Figure IX.6.6c is the HAADF and EDS images of LTMO particle carbon coated in the Ar/ H_2 environment where the thickness of the carbon coating varies from the 20 nm to 150 nm. In both carbon coated samples, the active TM and oxygen distribution remain uniform while the carbon thickness appeared to be nonuniform.

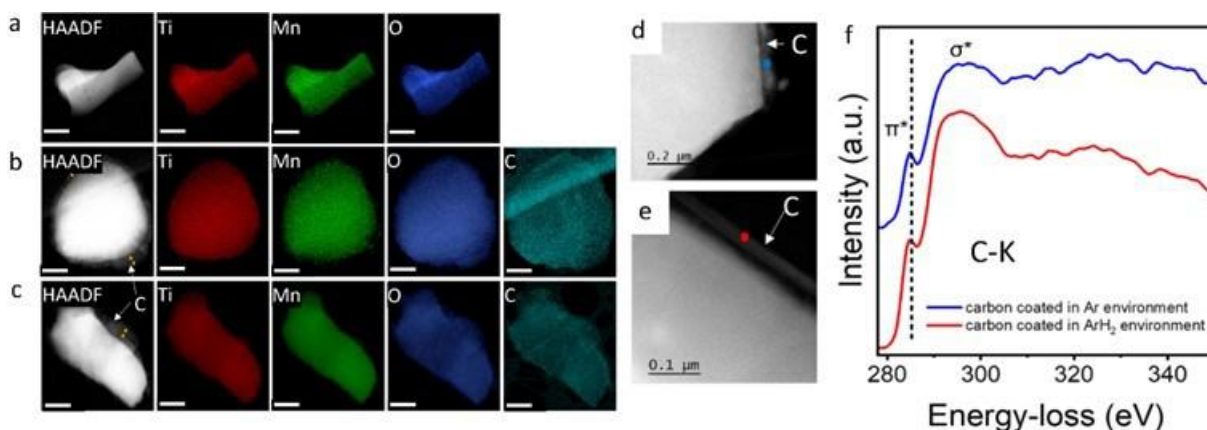


Figure IX.6.6 STEM-HAADF images, EDS elemental maps showing carbon spatial distribution, and EELS analysis showing the electronic structure of the carbon coating on DRX particles. (a) Pristine LTMOF, (b) LTMOF carbon coated in the Ar environment, (c) LTMOF carbon coated in the Ar/ H_2 environment. Scale bar is 500 nm. STEM-HAADF images of (d) LTMOF carbon coated in the Ar environment, (e) LTMOF carbon coated in the Ar/ H_2 environment showing carbon on the surface and the points from where the EELS spectra were taken, and (f) EELS spectra taken at C-K edge for particle (d) (blue) and (e) (red).

The carbon structure on LTMO particle surface was further studied by STEM-EELS. EELS was taken from the surface carbon region where C-K (π^*) edge was observed at 284.5 eV as shown in Figure 7d-f. The nature of the C-K (σ^*) peaks and the relative intensity of C-K (π^*) and C-K (σ^*) were analyzed which clearly revealed the amorphous nature of the carbon on particles coated in both Ar and Ar/H₂ environment. The study provides guidance on future optimization of carbon coating methods for better electrochemical performance of DRX cathodes.

Conclusions

In FY22, the Characterization and Modeling part of the “DRX deep-dive” program focused on developing fluorine quantification methodologies, understanding the impact of fluorination levels, and establishing techniques to characterize carbon coating. The discrepancy between the target composition and the actual stoichiometry obtained in DRX materials synthesized by conventional solid-state methods was demonstrated. The leading factors for the discrepancy, which include LiF volatility during the high temperature sintering and the intrinsic F solubility limit in DRX materials, revealed. Through the investigation of nanoscale structural and chemical changes upon cycling of a series of Mn-based DRX cathodes with varied F concentrations, we directly visualized the spatial distribution of Mn oxidation states near the surface, therefore gaining insight on the cathode surface oxygen loss upon battery cycling and their dependence on the F concentration. The chemical evolution of both the transition metals and CEI species on the surface of DRX electrodes in comparative electrolyte systems were also elucidated. We further accurately quantify CO₂ gasping rates within various voltage windows by using differential electrochemical mass spectrometry. Finally, characterization techniques were successfully applied to elucidate the nature of carbon coating on DRX particles.

Key Publications

1. J. Ahn, Y. Ha, F. R. Satish, R. Giovine, L. Li, J. Liu, M. J. Crafton, B. D. McCloskey, C. Wang, R. J. Clement, R. Kostecki, W. Yang and G. Chen, “Exceptional cycling performance enabled by local structural rearrangements in disordered rocksalt cathodes”, *Adv. Energy Mater.* 2200426 (2022)
2. N. Szymanski, Y. Zeng, T. Bennett, S. Patil, J. Keum, E. Self, J. Bai, Z. Cai, R. Giovine, B. Ouyang, F. Wang, C. Bartel, R.J. Clément, W. Tong, J. Nanda, G. Ceder, “Understanding the fluorination of disordered rocksalt cathodes through rational exploration of synthesis pathways”, *Chem. Mater.* 34, 7015–7028 (2022)
3. Y. Yue, Y. Ha, R. Giovine, R. J. Clément, W. Yang and W. Tong, “High-Voltage Reactivity and Long-Term Stability of Cation Disordered Rocksalt Cathodes”, *Chem. Mater.* 34, 1524–1532 (2022).
4. L. Li, J. Ahn, Y. Yue, W. Tong, G. Chen, and C. Wang, “Fluorination-Enhanced Surface Stability of Disordered Rocksalt Cathodes”, *Adv. Mater.* 2022, 2106256.
5. L. Li, Z. Lun, D. Chen, Y. Yue, W. Tong, G. Chen, G. Ceder and C. Wang, “Fluorination-Enhanced Surface Stability of Cation-Disordered Rocksalt Cathodes for Li-Ion Batteries”, *Adv. Funct. Mater.* 2021, 2101888.
6. M. J. Crafton, T.-Y. Huang, Y. Yue, R. Giovine, V. C. Wu, C. Dun, J. J. Urban, R. J. Clément, W. Tong, B. D. McCloskey, “Tuning Bulk Redox and Altering Interfacial Reactivity in Highly Fluorinated Cation-Disordered Rocksalt Cathodes”, *submitted*
7. M. J. Crafton, T.-Y. Huang, Y. Yue, R. Giovine, V. C. Wu, C. Dun, J. J. Urban, R. J. Clément, W. Tong, B. D. McCloskey, “Tuning Bulk Redox and Altering Interfacial Reactivity in Highly Fluorinated Cation-Disordered Rocksalt Cathodes”, *submitted, ACS Applied Materials & Interfaces.*
8. E. Spotte-Smith, R.L. Kam, D. Barter, X. Xie, T. Hou, S. Dwaraknath, S. M. Blau and K. A. Persson, *ACS Energy Lett.* 2022. 7(4), pp.1446-1453.
9. E. Spotte-Smith, T. Petrocelli, H. Patel, S. Blau and K. A. Persson, *ChemRxiv* 2022.

References

1. Spotte-Smith, E.W.C., Kam, R.L., Barter, D., Xie, X., Hou, T., Dwaraknath, S., Blau, S.M. and Persson, K.A., 2022. *ACS Energy Lett.*, 7(4), pp.1446-1453.

2. Borodin, O., Ren, X., Vatamanu, J., von Wald Cresce, A., Knap, J. and Xu, K., 2017. *Accounts of chemical research*, 50(12), pp.2886-2894.
3. Spotte-Smith, E., Petrocelli, T., Patel, H., Blau, S. and Persson, K., 2022. *ChemRxiv*.

Acknowledgements

Juhyeon Ahn, Oxana Andriuc, Vincent Battaglia, Tyler Bennet, Jordan Burns, Zijian Cai, Dongchang Chen, Guoying Chen, Jianli Cheng, Raphaele Juliette Clement, Matthew Crafton, Emily Foley, Yanbao Fu, Raynald Giovine, Yang Ha, Kenny Higa, Mathew Horton, Tzu-Yang Huang, Huiwen Ji, Robert Kostecki, Linze Li, Zhengyan Lun, Bryan McCloskey, Jagjit Nanda, Bin Ouyang, Kristin Persson, Rohit Satish, Ethan C. Self, Martin Siron, Wei Tong, Chongmin Wang, Ruoxi Yang, Wanli Yang, Yuan Yue, Yiman Zhang, Peichen Zhong

X Next-Gen Lithium-Ion Materials: Frontier Science at Interfaces

In lithium-ion batteries, most electrochemical reactions occur at the electrode-electrolyte interface. The interface components, surface structure and property determine battery performance. Thus, numerous efforts have been made to form or modify the electrode-electrolyte interface. In current commercial lithium-ion batteries, the important interface is the solid-liquid interface – and a non-aqueous liquid organic solvent is often the liquid electrolyte, generally made of lithium salt. It provides the lithium-ion transfer channels as the ion carrier; isolates the electron conduction, in favor of conductivity in the whole battery as the bridge connecting the cathode and anode.

The interface influences most of the reaction processes and parameters determining the battery performance. Furthermore, the side influence usually occurs between the electrode and electrolyte or on the surface of the electrode materials. To improve the performance of LIBs, the surface and interface in the battery can be efficiently modified and tuned.

The rest of this chapter contains detailed reports on the status of the following individual projects.

- Molecular-level Understanding of Cathode-Electrolyte Interfaces (University of Colorado, NREL)
- Interfacial Studies of Emerging Cathode Materials Lawrence Berkeley National Laboratory (LBNL)
- Understanding Modification of High-Energy Cathodes and Their Interfaces with Electrolytes for Next-Generation Li-ion Batteries (PNNL)
- Fluorinated Deep Eutectic Solvent (FDES)-Based Electrolytes (ANL)
- Developing In situ Microscopies for the Model Cathode/ Electrolyte Interface (NREL).

X.1 Molecular-level Understanding of Cathode-Electrolyte Interfaces (University of Colorado, NREL)

Michael F. Toney, Principal Investigator

Chemical and Biological Engineering
Materials Science and Engineering Program
University of Colorado, Boulder
Boulder, CO 80309
E-mail: michael.toney@colorado.edu

Tien Duong, DOE Technology Development Manager

U.S. Department of Energy
E-mail: Tien.Duong@ee.doe.gov

Start Date: October 1, 2018

End Date: September 30, 2022

Project Funding (FY22): \$450,000

DOE share: \$450,000

Non-DOE share: \$0

Project Introduction

Understanding the underlying reaction mechanisms accounting for cathode-electrolyte interphase formation is crucial to overcome present limitations and to develop stabilization strategies for next-generation lithium-ion batteries (NG-LIBs). To tackle this challenge, we combine theoretical modeling with X-ray surface scattering and spectroscopic studies along with electrochemical characterization using model thin-film cathode electrodes and high purity electrolytes. The collaboration team consists of researchers from SLAC National Accelerator Laboratory, U.S. Army Research Laboratory (ARL), the University of Colorado Boulder, and Oregon State University (OSU). Molecular-level modeling of cathode-electrolyte reactions are combined with diagnostics of cathode interphase evolution. This approach allows in-depth theoretical modeling and experimental probes to develop the necessary level of understanding into the interface degradation mechanisms and cathode stabilization strategies and it builds on our past success in related interfacial research [1–8]. To achieve our goals, we have employed high-voltage epitaxial thin film cathodes and carbonate-based and advanced fluorinated electrolytes. We have conducted synchrotron x-ray scattering and spectroscopy along with ion spectroscopies to elucidate underlying mechanisms of interfacial degradation of cathode surfaces and rationalization of cathode stabilization strategies through electrolyte design. Our approach will provide fundamental knowledge about how electrode surface and electrolyte design dictate interfacial reaction pathways and will help enable stabilization strategies for cathode interface.

Objectives

High-energy NG-LiB electrochemistry requires the utilization of high capacity and high voltage metal-oxide cathode materials. Their full potential has to date been hampered by the paucity of understanding the underlying chemistry and physics on the cathode-electrolyte reaction and the directed interphase. In particular, the practical implementation of NG-LIBs is to a large extent obstructed by the lack of a suitable electrolyte. While typical carbonate-based electrolytes have been reliable in commercial LiBs, there is degradation of electrolyte at high potentials. In combination with the highly reactive cathode metal oxide surface and surface defects, this creates an unstable cathode-electrolyte interface, which results in gas evolution, transition metal dissolution, active material consumption, and increased interfacial impedance. This is more problematic at elevated temperatures and/or during fast charging. Significant progress in mitigating these issues has been reported by using different electrolytes, such as nitriles [9], sulfones [10, 11], ionic liquids, and fluorinated carbonates [12]. However, stabilization of high voltage cathode-electrolyte interface (CEI) is unresolved due to a lack in mechanistic understanding of the degradation and stabilization strategy [13–14]. Our objective is to provide a detailed understanding of the interfacial reaction between the cathode and electrolyte. This includes an elucidation of the interphase evolution pathway and the changes on cathode structure and composition. We anticipate that our results will fill the gap in current understanding of the underlying chemistry and physics of

cathode-electrolyte reactions and will be disseminated through impactful publications. This knowledge can be utilized to guide the design of advanced electrolytes and the development of cathode stabilization strategies and will help to accelerate the development and deployment of NG-LIBs for various applications.

Approach

Our approach is to combine density functional theory (DFT) calculations and molecular dynamics (MD) simulations with advanced x-ray studies and precision electrochemical characterization using model thin-film electrodes. It starts with the purification of electrolytes and the controlled growth of low-Co, transition metal oxide thin films by Pulsed Laser Deposition (PLD) and Polymer-assisted Deposition (PAD). The reactivity and stability of cathode in electrolytes are probed by synchrotron-based X-ray scattering and spectroscopy studies. PLD-derived epitaxial lithium nickel-manganese-cobalt-oxide (NMC) thin-film as well as PAD synthesized spinels (LMO, LNMO, etc.) are used as well-defined, high voltage cathode materials. Utilization of epitaxial NMC532 thin films as model systems enables high resolution x-ray experiments and well-controlled electrochemical experiments that only contain contributions from the cathode rather than the parasitic reactions from the conductive additive or binder material. In order to achieve our objectives to identify the key cathode-electrolyte reactions, we plan a multimodal surface-sensitive probes, involving synchrotron-based x-ray scattering techniques (x-ray reflectivity or XRR, grazing incidence X-ray diffraction (GI-XRD) and surface X-ray diffraction or SXRD, as well as x-ray spectroscopy (x-ray absorption spectroscopy or XAS) measurements. XRR, GI-XRD and SXRD will yield information on the structural transformation of NMC and spinels thin film cathodes when they react with the electrolyte. XAS will unravel complementary chemical information and composition on cathode interphase. The obtained experimental results are compared with the molecular-scale modelling on the cathode-electrolyte interfacial reactions.

Results

In general, progress was dramatically slowed due to the covid-19 restrictions and lab-based research and access to synchrotron sources. This delayed many experiments at the Advanced Photon Source and the Stanford Synchrotron Radiation Lightsource and limited access to labs at SLAC, OSU, CU Boulder and the ARL. It was impossible to conduct in situ experiments at either SSRL or APS, as site access was eliminated for most user. From the experimental side, we focused on data analysis, some remote experiments and planning.

We first focus on the reactivity and stability of cathode thin-films in carbonate-based electrolyte. Here, NMC532 thin films with controlled surface structure and film thickness have been developed through PLD growth. Surface X-ray characterization showed that single-crystal 10 nm $\text{LiNi}_{0.5}\text{Mn}_{0.3}\text{Co}_{0.2}\text{O}_2$ (NMC532) thin-films have been successfully deposited on SrTiO_3 substrate with 15 nm SrRuO_3 as conductive buffer layer (Figure X.1.1). Non-specular phi scans confirmed the epitaxial relationship between NMC film and SrTiO_3 substrate (Figure X.1.1B). In order to probe the chemical reaction between cathode and carbonate-based electrolyte, the thin-film is subject to the solvent of ethylene carbonate (EC) - ethyl methyl carbonate (EMC) and electrolyte LP57 (1 M LiPF_6 in EC-EMC) for chemical soaking in glovebox for 2 hours. There are almost no changes on the SXRD peak position and profile of NMC films before compared to after chemical soaking (Figure X.1.1C), indicating negligible influence of chemical soaking on the out-of-plane structure of the NMC thin films.

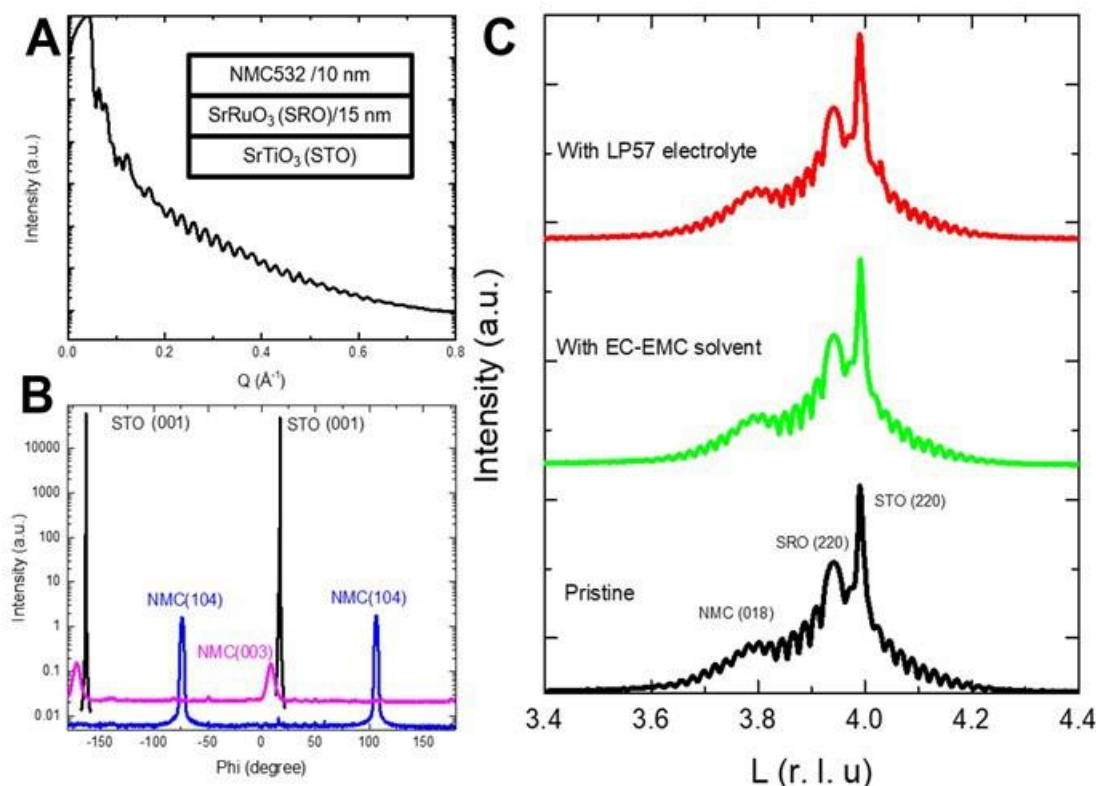


Figure X.1.1 Structural evolution of cathode thin-film with/without carbonate-based electrolyte (A) XRR of 10 nm NMC532 films grown on SrTiO_3 substrates with 15 nm SrRuO_3 buffer layers; (B) Off-specular ϕ -scans of STO {001}, NMC {104}, and NMC {003} of the film; (C) SXRD of NMC532 films before and after exposure to EC-EMC solvent and LP57 electrolyte

Although there are negligible structural transformations of NMC films upon chemical soaking, there are significant chemical transformations of NMC thin films. Total-reflection X-ray absorption near edge structure (XANES) of NMC thin-films has been utilized as a surface-sensitive probe to study the valence evolution of transition metals before and after the exposure to EC-EMC solvent and LP57 electrolyte. Ni K-edge XANES showed that compared to the pristine films, there are significant negative shifts of spectra toward lower energy after exposure to LP57 electrolyte (Figure X.1.2A). This indicated a dramatic reduction of Ni sites in NMC thin films after soaking in carbonate electrolyte. Such reduction phenomena can be also evidenced using EC-EMC solvent. After EC-EMC solvent soaking, the NMC thin-films showed similar spectra shifts at Ni K-edges, indicating the main contribution from carbonate solvent for Ni reduction, showing the LiPF_6 salt is plays a negligible role. Solvent-induced transition metal reduction is further evidenced in Co sites in NMC thin-films by the peak shifts after chemical soaking of NMC thin-films in EC-EMC solvent and LP57 electrolyte, while the peak shifts are smaller than Ni sites, indicating a decreased reduction degree for Co. Interestingly, there are negligible changes on the absorption peak position for Mn sites after the exposure to LP57 electrolyte and EC-EMC solvent under the same condition. Therefore, this shows the transition-metal-dependent degradation of NMC thin-films in carbonate-based electrolyte, and the EC-EMC solvent is believed to play a dominant role. Observation of different behaviors for transition metal reduction in carbonate-electrolyte is found to be consistent with the current understanding of the key contribution from Ni redox and partial contribution from Co redox in NMC cathode capacity, while Mn sites are believed to play a stabilization effect.

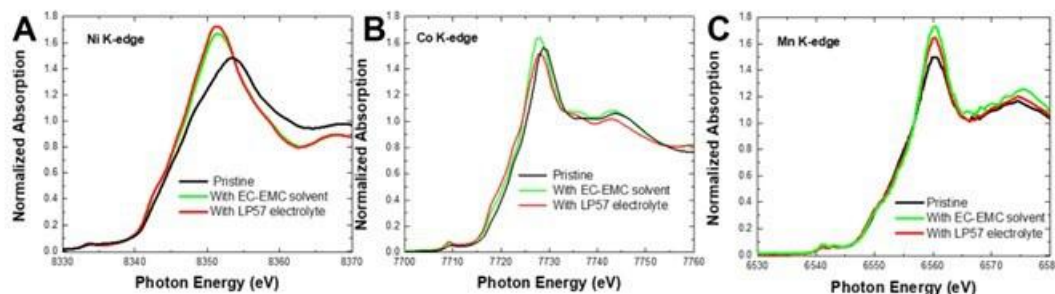


Figure X.1.2 Transition metal-dependent degradation of NMC cathode in carbonate-based solvent and electrolyte. Total-reflection X-ray absorption near edge structure (XANES) of NMC thin-films before and after exposure to EC-EMC solvent and LP57 electrolyte at Ni, Co, and Mn K-edges

To understand the chemical reaction between the cathode and carbonate-based electrolyte, density functional theory (DFT) calculations have been conducted using the Li_xNiO_2 model cathode surface at different stages of lithiation that mimics different battery state of charge. The LiFSI and LiPF_6 salts decomposed on the LiNiO_2 surface forming LiF [15, 16]. Carbonate solvents EC, EMC, fluoroethylene carbonate (FEC), propylene carbonate (PC) and additives 3,5-bis(trifluoromethyl)-1H-pyrazole, 1-methyl-3,5-bis(trifluoromethyl)-1H-pyrazole underwent H-transfer from solvent to the oxygen of Li_xNiO_2 surface [16, 17]. Solvent fluorination, complexation of the solvent with a Li^+ and increasing lithiation of Li_xNiO_2 cathode surface made this H-transfer reaction less favorable (Figure X.1.3). Cyclic carbonates undergo ring opening reaction after H-transfer and evolve CO_2 . Further DFT calculation showed the possible proton transport pathways in layered structure.

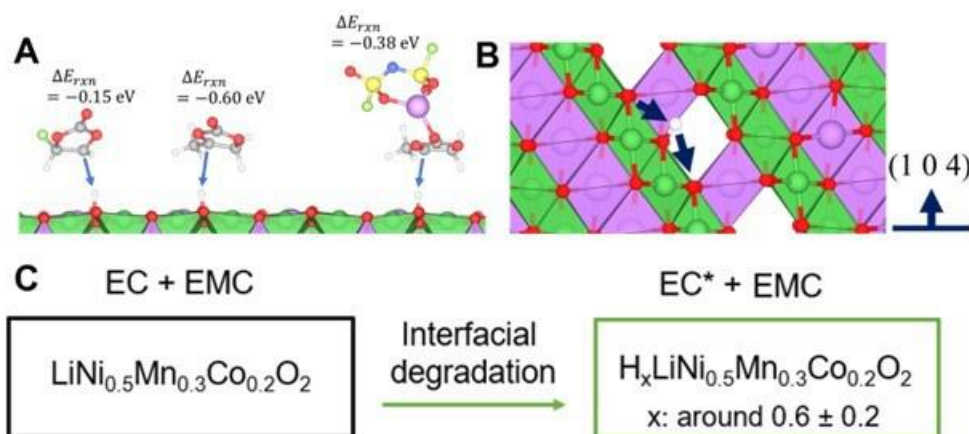


Figure X.1.3 Protonation reaction pathway between cathode and carbonate-based electrolyte. A) DFT calculation of EC and LiPF_6 salt decomposition reactions and their reaction activation energy on standard cathode $\text{Li}_{0.5}\text{NiO}_2$ surface; B) Illustration of the possible proton transfer pathways inside layered structure in cathode; C) Illustration of the interfacial degradation of NMC cathodes through surface protonation due to the deprotonation reaction of EC solvent on cathode surface

Therefore, when NMC thin-films are subject to a carbonate-based electrolyte, there are interfacial protonation reactions accounting for the degradation of cathode surface. The deprotonation of EC solvent at cathode can produce protons which would be transported in layered cathode, therefore reducing both Ni and Co sites, and generating radicals. Such a hypothesis is found to be consistent with our x-ray studies on the chemical transformation of NMC thin-films in carbonate-based electrolyte. Due to a fact that the proton is small, there are expected to be negligible changes on the out-of-plane structure in layered NMC. However, because of the positive charge that proton carries, the charge compensation mechanism will lead to significant reduction of Ni and Co sites. Therefore, SXRD showed negligible structural changes after chemical soaking of NMC thin film in carbonate electrolyte and solvent, however, significant chemical transformation of both Ni and Co sites have been evidenced by XAS. Since Ni and Co reduction origins from proton trapping, an estimation of proton

numbers in the NMC thin film has been conducted through a quantification of Ni and Co reduction degree (Figure X.1.3). More importantly, our hypothesis on the protonation degradation in NMC is found to be consistent with early theoretical prediction on the possibility of layered cathode hydrogenation [18, 19].

Such a hypothesis is further supported by a solvent fluorination effect on cathode stabilization. Based on the physical chemistry understanding, the fluorination of carbonate solvent leads to advanced solvent and electrolyte with enhanced chemical stability, therefore this can suppress the deprotonation reactions. NMC thin-film is then subject to carbonate-based solvent (EMC) and electrolyte (LP57), and the fluorinated electrolytes 1 M LiPF₆ in fluoroethylene carbonate (FEC)-EMC (labeled as 1F electrolyte) and 1 M LiPF₆ in fluoroethylene carbonate/3,3,3-fluoroethylmethyl carbonate/1,1,2,2-tetrafluoroethyl-2, 2, 2'-trifluoroethyl ether (FEC:FEMC:HFE, 2:6:2 by weight, labeled as 3F electrolyte) and HFE solvent. Soft-XAS collected in total electron yield with high surface sensitivity has been utilized to study the oxidation state of Ni and electronic properties of O when NMC thin-film is subject to different solvent and electrolyte (Figure X.1.4). As evidenced in Ni L₃-edge XAS, as compared to pristine sample, there is negative shift of spectra toward lower energy after NMC is exposed to LP57 electrolyte (1 M LiPF₆ in EC-EMC solvent), indicating a Ni reduction (Figure X.1.4A). However, such reduction is absent in NMC thin films after soaking in EMC solvent, indicating that the main deprotonation source comes from EC solvent. This result is found to be consistent with our theoretical modelling on EC deprotonation on cathode surface (Figure X.1.3A). Besides EMC, fluorinated solvent (HFE) and electrolytes (1F and 3F) are also found to be able to stabilize Ni sites in NMC, indicating the key contribution from solvent fluorination on cathode stabilization. The effect of solvent on cathode reactivity is further confirmed by O K-edge soft-XAS (Figure X.1.3B). The pre-edge peaks in O K-edge soft-XAS are a good indicator of transition metal oxidation states in NMC cathode since this comes from the hybrid orbital of transition metal 3d orbital and oxygen 2p orbital. As clearly shown, as compared to NMC films exposure to the fully fluorinated electrolyte 3F, there is slightly decreased intensity for pre-edge peak located around 530.2 eV for NMC films exposure to half-fluorinated 1F electrolyte, while the carbonate-based electrolyte LP57 leads to significant weakening in pre-edge peak intensity. This demonstrates that carbonate-based electrolyte tended to lead to NMC reduction, while the fluorinated solvents help to stabilize the cathode surface. The soft-XAS studies further support our hypothesis on interfacial degradation of NMC cathode by EC deprotonation reaction, since a replacement of hydrogen in solvent molecule by fluorine leads to fluorinated solvent with enhanced chemical stability toward deprotonation. Therefore, with an absence of solvent deprotonation, the stability of NMC cathode in electrolyte is enhanced.

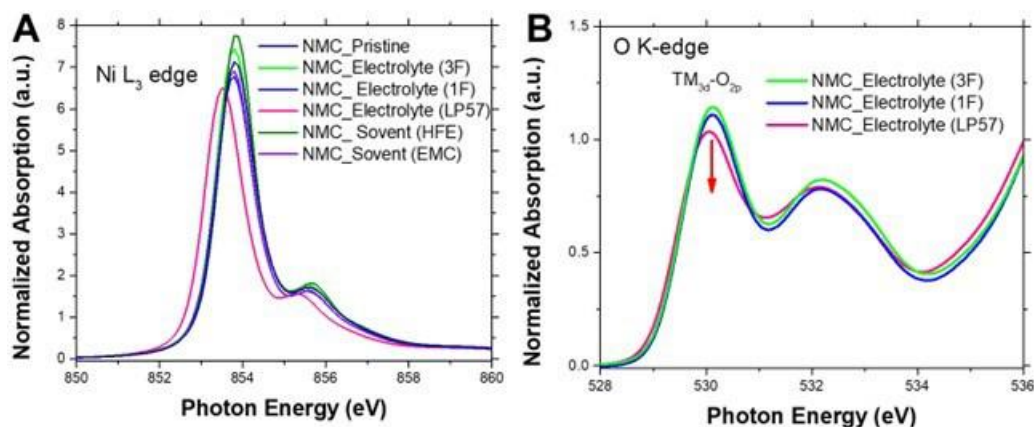


Figure X.1.4 Solvent effect on cathode degradation and stabilization. A) Ni L₃-edge XAS of NMC thin-film before and after exposure to carbonate electrolyte LP57, fluorinated electrolytes 1F and 3F; B) O K-edge XAS of NMC thin-films after exposure to carbonate electrolyte LP57 and fluorinated electrolytes 1F and 3F

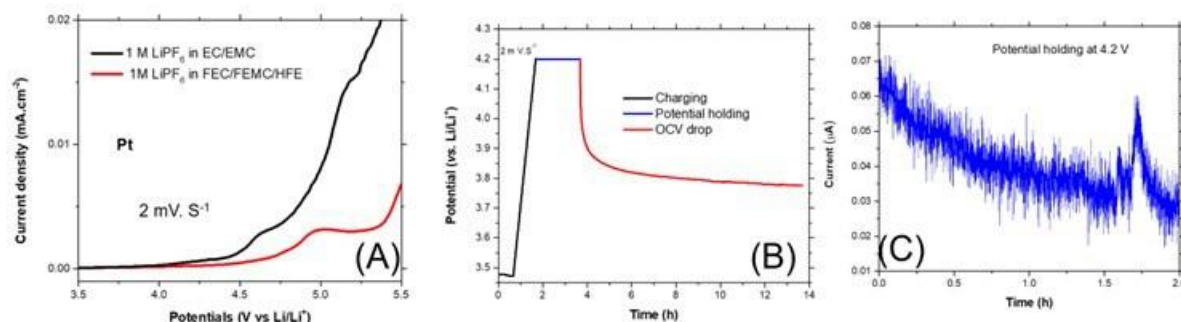


Figure X.1.5 (A) Electrochemical stability window of carbonate-based LP57 electrolyte and fluorinated electrolytes. (B) Voltage drop of NMC thin-films after charging to 4.2 V in LP57 electrolyte; (C) The leakage current of the NMC532 thin-films during the potential hold at 4.2 V

We have further investigated the self-discharge properties of the NMC532 thin film electrodes. Figure X.1.5 shows the stability of the electrolyte (A), the self-discharge, as observed from the potential drop after cathode charge to 4.2V (B), and the leakage current flow to the cathode charged to 4.2 V (C). This shows a strong self-discharge that we hypothesize is related to the deprotonation of the carbonate electrolyte at high potential and the proton insertion into the NMC532 metal-oxide cathode.

To confirm the presence of protons in the transition metal cathodes, we turn to time-of-flight secondary ion mass spectrometry (TOF-SIMS) performed at NREL (Steve Harvey). The electrodes were charged in deuterated EC:DMC with 1 M LiPF₆. These preliminary and not yet analyzed results are shown in Figure X.1.6 for NMC532 thin films cathode for pristine (A), charged to 4.2 V and relaxed to 4.15 V (B) and charged to 4.5 V and relaxed to 4.46 V (C). This suggests loss of Li near the surface for higher state of charge. Figure X.1.6(D) shows the deuterium signals and suggested more deuterium in the higher charge states, which will be confirmed. These compositional results are consistent with our model. Beyond the characterization of electrolyte stability with NMC532 electrodes, we are investigating the structural, chemical, and electrochemical aspects of the CEI using lithium manganese oxide (LMO). These studies employ the electrolyte LP58 (1.2 M LiPF₆ in EC: EMC=3:7) as a model electrolyte.

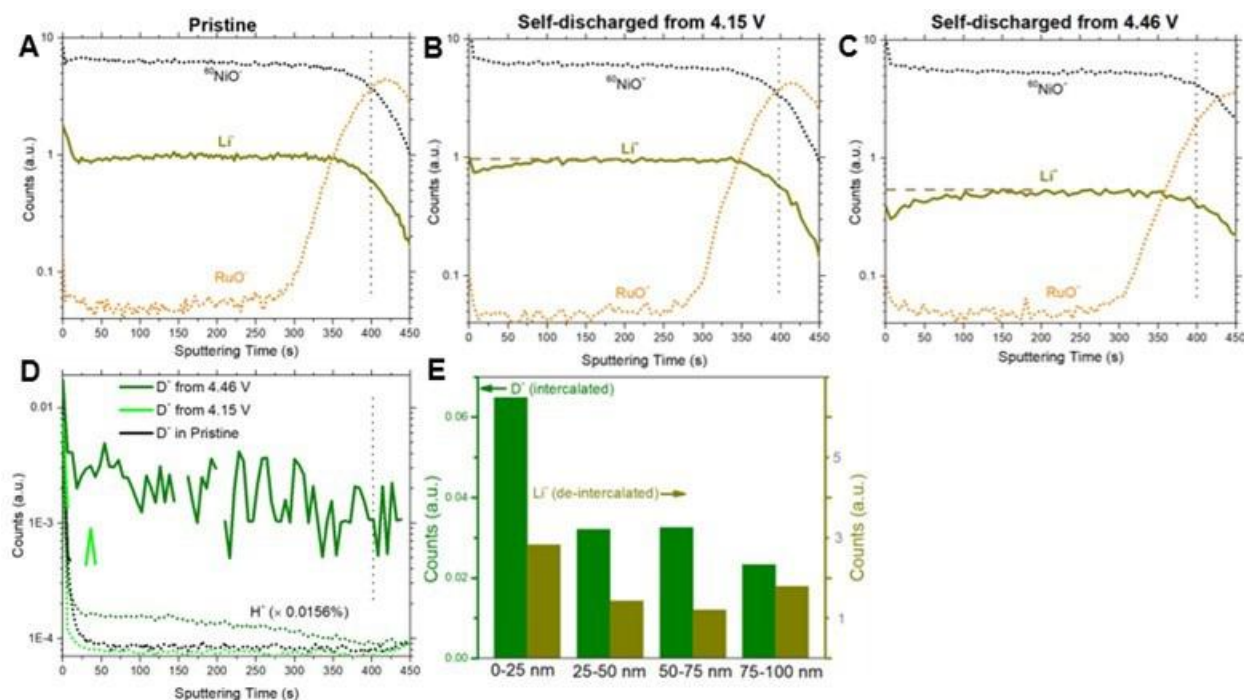


Figure X.1.6 Preliminary TOF-SIMS (A) pristine NMC. (B) charged to 4.2 V and relaxed. (C) charged to 4.5 V and relaxed. (D) and (E) deuterium TOF-SIMS summary.

The method for the fabrication of LMO thin film was guided by the work of Di *et al* [20]. Polymer-assisted deposition (PAD) is used to form a 25-50 nm thick continuous layer of LMO on an electrically conductive substrate. The substrate is a n-type doped Si wafer ($\rho = 5 \text{ m}\Omega\text{-cm}$) coated with 20 nm of Pt on the polished side and 40 nm Au back-coating. A 7-nm-thick layer of Cr improves the adhesion of the Pt and Au layers to Si, as shown in the inset of Figure X.1.7(A).

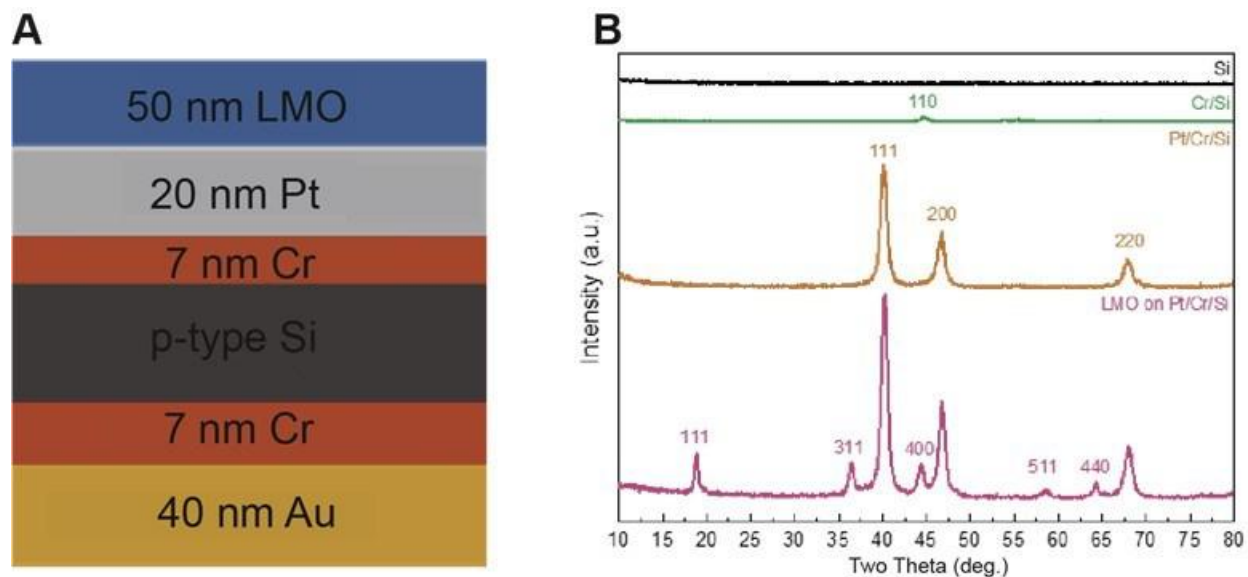


Figure X.1.7 Structural evolution of LMO thin-film during fabrication (A) LMO films grown on 20 nm Pt substrates with 7 nm Cr adhesive layers ; (B) GI-XRD of As-doped Si substrate, Cr coated Si, Pt/Cr coated Si, and LMO thin film on Pt/Cr/Si, respectively.

Lithium nitrate (LiNO_3), manganese (II) acetate tetrahydrate ($\text{Mn} [\text{CH}_3\text{CO}_2]_2 \cdot 4\text{H}_2\text{O}$), polyethylenimine (PEI), and ethylenediaminetetraacetic acid (EDTA) were purchased from Sigma-Aldrich. Lithium nitrate and manganese acetate tetrahydrate were dissolved in deionized water at 1.1:2 (Li/Mn molar ratio) to prepare the metal salt solution. A 10% excess lithium was added to compensate for the evaporation of lithium during calcination. EDTA and PEI (50 wt %) were mixed at a 1:2 mass ratio and dissolved in deionized water to prepare the polymer solution. The polymer solution and metal salts solution were mixed and stirred until the solution was homogeneous to obtain the final LMO precursor solution. The Pt-coated substrate was cut into smaller pieces of approximately $1\text{cm} \times 1\text{cm}$, and then cleaned in acetone, sonicated for 20 min, and then rinsed with acetone and deionized water. After drying in air, the substrate was cleaned in an ozone cleaner for 15 min. Approximately 50 μL of the LMO precursor solution was spin coated onto the substrate at 3000 rpm for 30 s. Eventually, the films were transferred into a single zone tube furnace and calcined from room temperature to 200°C ($1^\circ\text{C}/\text{min}$), held at 200°C for 2h and then to 540°C ($2^\circ\text{C}/\text{min}$) and held at 540°C for 1 h in air.

The crystal structure was measured using grazing incidence X-ray diffraction (GI-XRD) with a Rigaku SmartLab diffractometer equipped with a Cu source. LMO has a spinel structure with space group of $Fd\bar{3}m$. The GI-XRD patterns shown in Figure X.1.7(B) reveal a spinel phase of LMO with diffraction peaks that closely match the expected structure. Diffraction signatures for platinum, including the (111), (200) and (220) reflections are also observed, indicating that a single phase of LMO has been formed.

To verify that the LMO thin films were electrochemically active, we performed cycle voltammetry (CV) on using a customized cone cell.[21] The design of this cell makes it possible for eliminating the impact of SS caps, separators, current collectors, carbon black and binders in commonly seen coin cell tests. Also, it mitigates the issue of signal contamination in *in-situ/operando* X-ray characterization. The cone cell, illustrated in Figure X.1.8 (A), is supported by insulating PEEK, while the inner cone is made of highly durable and electrochemically inert Teflon. The LMO was placed under the cone and lithium metal wire serving as the counter and reference electrode was situated directly above the active area of LMO without contact to the LMO or cone. The cone cell was filled with electrolyte until the electrodes were immersed. An open-circuit voltage of 3.85 V vs. Li/Li^+ was observed for LMO, as shown in the beginning of the first cycle (red) in Figure X.1.8. The CV measurement was made within the potential range of 3.5–4.3 V at 1 mV/s by scanning first to the upper voltage limit and then back to the lower voltage limit, with this cycle repeated 10 times. The cyclic voltammograms in Figure X.1.8 show that the first anodic scan has peaks at 4.05 V and 4.22 V, which indicates a charge transfer process associated with the phase transformation of LiMn_2O_4 first to $\text{Li}_{1-x}\text{Mn}_2\text{O}_4$ ($0 < x < 1$) and then to $\lambda\text{-MnO}_2$. The cathodic scan shows two peaks at 4.13 V and 3.97 V, which is associated with the reversal of this two-step reaction. Starting from the 2nd cycle, that two peaks in the anodic scan have shifted to lower voltages, 4.02 V and 4.17 V, respectively, indicating that the energy barrier for the reduction of LMO decreases after the first cycle. One plausible hypothesis to explain the reduction of this energy barrier is that a CEI layer forms and stabilizes during the first anodic scan, consistent with previous work that suggests MnO may form on the top surface (1–2 nm) during the first delithiation of LMO [22]. It is possible that MnO is part of the constituent in the CEI. Comparing the 2nd to 10th cycles, it is clear that the electrochemistry using LMO films is reversible in CV, and the resulting CEI is representative to those of the real battery condition. The total charge of each half-cycle is $0.31 \pm 0.04 \mu\text{Ah}$, which indicates that the thickness of LMO film is $\sim 25\text{nm}$, assuming that all LMO in the active area is lithiated/delithiated during CV.

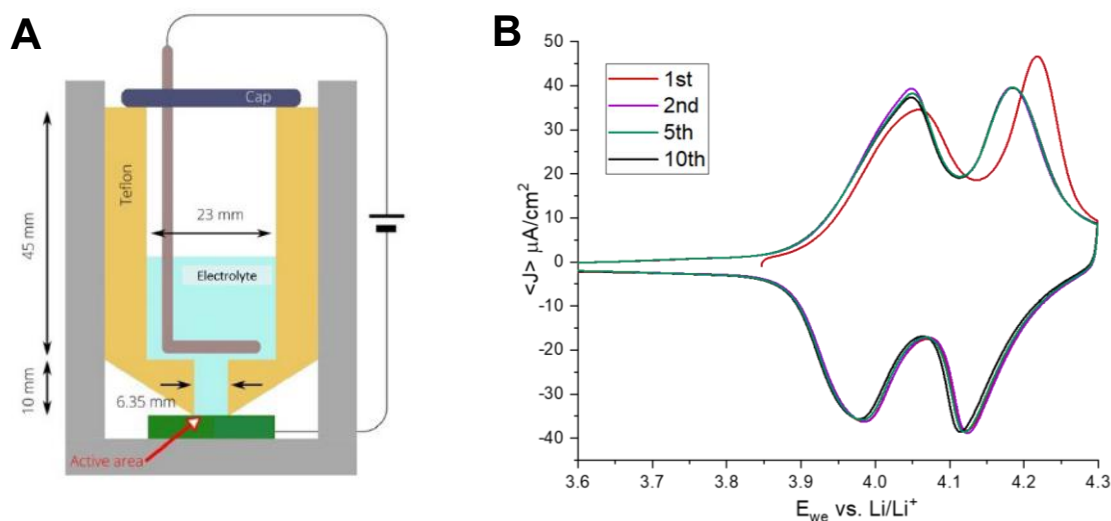


Figure X.1.8 Electrochemistry Tests for PAD-LMO films. (A) Schematic of A Cone Cell for Thin Film Electrochemistry Tests (B) Cycle Voltammetry (CV) of PAD-LMO film of the 1st, 2nd, 5th and 10th cycles

The composition of the CEI layer formed on LMO cathode materials after electrochemical cycling was probed using X-ray photoelectron spectroscopy (XPS). The surface compositions of pristine and electrochemically cycled LMO thin films were measured in this study. XPS measurements were performed on pristine LMO film was measured immediately following deposition. These films were subsequently transferred to an Ar glovebox and integrated into the previously describe cone cell. Full CV measurements were made using the same scan rate and potential range as decribed above and then rinsed in DMC. The cycled LMO films were then transferred into the XPS instrument for analysis. The XPS measurements are carried out with a Kratos AXIS Supra⁺. Transitions including O 1s, F 1s, Mn 2p, and Cr 2p are shown in Figure X.1.9. It is evident that fluorine contents increased dramatically after cycling, which suggests that the LiPF₆ in the electrolyte has decomposed and contributed F in the growth of the CEI. The evolution of the O 1s transition, on the other hand, shows a small uplifting shoulder after cycling, while the major peak has shrunk after cycling. This may indicate that the amount of a minor O contents has increased, while the major O component may have decreased, or covered by newly formed materials (possibly CEI layers) and leads to the attenuation of its O signals. The Mn 2p transitions have shifted to lower energy, indicating that the Mn valence gets reduced following cycling. This is consistent with the formation of MnO₂ from LMO in which the oxidation state of Mn reduces to 3⁺ from 4⁺. The intensity of the Mn peaks decreases after cycling, suggesting that the Mn concentration at the surface of the cylced film is lower that in the pristine LMO film. This is consistent with the formation of a CEI that incorporates organics/inorganics that contains lower Mn concentration.

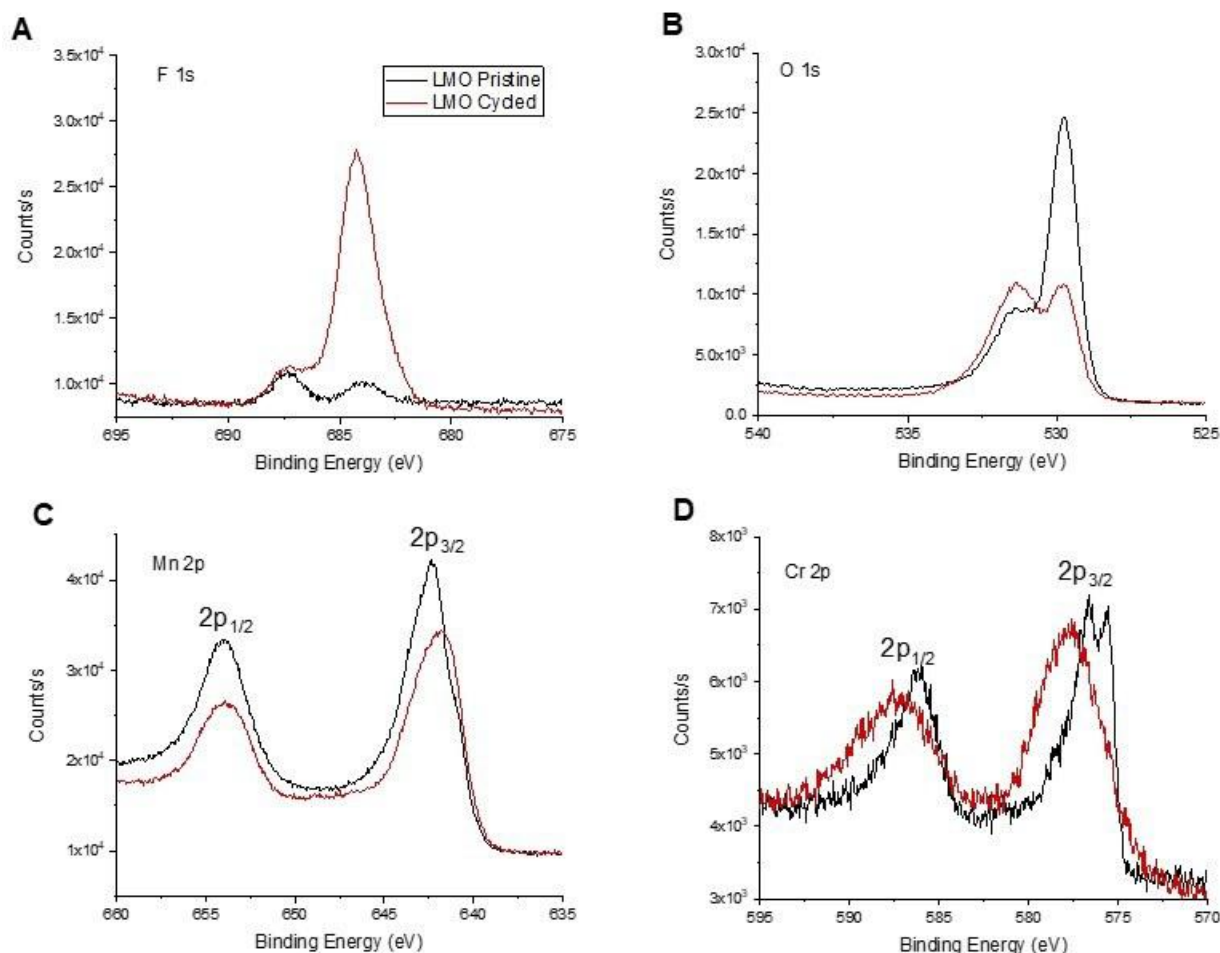


Figure X.1.9 XPS Results for PAD-LMO films before and after CV. The black curve stands for pristine LMO film and red curve for cycled LMO film.

A small amount of Cr can be detected on the top surface of LMO, either in pristine or cycled samples. This indicates that either there is Cr contamination in the precursor solution, possibly from Mn salt, or the Cr adhesive layer may have undergone some unknown process that leads to the uprising of Cr to the surface. Further study is needed to identify the origin of Cr at the surface of pristine and cycled LMO films and to evaluate whether the Cr is participating the CEI formation.

To further understand the constituents and evolution of CEI, a series of *ex situ* near-edge X-ray absorption fine structure (NEXAFS) measurements were made on LMO films that were cycled under systematically varied conditions. The samples are prepared, cycled and sealed in Ar at CU Boulder before being transferred to beamline 7-ID-1 of NSLS-II at Brookhaven National Lab. The XAS sample environment was UHV ($P = 10^{-9}$ Torr) at room temperature. The total electron yield (TEY), fluorescence yield (FY) and partial electron yield (PEY) were simultaneously recorded from each sample.

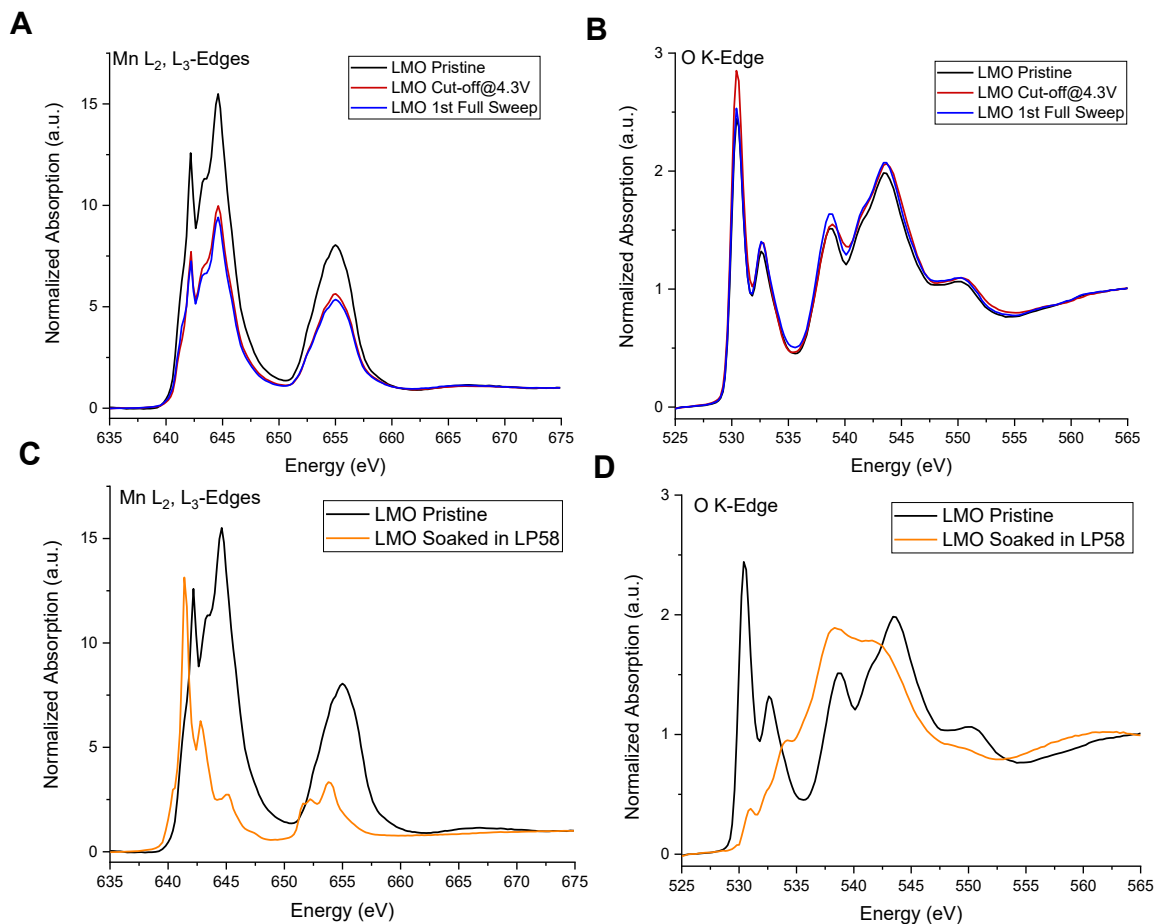


Figure X.1.10 NEXAFS Results for PAD-LMO films at pristine state (black curve), OCV (soaked in electrolyte, orange curve), cut-off at 4.3V (red curve) and after 1 full cycle (blue curve). (A) and (C): Manganese L₂ and L₃ edges, (B) and (D): Oxygen K-edge.

Figure X.1.10 shows the PEY collected at Mn and O edges for pristine and cycled LMO films in (A) and (B). Minimal shift in edge position is observed for Mn L₂ and L₃ edges, which indicates that the Mn components on LMO surface remains largely unchanged during the entire CV cycle. However, the normalized intensity of the 4.3V cut-off sample (fully delithiated, red curve) and the full sweep sample (fully lithiated blue curve) are almost the same and both significantly decreased in intensity in comparison to the pristine sample. This indicates that it is possible to have a newly formed layer is covering the LMO surface, as the PEY detection mode is very surface sensitive (<5 nm). The result shown in (B) for oxygen K-edge, however, doesn't seem to follow the same trend. Further follow-up experiments and analysis are needed to confirm this result.

Figure X.1.10 (C) and (D) show XAS at the O and Mn edges for pristine LMO and OCV state after soaking in LP58 electrolyte for 48 hours. The Mn L₂ and L₃ edges and O K-edge are all shifted in position and have profiles that differ significantly. This suggests that a surface reconstruction involving Mn and O results from soaking in electrolyte. Mn components on LMO surface are partially reduced to lower oxidation state and the oxygen environment has evolved. To understand the chemistry during OCV, further experiments and analysis are needed.

Conclusions

In summary, we have combined advanced x-ray surface scattering and x-ray spectroscopy studies with molecular modelling, we showed that the protonation reaction is the key to understanding the cathode-electrolyte reaction. The degradation of NMC cathode shows transition-metal dependent reduction behaviors in carbonate-based electrolyte, where the deprotonation from the solvent EC on cathode surface is believed to play a dominant role. We further show the rationalization for advanced electrolyte design to suppress such deprotonation reactions, therefore offering molecular-level insights into the degradation mechanisms of cathode in carbonate-based electrolytes and providing fundamental understanding for the development of cathode stabilization strategies.

Understanding the evolution and stabilization of the cathode interphase in electrolyte is of great significance for the development of NG-LiBs. In this project, we conducted surface X-ray scattering and spectroscopy studies using model epitaxial thin film cathodes in conjunction with theoretical modeling to probe key interfacial chemistry between thin-film cathodes and electrolytes. The structural and chemical evolutions of NMC cathode thin film in electrolytes has been experimentally and theoretically explored. As revealed by surface X-ray scattering and different x-ray spectroscopy probes, NMC thin films show transition metal dependent degradation behaviors in carbonate-based electrolyte and solvent, which we attribute to the interfacial protonation reaction between cathode and EC solvent. We further provide the molecular-level rationalization for advanced electrolyte design to suppress solvent deprotonation on cathode surface. We anticipate that our combined x-ray, electrochemistry, and molecular scale modeling approach will provide scalable insights into the understanding of the chemical and electrochemical stability of cathode surface in electrolyte, therefore promoting the rational design of advanced high-energy batteries.

Key Publications

1. Cho, S.-J.; Yu, D.-E.; Pollard, T. P.; Moon, H.; Jang, M.; Borodin, O.; Lee, S.-Y., Nonflammable Lithium Metal Full Cells with Ultra-high Energy Density Based on Coordinated Carbonate Electrolytes. *iScience* 2020, 23, 100844-100855.
2. Von Aspern, N.; Grünebaum, M.; Diddens, D.; Pollard, T.; Wölke, C.; Borodin, O.; Winter, M.; Cekic-Laskovic, I., Methyl-group functionalization of pyrazole-based additives for advanced lithium ion battery electrolytes. *J. Power Sources*. 2020, 461, 228159-228169.
3. Ko, J. S.; Paul, P. P.; Wan, G.; Seitzman, N.; DeBlock, R. H.; Dunn, B. S.; Toney, M. F.; Nelson Weker, J., NASICON $\text{Na}_3\text{V}_2(\text{PO}_4)_3$ Enables Quasi-Two-Stage Na^+ and Zn^{2+} Intercalation for Multivalent Zinc Batteries. *Chem. Mater.* 2020, 32, 3028-3035.
4. G. Wan, T.P. Pollard, L. Ma, M.A. Schroeder, C.-C. Chen, Z. Zhu, Z. Zhang, C.-J. Sun, H.L. Thaman, A. Vailionis, H. Li, S. Kelly, Z. Feng, J. Franklin, S.P. Harvey, Y. Zhang, Y. Du, Z. Chen, C.J. Tassone, H.-G. Steinrück, K. Xu, O. Borodin, M.F. Toney, Solvent-mediated Oxide Hydrogenation in Layered Cathodes, submitted to Nature Chemistry.

References

1. Cao, C., H. G. Steinrück, B. Shyam, K. H. Stone, and M. F. Toney. "In Situ Study of Silicon Electrode Lithiation with X-Ray Reflectivity." *Nano. Lett.* 16, no. 12 (Dec 14 2016): 7394-401. <https://doi.org/10.1021/acs.nanolett.6b02926>.
2. Cao, C. T., H. G. Steinrück, B. Shyam, and M. F. Toney. "The Atomic Scale Electrochemical Lithiation and Delithiation Process of Silicon." *Adv. Mater. Inter.* 4, no. 22 (Nov 23 2017): 1700771. <https://doi.org/ARTN 1700771>.
3. Horowitz, Y., H. G. Steinrück, H. L. Han, C. Cao, Abate, II, Y. Tsao, M. F. Toney, and G. A. Somorjai. "Fluoroethylene Carbonate Induces Ordered Electrolyte Interface on Silicon and Sapphire Surfaces as Revealed by Sum Frequency Generation Vibrational Spectroscopy and X-Ray Reflectivity." *Nano. Lett.* 18, no. 3 (Mar 14 2018): 2105-11. <https://doi.org/10.1021/acs.nanolett.8b00298>.
4. Steinrück, Hans-Georg, Chuntian Cao, Yuchi Tsao, Christopher J. Takacs, Oleg Kononov, Jenel Vatamanu, Oleg Borodin, and Michael F. Toney. "The Nanoscale Structure of the Electrolyte–Metal Oxide Interface." *Ener. Environm. Sci.* 11, no. 3 (2018): 594-602. <https://doi.org/10.1039/c7ee02724a>.

5. Franklin, J. B., B. Zou, P. Petrov, D. W. McComb, M. P. Ryan, and M. A. McLachlan. "Optimised Pulsed Laser Deposition of ZnO Thin Films on Transparent Conducting Substrates." *J. Mater. Chem.* 21, no. 22 (2011): 8178-82. <https://doi.org/10.1039/c1jm10658a>.
6. Hartung, S., N. Bucher, J. B. Franklin, A. M. Wise, L. Y. Lim, H. Y. Chen, J. N. Weker, *et al.* "Mechanism of Na⁺ Insertion in Alkali Vanadates and Its Influence on Battery Performance." *Adv. Ener. Mater.* 6, no. 9 (May 11 2016): 1502336. <https://doi.org/ARTN 1502336> 10.1002/aenm.201502336.
7. Wang, H. W., Y. Zhang, H. X. Ang, Y. Q. Zhang, H. T. Tan, Y. F. Zhang, Y. Y. Guo, *et al.* "A High-Energy Lithium-Ion Capacitor by Integration of a 3d Interconnected Titanium Carbide Nanoparticle Chain Anode with a Pyridine-Derived Porous Nitrogen-Doped Carbon Cathode." *Adv. Funct. Mater.* 26, no. 18 (May 10 2016): 3082-93.
8. Gauthier, M., T. J. Carney, A. Grimaud, L. Giordano, N. Pour, H. H. Chang, D. P. Fenning, *et al.* "Electrode-Electrolyte Interface in Li-Ion Batteries: Current Understanding and New Insights." *J Phys. Chem. Lett.* 6, no. 22 (Nov 19 2015): 4653-72. <https://doi.org/10.1021/acs.jpcclett.5b01727>.
9. Zhi, H., L. Xing, X. Zheng, K. Xu, and W. Li. "Understanding How Nitriles Stabilize Electrolyte/Electrode Interface at High Voltage." *J Phys. Chem. Let.* 8, no. 24 (Dec 21 2017): 6048-52. <https://doi.org/10.1021/acs.jpcclett.7b02734>.
10. Alvarado, J., M. A. Schroeder, M. H. Zhang, O. Borodin, E. Gobrogge, M. Olguin, M. S. Ding, *et al.* "A Carbonate-Free, Sulfone-Based Electrolyte for High-Voltage Li-Ion Batteries." *Mater. Today* 21, no. 4 (May 2018): 341-53. <https://doi.org/10.1016/j.mattod.2018.02.005>.
11. Su, Chi-Cheung, Meinan He, Paul Redfern, Larry A. Curtiss, Chen Liao, Lu Zhang, Anthony K. Burrell, and Zhengcheng Zhang. "Alkyl Substitution Effect on Oxidation Stability of Sulfone-Based Electrolytes." *ChemElectroChem* 3, no. 5 (2016): 790-97. <https://doi.org/doi:10.1002/celec.201500550>.
12. Suo, L., W. Xue, M. Gobet, S. G. Greenbaum, C. Wang, Y. Chen, W. Yang, Y. Li, and J. Li. "Fluorine-Donating Electrolytes Enable Highly Reversible 5-V-Class Li Metal Batteries." *Proc. Natl. Acad. Sci. U. S. A.* 115, no. 6 (Feb 6 2018): 1156-61. <https://doi.org/10.1073/pnas.1712895115>.
13. Borodin, O., and D. Bedrov. "Interfacial Structure and Dynamics of the Lithium Alkyl Dicarboxylate SEI Components in Contact with the Lithium Battery Electrolyte." *J. Phys. Chem. C* 118, no. 32 (Aug 14 2014): 18362-71. <https://doi.org/10.1021/jp504598n>.
14. Borodin, O., Guorong V. Zhuang, Philip N. Ross, and Kang Xu. "Molecular Dynamics Simulations and Experimental Study of Lithium Ion Transport in Dilithium Ethylene Dicarboxylate." *J. Phys. Chem. C* 117, no. 15 (April 18 2013): 7433-44. <https://doi.org/10.1021/jp4000494>.
15. Cho, S. J., D. E. Yu, T. P. Pollard, H. Moon, M. Jang, O. Borodin, and S. Y. Lee. "Nonflammable Lithium Metal Full Cells with Ultra-High Energy Density Based on Coordinated Carbonate Electrolytes." *iScience* 23, no. 2 (Feb 21 2020): 100844. <https://doi.org/10.1016/j.isci.2020.100844>.
16. Huang, Q., T. P. Pollard, X. Ren, D. Kim, A. Magasinski, O. Borodin, and G. Yushin. "Fading Mechanisms and Voltage Hysteresis in FeF₂-NiF₂ Solid Solution Cathodes for Lithium and Lithium-Ion Batteries." *Small* 15, no. 6 (Feb 2019): e1804670. <https://doi.org/10.1002/sml.201804670>.
17. Von Aspern, Natascha, Mariano Grünebaum, Diddo Diddens, Travis Pollard, Christian Wölke, Oleg Borodin, Martin Winter, and Isidora Cekic-Laskovic. "Methyl-Group Functionalization of Pyrazole-Based Additives for Advanced Lithium Ion Battery Electrolytes." *Journal of Power Sources* 461, (461 (2020/06/15/ 2020): 228159. <https://doi.org/10.1016/j.jpowsour.2020.228159>.
18. Benedek, R., M. M. Thackeray, and A. van de Walle. "Free Energy for Protonation Reaction in Lithium-Ion Battery Cathode Materials." *Chem. Mater.* 20, no. 17 (Sep 9 2008): 5485-90. <https://doi.org/10.1021/cm703042r>.
19. Fang, C. M., and G. A. de Wijs. "Local Structure and Chemical Bonding of Protonated Li_xMn₂O₄ Spinels from First Principles." *Chem. Mater.* 18, no. 5 (March 1 2006): 1169-73. <https://doi.org/10.1021/cm051564a>.
20. Di Huang, Chaiwat Engtrakul, Sanjini Nanayakkara, David W. Mulder, Sang-Don Han, Meng Zhou, Hongmei Luo, and Robert C. Tenent. "Understanding Degradation at the Lithium-Ion Battery Cathode/Electrolyte Interface: Connecting Transition-Metal Dissolution Mechanisms to Electrolyte

Composition." ACS Appl. Mater. Interfaces (Mar 4 2021): 13, 10, 11930–11939.

<https://doi.org/10.1021/acsami.0c22235>

21. Chuntian Cao, Travis P. Pollard, Oleg Borodin, Julian E. Mars, Yuchi Tsao, Maria R. Lukatskaya, Robert M. Kasse, Marshall A. Schroeder, Kang Xu, Michael F. Toney*, and Hans-Georg Steinrück, "Toward Unraveling the Origin of Lithium Fluoride in the Solid Electrolyte Interphase." Chem. Mater. 2021, 33, 18, 7315–7336 (Sep 14, 2021). <https://doi.org/10.1021/acs.chemmater.1c01744>
22. Xiang Gao, Yumi H. Ikuhara, Craig A. J. Fisher, Rong Huang, Akihide Kuwabara, Hiroki Moriwake, Keiichi Kohamac and Yuichi Ikuhara. "Oxygen loss and surface degradation during electrochemical cycling of lithium-ion battery cathode material LiMn_2O_4 ." J. Mater. Chem. A, 2019,7, 8845-8854 (Nov 30, 2018). <https://doi.org/10.1039/C8TA08083F>

Acknowledgements

Co-PIs, Oleg Borodin and Marshall Schroeder, conducted the DFT and MD and purified electrolytes, respectively. Co-PI, Zhenxing Feng growth PLD films. Use of the Stanford Synchrotron Radiation Lightsource, SLAC National Accelerator Laboratory, is supported by the U.S. Department of Energy, Office of Science, Office of Basic Energy Sciences under Contract No. DE-AC02-76SF00515. This research used resources of the Advanced Photon Source, a U.S. Department of Energy (DOE) Office of Science User Facility operated for the DOE Office of Science by Argonne National Laboratory under Contract No. DE-AC02-06CH11357.

X.2 Interfacial Studies of Emerging Cathode Materials Lawrence Berkeley National Laboratory (LBNL)

Marca M. Doeff, Principal Investigator

Lawrence Berkeley National Laboratory
1 Cyclotron Road
Berkeley, CA 94720
E-mail: mmdoeff@lbl.gov

Tien Duong, DOE Technology Development Manager

U.S. Department of Energy
E-mail: Tien.Duong@ee.doe.gov

Start Date: October 1, 2018

End Date: September 30, 2022

Project Funding (FY22): \$300,000

DOE share: \$300,000

Non-DOE share: \$0

Project Introduction

Recently, the discovery that reversible or partly reversible oxygen redox processes can occur in a variety of structures has opened up a new design space for cathode materials, with the tantalizing possibility of attaining capacities well beyond the 280 mAh/g theoretical limit of traditional intercalation layered oxides. Materials of interest include Li_2MnO_3 , [1] lithium and manganese rich NMCs (LMR-NMCs) [2] and Co-free analogs, [3] other types of lithium-rich layered oxides with structures similar to Li_2MnO_3 [4] and cation-disordered rock salts (DRX materials) [5]. Many of these materials exhibit capacities of 300 mAh/g or more, but suffer from poor rate capability, voltage hysteresis, and capacity fading [6]. In these cases, irreversible oxygen loss, [7] morphological [8] and structural changes [9] are to blame for the performance issues. Strategies such as partial fluorine substitution for oxygen [10, 11] appear to mitigate irreversible oxygen loss and result in improved behavior. For this work, we use an array of surface-sensitive and bulk techniques to understand what gives rise to processes that result in their degradation and attempt to mitigate them in selected materials.

Objectives

Reports of oxygen redox activity in materials with unusually high capacities are intriguing, but fairly little is known about how these materials actually work. There are a number of unanswered questions to which the work proposed here is designed to answer. First, how deep into the bulk does oxygen redox occur? Is it primarily a surface reaction? When does oxygen release occur, as opposed to reversible redox? Does the oxygen redox or oxygen release contribute to the structural instability that is often seen, and can this be prevented by, e.g., cationic or anionic substitutions, coatings, or other strategies? How do the surfaces of particles of charged or partially charged materials interact with the electrolytic solutions, and how does this contribute to capacity fading, rate limitations, and other performance issues? Once these questions are answered, strategies such as substitutions, coatings and particle morphology/size engineering can be considered to ensure robust cycling.

Approach

To answer the above questions, we synthesize materials with differing particle sizes/surface areas, compositions, or other properties, and characterize them using conventional laboratory techniques such as X-ray diffraction (XRD) and scanning electron microscopy (SEM). We then study their electrochemical properties in half-cell configurations, subjecting them to electrochemical charge, discharge, and cycling. In some cases, we may chemically delithiate them for further study. An array of surface and bulk sensitive techniques including synchrotron X-ray absorption spectroscopy (XAS), X-ray photoelectron spectroscopy (XPS), transmission X-ray microscopy (TXM), X-ray Raman (XRS), resonant inelastic X-ray scattering (RIXS) and microscopy are used to study materials at various states-of-charge, either in situ or ex situ. We

collaborate with the McCloskey group to do *in situ* differential mass spectroscopy (DEMS) experiments to understand oxygen loss. In FY22, we continued work begun in FY21 on $\text{Li}_4\text{Mn}_2\text{O}_5$ [12].

Results

In FY21, we studied synthetic parameters for making $\text{Li}_4\text{Mn}_2\text{O}_5$ and their effect on the electrochemistry. The material is made by reactive ball-milling of a Mn-containing precursor and a lithium source. The initial charge capacity is directly related to the degree of lithium excess used during synthesis, but there is little effect on the capacity of the subsequent discharge or cycling behavior. XRD on $\text{Li}_4\text{Mn}_2\text{O}_5$ made with a large excess of lithium shows reflections that can be attributed to Li_2O . This is a relatively insensitive technique for detecting small amounts of compounds made up of light elements, so is not useful for determining whether this impurity is present in samples made with lower levels of lithium excess. However, peaks due to lithia were also observed in the surface sensitive O K-edge XAS and bulk-sensitive X-ray Raman spectra of pristine $\text{Li}_4\text{Mn}_2\text{O}_5$ electrodes made with lower lithium excess, and disappeared in the spectra of fully charged electrodes. A signal due to lithium carbonate is observed in the electrode charged to 4.8V, suggesting a reaction with the electrolytic solution. These results indicate that decomposition of lithia contributes to the first charge capacity, but does not fully explain the origin of the large discharge capacities, which exceeds that which is predicted from the assumption that all of the trivalent Mn in the pristine material is oxidized to the tetravalent state upon extraction of lithium. Both Mn XRS and K-edge XAS on charged electrodes show no evidence of formation of pentavalent Mn.

While capacities over 300 mAh/g are initially obtained when cycling half-cells containing $\text{Li}_4\text{Mn}_2\text{O}_5$ between 4.5-1.5V, fading is rapid, hysteresis is evident, and the voltage profile gradually develops several plateaus similar to those seen for manganese oxide spinels, suggesting structural change is occurring. Increasing the lower voltage limit from 1.5 V to 2.5 V does not improve the capacity retention, implying the cycling behavior is sensitive to high-voltage operations. Reducing the upper voltage limit improves the cycling and delays the evolution of the voltage profile, but decreases the initial capacities. Of note is the small voltage polarization (ΔV , *i.e.*, the difference between average charge and discharge voltage) for these cells operated at high voltages, indicating that the cell resistance does not increase substantially and is not the primary cause of the rapid capacity fading. Mn K-edge XAS indicates that the average oxidation state of Mn falls below +3 upon cycling to 4.5V at the end of discharge, but is nearly unchanged if an upper voltage limit of 3.5V is used. Mn L-edge XAS data also shows evidence of re-reduction of Mn near the surface in electrodes charged to 4.8V, although it is oxidized at earlier stages of charge. While $\text{Li}_4\text{Mn}_2\text{O}_4\text{F}$ exhibits a lower initial capacity than $\text{Li}_4\text{Mn}_2\text{O}_5$, the evolution of plateaus in the voltage profile during cycling is less pronounced and capacity retention appears to be somewhat improved. Still, it appears that, while fluorination ameliorates the structural changes associated with the voltage profile changes, it does not prevent them entirely, nor does it result in greatly improved electrochemical characteristics.

Figure X.2.1 shows depth-profiling laboratory X-ray photoelectron spectra (XPS) of a $\text{Li}_4\text{Mn}_2\text{O}_5$ electrode charged to 4.8V, carried out this year. As etching time is increased, the technique probes deeper into the surface. The C1s and O1s XPS spectra show evidence of Li_2CO_3 and lithium alkyl carbonate formation, confirming the O K-edge results from FY21. A signal due to $(\text{CH}_2\text{CH}_2\text{O})_n^-$ is also present, implying a polymerization product. F1s and P2p spectra also show evidence of various decomposition products of LiPF_6 such as LiF , $\text{Li}_x\text{PF}_y\text{O}_z$, and phosphates. Interestingly, some of these reaction products such as Li_2CO_3 and lithium alkyl carbonates were already observed on surfaces of pristine electrodes exposed to electrolytic solution, although the polymerization product or decomposition products of LiPF_6 were not present (not shown). Li_2CO_3 may derive from reactions of adventitious Li_2O with CO_2 in air, or the electrolytic solution. These results suggest highly reactive active material surfaces and a cascade of side-reactions that take place at high potentials.

In FY22, we attempted a new tactic to ameliorate the various issues associated with cycling $\text{Li}_4\text{Mn}_2\text{O}_5$. Blending two different cathode materials is a common strategy used in Li-ion battery manufacture to overcome the shortcomings of each individual component [13]. There are sometimes synergistic effects. For example,

certain blends of manganese-containing spinel and NMC showed better storage characteristics than either component alone. By deliberately incorporating LiMn_2O_4 in with $\text{Li}_4\text{Mn}_2\text{O}_5$, we hoped to find a composition that cycled better without unduly compromising the high capacity that made $\text{Li}_4\text{Mn}_2\text{O}_5$ so initially promising. To that end, we carried out reactive ball-milling for 20 hours with various mixtures of LiMn_2O_4 and $\text{Li}_4\text{Mn}_2\text{O}_5$ (Table X.2.1). The XRD patterns (Figure X.2.2) show that the products are rock salt phases, with no spinel detected, clear from the absence of reflections at $2\theta=19^\circ$ and 59° .

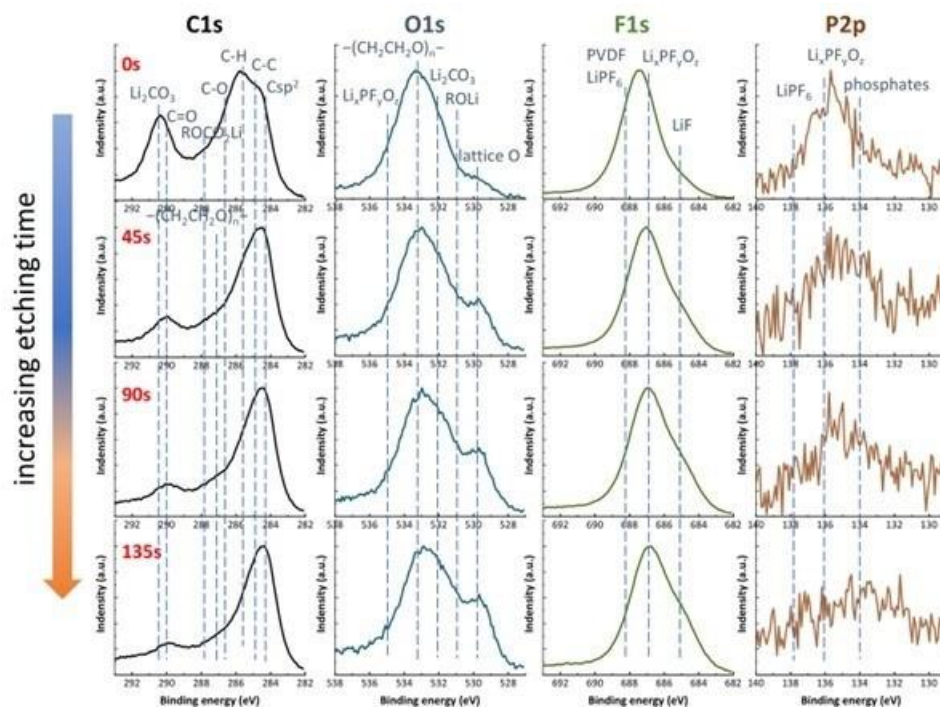


Figure X.2.1 XPS spectra on a $\text{Li}_4\text{Mn}_2\text{O}_5$ electrode charged to 4.5V as a function of etching time. Longer etching times probe deeper into the sample.

Table X.2.1 Compositions synthesized for this study

$n(\text{Li}_4\text{Mn}_2\text{O}_5)/n(\text{LiMn}_2\text{O}_4)$	Composition	Equivalent Composition	Theoretical capacity based on Mn redox (mAh/g)	Calculated average Mn oxidation state
1:0	$\text{Li}_4\text{Mn}_2\text{O}_5$	$\text{Li}_{1.6}\text{Mn}_{0.8}\text{O}_2$	246	3 ⁺
8.5:1.5	$\text{Li}_{3.55}\text{Mn}_2\text{O}_{4.85}$	$\text{Li}_{1.46}\text{Mn}_{0.82}\text{O}_2$	233	3.075 ⁺
8:2	$\text{Li}_{3.4}\text{Mn}_2\text{O}_{4.8}$	$\text{Li}_{1.42}\text{Mn}_{0.83}\text{O}_2$	229	3.1 ⁺
7.5:2.5	$\text{Li}_{3.25}\text{Mn}_2\text{O}_{4.75}$	$\text{Li}_{1.37}\text{Mn}_{0.84}\text{O}_2$	223	3.125 ⁺
7:3	$\text{Li}_{3.1}\text{Mn}_2\text{O}_{4.7}$	$\text{Li}_{1.32}\text{Mn}_{0.85}\text{O}_2$	220	3.15 ⁺
6.5:3.5	$\text{Li}_{2.95}\text{Mn}_2\text{O}_{4.65}$	$\text{Li}_{1.27}\text{Mn}_{0.86}\text{O}_2$	215	3.175 ⁺
6:4	$\text{Li}_{2.8}\text{Mn}_2\text{O}_{4.6}$	$\text{Li}_{1.22}\text{Mn}_{0.87}\text{O}_2$	211	3.2 ⁺

Incorporation of more LiMn_2O_4 into the structure should result in lower theoretical capacities calculated from the Mn redox capability (Table 1), since more Mn^{4+} is incorporated in the structure. However, the Mn K-edge XAS spectra (Figure X.2.2 center) shows a slight shifting to lower energies of the materials prepared with

LiMn_2O_4 , indicating that the average oxidation state is actually slightly lower than that of the parent compound. Similarly, the Mn L-edge spectra in TEY mode, which probes about 5 nm into the surface (Figure X.2.2 right) indicate a lower oxidation state for surface Mn. This implies that oxygen was lost to varying degrees during the reactive ball-milling process of the mixtures.

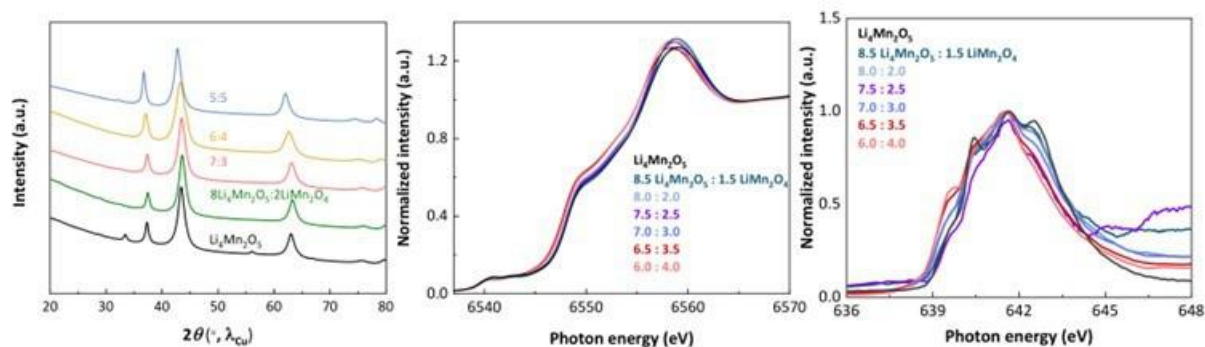


Figure X.2.2 (Left) XRD patterns of the compounds synthesized for this study. (Middle) Mn K-edge XAS spectra, and (right) Mn L-edge spectra in TEY mode.

Figure X.2.3 shows the first five cycles of half-cells containing the $\text{Li}_x\text{Mn}_2\text{O}_4$ compositions and capacity as a function of cycle number for twenty-two cycles at C/20 rate. As the LiMn_2O_4 content in the cathode materials was raised, the capacity in lithium half cells decreased somewhat, although the effect was less evident for materials made with smaller amounts of LiMn_2O_4 . Importantly, the first cycle coulombic efficiency and the capacity retention all improved steadily as LiMn_2O_4 content was increased in the cathode materials. Furthermore, the evolution of the voltage profiles upon cycling was less severe. Interestingly, the presence of a plateau near 3V similar to that found in manganese oxide spinel structures was already fairly pronounced in the first discharge profiles of cells containing the cathode materials made with high LiMn_2O_4 content. This suggests that micro- or nano-domains of spinel are already present in these materials, although microscopy needs to be carried out to confirm this. It should be noted that the evolution of the voltage profile towards one that resembles that of a spinel appears to depend on rate and voltage limits used, with more voltage fading evident at higher current densities and higher upper voltage limits (not shown).

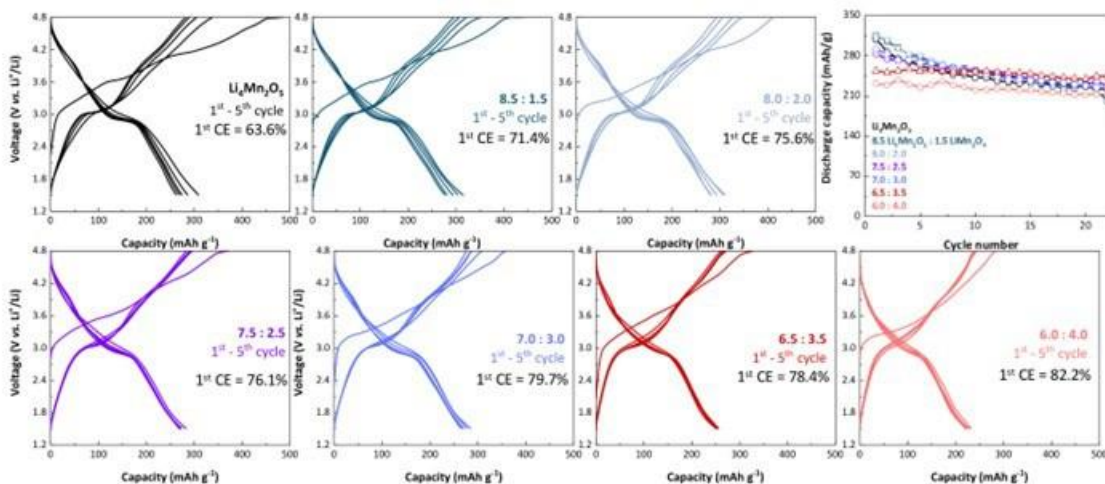


Figure X.2.3 First five cycles of cell containing the materials under study, cycled between 4.8-1.5V at C/20 rate. Upper right panel shows capacity retention as a function of cycle number for 22 cycles.

The best compromise between capacity and other electrochemical properties (first cycle coulombic efficiency, capacity and voltage retention) appears to be with the cathode material made in a 6.5 $\text{Li}_4\text{Mn}_2\text{O}_5$:3.5 LiMn_2O_4

ratio (nominal composition $\text{Li}_{1.27}\text{Mn}_{0.86}\text{O}_2$). This electrode delivers approximately 250 mAh/g initially between 4.8-1.5V, and shows the best cycling behavior both in terms of voltage and capacity retention. From this point onward, the report will focus on a comparison between this material and $\text{Li}_4\text{Mn}_2\text{O}_5$.

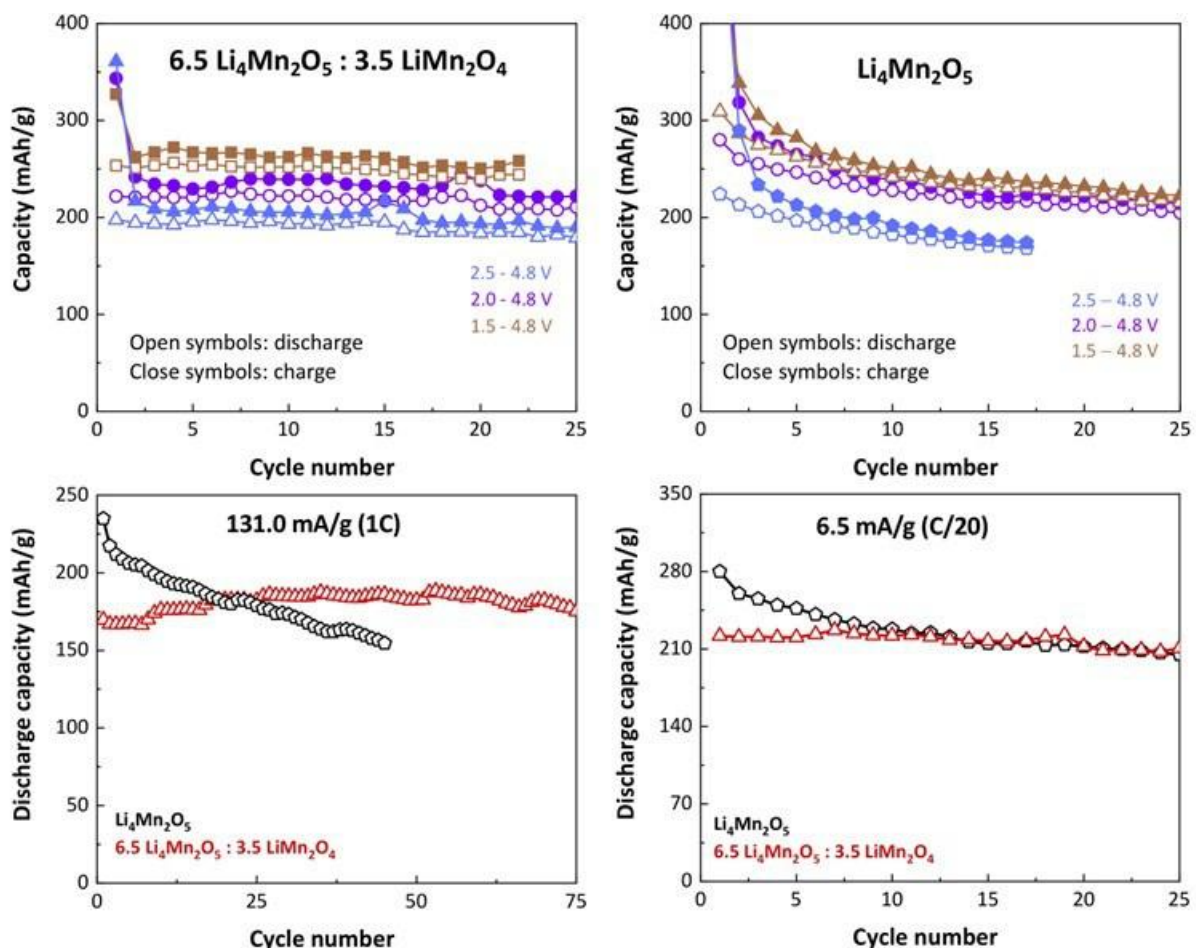


Figure X.2.4 Charge and discharge capacity as a function of cycle number between the indicated voltage limits for cells containing (upper left) $6.5 \text{ Li}_4\text{Mn}_2\text{O}_5 : 3.5 \text{ LiMn}_2\text{O}_4$ and (upper right) $\text{Li}_4\text{Mn}_2\text{O}_5$. Bottom panels show a comparison between capacity retention of cells containing $6.5 \text{ Li}_4\text{Mn}_2\text{O}_5 : 3.5 \text{ LiMn}_2\text{O}_4$ and $\text{Li}_4\text{Mn}_2\text{O}_5$ cycled at 1C rate (lower left) or C/20 rate (lower right) between 4.8-2.0V.

The improved cycling behavior of the $6.5 \text{ Li}_4\text{Mn}_2\text{O}_5 : 3.5 \text{ LiMn}_2\text{O}_4$ compared to $\text{Li}_4\text{Mn}_2\text{O}_5$ is evident in Figure X.2.4. No matter what voltage limits were used or what discharge rate was used, the former always outperformed the latter in terms of capacity retention.

To obtain a better understanding of what leads to the differences in electrochemical behavior, we carried out O K-edge mRIXS (m=mapping) experiments on the two types of electrodes (Figure X.2.5). Conventional O K-edge techniques such as XAS are not able to detect O redox processes in transition metal oxides (rather they probe the degree of TM-O covalency), but RIXS can [14]. In charged electrode materials that undergo oxygen redox, a telltale feature in the RIXS maps is observed at 523.8 eV emission energy using an excitation energy of 531 eV, attributable to oxidized oxygen. For the pristine, charged, and discharged $\text{Li}_4\text{Mn}_2\text{O}_5$ electrodes as well as the $6.5 \text{ Li}_4\text{Mn}_2\text{O}_5 : 3.5 \text{ LiMn}_2\text{O}_4$ ones, only a strong signal at the emission energy of 525 eV, characteristic of lattice oxygen, is observed (Figure X.2.5).

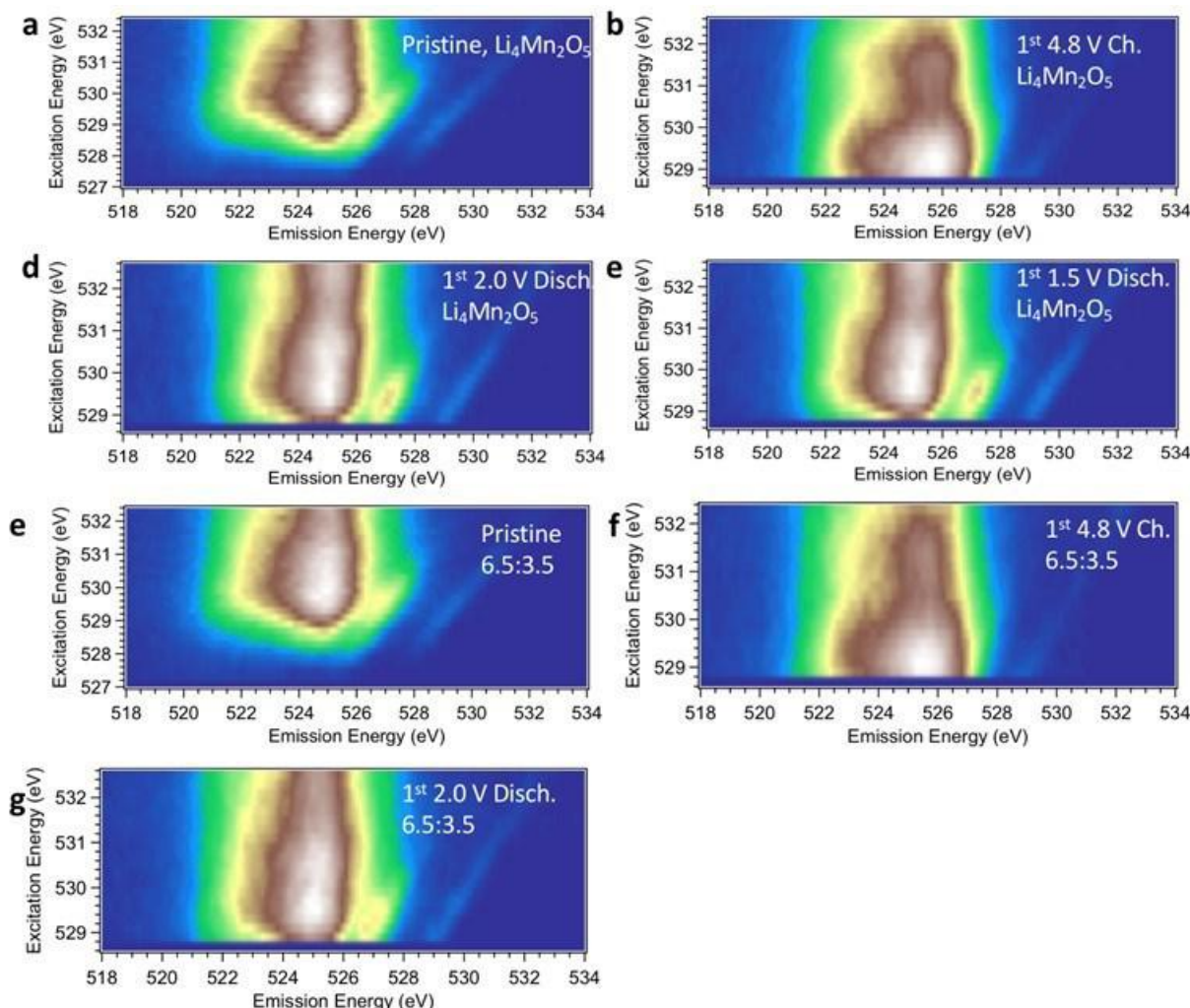


Figure X.2.5 RIXS maps of pristine, charged, and discharged $\text{Li}_4\text{Mn}_2\text{O}_5$ (a, b, c, d) and $6.5\text{Li}_4\text{Mn}_2\text{O}_5:3.5\text{LiMn}_2\text{O}_4$ electrodes (e, f, g). The prominent feature at an emission energy of 525 eV can be attributed to lattice oxygen. There is no signal at an emission energy of 523.8 eV and excitation energy of 531 eV, which would be characteristic of oxidized oxygen.

This result is somewhat puzzling, in light of the fact that these electrodes seem to deliver discharge capacities in excess of what is expected based solely on Mn redox initially. One possible scenario is that oxygen oxidation contributes to the first charge capacity, but is not reversible; rather the oxidized oxygen reacts with electrolyte or evolves as molecular oxygen. To test this further, we collaborated with the McCloskey group at U.C. Berkeley to do differential electrochemical mass spectroscopy (DEMS) on the two systems (Figure X.2.6 and Table X.2.2).

It is clear from these results that more gases are evolved from the $\text{Li}_4\text{Mn}_2\text{O}_5$ electrode than from the $6.5\text{Li}_4\text{Mn}_2\text{O}_5:3.5\text{LiMn}_2\text{O}_4$ one, close to the top of charge. Substantial amounts of carbon dioxide were detected in both types of cells, most likely stemming from decomposition of the electrolytic solution at high potentials either by the attack of reactive oxygen species (e.g., superoxide radicals) or electrochemical oxidation. Another potential source of CO_2 is from electrolytic decomposition of Li_2CO_3 , which was also detected in the pristine electrode in the XPS experiment described above. The H_2 gassing is caused by the crosstalk between cathode and anode; i.e., a protic oxidation species (R-H^+) from the electrolytic solution diffusing from the cathode to the anode and undergoing reduction there. The larger amounts of these gases detected in the DEMS of the $\text{Li}_4\text{Mn}_2\text{O}_5$ cell on the first cycle compared to the one with $6.5\text{Li}_4\text{Mn}_2\text{O}_5:3.5\text{LiMn}_2\text{O}_4$, which did not evolve

oxygen, suggests that 1) the oxygen release also exacerbates decomposition of electrolytic solution at high potentials, perhaps by reacting with it. 2) more oxidized oxygen species is formed in the $\text{Li}_4\text{Mn}_2\text{O}_5$ cell. While more experiments need to be done to understand the exact cause of gassing, one can clearly conclude that parasitic reactions are more severe in the cell made with a $\text{Li}_4\text{Mn}_2\text{O}_5$ electrode.

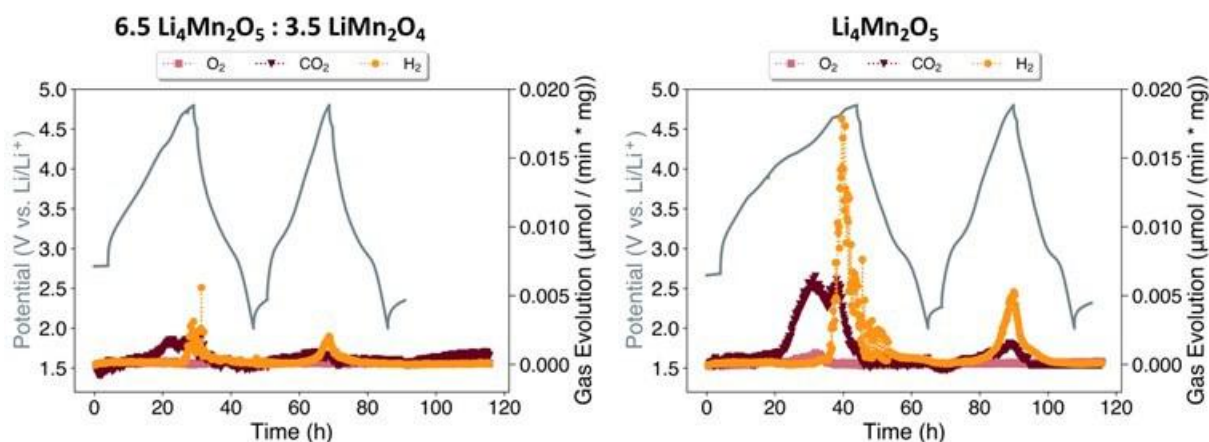


Figure X.2.6 DEMS results on cells containing 6.5 $\text{Li}_4\text{Mn}_2\text{O}_5$:3.5 LiMn_2O_4 (left) and $\text{Li}_4\text{Mn}_2\text{O}_5$ (right).

Table X.2.2 Gases detected during the first and second cycles of DEMS cells shown in adjacent figure

Material	Normalized amount of H_2 (umol/mg)		Normalized amount of CO_2 (umol/mg)		Normalized amount of O_2 (umol/mg)	
	cycle 1	cycle 2	cycle 1	cycle 2	cycle 1	cycle 2
6.5 $\text{Li}_4\text{Mn}_2\text{O}_5$:3.5 LiMn_2O_4	0.575	0.457	0.602	0.197	0	0
$\text{Li}_4\text{Mn}_2\text{O}_5$	1.88	0.793	1.61	0.336	0.142	0

The cycling of $\text{Li}_4\text{Mn}_2\text{O}_5$ electrodes also results in a gradual reduction of the average oxidation state of Mn below 3+ in the bulk, at the bottom of discharge, as noted earlier. A shift in the edge energies to lower values in the Mn K-edge XAS data of discharged electrodes cycled between various voltage limits in Figure X.2.7 is consistent with reduction of Mn. This is most likely associated with the loss of oxygen that is observed. The high discharge capacity of $\text{Li}_4\text{Mn}_2\text{O}_5$ over multiple cycles arises not only from the $\text{Mn}^{3+}/\text{Mn}^{4+}$ redox and very limited amount of anionic redox (if any, not detectable by mRIXS), but also from over-reduction of Mn^{3+} . In fact, theoretical discharge capacities taking in account the over-reduction, based on linear combination analysis of XAS data of electrodes discharged to various lower voltage limits, using MnO , Mn_2O_3 , and LiMn_2O_4 references, match the observed values seen for $\text{Li}_4\text{Mn}_2\text{O}_5$ well (not shown). The reduced Mn ions are prone to dissolve into the electrolyte, causing loss of active cathode materials and surface reconstruction. The dissolved Mn ions can also migrate to and deposit on the anode surface. These phenomena lead to capacity fading. In contrast, this Mn over-reduction is much less apparent in the 6.5 $\text{Li}_4\text{Mn}_2\text{O}_5$:3.5 LiMn_2O_5 electrodes, accounting for the better cycling stability.

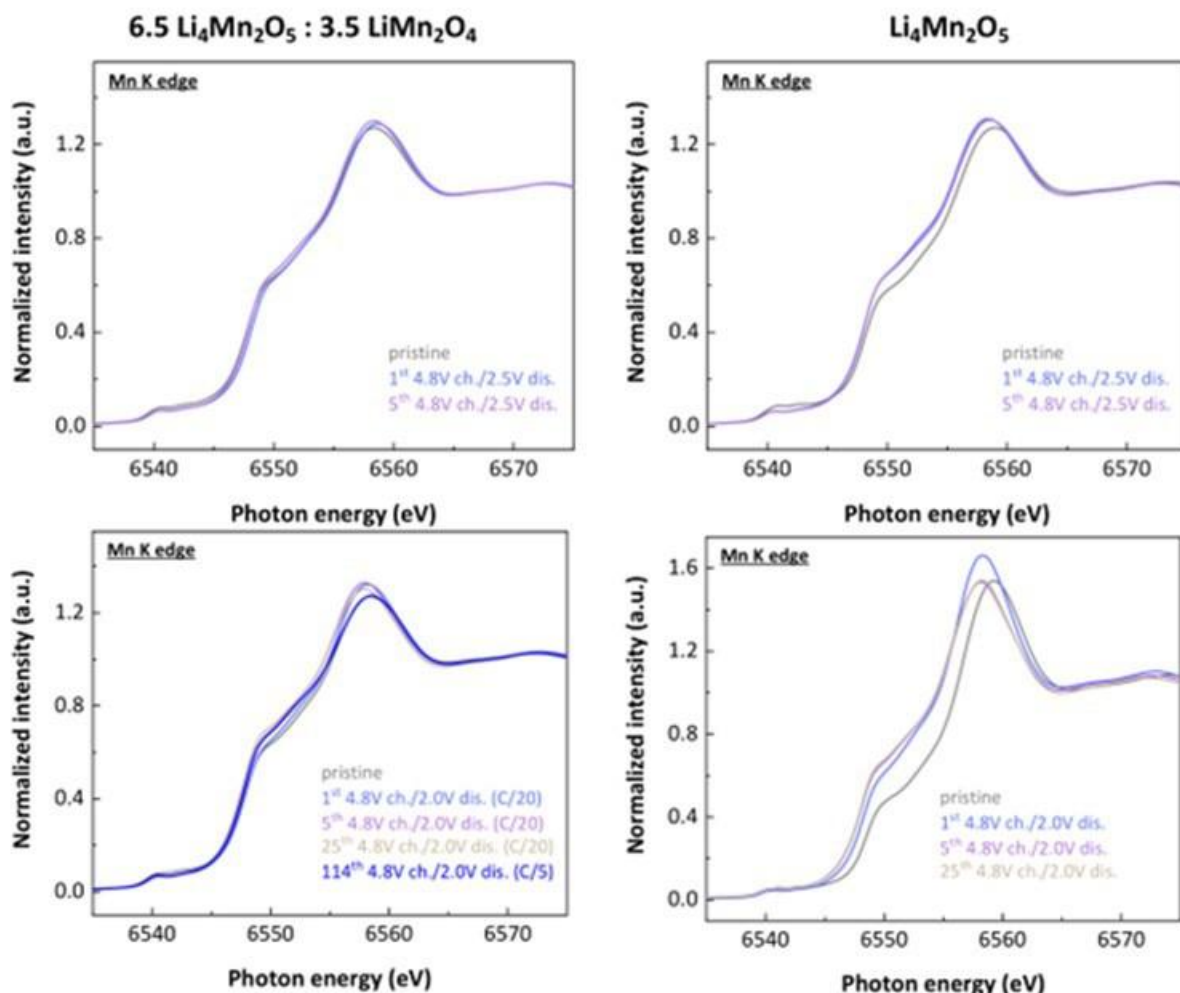


Figure X.2.7 Mn K-edge XAS data on (top left) pristine and $6.5\text{Li}_4\text{Mn}_2\text{O}_5:3.5\text{LiMn}_2\text{O}_4$ or (top right) $\text{Li}_4\text{Mn}_2\text{O}_5$ electrodes charged to 4.8V and discharged to 2.5V. Bottom left ($6.5\text{Li}_4\text{Mn}_2\text{O}_5:3.5\text{LiMn}_2\text{O}_4$) and right ($\text{Li}_4\text{Mn}_2\text{O}_5$) show results for electrodes charged to 4.8V and discharged to 2.0V for the designated number of cycles. Note that the $6.5\text{Li}_4\text{Mn}_2\text{O}_5:3.5\text{LiMn}_2\text{O}_4$ electrode on the bottom left underwent 114 cycles while the $\text{Li}_4\text{Mn}_2\text{O}_5$ one on the bottom right underwent only 25. All data obtained on electrodes in the fully discharged state.

These results definitively show that the approach of mixing $\text{Li}_4\text{Mn}_2\text{O}_5$ with LiMn_2O_4 results in dramatically improved performance.

Conclusions

$\text{Li}_4\text{Mn}_2\text{O}_5$ exhibit anomalously high discharge capacities early in their cycling histories that cannot be explained by oxidation to pentavalent Mn or reversible oxygen redox. Capacity and voltage fading occur rapidly upon cycling, and oxygen, hydrogen, and carbon dioxide are evolved during the initial cycles. The loss of oxygen from the structure causes a gradual decrease in the average Mn oxidation state in the bulk. Accounting for the over-reduced Mn explains the excess capacity that is observed for $\text{Li}_4\text{Mn}_2\text{O}_5$ electrodes. Reactive ball-milling of LiMn_2O_4 with $\text{Li}_4\text{Mn}_2\text{O}_5$ results in products that show better cycling retention, better 1st cycle coulombic efficiency, and less voltage fade when tested in half cells, although capacities are somewhat lower than that of the parent compound. The best of these materials has a composition of $6.5\text{Li}_4\text{Mn}_2\text{O}_5:3.5\text{LiMn}_2\text{O}_4$ and shows drastically better electrochemical behavior, much less gas evolution, and less tendency towards Mn reduction upon cycling.

Key Publications

1. Lee, S.-Y., Shangguan, J., Betzler, S., Harris, S. J., Doeff, M. M. and Zheng, H. "Lithium Metal Stripping Mechanisms Revealed Through Electrochemical Liquid Cell Electron Microscopy" *Nano Energy*, DOI:10.1016/j.nanoen.2022.107641 (2022)

References

1. Chen, H., and Islam, M. S., "Lithium Extraction Mechanism in Li-Rich Li_2MnO_3 Involving Oxygen Hole Formation and Dimerization" *Chem. Mater.* 28, (2016): 6656-6663.
2. Croy, J. R., Balasubramanian, M., Gallagher, K. G., and Burrell, A. K., "Review of the U.S. Department of Energy's "Deep Dive" Effort to Understand Voltage Fade in Li- and Mn-Rich Cathodes" *Acc. Chem. Res.* 48, (2015): 2813-21.
3. Luo, K., Roberts, M. R., Guerrini, N., Tapia-Ruiz, N., Hao, R., Massel, F., Pickup, D. M., Ramos, S., Liu, Y. S., Guo, J., Chadwick, A. V., Duda, L. C., and Bruce, P. G., "Anion Redox Chemistry in the Cobalt Free 3d Transition Metal Oxide Intercalation Electrode $\text{Li}[\text{Li}_{0.2}\text{Ni}_{0.2}\text{Mn}_{0.6}]\text{O}_2$ " *J. Am. Chem. Soc.* 138, (2016): 11211-11218.
4. Sathiyar, M., Rousse, G., Ramesha, K., Laisa, C. P., Vezin, H., Sougrati, M. T., Doublet, M. L., Foix, D., Gonbeau, D., Walker, W., Prakash, A. S., Ben Hassine, M., Dupont, L., and Tarascon, J. M., "Reversible Anionic Redox Chemistry in High-capacity Layered-oxide Electrodes" *Nature Mater.* 12 (2013): 827-835.
5. Seo, D. H., Lee, J., Urban, A., Malik, R., Kang, S., and Ceder, G., "The Structural and Chemical Origin of the Oxygen Redox Activity in Layered and Cation-disordered Li-excess Cathode Materials" *Nature Chem.* 8 (2016): 692-697.
6. Assat, G., Delacourt, C., Corte, D. A. D., and Tarascon, J.-M., "Practical Assessment of Anionic Redox in Li-Rich Layered Oxide Cathodes: A Mixed Blessing for High Energy Li-Ion Batteries" *J. Electrochem. Soc.* 163, (2016): A2965-A2976.
7. Xu, J., Sun, M., Qiao, R., Renfrew, S. E., Ma, L., Wu, T., Hwang, S., Nordlund, D., Su, D., Amine, K., Lu, J., McCloskey, B. D., Yang, W., and Tong, W., "Elucidating Anionic Oxygen Activity in Lithium-rich Layered Oxides" *Nature Commun.* 9, (2018): article no. 947.
8. Kan, W. H., Chen, D., Papp, J. K., Shukla, A. K., Huq, A., Brown, C. M., McCloskey, B. D., and Chen, G., "Unravelling Solid-State Redox Chemistry in $\text{Li}_{1.3}\text{Nb}_{0.3}\text{Mn}_{0.4}\text{O}_2$ Single-Crystal Cathode Material" *Chem. Mater.* 30, (2018): 1655-1666.
9. Mikhailova, D., Karakulina, O. M., Batuk, D., Hadermann, J., Abakumov, A. M., Herklotz, M., Tsirlin, A., Oswald, S., Giebeler, L., Schmidt, M., Eckert, J., Knapp, M., and Ehrenberg, H., "Layered-to-Tunnel Structure Transformation and Oxygen Redox Chemistry in LiRhO_2 upon Li Extraction and Insertion" *Inorg. Chem.* 55, (2016): 7079-7089.
10. Gent, W. E., Lim, K., Liang, Y., Li, Q., Barnes, T., Ahn, S. J., Stone, K. H., McIntire, M., Hong, J., Song, J. H., Li, Y., Mehta, A., Ermon, S., Tyliszczak, T., Kilcoyne, D., Vine, D., Park, J. H., Doo, S. K., Toney, M. F., Yang, W., Prendergast, D., and Chueh, W. C., "Coupling between Oxygen Redox and Cation Migration Explains Unusual Electrochemistry in Lithium-rich Layered Oxides" *Nature Commun.* 8, (2017): article no. 2091.
11. Lee, J., Papp, J. K., Clement, R. J., Sallis, S., Kwon, D. H., Shi, T., Yang, W., McCloskey, B. D., and Ceder, G., "Mitigating Oxygen Loss to Improve the Cycling Performance of High Capacity Cation Disordered Cathode Materials" *Nature Communications* 8, (2017): article no. 981.
12. Freire, M., Kosova, N. V., Jordy, C., Chateigner, D., Lebedev, O. I., Maignan, A., and Pralong, V. "A New Active Li-Mn-O Compound for High Energy Density Li-Ion Batteries" *Nature Mater.* 15, (2016): 173-177.
13. Chikkannanavar, S.B., Bernardi, D. M., and Liu, Lingyun "A Review of Blended Cathode Materials for use in Li-ion Batteries" *J. Power Sources* 248 (2014): 91-100.
14. Yang, W. and Devereaux, T.P. "Anionic and Cationic Redox and Interfaces in Batteries: Advances from Soft X-ray Absorption to Resonant Inelastic Scattering" *J. Power Sources* 389, (2018) 188-197.

Acknowledgements

We acknowledge contributions from the McCloskey group at U. C. Berkeley for DEMS experiments, and help with RIXS mapping experiments by Dr. Wanli Yang at the Advanced Light Source at LBNL. XAS experiments were carried out at the Stanford Synchrotron Radiation Lightsource.

X.3 Understanding Modification of High-Energy Cathodes and Their Interfaces with Electrolytes for Next-Generation Li-ion Batteries (PNNL)

Jie Xiao, Principal Investigator

Pacific Northwest National Laboratory
902 Battelle Blvd
Richland, WA, 99352
E-mail: jie.xiao@pnnl.gov

Yu-Jing Bi, Co-Principal Investigator

Pacific Northwest National Laboratory
902 Battelle Blvd
Richland, WA, 99352
E-mail: yujing.bi@pnnl.gov

Tien Duong, DOE Technology Development Manager

U.S. Department of Energy
E-mail: Tien.Duong@ee.doe.gov

Start Date: October 1, 2021

End Date: September 30, 2022

Project Funding (FY22): \$350,000

DOE share: \$350,000

Non-DOE share: \$0

Project Introduction

High-energy Ni-rich NMC ($\text{LiNi}_x\text{Mn}_y\text{Co}_{1-x-y}\text{O}_2$, $x \geq 0.6$) is one of the most promising cathode materials for next-generation high energy Li-ion batteries (LIBs) for electric vehicles. However, challenges exist for large-scale deployment of Ni-rich NMC. As more Ni is incorporated in the lattice, the material surfaces become more active, increasing both electrochemical and chemical reactivities of Ni-rich NMC in contact with electrolyte [1].

In the past few years, we have developed and optimized synthesis of Ni-rich NMC by using molten salt approach, which is then used as the model materials to study the interfacial reactions between cathode and electrolyte. We proposed mitigating gliding and microcracking of single crystal NMC76 through appropriate doping which demonstrated promising stability in full coin cells. This year we update the progress of doped single crystal NMC76 tested in 1Ah Li-ion pouch cells. Another challenge that needs to be addressed before large-scale development of Ni-rich NMC is gas generation [2], which also initiates from phase boundaries. Micron-sized single crystal Ni-rich NMC has a potential to address the common issues that polycrystals have. However, a quantifiable understanding of gas generation from single crystals and polycrystals is still lacking. In this report, the mechanism of gas generation from single crystal and polycrystalline $\text{LiNi}_{0.76}\text{Mn}_{0.14}\text{Co}_{0.1}\text{O}_2$ (NMC76) are investigated which provides different insights on the gas generation. The information from single crystal NMC76 also provides clues from material perspective to enhance the safety attributes of Ni-rich NMC cathodes.

Objectives

The objective of this project is to advance the fundamental understanding of the interfaces between electrolyte and Ni-rich NMC cathode by using high-performance single crystalline NMC76 as a model material. Ni-rich NMC single crystals will be doped to enhance cycling stability with a potential to eliminate gliding and cracking. By comparing single crystal and polycrystalline NMC76 in functioning electrochemical cells, the amounts of different gases generated upon cycling are quantified and compared in both coin and pouch cells to understand the impacts of reduced phase boundaries in single crystal NMC76.

Approach

- Dope single crystal NMC76 to enhance cycling stability with a potential to mitigate crystal gliding and cracking
- Develop a standard procedure of using in situ Differential Electrochemical Mass Spectrometry (DEMS) to ensure repeatable measurement results for gas quantification
- Monitor gas generation from single crystal and polycrystal NMC76.

Results

In FY21, we reported that doping can effectively improve the cycling stability of Ni-rich $\text{LiNi}_{0.76}\text{Mn}_{0.14}\text{Co}_{0.1}\text{O}_2$ (NMC76) single crystals in coin cells tests. Considering the different testing conditions in coin cells and pouch cells, in FY22, we cross validated the effectiveness of doping in NMC76 single crystals using 1 Ah pouch cells. Doped NMC76 single crystals have drum-like morphology (inset of Figure X.3.1a) with an average particle size of 3 μm . The particle size distribution of doped crystals seems to be more homogeneous than that of undoped NMC76 (data not shown here). The doped single crystals NMC76 are further validated in 1 Ah pouch cells cycled between 2.7 and 4.2V. Multi layers of cathodes and anodes alternately stacked together inside the 1 Ah pouch cells. On each side of the cathode Al current collector, the mass loading is 18 mg/cm^2 , corresponding to an areal capacity of 3.5 mAh/cm^2 . N/P ratio is controlled at 1.12 to avoid over lithiation on graphite anode. The first charge-discharge curve of the prototype pouch cells is shown in Figure X.3.1a. Without pre-lithiation of graphite anode, the first cycle efficiencies of the pouch cells cutoff at 4.2V is 83.62%. At C/10 (100mA) rate, the cell delivered 1.08 Ah. After three formation cycles at C/10, the pouch cells are further cycled at $\sim\text{C}/3$ rate (330 mA). Very stable cycling has been demonstrated from the graphite/single crystal NMC76 pouch cell with 89% capacity retention after 400 cycles (Figure X.3.1b). The cycling of the pouch cell is still in progress and the morphology of cycled single crystal will be updated later after the completion of cycling.

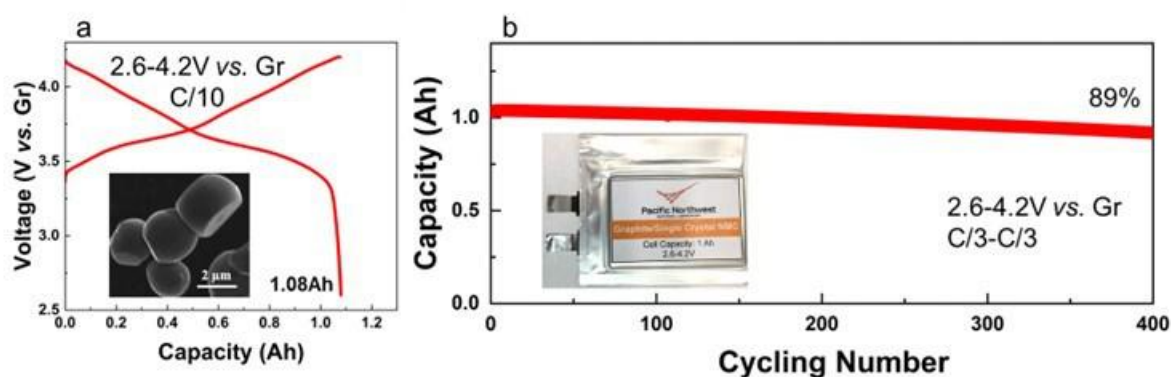


Figure X.3.1 Validation of doped single crystal NMC76 in 1Ah pouch cell using graphite anode. a, The first charge-discharge curve of the graphite/NMC76 single crystal pouch cell at C/10 cycled between 2.6-4.2V (vs. Graphite). b, Cycling stability of 1Ah Li-ion pouch cells employing as-prepared NMC76 single crystal cathode that demonstrates 89% capacity retention for 400 cycles (cycling still in progress).

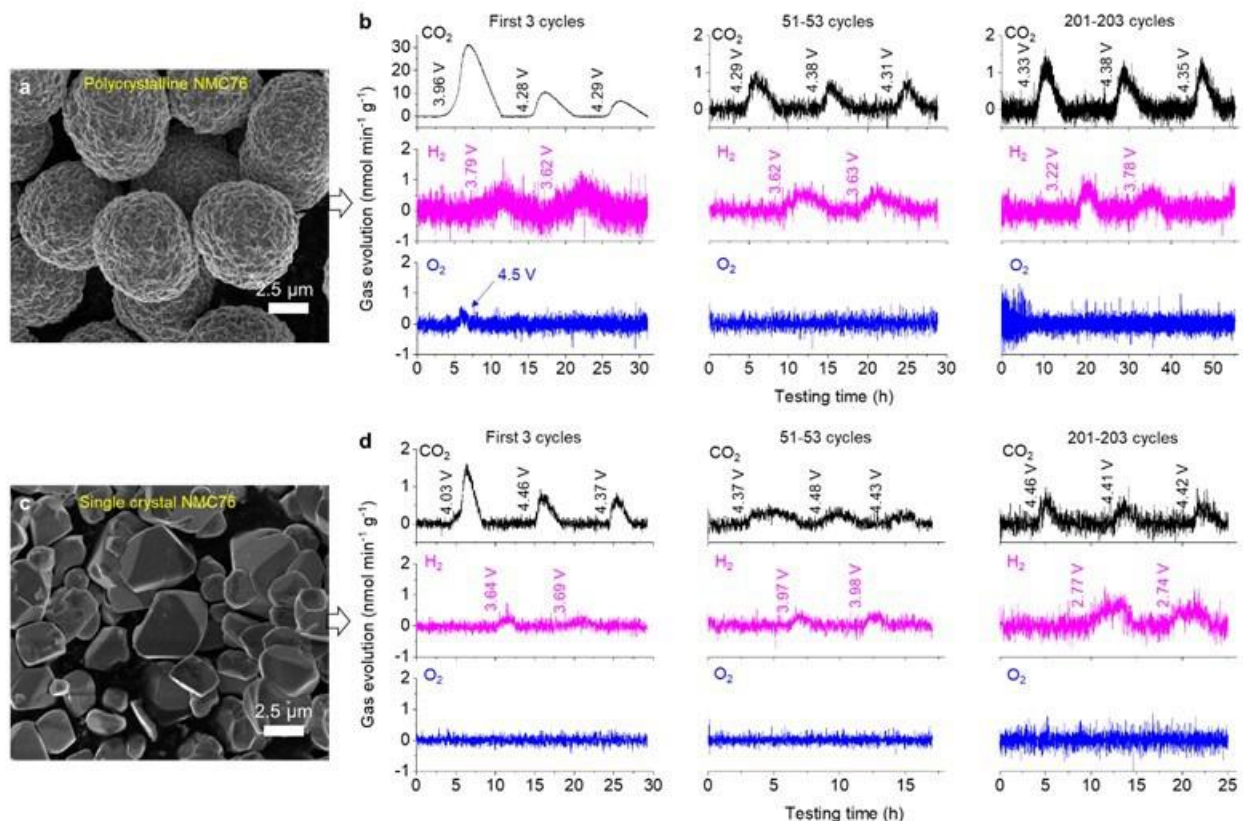


Figure X.3.2 Comparison of gas evolution from polycrystalline and single crystal NMC76 after different numbers of cycling. (a) and (c) display morphologies of pristine polycrystalline and single NMC76, respectively. (b) and (d) compare the evolution of CO₂, H₂, and O₂ at different cycles of polycrystalline and single crystal NMC76 electrodes, respectively. The cells cycled in DEMS are tested between 2.7 and 4.5 V.

This year we continue to study the gas generation mechanism from polycrystal and single crystal NMC76. Polycrystalline and single crystal NMC76 used in this project have average particle sizes of ca. 7 μm and 3 μm, respectively (Figure X.3.2a and c). CO₂, H₂, and O₂ gases detected at different cycles of polycrystalline and single crystal NMC76 are compared in Figure X.3.2 b and d. For polycrystalline NMC76, the detected amount of CO₂ is highest in the first cycle, mainly derived from the decomposition of residual lithium carbonate salt on the NMC surface. During the 2nd and 3rd cycle, the corresponding onset potentials of CO₂ generation are 4.26 V and 4.29 V, respectively, which is from chemical reactions between active lattice oxygen and electrolyte[3-5]. H₂ evolution can be assigned to the reduction of oxidized aprotic solvent (originally generated on the cathode side) on the anode. The cells for DEMS in Figure X.3.2b and d are cycled between 2.7 and 4.5 V, and R-H⁺ will be generated during the charge process, which is reduced on the anode side to produce H₂ with a delayed detection. The periodic occurrence of H₂ gas throughout the entire 200 cycles also suggests that H₂ is related to the electrolyte reaction driven by potentials. Compared to polycrystalline NMC76, the contents of CO₂ and H₂ produced from single crystal NMC76 are much less (Figure X.3.2d). After 50 and even 200 cycles (Figure X.3.2b), CO₂ and H₂ gases are still captured from both polycrystalline and single crystal NMC76. Only a trace amount of O₂ has been detected at 4.5 V during the first charge of polycrystalline NMC76, while there is no O₂ from single crystal charging throughout the entire 200 cycles. After the formation cycle, the complete vanishing O₂ signal in polycrystalline NMC76 may be related to the fast chemical reaction between highly reactive O with carbonate solvent such as EC, which has been well documented in Li-O₂ battery study[6-8]. To capture O₂ signal in a working electrochemical cell, a more significant amount of O released in a short time is needed[3].

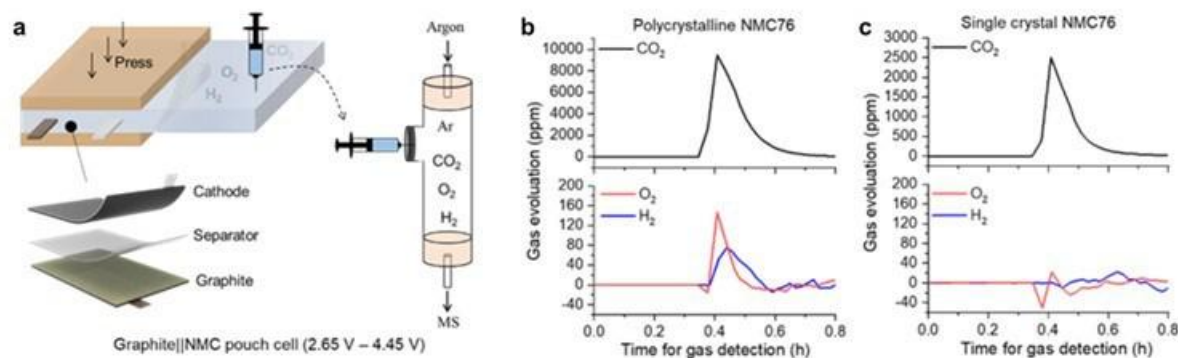


Figure X.3.3 a, Schemes for single layer pouch cell for gas collection and transfer. b,c) Quantified amounts of CO₂, O₂, and H₂ in pouch cells after 200 cycles of polycrystalline NMC76 (b) and single crystal NMC76 (c).

A group of Graphite||NMC76 single-layer pouch cells were cycled between 2.65 and 4.45 V (vs. graphite) for 200 cycles, to induce gas generation. The gradually generated gases are accumulated in a designed “gas room” in all the pouch cells (Figure X.3.3a). Gas is expelled to MS with carrier gas from each pouch cell after cycling. Unlike in half coin cells, O₂ is also detected from the pouch cells after 200 cycles (Figure X.3.3b) from polycrystal NMC76. The prominent observation of O₂ in pouch cells compared to the Li-metal coin cells can be assigned to the absence of highly active Li metal, which reacts with O species in the cell. The significantly reduced electrolyte (3.19 $\mu\text{L g}^{-1}$ in pouch cell vs. 26.45 $\mu\text{L g}^{-1}$ in DEMS cell) in the pouch cell also mitigates the fast reactions between ethylene carbonate (EC) and O, making it possible to capture more accumulated O₂ after extensive cycling. The simultaneous occurrence of O₂ and H₂ in Li-ion batteries with polycrystalline NMC76 cathode raises safety issue, especially during thermal runaway [9]. A single-layer pouch cell consisting of graphite and single crystal NMC76 is also studied. Again, there is no O₂ found in single crystals after 200 cycles (Figure X.3.3c) which can be assigned to the reduced phase boundaries of single crystal NMC76.

Conclusions

NMC76 single crystals have been doped to stabilize the lattice structure while mitigating gliding and cracking of crystals. The doped single crystal NMC76 has been validated in a 1Ah Li-ion pouch cell using graphite anode, which demonstrates a stable cycling of 89% capacity retention for 400 cycles. Microstructural changes of the extensively cycled single crystals will be further characterized and compared with undoped single crystals (cycling still in progress). The drastically reduced number of phase boundaries and oxygen deficiency in single crystal NMC76 alleviates surface side reactions, while the increased crystal size stabilizes lattice oxygen, both of which mitigate gas generation. It is also found that O₂ accumulated upon cycling of polycrystalline NMC76 is only observable in full pouch cells using graphite anode, highlighting the importance of selecting right testing platforms/protocols. The concurrence and accumulation of O₂ and H₂ in Ni-rich NMC need to be addressed before its large-scale deployment, while single crystal material indicates a potential pathway to enhance battery safety from a material perspective.

Key Publications

1. J. Xiao, “A granular approach to electrode design”, *Science*, 2022, 376, 455.
2. J. Hu, L. Li, Y. Bi, J. Tao, J. Lochala, D. Liu, B. Wu, X. Cao, S. Chae, C. Wang, J. Xiao, “Locking Oxygen in Lattice: A Quantifiable Comparison of Gas Generation in Polycrystalline and Single Crystal Ni-Rich Cathodes”, *Energy Storage Materials*, 2022, 47, 195-202.
3. J. Xiao, C. Anderson, X. Cao, H.-J. Chang, R. Feng, Q. Huang, Y. Jin, H. Job, J.-M. Kim, P. M. L. Le, D. Liu, L. Seymour, N. Shamim, L. Shi, B. Sivakumar, “Electrochemistry in Understanding and Designing Electrochemical Energy Storage Systems”, *Journal of The Electrochemical Society*, 2022, 169, 010524.

4. Y. Bi, Q. Li, R. Yi and J. Xiao, "To Pave the Way for Large-Scale Electrode Processing of Moisture-Sensitive Ni-Rich Cathodes", *Journal of the Electrochemical Society*, 2022, 169, 020521.

References

1. H. Hohyun Sun, Hoon-Hee Ryu, Un-Hyuck Kim, Jason A. Weeks, Adam Heller, Yang-Kook Sun, C. Buddie Mullins. 2020. "Beyond doping and coating: prospective strategies for stable high-capacity layered Ni-rich cathodes." *ACS Energy Letters* 5, 1136-1146. DOI:10.1021/acsenergylett.0c00191.
2. Toru Hatsukade, Alexander Schiele, Pascal Hartmann, Torsten Brezesinski, Jurgen Janek. 2018. "Origin of carbon dioxide evolved during cycling of nickel-rich layered NCM cathodes." *ACS Applied Materials & Interfaces* 10, 38892-38899. DOI: 10.1021/acsami.8b13158.
3. Roland Jung, Michael Metzger, Filippo Maglia, Christoph Stinner, Hubert A. Gasteiger. 2017. "Oxygen release and its effect on the cycling stability of $\text{LiNi}_x\text{Mn}_y\text{Co}_z\text{O}_2$ (NMC) cathode materials for Li-ion batteries." *Journal of Electrochemical Society* 164, A1361-A1377. DOI: 10.1149/2.0021707jes.
4. Johannes Wandt, Anna T.S. Freiberg, Alexander Ogrodnik, Hubbert A. Gasteiger. 2018. "Singlet oxygen evolution from layered transition metal oxide cathode materials and its implications for lithium-ion batteries." *Materials Today* 21, 825-833. DOI:10.1016/j.mattod.2018.03.037.
5. Roland Jung, Philipp Strobl, Filippo Maglia, Christoph Stinner, Hubbert A. Gasteiger. 2018. "Temperature dependence of oxygen release from $\text{LiNi}_{0.6}\text{Mn}_{0.2}\text{Co}_{0.2}\text{O}_2$ (NMC622) cathode materials for Li-ion batteries." *Journal of Electrochemical Society* 165, A2869-A2879. DOI: 10.1149/2.1261811jes.
6. J. Xiao, J. Hu, D. Wang, D. Hu, W. Xu, G. L. Graff, Z. Nie, J. Liu, J. Zhang. 2011. "Investigation of the rechargeability of Li-O_2 batteries in non-aqueous electrolyte" *Journal of Power Sources* 196, 5674-5678. DOI: 10.1016/j.jpowsour.2011.02.060.
7. B. D. McCloskey, A. Speidel, R. Scheffler, D.C. Miller, V. Viswanathan, J. S. Hummelshøj, J. K. Nørskov, A.C. Luntz. 2012. "Twin problems of interfacial carbonate formation in nonaqueous Li-O_2 batteries" *Journal of Physical Chemistry Letters* 3, 997-1001. DOI:10.1021/jz300243r.
8. Z. Zhang, J. Lu, R. S. Assary, P. Du, H.H. Wang, Y. Sun, Y. Qin, K. C. Lau, J. Greeley, P. C. Redfern, H. Iddir, L. A. Curtiss, K. Amine. 2011. "Increased stability toward oxygen reduction products for lithium-air batteries with oligoether-functionalized silane electrolytes" *Journal of Physical Chemistry C* 115, 25535-25542. DOI: 10.1021/jp2087412.
9. X. Wang, C. K. Law. 2013. "An analysis of the explosion limits of hydrogen-oxygen mixtures". *Journal of Chemical Physics* 138, 134305. DOI: 10.1063/1.4798459.

Acknowledgements

We thank the contribution from our collaborators Dr. Chongmin Wang at PNNL and Dr. Enyuan Hu at Brookhaven National Laboratory for characterizations.

X.4 Fluorinated Deep Eutectic Solvent (FDES)-Based Electrolytes (ANL)

Zhengcheng (John) Zhang, Principal Investigator

Argonne National Laboratory
9700 South Cass Avenue
Lemont, IL 60439
E-mail: zzhang@anl.gov

Tien Duong, DOE Technology Development Manager

U.S. Department of Energy
E-mail: Tien.Duong@ee.doe.gov

Start Date: October 1, 2019

End Date: September 30, 2022

Project Funding (FY22): \$500,000

DOE share: \$500,000

Non-DOE share: \$0

Project Introduction

The lithium-ion battery (LIB) is widely used in the devices supporting our digital and mobile lives; however, the LIB's adoption in electric vehicles (EVs) and more strategically smart grid applications has been limited by its energy density, high cost, and safety concerns. [1-4] Battery electrode materials with high theoretical capacity and high voltage are critical components and always desired for advancing the technology, and such battery materials for next-generation applications in electric vehicles have been reported in recent years. [5-7] However, new challenges arise from the non-aqueous electrolytes because the carbonate-based electrolytes are thermodynamically instable on charged cathode at voltages higher than 4.3 V vs Li^+/Li , [8-10] and these electrolytes are extremely reactive with the conversion-type, high-capacity anode such as silicon (Si), which leads to rapid deterioration in battery cycling performance. [11-13] Furthermore, there is severe safety concern of this highly flammable electrolyte due to the presence of highly volatile organic carbonate solvents. Due to its many advantages such as high conductivity, high electrochemical stability, and good passivation of the Al current collector, lithium hexafluorophosphate (LiPF_6) is still the dominating electrolyte salt in state-of-the-art electrolytes despite its thermal and chemical instability. Transition metal (TM) dissolution in the electrolyte and crosstalk with the anode have been widely reported for the high-voltage system; the reasons for these to occur have been ascribed to the cathode surface structure transformation and reconstruction. Nevertheless, even the pristine oxide cathode is in contact with the electrolyte, TM ions, for example Mn^{2+} dissolves simultaneously in the electrolyte due to the reaction of the weak acid HF, the hydrolysis product of LiPF_6 with a trace amount of moisture in the electrolyte, with oxide surface layer. [14-18] In both cases, diffusion and deposition of TM (mainly Mn^{2+}) on the anode side catalyzes the parasitic reactions, leading to active lithium loss and rapid capacity fade of the cell. [19-21] Therefore, demand is great for a new electrolyte that could enable the reversible and rapid positive/negative redox reactions and thus advance next-generation, high-voltage, high-energy LIB technology.

Objectives

The objective of this project is to develop fluorinated deep eutectic solvent (FDES, also called fluorinated ionic liquid-based aprotic electrolytes)-based electrolytes as new high voltage electrolytes to address the high reactivity of conventional organic electrolyte at the surface of the charged cathode and the safety concern associated with the organic electrolyte. The FDES are designed to provide thermodynamic stability on the charged cathode surface affording a stabilized cathode/electrolyte interface and should be highly compatible with anode including graphite and Si. The FDES is a new room-temperature molten salt comprising of new fluorinated organic cations and new fluorinated organic anions with a wide liquid window. FDES has superior thermal stability with no vapor pressure even heated to 300-400°C, and excellent fluidity at temperature lower than -20°C. Not only high performance, the FDES are non-flammable with significantly enhanced safety characteristic.

Approach

To solve the low conductivity and high viscosity issue of FDES electrolyte, an aqueous-organic hybrid electrolyte containing an ionic liquid N-methyl-N-propyl-piperidinium bis(fluorosulfonyl)imide was developed. Due to its tolerance to moisture and environment, the use of this electrolyte eliminates the critical environmental control employed for the state-of-the-art (SOA) electrolyte, electrode and cell fabrication thus reduces the cost of the battery mass production. Furthermore, this electrolyte addresses the most critical technical challenges associated with the EV batteries *i.e.* low energy density, safety, and high cost. In this paper, the benefits of this hybrid electrolyte were demonstrated for the first time in a high energy cell comprising a Ni-rich $\text{LiNi}_{0.5}\text{Mn}_{0.3}\text{Co}_{0.2}\text{O}_2$ (NMC532) as cathode coupled with a low potential lithium metal as anode.

Moreover, the physical and electrochemical properties could be systematically tuned by changing the structures of cations or anions. We have synthesized and evaluated two new ILs with fluorine and fluorinated alkyl functionalized cations, *i.e.* 1-methyl-1-propyl-3-fluoropyrrolidinium bis(fluorosulfonyl)imide (PMpyrF-FSI) and 1-methyl-1-(2,2,3,3,3-pentafluoropropyl)pyrrolidinium bis(fluorosulfonyl)imide (PMpyrF-FSI). Solvent purity is also critical for good cycling performance of Li-ion batteries. Different from the traditional synthesis method for ionic liquid, a facile one-step route was adopted for the FDES synthesis, which affords these materials with extremely high purity.

Results

Electrolyte stability

PMpyrF-FSI containing one fluorine in the pyrrolidinium cation ring was synthesized through a one-step quaternization method with methyl bis(fluorosulfonyl)imide (MeFSI) as methylating agent with 100% conversion (Figure X.4.1a-1b). Density function theory (DFT) calculations reveal that, in comparison with non-fluorinated counterpart, 1-methyl-1-propylpyrrolidinium (PMpyr^+), the presence of fluorine reduces the energy levels of both HOMO (from -13.18 eV to -13.29 eV) and LUMO (from -3.47 eV to -3.66 eV) of the cation (Figure X.4.1a). Such down shift in HOMO/LUMO energy indicates the increased resistance of the cation against oxidation but reduced resistance against reduction.

Potential energy surfaces were also constructed based on DFT calculations. The pyrrolidinium cation, either with or without the fluorine, binds equally strong to Li^0 surface (-2.12 eV and -2.10 eV, respectively), but much stronger than the FSI⁻ anion (-0.66 eV). However, PMpyrF^+ undergoes reductive decomposition with C-F cleavage, which is exothermic by -3.67 eV, as compared with C-H cleavage that is exothermic by -0.26 eV, followed by the ring opening process, which is exothermic by -0.87 eV (Figure X.4.1c). Therefore, the introduction of fluorine renders the reduction of PMpyrF^+ much more favored than PMpyr^+ , while such difference in reactivity is primarily due to the strong interaction between F and Li (110) surface. As indicated by the density of states, the significant orbital overlapping between Li-p orbital and F-s and p orbitals indicates the strong interaction. However, the overlapping cannot be found for H interacting with Li (110) surface. The strong interaction between F and Li (110) surface makes C-F cleavage more energetically favorable than C-H cleavage by -3.41 eV, which would preferentially generate inorganic or organic fluorides. Meanwhile, the FSI⁻ decomposition is also highly likely, as evidenced by the exothermic S-F bond cleavage of -5.97 eV, followed by exothermic dissociation of S-O bond, which is -2.94 eV. According to experience, the fluorides thus generated from the labile bonds in FSI⁻ would more likely exist in inorganic forms with heteroatom contents (P, S), and behave less protective as the fluorides generated from C-F bonds. To mimic the decomposition during charge state, the potential energy surface with consideration of e⁻ transfer after adsorption are constructed and shown in Figure X.4.1a and Figure X.4.1b. The reaction energy for the FSI⁻, PMpyrF^+ , and PMpyr^+ activations are -6.82 eV, -6.55 eV, and -3.14 eV, respectively. Thus, the corresponding reduction potential are 5.43 V, 5.16 V, and 1.75 V, according to equation S1 in Methods section. In a nutshell, the cations bind to Li (110) surface much stronger than anions, however, without F substitution, PMpyr^+ are not as active as FSI⁻ towards reduction. With F-substitution, PMpyrF^+ is more active towards reduction, almost as

active as FSI⁻ anion. Fortunately, the higher absorption preference of PMpyrf over FSI should lead to a more abundant fluorides from C-F origin thanks to the fluorinated cation.

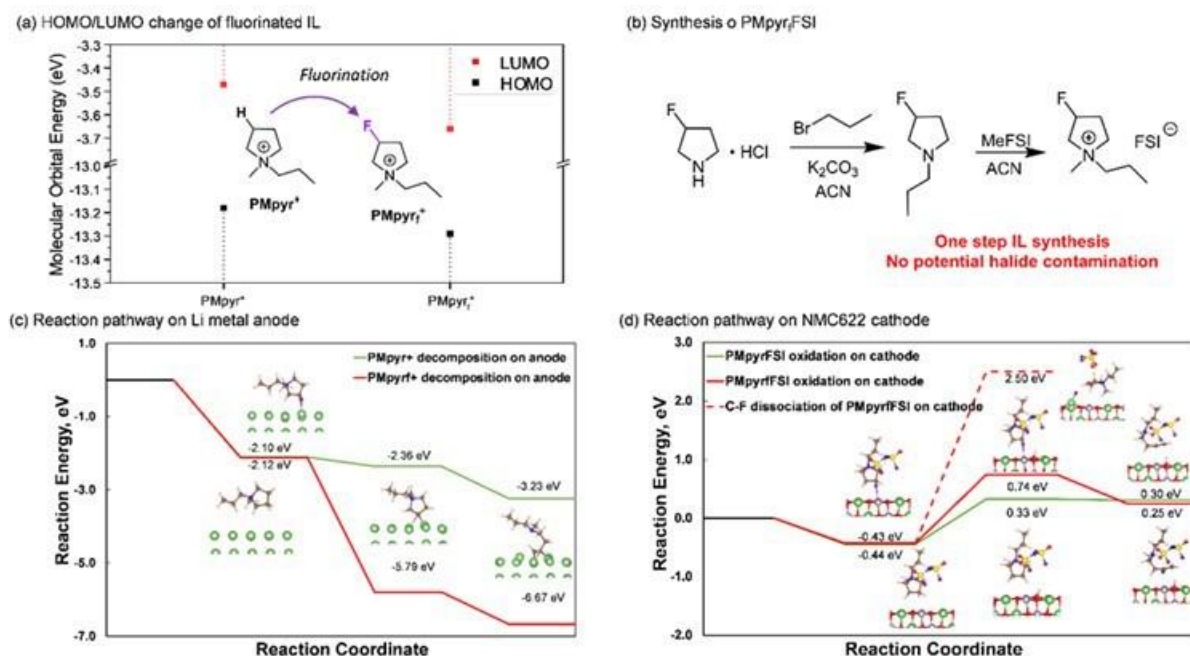


Figure X.4.1 Synthesis and DFT calculations of fluorine substituted cation PMpyrf⁺. (a) Comparison of HOMO/LUMO energy levels for PMpyr⁺ and PMpyrf⁺, (b) Synthesis route for PMpyrfFSI, (c) PMpyr⁺ and PMpyrf⁺ reduction pathway on Li metal, (d) PMpyr⁺ and PMpyrf⁺ oxidation pathway on NMC622 cathode.

On the NMC622 cathode side, PMpyrFSI and PMpyrfFSI bind equally strong with Mn sites through the cation part, with adsorption energy as 0.44 eV and 0.43 eV, respectively, however, the adsorption is much weaker when binding through anion part by 0.39 eV. Therefore, we will only consider cation oxidation during charging cycle. As indicated by Figure X.4.1d, PMpyrfFSI oxidation favors a deprotonation rather than C-F dissociation pathway, due to the lower potential energy for deprotonation compared with C-F cleavage (1.17 eV vs 2.93 eV). Furthermore, the C-N bond is weakened, followed by a ring opening process of deprotonated PMpyrfFSI, which results in a potential energy as -0.49 eV. However, in absence of fluorine, PMpyrFSI tends to be more easily oxidized with reaction potential energy as 0.77 eV for the deprotonation step, followed by exothermic ring opening process by -0.03 eV. This indicates that F substitution indeed renders PMpyrfFSI more resistant against oxidation, as predicted by the down shift of HOMO/LUMO energy. Apparently, what brought by fluorination is the improvement in thermodynamic stability against oxidation on cathode surface as well as strong tendency to decompose on Li⁰ anode. As we have learnt from the knowledge in LIB electrolytes, the latter strongly implies the preferential cation reduction to form interphases on Li⁰.

An ionic electrolyte (PMpyrf)_{0.8}Li_{0.2}FSI was formulated by dissolving LiFSI in PMpyrfFSI, whose performance was evaluated in a lithium-metal cell consisting of NMC622 cathode and a thin (20 μm) lithium-anode. Molecular dynamics (MD) simulation sheds light on the electrode/electrolyte interfacial structure in such batteries. Compared with its non-fluorinated cousin, the fluorine-presence on the cation (purple) makes it much easier to access and populate the inner-Helmholtz layers on both NMC622 cathode and Li metal anode (Figure X.4.2a and 2b), which suggest stronger surface interaction of PMpyrf⁺ cation with those electrode surfaces and predicts an interphasial chemistry with higher participation from PMpyrf⁺. The same insight was provided from the static distribution of the electrolyte components on both electrodes (Figure X.4.2d and Figure X.4.2e). On both Li⁰ and NMC622 cathode surfaces, the PMpyrf⁺ cations are much more populated within the inner-Helmholtz layer than its counterpart PMpyr⁺ without fluorine.

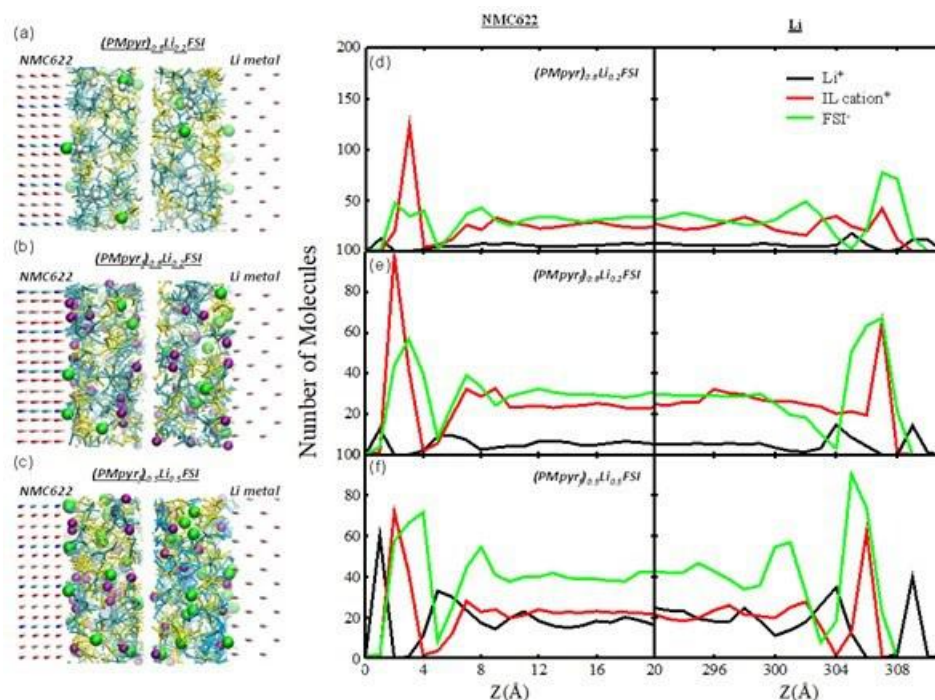


Figure X.4.2 MD simulation on electrolyte/electrode interaction. (a-c) Snapshot of electrolyte distribution on NMC622 and Li electrodes: cyan-IL cation⁺; white-H on the PMpyr⁺ backbone highlight in adjacent figure; purple-F on the PMpyr⁺ backbone; yellow-FSI⁻; green-Li⁺. (d-f) Molecular number density profiles along the z axis normal to the surface of the NMC cathode (left panels) and lithium anode (right panels). The center of mass of each molecule is used to calculate molecule distribution: (a, d) (PMpyr)_{0.5}Li_{0.5}FSI electrolyte, (b, e) (PMpyr)_{0.5}Li_{0.2}FSI electrolyte and (c, f) (PMpyr)_{0.5}Li_{0.5}FSI electrolyte.

Performance in battery

Although fluorination of cation favors the desired interfacial structure and interphasial chemistry of high fluorine abundance, excess PMpyr⁺ content in the electrolyte does increase bulk viscosity and leads to lower ion transport and higher interfacial impedance. Therefore, we must further optimize the electrolyte formulation by considering the impact of interfacial impedance. (PMpyr)_{0.5}Li_{0.5}FSI electrolyte is the composition that better balances these considerations. At this composition the interfacial structure as well as static distribution of the electrolyte components become less adsorbed on both electrode surfaces (Figure X.4.2c and Figure X.4.2f). Instead, more Li⁺ (green) are observed on both electrode surface, and the purple F-group from PMpyr⁺ cation is reduced, especially on Li metal surface.

The electrolyte interfacial structure alteration causes corresponding changes in solid-electrolyte-interphase (SEI) and cathode-electrolyte-interphase (CEI) chemistries, which are revealed by X-ray photoelectron spectroscopy (XPS) analysis. On Li metal surface (Figure X.4.3a), peaks observed in N 1s spectra are assigned to FSI⁻ decomposition peaks at 399.2 eV and 400.6 eV and PMpyr⁺ cation decomposition peak at 402.3 eV. At decreased PMpyr⁺ concentration, the peak relative intensity of 402.3 eV is substantially decreased for (PMpyr)_{0.5}Li_{0.5}FSI electrolyte, suggesting reduced PMpyr⁺ contribution to the SEI. This trend is confirmed by the corresponding changes in C-N peak of C 1s spectra at 286.3 eV. The LiF peak at 684.5 eV is much intensified for (PMpyr)_{0.5}Li_{0.5}FSI electrolyte, as well as for SO₂F peak observed at 687.8 eV in F 1s spectra, suggesting a higher FSI⁻ anion contribution to the SEI. This shift of interphasial chemistry from PMpyr⁺ cation to FSI⁻ anion is apparently a result of PMpyr⁺ cation reduction in interfacial region as well as the stronger coordination between Li⁺ and FSI⁻. The lower C atomic concentration and higher O atomic concentration observed in (PMpyr)_{0.5}Li_{0.5}FSI electrolyte are also consistent with reduced PMpyr⁺ cation decomposition, as C should have solely come from the cation and O from FSI⁻ anion, respectively. On NMC622 cathode, similar trend is observed, where the intensities of C-F peak and C-N peaks contributed from PMpyr⁺ cation decomposition are relative lower, which is replaced partially by LiF at higher intensity. A peak

at 529.2 eV is assigned to metal oxide (M-O) species in O 1s spectrum for (PMpyrf)_{0.5}Li_{0.5}FSI electrolyte, suggesting the cathode surface is visible now through a thinner CEI layer formed (Figure Figure X.4.3). Supporting this argument, both N and S are also observed in lower atomic concentration because of overall less cation and anion decomposition. While both PMpyrf⁺ cation and FSI⁻ anion participate in the SEI formation on Li metal anode and CEI formation on NMC622 cathode, the impact of PMpyrf⁺ cation concentration is more significant on Li metal.

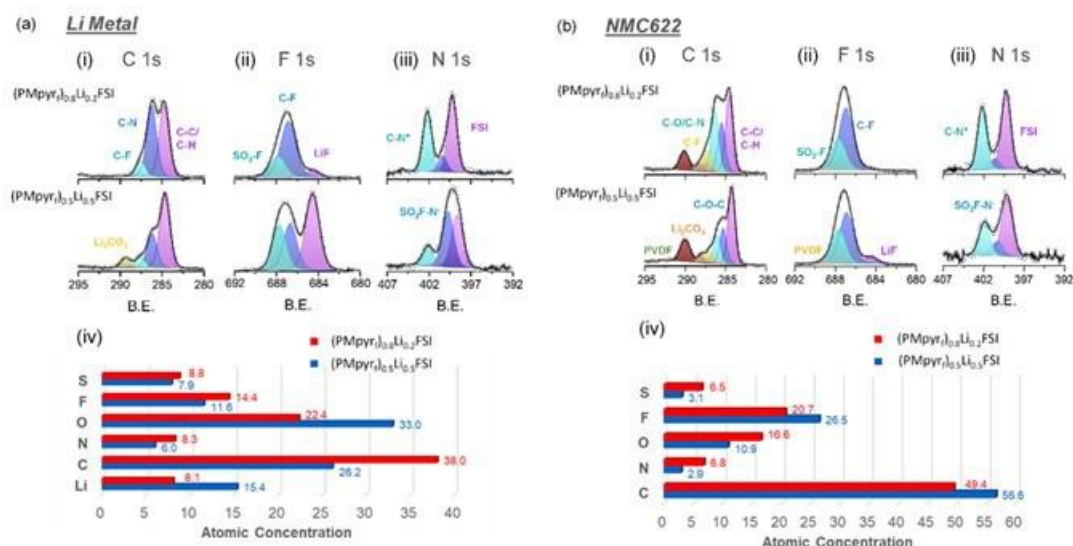


Figure X.4.3 XPS analysis of recovered electrodes. (a) Li metal anode and (b) NMC622 cathode harvested after formation using (PMpyrf)_{0.8}Li_{0.2}FSI and (PMpyrf)_{0.5}Li_{0.5}FSI electrolytes. (i) C 1s spectra, (ii) F 1s spectra, (iii) N 1s spectra and (iv) atomic concentration.

Stabilization of Li metal. The high stability of (PMpyrf)_{0.5}Li_{0.5}FSI toward Li metal was further confirmed in Li/Cu cells and Li/Li symmetric cells. The CE of Li metal anode cycling is measured in Cu/Li cells using Aurbach CE Protocol with Gen 2, (PMpyrf)_{0.8}Li_{0.2}FSI and (PMpyrf)_{0.5}Li_{0.5}FSI electrolytes at current density of 0.1 mA/cm² (Figure X.4.4a-Figure X.4.4c). Gen 2 electrolyte consumes all Li inventory within only 3 cycles and displays a low CE of 45.0%. Both PMpyrfFSI-based electrolytes demonstrated substantially higher CE, with (PMpyrf)_{0.5}Li_{0.5}FSI showing a higher CE of 97.9% compared to 96.5% for (PMpyrf)_{0.8}Li_{0.2}FSI. Similar performance is also observed in long-term cycling of Li/Cu cells (Figure X.4.4d). Li was plated on to Cu foil for 6 h and stripped to 1 V for 100 cycles with 0.1 mA/cm² current density. Gen 2 electrolyte shows lower than 35% CE throughout 100 cycles, while (PMpyrf)_{0.8}Li_{0.2}FSI and (PMpyrf)_{0.5}Li_{0.5}FSI show high CE of 99% after initial stabilization. With decreased PMpyrf⁺ cation concentration, (PMpyrf)_{0.5}Li_{0.5}FSI shows a higher first cycle CE than (PMpyrf)_{0.8}Li_{0.2}FSI, which suggests the SEI formed by (PMpyrf)_{0.5}Li_{0.5}FSI electrolyte is thinner and efficiently to protect Li surface from further degradation.

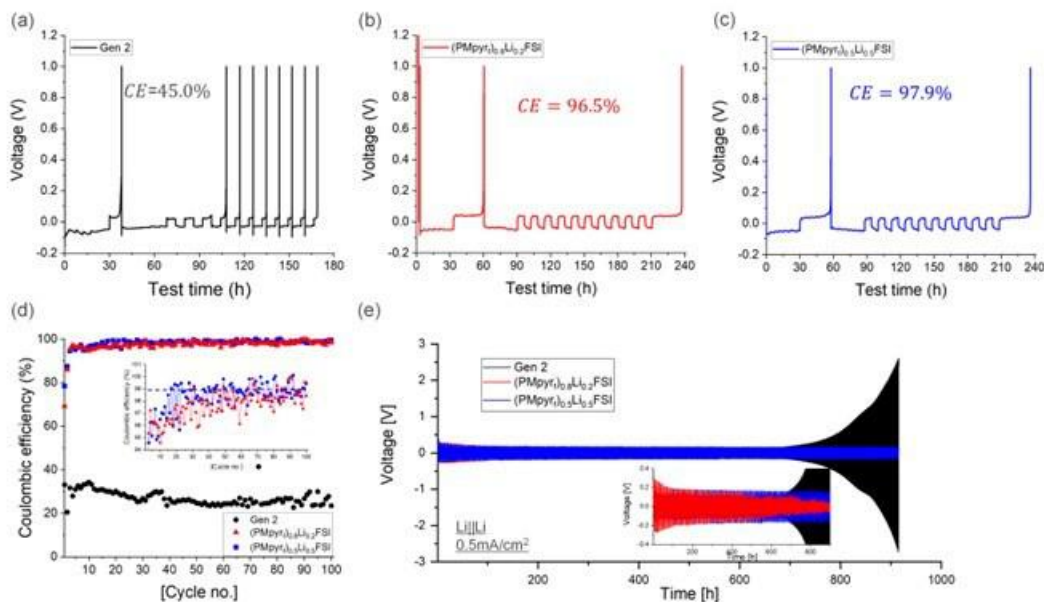


Figure X.4.4 Li/Cu and Li/Li symmetric cell performance. (a-c) Voltage profile of Aurbach test using (a) Gen 2, (b) (PMpyrf)_{0.8}Li_{0.2}FSI and (c) (PMpyrf)_{0.5}Li_{0.5}FSI. (d) Coulombic efficiency of Li/Cu cell cycled with current density of 0.1 mA/cm². (e) Voltage profile of Li/Li symmetric cell with current density of 0.5 mA/cm².

Gen 2, (PMpyrf)_{0.8}Li_{0.2}FSI and (PMpyrf)_{0.5}Li_{0.5}FSI electrolytes were also examined in Li/Li symmetric cells (Figure X.4.4e). For Gen 2 electrolyte, after the initial stabilization, the overpotential continues to increase and starts to polarize after 700 h, which correlates to the undesired side reactions between Gen 2 electrolyte and Li metal and results in accumulation of SEI layer, impedance buildup and electrolyte depletion. The voltage profile also demonstrates a characteristic “peaking” behavior that is ascribed to different resistances of dendrite formation (nucleation), dendrite dissolution, bulk dissolution and pitting from bulk Li surface. This type of voltage trace is typically correlated to a dendritic morphology on Li surface (Figure X.4.5a). For (PMpyrf)_{0.8}Li_{0.2}FSI electrolyte, the initial overpotential is slightly higher compared to (PMpyrf)_{0.5}Li_{0.5}FSI electrolyte, regardless of its lower viscosity, which suggests the excessive SEI formed by the fluorinated cation in (PMpyrf)_{0.8}Li_{0.2}FSI electrolyte has higher surface impedance. The overpotential continues decreases over cycling and cell experienced soft shorting issue after 600 h. This result is consistent with the higher portion of dendritic morphology observed in plated Li on Cu foil with (PMpyrf)_{0.8}Li_{0.2}FSI electrolyte (Figure X.4.5b). For (PMpyrf)_{0.5}Li_{0.5}FSI electrolyte, the voltage profile is stable over 900 h, which indicates that SEI formed by (PMpyrf)_{0.5}Li_{0.5}FSI sufficiently protects Li metal surface and minimizes the undesired side reactions. The stable overpotential also suggests that Li surface area is relatively maintained over Li plating/stripping, which could be due to the more densely packed columnar Li morphology in (PMpyrf)_{0.5}Li_{0.5}FSI electrolyte. The voltage profile of (PMpyrf)_{0.5}Li_{0.5}FSI (PMpyrf)_{0.5}Li_{0.5}FSI show the “arcing” behavior corresponding to a diffusion-controlled process. PMpyrfFSI based electrolyte show high Li metal compatibility as demonstrated in both Li/Cu and Li/Li cells, which could be contributed by the SEI formed by both PMpyrf⁺ cation and FSI⁻ anion. Moreover, with the PMpyrf⁺ cation concentration optimization, the SEI formed by (PMpyrf)_{0.5}Li_{0.5}FSI electrolyte shows lower impedance which enables uniform and highly densely packed Li morphology in Li plating.

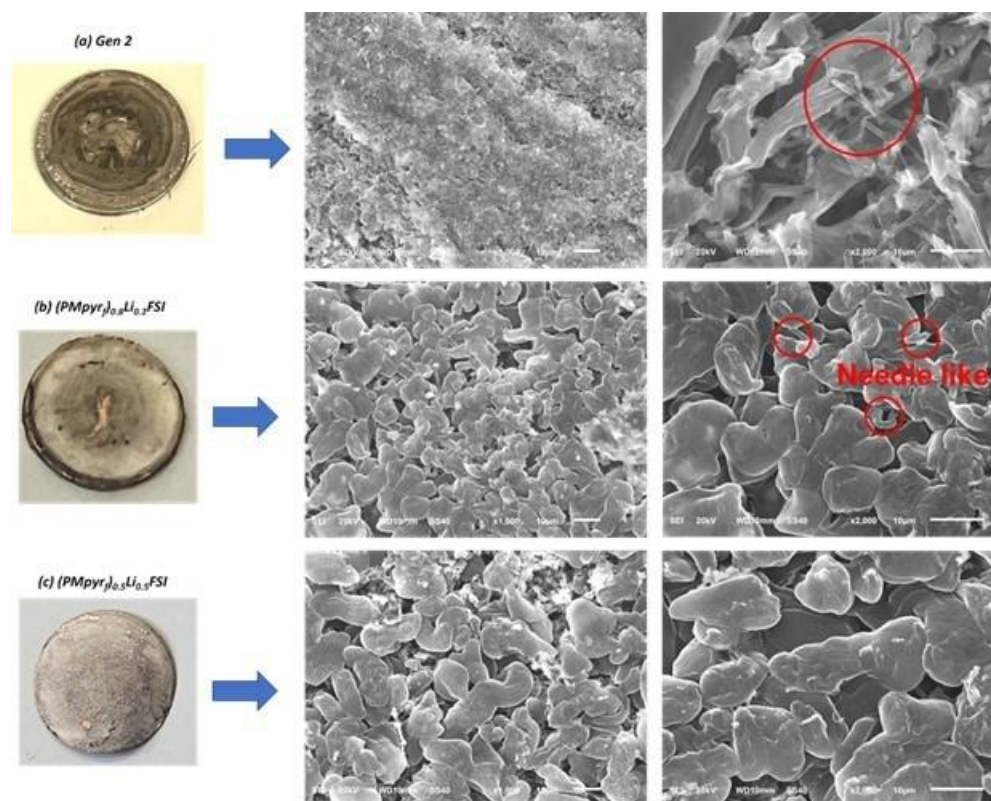


Figure X.4.5 Li/Cu and Li/Li symmetric cell performance. (a-c) Voltage profile of Aurbach test using (a) Gen 2, (b) (PMpyrf)_{0.8}Li_{0.2}FSI and (c) (PMpyrf)_{0.5}Li_{0.5}FSI. (d) Coulombic efficiency of Li/Cu cell cycled with current density of 0.1 mA/cm². (e) Voltage profile of Li/Li symmetric cell with current density of 0.5 mA/cm².

Conclusions

A fluorinated cation is synthesized for the first time, which makes it possible to formulate an ionic electrolyte that enables high voltage lithium metal battery. The fluorination brings unique interfacial structure and subsequent interphasial chemistries on both Li⁰ anode and high nickel cathode. Optimizing cation concentration, the strong electrode/cation surface interaction caused by fluorination can be attenuated, which lead to high Coulombic efficiency, densely packed Li morphology, as well as excellent cycling stability of the 4.6 V lithium-metal battery. STEM demonstrated that a highly protective CEI formed by (PMpyrf)_{0.5}Li_{0.5}FSI electrolyte maintains a thin cation mixing layer with minimum surface structure change. The new cation that carries fluorine will cast significant impact on emerging battery chemistries that desperately needs tailored interphasial chemistries.

Key Publications

1. Qian Liu, Wei Jiang, Jiayi Xu, Yaobin Xu, Zhenzhen Yang, Doo-Joo Yoo, Krzysztof Z. Pupek, Chongmin Wang, Cong Liu and Kang Xu, Zhengcheng Zhang. A Fluorinated Pyrrolidinium Cation-Regulated Electrode/Electrolyte Introduces New Interphasial Chemistries to Enable High-Voltage Lithium Metal Batteries. *Nat. Chem.*, 2022, under review.
2. Jianzhong Yang, Marco-Tulio Fonseca Rodrigues, Zhou Yu, Seoung-Bum Son, Kewei Liu, Nancy L Dietz Rago, Lei Cheng, Zhengcheng Zhang, Daniel Abraham and Chen Liao. Design of a Scavenging Pyrrole Additive for High Voltage Lithium-Ion Batteries. *J. Electrochem. Soc.*, 2022, 169 040507. DOI: 10.1149/1945-7111/ac613f
3. Qian Liu, Wei Jiang, Zhenzhen Yang, Zhengcheng Zhang. An Environmentally Benign Electrolyte for High Energy Lithium Metal Batteries. *ACS Appl. Mater. Interfaces*, 2021, 13, 58229–58237. (

4. Noah Johnson, Zhenzhen Yang, Ira Bloom, Zhengcheng Zhang. Enabling high-temperature and high-voltage lithium-ion battery performance through a novel cathode surface-targeted additive. *ACS Appl. Mater. Interfaces*, 2021, 13, 59538–59545. <https://doi.org/10.1021/acsami.1c18493>

References

1. Armand, M.; Tarascon, J. M., Building Better Batteries. *Nature* 2008, 451 (7179), 652-657.
2. Goodenough, J. B.; Park, K.-S., The Li-Ion Rechargeable Battery: A Perspective. *J. Am. Chem. Soc.* 2013, 135 (4), 1167-1176.
3. Nitta, N.; Wu, F.; Lee, J. T.; Yushin, G., Li-Ion Battery Materials: Present and Future. *Mater. Today* 2015, 18 (5), 252-264.
4. Li, M.; Lu, J.; Chen, Z.; Amine, K., 30 Years of Lithium-Ion Batteries. *Adv. Mater.* 2018, 30 (33), 1800561.
5. Tarascon, J. M.; Armand, M., Issues and Challenges Facing Rechargeable Lithium Batteries. *Nature* 2001, 414 (6861), 359-367.
6. Thackeray, M. M.; Wolverton, C.; Isaacs, E. D., Electrical Energy Storage for Transportation—Approaching the Limits of, and Going Beyond, Lithium-Ion Batteries. *Energy Environ. Sci.* 2012, 5 (7), 7854-7863.
7. Chen, S.; Wen, K.; Fan, J.; Bando, Y.; Golberg, D., Progress and Future Prospects of High-Voltage and High-Safety Electrolytes in Advanced Lithium Batteries: From Liquid to Solid Electrolytes. *J. Mater. Chem. A* 2018, 6 (25), 11631-11663.
8. Li, Q.; Chen, J.; Fan, L.; Kong, X.; Lu, Y., Progress in Electrolytes for Rechargeable Li-Based Batteries and Beyond. *Green Energy & Environment* 2016, 1 (1), 18-42.
9. Yang, H.; Zhuang, G. V.; Ross, P. N., Thermal Stability of Lipf6 Salt and Li-Ion Battery Electrolytes Containing Lipf6. *J. Power Sources* 2006, 161 (1), 573-579.
10. Campion, C. L.; Li, W.; Lucht, B. L., Thermal Decomposition of Lipf6-Based Electrolytes for Lithium-Ion Batteries. *J. Electrochem. Soc.* 2005, 152 (12), A2327.
11. Plakhotnyk, A. V.; Ernst, L.; Schmutzler, R., Hydrolysis in the System Lipf6—Propylene Carbonate—Dimethyl Carbonate—H₂O. *J. Fluorine Chem.* 2005, 126 (1), 27-31.
12. Kim, J.; Lee, J. G.; Kim, H.-s.; Lee, T. J.; Park, H.; Ryu, J. H.; Oh, S. M., Thermal Degradation of Solid Electrolyte Interphase (Sei) Layers by Phosphorus Pentafluoride (PF₅) Attack. *J. Electrochem. Soc.* 2017, 164 (12), A2418-A2425.
13. Wilken, S.; Treskow, M.; Scheers, J.; Johansson, P.; Jacobsson, P., Initial Stages of Thermal Decomposition of Lipf6-Based Lithium Ion Battery Electrolytes by Detailed Raman and Nmr Spectroscopy. *RSC Adv.* 2013, 3 (37), 16359-16364.
14. Campion, C. L.; Li, W.; Lucht, B. L., Thermal Decomposition of Lipf6-Based Electrolytes for Lithium-Ion Batteries. *J. Electrochem. Soc.* 2005, 152 (12), A2327.
15. Zhan, C.; Wu, T.; Lu, J.; Amine, K., Dissolution, Migration, and Deposition of Transition Metal Ions in Li-Ion Batteries Exemplified by Mn-Based Cathodes – a Critical Review. *Energy Environ. Sci.* 2018, 11 (2), 243-257.
16. Vetter, J.; Novák, P.; Wagner, M. R.; Veit, C.; Möller, K. C.; Besenhard, J. O.; Winter, M.; Wohlfahrt-Mehrens, M.; Vogler, C.; Hammouche, A., Ageing Mechanisms in Lithium-Ion Batteries. *J. Power Sources* 2005, 147 (1), 269-281.
17. Gilbert, J. A.; Shkrob, I. A.; Abraham, D. P., Transition Metal Dissolution, Ion Migration, Electrocatalytic Reduction and Capacity Loss in Lithium-Ion Full Cells. *J. Electrochem. Soc.* 2017, 164, A389.
18. Banerjee, A.; Shilina, Y.; Ziv, B.; Ziegelbauer, J. M.; Luski, S.; Aurbach, D.; Halalay, I. C., On the Oxidation State of Manganese Ions in Li-Ion Battery Electrolyte Solutions. *J. Am. Chem. Soc.* 2017, 139, 1738.
19. Zheng, L.-Q.; Li, S.-J.; Lin, H.-J.; Miao, Y.-Y.; Zhu, L.; Zhang, Z.-J., Effects of Water Contamination on the Electrical Properties of 18650 Lithium-Ion Batteries. *Russ. J. Electrochem.* 2014, 50 (9), 904-907.

20. Wu, X.; Ruan, D.; Tan, S.; Feng, M.; Li, B.; Hu, G., Effect of Stirring Environment Humidity on Electrochemical Performance of Nickel-Rich Cathode Materials as Lithium Ion Batteries. *Ionics* 2020, 26 (11), 5427-5434.
21. Li, J.; Daniel, C.; An, S. J.; Wood, D., Evaluation Residual Moisture in Lithium-Ion Battery Electrodes and Its Effect on Electrode Performance. *MRS Advances* 2016, 1 (15), 1029-1035.

Acknowledgements

The submitted manuscript has been created by UChicago Argonne, LLC, Operator of Argonne National Laboratory, which is supported by DOE Office of Science under Contract No. DE-AC02-06CH11357.

X.5 Developing In situ Microscopies for the Model Cathode/Electrolyte Interface (NREL)

Robert C. Tenent, Principal Investigator

National Renewable Energy Laboratory
16253 Denver West Parkway
Golden, CO 80401
E-mail: robert.tenent@nrel.gov

Tien Duong, DOE Technology Development Manager

U.S. Department of Energy
E-mail: Tien.Duong@ee.doe.gov

Start Date: October 1, 2018

End Date: September 30, 2022

Project Funding (FY22): \$336,000

DOE share: \$336,000

Non-DOE share: \$0

Project Introduction

The work presented here focuses on the development of new diagnostic techniques based on the scanning electrochemical microscope (SECM) to examine cell degradation processes occurring at the cathode/electrolyte interface. While lithium-ion batteries have developed significant market traction, key issues remain to be resolved for more broad adoption including developing a better understanding of degradation processes that limit cell life. Many commonly used cathode materials are known to degrade through various processes (transition metal dissolution and oxygen evolution, as examples). Products of this degradation are also known to diffuse through the cell and deposit at the anode SEI leading to performance loss. While these processes are known to occur, many open questions remain regarding the exact mechanisms by which they take place. As an example, while dissolution of manganese from cathode materials has been extensively studied, debate remains even regarding the oxidation state of Mn generated in the dissolution process.¹ This effort focuses on using the SECM format paired with complementary analytical techniques to detect and characterize cathode degradation products at and near to an active cathode/electrolyte interface

Objectives

This project seeks to employ SECM paired with complementary analytical techniques to study degradation processes occurring at the cathode/electrolyte interface. Specifically, we study degradation products evolving from model LiMn_2O_4 (LMO) and $\text{LiNi}_{0.5}\text{Mn}_{1.5}\text{O}_4$ (LNMO) cathode materials. We examine the impact of varied parameters on the degradation process as well as the properties of the resulting products. This will help develop understanding not only of how these degradation processes occur, but how degradation products may react elsewhere in the cell driving overall performance degradation.

Approach

The SECM is a scanning probe microscope which uses a small electrode to conduct electrochemical experiments near an active electrode/electrolyte interface. Figure X.5.1 shows a schematic of a typical SECM instrument which includes two working electrodes consisting of the small “tip” electrode as well as the underlying substrate sample. In the case of this work, the substrate would be a model cathode material under study. All electrodes are contained in an active electrochemical cell containing an electrolyte of interest. The tip and substrate electrode voltages are controlled by a bi-potentiostat using the same reference and counter electrodes. This configuration allows independent control of electrode voltages for both the substrate sample and the “sensing” tip electrode. This allows the tip to be used to conduct a variety of electrochemical experiments either in bulk electrolyte or near the substrate which can be held at a variety of voltages. A three-axis positioning system is used to place the tip electrode at various locations in the cell and across the substrate surface for measurements as required.

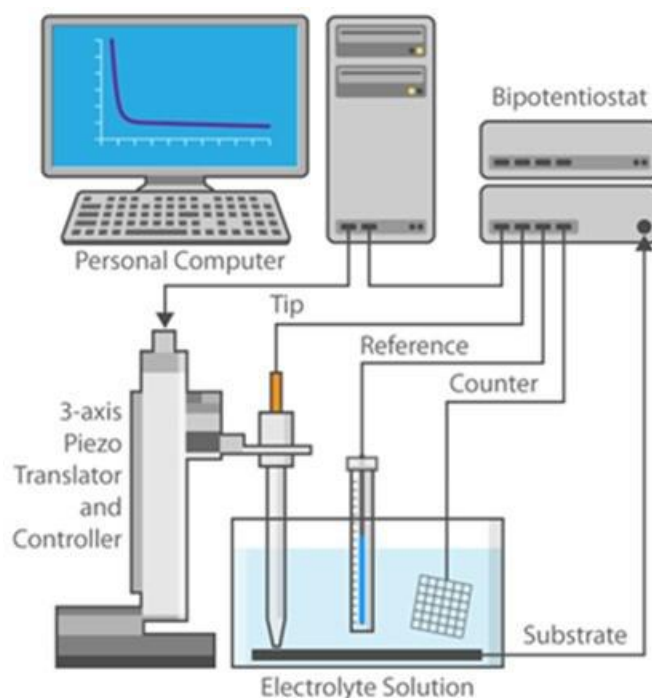


Figure X.5.1 Schematic of a typical scanning electrochemical microscopy / Al Hicks, NREL

The SECM can be employed in a variety of so-called “modes” which can be categorized broadly as imaging modes (as implied by the name of the technique) or as measurement modes. The work here focuses on applying SECM measurement modes to better understand cathode degradation products and their reactivity. In our case, we work with the “generation/collection” (GC) mode of SECM in which species generated at the substrate are detected or “collected” at the tip electrode. This approach is conceptually similar to the rotating ring disk electrode (RRDE) method commonly used in electrochemical characterization in which a species is generated at a disk electrode and then hydrodynamically driven to a surrounding ring electrode for detection and characterization. The key differentiator between the GC-SECM and RRDE methods is increased flexibility in the experimental conditions that can be used for detection at the tip electrode. In the case of this work, we employ cyclic voltammetry measurements made at the tip to characterize the electrochemical properties of cathode degradation products occurring both near the active cathode/electrolyte interface as well as in bulk electrolyte.

Results

Formation of Model Cathode Materials (LNMO)

Efforts over the last fiscal year have been focused, in part, on the isolation of electrolyte degradation processes from other, potentially coupled degradation processes. This effort began studies of the reactivity of both LMO and LNMO materials with model electrolyte systems. The electrolyte systems reported on here are 1M LiClO₄ in propylene carbonate (PC) and ethylene carbonate (EC) and are presently being paired with

evaluation using the LiPF₆ salt. Previous work was focused exclusively on reactions of LMO and Figure X.5.2 shows recent results for formation of LNMO using the polymer assisted deposition (PAD) technique. PAD is a simple technique that allows the deposition of films of mixed metal oxides using a solution-based technique (spin coating) followed by high temperature annealing in air.² Data in Figure X.5.3 includes cyclic voltammetric evaluation of the LNMO material compared to that for LMO. As expected, a similar response is observed for the LNMO to the LMO except for the relevant intercalation processes being shifted to higher voltage. XRD data is also shown indicating formation of the LNMO material. AFM data shows that the spin

coating process results in uniform, low surface roughness materials which eases near surface electrochemical studies.

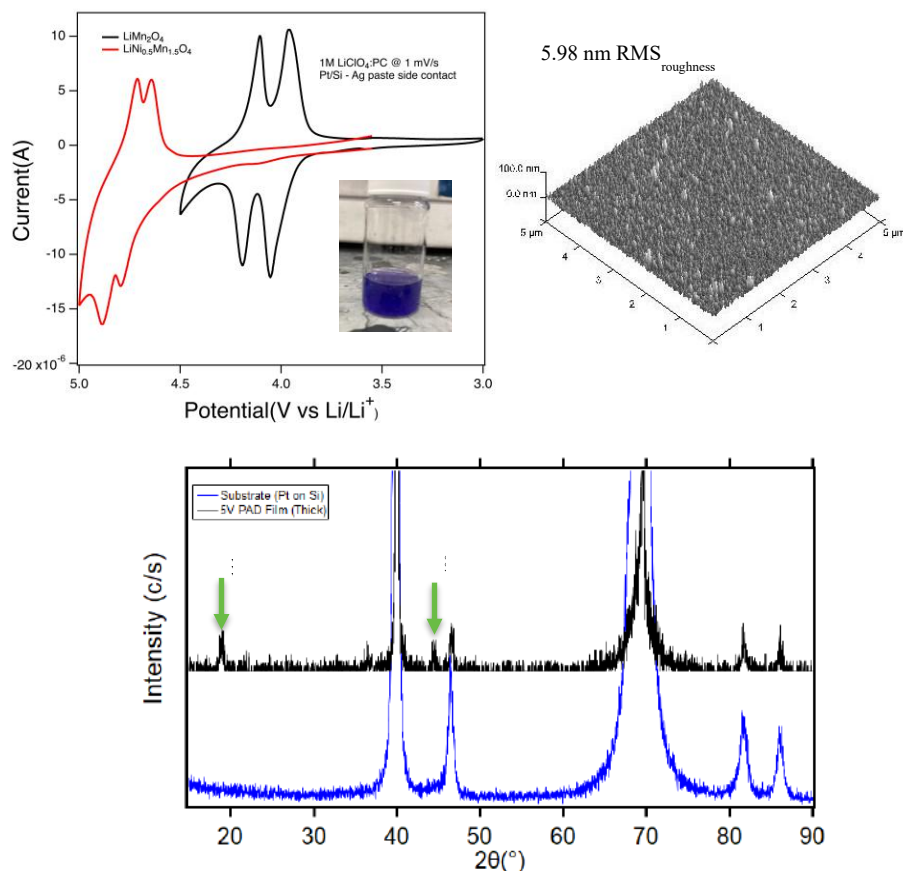


Figure X.5.2 Cyclic voltammetric, AFM and XRD data for LNMO deposited using the PAD technique

Studies of Electrolyte Oxidation Processes on Non-intercalating Electrodes

The oxidative stability of model electrolytes was initially studied on both Pt and GC electrodes to gain insight into the direct electrochemical oxidation of electrolyte components. This data serves as a basis for comparison to similar efforts evaluating these processes in the presence of the relevant model cathode materials which are believed to help drive the “chemical” oxidation of the electrolyte. The data in Figure X.5.3 shows results for electrolyte oxidation studies using Pt electrodes. These experiments were conducted using cyclic voltammetry (CV) to evaluate the electrochemical stability window of 1M LiClO₄ in both PC and EC for comparison. EC is suspected to be involved in the formation of reactive elements that drive the chemical oxidation of the electrolyte and PC is included for comparison. CV experiments were conducted with the extreme voltages of the range varied in order to determine the voltage at which electrolyte oxidation initiated. The data for the PC based system shows that the electrolyte oxidation starts at just below 5V with a well defined electron transfer reaction. Return voltage sweeps (that will drive reduction processes) show that the direct oxidation of the PC/ClO₄ based system leads to a well defined reduction process occurring at ~ 2.8V. For comparison, the EC based system shows a more varied response with a less well defined oxidation process and the formation of multiple electrochemically reactive species that are detected in the reduction sweep. Due to the simplicity of the observed direct oxidation products of the PC based electrolyte, this system was initially chosen for further comparison to model cathode electrodes as well as development of SECM-specific methods to detect reaction products. The more complex EC based system will be studied further going forward. In addition to the observed electrochemical processes in Figure X.5.3, it was noted that the measured capacitance of the electrochemical cells following electrolyte oxidation showed what appears to be an increase in capacitive

currents. This potentially indicates the formation of surface films as part of the direct oxidation of the relevant electrolyte species and will be studied further.

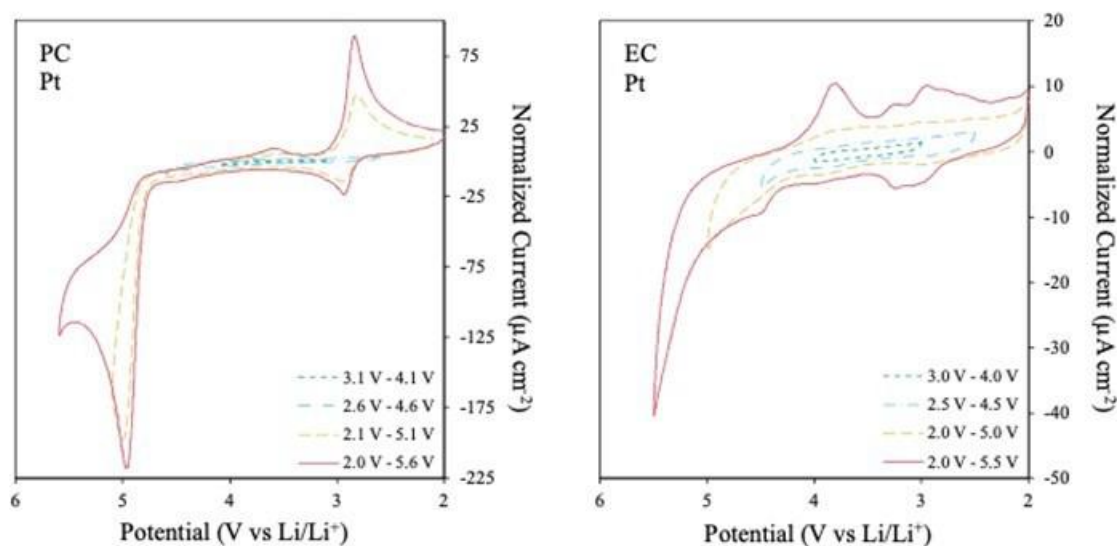


Figure X.5.3 Cyclic voltammetry data for 1M LiClO₄ in PC and EC at a 2mm Pt disk electrode

Comparison of Electrolyte Oxidation on Non-Intercalating Electrodes and Model Cathodes

Figure X.5.4 shows a comparison of CV data collected using the 1M LiClO₄:PC electrolyte using Pt as well as LMO and LNMO model cathodes. Data has been plotted as current density due to variations in electrode size. The top plot shows data for LMO compared to Pt for similar voltage windows. As compared to data in Figure X.5.3, within the voltage range for the LMO evaluation we have not yet pushed far enough positive for the direct oxidation of the electrolyte to occur. However, following the Li intercalation processes observed at ~ 3.9V and 4.1V a higher oxidative current is observed as compared to the Pt substrate. This increased current potentially indicates additional processes that may lead to the “chemical” oxidation of the electrolyte through a catalytic type of reactivity with the LMO. Interestingly, similar data for the LNMO material shows a less clear result with some increased current for the LNMO. However, this current nearly overlaps with that seen for the direct oxidation observed on Pt. This may be due to stabilization of the LNMO material through the addition of Ni to the LMO structure.³

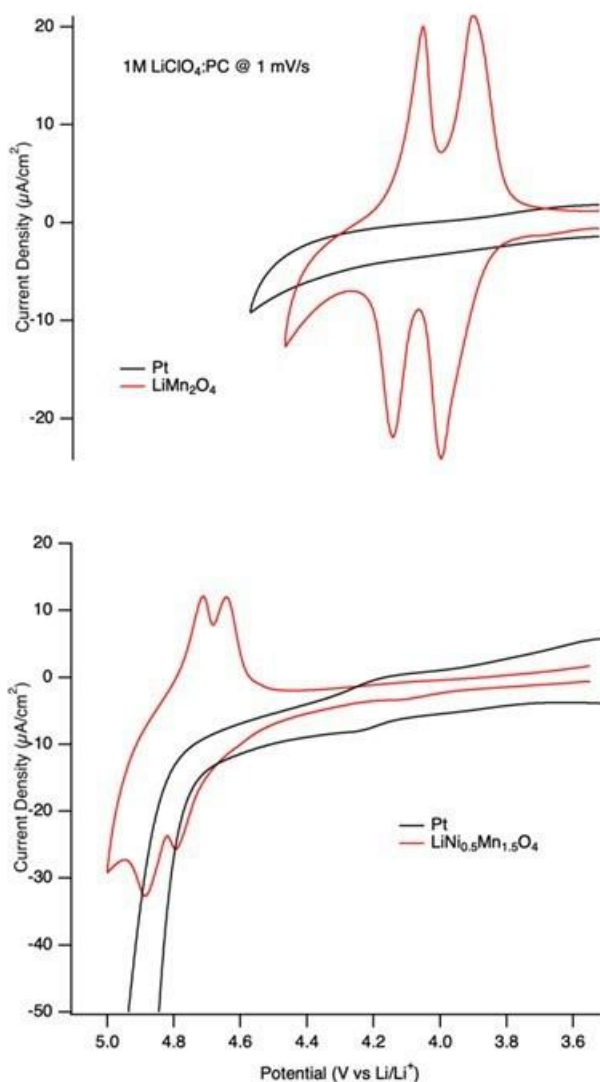


Figure X.5.4 Comparison of cyclic voltammetry data for LMO and LNMO with the “non-intercalating” Pt electrode.

Near Surface G/C SECM to Evaluate Direct Electrolyte Oxidation

Figure X.5.5 shows G/C SECM data collected for the direct oxidation of the LiClO₄:PC electrolyte at a Pt substrate with product detection occurring at a Pt tip electrode that was placed ~ 2 μm above the substrate. Positioning was accomplished using a redox mediator system as discussed elsewhere.⁴ The figure to the left plots the current measured at the Pt substrate as voltage was scanned from 3.5V out to 5.4V. The tip electrode was initial biased at 2.6V to allow the detection of the same reduction products earlier identified in Figure X.5.3. Note that as the substrate voltage increases, the reduction current detected at the tip electrode increases, eventually reaching a maximum and then decreasing. A second experiment was then conducted with the tip electrode biased at 3V. At this voltage, the tip should not be able to drive the reduction process observed in Figure X.5.3. Under these conditions little reduction current is measured (orange trace) at the tip electrode indicating that this electrode is detecting the direct oxidation product shown in Figure X.5.3.

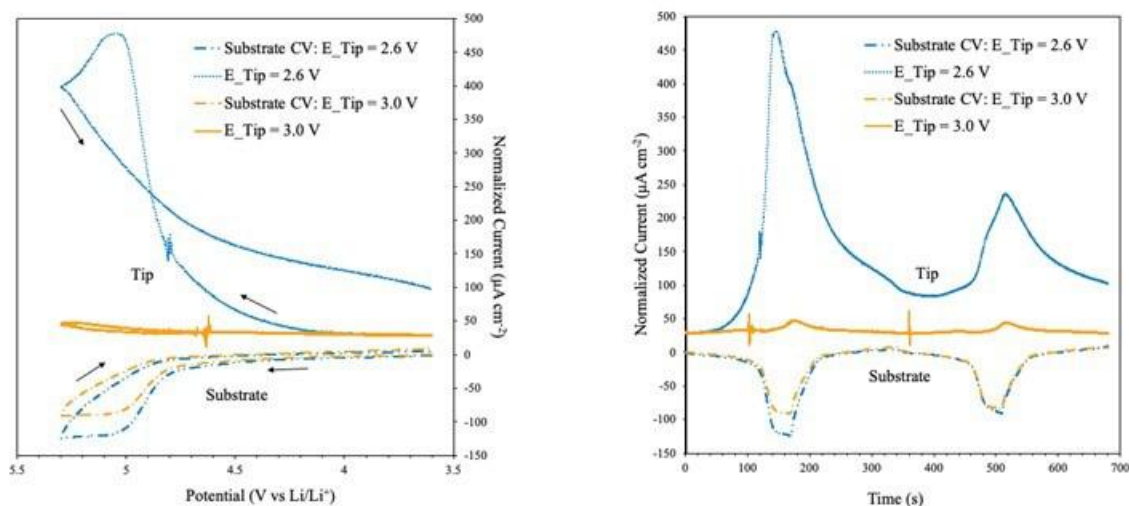


Figure X.5.5 G/C SECM data collected for a 10 μm Pt tip electrode placed $\sim 2 \mu\text{m}$ above a 2 mm Pt substrate.

The data to the right in Figure X.5.5 is the same as that shown on the left, however, is plotted versus time rather than substrate potential and was collected over the course of two scans of the substrate voltage out to 5.4V. Note that the current measured at the substrate and tip both decrease on the second scan. The difference in the tip electrode current is significantly more pronounced. This result is potentially consistent with the Pt substrate surface being passivated to some extent after the oxidation of the electrolyte possibly through deposition of a surface film. Interestingly, in a subsequent experiment, when the substrate was scanned to negative voltages the reactivity returned to that seen in the initial scan shown in Figure X.5.5. This potentially indicates that any film that may be formed on the Pt substrate can be removed through application of a negative voltage.

Initial G/C SECM Evaluation of Electrolyte Oxidation at Model Cathodes

Figure X.5.6 shows initial G/C SECM data collected for the detection of oxidation products formed at an LMO substrate using the 1M $\text{LiClO}_4\text{:PC}$ based electrolyte system. The tip electrode was a 10 μm Pt disk electrode placed near the substrate surface as discussed earlier. The data in Figure X.5.6 shows linear sweep voltammograms collected at the tip electrode with the underlying LMO substrate held at varied voltages. While the previous data set used distinct tip voltages to detect an expected reduction process, the approach described here enables detection of unexpected reduction products by sweeping through a range of tip voltages. Under these conditions, reduction processes will appear as inflections in the current versus potential curves rather than peaks. For this plot the tip current values had a deliberate current offset applied to allow differentiation of each sweep. The applied substrate voltage associated with each tip voltage scan is shown on the left side of each plot. The three vertical lines delineate areas where reduction products are detected at the tip electrode. In this case, we appear to see at least three distinct reduction products with processes detected at tip at voltages of $\sim 2.7\text{V}$, 3.2V and 3.55V . The process detected at 2.7V is potentially the same as that seen for the direct oxidation of the electrolyte while the processes observed at 3.2V and 3.55V appear to be distinct from the direct oxidation process. The process observed at 2.7V is present in all data sets and may be a residual product from an earlier scan (not shown). The process occurring at a tip voltage of 3.2V appears to develop at a substrate voltage of 4.6V . Interestingly this process also appears to begin to shift toward more negative tip voltages as substrate voltage increases. The final process at $\sim 3.55\text{V}$ appears to begin to develop above 5.4V applied at the substrate. This final process may be somewhat irrelevant as 5.4V is not likely to be employed in an actual cell, however the process observed at 3.2V tip voltage may be relevant for comparison to other high voltage cathode materials including the LNMO.

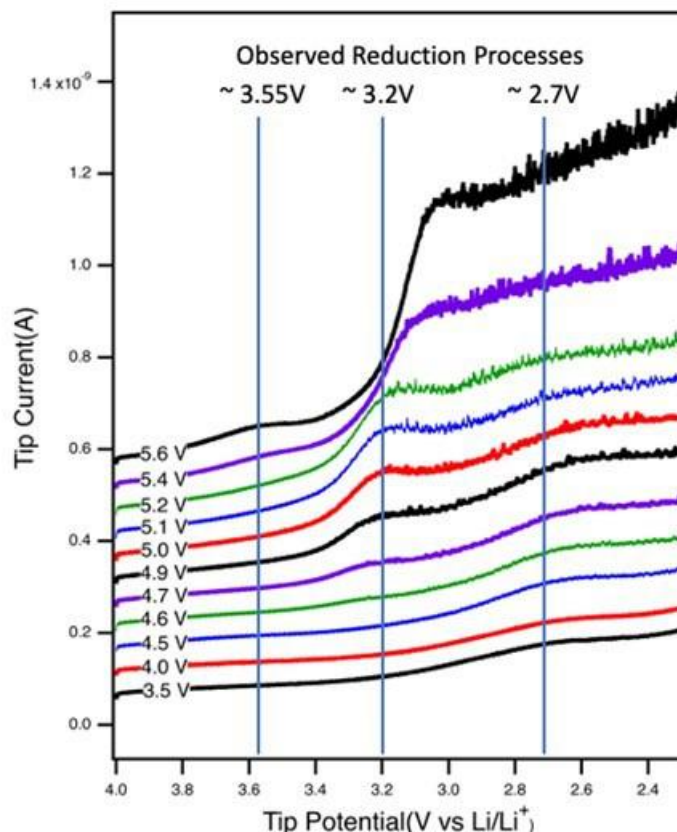


Figure X.5.6 G/C SECM tip linear sweep voltammetry (LSV) at varied substrate voltages.

Conclusions

Studies were conducted attempting to differentiate direct oxidation of model LIB electrolyte systems from “catalytic” oxidation of the electrolyte in the presence of model cathode materials. Focus was placed on comparing LMO and LNMO materials, largely evaluated with the 1M LiClO₄ and PC system. However, evaluation of alternate salts (LiPF₆) and carbonates (EC) has been initiated. Evaluation of the direct oxidation of our model electrolytes using both CV and SECM showed that the G/C SECM method can be used to detect oxidation products formed at the substrate electrode. Furthermore, direct oxidation studies appeared to indicate both the formation of soluble degradation products as well as potential surface films with indications from multiple approaches. Electrolyte oxidation stability windows were also characterized for LMO and LNMO model cathodes and compared to direct oxidation at Pt electrodes. This work was conducted both using cyclic voltammetry and G/C SECM methods. The G/C SECM data collected for a Pt tip near an LMO substrate biased at varied voltages appears to show multiple electrolyte oxidation products formed beyond those observed for direct oxidation using a Pt substrate. This result is still preliminary and will be explored further as this project moves forward with additional work on the LNMO material and a shift to the NMC 811 system which has been shown to also drive the “chemical” oxidation of the electrolyte.

Key Publications

1. Di Huang, Chaiwat Engtrakul, Sanjini Nanayakkara, David W. Mulder, Sang-Don Han, Meng Zhou, Hongmei Luo and Robert C. Tenent; Understanding Degradation at the Lithium-Ion Battery Cathode/Electrolyte Interface: Connecting Transition Metal Dissolution Mechanisms to Electrolyte Composition; (2021) *ACS Applied Materials and Interfaces*, 13(10), 11930-11939.
2. Rong He, Larissa Zhou, Robert C. Tenent and Meng Zhou; Basics of the Scanning Electrochemical Microscope and Its Application in the Characterization of Lithium-ion Batteries: A Brief Review; (2023) *Materials Chemistry Frontiers*, DOI: 10.1039/d2qm01079h

References

1. Zhan, C.; Wu, T.; Lu, J.; Amine, K., Dissolution, migration, and deposition of transition metal ions in Li-ion batteries exemplified by Mn-based cathodes – a critical review. *Energy & Environmental Science* **2018**, *11* (2), 243-257.
2. Jia, Q. X.; McCleskey, T. M.; Burrell, A. K.; Lin, Y.; Collis, G. E.; Wang, H.; Li, A. D. Q.; Foltyn, S. R., Polymer-assisted deposition of metal-oxide films. *Nature Materials* **2004**, *3* (8), 529-532.
3. Mohamedi, M.; Makino, M.; Dokko, K.; Itoh, T.; Uchida, I., Electrochemical investigation of $\text{LiNi}_{0.5}\text{Mn}_{1.5}\text{O}_4$ thin film intercalation electrodes. *Electrochimica Acta* **2002**, *48* (1), 79-84.
4. He, R.; Zhou, L.; Tenent, R.C.; Zhou, M., Basics of the Scanning Electrochemical Microscope and Its Application in the Characterization of Lithium-ion Batteries: A Brief Review; *Materials Chemistry Frontiers* **2023**, DOI: 10.1039/d2qm01079h

Acknowledgements

The authors would also like to thank Alfred Hicks in the NREL communications department for generating many of the graphics in this manuscript.

XI Next Generation Lithium-Ion Materials: Low-Cobalt/No Cobalt Cathodes

VTO battery R&D activity has historically been focused on developing a novel battery technology offering a combination of improved cost and performance. In the past, this was appropriate given that PHEVs and EVs did not perform as well as internal combustion engine powered vehicles (in terms of range or life) and they were more expensive. However, a combination of improved energy and lower cost materials being commercialized (e.g., NMC811) and an increasingly large volume of EVs being manufactured worldwide has led to a dramatic reduction in EV/PEV battery cost from well over \$1000/kWh in the mid 2000s to under \$150/kWh today. This, in turn, could lead to even greater EV sales in the near future. With EV cost and range improved, DOE recognized that EV/PEV batteries would need to be made, to the greatest extent possible, using only earth abundant materials.

In late 2018, the battery R&D program competitively awarded seven contracts to develop cells using low- or no-cobalt cathodes. The goals of these projects were to achieve a cobalt loading of less than 50mg/Wh, a cathode level specific energy greater than 600 Wh/kg, and to use that cathode to construct a cell that provide 80% capacity retention after 1000 cycles at a C/3 discharge rate. The contracts, now mainly completed, focused on high Ni NMC (Cabot Corp, University of Texas at Austin, University of California at Irvine, Pennsylvania State University), the 5V spinel $\text{LiMn}_{1.5}\text{Ni}_{0.5}\text{O}_4$ (LNMO) (Nexceris, University of California at San Diego) and a novel NiFeAl material at Oak Ridge National Laboratory.

Some selected highlights from these projects are as follows:

- UCSD, with project partners Tesla, LBNL, UT Austin, and Army Research Lab, used a dry electrode fabrication process along with a high voltage electrolyte formulation to demonstrate a 3mAh/cm² loading Gr/LNMO cell that achieved 70% capacity retention after 1000 cycles.
- UC Irvine, with partners from LBNL, PNNL, VA Tech, and American Lithium Energy developed a high-entropy doping strategy to fabricate a high-Ni, zero-Co layered cathode ($\text{LiNi}_{0.8}\text{Mn}_{0.13}\text{Ti}_{0.02}\text{Mg}_{0.02}\text{Nb}_{0.01}\text{Mo}_{0.02}\text{O}_2$) that has high thermal and cycling stability.. The resulting material exhibited 500 full cell cycles with just 5% capacity fade and zero strain during charge and discharge. In-situ heating experiments reveal that the thermal stability is significantly improved, reaching the level of NMC-532.

The rest of this chapter contains detailed reports on the status of the following individual projects.

- Aerosol Manufacturing Technology to Produce Low-Cobalt Li-ion Battery Cathodes (Cabot Corporation)
- Co-free Cathode Materials and their Novel Architectures (UCSD, UTA, LBNL)
- Enhancing Oxygen Stability in Low-Cobalt Layered Oxide Cathode Materials by Three-Dimensional Targeted Doping (UC Irvine)
- High-Nickel Cathode Materials for High-Energy, Long-Life, Low-Cost Lithium-Ion Batteries (UTA)
- Cobalt-Free Cathodes for Next Generation Li-Ion Batteries (Nexceris)
- High-Performance Low-Cobalt Cathode Materials for Li-ion Batteries (PSU).

XI.1 Aerosol Manufacturing Technology to Produce Low-Cobalt Li-ion Battery Cathodes (Cabot Corporation)

Toivo Kodas, Principal Investigator

Cabot Corporation
157 Concord Road
Billerica, MA, 01821
E-mail: Toivo.Kodas@cabotcorp.com

Haiyan Croft, DOE Technology Development Manager

U.S. Department of Energy
E-mail: Haiyan.Croft@ee.doe.gov

Start Date: October 1, 2018

End Date: September 30, 2022

Project Funding: \$2,749,057

DOE share: \$1,989,057

Non-DOE share: \$760,000

Project Introduction

Although considerable progress has been made with battery materials over the last 10 years, the cathode remains a major performance-limiting material in Li-ion battery (LIB) technology. New materials and battery chemistries will overcome some of the remaining challenges, but cathode materials must also be manufactured at a lower cost and with a smaller environmental footprint using new processes that can also enable improved control over stoichiometry, morphology, and compositional homogeneity. Cabot, Argonne National Laboratory and SAFT research teams are combining their extensive expertise in particle synthesis, battery materials and cell design to develop a low-cost, flexible aerosol manufacturing technology for production of high-performance cathode active materials (CAM). This project will develop low-Co CAMs via Reactive Spray Technology (RST) and Flame Spray Pyrolysis (FSP) to reach performance targets of < 50 mg Cobalt/Wh.

Objectives

The objective of this project is to research, develop, and demonstrate RST and FSP for production of low-Cobalt CAMs for use in high energy LIBs capable of the following (see Table XI.1.1):

Table XI.1.1 Project performance targets for cathode active material and cell made with this material

Beginning of Life Characteristics at 30 °C	Cell Level	Cathode Level
Useable Specific Energy @ C/3	---	≥60 Wh/kg
Calendar Life (< energy fade)	15 years	---
Cycle Life (C/3 deep discharge with <20% energy fade)	1,000	---
Cobalt Loading	<50 mg/Wh	---
Cost	≤\$100/kWh	---

Approach

To achieve the above targets, we have demonstrated the production of low-Cobalt particle compositions. Cabot has shown the feasibility of $\text{LiNi}_{0.8}\text{Mn}_{0.1}\text{Co}_{0.1}\text{O}_2$ (NMC811) by RST; for this project we are extending this to even lower Co amounts. This required us to identify approaches to solve key problems of phase stability, water sensitivity, interface degradation and others. The team has explored particle doping, coating, morphology, and size control on a robust platform that can be extended to other material configurations. We have leveraged the flexibility of RST and FSP to produce key low-Co cathode compositions relevant for achieving a scale up pathway. Cabot and ANL have identified the most suitable aerosol platform and process conditions to

synthesize low-Co cathode active material compositions. The optimization of low-Co electrodes includes new conductive additive formulations and improved low-Co cathode pastes that ensure percolation and mechanical stability of the film.

The performance goals in Table XI.1.1 drive us to new compositions, lower Cobalt than in NCM811 (such as $\text{LiNi}_{0.9}\text{Co}_{0.05}\text{Mn}_{0.05}$ and $\text{Ni}_{0.9-x}\text{Co}_{0.06}\text{Al}_x$ $x=0.005-0.03$), along with other materials systems comprising fluorine (Li-excess disordered rock salt, LxDRS). Composition must be optimized for performance, cycling, stability and operation, among others. Our proposed RST/FSP route will address these issues and allow doping, coating, gradients, and novel particle morphologies which can solve these problems.

Results

CAM particle morphology and structure optimization

Results obtained in budget period 2 (BP2) taught us that calcination and other post processing (surface washing/milling) steps greatly influence NCM9055 particle distribution and surface area. For instance, one-step calcination process at temperatures 750°C - 800°C (for 10-12h) destroys the green (as-prepared) powder structures and leads to sintering and particle agglomeration. These hard agglomerates needed to be milled, which due to the brittleness of NCM9055 created many fine particles seen by the high surface area of the final material (BET $3.5\text{-}6\text{ m}^2/\text{g}$) (referred to Figure XI.1.1). To this end, ANL has explored alternative ways to calcine the green powder to reduce/avoid particle sintering. Some initial work was done using a rotating oven (rotating kiln), but the results were not much different from the results using a static muffle furnace. In addition, dry aerosol (mimicking a fluidize bed) to keep the particles flowing during calcination with the intention to avoid sintering at elevated temperatures was also tried. The team also explored combining static calcination with dry aerosol calcination (DAC) process. After some trial using the DAC process alone and in combination with static (muffle furnace) calcination, the team realized that residence times are too short for full layered phase conversion, though the particle size and morphology were not changed from the original green powder. Though the signs for layered phase were not moving to the right direction (Figure XI.1.1). After extra experiments the team realized that DAC would need to use pure oxygen instead of air to get closer to the layered phase. Since the current DAC set up does not allow for that, we have abandoned that option.

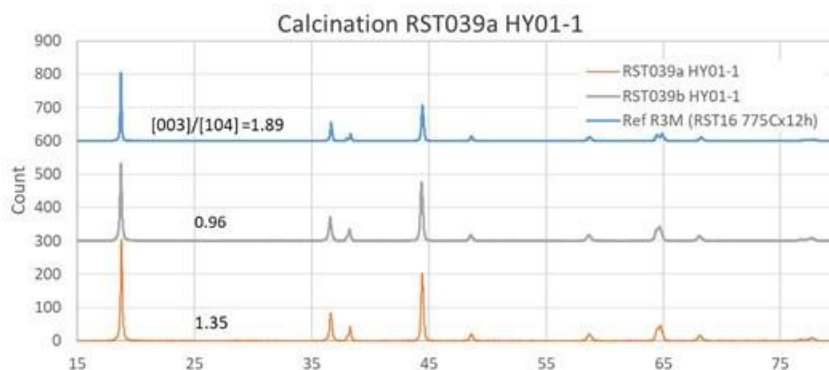


Figure XI.1.1 X-Ray diffraction plots for NCM9055 produced by RST (RST039) using improved calcination process HY01.

Based on discussions with the team members and other cathode scientist at ANL, we explored a two-step calcination. The first step was done at low temperature ($600^{\circ}\text{C} \leq T < 725^{\circ}\text{C}$) for $t > 12\text{h}$, followed by shorter second calcination at higher temperature ($> 725^{\circ}\text{C}$). The idea is to remove all surface carbonates and other volatile residues (from the RST synthesis) during the low-temperature static (muffle furnace) calcination. It is known that these residues can quickly melt at higher temperatures and promote particle necking creating large solid agglomerates. Though, this step will not fully convert the powder to the layered phase it starts the process (the powder seems to be a mixture of mainly spinel powder with some layered phase). Calcined powders were qualified by X-ray diffraction (XRD), particle size distribution (PSD), scanning electron microscopy (SEM)

and BET surface area. XRD studies are to confirm that we are obtaining the desirable layered structure (R3m). There are two main sign to look for when review XRD pattern (a) the ratio $[003/0104]$, which should be ~ 1.89 and the peak splitting around 64 degrees (Figure XI.1.1). SEM, PSD and BET will tell us particle morphology and size distribution. The green powder (after spray pyrolysis process) has an initial BET of $5.89 \text{ m}^2/\text{g}$. ANL was able to reduce porosity and particle surface area, while keeping particle morphology by using a 2-step static calcination to $1.11 \text{ m}^2/\text{g}$.

Additionally, ANL slightly modified the Li-excess and precursor solution concentration during spray pyrolysis synthesis. Based on previous experience, the latter leads to bigger particle size leading to process RST039. Spray pyrolysis (RST039) and calcination processes conditions (HY01) have been selected to produce NCM9055 with a surface area $\sim 1 \text{ m}^2/\text{g}$, these conditions will eliminate the need for particle surface washing and milling (Figure XI.1.2). The ANL team produced 4.5 kg of improved NCM9055 cathode powders having $0.96 \text{ m}^2/\text{g}$ and $D50 = 2.8 \mu\text{m}$ surface area and particle size respectively. Figure XI.1.3 shows XRD plots comparing progress toward obtaining improved crystallinity and particle morphology of the RST made NCM9055.

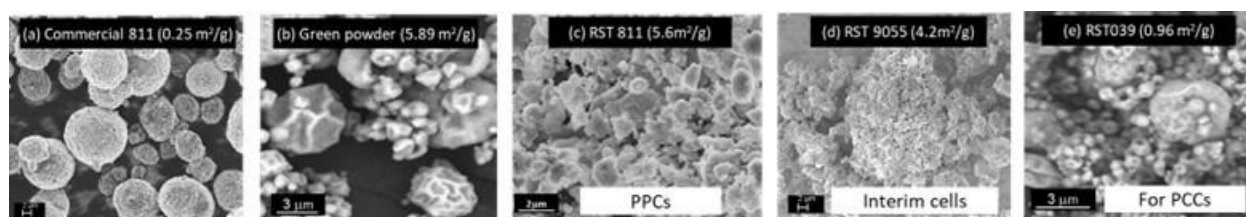


Figure XI.1.2 SEM images for different high nickel content NCMs (a) commercially available round NCM811; RST made cathode material (b) green powder, (c) NCM811, (d) NCM9055 and (e) improved NCM9055

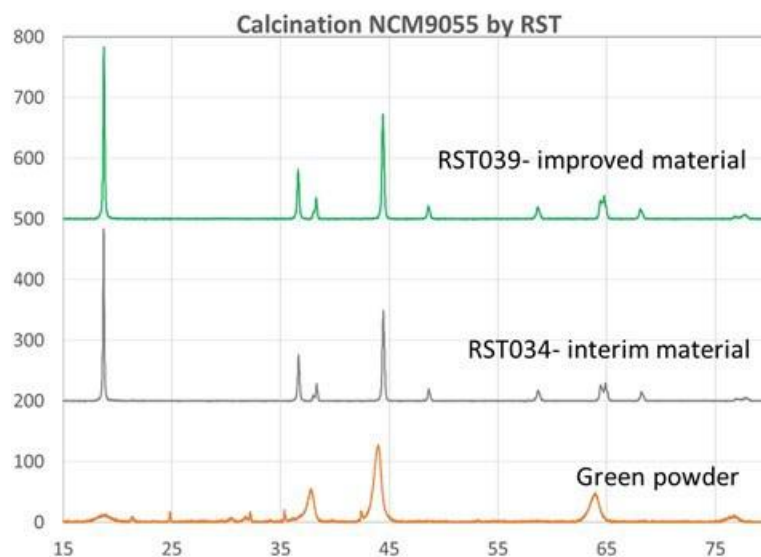


Figure XI.1.3 X-ray diffraction patterns for NCM9055 made by RST (a) green powder, (b) interim material used in BP2 to make pouch cells, (c) improved material to be used for final cell deliverables

Cathode particle surface modification

Cabot continued work to improve CAM surface coating properties using aluminum oxides with different surface areas FA-2 and FA-3 ($60 \text{ m}^2/\text{g} < \text{FA-1} < \text{FA-2} < \text{FA-3}$). The idea is to explore the effectiveness of higher surface area alumina on NCM particle coverage. It has been shown that FA-2 gives the best core particle surface coverage than our baseline FA-1 fumed alumina (used during BP2) and FA-3. It is worth mentioning that FA-3 has a different crystal phase composition (more amorphous) compared to the other two.

Additionally, initial results suggest that FA-2 can provide similar coating coverage with less amount of material to FA-1. This is particularly advantageous because it will limit the initial capacity reduction due to reaction of lithium with Al_2O_3 . Half coin cells (Figure XI.1.4.a) indicated that FA-2 could be a good option for RST made NCM9055, because these particles are smaller (D_{50} : 2-3 μm) needing a coating material with higher porosity and smaller particles (higher surface area). Full cell studies (Figure XI.1.4.b) using FA-1 and FA-2 (wt% < 2) to coat NCM811 (made by co-precipitation, D_{50} = 10 μm) were carried out. Electrode loadings were $\sim 3.5 \text{ mAh/cm}^2$ and were matched with graphite anodes. Cells were assembled and tested at 45°C from 2.8 to 4.2V using 1C charge/discharge rates. Between FA-1 and FA-2, there seems not to be significant difference in cycle-life (half and full coin cells), therefore both FA-1 and FA-2 will be used to surface coat NCM9055 (with 0.96 m^2/g BET surface area).

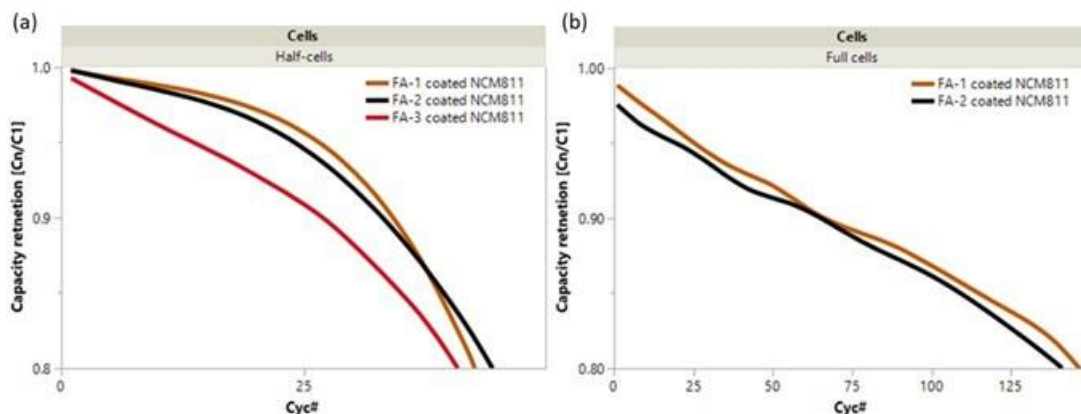


Figure XI.1.4 Electrochemical studies for NCM811 coated with different fumed alumina powders (FA-1, FA-2 and FA-3): (a) half coin cells and (b) full coin cells.

In addition, nano scale $\text{Li}_x\text{M}_y\text{O}_z$ was used to surface coat NCM811. As mentioned before, this type of coating particle can effectively protect the core Hi-Ni CAM while avoiding lithium consumption during formation. Li-metal oxides ($20 < \text{SA} < 50 \text{ m}^2/\text{g}$) with a fractal structure were made by flame spray pyrolysis (FSP). These particles were dispersed onto the surface of NCM811 (0.25 m^2/g) using a dry coating process. Due to their lower surface area compared to FA higher wt% were needed to obtain a good surface coverage ($D < E < 4 \text{ wt}\%$). Cell testing data indicates that Li-metal oxide coating reduces electrode resistance increase while improving cycle life testing. As shown in Figure XI.1.5 $\text{Li}_x\text{M}_y\text{O}_z$ has less impact on initial capacity than fumed alumina. The team will continue exploring this material as a next generation cathode coating option.

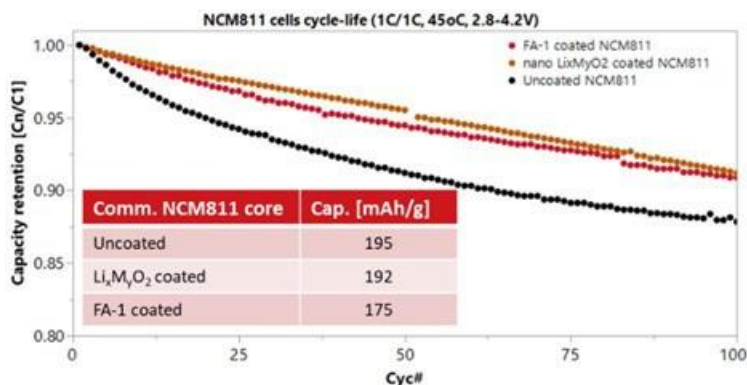


Figure XI.1.5 Full coin cell cycle life for cells made with NCM811 coated with FA-1 and with $\text{Li}_x\text{M}_y\text{O}_z$.

Fumed alumina coating optimization for RST NCM9055

Two types of fumed aluminas (FA-1 and FA-2) with differing in BET surface area were used to coat NCM9055 (BET SA=0.96 m²/g) made by RST. The loading of the alumina varied from 0 to 2 wt.% (A < B < C < D). The team also measure the influence of the coating layer on cathode surface interaction with water by measuring pH of the coated particles in an aqueous dispersion (measurements were taken after 24h soaking). As seen in Figure XI.1.6 a linear decrease in pH was highly correlated with fumed alumina loading, which is favorable to slurry processing, as elevated pH may cause slurry gelation.

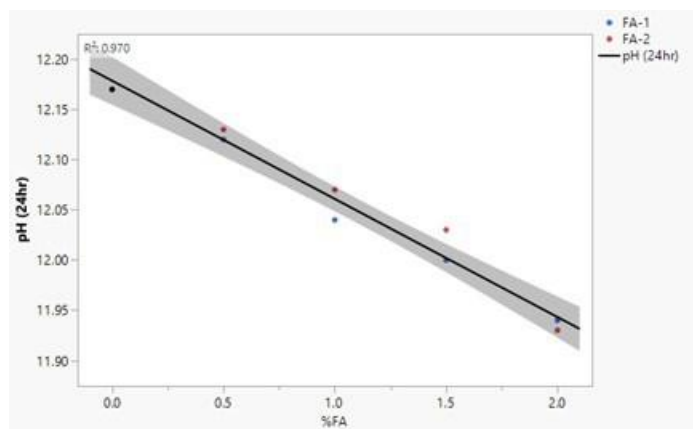


Figure XI.1.6 Correlation of pH after 24h and fumed alumina contents of RST9055-039 coated samples

Electrodes were coated on aluminum foil to assemble full 2032 coin-cells with constant n/p ratio of 1.2, and capacity area loading of 4.5 mAh/cm². The conductive carbon additive in the cathodes was 1.3% Blend C (CB+CNTs, more details in the next section), and binder was 1.2% Solef5130. Coin-cell initial capacity and first cycle efficiency were respectively 205 mAh/g and 90% for the uncoated particles and decreased with fumed alumina coating as shown on Figure XI.1.7.a. This is known to be caused by Li consumption by the alumina layer during cell formation. Highest capacity and 1st cycle efficiency of 196 mAh/g and 87% were achieved with 1 wt.% FA coating for both FA grades. Cycle-life testing performed at 45°C (1C/1D, 4.2-2.8V) confirmed beneficial effect of the surface coatings on capacity retention (Figure XI.1.7.b).

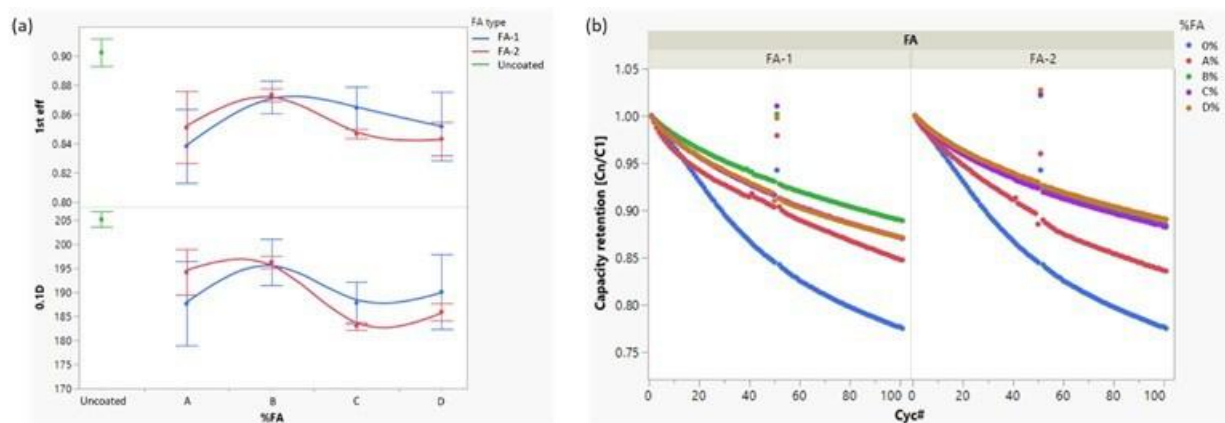


Figure XI.1.7 (a) 1st cycle efficiency and 1st C/10 capacity (4.2-2.8V) vs. fumed alumina contents of RST9055-039 coated samples. (b) 1C/1D, 45°C (4.2-2.8V) Capacity retention vs. cycles for RST9055-039 coated samples

Carbon Conductive Additives for Hi-Ni NCMs

This development continued using a better carbon nanotube dispersion CNT-C2. Previous study indicated that 1% CNT-C2 gave best cycle-life results with surface coated NCM811. The work done in this reporting

period was aimed at further improving cycle-life by blending with additional CB. Commercially available surface coated NCM811 was used as model for this purpose. The slurry formulations tested are listed in Table XI.1.2.

Table XI.1.2 Conductive carbon additives formulation tested using commercial NCM811 (a< 1wt%)

Conductive Carbon Additive (CCA) type	PVDF Binder	Loading	Density
0.5a % CNT-C2	1%	23 mg/cm ²	3.5 g/cc
a % CNT-C2	1.2%		
2a % CB	2%		
Blend C (0.5a % CNT-C2 + 0.8a % CB)	1.2%		

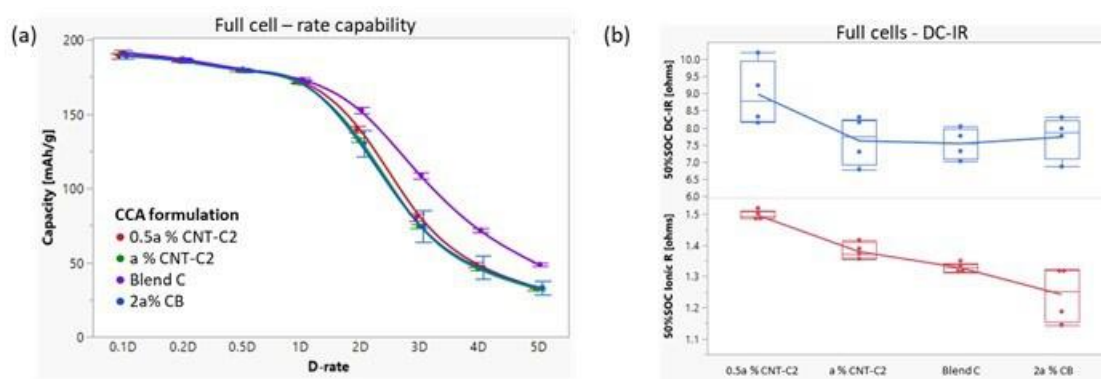


Figure XI.1.8 (a) Initial discharge rate capability of CCA formulations with NCM811. (b) Ionic and electronic resistance extracted from hppc testing of CCA formulations with NCM811

Cells were formed at C/10 CCCV and tested for discharge rate capability in 2.8-4.2V range. All formulations had 1st coulombic efficiency between 85-87%, and 0.1C capacity above 185 mAh/g. Rate capability results (Figure XI.1.8.a) shows that at higher discharge current the CB/CNT blend (Blend C) had significantly better discharge rate capability. We could attribute this effect to improved ionic conductivity in the electrodes due to the carbon black presence. This was proven by extracting ionic resistance from the hppc data at 50% SOC, where ionic resistance decreases with CB contents in the CCA formulation (Figure XI.1.8.b). Cycle-life testing was performed at 45°C using 1C-1D currents. The Blend of CNTs and CB outperformed all over formulations, both in capacity utilization and capacity retention (Figure XI.1.9). It is therefore the most promising choice to meet DOE targets of energy and capacity retention and will be tested with NCM9055 made by the RST process.

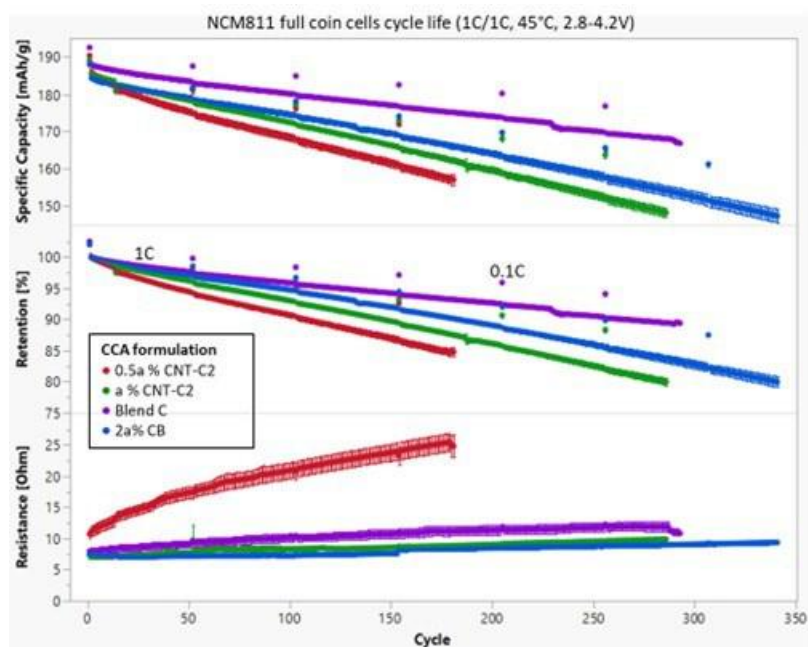


Figure XI.1.9 From top to bottom: Capacity utilization, retention, and DC-IR during cycle-life testing of CCA formulations with NCM811

Optimize electrode formulation and architecture.

NCM9055 made at ANL was surface coated using FA-1 and FA-2 at different loading amounts ($A < B < C < D < 2\text{wt}\%$). As mentioned earlier, the cathode initial capacity and pH (when dispersed in water) was influenced by the wt% of alumina. As the wt% increased the initial discharge capacity of the electrode decreased as well as the initial pH (w/o surface coating pH= 12.2) down to 11.4. Coin-cell initial capacity and first cycle efficiency were respectively 205 mAh/g and 90% for the uncoated particles and decreased with fumed alumina coating. This is known to be caused by Li consumption by the alumina layer during annealing of the coated particles. Highest capacity and 1st cycle efficiency of respectfully 196 mAh/g and 87% were achieved with $> A$ wt.% FA-2 coating. Based on formation results, cells made with FA-2 coated NCM9055 was selected for further cycling experiments. Cycle-life testing performed at 45°C (1C/1C, 4.2V-2.8V) confirmed beneficial effect of the coatings on capacity retention. Cells made with alumina coated NMC9055 (wt% $> A$) have reached about 300 cycles (with 80% capacity retention) at these conditions as show in Figure XI.1.10. The team has selected FA-2 (BET $> 100\text{m}^2/\text{g}$) due to the reduced capacity loss, lower DCIR and better cell performance.

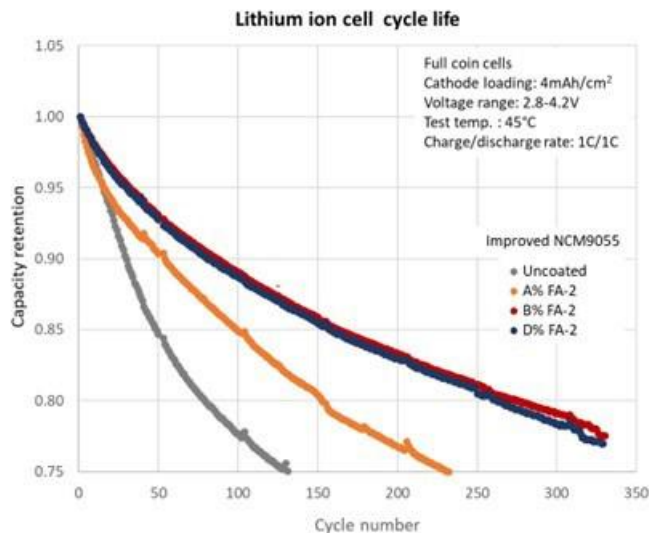


Figure XI.1.10 Full coin cells (4.3 mAh/cm²) cycle life results for different coated cathodes at 45 °C and 1C/1D charge/discharge rates

Cabot has increased the cathode dry coating process batch size from 50g to 1.5 kg. Analytical and electrochemical experiments were carried out using intermediate steps (100, 200, 500 1000g). Material characterization shows similar CAM (using NCM622) surface coverage for the different scales. And full coin cells show similar initial capacities and cycle life for cells made with cathode produced at different batch sizes. The scaled-up process was used to surface coat 4.5kg of NCM9055 made by RST. (See Figure XI.1.11.)

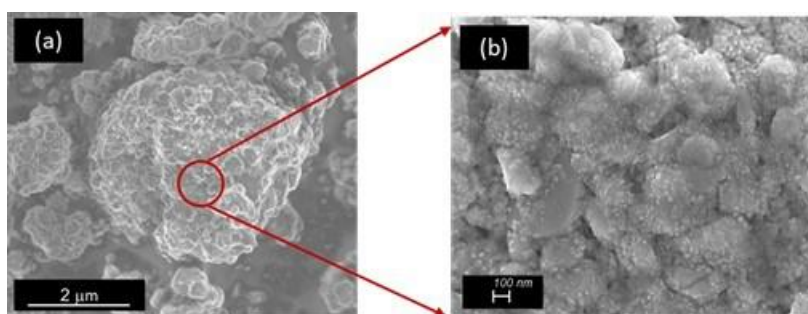


Figure XI.1.11 SEM images of FA-2 coated NCM9055 (a) secondary particle, (b) zoom-in view of the primary particles coated with fumed alumina

Project completion cell (PCC) fabrication and testing

The best alumina coated NCM9055 samples (based on cycle life) were selected and shipped to SAFT for slurry qualification and pouch cell testing. The surface coated RST9055 were tested for surface contamination, particle size and surface area. The slurries made with the RST samples passed qualification and were used to make double pouch cells (Figure XI.1.12). Figure XI.1.13 shows double layer pouch cells have shown 88% energy retention after 550 cycles (at 30°C, C/3) and projected to reach ~1000 cycles before drops below 80%. The pouch cycle life aligns with Cabot's results in full coin cells. Based on cycling data and initial capacities we calculated expected energy densities (cathode). Table XI.1.3 Compares cells made during the project and summarizes cathode energy densities for these cells at C/10 and C/3 (at 45°C). The final material cell initial energy density were 755Wh/kg and they retained 93% of it after 300 cycles.



Figure XI.1.12 SAFT experiments: slurry and cathode layer made with alumina surface coated RST 9055

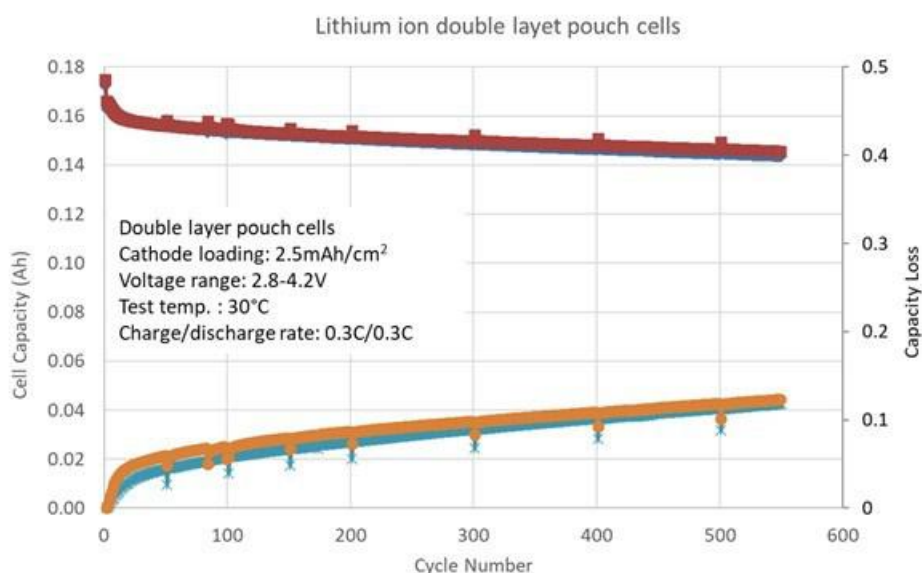


Figure XI.1.13 Double layer pouch cell made with optimized surface coated NMC9055

Table XI.1.3 Summary table showing initial cathode energy densities

Active material	Cathode Energy Density (Wh/kg)			
	Initial		After 300 cycles (C/3)	
	0.1C	0.33C	0.1C	0.33C
PPC: uncoated NCM811	650	610	515	450
Interim: NCM9055 v1	710	670	570	515
Final: NCM9055 v2	755	705	705	655

Conclusions

In FY2022, the team worked on improving NCM9055 particle morphology and reduce surface area. This was achieved by modifying and improving post processing steps (calcination and deagglomeration). After locking the process steps, the team focused on producing NCM9055 by RST for the final cell deliverables (project completion cells, PCC). ANL produced 4.5kg of NMC9055, with 0.96 m²/g and D50 = 2.8 μm surface area

and particle size respectively. The cathode powder was then surface coated by Cabot using the selected high surface area fumed alumina. The coated NCM9055 material has been sent to SAFT for qualification at small scale (200g) and large scale (1.5kg). Slurries made with the NCM9055 powder have passed SAFT standard testing (powder, slurry, and electrode coating qualification). Cabot has optimized and selected a new blend of carbon black and carbon nanotubes (Blend C) to be used for in Hi-Ni NCMs to be used in the fabrication of PCCs. SAFT has selected all other cell components (anode, binders, separator, and electrolyte). Double layer pouch cells made with the final NCM9055 material has shown an initial energy density of 755 Wh/kg and ~88% retention after 550 cycles (at 30°C, C/3) and projected to reach ~1000 cycles before drops below 80%.

Key Publications

1. “Aerosol Manufacturing Technology to Produce Low-Cobalt Li-ion Battery Cathodes”, BAT411_Aurora_2022_p, US DOE Vehicle Technologies Program Annual Merit Review, AMR, 2022.

Acknowledgements

We would like to acknowledge Dr. Joseph Libera and Dr. Eungje Lee at ANL; Mrs. Carine Steinway, Mrs. Serena Peterson, and Dr. Joong Sun Park at SAFT for their valuable contribution to this project.

XI.2 Co-free Cathode Materials and their Novel Architectures (UCSD, UTA, LBNL)

Ying Shirley Meng, Principal Investigator

University of California, San Diego
9500 Gilman Dr.
La Jolla, CA 92093
E-mail: shmeng@ucsd.edu

Arumugam Manthiram, Co-Principal Investigator

The University of Texas, Austin
Department of Mechanical Engineering
204 E. Dean Keeton Street, C2200
Austin, Texas 78712
E-mail: rmanth@mail.utexas.edu

Hieu Duong, Co-Principal Investigator

Tesla, Inc.
1 Tesla Rd
Austin, Texas, 78725,
E-mail: hiduong@tesla.com

Vince Battaglia, Co-Principal Investigator

Lawrence Berkeley National Laboratory
1 Cyclotron Road
Berkeley, CA 94720
E-mail: vsbattaglia@lbl.gov

Haiyan Croft, DOE Technology Development Manager

U.S. Department of Energy
E-mail: Haiyan.Croft@ee.doe.gov

Start Date: October 1, 2021
Project Funding: \$1,043,000

End Date: September 30, 2022
DOE share: \$834,000

Non-DOE share: \$209,000

Project Introduction

Since its discovery [1], $\text{LiNi}_{0.5}\text{Mn}_{1.5}\text{O}_4$ (LNMO) spinel-type cathode materials have long intrigued the transportation industry due to their high operating voltage (4.7 V) and capability to handle high charging rates. More recently, the strong desire to eliminate cobalt in cathode materials has sparked a renewed interest in this class of oxides. Various attempts to create LNMO/graphite batteries that exhibit high voltage, relatively high energy density, and high charging capabilities have been carried out worldwide, but they all have suffered from excessive degradation and short cycle life, especially when stored or cycled at elevated temperatures (55°C or higher) [2]. Our proposed work will solve the long-standing issues by 1) novel architecture of LNMO thick electrodes to enable 4-6 mAh/cm² loading, 2) new electrolyte formulation to suppress degradation in LNMO/Gr full cells, and 3) close collaboration among university-national lab-industry to demonstrate the feasibility of a Co free Li-ion cell with energy density exceeding 600 Wh/kg at cathode level. The main focus of this research is to solve the structural stability of LNMO and the interphase problems with electrolytes, including adopting an appropriate surface coating for the cathode; the development of a novel electrolyte (electrolyte additive, sulfone-based electrolyte); and the advancement of a new dry electrode processing method. In the past five years, our research team has made great progress on developing innovative synthesis techniques of high tap density cathode materials; conformal coating methods on powder samples; advanced

characterization techniques on the atomic scale, electrode scale, and at the cell level; we have also made significant inroads on thick-electrode-architecture cell prototyping. **UT Austin** has extensive experience in the co-precipitation synthesis of LNMO cathode materials with a batch tank reactor at above the kilogram scale. **UCSD** has achieved conformal coatings on cathode particles through polymer assisted deposition. **UCSD** has also demonstrated that cryo-(S)TEM is crucial for interphase studies as it can effectively preserve cathode electrolyte interphase (CEI) structure/chemistry from beam damage. **LBNL** has effective diagnostic methods for full cells at both the coin cell and pouch cell level. **Tesla, Inc.** possesses a unique dry battery electrode coating technology that offers extraordinary ionic and electronic conductivity for extremely thick electrodes. It is through these successful experiences and fundamental understanding of these high voltage cathode materials that we can successfully formulate strategies to optimize LNMO-based battery system.

Objectives

The proposed research aims to deliver a Co free Li-ion battery with energy density exceeding 600 Wh/kg at the cathode active material level. More specifically, the main goal of this project is to develop a high-performance and low-cost spinel-type $\text{LiNi}_{0.5}\text{Mn}_{1.5}\text{O}_4$ electrode and novel electrolyte formulation to suppress full cell degradation at high voltage and temperature. The best combination of high voltage electrode and electrolyte will achieve higher cell energy density, better safety performance, longer battery life, and greatly reduce the overall cost of the battery. The critical success factors in achieving that goal include:

1. Electrolyte stability and compatibility for both the cathode and anode materials under high charge and discharge voltage;
2. LNMO bulk and surface stability at high working temperature 55-60°C;
3. High areal cathode loading with new polymer binder and a dry-processing method to ensure adequate electronic and ionic transport for fast rates.

Approach

The main focus of this research is to solve the structural stability of LNMO and the interphase problems with electrolytes, including adopting an appropriate surface coating for the cathode; the development of a novel electrolyte (electrolyte additive, sulfone-based electrolyte); and the advancement of a new dry electrode processing method. In addition, to guide our research to determine which electrolyte system is more stable and compatible for LNMO electrode materials under high voltage cycling, we will develop a series of characterization techniques such as ex-situ X-ray photoelectron spectroscopy (XPS), ex-situ cryogenic transmission electron microscopy (cryo-TEM), ex-situ cryogenic focused ion beam microscope (cryo-FIB), in-situ Fourier-transform infrared spectroscopy (FTIR) and in-situ time-of-flight secondary-ion mass spectrometry (TOF-SIMS).

Results

The following progress has been achieved in FY22:

Enabling high performance LNMO using dry electrode method ($> 3 \text{ mAh/cm}^2$)

Dry electrode process was adopted to improve the performance of LNMO in the full cells. Unlike conventional slurry-based process, the dry process removes toxic NMP, solvent drying process as well as solvent recycling equipment cost. In addition to these environmentally benign features, the dry process can easily fabricate ultra-high loading electrodes without cracking, as shown in Figure XI.2.1a. The thick LNMO electrode up to 10 mAh/cm^2 was well optimized using carbon nanofibers as the conductive agent, PTFE as the binder, and etched Al as the current collector. Combining these inactive components with high-quality LNMO active material built a well-constructed thick film with a superior electronic conductive network. The electrochemical performance of this type of electrode at 3 mAh/cm^2 in the full cell is much better than the wet-coated electrode. In a practical condition, the LNMO/graphite full cell at 3 mAh/cm^2 level doubled the cycling life compared to slurry-based LNMO, as shown in Figure XI.2.1a and b. The success of dry LNMO electrodes is ascribed to reduced parasitic reactions, a well-built electronic percolation network, and robust mechanical properties.

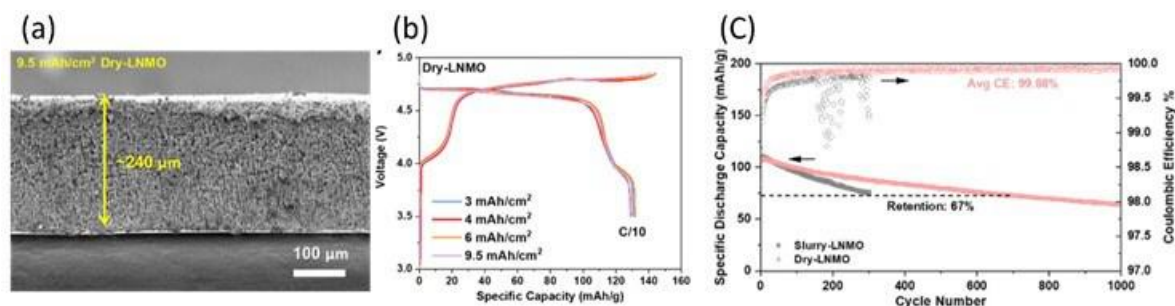


Figure XI.2.1 (a) SEM cross-section of a 240 μm dry-coated LNMO electrode. (b) Voltage profiles of dry-coated LNMO with various loadings in half cells. (c) Full cell cycling performance between dry-LNMO and conventional slurry-based LNMO.

Developing all-fluorinated novel electrolyte for high voltage cycling (3 mAh/cm²)

All-fluorinated electrolyte was developed during the project period. Fluorination of EC and EMC improved the oxidation stability of solvent molecules. This can be supported by the DFT calculation results. The reaction barrier of FEC is much higher than that of EC at different cathode facets. With the support of theoretical calculations, experimental investigations and analysis were carried out. LNMO/graphite full cells at 3 mAh/cm² level using 1M LiPF₆ in EC:EMC = 3:7 wt% (Gen2) and 1M LiPF₆ in FEC:FEMC = 3:7 wt% (FEC-FEMC) cycled at elevated temperature (55°C) were analyzed. Under such aggressive testing condition, full cells using Gen2 electrolyte experienced extremely unstable cycling, quick failure, and low average CE% (<99%) over the cycling. In contrast, full cells using FEC-FEMC electrolyte show excellent capacity retention (~68%) in 100 cycles with average CE% of ~99.4% (Figure XI.2.2). More importantly, the cycling data for FEC-FEMC electrolyte are reproducible which makes the improved cycling stability in all fluorinated electrolyte more valid.

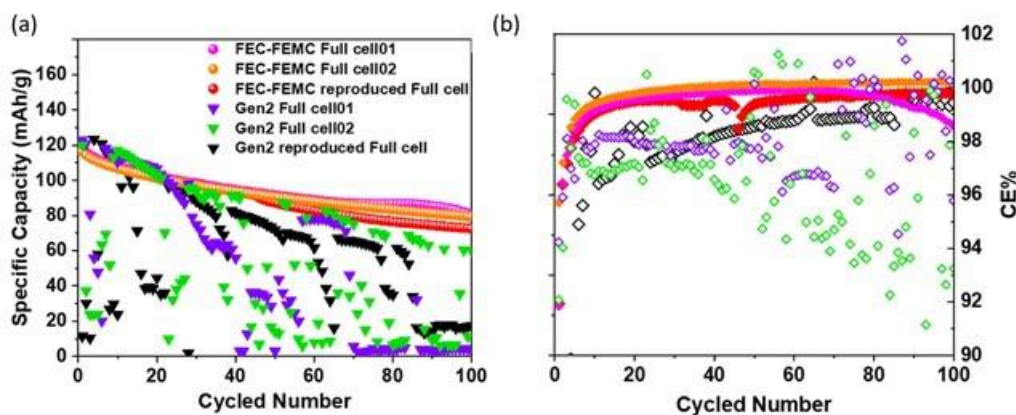


Figure XI.2.2 (a) Specific discharge capacity and (b) Coulombic efficiency (CE%) of high temperature (55 °C) LNMO/graphite full cell cycling.

Impact of a high-energy laser treatment on the surface chemistry of the Fe-LNMO cathode electrode

The morphologies of the pristine (referred to as baseline) and laser-treated Fe-LNMO cathode electrodes were explored with scanning electron microscopy (SEM, Figure XI.2.3a). As seen, the edges of laser-treated primary particles are not as sharp as the baseline sample, indicating the laser energy applied to the cathode particles is high enough to alter the primary particle morphology, which could induce changes in the structure and/or surface properties of the cathode electrode. In this regard, STEM are first carried out to understand any structural changes that could have been brought about by the laser treatment. STEM images (Figure XI.2.3b) of baseline and LT1 samples show a similar spinel lattice structure with no obvious difference. It should be

noted that the surface lattice structure with a thickness of about 2 nm is the Mn_3O_4 -type spinel. That phase is presented on both samples and is formed due to surface oxygen/Li deficiency instead of the laser treatment.

With respect to the surface chemistry evolution, XPS data were collected on the fresh baseline and LT1/LT2 electrodes before the electrochemical test. As shown in Figure XI.2.3c, the PVDF peaks at 286 eV and 290.3 eV (C1s spectra) of LT1 and LT2 are weaker than those of the baseline electrode, and such a decrease in the PVDF peak after the laser treatment can also be seen in the F 1s spectra, illustrating that the high energy laser treatment can induce the decomposition of the PVDF binder. Interestingly, a new LiF peak at about 685 eV in the F 1s spectra appears after the laser treatment. Theoretically, the formation of LiF should result from the reactions between the PVDF binder and Fe-LNMO active material, which are, respectively, the only source of fluorine and lithium in the electrode. Due to the formation of the LiF phase on the surface, the content of O-TM bonding in the O1s spectra (no sputtering) of LT1 and LT2 is less concentrated than that with the baseline sample. After 30s of Ar^+ sputtering, however, the O-TM content of LT1 and LT2 increases sharply and shows a concentration similar to that of the baseline sample. This indicates that the thickness of the surface LiF phase is only about 3 nm - 5 nm.

To understand the formation mechanism of the LiF phase, residual Li titration on fresh Fe-LNMO powder was first conducted to identify the Li source. As shown in Figure XI.2.3d, the pH of deionized water increases to about 9.5 after rinsing the fresh Fe-LNMO powder, clearly demonstrating the existence of surface residual Li species ($\text{LiOH}/\text{LiHCO}_3/\text{Li}_2\text{CO}_3$). Based on the titration result, it is determined that the concentration of surface residual Li is 174 ppm. Combining the XPS and titration data, a LiF formation mechanism is proposed in Figure XI.2.3e. Specifically, under the illumination of a high-energy laser, an elimination reaction may happen where the basic surface residual Li species (*e.g.*, Li_2CO_3) attack the proton on the PVDF binder, resulting in the formation of LiF as a product.

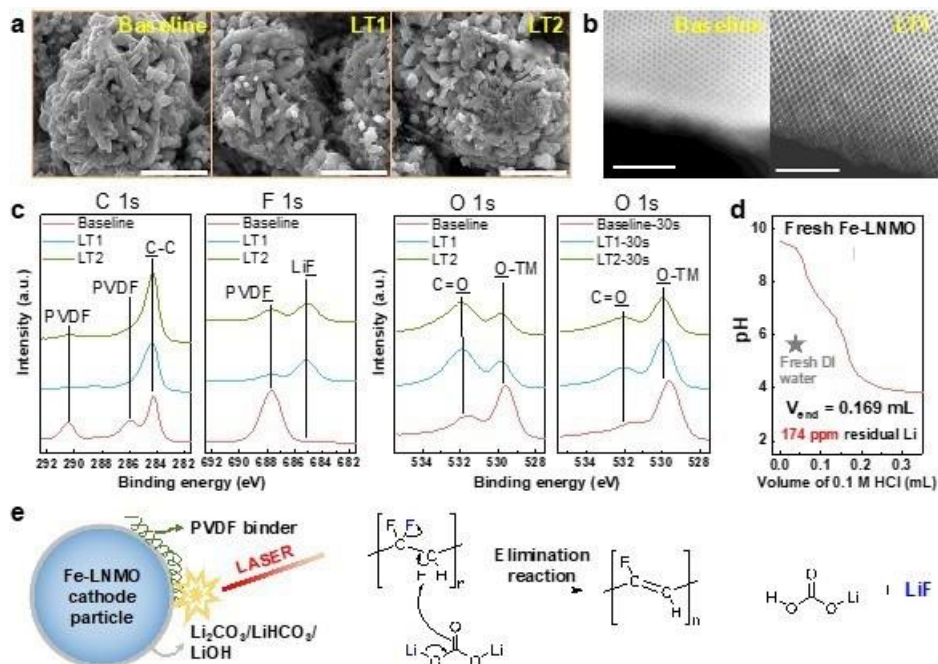


Figure XI.2.3 (a) Scanning electron microscope images of the pristine (baseline) and laser-treated (LT1 and LT2) Fe-LNMO cathode electrodes. (b) Scanning transmission electron microscope images of baseline and LT1 cathodes before electrochemical tests. (c) C1s, F1s, and O1s XPS data of baseline, LT1, and LT2 cathode electrodes before the electrochemical test. (d) Residual Li titration curve of Fe-LNMO cathode to determine the surface residual Li content. (e) Schematic illustration of a possible mechanism for the formation of surface LiF phase on the Fe-LNMO cathode. The scale bars in (a) and (b) are 5 μm and 5 nm, respectively.

Improved cycling performance of Fe-LNMO/graphite full cells by a high-energy laser treatment

Electrochemical performance tests were performed to understand any benefit that can be brought about by the laser treatment. The first cycle charge-discharge curves are displayed in Figure XI.2.4a. As seen, the LT1 and LT2 cells show capacities and coulombic efficiencies similar to the baseline cell, in great accordance with the TEM results, which displayed no structural changes induced by the laser treatment of Fe-LNMO. Furthermore, the rate performance was conducted in cells with Li-metal anodes to avoid active Li loss on the anode side. As shown in Figure XI.2.4b, the rate capability of the Fe-LNMO cathode is slightly worsened by the laser treatment. This is because of the loss of inter-particle contact in Fe-LNMO caused by the decomposition of the PVDF binder (Figure XI.2.4c). In this regard, further research on the laser treatment of cathode can focus on Figure XI.2.4c the optimization of binder content and laser energy to improve the rate performance.

The cycling performances of LT1 and LT2 cells were evaluated in a full cell configuration with graphite as the anode. As shown in Figure XI.2.4c, the LT1 and LT2 cells show consistently, and remarkably enhanced cycling stabilities compared to the baseline cell. Specifically, the LT1 and LT2 cells can deliver, respectively, 88% and 87% of their initial capacity (119 mA h g^{-1} at a C/2-1C rate) after 200 cycles; while the baseline cell with an initial capacity of 116 mA h g^{-1} (C/2-1C rate) only has a capacity retention of 77 %. The discharge profiles of LT1, LT2, and baseline cells are plotted in Figure XI.2.4d. During cycling, the voltages of the phase transformation plateaus of the LT1 and LT2 cells only slightly decreased; in contrast, the voltage of those plateaus of the baseline cell fades much faster. Electrochemical impedance spectroscopy (EIS) data in Figure XI.2.4e further demonstrate a lower interfacial impedance for the LT1 and LT2 cells compared to the baseline cell, as shown clearly with a higher magnification.

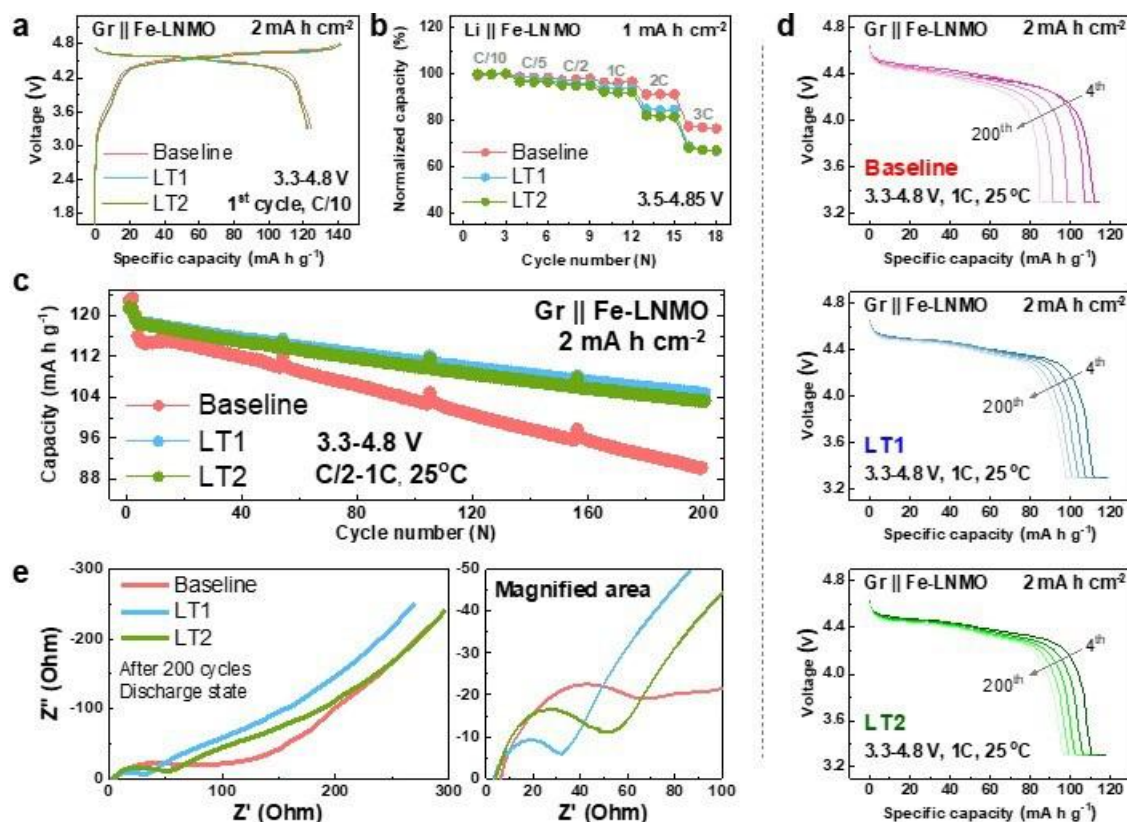


Figure XI.2.4 Electrochemical performance comparison of baseline, LT1, and LT2 cells. (a) First cycle charge-discharge curves, (b) rate capability test (based on Li || Fe-LNMO half cells), (c) cycle stability evaluation, (d) evolution of discharge curves, and (e) EIS plots of baseline, LT1, and LT2 full cells with graphite as the anode. The Li || Fe-LNMO and Gr || Fe-LNMO cells were operated at 3.5 V - 4.85 V and 3.3 V - 4.8 V, respectively. 1C equals 147 mA h g^{-1} .

Understand the degradation mechanisms of pristine and laser-treated Fe-LNMO/graphite full cells

XPS data on the cycled cathode electrode were collected to understand the chemistry of the cathode-electrolyte interphase (CEI). As shown in Figure XI.2.5a, the organic electrolyte decomposition species, represented by the C-O/C=O/ROCO₂R' peaks in C 1s and O 1s spectra, are more concentrated on the baseline cathode electrode than on the LT1 and LT2 cathode electrodes. This trend is also reflected in Figure XI.2.5b, where the O atomic concentration (representing mainly carbonates oxidation products) of the baseline cathode is higher than those of the laser-treated Fe-LNMO cathodes, especially LT1. Moreover, the content of LiF/TMF_x of the baseline cathode, standing for active material loss due to reactions between Fe-LNMO and LiPF₆ along with its decomposition products, is also significantly higher than those of LT1 and LT2 cathodes. In addition, the P atomic concentration of the baseline cathode is about 3%, which is three times higher than those of LT1 and LT2 (Figure XI.2.5b). These data clearly demonstrate that the surface LiF phase on LT1 and LT2 cathode can suppress the oxidation reaction between the cathode and electrolyte at high voltages. As a result, the intensity ratio of the O-TM peak over the C-O and C=O peaks of the baseline cathode is lower than those of LT1 and LT2 cathodes, demonstrating a thicker CEI on the baseline Fe-LNMO cathode. It should be noted that a robust CEI would not only protect the cathode from hazardous electrolyte attacks but can also reduce TM dissolution and acidic species formation, which will in turn prevent severe graphite anode degradation.

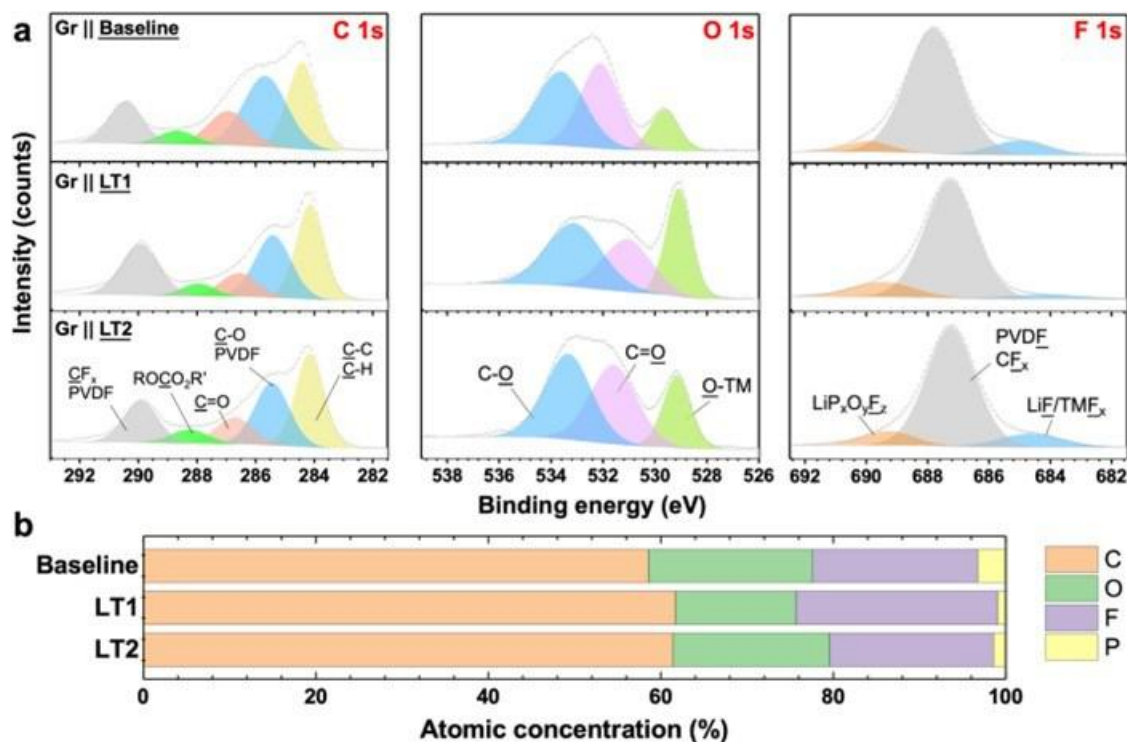


Figure XI.2.5 (a) C1s, O1s, and F1s XPS data of baseline, LT1, and LT2 cathode electrodes after 200 cycles in full cells with graphite as the anode. (b) XPS C, O, F, and P atomic concentrations of baseline, LT1, and LT2 cathode electrodes after 200 cycles in full cells.

In addition to XPS, NMR spectroscopy is utilized to quantitatively measure the P-containing acidic crossover species, such as HPO₂F₂, which according to previous reports, is generated from the side reactions of LiPF₆ involving oxidation reactions of ethylene carbonate (EC) and ethyl methyl carbonate (EMC). Figure XI.2.6 shows the concentration of HPO₂F₂ (−80 ppm and −18 ppm in the ¹⁹F and ³¹P spectra, respectively) generated chemically and electrochemically in the electrolytes cycled in the baseline and LT1 full cells. Clearly, the concentration of HPO₂F₂ in the LT1 cell is much less than that in the baseline cell after 200 cycles, in accordance with the XPS P atomic concentration measurement shown in Figure XI.2.5b. Interestingly, the concentration of HF is almost no difference in the LT1 and baseline cells. This suggests that HF formation may be irrespective of cathode reactivity, or it may participate in other reactions and get consumed. Overall,

the NMR data further demonstrate that the surface LiF phase can alleviate direct contact between the Fe-LNMO cathode and electrolyte, which significantly reduces the generation of HPO_2F_2 with an active proton. Other acid species, such as formic acid, ethanol/methanol, and water, have also been reported in the literature, and they have been deemed as one of the main culprits of cell failure.

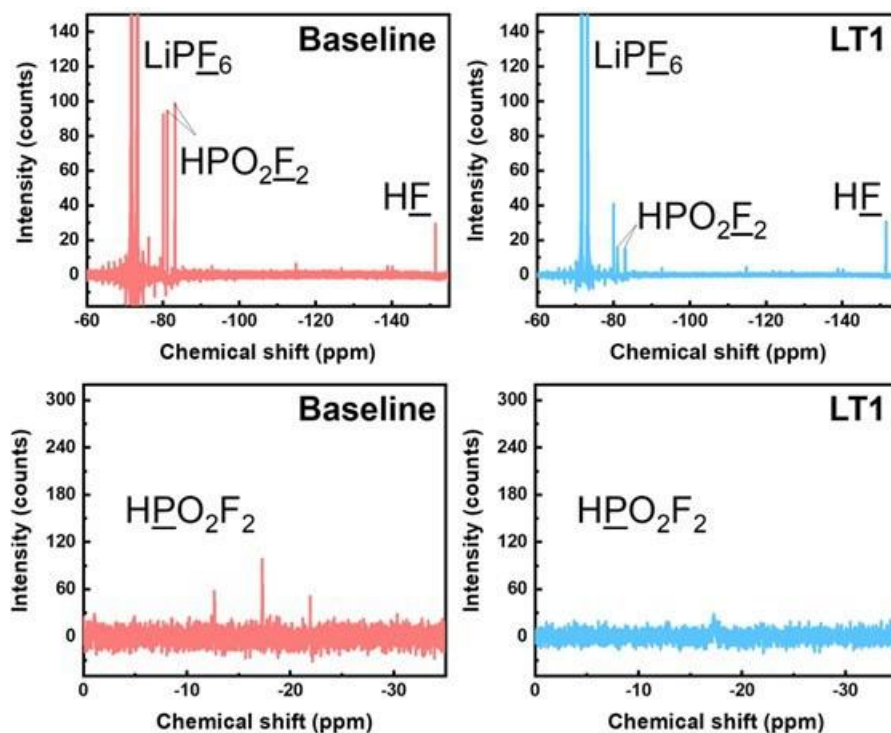


Figure XI.2.6 Normalized NMR ^{19}F and ^{31}P spectra of the retrieved electrolytes from baseline and LT1 full cells after 200 cycles.

Project complete cells (PCCs) deliverable

In the last quarter, the UCSD team has successfully delivered 26 PCCs to DOE and TARDEC laboratories. Out of 26 cells, 15 cells were shipped to Idaho National Laboratory (INL), 9 cells sent to TARDEC, and 2 cells delivered to ARL (Figure XI.2.7a and b). The capacity of each cell is estimated to be $\sim 3\text{Ah}$ with 10 layers of double-side coated LNMO at 2mAh/cm^2 level ($\sim 14\text{mg/cm}^2$ per side). In cells using Gen2 and FEC-FEMC electrolyte, Celgard 2325 separators are used since the FEC-FEMC electrolyte is not compatible with the Al_2O_3 -coated separators. For cells using Gen2 with 2 wt% LiDFOB, Al_2O_3 -coated separators are used. It was previously suggested that Dreamweaver could be a good separator candidate due to its larger porosity. However, mechanical failure constantly occurred during cell fabrication with Dreamweaver, and no cell could be fabricated. While the Dreamweaver separator can effectively mitigate the clogging issue during high voltage cycling, the future development of practical LNMO pouch cell needs to balance both separators' porosity and mechanical strength. In Figure XI.2.7c and d, it can be found that all three cell chemistries deliver consistent performance in both the formation cycle (C/20) and C/3 rate (0.99 A). Cells will be tested under various conditions such as high and low temperature storage and cycling.

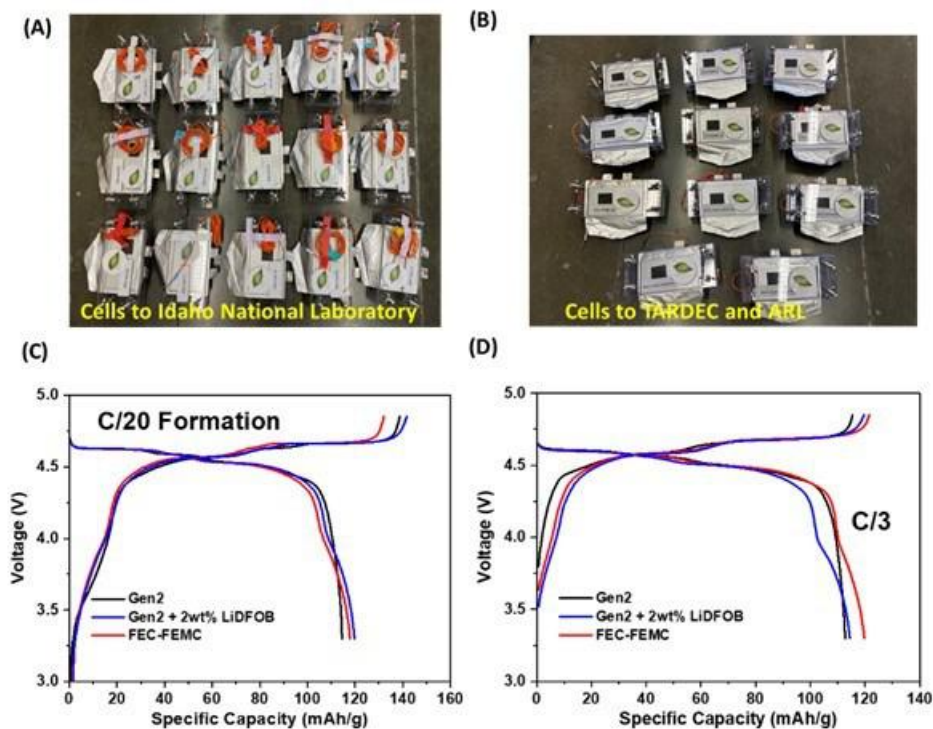


Figure XI.2.7 PCCs delivered to (A) INL and (B) TARDEC and ARL. First (C) formation and (D) C/3 cycle of each cell chemistry.

Conclusions

During the whole project period, several accomplishments have been made by the whole team as demonstrated above. We have successfully pushed forward both the understanding and commercialization of high voltage Co-free LNMO materials with practical loading and cell configuration. Last, we include a figure (see Figure XI.2.8) for performance comparison between our progress and recent to highlight the breakthrough in this project.

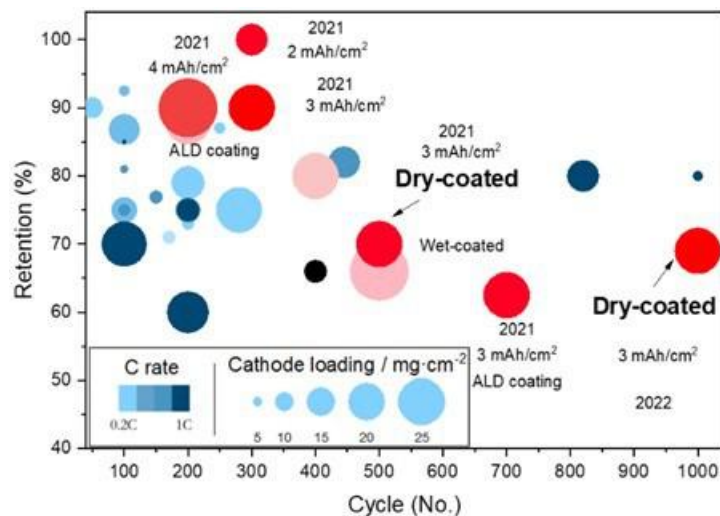


Figure XI.2.8 LNMO-Graphite full cell areal loading and cycling performance comparison between project progress and recent literature.

Key Publications

1. W. Li, M. Zhang, Y.S. Meng, et al., “Artificial cathode electrolyte interphase for improving high voltage cycling stability of thick electrode with Co-free 5 V spinel oxides”, *Energy Storage Materials*, 2022, 49, 77.
2. Z. Cui, F. Zou, H. Celio, and A. Manthiram, “Paving Pathways towards Long-Life Graphite LiNi_{0.5}Mn_{1.5}O₄ Full Cells: Electrochemical and Interphasial Points of View,” *Advanced Functional Materials*, 2022, 202203779.

References

1. Ohzuku, T.; Takeda, S.; Iwanaga, M. Solid-State Redox Potentials for Li[Me_{1/2}Mn_{3/2}]O₄ (Me: 3d-Transition Metal) Having Spinel-Framework Structures: A Series of 5 Volt Materials for Advanced Lithium-Ion Batteries. *J. Power Sources* **1999**, 81-82, 90–94.
2. Lu, J.; Lee, K. S. Spinel Cathodes for Advanced Lithium Ion Batteries: A Review of Challenges and Recent Progress. *Mater. Technol.* **2016**, 31 (11), 628–641.

Acknowledgements

Kang Xu and Marshall Schroeder from the Army Research Laboratory partnered on this project. We also thank Dr. Aaron D. Yocum (NETL manager), Dr. Yi Ding (TARDEC manager), Dr. Ahmad Pesaran (NREL manager), Dr. Jack Deppe (INL manager) for supporting our work.

XI.3 Enhancing Oxygen Stability in Low-Cobalt Layered Oxide Cathode Materials by Three-Dimensional Targeted Doping (UC Irvine)

Huolin Xin, Principal Investigator

University of California, Irvine
4129 Frederick Reines Hall
Irvine, CA, 92697-4575
E-mail: huolin.xin@uci.edu

Feng Lin, Co-Principal Investigator

Virginia Tech
Department of Chemistry
Blacksburg, VA, 24061
E-mail: fenglin@vt.edu

Kristin Persson, Co-Principal Investigator

University of California Berkeley,
210 Hearst Mining Building
Berkeley, CA, 94720
E-mail: kristinpersson@berkeley.edu

Wu Xu, Co-Principal Investigator

Pacific Northwest National Laboratory
902 Battelle Boulevard
Richland, WA 99354
E-mail: wu.xu@pnnl.gov

Jiang Fan, Co-Principal Investigator

American Lithium Energy Corporation
2261 Rutherford Rd
Carlsbad, CA 92008
E-mail: jfan@americanlithiumenergy.com

Haiyan Croft, DOE Technology Development Manager

U.S. Department of Energy
E-mail: Haiyan.Croft@ee.doe.gov

Start Date: October 1, 2018

End Date: December 31, 2022

Project Funding: \$2,150,000

DOE share: \$1,500,000

Non-DOE share: \$650,000

Project Introduction

In this project, we propose to develop a new concept and a generic platform that can lead to the greatly enhanced stabilization of all high-energy cathode materials, and in particular high-nickel (Ni) and low-cobalt (Co) oxides. The new concept is a 3D doping technology that hierarchically combines surface and bulk doping. We will use surface doping to stabilize the surface of primary particles and also introduce dopants in the bulk to further enhance oxygen stability, conductivity, and structural stability in low-Co oxides under high voltage and deep discharging operating conditions. This new concept not only will deliver a low-cost, high-energy cathode but also will provide a generic method that can stabilize all high-energy cathodes. The proposed novel 3D doping approach is poised to resolve some longstanding challenges in fundamental doping effects on

battery materials as well as to reduce Li-ion batteries' cost and improve their safety, energy density, and lifetime.

To tackle this problem, we have formed a highly complementary multi-university/national labs/industry team to enable a doping-central and systematic investigation of low-Co materials and create a knowledge base for many electrode materials to be used in advanced electric vehicles. The successful execution of the proposed project relies on five components that can be carried out by the complementary team members: (1) a theoretical investigation of the surface and bulk stabilizing dopants (Persson), (2) a precise synthesis of materials with targeted doping (Lin and Xin), (3) development of electrolytes for high-Ni low-Co oxides (Xu), (4) multi-scale characterization of the structures and their interfaces by scanning transmission electron microscopy (SEM) and synchrotron X-ray imaging and spectroscopy tools (Xin and Lin), and (5) pouch cell-level integration (Fan). The UCI-led project will enable a doping-central and systematic investigation of low-Co materials and create a knowledge base for many electrode materials to be used in advanced electric vehicles.

Objectives

The primary objectives of this project are:

- Displace Co while maintaining high-Ni content and high energy density: Cobalt concentration < 50 mg/Wh or No-Co, Energy density > 750 Wh/kg (C/3, 2.5-4.4 V) at cathode level, Cost ≤ \$100/kWh
- Improve cycle and calendar life by retaining oxygen through a 3D doping technology: Capacity retention > 80% at 1,000 cycles, energy retention > 80% at 1,000 cycles, calendar life: 15 years
- Deliver a theoretical model: High-throughput DFT calculations that rationalize the selection of oxygen-retraining surface and bulk dopants
- Develop electrolytes with functional additives to form high-quality surface protection layers on both high-Ni/low-Co layered oxides and graphite anode to help the whole project achieve the proposed energy and capacity retention target, i.e. >80% at 1,000 cycles. The FY19 work will focus on electrolyte formulating for NMC811 baseline cathode and graphite anode.
- Offer a knowledge base by performing proactive studies of thermal stability, oxygen loss, and the degradation of the cathode/electrolyte interfaces.

Approach

- We utilize a three-dimensional (3D) doping technology that is a hierarchical combination of surface and bulk doping: (1) Surface doping stabilizes the interface between the primary particles and the electrolyte. (2) Introduction of dopants to the bulk enhances oxygen stability, conductivity and structural stability in low-Co oxides under high voltage and deep discharging operating conditions. (3) A composition controlled and thermodynamics driven synthesis will be used to accurately achieve the desired 3D doping structures.
- Using first-principles calculations to predict surface dopants for oxygen retention at surface of LiNiO₂ and rationalize the effectiveness of dopants.
- Formulate new electrolytes that stabilize the cathode/electrolyte interfaces at deep charging conditions: (1) Coin cell testing of commercial baseline materials. Perform coin cell electrochemical studies of baseline commercial NMC811 cathode and graphite (Gr) anode using the baseline electrolyte to establish coin cell-level benchmarks. (2) Coin cell testing of NMC-D. Evaluate the capacity and cycle life of the synthesized 3D doped cathode materials at the coin cell level using the baseline electrolyte. The results will be compared with the commercial NMC811 baseline. (3) Electrolyte formulating. Formulate functional localized high-concentration electrolytes (LHCEs) to improve cycle life and safety of baseline commercial NMC811 cathode and Gr anode at the coin cell level, optimize electrolyte formulation for NMC-D-90532, and compare with electrolyte baseline for >200 cycles in Gr||NMC full cells at a 4.4 V cutoff.
- Advanced computational and characterization techniques are developed to study: (1) dopant environment and chemistry. (2) thermal stability, oxygen loss, and the degradation of the cathode/electrolyte interfaces.

Results

Scale-up synthesis of UCI Gen2 cathodes and electrochemical performance evaluations.

We performed scale-up synthesis of UCI Gen2 cathode. Figure XI.3.1a shows representative scanning electron microscopy (SEM) images of the synthesized UCI Gen2 cathode. It is seen that, after calcination optimization, secondary cathode particles with well controlled spherical morphology are obtained. The average diameter of the UCI Gen2 secondary particles is ~ 3 μm . Figure XI.3.1b shows the charge/discharge profiles of the cell containing the UCI Gen2 cathode at C/10 within 2.5–4.4 V. The UCI Gen2 cathode prepared by scale-up synthesis exhibits an excellent discharge capacity of ~ 210 mAh/g and a remarkable initial Columbic efficiency (CE) of $\sim 94\%$. The rate performance of UCI Gen2 cathode was evaluated in a typical coin cell from the rate of 0.1C to 5C (~ 3 mg/cm² loading; charge at different rate and discharge at 0.1C). The result (Figure XI.3.1c) shows that $\sim 94\%$ capacity is achieved at 1C, and $\sim 80\%$ capacity is achieved at 5C.

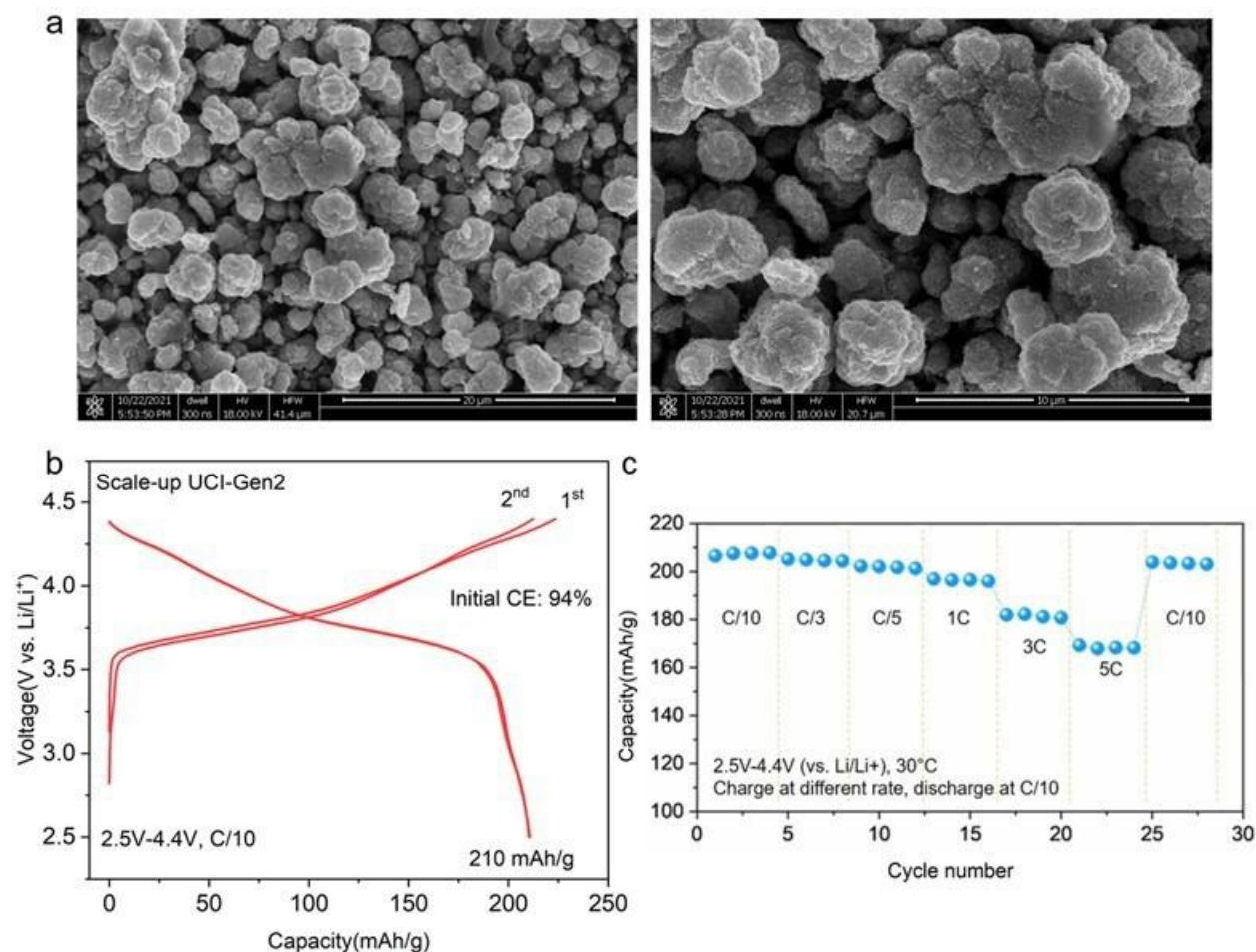


Figure XI.3.1 (a) Representative SEM images showing the morphology of the secondary particles of UCI Gen2 cathode. The average diameter of the UCI Gen2 secondary particles is ~ 3 μm . (b) Coin-cell test of the UCI Gen2 cathode at C/10 within 2.5–4.4 V. (c) Rate capability test of UCI Gen2 cathode at 30 °C.

Furthermore, we performed electrochemical tests (Figure XI.3.2) in half-cells at 50 °C to compare the capacity and thermal stability of NMC-811 and UCI Gen2 cathode. The results shown in Figure XI.3.2a demonstrate that more than 210 mAh/g initial discharge capacity is achieved at this temperature, which is comparable to the commercial NCM-811 material (Figure XI.3.2b). It is worth mentioning that although the cell was tested at 50 °C, the initial Columbic efficiency of UCI Gen2 cathode (94%) is significantly higher than that of the NCM-811 (85%), indicating much less side reaction in UCI Gen2 cathode compared with NMC-811. The cycling stability was also evaluated at this temperature with a cut-off voltage of 2.5V–4.4V. The result is shown in

Figure XI.3.2c. After 50 cycles, NMC-811 shows rapid degradation with 90.3% capacity retention, while UCI Gen2 cathode exhibits 96.6% retention, much higher than that of NMC-811.

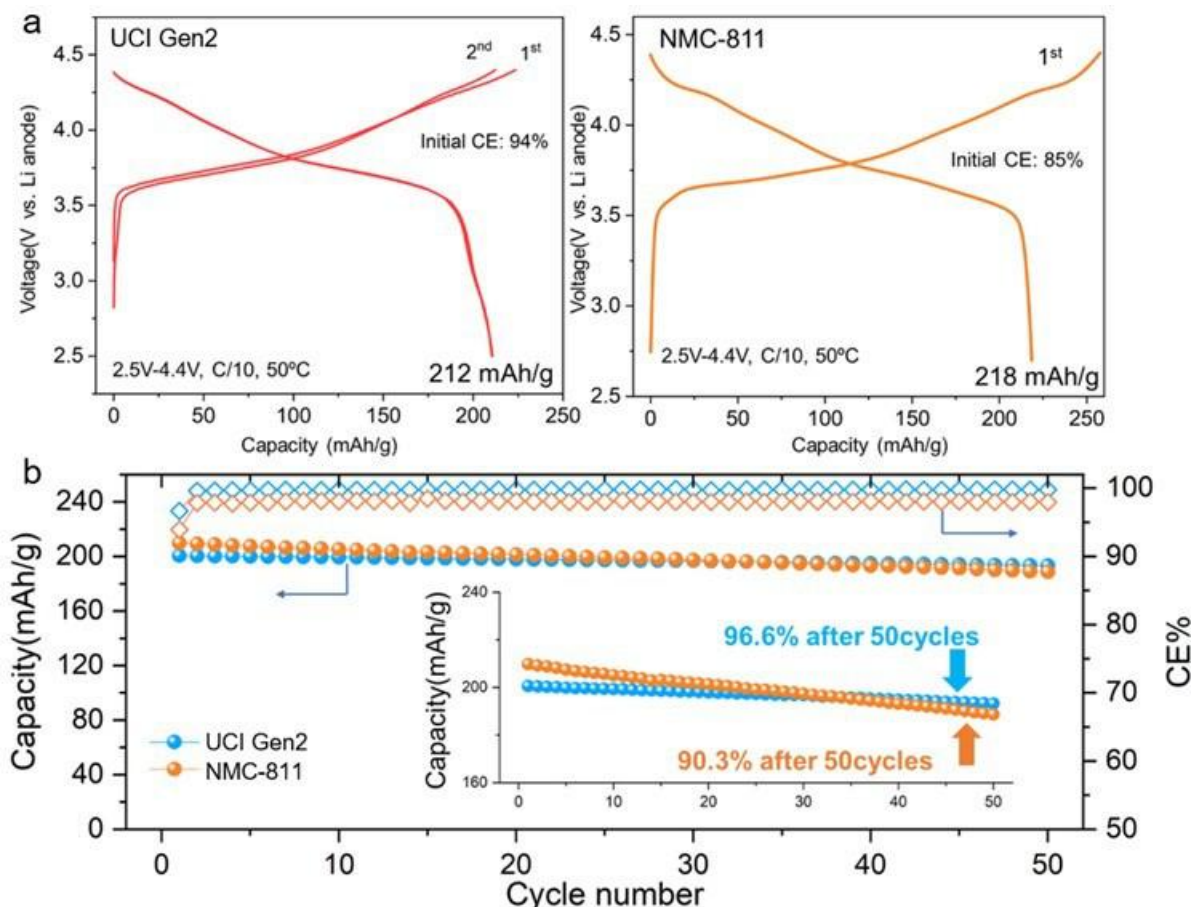


Figure XI.3.2 (a) Galvanostatic charge/discharge of UCI Gen2 cathode and NMC-811 at 50°C, C/10. (b) Cycling performance of UCI Gen2 cathode and NMC-811 at 50°C, C/2.

Mechanistic study of UCI-Gen2 cathode material.

We continued the mechanistic study on the UCI Gen2 cathode in this quarter. Figure XI.3.3a,b show that compared with the Ni-O bonding in NMC-811 which extends towards high-k direction which indicates that oxygen-related defects are formed in NMC-811, the Ni-O bonding in UCI Gen2 cathode remains stable even after long cycles. This suggests that UCI Gen2 cathode is highly robust in terms of oxygen retention. Oxygen loss is closely related to the nano-crack formation in the primary particles which has been demonstrated by our previous work [Matter, Volume 4, Issue 6, 2021, Pages 2013-2026]. Figure XI.3.3c shows electrochemical impedance spectroscopy (EIS) curves of the half-cells containing UCI Gen2, NMC-811, and LiNiO₂ cathodes. The results show that the UCI Gen2 cathode has the lowest impedance among all the cathodes, indicating more favorable reversibility and higher Li⁺ diffusion in UCI Gen2 cathode. Since the coordination change is closely related to the oxygen-release in layered oxide cathodes, wavelet-transformed EXAFS (WT-EXAFS) is applied to probe the Ni-O coordination in UCI Gen2 cathode in comparison with that in NMC-811.

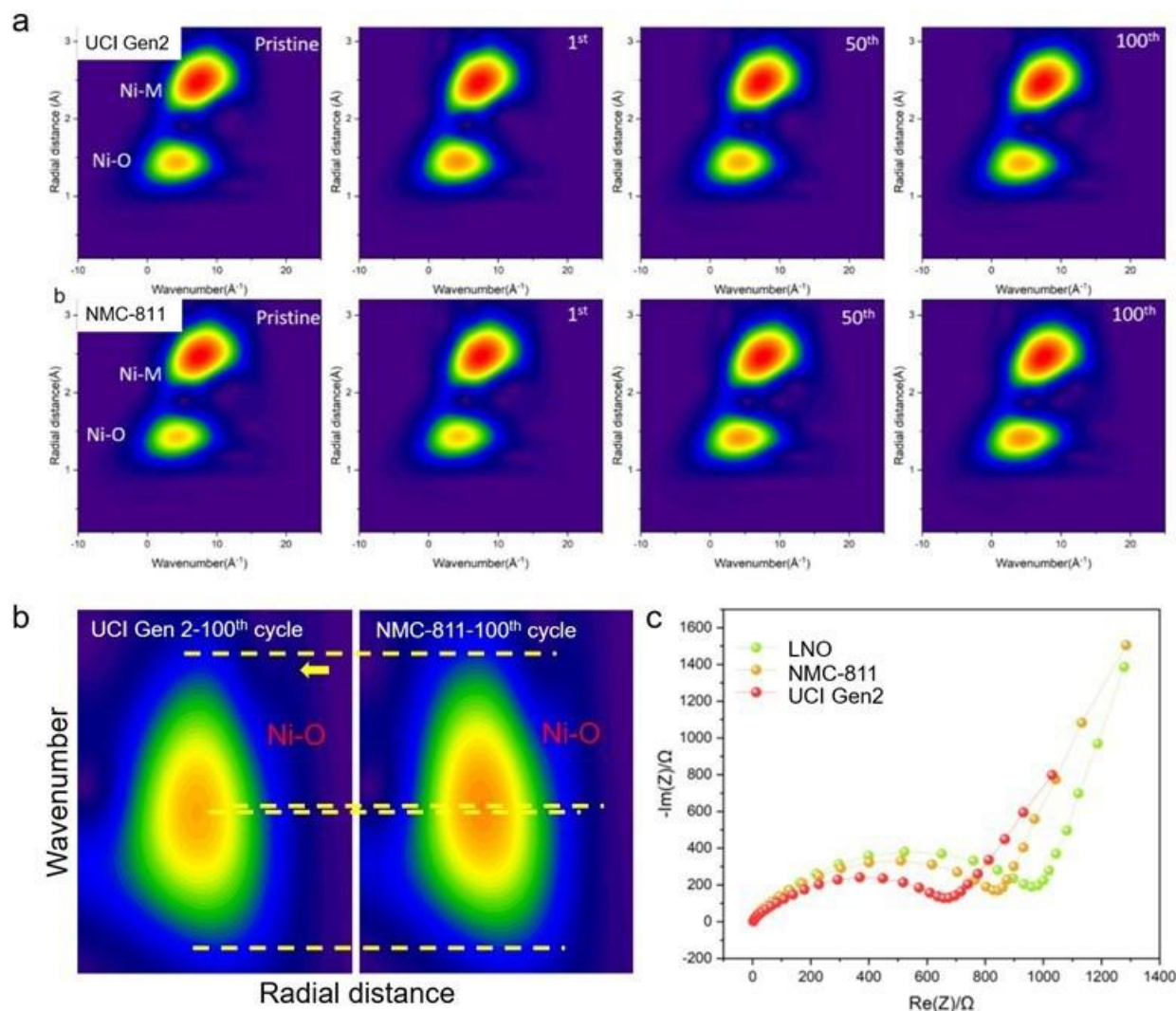


Figure XI.3.3 (a) Wavelet-transformed Ni-K edge EXAFS of UCI Gen 2 and NMC-811 cathode after different cycles. (b) Detailed comparison of the Ni-O bonding in both cathodes. (c) Electrochemical impedance spectroscopy (EIS) of LNO, NMC-811, and UCI Gen2 cathodes under the same cell conditions.

During thermal conditions or long-term electrochemical cycling process, oxygen release will lead to the formation of rock salt domains, accelerating the formation of nano-cracks owing to the lattice mismatch between the layered structure and rocksalt phase. These nano-cracks will nucleate, propagate, and finally lead to chemomechanical breakdown of layered cathodes. For example, as shown in Figure XI.3.4a,b, when heated up to 350°C, substantial cracks which preferentially lying on the (003) planes form in delithiated NMC-811 cathode; in stark contrast, there is no obvious crack formation in the delithiated UCI Gen2 primary particles, instead, only small void/pore are observed. This indicates that the thermal stability of the UCI Gen2 cathode is much more robust than the state-of-the-art NMC-811 cathode. To quantitatively evaluate the thermal stability of UCI Gen2 cathode in comparison with NMC-811, quantitative differential scanning calorimetry (DSC) was performed on both cathodes. Figure XI.3.4c shows the quantitative DSC results obtained by performing *in-situ* heating on both UCI-Gen2 and NMC-811 cathodes which are charged to the same cut-off voltage of 4.4V. To exclude the potential influence brought by the oxidation of aluminum foils, the experiments were performed with the protection of an argon atmosphere. The results show that the peak temperatures for UCI Gen2 and NMC-811 cathodes are 285 °C and 220 °C, respectively. With the electrode mass (kept the same for both cases) taken into consideration, the total enthalpy of exothermic peak of UCI Gen2 cathode is determined as 530 J/g, much lower than that of the NMC-811 cathode (983.9 J/g). The

quantitative results, which agree well with the previous TGA-MS measurements, demonstrate that the UCI Gen2 cathode has superior thermal stability and oxygen retention capability. Similar to the oxygen loss under thermal abuse conditions, long-term electrochemical cycling also results in oxygen loss and thereby surface rock salt reconstruction. To evaluate the structural stability of the UCI Gen2 cathode, the surface reconstruction of UCI Gen2 and NMC-811 after long-term cycling were characterized and compared. Figure XI.3.4d shows representative atomic structures of the cycled NMC-811 and UCI Gen2 primary particles. It is seen that, for the NMC-811, after long cycle, a thick (more than 15nm) degradation layer composed of rock salt phase and O1 phase forms on the particle's surface; in contrast, after long-term cycling, the O3 layered structure of UCI Gen2 cathode is well preserved, with only a thin layer (~3-4 nm in thickness) of rock salt formed on the surface. The above results, consistent with the thermal stability tests, indicates that the UCI Gen2 cathode is more robust than NMC-811 cathode in terms of oxygen retention.

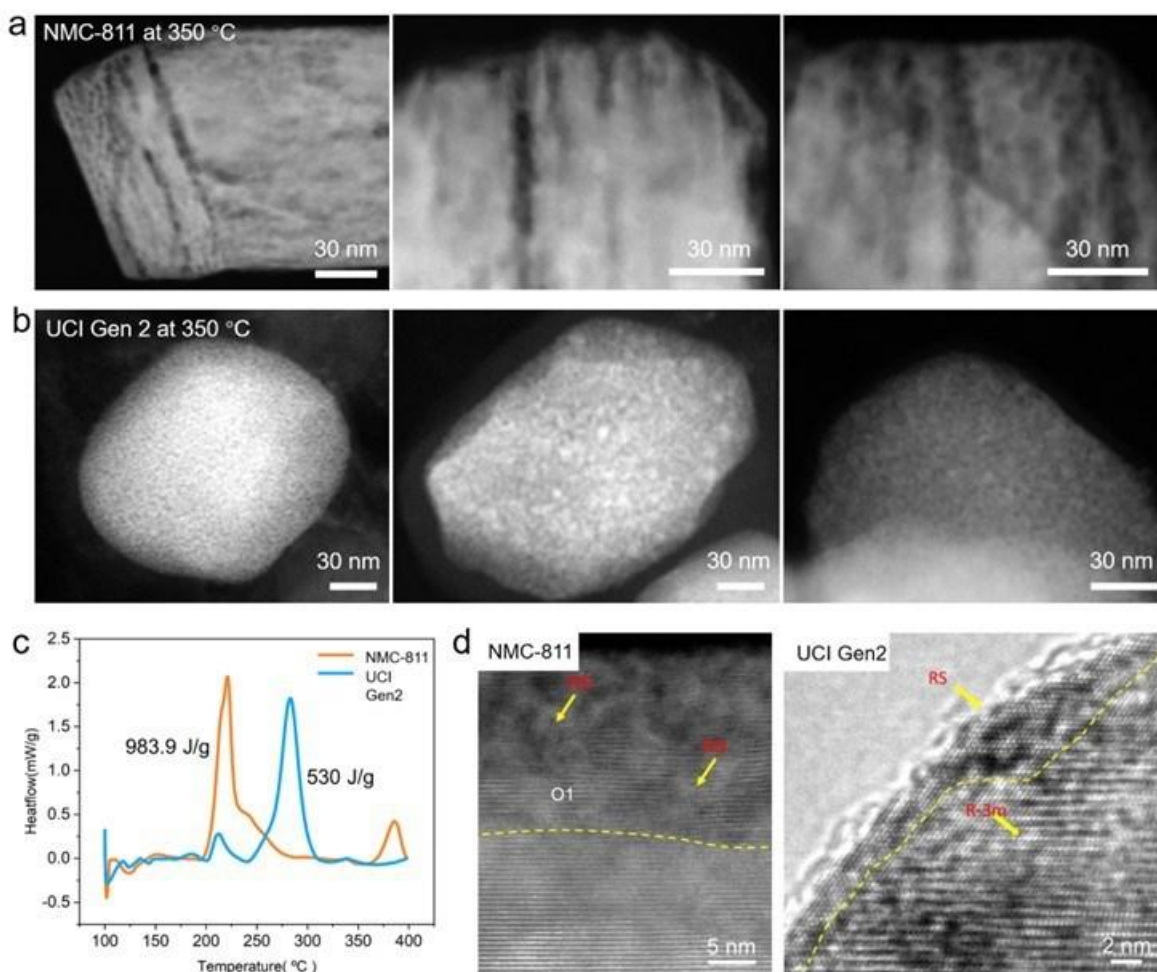


Figure XI.3.4 (a,b) HAADF-STEM images of delithiated NMC-811 and UCI Gen2 cathodes after at thermal abuse treatments at the same conditions. (c) Quantitative DSC result of charged (cut-off voltage 4.4V) NMC-811 and UCI Gen2 cathodes. (d) Atomic-resolution images showing the surface reconstruction of NMC-811 and UCI Gen2 cathodes after long-term cycling.

The dissolution of transition metals (TMs) on the graphite anode during long cycling was quantitatively investigated by synchrotron-based X-ray fluorescence (XRF). The UCI Gen2 cathode and NMC-811 (Provided by CAMP) cathode with the same loading ($3\text{mg}/\text{cm}^2$) are cycled in coin-type full cells between 2.5V-4.3V using Graphite (provided by CAMP) as anode. The graphite anodes after cycling at the same conditions (~250 cycles) are characterized using synchrotron-based XRF. Ni maps derived from the Ni-K edge of both anodes are shown in Figure XI.3.5. Graphite anode paired with NMC-811 has a significantly higher average Ni

concentration ($\sim 0.977 \mu\text{g}/\text{cm}^2$); in contrast, the graphite anode paired with UCI Gen2 cathode has an average Ni content as low as $0.682 \mu\text{g}/\text{cm}^2$, nearly 30% less than that in NMC-811 cathode. This indicates that the UCI Gen2 cathode has much higher stability in terms of mitigating TMs dissolution.

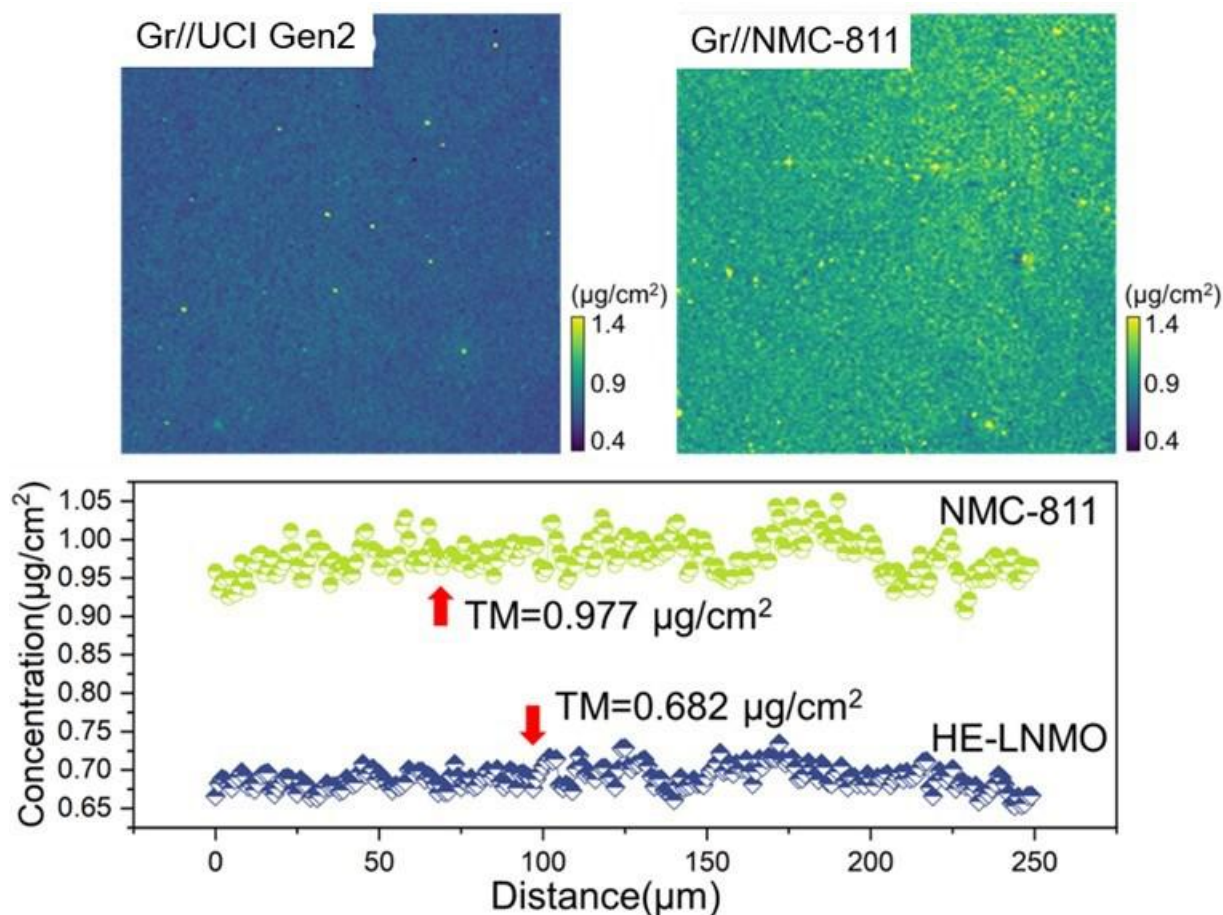


Figure XI.3.5 XRF result of Ni dissolution on Gr anodes (~ 250 cycles). Cycling condition: 2.5V-4.4V vs. Gr at 1C. Field of view: $0.25\text{mm} \times 0.25\text{mm}$.

Development of UCI-Gen2' cathode material.

we extended the doping strategies by replacing all the doping elements in UCI Gen2 cathode with a completely different set of dopants with similar concentrations. The new cathode is hereafter denoted as UCI Gen2' cathode. EDS elemental mapping in Figure XI.3.6 shows that Dopant 2, Dopant3, and Dopant4 are slightly enriched on the surface while Dopant1 is uniformly distributed across the primary particles. Figure XI.3.7 shows the second charge/discharge curve and dQ/dV curve of UCI Gen2' cathode compared with that of NMC-811. The results show that 195 mAh/g capacity can be delivered within 2.5V-4.4V, and the H2-H3 phase transition is significantly suppressed and delayed by 70mV in UCI Gen2' cathode. Long-term electrochemical tests (Figure XI.3.7) show that the UCI Gen2' cathode has better cycling stability than NMC-811 in half-cells. These results are obtained without fine optimization. We anticipate that with further calcination optimization, the performance of the UCI Gen2' cathode can be further improved.

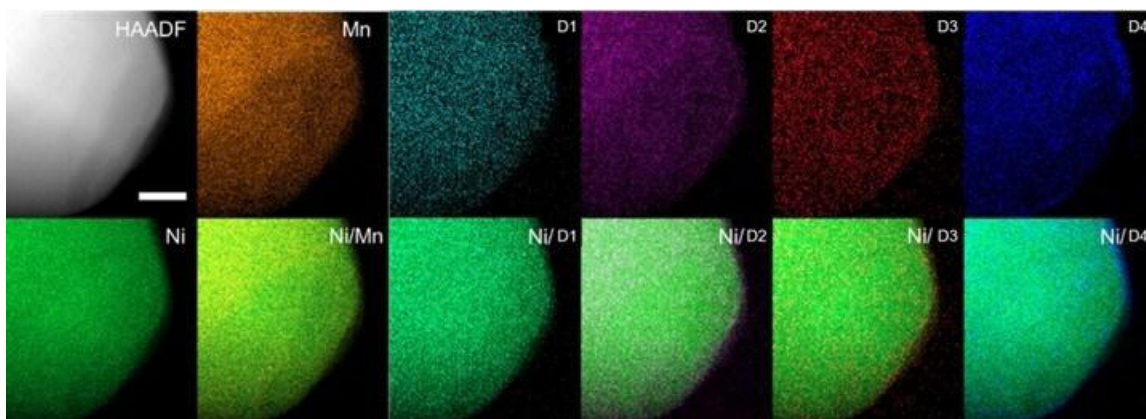


Figure XI.3.6 EDS elemental maps of UCI Gen2' cathode. The result shows similar element distribution as that in UCI Gen2 cathode.

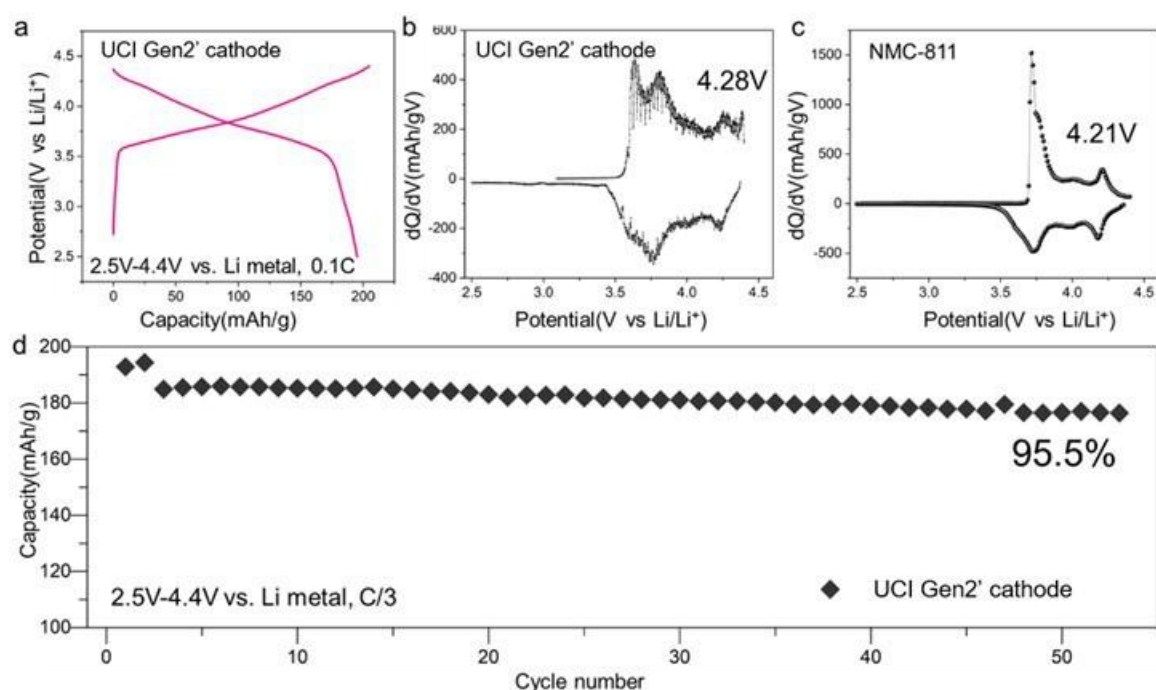


Figure XI.3.7 Electrochemical performance of UCI Gen2' cathode. a, charge/discharge profile of UCI Gen2' cathode. b-c, dQ/dV profile of UCI Gen2' cathode and NMC-811. d, cycling performance in half-cell.

Mechanistic study on the degradation pathway of a 'quasi' single-crystalline NMC-811 (QSC-811).

We extended the doping strategies by replacing all the doping elements in UCI Gen2 cathode with a completely we continued mechanistic study on the degradation pathway of a 'quasi' single-crystalline NMC-811 (QSC-811) in comparison with polycrystal (PC-811) and single-crystalline NMC-811 (NMC-811) cathodes. Electrochemical performances of SC-811, QSC-811, and PC-811 were evaluated and compared. Figure XI.3.8a shows the charge/discharge profile of different types of NMC-811. The result shows that the discharge capacity of SC-811 and QSC-811 is 209.5 mAh/g and 212.7 mAh/g, comparable with the 216.6 mAh/g of PC-811. This suggests that by tuning the "two-step" synthesis condition, the SC-811 and QSC-811 cathodes are capable to deliver discharge capacity comparable to the polycrystalline counterpart. However, as a well-known dilemma, as the number of grain boundaries decreases, the rate performance is getting worse owing to the sluggish bulk diffusion. The rate capacity shows that at 5C rate current (1C is set to 200mA/g), QSC-811 and SC-811 retain only 61.2% and 64.1% of their discharge capacity at 0.1C respectively,

significantly lower than the 69.3% of PC-811. This result is further evidenced by the galvanostatic intermittent titration technique (GITT) measurement shown in Figure XI.3.8c, showing that the Li-ion diffusion constant of PC-811 is slightly higher than that of QSC-811 and SC-811. Differential capacity (dQ/dV) curves of the initial charge/discharge cycle (Figure XI.3.8b) shows that the H2-H3 redox peak intensities in both SC-811 and QSC-811 are reduced compared with PC-811. This result indicates that the detrimental H2-H3 phase transition is to some extent suppressed in SC-811 and QSC-811 compared with PC-811. It's noted that although the H2-H3 redox peak intensity in QSC-811 is close to that of the SC-811, the peak position shifts to a more positive potential, indicating the mitigation of the H2-H3 phase transition during the delithiation of QSC-811. The cycling performances of the three types of NMC-811 cathodes are evaluated in 2032-type coin cells with Li chips as anodes (2.5V-4.4V, C/3). Figure XI.3.8d shows that the capacity retention of SC-811, QSC-811 and PC-811 after 100cycles are 92.6%, 79.5% and 79.2%, respectively. SC-811 delivers better cycling retention compared with QSC-811 and PC-811, which is in agreement with many reports on single-crystalline NMC cathodes.

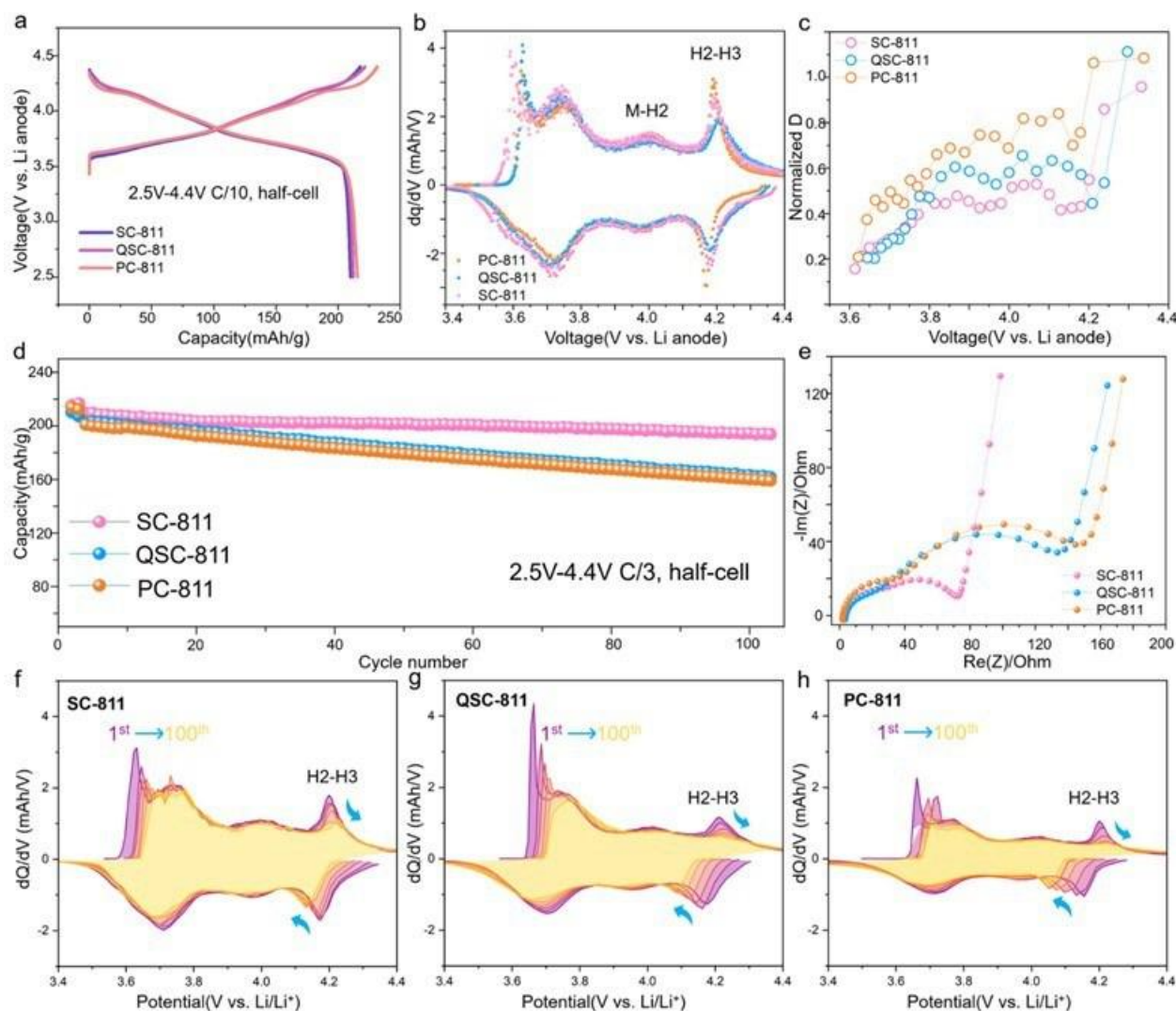


Figure XI.3.8 (a) Charge/discharge curve of PC-811, QSC-811 and SC-811, respectively. (b) dQ/dV curves of initial cycle. (c) Relative Li ion diffusion constant of three cathodes, respectively. (d) Long-term cycling stability (2.5V-4.4V, C/3). (e) EIS curve of after long cycling. (f-h) dQ/dV evolution with cycling.

To evaluate the impact of residual GBs on the phase transition during long-term cycling, dQ/dV curves of SC-811, QSC-811, and PC-811 at different cycling stages are performed. The results in Figure XI.3.8f-h show that

after 100 cycles, the H2-H3 redox peak of SC-811 remains prominent, while the corresponding redox peaks in both QSC-811 and PC-811 almost disappeared, indicating that more irreversible phase transition occurred during cycling in QSC-811 and PC-811. Moreover, the H2-H3 redox peaks in QSC-811 and PC-811 polarized significantly compared to SC-811 during long-term cycling, suggesting that both QSC-811 and PC-811 suffer higher impedance, which are usually associated with intergranular microcrack formation. Electrochemical impedance spectroscopy (EIS) in Figure XI.3.8e evidenced that after cycling, the impedance behavior in QSC-811 is close to PC-811 rather than SC-811. The above electrochemical performances show that although the residual GBs in the ‘quasi’-single-crystalline cathode didn’t cause serious initial capacity loss, they are prone to promote both the interfacial impedance and irreversible phase transition.

Transmission X-ray microscopes (TXM) tomography was applied to better visualize the degradation behavior of these residual GBs. As shown in Figure XI.3.9a, 3D reconstruction of a typical secondary particle of PC-811 shows that severe micro-cracks are formed after cycling, in agreement with the increased impedance and polarization in Figure XI.3.8h. As for SC-811, the single-crystalline particles remain intact as shown in Figure XI.3.8c, and no obvious crack forms owing to the absence of internal boundary. Interestingly, in cycled QSC-811 shown in Figure XI.3.9b, a few micro-cracks (usually 2~3 cracks) are observed in a single particle, which is analogous to the crack in PC-811. In general, single-crystalline cathode is proved to be crack-free during cycling because the anisotropic strain will no longer accumulate inside the particles. Nevertheless, these unobtrusive GBs in QSC-811 will lead to the inhomogeneous volume change, which breaks the QSC-811 into several primary particles.

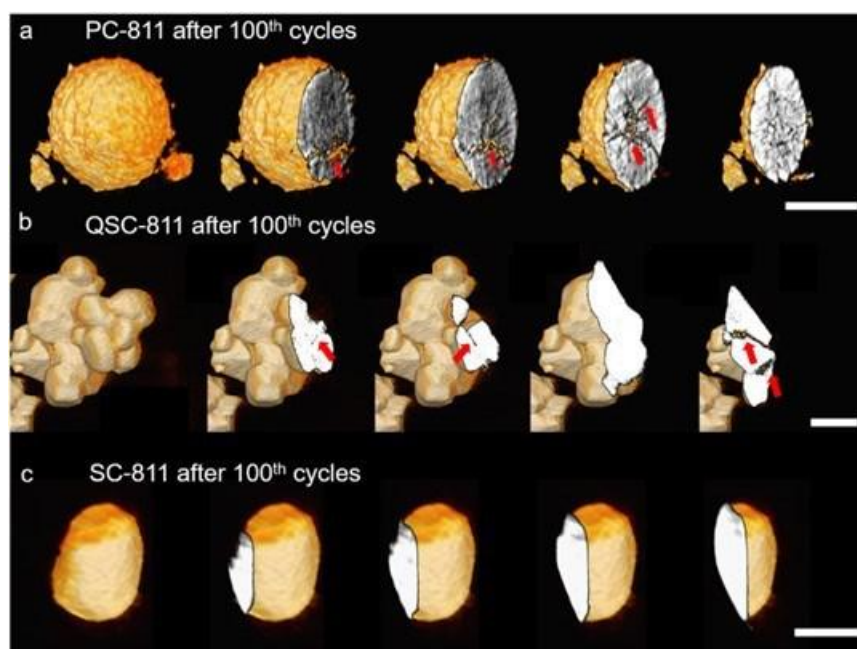


Figure XI.3.9 TXM tomography of long-term cycled PC-811, QSC-811 and SC-811. scale bar, 2 μ m.

Atomic resolution HAADF-STEM is performed to investigate the origins of increased impedance and polarization in QSC-811. As shown in Figure XI.3.10a, FIB cross-section shows that SC-811 cathode particle remains uncracked after cycling. Although a rocksalt reconstruction layer is formed on the surface, this layer is relatively thin and uniform with a thickness less than 5nm as shown in Figure XI.3.10b,c. In stark contrast, QSC-811 shows distinct and severe cracks after cycling shown in Figure XI.3.10d, matching well with the TXM result. The high-resolution images in Figure XI.3.10e-f show that the surface reconstruction layer around the crack is rather thick (more than 20nm) and disordered, with randomly distributed O1-stacking faults, edge dislocations, and rock salt phase. Next, AtomSegNet software based on deep-learning is employed to perform atomic column localization and segmentation. The super-resolution image in Figure XI.3.10g shows that a

large area of O1 stacking faults (highlighted in the upper right panel) along with prominent lattice distortion (lower right panel) are observed in the cycled QSC-811. However, as indicated in Figure XI.3.10h, SC-811 shows much more uniform surface reconstruction after cycling. Despite the thin layer of rocksalt phase and Li/TM interlayer mixing (upper right panel), most of the surface area remains intact R-3m layered structure (lower right panel). Compared with the uniform surface layer in SC-811, QSC-811 shows a much more unfavorable surface reconstruction layer. This unusual surface reconstruction indicates that the residual GBs not only break the intact particle into several primary particles with smaller sizes, more importantly, they also make the fresh surface around the cracks more “vulnerable” compared with the pristine surface. As a result, this thick and disordered surface reconstruction layer remarkably increases the impedance in QSC-811.

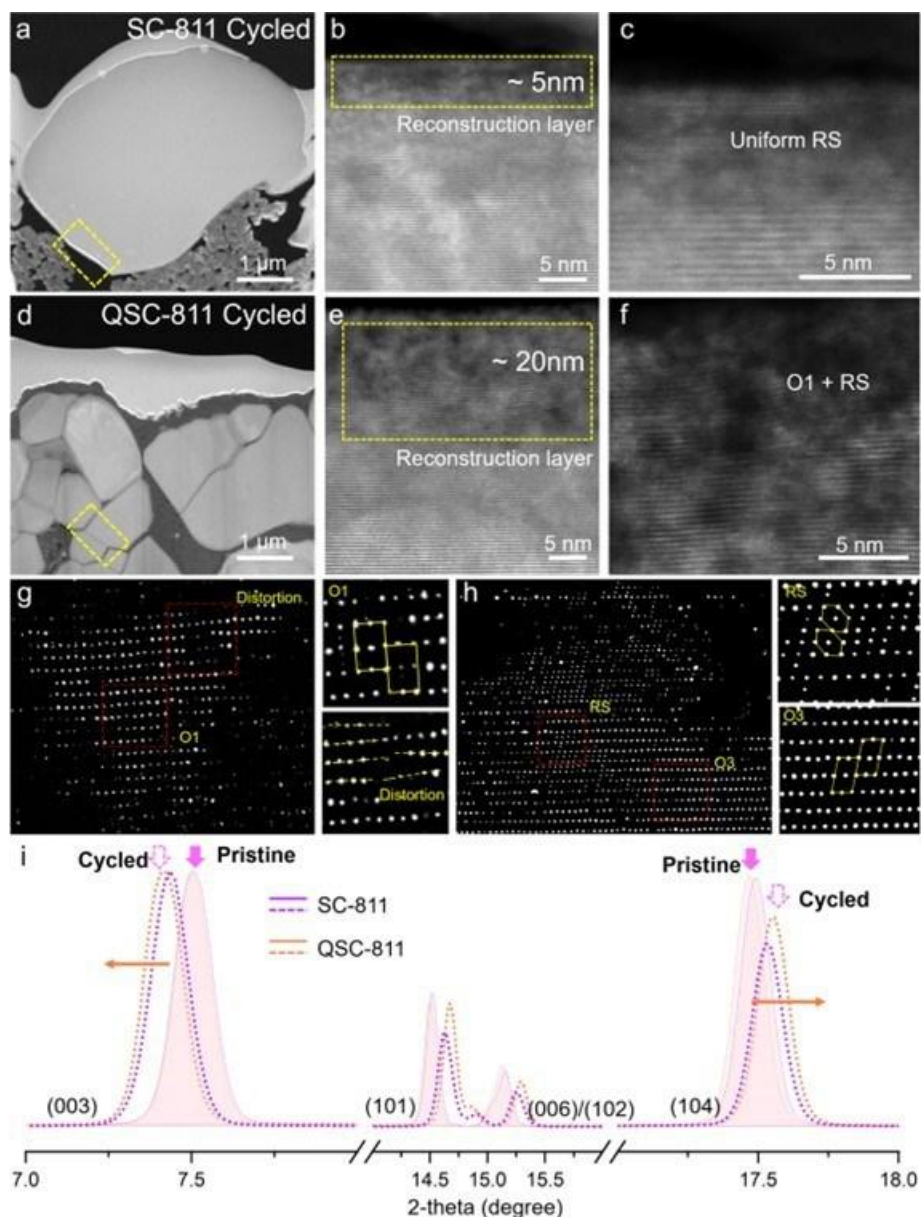


Figure XI.3.10 (a-c) HAADF-STEM images of cycled SC-811. (d-f) HAADF-STEM images of cycled QSC-811. (g-h) Super-resolution image corresponding to the (c) and (f) obtained by AtomSegNet. (i) XRD of SC-811 and QSC-811 before and after cycling (Pristine: solid line; Cycled: dashed line).

Conclusions

- We optimized the synthesis of UCI Gen2 cathode and performed electrochemical evaluations on the optimized UCI Gen2 cathode. A remarkable discharge capacity of ~210 mAh/g and an initial Columbic efficiency (CE) of ~94% were obtained.
- We further studied the thermal stability and cycling stability of UCI-Gen2 cathode in comparison with NMC-811 using quantitative DSC, TEM, and synchrotron-based X-ray techniques.
- The dissolution of transition metals (TMs) in UCI Gen2 cathode on the graphite anode during long cycling was quantitatively investigated by synchrotron-based X-ray fluorescence (XRF).
- The rate performance of UCI Gen2 cathode was evaluated in a typical coin cell from the rate of 0.1C to 5C (~3mg/cm² loading; same rate current for charge and discharge). The result (Figure 1) shows that ~70% capacity is achieved at 2C, and 55% capacity is achieved at 5C, comparable to many reported bare NMC-811 materials, which usually deliver ~60% capacity at 5C.
- We performed electrochemical tests in half-cells at 50 °C to compare the capacity and thermal stability of NMC-811 and UCI Gen2 cathode.
- UCI Gen2 cathode has been sent to ALE for project completion cell (PCC) fabrication.
- We extended the doping strategies by replacing all the doping elements in UCI Gen2 cathode with a completely different set of dopants with similar concentrations. UCI Gen2' cathode delivers an initial capacity of 195 mAh/g within 2.5V-4.4V without optimization, and long-term electrochemical tests show better cycling stability than NMC-811 in half-cells.
- We performed mechanistic study on the degradation pathway of a 'quasi' single-crystalline NMC-811 (QSC-811) in comparison with polycrystal (PC-811) and single-crystalline NMC-811 (NMC-811) cathodes. Our study shows that the residual GBs in QSC-811 caused by insufficient calcination time dramatically exacerbate the cathode's chemomechanical instability and cycling performance.

Key Publications

1. R. Zhang[#], C.Y. Wang[#], P. Zou, R. Lin, L. Ma, L. Yin, T. Li, W. Xu, H. Jia, Q. Li, S. Sainio, K. Kisslinger, S. Trask, S.N. Ehrlich, Y. Yang, A.M. Kiss, M. Ge, B. Polzin, S.J. Lee, W. Xu, Y. Ren, H.L. Xin*. Compositionally complex doping for zero-strain zero-cobalt layered cathodes. *Nature*, 610, 67-73 (2022).
2. R. Zhang[#], C.Y. Wang[#], M.Y. Ge, H.L. Xin*. Accelerated Degradation in a Quasi-Single-Crystalline Layered Oxide Cathode for Lithium-Ion Batteries Caused by Residual Grain Boundaries. *Nano Letters*, 22(9), 3818-3824 (2022).
3. C.Y. Wang, R. Zhang, F. Lin, L. Mu, H.L. Xin. In-Situ TEM Study of Chemo-Mechanical Degradation Pathways of LiNiO₂-Derived Layered Oxide Cathodes for Lithium-Ion Batteries. *Microscopy and Microanalysis*, 28 (S1), 172-174 (2022).
4. C. Wang, R. Zhang, C. Siu, M. Ge, K. Kisslinger, Y. Shin, and H. L. Xin*, Chemomechanically stable ultrahigh-Ni single-crystalline cathodes with improved oxygen retention and delayed phase degradations, *Nano Letters*, 21, 9797-9804 (2021)
5. H. Jia, Y. Xu, L. Zou, P. Gao, X. Zhang, B. Taing, B. E. Matthews, M. H. Engelhard, S. D. Burton, K. S. Han, L. Zhong, C. Wang, W. Xu*, Sulfone-based Electrolytes for High Energy Density Lithium-ion Batteries, *Journal of Power Sources*, 527, 231171 (2022).
6. J.-M. Kim, Y. Xu, M. H. Engelhard, J. Hu, H.-S. Lim, H. Jia, Z. Yang, B. E. Matthews, S. Tripathi, X. Zhang, L. Zhong, F. Lin, C. Wang, W. Xu*, Facile Dual-Protection Layer and Advanced Electrolyte Enhancing Performances of Cobalt-Free/Nickel-Rich Cathodes in Lithium-Ion Batteries, *ACS Applied Materials & Interfaces*, 14, 17405-17414 (2022).

XI.4 High-Nickel Cathode Materials for High-Energy, Long-Life, Low-Cost Lithium-Ion Batteries (UTA)

Arumugam Manthiram, Principal Investigator

University of Texas at Austin
Texas Materials Institute
University of Texas at Austin
Austin, TX 78712
E-mail: manth@austin.utexas.edu

Shriram Santhanagopalan, Co-Principal Investigator

National Renewable Energy Laboratory
15013 Denver West Parkway
Golden, CO 80401
E-mail: Shriram.santhanagopalan@nrel.gov

Haiyan.Croft, DOE Technology Development Manager

U.S. Department of Energy
E-mail: Haiyan.Croft@ee.doe.gov

Start Date: October 1, 2018	End Date: December 31, 2022	
Project Funding: \$3,000,000	DOE share: \$2,400,000	Non-DOE share: \$600,000

Project Introduction

Despite the success of lithium-ion technology, energy and cost requirements are extremely stringent for electric vehicle (EV) applications. Therefore, there is a need to further enhance the energy density of layered oxide cathodes ($\text{Li}[\text{Ni}_a\text{Co}_b\text{Mn}_c]\text{O}_2$ with $a + b + c = 1$, denoted as NCM-*abc* and $\text{Li}[\text{Ni}_{1-x-y}\text{Co}_x\text{Al}_y]\text{O}_2$, denoted as NCA). Moreover, the substantial dependence on the scarce and costly cobalt in these cathodes (*e.g.*, 12 wt.% Co in NCM-622) needs to be lowered for sustained mass market penetration of EVs. With the currently employed cathode formulations, demand for Co could outstrip supply by 2030 with surging global EV production, setting the stage for far higher prices. Although Co-free cathodes, such as LiFePO_4 and LiMn_2O_4 exist, their energy density cannot meet the requirements of next-generation EVs.

This project is focused on developing low-cobalt and cobalt-free, high-nickel layered $\text{LiNi}_{1-x}\text{M}_x\text{O}_2$ ($\text{M} = \text{Mn}, \text{Al}, \text{Mg}, \text{Zr}, \text{Ta}, \text{etc.}$ and $x \leq 0.15$) oxide cathode materials for lithium-ion batteries for EVs. With these high-nickel cathodes, high energy, high power, long lifetime over a wide temperature range, as well as excellent safety under abuse can be prioritized for varying market needs through careful compositional tuning. These efforts will also reduce or even eliminate the dependence of lithium-ion batteries on cobalt, thus leading to more secure supply chains, lower cost, and less adverse impacts on the environment. The cathode materials and understanding developed in this project will contribute to advancing the designs of low-cobalt or cobalt-free, high-energy-density lithium-ion batteries.

Objectives

The overall goal of this project is to achieve low-cobalt or cobalt-free lithium-ion cells with the following performance targets (See Table XI.4.1):

Table XI.4.1 Performance Targets

Beginning of Life Characteristics at 30 °C	Cell Level	Cathode Level
Useable Specific Energy @ C/3		≥ 600 Wh/kg
Calendar Life (<. energy fade)	15 Years	
Cycle Life (C/3 deep discharge with < 20% energy fade)	1,000	
Cobalt Loading		≤ 50mg/Whr
Cost	≤ \$100/kWh	

Approach

Low-cobalt and cobalt-free high-nickel layered $\text{LiNi}_{1-x-y}\text{M}_x\text{Co}_y\text{O}_2$ ($x \leq 0.15$, $y < 0.06$, $M = \text{Mn, Al, Mg, Zr, Ta, etc.}$) oxides are developed and assessed as cathodes in lithium-ion batteries with graphite anode. The materials are synthesized by hydroxide co-precipitation and lithiation annealing to maintain good thermal and cycling stability while achieving the 600 Wh kg^{-1} energy goal. Selected compositions are also subjected to atomic layer deposition (ALD) coatings at NREL and assessed with compatible ethylene carbonate (EC)-free electrolyte systems. Based on the results, an optimal cathode was selected to produce twenty-one 2 Ah pouch cells to deliver to DOE for independent evaluation/validation. Detailed experimental approaches for Year 4 are below:

1. Dopant Survey: Final evaluation of dopant effects on the electrochemical performance, surface stability, and safety of Co-free $\text{LiNi}_{1-x}\text{M}_x\text{O}_2$ ($x \leq 0.15$, $M = \text{Mn, Al, Mg, and more}$).
2. Synthesis Scale-Up: optimization and scale-up of best-performing $\text{LiNi}_{1-x}\text{M}_x\text{O}_2$ ($x \leq 0.15$, $M = \text{Mn, Al, Mg, and more}$) and delivery of 2 kg of selected cathode material to Tesla Inc. for fabrication of 2 Ah pouch cells.

Results

In conjunction with our efforts to scale up cathode synthesis in preparation for the final deliverable, we continued to investigate the stabilizing effect of dopants in high-Ni cathode materials. Our previous research indicates that Al and Mg are beneficial to the surface and structural stabilities of high-Ni cathode materials, yielding a wide combination of Al-Mg co-doped NMC composition. Besides cationic substitution, anionic substitution of oxygen with fluorine is also beneficial since fluorine bonds tightly with transition-metal ions and lowers their average valence state. Through fluorinating $\text{LiNi}_{0.95}\text{Mn}_{0.015}\text{Co}_{0.02}\text{Al}_{0.01}\text{Mg}_{0.005}\text{O}_2$ (NMCAM), we showed that 1% F-doping in high-Ni cathode materials yields better surface stability by reducing surface reactivity and polarization growth. We incorporated F into NMCAM using a solution-based method by mixing NH_4F and lithiated NMCAM in water and then reheating the sample at 400°C under oxygen flow. NH_4F reacts with surface residual species, such as LiOH and Li_2CO_3 , to form LiF on the surface of NMCAM. The measured residual lithium content of NMCAM was reduced after fluorination, indicating that NH_4F reacts with the surface residual lithium species successfully.

The electrochemical performance of 1F-NMCAM was studied in half cells and full cells. NMCAM and 1F-NMCAM delivered an initial discharge capacity of 224 and 195 mAh g^{-1} at C/3 rate, respectively (Figure XI.4.1a). The low initial discharge capacity for 1F-NMCAM is attributed to the insulating nature of fluorine at the surface. The voltage profiles for both materials look similar, but a slight charge/discharge overpotential is observed for 1F-NMCAM, which is attributed to the presence of a resistive LiF layer on the surface. The corresponding dQ/dV^{-1} curves show that fluorine coating assists in suppressing the phase transitions, especially the H2-H3 transition at high voltage (Figure XI.4.1b). In half cells, NMCAM retains 89% of its maximum capacity, while 1F-NMCAM retains 97% of its maximum capacity after 100 cycles (Figure XI.4.1c). The increase in capacity seen in 1F-NMCAM during initial cycles can be attributed to the hindered lithium diffusion kinetics by the insulating LiF coating, which is then alleviated later upon cycling due to electrolyte penetration into the bulk through microcracks at high state-of-charge. Rate performance of 1F-NMCAM is similar to the uncoated NMCAM sample (Figure XI.4.1d). We further examined the cycling stability of 1F-NMCAM in full cells with graphite anodes. The full cells were charged at C/3 rate and discharged at 1C rate

during cycling between 2.5 and 4.3 V. Higher voltage cutoff was utilized to exacerbate the surface reactivity of NMCAM so that the influence of fluorine coating can be distinguished. NMCAM delivers an initial discharge capacity of 197 mA h g⁻¹ as compared to 190 mA h g⁻¹ for 1F-NMCAM, which is consistent with half cells. The fluorine-coated sample exhibits a superior capacity retention of 71% at the end of 500 cycles whereas the uncoated sample exhibits a capacity retention of 59%. Polarization growth in the uncoated sample is higher than that of the coated sample, indicating that the LiF coating is effective in suppressing the grow of insulating surface species. The dQ dV⁻¹ plots for cycles recorded at C/3 rate before and at the end of cyclability tests are shown in Figure XI.4.2. For NMCAM, the reversibility in plateaus during charge and discharge decreased drastically, which can be attributed to rock salt formation and a thicker cathode-electrolyte interphase (CEI) formation at the surface (Figure XI.4.2b). On the contrary, dQ dV⁻¹ plots for fluorine coated sample showed high structural reversibility, suggesting that the surface coating also helps stabilize the layered structure and promotes high phase reversibility in high-Ni cathode materials (Figure XI.4.2d).

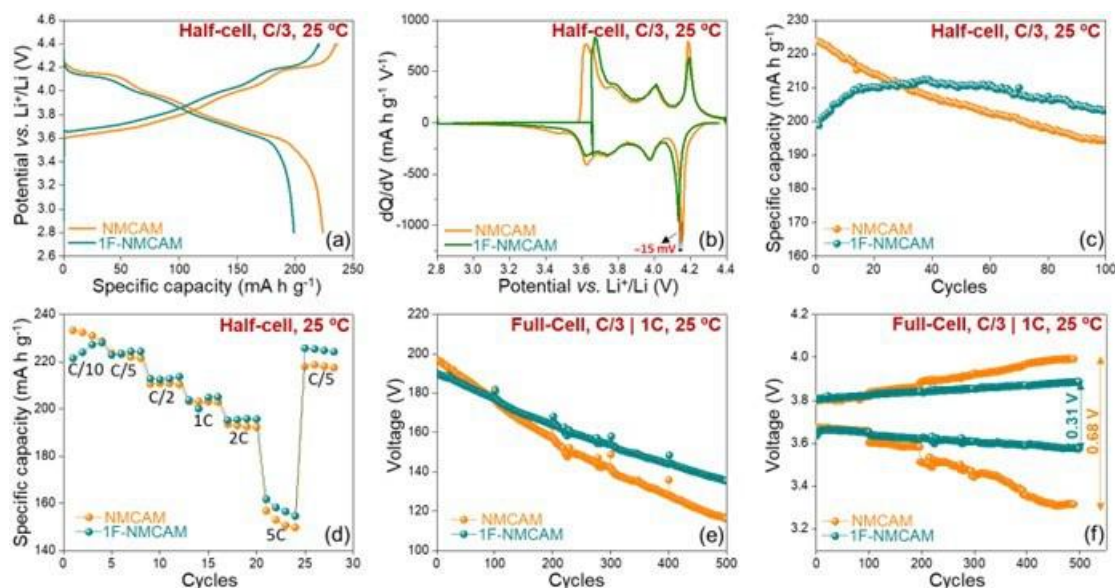


Figure XI.4.1 (a) First charge-discharge profiles of fluorine coated and uncoated samples in half-cell configuration, cycled at C/3 current rate at room temperature. The cycles were recorded after three formation cycles at C/10 current rate. (b) dQ dV⁻¹ curves corresponding to the first C/3 cycle. (c) Cycling performances of coated and uncoated samples in half cells at C/3 rate. (d) Rate capability of NMCAM and 1F-NMCAM. (e) Long-term cyclability of NMCAM and 1F-NMCAM in full cells cycled at C/3 charge and 1C discharge after three formation cycles. (f) Evolution of average charge and discharge voltages in full cells.

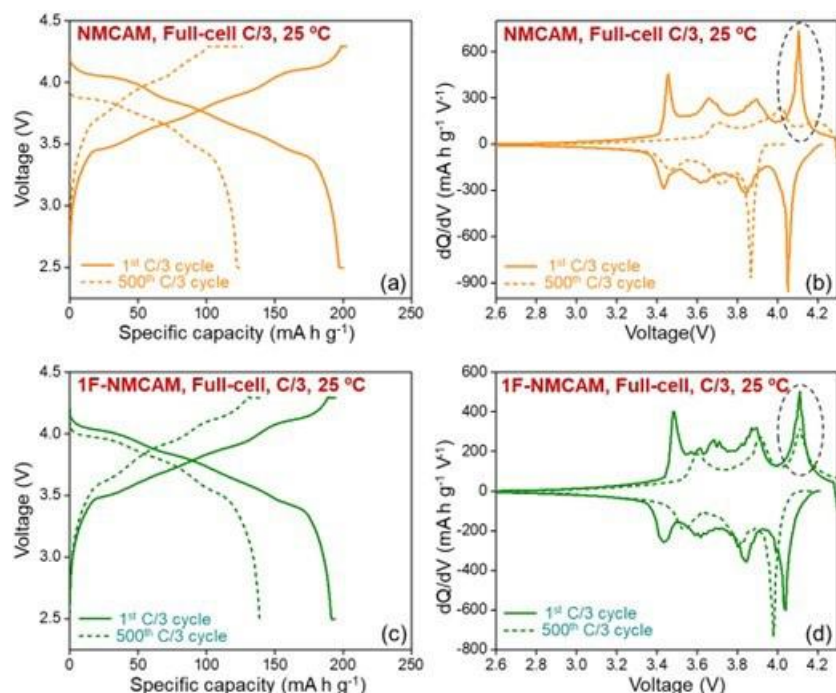


Figure XI.4.2 (a, b) Charge-discharge cycles recorded at C/3 rate before and after long-term cyclability for NMCAM and their corresponding dQ dV⁻¹ plots. (c, d) Charge-discharge cycles recorded at C/3 rate before and after long-term cyclability for 1F-NMCAM and their corresponding dQ dV⁻¹ plots.

Analysis of the cycled particle morphologies revealed little cracking in either sample. Instead, surface reactivity is the primary mechanism for performance fade in high-Ni cathodes. Surface reactivity of high-Ni cathode materials are accompanied by rock-salt formation, leading to a loss of active material and impedance growth. We examined the structural changes on the surface of 1F-NMCAM with high-angle annular dark-field scanning transmission electron microscopy (HAADF-STEM) imaging. Both samples show presence of cation mixing at the surface (Figure XI.4.3). Fast Fourier transform (FFT) was used to distinguish the rock-salt structure (red shade) from the layered structure (green shade). NMCAM shows 6 nm of rock-salt phase at the surface of the particle, while 1F-NMCAM contains only 2 nm of rock-salt phase on its surface. This further demonstrates the benefits of fluorine coating in reducing the surface reactivity of high-Ni cathode materials. In the future, we will combine our fluorination strategy with a formulated electrolyte to understand if both strategies can work synergistically to further improve the electrochemical performance of high-Ni cathode materials.

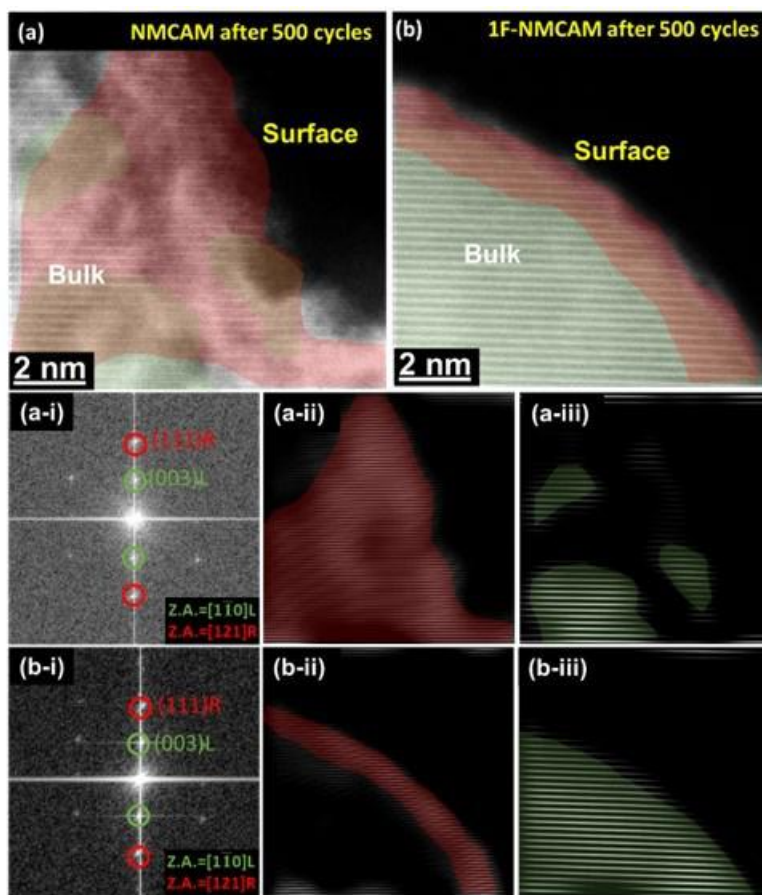


Figure XI.4.3 HAADF-STEM images acquired at the surface of (a) NMCAM and (b) 1F-NMCAM particles after 500 cycles. (a-i, b-i) Fast Fourier transformations of the area shown in a and b. R and L, respectively, corresponds to rock-salt and layered structures. (a-ii, a-iii) The areas corresponding to rock-salt and layered structure on the surface of NMCAM particle highlighted, respectively, in red and green. The areas were obtained by carrying out inverse FFT. (b-ii, b-iii) The areas corresponding to rock salt and layered structure on the surface of the 1F-NMCAM particle highlighted, respectively, in red and green.

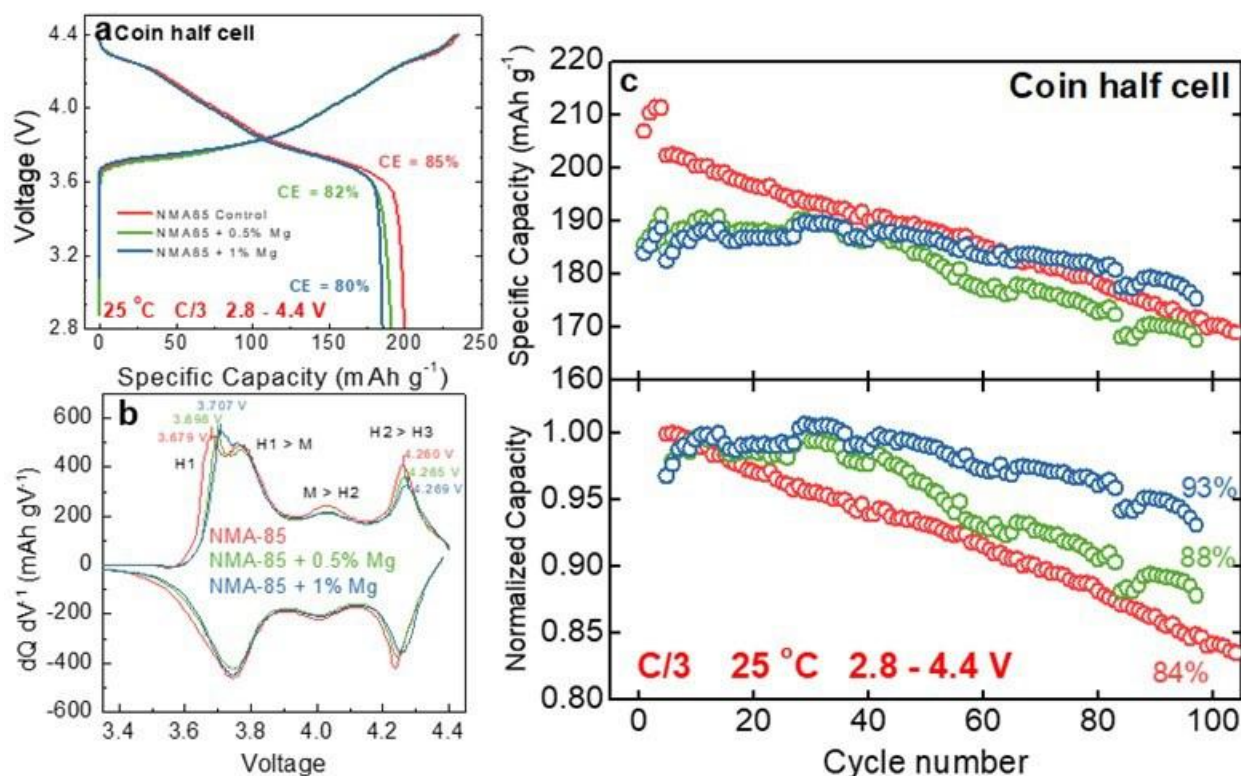


Figure XI.4.4 Electrochemical performances of NMA-85 at various levels of Mg incorporation in coin half cells. (a) Initial voltage profile at C/3 rate. (b) Corresponding differential capacity plot of the initial voltage profile. (c) Cycling performance and capacity retention over 100 cycles at C/3 rate.

In addition to fluorine doping, we also determined the optimal level of Mg inclusion to maximize performance of the final cathode composition. Mg has been shown to act as a pillaring ion, residing in the lithium plane and reinforcing the lattice against collapse at high SOC. A further desirable property of Mg is its facile incorporation into the coprecipitation process; Mg can be integrated during the initial precursor preparation and not as a foreign cation during calcination, greatly improving homogeneity. The electrochemical performances of pristine $\text{LiNi}_{0.85}\text{Mn}_{0.1}\text{Al}_{0.05}\text{O}_2$ (NMA-85) and NMA-85 with various concentrations of Mg incorporation are displayed in Figure XI.4.4. Increasing Mg content corresponds to a decrease in 1st cycle coulombic efficiency and discharge capacity. Furthermore, a decrease in the peak intensity and a shift to slightly higher potentials in the differential capacity plot corresponding to various phase transitions suggest a slight decrease in Li^+ diffusion kinetics, consistent with a higher valence ion present in the lithium plane. This is corroborated by the gradual increase in capacity during the first 20 cycles, which likely originates from an ordering of the Mg^{2+} ions within the lithium plane to the lowest energy configuration. The stability of these materials is improved to 93% capacity retention after 100 cycles, up from 84% retention in the undoped baseline. Mg, therefore, presents a simple means to improve the stability of a desired cathode when peak specific capacity is not the sole requirement.

The final composition selected for the end-of-project deliverable is $\text{Li}(\text{Ni}_{0.85}\text{Mn}_{0.10}\text{Al}_{0.05}\text{Mg}_{0.005})\text{O}_2$ (NMAM-85). We succeeded in producing and delivering 2 kg of NMAM-85 to Tesla Inc, pictured in Figure XI.4.5a. The material consists of a bimodal particle size distribution of 4 – 5 μm and 10 – 12 μm (Figure XI.4.5b). During the subsequent casting process, issues were encountered due to the delivered material containing a fraction of large agglomerates and small crucible fragments left over from synthesis. These unwanted impurities caused difficulties with the electrode casting process, causing some of the delivered material to go to waste. Sieving the cathode material addressed the issue, allowing enough electrodes for 16 large format pouch cells to be assembled. Preliminary cycling data performed in-house at Tesla are summarized in Figure XI.4.6 and Table XI.4.2. Cells were formed at 40°C and C/20 rate to promote uniform, stable

electrode/electrolyte interface formation. Subsequently, the cells were moved to a temperature-controlled chamber and cycled at 25°C, which resulted in unexpectedly low capacity, averaging 162 mA h g⁻¹ at the cathode level. DOE testing at INL stipulates the cells will be cycled at 30°C, and the cells at Tesla were cycled at this temperature to properly gauge their performance under the specified conditions. At this temperature, the cells achieve a cathode level specific capacity of 170 mA h g⁻¹. This corresponds to a cathode-level energy density of 630 Wh kg⁻¹, well in excess of the 600 Wh kg⁻¹ project goal. We are currently arranging for the cells to be shipped to INL for evaluation, and we expect them to arrive at INL in early December 2022.

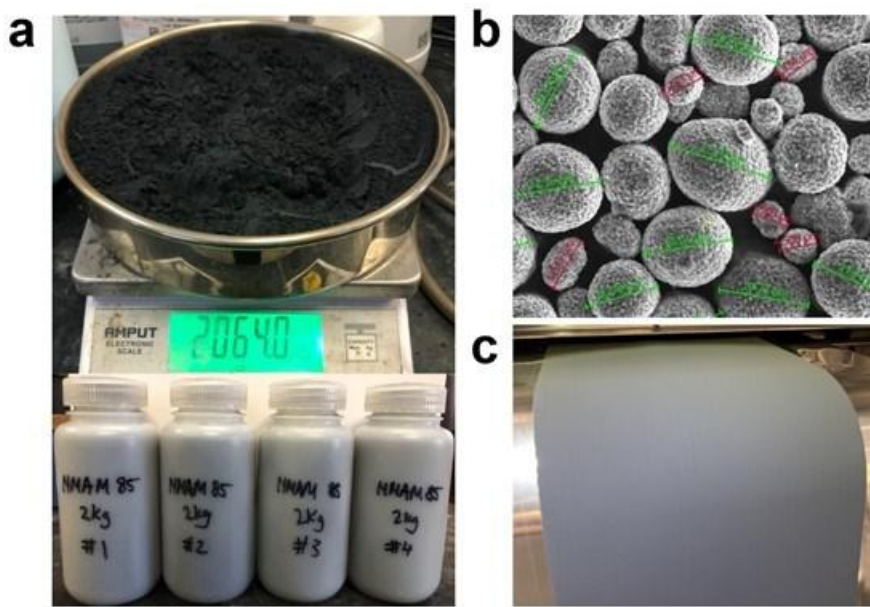


Figure XI.4.5 (a) photographs of the $\text{Li}(\text{Ni}_{0.85}\text{Mn}_{0.10}\text{Al}_{0.05}\text{Mg}_{0.005})\text{O}_2$ (NMAM-85) powder delivered to Tesla Inc, (b) SEM image of NMAM-85 with particle size measurement, and (c) casted cathode electrode done by Tesla Inc.

Table XI.4.2 Preliminary cycling metrics for the 2 Ah large-format pouch cells produced by Tesla Inc. using UT Austin's Co-free NMAM-85. The listed values are averages from the 16 individual cells.

C-rate	Temp, °C	Average cell capacity, Ah	Average cathode-level specific capacity, mA h g ⁻¹
C/20	40	2.22	194
C/10	25	1.98	173
C/3	25	1.86	162
C/3	25	1.86	162
C/3	25	1.86	162
C/10	30	2.25	196
C/3	30	1.97	171
C/3	30	1.94	169
C/3	30	1.95	170

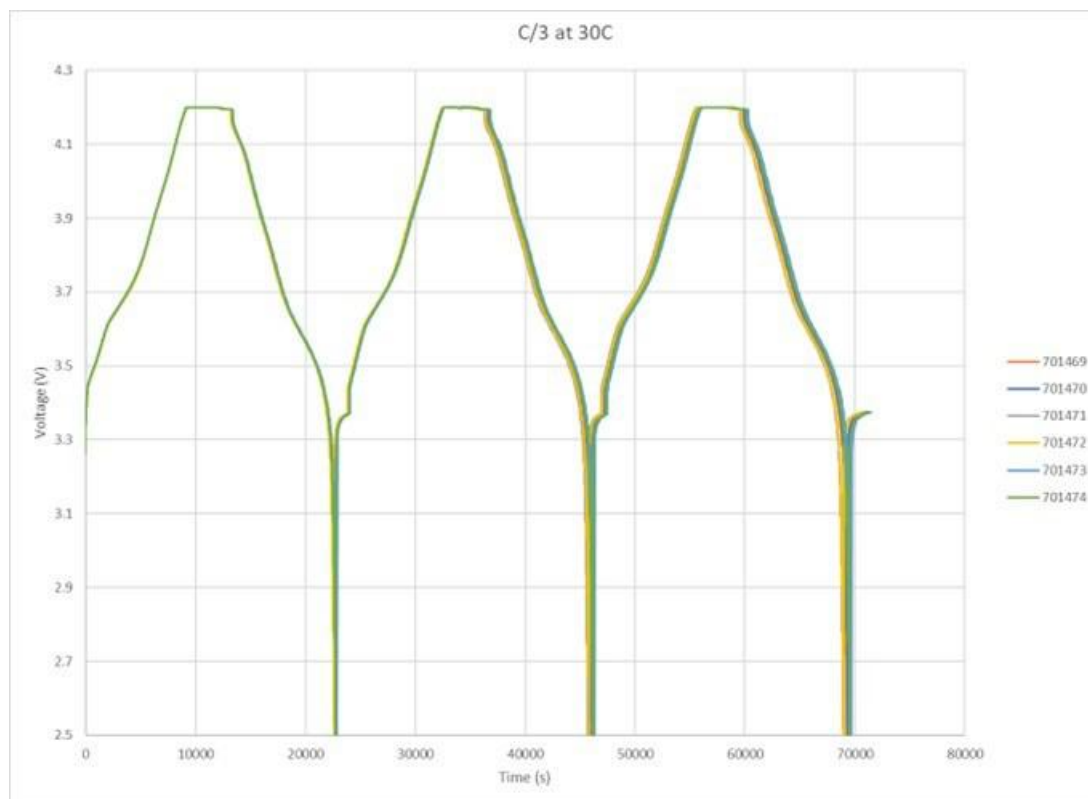


Figure XI.4.6 Voltage profiles of selected large-format pouch cells cycled between 2.5 and 4.2 V at C/3 rate, with cells maintained at 30°C. The average operating voltage on discharge is approximately 3.7 V.

Conclusions

In this year, UT Austin has explored various pathways to improve the performance and scale-up the synthesis of high-nickel layered oxide cathodes. Fluorine doping was found to be an effective strategy for improving the cycling stability and reduce the surface reactivity of high-nickel cathodes. Fluorine reacts with residual lithium species on the surface of the cathode, creating a stable LiF coating which passivates the surface. This greatly reduces the degree of electrolyte degradation that occurs during cycling, enabling superior cell lifetimes. Magnesium doping was also found to be beneficial in the chosen NMA for the final deliverable. Ultimately, a composition of $\text{LiNi}_{0.85}\text{Mn}_{0.10}\text{Al}_{0.05}\text{Mg}_{0.005}\text{O}_2$ (NMAM-85) was chosen to deliver to Tesla Inc. The synthesis of NMAM-85 was rigorously optimized to facilitate scale up of cathode production. The parameters for precursor coprecipitation were studied to ensure homogeneous deposition of hydroxide grains to produce dense, spherical particles. Crucible packing depths were optimized for high-yield calcination, allowing us to produce up to 600 g of cathode material in a single synthesis. The material was delivered to Tesla Inc. and Tesla fabricated into 2 Ah pouch cells, which show acceptable performance upon preliminary testing. The cells will be delivered to INL in the near future for DOE evaluation.

Key Publications

Reports

1. Four quarterly reports have been submitted to the DOE, one at the end of each quarter.

Publications

1. M. Yi, W. Li, and A. Manthiram, "Delineating the Roles of Mn, Al, and Co by Comparing Three Layered Oxide Cathodes with the Same Nickel Content of 70% for Lithium-ion Batteries," *Chemistry of Materials* **34**, 629-642 (2022).

2. Ruijun Pan, Zehao Cui, Michael Yi, Qiang Xie, Arumugam Manthiram, "Ethylene Carbonate-Free Electrolytes for Stable, Safer High-Nickel Lithium-Ion Batteries", *Advanced Energy Materials* **9**, 1901151: 1 - 11 (2022)
3. L. Sharma, M. Yi, E. Jo, H. Celio, and A. Manthiram, "Surface Stabilization with Fluorine of Layered Ultra-high-nickel Oxide Cathodes for Lithium-ion Batteries," *Chemistry of Materials* **34**, 4514–4522 (2022).
4. S. Lee and A. Manthiram, "Can Cobalt be Eliminated from Lithium-ion Batteries?" *ACS Energy Letters* **7**, 3058–3063 (2022).
5. R. R. Brow, A. W. Donakowski, A. Mesnier, D. J. Pereiral, K. X. Steirer, S. Santhanagopalan, and A. Manthiram, "Mechanical Pulverization of Co-free Nickel-rich Cathodes for Improved High Voltage Cycling of Lithium-ion Batteries," *ACS Applied Energy Materials* **5**, 6996–7005 (2022).
6. Mesnier, A. Manthiram, "Heuristics for molten-salt synthesis of single-crystalline ultrahigh-Ni layered oxide cathodes," *submitted*.
7. R. Pan, E. Jo, Z. Cui, and A. Manthiram, "Degradation Pathways of Cobalt-free LiNiO₂ Cathode in Lithium Batteries," *submitted*.
8. M. Yi, A. Dolocan, and A. Manthiram, "Stabilizing the Interphase in Cobalt-free, Ultrahigh-nickel Cathodes for Lithium-ion Batteries," *submitted*.

XI.5 Cobalt-Free Cathodes for Next Generation Li-Ion Batteries (Nexceris)

Neil Kidner, Principal Investigator

Nexceris
404 Enterprise Drive
Lewis Center, OH 43035
E-mail: n.kidner@nexceris.com

Haiyan Croft, DOE Technology Development Manager

U.S. Department of Energy
E-mail: Haiyan.Croft@ee.doe.gov

Start Date: October 1, 2018
Project Funding: \$3,083,213

End Date: March 31, 2022
DOE share: \$2,466,547

Non-DOE share: \$616,666

Project Introduction

This is a disruptive period for global automakers. Economic, political, and ecological pressures have hastened the global transition from internal combustion engine (ICE) to electric vehicles (EVs). In response, automakers are investing significant resources to accelerate the launch of EVs. However, to realize mass-market adoption of EVs, Li-ion battery costs must fall ($< \$100/\text{kWh}$), and performance must improve to alleviate customer concerns over driving range and lifetime. Today's commercial, state-of-the-art Li-ion batteries for EVs are based on high-energy-density layered oxides, and require cobalt, a metal of limited resources and subject to price speculation. There is, therefore, a need for new high-potential, and high-capacity cathode materials that are less reliant on critical materials to secure the supply chain and sustain rapid electrification of the U.S. transportation sector.

The spinel formulation $\text{LiNi}_{0.5}\text{Mn}_{1.5}\text{O}_4$ (LNMO) is a promising candidate based on its high specific energy (650 Wh/kg-cathode level) and cobalt-free formulation. Unfortunately, the adoption of this material has been limited by its poor cycle life, caused by oxidative decomposition of the electrolyte and a series of parasitic reactions occurring at the electrode-electrolyte interface^[1-2].

Objectives

The project goal was to develop a next-generation Li-ion battery based on a LNMO high-voltage spinel cathode material. LNMO is an attractive candidate cathode material, which already satisfies two of the project specifications, a usable specific energy (cathode level) of at least 600 Wh/kg, and a low-cobalt formulation that is compatible with a cell cost of less than \$100/kWh. The objective of this project was to develop and validate a stabilized, titanium-substituted lithium manganese nickel-oxide, $\text{LiNi}_{0.5}\text{Mn}_{1-x}\text{Ti}_x\text{O}_4$ (LNMTO) with improved cycle and calendar life, and a complementary cell chemistry (electrolyte formulation), for stable performance under aggressive high-voltage operating conditions.

Approach

The proposed project approach is shown schematically in Figure XI.5.1 To address limitations with poor cycle and calendar life of high-voltage LNMO cathode a microstructurally hierarchical LNMO/LNMTO core-shell cathode powder was proposed that enables the formation of a solid-electrolyte interface that effectively passivates the cathode surface. The microstructural enhancements of the cathode material focus on preferentially enriching the surface with titanium. In parallel, new, optimized LiPAA electrode binder and electrolyte chemistries will be incorporated to address degradation mechanisms associated with high-voltage systems.

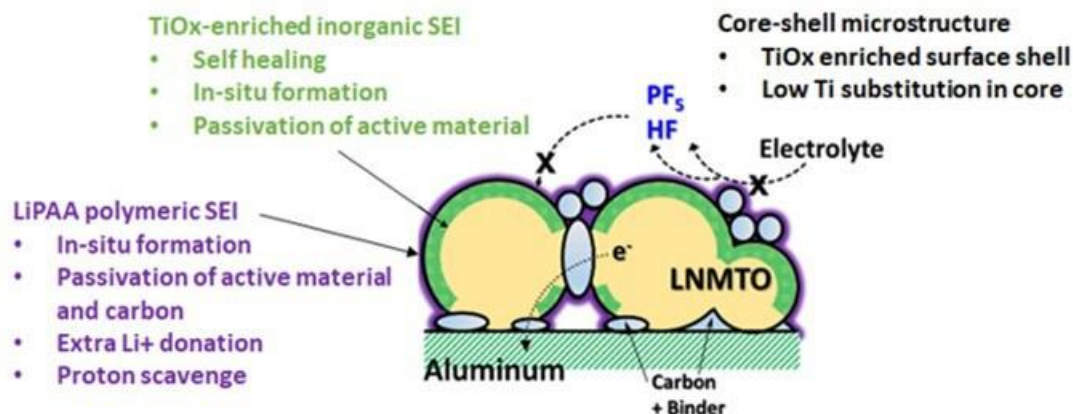


Figure XI.5.1 Schematic of the technical approach for creating high-performance LNMTO Li-ion cathodes.

In the first budget period the project team focused on producing LNMTO (and LNMO) powders by conventional solid-state synthesis methods, and fabricating LiB cells using these cathode materials, and test these cells to establish baseline performance levels. Analytical and testing protocols were established that were used throughout the project. Multiple large (2-Ah) cells were manufactured and fifteen of these Project Progress Cells (PPCs) delivered to Idaho National Laboratory (INL) for performance testing.

In the second budget period the project team built on the Year 1 results and continued to improve the performance of the LNMTO based cells. An alternative, *Hybrid Wet-Chemical Synthesis (HAWCS)* powder synthesis approach was developed and integrated to produce core-shell LNMO/LNMTO cathode microstructures. Electrolyte development continued to identify a complementary electrolyte formulation to pair with this high-voltage cathode. This budget period culminated with a set of down-selected 2-Ah cells that enabled an assessment of progress towards the overall project goals.

In the third budget period, a series of down-selected powder iterations were completed for single-layer pouch cell and 2-Ah cell testing. This approach, of frequent large-format testing of down-select LNMO/LNMTO core-shell powders enabled scale-up challenges to be better addressed and mitigated technical risk in the final Project Completion Cells (PCCs).

Results

The LNMO/LNMTO core-shell cathode powder has been systematically improved throughout the project, as shown in Figure XI.5.2 that compares single-layer pouch (SLP) cell performance of LNMO and LNMO/LNMTO core-shell cathodes from each year of the project.

In Year 1 a solid-state synthesis process was used to produce both homogeneous LNMO and LNMTO core powders. In Year 2 the *HAWCS* process was developed that improved the compositional and morphological uniformity of the LNMO powders. The LNMTO shell process was also integrated with the *HAWCS* derived LNMO core to produce the first iteration of LNMO/LNMTO core-shell powder. Finally, in Year 3 both the *HAWCS* and LNMTO shell deposition processes were optimized to produce a down-selected LNMO/LNMTO core-shell powder. For a given year the LNMO/LNMTO cathode provided a higher initial specific capacity and lower capacity degradation than the LNMO cathode. This is proposed to be due to the Ti substitution on the surface of the powder. The better uniformity of *HAWCS* powder compared to solid-state powder translated into significantly improved cycle life.

Optimization of the *HAWCS* process in Year 3 focused on increasing the effective powder particle, and the initial precipitation step. In addition, the LNMTO shell microstructure (shell thickness and Ti-substitution) was re-targeted to be integrated with the larger LNMO core powder. These process modifications were able to further improve the initial capacity and cycle-life of the high voltage LNMO/LNMTO core-shell cathodes.

Minimal capacity degradation was observed for SLP cells for LNMO/LNMTO core-shell cathodes with the following Ti-substitutions: $\text{LiNi}_{0.5}\text{Mn}_{1.35}\text{Ti}_{0.15}\text{O}_4$ (LNMTO-1), $\text{LiNi}_{0.5}\text{Mn}_{1.2}\text{Ti}_{0.3}\text{O}_4$ (LNMTO-2), and $\text{LiNi}_{0.5}\text{Mn}_{1.0}\text{Ti}_{0.5}\text{O}_4$ (LNMTO-3).

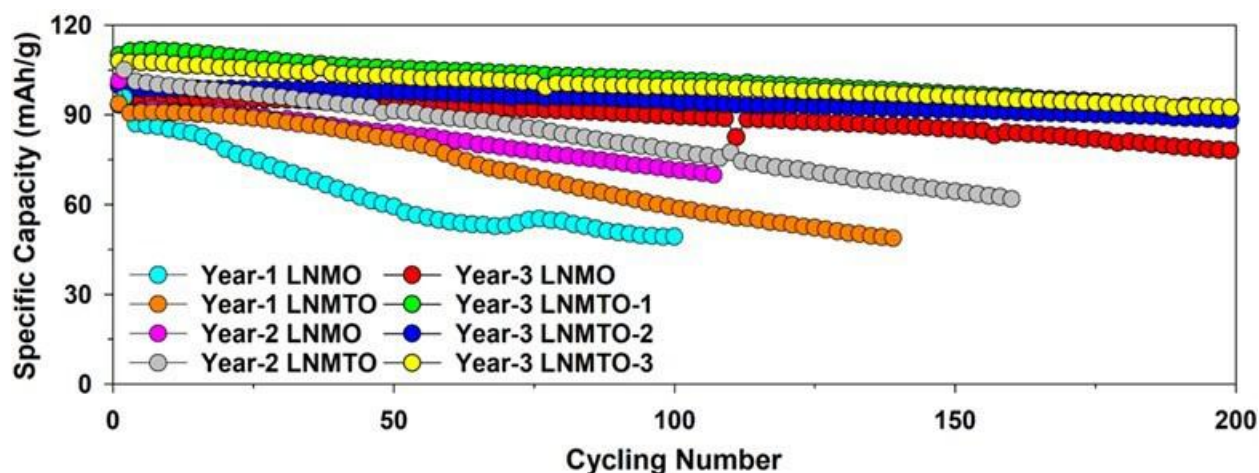


Figure XI.5.2 Cycle performance of SLP-cells capacity comparing homogeneous LNMO core (and homogeneous LNMTO for Year 1) and LNMO/LNMTO core-shell cathodes for each of the project years.

Microstructural characterization on the down-select LNMO core and LNMO/LNMTO core-shell powders has been completed to better understand the effect of process parameters on particle morphology and cell performance. Figure XI.5.3 shows SEM microstructures of LNMO and LNMO/LNMTO core-shell powders synthesized through the project.

The Year 1 solid-state process produced a small, irregular LNMO powder, composed of primary particles. The original (Year 2) *HAWCS* process consolidated these primary particles into an extremely uniform, spherical particle (second morphology) made up of distinct LNMO primary particles. In Year 3 process modifications were implemented to increase the measured powder particle size. A larger LNMO particle size improved the cycle life behavior of LNMO (likely due to a reduction in the LNMO surface area and detrimental surface interactions). SEM analysis identified that instead of growing the spherical secondary particles the larger Year 3 LNMO core powder consists of a tertiary agglomerated morphology. Subsequent application of the LNMTO shell smooths the tertiary LNMO/LNMTO core-shell morphology shown in Figure XI.5.3.

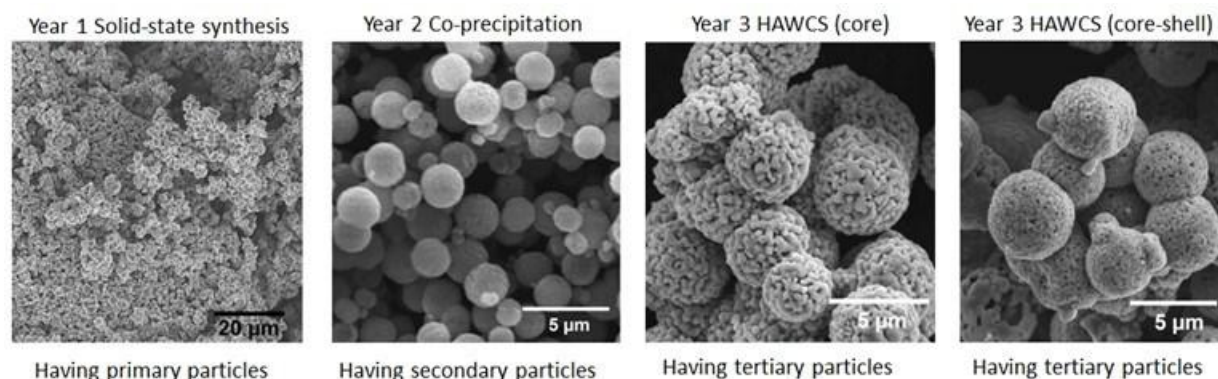


Figure XI.5.3 SEM of LNMO and LNMO/LNMTO core/shell powder synthesized throughout the project

LNMO/LNMTO core/shell cathodes from fresh and cycled SLP cells have been characterized by Raman Spectroscopy and Electrochemical Impedance Spectroscopy (EIS) (Figure XI.5.4) to develop a mechanistic understanding for the cell performance improvement demonstrated for the LNMO core/shell cathode versus

the homogeneous LNMO cathode. Raman spectra of Ti-rich $\text{LiNi}_{0.5}\text{Ti}_{1.5}\text{O}_4$ showed that cycled LNMTO-3 experienced sacrificial Mn dissolution and formation of the more-stable Ti-enriched CEI layer. Furthermore, EIS shows that the Ti-enriched core-shell cathodes reduce the interfacial impedance (R_{sf}) and charge-transfer (R_{ct}) resistance compared with LNMO cathodes.

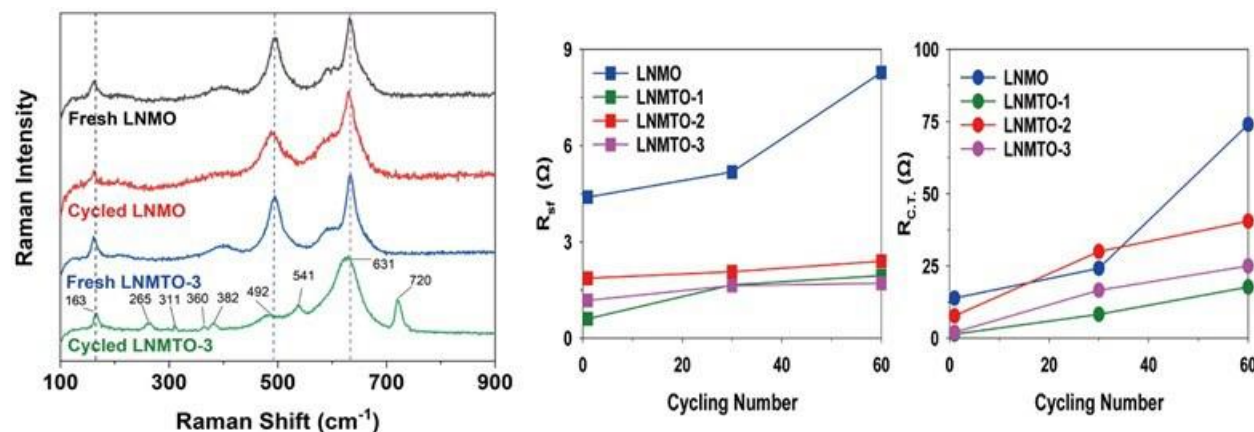


Figure XI.5.4 Raman spectra (left) and interfacial (R_{sf}) and charge-transfer (R_{ct}) impedance measured by impedance spectroscopy of fresh and cycled LNMO and LNMO/LNMTO core/shell cathodes (left). $\text{LiNi}_{0.5}\text{Mn}_{1.35}\text{Ti}_{0.15}\text{O}_4$ (LNMTO-1), $\text{LiNi}_{0.5}\text{Mn}_{1.2}\text{Ti}_{0.3}\text{O}_4$ (LNMTO-2), and $\text{LiNi}_{0.5}\text{Mn}_{1.0}\text{Ti}_{0.5}\text{O}_4$ (LNMTO-3).

The microstructure (density and porosity) of both the anode and cathode electrodes were found to have a significant effect on SLP cell performance, especially cycle-life. To further investigate this effect and optimize the electrode microstructure a systematic SLP study of different electrode configurations was completed. Six electrodes, three cathodes, and three anodes have been produced with a range of target densities and porosities. These electrodes were paired together and SLP cells fabricated. Figure XI.5.5 (left) shows the initial cycling that indicated higher cathode porosity improves cell performance, a result confirmed with 1-Ah cells, and used to downselect the electrode microstructure for the 2-Ah Project Completion Cells (PCCs).

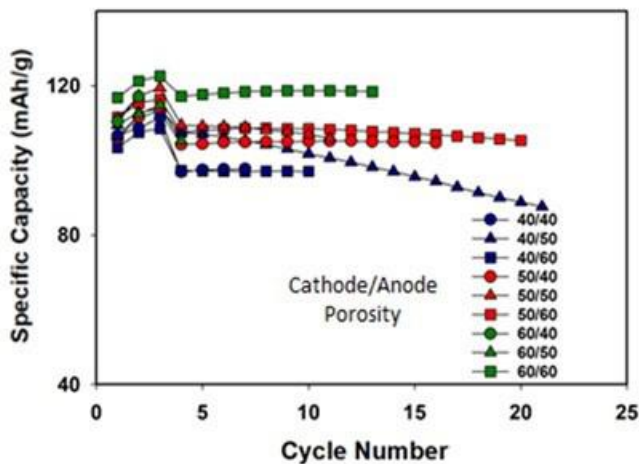


Figure XI.5.5 Initial cycling behavior of LNMO SLP-cells with different electrode (cathode/anode) porosities at 25 °C Electrolyte 1 M LiPF₆ in 1:1 wt. EC/EMC (no additive). Cycling conditions: Cycle 1-2: C/10 then C/3.

Thirty-four PCCs were fabricated using the down-select LNMO/LNMTO core-shell powder. Figure XI.5.6 shows the rated capacity and energy for the fifteen cells with the highest initial rated capacity. This information was used to finalize the PCC test plan. High voltage LNMO cathode likely have different gas-generation characteristics compared to standard cathode chemistries and different formation cycling procedures are expected. The modified formation cycling procedure developed during the project was unable to mitigate gas generation which degraded cell performance and impeded cell testing.

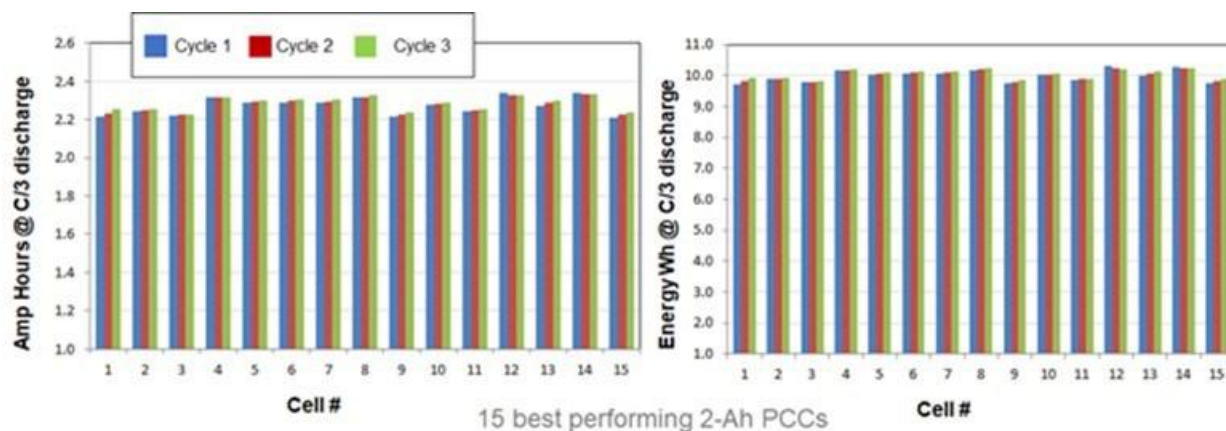


Figure XI.5.6 Rated capacity and energy of the fifteen 2-Ah PCCs with highest initial rated capacity.

Conclusions

In this project Nexceris, in collaboration with project partners; The Ohio State University and Navitas Advanced Systems advanced the technical maturity of a non-cobalt, $\text{LiNi}_{0.5}\text{Mn}_{1.5}\text{O}_4$ (LNMO) cathode for next-generation Li-ion batteries. To address limitations with poor cycle and calendar life a microstructurally hierarchical Ti-stabilized LNMO/LNMTO core-shell cathode powder has been developed and evaluated to address degradation mechanisms associated with high-voltage systems. Single-layer pouch cell and large-format 2-Ah cell testing have shown that an optimized LNMO/LNMTO core-shell cathode significantly improves initial cell capacity and cycle life compared to homogeneous LNMO cathode.

To support development and the fabrication of large-format cells a novel *Hybrid Alternative Wet-Chemical Synthesis (HAWCS)* process have been developed. This low-cost, synthesis approach enables the excellent compositional and particle morphology control achieved with co-precipitation without the strict process controls and associated expensive process equipment.

Key Publications

1. J.-H. Kim, N.P.W. Pieczonka, Z. Li, Y. Wu, S. Harris, B.R. Powell, Understanding the capacity fading mechanism in $\text{LiNi}_{0.5}\text{Mn}_{1.5}\text{O}_4$ /graphite Li-ion batteries, *Electrochimica Acta*. 90 (2013) 556–562.
2. J.-H. Kim, N.P.W. Pieczonka, L. Yang, Challenges and Approaches for High-Voltage Spinel Lithium-Ion Batteries, *ChemPhysChem*. 15 (2014) 1940–1954.

Acknowledgements

We would like to acknowledge the support of their project partners, Dr. Jung-Hyun Kim at The Ohio State University, and Dr. James Dong at Navitas Systems. Dr. Kim's team has provided excellent technical guidance and support for cell chemistry development and cell testing. Navitas Systems has provided feedback on the large-format cell manufacturing and testing. We would also like to thank the project's NETL manager, Adrienne Riggi for her project support and management, and Dr. Jack Deppe and Dr. Ahmad Pesaran for their technical guidance.

XI.6 High-Performance Low-Cobalt Cathode Materials for Li-ion Batteries (PSU)

Donghai Wang, Principal Investigator

Department of Mechanical Engineering
The Pennsylvania State University
University Park, PA 16802
E-mail: dwang@psu.edu

Chao-Yang Wang, Co-Principal Investigator

Department of Mechanical Engineering
The Pennsylvania State University
University Park, PA 16802
E-mail: cxw31@psu.edu

Jagjit Nanda, Co-Principal Investigator

SLAC National Accelerator Laboratory
2575 Sand Hill Rd
Menlo Park, CA 94025
E-mail: jnanda@stanford.edu

Chongmin Wang, Co-Principal Investigator

Environmental Molecular Sciences Laboratory
Pacific Northwest National Laboratory
Richland, WA 99352
E-mail: chongmin.wang@pnnl.gov

Haiyan Croft, DOE Technology Development Manager

U.S. Department of Energy
E-mail: Haiyan.Croft@ee.doe.gov

Start Date: October 1, 2018	End Date: December 31, 2022	
Project Funding (FY22): \$739,259	DOE share: \$591,407	Non-DOE share: \$147,852

Project Introduction

The layer-structured $\text{Li}[\text{Ni}_x\text{Co}_y\text{Mn}_{1-x-y}]\text{O}_2$ (NCM) cathode materials have become the industry's main choice for increasing the driving distance per charge of electric vehicles^[1-3] due to their high energy density and acceptable cycling stability. The price of cobalt (Co), a key element within cathode materials for stability, has nearly tripled over the past few years due to increased demand from the cell phone industry, current materials shortage, increased adoption of electrical vehicles, and speculation regarding a future global shortage,^[6-8] as mentioned in the DOE Funding Opportunity Announcement. To meet the requirement and sustainability of the next-generation long-range and low cost EVs, developing cathode materials with very low Co content while maintaining high energy density and low cost is both essential and urgent.

Objectives

The overarching objective of this work is to develop stabilized NCM cathode materials with low Co content (namely $\text{LiNi}_x\text{Co}_y\text{Mn}_{1-x-y}\text{O}_2$, $y \leq 0.04$) to meet DOE's goal of reducing Co loading to below 50 mg Wh^{-1} , while maintaining energy density greater than 600 Wh kg^{-1} based on the cathode material. The obtained NCM cathode paired with graphite anode shall deliver batteries with a high initial specific energy density of over 240 Wh kg^{-1} and low capacity fading rate of less than 20% in 1000 cycles under C/3 discharge rate.

Approach

To accomplish this goal, a multidisciplinary team has been formed from three organizations: The Pennsylvania State University (PSU), Oak Ridge National Laboratory (ORNL), and Pacific Northwest National Laboratory (PNNL). The PI and co-investigators are Dr. Donghai Wang (PI) from PSU with expertise in the synthesis of nanostructured materials and manipulation of interfacial properties of electrochemically active materials, Dr. Jagjit Nanda with substantial knowledge of and expertise in state-of-the-art cathodes from ORNL, Dr. Chao-Yang Wang with significant experience in advanced cell design and fabrication and cell diagnostics from PSU, and Dr. Chongmin Wang with world-wide known expertise of advance atomic scale characterization of electrode materials from PNNL. Furthermore, this project will leverage off and synergistically work with the current DOE-funded programs on battery materials at PSU and ORNL, and electrode materials characterization at PNNL.

Results

LFP-coated NMC811 cathode

This year, we continued to cycle the 2.5Ah pouch cells consisting of NCM811 cathode coated with 10wt% LFP vs. graphite anode, with the cathode loading of 17.5 mg/cm² and the N/P ratio of 1.1. These cells are cycled at 40°C as well as room temperature, as shown in Figure XI.6.1a. The cycling conditions are: C/3 CCCV to 4.2V until C/5, and aged cells are using a reference performance test (RPT) every 200 cycles, i.e., C/3 CCCV to 4.2V till C/20. It can be seen that LFP-coated NCM811 is very stable at room temperature, with capacity retention of 68.6% after 3217 cycles. At 40°C, the cell achieves 67.3% capacity retention after 1609 cycles. High temperature also leads to a fast increase in DCR, as shown in Figure XI.6.1b. The cell's capacity fading at elevated temperature is much faster than at room temperature due to low stability of the cathode material at high temperature (40°C).

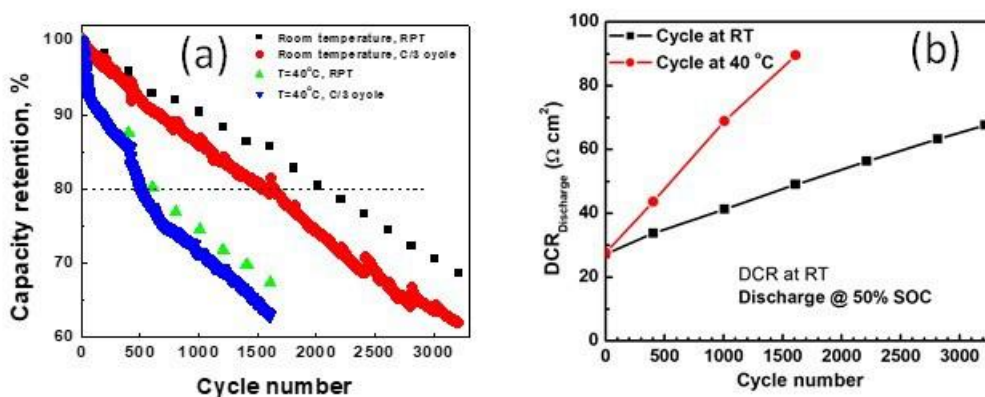


Figure XI.6.1 a) Capacity retention of the LFP-coated NCM/graphite cells during C/3 cycling at room temperature and 40°C. b) DCR of the LFP-coated NCM/Gr cells during C/3 cycling at room temperature and 40°C.

The impedance of the cell cycling is also analyzed. The result in Figure XI.6.2 shows that at 40°C, cathode impedance increases much faster than that cycling at room temperature. The EIS result agrees well with the DCR data above.

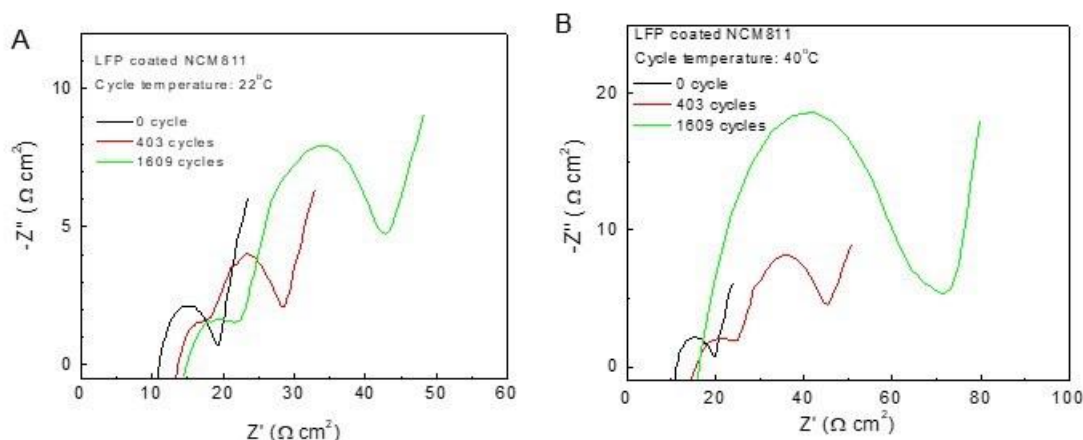


Figure XI.6.2 EIS over cycling at a) room temperature and b) 40°C of LFP-coated NCM811

Phosphate coating on $\text{LiNi}_{0.92}\text{Co}_{0.04}\text{Mn}_{0.04}\text{O}_2$

a) Al and P distribution after heat treatment of AlPO_4 coating:

Continuing last year's effort, we continued to explore the effect of phosphate/metaphosphate coating on $\text{LiNi}_{0.92}\text{Co}_{0.04}\text{Mn}_{0.04}\text{O}_2$ (NMC92)^{1,2}. STEM is obtained for the primary particle surface and interior to understand how dry coating of AlPO_4 nanoparticles can enhance better cycling performance of high-nickel cathode. Under STEM observation (Figure XI.6.3), Al is proved to be doped into the crystal structure, and none of Al is left on the primary particle surface. In contrast, P remains on the surface and there is no existence of P observed at the particle interior area. This result suggests a separation of Al and P from AlPO_4 during heat treatment. Al diffuses into the crystal structure and stays there as a doping element. At the same time, large radius PO_4^{3-} can only move along the primary particle boundaries and remains on the surface, acting as a coating layer.

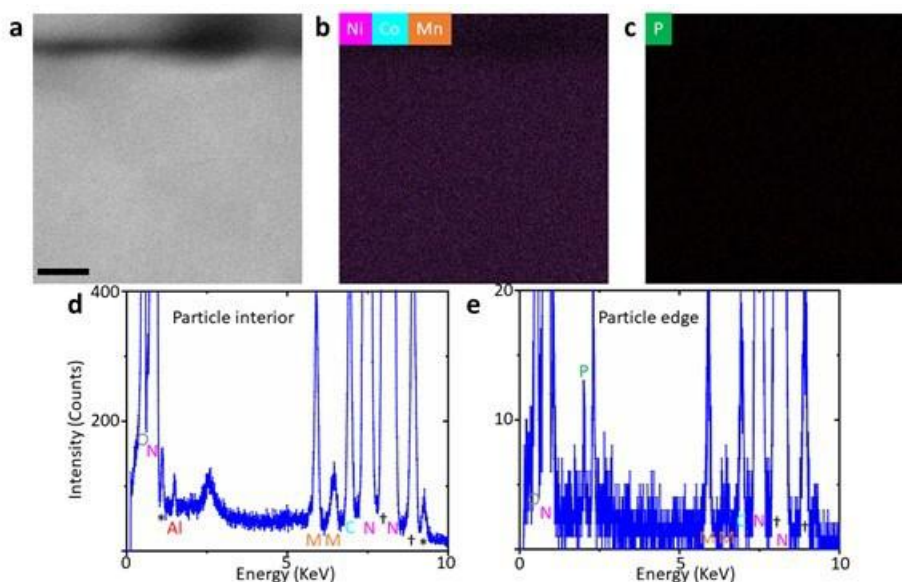


Figure XI.6.3 STEM studies on the primary particle of the pristine 1% AlPO_4 coated NCM92. a) Cross-sectional STEM-HAADF image captured at the edge of a primary particle along with b) the corresponding STEM-EDS Ni/Co/Mn mapping and c) the corresponding STEM-EDS P mapping in the same area with a) The scale bar in a) corresponds to 5 nm and applied to both b) and c). The STEM-EDS spectrum (d) is from the bottom part of a) inside the particle and the STEM-EDS spectrum (e) is from the particle edge.

b) Further development of NMC cathode surface protection:

Following the previous protective strategy, we developed other functional coatings, which demonstrated excellent cycling stability. As shown in Figure XI.6.4, with PSU-2 coating, the cell can have a cycle life (reaching 80% of initial capacity) over 400 cycles at 1C rate, an elevated performance compared to bare NMC92 reaching its cycle life after only 82 cycles. It is also worth noting that this strategy has universality and the PSU-1 coating with the same strategy also demonstrated an improved cycling performance.

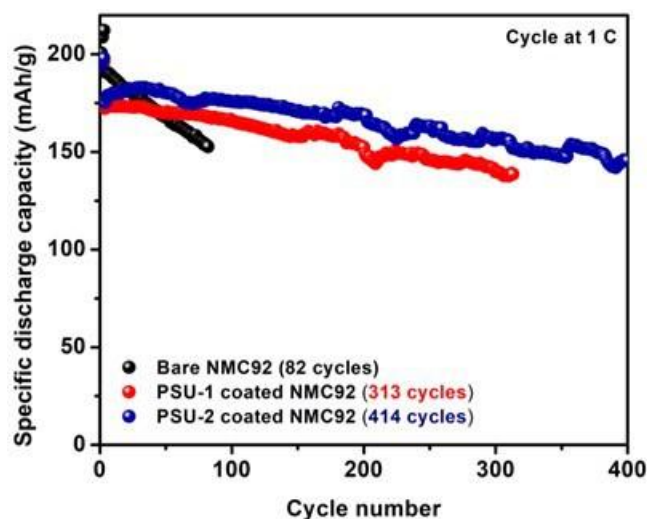


Figure XI.6.4 The comparison in electrochemical performance of bare, PSU-1 and PSU-2 coated high-nickel cathodes.

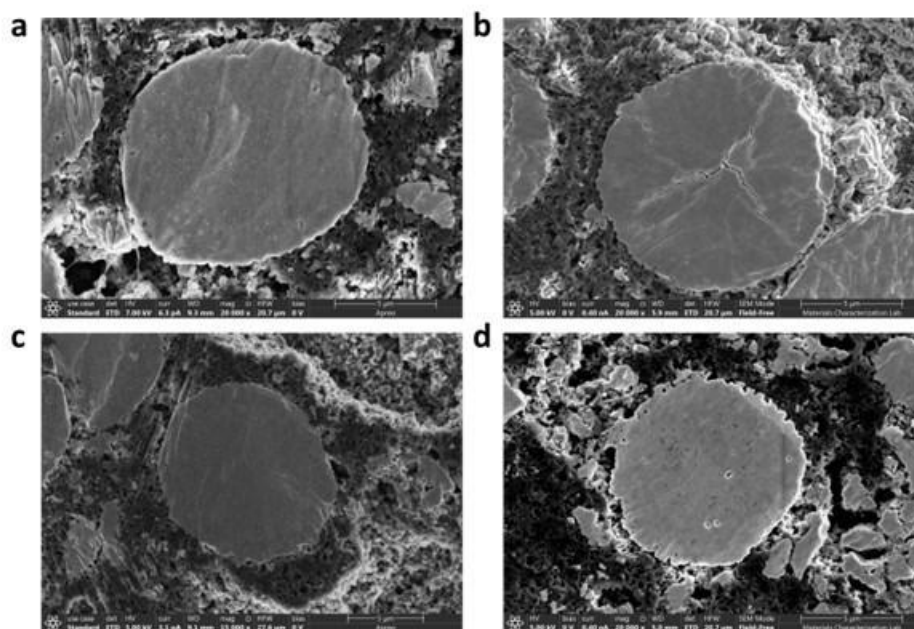


Figure XI.6.5 SEM images on cross-sections of: a) before and b) after 50 cycles of bare NMC92 cathode; c) before and d) after 50 cycles of PSU-1 coated cathode.

The cathode morphology after cycling has been thoroughly explored for a deeper understanding of the improvement of PSU-1 coated NMC92. After 50 cycles at a 1C rate, the cathodes are milled to observe the particle integrity at the delithiation state. In Figure XI.6.5b, the bare NMC92 cathode particle is damaged upon continuous volume expansion and contraction, generating cracks throughout the particles. These cracks are

assigned with more surface exposure with electrolytes and the increase of impedance over cycling. At the same time, PSU-1 coated NMC92 shows greatly intact morphology with no cracks observed.

Scaling up of high-nickel cathode material production

In our previous works, we have reported our efforts in exploring different coating and doping strategies that showed improvement in prolonging cell cycle life. This year, we continue scaling up high-nickel cathode material production, along with the coating method on large-scale production for pouch cell delivery.

After using different conditions of the calcination process for Ti-doped high-nickel cathode, we found the optimum conditions to be 30g/batch at 715°C under pure oxygen flow of 1.5L/h, where this procedure provides the best cycling performance of 97.0% capacity retention after 100 cycles.

Using these optimum conditions, 1kg of high-nickel cathode powder was synthesized and coupled with graphite anode into 30 2.7Ah pouch cells. The cells are sent to Idaho National Laboratory and are currently under testing. Control cells are cycled at Penn State University and show stable cycling with capacity retention of over 97% after 100 cycles at both 1C and C/3 current rates. (See Figure XI.6.6, Figure XI.6.7, and Figure XI.6.8.)

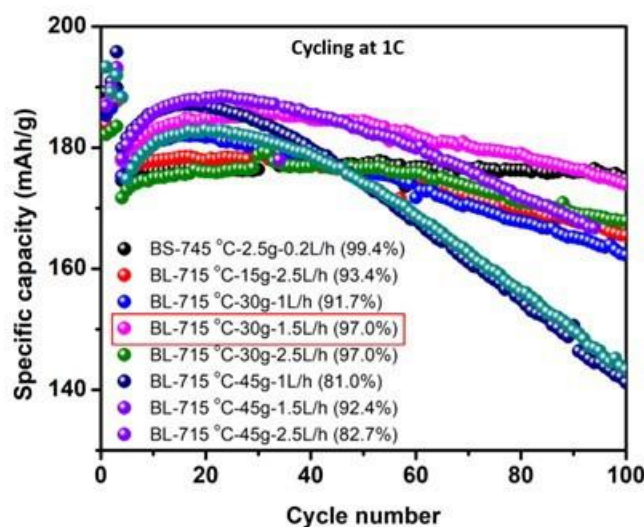


Figure XI.6.6 Comparison in cycling performance of Ti-doped NMC92 cathodes synthesized by different calcination conditions.

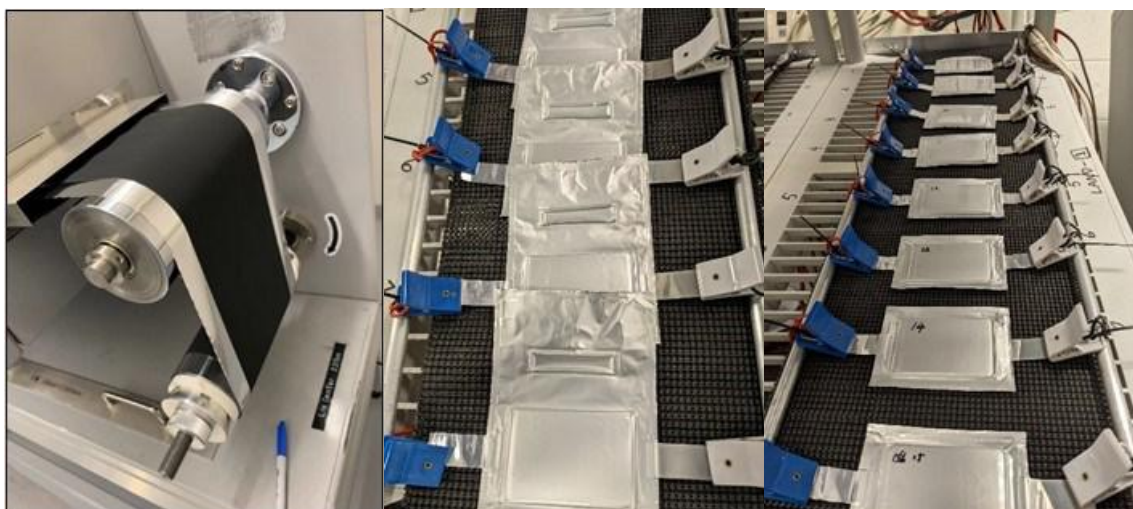


Figure XI.6.7 The Ti-doped high-nickel cathode is fabricated into electrode and pouch cells

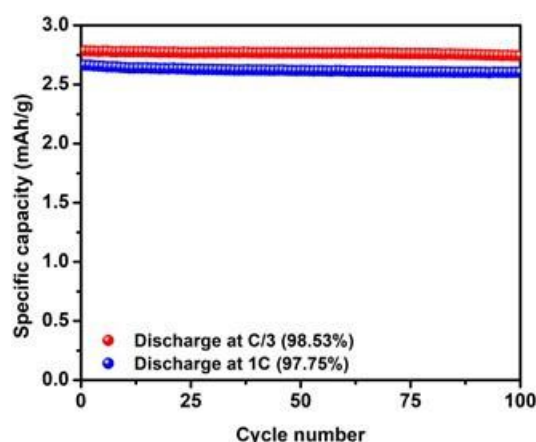


Figure XI.6.8 Cycling performance of pouch cell at C/3 and 1C rate

Conclusions

This year, we have worked on NCM811 and $\text{LiNi}_{0.92}\text{Co}_{0.055}\text{Mn}_{0.025}\text{O}_2$. We mainly focused on optimizing surface protection and deeply exploring the structural reconstruction at the surface and subsurface of the particles.

The 2.5 Ah LFP-coated NCM/graphite cells are ultra-stable with capacity retention at C/3 of 68.6% after 3217 cycles. At 40°C, the cell achieves 67.3% capacity retention after 1609 cycles.

For $\text{LiNi}_{0.92}\text{Co}_{0.055}\text{Mn}_{0.025}\text{O}_2$, we developed a surface protective mechanism. The phosphate coating can significantly inhibit the penetration of acidic components from the decomposition of electrolyte and trace water, which improves the cycling performance of high-nickel cathode material. Using the developed protective mechanism, we have found several better coating materials, e.g., PSU-1 and PSU-2, where PSU-2 coated cathode can maintain 80% capacity after 400 cycles at a current rate of 1C.

High-nickel $\text{LiNi}_{0.92}\text{Co}_{0.055}\text{Mn}_{0.025}\text{O}_2$ cathode material is successfully synthesized at a large scale. Ti-doped high-nickel is coupled with graphite to become 2.7Ah pouch cells. The cycling performance of these pouch cells is working at over 97% after 100 cycles.

Key Publications

1. Nguyen, Au, Peng Zuo, Heng Jiang, Chongmin Wang, and Donghai Wang. “Dual Protective Mechanism of AlPO_4 Coating on High-Nickel Cathode Material for High Energy Density and Long Cycle Life Lithium-Ion Batteries.” *Journal of The Electrochemical Society* 169, no. 5 (May 1, 2022): 050523.

Acknowledgements

We truly appreciated the support from the project manager Colleen Butcher at National Energy Technology Laboratory, Dr. Jack Deppe at Idaho National Lab, and Dr. Ahmad Pesaran at National Renewable Energy Lab.

XII Next Generation Lithium-Ion Materials: Diagnostics

The increasing demand for lithium-ion batteries requires advancements in diagnostics to observe capacity loss to maintain reliability as the capacity declines, identify anomalies to prevent catastrophic failures, and predict the end of battery life when the battery fades to a set capacity threshold. Well-developed battery test technologies must recognize all battery conditions and provide reliable results, even if the charge is low.

The rest of this chapter contains detailed reports on the status of the following individual projects.

- Interfacial Processes (LBNL)
- Advanced *in situ* Diagnostic Techniques for Battery Materials (BNL)
- Microscopy Investigation on the Fading Mechanism of Electrode Materials (PNNL)
- *In-Operando* Thermal Diagnostics of Electrochemical Cells (LBNL).

XII.1 Interfacial Processes (LBNL)

Robert Kostecki, Principal Investigator

Lawrence Berkeley National Laboratory
1 Cyclotron Rd.
Berkeley, CA 94720
E-mail: r_kostecki@lbl.gov

Tien Duong, DOE Technology Development Manager

U.S. Department of Energy
E-mail: Tien.Duong@ee.doe.gov

Start Date: October 1, 2021

End Date: September 30, 2022

Project Funding (FY22): \$440,000

DOE share: \$440,000

Non-DOE share: \$0

Project Introduction

Li-based batteries are inherently complex and dynamic systems. Although often viewed as simple devices, their successful operation relies heavily on a series of complex mechanisms, involving thermodynamic instability in many parts of the charge/discharge cycle and the formation of metastable phases. This paradigm of Li-battery system operation usually drives the battery toward irreversible physical and chemical conditions that lead to battery degradation and failure.

The requirements for long-term stability of Li batteries are extremely stringent and necessitate control of the chemistry at a wide variety of temporal and structural length scales. Progress towards identifying the most efficient mechanisms for electrical energy storage and the ideal material depends on a fundamental understanding of how battery materials function and what structural/electronic properties limit their performance. This in turn necessitates the development and use of new characterization tools to monitor these processes.

The design of the next generation of Li batteries requires a fundamental understanding of the physical and chemical processes that govern these complex systems. Although some significant advances have been made to prepare and utilize new materials efforts towards the understanding of their operation mechanisms and degradation modes have been insufficient and/or unsuccessful.

Instability and/or high resistance at the interface of battery electrodes limit electrochemical performance of high-energy density batteries. A better understanding of the underlying principles that govern these phenomena is inextricably linked with successful implementation of high energy density materials in Li-based cells for PHEVs and EVs. Pristine and cycled composite and thin film model electrodes are investigated using a variety of state-of-the-art techniques to identify, characterize and monitor changes in materials structure and composition that take place during battery operation and/or storage. This project constitutes an integral part of the concerted effort within the BMR Program and it supports development of new electrode materials for high-energy Li-metal based rechargeable cells.

Objectives

This collaborative project involves the development and application of advanced experimental methodologies to study and understand the mechanism of operation and degradation of high-capacity materials for rechargeable cells for PHEV and EV applications. The main objective of this task is to establish specific design rules toward the next generation of low impedance Li-metal rechargeable batteries that are capable of performing 1000 deep discharge cycles at CE > 99.9% and suppress lithium dendrites formation at high current densities (> 2 mA/cm²). This project aims at the following:

Apply far- and near-field optical multifunctional probes and synchrotron-based x-ray techniques to obtain detailed insight into the composition, structure and mechanism of reactions at Li/electrolyte interfaces at an adequate spatial and temporal resolution.

Design new *in situ* diagnostic techniques and experimental methodologies that are capable of unveiling the function and operation of hidden or buried interfaces and interphases that determine material, electrode and battery cell electrochemical performance and failure modes.

Understand the mechanism of operation and degradation of high energy density materials for rechargeable Li-metal batteries for PHEV and EV applications.

Propose effective remedies to address inadequate Li-metal rechargeable batteries calendar/cycle performance for PHV and EV applications.

The other goal is development and application of far- and near-field optical probes and synchrotron-based advanced X-ray techniques to obtain insight into the mechanism of Li^+ transport and interfacial reactions in lithium/liquid model systems. Through an integrated synthesis, characterization, and electrochemistry effort, this project aims to develop a better understanding of lithium / liquid electrolyte interface so that rational decisions can be made as to their further development into commercially viable Li-metal cells.

Approach

- The pristine and cycled composite electrode and model thin-film electrodes were probed using various surface- and bulk-sensitive techniques, including FTIR, ATR-FTIR, near-field IR and Raman spectroscopy/microscopy, and SPM to identify and characterize changes in materials structure and composition.
- Novel *in situ* / *ex situ* far- and near-field optical multi-functional probes in combination with standard electrochemical and analytical techniques are developed to unveil the structure and reactivity at interfaces and interphases that determine materials electrochemical performance and failure modes.

Results

Due to the extreme reactivity of Li metal, it has been a challenge to establish a reliable Li metal battery, which can provide high specific energy (500 Wh kg⁻¹). A key question is understanding the interface between Li metal and electrolytes since the solid-electrolyte interface (SEI) film affects the long-term stability and reversibility of Li metal anodes. There have been numerous studies shedding light on SEI composition and properties. It was shown that the SEI layer is heterogenous on the sub-micron level calling for the use of advanced characterization methods working beyond the diffraction limit, such as cryo-TEM, which requires a high vacuum to perform analysis. In contrast, we use characterization methods that work at ambient pressure to analyze the pristine SEI layer. This is achieved by the use of scattering-type Scanning Near-field Optical Microscopy (sSNOM), which makes it possible to image the chemical nature of the SEI layer in sub-diffraction limit in ambient conditions, which we applied to the Li metal battery system.

Sample preparation plays a crucial role in the analysis of the pristine SEI layer. Due to the reactivity of Li metal, it is important to ensure the cleanliness of the prepared Li metal foil to avoid any potential contamination. In laboratory settings, it is common practice to prepare Li metal anodes in a glovebox that contains liquid electrolytes. This leads to the accumulation of volatile organic compounds (VOC) which will react with and form a contamination film on the Li surface, even before coming in contact with an electrolyte. To address this issue, we have developed a transfer method ensuring the pristine condition of the Li surface before coming in contact with the electrolyte. Freshly rolled Li metal foil was prepared in a solvent-free glovebox and placed in a plastic bottle with a septum cap. It was then transferred into a glovebox containing liquid electrolytes. Microliters of GEN2 were then deposited onto the clean Li surface (free of a VOC-induced contamination layer) in a controlled way, through a septum, via a syringe.

Upon contact, Li metal reacts with the electrolyte, forming a thin film of products of the reaction: 1) inorganic components, such as LiF, Li_2O , Li_2CO_3 , etc; 2) organic Li salts, such as LiEDC (Lithium ethylene decarbonate), 3) organic products of electrolyte decomposition and 4) residual electrolyte. The literature suggests, that the latter groups (3 and 4) play little role in the passivation of Li metal anodes, and should be removed to analyze SEI components buried under. This can be achieved by washing the Li metal in DMC (dimethyl carbonate), which will clean the passivated Li metal surface of any components that are soluble in DMC

We have analyzed the effect of sample post-processing (washing, drying) on solid electrolyte interface components. The hypothesis is that inorganic Li salts such as LiF and Li_2CO_3 are less soluble compared to LiEDC, therefore some of the residuals of inorganic SEI components are going to stay on the Li surface, which will be revealed by ATR-FTIR. The far-field technique while lacking surface sensitivity and special resolution, is a good estimate of bulk SEI components. It is worth noting, that before analysis, samples were dried under vacuum for 24 hours, therefore any loosely physisorbed species and gasses that can be components of SEI, are removed from the film. Figure XII.1.1 shows that even after 24 hours under vacuum some of the EMC molecules are still present on the Li surface. The signal of Li metal exposed to GEN 2 electrolyte is dominated by P-F and LiEDC/electrolyte vibrations at $\sim 830\text{ cm}^{-1}$ and 1083, 1156, 1267, and 1654 cm^{-1} , respectively (Figure XII.1.1). Interestingly, the removal of the electrolyte by Celgard seems to remove most LiEDC peaks, indicating that LiEDC is mainly dissolved in the electrolyte. The region $1000 - 1400\text{ cm}^{-1}$ is still populated with peaks, showing that other lithium organic salts, such as butylene dicarbonate (Li_2BDC), $\text{LiO}-(\text{CH}_2)_2\text{CO}_2(\text{CH}_2)_2\text{OCO}_2\text{Li}$, and $\text{Li}(\text{CH}_2)_2\text{OCO}_2\text{Li}$ remain on the Li surface. Washing with DMC removes the majority of organic salts, leaving Li_2CO_3 on the surface as a dominant feature. The peak at 737 cm^{-1} is assigned to coordinated EC. The shoulder at lower wavenumbers is assigned to free EC and is present only in a sample with electrolyte dried under vacuum. Vibration at 927 cm^{-1} is assigned to free EMC molecules, and it shifts to 950 cm^{-1} in the case of Li-coordinated EMC molecules. Once the excess electrolyte is removed, either by Celgard or by washing, mostly bound electrolyte molecules are remaining.

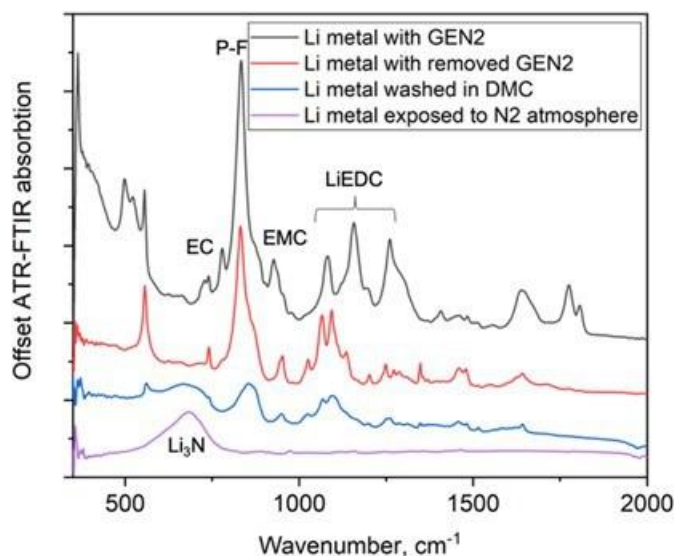


Figure XII.1.1 ATR-FTIR spectra of Li metal foil exposed to GEN 2 after various post-processing steps: (black) Li metal with dried electrolyte under vacuum (red) Li metal with electrolyte removed from the surface by a porous Celgard separator (blue) Li metal washed in DMC after the contact with GEN2 and (purple) fresh Li metal surface exposed to N_2 atmosphere of ATR-FTIR

To illustrate the effect of residual film covering SEI, we collected nano-FTIR spectra from Li metal surface exposed to GEN 2 electrolyte, where the excess electrolyte was removed. Optical microscopy indicates the presence of a thin film on the surface of Li metal (as shown in Figure XII.1.2a), due to the surface's iridescence. This thin film seems to cover a majority of the sample surface. Atomic force microscopy measurements indicate that the iridescent film's root means square roughness is approximately 1.2 nm.

Additionally, the nano-FTIR signal from that film is mainly dominated by P-F vibrations at 830 cm^{-1} . LiEDC vibrations, usually containing separated peaks with relatively narrow FWHM, are now forming one broad feature with multiple shoulders in the region $1000 - 1300\text{ cm}^{-1}$. The spectrum is consistent throughout the film. However, there are patches of the exposed surface under the iridescent film, where the nano-FTIR signal is dominated by Li_2CO_3 . LiEDC peaks are present as well, with no shoulders or broadening compared to the previous locations. The topography imaging (Figure XII.1.2b) revealed that those regions contain patches of absorbed species, which has a new peak at 930 and 764 cm^{-1} . These peaks could be attributed to free EC and EMC molecules. The rest of the area is uniformly covered with LiEDC, Lithium carbonate, and GEN 2 electrolyte components, indicating a strong bond between passivated Li surface and electrolyte molecules.

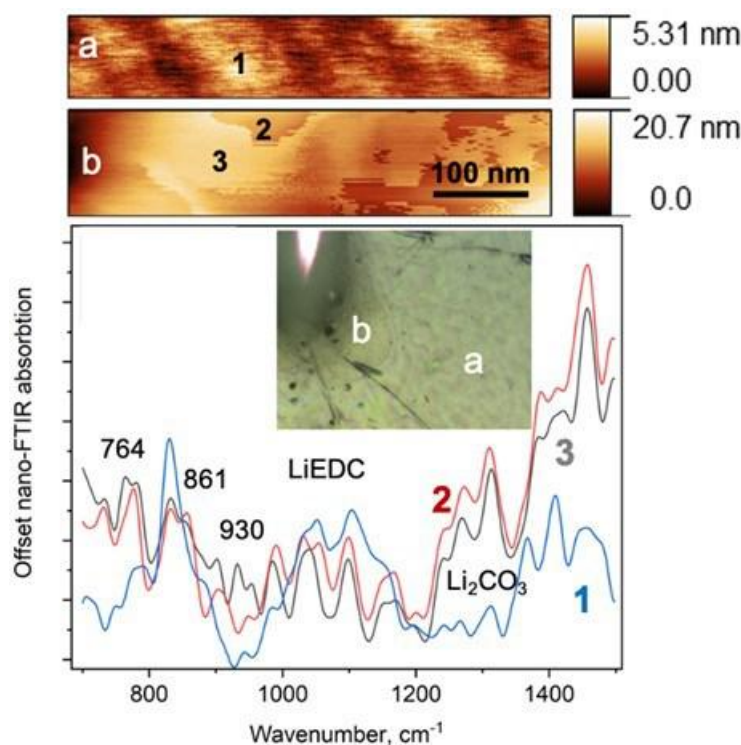


Figure XII.1.2 Topography and nano-FTIR spectra of Li metal surface after contact with GEN 2 electrolyte. The excess of electrolyte was removed by Celgard porous separator. Most of the Li metal surface is covered by thin iridescent film. a) topography of a patch of Li metal surface without a thin film b) topography of a thin film covering Li metal surface c) nano-FTIR spectra of different spots of the Li metal surface

It is important to note, that washing away organic components leads to potential damage of SEI and disturbs the passivation layer preventing Li from reacting with the environment. As an example, the rise of Li_3N peak in a washed Li metal surface can be explained by a reaction with N_2 gas, which is present in our nano-FTIR and ATR-FTIR systems. Notably, the undisturbed SEI stays inert in the N_2 environment even after a month of storage.

Interestingly, the effect of the residual film is less prominent when the Li was deposited electrochemically versus using Li foil. We used lithium iron phosphate (LFP) as a lithium source material, which undergoes a first-order phase transformation upon delithiation. This allows a steady Li^+ extraction from LFP and subsequent plating under constant potential. By controlling Li plating one can investigate species during the early SEI formation. We focused on investigating SEI components using nano-FTIR spectroscopy in ex-situ configuration. We assembled a 2-electrode cell with a thin-film Cu working electrode, lithium iron phosphate (LFP) counter electrode in GEN 2 electrolyte. After a cycle of stripping and plating Li at a current density $25\text{ }\mu\text{A}/\text{cm}^2$, we observed a change in copper electrode surface morphology, yielding congregated $\sim 500\text{ nm}$ nano

bubble with different chemical composition, as could be seen in Figure XII.1.3A, where the bubbles remain less reflective than the flat regions in infrared change.

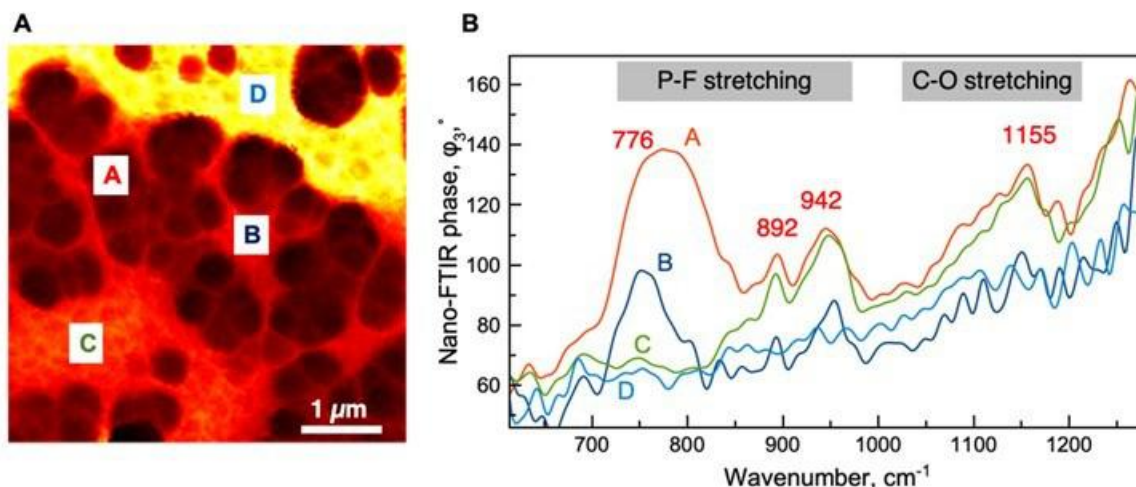


Figure XII.1.3 Nano-FTIR study of Cu surface after a cycle of plating and stripping Li A) Near-field infrared amplitude image (2nd harmonic) recorded in white light position B) Nano-FTIR phase ϕ_3 spectra recorded from selected locations A-D

Nano-FTIR spectra from the bubbles (Figure XII.1.3B) showed the presence of P-F stretching vibrations, where lower frequency corresponds to presence of PF_3 and higher for more oxygen-rich species like PFO_3^{2-} , which is a product of oxidation of LiPF_6 . Interestingly, smaller bubbles, located in area “C” in Figure XII.1.3A, contain only oxidized PF_6^- anions. At higher wavenumbers, $\sim 1155 \text{ cm}^{-1}$ corresponds to C-O stretching vibration of ethylene carbonate; however, the resolution quality is lacking due to the choice of laser. Notably, in the following experiments we have used sputtered Ni surface instead of Cu due to lesser effect of natural passivation in case of Ni. Additionally, we have switched to using current densities that are in the range of real-life LMB, in the range of $0.1 - 1 \text{ mA/cm}^2$

We prepared Li metal electrodes in a solvent-free glovebox and exposed their surfaces to pure liquid GEN 2 electrolyte. In this way we created an artificial SEI without introducing any unwanted components, like it was described above. This approach ensures minimal contamination of the Li metal surface during cell assembly. Pouch cells were subsequently assembled with Ni working electrodes and Li metal (with artificially created SEI) as counter electrodes. Then, 1 mAh/cm^2 of Li was plated galvanostatically on a Ni electrode with a current density of 0.5 mA/cm^2 . The oxidized Li metal counter electrode (“Li 10” in Figures) and plated Li on Ni working electrode (“Li-Ni 10” in Figures) were dried under vacuum for $\sim 1 \text{ hr}$ to allow residual electrolyte to vaporize. In another cell, after the Li plating step, the polarity of the cell was reversed and Li was stripped via similar but inverted protocols, leaving a reduced Li metal counter electrode (“Li 11” in Figures) and Ni working electrode with electrically disconnected, or “dead” Li on the surface. These *ex situ* electrodes were analyzed by infrared near-field imaging and Fourier transform infrared nano-spectroscopy (nano-FTIR).

Figure XII.1.4 shows “white light” (WL) imaging of the electrodes’ surfaces, showing a heterogeneous distribution of infrared reflection at the nanoscale. Since IR reflectivity can be correlated with the electronic conductivity of a material, Figure XII.1.1 likely shows the local distribution of SEI components with various electronic densities. Notably, Li 11 and Li-Ni 11 electrodes exhibit a similar pattern, with $\sim 50 \text{ nm}$ domains.

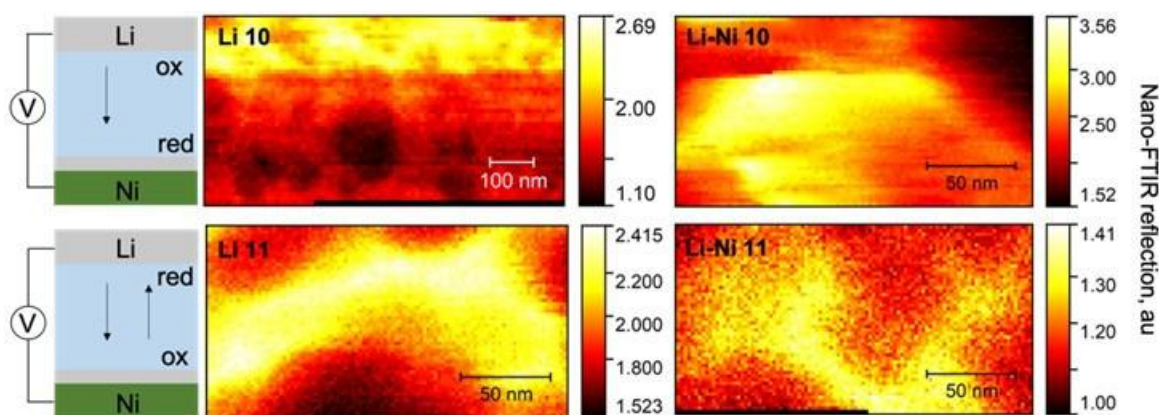


Figure XII.1.4 Nanoscale “white light” imaging of SEI layer on Lithium metal surface under various electrochemical conditions: a) Li metal electrode after oxidation under galvanostatic conditions b) Ni electrode after plating Li under galvanostatic conditions c) Li metal electrode after an oxidation-reduction cycle under galvanostatic conditions d) Ni electrode after a cycle of plating and stripping of Li

Figure XII.1.5 shows nano-FTIR spectra collected from the electrodes compared to the ATR-FTIR spectrum of dried electrolyte to reveal spectroscopic features of SEI components in each electrode. The data was collected at Berkeley Lab’s Advanced Light Source (ALS), Beamline 2.4 (capable of Synchrotron-based nano-FTIR and near-field Imaging), which allows using a bright and broadband infrared light source and a detector that allows probing vibrations at lower cutoff frequency $\sim 350\text{ cm}^{-1}$, which opens an opportunity to probe inorganic SEI components. Figure XII.1.2 shows that the majority of the spectral features are located in the region below 800 cm^{-1} . Oxidized electrodes, namely Li 10 and Li-Ni 11 show broad features above 1000 cm^{-1} , which can be attributed to the organic electrolyte components as well as organic Li salts, which are known to be present in the SEI layer. A feature at $400 - 450\text{ cm}^{-1}$ is present only on the working electrode, while a broad peak at $600 - 650\text{ cm}^{-1}$ is found in both Li metal electrodes and could be attributed to a LiF. Notably, the reduced Li metal electrode surface contains no significant peaks above 1000 cm^{-1} , indicating the minimal presence of organic components on the SEI. The knowledge obtained in ex-situ experiment will yield a better understanding of the results of in-situ studies, which is the next step in understanding SEI layer in LMB.

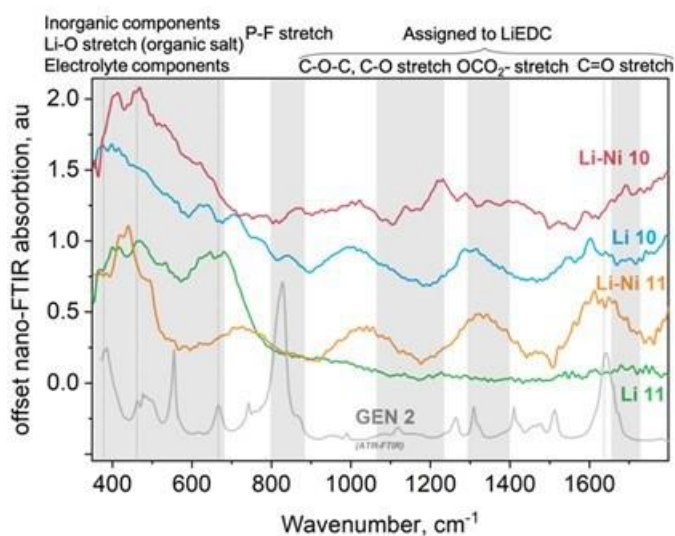


Figure XII.1.5 Nano-FTIR spectroscopy of SEI layer under various electrochemical conditions. Plated Li on Ni (red trace), oxidized Li surface (blue trace), plated and stripped Li “dead Li” (orange trace) and reduced Li surface after oxidation cycle (green trace). ATR-FTIR spectrum of dried GEN 2 electrolyte (grey trace)

In order to characterize SEI layer *in-situ*, we adopted a liquid cell design our lab has utilized successfully in the past, which generally enables the characterization of electrically biased solid/liquid interfaces, *in situ* and nondestructively, via near-field infrared nanospectroscopy (nano-FTIR). The experimental setup is illustrated in Figure XII.1.6, where an atomically thin and infrared transparent carbon membrane (graphene) functions as both an optical window and working electrode, while a metalized AFM probe opposite and adjacent to the interface enhances and confines incident infrared light. In this way, collection of nano-FTIR spectra from nanoscopic volumes subsurface to graphene (the interfacial region) are readily performed.

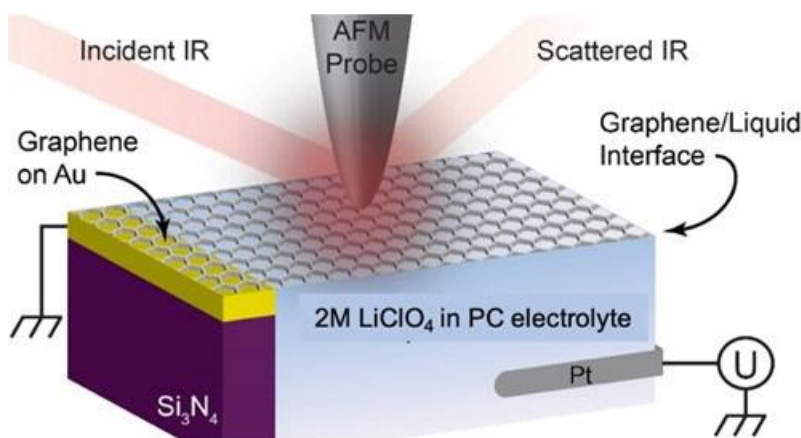


Figure XII.1.6 A schematic of experimental and device setup for graphene-liquid electrochemical in situ cell for infrared near-field imaging and nanospectroscopy, previously used in our group.

As described in the Q2 milestone, beyond the designing, building, and testing of the device, preliminary experiments were to be conducted which would build toward the eventual probing of the Li/liquid-electrolyte interface in future milestones. As a natural progression to this end, we opted to use an electrolyte which is less chemically complex than GEN2: 2M LiClO₄ in propylene carbonate (PC). Firstly, attenuated total reflection Fourier transform infrared spectroscopy (ATR-FTIR) of the bulk electrolyte was collected (top of Figure XII.1.7) and compared with nano-FTIR absorption of the graphene/liquid-electrolyte interface (bottom of Figure XII.1.7). It is clear by direct comparison that the molecular environment of the bulk and interface must be significantly different. Contributing to this discrepancy is likely the differences in average ion solvation between the bulk and interface. These measurements confirmed our device and experimental setup is capable of characterizing the interface, *in situ*.

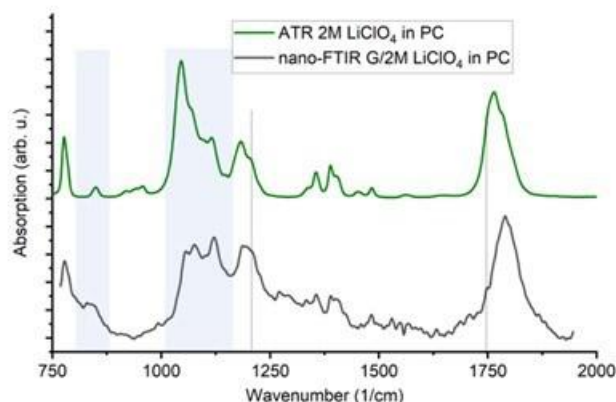


Figure XII.1.7 Comparison of ATR-FTIR of 2M LiClO₄ in PC (top green trace) and nano-FTIR spectra of the graphene / 2M LiClO₄ in PC interface (bottom black trace). Light blue bars and black vertical lines highlight measured differences in IR absorption between the bulk and interface.

Secondly, following the *in situ* methodology already described in the first paragraph, spatially-dependent nano-FTIR were collected along the graphene/liquid-electrolyte interface at roughly 100nm separations (and ca. 20nm resolution), while in an open circuit state. These spectra are plotted in Figure XII.1.8a, and possess subtle differences in a few regions, such as around 1200 and 1750 cm^{-1} (note the $\sim 1700\text{-}1900\text{ cm}^{-1}$ region corresponds to the carbonyl C=O group for PC). The modest heterogeneities in absorption may arise from *local* variations in (i) the concentration of free PC molecules (ii) the solvation state of interfacial ionic species, (iii) orientations of physisorbed ClO_4^- , and (iv) structure and composition of the electric double and diffuse layers. In any case, ultimately, these naturally occurring nanoscale heterogeneities in the infrared absorption spectra certainly point to *nanoscale* heterogeneities in the local molecular environments which together comprise the interface. As shown in our recently published work for polymer electrolyte systems, these heterogeneities may be the source for additional subsequent heterogeneities in Li plating and interphase formation - though additional work to verify this is still needed.

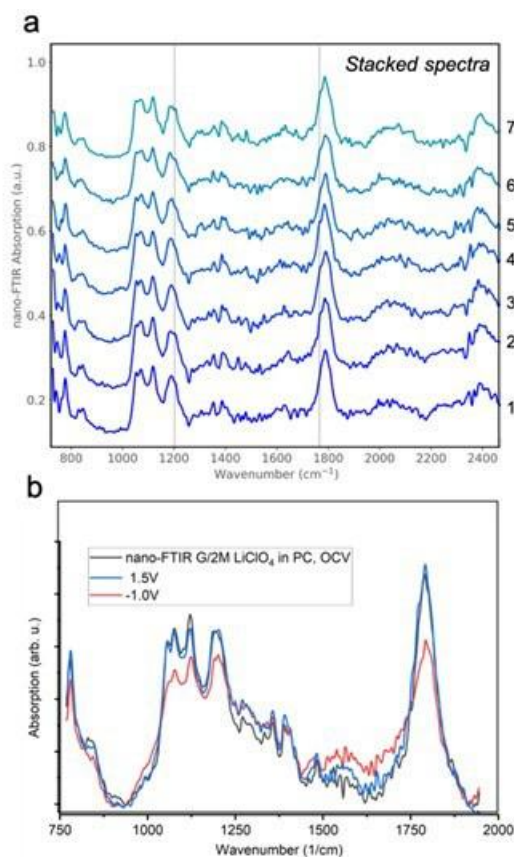


Figure XII.1.8 a) Spatially-resolved Nano-FTIR spectra across the graphene / 2M LiClO_4 in PC interface. Noted with the black lines are changes in shoulder of the peaks b) biased nano-FTIR data collected over single location

Thirdly, gold contacts to the graphene enable the biasing of the graphene working electrode with respect to a thin-diameter wire of choice which can be inserted into the liquid electrolyte reservoir (a few microliters in volume). For these preliminary measurements focused on demonstrating the device functionality and methodological transferability to a multiplicity of chemistries, we chose to conduct basic potential step experiments, to ensure the device was diffusion limited, and once a steady state was reached, collect nano-FTIR. To accomplish these *in-situ* bias-dependent measurements, we chose a silver wire. As the graphene electrode is biased, and charge is transferred to/from graphene proceeds, the graphene/liquid interface should respond, including the local distribution and concentration of electrolyte solution components. These changes

should be observable in the nano-FTIR if it is actually primarily probing the interface. Indeed, such findings are reflected in the bias-dependent nano-FTIR spectra we collected (Figure XII.1.8c).

We have also progressed towards the characterization of relevant interfaces and interphases, and the unveiling of key structures, chemistries, and mechanisms that originate therein, by proposing an *in situ* electrochemical cell. We find motivation from our recently published work (He, X., Larson, J. M., Bechtel, H. A., & Kostecki, R. (2022) *Nat Comm*, 13(1), 1-10.), to develop a new *in situ* cell (Figure XII.1.6 A.) that is compatible with non-polymer solid-state electrolytes. This device form should accommodate a number of solid-state electrolyte chemistries, but our first intended target will be lithium aluminum germanium phosphate (LAGP). With that in mind, before cell fabrication, we collected AFM (Figure XII.1.9. B), infrared white light images, and spatially dependent nano-FTIR (Figure XII.1.9. C) of an LAGP sample. Our initial exploratory data indicates that chemical heterogeneities exist on a spatial scale that can only be spectroscopically resolved with novel near-field techniques capable of sub-diffraction-limit characterization ($\lesssim 3$ micron spacing); similar to our recent work (He, X., Larson, J. M., Bechtel, H. A., & Kostecki, R. (2022) *Nat Comm*, 13(1), 1-10). These results support the continuation of this research trajectory, as mitigating such intrinsic heterogeneities and corresponding deleterious effects will be crucial for advanced energy storage schemes; and understanding such heterogeneities, and related phenomena, is a necessary first step toward this end.

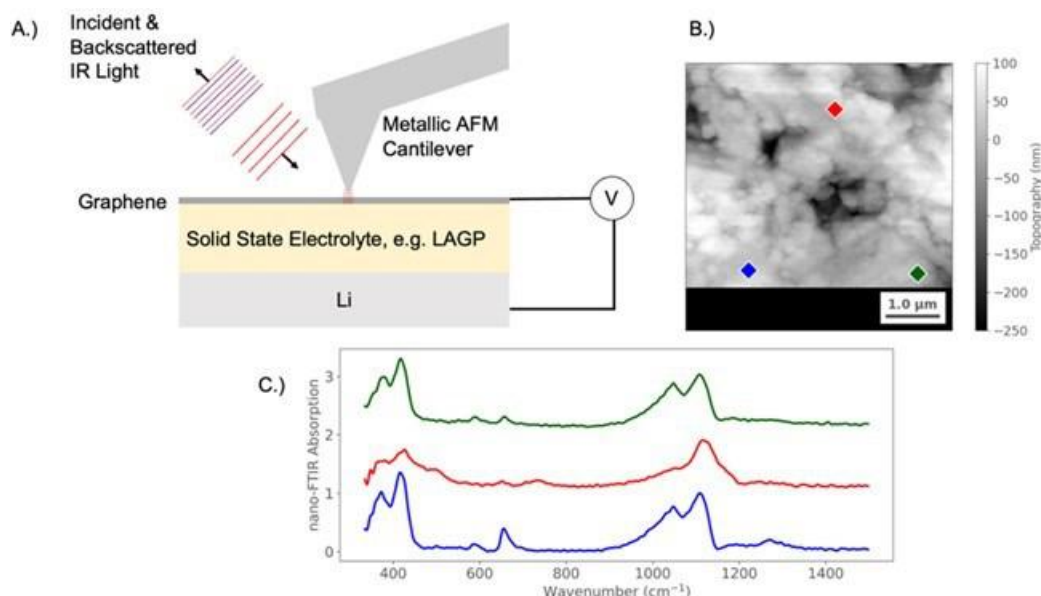


Figure XII.1.9 A.) Schematic of conceptualized *in situ* solid-state electrochemical cell to be prepared. B.) AFM topography data of a pristine LAGP surface. Colored diamonds indicate locations where nano-FTIR were collected. C.) Spatially dependent nano-FTIR absorption data which shows sub-diffraction-limit chemical heterogeneity across the LAGP surface; traces are color matched to the corresponding spatial locations shown in B.

Lastly, we have progressed in applying a complimentary method to nano-FTIR: Surface-enhanced Raman spectroscopy. To get a full picture of vibrational spectra of early SEI components and record Raman spectra, we employed Surface-enhanced Raman spectroscopy approach, where a metal nanostructure enhances Raman signal from molecules in ~ 10 -nm radius around the said structure. Although the lateral resolution does not break the optical limit, this technique is only sensitive to molecules absorbed on the metal surface. When the nanostructured Cu acts as a working electrode, it is possible to analyze SEI components in a close proximity to the electrode. It should be noted that the spectrum of GEN2 electrolyte both shows strong photoluminescence. With SERS, Raman scattering features could be seen over the photoluminescence background. Figure XII.1.10 shows Raman spectra of GEN 2 electrolyte collected through translucent current collector inert to Li: Cu and Ni. Although Ni plasmon resonance belongs to UV region, Raman features of GEN 2 electrolyte on Ni electrode

were still present. This could be explained by chemical mechanism of SERS through charge-transfer between metal substrate and electrolyte molecules.

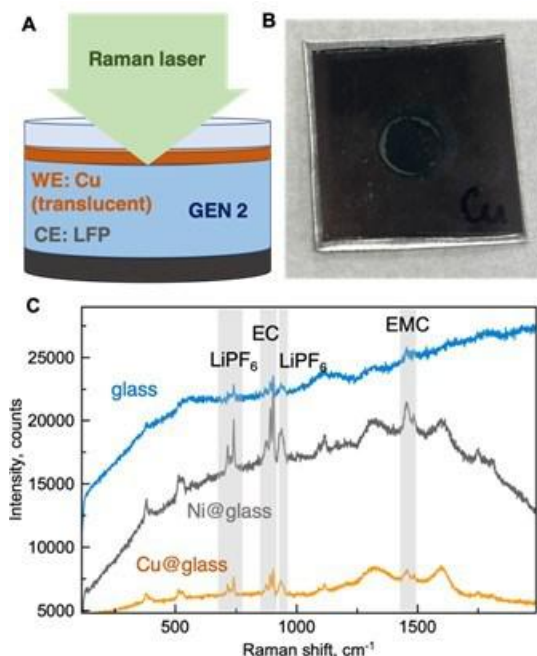


Figure XII.1.10 Surface-enhanced Raman spectroscopy (SERS) approach to investigate early SEI A) Schematic of in-situ SERS electrochemical cell. Thin translucent Cu thin film serves as working electrode and SERS substrate B) image of assembled 2-electrode electrochemical SERS cell.

In order to observe Li plating in-situ, we have assembled an electrochemical cell. In the designed experiment shown in Figure XII.1.11a, translucent Cu acts as a window and working electrode, used as a substrate to deposit Li via electroplating. Thin Cu films can enhance the Raman signal from molecules at the interface due to surface plasmon resonances. Since the effect is surface-sensitive, it is possible to probe reactions at the interface between working electrode and liquid electrolyte, *in situ*.

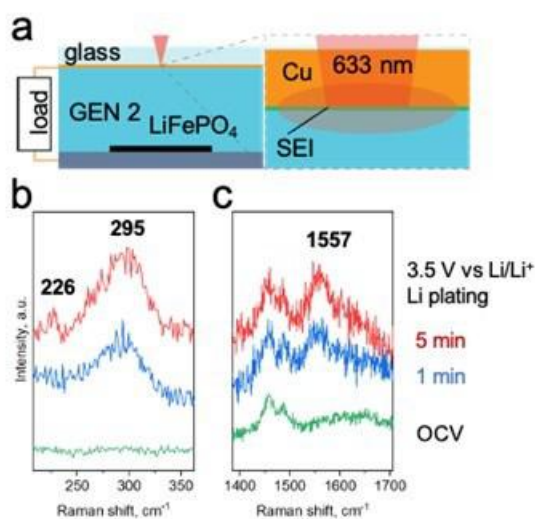


Figure XII.1.11 Probing Li/GEN2 electrolyte interface via Surface-enhanced Raman spectroscopy a) Schematic of SERS experimental setup b) and c) Raman spectra of Cu-GEN2 interface collected during Li plating

Peaks at 226 and 295 cm^{-1} (Figure XII.1.11b-c) emerge during steady Li plating in GEN 2 electrolyte. These peaks' intensities increase with the increasing time of Li plating. Such low frequencies were previously found to contain Li-Li vibrations in lithium clusters⁵. In the higher frequencies' region, a peak observed at 1557 cm^{-1} emerges which could be related to carbonate decomposition products. Further investigation of these phenomena will be an objective of following studies.

Conclusions

- Investigated SEI layer formed between Li metal and GEN2 electrolyte at nanometer resolution using *in situ* near-field IR nano-spectroscopy
 - Developed an effective strategy for preparing clean Li metal anodes with minimum contamination
 - Showed nanometer-scale inhomogeneities in Li metal SEI formed after the first cycle
 - Progressed towards applying same methodology to Garnet-type solid state electrolytes
- Pioneered *in situ* near-field IR experiments to investigate Li/carbonate-based liquid electrolyte interfaces at nanometer resolution
 - Successfully collected electrically biased spectra of graphene-carbonate electrolyte interface
 - Developed a complimentary technique to study SEI of Li metal in-situ based on Surface-enhanced Raman spectroscopy
- Developed and implemented a novel methodology, based on ATR-FTIR and near-field IR nano-FTIR, to interrogate buried and intact interfaces in a model solid-polymer-electrolyte (SPE) battery at various electrochemical states. In particular, this approach enabled *in situ* characterization of the SEI that forms at the Li/SPE interface. Moreover, we were able to identify that nanoscale heterogeneities implicit to the SPE are likely the source of heterogenous Li-plating, electrolyte decomposition, and SEI formation; and that molecular-level engineering will need to be used to overcome this challenge (He, X., Larson, J. M., Bechtel, H. A., & Kostecki, R. (2022) *Nat Comm*, 13(1), 1-10).

Key Publications

1. He, Xin, Jonathan M. Larson, Hans A. Bechtel, and Robert Kostecki. "In situ infrared nanospectroscopy of the local processes at the Li/polymer electrolyte interface." *Nature communications* 13, no. 1 (2022): 1-10.

Acknowledgements

This work has been performed in close collaboration with: V. Battaglia: ABMR program leads, ABMR Cathode and Anode Task Groups: ANL, LBNL, SUNY, UP, HQ, NREL and UU (R-C. Lee, J. Franklin, G. Chen, V. Battaglia, M. Doeff, K. Persson, V. Zorba, W. Yang, C. Ban, N. Balsara, B. McCloskey), Advanced Light Source (H. Bechtel, E. Rotenberg, E. Crumlin), University College London (P. Shearing, J. Franklin), University of Liverpool (UK) (L. Hardwick), Central Laser Facility, Research Complex at Harwell (UK), University of California, Berkeley, Umicore, and Farasis Energy, Inc.

XII.2 Advanced in situ Diagnostic Techniques for Battery Materials (BNL)

Xiao-Qing Yang, Principal Investigator

Chemistry Division, Brookhaven National laboratory
Bldg. 555, Brookhaven National Lab.
Upton, NY 11973
E-mail: xyang@bnl.gov

Enyuan Hu, Co-Principal Investigator

Chemistry Division, Brookhaven National laboratory
Bldg. 555, Brookhaven National Lab.
Upton, NY 11973
E-mail: enhu@bnl.gov

Tien Duong, DOE Technology Development Manager

U.S. Department of Energy
E-mail: Tien.Duong@ee.doe.gov

Start Date: October 1, 2021

End Date: September 30, 2022

Project Funding (FY22): \$425,000

DOE share: \$425,000

Non-DOE share: \$0

Project Introduction

This project is focused on the development of advanced diagnostic characterization techniques for the following issues: obtaining in-depth fundamental understanding of the mechanisms governing the relationship between the structure and the performance of battery materials; providing guidance and approaches to improve the properties of battery materials. The approach of this project is the development and application of combined synchrotron based in situ X-ray techniques such as x-ray diffraction (XRD), pair distribution function (PDF), hard and soft x-ray absorption (XAS and SXAS), together with other imaging and spectroscopic tools such as transmission electron microscopy (TEM), scanning transmission electron microscopy (STEM), mass spectroscopy (MS), X-Ray fluorescence microscopy (XRF) and transmission x-ray microscopy (TXM), as well as neutron-based techniques, such as neutron diffraction and neutron PDF (NPDF). For advanced Li-ion battery technologies, the revolutionary approaches using new generation of materials for cathode, anode, electrolyte, and separator are in the horizon. The new generation of cathode materials such as Li-rich high energy density $\text{Li}_{1+x}(\text{NiMnCo})\text{O}_2$ (NMC) composite materials, high Ni content, NMC cathode materials, and high energy density S-based cathode materials, together with high energy density lithium metal anode materials will significantly increase the energy density of the advanced Li-ion and beyond lithium-ion battery systems. However, many technical barriers must be overcome before the large-scale commercialization of these new materials can be realized. This project uses the time-resolved x-ray diffraction TR-XRD and absorption (TR-XAS) developed at BNL to study the kinetic properties of these materials with structural sensitivity (TR-XRD) and elemental selectivity (TR-XAS). This project develops and applies the HRTEM, TXM and PDF techniques, as well as neutron diffraction and neutron PDF to study the mechanisms of capacity and performance fading of cathode and anode materials. Another important issue is the thermal stability of new cathode materials which is closely related to the safety of the batteries. This problem has been studied using the combined TR-XRD, TR-XAS with mass spectroscopy (MS). This project also develops a novel in situ and ex situ X-ray fluorescence (XRF) microscopy combined with X-ray absorption spectroscopy (XAS) technique, which will enable us to track the morphology and chemical state changes of the electrode materials during cycling. In summary, this project supports the goals of VTO, the Battery and Electric Drive Technologies, and BMR program by developing new diagnostic technologies and applying them to the advanced Li-ion as well as beyond lithium-ion (such as Li-metal, Na-ion, and Li-S) battery systems and by providing guidance for new material development.

Objectives

The primary objective of this project is to develop new advanced in situ material characterization techniques and to apply these techniques to support the development of new cathode, anode, and electrolyte materials with high energy and power density, low cost, good abuse tolerance, and long calendar and cycle life for the next generation of lithium-ion batteries (LIBs) and beyond Li-ion batteries (Li-metal, Na-ion, and Li-S) to power plug-in hybrid electric vehicles (PHEV) and electric vehicles (EV). The diagnostic studies have been focused on issues relating to capacity retention, thermal stability; cycle life and rate capability of advanced Li-ion and beyond Li-ion batteries.

Approach

- Develop and apply advanced diagnostic techniques to study and improve the performance of high energy density LIBs and Li/S batteries.
- Using nano-probe beamline at NSLSII to study the elemental distribution of new solid electrolyte materials for Li-ion and Na-ion batteries
- Using hard X-ray fluorescence (XRF) imaging on the concentration gradient Ni-rich NCM cathode particles in a noninvasive manner with 3D reconstructed images through tomography scans to study the 3D Ni, Co, and Mn elemental distribution from surface to the bulk
- Using transmission X-ray Microscopy (TXM) studies on the concentration gradient Ni-rich NCM cathode particles with 3D reconstructed images through tomography scans.
- Using the S K-edge XRF imaging and XAS studies with examination of the reaction products on the sulfur cathode and Li-metal anode in high energy density Li/S cell.

Results

In FY2022, BNL has been focused on the development of new diagnostic techniques to study and improve the performance of beyond Li-ion batteries such as solid state batteries. Solid-state electrolyte is the key component of solid-state batteries. $\text{Li}_7\text{P}_2\text{S}_8\text{I}$ is one type of solid electrolyte with high ionic conductivity but poor stability against high voltage cathode such as $\text{LiNi}_{0.8}\text{Mn}_{0.1}\text{Co}_{0.1}\text{O}_2$ (NMC811). Its derivative $\text{Li}_7\text{P}_2\text{S}_8\text{I}_{0.5}\text{Br}_{0.5}$ (LPSIB) has improved high voltage stability but is still not stable against NMC811 above 4.5 V. The mechanism of such instability has not been clearly understood. Studies were planned in collaboration with Dr. Dongping Lu of PNNL to investigate such issue. Synchrotron-based XRD and PDF have been carried out for three samples: 1. Pristine LPSIB electrolyte; 2. NMC811 cathode charged to 4.5 V in liquid electrolyte; 3. Mixture of charged to 4.5 V NMC811 with LPSIB to study the interaction between them. Note that no reaction between NMC811 and LPSIB was involved for sample 2. Sample#3 is the same material of sample#2, but reacted with LPSIB. XRD data in Figure XII.2.1a shows that LPSIB has very few and broad peaks, suggesting that the crystallinity of LPSIB is very low. Charged NMC811 has the typical layered structure, and all its peaks can be indexed using the $R\bar{3}m$ space group. After mixing with LPSIB, both (003) and (110) peaks for sample 3 show obvious shift to the lower 2θ , suggesting both c and a axes lattices were expanded. PDF, as a total scattering technique, can probe both crystalline and amorphous phases and is the ideal tool for structural study of solid electrolyte. Figure XII.2.1b shows the PDF data of LPSIB and all the peaks in the low “ r ” region can be accounted for by chemical bonds or indirect correlations. Note that the broadening of peak at around 4 Å is due to the anion disorder or paddle wheel rotation effect. The long-range PDF data for LPSIB in Figure XII.2.1c confirms that LPSIB has no long-range order indicated by the almost flat line in 30-50 Å region. The long-range region data becomes weaker after NMC811 4.5V is mixed with LPSIB, suggesting poorer crystallinity. The short-range PDF data of NMC4.5 V has peaks at around 1.8 Å and 2.8 Å, corresponding to the transition metal (TM)-O bond and the TM-TM correlation respectively. Both peaks shift to higher “ r ” region after mixing with LPSIB, suggesting the oxidation state of TM in NMC811 was reduced. One possible reaction mechanism is that some S atoms replace O atoms in the NMC811 lattice and bonded with TM. This is supported by the fact that the intensity ratio between the first and the second peak increases after mixing.

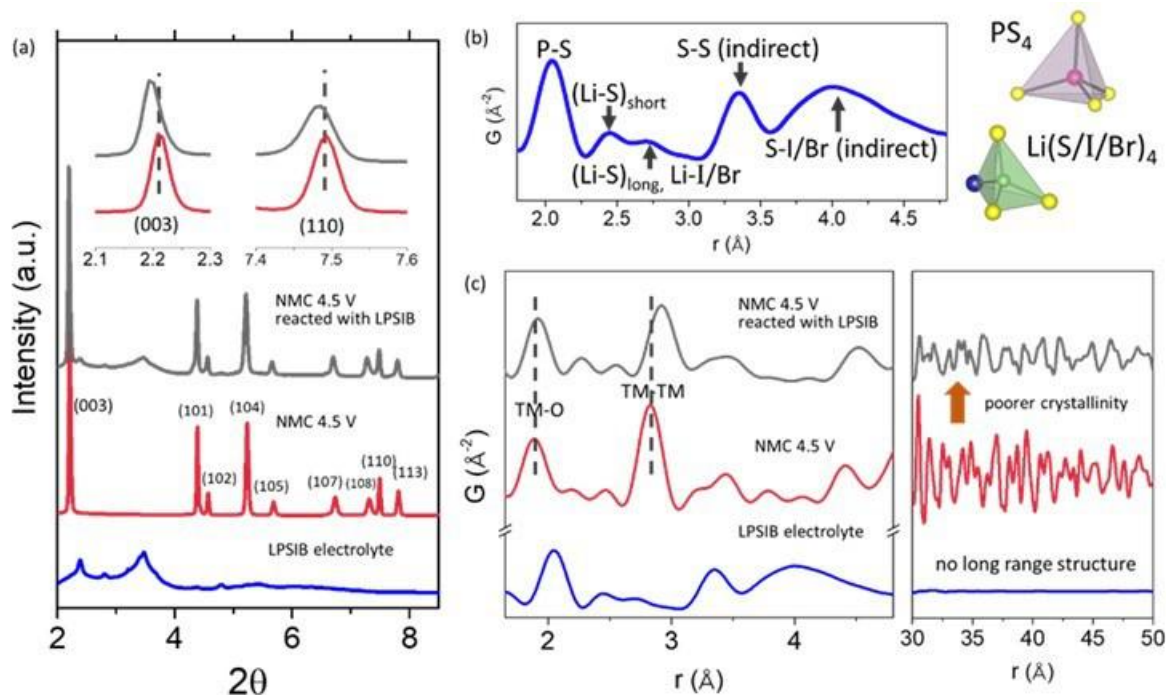


Figure XII.2.1 (a) Synchrotron XRD of #1. LPSIB (blue); #2. NMC8.11 charged to 4.5 V (red); #3. sample #2 mixed with LPSIB (black). (b) the short-range PDF data of LPSIB electrolyte with PS_4 and $\text{Li}(\text{S/I/Br})_4$ tetrahedra in the structure shown. (c) the short- and long-range PDF data of the samples #1, #2, and #3.

In FY2022 **BNL** also carried out the development of the advanced diagnostic techniques to achieve the thorough understanding of high energy density and long cycle life electrode materials. Li metal anode are regarded as one of the most promising anode materials for next generation Li-batteries because of the high theoretical capacity. However, the degradation of Li metal anodes related to unfavored interphase behaviors during electrochemical cycling is still a setback for its practical applications on electric vehicles. Great efforts have been devoted to solving the interphase problem for the Li metal anode by developing novel electrolytes in the past few years. For example, LiNO_3 has been widely used as an additive for the Li metal anode. However, the mechanism of how LiNO_3 improves the solid electrolyte interphase (SEI) for Li metal is still unclear, which greatly slows down the novel additive development. Therefore, the investigation of the effects of LiNO_3 on the Li metal anode was planned by using cryo-TEM. A cryo-electron microscopy study was carried out on the Li metal plated in the electrolyte with and without the LiNO_3 additive by **BNL** team. The cryogenic condition can greatly enhance the beam tolerance of Li metal and the SEI therefore reduce beam damage on the samples. As shown in Figure XII.2.2a and Figure XII.2.2b, the Li plated in the baseline electrolyte without LiNO_3 are in dendritic form. On the other hand, with LiNO_3 added, the Li are plated as uniform spheric Li particles and Li dendrite formation is greatly suppressed. Moreover, uniform and conformal SEI is formed with the help of LiNO_3 additive, which could be correlated with the improved capacity retention for LiNO_3 -added electrolyte. The fast Fourier transform pattern on a selected SEI area shows three different inorganic components in the SEI formed with LiNO_3 -added electrolyte.

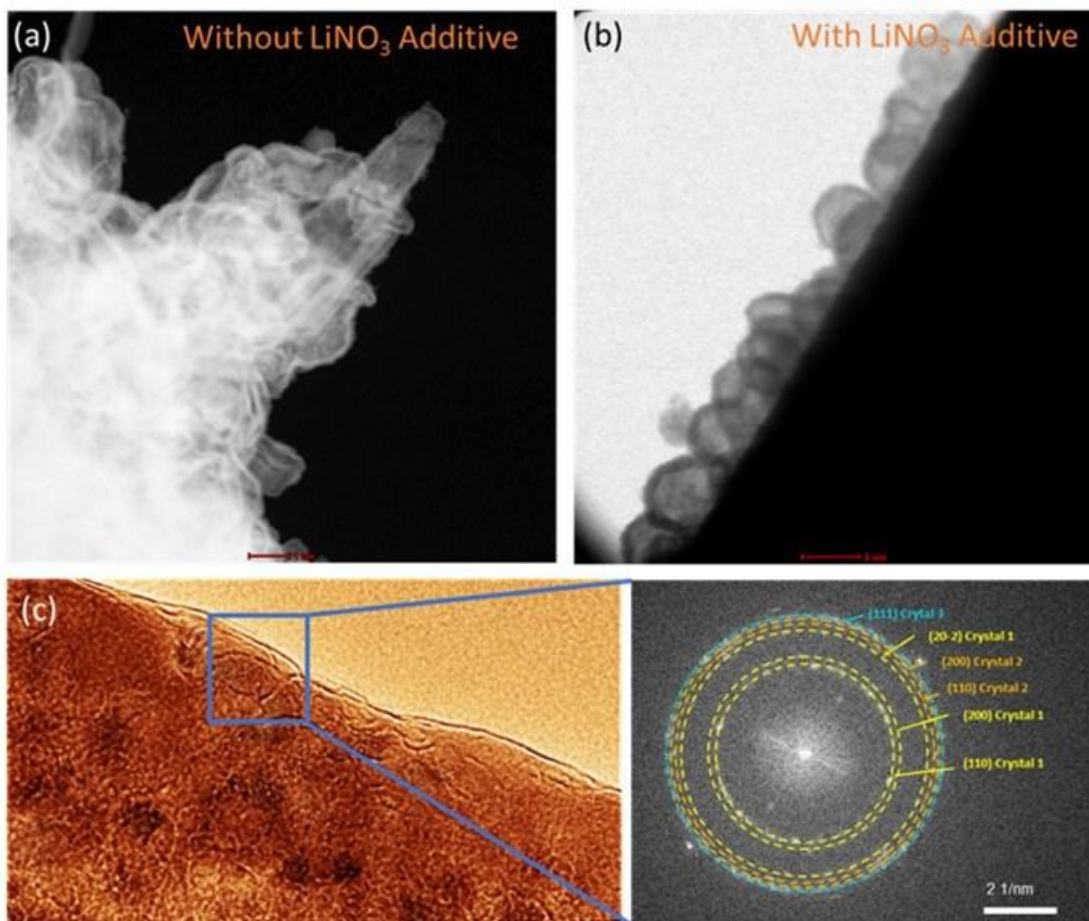


Figure XII.2.2 (a) Cryo-HAADF-STEM of plated Li dendrite in baseline electrolyte without LiNO_3 additive; (b) Cryo-bright field-STEM of plated Li particles in electrolyte with LiNO_3 additive; (c) Cryo-TEM and selected area diffraction of the SEI formed in electrolyte with LiNO_3 additive.

In FY2022, BNL team has been focusing on developing advanced diagnostic techniques to achieve the thorough understanding of high energy density and long cycle life electrode materials. $\text{LiNi}_{0.8}\text{Mn}_{0.1}\text{Co}_{0.1}\text{O}_2$ (NMC811), as an important high energy density cathode material for lithium batteries, suffers from capacity fading upon cycling. Several factors such as oxygen loss, surface reconstruction, and particle cracking have been identified to be responsible for the fading but whether these factors are independent or correlated has not been clearly understood yet. To answer this question, BNL team used multi-modal characterization tools at multi scale lengths to study long cycled NMC811 cathode (2.8-4.4V after 100 cycles). This work is done in collaboration with scientists at Stanford Synchrotron Radiation Lightsource, SLAC National Accelerator Laboratory. An electrode level computed tomography scan was done at the European Synchrotron Radiation Facility (ESRF) with results shown in Figure XII.2.3a, indicating after long cycling, the NMC811 particles experience various levels of morphological degradation. To study the chemical nature of these individual particles and therefore identify the possible correlation between chemical and morphological properties, the same electrode was characterized at National Synchrotron Light Source II (NSLS II) using a focused beam with beam size of around $10\text{ }\mu\text{m}$ for a particle-level characterization. Figure XII.2.3b shows the color-coded particles that have been labelled according to their morphological degradation extent (the bigger the number, the more serious degradation) and these labelled particles are further studied using x-ray absorption spectroscopy. Figure XII.2.3c, d, e show the details of representative particles that have different degrees of morphological degradation. Figure XII.2.3f shows the x-ray absorption near edge spectroscopy (XANES) results at Ni K-edge for selected particles p1, p2, p3, p4, and p5. The more damaged particles have lower edge energy which suggests lower oxidation state of the Ni, clearly indicating the correlation between

morphological degradation and chemical state. Such trend can be seen more clearly in Figure XII.2.3g, where the Fourier transformed extended x-ray absorption fine structure (ft-EXAFS) spectra show clear trend of the increased Ni-O bond distance at about 1.5 Å (not phase corrected) from p1 to p5, resulting from the reduced oxidation state of Ni. The decreased peak intensity going from p1 to p5 is likely due to oxygen vacancy induced by oxygen loss. These results demonstrated that the oxygen loss at high voltage charging plays an important role in the crack formation and capacity degradation of NMC811 particles. This study suggests that tuning the oxygen activity and suppressing the oxygen loss can potentially help to address the crack issue in NMC811 particles.

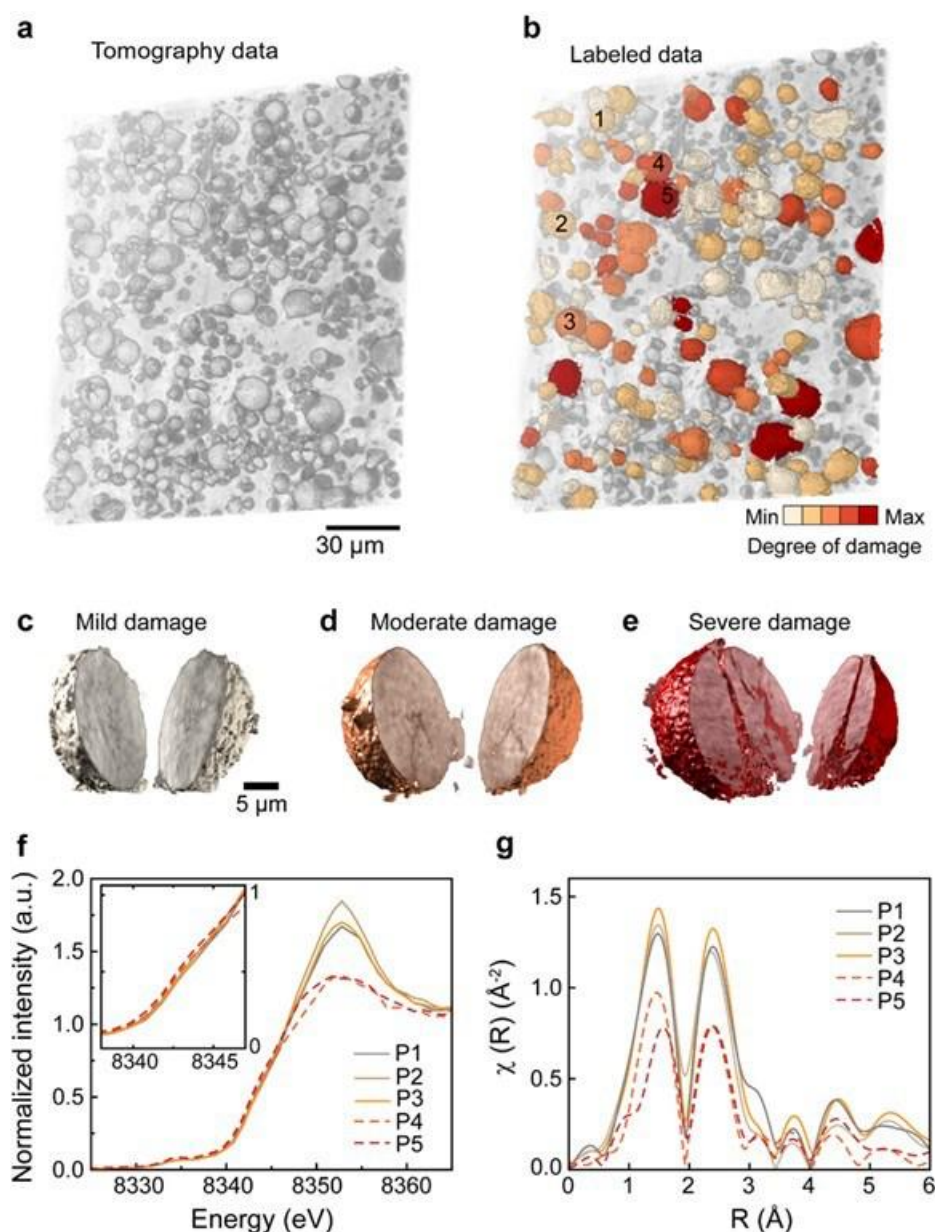


Figure XII.2.3 (a) computed tomography scan of cycled NMC811 electrode; (b) particles labelled based on their morphological damage extent; (c) to (e) details of representative particles having various degrees of damage; (f) XANES data of selected particles in (b); (g) ft-EXAFS data of selected particles in (b).

The *ex situ* soft X-ray absorption spectroscopy (sXAS) studies have been completed at **BNL** for polymeric sulfur (sulfurized polyacrylonitrile, or SPAN) cathode to understand how electrolytes influence the cathode-electrolyte-interphase (CEI). The work is done in collaboration with UCSD. Three types of electrolytes were used: 1. Localized high concentration electrolyte (LHCE): 1.8 M LiFSI in DEE/BTFE (DEE: diethyl ether; BTFE: bis(2,2,2-trifluoroethyl)ether; weight ratio 1:4) 2. Carbonate electrolyte: 1 M LiPF₆ in EC/EMC (EC: ethylene carbonate; EMC: ethyl methyl carbonate; volume ratio 3:7) 3. Ether electrolyte: 1 M LiTFSI in DOL/DME (DOL: 1,3-dioxolane; DME: dimethoxyethane; volume ratio 1:1). The data was collected in both total electron yield (TEY) mode and partial fluorescence yield (PFY) mode which has probing depth of 2~5 nm and >10 nm respectively.

The carbon K-edge sXAS results are shown in Figure XII.2.4. In the pristine sample, the peaks at ~285.5 eV and ~288.5 eV arise from different antibonding orbitals associated with the C=C bond in the SPAN pyridine rings. Other peaks corresponding to various functional groups in SPAN are indicated in the figure. Upon cycling, new peaks arise and evolve and their ways of evolution is highly dependent on the electrolyte used. Comparing the TEY data among different electrolytes, it is obvious that carbonate electrolyte leads to Li₂CO₃ formation in the CEI as indicated by the peak located at around 290.5 eV. Ether electrolyte generates semi-carbonates in the CEI as the corresponding peak is slightly lower in energy. This is probably due to the ring-opening and polymerization of DOL solvents. In contrast, LHCE does not generate any carbonate in the CEI. Instead, it may generate some esters as indicated by the growth of the peak at 288.6 eV. In all the electrolytes used, there are vinyl-group-containing species formed in the CEI as indicated by the peak at around 285.2 eV and close to the pyridinic $1\pi_{C=C}^*$ peak. Comparing among different cycles, LHCE forms a stable CEI even in the formation cycle as the spectra show little change from 1st cycle to the 50th cycle. However, both carbonate and ether electrolytes cannot form a stable CEI and the spectra keep evolving during cycling.

The PFY results are different from that of the TEY results, suggesting that CEI chemical compositions have depth-dependence. For example, the carbonate (either Li₂CO₃ or semi-carbonate) and ester peaks are much weaker in PFY than in TEY, indicating that these species are more likely on the top layer of CEI and on the side close to the electrolytes. Interestingly, PFY have peaks at around 284.1 eV that are absent in the TEY data. These low energy peaks typically arise from multi-ring molecules such as fused benzene/pyridine rings or their various derivatives with nitrogen substitution. Considering their close relationship to the SPAN structure which is built upon the network of pyridines, it is likely that these multi-ring molecules are the decomposition product of SPAN and lie in the bottom of CEI and on the side close to SPAN electrode. This study reveals the chemical composition and spatial distribution of SPAN CEI and how these are influenced by the electrolyte used.

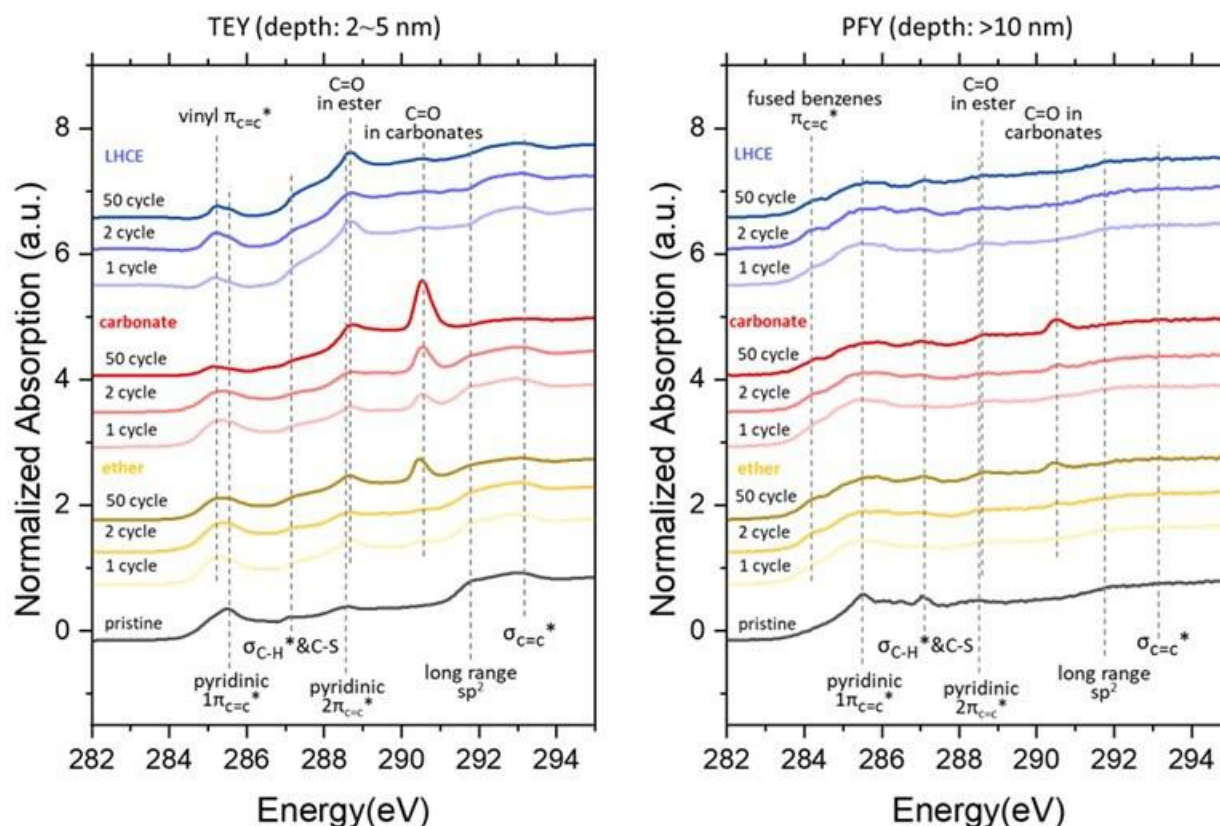


Figure XII.2.4 Carbon K-edge XAS both in TEY (left panel) and PFY (right panel) of ex situ SPAN electrodes cycled in various electrolytes.

Conclusions

This project, “Advanced in situ Diagnostic Techniques for Battery Materials (BNL)”, has been successfully completed in FY2022. All milestones have been completed. The publication records are very good. Extensive collaboration with other national Labs, US universities and international research institutions were well established.

Key Publications

1. Yunxian Qian, Yanli Chu, Zhongtian Zheng, Zulipiya Shadike, Bing Han, Shuhuai Xiang,, Yuanyuan Kang Shiguang Hu, Chaowei Cao, Ling Zhong, Qiao Shi, Muchong Lin, Hongbo Zeng, Jun Wang,, Enyuan Hu Conan Weiland, Xiao-Qing Yang, and Yonghong Deng, “A new cyclic carbonate enables high power/ low temperature lithium-ion batteries”, *Energy Storage Materials*, 45 (2022) 24-32, DOI: 10.1016/j.ensm.2021.11.030, Publication Date: November 24, 2021.
2. Sha Tan, Zulipiya Shadike, Jizhou Li, Xuelong Wang, Yang Yang, Ruqian Lin, Arthur Cresce, Jiangtao Hu, Adrian Hunt, Iradwikanari Waluyo, Lu Ma, Federico Monaco, Peter Cloetens, Jie Xiao, Yijin Liu*, Xiao-Qing Yang*, Kang Xu*, and Enyuan Hu*, “Additive engineering for robust interphases to stabilize high-Ni layered structures at ultra-high voltage of 4.8 V”, *Nature Energy*, VOL 7, June 2022 484–494 DOI: 0.1038/s41560-022-01020-x. Publication date: May 9, 2022.
3. Ruqian Lin1*, Yubin He, Chunyang Wang, Peichao Zou, Enyuan Hu, Xiao-Qing Yang*, Kang Xu, Huolin Xin*, “Characterization of the structure and chemistry of the solid-electrolyte interface by cryoEM leads to high-performance solid-state Li-metal batteries”, *Nature Energy*, DOI: 10.1038/s41565-022-01148-7. Publication date: June 30, 2022

XII.3 Microscopy Investigation on the Fading Mechanism of Electrode Materials (PNNL)

Chongmin Wang, Principal Investigator

Pacific Northwest National Laboratory
902 Battelle Boulevard, Mail Stop K8-93
Richland, WA 99352
E-mail: Chongmin.wang@pnnl.gov

Tien Duong, DOE Technology Development Manager

U.S. Department of Energy
E-mail: Tien.Duong@ee.doe.gov

Start Date: October 1, 2021

End Date: September 30, 2024

Project Funding (FY22): \$400,000

DOE share: \$400,000

Non-DOE share: \$0

Project Introduction

Li metal is intensively explored as anode for high energy density rechargeable. However, a range of fundamental questions regarding Li metal stripping and deposition need to be answered. It is well known that a SEI layer will initially be formed on the current collector, such as Cu. With continued decreasing potential, Li deposition will happen through nucleation and growth at the interface between Cu and the SEI layer formed on Cu. Apparently, the nucleation and growth behavior Li will be initially affected by characteristics of the SEI layer on the Cu. Therefore, the properties of the SEI layer on Cu, such as the mechanical strength, Li ion transport characteristics, and electrical conduction properties, will affect the features of the deposited Li. These properties have been only inferred, but not directly measured. We will focus on addressing the challenges related to the stability of Li metal anode, lithium nickel-manganese-cobalt oxide cathode, sulfur based solid electrolyte and interfaces defined by these active components in rechargeable batteries. The project will gain critical insights regarding the structural and chemical evolution of interfaces and their effect on electrode stability, which will form the foundation for addressing the key challenges of rechargeable batteries. The outcome of the proposed study will feed back to the battery materials fabrication group to aid in designing better materials with enhanced battery performance.

Objectives

The main objective is to explore interfacial phenomena in rechargeable Li-ion batteries of both solid-state electrolyte (SSE) and liquid electrolyte (LE) configuration, to identify the critical parameters that control the stability of interface and electrodes as well as solid electrolyte (SE). The outcome will be establishing correlations between structural-chemical evolution of active components of batteries and their properties. These correlations will provide insight and guidance to battery materials development groups for developing high-performance battery materials.

Approach

The project will use integrated advanced microscopic and spectroscopic techniques, including *in situ* and *ex situ* scanning transmission electron microscopy (STEM), environmental STEM, cryogenic electron microscopy, and *in situ* liquid secondary ion mass spectrometry, in collaboration with theoretical modeling, to directly probe the structural and chemical information of active materials in rechargeable batteries. Cryogenic STEM (cryo-STEM) with analytical tools, such as energy dispersive X-ray spectroscopy (EDS) and electron energy loss spectroscopy (EELS), will be used to gain chemical and electronic structural information at the interface between lithium metal and electrolyte of both solid-state and liquid configuration, which will allow direct correlation between the morphology and chemistry. STEM – high-angle annular dark-field atomic-level imaging and EDS/EELS will be used to probe the interface and bulk lattice stability of cathode and SE in

solid-state batteries (SSBs). The work will be in close collaboration with the battery development group within the BMR and U. S. – Germany Collaboration on Energy Storage.

Results

Revealing the dependence of SEI layer structure and composition on the Li local curvature

The biggest challenges for Li metal electrode is the controlled deposition and stripping. Existing knowledge indicates that the morphologies of Li deposits are affected by pressure, temperature, current density, electrolyte composition, and physical/chemical properties of solid electrolyte interphase (SEI) layer. Consequently, various approaches, mostly empirical in nature, have been explored intending to suppress irregular Li growth, including reducing local reaction rate, electric field regulation, and electrolyte modification. Although remarkable progress has been achieved in stabilizing Li electrodeposition, an in depth and comprehensive understanding of the underlying mechanism of Li nucleation and growth is still underdeveloped but is crucial for the practical use of Li-metal batteries.

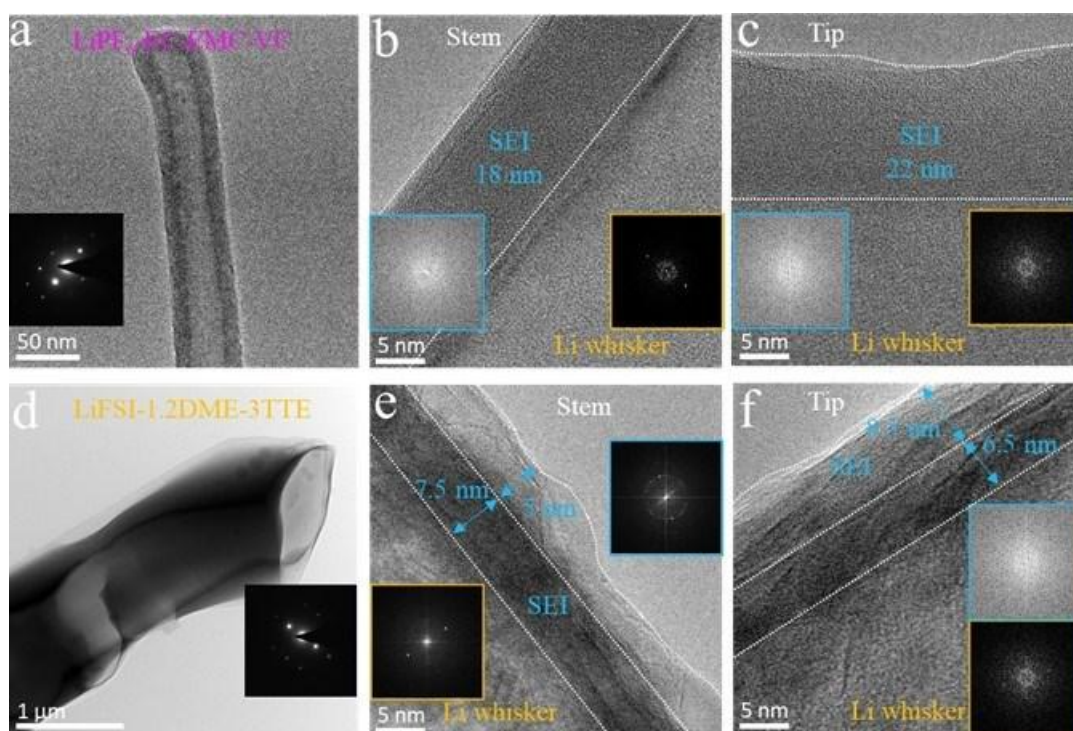


Figure XII.3.1 Microstructure of Li deposits and solid electrolyte interphase (SEI) formed in the different electrolytes. (a-c) Cryo-TEM images of Li deposits formed in the carbonate-based electrolyte: (a) TEM image of Li deposits with whisker morphology. (b) High-resolution TEM images acquired from the stem region of the Li whisker. (c) High-resolution TEM images acquired from the tip region of the Li whisker. (d-f) Cryo-TEM images of Li deposits formed in the ether-based LHCE: (d) TEM image of Li deposits with whisker morphology. (e) High-resolution TEM images acquired from the stem region of the Li whisker. (f) High-resolution TEM images acquired from the tip region of the Li whisker.

We use cryogenic transmission electron microscopy (cryo-TEM) to probe, at atomic level, the features of SEI on Li whisker formed in the carbonate-based electrolyte (LiPF₆-EC-EMC-VC) and ether based localized high concentration electrolyte (LHCE) with LiFSI-1.2DME-3TTE). We reveal that, with the carbonate-based electrolyte, most of the Li whiskers have a length of several micrometers as shown in Figure XII.3.1.a. Select area electron diffraction (SAED) pattern (inset of Figure XII.3.1.a) acquired from the Li whisker indicates that the Li deposits is crystalline Li metal, which is further substantiated by the high-resolution TEM image that taken from whisker stem region and tip region as shown in Figure XII.3.1.b and c. The SEI layer on the Li whisker stem region has a smooth surface, with a thickness of ~ 18 nm, as shown by the atomically resolved TEM image in Figure XII.3.1.1.b. High-resolution TEM image and corresponding FFT pattern (inset of Figure

XII.3.1.b with blue coded color) indicate its amorphous structure. The interface between Li whisker and SEI is atomically sharp (Figure XII.3.1.b). Similarly, the SEI layer on the Li tip region also exhibits amorphous structure but with thicker thickness (22 nm).

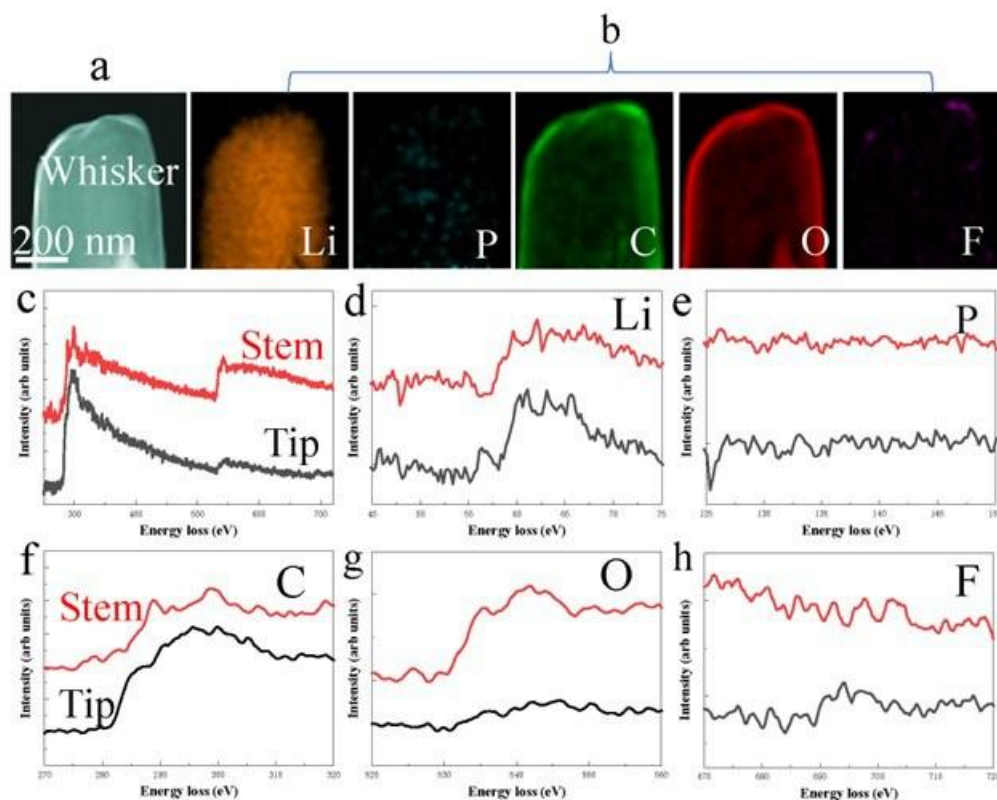


Figure XII.3.2 Structure and elemental composition of Li deposits and their SEIs formed in the carbonate-based electrolyte. (a) STEM-HAADF image showing the Li whisker. (b) EELS elemental mapping showing the elemental distribution of SEI. (c) EELS acquired from stem and tip region of the whisker. (d) EELS of Li. (e) EELS of P. (f) EELS of C. (g) EELS of O. (h) EELS of F.

While the Li deposit structure formed in LHCE is different from those formed in the carbonate-based electrolyte, featuring particle-shaped morphology except for very few Li whiskers, which is consistent with previous report that the ether-based LHCE is primarily lead to the formation of large Li particles during deposition. For Li deposits formed in the ether-based LHCE, SAED pattern (inset of Figure XII.3.1.d) and the atomically resolved TEM images (Figure XII.3.1.e and f) indicate that the whisker-shaped Li deposits are single-crystalline Li metals. The SEI layer on the Li whisker stem and tip region shows bilayer structure, which is characterized by an amorphous inner layer of 7.5 nm and a mosaic outer layer of 5 nm on the stem, while an amorphous inner layer of 6.5 nm and a mosaic outer layer of 8.5 nm on the tip. The mosaic outer layer is featured with an amorphous matrix dispersed with Li_2O particles (Figure XII.3.1. e and f).

We further investigated the chemical composition and fine structure of SEI layers by electron energy loss spectroscopy (EELS), revealing the elemental distribution and electronic structure with high spatial resolution. Compositionally, EELS maps (Figure XII.3.2) indicate that the SEI layers on the Li whisker stem and tip region formed in the carbonate-based electrolyte is similarly composed of O, C, F, and P (Figure XII.3.2), with O and C as the dominant components, indicating that the SEI is mainly derived from solvent reduction. However, the relative ratio of O and C on the stem is different from that on the tip as shown in Figure XII.3.3f and Figure XII.3.3g. In addition, tip region is rich of F, which indicates more Li salt decomposition happens in the tip region. Considering the difference on the reduction potential between solvent and Li salt, especially the LiPF_6 has higher reduction potential than solvent, more Li salt decomposition at the tip region is associated

with the potential difference between stem and tip region. It would be expected that the tip region has higher potential distribution than that at the stem region.

While in the ether-based LHCE, SEI layer on the tip region and stem region of the whisker are similarly composed of S, F, O, and N, but different in C. High concentration of S indicates SEI is mainly from reductive decomposition of Li salt, while C concentration near whisker tip region indicate enhanced solvent reduction on tip region. The difference of the composition of SEI layer at the tip and the stem of the whisker in those two electrolytes clearly show the nonuniform formation of SEI on Li whisker. Indicating the close correlation between the morphology of the whisker and SEI composition.

We reveal that composition of SEI formed on the tip and stem region of a Li whisker is different. As contrasted with the stem region, an enhanced electrical field at the tip region will lead to the preferential decomposition of certain component in the electrolyte, typically such as LiPF_6 salt around tip region. Further, an enhanced electrical field will also lead to preferential deposition of Li at the tip region, leading to a scenario of self-amplification effect for Li whisker growth. The observation of the distinctive difference of SEI on the tip and stem regions of Li whisker delineates insight on the direct correlation between features of SEI layer and Li morphology, leading to insight on possible tuning of crucial structural and chemical features of SEI to regulate the morphology of Li deposit.

Initial trigger of interfacial reactions between $\text{LiNi}_{0.8}\text{Mn}_{0.1}\text{Co}_{0.1}\text{O}_2$ (NMC811) secondary particle and $\text{Li}_7\text{P}_2\text{S}_8\text{Br}_{0.5}\text{I}_{0.5}$ (LPS) in solid state battery

Stability of cathode solid-state electrolytes interfaces represents a key challenge for using sulfide solid-state electrolytes. Chemical incompatibility, electrochemical reaction, and mechanical issues may all play a role in degrading battery performance. Although remarkable progress has been achieved in increasing interfacial conductivity and enabling high-rate cycling, an indepth and comprehensive understanding of the underlying mechanism of interface reaction between high nickle LiNiMnCoO_2 (NMC) cathode and surfliide solid electrolyte remain unclear.

Here, we use $\text{LiNi}_{0.8}\text{Mn}_{0.1}\text{Co}_{0.1}\text{O}_2$ (NMC811) secondary particle and $\text{Li}_7\text{P}_2\text{S}_8\text{Br}_{0.5}\text{I}_{0.5}$ (LPS) as model materials to investigate the initial trigger of interfacial reactions, revealing the interface structural change between NMC811 and LPS at pristine and after charge by transmission electron microscopy (TEM). We compare the structure of NMC811 secondary particles without embedding and embedded in LPS electrolyte at the state of pristine and after charged to 4.2 V using liquid electrolyte 1M LiPF_6 EC/DEC (V/V). To gain microstructural features, the microstructure of NMC811 secondary particle at pristine and after charged to 4.2 V is compared with NMC811/LPS and NMC811/LPS after charged to 4.2 V. To examine the mechanical damage accumulating in the cathode owing to repetitive lattice volume changes upon cycling, cross-sections of the NMC811 and NMC811/LPS charged to 4.2 V were investigated. We reveal that, during the initial charging, pure NMC811 cathode particles show high density of intergranular cracking. In contrast, the NMC811/LPS show no significant intergranular cracking. Apparently, introducing LPS into NMC811 cathode could effectively prevent the formation of intergranular cracking in the secondary particles.

To assess the interfacial reaction between NMC811 and LPS upon cycling of the battery, we use high resolution TEM to analyze the surface structural and chemical evolution of NMC811. Figure XII.3.3.a-d show the low magnification TEM images of the morphology of NMC811 and NMC811/LPS at pristine and after charging to 4.2 V. As shown in Figure XII.3.3.e-h, pristine NMC811 surface has a layer structure as confirmed by the high-resolution TEM image and the corresponding fast Fourier transforms (FFT). After charging to 4.2 V, a rock-salt layer with a thickness of ~ 2 nm is formed on the surface of NMC811 primary particle. A cathode electrolyte interphase (CEI) of ~ 3 nm on the surface of rock-salt layer, indicating the electrolyte permeation along the grain boundary of NMC811 secondary particle. Apparently, the formation of the CEI layer on the surface and along the crack of the cathode particles led to electrolyte consumption and salt depletion in the electrolyte.

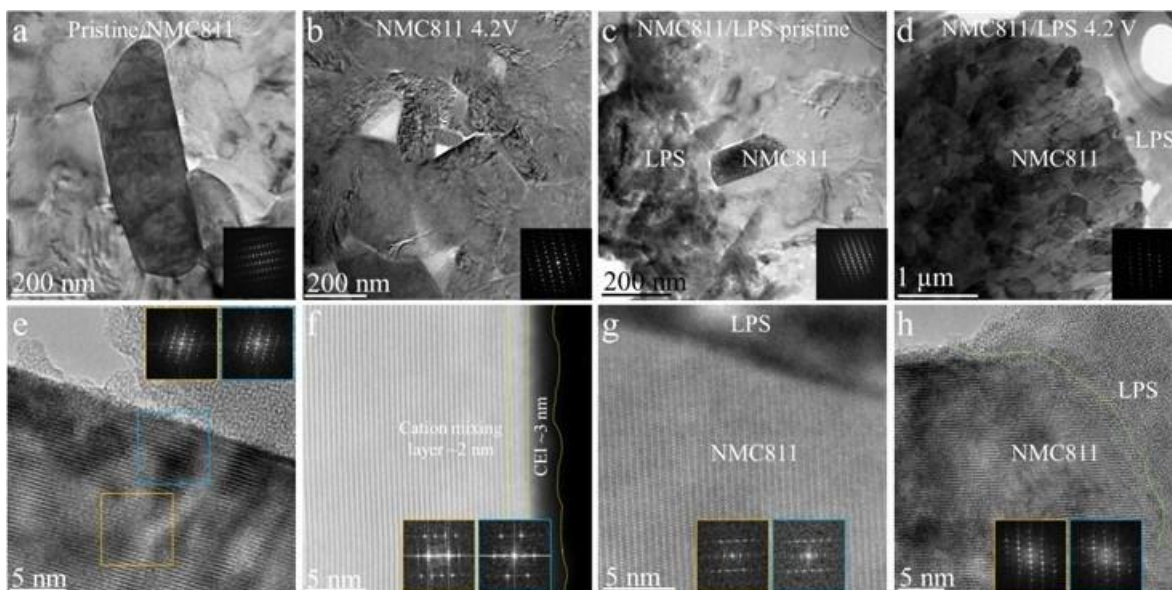


Figure XII.3.3 Microstructure of NMC811 and NMC811/LPS before and after charge. (a) pristine NMC811, (b) NMC811 charged to 4.2 V, (c) pristine NMC811/LPS, and (d) NMC811/LPS charged to 4.2 V. Insets are the selected area electron diffraction (SAED) patterns acquired from primary particle. High resolution TEM images of (e) pristine NMC811, (f) NMC811 charged to 4.2 V, (g) pristine NMC811/LPS, and (h) NMC811/LPS charged to 4.2 V. Insets are FFT patterns acquired from primary particle surface (orange color) and bulk region (blue color).

The pristine state of NMC811/LPS interface shows perfect layer structure indicates the chemical reaction between NMC811 and LPS solid state electrolyte does not affect cation mixing. After charging, the interface between NMC811 and LPS still remains as a layer structure as shown in Figure XII.3.3.h. These results demonstrate that the chemical reaction and electrochemical reaction between NMC811 and LPS solid state electrolyte will not affect the NMC811 surface structure. The absence of surface phase transformation on NMC811-LPS interface after charge indicates that NMC811-LPS interface is more stable than that of the NMC811-liquid electrolyte. Moreover, this shows that the direct contact of liquid electrolyte with the layer cathode plays a key role in initiating the widely documented layered-to-rock-salt transformation at the cathode surface.

We also acquired elemental mapping of NMC811 and NMC811/LPS before and after charging to 4.2 V as shown in Figure XII.3.4. The element distribution of pristine NMC811 is very uniform. However, after charge, there are very wide crack formed inside of NMC811 primary particle. As fluorine (F) and carbon (C) are components of the liquid electrolytes, but not the part of cathode particles, the spatial distribution of F and C can be used to trace the interaction of the liquid electrolyte and the cathode particles. As shown in Figure XII.3.4f, both F and C showed enrichment along the surface of intergranular crack, further confirming the penetration of the liquid electrolyte along the intergranular crack. The element distribution of pristine NMC811/LPS indicates a sharp interface between NMC811 and LPS as shown in Figure XII.3.4g, indicating a lack of element diffusion between the NMC811 and LPS. After charging to 4.2 V, phosphorus (P) and sulfur (S) show high concentration within the particle, indicating that LPS has electrochemically reacted with NMC811 particles, leading to the diffusion of S and P into NMC811 particle. This observation accounts for why the interface impedance between NMC811 and LPS is high.

In summary, we reveal the interfacial chemical and electrochemical reactions between NMC811 and LPS solid state electrolyte by a comprehensive analysis of SEM, FIB, TEM and STEM. We found that mixing NMC811 with LPS could form solid-solid interface, and this interface is stable than cathode-liquid interface. Direct contact of liquid electrolyte and NMC811 cathode plays a big role in initiating the widely documented layer to rock-salt phase transformation and intergranular crack formation inside of cathode particle.

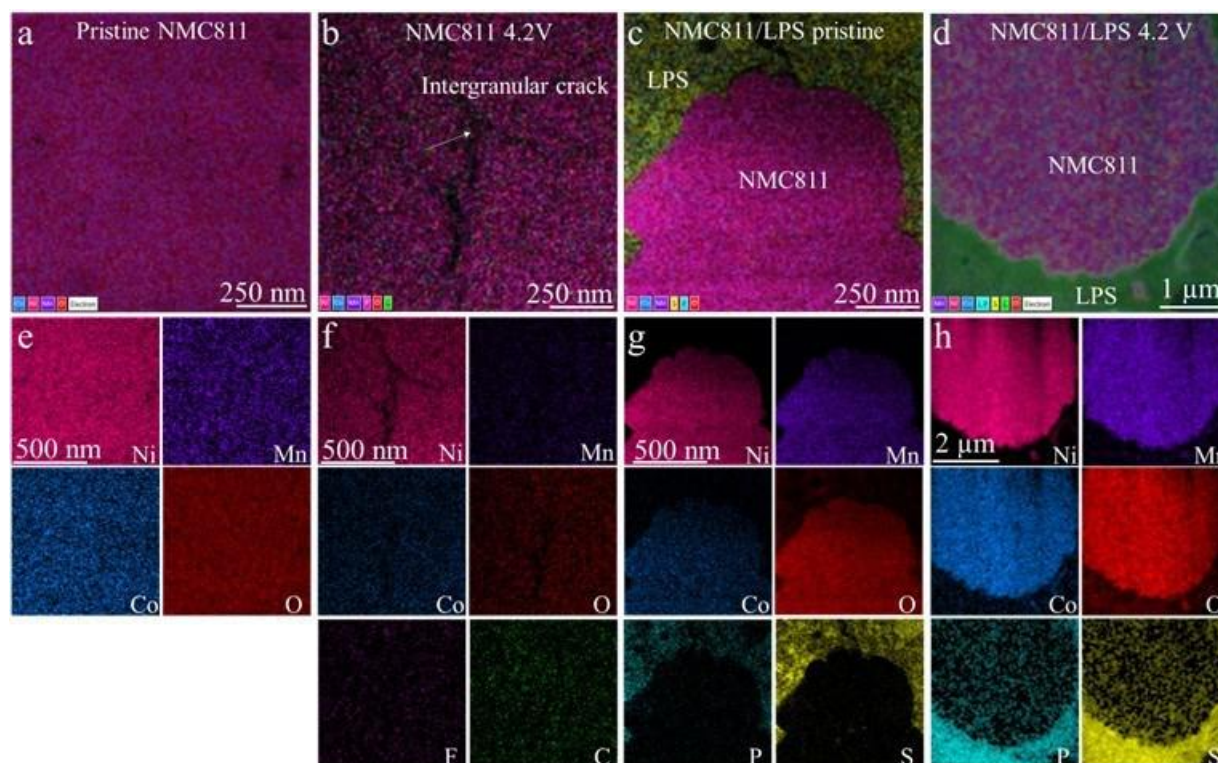


Figure XII.3.4 Elemental composition of NMC811 and NMC811/LPS before and after charge to 4.2 V. (a-d) Overlapped energy dispersive x-ray spectroscopy (EDS) elemental maps, showing the element distribution across the secondary particle interior and surface. (e-h) Elemental maps acquired from NMC811 and NMC811/LPS.

Detailed structural and chemical analysis reveals that the solid-solid interface provides a fast path for the lithium-ion transport and simultaneously prevents penetration of the liquid electrolyte into the cathode particle. This eliminates several detrimental factors, including the solid-liquid interfacial reaction, intergranular crack and layered to rock-salt phase transformation, which critically affects the battery cycle stability of both capacity and voltage. The interface between NMC811 cathode and LPS solid state electrolyte is unstable during electrochemical cycling as indicated by the diffusion of certain component of LPS into NMC811 particle, which could account for the large interfacial resistance between cathode and LPS. The present work provides insights for the rational design of solid-state electrolyte based all solid-state battery in future.

Conclusions

- For a Li dendrite, the composition of SEI formed on the tip and stem region is different. As contrasted with the stem region, an enhanced electrical field at the tip region will lead to the preferential decomposition of certain component in the electrolyte, typically such as LiPF_6 salt around tip region.
- An enhanced electrical field will also lead to preferential deposition of Li at the tip region, leading to a scenario of self-amplification effect for Li whisker growth.
- The observation of the distinctive difference of SEI on the tip and stem regions of Li whisker delineates insight on the direct correlation between features of SEI layer and Li morphology, leading to insight on possible tuning of crucial structural and chemical features of SEI to regulate the morphology of Li deposit.
- Mixing NMC811 with LPS could form solid-solid interface, and this interface is stable than cathode-liquid interface.
- The interface between NMC811 cathode and LPS solid state electrolyte is unstable during electrochemical cycling as indicated by the diffusion of certain component of LPS into NMC811 particle, which could account for the large interfacial resistance between cathode and LPS. The present

work provides insights for the rational design of solid-state electrolyte based all solid-state battery in future.

Key Publications

1. J.-M. Kim, Y. B. Xu, M. H. Engelhard, J. T. Hu, H.-S. Lim, H. Jia, Z. J. Yang, B. E. Matthews, S. Tripathi, X. H. Zhang, L. R. Zhong, F. Lin, C. M. Wang, W. Xu*. Facile Dual-Protection Layer Enhancing Performances of Cobalt-Free/Nickel-Rich Cathodes in Lithium-Ion Batteries. **ACS Appl. Mater. Interface**, **14**, 17405-17414 (2022).
2. E. Sebt, H. A. Evans, H. N. Chen, P. M. Richardson, K. M. White, R. Giovine, K. P. Koirala, Y. B. Xu, E. Gonzalez-Correa, C. M. Wang, C. M. Brown, A. K. Cheetham, P. Canepa, R. J. Clément. Stacking Faults Assist Lithium-Ion Conduction in a Halide-Based Superionic Conductor. **J. Am. Chem. Soc.**, **144**, 5795–5811 (2022).
3. Birger Horstmann, Jiayan Shi, Rachid Amine, Martin Werres, Xin He, Hao Jia, Florian Hausen, Isidora Cekic-Laskovic, Simon Wiemers-Meyer, Jeffrey Lopez, Diego Galvez-Aranda, Florian Baakes, Dominic Bresser, Chi-Cheung Su, Yaobin Xu, Wu Xu, Peter Jakes, Ru'diger-A. Eichel, Egbert Figgemeier, Ulrike Krewer, Jorge M. Seminario, Perla B. Balbuena, Chongmin Wang, Stefano Passerini, Yang Shao-Horn, Martin Winter, Khalil Amine, Robert Kostecki, and Arnulf Latz, "Strategies towards enabling lithium metal in batteries: interphases and electrodes", **Energy Envi. Sci.**, **14**, 5289(2021).
4. H. Yang, K. Tay, Y. B. Xu, B. Rajbanshi, S. Kasani, J. Bright, C. M. Wang, P. Bai, N. Q. Wu, "Nitrogen-Doped Lithium Lanthanum Titanate Nanofiber-Polymer Composite Electrolytes for All-Solid-State Lithium Batteries", **J. Electrochem. Soc.** **168**, 110507 (2021).
5. S. Chae, Y. B. Xu, R. Yi, H.-S. Lim, D. Velickovic, X. L. Li, C. M. Wang, J.-G. Zhang. Micron-Sized Silicon/Carbon Composite Anode Synthesized by Impregnation of Pitch in Nano-Porous Silicon. **Adv. Mater.** **33**, 2103095 (2021).
6. X. Han, S. Y. Wang, Y. B. Xu, G. M. Zhong, Y. Zhou, B. Liu, X. Y. Jiang, X. Wang, Y. Li, Z. Q. Zhang, S. Y. Chen, C. M. Wang, Y. Yang, W. Q. Zhang, J. L. Wang, J. Liu, J. H. Yang. All Solid Thick Oxide Cathodes Based on Low Temperature Sintering for High Energy Solid Batteries. **Energy Environ. Sci.** **14**, 5044 (2021).
7. X. H. Zhang, L. F. Zou, Z. H. Cui, H. Jia, M. H. Engelhard, B. E. Matthews, X. Cao, Q. Xie, C. M. Wang, A. Manthiram, J.-G. Zhang, W. Xu. "Stabilizing Ultrahigh-Nickel Layered Oxide Cathodes for High-Voltage Lithium Betal Batteries." **Materials Today** **44**, 15-24 (2021).
8. H. Jia, Y. B. Xu, X. H. Zhang, S. D. Burton, P. Y. Gao, B. E. Matthews, M. H. Engelhard, K. S. Han, L. R. Zhong, C.M. Wang, Wu Xu. "Advanced Low-Flammable Electrolytes for Stable Operation of High-Voltage Lithium-Ion Batteries." **Angew. Chemi. Intern. Edi.** **133**, 13109-13116 (2021).

XII.4 In-Operando Thermal Diagnostics of Electrochemical Cells (LBNL)

Ravi Prasher, Principal Investigator

Lawrence Berkeley National Lab
1 Cyclotron Rd
Berkeley, CA 94720
E-mail: RSPrasher@lbl.gov

Tien Duong, DOE Technology Development Manager

U.S. Department of Energy
E-mail: Tien.Duong@ee.doe.gov

Start Date: October 1, 2019

End Date: September 30, 2023

Project Funding (FY22): \$300,000

DOE share: \$300,000

Non-DOE share: \$0

Project Introduction

Characterizing electrochemical processes in Li-metal cells such as lithium deposition and dendrite growth at interfaces is of great significance for understanding and enhancing their electrochemical performance and reliability. In situ and operando 3-omega micro thermal sensors can provide significant information regarding the impact of buried interfaces as a function of time, material, voltage, current, and temperature, etc. Therefore, it is important to develop operando 3-omega micro thermal sensors and develop models relating those signals to electrochemical performance for beyond lithium-ion cells. The physics-based model relating thermal and electrochemical properties based on these measurements can facilitate future design of Li metal batteries.

Objectives

Transport at various interfaces in beyond lithium-ion cells will play a major role in electrochemical performance and reliability. It has not yet been possible to thermally profile a Li-metal cell during operation to provide a spatially resolved map of thermal transport properties throughout the cell. The objective of this research is to create a metrology capable of spatially resolved in operando thermal property profiling, and then relate thermal property to the quality of electrodes and interfaces and use the developed thermal metrology to understand electrochemical processes in Li-metal batteries such as dendrite growth, interface kinetics, and ionic transport.

Approach

To accomplish project goals, the team will utilize an in-house adapted 3-omega technique to probe thermal properties of a Li-metal cell while it is in operation, without affecting the operation of the cell. The 3 omega sensors will be deposited and fabricated on Li-metal cells based on previous learning on 3-omega sensor fabrication. The characteristic depth of the thermally probed region is defined by the wave's "thermal penetration depth, $\delta = \sqrt{D/2\omega}$, where D is the sample's thermal diffusivity, and 2ω is the heating frequency of the thermal wave (Lubner et al. 2020). By depositing the project's 3ω sensors on the battery's outer surface and adjusting ω , the team controls δ to span the full range from the top to the bottom layer, thereby noninvasively probing the thermal transport in subsurface layers and interfaces within the bulk of the battery. Thermal transport can be related to quality of the interface. By doing concurrent thermal transport and electrochemical performance measurements, the team plans to relate thermal transport to electrochemical performance. As frequency based thermal measurement techniques provide excellent spatial resolution within the cell, the team also plans to study heat generation at the electrolyte–Li-metal interface and relate the thermal signals to the interface kinetics and ionic transport. The frequency dependence of heat generated due to transport resistance is different from that due to kinetic resistance. The team plans to utilize this difference to separate the contributions of kinetic and transport resistance at the interface, which will enable understanding of interface kinetics and transport at the Li-metal–SSE interface.

Results

In the first quarter of this year, we worked on measuring the thermal contact resistance at the lithium-LLZO interface in symmetric solid-state cells. We studied the effect of pressure and cell cycling on the contact resistance, and correspondingly extracted the interface morphology related to the thermal measurements. Figure XII.4.1 (a) shows the schematic of a rough LLZO-lithium interface, with an average contact spot radius (a) and 'n' number of contacts per unit area and Figure XII.4.1 (b) illustrates the concept of thermal wave sensing to get spatially resolved thermal properties including the thermal contact resistance at the interface.

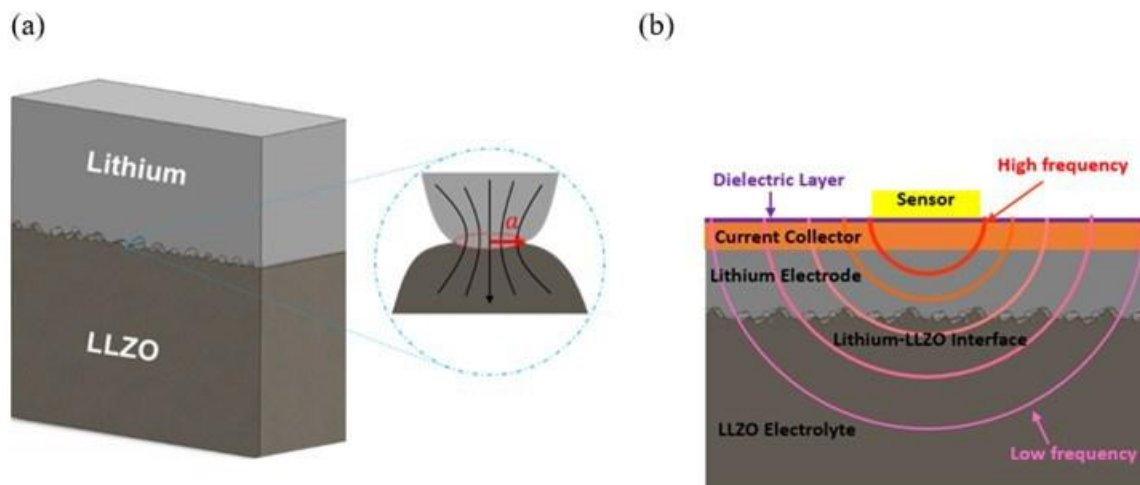


Figure XII.4.1 (a) Schematic of the rough lithium-LLZO contact with an expanded view of a single contact. The externally applied pressure leads to lithium deformation at the interface leading to an equilibrium distribution of lithium-LLZO contacts with average radius ' a ' and number of contacts per unit area ' n '. (b) Schematic of the frequency dependent thermal waves for measuring sub-surface thermal properties including the lithium-LLZO thermal contact resistance. The high frequency waves have shorter penetration depth and probe the properties of layers close to the sensor while the low frequency waves penetrate deeper up to the electrolyte. The variation in the measurement frequency allows spatially resolved probing of sub-surface thermal properties and the isolation of the lithium-LLZO interface resistance.

The thermal interface resistance extracted from the 3ω method is then used to extract the morphological parameters ' a ' and ' n ' by using a model developed by Yovanovic (Sridhar and Yovanovich, 1996). The thermal contact resistance is plotted as function of pressure in Figure XII.4.2 (a), and the extracted morphological parameters are plotted in Figure XII.4.2(c) and (d). We also did simultaneous EIS measurement (Figure XII.4.2(b)) to extract the electrochemical interface resistance and observed no significant change, most likely because the electrolyte was sputtered with gold before the cell fabrication, and the effective electrical contact between the lithium and the electrolyte was defined by the gold-electrolyte contact, which did not change with pressure.

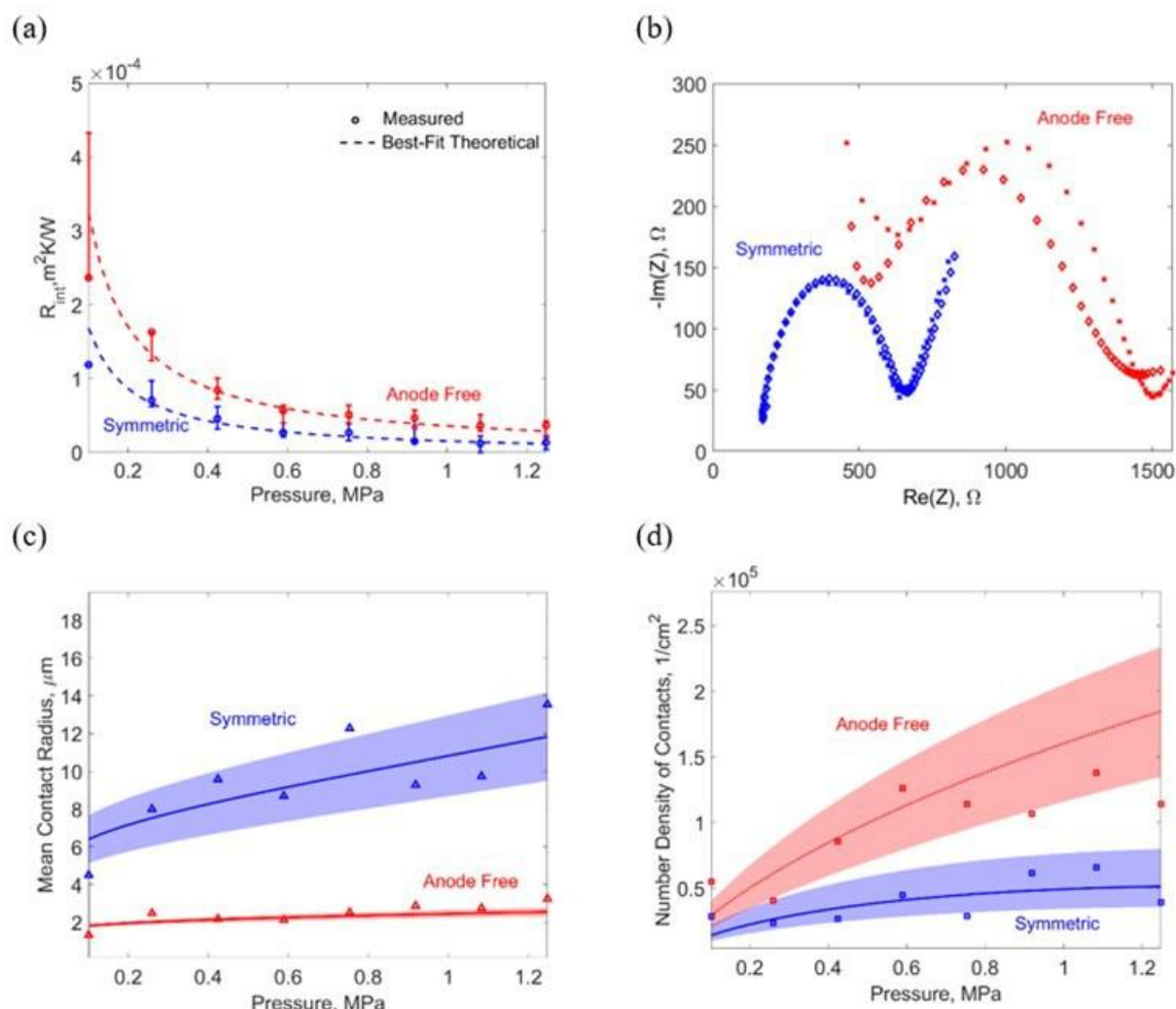


Figure XII.4.2 (a) Measured thermal interface resistance as a function of external stack pressure for anode-free (red) and symmetric (blue) cells. (b) EIS Nyquist plots for the symmetric (blue) and the anode-free (red) cells at atmospheric pressure (diamonds) and 1.25MPa (squares). There is no significant dependence of EIS spectra with pressure as the interface behavior is dominated by gold deposited on the electrolyte. Calculated mean contact radius (c) and number density of contacts (d) as a function of pressure for the symmetric (blue) and the anode-free (red) cells. The shaded areas show the error bands in the theoretical estimates from the 3ω measurements.

In the third quarter, we did optical profilometry to obtain the LLZO surface morphology before assembly and the morphology of lithium deposited on LLZO after 3 cycles. From the profilometry results, we calculated the mean contact spot size (a) and the density of contacts (n) and compared it against the results extracted from the 3-omega measurements. As shown in Figure XII.4.3 (a) and (b), the profilometry results (diamond) agree well with the thermal measurement results (triangles). Further, it is seen from the thermal measurements that as the number of cycles increases, the number density of contacts decreases while the average contact radius increases, indicating fewer larger contacts and an overall increase in the interface roughness with cycling. These results were verified qualitatively via ex-situ SEM characterization of two different cells done pre-cycling (uncycled, Figure XII.4.3(c)) and after 3 cycles (Figure XII.4.3 (d)).

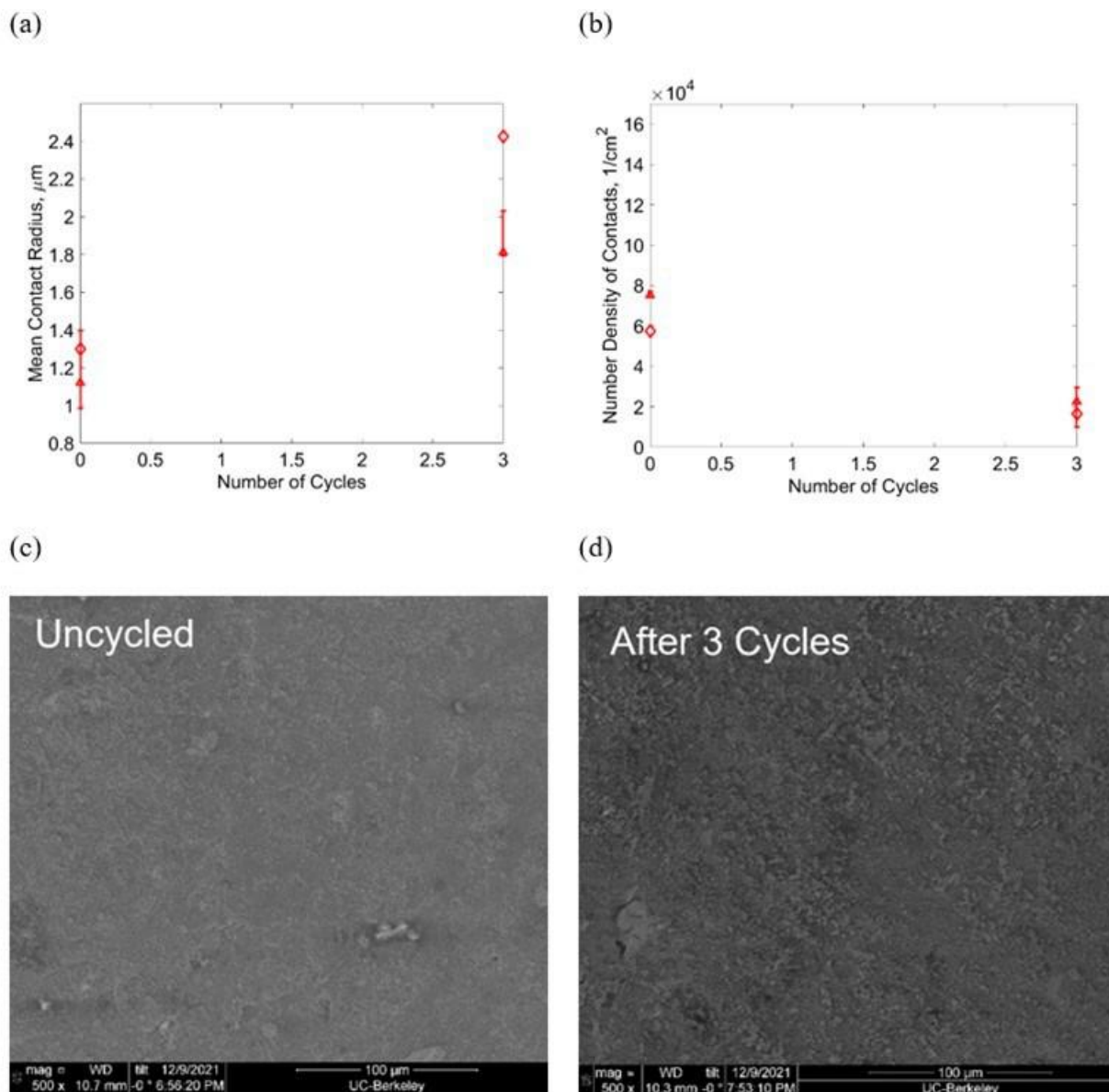


Figure XII.4.3 Measured mean contact radius (a) and number density of contacts (b) from thermal interface resistance (triangles) and profilometry (diamond) measurement. The results from thermal-contact resistance measurement agrees well with the results from profilometry and capture a general trend of interface degradation (decrease in contact density and increase in individual contact size) which is further verified by SEM images (c and d).

In the fourth quarter, we carried out self-heating study of thermally insulated solid-state cells. Because LAGP (Lithium aluminum germanium phosphate) is not air sensitive and easy to make with our lab's cold pressing and sintering process, we choose LAGP instead of LLZO as the electrolyte in the self-heating study. The cycling of solid-state cells was investigated under the excitation under high frequency alternate current (AC) from a function generator. The symmetric cells which have lithium metal at each side were assembled at first.

To do the thermal insulation, the cell stacks are sandwiched by the aerogel material and the power is supplied by copper wires instead of aluminum tabs. A small thermocouple is inserted between the aerogel and the Kapton film to monitor the temperature rise. And the LAGP-Lithium cell is sat on the Kapton film with additional Kapton tape for fastening. The solid-state cell is cycled under around 300 kPa pressure to enable good contact and electrochemical performance. The electrochemical impedance frequency response of the cell

is measured before the insulated heating experiments. The recorded temperature rise under different frequency of AC voltages are modeled with numerically using COMSOL. The required heat capacities of solid-state electrolyte are measured from differential scanning calorimeter (DSC). Other parameters are used from literature. From the results shown below, with the heat transfer coefficients fitted, the simulation results predicting the temperature rise due to self-heating and experiments results agree well. (See Figure XII.4.4.)

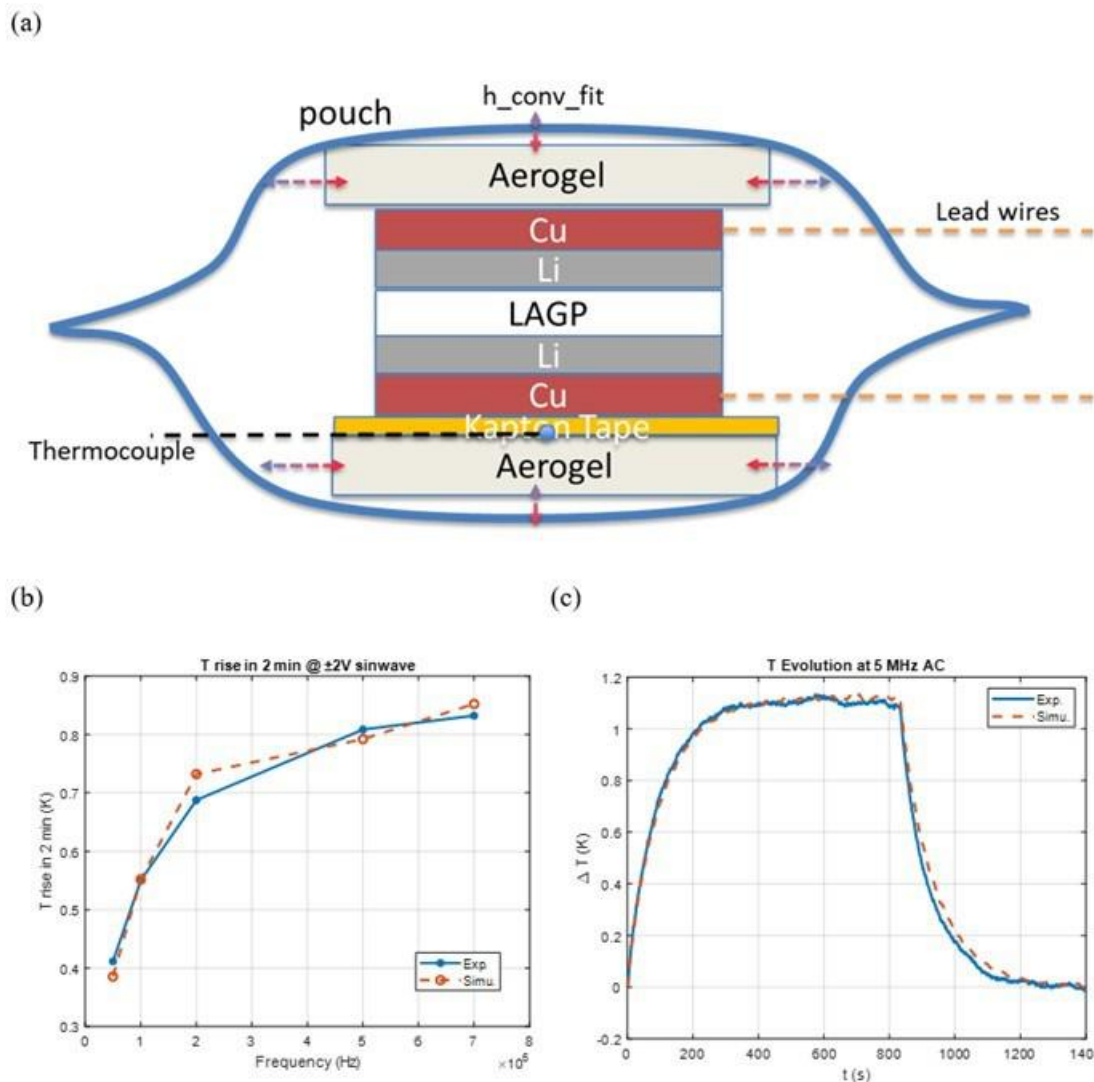


Figure XII.4.4 (a) The structure schematic of the assembled LAGP symmetric cell and insulation setup. (b) The temperature rises in 2 min under different frequency $\pm 2V$ sin wave. (c) The Example of fitting result between COMSOL simulation and experiments.

Conclusions

This year we performed in-situ monitoring of lithium-solid state electrolyte interface morphology from thermal interface resistance measurement enabled by thermal wave sensing based on the 3ω method. Morphological parameters such as the mean contact radius and the number density of contacts were extracted from the thermal measurements by considering the effect of morphology and contact mechanics on solid-solid thermal interface resistance. By utilizing the frequency dependence of the thermal penetration depth, the method provided spatial resolution to attribute the observed interface resistance to specific interfaces, an ability not available with techniques such as Electrochemical Impedance Spectroscopy (EIS). Further, we verified our observations with complementary ex-situ techniques such as optical profilometry and scanning electron microscopy (SEM). Finally, by considering the frequency-dependent heat generation rate and the thermal resistance of the cell, we

studied self-heating of lithium-solid state electrolyte cell and were able to predict the magnitude of the temperature rise using combined electrochemical-thermal simulations.

References

1. Lubner, Sean D., Sumanjeet Kaur, Yanbao Fu, Vince Battaglia, and Ravi Prasher. 2020. "Identification and Characterization of the Dominant Thermal Resistance in Lithium-Ion Batteries Using Operando 3-Omega Sensors." *Journal of Applied Physics* 127 (10). <https://doi.org/10.1063/1.5134459>.
2. M. R. Sridhar and M. M. Yovanovich, "Elastoplastic contact conductance model for isotropic conforming rough surfaces and comparison With Experiments," *J. Heat Transfer*, vol. 118, no. February, 1996, doi: 10.1115/1.2824241.

Acknowledgements

We thank Divya Chalise, Buyi Zhang, Dr. Yuqiang Zeng, Dr. Sean Lubner, Dr. Suman Kaur, Dr. Yanbau Fu, Dr. Vince Battaglia, Dr. Rob Jonson and Dr. Michael Tucker for their help in carrying out the research in this project.

XIII Next-Gen Lithium-Ion: Modeling Advanced Materials

Development of accurate, real-time models for rechargeable batteries is essential to ensure efficient battery management and safe operation. Using battery models, battery design parameters can be leveraged in developing strategies for optimal battery operation and improved efficiency. Optimal operation of battery results in prolonged battery life with maximum capacity by reducing losses while maintaining safety. This optimal operation is achieved by operating a battery with optimal charge discharge cycles (provided by an optimizer), through a controller. A model (representative of a battery) is involved as an integral component in the optimizer, controller, as well as state of charge (SOC) estimator. There are different states associated with batteries such as, SOC, voltage, current, capacity etc. – which all must be monitored and maintained at desired levels for optimal battery operation, and real time battery models can help realize such desirable performance. For a model to be useful, it should include all the significant phenomena that occur inside a rechargeable battery.

The rest of this chapter contains detailed reports on the status of the following individual projects.

- Electrode Materials Design and Failure Prediction (ANL)
- Characterization and Modeling of Li-Metal Batteries: Model-system Synthesis and Advanced Characterization (LBNL)
- Design of High-Energy, High-Voltage Lithium Batteries through First-Principles Modeling (LBNL)
- Modeling of Solid-State Conductors (LBNL).

XIII.1 Electrode Materials Design and Failure Prediction (ANL)

Venkat Srinivasan, Principal Investigator

Argonne National Laboratory
9700 South Cass Avenue
Lemont, IL 60439
E-mail: vsrinivasan@anl.gov

Tien Duong, DOE Technology Development Manager

U.S. Department of Energy
E-mail: Tien.Duong@ee.doe.gov

Start Date: October 1, 2021

End Date: September 30, 2022

Project Funding (FY22): \$580,000

DOE share: \$580,000

Non-DOE share: \$0

Project Introduction

In order to increase the energy density of next generation lithium ion batteries, it is necessary to enable lithium metal anodes due to the extremely large specific capacity and low reduction potential. Lithium deposition with liquid electrolytes faces several issues in terms of non-uniform deposition and formation of dendrites, which can short the cell. Solid electrolytes are adopted with the expectation that the mechanical stress fields that generate around dendritic protrusion will be capable of preventing their growth. Accordingly, both polymer and ceramic type solid electrolytes have been investigated for their capability to enable stable deposition of lithium. Unfortunately, ceramics demonstrate poor conformability, which leads to a decrease in the electrochemically active surface area during non-uniform deposition and dissolution of lithium, which can substantially hinder the overall cell performance. Also, ceramics are prone to fracture that can provide easy pathways for lithium dendrites to grow. Similarly, even for polymer electrolytes, non-uniform deposition of lithium can lead to development of dendritic protrusions, that can penetrate through the electrolyte and eventually short the cell. As a result, neither hard ceramics nor soft polymers are capable of completely stabilizing the lithium deposition process.

Polymer/ceramic composite electrolytes are introduced with the expectation of combining the advantages of polymers with that of the ceramics. Achieving facile transport of lithium ions from the polymer to the ceramic phase, and vice-versa, is a challenge, which can mostly be attributed to the relatively higher interfacial charge transfer resistance. On the other hand, some experimentalists claim that enhanced transport of lithium is possible through the polymer/ceramic interphase region, where some plasticization of the polymer chains adjacent to the ceramic particles increases their mobility. Accordingly, there exist several literatures that claim incorporation of ceramic particles within polymers enhance their conductivity; and several others claim the reverse, that addition of ceramic particles actually lead to a decrease in the conductivity of the composite electrolyte. In the present context, the desired polymer/ceramic interfacial resistance that can lead to an increase in the conductivity of the electrolyte, will be investigated.

Independent of the conductivity of the composite electrolyte, it is very important to note that both polymer and ceramic phases exist adjacent to the lithium electrode in the polymer/ceramic composites. Presence of these two different phases introduce heterogeneity in not only the transport properties but also the exchange current density associated with the polymer and the ceramic phases differs substantially. Hence, reaction current can get focused either at the polymer or at the ceramic regions if both the phases touch the lithium electrode. On the contrary, if only polymer touches lithium, the extent of reaction current heterogeneity at the electrode/electrolyte interface is expected to be smaller. However, depending on the thickness of the interfacial polymer layer, the extent of current focusing can be substantially large that can eventually lead to propagation of dendritic protrusions. This reaction current heterogeneity at the lithium/composite-electrolyte interface will also be studied as part of the present research.

Apart from the polymer ceramic composites, sulfide based soft inorganic solid electrolytes are also being investigated extensively for their inherent softness and possibly higher fracture toughness. These characteristics of the soft ceramic based solid electrolytes can potentially prevent crack propagation and maintain higher electrochemically active surface area, which is expected to stabilize the deposition of lithium. However, sulfide based soft ceramic electrolytes demonstrate grain/grain-boundary microstructure. Due to the heterogeneities associated with the transport and mechanical properties of the grain interiors and the grain boundary domains, it is possible to have reaction current focusing at, or around, these microstructural heterogeneities. The extent of reaction current focusing observed at the interface between lithium metal electrode and the soft inorganic solid electrolyte will be investigated as part of the present research.

Objectives

Development of computational methodologies for understanding the various degradation mechanisms for next-generation Li-ion batteries is the main objective of this project. This year's goal is to use the continuum-based mathematical model to estimate the conduction pathway through the polymer/ceramic composite type solid electrolytes and investigate interfacial stability between Li-metal electrodes and solid electrolytes during deposition and dissolution of lithium under externally applied currents. Effective conductivity and transference numbers of the composite electrolytes will be estimated here as a function of the ceramic volume fraction. Finally, the desired charge transfer resistances will be estimated that can lead to an enhancement in the effective conductivity of the composite electrolytes. On the other hand, development of strategies to minimize the reaction current heterogeneity at the lithium/composite-electrolyte interface, through the adoption of interlayers, is another major objective of the present project. To expand the modeling capabilities, other soft solid electrolytes, such as, sulfide-based soft ceramics will be investigated for their capability to stabilize the lithium deposition on metallic anodes.

Approach

A computational framework at the continuum level is developed in the present study to analyze the transport of ions and electrochemical reactions occurring within the composite electrolyte and at the electrode/electrolyte interface, respectively. Due to their single ion conducting behavior, ionic transport through the ceramic particles and electrolytes are modeling by solving a Laplace equation. However, lithium ion transport through the polymer phase can occur through both migration and diffusion, which necessitates solving for both the charge and mass balance relations while also allowing for the development of concentration gradients within the polymer electrolytes. Similar to the single ion conducting ceramic electrolytes, charge transport within lithium metal is again captured by solving Laplace equation, while using appropriate conductivities for the material of interest. Flow of current at the electrode/electrolyte interface is simulated through the adoption of the nonlinear Butler-Volmer equation. Finally, evolution of mechanical stress within the electrode and electrolytes, due to the deposition of lithium, is predicted by solving the mechanical equilibrium relations while taking into consideration the elastic-plastic deformation of the electrodes and the electrolytes. Impact of mechanical stress on the Butler-Volmer prescribed electrochemical reaction is also simulated computationally. Effective conductivities and the reaction current heterogeneities, as experienced by the composite and soft inorganic solid electrolytes, will be analyzed computationally in the next section of this report.

Results

Investigate the current focusing at the interface between lithium metal electrode and polymer/ceramic composite electrolyte: From a macroscopic standpoint composite electrolytes containing ceramic fillers and polymer matrix are expected to demonstrate high enough mechanical stiffness capable of preventing growth of lithium dendrites as well as show large enough deformability that can maintain good contact between the electrode and electrolyte domains (see Figure XIII.1.1(a)). Microscopically the polymers and ceramics demonstrate very different ionic conductivities, exchange current densities, and mechanical properties. The lithium metal anode can possibly see both the polymer and ceramic domains (as shown in Figure XIII.1.1(b)), or just the polymer region (depicted in Figure XIII.1.1(c)), depending on the adopted synthesis procedure. Transport of charge and ions in the electrode and electrolyte, and evolution of mechanical stress due to deposition of metallic lithium, have been solved in detail. Current focusing observed within the polymer

domain is depicted in Figure XIII.1.1(d) as a function of the elastic modulus of the soft polymer matrix. It is evident from the red squares that when the Li electrode can see both polymer and ceramic domains, major current focusing occurs in the ceramics. If the Li see only polymer, current focusing occurs in the polymer with a much smaller magnitude (see the cyan and blue lines in Figure XIII.1.1(d)). Also, increasing the thickness of the interfacial polymer layer (from 100 nm to 400 nm) leads to a decrease in the extent of current focusing within the polymer domain.

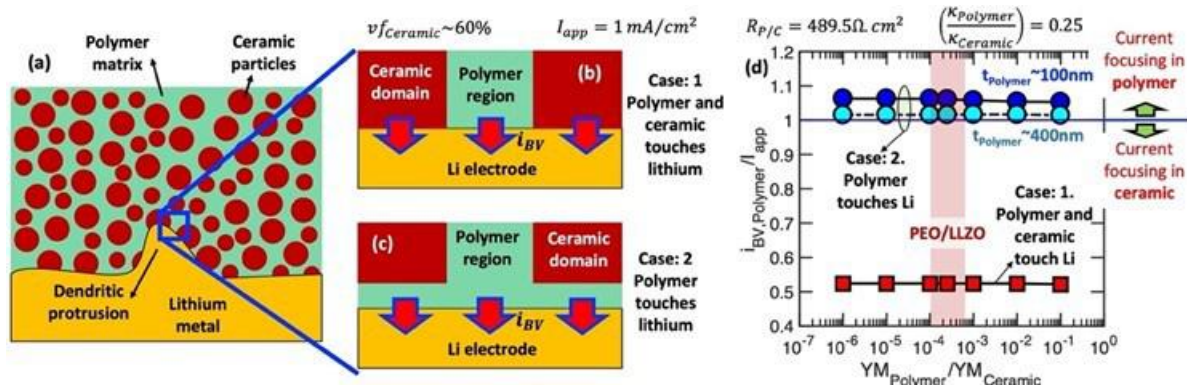


Figure XIII.1.1 (a) Schematic representation of the polymer/ceramic composite in contact with lithium metal. The brown domains are ceramics, and the green region is the polymer. (b) Zoomed in view at the electrode/electrolyte interface where both polymer and ceramic touch the lithium electrode. (c) Zoomed in view of the composite-electrolyte/lithium-metal interface where only polymer touches the electrode. (d) Current focusing within the polymer as a function of its elastic modulus. When both polymer and ceramic touch Li (red squares) major current focusing is observed in the ceramics. When only polymer touches Li (blue and cyan circles), current focusing is reduced substantially and occurs at the polymer domains.

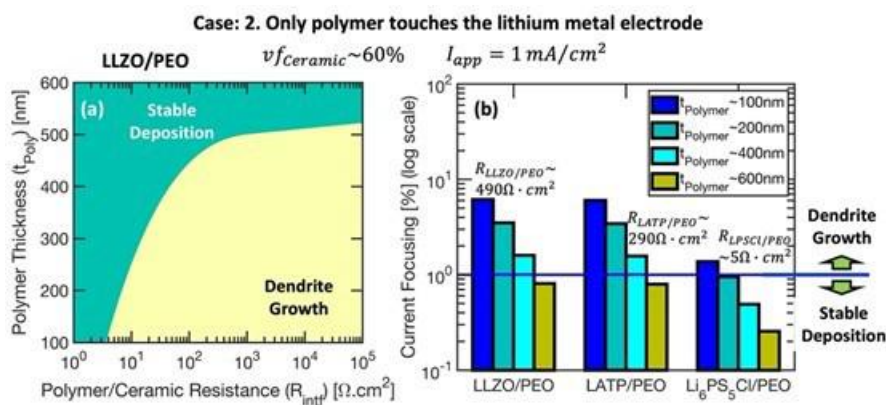


Figure XIII.1.2 In general only the polymer sees the Li electrode. (a) Phase map between polymer layer thickness and polymer/ceramic charge transfer resistance indicating domains of stable deposition (green) and regions with dendrite growth (yellow). (b) Current focusing at the polymer region for LLZO/PEO, LATP/PEO and Li_6PS_5Cl/PEO composite electrolytes with different thickness of the polymer layer at electrode/electrolyte interface.

Experimental observations reveal that majority of the cell fabrication procedures lead to only polymers seeing the Li electrode. A phase map between the polymer layer thickness and the polymer/ceramic interfacial resistance is depicted in Figure XIII.1.2(a), where it is clearly shown that increasing the thickness of the polymer layer at the electrode/electrolyte interface and decreasing the interfacial resistance between polymers and ceramics can help to stabilize the lithium deposition process. In the literature, several ceramic particles have been incorporated with PEO polymers for constructing composite electrolytes, such as, LLZO, LATP and Li_6PS_5Cl , and the current focusing experienced by each of them is depicted in Figure XIII.1.2(b). Due to the smaller interfacial resistance ($\sim 5 \Omega \cdot cm^2$), the sulfide based ceramic particles (Li_6PS_5Cl) tend to stabilize the lithium deposition most effectively. Finally, it can be concluded that irrespective of the ceramic particles, adoption of polymer interlayers with thickness larger than 600 nm should lead to stable deposition of lithium at

the electrode/electrolyte interface. Note that all the analysis being reported here did not take into consideration the presence of the solid electrolyte interphase (SEI) layer, which can introduce substantial heterogeneity during the lithium deposition process in a realistic environment.

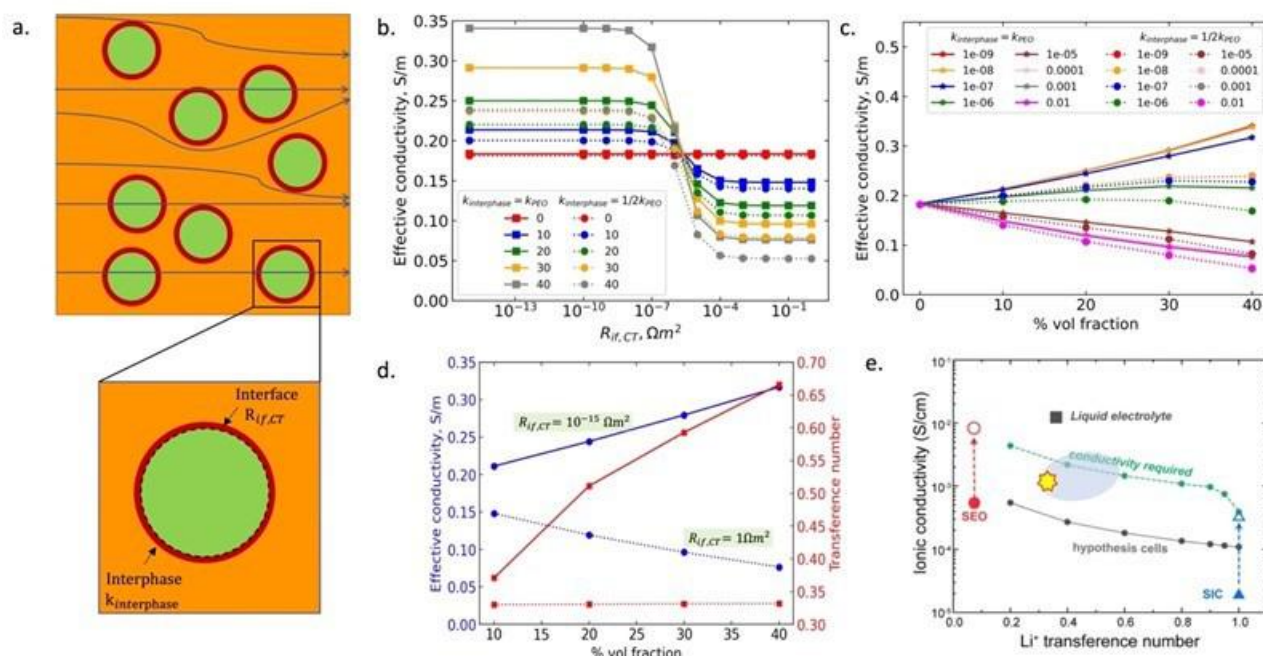


Figure XIII.1.3 Li ion transport mechanism study in PEO-LATP composite electrolyte at temperature 90°C. (a) Schematic representation of polymer and ceramic particles in composite electrolyte. Ceramic particles, polymer and interphase are represented in green, orange, and red respectively. Zoomed in view of ceramic particle depicts ceramic and polymer interface and interphase region near ceramic particle surface. (b) Effective conductivity of the composite electrolyte at a varying interface charge transfer resistance for different volume fractions of ceramics in polymer matrix. Solid lines represent case 1: $k_{interphase} = k_{PEO}$ and dotted lines represent case 2: $k_{interphase} = (1/2) k_{PEO}$. (c) Effective conductivity of the composite electrolyte at a varying volume fractions of ceramics in polymer matrix at different interface charge transfer resistance. Solid lines represent case 1: $k_{interphase} = k_{PEO}$ and dotted lines denote case 2: $k_{interphase} = (1/2) k_{PEO}$. (d) Transference number and Effective conductivity at low (solid line) and high (dotted line) interfacial charge transfer resistance. (e) Required ionic conductivity for the polymer electrolytes at different transference number for EV applications. Effective properties experienced by the composite electrolytes are represented by the blue oval patch. A yellow asterisk represents the current state of LATP-PEO system for $R_{CT} = 0.004 \Omega m^2$.

Elucidation of ion transport mechanism through the polymer and ceramic phases in a composite electrolyte: Composite electrolytes (CEs), consisting of polymer matrix and ceramic particles, are expected to possess higher transport parameters than polymer phase due to high ionic conductivity of ceramics. Li ions can possibly transport through 1) only polymer phase, and 2) polymer and ceramic phase in the composite electrolytes (Figure XIII.1.3(a)). Transport of lithium ions through the polymer/ceramic interphase layer is not taken into consideration. The higher ionic conductivity of Li ions can only be achieved by enabling Li ion transport through the ceramic particles. The charge transfer resistance between polymer and ceramic, R_{CT} , plays very important role to facilitate Li ion transfer through ceramic particle. At the surface of the ceramic particle, polymer chain motion gets impeded. This near surface region is defined as interphase and can possess lower conductivity than that of bulk, which is quantified by $k_{interphase}$ (Figure XIII.1.3(a)). At low R_{CT} , with increasing ceramic particle content, effective conductivity and transference number of the composite electrolyte increases. However, as R_{CT} value increases, this effect reverses and negatively affects the effective conductivity and transference number (Figure XIII.1.3(b) – (d)). At higher ceramic particle content (30-40 % volume fraction), interphase volume fraction is comparable with the polymer and significantly contributes to the effective conductivity. Lastly, interphase conductivity, $k_{interphase}$, dictates the quantification of the composite electrolyte conductivity, but the positive or negative effect of the ceramic particle content is dictated by R_{CT} . Interplay between $k_{interphase}$ and R_{CT} is necessary to predict the transport parameters of the composite

electrolyte. The present study of PEO-LATP composite system can meet the required targets of conductivity and transference number for electric vehicle (EV) application only at very low R_{CT} ($<10^{-6} \Omega m^2$) (Figure XIII.1.3(e)). Experimentally observed R_{CT} values at the PEO-LATP interface is around $0.004 \Omega m^2$ (denoted by the yellow asterisk in Figure XIII.1.3(e)), which is around three orders of magnitude larger than the desired charge transfer resistances. Hence development of better polymer/ceramic composites is necessary that can demonstrate a decrease in interfacial charge transfer resistance, and subsequently improvement in overall conductivity of the electrolyte.

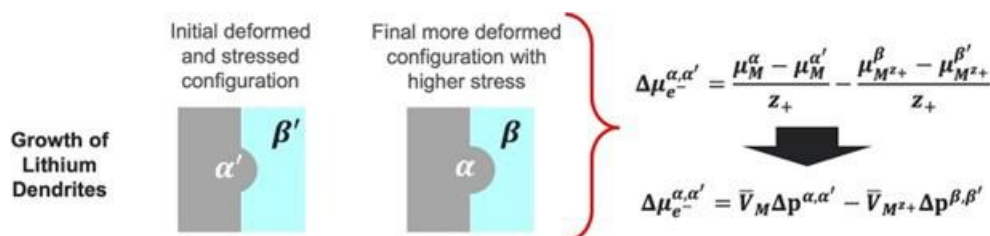


Figure XIII.1.4 During dendrite growth, change in stress induced electrochemical potential ($\Delta\mu_e^-$) depends on the lithium deposition induced increase in pressure within the electrode and electrolyte. Note that the change, or increase, in pressure is important, not the total pressure within the electrode and electrolyte.

Deciphering the influence of stress state on the exchange current density experienced by lithium metal electrodes in contact with solid polymer electrolytes during lithium deposition and stripping processes. Non-uniform lithium deposition while operating with solid electrolytes leads to mechanical stress evolution within both the lithium metal electrode and the solid electrolyte. Mechanical stress generation influences the electrochemical potential around the dendritic protrusion and overall reaction current density. This particular aspect is pointed out in Figure XIII.1.4.

During the nucleation process, the lithium deposit evolves on top of a flat electrode. For flat electrodes, both the electrode and electrolyte can be assumed to exist in stress free configurations. Hence, during lithium nucleation, the total stress within the electrode and the electrolyte influences the stress induced electrochemical potential term. However, during growth of the dendritic protrusion, both the electrode and electrolyte already exists in a stressed configuration. Further deposition of lithium helps to increase the stress. While estimating the change in stress induced electrochemical potential associated with the growth of dendritic protrusions, change in stress state within the electrode and electrolyte needs to be taken into consideration, instead of the total stress values. Accordingly, the expression for stress induced electrochemical potential, as shown in Figure XIII.1.4, is written as a function of increment in the stress state between the primed and the non-primed configurations.

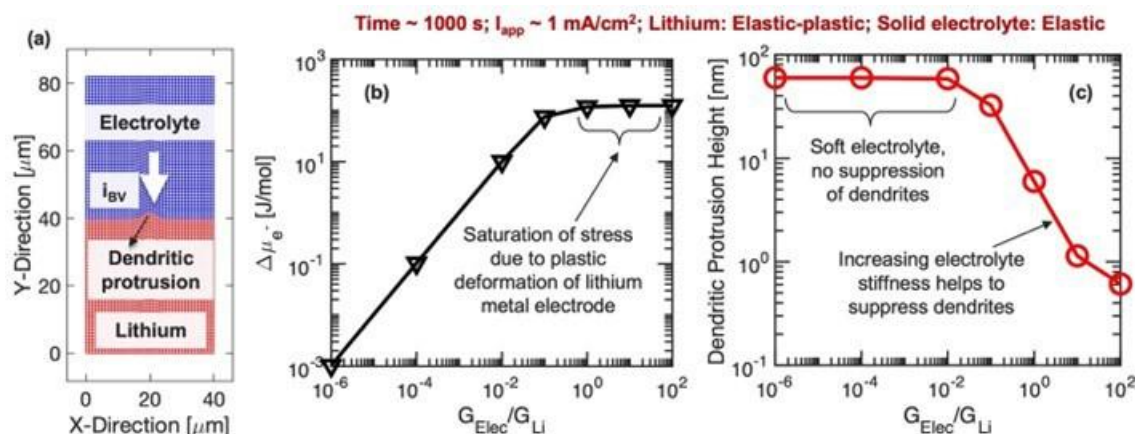


Figure XIII.1.5 (a) Schematic diagram of the lithium electrolyte interface with a dendritic protrusion at the middle. Butler-Volmer reaction is assumed at the electrode/electrolyte interface. (b) During lithium deposition at 1 mA/cm², evolution of stress induced electrochemical potential at the tip of the protrusion as a function of electrolyte modulus. (c) Increase in height of the dendritic protrusion as a function of electrolyte modulus. Softer electrolytes cannot suppress the dendrites. Stiffer electrolytes can successfully prevent dendrite growth due to plastic deformation of lithium metal.

A lithium metal electrode located adjacent to a solid electrolyte, containing a dendritic protrusion, is schematically demonstrated in Figure XIII.1.5(a). During dendrite growth, because of the fact that only the *increase* in stress within the electrode and electrolyte impacts the change in stress induced electrochemical potential, and not the *total* stress, the overall magnitude of stress induced electrochemical potential decreases substantially, which is depicted in Figure XIII.1.5(b). Even for very stiff electrolytes, the change in stress induced electrochemical potential is only around 100 J/mol, which is equivalent to only 1 – 2 mV. Increase in the height of the dendritic protrusion is shown in Figure XIII.1.5(c) during operation at 1 mA/cm² for 1000 seconds. It is evident that softer electrolytes cannot prevent the growth of dendrites, whereas the stiffer electrolytes block the dendrite growth through plastic deformation. Development of a computational model with corrected stress potential coupling will provide guidance to the next level of modeling efforts where dynamic growth of dendritic protrusions will be investigated.

Understanding the impact of grain boundaries in soft inorganic solid electrolytes (SEs) on the lithium deposition process and subsequent dendrite growth: Due to the extremely high stiffness of garnet type solid electrolytes (such as, LLZO), they do not conform to the depositing lithium, which can eventually lead to loss of contact between the lithium metal electrode and the solid electrolyte. This decrease in electrochemically active surface area can eventually lead to current focusing and dendrite growth within LLZO type stiff solid electrolytes. Sulfide based soft inorganics have been investigated due to their enhanced conformability and possibility of having enhanced electrochemically active surface area with lithium metal electrode. However, similar to garnets, sulfide based soft inorganics also demonstrate grain/grain-boundary (G/GB) microstructure. It has been reported earlier that softer grain boundaries of LLZO act as points for current focusing, which can eventually lead to cracking of the solid electrolyte and dendrites can grow through those crack openings. Since current focusing at the grain boundaries is assumed to be the main culprit that causes the formation and propagation of dendrites, the extent of current focusing at the grain boundaries for sulfide based soft inorganic solid electrolytes is worth investigating. Accordingly, reaction current distribution at the triple junction of lithium electrode, grain interior, and grain boundary of the solid electrolyte is investigated using the computational mesh shown in Figure XIII.1.6(a). The Butler-Volmer prescribed reaction current distribution at the lithium/electrolyte interface is plotted in Figure XIII.1.6(b), which contains contribution from electrochemical potential as well as mechanical stress. Enhanced reaction current at the grain boundary is evident, which increases with time, as is clearly demonstrated in Figure XIII.1.6(c). The blue dashed line indicates the applied current. Note that the ionic conductivity within the grain boundary region is assumed to be smaller than the grain interior, and the elastic modulus of the grain boundary region is assumed to be one order of magnitude smaller than the bulk electrolyte.

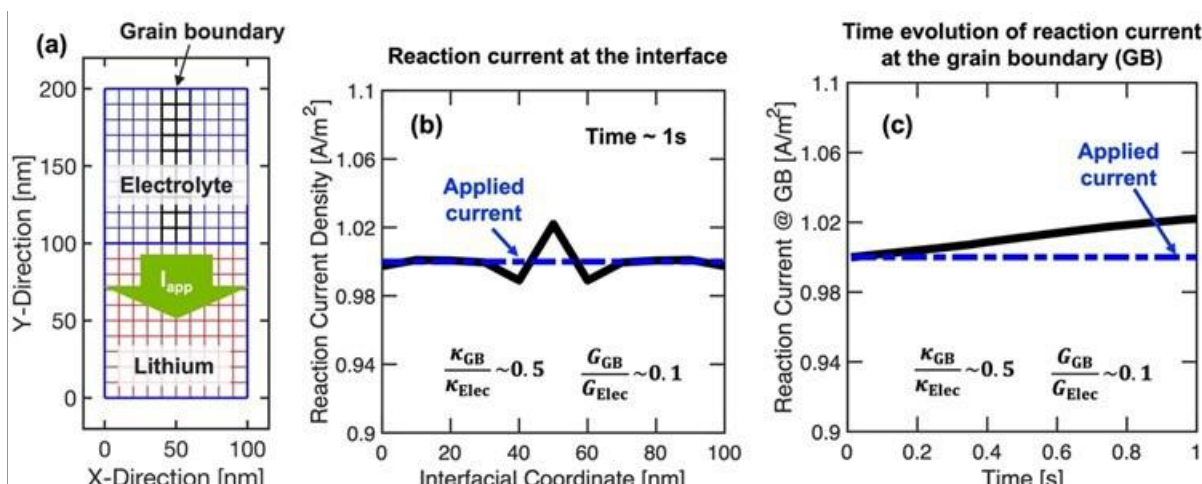


Figure XIII.1.6 (a) Lithium/solid-electrolyte mesh used in the present analysis. The grain interior and GBs are denoted by the blue and black regions respectively. Butler-Volmer reaction current is implemented at the lithium/solid-electrolyte interface. (b) Distribution of reaction current at the electrode/electrolyte interface (black line) after 1 s for GB conductivity and shear modulus being 50% and 10% of the grain interior, respectively. (c) Increase in reaction current density at the GB region with time, which demonstrates an increasing trend. In (b) and (c), the blue dashed line indicates the applied current density.

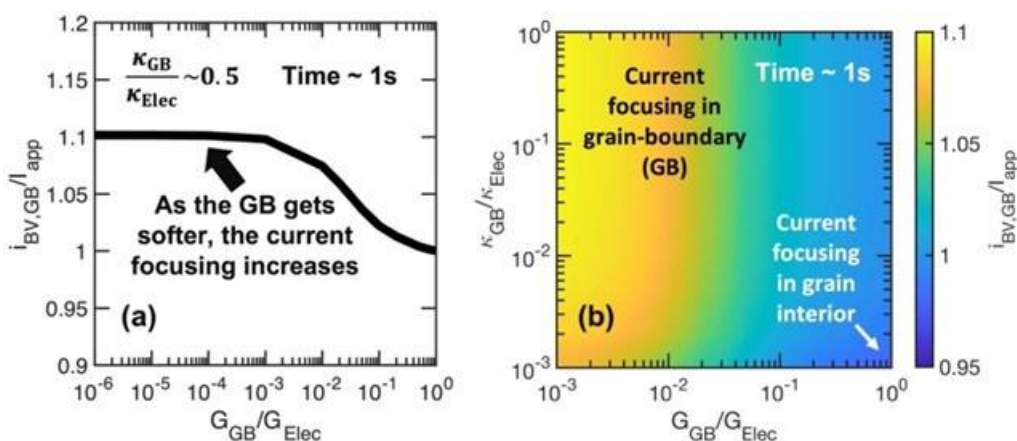


Figure XIII.1.7 (a) Current focusing at the grain boundary region after 1 s as a function of the shear modulus of the grain boundaries. Decreasing grain boundary modulus enhances the current focusing. (b) Phase map between conductivity and shear modulus of the grain boundaries indicating regions where current focusing should occur at the grain boundaries (yellow domain). Homogeneous distribution of reaction current can be achieved by adopting stiff grain boundary domains.

The extent of current focusing at the grain boundaries depend on the conductivity and shear modulus of the grain boundary region, which is demonstrated in Figure XIII.1.7(a) and Figure XIII.1.7(b). It is evident that the current focusing at the grain boundaries can be eliminated by the adoption of mechanically stiff grain boundary domains (right side Figure XIII.1.7(b)). Investigation of the current focusing at the grain boundaries of sulfide based soft inorganic solid electrolytes helps us to explain the propagation of lithium dendrites observed experimentally within these soft solids.

Conclusions

Lithium deposition mechanism at the lithium/solid-electrolyte interface was investigated over the last one year. It is evident that the presence of microstructural heterogeneity within the solid electrolytes can lead to substantial current focusing at the lithium/electrolyte interface, which can eventually result in formation and propagation of lithium dendrites. In composite electrolytes, decreasing the interfacial charge transfer resistance between the polymer and ceramic phases can not only help to enhance the overall conductivity of the solid electrolyte but also help to enable uniform deposition of lithium at the lithium-electrode/composite-electrolyte

interface. Even though it is argued that mechanical stress can substantially influence the nucleation of lithium, their impact on the growth of dendritic protrusions can be smaller than expected. The change in stress induced electrochemical potential ($\Delta\mu_{e^-}$) depends mostly on the change in the state of stress from the previous timestep (Δp), and not the total magnitude of stress (p). Finally, it is demonstrated that reaction current focusing is possible even at the grain boundaries of sulfide based soft ceramic type solid electrolytes. Hence, removal of microstructural heterogeneities is a necessity to enable stable deposition of lithium with solid electrolytes.

Key Publications

1. Hong Keun Kim, Pallab Barai, Kanchan Chavan, and Venkat Srinivasan. Transport and Mechanical Behavior in PEO-LLZO Composite Electrolytes. *Journal of Solid-State Electrochemistry* **26** 9 2059 – 2075 (2022).

XIII.2 Characterization and Modeling of Li-Metal Batteries: Model-system Synthesis and Advanced Characterization (LBNL)

Guoying Chen, Principal Investigator

Lawrence Berkeley National Laboratory
1 Cyclotron Road
Berkeley, CA 94720
E-mail: GChen@lbl.gov

Tien Duong, DOE Technology Development Manager

U.S. Department of Energy
E-mail: Tien.Duong@ee.doe.gov

Start Date: October 1, 2019

End Date: September 30, 2022

Project Funding: \$500,000

DOE share: \$500,000

Non-DOE share: \$0

Project Introduction

In order to develop mitigating approaches and rationally design advanced functional materials, a deep understanding of the relationships among structure, properties and function is essential. For Li-metal batteries employing a solid-state electrolyte (SSE), significant challenges, both at the material level and system level, prevent them from practical applications. It is well recognized that fundamental knowledge on the role of SSE microstructure in solid-state ion conduction and Li dendrite formation/propagation, performance-limiting processes and phase transition mechanisms in SSEs, and the dynamic evolution of the SSE/electrode interfaces are key to the development of high-energy Li-metal batteries with improved commercial viability. This project addresses these challenges in a systematic way, by synthesizing well-controlled SSE model systems and SSE/electrode model interfaces, obtaining new insights into the model materials and interfaces utilizing state-of-the-art analytical techniques, and subsequently establishing the correlations between specific property and function. The goal is to use these findings to properly design and synthesize advanced SSE materials and SSE/electrode interfaces with improved performance.

Objectives

This project will use a rational, non-empirical approach to design and develop SSE materials and interfaces for the next-generation Li-metal batteries. Combining a suite of advanced diagnostic techniques with well-controlled model-system samples, the project will perform systematic studies to achieve the following goals: 1) obtain understanding on the role of SSE grain and grain boundaries on Li ion conduction and dendrite formation, 2) obtain fundamental knowledge on rate- and stability-limiting properties and processes in SSEs when used in Li-metal batteries, 3) investigate the reactivities between SSE and electrodes and gain insights on the dynamic evolution of the interfaces, and 4) design and synthesize improved SSE materials and interfaces for safer and more stable high-energy Li-metal batteries.

Approach

The project will combine model-system synthesis and advanced diagnostic studies to investigate ion conduction and interfacial chemistry of SSE in Li-metal batteries. Single crystalline, polycrystalline and amorphous model samples with various grain and grain boundary properties will be synthesized. Model interfaces between the SSE and electrodes with controlled properties will also be developed. Both bulk-level and single-grain level characterization will be performed. Global properties and performance of the samples will be established from the bulk sample analysis, while the single-grain-based studies will utilize time- and spatially-resolved analytical techniques to probe the intrinsic redox transformation processes and failure mechanisms under Li-metal battery operating conditions.

Results

In order to investigate all-solid-state battery (ASSB) cathode interfaces in a controlled manner, we designed model systems with three key elements: 1) use of lithium metal halide solid electrolytes (SE) with a general formula of Li_3MCl_6 ($\text{M} = \text{Sc}, \text{In}, \text{Y}, \text{Er}, \text{and Yb}$). The halides exhibit a high ionic conductivity ($> 1 \times 10^{-4} \text{ S/cm}$ at room temperature), a wide electrochemical stability window (up to 4.5 V vs. Li/Li^+) and excellent ductility that enable them to be used with 4 V class lithium transition-metal oxide cathode active materials (CAM) without coating treatment. This allows diagnostic studies performed at the direct interface between CAM and SE; 2) use of single crystals (SC) CAM particles. Conventional polycrystalline (PC) samples such as $\text{LiNi}_{x-1}\text{Mn}_y\text{Co}_{1-x-y}\text{O}_2$ (NMC) are large spherical secondary particles made up of sub-micron primary grains with random orientations. This causes prolonged Li^+ diffusion pathways (higher tortuosity) and nonuniform Li concentration inside the particles, leading to stress and strain and eventual internal cracking along the grain boundaries. In liquid cells, electrolyte permeates into the pores and along the loose grain boundaries to enable the utilization of isolated CAMs. In ASSBs, however, cracking and volume change can lead to void formation, contact loss, impedance rise and capacity fade. Use of SC with controlled particle size can be expected to eliminate intergranular and intragranular cracking associated with volume expansion/contraction during cycling; 3) design and optimization of CAM SC surface facets for enhanced Li transport. It is known that PC particle surfaces are often terminated with a variety of crystalline facets that are not optimized for Li transport. For NMCs, (003) basal planes are Li impermeable and their interface with SE can become bottleneck for Li transport, increasing overall impedance and limiting rate capability. To this end, single-crystal based studies enables particle-level surface modification for optimal Li diffusion.

Figure XIII.2.1a and b show the scanning electron microscope (SEM) images of PC and SC $\text{LiNi}_{0.8}\text{Mn}_{0.1}\text{Co}_{0.1}\text{O}_2$ (NMC811) particles, respectively. While the PC sample is made of large secondary particles ($\sim 10 \mu\text{m}$) with many small primary grains ($\sim 1 \mu\text{m}$), the SC sample shows discrete particles in 3-5 μm size range, largely free of aggregation. Composite cathodes were prepared by combining PC- or SC-NMC811 particles, Li_3YCl_6 (LYC) and carbon black in a weight ratio of 57: 40.5:2.5, and referred to as PC and SC composite cathodes hereafter. Both types of NMC811 particles were used directly as cathode active materials without a coating. ASSB cells consisting of either a PC- or SC composite cathode, an LYC separator and a Li-In anode were assembled, and referred to as PC and SC cells hereafter. Figure XIII.2.1c-d show the cross-sectional SEM images of the cell, with the expanded view between the composite cathode and LYC separator (Figure XIII.2.1d) showing a clearly defined interface. The cells were cycled between 3.0 and 4.3 V (V vs. Li^+/Li) at C/2 under an external applied pressure of $\sim 8 \text{ Mpa}$, and the room temperature electrochemical performance are compared in Figure XIII.2.2. While the PC cell delivered a discharge capacity of $\sim 110 \text{ mAh/g}$ upon initial cycling, the SC cell delivered $\sim 150 \text{ mAh/g}$, a net gain of 36%. Gradual capacity decrease was observed in both cells, with a capacity retention of $\sim 70\%$ after 820 cycles and $\sim 90\%$ after 1000 cycles for PC and SC cells, respectively (Figure XIII.2.2a-c). The rate capability comparison is shown in Figure XIII.2.2d. As expected, both cells showed relatively poor rate performance due to the absence any liquid electrolyte. The SC cell, however, significantly outperformed the PC counterpart in both cycling stability and rate capability testing. We note that our SC cell performance represents one of the best performance reported on ASSB cells with a Ni-rich NMC cathode and a Li-metal based anode so far. It even surpasses those reported on cells equipped with a coated Ni-rich NMC cathode and a highly conductive SE such as sulfides.

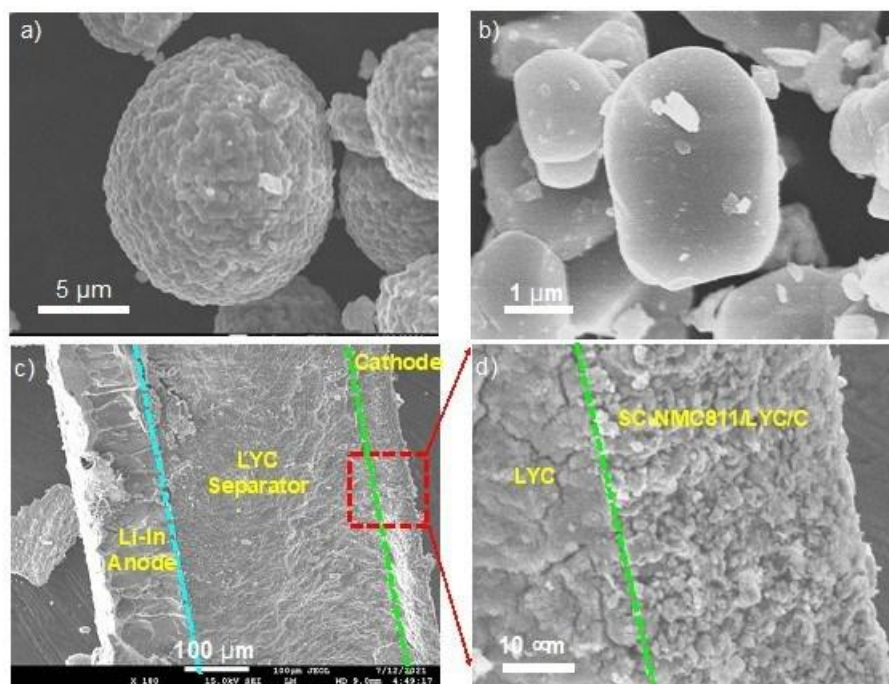


Figure XIII.2.1 SEM images of as-synthesized cathode particles: a) PC-NMC811 and (b) SC-NMC811. c, d) Cross-sectional SEM view of an assembled (SC-NMC811+LYC+C) | LYC | Li-In solid-state battery cell. An expanded view at the cathode side of the cell is shown in d).

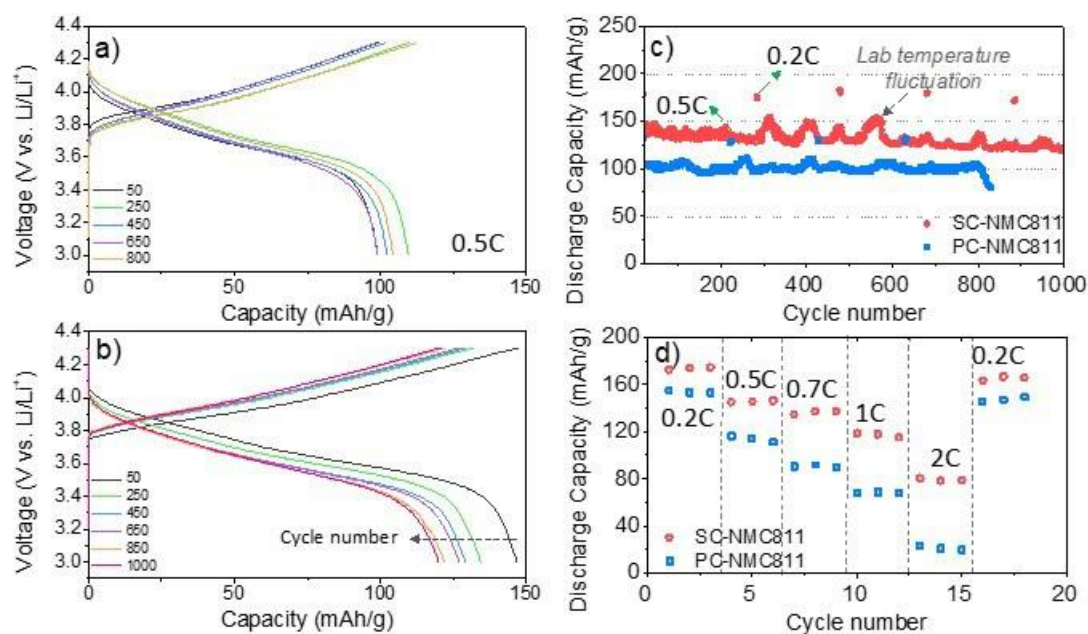


Figure XIII.2.2 a, b) Voltage profiles collected on PC-NMC811 and SC-NMC811 cells cycled at 0.5C, respectively. LYC was used as electrolyte and Li-In alloy used as anode. c) Comparison of discharge capacity as a function of cycle number and d) rate capability comparison of the cells.

To understand the superior performance of the SC cell, post-mortem analysis was carried out to examine the morphological changes in the PC and SC composite cathodes before and after cycling. Figure XIII.2.3 compares the SEM images collected in top-view as well as cross-sectional view using the focused ion beam (FIB) processing. While pristine PC-NMC811 consists of dense agglomerates of primary particles free of cracking (Figure XIII.2.3a and b), internal cracks with various sizes, shapes and lengths are clearly seen within the secondary particles after 820 cycles (Figure XIII.2.3c and d). In contrast to the intimate contact observed between the pristine NMC and LYC SE particles, large gaps are visible after cycling, leading to contact loss, isolated and inaccessible PC-NMC811 primary and secondary particles, and discontinuation in Li ion diffusion pathways. These changes are somewhat expected, considering the large anisotropic volume changes experienced by the cathode particles during cycling. A number of previous studies have demonstrated intergranular cracking in PC particles, both in solid and liquid electrolyte cells. On the other hand, no discernible changes were observed by comparing the pristine and cycled SC cathode composites. Both SEM and FIB-SEM images show crack-free SC-NMC811 particles before (Figure XIII.2.3e and f) and after long-term cycling of 1000 cycles (Figure XIII.2.3g and h). The contact between the SC-NMC811 and LYC SE particles remain nearly unchanged, enabling efficient Li ion migration during cycling. The two scenarios provide marked contrast in terms of the effect of cycling on the composite cathodes, with the former suffering significant loss of active materials due to isolation and inaccessibility, while the latter maintains the high utilization of the NMC cathode. The results support the performance differences observed on the two ASSB cells.

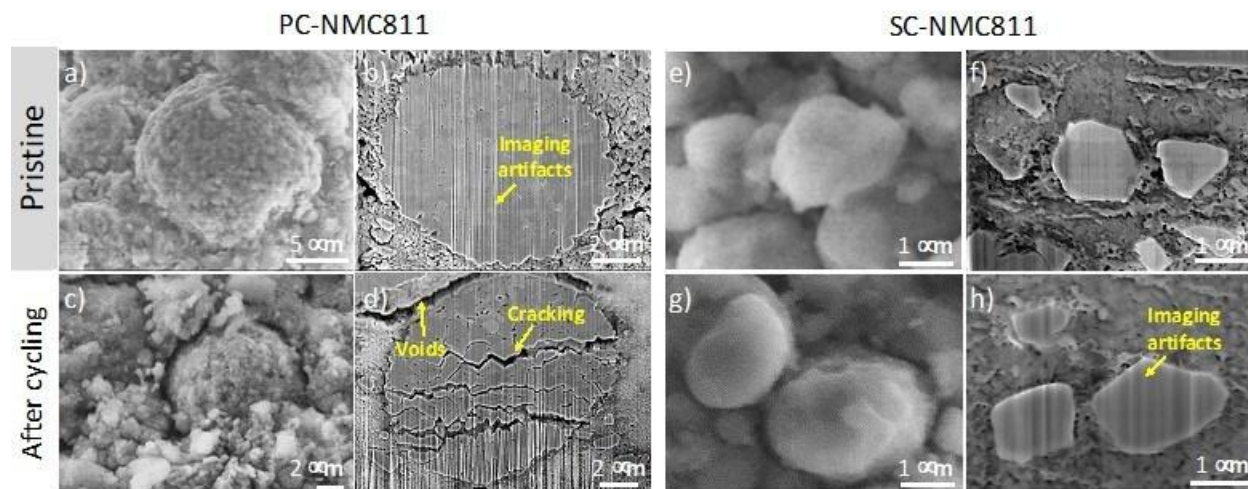


Figure XIII.2.3 SEM images (a, c, e, g) and cross-sectional FIB-SEM images (b, d, f, h) collected from as-prepared (a, b, e, f) and cycled (c, d, g, h) NMC811 composite cathodes. (a-d) collected from PC-NMC811 and (e-f) collected from SC-NMC811. The vertical lines in (b, d, f, h) are imaging artifacts from FIB processing.

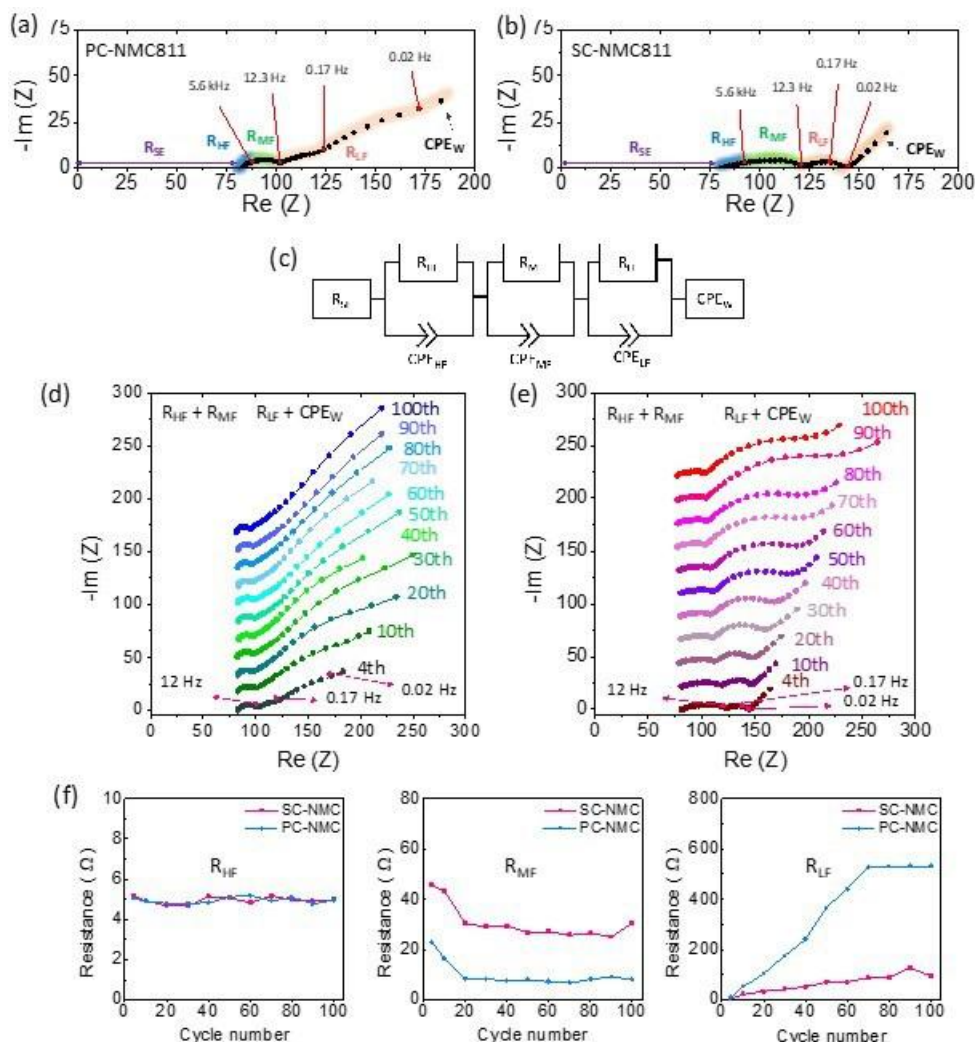


Figure XIII.2.4 (a, b) Nyquist plots collected at 3.67 V during the 4th discharge of the ASSB cells with a PC-NMC811 (a) and SC-NMC811 CAM (b). The colored lines are shown to guide the placement of the various semi-circle components on the Nyquist plots. (c) The equivalent circuit model for fitting the EIS data. (d, e) Nyquist plots obtained at 3.67 V during the discharge of PC-NMC811 (d) and SC-NMC811 (e) ASSB cells at the indicated cycle number. (f) Resistance values obtained from fitting the corresponding Nyquist plots in (d) and (e).

Further mechanistic understanding of the interface between the CAM and the SE were obtained using electrochemical impedance spectroscopy (EIS) analysis. Figure XIII.2.4a and b compare the Nyquist plots obtained at open circuit voltage, after 2-hour relaxation following the 4th discharge of the PC and SC cells to 3.67 V, respectively. The particular voltage of 3.67 V was chosen due to the known high diffusion coefficient at the corresponding state of charge of NMC811, allowing better differentiation of the impedance components in the ASSB cell. In both cases, the typical semi-circle shape along with the Warburg element appear in the examined frequency region (1 MHz - 1 mHz). According to previous reports, the bulk SE resistance from the separator layer (R_{SE}) appears at a very high-frequency region of > 1 MHz while the charge transfer resistance within the grain boundaries of SE evolves in the frequency region of 1 MHz - 1 kHz (R_{HF}). The semi-circle appeared in the mid-frequency region of 1 kHz - 10 Hz (R_{MF}) can be attributed to the charge transfer resistance at the interface between NMC811 CAM and LYC SE. In addition, the semi-circle at the low-frequency region of < 10 Hz (R_{LF}) can be assigned to the interfacial resistance between the LYC SE layer and the In-Li alloy anode as Li^+ ion diffusion impedance within the CAM. The latter component is also reflected in the subsequent Warburg region (CPE_W). The corresponding equivalent circuit is shown in Figure XIII.2.4c.

Figure XIII.2.4d and e compare the Nyquist plots of the 4th as well as every 10th discharge of the PC and SC cells to 3.67 V, respectively. In both cases, the R_{SE} resistance of the LYC SE separator layer was determined to be $\sim 80 \Omega$, corresponding to an electrolyte layer thickness of approximately 350 μm and an ionic conductivity of $0.3 \text{ mS}\cdot\text{cm}^{-1}$ in LYC. The R_{SE} values stay more or less constant throughout the cycling. The grain boundary resistance (R_{HF}) of LYC electrolyte evolves similarly in the frequency range of 0.15 MHz - 5.6 kHz. The R_{MF} component between 5.6 kHz and 12.3 Hz appears smaller in the PC cell, and the differences are likely a result of initial contact made between the CAM and the SE. While the PC particles are largely spherical and better for making surface contact, the SC particles are irregularly shaped. Furthermore, the measured Brunauer–Emmett–Teller (BET) surface areas of the PC-NMC811 and SC-NMC811 samples are 0.64 and 0.27 m^2/g , respectively, suggesting that more surface contact area is available for SE connection in the former. Regardless of the initial R_{MF} size, both cells showed a gradual reduction over the first 20 cycles, indicating a “break-in” process that establishes effective Li^+ ion migration pathways between NMC811 particles and LYC SE. This facilitates Li^+ ion migration upon initial cycling which is reflected by the small capacity increase in both cells (Figure XIII.2.2a and b). The R_{MF} component remained more or less constant in the subsequent cycles. The main differences between the two cells are observed in the R_{LF} and CPE_W region below 12 Hz, which includes impedance contribution from the SE and Li-In anode interface (12.3–0.17 Hz) as well as Li^+ diffusion within the CAM particles ($< 0.17 \text{ Hz}$). As shown in Figure XIII.2.4d and e, this component in both cells increases with cycling, however, the extent is significantly more severe in the PC cell. Further analysis was carried out by fitting the EIS data using the equivalent circuit shown in Figure XIII.2.4c, and the results are plotted in Figure XIII.2.4f. The initial R_{LF} values of $\sim 7\text{--}10 \Omega$ are similar, consistent with the pristine materials’ properties before cell cycling. Cycling leads to a continuous increase in R_{LF} in both cells. After 100 cycles, a large increase of over 60x was observed in the PC cell whereas in the SC cell, a much smaller increase of $\sim 10\text{x}$ was observed. Although the impedance evolution at the interface between LYC SE and Li-In anode also contributes to the increase in the R_{LF} component, it is expected that both cells experience similar changes at the anode interface as the same configuration was used for the study and the depth of discharge was carefully controlled during the experiment. Li^+ diffusion resistance within NMC811 CAM particles, therefore are considered as the main contributor to the observed differences in the R_{LF} and CPE_W components. The study demonstrates the unique advantage of using SC particles which provide improved Li^+ ion diffusion pathways upon continuous cell cycling due to their better mechanical properties.

Previous theory studies have predicted reduction of LYC to Y metal, Y_2Cl_3 and LiCl at the Li metal anode interface. Without effective protection, cells with a LYC SE are expected to have poor cycle life as metallic Y leads to an increase in electronic conduction and cell shorting over cycling. To this end, we also performed post-mortem analysis to understand interface evolution at the anode. Figure XIII.2.5 shows results collected at the cross-section of the cycled ASSB anode interface. A distinct interface layer was found between LYC electrolyte and Li-In anode (Figure XIII.2.5a), indicating reactivity at the anode. The SEM image shows an average interlayer thickness of $\sim 8 \mu\text{m}$ after 1000 cycles. Energy dispersive X-ray spectroscopy (EDX) analysis (Figure XIII.2.5b–d) reveals that the chemical composition of the interlayer includes In, Y and Cl, although Li may also exist which was not detectable by EDX. To further investigate the chemical nature of the interface layer, hard X-ray absorption spectroscopy (hXAS) and micro X-ray fluorescence (XRF) mapping were used to analyze Y oxidation state at the cycled anode interface. After removing the composite cathode and LYC layers, the sample was sandwiched between two Kapton tapes for measurements. The experiments were carried out at BL2-3 at Stanford Synchrotron Radiation Lightsource (SSRL). Figure XIII.2.5e compares the X-ray absorption near edge spectroscopy (XANES) profiles collected on the cycled interface as well as pristine LYC and Y metal standard for comparison. There is a white-line crossover between the pristine LYC and the cycled sample, indicating slight differences in atomic environment of Y. However, Y oxidation state largely remains at 3+ and metallic Y was not detected after the extensive cycling. This is further shown in the chemical map obtained by XRF (Figure XIII.2.5f), where a multi-energy map collected at 17053.99 eV, 17058.29 eV and 17180 eV was analyzed by linear combination fitting of Y hXAS data collected from Y metal and YCl_3 references. The oxidation state map of Y shows uniform distribution of Y^{3+} as well as the absence of metallic Y in the entire area examined. We believe this is related to the chemical nature as well as the higher potential of the Li_3In_7 alloy anode (0.6 V vs. Li/Li^+), which lead to modified interfacial reaction pathways and

the formation of a passivating interphase layer between LYC and the anode that enables stable-cycling of the ASSB cell.

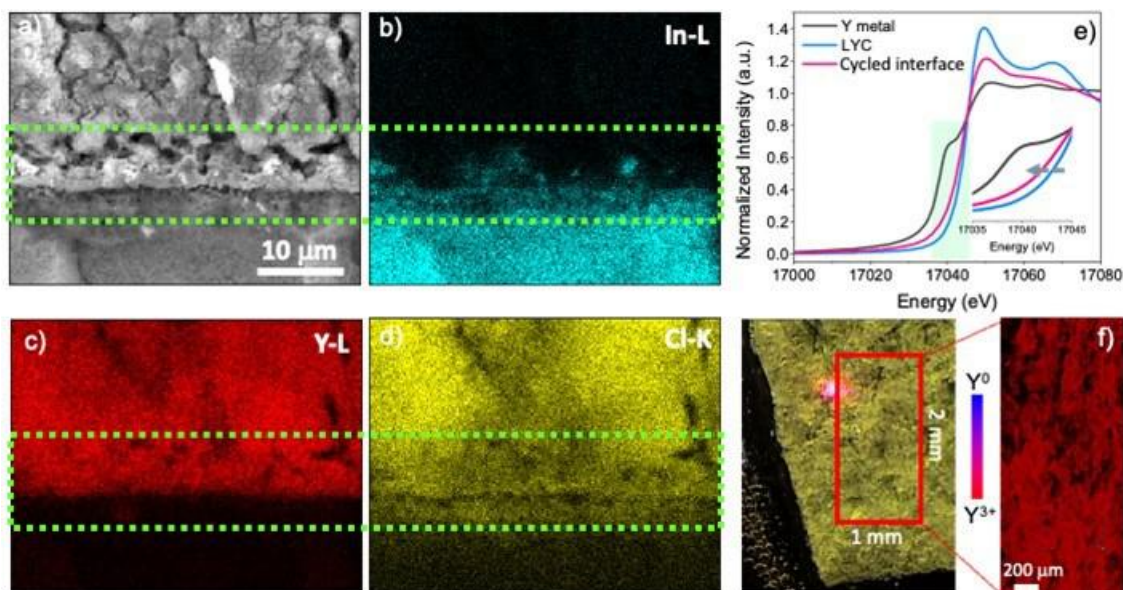


Figure XIII.2.5 Post-mortem analysis of the interface between LYC and Li-In anode after 1000 cycles. a) Cross-sectional SEM image, b-d) EDX maps of In-L, Y-L and Cl-K, respectively, e) Y K-edge XAS spectra collected on Y metal, pristine LYC and the interface after cycling, and f) Y chemical map obtained from XRF imaging.

Conclusions

Li-metal based ASSBs are currently facing a number of challenges. Among them are the oxidative instability of SSE in the composite cathodes, cracking and grain isolation associated with volume changes in cathode active materials, as well as chemical, electrochemical and mechanical instabilities at the SSE/electrode interfaces. Here we address these challenges by developing novel composite cathode structures featuring the following key design elements: 1) halide SE with high oxidative stability to enable direct use of uncoated 4 V-class CAM and 2) single-crystal CAM to eliminate intergranular cracking associated with volume changes and mechanical instability. We demonstrate exceptional performance achieved on such ASSB cells incorporating an uncoated SC-NMC811, an LYC SE, and a Li-In alloy anode, delivering a high discharge capacity of 170 mAh/g at C/5 and a superior capacity retention of nearly 90% after 1000 cycles. Through comparative studies on polycrystalline and single-crystal NMC811 composite cathodes, we reveal the working mechanism that enable such stable cycling in our composite design. At the anode interface, an interlayer between LYC and Li-In alloy evolves dynamically over cycling. A distinct layer with a thickness of $\sim 8 \mu\text{m}$ was observed after 1000 cycles. The chemical nature as well as the elevated potential of Li-In alloy enables the formation of a passivating interphase which largely contributes to the stable cycling of the ASSB cell. Our study highlights the importance in proper cathode composite design and interface engineering in developing future ASSBs with improved performance.

Key Publications

1. J. Ahn, Y. Ha, R. Satish, R. Giovine, L. Li, J. Liu, C. Wang, R. J. Clement, R. Kostecki, W. Yang and G. Chen, "Exceptional Cycling Performance Enabled by Local Structural Rearrangements in Disordered Rocksalt Cathodes," *Advanced Energy Materials*, 220042 (2022). DOI: 10.1002/aenm.202200426
2. M. Jung, S. Y. Kim, S.-B. Lee, M.-J. Kim, I.-J. Yang, W. Cho, J. Yu, G. Chen, K. Kim and K.-H. Park, "Anion Engineering for Halide Solid Electrolytes," under review (2022)
3. S. Y. Kim, H. Cha, R. Kostecki and G. Chen, "Composite Cathode Design for High-Energy All-Solid-State Lithium Batteries with Long Cycle Life," under review (2022)

4. Y. Lu, T. Zhu, E. McShane, B. D. McCloskey and G. Chen, “Single-Crystal $\text{LiNi}_x\text{Mn}_y\text{Co}_{1-x-y}\text{O}_2$ Cathodes for Extreme Fast Charging,” *Small* (2022). DOI: 10.1002/sml.202105833
5. M. Kim, L. Zou, S.-B. Son, I. D. Bloom, C. Wang and G. Chen, “Improving LiNiO_2 Cathode through Particle Design and Optimization,” *J. Mater. Chem. A* **10**, 12890 (2022). DOI: 10.1039/d2ta02492f

Patents and Invention Disclosures

1. U.S. Patent Application No. 17/838,457 titled “High-Energy and High Power Composite Cathodes for All Solid-State Batteries,” by G. Chen, S. Kim and Y. Lu, June 2022.
2. U.S. Patent Application No. 17/834,076 titled “Methods of Synthesizing Single-Crystal $\text{LiNi}_x\text{Mn}_y\text{Co}_{1-x-y}\text{O}_2$ Cathode Materials,” Y. Lu and G. Chen, June 2022.

Acknowledgements

This work was conducted by Se Young Kim and Shuhao Yang at LBNL.

XIII.3 Design of High-Energy, High-Voltage Lithium Batteries through First-Principles Modeling (LBNL)

Kristin A. Persson, Principal Investigator

Lawrence Berkeley National Laboratory

1 Cyclotron Rd

Berkeley, CA 94720

E-mail: kapersson@lbl.gov

Tien Duong, DOE Technology Development Manager

U.S. Department of Energy

E-mail: TGien.Duong@ee.doe.gov

Start Date: October 1, 2019

End Date: September 30, 2022

Project Funding (FY22): \$500,000

DOE share: \$500,000

Non-DOE share: \$0

Project Introduction

This project supports VTO programmatic goals by developing next-generation, high energy cathode materials and enabling stable cathode operation at high voltages through target particle morphology design, functional coatings, and rational design of electrolytes. We aim to provide fundamental insights into the atomistic mechanisms underlying surface reactivity and performance of Li-ion cathode materials and electrolytes with the ultimate goal to suggest improvement strategies, such as coatings, surface protection, novel electrolyte formulations, and particle morphology design. Transport modes as a function of solvent and salt concentrations will be clarified, and a data-driven reaction network framework will be designed and implemented to predict early SEI formation on lithium metal.

Objectives

The end-of-project goals include the following:

- Understanding of the factors that govern charge transport in nonaqueous, superconcentrated LEs.
- Critical surface and coating design and optimization strategies that will improve cycling of Li-ion battery cathodes by reducing cathode degradation from oxygen loss.
- Simulation and ML of the early formation of the SEI on Li-metal electrodes.

Approach

- First-principles calculations, both static and dynamic approaches, are used to model SSE material thermodynamics and kinetics. LEs are modeled through coupled classical MD and first principles methods to accurately capture solvation structure as well as reactivity of the liquid system.
- Examine different transport models to study the electron and ion mobility through the amorphous coating layer.
- The reaction network is built on large-scale first-principles data, using graph theory and machine learning (ML) models.

Results

One of the principal design obstacles of superconcentrated electrolytes is the a priori prediction of salt solubility – an open problem of physical chemistry. This problem is directly related to the electrolyte phase diagram construction (see Figure XIII.3.1 a). We developed a physical-chemical model which is intended for the dilute to moderate concentration range (up to ~1 molal) as a preliminary effort to addressing this open problem. This allows computation of the liquidus lines for selected carbonate electrolytes (e.g. LiPF₆ in PC) via calculation of the activity coefficients, and with certain assumptions regarding the eutectic composition, the glass transition and knowing neat solvent properties⁸. Classical molecular dynamics simulations, first

principles calculations and theoretical expressions are employed. The physical-chemical model computes the activity coefficients via accounting of solvent-ion and ion-ion interactions. These are quantified via Debye-Huckel theory, ion-pairing, the Born solvation equation and solvent entropic effects. We find that these contributions are all significant. These are all interrelated, for example the quantity of ion-pairing dictates the concentration-dependent dielectric constant, a quantity which the Born solvation equation and Debye-Huckel theory are dependent on. The dielectric increment of specific solvated species in solution (Figure XIII.3.1 c, free and LiPF_6 contact-ion pair species) are calculated via classical molecular dynamics simulations. Moreover, to account for ion-pairing, electronic structure calculations are used in order to find the association constant between such species. It is found that for test carbonate solutions, the herein developed physical-chemical model properly reproduces the activity coefficients and the relevant liquidus lines, as shown in Figure XIII.3.1 b.

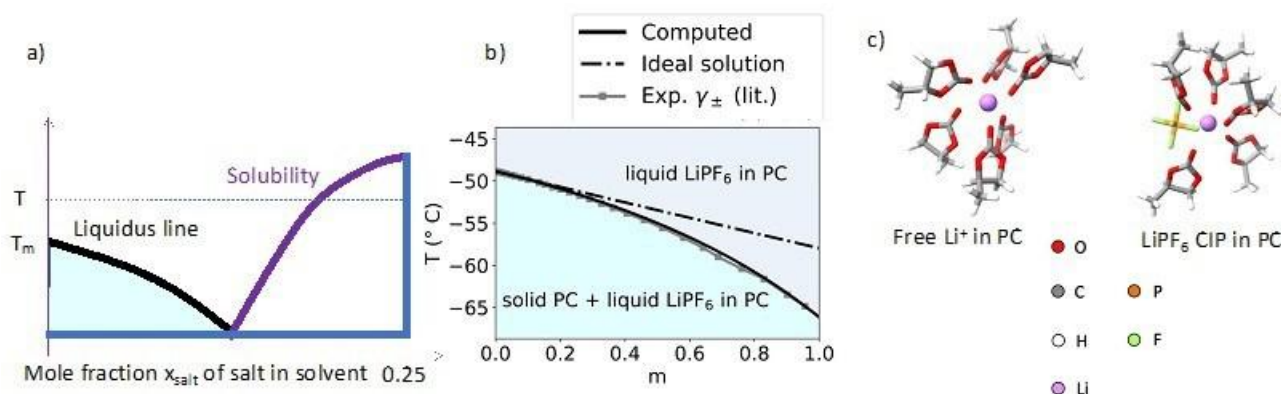


Figure XIII.3.1 [8] a) Schematic representation of the liquidus line (black) for a eutectic phase diagram. The line in purple shows the solubility, e.g. at a temperature T , the salt will not be soluble past the solubility line. b) Computed liquidus line based on activity coefficients calculated from the physical-chemical model developed. c) Sample structures of relevant species in solutions for the studied carbonate electrolyte, LiPF_6 in PC. These are the free Li^+ and contact-ion pair (CIP).

One of the principal design obstacles of superconcentrated electrolytes is the a priori prediction of salt solubility – an open problem of physical chemistry. This problem is directly related to the electrolyte phase diagram construction (see Figure XIII.3.1 a). We developed a physical-chemical model which is intended for the dilute to moderate concentration range (up to ~ 1 molal) as a preliminary effort to addressing this open problem. This allows computation of the liquidus lines for selected carbonate electrolytes (e.g. LiPF_6 in PC) via calculation of the activity coefficients, and with certain assumptions regarding the eutectic composition, the glass transition and knowing neat solvent properties⁸. Classical molecular dynamics simulations, first principles calculations and theoretical expressions are employed. The physical-chemical model computes the activity coefficients via accounting of solvent-ion and ion-ion interactions. These are quantified via Debye-Huckel theory, ion-pairing, the Born solvation equation and solvent entropic effects. We find that these contributions are all significant. These are all interrelated, for example the quantity of ion-pairing dictates the concentration-dependent dielectric constant, a quantity which the Born solvation equation and Debye-Huckel theory are dependent on. The dielectric increment of specific solvated species in solution (Figure XIII.3.1 c, free and LiPF_6 contact-ion pair species) are calculated via classical molecular dynamics simulations. Moreover, to account for ion-pairing, electronic structure calculations are used in order to find the association constant between such species. It is found that for test carbonate solutions, the herein developed physical-chemical model properly reproduces the activity coefficients and the relevant liquidus lines, as shown in Figure XIII.3.1 b.

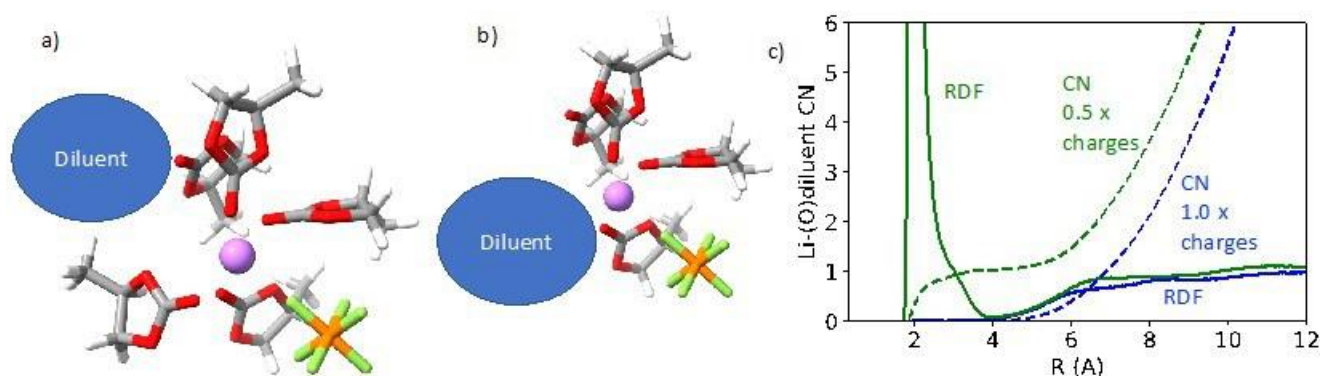
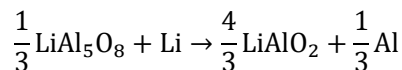


Figure XIII.3.2 [8] a) Molecular dynamics “snapshot” of the solvation structure of a Li cation in the high concentration electrolyte (HCE) formulation, with the diluent in the second solvation shell. b) Molecular dynamics “snapshot” of the solvation structure of a Li cation in the HCE formulation with the diluent, in this case present in the first solvation shell. Atoms are shown in purple (Li), red (O), white (H), green (F), and orange (P). c) Radial distribution functions and coordination numbers for lithium coordinating with the diluent for different classical molecular dynamics force field charge parameters of the diluent.

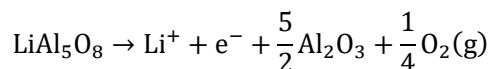
One of the main strategies to address the slow diffusivity of species in super concentrated electrolytes is to employ co-solvents. These co-solvents are often much less polar than their counterparts in solution and are in certain cases, when they are not expected to directly coordinate with the electroactive cation in the first solvation shell, referred to as diluents [1]. Figure XIII.3.2 a) shows the example of a diluent in an electrolyte – it is not present in the first solvation shell of the lithium cation. We investigated certain highly concentrated electrolytes, HCEs, [2] and highly concentrated electrolytes with co-solvents previously using classically molecular dynamics (unpublished). However, we found that in the HCEs with diluent investigated, the diluent appeared in the first coordination shell of lithium (Figure XIII.3.2 b). One example formulation is 3 M of salt, ratio of Li:PC:diluent 1:2:0.3 where the Li^+ counter anion is LiPF_6 . As such it became a question as to whether such first shell coordination was an artifact of the classical molecular dynamics forcefield or in fact the previously reported effects of the diluent were wrong (i.e. the diluent is effectively a conventional co-solvent). In order to evaluate the sensitivity of the forcefield, we scaled the charges of the diluent molecule by 0.5x the default charges (obtained from the OPLS force field). We found that the relevant structural motifs dramatically changed: in the 0.5x scaled charges the coordination number in the primary lithium solvation shell is 0 (Figure XIII.3.2 c, green). However, with default charges the coordination number is about 1, suggesting that the diluent is present in the primary solvation shell (Figure XIII.3.2 c, blue). This contradicts the design principle of HCEs with diluent where the diluent is chosen to allow the primary shell to be but the polar cosolvent (not the diluent). We also found that for the neat diluent, when studied in classical molecular dynamics, whether charges were scaled by 0.5, 1.0 or 1.2, the dielectric constant of the neat diluent surprisingly remained constant ($\epsilon=4$). Although requiring further investigation, we speculate that this is due to a tradeoff between magnitude of dipole moment and intermolecular interactions. The independence of the dielectric constant on charge scaling suggests that the dielectric constant alone may not be sufficient to use as a quantitative assessment of diluent molecular dynamics forcefields. It thus remains an open problem as to decisively distinguish between conventional co-solvent approaches and the HCEs for certain case studies via molecular dynamics, and generally as partial solvation is challenging to quantify both experimentally and theoretically.

Next, we report the method we have used to calculate the electrochemical stability window of amorphous coatings. The method combines formation energies calculated by density functional theory in the Materials Project [3], experimental thermochemical data for gaseous species and experimental electrochemical data for solvated ions. [4] The procedure is similar to the Pourbaix diagram formalism outlined by Persson et al [5]. To estimate the reaction potential (versus Li metal) in a high-throughput fashion, we make the following approximations: (1) For solid phases, we assume the entropy and $P\Delta V$ contributions to the Gibbs free energy of a reaction are negligible; (2) We assume a one-step single ion dissolution: $A = A^{n+} + ne^-$; (3) We assume

a unity of activity for condensed phases and all solvated ions. The electrochemical stability window consists of a reduction limit (V_{red}) at which the material starts lithiation during discharge and an oxidation limit ($-V_{ox}$) at which the material starts delithiation/decomposition during charge. Here we take Al_2O_3 and LiAl_5O_8 as examples to illustrate our method in calculating the electrochemical stability window of Li-containing and non-Li containing compounds. The lithiation compound of LiAl_5O_8 can be directly identified from a Li-Al-O phase diagram, see Figure XIII.3.3 a. Its discharge reaction can be expressed as:

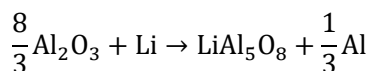


As all the reactants and products are in their solid phases, $V_{red} = -\frac{\Delta G}{zF} = -\frac{\Delta H}{zF} = 0.79 \text{ V}$, where z is the number of electrons transferred in the reaction and F is the Faraday's constant. As LiAl_5O_8 is a Li-containing compound, its delithiation takes place via a dissolution of Li^+ . From the Li-Al-O phase diagram, the delithiation reaction of LiAl_5O_8 can be expressed as:

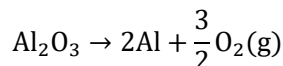


As the reaction involves oxygen gas evolution, we include the entropy value of O_2 taken from the JANAF tables [6]. Thus, $V_{ox} = -\frac{\Delta G}{zF} = -\frac{\Delta H - TS}{zF} = -3.96 \text{ V}$. Therefore, the electrochemical stability window of LiAl_5O_8 can be estimated as: $[V_{red}, -V_{ox}] = [0.79, 3.96]$.

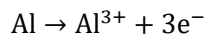
Similar to LiAl_5O_8 , the lithiation compound of Al_2O_3 can also be directly identified from a Li-Al-O phase diagram, see Figure XIII.3.3 b. Its discharge reaction can be expressed as:



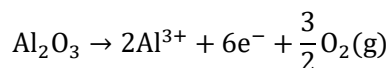
As all the reactants and products are in their solid phases, $V_{red} = -\frac{\Delta G}{zF} = -\frac{\Delta H}{zF} = 1.26 \text{ V}$. As Al_2O_3 is a non-Li containing compound, we assume its oxidation takes place via a dissolution of Al^{3+} . From the Li-Al-O phase diagram, the decomposition reaction of Al_2O_3 can be expressed as:



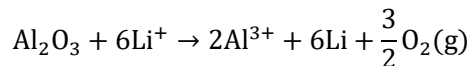
As the reaction involves oxygen gas evolution, we include the entropy value of O_2 . Thus, $\Delta G_1 = \Delta H - TS = 16.18 \text{ eV}$. Next, we add the standard free energy of Al^{3+} formation, ΔG_2 , to ΔG_1 .



$\Delta G_2 = -nFE_{\text{Al}^{3+}}^0 = -4.99 \text{ eV}$. n is the valence state of Al^{3+} and $E_{\text{Al}^{3+}}^0$ is the standard oxidation potential of Al^{3+} taken from the IUPAC publication [7].



$\Delta G_3 = \Delta G_1 + 2\Delta G_2 = 6.21 \text{ eV}$. Next, we reference the above equation to Li/Li^+ to calculate the reaction potential with $\text{Li}^+ + \text{e}^- \rightarrow \text{Li}$:



The standard oxidation potential of Li^+ is $E_{\text{Li}^+}^0 = 3.04 \text{ V}$. Thus, $\Delta G_4 = \Delta G_3 + 6nFE_{\text{Li}^+}^0 = 24.45 \text{ eV}$. Finally, the reaction potential V_{ox} can be obtained using the Nernst equation: $V_{ox} = -\frac{\Delta G_4}{zF} = -4.07 \text{ V}$. Therefore, the electrochemical stability window of Al_2O_3 can be estimated as: $[V_{red}, -V_{ox}] = [1.26, 4.07]$.

It should be noted that the actual dissolution process may involve multi-step/multi-ion dissolutions. Therefore, this method merely serves as an approximation that aims at broadly capturing the dissolution tendencies in a high-throughput fashion.

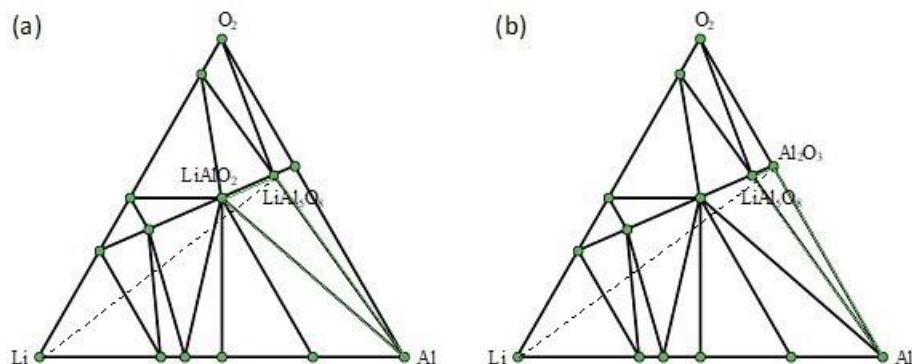


Figure XIII.3.3 [9]. Li-Al-O phase diagrams. (a) The first phase-region (green triangle) formed by LiAl_5O_8 , LiAlO_2 and Al for LiAl_5O_8 lithiation. (b) The first phase-region (green triangle) formed by LiAl_5O_8 , Al_2O_3 and Al for Al_2O_3 lithiation.

A coating material that participates in the redox reaction during extensive cycling may cause degradation of the surface film, thus a loss of the surface protection. Therefore, we retain only electrochemically stable compounds that can sustain the desirable voltage window. In this study, we select the compounds that exhibit a reduction limit smaller than 3 V and an oxidation limit above 4 V. Figure XIII.3.4 a illustrates the reduction and oxidation limits of the compounds that are thermodynamically stable. The electrochemical stability of each category is denoted by two violin plots: the left and right represent oxidation and reduction limits, respectively. We find that in general, fluorides, such as AlF_3 and LiAlF_4 , have the largest electrochemical stability window with high oxidation limits and low reduction limits. On the other hand, metal oxides, such as BaO and Bi_2O_3 , exhibit low oxidation limit, and nonmetal oxides, such as P_2O_5 and SeO_2 , have high reduction limit. The bar graph in Figure XIII.3.4 a summarizes the numbers of compounds for each category of materials that pass the electrochemical stability screening. After this screening tier, polyanionic oxides have the largest number of candidates, followed by fluorides and chlorides. There are only 12 metal oxides and 1 nonmetal oxide, B_2O_3 , left for further screening.

Next, we select cathode coatings that are inert to chemical reactions with both cathodes and electrolytes. The reaction energy ΔE_{rxt} is calculated using DFT-computed energies of the reactants and products, and a more negative ΔE_{rxt} indicates a more reactive chemical reaction. We set the criterion for chemically stable cathode coatings as: $\Delta E_{\text{rxt}} \geq -0.1$ eV per atom. We calculate ΔE_{rxt} between cathodes and coating materials using the commonly used cathodes, layered LiNiO_2 and LiCoO_2 , spinel LiMn_2O_4 , and olivine LiFePO_4 . Figure XIII.3.4 b shows that oxides coatings are less prone to react with cathodes than fluorides and chlorides. Specifically, all the electrochemically stable metal oxides exhibit low reactivity with common cathodes and pass the chemical stability descriptor. This round of screening returns 1790 compounds for further consideration with polyanionic oxides having the largest number of candidates (714).

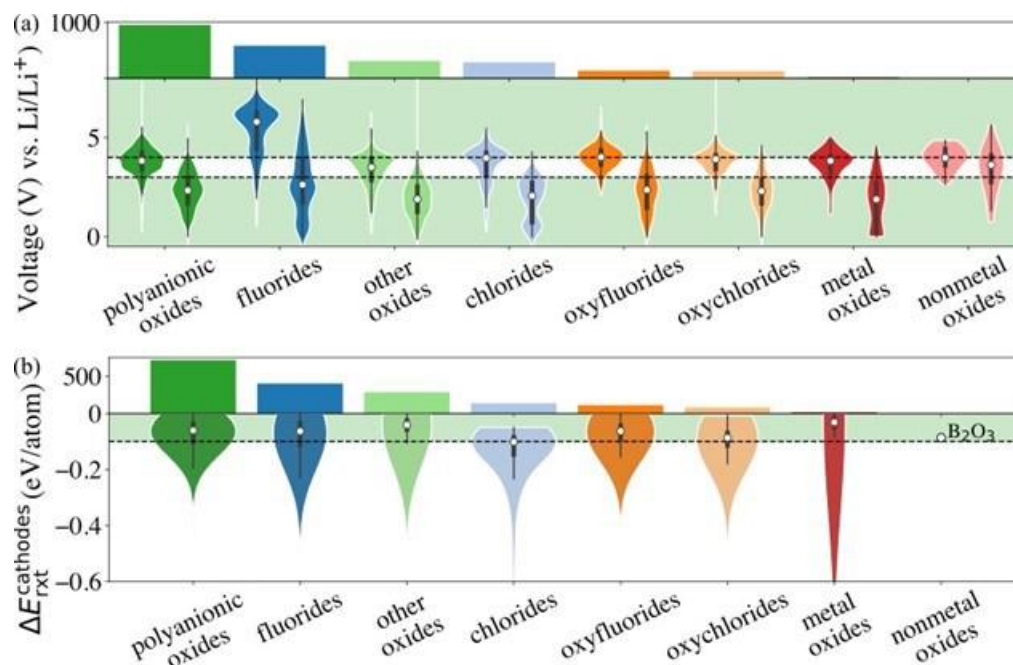


Figure XIII.3.4 [9] (a) Distribution of the reduction and oxidation limits for each category that pass thermodynamic stability descriptor. (b) Distribution of the reaction energy with LiNiO_2 , LiCoO_2 , LiMn_2O_4 and LiFeOP_4 cathodes for each category that pass electrochemical stability descriptor. The horizontal dash lines represent the limits of the descriptors. The histograms in (a) and (b) illustrate the numbers of compounds for each category that pass the descriptors.

Similarly, we calculate ΔE_{rxt} between coating materials and representative electrolyte components. In this study, we consider the commonly used Li_3PS_4 solid electrolyte and LiPF_6 -based non-aqueous liquid electrolytes, respectively, and categorize the coating materials based on their reactivity. In the case of LiPF_6 -based electrolytes, we calculate ΔE_{rxt} between coating materials and HF, which is known to react strongly with both cathodes and coating materials. Figure XIII.3.5 illustrates the distribution of ΔE_{rxt} with Li_3PS_4 and HF for the compounds that are chemically stable with the cathodes. We find that most fluorides and chlorides have lower chemical reactivity with both Li_3PS_4 and HF than oxides compounds, thus are chemically compatible with both the cathodes and electrolytes. On the other hand, most oxides compounds are not chemically inert in LiPF_6 -based liquid electrolytes due to a high reactivity with HF. This round of screening returns 902 and 508 coating candidates that are chemically compatible with Li_3PS_4 and LiPF_6 based electrolytes, respectively.

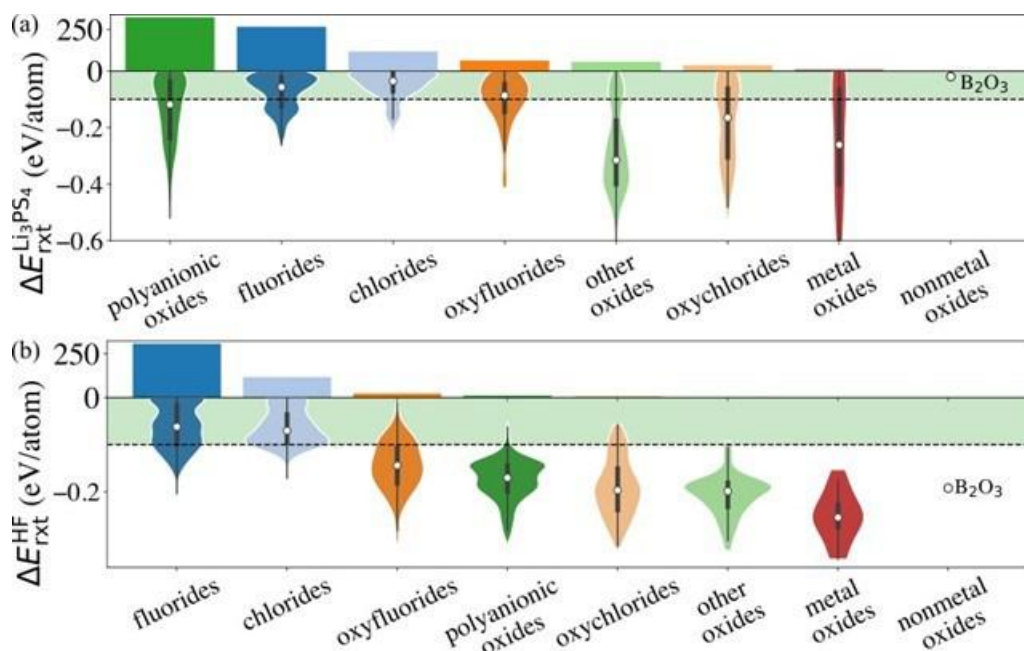


Figure XIII.3.5 [9] Distribution of the reaction energy ΔE_{rxt} with Li_3PS_4 (a) and HF (b) for each category that pass chemical stability with the cathodes descriptor. The horizontal dash lines represent the limits of the descriptors. The histograms in (a) and (b) illustrate the numbers of compounds for each category that pass the descriptors.

In addition, we find a correlation between Li^+ and O^{2-} diffusion, which can be explained by ionic conduction mechanism in amorphous structures. Our previous study showed that Li^+ and O^{2-} diffusion consists of discrete vibrational and translational motions. During vibrational motions, Li^+ is bonded to more O^{2-} ions than during translational motions, and its translation to another vibration site is activated by the Li-O bond breaking/formation process, which effectively explains the correlated transport between Li^+ and O^{2-} .

Conclusions

- Correlated electrolyte chemistry, and Li/SEI compositional structure determined for Li-EC-based electrolyte.
- Determined sensitivity of molecular dynamics (MD) parameters to diluent effect on transport in at least one superconcentrated electrolyte.
- Developed a high-throughput (HT) infrastructure for MD simulations.
- Determined chemistry and structural motifs that control cathode amorphous coating performance by screening over 50,000 inorganic compositions.

Key Publications

1. Tingzheng Hou, Wentao Xu, Xiaokun Pei, Lu Jiang, Omar M. Yaghi, and Kristin A. Persson, Ionic Conduction Mechanism and Design of Metal–Organic Framework Based Quasi-Solid-State Electrolytes, *J. Am. Chem. Soc.*, 144, 30, 13446, 2022.
2. Eric Sivonxay and Kristin A Persson, Density Functional Theory assessment of the lithiation thermodynamics and phase evolution in Si-based amorphous binary alloys, *Energy Storage Materials* 53 (2022) 42–50.
3. Julian Self, Nathan T. Hahn, and Kristin A. Persson, Solvation Effects on the Dielectric Constant of 1 M LiPF_6 in Ethylene Carbonate: Ethyl Methyl Carbonate 3:7, 2022.
4. Self, Julian, et al. A Theoretical Model for Computing Freezing Point Depression of Lithium-Ion Battery Electrolytes. *Journal of The Electrochemical Society* 168.12 (2021): 12
5. J. Cheng, Kara D. Fong, Kristin A. Persson, Materials Design Principles of Amorphous Cathode Coatings for Lithium-ion Battery Applications, *J. Mater. Chem. A*, 10, 22245, 2022.

References

1. Cao, Xia, Peiyuan Gao, Xiaodi Ren, Lianfeng Zou, Mark H. Engelhard, Bethany E. Matthews, Jiangtao Hu et al. "Effects of fluorinated solvents on electrolyte solvation structures and electrode/electrolyte interphases for lithium metal batteries." *Proceedings of the National Academy of Sciences* 118, no. 9 (2021).
2. Self, Julian, Kara D. Fong, and Kristin A. Persson. "Transport in superconcentrated LiPF₆ and LiBF₄/propylene carbonate electrolytes." *ACS Energy Letters* 4, no. 12 (2019): 2843-2849.
3. Jain, A. *et al.* Commentary: The Materials Project: A Materials Genome Approach to Accelerating Materials Innovation. *APL Materials* vol. 1 (2013).
4. Aykol, M. *et al.* High-throughput computational design of cathode coatings for Li-ion batteries. *Nat. Commun.* 7, 13779 (2016).
5. Persson, K. A., Waldwick, B., Lazic, P. & Ceder, G. Prediction of solid-aqueous equilibria: Scheme to combine first-principles calculations of solids with experimental aqueous states. *Phys. Rev. B - Condens. Matter Mater. Phys.* **85**, 235438 (2012).
6. Chase, M. W. *et al.* JANAF Thermochemical Tables, 1982 Supplement. *J. Phys. Chem. Ref. Data* **11**, 695–940 (1982).
7. Bard, A. J., Parsons, R. & Jordan, J. Standard Potentials in Aqueous Solution. *Stand. Potentials Aqueous Solut.* (2017) doi:10.1201/9780203738764/STANDARD-POTENTIALS-AQUEOUS-SOLUTION-ALLEN-BARD-ROGER-PARSONS-JOSEPH-JORDAN.
8. Self, Julian, et al. A Theoretical Model for Computing Freezing Point Depression of Lithium-Ion Battery Electrolytes. *Journal of The Electrochemical Society* 168.12 (2021): 12
9. J. Cheng, Kara D. Fong, Kristin A. Persson, Materials Design Principles of Amorphous Cathode Coatings for Lithium-ion Battery Applications, *J. Mater. Chem. A*, 10, 22245, 2022.

Acknowledgements

This research used resources of the National Energy Research Scientific Computing Center, a DOE Office of Science User Facility supported by the Office of Science of the U.S. Department of Energy under Contract No. DE-AC02-05CH11231. This research also used the Lawrence Livermore computational cluster resource provided by the IT Division at the Lawrence Berkeley National Laboratory (Supported by the Director, Office of Science, Office of Basic Energy Sciences, of the U.S. Department of Energy under Contract No. DE-AC02-05CH11231)

XIII.4 Modeling of Solid-State Conductors (Lawrence Berkeley National Laboratory) (LBNL)

Gerbrand Ceder, Principal Investigator

Lawrence Berkeley National Laboratory
1 Cyclotron Rd, MS: 33-146
Berkeley, CA, 94720
E-mail: gceder@berkeley.edu

Tien.Duong, DOE Technology Development Manager

U.S. Department of Energy
E-mail: Tien.Duong@ee.doe.gov

Start Date: October 1, 2021

End Date: September 30, 2022

Project Funding (FY22): \$460,000

DOE share: \$460,000

Non-DOE share: \$0

Project Introduction

Solid-state batteries promise to increase the safety and energy density of current Li batteries [1]. To enable their development, it is essential to develop superionic (SIC) electrolytes with high Li conductivity and electrochemical stability. Oxides provide a promising space for novel SICs, as they generally show increased electrochemical stability [6]. However, there are only a limited number of oxide SICs with acceptable Li conductivity of greater than 0.1 mS/cm [6]. The lack of known oxide SICs prompted a study to develop understanding of the transport mechanisms and so that design principles can be established to guide the discovery of new materials.

In this part of the BMR program, we use a range of first principles techniques to investigate the fundamental mechanisms behind facile Li transport in oxide SICs. From high-throughput computational screening, we identify structural motifs that lead to high Li conductivity and perform a detailed investigation of their mechanisms.

Objectives

Solid-state batteries are promising to achieve high energy density. The project objective is to determine the design principles needed to create solid-state electrolytes with high Li-ion conductivity, while also achieving stability against common Li-ion cathodes and Li-metal anodes.

Approach

High-throughput computation is used to screen suitable solid electrolytes (SEs) with high electrochemical stability and high ionic conductivity, incorporating the nudged elastic band and an *ab initio* molecular dynamics (AIMD) method. Density functional theory is used to calculate bulk elastic constants of materials, surface energies, and interface decohesion energies of grain boundaries. Thermodynamic interface stability is assessed from *ab initio* computed grand potential phase diagrams in which the lithium voltage can be controlled. Kinetic limits for SE decomposition are assessed by topotactic lithium insertion and removal from the SE.

Results

Oxy-argyrodite framework exhibiting high ionic conductivity

In the past year, we identified the topological features of the diffusion network in NASICON and garnets. These insights were used to perform a high-throughput screening to find novel solid electrolytes. One of the candidates identified from this search is $\text{Li}_6\text{PO}_5\text{Br}$ which has an oxy-argyrodite structure. Argyrodite sulfides can reach ionic conductivities > 10 mS/cm [1]. However, due to the 20% smaller lattice constant [2] and smaller polarizability of oxygen, the oxygen analogue $\text{Li}_6\text{PO}_5\text{Br}$ is a poor ionic conductor with an activation

energy that is 330 meV higher than its sulfide counterpart [2]. Despite this, we find that stuffing extra Li in the interstitial tetrahedral 16e (Li3 in Figure XIII.4.1) can still activate the diffusion network, and reduce the activation energy to ≈ 200 meV. Ab-initio simulations predict that room temperature ionic conductivity is expected to reach up to 3.2 mS/cm. The extra Li that is stuffed in the structure face-shares with two 24g Li-ions, facilitating the inter-cage diffusion [3]. Our analysis discovers that high ionic conductivity can be obtained in the oxide version of the argyrodite framework, and that the diffusion network of argyrodites shows similarity to that of NASICONs.

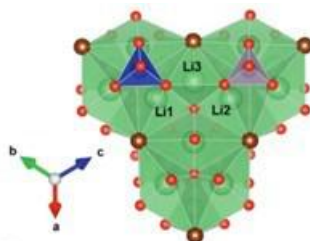


Figure XIII.4.1 Crystal structure of $\text{Li}_{6+1/4}\text{Si}_{1/4}\text{P}_{1-1/4}\text{O}_5\text{Br}$. Li-1 and Li-2 are the Li sites in the stoichiometric structure, and Li-3 is the site where additional Li is stuffed.

The framework of $\text{LiM}(\text{SeO}_3)_4$, another conductor we discovered, is a completely novel framework identified from our high-throughput screening. $\text{LiGa}(\text{SeO}_3)_2$ [4] and lithium-stuffed $\text{Li}_{1+1/4}\text{Mg}_{1/4}\text{Sc}_{1-1/4}(\text{SeO}_3)_2$ are predicted to have room temperature ionic conductivity exceeding 0.1 mS/cm. Various structural factors make this framework highly similar to that of NASICON. In the pristine form the Li ions reside in highly distorted tetrahedral sites as shown in Figure XIII.4.2a, similar to the distorted 6b octahedral Li site in stoichiometric NASICON $\text{LiTi}_2(\text{PO}_4)_3$. The $\text{LiM}(\text{SeO}_3)_2$ framework possesses a 3D homogeneous transport path, which also exists in the NASICON frameworks. Lastly, it contains a low-energy intermediate site (site X in Figure XIII.4.2b), which enables the bridging of neighboring Li-ions to facilitate their diffusion. These features make the $\text{LiM}(\text{SeO}_3)_2$ framework an intriguing candidate for in-depth investigation.

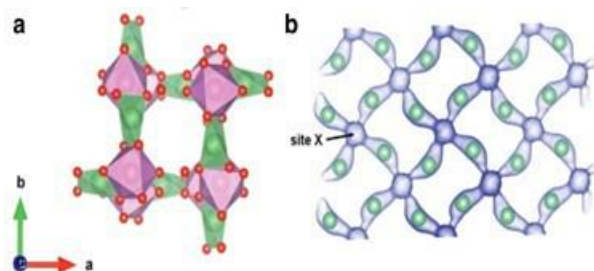


Figure XIII.4.2 a Crystal structure of $\text{LiGa}(\text{SeO}_3)_2$. Green and pink polyhedrons represent the coordination environment of lithium and gallium respectively. b The iso-surface of Li-ion probability density from AIMD simulation at 1000 K.

Corner-sharing frameworks as an important design principle for oxide SICs

The crystal structure of a typical Li-ion conductor can be constructed from its anion sublattice serving as a backbone hosting the mobile Li ions and immobile non-Li cations. By observing the crystal structure of well-known oxide-based superionic conductors (Figure XIII.4.3), such as NASICON-type $\text{Li}_{1+x}\text{Al}_x\text{Ti}_{2-x}(\text{PO}_4)_3$ [5], LiTa_2PO_8 [6] and $\text{Li}_{1+x}\text{Ta}_{1-x}\text{Zr}_x\text{SiO}_5$ [7], we identified a structural commonality among them: The non-Li cation polyhedrons in these materials are connected by a single oxygen anion vertex and have no edge- or face-sharing among the polyhedrons.

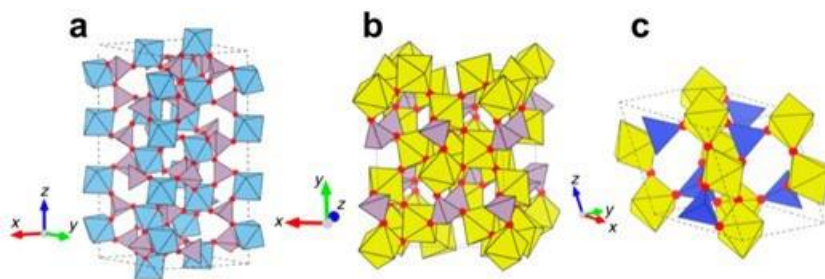


Figure XIII.4.3 Typical crystal structures of known superionic conductors with corner-sharing frameworks. (a) Structure $\text{Li}_{1+x}\text{Al}_x\text{Ti}_{2-x}(\text{PO}_4)_3$, (b) Structure of LiTa_2PO_8 , (c) structure of $\text{Li}_{1+x}\text{Ta}_{1-x}\text{Zr}_x\text{SiO}_5$.

We define a corner-sharing (CS) framework as a framework where all of the non-Li cation polyhedrons share one or fewer vertices. A non-corner-sharing (non-CS) framework is then a framework that has at least one edge- or face-sharing within the framework. To compare the Li environments in CS frameworks and non-CS frameworks, we employ a metric of distortion called continuous symmetry measure (CSM), which is 0 for a perfectly symmetric polyhedron and reaches a maximum value of 100 for completely distorted polyhedrons. In Figure XIII.4.4, we classify all of the quaternary lithium oxides from the Materials Project [8], based on if they have CS or non-CS frameworks. Then, we investigate how distorted the Li environment is. While a majority of Li environments in non-CS frameworks are highly symmetric with CSM values peaking near 0, the CS frameworks tend to provide a wide range of distorted Li environments (Figure XIII.4.4). From this observation, we propose that the highly distorted Li environment provided in CS frameworks is a major factor that can lead to low activation energy and high ionic conductivities.

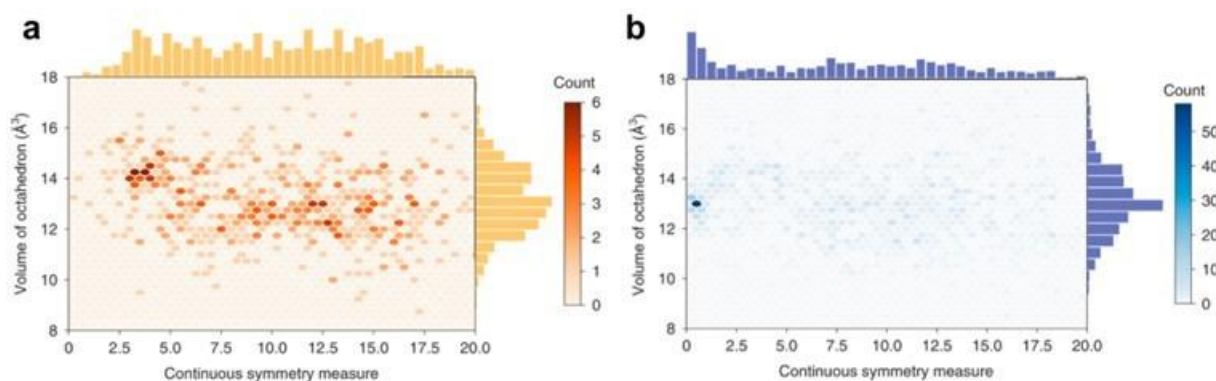


Figure XIII.4.4 Degree of distortion of octahedral Li environment in quaternary lithium oxide materials with (a) corner-sharing framework, and (b) non-corner-sharing frameworks.

While distortion is one aspect of why CS frameworks tend to show high ionic conductivities among the oxides, we identified another important advantage of CS frameworks: Due to the weak electrostatic screening and smaller radius of oxygen anions compared to sulfur anions, it is more challenging to achieve a flat energy landscape in oxides. We find that an important feature of CS frameworks is to provide reduced Li-cation interactions. In Figure XIII.4.5a, we compare the polyhedral packing ratio between CS and non-CS frameworks. The polyhedral packing ratio is defined as the volume of the non-Li polyhedrons divided by the volume of the unit cell. The non-Li cations in CS frameworks tend to occupy a smaller portion of the unit cell and leave more space for Li to occupy.

We also compare the likelihood of a Li site being distant from any non-Li cations. The site ratio β is defined as the ratio of Li sites that do not have any non-Li cations within the cutoff distance of 1.95 Å over all possible Li sites in the crystal structure. In Figure XIII.4.5b, we show that due to the low non-Li cation density in CS frameworks, a larger fraction of Li sites is located far away from any non-Li cations. Hence, Li ions in CS frameworks experience reduced electrostatic interaction from the non-Li cations. Defining a reduced-repulsion

(RR) channel as a percolating diffusion pathway of lithium sites that experience weak interaction between the non-Li cations, we find that the CS frameworks tend to have significantly higher dimensionality of RR-channels, as shown in Figure XIII.4.5c. The prevalence of the Li sites being located far away from any non-Li cations leads to a higher likelihood of such Li sites being connected and leads to higher dimensionality of RR-channels in CS frameworks.

For several exemplary SIC with a CS framework, we compare the RR-channel with the actual lithium diffusion pathways (Figure XIII.4.5d,e,f) which were computed using AIMD simulations. We confirmed that Li ions follow the RR-channel when diffusing through the CS frameworks, confirming our finding that the reduced interaction with non-Li cations is a key feature in allowing high Li ionic conductivity in oxide materials.

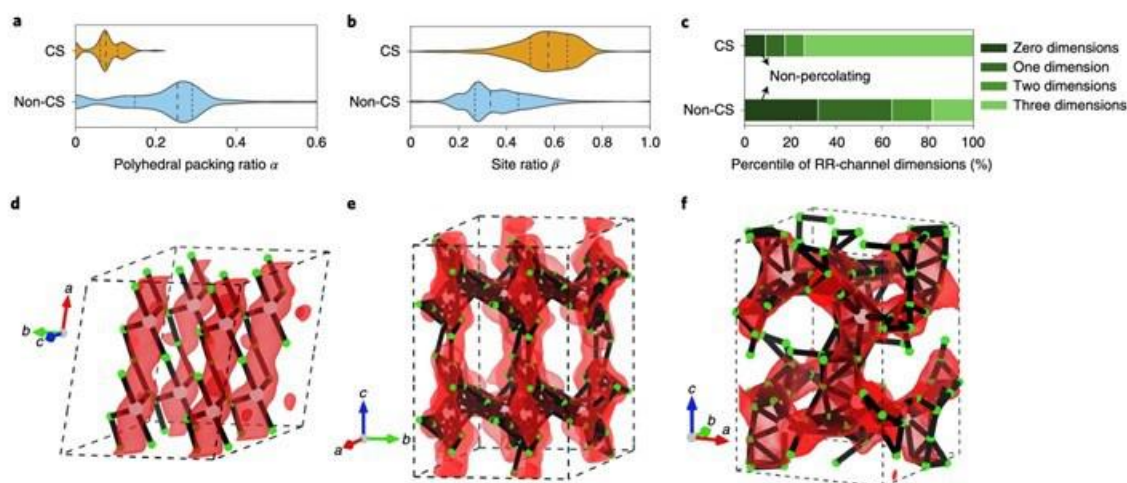


Figure XIII.4.5 Structural features of CS-frameworks and their RR channels a Comparing the polyhedral packing ratio α , b site-ratio β and c dimensionality of RR channels of CS and non-CS frameworks. In d-f, the lithium probability densities from ab-initio molecular dynamics simulations are shown in red with isosurfaces P0/100, P0/1000, P0/1000 respectively. The occupied and unoccupied lithium sites are shown in green and white spheres respectively. The RR-channels are shown with black edges.

Based on all the insights collected we performed a high-throughput screening to discover new lithium oxide SIC that contain the same feature of CS frameworks. The search was initialized from all of the quaternary Li containing oxides from the Materials Project database [8]. Among them, we identified 2,822 compounds in 637 distinct CS. We remove materials with band gaps smaller than 2 eV or compounds that contain unsuitable elements for solid electrolytes. In the last step, we prioritize experimentally synthesized compounds which lead us to 122 compounds in 56 distinct crystal structure groups. For one representative compound per group, we performed multi-step AIMD simulations to find the final candidate which has sufficiently high ionic conductivity (0.1 mS/cm) at 300K.

Table XIII.4.1 lists the ten fast Li-conducting frameworks discovered in this work. Our high-throughput screening using the feature of the CS framework gave a success rate of 39%. By imposing less strict criteria, we anticipate even more Li SIC could be discovered. Out of the above list we synthesize $\text{LiGa}(\text{SeO}_3)_2$ which shows remarkably high bulk ionic conductivity of 0.11 mS/cm at room temperature. This shows that our experimental results are in great agreement with our computational predictions, suggesting a new structural space for solid electrolytes.

Table XIII.4.1 Summary of Properties of 10 Screened Superionic Conductors with a CS Framework. The pristine and target composition extrapolated Li-ion conductivity of the target composition at 300 K ($\sigma_{300\text{K}}$), the activation energy of the target composition (E_a), pristine and target energy above the hull (E_{hull}), and dopant incorporation energy (E_d) are listed. The pristine and target compositions are the same if no dopants are introduced. bounds (error bar) are included.

Materials Project ID	ICSD ID	Pristine composition	Target composition	$\sigma_{300\text{K}}$ (mS/cm)	E_a (eV)	Pristine E_{hull} (eV/atom)	Target E_{hull} (eV/atom)	E_d (eV/defect)
mp-1198930	250868	LiGa(SeO ₃) ₂	LiGa(SeO ₃) ₂	0.212 (0.013, 3.57)	0.320 ± 0.070	0.0	0.0	N/A
mp-973966	422056	LiIn(IO ₃) ₄	LiIn(IO ₃) ₄	18.0 (3.57, 90.9)	0.155 ± 0.040	0.0	0.0	N/A
mp-559441	39761	LiTiPO ₅	Li _{1+1/16} Ti _{1-1/16} Ga _{1/16} PO ₅	1.70 (0.098, 29.7)	0.212 ± 0.071	0.013	0.019	0.79
mp-14646	65025	Li ₂ Mg ₂ (SO ₄) ₃	Li _{2+1/4} Mg ₂ (S _{11/12} P _{1/12} O ₄) ₃	2.74 (0.145, 52.0)	0.232 ± 0.073	0.0	0.011	0.81
mp-552663	161499	LiScAs ₂₀ ₇	Li _{1+3/8} Sc _{1-3/8} Mg _{3/8} As ₂₀₇	23.3 (4.26, 128)	0.177 ± 0.042	0.0	0.021	0.64
mp-1020018	428002	Li ₅ B(SO ₄) ₄	Li _{5+1/4} B(S _{15/16} P _{1/16} O ₄) ₄	0.330 (0.0368, 4.90)	0.330 ± 0.061	0.008	0.023	1.56
mp-1020022	248343	Li ₃ B(PO ₄) ₂	Li _{3+1/8} B(P _{15/16} Si _{1/16} O ₄) ₂	0.166 (0.00721, 3.83)	0.326 ± 0.078	0.014	0.028	1.63
mp-1020015	192496	Li ₂ B ₃ PO ₈	Li _{2+1/8} B ₃ P _{7/8} Si _{1/8} O ₈	0.251 (0.00744, 8.44)	0.269 ± 0.087	0.0	0.015	1.67
mp-1222376	260590	LiZnBO ₃	Li _{1+2/16} Zn _{1-1/16} BO ₃	0.605 (0.0104, 35.3)	0.220 ± 0.101	0.008	0.009	0.12
mp-556799	94355	Li ₃ In(BO ₃) ₂	Li _{3+1/8} In _{7/8} Zn _{1/8} (BO ₃) ₂	0.121 (0.0027, 5.33)	0.300 ± 0.094	0.004	0.009	0.50

Conclusions

From high throughput computational screening of structures with NASICON and garnet-based frameworks, we uncover oxy-argyrodite and LiM(SeO₃)₄ structures with high Li conductivity, which likely stem from similarity to NASICON frameworks. From observing several known oxide SICs, including the NASICON-type Li_{1+x}Al_xTi_{2-x}(PO₄)₃, we identify a common structural motif of CS frameworks, in which non-Li cation polyhedrons share one or less vertex. The features of CS frameworks that likely contribute towards facile Li diffusion include the more distorted Li environments, minimized electrostatic interactions between Li and other cations, and the occupation of a smaller volume of the unit cell, leaving more space for Li atoms.

By incorporating this design principle, we performed another computational screening, which uncovered new phases of promising SICs, significantly expanding the compositional search space for oxide SIC discovery. As a proof of concept, LiGa(SeO₃)₂ was experimentally realized and shown to have a high bulk Li conductivity of 0.11 mS/cm at room temperature. CS frameworks should thus prove to be an essential structural feature for discovering new classes of oxide SICs.

Key Publications

1. Huang, J., Zhong, P., Ha, Y., Lun, Z., Tian, Y., Balasubramanian, M., ... & Ceder, G. (2022). Oxygen Vacancy Introduction to Increase the Capacity and Voltage Retention in Li-Excess Cathode Materials. *Small Structures*, 2200343.
2. Sun, Y., Ouyang, B., Wang, Y., Zhang, Y., Sun, S., Cai, Z., ... & Ceder, G. (2022). Enhanced ionic conductivity and lack of paddle-wheel effect in pseudohalogen-substituted Li argyrodites. *Matter*, 5(12), 4379-4395.
3. Jun, K., Sun, Y., Xiao, Y., Zeng, Y., Kim, R., Kim, H., ... & Ceder, G. (2022). Lithium superionic conductors with corner-sharing frameworks. *Nature Materials*, 21(8), 924-931

References

1. Adeli, Parvin, et al. "Boosting solid-state diffusivity and conductivity in lithium superionic argyrodites by halide substitution." *Angewandte Chemie* 131.26 (2019): 8773-8778.
2. Kong, S. T., Deiseroth, H. J., Maier, J., Nickel, V., Weichert, K., & Reiner, C. (2010). Li₆PO₅Br and Li₆PO₅Cl: The first Lithium-Oxide-Argyrodites. *Zeitschrift für anorganische und allgemeine Chemie*, 636(11), 1920-1924.
3. De Klerk, N. J., Rosłoń, I., & Wagemaker, M. (2016). Diffusion mechanism of Li argyrodite solid electrolytes for Li-ion batteries and prediction of optimized halogen doping: the effect of Li vacancies, halogens, and halogen disorder. *Chemistry of Materials*, 28(21), 7955-7963.
4. Lee, D. W., & Ok, K. M. (2013). New alkali-metal gallium selenites, AGa (SeO₃)₂ (A= Li, Na, K, and Cs): effect of cation size on the framework structures and macroscopic centricities. *Inorganic Chemistry*, 52(9), 5176-5184.
5. Aono, H., Sugimoto, E., Sadaoka, Y., Imanaka, N., & Adachi, G. Y. (1990). Ionic conductivity of solid electrolytes based on lithium titanium phosphate. *Journal of the electrochemical society*, 137(4), 1023.
6. Kim, J., Kim, J., Avdeev, M., Yun, H., & Kim, S. J. (2018). LiTa₂PO₈: a fast lithium-ion conductor with new framework structure. *Journal of Materials Chemistry A*, 6(45), 22478-22482.
7. Xiong, S., He, X., Han, A., Liu, Z., Ren, Z., McElhenny, B., ... & Chen, H. (2019). Computation-guided design of LiTaSiO₅, a new lithium ionic conductor with sphene structure. *Advanced Energy Materials*, 9(22), 1803821.
8. Jain, A., Ong, S. P., Hautier, G., Chen, W., Richards, W. D., Dacek, S., ... & Persson, K. A. (2013). Commentary: The Materials Project: A materials genome approach to accelerating materials innovation. *APL materials*, 1(1), 011002.

XIV Next-Gen Li-ion: Low Temperature Electrolytes

Current Li-ion cells have demonstrated significant performance improvements in increasingly extreme conditions, including higher voltages, wider temperature range, and intense abuse conditions, and more recently, extreme fast charging. Yet, performance under these more extreme uses is often limited by the stability and properties of the liquid electrolytes within the cells. Traditional liquid electrolytes are composed of lithiumhexafluorophosphate (LiPF_6) salt dissolved in mixed carbonate solvents, which include ethylene carbonate (EC), propylene carbonate (PC), ethyl methyl carbonate (EMC), dimethyl carbonate (DMC) and/or diethyl carbonate (DEC), and an array of additives included to improve performance against the utilized electrodes. These volatile and flammable organic solvents can easily undergo drastic degradation processes, often act as a limiting factor in the performance under extreme conditions including operating at high voltage, in a wide temperature range, under extreme fast charging, and/or under extreme abuse. As such, there is a need to develop novel liquid electrolytes which can operate under those extreme conditions and can retain their enhanced performance and stability.

The rest of this chapter contains detailed reports on the status of the following individual projects.

- Ethylene Carbonate-Lean Electrolytes for Low Temperature, Safe Li-ion batteries (LBNL)
- Fluorinated Solvent-Based Electrolytes for Low Temperature Li-ion Battery (ANL)
- Synthesis, screening and characterization of novel low temperature electrolyte for lithium-ion batteries (BNL).

XIV.1 Ethylene Carbonate-Lean Electrolytes for Low Temperature, Safe Li-ion batteries (LBNL)

Bryan D. McCloskey, Principal Investigator

Lawrence Berkeley National Laboratory and University of California, Berkeley
201-D Gilman Hall
Berkeley, CA 94720
E-mail: bmcclosk@berkeley.edu

Tien Duong, DOE Technology Development Manager

U.S. Department of Energy
E-mail: Tien.Duong@ee.doe.gov

Start Date: October 1, 2019

End Date: September 30, 2022

Project Funding (FY22): \$650,000

DOE share: \$650,000

Non-DOE share: \$0

Project Introduction

Li-ion batteries suffer from performance limitations at low temperatures (sub- 0°C) due to a large rise in overall cell impedance. In prior years, we identified charge transfer resistance—an interfacial process—as the dominant limitation for low temperature battery performance, and that while charge transfer resistance is dominated by processes at the anode, the cathode charge transfer resistance also contributes substantially. In FY22, we aimed to understand how electrolyte composition impacts charge transfer resistance at both electrodes, with the ultimate goal of identifying an electrolyte that enables 70% of 30°C energy during a C/3 discharge at -20°C. Our work has primarily focused on identifying novel additives that impact the interfacial compositions.

Objectives

The research this year centered on investigating a new class of electrolyte additives to improve low temperature performance of Li-ion cells. Our objective was to investigate several analogs of this additive chemistry to understand its impact on the low temperature cell resistance to confirm that the additive did not have a negative impact on cycle life or coulombic efficiency. We further aimed to understand how cell resistance was influenced by this additive chemistry, and to perform a quantitative analysis of the solid electrolyte interface (SEI) and find the relation between the SEI composition and the resistance of the cell. Finally, we characterized key electrolyte transport and thermodynamic parameters as a function of temperature by developing reliable characterization techniques.

Approach

We selected three additive chemistries to investigate and characterized these additives at three concentrations (all less than 1 wt%). We tested graphite/NMC622 cells, with electrodes provided by Argonne's CAMP facility and electrolytes with novel additives prepared at LBNL. We used battery testers and impedance-capable potentiostats to conduct the work. In-situ and ex-situ mass spectrometry techniques are used for quantitative analysis of the SEI. Galvanostatic Electrochemical Impedance Spectroscopy (GEIS) is used to find the resistance of the cell during charge/discharge of the cell, and EIS spectra are deconvoluted using the distribution of relaxation times to quantify charge transfer and SEI resistances. Differential electrochemical mass spectrometry (DEMS) is used to quantify outgassing during formation cycling of cells comprised of various electrolytes. To measure electrolyte properties, our approach is to measure relevant transport and thermodynamic parameters, including conductivity, current fraction, diffusion coefficient, the thermodynamic factor, and the transference number. We do so through a combination of electrophoretic nuclear magnetic resonance spectroscopy (eNMR) and electrochemical measurements using Li-Li symmetric cells.

Results

Capacity and cycling performance characterization of electrolytes containing a new class of low-temperature additives.

This year we moved away from γ -butyrolactone and started considering inert nano-particles as a means of affecting the charge transfer resistance, whose rise limits the access of capacity at low temperature. We started with three slightly different chemical analogs of a nanomaterial that is generally considered inert. Figure XIV.1.1 gives the energy removed at -20°C from seven cells of different additives and concentrations that were brought to the top of charge at 30°C .

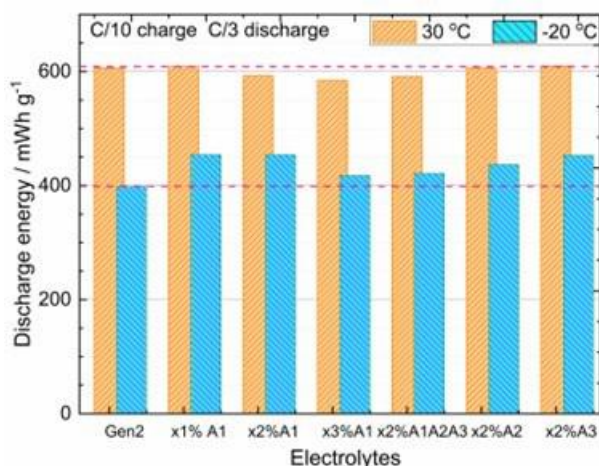


Figure XIV.1.1 Orange Energy removed at C/3 at 30°C . Blue Energy removed at -20°C . Gen 2 is the baseline electrolyte. x1, x2, x3 are 0.5, 0.75 and 1 % of the additive, respectively. A1, A2, A3 are three different analogs of the selected additive.

One sees from this chart that for the additive A1, the highest energy recovered on discharge at 30°C is for the smallest amount of the additive. We also see that the energy removed at 30°C using A1 at a quantity of x2 is less than that achieved for A2 and A3. However, for the different combinations and quantities of A1, A2, and A3 examined at -20°C , the highest level of energy recovered on discharge is for the A1 at 0.5 wt%. Interestingly, the energy recovered at -20°C is 70% of the energy recovered at 30°C , which is the stated USABC target and the overall objective of our project. Without the additive, for Gen2 electrolyte at -20°C , one recovers just 65% of the energy that is dischargable at 30°C .

With regard to cycle life, we see in Figure XIV.1.2 the early cycle life of two full cells of Graphite/NMC622 with Gen 2 electrolyte (1 M LiPF_6 in 3:7 EC:EMC) and Gen 2 electrolyte with our additive at 0.5%. We see that the cell with the additive shows the same cycle life as the cell without the additive. The coulombic efficiency is also provided in the graph and shows that the additive cell has slightly higher efficiency than the cell without the additive. It is possible that our additive is being slowly reduced on the cathode during discharge with each cycle to the extent that the coulombic efficiency appears to be slightly greater than 1. Further investigation is needed to understand this discrepancy.

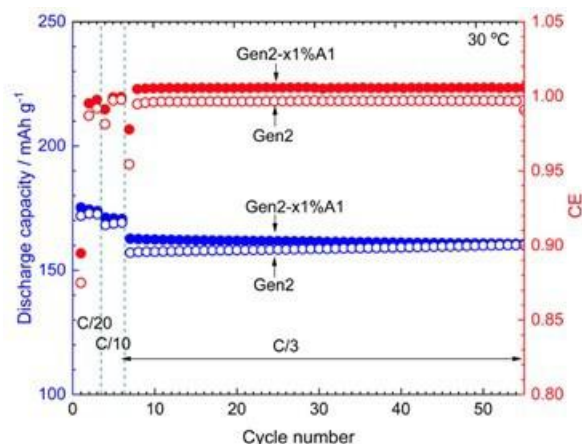


Figure XIV.1.2 Specific discharge capacity with regard to the cathode (in blue) and the coulombic efficiency (in red) versus cycle number. The open points are for Gen 2 and the filled points are for Gen 2 plus 0.5% A1.

To see if the impact of our additive carries to even lower temperatures, we measured the amount of energy that could be discharged from a cell fully charged at 30°C with Gen 2 electrolyte at 30°C, 20°C, 10°C, 5°C, 0°C, -5°C, -10°C, -15°C, -20°C, -25°C, and -30°C and compared the energies to a cell operating at the same conditions but with our additive. In Figure XIV.1.3 we see that the improvement to low temperature improvement continues to lower temperatures and that with our additive, one can extract twice the amount of energy from the cell at -30°C.

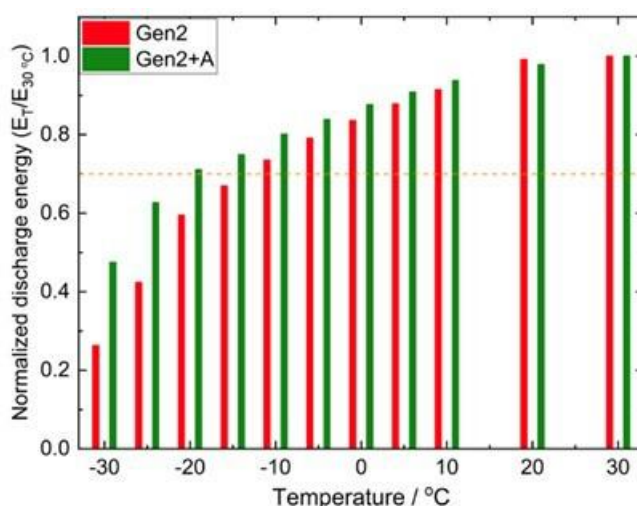


Figure XIV.1.3 Energy discharged from cells at different temperatures, one cell had the additive (green), that was fully charged at 30°C, normalized by the energy discharged at 30°C.

Electrochemical impedance analysis of cell employing our novel additive.

Previously acquired data indicated that low temperature energy improvement is associated with significant improvement in interfacial charge transfer resistance. To verify this, we measured the electrochemical impedance spectroscopy of cells with and without the additive at -20°C and -30°C. This data is presented in Figure XIV.1.4.

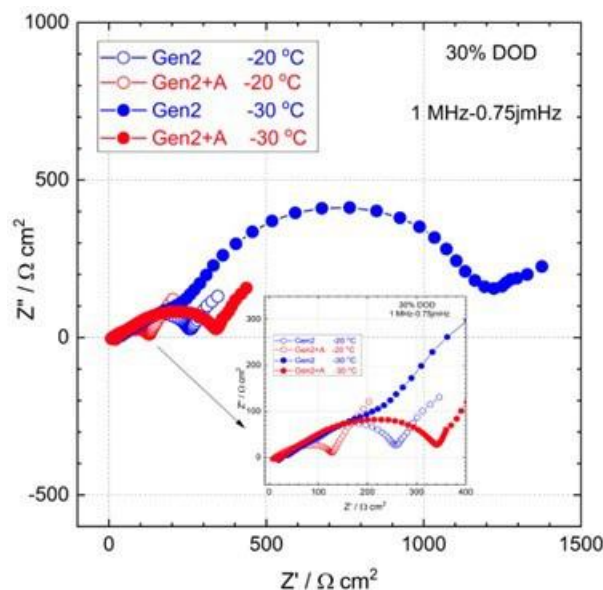


Figure XIV.1.4 Electrochemical impedance spectroscopy of two cells, one with and one without an additive, acquired at -20°C and -30°C . The filled data points are for the data taken at -30°C . The blue data points are for the cell without the additive.

One sees that the impedance of the cell with no additive at -30°C is much greater than the impedance at -20°C and that this impedance is greater than the impedance of the cell with the additive at -20°C . One also notices that the part of the impedance that grows the most with decrease in temperature is the mid-frequency semicircle, which corresponds to the characteristic frequency of charge transfer reactions.

We recognized that the improvement in the activation energy of the charge transfer kinetics appeared to be a result of changes that occur early in the formation of the cell. In the next set of experiments the impedance of the cells with and without the additive was measured at -20°C after the 1st, 2nd, 3rd formation cycles, as well as the 20th full C/3 cycle. One sees in Figure XIV.1.5a for the cell without the additive that the impedance of the ohmic and charge transfer resistance grew from the first cycle to the twentieth from 265 ohm-cm² to 450 ohm-cm². Whereas, in Figure XIV.1.5b, for the cell with the additive, one sees that the impedance of the first twenty cycles at -20°C is relatively constant at 180 ohm-cm². Thus, the additive has an immediate, stabilizing impact on the charge transfer kinetics.

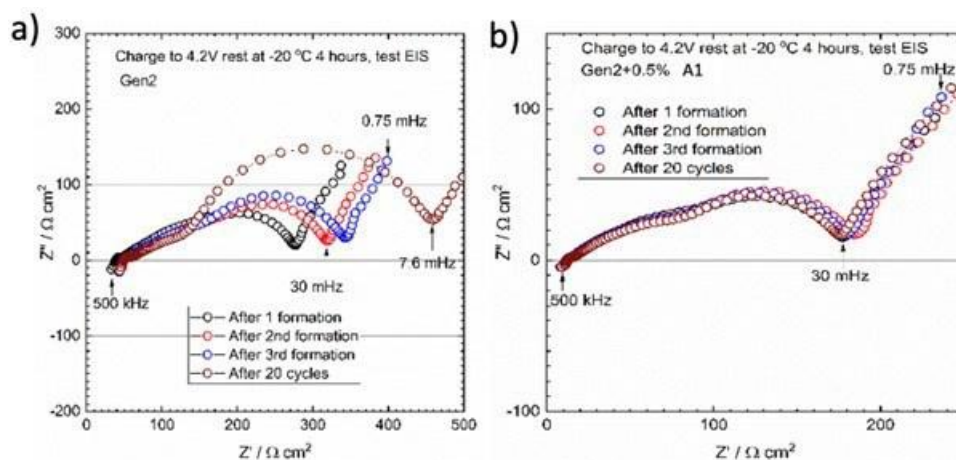


Figure XIV.1.5 a. Electrochemical impedance spectroscopy of a cell without the additive after the 1st, 2nd, 3rd, and 20th formation cycles acquired at -20°C . b. 6 Electrochemical impedance spectroscopy of a cell with the additive after the 1st, 2nd, 3rd, and 20th formation cycles acquired at -20°C .

We analyzed the performance of adding additive A to baseline electrolyte (1M LiPF₆ in 3:7 EC:EMC by wt%) using galvanostatic impedance spectroscopy (GEIS) in full coin cells. The results of GEIS experiments, as summarized in Figure XIV.1.6a, indicate that the total resistance significantly decreases on adding 0.75wt% additive A to the baseline electrolyte. Using the technique of Distribution of Relaxation Times (DRT), we deconvolute the total resistance into series (R_s), SEI (R_{SEI}) and charge-transfer resistance (R_{ct}). We see that, on adding additive A, SEI resistance increases (Figure XIV.1.6b) whereas charge-transfer resistance drastically decreases (Figure XIV.1.6c), which causes a decrease in total resistance at lower temperatures.

Quantification of outgassing during cell formation.

On performing Differential Electrochemical Mass Spectrometry (DEMS) on two-electrode full cells with the electrolyte containing additive A, we see that we have a significant increase in hydrogen evolution during the first formation cycle of the cell. The hydrogen evolution increases with increasing amounts of additive A (Figure XIV.1.7). We also see lower amounts of ethylene evolution. This data together indicates that there is a considerable change in the SEI (which is also confirmed by the increased SEI resistance in the system containing additive A).

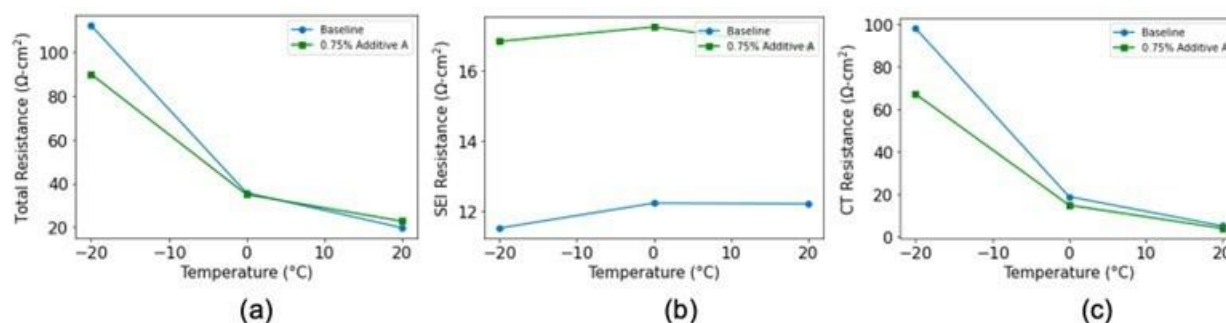


Figure XIV.1.6 (a) Total Resistance (b) SEI Resistance (c) Charge-transfer Resistance of Gr/NMC coin cell gathered at 50%SOC during a C/3 discharge at different temperatures in baseline electrolyte (1.0M LiPF₆ in 3:7 EC:EMC) with and without additive A.

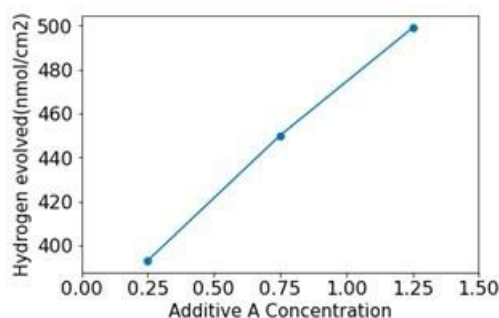


Figure XIV.1.7 Hydrogen evolution measured using DEMS during the formation cycle of Gr/NMC622 cells in the presence of different wt% of additive A, performed at room temperature.

Next steps for this work include combining results from GEIS and DEMS studies with titration mass spectrometry experiments on formed electrodes in an effort to quantify components of the SEI and observe how the quantities change in the presence of additive A. GEIS and DEMS studies on symmetric Gr/Gr and NMC/NMC cells will be helpful to realize the contribution of each of the electrodes towards the improved low temperature performance. Understanding additive A is improving the performance of cells at the structural level will help us have a better idea of the interfacial process in a cell.

Electrolyte transport characterization.

Most reports on measuring electrolyte transport coefficients use polarized symmetric lithium-lithium cells to measure transference numbers. Unfortunately, Li metal is notoriously unstable during stripping and plating in

liquid electrolytes. For the most extreme reactions, this could impact the surface area of the electrodes, change the salt concentration, and impact the overall characterization. For this reason, it's important to establish a reliable methodology to study transport and thermodynamic properties of liquid electrolytes at 30°C before extending this analysis to lower temperatures.

We have fully characterized an exemplary electrolyte, lithium bis(trifluoromethanesulfonyl)imide (LiTFSI) salt dissolved in tetraethylene glycol dimethyl ether (tetraglyme), at 30°C. We used x-ray tomography to image the interface between lithium and an electrolyte soaked separator in lithium-lithium symmetric cells and have determined the interface is stable when small polarizations are applied. To improve the accuracy of our characterization, we have incorporated electrophoretic NMR (eNMR), which directly measures cation, anion, and solvent velocities under an applied electric field. From eNMR we can directly obtain transference numbers with much higher certainty than can be determined indirectly using electrochemical methods. The more accurate determination of transference numbers have also enabled more accurate determination of the thermodynamic factor (see Figure XIV.1.8). These findings were published in Hickson et al. (see Key Publications).

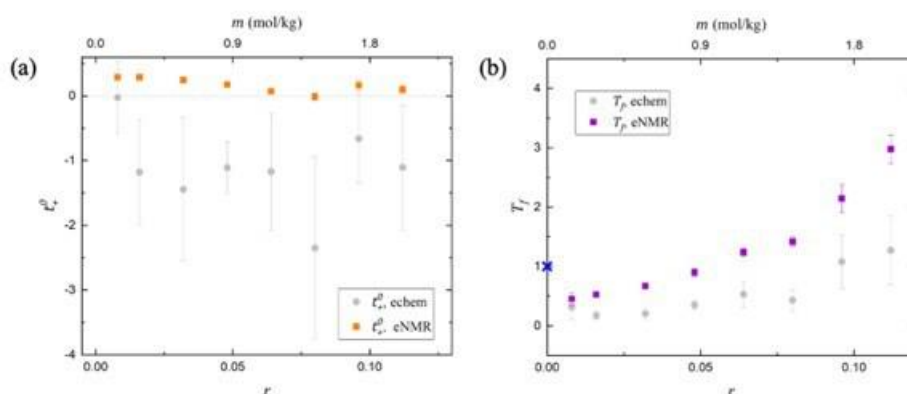


Figure XIV.1.8 Comparison of electrochemical techniques and electrophoretic NMR for (a) transference number and (b) thermodynamic factor. The thermodynamic factor is unity at $r = 0$, shown in blue, based on the thermodynamic requirement that all solutions are ideal in the limit of infinite dilution. Images are reprinted from Hickson et al.

We have begun extending this characterization to a wider temperature range, from 45°C to -20°C. Conductivity, a straightforward measurement not involving lithium metal, strongly decreases with temperature. Preliminary results indicate current fraction and diffusion coefficient also decrease with temperature, but it will be important to continue to study the reactive lithium – electrolyte interface for its stability as a function of temperature. The interfacial resistance increases substantially at lower temperatures, and the degree to which this impacts characterization will need to be investigated. We will continue to incorporate eNMR into this characterization to more precisely determine transference numbers and thermodynamic factors as a function of temperature.

Conclusions

The key conclusions from our research this year are:

1. Our newly discovered electrolyte additive provides a substantial increase in low temperature Li-ion battery energy. In certain embodiments (e.g., 0.5 wt% of A1 additive), we achieve the project target of 70% of 30°C energy density at -20°C when discharging at C/3 rate.
2. We confirm that the improved low temperature performance of our additives is a result of a sizable decrease in charge transfer resistance in the cell compared to the Gen 2 electrolyte baseline. Only a modest rise in SEI resistance is observed when employing our additive.
3. The chemistry of the formation cycling is clearly impacted by additive inclusion, as an increase in H₂ evolution is observed with increasing additive concentration.

4. Electrophoretic NMR is used to dramatically improve reproducibility of transference number and thermodynamic factor measurements of liquid electrolytes when compared to measuring these parameters using symmetric Li-Li cells.

Key Publications

1. Hickson, D. T.; Halat, D. M.; Ho, A. S.; Reimer, J. A.; Balsara, N. P. Complete Characterization of a Lithium Battery Electrolyte Using a Combination of Electrophoretic NMR and Electrochemical Methods. *Physical Chemistry Chemical Physics* **2022**, 24 (43), 26591–26599.
2. Hubble, D.; Brown, D. E.; Lau, J.; McCloskey, B. D.; Liu, G. “Liquid electrolyte development for low-temperature lithium-ion batteries.” *Energy & Environmental Science* **2022**, 15, 550-578.

Acknowledgements

This section was coauthored by co-PIs Kristin Persson, Gao Liu, Nitash Balsara, Vincent Battaglia, Robert Kostecki, and Wei Tong, as well as Yanbao Fu, Darby Hickson, and Triesha Singh. We also thank Stephen Trask, Andrew Jansen, Alison Dunlop, and their CAMP Facility colleagues for providing the graphite and NMC622 electrodes used in our studies.

XIV.2 Fluorinated Solvent-Based Electrolytes for Low Temperature Li-ion Battery (ANL)

Zhengcheng (John) Zhang, Principal Investigator

Argonne National Laboratory
9700 South Cass Avenue
Lemont, IL 60439
E-mail: zzhang@anl.gov

Tien Duong, DOE Technology Development Manager

U.S. Department of Energy
E-mail: Tien.Duong@ee.doe.gov

Start Date: October 1, 2019

End Date: September 30, 2022

Project Funding (FY22): \$600,000

DOE share: \$600,000

Non-DOE share: \$0

Project Introduction

Electric vehicles require Li-ion batteries (LIB) that not only have high energy/power densities at low cost, but also can achieve superior performances at low temperature (LT) environment ($< 0^{\circ}\text{C}$). However, current battery technology has not yet met the satisfactory LT performance requirement, in large part due to the limitation in the electrolyte and the electrolyte-derived electrode/electrolyte interfaces. Particularly at LT, the electrolyte ionic conductivity is significantly reduced, and the interface impedances are significantly increased, severely limiting the energy/power of LIB and potentially causing undesired lithium plating. [1] This project aims to improve the electrolyte performances at LT using fluorinated solvents.

Objectives

The objective is to develop electrolytes that enable LIB to deliver $> 70\%$ of usable energy at -20°C compared to the normal battery operating temperature (30°C) at C/3 rate, and to achieve excellent cycling performances and calendar life at high temperatures (40°C - 60°C).

Approach

Our first approach is to use fluorinated carbonates as co-solvents for the state-of-the-art (SOA) electrolyte. Due to the weaker polar-polar interaction in fluorine-containing groups, fluorinated carbonates are anticipated to show lower melting points than their non-fluorinated counterparts, which can be beneficial for LT application. Moreover, our previous studies demonstrated that fluorinated carbonates can significantly improve high temperature cycling performances of LIB. [2-4] Thus, incorporating fluorinated carbonates into the SOA electrolyte can potentially improve the performances of LIB at both low and high temperature.

Our second approach is to use fluorinated carboxylate esters as single solvents with solid-electrolyte interphases (SEI)-forming additives. Carboxylate esters generally have very low melting points, good dielectric constants, and low viscosities; thus, it is anticipated that carboxylate esters and its fluorinated derivatives can likely maintain excellent ionic conductivities at LT. Previous studies have reported the use of carboxylate esters or fluorinated carboxylate esters as co-solvents in the SOA electrolyte for LIB; [5, 6] however, their use as single solvents is less explored. The major challenge of using carboxylate esters is that carboxylate esters cannot form stable graphite SEI and thus SEI-forming additives are required.

Results

Design principle of fluorinated ester-based electrolytes

Compared to the conventional Gen 2 electrolytes with ethylene carbonate and ethyl methyl carbonate co-solvent (1.2 M LiPF_6 in EC/EMC w/w=3/7), the state-of-the-art electrolyte for low temperature performances includes ethyl acetate (EA) solvent with fluoroethylene carbonate (FEC) co-solvent. We reconfirmed the

superiority of EA solvent compared to ethyl butyrate (EB) solvent. Although EA has a low melting point and high ionic conductivity, it exhibits a stronger binding to Li^+ ions than EMC due to the absence of an electron-withdrawing ester group, resulting in a higher desolvation energy. To decrease the desolvation energy, one of the limiting factors of Li^+ ion kinetics at low temperatures, we functionalized the terminal methyl group ($-\text{CH}_3$) to trifluoro methyl group ($-\text{CF}_3$), a strong electron-withdrawing group. In addition, the fluorination enhances high voltage stability with reduced the highest occupied molecular orbital (HOMO) levels, preventing the possible oxidation of hydrogen at high voltage.

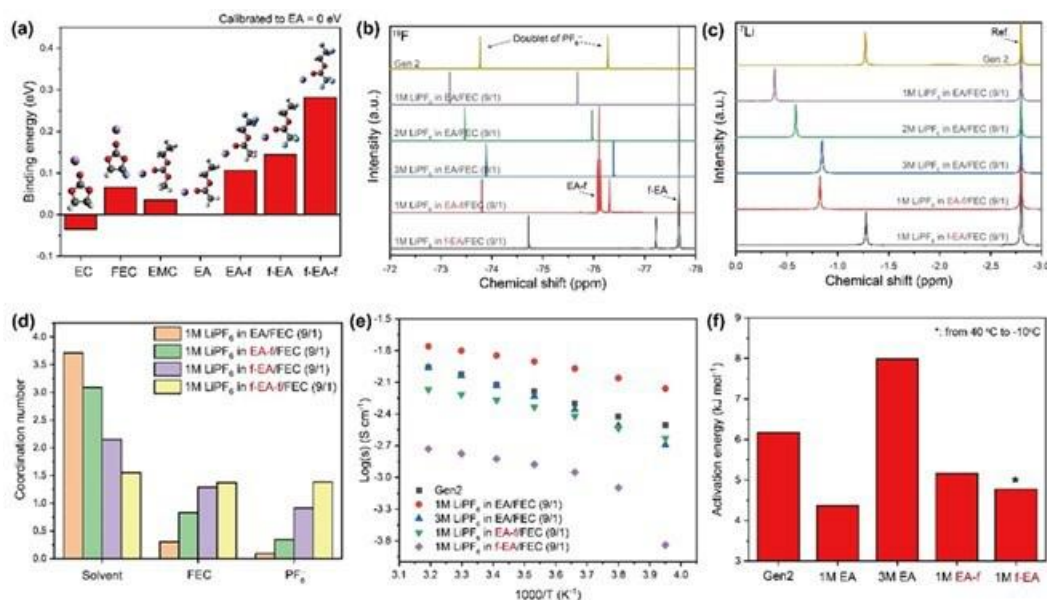


Figure XIV.2.1 (a) Binding energies of each solvent with Li ion. The dielectric constant for implicit solvation model was 6.02, and they were calibrated to EA = 0 eV. (b) ^{19}F - and (c) ^7Li -NMR spectra of different electrolytes. (d) Coordination number in Li solvation sheath of different electrolytes from MD simulation. (e) Ionic conductivities of different electrolytes at various temperatures, and (f) their calculated activation energies (E_a) from plots (e).

To further appreciate the different electron-withdrawing effect, we calculated binding energies of each solvent with a Li^+ ion (Figure XIV.2.1a). We applied implicit solvation effect for the calculations because Li^+ ions were chelated by f-EA and f-EA-f in gas phase, which is not feasible in electrolytes. The dielectric constant for implicit solvation effect was 6.02, and they were calibrated to EA = 0 eV. Note that a higher binding energy means relatively weaker binding to a Li ion. FEC had a higher binding energy (0.06 eV) than EC (−0.03 eV) due to the fluorination effect. In the case of EA-derivatives, EA-f, f-EA, and f-EA-f showed much higher binding energies of 0.11, 0.14, and 0.28 eV, respectively, than 0 eV of EA. The relative binding energies allow to expect solvation structures in co-solvent systems in a way that solvent with lower binding energy would aggressively solvate Li ions. It is noteworthy that while FEC has a higher binding energy than EA, EA-derivatives have higher binding energies than FEC. A weaker interaction between Li^+ and the solvent correlates with a higher participation of FEC in the Li solvation shell in EA-derivative electrolytes, however the interaction between the co-solvents as well as entropic effects can influence the speciation of the Li solvation.

Understanding solvation structures in electrolytes is important because solvents coordinated with Li are likely to be reduced to form the SEI layer. The degree of ion-pairing also affects solubility and ionic conductivity. We used FEC co-solvent with 10 vol% since pure EA or EA-f solvents cannot stabilize the SEI layer. To analyze the solvation structures, we conducted nuclear magnetic resonance (NMR) characterization for each electrolyte. From the ^{19}F -NMR spectra in Figure XIV.2.1b, the doublet of PF_6^- in 1 M LiPF_6 in EA/FEC (9/1) (EA electrolyte) was down-field shifted compared to Gen 2, indicating a lower ion-pair ratio. The peaks of PF_6^- were gradually up-field shifted as the concentration increased, showing ion-clustering at high

concentrations. While the peaks of PF_6^- in 1 M LiPF_6 in EA-f/FEC (9/1) (EA-f electrolyte) were comparable to those in 3 M EA electrolyte or Gen 2, the peaks of PF_6^- in 1 M LiPF_6 in f-EA/FEC (9/1) (f-EA electrolyte) were the most up-field shifted. f-EA-f electrolytes could not be measured because 1 M LiPF_6 was not soluble in f-EA-f/FEC (9/1) solvent even at room temperature.

The trend of peak shift was continued in the ^7Li -NMR spectra (Figure XIV.2.1c). As Li ions are solvated by solvents and anions, the corresponding Li peak shift can be considered as the sum of solvent and anion effects. Compared to -1.27 ppm in Gen 2, the Li peak in EA electrolyte was significantly down-field shifted to -0.39 ppm, implying a low portion of PF_6^- in solvation structures. As the concentration increased, the Li peaks were up-field shifted due to the participation of PF_6^- in solvation structures. The Li peak in EA-f electrolyte was comparable to 3 M EA electrolyte, and they were still significantly down-field shifted to -0.82 ppm compared to Gen 2, indicating the weak binding of EA-f to Li^+ ions. The Li peak in f-EA electrolyte was similar to Gen 2 because of the sum of high portion of ion-pair and weak binding of f-EA. The solvation structure modification was reconfirmed by molecular dynamics (MD) simulations (Figure XIV.2.1d). There is a strict trend in coordination number changes. In an order of EA, EA-f, f-EA, and f-EA-f, the coordination number of EA-derivative solvents decreased, and those of FEC or PF_6^- increased due to the weakened binding energies of EA-derivative solvents. This NMR characterization and MD simulation explain the modified solvation structures and energies in the EA-derivative electrolytes.

Ionic conductivities on various temperatures of different electrolytes were measured by electrochemical impedance spectroscopy (EIS) characterization using bulk electrolytes (Figure XIV.2.1e and Figure XIV.2.1f). As known in the literature, the EA electrolyte had higher ionic conductivity than Gen 2, due to its lower viscosity and lower ion-pair ratio (high dissociation). As the concentration increased to 3 M, the ionic conductivities decreased with a high activation energy of 8.0 kJ mol^{-1} because of the increased ion-pair ratio. In the case of EA-f electrolyte, the ionic conductivities were slightly lower than Gen 2, but they were high enough above 2.4 mS cm^{-1} to sustain ion transport at low temperatures. In the case of f-EA electrolytes, however, the ionic conductivity was significantly low to 1.5 mS cm^{-1} at room temperature, and it dropped to 0.2 mS cm^{-1} at -20°C because LiPF_6 salt in electrolytes was precipitated under -20°C . This confirmed that weak binding energy of fluorinated solvents leads to trade-offs between desirable physical properties.

SEI layers and interfacial resistance

In our previous paper, we unveiled that the SEI layer plays a crucial role in rate capability and stability at low temperatures.[7] With that in mind, we added 0.1M LiDFOB to EA-f electrolyte as an additive to modify the SEI layer. The optimized electrolyte was 0.9 M $\text{LiPF}_6 + 0.1 \text{ M LiDFOB}$ in EA-f/FEC (9/1). The SEI layer formation can be seen in dQ/dV profiles of NMC622/graphite cells at a first charging step. In the Figure XIV.2.2a, there was an EC reduction peak at 3.0 V in Gen 2. While there was a free FEC reduction peak at 2.7 V in EA electrolyte, Li^+ -coordinated FEC was reduced earlier at 2.3 V in EA-f electrolyte. This is well matched with the coordination number change of FEC in electrolytes from MD simulations. In the EA-f electrolyte with LiDFOB additive, DFOB^- was reduced earlier than Li^+ -coordinated FEC, forming an ion-conductive SEI layer. [8-9] In the case of f-EA electrolyte, f-EA solvent was reduced earlier than FEC and showed high peaks at 2.6 and 2.7 V due to the high reduction potential. In order to analyze the composition of SEI layers, we conducted X-ray photoelectron spectroscopy (XPS) characterization of graphite anodes in different electrolytes after three formation cycles. Based on the atomic ratio in Figure XIV.2.2b we observe that the prevalence of Li and O were higher in the EA-f electrolyte than EA electrolytes, likely due to the reduction of Li^+ -coordinated FEC. The fraction of O and C were further enlarged in EA-f electrolyte with LiDFOB additive, correlating to the active reduction of DFOB^- . Deconvolution of each element in the XPS spectra clarified the functional groups of reduction products. The participation of Li^+ -coordinated FEC in the EA-f electrolyte caused a large peak from the C=O bond at 532 eV in O 1s spectra. The addition of LiDFOB further modified the SEI layer, leading to less LiF and more organic compounds, exhibiting C=O , OCOO , and O-C=O bonds. In the case of cathodes in the different electrolytes, there was no significant difference in the components on the surface.

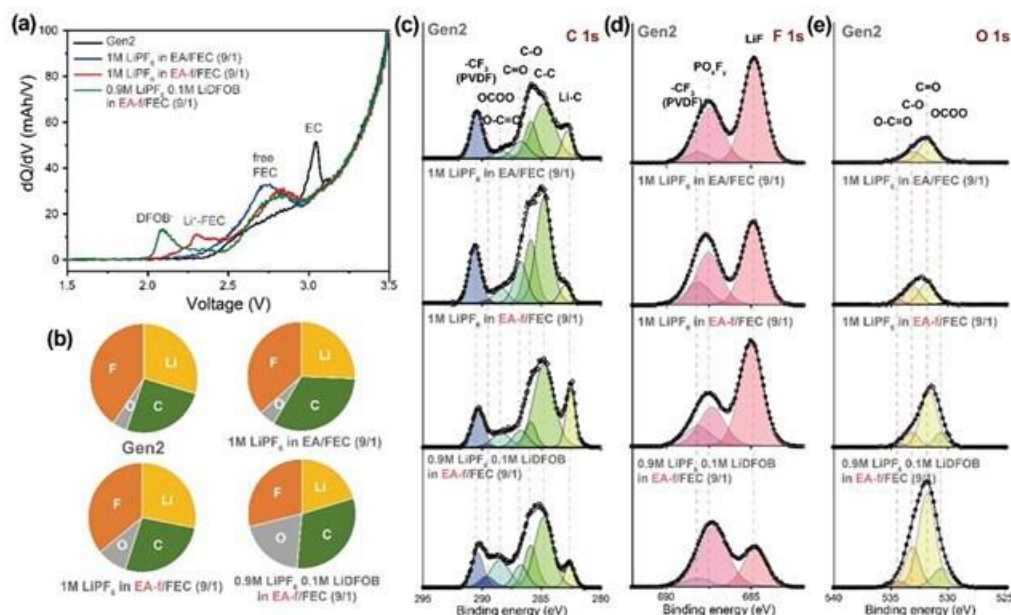


Figure XIV.2.2 (a) dQ/dV profiles of graphite|NMC622 cells with different electrolytes during 1st charging. (b) Atomic ratio and XPS spectra of (c) C 1s, (d) F 1s, and (e) O 1s of cycled graphite anodes after three formation cycles with different electrolytes.

To appreciate the effect of SEI layer and modified solvation structures to interfacial resistance, we measured temperature-dependent electrochemical impedance spectroscopy (EIS) for NMC622/graphite cells with different electrolytes at charged state to 3.7 V after three formation cycles (Figure XIV.2.3). It is evident that as the temperature decreased, the total resistances increased due to the lower thermal energy of Li⁺ ions for electrochemical reactions. While Gen 2 and EA electrolytes showed large total resistances to 365 Ω and 315 Ω at -20°C , respectively, EA-f electrolyte showed a much lower total resistance to 207 Ω at -20°C . In the case of the f-EA electrolyte, it showed the highest total resistance of 375 Ω at -20°C ; presumably due to low Li⁺ ion solubility and ionic conductivity at low temperatures. To compare each resistance component contribution, we deconvoluted and extracted the charge transfer resistance at the anode ($R_{\text{ct-anode}}$) and charge transfer resistance at the cathode ($R_{\text{ct-cathode}}$) from the measured data, since those two components are known as limiting factors at low temperatures (Figure XIV.2.3e and Figure XIV.2.3f). In the Arrhenius plot of $R_{\text{ct-anode}}$, Gen 2 showed the lowest resistance due to the ion-conductive SEI layer derived from EC reduction. While the EA electrolyte showed the highest resistance, EA-f and EA-f with LiDFOB additive showed relatively low resistances, likely due to the weaker solvation structure and modified SEI layer. In the case of $R_{\text{ct-cathode}}$, since there was no major difference in CEI layer composition, the weaker solvation effect was directly observed. While EA electrolyte showed similar resistances to Gen 2, EA-f and EA-f with LiDFOB additive showed much smaller resistances. The temperature-dependent EIS measurement shows that the weak solvation structures in EA-f electrolytes improve the interfacial kinetics with the support of a modified SEI layer.

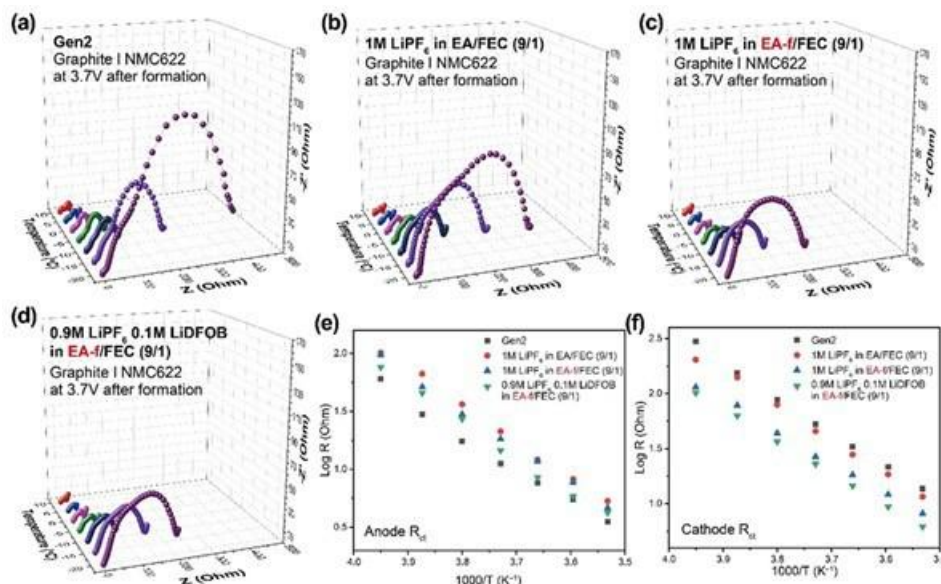


Figure XIV.2.3 Nyquist plots of graphite|NMC622 cells with (a) Gen 2, (b) 1M LiPF₆ in EA/FEC (9/1), (c) 1M LiPF₆ in EA-f/FEC (9/1), and (d) 0.9M LiPF₆ 0.1M LiDFOB in EA-f/FEC (9/1) electrolyte at various temperatures. Arrhenius plots of (e) R_{ct}-anode, and (f) R_{ct}-cathode fitted from (a-d).

Electrochemical performances

One of the advantages of fluorination is high oxidation stability. To compare the stability of electrolytes, we conducted a voltage holding test of NMC622/graphite cells with different electrolytes with a voltage step from 4.4 V to 4.9 V for 10 hours in each step (Figure XIV.2.4a). In the case of Gen 2, the leakage current sustained low up to 4.8 V, but started slightly increasing at 4.9 V. While the EA electrolyte showed a leakage current above 4.6 V, which rapidly increases at 4.9 V, EA-f and EA-f with LiDFOB additive maintained a low leakage current up to 4.9 V, indicating their superior oxidation stability. These results suggest the application of EA-f electrolytes to high voltage cathodes such as LiMn₂O₄ or LiNi_{0.5}Mn_{1.5}O₄. We measured rate capability of electrolytes at 25°C and -20°C (Figure XIV.2.4b and 4c). At room temperature, when various C-rates were applied from C/10 to 4 C, Gen 2 and EA electrolyte showed similar capacities of 116 and 113 mAhg⁻¹ at 4 C, respectively. In contrast, EA-f electrolyte with LiDFOB additive showed the best rate capability and delivered 138 mAhg⁻¹ at 4C due to the weak solvation structure and modified SEI layer. As shown in the voltage profiles with normalized capacity, the overpotential evolution of Gen 2 approached 0.62 V at 4 C, whereas that of EA-f electrolyte with LiDFOB additive maintained a low overpotential of 0.4 V at 4 C.

When the temperature decreased to -20°C, the difference in rate capability between the electrolytes was further diverged. When a current of 1C was applied at -20°C, Gen 2 only exhibited 33 mAhg⁻¹ capacity, while EA-f electrolyte with LiDFOB additive still maintained a high capacity of 70 mAhg⁻¹. In the voltage profiles of rate capabilities at -20°C Gen 2 showed a high overpotential of 1.1 V at 1 C while the EA-f electrolyte with LiDFOB additive remained at 0.77 V at 1 C. To exclude the effect of high ion-pair ratio in electrolytes, we tested 2 M and 3 M EA electrolytes with same test conditions, and in the case of 3 M EA electrolyte, it showed better rate capability than Gen 2 at 25°C, but poor capability at -20°C due to the ion clustering and low ionic conductivity. Poor performance was also observed in f-EA electrolyte, reconfirming the trade-off relation between the weak solvation structure and electrochemical performance. Finally, superior rate capabilities of EA-f electrolytes were found in Li metal batteries, showing the best capacity retention at 25°C and -20°C.

Long-term cyclability at high C-rates and low temperatures is considered as one of the challenging aspects in LIBs. To prove the superiority of our electrolytes, we conducted long-term cycling tests with various conditions (Figure XIV.2.4d-4f). When a current of 2 C was applied at 25°C, the EA electrolyte gradually decayed to a capacity retention of 73% after 400 cycles, while the EA-f electrolyte with LiDFOB additive

showed the best capacity retention of 91% after 400 cycles. This trend continues at a further high current of 6 C. While Gen 2 rapidly degraded to 34% within 50 cycles, the EA-f electrolyte with LiDFOB additive showed the best capacity retention of 85% even after 500 cycles. When a current of C/3 was applied at -20°C , Gen 2 and EA electrolytes showed a severe capacity degradation, corresponding to 7.5% and 34% capacity retention after 300 cycles, respectively. In stark contrast, the EA-f electrolyte with LiDFOB additive showed a negligible capacity loss and retained 97% capacity even after 300 cycles. This cycling test result reveals the superior stability of our electrolyte for fast charging and low temperature operations.

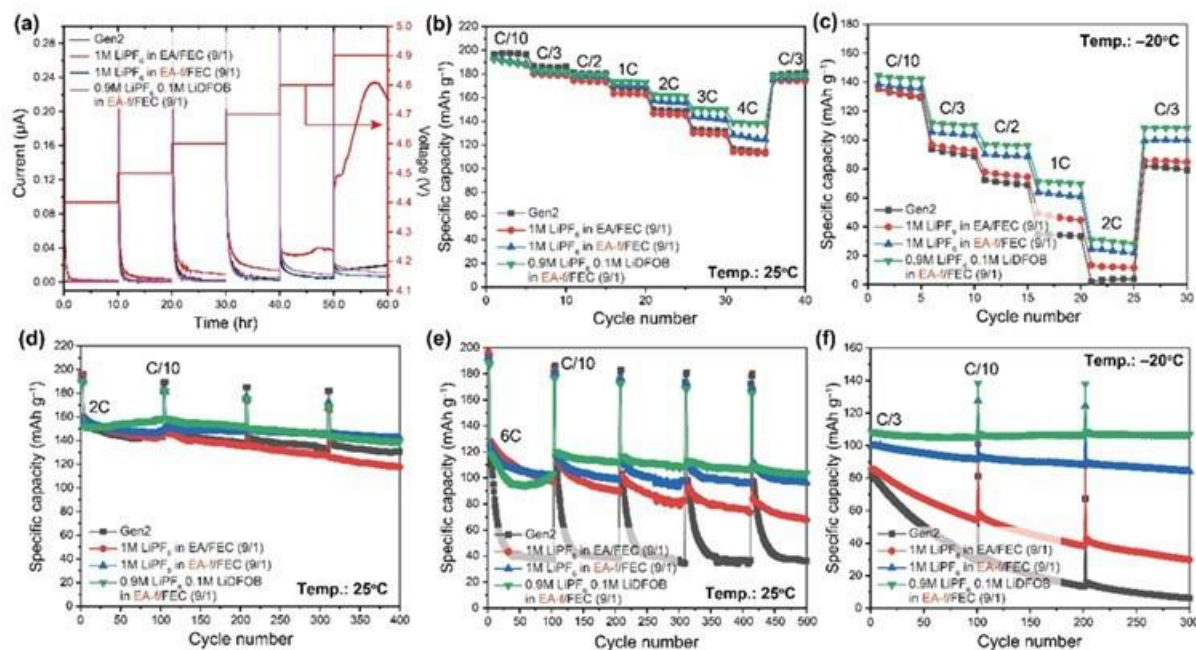


Figure XIV.2.4 (a) Voltage holding test of graphite|NMC622 cells with different electrolytes from 4.4 V to 4.9 V. C-rate capability with different electrolytes at (b) 25°C and (c) -20°C . Cyclability at (d) 2 C and (e) 6 C rate with different electrolytes at 25°C . (f) Cyclability at C/3 rate with different electrolytes at -20°C .

Conclusions

In summary, we have systematically investigated the effect of the position and degree of fluorination in EA solvent on electrochemical performances. We reveal that a high degree of fluorination or fluorination close to ester group imposes more electron-withdrawing effect, resulting in low atomic charges, low binding energies to Li^+ ions, low ionic conductivities, and poor solubilities at low temperatures. Since interfacial resistance is governed by the kinetics of Li^+ ion desolvation, charge transfer across the SEI and ion conductivity, EA-f electrolyte shows the best electrochemical performance at sub-zero temperature. EA-f effectively balances the property trade-offs associated with fluorination, outperforming both f-EA and f-EA-f based electrolytes. This study provides a deep insight on design principles of novel fluorinated electrolytes for LIBs operating at low temperatures.

Key Publications

1. Dong-Joo Yoo, Qian Liu, Orion Cohen, Minkyu Kim, Kristin A. Persson, and Zhengcheng Zhang. Rational Design of Fluorinated Electrolytes for Low Temperature Lithium-Ion Batteries. *Energy & Environmental Sciences* 2022, under review.
2. Xin Su, Ying Xu, Jianzhong Yang, and Zhengcheng, Zhang. Liquid electrolyte for low-temperature lithium batteries: main limitations, current advances, and future perspectives. *Energy Storage Materials* 2022, under review.

3. Dong-Joo Yoo, Qian Liu, Orion Cohen, Minkyu Kim, Kristin A. Persson, and Zhengcheng Zhang. Understanding the Role of SEI Layer in Low-Temperature Performance of Lithium-Ion Batteries. *ACS Applied Material & Interfaces* 2022, 14, 9, 11910–11918.

References

1. Choi, J. W.; Aurbach, D., Promise and reality of post-lithium-ion batteries with high energy densities. *Nature Reviews Materials* 2016, 1 (4), 16013.
2. Etacheri, V.; Marom, R.; Elazari, R.; Salitra, G.; Aurbach, D., Challenges in the development of advanced Li-ion batteries: a review. *Energy & Environmental Science* 2011, 4 (9), 3243-3262.
3. Dunn, B.; Kamath, H.; Tarascon, J.-M., Electrical Energy Storage for the Grid: A Battery of Choices. *Science* 2011, 334 (6058), 928-935.
4. Bandhauer, T. M.; Garimella, S.; Fuller, T. F., A Critical Review of Thermal Issues in Lithium-Ion Batteries. *Journal of The Electrochemical Society* 2011, 158 (3), R1-R25.
5. Gupta, A.; Manthiram, A., Designing advanced lithium - based batteries for low - temperature Conditions. *Advanced energy materials* 2020, 10 (38), 2001972.
6. Jow, T. R.; Delp, S. A.; Allen, J. L.; Jones, J.-P.; Smart, M. C., Factors Limiting Li⁺Charge Transfer Kinetics in Li-Ion Batteries. *Journal of The Electrochemical Society* 2018, 165 (2), A361-A367.
7. Ren, D.; Smith, K.; Guo, D.; Han, X.; Feng, X.; Lu, L.; Ouyang, M.; Li, J., Investigation of Lithium Plating-Stripping Process in Li-Ion Batteries at Low Temperature Using an Electrochemical Model. *Journal of The Electrochemical Society* 2018, 165 (10), A2167-A2178.
8. Jones, J.-P.; Smart, M. C.; Krause, F. C.; Bugga, R. V., The Effect of Electrolyte Additives upon Lithium Plating during Low Temperature Charging of Graphite-LiNiCoAlO₂ Lithium-Ion Three Electrode Cells. *Journal of The Electrochemical Society* 2020, 167 (2), 020536.
9. Xu, M.; Zhou, L.; Hao, L.; Xing, L.; Li, W.; Lucht, B. L., Investigation and application of lithium difluoro(oxalate)borate (LiDFOB) as additive to improve the thermal stability of electrolyte for lithium-ion batteries. *Journal of Power Sources* 2011, 196 (16), 6794-6801.

Acknowledgements

The submitted manuscript has been created by UChicago Argonne, LLC, Operator of Argonne National Laboratory, which is supported by DOE Office of Science under Contract No. DE-AC02-06CH11357.

XIV.3 Synthesis, screening and characterization of novel low temperature electrolyte for lithium-ion batteries (BNL)

Xiao-Qing Yang, Principal Investigator

Chemistry division, Brookhaven National laboratory
Bldg. 555, Brookhaven National Lab.
Upton, NY 11973
E-mail: xyang@bnl.gov

Enyuan Hu,, Co-Principal Investigator

Chemistry division, Brookhaven National laboratory
Bldg. 555, Brookhaven National Lab.
Upton, NY 11973
E-mail: enhu@bnl.gov

Tien Duong, DOE Technology Development Manager

U.S. Department of Energy
E-mail: Tien.Duong@ee.doe.gov

Start Date: October 1, 2021	End Date: September 30, 2022	
Project Funding (FY22): \$1,000,000	DOE share: \$1,000,000	Non-DOE share: \$0

Project Introduction

While the energy density and cost of batteries powering electric vehicles are becoming competitive with internal combustion engines, there are still several critical issues that need to be addressed. The low temperature performance of the batteries and the fast charge capability are two of them. Current lithium-ion batteries (LIB) experience a significant capacity drop down to about one fifth of its room temperature capacity at -30°C. Current LIB electrolyte is often based on ethylene carbonate (EC) as a major solvent component due to the high dielectric constant and formation of an excellent solid-electrolyte-interphase (SEI) on the graphite anode. Unfortunately, EC has a rather high melting point (37°C), leading to significantly increased viscosity and severely decreased Li⁺ conductivity at low temperatures. LIB also has high impedance at low temperature due to the sluggish Li⁺ transport through SEI. These issues result in the much-decreased capacity and poor cyclability at low temperature. Therefore, to improve the low temperature performance of LIB, it is critical to develop new electrolyte system that has low viscosity, high Li⁺ conductivity, and is able to form stable and low-impedance interphase on both anode and cathode. This consortium, with team members of Brookhaven National Laboratory (BNL), DEVCOM Army Research Laboratory (ARL), University of Maryland (UMD), and University of Rhode Island (URI), addresses the low temperature electrolyte challenge through integrated molecular modeling, electrolyte components design, synthesis, testing, and advanced characterization.

Objectives

The project objective is to develop next generation electrolyte formulations that enable the Li-ion batteries to deliver >70% of room temperature energy at -20°C, while still meeting the United States Advanced Battery Consortium (USABC) Operating Environment Conditions (-30°C to +52°C), fast charge capability, calendar life testing at 30°C, 40°C, 50°C, and 60°C.

Approach

Up to date, most low temperature electrolyte development efforts have been focused on adjusting a combination of different commercially available solvents only, and a decent low-temperature performance can only be achieved by sacrificing other properties such as high-temperature and high voltage performance. Keeping the goals of automobile application in mind, to achieve the desired low temperature performance while maintaining other performance, we need to design new electrolyte systems using an integrated approach

starting from theoretical calculations of the new electrolytes, understanding the electrolyte-electrode interphases, to the synthesis of new solvents, salts, and additives, as well as advanced characterizations of the electrolyte systems in actual battery environments. Molecular modeling has been used to predict the transport property, electronic structure and the initial solid electrolyte interphase (SEI) formation mechanisms to propose possible candidates that have high Li^+ conductivity, good stability, as well as low-impedance SEI. These candidates have been or will be synthesized and purified for experimental validation. The new electrolyte system is subject to a series of electrochemical testing and diagnostic studies for performance evaluation and mechanistic studies. These knowledges provide feedback to the theoretical model for better understanding and more accurate predictions.

Solvent candidates to be explored include but are not limited to ethers, esters, nitriles and their fluorine-substituted derivatives. Salt candidates include lithium tetrafluoroborate (LiBF_4), lithium hexafluorophosphate (LiPF_6), lithium bis(fluorosulfonyl) imide (LiFSI), lithium bis(trifluoromethanesulfonyl) imide (LiTFSI), lithium bis(oxalato) borate (LiBOB), and lithium difluoroxyoxalatoborate (LiDFOB) etc. Additive candidates include vinylene carbonate (VC), fluoro ethylene carbonate (FEC), phosphites, phosphates, sulfones, sultones, and sulfates.

New electrolyte systems are subject to a series of characterizations and theoretical calculations such as Infrared and Raman spectroscopies as well as x-ray and neutron pair distribution function (xPDF and nPDF) analysis. The results have been analyzed together with molecular dynamic (MD) calculations to understand the structure of the electrolyte. The SEI and cathode-electrolyte-interphase (CEI) components are subject to characterizations such as high energy x-ray photoelectron spectroscopy (HAXPES), resonant inelastic x-ray scattering (RIXS), x-ray absorption spectroscopy (XAS), x-ray photoemission electron microscopy (XPEEM), as well as cryo transmission electron microscopy (Cryo TEM) to obtain the structure, depth-profiling, and chemical distribution in the battery interphases.

Results

At **BNL**, new isoxazole-based electrolytes have been developed and their application for lithium metal batteries has been investigated. Isoxazole-based localized high concentration electrolytes (LHCEs) with FEC additive can significantly enhance the stability and functionality of SEI, and a high Coulombic efficiency (CE) of 98.6% was achieved, benefitted from the FSI^- and FEC derived better SEI with LiF and sulfur-rich components. With a lower isoxazole/TTE volume ratio in LHCE-TTE4.5, better SEI was formed, resulting in a superior electrochemical performance at low temperature. The Li/SPAN cell using LHCE-TTE4.5 delivered 340.7 mAh g^{-1} at -20°C and 273.8 mAh g^{-1} at -30°C , with 99.85% capacity retention after 50 cycles at -30°C as shown in Figure XIV.3.1. This work demonstrated the importance of SEI for low-temperature applications. Compared with the bulk ionic conductivity of electrolyte, the stability and impedance of the SEI have a significantly greater impact on the electrochemical performance at low temperatures. These results provide valuable information for developing and screening new electrolytes for low-temperature applications.

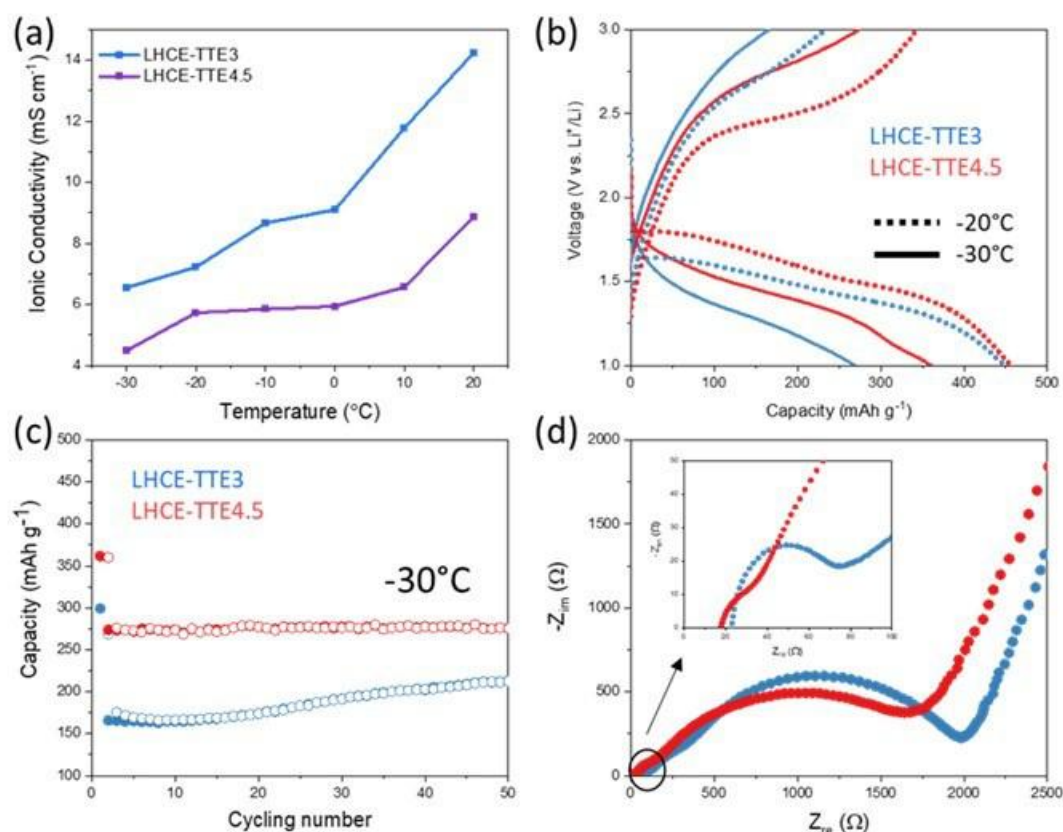


Figure XIV.3.1 (a) ionic conductivity of LHCE-TTE3 and LHCE-TTE4.5. (b) Charge-discharge voltage profile of Li/SPAN cells at -20 $^{\circ}\text{C}$ (dot line) and -30 $^{\circ}\text{C}$ (solid line) using LHCE-TTE3 (blue) and LHCE-TTE4.5 (red). (c) Li-SPAN cycling stability at -30 $^{\circ}\text{C}$ using LHCE-TTE3 (blue) and LHCE-TTE4.5 (red). (d) EIS results of Li/SPAN cells after 50 cycles at -30 $^{\circ}\text{C}$.

In LHCE electrolytes, the lowest unoccupied molecular orbital (LUMO) is shifted to the anion, generating an anion-derived interphase. (Sulfur is the unique element in FSI- only, not in any of the solvents. Therefore, sulfur K-edge XAS was carried out to identify the composition of the sulfur species from FSI- reduction in the interphase of cycled Li/Cu cells at **BNL**. As shown in Figure XIV.3.2(a), FSI anions were decomposed in both LHCE-TTE3 and LHCE-TTE4.5 electrolytes, generating Li_2S , SO_3^{2-} , and COSO_2^- species with similar intensity distribution. X-ray fluorescence (XRF) imaging was performed to investigate the spatial distribution of sulfur species. As shown in Figure XIV.3.2(b) and Figure XIV.3.2(c), relative homogenous sulfur species distribution was observed in both systems, indicating homogenous FSI- derived interphase formation. Higher sulfur signal intensity in (c) suggests more sulfur species in the interphase when using LHCE-TTE4.5 electrolyte, which is attributed to more anions located inside the solvation structure due to lower IZ amount in LHCE-TTE4.5. Compared with the solvent derived SEI generated using baseline electrolyte DOL/DME, which is consisting of mostly organic species, our LHCEs provided better Li metal passivation, enabling uniform and dense Li deposition and higher CE.

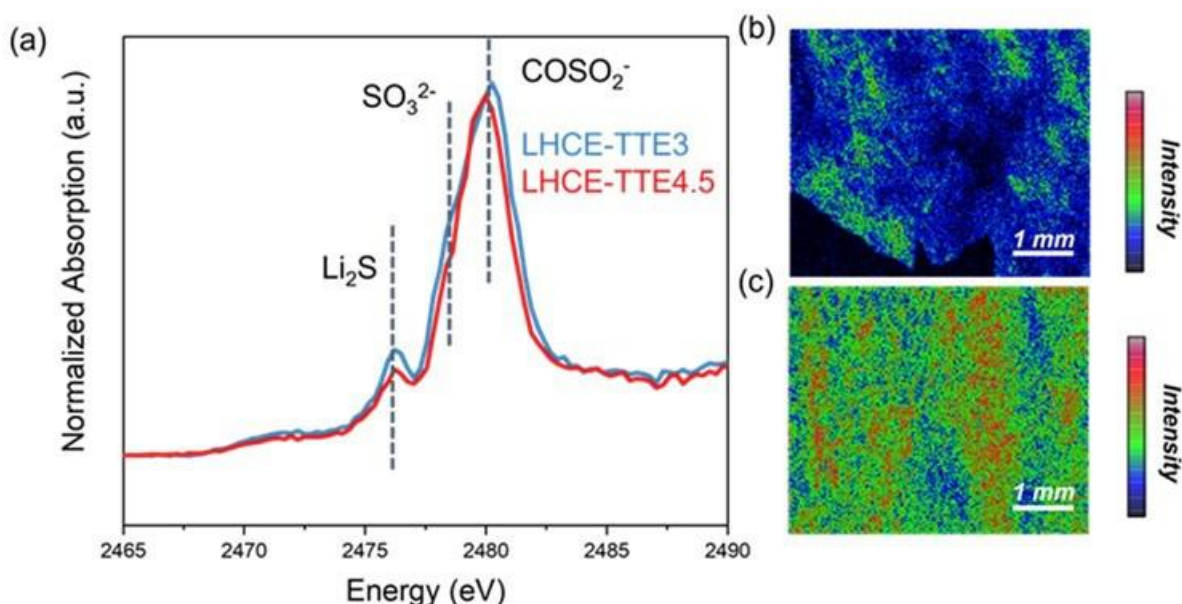


Figure XIV.3.2 (a) Sulfur K-edge X-ray absorption spectroscopy (XAS) of Cu foil with deposited lithium in Li/Cu cells. X-ray fluorescence images of sulfur species on Cu foil collected at 2482 eV using (b) LHCE-TTE3 and (c) LHCE-TTE4.5.

At University of Rhode Island (URI), various ester-based electrolytes using alternative Li salts have been systematically studied. Long term cycling performance at -20°C for ester-based electrolytes with alternative Li salts are presented in Figure XIV.3.3. Reversible capacities for cells cycled with methyl acetate (MA) and fluoroethylene carbonate (FEC) ester-based electrolyte for all the alternative Li salts outperformed cycling with the STD electrolyte (average capacity of 82 mAhg^{-1}) at the same conditions. While the best capacities were observed for the LiBF_4 -MA electrolyte (average capacity of 96 mAhg^{-1}), cells containing the LiDFOB salt in both MA/FEC (average capacity of 94 mAhg^{-1}) and in methyl propionate (MP)/FEC (average capacity of 87 mAhg^{-1}) have improved low temperature performance. The improved performance observed with MA/FEC is most likely due to the reduced viscosity coming from smaller molecule ester chain of MA compared to MP.

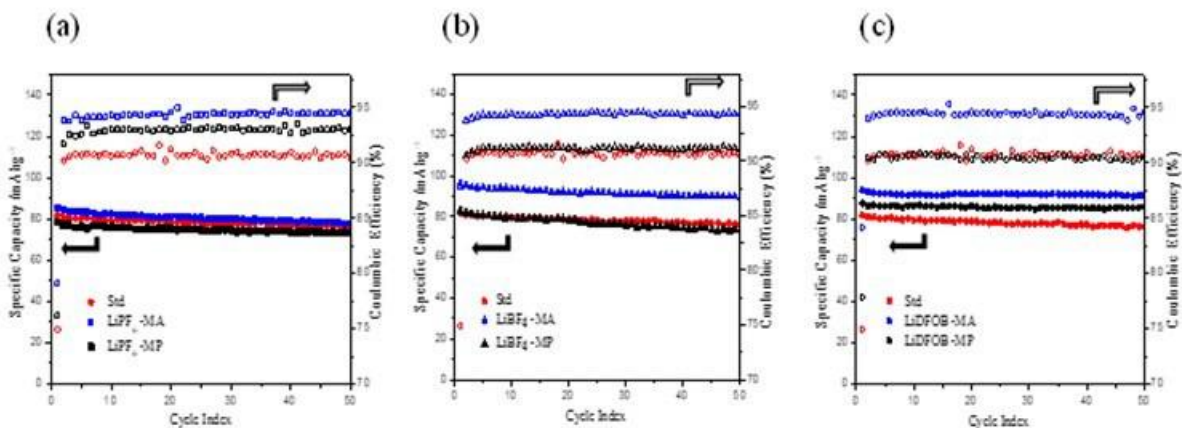


Figure XIV.3.3 Cycling performance of NMC 622 | graphite cells with (a) 1M LiPF_6 (b) 1M LiBF_4 (c) 1M LiDFOB as the salt at C/5 charge and C/3 discharge rate rates at -20°C .

The FE-SEM with EDX layered image and the elemental mapping images of the graphite electrodes after 50 cycles at -20°C with different electrolyte systems are provided in Figure XIV.3.4. After low temperature cycling, SEM images reveal significantly different morphology on the surface of the graphite particles in the two electrolyte systems containing LiPF_6 . Graphite particles cycled with the STD electrolyte have a grainy rough surface, the EDX elemental mapping reveals that the granular shaped particles have a high concentration of oxygen. The granular shaped particles are likely EC decomposition species such as Li_2CO_3 and lithium alkyl carbonates. Graphite anodes cycled with LiPF_6 -MA electrolyte generate a much smoother surface film on graphite. The spherical LiF particles formed on the graphite surface in cells containing LiBF_4 -MA during the initial formation cycling have not changed in shape or size upon the additional cycling. However, after the long-term cycling at -20°C , rod like structures are observed on the graphite particles which can be identified as plated lithium from the EDX mapping.

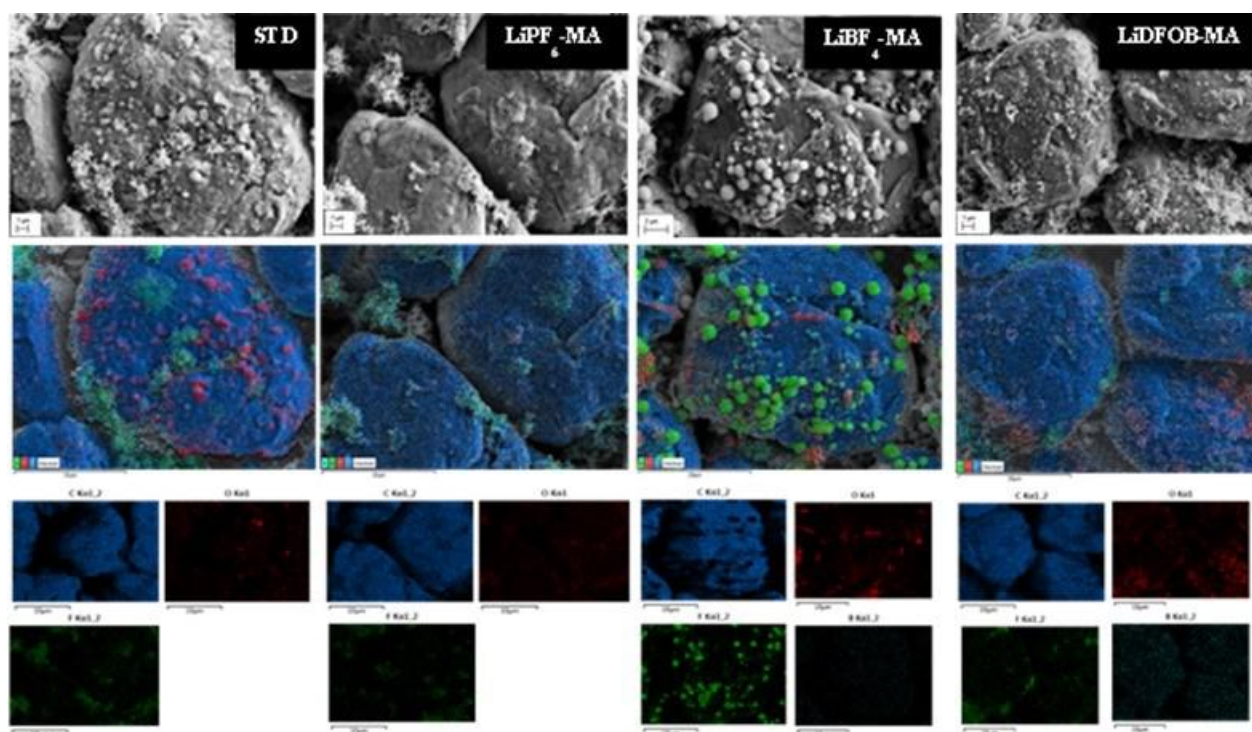


Figure XIV.3.4 FE-SEM (top) and SEM-EDX overlay images (center) and SEM-EDX elemental mapping (bottom, Blue- Carbon, Red- Oxygen, Green-Fluorine, light blue- Boron) of the SEI layer after 50 cycles at -20°C with each electrolyte formulation.

The University of Maryland at College Park (UMD) team developed a new innovative group of soft solvating electrolytes and the design principle for low temperature operation. As shown in Figure XIV.3.5a, the NMC811||graphite full cells using these new electrolytes with TTE diluent (F1, F2, F3) have significantly improved capacity retention than the EC/DEC baseline electrolyte. The F1 electrolyte enables the best capacity retention of 80.1% after 400 cycles with a high average CE of 99.94%. The F1 electrolyte also has excellent rate capability. As shown in Figure XIV.3.5b, the fast charging/discharging capability of the NMC811 (2.5 mAh/cm²) || graphite full cells using F1 electrolyte at 25°C are the the following: 202 mAh/g at 1C rate; 185 mAh/g at 2C rate; 169 mAh/g at 3C rate; and 140 mAh/g at 4C rate.

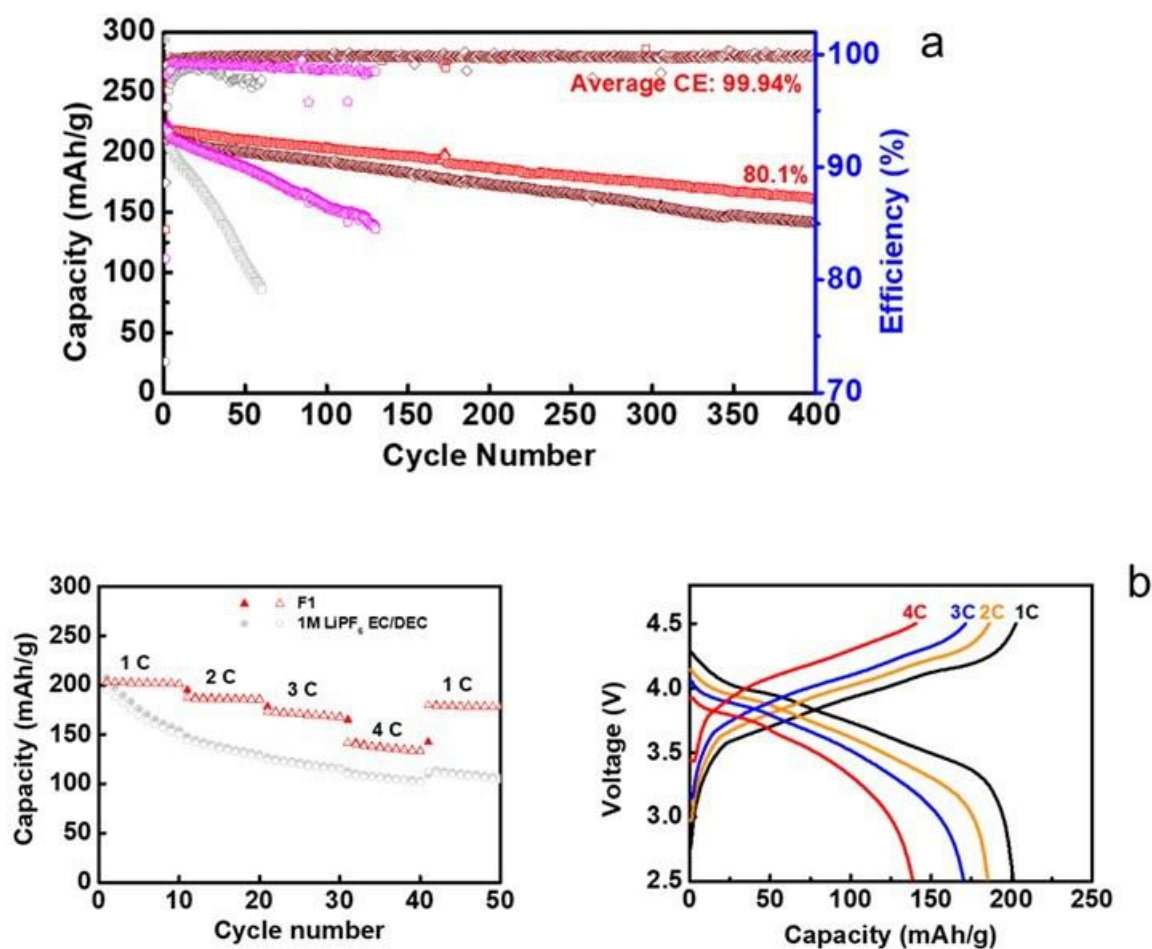


Figure XIV.3.5 (a). Cycling performance of TTE based new electrolytes in NMC811 (2.5 mAh/cm²) || graphite full cells in comparison with baseline electrolyte at 0.5 C rate under 25°C (3.0-4.5 V). (b) Rate performance of F1 electrolytes in NMC811 (2.5 mAh/cm²) || graphite full cells at 25°C, and corresponding voltage profiles

The NMC811||graphite full cells using F1 electrolytes exhibited exceptional low temperatures performance at -30°C and -40°C. As shown in Figure XIV.3.6a, at -30°C, the capacity retains 93.9% capacity after 260 cycles with an average Coulombic efficiency of 99.98%. In comparison, the EC/DEC baseline electrolyte completely failed to operate at -30°C due to the solidification of the EC in the electrolyte. Figure XIV.3.6b shows the cycling performance of F1 at 0.1 C rate under different temperatures (60°C, 25°C, 0°C, -20°C, -30°C, -40°C, -50°C, -60°C), and the voltage profiles of the cells using F1 electrolyte. The capacities at different temperatures and their percentage of room temperature are: 0°C: 206.8 mAh/g (95%), -20°C: 194.5 mAh/g (90%), -30°C: 188.7 mAh/g (87%), -40°C: 184.6 mAh/g (85%), -50°C: 161.0 mAh/g (75%), -60°C: 115.5 mAh/g (54%).

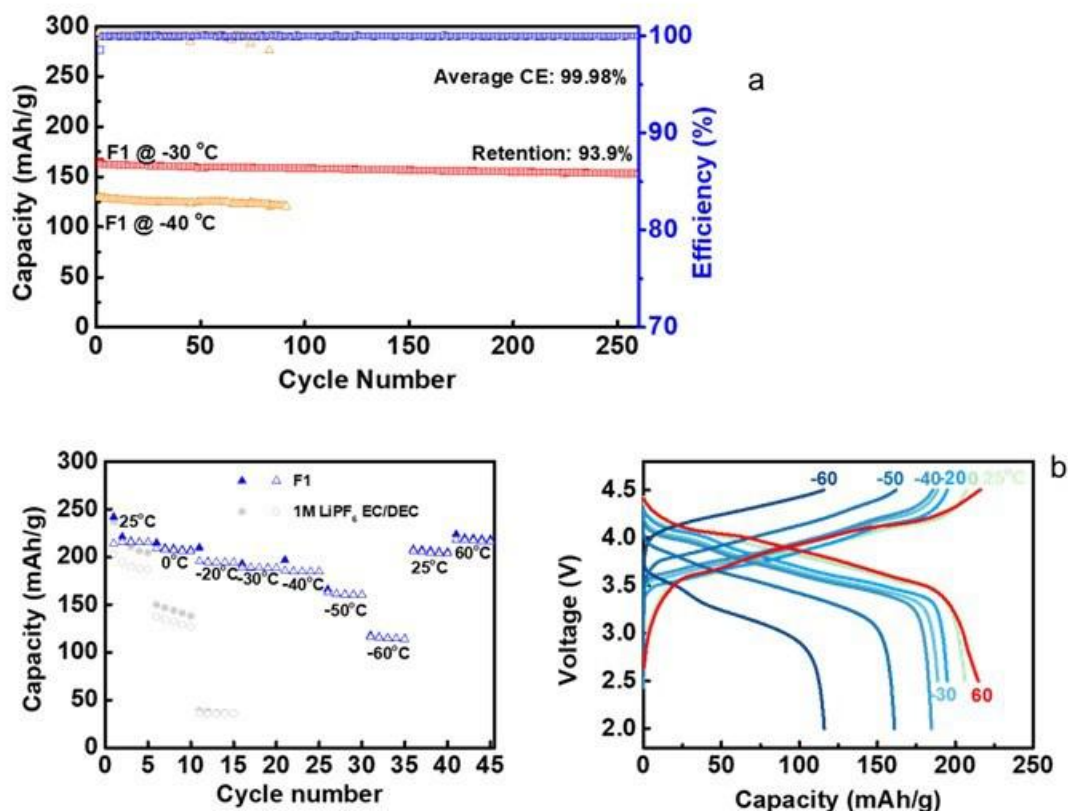


Figure XIV.3.6 (a). Long cycling performance of F1 electrolytes in NMC811 (2.5 mAh/cm²) || graphite full cells at 0.2 C rate at -30 °C / -40 °C. (b) Cycling performance at 0.1 C under different temperatures (60 °C, 25 °C, 0 °C, -20 °C, -30 °C, -40 °C, -50 °C, -60 °C), and voltage profiles using F1 electrolyte

Using this F1-based electrolyte, a NMC811||graphite pouch cells with N/P ratio of 1.1 and areal capacity of 2.5 mAh cm⁻² was built tested. As shown in Figure XIV.3.7, a charge/discharge capacity of 160.2 mAh/g at 0.2 C under -30 °C was obtained with average CE of 99.93% and capacity retention of 82.8% after 350 cycles. Even at higher C-rates of 0.3 C and 0.4 C, the pouch cell shows capacities of 152.6 mAh/g and 134.6 mAh/g respectively.

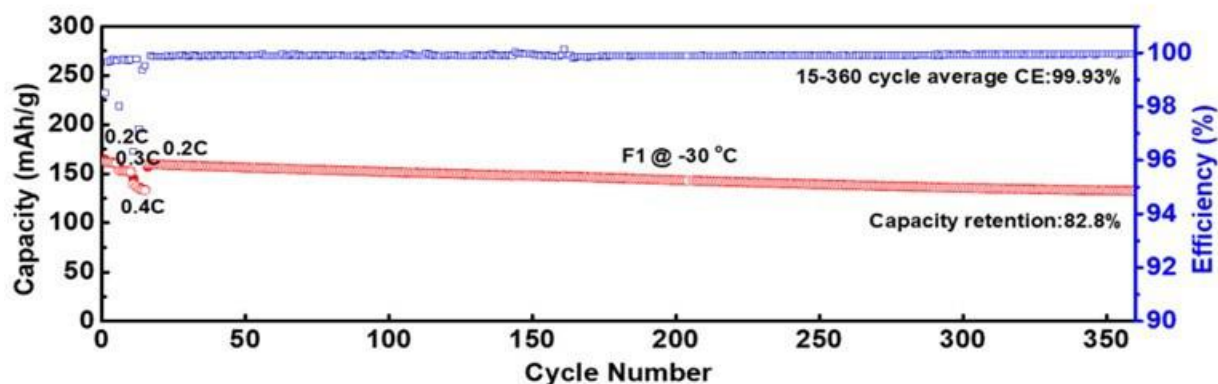


Figure XIV.3.7 Low temperature charge and discharge cycling performance of NMC811 || graphite pouch cell under -30 °C.

The ionic conductivity study at different temperature, Differential scanning calorimetry (DSC) measurement, and x-ray pair distribution function (PDF) study of these soft solvating electrolytes were carried out with the results shown in Figure XIV.3.8. As shown in Figure XIV.3.8a, the ionic conductivities of the soft-solvating electrolytes (F1, F2, F3) are much higher than those of the EC/DEC baseline electrolyte at temperatures below -20°C . The DSC results in Figure XIV.3.8b, shown that none of the F1-F3 electrolytes undergo a phase change over $\pm 90^{\circ}\text{C}$. As shown in Figure XIV.3.8c. The experimental x-ray PDF data was performed on the F1 electrolytes and its components including TTE diluent. An excellent agreement was observed between the experimentally measured PDF and molecular dynamic (MD) simulation predictions, indicating ability of the developed force field to accurately predict electrolyte and solvent structure in MD simulations in addition to the excellent agreement observed between MD predicted ionic conductivity and experiments shown in Figure XIV.3.8a.

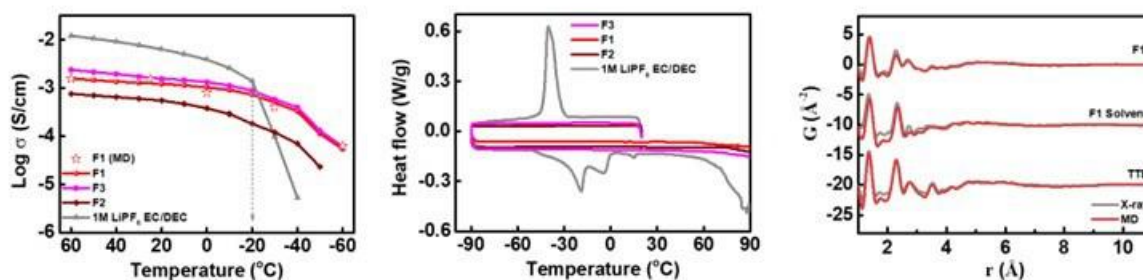


Figure XIV.3.8 (a) Temperature dependence of the conductivity of different electrolytes. For comparison, red stars represent conductivity values predicted with Molecular dynamics (MD). (b) Differential scanning calorimetry (DSC) cooling and heating curves of different electrolytes. Electrolytes were cooled to -90°C and then heated up to 90°C with $2^{\circ}\text{C}/\text{min}$, indicating wide temperature stability. (c) PDF data of F1 electrolyte, and single solvents. Greyline: experiment data; Redline: MD simulation predictions

A manuscript outlining the development methodology and performance of the soft solvating electrolytes demonstrating wide temperature battery operations has been accepted for publication in by *Nature* (2023). A US Provisional patent was filed for these new electrolytes on November 23, 2021 (US Provisional number 63/264504). Low-polarity-solvent electrolytes are introduced to enhance the Li^+ transport kinetics both in and across the electrode/electrolyte interphases at low temperatures, which enables the NMC811||graphite cell to operate in a wide temperature range from -40°C to 50°C , delivering a high capacity of 113 mAh g^{-1} (out of 117 mAh g^{-1} of the full cell) at 25°C and maintaining 81 % of its room-temperature capacity at -20°C at a current density of $1/3 \text{ C}$. The results were published on *Angewandte Chemie International Edition* in July 2022.

DEVCOM Army research Lab (ARL) carried out molecular modeling of the electrolytes structure and transport using molecular dynamics (MD) simulations combined with density functional theory (DFT) calculations aimed at understanding electrochemical stability window and initial decomposition pathways of the electrolyte solvents/diluents and salts.

An in-depth analysis of the structure and transport mechanism of the baseline 1M LiPF₆ in EC:DMC electrolyte was performed and published in 2022 in *Angew. Chem. Int. Ed* 2022, 61, e202205967, J. Electrochem. Soc 2022, 169, 100540. Unlike the relatively homogeneous structure found in the baseline electrolyte, a nano-domain structure was observed in MD simulations of the LiFSI(EMC)_{1.6} in TTE diluent electrolyte. A Li^+ cation has the highest affinity to carbonyl oxygens Oc(EMC) followed by the oxygens from FSI⁻ and is largely located in the LiFSI(EMC)_{1.6} domain with heavy salt aggregation with only a few percent of Li^+ situated in the TTE-rich domain. In agreement with FTIR performed by UMD, the majority (>97%) of carbonyl oxygens of EMC are coordinated to Li^+ , indicating an absence of free [not bound to Li^+] EMC solvent that would be more susceptible to oxidation than Li^+ EMC bond complexes. The presence of 0.11F from TTE coordinating a Li^+ and the absence of the Li^+ O(TTE) coordination reflects a weak interaction

between the LiFSI(EMC)_{1.6}-rich domains and TTE diluent, which is consistent with the FTIR result. A preferential reductive decomposition of LiFSI-based aggregates above 1.6 V and Li-TTE reduction are predicted by DFT calculations. A detailed analysis of the desolvation energy for the Li⁺ solvates revealed lower Li⁺ desolvation for the positively charged Li⁺ solvates in LiFSI(EMC)_{1.6} in TTE electrolyte compared to that in the baseline electrolyte in agreement with the lower activation energy for the interfacial resistance experimentally observed by UMD for LiFSI(EMC)_{1.6} in TTE electrolyte compared to baseline (see *Angew. Chem. Int. Ed* 2022, 61, e202205967). A difference in the SEI composition, desolvation energy and faster bulk transport at lower temperatures (below −30 °C) is responsible for the experimentally observed improved capacity retention at lower temperatures for graphite || NMC 811 cells by UMD.

MD simulations of the F1-based soft solvation electrolyte with an co-solvent and TTE diluent predicted the Li⁺ is largely located in the yellow domain coordinated by F1 solvent, while TTE diluent and co-solvents were located in a blue domain Figure XIV.3.9a. Despite high degree of contact ion pair formation and salt aggregation shown in Figure XIV.3.9(b-c), conductivity of the F1-based electrolyte exceeds that of the baseline electrolyte Figure XIV.3.8 below −30 °C. Much higher fraction of free Li⁺ (no counterion coordination) compared to free TFSI[−] rationalizes high transference number observed experimentally and in MD simulations. DFT calculations were performed on 20 solvents and identified a co-solvent with very high reduction potential that formation of the LiF-rich SEI on both anode and cathode leading to balanced interfacial resistance as observed by UMD (see *Nature* 2023).

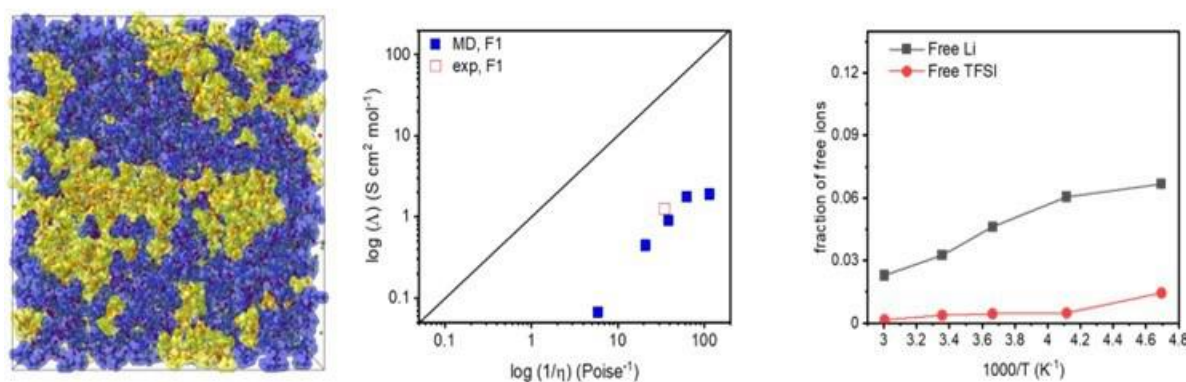


Figure XIV.3.9 MD simulation results: (a) a snapshot of the simulation box of F1 electrolyte. LiTFSI-F1 are highlighted by yellow isosurface, TTE and F4 by blue isosurface. (b) Walden plot for F1 electrolyte indicating strong ionic correlation. (c) Fraction of free Li⁺ and TFSI[−] defined as the ions not coordinated to any counterion within 5.0 Å of Li-N(TFSI) from MD simulations of F1 electrolyte. Low fraction of free ions is consistent with Walden plot.

In collaboration with Prof. Shirley Meng at University of California at San Diego (UCSD), the bulk structures of the 1M LiFSI-Me₂O and 1M LiFSI-Me₂O-TFE(1,1,2-tetrafluoroethane)-PFE(pentafluoroethane) electrolytes were studied via MD simulations using APPLE&P force field as a function of temperature after validating its ability to predict the solvent–Li⁺ binding energy obtained using quantum chemistry (QC) calculations. This study was carried out by Oleg Borodin at ARL. The Li⁺–Me₂O binding is the strongest, followed by Li⁺–TFE and Li⁺–PFE, indicating that TFE is more effective at salt dissociation than PFE. The MD simulations reveal a dominance of short, well-dispersed ionic aggregates in 1M LiFSI-Me₂O, although much larger aggregates were found in 1M LiFSI-Me₂O-TFE-PFE (Figure XIV.3.10d–f). A clear trend of an increasing extent of aggregation with increasing temperature is observed. This is consistent with increasing the Li⁺–FSI[−] coordination and decreasing the Li–ether oxygen coordination with increasing temperature (Figure XIV.3.10g). Through analysis of the radial distribution functions, representative solvates and coordination numbers reveal the strongest propensity for a Li⁺ to coordinate to the ether oxygen atoms of Me₂O followed by the oxygen atoms of FSI[−] and fluorine atoms of TFE. No coordination of Li⁺ to the fluorine of PFE is observed, in alignment with QC results, indicating that the weakest binding of Li⁺ is to the PFE solvent, in

agreement with the Raman data (Figure XIV.3.10b). Fast mobility of the Li^+ solvates dissociated from FSI^- anions in a low viscosity TFE/PFE diluent mixture combined with the increased population of such solvates with decreasing temperature and fast ionic exchange in aggregates resulted in a near constant conductivity of 1M LiFSI- Me_2O -TFE electrolyte in a wide temperature range from -78°C to $+80^\circ\text{C}$ enabling excellent low temperature battery performance as discussed in Nature Energy 2022, 7 (6), 548-559. Also, nearly all (>94%) Me_2O molecules are bound to Li^+ in 1 M LiFSI- Me_2O -TFE-PFE, resulting in improved oxidation stability due to a low fraction of “free” ether solvent that is known to undergo hydrogen transfer on the LiNiO_2 -like cathode surfaces.

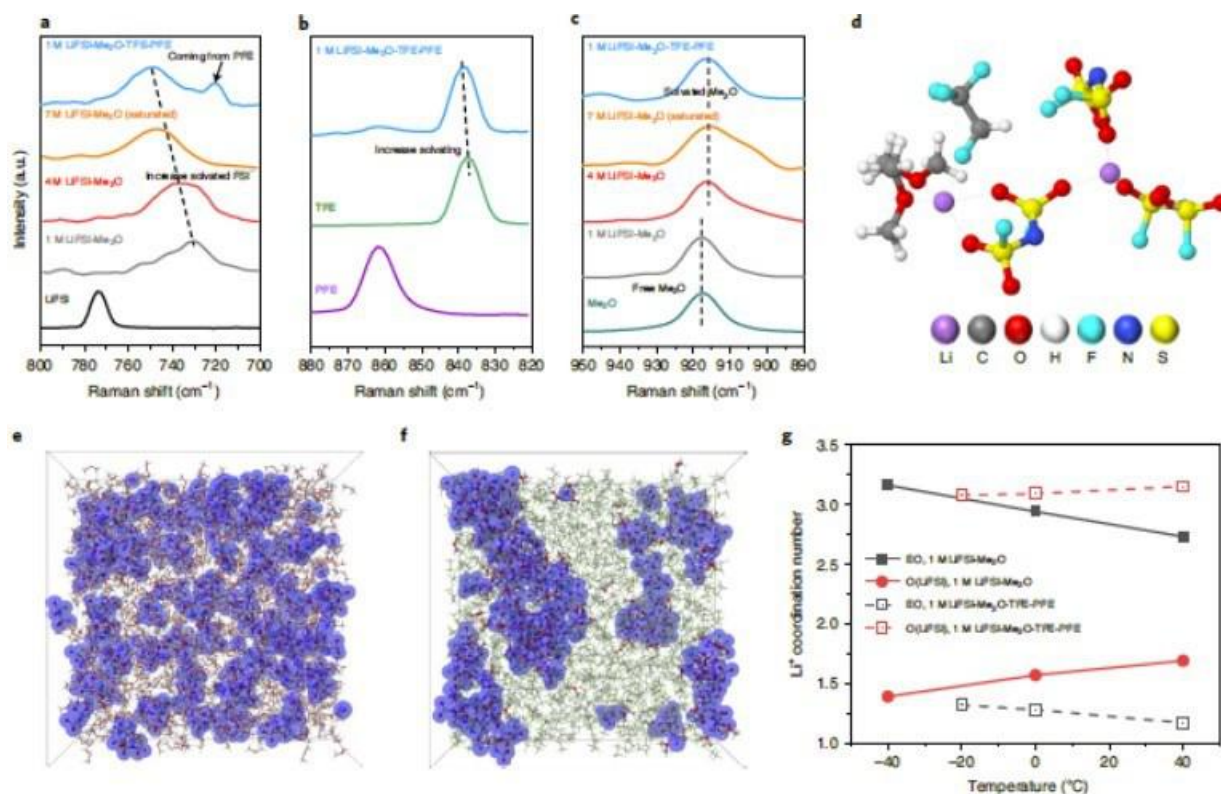


Figure XIV.3.10 Bulk structure and MD simulation results of the formulated electrolytes. **a–c**, Raman spectra of electrolytes at different LiFSI concentrations in Me_2O and the 1 M LiFSI- Me_2O -TFE-PFE mixture at $800\text{--}700\text{ cm}^{-1}$ (the S-N-S bending vibration of FSI^-) (**a**), $880\text{--}820\text{ cm}^{-1}$ (the C-F stretching vibration of TFE and PFE molecules) (**b**) and $950\text{--}890\text{ cm}^{-1}$ (the C-O-C stretching vibration of Me_2O) (**c**). **d–f**, Snapshots of the MD simulation cell containing the representative Li^+ solvates (**d**), 1 M LiFSI- Me_2O (**e**) and 1 M LiFSI- Me_2O -TFE-PFE (**f**) at 273 K. In **e,f**, the blue isosurfaces highlight the locations of Li^+ and FSI^- . Colors: Li, purple; C, grey; O, red; H, white; F, cyan; N, navy blue; S, yellow. **g**, Li^+ coordination numbers of Li-EO bonding and Li-O (from LiFSI) bonding at different temperatures. EO, ether oxygen.

Conclusions

This project, “Synthesis, screening and characterization of novel low temperature electrolyte for lithium-ion batteries (BNL)”, has been successfully completed in FY2022. All milestones have been completed with results being disseminated in numerous publications/patents. Extensive collaboration with other national Labs, US universities and international research institutions were well established.

Key Publications

Patents

1. A US Provisional patent was filed for these new electrolytes on November 23, 2021 (US Provisional number 63/264504).

Publications

1. Sha Tan, U. Nuwanthi D. Rodrigo, Zulipiya Shadike, Brett Lucht*, Kang Xu, Chunsheng Wang, Xiao-Qing Yang*, and Enyuan Hu*, “Novel Low-Temperature Electrolyte Using Isoxazole as the Main Solvent for Lithium-Ion Batteries”, *ACS Appl. Mater. Interfaces* 2021, 13, 24995–25001. DOI: 10.1021/acsami.1c05894, Publication date: May 19, 2021.
2. Nuwanthi D. Rodrigo*, Sha Tan, Zulipiya Shadike, Enyuan Hu, Xiao-Qing Yang, Brett L. Lucht*, “Improved Low Temperature Performance of Graphite/Li Cells Using Isoxazole as a Novel Cosolvent in Electrolytes”, *J. Electrochem. Soc.*, 2021, 168, 070527, DOI: 10.1149/1945-7111/ac11a6, Publication date: July 14, 2021.
3. Yunxian Qian, Yanli Chu, Zhongtian Zheng, Zulipiya Shadike, Bing Han, Shuhuai Xiang,, Yuanyuan Kang Shiguang Hu, Chaowei Cao, Ling Zhong, Qiao Shi, Muchong Lin, Hongbo Zeng, Jun Wang,, Enyuan Hu Conan Weiland, Xiao-Qing Yang, and Yonghong Deng, “A new cyclic carbonate enables high power/ low temperature lithium-ion batteries”, *Energy Storage Materials*, 45 (2022) 24-32, DOI: 10.1016/j.ensm.2021.11.030, Publication Date: November 24, 2021.
4. Sha Tan, Haodong Liu, Zhaohui Wu, Conan Weiland, Seong-Min Bak, Arthur Ronne, Ping Liu, M. Stanley Whittingham, Zulipiya Shadike*, Enyuan Hu*, Xiao-Qing Yang*, “Isoxazole-based Electrolytes for Lithium Metal Protection and Lithium-Sulfurized Polyacrylonitrile (SPAN) Battery Operating at Low Temperature”, *J. Electrochem. Soc.*, DOI: 10.1149/1945-7111/ac58c5, Publication date: February 25, 2022.
5. Nuwanthi D. Rodrigo*, Chamithri Jayawardana,* and Brett L. Lucht*, “Investigation of the Electrode-Electrolyte Interphase in Ester-Based Electrolytes in NCM523/Graphite Cells”, *J. Electrochem. Soc.*, DOI: 10.1149/1945-7111/ac5a19, Publication date: March 11, 2022.
6. Nan Zhang, Tao Deng, Shuoqing Zhang, Changhong Wang, Lixin Chen, Chunsheng Wang*, and Xiulin Fan*, “Critical Review on Low-Temperature Li-Ion/Metal Batteries”, *Advanced Materials*, 2022, 34, 2107899, DOI: 10.1002/adma.202107899, Publication date: December 02, 2021.
7. Bo Nan, Long Chen, Nuwanthi D. Rodrigo, Oleg Borodin, Nan Piao, Jiale Xia, Travis Pollard, Singyuk Hou, Jiaxun Zhang, Xiao Ji, Jijian Xu, Xiyue Zhang, Lin Ma, Xinzi He, Sufu Liu, Hongli Wan, Enyuan Hu, Weiran Zhang, Kang Xu,* Xiao-Qing Yang,* Brett Lucht,* Chunsheng Wang,* “Enhancing Li⁺ Transport in NMC811|| Graphite Lithium - Ion Batteries at Low Temperatures by Using Low - Polarity - Solvent Electrolytes” , *Angew. Chem., Int. Ed.*, 2022, 61, e202205967, DOI:10.1002/anie.202205967, Publication date: July 05, 2022.
8. Yijie Yin, Yangyuchen Yang*, Diyi Cheng, Matthew Mayer, John Holoubek, Weikang Li, Ganesh Raghavendran, Alex Liu, Bingyu Lu, Daniel M. Davies, Zheng Chen, Oleg Borodin* and Y. Shirley Meng*, “Fire-extinguishing, recyclable liquefied, gas electrolytes for temperature-resilient lithium-metal batteries”, *Nature Energy*, 7, pages 548–559 (2022), DOI: 10.1038/s41560-022-01051-4, Publication date: June 16, 2022.
9. Andersson, R., Borodin, O. & Johansson, P. Dynamic Structure Discovery Applied to the Ion Transport in the Ubiquitous Lithium-ion Battery Electrolyte LP30. *J. Electrochem. Soc* 169, 100540, doi:10.1149/1945-7111/ac96af (2022). Published 27 October 2022.

XV Beyond Li-ion R&D: Metallic Lithium

Rechargeable lithium metal batteries use metallic lithium as the negative electrode. The high specific capacity of lithium (3,860 mAh/g), very low redox potential (-3.040 V versus standard hydrogen electrode) and low density (0.59 g/cm³) make it the ideal anode material for high energy density battery technologies. Rechargeable lithium metal batteries could have a long run time due to the high charge density of lithium.

The rest of this chapter contains detailed reports on the status of the following individual projects.

- Lithium Dendrite Prevention for Lithium Batteries (PNNL)
- Integrated Multiscale Model for Design of Robust 3-D Solid-state Lithium Batteries (LLNL)
- Advanced Polymer Materials for Li-ion (SLAC)
- Anode-Free Lithium Batteries (PNNL).

XV.1 Lithium Dendrite Prevention for Lithium Batteries (PNNL)

Wu Xu, Principal Investigator

Pacific Northwest National Laboratory
902 Battelle Boulevard
Richland, WA 99354
E-mail: wu.xu@pnnl.gov

Tien Duong, DOE Technology Development Manager

U.S. Department of Energy
E-mail: Tien.Duong@ee.doe.gov

Start Date: October 1, 2021

End Date: September 30, 2022

Project Funding (FY22): \$400,000

DOE share: \$400,000

Non-DOE share: \$0

Project Introduction

Lithium (Li) metal is an ideal anode material for next-generation, high-energy-density, rechargeable batteries. However, the application of Li-metal anode has been hindered by concerns for safety and short cycle life. The safety concern regarding Li-metal batteries mainly arises from Li dendrite growth and electrolyte flammability; the short cycle life is largely associated with the high reactivity of Li metal with electrolyte and the Li loss due to formation of solid electrolyte interphase (SEI) and electrochemically inactive or “dead” Li during cycling. Although much progress has been achieved in suppressing Li dendrites and increasing Li Coulombic efficiency (CE) in liquid electrolytes in recent years, the intrinsic problems of Li-metal anode still exist. In FY21, we conducted three research areas: (1) continued to develop nonflammable polymer composite electrolytes (NPCEs) to enable improved safety feature of Li-metal batteries, (2) developed high thermal-stability separators that have high Li CE, suppress Li dendrites, and are stable with high-voltage cathodes, and (3) developed current collectors with three-dimensional (3D) structure for Li-metal anode. In this fiscal year, we continued the evaluation of the effectiveness of separators with high thermal stability in improving the thermal stability of Li-metal batteries, and the development of 3D porous current collectors for Li-metal anode to suppress Li dendrite growth, increasing the utilization of Li metal and consequently extending the cycle life of Li-metal batteries. Meanwhile, we also conducted mechanistic studies on Li deposition behavior to lay groundwork for future improvement of Li-metal batteries. The success of this project will increase safety and cycle life of Li batteries and accelerate market acceptance of EVs, as required by the EV Everywhere Grand Challenge.

Objectives

The objective of this project is to enable Li metal to be used as an effective anode in Li-metal batteries with good thermal stability and safety. The investigation in FY22 focused on the following aspects: (1) continuing evaluation of separators with high thermal stability in Li-metal batteries, (2) developing 3D-structured, lightweight, flexible current collectors for Li-metal anode and Li-metal batteries, and (3) obtaining mechanistic insight on Li-metal deposition/stripping behavior.

Approach

The approach has encompassed the following areas: (1) continue comparative evaluation of separators with high thermal stability in $\text{Li}||\text{LiNi}_{0.6}\text{Mn}_{0.2}\text{Co}_{0.2}\text{O}_2$ (NMC622) cells during cycling and heating process, (2) develop current collectors with 3D structure for Li-metal anode to suppress Li dendrite growth, increase Li utilization, and extend cycle life of Li-metal batteries, and (3) conduct mechanistic studies on Li deposition behavior to lay groundwork for future improvement of Li-metal batteries.

Results

1. Safe dual separator based on high thermal-stability polymers and conventional polyethylene

In FY21, polyimide, a high thermal stable polymer, was chosen to fabricate three-dimensionally ordered macroporous (3DOM) membrane and used as a separator in Li||NMC622 cells. The long-term cycling performances of Li||NMC622 cells using a single layer polyethylene (PE) separator (20 μm thick) and the PE-PI/3DOM dual separator (where the PE was 7 μm thick and the 3DOM PI was 11 μm thick) were compared. The PE-PI/3DOM dual separator based cells exhibited much longer cycle life compared to the single layer PE-based cells. To understand whether the improvement originates from the PI/3DOM, electrospun PI separator (hereinafter PI/electrospun) was fabricated as a reference for PI/3DOM in this fiscal year. The morphologies of 20 μm PE, 7 μm PE, PI/3DOM and PI/electrospun separators by scanning electron microscopy (SEM) are summarized in Figure XV.1.1a-c. It is seen that 3-DOM PI and electrospun PI have significant difference in morphology. Moreover, the 20 μm PE has a different morphology than the 7 μm PE (used in PE-PI dual separators). The 20 μm PE separator exhibits both larger pore size and wider distribution of pore size.

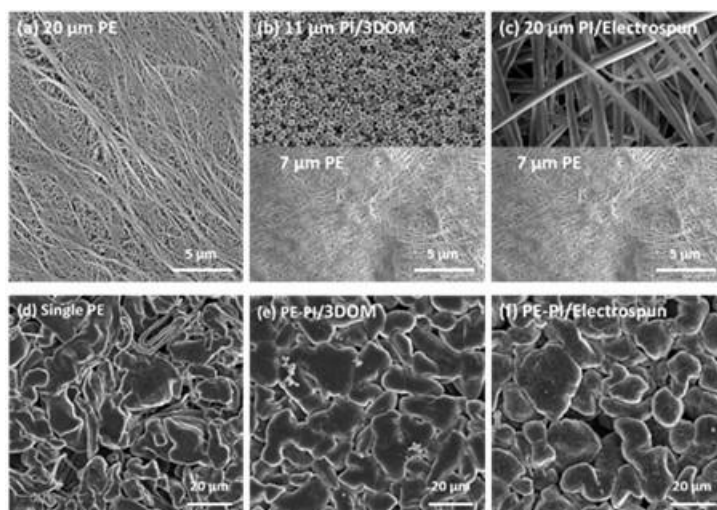


Figure XV.1.1 Morphologies of (a) single layer PE separator (20 μm), (b) 3DOM PI and 7 μm PE and (c) electrospun PI and 7 μm PE; (d), (e), (f) Morphologies of Li deposited on Cu with separators (a), (b) and (c) respectively, in the electrolyte of DME-LHCE (i.e. LiFSI-1.2DME-3TTE) at the current density of 0.4 mA cm^{-2} for 10 h.

When using these separators in Li||copper (Cu) cells to check Li morphologies deposited on Cu substrates (in cells using dual separators, the 7 μm PE was in contact with Cu, and 75 μL electrolyte of Li bis(fluorosulfonyl)imide (LiFSI) in 1,2-dimethoxyethane (DME) and 1,1,2,2-tetrafluoroethyl-2,2,3,3-tetrafluoropropyl ether (TTE) at 1:1.2:3 by mol., abbreviated as DME-LHCE), they lead to different Li deposits. As shown in Figure XV.1.1d, most Li deposits exhibit a granular morphology with sporadic dendrites when the 20 μm PE is used. However, after using the dual separators with 7 μm PE, the dendritic Li is not observed (Figure XV.1.1e,f). Li deposits exhibit similar morphologies in both dual separator cells, despite the PI membranes have significantly different morphologies. It suggests that the morphology of Li deposited on Cu substrate is mainly determined by the separator which is in direct contact with the Cu substrate.

To prove this hypothesis, Li||NMC622 cells using these separators were built where PE was in direct contact with Li electrode in all cells. As shown in Figure XV.1.2a, after substituting the 3DOM PI with electrospun PI in the PE-PI dual separator, the cycling performance of Li||NMC622 cells show nearly no difference, even though the two PI separators have significantly different morphologies. It indicates that the morphology of the PI separator that is in direct contact with positive electrode has minimal influence over the long-term cycling performance. Because the two PE-PI dual separators share the same 7 μm PE separator, they exhibit very similar long-term cycling performance. To further prove the separator that is in direct contact with Li is more influential over the cycling performance, Li||NMC622 cells using PE(7 μm)-PE(20 μm) and PE(20 μm)-PE(7

μm) dual separators were built. As shown in Figure XV.1.2b, after switching the PE separator that is in direct contact with Li, the cycling performance of the Li||NMC622 cells is changed. All evidence infers that the morphology of the separator that is in direct contact with Li plays a dominant role on Li deposition behavior and consequently cycling performance of Li||NMC622 cells.

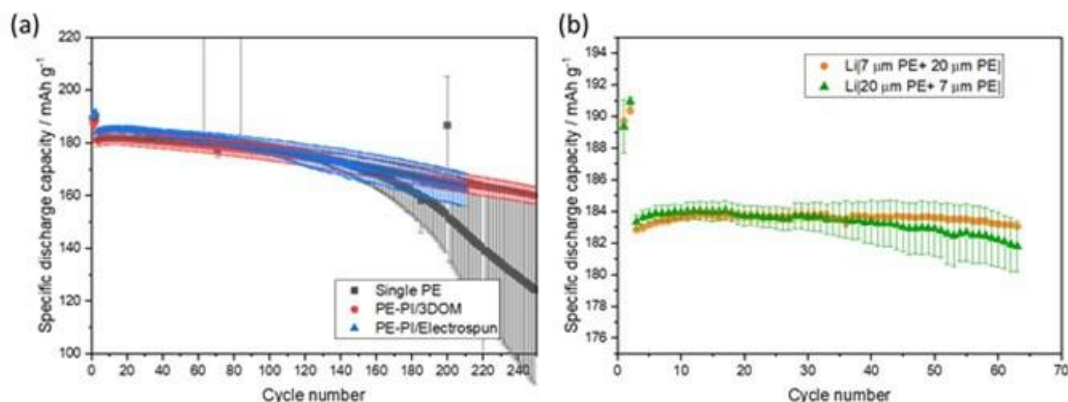


Figure XV.1.2 (a) Room temperature cycling performance of Li||NMC622 coin cells with three separators shown in the adjacent figure. (b) Room temperature cycling performance of Li||NMC622 coin cells with two dual separators. The cells contained 50 μm thick Li, 4.2 mAh cm⁻¹ NMC622, 75 μL DME-LHCE (LiFSI-1.2DME-3TTE), and were cycled between 2.5-4.4 V with C/10 charge and C/5 discharge after three formation cycles at C/10, where 1C=4.2 mA cm⁻².

Besides PI, polycarbonate (PC) and polysulfone (PS) were also chosen to fabricate electrospun membranes. The thermal stability and the cycling performance of dual separators based on PC and PS were evaluated. 20 μm thick PE separator was selected as the reference. As shown in Figure XV.1.3a, PE separator suffers from significant shrinkage after storage at 120°C for 1 min due to its low melting point, which poses a safety hazard to Li metal batteries since the shrinkage during thermal runaway readily leads to the internal shorting and then inevitably results in aggravated heat generation. In comparison, both PC and PS exhibit superior thermal stability (Figure XV.1.3b,c). The preliminary cycling performance of Li||NMC622 cells with PE and PS or PC dual separator and DME-LHCE electrolyte was evaluated and is shown in Figure XV.1.3d. PE-PS dual separator achieved comparable cycling performance to 20 μm single layer PE. In contrast, cells using PE-PC suffered from significant capacity loss, which is mainly due to the poor anodic stability of PC at about 3.7 V vs. Li/Li⁺.

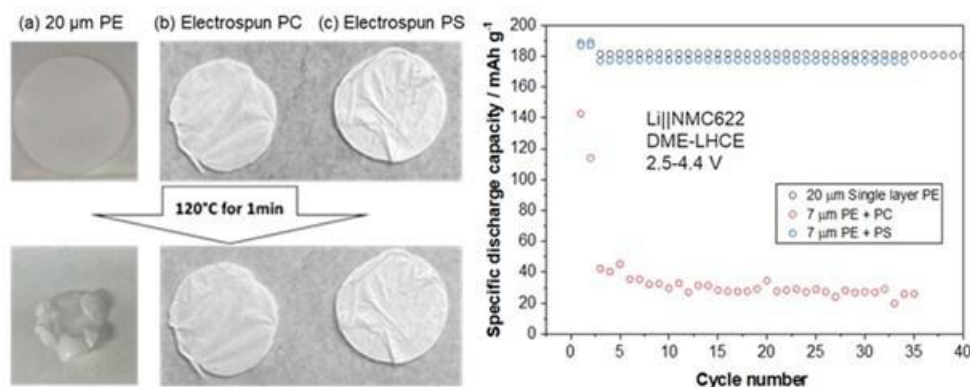


Figure XV.1.3 Thermal stabilities of (a) 20 μm single layer PE, (b) electrospun PC and (c) electrospun PS separators; (d) Cycling performance of Li||NMC622 cells using 20 μm single layer PE, 7 μm PE+PC and 7 μm PE+PS dual separators with DME-LHCE electrolyte (LiFSI-1.2DME-3TTE).

To verify the safety enhancement of PE-PI dual separator, differential scanning calorimeter (DSC) measurements on the Li||NMC622 micro cells comprising a single layer PE or a PE-PI with DME-LHCE

electrolyte (LiFSI-1.2DME-3TTE) were performed. Figure XV.1.4 shows the DSC curves of micro cells containing the studied separators. Both cells show two small endothermic peaks, one at $\sim 95^{\circ}\text{C}$ (for the evaporation of TTE diluent) and another at $\sim 128^{\circ}\text{C}$ (for the melting of PE separator). Starting at $\sim 130^{\circ}\text{C}$, both cells exhibit exothermic behavior, probably due to the reactions of electrodes and electrolyte. Counterintuitively, there is no serious exothermal reaction in the cell using the single layer $20\text{ }\mu\text{m}$ PE separator. The possible reason might be the lack of mechanical pressure between NMC622 and Li. Even after the PE separator shrank or melted at 128°C , the cell shorting between Li and NMC622 was not observed in the micro cell for DSC measurement. However, such contact is almost inevitable in real cells. Mechanical pressure will be introduced into the micro cells to simulate the environment of real Li metal batteries as part of future investigation.

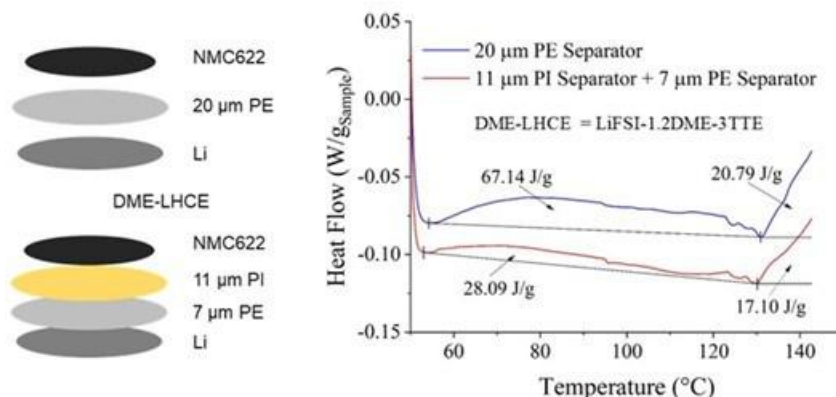


Figure XV.1.4 DSC curves of Li || NMC622 cells using a single layer $20\text{ }\mu\text{m}$ PE separator and $7\text{ }\mu\text{m}$ PE+PI separator. (NMC622 was charged to 4.4 V).

2. Development of 3D current collectors

A 3D current collector has great potential to suppress Li dendrite growth due to its increased surface area and pore volume that can improve Li utilization therefore increase the energy density of Li-metal batteries. However, the mainstream 3D current collectors are carbonaceous materials, which suffer from poor wettability with metallic Li and poor flexibility. To address these issues, a 3D current collector based on polymer fibers was designed and synthesized. Electroless plating was selected to transform the insulating polymer fibers to electronically conductive matrix.

Electrospun PI was selected as the precursor because of its high thermal stability. The Cu coated PI (Cu@PI) current collector was fabricated via electroless plating of PI porous membrane in an appropriate electroless plating solution containing Cu ions. The electroless plating conditions were carefully studied. The obtained composite materials were characterized with SEM. As shown in Figure XV.1.5a, the pristine electrospun PI fibers exhibit a smooth surface. Figure XV.1.5b exhibits the morphology of Cu@PI 3D porous membrane after electroless plating. It can be observed that a smooth layer of elemental Cu is covered on PI fiber surface. It is also worth noting that the Cu@PI sample was not sputtered with any electronically conductive material prior to the SEM characterization. Furthermore, the energy-dispersive X-ray spectroscopy (EDS) images in Figure XV.1.5c demonstrate the uniform coverage of Cu film on the surface of PI fibers, indicating that a porous, lightweight, and conductive current collector was successfully prepared. However, certain strands of the fiber are not fully covered with Cu as the C signals can still be observed, indicating that the synthesis process needs to be further optimized.

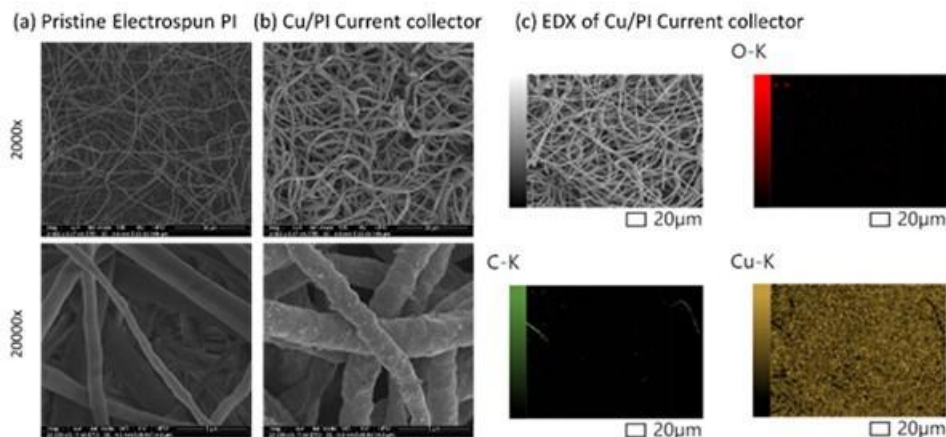


Figure XV.1.5 (a, b) SEM images showing morphologies of (a) pristine PI fiber and (b) polymeric 3D current collector (Cu@PI membrane). (c) EDS images showing Cu distribution of Cu@PI membrane.

The process of synthesizing 3D current collector of Cu@PI fibers was optimized. The SEM and EDS images, shown in Figure XV.1.6, demonstrate that the Cu is fully and uniformly coated on the PI fibers not only on the surface (Figure XV.1.6a) but also the inside (Figure XV.1.6b) of the PI membrane after the synthesis optimization. The EDS mapping images also indicate that the optimized synthesis process can provide a conductive 3D current collector. A 4 mAh cm^{-2} of Li was deposited on both 2D Cu foil (bare Cu) and the Cu@PI in DME-LHCE electrolyte (LiFSI-1.2DME-3TTE) at a current density of 0.4 mA cm^{-2} and the morphologies are shown in Figure XV.1.7. On the top surface, the Li deposits on bare Cu (Figure XV.1.7a) and Cu@PI (Figure XV.1.7b) show very similar morphologies with the same Li particle size. However, the cross-sectional images exhibit distinct morphologies (Figure XV.1.7c and d). The Li deposited on bare Cu is more porous and less dense than that deposited on Cu@PI. The thicknesses of Li deposited on Cu and Cu@PI are $\sim 20 \text{ μm}$ and $\sim 15 \text{ μm}$, respectively. This suggests that the Li deposited on Cu@PI may have less surface area, less contact and side reactions with liquid electrolyte, thus leading to longer cycling stability.

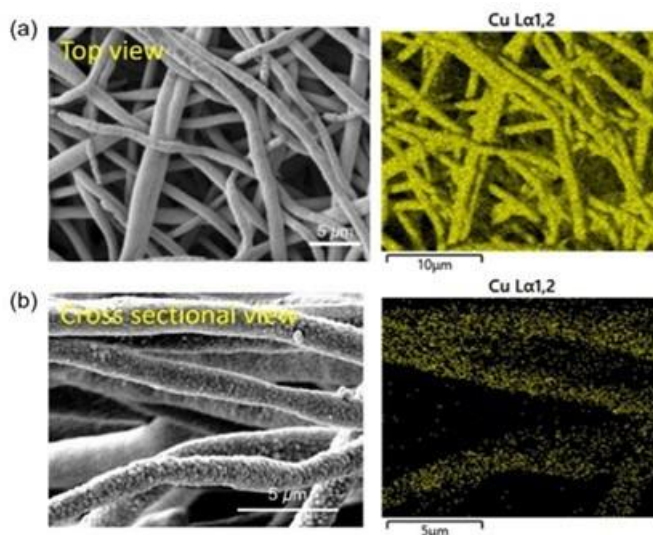


Figure XV.1.6 SEM images and EDS mapping images for Cu distribution on Cu@PI mat of (a) top-view and (b) their cross-sectional views.

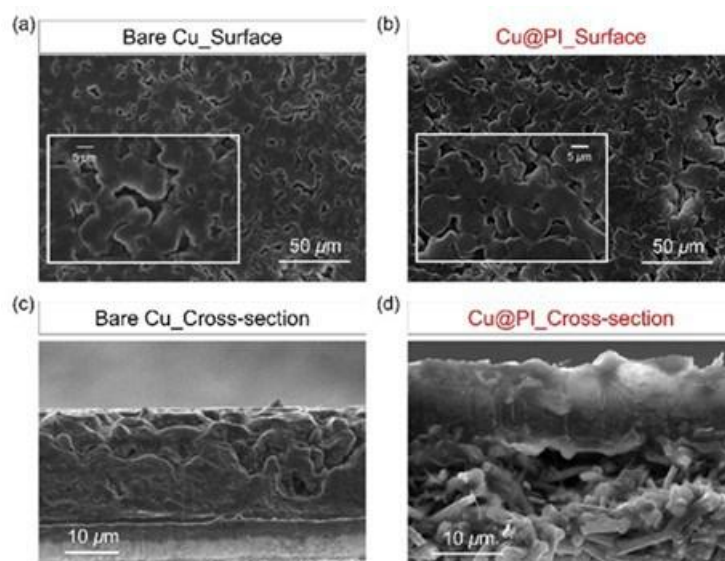


Figure XV.1.7 SEM images of deposited Li morphologies on (a, c) bare Cu foil and (b, d) Cu@PI mat.

To investigate the effect of Cu@PI 3D current collector on Li metal battery performance, Li||NMC622 coin cells were assembled and tested. Each cell contains 50 μm Li metal, 4 mAh cm^{-2} NMC622, 20 μm PE separator, and 75 μL DME-LHCE electrolyte (LiFSI-1.2DME-3TTE). The cycling performance of the Li||NMC622 cells was conducted at a current density of C/10 for charging and C/3 for discharging under a voltage range from 2.8 to 4.4 V (vs. Li/Li⁺) after two formation cycles at C/10, where 1C = 4.0 mA cm^{-2} . The Li||NMC622 cell with Cu@PI current collector has very similar performance to the Li||NMC622 cell with the bare Cu foil up to 30 cycles (Figure XV.1.8). Longer cycling stability and other cell performance are currently measured and will be updated in the future report.

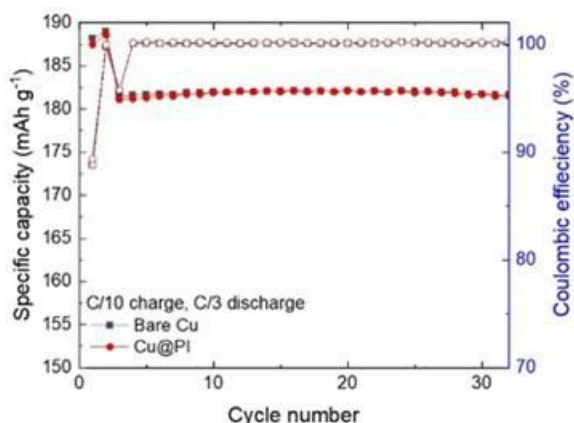


Figure XV.1.8 Room temperature cycling performance of Li || NMC622 coin cells using Cu@PI and bare Cu current collectors with DME-LHCE electrolyte (LiFSI-1.2DME-3TTE).

3. Investigation on SEI formation using reflection interference microscope

The quality of SEI dictates the performances of Li-metal batteries. We collaborated with Prof. Xiaonan Shan and Guangxia Feng at University of Houston to study the SEI formation behavior with *operando* reflection interference microscope (RIM) (Figure XV.1.9a). Two electrolytes, 1 mol L⁻¹ LiPF₆ in propylene carbonate (PC) with and without 50 ppm water (H₂O) were employed to study the effect of water additive on the SEI formation process. RIM exhibits extremely high sensitivity towards the SEI formation process. The

thicknesses of LiF-rich inner layer and organic-rich outer layer can be correlated to the intensities of the RIM signals (Figure XV.1.9c-e). It is revealed that the presence of trace amount of water (50 ppm) in the electrolyte induces a thicker and higher quality LiF-rich layer at the inner SEI and a much thinner organic-rich layer in the outer SEI, which leads to less electrolyte consumption, and more uniform Li nucleation on the electrode surface.

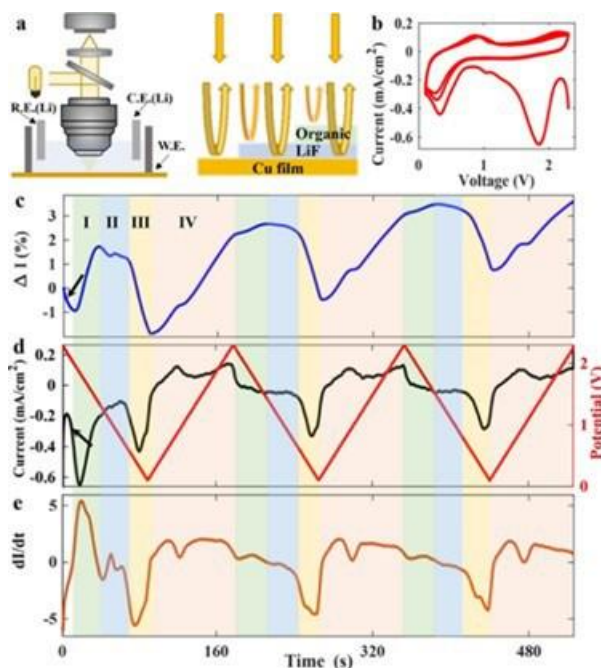


Figure XV.1.9 (a) Schematic diagram of using RIM to image the SEI formation dynamics. (b) Cyclic voltammetry (CV) curves of the first three cycles in 1 M LiPF₆/PC with 50 ppm H₂O as additive. (c) The optical reflection signal along with three CV cycles on Cu electrode in 1 M LiPF₆/PC with 50 ppm H₂O. (d) The corresponding current density (black curve and left axis) and voltage (red curve and right axis) in the first three cycles of CV scans. (e) The derivative of optical signals (the curve in c).

Conclusions

- Dual separators with a high thermal-stability porous membrane like PI and a conventional polyolefin separator like PE (where PE directly contacting Li metal) greatly enhance the long-term cycling stability of Li metal batteries with Ni-rich cathodes compared to the single PE separator.
- The morphology of the separator that is in direct contact with Li plays a dominant role on Li deposition behavior, and consequently cycling performance of Li||NMC622 cells.
- A 3D current collector based on Cu-coated PI fibers (i.e. Cu@PI) with full and uniform Cu coating on PI surface was successfully fabricated. The Cu@PI matrix leads to denser and thinner Li deposition than the regular Cu foil.
- RIM was successfully established to investigate the SEI formation and evolution processes on Cu and Li surfaces under *operando* condition. The correlation between the quality of the LiF-rich inner layer in the SEI and the thickness of the organic-rich outer layer has been clearly observed. The quality of the SEI also affect Li nucleation on the electrode surface.

Key Publications

1. G. Feng, Y. Shi, H. Jia, S. Risal, X. Yang, Z. Fan, W. Xu*, X. Shan*, “Imaging Lithium Nucleation Dynamics and Localized Overpotential Using Operando Reflection Interference Microscope”, *Advanced Sciences*, 2022, under review.
2. G. Feng[†], H. Jia[†], Y. Shi[†], X. Yang, Y. Liang, M. H. Engelhard, Y. Zhang, C. Yang, K. Xu*, Y. Yao*, W. Xu*, X. Shan*, “Imaging Solid-Electrolyte-Interphase Dynamics Using Operando Reflection Interference Microscopy”, *Nature Nanotechnology*, 2022, under revision after review.

3. H. Jia, and W. Xu*, “Electrolytes for High-Voltage Lithium Batteries”, *Trends in Chemistry*, 2022, **4** (7), 627-642. DOI:10.1016/j.trechm.2022.04.010. (Invited)
4. H. Jia, X. Cao, J.-G. Zhang, W. Xu*, “Electrolytes for Lithium-Ion and Lithium Metal Batteries”, *Encyclopedia of Energy Storage*, 2022, **4**, 108-122. DOI:[10.1016/B978-0-12-819723-3.00106-2](https://doi.org/10.1016/B978-0-12-819723-3.00106-2). (Invited)

Acknowledgements

Key contributors include Ji-Guang (Jason) Zhang, Hao Jia, Ju-Myung Kim, Hyung-Seok Lim, Chao Zeng, Mark H. Engelhard. Collaborators include (1) Chongmin Wang and Yaobin Xu of PNNL on characterization by TEM/SEM; (2) Marc Weber of Washington State University on nano-CT measurements; (3) Alex Bates, Yuliya Preger and Loraine Torres-Castro of Sandia National Laboratory on DSC microcell tests; (4) Yuepeng Zhang and Ashley Simmons of Argonne National Laboratory on electrospinning polyimide, polysulfone, and polycarbonate porous membranes; and (5) Xiaonan Shan and Guangxia Feng of University of Houston on studying SEI formation using *operando* reflection interference microscope.

XV.2 Integrated Multiscale Model for Design of Robust 3-D Solid-state Lithium Batteries (LLNL)

Brandon C. Wood, Principal Investigator

Lawrence Livermore National Laboratory
7000 East Avenue
Livermore, CA 94550
E-mail: wood37@llnl.gov

Simon Thompson, DOE Technology Development Manager

U.S. Department of Energy
E-mail: Simon.Thompson@ee.doe.gov

Start Date: October 1, 2021

End Date: September 30, 2024

Project Funding(FY22): \$375,000

DOE share: \$375,000

Non-DOE share: \$0

Project Introduction

Interfaces in solid-state batteries present critical impediments for both performance and cyclability. Particularly challenging is the cathode-electrolyte interface, which is often characterized by formation of unwanted chemical products and interphases, as well as the appearance of voids, gaps, or cracks that can accumulate during cycling. Chemical evolution and mechanical behavior at cathode-electrolyte interfaces are intrinsically linked and intimately connected to cycling behavior of solid-state batteries, as stresses accumulate within the solid electrolyte and in the cathode-electrolyte composite matrix. These interfacial stresses and reaction intermediates in turn affect desired transport properties, accelerate further chemical evolution, and promote mechanical failure. To advance and accelerate the development of solid-state batteries with high cyclability and lifetime, it is critical to understand how these degradation and failure modes are connected to specific interfacial features. Such understanding can aid in the development of more accurate and predictive lifetime models, as well as motivate changes in composition or processing. This project develops and applies advanced multiscale modeling approaches to assesses how chemical and microstructural evolution during cycling impact solid mechanics and transport at the cathode-electrolyte interface in solid-state batteries, with a view towards predicting conditions and materials features that ultimately lead to failure via fracture or catastrophic performance loss.

Objectives

The goal of the project is the development and application of multiscale, multiphysics models that connect composition, microstructure, and architecture to chemomechanical integrity at interfaces in 3-D solid-state batteries. The focus is on cathode-electrolyte interfaces and internal electrolyte interfaces in ceramic ($\text{Li}_{1-x}\text{La}_x\text{ZrO}_{12}$ [LLZO]) solid electrolytes, as well as other electrolyte formulations including halides (Li_3InCl_6) and/or inorganic/organic composites. The models integrate multiple computational methods from the atomistic to continuum scales, informed and validated through collaborations with complementary experimental efforts. The project addresses three objectives:

1. Develop multiphysics, multiscale chemomechanics models of cathode-electrolyte interfaces in solid-state batteries;
2. Assess interface- and microstructure-induced mechanical failure thresholds and high impedance;
3. Simulate chemomechanical evolution under battery operating conditions.

Approach

The team's approach integrates diverse computational methods—including density functional theory (DFT) calculations, molecular dynamics, machine learning, micromechanical modeling, and phase-field models—to predict the chemomechanical properties of cathode-electrolyte interfaces and internal grain boundaries at

different charge/discharge states. DFT and *ab initio* molecular dynamics are used to simulate interfacial chemistry and mechanical response with high accuracy, as well as to train interatomic potentials using machine learning methods for accessing much longer simulation times. These data parameterize micromechanics models and microstructure-aware continuum simulations, which establish microstructure-property relationships for ion transport and fracture. Phase-field simulations of cathode evolution during cycling provide a connection to battery operation. The integrated simulation techniques are also used to predict chemomechanical hotspots that are likely failure initiation zones under different operation conditions.

Results

Atomistic simulations of grain boundaries and interfaces in ceramic solid electrolytes

Although first-principles, DFT-based approaches provide excellent accuracy, their computational cost limits application to relatively simple systems and short times. This is problematic for complex interfaces with high structural and compositional disorder. Recognizing this limitation, the team prioritized development of a force field for LLZO based on machine learning (MLFF), trained on extensive DFT and *ab initio* molecular dynamics (AIMD) simulation data.¹ This MLFF can enable molecular dynamics simulations (MLMD) that are hundreds or thousands of times faster than fully first-principles approaches, while retaining much of their accuracy. The team carefully selected training data and a training procedure that would specifically render the MLFF suitable for interfacial and disordered models, rather than ideal crystals. MLMD correctly reproduced the vibrational and transport properties of AIMD on model systems. As further validation, MLMD was also able to capture LLZO thermal phase transitions, despite not being explicitly trained to do so. Figure XV.2.1a shows that the solid-solid transition from tetragonal to cubic LLZO is predicted at 850 K, close to the experimental observation of 923 K. The melting transition is also correctly captured.

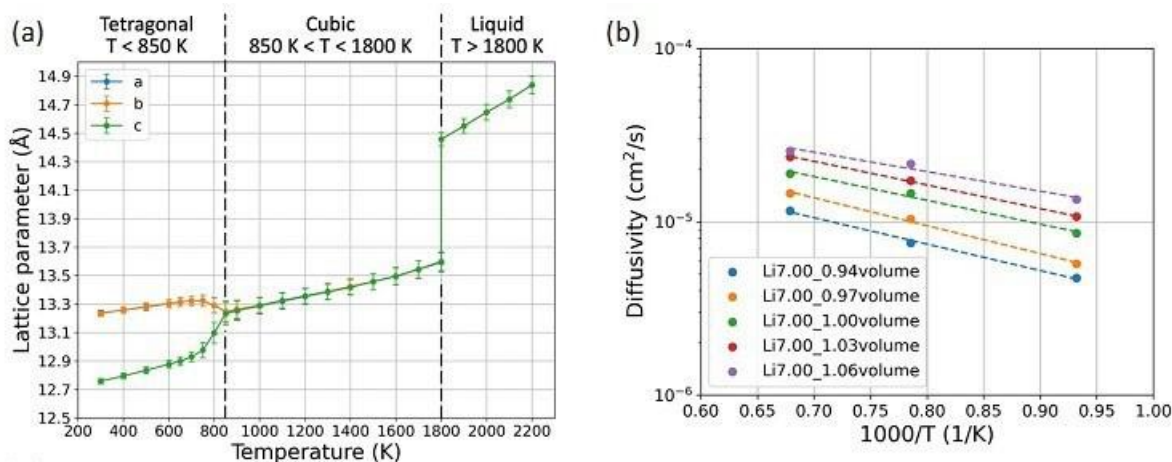


Figure XV.2.1 Temperature-dependent changes in (a) lattice parameters and (b) Li⁺ diffusivity under hydrostatic pressure, computed from 1536-atom MLMD of LLZO. Adapted from Ref. [1].

The team then applied MLMD to compute Li-ion diffusivities in response to mechanical stress/strain fields. They showed that the diffusivity tracks with hydrostatic strain (Figure XV.2.1b), and that uniaxial compressive strain has a particularly significant effect along the strain axis. This suggests that local regions under compressive strain would introduce significant impedance. The team plans to perform additional simulations of Li-ion diffusivity as a function of strain/stress, and the results will be used to parameterize a mesoscale model for evaluating the impacts of stress in complex polycrystalline LLZO and in LLZO/cathode composite architectures. The team also began directly simulating LLZO grain boundaries (GBs) using MLMD. They varied the tilt axis and further introduced local structural perturbations. It was found that the structural and chemical stability of GBs are highly sensitive to the local symmetry and atomic arrangement. The team plans to use these lower-angle GB models to augment fully disordered models, which are more representative of

high-angle GBs. Eventually, the transport and mechanical properties of these GBs will be incorporated into a microstructure-aware continuum model to assess larger-scale impacts under cycling conditions.

The team also probed the effects of chemical doping on the properties of LLZO. One avenue of study involved predicting the effects of chemical doping on mechanical deformability. This has implications not only for stress fracturing propensity, but also for processability, given that deformability is related to ease of sintering. A suite of computable metrics was devised as a proxy for plastic deformability and premelting, based on static, dynamic, and local structural variables.² The team suggested that these metrics, which were applied to Al-, Ba-, and Ta-doped LLZO as model systems, can be useful for quickly deriving trends, which can then be calibrated for use in larger-scale models. As a companion effort, the team also began development of an MLFF for doped systems by adding structural data across a wide range of temperatures. This will enable future simulations of GB and interface segregation effects on transport and mechanics, which the team hypothesizes could be closely related to interface-initiated failure mechanisms.

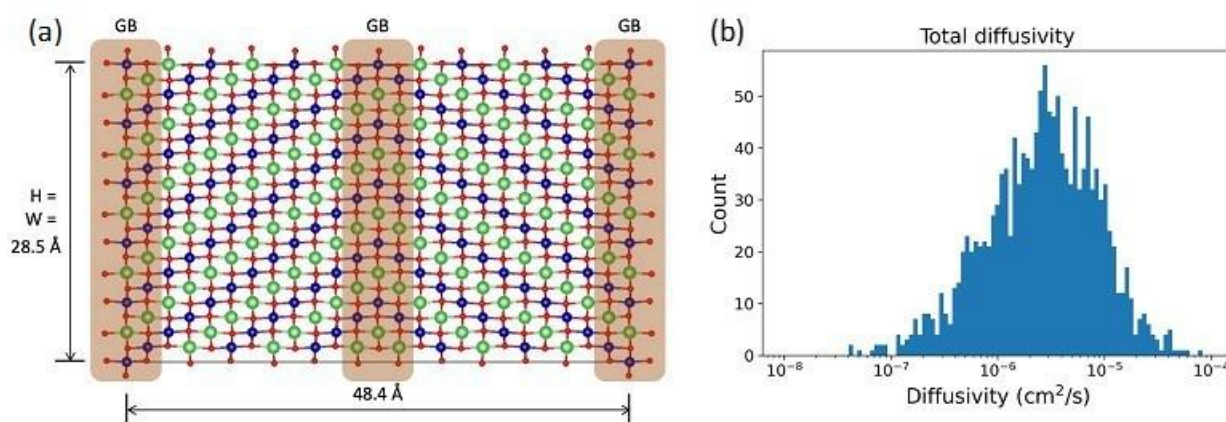


Figure XV.2.2 (a) $\Sigma 2(-1104)/[11-20]$ Model of a tilt grain boundary in LCO and (d) the histogram of diffusivities of individual Li⁺ ions in the grain boundary region from MLMD.

In preparation for simulations of the full cathode-electrolyte interface, the team also pursued development of an MLFF for an Li_xCoO_2 (LCO) cathode. The early version of this MLFF was used to compute Li-ion diffusivity at LCO GBs, reproducing expected dynamic and structural behavior from AIMD. The team applied this MLFF to analyze Li⁺ transport at eight different GB structures in LCO. Figure XV.2.2 shows an example LCO $\Sigma 2(-1104)/[11-20]$ tilt GB model with 4800 atoms. MLMD was performed to track Li atoms that stayed at the GB regions, evidencing that structural disorder at the interface generates a range of diffusivities. This range can be incorporated into mesoscale models and propagated across scales to determine likely effects on impedance, including in the presence of cycle-induced stresses.

Mesoscale modeling of microstructure effects on chemomechanical properties

As a first step towards incorporating the atomistic results into microstructural models, the team developed a new workflow that can quickly and efficiently reproduce digital representations of experimental microstructures, including electrolyte-cathode particle mixtures. The team previously explored the use of a phase-field grain-growth model; however, this approach has limitations in controlling topological features.³ The new workflow has three unique advantages: 1) it allows for generating porous microstructures consisting of two or more phases; 2) it enables better control over the microstructural topology; and 3) it is dramatically more efficient in generating 3D particulate microstructures (typically under one minute on a desktop computer, replacing several hours on a supercomputer). The new workflow first uses open-source software solutions to generate packings of irregular particles with prescribed size distributions. The data is then voxelized and labeled according to individual grains of each phase. Finally, this data is fed into the LLNL *MesoMicro* code, which further refines the microstructure within the phase-field approach. The *MesoMicro* code is then used to compute the effective ionic transport and elastomechanical response of the full microstructure.

The team applied the workflow to reproduce realistic microstructures of polycrystalline LLZO, which were then used as an initial basis for exploring microstructure-dependent chemomechanical effects. Figure XV.2.3a shows the predicted elastomechanical response of polycrystalline LLZO, parameterized using atomistic MLMD. To quantify the effect of the disordered GBs, comparative simulations were performed with and without GBs. It was found that the bulk modulus can vary by as much as 20 GPa due to the presence of GBs. The team also scanned the results to identify mechanical stress hotspots based on the computed local von Mises stress distributions within polycrystalline LLZO, highlighting local mechanical hotspots that exceed a critical stress threshold ($\sigma_{VM} > 1.0$ GPa; Figure XV.2.3b). These hotspots are mostly concentrated on the disordered GBs. Considering the elastic response with and without GBs (Figure XV.2.3b) shows that GBs relax the average stress and lead to a wider statistical distribution of local stresses. The increase in hotspot fraction with strain is also less sensitive when GBs are considered, again suggesting their role in tempering stress buildup. This new demonstration of hotspot prediction represents an important advance for predicting the likelihood of mechanical failure due to fracture or delamination, which are connected to the persistence and prevalence of such hotspots.

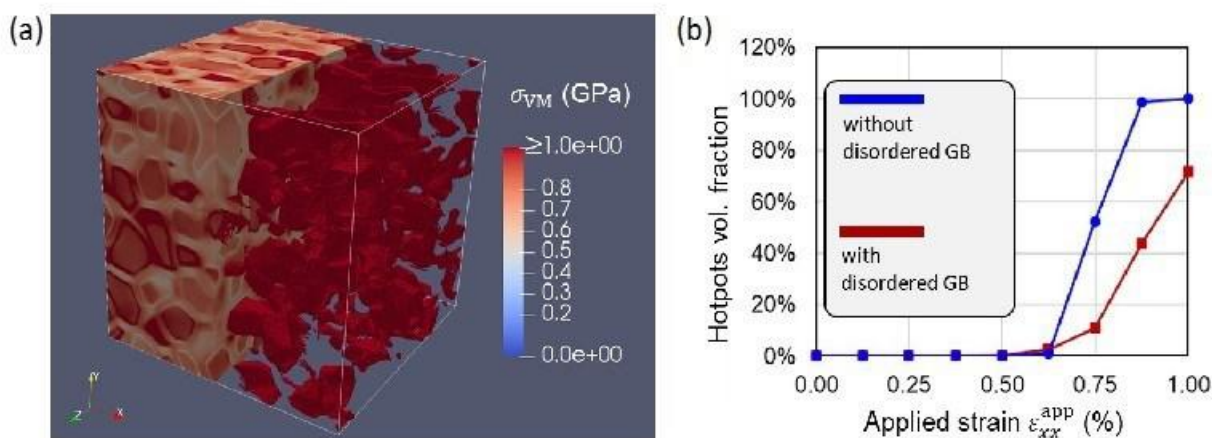


Figure XV.2.3 (a) Calculated von Mises stress distribution within a generated 3D polycrystalline microstructure of LLZO. Half of the structure shows stress hotspots as isosurfaces exceeding a threshold of 1.0 GPa. (b) Volume fraction of stress hotspots as a function of applied longitudinal strain.

The team's mesoscale models were also applied to a composite electrolyte material to determine effects on transport and mechanics. The ability to capture properties of a two-material system is key, as it will be required for cathode-electrolyte composites. The team collaborated with Dr. Ye (LLNL), who has been investigating the transport and mechanical properties of 3-D printed polymer/LLZO hybrid systems. Digital microstructure representations were reproduced from the experimental imaging, and LLNL's *MesoMicro* code was applied to compute the effective mechanical and transport properties of the composite with two different levels of porosity (Figure XV.2.4). For the more porous structure, the electrical current tends to concentrate within channels provided by the more conductive LLZO ceramic (Figure XV.2.4c), whereas the current density is more uniformly distributed in the dense structure. In addition, the more porous structure exhibits local stress hotspots between LLZO particles, while the dense structure results in stress hotspots concentrated at the roughened interfacial regions between the polymer and LLZO (Figure XV.2.4d). These results suggest that connectivity of LLZO particles is critical for enhanced Li ion conduction, and that mechanical failure is most likely to occur at the porous area of the LLZO layer at higher porosities and at LLZO/polymer interfacial regions for the denser structures.

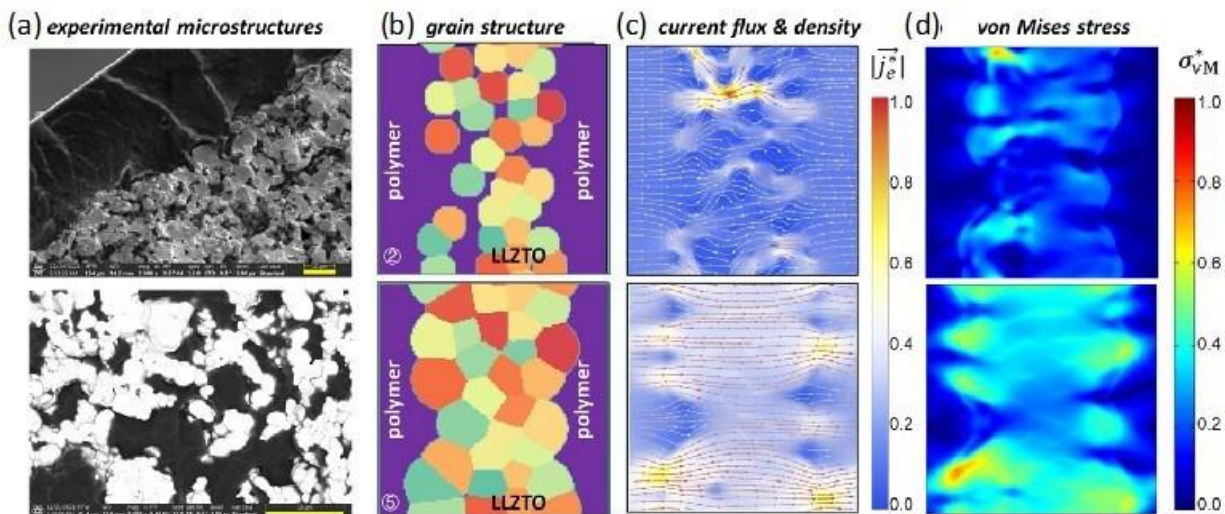


Figure XV.2.4 (a) Scanning electron microscopy of a polymer/LLZO/polymer system at the polymer/LLZO interface (top) and inside the porous bulk LLZO (bottom); scale bars are 10 μm . (b-d) Mesoscale modeling of (b) selected grain structures, (c) normalized electric current flux and density distributions, and (f) normalized von Mises stress distributions for two different representative microstructures (top: porous; bottom: dense).

Conclusions

The team's progress this year centered on two primary activities. First, at the atomistic scale, quantum simulations (DFT and AIMD) were used to train a machine learning interatomic force field that was specifically designed to tackle homogeneous and heterogeneous interfaces in LLZO and LCO. The team used this force field, which retains quantum accuracy with hundreds of times higher efficiency, to perform large-scale molecular dynamics. Results were analyzed to assess the effects of atomic structure and composition on local ion mobility, as well as the effects of stresses induced by volume changes during cycling or processing. They also developed a series of atomistic descriptors, largely derived from the dynamics, for predicting trends in processing temperatures and conditions for ceramic electrolytes. Second, at the microstructural scale, the atomistic simulations were used to parameterize continuum simulations for analyzing the effects of microstructure on mechanics and transport. The team used this multiscale modeling framework to explore the formation of stress and current hotspots—connected to chemomechanical failure—and their connection to grain boundaries and porosity. They also began examining multi-phase composites using both inorganic and organic electrolyte materials. Successful demonstration of this framework ensures it can also be applied to cathode/electrolyte composites, which the team plans to pursue next.

Key Publications

1. Dive, A., K. Kim, S. Kang, L.F. Wan, and B.C. Wood, "First-principles evaluation of dopant impact on structural deformability and processability of $\text{Li}_7\text{La}_3\text{Zr}_2\text{O}_{12}$." *Manuscript in review* (2022).
2. Yu, S., K. Kim, B.C. Wood, H.-G. Jung, and K.Y. Chung, "Structural design strategies for superionic sodium halide solid electrolytes." *Manuscript in review* (2022).
3. Ren, Y., T. Danner, A. Moy, M. Finsterbusch, T. Hamann, J. Dippell, T. Fuchs, M. Müller, R. Hoft, A. Weber, L.A. Curtiss, P. Zapol, M. Klenk, A.T. Ngo, P. Barai, B.C. Wood, R. Shi, L.F. Wan, T.W. Heo, M. Engels, J. Nanda, F.H. Richter, A. Latz, V. Srinivasan, J. Janek, J. Sakamoto, E.D. Wachsman, and D. Fattakhova-Rohlfing, "Oxide-based solid-state batteries: A perspective on composite cathode architecture," *Adv. Energy Mater.*, *in press* (2022).
4. Kim, K., A. Dive, A. Grieder, N. Adelstein, S. Kang, L.F. Wan, and B.C. Wood, "Flexible machine-learning interatomic potential for simulating structural disordering behavior of $\text{Li}_7\text{La}_3\text{Zr}_2\text{O}_{12}$ solid electrolytes," *J. Chem. Phys.* **156** (2022): 221101.

References

1. Kim, K., A. Dive, A. Grieder, N. Adelstein, S. Kang, L.F. Wan, and B.C. Wood, “Flexible machine-learning interatomic potential for simulating structural disordering behavior of $\text{Li}_7\text{La}_3\text{Zr}_2\text{O}_{12}$ solid electrolytes,” *J. Chem. Phys.* **156** (2022): 221101.
2. Dive, A., K. Kim, S. Kang, L.F. Wan, and B.C. Wood, “First-principles evaluation of dopant impact on structural deformability and processability of $\text{Li}_7\text{La}_3\text{Zr}_2\text{O}_{12}$.” *Manuscript in review* (2022).
3. Heo, T. W., A. Grieder, B. Wang, M. Wood, S.A. Akhade, L.F. Wan, L.-Q. Chen, N. Adelstein, and B.C. Wood, “Microstructural impacts on ionic conductivity of oxide solid electrolytes from a combined atomistic-mesoscale approach.” *npj Comp. Mater.* **7** (2021): 214.

Acknowledgements

This work was performed under the auspices of the U.S. Department of Energy by Lawrence Livermore National Laboratory under contract DE-AC52-07NA27344. The team gratefully acknowledges collaborations with Professor Nicole Adelstein (San Francisco State University) for modeling transport through disordered regions, Dr. Jianchao Ye (LLNL) for experimental results on LLZO/polymer composites, and Dr. Timo Danner (DLR, Germany) and the U.S.-Germany partnership on solid-state battery research for understanding impacts of microstructure.

XV.3 Advanced Polymer Materials for Li-ion (SLAC)

Zhenan Bao, Principal Investigator

Stanford University
Department of Chemical Engineering, Stanford University
Stanford, CA 94305
E-mail: zbao@stanford.edu

Yi Cui, Co-Principal Investigator

Stanford University
Department of Chemical Engineering, Stanford University
Stanford, CA 94305
E-mail: yicui@stanford.edu

Tien Duong, DOE Technology Development Manager

U.S. Department of Energy
E-mail: Tien.Duong@ee.doe.gov

Start Date: October 1, 2021

End Date: September 30, 2022

Project Funding (FY22): \$500,000

DOE share: \$500,000

Non-DOE share: \$0

Project Introduction

Batteries with lithium (Li) metal anode show great potential as the next generation energy storage devices for their high theoretical energy density (3860 kw kg^{-1}). However, lithium metal batteries (LMB) suffer from quick capacity fading and short cycle life. This is derived from the unstable interface between lithium metal and the electrolyte.

Specifically, the solid electrolyte interphase (SEI) formed when Li metal is in contact with the electrolyte is fragile and cracks during cycling. This inhomogeneity is further amplified throughout battery cycling, resulting in whisker-shaped deposited lithium and capacity fading.

Applying a polymer layer to the Li anode stabilizes this interface and promotes long-term operation of LMB. Polymers are desirable for this application due to their solution processability, programmable mechanical property, and tunable chemical composition. This polymer layer has both physical and chemical interactions with the underlying Li metal.

Physically, a viscoelastic polymer layer provides mechanical suppression to the growing lithium during the deposition process, which promotes homogeneous deposition of lithium while maintaining uniform coverage of the electrode during. By introducing moieties in the polymers that selectively interact with Li^+ or altering the Li^+ solvation environment, one can promote the transport of Li^+ at the interface.

Chemically, a polymer or polymer-based composite layer at the interface reacts with the underlying Li metal and produces a robust interfacial layer. This process generally aims to produce a “salt derived SEI”, which is found to promote stable operation of the Li anode, when compared with the alternative “solvent derived SEI”. However, to sustain this favorable SEI formation reaction, one relies on the limited reservoir of reaction materials in the polymer layer.

Here, we propose to sustain the salt derived SEI formation through physical interaction. Specifically, selective transport of salt over solvent is achieved at the electrode-electrolyte interface with a polymer layer.

We architected both salt affinitive and solvent phobic moieties in the polymer side chain to improve the selectivity of the material (Figure XV.3.1).

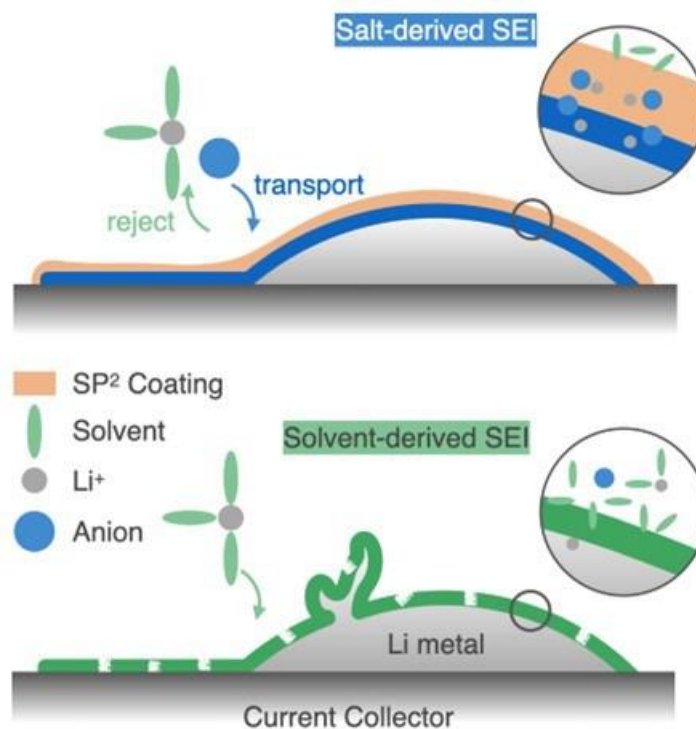


Figure XV.3.1 Illustration of how a salt philic solvent phobic (SP²) polymer coating on Li metal anode can induce the formation of desirable salt-derived solid electrolyte interphase (SEI).

Objectives

This project will develop new polymer materials for batteries. The team will develop polymer coatings with specific mechanical properties that can accommodate the volume expansion and contraction of the Li-metal anode associated with deposition and stripping (charging and discharging).

Approach

The project uses soft polymer coatings with dynamic crosslinking to give the resulting polymers liquid-like rheological properties and stretchable and self-healing properties. In previous work, the project has shown that such coatings resulted in uniform deposition/stripping of lithium metal and improved cycling stability of Li-metal electrodes. To understand the design rules for effective polymer coatings, the team chose a few representative polymers to systematically understand structure property relationships. Here, the team investigates the correlation between surface energy of the polymer and exchange current for lithium deposition.

Results Siloxane-based polymer has shown ability to improve the cycling performance of lithium metal anode. Beyond its relative chemical stability with lithium metal anode, the siloxane-based polymer chain is flexible and has a low glass transition point ($\sim -150^{\circ}\text{C}$). The fluid nature of the siloxane backbone offered us freedom on altering the chemical composition of the polymer via side chain engineering while maintaining the viscoelastic mechanical property of the polymer. Past studies have shown that a flowable interface maintains uniform coverage of Li metal anode during cycling, and is more beneficial than a rigid interface, which can crack and form pin holes. We selected four side chains to represent commonly used polymer chemistry in lithium metal battery: glyme, for the application of poly (ethylene oxide) in solid electrolyte; PyTFSI, for electrochemically stable ionic liquid based salt-solvation moieties; perfluorinated chain, for polyvinylidene fluoride (PVDF) or poly(vinylidene fluoride-co-hexafluoropropylene) (PVDF-HFP) based polymer in gel electrolyte and coating application; alkyl chain, for widely-used polyethylene chemistry in separator.

We first examined the salt affinities of these polymer side chains with DFT (density function theory) calculation. Figure XV.3.2.A showed the calculated interaction energy between these side chains and lithium cation. Glyme was known to form coordinated structures with lithium cations²⁸, which explains the high interaction energy ($356.6 \text{ kJ mol}^{-1}$). The alkyl chain has low interaction energy with Li^+ ($131.2 \text{ kJ mol}^{-1}$) due to their non-polar structure. The oxygen and fluorine on the perfluorinated chain forms coordinated structures with Li^+ with moderate interaction energy ($223.2 \text{ kJ mol}^{-1}$). The PyTFSI ionic liquid side chain also has high interaction energy ($355.4 \text{ kJ mol}^{-1}$) with Li^+ , attributed to the ionic interactions between the Li^+ and the TFSI⁻. The interaction energy of Li^+ with the glyme or PyTFSI side chains are nearly half the energy between Li^+ and anion (e.g., Li^+ -TFSI⁻, $582.7 \text{ kJ mol}^{-1}$)²⁹, indicating that these two side chains have limited ability to disassociate Li^+ -anion pairing, and their affinity to Li^+ can be extended to their affinity to Li^+ -anion salt complex.

Beyond salt affinity, we further characterized the solvent phobicity of various polymer side chains through contact angle measurements. We dropped $10 \mu\text{L}$ of either carbonate (1M LiPF_6 EC/DEC 10% FEC, 1M lithium hexafluorophosphate in ethylene carbonate and diethyl carbonate with 10% of fluoroethylene carbonate) or ether (1M LiTFSI DOL/DME, 1M lithium bis(trifluoromethanesulfonyl)imide in 1,3-dioxolane/dimethoxy ethane) electrolyte to a polymer-coated silica wafer. Classic compound electrolytes were used here to cover a wide range of ether and carbonate solvents. Although the glyme side chain shows affinity to lithium salt, it is also electrolyte philic, demonstrated by the low ($<10^\circ$) contact angles for both ether and carbonate electrolyte. In comparison, the other salt affinitive PyTFSI side chain has less attraction to solvents ($\sim 20^\circ$ contact angles). Both the alkyl and perfluorinated chains showed higher levels of solvent resistance with contact angles of $\sim 40^\circ$ for ether electrolytes and $>50^\circ$ for carbonate electrolyte (Figure XV.3.2.B).

Here we identified the PyTFSI side chain as salt affinitive with moderate electrolyte repelling ability. To further increase the solvent repelling capability of the polymer, we replaced 40% of the PyTFSI side chain with the perfluorinated chain. This dual side chain design strategy increased the contact angle from 22° to 36° in ether electrolyte, and from 29° to 45° in carbonate electrolyte, preserving the salt affinity of the polymer while increasing its solvent phobicity (Figure XV.5.2.C). We name this designer polymer as “SP²” (Salt Philic Electrolyte Phobic).

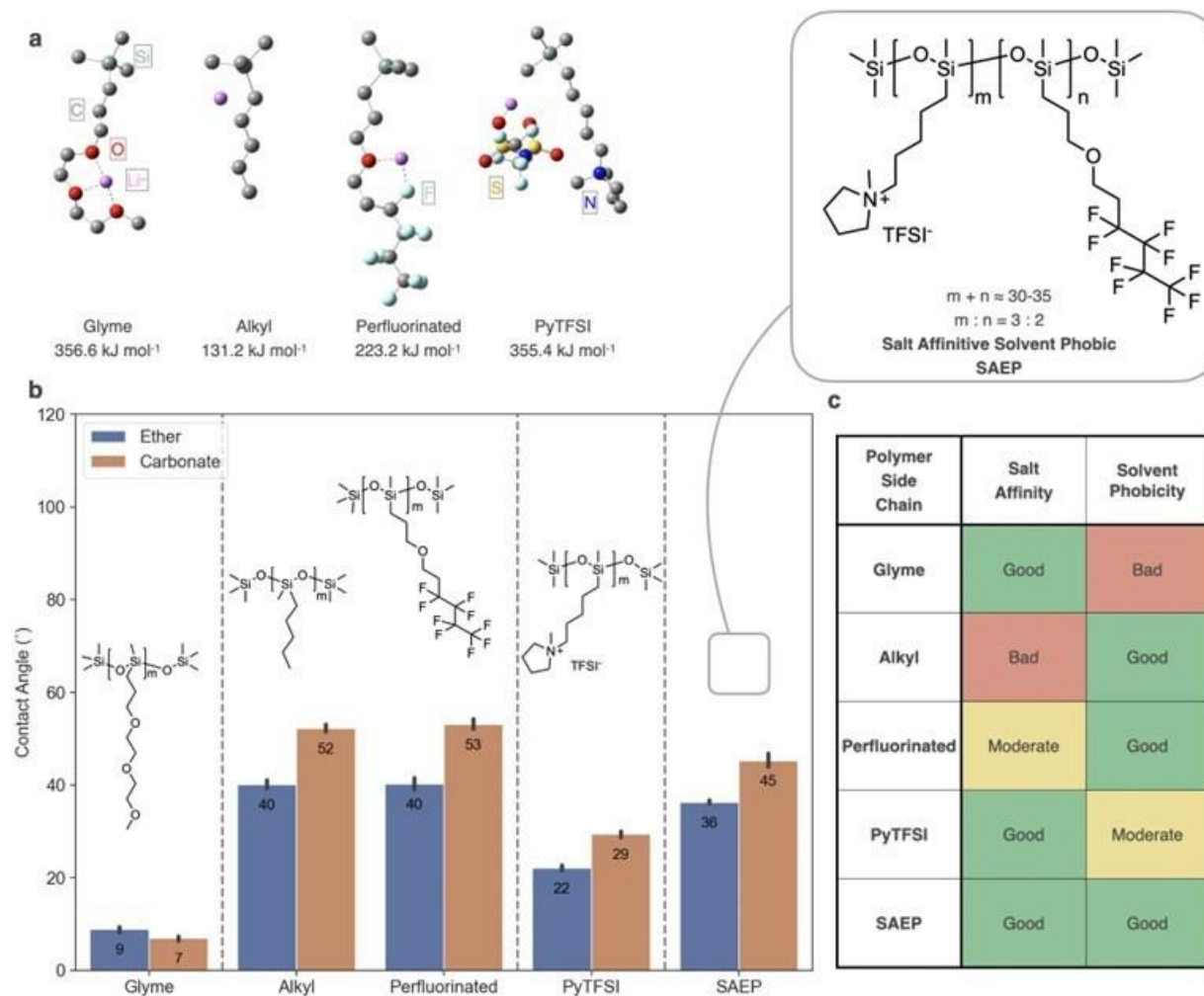


Figure XV.3.2 Characterization of salt affinity and solvent phobicity: **A**, density functional theory (DFT) based calculation of Li⁺'s interaction energy with various polymer side chains; **B**, contact angle measurement of polymer coated Si wafer with ether (1M LiTFSI DME) or carbonate (1M LiPF₆ EC/DEC 10% FEC) electrolyte; **C**, comparison of salt affinity and solvent phobicity of various polymer side chain. SAEP is SP²

To demonstrate the selectivity of the SP² polymer, we designed a H-cell experiment (Figure XV.3.3.A). The LHS (left-hand side) of the H-cell was filled with 3 mL of 1M LiTFSI DME (Lithium bis(trifluoromethanesulfonyl)imide, Dimethoxyethane) electrolyte, and the RHS (right-hand side) was filled with 6 mL DME solvent. The two sides were separated by two layers of separators with 100 mg of polymer sandwiched. As the system equilibrates, the concentration difference drives the diffusion of salt from LHS to RHS and vice versa for DME. To avoid vacuum build-up upon solvent flow, the caps of the H-cell were loosened. Visually, the lowering of the liquid line on the RHS represents DME migration from right to left. The salt concentration was evaluated after 3 hrs with ¹⁹F NMR, and the measured concentrations of LiTFSI were listed in Figure XV.3.3.B. When there were no polymer present, liquid levels of the two sides matched after 3 hrs, indicating significant DME diffusion from right to left. When the SP² polymer was inserted in the H-cell, the liquid level difference was maintained after 3 hours. NMR spectrum revealed that LiTFSI salt has migrated from left to right, resulting in 0.025M of LiTFSI in RHS. We noted the LiTFSI concentration remained at 1M on LHS, instead of lowering, and we argue that the slight evaporation of DME compensated for the salt diffusion and maintained the salt concentration on the LHS. To examine the necessity of introducing a second solvent phobic side chain to the salt affinitive polymer, we conducted H-cell experiment with just PyTFSI polymer. When there is only salt affinitive polymer present, the liquid level on the RHS

almost matched that of the LHS, indicating significant solvent migration. There is also salt migration from left to right, and the RHS reached 0.051M LiTFSI after 3 hrs of resting.

The presence of an electrolyte phobic side chain also limited the swelling of the polymer in 1M LiTFSI DME electrolyte. Specifically, we compared the mechanical properties and ionic conductivities of the PyTFSI (only salt affinitive polymer, Figure XV.3.3.C) and SP² (Figure XV.3.3.D) polymer before and after soaking in the electrolyte for 8 hours. We characterized the frequency dependent modulus of the polymer in rheological measurements: the loss modulus (G'') represents the liquid characteristic, and the storage modulus (G') represents the solid characteristic. Before soaking, both the SP² and the PyTFSI polymer showed viscous behavior with G'' higher than G' in the characterized frequency range. After swelling, the polymer showed decrease in both storage and loss moduli, indicating reduction in mechanical strength. Specifically, we characterized the relative liquid to solid characteristic of the polymer by calculating the $\tan(\delta)$ (ratio between G'' and G') at the angular frequency of 10 rad s⁻¹. For the PyTFSI polymer, the $\tan(\delta)$ increased close to an order (1.7 to 16) upon soaking, while the SASP polymer's $\tan(\delta)$ remained relatively constant (2.3 to 2.4). Although SP² and PyTFSI polymers can both be swelled by the solvent, SASP maintained its relatively solid-liquid characteristics, while the PyTFSI polymer becomes more liquid-like, indicating it is less resistive to solvent swelling.

Beyond changes in mechanical properties, we also measured the ionic conductivities of the polymer before and after soaking (Figure XV.3.3.E) with EIS (electrochemical impedance spectroscopy) at 25 °C. The ionic conductivity in the dry state is attributed to ionic dissociation of PyTFSI moieties, and the wet state ionic conductivity is contributed by both the tethered ionic moieties as well as salt in the electrolyte. After soaking the polymer in the electrolyte, the conductivities of PyTFSI increased for an order (0.012 to 0.116 mS cm⁻¹) while the conductivities of SP² remained within one order (0.013 to 0.043 mS cm⁻¹). This is due to the higher solvent resistance for the SP² polymer. Based on both the mechanical characterization and ionic conductivity measurements, we can conclude that the addition of solvent phobic side chain can improve the solvent resistance of the polymer.

We further examined SP² polymer's ability to induce salt derived SEI formation with surface analysis technique X-ray photoelectron spectroscopy (XPS). We assembled Li|Cu cell with polymer-coated Cu current collector. We stripped and plated Li through the polymer layer in 1M LiTFSI DME electrolyte for 10 cycles to produce a layer of SEI underneath the polymer coating. After that, the cell was disassembled, and the Cu foil was transported to the XPS chamber in an air-free transfer process. The O1s spectra of the cycled Cu electrode after 2 min of sputtering were shown in Figure XV.3.3.F. We attributed the peak at 530.9 eV to -NO_x/SO_x (LiTFSI salt breakdown), and the peak at 533.8 eV to -RO-CO_x-Li (DME breakdown). By calculating the percentage of the peak area attributed to salt/solvent breakdown, we can quantify the polymer coating's ability to form salt derived SEI. When there was no coating, 56% of the SEI was attributed to salt decomposition. When the PyTFSI polymers were present, the salt derived SEI content was increased to 63%. This content can be further improved to 73% when SP² coating was presented. Due to the selective transporting ability of the SP² polymer, lithium anode has limited access to solvent molecules, and the percentage of salt derived SEI content was increased.

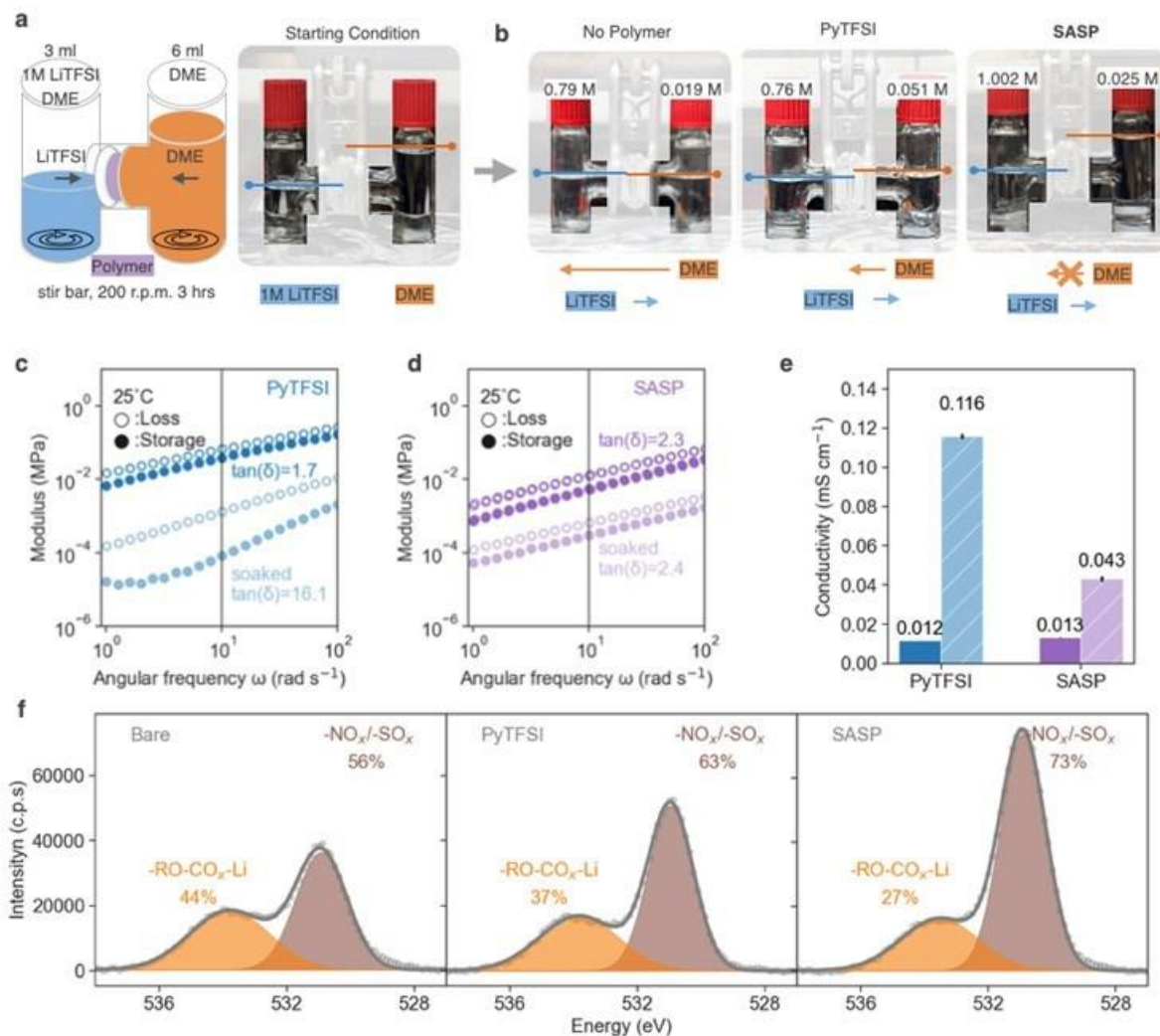


Figure XV.3.3 Selectivity of PyTFSI and SASP polymer: **A**, experimental set-up for H-cell experiments; **B**, H-cell experiment with the polymer sandwiched in the middle, images taken after 3 hrs with the measured LiTFSI concentration labelled on the graph; rheological frequency sweep of the polymer after soaked in 1M LiTFSI DME electrolyte for 8 hrs, with the $\tan(\delta)$ at 10 rad s⁻¹ marked; **C**, PyTFSI; **D**, SASP; **E**, conductivity (25 °C) of the polymer before and after soaked in 1M LiTFSI DME for 8 hrs ; **F**, Oxygen 1s XPS of SEI on the anode, and the signals attributed to either salt or solvent decomposition were separated with their relative percentage marked out. SASP is SP²

The ability of SP² polymer to improve SEI composition leads to upgrades in electrochemical performance in Li|Cu cycling. As shown in Figure XV.3.4.A, we compared the coulombic efficiency (C.E.) for the two cases with and without SP² coating under a short-term 10 cycles 0.5 mA cm⁻¹ 1mAh cm⁻¹ cycling protocol¹. In 1M LiTFSI DOL/DME 1wt% LiNO₃ electrolyte, the C.E. increased from 98.3% to 99.5% with SP². We also examined the C.E. in carbonate (1M LiPF₆ EC/DEC with 10% FEC), as well as 1M LiFSI in FDMEB² electrolyte. In carbonate electrolyte, the C.E. increased from 96.0% to 97.0%. In FDMEB electrolyte, since the baseline electrolytes already achieves high C.E. in this short-term cycling protocol, we observed a small increase with the addition of a SP² coating (99.4% to 99.5%). We also paired the SP² coating with the state-of-the-art Li metal electrolyte: 1.2M LiFSI in 2-(2-(2,2-difluoroethoxy)ethoxy)-1,1,1-trifluoroethane (F5DEE)³ and the C.E. increased from 99.5% to 99.6%. These is less room for C.E. improvement when the baseline C.E. is already high. However, in long-term tests, small increasements of C.E. still translated to longer cell cycle life, as we show in the following section.

Since both the EC/DEC and FDMB electrolytes were cycled with Li|NMC configuration, we characterized how SP² coating affects electrolytes' stability with Li metal anode through EIS and long-term cycling in Li|Li symmetric cell. Figure XV.3.4.B shows the interfacial impedance of SP² coated Li in carbonate or FDMB electrolyte for different length of time. The uncoated ones were used as comparison. For both electrolytes, SP² layer was observed to suppress the interfacial impedance increase. We quantified the increase with this formula: $(I_{100} - I_0)/I_0$ (%). For the first 100 hrs, SP² reduced the impedance increase from 104% to 33% in carbonate electrolyte, and from 153% to 42% in FDMB electrolyte Figure XV.3.4.C. Since the polymer was coated on Li surface with the THF solvent, we also examined THF's influence on interfacial impedance. We treated bare Li metal with THF and tracked its impedance evolution in carbonate electrolyte. With or without THF treatment, Li electrodes experienced similar ~100% impedance increase, indicating that SP² polymer is the reason of reduced impedance growth.

We also cycled Li|Li symmetric cells at 1 mA cm⁻¹ current density and 1mAh cm⁻¹ capacity (Figure XV.3.4.D). For the carbonate electrolyte, the addition of SP² coating resulted in a higher deposition overpotential, which was stable over cycles. For the uncoated Li anode, the overpotential decreased between 25 and 40 cycles. This is due to increased surface area from irregular whisker-shaped lithium deposition⁵, which was verified by SEM (Figure XV.3.4.E). The addition of SP² coating promoted homogeneous deposition, as opposed to whisker-shaped deposition. For the FDMB electrolyte, a layer of SP² polymer maintained a stable overpotential over time. Without the SP² coating, FDMB electrolyte continued to react with lithium metal and increased the deposition overpotential². In both cases, a layer of SP² coating limited the solvent breakdown at the Li electrode and sustained stable operation.

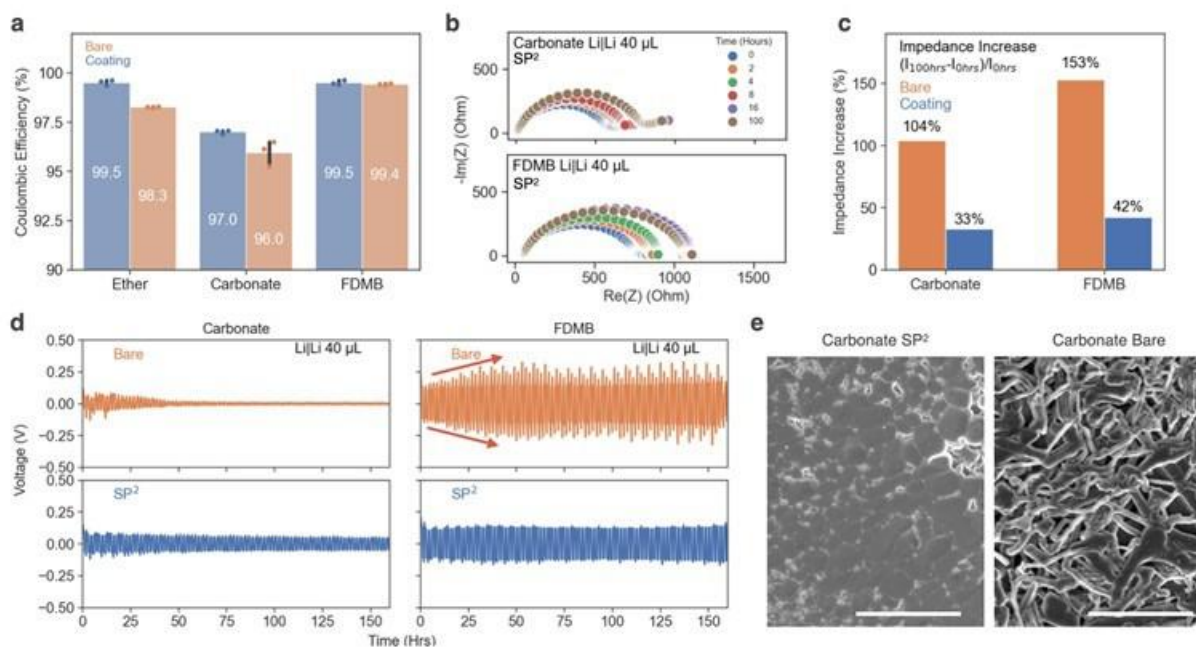


Figure XV.3.4 Electrochemical characterization of SP² with different electrolytes: **A**, coulombic efficiency measured of coated Cu in Li|Cu geometry with 40 μ L of ether (1M LiTFSI DOL/DME 1wt% LiNO₃), carbonate (1M LiPF₆ EC/DEC 10% FEC) or FDMB (1M LiFSI FDMB) electrolyte; **B**, EIS measurement overtime with either SP² coated Li|Li symmetric cell in electrolytes; **C**, calculated impedance increase (%) over 100 hours; **D**, voltage curve of Li|Li symmetric cell with and without SP² coating; **E**, SEM top view image of deposited Li on Cu electrode in carbonate electrolyte, scale bar 10 μ m.

Since SP² (salt-philic solvent-phobic) coating showed improvement in carbonate electrolyte, SP² coated thin Li anodes (50 μ m) were also assembled into Li|NMC cells. They were cycled at different C-rates, and we found reasonable capacity (>200 mAh g⁻¹) can be achieved at C/10 and C/3 for carbonate electrolyte (Figure

XV.3.5.A). We proceeded with C/5 charging and C/3 discharging in long-term cycling. Figure XV.3.5.B showed the discharge capacity over cycles when pairing with 2.5 mAh cm^{-2} NMC cathode for carbonate and a cycle life of ~ 250 was reached. The C.E. of each cycle were shown in Figure XV.3.5.C. Our polymer coating polymer design is a marked improvement in full cell cycle life vs. capacity when compared with other state-of-the-art Li anode modification strategies (Figure XV.3.5.D). [6,7,16,17,8–15]

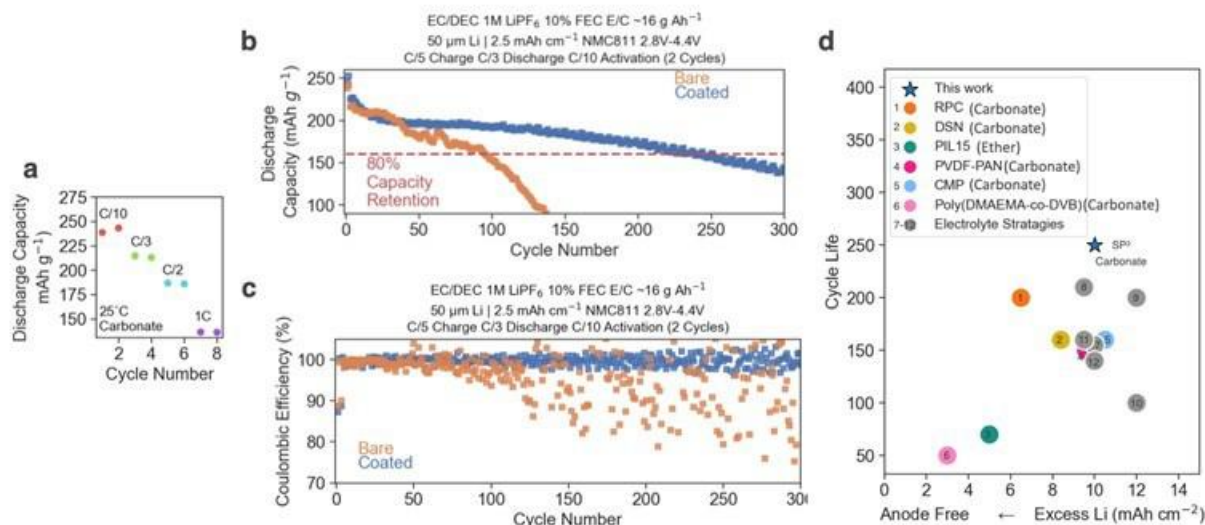


Figure XV.3.5 Cycling of SP² coated Li anode in Li|NMC cells: **A**, rate capabilities; **B**, cycle life and capacity; **C**, coulombic efficiency of each cycle. **D**, comparison of cycle life (80% capacity retention) plotted against access lithium amount of the SP² coating with other coatings/ electrolyte strategies; The x axis locations of 4, 5, 7, 11, and 12 are 10 mAh cm^{-2} , and they are adjusted slightly to dodge.

Conclusions

Overall, we developed SP² polymer coating on Li metal anode. This coating allows selective transport of lithium salt instead of solvent molecules. When salt has a higher probability to be in physical contact with Li metal, salt-derived SEI formation is promoted. SP² was found to be applicable to several typical electrolyte chemistry and showed improvement in cycling performance for ether, carbonate, and fluorinated ether electrolytes.

Key Publications

1. Z. Huang, J-C Lai, S-L Liao, Z Yu, Y. C.W.Yu, H. Gong, Y.Yang, X Gao, Y. Cui, and Z. Bao " A salt-philic solvent-phobic (SP²) interfacial coating design for lithium metal electrodes " under review, (2022)
2. Yu, Z., Rudnicki, P.E., Zhang, Z. Y Cui, Z Bao, *et al.* Rational solvent molecule tuning for high-performance lithium metal battery electrolytes. *Nat Energy* 7, 94–106 (2022). <https://doi.org/10.1038/s41560-021-00962-y>
3. Kim, M.S., Zhang, Z., Rudnicki, P.E. Z Bao, Y Cui, *et al.* Suspension electrolyte with modified Li⁺ solvation environment for lithium metal batteries. *Nat. Mater.* (2022). <https://doi.org/10.1038/s41563-021-01172-3>
4. H Wang, Z Yu, Z Bao, Y Cui, Liquid electrolyte: The nexus of practical lithium metal batteries, *Joule*, <https://doi.org/10.1016/j.joule.2021.12.018>
5. Z Huang, S Choudhury, N Paul, R Gilles, Z Bao, *et al.* Effects of Polymer Coating Mechanics at Solid-Electrolyte Interphase for Stabilizing Lithium Metal Anodes, *Advanced Energy Materials* (2022). <https://doi.org/10.1002/aenm.202103187>

6. H.Wang, Z.Bao, Y.Cui, Liquid electrolyte: The nexus of practical lithium metal batteries, *Joule*, <https://doi.org/10.1016/j.joule.2021.12.018>
7. Z Yu, S Seo, Z Bao, et al, A Solution-Processable High-Modulus Crystalline Artificial Solid Electrolyte Interphase for Practical Lithium Metal Batteries, *Advanced Energy Materials*, (2022). <https://doi.org/10.1002/aenm.202201025>
8. W Yu, Z Yu, Y Cui, Z Bao, Degradation and speciation of Li salts during XPS analysis for battery research, *ACS Energy Letter*, (2022). <https://doi.org/10.1021/acseenergylett.2c01587>

References

1. J. Xiao, Q. Li, Y. Bi, M. Cai, B. Dunn, T. Glossmann, J. Liu, T. Osaka, R. Sugiura, B. Wu, J. Yang, J.-G. Zhang, M. S. Whittingham, *Nature Energy* **2020**, *5*, 561.
2. Z. Yu, H. Wang, X. Kong, W. Huang, Y. Tsao, D. G. Mackanic, K. Wang, X. Wang, W. Huang, S. Choudhury, Y. Zheng, C. V Amanchukwu, S. T. Hung, Y. Ma, E. G. Lomeli, J. Qin, Y. Cui, Z. Bao, *Nature Energy* **2020**, *5*, 526.
3. [Z. Yu, P. E. Rudnicki, Z. Zhang, Z. Huang, H. Celik, S. T. Oyakhire, Y. Chen, X. Kong, S. C. Kim, X. Xiao, H. Wang, Y. Zheng, G. A. Kamat, M. S. Kim, S. F. Bent, J. Qin, Y. Cui, Z. Bao, *Nature Energy* **2022**, *7*, 94.
4. X. Cao, H. Jia, W. Xu, J.-G. Zhang, *Journal of The Electrochemical Society* **2021**, *168*, 010522.
5. G. Bieker, M. Winter, P. Bieker, *Phys. Chem. Chem. Phys.* **2015**, *17*, 8670.
6. Y. Gao, Z. Yan, J. L. Gray, X. He, D. Wang, T. Chen, Q. Huang, Y. C. Li, H. Wang, S. H. Kim, T. E. Mallouk, D. Wang, *Nature Materials* **2019**, *18*, 384.
7. Z. Yu, D. G. Mackanic, W. Michaels, M. Lee, A. Pei, D. Feng, Q. Zhang, Y. Tsao, C. V Amanchukwu, X. Yan, H. Wang, S. Chen, K. Liu, J. Kang, J. Qin, Y. Cui, Z. Bao, *Joule* **2019**, *3*, 2761.
8. Z. Huang, S. Choudhury, H. Gong, Y. Cui, Z. Bao, *Journal of the American Chemical Society* **n.d.**, *142*, 21393.
9. D. Wang, H. Liu, F. Liu, G. Ma, J. Yang, X. Gu, M. Zhou, Z. Chen, *Nano Letters* **2021**, *21*, 4757.
10. K. Zhang, W. Liu, Y. Gao, X. Wang, Z. Chen, R. Ning, W. Yu, R. Li, L. Li, X. Li, K. Yuan, L. Ma, N. Li, C. Shen, W. Huang, K. Xie, K. P. Loh, *Advanced Materials* **2021**, *33*, 2006323.
11. S. Stalin, P. Chen, G. Li, Y. Deng, Z. Rouse, Y. Cheng, Z. Zhang, P. Biswal, S. Jin, S. P. Baker, R. Yang, L. A. Archer, *Matter* **2021**, *4*, 3753.
12. X. Cao, X. Ren, L. Zou, M. H. Engelhard, W. Huang, H. Wang, B. E. Matthews, H. Lee, C. Niu, B. W. Arey, Y. Cui, C. Wang, J. Xiao, J. Liu, W. Xu, J.-G. Zhang, *Nature Energy* **2019**, *4*, 796.
13. X. Cao, L. Zou, B. E. Matthews, L. Zhang, X. He, X. Ren, M. H. Engelhard, S. D. Burton, P. Z. El-Khoury, H.-S. Lim, C. Niu, H. Lee, C. Wang, B. W. Arey, C. Wang, J. Xiao, J. Liu, W. Xu, J.-G. Zhang, *Energy Storage Materials* **2021**, *34*, 76.
14. W. Xue, Z. Shi, M. Huang, S. Feng, C. Wang, F. Wang, J. Lopez, B. Qiao, G. Xu, W. Zhang, Y. Dong, R. Gao, Y. Shao-Horn, J. A. Johnson, J. Li, *Energy Environ. Sci.* **2020**, *13*, 212.
15. W. Xue, M. Huang, Y. Li, Y. G. Zhu, R. Gao, X. Xiao, W. Zhang, S. Li, G. Xu, Y. Yu, P. Li, J. Lopez, D. Yu, Y. Dong, W. Fan, Z. Shi, R. Xiong, C.-J. Sun, I. Hwang, W.-K. Lee, Y. Shao-Horn, J. A. Johnson, J. Li, *Nature Energy* **2021**, *6*, 495.
16. W. Zhang, Z. Shen, S. Li, L. Fan, X. Wang, F. Chen, X. Zang, T. Wu, F. Ma, Y. Lu, *Advanced Functional Materials* **2020**, *30*, 2003800.
17. S. Li, W. Zhang, Q. Wu, L. Fan, X. Wang, X. Wang, Z. Shen, Y. He, Y. Lu, *Angewandte Chemie International Edition* **2020**, *59*, 14935.

XV.4 Anode-Free Lithium Batteries (PNNL)

Ji-Guang Zhang, Principal Investigator

Pacific Northwest National Laboratory
902 Battelle Boulevard
Richland, WA 99354
E-mail: jiguang.zhang@pnnl.gov

Xia Cao, Co-Principal Investigator

Pacific Northwest National Laboratory
902 Battelle Boulevard
Richland, WA 99354
E-mail: xia.cao@pnnl.gov

Tien Duong, DOE Technology Development Manager

U.S. Department of Energy
E-mail: Tien.Duong@ee.doe.gov

Start Date: October 1, 2021

End Date: September 30, 2024

Project Funding (FY22): \$300,000

DOE share: \$300,000

Non-DOE share: \$0

Project Introduction

Ever increasing need for electrical vehicles (EVs) continually pushes the boundary of high-energy-density storage systems. To date, the state of the art of lithium (Li) ion batteries (LIBs) consisting of graphite anode and high voltage Li intercalation cathodes cannot satisfy the energy demand from these applications. By replacing graphite anode with Li metal anode (LMA), specific energy density of Li metal batteries (LMBs) can increase by more than 50% because LMA has a much higher specific capacity (3820 mAh g^{-1}) than that of graphite (372 mAh g^{-1}).¹ To further increase the energy density of Li batteries, the concept of “anode-free” Li batteries (AFLBs) has been explored. An as-assembled or fully discharged AFLB consists of a Li-containing cathode and an anode current collector (such as copper (Cu)).² All Li source is stored in cathode. This cell design not only increases energy density of the battery, but also improves the safety of the battery because there is no Li metal present in the battery in its as-assembled or discharged state. Neudecker et al. first demonstrated the feasibility of this concept in solid state thin film batteries based on LiPON electrolyte.³ Adams and Zhang et al. demonstrated the feasibility of AFLB in coin-cells with non-aqueous liquid electrolytes.² Recently, Niu, Xiao, and Liu et al. investigated the performance of LMBs and AFLBs with different thicknesses of LMA (100 μm , 50 μm , 20 μm , and 0 μm (AFLB)).⁴ They found that too thick or too thin (such as 0 μm in the case of AFLB) Li will lead to faster capacity fade. Therefore, there are still significant barriers needing to be overcome before the practical application of AFLBs. AFLBs share many similarities with LMBs except that the optimization of AFLBs need to be done in the case of no Li available in anode in an as-assembled cell. Both AFLB and LMB need a highly efficient electrolyte to reach ultra-high Li Coulombic efficiency (CE) and a highly reversible cathode CE. Therefore, there is an urgent need to understand the correlation between Li CE, cathode CE and electrolyte (including its electrochemical properties and consumption) as well as Li dendrite growth and the formation of “dead” Li, so that LMBs and AFLBs can be designed to achieve desired energy density and cycle life.

Objectives

The main objective of this project is to explore the feasibility of anode-free lithium batteries (AFLBs) for high-energy-density energy storage systems. In this project, we will investigate the main factors affecting the performance of AFLBs and identify the solutions to enable long-term cycling and safety of these batteries. The Li dendrite suppressing principles and strategies for both liquid and solid-state AFLBs, ranging from materials design (electrolytes, cathodes, current collectors), cell fabrication, and operation controls will also be

investigated in order to enable a high CE of AFLB to be above 99.7% and maximize the cycling stability of the AFLBs. Because of the many similarities among AFLBs, Li-metal batteries, and Li-ion batteries, experiences and approaches developed for AFLBs can also be applied to Li-metal and Li-ion batteries, thus accelerating the market penetration of Li-based rechargeable batteries.

Approach

1. Analyze the Li loss due to solid electrolyte interphase (SEI) formation and “dead” Li generation by dendrite growth during the Li deposition and stripping processes.
2. Identify the electrolytes that enable the formation of a SEI layer with high surface energy with Li metal anode. The new electrolytes promote the formation of lithiophobic/robust SEI and facilitate the reuse of SEI layer so the continuous loss of Li and electrolyte can be minimized. Special attention is made to minimize the dissolution of SEI. Two strategies are used to mitigate the SEI dissolution by the electrolyte engineering: one is manipulating the electrolyte decomposition pathway to form insoluble SEI components; another is reducing electrolyte solvation ability to SEI by developing a near-saturated electrolyte (such as localized high concentration electrolyte with minimal free-solvents).
3. Stabilize anode current collector and reduce initial Li loss. Two approaches to stabilize Cu substrate are investigated, including three-dimensional (3D) substrate construction and polymer coatings.
4. Optimize cycling parameters of AFLBs to improve their cycle life. Different cut-off charge/discharge voltages of AFLB are investigated to minimize the Li nucleation and suppress the continuous SEI/CEI formation.

Results

Optimize the charge/discharge parameters of AFLBs

AFLB shares many similarities with LMB because the AFLB is actually an extreme case of LMBs where Li reservation on the anode is 0. However, beyond the issues of Li metal in LMBs, AFLB has several additional problems due to the lack of Li on Cu anode as assembled. It mainly includes the Cu redox reaction at open circuit voltage (OCV) of the cell, the repeated Li nucleation on Cu anode at the beginning of each cycle, and the increased Li galvanic corrosion that is caused by the Li||Cu galvanic cells at the early state of Li plating. All these undesired reactions result in the loss of active Li and increase of cell resistance that further led to fast capacity decay of the AFLB. Therefore, the testing protocol has significant influence on the AFLBs. In this work, all the cells were rested at 1.5 V for wetting to avoid the Cu redox at OCV, and different depth of discharge (DOD) were applied to avoid the repeated Li nucleation and minimize the Li galvanic corrosion. Figure XV.4.1 shows the schematic of Li reservation on Cu at different DODs by adjusting the discharge cut-off voltage. Cut-off discharge voltage of V2 (see Figure XV.4.1) is an optimized voltage for Cu||NMC622 AFLB with a complete Li nucleation layer formed on the Cu. At this condition, Cu||NMC622 cell could balance the energy and cycling stability.

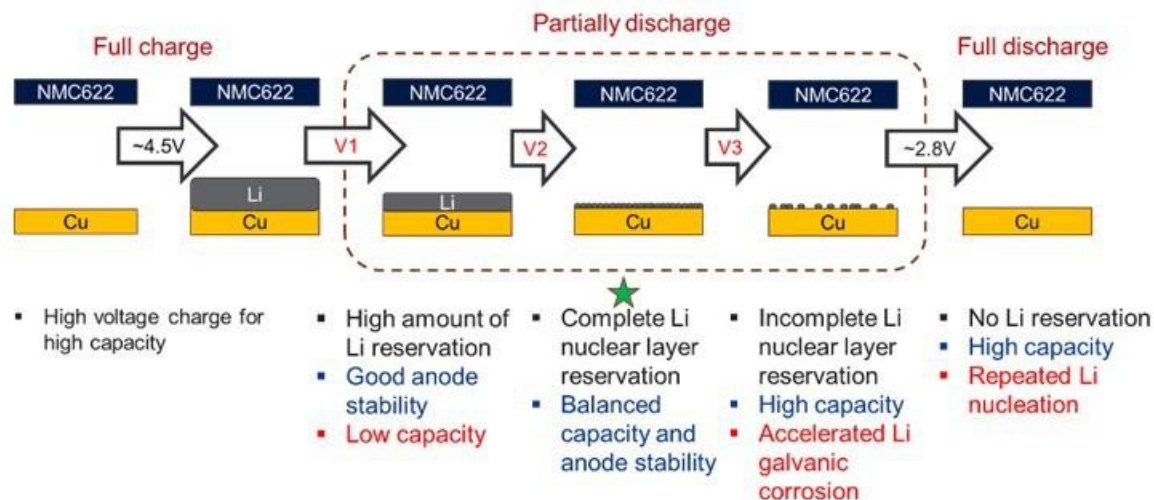


Figure XV.4.1 Schematic Li reservation on Cu (Li from cathode) by voltage optimization

Figure XV.4.2 shows the electrochemical performance of Cu||NMC622 cells charged to 4.5 V and discharged to different cut-off voltages. With the increase of cutoff voltage (lower DOD), cells deliver decreased capacity while cycling stability increased. The details of the cell performance are summarized in Table XV.6.1. Cut-off voltage of 3.5 V for discharge can be considered as optimised with a balanced energy and energy-retention.

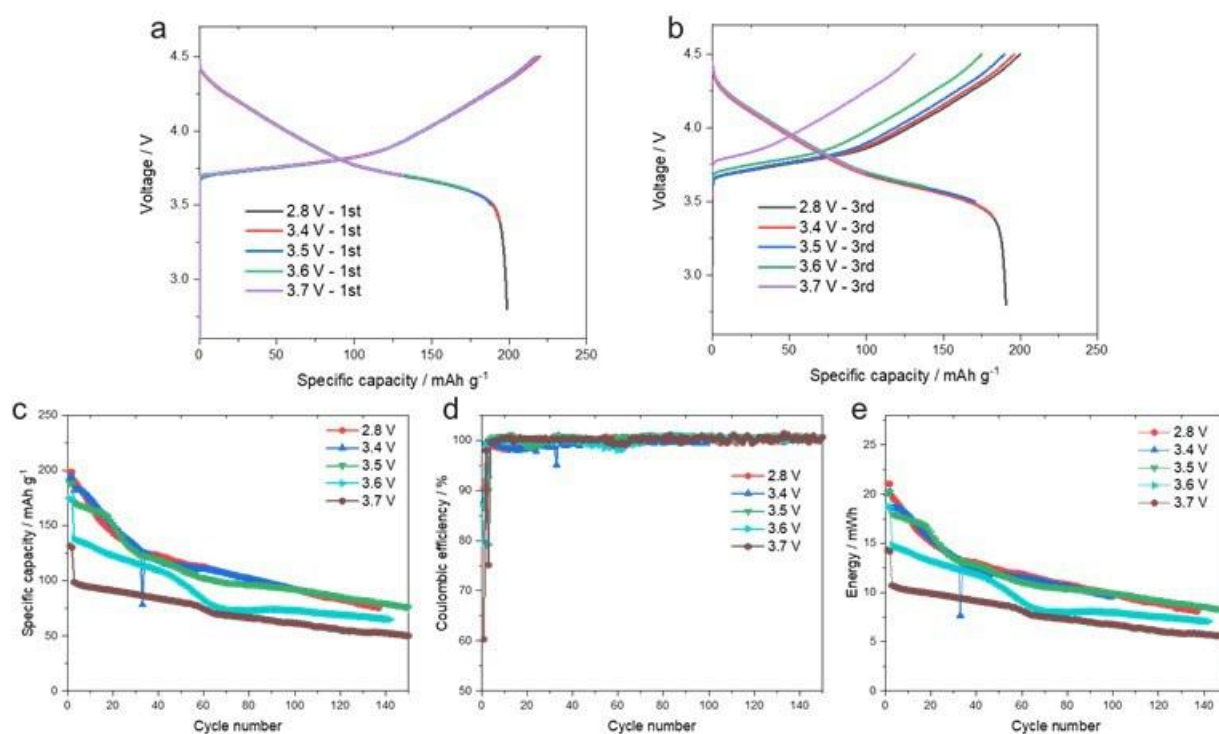


Figure XV.4.2 Cu || NMC622 cell performance at different discharge cutoff- voltages.

Table XV.4.1 Summarized performance of Cu || NMC622 cells at different discharge cutoff-voltages

	Formation cycle		Cycling			
Cut-off voltage / V	Initial cap. / mAh g ⁻¹	Initial CE / %	Initial cap. / mAh g ⁻¹	Initial CE / %	Cap. Retention / % (100 cycles)	Average CE / %
2.8	198.6	90.42	190.6	95.46	52.5	99.7
3.5	188.3	86.66	170.6	89.95	54.1	100.2
3.6	174.5	79.9	138.6	79.22	53.4	99.8
3.7	131.6	60.35	98.6	75.14	62.4	99.8

In addition to the optimized discharge cut-off voltage of 3.5 V for Cu||NMC cells, we also further optimized the operation range of Cu||NMC cells by investigating the effect of charge cut-off voltage on the cell performance. In parallel to the Cu||NMC622 cells, we also studied Cu||NMC811 cells. Figure XV.4.3a shows the electrochemical performance of Cu||NMC622 and Cu||NMC811 cells. In the cut-off voltage of 3.5 to 4.5V, the Cu||NMC811 cell demonstrate better capacity and cycling stability than Cu||NMC622 cell. Therefore, Cu||NMC811 cell were further investigated using a charge cut-off voltage between 4.4 to 4.7 V with the same discharge cut-off voltage of 3.5 V. The results in Figure XV.4.3b and 3c show that the cell cycled with a charge cut-off voltage of 4.4 V exhibits the most stable cycling stability (63% at 100th cycle) with a highest cycling Coulombic efficiency (99.65% at 100th cycle). Thus, 4.4 V is considered optimized charge cut-off voltage when matched with an optimized discharge cut-off voltage of 3.5V.

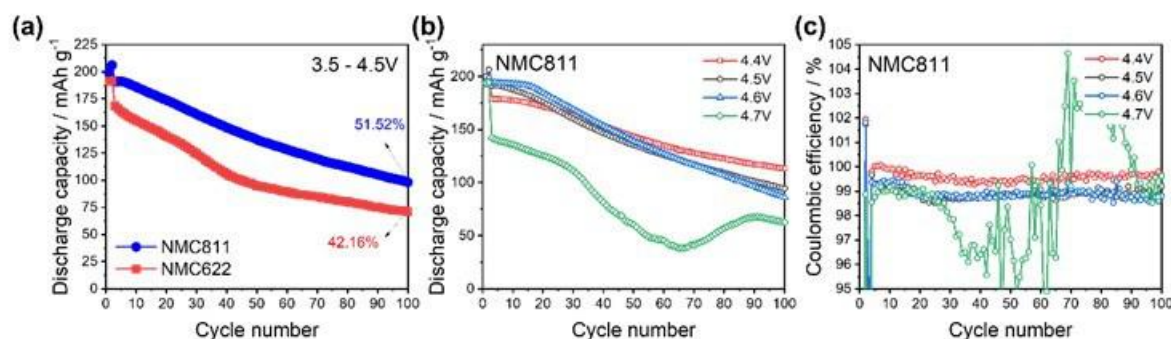


Figure XV.4.3 (a) Cycling performances of Cu || NMC622 and Cu || NMC811 cells cycled between 3.5 – 4.5V. (b) Cycling performances and (c) Coulombic efficiencies of Cu || NMC811 cells cycled with different charge cut-off voltages.

Stabilize anode current collector

The surface stability of Cu anode is another important factor on the cycle life of AFLBs. The side reactions between the interface of Cu current collector and liquid electrolyte during operation of AFLB will consume both Li and electrolyte, therefore leads to reduced CE. To address this problem, an artificial protection layer (containing PEO coordinated with Li salt (named PL_RX)) has been coated on the surface of Cu anode in a process illustrated in Figure XV.4.4a and 4b. The main role of this coating layer is to smooth the Li deposition and stripping, particularly after Li stripping, the residue Li morphology with the coating layer is much smoother than the one without coating layer as shown in Figure XV.4.4d and 4e, which means the residue Li in the coated condition has much less surface area. Figure XV.4.4c shows the voltage profiles of Li||Cu cells and the calculated average CE of Li||Cu cells with or without PL_RX layer. The results shows that cells with and without PL_RX protected Cu substrate exhibit a coulombic efficiency of 99.65% and 99.3%, respectively. This is consistent with smoother surface morphology shown in Figure XV.4.4e as compared to those of Figure XV.4.4d.

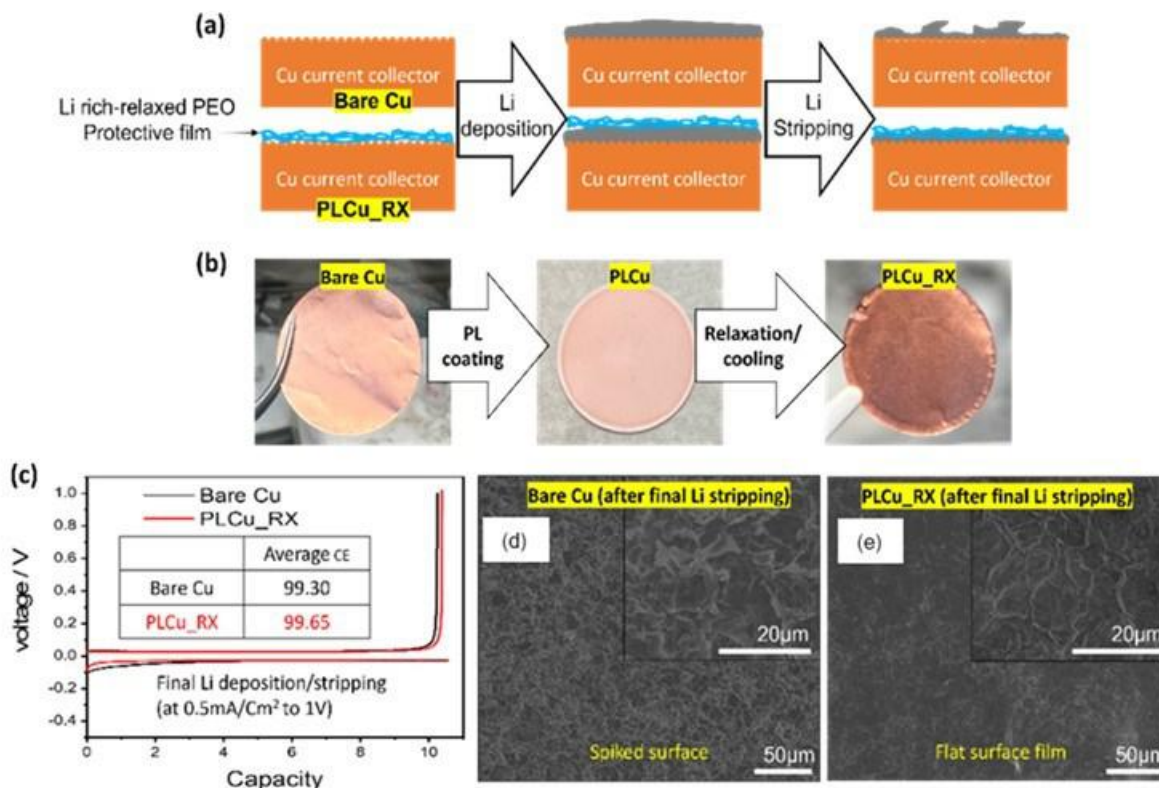


Figure XV.4.4 (a) The schematic of Li deposition/stripping on Cu with and without PL_RX layer. (b) Digital photographs of the bare Cu, PLCu and PLCu_RX. (c) Li deposition/stripping voltage profiles of the bare Cu and PLCu_RX with an average CE value. (d) SEM images of the Cu surfaces after Li stripping from bare Cu substrate and (e) PL_Rx coated Cu substrate.

To further improve the coating layer performance, we also introduced additional additives into the coating layer. As shown in Figure XV.4.5a and 5b, The PLCu-RX is best coating layer among the investigated samples, it gives the highest Li CE of 99.65% while the bare Cu has CE of 99.3%. As a result, in the Cu||NMC811 cells, the cells with the PLCu-RX coating layer have an apparent improved cycling stability as shown in XV.6.5c and 5d.

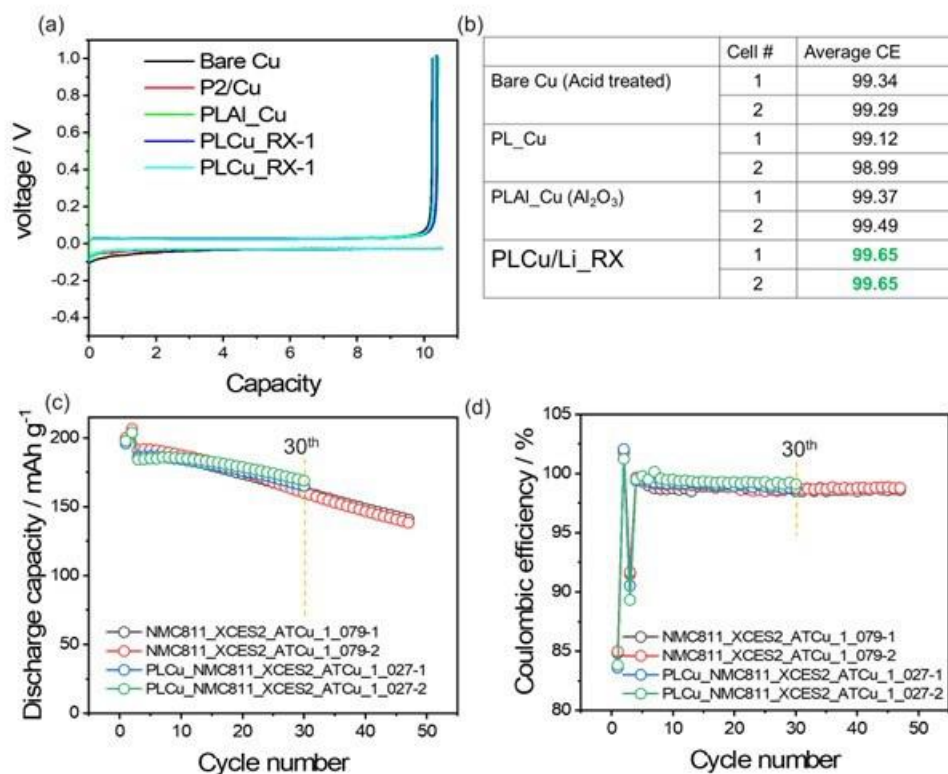


Figure XV.4.5 (a) The voltage profiles and (b) Coulombic efficiency of the Li || Cu cells with different coating layers. (c) Discharge capacity and (d) Coulombic efficiency of the Cu || NMC811 with and without optimized coating layer.

Electrolyte development

Electrolyte is one of the most important factors determining the cycle life of AFLBs. We started with LHCEs, which have high Li CE of above 99.4% and stable cycling in LMBs. Figure XV.4.6 is the result of the 200 mAh pouch cells using several of our LHCEs (Cu||NMC532 dry cells were acquired from commercial source), and 68.4% and 65.4% capacity retention are obtained in the optimized LHCE after 100 cycles.

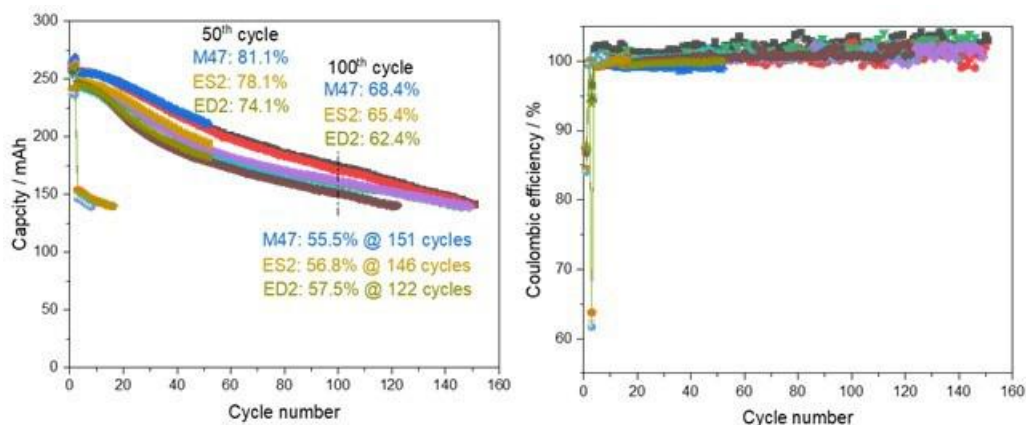


Figure XV.4.6 (a) Discharge capacity and (b) Coulombic efficiency of the 200 mAh Cu || NMC532 pouch cells with different types of LHCEs.

To further optimize the electrolyte, advanced additive is also studied in the work, forming additive containing LHCEs (E1-E4). When tested in Cu||Li cells, all these four electrolytes lead to very high Li CEs of 99.45%-99.7% as shown in Figure XV.4.7a. When paired with NMC811 cathode, electrolytes E1, E3 and E4 show stable cycling behavior as shown in XV.6.6b-6d. Among them, cell with E4 electrolyte demonstrates the best cycling stability with a capacity retention of 74.5% in 100 cycles for AFLBs.

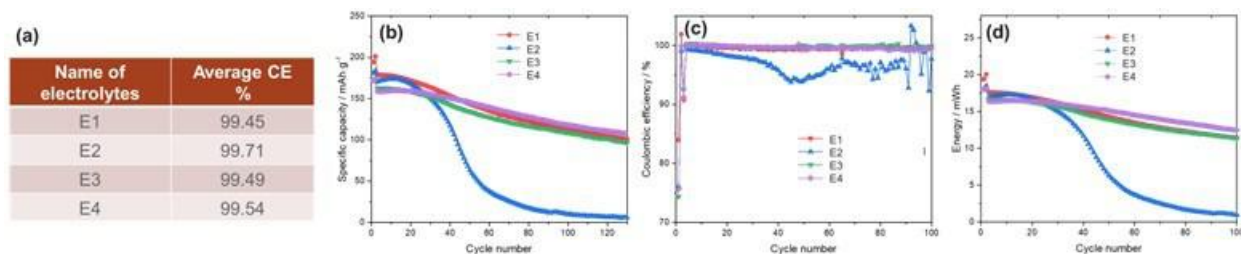


Figure XV.4.7 (a) The Coulombic efficiency of the Li||Cu cells with additives. (b) Discharge capacity and (c) Coulombic efficiency and (d) energy of the Cu||NMC811 with the LHCE with additives.

Pressure effect in coin cells

For the anode-free batteries, the uniform/dense lithium (Li) deposition is critical for long-term cell operation. However, when a coin type cell is used to investigate battery performance, non-uniform pressure introduced by the spacer and spring used in coin cells may lead to non-uniform deposition of Li, preautered local failure, and shortend cycle life of batteries. This is especially important for AFLBs that has no cushion layer (such as Li metal anode in the case of Li metal batteies or graphite anode in the case of Li ion batteries) to mitigate the pressure non-uniformity in a typical coin cell. In this work, we found that Li deposition in AFLBs is more porous in the center but more dense on the edge of cells (Figure XV.4.8 b and c) after the cell was charged to 4.5V (Figure XV.4.8a). This non-uniformity is directly related to the non-uniform thickness of commercial stainless steel spacers (SSS) and springs used in coin cells which can exert an non-uniform pressure on Cu substrate as shown in Figure XV.4.8d). The non-uniform pressure distribution leads to poor cycling performance (Figure XV.4.8e). Although coin cell is a convinent battery structure for testing of conventional batteries, non-uniform pressure distribution in coin cells is a clear barrier for investigation of AFLBs which is highly sensitive to pressure uniformity. In the next year, a small pouch cell with a more uniform distribution of pressure will be used to ellinate the effect of pressure non-uniformity observed in coin-cells and further improve the performance of AFLBs.

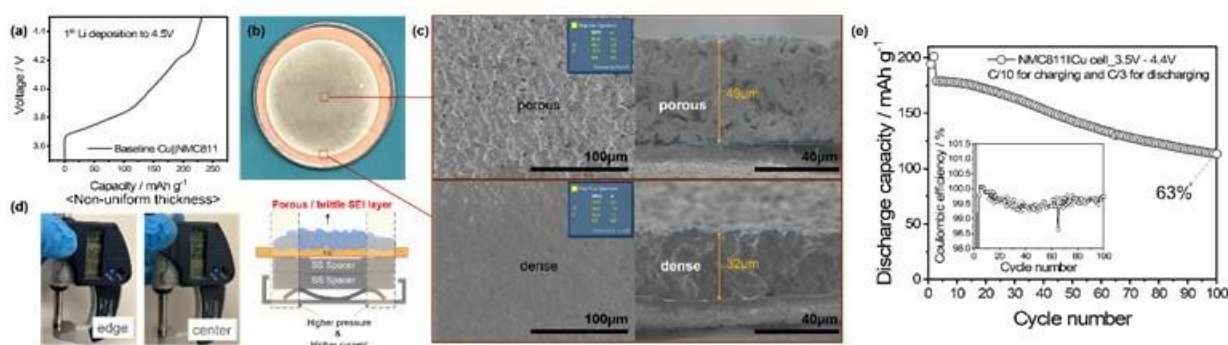


Figure XV.4.8 (a) Voltage profile of Li||NMC811 baseline cell charged to 4.5V, (b) digital photograph of Cu electrode after the 1st Li deposition to 4.5V, (c) SEM images with EDX data (insets) for the top (left) and cross-sectional (right) views of the center (upper) and edge (lower) regions of the Cu electrode after the 1st Li deposition to 4.5V, (d) digital photographs displaying the non-uniform thickness of the SSS with a schematic illustration of the non-uniform Li deposition leading to a porous/brittle SEI layer by non-uniform pressure/current distribution on Cu electrode, and the cycling performance of Cu||NMC811 cell cycled between 3.5V – 4.4V with the commercial 2032 coin cell set.

Conclusions

- The cycling parameter, particular the voltage range is optimized for AFLBs using PNNL developed LHCE electrolyte in Cu||NMC622 and Cu||NMC811 cells. 3.5-4.4V is found to be the best operation voltage window to balance the capacity and capacity retention of the AFLBs with NMC cathode. A thin Li nucleation layer remains on the Cu anode after discharge at this condition, which can avoid continuous Li nucleation and minimize the active Li loss and electrolyte depletion.
- For the Cu anode stabilization, an advanced coating layer (PLCu-LiRX) leads to smooth morphology of Li deposition and stripping. With this coating layer, the CE of Li||Cu cells can be improved from 99.4% to 99.65% and the cycling stability of the Li||NMC811 cells is also improved compared to using the bare Cu without any coating. This work point to a new type of coating to address the challenges on initial Li loss in AFLBs. The possible long term cycling stability will be further investigated during next year.
- An advanced additive for LHCE is proposed in electrolyte development. As LHCE already has high Li stability (Li CE of 99.4%) compared to most other electrolytes by forming a robust anion-derived SEI, further improvement of the LHCE is challenging. However, an even higher Li CE is required for the cycling stability of the AFLBs because there is no Li reserve in anode. Among various organic and inorganic additives we investigated for LHCE, one additive stands out to be promising for LHCE in this work. By using this additive, the Li CE is improved to 99.7% and a high-capacity retention of 74.5% after 100 cycles is obtained in the Cu||NMC811 cells.
- Pressure effect in coin cell is studied in this work and uneven pressure distribution issue has been analyzed. In the next year, a small pouch cell with a more uniform distribution of pressure will be used to investigate the performance of AFLBs.

Key Publications

Presentation

1. Anode-Free Li Metal Batteries with localized high concentration electrolytes, Xia Cao, Phung M Le, Yan Jin, Wu Xu, and Ji-Guang Zhang, 241st ECS meeting, Vancouver, BC, Canada, May 2022.

References

1. J. Liu, Z. Bao, Y. Cui, E. J. Dufek, J. B. Goodenough, P. Khalifah, Q. Li, B. Y. Liaw, P. Liu, A. Manthiram, Y. S. Meng, V. R. Subramanian, M. F. Toney, V. V. Viswanathan, M. S. Whittingham, J. Xiao, W. Xu, J. Yang, X.-Q. Yang and J.-G. Zhang, *Nature Energy*, 2019, 4, 180-186.
2. J. Qian, B. D. Adams, J. Zheng, W. Xu, W. A. Henderson, J. Wang, M. E. Bowden, S. Xu, J. Hu and J.-G. Zhang, *Advanced Functional Materials*, 2016, 26, 7094-7102.
3. B. J. Neudecker, N. J. Dudney and J. B. Bates, *Journal of The Electrochemical Society*, 2000, 147, 517.
4. C. Niu, D. Liu, J. A. Lochala, C. S. Anderson, X. Cao, M. E. Gross, W. Xu, J.-G. Zhang, M. S. Whittingham, J. Xiao and J. Liu, *Nature Energy*, 2021, 6, 723-732.

Acknowledgements

Key contributor: Hyung-Seok Lim.

XVI Beyond Li-ion R&D: Solid-State Batteries

Lithium-ion batteries have made tremendous progress in the last two decades and are now instrumental in creating worldwide demand for electric vehicle (EVs), but the liquid organic electrolyte in lithium-ion battery cells is highly reactive and flammable. There is growing interest in the use of solid lithium-ion conducting materials in place of the liquid electrolyte. Solid electrolyte materials are non-flammable, and they not only allow more robust cell operation but also the integration of metal-based anodes needed to achieve VTO's aggressive cost, energy density, and cycle life targets. Solid electrolyte materials face challenges, however, including low conductivity, poor voltage stability, and inadequate mechanical properties. VTO research in this area attempts to overcome these challenges by research of new solid electrolytes that can address materials challenges and enable next-generation chemistries, complementary diagnostics, and modeling techniques to ensure materials development progress.

The rest of this chapter contains detailed reports on the status of the following individual projects.

- Lithium Dendrite-Free Solid Electrolytes for High Energy Lithium Batteries (University of Maryland, College Park)
- All Solid State Batteries Enabled by Multifunctional Electrolyte Materials (Solid Power Inc.)
- Development of Thin, Robust, Lithium-Impenetrable, High-Conductivity, Electrochemically Stable, Scalable, and Low-Cost Glassy Solid Electrolytes for Solid-State Lithium Batteries (Iowa State University)
- Physical and Mechano-Electrochemical Phenomena of Thin Film Lithium-Ceramic Electrolyte Constructs (University of Michigan)
- Low Impedance Cathode/Electrolyte Interfaces for High Energy Density Solid-State Batteries (University of Maryland, College Park)
- Molecular Ionic Composites: A New Class of Polymer Electrolytes to Enable All Solid-State and High Voltage Lithium Batteries (Virginia Polytechnic Institute and State University)
- Hot Pressing of Reinforced All-solid-state Batteries with Sulfide Glass Electrolyte (General Motors LLC)
- Developing Materials for High-Energy-Density Solid State Lithium-Sulfur Batteries (Penn State University, University Park)
- Developing an In-situ Formed Dynamic Protection Layer to Mitigate Lithium Interface Shifting: Preventing Dendrite Formation on Metallic Lithium Surface to Facilitate Long Cycle Life of Lithium Solid State Batteries (University of Wisconsin-Milwaukee)
- Fundamental Understanding of Interfacial Phenomena in Solid-State Batteries (General Motors)
- Multidimensional Diagnostics of the Interface Evolutions in Solid-State Lithium Batteries (University of Houston)
- First-Principles Modeling of Cluster-Based Solid Electrolytes (Virginia Commonwealth University)
- Predictive Engineering of Interfaces and Cathodes for High-Performance All Solid-State Lithium-Sulfur Batteries (University of Louisville)
- Design of Strain Free Cathode – Solid State Electrolyte Interfaces Using Chemistry-Informed Deep Learning (ANL)
- Enabling continuous production of defect-free, ultrathin sulfide glass electrolytes for next generation solid state lithium metal batteries (ANL)
- Stable Solid-State Electrolyte and Interface for High-Energy All-Solid-State Lithium-Sulfur Battery (PNNL)
- Scale-Up of Novel Li-Conducting Halide Solid State Battery Electrolyte (LBNL)
- Low-Pressure All Solid State Cells (NREL)
- 3D Printing of All-Solid-State Lithium Batteries (LLNL)
- Substituted Argyrodite Solid Electrolytes and High-Capacity Conversion Cathodes for All-Solid-State Batteries (Oak Ridge National Laboratory).

- Multifunctional Gradient Coatings for Scalable, High-Energy-Density Sulfide-Based Solid-State Batteries (ANL)
- Thick Selenium-Sulfur Cathode Supported Ultra-thin Sulfides Electrolytes for High-energy All-solid-state Lithium Metal Batteries (ANL)
- Synthesis of Composite Electrolytes with Integrated Interface Design (ANL)
- Polymer Electrolytes for Stable Low Impedance Solid State Battery Interfaces (ORNL)
- Inorganic-Polymer-Composite Electrolyte with Architecture Design for Lithium Metal Solid State Batteries (BNL)
- Ion Conductive High Li⁺ Transference Number Polymer Composites for Solid-State Batteries (LBNL)
- Precision Control of the Li Surface for Solid-state Batteries (Oak Ridge National Laboratory)
- Lithium Halide-Based Superionic Solid Electrolytes and High Voltage Cathode Interfaces (ORNL)
- Polyester-Based Block Copolymer Electrolytes for Lithium-Metal Batteries (UCB)
- Development of All Solid-State Battery using Anti-Perovskite Electrolytes (ANL)
- High-Conductivity and Electrochemically Stable Lithium Thioborate Solid-State Electrolytes for Practical All-Solid-State Batteries (Stanford University)
- Solid state batteries with long cycle life and high energy density through materials design and integration (LBNL).

XVI.1 Lithium Dendrite-Free Solid Electrolytes for High Energy Lithium Batteries (University of Maryland, College Park)

Chunsheng Wang, Principal Investigator

University of Maryland, College Park
Room 3236 Jeong H. Kim Engineering Building
College Park, MD 20742
E-mail: cswang@umd.edu

Tien Duong, DOE Technology Development Manager

U.S. Department of Energy
E-mail: Tien.Duong@ee.doe.gov

Start Date: October 1, 2019
Project Funding: \$1,250,000

End Date: December 30, 2022
DOE share: \$1,000,000

Non-DOE share: \$250,000

Project Introduction

The development of all-solid-state Li metal batteries (ASSLBs) using nonflammable inorganic or organic solid-state electrolytes (SSEs) was reckoned as the promising direction due to their enhanced safety and high energy density. However, lithium dendrite growth during charge/discharge cycles still limits the use of all-solid-state batteries.

In our project, a criterion for lithium dendrite suppression that is developed through systematical investigation on thermodynamics and kinetics of lithium dendrite growth was proposed to guide the SSE design and Li/SSE interface modification. $\text{Li}_7\text{N}_2\text{I-LiOH}$ and Li_3YCl_6 solid electrolyte with high ionic conductivity and low electronic conductivity was used to validate the criterion for lithium dendrite suppression and achieve the project objective. Different surface modifications were also explored to enhance the dendrite suppression capability of SSEs.

Objectives

The objective of this project is to research, develop, and test Li-metal-based batteries that implement solid Li-ion conductors (LICs) equipped with $\text{Li}_7\text{N}_2\text{I-LiOH}$ SSE capable of achieving cell performance of 350 Wh/Kg energy density for 1000 cycle life with a cost of $\leq \$100/\text{kWh}$. To achieve these, the team will 1) establish the relationship among interface energy, lithium plating/stripping overpotential, interface resistance, SSE stability with lithium, and critical current density (CCD). 2) The dendrite suppression criterion will be developed based on the relationship. 3) The dendrite suppression capability for the $\text{Li}_7\text{N}_2\text{I-LiOH}$ pellet will be evaluated by testing the CCD. 4) The $\text{Li}_7\text{N}_2\text{I-LiOH}$ electrolytes and $\text{Li}_7\text{N}_2\text{I-LiOH/Li}_3\text{YCl}_6$ bi-layer electrolytes will be used to validate the developed dendrite suppression criterion and support Nickel Manganese Cobalt oxides (NCM) cathodes. 5) New engineering methods would be developed to suppress the Li dendrite to realize ASSLB.

Approach

Li metal surface will be engineered with the interface to suppress dendrite growth and maintain cycling stability. Thin-film solid electrolytes will be fabricated by reducing particle sizes and a polymer binder. A high energy density solid-state battery will be assembled by combining Li modification, thin-film solid electrolyte, and the thick and stable positive electrode.

Results

Suppressing Li dendrite by introducing a composite polymer layer (CPI)

Generally, the interface film or SEI will be formed between the SSEs and Li anode via electrochemical or chemical reactions. Compared with the SSE-derived SEI, the introduced SEI can be denser and more ion-conductive via interface engineering. Figure XVI.1.1.a shows the prepared gel-electrolyte, which is solid at

room temperature and melts after heating to 40°C or higher. The composite polymer has been reported to enable stable cycling of Li||Li cells over 1000 h, indicating a uniform Li dissolution/deposition based on a dynamic stability mechanism because of the formation of robust SEI and the confinement of the solvent molecule of the polymer. The CPI was then applied to the full cell to evaluate its performance. Figure XVI.1.1.b shows the schematic of the ASSLMB, which utilizes the LPSC and LYC film as the thin electrolyte. The ratio of NMC622, LYC, and carbon black is 70:26:4, while the Li with a design of CPI (eLi) is used as the anode. The eLi/LPSC-LYC/NMC622 full cells were tested between 2.8 V and 4.2 V at RT under a stacking pressure of 8-10 MPa. The ASSLMB based on the designed eLi anode presents excellent rate capability when charged/discharged with different C-rates ranging from 0.1 to 1.0 C (Figure XVI.1.1.c and d). The cell can deliver high capacities of 165, 147, 118, and 76 mAh g⁻¹ at C-rates of 0.1, 0.2, 0.5 and 1.0 C, respectively, while showing a high average CE of >99%. Long-term cycling performance was also evaluated with the full cell at 0.15 C as shown in Figure XVI.1.1.D.e. The proposed SSB has an 81 % capacity retention after 100 cycles without a sharp capacity drop, which is benefited from the robust SEI layer formed by the CPI. The CE of a full cell with eLi is around 99.5% on average, which is much higher than the cell with a fresh Li anode.

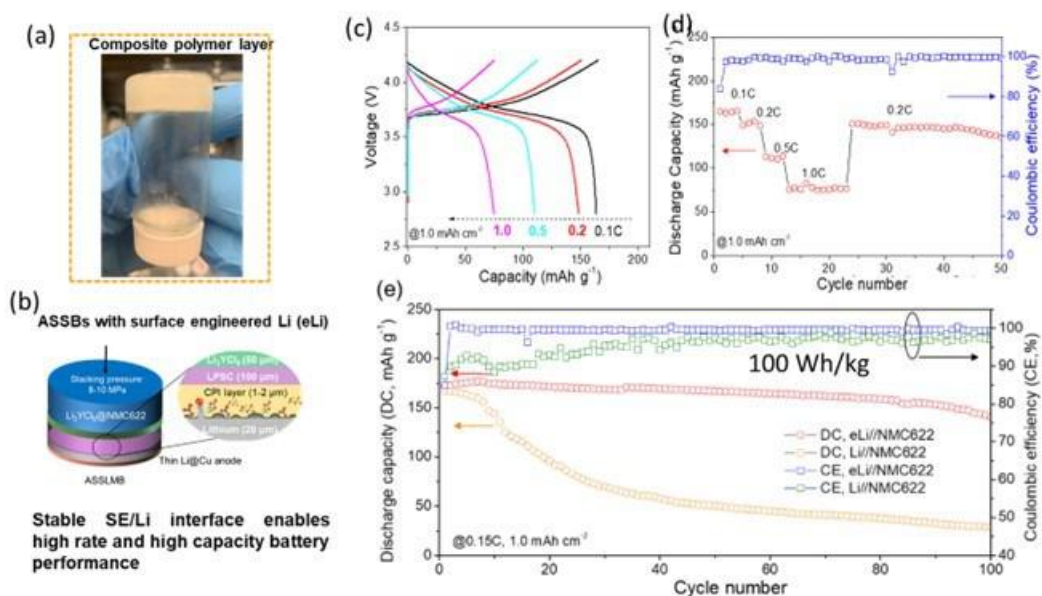


Figure XVI.1.1 (a) Digital image of the gel-like electrolyte. (b) Schematic of the solid-state full cell with the designed eLi anode. (c) Charge-discharge curves of the cell at rates of 0.1, 0.2, 0.5, and 1.0 C. (d) Cycling performance of eLi/LPSC/NMC622 solid cell at 0.2 C with an areal capacity of 1.0 mAh cm⁻², 1C = 160 mA g⁻¹. (e) Comparison of the cycling performance of NMC622 solid full cell with fresh Li and eLi anodes at 0.15C, the cathode has an areal capacity of 1.0 mAh cm⁻².

Fabricating thin-film LPSC-polymer composite electrolytes for high energy density

In order to achieve a high energy density of the ASSLB, a thin and robust solid electrolyte is required as illustrated in Figure XVI.1.2.a. To fabricate a free-standing thin-film electrolyte, 0.5wt% of acrylonitrile butadiene rubber (NBR) binder was mixed with wet-milled LPSC powder and pressed at 180 MPa. With the free-standing thin film electrolyte, we are able to design ASSBs with high energy density. Two designs are reported (Figure XVI.1.2.b). In design I, 31.25 mg of the composite cathode, 15 mg electrolyte, and thin Li were used, which can reach an energy density of 350 Wh/kg. Figure XVI.1.2.c shows the SEM image and EDS mapping of the full cell using the design I. As we can see, a ~ 50 μm thin electrolyte is sandwiched between Li and composite cathode. However, the cell was short-circuited during 1st charge, probably due to heterogeneous stress distribution during Li plating, which will lead to electrolyte crack and cell short-circuit. To avoid mechanical breakdown, we increase the electrolyte mass to 30mg and reduce the cathode load to 12.5 mg, which was marked as design II. The designed thin-film battery with lower cathode loading can be

charged/discharged for 9 cycles (Figure XVI.1.2.d) and the cell can deliver a theoretical energy density of 153.5 Wh/kg.

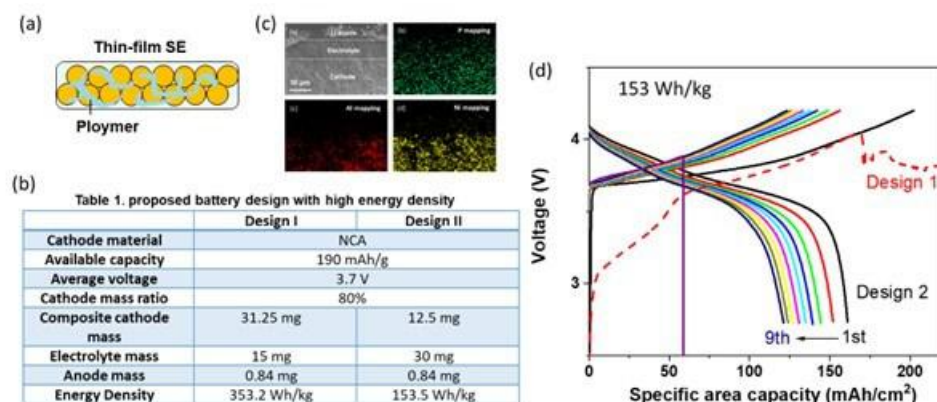


Figure XVI.1.2 (a) Schematic of the proposed thin-film solid electrolyte. (b) EDS mapping of the full cell with the thin-film electrolyte of design 1. (c) charge-discharge curves of full cells with design 1 (dash line) and design 2 (solid line) in Table 1. (d) table of the proposed battery with a different structure.

High mass loading cathode enabled by Li anode modification

Li anode modification is also an effective way to increase the energy density of full cells. As shown in Figure XVI.1.3.a, we developed a modified Li anode that shows a high critical current density of 8.0 mA/cm² at a fixed capacity of 4.0 mAh/cm² at a temperature of 80°C. Due to the high Li dendrite suppression capability of the modified Li anode, a high cathode loading was able to match with modified Li to assemble the NMC811||Li full cell, which can provide a high capacity of 7.9 mAh/cm² at a current density of 1 mA/cm² and temperature of 80°C (Figure XVI.1.3.b). The schematic of the structure was shown in Figure XVI.1.3.c. The cells were assembled by 70 mg of composition cathode with NMC811 weight ratio of 60% and the high weight of the electrolyte layer (25mg). The cell-level energy density was 223.8 Wh/kg for the assembled NMC811 full cell using the modified Li anode (Figure XVI.1.3.d).

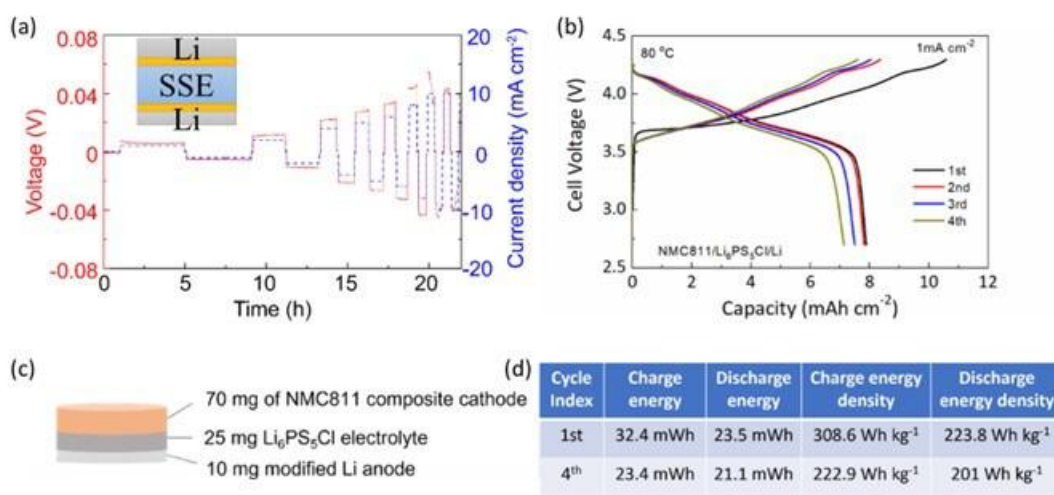


Figure XVI.1.3 (a) Critical current density of Li/LPSC/Li symmetric cell at fixed capacity of 4 mAh/cm² under 80 °C. (b) Cycling performance of the Li || NMC811 cell. (c) Schematic of the proposed thick cathode solid-state battery. (d) Table of calculated energy density of the corresponding battery.

Optimizing the structure of solid-state batteries for higher energy density and lower cost

In the previous sections, we evaluated three cell structures for high energy density, long cycling stability, and low cost. The energy density comparisons were shown in Figure XVI.1.4.a and the detailed structural parameters were listed in Figure XVI.1.4.b. Structure 1 could provide stable cycling performance with 81% of retention after 100 cycles (Figure XVI.1.1.e). However, the use of double-layer electrolytes limits the energy density. Moreover, yttrium(III) chloride is an expensive ingredient to prepare LYC electrolytes, which also increases the cost. Structure 2 replaces the double-layer electrolyte with solvent-modified LPSC. As a result, the energy density increases from 100 Wh/kg to 153 Wh/kg (Figure XVI.1.2.c). The energy density change is not significant because the cathode loading is still small. To solve the remaining issue, a modified Li anode was used to match with 78.5 mg of composite NMC811 cathode. The structure 3 NMC811||Li full cell can provide a high capacity of 7.9 mAh/cm² at a current density of 1 mA/cm² and temperature of 80°C. The cell-level energy density was >250 Wh/kg for the assembled NMC811 full cell using the modified Li anode. The low energy density is caused by the low weight ratio (60%) of NMC811 in the composite cathode and the high weight of the electrolyte layer (25mg). If the weight of the LPSC electrolyte layer can decrease to 10 mg, and the weight ratio of NMC811 in the composite cathode can be improved to 85%, the whole weight of the cell will be reduced from 105 mg to 69.4 mg, which will increase the cell-level energy density to 338.6 Wh/kg. We will further optimize the NMC811 composite cathode and the thin-film electrolyte layer in our further work.

Since structure 3 is the most promising design to reach higher energy density, the cost evaluation was further performed. Pie chart in Figure XVI.1.4c shows that solid electrolytes will take up 91.91% of cell cost if the commercial LPSC electrolyte was used. This is because the manufacturing of solid electrolytes is still in its infancy. Therefore, the unit price of a solid electrolyte is much higher than that of an anode and cathode. By adopting the price of raw material for solid electrolytes (Figure XVI.1.4.d), the cost percentage of LPSC electrolytes in design 3 was dramatically reduced to 57%. The estimated cost for structure 3 is \$208.8 /kWh. 90% further price reduction can be expected with the large-scale manufactory of the solid electrolyte. Due to the absence of transition metal, the speculation is reasonable. Therefore, structure 3 using a modified Li anode and thin LPSC electrolyte is a promising choice to realize high energy density solid-state batteries.

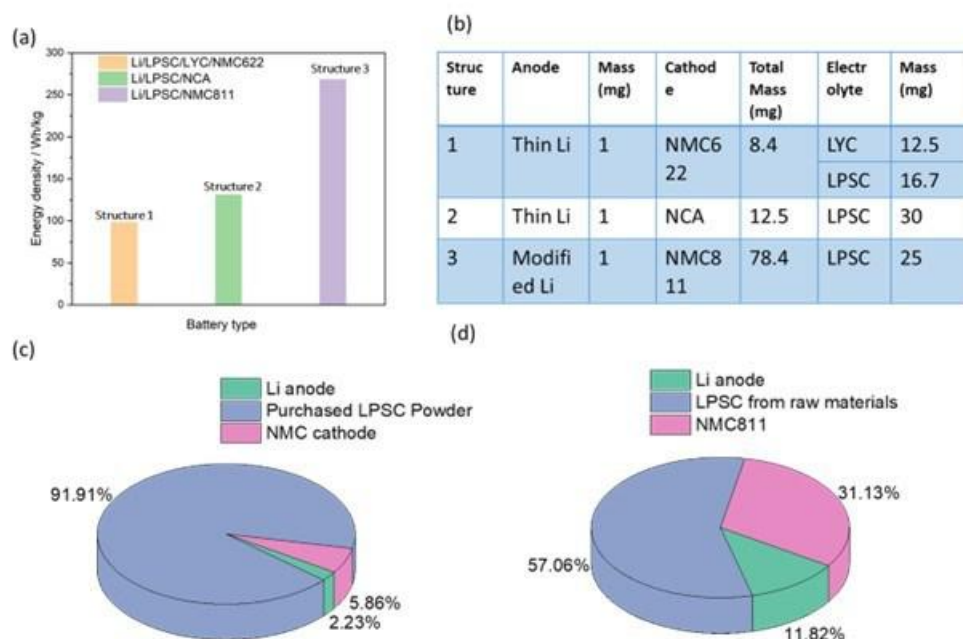


Figure XVI.1.4 (a) Calculated energy density of three structural designs. (b) Structural parameters of three evaluated cell structure (c) Cycling performance of the Li||NMC811 cell. (c,d) Cost evaluation for structure design 3. The prices of LPSC was adopted from commercial in c and from raw materials in d.

Conclusions

1. We engineered Li anode with a rationally designed gel-electrolyte to achieve stable cycling of NMC622 solid full cell with an energy density of 100 Wh/kg for 100 cycles with a retention of 81%.
2. We fabricated NCA || Li full cell using a thin film composite electrolyte of polymer and microstructural optimized LPSC to reach an energy density of 153 Wh/kg.
3. A high critical current density of 8 mA/cm² at a fixed capacity of 4.0 mAh/cm² was achieved using a modified Li anode.
4. We developed a NMC811||Li full cell with high specific energy design of 223 Wh/kg, low cost by matching a thick electrode with a modified Li anode.

Key Publications

1. X. He, X. Ji, B. Zhang, N. Rodrigo, S. Hou, K. Gaskell, T. Deng, H. Wan, S. Liu, J. Xu, B. Nan, B. Lucht, C. Wang, Tuning interface lithiophobicity for lithium metal solid-state batteries, *ACS Energy Lett.*, 2022, 7 131-139.
2. T. Deng, X. Ji, L. Zou, O. Chiekezi, X. Fan, L. Cao, T. R. Adebisi, H. Chang, H. Wang, B. Li, X. Li, C. Wang, D. Reed, J.-G. Zhang, V. Sprenkle, C. Wang, X. Lu, Interfacial engineering enabled practical low-temperature sodium metal battery, *Nat. Nanotechnol.*, 2022, 17, 269-277.
3. Hongli Wan, Zeyi Wang, Sufu Liu, Tao Deng, Xinzi He, Weiran Zhang, Chunsheng Wang, Critical Interphase Overpotential as a Lithium Dendrite Suppression Criterion for All-Solid-State Lithium Battery Design. *Nature Energy*, Under Revise.
4. Xiao Ji, Xinzi He, Chi Chen, Singyuk Hou, Jijian Xu, Bao Zhang, Yunjun Ruan, Jiaxun Zhang, Tao Deng, Ji Chen, Chunsheng Wang, Void Suppressive Lithium Anodes for All-Solid-State Batteries, *Nature Materials*, Under review.
5. H. Wan, B. Zhang, S. Liu, J. Zhang, X. Yao, C. Wang, Understanding LiI-LiBr Catalyst Activity for Solid State Li₂S/S Reactions in an All-Solid-State Lithium Battery, *Nano Lett.* 2021, 21, 8488-8494.
6. H. Wan, S. Liu, T. Deng, J. Xu, J. Zhang, X. He, X. Ji, X. Yao, C. Wang, Bifunctional Interphase-Enabled Li₁₀GeP₂S₁₂ Electrolytes for Lithium-Sulfur Battery, *ACS Energy Lett.*, 2021, 6, 862-868.
7. X. Ji, S. Hou, P-F. Wang, X. He, N. Piao, X. Fan, C. Wang, Solid-State Electrolyte Design for Lithium Dendrite Suppression, *Adv. Mater.* **2020**, 2002741.

XVI.2 All Solid State Batteries Enabled by Multifunctional Electrolyte Materials (Solid Power Inc.)

Pu Zhang,, Principal Investigator

Solid Power Inc.
486 S Pierce Ave, Suite E
Louisville, CO 80027
E-mail: pu.zhang@solidpowerbattery.com

Tien Duong, DOE Technology Development Manager

U.S. Department of Energy
E-mail: Tien.Duong@ee.doe.gov

Start Date: October 1, 2019
Project Funding: \$398,544

End Date: September 30, 2022
DOE share: \$319,246

Non-DOE share: \$79,298

Project Introduction

Solid Power is teaming with University of California San Diego (Prof. Shirley Y. Meng) to develop a high energy, long life, low cost, and safe all-solid-state-battery (ASSB). The battery is enabled by a multifunctional solid state electrolyte (SSE). The project will enable scalable production of large format solid state batteries required by the vehicle market and building domestic battery manufacturers as leaders in the global vehicle ASSB production.

Objectives

The project objective is to develop Li-metal solid batteries enabled by multifunctional SSEs for EV application. The ultimate goal is scalable production of large-format ASSBs able to deliver ≥ 350 Wh/kg specific energy, ≥ 1000 cycle life, and $\leq \$100/\text{kWh}$ cost.

Approach

The project will develop a high-performance Li-metal all-solid-state cell enabled by a multifunctional SSE. The new SSE will: (1) have high conductivity (up to 10 mS/cm), (2) be stable against lithium metal and high-voltage cathode (0-4.5 V), (3) promote uniform lithium plating (enabling $> 2C$ charge rate), and (4) be compatible with large-scale manufacturing processes. The specific cell chemistry to be demonstrated will be the SSE with Li-metal anode and high-nickel-content Li-metal oxide cathode. The all-solid-state cell will be assembled by scalable roll-to-roll processes developed by Solid Power.

Results

SSE material optimization

Solid Power's halogenated LPS material was used as a starting point. Li_2S , P_2S_5 , a halogen and other selected dopants were mechanically milled to form glassy sulfide electrolytes. A subsequent heat-treatment was conducted to obtain glass-ceramic solid electrolytes. The electrolyte compositions and synthesis processes have been developed and optimized by using a "Design of Experiments" technique. Li ion conductivity and critical current density (CCD) with Li are the key criteria to qualify the electrolyte materials, followed by a full cell performance confirmation. The optimized electrolyte has shown a Li ionic conductivity of 6 mS/cm at 25°C and 2 mS/cm at 0°C. A CCD of 20 mA/cm² at 70°C is also demonstrated with the electrolyte. The progress of the electrolyte development is shown in Figure XVI.2.1.

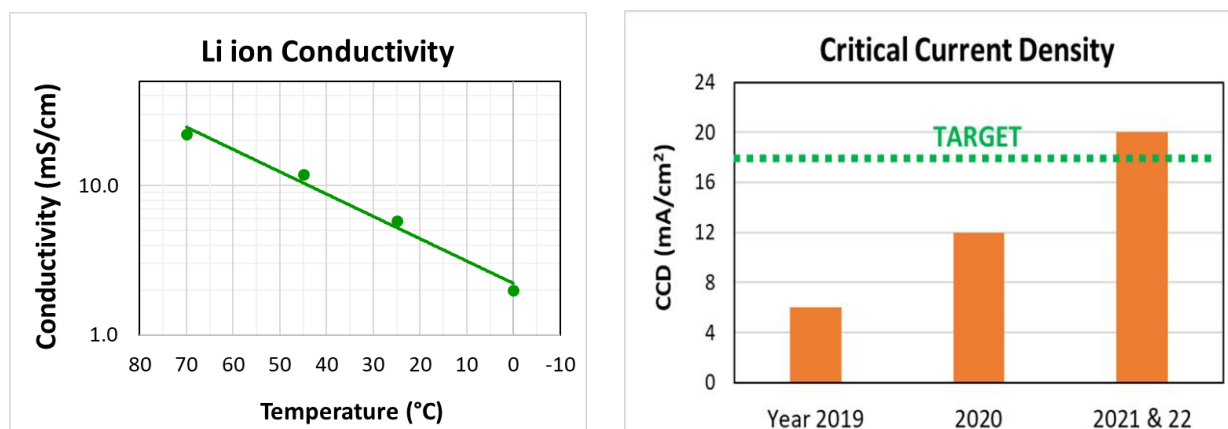


Figure XVI.2.1 The electrolyte development progress: Li ion conductivity and CCD at 70°C

SSE separator fabrication

The SSE separator coating process has been developed at pilot scale. A separator slurry was prepared by mixing the SSE powder, a binder, and a solvent by using a planetary mixer. The slurry was then cast on a carrier film on a slot-die coater. A roll-to-roll separator (≥ 100 m and ≤ 40 μ m) has been demonstrated. Figure XVI.2.2 shows a separator coating on the slot-die coater at Solid Power.



Figure XVI.2.2 A solid-state-electrolyte separator coating on a slot-die coater

Full pouch cell cycle life

A single layer pouch cell (at 6 mAh) was assembled for performance demonstration. The cell contained a NMC 622 composite cathode (at 3 mAh/cm²), a thin Li metal anode, and a SSE separator. When tested at C/5 - C/5, 2.8V - 4.2V, and 45°C, the cell showed 87% capacity retention after 750 cycles (in Figure XVI.2.3). It should be noted that the cell contains a pure Li anode. Surface modification of the Li anode is expected to improve the cycling stability further.

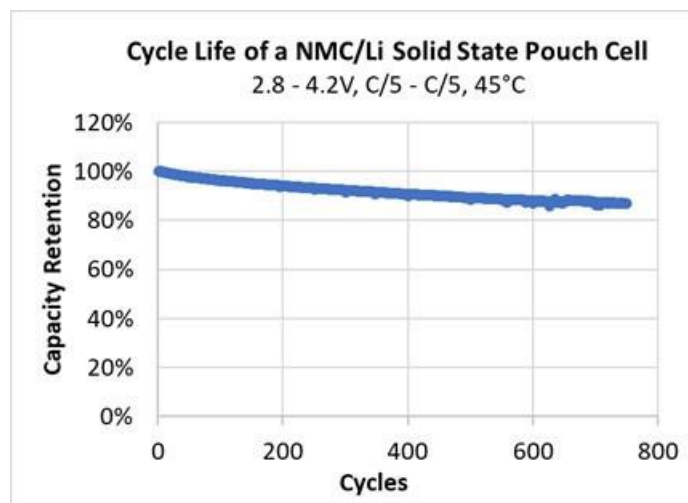


Figure XVI.2.3 Cycle life of an NMC/Li metal solid state pouch cell

Full pouch cell calendar life

The calendar life was evaluated in a 6 mAh Li-NMC pouch cell. The cell was formed at 2.5V-4.2V at C/10 and 45°C. It was then charged to 4.2V at C/10 & 45°C (100% SOC) and stored at 60°C for 30 days. After the storage, the cell was discharged to 2.5V (“capacity retention”), recharged to 4.2V, and discharged again to 2.5V (“capacity recovery”) at C/10 and 45°C. As shown in Figure XVI.2.4, the cell capacity retention is 87% and recovery is 95%, when compared to the initial discharge capacity, after the storage. Both the capacity retention and recovery from the ASSB cell are comparable to or better than the conventional Li ion battery cell at the same testing conditions. The storage result confirms long term stability of the solids state electrolyte and suggests the ASSB cell having a calendar life > 10 years.

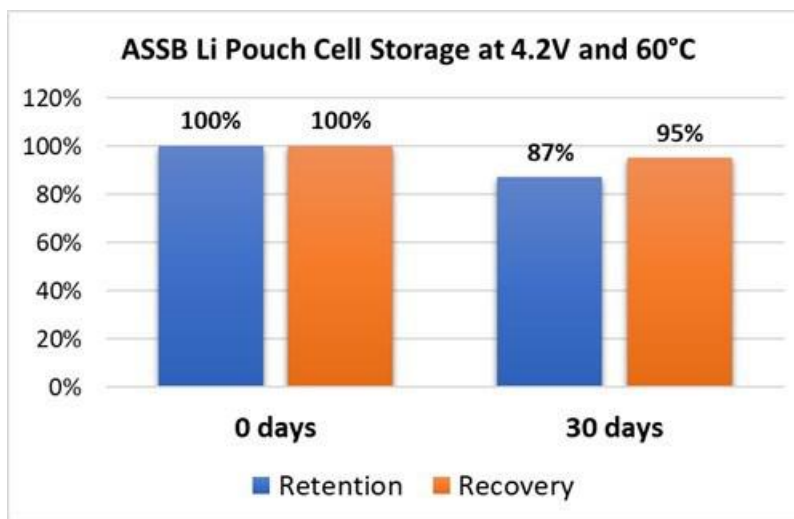


Figure XVI.2.4 Storage test of an NMC/Li metal solid state pouch cell at 60°C

Conclusions

Multifunctional SSE materials have been developed and optimized with high conductivity and electrochemical stability. SSE separator films have been coated by using a roll-to-roll process. All-solid-state NMC-Li pouch cells containing the developed SSE have been assembled in a pouch format. A cycle life of > 750 at 100% DOD and 45°C has been demonstrated in a full pouch cell.

XVI.3 Development of Thin, Robust, Lithium-Impenetrable, High-Conductivity, Electrochemically Stable, Scalable, and Low-Cost Glassy Solid Electrolytes for Solid-State Lithium Batteries (Iowa State University)

Steve W. Martin, Principal Investigator

Iowa State University
528 Bissell Rd
Ames, IA, 50011-1096
E-mail: swmartin@iastate.edu

Tien Duong, DOE Technology Development Manager

U.S. Department of Energy
E-mail: Tien.Duong@ee.doe.gov

Start Date: October 1, 2019
Project Funding: \$1,252,595

End Date: September 30, 2022
DOE share: \$1,000,000

Non-DOE share: \$252,595

Project Introduction

The development of thin, < 50 microns, mixed oxy-sulfide-nitride (MOSN) mixed glass former (MGF) glassy solid electrolyte (GSE) films that yield superior performance in a safer, lower-cost, and Li-dendrite impenetrable form will be used to develop new solid-state lithium batteries (SSLBs). It is expected that high rate and long cycle life SSLBs can be achieved using thin-film MOSN GSEs. The new GSEs in SSLBs are anticipated to increase the energy density (anode basis) from ~ 300 mAh/g to ~ 4,000 mAh/g, enabling replacement of internal combustion engines in both light and heavy-duty vehicles. Each 20% reduction in the ~ 1.6 billion liters of gasoline used per day in the United States would reduce CO₂ emissions by ~ 4 billion kg CO₂ per day. The team will also increase scientific and engineering knowledge of thin-film GSEs in SSLBs.

Objectives

The objective of this project is to develop new high Li⁺-conducting MOSN GSE thin-films, < 50µm, that are impermeable to lithium dendrites, scalable through low-cost glass manufacturing, chemically and electrochemically stable, and will enable low-cost, high-energy-density SSLBs. It is expected that the SSLBs constructed from these new MGF MOSN GSEs will meet and exceed all program objectives: useable specific energy @ C/3 ≥ 350 Wh/kg, calendar life 15 years, cycle life (C/3 deep discharge with < 20% energy fade) 1,000, and cost ≤ \$100/kWh.

Approach

The MOSN MGF GSEs have been prepared and optimized in previous work in bulk glass form and exhibit high ionic conductivity and the necessary thermal stability to be successful in drawing into a thin film. In this project, the glass chemistry has been further improved to further optimize thermal stability and electrochemical properties. Optimized glass chemistries have been cast into large preforms, 10 cm x 30 cm x 1 cm and the drawing conditions have started to be optimized to generate thin-films, 50 µm x 5 cm, for use at the cell level.

Results

Compositional optimization and characterization of MOSN MGF GSEs

Several glass compositions have been studied in the previous two years of the project, with most research being conducted on the MOS ISU-6, based in the Li₂S – SiS₂ – LiPO₃ system, and the MOSN ISU-7 series, based in the Li₂S – SiS₂ – LiPO₃ – LiPON system. Previous work has shown that these glasses possess good stability against lithium metal from 0-5 V, stable cycling at low current densities, high conductivity near 10⁻³ S/cm, and a high working range (difference of crystallization temperature (T_c) and glass transition temperature

(T_g) greater than 100°C . While the working range can be a simple method to predict the drawability of a glass, it has been determined that it is not a complete picture of the thermal properties of a glass to fully predict the drawing abilities.

It was determined that a series of isothermal differential scanning calorimetry (DSC) experiments would be a good method to determine the crystallization behavior of various glasses. To determine the effect of the anion exchange between sulfur, oxygen, and nitrogen, three different glasses comparable to ISU-6 were synthesized: a pure sulfide, where the LiPO_3 was replaced with LiPS_3 ; the MOS ISU-6; and a MOSN where a portion of the LiPO_3 was replaced with LiPON .

Using the Johnson-Mehl-Avrami-Kohnogorov model [1], a time-temperature-transition (TTT) model was developed to determine the crystallization behavior during isothermal heating and cooling. Along with this, the Mauro-Yue-Ellison-Gupta-Allan (MYEGA) [2] model was utilized to determine the viscosity of each glass using simple DSC experiments. Figure XVI.3.1A shows the TTT model for the sulfide, MOS, and MOSN glasses studied, and Figure XVI.3.1B shows the expected viscosity behavior of these glasses as well. From these figures, we can see that the MOS glass shows the best viscosity and crystallization behavior for drawing, and as such, the ISU-6 composition was scaled up for drawing.

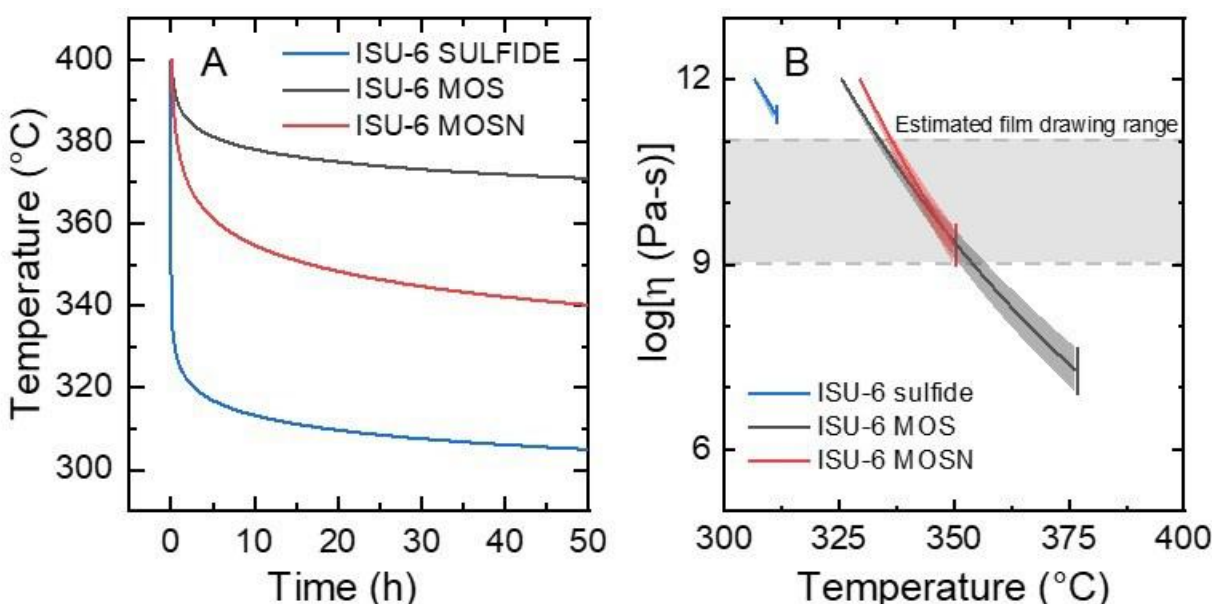


Figure XVI.3.1 A) Modeled TTT curves showing the 10% crystallization threshold for the pure SULFIDE, MOS, and MOSN glasses. B) Modeled viscosity curves for the three-glass series. Cutoffs for the curves are at the 15-hour mark of each glass on the TTT curve.

Optimization of processing conditions for the production of thin-film MOS MGF GSE ribbons

Several advancements have been made in optimizing the processing of thin-film ISU-6. Through careful control of the small-scale batches (~ 10 g), a ~ 200 g preform was able to be cast and annealed. This preform, shown in Figure XVI.3.2A, was then loaded into our custom-built draw tower and heated to a temperature around 355°C . While more difficult to draw than a pure oxide, small sections of thin-film ribbons have been generated with thicknesses around $60\text{ }\mu\text{m}$, shown in Figure XVI.3.2C, and large sections of thin-film ribbons have been synthesized with thicknesses around $200\text{ }\mu\text{m}$, shown in Figure XVI.3.2B. In this process, it has been noticed that control of the composition, and defects inside the glass are extremely important to allow for the drawing of high-quality films less than $100\text{ }\mu\text{m}$. More work is still being conducted to further improve the quality of the preform to generate larger amounts of thinner films.

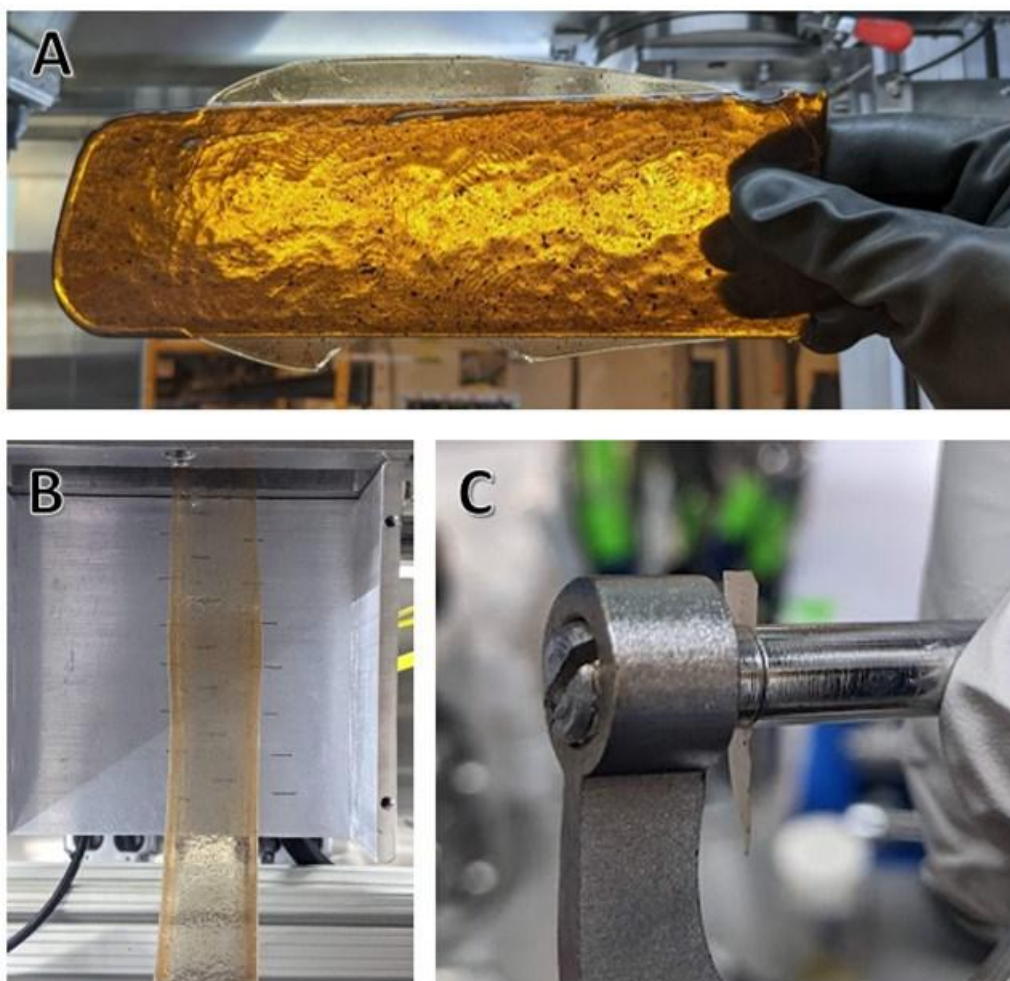


Figure XVI.3.2 A) An image of the ISU-6 preform following casting and annealing, approximately 10 cm x 25 cm x 0.5 cm. B) An image of thin film ISU-6 being drawn of around 200 μm in thickness. C) An image of a small piece of 60 μm thin film produced from the drawing process.

Fabricate and test ASSLBs utilizing GSEs in small-area planar format

Small samples of the drawn thin film were taken and placed into Li | GSE | Li symmetric cells and tested to determine the conductivity of the thin-film after drawing. Each cell was fabricated and allowed to rest for 24 hours with electrochemical impedance spectroscopy (EIS) scans conducted every 30 minutes at room temperature. It is to be noted, that the impedance arc associated with interfacial impedance decreased in size over time, indicating the formation of a lower resistance interface. Following this rest, the symmetric cells were tested in a Novocontrol Dielectric Spectrometer to determine the temperature dependent ionic conductivity. These results can be seen in Figure XVI.3.3A. These results were also normalized to area specific resistance (ASR) and compared to the expected ASR calculated from the bulk conductivity of ISU-6, shown in Figure XVI.3.3B. From these graphs, we can see a very good match in the activation energy for conduction indicating that the conduction mechanism is consistent, and we see a slight decrease in the conductivity typically. This lower conductivity may be due to the bulk conductivity being determined through blocking sputtered gold electrodes with well defined areas, and the thin film conductivity being with thicker lithium electrodes that may be reacting slightly with the surface of the film. More work is being conducted to generate thinner films for electrochemical testing, including symmetric cell cycling.

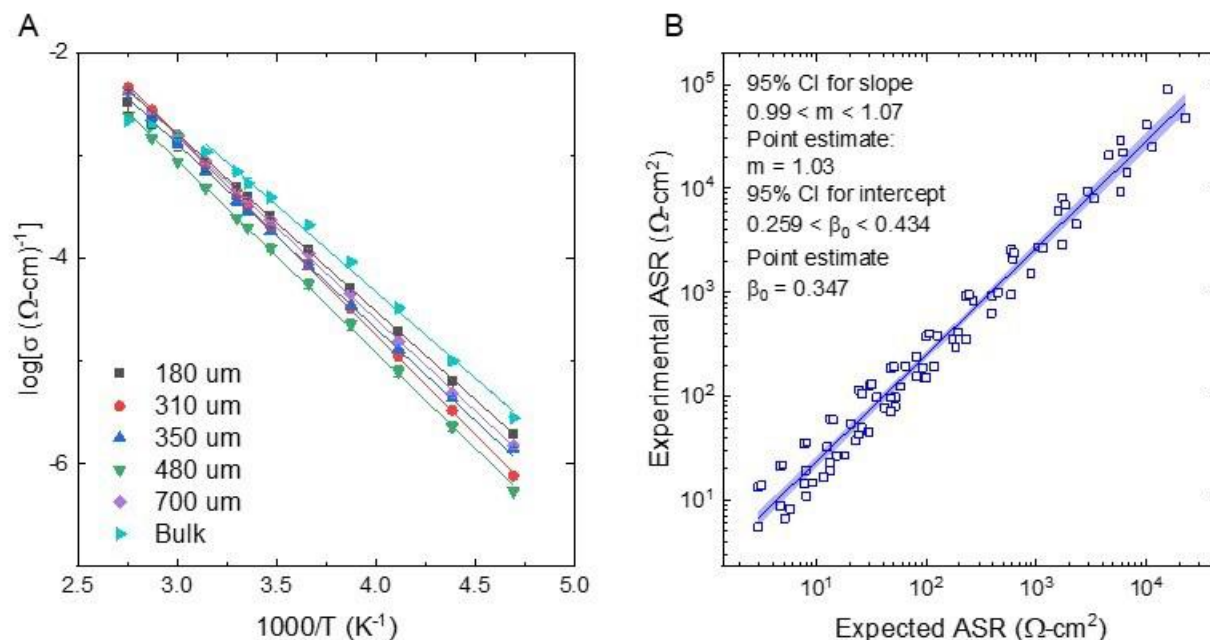


Figure XVI.3.3 A) Arrhenius plot showing conductivity of various thin-film samples compared to the conductivity of a bulk glass piece. B) Expected ASR compared to experimental ASR showing that the thin films exhibit behavior close to what is expected.

More full cell studies were conducted this fiscal year, primarily with LiFePO_4 active materials. Recently a hybrid cell architecture has shown good promise, comprised of a lithium foil anode, a bulk piece of ISU-6, and a tape-cast composite cathode containing GSE, LiFePO_4 , conductive carbon, and a binder. At the electrolyte-cathode interface, around 0.5 μL of an ionic liquid triglyme + LiTFSI was added to improve interfacial properties. A cell made with this architecture exhibited excellent behavior with an initial specific capacity over 100 mAh/g, and with a Coulombic efficiency over 99% for most of the 100 cycles it was cycled at $C/50$, as can be seen in Figure XVI.3.4. It is believed that the outlier data points for various cycles are due to differences in room temperature throughout the day, and power outages experienced during the months-long cycling. Other work is being done to develop Li-S based composite cathodes for use with these GSEs, but this is still at the beginning stages of testing.

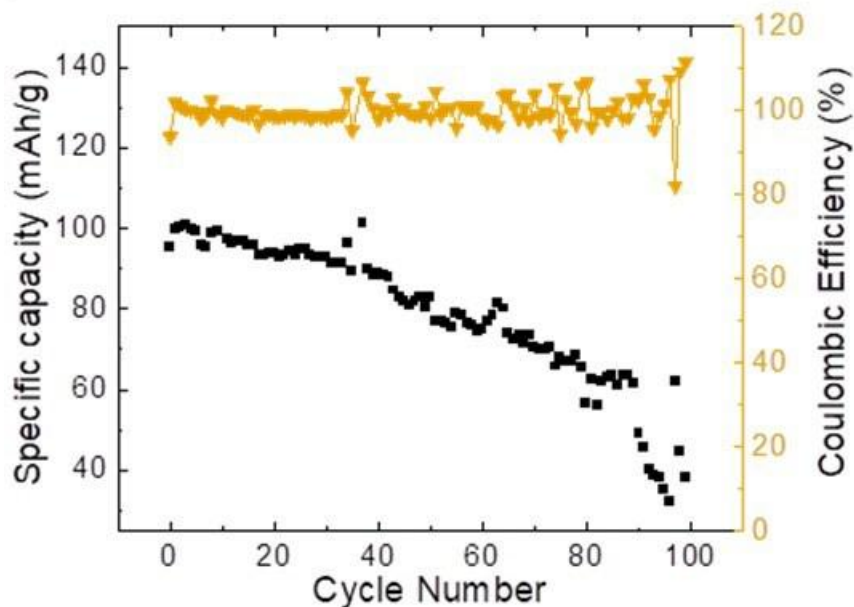


Figure XVI.3.4 Specific capacity and coulombic efficiency of an LiFePO₄ hybrid style cell cycled for 100 cycles.

Conclusions

In FY 2022, we have continued the optimization and characterization of our MOSN GSEs, including through developing a more rigorous understanding of the crystallization and viscosity behaviors of our glasses as relates best to the glass drawing process. The first drawn thin film glassy electrolytes have been synthesized using a MOS GSE showing a conductivity greater than 10^{-4} S/cm after the drawing process. Current work is being done to synthesize more thin film to test in further electrochemical experiments and in full cells, with the LiFePO₄ composite cathodes. Investigations into composite cathodes have shown excellent preliminary results, with more work being conducted. Further work is being conducted to optimize the thin film drawing and the composite cathode.

Key Publications

1. "NaPON doping of Na₄P₂S₇ glass and its effects on the structure and properties of mixed oxy-sulfide-nitride phosphate glass," Inorganic Chemistry, Madison Olson, Steven Kmiec and Steve W. Martin, Published on line October 24, 2022, <https://pubs.acs.org/doi/10.1021/acs.inorgchem.2c02300>
2. "Interpretation of the Na⁺ Ionic Conductivity in Na₄P₂S_{7-x}O_x Mixed Oxy-Sulfide (MOS) Glasses: Effects of Diverse Sodium Environments," Steven Kmiec, Madison Olson, Matthew Kenney, Steve W. Martin, Chemistry of Materials, On line published, October 26, 2022, <https://pubs.acs.org/doi/10.1021/acs.chemmater.2c01934>
3. "Grain-Boundary-Free Glassy Solid Electrolytes based on Sulfide Materials: Effects of Oxygen and Nitrogen Doping on Electrochemical Performance," Ran Zhao, Guantai Hu, Steven Kmiec, Jacob Wheaton, and Steve W. Martin, Batteries and Supercapacitors, e2021000356-1-13, 2022, <https://doi.org/10.1002/batt.202100356>
4. "An electrochemically stable defect-free glassy electrolyte formed at room temperature for all-solid-state sodium batteries, Xiaowei Chi, Ye Zhang, Fang Hao, Steven Kmiec, Hui Dong, Rong Xu, Kejie Zhao, Liang Wang, Lihong Zhao, Liqun Guo, Huolin Xin, Steve W. Martin, Yan Yao, Nature – Communications, 13:2854 (2022), <https://doi.org/10.1038/s41467-022-30517-y>

References

1. Fanfoni, M., and M. Tomellini. "The Johnson-Mehl- Avrami-Kohnogorov Model: A Brief Review." // *Nuovo Cimento D* 20, no. 7 (1998/07/01 1998): 1171-82.

2. Mauro, John C., Yuanzheng Yue, Adam J. Ellison, Prabhat K. Gupta, and Douglas C. Allan. "Viscosity of Glass-Forming Liquids." *Proceedings of the National Academy of Sciences* 106, no. 47 (2009): 19780.

Acknowledgements

We would like to acknowledge collaboration with Dr. Sara Cady of the Chemical Instrumentation Facility at Iowa State University for her help with conducting MAS NMR and CHNS experiments. We would also like to acknowledge Dr. Dapeng Jing from the Materials Analysis and Research Laboratory at Iowa State University for his help with collecting XPS spectra.

XVI.4 Physical and Mechano-Electrochemical Phenomena of Thin Film Lithium-Ceramic Electrolyte Constructs (University of Michigan)

Jeff Sakamoto, Principal Investigator

University of Michigan
Mechanical Engineering
2350 Hayward Ave.
Ann Arbor, MI, 48109
E-mail: jeffsaka@umich.edu

Tien Duong, DOE Technology Development Manager

U.S. Department of Energy
E-mail: Tien.Duong@ee.doe.gov

Start Date: October 1, 2019
Project Funding: \$1,250,000

End Date: September 30, 2022
DOE share: \$1,000,000

Non-DOE share: \$250,000

Project Introduction

While a small number of solid electrolytes exhibit high ionic conductivity ($\sim 1 \text{ mS cm}$ at 298K), few are stable against Li metal. The garnet-type solid electrolyte, based on the nominal formula $\text{Li}_7\text{La}_3\text{Zr}_2\text{O}_{12}$ (LLZO), is unique in that it is a fast ion conductor and – as we demonstrated in our recent project (DE-EE-00006821) – is stable against Li. Moreover, our former project successfully demonstrated a decrease in Li-LLZO interface resistance from 12,000 to 2 Ohms/cm^2 and stable cycling at 1 mA/cm^2 for 100 cycles ($\pm 15 \text{ } \mu\text{m}$ Li per cycle). Although the past project (DE-EE-00006821) demonstrated LLZO is a viable solid electrolyte for enabling Li metal solid-state batteries (LMSSB), the studies used thick pellets (1mm) and thick anodes ($\sim 500 \text{ } \mu\text{m}$). To achieve commercial relevance, performance must be demonstrated using substantially lower LLZO and Li thickness in the range of $< 30 \text{ microns}$ and $< 20 \text{ microns}$, respectively.

Objectives

The objective of this project is to understand the underpinning mechanisms that comprise these knowledge gaps to advance LLZO thin film technology. At the University of Michigan (UM), **Sakamoto-Dasgupta-Siegel** have an established history of research with LLZO, batteries, solid-state batteries, computation related to batteries, interface engineering, and the manufacturing research of batteries.

Approach

The approach to achieve the project objectives is to use LLZO as a model system to study the mechano-electrochemical phenomena the control the stability and kinetics of the Li-solid electrolyte interface. The physical and mechano-electrochemical behavior of thin Li was studied. In the initial stages, thin Li, made through *in situ* plating, is used together with conventional lab-scale thick LLZO pellets. In the latter stages of the project, thin Li was to be used together with thin LLZO.

Results

Li-free or Anode-free manufacturing of LMSSB is rapidly becoming an important area of research and of significant commercial interest. In response, this project focused on understanding the underpinning mechanisms that affect solid-state electrochemical deposition and understanding the electrochemical and mechanical behavior of *in situ* deposited Li. To complement the work on the anode, this project studied the compatibility between S cathodes and state-of-the-art sulfur catholyte with LLZO membranes. Summaries of the major project achievements are provided immediately below. Details of these major achievements follow the bulleted list.

Major Project Achievements:

- First to understand the cycling behavior of homogeneous *in situ* formed, thin Li electrodes with LLZO
- First to confirm adhesion at the Li-LLZO electrolyte interface creates hydrostatic stress
- First to observe the cycling behavior of *in situ* formed Li is dramatically different vs Li foil
- *operando* analysis of in situ Li formation enabled a deeper understanding of Li-free manufacturing
- The visual *operando* platform established in the project will enable other important *operando* studies of Li/Na cycling
- First to understand the chemical compatibility between LLZO and sulfur-electrolytes
- Understanding the reaction pathways between LLZO and liquid electrolytes enabled functionalization and stabilization of LLZO.
- In close collaboration with Professor Linda Nazar at the University of Waterloo, we were the first to demonstrate the theoretical capacity of S (1,300 mAh/g) using ether-based electrolyte and using LLZO to protect the Li anode.

Perspective on Solid-state Battery Technology for EVs¹

Owing to the potential to achieve $>1200 \text{ Wh L}^{-1}$, improve safety, and reduce cost compared to Li-ion, there is significant interest in commercializing solid-state batteries. However, solid-state batteries are currently not competitive with Li-ion on either a cost or performance basis and are not yet widely available on a commercial scale. Due to the solid nature of the individual components, solid-state batteries possess a unique set of design criteria that are dictated by the combination of their electrochemical, mechanical, and thermal properties. While significant scientific progress has been made in the past decade, in order to achieve commercial success, these criteria must be considered at each stage of the battery design, from the materials to the systems level.

Our perspective article¹ provides an overview of the couplings between the material properties of each component and how these links play a role in solid-state battery design, manufacturing, and operation (Figure XVI.4.1). Of the many industries that may benefit from solid-state batteries, automakers currently provide the largest impetus for their development due to the strict requirements for performance, safety, and costs for electric vehicles. Therefore, this perspective offers specific insight into the challenges facing solid-state batteries for electric vehicles, with input from three global automakers to provide targeted guidelines for continued solid-state battery research and development.

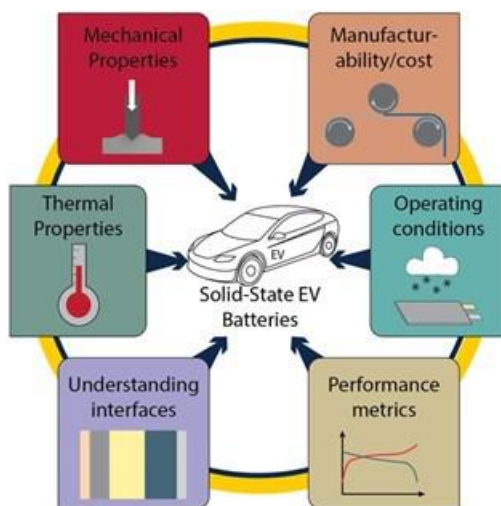


Figure XVI.4.1 Our Perspective¹ article accepted in Joule provides insight into the technological status of solid-state batteries and provides a guide for future challenges and opportunities to work with OEMs to advance the technology readiness level (TRL).

Key aspects and challenges for solid-state batteries from academic and industrial perspectives

It is hoped that the guidelines proposed in the perspective will help to further the state-of-understanding of a range of phenomena discussed herein, leading to accelerated progress in the community. In addition to the many phenomena already mentioned, there remain many outstanding questions that if answered, could make dramatic impacts on the trajectory of these technologies. In summary, we offer a list of a subset of these questions that were most frequently discussed in our discussions with industry and the community:

How will the Li plating/stripping processes change with variable vehicle charging and driving (discharge) profiles and with changing temperatures? In particular, can the electrochemical response to variable current draws be linked to the intrinsic time-dependent mechanical properties of the Li metal? For example, interspersing occasional “fast charge events”, into the cycling protocol may be used to simulate the habit of EV customers who typically operate using low charge/discharge rates with the occasional fast charging to meet immediate demands. Lesser used techniques, like direct current internal resistance (DCIR) measurements may provide additional insight on the battery behavior under these conditions. Furthermore, can the causes of Coulombic efficiency loss be identified and used to predict how these external factors affect the lifetime of the battery?

Can we improve manufacturability and costs of solid-electrolytes while maintaining high conductivity? This may include reducing the costs of extraction of rare-earth metals and other critical elements or minimization of time/energy intensive steps such as drying and densification.

How can mechanical fatigue induced by cyclic strains in the cell be managed? These effects may be related to swelling induced by the growth and shrinkage of a Li metal anode, or by cyclic cathode strains.

How can the rate capability of composite cathodes be increased to compete with state-of LIBs without requiring elevated temperatures?

Can solid state batteries provide life-cycle benefits such as improved/simpler recycling of components, and reduced need for supply-limited or hazardous materials?

The effect of aspect ratio on the mechanical behavior of Li metal in solid-state cells²

While tensile creep experiments have reliably determined the creep mechanism for Li metal, compressive creep experiments more accurately reflect the stress state of Li metal under stack pressure in a solid-state battery. In this study, the effects of the applied compressive stress and Li thickness on the strain and strain rate of Li metal coupled with Li_{6.5}La₃Ta_{0.5}Zr_{1.5}O₁₂ SSE and a Ni current collector were evaluated. The degree of Li/LLZO adhesion was controlled for all symmetric cells by measuring the Li/LLZO interfacial resistance using electrochemical impedance spectroscopy. All Li/LLZO interfacial resistances were measured to be < 15 Ω cm² and differences in interfacial resistance did not correlate with creep strain, suggesting good Li/LLZO adhesion for all tests. It was shown that as the Li thickness decreased, the effects of friction from the Li/LLZO and Li/Ni interfaces were amplified, resulting in lower creep strain for thinner Li foil samples (Figure XVI.4.2). At 1 MPa applied stress, the measured strain rate for all foil thicknesses was almost four orders of magnitude smaller than the steady-state strain rate predicted from tensile creep tests of Li. The frictional effects of the interfaces prevented the determination of a stress exponent, but it was seen that strain rates were a function of both Li metal thickness and applied stress, decreasing as the thickness and applied stress decreased. We propose that frictional effects from the Li/LLZO and Li/Ni interfaces induce regions of hydrostatic stress in Li metal, thereby lowering the volume of material free to deform, which becomes more pronounced at lower aspect ratios. Overall, the results of this study have implications for stack pressure requirements in solid-state batteries, where the mechanical behavior of the Li metal anode may change with aspect ratio during battery operation. The proposed hydrostatic stress state of Li is also of great importance to accurately model failure mechanisms on the < 100 μ m length scale, including SSE crack propagation during plating and Li void formation during stripping.

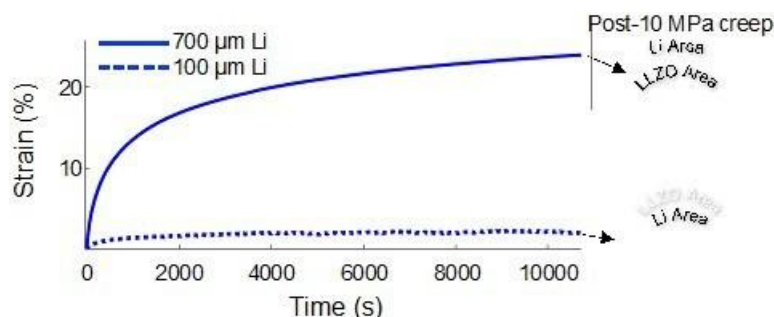


Figure XVI.4.2 Mechanical strain % vs time plot of Li-LLZO-Li cells consisting of thick (700 micron) and thin (100 micron) Li anodes. When Li was ≤ 100 microns thick, negligible deformation occurred. This behavior suggests that Li-LLZO frictional or adhesion likely created hydrostatic stress in Li, thus limiting deformation when Li is thin (≤ 100 microns).

Understanding Coupled Electro-Chemo-Mechanics During *In Situ* Li Metal Anode Formation in Solid-State Batteries³

Solid-state batteries (SSBs) could enable the use of Li metal anodes, giving a major advantage for energy density. Unfortunately, Li presents challenges in manufacturing stemming from the reactivity and the difficulty of fabricating thin Li films and high-quality Li/Electrolyte interfaces. Recently, *in situ* anode formation has shown promise for overcoming these challenges. In this approach, cells are assembled without an anode (“Anode-free”), and Li is plated out from the positive electrode after fabrication. This reduces the need for inert atmospheres, reduces cell complexity, and potentially lowers cost.

As the Li is plated out at the Li/Electrolyte interface, mechanical stresses evolve due to the volume changes in the cell. These stresses play an important role in the uniformity and quality of the resulting *in situ* formed Li electrode. The coupling between mechanics and electrochemistry also plays a key role in this process. This work utilizes *operando* 3D optical video microscopy to characterize electrode morphology evolution during *in situ* anode formation on one of the most promising solid electrolytes, $\text{Li}_7\text{La}_3\text{Zr}_2\text{O}_{12}$ (LLZO). These morphology changes are linked to corresponding electrochemical signatures in three regimes and linked to the mechanical stresses at the Li/LLZO interface. A mechanistic framework is built to understand these factors, which is then used to provide insight into the parameters that control uniformity and how systems can be designed to improve the resulting electrode properties. The role that stack pressure plays and the importance of stack pressure uniformity are highlighted. The impacts of interfacial toughness, current collector properties, and cell geometry are discussed. Based on the mechanistic framework, improved areal Li coverage is demonstrated, providing insight for future works to enable *in situ* anode formation in a range of material systems and cell architectures. The details of this study were published in a manuscript titled, “Understanding Coupled Electro-Chemo-Mechanics During *In Situ* Li Metal Anode Formation in Solid-State Batteries”, by Eric Kazyak, Michael Wang, Kiwoong Lee, Srinivas Yadavalli, Adrian J. Sanchez, M. D. Thouless, Jeff Sakamoto, and Neil P. Dasgupta.

Understanding Coupled Electro-Chemo-Mechanics During *In Situ* Li Metal Anode Formation in Solid-State Batteries⁴

The transition from laboratory-scale thick Li-metal anodes ($>500 \mu\text{m}$) to thin ($\sim 10\text{--}30 \mu\text{m}$) Li anodes is necessary for the successful implementation of Li-metal solid-state batteries (LMSSB). However, the mechanical deformation of Li along an interface depends on its thickness, making it essential to understand the interface mechanics between thin Li layers and solid electrolytes. We investigate the stripping behavior of thin Li electrodes that are formed using *in situ* plated (anode-free) Li on $\text{Li}_7\text{La}_3\text{Zr}_2\text{O}_{12}$ garnet-type solid electrolytes. We demonstrate that the accessible discharge capacity increases as current density decreases and as the Li anode thickness increases. It is shown that two different mechanisms restrict the stripping of thin Li electrodes, depending on the current density. We demonstrate that de-wetted Li/LLZO interfaces during stripping can be reestablished using a simple thermal treatment. This approach could be integrated into future charging protocols, and the findings provide insight into LMSSB design, implementation, and operation. (See Figure XVI.4.3.)

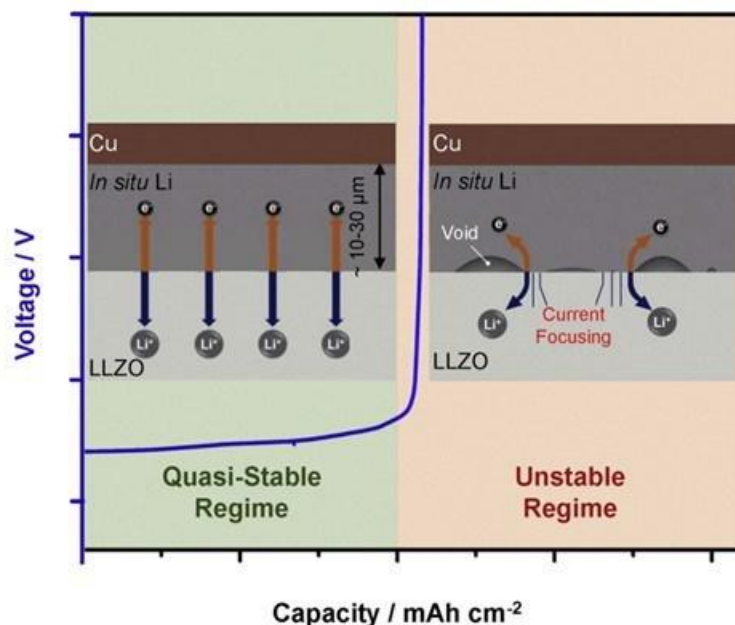


Figure XVI.4.3 Two distinct behaviors were observed when stripping in situ formed Li electrodes.

Demonstrating the efficacy of LLZO membranes to protect Li anodes in Li – S technology (In collaboration with Professor Linda Nazar, University of Waterloo).

Because initial success was achieved in stabilizing the sulfur catholyte and LLZO interface, the project resources were redirected from the study of ALD coatings to suppress potential reactions between LLZO and the organic electrolyte to treating the native LLZO interface. This work closely involves pre-PhD candidate Max Palmer at the University of Michigan and Prof. Linda Nazar and her PhD students Abhi Shayamsunder and Ivan Kochetkov from the University of Waterloo, Canada. (See Figure XVI.4.4.)

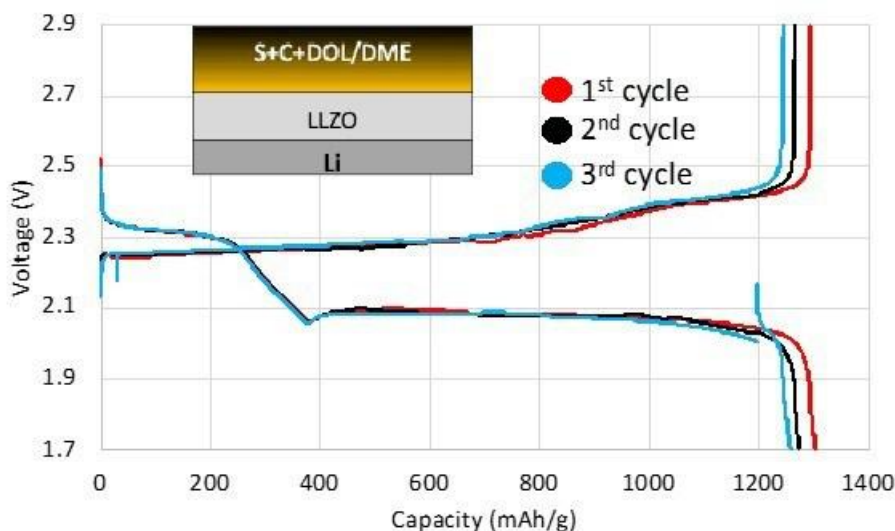


Figure XVI.4.4 Cycling at 108 $\mu\text{A}/\text{cm}^2$ at room temperature with carbon paper. A Li-LLZO-DOL/DME/S hybrid battery can be discharged to 1,300 mAh/g and be cycled 3 times with minimal capacity loss.

In this collaboration, it was determined that residual adventitious compounds on the LLZO surface, react state-of-the-art Li-S organic electrolytes. A reaction pathway was hypothesized and validated, enabling the design

and implementation of a treatment process to stabilize the native LLZO surface using DOL/DME 1.0M LiTFSI as the catholyte. An interface resistance of 30 Ohms/cm² was achieved and exceeds the goal of 40 Ohms/cm². Demonstrating the compatibility between LLZO and the liquid electrolyte, hybrid Li-S cells were made using LLZO to protect the Li electrode and DOL/DME 1.0M LiTFSI as the catholyte for S+carbon prototype cells (Figure XVI.4.4). The goal of the initial cycling study was to demonstrate stable cycling and to demonstrate that LLZO can protect the Li anode to protect fouling of the Li anode with soluble polysulfides. The data in Figure 1 show that the Li-LLZO-S cell closely resembles a standard all-liquid Li-S, but it uses LLZO to protect the Li anode. The fact that the profile closely resembles a liquid Li-S, shows potential as an effective cell configuration to ameliorate the side reactions that limit traditional Li-S cells, such as passivation of the Li anode from deleterious side reactions with soluble polysulfides.

Conclusions

The focus of this project was to study the mechano-electrochemical phenomena of thin Li electrodes integrated with relevant model LLZO solid electrolyte and to evaluate LLZO compatibility with S-based cell chemistries. In one study, new insight into the mechanical behavior of thin Li was found that could help guide efforts to understand the stability and kinetics of thin (< 20 micron) commercially-relevant Li electrodes in solid-state batteries. In a second study, an *operando* visualization platform was used to better understand correlations between *in situ* Li plating conditions and Li areal and topographic homogeneity. In a third study, the stripping behavior of thin, *in situ* Li was investigated. It was determined that the stripping behavior of *in situ* formed Li is dramatically different compared to previous studies using Li foil. It is likely that the purity of *in situ* formed Li metal and the interface that it forms with the solid electrolyte are dramatically different compared to many previous studies that involve Li foil that was placed on a solid electrolyte. In a fourth study, it was shown that by understanding the reactions between untreated-LLZO and treated-LLZO, that it is possible to develop a viable approach for eliminating reactions between LLZO and S electrolytes.

Key Publications

1. Wang, Michael J., Eric Kazyak, Neil P. Dasgupta, and Jeff Sakamoto. "Transitioning solid-state batteries from lab to market: Linking electro-chemo-mechanics with practical considerations." *Joule* 5, no. 6 (2021): 1371-1390.
2. Haslam, Catherine G., Jeffery B. Wolfenstine, and Jeff Sakamoto. "The effect of aspect ratio on the mechanical behavior of Li metal in solid-state cells." *Journal of Power Sources* 520 (2022): 230831.
3. Kazyak, Eric, Michael J. Wang, Kiwoong Lee, Srinivas Yadavalli, Adrian J. Sanchez, M. D. Thouless, Jeff Sakamoto, and Neil P. Dasgupta. "Understanding the electro-chemo-mechanics of Li plating in anode-free solid-state batteries with operando 3D microscopy." *Matter* (Online) 5, no. 11 (2022).
4. Lee, Kiwoong, Eric Kazyak, Michael J. Wang, Neil P. Dasgupta, and Jeff Sakamoto. "Analyzing void formation and rewetting of thin *in situ*-formed Li anodes on LLZO." 6, 11 *Joule* (2022): 2547.

Acknowledgements

Adrienne Riggi (Adrienne.Riggi@netl.doe.gov) served as the NETL program manager for this project. The Co-PIs included Associate Professor Neil Dasgupta, University of Michigan, Mechanical Engineering and Professor Don Siegel, University of Texas, Austin, Mechanical Engineering. The PIs would like to acknowledge the significant contributions to the LLZO-S compatibility studies from Professor Linda Nazar (University of Waterloo)

XVI.5 Low Impedance Cathode/Electrolyte Interfaces for High Energy Density Solid-State Batteries (University of Maryland, College Park)

Eric Wachsman, Principal Investigator

University of Maryland College Park
1206 Engineering Laboratory Building
University of Maryland
College Park, MD 20742
E-mail: ewach@umd.edu

Yifei Mo, Co-Principal Investigator

University of Maryland College Park
1137 Engineering Laboratory Building
University of Maryland
College Park, MD 20742
E-mail: yfmo@umd.edu

Tien Duong, DOE Technology Development Manager

U.S. Department of Energy
E-mail: Tien.Duong@ee.doe.gov

Start Date: October 1, 2019
Project Funding: \$1,250,000

End Date: February 23, 2023
DOE share: \$1,000,000

Non-DOE share: \$250,000

Project Introduction

All-solid-state batteries (ASSBs) using a ceramic fast Li-ion conductor as a solid-state electrolyte (SSE) have been proposed as a promising strategy to significantly increase the energy density of lithium batteries. Due to their high ion conductivity and excellent stability, Li-stuffed garnets exhibit the most promising physical and chemical properties for SSEs. However, the typical microstructure, thick ($>100\ \mu\text{m}$) bulk electrolyte and simple planar electrode/electrolyte interfaces, combined with poor electrode wetting of the garnet result in excessively high area specific resistances (ASRs) that severely limit achievable current density and cell energy density.

Recently, the University of Maryland PIs have pioneered thin garnet-based solid-state batteries that effectively address the interfacial impedance at the Li metal side. We have demonstrated the ability to overcome the solid-electrolyte/solid-electrode interfacial impedance using interfacial engineering [1] of solid-state garnet (e.g. $\text{Li}_7\text{La}_3\text{Zr}_2\text{O}_{12}$ LLZ) electrolytes under BMR contract DEEE0006860. Further, we have demonstrated Li-metal anodes with unique porous-dense-porous trilayer LLZ architectures achieving excellent stability and high current density ($10\ \text{mA}/\text{cm}^2$) for Li-cycling with no electrical shorting [2] successfully solving the high Li-garnet interfacial impedance that severely limited achievable current density. We have also developed state-of-the-art Li-metal solid-state batteries using this technology demonstrating high energy density ($\sim 300\ \text{Wh}/\text{kg}$) with both NMC high-voltage [3] and S high-capacity [4] cathodes using these trilayer garnet structures. However, cycling rate in full cells is orders of magnitude lower than Li-symmetric cells as issues remain with regard to properties evolving at the cathode-electrolyte interface. Today's processing routes require temperatures of $\geq 1000^\circ\text{C}$ for the garnet, which unavoidably leads to enhanced ion diffusion at the interface, thereby raising the issues of material compatibility and the formation of possible interphases that influence the total cell resistance for desired cathode/electrolyte co-sintering. In addition, even with cathodes infiltrated into pre-sintered garnet structures major challenges still exist at the cathode interfaces for all-solid-state batteries, including (1) high cathode interfacial resistance and (2) limited processing techniques that incorporate active cathode materials within the solid electrolyte.

Objectives

The project objective is to integrate computational and experimental research to develop and test Li-metal-based batteries that implement solid SSEs equipped with NMC cathodes integrated into the Li-metal/LLZ tri-layer architecture. Specifically, the team is achieving the following: (1) identify and demonstrate interfacial layers to achieve low-impedance and stable NMC/LLZ interfaces; (2) develop novel processing techniques to fabricate NMC/LLZ composite cathodes with low interfacial resistance; and (3) enable high-performance ASSBs with an energy density of 450 Wh/kg and 1400 Wh/L and negligible degradation for 500 cycles.

Approach

In this new project, the team is building on their demonstrated expertise with garnet electrolytes and ASSBs to accomplish the following: (1) engineer interfaces to overcome high NMC/LLZ interfacial impedance and interfacial degradation; (2) develop processing and fabrication techniques to achieve high-loading NMC/LLZ composite cathodes with low resistance and high cyclability; and (3) integrate the NMC/LLZ cathodes into all-solid-state Li-metal/LLZ cells to achieve high-energy-density batteries.

Results

COVID-19 Impact

Progress on experimental results were impacted by COVID19 which closed labs for several months resulting in a 6 month no-cost extension.

Thermochemical stability between LLZ and interface coated NMC (Experimentally determined)

Previous XRD results of sintered NMC/Li_{6.75}La₃Zr_{1.75}Ta_{0.25}O₁₂ (LLZTO) pellets suggested that NMCs with higher Ni contents (e.g., NMC811) are more reactive towards garnet than those with lower amounts of Ni. NMC811/LLZTO pellets demonstrated near complete loss of peak intensity in XRD when sintered at 1000°C. To further investigate this effect, TGA/DSC was performed on samples of the pristine NMCs in both Ar and O₂ atmosphere as literature reports indicate NMC loses O₂ from the lattice at high temperatures. The TGA results are shown in Figure XVI.5.1, and show that the higher the Ni content of NMC, the greater the mass loss with an earlier onset temperature. Furthermore, the samples heated in an O₂ environment show decreased mass loss with increase in the onset temperature across all compositions of NMC. This stabilization of the NMC is significant enough that NMC111 demonstrates nearly no mass loss up to 1100°C in O₂. Additionally, coating NMC622 with a 4nm layer of alumina further reduces the mass loss of NMC622, such that in O₂ atmosphere the sample loses less than 0.5wt%. This suggests that careful selection of co-sintering environment, use of a protective ALD coating, as well as the NMC composition should be done when co-sintering NMC and LLZTO.

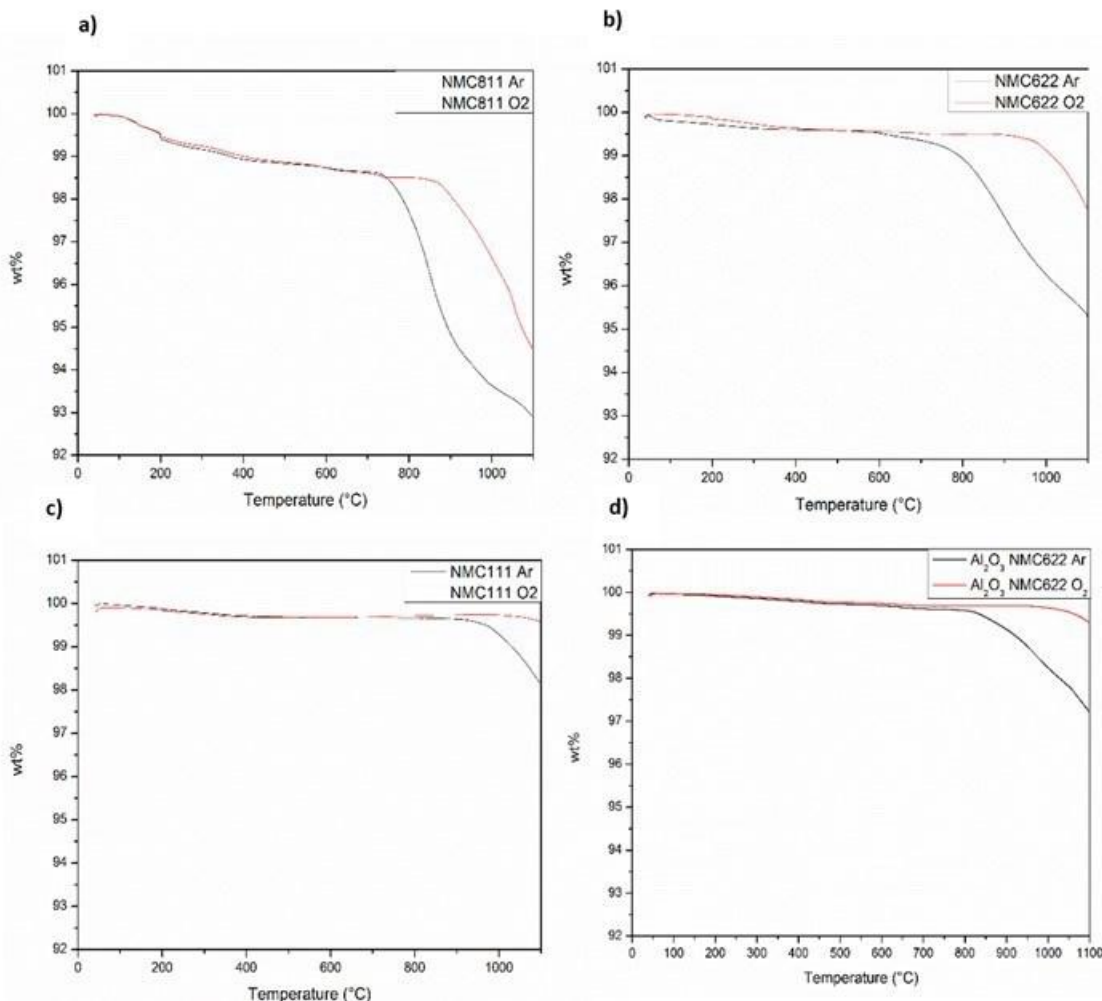


Figure XVI.5.1 TGA results of a) NMC811, b) NMC622, c) NMC111, and d) Al₂O₃ coated NMC622 in both Ar and O₂ atmospheres.

Figure XVI.5.2 contains the summarized phase weight percentage results of the Rietveld Refinement of the powder XRD spectra. The samples consisted of NMC and LLZTO in a 1:1 weight ratio co-sintered at 900°C for 3hrs in Ar and O₂. The results for samples co-sintered in air are not included as they show similar results to those processed in O₂ except that the weight percent of NMC is slightly lower indicating intermediate thermochemical stability between Ar and O₂ of NMC. Across all NMC compositions, the wt% of NMC decreases with increasing Li content of the LLZO, indicating either a loss of NMC crystallinity or formation of amorphous decomposition phases. For higher Ni content NMCs, the increase in Li content is also correlated with an increase in the formation of a perovskite-like decomposition phase, La₂Li_{0.5}M_{0.5}O₄ (M=Ni, Mn, Co). It is unclear what the exact composition of the transition metal site is because all these compositions have very similar XRD patterns. Furthermore, more perovskite is formed when NMC811 is co-sintered than NMC622. This combined with previous TGA/DSC results seems to indicate that the lower the thermochemical stability of the pure NMC and higher Li content in the LLZO leads to greater formation of the perovskite decomposition phase (NMC811 demonstrated greater O₂ mass loss starting at lower temperatures than NMC622). This trend holds true regardless of the co-sintering atmosphere.

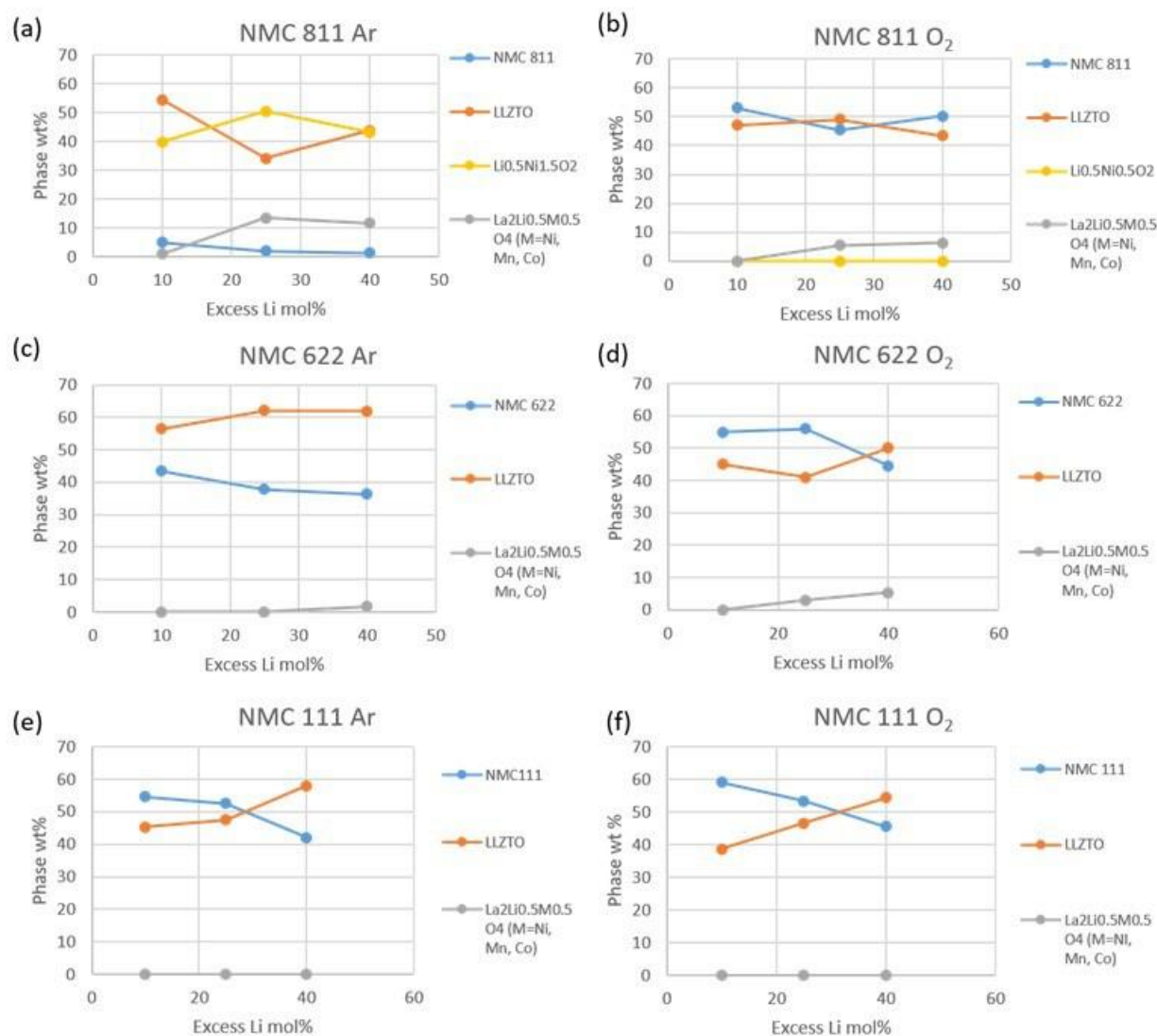


Figure XVI.5.2 XRD and Rietveld Refinement Analysis of a-b) NMC811, c-d) NMC622, and e-f) NMC111 co-sintered in a 1:1 wt ratio with LLZTO of varying amounts of excess Li in both Ar and O₂ atmospheres

Across all NMC compositions, the wt% of NMC is lower for samples sintered in Ar than those sintered in O₂. This reinforces the importance of having high oxygen partial pressure to prevent O₂ loss from the NMC that leads to subsequent decomposition. This difference is smaller for NMC111 and becomes greater for NMC622 and greatest for NMC811. It is notable that for NMC811 co-sintered in Ar, less than 10wt% is still the NMC phase, as a high Ni-content lithiated spinel phase (Li_{0.5}Ni_{1.5}O₂) is detected instead. In O₂, the NMC811 phase is largely preserved. Additionally, the weight fraction of the perovskite decomposition phase is higher for NMC811 co-sintered in Ar than in O₂. This suggests that stabilizing the NMC is of the utmost importance to prevent formation of decomposition products like La₂Li_{0.5}M_{0.5}O₄ (M=Ni, Mn, Co).

Various coatings of lithium silicates and lithium aluminates with varying lithium content and at varying sintering atmosphere was studied. Thin layers of lithium silicates and aluminates were coated over NMC622 through solution-based synthesis route. (Please note in the following experiments we have used NMC622 for the studies). Figure XVI.5.3 shows the summarized phase weight percentage results of the Rietveld Refinement of the powder XRD spectra of LLZTO and lithium silicate coated NMC622. Two species of lithium silicate was used: Li₂SiO₃ and lithium rich Li₄SiO₄. With 40mol% excess Li, for uncoated NMC

sample about 2 wt% of perovskites were formed. In addition, with the silicate coated sample, NMC phase % was higher when sintered in O₂ atmosphere (45%) compared to the uncoated sample (35%). Further, when the samples were sintered in Ar atmosphere La₂Li_{0.5}M_{0.5}O₄ (M=Ni, Mn, Co) phase increases with increasing Li content.

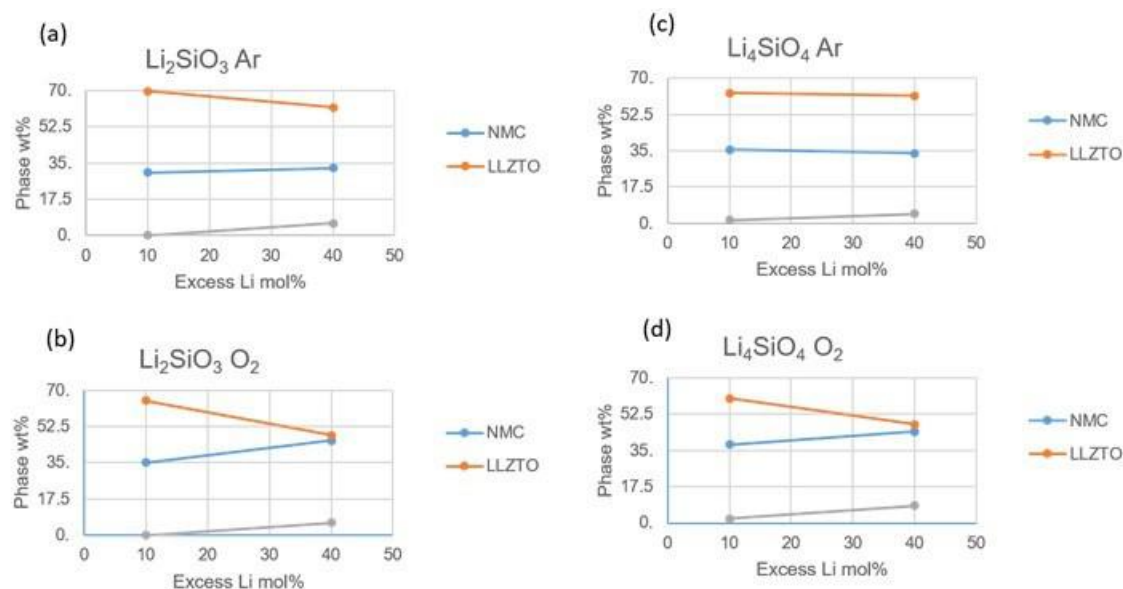


Figure XVI.5.3 Rietveld Refinement Results of XRD of Li₂SiO₃-NMC622 co-sintered in a 1:1 wt ratio with LLZTO onto LLZTO trilayers at 900 °C in (a) Ar atmosphere and (b) O₂ atmosphere. Similarly, Rietveld refinement results of XRD of Li₄SiO₄-NMC622 sintered in (c) Ar and (d) O₂ atmosphere.

Figure XVI.5.4 shows the Rietveld refinement analysis of lithium aluminate coated NMC with garnet solid electrolyte sintered at different sintering atmosphere (Ar and O₂). When sintered in Ar atmosphere, the phase wt% of NMC is unchanged and the presence of coating phase decreased the formation of La₂Li_{0.5}M_{0.5}O₄ (M=Ni, Mn, Co) decomposition phase.

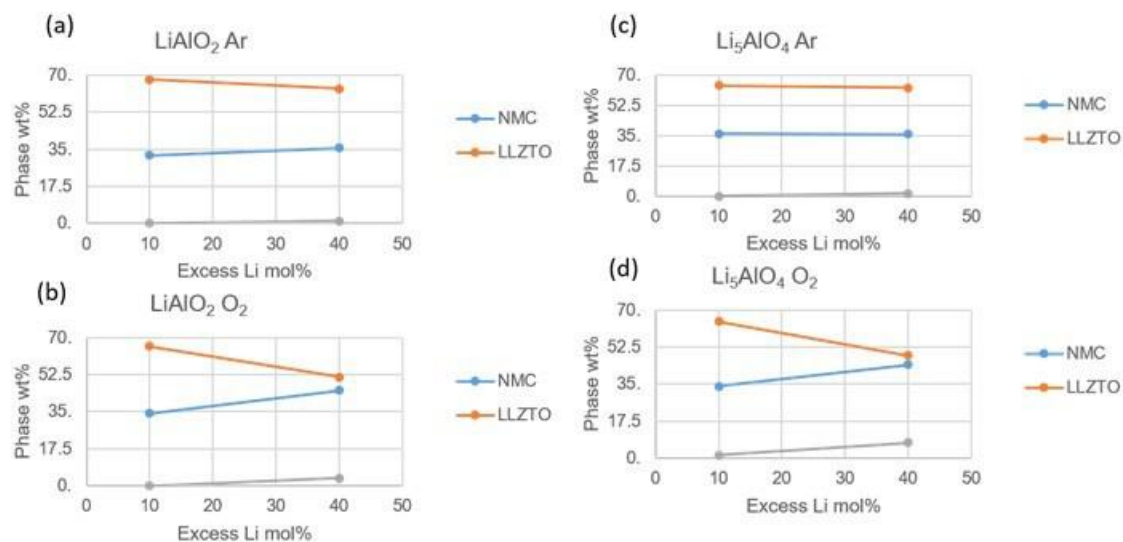


Figure XVI.5.4 Rietveld Refinement Results of XRD of LiAlO₂-NMC622 co-sintered in a 1:1 wt ratio with LLZTO onto LLZTO trilayers at 900 °C in (a) Ar atmosphere and (b) O₂ atmosphere. Similarly, rietveld refinement results of XRD of Li₅AlO₄-NMC622 sintered in (c) Ar and (d) O₂ atmosphere.

Computational results and model refined for process optimization

The computation model results for interface side reactions were compared with experimental results. The experimental results reported the formation of delithiated phases as side products in agreement with our computation predictions. For the process optimization, experimental results shown improvement in interface stability using oxygen gas environment. To improve our model to account for the process optimization, we include the sintering environment into our computation model using the grand potential phase diagram approach. In the improved model, the external environment is open to the interface for the potential reaction evaluations. Our models consider the environment in two ways. One way is through the control of Li chemical potential (Table XVI.5.1), which is a key element loss during sintering, and can be strongly interacting with the environment. Thus, the environment chemical potential can be translated into the Li chemical potential. In our results, we observe having an appropriate range of Li chemical potential can reduce Li loss and also promote the formation of passivation layer such as Li_2O , which can kinetically limit Li loss and mitigate the side reaction (Table XVI.5.1). In another model, we directly consider the oxygen gaseous environment (Table XVI.5.2). In this model, we observe significant stabilization of the cathode materials (Table XVI.5.2), in agreement with the previously reported experimental results. In summary, computation models for process optimization were developed achieving good agreement with experiment. In addition, as shown above, the experimental results for inter-layer materials are compared with previous computation results. The coating layer materials predicted by computation are now verified by experiments. These coating layers show good stabilities and good conductive properties, confirming and verifying the computation prediction of the stable coating between garnet and cathode.

Table XVI.5.1 Stability of LLZO–NMC 111 Under Varying Li Chemical Potential.

μLi (eV)	ratio of NMC	ratio of LLZO	Mutual Rxn. E. (meV/atom)	Phase equilibria
0	0.43	0.57	-81	La_2O_3 , Li_2O , ZrCo_2 , ZrMn_2 , ZrNi_3
-0.25	0.75	0.25	-29	La_2O_3 , Li_2O , MnCo , $\text{Zr}_6\text{Co}_{23}$, ZrNi_3
-0.5	1.00	0.00	0.00	Co , Li_2O , MnCo , MnNi_3
-1	0.53	0.47	-27	Co , $\text{La}_2\text{MnCoO}_6$, Li_2O , $\text{Li}_6\text{Zr}_2\text{O}_7$, MnNi_3
-1.25	0.43	0.57	-87	Co , $\text{La}_2\text{MnCoO}_6$, Li_2O , $\text{Li}_6\text{Zr}_2\text{O}_7$, Ni
-1.75	0.43	0.57	-155	$\text{La}_2\text{MnCoO}_6$, Li_2O , Li_6CoO_4 , $\text{Li}_6\text{Zr}_2\text{O}_7$, Ni
-2	0.43	0.57	-151	$\text{La}_2\text{MnCoO}_6$, Li_2O , $\text{Li}_6\text{Zr}_2\text{O}_7$, LiCoO_2 , Ni
-2.25	0.43	0.57	-139	$\text{La}_2\text{MnCoO}_6$, Li_2O , $\text{Li}_6\text{Zr}_2\text{O}_7$, LiCoO_2 , NiO
-2.75	0.43	0.57	-125	$\text{La}_2\text{MnCoO}_6$, Li , Li_2NiO_3 , Li_2O , $\text{Li}_6\text{Zr}_2\text{O}_7$, LiCoO_2
-3	0.43	0.57	-138	$\text{La}_2\text{MnCoO}_6$, Li , Li_2NiO_3 , Li_2O_2 , $\text{Li}_6\text{Zr}_2\text{O}_7$, LiCoO_2
-3.25	0.43	0.57	-146	$\text{La}_2\text{MnCoO}_6$, Li , Li_2NiO_3 , Li_2O_2 , Li_2ZrO_3 , LiCoO_2
-3.5	0.43	0.57	-140	$\text{La}_2\text{MnCoO}_6$, Li , Li_2NiO_3 , LiCoO_2 , O_2 , ZrO_2
-3.75	0.43	0.57	-158	$\text{La}_2\text{MnCoO}_6$, Li , $\text{Li}(\text{CoO}_2)_2$, NiO , O_2 , ZrO_2
-4	0.43	0.57	-168	CoO_2 , $\text{La}_2\text{MnCoO}_6$, Li , NiO , O_2 , ZrO_2

Table XVI.5.2 Stability of LLZO–NMC 111 Interface Under Varying O_2 Chemical Potential

μO (eV)	ratio of NMC	ratio of LLZO	Mutual Rxn. E. (meV/atom)	Phase equilibria
0.00	0.43	0.57	-141	$\text{La}_2\text{MnCoO}_6$, Li , Li_2NiO_3 , Li_2O_2 , $\text{Li}_6\text{Zr}_2\text{O}_7$, LiCoO_2
-0.25	0.43	0.57	-145	$\text{La}_2\text{MnCoO}_6$, Li , Li_2NiO_3 , Li_2O_2 , Li_2ZrO_3 , LiCoO_2
-0.50	0.43	0.57	-141	$\text{La}_2\text{MnCoO}_6$, Li , Li_2NiO_3 , LiCoO_2 , O_2 , ZrO_2
-0.75	0.43	0.57	-160	$\text{La}_2\text{MnCoO}_6$, Li , $\text{Li}(\text{CoO}_2)_2$, NiO , O_2 , ZrO_2
-1.00	0.43	0.57	-168	CoO_2 , $\text{La}_2\text{MnCoO}_6$, Li , NiO , O_2 , ZrO_2

Demonstrating 10X reduction in interfacial resistance between coated and uncoated LLZ/NMC interfaces

Various interlayer coatings identified by previous computational work were synthesized on the surface of NMC622 via a solution-based process. These include LiAlO_2 , Li_2SiO_3 , and Li_2ZrO_3 . These coated NMC powders were then co-sintered in a 1:1 weight ratio of NMC: LLZTO at 1000°C in O_2 onto LLZTO trilayers to fabricate symmetric cells for EIS testing. These results for varying coating thicknesses are summarized in Figure XVI.5.5. Shown in Figure XVI.5.5a-b, 2.5mol% was the optimal coating thickness for the Li_2ZrO_3 leading to a 2.5X reduction in the impedance. For the LiAlO_2 and Li_2SiO_3 coatings, 10mol% was optimal both leading to a 4X reduction in the impedance.

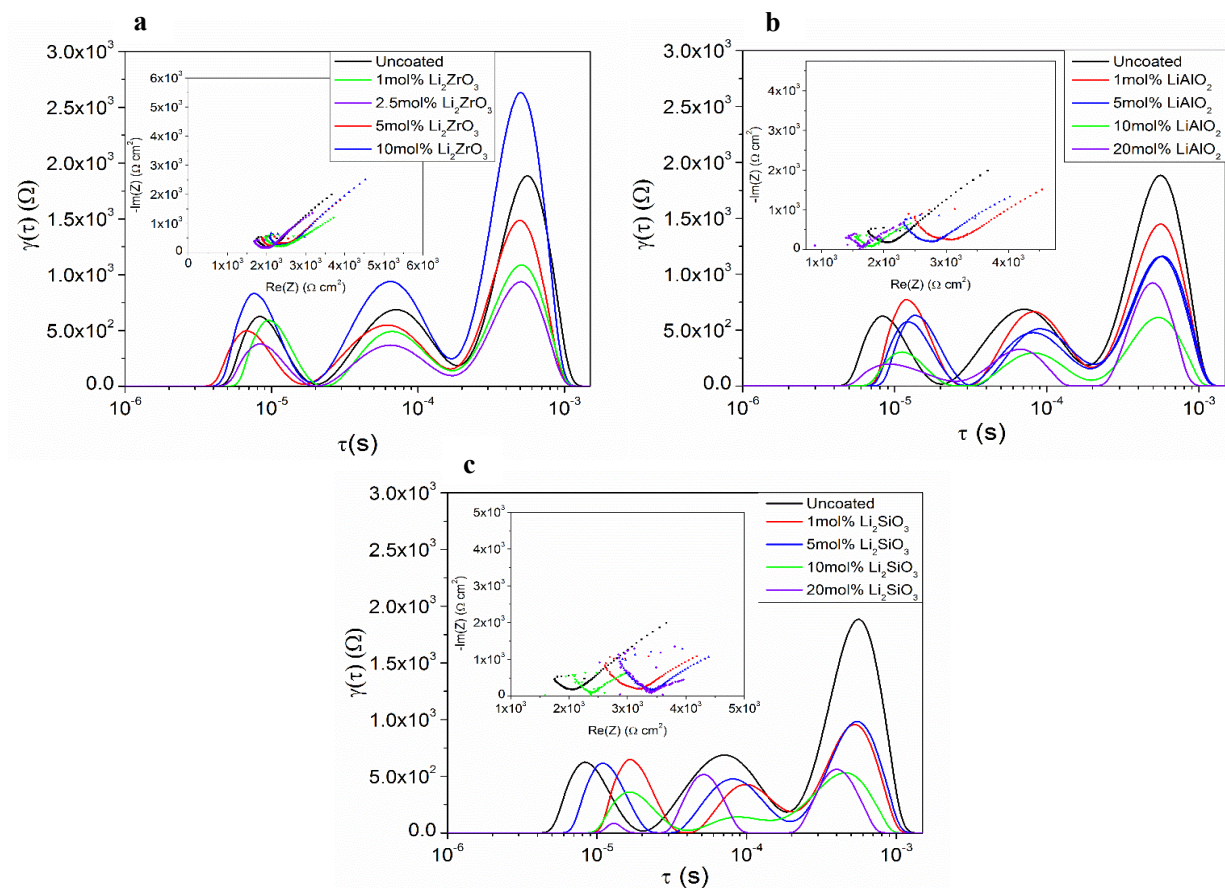


Figure XVI.5.5 Nyquist plots and Distribution of Relaxation Times Analysis of EIS of a) Li_2ZrO_3 -NMC622, b) LiAlO_2 -NMC622, and c) Li_2SiO_3 -NMC622 co-sintered in a 1:1 wt ratio with LLZTO onto LLZTO trilayers at 1000°C in O_2 .

Since the computational results indicated that the Li concentration gradient between NMC and LLZO is the main driving force for the reaction, more lithiated versions of the silicate and aluminate coatings (Li_5AlO_4 and Li_4SiO_4) were also synthesized and coated on NMC622. These EIS results are shown in Figure XVI.5.6. At the same molar concentration, the higher lithium content aluminate and silicate reduced the impedance 2x more than their less lithiated counterparts. In addition, 5X reduction in interface resistance was attained for 10mol% excess lithium containing Li_5AlO_4 coated NMC and a 10X reduction in interface resistance was attained with 10mol% of excess lithium for Li_4SiO_4 coated NMC compared to the uncoated samples. This confirms the computational results that reducing the difference in the Li concentration at the interfaces attenuates the interfacial reaction of NMC and LLZTO.

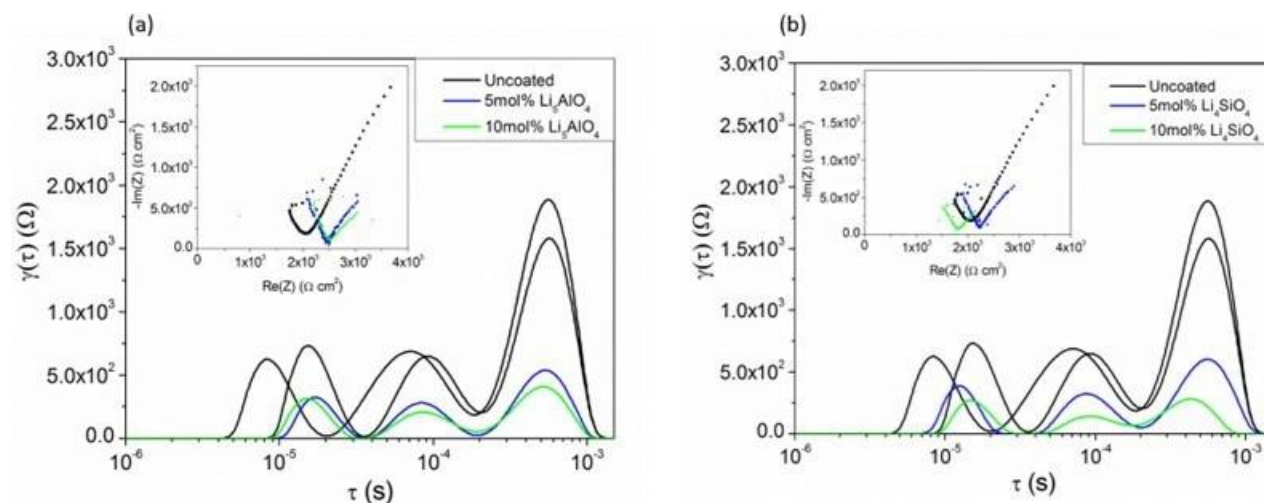


Figure XVI.5.6 Nyquist plots (inset) and Distribution of Relaxation Times Analysis of EIS of a) Li_5AlO_4 -NMC622, and b) Li_4SiO_4 -NMC622 co-sintered in a 1:1 wt ratio with LLZTO onto LLZTO trilayers at 1000 °C in O_2 .

Table XVI.5.3 summarizes the EIS reduction with various coating materials. From the materials studied Li_4SiO_4 coated NMC with 10mol% excess Li co-sintered sample exhibited 10X reduction in interface resistance compared to the uncoated sample.

Table XVI.5.3 Comparison on EIS Reduction with Respect to Various Coating Material

Coating	Li_2ZrO_3					
mol%	2.5					
EIS Reduction		1.33X	4x	5x	4x	10x

Trilayer cell with composite NMC-LLZ cathode layer

Efforts to fabricate a full cell via sintering a tape casted NMC622/LLZTO composite cathode, dense LLZTO layer, and LLZTO porous anode for Li metal are currently underway. Despite the shrinkage mismatch between the porous anode tape and the initial formulations of the composite NMC tapes causing extreme curling, some full cells were successfully fabricated and infiltrated with Li metal. Figure XVI.5.7 contains a Nyquist plot of NMC|LLZTO|Li Metal full cells with both Li_4SiO_4 coated NMC622 and uncoated NMC622. The impedance drops by nearly an order of magnitude highlighting the ability of this interfacial coating to improve the interface between LLZTO and NMC622. (Note: This is lower than interface resistance obtained from symmetric cell studies as the sintering temperature here was increased to 1050°C, suggesting that the coating is less effective at reducing the interfacial impedance as the sintering temperature increases past a certain point.). The sintering temperature was increased in order to ensure complete densification of the LLZTO dense layer in the trilayer structure. Cycling data is forthcoming for these cells.

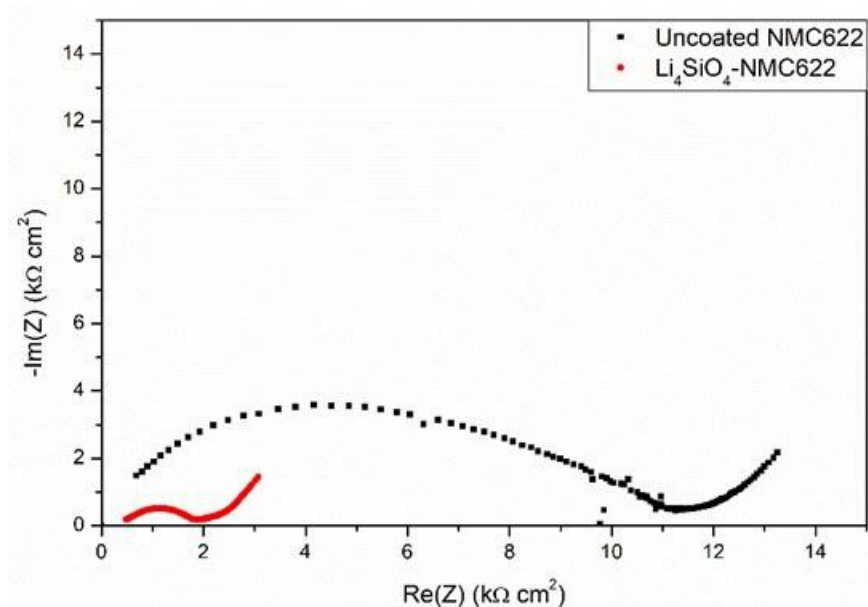


Figure XVI.5.7 Nyquist of EIS of uncoated and Li₄SiO₄ coated NMC622 Li metal full cells co-sintered in a 1:1 wt ratio with LLZTO onto LLZTO trilayers at 1050 °C in O₂.

Conclusions

The reactivity of NMC with LLZTO increases with increasing Ni content. The reaction is mainly caused by Li deficiency at high temperature. Apart from optimum Li content effect of sintering atmosphere was also studied. O₂ atmosphere is suitable for the co-sintering studies of NMC with LLZT. Further, with interface coated NMC and with optimum amount of excess Li the formation of perovskite phase can be reduced. First-principles computation was used to study the trends in stability with LLZO and NMC through varying Li and O₂ chemical potential. EIS measurement on NMC/trilayer LLZTO/NMC symmetric cells found that Li₄SiO₄ is better than any other interface coating material at improving the interfacial impedance. Moreover, increasing the amount of available Li during co-sintering can dramatically reduce the reaction of NMC and LLZTO achieving a 10X reduction in interfacial ASR. Preliminary studies on all-solid-state full cells were conducted and the Li₄SiO₄ interface coating reduced the overall impedance by nearly an order of magnitude compared to the cell with no interface coating.

Key Publications

Papers

1. Y. Ren, T. Danner, A. Moy, M. Finsterbusch, T. Hamann, J. Dippell, T. Fuchs, M. Müller, R. Hoft, A. Weber, L.A. Curtiss, P. Zapol, M. Klenk, A.T. Ngo, P. Barai, B. Wood, R. Shi, S. Wan, T. Wook, M. Engels, J. Nanda, F. Richter, A. Latz, V. Srinivasan, J. Janek, J. Sakamoto, D. Fattakhova-Rohlfing, and E.D. Wachsman, "Oxide-Based Solid-State Batteries: A Perspective on Composite Cathode Architecture," *Advanced Energy Materials*, 2201939 (2022).
2. Y. Ren and E.D. Wachsman, "All Solid-State Li/LLZO/LCO Battery Enabled by Alumina Interfacial Coating," *Journal of The Electrochemical Society*, **169**, 040529 (2022).
3. A. Neumann, T. R. Hamann, T. Danner, S. Hein, K. Becker-Steinberger, E. D. Wachsman, and A. Latz, "Effect of the 3D Structure and Grain Boundaries on Lithium Transport in Garnet Solid Electrolytes," *ACS Applied Energy Materials*, **4**, 4786-4804 (2021)
4. A. M. Nolan, D. Wickramaratne, N. Bernstein, Y. Mo*, M. D. Johannes*, "Li+ Diffusion in Amorphous and Crystalline Al₂O₃ for Battery Electrode Coatings", *Chemistry of Materials* **33**, 19, 7795–7804 (2021)

Presentations

1. E. D. Wachsman, “A Solid Transformation of Energy Storage,” World Conference on Solid Electrolytes for Advanced Applications, October 25-27, 2021, Webinar (Invited)
2. Y. Mo, “Interfacial Failure of Lithium Metal in Solid-State Batteries : Insight from Large-Scale Atomistic Modeling”, the International Battery Materials Association(IBA) 2021 Annual meeting in Xiamen, China (virtual) (10/2021) (Invited)
3. Y. Mo, “Data-Driven Discovery of New Materials for Solid-State Batteries”, 5th Forum of Materials Genome Engineering, Zhengzhou, China (virtual) (12/2021) (Invited)
4. E. D. Wachsman, “A Solid Transformation of Energy Storage,” Materials Research Society, December 6-8, 2021, Boston (Invited)
5. E. D. Wachsman, “Enabling High Rate Metal Anodes by Tailored Structures and Interfaces,” Lithium Metal Anodes and their Application in Batteries, February 9-10, 2022, Webinar - Keynote
6. Y. Mo, “Interfacial Failure of Lithium Metal in Solid-State Batteries : Insight from Large-Scale Atomistic Modeling”, World Conference on Solid Electrolytes for Advanced Applications (virtual) (10/2021) (Invited)
7. Y. Mo, “Computation Guided Design of Materials for Solid-State Batteries”, Battery Energy Webinar (virtual) (03/2022) (Invited)
8. E. D. Wachsman, “Enabling High Rate Metal Anodes by Tailored Structures and Interfaces,” 23rd International Conference on Solid State Ionics, July 17-22, 2022, Boston (Keynote)
9. Y. Mo, “Interfacial Atomistic Mechanisms of Lithium Metal Stripping and Plating in Solid-State Batteries”, The 10th International Conference on Multiscale Materials Modeling (MMM10), Baltimore MD (10/2022)
10. Y. Mo, “Data-Driven Discovery of Materials for Next-Generation Batteries”, “Frontiers in Computational Materials Science”, UW-Madison Computation In Engineering Forum 2022 (10/2022) (Invited)
11. Y. Mo, “Computation Guided Design of Materials for Solid-State Batteries”, Department of Chemical Engineering, Columbia University (10/2022) (Invited)

References

1. A.M. Nolan, Y. Zhu, X. He, Q. Bai, Y. Mo, “Computation-Accelerated Design of Materials and Interfaces for All-Solid-State Lithium-Ion Batteries”, *Joule*, 2, 2016-2046 (2018)
2. X. He, Y. Zhu, Y. Mo, “Origin of Fast Ion Diffusion in Super-Ionic Conductors”, *Nature Communications*, 8, 15893 (2017)
3. X. Han, Y. Gong, X. He, G.T. Hitz, J. Dai, Y. Mo, V. Thangadurai, E.D. Wachsman, L. Hu “Negating Interfacial Impedance in Garnet-Based Solid-State Li-Metal Batteries”, *Nature Materials*, 16, 572 (2017)
4. W. Luo, Y. Gong, Y. Zhu, K. Fu, J. Dai, S. Lacey, C. Wang, B. Liu, X. Han, Y. Mo, E.D. Wachsman, L. Hu “Transition from Super-lithiophobicity to Super-lithiophilicity of Garnet Solid-State Electrolyte”, *Journal of the American Chemical Society*, 138, 12258-12262 (2016)

XVI.6 Molecular Ionic Composites: A New Class of Polymer Electrolytes to Enable All Solid-State and High Voltage Lithium Batteries (Virginia Polytechnic Institute and State University)

Louis A. Madsen, Principal Investigator

Department of Chemistry
Virginia Tech
319 Davidson Hall
1040 Drillfield Dr.
Blacksburg, VA 24061
E-mail: lmadsen@vt.edu

Feng Lin, Co-Principal Investigator

Department of Chemistry
Virginia Tech
323 Davidson Hall
1040 Drillfield Dr.
Blacksburg, VA 24061
E-mail: fenglin@vt.edu

Tien Duong, DOE Technology Development Manager

U.S. Department of Energy
E-mail: Tien.Duong@ee.doe.gov

Start Date: January 1, 2022

End Date: December 31, 2022

Project Funding (FY22): \$394,426

DOE share: \$327,245

Non-DOE share: \$67,181

Project Introduction

Based on a newly discovered class of solid polymer electrolyte materials, which we term molecular ionic composites (MICs), we are developing Li solid electrolytes targeted for use in transportation applications. MICs form a mechanically stiff (~ 1 GPa modulus), electrochemically stable, and highly thermally stable matrix that can resist dendrite formation with metal anodes, allow high voltage operation, provide robust safety against fire, and enable fast charging/discharging over a wide temperature range. The component molecules in MICs are inexpensive and MICs can be processed to yield a large area format at room temperature and generally in ambient atmosphere and with relatively safe solvents. Our team is advancing this class of polymer electrolytes to promote uniform lithium plating, inherent safety, and long-term stability against both lithium metal anodes and high voltage layered oxide cathodes.

Objectives

Utilizing molecular ionic composite (MIC) solid polymer electrolytes, the overall objective is to develop solid-state lithium conductors targeted for use in transportation applications. MICs form a mechanically stiff, electrochemically stable, and thermally stable matrix.

Specific objectives include the following: (1) Development of robust MIC electrolyte thin films (down to ~ 20 μm) to serve as simultaneous nonflammable separators and dendrite-blocking Li^+ conductors that enable the use of Li metal anodes, (2) electrochemical quantification of key performance metrics including electrolyte stability, interfacial reactions, and suitability/compatibility with a range of electrode materials, and (3) comprehensive investigation of ion transport mechanisms and electrode-electrolyte interfacial reactivity under practical operating conditions using NMR and synchrotron X-ray analyses.

Approach

MICs rely on a unique polymer “PBDT” that is similar to Kevlar® in its strength, stiffness, and thermal stability, but with densely spaced and ordered ionic groups that serve to form an electrostatic network that permeates mobile ions in the MIC. The team can tailor the ion concentrations and types to yield MIC electrolyte films that are electrochemically compatible with Li-metal anode as well as a range of high-voltage layered cathodes. The team is searching the composition space of lithium salts, electrochemically compatible ionic liquids, and polymer (PBDT) molecular weight to determine best composition windows for MIC electrolytes. The team is also investigating best methods for casting or spraying thin films in terms of temperature, solvent/evaporation conditions, and control over the initial liquid crystalline gel formation point. Concurrently, the team is testing MIC films in various electrochemical cells, quantifying transport and structural/morphology parameters with NMR and X-ray techniques, and measuring key mechanical (dynamic mechanical thermal analysis, stress-strain) and thermal (DSC, TGA) properties.

Results

Over this year, we showed that MIC solid electrolytes made with Pyr_{13}^+ cations and FSI^- anions, demonstrated enhanced rate capability. In order to characterize this MIC material in detail, we measured the diffusion coefficients of these cations and anions in MICs with 10 wt% PBDT and either 10 wt% or 20 wt% of two different Li salts (LiFSI and LiTFSI). As shown in Figure XVI.6.1, the diffusion coefficients decrease when increasing the polymer content in the MIC, and when comparing the $\text{Pyr}_{13}\text{FSI}$ and $\text{Pyr}_{14}\text{TFSI}$ based MICs, both the cation and anion in $\text{Pyr}_{13}\text{FSI}$ based MIC show substantially faster diffusion coefficients, indicating that the lithium ion will also likely diffuse faster, and this could explain the higher rate capability of the new MICs.

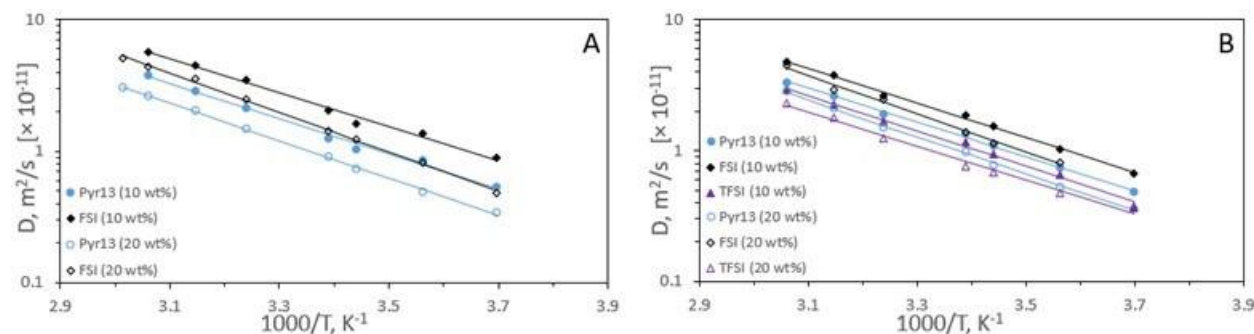


Figure XVI.6.1 Temperature dependence of diffusion coefficients of Pyr_{13}^+ and FSI^- in MICs with 10 wt% PBDT and LiFSI or LiTFSI salt. (A) shows the effect of LiFSI wt% (10% or 20%) on the diffusion coefficients while (B) shows again the $\text{Pyr}_{13}\text{FSI}$ IL but with LiTFSI at 10 or 20 wt%. In both cases, the diffusion coefficients are a factor of 3 faster than when using $\text{Pyr}_{14}\text{TFSI}$ IL with these salts. There is also noticeably faster diffusion for the LiFSI salt system as compared to LiTFSI, and only a modest decrease in ion diffusion when using 20 wt% salt as opposed to 10 wt%. Battery cell testing is underway with these and related systems (see also the figure below).

Furthermore, our team has made progress toward incorporation of high energy density Ni-rich cathodes with MIC electrolytes. The electrochemical data shows a high energy density of 558 Wh/kg (half cell, materials basis) with good capacity retention (92%) for 50 cycles. In this example coin cell, $\text{Li} \parallel \text{MIC} \parallel \text{Ni-rich cathode}$, was cycled between 2.5 and 4.2V at C/3 rate. Figure XVI.6.2 overviews these results. The team is currently exploring strategies to maintain capacity with a higher upper cut off voltage and has recently reached 4.4 V cutoff. Compared to conventional polymer electrolytes, our MICs demonstrated high energy density with good capacity retention. More recent studies (August - October 2022, not shown) have demonstrated similar systems with up to 700 Wh/kg and 90% capacity retention for 100 cycles.

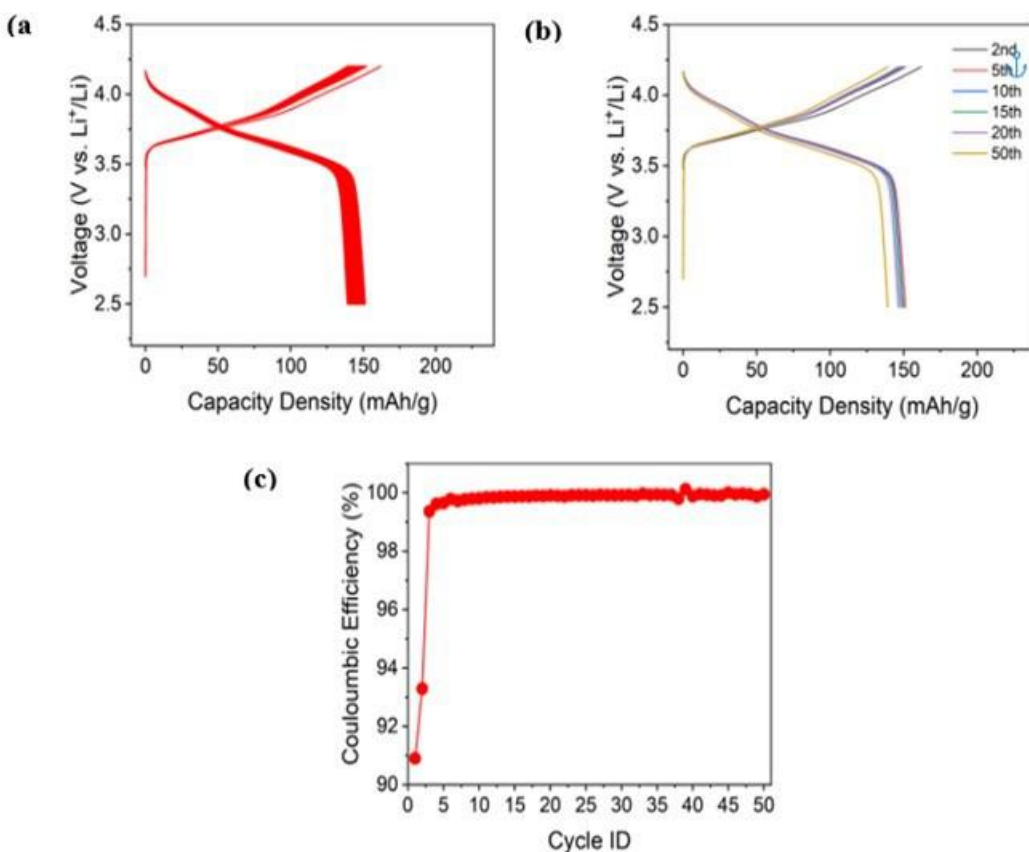


Figure XVI.6.2 Li/MIC/NMC622 cathode coin cell cycled at 60°C at C/3. The mass loading of the cathode material is 3.36mg/cm². (a) Galvanostatic charge/discharge profiles at C/3 for 50 cycles. (b) Charge/discharge profiles by different cycle numbers. (c) Coulombic efficiency (%) for 50 cycles.

This year, the team has also evaluated in detail the performance of PBDT as a polymer binder for LiFePO_4 (LFP) cathodes (and eventually others), and we have incorporated these cathodes into battery cells for testing. Use of this PBDT binder eliminates the traditional fluorinated polymer PVDF from the battery, and enables processing in water, removing the need for harmful solvents such as NMP. The long-term cycling stability of such cathodes with 3% PBDT binder is quite comparable to cathodes made with 3% PVDF binder. Figure XVI.6.3 shows the specific discharge capacity of LFP electrodes cycled at 4C rate for 1000 cycles at 22°C following 5 initial cycles at 0.2C. We can see that the 3% PVDF-LFP electrodes have only a slightly higher specific capacity at 4C rate than the 3% PBDT-LFP, which is likely due to the higher electrolyte uptake of PVDF, as reported previously. However, a notable capacity decay, from 127 mAh/g to 120 mAh/g, is observed for the 3% PVDF-LFP electrodes after 560 ~ 800 cycles, while the capacity of 3% PBDT-LFP remains nearly constant for 1000 cycles. Further experiments show that 3% PBDT-LFP electrodes start to show capacity decay only after 1100 ~ 1500 cycles. Thus, the LiFePO_4 electrode prepared with PBDT as binder has comparable or better cycling stability over PVDF, making PBDT a promising fluorine-free binder material to enable lithium ion batteries with no significant performance decay over long-term cycling at high rates.

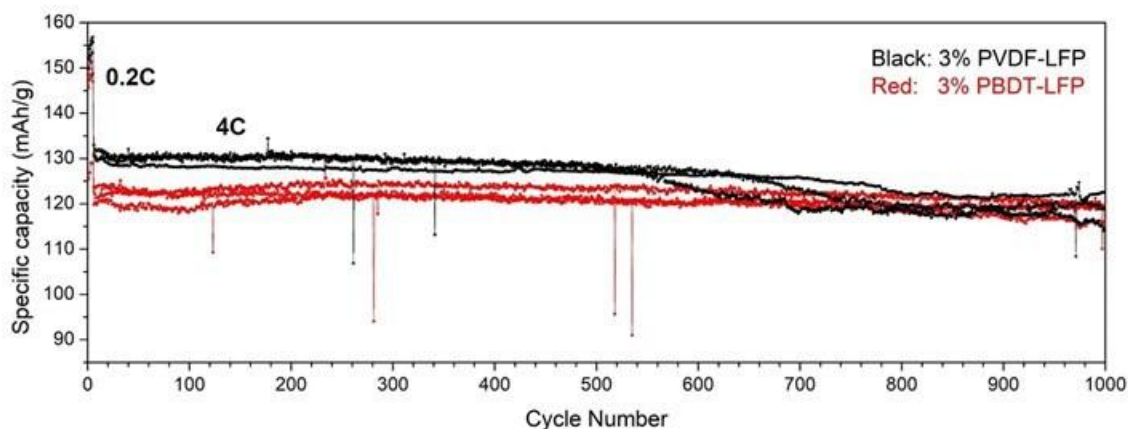


Figure XVI.6.3 Specific discharge capacity of LiFePO_4 electrodes prepared with 3% PBDT (red) and 3% PVDF (black) as binder over long-term cycling at 22°C . Performances of three cells are shown for each type of electrode. The cells are cycled at 0.2C for 5 cycles followed by 1000 cycles at 4C rate. Occasional pausing of the battery tester causes a few inconsistent data points in the plot. Electrodes with PBDT binder demonstrate better long-term cycling stability in spite of their slightly inferior capacity compared to their PVDF counterparts. The PBDT cells were run longer, up to 2000 cycles, with only minimal loss (10%) in specific capacity.

Besides this long-term cycling performance, the team has also evaluated the mechanical integrity of these electrodes in order to characterize the binding strength of PBDT vs. PVDF. LFP electrodes were cut into slices and adhered to a tape and then peeled off (Figure XVI.6.4). For the 3% PVDF-LFP electrode, the LiFePO_4 and carbon black particles peel off easily and the carbon coating layer on the aluminum substrate is almost intact. This suggests that the binding strength between the carbon coating layer and the electrode particles is weak. When using PBDT as the binder, a higher force is needed to peel the electrode off as evidenced by the curling of the current collector (carbon-coated aluminum) after the test. Some of the carbon coated on the aluminum also peels off during the test, leading to exposure of the metallic luster of the aluminum. This strongly suggests that PBDT endows higher binding strength between the electrode particles and the current collector. In combination with the better long-term cycling stability discussed above and the similar rate capability of 3% PBDT-LFP electrodes compared to the 3% PVDF-LFP electrodes, the team believes PBDT holds great potential as a polymer binder for commercial electrodes.

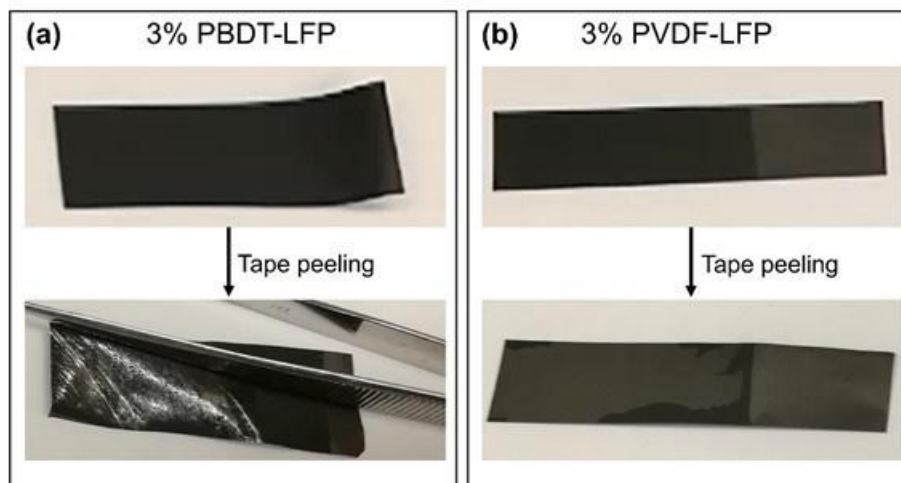


Figure XVI.6.4 Images of the electrodes before and after tape peeling tests. The electrodes are pressed on an adhesive tape and then peeled off. The thin carbon coating layer on the aluminum substrate stays intact after the peeling test when using PVDF as the binder. However, when using PBDT as the binder, the majority of the carbon coating layer is peeled off along with the LiFePO_4 and carbon particles, exposing the metallic luster of the aluminum substrate. These tests strongly indicate that PBDT has higher binding strength than PVDF.

The team has also probed the evolution of ionic heterogeneity as well as degradation processes of molecular ionic composites (MICs) electrolyte for high voltage, solid-state lithium batteries. Figure XVI.6.5 shows examples of X-ray absorption spectroscopy (XAS) and X-ray fluorescence imaging (XRF) obtained at the TES beamline (8-BM, tender energy X-ray absorption spectroscopy) at NSLS-II. The distinct absorption features of the sulfur K-edge allowed us to interpret oxidation state, the characteristic bonding between the sulfur atom and its neighboring elements. An energy range of 1 to 5 keV and spatial resolution of 2 μm are suitable for imaging of the ionic species in the MIC electrolyte. The capability of TES 8-BM also facilitates the characterization of spatial heterogeneity of ionic species inside our novel polymer electrolyte via in situ 3D fluorescence imaging and tomography. Initial XAS results are enabling identification of the evolution of chemical species from their characteristic X-ray absorption near edge structure (XANES) information. As we further improve, analyze, and interpret these experiments/results, we envision that our discovery will provide fundamental knowledge about the ion dynamics and polymer electrolyte decomposition process to better understand cell failure mechanisms.

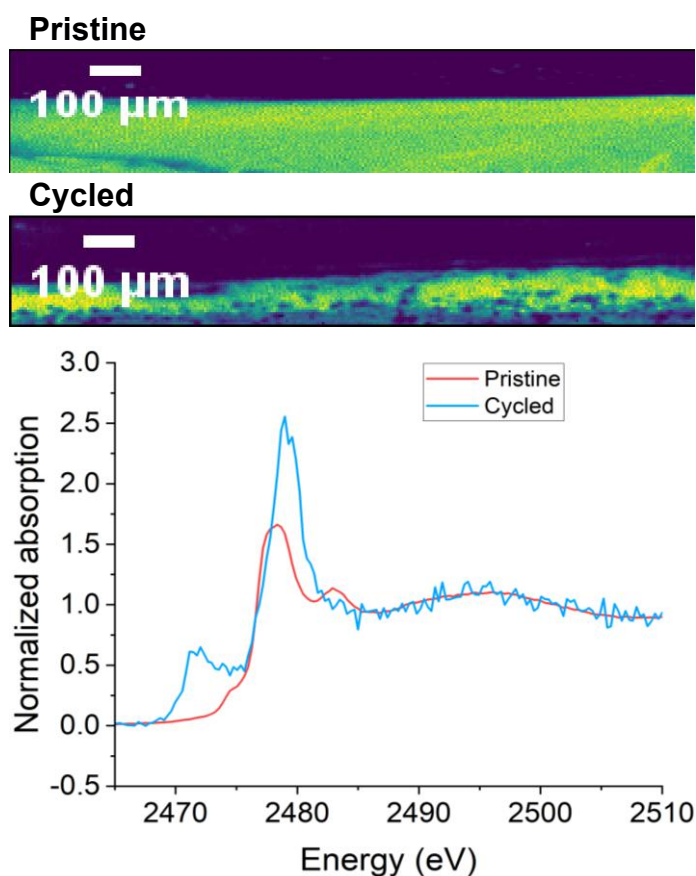


Figure XVI.6.5 X-ray fluorescence imaging and X-ray absorption spectroscopy results of pristine and cycled molecular ionic composite (MIC) electrolytes. The cycled MIC sample displayed a heterogeneous distribution of sulfur species compared to the pristine sample. The evolution of decomposed sulfur species is revealed from distinct XANES.

The team has also screened various types of additives to the molecular ionic composite (MIC) electrolytes to improve lithium symmetric cell performance at 23°C (Figure XVI.6.6). Additives are incorporated into MIC electrolytes based on our (now traditional) TFSI-based compositions to aid in formation of stable solid electrolyte interphase (SEI) films. Additives such as fluoroethylene carbonate (FEC), lithium difluoro(oxalate) borate (LiDFOB) salt, and lithium bis(oxalate)borate (LiBOB) salt showed enhanced limiting current density compared to that of MIC membranes without additives.

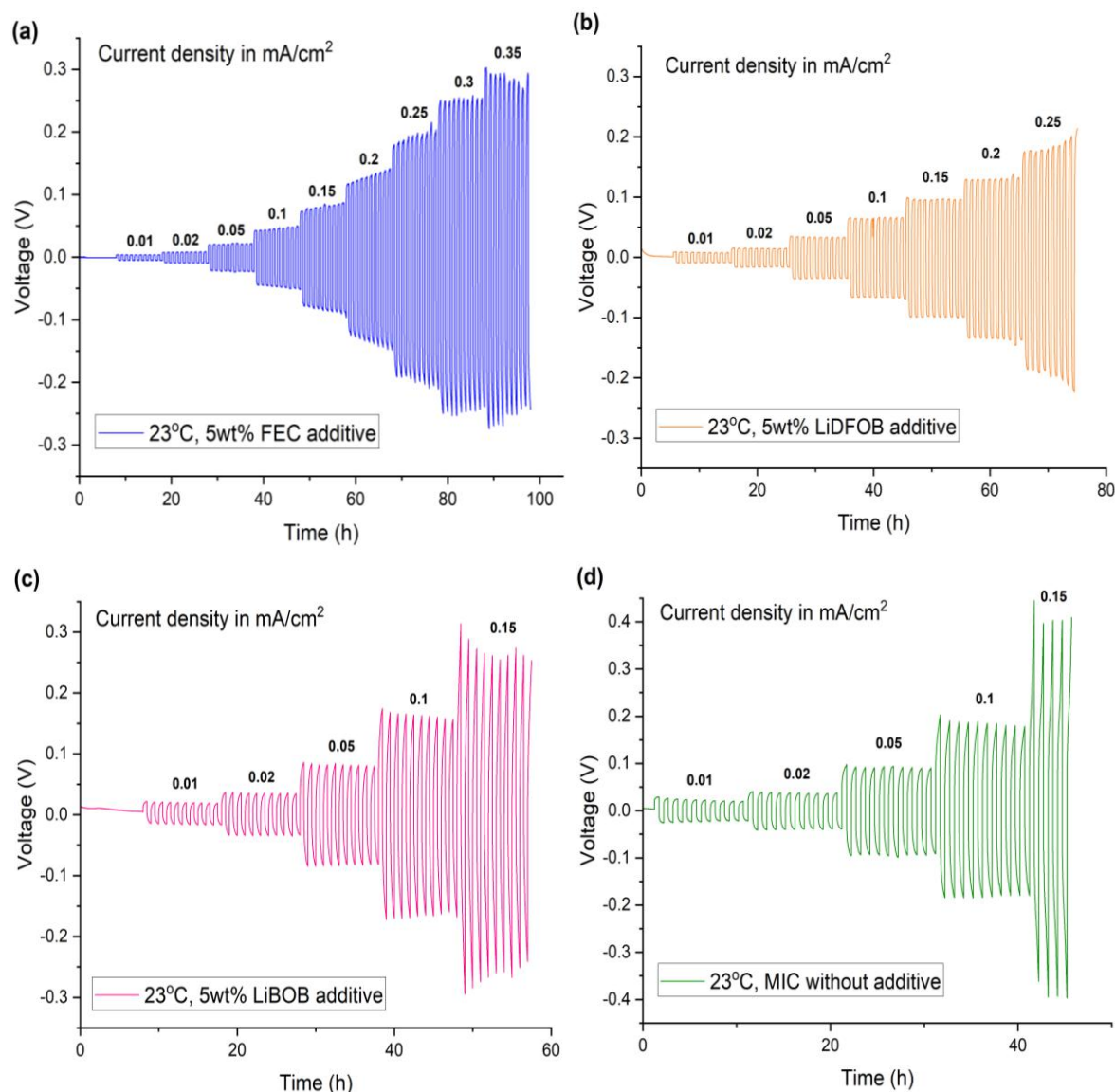


Figure XVI.6.6 Lithium symmetric cell performance with and without selected additives to aid in SEI formation. All plots are voltage profiles of symmetric cells cycled at 23 °C with increasing steps of current density. The charge and discharge times are 0.5 h, respectively, and the current density is stepped every 10 cycles. (a) 5 wt% of fluoroethylene carbonate (FEC), (b) lithium difluoro(oxalate)borate (LiDFOB) salt, (c) lithium bis(oxalate)borate (LiBOB) salt, and (d) without additives. We observe significant gains (up to 2.3X) in limiting current for the FEC and LiDFOB additives. Future goals include exploration of a range of other additives, focusing on non-volatile compounds, spatial separation of additives near interfaces, and additives that can largely be consumed during dominant SEI formation.

This year, the team has also investigated how MIC electrolytes impact the bulk properties of cathodes in batteries. We evaluated the bulk stability of NMC811 cathodes by hard X-ray absorption spectroscopy (XAS) after charging in contact with MIC electrolytes. As Ni is the primary charge compensating element in nickel-rich layered oxides at 2.5–4.4 V, we mainly focus on the evolution of Ni oxidation states. During the first cycle, the Ni K-edge exhibits a reversible energy shift upon charging and discharging (Figure XVI.6.7a). After 35 cycles, the pre-edge region feature is well-preserved and the edge position of the charged cathode shows a minor shift compared to the initially charged cathode, suggesting that the bulk structural properties (e.g., symmetry) of long-time cycled cathode is maintained. The extended X-ray absorption fine structure analysis (EXAFS) in Figure XVI.6.7b reveals that the interatomic distances of Ni-O and Ni-TM in charged materials remain unchanged after cycling, which is another positive indicator of structural stability. More detailed

properties at the particle level are analyzed through transmission x-ray microscopy (TXM), which can pinpoint spatial redox reactions in a specific particle and provide information related to Li diffusion pathways. The color code in the TXM images corresponds to different Ni oxidation states. Compared to the pristine particles (Figure XVI.6.7c), a significant charge heterogeneity can be observed in the particles once they undergo initial charging (Figure XVI.6.7d, f), which can be attributed to the non-uniform redox reactions caused by the local limitations of electronic and ionic transport. The charged particles also demonstrate a holistic core-shell structure, with a higher oxidation state at the sub-surface region while a lower oxidation state in the bulk (Figure XVI.6.7g). After prolonged cycling, the charge heterogeneity increases, with the appearance of some minor inactive domains (Figure XVI.6.7e). Nevertheless, considering the consistency of hard XAS results for charged electrodes before and after long-time cycling, the bulk structure is stable in the MIC-based solid-state systems.

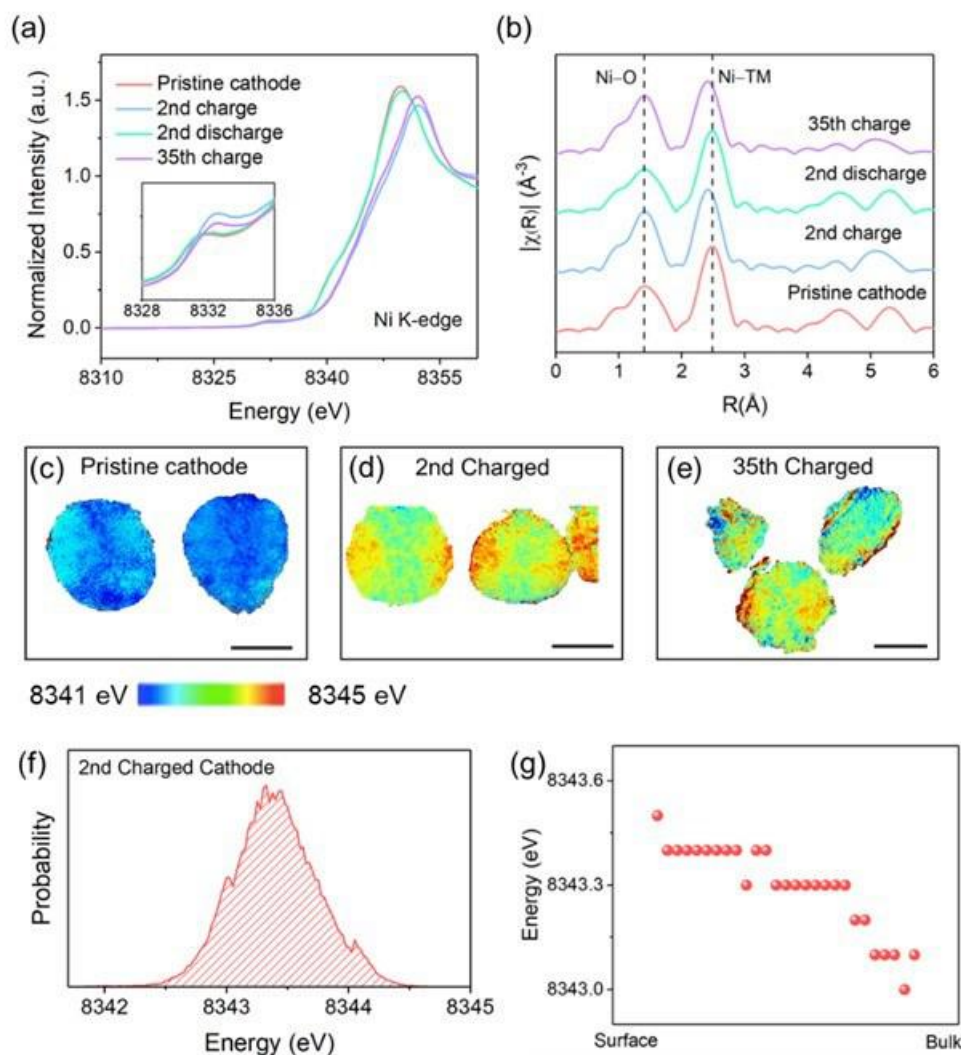


Figure XVI.6.7 (a) X-ray absorption near-edge spectroscopy and (b) extended X-ray absorption fine structure results of pristine and charged NMC811 cathodes in contact with MIC electrolytes; the transmission X-ray microscopy results of (c) pristine cathode, (d) 2nd charged cathode and (e) 35th charged cathode; The scale bars in c-e are all 5 μm. (f) the histogram of Ni K-edge energy distribution and (g) the depth-dependent Ni K-edge energy variation in the 2nd charged cathode.

The team has also conducted advanced NMR analyses on MIC electrolytes, now on samples that have been cycled or charged and then removed intact from disassembled cells. We have investigated coin cell crimping pressure over a range of 0.2 to 0.6 tons (employing a 0.9 cm² active cell area) to find the optimal cell

performance in the range of 0.3 to 0.4 tons. After cell disassembly, MIC electrolytes are fully intact and can be peeled off the electrodes. In all these cases, the MIC electrolytes display a single component NMR diffusion signal curve, verifying that no significant heterogeneity (e.g., cracking, surface modification, ion/salt loss) occurs during cell assembly/disassembly and cycling. Figure XVI.6.8 shows a representative normalized ^1H NMR signal intensity (Stejskal-Tanner) plot of a cycled coin cell that was assembled with a crimping pressure of 0.3 tons.

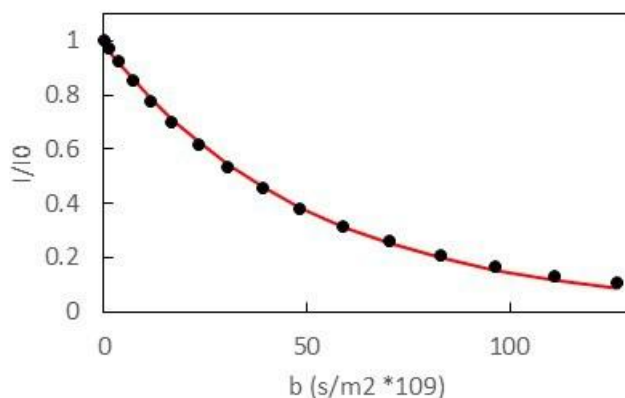


Figure XVI.6.8 Proton (Pyr_{14} cation) NMR signal attenuation curve (I/I_0 vs. NMR diffusometry parameter b) showing a diffusion coefficient $D = 2.0 \times 10^{-11} \text{ m}^2/\text{s}$ for a $\text{Li}|\text{Li}$ cell charged/discharged for 100 cycles. Best fit to the data (black points) with a single diffusing component (red line) shows no significant heterogeneity introduced into the sample. The sample was sealed in glass under vacuum at room temperature after cell disassembly and cycling and measured on our 400 MHz NMR spectrometer.

Further investigations in this area include using NMR diffusometry to quantify and understand ion dynamics within the MIC films at various states of charge and total cycling times in cells with LiFePO_4 (LFP) cathodes as well as in cells with NMC811 cathodes. The composition of these films is 10 wt% PBDT, 10 wt% LiTFSI and 80 wt% $\text{Pyr}_{14}\text{TFSI}$, consistent with our baseline optimal/robust MIC formulation. To investigate ion dynamics in the film, we measured the diffusion coefficients of the mobile cations and anions, Pyr_{14}^+ and TFSI^- , respectively, from room temperature to 80°C as shown in Figure XVI.6.9. All samples measured had diffusion coefficients ranging from 2×10^{-12} to 6×10^{-11} (depending on temperature and history), with the uncycled films having somewhat higher diffusion coefficients (by 30-80%) compared to those MIC films collected from cycled cells. This may be due to some of the mobile ions being pushed out of the film and dispersed into the porous cathode when assembling the coin cell, or possibly due to degradation of some fraction of the ions. Comparing to the cation and anion diffusivities of uncycled MIC films reported in a previous paper we published (Yu et al, *Advanced Energy Materials*, 2021 – see Key Publications list below), the diffusion coefficients of the uncycled films match within errors. The cell with the NMC cathode was charged to 4.4 V at 60°C with a charging rate of 0.1 C then disassembled at this charged state and sealed into a glass NMR tube under vacuum before performing diffusometry experiments. The $\text{Li}/\text{MIC}/\text{LFP}$ cells were cycled 20 times at room temperature before disassembly. The charge/discharge cycles were run 5 times at different constant current densities of 0.01 mAh/cm^2 , 0.02 mAh/cm^2 , 0.05 mAh/cm^2 , and 0.1 mAh/cm^2 . Both cells have comparable diffusion coefficients. These results indicate high overall film stability (electrochemical, chemical, and structural) of MIC electrolytes up to 4.4 V and at 60°C . Figure XVI.6.10 and Figure XVI.6.11 show the charging and cycling steps used for preparing these cells for NMR diffusometry measurements.

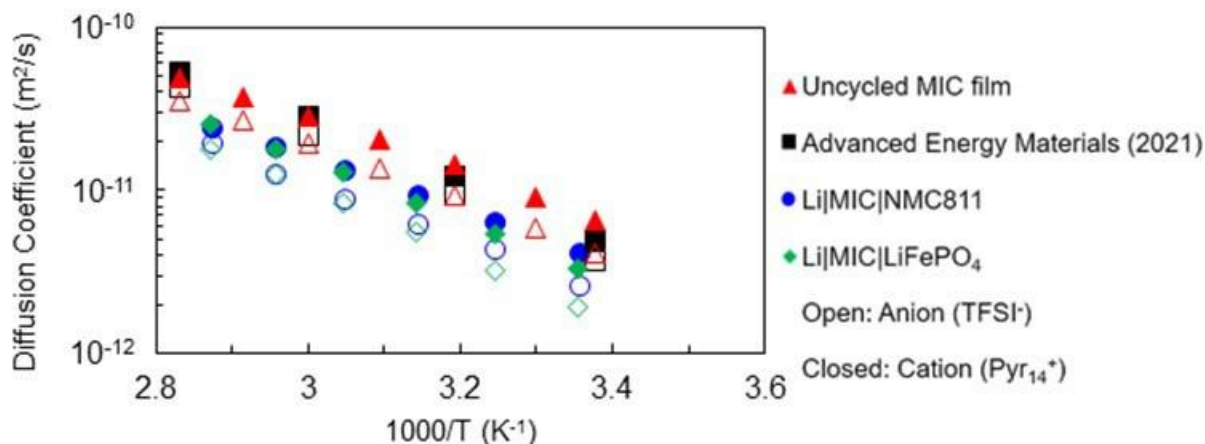


Figure XVI.6.9 Temperature dependence of the cation (Pyr_{14}^+) and anion (TFSI^-) diffusion coefficients in cycled/charged MIC films.

The solid data points represent the cation diffusion coefficients and the open data points represent the anion diffusion coefficients. The red triangles are the diffusion coefficients of the uncycled MIC film before assembly into a battery, and the diffusion coefficients agree with the uncycled MIC film reported in the Yu et al, *Advanced Energy Materials* 2021 paper (black squares). The blue circular data points are of the MIC film after charging to 4.4 V in a Li/MIC/NMC811 cell, and the green diamonds are of the MIC film after 20 cycles in a Li/MIC/LFP cell. Both MIC membranes collected after cell assembly and then charging, and/or cycling have similar diffusion coefficients, which are approximately half as high as the uncycled MIC material, possibly due to some mobile ions pushed into the porous cathode during cell assembly. These data provide critical information for further optimizing MIC composition, casting process, SEI/interface assessment and optimization, and cell assembly.

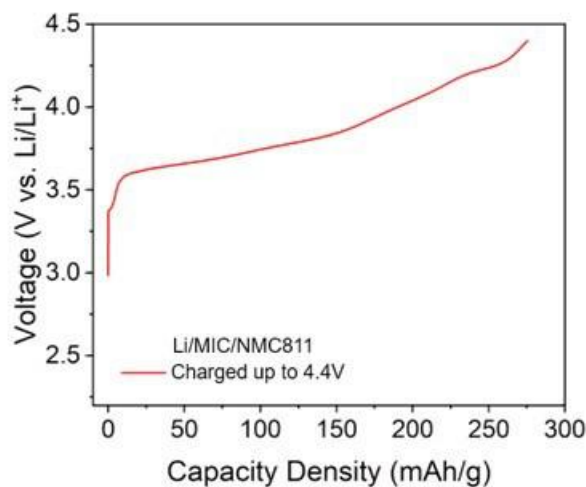


Figure XVI.6.10 Constant current charging step of Li/MIC/NMC811 cell, run at 60 °C with a 0.1C charging rate and an upper cut off voltage of 4.4V.

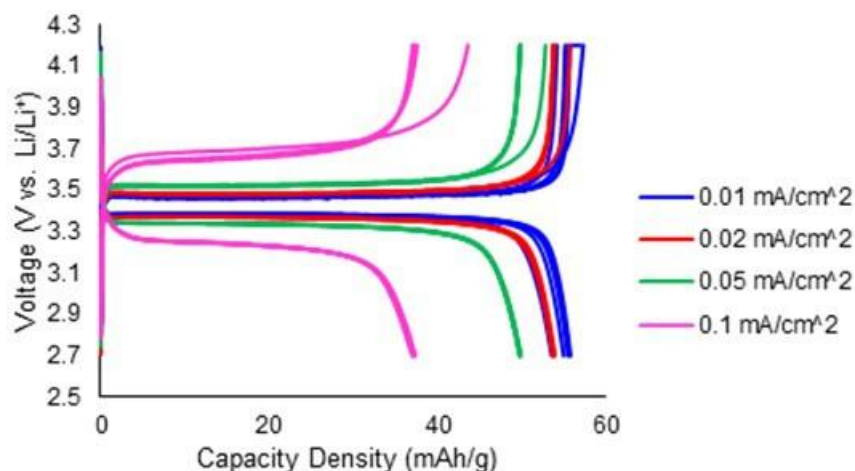


Figure XVI.6.11 Charge/discharge profile of Li/MIC/LiFePO₄ cell at room temperature. The cell was run at each constant current density for 5 cycles before increasing current density, for a total of 20 cycles.

The previous baseline-optimized MIC electrolyte with 10 wt% PBDT, 10 wt% LiTFSI and 80 wt % Pyr₁₄TFSI shows excellent thermal stability and mechanical properties, but the rate capability is still limited due to a relatively low Li⁺ transference number (~ 0.2). During the past year, the team has incorporated new mobile ions (Pyr₁₃⁺, FSI⁻, BOB⁻ and DFOB⁻) into the MIC electrolyte to improve its rate capability. Figure XVI.6.12 shows a comparison of the specific capacity of Li/MIC/NMC811 cells using the previous MIC and the new engineered MIC electrolyte. Incorporating a new ion composition substantially increases the rate capability. The team has also recently seen even larger gains with other salt combinations. Clearly, substantial rate capability improvements are in store for MIC electrolytes by further tuning ionic composition.

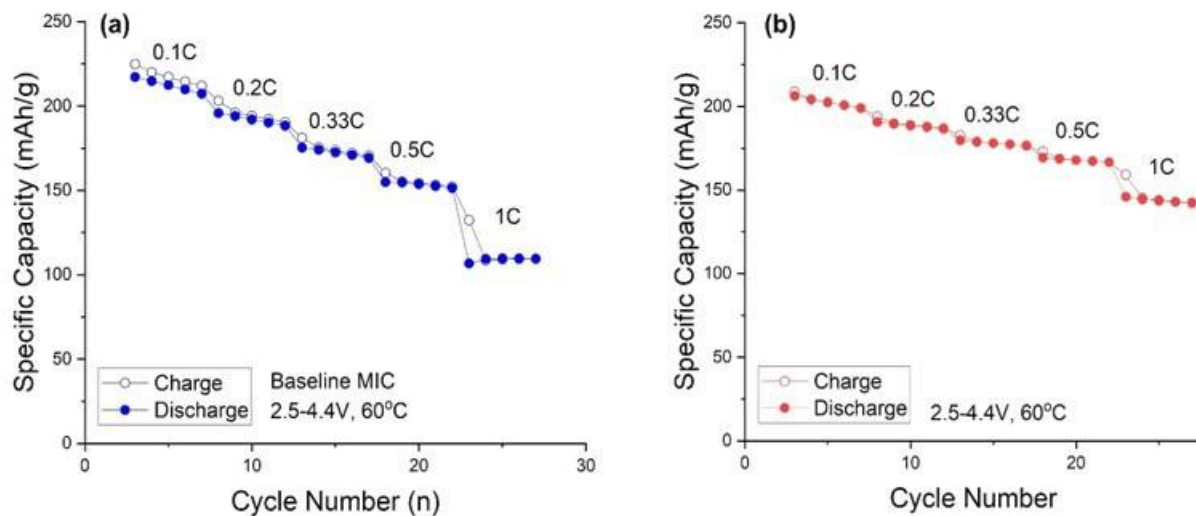


Figure XVI.6.12 Specific capacity of Li/MIC/NMC811 cells with (a) previous MIC composition and (b) modified MIC with mixed ion composition measured at 60 °C when cycled between 2.5 V and 4.4 V.

Conclusions

In summary, the team at Virginia Tech has made significant progress in year 3 of the project. The team has established NMR characterizations of battery cell components at different states of charge and after different cycling protocols. The team has evaluated and confirmed the compatibility of MIC electrolytes with different cathode materials, including LiFePO₄, NMC622, and NMC811. The team has found that MIC electrolytes can enable high-voltage (up to 4.4 V) cycling with NMC cathodes and Li metal anodes, with capacity retention of

up to 90% for 100 cycles. The team is continuing to optimize the cycling conditions and cell testing environments. The team has undertaken advanced X-ray spectroscopy and fluorescence imaging to evaluate electrolyte and interfacial stability after assembly and cycling. The team has also demonstrated that the highly charged, double helical, and thermally stable polymer we use (PBDT) can serve as a robust cathode binder that eliminates fluorinated polymers and involves only water processing. Going forward in the last few months of this project, the team is incorporating newly developed MIC compositions and thinner solid electrolyte films into full-cell testing to reach higher energy densities (up to and beyond 700 Wh/kg on a materials/half-cell basis) and at least 3X higher rate capability than previous versions. Furthermore, the team is developing key understanding of failure mechanisms and SEI formation to achieve more stable cycling with different types of electrodes.

Key Publications

1. Deyang Yu, Linqin Mu, Xu Feng, Feng Lin, and Louis A. Madsen. "Rigid-Rod Sulfonated Polyamide as an Aqueous-Processable Binder for Li-Ion Battery Electrodes." *ACS Appl. Energy Mater.* (2022), 5, 12531-12537. doi: 10.1021/acsam.2c02173.
2. Joshua E. Bostwick, Curt J. Zanelotti, Deyang Yu, Nicholas F. Pietra, Teague A. Williams, Louis A. Madsen, and Ralph H. Colby. "Ionic interactions control the modulus and mechanical properties of molecular ionic composite electrolytes" *Journal of Materials Chemistry C* (2022), 10, 947-957. doi: 10.1039/d1tc04119c.

Acknowledgements

The team acknowledges collaborations with T. J. Dingemans' group at University of North Carolina (UNC) Chapel Hill in which they are forming composites based on PBDT polymer with carbon materials such as graphene oxide and are beginning to develop new charged rigid-rod polymers that build on PBDT. The team also acknowledges collaborations with Prof. R. H. Colby at PSU on shear rheology and broadband dielectric spectroscopy to understand mechanical properties and conduction mechanisms. The team also acknowledges collaborations with Dr. D. Nordlund and Dr. Y. Liu at SLAC National Accelerator Laboratory (SLAC), and S.-M. Bak of Brookhaven National Lab, for conducting synchrotron X-ray studies on MIC films and composite electrodes. The team also appreciates the collaboration with Prof. Y. Yao at University of Houston for establishing the solid-state battery testing platform and Prof. P. Dong, George Mason University (GMU) for advanced mechanical testing, and Prof. D. Troya for molecular dynamics simulations of ion transport processes.

XVI.7 Hot Pressing of Reinforced All-solid-state Batteries with Sulfide Glass Electrolyte (General Motors LLC)

Thomas A. Yersak, Principal Investigator

General Motors LLC
GM Global Research and Development
30470 Harley Earl Blvd.
Warren, MI 48092
E-mail: thomas.yersak@gm.com

Tien Duong, DOE Technology Development Manager

U.S. Department of Energy
E-mail: Tien.Duong@ee.doe.gov

Start Date: October 1, 2019
Project Funding: \$1,250,000

End Date: September 30, 2023
DOE share: \$1,000,000

Non-DOE share: \$250,000

Project Introduction

The performance of all-solid-state batteries (ASSBs) with sulfide solid-state electrolytes (SSEs) is limited because they are 10% - 20% porous. Porosity limits energy density of the composite cathode and provides a conduit for Li-metal deposits through the separator if operating specifications (i.e. current density, operating temperature, and pressure) are not strictly controlled. This project intends to demonstrate that hot press cell processing and appropriately formulated sulfide glass SSEs can eliminate porosity to enable Li-NCM ASSBs with energy density of > 350 Wh/kg.

Objectives

The objective of this project is to research, develop, and test Li-NCM ASSBs capable of achieving program performance metrics by implementing appropriately formulated sulfide glass SSEs and hot press cell processing in a dry room environment. In the composite cathode, hot pressing eliminates porosity to increase energy density by enabling thick composite cathodes with high active material loading. In the separator, hot pressing eliminates porosity that may otherwise provide a conduit for Li metal deposits to short the cell. Unfortunately, hot press cell processing may cause a deleterious side-reaction between sulfide SSE and NCM active material even though sulfide SSEs are kinetically stable versus NCM at room temperature. For this reason, work conducted during this project's first budget period focused on enabling the hot press processing of composite cathodes with the objective of demonstrating a reversible capacity of > 120 mAh/g after hot pressing.

Approach

The sulfide SSE used in the composite cathode, otherwise known as the catholyte, will dictate the processing specifications for ASSB hot pressing. Thermal stability can be achieved by NCM passivation and proper catholyte formulation. Work conducted during this project's first budget period systematically evaluated different NCM coatings, catholyte formulations, and hot press cell processing conditions (i.e. temperature, time, and pressure). Having established the feasibility of hot-pressed composite cathodes, work transitioned to this project's second budget period, which is focused solely on the separator. Separator glass electrolyte compositions will be systematically studied for processability and compatibility with secondary electrolyte phases. The functional characteristics of process glass electrolyte separators such as ionic conductivity and critical current density will then be determined. In the final budget period of this project, full ASSB stacks will be hot-pressed to realize thickness targets for cathode-supported separators.

Results

In our first budget period, we studied the electrochemical performance of hot-pressed cathode composites with NCM cathode active material (CAM) and sulfide solid state electrolyte (SSE) catholytes. We reported that a cathode composite of NCM622 and $75\text{Li}_2\text{S} \cdot 25\text{P}_2\text{S}_5$ (glassy Li_3PS_4) retained adequate cyclability after hot-pressing at 200°C [1]. Hot-pressing of a cathode/separator stack consolidates SSE to improve the energy density of the cathode composite and to block Li deposits from shorting the separator. The second budget period therefore focuses on the study of SSE materials for cathode-supported separators. Three topics will be covered in this first section; namely, the process rheology of ternary glasses, the implementation of a 3-electrode test cell, and the evaluation of a multifunctional reinforcement.

The process rheology of glass electrolytes was assessed to improve the consolidation of cathode-supported separators during hot pressing. This work supports the overall goal for Budget Period 2. We studied the binary $70\text{Li}_2\text{S} \cdot 30\text{P}_2\text{S}_5$ and the ternary $70\text{Li}_2\text{S} \cdot (30-x)\text{P}_2\text{S}_5 \cdot xA$ glass compositions, where A represents a third glass component. We assessed process rheology by measuring porosity and sample diameter before and after hot pressing. A picture of samples after processing (Figure XVI.7.1a) shows that the ternary glass composition decreases the load required to achieve adequate consolidation. In fact, the ternary sample's diameter increased by 79% under a 1 metric ton load (74 MPa nominal pressure) whereas the binary sample's diameter increased by only 12.6% under a higher 5 metric ton load (370 MPa nominal pressure). Our previous work showed that NCM is susceptible to microcracking when consolidated at a 370 MPa pressure [1]. Decreasing the process load is critical to preserve the mechanical integrity of high-Ni content polycrystalline NCM particles within the cathode support. Current work investigates lowering the process temperature and residence time to limit degradation of the NCM/catholyte interface within the cathode support.

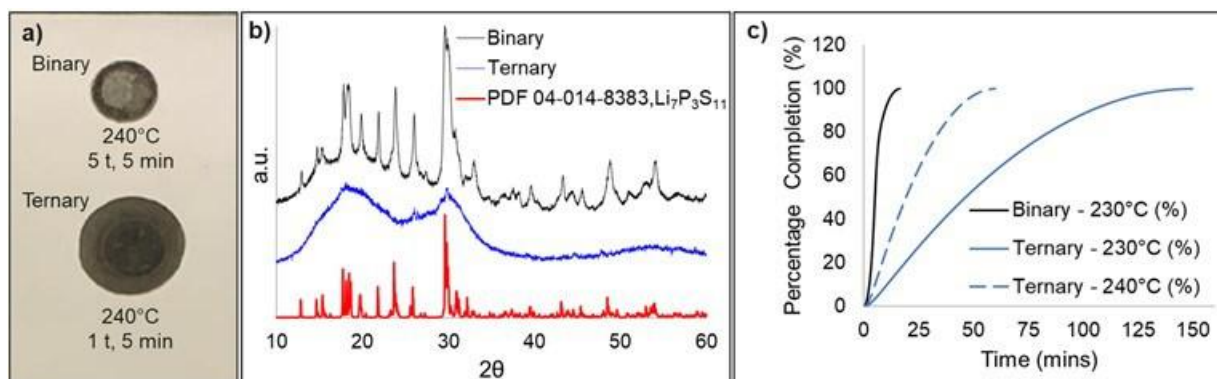


Figure XVI.7.1 a) Picture of reinforced SSE pellets after hot pressing at 240°C for 5 minutes. b) XRD profiles of hot-pressed SSE pellets. The binary sample devitrifies to $\text{Li}_7\text{P}_3\text{S}_{11}$ while the ternary sample remains a glass. c) Fractional extent of devitrification for binary and ternary samples as determined by the integration of a DSC exothermic feature.

To understand the ternary phase's improved process rheology, we investigated the glasses with both X-ray diffraction (XRD) and differential scanning calorimetry (DSC). Figure XVI.7.1b presents the diffraction patterns of both binary and ternary glasses after hot pressing at 240°C for 10 minutes and the patterns are indexed to the reflections of $\text{Li}_7\text{P}_3\text{S}_{11}$ (pdf #04-014-8383). The binary glass devitrified during hot pressing while the ternary glass remained largely amorphous. It is well known that the viscosity of glasses increases substantially upon devitrification as crystallites grow and physically interact. We therefore attribute the superior processability of the ternary glass to its more sluggish crystallization kinetics. To confirm this suspicion, we conducted DSC experiments on both the binary and ternary glasses. The binary glass had a crystallization onset of 272.79°C when dynamically heated at $10^\circ\text{C}/\text{min}$ while the ternary glass had a higher crystallization onset of 294.25°C under the same conditions. Additionally, we also measured the time required to complete full crystallization (Figure XVI.7.1c). It took the ternary glass over 2 hours to fully devitrify at 230°C while the binary glass fully crystallized in less than 10 minutes at 230°C .

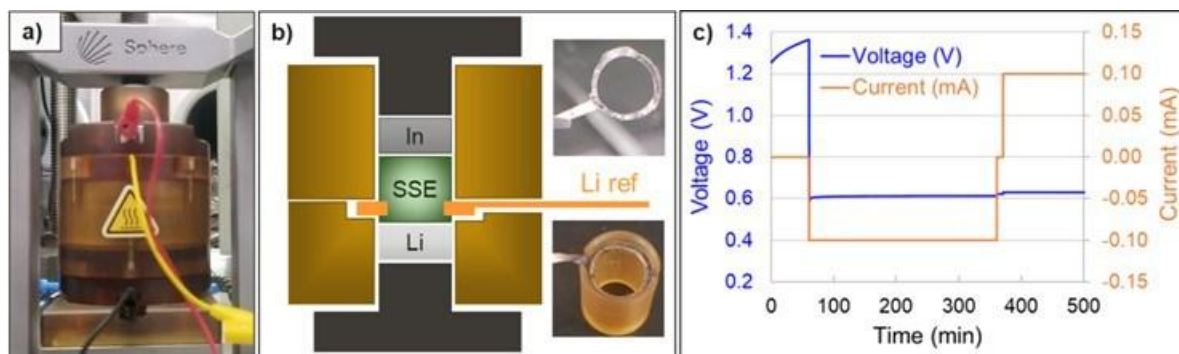


Figure XVI.7.2 a) Picture of a 3-electrode test cell used in this study. b) Schematic of the 3-electrode test cell. The reference electrode is an annular Cu foil disc with Li metal coating held in place with a two-part sleeve. c) Voltage and current versus time for a 3-electrode cell with a Li metal counter electrode, an indium working electrode, and a Li reference electrode.

A 3-electrode test cell was implemented to meet Q4 FY2021's Milestone and support the failure analysis of SSE separators. A picture of the 3-electrode test cell is provided in Figure XVI.7.2a and a schematic of the 3-electrode test cell's cross section is provided in Figure XVI.7.2b. It consists of a two-piece polyethylenimine (PEI) sleeve, 8 mm diameter stainless steel current collectors, and a reference electrode. The reference electrode is a ring of 30 μm thick Li foil supported by 10 μm thick Cu foil (Figure XVI.7.2b inset). The inside of the Li ring is embedded within the SSE sample prior to testing. In our initial test the working electrode was indium metal, the counter electrode was Li metal, and the reference electrode was Li metal. As shown in Figure XVI.7.2c, once the indium working electrode is alloyed with Li upon the application of a negative current, the reference electrode measures the correct voltage of 0.6V. This 3-electrode cell is appropriate for all-solid-state test cells, however, its utility for semi-solid test cells remains to be evaluated. Further work is needed to provide a seal between the two pieces of the PEI sleeve to prevent leakage of a secondary electrolyte phase.

Multifunctional reinforcement was evaluated to replace insulating aramid fibers to meet Q1 FY2022's Milestone and reduce the resistance of reinforced SSE separators. Al-doped LLZO fibers were obtained from a commercial vendor and a SEM image of the fibers is provided in Figure XVI.7.3a. XRD analysis (Figure XVI.7.3b) showed that the fibers were not pure cubic phase $\text{Li}_7\text{La}_3\text{Zr}_2\text{O}_{12}$. A baseline separator of Li_3PS_4 + 3 wt.% Kevlar fiber had an ionic conductivity of 0.187 mS/cm at room temperature. Li_3PS_4 separators with 3 wt.% and 10 wt.% LLZO fiber reinforcement had lower conductivities of 0.103 and 0.08 mS/cm, respectively. LLZO fiber reinforcement is therefore not considered for future work.

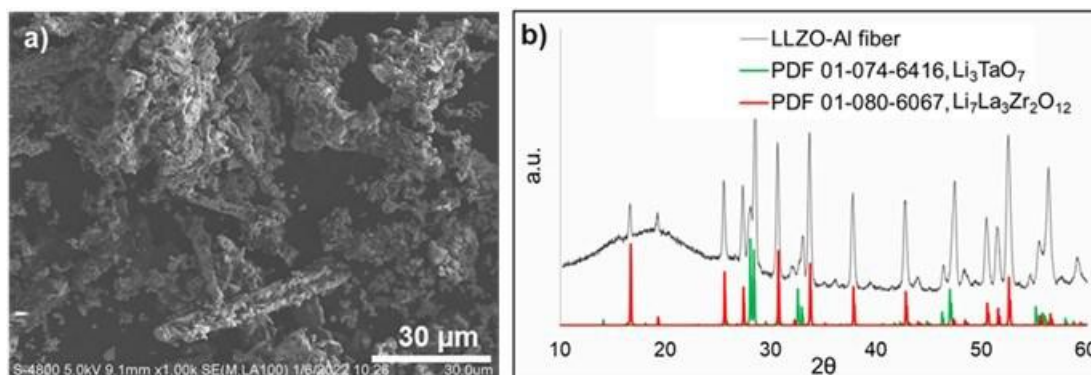


Figure XVI.7.3 a) SEM image of LLZO fibers obtained from a commercial vendor. b) XRD profile of the LLZO fibers indicate a significant Li_3TaO_7 impurity.

This second section describes the moisture stability of sulfide-based solid-state electrolytes (SSE) when exposed to a dry room environment. The poor moisture stability of sulfide SSEs presents a major obstacle to the commercialization of solid-state batteries (SSBs) utilizing these SSEs. If SSBs are to be manufactured using the same capital equipment and facilities as those used to make conventional Li-ion batteries, then the moisture stability of sulfide SSEs must be improved. Here, we report a systematic study of moisture stability as a function of sulfide SSE composition and dewpoint. We propose that moisture stability should be defined not only as H_2S generation, but also as ionic conductivity reduction. Furthermore, we show that sulfide SSEs composed primarily of PS_4^{3-} structural units are the most stable and that anhydrous solvents protect sulfide SSEs from hydrolysis during processing.

In the first experiment of this study, a variety of sulfide SSE powders were exposed to a -40°C dew point dry room environment for 30 minutes as shown in Figure XVI.7.4a. During this experiment H_2S gas generation was monitored and the data are provided in Figure XVI.7.4b. Our results are consistent with the findings of previous studies with respect to the influence of glass modifier (Li_2S) content, glass co-modifier (Li_2O), and LiI dopant on H_2S generation. First, sulfide SSEs with 75 mol% glass modifier produced the least amount of H_2S gas [2]. $(\text{Li}_2\text{S})_{75}(\text{P}_2\text{S}_5)_{25}$ (75-25 LPS), $(\text{Li}_2\text{O})_7(\text{Li}_2\text{S})_{68}(\text{P}_2\text{S}_5)_{25}$ (7-68-25 LPSO), and $(\text{Li}_2\text{S})_{75}(\text{P}_2\text{S}_5)_{25} + 20 \text{ mol\% LiI}$ (75-25 LPSI) all generated a maximum of 0.1 g/cc H_2S , whereas $(\text{Li}_2\text{S})_{70}(\text{P}_2\text{S}_5)_{30}$ (70-30 LPS) and $(\text{Li}_2\text{O})_7(\text{Li}_2\text{S})_{63}(\text{P}_2\text{S}_5)_{30}$ (7-63-30 LPSO) generated a maximum of 0.6-0.7 g/cc H_2S . Second, a Li_2O co-modifier modestly reduced the H_2S generation of sulfide SSEs [3-5].

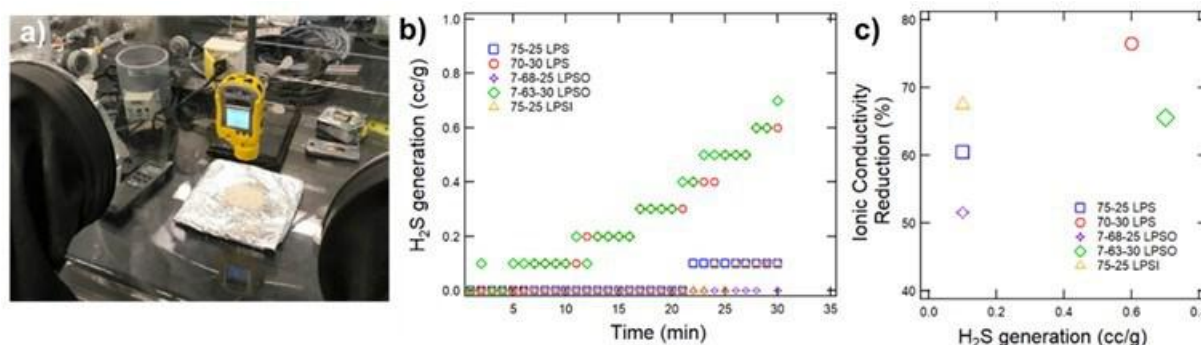


Figure XVI.7.4 a) A picture of the experimental setup used to expose sulfide SSE powders to a dry room environment. The setup includes a 300L volume tabletop glovebox, a cartridge-based desiccant system, a microcontroller system to control the moisture setpoint, a personal H_2S detector, and a fan to continuously mix the glovebox air. b) H_2S generation of different SSEs in a -40°C dew point dry room as a function of time. c) Reduction in ionic conductivity versus maximum H_2S reading for different sulfide SSEs.

In addition to monitoring H_2S gas generation, this study reports on the ionic conductivity of sulfide SSEs before and after exposure to a -40°C dew point dry room environment and the data are provided in Figure XVI.7.4c. Every sample experienced a significant drop in ionic conductivity with 70-30 LPS having the largest drop of 76.5% and 7-68-25 LPSO having the smallest drop of 51.6%. The products of sulfide SSE hydrolysis may include compounds such as LiOH [2], Li_3PO_4 [6], and $\text{LiI} \cdot \text{H}_2\text{O}$ [7]. These compounds are poor ionic conductors, and if formed on the surface of sulfide SSE particles will act to substantially increase interparticle impedance once the powders are consolidated into pellets or films. We conclude that H_2S generation is not a sufficient metric for the moisture stability of sulfide SSEs and that moisture stability should also comprehend functional characteristics like ionic conductivity.

The local structures of sulfide SSEs before and after exposure were determined by Raman spectroscopy and the data are provided in Table XVI.7.1. The spectra for 70 mol% Li_2S modifier content SSEs are dominated by a single feature, which may be deconvoluted into multiple peaks attributable to PS_4^{3-} (421 cm^{-1}), $\text{P}_2\text{S}_7^{4-}$ (406 cm^{-1}), and $\text{P}_2\text{S}_6^{4-}$ (387 cm^{-1}) structural units. After exposure the relative abundance of the PS_4^{3-} structural unit increases, which indicates that it is comparatively more stable than $\text{P}_2\text{S}_7^{4-}$ and $\text{P}_2\text{S}_6^{4-}$ structural units. Sulfide SSEs with 75 mol% Li_2S modifier content therefore produce less H_2S because they are primarily composed of

PS_4^{3-} structural units, which react with moisture at a slower rate than the larger structural units found in sulfide SSEs with 70 mol% modifier content.

In the next experiment, the moisture stability of 75-25 LPSI was measured as a function of dew point and the data are provided in Figure XVI.7.5. H_2S generation is not reported since the maximum value at the end of each 30 minute exposure was below the 0.1 ppm detection limit of our sensor. Pristine 75-25 LPSI has an ionic conductivity of 1.21 mS/cm at room temperature when only handled inside an inert glovebox with 1 ppm H_2O (-76°C dewpoint). Exposing 75-25 LPSI powder to a dry room environment results in degradation of ionic conductivity that trends as the negative log of moisture content. This result implies that over-sizing dry room air handling equipment may not adequately address the poor moisture stability of sulfide SSEs. Fortunately, sulfide SSEs can be handled in a dry room while immersed in an anhydrous solvent. An example would be a slurry prepared for film tape casting. When 75-25 LPSI is exposed to a dry room environment while immersed in dodecane, it retains an ionic conductivity of 1.04 mS/cm (Figure XVI.7.5; star).

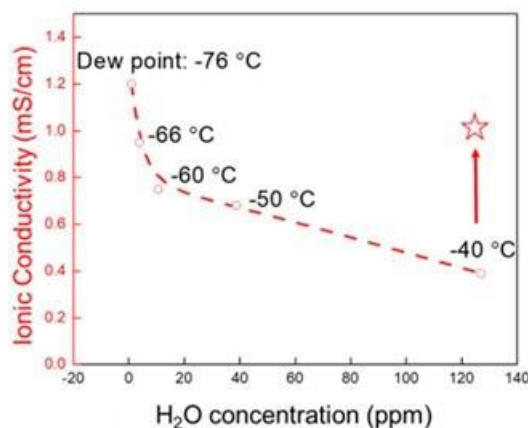


Figure XVI.7.5 Ionic conductivity of LPSI sulfide SSE after exposure as a dry powder to different dry room environments for 30 minutes. The star marks the ionic conductivity of LPSI sulfide SSE after exposure to a -40°C dew point dry room for 30 minutes while immersed in anhydrous dodecane.

Table XVI.7.1 Summary of Raman spectroscopic data of sulfide and oxysulfide glass SSEs before and after exposure to a dry room environment. Fractional peak areas are assigned to the vibrational modes of different glass structural units.

Sample	PS_4^{3-} (421 cm^{-1})	$\text{P}_2\text{S}_7^{4-}$ (406 cm^{-1})	$\text{P}_2\text{S}_6^{4-}$ (387 cm^{-1})
Pristine $(\text{Li}_2\text{S})_{70}(\text{P}_2\text{S}_5)_{30}$	27.0%	60.2%	12.8%
Exposed $(\text{Li}_2\text{S})_{70}(\text{P}_2\text{S}_5)_{30}$	28.2%	57.8%	14.0%
Pristine $(\text{Li}_2\text{O})_7(\text{Li}_2\text{S})_{63}(\text{P}_2\text{S}_5)_{30}$	25.3%	59.7%	15.0%
Exposed $(\text{Li}_2\text{O})_7(\text{Li}_2\text{S})_{63}(\text{P}_2\text{S}_5)_{30}$	33.1%	53.3%	13.6%

This third section describes progress towards achieving a solid-state electrolyte separator performance metric. Here, we present two datasets. In the first dataset a melt cast LiPSiS glass wafer was combined with an ether-based liquid electrolyte to achieve a critical current density of $3.0 \text{ mA}/\text{cm}^2$ at a stack pressure of only 0.1 MPa [8]. In the second dataset 3rd party testing showed a cycle life of nearly 100 cycles at current density of $2 \text{ mA}/\text{cm}^2$ for a hot-pressed, reinforced LiPS pellet. Detailed descriptions for each dataset are provided below. We conclude with a summary of the strategy we employed to reduce this technology to practice.

Dimethoxyethane (DME) and 1,3 dioxolane (DOL) are popular liquid electrolyte solvents for lithium metal batteries. We therefore evaluated the solubility of $(\text{Li}_2\text{S})_{60}(\text{SiS}_2)_x(\text{P}_2\text{S}_5)_{40-x}$ ($0 \leq x \leq 40$) sulfide glass SSEs in 1:1 (v/v) DME:DOL and the data are provided in Figure XVI.7.6 [8]. SiS_2 -rich glasses within the compositional range of $x \geq 28$ were found to be insoluble in DME:DOL (Figure XVI.7.6). Insolubility of $x \geq 28$ compositions was confirmed with Raman spectroscopy (Figure XVI.7.6b and c). Glass wafers with a composition of $(\text{Li}_2\text{S})_{60}(\text{SiS}_2)_{12}(\text{P}_2\text{S}_5)_{28}$ were prepared by melt casting as previously described [9]. Hybrid symmetric lithium test cells with a thin liquid electrolyte layer (0.6M LiTFSI + 0.4M LiNO_3 in 1:1 (v/v) DME:DOL) at the interface between lithium metal electrodes and an insoluble $(\text{Li}_2\text{S})_{60}(\text{SiS}_2)_{28}(\text{P}_2\text{S}_5)_{12}$ glass wafer were tested. Hybrid test cells delivered a critical current density of 3.0 mA/cm^2 at 25°C and 0.1 MPa, which is nearly double the CCD of comparable dry symmetric test cells cycled at 10x higher stack pressure (Figure XVI.7.7).

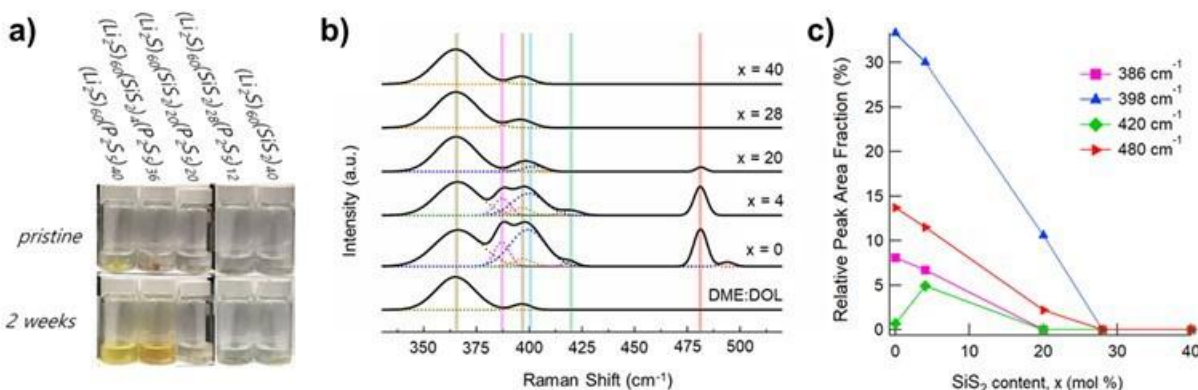


Figure XVI.7.6 a) Solubility times series for $(\text{Li}_2\text{S})_{60}(\text{SiS}_2)_x(\text{P}_2\text{S}_5)_{40-x}$ ($x = 0, 4, 20, 28, 40$) glasses soaked in 1:1 (v/v) DME:DOL. After 2 weeks the $x = 0, 4$ and 20 sample solutions show signs of discoloration, which is attributed to dissolution of the glass. The $x = 28$ and 40 sample solutions remain clear over the course of the experiment. b) Raman spectra of pristine DOL:DME solvent and solutions obtained by soaking $(\text{Li}_2\text{S})_{60}(\text{SiS}_2)_x(\text{P}_2\text{S}_5)_{40-x}$ ($x = 0, 4, 20, 28, 40$) glasses in DME:DOL. The location of structural unit vibrational modes are indicated with colored bars from left to right; namely, $\text{P}_2\text{S}_7^{4-}$ (pink), $\text{P}_2\text{S}_6^{4-}$ (blue), PS_4^{3-} (green), and S_8 (orange). Two vibrational modes of DME:DOL are also indicated (brown). c) Summary of dissolved species as a function of glass composition.

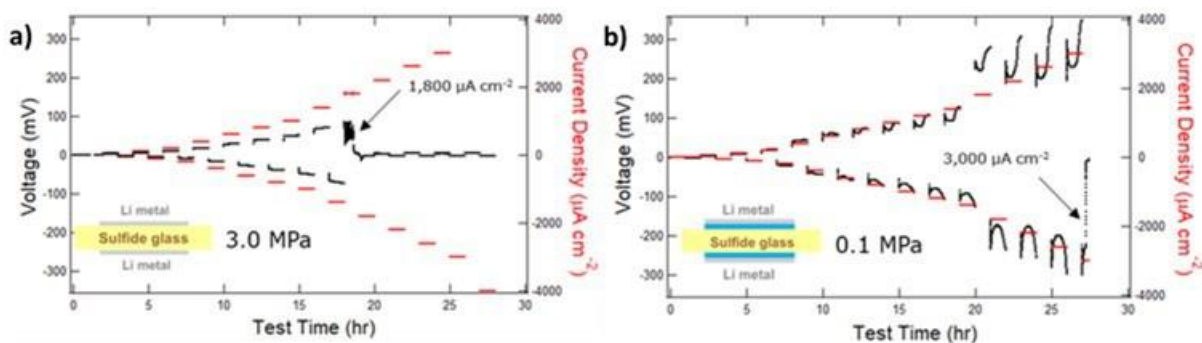


Figure XVI.7.7 CCDs of symmetric Li/SSE/Li test cells with or without a liquid electrolyte interlayer and a different stack pressures at 25°C . The SSE separators are $(\text{Li}_2\text{S})_{60}(\text{SiS}_2)_{28}(\text{P}_2\text{S}_5)_{12}$ glass wafers of approximately $600 \mu\text{m}$ thickness. a) A test cell with direct Li/SSE contact and 3 MPa stack pressure experiences shorting failure at a CCD of $1,800 \mu\text{A cm}^{-2}$. b) A hybrid test cell with liquid electrolyte Li/SSE interlayer and a 0.1 MPa stack pressure experiences shorting failure at a CCD of $3,000 \mu\text{A cm}^{-2}$. Note: the test was paused for two days at 20 hours due to a planned facility power outage.

LiPSiS melt cast wafers are not practical for two reasons. First, sulfide glass melts are extremely volatile and corrosive and require process temperatures above 1000°C . Second, glass wafers are very brittle and easy to break. For these reasons, our previous work demonstrated that $(\text{Li}_2\text{S})_{70}(\text{P}_2\text{S}_5)_{30}$ sulfide glass could be fully

consolidated by hot pressing at 240°C and 370 MPa pressure [10]. Several hot-pressed, reinforced SSE pellets with dimensions of approximately 25 mm in diameter and 1 mm in thickness were sent to a 3rd party for testing and the results are provided in Figure XVI.7.8. The pellet was cycled under progressively higher current densities from 0.1 mA/cm² to 2.0 mA/cm². Nearly 100 hundred cycles were achieved with a current density of 2.0 mA/cm² and an areal capacity of 2.0 mAh/cm².

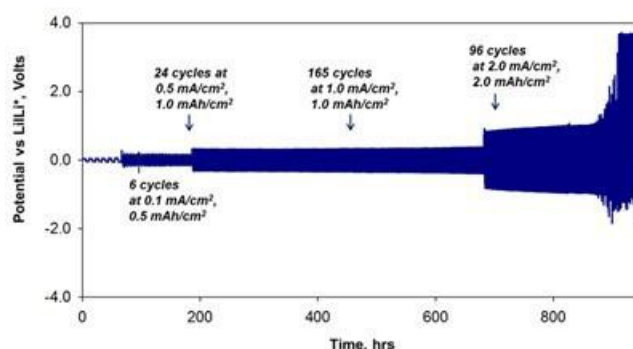


Figure XVI.7.8 3rd party validation of a 1 mm thick hot-pressed LiPSO sulfide glass pellet reinforced with Kevlar fiber pulp.

To translate this result to practice we considered a different solid state electrolyte composition. The sulfide glass composition was tuned for manufacturability by adding a third glass component, A. Component A slows down glass crystallization kinetics by a factor of 10 to enable processing at low pressure and short time. With a $(\text{Li}_2\text{S})_{70}(\text{P}_2\text{S}_5)_{25}(\text{A})_5$ glass composition we fabricated a 40 cm² standalone separator with non-woven aramid fiber reinforcement, a porosity of 8.6%, a thickness of approximately 110 μm thick, and an ionic conductivity of 0.75 mS cm⁻¹ (Figure XVI.7.9). These separators will be used in future pouch cell studies.



Figure XVI.7.9 Ternary glass separator with 0.75 mS/cm ionic conductivity and 110 μm thickness.

This final section describes custom laboratory hardware and a semi-solid electrolyte system. First, we present custom laboratory hardware that will be used to simulate a dry room environment. Demonstration of this hardware meets the Q4 FY2022 deliverable. Second, we outline a semi-solid electrolyte system based on solid-state electrolyte (SSE) and solvate ionic liquid (SIL) that will be used to meet future project deliverables. Finally, micro-CT images of all-solid-state separators *post-mortem* are presented to motivate the need for the aforementioned semi-solid electrolyte system.

A tabletop glovebox was modified with a custom moisture control system to conveniently simulate a dry room environment at any moisture setpoint ranging from -80°C to -40°C dewpoint. For reference, an inert glovebox will have a moisture level of about -80°C dewpoint while a cell assembly dry room will have a moisture level of about -40°C dewpoint. A picture of the setup is provided in Figure XVI.7.10a. It consists of a moisture probe, a microcontroller, a solid-state relay, and a cartridge-based desiccant system. As shown in Figure

XVI.7.10b, the microcontroller is programmed to turn the cartridge-based desiccant system on and off to keep the moisture setpoint within a desired range.

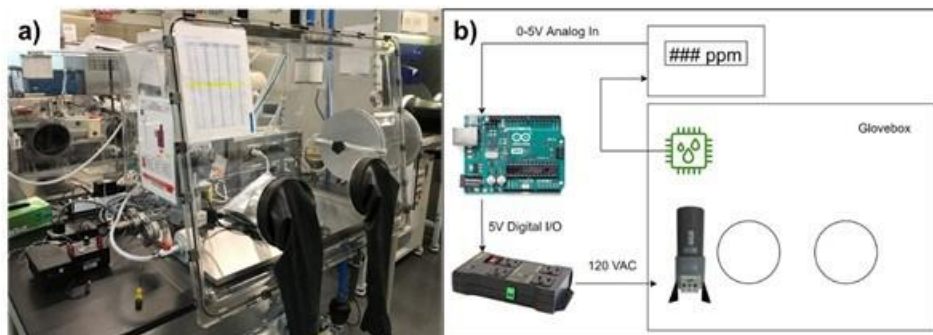


Figure XVI.7.10 a) Picture of the retrofitted glovebox. The glovebox is equipped with a custom system to maintain a dry room environment within a predetermined moisture setpoint range. b) Schematic of the glovebox moisture control system. It consists of a moisture probe, a microcontroller, a solid-state relay, and a cartridge-based desiccant system.

X-ray computed microtomography (micro CT) was used to image all-solid-state solid-state electrolyte (SSE) separators after failure by internal shorting (Figure XVI.7.11). The SSE was a glass powder with composition $70\text{Li}_2\text{S} \cdot 25\text{P}_2\text{S}_5 \cdot 5\text{A}$, where A is a third glass component. The separators were fabricated by consolidating the glass powder into 13 mm diameter Kevlar[®] fiber reinforced pellets at room temperature (cold-pressed, CP) or 240°C (hot-pressed, HP) and 300 MPa. Symmetric Li/SSE/Li cells were constructed with these pellets and cycled at progressively higher current densities under a 3 MPa stack pressure as previously described [10]. The separators were collected after failure, sectioned into $2\text{ }\mu\text{m} \times 2\text{ }\mu\text{m} \times 0.5\text{ }\mu\text{m}$ (length x width x thickness) pieces, and embedded inside UV curable epoxy. The samples were scanned using a Zeiss Xradia Versa 520 3D X-ray microscope with diffraction contrast tomography (DCT) module at a voxel size of $0.7\text{ }\mu\text{m}$ and an X-ray voltage of 40 kV. The micro CT image of the CP sample is provided in Figure XVI.7.11a and red arrows point to large deposits of Li metal. Closer inspection reveals that the SSE is denser at the boundary with the Li deposit. The micro CT image of the HP sample is provided in Figure XVI.7.11b and a red arrow pointing to a Li deposit expanding an incipient SSE microcrack. In both cases, high stresses are generated at the SSE/Li interface when Li deposition is volumetrically confined under a high stack pressure. As a result, Li deposits penetrate both CP and HP separators. The design of a semi-solid system is therefore required to dissipate the stresses at the SSE/Li interface.

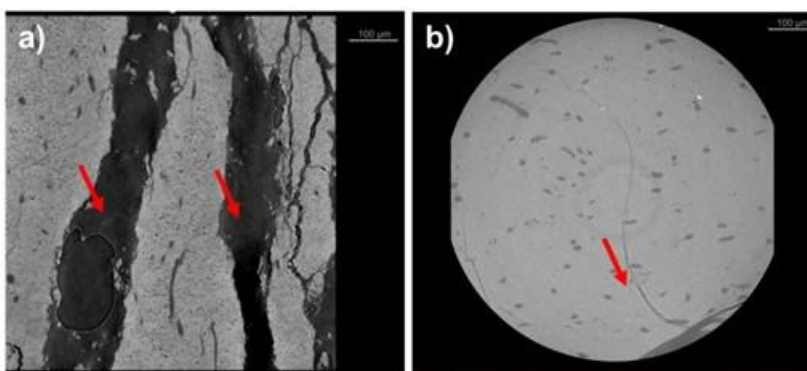


Figure XVI.7.11 a) Micro-CT image of a cold-pressed separator after a critical current density experiment. Red arrows point to Li metal deposit. b) Micro-CT image of a hot-pressed separator after a critical current density experiment. A red arrow points to a Li deposit that has expanded an incipient micro-crack. For both images the vertical direction corresponds to the thru plane, transverse direction of the separator. Large speckles in both images are attributed to the Kevlar[®] reinforcing fibers.

Finally, we evaluated the stability of a semi-solid electrolyte system. A secondary electrolyte phase reduces the need for a high stack pressure [8], which may alleviate deleterious stresses generated at the SSE/Li interface

during confined Li deposition. A SIL was prepared by combining lithium bis(trifluoromethanesulfonyl)imide salt (LiTFSI) and triethylene glycol dimethyl ether (G3) in a molar ratio of 1:1. Dilute liquid electrolytes were also prepared by combining LiTFSI and G3 in molar ratios of 1:2, 1:3, or 1:4. Glass electrolytes were prepared with varying content of a third glass component according to the compositional formula $70\text{Li}_2\text{S} \cdot (30-x)\text{P}_2\text{S}_5 \cdot x\text{A}$ ($x = 0, 2, 5, 10$). Solubility tests were conducted by immersing SSE chunks in liquid electrolyte. After 1 week, we measured the solids mass loss and conducted UV-Vis absorption spectroscopy with the liquid phase. The solids mass loss was measured by filtering the solutions and drying the remaining solids at 60°C and the results are provided in Figure XVI.7.12a. No mass loss was observed for SSEs soaked in $\text{Li}(\text{G3})\text{TFSI}$, while significant mass loss was observed for SSE samples soaked in dilute liquid electrolytes. The stability of SSEs in $\text{Li}(\text{G3})\text{TFSI}$ can be explained by the strong complexation of G3 with Li salts [11]. In dilute liquid electrolytes, oxygen in G3 attacks the electropositive elements (e.g. P) of the sulfide SSEs by nucleophilic attack. The composition of the SSE also influences the stability of the semi-solid electrolyte system. We find that the solubility of glasses in dilute solutions decreases as A content increases. UV-Vis spectroscopy was conducted to corroborate the data outlined above and the data are provided in Figure XVI.7.12b and c. In conclusion, future work will employ the use of a semi-solid electrolyte system containing $\text{Li}(\text{G3})\text{TFSI}$ SIL and SSE with A content.

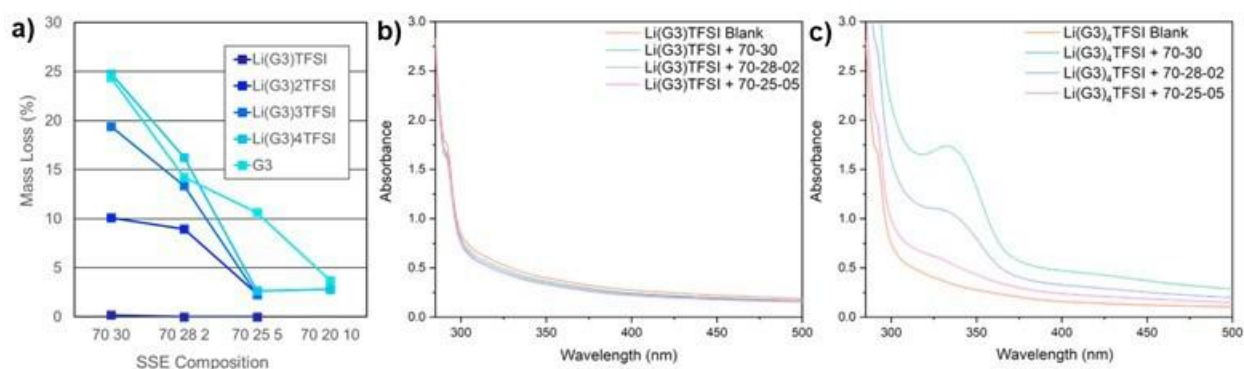


Figure XVI.7.12 a) $70\text{Li}_2\text{S} \cdot (30-x)\text{P}_2\text{S}_5 \cdot x\text{A}$ SSE solids mass loss after soaking in a variety of liquid electrolyte formulations. All SSEs soaked in $\text{Li}(\text{G3})\text{TFSI}$ solvate ionic liquid are stable. b) UV-Vis molecular absorption spectroscopy results for $70\text{Li}_2\text{S} \cdot (30-x)\text{P}_2\text{S}_5 \cdot x\text{A}$ SSE samples soaked in $\text{Li}(\text{G3})\text{TFSI}$ solvate ionic liquid electrolyte and c) $\text{Li}(\text{G3})_4\text{TFSI}$ liquid electrolyte.

Conclusions

The topics studied this year include the process rheology of ternary solid-state electrolyte glass compositions, the moisture stability of sulfide-based solid-state electrolytes, and the stability of sulfide-based solid-state electrolytes towards several liquid electrolytes. The results outlined above suggest that progress toward delivering a single layer pouch cell is on track.

Key Publications

1. Yersak, Thomas A., Fang Hao, Chansoon Kang, James R. Salvador, Qinglin Zhang, Hernando Jesus Gonzalez Malabet, and Mei Cai. "Consolidation of composite cathodes with NCM and sulfide solid-state electrolytes by hot pressing for all-solid-state Li metal batteries." *Journal of Solid State Electrochemistry* 26, no. 3 (2022): 709-718.
2. Yersak, Thomas A., Chansoon Kang, James R. Salvador, Nicholas PW Pieczonka, and Mei Cai. "Sulfide glass solid-state electrolyte separators for Li metal batteries: using an interlayer to increase rate performance and reduce stack pressure." *Materials Advances* 3, no. 8 (2022): 3562-3570.
3. Yersak, Thomas A., Yubin Zhang, Fang Hao, and Mei Cai. "Moisture Stability of Sulfide Solid-State Electrolytes." *Frontiers in Energy Research* 10:882508 (2022).
4. T.A. Yersak. "Process Rheology of Oxysulfide Solid-State Electrolyte Separators for Solid-State Batteries." American Chemical Society Fall Meeting, 22 August 2022. Invited seminar.

References

1. Yersak, Thomas A., Fang Hao, Chansoon Kang, James R. Salvador, Qinglin Zhang, Hernando Jesus Gonzalez Malabet, and Mei Cai. "Consolidation of composite cathodes with NCM and sulfide solid-state electrolytes by hot pressing for all-solid-state Li metal batteries." *Journal of Solid State Electrochemistry* 26, no. 3 (2022): 709-718.
2. Muramatsu, Hiromasa, et al. "Structural change of $\text{Li}_2\text{S}-\text{P}_2\text{S}_5$ sulfide solid electrolytes in the atmosphere." *Solid State Ionics* 182.1 (2011): 116-119.
3. Ohtomo, Takamasa, Akitoshi Hayashi, Masahiro Tatsumisago, and Koji Kawamoto. "Characteristics of the $\text{Li}_2\text{O}-\text{Li}_2\text{S}-\text{P}_2\text{S}_5$ glasses synthesized by the two-step mechanical milling." *Journal of non-crystalline solids* 364 (2013): 57-61.
4. Ohtomo, Takamasa, et al. "Glass electrolytes with high ion conductivity and high chemical stability in the system $\text{LiI}-\text{Li}_2\text{O}-\text{Li}_2\text{S}-\text{P}_2\text{S}_5$." *Electrochemistry* 81.6 (2013): 428-431.
5. Ohtomo, Takamasa, et al. "All-solid-state batteries with $\text{Li}_2\text{O}-\text{Li}_2\text{S}-\text{P}_2\text{S}_5$ glass electrolytes synthesized by two-step mechanical milling." *Journal of solid state electrochemistry* 17.10 (2013): 2551-2557.
6. Ohtomo, Takamasa, et al. "Suppression of H_2S gas generation from the $75\text{Li}_2\text{S}\cdot 25\text{P}_2\text{S}_5$ glass electrolyte by additives." *Journal of Materials Science* 48.11 (2013): 4137-4142.
7. Calpa, Marcela, et al. "Chemical stability of $\text{Li}_4\text{PS}_4\text{I}$ solid electrolyte against hydrolysis." *Applied Materials Today* 22 (2021): 100918.
8. Yersak, Thomas A., Chansoon Kang, James R. Salvador, Nicholas PW Pieczonka, and Mei Cai. "Sulfide glass solid-state electrolyte separators for Li metal batteries: using an interlayer to increase rate performance and reduce stack pressure." *Materials Advances* 3, no. 8 (2022): 3562-3570.
9. Yersak, Thomas A., James R. Salvador, Nicholas PW Pieczonka, and Mei Cai. "Dense, melt cast sulfide glass electrolyte separators for Li metal batteries." *Journal of The Electrochemical Society* 166, no. 8 (2019): A1535.
10. Yersak, Thomas, James R. Salvador, Robert D. Schmidt, and Mei Cai. "Hot pressed, fiber-reinforced $(\text{Li}_2\text{S})_{70}(\text{P}_2\text{S}_5)_{30}$ solid-state electrolyte separators for Li metal batteries." *ACS Applied Energy Materials* 2, no. 5 (2019): 3523-3531.
11. Oh, Dae Yang, et al. "Excellent compatibility of solvate ionic liquids with sulfide solid electrolytes: toward favorable ionic contacts in bulk-type all-solid-state lithium-ion batteries." *Advanced Energy Materials* 5.22 (2015): 1500865.

Acknowledgements

The PI (Thomas A. Yersak) would like to provide recognition to our NETL managers, Adrienne L Riggi and Coriana H. Fitz. Special thanks is also given to Dr. Yubin Zhang, Dr. Hernando Jesus Gonzalez Malabet and Mr. Aaron Ketchum for their important contributions to the project.

XVI.8 Developing Materials for High-Energy-Density Solid State Lithium-Sulfur Batteries (Penn State University, University Park)

Donghai Wang, Principal Investigator

Penn State University
134 Energy & Environmental Laboratory
University Park, PA 16802
E-mail: dwang@psu.edu

Tien Duong, DOE Technology Development Manager

U.S. Department of Energy
E-mail: Tien.Duong@ee.doe.gov

Start Date: October 1, 2019	End Date: December 30, 2022	
Project Funding (FY22): \$425,259	DOE share: \$339,358	Non-DOE share: \$85,901

Project Introduction

Lithium-sulfur (Li-S) all-solid-state battery (ASSB) is a promising candidate to replace existing Li-ion batteries for application in electric and plug-in hybrid electric vehicles (EVs and PHEVs) due to its high energy density and superior safety. Moreover, recent advances in improving ionic conductivities ($\approx 10^{-2} \text{ S cm}^{-1}$) of sulfide-based solid-state electrolytes (SSEs) put us one step closer to the practical application of Li-S ASSBs¹. In Li-S ASSBs, the polysulfide shuttling and self-discharges in liquid-type Li-S batteries could be fundamentally resolved². Furthermore, as added benefits, sulfide-based SSEs possess improved safety due to the absence of flammable organic electrolytes^{3,4}. However, despite those encouraging characteristics of ASSBs, there are technological challenges such as low sulfur utilization and increased interfacial resistance due to poor contact, large volume expansion of sulfur upon cycling and unoptimized microstructure of sulfur-carbon-SSEs composites in the solid cathode, poor charge/discharge rate due to the low conductivity of SSEs, and SSEs' chemical instability against moisture and lithium/lithium alloy anodes. The challenges are fundamentally attributed to the properties of the solid materials and their interfaces in electrodes.

In brief, we shall address the following three problems of Li-S ASSBs in this project. First, we aim to construct electron and ionic transport pathways in the cathode to improve sulfur utilization upon cycling and boost overall energy density. Second, we target generating a favorable interface between carbon-sulfur composite and solid-state electrolytes with novel solid additives or approaches. Third, we plan to develop new sulfide-based solid electrolytes with high ionic conductivity and improved stability against moisture and lithium alloys for all.

Objectives

The project objectives are to develop materials involving advanced S-C composite materials, solid additives, and sulfide-based SSEs and acquire knowledge of Li-S ASSBs. Li-S ASSBs with high areal sulfur loading ($\geq 5 \text{ mg cm}^{-2}$) and high sulfur content ($\geq 50 \text{ wt\%}$ in cathode), pairing with lithium or lithium alloy anode, shall deliver a high initial specific capacity of over 1200 mAh g^{-1} at high charge/discharge rate ($> 0.3 \text{ C}$) for 500 cycles with over 80% capacity retention. The out-year goals are as follows: (1) develop and optimize sulfur cathode materials and synthesize new solid electrolytes (ionic conductivity $> 5 \text{ mS cm}^{-1}$ at room temperature) (2) conduct characterization and performance tests on both material and electrode levels. The final demonstration will be all-solid-state sulfur cathodes with $> 1200 \text{ mAh g}^{-1}$ discharge capacity at 0.3 C discharge rate and 50 wt% sulfur content for 500 cycles at room temperature.

Approach

The project goal will be accomplished by developing new materials, together with the in-depth characterization of sulfur cathodes. Specifically, approaches to realize the project objectives include the following:

- (1) development of new carbon material with unique structure, high surface area, and large pore volume;
- (2) development of new S-C and S-C-M_xS_y materials (M = Li, Co, Ti, Mo, etc.) to facilitate electron/ion transport;
- (3) development of novel additives to tune interfacial behavior among components in the cathode;
- (4) development and optimization of new SSE through cation and anion doping with superior properties such as high ionic conductivity, good moisture, and stability; and
- (5) diagnostics, characterization, and cell tests on the developed new material or advanced sulfur cathode.

Results

In this budget period, we mainly focused on the following three aspects: (1) the development of sulfide-based SSEs with high ionic conductivity and their application in sulfur cathode; (2) the development of advanced materials for sulfur cathode and its utilization in Li-S all-solid-state batteries; (3) development of alloy anode material for solid-state Li-S batteries. Meanwhile, we were working on novel characterization techniques for the Li-S ASSBs to acquire knowledge of the electrochemical system and degradation mechanism. In the following part, we shall elucidate our accomplishments that have been achieved so far.

(1) Sulfide-based SSEs with high ionic conductivity

SSE plays a critical role in determining the performance of Li-S ASSBs. An ideal SSE should possess the following properties: (1) high ionic conductivity ($>5 \text{ mS cm}^{-1}$) at room temperature; (2) good compatibility with lithium metal anode; (3) good formability; (4) good moisture stability. In this budget period, we developed sulfide-based SSEs for Li-S ASSBs, namely, LPB, which possesses the above-mentioned characteristics.

The LPB SSE was synthesized via a facile liquid-phase synthesis method with a low annealing temperature of 160°C . The LPB SSE exhibited a high ionic conductivity of 6.09 mS cm^{-1} at 25°C with a low activation energy of 0.212 eV (Figure XVI.8.1a). The result is among the highest ionic conductivities reported for liquid-phase synthesized sulfide SSEs (Figure XVI.8.1b) and meets our proposed milestone for developing sulfide SSE.

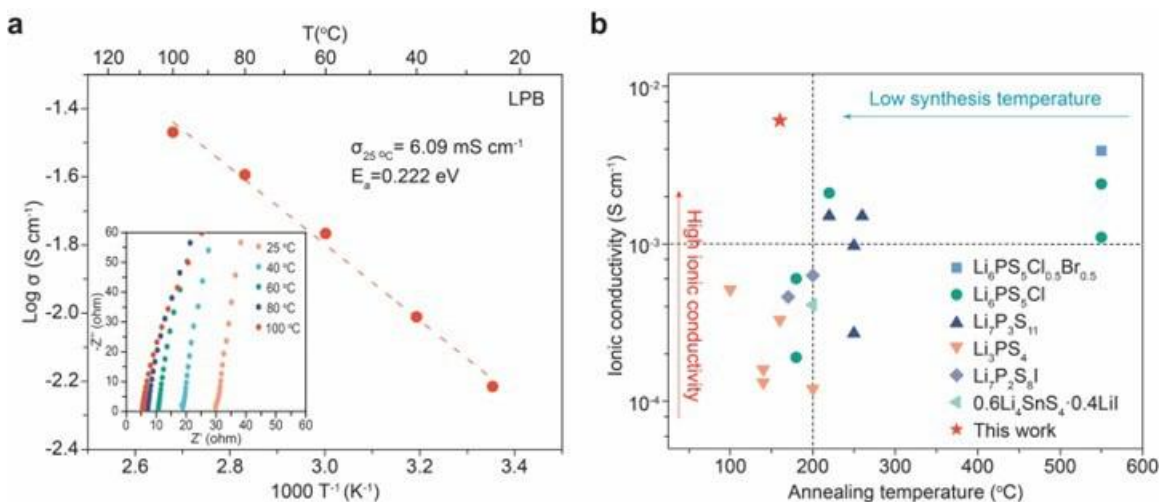


Figure XVI.8.1 (a) Arrhenius and Nyquist impedance plots for hot-pressed LPB SE pellet from 25 to 100°C . (b) Comparison of room-temperature ionic conductivity and synthesis temperature of LPB SSE and reported liquid-phase synthesized sulfide SSEs.

Solid-state sulfur cathodes and Li-S ASSBs were fabricated and evaluated. The cathode powders constituted of sulfur, conductive carbon (Ketjenblack, KB), and SSEs were prepared by ball milling with a remarkably high sulfur content of ~ 60 wt% (KB/S/SSE=10/50/24, w/w/w). LPB, L_3PS_4 (LPS), and $\text{Li}_{10}\text{GeP}_2\text{S}_{12}$ (LGPS) SSEs were used to fabricate the sulfur cathodes (S-C-LPB, S-C-LPS, and S-C-LGPS). The assembled Li-S ASSBs (Li-In/LPB/S-C-SSE) were electrochemically evaluated in a Swagelok cell at 60°C under ambient air. The S-C-LPB cathode also showed excellent rate performance compared with S-C-LPS and S-C-LGPS cathodes (Figure XVI.8.2a), presenting much higher discharge capacities of 1144.6, 1024, 907.8, and 663 mAh g^{-1} at 0.1, 0.3, 0.5, and 1 C, respectively. The superior performance of the S-C-LPB cathode at 0.1 C is equivalent to a high cathode-level specific energy of $1318.7 \text{ Wh kg}^{-1}$ and volumetric energy density of 2561.8 Wh L^{-1} with an average discharge voltage of 1.935 V (vs. Li/Li^+). The cycling stability of the S-C-LPB cathode was investigated as well. A Li-S ASSB cell with an areal sulfur loading of $\sim 2.57 \text{ mg cm}^{-2}$ was tested at 0.5 C under a constant current, constant voltage (CCCV) mode between 0.8–2.5 V (Figure XVI.8.2b). Impressively, the S-C-LPB cathode cycled stably for over 800 cycles with a high initial discharge specific capacity of $\sim 1004.6 \text{ mAh g}^{-1}$ and a low fading rate of $\sim 0.028 \%$ per cycle.

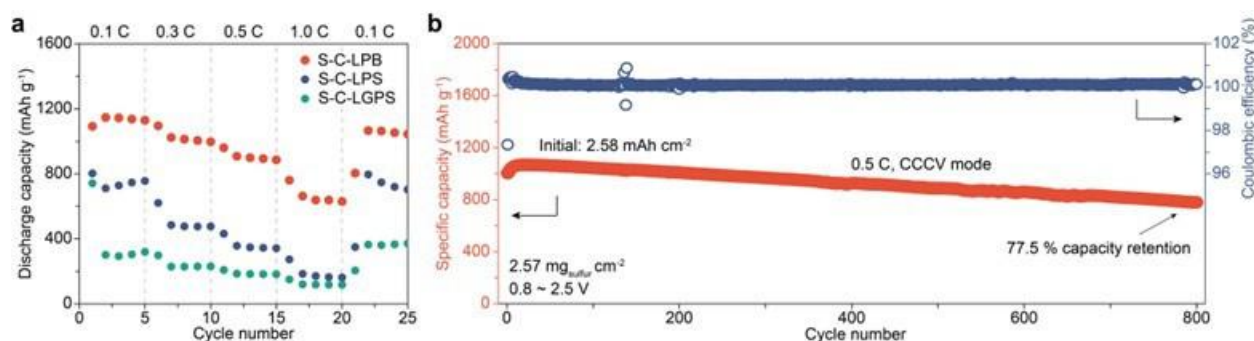


Figure XVI.8.2 (a) Rate performance of different sulfur cathodes. (b) Cycling performance of the S-C-LPB cathode at 0.5 C under CCCV mode (cutoff current, 0.1 C; cutoff voltage, 2.5 V vs. $\text{Li-In}/\text{Li}^+$) between 0.8 and 2.5 V at 60°C .

Through post-characterization, we found that the root cause for the superior performance of the S-C-LPB cathode is the low density of LPB (1.491 g cm^{-3}), much lower than that of LPS (1.83 g cm^{-3}), LGPS (2.04 g cm^{-3}), and other conventional inorganic SSEs, which ensure sufficient SSE volume content and ionic transport pathways in sulfur cathodes with an ultrahigh sulfur content of ~ 60 wt%. As shown in the SEM images (Figure XVI.8.3a, e), the S-C-LPB cathode aggregate powders are smaller than the S-C-LPS aggregate. Upon pressing the powders into electrodes, the formed S-C-LPB cathode made from small powders seems relatively denser than the S-C-LPS sulfur cathode with many voids on the surface (Figure XVI.8.3c, g). In addition, locally high-intensity sulfur signals are detected (marked in dashed circles) in the EDS mapping of the S-C-LPS electrode (Figure XVI.8.3c), indicating the presence of bulky sulfur particles. After lithiation, massive aggregated Li_2S emerges and separates from carbon (Figure XVI.8.3d). Given the poor electronic and ionic conductivity of sulfur/ Li_2S , the lithiation/delithiation of bulky sulfur/ Li_2S is kinetically less favorable than small sulfur/ Li_2S particles, thus leading to higher resistance and lower sulfur utilization of the S-C-LPS cathode. In stark contrast, the S-C-LPB cathode exhibits excellent content uniformity with homogenous distribution of all elements before and after lithiation (Figure XVI.8.3g, h). Such observations are also supported by the XRD results illustrated in Figure XVI.8.3b, f, indicative of large crystalline sulfur particles in the S-C-LPS cathode in contrast to the small amorphous sulfur particles in the S-C-LPB cathode.

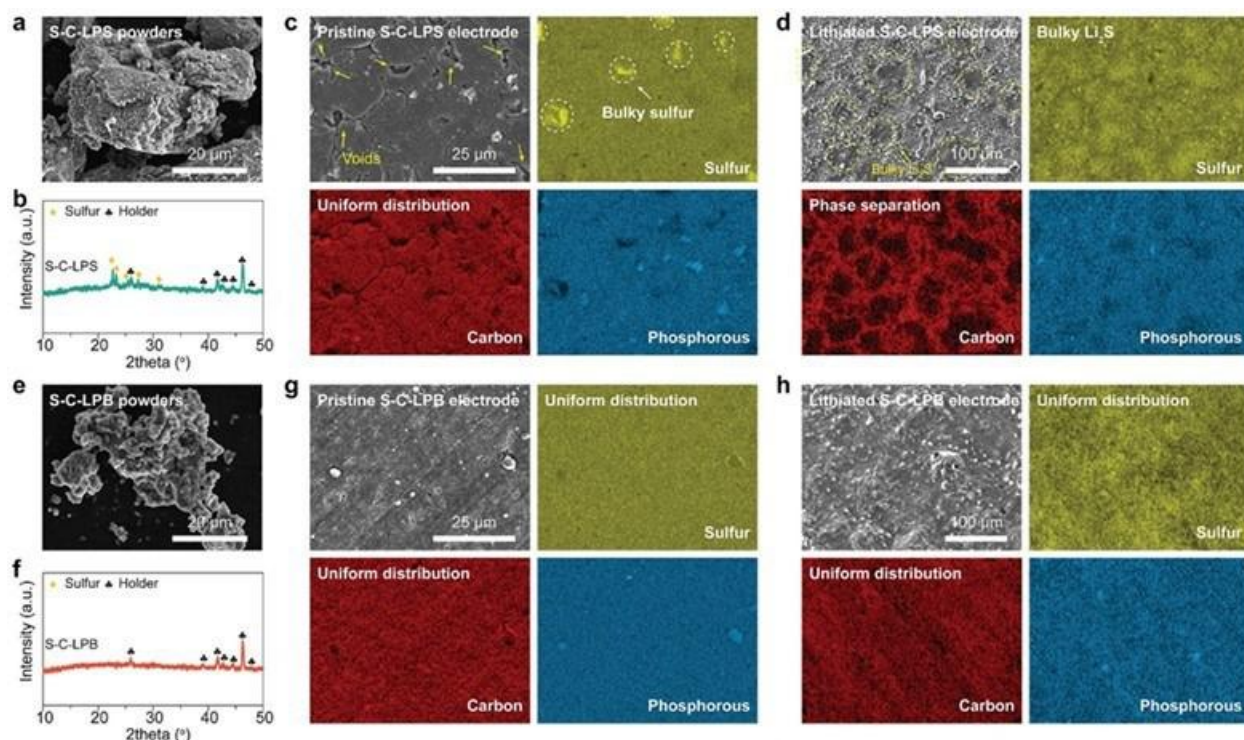


Figure XVI.8.3 (a and e) SEM images of S-C-LPS (a) and S-C-LPB (e) cathode powders. (b and f) XRD of S-C-LPS (b) and S-C-LPB (f) cathode powders. (c and d) SEM and EDS mapping images of S-C-LPS cathode before (c) and after (d) lithiation. (g and h) SEM and EDS mapping images of S-C-LPB cathode before (g) and after (h) lithiation.

(2) Sulfur cathode for Li-S all-solid-state batteries

In this budget period, we also developed advanced sulfur cathode material for Li-S all-solid-state batteries, which could deliver a higher discharge capacity of over 1000 mAh g⁻¹ at room temperature. Our previous findings revealed that a highly efficient ionic and electronic pathway within cathode composites plays an important role in improving the electrochemical performance of sulfur cathodes. Thus, we focused on developing novel advanced sulfur cathode materials with good components uniformity and efficient ionic and electronic pathways for Li-S all-solid-state batteries. Moreover, combined with the optimization of cathode compositions, cathode additives, and preparation processes, the new advanced sulfur cathode materials enabled superior sulfur utilization at room temperature. The cycling performance of the developed advanced sulfur cathode is illustrated in Figure XVI.8.4. The sulfur cathode was first electrochemically activated at 0.05 A g⁻¹ (based on the weight of the whole sulfur cathode) for the three cycles and then subsequently cycled at 0.1 A g⁻¹ (= 0.12 C). During the first few cycles, the discharge specific capacity can reach up to 1200 mAh g⁻¹. After increasing the current rate to 0.12 C, the cell can still achieve above 1000 mAh g⁻¹ discharge capacity at room temperature. The sulfur cathode with moderate sulfur loading of 2.055 mg cm⁻² and high sulfur content of 50 wt% shows superior cycling stability for over 250 cycles. Even after 250 cycles, the discharge specific capacity remains high at 987.8 mAh g⁻¹.

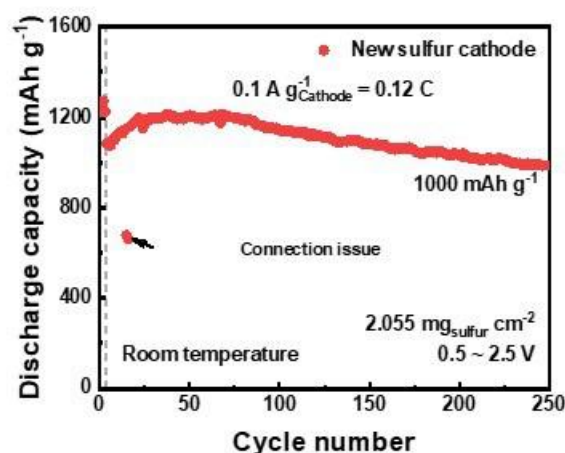


Figure XVI.8.4 Long-term cycling performance of the new sulfur cathode composite under 0.1 A g^{-1} ($= 0.12 \text{ C}$) between 0.5 to 2.5 V at room temperature. The discharge capacity is based on the weight of sulfur.

We further investigated the performance of sulfur cathodes under different testing conditions (e.g., temperatures, cathode sulfur loading, membrane thickness, cathode compositions, operation pressure, etc.). We found that sulfur cathode performance would significantly deteriorate with lower first-cycle Coulombic efficiency and discharge capacities upon increasing sulfur loading or decreasing temperatures (Figure XVI.8.5a, b). Through detailed analysis, we discovered that the primary cause of this problem is the high internal resistance of the cell, particularly the sulfur cathode, at room temperature or high areal sulfur loading. Therefore, based on such discovery, we then attempted to reduce the membrane thickness, employ solid electrolytes with higher ionic conductivity, optimize cathode compositions, and develop new sulfur cathode materials to minimize batteries' internal resistance.

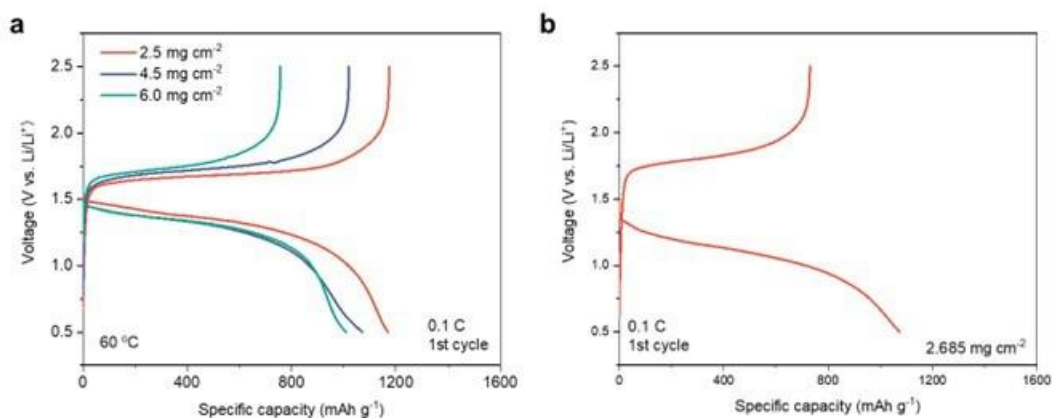


Figure XVI.8.5 The 1st-cycle galvanostatic charge-discharge curves of sulfur cathodes evaluated (a) with different areal sulfur loading of 2.5 – 6.0 mg cm^{-2} under 60°C and (b) with areal sulfur loading of $\sim 2.685 \text{ mg cm}^{-2}$ at room temperature. The current rate is 0.1 C .

Consequently, two newly synthesized sulfur cathodes, i.e., PSU-1 and PSU-2, were developed with enhanced electronic and ionic transport (lower resistance). The rate performance of the two cathodes with areal sulfur loading of 2 – $3 \text{ mg}_{\text{sulfur}} \text{ cm}^{-2}$ was evaluated and summarized in Figure XVI.8.6. Specifically, PSU-1 delivered a good discharge specific capacity of over 1150 mAh g^{-1} at 0.1 C . However, upon increasing the current rate to 0.5 C , the discharge specific capacity of the PSU-1 cathode dropped sharply to $\sim 550 \text{ mAh g}^{-1}$, showing that the electron/ion transport within the cathode still needs further optimization and improvement. By optimizing

the cathode compositions, preparing procedures, and employing solid electrolytes with higher ionic conductivity, PSU-2 sulfur cathodes were successfully developed, which delivered a superior specific capacity of over 1200 mAh g⁻¹ at a high current rate of 0.5 C and room temperature.

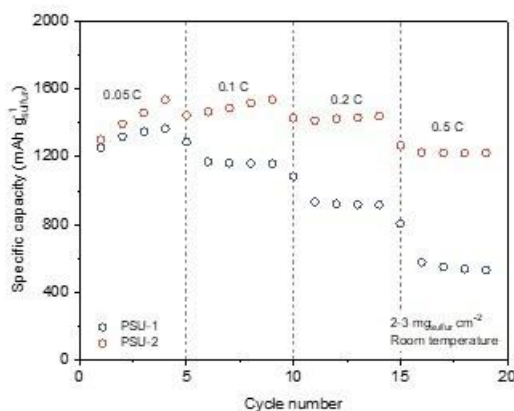


Figure XVI.8.6 Rate performance of two developed sulfur cathodes, i.e., PSU-1 and PSU-2. The areal sulfur loading of the cathodes is 2-3 mg_{sulfur} cm⁻². Cells were tested at room temperature.

Besides the above two cathodes, we successfully prepared another sulfur cathode with optimized cathode components, compositions, and preparation procedures, demonstrating superior electrochemical performance at high areal sulfur loading. As shown in Figure XVI.8.7, the sulfur cathode with areal sulfur loading of 5.39 mg cm⁻² and sulfur content of 50 wt% delivered a high discharge specific capacity of over 1200 mAh g⁻¹ at room temperature. After 10 cycles, the discharge specific capacity remained as high as ~ 1400 mAh g⁻¹.

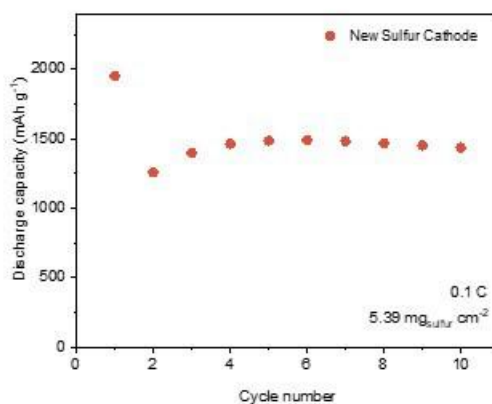


Figure XVI.8.7 Cycling performance of the Li-S ASSBs using the new sulfur cathode at 0.1 C with high sulfur loading and content under room temperature.

(3) Lithium alloy anodes for Li-S all-solid-state batteries

To increase the energy density of Li-S all-solid-state batteries, instead of using Li-In alloy anode, we developed and utilized different types of lithium alloy anodes, such as Li-Si, Li-Ge, or Li-Sn alloy with higher specific capacity and energy density than Li-In. We synthesized various lithium alloy anodes by the high-energy ball-milling method for fabricating high-energy-density Li-S all-solid-state batteries (Li-S ASSBs). To avoid the interfacial issues between Li metal and solid electrolytes, using alloy anodes could mitigate the interfacial resistance increase and the lithium dendrite growth. In addition, owing to the stable and reversible plating/stripping of alloy anodes, we can develop stable and durable Li-S ASSBs with high sulfur utilization

(high discharge capacity). After optimizing the composition and synthesis procedures, we found a type of alloy anode (Lithium alloy-2) can cycle stably and enable Li-S ASSBs with high discharge specific capacity, which remained $1368.6 \text{ mAh g}^{-1}$ after 150 cycles, as shown in Figure XVI.8.8. The full cells were cycled under 0.1 C at 60°C , and the sulfur cathode loading was around 2.19 mg cm^{-2} . Other than that, the other two types of lithium alloy anode behaved differently. The Li-S ASSB using Lithium alloy-1 exhibited a high initial discharge capacity of around 1400 mAh g^{-1} but suffered from short-circuiting after 20 cycles. The Li-S ASSB with Lithium alloy-3 also had good reversibility and still showed a high discharge specific capacity of $1162.4 \text{ mAh g}^{-1}$ after 150 cycles. It shows that the lithium alloy anodes could be utilized for Li-S ASSBs, delivering high discharge specific capacities and good capacity retention. We are investigating the mechanism of the short-circuiting behavior and trying to gain more knowledge of how different lithiation states of alloy anodes affect the full cells' stability and electrochemical performance, which shall guide us to fabricate Li-S ASSBs with prolonged and excellent electrochemical performance.

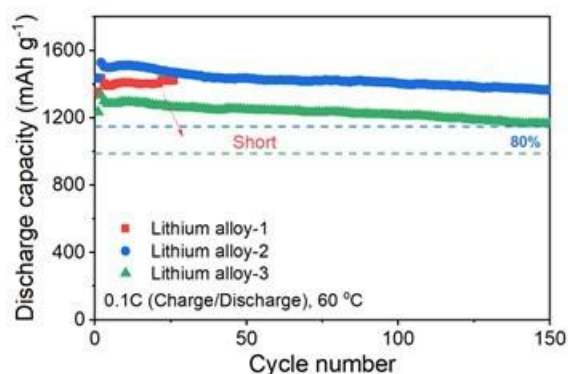


Figure XVI.8.8 Cycling performance of the Li-S ASSBs using the as-synthesized alloy anodes. The cells were tested at 0.1 C under 60°C , and the specific capacity is based on the weight of sulfur.

(4) Capacity fading and degradation mechanism characterization

Since Li-S ASSBs still face continuous capacity decay upon cycling, we studied their origin using X-ray photoelectron spectroscopy (XPS) and found that the electrochemical and chemical degradation of sulfide SSE is the culprit. As shown in Figure XVI.8.9, $\text{P-S}_x\text{-P}$ in $\text{P } 2p$ spectra and sulfate species in $\text{S } 2p$ spectra were observed in the cathode after cycling. The former is induced by the electrochemical oxidation of sulfide SSE, while the latter might be caused by the reaction of sulfide SSE or Li_2S with moisture in the air. Together, the continuous electrochemical and chemical degradation of SSE will cause the destruction of ionic transport pathways, giving rise to the continuous growth of internal resistance and, thus, capacity fading of Li-S ASSBs.

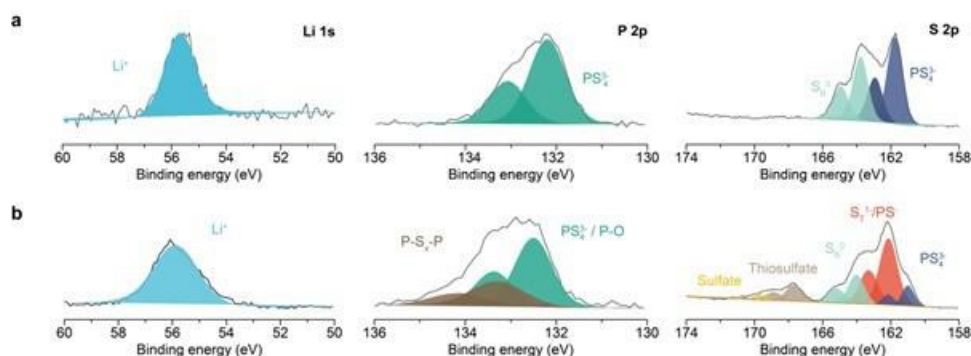


Figure XVI.8.9 XPS spectra of the S-C-LPB cathode (a) before and (b) after cycling at charged state.

Conclusions

In conclusion, we have accomplished our goals for the budget period 1 and 2 and obtained the following main achievements: (1) We successfully synthesized a glass-ceramic solid-state electrolyte by a facile liquid-phase

method with a high ionic conductivity of $\sim 6.09 \text{ mS cm}^{-1}$ at 25°C , and good electrochemical stability against lithium metal anode. (2) We developed an advanced sulfur cathode for Li-S all-solid-state batteries for over 250 cycles with a high discharge capacity of above 1000 mAh g^{-1} at room temperature. (3) The effects of sulfur loadings, sulfur contents, and testing temperature on the electrochemical performance were also investigated to help acquire the knowledge of internal impedance and electron/ion transport mechanism accompanied by various characterization techniques. (4) A new sulfur cathode was developed and can deliver a discharge capacity of $\sim 1400 \text{ mAh g}^{-1}$ with high areal sulfur loading of 5.39 mg cm^{-2} and sulfur content of 50 wt% at room temperature. (5) Alloy anodes were utilized to facilitate Li-S ASSBs with superior electrochemical performance for over 150 cycles with good capacity retention at 60°C . (6) We have investigated the capacity fading mechanism of Li-S ASSBs using XPS.

Key Publications

1. Wang, Daiwei, Li-Ji Jhang, Meng Liao, Shiyao Zheng, Atif AlZahrani, Tianhang Chen, Yue Gao, Donghai Wang. "New conductive lithium thiophosphate solid electrolyte for all-solid-state lithium-sulfur batteries with high sulfur utilization." *In preparation*.
2. Wang, Daiwei, Li-Ji Jhang, Rong Kou, Meng Liao, Shiyao Zheng, Heng Jiang, Pei Shi, Guo-Xing Li, Kui Meng, Donghai Wang, "Realizing high-specific-energy sulfur cathode for all-solid-state lithium-sulfur batteries using a low-density inorganic solid electrolyte." *Under review*.

References

1. Kamaya, Noriaki, Kenji Homma, Yuichiro Yamakawa, Masaaki Hirayama, Ryoji Kanno, Masao Yonemura, Takashi Kamiyama, Yuki Kato, Shigenori Hama, Koji Kawamoto, and Akio Mitsui. 2011. "A lithium superionic conductor." *Nature Material* 10: 682-686.
2. Hayashi, Akitoshi, Takamasa Ohtomo, Fuminori Mizuno, Kiyoharu Tadanaga, and Masahiro Tatsumisago. 2003. "All-solid-state Li/S batteries with highly conductive glass-ceramic electrolytes." *Electrochemistry Communications* 5, no. 8 (August): 701-705.
3. Inoue, Takao, and Kazuhiko Mukai. 2017. "Are All-Solid-State Lithium-Ion Batteries Really Safe? – Verification by Differential Scanning Calorimetry with an All-Inclusive Microcell." *ACS Applied Materials & Interfaces* 9, no. 2 (January): 1507-1515.
4. Tatsumisago, Masahiro, Motohiro Nagao, and Akitoshi Hayashi. 2013. "Recent development of sulfide solid electrolytes and interfacial modification for all-solid-state rechargeable lithium batteries." *Journal of Asian Ceramic Societies* 1, no. 1 (March): 17-25.

Acknowledgements

We appreciate the support from Colleen Butcher at National Energy Technology Laboratory and Patricia Smith from DOE.

XVI.9 Developing an In-situ Formed Dynamic Protection Layer to Mitigate Lithium Interface Shifting: Preventing Dendrite Formation on Metallic Lithium Surface to Facilitate Long Cycle Life of Lithium Solid State Batteries (University of Wisconsin-Milwaukee)

Deyan Qu, Principal Investigator

University of Wisconsin-Milwaukee
3200 N Cramer Street
Milwaukee, WI 53211
E-mail: qud@uwm.edu

Tien Duong, DOE Technology Development Manager

U.S. Department of Energy
E-mail: Tien.Duong@ee.doe.gov

Start Date: October 18, 2019

End Date: October 17, 2022

Project Funding (FY22): \$411,235

DOE share: \$327,899

Non-DOE share: \$83,336

Project Introduction

The next-generation battery innovations for EV without ICE will have to enable the vehicle to drive for long distances. Marginal improvements of state-of-art Li-ion technology cannot meet this challenge. Any “beyond Li-ion” technologies, which aim to achieve cell performance targets of $\geq 350\text{Wh/Kg}$, over 1000 cycles at C/3 rate, 15 year shelf life and $< \$100/\text{KWh}$ cost, will need a metallic Li anode ($\sim 3862\text{ mAh/g}$). Applications of Li anodes in batteries are hindered by the dendrite formation during the battery operation leading to serious safety issues. Previous efforts to suppress the dendrite formation on lithium metal anodes by altering the electrolyte, modifying the Li surface, or optimizing the cell structure fell short because they did not solve the root causes of the dendrite formation during the interface shift of Li anodes during cycling. We propose to investigate interface shift, surface homogeneity and surface Li^+ concentration. Our work will focus on creating a dynamic protection layer during the interface shift to prevent dendrite formation throughout the battery operation, potentially enabling the commercialization of a safe metallic Li battery with a long cycle life. This is particularly important in a solid-state-electrolyte battery, since the interfacial changes between the Li anode and the electrolyte could create a physical gap which hinders the electrochemical reaction.

In FY2022, we demonstrated:

1. A prelithiated Si anode for a long cycle Li-S all-state-state-battery (ASSB).
2. A flexible, highly conductive and thin solid-state-electrolyte (SSE) membrane.
3. Organic cathode material in ASSB
4. An Li-S ASSB in a pouch cell.

Objectives

The objectives of this project are to research, develop, and test lithium metal-based batteries that implement solid lithium-ion conductors equipped with a formed dynamic protection layer. The proposed project aims to enable safe, long cycle Li anodes achieving cell performance targets of 400Wh/Kg , over 100 cycles, 15-year shelf life and $< \$100/\text{KWh}$ cost.

Our efforts are to contribute an *in-depth* understanding of the Li interface and dendrite growth prevention to the field of Li metal batteries, which will pave the way for the eventual development of high energy density, low cost and long-lasting Li batteries. This advancement could be a crucial selling point for the greater adoption of electric vehicles (EV). This project will make possible the translation of fundamental research into

the practical implementation of high energy Li anodes, enabling the eventual achievement of the cell performance targets.

Approach

The novelty of our approach is that we intend to mitigate the dendrite problem by creating a dynamic protection layer during the interface shift to prevent dendrite formation throughout the battery operation. Four approaches will be explored: 1) Surface with homogeneous activity; 2) Artificial interface to “alloy” Li dendrites; 3) Dissolution and re-deposition of Li through re-distribution of Li-carrier complex; 4) Control local Li concentration.

Results

The novelty of our approach is that we intend to mitigate the dendrite problem by creating a dynamic protection layer during the interface shift to prevent dendrite formation throughout the battery operation. Four approaches will be explored: 1) Surface with homogeneous activity; 2) Artificial interface to “alloy” Li dendrites; 3) Dissolution and re-deposition of Li through re-distribution of Li-carrier complex; 4) Control local Li concentration.

Results

Fully prelithiated all-electrochem-active Si anode for the mitigation of dendrite growth.

The development of all-solid-state Li-S batteries has been greatly impeded by dendrite growth and dendrite penetration, which are both related to the Li metal anode. As a compromised alternative, we report lithium silicide (Li_xSi) as a dendrite-free and high-capacity anode with Li source. The as-synthesized Li_xSi is relatively soft, highly electronically conductive, and with a high Li diffusivity. These distinctive properties make Li_xSi anode viable as an “all-electrochem-active” electrode (consisted of 100 wt.% Li_xSi). Compared with the typical composite electrode, the all-electrochem-active electrode not merely maximizes the electrode-level energy density but also minimizes the electrolyte-related interfacial degradation. Li_xSi symmetric cell demonstrates a reversible cycling at 4 mA cm^{-2} for over 320 h. Stress change and morphological evolution of the Li_xSi electrode are investigated upon dealloying/alloying. When paired with a S cathode (active mass loading of 3 mg cm^{-2}), Li_xSi -S full cell shows a good cycling behavior over 500 cycles and rate performance (69% capacity retained at 1.2C) even at 25°C .

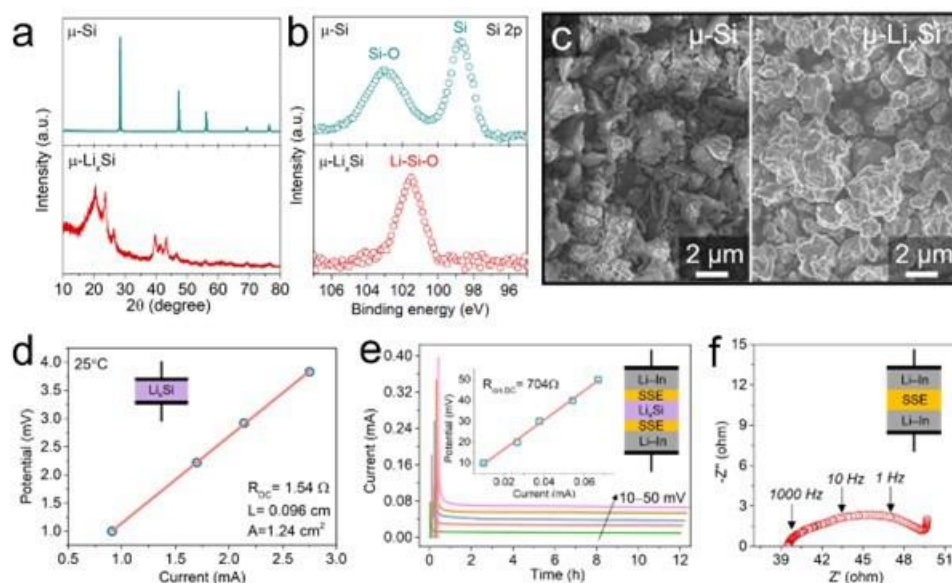


Figure XVI.9.1 a) X-ray diffraction profiles. b) XPS spectra of the Si 2p region. c) SEM images of the pristine $\mu\text{-Si}$ and the as-synthesized $\mu\text{-Li}_x\text{Si}$. d) Electronic conductivity measurement of $\mu\text{-Li}_x\text{Si}$. e) DC polarization measurement of Li-In|SSE| $\mu\text{-Li}_x\text{Si}$ |SSE|Li-In symmetric cell. f) AC impedance measurement of Li-In|SSE|Li-In symmetric cell.

Figure XVI.9.1a displays the X-ray diffraction (XRD) profiles. After prelithiation process, the pristine crystalline μ -Si (Figure XVI.9.1a, up) transformed to amorphous $\text{Li}_{3.75}\text{Si}$ ($\text{Li}_{15}\text{Si}_4$) phase (Figure XVI.9.1a, bottom), as indicated by the newly emerged peaks at ca. 21° , 24° , 27° , 40° , and 43.5° . Despite the Li/Si molar ratio of the precursors is 4.4/1, ca.10% extra Li is still required to obtain a phase pure $\text{Li}_{4.4}\text{Si}$ ($\text{Li}_{22}\text{Si}_5$) compound. Since some unavoidable side reactions related with the surface impurities of the pristine Si particles need to consume extra Li during milling process. The as-synthesized $\text{Li}_{3.75}\text{Si}$ compound (denoted as $\mu\text{-Li}_x\text{Si}$ thereafter) was then used for the following study. X-ray photoelectron spectroscopy (XPS) analysis of the pristine μ -Si in Figure XVI.9.1b shows two peaks in the region Si 2p, representing the Si–Si bond (98.5 eV) and the Si–O bond (103 eV). The Si–O bond originated from the native oxide layer (SiO_2) existed on the surface of Si particles. After lithiation, the new peak occurring at 101.5 eV was assigned to the Li–Si–O bond formed within Li_xSi matrix. Scanning electron images (SEM) show that the pristine μ -Si were separate particles with rigid edges (Figure XVI.9.1c, left), while the particles became expanded and interconnected with smoother edges after lithiation (Figure XVI.9.1c, right).

The pristine μ -Si showed an electronic conductivity of $10\text{--}2\text{ mS cm}^{-1}$ and barely had any ion diffusivity. After lithiation, $\mu\text{-Li}_x\text{Si}$ exhibited three orders of magnitude higher electronic conductivity (50.3 mS cm^{-1}) (Figure XVI.9.1d). To evaluate the Li conductivity of $\mu\text{-Li}_x\text{Si}$, direct current (DC) polarization measurement was carried out on $\text{Li-In|SSE}|\mu\text{-Li}_x\text{Si}|\text{SSE}|\text{Li-In}$ cell, where the SSE layer acted as an electron-blocking electrode. As illustrated in Figure XVI.9.1e, the overall DC resistance includes two SSE layers ($2R_{\text{ion,SSE}}$), two Li-In|SSE interfaces ($2R_{\text{Li-In|SSE}}$), one $\mu\text{-Li}_x\text{Si}$ layer ($R_{\text{ion},\mu\text{-Li}_x\text{Si}}$), and two $\mu\text{-Li}_x\text{Si}|\text{SSE}$ interfaces ($2R_{\mu\text{-Li}_x\text{Si}|\text{SSE}}$). To estimate the resistance contributed by the SSE layer and the Li-In|SSE interface, a Li-In|SSE|Li-In cell was further fabricated; its AC impedance is shown in Figure XVI.9.1f. The resistance of SSE layers ($2R_{\text{ion,SSE}}$) and Li-In|SSE interface ($2R_{\text{Li-In|SSE}}$) was around $49.5\ \Omega\text{ cm}^2$. Therefore, the Li conductivity of the $\mu\text{-Li}_x\text{Si}$ layer was roughly calculated to be $> 0.1\text{ mS cm}^{-1}$, since it was hard to decouple the resistance of $\text{Li}_x\text{Si}|\text{SSE}$ interface from the overall resistance.

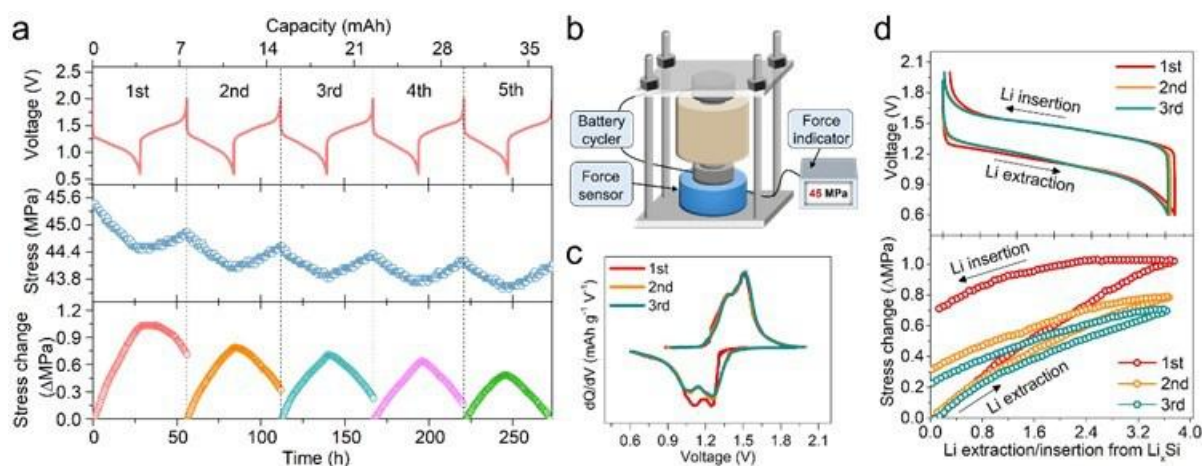


Figure XVI.9.2 a) The voltage profiles of $\mu\text{-Li}_x\text{Si}|\text{SSE}|\text{LTO}$ cell (up) along with correlated evolution of stress (middle) and stress change (bottom). b) Schematic of pressure-monitoring cell. c) Corresponding dQ/dV curves. d) Voltage and stress change plotted as a function of the molar amount of lithium extracted from or inserted into the $\mu\text{-Li}_x\text{Si}$ phase.

The volume change of $\mu\text{-Li}_x\text{Si}$ electrode was explored by *in-situ* monitoring the dynamic pressure change of $\mu\text{-Li}_x\text{Si}|\text{SSE}|\text{Li}_4\text{Ti}_5\text{O}_{12}$ full cell. Since the phase transition of $\text{Li}_4\text{Ti}_5\text{O}_{12}$ (LTO) cathode causes negligible volume change, the net stress change of the full cell is governed by the $\mu\text{-Li}_x\text{Si}$ anode alone. Voltage profiles of full cell (Figure XVI.9.2a, up) along with the correlated evolution of stress (Figure XVI.9.2a, middle) and the stress change (Figure XVI.9.2a, bottom) were recorded over five consecutive cycles. Figure XVI.9.2b illustrates the stress measurement setup and Figure XVI.9.2c shows the corresponding dQ/dV curves. With an areal capacity of $\approx 3\text{ mAh cm}^{-2}$, the full cell exhibited $\approx 0.7\text{ MPa}$ stress swing upon cycling, with a stress decrease during discharge (Li extracted from $\mu\text{-Li}_x\text{Si}$) and an increase during charge (Li inserted to $\mu\text{-Li}_x\text{Si}$).

Theoretically, the stress change only depends on the quantity of Li inserted or extracted from the $\mu\text{-Li}_x\text{Si}$ electrode, which is proportional to the areal capacity. But in real scenarios, the stress change can be weakened due to the elastic deformation of SSE layer and the presence of pores and void spaces within the cell. For example, the thicker the SSE layer is, the smaller stress change would be detected. As shown in Figure XVI.9.2a (bottom) and Figure XVI.9.2d (bottom), a relatively large stress hysteresis (irreversibility of stress change) is revealed from the initial cycle, which gradually vanishes in the subsequent cycles. At the 5th cycle, the stress change became highly reversible upon charge/discharging (Figure XVI.9.2a, bottom). The weakening of stress hysteresis could be attributed to the rearrangement of pristine void space within the cell along the contraction and expansion of $\mu\text{-Li}_x\text{Si}$ at the initial cycles. Also, stress hysteresis caused by the irreversible trap of some active Li inside the LTO structure during the 1st cycle, as revealed by the initial Coulombic efficiency of 97.0% (Figure XVI.9.2d, up), would disappear in the following cycles.

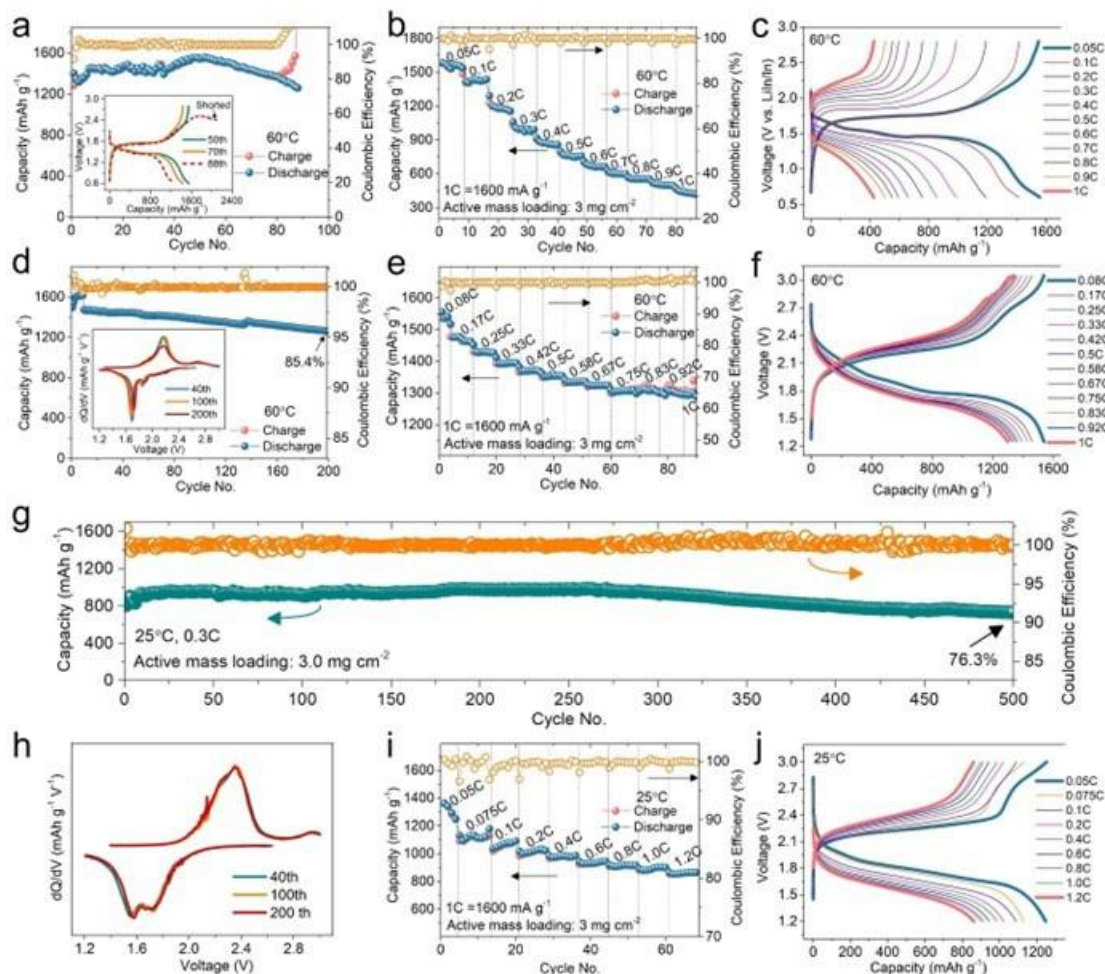


Figure XVI.9.3 a) Cycling and b-c) rate performance of Li-In|SSE|S full cell at 60°C. d) Cycling and e-f) rate performance of $\mu\text{-Li}_x\text{Si}$ |SSE|S full cell at 60°C. g) Cycling and e-f) rate performance of $\mu\text{-Li}_x\text{Si}$ |SSE|S full cell at 25°C.

Full cell performance was evaluated by pairing a S cathode with a pure Li anode, a Li-In alloy anode, and a $\mu\text{-Li}_x\text{Si}$ alloy anode, respectively. All cells with an areal S loading of 3 mg cm⁻² were first tested under 60°C and ≈ 50 MPa. Li|SSE|S cell became quickly shorted in the initial charging process, induced by Li dendrite formation during Li plating. Li_xSi|SSE|S cell (Figure XVI.9.3f) displayed a discharge voltage plateau of 1.75 V, which is 280 mV higher than that compared with Li-In|SSE|S cell (Figure XVI.9.3c). The discharge plateau represented the solid–solid conversion between S and Li₂S occurred within the S cathode. Long-term cycling tests were next carried out. Li-In|SSE|S cell in Figure XVI.9.3a showed a rapid capacity fading after 50 cycles

and became shorted at the 88th cycle. It is noteworthy that a relatively high mass loading and high current condition could cause cavity formation at the Li-In/SSE interface and unexpectedly Li-In filament growth, which would result in capacity decay and cell failure. In comparison, $\mu\text{-Li}_x\text{Si|SSE|S}$ cell in Figure XVI.9.3d showed stable cycling and retained 85.4% capacity after 200 cycles. Under high current of 1C ($1\text{C}=1600\text{ mA g}^{-1}$), Li-In/SSE|S cell only delivered 427 mAh g^{-1} (Figure XVI.9.3b-c), whereas $\mu\text{-Li}_x\text{Si|SSE|S}$ cell can deliver 1301 mAh g^{-1} (Figure XVI.9.3e-f), again implying the more favorable dealloying/alloying kinetics of $\mu\text{-Li}_x\text{Si}$ alloy compared with Li-In alloy.

Room-temperature operation has been a long-standing challenge to achieve ideal practical application of ASSBs. Therefore, cycle life and rate capability of $\mu\text{-Li}_x\text{Si|SSE|S}$ cell were evaluated at 25°C . Figure XVI.9.3g shows 76.3% capacity was retained after 500 cycles under 0.3C. Under 1.2C, an accessible capacity of 866 mAh g^{-1} was achieved, corresponding to 69% of the capacity under 0.05C (1249 mAh g^{-1}).

A flexible, highly conductive thin SSE and the fabrication of a Li-S pouch cell

Despite the successful efforts on boosting the material- and electrode-level energy density, strategies to increase the cell-level energy density have rarely been reported. Most of the reported cells were based on a pellet-type configuration manufactured by dry powder die compression. The obtained SSE separator was rather thick (0.5–1.0 mm) and the cathode areal loading was relatively low ($< 2\text{ mg cm}^{-2}$), resulting in an extremely low cell-level energy density ($< 50\text{ Wh kg}^{-1}$) and a high cell internal resistance. The major challenge for reducing the separator thickness is the brittleness of ceramic materials, a problem which is exacerbated under a practical condition, as the area to thickness ratio of the separator increases. Therefore, developing feasible technology to manufacture thin but robust SSE is an imperative need for exploiting commercialization-driven ASSBs.

During FY2022, we fabricated a remarkable free-standing SSE membrane, which was merely $46\text{ }\mu\text{m}$ thick, and an ultralow areal resistance of $3.3\text{ }\Omega\text{ cm}^2$ was achieved, more than tenfold lower than that of reported SSE pellets.

A thick SSE can not only reduce the cell-level energy density but also cause an exceptionally high areal resistance, based on the equation $R = l/\sigma$, where $R\text{ (}\Omega\text{ cm}^2\text{)}$ is the areal resistance, $l\text{ (cm)}$ is the thickness, and $\sigma\text{ (S cm}^{-1}\text{)}$ is the conductivity, respectively. Such a high areal resistance would inevitably result in a high cell resistance and poor power performance, undermining the intrinsic benefits of high conductivity of sulfide superionic conductors. Therefore, developing a thin ($< 50\text{ }\mu\text{m}$) but robust SSE membrane should take precedence over other factors in commercializing sulfide-based Li-organic batteries. In this study, the dry process was used to manufacture $\text{Li}_6\text{PS}_5\text{Cl}$ membrane. Despite the binder content being merely 0.2 wt.%, the as-fabricated SSE membrane in Figure XVI.9.4a was free-standing and demonstrated a high flexibility. After cold pressing, the SSE thickness was reduced from $70\text{ }\mu\text{m}$ (Figure XVI.9.4c) to $46\text{ }\mu\text{m}$ (Figure XVI.9.4c), with a compaction density of 2.6 g cm^{-3} . As marked by the arrows, the PTFE fibrils were well retained within the much-densified SSE structure. The ionic conductivity of SSE membrane was measured to be 1.4 mS cm^{-1} (Figure XVI.9.4d), which was slightly lower than that of the binder-free SSE pellet (1.8 mS cm^{-1}), owing to the ionic insulating nature of PTFE. Despite this fact, the areal resistance was a mere $3.3\text{ }\Omega\text{ cm}^2$, more than tenfold lower than the SSE pellet ($39\text{ }\Omega\text{ cm}^2$, we used 0.7 mm thickness in the calculation).

It is worth mentioning that PTFE would decompose once in contact with lithium to generate defluorinated carbon, which is electronically conductive. The propagation of the reaction will eventually cause the short of the membrane. We are in the process of overcoming the obstacle, but in the meantime, $\text{Li}_{38}\text{In}_{62}$ alloy (0.62 V vs. Li^+/Li) was used as an anode. In order to test the flexible SSE membrane, a polyimide was used as the cathode in a sheet-type polyimide| $\text{Li}_6\text{PS}_5\text{Cl}$ |LiIn full cell. Polyimide is a durable and low-cost engineering plastic with high thermal resistance, chemical inertness, and insolubility in common organic solvents. It was also proven to be a high-performance cathode material in lithium-ion batteries and tested in many stationary energy storage systems. We chose the material to be a cathode test vehicle. The polyimide| $\text{Li}_6\text{PS}_5\text{Cl}$ |LiIn full cell in Figure XVI.9.4e shows a discharge plateau of 2.2 V (vs. Li^+/Li) and an attainable capacity of $\sim 180\text{ mAh}$

g^{-1} , which is consistent with that of the pellet-type cells. Cycling performance in Figure XVI.9.4f shows almost no capacity decay with an average Coulombic efficiency $>99\%$ over 30 cycles. To the best of our knowledge, this is the first demonstration of a sulfide-based organic ASSB with a sheet-type cell design. Energy densities were compared among these works based on considering only the cathode and the SSE part, since the anode can be further optimized. The calculated volumetric energy density was 164.2 Wh L^{-1} and the gravimetric energy density was 100.3 Wh kg^{-1} . The energy density was more than tenfold higher than the value of other works despite the mediocre intrinsic capacity of polyimide. It should be noted that PI was only employed as a test vehicle here, but the dry-film technique can be extended to many other thermally stable and sulfide SSE-compatible cathodes.

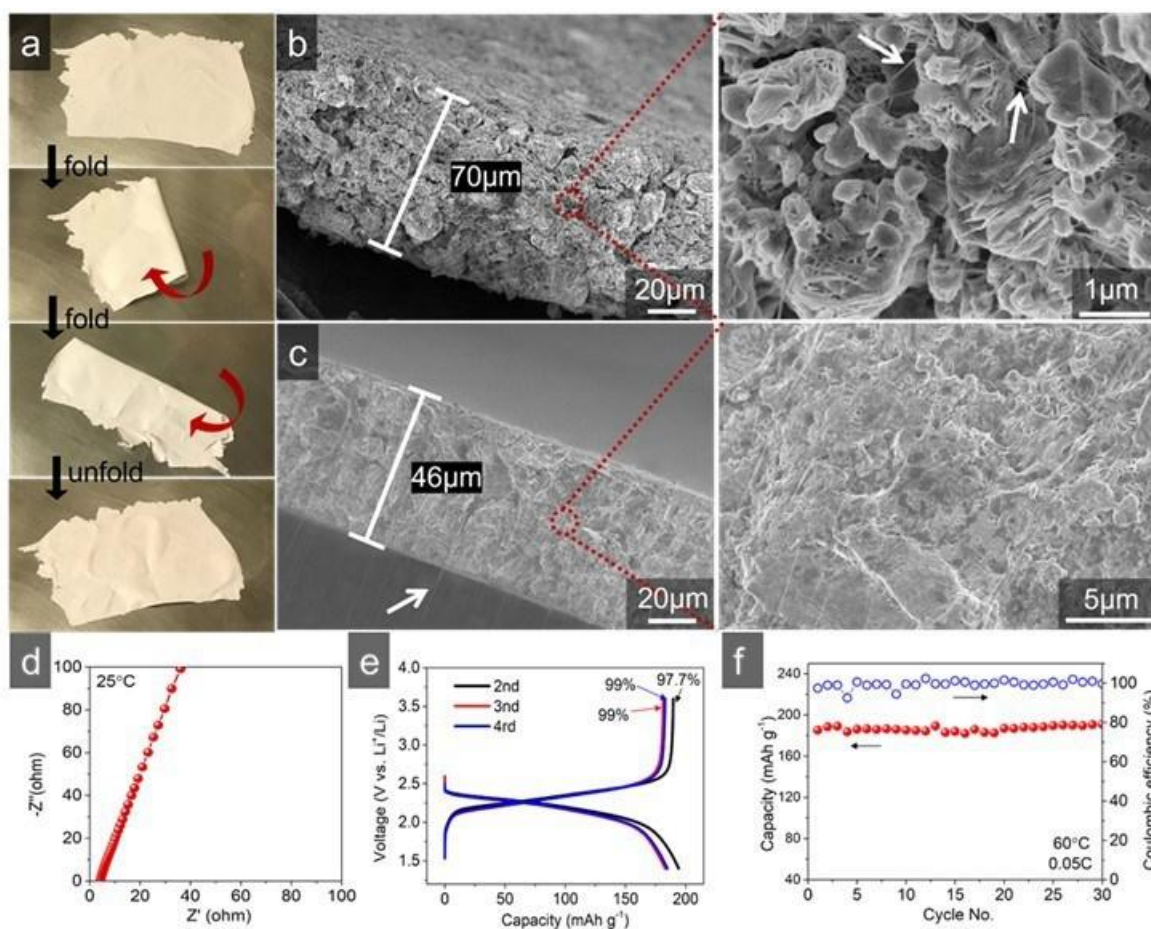


Figure XVI.9.4 a) Flexibility test of the free-standing SSE membrane. b) Cross-sectional SEM images of SSE membrane b) before and c) after cold pressing. d) Ionic conductivity measurement of SSE membrane at 25°C . e) Galvanostatic voltage profiles and f) cycling performance of sheet-type Polyimide | $\text{Li}_6\text{PS}_5\text{Cl}$ | LiIn cell at 60°C .

The ultimate goal of the flexible SSE is to fabricate a large format pouch cell. After verifying the electrochemical performance of the PTFE bond flexible SSE, a sulfur/ $\text{Li}_6\text{PS}_5\text{Cl}$ / LiIn full cell in a pouch cell format was built. Figure XVI.9.5 shows the 2x3 inch pouch cell, the test fixture and the first a few cycles of the cell. The initial capacity of the cell was above 1100 mAh/g (of sulfur). As shown in the figure, although the ASSE Li-S cell can light a LED without external pressure, about 500 KPa was still applied to discharge the cell.

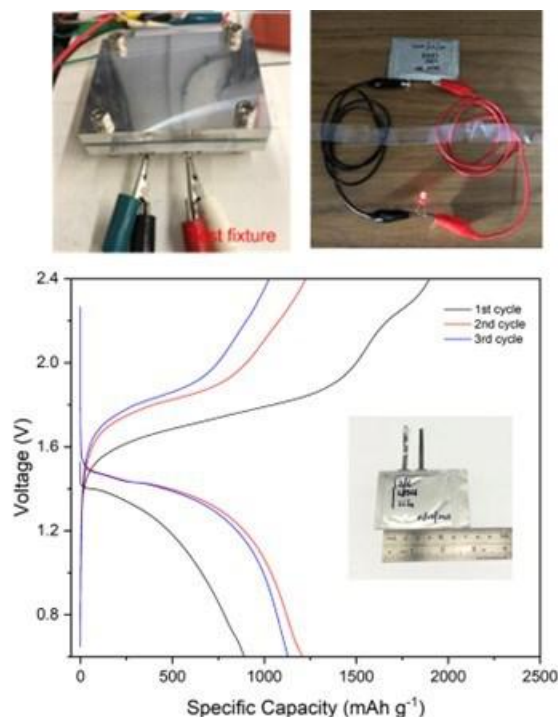


Figure XVI.9.5 All solid-state sulfur | $\text{Li}_6\text{PS}_5\text{Cl}$ | LiIn cell pouch cell (full cell, 2x3 inch), cell under test in a pressure fixture and first 3 cycles @60°C.

Conclusions

A fully lithiated Si electrode materials was made. Derived from its distinctive properties, an all-electrochem-active $\mu\text{-Li}_x\text{Si}$ electrode architecture has been validated to be feasible. When paired with S cathode, the all-solid-state $\text{Li}_x\text{Si-S}$ batteries show appealing rate and cycling performance at room temperature. To fully unleash the potential of Si-based anode, advanced cell designs with a thinner electrolyte film and a lower stack pressure need to be further explored. Overall, this work paves a pathway to solve the longstanding interface-related issue of Li_xSi anode and advances the development of high-performance and high-energy-density Li-S ASSBs.

A dry-film approach was used to fabricate an ultrathin $\text{Li}_6\text{PS}_5\text{Cl}$ membrane. The performance of the flexible membrane was proven in a polyimide- LiIn ASSB, and followed by assembling into an 2x3 inch LiIn-Sulfur ASSB cell. The free-standing $\text{Li}_6\text{PS}_5\text{Cl}$ membrane was merely 46 μm thick, with an ultralow areal resistance of 3.3 $\Omega \text{ cm}^2$. We believe the dry-film approach could be used for the manufacture of large format ASSB.

References

1. Weixiao Ji, Xiaoxiao Zhang, Le Xin, Avery Luedtke, Dong Zheng, He Huang, Tristan Lambert, Deyang Qu*, "A high-performance organic cathode customized for sulfide-based all-solid-state batteries", *Energy Storage Material*, 45(2022)680
2. Weixiao Ji, Xiaoxiao Zhang, Huainan Qu, Le Xin, Avery T. Luedtke, He Huang, Tristan H. Lambert, Deyang Qu*, "Polyimide as a durable cathode for all-solid-state $\text{Li}(\text{Na})$ -organic batteries with boosted cell-level energy density", *Nano Energy* 96 (2022)107130.
3. Weixiao Ji, Xiaoxiao Zhang, Dong Zhang, He Huang, Tristan Lambert, Deyang Qu*, "Practically Accessible All-Solid-State Batteries Enabled by Organosulfide Cathodes and Sulfide Electrolyte", *Adv. Funct. Mater.* 2022 2202919.
4. Weixiao Ji, Xiaoxiao Zhang, Miao Liu, Tianyao Ding, Huainan Qu, Dantong Qiu, Dong Zheng, Deyang Qu*, "High-performance all-solid-state Li-S batteries enabled by an all-electrochem-active prelithiated Si anode", *Energy Storage Material*, 53(2022)613-620

Acknowledgements

The PI and his staff researchers are grateful to Patricia Smith, Simon Thompson, Colleen Butcher and Tiffany Zachry for their guidance and supports. Such helps were extremely important to the success of our research during the pandemic of COVID. The PI in UWM (DYQ) is grateful to Professor T.H. Lambert and Dr. H Huang of Cornell, and Drs. Le Xin and Avery Luedtke of Millipore Sigma for the synthesis of the materials.

XVI.10 Fundamental Understanding of Interfacial Phenomena in Solid-State Batteries (General Motors)

Xingcheng Xiao, Principal Investigator

General Motors Research and Development Center
30470 Harley Earl Blvd.
Warren, MI 48092-2031
E-mail: xingcheng.xiao@gm.com

Tien Duong, DOE Technology Development Manager

U.S. Department of Energy
E-mail: Tien.Duong@ee.doe.gov

Start Date: October 1, 2019	End Date: May 31, 2023	
Project Funding (FY22): \$1,333,325	DOE share: \$1,000,000	Non-DOE share: \$333,325

Project Introduction

Solid-state batteries (SSBs) are considered the next generation battery technology for resolving the intrinsic limitations of current lithium-ion batteries, such as poor abuse tolerance, insufficient energy density, and short cycle life. However, the main hurdle for SSB in electric vehicle (EV) applications is the complexity caused by material interfaces, such as Li metal/solid electrolyte (SE) and SE/cathode interfaces, leading to increased impedance and shortened cycle life. Although interfaces in SSBs are one of the key factors, a clear understanding of their properties and functions is still unavailable, partly due to the difficulty in characterizing buried solid-solid interfaces and interphases formed during battery cycling.

Objectives

The project objective is to develop a comprehensive set of in situ diagnostic techniques combined with atomic/continuum modeling schemes to investigate and understand the coupled mechanical/chemical degradation associated with dynamic interfacial phenomena in SSBs. Specifically, in situ observations and characterizations of lithium plating-stripping processes, lithium dendrite formation, interphase formation, and the induced interfacial stresses, as well as the mechanical and electrochemical properties of interfaces and interphases, are paramount. The study will provide useful guidelines for optimizing cell structure design and engineering interfaces and interphases to enable SSBs. In addition, it will establish a critical guideline to design safe and durable SSBs with energy density > 500 wh/kg for EV applications.

Approach

The multiscale in situ diagnostic tools, including AFM, nanoindentation, dilatometer, stress sensors, and pressure cells, will be used to investigate mechanical behavior and microstructure evolution at interface/interphase during lithium plating and stripping. The information (along with Li-ion transport properties and microstructure evolution obtained using the advanced spectroscopic ellipsometry, and in situ TEM) will be correlated with electrochemical performance toward high cycle efficiency and dendrite-free SSBs. The goal of this understanding is to develop strategies for surface and interface engineering, apply them to commercially available SEs (including powder, pellets, and foils), and assemble SSBs for further validation and optimization, eventually extending cycle life for EV application.

Results

In-situ observations of surface passivation layer growth on lithium metal

Many of our models of the interface between lithium metal and solid electrolytes assume an ideal contact, where only pure lithium metal is in contact with the solid electrolyte. Here we report an in situ spectroscopic study demonstrating that even when lithium metal is rigorously polished and cleaned, there still exists a surface layer that is tens of nanometers thick (Seo 2022, 211602).

Figure XVI.10.1 shows x-ray photoemission spectroscopy (XPS) of the surface of cleaned and polished lithium foil as the surface is etched with an argon ion beam. The XPS data reveals that Li_2CO_3 and Li_2O both still exist near the top surface after cleaning and polishing. XPS does not provide any information on the thickness of these layers since the etching rate of these layers is not known. An in situ optical spectroscopic ellipsometry (OSE) study was conducted to measure the thickness of the surface layer as it is exposed to air.

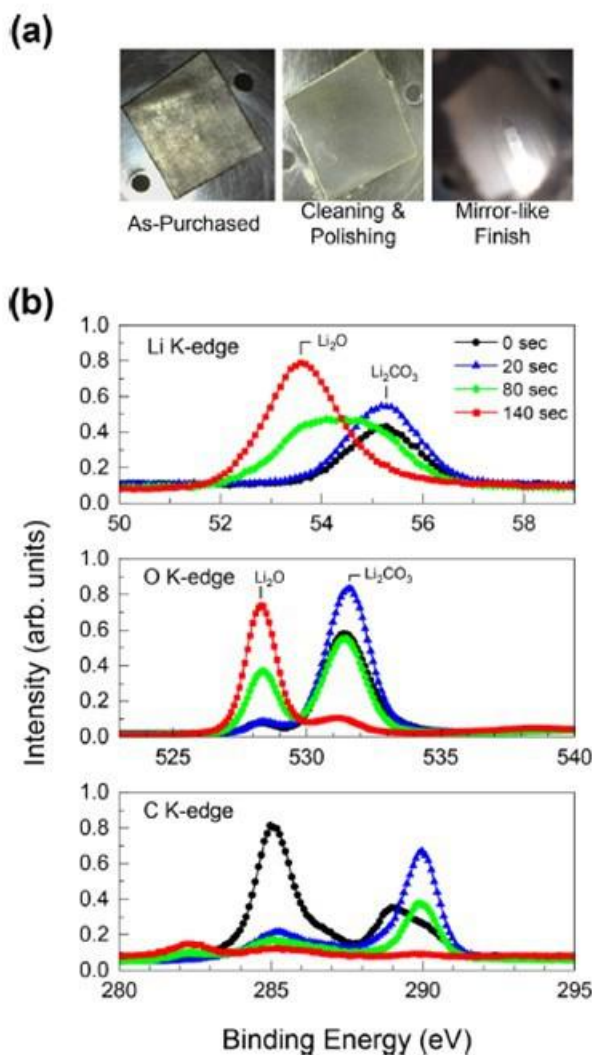


Figure XVI.10.1 (a) Photos of Li foil as it is cleaned and polished. (b) XPS at the K-edge of Li, O, and C, respectively, as its surface layer is slowly removed by the Ar-ion milling process

Figure XVI.10.2 shows the thickness of the top surface layer as a function of exposure time to air. Up until 5 minutes, the film is initially about 50 nm thick and increases linearly in time at a rate of 24 nm/min. This indicates that the initial growth of the film is an interface-controlled process rather than a diffusion-controlled. A future study will look at how this process depends on temperature.

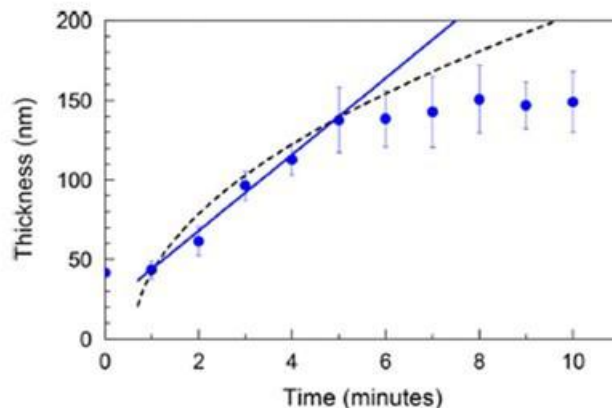


Figure XVI.10.2 Thickness of the surface layer as a function of time after the sample is exposed to air. The solid and dashed lines are linear and parabolic functions for interface-controlled and diffusion-controlled processes, respectively.

Development of the analytical model to predict the CCD for Li/SE interfaces

The combined impacts of the interface and compressive stress (stack pressure) on the Li surface morphology are considered to predict the critical current density (CCD) at the Li/solid electrolyte (SE) interface during the stripping process. To take these two impacts into consideration in an analytical model, the Li flux contributed by the vacancy hopping and creep effects should be quantified. The representative Li/Li₂O (lithiophilic), Li/LiF (lithiophobic) and the experimentally intensively studied Li/LLZO interfaces are chosen to justify this model.

The flux due to hopping is calculated based on the hopping rates, which are obtained from DFT calculated hopping barriers. Considering three consecutive Li layers ($j-1, j, j+1$), the hopping flux across the j th layer ($\frac{dN_j}{dt}$) is defined as

$$\frac{dN_j}{dt} = \frac{1}{2}k_{f,j+1}(N_{j+1} - N_j) - \frac{1}{2}k_{f,j}(N_j - N_{j-1}) - \frac{1}{2}k_{b,j}(N_j - N_{j+1}) + \frac{1}{2}k_{b,j-1}(N_{j-1} - N_j), \quad (1)$$

where $k_{f,i}$ is the forward hopping rate, $k_{b,i}$ is the backward hopping rate and N_i is the number of Li atoms on the i th Li layer ($i = j-1, j, j+1$).

Since Li atoms are stripped from the Li surface (the first layer), the hopping flux on the first layer is

$$\frac{dN_1}{dt} = \frac{1}{2}k_{f,2}(N_2 - N_1) - \frac{1}{2}k_{b,1}(N_1 - N_2). \quad (2)$$

When hopping can catch up with the vacancies generated during stripping, the concentration on the first layer does not change, which requires that

$$\frac{dN_1}{dt} = \frac{1}{2}k_{f,2}(N_2 - N_1) - \frac{1}{2}k_{b,1}(N_1 - N_2) - k_s N_1 = 0, \quad (3)$$

where k_s is the stripping rate applied on a unit area. When the forward and backward hopping events are symmetric ($k_{f,2} = k_{b,1}$), Eqn. (3) becomes

$$\frac{dN_1}{dt} = k_{f,2}(N_2 - N_1) - k_s N_1 = 0. \quad (4)$$

Then the stripping rate is related to the hopping rates according to

$$k_s = \frac{k_{f,2}(N_2 - N_1)}{N_1} = k_{f,2}\Delta N/N_1, \quad (5)$$

where $\Delta N = N_2 - N_1$. Because the current density is defined as current per unit area, the critical current density (i_c) is calculated using

$$i_c = \frac{qk_s}{A_0} = \frac{qk_{f,2}}{A_0} * \frac{\Delta N}{N_1}, \quad (6)$$

where q is the electric charge of an electron and A_0 is the unit area on the Li (001) plane. The backward hopping events always happen, and the stripping is more related to the forward hopping, therefore, Eqn. (6) can be used to predict the CCD at any Li/SE interface when the forward hopping rates from the second layer to the first layer ($k_{f,2}$) are available. It should be mentioned that Eqn. (6) holds in a short time (dt), which requires $\frac{\Delta N}{N_1}$ is small.

The creep induced flux (\dot{n}_p) over a unit area is a function of the applied strain rate ($\dot{\epsilon}$) according to

$$\dot{n}_p = \frac{N_A A_0 L \dot{\epsilon}}{V_{Li}}, \quad (7)$$

where N_A is the Avogadro's constant, L is the thickness of the Li metal and V_{Li} is the molar volume of Li. The strain rate ($\dot{\epsilon}$) is a function of the stack pressure (σ) and the temperature (T)

$$\dot{\epsilon} = \sigma^m A_c \exp\left(-\frac{Q_c}{RT}\right), \quad (8)$$

where m , A_c and Q_c are constants measured from experiments (LePage et al, 2019, A89) and R is the gas constant. Combining Eqn. (7) and (8), \dot{n}_p is expressed as a function of L , σ and T using

$$\dot{n}_p = \frac{N_A A_0 L}{V_{Li}} \sigma^m A_c \exp\left(-\frac{Q_c}{RT}\right). \quad (9)$$

Since the polynomial effect of σ ($m = 6.6$) is more prominent than the effects of L and T on \dot{n}_p , L ($L = 100 \mu\text{m}$) and T ($T = 298 \text{ K}$) are treated as constants and thus \dot{n}_p is only dependent on the applied stack pressure. When both the hopping flux and the creep induced flux are considered, i_c is expressed as

$$i_c = \frac{qk_s}{A_0} = \frac{q(k_{f,2} + \dot{n}_p)}{A_0} * \frac{\Delta N}{N_1}. \quad (10)$$

Prediction of critical current densities for Li/Li₂O, Li/LiF and Li/LLZO interfaces using the analytical model.

Table 1 lists the CCD ($\frac{\Delta N}{N_1} = 10^{-6}$) predicted for Li/Li₂O, Li/LiF and Li/LLZO interfaces. The predicted CCD here are consistent with our previous KMC simulations considering the hopping events for Li/Li₂O and Li/LiF (Yang 2021, 2814). Although the CCD for LLZO is higher than the experimental values by 2 orders of magnitude (Wang 2019 842), the LLZO surface in experiments is normally covered with some Li₂CO₃ (not a flat surface), which limits the measured CCD.

Table XVI.10.1 $k_{f,2}$ and predicted CCD for Li/Li₂O, Li/LiF and Li/LLZO interfaces without the creep effects.

	Li ₂ O	LiF	LLZO
$k_{f,2} (s^{-1})$	3.31e10	3.76e3	2.14e8
CCD (A/cm ²)	43.0	4.88e-6	0.277

Figure XVI.10.3 shows i_c at different stack pressure for Li/Li₂O, Li/LiF and Li/LLZO interfaces using Eqn. (10) assuming $\frac{\Delta N}{N_1} = 10^{-6}$. For the lithiophilic Li/Li₂O interface (wetting angle 0°), no stack pressure is required to reach a current density of 10 mA/cm². In contrast, for the lithiophobic Li/LiF interface (wetting angle 108.7°), a stack pressure around 4 MPa is necessary to achieve the goal of 10 mA/cm². For another lithiophilic interface (Li/LLZO, wetting angle 60.2°), the stack pressure is not necessary to reach a stripping current density of 10 mA/cm². As the Li/LLZO is not as lithiophilic as the Li/Li₂O, the CCD is smaller than that of the Li/Li₂O interface but larger than that of the Li/LiF interface, suggesting that the analytical model captures the trends of CCD among different Li/SE interfaces.

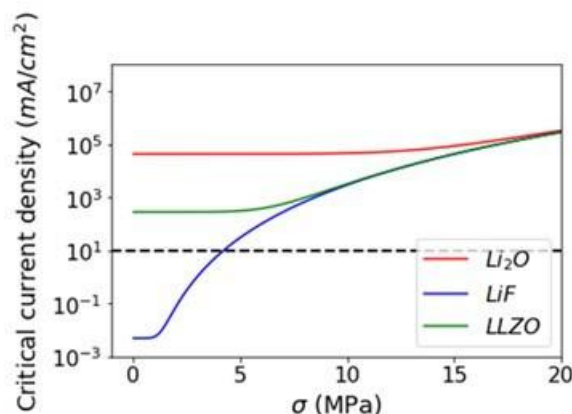


Figure XVI.10.3 Predicted critical current density at different stack pressures for Li/Li₂O, Li/LiF and Li/LLZO interfaces considering Li hopping and creep induced Li flux.

Mechanical characterization of interlayer for stabilizing the interface between Li metal and solid electrolyte

Environmental nanoindentation was performed along a lithium-rich cross-section of LLZTO solid electrolyte. A LLZTO pellet was cycled until failure in a Swagelok type cell with lithium metal foil as both electrodes. After disassembly of the cell, the LLZTO pellet was fractured into two halves exposing a metallic lithium-rich cross-section as shown in Figure XVI.10.4 (a). One half of the LLZTO pellet was taken to SEM and imaged. The lithium microstructure can be seen in Figure XVI.10.4 (b). The other half of the LLZTO pellet was mounted in epoxy and lightly polished in order to provide a smooth surface for safe nanoindentation along the lithium-rich cross-section. Figure XVI.10.4 (c) shows the mounted and polished LLZTO cross-section. 120 indents were made along the cross-section in a 3 x 40 matrix as shown by the overlaying groupings A, B, and C in Figure XVI.10.4 (c). Nanoindentation was performed in an argon-filled glovebox to minimize exposure to air and the growth of any passivation films. The elastic modulus of the entire cross-section was 117.60 ± 18.11 GPa, while the hardness was 5.41 ± 1.63 GPa. A statistical t-test showed that the results for both mechanical properties were not statistically significant compared to the surface nanoindentation results of the same pellet prior to electrochemical cycling. If the excess lithium shown in the cross-section were to influence the mechanical properties of the pellet, then group A would show the most change as it covers the most lithium-rich area. Group B covers a lower percentage of lithium-rich area while group C does not cover any of the lithium morphology. However, when comparing the mechanical properties between all three groups, there was no significant difference. Figure XVI.10.4 (d) compares the elastic modulus between the three groups. If the excess lithium does influence the mechanical properties of the LLZTO pellet, then it must be localized and does not extent far into the pellet. Thus, mechanical polishing method used in this study could remove the influence of the lithium metal. More precise measurements of local mechanical properties, such as atomic force microscopy (AFM)-based indentation, and better sample preparation methods will be used properly perform nanoindentation of a cross-section.

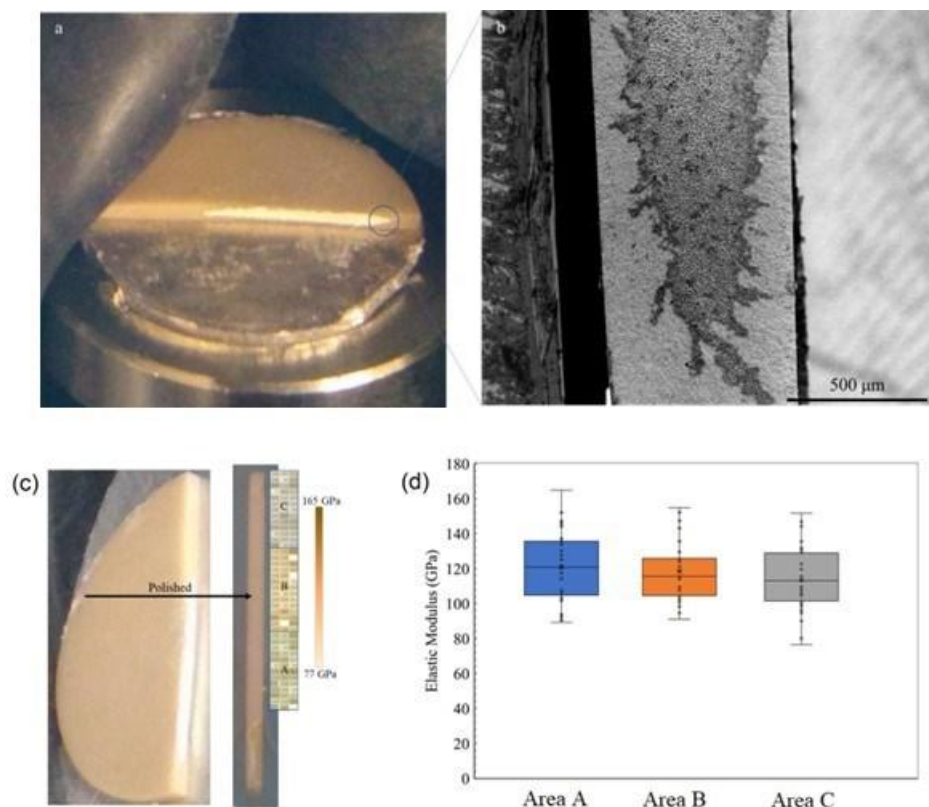


Figure XVI.10.4 (a) Photo of the LLZTO lithium-rich cross-section. (b) SEM image of the lithium-rich cross-section highlighting the lithium microstructure. (c) Diagram depicting the mounted and polished lithium-rich cross-section with an overlay showing the indentation groupings. (d) Elastic modulus results for the lithium-rich cross-section grouped by area.

Investigation of different polymer nanocomposite-based interlayers to reduce the interfacial resistance of solid-state batteries.

Recently, we have developed a polymer nanocomposite as the interlayer to maximize the interfacial contact between lithium metal and solid electrolyte, therefore, to facilitate the ion transport through the interface. We first deposited a thin film on Li-metal surface by soaking it in DTL solution, which stands for (1,2-dimethoxyethane (DME) solvent with trimethyl phosphate (TMP) and LiNO_3 additives). In addition, we also replaced DME with DOL (1,3-Dioxolane) for form more flexible coating. The electrochemical impedance spectroscopy shows the interlayer can significantly reduce the impedance by almost two orders of magnitude, as shown in Figure XVI.10.5.

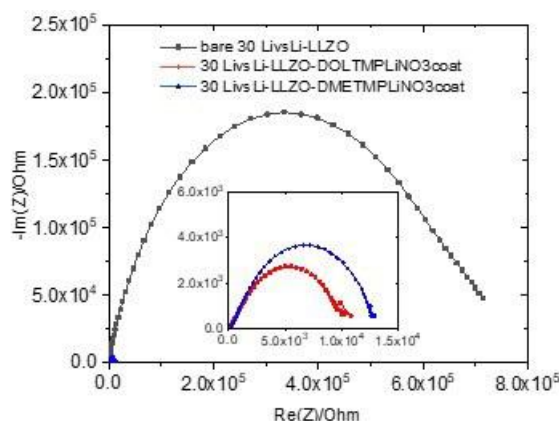


Figure XVI.10.5 The comparison of interfacial impedance of Li vs. LLZO with different interlayers.

To correlate the battery performance and the components and properties of the coating layer formed in the soaking process, Density Functional Theory (DFT)-based molecular dynamics (AIMD) simulations together with experimental investigation were performed to study the reaction mechanism of the DTL solution on Li metal surface. When constructing the structures for Li metals covered by the DTL solution, to resemble the 0.8 M LiNO_3 in DME/TMP (volume ratio = 5:1) solution in the experiment, 6 DME molecules, 1 TMP molecule and 1 LiNO_3 molecule were packed as the liquid solution, relaxed, and formed an interface with Li (001) surface. The AIMD simulation using the NVT ensemble was performed at 400 K with the Nose-Hoover thermostat. The higher temperature (below the Li melting point, 454 K) was used to accelerate the calculations. The system was firstly run for 5 ps with a time step of 1 fs. If no bond breakage or decomposition was observed, another 15 ps was added.

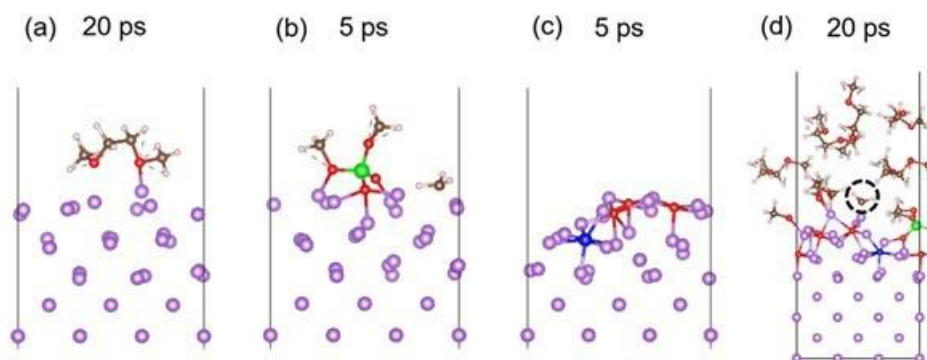


Figure XVI.10.6 Structures after AIMD simulations. (a) DME molecule (b) TMP molecule, (c) LiNO_3 molecule, and (d) DTL solution on the Li metal. Purple: Li, Brown: C, White: H, Red: O, Blue: N, Green: P. The colors for different elements are consistent in all the figures

Figure XVI.10.6 a-c show the final structures of one molecule on the Li metal after the AIMD simulations. No reactions occur between DME and the Li metal after 20 ps (Figure XVI.10.6a). In contrast, after 5 ps, one of the C-O bonds breaks in TMP (Figure XVI.10.6b), forming a CH_3 radical, while the LiNO_3 completely decomposes to nitrides and oxides (Figure XVI.10.6c). These observations are consistent with the SEM images for Li surfaces soaked in DME or TMP for 1 hour.

The DME/TMP/ LiNO_3 interlayer synthesized by simple soak coating approach can form a soft organic-inorganic composite layer on Li metal surface. Such DTL interlayer can effectively protect Li metal by suppressing Li volume change during cycling. The interlayer can also uniformly distribute the stress generated during cycling. The reduced strain rate during the initial stage of plating can mitigate SEI delamination and cell failure. With the interlayer applied between Li and LLZO, intensive polishing is no longer necessarily

needed. Further investigation is be focused on studying the chemical composition of the DTL layer and understanding the reaction mechanism and how the interlayer impacts the critical current density.

To help mitigate this surface layer formation and to decrease the interfacial resistance between lithium foil and the solid electrolyte in all-solid-state batteries, researchers are looking into coating an artificial solid-electrolyte interphase onto lithium foil (Li 2016, 1853 and Liu 2020, 2002297). Here we present measurements on the interfacial resistance of coated lithium foil and its dependence on applied external pressure. Lithium foil was coated in a solution of Dimethyl ether, trimethylpropane, and Lithium Nitrate (DTL). DTL coated and uncoated lithium foil samples were prepared at General Motors Global Research and Development Center. Samples were then assembled, and vacuum sealed in a pouch cell for pressure cell studies. Figure XVI.10.7 shows Electrochemical Impedance Spectroscopy (EIS) data that suggests that the interfacial resistance significantly decreases when lithium foil is coated with DTL, and that under externally applied pressure both coated and uncoated samples show a significant decrease in their interfacial resistances.

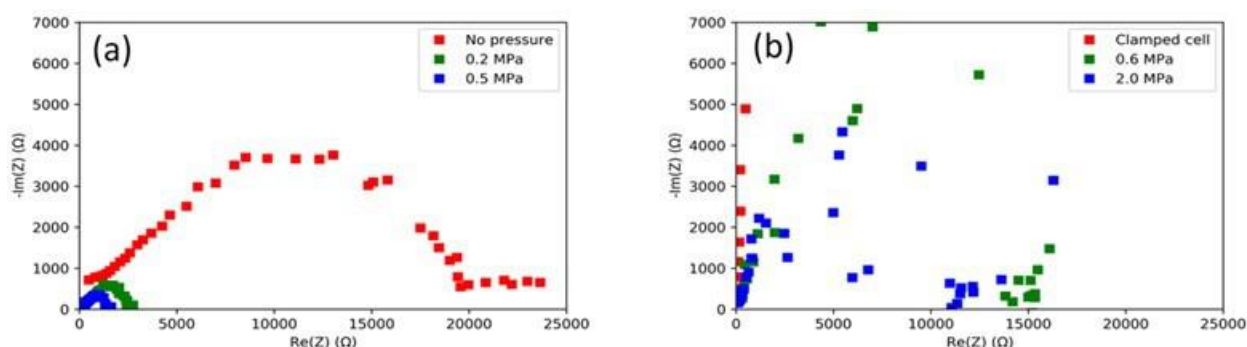


Figure XVI.10.7 (a) EIS spectra taken on DTL-coated Li symmetric pouch cell. (b) Bare lithium symmetric pouch cell EIS data. The inset at the top right shows the spectra when the pouch cell is clamped. Note that the clamped cell interfacial impedance is too large to be shown on the plot in (b).

Mechanical properties of interlayer materials

Determining the mechanical properties of interlayer materials is vital for long-term cycling in lithium metal batteries. It has been proposed that the shear modulus of a solid electrolyte in a solid-state lithium metal battery is an important parameter for preventing dendritic growth, for instance (Monroe and Newman, 2005 A396). The measured elastic modulus of nanoindentation experiments on thin films can be influenced by the substrate. To see the influence of the substrate, environmental nanoindentation was performed on two different samples of dip-coated thin films grown on lithium foil using a Berkovich tip. Figure XVI.10.8 shows that the average modulus decreased as the dip-coat time increased, and that the modulus of the maximum dip-coat time sample of 2 hours is similar to the average results for the 1-hour sample. These results provide more confidence that the previous results found are probing the polymer film. Figure XVI.10.9 shows histograms representing the spread of the data comparing each sample with lithium foil.

The error bars in Figure XVI.10.8 show that the measured modulus varies significantly across every sample. For lithium foil, this may be explained by how Lithium has a very high anisotropy factor (Herbert, 2018 1335), and since lithium foil is polycrystalline, it is expected to see moduli ranging by 17 GPa. It is proposed that one reason for such large variations in the thin film samples has to do with variations in the morphology of the film. Figure XVI.10.10 shows an example of three AFM images taken at different locations on the DME 15-minute sample, showing differences in the local morphology of the film at different locations.

It is also plausible that the sharpness of the Berkovich tip makes it difficult to detect the surface of such a soft polymer layer, as reported previously (VanLandingham 2001, 1). To build more confidence in these results, flat punch indentation will be performed next. Creep studies will also be performed with this indenter to

extract the time-dependent modulus to characterize the viscous behavior of the polymer film. These results will aim to better understand why coated lithium metal anodes outperform uncoated ones during long-term cycling tests. Finally, finite element method (FEM) will be applied to this system to determine whether the results presented here are in isolation of the substrate.

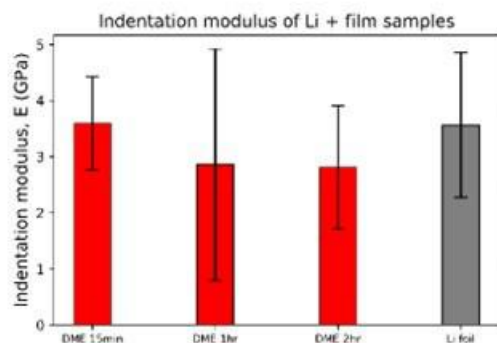


Figure XVI.10.8 Indentation modulus results on different thin films on Li-foil.

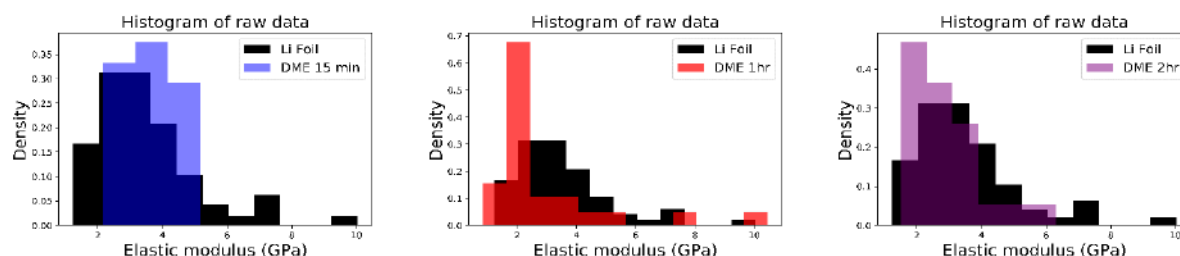


Figure XVI.10.9 Histogram of the moduli in previous figure.

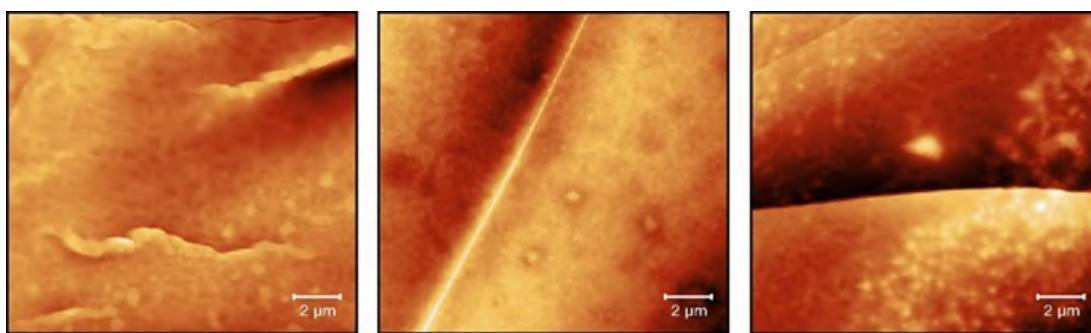


Figure XVI.10.10 Three AFM images at different locations of the DME 2 hr. sample.

Future work

Figure XVI.10.11 shows the forward and backward hopping barriers in the three Li/SE interfaces at different stack pressures. When the stack pressure is applied ($\sigma > 0$ MPa), the forward hopping barrier (E_f) is decreased by half of the mechanical bias (E_p), while the backward hopping barrier is increased by half of E_p (the method to solve E_p from n_p will be summarized in the next quarter). For Li/Li₂O and Li/LiF interfaces, all the barriers have been calculated. For the Li/LLZO interface, more NEB calculations will be performed to get all the hopping barriers at 0 MPa and then the modified barriers can be obtained at different stack pressures.

With the modified barriers due to creep effects, the KMC simulations of the vacancy evolution during stripping can be performed at different stack pressures and provide the range of CCD. With the CCD and critical pressure predicted from the analytical model and the KMC simulations, the interface and creep effects on the

Li surface morphology can both be studied and provide clues to design the Li/SE interface and keep it flat during stripping.

In addition, the optimized interlayers will be applied between Li metal electrode and solid electrolyte to test the critical current density. Based on that, the cycle life tests will be performed to investigate how the interlayer can improve the cycle stability of all solid-state batteries

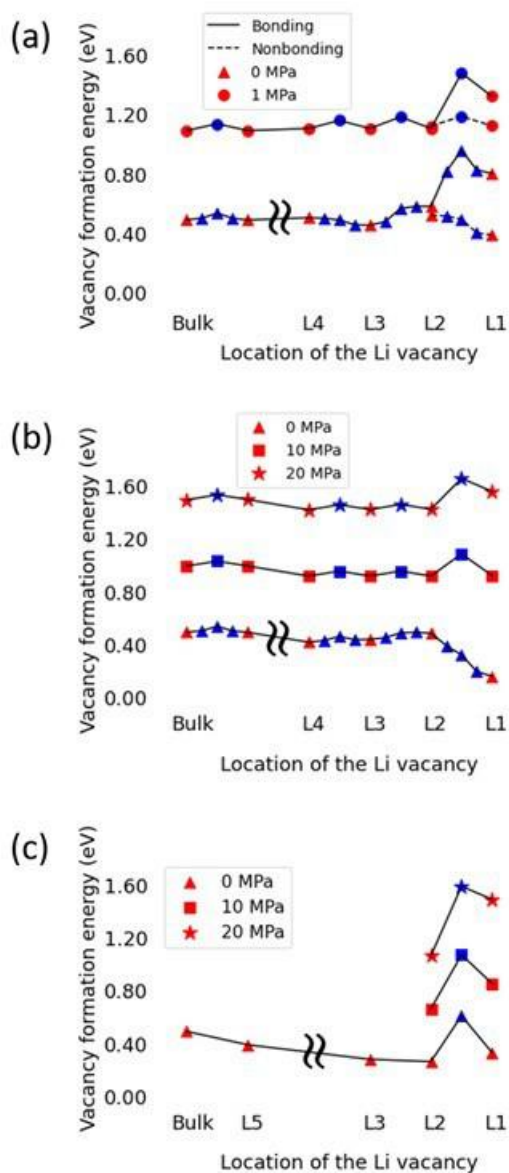


Figure XVI.10.11 Forward and backward barriers for at different stack pressures for Li/Li₂O (a), Li/LiF (b) and Li/LLZO interfaces (c) for later KMC simulations. The red markers represent the vacancy formation energy and blue ones stand for the transition state energy. For the Li/LLZO interface, more NEB calculations will be performed to get all the necessary hopping barriers to perform the KMC simulations.

Conclusions

- The surface passivation layer of lithium metal exists even after rigorously preparing its surface inside a glovebox. The potential impact of this lithium passivation layer should be considered when understanding the interface phenomena between lithium metal and solid-state electrolytes.

- Both the analytical model and KMC simulations suggest that a lithiophobic interface (Li/LiF, Li/Li₂S) requires a larger stack pressure compared to a lithiophilic interface (Li/Li₂O, Li/LLZO) to maintain a flat surface.
- A nanocomposite interlayer DTL coating has been developed to significantly reduce the interfacial impedance. The polymer matrix makes the coating flexible and maximizes the interfacial contact between solid electrolyte and lithium metal.

Key Publications

1. Meyer, Andrew, Xingcheng Xiao, Mengyuan Chen, Ambrose Seo, and Yang-Tse Cheng. "A Power-Law Decrease in Interfacial Resistance Between Li₇La₃Zr₂O₁₂ and Lithium Metal After Removing Stack Pressure." *Journal of The Electrochemical Society* 168, no. 10 (2021): 100522.
2. Cho, Jung Hwi, Kunjoong Kim, Srinath Chakravarthy, Xingcheng Xiao, Jennifer LM Rupp, and Brian W. Sheldon. "An Investigation of Chemo-Mechanical Phenomena and Li Metal Penetration in All-Solid-State Lithium Metal Batteries Using in Situ Optical Curvature Measurements." *Advanced Energy Materials* (2022): 2200369.
3. Feng, Min, Chi-Ta Yang, and Yue Qi. "The Critical Stack Pressure to Alter Void Generation at Li/Solid-Electrolyte Interfaces during Stripping." *Journal of the Electrochemical Society* 169, no. 9 (2022): 090526.
4. Seo, A., Meyer, A., Shrestha, S., Wang, M., Xiao, X. and Cheng, Y.T., 2022. Observation of the surface layer of lithium metal using in situ spectroscopy. *Applied Physics Letters*, 120(21), p.211602.
5. Xingcheng Xiao, A process to reduce the interfacial impedance in all solid-state batteries, GM patent number, P103667

References

1. Herbert, Erik G., Stephen A. Hackney, Nancy J. Dudney, and P. Sudharshan Phani. "Nanoindentation of high-purity vapor deposited lithium films: The elastic modulus." *Journal of Materials Research* 33, no. 10 (2018): 1335-1346.
2. LePage, William S., Yuxin Chen, Eric Kazyak, Kuan-Hung Chen, Adrian J. Sanchez, Andrea Poli, Ellen M. Arruda, M. D. Thouless, and Neil P. Dasgupta. "Lithium mechanics: roles of strain rate and temperature and implications for lithium metal batteries." *Journal of The Electrochemical Society* 166, no. 2 (2019): A89.
3. Li, Nian - Wu, Ya - Xia Yin, Chun - Peng Yang, and Yu - Guo Guo. "An artificial solid electrolyte interphase layer for stable lithium metal anodes." *Advanced materials* 28, no. 9 (2016): 1853-1858.
4. Liu, Wei, Pengcheng Liu, and David Mitlin. "Review of emerging concepts in SEI analysis and artificial SEI membranes for lithium, sodium, and potassium metal battery anodes." *Advanced Energy Materials* 10, no. 43 (2020): 2002297.
5. Monroe, Charles, and John Newman. "The impact of elastic deformation on deposition kinetics at lithium/polymer interfaces." *Journal of The Electrochemical Society* 152, no. 2 (2005): A396.
6. Seo, A., Meyer, A., Shrestha, S., Wang, M., Xiao, X. and Cheng, Y.T., 2022. Observation of the surface layer of lithium metal using in situ spectroscopy. *Applied Physics Letters*, 120(21), p.211602.
7. VanLandingham, Mark R., et al. "Nanoindentation of polymers: an overview." *Macromolecular symposia*. Vol. 167. No. 1. Weinheim: WILEY-VCH Verlag GmbH, 2001.
8. Wang, Michael, Jeffrey B. Wolfenstine, and Jeff Sakamoto. "Temperature dependent flux balance of the Li/Li₇La₃Zr₂O₁₂ interface." *Electrochimica Acta* 296 (2019): 842-847.
9. Yang, Chi-Ta, and Yue Qi. "Maintaining a Flat Li Surface during the Li Stripping Process via Interface Design." *Chemistry of Materials* 33, no. 8 (2021): 2814-2823.

Acknowledgements

The PI (Dr. Xingcheng Xiao) and co-PIs (Profs. Brian W. Sheldon, Yue Qi, Yang-Tse Cheng, and Ambrose Seo) would like to thank Tien Duong, Tricia Smith, Adrienne Riggi, and Coriana H. Fitz at DoE for program management, and all the students and postdocs involved in this project Yifan Zhao (General Motors), Juny Cho, Min Feng (Brown University), and Jacob Hempel (University of Kentucky).

XVI.11 Multidimensional Diagnostics of the Interface Evolutions in Solid-State Lithium Batteries (University of Houston)

Yan Yao, Principal Investigator

University of Houston
4800 Calhoun Rd
Houston, TX 77004
E-mail: yyao4@uh.edu

Tien Duong, DOE Technology Development Manager

U.S. Department of Energy
E-mail: Tien.Duong@ee.doe.gov

Start Date: October 1, 2019
Project Funding: \$1,2500,000

End Date: March 31, 2023
DOE share: \$1,000,000

Non-DOE share: \$250,000

Project Introduction

The failure of a solid-state Li battery may be briefly attributed to two main causes: interfacial resistance increase and Li dendrites growth. The former may be further attributed to electrolyte decomposition and interfacial void formation (*i.e.* loss of physical contact). Electrolyte decomposition happens in two ways: oxidative decomposition at the cathode active material–electrolyte interface and reductive decomposition at the Li (including dendrites)–electrolyte interface. Void formation occurs at the same two interfaces. The complex origins of battery failure call for multidimensional diagnostics utilizing not one but a combination of tools that can quantify the formed void and dendrites, identify the chemical and mechanical natures of the Li dendrites and electrolyte decomposition products, and *in situ* monitor the evolution of the processes. The tools also need to cover a sufficiently large scale (up to $\sim 100\ \mu\text{m}$), have spatial resolutions of a few nanometers, and be sensitive enough to detect subtle changes in chemical and mechanical properties. These considerations lead us to a toolset of FIB-SEM tomography, ToF-SIMS, and nanoindentation (inside SEM chamber, *i.e.* in-SEM nanoindentation) and atomic force microscopy (AFM; inside SIMS chamber, *e.g.* in-SIMS AFM)-based stiffness mapping for structural, chemical, and mechanical characterizations, respectively. We will acquire detailed information of interfaces and dendrites evolutions including but not limited to (1) real-time visualization of Li dendrites growth within the whole thickness of electrolyte layer, (2) chemical composition, mechanical property, and evolution of electrolyte decomposition products, including intermediate and metastable ones, at both cathode and anode interfaces, (3) potential correlation of the induction and propagation of Li dendrites with electrolyte decomposition, and, (4) quantitative correlation between electrolyte decomposition, void formation, and cell performance. These in-depth understandings will allow us to effectively predict and optimize the physical and chemical changes of components within solid-state Li batteries during charge and discharge.

Objectives

The project objective is to develop a platform in combination of FIB-SEM tomography, ToF-SIMS, and in-SEM nanoindentation-based stiffness mapping for structural, chemical, and mechanical characterizations in solid-state Li batteries. Assessment of the influence of cell design and testing conditions (external pressure, current density, temperature) on the evolutions of interfaces will be performed.

Approach

Space- and time-resolved structural, chemical, and mechanical characterizations of the cathode–electrolyte and anode–electrolyte interfaces will be performed on all-solid-state Li batteries using FIB-SEM, ToF-SIMS, in-SEM nanoindentation. Tasks include (1) development of solid-state cell thin stacks and test-cell configurations that are suitable for in-situ characterizations, (2) quantitative characterization and in-situ tracking of interfacial voids formation within composite cathode and electrolyte layer; (3) identification and in-situ tracking of the

chemical composition, spatial distribution, and mechanical properties of electrolyte decomposition products at the Li- and cathode-electrolyte interfaces; (4) visualization, chemo-mechanical properties detection, and in-situ tracking of Li dendrites grown within solid electrolyte layer.

Results

The project objective is to develop a platform in combination of structural, chemical, and mechanical characterizations in solid-state Li batteries. Our previous operando SEM analyses successfully showcased the morphological evolution of solid-state battery interface during lithiation and delithiation. This year, we further extended our characterization capability to acquire chemical information at the electrolyte–electrode interface during cell operation, as well as to link chemical and mechanical properties together.

Time-of-Flight Secondary Ion Mass Spectrometry (ToF-SIMS) analyses were conducted to understand the interfacial reactions between lithium (Li) anode and Li_3PS_4 glass-ceramic (LPS) electrolyte. As shown in Figure XVI.11.1, a “pristine LPS” sample was prepared by stacking Li foil onto an LPS pellet, heating at 60°C for 1 h, then carefully peeling off the Li foil. In comparison, a “plated LPS” sample was obtained after charging a Li|LPS|Li symmetric cell at 0.28 mA cm^{-2} for 10 h and then peeling off the Li foil at the negative side. ToF-SIMS measurements were performed using a ToF-SIMS NCS (ION-TOF GmbH), the samples were transferred from the glove box using an air-free transfer vessel. Depth profile analysis was conducted by Cs^+ sputtering to acquire spatial–chemical information across the interface between Li and LPS for both samples.

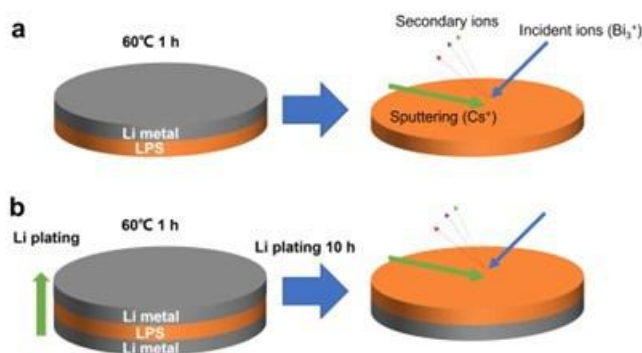


Figure XVI.11.1 Experimental setup of ToF-SIMS analysis. (a) Schematic illustration of the preparation of pristine LPS, (b) schematic illustration of the preparation of plated LPS.

The mass spectra of pristine LPS and plated LPS were collected to identify the chemical evolution of the LPS electrolyte during Li plating. As shown in the high-resolution spectra measured in positive polarization mode (Figure XVI.11.2a-c), obvious peak intensity increases occurred at m/z of ~ 37.04 (Li_3O^+) and ~ 184.93 (CsLi_3P^+). The Li_3O^+ peak can be ascribed to the plated Li metal near the surface of the sample pellet. Formation of CsLi_3P^+ fragment is due to the combination of Cs^+ and Li_3P fragments during Cs^+ sputtering, representing the formation of reduced electrolyte product Li_3P . The PS^+ fragment represents the LPS electrolyte, and the slight decrease of the PS^+ intensity in plated LPS indicated the decomposition of LPS at the interface. The decomposition product of LPS can also be observed in the negative polarization mode shown in Figure XVI.11.2f. The Li_2PS_4^- peak ascribed to LPS shows a dramatic decrease in plated LPS. Similarly, the increase of LiO^- peak in Figure XVI.11.2d further proves the existence of plated Li metal at the interface. The LiS^- peak, supposedly representing another reduction product Li_2S was also observed in Figure XVI.11.2e.

To further understand the distribution of plated Li metal, LPS, and interfacial reduction products across the interface on the plated LPS, the ToF-SIMS spectra were collected during prolonged Cs^+ sputtering. The depth profiles of various secondary ions are shown in Figure XVI.11.3. For pristine LPS (Figure XVI.11.3a), slight decrease in the intensity of Li_3O^+ and CsLi_3P^+ peaks was observed at the very beginning of the Cs^+ sputtering, which may imply the minor reactions happened between Li and LPS during their contact at 60°C . The intensity of the peaks became relatively stable once the Cs^+ sputtered away the surface layer.

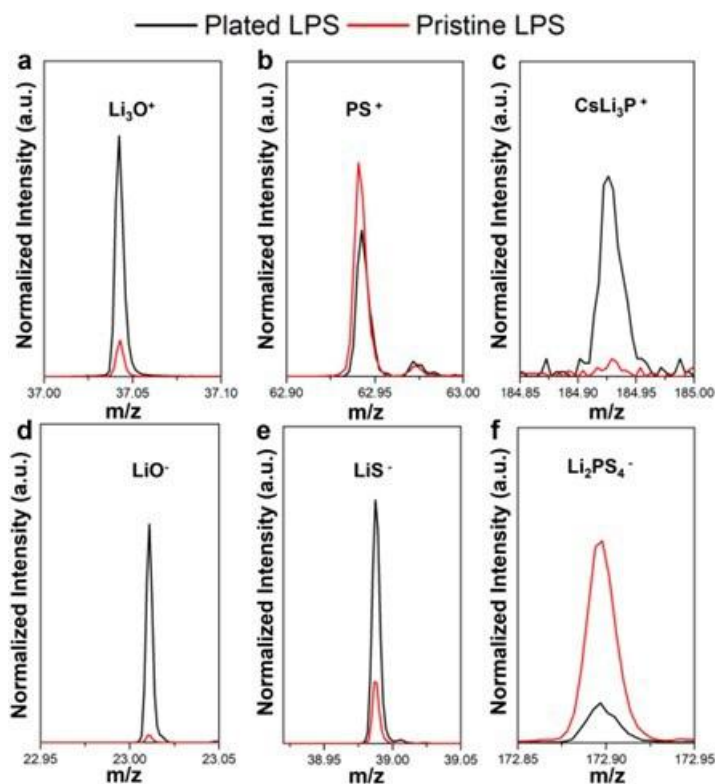


Figure XVI.11.2 ToF-SIMS analysis of plated and pristine LPS surface. (a-c) Mass spectra of pristine LPS and plated LPS in positive polarization mode. (d-f) The mass spectra of pristine LPS and plated LPS samples in negative polarization mode.

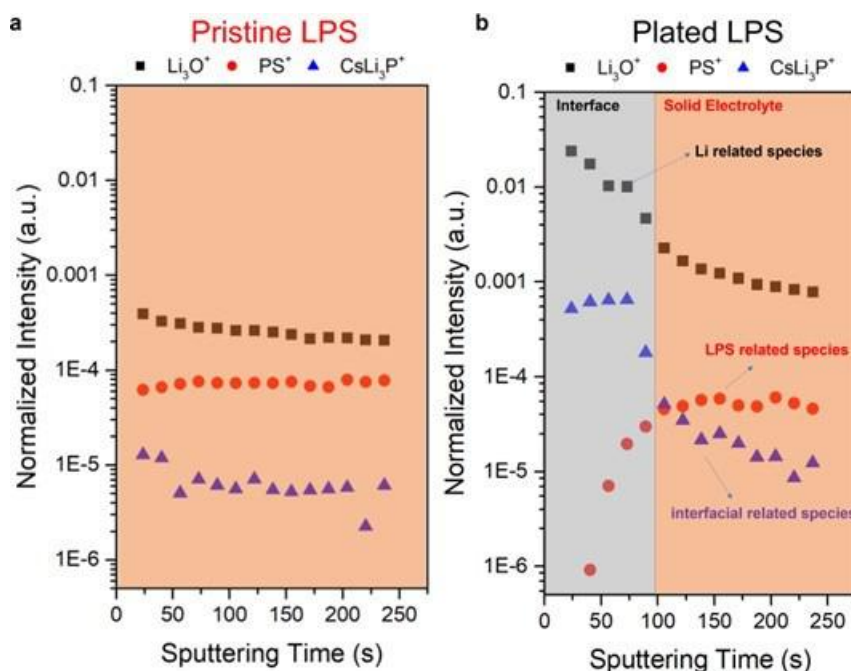


Figure XVI.11.3 Depth profile of Li_3O^+ , PS^+ and CsLi_3P^+ fragments in (a) pristine LPS and (b) plated LPS.

For the plated LPS, variations of Li_3O^+ , PS^+ , and CsLi_3P^+ can be observed across the interfacial layer shown in Figure XVI.11.3b. The much higher Li_3O^+ intensity in this sample compared to that in Figure XVI.11.3a indicated the existence of plated Li metal at the surface. The fragment of CsLi_3P^+ in Figure XVI.11.3b

remained stable throughout the interfacial layer and dropped significantly into the LPS phase. In contrast, LPS-related species were negligible at the surface of the interfacial layer but rapidly increased to a similar level of pristine LPS. The depth profile data demonstrated the self-passivation reaction between Li anode and LPS electrolyte during Li plating. We are further characterizing and monitoring the evolution of interfacial layer to better understand the extent of interfacial reactions, their impact on interfacial resistance and electrode performance.

To investigate the chemical information at the interface, a customized-built time-of-flight secondary ion mass spectrometry (ToF-SIMS) stage was designed for in situ biasing of the specimen inside a ToF-SIMS (Figure XVI.11.4). The in situ biasing stage allows electrochemical biasing and ToF-SIMS imaging at the same time. For conducting operando ToF-SIMS diagnosis, a solid cell with the structure of NMC|Li₆PS₅Cl|Ag-C was fabricated and polished with an Ar-ion polisher. (Figure XVI.11.5, left) The cell was mounted vertically on the stage and protected during the sample transfer from a glovebox to the ToF-SIMS by employing an air-free transfer vessel. A 100 × 100 μm² area at the interface between the electrolyte and the interlayer was chosen for the operando characterization.

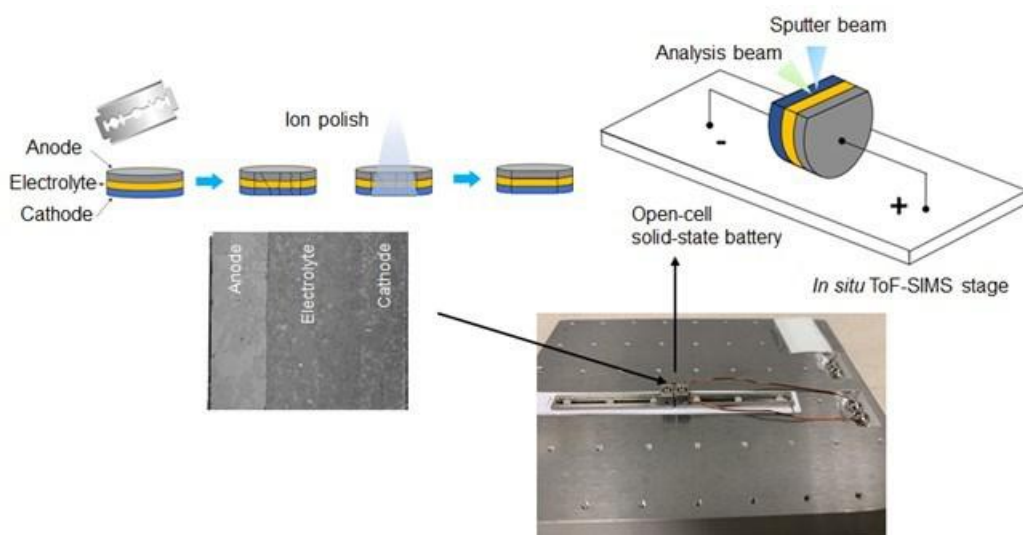


Figure XVI.11.4 Schematic illustration of an in situ ToF-SIMS stage and open-cell setup on the stage.

The ToF-SIMS mapping of the cell during a 3-hour charging is shown in Figure XVI.11.5. Before charging (0 min), there is a clear distinction between the solid electrolyte layer and the interlayer, characterized by Li⁺ and Ag⁺ signals, respectively. As charging proceeds, Li⁺ signal gradually extends into the interlayer, indicating lithiation and/or lithium growth. The moving front of Ag⁺ signal retreats as Li⁺ progresses, which may be interpreted either as a decrease of Ag element in the lithiated region or Ag⁺ signal being overwhelmed by the more intensive Li⁺ signal.

The signal intensity of both Ag⁺ and Li⁺ is plotted against distance and compared in Figure XVI.11.6. Both signals show gradient distribution in the lithiation front, indicating a gradual, possibly multi-step lithiation process. These intensity–distance profiles can be fed into modeling of diffusion and reveal the lithiation and lithium growth mechanism in the interlayer. Further efforts on distinguishing different Ag and Li species, from which details on the chemical status of the lithiated species can be extracted, are ongoing. With an improved understanding of the working mechanism of the interlayer, further engineering can be done for improvement.

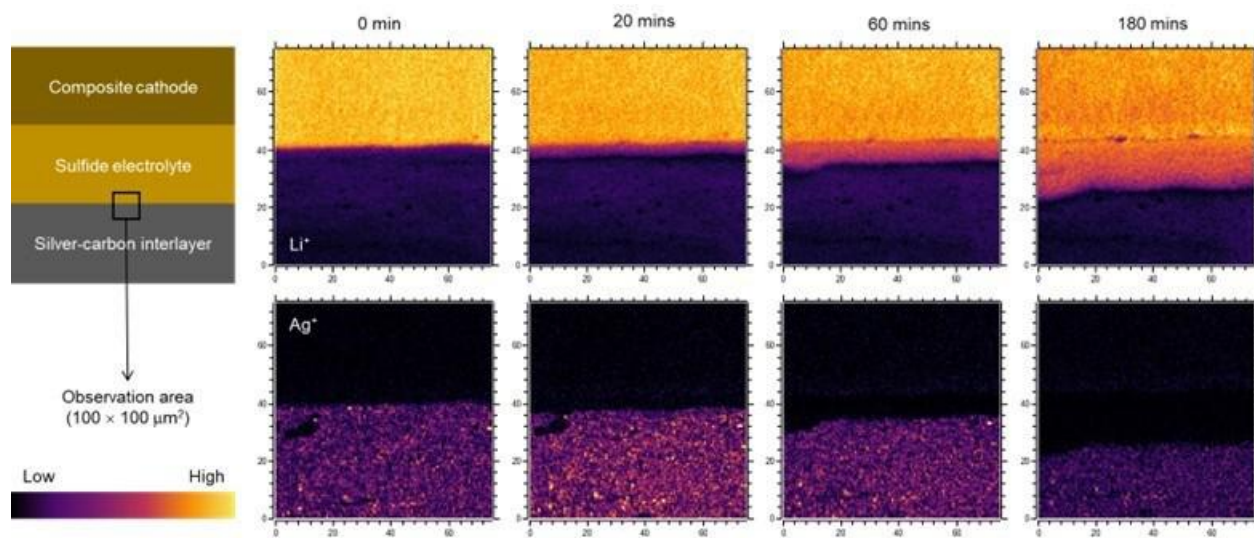


Figure XVI.11.5 Operando ToF-SIMS mapping of Li^+ and Ag^+ at the electrolyte–silver-carbon interface. The x- and y-axis represent the spatial coordinates in μm . The brightness in color represents the ion count. (Left column) Structure of the solid-state lithium metal cell used in the observation; the observation area is marked with a black square. (Top row) Mapping of Li^+ ; the strong Li^+ signal in the top region ($40 < y < 75$) originates from the solid electrolyte. (Bottom row) Mapping of Ag^+ ; Ag^+ signal is only present within the silver-carbon layer ($y < 40$).

The operando chemical monitoring with spatial resolution can be readily applied to other interfaces and bulk phases in the same cell. Application of the method to material evolution in the cathode, anode, and related interfaces will shed light on a series of questions of interest, including passivation, material failure, and dendrite growth. The method is complementary to our previously reported operando methods concerning microstructural and mechanical evolution. Our air-free transfer vessels allow spatially aligned cross-reference between these methods.

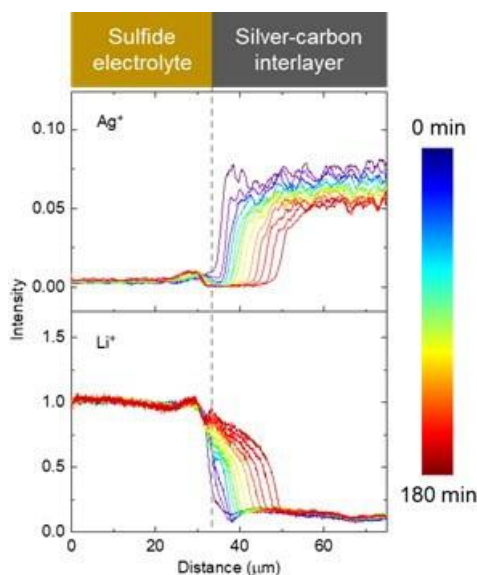


Figure XVI.11.6 Evolution of the spatial distribution of Ag^+ and Li^+ during charging. Curves processed from ToF-SIMS spectra such as those displayed in adjacent figure.

In solid-state batteries, mechanical properties of cell components are often as crucial as their chemical information. Understanding the chemo-mechanical behaviors of electrodes is critical to the rational

engineering of solid-state battery systems with robust solid-solid contact during operation. Here, pyrene-4,5,9,10-tetraone (PTO) / $\text{Li}_6\text{PS}_5\text{Cl}$ composite cathode was chosen as a model materials system to demonstrate our capability on probing the chemo-mechanical behavior of solid-state batteries. The chemical and mechanical characterizations of composite electrode were performed by combining Time-of-Flight Secondary-Ion Mass Spectroscopy (ToF-SIMS) with in-SEM nanoindenter system. First, PTO/ $\text{Li}_6\text{PS}_5\text{Cl}$ composite cathode sample was prepared by Ar-ion polishing to achieve a clean and smooth cross-section for characterization. The cross-section image of the composite cathode is presented in Figure XVI.11.7a, where the domains with low and high contrast correspond to the PTO and $\text{Li}_6\text{PS}_5\text{Cl}$ phases, respectively. ToF-SIMS analysis was performed to acquire the composition and spatial distribution of composite cathode. First, the mass spectra of the pristine PTO, the pristine $\text{Li}_6\text{PS}_5\text{Cl}$ and the composite cathode have been compared to identify the chemical characteristic ions of PTO and $\text{Li}_6\text{PS}_5\text{Cl}$ species, as shown in Figure XVI.11.7b. Li_xPTO fragments (LiC_2^- at m/z of 31.0166 and LiC_4^- at m/z of 55.0166) can be clearly localized in the composite cathode sample, which has confirmed the lithiation of PTO species. Smaller peaks at m/z of 31.0166 and 55.0166 in pristine $\text{Li}_6\text{PS}_5\text{Cl}$ and pristine PTO samples may originate from contaminations during sample preparation. Additionally, the peak intensity ratio between PO_2^- and PS^- was dramatically increased in the composite cathode as compared to the pristine $\text{Li}_6\text{PS}_5\text{Cl}$, which implied the occurrence of the oxidation of the $\text{Li}_6\text{PS}_5\text{Cl}$ electrolyte in the composite cathode. Similar intensity changes in the peak ratio were also observed between PO_3^- and PSO^- fragments. PO_x^- (PO_2^- , PO_3^-) fragments were also observed in pristine $\text{Li}_6\text{PS}_5\text{Cl}$ sample, which can be explained by the high reactivity of $\text{Li}_6\text{PS}_5\text{Cl}$ with trace amount (ppm) of oxygen and water, leading to the slight oxidation of the electrolyte during storage in the glovebox or transportation through the transfer vessel. ToF-SIMS secondary ion (SI) images were then used to confirm the chemical evolution in the composite cathode. To spatially identify the chemical changes in the composite cathode, ion mapping of the composite cathodes from the same region was also performed, as shown in Figure XVI.11.7a. Figure XVI.11.7c shows the 2D-distribution of fragments corresponding to the $\text{Li}_6\text{PS}_5\text{Cl}$ (red, Cl^-), PTO (blue, C_2H^-), interphase component (green, PO_x^-) and Li_xPTO (gold, Li_2OH^+). The Li_2OH^+ species was used to represent the distribution of Li_xPTO due to its strong signal in the image mode. The oxidation fragments (PO_x^-) from $\text{Li}_6\text{PS}_5\text{Cl}$ can be observed at the interface, which indicates the occurrence of chemical reactions at the PTO and $\text{Li}_6\text{PS}_5\text{Cl}$ electrolyte interface. Meanwhile, the Li_xPTO -related fragments can also be found inside the PTO domains. We believe these fragments originated from the spontaneous redox reactions between PTO and $\text{Li}_6\text{PS}_5\text{Cl}$. In summary, the ToF-SIMS analysis has allowed highlighting the chemical evolution of PTO electrode and $\text{Li}_6\text{PS}_5\text{Cl}$ electrolyte with a sufficient spatial resolution.

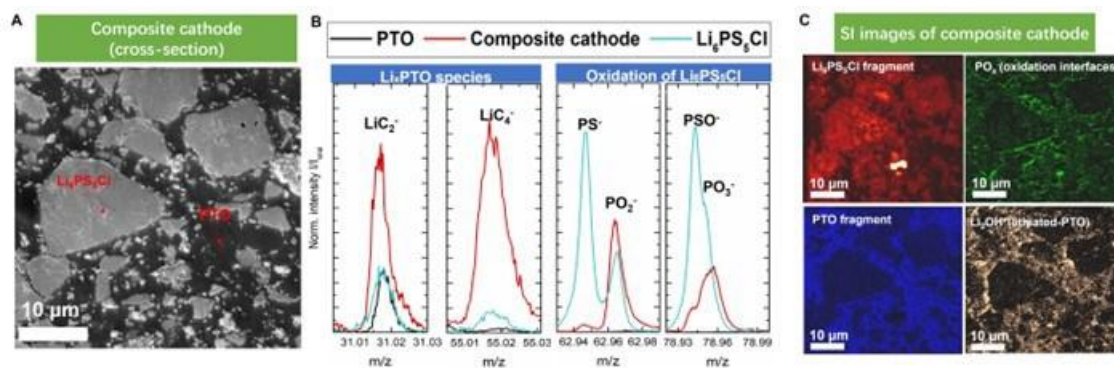


Figure XVI.11.7 Spatially resolved chemical analysis of composite cathode. (a) Cross-section SEM image of the composite cathode pellet. (b) Zoomed-in mass spectra of pristine PTO, $\text{Li}_6\text{PS}_5\text{Cl}$ electrolyte and composite cathode (c) Secondary ion images of $\text{Li}_6\text{PS}_5\text{Cl}$ fragments, PO_x fragments, PTO fragments, and Li_2OH^+ fragments in composite cathode, respectively.

Effects of such important chemical evolution on mechanical properties of composite cathodes were seldom reported, mainly due to the limited spatial resolution of nanoindentation tests under an optical microscope. To overcome this limitation, in-SEM nanoindentation tests were performed on the composite cathodes and mechanical properties of different phases were measured with much higher spatial resolutions, as shown in Figure XVI.11.8a. Mechanical properties of pristine PTO and pristine $\text{Li}_6\text{PS}_5\text{Cl}$ were also tested as references.

More details about in-SEM nanoindentation measurements on different phases are demonstrated in supplemental movies. Typical load-displacement curves of PTO and $\text{Li}_6\text{PS}_5\text{Cl}$ in the composite cathode are shown in Figure XVI.11.8b and c, respectively. The average Young's modulus (using Oliver-Pharr method^[1]) of PTO and $\text{Li}_6\text{PS}_5\text{Cl}$ in the composite cathode were measured as 15.0 ± 2.5 GPa and 30.3 ± 4.5 GPa, respectively. The average hardness of PTO and $\text{Li}_6\text{PS}_5\text{Cl}$ in the composite cathode were measured as 0.92 ± 0.27 GPa and 1.56 ± 0.27 GPa. More deformation should have occurred in the softer PTO phase when preparing the composite cathode by mortar mixing and uniaxial compaction, resulting in $\text{Li}_6\text{PS}_5\text{Cl}$ fragments surrounded by the PTO domains. The Young's modulus and hardness of pristine PTO were measured as 5.6 ± 0.7 GPa and 0.28 ± 0.05 GPa, respectively, which is consistent with the reported values. The Young's modulus and hardness of pristine $\text{Li}_6\text{PS}_5\text{Cl}$ electrolyte were measured as 25.7 ± 4.0 GPa and 1.19 ± 0.29 GPa, respectively, which is in the same order as the theoretical value reported by Deng et al.^[2] The average Young's modulus and hardness of pristine PTO, pristine $\text{Li}_6\text{PS}_5\text{Cl}$, PTO in composite cathode and $\text{Li}_6\text{PS}_5\text{Cl}$ in composite cathode are shown in Figure XVI.11.8d. The Young's modulus and hardness value of PTO in composite cathode dramatically increased compared to the pristine PTO, while the $\text{Li}_6\text{PS}_5\text{Cl}$ didn't. We believe that the dramatic modulus and hardness increase in the PTO in composite cathode should be originated from the partial lithiation of PTO in the composite cathode during the sample preparation process. As mentioned in the earlier ToF-SIMS analysis, chemical reactions did occur in the composite cathode. In this regard, the average Young's modulus and hardness data of different phases in the composite cathodes are insufficient to reflect the actual composition variations in such cathodes.

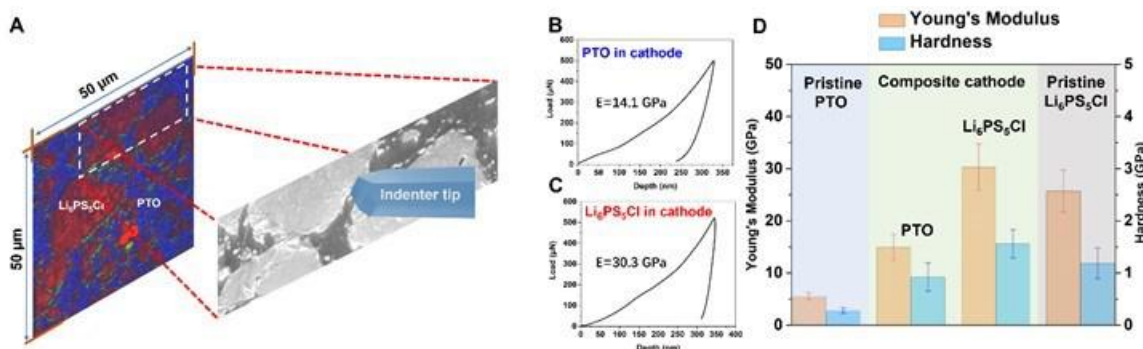


Figure XVI.11.8 Spatially resolved mechanical analysis of composite cathode. (a) Schematic illustration of in-SEM nanoindentation test on the identical region of interests for ToF-SIMS characterizations. (b and c) load-displacement curves of PTO and $\text{Li}_6\text{PS}_5\text{Cl}$ in composite cathode, respectively. (d) comparison of mechanical properties of pristine PTO, pristine $\text{Li}_6\text{PS}_5\text{Cl}$, PTO in composite cathode and $\text{Li}_6\text{PS}_5\text{Cl}$ in composite cathode.

Figure XVI.11.9a and b show Young's modulus and hardness mapping of the PTO phase at a specific location of interest. Figure XVI.11.9c shows the lithium distribution in the same area by ToF-SIMS analysis. The secondary ion image of Li^+ fragment in PTO domains confirmed the lithiation of PTO even before the electrochemical operation of the cathode. It is important to note that the normalized lithium intensity here does not directly reflect the quantitative lithium concentration in the material. Still, the intensity variation provides information about the distribution of the Li^+ concentration difference in the PTO domains. Figure XVI.11.9d shows Young's modulus and hardness of the pristine PTO and the Li_xPTO with different Li concentrations. All Li_xPTO phases are stronger than the pristine PTO, and the Li_xPTO with higher Li concentration shows higher Young's modulus and hardness. The above trend effectively illustrates the chemical reaction affected mechanical properties in the PTO domains and potentially provides a new dimension for understanding the chemo-mechanical behaviors in all-solid-state batteries.

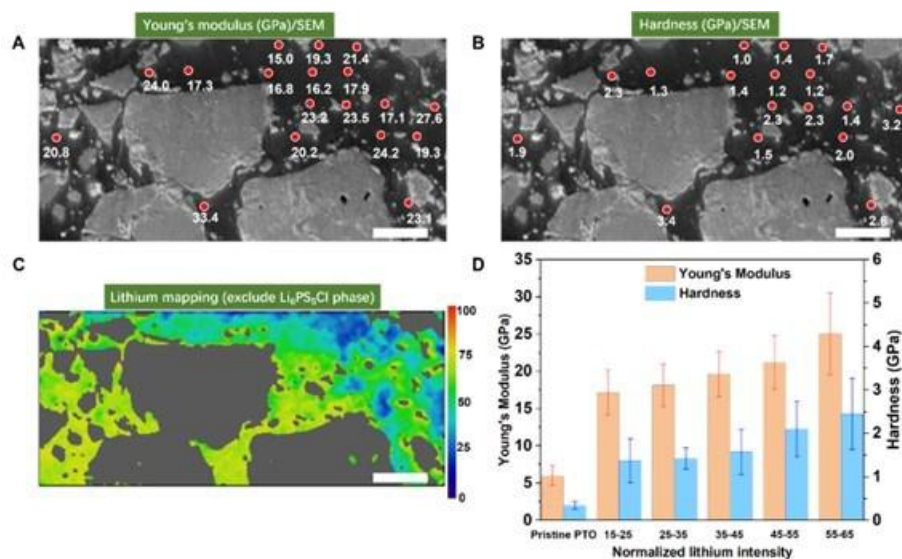


Figure XVI.11.9 Correlating chemical and mechanical properties. (a) Young's modulus mapping results in the PTO domains of the composite cathode, scale bar 5 μm . (b) Hardness mapping results in the same PTO domains of the composite cathode, scale bar 5 μm . (c) Lithium distribution mapping in PTO domains overlapping with the indented area, the intensity is normalized by the total ion counts from ToF-SIMS analysis, scale bar 5 μm . (d) Mechanical properties of PTO domains with different lithium concentrations.

Conclusions

We have developed an operando characterization platform for space- and time-resolved structural, chemical, and mechanical characterizations of the cathode–electrolyte and anode–electrolyte interfaces of all-solid-state Li batteries. The electrolyte decomposition products are identified under different cycling conditions. An operando ToF-SIMS setup is developed to serve as a platform for investigating the evolution of structural and chemical properties with a high spatial and chemical resolution during cell operation. The platform also enables us to spatially correlate the chemical and mechanical properties of different components within a composite electrode. Probing chemo-mechanical properties and their evolution during cycling allows us to understand cell kinetics and rationally design solid-state batteries to achieve improved performance.

References

1. Oliver, Warren Carl, and George Mathews Pharr. "An improved technique for determining hardness and elastic modulus using load and displacement sensing indentation experiments." *Journal of Materials Research* 7, 1992: 1564.
2. Deng, Zhi, Zhenbin Wang, Iek-Heng Chu, Jian Luo, and Shyue Ping Ong. "Elastic properties of alkali superionic conductor electrolytes from first principles calculations." *Journal of the Electrochemical Society* 163, 2015: A67.

Acknowledgements

We thank our UH team members Prof. Zheng Fan and Prof. Yanliang Liang and our collaborators Prof. Jun Lou and Prof. Hua Guo at Rice University. We appreciate the support from Tien Duong, DOE Technology Development Manager, and Ms. Colleen Butcher at NETL for project management.

XVI.12 First-Principles Modeling of Cluster-Based Solid Electrolytes (Virginia Commonwealth University)

Puru Jena, Principal Investigator

Virginia Commonwealth University
Department of Physics
701 W Grace St
Richmond, VA 23284
E-mail: pjena@vcu.edu

Hong Fang, Co-Principal Investigator

Virginia Commonwealth University
Department of Physics
701 W Grace St
Richmond, VA 23284
E-mail: hfangtom@gmail.com

Tien Duong, DOE Technology Development Manager

U.S. Department of Energy
E-mail: Tien.Duong@ee.doe.gov

Start Date: October 1, 2019

End Date: December 31, 2022

Project Funding: \$341,735

DOE share: \$273,409

Non-DOE share: \$68,326

Project Introduction

The current modeling schemes to develop advanced solid electrolytes are focusing on materials in which the building blocks are individual atoms. Our theoretical approach is a paradigm shift in solid electrolyte design. Instead of atoms, we focus on clusters as the building blocks and model these solid electrolytes and their interfaces with electrodes, especially Li-metal anode, for their successful implementation in solid-state batteries. The advantage of using the cluster-ions to replace elemental-ions is that the size, composition, and shape of the former can be tailored to achieve higher superionic conductivity, electrochemical stability and charge transfer across solid-solid interfaces than conventional materials. Specifically, our proposed project includes: (1) Developing cluster-based solid electrolytes, where the halogen components are replaced by cluster-ions that mimic the chemistry of halogens but are characterized by additional degrees of freedom, including the size, shape, and composition. (2) Providing a fundamental understanding of the ionic conduction mechanism in the newly-developed cluster-based solid electrolytes; (3) Modeling the interfacial properties (*i.e.*, structural, chemical and transport) between the cluster-based solid electrolytes and electrodes at the atomic level. For the cluster-based solid electrolytes incompatible with the Li-metal anode or cathode materials, potential candidates for interfacial coatings will be identified and studied. (4) Providing a theoretical framework towards optimizing critical parameters, such as current density, kinetic and mechanical stability, that will guide experimentalists to attain desired electrolyte-electrode interface for the developed cluster-based solid electrolytes.

Objectives

The objective of the project is to use cluster-ions, which are stable atomic clusters that mimic the chemistry of individual atoms, as the building blocks of new solid electrolytes (SEs) for Li-ion batteries and the corresponding battery system. The advantages of using cluster-ions to replace elemental ions is that the size, shape, and composition of the former can be tailored to achieve higher superionic conductivity, electrochemical stability, and charge transfer across the solid-solid interfaces than the conventional materials. More specifically, the goal is to develop superior SEs based on cluster-ions and to model these SEs and their interfaces with electrodes, especially with the Li-metal anode, for successful integration into high performance

SSBs for EVs. The team will model and screen cluster-based SEs that, compared to conventional SEs, have low activation energies, practical room-temperature ionic conductivities, wide electrochemical stability windows, and desired mechanical properties that, for example, can inhibit the Li-metal anode dendrite growth. They will provide a fundamental understanding of the ionic conduction mechanism in the newly developed, cluster-based SEs and identify means to further improve property metrics via chemical and defect engineering. The team will model the interfacial properties, such as the structural, chemical, electrochemical, and ion/charge transfer properties, between the cluster-based SEs and electrodes at the atomic level, as well as find the interfacial coating materials with desired properties. Based on accumulated data from modeling, they will establish links between the basic parameters of the cluster-ions and the bulk/interface properties, which can directly guide experiments. Meanwhile, the team will work closely with experimentalists in the BMR Program to complement the project's theoretical efforts and to guide them in focused development of the predicted cluster-based SEs and the interfaces.

Approach

1. *Developing new cluster-based solid electrolyte materials using selected cluster-ions from the established database of clusters.*

The possible crystal structures of the newly developed materials will be determined using structure prediction techniques, such as the particle swarm optimization and the evolutionary algorithm [1-2]. The most stable phases that contain the cluster-ion from the search will be considered as the initial structures, subject to further investigation. Each cluster-based solid electrolyte material with the determined crystal structure will be fully optimized (for both the ion positions and lattice parameters) to its energy minimum using DFT calculations [3-4]. The lattice dynamic stability of the structure will then be tested by phonon calculations based on the optimized structure; absence of imaginary frequency would define a stable structure. The formation energy of the lattice-dynamically stable cluster-based solid electrolyte material will be calculated. Its thermodynamics stability will be investigated by calculating the pair correlation function and the position correlation function using the structural data from MD simulations at different temperatures. For each cluster-based solid electrolyte that is thermally stable, possible defects involving Li⁺ in the material will be studied by calculating their formation and binding energies. Next, for each cluster-ion based solid electrolyte, a supercell system with the relevant defect will be subjected to MD simulations with constant volume at different temperatures. MSD of the Li-ions will be calculated using our own programs. The diffusion coefficients and the ionic conductivity at different temperatures will be calculated from the MSD using the Nernst-Einstein relation. The room temperature ionic conductivity and the activation energy of the material will be obtained by fitting to the Arrhenius relationship. The relevant electronic properties, including the bandgap, the band edges and the electronic conductivity will be calculated using DFT. The hybrid functional (e.g. HSE [5]) or meta-GGA (e.g. mBJ [6]) will be applied. All the obtained results from the above process will be collected into a database.

2. *Modeling the ionic conduction mechanism in the cluster-based solid electrolyte materials.*

To study the ionic conduction mechanism, we first investigate the channel size inside the solid electrolyte for Li⁺ migration, created by different cluster-ions. Next, the migration routes of Li⁺ in the presence of the chosen defect will be studied. Given the non-spherical nature of the cluster-ion, there are a number of inequivalent migration routes. The energy barrier for each of these will be calculated using the NEB method. The effect of the changing orientation of the cluster-ions on the ionic conductivity of the material will be studied by building a Boltzmann model for different orientational configurations and selective dynamic simulations. The pattern of Li⁺ motions inside the cluster-based solid electrolytes will be investigated using statistical analysis, such as computing the distinct van Hove time correlation function in the modeled system. From the above studies, the dependence of the solid electrolyte performance on the size, shape (symmetry), internal charge distribution, electron affinity, as well as the dynamics of the cluster-ion will be established.

3. *Modeling and optimizing the chemical mixing and doping in the cluster-based solid electrolyte materials.*

Different phases with mixed halides and clusters will be created via chemical mixing. Their structures with different ratio will be fully optimized using DFT energy calculations. Each optimized system will then be investigated using DFT calculations and MD simulations to reveal its formation energy, ionic conduction properties, electrochemical properties, and mechanical properties against the original phase. The ratio that can enable the highest ionic conductivity while maintaining merits in other aspects will be recorded in the database.

4. *Modeling and optimizing the defect formation and concentration.*

Models will be built for the cation-doped cluster-based solid electrolyte systems with supercells that contain different concentrations of the Li-vacancy defects. The structure of these systems will first be energetically optimized using DFT calculations. Then, the structures will be studied using MD simulations at fixed temperature. The ionic conduction properties of the resulting structures will be investigated. The defect concentration that can entail the highest ionic conductivity in the cluster-based solid electrolyte will be revealed.

5. *Modeling the electrolyte-electrode interfaces.*

Given that many of the cluster-based solid electrolytes material are metastable, the possible equilibrium phases at the interfaces when the solid electrolyte is in contact with the electrode will be first identified by building lithium grand potential diagrams at different battery voltages (modeled by the lithium chemical potential) using the crystal data from the material database, e.g. the Materials Project [7]. Next, DFT calculations and MD simulations will be conducted to study the stability, electronic and ionic conduction properties of the obtained equilibrium phase at the interface. The interface between the cluster-based solid electrolyte and the equilibrium phase, or between the equilibrium phase and the electrode will be modeled using stacked slabs of the active materials. The local bonding reconstruction and charge transfer, as well as possible amorphization of the interface will then be studied using MD simulations. If the interface cannot form a Li-conducting layer, or will destroy the structure of the solid electrolyte through reaction, potential coating materials that are chemically/electrochemically stable, Li-conducting and having little lattice mismatch with the active materials, will be identified. The structural, electrochemical and transport properties of the coating materials will be studied using DFT calculations and MD simulations.

6. *Modeling and optimizing the interface between the cluster-based solid electrolyte and the identified coating materials.*

Possible alloying phases between the cluster-based solid electrolyte and the coating material will be investigated using the cluster expansion method [8-9]. The alloys that appear on or near the built convex hull will be selected as the stable phases and their relevant properties, e.g., the ionic conductivity, will be studied using DFT calculations and MD simulations. The alloying phase that can entail the highest ionic conductivity will serve as a good candidate for coating. The results regarding the identified coating materials and their possible alloying phases will be included in our database.

7. *Establishing links between the key parameters of the cluster-ion and the bulk and interfacial properties of the cluster-based solid electrolyte materials.*

With the data accumulated in our database, links between the key parameters (such as the size, shape, composition, charge distribution, and electron affinity) of the cluster-ion and the cluster-based solid electrolyte as well as its interfaces can now be drawn by using machine learning techniques. The established links aim to guide experiments in terms of which cluster-ions to choose that can entail high-performance cluster-based solid electrolytes and interfaces with the electrodes, especially with the Li-metal anode. The PI and team at VCU will work in close collaboration and coordination (unfunded) with VTO-BMR (Vehicle Technology Office's Battery Materials Research) Program PIs working at multiple DOE National Laboratories on solid electrolyte modeling and interfaces and specifically with experimental groups working on synthesis and interfacial characterization of Li-based solid electrolytes.

Results

1. Phase analysis for the interfaces between the cluster-based solid electrolyte and electrodes. (Q1, FY 2022; Completed, December 31, 2021):

Phase analysis and reactivity prediction on the interface of anode (Li-metal)-electrolyte and the interface of cathode-electrolyte have been conducted. The intrinsic electrochemical windows of the studied cluster-based solid electrolytes are evaluated. The decomposition phases at the electrode/electrolyte interfaces are identified at different cell voltages. Also identified are the possible chemical reactions at the interfaces and their reaction energies which measure the driving force for the reactions to occur. Commonly used cathode materials as well as coating materials of cathodes are considered. For each studied solid electrolyte, the compatible cathode and coating materials are identified.

It is found that most cluster-based solid electrolytes (CBSEs) exhibit small intrinsic electrochemical windows as the known lithium sulfides. Nearly all the CBSEs exhibit significantly smaller reaction energies than those of the well-known LGPS and lithium argyrodite. The decomposition phases of the CBSEs at the Li-metal side are found to be electronically insulating and lithium conductive with large electrochemical windows. At a high cell voltage on the cathode side, the decomposition phases of the CBSEs are also electronically insulating. These decomposition phases can effectively “shield” the solid electrolytes from further decomposition, leading to large overpotentials that significantly expand their electrochemical windows.

2. Modeling structural properties of the cluster-based solid electrolyte interfaces. (Q2, FY 2022; Completed, March 31, 2022):

Besides the previous interfacial studies using phase diagrams and reactivity prediction under full thermodynamic equilibrium, explicit interface modeling and simulations at finite temperatures are conducted to capture the more realistic kinetic effects of different species at the interface. Interface models between the studied cluster-based solid electrolytes and the Li-metal anode are constructed. Each model is built as a coherent heterointerface which allows both the solid electrolyte and the Li-metal anode superlattices form periodicities along the interfacial plane. In particular, slabs of the solid electrolytes and the Li-metal anode are cleaved according to different Miller indices (hkl). Then, the lattices of each slab-couple are matched according to the epitaxial constraint with the restriction of maximal surface area of 300 \AA^2 , maximal lattice length mismatch of 0.03 \AA and maximal lattice angle mismatch of 0.01 radians. For each as-built interface, there are still a few different configurations with different terminal species at the interface. The initial distances between the electrolyte slab and the anode slab are set to about 60% of the sum of van der Waals radii of the terminal elements in the closest contact. A vacuum padding greater than 12 \AA is also included in each structure to minimize the interactions between the cell images perpendicular to the interface.

For example, Figure XVI.12.1(A) shows the interface model of the CBSE $\text{Li}_6\text{PS}_5(\text{BH}_4)$ and the Li-metal anode as a coherent epitaxial interface with the minimum surface area of 114.67 \AA^2 . The interface exhibits a very low misfit strain (measured by the von Mises strain) of 0.008 . The model contains 12 formula units of the CBSE and 5 atomic layers of the Li-metal. There are three configurations of the interface model with different types of atomic terminal groups at the interface, including H_2 , B and LiS. Based on the optimized (in both the lattice and ionic position) interface model, molecular dynamics simulations are conducted and the resulting interfacial structures are characterized by the evolution of local bonding structure and the interphase along the simulation time. It is found that the major interfacial reaction is the reduction of P in the argyrodite composition, as suggested by the continuing disintegration of the PS_4 units represented by the progressive P-S bond breaking. As shown in Figure XVI.12.1(B), more than 10% P-S bonds are broken within 20 ps. On the other hand, the cluster-ions BH_4^- introduced in the solid electrolyte maintain their completeness throughout the time, per Figure XVI.12.1(B). This is different from the results of the phase diagram based on phases at full thermodynamic equilibrium, where decomposed phases such as LiB and LiH are predicted at the interface based on the premise that the BH_4^- units will disintegrate. While, in practice, the BH_4^- clusters are unlikely to break due to large kinetic barrier originated from the strong B-H covalent bonding. Thus, the instability of the CBSE against Li-metal anode is not due to the introduced cluster-ion that can greatly enhance the low-

temperature ionic conductivity. Rather, the instability is due to the phosphate species already included in the argyrodite system. Note that, compared to the semiconducting LiH and electrically conductive LiB, LiBH_4 is a good insulator and has much better electrochemical stability as well as ionic conductivity. This suggests that the cluster-based solid electrolyte $\text{Li}_6\text{PS}_5(\text{BH}_4)$ should have a much better electrochemical stability against Li-metal anode than that evaluated by only considering the thermodynamic equilibrium phases.

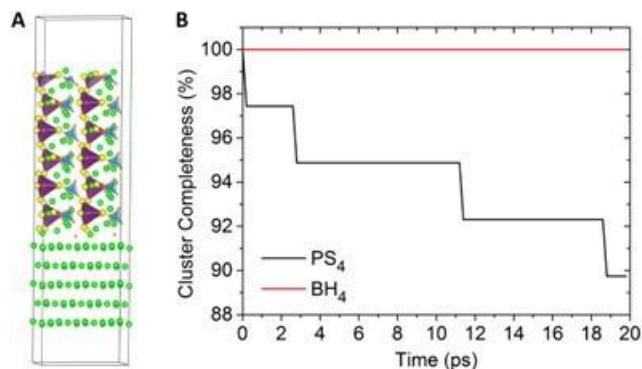


Figure XVI.12.1 (A) Interface model between a CBSE and Li-metal anode. Li atoms are in green, BH₄ units in light blue with H in pink, and PS₄ units in purple with S in yellow. (B) Evolution of P-S and B-H bonds vs. simulation time.

3. Modeling chemical/electrochemical and transport properties of the cluster-based solid electrolyte interfaces. (Q3, FY 2022; Completed, June 30, 2022):

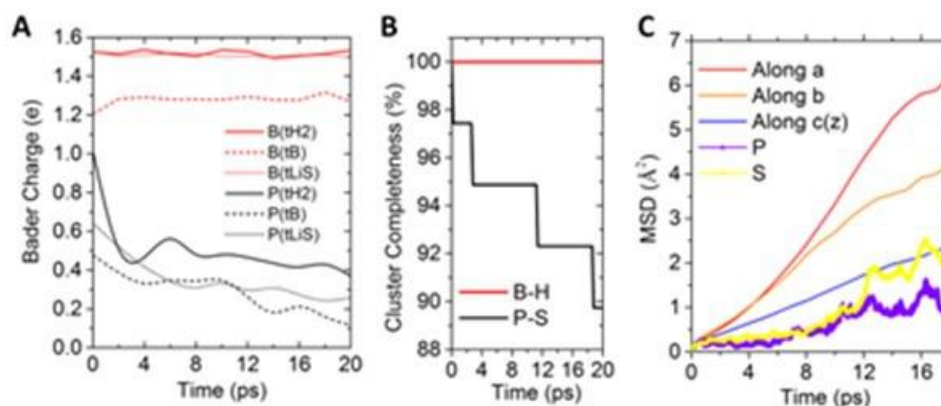


Figure XVI.12.2 Chemical/electrochemical stability and ion transport properties at the $\text{Li}_6\text{PS}_5(\text{BH}_4)\text{-Li}$ interface. (A) The charge transfer at the P and B sites for different terminal (t) groups (H2, B and LiS) at the interface. (B) Bond completeness for the clusters. (C) Calculated mean-square displacement of Li-ions as well as P and S along different directions, with the c-axis the direction perpendicular to the interfacial plane.

Further explicit simulations for the electrolyte-electrode interface to study the chemical/electrochemical stability and the transport property. The studies are based on the models between the studied cluster-based solid electrolytes (CBSEs) and the Li-metal anode as well as selected cathode materials. Each model is a coherent heterointerface which allows both the solid electrolyte and the anode/cathode supercell lattices form periodicities along the interface. Molecular dynamics simulations are conducted at finite temperatures, and the obtained data are analyzed by charge analysis and ionic diffusion. Specifically, for the CBSE-Li interface models, we analyzed the charge transfer for the relevant species based on the models built in our previous studies. For example, Figure XVI.12.2 shows the results for the $\text{Li}_6\text{PS}_5(\text{BH}_4)\text{-Li}$ interface with different terminal atomic groups (including H2, B and LiS). Per Figure XVI.12.2(A), P from the PS_4^{3-} moieties will gain electrons (being reduced), which is accompanied with the continued breaking of the P-S bonds as shown in Figure XVI.12.2(B). This is the dominant contributor for the CBSE-Li interfacial reaction. The functional clusters BH_4^- on the other hand will not react, as indicated by the constant charge state of B and the intactness

of the B-H bonds, per Figure XVI.12.2(A)-(B). Such a phenomenon is independent from the terminal group at the interface, as shown in the figure. The ionic transport study in Figure XVI.12.2(C) shows that the Li-ion diffusion becomes anisotropic in the interface, with the fastest ion-diffusion along the a-axis and the slowest diffusion across the interface. Some P and S ions also start moving across the interface into the surface of Li metal anode due the break-up of the PS_4^{3-} moieties around the interface.

4. Identifying potential coating materials, and modeling electrolyte-coating-electrode interfaces. (Q4, FY 2022; Completed, September 30, 2022):

Coating materials are selected to stabilize the interfaces between the cluster-based solid electrolytes (CBSEs) and the electrodes, in particular, the Li-metal anode. This is done by first using phase diagram and reactivity analyses, and then, using explicit interface modeling at room temperature. The results show that the selected coating materials can stabilize the interfaces under study.

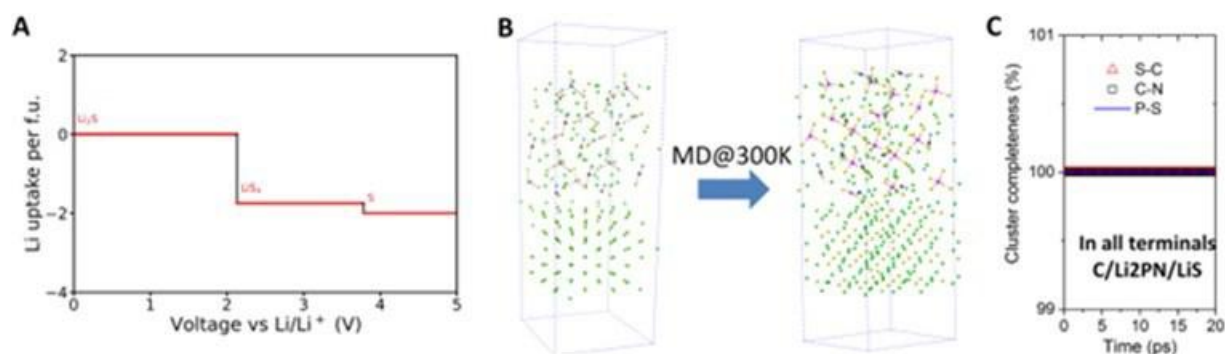


Figure XVI.12.3 (A) Li-uptake plot of Li_2S against the voltage. (B) Modeled structures at the $\text{Li}_6\text{PS}_5(\text{SCN})$ - Li_2S interface before and after the simulation run. (C) The analysis of the cluster completeness of the interfacial models with different terminal groups.

For example, it is found that the CBSEs containing the SCN^- cluster are not stable against Li-metal anode due to the breaking-up of the cluster to S and C-N. We found that Li_2S can serve as a coating layer to stabilize the $\text{Li}_6\text{PS}_5(\text{SCN})$ -Li interface. Phase and reactivity analysis under the thermodynamically equilibrium condition predict that Li_2S is stable against Li metal, as shown in Figure XVI.12.3(A). Explicit simulations based on the $\text{Li}_6\text{PS}_5(\text{SCN})$ - Li_2S interfacial models show that the CBSE is stable against Li_2S without any reaction. Figure XVI.12.2(B)-(C) show that both phases will remain intact at the interface, and the SCN^- anion clusters will not break. The PS_4^{3-} clusters from the argyrodite component are also stabilized with the coating, regardless of the different terminal groups in contact with Li_2S . Further radial distribution function analyses on P-S, C-S, and C-N pairs confirm that crystalline phases and the long-range structures of the active materials at the interface are indeed stable. Li_3PO_4 is identified as another coating material that can stabilize the CBSE-electrode interfaces, according to the phase diagram analysis and reactivity prediction. Figure XVI.12.4 shows the simulation results for the $\text{Li}_6\text{PS}_5(\text{SCN})$ - Li_3PO_4 interface. The CBSE is stable against Li_3PO_4 with no reactions of the anion clusters PS_4^{3-} , PO_4^{3-} , and SCN^- .

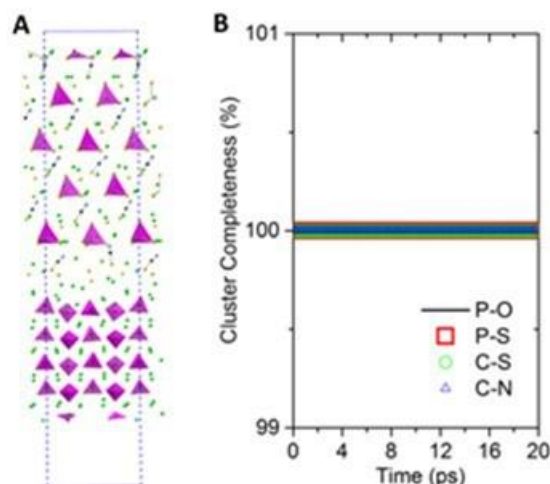


Figure XVI.12.4 (A) The built $\text{Li}_6\text{PS}_5(\text{SCN})\text{-Li}_3\text{PO}_4$ interface model, where PS_4 clusters are in bigger tetrahedra, PO_4 cluster in smaller ones, SCN clusters in yellow-black-cyan, and Li in green. (B) The completeness analyses for PS_4 , PO_4 , and SCN clusters.

Conclusions

The major conclusions obtained from the studies include:

1. The introduced anion clusters, except for SCN^- , will not affect the interfacial stability of the solid electrolytes against Li metal or regular cathode materials. In some cases, these cluster ions can effectively stabilize the interfaces by forming favorable ionically conductive interphases that are self-terminating and electrically insulating.
2. The cluster-based solid electrolytes can be further stabilized at the interfaces using coating materials such as Li_2S and Li_3PO_4 .
3. Methodologically, it is necessary to conduct explicit modeling for the cluster-based solid electrolyte interfaces, besides the phase analysis and reactivity prediction based on the ground-state energies of the active phases.

Key Publications

1. R. L. Sacci, T. H. Bennett, H. Fang, P. Jena, J. Nanda *et al.*, *J. Mater. Chem. A* **10**, 15731, 2022.
2. H. Fang and P. Jena, *Nature Communications* **13**, 2078, 2022.
3. H. Fang, P. Jena, J. Nanda, D. Mitlin *et al.*, *Joule* **6**, 543, 2022.
4. H. Fang, P. Jena, J. Nanda, D. Mitlin *et al.*, *Angew. Chem.* **60**, 26158, 2021.
5. H. Fang, P. Jena, Y. Wu *et al.*, *J. Phys. Chem. Lett.* **12**, 7120, 2021.

References

1. Y. Wang, J. Lv, L. Zhu, Y. Ma, *CALYPSO: A Method for Crystal Structure Prediction*, *Comput. Phys. Commun.* **2012**, 183, 2063.
2. A. R. Oganov, C. W. Glass, *Crystal Structure Prediction Using Evolutionary Algorithms: Principles and Applications*, *J. Chem. Phys.* **2006**, 124, 244704.
3. S. J. Clark, M. D. Segall, C. J. Pickard, P. J. Hasnip, M. J. Probert, K. Refson, M. C. Payne, *First Principles Methods Using CASTEP*, *Zeitschrift fuer Kristallographie*. **2005**, 220, 567.
4. G. Kresse, J. Furthmüller, *Efficiency of Ab Initio Total Energy Calculations for Metals and Semiconductors Using a Plane-Wave Basis Set*, *Int. J. Comput. Mater. Sci. Eng.* **1996**, 6, 15.
5. A. V. Krukau, O. A. Vydrov, A. F. Izmaylov, G. E. Scuseria, *Influence of the Exchange Screening Parameter on the Performance of Screened Hybrid Functionals*, *J. Chem. Phys.* **2006**, 125, 224106.
6. J. Sun, A. Ruzsinszky, J. P. Perdew, *Strongly Constrained and Appropriately Normed Semilocal Density Functional*, *Phys. Rev. Lett.* **2015**, 115, 036402.

7. A. Jain, S. P. Ong, G. Hautier, W. Chen, W.D. Richards, S. Dacek, S. Cholia, D. Gunter, D. Skinner, G. Ceder, K.A. Persson, *The Materials Project: A Materials Genome Approach to Accelerating Materials Innovation*, APL Materials. **2013**, 1, 011002.
8. A. V. D. Walle, G. Ceder, *Automating First-Principles Phase Diagram Calculations*, J. Phase Equilib. **2002**, 23, 348.
9. A. V. D. Walle, M. Asta, G. Ceder, *The Alloy Theoretic Automated Toolkit: A User Guide*, Calphad. **2002**, 26, 539.

XVI.13 Predictive Engineering of Interfaces and Cathodes for High-Performance All Solid-State Lithium-Sulfur Batteries (University of Louisville)

Badri Narayanan, Principal Investigator

University of Louisville
332 Eastern Parkway
Louisville, KY 40292
E-mail: badri.narayanan@louisville.edu

Tien Duong, DOE Technology Development Manager

U.S. Department of Energy
E-mail: Tien.Duong@ee.doe.gov

Start Date: October 1, 2019
Project Funding: \$1,250,000

End Date: December 31, 2022
DOE share: \$1,000,000

Non-DOE share: \$250,000

Project Introduction

All solid lithium-sulfur battery (ASLSB) is a promising next-generation energy storage technology due to its high theoretical capacity (~ 1675 Ah/kg; ~ 5 -6 times higher than state-of-the-art Li-ion batteries), high promised energy density (400 Wh/kg), safety, no polysulfide-shuttling, and natural abundance of sulfur. Sulfide (Li_2S - P_2S_5) solid electrolytes (SSEs) possess high Li-ion conductivity ($\sim 10^{-3}$ S/cm), good elastic stiffness (~ 30 GPa), good stability against Li metal, and low flammability. Such a collection of unique properties make them promising for use in long-lived, safe, high-capacity Li-S batteries for all-electric transportation. Despite this promise, ASLSBs (even using SSEs) remain far from commercialization due to unresolved issues at the electrode-electrolyte interfaces, including (a) poor contact, and high resistance to Li^+ ion transport across the cathode/SSE interface, (b) poor ionic/electronic conduction within the cathode, and (c) dendrite growth at the Li/SSE interface. Most of these daunting challenges arise primarily from a lack of fundamental understanding of electrochemical/chemical and transport processes that occur at electrode/electrolyte interfaces, especially at atomic to mesoscopic scales.

Here, we propose to bridge this knowledge gap and address the interfacial issues by developing highly accurate materials models at atomic-to-mesoscopic length/time scales using data-centric and machine learning methods.. Successful development of these models will significantly advance the current state-of-the-art in fundamental understanding of reaction chemistry, kinetics, charge transfer, and dendrite growth at electrified solid-solid interfaces. Multi-scale simulations based on the newly developed models, alongside our wet-chemistry synthesis and advanced characterization will unravel novel strategies to mitigate interfacial resistance, enable precise control over the composition/morphology of solid electrolyte interphase (SEI) and design cathodes with high sulfur loading. Broadly, fundamental knowledge gained by this work will enable development of high-performance ASLSBs that meet DOE targets of specific energy (350 Wh/kg @C/3), sulfur loading (> 6 mg/cm²), and high cycle life (1000).

Objectives

The primary goal of this project is to leverage data-driven methods and ML strategies to develop accurate multi-physics models for all-solid-state Li-S battery (ASLSB) materials that can capture electrochemical and transport phenomena over atomic-to-mesoscopic length/timescales; these models will be rigorously validated by synthesis and advanced characterization experiments. The team will leverage the predictive power of these models, alongside synthesis/characterization experiments and battery fabrication to address longstanding issues at the electrode/electrolyte interfaces in ASLSBs. The project's proposed technology involves the following: (1) halide-doped solid sulfide electrolytes that can concurrently provide high Li^+ ion conductivity and suppress dendrite growth; (2) novel mesoporous cathode composed of interconnected carbon nano-cages co-infiltrated

with sulfur and sulfide electrolyte, which hold potential to allow high sulfur loading and optimal ion/electron pathways; and (3) functionalization of sulfide electrolyte with ionic liquids to improve physical contact and minimize impedance at the cathode/electrolyte interface.

Approach

The project brings together innovative solutions in multi-scale materials modeling, electrolyte synthesis, fabrication of cathode architecture, and electrolyte functionalization to overcome the issues at electrode-electrolyte interfaces in ASLSBs. The central idea is to employ a data-driven and ML-based approach to develop accurate multi-physics battery models at atomic-to-mesoscale scales. This approach overcomes critical problems with existing model development methods by foregoing need for pre-defined functional forms, introducing deep-learning technique to describe reactivity, and employing optimization methods that do not require human intuition. Multi-scale simulations based on the newly developed models will provide insights into electrochemical phenomena at electrode/electrolyte interfaces.

Results

1. Understanding atomic-scale processes at electrified interfaces with argyrodite electrolytes using reactive molecular dynamics simulations

To significantly advance the fundamental understanding of electrochemical processes in ASLSBs featuring argyrodite electrolytes, we developed a reactive force field (ReaxFF) to accurately describe the interactions between Li, P, and S atoms using our well-established machine learning framework.[1-4] We trained the ReaxFF model against an extensive dataset of energies, forces, charges, structural/elastic properties for a wide range of configurations that amply sample different regions of the potential energy landscape (i.e., stable, unstable and transition states) derived from first principles calculations. Importantly, the training set included several tens of *ab initio* molecular dynamics (AIMD) trajectories that provide a good sampling of (a) Li^+ ion migration pathways through argyrodite electrolytes, and (b) interfacial reactions. Our newly developed ReaxFF can accurately predict (a) lattice parameters (within $\sim 1\%$ of DFT), (b) heat of formation (\sim within 15 meV/atom of DFT), (c) elastic constants (within $\sim 20\%$ of DFT), and (d) lithium-ion conduction in sulfide electrolytes (room temperature conductivity in the same order of magnitude as experiments). Additionally, the predicted interfacial energies for various $\text{Li} \parallel \text{Li}_7\text{PS}_6$, $\text{S}_8 \parallel \text{Li}_7\text{PS}_6$, and $\text{Li}_2\text{S} \parallel \text{Li}_7\text{PS}_6$ are within 0.2 J/m^2 of DFT values; while the atomic charges in the interface are close to Bader charges predicted by DFT calculations.

We employed large-scale reactive molecular dynamics (RMD) simulations using our newly developed ReaxFF interatomic potential to study the dynamic evolution of two representative interfaces, namely (a) $\text{Li} (001) \parallel \text{Li}_7\text{PS}_6 (001)$ (i.e., anode-electrolyte) and (b) $\text{S}_8(001) \parallel \text{Li}_7\text{PS}_6(001)$ (i.e., cathode-electrolyte) both in the absence and under applied electric field. To study interface between argyrodite Li_7PS_6 (cubic) electrolyte with Li metal (body-centered cubic) anode, we employed a symmetric Li-cell model $\text{Li} (001) \parallel \text{Li}_7\text{PS}_6 (001) \parallel \text{Li} (001)$ with dimensions of $8.6 \text{ nm} \times 8.6 \text{ nm} \times 26.3 \text{ nm}$. Periodic boundary conditions are employed along all directions; note the supercell size for the individual components (Li, Li_7PS_6) in the plane of the interface are chosen such that the epitaxial strain is less than 1% . We study the formation of the solid electrolyte interphase (SEI) in the absence/presence of applied electric field using RMD simulations within canonical ensemble (NVT) under ambient conditions for 1 ns. Most argyrodite (sulfide) electrolytes are known to be unstable against Li metal. Indeed, our RMD simulations indicate that Li_7PS_6 undergoes reductive decomposition near the $\text{Li} \parallel \text{Li}_7\text{PS}_6$ interface via progressive breakdown of the PS_4^{3-} motifs present in the electrolyte (Figure XVI.13.1(a)). These species bind with Li atoms of the anode to form a SEI; as the SEI builds up new bonds between anodic lithium ($\text{Li}(a)$) and the P/S atoms from the electrolyte (i.e., $\text{P}(e)$, $\text{S}(e)$) continue to appear (Figure XVI.13.1(b,c)). Clearly, applied electric field significantly promotes the decomposition of PS_4 motifs, as indicated by a higher fraction of broken P-S bonds at $E = 0.5 \text{ eV/nm}$ in Figure XVI.13.1(a). Interestingly, the thickness of the as-formed SEI layer reaches an equilibrium at $\sim 0.6 \text{ ns}$. On the other hand, applying electric field (0.5 eV/nm) normal to the interface causes the SEI to grow progressively even until 1 ns (Figure XVI.13.1(d)).

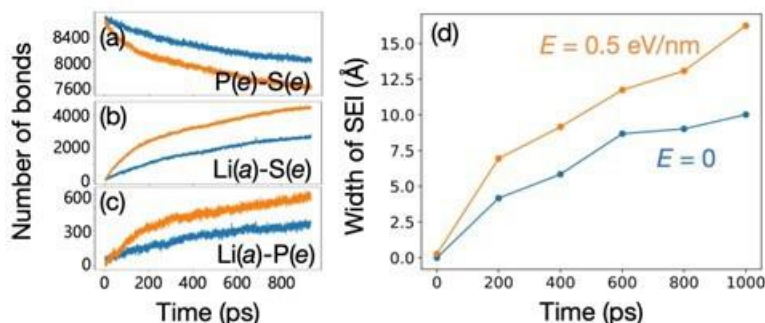


Figure XVI.13.1 Build-up of SEI at Li (001) || Li₇PS₆ (001) studied using reactive molecular dynamics simulations. Temporal evolution of the number of (a) P(e) – S(e), (b) Li(a) – S(e), and (c) Li(a) – P(e) at the interface under no bias (blue) and applied electric field of $E = 0.5$ eV/nm normal to the interface (orange). (d) Time-evolution of the thickness of the as-formed SEI. Li(a) denotes lithium atoms belonging to anode, while S(e) and P(e) are sulfur and phosphorus atoms belonging to the electrolyte respectively.

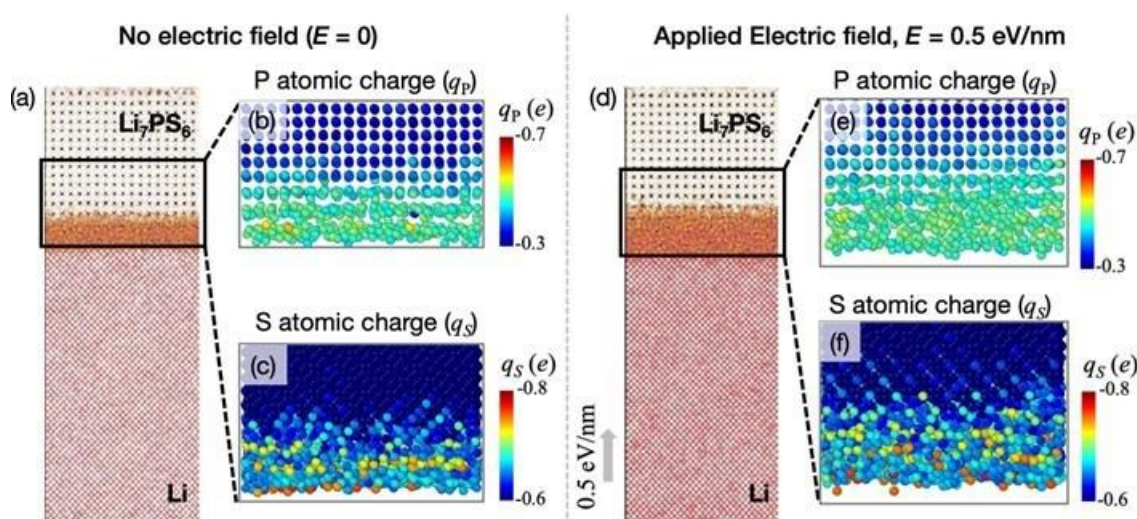


Figure XVI.13.2 Composition of the SEI formed at interface formed between Li metal anode and Li₇PS₆ electrode obtained by RMD simulations. Evolution of the interface is studied (a-c) in absence of electric field ($E = 0$), and (d-f) under applied electric field $E = 0.5$ eV/nm along the positive z-direction (i.e., normal to the Li (001) || Li₇PS₆ (001) interface). Atomic snapshot of the Li (001) || Li₇PS₆ (001) interface after 1 ns are shown in panels (a) and (c) for $E = 0$ and $E = 0.5$ eV/nm respectively. The P atoms (panels (b, e)) and S (panels (c, f)) are colored by their charges.

Next, we analyzed the composition of the SEI by analyzing the charge state of the P and S atoms in the as-formed SEI. In the pristine electrolyte, Li₇PS₆, the P and S atoms are present in their unreduced states with charges of $-0.4e$ and $-0.57e$ respectively. During reductive decomposition of Li₇PS₆, the atomic charges of P (q_P) and S are expected to become more negative, up to $-0.73e$ for P (corresponding to Li₃P) and $-0.7e$ (corresponding to Li₂S) in their fully reduced states. Applied electric field enables vigorous decomposition of Li₇PS₆, which in turn, yields more reduced species, as indicated by the largely more negative charges on P and S atoms in the SEI, as compared to that at $E = 0$ (Figure XVI.13.2). Direct visualization of the atomic snapshot at the end of the RMD runs clearly shows that the thickness of as-formed SEI is significantly higher under applied electric field (Figure XVI.13.2(a,c)). Our analysis of the atomic charges showed that the P atoms do not get fully reduced (i.e., do not form Li₃P) even under applied bias (Figure XVI.13.2(b,d)). Importantly, $\sim 33\%$ and $\sim 37\%$ of P atoms reduce partially at $E = 0$ and $E = 0.5$ eV/nm respectively, with atomic charges $-0.6 < q_P < -0.45$ (Figure XVI.13.2(b,d)). In other words, PS₄³⁻ motifs decompose only down to PS₃, PS₂ and PS species, which bind with lithium to form LiPS_x phases, with the more reduced phases occurring at $E = 0.5$

eV/nm (i.e., more negative q_P). On the other hand, $\sim 10\%$ of S atoms get fully reduced to form Li_2S in the SEI even in the absence of electric field; under applied field ($E = 0.5$ eV/nm), slightly higher fraction of S ($\sim 12\%$) gets fully reduced (Figure XVI.13.2(c,e)). In addition, a significant fraction of S atoms ($\sim 18\%$, $\sim 21\%$ at $E = 0$, 0.5 eV/nm respectively) reduce partially to form Li_xS phases (Figure XVI.13.2(c,e)). Essentially, the SEI is composed of Li_xS , Li_2S and LiPS_x phases.

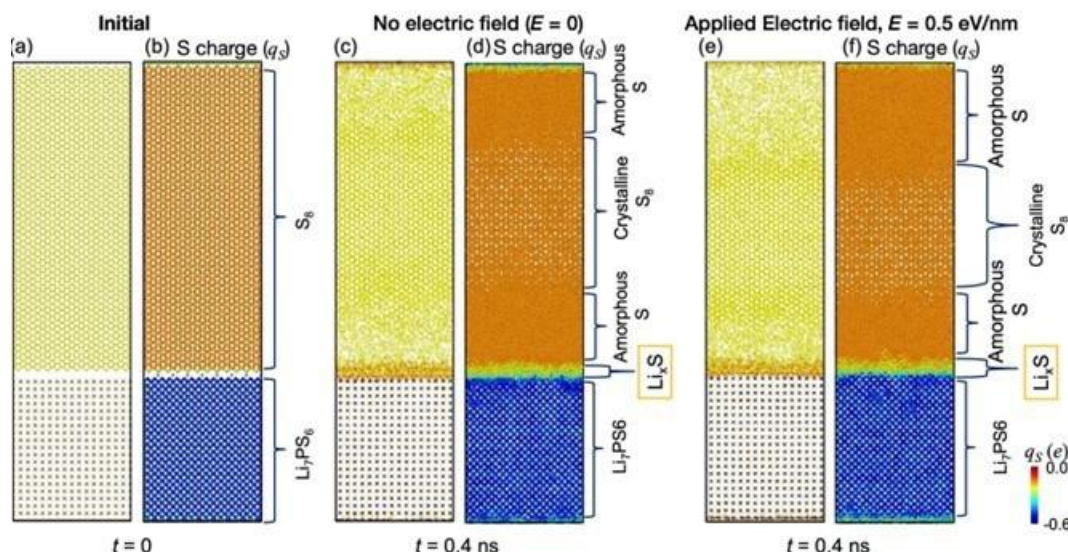


Figure XVI.13.3 Structural evolution of the interface between S_8 cathode and Li_7PS_6 electrode obtained by RMD simulations. (a) Initial configuration of the symmetric S_8 (001) || Li_7PS_6 (001) || S_8 (001) slab, and (b) distribution of charges in the sulfur atoms in the initial configuration. Evolution of the interface is studied (c,d) in absence of electric field ($E = 0$), and (e,f) under applied electric field $E = 0.5$ eV/nm along the positive z-direction (i.e., normal to the S_8 (001) || Li_7PS_6 (001) interface). Atomic snapshot of the S_8 (001) || Li_7PS_6 (001) interface after 0.4 ns are shown in panels (c) and (e) for $E = 0$ and $E = 0.5$ eV/nm respectively.

Panels (b), (d), (f) show only the S atoms (colored by their charge) in the snapshots shown in (a), (c), and (e) respectively.

To investigate the electrochemical reactions at the cathode-electrolyte interface, we performed RMD simulations on symmetric model of S_8 (001) || Li_7PS_6 (001) || S_8 (001) composed of $\sim 100,000$ atoms (~ 8.8 nm \times 5.9 nm \times 30 nm) with minimal epitaxial strain at the interface ($< 1\%$). Detailed analysis of our simulation trajectories reveals that the Li atoms from the electrolyte move into the cathode, reduces the nearby S, and causes opening of the S_8 rings (Figure XVI.13.3). Similar reactions are observed regardless of the applied electric field (Figure XVI.13.3). Interestingly, the applied electric field does not cause significant acceleration of CEI formation. The reduction of the S atoms near the S_8 (001) || Li_7PS_6 (001) is clearly evidenced by their more negative charges ($q_S \sim -0.45$ e) as compared to that in S_8 ($q_S \sim 0$) (Figure XVI.13.3(b,d)). Notably, the S atoms do not reduce fully down to Li_2S ($q_S \sim -0.7$ e) but form partially reduced Li_xS phase. The growth the as-formed Li_xS layer is rapid initially, but it becomes stagnant at ~ 0.2 ns. The extent of reduction of S reduces as we move away from the interface. Interestingly, the sulfur proximal to the Li_xS region amorphize, possibly due to the strain induced by the Li_xS layer (Figure XVI.13.3(a,c)).

2. Development of highly conductive iodine and fluorine dual-doped argyrodite solid electrolyte for lithium-metal batteries:

The argyrodite-class Li_7PS_6 SE and its halogen-doped derivatives $\text{Li}_6\text{PS}_5\text{X}$ ($\text{X} = \text{Cl}, \text{Br}, \text{I}$) have received a lot of attention owing to their high Li-ion conductivity (among solid-state materials), and tunable interfacial stability against Li-metal. In particular, the halide dopants are known to introduce anion site-disorder by partially replacing the S^{2-} ions in $4a/4d$ crystallographic sites; such disorder can introduce facile pathways for Li^+ hops, and in turn enhance the Li^+ ion conduction by 3-4 times that for pristine Li_7PS_6 . [5-7] More importantly, the halogen dopants (particularly F) can produce a stable SEI against Li-metal, which enhance the electrochemical stability against Li-metal, as shown by our work in Year 1 on F- and Cl- doped SEs. [8] However, previous solid-state synthesis works have shown that iodine (I) doped argyrodite possess Li^+

conductivity (1-2 orders of magnitude lower than its Cl/Br counterparts) due to the lack of disorder in its crystal structure; specifically, unlike Cl/Br, I⁻ anions do not coinhabit both the 4a and 4d sites, preferring to reside only in the former.[5] In this work, we introduced disorder in I-doped argyrodites using our liquid-phase synthesis method (developed in Year 1 of this project) in two ways: (a) heat-treatment schedule that causes segregation of I⁻, and (b) dual-doping with I⁻ and F⁻ anions to achieve favorable anion site-disorder.

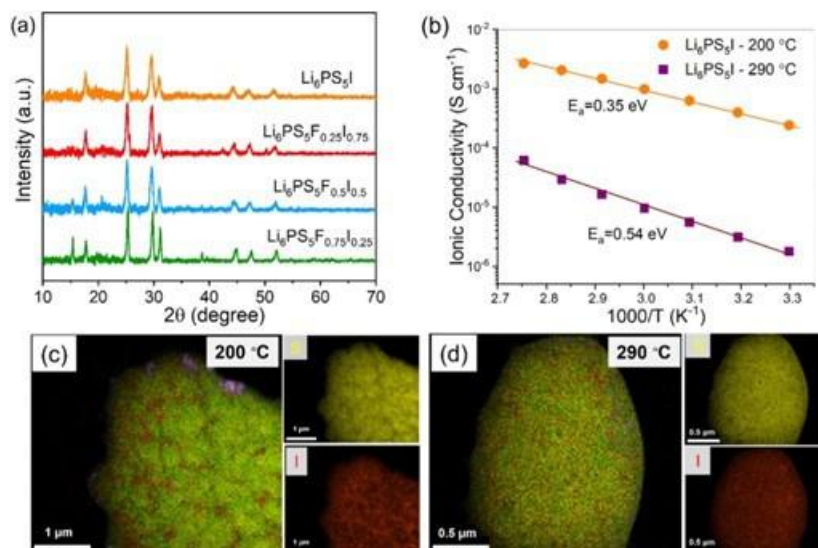


Figure XVI.13.4 Solvent-based synthesis of iodine and fluorine doped argyrodite electrolytes. (a) XRD patterns for as-synthesized $\text{Li}_6\text{PS}_5\text{I}$, $\text{Li}_6\text{PS}_5\text{F}_{0.25}\text{I}_{0.75}$, $\text{Li}_6\text{PS}_5\text{F}_{0.5}\text{I}_{0.5}$ and $\text{Li}_6\text{PS}_5\text{F}_{0.75}\text{I}_{0.25}$ indicating high phase-purity of the argyrodites, (b) Arrhenius plots of solvent synthesized $\text{Li}_6\text{PS}_5\text{I}$ after two different heating treatment temperatures (200 °C, 290 °C); TEM elemental mapping of synthesized $\text{Li}_6\text{PS}_5\text{I}$ argyrodite after heating treatment at (c) 200 °C and (d) 290 °C. (S in Yellow, I in Red, O in Pink).

A. Heat treatment schedule to introduce structural disorder:

We synthesized $\text{Li}_6\text{PS}_5\text{I}$, $\text{Li}_6\text{PS}_5\text{F}_{0.25}\text{I}_{0.75}$, and hybrid-doped $\text{Li}_6\text{PS}_5\text{F}_{0.25}\text{I}_{1-x} \cdot (x-0.25)\text{LiF}$ ($x = 0.5, 0.75$) argyrodites using our solvent-based approach (Figure XVI.13.4). The X-ray diffraction (XRD) patterns of the as-synthesized SEs show characteristic diffraction peaks at $2\theta = 17.7^\circ$, 25.2° , 29.6° , and 31.0° , corresponding to the planes of (200), (220), (311), and (222) in argyrodite structure, indicating high phase purity (especially in I-only case) (Figure XVI.13.4(a)). Notably, while synthesized $\text{Li}_6\text{PS}_5\text{I}$ is a pure phase argyrodite, the addition of 0.25 mols of F⁻ to synthesize $\text{Li}_6\text{PS}_5\text{F}_{0.25}\text{I}_{0.75}$ appears to make it difficult for iodine to fully incorporate, as small secondary peaks corresponding to LiI can be observed at $2\theta = 42.4^\circ$ and 50.2° (Figure XVI.13.4(a)). With higher F-doping content, the LiI peaks disappear. Instead, a minor impurity peak at $2\theta = 39.1^\circ$ starts to appear which is attributed to a small amount of secondary LiF phase (Figure XVI.13.4(a)). Nevertheless, at any composition, the structure of the as-synthesized sample is primarily argyrodite. This is further evidenced by Raman spectroscopy; for all compositions, we observed strong bands around 420 cm^{-1} , with smaller bands appearing at 575 cm^{-1} and 200 cm^{-1} – both associated with PS_4^{3-} tetrahedra. To understand the effect of heat-treatment schedule on the structure (and consequent Li^+ conductivity), we synthesized $\text{Li}_6\text{PS}_5\text{I}$ using two different heat treatment temperatures (200 °C and 290 °C). At room temperature, the 290 °C-treated $\text{Li}_6\text{PS}_5\text{I}$ sample shows an ionic conductivity of $1.8 \times 10^{-6} \text{ S cm}^{-1}$, which is consistent with previous reports from solid-state synthesis methods (Figure XVI.13.4(b)). In contrast, lower heat treatment temperature at 200 °C results in $\text{Li}_6\text{PS}_5\text{I}$ displaying a high ionic conductivity of $2.5 \times 10^{-4} \text{ S cm}^{-1}$ at room temperature, which is amongst the highest value for $\text{Li}_6\text{PS}_5\text{I}$ argyrodite reported thus far (Figure XVI.13.4(b)). This conductivity is even higher than that reported for solid-synthesized $\text{Li}_6\text{PS}_5\text{I}$ after additional high-energy ball-milling treatment ($2 \times 10^{-4} \text{ S cm}^{-1}$), which introduces extra structural disorder. In addition, the 200 °C- $\text{Li}_6\text{PS}_5\text{I}$ not only exhibits higher ionic conductivity than the 290 °C-sample in the temperature range of 30 °C -90 °C, but also shows much lower activation energy (0.34 eV vs. 0.55 eV, respectively). Transmission electron microscopy (TEM) was performed to analyze the morphology and elemental distribution of $\text{Li}_6\text{PS}_5\text{I}$ samples

after 200°C and 290°C heat treatments, respectively (Figure XVI.13.4(c,d)). Compared to the homogenous distribution of S and I elements for the 290°C-sample (Figure XVI.13.4(d)), the 200°C-treated sample displays a mismatched distribution with iodine (I) aggregating at the edges while the sulfur remains in the inner region. Such elemental distribution is considered to contribute to the observed fast ion transport in 200°C-treated $\text{Li}_6\text{PS}_5\text{I}$, similar to the reduced impedance at grain boundaries seen in previous reports.

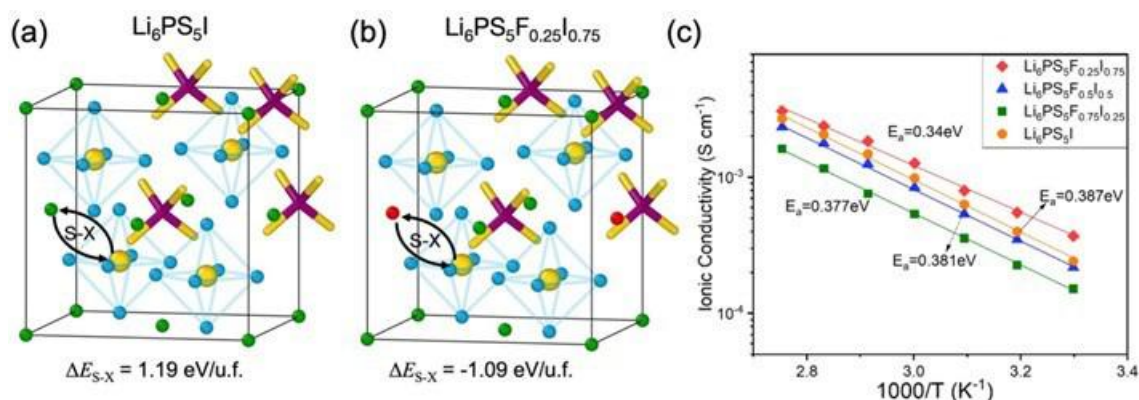


Figure XVI.13.5 Anion-disorder in dual-doped argyrodite SEs and its impact on Li-ion conduction. Atomic-scale structures of (a) $\text{Li}_6\text{PS}_5\text{I}$, and (b) $\text{Li}_6\text{PS}_5\text{F}_{0.25}\text{I}_{0.75}$ optimized by DFT. In each panel, the energy change associated with swapping a S atom at 4d site (cage-center) with a halogen (I in panel (a), and F in panel (b)) are indicated. The Li, P, S, F and I atoms are depicted as blue, purple, yellow, red, and green spheres, respectively. (c) Arrhenius plots (30–90°C) of $\text{Li}_6\text{PS}_5\text{I}$ and hybrid-doped argyrodites obtained from EIS measurements.

B. Dual-doping with fluorine and iodine to introduce anion-site disorder.

We performed DFT calculations to elucidate the energetics of anion-disorder during dual doping of argyrodite with F^- and I^- (Figure XVI.13.5). We found that $\text{Li}_6\text{PS}_5\text{I}$ exhibits a perfect argyrodite structure with face-centered cubic symmetry (space group: $Fm\bar{3}m$) consisting of PS_4^{3-} building blocks (Figure XVI.13.5(a)) and I atoms at the corners/face centers (i.e., 4a Wyckoff sites). The S atoms belonging to the PS_4^{3-} occupy the Wyckoff 16e sites; while other S occupy the 4d sites. The Li atoms partially occupy the 48h/24g positions, which form a cage-like structure around the S-atoms placed at the 4d sites (Figure XVI.13.5(a)) consistent with previous DFT works. Notably, our DFT-predicted lattice parameter (10.3 Å) is close (within 2%) to those obtained from our XRD measurements in Figure XVI.13.5(a) (10.12 Å). Li-ion transport through such an atomic structure has been reported to consist of three types of jumps: (i) localized jumps between adjacent 48h sites (doublet), (ii) jumps within a cage centered at a given S/X atom at 4d site, and (iii) inter-cage jumps, the latter of which is the primary bottleneck for Li ion mobility. As opposed to the fast ion transport in $\text{Li}_6\text{PS}_5\text{Cl}$ and $\text{Li}_6\text{PS}_5\text{Br}$ argyrodites, $\text{Li}_6\text{PS}_5\text{I}$ has been reported to exhibit poor ionic conductivity due to the absence of anion site disorder. Consistent with these reports, our DFT calculations show that inducing an anti-site disorder by swapping a pair of S and I between 4d and 4a is significantly endothermic ~ 1.19 eV/u.f (Figure XVI.13.5(a)). Such energetic penalty against anion-disorder in $\text{Li}_6\text{PS}_5\text{I}$ can be attributed to the substantial larger size of I^- (2.06 Å) as compared to S^{2-} (1.85 Å). On the other hand, in F/I co-doped $\text{Li}_6\text{PS}_5\text{F}_{0.25}\text{I}_{0.75}$, an anti-site defect involving S and F atoms (with smaller ionic radius: 1.33 Å) is thermodynamically favorable, with the anion-disordered structure being ~ 1.09 eV/u.f. lower in energy than the pristine case (Figure XVI.13.5(b)). This energetic preference for halogen disorder in F/I co-doped $\text{Li}_6\text{PS}_5\text{F}_{0.25}\text{I}_{0.75}$ would enhance the frequency of inter-cage hops, owing to difference in electronegativity between S and F ions as suggested by previous DFT studies. Indeed, our DFT predictions are consistent with our Electrochemical impedance spectroscopy (EIS) measurements (Figure XVI.13.5(c)), which show that addition of small amounts of F^- into the $\text{Li}_6\text{PS}_5\text{I}$ argyrodite to obtain $\text{Li}_6\text{PS}_5\text{F}_{0.25}\text{I}_{0.75}$ increase the ionic conductivity at room temperature (3.5×10^{-4} S cm^{-1}) as compared to $\text{Li}_6\text{PS}_5\text{I}$ (2.5×10^{-4} S cm^{-1}). However, additional F-doping content results in slightly slower ion transportation, with $\text{Li}_6\text{PS}_5\text{F}_{0.25}\text{I}_{0.5}\cdot 0.25\text{LiF}$ and $\text{Li}_6\text{PS}_5\text{F}_{0.25}\text{I}_{0.25}\cdot 0.5\text{LiF}$ samples showing ionic conductivities of 2.4×10^{-4} S cm^{-1} and 1.5×10^{-4} S cm^{-1} , respectively. The decreased ionic conductivity is

attributed to the increased secondary phase (LiF) content in argyrodite structure (see XRD in Figure XVI.13.4(a)).

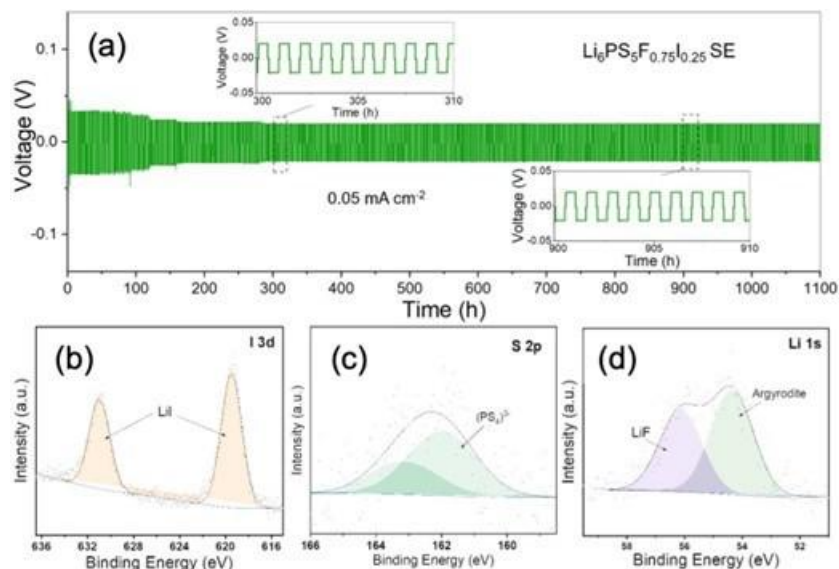


Figure XVI.13.6 Electrochemical stability of $\text{Li}_6\text{PS}_5\text{F}_{0.75}\text{I}_{0.25}$ SE against Li-metal obtained from cycling performance of Li-symmetric cell. (a) Voltage profiles of $\text{Li}_6\text{PS}_5\text{F}_{0.25}\text{I}_{0.25}\cdot 0.5\text{LiF}$ -based symmetric cell cycling up to 1,100 hours (0.05 mA cm^{-2}). XPS spectra of cycled symmetric cell with $\text{Li}_6\text{PS}_5\text{F}_{0.25}\text{I}_{0.25}\cdot 0.5\text{LiF}$ SE: (b) I 3d, (c) S 2p, and (d) Li 1s.

The electrochemical stability of $\text{Li}_6\text{PS}_5\text{I}$ and hybrid-doped argyrodites towards metallic Li anode was examined by cycling in Li symmetric cells (Figure XVI.13.6). We observed that the polarization voltage of the $\text{Li}_6\text{PS}_5\text{I}$ -based cell increases from its initial value of 0.18 V to 0.37 V after 100 cycles, while those containing F showed very stable voltage profiles. Among them, the $\text{Li}_6\text{PS}_5\text{F}_{0.25}\text{I}_{0.25}\cdot 0.5\text{LiF}$ -based cell shows the lowest polarization voltage at 0.03 V, suggesting that the most stable interface is formed between $\text{Li}_6\text{PS}_5\text{F}_{0.25}\text{I}_{0.25}\cdot 0.5\text{LiF}$ and Li metal. Such a stable interface is further confirmed by the comparison between the impedance spectra of $\text{Li}_6\text{PS}_5\text{F}_{0.25}\text{I}_{0.25}\cdot 0.5\text{LiF}$ -based Li symmetric cell before and after 100 cycles under 0.05 mA cm^{-2} in which a minor variation of total resistance ($2,950$ vs $2,780 \Omega$) is observed. Figure XVI.13.6(a) presents the long-term cycling stability of the Li symmetric cell using $\text{Li}_6\text{PS}_5\text{F}_{0.25}\text{I}_{0.25}\cdot 0.5\text{LiF}$ as SE, which runs continuously for 1,100 hours without short circuit. The initial polarization of $\sim 0.03 \text{ V}$ is slightly dropped to 0.025 V over the first 150 hours due to interfacial reactions. After this, the formation of stable SEI layer contributes to a stable voltage ($\sim 0.022 \text{ V}$) and cycling for the remaining 950 hours. X-ray photoelectron spectroscopy (XPS) was performed on the $\text{Li}_6\text{PS}_5\text{F}_{0.25}\text{I}_{0.25}\cdot 0.5\text{LiF}$ -based cell after Li plating/stripping to investigate the chemical compositions and to understand the reactions occurring at the interface. In the XPS spectra of $\text{Li}_6\text{PS}_5\text{F}_{0.25}\text{I}_{0.25}\cdot 0.5\text{LiF}$ SE, the doublet peaks for I 3d (Figure XVI.13.6(b)) at 619.4 eV and 630.5 eV originated from Li-I bonding, while the peak at 56.2 eV for Li 1s (Figure XVI.13.6(d)) is attributed to Li-F bonding. This observation indicates that interfacial reactions between $\text{Li}_6\text{PS}_5\text{F}_{0.25}\text{I}_{0.25}\cdot 0.5\text{LiF}$ and Li metal form an SEI layer that contains both LiF and LiI during the long-term cycling of Li symmetric cells. Moreover, high F-doping content in $\text{Li}_6\text{PS}_5\text{F}_{0.25}\text{I}_{0.25}\cdot 0.5\text{LiF}$ results in an increase of interfacial LiF, which has been shown to play a prominent role in both interface stabilization and the prevention of Li dendrites. At the interface between halide doped argyrodites ($\text{Li}_6\text{PS}_5\text{X}$, $\text{X} = \text{Br}, \text{Cl}$) and Li metal, the participation of halide ions X^- has been reported to form LiX (Br, Cl), which contributes to the enhancement of interfacial stability. In this study, the observed behaviors of dual-doped argyrodites suggests that the dopant composition has significant impacts on both interfacial reactions and electrochemical stability at the interface.

3. Fabrication of Battery with Optimized Cathode at high S-loading, SSE, and Li anode:

At high S-loading, the low capacity of solid-state lithium-sulfur battery can be attributed to poor sulfur utilization and lower ionic (Li) conductivity of the S-cathode. To address these issues, we successfully

incorporated SE ($\text{Li}_6\text{PS}_5\text{F}_{0.5}\text{Cl}_2$) into the cathode (Super-P carbon-sulfur) at high S- loading (4 mg/cm^2) by pressing it together. This was possible after we learned how to handle the entire battery assembly including the cathode formulation inside the glove box. In all cases, cathode containing SSE powder (balled milled together) was pressed together with the SSE powder in a stainless-steel pellet die inside the glove box, and a prescribed amount of ionic liquid (LiTFSI in $\text{PYR:DOL}(1:3)$ at 3M) to ensure sufficient wetting.

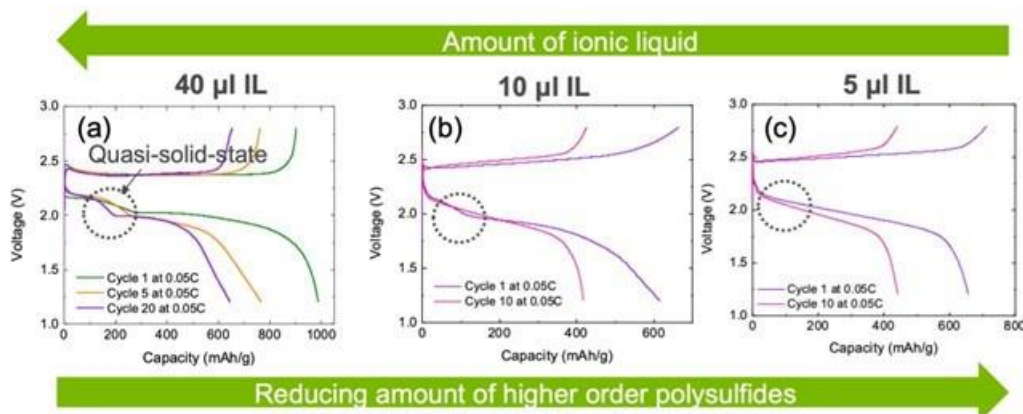


Figure XVI.13.7 Effect of amount of functionalizing IL on the discharge profiles for batteries consisting of Li anode, SPS cathode with 4.0 mg/cm^2 loading and 30% SE, and $\text{Li}_6\text{PS}_5\text{F}_{0.5}\text{Cl}_2$ electrolyte. Discharge profiles at selected cycles are shown for different amounts of functionalizing IL (LiTFSI in $\text{PYR:DOL}(1:3)$ at 3M) at the cathode-SSE interface at 30°C , namely, (a) $40 \mu\text{L}$, (b) $10 \mu\text{L}$, and (c) $5 \mu\text{L}$. As the amount of IL decreases, the discharge profile changes from a two-plateau (at $40 \mu\text{L}$), indicative of a quasi-solid-state behavior to a single slope (at $5 \mu\text{L}$) akin to an all-solid-state Li-S battery.

First, we systematically investigated the effect of amount of functionalizing IL on the electrochemical performance of the batteries during cycling for cathodes containing 30% $\text{Li}_6\text{PS}_5\text{F}_{0.5}\text{Cl}_2$ (Figure XVI.13.7). At high amount of IL ($40 \mu\text{L}$), the discharge profile indicate two plateaus at $\sim 2.2 \text{ V}$ and $\sim 2.0 \text{ V}$, showing formation of higher-order polysulfides and is indicative of a quasi-solid-state battery (Figure XVI.13.7(a)). As the amount of IL decreases, the two-plateau profile changes to a single-slope behavior, which resembles an all-solid-state battery (Figure XVI.13.7(b,c)). We find that $5 \mu\text{L}$ of IL provides sufficient wetting, while still maintaining a near-all-solid-state like discharge profile (Figure XVI.13.7(c)). The quasi-solid-state behavior in the batteries containing high amount of functionalizing IL affords a higher initial discharge capacity $\sim 1000 \text{ mAh/g}$; however, the capacity fades quickly and yields $\sim 200 \text{ mAh/g}$ after 100 cycles, possibly due to burn out of the IL. At lower amounts of IL, although the initial discharge capacity reduces to $\sim 650 \text{ mAh/g}$, it fades slowly (Figure XVI.13.7(c)).

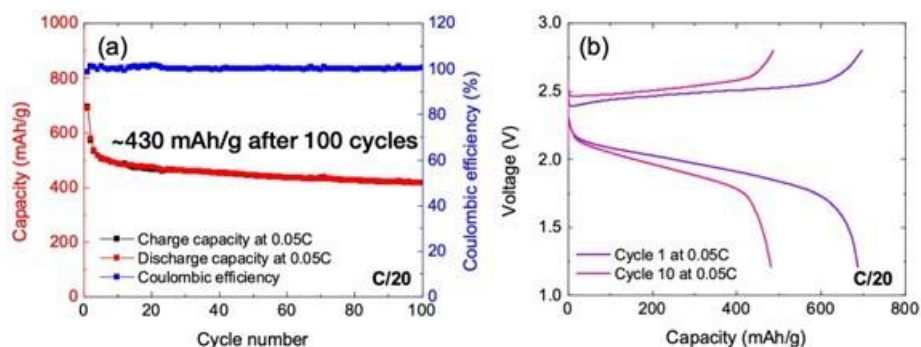


Figure XVI.13.8 Electrochemical cycling performance of batteries consisting of Li anode, SPS cathode with 4.0 mg/cm^2 loading pressed with 25% SE, $\text{Li}_6\text{PS}_5\text{F}_{0.5}\text{Cl}_2$ SE with $5 \mu\text{L}$ of ionic liquid (LiTFSI in $\text{PYR:DOL}(1:3)$ at 3M) at the cathode-SSE interface. (a) Capacity variation, and Coulombic efficiency as a function of cycles at 60°C at $\text{C}/20$, (b) Discharge profiles at selected cycles.

We optimized the amount of SE in the cathode, while keeping the amount of IL fixed at $5 \mu\text{L}$ to further enhance the Li^+ ion conductivity of the cathode, and consequently, its capacity (Figure XVI.13.8). We find that

the battery with 25% SSE in the cathode showed the best performance with an initial discharge capacity of ~ 700 mAh/g, and retention of ~ 430 mAh/g after 100 cycles (@C/20) at 60°C (Figure XVI.13.8(a)). Indeed, the discharge profiles show a solid-state-like behavior, which shows that the $5\ \mu\text{L}$ of IL is still low enough to suppress formation of higher-order polysulfides (Figure XVI.13.8(b)). Interesting, the capacity fade is appreciable only over the initial 5 cycles (where it drops from ~ 700 mAh/g to ~ 480 mAh/g); thereafter, the capacity remains nearly stable, with a slow drop down to ~ 430 mAh/g at 100 cycles. This indicates that the interphase at the cathode-electrolyte interface does not form fully in the first few cycles; we are currently running a few battery tests with slow-rate for the initial discharge; before beginning the cycling tests.

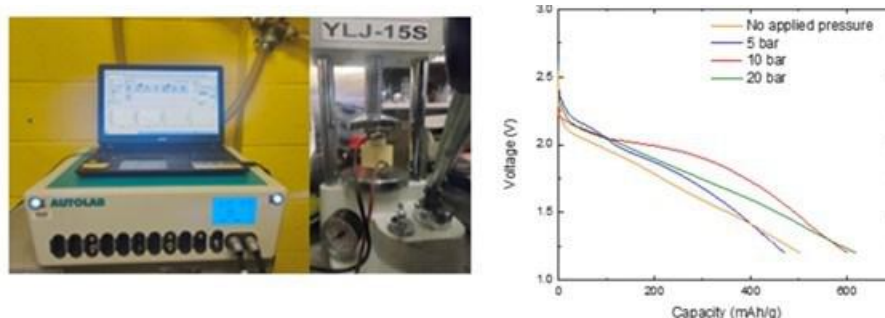


Figure XVI.13.9 Electrochemical cycling performance of batteries consisting of Li anode, SP-S cathode with $4.0\ \text{mg}/\text{cm}^2$ loading pressed with 25% SE, $\text{Li}_6\text{PS}_5\text{F}_{0.5}\text{Cl}_2\text{SE}$ with $5\ \mu\text{L}$ of ionic liquid (LiTFSI in PYR:DOL(1:3) at 3M) at the cathode-SSE interface under applied pressure. (a) A picture of the specialized cell being tested inside the glove box under applied pressure (b) Initial discharge curve at 0.05 C for batteries tested under tested under 0, 5, 10, and 20 bar.

Furthermore, we studied the effect of pressure on the initial discharge capacity using a specially designed pressure controlled split cell (Figure XVI.13.9(a)). Cells with cathode (SP-S:CNT:SSE (30:45:25), S-loading: $4\ \text{mg}/\text{cm}^2$, 25%SE), $5\ \mu\text{L}$ of functionalizing IL at cathode-electrolyte interface, and Li-anode were assembled and tested inside the Ar filled glove box using the Autolab (Nova 2.1) system. Our battery tests under applied pressures showed that initial discharge capacities increased marginally with applied pressure (up to 20 bar) (Figure XVI.13.9(b)); beyond this pressure, batteries failed due to short circuit issues. Although initial discharge capacity shows little pressure dependence, at an optimal 10 bar pressure, the plateau $\sim 2.1\ \text{V}$ has become more prominent implying improved reaction forming Li_2S . This shows that the applied pressure facilitates the kinetics of interphase formation at cathode-electrolyte interface.

Conclusions

Classical molecular dynamics simulations based on our newly developed ReaxFF provided atomic-scale insights into the electrochemical processes that occur at electrode-electrolyte interfaces in ASLSBs with argyrodite electrolytes (Li_7PS_6) under electric field. At the anode, we find that the electrolyte undergoes reductive decomposition, wherein the PS_4^{3-} motifs break down to form a solid-electrolyte interface containing Li_xS , Li_2S and LiPS_x . Applied electric field accelerates the kinetics of SEI-formation, and yields thicker SEI at equilibrium; nevertheless, the interfacial reactions (and consequently, the composition of SEI) are identical to those that occur in the absence of any bias. On the cathode side, sulfur reduces partially to form Li_xS ; strain associated with the higher volume of the as-formed Li_xS causes amorphization of the S-cathode. Interestingly, applied electric field has negligible effect on the kinetics of interfacial reactions at the cathode, as well as on the width of the cathode-electrolyte-interphase.

We employed a solvent-based synthesis method to produce highly conductive I-containing argyrodites: $\text{Li}_6\text{PS}_5\text{I}$ and hybrid-doped $\text{Li}_6\text{PS}_5\text{F}_{0.25}\text{I}_{0.75}$ and $\text{Li}_6\text{PS}_5\text{F}_{0.25}\text{I}_{1-x} \cdot (x-0.25)\text{LiF}$ ($x = 0.5, 0.75$). The solvent-synthesized $\text{Li}_6\text{PS}_5\text{I}$ shows an impressive ionic conductivity of $2.5 \times 10^{-4}\ \text{S cm}^{-1}$ at room temperature, while an even higher value ($3.5 \times 10^{-4}\ \text{S cm}^{-1}$) is observed for $\text{Li}_6\text{PS}_5\text{F}_{0.25}\text{I}_{0.75}$ argyrodite with dual F/I⁻ dopants. Density functional theory calculations indicate that co-doping argyrodite with F/I ions makes anion-disordering energetically favorable, which in turn, facilitates faster Li-ion transport. When $x = 0.25$, $\text{Li}_6\text{PS}_5\text{F}_{0.75}\text{I}_{0.25}$ with higher F-doping content displays the best electrochemical stability towards Li metal. Li symmetric cells display stable voltage

profiles up to 1100 hours, which is due to the formation of a stable SEI layer that contains both LiI and LiF. In addition, $\text{Li}_6\text{PS}_5\text{F}_{0.75}\text{I}_{0.25}$ SE-based Li metal batteries show great cycling performance, retaining a specific capacity of 105 mAh g⁻¹ after 200 cycles.

Finally, we addressed the key issues surrounding low S-utilization, and low Li-ion conductivity of cathodes at high S-loading (4 mg/cm²) by optimizing the cathode architecture (using mixture of carbon nanotubes, super-P, and acetylene black), incorporating argyrodite electrolyte ($\text{Li}_6\text{PS}_5\text{F}_{0.5}\text{Cl}_{0.5}$) into the cathode via pressing, and using ionic liquid (LiTFSI in PYR:DOL(1:3) at 3M) to ensure sufficient wetting. We find that using small amount of ionic liquid (5 μL) provides sufficient wetting, while still maintaining a near-all-solid-state like discharge profile. Furthermore, we found that 25% SSE in the cathode showed the best performance with an initial discharge capacity of ~ 700 mAh/g, and retention of ~ 430 mAh/g after 100 cycles (@C/20) at 60°C.

Key Publications

1. B. Narayanan, *Computational Modeling of Battery Materials*, in *Encyclopedia of Energy Storage*, L.F. Cabeza, Editor. 2022, Elsevier: Oxford. p. 278-290. DOI: [10.1016/B978-0-12-819723-3.00156-6](https://doi.org/10.1016/B978-0-12-819723-3.00156-6)
2. W. Arnold, V. Shreyas, Y. Li, M. Koralalage, J. Jasinski, A. Thapa, G. Sumanasekera, A. Ngo, B. Narayanan*, and H. Wang*. Synthesis of fluorine-doped lithium argyrodite solid electrolytes for solid-state lithium metal batteries. *ACS Applied Materials and Interfaces* 14, 11483 (2022) DOI: <https://doi.org/10.1021/acsami.1c24468> (*Corresponding Authors)
3. W. Arnold, V. Shreyas, S. Akter, Y. Li, J. Jasinski, G. Sumanasekera, B. Narayanan, and H. Wang. Highly Conductive Iodine and Fluorine Dual-Doped Argyrodite Solid Electrolyte for Lithium Metal Batteries. *Manuscript submitted* (2022).
4. V. Shreyas, S. Gupta, W. Arnold, S. Akter, H. Wang, and B. Narayanan. Mechanism for superionic lithium conduction in fluorinated argyrodites. *Manuscript submitted* (2022).
5. M. Koralalage, V. Shreyas, W. Arnold, S. Akter, A. Thapa, J. Jasinski, H. Wang, G. Sumanasekera, B. Narayanan. Functionalizing cathode-electrolyte interface with ionic liquids for high-performance quasi-solid-state lithium-sulfur batteries. *Manuscript submitted* (2022).

References

1. Chan, H., et al., *Machine learning coarse grained models for water*. *Nature Communications*, 2019. **10**(1): p. 379.
2. Chan, H., et al., *Machine Learning Classical Interatomic Potentials for Molecular Dynamics from First-Principles Training Data*. *The Journal of Physical Chemistry C*, 2019.
3. Narayanan, B., et al., *Accurate quantum chemical energies for 133 000 organic molecules*. *Chemical Science*, 2019. **10**(31): p. 7449-7455.
4. Narayanan, B., et al., *Machine learnt bond order potential to model metal-organic (Co-C) heterostructures*. *Nanoscale*, 2017. **9**(46): p. 18229-18239.
5. Arnold, W., et al., *Halide doping effect on solvent-synthesized lithium argyrodites $\text{Li}_6\text{PS}_5\text{X}$ (X= Cl, Br, I) superionic conductors*. *Journal of Power Sources*, 2020. **464**: p. 228158.
6. Wang, H., et al., *A lithium argyrodite $\text{Li}_6\text{PS}_5\text{Cl}_{0.5}\text{Br}_{0.5}$ electrolyte with improved bulk and interfacial conductivity*. *Journal of Power Sources*, 2019. **412**: p. 29-36.
7. Boulineau, S., et al., *Mechanochemical synthesis of Li-argyrodite $\text{Li}_6\text{PS}_5\text{X}$ (X=Cl, Br, I) as sulfur-based solid electrolytes for all solid state batteries application*. *Solid State Ionics*, 2012. **221**: p. 1-5.
8. Arnold, W., et al., *Synthesis of Fluorine-Doped Lithium Argyrodite Solid Electrolytes for Solid-State Lithium Metal Batteries*. *ACS Applied Materials & Interfaces*, 2022.

Acknowledgements

This project involves three co-investigators: Dr. Hui Wang, Dr. Gamini Sumanasekera, and Dr. Jacek Jasinski at the University of Louisville. A part of this work was performed in collaboration with Prof. Anh Ngo (University of Illinois-Chicago, Argonne National Laboratory), Prof. Subramanian Sankaranarayanan (University of Illinois-Chicago, Argonne National Laboratory), and Prof. Arunkumar Subramanian (University of Illinois-Chicago). This research used resources of the National Energy Research Scientific Computing

Center, a DOE Office of Science User Facility supported by the Office of Science of the U.S. Department of Energy under Contract No. DE-AC02-05CH11231. Use of the Center for Nanoscale Materials was supported by the U. S. Department of Energy, Office of Science, Office of Basic Energy Sciences, under Contract No. DE-AC02-06CH11357.

XVI.14 Design of Strain Free Cathode – Solid State Electrolyte Interfaces Using Chemistry-Informed Deep Learning (ANL)

Hakim Iddir, Principal Investigator

Argonne National Laboratory
9700 South Cass Avenue
Lemont, IL 60439
E-mail: iddir@anl.gov

Tien Duong, DOE Technology Development Manager

U.S. Department of Energy
E-mail: Tien.Duong@ee.doe.gov

Start Date: October 1, 2019

End Date: September 30, 2022

Project Funding (FY22): \$300,000

DOE share: \$300,000

Non-DOE share: \$0

Project Introduction

Structure-property relationships are at the heart of most fundamental scientific approaches. However, the link between structure and property remains a challenge in the materials science of complex systems, such as the oxides that form battery components. **In particular, the chemical and mechanical stability of the cathode-SSE interface presents a challenge to the development of solid-state batteries.** High performance Density Functional Theory (DFT) calculations provide the necessary framework to understand such systems.

Unfortunately, given the limited number of atoms and time scales accessible by the method and the myriad calculations required to achieve satisfactory results, the computational cost of simulating all the possible configurations of a multicomponent oxide is prohibitive. In this work, we augment the DFT data with Machine Learning (ML) – especially deep learning – techniques that allow us to access large system sizes and longer time scales necessary to build thermodynamic models. We focus on understanding the nature of benchmark $\text{Li}_{1-a}\text{Ni}_{1-x-y-z}\text{Mn}_x\text{Co}_y\text{M}_z\text{O}_2$ structures (M dopant, $\alpha, x, y, z < 1$), their volume change with Li content, nature and concentration of the dopants, as well as the chemical stability of the SSE-cathode interface. The DFT and ML approach will provide new cathode compositions that will reduce the strain of the SSE-cathode interface and hence improve its mechanical and chemical stabilities

In this project we aim at developing a methodology that will allow us to explore and expand the configurational space using High-Performance Computing (HPC) approaches in a systematic and efficient way. The methodology will encompass, DFT, Ab-Initio Molecular Dynamics (AIMD), Molecular Dynamics, and ML. The methodology will also take advantage of the variety of software already developed at Argonne and at other DOE laboratories, such as BALSAM to automate, manage and control the large number of calculations needed to achieve our goal.

Objectives

Structure-property relationships are at the heart of most fundamental scientific approaches. However, the link between structure and property remains a challenge in the materials science of complex systems, such as the oxides that form battery components. **In particular, the chemical and mechanical stability of the cathode-SSE interface presents a challenge to the development of solid-state batteries.** High performance Density Functional Theory (DFT) calculations provide the necessary framework to understand such systems. Unfortunately, given the limited number of atoms and time scales accessible by the method and the myriad calculations required to achieve satisfactory results, the computational cost of simulating all the possible configurations of a multicomponent oxide is prohibitive. In this work, we augment the DFT data with Machine Learning (ML) – especially deep learning – techniques that allow us to access large system sizes and longer time scales necessary to build thermodynamic models. We focus on understanding the nature of benchmark $\text{Li}_{1-a}\text{Ni}_{1-x-y-z}\text{Mn}_x\text{Co}_y\text{M}_z\text{O}_2$ structures (M dopant, $\alpha, x, y, z < 1$), their volume change with Li content, nature and

concentration of the dopants, as well as the chemical stability of the SSE-cathode interface. The DFT and ML approach will provide new cathode compositions that will reduce the strain of the SSE-cathode interface and hence improve its mechanical and chemical stabilities

In this project we aim at developing a methodology that will allow us to explore and expand the configurational space using High-Performance Computing (HPC) approaches in a systematic and efficient way. The methodology will encompass, DFT, Ab-Initio Molecular Dynamics (AIMD), Molecular Dynamics, and ML. The methodology will also take advantage of the variety of software already developed at Argonne and at other DOE laboratories, such as BALSAM to automate, manage and control the large number of calculations needed to achieve our goal.

Approach

All calculations will be performed by spin-polarized DFT as implemented in the Vienna Ab Initio Simulation Package (VASP).^{1,2} To make sure all the oxidation state of ions are correct, after geometry optimization within the DFT+U framework, electronic relaxation will be performed using a single point calculation with the hybrid functional HSE06.³ For production calculations we will use the MPI parallelized version of VASP.

Exploration of the potential energy surface (PES) is needed to predict the structure of solid materials and interfaces. Such calculations are infeasible using MD or DFT calculations alone. Thankfully, the PES of a system can be represented by the sum of the energies of the local neighborhoods surrounding each atom. This enables the use of ML surrogate models trained with DFT calculations to capture the energies in local neighborhoods. The input to the ML surrogate must be a unique representation of the system under study. Consequently, the local environment of each ion is described using a local environment descriptor that renders the atomic configuration invariant to rotations, translations, and permutations of the atoms. In recent years, several different descriptors have come to prominence with advantages and disadvantages. Once the ML surrogate is trained, the total energy and forces over all the ions of any structural configuration can be determined. Such information can be used for atomistic simulations, namely, MD and Monte Carlo (MC).

In this project, we propose to use the open-source DeepMDkit python/C++ package to construct the ML PES and force fields. The promise of DeepMDkit in this work is to provide near-DFT accuracy at orders of magnitude lower computational expense, comparable to traditional molecular dynamic simulations. Efficiency in training is facilitated through integration with TensorFlow and MPI/GPU support.

One of the challenges of the development of a ML PES is achieving accurate predicted forces and energies across the entire configurational space, while minimizing the total number of calculations required for training. In recent years, active learning has been highlighted for its ability to target training examples most likely to improve the model quality or to achieve some other objective (i.e. maximizing a predicted material property). DP-GEN, an open source python package based on DeepMDkit, implements a similar active learning scheme with HPC support, and has been employed to construct a ML PES with accuracy approaching DFT and sometimes exceeding embedded atom potential for experimentally measured properties of interest.⁴ In this work, we propose to leverage DeepMDkit and DP-GEN to efficiently generate ML-PESs for cathode-electrolyte systems including a variety of dopants.

Results

The cathode volume change upon delithiation is the leading cause of cathode-solid electrolyte interface strain. To design doping strategies that minimizes strain, the distribution of the dopant and the effect on the cation arrangements must be determined. We have shown our strategy to understand the distribution of elements and the subsequently volume change upon delithiation. We have chosen $\text{LiNi}_{0.8}\text{Mn}_{0.1}\text{Co}_{0.1}\text{O}_2$ (NMC811) as the baseline cathode material, given its widespread use and favorable electrochemical properties. We have tested Ti, Zr, Al, Fe, Ca, Mg, Y, W, Nb, B, and La as dopants and candidates for Co substitutes. As an example of the collected data Figure XVI.14.1 shows the energy landscape for Zr doped NMC811, where Zr substitute 1/3 of the Co sites. The lowest energy configuration presents pairs of uniformly distributed Mn-Co or Mn-Zr pairs.

The highest energy configuration shows Zr-Mn-Co clusters and some Li/Ni antisite defects in contiguous layers. We also collected data for Zr substituting 2/3 and all the Co sites. All the calculations have been performed using the R2SCAN + D3 functional and Van der Waals correction, which have been demonstrated previously to offer very accurate structural and energetic features for cathode materials. All the data produced is being used to train a machine learning potential that would be used to further explore the cation distributions in much larger simulation cells. The ML fitting is being performed using DeepMDkit.

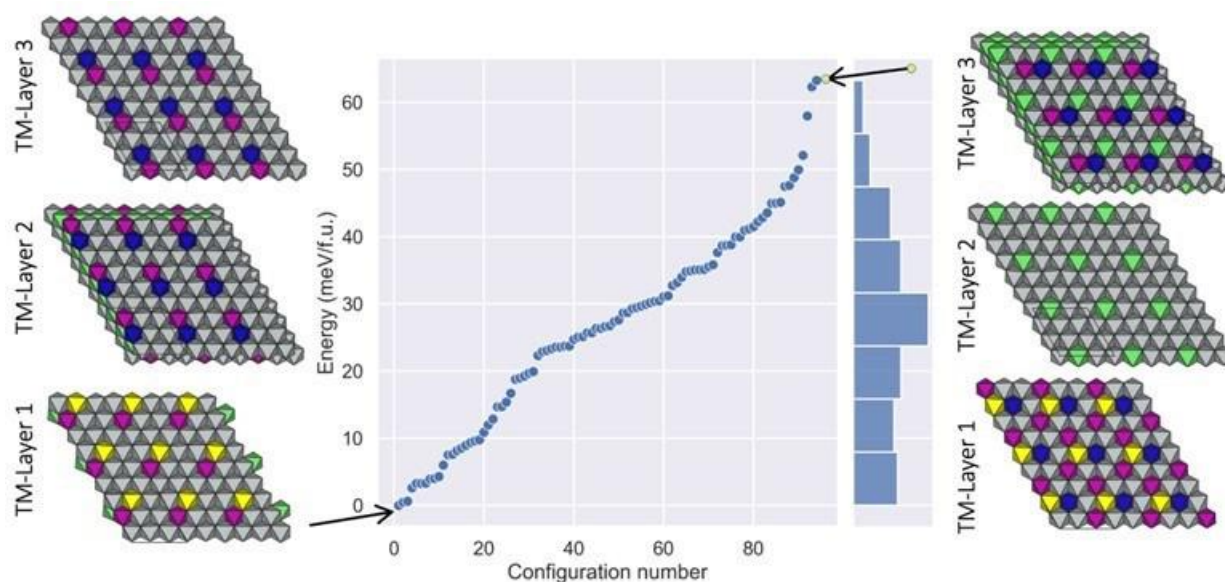


Figure XVI.14.1 Zr doped (1/3 of Co sites) NMC811 energy distribution for several random cationic configurations. Insets show top view of three TM layers in the simulation cell for the lowest and highest energy configurations. Purple, blue grey, yellow and green tetrahedrons represent Mn, Co, Ni, Zr and Li sites.

Bayesian optimization strategies are used to identify low energy configurations of dopants in the NMC811 structure. We leverage the technology described in Garcia et al. (2021) wherein each member of an ensemble of MLFFs is trained with a subsampling with replacement of the dataset. This provides an estimate of the uncertainty propagated to the energy predictions from the variability of the MLFF parameters. By selecting configurations that best balance high uncertainty and low energy, configurations with potentially very low energies can be identified.

Using the DFT data to estimate volume change for the baseline cathode material, some differences with our previous work on LiNiO_2 (LNO) volume change (see publications) are observed. Specifically, the distribution of vacancies in NMC811 follows a solid solution model without any apparent clustering (see Figure XVI.14.2). Hence, only one phase is being observed at high state of charge (highly delithiated system). The volume change, however, remains similar for NMC811 and LiNiO_2 . The c-lattice parameter for LNO decreases by 8% while for NMC811 decreases by 7.5%.

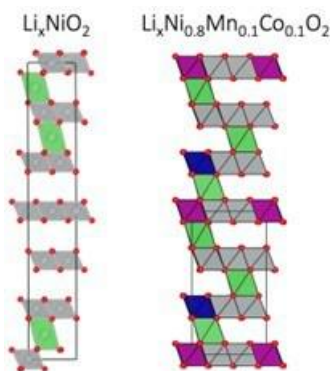


Figure XVI.14.2 Side view schematic simulation cells comparing LNO and NMC811 lowest energy Li distribution (Li content: $x = 0.12$). Purple, blue grey, and green tetrahedrons represent Mn, Co, Ni and Li sites. Small red spheres represent oxygen ions.

As a first step towards the evaluation of the volume changes upon de-lithiation of NMC811 with added dopants, DFT calculations were performed to provide training data for the DeepMDkit machine learning force fields (MLFFs). The potential energy surface was thoroughly explored to determine the most likely cation configurations and provide high quality data for the MLFFs. Figure XVI.14.3 shows the probability of occurrence for the tested conformations with one and two dopants (Zr case) in the simulation cell (3.7% and 7.4% TM atom %). The probability of occurrence for each configuration is computed using DFT energies, configurational density of states and the Boltzmann factor at three different temperatures. The configurational entropy increases the probability of occurrence of high-energy configurations w.r.t the ground state computed at 0K, and dopant concentration seem to impact the probability distribution. The volume change upon de-lithiation to a very high state of charge (SOC 2%), (see publications section) show a volume decrease by $\sim 7\%$ for pure LiNiO_2 . A decrease of $\sim 6.5\%$ in volume for the doped (Al, B, Fe, Nb, Ti, W, Zr) NMC811 cathode is calculated, showing a minimal impact. However, dopants (La, Mg, Ca) with a preference for the Li layer sites, presented a smaller decrease ($\sim 4\%$). Dopants in the Li layer act as pillars, avoiding the lattice inter-slab space collapse. The data is being processed to be presented in a publication currently in preparation.

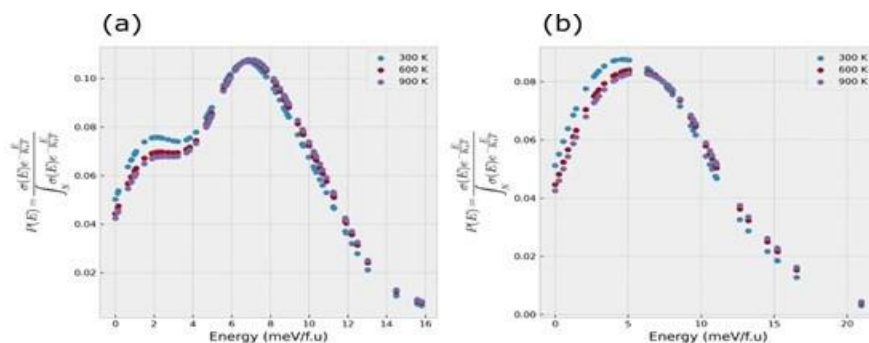


Figure XVI.14.3 Probability of occurrence of a given configuration of Zr-doped $\text{LiNi}_{0.8}\text{Mn}_{0.1}\text{Co}_{0.1}\text{O}_2$ (a) one dopant per cell [3.7% of total transition metal content] (b) two dopants per cell [7.4% of total transition metal content].

Aluminum and magnesium dopants were selected for a preliminary study to demonstrate the methodology. For a given NMC volume, the Co atoms were replaced with either 1, 2 or 3 Al or Mg atoms. The dopants were either placed in the transition metal layer or the Li-layer. From these DFT calculation results, an ensemble of five MLFFs were trained for each of Al and Mg. Ensembles were successfully trained for each dopant type with R^2 values of .987 and .998 for Al and Mg, respectively. These ensembles can be employed to estimate the uncertainty in the MLFF predictions and are therefore a critical component in the use of Bayesian optimization to identify low energy structures (as in the team's previous work with LiNiO_2). In the next quarter, these MLFF ensembles will be employed to identify the lowest energy configurations for each dopant type and concentration (for a total of 6 structures), and then to determine the volume change with de-lithiation with

estimated uncertainties. Figure XVI.14.4 shows the parity plots for the MLFF predictions of energies compared with the DFT data for Al and Mg (as representative examples of the data).

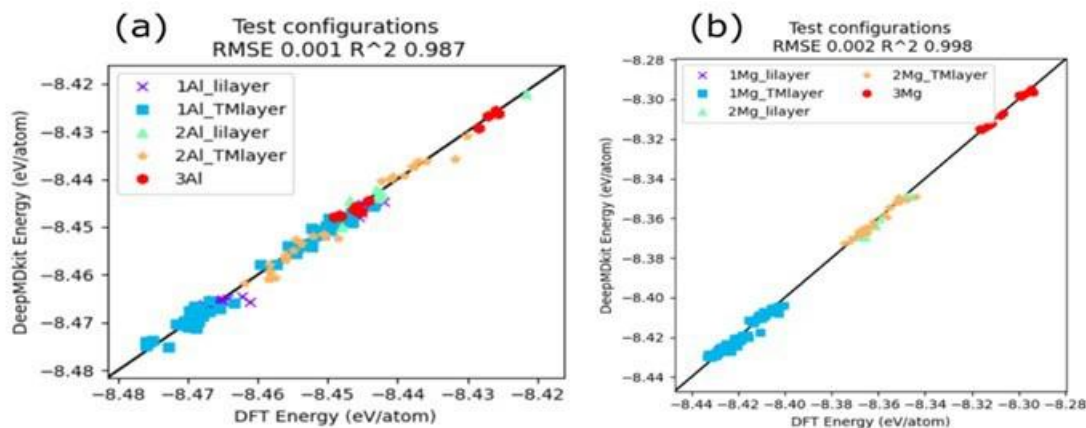


Figure XVI.14.4 Parity plots of machine learning model energies for (a) Al doped NMC811 and (b) Mg doped NMC811

We have previously demonstrated (see publication section) that the decrease in Li slab space is the main cause of volume change during charging for Ni rich materials. The Li slab space is the distance between oxygen layers adjacent to a Li layer. NMC811 has a very similar behavior to LiNiO_2 . Upon delithiation at very high SOC, the Li slab space collapses. For NMC811 the Li slab space goes from 2.58 Å when fully discharged to 2.35 Å when fully charged (0% Li), a 9.8% total decrease (see Figure XVI.14.5a). Ti, Zr, Al, Fe, Mg, Nb, B and W dopants do not have a major effect on the Li slab space collapse. They all prefer to stay in the transition metal layer of NMC811. For these dopants in the transition metal layer, the coulombic repulsions between adjacent oxygen layers at high SOC remain similar to the ones of undoped compositions. On the contrary, Ca, La and Y dopants prefer to be in the Li layer, mainly because of their size comparable or larger than Li ions. Upon delithiation these dopants stay in their octahedral position in the Li layer, acting as pillars. We found that for Ca the Li slab space decreases from 2.66 Å to 2.45 Å (see Figure XVI.14.5b), a 7.8% total decrease (compared to 9.8%). For La the Li slab space changes from 2.68 Å to 2.49 Å (see Figure XVI.14.5c), a 7.0% total decrease. Y doped NMC811 simulations present similar trends.

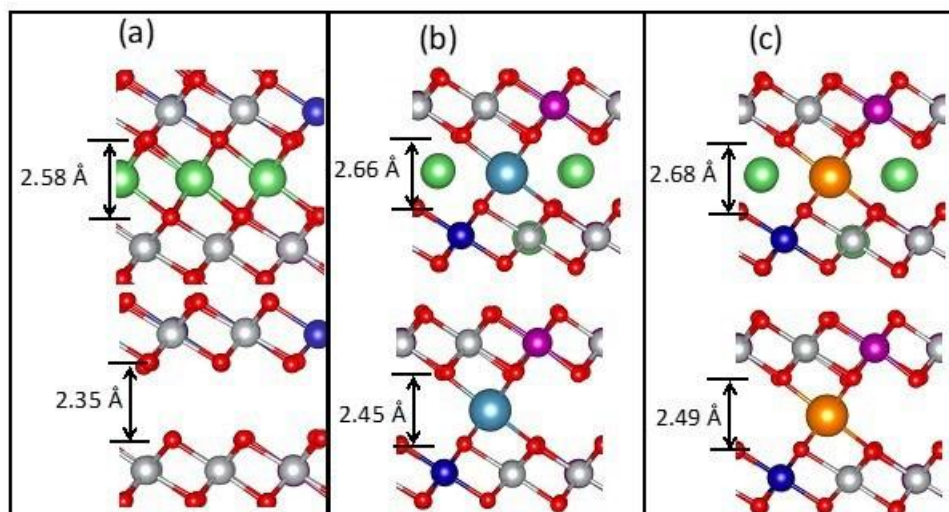


Figure XVI.14.5 Schematic representation of atomic arrangements for (a) NMC811, (b) Ca doped NMC811 and (c) La doped NMC811. Red, green, gray, purple, blue, light blue and orange spheres represent O, Li, Ni, Mn, Co, Ca and La respectively. Li slab space is also indicated.

The distribution of the dopants plays a major role in the structural characteristics of layered materials. We have tested hundreds of configurations with the dopants dispersed in NMC811. To understand the effect of temperature we have calculated the configurational density of states, that accounts for the configurational entropy of the system. Multiplying the configurational density of states by the Boltzmann factor and normalizing, we obtained the probability of occurrence of a given configuration. The probability of occurrence is equivalent to the mole fraction of a configuration in the material. Figure XVI.14.6 shows two examples of the probabilities of occurrence for Ca (Figure XVI.14.6a) and La (Figure XVI.14.6b). Given the moderate range of possible energies for these materials, the temperature has a minimal significant effect on their dispersion. For Ca (see Figure XVI.14.6a), the lowest energy configurations are characterized by Ca well dispersed and located in the Li layer. However, given the probability of finding other configurations is also high, a mixed of Ca in the Li layer and Co layer and even some clustering is possible. La dopant also prefers the Li layer. Given a narrower distribution near the ground state, La will not form clusters or be in the Co layer. Hence, La should be a suitable candidate as a dopant.

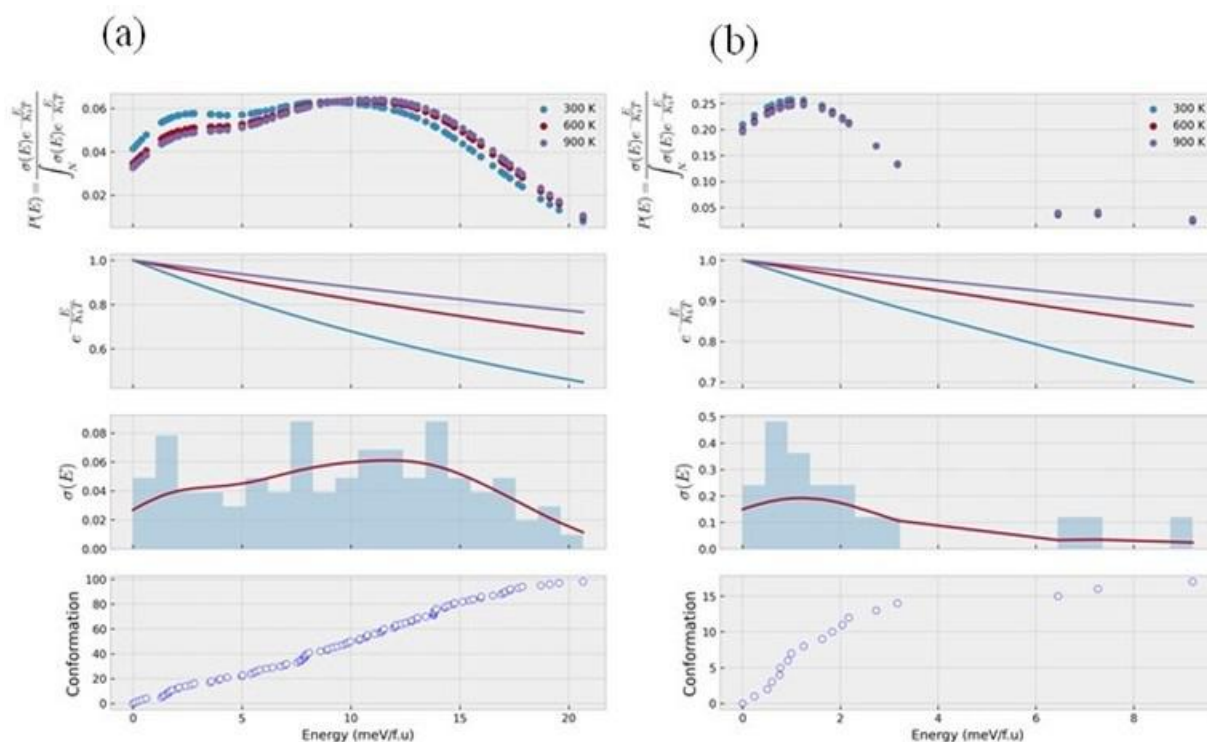


Figure XVI.14.6 Energy of configurations, configurational density of states, Boltzmann factor and probability of occurrence of each tested configuration for (a) Ca and (b) La.

A major project deliverable will be the determination of dopant/concentration that will inhibit volume contraction with cathode delithiation. This requires first determining low energy structure for different dopant configurations and concentration levels. To this end, we employ an ensemble of previously trained MLFFs to predict the total energies for many configurations and employ a batch Bayesian optimization strategy to identify a lowest energy structure via density functional theory. Figure XVI.14.7 shows the ensemble mean and standard deviation of total energies for 100,000 structures, and the structure batch Bayesian optimization would select with access to different random subsets. The figure illustrates that there is little difference between the “best” 50 structures overall and the best 50 structures selected from ten random subsets of 10,000 structures. There are six classes of configurations that must be explored. There are three different dopant concentrations (i.e. where 1, 2 or 3 out of 3 Co atoms are replaced by the dopant atom) and two mechanisms (replacement in the transition metal layer or insertion into the lithium channels), corresponding to six total

categories. The team is writing a manuscript that highlights this methodology and illustrates its use in identifying promising dopants for reducing volume changes in high-Ni battery cathode materials.

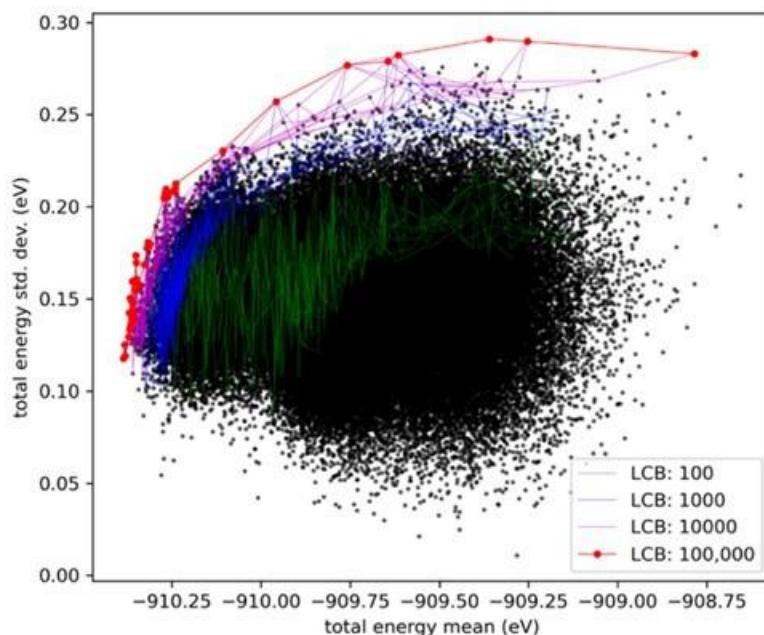


Figure XVI.14.7 The predicted ensemble mean and standard deviation total energies are plotted for each of 100,000 structures for the case where one Co atom is replaced by Mg in the transition metal layer. Structures with the best combination of low mean and high standard deviation total energy are plotted for all structure in red, and then in other colors corresponding to the most promising structures from selected subsets of structures.

It is important to highlight that the major issues in solid state batteries happen under the extreme conditions of high SOC. Structural changes in Li_xNiO_2 , as Li is removed during charging, are known to cause damage to microcrystallites of Li_xNiO_2 , limiting the lifetime and state of charge in Nickel-rich Li-ion batteries. The stacking of NiO_2 layers has been observed to change from O3 to O1 in the limit of zero Li (NiO_2). Theoretically, the energy difference between O1 and O3 stacking in NiO_2 is too small to predict reliably with DFT. Different levels of DFT theory will predict different relative energetics for O1 and O3. However, DFT predicts larger, more reliable energy differences between the stacking of layers in NiO_2 with defects and can be used to rationalize why the stacking of Li_xNiO_2 changes when x approaches zero.

To provide a possible explanation for the experimental observation of the O1 phase at high SOC, we studied the effect of proton defects in the phase transformations at high SOC of Ni-rich materials. This effort has resulted in a paper already submitted for review. We and others have examined the relative energy of O1 and O3 stacking in NiO_2 with several flavors of DFT. Gradient corrected DFT with van der Waals terms favor O1 stacking, while DFT+U, meta-functionals, and hybrid exchange with van der Waals terms favor O3 stacking. Table XVI.18.1 contains the lattice constants, volumes, energies, and relative energies for O1 and O3 stacking of NiO_2 calculated with five density functionals and experiments.

Table XVI.14.1 NiO₂ Cell parameter and energies for different oxygen stacking sequences and DFT functionals

	O1 NiO ₂				O3 NiO ₂				
	a	c	volume	Energy	a	c	Volume	Energy	E(O1-O3)
	(Å)	(Å)	(Å ³)	(eV/cell)	(Å)	(Å)	(Å ³)	(eV/cell)	(eV/cell)
Experiment (Ref.[4])	2.822	13.04	89.93						
optB86b-vdW (Ref.[1])	2.808	12.834	87.63	-31.8204	2.806	13.061	89.08	-31.8080	-0.0124
optB86b-vdW+U	2.779	13.082	87.51	-19.6138	2.779	13.200	88.26	-19.6139	0.0001
R2SCAN+D4 (Ref.[2])	2.785	13.119	88.10	-80.5317	2.784	13.218	88.75	-80.5350	0.0033
HSE06+DFTd4 (Ref.[3, 4])	2.765	13.253	87.74	-69.0278	2.766	13.238	87.72	-69.0341	0.0063

Although the optB86b-vdW predicts a geometry in reasonable agreement with experiment for structural parameters for layered materials, strong correlation is needed to predict accurate energies with changes in oxidation state associated with charging Li_xNiO₂.¹ Note that optB86b-vdW+U gives the best agreement with experiment for the c lattice parameter.

R2SCAN+DFTd4 yields a unit cell volume that agrees the best with experiment. All the methods, which include strong correlation, have c lattice parameters that are slightly longer than experiment. All density functionals in Table XVI.18.1 predict lattice constants within 2% of the experimental lattice constant. DFT correctly ranks the relative energies of phases that differ by less than 10 meV/atom about 80% of the time. Our results are consistent with perfect crystals of O1 and O3 NiO₂ having essentially the same energy. However, DFT is reliable for larger energy differences which is the focus of this study.

We decided to use the R2SCAN+D4 functional for calculations involving supercells needed for defect calculations and molecular dynamics. R2SCAN+D4 includes dispersion and predicts the lattice energies of molecular crystals to within 1 kcal/mol. Although R2SCAN+D4 is not as accurate as a nonlocal functional, it is significantly less expensive and approaches the accuracy of hybrid functionals.

We find that a proton defect favors O1 stacking over O3 in a Ni₃₆O₇₂ supercell by 90 meV. Figure XVI.14.8 compares the geometries of proton defects for O1 and O3 stacking of NiO₂. For O3 stacking, the proton points between two oxygen atoms above the hydroxyl. For O1 stacking, the O-H bond points directly at an oxygen atom in the layer above the hydroxyl. This leads to shorter (1.725 Å) and stronger H-bonds favoring O1 stacking over O3 stacking. Higher proton concentrations are expected to further enhance the stability of O1 over the O3 phase.

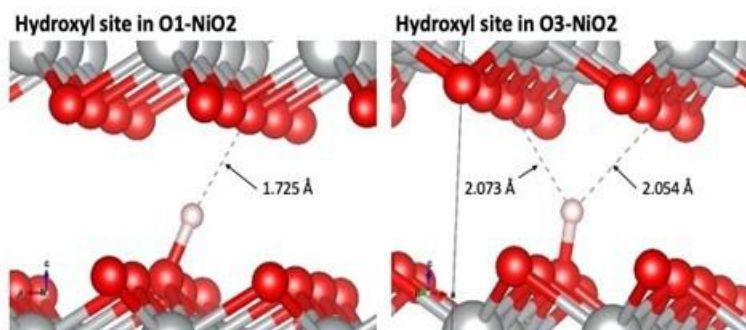


Figure XVI.14.8 Comparison of a proton defect in O1-NiO₂ and O3-NiO₂. O1-NiO₂ is on the left. O3-NiO₂ is on the right.

We have also carried out ab initio molecular dynamics (AIMD) simulations for proton motion between layers of NiO_2 . Figure XVI.14.9 shows an AIMD trajectory of a proton. The proton is bonded to oxygens in different layers at the start and end of the trajectory. Movement this fast is consistent with small barriers to proton transfer observed in the NEB calculation.

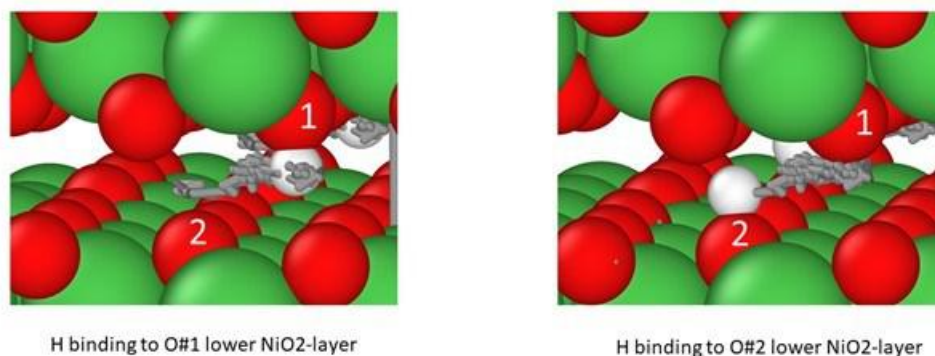


Figure XVI.14.9 A trajectory for proton motion in NiO_2 .

Reactions with the electrolyte and air generate protons that diffuse into the bulk of NiO_2 . We predict that proton defects favor the O1 phase over the O3 phase. We show that protons can diffuse in the space between layers of NiO_2 . Protons combined with oxygen defects drive the transformation from O3 stacking to O1 stacking in NiO_2 . Although O1 stacking may be thermodynamically stable relative to O3 stacking, proton defects and oxygen defects favor O1 stacking and drives the transition from O3 to O1 stacking. Modifications to NiO_2 , which suppresses the proton insertion or oxygen loss, will minimize the thermodynamics driving the change from O3 to O1 stacking and prevent structural damage to Li_xNiO_2 at a high state of charge.

Experimental validation

We have shown that dopants with the greatest impact in decreasing volume change upon delithiation are preferentially located in the Li layer. Upon delithiation these dopants stay in their octahedral position in the Li layer, acting as pillars. We found that for Ca the Li slab space decreases from 2.66 Å to 2.45 Å, a 7.8% total decrease (compared to 9.8% for the undoped system). For La the Li slab space changes from 2.68 Å to 2.49 Å, a 7.0% total decrease. In the last quarter we have been using an ensemble of previously trained machine learning force fields (MLFF) to predict the total energies for many configurations and employ a batch Bayesian optimization strategy to identify a lowest energy structure via density functional theory.

Based on the results of the dopant screening, we have started the experimental validation of the results. We have started the solubility study of La in MNC811. The doped material was prepared mixing $\text{La}(\text{NO}_3)_3$ with $\text{Ni}_{0.8}\text{Mn}_{0.1}\text{Co}_{0.1}(\text{OH})_2$, dry it overnight in a N_2 atmosphere and then calcine at 720 °C for 12 hours in an oxygen atmosphere. We tested 1%, 3% and 5% target La compositions. According with the preliminary data the solubility of La in MNC811 is less than 1%. A side phase is formed during synthesis. As seen in the X-ray diffraction on Figure XVI.14.3 the phase $\text{La}_2\text{Li}_{0.5}\text{M}_{0.5}\text{O}_4$ ($\text{M}=\text{Ni}, \text{Co}$) is present. However, the lattice parameter of the doped material changed with the respect to pure MNC811. This may be evidence of some La insertion. Refinement of experimental conditions and lattice parameters upon delithiation is in progress.

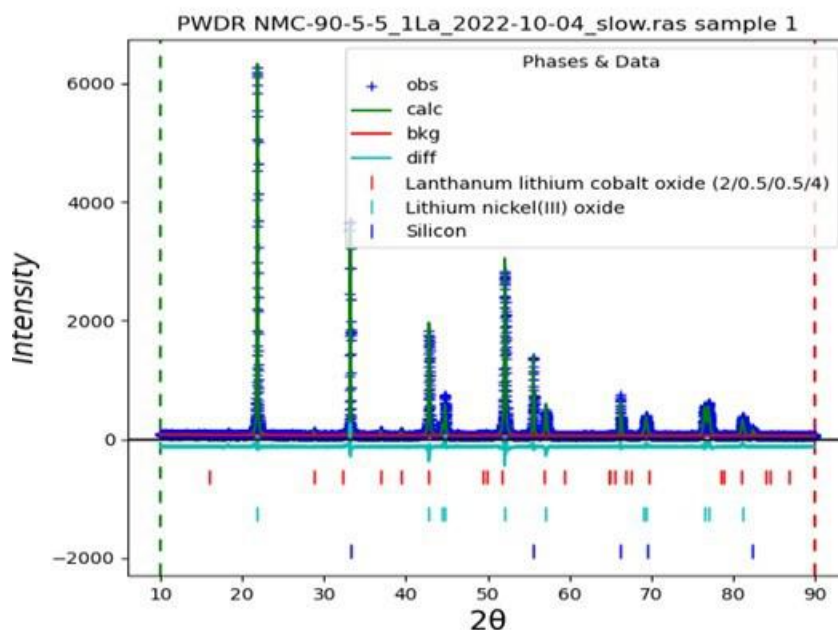


Figure XVI.14.10 X-ray diffraction of La doped NMC811 material.

Conclusions

A machine learning methodology was developed and tested to investigate the effect of Li content and dopants on the volume change in Ni—rich cathode materials. The results obtained using state-of-the-art DFT methods show that the volume collapse at high state of charge is mostly independent of the oxygen stacking sequence. DFT results suggest that large ions prefer to be in the Li layer act as pillars and reduce the collapse of the c lattice parameter at high state of charge. Experimental validation is in progress to test other factors such as the feasibility of doping the material at the right concentration.

Key Publications

Papers

1. Garcia, J. C.; Gabriel, J.; Paulson, N. H.; Low, J.; Stan, M.; Iddir, H. Insights from Computational Studies on the Anisotropic Volume Change of Li_xNiO_2 at High States of Charge ($x < 0.25$). *J. Phys. Chem. C* **2021**. <https://doi.org/10.1021/acs.jpcc.1c08022>.
2. Low, J.; Garcia, J. C.; Iddir, H. On proton defects and the phase transformation of NiO_2 . (revision submitted to *J. Phys. Chem. C*)
3. Garcia, J. C.; Paulson, N. H.; Low, J.; Iddir, H. Effect of dopants on volume change at high state of charge for Ni rich cathode materials. (In preparation)

Presentations

1. Gabriel, Joshua, Juan Garcia, Noah Paulson, John Low, Marius Stan and Hakim Iddir. "Machine Learning Force Fields for high Nickel Li ion cathodes." Abstract of presentation at the 2021 AIChE Midwest Regional Virtual Conference, March 17, 2021 - March 18, 2021.
2. Paulson, N.H., "Deep-Learned Interatomic Potentials to Simulate Volume Change in Cathode Materials" NREL Machine Learning for Batteries Virtual Workshop, March 23, 2021.
3. Alex Tai, Joshua Gabriel, Noah Paulson, Juan Garcia, John Low, Hakim Iddir, **Exploring Solid State Cathode Materials Space** (2021 NAISE Undergraduate Interns Symposium - (US, 08/01/21-08/16/21))

References

1. Kresse, G.; Furthmüller, J. Efficiency of Ab-Initio Total Energy Calculations for Metals and Semiconductors Using a Plane-Wave Basis Set. *Comput. Mater. Sci.* **1996**, *6* (1), 15–50. [https://doi.org/10.1016/0927-0256\(96\)00008-0](https://doi.org/10.1016/0927-0256(96)00008-0).
2. Kresse, G.; Hafner, J. Ab Initio Molecular Dynamics for Liquid Metals. *Phys. Rev. B* **1993**, *47* (1), 558–561. <https://doi.org/10.1103/PhysRevB.47.558>.
3. Heyd, J.; Scuseria, G. E.; Ernzerhof, M. Hybrid Functionals Based on a Screened Coulomb Potential. *J. Chem. Phys.* **2003**, *118* (18), 8207–8215. <https://doi.org/10.1063/1.1564060>.
4. Zhang, L.; Han, J.; Wang, H.; Saidi, W.; Car, R.; E, W. End-to-End Symmetry Preserving Inter-Atomic Potential Energy Model for Finite and Extended Systems. In *Advances in Neural Information Processing Systems 31*; Bengio, S., Wallach, H., Larochelle, H., Grauman, K., Cesa-Bianchi, N., Garnett, R., Eds.; Curran Associates, Inc., 2018; pp 4436–4446.
5. Croguennec, L.; Pouillier, C.; Mansour, A. N.; Delmas, C. Structural Characterisation of the Highly Deintercalated $\text{Li}_x\text{Ni}_{1.02}\text{O}_2$ Phases (with $x \leq 0.30$). *J. Mater. Chem.* **2001**, *11* (1), 131–141. <https://doi.org/10.1039/B003377O>.
6. Xu, C.; Reeves, P. J.; Jacquet, Q.; Grey, C. P. Phase Behavior during Electrochemical Cycling of Ni-Rich Cathode Materials for Li-Ion Batteries. *Adv. Energy Mater.* **2021**, *11* (7), 2003404. <https://doi.org/10.1002/aenm.202003404>.
7. Park, K.-Y.; Zhu, Y.; Torres-Castaneda, C. G.; Jung, H. J.; Luu, N. S.; Kahvecioglu, O.; Yoo, Y.; Seo, J.-W. T.; Downing, J. R.; Lim, H.-D.; Bedzyk, M. J.; Wolverton, C.; Hersam, M. C. Elucidating and Mitigating High-Voltage Degradation Cascades in Cobalt-Free LiNiO_2 Lithium-Ion Battery Cathodes. *Adv. Mater.* **2022**, *34* (3), 2106402. <https://doi.org/10.1002/adma.202106402>.
8. Lee, S. H.; Rasaiah, J. C. Proton Transfer and the Mobilities of the H^+ and OH^- Ions from Studies of a Dissociating Model for Water. *J. Chem. Phys.* **2011**, *135* (12), 124505. <https://doi.org/10.1063/1.3632990>.
9. Park, J.-S. Comparison Study of Exchange-Correlation Functionals on Prediction of Ground States and Structural Properties. *Curr. Appl. Phys.* **2021**, *22*, 61–64. <https://doi.org/10.1016/j.cap.2020.12.005>.

Acknowledgements

This work is performed by the Strain-Free project team: Juan Garcia, Noah Paulson, John Low and David Carter from Argonne National Laboratory, using the computational resources at NREL and ANL (LCRC).

XVI.15 Enabling continuous production of defect-free, ultrathin sulfide glass electrolytes for next generation solid state lithium metal batteries (ANL)

Tim Fister, Principal Investigator

Argonne National Laboratory
9700 South Cass Avenue
Lemont, IL 60439
E-mail: fister@anl.gov

Simon Thompson, DOE Technology Development Manager

U.S. Department of Energy
E-mail: Simon.Thompson@ee.doe.gov

Start Date: October 1, 2020

End Date: September 30, 2023

Project Funding (FY22): \$167,000

DOE share: \$167,000

Non-DOE share: \$0

Project Introduction

Sulfide glass materials are one of the most appealing candidates for solid state batteries due to their superior performance using relatively inexpensive raw materials. Glass materials prepared from a melt, unlike ball milled sulfides or polycrystalline electrolytes, also lack the void space and grain boundaries that are often weak points for lithium dendrites or decomposition species. In practice these glasses are not entirely defect free and can have isolated defects such as bubbles or crystalline inclusions formed during manufacture and processing. Recent advances from PolyPlus have demonstrated the ability to draw glasses to thicknesses approaching 10-20 microns. These thicknesses produce a flexible glass that is compatible with roll-to-roll manufacturing, but impurities become an even more negative design parameter in this regime.

Objectives

The goal of this project is to identify the source of defects in sulfide glasses and understand their impact on the mechanical and electrochemical stability of the solid electrolyte. Understanding the distribution, size, and composition of these defects, and identifying ways to mitigate them, is a critical requirement for achieving ultrathin glass sheets necessary for a roll-to-roll manufacturer to build them into cylindrical format cells.

Approach

This project focuses on sulfide glasses developed and produced at PolyPlus and uses advanced synchrotron and optical methods at Argonne National Laboratory to identify and analyze defects in glass samples ranging from 20-1000 μm in thickness. Analytical methods developed in this project will focus on buried defects within the glass and reactions that form at the surface and electrode interface, both from processing and electrochemical treatments, as illustrated in Figure XVI.15.1.

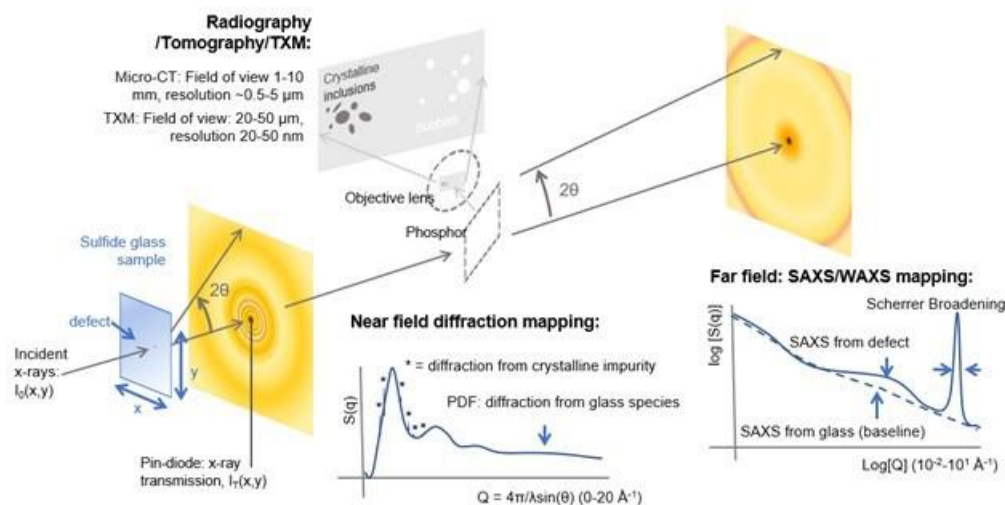


Figure XVI.15.1 Schematic of multimodal synchrotron analysis of sulfide glass samples.

During the second two quarters of this project, Argonne and PolyPlus established processing parameters to improve homogeneity and reduce crystalline impurities. Argonne developed phase analysis approaches to screen for crystalline impurities or phase heterogeneity in the sulfide glass using the x-ray diffraction measurements that mapped over the entire volume of sulfide glass samples provided by PolyPlus. These feasibility measurements showed that these techniques are uniquely sensitive to the atomic structure of the glasses and that the x-rays were easily capable of measuring 100 μm thick glass samples and will be able to resolve structure in the final ultrathin samples. A multi-modal approach was also developed to provide simultaneous x-ray and optical characterization (Figure XVI.15.2). Preliminary Raman experiments provide similar data to previous characterized Li-S-B glasses.

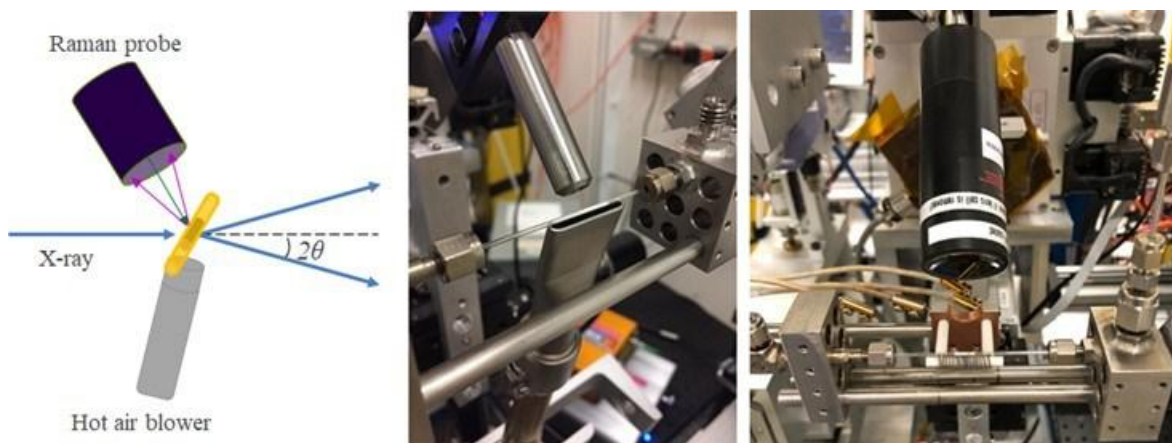


Figure XVI.15.2 Schematic of an in-situ Raman and diffraction technique for multiple sample environments.

Development of low discharge optical emission spectroscopy (GDOES) is ongoing but has demonstrated elemental sensitivity on elements as light as Li, although the setup requires further optimization including minimized re-deposition, calibration standards for each element, and sputtering rate (Figure XVI.15.3).

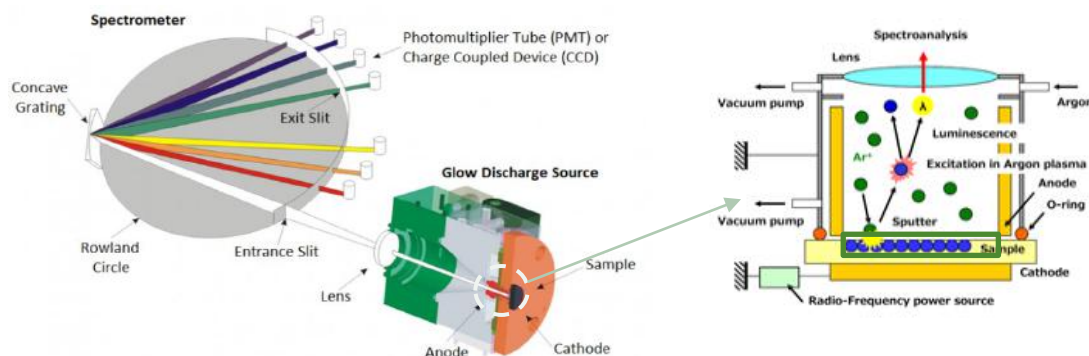


Figure XVI.15.3 Schematic of GDOES chemical composition depth profiling instrumentation.

Results

Synchrotron x-ray experiments at the Advanced Photon Source (APS) focused on determining the differences in glass manufacture and processing using a phase analysis approach to identify possible sources for impurity inclusions and ways to mitigate removal. The phase analysis approach maps the impurities with x-ray scattering from the sulfides in XRD regimes as shown in Figure XVI.15.4. The phase analysis approach developed uses principal component analysis or a K-means clustering algorithm to screen for crystalline impurities or phase heterogeneity in the sulfide glass itself.

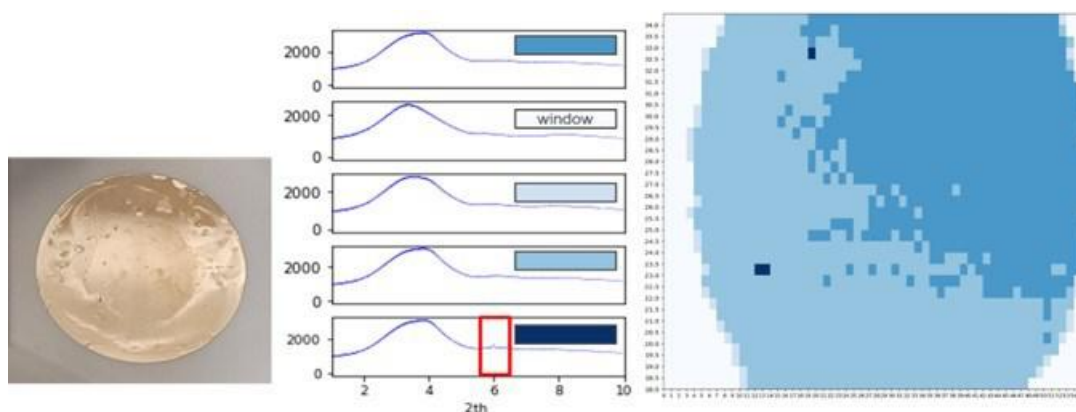


Figure XVI.15.4 K-means clustering phase analysis of a Li-B-S glass with both phase heterogeneity due glass thickness and noncrystalline impurities.

Processing parameters tested to improve homogeneity and reduce crystalline impurities are listed in Table XVI.15.1. The impact from differences in the post-processing parameters on the crystalline impurities or phase heterogeneity in the sulfide glass is shown in Figure XVI.15.5, with an ion gun post-processing treatment significantly reducing the crystalline impurities. Pre-processing parameters that mitigate air contamination minimize the crystalline impurities. Since diffraction peaks were largely related to crystallized forms of the glass, the concentration of defects could be quantified simply by normalizing the integrated intensity of the Bragg peaks by the overall glass signal.

Table XVI.15.1 Processing parameters to reduce or remove crystalline impurities

Sample	Standard	Hot press	Post-processing	
			Ion gun	Polished
1	X			
2			X	
3		X	X	
4		X		X
5	X	X		

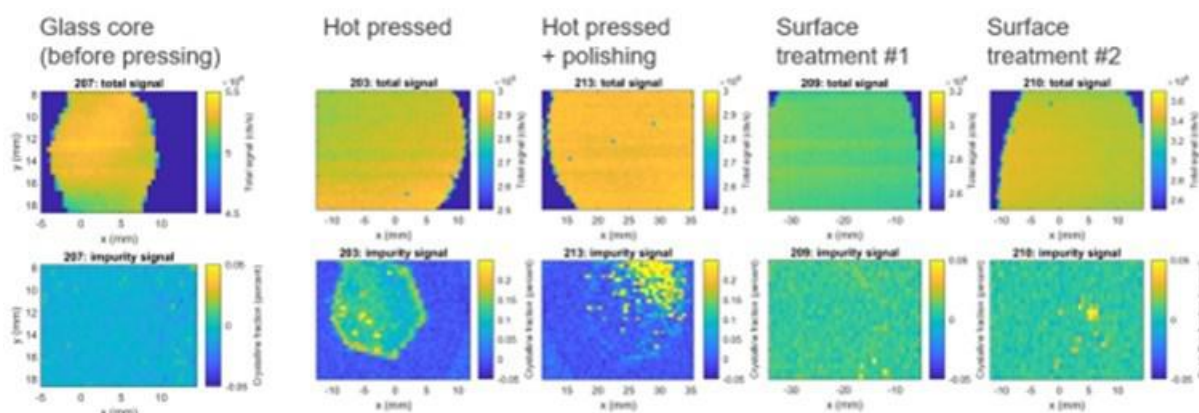


Figure XVI.15.5 Phase analysis maps show the influence of different processing parameters on crystalline impurities. Note that synchrotron XRD can measure crystalline impurity levels to $\sim 0.01\%$.

An in-situ Raman and diffraction technique has been developed to probe the structural properties of both the bulk material and impurities. The complementary methods provide simultaneous x-ray and optical characterization. Preliminary Raman spectra are shown in Figure XVI.15.6 for two Li-B-S glasses are similar to reported LiBS_2 glasses.¹ Future phase analysis of glass electrolytes will include this multi-modal approach.

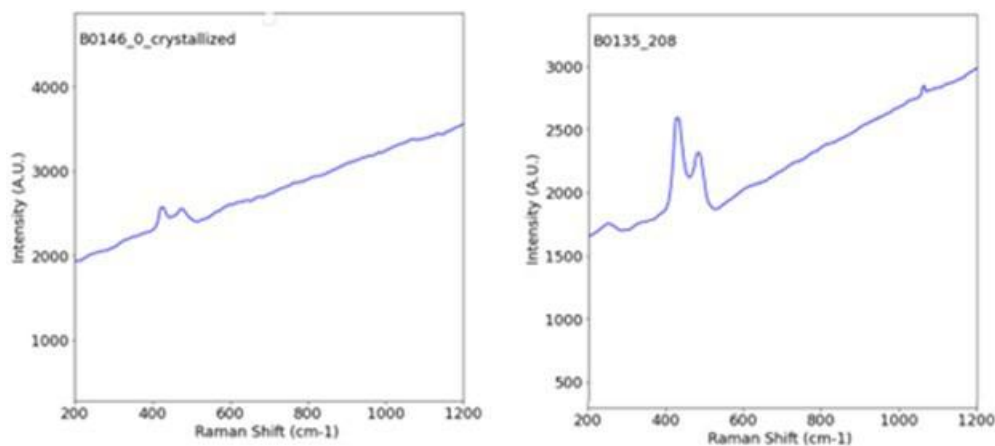


Figure XVI.15.6 The Raman spectra for two Li-B-S glasses, the first of which was intentionally crystallized.

Changes in composition near-surface and in the bulk of glass electrolytes were evaluated using GDOES to identify extra species related to processing of glass disks (Figure XVI.15.7). The sputtering power was optimized from 2.5 W (mild) to 5 W to probe from the surface to the bulk region of the glass electrolytes. Preliminary GDOES results for the surface composition show the major components are B, Li, and S with

some surface enrichment of Li and S regions. Both Mg and N impurities were found in the bulk composition. Development of a transfer chamber to avoid air exposure is underway for GDOES as the commercially available is not air tight. Interfacial characterization of the glass materials will be emphasized in the coming year of this project. This will include optical analysis of features within the glass and at an electrode/glass interface using digital holographic microscopy and x-ray imaging methods.

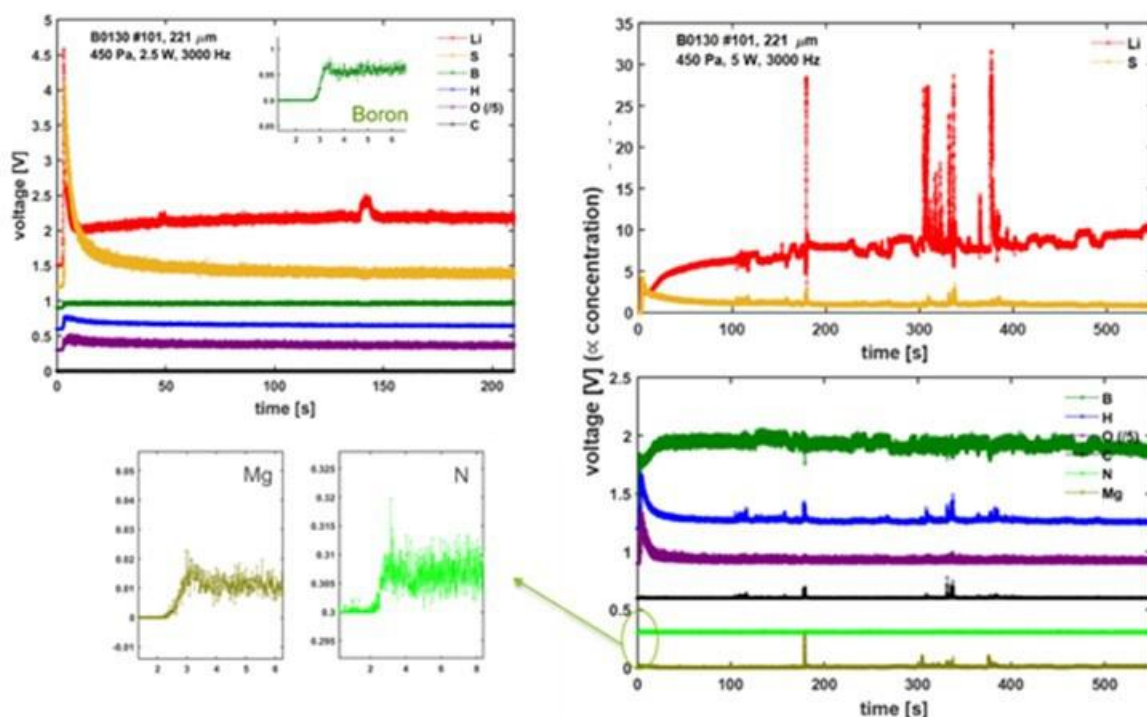


Figure XVI.15.7 Changes in composition near-surface and in the bulk of Li-B-S electrolytes were evaluated using GDOES.

Conclusions

- Used K-means clustering algorithm to quantify heterogeneity in both crystalline and amorphous species for characterizing bulk structure of sulfide glass electrolytes ranging from 100-1000 μm thick.
- Determine pre and post-processing procedures that improve homogeneity by reducing crystalline impurities.
- Developed a multi-modal approach to provide simultaneous x-ray and optical characterization.
- Initial GDOES measurements show sensitivity to composition gradients at the surface or bulk glass samples.

References

1. Tatsumisago, M. et al. *J. Am. Ceram. Soc.*, 71 (9) 766-769 (1988)

XVI.16 Stable Solid-State Electrolyte and Interface for High-Energy All-Solid-State Lithium-Sulfur Battery (PNNL)

Dongping Lu, Principal Investigator

Pacific Northwest National Laboratory
902 Battelle Blvd.
Richland, WA 99354
E-mail: dongping.lu@pnnl.gov

Simon Thompson, DOE Technology Development Manager

U.S. Department of Energy
E-mail: Simon.Thompson@ee.doe.gov

Start Date: January 31, 2022

End Date: September 30, 2027

Project Funding (FY22): \$700,000

DOE share: \$700,000

Non-DOE share: \$0

Project Introduction

All solid-state-lithium batteries (ASSLBs) have potential to achieve higher energy and power density, extending the range of electric vehicles and reducing charging time simultaneously. Although oxides are intrinsically more stable than sulfides, sulfide solid state electrolytes (S-SSEs) are arguably more viable for bulk-type ASSLBs. This stems from sulfides' low material density, low elastic modulus, and high ionic conductivity, which allows intimate contact with active materials and practical processibility through industrial slurry or dry processing. Following the work on $\text{Li}_{10}\text{GeP}_2\text{S}_{12}$ (LGPS), a series of sulfide-based compounds displaying extremely high ionic conductivities ($> 10^{-2}$ S/cm) have been developed. By using surface coated cathodes and S-SSEs, stable cycling of LiCoO_2 cells and high energy $\text{LiNi}_x\text{Mn}_y\text{Co}_{(1-x-y)}$ cells have been demonstrated, proving viability of S-SSEs for high performance ASSLBs. More promisingly, S-SSEs are compatible with sulfur both chemically and electrochemically and thus are feasible for direct sulfur cathode application without using any protective cathode coating. Despite high expectations for S-SSEs, there are significant materials and interfacial challenges that need to be addressed before practical technology deployment. These challenges include materials moisture sensitivity, Li/SSE interfacial stability, and scalable processing of SSE film and SSE contained cathodes. Moreover, to improve energy in ASSLBs, the SSE membrane thickness should be minimized while the cathode mass loading should be practically high. This is especially important in all solid-state Li-S battery due to the relative low working voltage of S (1.9 V vs. Li). To reach a cell level energy > 500 Wh/kg in a 2 Ah pouch cell, the S cathode areal capacity should be > 8 mAh/cm², which must in turn be charge balanced by the same amount of Li stripping/plating at the anode side. However, such deep Li cycling causes significant challenges to the metallic Li anode including large volume change, reaction nonuniformity, pressure variation, and Li dendrite formation. Although S-SSEs allow Li metal cycling at certain current densities and areal capacities, stable Li cycling at the capacities matching high-areal-capacity S cathodes is still beyond reach. This is why most long cycling of S cathodes had to use Li-In or other alloy-based anodes, which unfortunately sacrifices cell energy due to the heavy material (In: 7.3 g/cm³) and its high working voltage (0.6 V vs. Li). Thus, in addition to the challenges of ionic conductivity, chemical stability, and interfacial properties, achieving highly reversible Li plating/stripping at high areal capacities is another key step toward stable operation of ASSLBs. Comprehensive strategies built on innovations of material development, interfacial design, chemo-mechanical management, and viable processing are essential to overcome the existing barriers faced by the practical ASSLBs.

Objectives

This project focuses on addressing material and interfacial barriers of sulfide-based solid-state electrolyte (SSE) for deep cycling of Li metal anode in all-solid-state Li batteries (ASSLBs). The ultimate goals are:

1. Development of Li metal compatible S-SSEs with low Li/SSE interfacial resistance and high room-temperature Li^+ conductivity
2. Enabling safe Li plating/stripping at a critical current density $> 1 \text{ mA/cm}^2$ for long-term cycling
3. Ultra-thin multifunctional interlayer to enable deep and stable Li cycling.
4. Dry extrusion-lamination processing of a SSE/interlayer bilayer assembly ($< 100 \text{ }\mu\text{m}$) with an overall ionic conductivity $> 1 \text{ mS/cm}$.
5. Validation test of solid electrolytes and processing technology in realistic Li-S pouch cells with an energy target of 500 Wh/Kg .

Approach

1. Develop halogen doped sulfide SSE to minimize Li/SSE areal interfacial resistance ($\text{AIR} < 5 \text{ }\Omega\text{cm}^2$) and improve room temperature (r.t.) Li^+ conductivity ($\sigma \sim 6 \text{ mS/cm}$).
2. Development of surface treatment approach to improve moisture stability of sulfide solid electrolyte.
3. Optimization, characterization, and simulation of Li/SSE interface and its dynamics.
4. Electrolyte composition and cell optimization to improve critical current density ($\text{CCD} > 1 \text{ mA/cm}^2$) and Li/SSE/Li cycle life (> 400 cycles).

Results

Development of sulfide solid electrolytes with low lithium interfacial resistance ($\text{AIR} < 5 \text{ }\Omega\text{cm}^2$) and high r.t. Li^+ conductivity ($\sigma > 5 \text{ mS/cm}$).

The dual-halogen-doped sulfide SSE $\text{Li}_7\text{P}_2\text{S}_8\text{Br}_{1-x}\text{I}_x$ ($0 \leq x \leq 1$) was synthesized by a mechanochemical method through careful control of types and relative contents of the halogen dopants. Figure XVI.16.1a compares the powder X-ray diffraction (XRD) patterns of the $\text{Li}_7\text{P}_2\text{S}_8\text{Br}_{1-x}\text{I}_x$ ($0 \leq x \leq 1$) by varying the halogen dopants of Br and I. Diffraction peaks of Beryllium (Be) from the sample holder are marked and used as an internal reference. Peaks centered at 28.2° and 32.6° are detected in $\text{Li}_7\text{P}_2\text{S}_8\text{Br}$ ($x=0$) and ascribed to the unreacted LiBr. We gradually decreased the content of LiBr in $\text{Li}_7\text{P}_2\text{S}_8\text{Br}_x$ until it disappeared in XRD and found the corresponding composition was $\text{Li}_{6.7}\text{P}_2\text{S}_8\text{Br}_{0.7}$. Therefore, the $\text{Li}_7\text{P}_2\text{S}_8\text{Br}$ is in a composite form with actual composition of $\text{Li}_{6.7}\text{P}_2\text{S}_8\text{Br}_{0.7}-(\text{LiBr})_{0.3}$. With increase of LiI content in $\text{Li}_7\text{P}_2\text{S}_8\text{Br}_{1-x}\text{I}_x$, the peak at around 29.6° , corresponding to plane (211) of $\text{Li}_{6.7}\text{P}_2\text{S}_8\text{Br}_{0.7}$, shifts to a smaller angle (Figure XVI.16.1a). Considering the larger ionic radius of I^- ($2.06 \text{ }\text{\AA}$) versus Br^- ($1.82 \text{ }\text{\AA}$), this suggests that element Br^- was successfully substituted by I^- in the structure. Moreover, the intensity of LiBr peak decreases with the increase of LiI and completely disappears after x approaches 0.5. When $x \geq 0.8$, two new peaks, centered at around 21° and 31° , show up in $\text{Li}_7\text{P}_2\text{S}_8\text{Br}_{1-x}\text{I}_x$, suggesting the formation of a $\text{Li}_4\text{PS}_4\text{I}$ -type phase (also considered as $\text{Li}_7\text{P}_2\text{S}_8\text{I}$ high temperature phase). No LiI peaks are detected in all XRD patterns. Given the phase evolutions upon incorporating LiI into $\text{Li}_7\text{P}_2\text{S}_8\text{Br}_{1-x}\text{I}_x$ ($0 \leq x \leq 1$), we believe that partial amounts of LiI contribute to the sulfide phase formation and the rest stay as amorphous LiI when $x \geq 0.5$, forming a mosaic composite structure where the conductive sulfides are the cores.

The halogen doping has an important effect on ionic conductivity of the SSEs. Figure XVI.16.1b shows Li^+ conductivity of $\text{Li}_7\text{P}_2\text{S}_8\text{Br}_{1-x}\text{I}_x$ ($0 \leq x \leq 1$) as a function of x at 20°C . Without any I, the $\text{Li}_7\text{P}_2\text{S}_8\text{Br}$ ($x=0$) has a Li^+ conductivity (σ) of 1.9 mS cm^{-1} . With increase of I concentration, the ionic conductivity of $\text{Li}_7\text{P}_2\text{S}_8\text{Br}_{1-x}\text{I}_x$ increases, which is believed due to the formation of I substituted phase and existence of amorphous LiI. The LiI possesses a relatively high intrinsic ionic conductivity ($10^{-5} \text{ mS cm}^{-1}$ at 25°C), and its amorphous state and uniform distribution among the sulfide particles form an ionic conductive network, lowering solid-solid boundary resistance. The ionic conductivity reaches an extremely high value of 5.9 mS cm^{-1} at $x = 0.5$, suggesting an optimal crystal/amorphous ratio in the mosaic structure. Beyond the point $x = 0.5$, a decreasing trend of σ was observed from 4.4 mS cm^{-1} for $\text{Li}_7\text{P}_2\text{S}_8\text{Br}_{0.2}\text{I}_{0.8}$ to 3.6 mS cm^{-1} for $\text{Li}_7\text{P}_2\text{S}_8\text{I}$. This is because the excess of I is barely doped into the crystalline phase; instead, it increases the thickness of the amorphous layer and thus its interfacial resistance. In comparison with other reported electrolytes, the $\text{Li}_7\text{P}_2\text{S}_8\text{Br}_{0.5}\text{I}_{0.5}$ through cold pressed pellet shows a comparable ionic conductivity with other LISICON, $\text{Li}_7\text{P}_3\text{S}_{11}$, and $\text{Li}_{10}\text{GeP}_2\text{S}_{12}$ electrolytes.

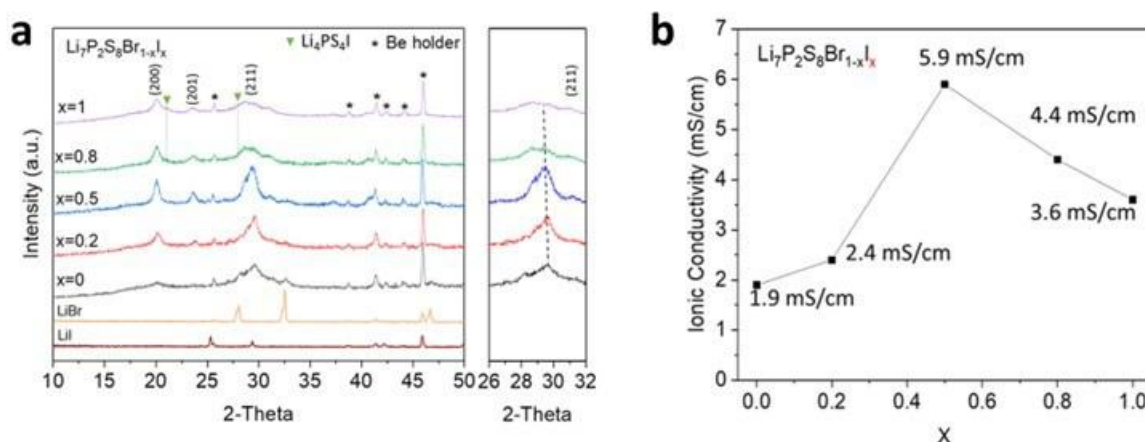


Figure XVI.16.1 (a) XRD patterns and (b) ionic conductivities of $\text{Li}_7\text{P}_2\text{S}_8\text{Br}_{1-x}\text{I}_x$ ($0 \leq x \leq 1$) at 20 °C.

Amphipathic molecular coating to improve moisture stability of sulfide solid electrolytes

Sulfide-based solid-state electrolytes (SSEs) have merits of low density, high ionic conductivity, and favorable mechanical properties compared to the oxide ceramic and polymer materials. However, mass production and processing of sulfide SSEs remain an ongoing challenge due to their poor moisture stability. To address those issues, we developed a reversible surface coating strategy for enhancing the moisture stability of sulfide SSEs by using amphipathic organic molecules (AOMs). An ultra-thin amphipathic organic layer (1-Bromopentane) was coated on the sulfide SSE surface (e.g., $\text{Li}_7\text{P}_2\text{S}_8\text{Br}_{0.5}\text{I}_{0.5}$ (LPSBI)) via van der Waals forces. 1-Bromopentane has more negative adsorption energy with SSE than H_2O based on first-principles calculations, thereby enhancing the moisture stability of SSE because the hydrophobic long-chain alkyl tail of 1-Bromopentane repels water molecules. The weight gained after the process was measured at 0.97 wt.%, indicating that a very thin layer of molecules was coated on the surface of LPSBI. Moreover, this amphipathic molecular layer has a negligible effect on ionic conductivity and can be removed reversibly by heating at low temperatures (e.g., 160 °C).

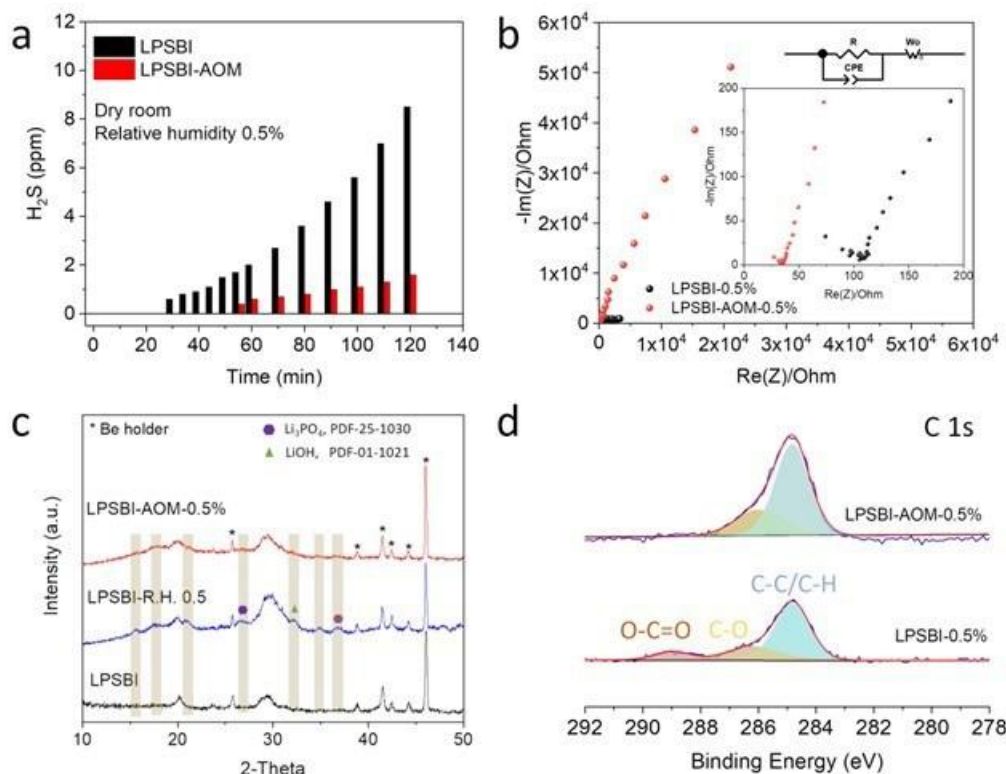


Figure XVI.16.2 a) Measurement of H_2S release, b) electrochemical impedance spectra (EIS), c) XRD patterns, and d) high-resolution C 1s spectra of $Li_7P_2S_8Br_{0.5}I_{0.5}$ powders with/without amphipathic organic molecules coating exposed to air with a relative humidity of 0.5% in a dry room.

To investigate the effects of AOM coating on the moisture stability of LPSBI, we monitored the H_2S generation from LPSBI and LPSBI-AOM during dry-room exposure (R.H. = 0.5%) for 120 minutes. As shown in Figure XVI.16.2a, the concentration of H_2S gas released from pristine LPSBI increases to 8.9 ppm at 120 min. In sharp contrast, the concentration of H_2S gas is as low as 1.6 ppm for LPSBI-AOM during the 120 min exposure, which is 82% less than the amount from pristine LPSBI. When comparing the accumulated H_2S in the first 40 minutes, which is a typical processing time for electrodes or solid separators in mass production, the H_2S concentration is below the detection limit. This indicates that the AOM coating almost completely shuts down the reactions between LPSBI and H_2O and dramatically enhances the moisture stability of LPSBI. Figure XVI.16.2b compares the EIS of LPSBI before and after exposure to air with an R.H. of 0.5%. The data is analyzed by fitting the spectra to an equivalent electrical circuit, composed of a constant phase element (CPE) in parallel with an Ohmic resistance (R), representing the impedance of Li-ion transport through the bulk/grain and grain boundary, and a Warburg impedance (W_o), representing impedance contributions from the electrode. Upon exposure, a semicircle is detected in the EIS of LPSBI-0.5%, corresponding to an overall impedance due mainly to the reactions between LPSBI and H_2O . The calculated ionic conductivity of LPSBI-0.5% is 0.8 mS cm^{-1} , an 85% drop compared with that of the pristine LPSBI before exposure (5.3 mS cm^{-1}). In contrast, the calculated ionic conductivity for LPSBI-AOM-0.5% is 2.5 mS cm^{-1} , which is three times higher than that for LPSBI-0.5%. The powder XRD patterns of the exposed LPSBI with/without AOM are presented in Figure XVI.16.2c. Compared to the pristine LPSBI, additional peaks are observed in both LPSBI-0.5% and LPSBI-AOM-0.5%, some of which are indexed to Li_3PO_4 and $LiOH$, indicating reactions between sulfide samples and moisture. In addition, these peaks appear to be much sharper in the LPSBI-0.5% sample, especially for the peaks corresponding to Li_3PO_4 and $LiOH$, suggesting more severe reactions between LPSBI and moisture, which corresponds with the observations of H_2S formation. To study details of the surfaces of these samples before and after exposure, XPS measurements were conducted on LPSBI-0.5% and LPSBI-AOM-0.5% powders. Figure XVI.16.2d shows the high-resolution C 1s spectra of these powders. In

comparison to LPSBI-AOM-0.5% XPS results, a peak centered at ~ 288.8 eV, corresponding to $\text{O}-\text{C}=\text{O}$, is detected in LPSBI-0.5%, indicating that carbonate species could be the products of the reactions between LPSBI and $\text{H}_2\text{O}/\text{CO}_2$ in air.

Optimization, characterization, and simulation of coated sulfide solid electrolytes and the Li/SSE interfaces

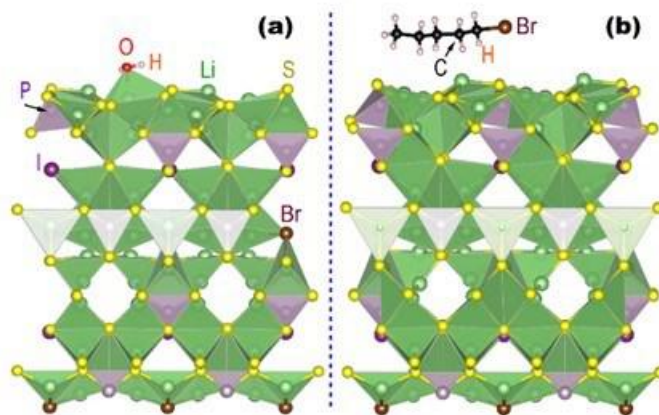


Figure XVI.16.3 Adsorption of a) H_2O or b) 1BR on the stable surface of $\text{Li}_7\text{P}_2\text{S}_8\text{Br}_{0.5}$ (LPSBI). The adsorption of 1BR on LPBSI with $E_{\text{ad}} = -0.9 \pm 0.7$ eV/adsorbate-atom is favorable compared to H_2O on LPSBI with $E_{\text{ad}} = -0.1 \pm 0.8$ eV/adsorbate-atom.

The mechanism of improved moisture stability due to the introduced 1-Bromopentane (1BR) coating was studied by examining the adsorption energy of adsorbate (H_2O vs. 1BR molecule) on the LPSBI surface through first-principles calculations based on density functional theory (DFT). $E_{\text{ad}} = E_{\text{adsorbate/LPSBI}} - E_{\text{adsorbate}} - E_{\text{LPSBI}}$ (1), where $E_{\text{adsorbate/LPSBI}}$ is the total energy of the adsorbed H_2O or 1BR on the surface of LPSBI, $E_{\text{adsorbate}}$ is the total energy of an isolated H_2O or 1BR molecule, and E_{LPSBI} is the total energy of the relaxed bare LPSBI slab. Equation (1) indicates that a negative adsorption energy (E_{ad}) corresponds to a favorable adsorption process (i.e., a strong bonding of adsorbate with respect to 1BR), and *vice versa*. Figure XVI.16.3 illustrates the adsorptions of H_2O and 1BR, respectively, on the surface of LPSBI after structural relaxations by first-principles calculations. It is indicated that the atom O in H_2O is connected to Li^+ with a bond length of 2.05 Å, while O is far from the other ions (P^{5+} , S^{2-} , Br^- , and I^-) on the surface of LPSBI (> 3.2 Å). For 1BR, the atom Br does not have a distinct bonding preference associated with the ions on the surface of LPSBI, as suggested by its long bond lengths (> 4.2 Å) with respect to the ions of S, Li, and P. The longer bond length of 1BR with respect to LPSBI compared with that of H_2O is due mainly to the larger volume of 1BR molecule and Br ion (e.g., the atomic radius is 120 pm for Br, while it is 66 pm for O). However, when extracting the absorption energy, the adsorption of 1BR on LPBSI is very favorable (i.e., showing a stronger bonding) compared to that of H_2O on LPSBI. The adsorption of 1BR on LPBSI has a $E_{\text{ad}} = -0.9 \pm 0.7$ eV (per adsorbate-atom), which is much lower than that of H_2O ($E_{\text{ad}} = -0.1 \pm 0.8$ eV). This suggests that the 1BR coating is more easily formed thermodynamically on the surface of LPSBI than the adsorption of H_2O , and in turn, provides protection against H_2O vapor attacking, as verified by the present experiments.

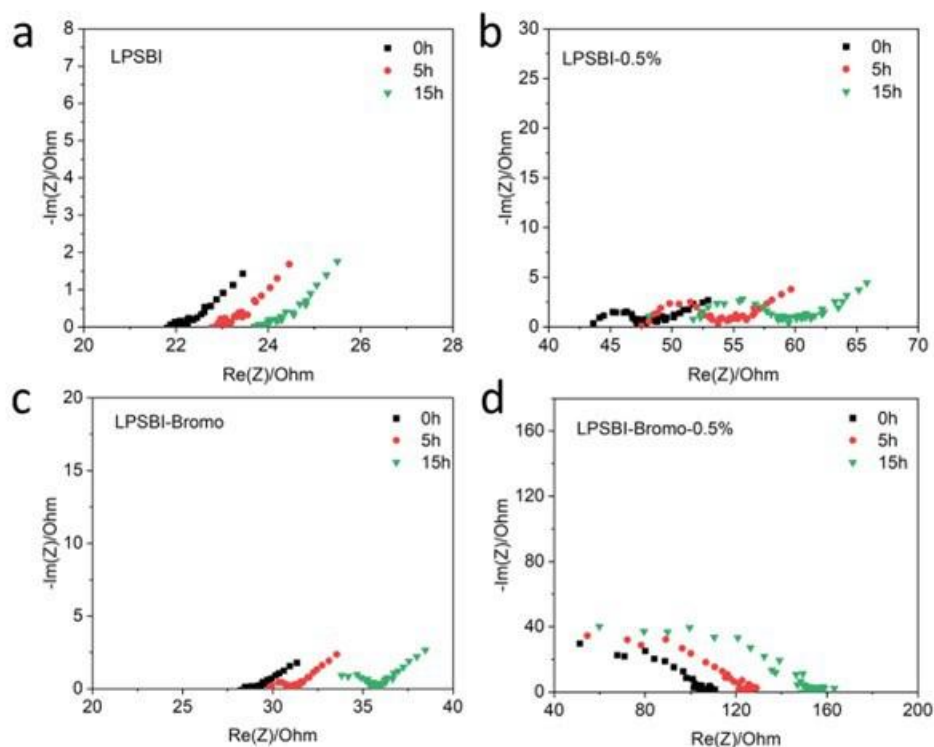


Figure XVI.16.4 Time-dependent EIS of Li/SSE/Li cells. a) Li/LPSBI/Li, b) Li/LPSBI-0.5%/Li, c) Li/LPSBI-Bromo/Li, and d) Li/LPSBI-Bromo-0.5%/Li.

The Li/LPSBI interfacial behaviors with/without 1BR coating were studied at different conditions. Figure XVI.16.4 compare time-dependent electrochemical impedance spectra (EIS) of the LPSBI with/without coating and before/after air exposure (dry room, 0.5% relative humidity). All the LPSBI pellets were pressed under 350 MPa with 700 μm in thickness for EIS measurement. Figure XVI.16.4 a show that the areal interfacial resistance of pristine LPSBI/Li only increased by 2 ohm after contacting with Li for 15h. With 1-BR on the surface, areal resistance increased by 8 ohm after 15h (Figure XVI.16.2c), which is due to the presence of 1-BR coating. After air exposure in dry room, the interfacial resistance of LPSBI-0.5%/Li increased by 50 ohm (Figure XVI.16.4b), indicating that water reaction products on the surface of LPSBI are not stable against Li metal and deteriorate the interfacial stability. In contrast, LPSBI-Bromo-0.5%/Li showed only 12 ohm increasing in interfacial resistance (Figure XVI.16.2b), similar with LPSBI-Bromo, indicating a good protection effect from 1-BR against moisture.

Optimization of solid electrolyte composition to improve Li plating critical current density and Li/SSE/Li cycle life

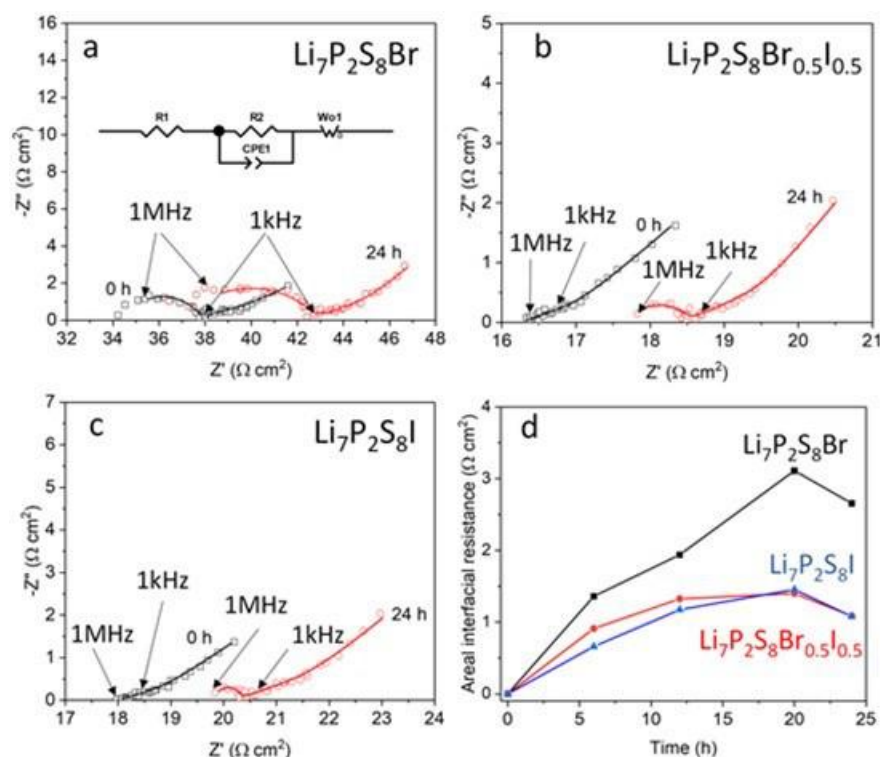


Figure XVI.16.5 Nyquist plots of a) Li/Li₇P₂S₈Br/Li, b) Li/Li₇P₂S₈Br_{0.5}I_{0.5}/Li, and c) Li/Li₇P₂S₈I/Li cell with equivalent circuit fitting at 20°C. d) Evolution of areal interfacial resistance of each cell with time at 20°C.

Interfacial stability of dual-halogen-doped sulfide solid state electrolytes (S-SSEs, $\text{Li}_7\text{P}_2\text{S}_8\text{Br}_{1-x}\text{I}_x$, $0 \leq x \leq 1$) against Li metal was studied and correlated to the unique properties of the halogen doped SSEs. Effects of halogen doping especially the LiI was studied by monitoring the impedance evolutions of the Li/Li₇P₂S₈Br_{1-x}I_x/Li symmetric cells. The Nyquist plots of the cells with equivalent circuit fitting are shown in Figure XVI.16.5. A clear semicircle is detected in the initial EIS spectra of Li₇P₂S₈Br at 20°C. Given the short contacting time, the semicircle is ascribed to the SSE grain boundary resistance rather than interfacial resistance between Li₇P₂S₈Br and Li. In contrast, no semicircle is detected for Li₇P₂S₈Br_{0.5}I_{0.5} and Li₇P₂S₈I at 0 h, suggesting a small or negligible grain boundary resistance for both electrolyte containing LiI dopant. After 24 h, overall resistance of the cell Li/Li₇P₂S₈Br/Li increases from 37.2 to 42.5 Ω cm² with appearance of a second semicircle, corresponding to the deterioration of Li₇P₂S₈Br/Li interface. The measured areal interfacial resistance (AIR) of Li₇P₂S₈Br/Li is 2.65 Ω cm². The evolutions of AIR along with exposure time are shown in Figure XVI.16.5d. In contrast to Li₇P₂S₈Br, the AIR of Li₇P₂S₈Br_{0.5}I_{0.5}/Li and Li₇P₂S₈I/Li after 24 h are only 1.09 and 1.08 Ω cm², respectively. Moreover, both SSEs with LiI (Li₇P₂S₈Br_{0.5}I_{0.5} and Li₇P₂S₈I) display an exceptionally stable and low AIR, indicating that the presence of LiI facilitates building a superior stable and highly Li⁺ conductive solid electrolyte interface (SEI).

Thanks to the stable and low-resistance SSE/Li interface featuring a LiI-rich interface, the Li₇P₂S₈Br_{0.5}I_{0.5} enables long-term Li cell cycling at different conditions. Figure XVI.16.6a shows cycling performance of a Li/Li₇P₂S₈Br_{0.5}I_{0.5}/Li cell at 20°C at 0.5 mA cm⁻² with a charge/discharge capacity of 0.25 mAh cm⁻². No sign of shorting is observed throughout the cycling of 1000 h. Promisingly, stable cell cycling (>1000 h) is also achieved at 60°C at 1 mA cm⁻² with a charge/discharge capacity of 0.5 mAh cm⁻² and at 100°C at 2 mA cm⁻² with a charge/discharge capacity of 1 mAh cm⁻². Both the exceptionally high ionic conductivity and outstanding dendrite suppression capability suggest Li₇P₂S₈Br_{0.5}I_{0.5} a promising SSE for all solid-state Li metal batteries.

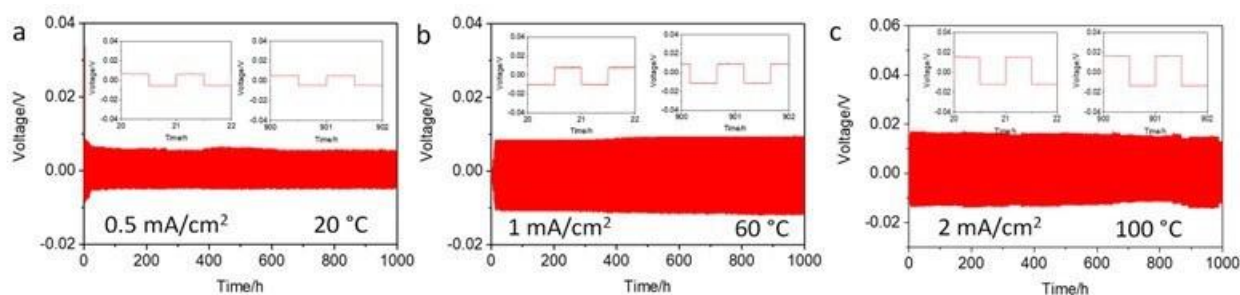


Figure XVI.16.6 a-c) Long term cycling of a Li/Li₇P₂S₈Br_{0.5}I_{0.5}/Li cell at a) 0.5 mA cm⁻² with a charge/discharge capacity of 0.25 mAh cm⁻² at 20 °C, b) 1 mA cm⁻² with a charge/discharge capacity of 0.5 mAh cm⁻² at 60 °C, and c) 2 mA cm⁻² with a charge/discharge capacity of 1 mAh cm⁻² at 100 °C.

Conclusions

A glass-ceramic phase sulfide solid electrolyte Li₇P₂S₈Br_{1-x}I_x (0 ≤ x ≤ 1) was developed by solvent-assisted mechanochemical synthesis followed by low-temperature heat treatment. Preferred organic solvents with low relative polarity (<2.4) was identified for the synthesis.

The halogen dopant has an important effect on ionic conductivity. The Li₇P₂S₈Br_{0.5}I_{0.5} shows the highest ionic conductivity (5.9 mS/cm) among Li₇P₂S₈Br_{1-x}I_x (0 ≤ x ≤ 1) and supports a critical current density of 1.4 mA/cm² in Li/Li symmetric cells at 20 °C and even higher currents at elevated temperatures.

The LiI doped SSEs (e.g., Li₇P₂S₈Br_{0.5}I_{0.5} and Li₇P₂S₈I) show an exceptionally stable and low Li/SSE interfacial resistances when contacting with Li metal (1.09 and 1.08 Ω cm², respectively), facilitating a stable and low resistant for all solid-state batteries with metallic Li as anode.

Scaling up of the highly conductive Li₇P₂S₈Br_{0.5}I_{0.5} was achieved at 200 g/batch with ionic conductivity of 3.14 mS/cm by industrial partner Ampcera Inc.

Key Publications

1. Yu, Z.; Shang, S.; Ahn, K.; Marty, D.; Feng, R.; Engelhard, M.; Liu, Z.; and Lu, D.; Enhancing Moisture Stability of Sulfide Solid-State Electrolytes by Reversible Amphipathic Molecular Coating, *ACS Appl. Mater. Interfaces*, **2022**, 14, 28, 32035
2. Strange, L.; Engelhard, M.; Yu, Z.; and Lu, D.; Li₇P₂S₈Br_{0.5}I_{0.5} solid state electrolyte by XPS, *Surf. Sci. Spectra*, **2022**, 29, 2, 024008
3. Zhou, J.; Chen, Y.; Yu, Z.; Bowden, M.; Miller, Q. R.; Chen, P.; Schaefer, H. T.; Mueller, K. T.; Lu, D.; Xiao, J., Wet-chemical synthesis of Li₇P₂S₈I with tailored particle size for solid state electrolytes. *Chemical Engineering Journal* **2022**, 429, 132334.
4. Yu, Z.; Lu, D.; Xiao, J.; Liu, J.; “Air-stable solid-state electrolyte”, U.S. Patent Application No. 17/507,432.
5. Yu, Z. and Lu, D.; “Lithium-metal compatible solid-state electrolyte for all-solid-state battery” Patent Application, No. 17/945,447, No. PCT/US2022/043609.
6. Zhang, X.; Zhou, J.; Wang, W.; Lu, D.; Bowden, M. E., Method for preparing lithium phosphate sulfide solid electrolytes. US Patent App. 17/580,306.
7. Lu, D.; Scaling-Up and Roll-to-Roll Processing of Highly Conductive Sulfide Solid-State Electrolytes, The 2022 Vehicle Technologies Office (VTO) Annual Merit Review, June 21-23, **2022**
8. Yu, Z.; Marty, D.; and Lu, D.; Highly Conductive and Li Stable Sulfide Solid-State Electrolytes for All-Solid-State Li Battery, ACS Fall, Chicago, IL, August 21 - 25, **2022**

Acknowledgements

Zhaoxin Yu, Michael Kindle, Daniel Marty, Yaobin Xu, Chao Zeng, Chongmin Wang, Jie Bao and Zhijie

Xu (PNNL); Jun Liu (University of Washington); Deyang Qu (University of Wisconsin-Milwaukee); Shunli Shang (Pennsylvania State University); Emery Brown and Ryan Du (Ampcera Inc).

XVI.17 Scale-Up of Novel Li-Conducting Halide Solid State Battery Electrolyte (LBNL)

Mike Tucker, Principal Investigator

Lawrence Berkeley National Laboratory
1 Cyclotron Rd
Berkeley, CA 94720
E-mail: MCTucker@LBL.gov

Simon Thompson, DOE Technology Development Manager

U.S. Department of Energy
E-mail: Simon.Thompson@ee.doe.gov

Start Date: October 1, 2021

End Date: September 30, 2022

Project Funding (FY22): \$400,000

DOE share: \$400,000

Non-DOE share: \$0

Project Introduction

LBNL and project partner Saint Gobain (SG) will demonstrate scalable processing of halide-based solid state batteries. SG's innovative halide-based SSE utilized in this project is inherently scalable: it can be compressed into a dense electrolyte sheet at room temperature under moderate pressure, can be processed in dry air, and does not present any safety issues during processing or end use. The halide material will form the dense electrolyte layer, and be dispersed in the thick cathode to form a highly conductive path for Li ions. The halide will also be in contact with various environments and other materials (solvents, binders, processing equipment, etc.) throughout the battery manufacturing process, and must be stable in contact with cathode and anode materials during operation. R&D efforts commonly use thick pellets of SSE materials to interrogate the relevant interactions, however such studies do not usually reflect the challenges and processing constraints of commercially-relevant thin electrolyte layers. To establish the scalability of this promising material, full cells must be fabricated using a thin electrolyte layer and scalable processing techniques, and any issues encountered during scale-up and processing must be thoroughly characterized and addressed before pilot manufacturing can commence. In this project, SG produces halide powders with Li_3YBr_6 (LYB) and proprietary compositions, and LBNL focuses on fabricating thin electrolyte and thick cathode layers incorporating these powders.

Objectives

The key objectives are: identification of processing and cell materials that are compatible with the halide material; demonstration of full cells with thin electrolyte and thick cathode prepared by scalable techniques; and, scale-up to pouch-size cells. The final objective is a 10 mAh, ~3x4 cm pouch cell providing 300 Wh/kg.

Approach

Initially, the compatibility of the halide powder with processing materials (solvents, binders, processing equipment surfaces) and cell materials (current collectors, cathode active materials, carbon, anode-side solid secondary electrolytes (SSE-A)) will be evaluated. Tape casting will be used to prepare thin (<40 μm) electrolyte and SSE-A layers, and thick (>100 μm) cathode layers, which will be laminated for adhesion and densification. If tapecasting materials are not compatible with the halide, then alternative processing approaches will be evaluated. Once compatible materials and processing techniques are identified, the processing parameters and cell architecture will be optimized for performance and cycling stability at the coin cell level. Finally, pouch cells will be fabricated to demonstrate scalability. Throughout the project, advanced characterization techniques will be used as needed to evaluate materials interactions and cell architecture.

Results

Solvent and binder screening is studied with LYB raw powder. The particle size is up to 20 μm . Solvents were mixed with LYB powder separately overnight and then solvents were evaporated before ionic conductivity measurement. LYB reacted with cyclohexanone, 2-butanone, DMF, DMSO, acetonitrile, 2-butanol and NMP with color or phase changing. No changes or XRD impurity peaks were observed for LYB powder mixed with hexane, heptane, xylene, toluene and cyclohexane. The ionic conductivity of LYB after mixing with the compatible solvents, shown in Figure XVI.17.1, is comparable to the ionic conductivity of fresh LYB powder. In summary, LYB is compatible with the low polarity solvents.

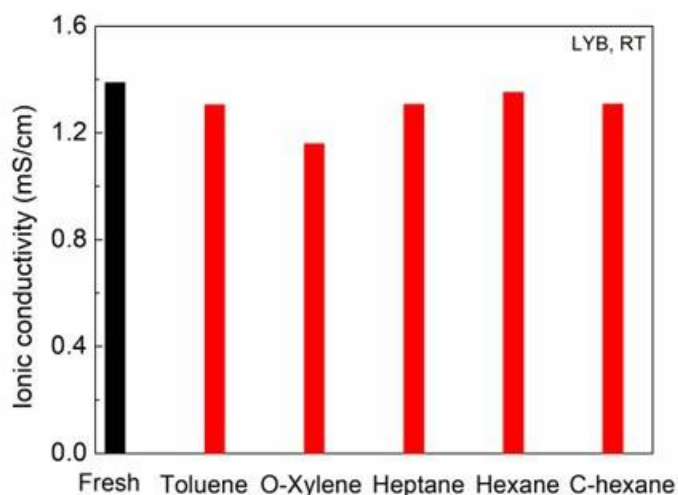


Figure XVI.17.1 Ionic conductivities of fresh and solvent-processed LYB powders at room temperature

Toluene is used as the interim solvent for binder screening and the following tape cast study. Most conventional battery industry binders don't dissolve in these solvents. A selected binder was mixed with LYB and toluene. The mixture was ball milled overnight and then tape cast on a Mylar substrate in a glove box. After drying at 100°C for 20 h, the LYB tape was peeled off as a free-standing sheet, Figure XVI.17.2(Left). An electrolyte was punched and its ionic conductivity was measured in a Sphere Energy sealed cell setup at 100 MPa. The ionic conductivity is 5.6×10^{-5} S/cm. The ionic conductivity of the LYB tape changes with time under pressure. As seen in Figure XVI.17.2(Right), the ionic conductivity remains low for ~100 h and then increases dramatically. The final ionic conductivity of the tape is even higher than that of fresh LYB powder. The cell was disassembled and the tape was partially liquefied starting from the edge, indicating reaction during the high-pressure hold. A parallel study demonstrates the stability of the LYB tape stored in a glove box without pressure. Thus, the tape decomposed under pressure, in contact with stainless steel plungers.

The halide material is incompatible with Li metal as halide decomposes at low voltage (~0.6 V). The voltage of Li/halide/Li symmetric cells increase when cycled at a constant current density, showing the incompatibility between the halide electrolytes and Li metal electrode. Although Li/In alloy shows good compatibility with halide electrolyte and is being used in halide material studies, it reduces the energy density and increases cost. In this study, several interlayers (SSE-A) are explored to inhibit the reaction between Gen2.2 halide and Li metal.

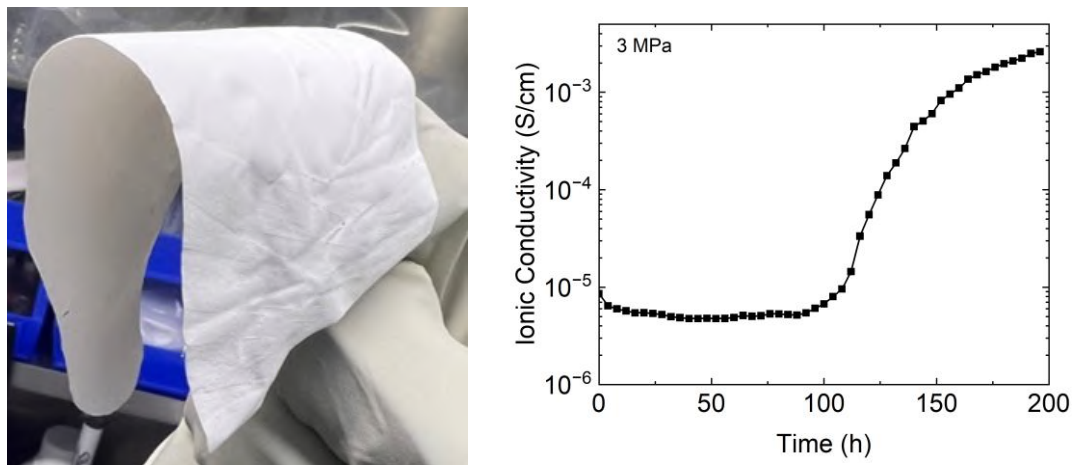


Figure XVI.17.2 (Left) Free-standing LYB tape with binder; (Right) Ionic conductivity of LYB tape changes with time under pressure

A promising SSE-A was tested as an interlayer between Gen2.2 halide and Li metal to obtain the SSE-A/halide/SSE-A sandwich structure, pressed at 150 MPa. Li metal was used as the electrode and pressed at 10 MPa. The Li/SSE-A/halide/SSE-A/Li symmetric cell was cycled at 0.2 mA/cm², Figure XVI.17.3(Left). The voltage is relatively stable for 200 h. The SSE-A interlayer is effective to mitigate the reaction between Gen2.2 halide and Li metal. A full cell was assembled with NMC811 cathode and SSE-A added between Gen2.2 halide SSE and Li metal anode. The cell was cycled between 3 to 4.2 V. The initial discharge capacity is 125 mAh/g (Figure XVI.17.3(Right)), which is 77% of the capacity for a NMC811/Gen2.2/Li-In cell.

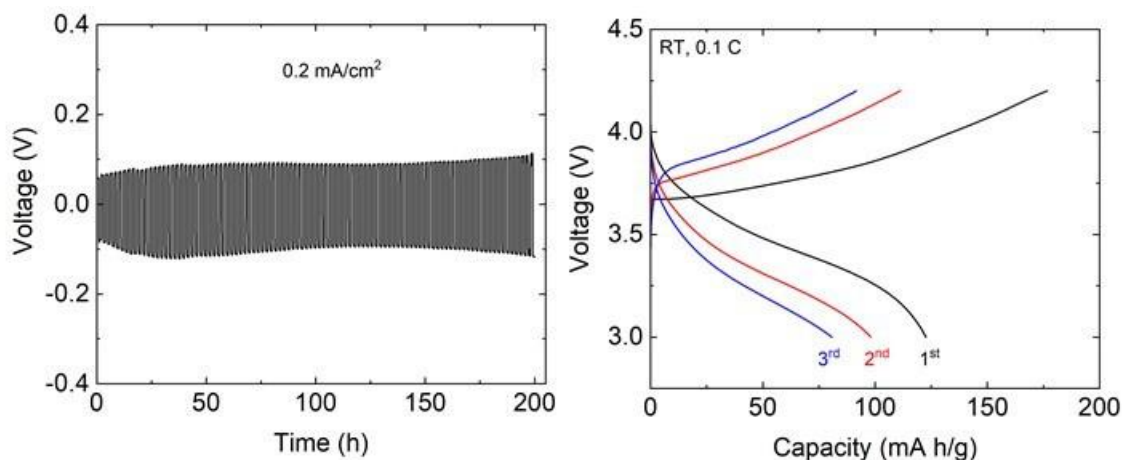


Figure XVI.17.3 (Left) Galvanostatic cycling voltage profiles for a Li/SSE-A/halide/SSE-A/Li symmetric cell; (Right) Charge-discharge curves of the NMC811/halide/SSE-A/Li cell at room temperature with a rate of 0.1 C

Conclusions

Solvents were screened and solvents with low polarity are compatible with halide materials. Binder screening is still on-going. Free-standing tapes were prepared, but LYB decomposed with the binder under pressure. Promising interlayers were identified to mitigate the reaction between halide and Li metal. The voltages of the Li symmetric cells are stable at low current densities. Further study will focus on reducing the thickness of the interlayers.

Acknowledgements

We thank Mike McGahan, Xin Qian, and John Pietras at Saint Gobain for helpful discussion and providing powder samples. Kris Shen produced all of the results presented in this report. Marca Doeff and Vince Battaglia are key personnel on this project.

XVI.18 Low-Pressure All Solid State Cells (NREL)

Anthony K. Burrell, Principal Investigator

National Renewable Energy Laboratory
15013 Denver West Parkway
Golden, CO, 80401
E-mail: Anthony.Burrell@nrel.gov

Simon Thompson, DOE Technology Development Manager

U.S. Department of Energy
E-mail: Simon.Thompson@ee.doe.gov

Start Date: October 1, 2021	End Date: September 30, 2027	
Project Funding (FY22): \$1,240,000	DOE share: \$1,240,000	Non-DOE share: \$0

Project Introduction

One of the major options for significantly increasing the energy density of batteries is the deployment of lithium anodes coupled with high-capacity cathodes. The development of advances in high-energy-density All-Solid-State Batteries (ASSBs) technologies are predicated upon identifying solid electrolyte materials with high room-temperature ionic conductivity ($> 1 \text{ mS/cm}$), chemical and electrochemical stability at the electrodes ($0 \text{ V} - 4.5 \text{ V vs. Li/Li}^+$), and desirable mechanical properties that ensure good electrode-electrolyte contact and inhibit growth of lithium dendrites upon cycling at high current densities necessary for electric-vehicle applications.

Objectives

The goal of this project is to develop all-solid-state batteries using four classes of solid-state electrolytes (SSEs) and/or electrode modifiers that can be used to achieve the final 500-Wh/kg cell target. These materials will be downselected using full-cell testing and advanced characterization to achieve cell targets at cell pressures less than 100 psi.

Approach

Many factors limit the performance of all-solid-state batteries, and this project seeks to address the interface stability of both the lithium interface and the high-voltage cathode. The combination of multiple ionic conductors coupled is specifically targeted to allow solution processing, and low-pressure cell outcome will enable lower-cost deployment of solid-state cells in automotive applications.

To achieve the goal of low-pressure all-solid-state batteries, the team is utilizing three classes of solid ion conductors, sulfide materials, melt-processable lithium carboranes, and multinary metal halides. These materials can be chemically modified to optimize ionic conductivity and voltage stability in single conductor modes or in combinations to effect interface modification for full-cell development. Specifically, the use of flexible ionic conductors at the cathode interface will enable the mechanical effects of cathode expansion and contraction to be mitigated. In combination with the materials discovery work, the project has an extensive characterization team to help determine the impacts of interface, chemical, electrochemical, and mechanical factors on system performance. Full-cell assembly and development, targeting approaches that are readily scalable and compatible with roll-to-roll processes, will drive the materials innovation and development.

Results

Fabrication of Solid-State Cells Using High-Volume Manufacturing Techniques

Argyrodite SSE is used as a baseline solid electrolyte material to develop slurry and tape-casting methods, composite cathodes and anodes, cell fabrication, and cell testing capability with controlled pressure. Composite cathodes containing $>60 \text{ wt } \% \text{ LiCoO}_2$ and anodes containing $>60 \text{ wt } \% \text{ graphite}$ were slurry coated

onto Al and Cu substrates, respectively. These films were each coated with a thin layer of argyrodite SSE and assembled into full-cell stacks in coin cells. The load frame is designed to apply pressures up to 20 MPa without shorting the cells (Figure XVI.18.1). At present, the load frame does not have any load cells on it. The cell testing team developed appropriate components and procedures to enable electrical isolation and prevent misalignment during mechanical loading of cells. Cells fabricated using this method display steady voltage curves and reasonable capacity. Figure XVI.18.2 illustrates cell potential for a solid-state graphite/LCO cell during initial CC cycling at $\sim C/20$. The measured specific capacity was >90 mAh/g LCO with modest voltage windows of 3.0–4.2 V. Thus, roughly 65% of the theoretical cathode capacity was accessed at an unknown/modest pressure. In the coming months, we will add load cells to the load frames to explicitly measure force. This will allow for pressure-dependent electrochemical measurements on tape-cast electrodes incorporating novel solid-electrolyte or interfacial materials. After demonstrating the ability to reliably make large-area cells with a reasonable/repeatable capacity, the team will start to make cells using novel electrolyte materials from the materials development team to enable good cell performance at more modest pressures.

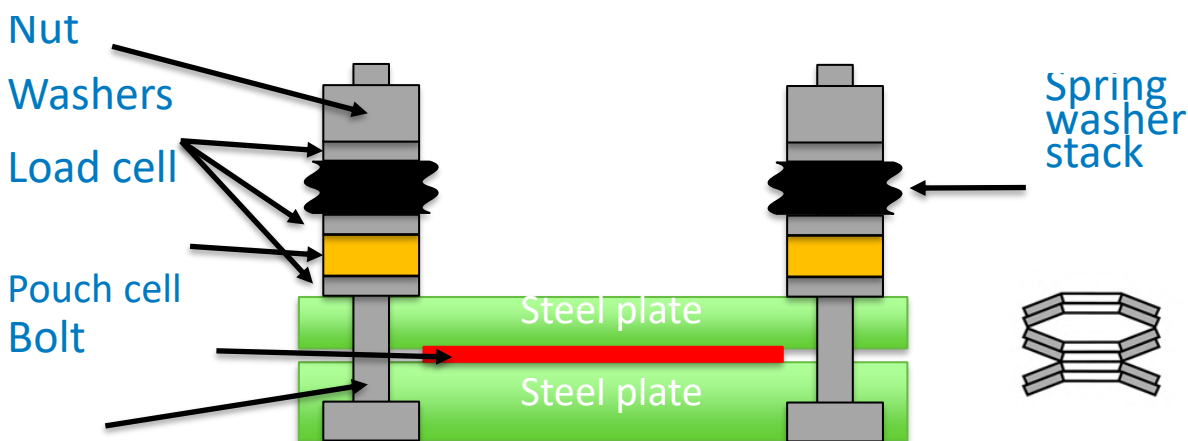


Figure XVI.18.1 Cell testing hardware for SSE can be used to measure pressure in real time or to calibrate individual spring stacks (top)

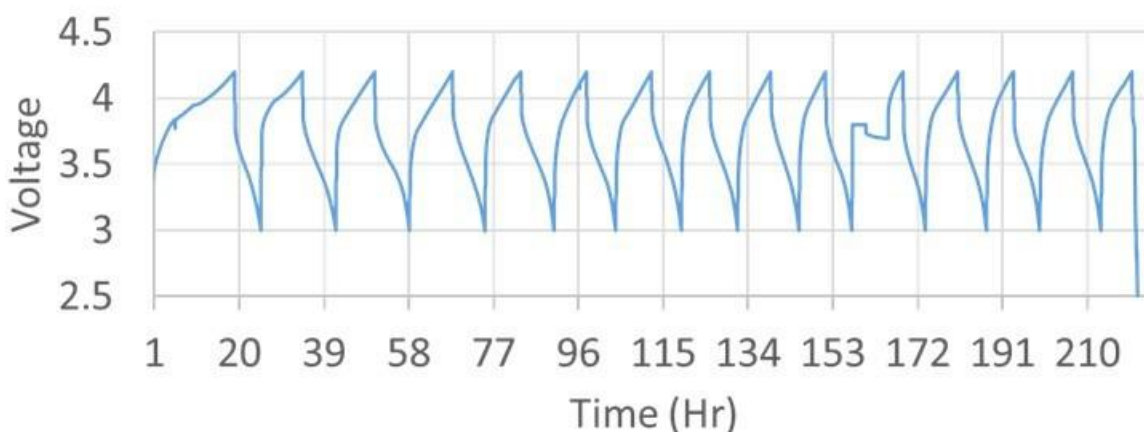


Figure XVI.18.2 Representative cell potential for small-area SSE graphite/LCO cell cycling at $C/20$ between 3.0 and 4.2V. The applied pressure is unknown but will be measured in coming months.

Low-Tortuosity Catholyte via Ultrafast Laser Patterning for Improved Solid-State Batteries

In the fabrication of a solid-state battery, the SSE is usually formed first and then the composite cathode and the anode are added in subsequent steps. This approach results in an SSE/cathode interface susceptible to mechanical instability and high contact resistance that limits the allowable current density during battery

operation. Furthermore, the planar interface limits how far lithium ions can diffuse away from the interface, which constrains the thickness of the cathode and limits the overall energy density. We propose that microstructuring the cathode via ultrafast laser ablation will yield a much higher surface area that (1) greatly increases contact points between the SSE and cathode and (2) allows both vertical and lateral lithium-ion diffusion through lower-tortuosity pathways into the cathode. We believe these improvements will be the key to achieving target current densities $>1 \text{ mA/cm}^2$. Furthermore, reducing the diffusion barriers enables the use of thicker cathode films that increase the overall energy storage capacity, which is crucial to meet the energy density target of 500 Wh/kg . Figure XVI.18.3 illustrates this concept. Microstructures with tunable micrometer dimensions will be created in the cathode using already-established laser ablation capabilities at our facilities. Our sulfide-based SSEs are amenable to filling in the cathode microstructures and creating a greatly enhanced interface.

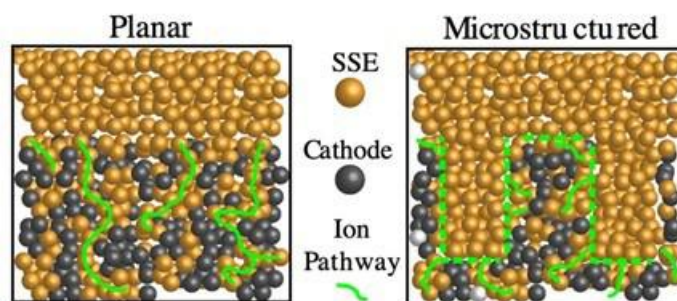


Figure XVI.18.3 A microstructured interface between the SSE and catholyte has many more less-tortuous pathways for ion conduction compared to a typical planar interface

Sample Holder

Introduction of the sulfur-based SSE in the cathode to form a “catholyte” requires moisture-free processing. To start, we have constructed an air-free holder with 2-in-diameter sapphire windows. The catholyte sample is mounted in the cell on the bottom window inside an argon-filled glovebox and then sealed by using a retaining ring to compress the windows onto an O-ring. Laser patterning is done through the top sapphire window. Figure XVI.18.4a shows a catholyte sample of NMC811/LPSCI composite film in the air-free holder.

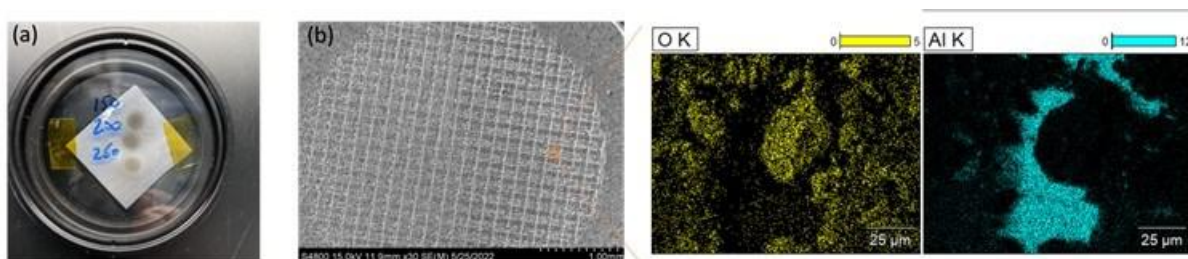


Figure XVI.18.4 (a) NMC811/LPSCI catholyte sample in custom air-free holder with sapphire windows; (b) SEM image of a laser-ablated catholyte revealing the crosshatch channel pattern made using ultrafast laser ablation, as well as EDS of a region inside one of the channels.

Laser Ablation

Micrometer-sized channels were ablated using an ultrafast laser with ~ 600 -fs pulse duration and near-infrared (NIR) emission ($1,030 \text{ nm}$). The laser beam is steered across the sample using galvanometer-controlled mirrors. The depths of the channels are controlled by adjusting the power of the laser. Initially, we tried a crosshatch of channels with $180\text{-}\mu\text{m}$ spacing between channels. Scanning electron microscope (SEM) imaging confirms the patterning was successful (Figure XVI.18.4b). In addition, energy-dispersive X-ray spectroscopy (EDS) was measured in a small area inside one of the channels, showing that some regions in the channel still contain some of the cathode based on the oxygen signature. In other areas, all of the materials had been removed, exposing the aluminum current collector underneath based on the Al signature.

To test the effects of microstructures in the catholyte, we will construct a symmetric cell with solid electrolyte and measure the pressure-dependent EIS. This will indicate whether the microstructures improve the ionic resistance within the cathode and interfacial resistance between the cathode and solid electrolyte. We will refine the laser ablation (e.g., the size, shape, and density of microstructures) to determine more optimal interfaces. In addition, a larger air-free holder will be designed and built to accommodate a much larger (>4-in diameter) sample of catholyte. This will facilitate slurry casting of the SSE onto the laser-patterned catholyte.

The cell build team has primarily focused on the incorporation of high-energy-density active materials into a solid-state system. The cathode of interest is the no-cobalt, nickel-rich cathode NMA ($\text{LiNi}_{0.9}\text{Mn}_{0.05}\text{Al}_{0.05}\text{O}_2$), capable of generating 230 mAh/g. This NMA has been ALD-coated with Al_2O_3 to mitigate known side reactions between transition metal oxides and the chlorinated argyrodite ($\text{Li}_6\text{PS}_5\text{Cl}$) used in our solid-state system. A mixture of NMA (65 wt %), argyrodite (30 wt %), VGCF (2.5 wt %), and Oppanol (2.5 wt %) combined with xylene was mixed in a mortar and pestle. The slurry was blade-coated onto Al foil and dried in a glovebox with a loading of 0.7 mAh/cm². The anode consists of Si nanoparticles (Paraclete Energy, Batch G18) mixed with a 0.5-wt % solution of PVDF in NMP such that the Si nanoparticles and the dissolved PVDF were 99 and 1 wt % of the mixture, respectively. While the cathode must contain both SSE and carbon to increase the electrode's ionic and electronic conductivity, the silicon electrode does not need to contain carbon due to its higher conductivity ($3 \times 10^{-5} \text{ S cm}^{-1}$ for Si and $\sim 10^{-6}$ to $10^{-4} \text{ S cm}^{-1}$ for NMA) and can avoid the degradation that occurs at the SSE/carbon interface. The slurry was mixed with a planetary mixer and was blade-coated onto a Cu foil with a roughened surface using a wet gap of 75 μm . The resulting electrode was dried under vacuum at 80°C for 12 hours before being calendared.

An SSE electrolyte layer was printed onto both the Si and NMA electrodes with a slurry consisting of 95 wt % argyrodite and 5 wt % Oppanol with a thickness of 40 μm and 70 μm , respectively. A separate SSE film was coated on a polished stainless steel surface and dried in a glovebox. This film was removed with a carbon-steel blade and was used as a free-standing electrolyte layer (30- μm thickness) between the electrolyte-coated cathode/anode (Figure XVI.18.5), giving a total electrolyte thickness of 140 μm . Punches were then removed from the electrodes and placed into a coin cell, which was pressed in a high-pressure setup at approximately 125 MPa.

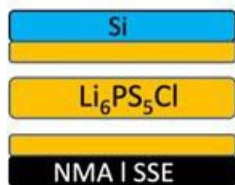


Figure XVI.18.5 Diagram of the electrode and electrolyte stack

Results from the NMA vs. Si cell are shown in Figure XVI.18.6.

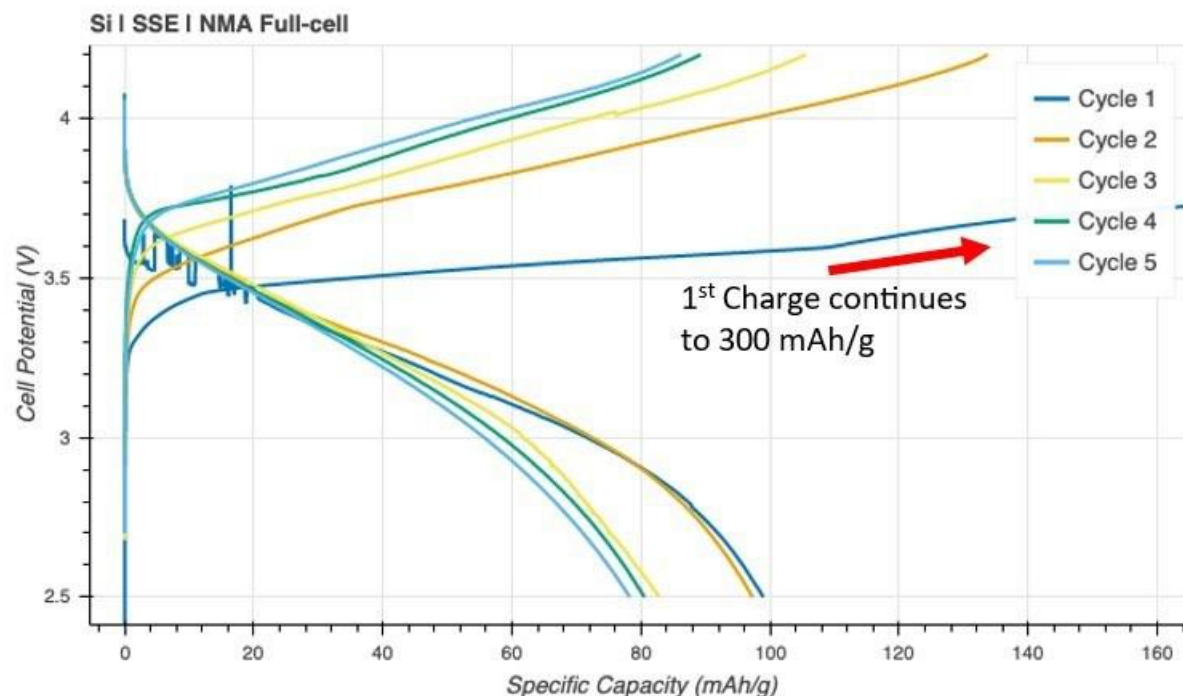


Figure XVI.18.6 Cycling data for the NMA vs. Si cell cycled at Room Temp and C/20. Erratic voltage profiles for the first charge/discharge can be caused by a loss of physical contact between active particles and the electrolyte.

Conclusions

As expected, there is a large disparity between the first charge and discharge that can be caused by several aspects including: (1) chemical diffusion between the electrolyte and active material, (2) consumption of the active materials, (3) formation of a space-charge layer, and (4) change in chemical composition in the interface between the SSE and the contraction of NMA particles during delithiation. The low specific capacity of 100 mAh/g of subsequent cycles can partially be attributed to the conservative charge voltage (4.2 V). This is the first report of an NMA vs. Si solid-state battery to our knowledge. Future work will aim to increase the specific capacity of these Si/NMA SSE systems and to develop methods for low-pressure cycling.

XVI.19 3D Printing of All-Solid-State Lithium Batteries (LLNL)

Jianchao Ye, Principal Investigator

Lawrence Livermore National Laboratory
7000 East Avenue
Livermore, CA, 94550
E-mail: ye3@llnl.gov

Simon Thompson, DOE Technology Development Manager

U.S. Department of Energy
E-mail: Simon.Thompson@ee.doe.gov

Start Date: January 10, 2022

End Date: January 9, 2025

Project Funding (FY22): \$375,000

DOE share: \$375,000

Non-DOE share: \$0

Project Introduction

All-solid-state lithium metal batteries (ASSLBs) have attracted attention due to their potential for mitigating safety issues and addressing energy density limitations of conventional lithium-ion batteries (LIBs). While solid-state electrolytes (SSEs) with room-temperature ionic conductivities greater than that of their liquid electrolyte counterparts have been discovered, integration of the different solid components of ASSLBs is not trivial. Taking garnet $\text{Li}_7\text{La}_3\text{Zr}_2\text{O}_{12}$ (LLZO) electrolyte as an example, problems for this SSE include brittleness, high temperature processing for densification, poor contact with electrodes, and lack of scalable manufacturing methods. These obstacles must be overcome before LLZO becomes commercially viable for ASSLB applications.

Realistic shape factors. Commercially available or lab-developed SSE discs must be thick (e.g., hundreds of micrometers to millimeters) to be mechanically robust enough to overcome their brittle nature, which unfortunately increases the cell impedance and accounts for the majority of overall cell weight and volume, leading to dramatically decreased power and energy densities. To increase energy density, membrane thickness has to be less than 100 μm and ideally $< 20 \mu\text{m}$. However, poor mechanical properties such as brittleness for pure oxide SSEs and low stiffness for polymer SSEs increase processing difficulty and promote defect-induced Li penetration. Ultrathin, flat and dense SSE membranes show high flexibility and thus can be stacked together with other electrode components for large scale battery assembly, though that the community suffers from a lack of cost-effective precision manufacturing methods for this purpose. Alternatively, composite polymer electrolytes with requisite active filler content and proper organization may increase mechanical flexibility while reducing manufacturing cost. However, these materials still suffer from conductivity, mechanical stiffness, and electrochemical stability issues which all must be addressed.

Electrode integration. Wetting of SSEs with metallic Li has been partially addressed by introducing lithiophilic interfaces, while the uniformity and cost of the artificial layer still need to be optimized. In addition, achieving good contact of SSEs with the cathode is still an issue. On one hand, co-sintering has been investigated to enhance the cathode contact via solid-state densification while kinetically limiting the chemical reactions. Our work on composite pellet co-sintering and slurry-based co-sintering has shown reasonable thermal stability between Ta-doped LLZO (LLZTO) and NMC 622 at 900 °C. However, issues like mechanical robustness due to relatively high porosity still need to be solved. In addition, carbon additives need to be introduced to provide electronically conductive pathways for these relatively thick electrodes. On the other hand, cathode slurries with polymer binders have often been spread on the sintered LLZO films for cell assembly. The use of polymer binder may sacrifice the operational temperature and lower electrochemical stability. A small amount of liquid electrolyte/solvent is usually applied to enhance the contact, which negates some of the safety benefits of all-solid-state batteries. A highly conductive solid catholyte with stable and good contact with cathode will be necessary to facilitate Li^+ transport.

Scaling up approach. Unlike liquid electrolyte-based LIBs for which roll-to-roll (R2R) methods have been developed for large scale manufacturing, scaling up of SSBs is likely different. Although soft and glassy sulfide-based SSBs are promising candidates for R2R manufacturing, their interfacial stability with electrodes must be resolved. For garnet LLZO-based SSBs, composite polymer electrolytes may be most ready for meaningful demonstrations of scaling up, though their Li^+ conductivity still needs improvement. Pure ceramic-based SSBs will likely require one-step formation to avoid repeated deformation induced cracking.

Cycling stability. Even with successful manufacturing of an ASSLB, poor cycling stability can still limit performance. Several failure mechanisms must be overcome include (but are not limited to): 1) void formation at the Li anode side during Li stripping; 2) Li dendrite nucleation and penetration; and 3) cracking/delamination on the cathode side. Effective characterization methods that help shed light on the failure mechanisms will be critical for designing better materials and manufacturing approaches that stabilize the long-term cycling performance.

Objectives

Specific Objective 1: Down select 3D printing and post processing approaches for SSE/cathode integration
Specific Objective 2: Understand battery failure mechanisms via ex situ and in situ characterization

Approach

The technical approaches include advanced manufacturing based on 3D printing and related techniques, ex situ/in situ characterizations, and battery testing. In addition to experimental efforts, the team will work closely with the computational partner (PI: Brandon Wood) to better understand battery failure mechanisms and design new battery architectures and chemistries for performance improvement. 3D printing approaches will be optimized and down selected to fabricate 3D interfaces for battery performance evaluation. Three approaches including sintering-free, hybrid, and co-sintering will be studied. Ex situ and in situ characterizations will be developed to understand battery failure mechanisms. Routine electrochemical and basic characterizations will be used for troubleshooting. In situ Raman and KPFM techniques will be conducted to analyze the electro-chemo-mechanical evolution of printed ASSLBs.

Results

LLZTO/SPE hybrid electrolyte

The team evaluated hybrid electrolytes using the porous LLZTO as scaffold and solid polymer electrolyte (SPE) as flexible and conductive filler, aiming at improving conductivity and cracking resilience. PEGDA/PEGMEA/PEO/LiTFSI SPE was chosen as the infilling polymer electrolyte based on the teams' previous studies on SPEs. Figure XVI.19.1 shows the SEM images of a pristine LLZTO porous film as well as the hybrid system after infilling and curing of corresponding monomers. Most of the pores were filled with the SPE, although gaps can be observed in the fracture surface, implying that the wetting between the pristine LLZTO and SPE may not be sufficiently well. The pristine porous LLZTO films showed a poor room temperature ionic conductivity of 1.16×10^{-5} S/cm. After the LLZTO films were acid treated with H_3PO_4 , the overall resistance decreases due to the removal of the surface contaminants such as Li_2CO_3 and thus the conductivity increased to 3.58×10^{-5} S/cm. By adding SPE in the pores of the LLZTO films, it is expected to introduce extra Li^+ transport channels and thus further improve the overall conductivity. As shown in Table XVI.25.1, the total ionic conductivity of the SPE/infilled pristine LLZTO (SPE/LLZTO/SPE) is 1.27×10^{-5} S/cm, higher than SPE alone (7.1×10^{-6} S/cm). After removing the contributions from the SPE layers top and bottom of the SPE/LLZTO/SPE hybrid system, the conductivity of the SPE infilled pristine LLZTO layer is 2.5×10^{-5} S/cm, higher than pristine LLZTO film, but slightly lower than the acid treated LLZTO film only, which may be partially due to the gaps observed in Figure XVI.19.1. The ionic conductivity at 60 °C, Li^+ transference number and critical current density values are also improved with the LLZTO scaffold as shown in Table XVI.19.1.

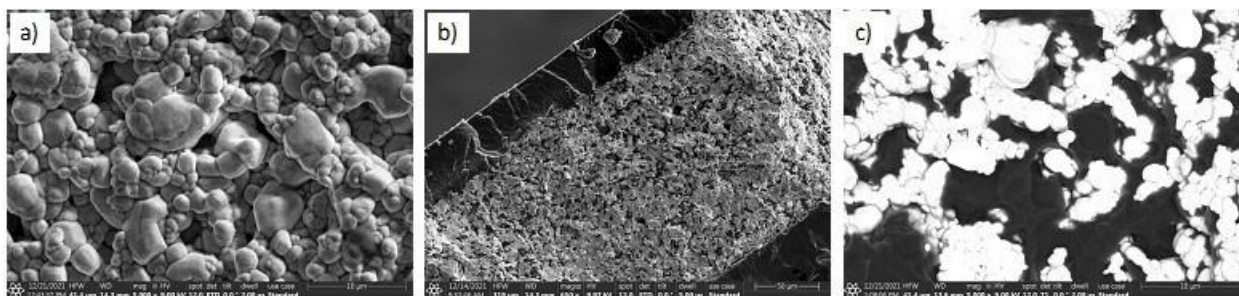


Figure XVI.19.1 SEM images of a) pristine LLZTO film; b) SPE infilled LLZTO films, c) Backscattered electron image of the LLZTO/SPE system.

Table XVI.19.1 Ionic conductivity (σ_{Li}) at RT and 60 °C, activation energy (E_a) at 60 °C, transference number (t_{Li+}) at 60 °C, and critical current density (CCD) at 60 °C of the polymer SE and hybrid system (LLZTO/ Polymer) with different acid treatments conducted on LLZTO films.

Composition	Total σ_{Li} @ RT (mS/cm)	Total σ_{Li} @ 60 °C (mS/cm)	E_a @ 60 °C (eV)	t_{Li+} @ 60 °C	CCD @ 60 °C (mA/cm ²)
Polymer SE	0.0071±0.002	0.12	-----	0.24±0.03	0.13
SPE/ LLZTO/SPE	0.0127±0.0002	0.173±0.027	0.46	0.41±0.07	0.25±0.02
SPE/HCl- LLZTO/SPE	0.017±0.005	0.171±0.056	0.51	0.44±0.02	0.22±0.04
SPE/H ₃ PO ₄ -LLZTO/SPE	0.0076±0.0007	0.153±0.051	0.45	0.59±0.01	0.28±0.02

To remove a possible ion-blocking effect due to the presence of the surface Li_2CO_3 contaminant layer, different treatments using HCl acid and H_3PO_4 acid to either remove Li_2CO_3 or convert it into other Li species were carried out on the porous LLZTO films. Figure XVI.19.2 shows the XPS analysis of the pristine and acid treated LLZTO films. The La and Zr peaks in pristine LLZTO are very weak due to the existence of Li_2CO_3 surface layer, in contrast, these peaks are observed for the acid treated LLZTO films. As expected, the surface of the acid treated film is decorated with either Cl^- from HCl or PO_4^{3-} species from H_3PO_4 (Figure XVI.19.2e-f).

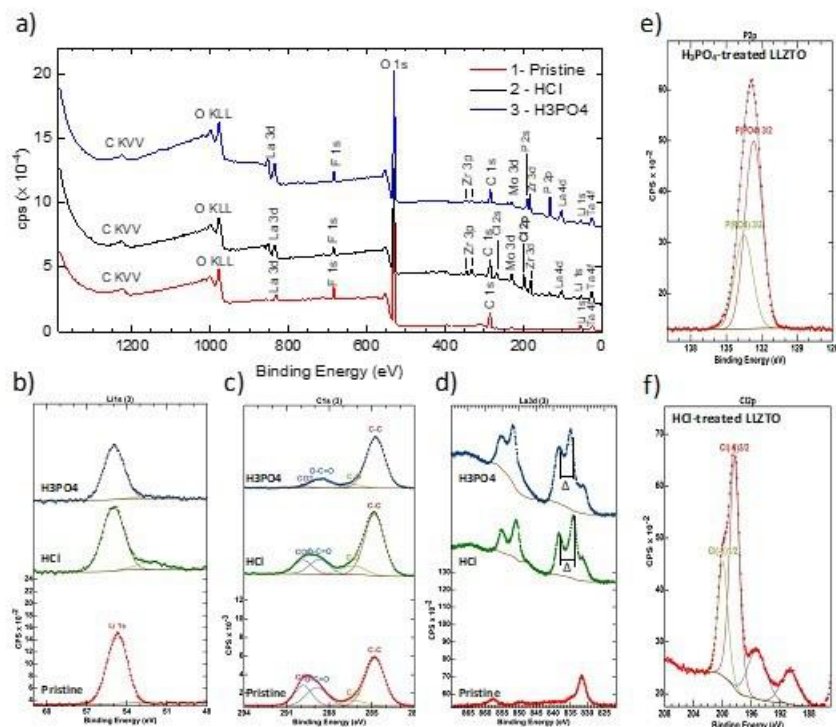


Figure XVI.19.2 XPS survey scan of a) Pristine LLZTO film and acid treated LLZTO films, HCl and H₃PO₄; b) High resolution Li 1s XPS spectra; c) High resolution C 1s XPS spectra; d) High resolution La 3d XPS spectra; e) High resolution P 2p XPS spectra; e) High resolution Cl 2p XPS spectra.

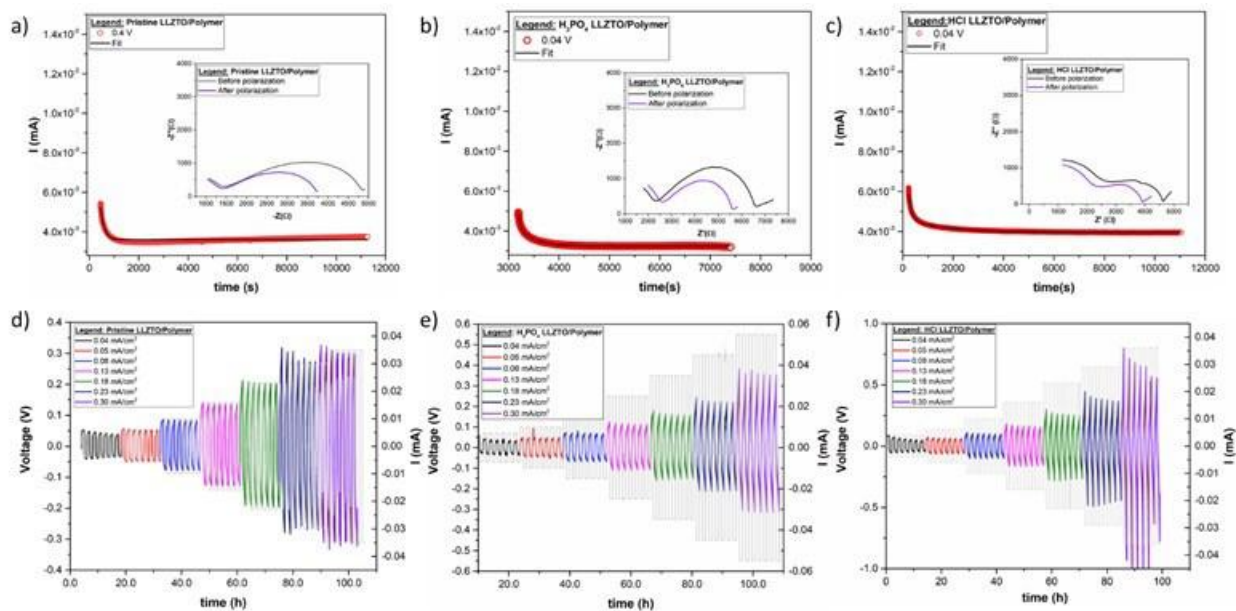


Figure XVI.19.3 a)-c) DC polarization curves for determining the Li⁺ transference number under an applied voltage of 0.04 V at 60 °C. a) Pristine LLZTO film; b) H₃PO₄ treated films; c) HCl treated film. The inset shows the impedance taken just before and immediately after the DC polarization experiment. The curves were fitted with a decay function and the steady state at the end of the curve was extrapolated. d)-f) Voltage vs. time plots of plating-stripping at different current densities. d) Pristine LLZTO film; e) H₃PO₄ treated films; f) HCl treated film.

Figure XVI.19.3a-c shows the chronoamperometry (CA) plots and the EIS plots before and after DC polarization. Decreased charge transfer resistances were observed after Li plating/stripping, implying an improved interfacial contact between Li and SPE in Li/SPE/LLZTO/SPE/Li. The transference numbers were further increased especially for the H_3PO_4 treated sample, up to 0.59 (Table XVI.25.1). The CCD value for HCl treated LLZTO film is lower than that of the pristine film (0.22 mA/cm^2 vs 0.25 mA/cm^2), while H_3PO_4 treatment slightly increases the CCD to 0.28 mA/cm^2 . However, the total ionic conductivity of H_3PO_4 treated LLZTO sample after SPE infilling is the lowest.

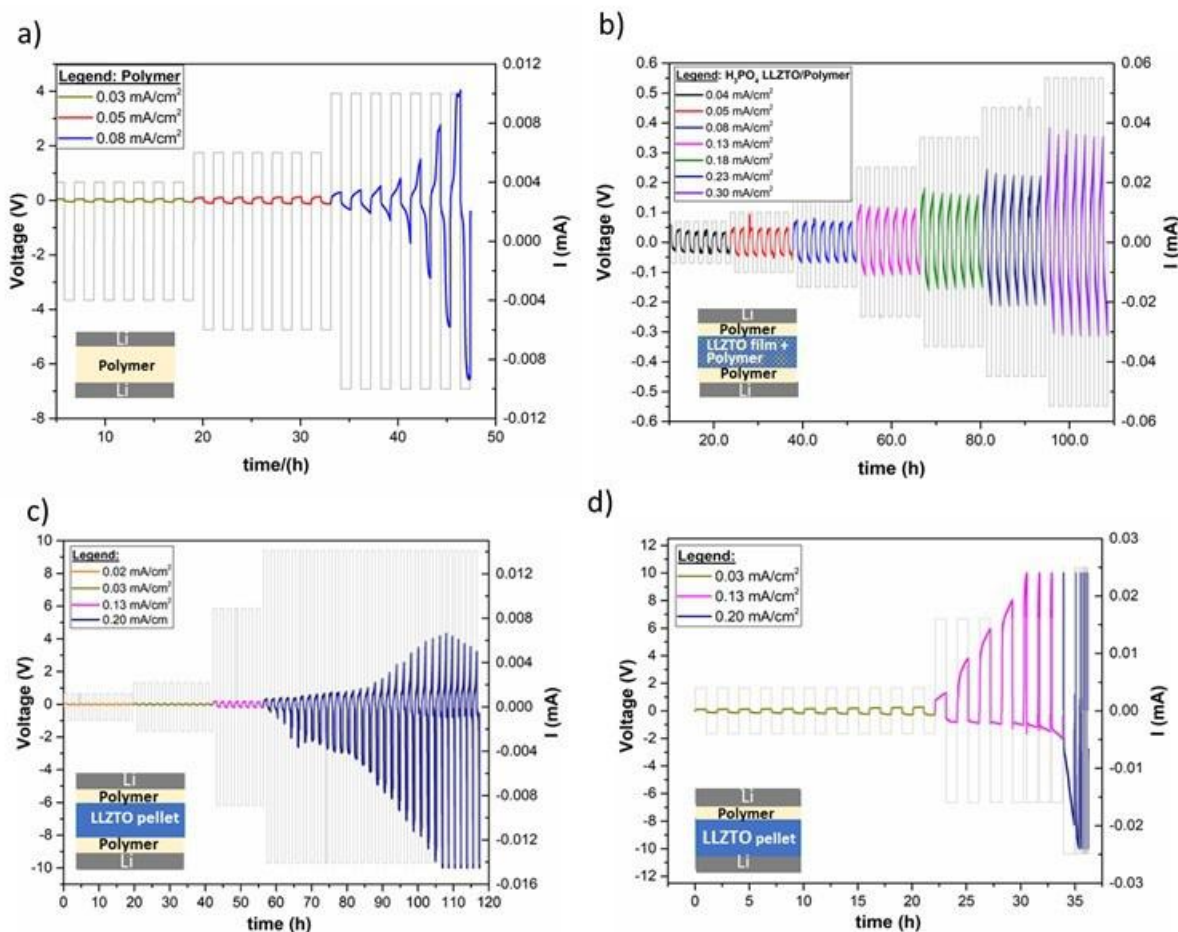


Figure XVI.19.4 Voltage vs time plots at 60°C of the four model systems assembled to understand the conductivity differences: a) single SPE layer; b) SPE infilled porous LLZTO film (H_3PO_4 treated); c) stacked SPE, densified LLZTO pellet (H_3PO_4 treated) and SPE; d) stacked SPE and densified LLZTO pellet (H_3PO_4 treated) bilayers with the polymer side initially connected to the positive electrode. Their corresponding cycling stability tests showing symmetric and asymmetric cycling behaviors.

To simplify the 3D interface problem, the team designed different control experiments to compare the cycling behaviors of four model Li symmetric cells: 1) Li|SPE|Li; 2) Li|SPE|infilled-LLZTO|SPE|Li; 3) Li|SPE|LLZTO-1100C|Li; 4) Li|SPE|LLZTO-1100C|SPE|Li. The first two cell configurations (1 and 2) (Figure XVI.19.4a-b) show symmetric voltage profiles, suggesting Li^+ transport along both directions is similar. This symmetry seems to be intuitive for a symmetric cell setup. However, when the SPE infilled LLZTO layer is replaced with a well densified LLZTO pellet, e.g., in the configuration of Li|SPE|LLZTO-1100C|SPE|Li (Figure XVI.19.4c), the team observed an asymmetric cycling behavior. The overpotential in the second half cycles increases more rapidly than the opposite direction. This abnormal asymmetry in a symmetric cell is still a mystery. Given the only difference between the above two setups (LLZTO infilled SPE and LLZTO/SPE) is that Li^+ ions can transport in both polymer and LLZTO channels in the infilled LLZTO case, versus Li^+ ions must transport from polymer to LLZTO and from LLZTO to polymer in the dense LLZTO case, the team

suspect that the ion transport via LLZTO/SPE interface is the origin of this asymmetric behavior. In fact, in an SPE asymmetric cell using a densified LLZTO pellet stacked with only one SPE film (Figure XVI.19.4d), the similar asymmetric behavior is observed, where Li^+ transport in the direction of LLZTO to SPE becomes much more difficult at current densities of 0.13 mA/cm^2 or above. The observed accelerated degradation is found in Li|SPE|Li , $\text{Li|SPE|LLZTO-1100C|Li}$, and $\text{Li|SPE|LLZTO-1100C|SPE|Li}$, but not in $\text{Li|SPE|infilled-LLZTO|SPE|Li}$. The observations suggest an advantage in using the SPE infilled LLZTO, while detailed understanding of the degradation mechanism is still needed. Possible explanations to be scrutinized in future work include: 1) charge accumulation and clogging at the LLZTO/SPE interface due to the sluggish charge transport from LLZTO to SPE; 2) Polymer/Li interface degradation at high voltages. To further enhance the performance of the hybrid electrolyte, the ionic conductivity of SPEs, and their compatibility with LLZTO shall be improved, which will be the next research focus area.

Composite polymer electrolyte approach

Mechanical properties (Modulus E and hardness H) of PEGDA/PEGMEA/PEO/LiTFSI solid polymer electrolytes (SPEs) were measured using spherical indentation, as shown in Figure XVI.19.5. The Young's modulus ranges from 290 kPa up to 10 MPa, while hardness from 9 kPa to 300 kPa, depending on the composition of the SPEs. Both E and H increase with higher PEGDA content (Figure XVI.19.5b and d), which forms 3D crosslink network. Increasing the ratio of PEO/PEGMEA can further improve E (Figure XVI.19.5a), but shows little effects on H (Figure XVI.19.5c), likely because the two are both with straight polymer chains. One composition used for further studies (PEGDA:PEGMEA:PEO = 1:8:1) shows E of $\sim 2.58 \text{ MPa}$ and H of $\sim 156 \text{ kPa}$, which delivers an ionic conductivity of 10^{-5} S/cm at room temperature. Reducing PEGDA and PEO contents can increase the ionic conductivity up to $6 \times 10^{-5} \text{ S/cm}$, however, E reduces to 0.29 MPa , and H to 12 kPa .

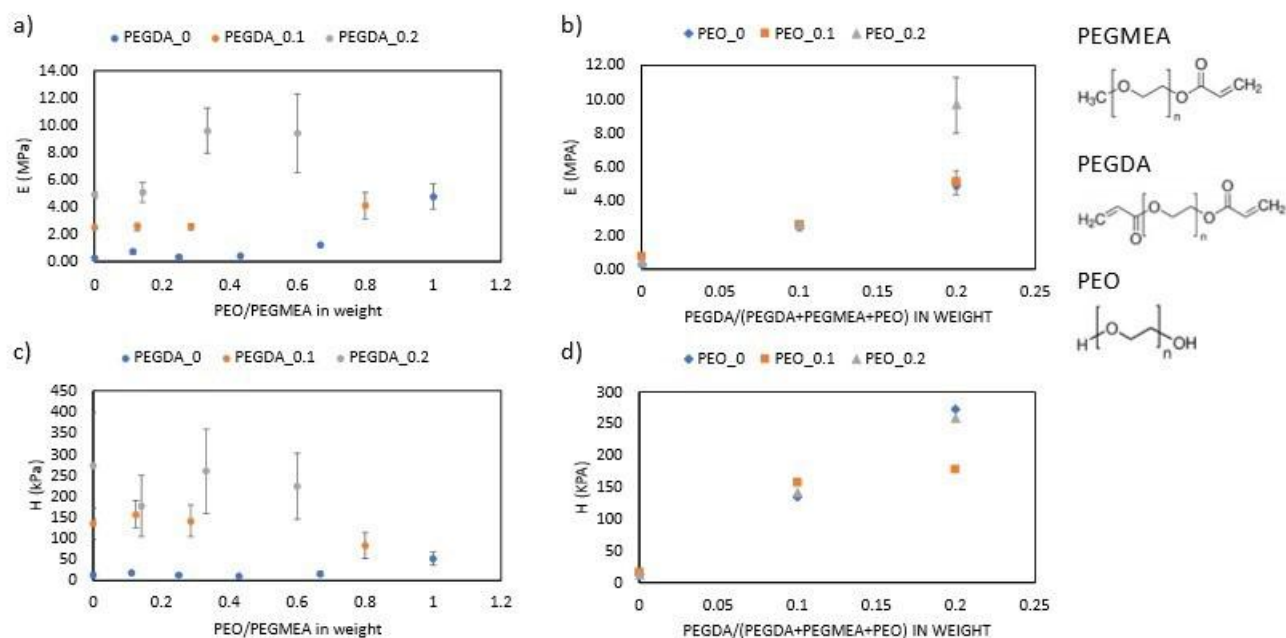


Figure XVI.19.5 Young's modulus (E) and hardness (H) measured using spherical indentation.

To further improve the ionic conductivity of polymer electrolytes, LLZTO “active” filler nanoparticles were introduced in the 1PEGDA-8PEGMEA-1PEO/LiTFSI matrix. A series of LLZTO contents from 7wt% up to 31wt% were prepared. The highest ionic conductivity of $6.6 \times 10^{-5} \text{ S/cm}$ was obtained for 7wt% LLZTO (Figure XVI.19.6a). Further increasing the LLZTO content however leads to the decrease of ionic conductivity. Detailed optimization of the LLZTO content can be conducted in the range below 13wt% to pin down the peak conductivity. The highly conductive LLZTO particles seems to be not involved in the overall

Li^+ conduction. The addition of LLZTO particles helps to reduce the crystallinity of PEG polymers and thus improves the conductivity. However, further addition of the particles increases the interfacial area and the impedance between LLZTO and polymer electrolyte could hinder the Li^+ ion transport. Therefore, to improve the conductivity of high-LLZTO-content composite polymer electrolytes, one strategy is to form bicontinuous LLZTO/polymer networks, which is being explored in the sintering-refilling hybrid approach. Another strategy is to improve the Li^+ ion transport between the LLZTO/polymer interface.

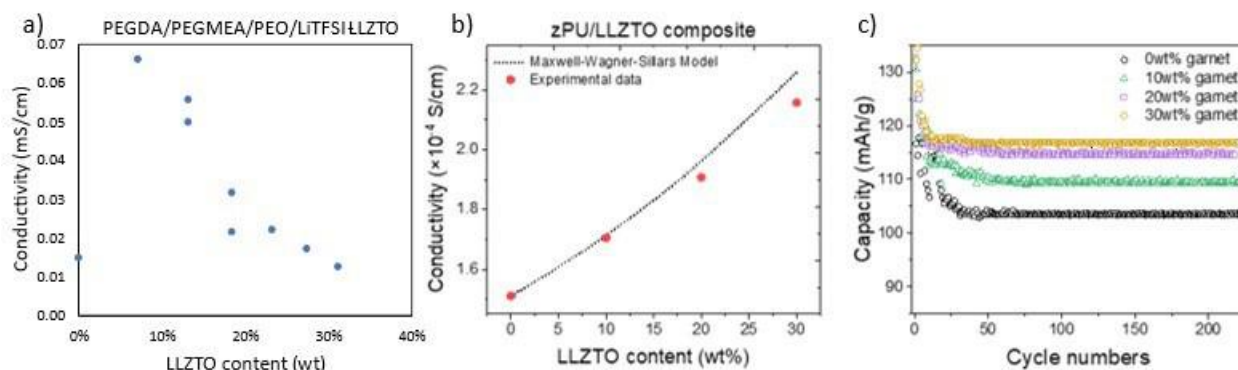


Figure XVI.19.6 Conductivity of composite polymer electrolytes made from a) PEG/LLZTO and b) zPU/LLZTO recipes. c) Cycling tests of Li|zPU/LLZTO|LFP solid state batteries at 1C rate, room temperature.

To achieve that, the team is collaborating with researchers at University of Illinois at Chicago to develop zwitterionic polyurethane (zPU)/LLZTO composite polymer electrolyte. The high surface energy of the zPU/LiTFSI polymer electrolyte improves the wetting with LLZTO particles. The high LiTFSI content (up to 80wt%) increases the Li^+ concentration in polymer matrix and facilitates the ion transport between zPU and LLZTO. As a result, as shown in Figure XVI.19.6b, the Li^+ conductivity of the composite polymer electrolyte (CPE) continuously increases from 1.5×10^{-4} S/cm to 2.2×10^{-4} S/cm (at RT) with the increase of LLZTO content up to 30wt%. The increasing trend can be fit using a Maxwell-Wagner-Sillars conductivity model. The LFP|zPU-LLZTO CPE|Li full cells also show improved capacity at 1C rate with the increase of LLZTO content (Figure XVI.19.6c), likely attributed from the higher conductivity. There are significant capacity drops in the first 10-20 cycles for all the zPU cells, though the addition of LLZTO facilitates the stabilization. After ~50 cycles, cell capacity is very stable with little decrease in the next 200 cycles. With such promising results, the team moves forward to introduce 3D printed cathodes to integrate with the zPU/LLZTO CPE. Representative prints are shown in Figure XVI.19.7.

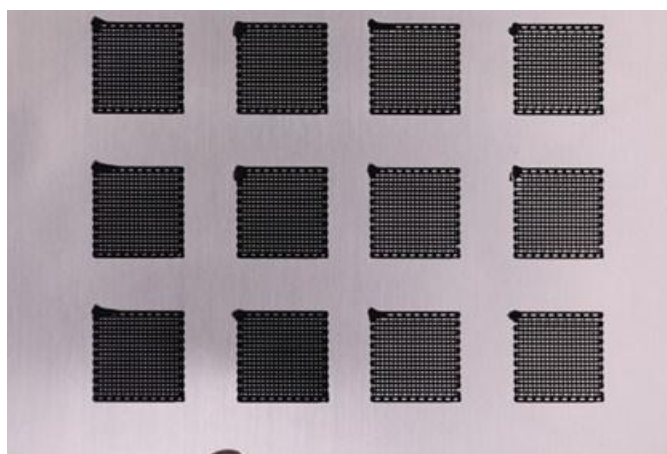


Figure XVI.19.7 Direct ink writing printed single-crystal NMC811 cathode. Nozzle diameter is 200 μm , hatch spacing is 400 μm , and mass loading is ~ 10 mg/cm².

Co-sintering approach

The team previously showed co-sintering results for cathode composites made with 50 wt% NMC 622 / 50 wt% LLZTO ($\text{Li}_{6.4}\text{La}_3\text{Zr}_{1.4}\text{Ta}_{0.6}\text{O}_{12}$). In order to better approximate the conditions of an actual solid-state cell, the team recently studied co-sintering outcomes using cathode composites made with less electrolyte (75 wt% NMC 622 / 25 wt% LLZTO), as well as with LCO (LiCoO_2) as the cathode material (75 wt% LCO / 25 wt% LLZTO). To test the electrochemical performance of these co-sintered materials, the cathode and electrolyte were mixed with a small amount of binder and coated on top of pre-sintered LLZTO pellets (Figure XVI.19.8a). The samples were then co-sintered at 750°C or 900°C for 2h in either air or argon to determine the effect of temperature and sintering environment on stability and performance (Figure XVI.19.8b-c). For all the samples, a definite color change throughout the LLZTO pellet from white to green after co-sintering was observed, with the color intensity corresponding to the temperature and the environment. This is likely due to cobalt diffusion from the cathode into the LLZTO. Figure XVI.19.8d shows an optical image of the back side of the LLZTO pellets after co-sintering, and a few trends can be observed. First, the green color change is more intense at higher temperatures and in argon vs. air, indicating a greater degree of reaction under these conditions. Even after sintering at 750°C in air (the least reactive condition), the LLZTO pellet still changes to a yellow color for both LCO and NMC 622, suggesting some amount of cathode/electrolyte reaction. Second, the green color change is more significant for LCO compared to NMC 622, likely due to the greater cobalt content in LCO relative to NMC 622.

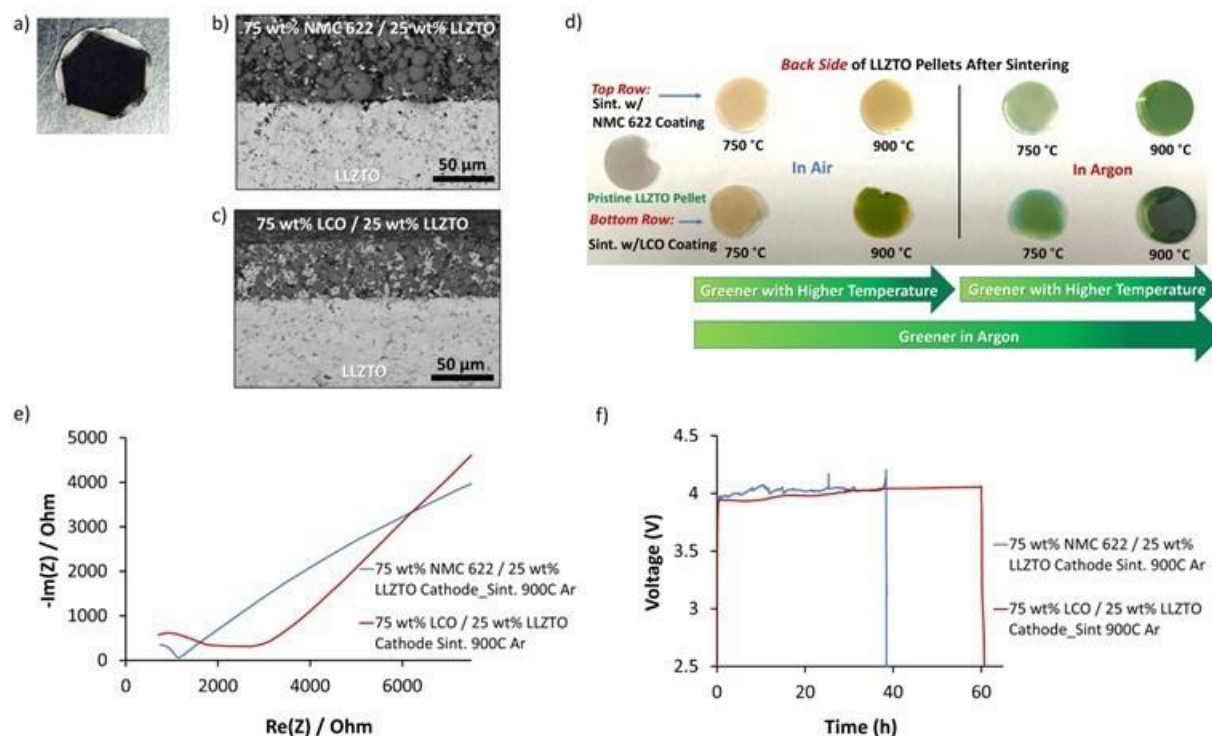


Figure XVI.19.8 Backscattered SEM cross-sections of composite cathodes coated on pre-sintered LLZTO pellets and co-sintered at 900°C for 2h in Ar (b-c). Optical image before sintering (a). d) Optical images of the back side of the LLZTO pellets after co-sintering at different temperatures and in different environments (air vs. Ar). Electrochemical measurements using Li as the anode: e) EIS comparison before cycling. f) Voltage profiles for the 1st charge/discharge cycle at C/20.

The electrochemical performance of these cells was evaluated by sputtering gold onto the cathode to form a conductive contact and assembling cells with Li as the anode. All of the samples co-sintered at 750°C (in both air and argon) hit the upper cutoff voltage immediately. This is probably due to high resistance in the cell from the poor sintering between the cathode and electrolyte at these temperatures, which results in a discontinuous ion transport pathway. For the LCO sample sintered at 900°C in Ar, the cell continued to charge for a very

long time and never hit the upper cutoff voltage (it hit the time limit set in the program instead), while the NMC 622 cell sintered at 900°C in Ar also charged for a long time and had a bumpy voltage profile before finally hitting the upper cutoff voltage. Both cells hit the lower cutoff voltage very quickly upon discharge (Figure XVI.19.8f). This poor performance could be due to a combination of interfacial contact issues, cathode degradation, and secondary phase formation.

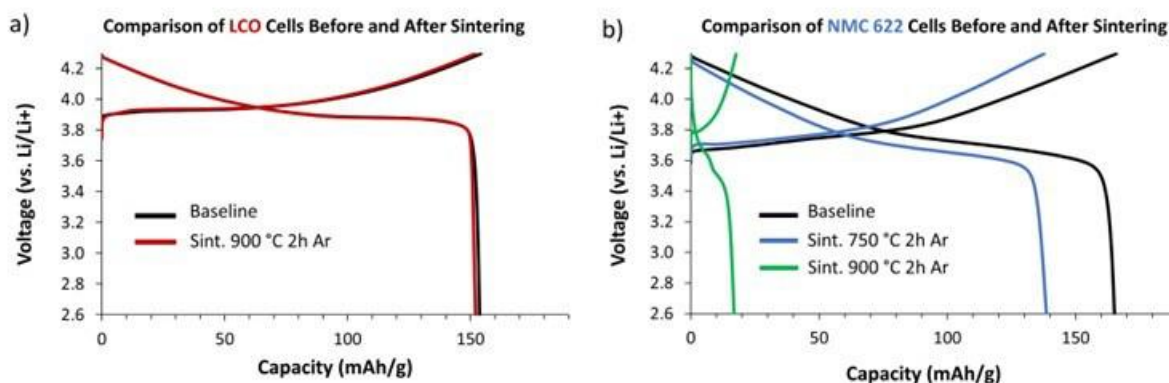


Figure XVI.19.9 Representative voltage vs. capacity profiles for cathode materials sintered at 750 °C and 900 °C for 2h in Ar before electrode preparation. Half cells were cycled at C/10 charge/discharge using liquid electrolyte (1.2M LiPF₆ in 3:7 wt% EC/EMC) and Li as the anode. (a) LCO and (b) NMC 622.

To determine if some of the observed degradation during co-sintering is due to degradation of the cathode material itself, the stability of each cathode at high temperatures was studied independently. To accomplish this, each cathode powder was pressed into a pellet (to mimic the co-sintering conditions) and then sintered at 900°C for 2h in Ar. The pellets were then crushed into a powder, mixed with carbon black and binder to create a conventional cathode slurry, and tape cast. The cathodes were assembled into coin cells with liquid electrolyte (1.2M LiPF₆ in 3:7 wt% EC/EMC) and cycled at C/10 to monitor capacity changes (Figure XVI.19.9). For LCO, the capacity and voltage profiles are very similar before and after sintering at 900°C (154 mAh/g vs. 152 mAh/g, respectively), indicating that the sintering does not cause initial capacity loss. However, for NMC 622, there is a substantial decrease in capacity from 165 mAh/g to 17 mAh/g after sintering at 900°C. Another set of NMC 622 samples was sintered at 750°C for 2h in Ar as a comparison. While the capacity after sintering at this lower temperature is much better than after sintering at 900°C, there is still a significant decrease compared to the baseline (139 mAh/g vs. 165 mAh/g). These results indicate that while co-sintering at these higher temperatures may be feasible for LCO, it must be done at much lower temperatures for NMC 622 to prevent degradation.

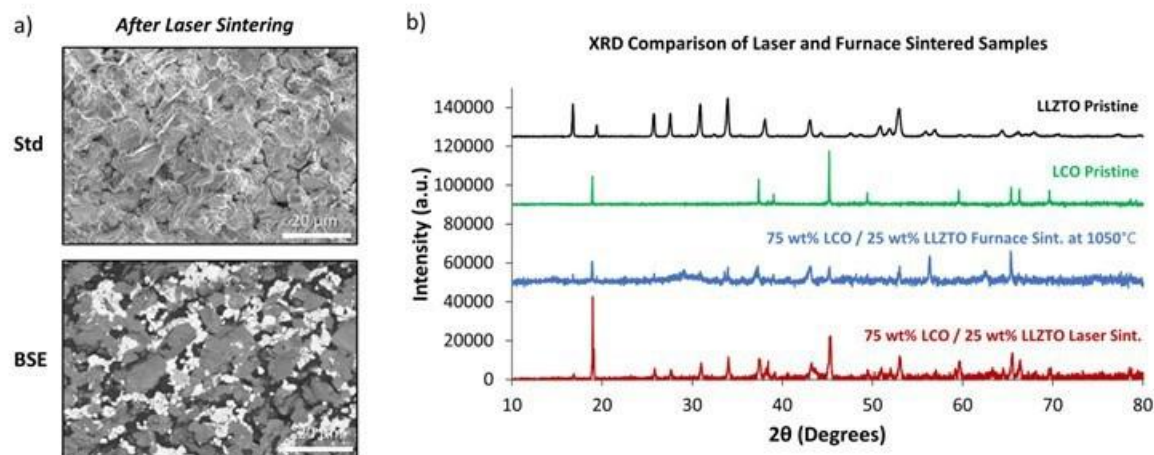


Figure XVI.19.10 75 wt% LCO / 25 wt% LLZTO pellets laser co-sintered at 26 W for 90 s using a laser diode array. a) Standard and backscattered SEM images of cross-sections after co-sintering. b) XRD comparison of laser and furnace co-sintered samples.

The team has recently been exploring laser sintering of LLZTO [1] and laser co-sintering as a way to minimize the detrimental effects of conventional high-temperature furnace sintering. Using a rapid laser heating decreases the overall sintering time significantly (minutes compared to hours), which should help limit cathode/electrolyte reactions and help prevent the formation of secondary phases. Figure XVI.19.10 shows some preliminary results for a 75 wt% LCO / 25 wt% LLZTO composite pellet sintered at 26 W for 90 s ($\sim 1215^{\circ}\text{C}$) using a 1000 nm laser diode array. The cross-sectional SEM images (Figure XVI.19.10a) show a significant degree of sintering between the cathode and LLZTO particles, and the XRD results (Figure XVI.19.10b) indicate fewer secondary phases are formed during the short laser sintering period relative to the furnace sintered sample. The sintering parameters will be further tuned in the future, but these initial results demonstrate the potential for laser sintering to minimize interfacial reactions during co-sintering. Laser co-sintering will be further explored under this project.

Conclusions

In FY22, we continued optimizing the conductivity of the solid-state electrolytes. Over 1×10^{-4} S/cm ionic conductivity was achieved in zPU/LLZTO CPEs, and 6×10^{-5} S/cm in PEGDA/PEGMEA/PEO/LLZTO CPEs. The conductivity decreasing with further increasing of LLZTO powder content in PEG and the asymmetric cycling behavior in LLZTO/PEG suggested the resistance for Li^{+} transport from LLZTO to PEG is large, which shall be resolved to achieve both good ionic and mechanical properties. The co-sintering studies found that 750°C or above temperature heat treatment leads to deteriorate of the NMC's electrochemical properties. To make this co-sintering approach work, the sintering temperature/time must be further reduced.

Key Publications

Papers

1. Hammons, J.; Espitia, J. A.; Guzman, E. R.; Shi, R.; Meisenkothen, F.; Wood, M.; Ceron, M. R.; Ye, J. Pore and Grain Chemistry during Sintering of Garnet-type $\text{Li}_{6.4}\text{La}_3\text{Zr}_{1.4}\text{Ta}_{0.6}\text{O}_{12}$ Solid-state Electrolytes. *J. Mater. Chem. A* **2022**.

Presentations

1. Marissa Wood, Liwen Wan, Anirudda Dive, Jianchao Ye. Co-sintered solid electrolyte/cathode interfaces in solid-state batteries. 2022 MRS Spring Meeting & Exhibit, Honolulu, Hawai'i, USA
2. VTO Solid-State Battery Review Meeting, Berkeley, CA (Aug 2022): "3D Printing of All-Solid-State Lithium Batteries"; E. Ramos, M. Wood, Y. Zhang, J. Schwartz, S. Huang, S. Liang, X. Gao, A. Espitia, M. Williams, F. Hall, J. Ye.

3. Solid-State Battery Summit, Chicago, IL (Aug 2022): “Additive Manufacturing of Solid State Batteries”; E. Ramos, A. Browar, M. Wood, J. Roehling, A. Santomauro, J. Forien, A. Martin, J. Yoo, J. Tong, J. Ye.

References

1. Ramos, E., et al., *CO₂ Laser Sintering of Garnet-Type Solid-State Electrolytes*. ACS Energy Letters, 2022. 7: p. 3392-3400.

Acknowledgements

LLNL Team members who have contributed to the project in FY22 include Erika Ramos, Marissa Wood, Yuliang Zhang, Sijia Huang and Johanna Schwartz. We also acknowledge our collaborators from LLNL simulation group include Bo Wang, Tae Wook Heo, and Brandon Wood, as well as our external collaborators from University of Illinois at Chicago include Sangil Kim, Kun Wang, Yuechen Gao, and Gang Cheng.

XVI.20 Substituted Argyrodite Solid Electrolytes and High-Capacity Conversion Cathodes for All-Solid-State Batteries (Oak Ridge National Laboratory)

Jagjit Nanda, Principal Investigator

Oak Ridge National Laboratory
1 Bethel Valley Road
Oak Ridge, TN, 37831
E-mail: jnanda@slac.stanford.edu

Simon Thompson, DOE Technology Development Manager

U.S. Department of Energy
E-mail: Simon.Thompson@ee.doe.gov

Start Date: October 1, 2021

End Date: September 30, 2022

Project Funding (FY22): \$650,000

DOE share: \$650,000

Non-DOE share: \$0

Project Introduction

Advances in solid electrolytes (SEs) with superionic conductivity and stabilized electrode-electrolyte interfaces are key enablers for all-solid-state batteries (SSBs) to meet the energy density and cost targets for next-generation batteries for electric vehicles. The project aims at the synthesis and fabrication of Li-ion conducting argyrodite SEs with the nominal composition $\text{Li}_6\text{PS}_5\text{X}$, where $\text{X} = \text{Cl}, \text{Br}, \text{and/or I}$. The team will combine electrochemical impedance spectroscopy (EIS) with complementary *in situ* spectroscopy and microscopy to probe buried solid-solid interfaces and quantify the voltage losses associated with side reactions involving the SE. Specifically, they plan to investigate the interfacial reaction between various $\text{Li}_6\text{PS}_5\text{X}$ SEs and Li-ion cathodes belonging to different structural families [transition metal (TM)-based sulfides and fluorides (for example, FeS_2 and FeF_2) and high-voltage layered oxides (for example, $\text{LiNi}_{0.8}\text{Mn}_{0.1}\text{Co}_{0.1}\text{O}_2$, NMC-811). New dopants such as niobium and partial substitution of sulfur with oxygen will be explored to improve the stability of argyrodite SEs against lithium metal and high-voltage cathodes.

Objectives

1. Produce $\text{Li}_6\text{PS}_5\text{X}$ ($\text{X} = \text{Cl}, \text{Br}, \text{and/or I}$) SEs using solvent-mediated routes with ionic conductivity $\geq 1 \times 10^{-3} \text{ S/cm}^{-1}$ at room temperature
2. Optimize synthesis and annealing conditions to obtain phase-pure SE $\text{Li}_6\text{PS}_5\text{X}$ powders. Evaluate structure using X-ray diffraction (XRD), Raman spectroscopy, and neutron scattering.
3. Compare the structure and Li^+ conductivity of $\text{Li}_6\text{PS}_5\text{X}$ prepared through solvent-mediated versus mechano-chemical and solid-state routes.
4. Integrate $\text{Li}_6\text{PS}_5\text{X}$ SE separators with working cathodes and thin Li metal anodes for SSB testing and performance optimization.

Approach

Scalable solution-based processing routes will be developed to produce freestanding sulfide/binder solid-state separators with thicknesses $< 50 \mu\text{m}$ and area-specific resistance (ASR) $< 50 \Omega \text{ cm}^2$. These ultra-thin separators will be integrated with Li-metal anodes and high areal capacity cathodes (for example, Ni-rich NMC, S, FeS_2 , and FeF_3) to demonstrate lab-scale prototype SSBs. As a cross-cut activity, various *in situ* and *ex situ* passivation methods will be combined with enabling characterization techniques to facilitate Li^+ transport across electrode/SE interfaces.

Results

Precursor mixing has a major impact on key properties (e.g., phase purity, morphology, and ionic conductivity) of solid electrolytes (SEs) synthesized through solid-state routes. The first phase of this fiscal year's activities focused on the solid-state synthesis of $\text{Li}_6\text{PS}_5\text{X}$ ($\text{X} = \text{Cl}, \text{Br}$) SEs where two precursor mixing strategies were explored. The first method involved hand grinding (HG) stoichiometric amounts of Li_2S , LiCl , and P_2S_5 in an agate mortar and pestle followed by pelletizing and heating at 550°C ($5^\circ\text{C}/\text{min}$) for 10 hours under flowing Ar. To investigate the effect of higher energy mixing on the product's conductivity and purity, we also used a planetary mill (PM) assisted route where precursors were blended with zirconia milling media for 1 h at 100 RPM. After milling, the resulting mixtures were pelletized and annealed at the same conditions as the HG samples.

The ionic conductivity of the SEs was evaluated using EIS in a blocking cell configuration. As shown in Figure XVI.20.1(a), all samples had ionic conductivities on the order of $1 \text{ mS}/\text{cm}$ at room temperature. The $\text{Li}_6\text{PS}_5\text{Cl}$ samples exhibited higher ionic conductivities across both the HG and PM samples. This trend is attributed to greater anion site disorder for the Cl-based sample which facilitated Li^+ transport as reported previously.¹⁰ For a given composition, the ionic conductivity of the PM samples exhibited higher conductivity, presumably due to more intimate precursor mixing prior to annealing.

Raman spectroscopy and XRD were used to characterize the materials' bulk and local structures. Figure XVI.20.1(b) shows a Raman spectrum of each sample highlighting the principal Raman band near 430 cm^{-1} which is indexed to the ortho-thiophosphate units PS_4^{3-} . This band was slightly blue-shifted for the Cl-containing samples, suggesting that different halide substitutions influence P-S bond lengths. XRD patterns in Figure XVI.20.1(c) show that all samples had the expected argyrodite peaks along with minor phase impurities including LiCl and Li_2S . Sloping backgrounds near $2\theta=30^\circ$ are due to Kapton tape which was used to prevent air exposure during the measurements. Overall, these results demonstrate that HG and PM blending routes did not have a discernable impact on the materials' structure as determined by Raman and XRD. These findings suggest that the differences in ionic conductivity may be influenced by amorphous phases or other subtle factors.

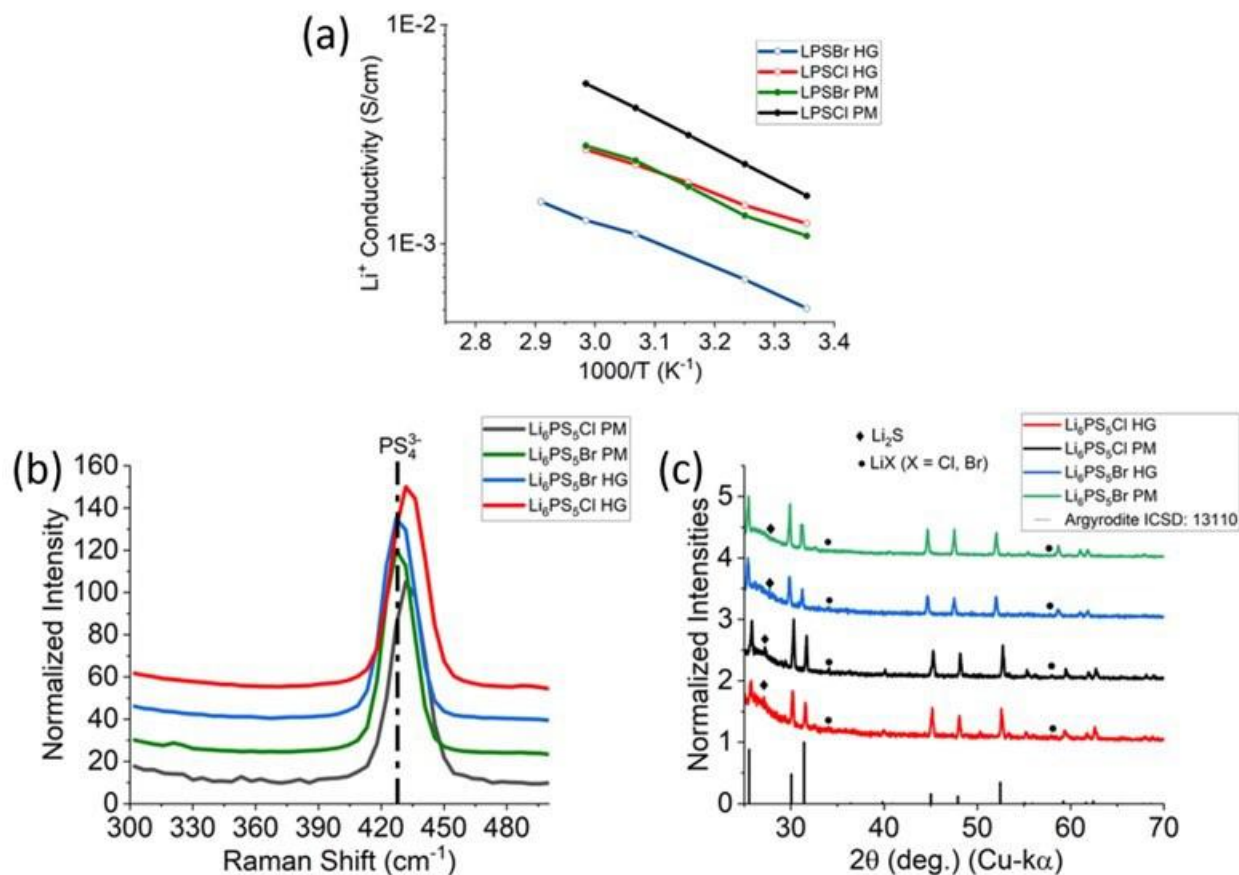


Figure XVI.20.1 (a) Temperature-dependent Li⁺ conductivity measurements for Li₆PS₅X (X = Cl, Br) prepared by HG and PM. (b) Raman spectra and (c) powder XRD patterns for Li₆PS₅X (X = Cl and Br) prepared by HG and PM methods.

In addition to SE synthesis, we also investigated how different SEs impact the performance of SSBs containing composite NMC811 cathodes. Unlike conventional sulfide SEs (e.g., β -Li₃PS₄, LPS), which are unstable at potentials > ca. 2.6 V vs. Li/Li⁺, halide-containing compositions [e.g., Li₆PS₅Cl (LPSCl) and Li₃InCl₆ (LIC), obtained through a collaboration with Halide Team – Task 1.14], have outstanding oxidative stability which is anticipated to facilitate the formation of stable NMC/SE interfaces. As shown in Figure XVI.20.2(a) and (b), we evaluated pellet-type cells containing: (i) a single-layer sulfide separator and catholyte (LPSCl) and (ii) a bilayer sulfide/halide LPSCl/LIC separator and LIC catholyte. The composite cathodes were prepared by blending NMC811 (uncoated), SE powder (either LPSCl or LIC), and carbon nanofibers on a Turbula T2F shaker. The cathodes were tested against In metal anodes where the Li_xIn alloy (0 < x < 1) was electrochemically formed *in-situ* during charging. Similar cells containing Li metal anodes were also prepared and tested, but these results are not shown here due to internal shorts caused by Li dendrites when the current density exceeded 100 μ A/cm².

Figure XVI.20.2 (c) and (d) show galvanostatic voltage profiles for SSBs containing single-layer (LPSCl) and bilayer (LPSCl+LIC) separators, respectively. The voltage profiles suggest that the charge compensation is almost entirely through the NMC811 active material, and neither LPSCl nor LIC exhibited significant oxidative decomposition during charge steps. The initial reversible capacity of the LPSCl cell was 13% higher than that of the LPSCl+LIC cell (161 and 142 mAh/g_{NMC}, respectively), possibly due to the higher Li⁺ conductivity of LPSCl (~2 mS/cm at room temperature vs. 0.5 mS/cm for LIC). Both cells exhibited significant capacity fade and retained only ~25 mAh/g_{NMC} after 40 cycles (see Figure XVI.20.2(e)). Interestingly, the cells' operating voltage gradually increased during cycling due to the cumulative irreversible capacity losses that were potentially caused by: (i) negative drifting of the Li_xIn anode potential

and/or (ii) positive drifting of the cathode's state-of-charge. After 40 cycles, the LPSCl and LPSCl+LIC cells had cumulative irreversible capacity losses of 2.04 and 1.58 mAh, respectively. These losses correspond to anode stoichiometries of $\text{Li}_{0.12}\text{In}$ and $\text{Li}_{0.09}\text{In}$, respectively, indicating the anodes remained within desired $\text{In}/\text{Li}_x\text{In}$ two-phase region ($0 < x < 1$, 0.622 V vs. Li/Li^+) throughout the experiments. As such, the cells' potential drift during cycling was due to Li inventory loss in the NMC active material. More specifically, the total irreversible capacity was 194 and 150 mAh/g_{NMC} for the LPSCl and LPSCl+LIC cells, respectively. Interestingly, this drifting behavior was not observed in our team's prior results acquired on SSBs containing NMC811+LPS+C cathodes and LPS separators (reported in FY21).

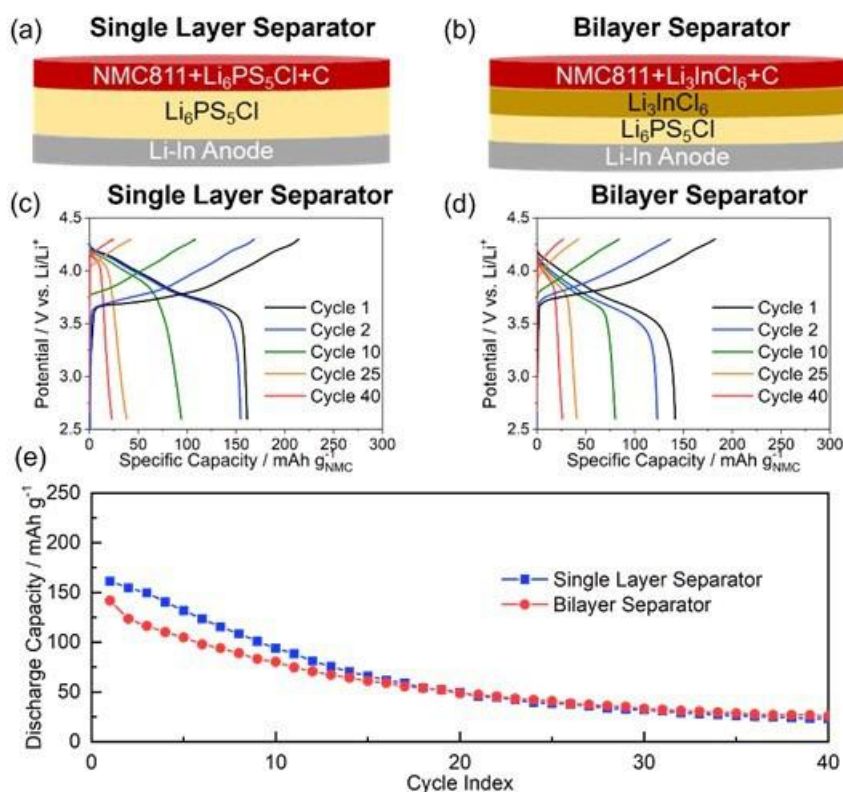


Figure XVI.20.2 Electrochemical performance of SSBs containing NMC811 composite cathodes and Li_xIn anodes. (a,b) Schematics of the cell designs. Voltage profiles for cells containing (c) single layer $\text{Li}_6\text{PS}_5\text{Cl}$ and (d) bilayer $\text{Li}_6\text{PS}_5\text{Cl}/\text{Li}_3\text{InCl}_6$ separators. (e) Discharge capacity over 40 cycles. Cells were cycled by polarizing the cathode between 2.6 – 4.3 V vs. Li/Li^+ at a constant current of $\pm 66 \mu\text{A}/\text{cm}^2$ (cycle 1) and $\pm 127 \mu\text{A}/\text{cm}^2$ (cycles 2-40). Due to the use of Li_xIn anodes, potentials were referenced against Li/Li^+ by adding 0.622V to the measured cell potential.

Operando Raman spectroscopy was used to explore how the cathode/SE interface in SSBs evolves during cycling. For these measurements, the team designed a hermetically sealed cell (Figure XVI.20.3) comprised of a c-shaped clamp (provides stack pressure up to ~ 50 MPa), a pair of stainless-steel rod current collectors, and a G10 composite tube as the cell body. At different states of charge, a Raman mapping frame was acquired on Li/SE/NMC full cells to monitor changes in the NMC/SE interfacial chemistry.

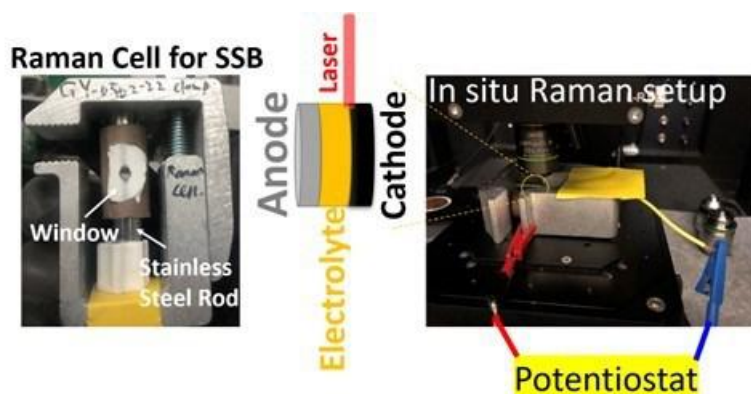


Figure XVI.20.3 (left) Photograph of an in-house developed Raman cell, (middle) schematic of the Raman mapping measurements to probe the NMC/SE interface, and (right) experimental setup for the *in-situ* Raman measurements.

An optical microscope image of the NMC/SE interface is shown in Figure XVI.20.4(a). The scanned area was set to $60 \times 120 \mu\text{m}^2$, with a step size of $1 \mu\text{m}$, and each resultant map contains 7,200 spectra. A typical spectrum of the bulk sulfide SE is shown in Figure XVI.20.4(b). A peak centered at 425 cm^{-1} is assigned to P-S stretching of the PS_4^{3-} tetrahedra. By scaling the intensity of the 425 cm^{-1} peak, a Raman mapping frame (Figure XVI.20.5(c)) representing the PS_4^{3-} distribution within the scanned area was prepared. Notably, Raman maps based on a single peak intensity do not distinguish distribution of other species which may be present at the NMC/SE interface.

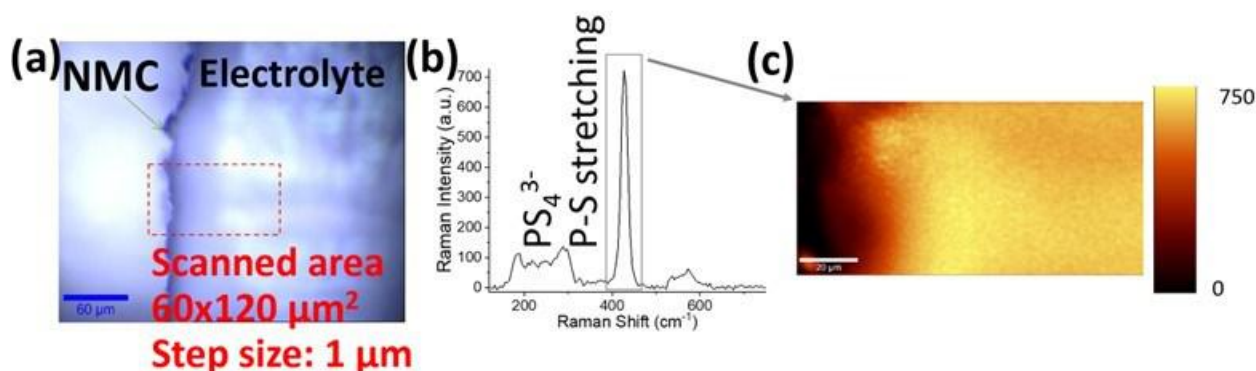


Figure XVI.20.4 (a) Optical microscope image of the NMC/SE interface. (b) Raman spectrum taken from the bulk SE. (c) Raman map based on scaling single peak intensity of the P-S stretching mode centered at 425 cm^{-1} .

To distill the interfacial chemistry of the Li/SE/NMC SSB, an unsupervised machine learning method (K-means clustering) was developed to process each Raman mapping frame. The basic idea of K-means clustering algorithm is to partition the total number of Raman spectra (7,200 in this case) in a mapping frame into K groups. Each group contains Raman spectra of a certain level of similarity, and different groups are color-coded. Consequently, the NMC/SE interface can be extracted as shown in Figure XVI.20.5(a). The average spectrum (so-called centroid spectrum) of each group can be used as its characteristic spectrum. Through this analysis method, we compared the NMC/SE interfacial chemistry at different states of charge as shown in Figure XVI.20.5(b). The results indicate that sulfur and polysulfidophosphate are the oxidative byproducts formed after charging the cathode to 4.2V vs. Li/Li^+ . After the 1st charge/discharge cycle, the P-S stretching mode redshifts to a lower frequency (Figure XVI.20.5(c)), indicating the generation of other sulfide compounds, such as $\text{Li}_4\text{P}_2\text{S}_6$ or $\text{Li}_7\text{P}_3\text{S}_{11}$. Notably, discharging the cell to 2.7 V did not restore the original NMC/SE interfacial chemistry, confirming that oxidative decomposition of the SE is irreversible which is consistent with our prior electrochemical investigations.

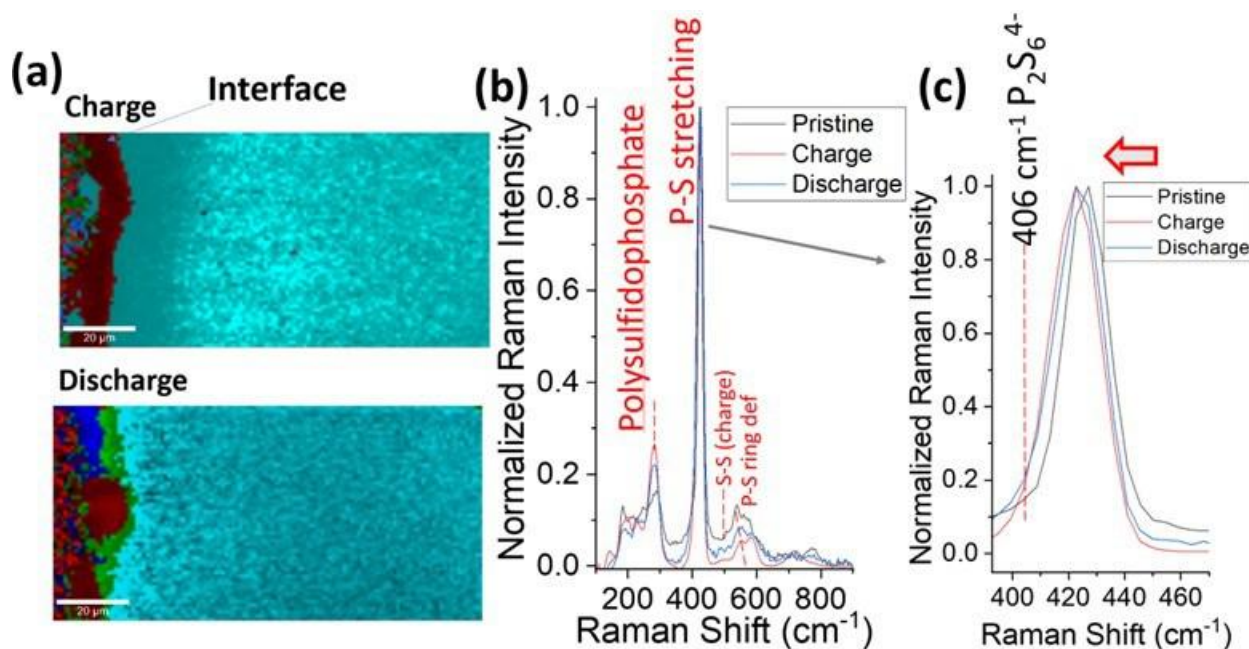


Figure XVI.20.5 (a) Raman mapping of the NMC/SE interface after K-means clustering analysis. (b) Comparison of the centroid spectra taken at the NMC/SE interface at different states of charge. (c) Magnified view of the P-S stretching mode in (b).

Conclusions

Overall, we have shown that the properties of Li₆PS₅X (X = Cl, Br) SEs are affected by anion selection and the precursor mixing process. Our SSB full-cell testing results demonstrate that incorporating oxidatively stable SEs in composite cathodes does not necessarily ensure the formation of robust NMC/SE interfaces, and cumulative irreversible capacity losses in such cells can yield rapid performance decline. Rather than SE decomposition, the capacity fade in LPSCl and LIC-based SSBs is most likely due to active material isolation resulting from repeated volume changes during cycling. As such, an additional understanding of the mechanics of solid-solid interfaces will be critical to address key performance bottlenecks for Li metal SSBs. The operando Raman cell developed in this program enables the exploration of the electrode/electrolyte interfacial structure and chemistry in SSBs. Ongoing efforts are aimed at optimizing full cell cycling performance by exploring how stack pressure and cathode composition (e.g., carbon/SE content and particle morphology) impact cycling stability for cells prepared with free-standing thin film argyrodite and/or halide SEs.

Key Publications

Presentations

1. E. C. Self, W.-Y. Tsai, A. S. Westover, K. L. Browning, G. Yang, J. Nanda "Benchmarking Solid-State Batteries Containing Sulfide Separators: Effects of Electrode Composition and Stack Pressure" *J. Electrochem. Soc.* **2022**, 169, 100510.

Presentations

1. Yang G, Zhang Y, Self E, Brahmabhatt T, Bilheux JC, Bilheux H, Nanda J. Initial Capacity Loss Mechanism of All-Solid-State Lithium Sulfide Battery Unraveled by in Situ Neutron Tomography. In ECS Meeting Abstracts 2022 Jul 7 (No. 2, p. 205). IOP Publishing. (Invited)
2. Nanda J, Sacci R. Self E.C, Yang G, Brahmabhatt T, Tsai, W- Substituted Argyrodites based solid-electrolytes for all solid-state batteries, ACS Fall Meeting Chicago 2022 (Invited)
3. Self E.C., Delnick F.M., Yang G, Brahmabhatt T, Tsai W-Y, Nanda J. All-Solid-State Batteries Containing Lithium Thiophosphate Separators. In TechConnect World Innovation Conference Expo 2022 Jun 13

References

1. Kraft, Marvin A., et al. "Influence of lattice polarizability on the ionic conductivity in the lithium superionic argyrodites $\text{Li}_6\text{PS}_5\text{X}$ ($\text{X} = \text{Cl}, \text{Br}, \text{I}$).*" Journal of the American Chemical Society* 139.31 (2017): 10909-10918.

Acknowledgements

The PI sincerely appreciates support from the team consisting of Co-PIs: Drs. Ethan Self, Frank Delnick, Guang Yang, Wan-Yu Tsai and graduate student Mr. Teerth Brahmbhatt. The project collaborators include Prof. Daniel Hallinan and Ms. Anna Mills (Graduate Student) from Florida A&M University and Florida State University (FAMU-FSU), who are responsible for the development of thin sulfide separators through a sub-contract.

XVI.21 Multifunctional Gradient Coatings for Scalable, High-Energy-Density Sulfide-Based Solid-State Batteries (ANL)

Justin Connell, Principal Investigator

Argonne National Laboratory
9700 South Cass Avenue
Lemont, IL 60439
E-mail: jconnell@anl.gov

Simon Thompson, DOE Technology Development Manager

U.S. Department of Energy
E-mail: Simon.Thompson@ee.doe.gov

Start Date: November 1, 2021

End Date: December 31, 2026

Project Funding (FY22): \$530,000

DOE share: \$530,000

Non-DOE share: \$0

Project Introduction

All-solid-state batteries (ASSBs) have great potential to significantly improve the safety of lithium batteries by replacing flammable liquid electrolytes with solid-state electrolytes (SSEs), but interfacial stability remains a key barrier to commercialization. Among various classes of solid electrolytes that have been investigated, sulfide-based SSEs deliver the highest Li-ion conductivities (≥ 10 mS/cm) compared to polymer and oxide SSEs across a wide range of temperatures with favorable mechanical properties and low temperature processability. The majority of recent developments in ASSBs have focused primarily on improving cycle life by protecting the lithium metal and suppressing lithium dendrites on the anode side. Significantly less has been done to improve the integration of cathode materials into ASSBs; however, for ASSBs to compete in the electric vehicle (EV) market, they must incorporate stable, high-energy cathodes and utilize low-cost processes. In particular, industry needs a strategy to stabilize ASSBs integrating both Li metal anodes and high energy density cathodes, and manufacturability is paramount.

Sulfide SSEs face three primary limitations to their large-scale deployment. The first is their incompatibility with environmental conditions, even those in dry room environments, due to the high reactivity of sulfide materials with both H_2O and O_2 , which leads to material degradation and toxic H_2S evolution. The extent of this reactivity can be mitigated depending on the specific chemistry of the material, but in all cases some degree of air-sensitivity is present, motivating new strategies to make sulfide SSEs more amenable to processing at scale. The second limitation is the intrinsic instability of the anode and cathode interface with sulfide SSEs. Particularly concerning is evidence that direct contact between oxide cathodes and sulfide SSEs leads to chemical intermixing and electrochemical reactivity to form deleterious interfaces that block lithium ion transport. Due to this incompatibility, coatings are required to stabilize the anode and cathode interfaces, with direct coating of the oxide and Li metal surfaces serving as the primary approach for stabilization to date. Despite some success of such coating strategies, the need for separate coating steps for each interface adds significant cost and complexity when considering scalability of this technology. The third, less explored but equally critical issue that must be mitigated is the formation of space-charge layers at oxide-sulfide interfaces, which can lead to high interfacial impedance at the SSE-cathode interface. Such space charge layers are formed due to the mismatch in chemical potential between oxide and sulfide materials, and result in the formation of a Li depletion region within the sulfide during charging of the cathode.

Objectives

This task seeks to develop scalable approaches to synthesize gradient-coated sulfide solid-state-electrolyte (SSE) particles to improve their air/moisture tolerance and provide chemical compatibility with Li-metal anodes and high-voltage oxide cathodes. The compositional gradient is targeted to provide the additional

advantage of lower interfacial impedance due to mitigation of detrimental, spontaneously formed space-charge layers and/or elemental interdiffusion at the sulfide SSE-oxide cathode interface.

Approach

The team will leverage a surface science-based, integrated experimental-theoretical approach to synthesize gradient-coated SSE powders, characterize the structure, composition, and intrinsic stability of coated SSEs in contact with reactive electrodes, and directly correlate this understanding with their electrochemical performance. Gradient coatings will be developed using atomic layer deposition (ALD) and/or physical mixing methodologies viable at the kg/ton scale, ensuring technical and commercial relevance of the final, optimized coating process. Well characterized, model surfaces will be used to understand the electronic structure and chemical stability of the gradient coatings as a function of gradient composition and thickness to understand the effect of space-charge layers and chemical reactions on interface resistance. They will accelerate development and optimization of the gradient coatings for improved performance in full cells by establishing a tight feedback loop between materials synthesis and experimental/computational characterization of interfacial (electro)chemistry.

Results

Among the various classes of solid-state electrolytes (SSEs) that have been investigated to date, argyrodite-based SSEs with the general formula $\text{Li}_{7-y}\text{PS}_{6-y}\text{X}_y$ (LP SX; X = Cl, Br, I), have emerged as one of the most promising families of sulfide-based materials due to the wide range of compositional control and structural (dis)order achievable depending on the nature and chemistry of the halide dopant incorporated into the material. As a result, we have focused our efforts on this family of materials as a platform for developing our gradient coating chemistries. All materials studied have the nominal formula $\text{Li}_6\text{PS}_5\text{Cl}$ (LPSCl), and we have evaluated LPSCl materials synthesized in-house at ANL, as well as material obtained from the commercial suppliers NEI and Ampcera.

Structural and (Electro)chemical Characterization of Uncoated LPSCl.

Figure XVI.21.1a shows representative X-ray diffraction (XRD) patterns for LPSCl from ANL, NEI, and Ampcera. An XRD pattern of the Kapton background signal is also provided for comparison. In all three SSEs, the powder crystallizes in the cubic F-43m space group, as expected, with no detectable impurity phases. Electrochemical impedance spectroscopy (EIS) measurements of pellets pressed from each SSE powder indicate room-temperature ionic conductivities of 1.2, 0.9 and 1.4 mS/cm for the ANL, NEI, and Ampcera materials, respectively. Temperature-dependent conductivity measurements derived from EIS analysis (Figure XVI.21.1b) allow for determination of the activation energy (E_a) for Li^+ transport according to the Arrhenius equation $\sigma(T) = A \exp(-E_a/kT)$, where A is a pre-exponential factor, k is the Boltzmann constant, and T is the absolute temperature. The E_a for the LPSCl solid-state electrolytes from NEI was calculated to be 0.31 eV while the ANL and Ampcera electrolytes have an E_a of 0.30 eV, providing a baseline for Li^+ mobility to compare against coated SSE materials. Representative electrochemical characterization data for $\text{Li}|\text{LPSCl}|\text{Li}$ symmetric cells made from the ANL-synthesized LPSCl and NEI solid-state electrolyte are summarized in Figure XVI.21.1c. In both cases, the LPSCl materials exhibit close-to-uniform plating/stripping profiles at current densities up to 0.35 mA/cm². At current densities >0.35 mA/cm² the plating/stripping profiles of both LPSCl materials become unstable, showing sharp voltage drops indicative of nonuniform Li plating and/or internal short-circuiting. Returning to lower current densities (≤ 0.1 mA/cm²) with the NEI material recovers the same symmetric plating/stripping behavior observed initially, indicating hard short-circuits do not form up to 0.75 mA/cm² (~ 1.8 μm Li plated per cycle).

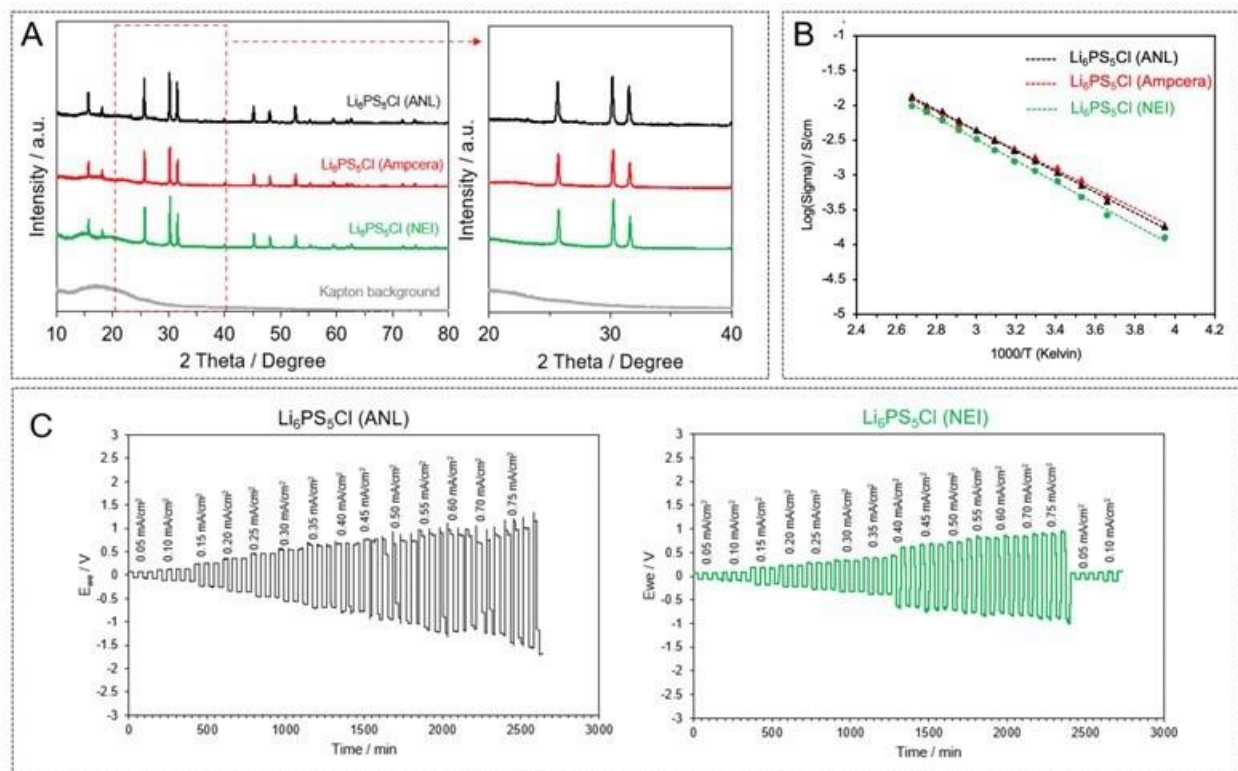


Figure XVI.21.1 (a) X-ray diffraction patterns for pristine $\text{Li}_6\text{PS}_5\text{Cl}$ (LPSCI) from ANL, NEI, and Ampcera (the XRD pattern for the Kapton background is shown for comparison). (b) Arrhenius plots for the total Li^+ conductivity of LPSCI from ANL, NEI and Ampcera in the temperature range of -20°C to 100°C . (c) Cycling stability of pristine LPSCI from ANL (black) and NEI (green) in $\text{Li} || \text{Li}$ symmetric cells at 65°C .

Surface characterization of LPSCI materials via X-ray photoelectron spectroscopy (XPS) was also performed to assess the nominal composition and surface chemistry of the starting materials and establish a baseline prior to applying coatings (Figure XVI.21.2). Utilizing our glovebox-connected ultrahigh vacuum (UHV) system, it is possible to analyze the LPSCI materials without any ambient air exposure prior to analysis. XPS core level spectra of the as-received Ampcera LPSCI powders reveals a surface exhibiting little to no impurity species and minimal (but non-zero) surface oxidation. The dominant species observed in both the S 2p and P 2p core levels (Figure XVI.21.2a-b) are assigned to PS_4^{3-} tetrahedra in LPSCI. Evidence of S^{2-} species is also present in the S 2p, consistent with the presence of Li_2S . Negligible (≤ 0.5 at%) amounts of S^0 and $\text{P}_2\text{S}_5/\text{Li}_3\text{PO}_4$ can also be fit to the spectra, indicating possible residual precursor materials or some degree of surface oxidation, but are within the experimental error and are therefore not confidently assigned as present. The Cl 2p core level (Figure XVI.21.2c) indicates a single species that is consistent with Cl^- in the LPSCI structure. Surface oxide species (Figure XVI.21.2d) are partially due to carbonaceous contaminants that are inherent to XPS analysis (R-C-O and O-C-O), as well as suggest a small amount of surface carbonate or phosphate formation, perhaps due to some air exposure during the materials manufacturing and/or shipment. Quantitative composition analysis of the Ampcera sample indicates the surface oxygen content is approximately 10% of the total signal, suggesting a thin layer of surface oxidation is present. Similar surface speciation is observed from NEI and ANL-synthesized materials, with surface oxidation at or below the levels observed in the Ampcera material. Overall, the XPS analysis indicates high quality materials suitable for testing the impact of SSE coating on (electro)chemical stability and performance.

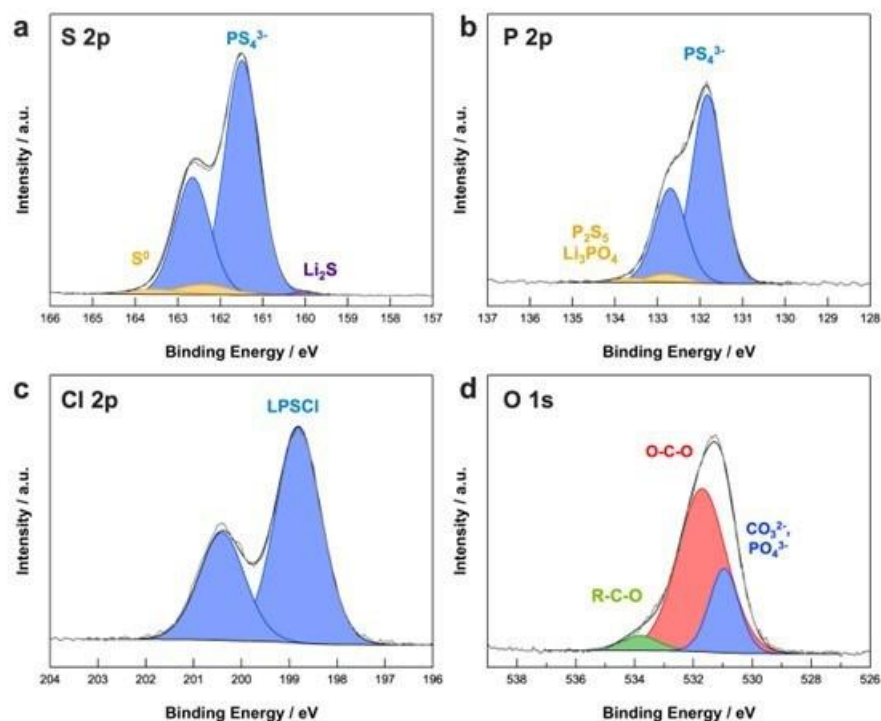


Figure XVI.21.2 (a) S 2p, (b) P 2p, (c) Cl 2p and (d) O 1s XPS core level spectra for the Ampcera LPSCI SSE.

Chemical Stability of LPSCI to ALD Coating

Having established performance baselines for Li-Li symmetric cells with uncoated LPSCI and benchmarked the surface chemistry of the starting material, we turn our attention to the chemical stability of these materials to atomic layer deposition (ALD) coating and contact with Li metal. In order to analyze the stability of LPSCI to coating via ALD, pressed SSE pellets were prepared and inserted into the ALD reactor alongside powders. This provides extended surfaces for XPS analysis while ensuring that surface characterization is done on the exact same reaction conditions for coating powders used for subsequent electrochemical characterization. ALD Al_2O_3 coatings were applied at 150°C with each ALD cycle consisting of alternating exposures to trimethylaluminum (TMA) followed by H_2O exposure. The intensity of the Al 2p and O 1s signals increases with increasing ALD cycles (Figure XVI.21.3), consistent with the deposition of Al_2O_3 and a small fraction of Li_xAlO_y onto the SSE. Analysis of the S 2p, P 2p and Cl 2p core levels further reveals that the LPSCI materials are surprisingly robust to the ALD coating chemistry (Figure XVI.21.3). Specifically, the only chemical reactivity observed on ALD-coated SSEs relative to uncoated materials were found in the S 2p core level, where a small fraction of Li_2S formation is observed ($\leq 10\%$ of the total signal after 10 ALD cycles). No other chemical changes are observed in the P or Cl core levels after ALD, indicating the small amount of reaction observed is confined to S species in LPSCI. This result is particularly surprising given that each ALD cycle incorporates exposure to H_2O vapor as the oxygen source for the Al_2O_3 . Despite the exposure of the surface to H_2O vapor at 150 °C, there is no evidence of oxidation – *e.g.*, SO_3^{2-} formation, which would be observed at ~ 167 eV in the S 2p core level spectrum. Identical reactivity is observed on material made at ANL or sourced from NEI, as well as on coated powders, indicating this result is general to LPSCI materials, regardless of supplier or form factor. We speculate that the exposure of the SSE surface to TMA, which is highly reducing, leads to the formation of a thin Li_2S layer that passivates the surface to further reaction with TMA and H_2O . Regardless of the mechanism, however, the results are unambiguous that ALD coating of sulfide SSEs is feasible, and results in negligible reaction with the underlying material.

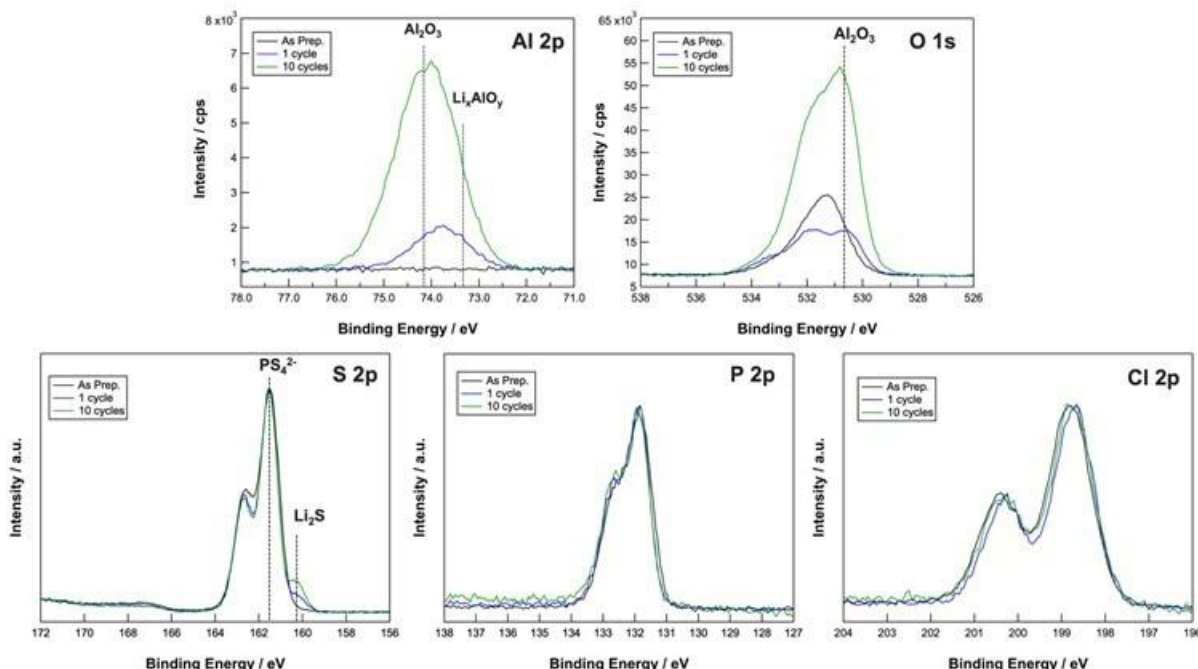


Figure XVI.21.3 Al 2p, O 1s, S 2p, P 2p, and Cl 2p core level spectra for Ampcera LPSCI SSE with varying numbers of ALD Al_2O_3 coating cycles. Intensities of the S 2p, P 2p and Cl 2p spectra are normalized for comparison.

Chemical Stability of Coated LPSCI to Reactivity with Li Metal.

Not only is LPSCI robust to the ALD coating chemistry, but coating of the SSE with ~ 1 nm ALD Al_2O_3 (10 cycles) results in significantly more stable interfaces with Li metal. Approximately 10 nm of Li metal was deposited onto the same SSE pellets analyzed in Figure XVI.21.3, and utilizing our unique, air-free UHV transfer line, we were able to perform XPS to directly measure the reactivity of coated and uncoated materials at the pristine Li-SSE interface. Analysis of the S 2p and P 2p core levels of coated and uncoated material before and after Li deposition reveals significantly less reduction of LPSCI that was coated by 10 ALD Al_2O_3 cycles (Figure XVI.21.4). In both cases, S 2p core level spectra reveal the reduction of PS_4^{2-} species to Li_2S by Li metal; however, the relative fraction of Li_2S formed on coated material is significantly lower: $\sim 61\%$ vs. 81% of the total signal for coated and uncoated material, respectively. This difference is even more significant considering that $\sim 10\%$ of the coated SSE was already converted to Li_2S during the ALD process. Analysis of the P 2p core level spectra reveals that P species are even more protected from reduction by Li metal than S species. Specifically, approximately 78% of the P species on the uncoated material are reduced, whereas only 53% of the coated material is reduced by contact with Li. Furthermore, the majority of the species formed on uncoated LPSCI are assigned to fully reduced Li_3P , whereas a more or less equal fraction of Li_3P and less reduced Li_xP and $\text{Li}_{(x-1)}\text{P}$ species are observed on ALD-coated SSE, indicating a greater degree of protection.

Collectively, these results indicate the significant promise of our ALD coating strategy. Not only are sulfide SSEs surprisingly robust to the ALD Al_2O_3 process comprising exposure to TMA and H_2O vapors, but they also significantly improve the materials stability against the highly reducing Li metal anode. We anticipate a wide spectrum of ALD coating chemistries will provide similar benefits to materials stability against reactive electrodes while preserving the underlying SSE chemistry. With these results in mind, we will continue developing additional ALD coating chemistries through a combination of computational assessment and experimental validation of materials stability, electronic structure, and electrochemical performance. In order to perform such an analysis, however, greater understanding of the intrinsic stability and electronic properties of these coatings is needed.

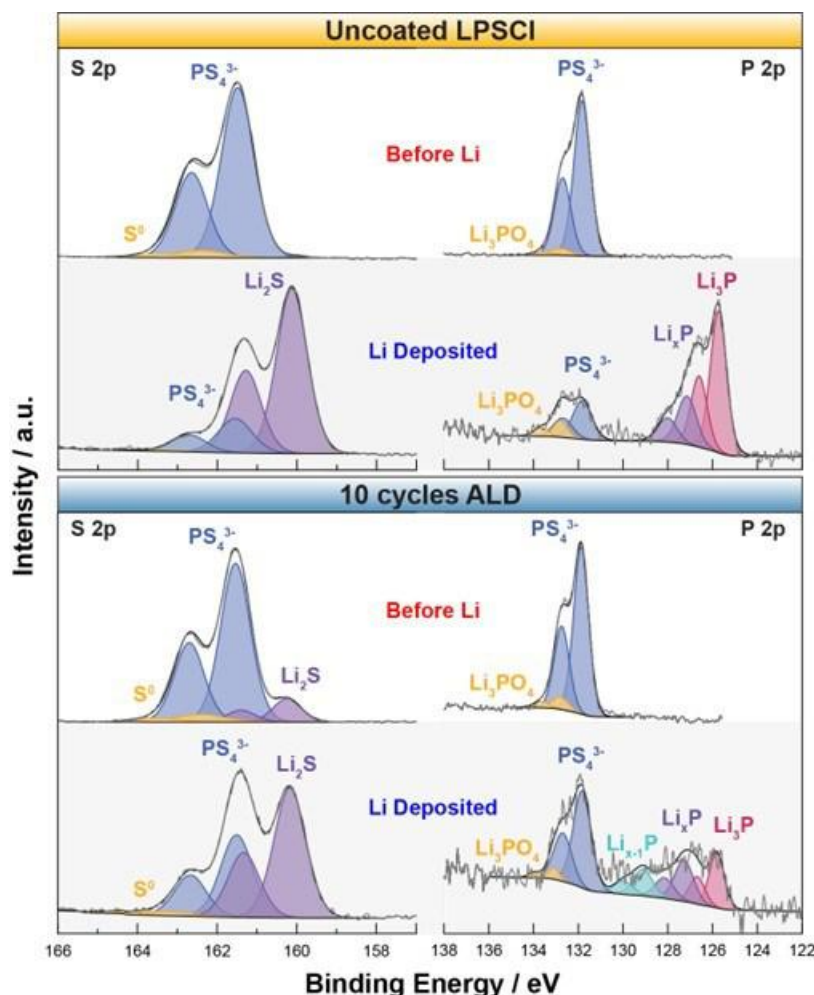


Figure XVI.21.4 S 2p (left) and P 2p (right) core level spectra of uncoated LPSCI (top) and LPSCI coated with 10 ALD cycles (bottom) before and after Li metal deposition.

Computational Assessment of Origins of Materials Stability

In order to understand the origin of the surprising robustness of LPSCI materials to ALD coating and the subsequent improvement in stability against Li metal, computational assessment of the thermodynamic stability and electronic properties for the coatings at interfaces of argyrodite particles was performed. In order to analyze the electronic structure of the coatings, we started with density functional theory (DFT) calculations for LPSCI with different degrees of oxygen substitution. The electronic density of states (Figure XVI.21.5) shows an increase of the bandgap from 3.32 eV to 3.55 eV when 5% of S atoms are substituted by oxygen. Calculations for the isostructural analogue where all of the S atoms are substituted by O atoms produces an even larger increase in band gap to 7.04 eV; however, the lattice constant of argyrodite decreases considerably. Substituting oxygens into the Cl positions was found to be less energetically favorable than substitution into tetrahedral S positions, and substitution of O atoms into P positions is unfavorable. Our results point to the possibility that ALD coatings of oxide or oxysulphide materials will result in lower electronic conductivity because of an increased band gap deriving from exchange of some sulfur for oxygen at the interface.

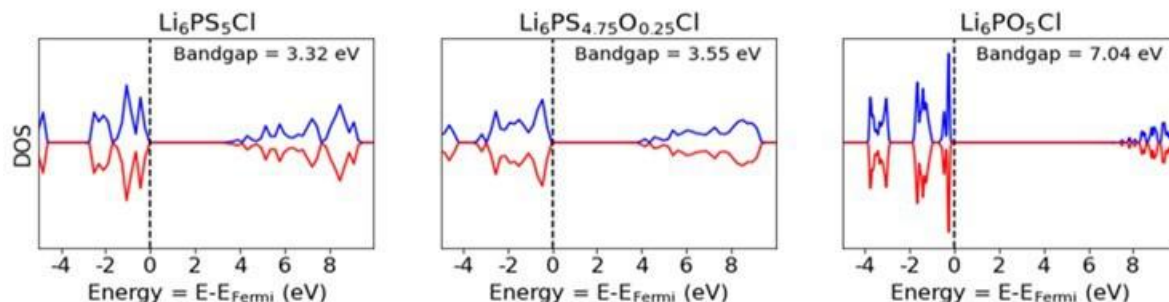
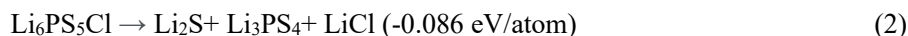
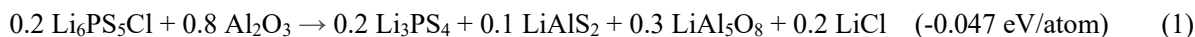


Figure XVI.21.5 Calculated densities of states for LPSCl SSE with varying concentration of oxygen.

To gain further insights into the stability and transport properties of oxide coatings, we consider computational models of LPSCl with ALD alumina coatings. First, we have calculated the work functions for amorphous alumina and LPSCl to determine the relative band alignment at their interface. The results indicate that work function for LPSCl (4.6 eV) is considerably smaller than the work function for amorphous alumina (average 6.5 eV). Our calculations for amorphous LPSCl with the same composition as a crystalline argyrodite produce a work function very close to the value for the crystal, suggesting that electronic transport through LPSCl interfaces is easier than through alumina-LPSCl interfaces.

As the XPS results in Figure XVI.21.3 indicate a thin, but detectable reaction layer formed at the alumina-LPSCl interface, we also need to consider electronic and ionic transport properties for reaction products that could be present at interfaces depending on synthesis and processing conditions. Considering possible chemical reactivity between argyrodite and the alumina coatings, we have determined two compositions in the range between $\text{Li}_6\text{PS}_5\text{Cl}$ and Al_2O_3 corresponding to the points on the convex hull according to the following reactions:



Notably, LPSCl decomposition (Eqs. 1-2) is found to be favorable, resulting in the formation of Li_2S and lithiated Al oxides/sulfides. This result is consistent with the XPS results that indicate the formation of a thin layer of Li_2S (Figure XVI.21.3) and reduced Al species (either LiAlO_x or LiAlS_x) after ALD coating. Calculations of barriers for Li^+ hopping through some of these interfacial phases, some of which could impede ionic transport, produce the lowest values for the barriers in LiAlS_2 , LiCl , and Li_2S , which range from about 0.2 eV to 0.4 eV (Figure XVI.21.6). These relatively low transport barriers indicate that Li ionic transport is feasible through the reaction products that may form at the interface between ALD alumina and LPSCl. Taken together, these results provide a baseline for assessing potential ALD coating chemistries. Electronic band structure, work functions, interface reaction enthalpies, and barriers for Li ion transport will be assessed for candidate chemistries to further establish their contributions to possible space charge layer formation at interfaces and resulting increases in interfacial impedance. Continued development of screening criteria for target chemistries and compositional distributions across the interfaces will target materials stability and electrochemical properties as well, providing a framework for design of new coatings that is guided by both computation and experiment.

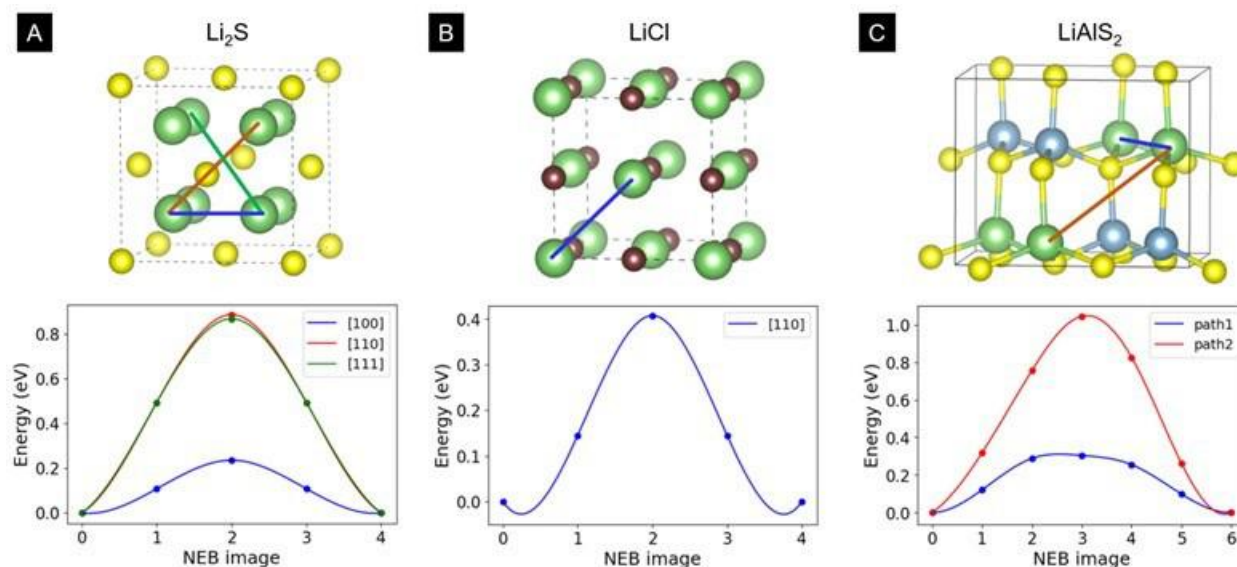


Figure XVI.21.6 Calculated barriers for Li hopping in predicted reaction products of alumina with LPSCI – (a) Li_2S , (b) LiCl and (c) LiAlS_2 – indicate feasibility of Li ionic transport through the interfacial layers.

Conclusions

Utilizing a surface science-based, integrated experimental-theoretical approach, we have demonstrated a new, scalable method for stabilizing sulfide-based SSEs against environmental exposure and contact with reactive electrodes. Through structural, spectroscopic, and electrochemical methods, we have fully characterized and benchmarked a number of LPSCI materials from different sources in order to understand their baseline performance characteristics. We have further demonstrated that it is possible to coat argyrodite powders using ALD, and that the ALD processing conditions result in minimal reactivity to the underlying material, suggesting that ALD on argyrodite materials is a viable path forward to scalable coating of sulfide-based SSEs. Al_2O_3 -coated LPSCI materials exhibit much less reactivity after contact with Li metal relative to uncoated materials, indicating significant benefits of the coated materials for creating stable interfaces with reactive electrodes. The origin of the enhanced materials stability was determined using DFT calculations, which support the reaction product chemistries observed via XPS. DFT calculations further suggest these reaction products should increase the barrier for electron transport, while nudged elastic band calculations indicate that the reaction products formed possess reasonable barriers for Li^+ transport. Overall, the calculations indicate favorable interfacial properties for integration into symmetric and full cells. Leveraging our combined experimental-theoretical approach, we anticipate the development of many new coating chemistries and deeper understanding of the coupled (electro)chemical properties that result in stable and conductive interfaces between anode and cathode materials in full cells.

Key Publications

Invention Disclosures

1. **Multifunctional Coatings for Solid State Electrolyte Powders.** Connell, J. G.; Elam, J. W.; Hood, Z. D.; Mane, A. U. ANL-IN-22-023.

Acknowledgements

The PI is grateful to his collaborators Collin Becker (Solid Power), Josh Buettner-Garrett (Solid Power), Jeffery Elam (ANL), Zachary Hood (ANL), Taewoo Kim (ANL), Eungje Lee (ANL), Anil Mane (ANL), Sanja Tepavcevic (ANL), Aditya Sundar (ANL), Peter Zapol (ANL) and Pu Zhang (Solid Power), for data collection and analysis and their many other valuable contributions to the project.

XVI.22 Thick Selenium-Sulfur Cathode Supported Ultra-thin Sulfides Electrolytes for High-energy All-solid-state Lithium Metal Batteries (ANL)

Guiliang Xu, Principal Investigator

Argonne National Laboratory
9700 South Cass Avenue
Lemont, IL 60439
E-mail: xug@anl.gov

Simon Thompson, DOE Technology Development Manager

U.S. Department of Energy
E-mail: Simon.Thompson@ee.doe.gov

Start Date: January 1, 2022

End Date: October 31, 2026

Project Funding (FY22): \$500,000

DOE share: \$500,000

Non-DOE share: \$0

Project Introduction

Lithium/sulfur (Li/S) battery constitute a serious contender for energy storage application because of its high theoretical energy density (~ 2600 Wh/kg) and the nature abundance of sulfur.[1] All solid-state lithium/sulfur batteries (ASSLSBs) using solid-state electrolytes (SSEs) can effectively eliminate the polysulfide shuttle and stabilize Li metal anode to improve the cycling stability and safety.[2] However, the lack of SSEs that can improve their power characteristics and energy densities significantly hinders their implementation. Two essential criteria for SSEs to achieve 500 Wh/kg are (1) comparable RT ionic conductivity ($>10^{-2}$ S/cm) with liquid electrolytes that can boost the utilization of cathode active materials; and (2) thin and lightweight that can reduce the percentage of inactive components in the whole cells. Nevertheless, the fabrication of ultra-thin and mechanically stable sulfides SSEs remain technically challenging.[3] In particular, most sulfides SSEs are not stable under ambient condition, limiting the conventional processing approaches.[4] Moreover, stabilization of the SSE/cathode interface and the SSE/Li anode interface to maintain intimate solid-solid contact and negligible interfacial resistance during charge/discharge remain formidable challenge.[5]

The team led by Dr. Guiliang Xu at Argonne National Laboratory is focusing on the development of ultra-thin sulfides SSEs with high RT ionic conductivity and high air/mechanical/electrochemical stability as well as intimate solid-solid contact when coupling with high-capacity Li metal anode and Se-S cathode.

Objectives

The project objective is to develop ultra-thin (< 30 μm) sulfide SSEs with high room temperature ionic conductivity ($> 10^{-2}$ S/cm) and high chemical/mechanical/electrochemical stability, and further integrate them with lithium metal and high-loading selenium-doped sulfur (Se-S) cathodes through rational interface engineering to develop all-solid-state Li-S batteries (ASSLSBs) with high cell energy density of > 500 Wh/kg and stable cycle life of > 300 cycles at a current density of > 1 mA/cm².

Approach

The thickness and chemical/interfacial stability of sulfide SSEs are the critical challenges for energy density, cycle life, and mass production of all-solid-state Li/S pouch cells. The team will combine innovative material design, electrode architecture fabrication, and advanced diagnostics tools to address these challenges. Specifically, the approaches include: (1) improving air stability and ionic conductivity of sulfides through synthetic control and cation/anion doping, (2) fabrication of flexible thick SeS cathode supported thin sulfide electrolytes to ensure intimate contact and increase the energy density, (3) stabilizing Li-metal/sulfide electrolytes interface via interlayer and additives design to increase the critical current density (CCD) of lithium stripping/plating, (4) advanced Li/S pouch cell design, and (5) multiscale advanced diagnostic such as

in situ X-ray diffraction (XRD), X ray absorption spectroscopy (XAS), X-ray imaging, and focused ion beam-scanning electron microscopy (FIB-SEM) to understand and overcome the degradation pathways.

Collaboration

- Processing of sulfides: Dr. Jieun Lee (CSE, ANL)
- Synthesis of sulfides: Dr. Chen Zhao (CSE, ANL), Dr. Xingkang Huang (UChicago)
- Synchrotron X-ray diffraction: Dr. Dongzhou Zhang, Dr. Wenqian Xu (APS of ANL)
- Synchrotron X-ray absorption spectroscopy: Dr. Cheng-Jun Sun (APS of ANL)
- Electron microscopy: Dr. Yuzi Liu (CNM of ANL).

Results

Set up a dedicated lab for synthesis, processing, and test of sulfides SSEs at Argonne

To achieve our goal in developing 500 Wh/kg ASSLSBs, during the first year of this project, we have set up a dedicated lab for the synthesis, processing, and test of sulfides SSEs. Sulfides SSEs are moisture sensitive, which currently require the use of Argon-filled glovebox. Figure XVI.22.1a and 1b show the digital photos of our lab that contains battery cycler, slurry mixer, thin film coater, furnace, and pellet presser inside glovebox as well as high-energy ball-milling with gas-protected jars. Meanwhile, we have set up an in-house electrospinning equipment that is used to develop thin sulfides SSEs, which is critical to increase the cell energy density of ASSLSBs.

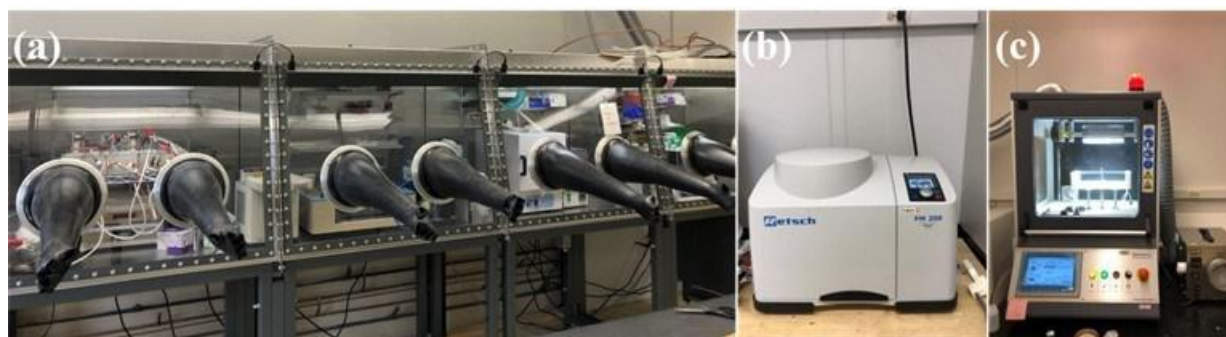


Figure XVI.22.1 Digital photos of all-solid-state sulfide lab at chemical sciences and engineering division of Argonne: (a) glovebox for synthesis, processing, and test of sulfides SSEs. (b) High-energy ball-milling with gas-protected jars for the synthesis of sulfides SSEs. (c) in-house electrospinning for the fabrication of thin sulfides SSEs.

High throughput screening synthesis of $\text{Li}_6\text{PS}_5\text{Br}$ with various dopants via in situ synchrotron X-ray diffraction

Among all the sulfides SSEs, argyrodite family with a general formula of $\text{Li}_6\text{PS}_5\text{X}$ ($\text{X}=\text{Cl}$, Br , and I) is of particular interest due to their high ionic conductivity (above 10^{-3} S/cm) at room temperature, low cost, and good compatibility towards Li metal. Unlike $\text{Li}_6\text{PS}_5\text{I}$ comprising fully ordered S^{2-} and I^- , $\text{Li}_6\text{PS}_5\text{Cl}$ comprising fully disordered S^{2-} and Cl^- , $\text{Li}_6\text{PS}_5\text{Br}$ comprises a mixture of ordered and disordered structures, thus demonstrating the fastest theoretical Li^+ mobility in the $\text{Li}_6\text{PS}_5\text{X}$ family. However, $\text{Li}_6\text{PS}_5\text{Br}$ still suffers from insufficient ionic conductivity and poor moisture stability, which significantly hinder its practical application. Figure XVI.22.2 shows our material design principles. Based on the classical hard-soft acid-base concept, We plan to use anion (e.g., O^{2-}) doping and cation doping (e.g., Sn^{4+} , Sb^{5+}) to improve the air stability of $\text{Li}_6\text{PS}_5\text{Br}$ due to the higher binding strength between phosphorus and oxygen or between cation dopants and sulfur, which however might lead to reduced ionic conductivity. We hence will further explore the effect of halogen doping (e.g., Br) to compensate the ionic conductivity. Nevertheless, the successful incorporation of multi dopants in the $\text{Li}_6\text{PS}_5\text{Br}$ would require a significantly increased efforts on the synthetic control, which is time consuming.

Unlike the conventional approaches that are mostly based on trial-and-error experiments, the in situ synchrotron X-ray diffraction (SXRD) at Advanced Photon Source (APS) could allow us to directly probe the

phase transition and crystal structure evolution during formation of $\text{Li}_6\text{PS}_5\text{Br}$ SSEs with various dopants. We could also monitor the structural evolution during holding (e.g., effect of time) and cooling process (quenching vs. slow cooling). Moreover, through Rietveld refinement, we will be able to obtain the evolution of cell lattice parameter, and microstrain and Br/S^{2-} site disorder during synthesis. These information would be very valuable for us to design better sulfides SSEs. Figure XVI.22.3a shows the in situ SXR set up that we have built at APS, which include X-ray beam, gas-blower heater, and a camera. Figure XVI.22.3a shows a snapshot during the in situ heating experiment, in which the gas-blower directly heated the sample, while the X-ray penetrated through the samples to collect the SXR patterns during synthesis process.

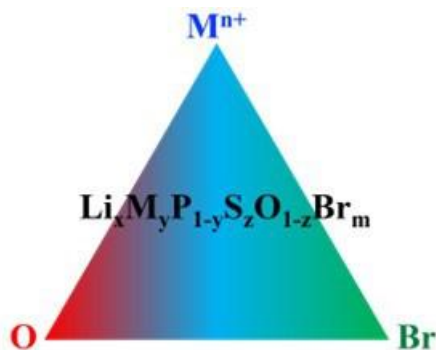


Figure XVI.22.2 Design principle of Argyrodite sulfide electrolytes with multi dopants. M represents cations.

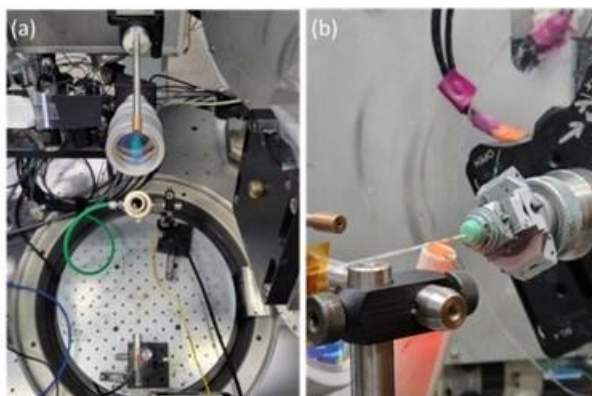


Figure XVI.22.3 (a) A digital photo of in situ SXR set up at Advanced Photon Source (APS) to probe the synthesis of sulfides SSEs. (b) A snapshot during in situ heating process.

In order to understand the effect of O and Br doping, we have designed five samples with formula of $\text{Li}_6\text{PS}_5\text{Br}$, $\text{Li}_6\text{PS}_{4.8}\text{O}_{0.2}\text{Br}$, $\text{Li}_{5.5}\text{PS}_{4.5}\text{Br}_{1.5}$, $\text{Li}_{5.5}\text{PS}_{4.3}\text{O}_{0.2}\text{Br}_{1.5}$, and $\text{Li}_{5.5}\text{PS}_{4.4}\text{O}_{0.1}\text{Br}_{1.5}$, respectively. The type and concentration of dopants can significantly affect the synthesis process of $\text{Li}_6\text{PS}_5\text{Br}$ electrolytes. Hence, we used in situ SXR to investigate the formation process of these electrolytes. Before the in situ SXR experiment, Li_2S , LiBr , P_2S_5 and Li_2O with appropriate molar ratio were mixed homogeneously by ball-milling at 500 rpm for 8 h. We then loaded the samples into quartz tubes and sealed with Kapton tape to prevent the moisture contamination during the experiment.

Figure XVI.22.4a shows the in situ SXR pattern during formation of $\text{Li}_6\text{PS}_5\text{Br}$ by direct heating the $\text{Li}_2\text{S}/\text{LiBr}/\text{P}_2\text{S}_5$ mixture from room temperature (RT) to 600°C with a heating rate of $5^\circ\text{C}/\text{min}$ followed by rapid cooling ($30^\circ\text{C}/\text{min}$). As shown, the reaction process can be separated into three regions: (I) starting materials; (II) formation of $\text{Li}_6\text{PS}_5\text{Br}$; (III) quenching process. Figure XVI.22.4b shows the zoom-in view at 2θ range of $6-9.5^\circ$. As shown, upon heating, the peaks of starting materials— Li_2S (111 and 200), LiBr (111 and 200) and P_2S_5 (012 and 2-2-1) gradually decreased. At a temperature of $\sim 270^\circ\text{C}$, three new peaks corresponding to the (220), (311) and (222) peaks of $\text{Li}_6\text{PS}_5\text{Br}$ emerged, indicating formation of $\text{Li}_6\text{PS}_5\text{Br}$. Further heating from 270°C to 600°C results in the increase of XRD peak intensity due to the growth of

particle size and disappearance of other impurities. We have conducted Rietveld refinement on the SXRD pattern at 600°C. As shown in Figure XVI.22.5, the formed $\text{Li}_6\text{PS}_5\text{Br}$ is well consistent with the standard $\text{Li}_6\text{PS}_5\text{Br}$ with a space group of F-43m and cell lattice parameter of $a=b=c=10.097443 \text{ \AA}$ and $\alpha=\beta=\gamma=90^\circ$. During quenching (rapid cooling), we can see there is no phase transition, indicating the reservation of pure $\text{Li}_6\text{PS}_5\text{Br}$ phase.

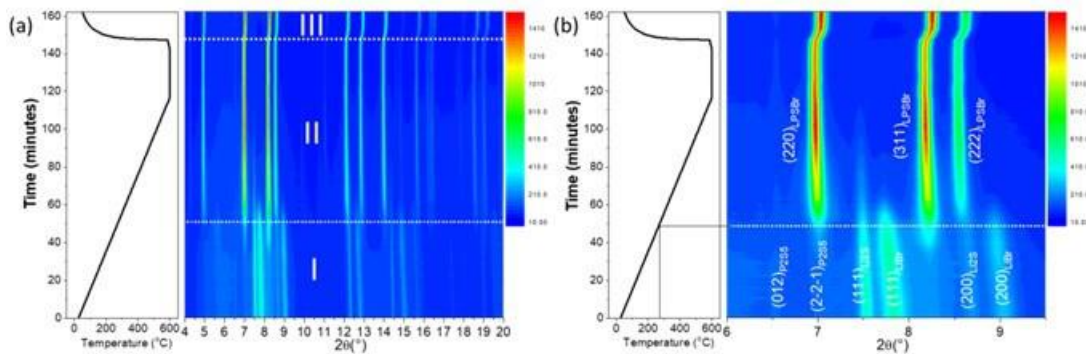


Figure XVI.22.4 (a) 2D Contour plot of in situ SXRD patterns during formation of $\text{Li}_6\text{PS}_5\text{Br}$. (b) Zoom-in view of 2θ range of 6.0-9.5°.

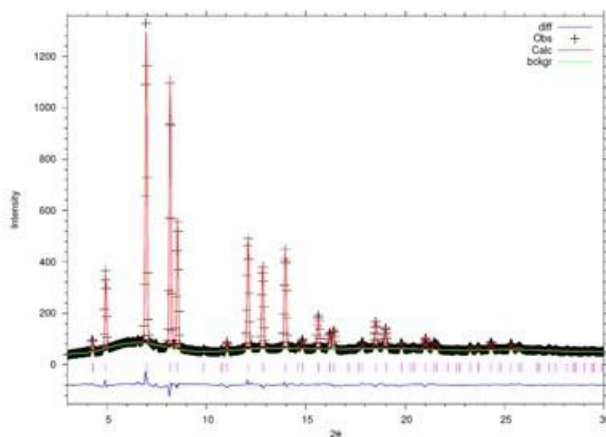


Figure XVI.22.5 Rietveld refinement of in situ SXRD pattern at 600°C during synthesis of $\text{Li}_6\text{PS}_5\text{Br}$.

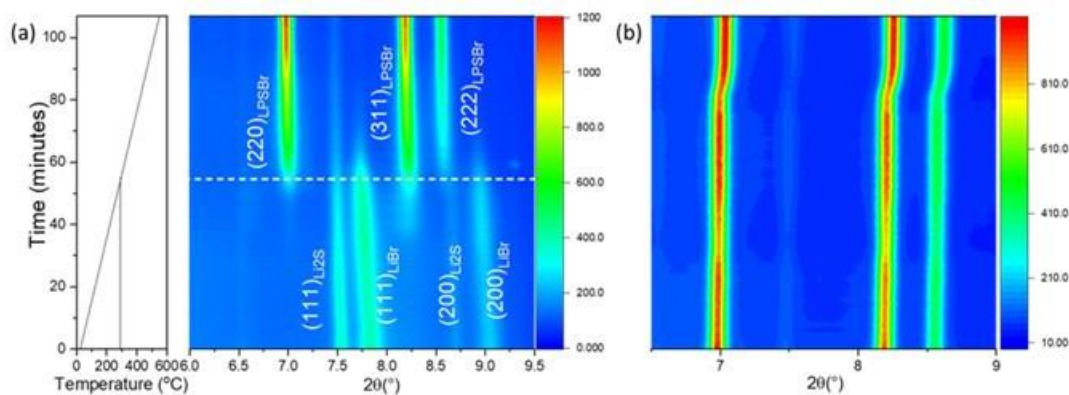


Figure XVI.22.6 2D Contour plot of in situ SXRD patterns during formation of $\text{Li}_6\text{PS}_{4.8}\text{O}_{0.2}\text{Br}$: (a) heating from RT to 550°C; (b) 550°C holding for 8 h followed by quenching (30°C/min).

We further investigated the case of $\text{Li}_6\text{PS}_{4.8}\text{O}_{0.2}\text{Br}$ with oxygen doping. As shown in Figure XVI.22.6a, the synthesis process of $\text{Li}_6\text{PS}_{4.8}\text{O}_{0.2}\text{Br}$ generally follows similar reaction process by converting Li_2S , LiBr , P_2S_5 and Li_2O to form $\text{Li}_6\text{PS}_{4.8}\text{O}_{0.2}\text{Br}$. However, compared to the result of $\text{Li}_6\text{PS}_5\text{Br}$, the starting temperature for the evolution of (220) peak of $\text{Li}_6\text{PS}_5\text{Br}$ in the oxygen-doped one was postponed to around 300°C . Meanwhile, it can be clearly seen that even after heated to 550°C , there are still some peaks remaining, which are corresponding to Li_2S and LiBr , respectively. The results indicate that the incorporation of Li_2O will compete with Li_2S for site occupancy during the formation of $\text{Li}_6\text{PS}_{4.8}\text{O}_{0.2}\text{Br}$. Even after heating at 550°C for 8 h, the peaks of Li_2S still remained (Figure XVI.22.6b).

To balance the moisture stability and ionic conductivity, we have further explored O-/Br co-doped argyrodite electrolytes— $\text{Li}_{5.5}\text{PS}_{4.3}\text{O}_{0.2}\text{Br}_{1.5}$. Figure XVI.22.7a shows the in situ SXR patterns during heating a ball-milled mixture of $\text{Li}_2\text{S}/\text{P}_2\text{S}_5/\text{P}_2\text{O}_5/\text{LiBr}$ from room temperature to 600°C to form $\text{Li}_{5.5}\text{PS}_{4.3}\text{O}_{0.2}\text{Br}_{1.5}$. The results show that in addition to the cubic structure argyrodite solid electrolytes, there are significant residue of LiBr in the final product even when the temperature reached 600°C , indicating that Br has not been successfully incorporated into the 4a sites. This could be due to the larger ionic radii of Br^- (182 pm) than S^{2-} (170 pm). The results also indicated that higher temperature might be necessary to substitute more Br in the $\text{Li}_6\text{PS}_5\text{Br}$.

Figure XVI.22.7b show the selected SXR patterns during cooling from 600°C to 50°C with a cooling rate of $30^\circ\text{C}/\text{min}$. Strikingly, in addition to the peak shift to higher 2-theta degree due to lattice contraction, it is obvious to observe a series of new peaks, as marked at 8.50° , 12.07° , 12.78° and 14.26° , indicating formation of new phases during rapid cooling. This is different from the results in the $\text{Li}_6\text{PS}_5\text{Br}$ and $\text{Li}_6\text{PS}_{4.8}\text{O}_{0.2}\text{Br}$, in which the rapid cooling does not induce formation of new phases.

To successfully dope Br and O in the $\text{Li}_6\text{PS}_5\text{Br}$, we have further developed a two-step calcination process to synthesize pure phase $\text{Li}_{5.5}\text{PS}_{4.5}\text{Br}_{1.5}$ and $\text{Li}_{5.5}\text{PS}_{4.4}\text{O}_{0.1}\text{Br}_{1.5}$. Different from previous one-step calcination process, in which we directly heated the precursor mixture (Li_2S , LiBr and P_2S_5) from room temperature to 500 – 600°C , we pre-calcined the mixture at 300°C for 12 h because our previous in situ SXR results showed that $\text{Li}_6\text{PS}_5\text{Br}$ started to form at $\sim 300^\circ\text{C}$. We then used in situ SXR to monitor the phase transition process during heating of pre-calcined mixture. As shown in Figure XVI.22.8, before heating, the pre-calcined mixture shows clear XRD peaks that belong to $\text{Li}_6\text{PS}_5\text{Br}$. Meanwhile, signature XRD peaks of LiBr can be observed. During heating from 25°C to 550°C , all the peaks gradually shifted to lower 2-theta degree, corresponding to thermal expansion. When the temperature is higher than 550°C , the (111), (200), (220), (311), (400), (331), (420), (422), (511), (531) and (442) peaks of LiBr suddenly disappeared, accompanied by the emergence of (111), (200), (220), (311), (222), (422), (333), (440), (620), (533), (622), (642) and (553) peaks of $\text{Li}_6\text{PS}_5\text{Br}$. The results indicate that pre-calcination step is important to successfully dope high Br content into $\text{Li}_6\text{PS}_5\text{Br}$ and synthesize pure-phase $\text{Li}_{5.5}\text{PS}_{4.5}\text{Br}_{1.5}$.

We further studied the case of $\text{Li}_{5.5}\text{PS}_{4.4}\text{O}_{0.1}\text{Br}_{1.5}$, in which both O and Br were introduced. Our previous experiment by single-step calcination shows that a significant amount of LiBr residue. By sharp contrast, as shown in Figure XVI.22.9, the synthesis process of $\text{Li}_{5.5}\text{PS}_{4.4}\text{O}_{0.1}\text{Br}_{1.5}$ via two-step calcination undergo similar process as that of $\text{Li}_{5.5}\text{PS}_{4.5}\text{Br}_{1.5}$. At a temperature of $\sim 520^\circ\text{C}$, the formation of pure phase $\text{Li}_{5.5}\text{PS}_{4.4}\text{O}_{0.1}\text{Br}_{1.5}$ was observed, indicating both O and Br have been successfully doped into $\text{Li}_6\text{PS}_5\text{Br}$.

Furthermore, we have investigated the effect of holding time on the crystal structures of final products during quenching or rapid cooling ($\sim 30^\circ\text{C}/\text{min}$). Figure XVI.22.10a shows the results of SXR patterns after holding at 600°C for 0.5 h and rapid cooling to 25°C . A generation of new peaks belong to LiBr was observed during rapid cooling, indicating holding at high-temperature for short period of time is not enough to maintain the argyrodite crystal structure. By contrast, a process of 10 h holding can lead to maintained pure phase $\text{Li}_{5.5}\text{PS}_{4.4}\text{O}_{0.1}\text{Br}_{1.5}$ during rapid cooling (Figure XVI.22.10b).

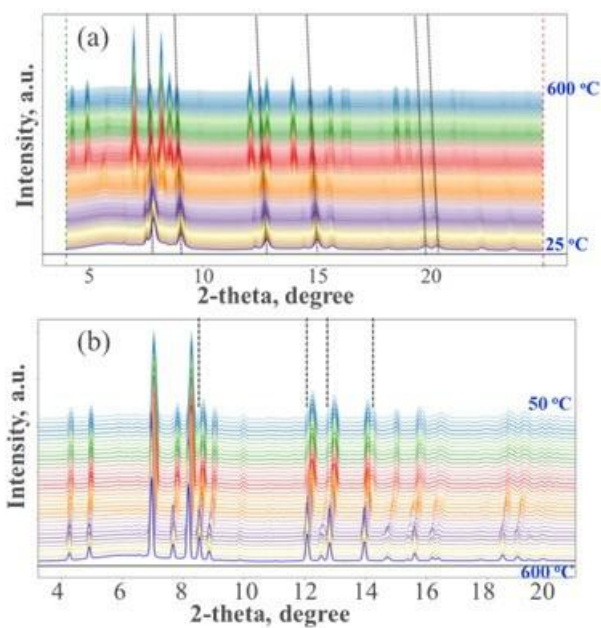


Figure XVI.22.7 In situ SXR D patterns during (a) heating (25 °C to 600 °C) and (b) rapid cooling (30 °C/min) of a ball-milled mixture of $\text{Li}_2\text{S}/\text{P}_2\text{S}_5/\text{P}_2\text{O}_5/\text{LiBr}$ to form $\text{Li}_{5.5}\text{PS}_{4.3}\text{O}_{0.2}\text{Br}_{1.5}$.

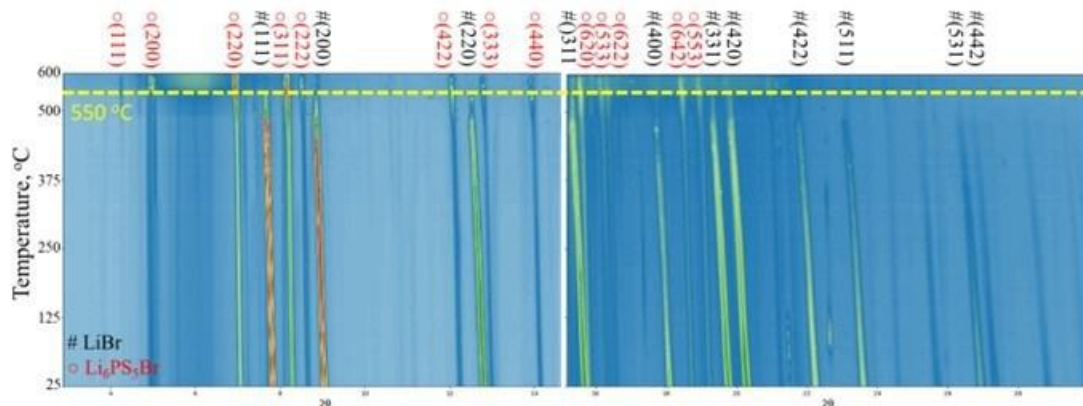


Figure XVI.22.8 Contour plot of in situ SXR D pattern during synthesis of $\text{Li}_{5.5}\text{PS}_{4.5}\text{Br}_{1.5}$ from 25 °C to 600 °C. The heating rate is 5 °C/min, and the time interval between two successive XRD patterns is 30 s. The color represent intensity, with blue and red represent low and high, respectively.

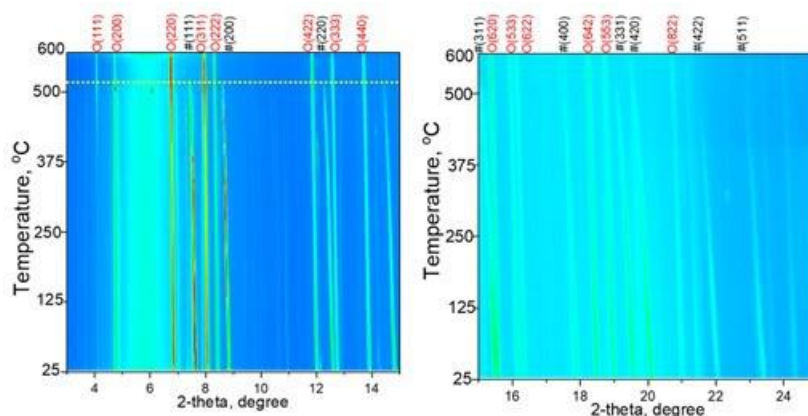


Figure XVI.22.9 (Contour plot of in situ SXR D pattern during synthesis of $\text{Li}_{5.5}\text{PS}_{4.4}\text{O}_{0.1}\text{Br}_{1.5}$ from 25 °C to 600 °C. The heating rate is 5 °C/min, and the time interval between two successive XRD patterns is 30 s. The color represent intensity, with blue and red represent low and high, respectively.

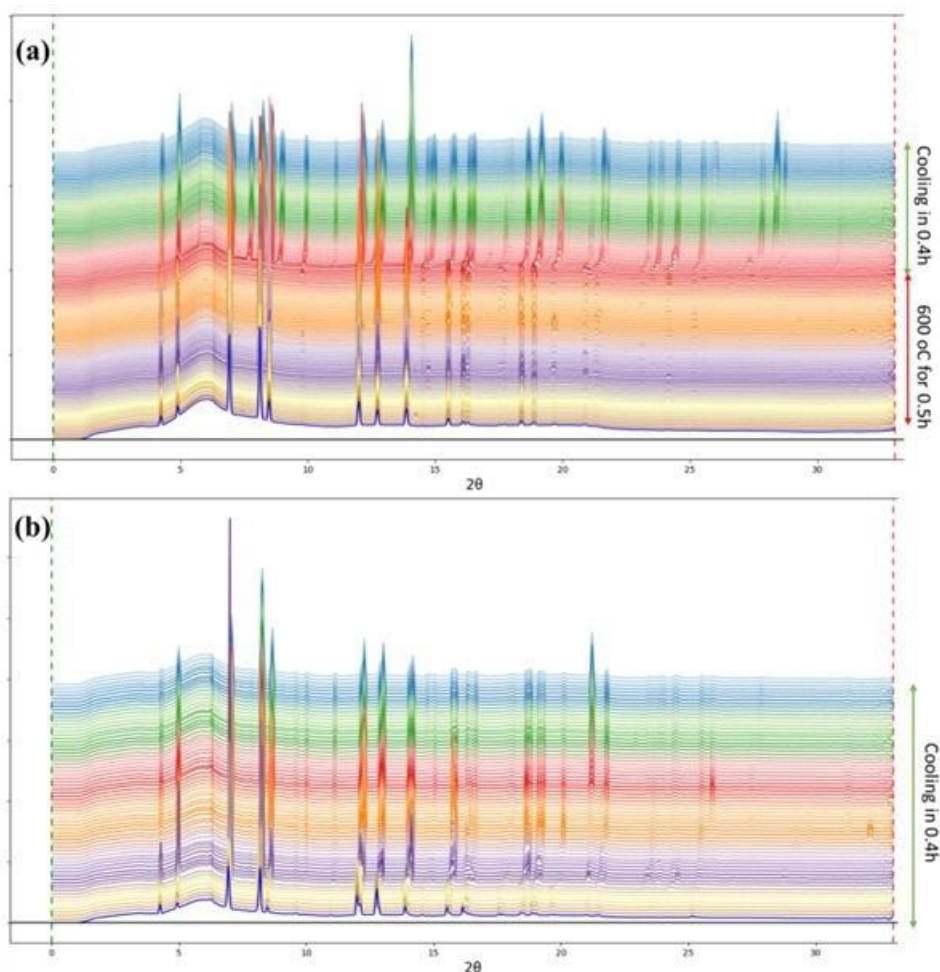


Figure XVI.22.10 The effect of holding time on the crystal structures of final products during rapid cooling: (a) 0.5 h; (b) 12 h.

Understanding of relationship between local crystal structure and ionic conductivity/moisture stability

To reveal the relationship between synthetic conditions, local crystal structure (lattice parameter, cell volume, phase fraction, microstrain, $\text{S}^{2-}/\text{Br}^-$ site disorder) and ionic conductivity/moisture stability of $\text{Li}_{6-x}\text{PS}_{5-x-y}\text{O}_y\text{Br}_{1+x}$, we have performed Rietveld refinement using general structure analysis systems (GSAS) on all the

SXRD patterns during synthesis of $\text{Li}_6\text{PS}_5\text{Br}$, $\text{Li}_6\text{PS}_{4.8}\text{O}_{0.2}\text{Br}$, $\text{Li}_{5.5}\text{PS}_{4.5}\text{Br}_{1.5}$, $\text{Li}_{5.5}\text{PS}_{4.3}\text{O}_{0.2}\text{Br}_{1.5}$, and $\text{Li}_{5.5}\text{PS}_{4.4}\text{O}_{0.1}\text{Br}_{1.5}$. Figure XVI.22.11 shows the representative Rwp value of Rietveld refinement results and selected refined in situ XRD patterns at different temperature in the case of $\text{Li}_6\text{PS}_5\text{Br}$. As shown, the Rwp value of all refined 116 patterns are below 7%, indicating a good fitting result. The refined SXRD patterns also exhibit a good match between experimental and calculated results.

Figure XVI.22.12a shows the evolution of lattice parameter during synthesis of $\text{Li}_6\text{PS}_5\text{Br}$. During heating, the lattice parameter exhibits a gradual increase due to thermal expansion and undergo a sudden decrease during rapid cooling because of thermal contraction. The refinement could also provide the evolution of phase fraction during heating/cooling process. As shown in Figure XVI.22.12b, starting at 400°C, $\text{Li}_6\text{PS}_5\text{Br}$ accounts for 97.5% and then gradually increased to 100% along with increasing temperature to 600°C and stayed at ~100% during cooling process.

$\text{S}^{2-}/\text{Br}^-$ site disorder is a key factor that can significantly affect the transport of Li^+ , particularly the shorter interstage jump that is the limiting step. Figure XVI.22.13 shows the crystal structure of $\text{Li}_6\text{PS}_5\text{Br}$ with space group of F-43m. As shown, S^{2-} nominally occupies the 4d site, but it can exchange with the Br^- anion on 4a site. As each S^{2-} on 4d is surrounded by six Li^+ that are highly related to the Li^+-Li^+ jump distances, the $\text{S}^{2-}/\text{Br}^-$ site disorder would therefore affect the Li^+-Li^+ jump particularly the interstage jump that has been identified as limiting step. Through Rietveld refinement, we are able to obtain the change of site disorder as a function of synthetic conditions. Taking $\text{Li}_6\text{PS}_5\text{Br}$ as an example, we can see that the gradual heating process has led to gradual decrease of $\text{S}^{2-}/\text{Br}^-$ site disorder, which should be due to more and more incorporation of S in the 4d and 16e sites during heating. Noted that the SXRD peak of LiBr disappeared ahead of Li_2S , indicating Br might hence occupy 4a and 4d during the early heating process. The site disorder has reached a minimal value of ~21% between 500–600°C. While it should be noticed that the rapid cooling process can cause a significant increase of site disorder, which might hence help to improve the ionic transport.

We have conducted Rietveld refinement to compare the lattice parameters and percentage of site disorder in the $\text{Li}_6\text{PS}_5\text{Br}$, $\text{Li}_6\text{PS}_{4.8}\text{O}_{0.2}\text{Br}$, $\text{Li}_{5.5}\text{PS}_{4.5}\text{Br}_{1.5}$ and $\text{Li}_{5.5}\text{PS}_{4.4}\text{O}_{0.1}\text{Br}_{1.5}$. As shown in XVI.29.14, higher amount of O doping caused decrease of both lattice parameter and percentage of $\text{Br}^-/\text{S}^{2-}$ site disorder, and hence would cause the reduction of ionic conductivity. While high Br content could compensate for both lattice parameter and percentage of $\text{Br}^-/\text{S}^{2-}$ site disorder and would thus improve the ionic conductivity. These results provided evidence for synthetic control to tailor the site disorder in the argyrodite sulfide solid electrolytes.

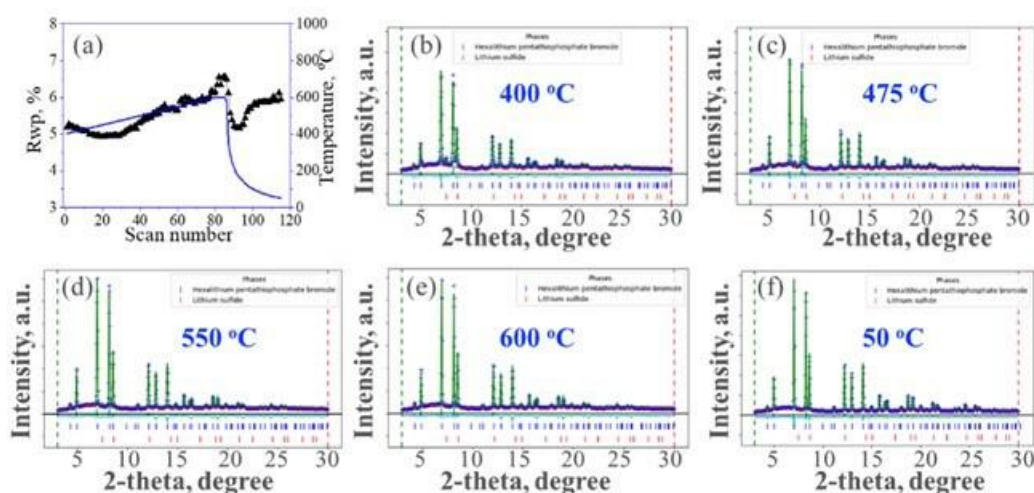


Figure XVI.22.11 (a) Representative Rwp value of Rietveld refinement results and (b-f) selected refined in situ XRD patterns at different temperatures during synthesis of $\text{Li}_6\text{PS}_5\text{Br}$. Rwp represents the weighted profile residual, which is an indicator of refinement results.

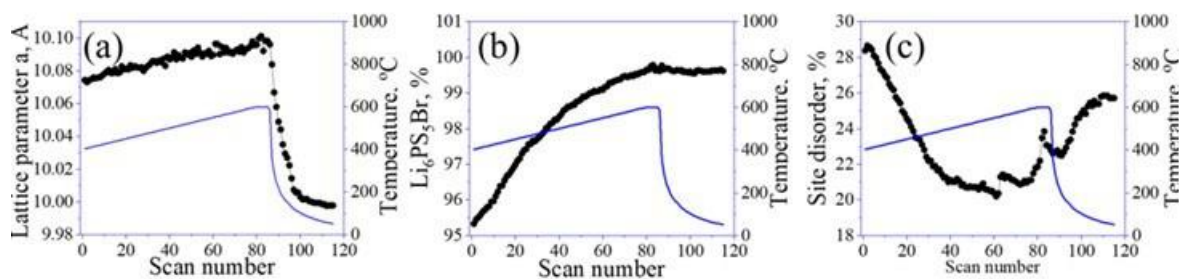


Figure XVI.22.12 (a) Lattice parameter a , (b) phase fraction of $\text{Li}_6\text{PS}_5\text{Br}$ and (c) percentage of site disorder as a function of temperature during synthesis of $\text{Li}_6\text{PS}_5\text{Br}$. Blue curves in (a-c) represent the temperature profile.

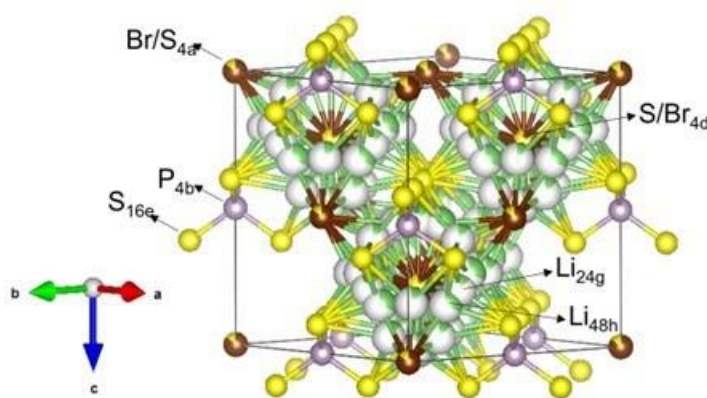


Figure XVI.22.13 Crystal structure of $\text{Li}_6\text{PS}_5\text{Br}$ shown in $\text{S}^{2-}/\text{Br}^-$ site disorder.

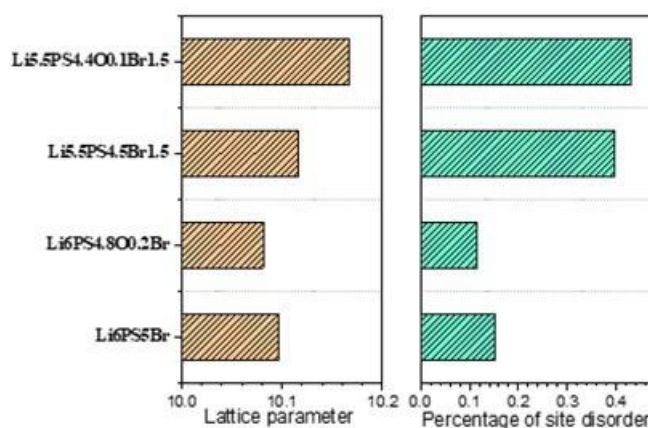


Figure XVI.22.14 Comparison on the lattice parameter and percentage of site disorder of $\text{Li}_6\text{PS}_5\text{Br}$, $\text{Li}_6\text{PS}_{4.8}\text{O}_{0.2}\text{Br}$, $\text{Li}_{5.5}\text{PS}_{4.5}\text{Br}_{1.5}$ and $\text{Li}_{5.5}\text{PS}_{4.4}\text{O}_{0.1}\text{Br}_{1.5}$.

Conclusions

In summary, during the first year of this project, we have set up a dedicated lab to synthesize, process and test sulfides solid state electrolytes. We have further used in situ synchrotron X-ray diffraction to probe the effect of dopants (Br and O) on the synthesis process of $\text{Li}_{6-x}\text{PS}_{5-x-y}\text{O}_y\text{Br}_{1+x}$, aiming to simultaneously improve the ionic conductivity and moisture stability of argyrodite sulfide electrolytes. A two-step calcination process has been developed to synthesize pure phase material, and the correlation between synthetic conditions, local crystal structure and ionic conductivity/moisture stability has been revealed. In FY23, we will use these valuable guideline to accelerate the development of Br/O co-doped $\text{Li}_{6-x}\text{PS}_{5-x-y}\text{O}_y\text{Br}_{1+x}$ electrolytes, and measured their ionic conductivity/moisture stability and electrochemical properties as well as performance in all-solid-state lithium/sulfur batteries.

Key Publications

Presentations

1. Xu, Gui-Liang. "Probing the degradation and synthesis of sulfides solid electrolytes by in situ synchrotron XRD." Invited oral presentation at the 2022 American Chemical Society Fall Meeting, , August 21, 2022 - August 25, 2022.
2. Lee, Jieun and Xu, Gui-Liang. Electrode design strategies for high energy density all-solid-state Li-S batteries." Poster presented at the 242nd Electrochemical Society Meeting, Atlanta, GA US, October 9, 2022-October 13, 2022.

References

1. Zhao, C.; Xu, G. L.; Yu, Z.; Zhang, L.; Hwang, I.; Mo, Y.-X.; Ren, Y.; Cheng, L.; Sun, C. -J.; Ren, Y.; Zuo, X.; Li, J.-T.; Sun, S.-G.; Amine, K. and Zhao, T. A high-energy and long-cycling lithium-sulfur pouch cell via a macroporous catalytic cathode with double-end binding sites. *Nature Nanotechnol.*, 2021, 16, 166-173.
2. Ding, B.; Wang, J.; Fan, Z.; Chen, S.; Lin, Q.; Lu, X.; Dou, H.; Nanjundan, A. K.; Yushin, G.; Zhang, X.; Yamauchi, Y. Solid-state lithium-sulfur batteries: Advances, challenges and perspectives. *Mater. Today* 2020, 40, 114-131.
3. Yang, X.; Adair, K. R.; Gao, X.; Sun, X. Recent advances and perspectives on thin electrolytes for high-energy-density solid-state lithium batteries. *Energy Environ. Sci.* 2021, 14, 643.
4. Li, Y.; Daikuhar, S.; Hori, S.; Sun, X.; Suzuki, K.; Hirayama, M.; Kanno, R. Oxygen Substitution for Li-Si-P-S-Cl Solid Electrolytes toward Purified $\text{Li}_{10}\text{GeP}_2\text{S}_{12}$ -Type Phase with Enhanced Electrochemical Stabilities for All-Solid-State Batteries. *Chem. Mater.* 2020, 32, 8860-8867.
5. Wang, C.; Liang, J.; Zhao, Y.; Zheng, M.; Li, X. and Sun, X. All-solid-state lithium batteries enabled by sulfide electrolytes: from fundamental research to practical engineering design. *Energy Environ. Sci.* 2021, 14, 2577.

Acknowledgements

Support from Simon T. Thompson of the U.S. DOE's Office of Vehicle Technologies Program is gratefully acknowledged. Use of the Advanced Photon Source, an Office of Science User Facility operated for the DOE Office of Science by Argonne National Laboratory, was supported by DOE under contract no. DE-AC02-06CH11357.

XVI.23 Synthesis of Composite Electrolytes with Integrated Interface Design (ANL)

Sanja Tepavcevic, Principal Investigator

Argonne National Laboratory
9700 South Cass Avenue
Lemont, IL 60439
E-mail: sanja@anl.gov

Simon Thompson, DOE Technology Development Manager

U.S. Department of Energy
E-mail: Simon.Thompson@ee.doe.gov

Start Date: October 1, 2021

End Date: October 1, 2027

Project Funding (FY22): \$550,000

DOE share: \$550,000

Non-DOE share: \$0

Project Introduction

Making safe, strong, and stable solid-state electrolytes (SSEs) is essential for high density Li metal batteries. Using combined experimental- and computational-based methodologies, we previously gained interdisciplinary, atomic-level insights into solid electrolyte interfaces with metallic Li by studying LLZO and PEO thin films as model systems. This proposal will transfer and build upon the knowledge gained on thin films to create more refined composite ceramic-polymer electrolytes (CPEs) that can be synthesized in a real-world manufacturing process. We will focus on an integrated design of critical interfaces to improve CPE ionic conductivity and guide homogeneous ion distribution across both anode and cathode interfaces. The study will be focused on the LLZO-PEO system, where nanofiber LLZO will be used to improve ion transport and electrochemical stability. Investigations into CPEs based on polyethylene oxide (PEO) showed that integrating ceramic fillers with polymers increased Li^+ transport by decreasing the crystallinity of the conducting polymer and creating space charge regions that can enhance Li^+ diffusion. The combination of Li^+ -conducting ceramics and polymers offers a new pathway to create better electrolytes with both high ionic conductivity and good mechanical properties.

Objectives

This project aims to develop well-controlled, scalable LLZO nanofiber and CPE synthesis processes that will address the manufacturing challenges of current SSEs and demonstrate the fabrication of large-area, thin CPE membranes with outstanding electro-chemomechanical properties. The outcome of this proposal will be a transformative manufacturing solution that can create large-area, mechanically and (electro)chemically stable SSEs (0 V to 4.5 V versus Li/Li^+) with Li^+ conductivity of $\geq 10^{-3}$ S/cm at room temperature enabling $\geq 1\text{C}$ charging rates.

Approach

To commercialize all-solid-state lithium-ion battery technology, further advances will require the application of knowledge, concepts, and tools from a variety of fields including materials science, physics, engineering, theory, and interfacial electrochemistry. The team's research philosophy is to establish a synthesis-material characterization-computation cycle that advances synthesis, chemistry, microstructure, interfaces, and transport in CPEs by a coordinated, interdisciplinary approach. The team's diverse expertise will allow them to understand, create, and rapidly scale up composite electrolytes to meet ambitious conductivity, energy, and power density targets.

Results

Electrolyte Membrane Synthesis and Optimization.

Three different routes for electrolyte membrane fabrication were explored (Figure XVI.23.1). First, we attempted to create cubic $\text{Li}_7\text{La}_3\text{Zr}_2\text{O}_{12}$ (LLZO) pellets directly from nanofibers at room temperature by hydraulic pressing with a 1-inch diameter die under 40 MPa pressure. Pure nanofiber pellets were brittle and porous, with highest relative density $\sim 65\%$, high impedance, and low ionic conductivity around $1.3 \times 10^{-5} \text{ S/cm}$ at 100°C . In order to achieve improved density, mechanical strength, and electrochemical performance, we developed LLZO fiber-polymer composites with the polymer matrix reinforced by nanofibers. Ideally, interconnected LLZO nanofiber networks form the basis of the composite, with the polymer present within the fiber “scaffold” to increase flexibility and provide soft interfacial contacts for the anode and cathode. Al-doped cubic $\text{Li}_7\text{La}_3\text{Zr}_2\text{O}_{12}$ nanofibers were formed from electrospun polymer precursor fibers after annealing at 750°C for 2 h. LLZO fibers of a desired loading (50 wt%) were mixed with a LiTFSI-PEO solution into a well-dispersed slurry (EO: $\text{Li}^+ = 15\text{--}20$ (molar ratio) LLZO:PEO = 1.4 (mass ratio)) and drop cast on Al foil or slot-die coated on a fast-moving web to form thin membranes.

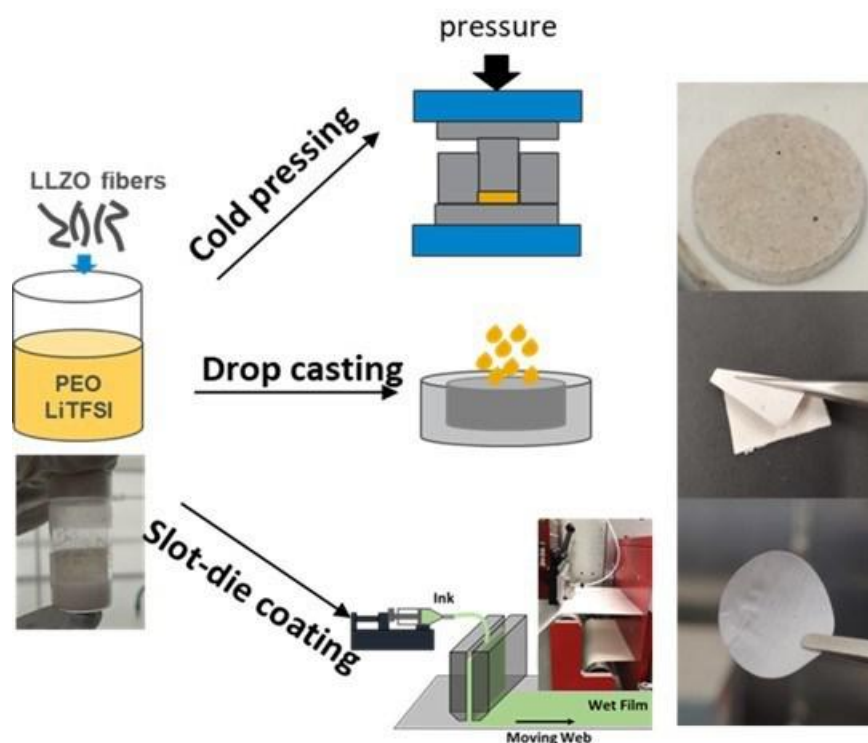


Figure XVI.23.1 *Electrolyte Membrane Synthesis and Optimization.* Schematics of cold pressing, drop casting and slot-die coating techniques with optical photographs of the resulting electrolyte membranes.

Cross-sectional scanning electron microscopy (SEM) images of composite membranes are shown in Figure XVI.23.2. Manually dropcast samples (Figure XVI.23.2a) have an average thickness of $150 \mu\text{m}$ and showed surface roughness, voids, and non-uniform fiber distribution. Membranes created by our slot-die technique (Figure XVI.23.2b) have controllable thicknesses of $80\text{--}150 \mu\text{m}$ and show good ductility and uniform fiber distribution in the polymer. By accurately controlling coating pressure and gap, as well as web moving speed, uniform membranes of low thickness ($\leq 20 \mu\text{m}$) can be obtained. We will continue to improve microstructure with respect to nanofiber loading and spatial distribution, coating defect control, and membrane thickness by further optimizing ink composition and mechanical fluidic properties and coating process parameters to ensure dense, low-defect membranes with good LLZO fiber percolation networks.

To further determine the impact of coating procedure, we compared cycling of LLZO-polymer composite membranes with 50 wt% LLZO nanofibers. Critical current density (CCD) measurements confirmed superior microstructure resulted in better electrochemical performance by slot-die membranes, with CCD values of $120 \mu\text{A}/\text{cm}^2$ for drop-cast and $160 \mu\text{A}/\text{cm}^2$ for slot-die coated membranes in Li-PEO-LiTFSI-LLZO-Cu cell configurations (Figure XVI.23.2c). While neither sample has adequate ionic conductivity ($0.2 \text{ mS}/\text{cm}$ at 60°C), we will continue to adjust and optimize nanofiber distribution to form a good percolation network to achieve high room temperature conductivity. Numerous parameters can be adjusted to improve Li^+ conductivity: LLZO loading and composition, nanofiber size and morphology, LiTFSI ratio, and synthetic polymer modifications.

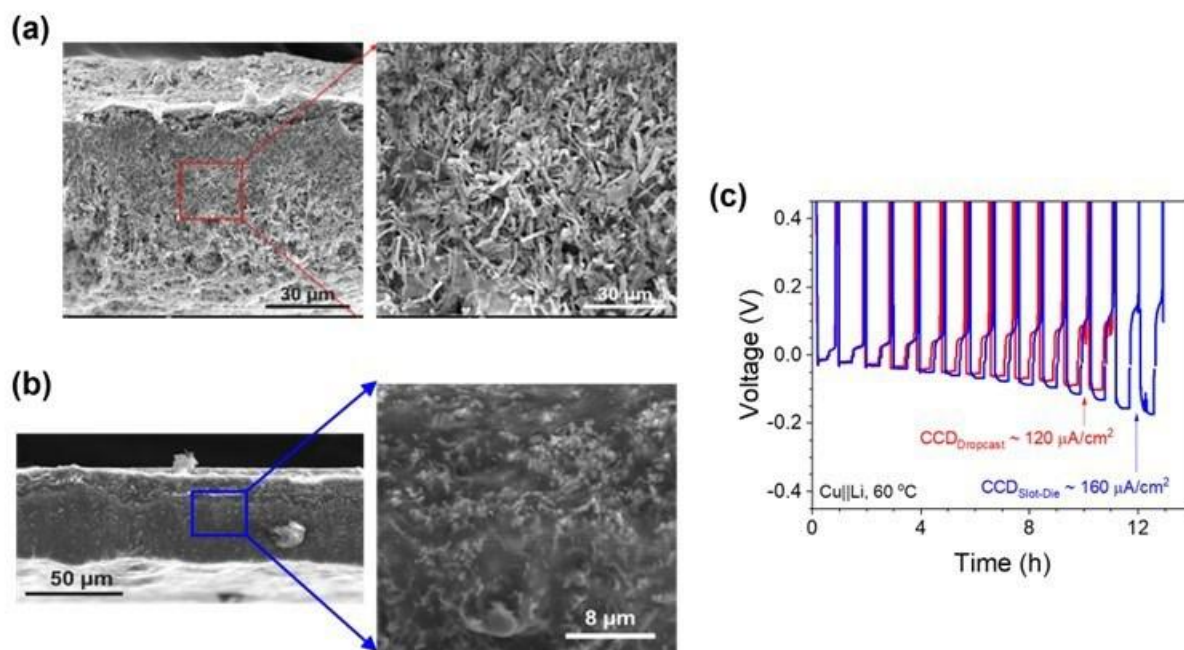


Figure XVI.23.2 *Characterization of Composite Membranes*. Cross-section SEM of flexible LLZO fiber-PEO-LiTFSI CPEs prepared by (a) dropcasting and (b) slot-die coating. (c) Critical current density determination for drop-casted (red) and slot-die coated (blue) membranes in Cu-Li half-cell configuration (d) Arrhenius plot of bulk ionic conductivity for composite and polymer solid state electrolytes.

Effect of Nanofibers on the Composite-Anode Interface

The formation of a stable solid-electrolyte interphase (SEI) is critical for safe, long-life lithium metal batteries (Figure XVI.23.3a). It is an open question how the ceramic component in CPEs affects the SEI. To explore this, we performed in situ X-ray photoelectron spectroscopy (XPS) measurements on LLZO nanofiber CPEs before and after exposure to lithium metal. From initial XPS measurements (Figure XVI.23.3b), it is clear there is no LLZO at the near surface ($\sim 5 \text{ nm}$) of the composite. The sample was then coated with 10 nm of Li metal via e-beam deposition, and core-level spectra were taken over time to determine reaction products between the composite and Li^0 (Figure XVI.23.3c). The products formed are entirely derived from PEO and LiTFSI, with no LLZO participation in the reaction. Inorganic, salt-derived species like LiF , Li_2O , and Li_2S form rapidly upon contact with lithium. Over longer timescales, polymer-derived products like lithium alkoxides (Li-OR) and alkyllithium species (Li-R) appear, indicating much slower reaction kinetics. This presents a heterogeneous SEI made of hard inorganics and soft organic compounds and is virtually identical to that of PEO-LiTFSI without LLZO.

Electrochemical impedance spectroscopy (EIS) analysis of coin cells with 0 wt% and 50 wt% LLZO composites shows that the (electro)chemically formed SEIs are nearly identical, with similar interface resistances around $700 \Omega \text{ cm}^2$ (Figure XVI.23.3d). However, galvanostatic cycling of different composites

shows that the inclusion of 50 wt% LLZO nanofibers increases the critical current density by a factor of three compared to 0 wt% LLZO (Figure XVI.23.3e). This increase is unlikely to be due to interface differences and must be related to bulk structural changes from LLZO.

To investigate this further, we used mesoscale modelling to compare lithium plating on electrodes with bad and good SEIs. A heterogeneous, thin, and soft SEI will lead to non-uniform Li deposition and dendrite formation, while a homogeneous, strong SEI will help suppress dendrites (Figure XVI.23.3f). We calculated the effective dendrite growth velocity as a function of bulk electrolyte modulus relative to the modulus of lithium metal ($G_{\text{elec}}/G_{\text{Li}}$) for the two SEI conditions. Given the soft bulk properties of our CPEs with or without LLZO, only a quality SEI can inhibit dendrite growth, and the SEI in all cases is weak due to the heterogeneous mixture of inorganic and organic products. To help explain our CCD results, we also incorporated the microstructure of 50 wt% LLZO nanofibers explicitly into the bulk of the model electrolyte (Figure XVI.23.3g). Since LLZO is stronger than Li, the dendrite is forced to push or grow around the fiber as lithium plates. This effectively slows the dendrite growth velocity by up to 87% at 0.2 mA/cm² and is current-density-dependent. These results show that while the nanofiber microstructures may help slow dendrites, only a strong SEI at the anode interface will prevent dendrites in the first place. Thus, we are actively investigating directed SEI formation to achieve higher current densities.

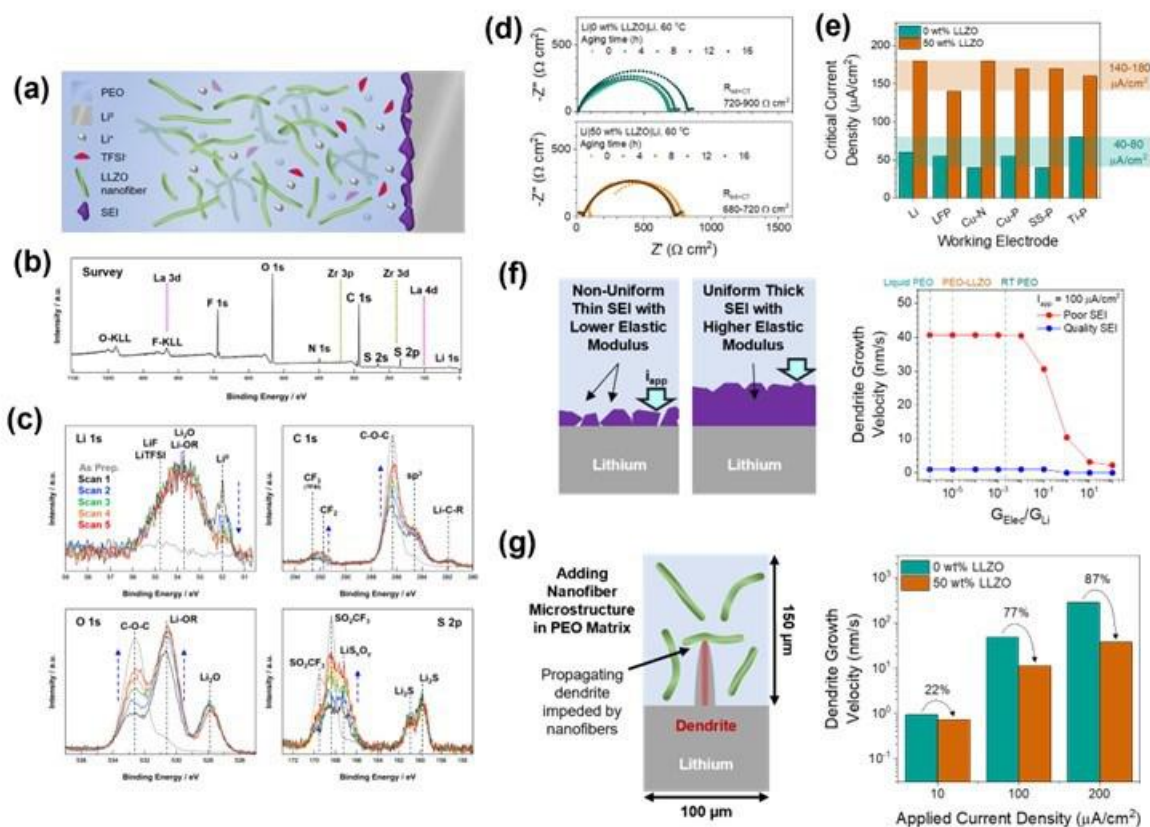


Figure XVI.23.3 *Nanofibers at the Interface*. (a) Schematic of the composite electrolyte-lithium metal interface. (b) XPS survey scan of the composite, showing no LLZO and only PEO-LiTFSI at the surface. (c) XPS core level spectra of the composite before and after 10 nm of Li metal was vacuum deposited. Scans 1-5 represent ~1 hour of reaction time. (d) EIS data from Li-Li symmetric cells with 0 wt% and 50 wt% LLZO nanofiber composites over 20 hours. (e) Critical current densities for 0 and 50 wt% LLZO composite electrolytes with different working electrodes and Li counter electrodes. (f) Schematic of mesoscale model used to determine the dendrite growth velocity with poor and good quality SEIs, which shows that stronger, homogeneous SEIs slow dendrite growth more than heterogeneous, thin, weak SEIs. (g) Addition to the model in (f) where LLZO nanofibers can physically block growing lithium dendrites, showing that dendrites can slow dendrite growth and prolong cell shorting by up to an order of magnitude depending on the current density.

Determining Percolation Thresholds in the Composite Matrix.

Effective conductivity of a fiber-reinforced composite can be estimated using “effective medium theories”. In this particular approach, the fibers are placed in the matrix material, the perturbation in the electric field due to the presence of the foreign inclusion is calculated, and finally the effective conductivity of the composite is estimated as a function of the corresponding conductivity and volume fraction of the fibers and the matrix material. During this effective property estimation process, the total current and electric fields are assumed to be volume average of the currents and electric fields in individual phases. The advantage of these effective medium theories is that they can successfully estimate the effective conductivity of the composite from very small (~0.0 vol%) to extremely large (~100 vol%) volume fractions of the fiber materials and is not limited by any dilute approximations. The magnitude of the percolation threshold is estimated from the expression of effective properties through the assumption of a completely insulating matrix phase. With an insulating matrix, the minimum volume fraction of fibers that leads to a non-zero magnitude of the effective conductivity of the composite is characterized as the percolation threshold. It is interesting to note that the magnitude of the percolation threshold does not depend on the conductivity of the individual phases and depends only on the geometry of the fibers. In the present context, percolation threshold for LLZO fibers in PEO matrix is estimated using the “effective medium theory” based technique[1]. Because of the isotropic conductivity demonstrated by LLZO fibers, the conductivity of both the fiber inclusions and PEO polymers are assumed to be isotropic. However, due to the geometric anisotropy associated with the shape of the fibers, the individual fibers are assumed to be randomly oriented, and an orientational averaging is conducted before estimating the effective conductivity and percolation threshold of the composite material.

In the effective medium theory, each fiber is approximated as an ellipsoid with a certain length and diameter. The percolation threshold in terms of the volume percentage of the LLZO fibers is shown in Figure XVI.23.4a. It is evident that as the aspect ratio of the fibers increase, percolation can be achieved with smaller fraction of fibrous inclusions. The percolation thresholds in weight percentage of LLZO is also, which indicates that more than 20 wt% LLZO fibers are needed to obtain percolation with elongated fibers of aspect ratio 10. The theoretical analysis presented here has several approximations: the interface between the LLZO fiber and the PEO matrix is assumed to be perfect and without any impurities, which is very far from the realistic observations; and the connection between individual fibers is expected to be perfect, such that as soon as two fibers touch each other, it is assumed that they start behaving as a single fiber. The interfacial resistance associated with ion transport from one fiber to the next is neglected.

Determining LLZO Nanofiber Participation in Conductivity of Slot-Die Coated CPes

Composite polymer electrolytes were prepared via slot-die coating while varying the weight percent of LLZO from 0 to 50 wt%. This shows a small increase in bulk ionic conductivity with small amounts of LLZO, then a decrease in conductivity with higher LLZO (>10 wt%), as shown in Figure XVI.23.4b. Notably, at 50 wt% LLZO, we are above the expected percolation threshold and should achieve high conductivity if the nanofibers are in contact with each other in a percolation network. Our results indicate that this is not the case. Interestingly, two regions below and above 55°C (the nominal melting point of the polymer phase) are seen in all samples, with activation energies around 1.2 eV and 0.5 eV, respectively. This indicates further that ionic transport in these electrolytes is still dominated by the PEO-LiTFSI polymer phase. SEM imaging in Figure XVI.23.4c shows that our preparation method for coating from a concentrated ink results in the LLZO nanofibers being coated uniformly by the PEO-LiTFSI polymer matrix. This inhibits the percolation network since there is a high barrier for ion transport between LLZO and PEO. Future work will focus on adjusting the properties of the coating inks and slot-die parameters to ensure more intimate LLZO-LLZO contact between fibers while still maintaining a dense composite matrix.

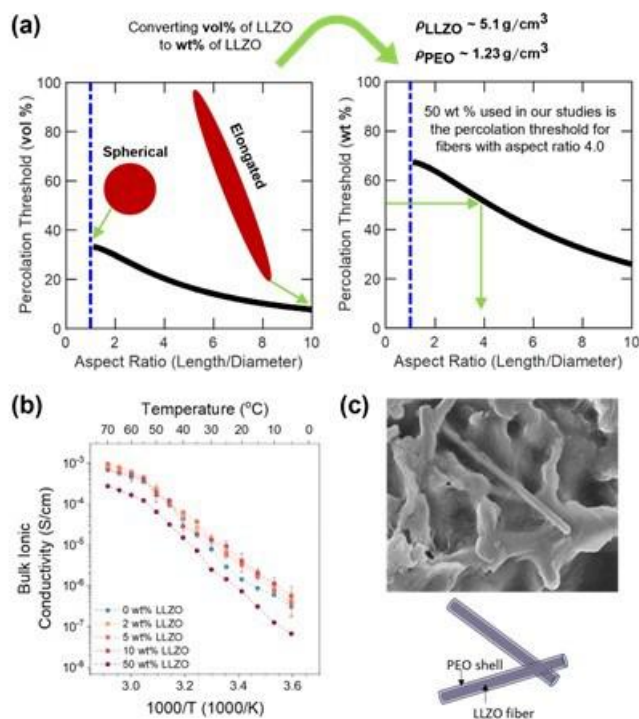


Figure XVI.23.4 *Nanofiber Percolation Threshold and Conductivity in CPEs.* (a) Schematic of percolating object aspect ratio and calculated percolation thresholds (volume and weight percent) for LLZO nanofibers in a PEO-LiTFSI matrix. (b) Ionic conductivity of composite polymer electrolytes with 0, 2, 5, 10, and 50 weight percent LLZO nanofibers. 50 wt% corresponds to 20 vol% of the LLZO filler in the polymer matrix. (c) Scanning electron micrograph of the as-prepared composite electrolyte, showing that nanofibers are coated with thin layers of polymer and are likely not in direct contact with each other.

Synthesis of Nanofibers: Dopant-Free and with Al and Ga Dopants

Al^{3+} and Ga^{3+} dopants, when inserted into bulk LLZO, are directly substituted into the lithium sublattice of interconnected tetrahedral and octahedral sites and show relatively little difference in formation energy with respect to defects on the lithium sublattice. While electrochemical impedance spectroscopy (EIS) measurements with blocking electrodes showed that Al-doped LLZO can achieve an ionic conductivity of 6×10^{-4} S/cm (data not shown), Ga-doped LLZO pellets with the high purity cubic phase demonstrated a higher ionic conductivity of 2.3×10^{-3} S/cm, being the highest among all the reported dopants. Despite the high conductivity of Ga-doped cubic LLZO, we have demonstrated previously that with prolonged contact between Li and Ga-LLZO, interfacial resistance decreased while charge transfer resistance continuously increased over time due to chemical reactions at the Li|Ga-LLZO interface.[2] Our LLZO-polymer composites have the unique advantage of utilizing the high conductivity Ga-doped LLZO for bulk Li^+ transport while preventing its detrimental contact with the Li electrode since the LLZO is physically separated from the electrode by the PEO-LiTFSI polymer phase.

We have investigated the synthesis of LLZO nanofibers without and with Al^{3+} or Ga^{3+} dopants. Figure XVI.23.5a shows X-ray diffraction data for three nanofiber samples fabricated by annealing at 750°C for 2 h. All LLZO phases are cubic, the necessary phase for fast Li^+ conduction. Minor impurity phases like $\text{La}_2\text{Zr}_2\text{O}_7$ were observed in some samples, suggesting further optimization of Li content and/or precursor compositions is needed. Figure XVI.23.5b & Figure XVI.23.5c show STEM HAADF images and EDX elemental mapping of Al- and Ga-doped LLZO nanofibers. Both Al and Ga dopants showed a homogeneous distribution within fibers, which is critical for obtaining a highly conductive Li^+ transport network. Importantly, we are able to generate cubic nanofibers with all dopants with both lab-scale and large roll-to-roll nanofiber fabrication equipment, showing this approach is scalable for generating Ga-doped LLZO nanofibers.

Composite polymer electrolyte membranes made with the three different fibers (undoped, Al-doped, and Ga-doped) show identical flexibility and mechanical performance, indicating dopant does not impact macroscale electrolyte properties. Preliminary measurements with composite electrolytes show no significant change in bulk ionic conductivity with changing dopant, as the PEO-LiTFSI matrix still dominates conductivity ($\sim 10^{-6}$ S/cm at 25°C and $\sim 10^{-4}$ S/cm at 60°C) for the reasons discussed above.

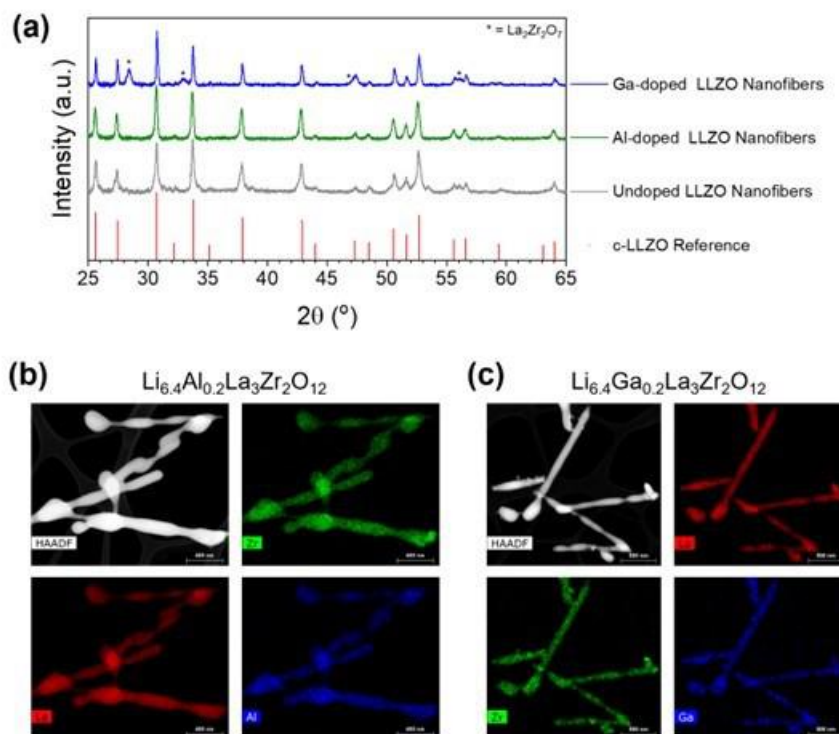


Figure XVI.23.5 Undoped, Al-Doped, and Ga-Doped LLZO Nanofibers. (a) XRD of LLZO nanofibers without added dopants and with Al³⁺ and Ga³⁺ dopants, all showing cubic phase. STEM HAADF images and EDX elemental mapping of (b) Al-doped and (c) Ga-doped LLZO nanofibers showing uniform dopant distribution across multiple nanofibers.

Conclusions

We have accomplished several steps on the path to integrated interface design in composite polymer electrolytes. Slot-die coating proved the best scalable method for creating dense, uniform composites with LLZO nanofibers and PEO-LiTFSI polymer matrix. We are able to achieve uniform coatings of 50 wt% LLZO composites at thicknesses as low as 15 μ m. The interface of the CPE with lithium metal anodes is dominated by the polymer phase, forming mixed inorganic and organic components. This heterogeneous SEI is unfavorable for high current densities, and only the microstructure of the strong LLZO fibers in the bulk of the electrolyte helps slow dendrite formation. Our future work will focus on two keys interfaces: 1) the interface between neighboring LLZO nanofibers and the nanofibers with PEO-LiTFSI, and 2) the electrolyte-anode interface. Synthetic efforts will ensure proper LLZO-LLZO contact in the matrix to improve the percolation network and modify the LLZO surface to lower the Li⁺ transport barrier between polymer and ceramic phases. We have successfully synthesized single-crystal LLZO nanofibers with high aspect ratio to assist in establishing a robust percolation network. At the same time, we will investigate the use of additives and secondary coatings on the anode surface to create strong, inorganic, homogeneous SEIs with low resistance and optimal mechanical properties to prevent dendrites at high current densities. Using our roll-to-roll slot-die coating techniques, we have generating artificial SEI layers to help lower interfacial resistance. We are also currently working with Prof. Candance Chan at Arizona State University and Drs. Marca Doeff and Mike Tucker at Berkeley Lab to determine the inherent conductivity of our numerous LLZO fiber compositions.

References

1. Wang, Yang and Weng, George J. 2018. “Electrical Conductivity of Carbon Nanotube and Graphene Based Nanocomposite.” In *Micromechanics and Nanomechanics of Composite Solids*, edited by S.A. Meguid and G.J. Weng, 123-156. Springer International Publishing AG.
2. Tsai, Chih-Long, Ngoc Thanh Thuy Tran, Roland Schierholz, Zigeng Liu, Anna Windmüller, Che-an Lin, Qi Xu, Xin Lu, Shicheng Yu, Hermann Tempel, Hans Kungl, Shih-kang Lin, and Rüdiger-A. Eichel. 2022. “Instability of Ga-substituted $\text{Li}_7\text{La}_3\text{Zr}_2\text{O}_{12}$ toward metallic Li.” *Journal of Materials Chemistry A* 10 (April), 10998-11009.

Acknowledgements

The PI is grateful to our team members Yuepeng Zhang, Michael Counihan, Devon Powers, Shiyu Hu, Pallab Barai, Justin Connell, Kanchan Chavan, Larry Curtiss and Venkat Srinivasan for data collection and analysis and their valuable contributions to the project. We also thank Xinwei Zhou, Yuzi Liu, Ashley Simmons, Byeongdu Lee for help with materials synthesis and characterization.

XVI.24 Polymer Electrolytes for Stable Low Impedance Solid State Battery Interfaces (ORNL)

Xi (Chelsea) Chen, Principal Investigator

Oak Ridge National Laboratory
PO Box 2008, MS6124
Oak Ridge, TN, 37830
E-mail: chenx@ornl.gov

Simon Thompson, DOE Technology Development Manager

U.S. Department of Energy
E-mail: Simon.Thompson@ee.doe.gov

Start Date: October 1, 2021

End Date: September 30, 2026

Project Funding (FY22): \$500,000

DOE share: \$500,000

Non-DOE share: \$0

Project Introduction

This work aims at developing stable and low impedance polymer/electrode interfaces for the integration of a thin solid composite electrolyte into a battery, to achieve chemical stability at the electrodes, high energy density (500 Wh/kg), high rate (1 mA/cm²) and long cycle life (80% capacity retention for 300 cycles), demonstrated in pouch cells.

Our main design principle is to use an oxide ceramic as the main ion transporting phase in the electrolyte and a polymer electrolyte to form optimized interfaces with the electrodes as well as to provide flexibility to the electrolyte membrane. Oxide ceramics have the advantages of high ionic conductivity, high Li ion transference number and high mechanical modulus. Polymer electrolytes are soft and flexible and capable of maintaining good contact at interfaces. However, the adoption of composite electrolyte in a solid-state battery has two main technical barriers:

- 1) Internal interface: a large interfacial resistance between the polymer and the ceramic electrolyte must be overcome. Even with an interconnected ceramic pathway to deliver good conductivity, the polymer-ceramic interface issue cannot be bypassed. Because we still rely on polymer to make contact and bridge the ceramic with the electrodes.
- 2) External interface: stable and low impedance interfaces between the polymer and the electrodes (including the anode and the cathode) must be achieved, as this is crucial for high rate and long cyclability of a solid-state battery.

Objectives

The overall objective of this project is developing stable and low impedance polymer/electrode interfaces for the integration of a thin solid composite electrolyte into a battery, to achieve chemical stability at the electrodes, high energy density (500 Wh/kg), high rate (1 mA/cm²) and long cycle life (80% capacity retention for 300 cycles), demonstrated in pouch cells.

The main objective can be dissected into 4 tasks: Task 1 is the synthesis and characterization of fluoropolyether polymers, or other model polymer electrolytes. Task 2 focuses on understanding and optimizing polymer-cathode interface. Task 3 focuses on understanding and optimizing polymer-anode interface. Task 4 is the integration of a thin composite electrolyte into a solid-state battery.

Approach

The team's main design principle is to use an oxide ceramic as the main ion transporting phase in the electrolyte and a fluorinated polyether-based polymer electrolyte to form optimized interfaces as well as to

provide flexibility to the electrolyte membrane. Compared with inorganic electrolytes, polymer electrolytes are soft and flexible and capable of maintaining good contact at interfaces. However, several technical barriers remain. On the Li-metal side, the interface between polymer electrolytes and thin-Li and Li-free anodes is still at an early stage of investigation. Interface optimization using thin-Li and Li-free designs is crucial to reaching the DOE 500 Wh/kg target. On the cathode side, studies on the polymer/cathode interface are scarce. The interface resistance between polymer (catholyte) and cathode active material is not well understood. In addition, with a target voltage stability of 0–4.5 V versus Li/Li⁺, a polymer with oxidative stability up to 4.5 V is needed. Fluorinated polyethers have the potential to form stable and low impedance interfaces at both the cathode side and the anode side. By systematically examining the effects of fluorine content, polymer chain length and structure, and plasticization on the interfacial resistance with the cathode and the anode, a balance between the desolvation kinetics of Li⁺ and diffusion rate will be achieved to optimize the interface ion transport. A fundamental understanding of the origin of interfacial impedance with the cathode as well as Li-metal anode will be developed alongside the optimization process to generate design rules for polymers with optimized interfaces. The team will also develop a processing procedure to integrate a thin composite electrolyte that was previously developed into a full cell. The composite electrolyte features an interconnected ceramic structure. It will be backfilled with the newly developed fluorinated polymer electrolytes. The mechanical properties of the composite electrolytes will be optimized to accommodate roll-to-roll processing.

Results

In FY22, efforts were focused on Task 1, the synthesis and characterization of fluoropolyether polymers; and Task 4, the integration of a thin composite electrolyte into a solid-state battery. Results on the progress of these two tasks are summarized below.

The synthesis and characterization of fluoropolyether polymers.

The synthetic scheme of fluorinated polyether-containing polymer electrolyte membranes is shown in Figure XVI.24.1a. Two precursor oligomers were used, a perfluoropolyether (PFPE) with bifunctional urethane methacrylate (Fluorolink® MD700, Solvay), and a polyethylene glycol dimethacrylate (PEGDMA, molecular weight 1000 g/mol, Polysciences). The precursors were mixed in a desired weight ratio in a mixed solvent. Two mixed solvent systems were found to be able to co-dissolve PEGDMA/PFPE precursors: an acetonitrile (ACN)/hexafluorobenzene (HFB) mixed solvent system and a tetrahydrofuran (THF)/*N*-methyl-2-pyrrolidone (NMP) mixed solvent system. The mixtures were stirred for overnight. 0.1% initiator, azobisisobutyronitrile (AIBN), was then added to the mixture and vortexed for approximately 5 mins to dissolve it. The crosslinking reaction was carried out between two glass plates separated by cover glass slips with a thickness of 0.17 mm. The reaction was performed at 75 °C for 1 hr. The crosslinked membrane was peeled off the glass plate and dried in vacuum oven at 80 °C for overnight. Figure XVI.24.1b and c show the membrane morphology from the two mixed solvent systems. A representative composition, 60:40 w/w PFPE:PEO is shown. ACN/HFB solvent system produced an optically clear membrane with no mesoscopic (micrometer level) phase separation. THF/NMP solvent system produced an optically cloudy membrane. The phase separation length scale is on the order of a few micrometers. For the rest of the work, we chose to use ACN/HFB solvent system to prepare the crosslinked PEO-PFPE copolymer membranes.

After crosslinking and drying of the membranes, lithium bis-trifluoromethanesulfonimide (LiTFSI) salt was infused into the membranes by soaking the membranes in 1M LiTFSI solution in a mixture of ethylene carbonate and dimethyl carbonate (1 : 1 volume ratio) solvents for 12 hrs. The dry membranes were subsequently thoroughly dried in a vacuum oven at 80°C for overnight. The plasticized membranes were used without drying.

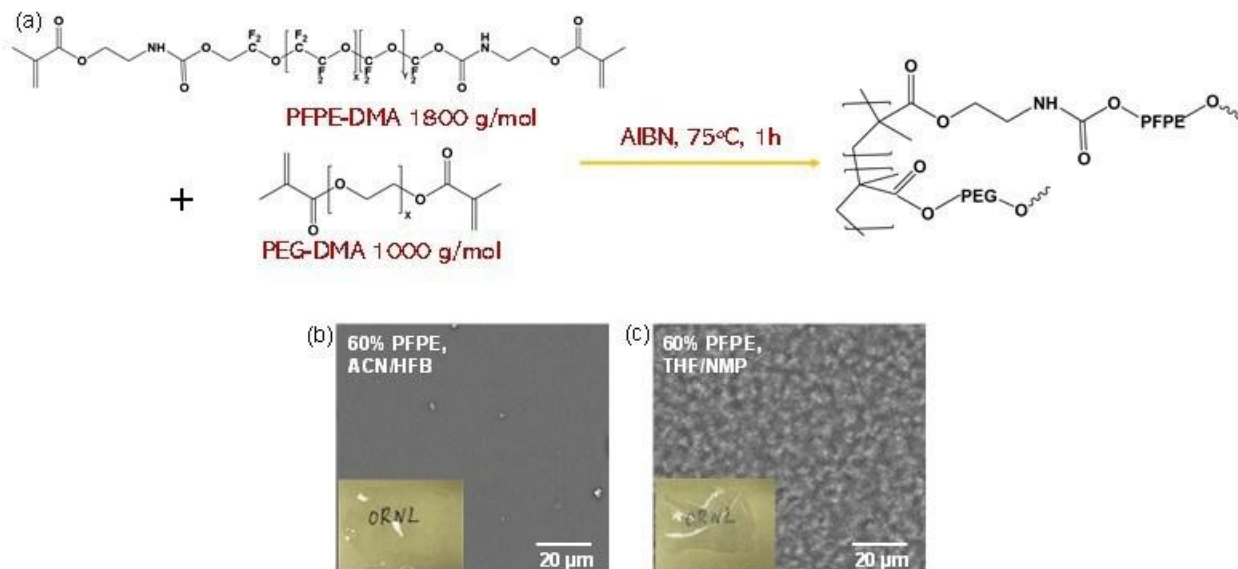


Figure XVI.24.1 Synthesis of crosslinked PEO-PFPE copolymer membrane. (a) Synthesis scheme; (b, c) Scanning electron microscopy (SEM) images of 60w:40w PFPE:PEO membranes made using acetonitrile (ACN)/hexafluorobenzene (HFB) (a) and tetrahydrofuran (THF)/*n*-methyl-2-pyrrolidone (NMP) (b) mixed solvents. Inset of (b,c), digital pictures of the membranes.

The structure and thermal properties of a series of crosslinked PEO-PFPE membranes were thoroughly investigated. The weight ratio of PFPE to PEO varied from 0:100 to 100:0, as described in Table XVI.24.1. Figure XVI.24.2a and b show the structure of dry membranes obtained using small angle X-ray scattering (SAXS) and wide-angle X-ray scattering (WAXS). In SAXS, crosslinked PEO (xPEO) did not show any features, indicating a homogeneous one phase morphology, both in the pristine form and after infusing with LiTFSI salt. Pristine PFPE membrane showed a peak at $Q = 1.5 \text{ \AA}^{-1}$, where Q is the scattering wave vector. This peak arises due to the microphase separation between the hydrocarbon part of the PFPE molecules and the fluorocarbon part of the PFPE molecules^{1, 2}. In 40PFPE and 60PFPE membranes, a broad peak can be observed, again indicating a microphase separated morphology in these membranes. The average domain spacing, D , can be calculated using $D = 2\pi/Q_{\text{max}}$, where Q_{max} is the Q position of the peak maxima. The D -spacing results are summarized in Table XVI.24.1. In pristine PFPE, $D = 4.2 \text{ nm}$. The addition of LiTFSI salt did not change this spacing. Since pristine PFPE is a fluorine-rich oligomer, we interpret the morphology as small hydrocarbon domains dispersed in a fluorine-rich matrix, with the average nearest domain spacing being 4.2 nm. When PEO and PFPE were mixed and crosslinked together (40PFPE and 60PFPE), the copolymer became hydrocarbon rich. SAXS results of 40PFPE and 60 PFPE copolymers suggest a microphase separated morphology where fluorocarbon-rich domains are dispersed in a PEO-rich matrix, with the average D -spacing being 8.4 and 7.8 nm, respectively. Compared with pristine PFPE, the peaks in 40PFPE and 60 PFPE are broader, indicating the distributions of the D -spacings in these two samples are larger. With the addition of salt, the intensity of the peak decreased. This indicates that LiTFSI was infused into both the PFPE-rich phase and the PEO-rich phase, which decreased the contrast between the two phases. On the other hand, the domain spacing did not change significantly, with the addition of LiTFSI. The SPM image in Figure XVI.24.2c revealed a finely phase separated morphology of 60PFPE membrane, where PFPE-rich domains (the dark domains) on the order of 10 nm in size dispersed homogeneously in the PEO-rich matrix. This is in agreement with SAXS results. Pristine PFPE showed two peaks in WAXS, and pristine xPEO showed three peaks in WAXS. These peaks are associated with interchain spacings^{1, 2}. 40PFPE and 60 PFPE's peaks are convolutions of the pristine PFPE and xPEO's peaks.

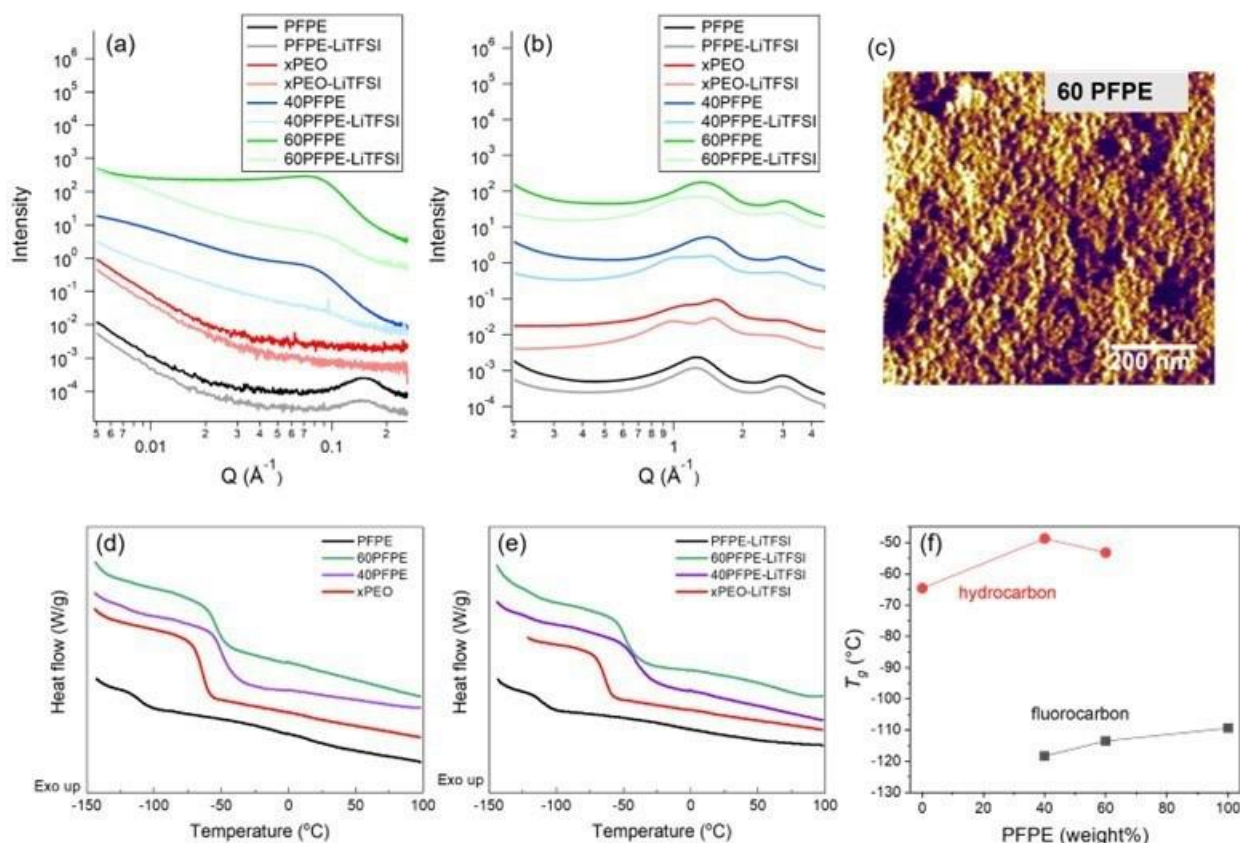


Figure XVI.24.2 Structure, morphology and thermal properties of crosslinked PEO-PFPE copolymer membranes. (a, b) Small angle X-ray scattering (SAXS) (a) and wide angle X-ray scattering (WAXS) (b) profiles of PFPE, xPEO, 40 PFPE and 60 PFPE in the pristine form and with LiTFSI salt. SAXS and WAXS measurements were taken at room temperature. (c) A scanning probe microscopy (SPM) phase image showing the surface morphology 60 PFPE electrolyte membranes at the nanometer scale. (d-f) Differential scanning calorimetry (DSC) of dry xPEO/PFPE electrolytes. (d) DSC thermogram (2nd heating) of pristine xPEO, PFPE, 60PFPE and 40PFPE. (e) DSC thermogram (2nd heating) of xPEO, PFPE, 60PFPE and 40PFPE infused with LiTFSI salt. (f) Glass transition temperature (T_g) of the hydrocarbon and fluorocarbon phases of the membranes as a function of PFPE weight%. The values used in this plot are from samples without LiTFSI salt.

Table XVI.24.1 Sample description and SAXS/WAXS/DSC results

Sample	PFPE:PEGDMA (w:w)	LiTFSI wt%	D-spacing (nm)	T_g hydrocarbon (°C)	T_g fluorocarbon (°C)
xPEO	0:100	0	N/A	-64.6	N/A
xPEO-LiTFSI	0:100	45	N/A	-54.3	N/A
PFPE	100:0	0	4.2	10 - 20	-109.4
PFPE-LiTFSI	100:0	12	4.2	10 - 20	-109.8
60PFPE	60:40	0	7.8	-53.2	-113.5
60PFPE-LiTFSI	60:40	23	7.4	-47.0	-115.6
40PFPE	40:60	0	8.4	-48.7	-118.3
40PFPE-LiTFSI	40:60	43	7.4	-40.7	-118.0

Figure XVI.24.2d-f show the differential scanning calorimetry (DSC) of dry crosslinked PEO-PFPE electrolytes. Pristine xPEO showed one glass transition temperature (T_g) at -64.6°C (Table XVI.24.1). After infusing with LiTFSI, the glass transition temperature increased to -54.3°C, due to the EO-Li⁺ coordination.

Pristine crosslinked PFPE showed a T_g at -109.4°C . With LiTFSI, the T_g remained very similar, at -109.8°C . This indicates that fluoroether does not form tight coordination with Li^+ , i.e., the presence of Li^+ does not significantly influence the segmental dynamics of PFPE. Looking very closely, the DSC thermogram of PFPE has another weak glass transition, in the 10°C to 20°C range. This glass transition has been reported in several other crosslinked PFPE systems^{3,4}. It's the glass transition of the hydrocarbon portion of the crosslinked PFPE membranes. Although in our system, this transition is too weak to be determined accurately, it actually plays a very important role in the xPEO-PFPE copolymer's ion transport properties, which will be explained immediately after the DSC results.

In 40PFPE and 60PFPE copolymer membranes, two T_g s are observed in the DSC thermograms, one near -110°C , which is associated with the PFPE-rich phase, and one near -50°C , which is associated with the PEO-rich phase. The T_g s as a function of PFPE's weight percentage is plotted in Figure XVI.24.2f. Evidently the PEO phase (the hydrocarbon phase)'s T_g exhibited greater than 10°C increase compared with pristine xPEO. Since the hydrocarbon in PFPE is highly miscible with PEO and has high T_g , it significantly increased the T_g of the PEO phase. The PFPE phase's T_g also increased with PFPE's weight percentage. This is likely due to the chain connectivity between the PFPE phase and PEO phase, since the domain sizes are small and the domains are crosslinked together.

The ion transport and electrochemical properties of crosslinked PEO-PFPE membranes were evaluated and summarized Figure XVI.24.3 and Table XVI.24.2. In the dry state, crosslinked PFPE membrane showed an extremely low ionic conductivity of 3×10^{-10} S/cm at 70°C . The incorporation of PFPE into PEO caused dramatically decreased ionic conductivity – at least one order of magnitude lower than the dry xPEO-LiTFSI membrane. **The low ionic conductivity is the result of two main contributing factors: first, the increased T_g of the PEO-rich phase in the copolymer membrane. Since the Li^+ transport is strongly coupled to the segmental motion of PEO chains, an increase in T_g (decrease in the segmental mobility) leads to decreased Li^+ mobility. Second, due to the finely phase separated morphology of the xPEO-PFPE membrane, the PEO phase's tortuosity significantly increased. Li ions have to move through a much more tortuous path to cross the membrane to reach the electrode. This also contributed to decreased Li^+ transport rate.**

The ionic conductivities of all the plasticized membranes were 1-2 orders of magnitude higher compared to the dry membranes. However, the room temperature ionic conductivity of plasticized 60PFPE-LiTFSI (1.7×10^{-5} S/cm) is still nearly 1 order of magnitude lower than plasticized xPEO-LiTFSI (1.1×10^{-4} S/cm).

The electrochemical oxidative stability of dry and plasticized 60PFPE-LiTFSI was evaluated and compared with xPEO-LiTFSI (Figure XVI.24.3c-f). A Li||Mo cell was constructed and a potentiostatic hold method was used to obtain the oxidative stability of the membranes. In this method, the cell voltage was increased from open circuit voltage to 6 V with an interval of 0.1 V. At each voltage step, the voltage was held for 1 hr while the current response was recorded. Figure XVI.24.3c and e show the current response of each potentiostatic hold from 3.1 V to 5 V. The current at the end of each 1 hr hold is plotted as a function of the step voltage, plotted in Figure XVI.24.3d and f. In the dry state, both 60PFPE-LiTFSI and xPEO-LiTFSI are stable up to 3.8V. In the plasticized state, both are stable up to 3.7 V. Although fluorine-containing compound is known to have high oxidative stability⁵, the incorporation of PFPE segments into xPEO did not effectively improve the oxidative stability of xPEO-PFPE membranes. This is likely because the PFPE segments formed microphase separation with xPEO segments and the PFPE-rich domains do not conduct Li ions effectively.

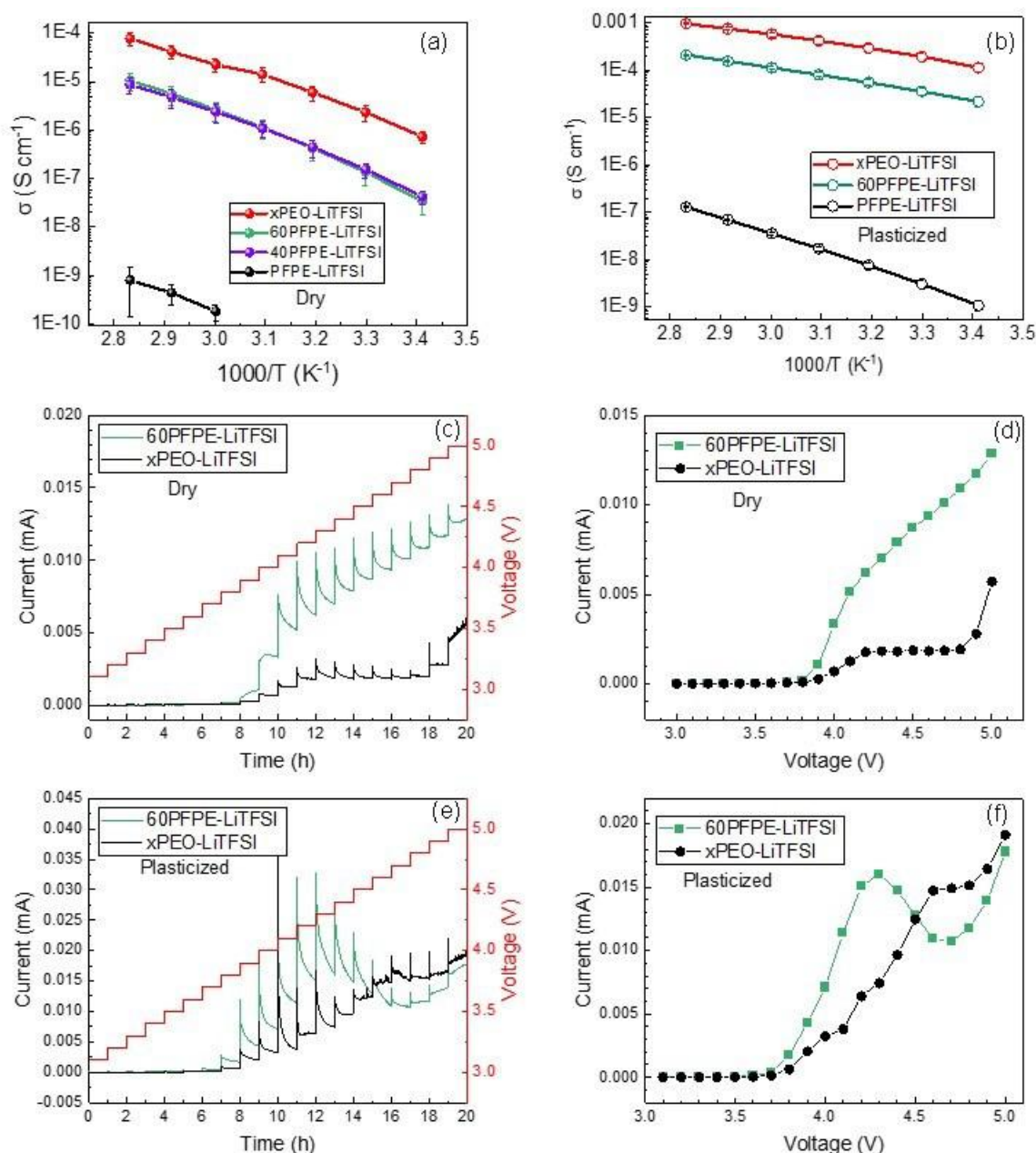


Figure XVI.24.3 Ionic conductivity and oxidative stability of crosslinked PEO-PFPE membranes. (a,b) Ionic conductivity of crosslinked PEO-PFPE in dry (a) and plasticized (b) states. (c-f) The potentiostat hold method to determine the electrochemical stability window of 60PFPE-LiTFSI and xPEO-LiTFSI. (c, e) Current vs time (left vertical axis) and potential vs time (right vertical axis). The hold time at each voltage step was 1 hr. (d, f) Current at 1 hr vs potential.

Table XVI.24.2 shows the Li^+ transference number, t_+ results of xPEO-LiTFSI and 60PFPE-LiTFSI membranes. Compared with xPEO-LiTFSI, 60PFPE's t_+ decreased slightly, in both dry and plasticized states. It's been reported that liquid PFPE oligomers may be pseudo single-ion conductors with very high t_+ values.⁶ Our results show that the incorporation of PFPE segments into xPEO did not improve the transference number of the copolymer membrane. This is again likely due to the phase separated morphology and the fact that PFPE-rich phase does not contribute significantly to Li ion transport of the membranes.

Table XVI.24.2 Li ion transference number of xPEO-LiTFSI and 60PFPE-LiTFSI

Sample	Measuring Temperature (°C)	t_+
xPEO-LiTFSI dry	70	0.20
xPEO-LiTFSI plasticized	20	0.066
60PFPE-LiTFSI dry	70	0.14
60PFPE-LiTFSI plasticized	20	0.044

The integration of a 3-D interconnected ceramic based composite polymer electrolyte into a solid-state battery.

We synthesized and characterized a 3-dimensionally interconnected polymer-ceramic composite electrolyte (referred later in the text as “Trilayer with Porous LICGC™ Scaffold”) via a tape casting approach, that is in the form of a ~145 μm thick free-standing membrane. Figure XVI.24.4a shows schematically the fabrication process. First, a slurry of 1 μm LICGC™ (doped lithium aluminum titanium phosphate) particles was prepared which was tape cast on to mylar foils. After the drying, the green tape was flexible and could be easily peeled off from the mylar substrate. Small discs were subsequently punched out from the green tape which were then sintered in dry air (1000 °C, 3h) to obtain porous, partially sintered LICGC™ ceramic scaffolds. Freshly prepared thermally cross-linkable polymer precursor solution was used to infiltrate the scaffolds. Briefly, O,O'-Bis(2-aminopropyl) polypropylene glycol-block-polyethylene glycol-block-polypropylene glycol (Jeffamine ED2003) and LiTFSI were dissolved in ethanol until a clear solution was obtained. The ethanol was dried off in a vacuum oven at RT overnight to get rid of the ethanol. Next day, poly(ethylene glycol) diglycidyl ether (PEGDGE, molecular weight 500 g/mol) was stirred in for an hour or so to obtain a viscous precursor solution. The amount of solution to be infiltrated was calculated based on the porosity of the disc to be infiltrated. After letting the solution infiltrate at RT overnight, the sample was placed in an oven at 100 °C for complete curing. No liquid plasticizer is present in the samples. Next, thin layers (1-5 μm) of linear-PEO+LiTFSI electrolyte were spray coated on both surfaces of the infiltrated samples to obtain the Trilayer with Porous LICGC™ Scaffold. Spray coating allowed application of uniform surface polymer layers of controllable thickness, which are needed to act as a physical barrier between the Li electrode and LICGC™ ceramic as it is unstable with Li. Besides, the soft linear-PEO+LiTFSI layer can form a conformal interface with the lithium metal anode, and is known to be chemically stable with lithium metal. These surface layers also allowed to understand their role in an interconnected composite electrolyte design. Figure XVI.24.4b shows an SEM image of the surface of the green tape with uneven shaped ceramic particles with an average diameter of 1 μm . Figure XVI.24.4c and d show the ceramic tape cross-section after partial sintering. A 3D-interconnected scaffold containing uniform sized interconnected particles can be observed after sintering. Figure XVI.24.4e-g show the cross-section images of the Trilayer with Porous LICGC™ Scaffold highlighting the middle, bottom surface, and top surface of the membrane. A complete infiltration of the LICGC™ scaffold with crosslinked-PEO+LiTFSI can be clearly seen in these images. The linear-PEO+LiTFSI layers on both surfaces are thin (<5 μm), uniform, and well adhered to crosslinked-PEO+LiTFSI infiltrated ceramic middle layer.

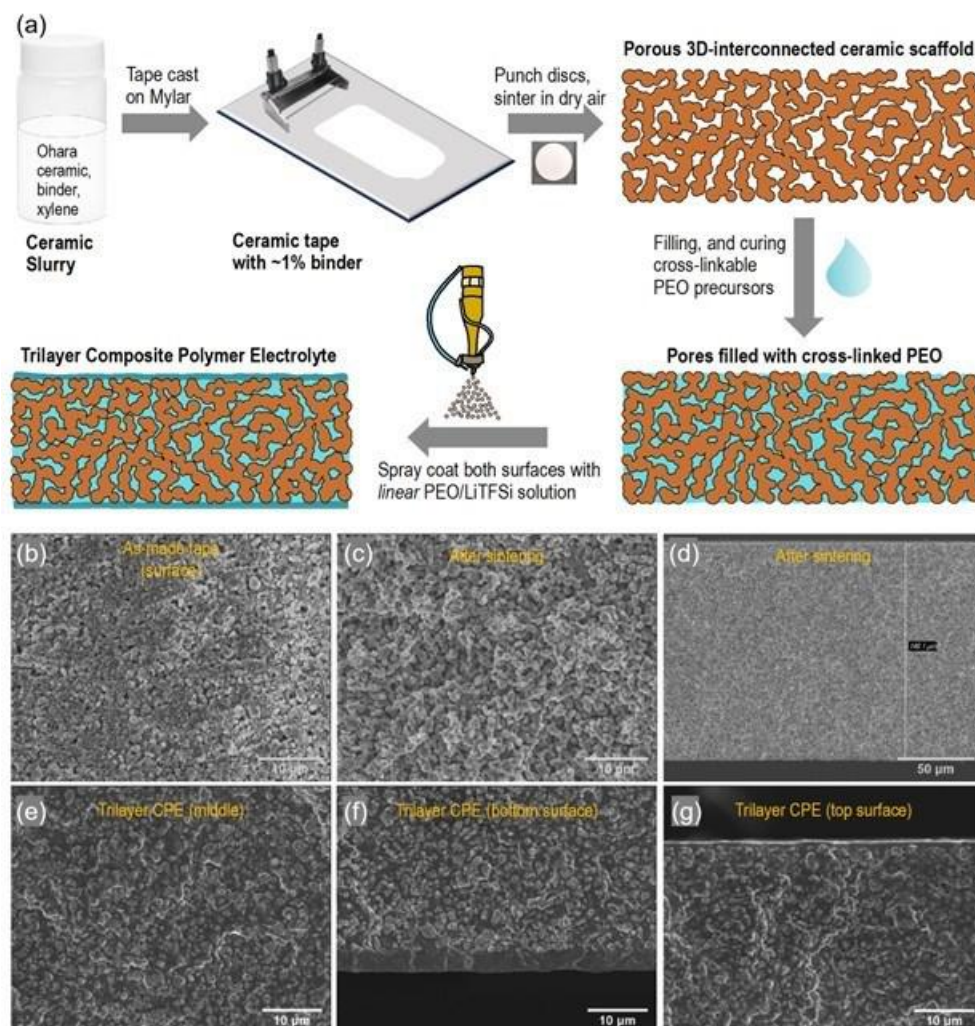


Figure XVI.24.4 (a) Schematic representation of the fabrication process of Trilayer with Porous LICGCTM Scaffold. (b-g) SEM images of surface of the as-cast green ceramic tape (b), cross-section of the sintered tape (c-d), cross-section of the sintered tape after filling with crosslinked-PEO+LiTFSI and spray coating the two surfaces with linear-PEO+LiTFSI ("Trilayer with Porous LICGCTM Scaffold") (e-g).

We had also performed sintering of green LICGCTM tapes with various sintering profiles to study their effect on the resulting porosity and ionic conductivity of the resulting ceramic scaffolds, shown in Figure XVI.24.5a. Effect of slurry formulation in green tape was also explored, and was found to have significant impact on the ionic conductivity of the resulting scaffold for a given sintering profile. Based on the weight, dimensions of the sintered discs, and theoretical density of LICGCTM (3.05 g/cm^3), the porosity (in volume %) was estimated. As expected, higher sintering temperatures and longer sintering times led to reduced porosity and higher ionic conductivity. The sample porosities ranged between 40-52 vol.%. The sample sintered at the highest temperature of 1100°C for 3 hours experienced significant densification (9 vol.% porosity). Although curiously its ionic conductivity was still only $\sim 17\%$ of that of the commercially obtained dense LICGCTM plate with $\sim 0\%$ porosity. To note a few more data points here, partial sintering at 1000°C for 3h of a hydraulically pressed LICGCTM green pellet without any binders resulted in an ionic conductivity of $1.8 \times 10^{-5} \text{ S/cm}$, compared to $2.6 \times 10^{-6} \text{ S/cm}$ for a green tape made with low solids slurry, and $1.2 \times 10^{-5} \text{ S/cm}$ for a green tape made with high solids slurry.

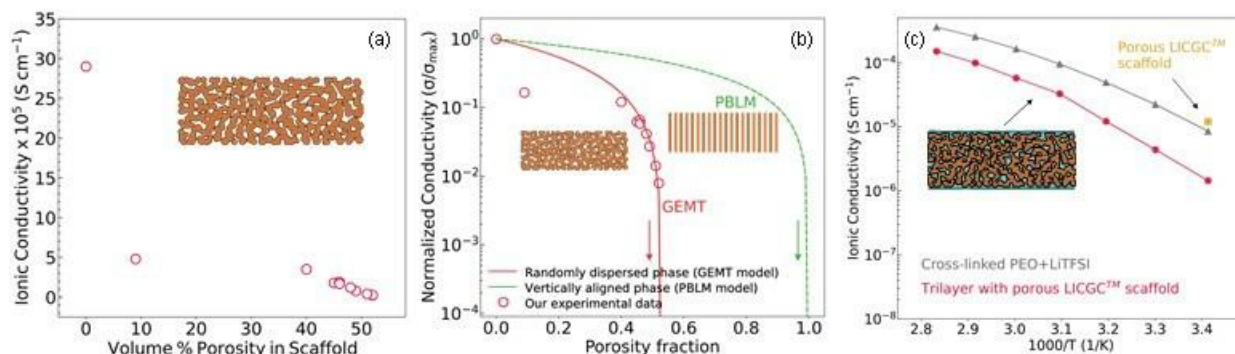


Figure XVI.24.5 (a) Ionic conductivity of the unfilled LICGCTM scaffolds as a function of volume % of their porosity. (b) Ionic conductivity of the scaffolds compared to effective medium theory (EMT) calculations. The measured conductivities of the scaffold fall nicely on the GEMT curve, which predicts the conductivity of randomly dispersed percolated particles. Conductivity of another morphology – vertically aligned percolated particles – is also modelled using PBLM model as a comparison. (c) Arrhenius plot of the ionic conductivity of the Trilayer with Porous LICGCTM Scaffold.

Figure XVI.24.5a provided an opportunity to analyze the conductivity data with respect to the effective medium theories (EMT) and estimate the highest theoretical conductivity achievable in the scaffolds. The McLachlan Generalized EMT (GEMT) is often used to describe the effective properties of particulate composites with randomly dispersed phases.⁷ The equation for the effective conductivity, σ_{eff} is

$$\frac{g(\sigma_f^{1/t} - (\sigma_{eff})^{1/t})}{\sigma_f^{1/t} + \left(\frac{1-g_e}{g_e}\right)(\sigma_{eff})^{1/t}} + \frac{(1-g)(\sigma_m^{1/t} - (\sigma_{eff})^{1/t})}{\sigma_m^{1/t} + \left(\frac{1-g_e}{g_e}\right)(\sigma_{eff})^{1/t}} = 0 \quad (2)$$

where g , and g_e are the volume fraction of the conductive particles in the composite and the percolation threshold respectively, t is the percolation slope, and σ_m is the conductivity of the “matrix”, i.e. the material containing filler particles of conductivity σ_f . Equation 2 was solved numerically for σ_{eff} and the results are shown together with the experimental values of the conductivity of the LICGCTM scaffold in Figure XVI.24.5b. These are obtained for the percolation threshold of 0.5, i.e. loose random packing limit. The conductivity values are normalized with respect to the maximum achievable conductivity in fully dense LICGCTM plate which is equal to 2.9×10^{-4} S/cm. The conductivity of the empty space was taken four orders of magnitude smaller than this value (to perform numerical solution with sufficiently small value), and the arrows indicate drop of the effective conductivity to zero. The measured conductivities of the scaffold fall nicely on the GEMT curve. The nice match between theoretical GEMT calculation and the experimental data solidly demonstrates that around the porosity of 50 vol%, the conductivity of randomly packed interconnected ceramic network is very sensitive to small changes of porosity. Specifically, a porosity increase from 46% to 51% caused more than 1 order of magnitude decrease in the resulting ionic conductivity of the ceramic network. Furthermore, at this porosity value, the highest reasonable conductivity that can be achieved is approximately 1/10 of the dense plate’s conductivity. This value is significantly lower than that of the dense ceramic plate. And yet 50% porosity is likely a sweet spot for the scaffold to achieve in order maintain the connectivity of the polymer phase to ensure good flexibility. Therefore, limited ionic conductivity is one of the intrinsic weaknesses of such randomly oriented interconnected ceramic network. In addition to the predictions for the percolation driven behavior in composites, we placed the predicted conductivity based on the parallel brick layer model (PBLM) in Figure XVI.24.5b which provides the upper limit of conductivity achievable in the most favorable configuration – layers of LICGC parallel to the electric field. At volume fraction corresponding to the percolation threshold of particulate composite, the conductivity of brick layered structure is 1.39×10^{-4} S/cm. This is the ideal conductivity of the vertically aligned LICGC structure taking 48 % of the

volume, which is approximately 50% of the dense plate's value and much higher than the randomly-oriented case. We would like to confirm this effect of ceramic network architecture experimentally in near future.

The ceramic scaffold obtained from the high solids slurry (ionic conductivity of 1.2×10^{-5} S/cm) was selected for composite electrolyte preparation and testing. Arrhenius plot of the ionic conductivity of the Trilayer with Porous LICGC™ Scaffold is presented in Figure XVI.24.5c. The membrane has an ionic conductivity of 1.4×10^{-6} S/cm at 20 °C and 4.4×10^{-6} S/cm at 30 °C. This is almost an order below the RT ionic conductivity measured for the unfilled ceramic scaffold (1.2×10^{-5} S/cm). This is due to the high interfacial impedance at the polymer/ceramic electrolyte with excess polymer layers present at the top/bottom surfaces of the composite membrane that dominates the overall impedance, resulting in an order lower ionic conductivity. The ionic conductivity of the Trilayer with Porous LICGC™ Scaffold was found to be lower than a pure crosslinked-PEO+LiTFSI polymer electrolyte membrane at all temperatures.

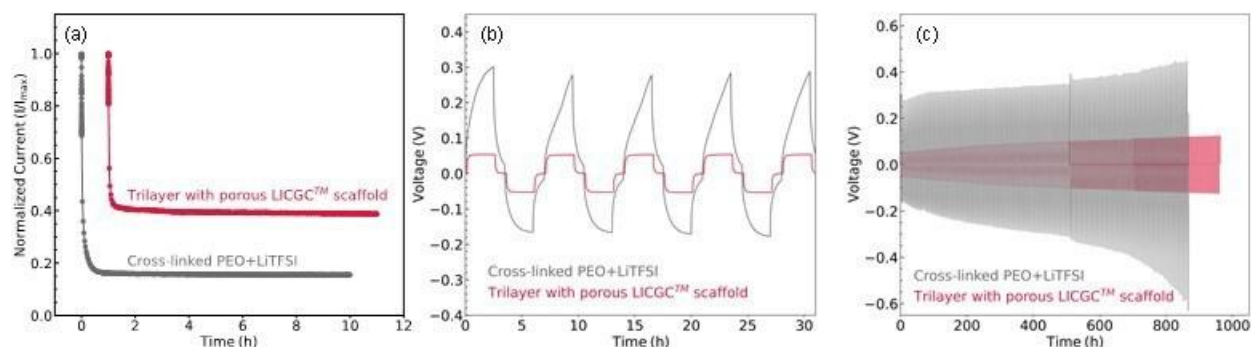


Figure XVI.24.6 (a) Current v. time obtained during the transference number measurement, comparing the steady state current obtained after 10h of polarization, for the Trilayer with Porous LICGC™ Scaffold and the pure crosslinked-PEO+LiTFSI electrolytes.

Note, one of the plots is shifted by an hour on the x-axis for ease of viewing the initial current values. (b) Voltage profiles of symmetric cells made with Trilayer with Porous LICGC™ Scaffold and crosslinked-PEO+LiTFSI electrolytes, cycled at 0.2 mA/cm², 2.5 h each strip/plate, at 70 °C. (c) Long-term cycling of the two symmetric cells shown in (b).

On the other hand, the transference number was determined to be almost three times higher for the Trilayer with Porous LICGC™ Scaffold (~0.3) compared with the pure polymer electrolytes (~0.1 for both the crosslinked-PEO+LiTFSI and linear PEO+LiTFSI) (Figure XVI.24.6a). A ceramic electrolyte has a transference number of nearly 1.0. Hence the reduction from 1.0 to 0.3 is likely due to contributions from the crosslinked-PEO+LiTFSI phase, linear-PEO+LiTFSI phase and the polymer/ceramic interface. A low transference number leads to generation of salt concentration gradients within the electrolyte upon passage of current, and at high currents when the diffusion rate cannot compensate for the rate of Li⁺ consumption on the reducing electrode, a complete depletion of lithium salt can occur which are reflected in steep overpotentials during Li//Li symmetric cell cycling. Indeed, because of the higher transference number of the Trilayer with Porous LICGC™ Scaffold, flatter overpotentials are observed during cycling of the Li//Li symmetric cells (@0.2 mA/cm² for 2.5h at 70 °C) compared to that of a pure crosslinked-PEO+LiTFSI membrane (Figure XVI.24.6b) of similar thickness, despite its lower ionic conductivity. In terms of long-term Li//Li cycling, the Trilayer with Porous LICGC™ Scaffold cycled without shorting under the above-mentioned cycling conditions for at least ~1000 h (Figure XVI.24.6c). The pure crosslinked-PEO+LiTFSI was also stable towards dendrite formation under these conditions for the test duration. Comparison of dendrite formation at higher current densities was not obtained as the crosslinked-PEO+LiTFSI developed steep overpotentials due to its low transference number, reaching cut-off voltage soon after cycling is begun (data not shown).

Conclusions

In Task 1, we synthesized fluorinated polyether copolymers consisting of crosslinked network of PEO segments and PFPE segments. The structure, morphology, thermal and electrochemical properties of xPEO-PFPE copolymer electrolytes were thoroughly investigated. Neat crosslinked PFPE electrolyte is a very poor

ion conductor with ionic conductivity of 3×10^{-10} S/cm at 70°C. The microphase separated morphology of xPEO-PFPE copolymers as well as the increased glass transition temperature of the main ion-transporting PEO-rich domains caused xPEO-PFPE's ionic conductivity to decrease by more than one order of magnitude compared neat crosslinked PEO polymer electrolyte. Also due to the microphase separated morphology, xPEO-PFPE copolymer electrolyte did not exhibit improved Li ion transference number or improved oxidative stability, compared to neat xPEO polymer electrolyte, likely because the PFPE rich domains did not contribute to ion transport significantly. Due to the unsatisfactory performance of xPEO-PFPE, in FY23 we will switch to other model polymer electrolytes.

In Task 4, a 3D-interconnected composite polymer electrolyte with a well-controlled architecture was prepared in a multi-step approach, and its electrochemical properties and cycling performance were investigated. Interconnected porous scaffolds were obtained via partial sintering of green tapes made from tape casting of commercial ceramic LICGCTM powders. The ionic conductivity of the unfilled porous scaffolds as a function of porosity was obtained by both experiment and theoretical modelling, to evaluate the maximum conductivity that can reasonably be achieved with this approach. The experimental results match well with theoretical conductivity of randomly dispersed percolated particles modelled with McLachlan GEMT theory. At a porosity of around 50%, the conductivity of the scaffold is very sensitive to the volume fraction of voids, and its maximum conductivity is approximately 1/10 that of the dense plate.

The scaffold with ionic conductivity of 1.2×10^{-5} S/cm and 48 vol% porosity was infiltrated with dry cross-linked PEO based polymer electrolyte and covered on two surfaces with thin layers of linear PEO based dry polymer electrolyte, to understand the role of excess surface polymer layers and also to act as a physical barrier between the lithium electrode and LATP-based ceramic. The interconnected ceramic framework avoids the high interfacial impedance at the polymer/ceramic electrolyte interface within the bulk of the composite electrolyte. However, the high impedance of such an interface with excess polymer layers present at the top/bottom surfaces of the composite membrane dominates the overall impedance, resulting in an order lower ionic conductivity (1.4×10^{-6} S cm⁻¹ at 20 °C) compared to the unfilled ceramic scaffold (1.2×10^{-5} S/cm at RT).

Finally, an improvement in transference number is observed for the trilayer composite (~0.3 vs. ~0.1) compared to the pure polymer electrolytes used. The trilayer composite exhibited improved Li symmetric cell cycling characteristics, including higher rate capability and lower overpotential. The trilayer composite membrane also has improved resistance to fracture compared to a control trilayer prepared with a 100% dense LICGCTM ceramic plate in the middle, as was qualitatively demonstrated from the fact the former can survive coin-cell crimping without fracturing while the later severely fractures and could not therefore be cycled. In FY23 we will investigate methods to minimize the interfacial resistance between the surface polymer layer and the bulk composite.

Key Publications

1. U.S. Patent Application 17/675,070, "Gel Composite Electrolyte Membrane for Lithium Metal Batteries", Filed February 18, 2022; UTB Ref. 4191.1; WNJ Ref. 138974.200994-US
2. Tsai, W.-Y.*; Chen, X. C.*; Kalnaus, S.; Sahore, R.; Du, Z.; Westover, A. S., Li Morphology Evolution during Initial Cycles in a Gel Composite Polymer Electrolyte. *ACS Applied Energy Materials* **2022**.

References

1. Chintapalli, M.; Timachova, K.; Olson, K. R.; Banaszak, M.; Thelen, J. L.; Mecham, S. J.; DeSimone, J. M.; Balsara, N. P., Incipient microphase separation in short chain perfluoropolyether-block-poly(ethylene oxide) copolymers. *Soft Matter* **2017**, *13* (22), 4047-4056.
2. Chintapalli, M.; Timachova, K.; Olson, K. R.; Mecham, S. J.; DeSimone, J. M.; Balsara, N. P., Lithium Salt Distribution and Thermodynamics in Electrolytes Based on Short Perfluoropolyether-block-Poly(ethylene oxide) Copolymers. *Macromolecules* **2020**, *53* (4), 1142-1153.

3. Hu, Z.; Chen, L.; Betts, D. E.; Pandya, A.; Hillmyer, M. A.; DeSimone, J. M., Optically Transparent, Amphiphilic Networks Based on Blends of Perfluoropolyethers and Poly(ethylene glycol). *Journal of the American Chemical Society* **2008**, *130* (43), 14244-14252.
4. Lopez, G.; Ameduri, B.; Habas, J.-P., A Versatile Strategy to Synthesize Perfluoropolyether-Based Thermoplastic Fluoropolymers by Alkyne-Azide Step-Growth Polymerization. *Macromolecular Rapid Communications* **2016**, *37* (8), 711-717.
5. Amanchukwu, C. V.; Yu, Z.; Kong, X.; Qin, J.; Cui, Y.; Bao, Z., A New Class of Ionically Conducting Fluorinated Ether Electrolytes with High Electrochemical Stability. *Journal of the American Chemical Society* **2020**, *142* (16), 7393-7403.
6. Wong, D. H. C.; Thelen, J. L.; Fu, Y.; Devaux, D.; Pandya, A. A.; Battaglia, V. S.; Balsara, N. P.; DeSimone, J. M., Nonflammable perfluoropolyether-based electrolytes for lithium batteries. *Proceedings of the National Academy of Sciences* **2014**, *111* (9), 3327-3331.
7. McLachlan, D. S.; Blaszkiewicz, M.; Newnham, R. E., Electrical resistivity of composites. *Journal of the American Ceramic Society* **1990**, *73* (8), 2187-2203.

Acknowledgements

We would like to thank Dr. Wan-Yu Tsai for leading the publication “Li Morphology Evolution during Initial Cycles in a Gel Composite Polymer Electrolyte.”

XVI.25 Inorganic-Polymer-Composite Electrolyte with Architecture Design for Lithium Metal Solid State Batteries (BNL)

Enyuan Hu Principal Investigator

Chemistry division, Brookhaven National laboratory
Bldg. 555, Brookhaven National Lab.
Upton, NY 11973
E-mail: enhu@bnl.gov

Simon Thompson, DOE Technology Development Manager

U.S. Department of Energy
E-mail: Simon.Thompson@ee.doe.gov

Start Date: October 1, 2021

End Date: September 30, 2022

Project Funding (FY22): \$500,000

DOE share: \$500,000

Non-DOE share: \$0

Project Introduction

This project aims to leverage the strong expertise and close collaboration of the team (Brookhaven National Laboratory, Harvard University and University of California Irvine) to address issues facing solid electrolyte lithium metal batteries and achieve goals set by DOE. We propose to use inorganic-polymer-composite electrolyte coupled with architecture design to address the issue. Composite electrolyte can inherit the merits of both the inorganic electrolyte part (high ionic conductivity, compatibility with cathode, good mechanical strength and so on) and the polymer part (good interfacial contact, tunable stability with lithium metal, facile thickness control, flexibility, easy roll-to-roll processing and so on). It is worth noting that the proposed organic-inorganic hybrid strategy is built upon the demonstrated success of a ‘combination’ strategy for liquid electrolyte optimizations in which combines ethylene carbonate (excellent interphase formation capability but poor conductivity) and some linear carbonate (great conductivity but cannot form good interphase).

The importance and success of the architecture design for solid electrolyte, especially in addressing the lithium dendrite penetration issue, has been recently demonstrated by the team. We will generalize this strategy to composite electrolytes that include broad types of ceramic and polymer electrolytes. We will optimize the composite electrolyte structure—sandwiched, interpenetrated, or dispersed to strike a balance between ionic conductivity, mechanical stability, and electrochemical (interface) stability.

The advantage of high energy density of solid-state batteries can only be realized by a lithium metal anode. Therefore, stability against lithium metal is a key property required for solid electrolyte and lithium metal protection is needed if the electrolyte does not have sufficient thermodynamic stability against lithium. The lithium metal stability issue can be addressed by engineering the interphase, a strategy that has been proven to be successful in liquid-electrolyte-based lithium metal batteries. It was shown that through tuning the solvation structure and the additive, the property of solid-electrolyte-interphase (SEI) can be engineered to favor lithium-ion transport across the interphase and stabilize the lithium metal anode. We propose to use similar strategies for the composite solid electrolyte and engineer the lithium metal SEI through the optimization of the polymer electrolyte composition, especially the choice of additives.

We also aim to apply the advanced characterization tools including synchrotron and cryoEM, to help us understand both the interphases and the bulk properties. The interphases include lithium metal SEI, cathode-electrolyte-interphase (CEI), and also very importantly, the interphase between polymer and ceramic in the solid electrolyte which is critical to the overall electrolyte performance but was very little characterized and understood.

Objectives

This project targets the following goal: the composite electrolytes will be thin ($< 100 \mu\text{m}$) and have high Li-ion conductivity ($\geq 10^{-3} \text{ S/cm}$ at room temperature), low interfacial impedance, and desirable mechanical properties. When used in the solid electrolyte (SE) Li-metal battery, a current density $> 1 \text{ mA/cm}^2$ and an areal capacity of $2\text{-}3 \text{ mAh/cm}^2$ can be achieved with more than 300 cycles. The constructed $\text{LiNi}_x\text{Mn}_y\text{Co}_{1-x-y}\text{O}_2$ (NMC)/ $\text{LiCoO}_2 \parallel$ composite electrolyte \parallel Li-metal cell can be operated at up to 4.5 V versus Li^+/Li . The SE will also be compatible with high loading cathodes in achieving high energy density at the coin or pouch-cell level.

Approach

The project approaches are as follows: (1) design and synthesize polymer with anion-tether strategy for high transference number, (2) through theories and experiments, design hierarchical inorganic electrolyte for suppressing lithium dendrite penetration, (3) optimize the composite electrolyte composition and structure, (4) use additives for Li-metal anode and NMC cathode protection, and (5) use synchrotron and cryogenic electron microscopy characterization to understand the bulk electrolyte and interphases.

Results

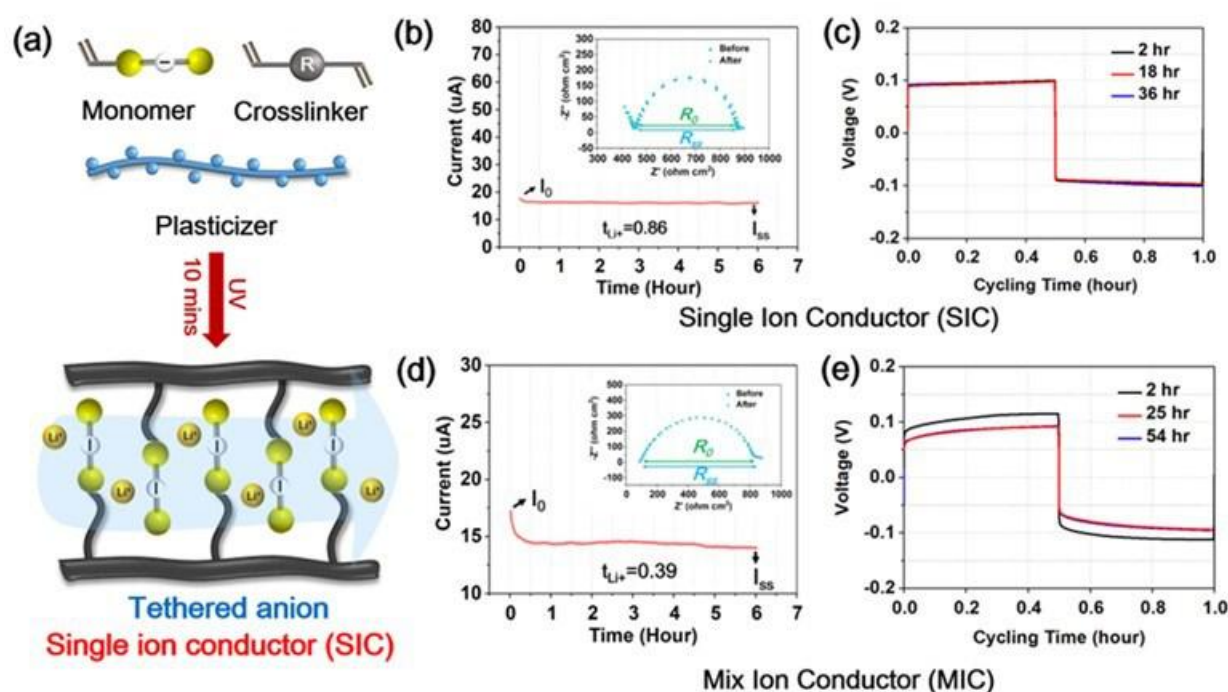


Figure XVI.25.1 (a) Schematic illustration showing the UV-polymerization route to synthesize the single lithium ion conducting SPE from the anionic monomer, crosslinker, and plasticizer. (b) Li^+ transference number measured by the potentialstatic polarization method of SIC-SPE. (c) Voltage-time profile of the Li-Li symmetric cells when cycling at 0.2 mA/cm^2 and 0.1 mAh/cm^2 showing the concentration overpotential of SIC-SPE. (d) Li^+ transference number measured by the potentialstatic polarization method of MIC-SPE. (e) Voltage-time profile of the Li-Li symmetric cells when cycling at 0.2 mA/cm^2 and 0.1 mAh/cm^2 showing the concentration overpotential of MIC-SPE.

In FY2022, the team has established a UV-polymerization platform to synthesize the single lithium ion-conducting polymer electrolyte (SIC), as shown in Figure XVI.25.1a. An anionic monomer with ionizable Li^+ counter-cation was co-polymerized with a crosslinking reagent to adjust the Li^+ concentration and regulate the mechanical properties. The role of the plasticizer is to facilitate the solvation and dissociation of Li^+ to improve the ionic conductivity. In sharp contrast to conventional polymer electrolytes, all the anions in SIC were covalently tethered to the polymer backbones, and the Li^+ is the sole charge carrier. As a result, the unique polymer architecture design has delivered a high Li^+ transference number (t_{Li^+}) of 0.86 (Figure

XVI.25.1b), which is four-fold higher than the conventional poly-ethylene oxide (PEO) SPE. Benefiting from this high t_{Li^+} , i.e., the migration and accumulation of electrochemically non-reactive anions at the SPE-electrode interface are largely avoided. Figure XVI.25.1c shows the voltage-time curve of Li/SIC-SPE/Li cell at different cycling time. The SIC-SPE exhibits total overpotential of 100 mV, and a low concentration overpotential of 10 mV when cycling at 0.2 mA/cm^2 and 22°C (Figure XVI.25.1c). For comparison, we also synthesized a mixed ion-conducting SPE (MIC) containing free-mobile anions. The Li^+ concentration, crosslinking degree, and plasticizer content of MIC were controlled to be the same as SIC, while a much lower t_{Li^+} of 0.39 (Figure XVI.25.1d) was observed. As expected, the Li-Li symmetric cell with MIC also showed a high concentration overpotential of $\sim 50 \text{ mV}$ (Figure XVI.25.1e). The above results preliminarily revealed the critical role of t_{Li^+} in dominating the electrochemical behavior of solid-state batteries. We will investigate its effect on dendrite suppression, SEI formation, and full cell durability in the next stage.

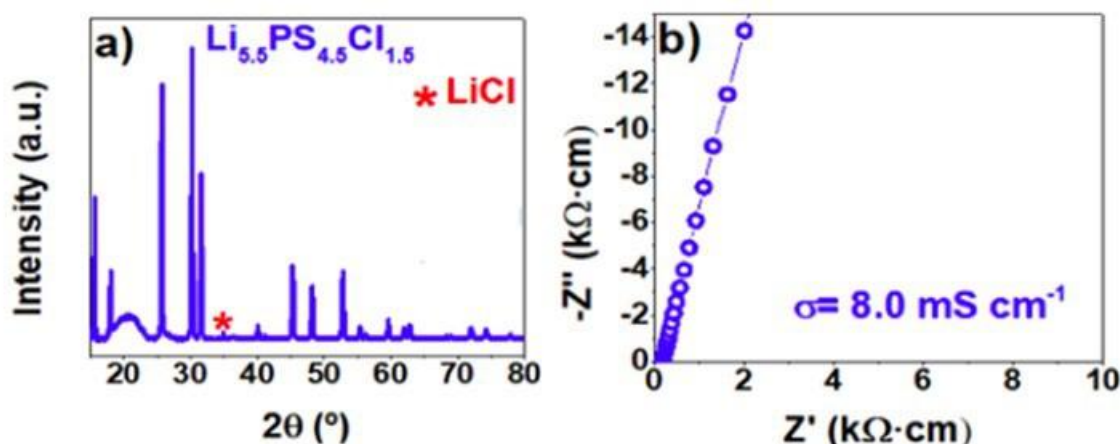


Figure XVI.25.2 (a) Powder XRD (a) and impedance (b) at room temperature of as-synthesized $\text{Li}_{5.5}\text{PS}_{4.5}\text{Cl}_{1.5}$.

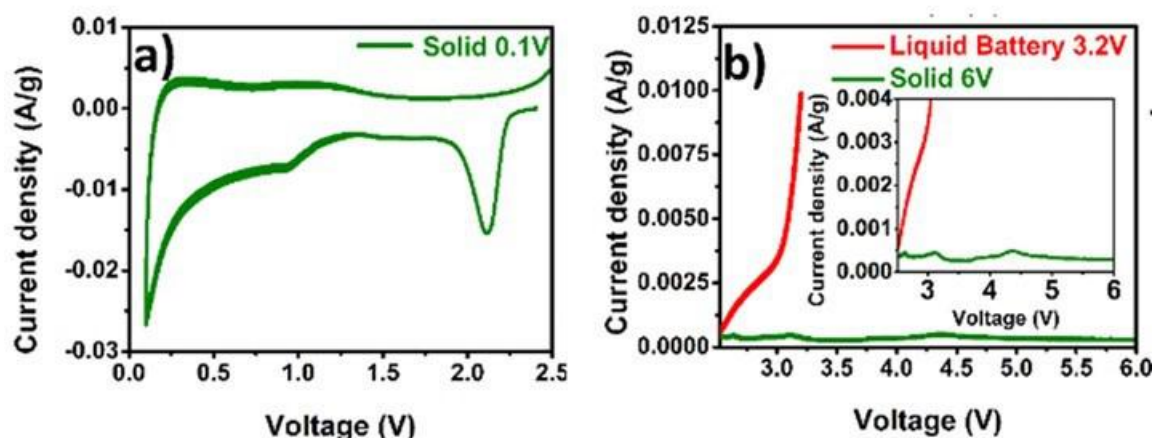


Figure XVI.25.3 $\text{Li}_{5.5}\text{PS}_{4.5}\text{Cl}_{1.5}$ (LPSCl_{1.5}) show a voltage stability to Li metal (a) and up to 6.0 V (b) in solid state batteries in cyclic voltammetry (CV) tests. Li/LPSCl_{1.5}/LPSCl_{1.5}-C (cathode composition 0.9:0.1- LPSCl_{1.5}:Carbon black (w/w)) were collected on a Solartron 1455A with a voltage sweeping rate of 0.1 mV s^{-1} from 0.1 to 6 V.

In FY2022, we also designed a solid electrolyte with the chemical composition of $\text{Li}_{5.5}\text{PS}_{4.5}\text{Cl}_{1.5}$ within the argyrodite phase through the optimized chemical synthesis route (Figure XVI.25.2a). The electrolyte in our impedance measurement shows an ionic conductivity of 8 mS/cm at room temperature (Figure XVI.25.2b). In the cyclic voltammetry (CV) test, it shows a wide voltage stability window. The decomposition current down to 0 V in a direct contact with Li metal anode (Figure XVI.25.3a) is very small, and the same for the battery charged up to 6 V (Figure XVI.25.3b) in solid state batteries. For the low voltage region, cells were scanned from Open Circuit Voltage (OCV) to 0.1 V and then back to 2.5 V. For the high voltage region, cells were

tested from OCV to 6 V and subsequently scanned back to 2.5 V. All cells were previously pressed at 125 MPa and an external pressure of 38 MPa was applied during test.

In FY2022, synchrotron soft x-ray absorption spectroscopy (sXAS) and total scattering technique pair distribution function (PDF) characterization of polymer electrolytes have been completed. The polymer used is polyvinylidene fluoride (PVDF) and the salts used include both lithium bis(trifluoromethanesulfonyl) imide (LiTFSI) and lithium bis(sulfonyl fluoride) imide (LiFSI). The polymer electrolyte was prepared by solvent casting method. PVDF and salts were first dissolved into N-methyl-2-pyrrolidone (NMP) and stirred for 24 hours, followed by vacuum drying at 60 °C for one day to form the polymer electrolyte.

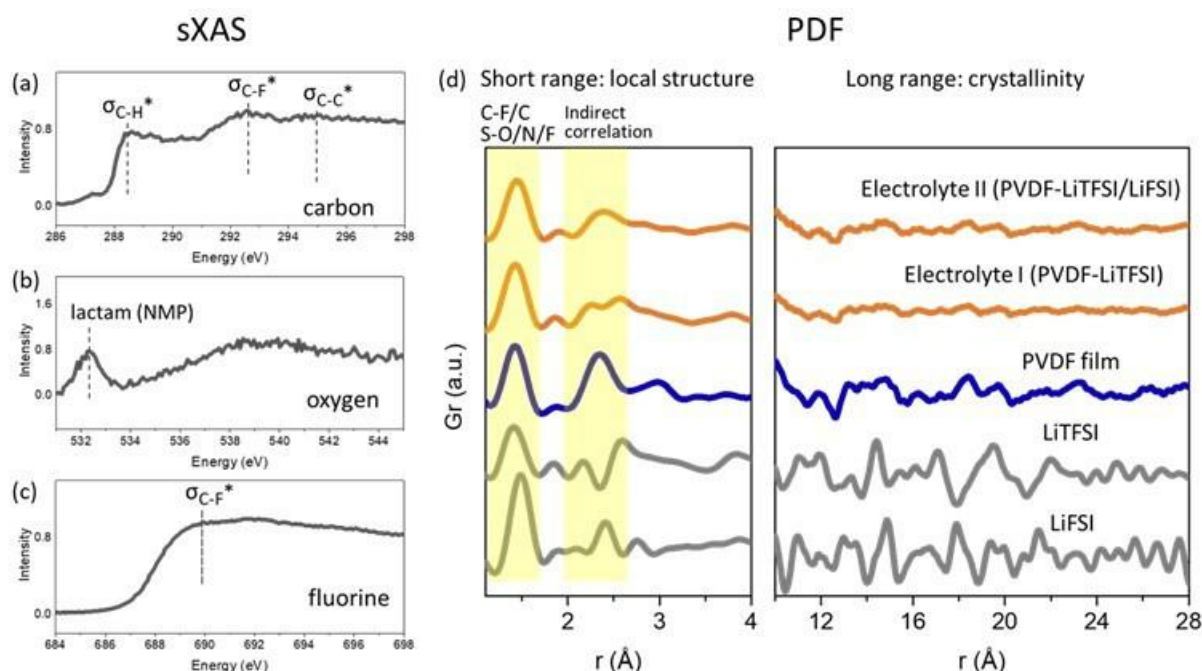


Figure XVI.25.4 sXAS and PDF characterization of the polymer electrolytes. (a) carbon (b) oxygen (c) fluorine K-edge sXAS of PVDF mixed with NMP and vacuum dried. (d) PDF results of polymer, salts and polymer electrolytes.

Carbon, oxygen and fluorine K-edge sXAS of blank polymer (mixed with NMP and vacuum dried without adding the salts) are shown in Figure XVI.25.4a, Figure XVI.25.4b and Figure XVI.25.4c respectively. All data are measured in partial fluorescence yield mode. In Figure XVI.25.4a, the peaks at 288.4 eV, 292.8 eV and 295 eV correspond to the excitation of core electrons to the C-H, C-F and C-C antibonding orbitals respectively. Surprisingly, Figure XVI.25.4b shows there is clear oxygen signal from the blank polymer. Since PVDF itself does not contain any oxygen, the only possible oxygen source is the amide group in NMP which is also known as lactam (cyclic amide). The 532.2 eV peak in Figure XVI.25.4b indeed corresponds to the carbonyl antibonding associated with the amide group. Figure XVI.25.4c shows the fluorine sXAS which has the peak at around 689.8 eV corresponding to the σ C-F antibonding in PVDF. Figure XVI.25.4d shows the PDF results of PVDF (pure powder without going through mixing with NMP), salts and the polymer electrolytes. In general, the PDF data can be divided into the short-range region associated with the local structure and the long-range region that indicates the crystallinity of the materials. In the short-range region, the first peak (shaded) at around 1.5 Å relates to the shortest bond in these materials which can be C-F/C as in PVDF and S-O/N/F as in LiTFSI and LiFSI salts. The second shaded region at around 2.3 Å correspond to indirect correlations between atoms that are not directly bonded to each other but connected through an atom bonding to both simultaneously. For example, it could be the correlation between two oxygen atoms in the sulfonyl group. In the long-range region, it is obvious that pristine PVDF, LiTFSI and LiFSI all have good crystallinity as indicated by the strong oscillating peaks. After making them into polymer electrolyte, the magnitude of oscillation considerably decreases, suggesting the loss of crystallinity during electrolyte making.

This study shows how wet method affects the composition and the crystallinity of the polymer electrolyte. Future studies will be devoted to understanding its influence on the cell electrochemistry.

Conclusions

In conclusion, we established a UV-polymerization platform to synthesize the single lithium ion-conducting polymer electrolyte with high ionic conductivity and high transference number. We also designed and synthesized a ceramic electrolyte with the chemical composition of $\text{Li}_{5.5}\text{PS}_{4.5}\text{Cl}_{1.5}$ having the argyrodite structure. It shows high ionic conductivity of 8 mS/cm at room temperature and high voltage stability. We applied synchrotron-based characterizations to understand the structure of PVDF-based polymer electrolyte.

Key Publications

1. Ruoqian Lin, Yubin He, Chunyang Wang, Peichao Zou, Enyuan Hu, Xiao-Qing Yang, Kang Xu, Huolin Xin*, “Characterization of the structure and chemistry of the solid-electrolyte interface by cryoEM leads to high-performance solid-state Li-metal batteries”, *Nature Nanotechnology*, 2022, 17, 768. DOI: 10.1038/s41565-022-01148-7.
2. Bowen Shao, Sha Tan, Yonglin Huang, Lifu Zhang, Jian Shi, Xiao-Qing Yang, Enyuan Hu*, Fudong Han*,
3. “Enabling Conversion-Type Iron Fluoride Cathode by Halide-Based Solid Electrolyte”, *Advanced Functional Materials*, DOI: 10.1002/adfm.202206845.
4. Materials, DOI: 10.1002/adfm.202206845.

Acknowledgements

E. Hu acknowledges the help from Prof. Fudong Han in Rensselaer Polytechnic Institute for the help on designing and making in situ cells for charactering the solid-state electrolyte using synchrotron.

XVI.26 Ion Conductive High Li⁺ Transference Number Polymer Composites for Solid-State Batteries (LBNL)

Bryan D. McCloskey, Principal Investigator

Lawrence Berkeley National Laboratory and University of California, Berkeley
201-D Gilman Hall
Berkeley, CA 94720
E-mail: bmcclosk@berkeley.edu

Simon Thompson, DOE Technology Development Manager

U.S. Department of Energy
E-mail: Simon.Thompson@ee.doe.gov

Start Date: October 1, 2021

End Date: September 30, 2026

Project Funding (FY22): \$280,000

DOE share: \$280,000

Non-DOE share: \$0

Project Introduction

This project seeks to develop polymer-inorganic composites that have an optimal combination of conductivity, processability, and low interfacial resistance at both a Li metal anode and a porous Li[Ni, Co, Mn]O₂ (NMC) cathode. In an effort to enable Li metal anodes, mechanically rigid solid-state Li⁺ conductors, such as Li₇La₃Zr₂O₁₂ (LLZO), Li_{1+x}Al_xTi_{2-x}(PO₄)₃ (LATP), and Li₂S-P₂S₅ glasses (LPS), have been employed due to their high Li⁺ ion conductivity and, when engineered to eliminate interfacial defects, appropriate stiffness to suppress Li metal dendrite formation. However, for these materials to result in batteries that compete against current commercial cells in terms of energy density and cost per kWh, they would need to be manufactured at no more than 50 microns thickness and cost no more than \$5 per square meter. The materials would also need to be engineered to be defect free (to disallow Li dendrite growth) and have anode and cathode interfacial resistances that remained low over 100s of cycles. These metrics are daunting for pure thin-film inorganic ion conductors, particularly when a porous, thick cathode also needs to be used to achieve competitive cell energy densities.

To overcome these challenges, this project aims to develop polymer-inorganic composites, where high Li⁺ transference number polymer electrolytes serve as a binder for inorganic ion conducting particles. By optimizing the composition of this composite electrolyte, we aim to marry the processability and interfacial mechanical compliance of polymers with the impressive transport properties of inorganic composites, thereby enabling roll-to-roll manufacturing to allow thin (<50 micron) layers of high conductivity solid-state conductors to be cost-effectively incorporated into batteries.

Objectives

In FY22, we focused on the synthesis and development of a polymer matrix for our composite electrolyte. Our objective is to create a high transference number polymer electrolyte using strategies inspired by our prior molecular dynamics simulations. We focused on high Li⁺ transference number polymers—those in which current passed through the polymer electrolyte is carried predominantly by the Li⁺ and not its anion—as inspired by Mehrotra, Srinivasan et al., who intriguingly hypothesized that ion transport through polymer-inorganic interfaces is improved when both phases have similar transference numbers. We aimed to develop polymers in which trifluoromethane sulfonyl imide anions (TFSI) are appended to the polymer backbone due to the availability of such monomers and our experience with them. TFSI also provides high charge delocalization, thereby imparting high ion dissociation compared to other potential appended anions (e.g., sulfonates). An additional objective was to perform studies on procured ceramic particles to quantify surface impurities, namely lithium carbonate (Li₂CO₃) on LLZO particles, so that we may understand the role of these impurities on ion transport through the ceramic-polymer interface.

Approach

Our approach relies on the following key steps in FY22: 1. Using monomers with TFSI anions appended to them, synthesize and characterize polyanionic polymer electrolytes with high Li^+ transference number and conductivity. 2. Through systematic material structure-property characterization, understand how to reduce interfacial ion transport impedance between inorganic ion conductors (specifically, thin film inorganic conductors such as LLZTO, LATP, and LPS) and high Li^+ transference number polymer electrolytes. 3. Use acid titrations to quantify Li_2CO_3 on as-received LLZO particles.

Results

In FY22, we developed a reversible addition-fragmentation chain-transfer (RAFT) polymer synthesis procedure to reliably produce poly((trifluoromethane)sulfonimide lithium methacrylate) (PLiMTFSI) at a controlled molecular weight. We have produced 20,000 g/mol and 60,000 g/mol molecular weight PLiMTFSI, with molecular weight confirmed by ^1H nuclear magnetic resonance spectroscopy (NMR) end-group analysis and gel permeation chromatography (GPC). NMR was also used to characterize the reaction kinetics of the 20K PLiMTFSI and determine conversion and molecular weight as a function of time, as shown in Figure XVI.26.1. The molecular weight predicted by conversion was verified by NMR end-group analysis and GPC. No melting was detected via differential scanning calorimetry (DSC) indicating the lack of crystalline domains in the PLiMTFSI. X-ray diffraction (XRD) results confirmed the amorphous nature of polymer, with only a broad XRD peak evident as shown in Figure XVI.26.2. No glass transition temperature was detected via initial DSC test within the range of -80°C to 250°C , however further DSC studies will be necessary to rule out any glass transition behavior in this temperature range.

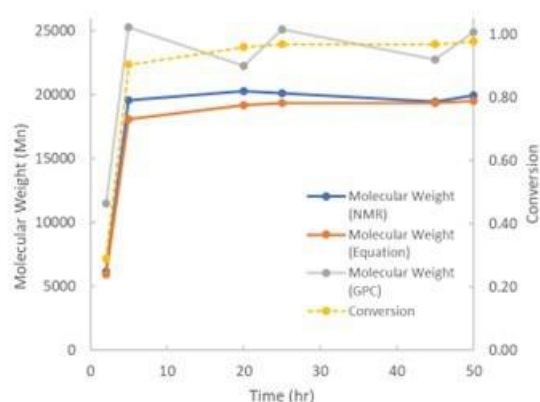


Figure XVI.26.1 Conversion and molecular weight data from a 20K PLiMTFSI synthesis.

Once we successfully synthesized these PLiMTFSI polymers, we cast free-standing films to begin measuring conductivity of our neat polymers. Solvent choice and polymer concentration was found to be important, with 30 wt.% PLiMTFSI in methanol the best solution composition for film casting. Drop casting directly onto stainless steel led to usable films for conductivity measurements, but we were unable to remove films from the stainless steel after drop casting. We attempted to create a free-standing film using solvent casting with a doctor blade to control the thickness. After casting onto a Teflon surface we were able to remove the PLiMTFSI; however, the film was brittle and difficult to transfer to an electrochemical cell without it breaking.

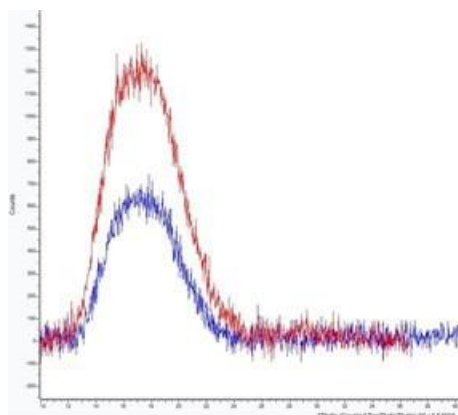


Figure XVI.26.2 XRD data showing characteristic amorphous peak for both the 60K (red) and 20K (blue) PLiMTFSI.

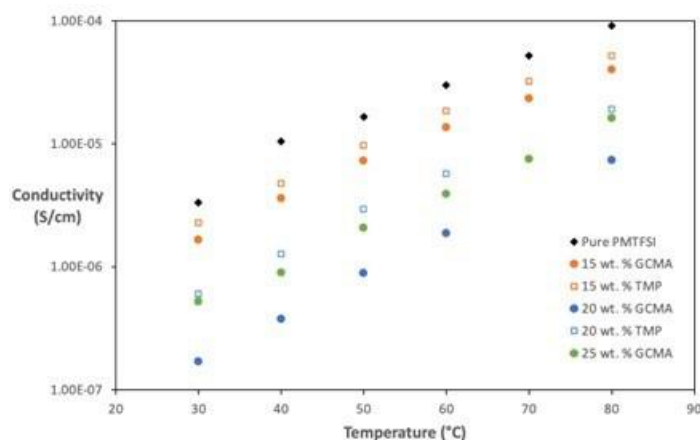


Figure XVI.26.3 Conductivity of prepared PLiMTFSI single-ion conducting polymer films as a function of temperature and plasticizer (TMP and GCMA) content.

To impart polymer mechanical properties that allow good film formation (and to reduce film brittleness), we incorporated two plasticizers in film compositions that also contained PLiMTFSI. Glycerol carbonate methacrylate (GCMA) and acetone-protected trimethylolpropane methacrylate (TMPMA) allowed us to explore methods of creating flexible, free-standing films, whereas films prepared from PLiMTFSI by itself were brittle and difficult to handle, as was expected given its high ion content. While a reliable method to produce these free-standing films at a thickness of less than 100 μm is still ongoing, we were able to measure conductivity of various polymer/plasticizer combinations using stainless steel symmetric cells. The conductivity values are given in Figure XVI.26.3, which show the plasticizer content had an impact on the conductivity of PLiMTFSI. While the plasticizers reduced the film conductivity, future refinements to the film composition, including the incorporation of plasticizers with good ion solvating properties, should provide improved ion conductivity.

The plasticizers we examined above were small molecule methacrylates, and large quantities (i.e. 60 wt%) were required in order to observe appreciable mechanical changes in the film, which ultimately reduced ion content in the film and therefore conductivity. In light of these observations, we developed RAFT polymer synthesis of the methacrylates, GCMA and TMPMA. By using polymer blends of PLiMTFSI with polymerized GCMA and TMPMA, we hope to create systems that need less plasticizer to produce the same mechanical properties we saw with the small molecule additives. Polymerizing GCMA was the focus of our investigation. Additionally, identification of a suitable solvent for the TMPMA polymer synthesis proved challenging, as the polymer was found to be insoluble in many common solvents. We used several procedures

to synthesize a GCMA polymer with a molecular weight comparable to our PLiMTFSI. Figure XVI.26.4 below details the ^1H NMR data for a RAFT synthesis using the initiators Azobisisobutyronitrile (AIBN) in DMSO (top) and 4,4'-Azobis(4-cyanopentanoic acid) (ACPA) in acetonitrile (bottom). The reaction in AIBN produced a conversion of near unity, but removing the DMSO from the product has proven time consuming and detrimental to the reaction yield. On the other hand, our reaction in ACPA has a lower conversion (around 85%), so the need to purify our product impacted the yield.

In addition to polymer film synthesis and characterization, we have initiated studies on as-received LLZO ceramic powder. Through an acid titration technique developed in our lab, we determined that our LLZO particles have significant amounts of lithium carbonate present, and through X-ray Photoelectron Spectroscopy (XPS) verified that carbonate is present on the particle surface. Previous research shows that carbonate can have a significant impact on electrochemical performance and ion transport across interfaces, so we investigated how we might be able to change the amount of carbonate on the surface. Exposing the LLZO particles to air for 12 hrs resulted in more carbonate forming (Table XVI.26.1, air-exposed), suggesting that the particles' surface as received are not passivated and that the carbonate surface layer is not dense. Furthermore, a simple water washing procedure (exposure to air-free water for 5 minutes) resulted in approximately half of the carbonate being removed from our LLZO sample (Table XVI.26.1, washed). These data are listed below in Table XVI.26.1, and demonstrate that we now have an additional, largely unstudied, knob that we can turn to examine its impact on Li transport properties.

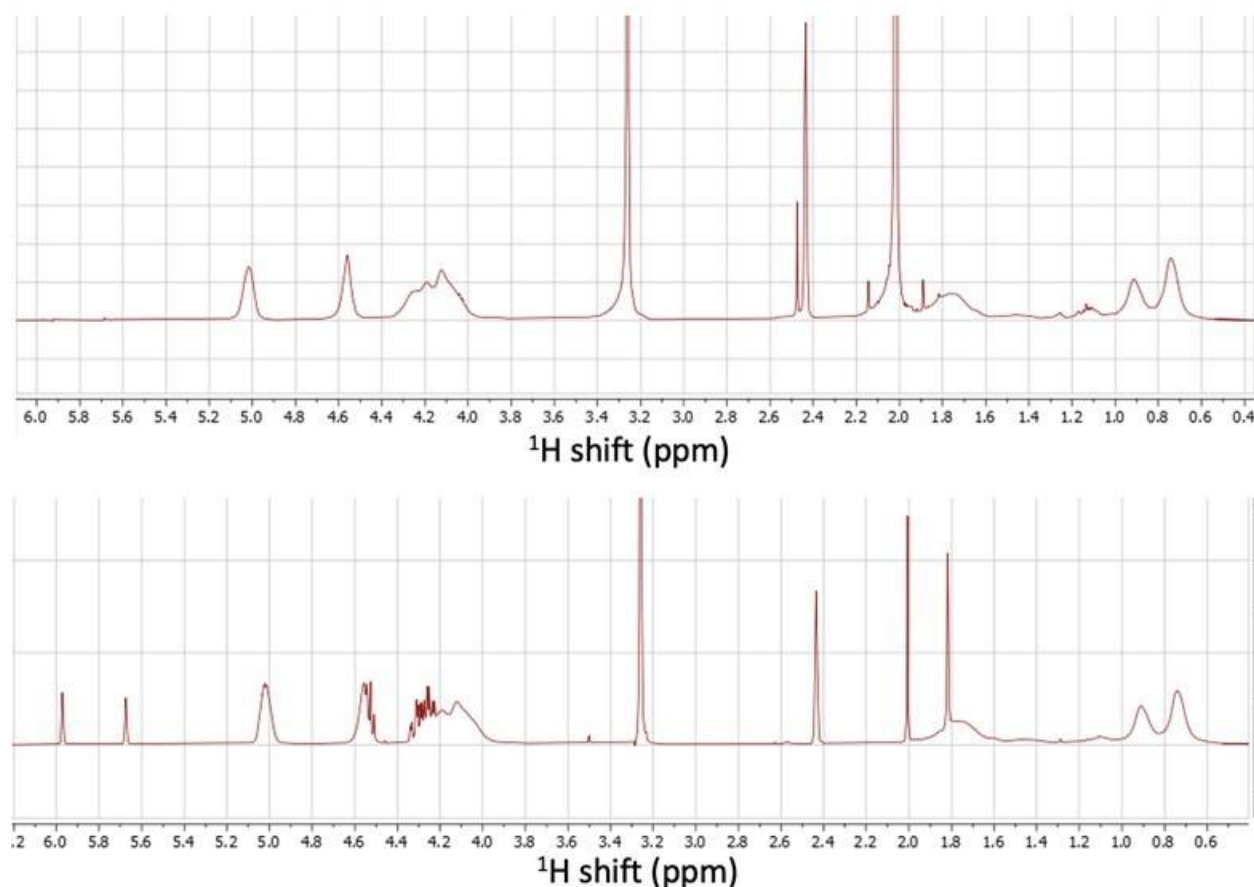


Figure XVI.26.4 NMR data for GCMA polymerization with AIBN in DMSO (top) and ACPA in acetonitrile (bottom). The peaks at 5.7 and 6.0 correspond to the monomer, while the double-humped peak from 0.6-1.0 represent the polymer.

Table XVI.26.1 Lithium Carbonate content of various LLZO samples

LLZO Sample Type	Li ₂ CO ₃ wt. %
As-received	5.56
Air-exposed	16.17
Washed	2.40

Conclusions We have successfully synthesized single ion conducting PMLiTFSI polymers with controlled molecular weight. Additionally, we have successfully synthesized two additional polymers (polymerized GCMA and TMPMA) that serve as promising blending polymers to improve PMLiTFSI film forming properties and ion conductivity. Finally, we have employed acid titrations to quantify Li₂CO₃ surface impurities on as-received ceramics, and show that LLZO is air-sensitive (carbonate content increases after air exposure) and that simple washing techniques can reduce carbonate impurities in LLZO powders.

Key Publications

1. Tronstad, Z.; McCloskey, B. D. “Ion Conductive High Li⁺ Transference Number Polymer Composites for Solid-State Batteries.” Presented at the American Institute of Chemical Engineering Annual Meeting, Nov. 2022.

Acknowledgements

This section was coauthored by Zachary Tronstad (LBNL).

XVI.27 Precision Control of the Li Surface for Solid-state Batteries (Oak Ridge National Laboratory)

Andrew S. Westover, Principal Investigator

Oak Ridge National Laboratory
PO Box 2008, MS6124
Oak Ridge, TN 37830
E-mail: westoveras@ornl.gov

Simon Thompson, DOE Technology Development Manager

U.S. Department of Energy
E-mail: Simon.Thompson@ee.doe.gov

Start Date: January 1, 2022

End Date: September 30, 2026

Project Funding (FY22): \$800,000

DOE share: \$800,000

Non-DOE share: \$0

Project Introduction

The knowledge of lithium surface engineering and the implications for cell design of Li-metal-batteries will improve commercialization efforts for solid-state Li-metal batteries. There is very little standard knowledge about variations in the impurity level in different lithium sources, the surface chemistry of different lithium surfaces, and their impact on performance. Furthermore, the strategies developed to engineer the surface of the lithium metal for integration into Li-metal batteries will provide significant performance increases, ideally enabling successful commercialization.

Objectives

This project has three primary objectives. 1) Understand the chemistry and mechanics of native Li and its surfaces and correlate with electrochemical performance 2) engineer the Li surfaces to minimize interfacial resistance and optimize stress relief along the interface and 3) demonstrate that the engineered surface coating can enable batteries with a specific energy of 500 Wh/kg for at least 300 cycles.

Approach

This project is broken into two parts. First, the team is focused on thoroughly understanding the purity, mechanics, and surface chemistry of multiple lithium sources and how these parameters impact performance. Second, they will focus on intentional engineering of the lithium purity and surface chemistry to control the mechanical properties, electrochemical stability, and electrochemical performance. They will explore three approaches to engineer the surfaces: gas-phase passivation, deposition of thin metal coatings, and deposition of thin inorganic coatings. To test electrochemical performance, they will use standard ceramic and polymer electrolytes to demonstrate the impact of purity and surface chemistry. The program will also employ a range of standard and specialized characterization techniques, including a significant focus on understanding the mechanics of lithium metal using nanoindentation and adhesion measurements using surface probe microscopy.

Results

This first year has focused on obtaining and characterizing multiple different Lithium sources. In all the project studied five different Li sources labeled Supplier #1, Supplier #2, Supplier #3, and Supplier #4, and ORNL evaporated Li produced in-house. The Supplier #1, Supplier #2, Supplier #3, and Supplier #4 Li are all rolled Li metal foils with a thickness of $\sim 40 \mu\text{m}$, except for the Supplier #4 which as a standard $600 \mu\text{m}$ thick Li. Each of the purchased Li sources was stored in its original packaging in an Ar-filled glovebox with minimal O_2 and H_2O content before characterization. The Supplier #1, Supplier #2, and Supplier #4 Li films were freestanding, while the Supplier #3 Li was laminated onto Cu foil. The ORNL Li was evaporated in a custom-designed chamber using an Alfa Aesar rolled Li foil as the precursor. The Alfa Aesar foil was placed into a Ta

crucible and evaporated onto Cu foil at ~ 170 Å/s. After deposition, the chamber and all the associated Li were allowed to cool for several hours before 95% Ar/ 5% CO₂ (99.9999% pure) gas mixture was used to vent the system before bringing the evaporated Li metal into the same glove box used to store the other Li foils. To perform the initial characterization of the films, the team performed infrared spectroscopy measurements in the same Ar-filled glovebox using a Bruker Alpha II Fourier Transform Infrared Spectrometer (FTIR) with Attenuated Total Reflection (ATR) diamond crystal module. The data is presented in Figure XVI.27.1. As can be seen in the data, all the Li films have some amount of lithium carbonate and lithium oxide on the surface, as seen by the characteristic Li oxide/ Li/salt peaks from ~ 400 -700 cm⁻¹ and the characteristic Li carbonate peaks at 800 cm⁻¹ and 1400-1600 cm⁻¹. In addition, the rolled foils all have some amount of hydrocarbon, indicated by the series of peaks between 2800 and 3000 cm⁻¹. The Supplier #4 Li has an especially intense hydrocarbon peak suggesting a hydrocarbon coating on the surface that may or may not be intentional. On the other hand, the Supplier #3 Li has a faint but distinct silicone-based hydrocarbon signature with the characteristic Si-H peak at 780 cm⁻¹ and Si-O-Si peaks between 900-1100 cm⁻¹. While the Supplier #1 and Supplier #2 Li don't have intense hydrocarbon peaks, the Supplier #1 Li has a particularly intense Li carbonate signature, and the Supplier #2 Li has a particularly intense Li oxide signature. The ORNL Li only has relatively low-intensity Li oxide and Li carbonate peaks.

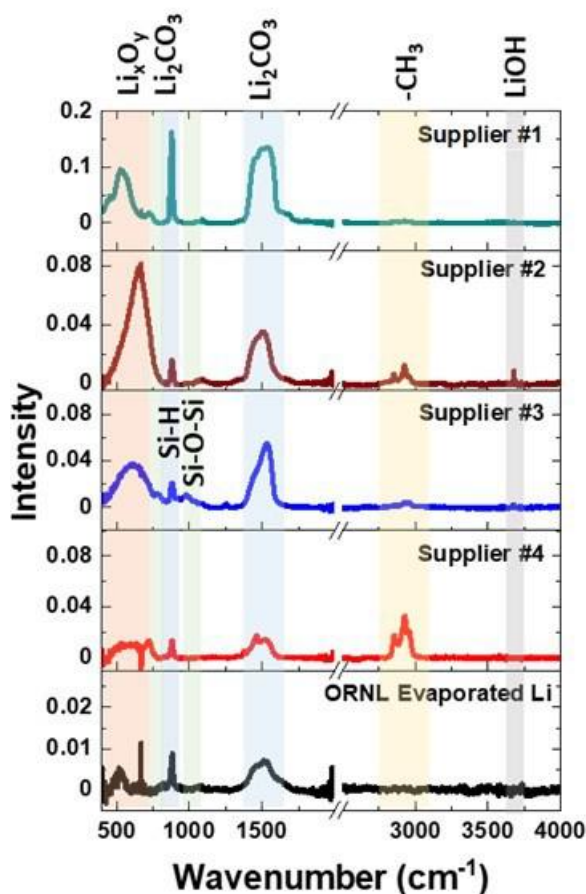


Figure XVI.27.1 ATR data of the 5 Li sources studied: Supplier #1, Supplier #2, Supplier #3, Supplier #4 and ORNL Evaporated Li from 400 cm⁻¹ to 4000 cm⁻¹.

Table XVI.27.1 Surface Composition from XPS (at.%) Before Etching

	Li	O	C	F	Si	S	N	Cl
Supplier #1	30.4	43.1	26.3	0.1	0.1	0.0	0.0	0.1
Supplier #2	22.3	21.9	55.2	0.2	0.0	0.0	0.4	0.0
Supplier #3	24.8	32.1	41.4	0.2	1.6	0.0	0.0	0.0
Supplier #4	18.8	16.6	64.6	0.0	0.0	0.0	0.0	0.0

The project further characterized the samples using X-ray Photoelectron Spectroscopy (XPS), as shown in Table XVI.27.1 and Figure XVI.27.1. Table XVI.27.1 presents the relative composition from an initial survey scan. All the samples have a significant amount of O and C on the surface, with the ORNL evaporated Li having the highest Li concentration. Other trace impurities, including N, F, S, Si, and Cl, are found in trace amounts throughout a few samples but are not significant enough to merit much discussion except for the Si concentration in the Supplier #2 samples. There is an appreciable amount of Si in the Supplier #2 Li amounting to ~1.6 at.%. This data corroborates and supports the IR data, which shows the characteristics of a Si-based hydrocarbon such as Silicone. A detailed look at the Li1s, C1s, and O1s (Figure XVI.27.2) reveals the presence of a significant amount of Li carbonate, C-C based material, a small amount of Li oxide, and a small amount of Li carbide in the ORNL evaporated Li. The C1s data is particularly intriguing. It suggests that Li carbonate-based species dominate the surface layer of the ORNL Li and the Supplier #1 Li, but that of the Supplier #2, Supplier #3 and Supplier #4 Li are dominated by the C-C species, likely a hydrocarbon. This observation aligns with the IR data where there are distinct hydrocarbon species in the Supplier #2, Supplier #3, and Supplier #4 Li samples. The lack of significant Li oxide peaks in the initial scan deviates from the IR data. It suggests that the Li oxide components prevalent in much of the IR data come from species that are deeper under the surface as IR probes several hundred nm at once while XPS only probes the few nanometers on the very outer surface. To get a better picture of the surface composition of the Li metal sources and how they change a function of depth, the project used the etching capability integrated into the XPS system, where the instrument can sputter off the surface and explore the surface composition as a function of depth. This data is presented in Figure XVI.27.3, focusing on the Li1s, C1s, and O1s in Figure XVI.27.3 (a),(b,) and (c), respectively. The carbon-based surface species quickly disappear in all the samples after <60 s of etching. The lone exception to this is the Supplier #1 Li, where the C-C based peak immediately disappears, but the Li carbonate peak remains for 250 s of etching (~50 nm). While the carbon species are etched away relatively quickly, rather than a pure Li metal signal appearing, a distinct Li-oxide signal appears in all the Li samples. This oxide is also etched away after ~300s (~60nm) for the evaporated Li, 1500s (~300 nm) for the Supplier #4 Li, 1500s (~300 nm) for the Supplier #3 Li, 2000s (~400 nm) for the Supplier #3 Li, and 3200s (~640nm) for the Supplier #1 Li. While the Supplier #3, Supplier #4, and ORNL Li all have a quick decline in intensity suggesting a more mixed composition, the Supplier #1 and Supplier #2 Li both have a very distinct Li oxide layer that persists for >1000 s of etching followed by a more gradual decay in the Li oxide content. This buried oxide directly aligns with the IR data.

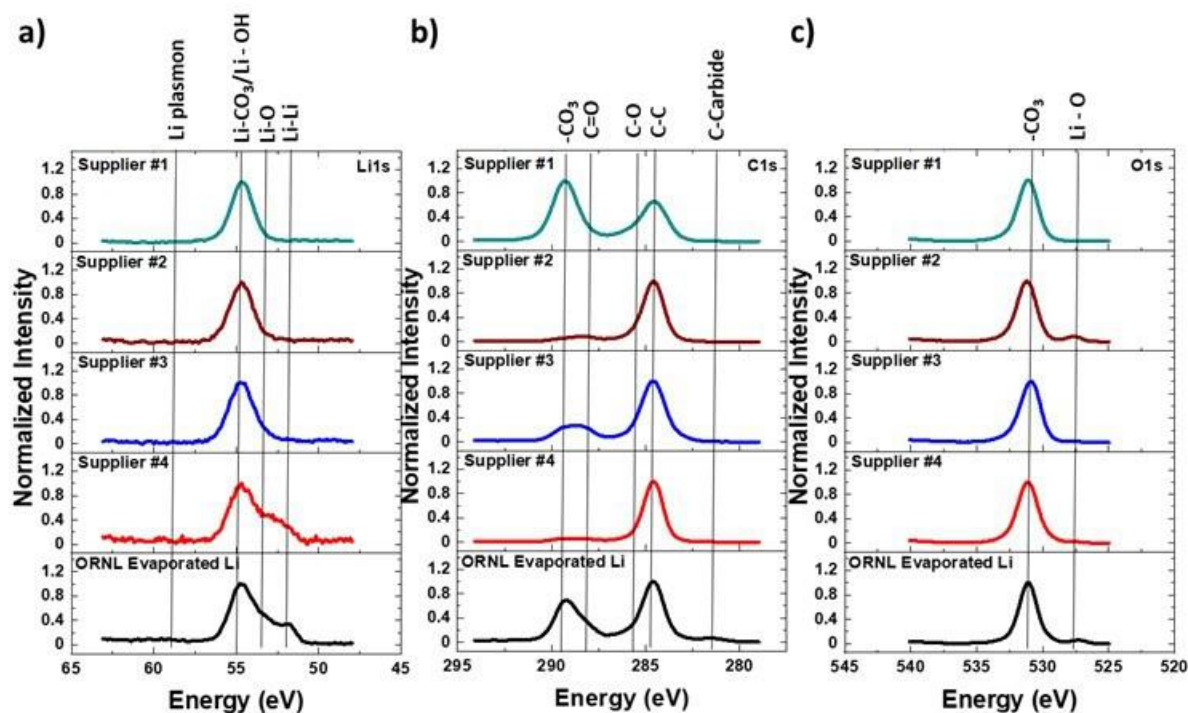


Figure XVI.27.2 Initial XPS data of the 5 Li sources studies: Supplier #1, Supplier #2, Supplier #3, Supplier #4 and ORNL Evaporated Li, focused on the Li1s (a), the C1s (b), and the O1s (c) peaks.

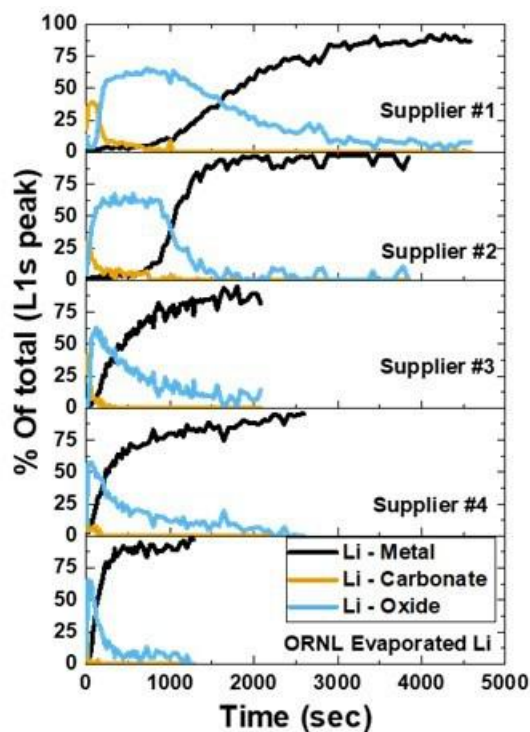


Figure XVI.27.3 Depth profiling XPS data of the 5 Li sources studies Supplier #1, Supplier #2, Supplier #3, Supplier #4 and ORNL Evaporated Li focused on the Li1s peaks with the different Li, C, and O species denoted as a function of etching time. The estimated etching rate based on a SiO_2 standard was 12 nm/min for an estimated etch depth of ~ 200 nm per 1000s.

After the Li etching was completed, the team again took survey scans of each Li sample (Table XVI.27.2). The dominant signal was Li metal at greater than >97% in all cases. Each of the samples had some residual oxygen due to the outgassing of O from the XPS chamber walls. All other impurities, including the C and Si, were eliminated from the samples. The most notable impurity is Na, which appeared in appreciable amounts in both the Supplier #2 and Supplier #4 Li. As Na is the most common impurity in Li metal, this is likely a real impurity. Based on the atomic percentages from XPS, this would place the Supplier #3 and Supplier #1 Li at ~99.6% pure. There were trace amounts of Cu identified for the Supplier #4 and the ORNL evaporated Li, but this is an artifact of the etching process as both have Cu substrates. A small amount of re-sputtering of Cu onto the surfaces is not unexpected.

Table XVI.27.2 Surface Composition from XPS (at.%) Before Etching

	Li	O	C	Cu	Na
Supplier #1	96.8	2.8	0.0	0.0	0.4
Supplier #2	98.2	1.3	<0.1	0.0	0.3
Supplier #3	98.0	2.0	0.0	<0.1	0.0
Supplier #4	97.8	2.2	0.0	0.0	0.0

Building on the initial chemical characterization of the surface the team also performed nanoindentation and liquid based Li plating and stripping with the same Li sources. Nanoindentation experiments have been performed on metallic lithium from commercial supplier 1 and commercial supplier 3. Representative load-displacement curves obtained at a target strain rate of 0.05 1/s are shown in Figure XVI.27.4 (a) and (b), respectively. The poor reproducibility from one test to the next and the stochastic nature of each test are wholly consistent with previously published¹ load-displacement curves obtained at very similar strain rates in high-purity, evaporated lithium. Although not explicitly shown in Figure XVI.27.4, the in-situ surface detection was triggered at a contact stiffness of 40 N/m and the point of contact between the indenter tip and the surface of the test specimen was accurately determined to within 5 nm or less. Among the more than 200 measurements performed in the two commercial sources, there was no significant experimental evidence of indenter tip contamination. In addition, nanoindentation results obtained in a fused silica reference block show no discernable change in the indenter tip geometry before and after the experiments performed in lithium.

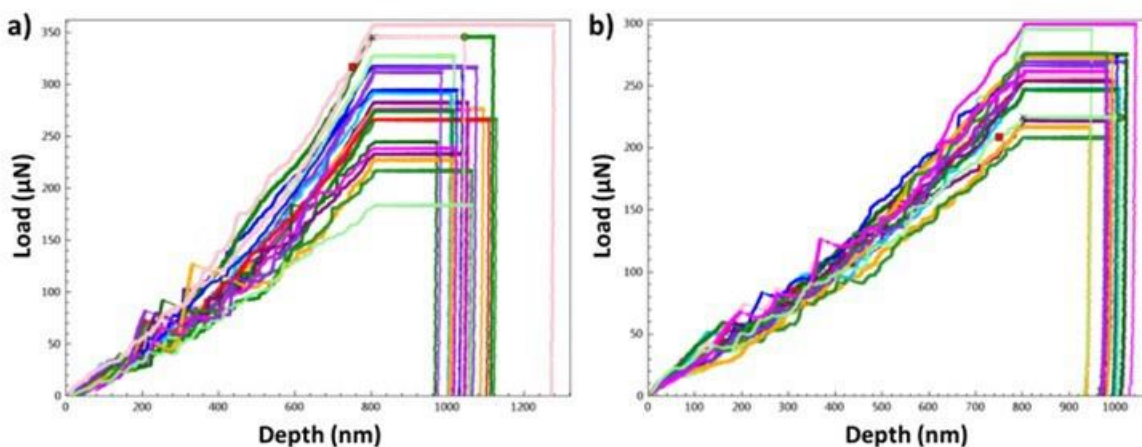


Figure XVI.27.4 Representative load-displacement curves obtained in metallic lithium from a) commercial supplier 1 and b) commercial supplier 2. The data were obtained using a diamond Berkovich indenter tip, a target strain rate 0.05 1/s, and a target depth of 800 nm.

Figure XVI.27.5 (a) shows the average elastic modulus measured as a continuous function of indentation depth. The scatter in the data reflect the variability and stochastic nature of the load-displacement curves shown in Figure XVI.27.4. The measured modulus is well within the expected range of lithium, which is nominally 3 to 22 GPa depending on the crystallographic orientation. The average modulus shown in Figure XVI.27.5 (a) suggests both sources have very similar texture. The slight depth dependence observed in the modulus (from both suppliers) is unexpected and its origin is currently under investigation. Among the experimental factors that could potentially cause or contribute to the observed depth dependence, thermal drift, a systematic error in the indenter tip area function, an error in the frame stiffness, the plasticity effect, the amplitude of the harmonic oscillation, and substrate effects have effectively been eliminated. One possible explanation is a breakdown in the geometric self-similarity of the contact geometry brought about by the strong depth dependence observed in the measured hardness. Figure XVI.27.5 (b) shows the average hardness measured as a continuous function of depth. For the sake of clarity, the scatter bars have been omitted from the plot. For comparative purposes, the plot shows the average hardness measured at similar strain rates in an evaporated lithium deposited at ORNL. These data were published in 2018 [1]. In stark contrast to the measured elastic modulus shown in Figure XVI.27.5 (a), Figure XVI.27.6 (b) shows the hardness exhibits a very strong depth dependence. This general observation is well-documented in evaporated lithium [1]. The interesting observation here is that despite significant variations in the purity of the lithium surface, test specimens from commercial suppliers #1 & #3 exhibit similar behavior to that of the high-purity, evaporated lithium. That said, based on work characterizing the surface of the films Supplier 1 Li had a very thick surface layer that was characterized by ~ 50 nm of Li_2CO_3 followed by a distinct Li_2O layer. Commercial Supplier 2 on the other hand had a much thinner surface layer with an organic silicone layer followed by a mixed $\text{Li}_2\text{O}/\text{Li}$ layer. The difference in the surface chemistry of the three different Li sources may be part of the difference in the mechanics. More detailed analysis and understanding will be developed in the next year.

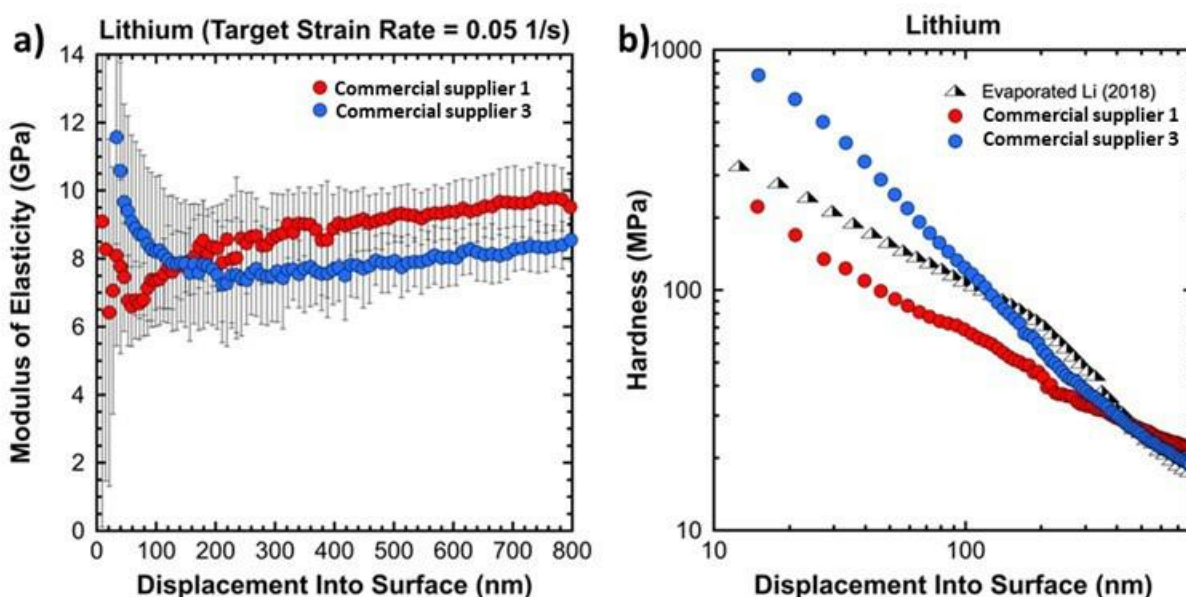


Figure XVI.27.5 a) The average elastic modulus of lithium obtained from the two commercial suppliers. (b) The average hardness of lithium obtained from the two commercial suppliers and an evaporated lithium deposited at ORNL (data from the ORNL specimen were published in 2018).

In addition to the mechanical measurements, the project also compared the electrochemical performance of all five Li sources in liquid electrolytes. To perform the tests, Li//Li symmetric coin cells were made using one type of lithium metal as both the electrodes, with the diameter of one electrode slightly larger than the other to ensure a well-defined active area ($1/2''$ and $7/16''$). Gen 2 (1.2M LiPF₆ in EC/EMC (3:7 by wt.)) was used as the liquid electrolyte (25 μL per cell), and Celgard® 2325 as the separator. After a 24 h rest at room

temperature, AC impedance was measured, followed by galvanostatic cycling at 0.2 mA/cm^2 for 2.5 h at room temperature. The results are presented in Figure XVI.27.6.

Figure XVI.27.6 (a) shows the cycling of all five Li sources. Initially there is a significant disparity in the Li deposition overpotential with the lowest resistance for the evaporated Li. From there the overpotential of the Li sources increases in the order of Supplier 4 < Supplier 3 < Supplier 1 < Supplier 2. After 8 cycles the resistances levels off a bit but have the same trends in overpotential. This matches with the total magnitude of the resistance measured in the electrochemical impedance spectroscopy (EIS) curves from 100 kHz to 0.1 Hz in Figure XVI.27.6 (b). The EIS curves also clearly show at least 2 semicircles consistent with the heterogenous surface layers demonstrated in XPS and IR characterizations.

In addition to the trends in overpotential, the commercial Li sources, all of which were rolled, have irregular plating and stripping profiles. Literature works point to the fact that these irregularities correspond to non-homogenous Li plating and stripping, and the formation of mossy Li and dead Li.² After 200+ hours of plating and stripping, the plating and stripping profiles of all but the Li from Supplier #2 have flat plating and stripping profiles with much lower resistance than the initial plating and stripping measurements. The evaporated Li still has the lowest resistance but followed closely by the Li from Supplier #4. The final three Li metal sources had very similar overpotentials, but while the deposition profiles for the Li from Suppliers #1&2 have flat deposition profiles, the Li from Supplier #3 had wide swings in the deposition overpotential that started to get worse with each cycle after about 150 hours of cycles. Notably, the Li from Supplier #3 was the only Li source that had a silicon signature in the surface layer.

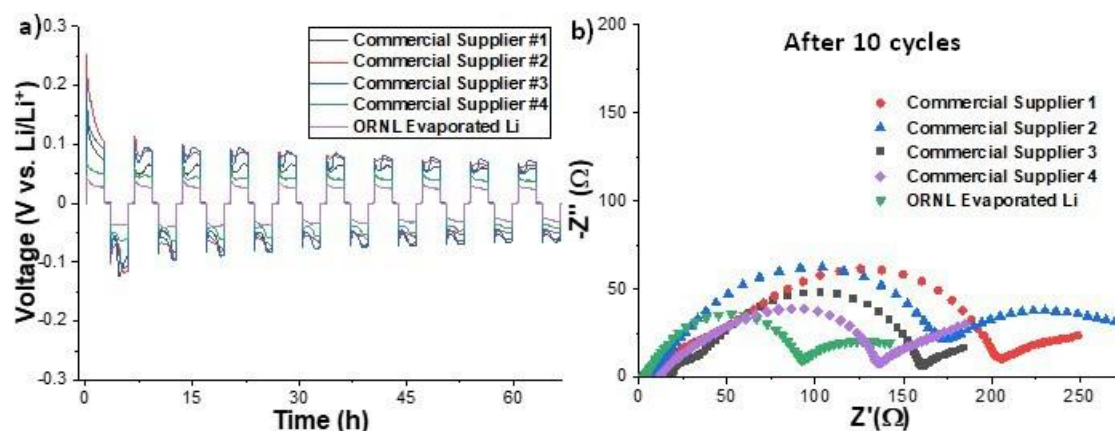


Figure XVI.27.6 a) plating and stripping data for symmetric Li/liquid electrolyte/Li cells at a current density of 0.2 mA/cm^2 for 2.5 hours per cycle. b) EIS data after 10 cycles.

Building on the Li cycling in liquid electrolytes, the project also performed symmetric testing with both standard polymer electrolytes and with sulfide based argyrodite solid electrolytes. Figure XVI.27.7 shows symmetric Li/electrolyte/Li cell cycling of the five different Li sources using a standard PEO-LiTFSI electrolyte tested at 0.1 mA/cm^2 for 10 hours (1 mAh/cm^2) at 70°C . The polymer electrolyte membrane was prepared by the solution casting method, where a 5 wt.% solution of linear PEO (M.W. 400,000) and LiTFSI salt (3:1 by weight) in acetonitrile was cast into a Teflon dish and ambient dried. The membrane is further heat dried ($50\text{--}60^\circ\text{C}$) under vacuum before transferring to a glove box for coin-cell assembly. The electrolyte used for all tests was made in the same batch. It is difficult to precisely control pressure in a coin cell format, however, the number of spacers per coin cell was adjusted to keep the total stack thickness roughly constant in order to account for the variation in thickness of lithium foils from various sources. Each source had different performance in the symmetric cell tests. The first key difference was the overpotential. For the most part the overpotential directly correlates with the thickness of the interphase as measured by XPS as can be seen in Figure XVI.27.7 (f). The films with the highest resistance were Suppliers 1&2 which both had thick distinct

Li_2CO_3 and Li_2O layers. These were followed by the Suppliers 2&3 which had a silicone based and organic based surface layers followed by thin Li_2O layers. The lowest resistance was for the evaporated Li metal which also had the thinnest interphase. The second key difference was in the capacity plated and stripped before failure. The best performance was from suppliers 3&4 which had the organic surface and thin interphase. The quickest sample to fail though was the ORNL evaporated Li which had the thinnest interphase. This discrepancy cannot be simply explained based on the chemistry of the surface by itself. It is possible that the microstructure of the Li metal itself also plays a key role in dictating the capacity plated before failure. Regardless in all cases, the cells failed before reaching 25 cycles or 25 mAh/cm^2 of cumulative capacity plated each direction. The dramatic difference in overpotential and subsequent failures also emphasizes the effect that Li source to source variation can have on performance even with nominally the same solid electrolyte.

In addition to developing a baseline with the standard PEO-LiTFSI electrolyte the program is also developing baselines for argyrodite ($\text{Li}_6\text{PS}_5\text{Cl}$) sulfide solid electrolytes (NEI corporation, 3-5 μm particle size) and LLZTO (Toshiba LLC.). Figure XVI.27.8 shows some initial results from the argyrodite solid electrolytes tested in symmetric Li/argyrodite/Li cells. In this case the cells used an argyrodite electrolyte powder that was directly compacted in a PEEK cell along with Li metal electrodes. For these cells the argyrodite powder separators were consolidated using pressure alone. The project compared two different Li sources, supplier #3 and our evaporated Li. The cells were tested at room temperature, at a current density of 0.1 mA/cm^2 for 10 hours under 5-6 MPa of pressure. Here one can see that the initial overpotential is virtually the same for both Li sources. This could be due to the high pressures being used. While the first cycle for both Li sources are almost the same, from the second cycle one can see a rapid rise in the resistance for the evaporated Li cell that gets worse each cycle. This voltage rise has been identified with voiding during stripping resulting in contact loss. This can be further confirmed as the overpotential during the rest period after cycling returns to 0V suggesting that there is still Li remaining at the surface. Notably, the mechanical nanoindentation data showed that the Li from Supplier #3 had on average a lower hardness at the small length scales compared to the evaporated Li metal. This is directly related to the ability of Li to self-diffuse relieving stress. This difference correlates with this rapid rise in voltage for the evaporated Li metal cells.

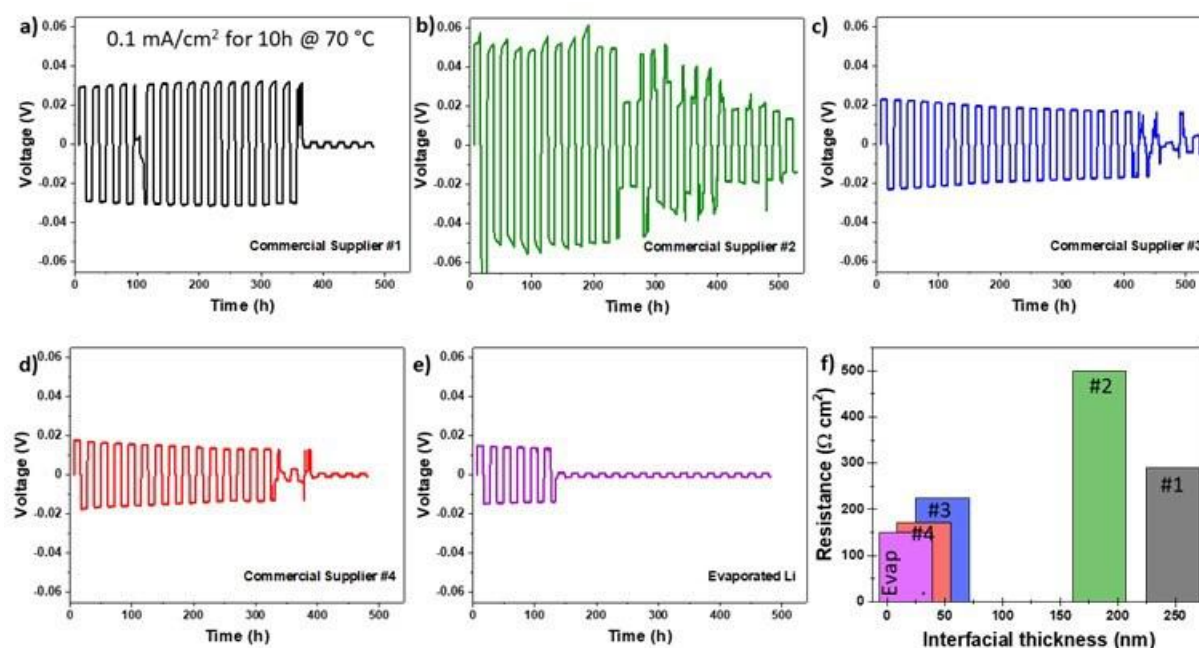


Figure XVI.27.7 Li/PEO-LiTFSI/Li symmetric cycling. All cells were cycled under the same conditions at 0.1 mA/cm^2 for 10 hours at 70°C . a) Commercial supplier #1, b) commercial supplier #2, c) commercial supplier #3, d) commercial supplier #4, and e) evaporated Li. f) A plot of the thickness of the estimated interface including the surface layer and distinct Li_2O layers (excluding the mixed Li_2O /Li metal layer) vs. the resistance determined from the plating overpotential.

Based on both the polymer, sulfide argyrodite, and liquid electrolytes it is clear that the Li source clearly plays a key role in determining the performance and ultimate failure. The data also suggests that while the overpotential is strongly influenced by the surface layers, the failure may also be significantly impacted by the microstructure or differences in the bulk Li metal.

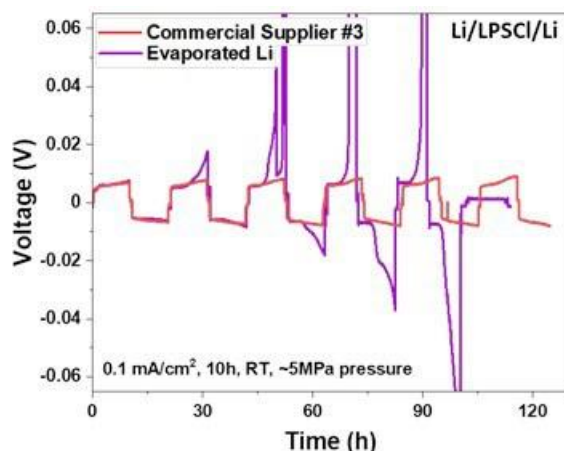


Figure XVI.27.8 Li/LPSCI Argyrodite (NEI)/Li test under 5MPa of pressure at room temperature at a current density of 0.1 mA/cm² for 10 hours. Red – Commercial supplier #3, Purple – Evaporated Li.

Conclusions

- The surface of Li metal strongly depends on the source. Different manufacturing process and storage processes dramatically impact the thickness and composition of the Li metal surface.
- The thickness and composition of the surface layer directly effects the interfacial resistance of Li metal in both liquid electrolytes and in solid polymer electrolytes.
- The failure mechanisms for solid electrolytes, while impacted by the surface, is not the only property of the Li metal that impacts the ultimate failure. Microstructure and its associated mechanics also appear to play a critical role in determining when Li filaments will penetrate solid electrolytes causing failure.

Key Publications

1. Tsai, W.-Y; Chen, X; Kalnaus, S. K.; Sahore, R.; Du, Z.; and Westover, A. S., “Li morphology evolution during initial cycles in a gel composite polymer electrolyte”, *ACS Appl. Energy Mater.* 2022, 5, 9, 11362–11369.

References

1. Herbert, E. G.; Hackney, S. A.; Thole, V.; Dudney, N. J.; Phani, P. S., Nanoindentation of high-purity vapor deposited lithium films: A mechanistic rationalization of diffusion-mediated flow. *Journal of Materials Research* 2018, 33 (10), 1347-1360.
2. Wood, K. N.; Noked, M.; Dasgupta, N. P., Lithium metal anodes: toward an improved understanding of coupled morphological, electrochemical, and mechanical behavior. *ACS Energy Letters* 2017, 2 (3), 664-672.

Acknowledgements

Key work in this project was performed by ORNL researchers Dr. Ritu Sahore, Dr. Erik Herbert, Dr. Sergiy Kalnaus, Dr. Wan-Yu Tsai, and Dr. Robert Sacci. The authors would also like to acknowledge the support and input of Dr. Nancy Dudney and Dr. Jagjit Nanda both former staff scientists at ORNL.

XVI.28 Lithium Halide-Based Superionic Solid Electrolytes and High Voltage Cathode Interfaces (ORNL)

Robert L. Sacci, Principal Investigator

Oak Ridge National Laboratory
P.O. Box 2008, MS6124
Oak Ridge, TN 37830
E-mail: saccirl@ornl.gov

Jagjit Nanda, Co-Principal Investigator

SLAC National Accelerator
2575 Sand Hill Rd
Menlo Park, CA 94025
E-mail: jnanda@slac.stanford.edu

Simon Thompson, DOE Technology Development Manager

U.S. Department of Energy
E-mail: Simon.Thompson@ee.doe.gov

Start Date: October 1, 2022

End Date: September 30, 2026

Project Funding (FY22): \$1,250,000

DOE share: \$1,250,000

Non-DOE share: \$0

Project Introduction

The realization of practical SSBs requires addressing several critical gaps in materials, synthesis, and processing, *simultaneously*. Advances in scalable processing of superionic solid electrolytes (SEs), stabilizing electrode-electrolyte interfaces and promoting long cycle life are all needed to meet the energy density and cost targets for next-generation batteries for electric vehicles. For SSBs to attain both high energy density and long cycle life, one of the most critical issues to solve is the electrolyte-cathode interface, where significant losses occur due to oxidative instabilities, poor wettability, and interfacial contact loss during cathode volumetric expansion. This problem is exacerbated in the case of high voltage cathodes, where the electrolyte instability leads to the formation of reactive interphase that could block lithium transport and increase area-specific resistance (ASR) between the cathode-SE.

Objectives

The project aims to develop low-temperature solution-based synthesis strategy for high ionic conducting halide-based solid electrolyte (SE) and to enable approaches to develop a scalable process for integrating halide-based SE within porous high-voltage Li-ion cathode matrix. The proposed tasks and metrics aim at addressing the long-term Vehicle Technologies Office goal for developing SSBs at ambient temperature with energy density in the range of 500 Wh/Kg and 1000 Wh/L for electric drive vehicles. We will demonstrate single-layer, pouch-cell SSB containing a thin halide SE separator coupled with high-voltage cathodes with 70% capacity retention over 300 cycles at 2 mA/cm² in an anode-free SSB configuration that can attain 1000 Wh/L in prototype cells. If successful then we will decrease the cost of SSB manufacturing while enabling high energy density cathode architectures.

Approach

The project employs a multifaceted approach: (1) conduct solution-based synthesis of the metal halide superionic conductor as the platform to enable robust cathode-electrolyte interface processing for SSBs, (2) infiltrate pore structures using solution-based processing that deposits high-conductivity SEs within cathode pores, and (3) facilitate lithium transport and improve stability using cation doping (divalent to introduce lithium vacancies, and lanthanum to prevent indium redox).

Our approach for the Years 1 and 2 aim at developing low-cost, solution-based synthesis routes to produce a halide class of superionic conductor belonging to Li_3MX_6 (where $\text{M} = \text{Sc}, \text{Y}, \text{La}, \text{Er}, \text{In}$, and $\text{X} = \text{Cl}, \text{Br}, \text{I}$) along with enabling electrochemical and structural characterization.

Results

To-Date Milestone overview:

1. Produce gram-scale quantities of Li_3InCl_6 SE using solvent-phase synthesis. (Completed)
2. Obtain phase-pure Li_3InCl_6 thin pellets with $\sim 1 \text{ mS/cm}^{-1}$ conductivity (Completed).
3. Utilize neutron diffraction, XPS, and Raman and electron microscopy to characterize Li_3InCl_6 SE (Completed)
4. Compare the structure and Li^+ conductivity of Li_3InCl_6 prepared through solvent-mediated vs. mechanochemical $>5\text{g}$ batch of with ionic conductivity in the range of 1 mS/cm^{-1} (Completed).

Our first goal was scaling up Li_3InCl_6 synthesis from two solvent systems: ethanol and water (Q1 and Q2 objectives). We weighed out stoichiometric amounts of InCl_3 and LiCl in a 1:3 ratio. We then dissolved this salt mixture in solvent, about 20 mL per 2 g for water or 50 mL per 2 g for alcohols. Solutions were sonicated while heating at 60°C for 1 h, before loading onto a rotovap for *in vacu* solvent removal. The rotovap bath was set to 50°C for 1 h then 80°C for an additional hour. The resulting clear/colorless syrup was then placed in a 10^{-4} torr vacuum over at 80°C overnight. The material was then brought into an Ar-filled glovebox and loaded into a vacuum tube furnace and heated at 150°C for 4 hours (ramp rate was 2°C/min) and naturally cooled to room temperature. Conductivity was measured on a 10 MPa cold pressed pellet using a SP240 Biologic potentiostat.

The largest product yield to date is 11 g at 97% yield and was only limited by the rotovap flask volume. At the beginning our major impurity was LiCl ; in fact, this impurity tends to plague some batches. We found that adding 10% stoichiometric excess of InCl_3 drastically reduces LiCl impurity level. However, this appeared initially to come at the cost of conductivity. The best room temperature conductivity to date is 0.1 mS cm^{-1} . The addition of excess InCl_3 increases the apparent grain boundary resistance. Our working hypothesis is that the excess InCl_3 fills in occupancies within the structure, which is a layered structure that houses Li within the galleries. Because all the In sites are at full occupancy, pressing a pellet introduces anisotropic effects on conductivity. Our next step is to test this hypothesis by combining high resolution XRD with pressure-resolved impedance spectroscopy on pellets. From this we should be able to relate excess indium loading with In site occupancies/anisotropic strain with ionic conductivity.

After successfully scaling up the synthesis of Li_3InCl_6 in two solvent systems: ethanol and water we turned to improving the time it takes to synthesize large batches of Li_3InCl_6 is on the order of 3 hours, with the rate limiting step being removal of bulk solvent. Before, LiCl was the major impurity and was present in 0-5% by mass (estimated via XRD). We found that synthesis from ethanol produced greater LiCl impurities and were less consistent. To probe this fact, we systematically increased the amount of InCl_3 from 0% excess to 20%. We found that 10% excess of InCl_3 was enough to force the reaction to completion (see Figure XVI.28.1). This systematic increase was also done for synthesizing from H_2O . The XRD showed little change as synthesis from H_2O is robust, producing pure product with little art required. However, the ionic conductivity increased with the addition of 10 and 20% excess InCl_3 . This is different from the ethanol-derived sample where we see a *decrease* in overall conductivity. This decrease seems to come from grain boundary issues. In conclusion, the addition of rare earth improves synthesis purity and may improve overall ionic conductivity.

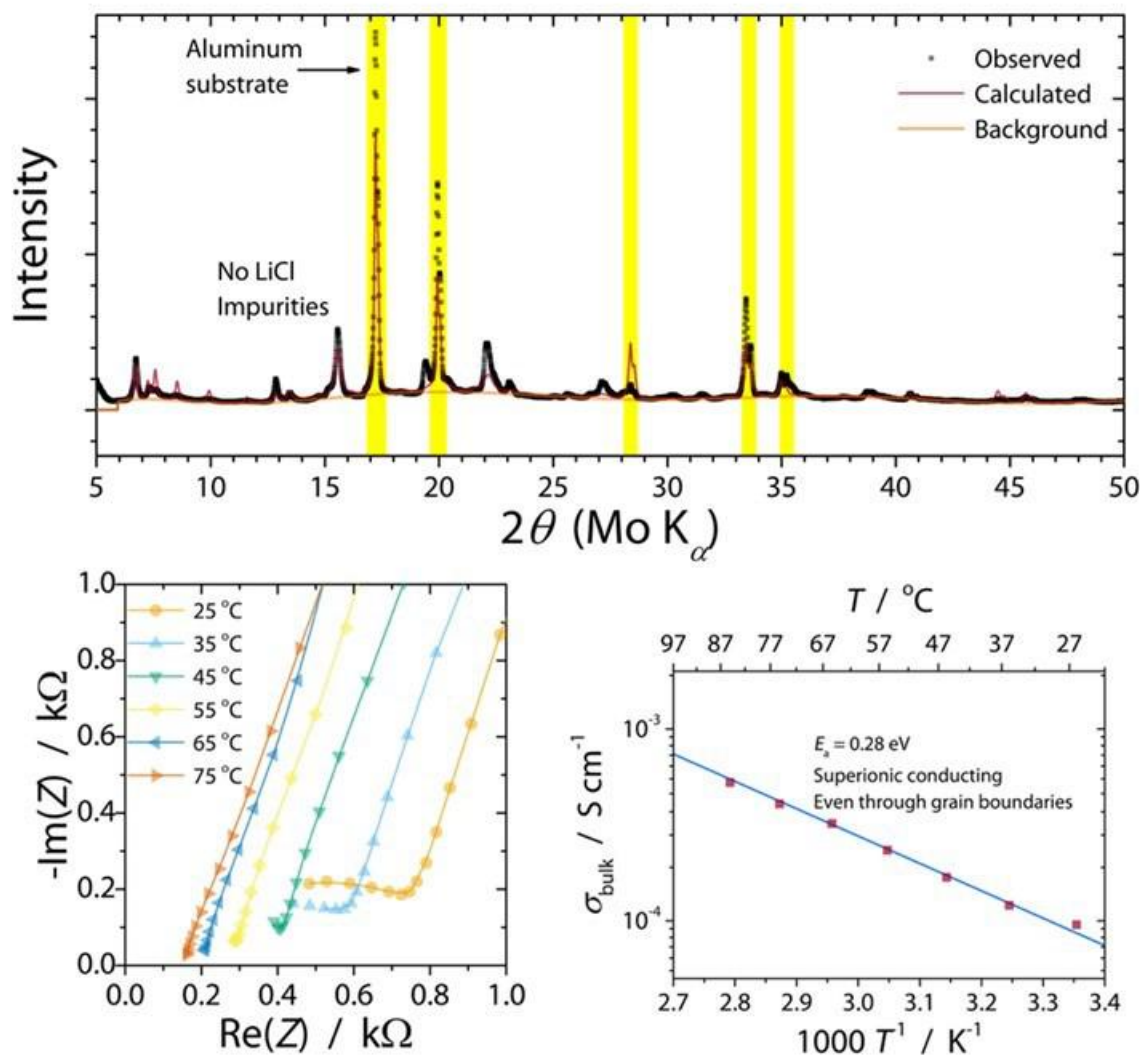


Figure XVI.28.1 Results of the large scale Li_3InCl_6 synthesis with 10% excess InCl_3 from Ethanol solution. Top: XRD shows no impurities other than Al substrate. Bottom left: Nyquist plot shows electrolyte is highly conductivity with some grain boundaries present after pressing at 5 MPa. Bottom right: Arrhenius plot shows product is a superionic conductor with low activation energy.

The suggestion above is further supported by the results from the mechanical synthesis route (Figure XVI.28.2). We systematically adjusted the amount of excess InCl_3 from 0 to 20%. We milled the precursors for 16 h in a planetary mill. The milling was enough to obtain near phase pure product though the XRD shows very broad diffraction peaks suggesting the product is nanocrystalline or highly defective/disordered. The conductivity was found to be high, 0.25 mS cm^{-1} at room temperature with energy of activation being 0.32 eV . Annealing at 150°C for 5 h improved the ambient ionic conductivity, 0.40 mS cm^{-1} with 0.30 eV . These results are in line with H_2O -based synthesis and therefore different from ethanol-based. This supports the idea that the Li_3InCl_6 , synthesized from ethanol is different. Although this difference may just be surface level, this is the very region that results in grain boundaries and impedes overall ion transport. In conclusion, mechanical and H_2O -based synthesis have little grain boundary resistances while Ethanol-based had significantly more, suggesting surface termination difference.

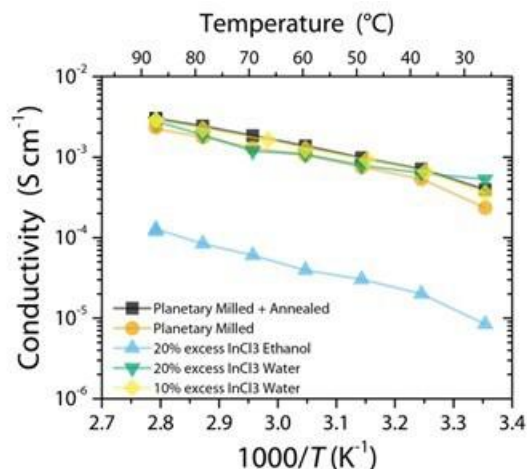


Figure XVI.28.2 Arrhenius plot of overall conductivity of Li_3InCl_6 as a function of different synthesis methods and Li_3InCl_6 excess amounts.

We tested the hypothesis that the excess InCl_3 fills in occupancies within the structure, which is a layered structure that houses Li within the galleries (Figure XVI.28.3). This means that the material becomes a more layered-like structure with increased InCl_3 and therefore the application of pressure (to make a device) may induce some anisotropic effects on conductivity. We conducted a pressure-resolved measurement and show that the conductivity increases with pressure until ~ 33 MPA. After this the conductivity decreases substantially. When the pressure is released back to the starting value the conductivity slowly improves. This suggests that high pressure induces some change to the bulk material, either aligning it or chemically changing it. This is important information to know when we start making full-cell devices in years 3-4. We can now expect that while high pressures may improve cathode-electrolyte adhesion, they will affect bulk properties, perhaps negatively. In conclusion, excessive pressure induces structural or bulk alignment changes in bulk Li_3InCl_6 that results in decreased overall conductivity (increased grain boundary resistivity).

We have made our first Li_3InCl_6 infiltrated membrane, pictured below in Figure XVI.28.4. We tried infiltrating commercial polypropylene (Celgard); however, neither H_2O nor Ethanol solutions wet the material and therefore do not penetrate. That said, it does appear visually that a thin yet inhomogeneous Li_3InCl_6 layer can be deposited atop this membrane. The successful infiltration occurred when we used a highly porous polyaramid membrane (Dreamweaver Gold). The Li_3InCl_6 coats the fibers from ethanol very well. We are in the process of pressing these membranes and taking conductivity measurements. We speculate membranes with porosity of $>70\%$ and little-to-no micropores is required for successful infiltration and electrolyte synthesis in this form factor. Figure XVI.28.4 shows that the Li_3InCl_6 -coated separator becomes more textured and contains a large number of small sparkling deposits. That said, the loading for this sample was poor and the resulting conductivity neigh nonexistent. We are progressing by using dip casting into hot (80°C solutions) as we believe that the poor loading is due to using overly dilute solutions.

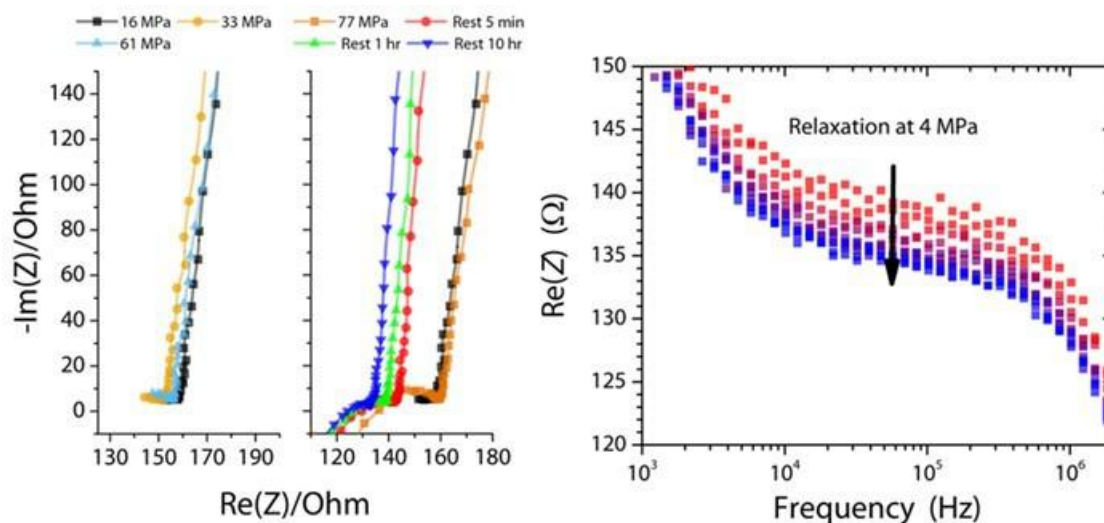


Figure XVI.28.3 Nyquist plot (left) and Bode plot (right) showing pressure induced effects of Li_3InCl_6 conductivity.

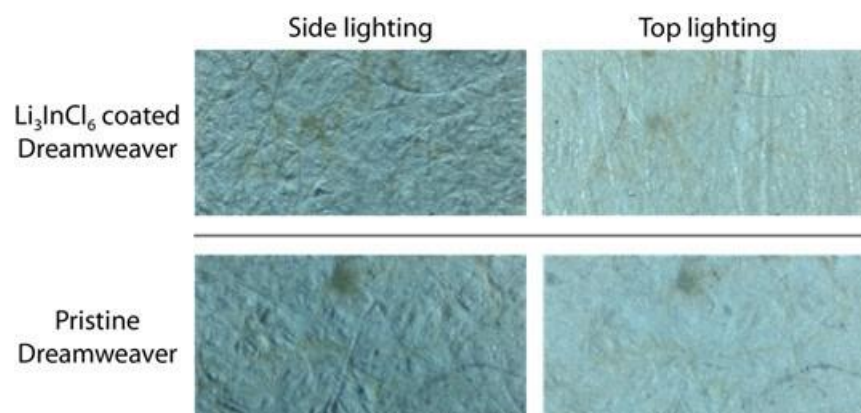


Figure XVI.28.4 Optical micrographs of Dreamweaver Gold porous membranes before and after Li_3InCl_6 infiltration from ethanol solution precursor.

We have been successful in using neutron scattering to probe the difference between H_2O -mediated synthesis and ethanol-mediated synthesis of Li_3InCl_6 . Figure XVI.28.5 shows that ethanol-mediated synthesis occurs differently than H_2O -mediation. Here, we see that upon a base drying at 60°C , LiCl and InCl_3 are seen along with a third unknown phase. Heating this solution to near 100°C shows that the InCl_3 and the unknown phase drop out, and is replaced by an intermediate phase. The presence of LiCl does not change though, the peaks corresponding to LiCl does decrease by 20%. Heating to 120°C , shows that the Li_3InCl_6 product forms along with further decrease in LiCl signals. At 150°C phase pure product is achieved. For H_2O (reported in [1]), there was two intermediate phases and there was no detection of LiCl . This suggests that for ethanol-synthesized samples, LiCl may exist in trace amounts or be more descriptive of the grain boundaries. This key difference led us to investigate how Li_3InCl_6 synthesized from ethanol evolved during full cell cycling.

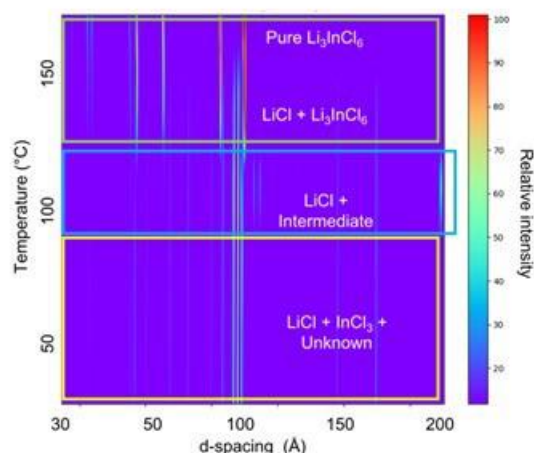


Figure XVI.28.5 *In situ* neutron diffraction of Li_3InCl_6 being synthesized from ethanol solution.

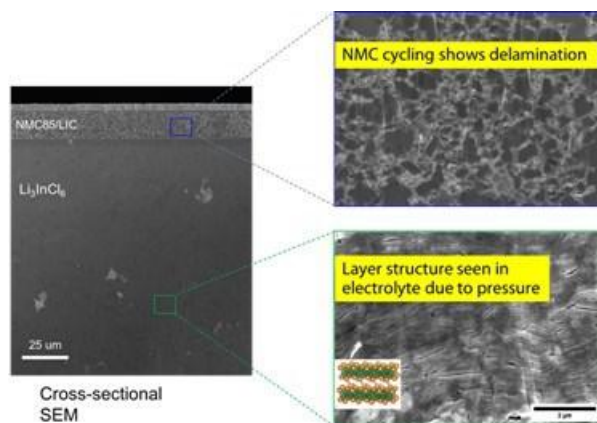


Figure XVI.28.6 Scanning electron micrograph (SEM) cross-sections of a Li-In alloy/NMC85 full cell that uses ethanol-derived Li_3InCl_6 as the bulk solid electrolyte and the electrolyte within the cathode. After 50 cycles we see extensive delamination in both the cathode- Li_3InCl_6 composite and also the bulk Li_3InCl_6 itself.

Yan Yao's group at the University of Houston have been testing the full cell cycling stability of the Li_3InCl_6 solid electrolytes. Thus far, the material has been used to access 170 mAh of the NMC85's 220 mAh theoretical capacity during the first cycle; however, the capacity rapidly decays. These cells were pressurized at 5 MPa, which is significantly lower than literature reports of 200 MPa. Figure XVI.28.6 reveals the likely cause capacity fade is the solid electrolyte delaminating from the NMC cathode. We can see that the grains become readily distinguishable in the SEM and voids can be seen. Interestingly, in the bulk we see similar delamination and void formation. It appears, therefore, that pressure and/or cycling induces large scale relaxations. We also saw in the previous quarter that grain boundary impedance is highest in ethanol synthesized products. Putting all this together, it seems that ethanol-synthesized samples may contain trace LiCl that may collect at gains. These nano sized LiCl domains affect cycling performances by leading to more and more delamination that cannot be overcome by mere addition of pressure.

We have concluded that while alcohol-based synthesis is indeed faster and can occur at lower temperatures, LiCl forms during ethanol drying and then reacts with an intermediate phase. This means that trace LiCl may remain after heating to 150°C. We will test the overall performance of these materials after annealing at 200°C to see if they are more robust.

Conclusions

1. We confirmed that aqueous synthesis of Li_3InCl_6 is robust, supplying reproducible products at large scale. We found that while alcohol-based synthesis methods result in fairly pure products, LiCl remains the principal form of impurity. That said, this impurity does not affect lattice conductivity, rather it seems to adversely affect the grain boundary resistance
2. There is little difference between mechanochemical synthesized product and the aqueous phase. Annealing the mechanochemical synthesized product does increase the grain boundary resistance. This suggests that the as-milled powder could be cold pressed in a roll-to-roll processing stream.
3. Grain boundary effects on ionic conductivity is affected by pressure and Li_3InCl_6 delaminates after extensive cell cycling. We confirmed that the processing and perhaps final annealing of the solid electrolyte plays a major role in device performance.

For year 2 we will focus on Li_3YCl_6 and testing compatibility with low to zero strain cathodes and continue in developing thin films less than 100- μm thick.

Key Publications

Invited Talk

1. Robert Sacci and Jagjit Nanda, Substituted Argyrodites and halide-based solid electrolytes for all solid-state batteries, ACS Fall 2022, Chicago IL

References

1. Sacci, R.L.; Bennett, T.H.; Drews, A.R.; Anandan, V.; Kirkham, M.J.; Daemen, L.L.; Nanda, J., *J. Mater. Chem. A*, 2021, **9**, 990-996

Acknowledgements

These researchers provided important insights and assistance with the programs: Teerth Brahmabhatt, Bredesen Center, University of Tennessee, Knoxville, Prof. Yan Yao and Liqun Guo, University of Houston.

XVI.29 Polyester-Based Block Copolymer Electrolytes for Lithium-Metal Batteries (UCB)

Dr. Nitash P. Balsara, Principal Investigator

Department of Chemical and Biomolecular Engineering
University of California, Berkeley
Berkeley, CA 94720
E-mail: nbalsara@berkeley.edu

Tien Duong, DOE Technology Development Manager

U.S. Department of Energy
E-mail: Tien.Duong@ee.doe.gov

Start Date: October 1, 2021

End Date: September 30, 2022

Project Funding (FY22): \$400,000

DOE share: \$400,000

Non-DOE share: \$0

Project Introduction

Polymer electrolytes (PEs) offer increased stability in lithium batteries in comparison to more widely used liquid electrolytes (LEs). Block copolymer-based electrolytes containing both soft, ion-conducting domains and rigid, nonconducting domains offer the opportunity to tune both mechanical and electrical properties separately. Most block copolymer electrolytes studied thus far comprise PEO as the conducting domain. The team hopes to develop polyester-based electrolytes that exhibit much higher transport properties and limiting currents than PEO-based electrolytes. An all-solid full cell with this new block copolymer electrolyte, a Li-metal anode, and an NMC cathode will have much higher energy density than current Li-ion technology.

Objectives

The project objective is to design and synthesize polyester based block copolymer electrolytes that can enable full-cell cycling at 1 mA/cm² or greater for 300 cycles. The cell comprises Li-metal anode, 4.5 V NMC cathode, and thin separators (20-50 μ m) casted from the aforementioned block copolymer.

Approach

The team will begin by synthesizing several series of polyester homopolymers and fully characterizing their blends with lithium salts as PEs in Li-Li symmetric cells. Next, they will make block copolymer electrolytes based on the most promising homopolymer candidate and measure the electrochemical and mechanical properties thoroughly. Finally, they will assemble full cells with the optimum block copolymer electrolytes together with lithium metal and a 4.5 V NMC cathode.

Results

New Project: Design and synthesis of new polyester-based electrolytes

We developed a general and efficient synthesis platform to make polyesters. Several poly(alkylene malonates) were synthesized through condensation polymerization of dimethyl malonate and the corresponding diol, as shown in Figure XVI.29.1 (Scheme 1). Ethylene glycol, 1,3-propanediol, 1,5-pentanediol, and 1,6-hexanediol were employed individually to make poly(ethylene malonate) (PEM), poly(trimethylene malonate) (PTM), poly(pentylene malonate) (PPM), and poly(hexylene malonate) (PHM). Heat and vacuum are employed for complete condensation but different conditions are required for each monomer. For PPM and PHM, transesterification catalyst Ti(OiPr)₄ was used to aid polycondensation reaction at a lower temperature. Molecular weights of these polymers were in the range of 4–10 kDa based on the end group analyses of their ¹H NMR spectra. Gel permeation chromatography (GPC) revealed the polydispersity to be around 2 by virtue of condensation polymerization. Differential scanning calorimetry (DSC) shows that all these polymers are amorphous and the glass transition temperature (*T*_g) value decreases with increasing chain length of diol (*n*). Very high -OH end group functionality (>95%) is observed in PPM. This feature allows us to functionalize the

chain ends and make block copolymers in the future. More recently, we are able to make PPM with a molecular weight as high as 35 kDa.

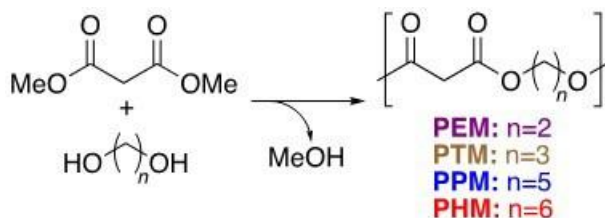


Figure XVI.29.1 Scheme 1. Synthetic scheme and nomenclature of polyesters made for this project.

All four polyesters form soluble complex with lithium bis(trifluoromethanesulfonyl)imide (LiTFSI) salt. Blends of 40 wt% LiTFSI and 60 wt% polymer are amorphous. Their T_g values increased compared to homopolymers. The physical properties of these four polymers and blends are summarized in Table XVI.29.1. We then examined the T_g of PPM/LiTFSI electrolytes under a wide range of salt concentrations. In Figure XVI.29.2, we are showing a comparison of T_g data with PEO. While T_g of PEO/LiTFSI blends has a nonmonotonic dependence on salt concentration (r), T_g of PPM/LiTFSI blends increase linearly with increasing r . Moreover, all PPM/LiTFSI blends are fully amorphous. These thermodynamic studies show great promise of these polyester/LiTFSI blends to be electrolytes in lithium batteries.

Table XVI.29.1 Structural characterization of polyesters made for the current project

Name	Mn (kg mol ⁻¹)	\bar{D}	Tg of pure polymer (°C)	Tm of pure polymer (°C)	Tg of electrolyte (°C)
PEM	3.7	2	-20	NA	0
PTM	10.3	2	-35	NA	-10
PPM	9.6	2	-50	NA	-20
PHM	5.8	2	-60	NA	-25

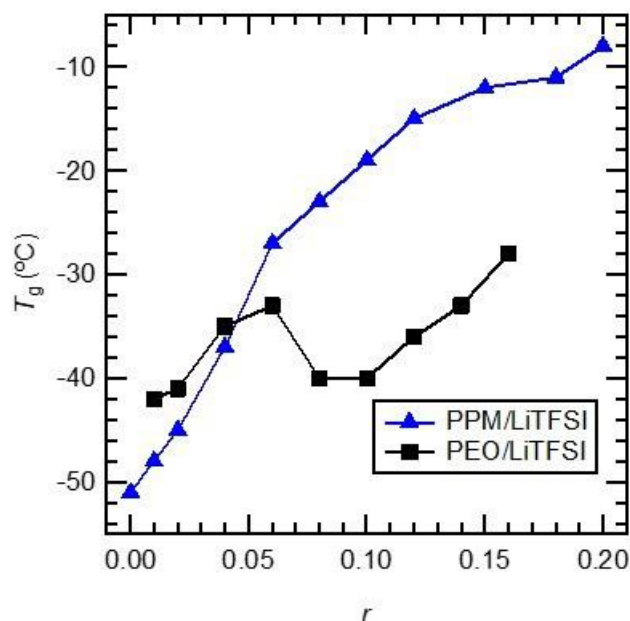


Figure XVI.29.2 Effect of salt concentration (r) on the T_g of PPM/LiTFSI and PEO/LiTFSI electrolytes.

Conductivity measurements of the polyester electrolytes

Once the polyester synthesis method was standardized, we measured the conductivity of electrolytes based on all four polymers. The structures of the four polymers are shown in Figure XVI.29.3a. We made four polymer electrolytes comprising 40 wt% of lithium bis(trifluoromethanesulfonyl)imide (LiTFSI) salt and 60 wt% of each polymer. We define salt concentration as $r = [\text{Li}]/[\text{O}]$, where all the oxygen atoms in the polymer are counted (a total of four in every repeating unit in Figure XVI.29.3a). Due to the difference in molecular formula of these polymers, r falls between 0.07–0.11. The well-studied PEO/LiTFSI system exhibits a broad maximum in conductivity in this range of r values.¹ In Figure XVI.29.3b, we show ionic conductivity (κ) values of these electrolytes measured in lithium-polymer-lithium symmetric cells at 90°C, along with their glass transition temperature (T_g) values. Ionic conductivity increases drastically with the increasing chain length of diol until $n = 5$. This is expected because ion transport is usually facilitated by low T_g polymers. PPM/LiTFSI electrolyte almost has an order of magnitude higher conductivity than the PEM/LiTFSI electrolyte, reaching 10^{-3} S/cm at 90°C. This is comparable with PEO/LiTFSI electrolytes reported in literature.¹ The ionic conductivity decreased when n was increased from 5 to 6. This preliminary screening suggests that PPM/LiTFSI electrolyte has the optimum ionic conductivity among this series of polyester-based electrolytes.

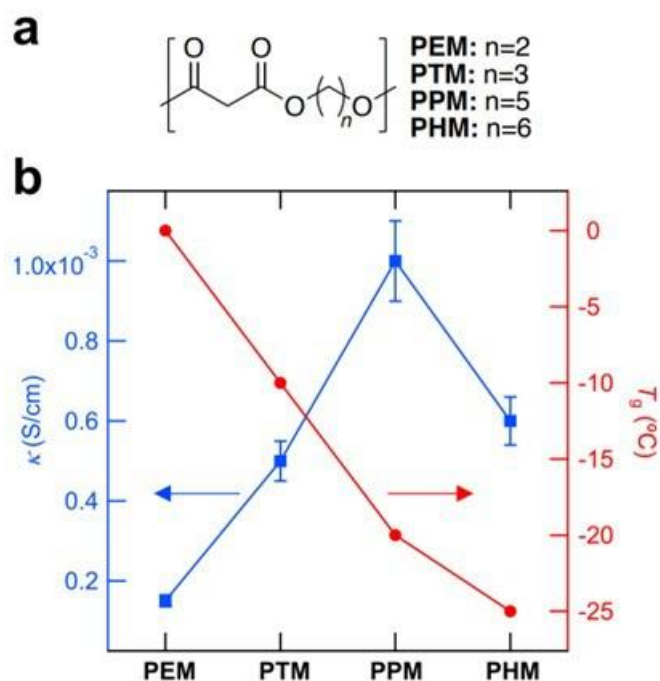


Figure XVI.29.3 a) Structures of a series of poly(alkyl malonates) synthesized for this project. b) Ionic conductivity (κ) (blue squares) and glass transition temperature (T_g) (red circles) of polymer electrolytes comprising 40 wt% of LiTFSI salt at 90°C.

The effect of salt concentration (r) on κ of PPM/LiTFSI electrolytes is shown in Figure XVI.29.4. Also shown in this figure are values of the same parameters for PEO/LiTFSI electrolytes as reported in literature.¹ The conductivity of PPM/LiTFSI electrolytes in the range $0.02 \leq r \leq 0.10$ is about 10^{-3} S/cm. These values are close to the conductivity of PEO/LiTFSI electrolytes. In the range $0.10 \leq r \leq 0.20$, κ of PPM/LiTFSI electrolytes drifts towards values that are significantly lower than PEO/LiTFSI electrolytes.

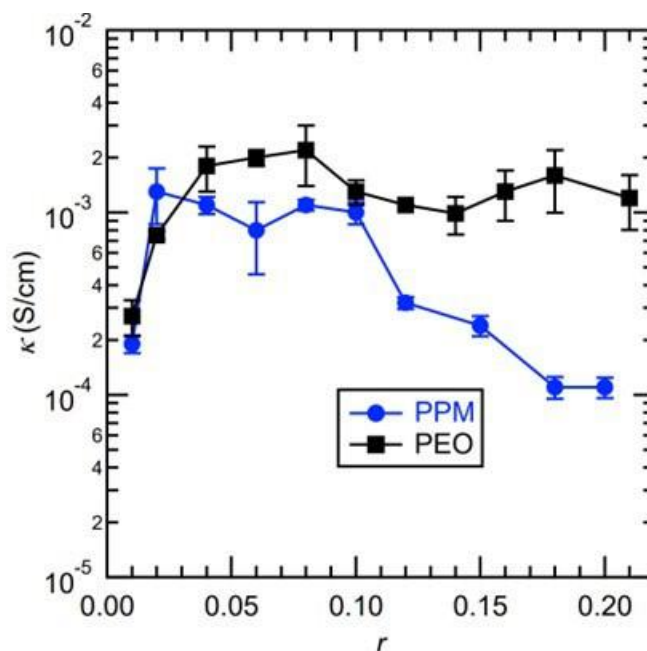


Figure XVI.29.4 The effect of salt concentration r on ionic conductivity, κ , of PPM/LiTFSI (blue circles) and PEO/LiTFSI (black squares) electrolytes at 90°C. Data for PEO/LiTFSI electrolytes were taken from previous work.¹

Symmetric cell characterization

We first examined the effect of polymer structure on the current fraction of different polyester electrolytes. The structures of the four polyesters, poly(alkyl malonates), are shown in Figure XVI.29.5a. We made four polymer electrolytes comprising 40 wt% of lithium bis(trifluoromethanesulfonyl)imide (LiTFSI) salt and 60 wt% of each polymer. We define salt concentration as $r = [\text{Li}]/[\text{O}]$, where all the oxygen atoms in the polymer are counted (a total of four in every repeating unit in Figure XVI.29.5a). Due to the difference in molecular formula of these polymers, r falls between 0.07–0.11. The well-studied PEO/LiTFSI system exhibits a broad maximum in electrolyte efficacy in this range of r values.¹

The symmetric cells were assembled by placing the electrolytes within silicon spacer with an inner hole diameter of 3.175 mm and 254 μm thickness. It was then sandwiched between nickel backed lithium electrodes. Finally, it was attached with nickel current collector and sealed within a pouch material. In Figure XVI.29.5b, we show current fraction (ρ_+) values of these electrolytes measured in lithium-polymer-lithium symmetric cells at 90°C. We observed very high current fraction values (around 0.6) for all four polyester electrolytes. This is about six-fold of the current fraction of PEO/LiTFSI electrolyte (less than 0.1). From our study on conductivity we know that PPM/LiTFSI has the best conductivity among the four polyester electrolytes. Thus, we decide to focus on PPM/LiTFSI for the rest of our study.

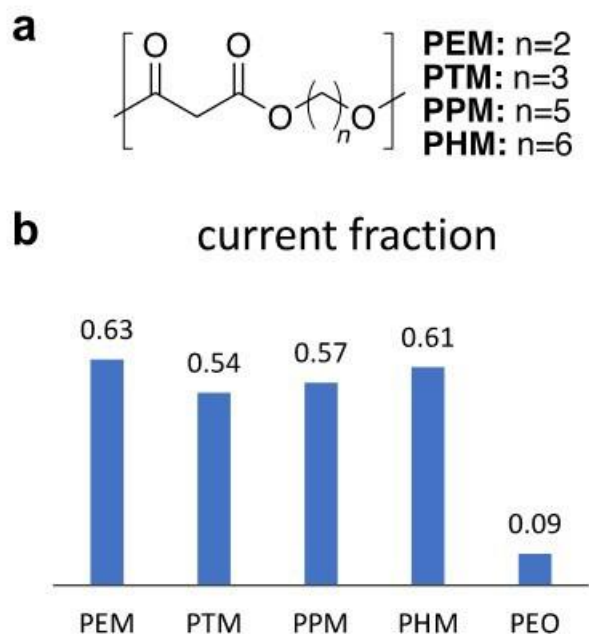


Figure XVI.29.5 a) Structures of a series of poly(alkyl malonates) synthesized for this project. b) current fraction of polymer electrolytes comprising 40 wt% of LiTFSI salt at 90°C. PEO stands for benchmark poly(ethylene oxide).

The effect of salt concentration (r) on the current fraction (ρ_+) and electrolyte efficacy ($\kappa\rho_+$) of PPM/LiTFSI electrolytes is shown in Figure XVI.29.6. Also shown in this figure are values of the same parameters for PEO/LiTFSI electrolytes as reported in literature.¹ The ρ_+ values of all PPM/LiTFSI electrolytes are all about 0.6 in the range $0.01 \leq r \leq 0.15$, while the ρ_+ values of PEO/LiTFSI decrease from 0.18 to 0.07 with increasing r from 0.01 to 0.14. The $\kappa\rho_+$ value of PPM/LiTFSI electrolytes are higher than PEO/LiTFSI electrolytes across all salt concentrations, with a maximum of 3×10^{-4} S/cm at $r = 0.06$. This is about 50% higher than the best efficacy of PEO/LiTFSI electrolyte observed at $r = 0.08$.

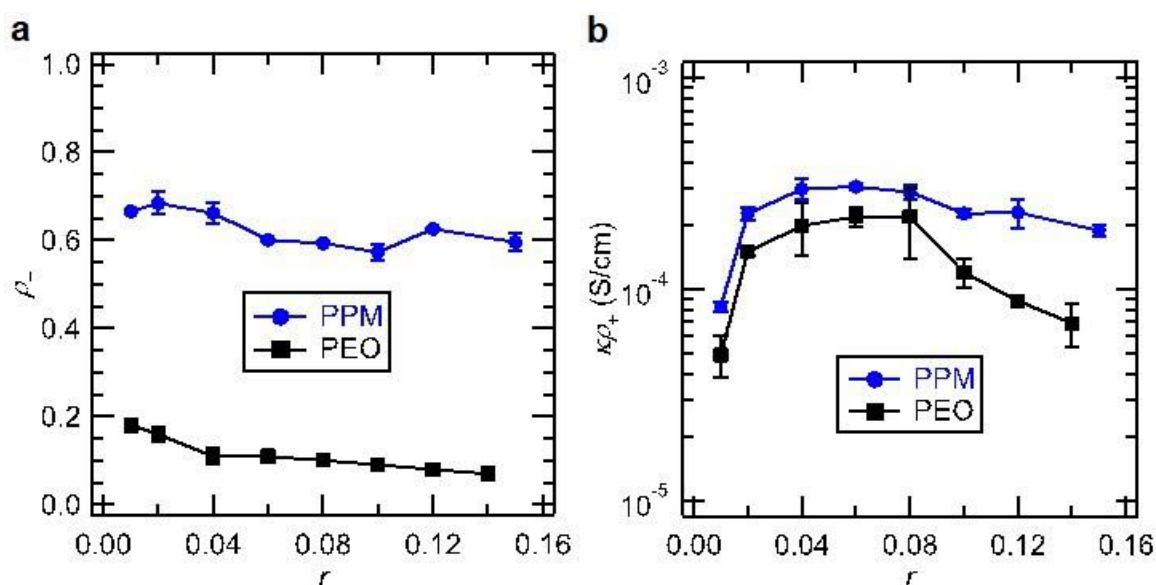


Figure XVI.29.6 The effect of salt concentration r on a) current fraction, ρ_+ , b) electrolyte efficacy, $\kappa\rho_+$, of PPM/LiTFSI (blue circles) and PEO/LiTFSI (black squares) electrolytes at 90°C. Data for PEO/LiTFSI electrolytes were taken from previous work.¹

We further examined the effect of salt concentration (r) on the salt diffusion coefficient (D) of PPM/LiTFSI electrolytes is shown in Figure XVI.29.7. The D values of all PPM/LiTFSI electrolytes are near 10^{-7} cm²/s, the same magnitude as PEO/LiTFSI electrolytes.

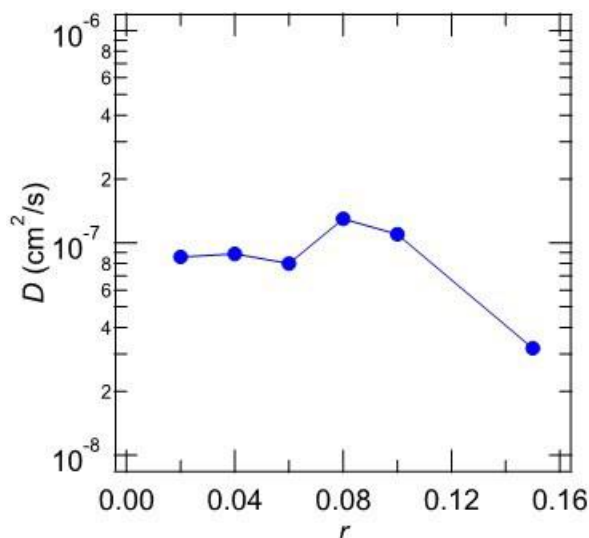


Figure XVI.29.7 The effect of salt concentration r on salt diffusion coefficient, D , of PPM/LiTFSI (blue circles) electrolytes at 90°C.

The concentration cell was prepared by creating a channel of (4 cm X 1.5 mm) dimensions in a 250 μ m thick silicone spacer. Half of the channel was filled by electrolyte of reference salt concentration ($r = 0.08$) whereas the other half was filled by electrolytes of different salt concentrations, r . Nickel backed lithium electrodes were placed at the two sides of the channels and the assembly was vacuum sealed. The cells were annealed at 90°C for 24 h before the cell potential, U , was recorded. Experiments were repeated with 3-4 different cells at each salt concentration to ensure the reproducibility. (See Figure XVI.29.8.)

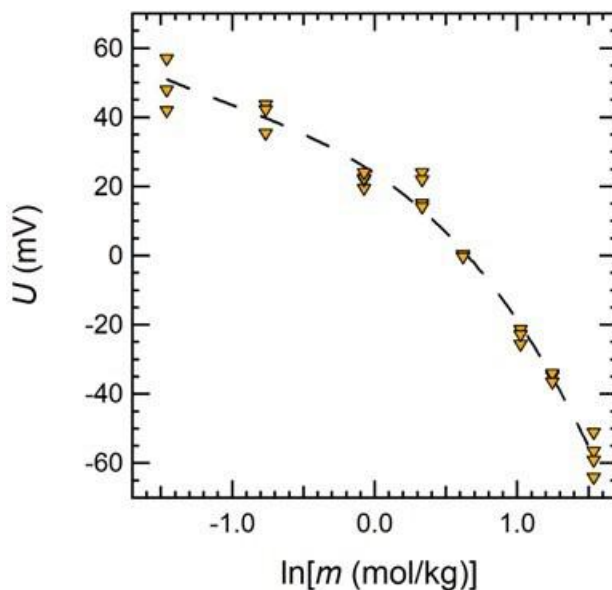


Figure XVI.29.8 Concentration cell open-circuit potential (U) as a function of natural log molality ($\ln[m]$) at 90°C. The fit is shown in dashed line. Three data points at each salt concentration represents reproducibility of the data.

Finally, oxidative stability of the PPM electrolytes was compared against PEO electrolytes using linear sweep voltammetry technique in a lithium / polymer ($r = 0.02$) / stainless steel cell. Figure XVI.29.9 shows that PEO based electrolyte gave rise to oxidation currents above 0.01 mA/cm^2 in the $3.5 - 5 \text{ V}$ window, whereas, the PPM electrolyte exhibited current densities below 0.01 mA/cm^2 in the $3.5 - 5 \text{ V}$ window. Thus, PPM exhibits higher oxidation current than PEO electrolyte.

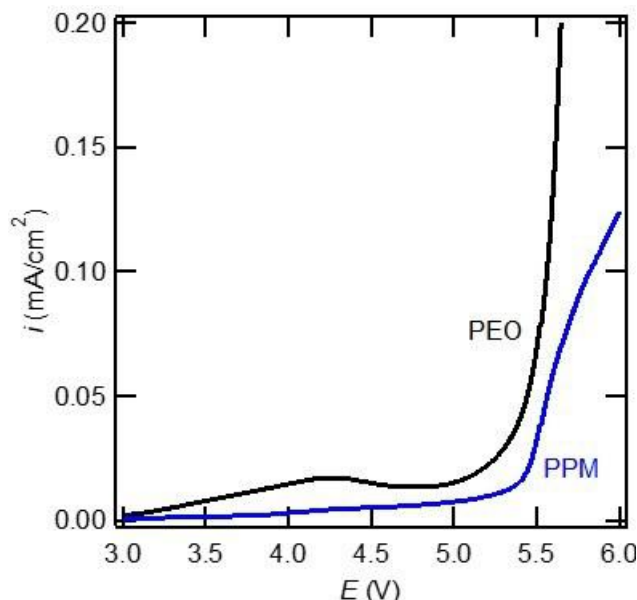


Figure XVI.29.9 Linear sweep voltammetry (3–6 V vs Li^+/Li) of PPM and PEO electrolytes at 90°C . The scanning rate is 1 mV/s .

The efficacy of PPM polymer to conduct sodium metal ion is tested by making electrolyte of PPM/NaTFSI at $r = 0.06$ ($r = [\text{Na}^+]/[\text{O}]$). Figure XVI.29.10 represents the chronopotentiometry data of sodium / polymer ($r = 0.06$) / sodium cells at a current density of 0.125 mA/cm^2 . The inset represents the impedance spectra before and after the polarization. Based on the experiment the conductivity (κ) and current fraction (ρ_+) of the electrolyte is $\kappa = 6 \times 10^{-4} \text{ S/cm}$ and $\rho_+ = 0.54$ at 80°C and the electrolyte was found to be stable against sodium metal electrodes.

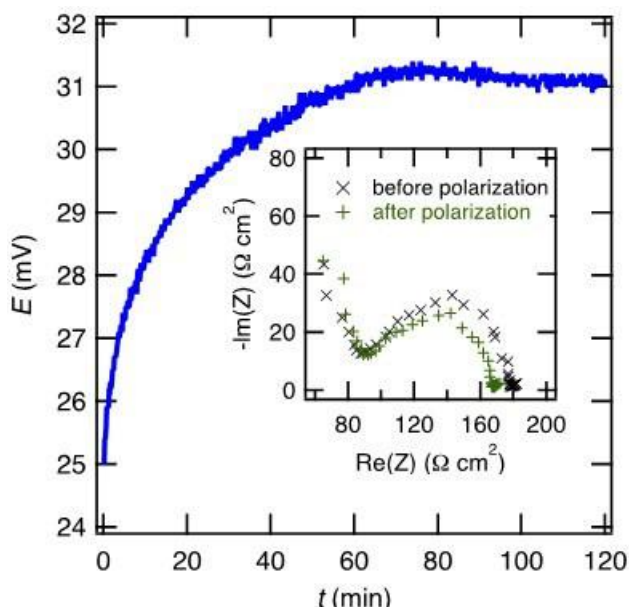


Figure XVI.29.10 Chronopotentiometry curve of a sodium/polymer/sodium symmetric cell with a PPM/NaTFSI electrolyte at $r = 0.06$, under a current density of 0.125 mA/cm^2 at 80°C . The inset is the normalized Nyquist plot before and after polarization.

Conclusions

In the present research, the efficiency of new polyester-based electrolyte against lithium metal has been investigated. The major conclusions are summarized below

- A variety of polyester based electrolytes of varying chain lengths were successfully designed and synthesized. Among various polyesters, poly(pentyl malonate) (PPM) exhibited highest conductivity and current fraction value
- The conductivity of PPM electrolytes is similar to PEO electrolytes however PPM exhibit almost 50% higher current fraction value. Therefore, the effective conductivity of PPM is higher than PEO making it a better electrolyte
- PPM also exhibited higher oxidative stability than PEO electrolytes
- The polymer could also act as a promising candidate for sodium ion battery.

Key Publications

1. Chakraborty, S.; Sethi, G. K.; Frenck, L.; Ho, A. S.; Villaluenga, I.; Wantanabe, H.; Balsara, N. P. Effect of Yield Stress on Stability of Block Copolymer Electrolytes against Lithium Metal Electrodes. *ACS Appl. Energy Mater.* **2021**, *5*, 852
2. Yu, X.; Hoffman, Z. J.; Lee, J.; Fang, C.; Gido, L. A.; Patel, V.; Eitouni, H. B.; Wang, R.; Balsara, N. P. A Practical Polymer Electrolyte for Lithium and Sodium Batteries: Poly(pentyl malonate). *ACS Energy Lett.* **2022**, *7*, 3791–3797.

References

1. Pesko, D. M.; Feng, Z. G.; Sawhney, S.; Newman, J.; Srinivasan, V.; Balsara, N. P. Comparing Cycling Characteristics of Symmetric Lithium-Polymer-Lithium Cells with Theoretical Predictions. *J. Electrochem. Soc.* **2018**, *165*, A3186–A3194.

Acknowledgements

The Principal Investigator acknowledges the important contributions of the students and post-docs supported by the BMR program, Saheli Chakraborty, Gumi Sethi, Xiaopeng Yu, Vivaan Patel and Lilly Gido.

XVI.30 Development of All Solid-State Battery using Anti-Perovskite Electrolytes (ANL)

Zonghai Chen, Principal Investigator

Argonne National Laboratory
9700 South Cass Avenue
Lemont, IL, 60439
E-mail: Zonghai.chen@anl.gov

Tao Li, Co-Principal Investigator

Argonne National Laboratory
9700 South Cass Avenue
Lemont, IL, 60439
E-mail: taoli@anl.gov

Simon Thompson, DOE Technology Development Manager

U.S. Department of Energy
E-mail: Simon.Thompson@ee.doe.gov

Start Date: October 1, 2021

End Date: September 30, 2026

Project Funding (FY22): \$585,000

DOE share: \$585,000

Non-DOE share: \$0

Project Introduction

In the past decades, a continuous effort has been paid to developing high-energy density lithium-ion chemistries without sacrificing their safety performance for automobile applications. Conventional non-aqueous electrolytes have been the bottleneck for further increase in both the energy density and safety while solid-state electrolytes are promising to take the seat and continue the journey. Giving top priority to the processability of the electrolyte material for scalable manufacturing, the project team will develop a high-performance anti-perovskite solid-state electrolyte with stabilized electrode/electrolyte interfaces for scalable fabrication of liquid-free solid-state batteries. In line with this project's objectives, the project consists of four over-arching goals.

- Development of high-performance anti-perovskite electrolytes.
- Accessing the air stability and proton mobility.
- Stabilizing the solid/solid interface through interfacial engineering.
- Prototyping liquid free cells using anti-perovskite electrolyte.

Objectives

The objective of this project is to develop an optimized anti-perovskite electrolyte with a stabilized interface for scalable fabrication of liquid-free solid-state batteries.

Approach

The project approach is multifold: (1) chemistry design: multiple doping at anion sites will be pursued to improve structural stability, ionic conductivity and environmental compatibility; (2) interfacial design: surface coating will be deployed to improve the chemical and mechanical stability of solid/solid interface; and (3) process development: a scalable fabrication process based on melt-infiltration or dry lamination will be developed for the fabrication of all solid state lithium batteries.

Results

Synthesis of anti-perovskite electrolytes

The synthesis of anti-perovskite electrolytes is a one-step solid-state reaction. The starting materials are LiOH and lithium halide (LiCl, LiBr, and LiI). Anti-perovskite materials can be easily synthesized by heating the mixture of starting materials at about 300°C under vacuum conditions. Figure XVI.30.1 shows the evolution of high-energy X-ray diffraction (HEXRD) patterns collected during the thermal treatment of Li_3OCl . The in situ HEXRD results clearly show that the anti-perovskite material (Li_3OCl) is formed at about 225°C and melts at about 280°C. During the cooling process, anti-perovskite Li_3OCl crystallizes when the temperature is below 280°C. In the lab-scale synthesis, it was found that the synthesized materials were firmly stuck to the crucible wall. This chemically originated from the strong chemical bonding between the Li_2O moiety and various oxide materials. The chemical interaction between the crucible and the formed electrolyte increases the difficulty in recovering desired materials and potentially unbalanced loss of starting materials due to the interfacial reaction with the crucible, leading to the deviation of desired stoichiometry. To overcome this difficulty, we tried crucibles made from different materials (Al_2O_3 , quartz, porcelain, and MgO-coated Al_2O_3) without much success. Progress was made by using metallic crucibles and polytetrafluoroethylene (PTFE) crucibles. When extremely chemically resistive tungsten or PTFE crucible was used for the synthesis, the material could be easily recovered, and a pure anti-perovskite material was obtained.

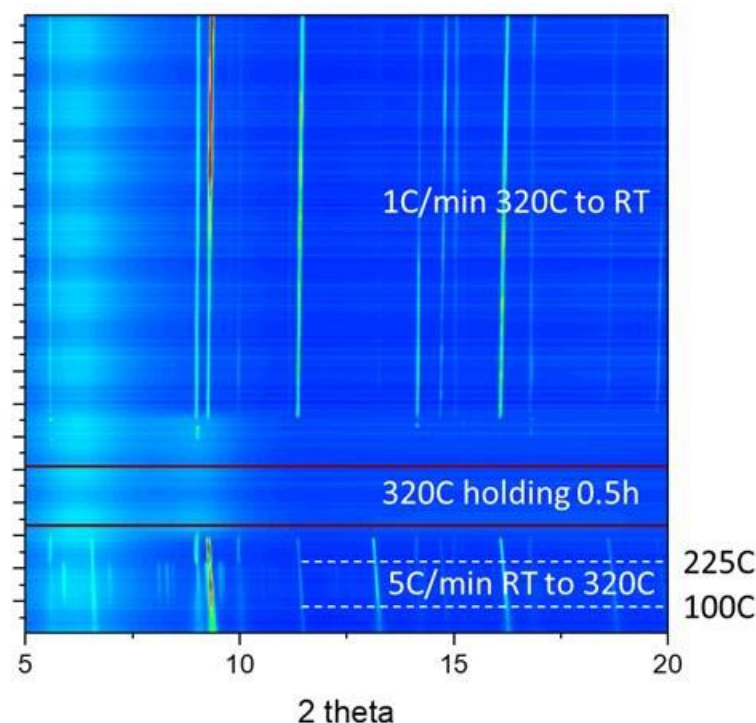


Figure XVI.30.1 Evolution of HEXRD patterns during solid-state synthesis of Li_3OCl .

With the established synthesis process, we were able to synthesize the phase-pure cubic form of protonated Li_2HOCl solid state electrolyte. In order to measure the Li^+ conductivity of synthesized electrolytes, a protonated anti-perovskite powder, Li_2HOCl , was cold-pressed into a half inch pellet, and symmetrical cells using indium foil as the conducting layers were assembled for electrochemical impedance spectroscopy (EIS) measurement. The measured Li^+ conductivity at different temperatures is consistent with the best-reported results (G. Yushin, et. al., *Advanced Energy Materials*, 2017, 1700971).

Structure stability of protonated $\text{Li}_2\text{HOCl}_{1-x}\text{Br}_x$ ($0 \leq x \leq 1$) anti-perovskite electrolytes

One simple way to manipulate the structure of anti-perovskite electrolytes is anion substitution at the dodecahedral site. We initially focused on the synthesis of protonated $\text{Li}_2\text{OHCl}_{1-x}\text{Br}_x$ ($0 \leq x \leq 1$) using $\text{LiOH} \cdot \text{H}_2\text{O}$ and different ratios of LiCl and LiBr salt mixture as the starting materials. Figure XVI.30.2a shows high energy X-ray diffraction (HEXRD) results of five synthesized electrolytes. Four Br-substituted electrolytes can be directly indexed to a cubic phase with Pm-3m space group. The enlarged views near (110) and (200) are shown in Figure XVI.30.2b. The peak splitting suggests a lattice distortion in the synthesized Li_2OHCl electrolyte, resulting in an orthorhombic phase where $a \neq b \neq c$. These results show 25% Br substitution can effectively preserve the cubic phase of anti-perovskite electrolyte, which may lead to an improved ion conductivity at room temperature. Shifting of peaks to the lower angle with increased Br content, as shown in Figure XVI.30.2 also implies a lattice volume expansion with Br doping. Detailed results for Rietveld refinement reveal a $\sim 2.9\%$ lattice volume increase with every 25% Br substitution. In addition, a small amount of LiCl impurities was observed in the synthesized Li_2OHCl powder (highlighted by the red arrows in Figure XVI.30.2a), indicating a loss of LiOH during the solid-state synthesis.

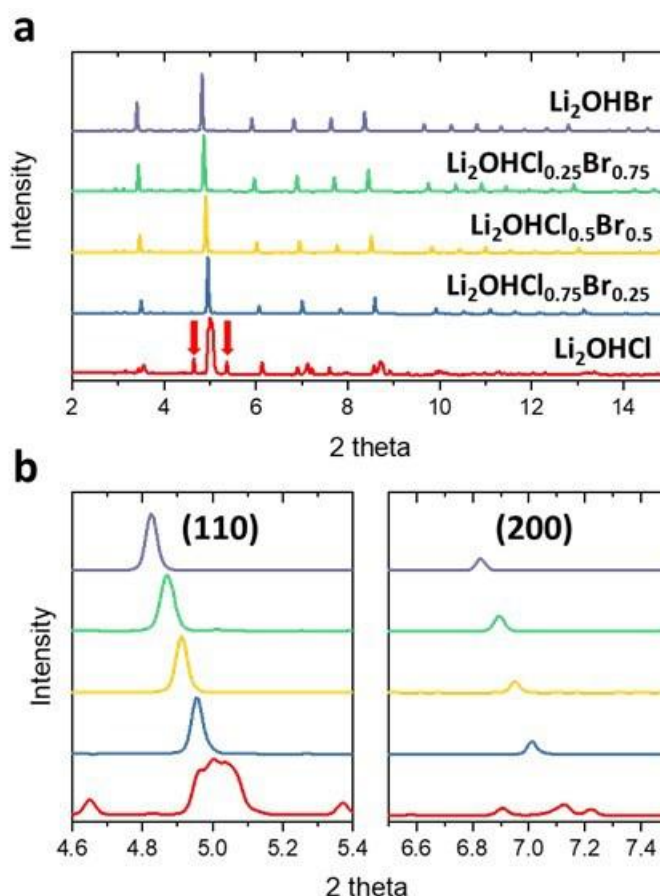


Figure XVI.30.2 a) HEXRD results of the anti-perovskite electrolytes with different Cl and Br ratios. Red arrows indicate the LiCl impurities in Li_2OHCl , and b) HEXRD spectra near (110) and (200) peaks.

The structural evolution of protonated $\text{Li}_2\text{HOCl}_{1-x}\text{Br}_x$ ($0 \leq x \leq 1$) at elevated temperatures were studied by differential scanning calorimetry (DSC). Li_2OHCl shows an endothermal peak at 44°C as indicated by a red arrow in the bottom panel of Figure XVI.30.3, contributed from the orthorhombic to cubic phase transformation for undoped electrolytes. This peak was not seen in other Br-substituted electrolytes, which agrees with their single cubic phase at room temperature observed from HEXRD measurements. It was observed that Li_2OHCl melted at 296°C , and the melting point decreases with the content of Br dopant.

Additional DSC peaks were observed for Br doped electrolyte samples, suggesting additional phase transformation induced by Br doping.

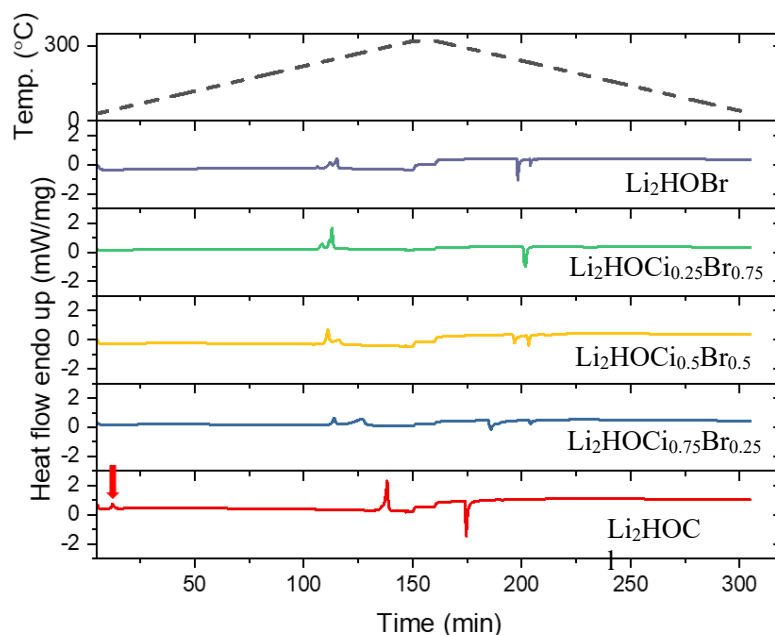


Figure XVI.30.3 DSC results of the anti-perovskite electrolytes with different Cl and Br ratios. Red arrow points to the endothermal peak from the orthorhombic to cubic phase transformation in Li_2HOCl .

Li⁺ conductivity of protonated $\text{Li}_2\text{HOCl}_{1-x}\text{Br}_x$ ($0 \leq x \leq 1$) anti-perovskite electrolytes

Initially, a cold press was used to prepare electrolyte pellets using the synthesized electrolytes. Figure XVI.30.4 shows the measured lithium-ion conductivity of the cold press samples at various temperatures. Worth mentioning is that Li_2HOCl exists as a tetragonal form at around room temperature, showing substantially lower lithium-ion conductivity than others. When the temperature is higher than 40°C, Li_2HOCl converts to its cubic form with a much higher Li^+ conductivity, as shown in Figure XVI.30.4. Overall, it is observed that partially replacing Cl with Br can improve the Li^+ conductivity and the conductivity peaks at the composition of $\text{Li}_2\text{HOCl}_{0.75}\text{Br}_{0.25}$. Nevertheless, the room temperature conductivity for all these samples is still far below expectation. The cold-pressed pellet samples were further surveyed using scanning electron microscopy (SEM). Without many surprises, the cold-pressed samples have a porous structure (see Figure XVI.30.5). Therefore, further densification using hot-press is needed to improve their nominal Li^+ conductivity.

The electrolyte powder was heated to 200°C and a pressure of 1000 MPa was applied to densify the pellet. Mechanically strong pellets were obtained through the hot-press approach. The temperature-dependent Li^+ conductivity of these hot-pressed pellet samples was also measured. A similar slope was observed for all electrolytes, implying similar activation energy for lithium-ion conduction. The linear fitting results show that the samples have an activation energy of about 0.6 eV, which is very close to the numbers measured for cold-pressed pellets. This suggests that the hot-press process didn't alter the electrolytes' chemical nature. Compared to the conductivity measured for cold-pressed samples, the conductivity was generally improved by 2-3 folds using the hot-press process. Our current exercise was limited to 200°C to avoid the extra phase transformation occurring for Br doped samples at about 250°C (see Figure XVI.30.3). A careful optimization of hot-press process beyond 250°C will be conducted to improve the densification of anti-perovskite electrolyte pellets further.

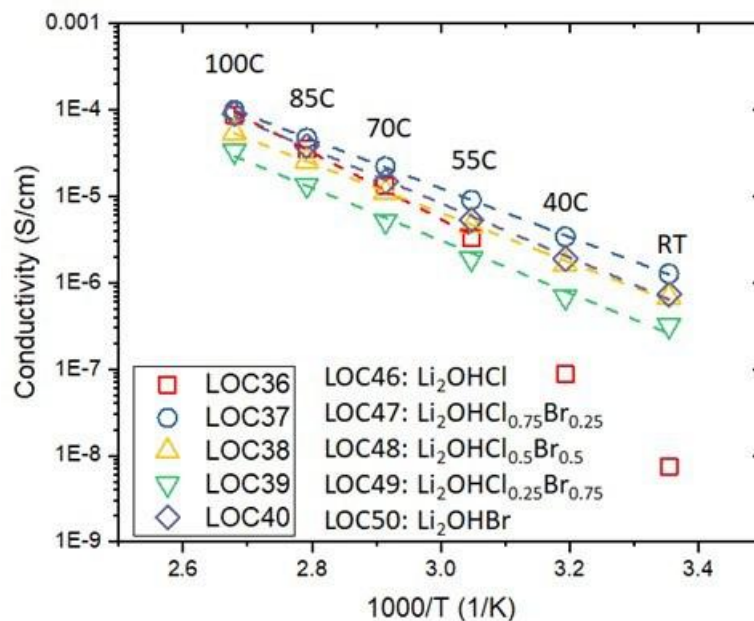


Figure XVI.30.4 Measured Li⁺ conductivity of protonated anti-perovskite electrolyte pellets prepared using cold press.

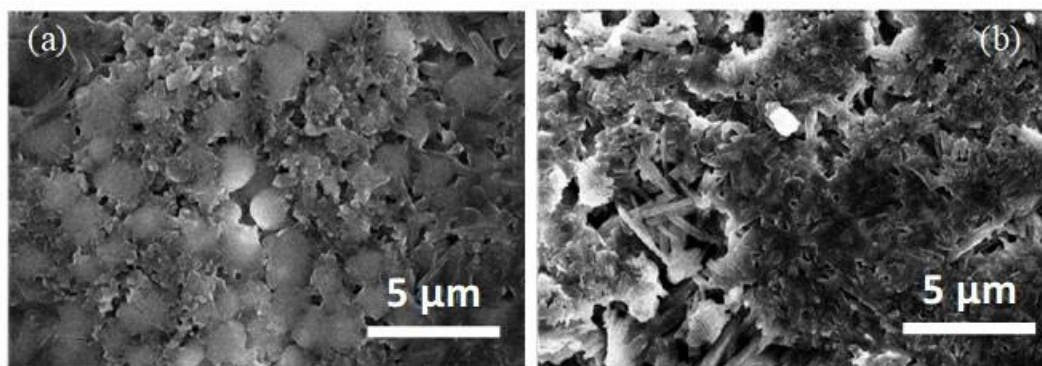


Figure XVI.30.5 Scanning electron microscopy images of cold-pressed electrolyte pellets from a) Li₂HOCl, and b) Li₂HOCl_{0.75}Br_{0.25}, showing the presence of big voids in pellets that can significantly reduce the nominal lithium-ion conductivity of the electrolyte pellets.

Chemical stability of anti-perovskite electrolytes against metallic lithium

One of the significant advantages of anti-perovskite electrolyte is that all the elemental components are already at their lowest valence state; hence, the electrolyte will be thermodynamically compatible with metallic lithium. As a demonstration of their chemical stability, a small amount of Li₃OCl and metallic lithium was sealed in a quartz tube for *in situ* HEXRD observation. The sealed sample was then slowly heated to 220°C and held at 220°C for an hour. The HEXRD patterns of the sample were continuously collected during the experiment. Figure XVI.30.6 shows that the lithium melted at about 180°C. However, the structure of Li₃OCl was maintained even when heated and held at 220°C with the metallic lithium. No chemical reaction between the electrolyte and metallic lithium was observed.

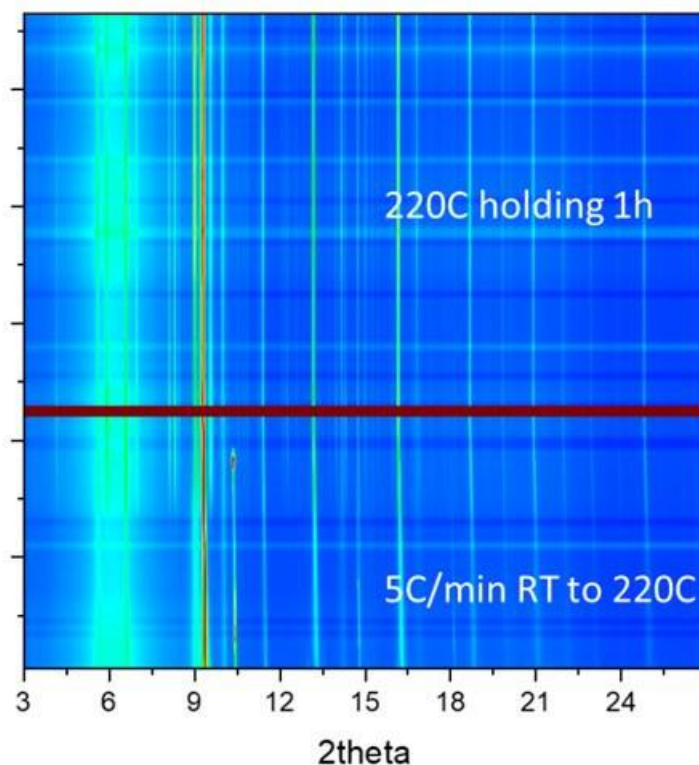


Figure XVI.30.6 Evolution of HEXRD patterns showing the interaction between metallic lithium and Li_3OCl electrolyte during heating, showing great chemical compatibility up to 220°C .

Investigating the environmental compatibility of anti-perovskite electrolytes

It is also anticipated that the synthesized anti-perovskite electrolytes are sensitive to moisture. Figure XVI.30.7 compares X-ray diffraction (XRD) patterns of Li_3OBr powder before and after aging in a glovebox for one month. Before aging, the material was dominated by a cubic structure, with a small amount of impurity phase. After aging, a clear growth of impurities phase was observed, even though the sample was stored inside the glovebox. Therefore, it is of our interest to further study the moisture sensitivity of the electrolytes, and to search for electrolyte candidates that can at least survive in a dry room environment.

Figure XVI.30.8a shows the conceptual design of a simple sample holder to investigate the interaction between anti-perovskite electrolyte and the moisture in the air. In this design, an inert gas carrying a certain level of moisture will pass through the sample holder to provide a constant level of moisture in the sample holder. CAPTON windows on both sides provide a good X-ray pathway to track the structure evolution of the electrolyte material held inside the sample holder. Figure XVI.30.8b shows an image of the implemented sample holder that is compatible with the working environment offered at sector 17BM of Advanced Photon Sources (APS) at Argonne National Laboratory. Controlling the moisture level at 40% relative humidity (RH) (~ 1070 Pa moisture partial pressure), we were able to follow the conversion reaction from the cubic Li_3OBr to the unidentified impurity phase using high energy X-ray diffraction (HEXRD). Using the ratio of peak intensity between cubic Li_3OBr and impurity phase as a quantitative indicator, the evolution from Li_3OBr to the impurities phase can be obtained, as shown in Figure XVI.30.8c. Although a catastrophic decomposition was observed after exposure to high moisture level for about 3 hours, a continuous slow decomposition was also confirmed at the beginning of the experiment. It is worth mentioning that a fairly high moisture level (40% RH) was used to shorten the need for beam time. A good dry room generally operates at $\sim 1\%$ RH. Good stability in dry room can be expected, and needs to be validated in the future.

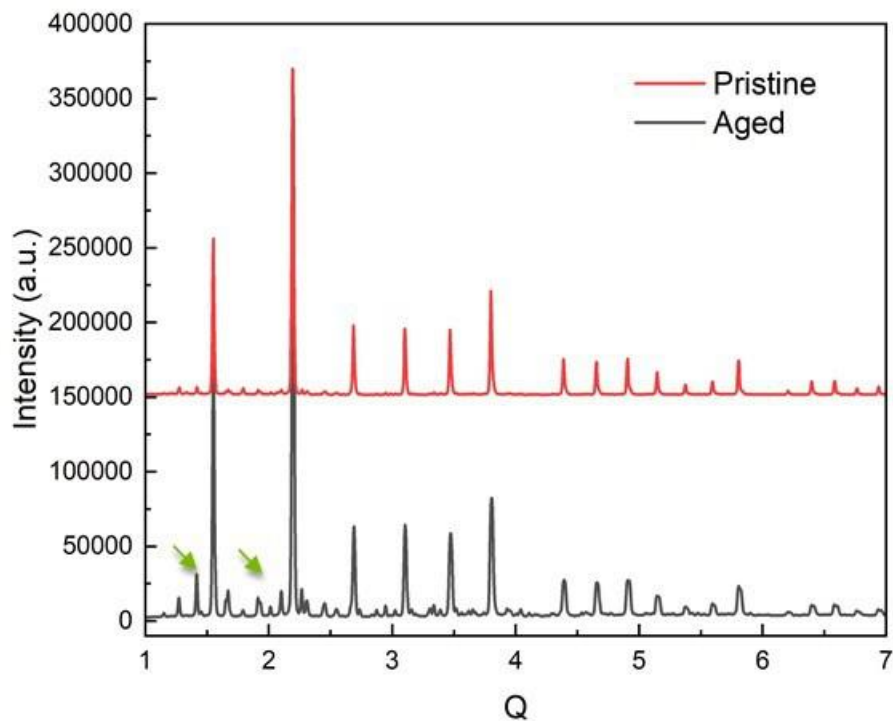


Figure XVI.30.7 Comparison of X-ray diffraction patterns of Li_3OBr before and after aging in the glovebox for 1 month, showing a slow degradation of Li_3OBr during storage.

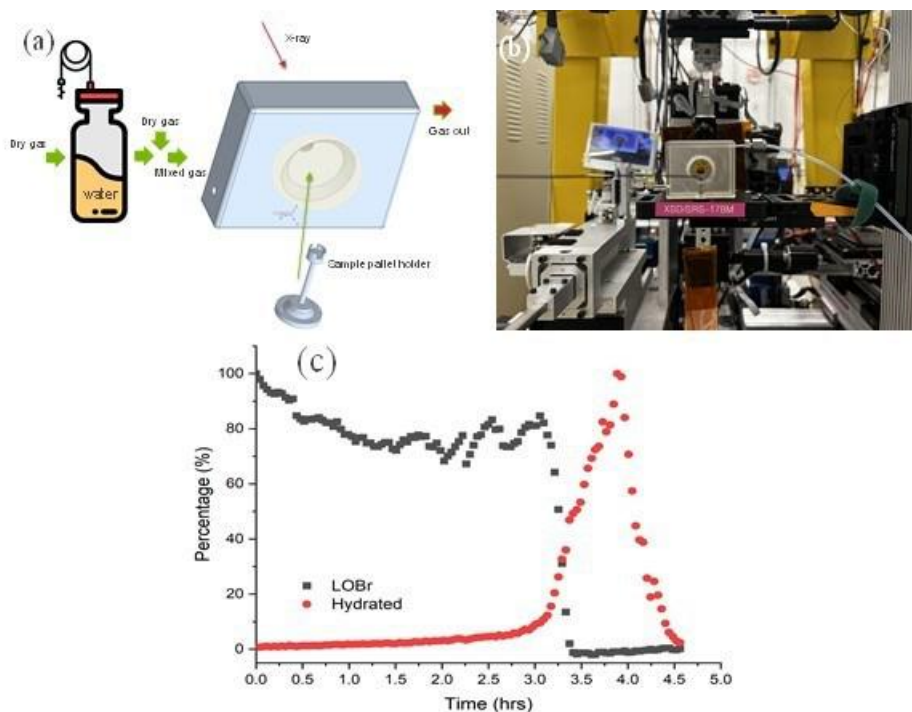


Figure XVI.30.8 (a) Illustration of a sample environment to study the moisture sensitivity of electrolyte samples; (b) image of the working sampler holder integrated in sector 17BM of Advanced Photon Sources; and (c) evolution of Li_3OBr and its decomposition product during the exposure to 40% humidity (~1070 Pa moisture partial pressure).

Conclusions

A simple one-step solid state route was established to synthesize anti-perovskite electrolytes. Br-doping is an effective approach to stabilize the electrolyte materials in cubic format with improved lithium-ion conductivity. The protonated anti-perovskite electrolytes have a low melting point below 280°C, which is beneficial for developing a scalable process for creating a strong electrode/electrolyte interface. The best Li⁺ conductivity obtained is at 10⁻⁵ S/cm, which is below expectation. Substantial improvement in electrolyte chemistry and densification process is needed to improve the Li⁺ conductivity further.

Acknowledgements

This report is coauthored by Dr. Jiantao Li, Dr. Fan Wang, Dr. Yingying Xie, and Ms. Xinyi Liu. Dr. Yuzi Liu and Dr. Xinwei Zhou are also acknowledged for their help in electron microscopy characterization. We thank Dr. Tianyi Li and Dr. Wenqian Xu of Advanced Photon Source (APS) at ANL for assistance in structural characterization using high energy X-ray diffraction. We also sincerely acknowledge the collaboration with Dr. Xianghui Xiao of Brookhaven National Laboratory for Transmission X-ray Microscopy characterization and Dr. Xiangbo Meng of Arkansas University for material protection using atomic layer deposition.

XVI.31 High-Conductivity and Electrochemically Stable Lithium Thioborate Solid-State Electrolytes for Practical All-Solid-State Batteries (Stanford University)

Yi Cui, Principal Investigator

Stanford University
450 Serra Mall
Stanford, CA, 94305
E-mail: yicui@stanford.edu

Simon Thompson, DOE Technology Development Manager

U.S. Department of Energy
E-mail: Simon.Thompson@ee.doe.gov

Start Date: October 1, 2021	End Date: September 30, 2022	
Project Funding (FY22): \$200,000	DOE share: \$200,000	Non-DOE share: \$0

Project Introduction

This project aims to develop novel lithium thioborates (Li-B-S, LBS) as a new class of solid-state electrolytes (SSEs) to realize high-performance all-solid-state batteries (ASSBs), with a particular focus on addressing the technical challenges in electrolyte synthesis, cell integration, failure diagnostics, and scale-up. The approach will be technologically transformative to the current solutions for ASSB development.

Objectives

We plan to develop doped and undoped lithium thioborates for high-energy-density, all-solid-state lithium metal batteries. For the final deliverables, ASSBs with the ability to reach an energy density of 500 Wh/kg and maintain 80% capacity for at least 300 cycles will be demonstrated.

Approach

The long-term project has a multistep approach toward integration of LBS with high-voltage cathodes, with steps 1-3 as the focus for this year:

1. Fabricate undoped LBS powders using an all-solid-state synthesis method to achieve high ionic conductivity, low electronic conductivity, and a wide operational voltage window.
2. Integrate LBS SSEs into symmetric Li/LBS/Li cells and into full batteries using high-voltage cathodes including lithium Ni-Mn-Co (NMC) oxide.
3. Study atomic, particle, and cell-scale Li-metal-SSE interface development and dendrite growth mechanisms in SSEs using advanced characterization tools. Use knowledge to better develop SSEs and modify interfaces for stable cycling in full cells.
4. Fabricate doped LBS powders and develop particle/surface modifications to increase ionic conductivity as well as stability in full batteries and in air for glovebox-free synthesis.
5. Use density functional theory to guide development of new doped LBS materials and to explore interactions at solid-solid interfaces.

Results

We developed a multigram-scale synthetic procedure to produce $\text{Li}_{10}\text{B}_{10}\text{S}_{20}$. The synthesis involves grinding of the precursor materials, Li_2S , S, and B; loading the precursors into a boron nitride crucible; sealing the crucible in a quartz tube; sintering; and unloading the material to retrieve the powders (Figure XVI.31.1a). We retrieved white powders that pressed into a dense pellet that could be held by tweezers.

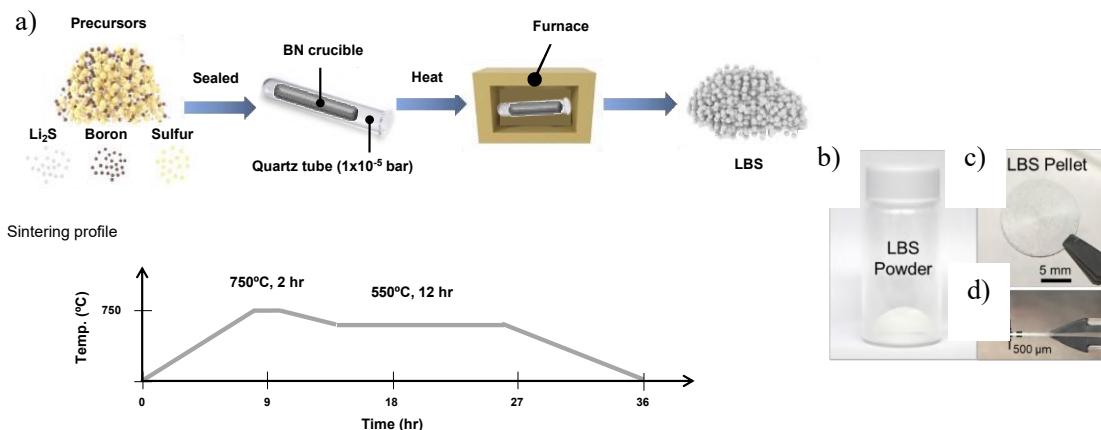


Figure XVI.31.1 (a) Synthesis procedure and sintering profile for $\text{Li}_{10}\text{B}_{10}\text{S}_{20}$. (b-d) LBS powders optical images.

We performed X-ray diffraction on the LBS powders and compared this spectrum to the calculated spectrum (retrieved from [1]). We found a close match and confirmed the purity of the powders retrieved from this synthesis. (See Figure XVI.31.2.)

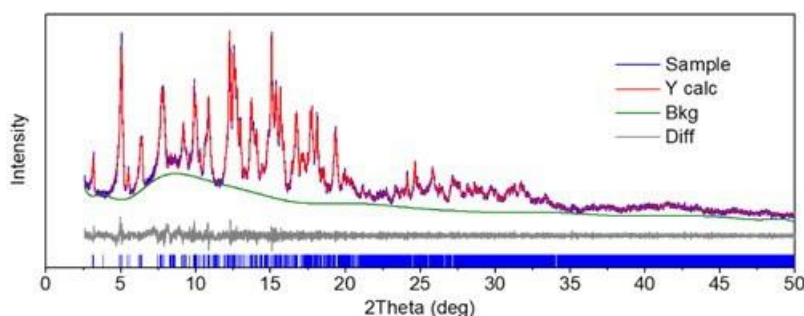


Figure XVI.31.2 X-ray diffraction of $\text{Li}_{10}\text{B}_{10}\text{S}_{20}$ in blue, compared to calculated spectrum in red.

We have synthesized high-purity $\text{Li}_{10}\text{B}_{10}\text{S}_{20}$ SSE with total resistance of 220 Ω and ionic conductivity of $3.4 \times 10^{-4} \text{ S cm}^{-1}$ (Figure XVI.31.3a) under 360 MPa pressure with stainless steel electrodes. In Li - $\text{Li}_{10}\text{B}_{10}\text{S}_{20}$ -SS asymmetric cells, we measured the voltage stability window to be 1.3-3.0V vs. Li/Li^+ when measured at room temperature, with a scan rate of 0.1 mV/s (Figure XVI.31.3b-c)

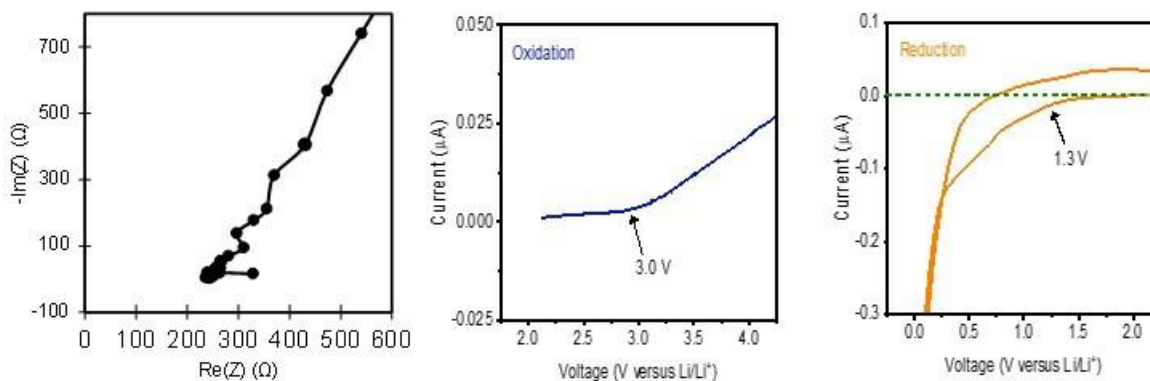


Figure XVI.31.3 (a) Electrochemical impedance spectroscopy of 450-micron pellet of $\text{Li}_{10}\text{B}_{10}\text{S}_{20}$ using 360 MPa pressure, stainless steel electrodes. (b) voltage stability window of $\text{Li}_{10}\text{B}_{10}\text{S}_{20}$ using carbon-LBS composite cathode, Li metal anode.

We assembled Li-LBS-Li symmetric cells using a split cell configuration with 35 MPa pressure to assess the chemical electrochemical stability of LBS with Li metal. When in contact with lithium metal in a symmetric Li-LBS-Li cell, $\text{Li}_{10}\text{B}_{10}\text{S}_{20}$ is semi-stable, forming a slightly resistive interfacial layer (Figure XVI.31.4). The ionic conductivity remains stable over time in the cell and the interfacial layer does not grow (Figure XVI.31.4)

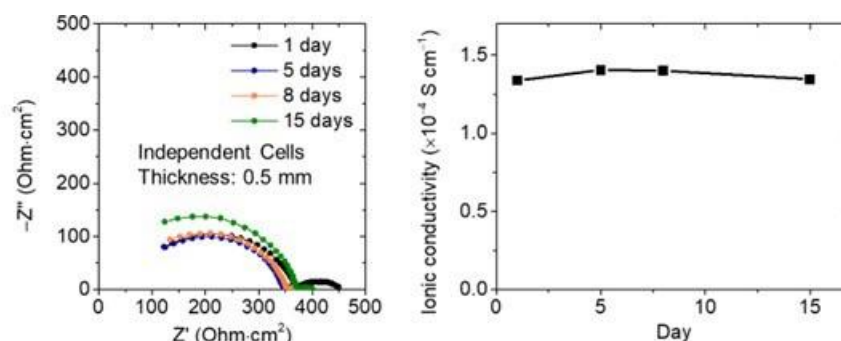


Figure XVI.31.4 (a) Electrochemical impedance spectroscopy over several days of 450-micron pellet of $\text{Li}_{10}\text{B}_{10}\text{S}_{20}$ using 35 MPa pressure, Li metal electrodes. (b) The ionic conductivity of this pellet over 15 days.

To determine the suitability of $\text{Li}_{10}\text{B}_{10}\text{S}_{20}$ as an SSE with Li metal anodes, we have used X-ray photoelectron spectroscopy to analyze the species at the surface of $\text{Li}_{10}\text{B}_{10}\text{S}_{20}$ before (Figure XVI.31.5 a-c) and after (Figure XVI.31.5 d-f) contact with lithium metal. We found the new peaks appear after $\text{Li}_{10}\text{B}_{10}\text{S}_{20}$ comes in contact with Li (Figure XVI.31.5 d-f): in the B1s region, elemental boron appears, and in the Li1s and S2p regions, Li_2S peaks appear. Both B and Li_2S peaks are small in comparison to $\text{Li}_{10}\text{B}_{10}\text{S}_{20}$, suggesting minimal reaction.

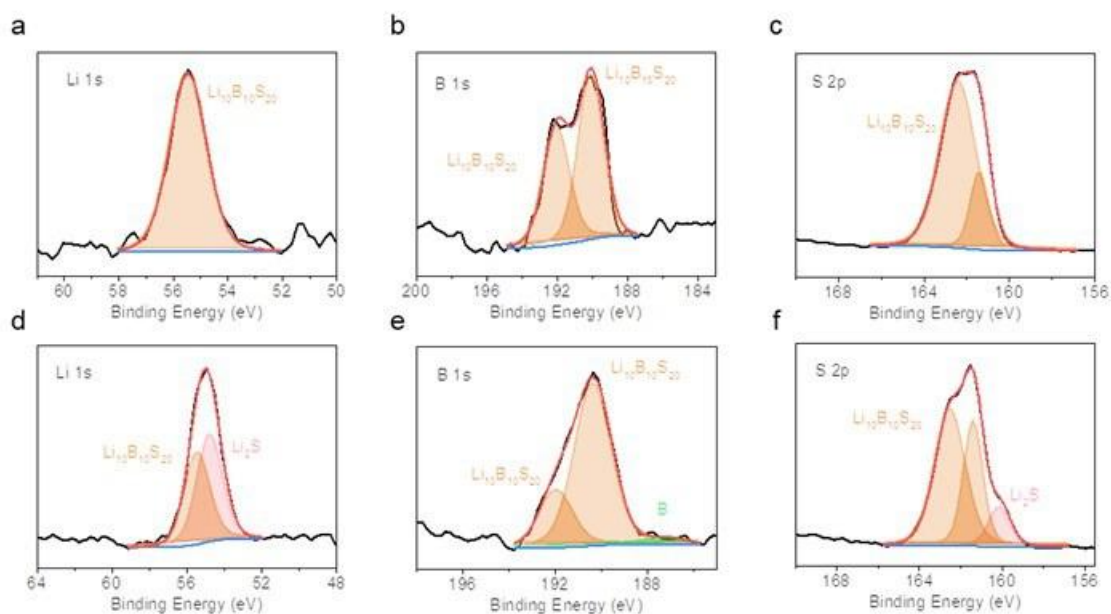


Figure XVI.31.5 (a-c) XPS of $\text{Li}_{10}\text{B}_{10}\text{S}_{20}$ powder: (a) Li1s; (b) B1s; (c) S2p. (d-f) XPS of $\text{Li}_{10}\text{B}_{10}\text{S}_{20}$ powder after reaction with Li metal: (d) Li1s; (e) B1s; (f) S2p.

We measured the critical current density of Li-LBS-Li cells to be 1.0 mA cm^{-2} at room temperature. We cycled Li-LBS-Li cells at 35 MPa, room temperature, and the cells cycled for over 100 hours with little interfacial resistance increase (Figure XVI.31.6).

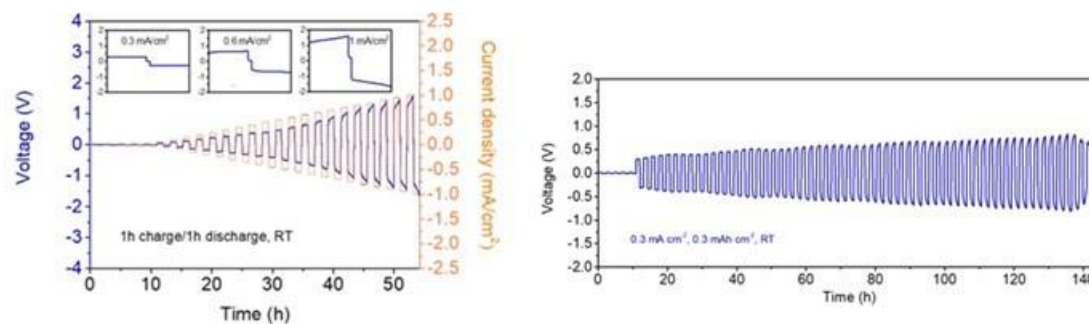


Figure XVI.31.6 Critical current density and constant current (0.3 mA cm⁻², 0.3 mAh cm⁻²) testing of Li-LBS-Li cells at room temperature, 35 MPa pressure.

Conclusions

To conclude, we have made significant progress on our stable lithium thioborate solid electrolyte for lithium metal batteries. We developed a consistent, scalable, gram-scale synthesis of LBS phases that results in pure and crystalline LBS as determined by XRD. We have demonstrated high ionic conductivity, $3.4 \times 10^{-4} \text{ S cm}^{-1}$, at room temperature of Li₁₀B₁₀S₂₀. We also report high critical current density, 1.0 mA cm⁻², and stable cycling of this phase.

References

1. Zum Hebel, P. "Preparation, Crystal Structure and ⁷Li NMR of Li_{6+2x}[B₁₀S₁₈]S_x(X≈)." *Solid State Ionics* 43 (November 1990): 133–42.

XVI.32 Solid state batteries with long cycle life and high energy density through materials design and integration (LBNL)

Gerbrand Ceder, Principal Investigator

Lawrence Berkeley National Laboratory
1 Cyclotron Rd.
Berkeley, CA, 94720
E-mail: gceder@lbl.gov

Haegyum Kim, Co-Principal Investigator

Lawrence Berkeley National Laboratory
1 Cyclotron Rd.
Berkeley, CA, 94720
E-mail: haegyumkim@lbl.gov

Simon Thompson, DOE Technology Development Manager

U.S. Department of Energy
E-mail: Simon.Thompson@ee.doe.gov

Start Date: January 28, 2022

End Date: September 30, 2026

Project Funding (FY22): \$1,875,000

DOE share: \$1,875,000

Non-DOE share: \$0

Project Introduction

Solid-state Li metal batteries hold tremendous promise as a safer and higher energy-density technology than current Li-ion systems. By replacing the liquid electrolyte with a solid electrolyte (SE), the temperature at which a cell experiences thermal runaway can be increased, thereby preventing fire. In addition, the use of a Li metal anode can lead to a significant increase in energy density. However, several challenges need to be addressed before any solid-state lithium metal battery can be competitive and surpass the specific energy, energy density, and cycle life of lithium ion.

Objectives

This project aims to create solid-state Li-metal batteries (SSLMBs) with high specific energy, high energy density, and long cycle life using scalable processing techniques. The team will achieve this by addressing fundamental challenges associated with (1) interfacial reactivity, (2) Li-metal plating, and (3) cathode loading. Addressing these challenges supports the broader Vehicle Technologies Office goal of solid-state batteries with increased cycle life and energy density. Ultimately, this project will develop an understanding of how to prevent interfacial reactions, make uniform Li-metal plating, and increase cathode loading significantly. The knowledge obtained from this project will be used to design SSLMBs with high specific energy of 500 Wh/kg, 80% capacity retention for at least 300 cycles, and critical current density (CCD) $> 1 \text{ mA/cm}^2$.

Approach

This project addresses several fundamental challenges and makes the SSLMB competitive, surpassing the specific energy, energy density, and cycle life of Li-ion batteries:

- Create *homogeneous lithium deposition* on the anode without penetration of lithium metal through the separator to achieve **high cycle life** and **high safety**. The team will achieve this with the use of an active buffer layer (ABL) that combines active and inactive components to homogenize lithium plating and to keep the lithium plating potential away from the solid electrolyte (SE) separator.
- Limit *chemical reactivity* and *mechanical decohesion* between the SE, carbon, and cathode material in the composite cathode so that **high cycle life** can be achieved. The team will limit chemical reactivity by protecting the carbon from the SE, by using novel cathode coatings designed to be stable to high

voltage and that do not react with the SE, by using novel solid halide catholyte conductors, and by using inorganic/organic solid composite electrolytes in the cathode.

- Achieve *high volumetric loading* of the active cathode material in the composite cathode to achieve **high energy density** and **high specific energy**. The team will achieve high volumetric cathode loading by creating thin highly porous conductor scaffolds that are infiltrated with cathode, by tailored particle size distributions of deformable lightweight conductors, and by the use of organic/inorganic hybrids.
- Create *inexpensive materials* and *processes* to fabricate SSBs so that they can be **cost-competitive** with Li ion batteries. The team will create solution-processable organic/inorganic hybrids to be used as separator and to blend in the composite cathode; they will use inexpensive, scalable ceramics processing techniques to create high loading composite cathodes.

Results

Task 1: Buffer layers to stabilize the Lithium/SE interface and create uniform lithium plating.

Thin ABL electrode fabrication optimization:

This task aims to develop ABLs to reduce interfacial resistance and stabilize interfaces at lithium/SE, and to avoid dendritic lithium growth. Recent studies have shown that a silver (Ag)-carbon composite layer between the current collector and the SE can prevent dendrite formation in solid-state batteries where lithium plating and stripping takes place. The initial goal of this project is to understand the mechanism of lithium plating in the presence of such a buffer layer and to understand what causes more uniform, favorable lithium deposition. To understand such mechanisms, it is important to reproduce some parts of the full cell. A major part of is the construction of the buffer layer itself which consists of an Ag-carbon composite. One of the major challenges has been to identify the percentage of binder that needs to be in the coating. Second, the buffer layer and current collector need to be combined with a compatible solid electrolyte and a lithium source to make a cyclable cell.

The team has tested and optimized several important parameters, including (1) binder content, (2) mixing conditions, (3) drying conditions, (4) calendaring conditions, (5) surface roughness of the stainless-steel (hereafter, SUS or SS) current collector. For example, different carbon and binder ratios were used with different mixing protocols to achieve a reasonable conductivity of the layer. Slurry was mixed using a rotor-stator homogenizer with high molecular weight polyvinylidene fluoride (PVDF) binder and N-Methyl-2-pyrrolidone (NMP) as the solvent. Surface resistance of the layer was relatively lower for higher binder contents vs. the lower binder contents. This could be due to the porosity of the electrode decreasing with the introduction of higher amounts of binder. Higher binder contents reduce the overall conductivity of the system; therefore, lower amounts of binder were used. In the Ag-carbon composite, we found that the percentage of carbon in the electrode coating determines the initial porosity of the coating. The higher the carbon content, the higher the porosity of the coating, which could cause higher interfacial resistance. Higher carbon content also causes the slurry to show more shear thinning properties. This would govern the determination of the wet thickness of the cast that would give the correct dry thickness. The dry thickness of the final coating was 15 μm prior to calendaring. After the calendaring, the coating layer becomes $\sim 10 \mu\text{m}$. (Figure XVI.32.1). The team is investigating the thickness uniformity and distribution of Ag nanoparticles in the ABL, which might determine the Li plating and stripping performance.



Figure XVI.32.1 Image of final electrode coating.

Computational investigation to understand the role Ag nanoparticles in ABL:

Understanding the role of Ag particles in Ag-carbon ABL is crucial to design new ABLs with an inexpensive active metal component. As an effort to understand the thermodynamics in the lithiation of Ag in the Ag-carbon buffer layer, the team performed *ab-initio* calculations to compute the formation energy and voltage profile of Ag-Li alloys. In these calculations, the team considered three types of lattice geometries: BCC, FCC and γ -brass as suggested by experiments. For each lattice type, the electronic energy of 150 different configurations were computed. A cluster-expansion model was fitted for each lattice type, from which ground-state structures were predicted. Figure XVI.32.2 shows the DFT formation energies and configurations of predicted ground states. Besides experimentally reported structures (e.g., CsCl-type BCC structure, I41 FCC structure, and γ -Ag₅Li₈), other ordered ground-state structures have also been found (e.g., FCC AgLi₃ structure, and γ -Ag₂Li₁₁). The team aims to further include phonon corrections with DFT electronic energies in the current cluster-expansion model, in order to match the experimental phase stability and thus to calculate an accurate lithiation voltage profile for bulk Ag-Li system.

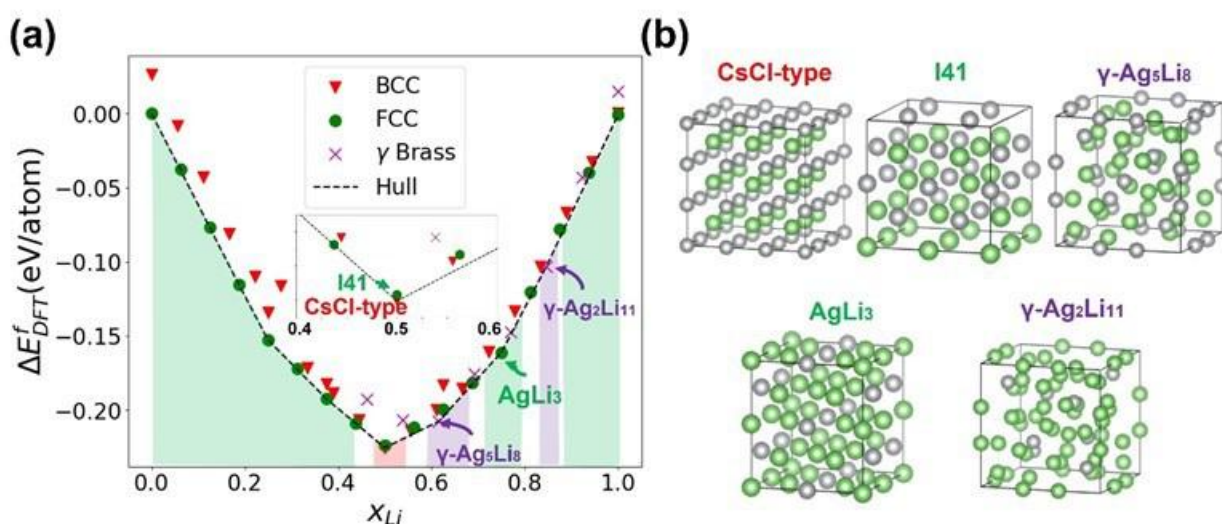


Figure XVI.32.2 (a) Computed DFT formation energy for ground-state structures predicted by cluster expansion in BCC (red triangle), FCC (green dot) and γ -brass (magenta cross) lattice types. The convex hull of formation energy is marked with dashed line, under which single-phase regions are shaded with light red (BCC), light green (FCC) and light magenta (γ). The composition range $0.4 < x_{Li} < 0.6$ is enlarged in the middle. Phonon energy and entropy contributions are not included. (b) Predicted ground-state structures as marked with arrows in (a).

Understanding role of carbon structure in ABL:

Carbon is another important component of ABLs. We hypothesized that the carbon structure will impact the Li plating performance significantly because the Li diffusivity in the carbon varies depending on its structure. Here, we tested and compared two distinct types of carbon: amorphous carbon (Super P) and graphite (natural graphite with particle size of $\sim 20\ \mu\text{m}$) as ABLs without metallic component. These two carbon materials will have very different Li diffusion behavior when they are in thin electrode form. The sphere-like amorphous carbon will have three-dimensional Li diffusion pathways once it is lithiated. In this respect, amorphous carbon ABL can provide Li diffusion and electron transport pathways between a SE and a current collector (Figure XVI.32.3a). In contrast, in the plate-like graphitic carbon, Li ions can transport rapidly along *ab*-plane, but Li migration along the *c*-direction is not feasible because of the very high migration barrier $> 8\ \text{eV}$. [1] In the electrode film, the graphitic carbon plates stack on top of each other because of their two-dimensional morphology. Therefore, the graphitic carbon electrode film will have very low Li diffusivity along the *c*-direction while maintaining a high electrical conductivity (Figure XVI.32.3b). Therefore, the amorphous carbon can represent an ABL with a high Li diffusivity and a high electrical conductivity and the graphitic carbon can represent the ABL with a low Li diffusivity but with a high electrical conductivity. In our experiments, we prepared the ABL by mixing carbon (the amorphous carbon and graphitic carbon) and polytetrafluoroethylene (PTFE) binder in 70 wt% (carbon): 30 wt%(PTFE) ratio and a subsequent roll pressing method. The Li_3PS_4 SE is pressed under 500 MPa to make a dense pellet. Then, an asymmetric Li half-cell is prepared with a Li_3PS_4 solid electrolyte pellet as shown in Figure XVI.32.3c. We used a copper (Cu) film as a current collector. The asymmetric cells are discharged for 60 hours under a constant current of $27.3\ \mu\text{A}$ ($0.115\ \text{mA}/\text{cm}^2$). Figure XVI.32.3d shows the discharging profile of the asymmetric cell. Figure XVI.32.3e-f shows the optical microscope images of amorphous carbon and graphitic carbon after Li plating (total capacity: $6.9\ \text{mAh}/\text{cm}^2$). We found that the Li plating preferentially occurs on the interface between the amorphous carbon and Cu current collector. Figure XVI.32.3e shows the amorphous carbon ABL film facing the Cu current collector, where we found a shiny Li metals on the carbon surface. We suspect that Li metal fills the pores in the amorphous carbon film. In contrast, it is clearly visible that Li metal is plated at the interface between graphitic carbon and Li_3PS_4 SE (Figure XVI.32.3f). The goldish color of the ABL indicates that Li ions intercalate into graphitic carbon. We speculate that the Li plating occurs first and the plated Li metal is squeezed in the pores of the graphitic carbon electrode. Therefore, lithation to graphitic carbon can occur along the *ab*-plane. This work demonstrates that the Li diffusivity along the direction which is perpendicular to the current collector serves an important role in determining Li plating behaviors.

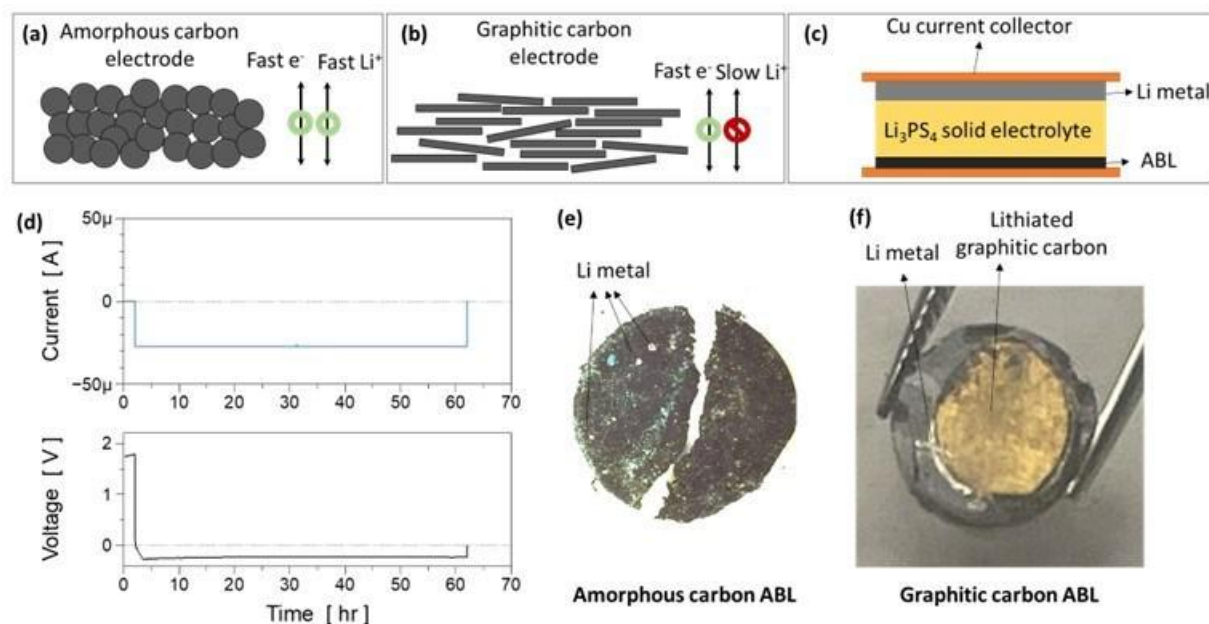


Figure XVI.32.3 Schematics of (a) amorphous carbon and (b) graphitic carbon electrodes. (c) Schematic of an asymmetric cell with ABL. (d) Discharging profile of the asymmetric cell. Optical microscopy images of (e) amorphous carbon and (f) graphitic carbon ABLs after Li plating.

Task 2: Composite cathode: high voltage stability, chemical and mechanical degradation issue.

Carbon-cathode composite design:

Currently there are two main fundamental challenges limiting the cyclability of composite cathodes: (1) chemical and electrochemical degradation at the cathode/SE and SE/carbon interfaces and (2) mechanical contact loss at the cathode/SE interface due to repeated expansion and contraction of the cathode particles. In FY22, we aimed to evaluate the strategy of tailoring coatings to the chemistry of the cathode. The novel 3-dimensional (3D) composite developed in this task consists of 3D carbon frame as a core which is coated with the cathode particles. The structure limits (or at least reduces) direct contact between carbon and SE and therefore minimizes the degradation of cathode composite. In addition, the soft and pliable carbon framework can accommodate the volume change of cathode active material (CAM) thus prevent the mechanical contact loss at the cathode/SE interface.

Three different routes were taken to synthesize the carbon/CAM composite: (i) directly deposit CAM particles outside the crystalline carbon framework surface and improve the conductivity by thermal annealing or CNT integration, (ii) synthesize 3D porous rGO (reduced graphene oxide) networks and then integrate them with the CAM particles, and (iii) direct integration of CAM on 2-dimensional (2D) rGO micro-flakes. To achieve controlled uniform coatings in routes (i) and (ii), we adopted a dual ligand modification method to deposit CAM around the carbon core with the assistant of poly(vinylpyrrolidone) (PVP) and Polyethylenimine (PEI) polymers on the surface. While the former promoted the dispersion of particles, the amino groups in the latter can improve the binding. In the first route, we used molecular organic framework (MOF) particles as an example to optimize the synthesis conditions. Covalent organic frameworks (COFs) were chosen as the carbon material due to their highly ordered structure, which can provide large surface area and 1-D channels to facilitate efficient ion transport. After thermal annealing under inert Ar atmosphere, the inner COFs transform to porous carbon material with the structure retained. The reverse design was investigated first in which COFs were directly grow outside the particles just for demo. Based on experimental results, the thickness of COFs shell can be tuned from ~10 nm to ~50 nm or more (Figure XVI.32.4). The successful synthesis of the core/shell particle/carbon structures validate the potential of uniform deposition of CAM as a shell with the assistant of dual ligands.

Attempts were also made to improve the crystallinity of the COFs shell to achieve the 1-D ion transport channel as well as the use of other particles as core to demonstrate the generality of our method. We first modified the particles with PVP and PEI before directly disperse the particles into the COFs monomer solution with certain concentrations. After aging for 2 hours, solvothermal method was applied to achieve the core/shell composite structure. In the next step, we will prepare the samples with particles as shell and carbon as core by using the same method in the demo reactions.

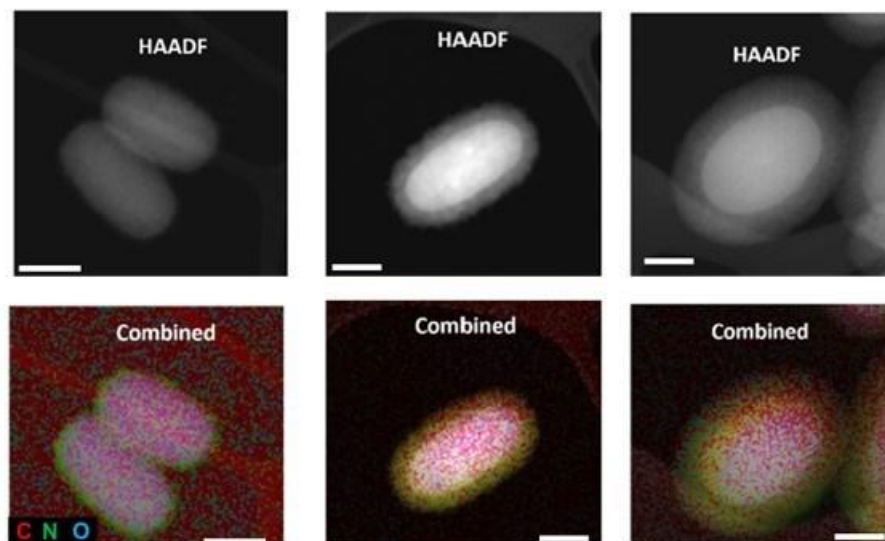


Figure XVI.32.4 Characterization of core-shell structures. TEM confirms the shell thickness can be tunable. (Scale bar: 250 nm)

In the third route, we used graphite oxide (GtO), which is obtained by oxidization from commercially available graphite, as a starting material. GtO is dispersed in deionized water and sonicated for 1.5h to exfoliate graphene layers. Commercially available $\text{LiNi}_x\text{Mn}_y\text{Co}_{1-x-y}\text{O}_2$ (NCM) CAM is added to the exfoliated graphene oxide solution and homogeneously mixed. After the mixed solution is stirred for 20 h at 90°C (oil bath) after adding Urea (a reducing agent), the powder is filtered and dried. Figure XVI.32.5a-d show the morphologies of NMC before hybridization (Figure XVI.32.5a-b) and after hybridization (Figure XVI.32.5c-d). Two main observations can be made: (i) rGO flakes are attached on large NMC particles and (ii) small NMC particles are decorated on rGO surface. XRD confirms that the crystallinity of NMC does not change after the synthesis (Figure XVI.32.5e). From the thermogravimetric (TGA) analysis, it is verified that the carbon content in the composite is ~ 9 wt% as shown in Figure XVI.32.5f. Synthesis conditions are being optimized by controlling several important parameters, including sonication time, CAM/graphene ratio, and CAM particle size.

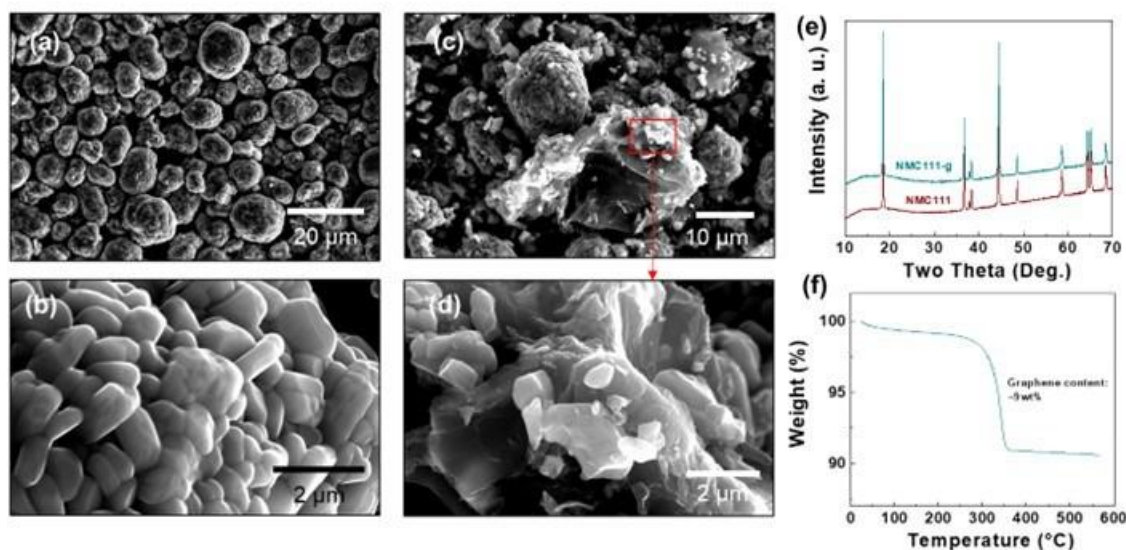


Figure XVI.32.5 Scanning electron microscope (SEM) images of (a-b) NMC and (c-d) NMC/graphene composite. (e) XRD of NMC and NMC/graphene composite. (f) TGA result of NMC/graphene composite.

Halide-based SE development for high voltage stability:

New Li_3MX_6 halides containing rare earth (RE) elements are also being developed as high-voltage stable SEs. So far a number of Li_3MCl_6 ($\text{M} = \text{Sc}, \text{In}, \text{Y}, \text{Er}, \text{Yb}$) chlorides have been reported to have a high ionic conductivity (up to 10^{-3} – $10^{-4} \text{ S}\cdot\text{cm}^{-1}$) and a wide electrochemical stability window (up to 4.3 V vs. Li/Li^+). In the Li_3REX_6 -family of compounds, it is fairly common for the halides to go through polymorphic transformations, especially under thermal treatments. For example, by means of solid-state reactions using relatively low annealing temperatures, metastable phases of Li_3RECl_6 (such as $\beta\text{-Li}_3\text{YCl}_6$ and trigonal Li_3YbCl_6) can be obtained, which were found to have higher ionic conductivities compared to their corresponding thermodynamically stable phases ($\alpha\text{-Li}_3\text{YCl}_6$ and orthorhombic Li_3YbCl_6). We aim to engineer new compositions and phases of Li_3REX_6 that may have better ionic transport properties, wider electrochemical stability windows and/or better mechanical properties. Synthesis conditions will be optimized according to thermal analysis using variable-temperature X-ray diffraction (XRD), thermogravimetry (TGA) and differential scanning calorimetry (DSC) measurements. Both variable-temperature XRD and DSC measurements can provide insights on phase transformations and may lead to the discovery of new phases, especially high-temperature phases. By recognizing the heat effects in phase transitions (endothermic or exothermic), the energetic relationships between different phases can also be obtained.

Li_3REX_6 -family (RE = rare earth) of halides often crystallize in three types of phases: monoclinic (C2/m structure), trigonal (P-3m1 structure) and orthorhombic (Pnma structure). It is well recognized that polymorphic transformations are common among the halides, especially under thermal treatment conditions. However, the impact of crystal structure on halide properties are not well understood. In FY22, the team investigated the synthesis-composition-structure-property relationships in the Li-Y-Cl system. Three synthesis routes, solid-state (SS), co-melting (CM) and mechanochemical (MC) methods, were used to prepare Li_3YCl_6 -type SEs. The precursors were heated at 450°C in SS synthesis and 550°C in CM synthesis, with the latter corresponding to synthesis under the melting condition of the precursors. High-energy ball milling was used in the MC synthesis.

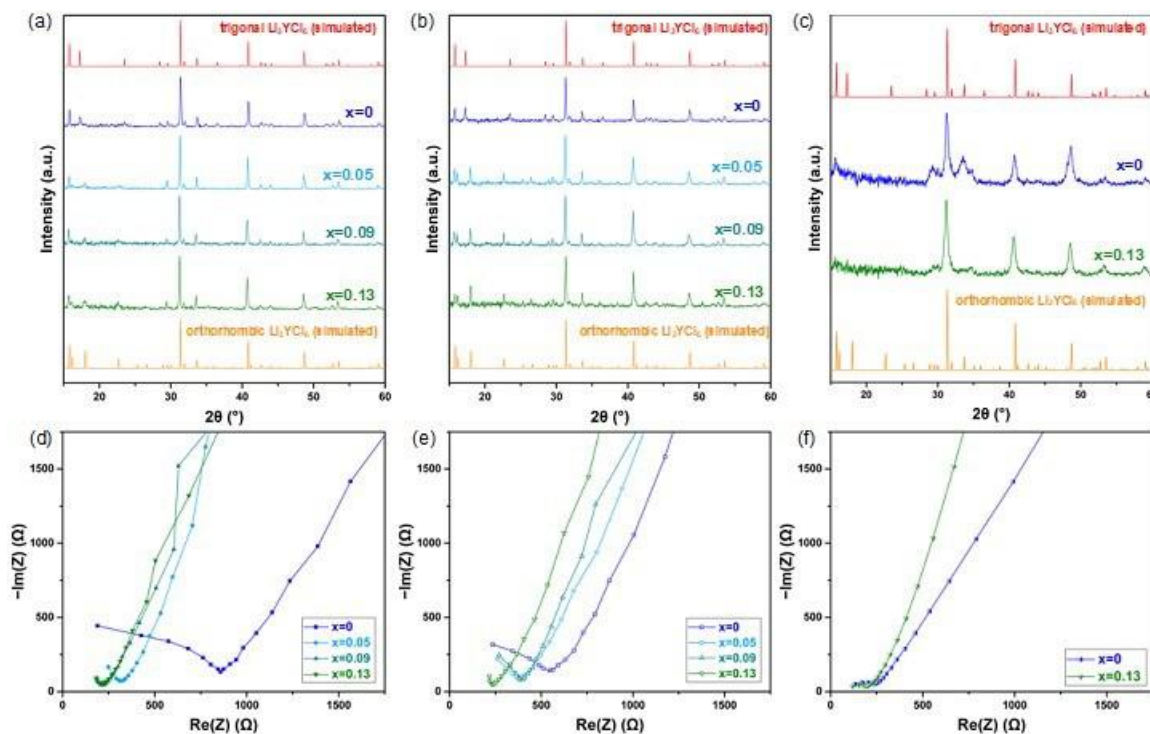


Figure XVI.32.6 (a, b, c) XRD patterns and (c, d, e) Nyquist plots of $\text{Li}_{3-x}\text{Y}_{1+x}\text{Cl}_6$ ($0 \leq x \leq 0.13$) samples prepared from solid-state (a, d), co-melting (b, e) and mechanochemical synthesis (c, f).

Figure XVI.32.6 shows XRD patterns obtained on various synthesized samples as well as the Nyquist plots from the electrochemical impedance spectroscopy (EIS) measurements. When the stoichiometric ratio (1:3) of YCl_3 and LiCl was used, Li_3YCl_6 with the trigonal phase was obtained from both SS and CM synthesis (Figure XVI.32.6a and b). Increasing the amount of YCl_3 precursor, on the other hand, leads to the formation of nonstoichiometric $\text{Li}_{3-x}\text{Y}_{1+x}\text{Cl}_6$ compounds with the orthorhombic phase. This is clearly shown by the splitting of the diffraction peak at $\sim 15.8^\circ$, the absence of the peak at $\sim 17.3^\circ$, and an additional peak appears at $\sim 18.0^\circ$ on the XRD pattern in Figure XVI.32.6a and b. We found that the synthesis method plays an important role as the trigonal-to-orthorhombic transition occurs at a different level of YCl_3 excess in SS and CM synthesis, with the former requiring a much higher amount than that in the latter. In comparison, the samples prepared by the MC method show significantly broader diffraction peaks. This is likely due to the lower crystallinity from high-energy ball milling synthesis as well as increased cation disordering in the lattice.

Synthesis methods also affect the lattice dimension of $\text{Li}_{3-x}\text{Y}_{1+x}\text{Cl}_6$. Figure XVI.32.7a shows the normalized unit cell volume (V/Z , where Z denotes the number of the chemical formula in the unit cell) obtained from the refinement of the XRD patterns. Among trigonal Li_3YCl_6 samples prepared by the different methods, the V/Z value follows the following order: MC > SS > CM. Room-temperature ionic conductivities (σ_{25}) obtained from EIS measurements are also shown in Figure XVI.32.7b. Consistent with previous reports, the values are 0.049 and 0.081 mS cm^{-1} for SS- Li_3YCl_6 and CM- Li_3YCl_6 , respectively. The conductivity increases with the increase of Y content in the composition, reaching 0.197 and 0.187 mS cm^{-1} for $\text{Li}_{3-x}\text{Y}_{1+x}\text{Cl}_6$ ($x = 0.13$) prepared by SS and CM, respectively. Overall, higher conductivities are obtained on ball-milled samples, achieving 0.179 and 0.233 mS cm^{-1} for $x=0$ and $x=0.13$, respectively (Figure XVI.32.7b). The σ_{25} of nonstoichiometric $\text{Li}_{3-x}\text{Y}_{1+x}\text{Cl}_6$ appears to be less dependent on the synthesis methods. These differences may be associated with the structural characteristics of trigonal and orthorhombic phases, such as the cation disorder and defect concentration, which will be further investigated in the future research.

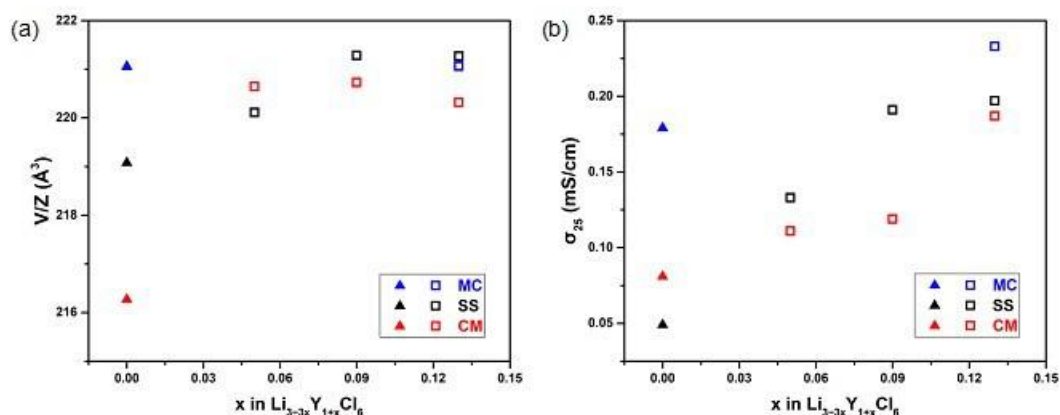


Figure XVI.32.7 Comparison of normalized unit cell volumes (a) and room-temperature ionic conductivities (b) of $\text{Li}_{3-x}\text{Y}_{1+x}\text{Cl}_6$ ($0 \leq x \leq 0.13$) samples prepared by different synthesis methods. \blacktriangle indicates trigonal phase and \square indicates orthorhombic phase.

Task 3. High-loading composite cathodes.

Thin SE layer development:

In this task, tape casting is used to fabricate a thin (target thickness 20 μm) Lithium Lanthanum Zirconium Oxide (LLZO) electrolyte separator. Figure XVI.32.8 shows the overall process to fabricate LLZO thin film. The tape casting and associated processes should be optimized to obtain high density, ionic conductivity, and mechanical properties of the prepared thin LLZO electrolyte. We optimized variables such as the lamination pressure, debinding time, and sintering time. Firstly, the effect of lamination pressure on green body density and fabricated thin LLZO film was investigated. Lamination is a step to bind separate tape casted LLZO sheets into one sheet (green body) by exerting pressure at an elevated temperature (Figure XVI.32.8, right). Lamination pressures between 4500 to 20000 lb for an area of 2.27 cm^2 were scanned. At a lamination pressure of 9000 lb at 90°C, the green density reached 2.07 g/cm^3 . The green density did not increase further with pressure. Thus, we decided to fix 9000 lb as an appropriate lamination pressure for the LLZO film fabrication.

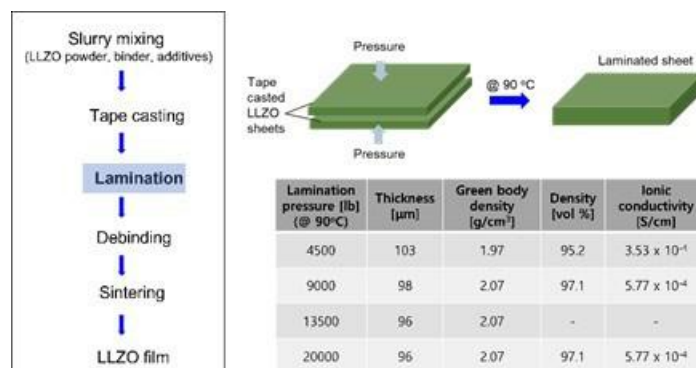


Figure XVI.32.8 Thin LLZO film fabrication process (left). Schematic illustration of lamination step and effect of lamination pressure on properties of fabricated LLZO film (right).

The effect of debinding time on densification of LLZO film was also investigated. Debinding involves the burning off of the binder and additives at a high temperature. If these are not fully removed through the debinding process, the residual hinders densification. Figure XVI.32.9 shows the relationship between debinding time and the green body weight. The weight of the green body keeps decreasing even after 12 hours of debinding at 675°C. This result indicates that a longer debinding time or higher debinding temperature is necessary. After several experiments, we optimized the debinding temperature at 690°C and the debinding process was completed after 4 hours.

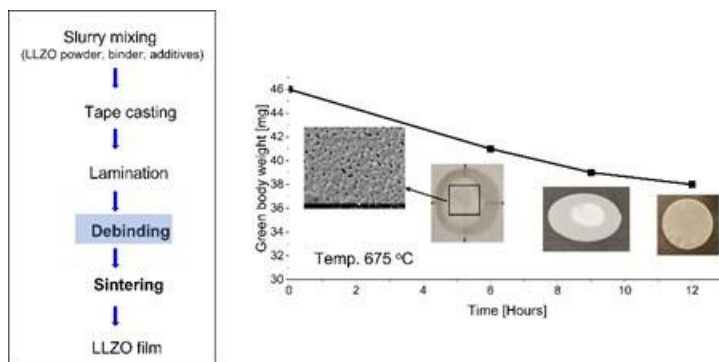


Figure XVI.32.9 Debinding time vs. green body weight. The inset pictures are fabricated LLZO film with different debinding times. The white area in the central area of the LLZO film has a relatively low density because of incomplete debinding.

The team has also optimized the procedure to fabricate a flat LLZO film. The LLZO film was sintered under a dead weight to prevent curving (Figure XVI.32.10). The loading should be heavy enough to prevent the curve, but it should not be so heavy that it breaks the sample. A graphite plate was used as a weight because it is chemically inert with LLZO at high temperatures. Different loadings from 1 to 3 g/cm² were tested. As shown in Figure XVI.32.10, the sintered LLZO film was severely curved with the 1 g/cm² loading. The 2 g/cm² loading resulted in less curving than the 1 g/cm², but curving was still evident. The 3 g/cm² loading was enough to prevent curving without breaking the sample.

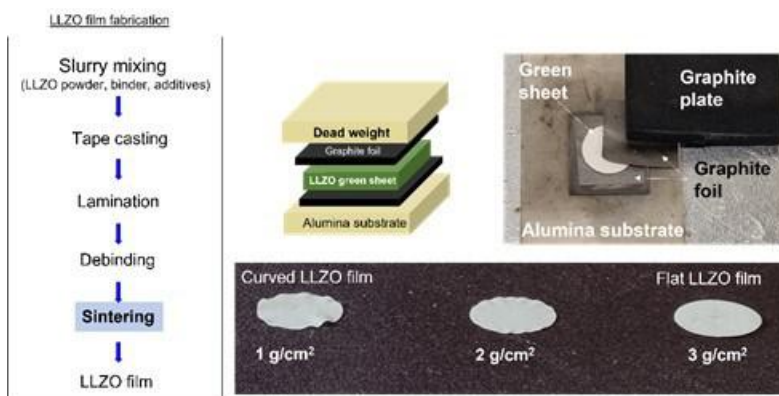


Figure XVI.32.10 Schematic view of sintering condition (upper) and effect of dead weight on the flatness of the sintered thin LLZO film (below).

The sintering temperature was also explored in the range of 1050°C to 1180°C. The sintering behavior of thin LLZO may be different from thick LLZO pellets because it can undergo relatively more Li loss and more severe shrinkage during sintering. All the samples were sintered with 3 g/cm² loading under an argon atmosphere. Up to the sintering temperature of 1150°C, the LLZO films were flat and semi-translucent as shown in Figure XVI.32.11. But a sample treated at 1180°C had a surface color change and relatively poor flatness. These results show that the optimum sintering temperature needs to be below 1180°C.

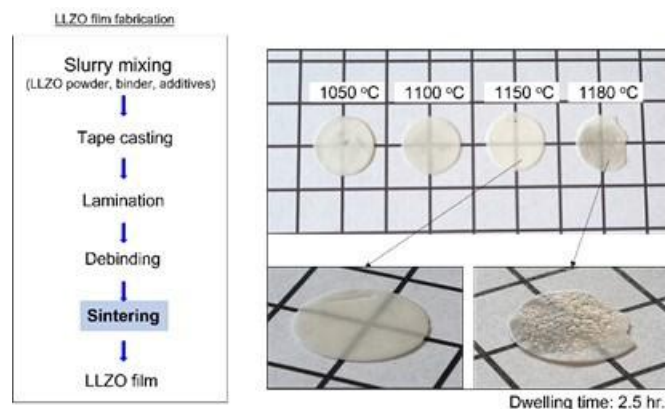


Figure XVI.32.11 Picture of sintered LLZO films that were sintered at different temperatures.

Mechanical properties of thin LLZO film:

We have started the investigation of the mechanical properties of the films. The mechanical properties of thin LLZO films need to be characterized and enhanced because the thin LLZO is currently highly fragile. Preliminary mechanical property testing has been conducted with thick LLZO pellets ($\sim 700\ \mu\text{m}$) because the LLZO film synthesis needs more optimization. In this report, we fabricated LLZO pellets at LBNL using the same recipe as for the LLZO thin films and evaluated mechanical properties such as hardness (H) and fracture toughness (K_{IC}). Hardness (H) was evaluated using micro-indentation. Indentation with 5 different loads (50, 100, 300, 500, and 1000 gf) was conducted, and the diagonal lengths of the indented points were plotted. By fitting the diagonal length vs. applied force, we obtained a hardness of 10.02 GPa, in the range of hardness reported in the literature for LLZO pellets. Fracture toughness (K_{IC}) was also evaluated using the direct crack length observation method. The length of the cracks at the corners of the indented points was measured. Using the above-obtained hardness and observed crack length, the fracture toughness (K_{IC}) could be obtained using the Niihara equation. The K_{IC} was $1.367\ \text{MPa}\cdot\text{m}^{0.5}$, again in good agreement with previously reported values of fracture toughness of LLZO pellets.

Secondary SE development and integration:

The team has tested cathode composites containing secondary SEs. The cathode composite consists of cathode active material (CAM) and secondary SE. In this study, we used NMC111 ($\text{Li}_{1.05}\text{Ni}_{0.33}\text{Mn}_{0.33}\text{Co}_{0.33}\text{O}_2$) as a CAM. As a secondary SE, Succinonitrile (SN) with lithium salts were investigated because they have good oxidative stability and high Li^+ ion conductivity. LiTFSI (Lithium bis(trifluoromethanesulfonyl) imide) was used as the lithium salt because it is known to be stable with LLZO. SN+LiTFSI was prepared by mixing molten SN and LiTFSI at 80°C . The ionic conductivity, electronic conductivity, and voltage stability window of the secondary SE were evaluated. Symmetric cells (SUS/SN+ LiTFSI/SUS,) were fabricated to evaluate ionic conductivity and electronic conductivity, then electrochemical impedance spectroscopy (EIS) and direct current (DC) polarization were conducted. The Nyquist plots from the EIS are plotted in Figure XVI.32.12a. The diameter of the semicircle significantly decreased with higher LiTFSI concentrations indicating that it has a higher ionic conductivity. The ionic conductivity increased more than 10 times from $2.39 \times 10^{-4}\ \text{S/cm}$ (1.6 mol%) to $3.47 \times 10^{-3}\ \text{S/cm}$ (5.0 mol%). DC polarization curves are shown in Figure XVI.23.12b, and all the SN+LiTFSI samples showed similar electronic conductivity $\sim 1 \times 10^{-9}\ \text{S/cm}$. These EIS and DC polarization results show that the SN+LiTFSI is highly ionic conductive but electronically insulating. In order to observe the stable voltage window of the SN+LiTFSI, Li/SN+LiTFSI/SUS cells were fabricated, and linear sweep voltammetry was conducted (Figure XVI.32.12c). Up to 4.7 V vs. Li/Li^+ , negligible current was detected for all the SN+LiTFSI samples. This indicates that SN+LiTFSI has a wide enough voltage window to be used with high-voltage cathode active materials. The team will further explore other secondary SEs, including other salts such as LiBOB and mixtures with LiTFSI, and will assess compatibility of secondary SEs with cathode materials. The team will also attempt to build liquid-free cells using a mixture of SSE, CAM and conductive additives for the cathode, with LLZO separators.

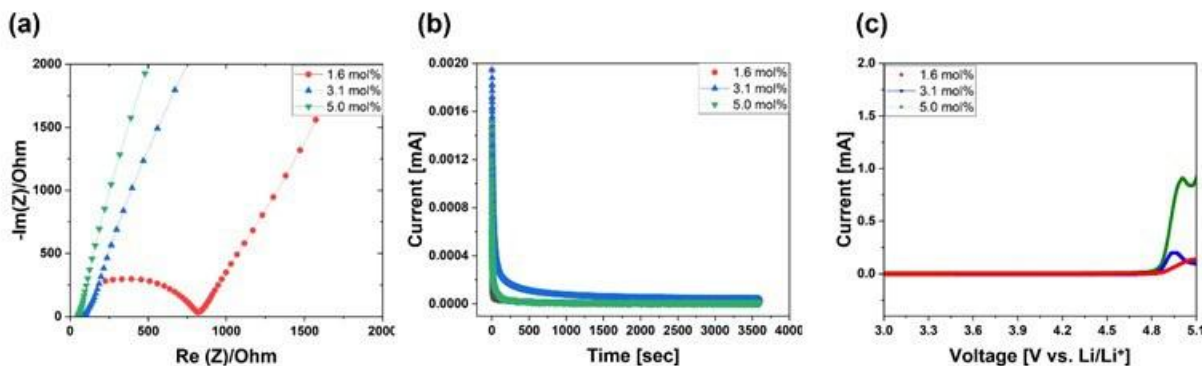


Figure XVI.32.12 Property testing of different mol% of LiTFSI in SN. (a) Nyquist plot. (b) DC Polarization. (c) LSV.

Task 4. Glass composite solid electrolyte by low-temperature solution-phase synthesis.

This task aims to develop a sulfide glass separator that is both thin and resisting Li dendrite penetration from the lithium metal anode side. Solution processable separators would be more easily integrated with solid-state batteries through low-cost processing. In addition, solution processable SEs could be directly integrated with cathode materials to form a composite cathode through conventional slurry coating. Our objective is therefore to develop the processes to synthesize hybrid SEs from inorganic conductors and polymer through solution-based processes, and which combine high ionic conductivities ($>10^{-3} \text{ S cm}^{-1}$) and high fracture toughness ($>10 \text{ MPa m}^{1/2}$). We will initially focus on sulfide-based materials, but will also consider other inorganic conductors later in the process. The sulfide coupled with a functional polymer network will be deposited through the solution-phase as a thin film onto a protected lithium metal surface. As the solvent evaporates, an intimate mixture of sulfide glass and polymer network is formed within a homogeneous film. Replicating the biomineralization processes that occur in natural structural materials, the polymer functional groups will strongly interact with the sulfide glass to form a material with high fracture toughness. The composition of the sulfide glass can also be modified using various dopants to tune the chemical and electrochemical properties of the SE.

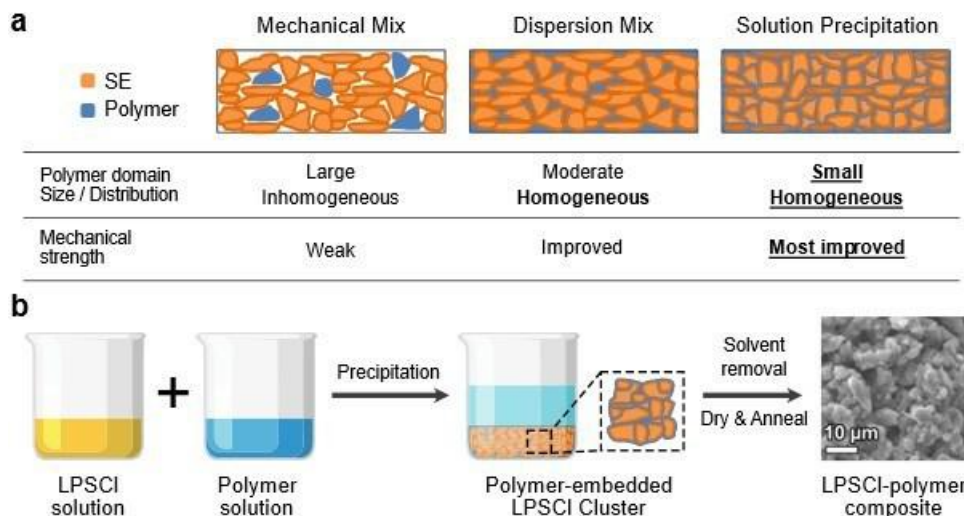


Figure XVI.32.13 (a) Comparison of three possible methods for preparing the solid electrolyte-polymer composites. Note that the solution-precipitation method has an advantage of a high mechanical strength owing to its smaller polymer-domain size and uniformly distributed microstructure. (b) Schematic showing the preparation process of the solution-precipitation method.

There are three different methods that can mix functional polymers with solid-state ceramic materials – direct mechanical mixing, slurry dispersion, and solution precipitation as shown in Figure XVI.32.13. The

morphology of the mixture is very different among the three methods. Mechanical mixing tends to yield the most inhomogeneous composite, since the particles' size determines the mixing uniformity. The slurry dispersion allows the polymer particles to dissolve in the slurry solvent, therefore the polymers tend to coat on the ceramic particles. In this case, the finer the ceramic particles, the better the dispersion. Solution precipitation dissolves both the polymer adhesive and ceramic particles in the solvents, and precipitated both polymer and ceramic out concurrently and instantaneously in nonsolvent. The mixture could form nanoscale or even molecular level mixture depending on the polymer and ceramic cluster interactions. This task mainly focuses on the developing, understanding, and controlling of the processes of the slurry dispersion and solution precipitation method. A novel solution-precipitation approach was employed to prepare LPSCl-polymer composites using polyethylene oxide (PEO) and polyphenylene oxide (PPO) polymers. PEO can strongly interact with Li-ion through the oxygen elements in PEO. PPO also has oxygen elements, which can interact with lithium-ion. PPO also have higher thermally stability. Ethanol (EtOH) is used as a solvent to dissolve the LPSCl solid form to a soluble cluster form. However, the overall liquid process time must be controlled to retain the cluster structure and subsequent argyrodite structure. Thus, we first investigate the effect of dissolution time on the LPSCl structure properties, as shown in Figure XVI.32.14. SEM images (Figure XVI.32.14a-c) show the decrease in the grain size of the SE with the dissolution time in EtOH, and it appears to form a more amorphous-like shape at a longer dissolution time (30-min). In addition, XRD results show a decrease in the signal for both cases compared to the pristine LPSCl, but the 30-min sample shows the lowest intensity of XRD peaks among the samples (Figure XVI.32.14d). A decrease in the ionic conductivity with the dissolution time is also observed (Figure XVI.32.14e). 30-min sample shows a comparatively lower conductivity (0.01 mS/cm) than 5-min sample (0.04 mS/cm). These results suggest that the dissolution of LPSCl in EtOH will affect the overall crystal structure and ionic conductivity of the recovered precipitates and those properties are strongly dependent on the dissolution time. Thus, the solution-precipitation method requires the minimum exposure of LPSCl to EtOH to minimize the depletion of the crystal structure of LPSCl and additional heat treatment to recover some crystal structure and ionic conductivity of LPSCl.

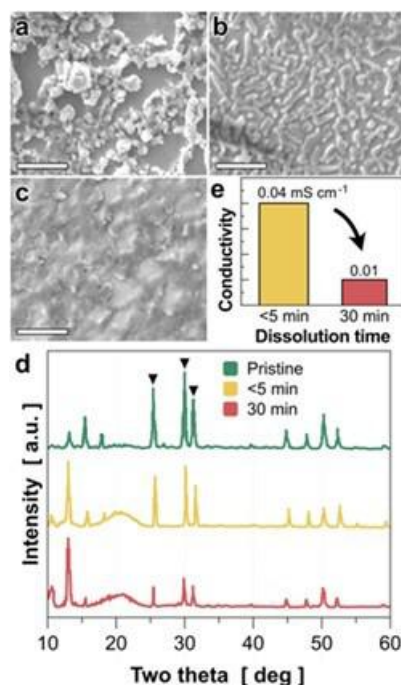


Figure XVI.32.14 Morphological and structural changes with dissolution time in EtOH. (a-c) SEM images of (a) pristine LPSCI powder, (b) LPSCI precipitate after dissolution in EtOH for 5 min, and (c) after dissolution for 30 min. Scale bars in SEM images are 10 μm . (d) XRD results of LPSCI with a different dissolution time in EtOH. As the time increases, the intensities of the representative LPSCI peaks (denoted as a triangle) decreases. Please note that the sharp peak at $\sim 13^\circ$ and the bump peak at $\sim 20^\circ$ were from a different airtight XRD holder used in yellow and red patterns. (e) Ionic conductivities of LPSCI with different dissolution times. Note that a shorter dissolution time of LPSCI is preferred to exhibit a higher conductivity.

To evaluate the proposed solution-precipitation method, we comparatively investigated the morphological and mechanical properties of the LPSCI-polymer composites with the other preparation methods. First, we discuss the morphology of LPSCI-PEO composites using SEM images in Figure XVI.32.15. Regardless of the polymer content, all composites displayed similar morphology with crystal grain sizes between 1 and 10 μm . Unlike the size of LPSCI decreased after the precipitation without polymer, the feature size of the polymer composite appears to be preserved when the precipitation was performed in the polymer solution. This result suggests that the polymer promotes LPSCI precipitation and possibly limits ethanol accessibility to LPSCI. Because we could not identify the polymer phase in SEM images, we performed transmission electron microscope (TEM)-energy dispersive X-ray spectroscopy (EDS) analyses to track how the polymer distributes on the composites. For the TEM analyses, we used an air-tight sample transfer TEM holder to avoid any potential degradation of the composite due to air exposure. Figure XVI.32.16 shows the comparative results between LPSCI-PEO composites by dispersion method (Figure XVI.32.16a) and the composites via the solution-precipitation method (Figure XVI.32.16b). Considering all sample preparation procedures were conducted without air exposure, oxygen (O) elemental distribution in the EDS maps is expected to represent the presence of PEO along with the LPSCI phase. To compare the elemental distribution clearly, we put bi-elemental maps of P-O and P-Cl right next to each STEM-HAADF image. For the 2 wt.% polymer composites prepared by the dispersion mix method, a non-uniform distribution of PEO is clearly observed as shown in Figure XVI.32.16a. In contrast, the solution-precipitation method creates a uniform distribution of PEO in LPSCI composites (Figure XVI.32.16b). These results confirm a solution-precipitation method is better than the dispersion mix one in order to produce a uniform distribution of the polymer and ceramic phase.

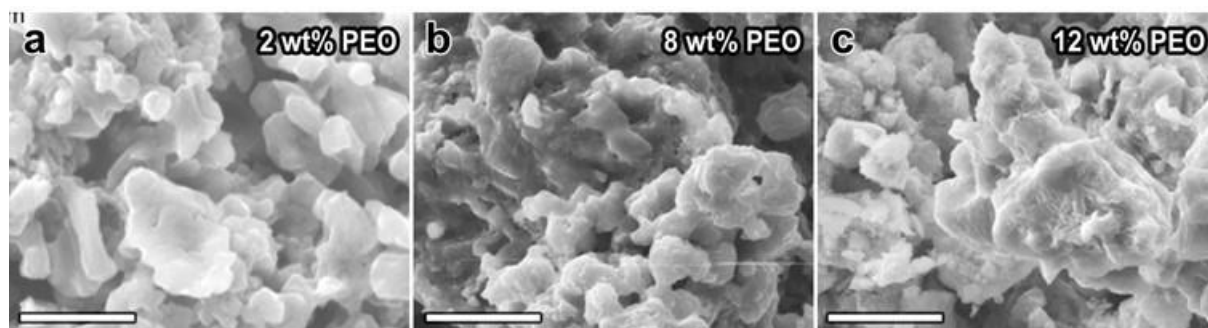


Figure XVI.32.15 Scanning electron microscope (SEM) images of LPSCI-PEO composites with the polymer content of 2%w, 8%wt, and 12% wt (from left to right).

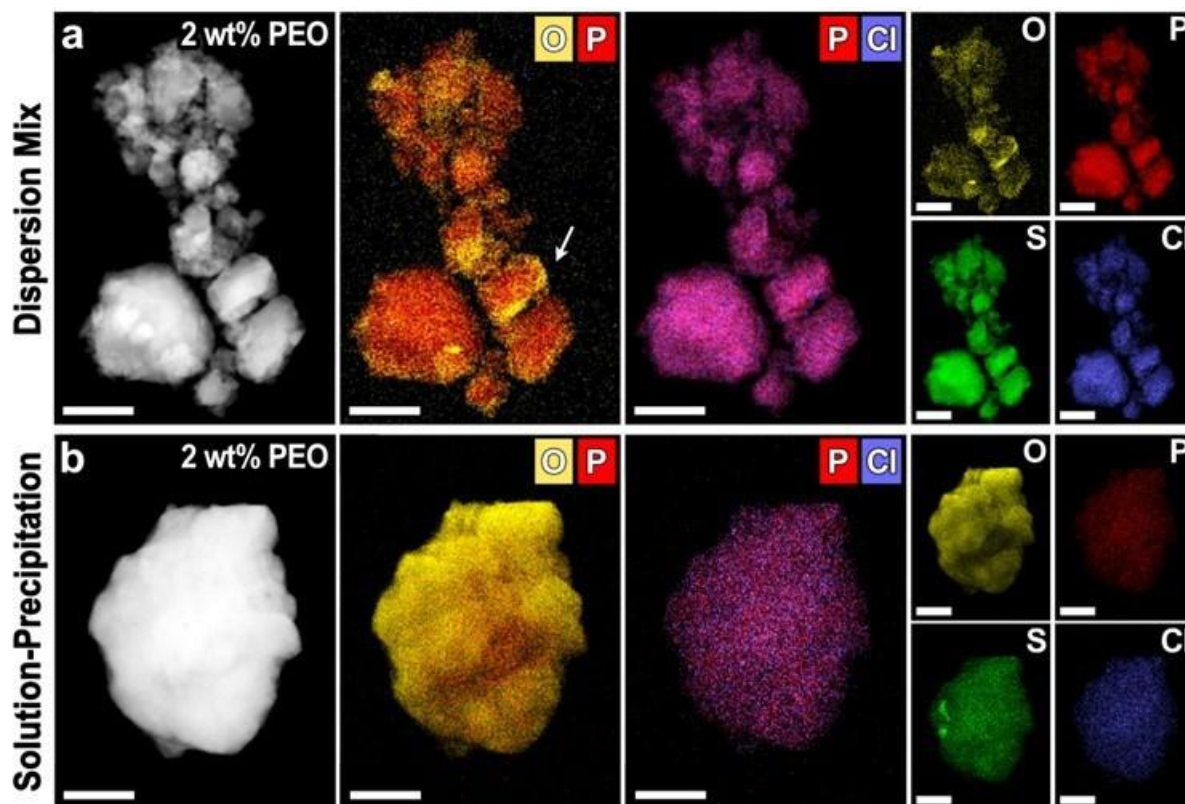


Figure XVI.32.16 Chemical and Mechanical evaluations of LPSCI-PEO composite. (a-b) Elemental mappings of (O, P, S, Cl) in LPSCI-PEO composites with 2 wt.% polymer content. Note that the composites are prepared by two different methods: (a) dispersion mix and (b) solution-precipitation methods. (Scale bar: 1 μ m)

Conclusions

This project has four main tasks: (1) ABL development, (2) chemically and mechanically stable cathode composite development, (3) high loading cathode composite design, and (4) glass composite solid electrolyte development. For task 1, the team has optimized the thin ABL film fabrication process (~ 10 μ m), investigated the lithiation process in Ag by computations to understand how Ag nanoparticles in ABL help to uniform Li metal plating, and studied how the carbon structure affect the Li metal plating behaviors. For task 2, the team has evaluated their approaches to make CAM-carbon composite electrodes that can provide high electronic conductivity but minimize detrimental carbon-SE interfaces. In addition, the team investigated the synthesis-

composition–structure–property relationships in the Li–Y–Cl halide SEs. By increasing Y content in $\text{Li}_{3-x}\text{Y}_{1+x}\text{Cl}_6$ ($0 \leq x \leq 0.13$), they observed higher ionic conductivities. Task 3 focuses on the optimization of thin LLZO separator and development of secondary SE for the cathode composite. They developed thin ($<100 \mu\text{m}$) LLZO separators but further optimization is underway to achieve $<20 \mu\text{m}$. The team has studied SN-based plastic crystal SEs to be used as catholytes. In the efforts of Task 4, the team has developed glass ceramic hybrid SEs consisting of PEO and LPSCl. They found the solution-precipitation method can make uniform mixing of PEO and LPSCl in contrast to mechanical mixing and slurry dispersion methods.

Key Publications

1. Hao Shen, Kai Chen, Jiawei Kou, Zhanghui Jia, Nobumichi Tamura, Weibo Hua, Wei Tang, Helmut Ehrenbert, and Marca Doeff “Spatiotemporal Mapping of Microscopic Strains and Defects to Reveal Li-dendrite-induced Failure in All-Solid-State Batteries” *Materials Today*, 57, 180-191 (2022). DOI: 10.1016/j.mattod.2022.06.005

References

1. Sascha Thinius, Mazharul M. Islam, Paul Heitjans, and Thomas Bredow. “Theoretical Study of Li Migration in Lithium–Graphite Intercalation Compounds with Dispersion-Corrected DFT Methods” *J. Phys. Chem. C* 118, 5, 2273–2280 (2014). <https://doi.org/10.1021/jp408945j>

Acknowledgements

This project collaborates with the following co-PIs: V. Battaglia, G. Chen, M. M. Doeff, G. Liu, M. Scott, M. Tucker, and J. Urban, all at LBNL.

XVII Beyond Li-Ion R&D: Lithium Sulfur Batteries

Lithium-sulfur (Li-S) battery technology has the potential to offer affordable, lighter-weight batteries that also have a safety advantage over present systems. In these batteries, the metal-rich cathode of Li-ion cells is replaced with a comparatively cheap and abundant elemental sulfur, a material that offers the theoretical potential for a five-fold improvement in capacity for the same weight. By using sulfur, lightweight cells can be produced using more cost-effective materials, while also reducing the environmental and social concerns surrounding the production of nickel and cobalt. Whereas such battery types as Li-ion and Na-ion employ an intercalation mechanism for Li-ions to shuttle between electrodes, Li-S batteries operate by a ‘conversion mechanism’ in which elemental sulfur and lithium react to form a series of lithium-containing sulfur compounds (polysulfides) to deliver the energy stored in the cell. There are several key challenges associated with this technology including the poor electronic conductivity of sulfur, the dissolution of discharge products (shuttle effect) and the poor reversibility of lithium.

The rest of this chapter contains detailed reports on the status of the following individual projects.

- A Novel Chemistry: Lithium-Selenium and Selenium-Sulfur Couple (ANL)
- Development of High Energy Lithium-Sulfur Batteries (PNNL)
- Mechanistic Investigation for the Rechargeable Li-Sulfur Batteries (Brookhaven National Laboratory & University of Wisconsin-Milwaukee)
- New electrolyte binder for Lithium sulfur battery (LBNL)
- Strategies to Enable Lean Electrolytes for High Loading and Stable Lithium-Sulfur Batteries (UCSD)
- New Engineering Concepts for High Energy Density Li-S Batteries (UPitt)
- Development of Li-S Battery Cells with High Energy Density and Long Cycling Life (PSU)
- Nanostructured Design of Sulfur Cathodes for High Energy Lithium-Sulfur Batteries (Stanford University).

XVII.1 A Novel Chemistry: Lithium-Selenium and Selenium-Sulfur Couple (ANL)

Khalil Amine, Principal Investigator

Argonne National Laboratory
9700 South Cass Avenue
Lemont, IL 60439
E-mail: amine@anl.gov

Tien Duong, DOE Technology Development Manager

U.S. Department of Energy
E-mail: Tien.Duong@ee.doe.gov

Start Date: October 1, 2013

End Date: September 30, 2022

Project Funding (FY22): \$500,000

DOE share: \$500,000

Non-DOE share: \$0

Project Introduction

Lithium/sulfur (Li/S) batteries have attracted extensive attention for energy storage applications due to the high theoretical energy density (2600 Wh/kg) and earth abundance of sulfur.[1] Recently, selenium and selenium-sulfur systems have also received considerable attention as cathode materials for rechargeable batteries because of the high electronic conductivity (20 orders of magnitude higher than sulfur) and high volumetric capacity (3254 mAh cm⁻³) of selenium.[2] Selenium-sulfur (Se-S) mixtures are miscible in a wide concentration range, and many Se-S composites can be prepared, including Se₅S, Se₅S₂, Se₅S₄, SeS, Se₃S₅, SeS₂, SeS₇, and even materials with a small amount of Se such as SeS₂₀. [2] These Se-S composites offer higher theoretical specific capacities than Se alone and improved conductivity compared to pure S. However, similar to Li/S batteries, two major obstacles resulting from lithium polysulfides/polyselenides (LiPSs/LiPSes) shuttle and lithium dendrite formation remain huge challenges for long-life Li/Se-S batteries.[3] The former is due to the dissolution and migration of polysulfides/polyselenides intermediates in the conventional ether-based electrolytes, which could induce severe parasitic reactions with Li metal and hence formation of porous or mossy Li metal. The latter is originated from the parasitic reactions of lithium metal with the electrolytes, leading to the formation of fragile solid electrolyte interphase (SEI) on Li metal, further uncontrolled lithium dendrite growth and eventually dead lithium. These parasitic reactions are the direct cause for the rapid capacity fade and poor coulombic efficiency of Li/S and Li/Se-S batteries.

Via advanced diagnostic tools including synchrotron X-ray probes and computational modeling, the team led by Dr. Khalil Amine and Dr. Guiliang Xu at Argonne National Laboratory (ANL) is focusing on the development of rational cathode structure designs and exploration of novel electrolytes to effectively eliminate these parasitic reactions and simultaneously suppress the shuttle effect and lithium dendrite formation during long-term cycling.

Objectives

The objective of this project is to develop novel Li/Se-S batteries with high energy density (500 Wh/kg) and long life (>500 cycles) along with low cost and high safety.

Approach

To prevent the dissolution of polysulfides and increase the active material utilization, S or Li₂S is generally impregnated in a conducting carbon matrix. However, this approach makes it difficult to increase the loading density of practical electrodes. It is proposed here to solve the above barriers by the following approaches: (1) partial replacement of S with Se, (2) confinement of the Se-S in a porous conductive matrix with high pore volume, and (3) exploration of advanced electrolytes that can suppress shuttle effect and lithium dendrite growth.

Collaboration

- Synchrotron X-ray diffraction: Dr. Wenqian Xu, APS of ANL
- Synchrotron X-ray absorption spectroscopy: Dr. Chengjun Sun, APS of ANL

Results

Development of 1Ah-level Li/S pouch cell with 300 Wh/kg cell energy density and stable cycle life via a double-end binding host design

Currently, most of the reported Li/S batteries were evaluated in coin cells only, while the performance in practical pouch cells showed disappointingly lower specific energy and shorter cycle life. In FY21, we have developed an advanced sulfur cathode using a host with double-end binding sites (denoted as 3d-omsh/ZnS,Co-N-C/S). In FY22, we have been focusing on fabrication of Ah-level Li/S pouch cell with high cell energy density and stable cycle life using this cathode. We have calculated the cell energy density of Li/S pouch cell as a function of areal S loading and electrolytes/sulfur (E/S) ratio, see Figure XVII.1.1a. The results show that in order to reach the goal of 300 Wh/kg, the E/S ratio should be maintained below 4 $\mu\text{L}/\text{mg}$ and the areal capacity should be at least 6 mAh/cm^2 . We therefore proposed a multilayers and interdigitated type battery for the pouch cell stacking (Figure XVII.1.1b). As a result, we have fabricated a four-layers Li/S pouch cell using 3d-omsh/ZnS,Co-N-C/S cathode with a areal S loading of $\sim 6.25 \text{ mg}/\text{cm}^2$ (6mm*8 mm) and total S amount of 1.2 gram. The electrolytes used in the test was conventional dioxolane (DOL)/ dimethoxyethane (DME)-based electrolytes and the electrolyte/sulfur ratio is controlled at 4 $\mu\text{L}/\text{mg}$. The negative/positive capacity ratio is around 2.6.

Figure XVII.1.2a shows the charge/discharge curves of 1.2g-sulfur pouch cell at different current densities. As shown, the as-assembled cell could deliver a high specific capacity of $> 1200 \text{ mAh}/\text{g}$ at 41.67 mA/g , indicating a high sulfur utilization even under operation with a lean electrolyte and high areal S loading condition. The specific energy of the pouch cell was evaluated on the basis of the equation (1):

$$E_g = \frac{vc}{\sum m_i} \quad (1)$$

where E_g is the cell specific energy (Wh/kg), V is the output voltage (V), C is the output capacity (mAh), and m_i is the weight (g) of each component of the pouch cell. The total weight taken into consideration includes the weight of the cathode (including sulfur, binder, carbon black, and carbon host), Li metal foil (100 μm), electrolyte ($\rho_{\text{electrolyte}} = 1.0 \text{ g}/\text{cm}^3$), separator ($\rho_{\text{separator}} = 0.95 \text{ g}/\text{cm}^3$), Al foil ($\rho_{\text{Al}} = 2.70 \text{ g}/\text{cm}^3$) current collector, and Cu foil ($\rho_{\text{Cu}} = 8.96 \text{ g}/\text{cm}^3$) current collector. The weight percentage of each component is summarized in Figure XVII.1.3. As a result, it could enable a high practical cell energy density of 317 Wh/kg.

When the current density was increased by 4X, the specific capacity was decreased to around 950 mAh/g with increased voltage polarization. This should be due to the insufficient ion transport in the thick cathode under lean electrolytes condition, indicating further improvement is needed to boost the performance at higher current densities. Figure XVII.1.2b shows the corresponding cycle performance of the Li/S pouch cell at 83.33 mA/g and E/S ratio of 4 $\mu\text{L}/\text{mg}$. Surprisingly, even under the influence of side reactions between the bare lithium metal and the DOL/DME-based electrolyte, our Ah-level Li/S pouch cell still delivered high Coulombic efficiency ($> 95\%$) and stable cycling performance for 80 cycles ($\sim 74\%$ capacity retention), supporting the effectiveness of the double-end binding sites in immobilizing polysulfides and eliminating Li metal corrosion. We have compared our results with the reported performance in the literature, and found that in terms of specific energy, cycle life and capacity retention, our Li/S pouch cell based on the macroporous host with double-end binding site design clearly represents a significant advance. While you could see the fluctuation of capacity after tens of cycles, which should be attributed to the inherent instability of Li metal with the conventional ether electrolytes. With further Li metal protection (e.g., host design or electrolytes modulation) and cell configuration optimization (e.g., internal pressure), we believe the performance could be further improved.

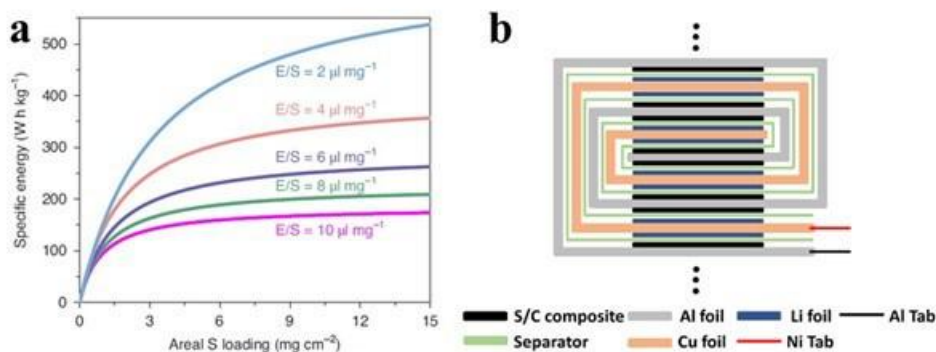


Figure XVII.1.1 (a) Calculated specific energy versus areal S loading for Li/S pouch cells with different E/S ratios assuming that the specific capacity and the average discharge voltage are 1,000 mAh/g and 2.05 V, respectively. (b). Configuration of interdigitated type battery winding for the pouch cell stacking.

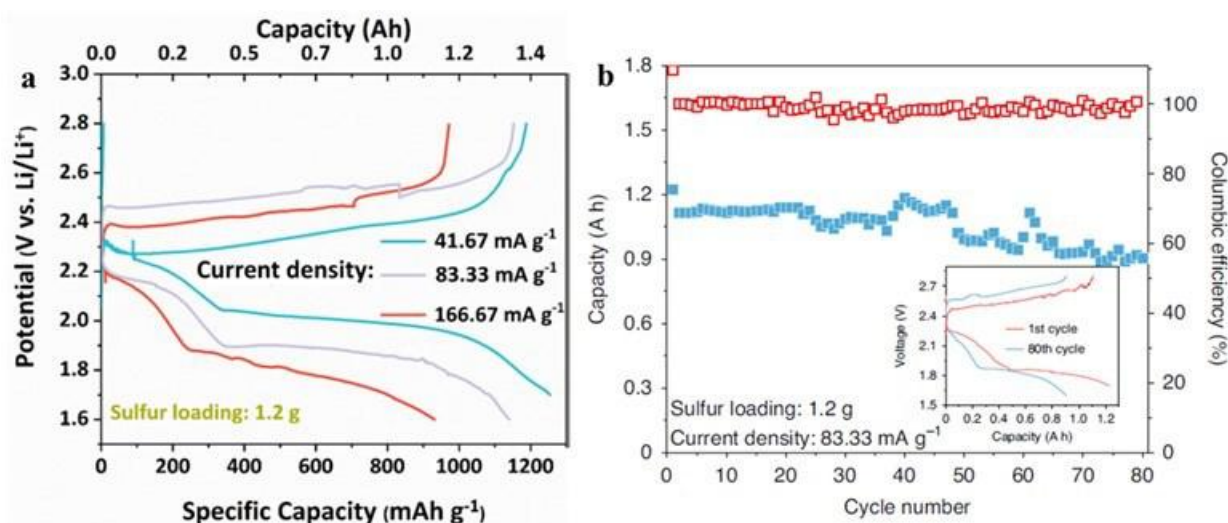


Figure XVII.1.2 (a) Charge/discharge curves of 1.2 g-sulfur pouch cell using sulfur/macroporous host with double-end binding cathode under different current density ranging from 41.67 mA/g to 166.67 mA/g. (b). Cycling performance of 1.2-g-sulfur pouch cell using sulfur/macroporous host with double-end binding cathode at 83.33 mA/g.

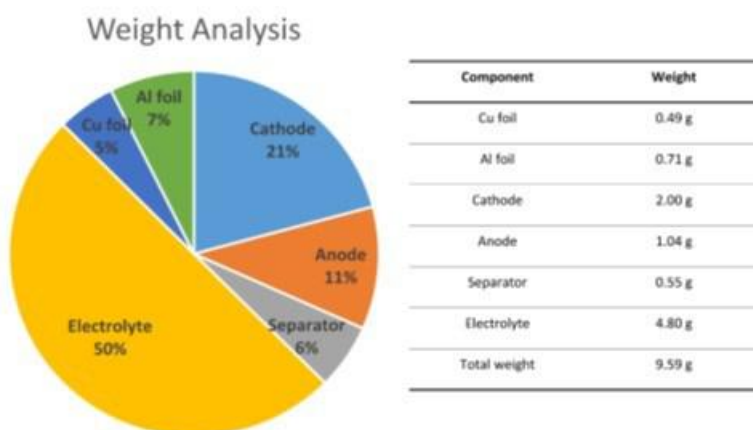


Figure XVII.1.3 Weight analysis pie chart of the 1.2-g-sulfur pouch cell through interdigitated type battery winding.

Advanced characterization of sulfur/double-end binding composite during charge/discharge

To clearly understand the underlying mechanism for the significantly improved performance of the aforementioned Li/S pouch cell using double-end binding host, we have conducted a series of in situ and ex situ characterization.

First of all, we used in situ synchrotron high-energy X-ray diffraction (HEXRD) to reveal the reaction mechanism of 3d-omsh/ZnS,Co-N-C/S cathode during charge/discharge at C/10. As shown in Figure XVII.1.4, four peaks located at 2.05° , 2.37° , 3.35° and 3.92° can be assigned to the Li_2S crystal phase, which started to emerge at the same depth of discharge (Point A, 2.14 V). The peak intensities for the solid Li_2S keep increasing with further lithiation to 1.8 V, suggesting the continuous precipitation of Li_2S during discharge. Moreover, four X-ray diffraction peaks at $\sim 2.02^\circ$, 2.18° , 3.40° and 3.96° , which appeared slightly later (Point B, 2.13 V) than that for Li_2S and then disappeared (Point C, 2.10 V) during further discharge, can be attributed to the solid Li_2S_2 intermediates. This is consistent with the previous observation of Li_2S_2 and resolves the debate on the existence of Li_2S_2 during charge/discharge of Li/S batteries. During the subsequent charging process, the peak intensities assigned to Li_2S gradually decrease and completely disappear after charge beyond point D, 2.30 V. In addition, the formation/decomposition of the crystalline Li_2S_2 intermediate that was observed during discharge did not occur during charge, which is due to the fast and efficient conversion of solid Li_2S_2 to liquid LiPSs by the DEB sites.

Furthermore, in situ UV-visible (UV-vis) spectroscopy characterization during discharge of the 3d-omsh/ZnS,Co-N-C/S cathode directly confirmed no migration of polysulfides species on the Li anode side, indicating no polysulfides shuttling or Li metal corrosion. As shown in Figure XVII.1.5a, during the discharge of the cell with Ketjenblack (KB)/S cathode at 0.1 C (discharge curve is shown on right), we identified a very sharp peak located at the wavelength of 535 nm after being discharged to 1.8 V, suggesting a large amount of diffusion of Li_2S_6 to the anode side. Moreover, other polysulfide species S_8^{2-} , S_4^{2-} , and S_2^{2-} located at the wavelengths of 570 nm, 510 nm, and 450 nm, respectively, were also identified, indicating a severe shuttle effect in the KB/S cathode. The digital photograph of the test cell (inset of Figure XVII.1.5a) shows a clear color change of the separator to dark brown, further revealing the migration of LiPSs to the Li metal side. by contrast, the test cell with 3d-omsh/ZnS,Co-N-C/S cathode exhibited very weak lithium polysulfides peaks for S_8^{2-} , S_6^{2-} , S_4^{2-} , and S_2^{2-} . This result indicates that the double-end binding site has a strong binding ability towards lithium polysulfides to prevent their diffusion to the Li anode side. The digital photographs of the cell after being discharged to 1.8 V (inset of Supplementary Figure XVII.1.5b) show that the color of the separator remained unchanged, confirming the capability of relieving the shuttle effect by the 3d-omsh/ZnS,Co-N-C host material.

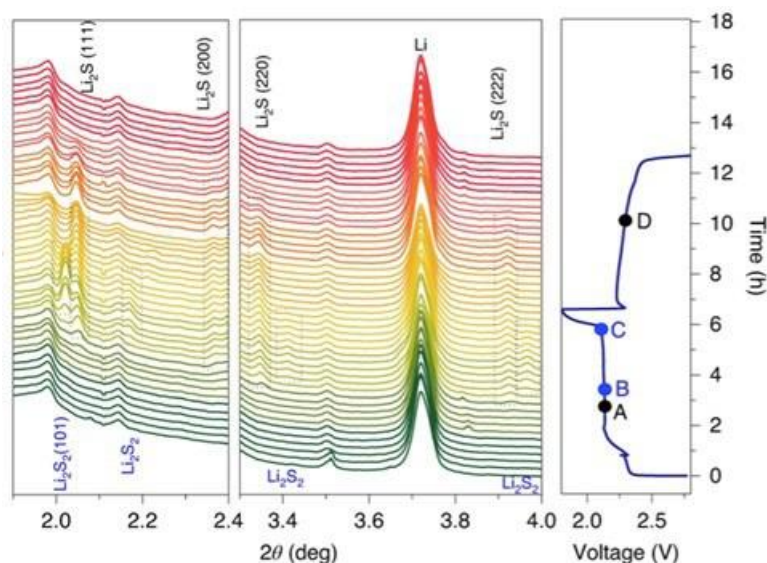


Figure XVII.1.4 Charge/discharge curve of the 3d-omsh/ZnS,Co-N-C/S cathode at 0.1 C and the corresponding in situ HEXRD patterns. Points A/D and B/C indicate the critical voltage point of the appearance/disappearance of Li_2S (marked by the black boxes in HEXRD) and Li_2S_2 (marked by the blue boxes in HEXRD), respectively.

We have further conducted Time-of-Flight Secondary Ion Mass Spectrometry (ToF-SIMS) characterization on the cycled sulfur cathode and cycled Li metal anode using different hosts. As shown in the ToF-SIMS depth profiles of S^- secondary ions in various cycled S cathodes at 1 C for 100 cycles (Figure XVII.1.6a), the cycled KB/S and macroporous carbon/S cathodes exhibited the highest intensities of the S migration layer caused by the LiPSs shuttle, while the intensities of the S^- peaks in the case of macroporous carbon/ZnS/S and macroporous carbon/Co-N-C/S became weaker but still existed. No S migration layer for the cycled macroporous carbon/ZnS, Co-N-C/S can be observed, confirming the effectiveness of double end binding sites in immobilizing polysulfides. Figure XVII.1.6b compares 3D S element reconstructions of the cycled sulfur cathodes, which show that the thickness of the S migration layer follows a trend of macroporous carbon/ZnS,Co-N-C/S (Figure XVII.1.6b-V) << macroporous carbon/Co-N-C/S (Figure XVII.1.6b-IV) < macroporous carbon/ZnS/S (Figure XVII.1.6b-III) < macroporous carbon/pure carbon/S (Figure XVII.1.6b-II) < KB/S (Figure XVII.1.6b-I). ToF-SIMS on the cycled Li metal was also conducted to directly probe Li metal corrosion. As shown in Figure XVII.1.6c, many S agglomerates were identified on the surface of cycled Li metal anodes in the cells with KB/S (Figure XVII.1.6c-I) and macroporous carbon/pure carbon/S (Figure XVII.1.6c-II) cathodes, indicating a severe shuttle effect and Li metal corrosion. The intensities of the S element on the surface of the cycled Li metal anodes became weaker in the case of the SEB sites (Figure XVII.1.6c-III and IV) but were still visible, illustrating that the SEB sites cannot eliminate the shuttle effect and Li metal corrosion. By sharp contrast, only a very weak S signal due to the formation of a S-containing solid-electrolyte interphase layer can be found on the surface of the cycled Li metal anode using the double-end binding host (Figure XVII.1.6c-V).

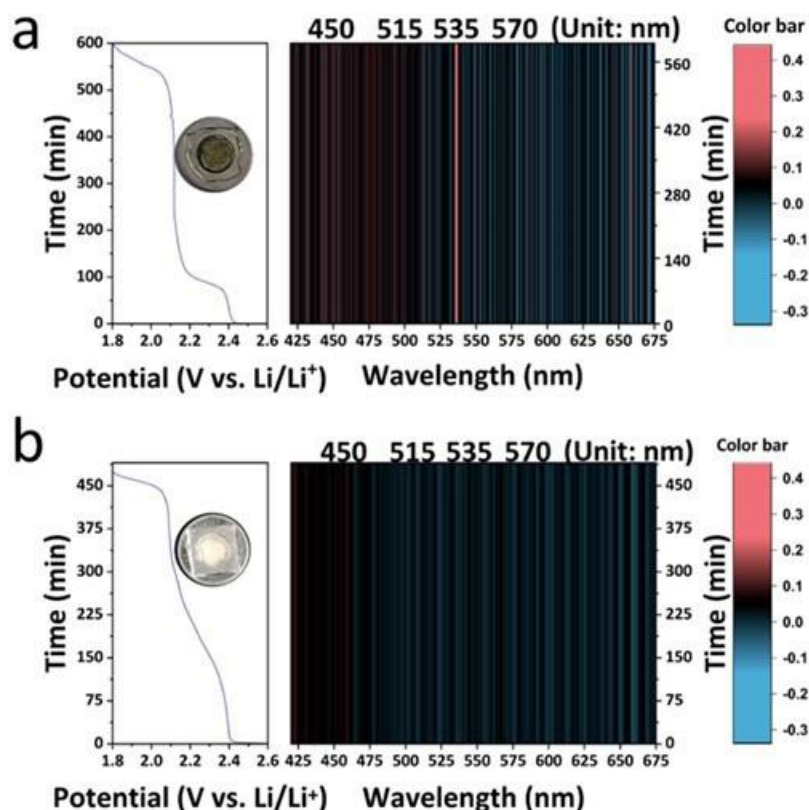


Figure XVII.1.5 In situ UV-vis observations and the corresponding discharge curves of (a) KB/S and (b) 3d-omsh/ZnS,Co-N-C/S cathodes at 0.1 C. Inset of (a): digital photograph of the in situ cell of KB/S cathode after testing; inset of (b): digital photograph of the in situ cell of 3d-omsh/ZnS,Co-N-C/S cathode after testing. The color bars indicate the derivative of reflectance, with pink color means positive number, blue color corresponds to negative number.

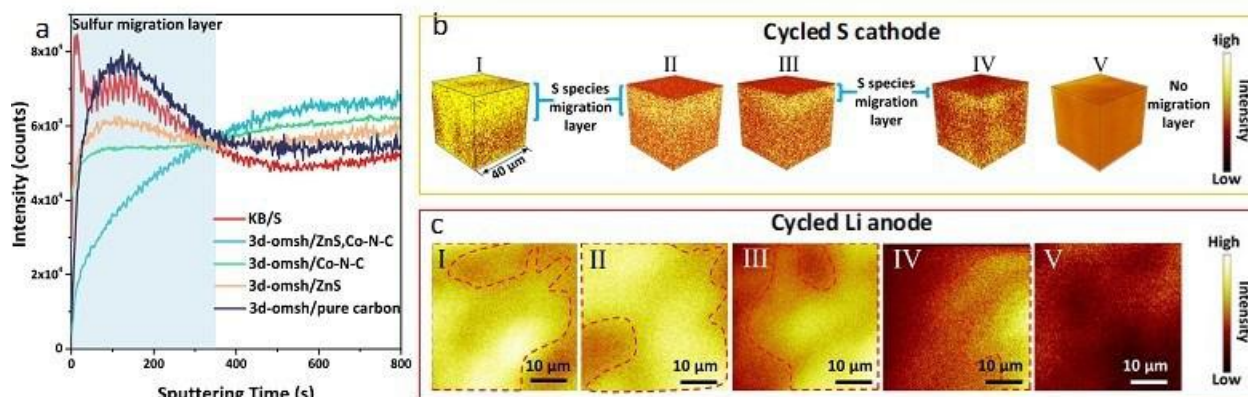


Figure XVII.1.6 ToF-SIMS (a) depth profiles and (b) 3D rendering of S- secondary ions distribution of cycled (I) KB/S, (II) ANL- macroporous carbon/S, (III) Macroporous carbon/ZnS/S, (IV) Macroporous carbon/Co-N-C/S, and (V) Macroporous carbon/ZnS,Co-N-C/S cathodes after 100 cycles at 1 C. (c) ToF-SIMS S-element mappings on the surface of cycled Li metal anode of (I) Li-KB/S, (II) Li-Macroporous carbon/S, (III) Li-Macroporous carbon/ZnS/S, (IV) Li-Macroporous carbon/Co-N-C/S, and (V) Li-Macroporous carbon/ZnS,Co-N-C/S cells after 100 cycles at 1 C. The color bar in (b) and (c) represents the signal intensity, with yellow color represent high intensity and black color represent low intensity. The region outlined by red dash-line in (c) indicated the location of migrated sulfur species.

Performance evaluation and mechanistic understanding of Li/S pouch cells under low E/S ratio

To further increase the cell energy density of Li/S pouch cells using double-end binding host, we have reduced the electrolytes/sulfur ratio from 4 to 2.5 $\mu\text{L}/\text{mg}$. As shown in Figure XVII.1.7a, the cell exhibits a main discharge working plateau of 2.05 V versus lithium and a specific capacity of $\sim 1000 \text{ mAh/g}$. By considering the weight of all the cell components (cathode, anode, electrolytes, current collector, separator, etc.), the cell energy density is calculated to be 352.43 Wh/kg. Furthermore, as shown in the simulation results by using BatPaC (<https://www.anl.gov/cse/batpac-model-software>), when the cell capacity of Li/S pouch cells is increased to $\sim 50 \text{ Ah}$, the cell energy density could be further increased to $\sim 450 \text{ Wh/kg}$ (Figure XVII.1.7b). Moreover, the cost of our Li/S pouch cells will be significantly lower than that of current lithium-ion batteries. In addition, the natural abundance of sulfur could mitigate the critical raw material supply chain challenge of lithium-ion batteries that use expensive and scarce Ni and Co elements. However, under a low E/S ratio of 2.5 $\mu\text{L}/\text{mg}$, the cell could only sustain few cycle of charge/discharge and then exhibits a sudden failure.

In Li/S battery, the Li ion transfer changes depend on the amount of electrolytes. In general, the lower the electrolyte amount in the cell, the slower the Li ion transfer. To understand the rapid cell failure of the Li/S batteries under lean electrolytes, we have used electrochemical impedance spectroscopy (EIS) to reveal the impedance evolution during discharge of high mass loading sulfur electrodes at different E/S ratios. Figure XVII.1.8a-c shows the 1st discharge curve of sulfur cathode with an areal S loading of 14.3 mg/cm^2 at E/S ratio of 10, 4, and 2 $\mu\text{L}/\text{mg}$, respectively. Figure XVII.1.8d-f show the corresponding EIS spectra at the 1st discharged state, which exhibit two semi circles at high and low frequency region, corresponding to interfacial (R_{int}) and charge-transfer (R_{ct}) resistances. As shown, for the cell with E/S ratio of 10 $\mu\text{L}/\text{mg}$ (Figure XVII.1.8a) and 4 $\mu\text{L}/\text{mg}$ (Figure XVII.1.8b), the cell can still exhibit two distinct discharge plateaus with R_{int} and R_{ct} resistances below 20 Ω (Figure XVII.1.8d) and 200 Ω (Figure XVII.1.8e), respectively. By contrast, when the E/S ratio is further reduced to 2 $\mu\text{L}/\text{mg}$ (Figure XVII.1.8c), it shows only a short discharge plateau and increased R_{int} of the 400 Ω and R_{ct} of 1800 Ω (Figure XVII.1.8f), which is mainly likely due to the substantial Li ion transfer constraint at the interface. Figure XVII.1.8g-i further shows the impedance evolution of high loading S electrodes during discharge at different E/S ratio, which shows that low E/S ratio significantly increase the resistance.

Indeed, it has been well discussed in Li/S community that Li metal failure and electrolytes deterioration will play a dominant role in the performance of Li/S batteries under high-loading cathode and lean electrolytes condition. Meanwhile, it has been well known that the conventional DOL/DME electrolytes cannot enable efficient reversible Li stripping/plating. For example, under a high S loading of 14.3 mg/cm^2 and 167.5 mA/g , the absolute current density applied onto Li metal is as high as 2.4 mA/cm^2 , raising critical challenge (e.g., dendrite formation) for the stabilization of Li metal. On the other hand, lithium metal is highly reactive in contact with non-aqueous ether-based electrolyte solutions, which will inevitably consume considerable amount of electrolytes to form solid-electrolyte interphase (SEI). Under lean electrolytes condition, the continuous parasitic reactions between Li metal and electrolytes could result in electrolytes depletion of the cell, leading to large increase of the internal cell resistance (as shown in Figure XVII.1.8) and hence sluggish reaction kinetics of sulfur cathodes. Hence, further Li metal protection technologies and cell configuration optimization (for example, internal pressure and tortuosity/porosity) are required to extend the cycle life.

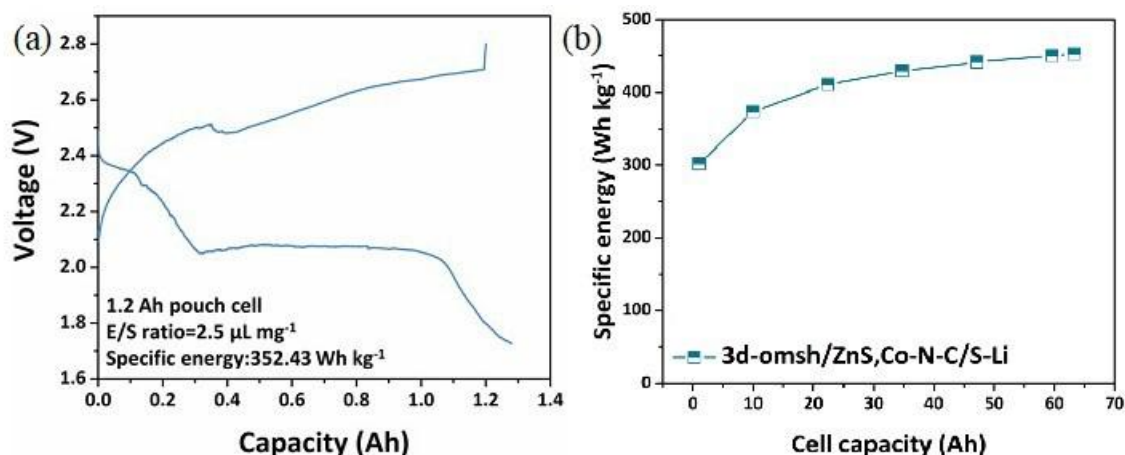


Figure XVII.1.7 (a) The charge/discharge curve of the Li/S pouch cell using ANL double-end binding host with an E/S ratio of 2.5 $\mu\text{L}/\text{mg}$. (b) BatPaC simulation of the cell specific energy of our Li/S pouch cell based on various cell capacities.

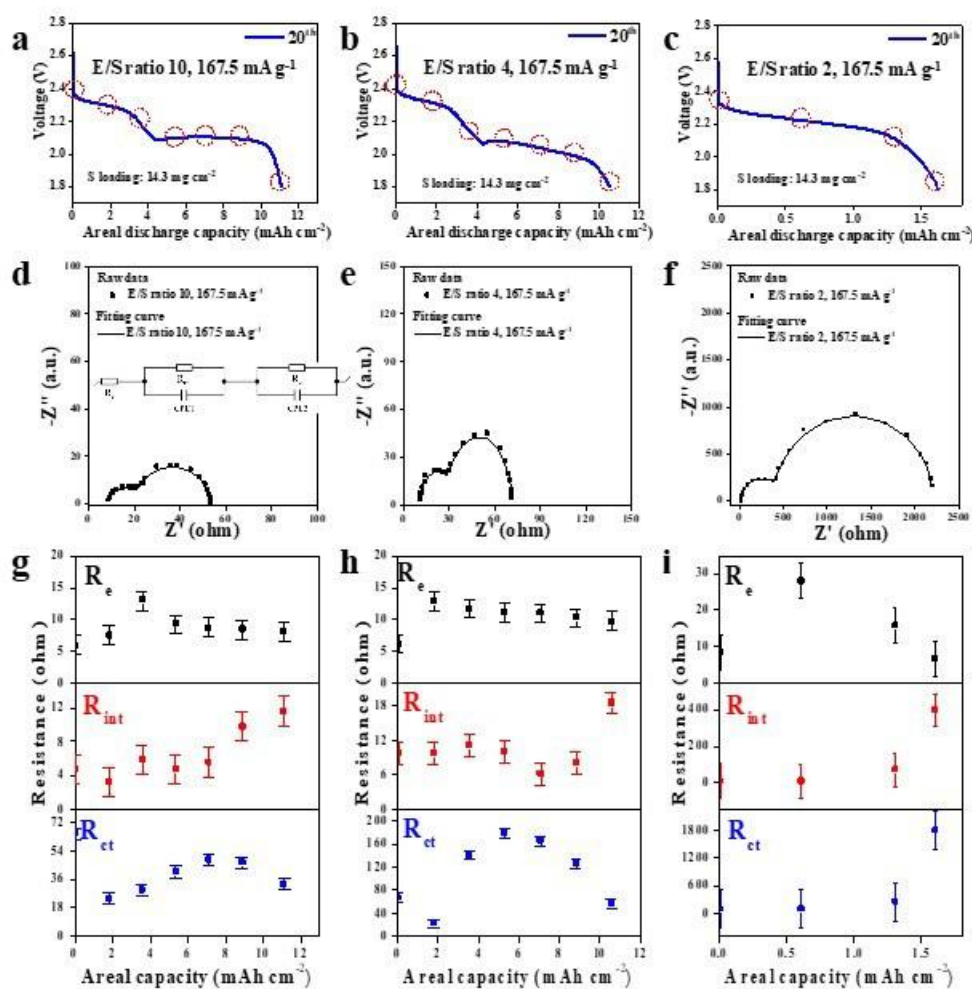


Figure XVII.1.8 Electrochemical characterization of Li/S cells at various E/S ratios. The 1st discharge voltage curves and EIS results of sulfur cathode with S loading of $14.3 \text{ mg}/\text{cm}^2$ at $167.5 \text{ mA}/\text{g}$ and E/S ratios of (a, d) $10 \text{ } \mu\text{L}/\text{mg}$, (b, e) $4 \text{ } \mu\text{L}/\text{mg}$, and (c, f) $2 \text{ } \mu\text{L}/\text{mg}$. Inset in (d) shows the equivalent circuit. (g-i) shows the impedance evolution during discharge process at (g) $10 \text{ } \mu\text{L}/\text{mg}$, (h) $4 \text{ } \mu\text{L}/\text{mg}$, and (i) $2 \text{ } \mu\text{L}/\text{mg}$. The red dotted circles in Figure a-c correspond to the ex situ point shown in Figure g-i.

Development of novel SeS cathode with high areal capacity of $> 4 \text{ mAh/cm}^2$ for 100 cycles

To further increase the cycling performance and suppress the self-discharge of Li/S batteries during charge/discharge at a wide temperature range (0°C - 50°C). This would require both control on the cathode structures and electrolyte structures to simultaneously suppress the shuttle effect and stabilize Li stripping/plating process.

We prepared the ordered macroporous sulfur host (OMSH). As shown in the scanning electron microscopy (SEM) image of OMSH (Figure XVII.1.9a), the ordered macroporous structure with a pore diameter of $\sim 180 \text{ nm}$ was successfully constructed. We then infiltrated $\sim 80 \text{ wt.}\%$ Se doped S (Se:S=1:9 in mass ratio) into the hollow chamber of OMSH through the molten-diffusion method at a temperature of 155°C for 12 h. The obtained cathode material was denoted as OMSH-Se/S. The transmission electron microscopy (TEM) image of OMSH-Se/S (Figure XVII.1.9b) shows that the macropores of OMSH are filled with Se doped S particles. The energy-dispersive X-ray spectroscopy (EDS) images of OMSH-Se/S (Figure XVII.1.9c) indicates that S and Se elements are uniformly distributed inside the cathode material, confirming the successful encapsulation of Se-S into the ordered macroporous structure. Meanwhile, the uniform distribution of Zn and Co elements suggests the existence of double-end binding sites inside the OMSH-Se/S, which can enhance the electrochemical kinetics of redox. X-ray photoelectron spectroscopy (XPS) characterization of OMSH-Se/S (Figure XVII.1.9d) reveals the existence of Se bonding as the Se $3p_{1/2}$ (168.31 eV) and Se $3p_{3/2}$ (161.82 eV) can be identified. Meanwhile, the Se-S (56.0 eV & 57.0 eV) and Se-Se (55.49 eV & 56.35 eV) bonds in OMSH-Se/S cathode material (Figure XVII.1.9e) confirmed the formation of a new phase of Se/S compound after Se doping, rather than a simple physical mixture of Se and S. The formation of the Se/S phase can enhance the electronic conductivity and reversibility of cathode composite in comparison with pure S phase. The content of Se/S in the OMSH-Se/S was measured to be $79.11 \text{ wt.}\%$ by thermogravimetric analysis (TGA, Figure XVII.1.9f).

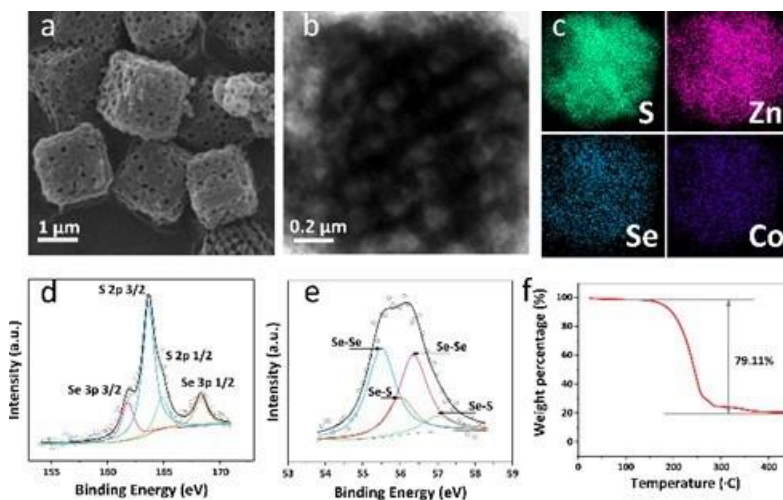


Figure XVII.1.9 Structure and composition analysis of cathode material. (a) SEM image of OMSH host material. (b, c) TEM and corresponding EDS chemical mapping of OMSH-Se/S (interesting elements are S, Zn, Se, and Co). High-resolution XPS spectra of (d) S 2p and (e) Se 3d of OMSH-SeS cathode material. (f) TGA curve of OMSH-SeS cathode material under argon atmosphere from room temperature to 450°C .

The HFE-based electrolyte that we invented during this project can significantly suppress the solubility of LiPSs, leading to suppressed shuttle effect. Meanwhile, Se doping and the ordered macroporous host structure can greatly enhance the electrical conductivity and the ion transport of the cathode composite even under high S content conditions. Thus, as shown in Figure XVII.1.10a, the OMSH-Se/S cathode material can deliver a reversible specific capacity of 1065.25 mAh/g^1 and

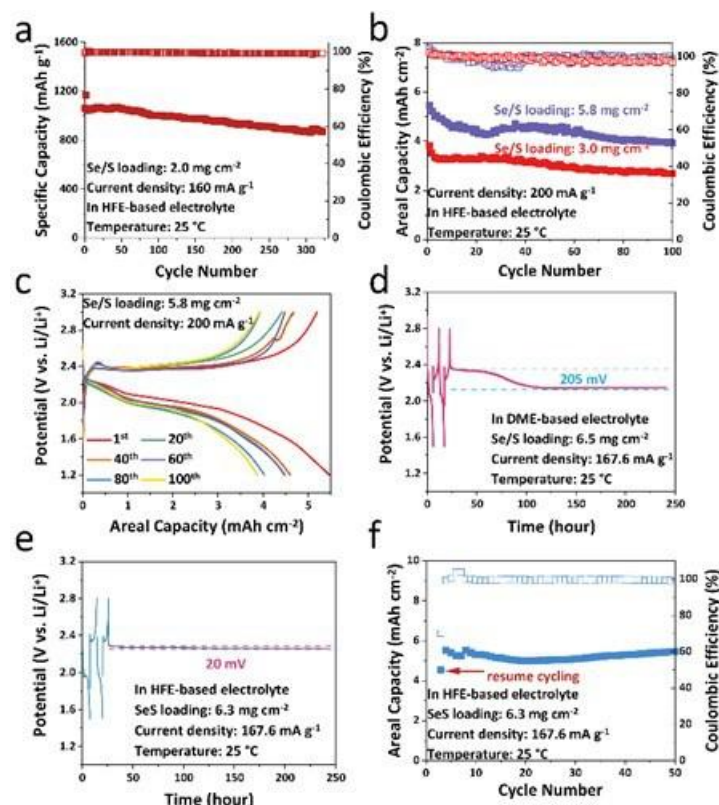


Figure XVII.1.10 Electrochemical characterizations of OMSH-Se/S cathode material. a) Cycling performance of OMSH-Se/S cathode in HFE-based electrolyte at 160 mA g^{-1} with a areal Se/S loading of 2 mg cm^{-2} . b) Cycling performance of OMSH-Se/S cathode with higher areal Se/S loading conditions (3.0 mg cm^{-2} and 5.8 mg cm^{-2}) in HFE-based electrolyte at 200 mA g^{-1} . c) Voltage profiles of various cycles of OMSH-Se/S cathode under high areal Se/S loading (5.8 mg cm^{-2}) condition in HFE-based electrolyte. Voltage profiles of OMSH-Se/S cathode ($\sim 6.5 \text{ mg cm}^{-2}$) that rested for 1 week after 2 initial cycles in d) DME- and e) HFE-based electrolytes. f) Cycling performance of OMSH-Se/S cathode after resting for 1 week in HFE-based electrolyte. Hollow and solid symbols in (a, b, f) represent coulombic efficiency and discharge capacity, respectively.

a high coulombic efficiency ($>99.5\%$) at a current density of 160 mA g^{-1} . Moreover, a high-capacity retention rate of 81.77% for 300 cycles can be achieved with an areal Se/S loading of 2 mg cm^{-2} . We also characterized the electrochemical performance of OMSH-Se/S cathode under higher areal Se/S loading and controlled E/S ratio ($10 \mu\text{L/mg}$). As shown in Figure XVII.1.2b, when increasing the areal Se/S loading to 3.0 mg cm^{-2} , the cell can deliver a high areal capacity of 3.82 mAh cm^{-2} at 200 mA g^{-1} , and maintain 2.70 mAh cm^{-2} after 100 cycles. Moreover, when we further increased the areal Se/S loading to 5.8 mg cm^{-2} , the cathode can still deliver 5.47 mAh cm^{-2} at 200 mA g^{-1} (Figure XVII.1.10b & 10c), corresponding to a specific capacity of $943.10 \text{ mAh g}^{-1}$. The high active material utilization of OMSH-Se/S under high areal Se/S loading indicates that the ordered macroporous host combined with Se doping can effectively enhance the electrochemical redox kinetics. As a result, the OMSH-Se/S can achieve a high coulombic efficiency of $>99.2\%$ and a high-capacity retention rate (71.77% for 100 cycles) even under high areal Se/S loading (5.8 mg cm^{-2}) conditions.

Conclusions

In summary, we have developed a high-energy Li/S pouch cell with high cell energy density of $> 300 \text{ Wh/kg}$ and stable cycle life via using a double-end binding host. We have conducted a series of advanced characterization to reveal the strong binding and catalytic effect of double-end binding host towards polysulfides, highlighting the importance of host design in enabling high-energy and long-life Li/S pouch cells. We have further investigated the degradation mechanism of Li/S batteries under low electrolytes/sulfur ratio, which can be attributed to the depletion of electrolytes and the significantly increased cell resistance due to the high reaction activity of Li metal and electrolytes. We have further combined the double-end binding host and fluorinated electrolytes to improve the cycling stability and self-discharge of Li/S batteries.

Key Publications

Publications

1. Zhao, C.; Daali, A.; Hwang, I.; Li, T.; Huang, X.; Robertson, D.; Yang, Z.; Trask, S.; Xu, W.; Sun, C. J.; Xu, G. L.(*); Amine, K(*). Pushing lithium-sulfur batteries towards practical working conditions through cathode-electrolyte synergy. *Angew. Chem. Int. Ed.* 2022, e202203466. Publication date: April 24, 2022.
2. Lee, B. J.; Zhao, C.; Yu, J.-H.; Kang, T. H.; Park, H. Y.; Kang, J.; Jung, Y.; Liu, X.; Li, T.; Xu, W.; Zuo, X. B.; Xu, G. L.(*); Amine, K.(*); Yu, J. S.(*). A redox-active interlayer for high-energy and long-cycling lithium-sulfur batteries. *Nature Communications*, 2022, 13, 4629. Publication Dates: 08 August 2022.

Presentations

1. Gui-Liang Xu (Invited talk), Khalil Amine. Advanced Cathode and Electrolytes Design for High-Energy Li/S pouch cells. 39th Annual International Battery Seminar & Exhibit. Orlando, FL, March 28-31, 2022
2. Chen Zhao, Gui-Liang Xu, and Khalil Amine. "Cathode engineering for high energy and stable lithium sulfur batteries under practical pouch cell condition." Poster presented at the 21st International Meeting on Lithium Batteries (IMLB 2022), Sydney Australia, June 26, 2022-July 1, 2022.

Patents

1. HIGH ENERGY METAL SULFUR OR SELENIUM-SULFUR BATTERY. Chen Zhao, Gui-Liang Xu and Khalil Amine. US Patent application, filed on Sep 28, 2022, no. 17/954,939.

References

1. Z.W. Seh, Y. M. Sun, Q. F. Zhang, and Y. Cui. "Designing High-Energy Lithium-Sulfur Batteries." *Chemical Society Reviews* 45, no. 20 (2016): 5605-34. DOI:10.1039/c5cs00410a.
2. A. Abouimrane, D. Dambournet, K. W. Chapman, P. J. Chupas, W. Weng, and K. Amine. "A New Class of Lithium and Sodium Rechargeable Batteries Based on Selenium and Selenium-Sulfur as a Positive Electrode." *Journal of the American Chemical Society* 134, no. 10 (2012): 4505-08. DOI: 10.1021/ja211766q.
3. Y. Cui, A. Abouimrane, J. Lu, T. Bolin, Y. Ren, W. Weng, C. Sun, et al. "(De)Lithiation Mechanism of Li/SeS_x (X = 0-7) Batteries Determined by in Situ Synchrotron X-Ray Diffraction and X-Ray Absorption Spectroscopy." *Journal of the American Chemical Society* 135, no. 21: 8047-56. DOI: 10.1021/ja402597g.

Acknowledgements

Use of the Advanced Photon Source, an Office of Science User Facility operated for the DOE Office of Science by Argonne National Laboratory, was supported by DOE under contract no. DE-AC02-06CH11357.

XVII.2 Development of High Energy Lithium-Sulfur Batteries (PNNL)

Dongping Lu, Principal Investigator

Pacific Northwest National Laboratory
902 Battelle Blvd.
Richland, WA 99354
E-mail: dongping.lu@pnnl.gov

Jun Liu, Co-Principal Investigator

Pacific Northwest National Laboratory
902 Battelle Blvd.
Richland, WA 99354
E-mail: jun.liu@pnnl.gov

Tien Duong, DOE Technology Development Manager

U.S. Department of Energy
E-mail: Tien.Duong@ee.doe.gov

Start Date: October 1, 2015

End Date: September 30, 2023

Project Funding (FY22): \$300,000

DOE share: \$300,000

Non-DOE share: \$0

Project Introduction

Lithium-sulfur (Li-S) battery has a high theoretical energy and low cost, making it one of the most promising battery technologies to meet the DOE battery cost target of < \$80/kWh for vehicle electrification. Despite advances in Li-S battery, deployment of the technology is still hindered by the low practical energy and limited cycle life. Achieving a high energy Li-S cell is feasible only through the simultaneous integration of a high-loading S cathode, thin Li anode, and most importantly a very lean amount of electrolyte. However, a simple combination of these parameters in a high-energy cell often leads to both a low reversible capacity and a very limited cycling life. Clear understanding of fundamental mechanisms of the cell failure at realistic conditions still need more efforts. Our study of high-energy Li-S pouch cells indicates that 1) electrolyte amount has a nearly linear correlation with the cumulative cell capacity (i.e., overall capacities delivered during the lifespan); and 2) electrolyte diffusion/ redistribution is hindered by the high tortuosity sulfur electrodes, which leads to the reaction heterogeneity and accelerated cell-failure. To improve cell cycle life and maintain high energy density of the cell at the same time, new designs of materials and electrode architectures addressing the above issues are essentially needed. Rational designs should be targeted to increase effective electrolyte supply, facilitate electrolyte infiltration and distribution, reduce electrolyte consumption, maintaining a durable Li-ion conduction network under realistic cell operation conditions. First, reducing electrode porosity is critical to conserving more electrolyte for cell cycling. For a given areal capacity, sulfur cathodes are much thicker and more porous (>60%) compared to the dense NMC cathodes due to the use of low density and porous S/C materials. This severely diminishes cell energy while also requiring more electrolyte for pore filling. However, reducing electrode porosity through direct pressing proves challenging if using the materials originally designed for highly porous cathodes. This is because the electrodes featuring low porosity and high tortuosity have slow electrolyte diffusivity, reducing the sulfur reaction kinetics and utilization rate. Therefore, a clear understanding of the effect that electrode porosity/tortuosity has on the electrolyte transport, sulfur reaction kinetics and cell life is critical for the rational design of materials and electrode architectures. Approaches that reduce the tortuosity in a low-porosity cathode are required to ensure the quick electrode wetting. Second, Li-ion conduction pathways should be maintained by either developing stable electrolytes/additives or through building durable quasi-solid Li⁺ conduction networks. So far, the ether-based liquid solutions combined with LiNO₃ additive remain the most viable option for Li-S electrolytes. However, consumption and depletion continue through chemical and electrochemical reactions. The “non-solvating” electrolytes, localized concentrated electrolytes, and solid electrolytes received widespread attention for prolonging the cycle life of

the Li metal batteries. These electrolytes may also be helpful in Li-S cells but need an optimal electrode architecture that can take advantages of novel electrolytes.

The objective of this project is to develop high-energy Li-S batteries with a long lifespan. In FY22, we focused on the development of cathode materials, electrode architecture, and processing to realize operation of low-porosity electrodes at very lean electrolyte conditions.

Objectives

- Realize S utilization rate >1100 mAh/g in low-porosity (porosity $\leq 40\%$) and high-loading (> 4 mg/cm²) S electrodes through optimization of materials and electrode architectures.
- Scale-up preparation of the optimized materials and high-loading and dense sulfur electrodes to support Li-S pouch cell demonstration and evaluation.

Approach

1. Build 3D S electrode models and simulate electrolyte transport and S reactions in high-loading and low-porosity electrodes.
2. Optimize S/C material and electrode architecture to realize S utilization >1100 mAh/g in high loading electrode (>4 mg S/cm²) with S content $>70\%$.
3. Study impacts of electrode architecture and topography on S reactions and cell cycling.
4. Process and validate high-loading (>4 mg/cm²) and dense ($<40\%$ porosity) S electrodes at a relevant scale.

Results

1. Understand electrolyte transport and S reactions in low-porosity and high-loading S electrodes through 3D electrode simulation

The three-dimensional (3D) pore-scale S electrode model was built to understand electrolyte propagation in the high-mass-loading and tortuous S cathodes and its impacts on S reactions. The 3D flow simulation would provide new insights on the optimization of materials structures and electrode architectures, which was validated experimentally by Micro-computed tomography (Micro-CT) and material analysis. In the pore scale model, the electrode and electrolyte infiltration were simulated using the discrete element method (DEM) and multiple flow simulation, respectively. To investigate the effects of particle size on electrolyte wettability, small particle cathode (SPC, particle size of 20 μm) and large particle cathode (LPC, particle size of 90 μm) models were generated with the same electrode porosity (Figure XVII.2.1a and e). Both the electrodes have a thickness of 120 μm to mimic the thick electrode; the SPC has 6-8 layers of particles (Figure XVII.2.1a) whereas the LPC has 1 to 2 layers of particles (Figure XVII.2.1e). At the initial wetting stage, driven by gravity and surface tension, the added electrolyte will flow through the voids and diffuse into the electrode pores, pushing the air outside the electrode. After reaching steady state, air is still observed occupying a portion of the pore channels due to non-uniform electrolyte flow and surface tension, which is dictated by material/electrode properties. While the SPC electrode has more challenges in wetting due to narrow and even closed pores, the LPC, in contrast, revealed a much better wetting with only a small portion of the air trapped inside the electrode. Accordingly, the nonuniform wetting effect of SPC and LPC was quantified. The electrode volume (ϵ_d) is set at a constant value of 0.55, which consists of loaded S (ϵ_s) and the carbon materials volume (ϵ_c). The volume fraction of the electrolyte and air was calculated by the cross-section average distribution profile along the thickness direction from the 3D pore-scale model. As shown in Figure XVII.2.1f, for LPC, at the separator-electrode interface ($x = 25$ μm), the electrode is fully wetted without trapped air. Starting from the $x = 50$ μm , the air volume begins to increase slightly and reaches the maximum volume fraction of 8.2% at $x = 85$ μm (bottom of electrode). The average air fraction inside the LPC is only 3.5%, indicating the liquid electrolyte can access the most pores. In contrast, the SPC electrode has a 11.1% air fraction even at the separator-electrode interface. The air volume increases along the electrode thickness direction and reaches a plateau around 23% at $x > 60$ μm . The average air fraction in SPC is as high as nearly 50% (Figure XVII.2.1b). The multiple flow simulation from the 3D pore-scale electrode model suggests that using large particles to reduce particle stacking layers is helpful in facilitating the wetting of high-loading

electrodes. Experimentally, carbon particles of different sizes were synthesized to fabricate high-loading ($> 4 \text{ mg/cm}^2$) and dense S electrodes (porosity 45%). The structures of SPC and LPC were studied using X-ray Micro-CT. Three phases—S/C particles, binder/carbon additives, and voids—were separated and colored yellow, grey, and blue, respectively (Figure XVII.2.1c and g). Consistent with the simulation results, small particles tend to form a compact layer in SPC and generate horizontally aligned pores along the plane direction (Figure XVII.2.1c: top and cross-sectional view), blocking electrolyte infiltration. The Micro-CT results of the LPC indicate that large particles form through-pores perpendicularly across the electrode (Fig. XVII.2.1g). The measured electrode tortuosity of SPC and LPC are 2.01 and 1.16, respectively, along the perpendicular direction. The lower tortuosity indicates better electrolyte wetting inside the dense electrodes, which is critical to improving sulfur utilization rate and reaction kinetics.

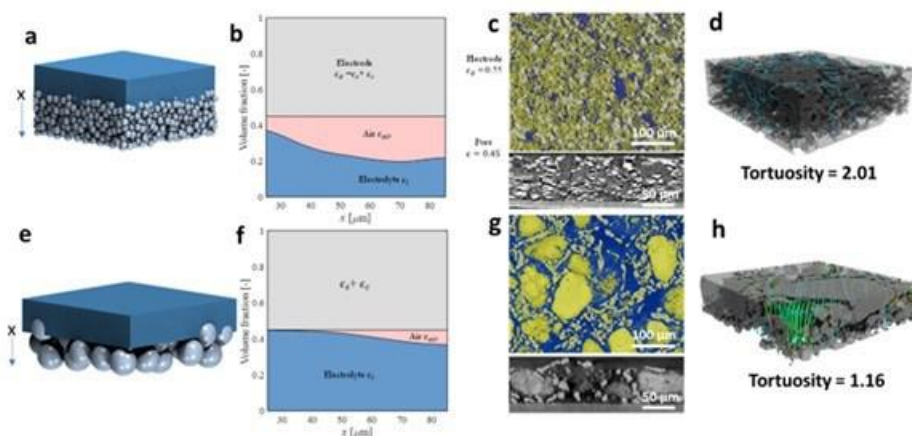


Figure XVII.2.1 3-D pore-scale models for SPC (a) and LPC (e); The electrolyte and air distribution along the electrode depth x for SPC (b) and LPC (f); Top and cross-sectional view of Micro-computed tomography (micro-CT) images of SPC (c) and LPC (g); Tortuosity and flow path of SPC (d) and LPC (h).

2. Develop low-tortuosity sulfur cathode and realize sulfur utilization $> 1100 \text{ mAh/g}$ at high sulfur loading ($> 4 \text{ mg S/cm}^2$) and lean electrolyte conditions ($E/S \text{ ratio} = 4 \text{ } \mu\text{L/mg}$)

According to the 3D pore electrode simulation, in order to lower electrode porosity, we proposed a single-particle-layer electrode concept (i.e. one particle thick electrode) and experimentally realized it through materials synthesis optimization. With the single-particle-layer electrodes, a high discharge capacity of 1100 mAh/g can be obtained in high loading electrodes ($> 4 \text{ mg S/cm}^2$) with sulfur content $> 70\%$ and porosity $< 40\%$ at lean electrolyte conditions ($E/S \text{ ratio} = 4 \text{ } \mu\text{L/mg}$).

As illustrated in Figure XVII.2.2a, to realize single-particle-layer electrode coating, the diameter of the S/C secondary particles should be equal or slightly larger than the designed electrode thickness. By controlling the wet coating thickness followed by appropriate electrode calendaring, the large S/C secondary particles will be distributed evenly to form a single-particle-layer electrode, featuring a low-tortuosity electrode structure in both vertical and planar directions. This unique electrode structure not only uniform electrolyte transport among the cathode particles but also benefits sulfur reaction homogeneity, which promotes uniform SEI formation on the Li anode side and hence extends cycling life. Based on our calculation, in order to prepare 4 mg/cm^2 electrodes with 70% sulfur content and 35% porosity, the electrode thickness should be around $45 \text{ } \mu\text{m}$. Accordingly, $50 \text{ } \mu\text{m}$ S/C secondary particles (Figure XVII.2.1b) were specifically synthesized and the sulfur content in S/C composite was controlled as high as 90%. After adding carbon additive and binder, the electrode with a S/C: carbon:binder mass ratio of 8:1:1 and 72% sulfur in the whole cathode was prepared. The electrode porosity was reduced from 70% to 35% through calendaring. The single-particle-layer electrode structure was characterized by micro-CT and reconstructed into a 3D image (Figure XVII.2.2c). The individual S/C particles are highlighted with yellow dotted line. It is clear that the large particles occupied the electrode from bottom to very top and formed through-pores between the particles. Such through-pores have low tortuosity and provide diffusing channels for quick electrolyte infiltration and distribution. Benefiting from

sufficient electrolyte wetting, the single-particle-layer electrode can deliver a high sulfur utilization rate of 1100 mAh/g (at 0.05 C) even under harsh low porosity and lean electrolyte conditions. Compared to 70% porosity electrode, the 35% porosity electrode shows a better overall performance in terms of sulfur utilization rate and capacity retention. This suggests that reduced porosity of the single-particle-layer electrode does not affect the sulfur reaction kinetics. However, when switched to a multi-particle-layer electrode composed of relatively smaller particles ($< 20\ \mu\text{m}$), the cell suffered from obvious capacity fluctuation and readily failed after only 20 cycles. The poor performance of the multi-particle-layer electrode is due to the highly tortuous electrode structure formed by stacking of multi-layer small particles.

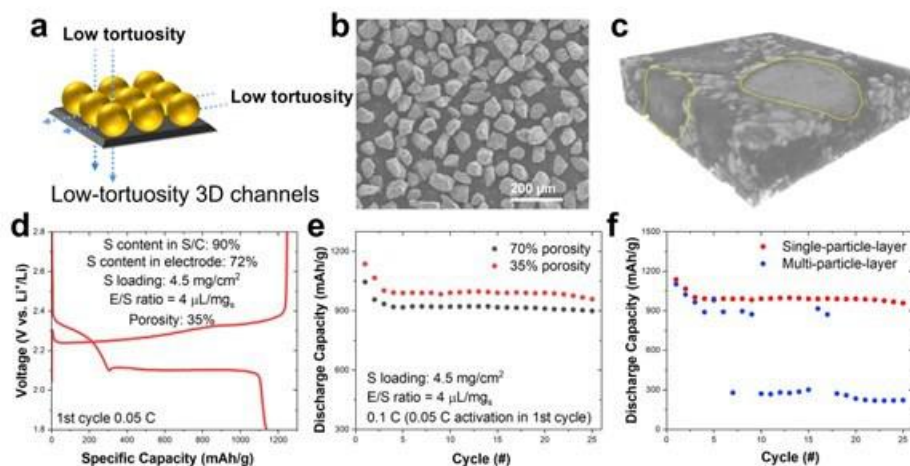


Figure XVII.2.2 (a) Schematic of a single-particle-layer electrode with low tortuosity in vertical and planar direction. (b) SEM image of sulfur/carbon materials around 50 μm . (c) Reconstructed micro-CT image of single-particle-layer electrode. (d) Discharge and charge curves of the single-particle-layer electrode during first cycle. (e) Cycling performance of single-particle-layer electrode at different porosity. (f) Cycling performance of single/multi-particle-layer electrodes.

3. Impacts of electrode architectures on sulfur reaction pathway and kinetics and cell cycling

To understand the sulfur reaction processes in LPC, a high-resolution synchrotron X-ray diffraction (XRD) study was performed and compared with small particle cathode (SPC) with a multi-particle-layer structure.

Both LPC and SPC cathodes were charged/discharged to the designed voltages, and the transmission ex-situ XRD were collected. Figure XVII.2.3a and c show the first discharge/charge profiles of the LPC and SPC electrodes under lean-electrolyte conditions ($E/S = 4$), respectively, where significant difference was observed for both reversible capacities and voltage plateaus. The corresponding phase evolutions of S_8 , lithium polysulfides (LiPS), and Li_2S were also clearly identified by XRD for the SPC and LPC (Figure XVII.2.3b and d). For simplicity, the comparison is focused on the main phases of S_8 , LiPS, and Li_2S by tracking their respective characteristic diffraction peaks: 2.86° , 3.2° for S_8 ; 1.2 – 2.6° , 2.4 – 2.6° and 2.95 – 3.15° for LiPS; and 3.38° and 3.89° for Li_2S .

Before discharging, both the pristine LPC and SPC cathodes have an α - S_8 phase but in an amorphous or nanocrystalline state. For the LPC electrode (Figure XVII.2.3b), once the discharge process starts (cutoff at 2.2 V), the α - S_8 peaks become very weak quickly, indicating fast reaction kinetics due to the sufficient electrode wetting. Accompanying this, a new set of diffraction peaks was observed in the 2-theta ranges of 2.4° – 2.6° and 2.95° – 3.15° (labeled with orange dashed squares), indicating conversions of S_8 to LiPS. The intensity of the new peaks decreases in the subsequent discharging (cutoff: 2.1 V), indicating continuous reactions of LiPS. In the voltage range of 2.1 to 1.9 V, with the decrease in LiPS diffraction intensity, a new set of peaks grow at 3.38° and 3.89° (labeled with violet dashed lines), corresponding to cubic-phase Li_2S . While in the SPC electrodes, distinct behaviors were identified for each voltage range. In contrast to the quick disappearance of S_8 in the SPC electrode, the S_8 phase still maintains at a high content after discharging to 2.2 V and coexists with the LiPS phase until 2.1 V. This suggests sluggish kinetics of the S-to-LiPS conversion of SPC. At the

end of discharge, only very weak diffractions of Li_2S were identified, while the LPS diffractions stayed strong (Figure XVII.2.3d). Compared to the LPC electrode, the SPC electrode has much slower S-to-LiPS reaction kinetics and lower conversion degree, which may be caused by restricted electrolyte wetting of highly tortuous electrode structure. In addition, the LiPS diffuses out more quickly in the SPC and accumulates outside the electrode. During the next step, the LiPS-to- Li_2S conversion, only part of the LiPS can re-access the active surface and form Li_2S (or Li_2S_2) passivation layers, blocking the inflow of LiPS. As a result, blocked LiPS inflow would speed up sulfur irreversible loss (Figure XVII.2.3c), which explains the low capacity and very weak Li_2S diffractions in the SPC at the end of discharge (Figure XVII.2.3d). More details of this study have been published at *Energy & Environmental Science*, 2022 15 (9), 3842-3853.

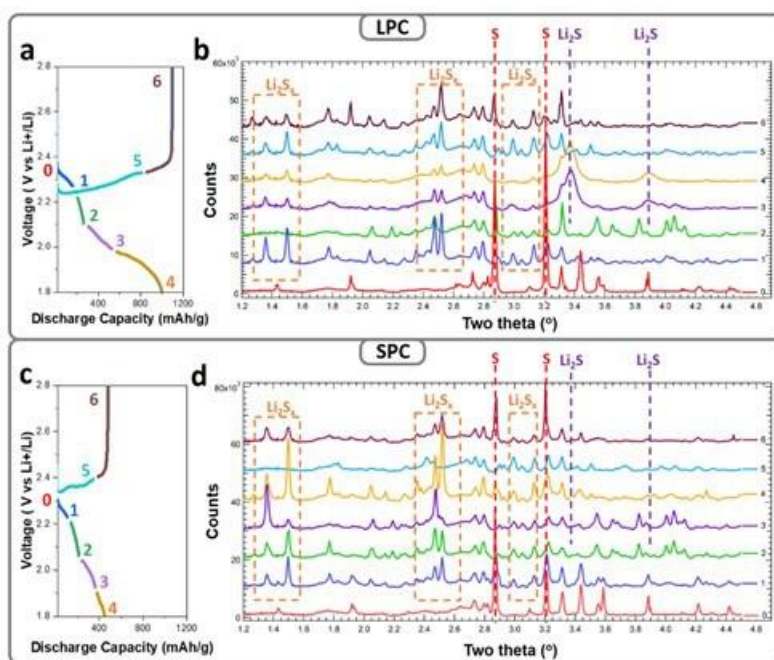


Figure XVII.2.3 Ex situ synchrotron XRD characterization of the LPC and SPC at different depths of discharge. Typical first cycle discharge/charge curves and the corresponding XRD patterns ($\lambda = 0.19316$) for the LPC (a, b) and SPC (c, d). Successive diffraction patterns are vertically offset by 6,000 relative to that of the pristine cathode (point 0, no offset).

4. Materials optimization and scaling up for low-porosity and high-loading electrodes

To further improve cathode energy density, sulfur content need be improved through optimizing the structures of the sulfur host materials. In addition to critical materials properties of pore volume and specific surface area, we identified that pore connectivity of carbon host is an important factor that should be considered carefully when designing the large size secondary carbon host materials.

The nitrogen doped integrated Ketjen Black (NKB) particles with different pore conductivity (NKB11, NKB12, and NKB15) were synthesized by integrating KB particles by poly(melamine-co-formaldehyde) methylated (PMF) at different PMF/KB ratio (1:1, 1:2, and 1:5, respectively), where PMF acts as both an integration reagent and nitrogen resource. After sulfur was infiltrated at 155°C (80 wt.% S), the sulfur distribution in different NKBs was studied by X-ray nano-computed tomography (nano-CT). Fig. XVII.2.4a-c exhibit the re-constructed 3D images of NKB/S materials, the red color represents a high contrast of sulfur, and the evolution from red to blue color means a decrease of relative sulfur concentration. In the NKB11/S (Figure XVII.2.4a), the red and yellow areas are close to the center part of the secondary particle while the blue and green areas are around the surface region. This indicates during heat treatment, sulfur tends to concentrate at the center of NKB11, exhibiting a descent sulfur concentration gradient from inside to outside. This is due to the high pore connectivity of the NKB11 at a lower integration degree (PMF/KB=1/1). Driven by the capillarity, such high surface area as well as sufficient pore connectivity facilitate sulfur diffusion and

distribution. On the contrary, with an increase of PMF/ KB ratio from 2:1 to 5:1, bigger size sulfur aggregation was observed across the particle. This is because with increase of amorphous carbon content, both NKB particle surface and inside pores get blocked, reducing both the pore volume and connectivity as proved by the BET (not shown here) and nano-CT analysis. As a result, the fused sulfur has a limited accessibility to the mesopores of the NKB. Instead, the sulfur stays in the voids between the individual KB particles and forms such a connected sulfur framework, which has a high contrast in CT.

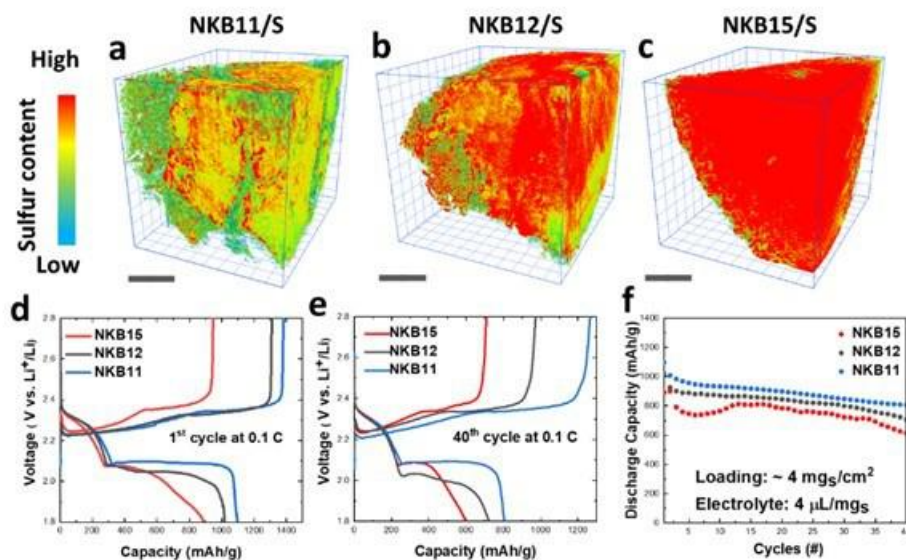


Figure XVII.2.4 X-ray nano-computed tomography (X-ray nano-CT) images of sulfur concentration distribution in (a) NKB11, (b) NKB12 and (c) NKB15, respectively. The scale bar is 6 μm . (d) Discharge/charge curves of different NKB/S electrodes in the first cycle. (e) Discharge/charge curves different NKB/S electrodes after 40 cycles. (f) Cycling performance of different NKB/S electrodes in 40 cycles at low E/S ratio.

Effects of KB integration degree and sulfur distribution on cell performance were studied in coin cells. The electrochemical performance of different NKB/S materials was evaluated at practical conditions of high sulfur loading ($\geq 4 \text{ mg/cm}^2$) and lean electrolyte (E/S ratio $4 \mu\text{L/mg}_\text{S}$). Figure XVII.2.4d and e compare the discharge/charge curves of different NKB/S materials at the 1st and 40th cycles. With an increase of PMF/KB ratio, the cell shows a decreasing trend of sulfur utilization rate from 1100, 1020, to 890 mAh/g. A close comparison of discharging profiles indicates that all the three NKB/S materials show similar capacities of $\sim 250 \text{ mAh/g}$ for the first discharge plateau at 2.3V, suggesting a similar conversion extent from elemental sulfur to Li polysulfides. An obvious performance deviation was observed for the second discharge plateau: bigger polarization and lower discharge capacity at higher PMF/KB ratio. Such a trend was maintained during cycling. After 40 cycles, NKB11/S has a reversible capacity of 800 mAh/g with a similar discharge voltage, while the NKB12/S and NKB15/S suffer from an increased polarization and a quicker capacity fading. This performance deviation was ascribed to the differences of NKB structures and sulfur distribution. As proved by nano-CT and EDS (not shown here), NKB11 has a more open structure and better pore connectivity, forming a decrescent sulfur distribution from inside to outside. The sulfur-lack carbon shell provides more active sites for polysulfides deposition before diffusing outside of the particles. While for NKB12 and NKB15 having lower surface area and less pore accessibility, sulfur has slower reaction kinetics and more serious irreversible loss. As a result, the generated polysulfides will either directly deposit on the particle surface or diffuse outside secondary particles, causing the capacity loss of the second discharge plateau. Without sacrificing the rigidity and processability of the secondary particles, PMF:KB = 1:1 is an optimal ratio for the synthesis of high performance NKB/S cathode.

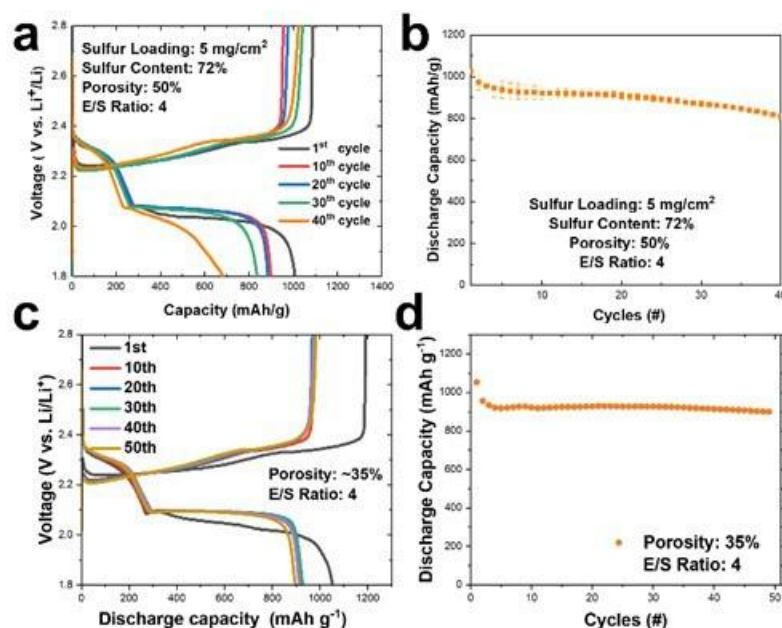


Figure XVII.2.5 (a) Discharge/Charge curves of 5mg/cm² NKB11/S electrode at different cycles. (b) Cycling performance of the 5mg/cm² NKB11/S electrode. (c) Discharge/Charge curves of NKB11/S-Polymer electrodes at different cycles. (d) Cycling performance of NKB11/S-Polymer cathodes.

The NKB11/S was scaled up to ~40 g per batch at the lab for large area electrode processing. Feasibility of the materials was further validated by increasing both sulfur content in the NKB/S composite and sulfur loading of the electrode. For the 50% porosity cathode with overall sulfur content of 72%, the 5 mg/cm² electrode still delivers a high discharge capacity of ~1000 mAh g⁻¹ under lean electrolyte conditions (E/S 4) (Figure XVII.2.5a and b). Compared to the 64% S electrodes, although the discharge specific capacity was decreased slightly from ~1100 to ~1000 mAh g⁻¹ in a 72% S electrode, the overall specific capacity (based on whole weight of the electrode) was instead improved from 704 to 720 mAh/g because of the reduction of parasitic weight. After 40 cycles, the cell can maintain a capacity of 817 mAh/g, 80% of its initial capacity. By integrating our recently developed polymer additives, the very dense sulfur cathode (35% porosity) can still deliver a large discharge capacity and maintain stable cycling of 50 cycles at a low E/S ratio of 4 (Figure XVII.2.5c and d). This further validates the feasibility of the NKB11/S for large area electrode coating and Li-S pouch fabrication.

Conclusions

1. Electrolyte wetting issue in low-porosity S electrodes was studied by experimental characterization and theoretical simulation.
2. A single-particle-layer electrode (SPLE) approach was proposed and validated for low tortuosity electrode fabrication.
3. The SPLE composed of large-size integrated KB (IKB) particles shows better electrolyte wetting and lower polysulfide shuttling, improving both S specific capacity and cycling stability.
4. By controlling electrode structure, high-mass-loading S electrodes (>4 mg cm⁻²) with low porosity of ~35% can deliver a high S utilization rate (>1100 mAh g⁻¹) at very lean electrolyte conditions (E/S=3 μL mg⁻¹).
5. The large-size NKB materials were scaled-up synthesized and transferred to Battery500 for pouch cell fabrication.

Key Publications

1. Feng S., Singh R., Li Z., Wang Y., Fu Y., Anderson C., Bao J., Xu Z., Shi L., Lin Y., Khalifah P., Wang W., Liu J., Xiao J., and Lu D., Low-Tortuous Single-Particle-Layer Electrode for High-Energy Lithium-Sulfur Batteries, *Energy & Environmental Science*, 2022 15 (9), 3842-3853.
2. Shi L., Anderson C., Mishra L., Qiao H., Canfield N., Xu Y., Wang, C. Jang T., Yu Z., Feng S., Le P., Bak S., Subramanian V., Wang C., Liu J., Xiao J., Lu D., Early Failure of Lithium-sulfur Batteries at Practical Conditions: Crosstalk between Sulfur Cathode and Lithium Anode, *Advanced Science*, 2022, 9 (21), DOI:10.1002/advs.202201640.
3. Feng S., Liu J., Zhang X., Shi L., Anderson C., Lin Y., Song M., Liu J. Xiao J., Lu D. Rationalizing nitrogen-doped secondary carbon particles for practical lithium-sulfur batteries, *Nano Energy*, 2022, 103, 107794.
4. Lu D. and Liu J., Development of High-Energy Lithium-Sulfur Batteries, The 2022 Vehicle Technologies Office (VTO) Annual Merit Review, 2022, June 21-23.
5. Shi L., Anderson C., Liu D., Xiao J., and Lu D., Effects of Sulfur Cathode Topography on Cycling of Practical Li-S Batteries, 242nd ECS Meeting, October 9-13, 2022, Atlanta, GA

Acknowledgements

Shuo Feng, Lili Shi, Rajesh Kumar Singh, Jie Bao, Zhijie Xu, Yucheng Fu, Jie Xiao and Ji-Guang Zhang (PNNL); Peter Khalifah (BNL); Zhao Liu, Adam Stokes (Thermo Fisher Scientific)

XVII.3 Mechanistic Investigation for the Rechargeable Li-Sulfur Batteries (Brookhaven National Laboratory & University of Wisconsin-Milwaukee)

Enyuan Hu, Principal Investigator

Chemistry division, Brookhaven National Laboratory
Bldg. 555, Brookhaven National Lab.
Upton, NY 11973
E-mail: enhu@bnl.gov

Deyang Qu, Co-Principal Investigator

University of Wisconsin Milwaukee
3200 N Cramer Street
Milwaukee, WI, 53211
E-mail: qud@uwm.edu

Tien Duong, DOE Technology Development Manager

U.S. Department of Energy
E-mail: Tien.Duong@ee.doe.gov

Start Date: October 1, 2021

End Date: September 30, 2022

Project Funding (FY22): \$235,000

DOE share: \$235,000

Non-DOE share: \$0

Project Introduction

Rechargeable lithium-sulfur (Li-S) batteries have been considered as a potential candidate of beyond Li-ion chemistry to replace the state-of-art Li-ion batteries in EV applications, owing to the high theoretical energy density ($1672\text{mAh}\cdot\text{g}^{-1}$), safety, and low cost. The energy density of a Li-S battery could potentially reach 2-3 times higher than that of a state-of-art Li-ion battery. However, to realize the full potential of Li-S chemistry, one has to overcome the “shuttle-effect” caused by dissolved polysulfide ions. On the Li-S cell level, this phenomenon causes high self-discharge, low Coulombic efficiency, low active materials utilization, and short cycle life. The dendrite growth and “dead” Li formation on a Li anode still remain as major technical difficulties.

In the past few years, we developed the MS-HPLC essays for the quantitative and qualitative identification of dissolved polysulfide ions in various electrolytes. Couple with *in-situ* electrochemical method, the change of the dissolved polysulfides during the battery operation was determined. The mechanisms for the sulfur redox reaction which including the equilibrium between dissolved polysulfide ions and element sulfur were revealed. So the continuous decay of the capacity during cycling, “shuttle-effect” and high self-discharge during the storage became better understood. We concluded that 1) The shuttle-effect can be mitigated by using alternative anodes that do not react with dissolved polysulfides; 2) The shuttle-effect can be mitigated by forming short-chain polysulfide ions, which are much less reactive than longer chain polysulfide ions.

Although the mechanism and behaviors of the dissolved polysulfide ion in the electrolyte were very well understood from our previous investigation, the reaction mechanism of the polysulfides and sulfur in the cathode side in solid phase has not been thoroughly studied yet, especially the sulfur redeposition and distribution during charging. Collaborating between UWM and BNL, we started investigating the sulfur redox reaction in the solid phase taking the advantage of synchrotronic techniques in BNL and electrochemical analytical techniques in UWM.

In FY2022, the interim goal was to develop a Li-sulfur battery with sulfur containing cathode of 600-800 mAh/g capacity with the mitigation of the “shuttle effect”. The objective has been achieved. We demonstrated in FY2022:

1. A small molecular organosulfide cathode that delivered 600 mAh/g in a solid-state Li-S cell after 500 cycles.
2. A carbon/sulfur cathode that delivered over 1000 mAh/g capacity in a traditional Li-S liquid pouch cell after 100 cycles with the mitigation of “shuttle-effect”.

Objectives

The primary objectives were as follows:

1. To optimize and down select polymeric sulfur electrode. We will focus on the overall dissolution of polysulfide in an electrolyte and effectiveness of polymeric sulfur electrodes.
2. To develop small organosulfur materials for all solid-electrolyte Li-S batteries.
3. To continue developing the alternative anode materials having low reactivity with dissolved polysulfide ions.
4. To continue investigating the interaction of polysulfides in the cathode solid phase.

Approach

In this collaborative project, we first down selected the cross-linked polymerized sulfur compounds, in which sulfur was attached to the conductive backbone with covalent bonds, therefore the polysulfides can be immobilized within the matrix. We also explored the small organosulfur molecules in all-solid-state Li-S batteries. We continued exploring the alternative anode materials which can cycle well and did not react with dissolved polysulfide and sulfur in the electrolyte in order to mitigate the “shuttle effect”. In addition, we continued to engage in the fundamental *in-situ* electrochemical investigations of the sulfur redox mechanisms in order to guide the material and engineering designs. We also continued to optimize the alternative electrode fabrication processes.

Results

Small molecular organosulfide cathode in an All-Solid-State Battery

In the past few years, we have successfully developed the MS-HPLC essays for the quantitative and qualitative identification of dissolved polysulfide ions in various electrolyte. Couple with *in-situ* electrochemical method, the change of the dissolved polysulfides during the battery operation can be determined. The mechanisms for the sulfur redox reaction which including the equilibrium between dissolved polysulfide ions and element sulfur were revealed. So the continuous decay of the capacity during cycling, “shuttle-effect” and high self-discharge during the storage became better understood. With the *in-situ* analytical method, we also revealed that the short chain-length polysulfide ions e.g. S_4^{2-} and S_3^{2-} are much less reactive with Li than the longer chain polysulfide ions. To mitigate the problem caused by the soluble long-chain polysulfides in a Li-S battery, sulfur/organic polymer materials were synthesized as alternative cathode materials instead of elemental sulfur (S_8). We have exhausted many sulfur/organic polymer materials last year. However, the sulfur to polymer ratio must be limited to certain value to avoid the existence of elemental sulfur e.g. 4:1 S_8 :PAN ratio. In addition, a substantial low discharge voltage was also observed. To mitigate the problem, we tried to explore small organo-sulfur compounds. Such organo-sulfur compounds are highly soluble in a liquid electrolyte, so they have attracted little attention as Li-S cathode. But if used in an all-solid-state (ASSB) Li cell, the small organo-sulfur compounds demonstrated high reversibility, high capacity and potential to operate at room temperature.

A small molecular organic sulfur electrode materials offer unparalleled advantages over the polymeric sulfur compounds in terms of easy processability, easy synthesis, high energy density, high potential and better electrochemical reversibility. However, the notorious dissolution issue of small organosulfide compounds in organic liquid electrolytes can cause detrimental “cross-talks” between the electrodes, which is regarded as the major obstacle toward a long cycle life. The integration of the small organosulfide cathode materials into an

ASSB system, in which the dissolution can be suppressed by taking advantage of the inherent immobility of solid-state electrolytes (SSEs), could be an ultimate solution.

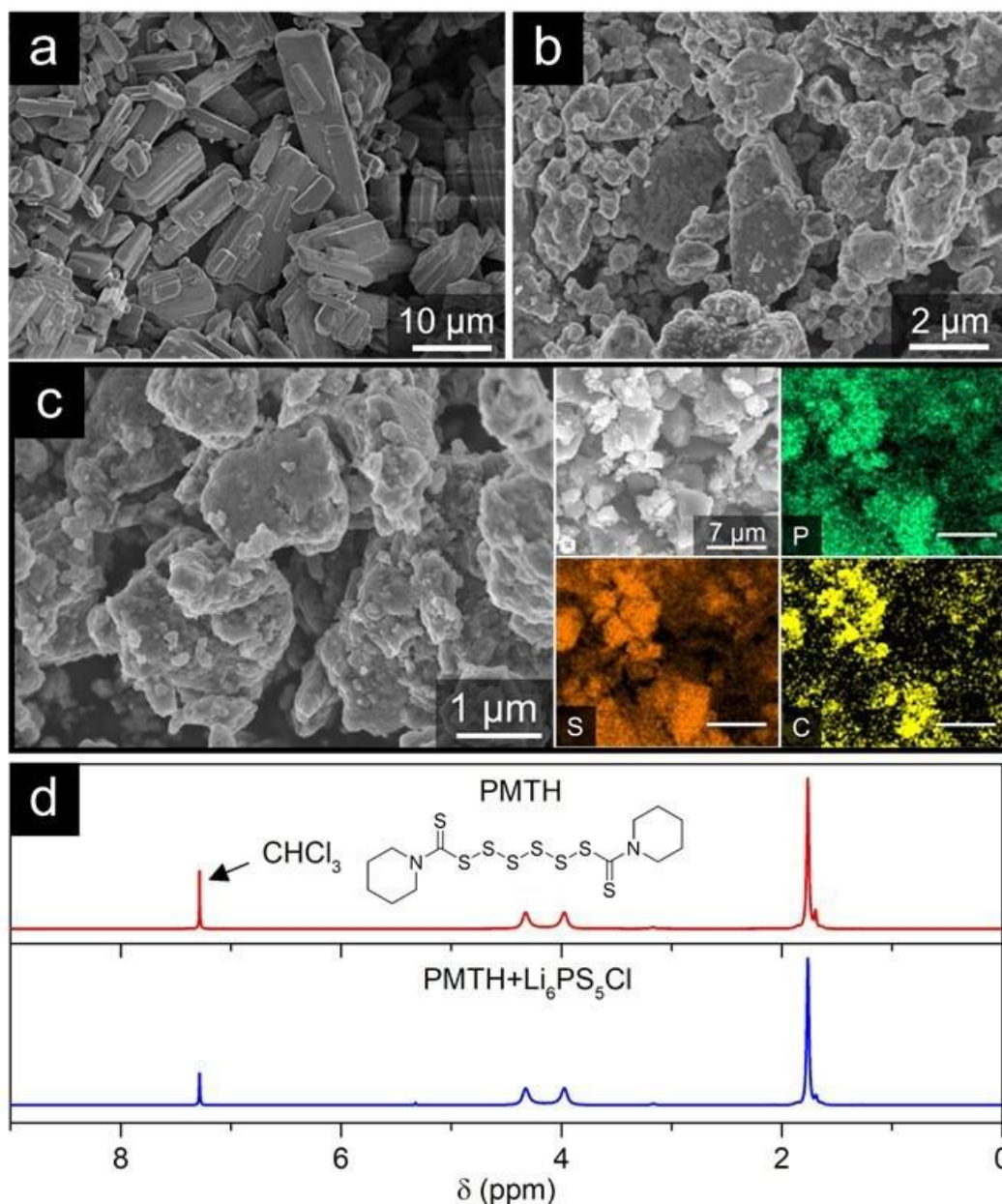


Figure XVII.3.1 SEM images of the pristine a) PMTH and b) $\text{Li}_6\text{PS}_5\text{Cl}$. c) SEM image and EDS mapping of the ball-milled PMTH cathode composite. d) Comparison of ^1H NMR spectra between the pristine PMTH and the ball-milled PMTH cathode composite.

Herein, we report the first application of thiuram polysulfide as an organic cathode material in solid-state batteries based on sulfide electrolytes. Dipentamethylenethiuram hexasulfide (PMTH) was selected as a representative cathode material. A discharge capacity of $\sim 600 \text{ mAh g}^{-1}$ was obtained under 82 mA g^{-1} at 25°C . The cell retained 80.8% of its capacity for 500 cycles at 200 mA g^{-1} . Upon cycling, an electrochemically reversible cathode/electrolyte interface was revealed; an oscillating stress change of the entire cell was also observed, which was dominated by stress evolution of the anode side demonstrating the good mechanical properties of the material during cycling. The energy density was 1140 Wh kg^{-1} at the material level and 376

Wh kg^{-1} at the electrode level, outperforming all other organic cathodes reported in ASSBs. An areal capacity of 10.4 mAh cm^{-2} was achieved with a high mass loading electrode.

To construct an ASSLB, argyrodite-type $\text{Li}_6\text{PS}_5\text{Cl}$ was selected as SSE and $\text{Li}_{38}\text{In}_{62}$ alloy (0.62 V vs. Li^+/Li) was employed as anode. PMTH cathode composite was prepared by high-energy ball-milling process. Pristine PMTH and conductive carbon were pre-milled sufficiently before adding $\text{Li}_6\text{PS}_5\text{Cl}$, aiming to minimize the degradation of $\text{Li}_6\text{PS}_5\text{Cl}$ in the presence of carbon during long-term milling considering the narrow ESW of $\text{Li}_6\text{PS}_5\text{Cl}$ (1.7–2.0 V vs. Li^+/Li). Figure XVII.3.1a-c show the scanning electron microscopy (SEM) images and energy dispersive spectroscopy (EDS) mappings of the pristine PMTH, $\text{Li}_6\text{PS}_5\text{Cl}$, and the ball-milled cathode composite, respectively. The pulverization process can not only downsize the coarse PMTH crystals to achieve intimate contact between cathode components, but also homogenize the dispersion of cathode components to enable non-blocked conduction pathways within the cathode. Both are indispensable prerequisites for achieving high active material utilization and fast redox kinetics at room temperature. The chemical compatibility of PMTH molecule against sulfide SSE after milling is validated by ^1H nuclear magnetic resonance (NMR) spectra (Figure XVII.3.1d).

Pellet-type PMTH| $\text{Li}_6\text{PS}_5\text{Cl}$ |LiIn cells were assembled and cycled between 0.4–3 V (vs. In/LiIn). Ideally, the redox chemistry of PMTH cathode involves ten-electron transfer (Figure XVII.3.2a), corresponding to a theoretical capacity of 597 mAh g^{-1} . CV profiles in Figure XVII.3.2b display only one pair of redox peaks occurring at $\sim 1.65 \text{ V}/3.1 \text{ V}$, implying a direct conversion between the charged state (PMTH) and the discharged state ($\text{Li}_2\text{S}+\text{C}_6\text{S}_2\text{H}_{10}\text{Li}$), which is different from the multi-staged redox mechanism in liquid electrolytes. Also, the overpotential was higher compared to that in the liquid cells, which stemmed from the more sluggish conversion reaction in solids. The irreversible capacity and electrochemical polarization at the first cycle could be attributed to the oxidative decomposition of SSE, forming products with poor ionic conductivity and therefore increasing the interfacial resistance. Some oxidation products of SSE, such as sulfur or polysulfide, are redox-active and could contribute to an extra capacity. The reversible capacity of SSE decomposition products is found to be $\sim 30 \text{ mAh g}^{-1}$ at 25°C . Figure XVII.3.2c shows highly consistent voltage profiles at the 20th and 50th cycles, with an attainable capacity of $\sim 595 \text{ mAh g}^{-1}$ and a nearly full material utilization. The inset dQ/dV curves display a pair of highly reversible redox peaks at around 2.5 V/1.9 V. After 260 cycles, the ball-milled cell in Figure XVII.3.2d retained a 91.4% capacity with a stable Coulombic efficiency (C.E.) of $\sim 100\%$ throughout cycling. The high utilization of the well-processed cathode should also be attributed to the high dispersity of S active sites inherited from the linearly structured organic matrix of PMTH.

Figure XVII.3.2e displays the rate performance from 0.12C (70 mA g^{-1} , 0.14 mA cm^{-2}) to 1.2C (710 mA g^{-1} , 1.42 mA cm^{-2}). An accessible capacity of $\sim 341 \text{ mAh g}^{-1}$ was delivered even at 1.2C, corresponding to 57 % of the capacity at 0.12C. Usually, the limitation under high rates stems from the spatial inhomogeneity of local state-of-charge (SOC) within the electrode, including the SOC distribution across the through-plane direction and within the active material domains, respectively. Along electrode through-plane direction, the local SOC decreased away from the bulk SSE phase, due to the Ohmic drop of SSE. While within the active material domains, the local SOC decreased from the Active material |SSE interface to the core of active material particles, due to the limitation of solid-state diffusion. To ameliorate SOC distribution inhomogeneity, electrode engineering strategies such as reducing the electrode tortuosity can be explored in future work.

Cross-sectional SEM images before and after cycling were compared. The thickness of the cathode and the SSE in Figure XVII.3.2f is $\sim 63 \text{ }\mu\text{m}$ and $\sim 420 \text{ }\mu\text{m}$ before cycling, respectively. After cycling, the cathode thickness remains almost unchanged (Figure XVII.3.2g). EDS mappings in Figure XVII.3.2h-i display that the cathode interface keeps intimate contact throughout cycling except for becoming less distinguishable after cycling. Top-view SEM images in Figure XVII.3.2j-k exhibit almost no crack formation for both the cathode and the SSE layer throughout cycling, indicating a moderate volumetric variation during repetitive conversion process.

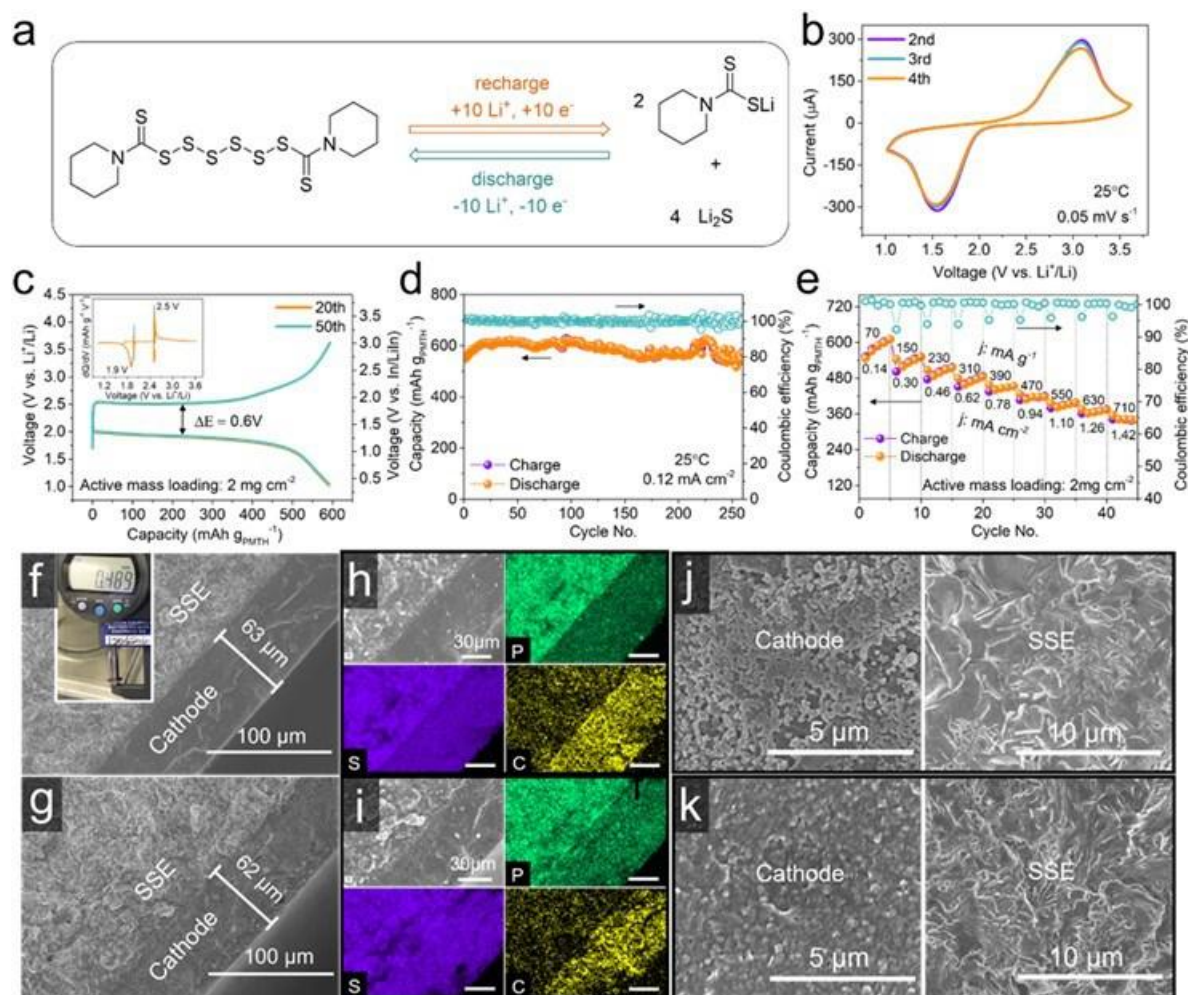


Figure XVII.3.2 a) Conversion reaction mechanism of PMTH molecule. b) CV profiles at 0.05 mV s^{-1} . c) Galvanostatic voltage profiles and corresponding dQ/dV curves. d) Cycling performance at 0.1 C and e) rate performance at 25°C . Cross-sectional SEM images of the cathode-SSE pellet f) before (inset is the thickness measurement) and g) after cycling. EDS mapping of cathode|SSE interface h) before and i) after cycling. Top-view SEM images of cathode and SSE surface j) before and k) after cycling.

To explore the practical applicability of PMTH cathode, prolonged cycling test under a higher current ($\sim 0.3\text{C}$, 200 mA g^{-1}) was carried out. All cells were cycled under 60°C , aiming to improve the reaction kinetics and interfacial contact within the cell. Figure XVII.3.3a displays an attainable capacity of $\sim 600 \text{ mAh g}^{-1}$ and excellent cyclability, retaining 80.8% of capacity after 500 cycles, which is record-breaking for Li-organic ASSBs to date.

Recently, developing high mass loading electrodes has become a popular trend for electric vehicle (EV) batteries, since the amount of energy stored in a given cell is largely dependent on the mass loading of the active material. Therefore, the performance of a high mass loading PMTH cathode is investigated. With an active mass loading of 17 mg cm^{-2} , the PMTH cathode in Figure XVII.3.3b displays an ultrahigh areal capacity of 10.4 mAh cm^{-2} . The voltage profiles are similar to those of the cells with a moderate active mass loading (2 mg cm^{-2}). A relatively small current (0.05 C) can promote the SOC distribution within the composite cathode and also prevent potential vibrant stress change caused by both electrodes. The high mass loading cell in Figure XVII.3.3c retained 96.2% of capacity after 50 cycles and possessed nearly 100% C.E. throughout cycling.

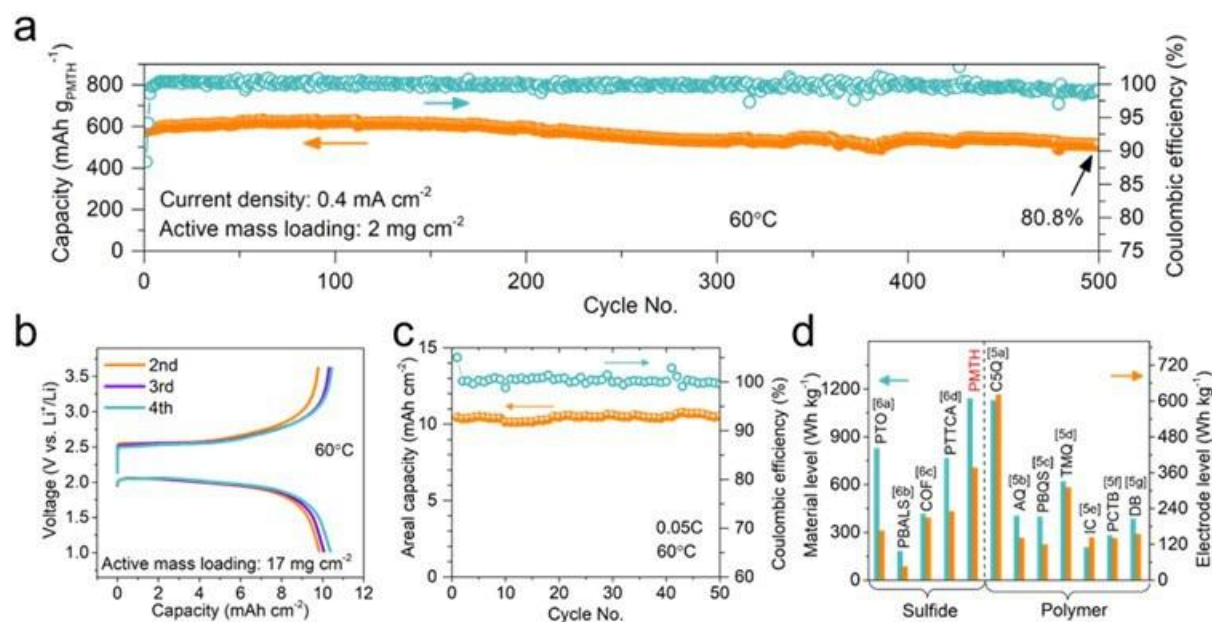


Figure XVII.3.3 a) Prolonged cycling performance at 60 °C. b) Galvanostatic voltage profiles of high active mass loading PMTH cathode and c) its cycling performance at 0.05 C. d) Energy density comparison of the state-of-the-art organic cathodes reported in Li-organic ASSBs.

Figure XVII.3.3d compares the gravimetric energy density of PMTH with previously reported organic cathodes for Li-organic ASSBs. The material-level energy density was 1140 Wh kg⁻¹, surpassing the records of all literatures. Notably, the theoretical capacity of organosulfide could be further improved by devising the end caps and increasing the number of linear S atoms. The electrode-level energy density was 376.2 Wh kg⁻¹, which was the highest among sulfide-based ASSBs but the second highest when compared with SPE-based ASSBs. This is due to the lightweight property of SPEs compared with sulfide electrolytes. To further enhance the electrode-level energy density of PMTH, future work can reduce the SSE volume fraction within the composite cathode through adopting more ionically conductive sulfide SSEs.

A carbon/sulfur with the mitigation of “shuttle-effect”

We successfully developed an *in-situ* HPLC/MS-electrochemical method, so the dissolved polysulfides during the battery operation can be qualitatively and quantitatively determined. The equilibrium reactions between dissolved polysulfides and elemental sulfur (polysulfide shuttle), were determined as the major reason for the continuous decay of the capacity during cycling and high self-discharge during storage or so-called “shuttle-effect”.

As part of our continuous efforts of mitigating the “shuttle-effect”, we synthesized a bio-inspired porous carbon material (NC) as a host carbon for a sulfur (S₈) in a cathode. We conducted a qualitative and quantitative analysis on the catalysis of the NCs to the disproportionation reaction of dissolved polysulfide ions. A polysulfide solution with 5 mM of stoichiometry Li₂S₆ were prepared by mixing S₈ and Li₂S in DME/DOL (1:1 vol%). The same amount of different NC samples synthesized at various temperatures was added into the mixtures and resting for 24 h. SuperC65 and PWA were also tested for a comparison. Figure XVII.3.4a shows the color of the blank solution with 5 mM Li₂S₆ and the same solution with the addition of NC750 (synthesized at 750 °C and so on), NC800, NC900, NC950, and SuperC65, respectively. The original baseline mixture solution displayed a green color because of the low polysulfides concentration and the relatively higher content of S₄²⁻ in the solution. After resting for 24 h, the color of the baseline and SuperC65 samples remained unchanged, while the color of the solutions with NCs faded to a lighter color, especially the solutions with NC750 and NC800, which were almost transparent. This phenomenon implied the activity of the NCs to the polysulfides in the electrolyte. The concentration and distribution of the polysulfide anion species were

changed with the addition of the bio-inspired NCs. The resulted mixture solutions were then derivatized with a methyl triflate and analyzed using a HPLC to obtain the distribution of the polysulfide species in the electrolyte, thus the further investigation of the induced reaction of polysulfides induced by the NCs quantitatively and qualitatively. The corresponding chromatograms of different samples are shown in Figure XVII.3.4b. Peaks appearing at 12.1, 13.2, 14.0, 14.7, 15.3, 15.9, and 17.0 min can be attributed to $\text{CH}_3\text{S}_3\text{CH}_3$, $\text{CH}_3\text{S}_4\text{CH}_3$, $\text{CH}_3\text{S}_5\text{CH}_3$, $\text{CH}_3\text{S}_6\text{CH}_3$, $\text{CH}_3\text{S}_7\text{CH}_3$, $\text{CH}_3\text{S}_8\text{CH}_3$, and S_8 , respectively. The SuperC65 sample displayed the same patterns as the baseline sample, indicating that SuperC65 did not induce the shift of the chemical equilibrium of the polysulfide species.

By comparison, $\text{CH}_3\text{S}_n\text{CH}_3$ ($n = 3-8$) peaks of the solutions with NC750, NC800, NC900, and NC950 almost disappeared, and the intensity of the elemental sulfur peak increased drastically. In addition, the relative ratios of peaks also changed. These results indicate the occurrence of disproportionation of S_n^{2-} induced by the NCs, which transferred most of the dissolved polysulfide anions to possibly insoluble Li_2S_n ($n < 2$) and dissolved S_8 .

This conclusion was further verified by the chromatograms of the derivatized polysulfides mixtures with PWA, which was an activated carbon with only oxygen functional groups on the surface and a similar specific surface area with NCs. As shown in Figure XVII.3.4c, the chromatogram of PWA also displayed decreased intensities for $\text{CH}_3\text{S}_n\text{CH}_3$ ($n = 3-8$) peaks and increased intensity for S_8 peak, but not as much as NCs samples. Therefore, it can be speculated that the nitrogen atoms in the NCs play a critical role for the shift of chemical equilibrium of S_n^{2-} toward elemental sulfur. The “shuttle-effect” that related to the dissolved polysulfides can, therefore be mitigated. In addition, due to the relatively low specific surface area and pore volume, NC750 did not trap as much sulfur as that of NC800. Hence, although NC750 can interact with polysulfide anions chemically and promote the S_n^{2-} transfer into S_8 , it still exhibited the lowest specific capacity among all the S/NC cathodes.

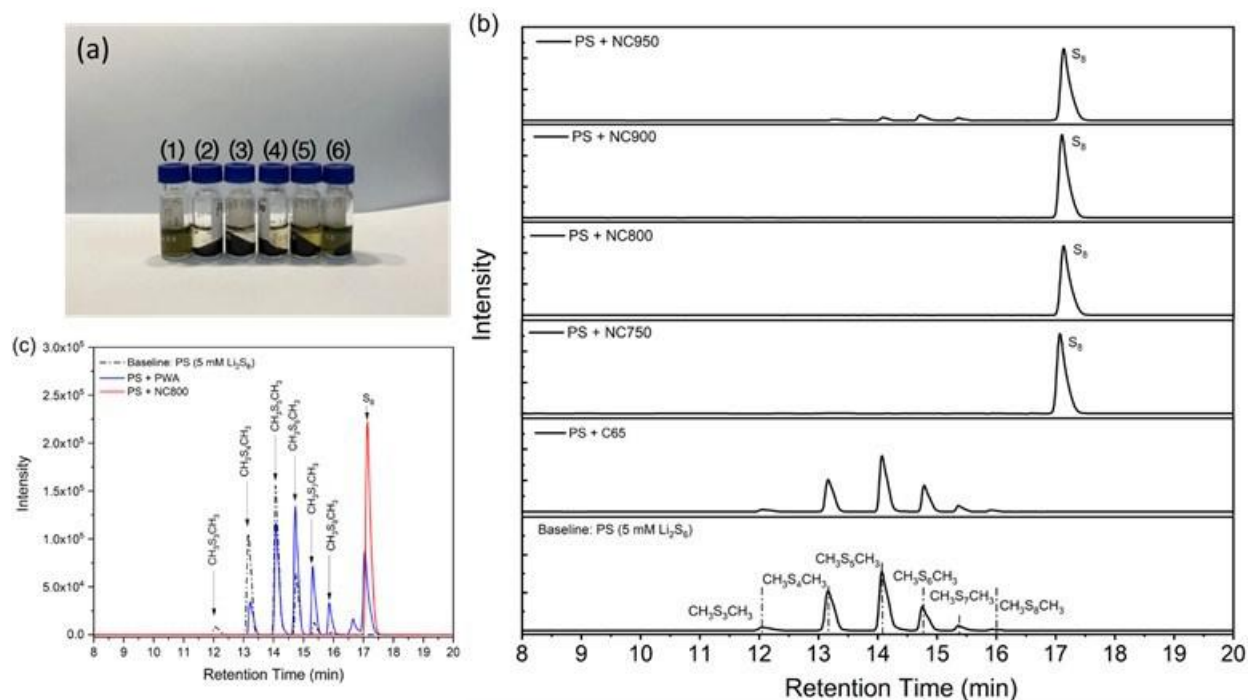


Figure XVII.3.4 (a) Color changes of 5 mM Li_2S_6 solution with different carbon samples of (1) baseline, (2) NC750, (3) NC800, (4) NC900, (5) NC950, and (6) SuperC65; (b) Corresponding HPLC chromatograms of the derivatized polysulfides mixtures; (c) HPLC chromatograms of the derivatized polysulfides (5 mM Li_2S_6) mixtures with NC800 and PWA.

A Li-S pouch cell was assembled to evaluate the electrochemical performance by using S/NC800 cathode and an S/Ketjen Black cathode for comparison. S/Ketjen Black cathode was known for the “shuttle-effect”. As

shown in Figure XVII.3.5a, after being activated at 0.05C for two cycles, the cell with NC800 delivers an initial specific capacity of 905 mAh g⁻¹ at the rate of 0.2C and displays an incremental capacity increase during the first 50 cycles. The capacity increase can be ascribed to the slow penetration of the electrolyte during the discharge and charge processes. The capacity of the pouch cell was stabilized after 50 cycles and remained at 1031 mAh g⁻¹ after 100 cycles. The nearly unchanged upper plateau of the charge/discharge curves shown in Figure XVII.3.5b also demonstrates the ability of NC800 to mitigate the “shuttle-effect” that occurred during the cycling process. HPLC analysis was then carried out to determine polysulfides in the electrolyte during cycling. The pouch cells were disassembled after cycling for three cycles. The electrolyte was then taken out from the separators and derivatized with the methyl triflate to form stable dimethyl polysulfides. As shown from the HPLC chromatographs displayed in Figure XVII.3.5c, the S/NC800 sample exhibits lower intensities for polysulfide peaks and higher intensity for S₈ peak in comparison with the S/Ketjenblack sample. These results confirmed the interactions between NC800 and polysulfides and facilitation of the formation of elemental sulfur. The solubility of S₈ in electrolyte is much lower than that of the polysulfide species, hence it can be better absorbed in the porous cathode matrix instead of shuttling to the anode.

With the solid evidence, both from the diagnosis and pouch cell cycling, the bio-inspired carbon can induce the conversion of polysulfides to possibly insoluble short-chain (n<2) polysulfides and elemental sulfur. Hence the “shuttle-effect” was mitigated. However, the detailed mechanisms are still needed to be understood.

Conclusions

In conclusion, thiuram polysulfide was explored as a low-cost and high-capacity cathode material for practically feasible all-solid-state organo sulfide batteries based on sulfide electrolytes. The feasibility of thiuram hexasulfide (PMTH) cathode was validated in a PMTH|Li₆PS₅Cl|LiIn cell. The cells delivered a capacity of ~600 mAh g⁻¹ and retained 80.8% capacity after 500 cycles. An oscillating-stress change up to 0.6 MPa was disclosed upon cycling. Meanwhile, the evolution of cathode interface upon cycling was proven to be reversible. The specific energy was determined to be 1140 Wh kg⁻¹ at the material level and 376 Wh kg⁻¹ at the electrode level. The cell delivered an areal capacity of 10.4 mAh cm⁻² under a high active mass loading condition.

In addition, a bio-inspired nitrogen-doped carbon was made. The carbon was used as the host of a sulfur cathode in a Li-S battery. The existence of these nitrogen atoms induces the chemical reaction to shift the chemical equilibrium of dissolved S_n²⁻ in the electrolyte toward formation of S₈, which has lower solubility in the electrolyte than polysulfides. The formed S₈ is deposited at the cathode side during the cycling process instead of transferring to the lithium anode side through the electrolyte. The as-prepared NCs also possessed a unique porous structure with a high specific surface area, which can physically trap the S₈ at the cathode side. Therefore, the synergistic effects of these remarkable characteristics effectively suppressed the dissolution and migration of high-order lithium PS, resulting in a stable electrochemical performance of Li-S cells.

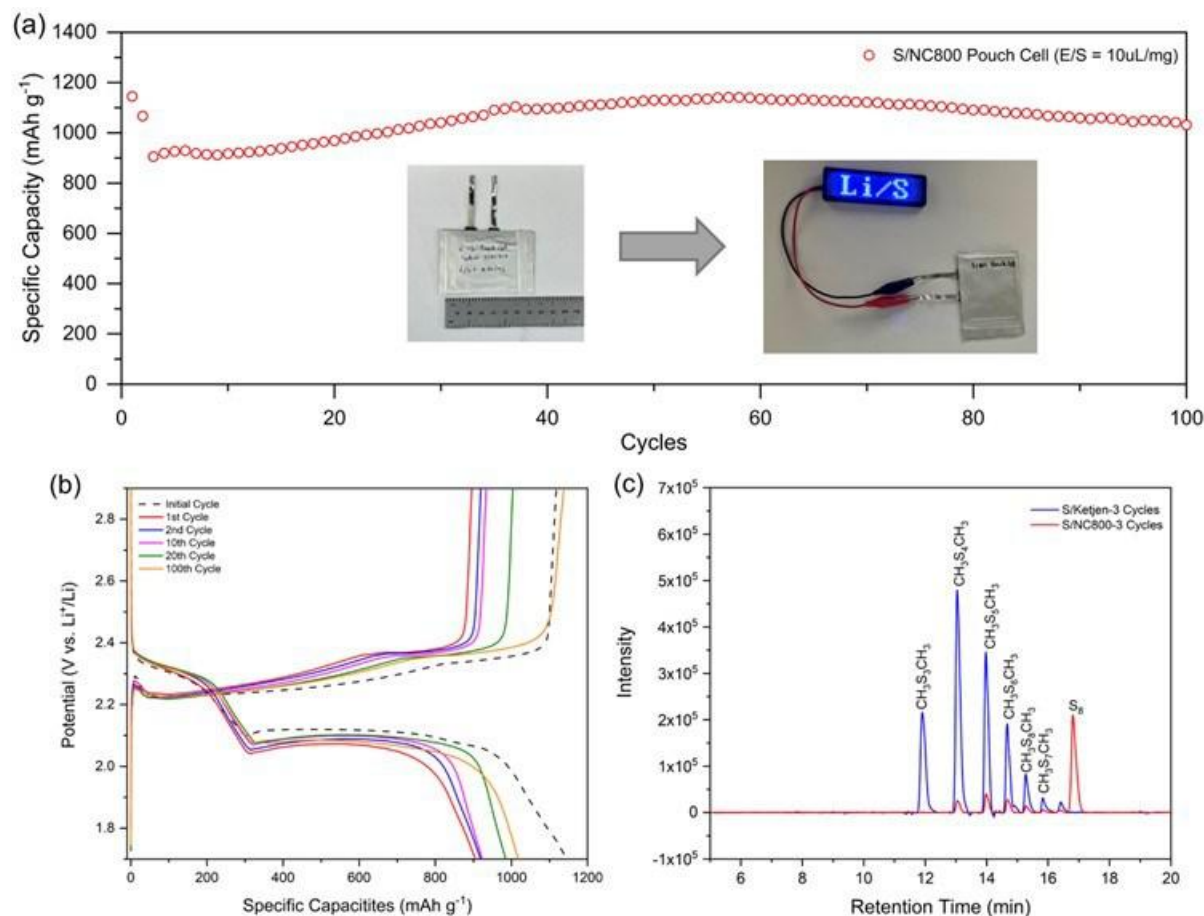


Figure XVII.3.5 (a) Cycling performance and (b) Galvanostatic charge-discharge curves of S/NC800 pouch cell with the E/S ratio of $10 \mu\text{L mg}^{-1}$; (c) HPLC chromatograms of S/NC800 and S/Ketjenblack pouch cells after 3 cycles.

Key Publications

1. Weixiao Ji, Xiaoxiao Zhang, Miao Liu, Tianyao Ding, Huainan Qu, Dantong Qiu, Dong Zheng, Deyang Qu*, "High-performance all-solid-state Li-S batteries enabled by an all-electrochem-active prelithiated Si anode", *Energy Storage Mater.* 2022, 53, 613-620.
2. Weixiao Ji, Xiaoxiao Zhang, Dong Zhang, He Huang, Tristan Lambert, Deyang Qu*, "Practically Accessible All-Solid-State Batteries Enabled by Organosulfide Cathodes and Sulfide Electrolyte", *Adv. Funct. Mater.* 2022 32, 2202919
3. Dong Zheng, Dantong Qiu, Tianyao Ding, Deyang Qu*, "Examining the Chemical Stability of Battery Components with Polysulfide Species by High Performance Liquid Chromatography and X-ray Photoelectron Spectroscopy", *Ind. Eng. Chem. Res.* 2022, 61, 3055-3062.
4. Zulipiya Shadike, Sha Tan, Qin-Chao Wang, Ruqian Lin, Enyuan Hu, Deyang Qu, Xiao-Qing Yang, "Review on Organosulfur Materials for Rechargeable Lithium Batteries", *Mater. Horiz.* 2021, 8, 471-500.

Acknowledgements

The PI in UWM (DYQ) is grateful to Professor T.H. Lambert and Dr. H Huang of Cornell for the synthesis of the materials.

XVII.4 New electrolyte binder for Lithium sulfur battery (LBNL)

Gao Liu, Principal Investigator

Lawrence Berkeley National Laboratory
Berkeley, California, 94720
E-mail: gliu@lbl.gov

Tien Duong, DOE Technology Development Manager

U.S. Department of Energy
E-mail: Tien.Duong@ee.doe.gov

Start Date: October 1, 2020

End Date: September 30, 2023

Project Funding (FY22): \$420,000

DOE share: \$420,000

Non-DOE share: \$0

Project Introduction

A strong demand for low-cost and high-energy-density rechargeable batteries has spurred lithium-sulfur (Li-S) rechargeable battery research. First, sulfur is an abundant and low-cost material. Second, the Gibbs energy of the lithium (Li) and sulfur reaction is approximately 2,600 Wh/kg, assuming the complete reaction of Li with sulfur to form Li_2S , more than five times the theoretical energy of transition metal oxide cathode materials and graphite coupling. With these advantages, Li-S batteries could be both high energy density and low cost, satisfying demand in energy storage for transportation application. The major obstacle is the loss of sulfur cathode material as a result of polysulfide dissolution into common electrolytes, which causes a shuttle effect and significant capacity fade. The polysulfide shuttle effect leads to poor sulfur utilization and fast-capacity fade, which have hindered widespread use of rechargeable Li-S batteries. This proposed work of new electrolyte development in understanding the thermodynamics and kinetics of polysulfide dissolution and precipitation will yield new approaches for electrolytes of Li-S rechargeable batteries.

Objectives

This project aims to develop new electrolytes and additives and electrode binders for Li-S battery. The properties of the ideal electrolyte for sulfur electrode would be high ion conductivity, stable towards polysulfide, and promoting the polysulfide affiliation with the electrode substrate to prevent polysulfide dissolution. The first objective is to understand the electrode substrate interaction with the polysulfides in different electrolytes. This will lead to better understandings of the polysulfide nucleation and precipitation mechanisms in common electrolytes. The second objective is chemically modifying the structures of the solvent and salt electrolyte molecules to increase electrolyte stability and ionic conductivity and to prevent polysulfide dissolution and promote polysulfides precipitation.

Approach

This project aims to develop new electrolytes and additives, and electrode binders for Li-S battery. The properties of the ideal electrolyte for sulfur electrode would be high ion conductivity, stable towards polysulfide, and promoting the polysulfide affiliation with the electrode substrate to prevent polysulfide dissolution. The project is designed to first understand the electrode substrate and binder interaction with the polysulfides in different electrolytes. This leads to better understandings of the polysulfide nucleation and precipitation mechanisms in common electrolytes. The second stage of the project will focus on chemically modifying the structures of the solvent and salt electrolyte molecules, and electrode binders to increase electrolyte stability and ionic conductivity and to prevent polysulfide dissolution and promote polysulfides precipitation.

Results

Electrolyte additive synthesis and electrolyte formulation

The 1,1,1,2,2,3,3,4,4-nonafluoro-6-(2-methoxyethoxy)hexane (F_4EO_2) electrolyte additive was prepared by following our previous works [8] and the synthesis scheme of the F_4EO_2 additive is shown in Figure XVII.4.1. Briefly, 13.70 g (0.180 mol) of 2-methoxy ethanol in 540 mL DCM and 36.03 g of (0.189 mol) 4-toluenesulfonyl chloride were mixed into a 1000 mL two-neck round bottom flask, and equipped with an air condenser, argon flow, and a magnetic stirrer. After that, 50 mL (0.360 mol) of dried TEA (distilled from CaH_2), was slowly added via a dropping funnel and the mixture was stirred for 12 h at 25 °C. The crude product was washed with distilled H_2O , diluted HCl, and saturated $NaHCO_3$. After evaporation of the DCM, the yellowish liquid product (2-methoxyethyl 4-methylbenzenesulfonate) (42.0 g, 96% yield), was used for the next step without any additional purification. 35.00 g (0.152 mol) of 2-methoxyethyl 4-methylbenzenesulfonate and 20.07 g (0.076 mol) of 1H,1H,2H,2H-perfluorohexan-1-ol were mixed in NMP (46 mL) and aqueous KOH (45 wt%, 46 mL). The reaction mixture was stirred for 5 h at 50 °C and then the temperature was increased up to 70 °C and stirred for 2 h. After completion of the reaction, the product was extracted with ether, washed with water and brine, and dried over $MgSO_4$, and concentrated under reduce pressure to yield crude yellowish color oil. Finally, a colorless liquid F_4EO_2 product (22.02 g, 75% yield) with high purity was obtained by distillation under high vacuum of the crude oil. 1H NMR (500 MHz, $CDCl_3$): δ = 2.40-2.50 (m, 2H); 3.39 (s, 3H); 3.54-3.64 (m, 4H), 3.78 (t, J = 7.08 Hz, 2H). The prepared electrolyte additive was further dried with molecular sieves and stored inside the inert atmosphere glove box.

TTE, DOL, LiFSI, LiTFSI, and F_4EO_2 were used to prepare electrolyte solutions. The electrolyte solutions are denoted as TDLiTFSI, T5FDLiTFSI, T10FDLiTFSI, T20FDLiTFSI, T5FDLiFSI and T5FDLiTFSI-FSI. The details of the composition of the electrolyte solutions are shown in Table XVII.4.1.

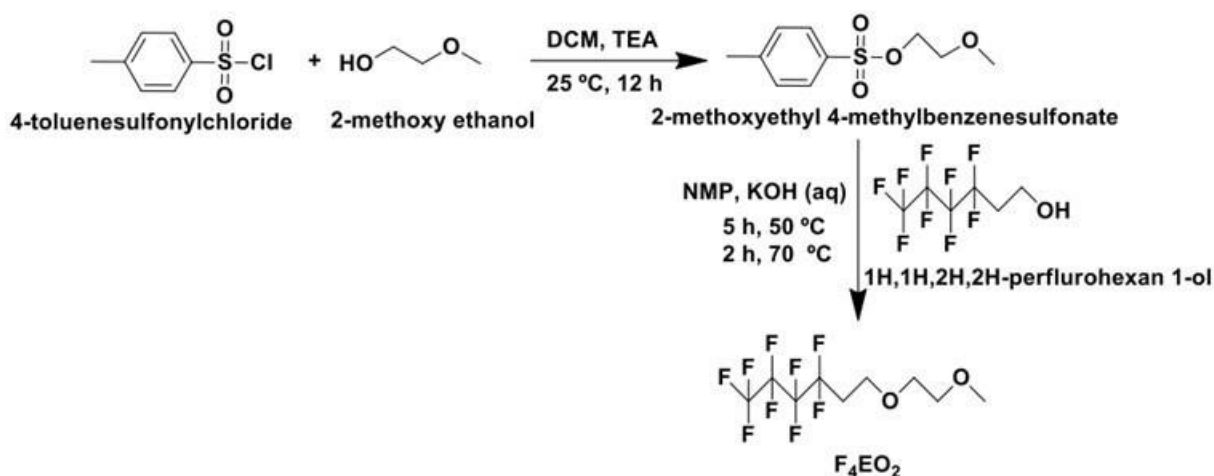


Figure XVII.4.1 The synthesis scheme of 1,1,1,2,2,3,3,4,4-nonafluoro-6-(2-methoxyethoxy)hexane (F_4EO_2).

Table XVII.4.1 Structural characterization of polyesters made for the current project

Acronym of the Electrolyte Solution	Ratio TTE:F ₄ :EO ₂		DOL (vol%) in the electrolyte	Concentration LiTFSI (M)	Concentration LiFSI (M)
	TTE	F ₄ :EO ₂			
TDLiTFSI	5	-	10%	0.5	-
T5FDLiTFSI	5	1	10%	0.5	-
T10FDLiTFSI	10	1	10%	0.5	-
T20FDLiTFSI	20	1	10%	0.5	-
T5FDLiTFSI	5	1	10%	0.5	0.5
T5FDLiTFSI-FSI	5	1	10%	0.5	0.25

Li-S cell performances

The new electrolytes were tested using the coin cell configuration of Li//electrolyte//S/C composite cathode at 30 °C. The sulfur material was used as an active cathode material because of its high theoretical specific capacity (1675 mAh/g), low cost, abundance, and safety. The charge-discharge capacity of the cells was measured over a voltage range of 1.7 to 2.8 V at 0.1 C. Figure XVII.4.2 depicts the galvanostatic cycling capacity and Coulombic efficiency of the first 20 cycles. The discharge gravimetric specific capacities using these electrolyte solutions were 866, 1331, 1124, 1013, 1025, and 982 mAh/g, respectively, at the first cycle, which are comparable to or higher than other reported Li-S battery chemistries. Furthermore, the discharge capacities were 526, 1222, 1129, 1128, 692, and 584 mAh/g, respectively, after 20 cycles. The cycling capacity of the cell with TDLiTFSI electrolyte solutions without F₄EO₂ additive showed lower capacity than those of the cells with other electrolytes with the additive with LiTFSI salt. The performance of the Li-S cells with the prepared electrolytes is consistent with the electrolytes electrochemical stability, and ionic conductivity results. The capacity retention of the cells with T5FDLiTFSI, T10FDLiTFSI, and T20FDLiTFSI electrolyte solutions was excellent even though only 0.5 M LiTFSI salt concentration was used (lower than the standard salt concentration). In this study, we demonstrate the formation of a robust SEI layer and S electrode stabilization by F₄EO₂ additive and TFSI anion. The Coulombic efficiencies of the cells with T5FDLiTFSI, T10FDLiTFSI, and T20FDLiTFSI electrolyte solutions were 100%, 99.93%, and 99.92%, respectively, after 20 cycles. However, the Coulombic efficiencies were significantly decreased after 20 cycles of the cells with T5FDLiTFSI-FSI, and T5FDLiFSI electrolytes, at 88.18%, and 88.79%, respectively. This could attribute to the only difference of the presence of FSI ion in the T5FDLiTFSI-FSI, and T5FDLiFSI electrolytes. It is also reported the TFSI anion is more chemically stable compared to the FSI anion toward lithium metal surface.

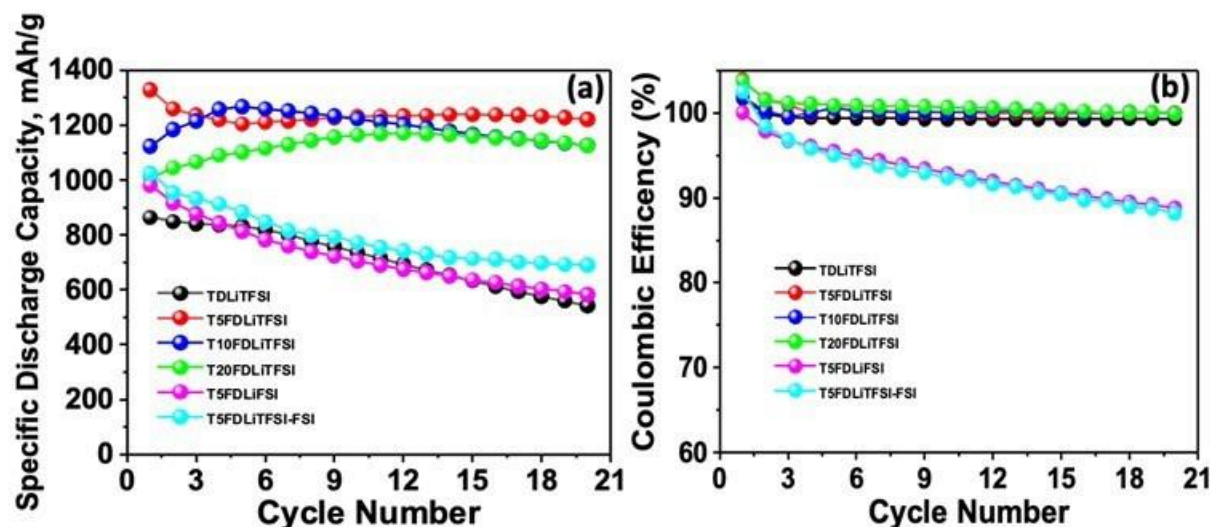


Figure XVII.4.2 Li-S cell cycling results as a function of cycle number at 0.1 C rate with different electrolyte compositions. (a) Sulfur specific gravimetric discharge capacities. (d) Coulombic efficiencies.

Morphological analyses of the electrodes

The surface morphology of the electrodes was analyzed by SEM to better understand the impact of the F_4EO_2 additive and anionic structure of the imide salts (FSI^- vs. $TFSI^-$) to the cathode and anode electrodes. All of the cycled Li-anodes and S cathodes were washed with DOL and dried before SEM and XPS analysis. Figure XVII.4.3 is the SEM surface images of the sulfur cathode and lithium metal anode electrode from the different electrolyte chemistries after cell cycling. The surface of the original Li-metal anode was neat and smooth. The Li-metal anode harvested from the cell using T5FDLiTFSI electrolyte solution exhibited a smoother, less crack, and compact surface, and the photo image of the lithium metal is also shining with no black residues. However, the lithium surface with T5FDLiTFSI-FSI, and T5FDLiFSI electrolytes exhibited rough and irregular surfaces due to the growth of SEI layers. These results suggest that Li-metal anode interface is easily degraded in the FSI anion containing electrolytes, resulting in a less stable SEI layers formed on the Li metal anode with LiFSI $^-$ containing electrolyte in Li-S cells.

Moreover, the surfaces of the cycled S/C composite cathodes were also characterized by SEM images to evaluate the effect of cathode/electrolyte interphases during cycling. There were no significant changes observed on the surfaces of S/C composite cathodes before and after cycling with all of three electrolyte compositions, suggesting that the electrode/electrolyte interphases formed on the S/C cathode are stable and not the predominating factor responsible for cell performance variation. However, there are some changes observed on the cathode surfaces after cycling, which may be due to the volume change of the S/C cathode during the CD cycling. Therefore, it is clear that the cycling stability of the SEI layers on the Li-metal anode plays a significant role in cycling performance variation of this groups of electrolytes.

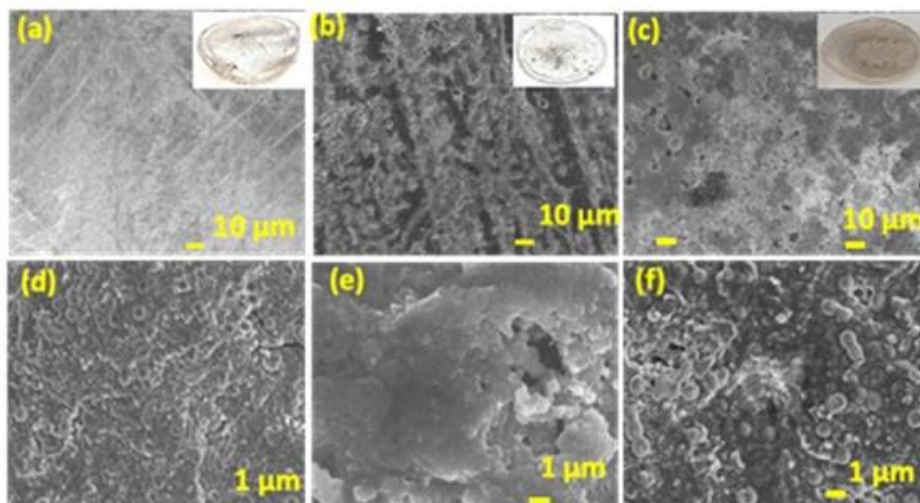


Figure XVII.4.3 SEM surface images of the cycled Li-S battery electrode using different electrolyte solutions. (a-c) Li-anodes, and inset photo images are the surface of Li metal. (d-f) sulfur cathodes. (a,d) T5FDLiTFSI electrolyte. (b,e) T5FDLiTFSI-FSI electrolyte. (c,f) T5FDLiFSI electrolyte.

Chemical analysis of the lithium metal electrode

Full XPS scans were performed on both cycled lithium anodes and cathodes from cells using the different electrolytes. The chemical composition on the surface of the cycled S/C cathode electrodes was almost identical for all the cells with different electrolytes. The differences are from the lithium metal anodes. Figure XVII.4.4 show the XPS analyses of the surface of the Li-anode after cycling, focusing on the fluorine and sulfur elements. Figure XVII.4.4a depicts the F 1s spectra of the cycled Li anode with TDLiTFSI, T5FDLiTFSI, T10FDLiTFSI, T20FDLiTFSI, T5FDLiTFSI-FSI, and T5FDLiFSI electrolytes. The main peak was observed at 685.51 eV for cycled Li anode with T5FDLiFSI electrolyte, which corresponds to LiF compound, produced from the degradation of FSI anion. There is also a noticeable shoulder peak around 688 eV for the electrolyte with FSI anions, indicating a distinctive configuration of the LiF formed with LFI anion salt. The intensity of the LiF peak consistently decreased with the increased amount of LiTFSI salt and F_4EO_2 additive in the electrolyte solutions, and the main peak position shift to higher energy. Overall, TFSI anion based electrolytes tend to facilitate the smooth lithium deposition with fewer LiF by products formation, whereas the FSI anion has higher reactivity toward lithium metal.

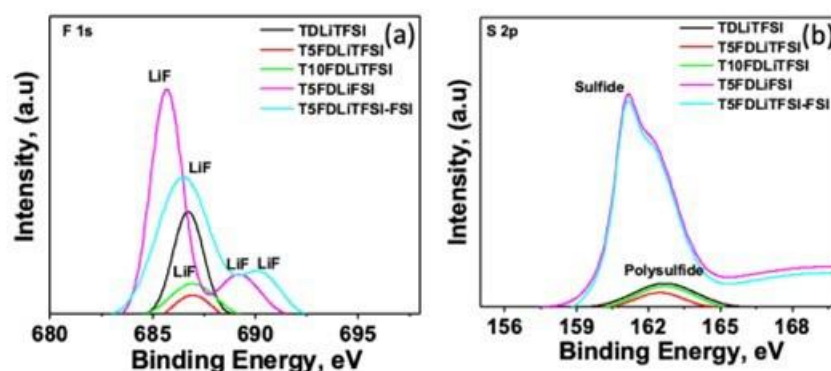


Figure XVII.4.4 High-resolution XPS spectra of the surface of cycled Li-anode after washing off the electrolyte. (a) fluorine 1s and (b) sulfur 2p.

The reactivity of the FSI anion based electrolyte toward lithium metal is coupled with reactions of polysulfides on the lithium metal surface. With the TFSI anion based electrolyte such as T5FDLiTFSI, the sulfur 2p spectra of the cycled Li-metal anode is no as prominent. However, with increasing the FSI anion concentration of T5FDLiTFSI-FSI, and T5FDLiFSI electrolytes, there is a large accumulation of both Li_2S and polysulfides species. The TFSI anion stability toward both the electrolyte and polysulfides explains the superb Li-S cell cycling performance of the T5FDLiTFSI, T10FDLiTFSI, and T20FDLiTFSI group of electrolytes.

Conclusions

We have synthesized a highly fluorinated ether-based bifunctional micelle electrolyte additive, F_4EO_2 , and applied a unique strategy to suppress polysulfide dissolution and enhance lithium metal stabilization in Li-S battery. With this bifunctional additive, we have prepared different electrolyte solutions by using F_4EO_2 , TTE, LiTFSI, LiTFSI, and DOL, respectively, for Li-S battery application. The LiTFSI imide electrolyte with F_4EO_2 additive showed excellent compatibility with Li-metal anode, good electrochemical stability, cycling stability, and high specific discharge capacity of ca. 1350 mAhg^{-1} with the battery configuration of Li//electrolyte//S/C composite at 0.1C. The FSI anion has high reactivity with the Li-metal anode, and forms a large amount of LiF and sulfides deposits on the surface of the Li-metal anode, leading to cell performance degradation. Concurrently, the micelle-like F_4EO_2 additive improves the battery performance substantially. The results demonstrated that the Li-S battery with T5FDLiTFSI electrolyte using F_4EO_2 additive showed excellent cycling performance, with good capacity retention and high coulombic efficiency (99.98%), by suppressing polysulfides dissolution and stabilizing lithium metal anode.

References

1. G. Zhou, H. Chen, Y. Cui, 2022, 7, DOI 10.1038/s41560-022-01001-0.
2. N. Wang, X. Zhang, Z. Ju, X. Yu, Y. Wang, Y. Du, Z. Bai, S. Dou, G. Yu, Nat. Commun. 2021, 12, 1–10.
3. N. Wang, X. Zhang, Z. Ju, X. Yu, Y. Wang, Y. Du, Z. Bai, S. Dou, G. Yu, Nat. Commun. 2021, 12, 1–10.
4. M. Zhao, B. Q. Li, X. Q. Zhang, J. Q. Huang, Q. Zhang, ACS Cent. Sci. 2020, 6, 1095–1104.
5. Q. Pang, X. Liang, C. Y. Kwok, L. F. Nazar, Nat. Energy 2016, 1, 1–11.
6. J. Lei, T. Liu, J. Chen, M. Zheng, Q. Zhang, B. Mao, Q. Dong, Chem 2020, 6, 2533–2557.
7. Q. Ma, B. Tong, Z. Fang, X. Qi, W. Feng, J. Nie, Y.-S. Hu, H. Li, X. Huang, L. Chen, Z. Zhou, J. Electrochem. Soc. 2016, 163, A1776–A1783.
8. Y. Zhao, C. Fang, G. Zhang, D. Hubble, A. Nallapaneni, C. Zhu, Z. Zhao, Z. Liu, J. Lau, Y. Fu, G. Liu, Front. Chem. 2020, 8, 1–9.
9. W. Xue, Z. Shi, L. Suo, C. Wang, Z. Wang, H. Wang, K. P. So, A. Maurano, D. Yu, Y. Chen, L. Qie, Z. Zhu, G. Xu, J. Kong, J. Li, Nat. Energy 2019, 4, 374–382.

10. J. Sun, K. Zhang, Y. Fu, W. Guo, *Nano Res.* 2022, DOI 10.1007/s12274-022-4361-z.
11. T. van Ree, *Curr. Opin. Electrochem.* 2020, 21, 22–30.
12. S. Gu, C. Sun, D. Xu, Y. Lu, J. Jin, Z. Wen, *Electrochem. Energy Rev.* 2018, 1, 599–624.
13. X. Li, M. Banis, A. Lushington, X. Yang, Q. Sun, Y. Zhao, C. Liu, Q. Li, B. Wang, W. Xiao, C. Wang, M. Li, J. Liang, R. Li, Y. Hu, L. Goncharova, H. Zhang, T. K. Sham, X. Sun, *Nat. Commun.* 2018, 9, 1–10.
14. K. Sun, Q. Wu, X. Tong, H. Gan, *ACS Appl. Energy Mater.* 2018, 1, 2608–2618.
15. Fang, G. Zhang, J. Lau, G. Liu, *APL Mater.* 2019, 7, DOI 10.1063/1.5110525.
16. S. S. Zhang, *J. Power Sources* 2013, 231, 153–162.
17. J. Scheers, S. Fantini, P. Johansson, *J. Power Sources* 2014, 255, 204–218.
18. S. Zhang, K. Ueno, K. Dokko, M. Watanabe, *Adv. Energy Mater.* 2015, 5, DOI 10.1002/aenm.201500117.
19. R. Xu, I. Belharouak, J. C. M. Li, X. Zhang, I. Bloom, J. Bareño, *Adv. Energy Mater.* 2013, 3, 833–838.
20. D. J. Lee, M. Agostini, J. W. Park, Y. K. Sun, J. Hassoun, B. Scrosati, *ChemSusChem* 2013, 6, 2245–2248.
21. D. J. Lee, M. Agostini, J. W. Park, Y. K. Sun, J. Hassoun, B. Scrosati, *ChemSusChem* 2013, 6, 2245–2248.
22. D. Aurbach, E. Pollak, R. Elazari, G. Salitra, C. S. Kelley, J. Affinito, *J. Electrochem. Soc.* 2009, 156, A694.
23. H. L. Wu, M. Shin, Y. M. Liu, K. A. See, A. A. Gewirth, *Nano Energy* 2017, 32, 50–58.
24. L. Suo, Y. S. Hu, H. Li, M. Armand, L. Chen, *Nat. Commun.* 2013, 4, 1–9.
25. J. Park, K. Ueno, N. Tachikawa, K. Dokko, M. Watanabe, 2013.
26. J. W. Park, K. Yamauchi, E. Takashima, N. Tachikawa, K. Ueno, K. Dokko, M. Watanabe, *J. Phys. Chem. C* 2013, 117, 4431–4440.
27. X. Ren, S. Chen, H. Lee, D. Mei, M. H. Engelhard, S. D. Burton, W. Zhao, J. Zheng, Q. Li, M. S. Ding, M. Schroeder, J. Alvarado, K. Xu, Y. S. Meng, J. Liu, J. G. Zhang, W. Xu, *Chem* 2018, 4, 1877–1892.
28. R. Cao, J. Chen, K. S. Han, W. Xu, D. Mei, P. Bhattacharya, M. H. Engelhard, K. T. Mueller, J. Liu, J. G. Zhang, *Adv. Funct. Mater.* 2016, 26, 3059–3066.
29. A. Singh, A. Rafie, V. Kalra, *Sustain. Energy Fuels* 2019, 3, 2788–2797.
30. [30] C. Weller, J. Pampel, S. Dörfler, H. Althues, S. Kaskel, *Energy Technol.* 2019, 7, DOI 10.1002/ente.201900625.

Acknowledgements

Dr. Faiz Ahmet, Dr. Thanh-Nhan Tran, Dr. Chen Fang performed experimental work, and analyzed data.

XVII.5 Strategies to Enable Lean Electrolytes for High Loading and Stable Lithium-Sulfur Batteries (UCSD)

Ying Shirley Meng, Principal Investigator

University of California, San Diego
9500 Gilman Dr.
La Jolla, CA 92093
E-mail: shmeng@ucsd.edu

Hui Du, Co-Principal Investigator

Ampcera, Inc.
Tucson Tech Park
1700 E 18th St Ste 102
Tucson, AZ 85719-6552
E-mail: hdu@ampcera.com

Mei Cai, Co-Principal Investigator

General Motors.
30470 Harley Earl Blvd.
Warren, MI 48092
E-mail: mei.cai@gm.com

Haiyan Croft, DOE Technology Development Manager

U.S. Department of Energy
E-mail: Haiyan.Croft@ee.doe.gov

Start Date: October 1, 2021

End Date: December 31, 2022

Project Funding (FY22): \$569,109

DOE share: \$428,175

Non-DOE share: \$140,934

Project Introduction

Lithium-sulfur (Li-S) batteries offer the potential for higher energy densities due to the high theoretical capacities of the sulfur cathode (1675 mAh g^{-1}). Moreover, by using abundant elemental sulfur, they also benefit from lower material costs than conventional lithium-ion batteries (LIBs) which are still largely based on costly transition metal oxides materials such as nickel and cobalt.¹ Sulfur-based cathodes also offer improved safety factors due to their conversion-based reaction mechanisms which reduce the risks of thermal runaway typical of host-type materials.² Moreover, the environmentally benign nature of elemental sulfur also reduces the potential environmental impact of cells when they reach their end of life. However, the commercialization of Li-S still faces several technical barriers that impede its commercialization:

1. Inability to enable lean electrolyte conditions necessary for high energy densities.
2. Polysulfide dissolution resulting in sulfur inventory loss & continuous electrolyte consumption.

To achieve targets of 500 Wh/kg under realistic sulfur cathode loadings ($\geq 64 \text{ wt\%}$), lean electrolyte conditions of $< 3 \text{ g/Ah}$ are needed, an ambitious goal currently unachievable with the state of the art. The highly porous nature of low-density carbon-sulfur (C-S) composite cathodes makes it difficult to prepare compact electrodes with high sulfur loading, often resulting in cracking during the fabrication process. Continuous electrolyte consumption originating from high cathode porosity also results in the need for a large excess of liquid electrolytes to achieve reasonable sulfur utilization and cycle life. There is an urgent need to develop compact electrodes with high sulfur loading and low porosity, with a focus on balancing high tap density and sufficient intrinsic porosity to allow wettability as well as efficient polysulfide adsorption. Recent attempts to reduce electrolyte excess include efforts to improve electrolyte diffusion within porous electrodes, as well as the use

of 3D nanoporous sulfur host structures to improve wettability and reduce tortuosity.³ However, these studies have yet to demonstrate efficacy under lean electrolyte conditions and high sulfur areal loadings ($>10 \text{ mAh cm}^{-2}$). Comparatively, our promising strategies to enable lean electrolytes for high-loading and stable Lithium-Sulfur batteries are via adopting redox active dense stacking polymers as Li-S cathodes. Our bulky hexaazatrinaphthylene (HATN) polymer reduces the stacking porosity to achieve a high bulk density of 1.6 g cm^{-3} by the melting polymerization process, while its intrinsic porosity based on *s*-triazine bonding is maintained.⁴ The bulky HATN polymer serves as an Sulfur host material, which shows high S loading with a low porosity in Li-S batteries using a limited amount of electrolyte; regulates the lithium polysulfide deposition; accommodates the cathode volume change from S to Li_2S .

This project is led by UCSD with the collaboration of **Ampcera Inc.** and **General Motors (GM)**. Our UCSD team has established the baseline setup for the HATN lab-scale synthesis; built the cryogenic characterization toolbox for Li-S batteries; developed the quantitative methodologies to analyze the degradation of Li-S batteries. **Ampcera Inc.** is a company possessing the technology of solid-state chemical synthesis, which dedicates the effort to scaling up the synthesis of HATN polymer (kg-scale) in this project. **GM** contributes to the large-size Li foil supply and large-capacity cell assembly owing to their robust facilities and resources for pouch cell production. Upon effort of the entire team, we can insight into the root limitations of high-energy-density Li-S batteries and develop strategies to sort them out.

Objectives

The objective of the project is to develop high energy density ($>500 \text{ Wh/kg}$) and low cost ($<68 \text{ \$/kWh}$) Li-S pouch cells. More specifically, the main goal of this project is to develop a high-performance and low-cost polymer-based S electrode (HATN-S) and novel electrolyte formulation to enable long-term stable cycling. The best combination of novel cathode synthesis process, new electrolyte formula and full cell design will provide us a high energy Li-S pouch cell. The critical success factors in achieving that goal include:

- Develop novel electrode architectures and electrolyte chemistries including HATN polymer-Sulfur composite electrode, and state-of-the-art liquid electrolyte systems to enable Li-S pouch cell that use high areal loading ($>10 \text{ mAh cm}^{-2}$) and low porosity (30%) cathode with high full cell energy density ($>500 \text{ Wh/kg}$).
- Utilize advanced characterization, and diagnosis tools for resolving the root causes of capacity fade and identify electrode architectures that improve the cycle life of Li-S pouch cells.
- Close collaboration between university-industry to deliver practical pouch type cells with low cost ($<68 \text{ \$/kWh}$).

Approach

To achieve that, novel electrode architectures using the HATN polymer-sulfur composite electrode will be explored to achieve the low cathode porosity and the high S active loading of the composite electrode. Additionally, advanced electrolyte systems and the optimization of Li metal anode will be applied further to increase the energy density of the Li-S pouch cell. If successful, the proposed HATN polymer-sulfur composite electrode will achieve less than 30% porosity, significantly decreasing electrolyte usage with high areal capacities of $>10 \text{ mAh cm}^{-2}$, enabling lean electrolyte conditions $<3 \text{ g/Ah}$ in the full Li-S pouch cell.

Results

In budget plan 1 (BP1), the characterization toolbox, including thermogravimetric analysis (TGA), cryogenic focused ion beam-scanning electron microscopy (cryo-FIB-SEM), titration-gas chromatography (TGC), and High-performance liquid chromatography- ultraviolet spectroscopy (HPLC-UV), was constructed to quantify the Li and S inventory loss in Li-S batteries (Q1). It revealed that Li losses are more severe under lean electrolyte conditions (baseline electrolyte: $1 \text{ M LiTFSI DOL/DME}$, vol/1:1, 2 wt.% LiNO_3) due to the consumption of limited LiNO_3 reservoir in lean electrolyte conditions (Q2). HPLC-UV methodology was introduced to quantify the LiNO_3 consumption of the electrolyte, and the calibration curve of LiNO_3 concentration was established (Q3). The LiNO_3 depletion in nanostructured C-S cathode-based Li-S batteries

is tremendously larger than in bulky S cathode-based ones (Q3) due to larger cathode porosity (larger cathode surface area). These results suggest the importance of using bulk S cathode materials to decrease LiNO_3 consumption. The above results validate the purpose of using the bulky HATN-S materials to achieve lean electrolyte usage for high-energy-density Li-S batteries. In Q2, it was demonstrated that HATN-S cathode could enable lean electrolyte usage in Li-S batteries with electrolyte-to-sulfur, E/S ratio of $6 \mu\text{l mg}_{\text{sulfur}}^{-1}$ paired with thin lithium ($100 \mu\text{m}$).

Further efforts were dedicated to optimizing the synthesis of HATN/CNT polymer composite (a 10 g-lab scale) to construct a good 3D ion and electron conduction network (Q3). The optimized HATN/CNT-S cathode was evaluated using a lean baseline electrolyte (E/S ratio of $6 \mu\text{l mg}_{\text{sulfur}}^{-1}$) by pairing it with $100 \mu\text{m}$ Li metal foils. Long cycling stability of 680 cycles with an areal capacity of $\sim 2 \text{ mAh cm}^{-2}$ was achieved (Q3), which is far more excellent than the nanostructured C-S cathode with only 75 cycles in baseline electrolyte. In Q4, the HATN/CNT-S cathode was ultimately optimized by mixing elemental sulfur with the HATN/CNT host materials in the process of electrode preparation. Thus, S is infiltrated into the host during initial discharge and charge (electrochemical infusion), which circumvents the conventional S melt infusion method. It is shown that this optimized HATN/CNT-S presents the highest S-specific capacity of $\sim 1250 \text{ mAh g}_{\text{sulfur}}^{-1}$ (high S utilization) and the highest discharge plateau (fast polysulfide kinetics) under the lean electrolyte condition. Besides, it is illustrated that the HATN/CNT host accommodates the volume change from S to Li_2S , while the C-S cathode suffers from a large volume change. By using a lean baseline electrolyte (Electrolyte-to-Sulfur, E/S ratio of $\sim 6 \mu\text{l mg}_{\text{sulfur}}^{-1}$ or Electrolyte-to-Capacity, E/C ratio of $\sim 5 \text{ g Ah}^{-1}$) and pairing with $100 \mu\text{m}$ Li metal foils (N/P ratio of 2.6) received from our collaborators at GM, the HATN/CNT-S cathode delivers a high cycling areal capacity of $\sim 5.5 \text{ mAh cm}^{-2}$ at 0.1 C in Li-S batteries (coin-cell). Besides, the GM C-S cathode was evaluated under the E/S ratio of $\sim 10 \mu\text{l mg}_{\text{sulfur}}^{-1}$, presenting a similar limited cycling behavior to the UCSD nano C-S cathode with drastic capacity decay (Q1-Q3). The milestone of an initial areal capacity of 5 mAh cm^{-2} has been achieved, and future work will be focused on the assembly of a small pouch cell to make the most use of the electrolyte for high energy density.

As decomposition-based LiNO_3 is required in the charge and discharge of Li-S batteries, a stable alternative is necessary to avoid continuous depletion of its critical function. Thus, a new electrolyte (NewEle) system is proposed to avoid reliance on LiNO_3 , using an alternative additive that is stable at the Li metal anode. In applying this new electrolyte system to the C-S cathode that involves S redox chemistry only, stable cell cycling with a capacity retention of $\sim 75\%$ after 320 cycles is achieved using lean electrolyte conditions, compared to the baseline LiNO_3 containing electrolyte that shows severe degradation after 75 cycles. The NewEle would be extended to HATN/CNT-S cathode for even longer cycling performance of high-energy-density Li-S batteries.

Investigating the Li-S batteries under lean lithium and electrolyte conditions

To establish a reference for comparison, the HATN-S electrodes will be tested against the conventional C-S electrode composite. In Li-S battery research, there is extensive work on nanostructured C-S cathode materials to not only resolve the weakness of insulating S but also enhance the absorption of polysulfide for a good cycling behavior. Figure XVII.5.1a and Figure XVII.5.1b show the nano C-S cathode with porous honeycomb structure prepared in BP1. The Li-S community has been increasing the awareness of decreasing electrolyte usage to achieve high energy density. To investigate the practical cyclability of S cathode, all the work is under stringent conditions of lean electrolyte and lithium as recommended through findings at the Battery500 consortium. Figure XVII.5.1c shows charge-discharge curves of the C-S composite cathode at different C-rates using a $100 \mu\text{m}$ Li metal foil anode and an E/S ratio of $\sim 10 \mu\text{l mg}_{\text{sulfur}}^{-1}$. The nanostructured C-S composite cathode delivers areal capacities of 3 mAh cm^{-2} , 2.5 mAh cm^{-2} , and 2 mAh cm^{-2} at 0.05 C, 0.1 C, and 0.2 C respectively. The initial discharge plateaus are observed to be lower compared to cells operating with extremely excessive electrolyte, as S redistribution in the cathode is prohibited due to slower polysulfide diffusion in lean electrolyte conditions. The C-S cathode cycles at 0.2 C for less than 100 cycles (Figure XVII.5.1d) before complete failure. Interestingly, severe degradation is observed at the 74th and 75th cycles, wherein the cell displayed an abnormal charge voltage profile (inset), likely due to severe polysulfide shuttle

(inset of Figure XVII.5.1d). Such phenomena are not observed in Li-S cells when large excess electrolytes are used, highlighting the need to understand the root causes for practical Li-S cells to be realized.

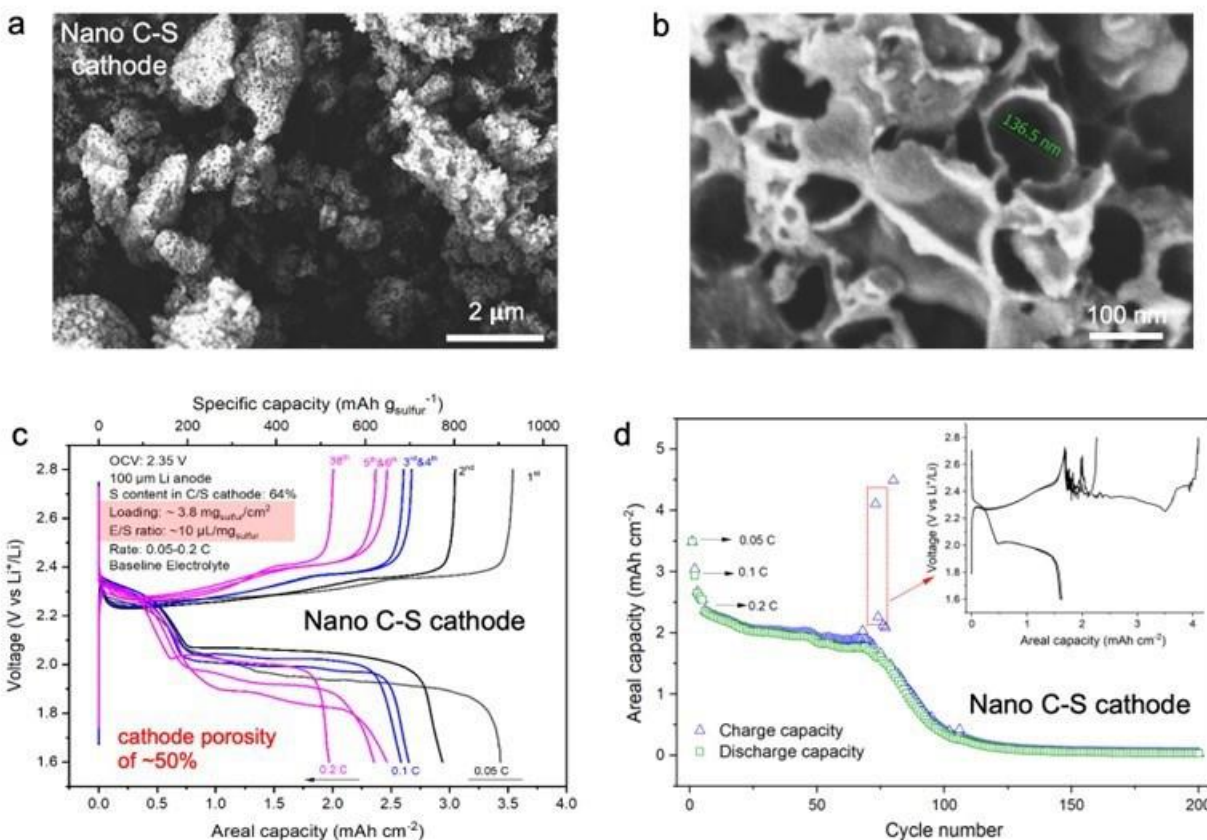


Figure XVII.5.1 (a and b) SEM images of the nanostructured C-S cathode, (c) Voltage profiles of C-S composite electrodes at different C-rates using 100 μm Li and E/S ratio of 10 $\mu\text{L mg}_{\text{sulfur}}^{-1}$ and (d) the corresponding cycling stability.

Quantifying the Li and S inventory loss in Li-S batteries.

We also established a series of characterization tools to elucidate the root cause of the low cycling life of C-S system. In the Q1&Q2, we developed TGA as a valid tool for quantification of S mass (Figure XVII.5.2a), and in turn, S inventory losses with cycling. In Q2, we proceeded to analyze the S inventory loss of the cycled electrode materials under lean electrolyte conditions. To do so, the cycled electrode at the charged state from Figure XVII.5.2d was extracted and its S content was analyzed using TGA. From an initial S mass of 3.1 mg at the pristine state, only 0.6 mg of active S was found after 200 cycles, as shown in Figure XVII.5.2b and Figure XVII.5.2c. The TGA measured for the C-S cathode illustrates a drastic S inventory loss (80.6%), a contrasting conclusion from what was previously reported using a large excess of electrolyte. From these initial results, it indicates that capacity fade in the Li-S cells is due to both Li and S inventory losses, with more severe depletion of S inventory under lean electrolyte conditions. Thus, the consumption of LiNO_3 in lean Li and electrolyte Li-S system might be the pivotal factor that limits the Li-S cycling performance.

Previously, our group has successfully developed the Titration Gas Chromatography (TGC) method to quantify the metallic Li mass in the cycled electrodes. The TGC method has been expanded recently to accommodate the Li-S system (Figure XVII.5.2d). A new calibration curve with a range of up to 2.5 mg of Li was established for measuring larger quantities of Li used in this project. With the new calibration curve, the remaining metallic Li mass in the cycled Li metal electrode from Li-S cells can be quantified. Herein, we used the baseline C-S electrode system as it undergoes a quicker and more severe failure route to facilitate analysis. The cycled Li metal was divided into 3 samples to fit the mass range of the new calibration curve. The yellow

residues of sulfur species of those 3 samples (brown solution) suggest a large amount of polysulfide that reacts with Li metal (polysulfide shuttle). The TGC quantified that the Li anode undergoes a large Li inventory loss of 47.00% (Figure XVII.5.2e). A calculated total of $\sim 10 \text{ mAh cm}^{-2}$ Li anode capacity is lost in the cycled cell despite a total cathode capacity of only $\sim 2 \text{ mAh cm}^{-2}$, indicating that the polysulfide shuttle can induce a disproportionate amount of Li inventory losses in the cell. Therefore, we can infer that without sufficient Li passivation, polysulfides will shuttle to the Li anode side, inducing a combination of both Li and S inventory losses. Thus, a potentially effective approach to mitigate both Li and S inventory losses would be to protect Li using an additive more stable and effective than LiNO_3 , which will be discussed later.

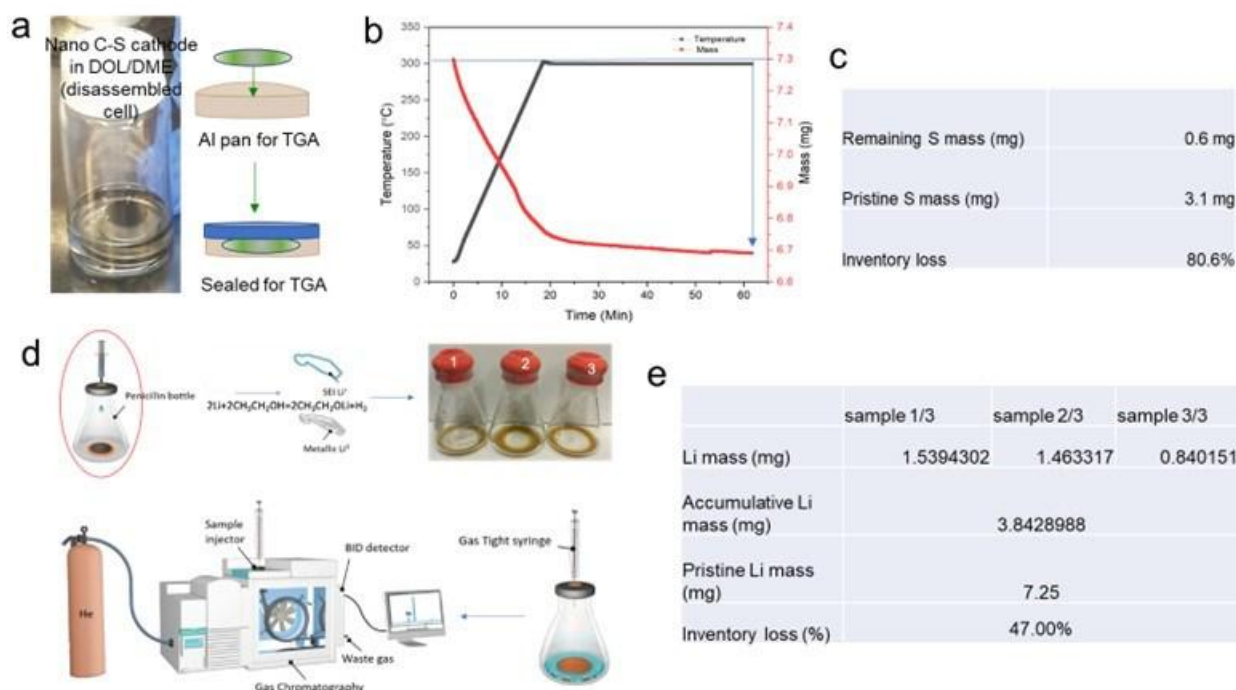


Figure XVII.5.2 (a) Photo of the C-S cathode from the disassembled cell after 200 cycles (Previous figure, d) and immersed in DOL/DME solvents and the schematic of protecting S samples for TGA Photo of Li metal from the disassembled cell after 200 cycles; (b and c) TGA curves and the data table of the above cycled C-S cathode; (d) The schematic of TGC quantification of Li metal loss including the sample of the cycled Li metal by polysulfide shuttle from the disassembled cell after 200 cycles (Previous figure, d); (e) The Li mass quantified by TGC.

Quantifying the LiNO_3 depletion in nano C-S and bulk C-S cathodes

In Q2, the HPLC-UV methodology was introduced to quantify the consumption of LiNO_3 . In Figure XVII.5.3a, the cycled cell was disassembled and dissolved by DOL/DME solvent, which generates a homogeneous liquid sample (electrolyte). The samples were injected into the HPLC column chromatography for separation and then characterized by the UV detector. Based on the polarity of different species in the sample, LiNO_3 was first eluted out.

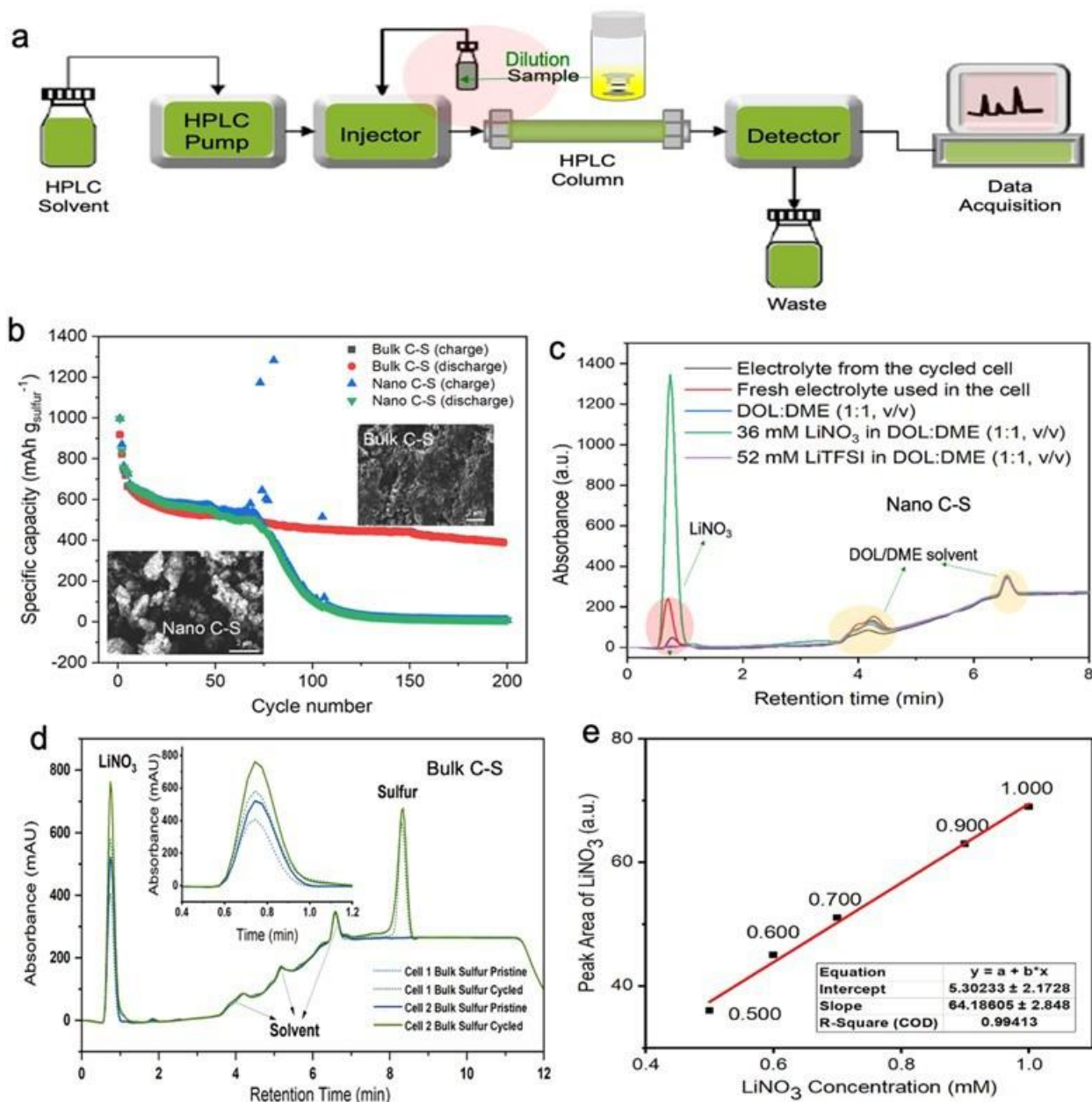


Figure XVII.5.3 (a) The schematic of the HPLC-UV methodology used to investigate the LiNO_3 amount; (b) The cycling behavior of the nanostructured C-S and the bulk C-S cathode in baseline electrolyte with E/S ratio of $10 \mu\text{l mg}_{\text{sulfur}}^{-1}$ and $100 \mu\text{m Li}$. The S loading of is $3.8 \text{ mg}_{\text{sulfur}} \text{ cm}^{-2}$ of the nano C-S and $2.52 \text{ mg}_{\text{sulfur}} \text{ cm}^{-2}$ of the bulk C-S; (c) HPLC-UV spectra of the fresh electrolyte, DOL/DME solvent, LiNO_3 and LiTFSI in DOL/DME solvent, and the cycled electrolyte of the nano C-S cathode; (d) HPLC-UV spectra of the pristine electrolyte and cycled electrolyte for bulk C-S cathode; (e) The standard curve of LiNO_3 concentration ranging from 0.5 mM to 1 mM.

It is known that cathode porosity and tortuosity impact electrolyte usage and wettability. To investigate the influence on electrolyte consumption, both the nano C-S cathode and the bulky C-S cathode are evaluated for comparison (Figure XVII.5.3b). Note that the bulky C-S cathode was prepared by a simple mix of bulk S and super P (low surface area). Since these two cathodes are using the same E/S ratio of $10 \mu\text{l mg}_{\text{sulfur}}^{-1}$ and the lithium anode is still excessive, the S utilization (practical S-specific capacity/ S theoretical capacity) can affect the electrolyte utilization. Figure XVII.5.3b shows that the Bulky C-S cathode delivers a similar S-specific capacity to that of the Nano C-S cathode indicating a similar S utilization. However, the bulky C-S

cathode sustains superior cycling in sharp contrast to the nano C-S cathode with a limiting cycle life. It has been verified the consumption of LiNO_3 in the nano C-S cathode is severe while there is minor LiNO_3 depletion in the bulky C-S cathode (Figure XVII.5.3c and Figure XVII.5.3d). It is evidenced that the LiNO_3 peak intensity of the cell after C-S cycling in baseline electrolyte is fragile, suggesting the depletion of LiNO_3 . Further, a standard curve of LiNO_3 concentration vs UV adsorption was established (Q3, Figure XVII.5.3e), and it can be used to retrieve the accurate concentration of the LiNO_3 at different stages. This huge difference in the LiNO_3 depletion is correlated to the high surface area of both the carbon host and S. Since the S redox chemistry is an interfacial reaction on the conductive carbon host materials, the nano C-S consumes far more LiNO_3 during the charge and discharge. Hence, to achieve lean electrolyte utilization for high energy density, the S cathode should be of less porosity and tortuosity instead of the conventional cathode design principle of the nanostructured C-S cathode.

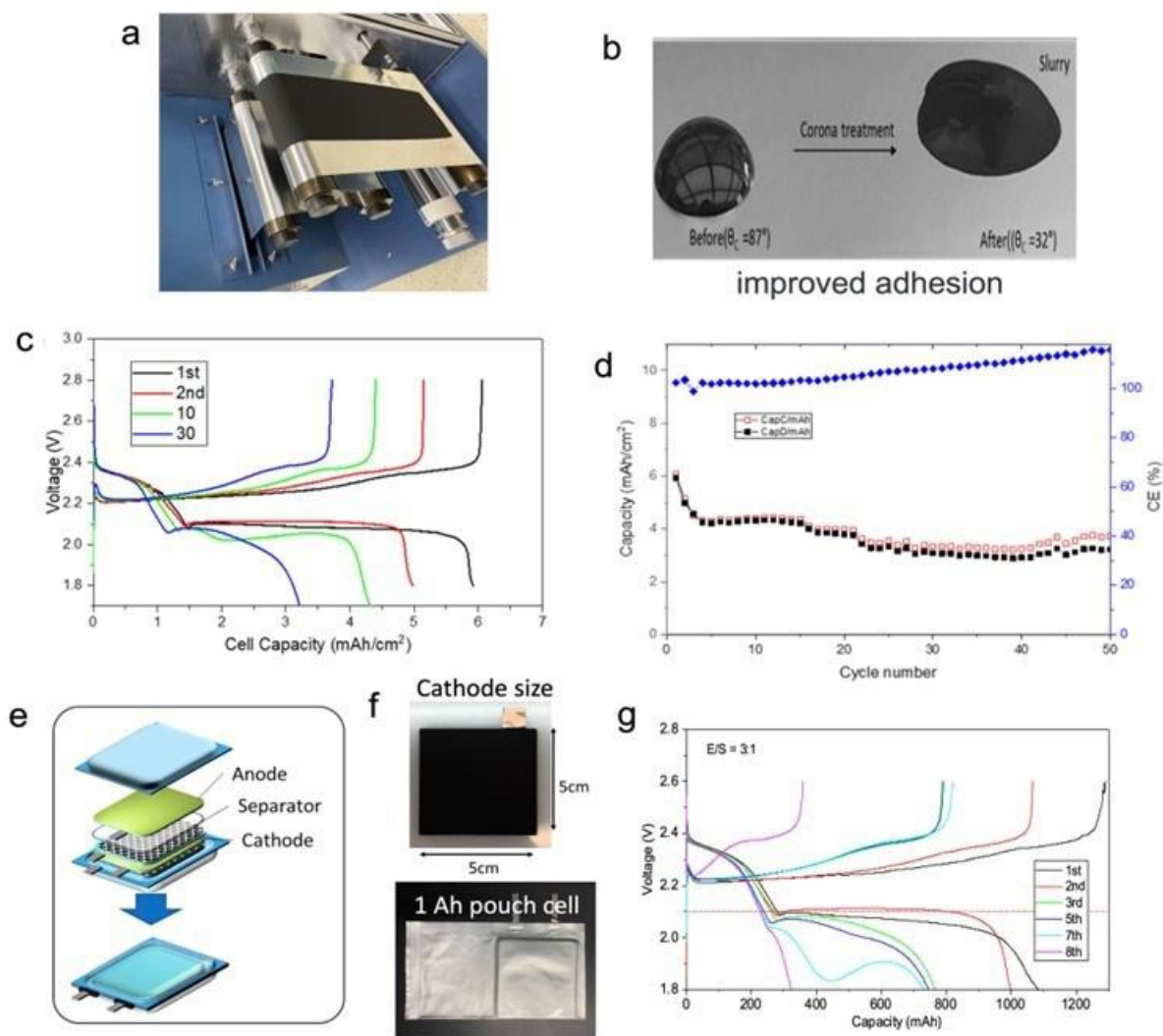


Figure XVII.5.4 (a) The roll-to-roll S electrode casting at GM; (b) The corona treatment by plasma to increase the adhesion to the Al current collector; (c) Electrochemical performance of $5.2 \text{ mg}_{\text{sulfur}} \text{ cm}^{-2}$ sulfur cathode electrode, c) charge-discharge profiles and d) discharge-discharge capacities and CE vs. cycle number; (e and f) The schematic and the photos of the design of a Li-S pouch cell; (g) The voltage profiles of various cycles of the 1 Ah Li-S pouch cell delivering a super high energy density of 400 Wh kg^{-1} .

Baseline C-S cathode performance and the high-energy-density Li-S pouch cell with limited cycle life (General Motors).

In the benchmarking scope of work, all the C-S baseline composite electrodes were studied using a low electrode loading. Thus, the loadings of the C-S reference electrodes need to be increased for meaningful comparisons. However, due to the limitations of the slurry-based casting of low-density C-S-based composites, it is difficult to achieve such high-loading cast layers at the laboratory scale. To this end, GM has produced C-S cathode (nanostructured) electrodes with high loading of $>5 \text{ mg}_{\text{sulfur}} \text{ cm}^{-2}$ by developing new slurry coating technology (e.g., plasma treatment of Al substrate) and further optimizing slurry compositions (Figure XVII.5.4a and Figure XVII.5.4b).

Figure XVII.5.4c shows the potential vs. specific capacity retention curves of the GM C-S cathode with $5.2 \text{ mg}_{\text{sulfur}} \text{ cm}^{-2}$. The areal discharge capacity can reach up to $\sim 6 \text{ mAh cm}^{-2}$ initially under the first formation cycle at 0.05 C with an E/S ratio of $8 \text{ } \mu\text{l mg}_{\text{sulfur}}^{-1}$, which quickly stabilized at 4 mAh cm^{-2} after switching to the discharge current rate of 0.1 C for the following cycles. The cell lasts for about 50 cycles till the discharge capacity decreases to below 60% retention (Figure XVII.5.4d). GM C-S cathode also shows major capacity decay by using the lean electrolyte. In Q3 and Q4, GM finished the delivery of two batches of the GM C-S cathode to UCSD with the S loading of ~ 5 and $\sim 3.26 \text{ mg}_{\text{sulfur}} \text{ cm}^{-2}$. In the coming budget year, UCSD will work closely with GM to evaluate the electrochemical performance of the GM C-S cathode and use it as the baseline for future studies.

Figure XVII.5.4e and Figure XVII.5.4f show the design and assembly of a 1-Ah Li-S pouch cell at GM and it was evaluated with lean electrolyte usage of $\text{E/S} = 3 \text{ } \mu\text{l mg}_{\text{sulfur}}^{-1}$. The pouch cell delivers a super high energy density of 400 Wh kg^{-1} . However, the cycling is limited, which is identical to the coin cell performance. All these results demonstrate the electrolyte depletion in conventional nanostructured C-S cathode is severe, which deters the cycling stability. Nevertheless, the bulky S cathode materials can be the solution to this bottleneck problem.

The optimization of the bulky HATN/CNT-S cathode with a low porosity and tortuosity

This project focuses on the bulky dense-stacking HATN polymer as S host materials. In BP1, carbon nanotubes (CNTs) were incorporated into the HATN polymerization to construct a good 3D ion and electron conduction network (Figure XVII.5.5a), while maintaining a high tap density and bulky size ($\sim 17 \text{ } \mu\text{m}$) of the HATN/CNT composite (Figure XVII.5.5b) owing to the melting polymerization of the HATN host (Q3-Q4). Elemental S was mixed with the HATN/CNT host during the electrode preparation, S was incorporated into this host material by the electrochemical infusion during initial discharge and charge. This circumvents the conventional S melting infusion to decrease the cathode cost of Li-S batteries. A slurry recipe containing HATN/CNT (26 wt.%), S (64 wt.%), a small amount of binder (5 wt.%), and carbon additive (super P, 5 wt.%) was applied to prepare the cathode electrode sheet using carbon-coated Al foil as the current collector for better adhesion.

Figure XVII.5.5c shows that despite lean electrolyte usage, the second discharge plateau of the optimized HATN/CNT cathode typically lies at a higher voltage of $\sim 2.1 \text{ V}$ at the formation cycle (0.05 C, $1\text{C}=1000 \text{ mA g}^{-1}$) than that using conventional S infusion. This indicates faster polysulfide redox reaction kinetics for better S redistribution in the cathode under lean electrolyte conditions. The coin-cells were assembled by pairing against the $100 \text{ } \mu\text{m}$ Li metal foil obtained from our collaborator GM and a lean electrolyte (E/S ratio of $\sim 6 \text{ } \mu\text{l mg}_{\text{sulfur}}^{-1}$) using baseline electrolyte (1 M LiTFSI in a DOL/DME mixture (1:1, v/v) with 2 wt% LiNO_3). HATN/CNT-S delivers a higher S-specific capacity of $\sim 1250 \text{ mAh g}_{\text{sulfur}}^{-1}$ than either $\sim 900 \text{ mAh g}_{\text{sulfur}}^{-1}$ for the HATN-S cathode (Q2) or $\sim 1050 \text{ mAh g}_{\text{sulfur}}^{-1}$ for the HATN/CNT-S cathode via S melt infusion (Q3). And an areal capacity of $\sim 3.0 \text{ mAh cm}^{-2}$ at 0.05 C was achieved. Figure XVII.5.5d shows the cryogenic focused ion beam scanning electron microscopy (Cryo-FIB SEM) image of the cross-section of the UCSD nano C-S cathode as a reference, which is highly porous. However, the HATN/CNT-S cathode via electrochemical infusion features a bulky particle size of $>10 \text{ } \mu\text{m}$ (Figure XVII.5.5e) with a low porosity of $\sim 30\%$, the same as that of bare HATN-S cathode (29%, Q1). Further, the quantification of the 2-D tortuosity of this optimized

HATN/CNT-S cathode is based on a simplified mathematical equation ($\tau = C/L$), wherein C is the electrolyte diffusion curve length and L is the distance between the curve ends. Thus, $\tau=1$, $\tau=1.57$, and $\tau=\infty$ are defined as paths of a straight line, a semicircle, and a circle, respectively. Herein, three diffusion paths in the above cross-section were measured, which exhibits a low average 2-D tortuosity (τ) of 1.22 based on $\tau_1=1.14$, $\tau_2=1.15$, and $\tau_3=1.37$ within 1.57 of a semicircle path. The EDX spectrum of Figure XVII.5f corresponds to the uniform S-element distribution of the HATN/CNT-S cathode. Its low cathode porosity decreases the electrolyte usage, and the low cathode tortuosity facilitates electrolyte wettability, which ultimately yields a high S utilization and a high working voltage. All these results show the effectiveness of the electrochemical S infusion into a bulky ion/electron conductive network.

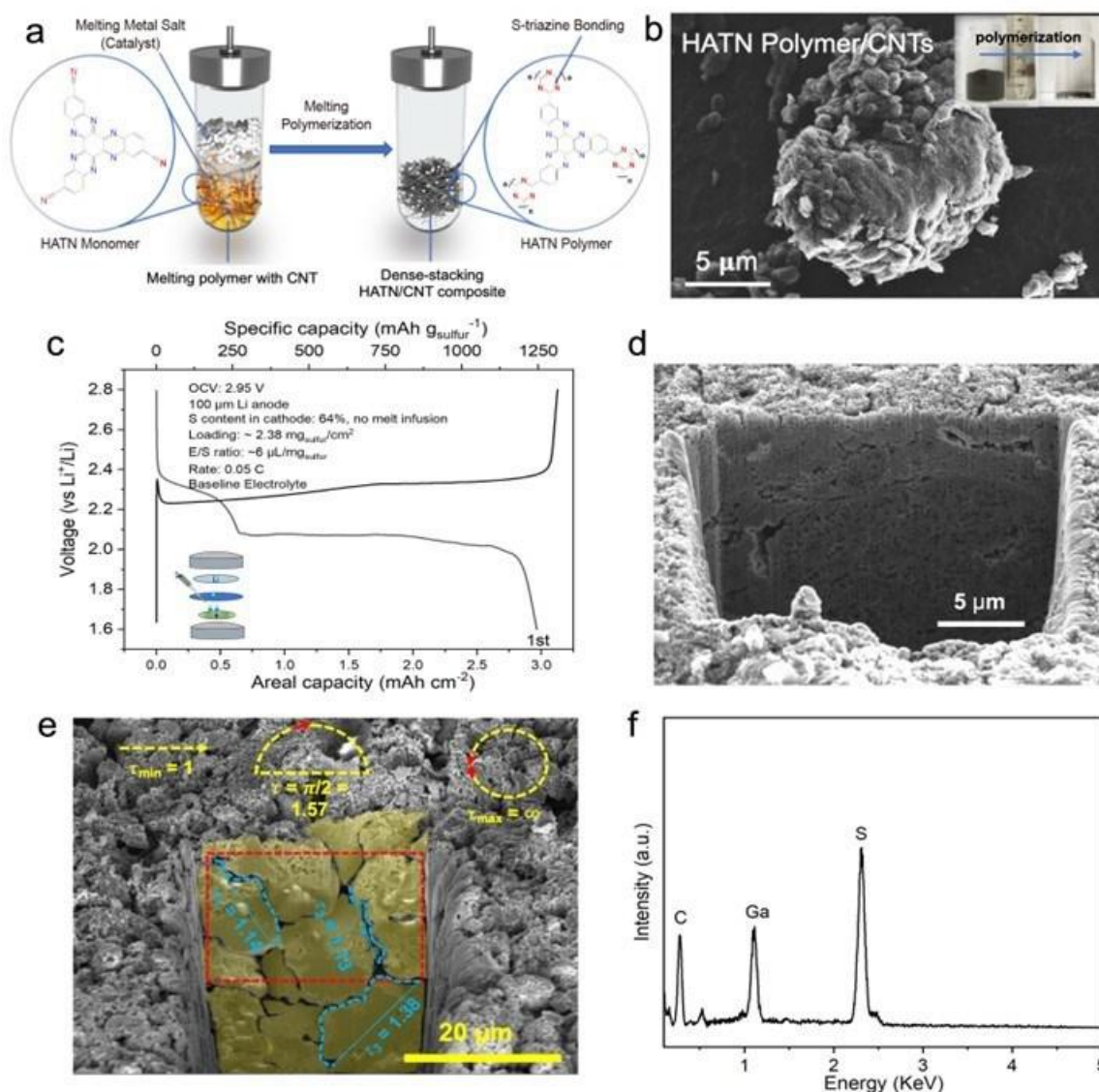


Figure XVII.5 (a) The schematic of the synthesis of the HATN/CNT composite; (b) the SEM image of HATN/CNT, and the digital photo of the composite before and after polymerization (inset); (c) The voltage profile of HATN/CNT-S cathode without S melt infusion in baseline electrolyte of 1 M LiTFSI in a DOL/DME mixture (1:1, v/v) with 2wt.% LiNO₃, using 100 μm Li and E/S ratio of 6 μL mg_{sulfur}⁻¹; (d) The Cryo-FIB SEM image of the cross-section of the UCSD nano C-S cathode with highly porous structure; (e) The Cryo-FIB SEM image of the cross-section of the HATN/CNT-S cathode via electrochemical infusion, which is highlighted with a low average 2-D tortuosity (τ) of 1.22 and a bulky particle size of >10 μm; (f) The EDX spectrum of the selected area (red rectangle in 4e), showing the successful electrochemical S infusion.

Evaluating the optimized HATN/CNT-S cathode

The destruction of electrode structural integrity during cycling is one of the bottleneck problems of Li-S batteries, because the conversion of S ($2.07 \text{ g} \cdot \text{cm}^{-3}$) into Li_2S ($1.66 \text{ g} \cdot \text{cm}^{-3}$) intrinsically sustains from a large volume expansion of 180% ($V_{\text{Li}_2\text{S}}/V_{\text{S}}$, normalized to 1 mol) or a volume change of 80% ($V_{\text{Li}_2\text{S}} - V_{\text{S}}/V_{\text{S}}$, normalized to 1 mol). Thus, the selection and design of S cathodes are of great importance. Figure XVII.5.6a and Figure XVII.5.6b exhibit the top view of the cryo-FIB SEM images of HATN/CNT-S from the pristine to the initially discharged respectively, under a small magnification, which is for the analysis of cathode volume change from a broad perspective. The minimal particle size evolution demonstrates that our HATN/CNT-S cathode can accommodate the large volume change during the charge and discharge processes. This is attributed to a vacant bulky HATN/CNT host that can contain the active liquid S species (Sulfur and polysulfide) much better than an S solid-infused HATN/CNT host (melt infusion).

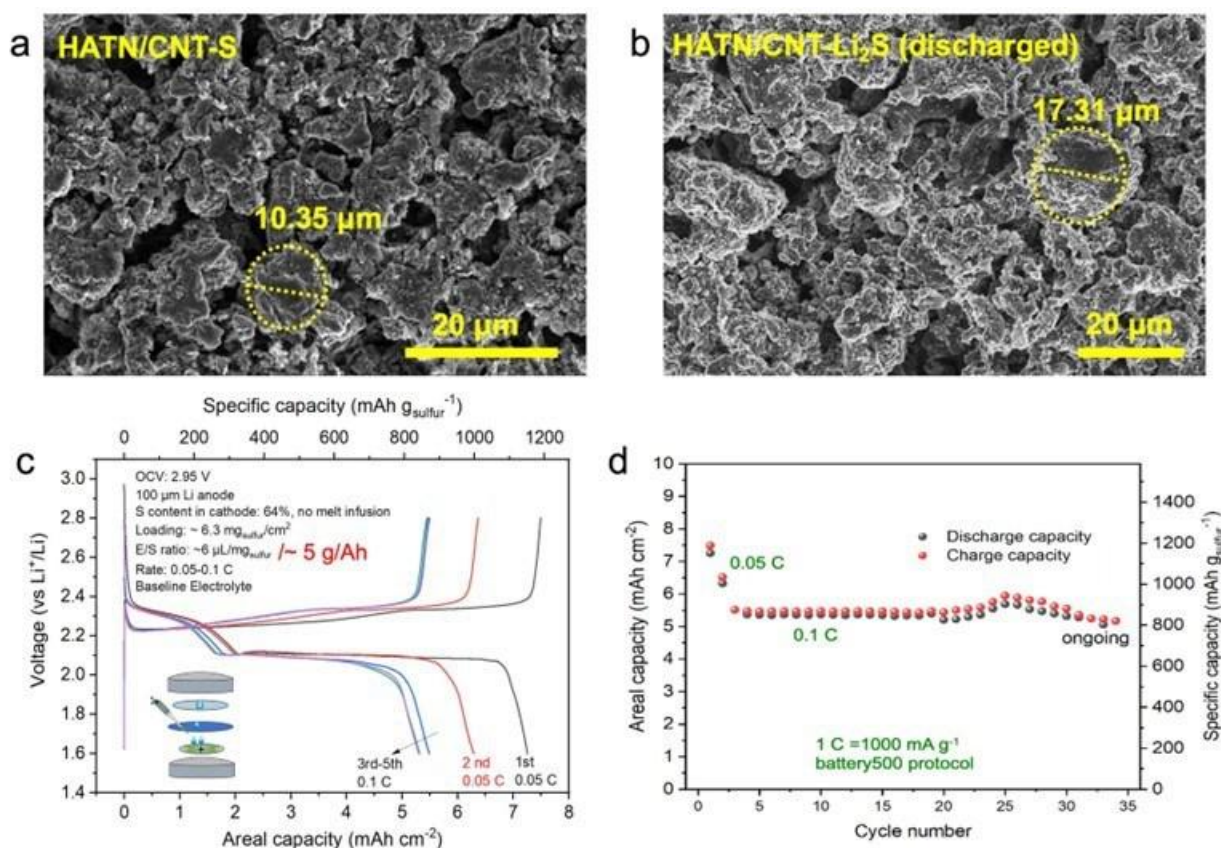


Figure XVII.5.6 (a) The top-view of SEM images of the pristine HATN/CNT-S cathode and after 1st discharge (b) with a similar S loading of $\sim 5 \text{ mg cm}^{-2}$ under a small magnification; (c) Voltage profiles of the HATN/CNT-S cathode with $\sim 6.30 \text{ mg}_{\text{sulfur}} \text{ cm}^{-2}$, using 100 μm Li with an E/S ratio of $6 \mu\text{L mg}_{\text{sulfur}}^{-1}$ and an E/C ratio of 5 g/Ah. The inset schematics illustrates the cell assembly; (d) The cycling behavior of the optimized HATN/CNT-S cathode at 0.1 C, 1 C = 1000 mA g⁻¹.

To achieve high-energy-density Li-S batteries, the cathode porosity of HATN/CNT-S needs to be decreased, and the S loading needs to be increased. At the early stage, the HATN/CNT-S cathode with a small areal capacity of 2.5 mAh cm^{-2} was achieved with a stable cycling behavior (680 cycles, Q3). Q4 mainly focuses on preparing high-areal-capacity HATN/CNT-S cathodes by increasing the S-specific capacity via electrochemical infusion (Figure XVII.5.6). The milestone of a starting areal capacity of 5 mAh cm^{-2} , recommended by the DOE, has been completed by increasing the S loading to $\sim 6.30 \text{ mg}_{\text{sulfur}} \text{ cm}^{-2}$. The areal discharge capacity can reach up to $\sim 7.4 \text{ mAh cm}^{-2}$ initially under the first 0.05 C (0.315 mA cm^{-2}) formation cycle with a low N/P ratio of 2.6 and a low E/S ratio of $6 \mu\text{L mg}_{\text{sulfur}}^{-1}$ or 5 g Ah^{-1} , which quickly stabilized at 5.5 mAh cm^{-2} after switching to the 0.1 C discharge current rate for the following cycles (Figure XVII.5.6d). Notably, the initial discharge plateaus are consistent with the subsequent, which reflects the good wettability

and polysulfide diffusion in the HATN/CNT cathode. The cell is ongoing stably with high capacity retention after 35 cycles. The Post-Mortem analysis of the cycled cell will be conducted to quantify the Li and LiNO_3 inventory loss. Herein, the cells of the HATN/CNT-S cathodes were prepared using 100 μm Li anodes (inset of Figure XVII.5.6c) aiming for a low N/P ratio. Our coin-cell performance, under such stringent conditions of lean electrolyte and lean lithium, indicates that it is worth moving closer to the target of $<3 \text{ g Ah}^{-1}$ electrolyte amount. Further, UCSD and GM will work closely to prepare single-layer or few-layer pouch cells using even leaner electrolytes, demonstrating the cyclability of pouch cells.

The scaling up of HATN synthesis at Ampcera

The HATN polymer synthesis has been improved to a 10-g scale at the UCSD lab. Ampcera has assembled a lab-scale synthesis as part of the scale-up process. A dozen of trials have been conducted to optimize the monomer synthesis process to obtain the beige yellow product (Figure XVII.5.7a and Figure XVII.5.7b). A preliminary batch of HATN monomer (synthesized at Ampcera) was received by UCSD for NMR conformation. However, validation has been delayed due to supply chain issues associated with the NMR solvent. Finally, trial 14 has the best quality with minor impurities. In Q4, UCSD has worked on the scale-up synthesis by collaborating with Ampcera by on-site visiting. Using a proprietary polymerization process, Ampcera has been able to form the HATN polymer which will be validated by UCSD using FTIR and BET analysis. Further, Ampcera has already established the setup of scaling-up of the synthesis of the HATN monomer (Figure XVII.5.7c). By on-site visit to Ampcera, the baseline synthesis of 2 g-batch was established. The yield has recently been improved to $>80\%$ with high reproducibility, and the monomer synthesis will be scaled after NMR validation by the end of BP1.

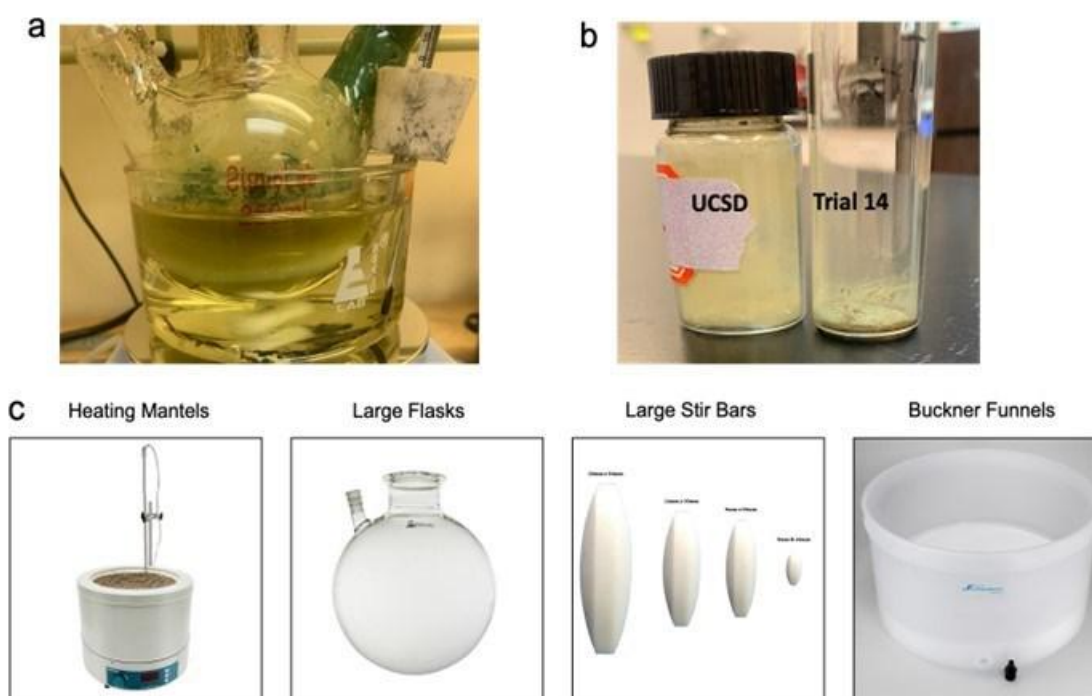


Figure XVII.5.7 (a and b) The lab-scale trial of the HATN monomer synthesis at Ampcera; (c) The scaling-up synthesis of HATN monomer at Ampcera.

Reporting a NewEle Li-S system with long cyclability

Q2 has revealed that the LiNO_3 reservoir limits the cycling life of Li-S batteries in the baseline electrolyte, and there is a tradeoff between energy density and cycling stability. To realize the long cycling life and high energy density of Li-S batteries, efforts are put into developing alternative electrolytes. The electrolyte design is based on Li metal compatibility and polysulfide solubility considerations. In Q1, the localized high concentration

electrolyte (LHCE) of LiFSI:DME:TTE with a 1:1.2:3 molar ratio was studied. Li-S battery using this LHCE generates large polarization and very low S-specific capacity, though LHCE enables large granular Li deposition morphology and high Coulombic efficiencies.

In BP1, we designed a New Electrolyte that does not contain LiNO_3 . A new type of N-containing salt is synthesized in the lab. The resulting electrolyte shows high chemical compatibility with Li metal, verified from the shining Li kept in our electrolyte for 48 h (Figure XVII.5.8a). Using this NewEle system, the Li-S battery can undergo a successful charge-discharge process without any over-charge issue that happens without LiNO_3 . It also demonstrates that NewEle additive salt and LiNO_3 are more active and pivotal in the cathode part to preclude the over-charge problem, which is used to be deemed as the “polysulfide shuttle” effect. It has been reported that NewEle contains only 10 mM of the as-synthesized additive, which is much smaller than ~ 0.4 M of LiNO_3 in the baseline electrolyte (2wt.% LiNO_3). In the NewEle system, the C-S cathode delivers a similar initial specific capacity of $\sim 1000 \text{ mAh g}_{\text{sulfur}}^{-1}$ at a formation current density of 0.05 C with a low E/S ratio of $10 \mu\text{l mg}_{\text{sulfur}}^{-1}$, compared to that of baseline electrolyte (Figure XVII.5.8b). The C-S cathode delivers a higher S-specific capacity of $800 \text{ mAh g}_{\text{sulfur}}^{-1}$ than $600 \text{ mAh g}_{\text{sulfur}}^{-1}$ in the baseline electrolyte when cycling at 0.2 C, indicating higher S utilization (practical S-specific capacity/theoretical S-specific capacity) in NewEle (Figure XVII.5.8b). Finally, the cycling life of the C-S cathode is boosted with capacity retention of $\sim 75\%$ after 320 cycles using lean NewEle (Figure XVII.5.8b). In contrast, the cells can only cycle for ~ 75 cycles before a drastic capacity drop in the baseline electrolyte (Figure XVII.5.8b).

Focused ion beam (FIB) systems use a finely focused beam of ions (usually gallium) that can be operated at low beam currents for imaging or high beam currents for site-specific sputtering or milling. FIB can also be incorporated into a system with both electron and ion beam columns, allowing the same feature to be investigated using either of the beams. Cryo-FIB-SEM allows samples to be cooled to cryogenic temperatures (Figure XVII.5.8c), which preserves the structure of sensitive samples such as lithium and sulfur. Figure XVII.5.8d presents the Cryo-FIB images of the cross-section Li metal anode after cycling (320 cycles) in the NewEle system. It is shown that the Li surface has bulky Li deposition in the NewEle system, and there is a large quantity of reacted Li metal in the bulk of Li metal. The cycled Li (red dash zone) was further investigated by the EDX to analyze the composition of cycled Li. Figure XVII.5.8e exhibits the Energy-dispersive X-ray spectroscopy (EDX) spectrum of Figure XVII.5.8d with the major signal of O and S and a minor signal of N. Since LiTFSI (the major Li salt of the electrolyte) has been proved to be stable during the cycling of Li-S batteries, our N-O-containing alternative additive has a minor decomposition issue. It suggests that the passivation layer on the Li metal in NewEle contains both Li_2O and Li_2S with a close amount of atomic percentage of $\sim 30\%$ (inset of Figure XVII.5.8e). This demonstrates that Li_2S is at a low amount of acting as a component of the passivation layer like Li_2O , a common inorganic component of Li solid-electrolyte-interface (SEI). Hence, the reaction between polysulfide and Li (polysulfide shuttle) that generates Li_2S is inhibited, which keeps the Li inventory for the long cycling stability of Li-S batteries. The above results show that our promising NewEle system can offer a solution to future stable high-energy Li-S batteries.

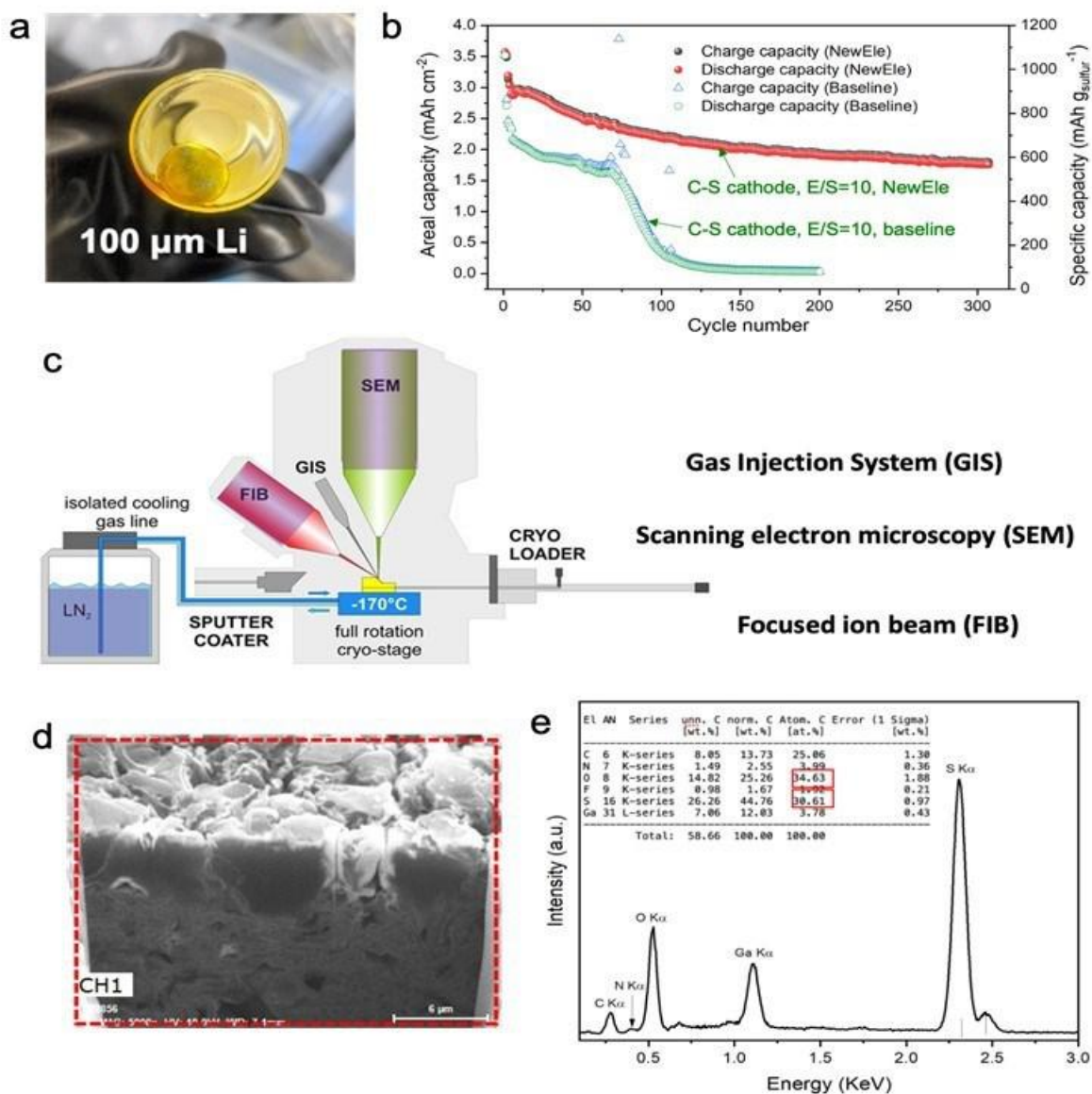


Figure XVII.5.8 (a) The photo of Li chip immersed into NewEle for 2 days; (b) The cycling behavior of the UCSD Nano C-S cathode in baseline electrolyte of 1 M LiTFSI in a DOL/DME mixture (1:1, v/v) with 2wt.% LiNO₃ and in 10 mM this NewEle additive, using 100 μm Li and E/S ratio of 10 μl mg_{sulfur}⁻¹. Cycling behavior by S-specific capacity and areal capacity; (c) The schematic of Cryo-FIB-SEM used to characterize lithium and sulfur in this project; (d) Cryo-FIB images of the cycled Li in the NewEle system (cross-section), and (e) the EDX spectrum of the red dash zone of the cycled Li metal with quantitative elemental analysis.

Conclusions

In BP1, a characterization toolbox has been established to investigate the Li and S inventory loss, electrolyte depletion, and electrode structural evolution. HATN polymer composite S cathode has been optimized to HATN/CNT-S cathode featuring a 3D ion and electron conduction network. The milestone of a starting areal capacity of >5 mAh cm⁻² has been completed by increasing the S loading to ~6.30 mg_{sulfur} cm⁻². The areal discharge capacity can reach up to ~7.4 mAh cm⁻² initially under the first 0.05 C (0.315 mA cm⁻²) formation cycle with a low N/P ratio of 2.6 and a low E/S ratio of 6 μl mg_{sulfur}⁻¹ or 5 g Ah⁻¹, which quickly stabilized at 5.5 mAh cm⁻² after switching to the 0.1 C discharge current rate for the following cycles. Notably, the initial discharge plateaus are consistent with the subsequent, which reflects the good wettability and polysulfide diffusion in the HATN/CNT cathode. This is attributed to the low porosity of 30% of HATN/CNT-S cathode in contrast to 50% of the nanostructured C-S cathode and the low tortuosity of HATN/CNT-S the cathode for

good electrolyte wettability into its bulky structure. Besides, to replace the decomposition-based LiNO_3 additive, the NewEle system has been introduced. The NewEle additive was evaluated using a C-S cathode that only involves S redox, which shows 320 cycles of cycle life with 75% capacity retention using lean electrolyte and lithium. Further, the Cryo-FIB morphology characterization of the cycled Li in the NewEle system coupling with the EDX results validate the inhibition of polysulfide shuttle reaction with Li and the non-sacrificial property of the NewEle alternative additive. The NewEle will be extended to the HATN/CNT-S cathode, essential to achieving stable high-energy-density Li-S batteries. For the large scale HATN production, UCSD has helped Ampecera to establish the setup of scaling-up of the synthesis of the HATN monomer. Ampecera is now able to synthesize the HATN monomer in small batch with a very high yield of >80%, which can be readily scaled up based on Ampecera's facilities. GM has demonstrated the capability of making large-format Li-S pouch cells. Once the enough HATN/CNT-S active material is synthesized, GM will start to make Ah level Li-S pouch cells with the newly design S-based cathode.

Key Publications

1. Non-disclosure invention regarding the new electrolyte additive and formula (in preparation).

References

1. Mauler, L.; Duffner, F.; Zeier, W. G.; Leker, J., Battery cost forecasting: a review of methods and results with an outlook to 2050. *Energy Environ. Sci.* **2021**, *14* (9), 4712-4739.
2. Manthiram, A.; Fu, Y.; Chung, S. H.; Zu, C.; Su, Y. S., Rechargeable lithium-sulfur batteries. *Chem. Rev.* **2014**, *114* (23), 11751-11787.
3. Shi, L.; Bak, S.-M.; Shadike, Z.; Wang, C.; Niu, C.; Northrup, P.; Lee, H.; Baranovskiy, A. Y.; Anderson, C. S.; Qin, J.; Feng, S.; Ren, X.; Liu, D.; Yang, X.-Q.; Gao, F.; Lu, D.; Xiao, J.; Liu, J., Reaction heterogeneity in practical high-energy lithium-sulfur pouch cells. *Energy Environ. Sci.* **2020**, *13* (10), 3620-3632.
4. Wang, X.; Yang, Y.; Lai, C.; Li, R.; Xu, H.; Tan, D. H. S.; Zhang, K.; Yu, W.; Fjeldberg, O.; Lin, M.; Tang, W.; Meng, Y. S.; Loh, K. P., Dense-Stacking Porous Conjugated Polymer as Reactive-Type Host for High-Performance Lithium Sulfur Batteries. *Angew. Chem. Int. Ed.* **2021**, *60* (20), 11359-11369.

XVII.6 New Engineering Concepts for High Energy Density Li-S Batteries (UPitt)

Prashant N. Kumta, Principal Investigator

University of Pittsburgh
815C Benedum Hall,
3700 O'Hara St.
Pittsburgh, PA 15261
E-mail: pkumta@pitt.edu

George E. Blomgren, Co-Principal Investigator

Blomgren Consulting Services, Ltd.
Oberlin, OH 44074
E-mail: geblomgren@prodigy.net

Oleg I. Velikokhatnyi, Co-Principal Investigator

University of Pittsburgh
815C Benedum Hall,
3700 O'Hara st,
Pittsburgh, PA 15261
E-mail: olv3@pitt.edu

Start Date: October 1, 2021
Project Funding: \$512,629

End Date: September 30, 2022
DOE share: \$409,984

Non-DOE share: \$102,645

Project Introduction

Lithium (Li)-Sulfur (S) batteries (LSBs) with energy densities ≥ 500 Wh/kg @C/5 and >1000 cycles, cycle life operating over wide temperatures is key for meeting the increasing and incessant global energy demands. The system has been studied extensively for several years. Progress is however very much, limited due to the hurdles of: (a) poor Li^+ reaction kinetics (conductivity/diffusivity) for full reversible S conversion to Li_2S , (b) inferior electron (e^-) conductivity, capacity and cycle life due to electrolyte soluble polysulfides (PSs) that are formed which migrate to the anode and also react with the anode causing corrosion of the anode, (c) unstable solid electrolyte interphase (SEI) formation and (d) dendrite formation on the anode which pose a safety risk owing to the short-circuit potential caused by puncturing of the separator. Furthermore, the dendrites formed on the Li anode limit the cycle life due to polarization at solid/liquid interfaces causing safety, inferior capacity, energy density, rate, and cycle life issues. The creation and fabrication of economical $\leq \$80/\text{kWh}$, high energy density LSBs is vital for their widespread commercial use in current and next generation electric vehicles.

Objectives

The major objectives/goals of this DOE funded project are to develop a lithium sulfur pouch cell with a cell capacity >300mAh with energy density ≥ 500 Wh/kg, ≥ 750 Wh/L with cycling over 1000 cycles @C/3 rate, cycle life of 1000 at C/3 and $\leq 20\%$ fade in energy @ C/10-C/3 rates, and an affordable and attractive cost of $\leq \$80/\text{kWh}$. To achieve these proposed objectives, the following **major goals** will be attained in year 1 of the three-year funded project. (a) Identification of effective functional electrocatalysts (ECs) and Li-ion conductors (LICs) lowering the activation barrier; (b) In situ synthesis of the functional ECs and LICs dispersed complex carbon-based framework materials (CFM) and sulfur (S) nanocomposite with S content $\geq 90\text{wt. \%}$; (c) Achieve at minimal at least $\sim 15\text{mAh}/\text{cm}^2$ areal capacity of the S electrode with S loading at the least $\geq 10\text{mg}/\text{cm}^2$; (d) Synthesis of Li-structurally isomorphous (SIA) alloy and multicomponent alloys (MCAs) exhibiting at minimal ≥ 1000 cycle with at least $15\text{mAh}/\text{cm}^2$ areal capacity @C/3 rate; (e) Identification of the

optimal electrolyte compositions with suitable additives giving Li^+ conductivities that are at minimal $\sim 10^{-2}$ S/cm and polysulfide (PS) dissolution < 1 ppm in the modified electrolytes.

Approach

Work involves executing a first principles density functional theory (DFT) driven study directed at identification of functional electrocatalyst (ECs) for efficient conversion of polysulfides (PSs) to Li_2S during the forward discharge process and backward charge process to elemental sulfur and Li. Also, first principles computational approaches will be applied to identify solid-state LICs with conductivity equal or more than, $> 10^{-4}$ S/cm. Employing the expertise in the PI's laboratory, suitable low temperature ($< 240^\circ\text{C}$) scalable synthesis techniques developed and already in existence will be used to generate theoretically identified functional ECs and LICs. Low PS solubility and stable solid electrolyte interphase (SEI) forming electrolytes will then be prepared from commercially available solvents, additives, and salts. The effectiveness of the functional ECs and LICs to improve the PS to Li_2S transformation kinetics and moreover, the ability to achieve the targeted specific capacity by trapping PSs including desired structural transformation during charging/discharging will be assessed, and accordingly suitable modification of functional ECs and LICs will be performed followed by modification of the synthesis approaches to generate the ideal microstructures. Suitable modification if required of Li alloy as anode will also be performed by alloying with other identified metals to improve the Li ion diffusivity kinetics and the Gibb's Thomson Parameter. The scalable approaches developed will be further refined to optimize the sulfur utilization in the cathode, engineer the surface and bulk structure of the novel Li-SIA and Li-MCA anodes to yield the desired areal capacity with optimal coulombic efficiency, and finally optimize the electrolyte structure to minimize and eliminate PS dissolution with the desired Li^+ conductivities. Finally, the developed systems will be scaled up, fabricated, and tested in pouch cell configurations.

Results

Over the past year of this funded project, a significant amount of work was performed to computationally identify functional ECs and LICs which would help achieve 80% lower activation barriers of PS to Li_2S transformation and gain a 10X improvement in the reaction kinetics. Another goal of the initial study was to synthesize and characterize $\sim 20\text{nm}$ sized ECs and LICs homogeneously dispersed in the CFM/S. Also, dendrite free growth study of the newly developed alloy was planned to be conducted for achieving ≥ 1000 cycles cyclability tests @C/3 rate. To achieve these targeted objectives, initial theoretical work focused on identification of suitable binary and ternary functional ECs to improve the forward and backward reaction kinetics of polysulfide conversion to Li_2S and vice versa to elemental Li and S. This study has been conducted using first principles computations which were initiated in the early months of the project and the computational units for conducting these studies have been allocated through the Extreme Science and Engineering Discovery Environment (XSEDE) services supported by the National Science Foundation grant number ACI-1548562. As mentioned above, this theoretical component of the work identified binary and ternary functional electrocatalysts that have been used in the experimental component of the present project. The work conducted during the initial first quarter of the funded project focused on studying the kinetics of the transformation reaction converting the recalcitrant Li_2S_2 to Li_2S as a final product as well as identifying new functional electrocatalysts to favor this reversible reaction.

In addition, work was performed to synthesize the theoretically identified binary functional ECs in nanometer scales ($\sim 20\text{nm}$) along with in situ generation of dispersion of these functional ECs in the S infiltrated complex carbon-based framework materials (CFM-S). The synthesized functional ECs dispersed CFM-S structures were tested in the lean electrolyte conditions ($\text{E/S} = 4\mu\text{l mg}^{-1}\text{ S}$) against Li metal and Li metal alloy to study the effectiveness of the functional ECs. A significant improvement in the initial charge and discharge capacity ($\sim 1000\text{mAh g}^{-1}\text{ S} - 1200\text{mAh g}^{-1}\text{ S}$) of the ECs embedded CFM-S were observed @ C/25 rate using 1.8M LiTFSI (in DOL:DME) +0.4M LiNO_3 electrolyte with moderate S loading of 2.8mg cm^{-2} under lean electrolyte conditions (Figure XVII.6.1). However, the system shows poor cyclability and a drop in capacity in the 1st 10 cycles is observed which could be improved using theoretically identified lithium-ion conductors as coating materials with the generation and incorporation of homogeneous dispersions of polysulfide trapping

agent (PTA). These studies were conducted during subsequent months with corresponding higher S loadings and are discussed in the later sections of the present report. Additionally, the potential of highly porous electronically conducting materials were identified as modified framework materials (ECMF) with the realization of high S loadings of 4.2-4.6 mg cm⁻². These ECMFs show excellent cyclability/stability when S is infiltrated into the ECMF due to their promising PS adsorption and encapsulation capability of ECMF (Figure XVII.6.2 and Figure XVII.6.3). Consequently, these porous ECMF materials will be used for S encapsulation along with generation of uniform functional ECs dispersion which will be expected to achieve higher specific capacity (> 1000 m Ah g⁻¹ S) as well as better cycle life of the ECs embedded electronically conducting framework structures.

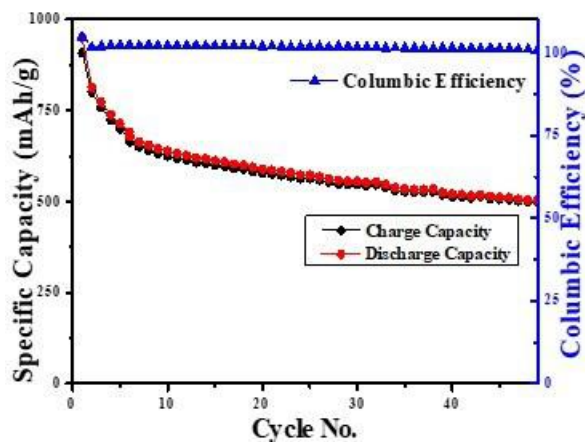


Figure XVII.6.1 Cycling performance of functional ECs embedded CFM-S (Li anode) cycled in coin cell configuration with S loading 2.8 mg cm⁻² and electrolyte (E)/ sulfur (S); E/S = 4 μ l mg⁻¹ S.

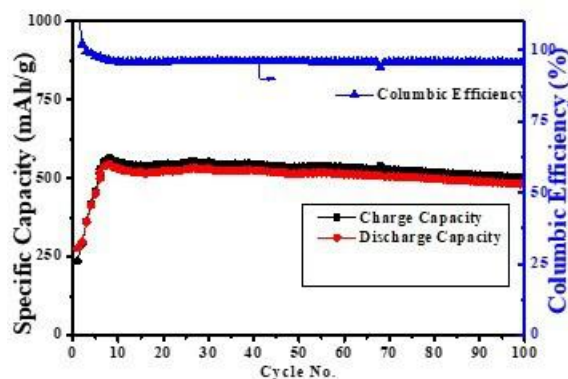


Figure XVII.6.2 Cycling performance of S infiltrated electronically conducting framework materials cycled in coin cell configuration with S loading 4.6 mg cm⁻² and electrolyte (E)/ sulfur (S); E/S = 4 μ l mg⁻¹ S.

Additionally, novel dendrite free structurally isomorphous binary and ternary Li metal alloy (Li-SIA) anode was developed for use in the proposed Li-S batteries to achieve the targeted areal capacity (~ 15 mAh cm⁻²) of the anode in realizing the targeted energy density ≥ 500 W h kg⁻¹ of the Li-S cell. The plating and stripping polarization curve of Li-SIA in a symmetrical cell at 2.5 mA cm⁻² current density with 5 mAh cm⁻², areal discharge capacity showed excellent cyclability for 500 cycles without dendrite formation. Electrochemical testing of the Li-SIA alloy after further crystallographic and compositional structural modification is currently on-going to achieve a higher areal capacity of ~ 10 mAh cm⁻² -15 mAh cm⁻² at C/4 rates (2.5 mA cm⁻²) to

determine the feasibility of this anode system to sustain the targeted areal capacity $\sim 15 \text{ mAh cm}^{-2}$ for Li-S batteries for prolonged cycles.

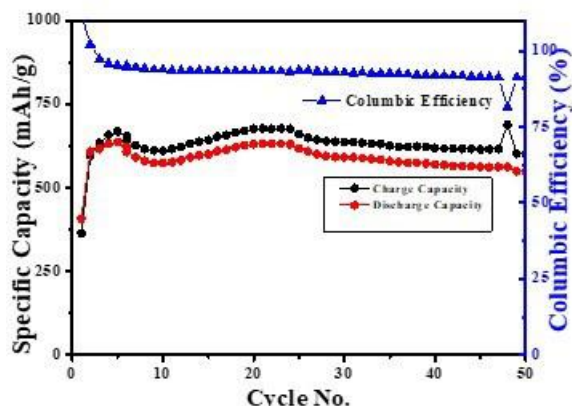


Figure XVII.6.3 Cycling performance of S infiltrated carbon coated electronically conducting framework materials cycled in coin cell configuration with S loading 4.2 mg cm^{-2} and electrolyte (E)/ sulfur (S); E/S = $4 \mu\text{l mg}^{-1} \text{ S}$.

Preliminary work was also initiated in this past year related to fabrication of new sulfur confinement cathodes and is also reported here. With the goal of generating advanced cathode architectures, attempts were made to modify the catholyte using functional additives. These functional monomer additives not only can finetune the dissolution of polysulfides but also they can modify the electrolyte/electrode interface on the Li anodes. Therefore, additives can play a vital role in improving the cycle life of Li-S batteries. In this report accordingly, the use of functional monomer additive molecule (FAM) as a promising stabilizer for use in Li-S batteries to improve the cycle life is described. It was observed that the FAM-short chain polysulfides complexes formed during charge-discharge processes not only modify the kinetics of formation of short-chain polysulfides but also reduce the polysulfide dissolution. The results highlight the importance of use of appropriate amounts of FAM and carbon matrix serving as the sulfur host material for the efficient functioning of the functional monomer additive molecule (FAM) in Li-S batteries. The electrochemical cycling performance of sulfur infiltrated carbon-based complex framework materials, CFM termed as, CFM-S cathodes containing the FAM, tested in Li-S battery is shown in Figure XVII.6.4. The CFM-S containing FAM were cycled at 0.05C with an average electrode loading of 3.8 mg cm^{-2} electrode area. The CFM-S shows an initial discharge capacity of $\sim 875 \text{ mAh g}^{-1}$ which stabilizes at $\sim 625 \text{ mAh g}^{-1}$ after the 6th cycle. Upon prolonged cycling, the CFM-S shows a very stable capacity of $\sim 550 \text{ mAh g}^{-1}$ for over 26 cycles. The electrolyte (E)/sulfur (S) ratio was $4 \mu\text{l mg}^{-1}$. Efforts to increase the S loadings with use of Li-ion conductors and electrocatalysts to enhance the specific capacity are currently ongoing.

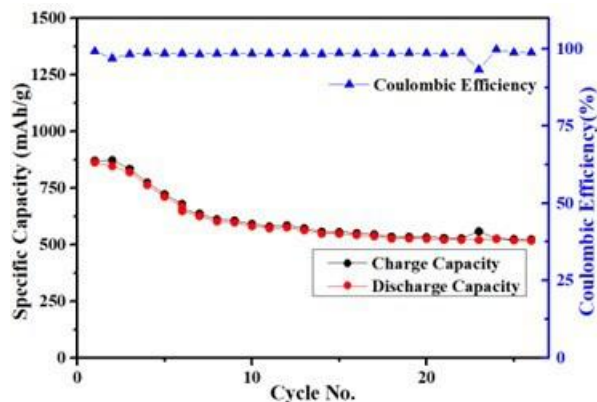


Figure XVII.6.4 Electrochemical cycling performance and Coulombic efficiency of CFM-S containing FAM cycled between 1-7-2.8V.

Another system that was studied included the synthesis of redox-active porous inorganic-organic framework materials (IOFM) as cathode in Li-S battery. These systems serve as a Li_2S_x reactive-type hosts to regulate polysulfide electrochemistry, facilitating its transformation into nanostructured Li_2S and S within the porous IOFM matrix. The IOFM was selected since it provides good surface area of $\sim 1000 \text{ m}^2 \text{ g}^{-1}$, which enables compact electrode preparation with high sulfur loading on carbon-coated Al foil. Thus, the IOFM/S cathode was tested for Li-S battery performance, and the electrochemical cycling performance of IOFM-S is shown in Figure XVII.6.5. The IOFM-S cells were cycled at 0.05C with an average electrode loading of 2.6 mg cm^{-2} electrode area. The IOFM-S shows an initial discharge capacity of $\sim 500 \text{ mAh g}^{-1}$ which stabilizes at $\sim 650 \text{ mAh g}^{-1}$ after the 4th cycle. The low initial discharge capacity observed, and the subsequent increase is likely due to wettability issues due to the low electrolyte (E)/sulfur (S) ratio of $4 \mu\text{l mg}^{-1}$. Upon prolonged cycling, the IOFM-S shows a stable capacity of $\sim 550 \text{ mAh g}^{-1}$ for over 25 cycles. Efforts to increase the S loading with use of Li-ion conductors and appropriate electrocatalyst to increase the specific capacity of these systems are currently ongoing.

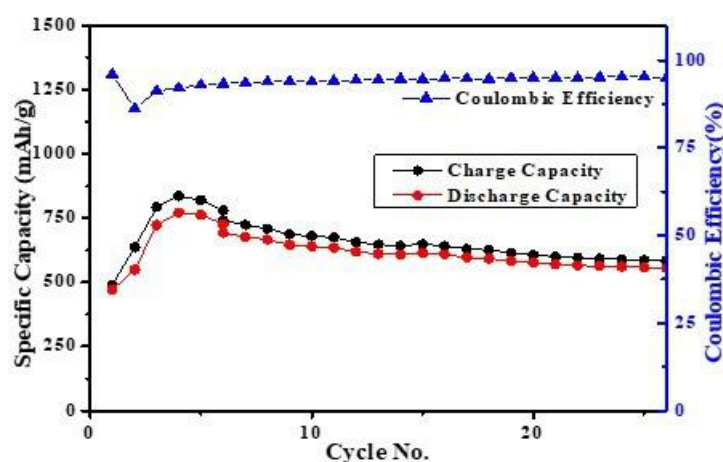


Figure XVII.6.5 Electrochemical cycling performance and Coulombic efficiency of IOFM-S cycled between 1.7-2.8V.

Furthermore, during this period, first principles computational study was also conducted with the goal to identify multi-component alloy (MCA) anodes. These MCA anodes were identified using density functional theory (DFT) methods to demonstrate formation of uniformly disordered, metastable, *bcc* solid solution. Based on the first principles theoretical studies, the ability of the MCA anodes to incorporate large amounts of Li (above 50 at. %) was studied in the first year of this project. The aim being that these systems will be able to electrochemically alloy theoretically demonstrated amounts of Li ($> 50 \text{ at. \%}$) during electrochemical cycling without the formation of lithium dendrites. Additionally, the goal here is to explore the ability of the system to cycle for greater than 100 cycles attaining a targeted specific capacity of at least at minimal or greater than 15 mAh cm^{-2} . In the previous experimental study conducted in an earlier DOE funded project, the synthesis of a specific Fe-based MCA, FMCA1 also later denoted as MCA1 was demonstrated exhibiting an areal specific capacity of 4 mAh cm^{-2} without dendrite formation up to 300 cycles when cycled at a current of $\text{C}/2$ rate. However, the low areal specific capacity is due to insufficient amounts of Li that is accommodated or alloyed by the host alloy, FMCA1, exhibiting the *bcc* crystal structure preventing the widespread use of this material as an anode in the lithium-ion batteries. Thus, there is a need to identify better alloys with lower atomic weight and stronger ability of the base alloy structure to accept higher Li content without inducing phase separation and intermetallic phase formation.

Phase stability analysis was therefore conducted, and correspondingly, calculation of the phase stability is shown in Figure XVII.6.6(a, b). The results of the studies shown in the figure indicate that the metastable MCA1, alloy exhibiting the *bcc* phase can accommodate only up to $\sim 33 \text{ at. \%}$ of Li without causing phase

separation (black line and arrow in Figure XVII.6.6(b)), which is clearly insufficient to yield the desired target areal specific capacity of 15mAh cm^{-2} . To achieve this target areal specific capacity, there is a need to incorporate at least 50 at. % of Li into the structure and also use lighter constituent elements to reduce the total weight of the assembled anode and the ensuing fabricated full battery. Thus, in the present computational study, lighter elements were selected and the corresponding phase stability of the several compositions studied were calculated. As shown in Figure XVII.6.6(b), there are several MCAs which can incorporate significantly higher amount of Li than the earlier identified and generated MCA1 alloy. For example, MCA2 can accommodate more than 60at. % of Li ions resulting in more than 15mAh cm^{-2} areal specific capacity. Also, MCA2, MCA4 and MCA5 demonstrate much lower gravimetric density than that of MCA1, thus rendering it possible to increase the specific capacity of the current collector as a Li-anode even further permitting the possibility of generating anode-free Li-S batteries.

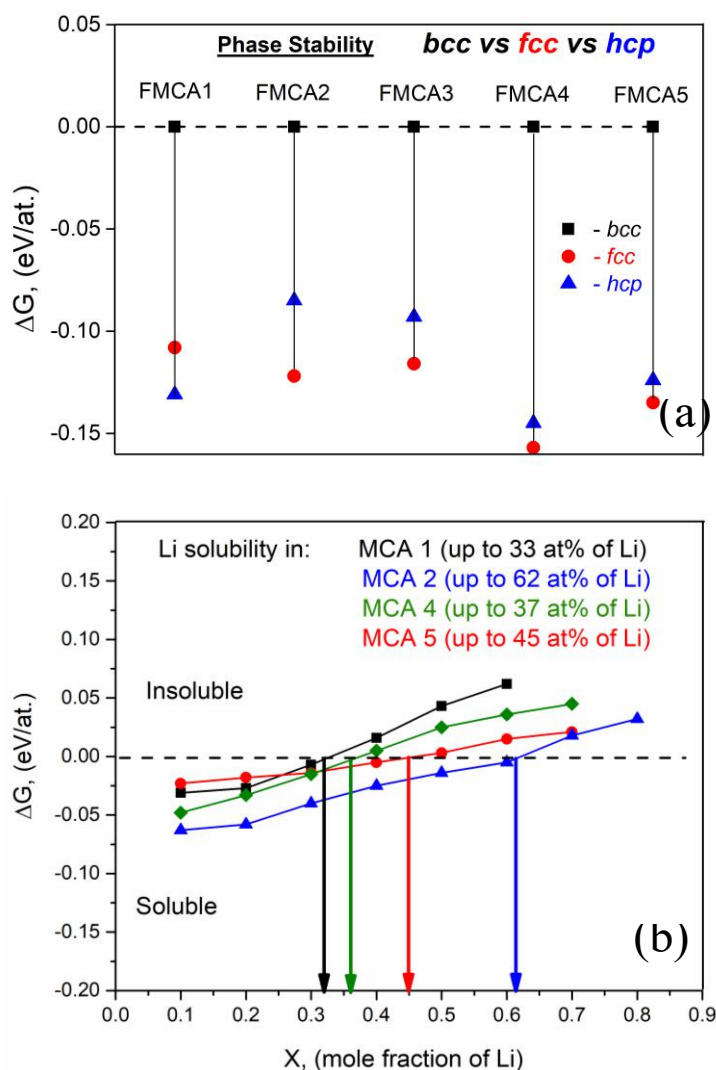


Figure XVII.6.6 First principles theoretical calculations showing (a) phase stability of non-lithiated alloys; (b) lithiated alloy phase stability.

Also, over the past year of this project, preliminary work was initiated related to fabrication of new sulfur confinement cathodes the results of which are reported here. With the goal of generating advanced cathode architectures in mind, attempts were made to modify the aqueous polymer binder with functional group

additives. These functional polymer binders contain sugar monomer repeating units which not only can finetune the dissolution of polysulfides but also serve to modify the electrode interface on the cathode. Therefore, the studies conducted by this team further report on an aqueous processable biopolymer for sulfur cathodes. The polymer binder can play a vital role in improving the cycle life of Li-S batteries. In this report accordingly, the use of this functional polymer binder with repeating cyclic monomer or new sugar molecule serving as a promising stabilizer for use in Li-S batteries to improve the cycle life is described. It was observed that during electrochemical cycling, the polymer binder-short chain polysulfides complexes likely formed during charge-discharge processes not only modify the kinetics of formation of short-chain polysulfides but also reduce the polysulfide dissolution. The results presented here highlight the importance of use of appropriate amounts of the polymer binder and carbon framework matrix serving as the sulfur host material for the efficient functioning of the functional groups with repeating cyclic monomer units in Li-S batteries. The electrochemical cycling performance of sulfur infiltrated high surface area carbon-based complex framework materials, HCFM termed as, HCFM-S cathodes containing the aqueous polymer binder, tested in Li-S battery is shown in Figure XVII.6.7. The HCFM-S containing were cycled at 0.05C with an average electrode loading of 4.3 mg cm^{-2} electrode area. The HCFM-S shows an initial discharge capacity of $\sim 1090 \text{ m Ah g}^{-1}$ which stabilizes at $\sim 725 \text{ m Ah g}^{-1}$ after the 12th cycle. Upon prolonged cycling, the HCFM-S shows a very stable capacity of $\sim 725 \text{ m Ah g}^{-1}$ for over 25 cycles. The electrolyte (E)/sulfur (S) ratio used here was $8 \mu\text{l mg}^{-1}$. Efforts to increase the S loadings with use of *in-situ* synthesized Li-ion conductors and functional electrocatalysts identified by theoretical studies mentioned earlier to enhance the specific capacity are currently ongoing. Results of these studies will be reported in the next annual report.

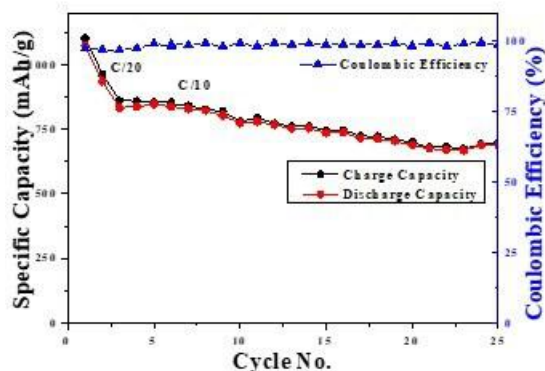


Figure XVII.6.7 Electrochemical cycling performance and Coulombic efficiency of CFM-S electrode cycled between 1.8-2.8V at C/20 and 1.7-2.8V at C/10 current rates.

Research work to identify new sulfur confinement cathodes continued further this past year. This work included identification and fabrication of these new sulfur confinement systems. With the goal of generating advanced cathode architectures in mind, attempts were made to modify new porous organic framework materials (POFM1) with pre-designed and customized properties which have been employed as sulfur storage cathode materials for lithium-sulfur (Li-S) batteries. These POFM1 materials are composed of light weight elements including carbon and oxygen and are connected by covalent bonds with the functional group additives. These lightweight elements containing functional cathode materials comprise repeating units of monomer which not only finetune the dissolution of polysulfides but also serve to modify the electrode interface due to the multifunctional cathode chemistry. Furthermore, the lightweight elements present in the polymer framework and backbone could serve as polysulfide trapping species thereby stabilizing the cathode structure and exhibiting stable cycling behavior. Therefore, the studies were conducted by the team herein in this report on the synthesis of the POFM1 material useful for sulfur cathodes. The POFM-1 electrode can play a vital role in improving the cycle life of Li-S batteries. In this report accordingly, the use of functional monomer with repeating cyclic metal-carbon-oxygen ring or new monomer molecule serving as a promising stabilizer for use in Li-S batteries to improve the cycle life is described. It is observed that during

electrochemical cycling, the POFM1-short chain polysulfides complexes likely formed during charge–discharge processes not only modify the kinetics of formation of short-chain polysulfides but also reduce the polysulfide dissolution. The results so far highlight the importance of use of appropriate functional monomer units of the POFM1 system with the porous organic framework matrix serving as the sulfur host material facilitating efficient functioning of the functional groups with repeating cyclic monomer units in Li–S batteries.

The electrochemical cycling performance of these sulfur infiltrated porous polymer framework structures, POFM1, termed as, POFM1-S cathodes containing the organic solvent-based polymer binder, tested in Li-S battery is shown in Figure XVII.6.8. The POFM1-S electrodes were cycled at 0.05C for the initial cycling with an average electrode loading of 3.2 mg cm^{-2} electrode area for the entire test. The POFM1-S electrode shows an initial discharge capacity of $\sim 950 \text{ m Ah g}^{-1}$ which stabilizes at $\sim 625 \text{ m Ah g}^{-1}$ after the 10th cycle. Upon prolonged cycling at 0.1C, the POFM1-S electrode shows a very stable capacity of $\sim 480\text{--}490 \text{ m Ah g}^{-1}$ for over 230 cycles. The electrolyte (E)/sulfur (S) ratio used here was $8 \mu\text{l mg}^{-1}$. Although these systems show moderate capacities of $\sim 490 \text{ m Ah g}^{-1}$, the cycling results show the potential of these new porous organometallic polymeric structures to stabilize the polysulfide dissolution characteristics exhibiting stable capacities for over 230 cycles. There is still the challenge to achieve higher specific capacities to values of $\sim 1000 \text{ mAh g}^{-1}$ desired. This challenge will require improvements in design, fabrication as well as engineering of the composite architectures containing the active material, functional electrocatalysts as well as Li-ion conductors. This challenge is presented in the form of accurate design to result in an optimal matrix material which can provide suitable pore-size environment to trap the soluble intermediate lithium polysulfides (LiPSs). Work is currently ongoing to achieve these objectives requiring a combination of synergistic experimental and theoretical studies to be conducted in tandem to meet the requirements of the project. Results of these planned studies will be compiled and reported in the next annual report.

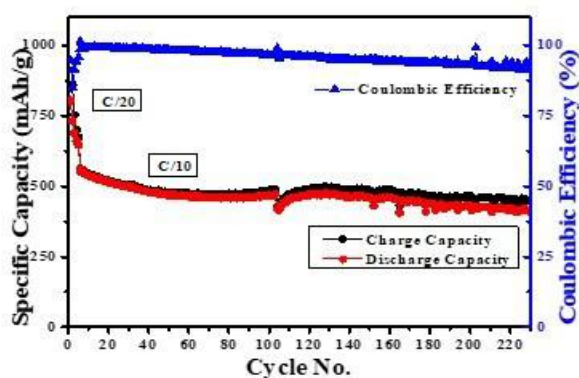


Figure XVII.6.8 Electrochemical cycling performance and Coulombic efficiency of POFM1-S electrode cycled between 1.8–2.8V at C/20 and 1.7–2.8V at C/10 current rates.

Additionally, during this period of funding over the last year as mentioned above, computational study was conducted with the goal to identify multi-component alloy (MCA) anodes that can, not only function as functional dendrite-free anodes but also serve as dendrite-resistant anode current collectors. The use of anode current collectors that are dendrite-resistant offers the unique opportunity to use these alloy systems in anode-free configuration thereby leading to lower battery component weight of the overall assembled battery. As a result, this opens the possibility of achieving higher energy density meeting the target objectives of the project outlined earlier. These MCA anodes were identified using density functional theory (DFT) methods to demonstrate formation of uniformly disordered, metastable, *bcc* solid solution alloys isostructural with metallic lithium. Based on theory, the ability of the MCA anodes to incorporate large amounts of Li (above 50 at. %) was studied and discussed earlier in the present report. The aim being that these systems will be able to

electrochemically alloy theoretically demonstrated amounts of Li (> 50 at. %) experimentally in prototype coin cells during electrochemical cycling without the formation of pernicious lithium dendrites.

Another important and required goal of this project as mentioned earlier is to explore the ability of the system to cycle more than 100 cycles attaining a targeted specific capacity larger than 15 mAh cm^{-2} . In the previous experimental study of an earlier DOE funded project as mentioned above, the synthesis of a specific steel-based MCA, namely, MCA1 was demonstrated exhibiting an areal specific capacity of 4 mAh cm^{-2} without dendrite formation up to 300 cycles at $C/2$ rate. Additionally, as discussed and mentioned earlier, the low areal specific capacity is due to insufficient amounts of Li that is accommodated by the parent material or alloyed by the host alloy, MCA1, displaying the metastable *bcc* crystal structure therefore preventing this material from being widely used as an anode in the lithium-ion batteries. Thus, there is a need to identify better alloys containing lower atomic weight elements and displaying stronger ability of the base alloy structure to accept higher Li contents without inducing phase separation and/or formation of any intermetallic phases that undergo structural as well as large volumetric phase changes consequently, leading to failure of the electrodes and the cells. Incorporation of lightweight elements would generate low density alloys and current collectors that would offer significant advantages in terms of reducing the overall weight of the assembled battery thereby resulting in higher energy densities. Studies are therefore being conducted to refine the alloy system and develop economic scalable fabrication approaches to generate these new current collectors for direct use in the coin cell as well as pouch cell. Results of these studies will be discussed and reported in the annual report next year.

Another computational task that was conducted during the past year of this funded project was identifying alloying elements facilitating the likely enhancement of Li-ion mobility in the identified multicomponent alloys, MCAs and thus, to improve the overall cyclability and performance of the MCA anode. Using first principles climbing nudged elastic band approach the activation barriers for Li-ion diffusivity were calculated and collected in Figure XVII.6.9. The higher the barrier, the lower the Li-ion mobility in the alloy. One can see that the alloying elements EI1, EI2, and EI3 exhibit a higher barrier and thereby decrease the Li-ion mobility compared to pure Li-bcc metal, while EI4, EI5 and EI6 are more favorable and thus will noticeably likely enhance the Li-ion mobility.

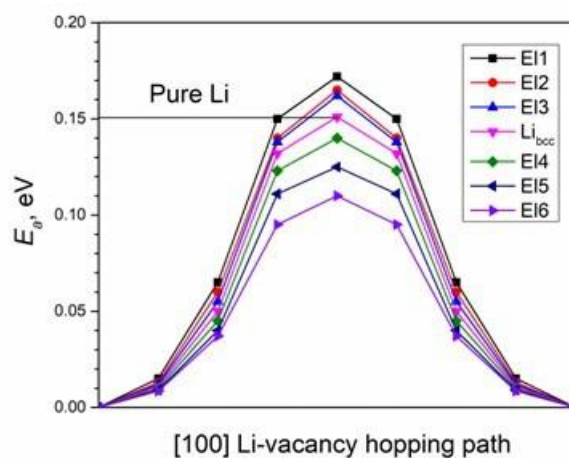


Figure XVII.6.9 Activation barriers for Li-vacancy hopping.

The team also studied the system of MCA as a dendrite free anode material that was synthesized by a simple high energy mechanical milling process to validate the theoretical findings presented in Figure XVII.6.6(b). The structurally isomorphous system, MCA4 having similar lattice registry to metallic Li, prevents Li dendrite growth by forming a solid solution with the reacting Li-ions electrochemically presented to it from the metallic Li foil serving as the counter electrode. The ensuing electrochemical alloying reaction allows a significant amount of Li to solubilize into the parent MCA4 alloy causing minimal change in volume due to the solid

solution formation. The crystallographic arrangements of the atoms in the MCA4 alloy being similar to that of Li thus serves to preserve the overall crystallographic symmetry and allows the formation of a solid solution with optimal interfacial energy. The MCA4 alloy also improves the lithium diffusion preventing surface segregation while continuing to maintain dendrite - free cycling, hence, serving as effective anodes as well as current collectors in Li-S batteries corroborating the theoretical findings. The MCA4 alloy was generated by a simple high energy alloying approach and the anode electrode for electrochemical testing was prepared by standard slurry casting method followed by electrochemical testing in a coin cell configuration, the results of which are shown in Figure XVII.6.10. The MCA4 cells were cycled for 1 m Ah/cm² at 1 C-rate with an average electrode loading of 3.2 mg cm⁻². The MCA4 cells show excellent plating/stripping behavior affording a stable areal capacity of ~1 m Ah/cm² for continuous 30 cycles. The propensity of the MCA4 alloy electrode to demonstrate reversible Li cycling (plating/stripping) is seen in Figure XVII.6.10 as the overpotential of the cell decreases with cycle number. Further electrochemical testing of the cells with the various other MCAs electrodes are also currently on-going. Additionally, efforts are being directed at fabricating free standing dense pellets of the MCAs to serve as dendrite-resistant anode current collectors for reversibly cycling Li ions. These studies will be completed in the coming months of the funded project. Correspondingly, results of the ongoing current studies conducted on the MCAs electrodes and the electrochemical testing results of the dense pellet of MCAs serving as current collectors will be described and discussed in the annual report for next year.

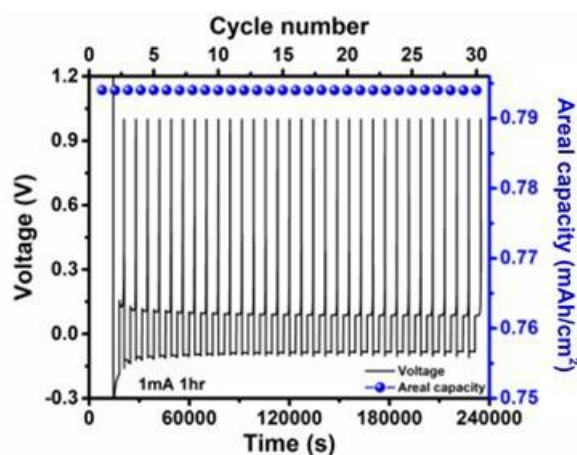


Figure XVII.6.10 Electrochemical cycling performance and areal discharge capacity of synthesized MCA4 electrode cycled at 1 mA current for 1 h for alloying and de-alloying, respectively for 30 cycles.

As already mentioned earlier in the present report, computational DFT studies have been executed with the goal to identify MCA anodes that can, not only function as functional dendrite-free anodes but also serve as dendrite-resistant anode current collectors validating the experimental results described above. These alloys demonstrated the unique ability to form uniformly disordered, metastable, *bcc* solid solution isostructural with metallic lithium. One of the criteria for generating a morphologically stable interface preventing dendrite formation is the design of an alloy exhibiting the *bcc* alloy structure with matched interfacial enthalpy resulting in optimal values (close to zero) thereby preventing dendrite formation. Using the macroscopic atom model, the team estimated the interfacial enthalpy between Li layer and various MCA compositions and thereby identified the best alloys satisfying this criterion. The following equations have been used for these calculations:

$$\Delta H_{Li \text{ in } ABC \text{ (bcc)}}^{inter} = c^{Li \text{ in } ABC} (x \Delta H_{Li \text{ in } A}^{inter} + y \Delta H_{Li \text{ in } B}^{inter} + (1 - x - y) \Delta H_{Li \text{ in } C}^{inter}) \quad (1)$$

$$\Delta H_{inter}^{Li-A} = \frac{V_{Li}^{2/3}}{(\eta_{ws}^{1/3})_{av}} \left[-P(\Delta\phi^*)^2 + Q \left(\eta_{ws}^{1/3} \right)^2 \right] \quad (2)$$

$\left(\eta_{ws}^{1/3}\right)_{av}$ – is the average value of the electron density at the boundary of Wigner Seitz cell

$\Delta\phi^*$ – the difference between ϕ_{Li}^* and ϕ_A^* defined as the work function of the pure metals Li and A

V_{Li} – atomic volume of Li

$P = 14.2 \text{ kJ}/(\text{mol cm}^2 \text{ V}^2 (\text{density unit})^{1/3})$

$Q = 133.5 \text{ kJ}/(\text{mol cm}^2 (\text{density unit}))$

All the parameters are tabulated and available in the literature and can also be calculated from first principles for elements not documented in the literature. Table XVII.6.1 shows the calculated interfacial energy of the different MCAs considered in the present study with Li metal at zero-degree temperature. Table XVII.6.1 shows that MCA4 and MCA5 alloys demonstrate interfacial energies very close to zero value for 5 at. % of Li. Furthermore, it can be construed that the values will not be too large even at higher Li-concentration in contrast to the other three MCAs collected in Table XVII.6.1. Thus, MCA4 and MCA5 could be considered as promising Li-anode materials exhibiting favorable conditions for suppressing dendrite formation during electrochemical cycling.

The experimental validations of these theoretical findings are already demonstrated for the MCA4 alloy generated by high energy alloying described and discussed above. The electrochemical cycling results of this alloy is also shown in Figure XVII.6.10 above. The experimental synthesis of the other alloys and the corresponding electrochemical cycling studies for the other alloys are ongoing and are planned to be completed in the coming months of the funded project. Results of these studies will be reported in the consecutive quarterly reports as well as the annual report of the project for next year.

Table XVII.6.1 ΔH interface for $c_{Li} = 5$ at. % for the different MCAs considered.

MCAs	ΔH_{int} in kJ/mol
MCA1	+1.5
MCA2	+1.8
MCA3	+1.4
MCA4	+0.07
MCA5	-0.3

Conclusions

Research work was conducted in three areas of the project. These include experimental identification and synthesis of new confinement cathodes for embedding sulfur and preventing polysulfide migration. The second aspect of the project related to conducting theoretical studies to identify functional electrocatalysts for promoting the complete conversion of polysulfides to Li_2S and back to elemental sulfur. The work also related to calculation of the activation barriers and identification of electrocatalysts that will lower the activation barriers. A third aspect of the work was directed at theoretical identification of alloying elements and composition of alloys that will exhibit solid solution formation with lithium during electrochemical cycling yielding high areal capacities of 10 m Ah cm^{-2} and above without inducing phase separation. This portion of the work also included experimental synthesis of these alloys determined and identified by theory. Experimental cell fabrication and testing was also conducted. All aspects of these three components have been successfully conducted and completed in this first year of the project. This project has therefore been successfully completed in FY2022. All anticipated aims planned to be completed in year 1 have been achieved.

One book and one book chapter were also published as well as two invited presentations were delivered in FY2022. Extensive collaboration between the team members helped achieve very fruitful results.

Key Publications

Publications

1. Moni K. Datta, Ramalinga Kuruba, T. Prasada Rao, Oleg I. Velikokhatnyi, and Prashant N. Kumta, “New approaches to high-energy density cathode and anode architectures for lithium-sulfur batteries”, in *Lithium-Sulfur Batteries, Advances in High-Energy Density Batteries*, Edited by Prashant N. Kumta, Aloysius F. Hepp, Moni K. Datta and Oleg I. Velikokhatnyi, Elsevier Publications, 2022, 354 – 439, ISBN: 978-0-1-819676-2.
2. *Lithium-Sulfur Batteries, Advances in High-Energy Density Batteries*, Edited by Prashant N. Kumta, Aloysius F. Hepp, Moni K. Datta and Oleg I. Velikokhatnyi, Elsevier Book Publications, 2022, ISBN: 978-0-1-819676-2.

Presentations

1. Prashant N. Kumta, “Perspectives on Materials for Energy Applications”, Lehigh University, Bethlehem, PA, April 19, 2022 (invited).
2. Prashant N. Kumta, Oleg Velikokhatnyi, and Ramalinga Kuruba, “From Lithiated Transition Metal Oxides to Silicon and Lithium-Sulfur Systems: An Evolution of Electrochemically Active Materials”, presented at the 242nd Electrochemical Society Symposium on Research and Development of Primary and Secondary Batteries in honor of George E. Blomgren, October 9-12, 2022 (Invited).

Acknowledgements

The principal investigator and co-investigators cordially and gratefully acknowledge the funding and support from DOE, vehicle technology office (VTO) as well as profusely thank Tien Duong and Haiyan Croft, the program managers for their constant encouragement. The team is particularly thankful for the deep insights and extremely valuable suggestions of Tien Duong during all the quarterly review discussions throughout the past year of the project. Finally, the principal investigator and co-investigators acknowledge the perseverance and dedicated effort of the fellow team members, Dr. Ramalinga Kuruba and Dr. Mayur Gaikwad who contributed extensively with their motivation and steadfast diligence to complete all aspects of the present project.

XVII.7 Development of Li-S Battery Cells with High Energy Density and Long Cycling Life (PSU)

Donghai Wang, Principal Investigator

Pennsylvania State University
134 Energy & Environmental Laboratory
University Park, PA 16802
E-mail: dwang@psu.edu

Haiyan Croft, DOE Technology Development Manager

U.S. Department of Energy
E-mail: Haiyan.Croft@ee.doe.gov

Start Date: January 1, 2022

End Date: December 31, 2022

Project Funding (FY22): \$580,748

DOE share: \$464,598

Non-DOE share: \$116,150

Project Introduction

The Li-S battery, based on reversible lithiation/delithiation of sulfur ($16 \text{ Li} + \text{S}_8 \rightarrow \text{Li}_2\text{S}_n + 8 \text{ Li}_2\text{S}$), is believed to be a next-generation high-energy power source for electric vehicle applications due to its high theoretical energy density (specific energy density of 2450 Wh/kg and volumetric energy density of 2899 Wh/L for the cathode, 3 times that of the traditional Li-ion battery cathode) and the low cost of sulfur [1]. Despite the numerous advantages, practical application of Li-S battery technology is encountering several challenges for both sulfur cathode and lithium anode [2]. First, the electric and ionic insulating nature of sulfur makes it difficult to obtain high capacity at useful charge/discharge rates. It requires conductive additives during the fabrication of electrodes to access large portions of the sulfur which reduces the practical energy density [3]. Second, the lithium polysulfide (Li_2S_x , $x = 4 \sim 8$) can dissolve in the liquid electrolyte and be reduced on the anode surface causing multiple issues during cell cycling, such as shuttling effect, self-discharge, and continuous capacity fading [4]. Finally, electrolyte depletion due to growth of Li dendrites and electrolyte reaction with the Li anode shall lead to poor cycle life [5].

In brief, the most challenging issue is still polysulfide dissolution and its shuttling phenomena. We shall develop a new soluble-polysulfide-free sulfur cathode with high sulfur content ($> 50 \text{ wt}\%$). With this polysulfide-free cathode, accompanied with the development of functional binders, optimization of electrolyte compositions and electrode fabrication, and protected Li metal anode, advanced Li-S batteries with high energy density and long cycle life are achievable.

Objectives

The objective of this project is to develop a new soluble-polysulfide-free sulfur cathode (*i.e.*, sulfur polymerized composite (SPC)-derived sulfur composite materials) with a high sulfur content ($> 50 \text{ wt}\%$) and high discharge specific capacity ($> 700 \text{ mAh/g}$, based on the weight of the whole cathode), and demonstrate the performance of the sulfur electrode at high electrode capacity ($> 7 \text{ mAh/cm}^2$, low N/P ratio (< 2) and low electrolyte/sulfur (E/S) ratio ($< 2.5 \text{ }\mu\text{L/mg}$). A prototype 0.5 Ah Li-S battery cells with the predicted energy density of 400 Wh/kg and 80% capacity retention for over 300 cycles using conventional electrolyte and lithium metal anodes with a protective layer developed from PI's group will be demonstrated.

Approach

The overall approach will focus on synthesizing and optimizing a novel polysulfide-free sulfur composite active material and functional binders. Specifically, approaches to realize the project objectives include the following: (1) development of novel polysulfide-free sulfur composite active materials, (2) development of new functional polymer binders to facilitate Li^+ transport and trap residual lithium polysulfide; and (3) diagnostics, characterization, theoretical simulation, and cell tests on the developed materials in Li-S batteries.

Results

In this budget period, we mainly focused on the following aspects: (1) optimization of the synthetic procedures for sulfurized polyacrylonitrile (SPAN) cathode baseline; (2) development of sulfur polymerized composite (SPC) with incorporated heteroatoms as high-performing cathode materials (SPC-1) for Li-S batteries; and (3) development of high sulfur content SPC-2 cathode materials for Li-S batteries with enhanced specific capacity. Meanwhile, we were working on the in-depth characterization and computational simulation on our materials and systems. In the following part, we shall elucidate our accomplishments that have been achieved so far.

1. Optimization of sulfurized polyacrylonitrile (SPAN) baseline

The sulfur content of cathode materials plays a critical role in determining the specific capacity of Li-S batteries. In this regard, different types of SPAN active materials have been prepared and tested. The key synthesis conditions were tuned to yield expected enhancements in electrochemical performances. We mainly explored the dependence of the heating procedure on the initial specific capacity of obtained SPAN samples since it largely affected the chemical composition (*e.g.*, sulfur content) and directly determined the theoretical capacity of SPAN cathode materials (Figure XVII.7.1a). In detail, SPAN cathodes were prepared upon different heating procedures with varying heating time of 2, 4, 6, and 7.5 hours. SPAN cathodes prepared with reduced heating time were deemed to deliver higher sulfur content and so as enhanced initial capacities. As shown in Figure XVII.7.1b, SPAN powders synthesized from procedures with a heating time of 4-7.5 h exhibited amorphous structures according to their XRD patterns, indicating the good confinement of PAN to sulfur and the accessibility for the construction of polysulfide-free cells. While upon a reduced heating procedure of 2 h, the obtained powder showed the crystal structure of sulfur, demonstrating the remaining, not-well confined sulfur (*i.e.*, ring-structured S₈). Therefore, although this batch of SPAN powders could provide very high initial capacities due to the intrinsically high sulfur content, the as-fabricated cells would suffer from low cycling stability resulting from the undesirable side-reactions between the polysulfide and carbonate electrolyte. For electrochemical performance evaluation, sulfur cathodes using the above SPAN powders were fabricated with 80 wt% of active material and an areal loading of ~2 mg SPAN/cm². Their electrochemical performances were tested in conventional ether-based electrolytes and shown in Figure XVII.7.1c. After optimization, the initial discharge specific capacity of the SPAN (2 and 4 h) cathode after activation could reach > 700 mAh g⁻¹ (based on the weight of the whole cathode). Such initial discharge specific capacity fulfills the target for this reporting period. Two voltage plateaus at 2.36 and 2.17 V were well defined upon discharging. Despite its enhanced initial capacity, SPAN cathode (2 h) demonstrated relatively fast capacity decay and limited cycling stability. Therefore, a balance should be further struck between reduced heating time (*i.e.*, sulfur content) and cycling stability to maximize the advantages of polysulfide-free Li-S cathodes in carbonate electrolyte.

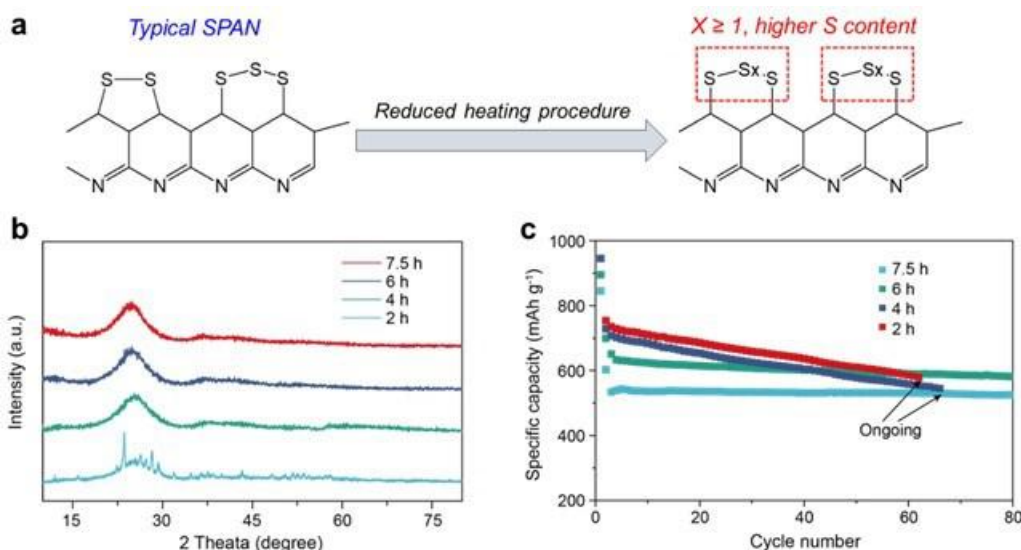


Figure XVII.7.1 (a) Reduced heating procedure (*i.e.*, decreased heating time upon SPAN synthesis) was used to increase the sulfur content in obtained SPAN powders so as the specific capacity. (b) XRD spectra of SPAN cathodes synthesized with varying heating time from 2 to 7.5 h. (c) Cycling performances of SPAN cathodes synthesized with varying heating time from 2 to 7.5 h.

2. Development of sulfur polymerized composite cathode material generation-1 (SPC-1)

The sulfur polymerized composite cathode materials were fabricated for polysulfide-free cathode materials in Li-S batteries. In our proposed SPC-1 materials, heteroatoms are introduced to modify the backbones and side chains of the polymeric parts. The type of heteroatoms determines their binding energy with sulfur atoms and thus the reversibility of conversion reactions in Li-S batteries. Therefore, three types of heteroatoms (denoted as a, b, and c) were first introduced into the synthetic routes of the SPC-1 materials (denoted as SPC-1a, SPC-1b, and SPC-1c) and then screened by the initial specific capacity of the yielded batteries. Cathodes based on SPC-1a, b, and c were fabricated with 80 wt% of active material and areal loading $\sim 2 \text{ mg}_{\text{SPC-1}}/\text{cm}^2$. The Li-S batteries based on the above cathodes were tested in carbonate-based electrolyte because it is safer, cheaper than the ether-based electrolyte, and proves to contribute a polysulfide-free conversion reaction with improved cycling performance. As a result, batteries based on SPC-1a cathodes demonstrated the highest initial specific capacity ($\sim 530 \text{ mAh/g}$) over its counterparts, including batteries based on SPC-1b, and SPC-1c cathodes (Figure XVII.7.2a). The selected heteroatom-a has better electronic conductivity than sulfur, demonstrates good compatibility with carbonate electrolyte, and can serve as extra bond sites for sulfur species to enhance sulfur utilization. However, the theoretical capacity of heteroatom-a is limited. Therefore, the trade-off between the amount of heteroatom-a in SPC-1a and the yielded capacity needs to be clarified for optimized electrochemical performance. In this regard, SPC-1a containing various weight percentages of heteroatom-a (*i.e.*, 2, 6, and 10 wt%, denoted as SPC-1a2, 1a6, and 1a10) were synthesized and evaluated in full cells (Figure XVII.7.2b-d). Consequently, among SPC-1a2, SPC-1a6, and SPC-1a10 composite active materials, SPC-1a6 cathode shows the highest initial discharge capacity of $\sim 530 \text{ mAh/g}$ as well as more desirable cycling stability.

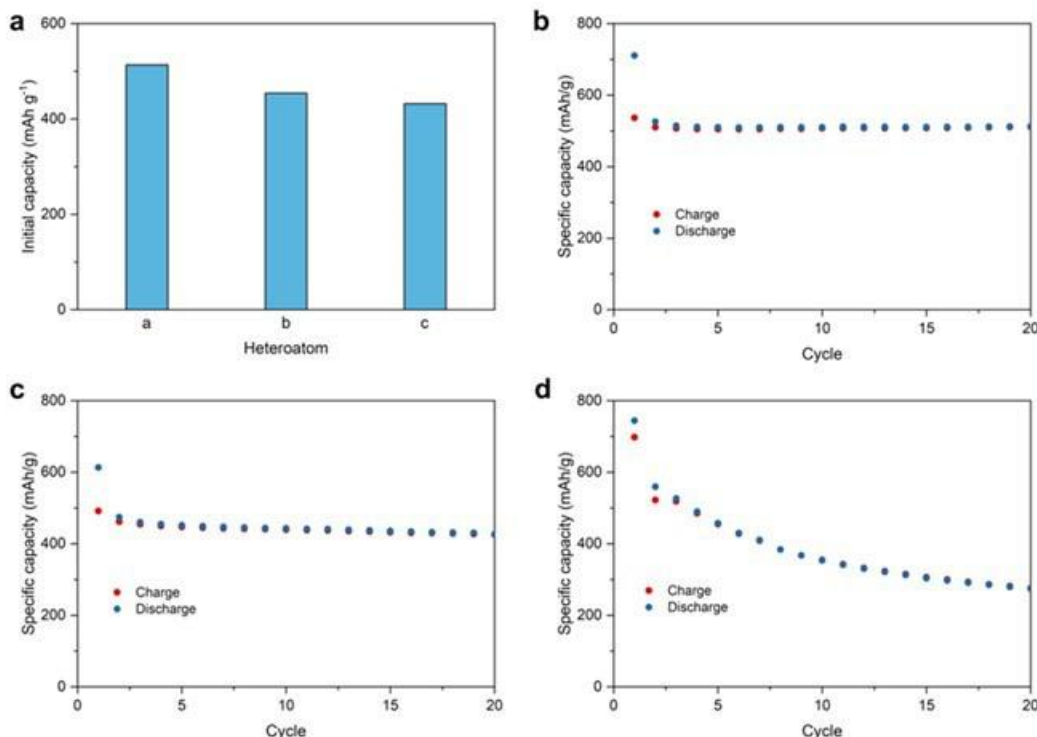


Figure XVII.7.2 (a) Initial capacities of SPC-1a, SPC-1b, and SPC-1c cathodes. (b)-(d) Cycling performance of SPC-1a2 (b), SPC-1a6 (c), and SPC-1a10 (d) cathodes in carbonate electrolytes. The areal active material loading is around 2 mg/cm². The cells were activated at 0.05 A/g (based on composite weight) for the 1st cycle and then cycled at 0.1 A/g.

Following with that, according to the optimized synthetic strategy from our SPAN baseline shown above, we also leveraged an optimized fabrication method with reduced heating time (*i.e.*, 4 hours) for the synthesis of SPC-1 with both high initial capacity (sulfur content) and cycling stability. As a result, batteries based on optimized SPC-1 (4 h) demonstrated enhanced initial specific capacity over 650 mAh/g (Figure XVII.7.3a). Such initial discharge specific capacity meets the target for this reporting period. Besides, due to the stabilization of introduced heteroatom in the sulfur chain, the obtained SPC-1 cathode also delivered high cycling stability. Benefiting from the combined advantages of introduced heteroatom and reduced heating procedure, the SPC-1-based Li-S cells demonstrated enhanced specific capacity and cycling performances compared with the SPAN baseline (Figure XVII.7.3b).

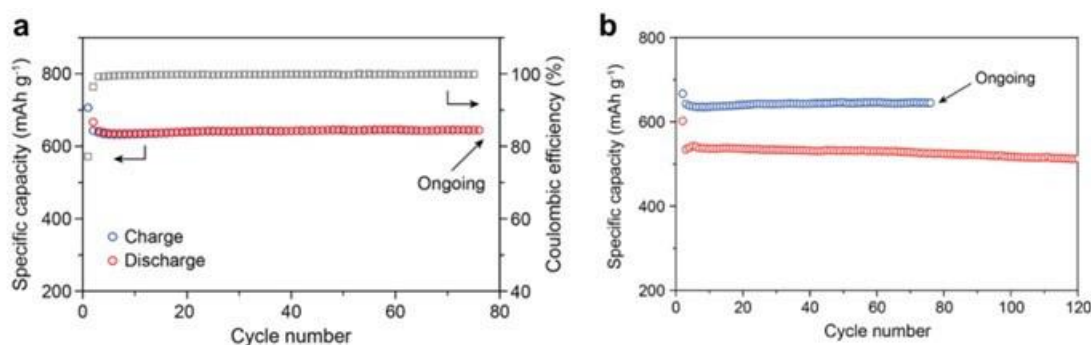


Figure XVII.7.3 (a) Cycling performances of optimized SPC-1 cathodes with reduced heating procedure of 4 h in carbonate electrolyte. (b) Optimized SPC-1 cathodes (blue) delivered enhanced specific capacities over 630 mAh/g compared with SPAN baseline (red) in carbonate electrolyte.

3. Development of sulfur polymerized composite cathode material generation-2 (SPC-2)

The SPC preparation was further optimized to SPC-2 with higher S content because it could afford the resultant SPC material with higher specific capacity. The composition and micro-structures in the resultant cathode composite may also be affected by the heating procedure upon synthesis. Previously we showed that SPAN baseline with much improved specific capacity could be obtained by reducing the heating time and decreasing the heating temperature. Therefore, in this quarter, we applied optimized synthetic strategy and parameters to the preparation of our SPC-2 cathode materials. In specific, we reduced the heating time and the heating temperature of SPC-2 cathode materials and then tested them in carbonate electrolyte (Figure XVII.7.4). For electrochemical performance evaluation, sulfur cathodes using the above SPC-2 powders were fabricated with 80 wt% of active material and an areal loading of $\sim 2 \text{ mg SPC-2/cm}^2$. Their electrochemical performances were tested in carbonate electrolytes (Figure XVII.7.4a). After optimization, the initial discharge specific capacity of the SPC-2 cathode after activation could reach $> 700 \text{ mAh/g}$ (based on the weight of the whole cathode). Such initial discharge specific capacity fulfills the target for this reporting period. The optimized SPC-2 also showed cycling stability with capacity retention $> 90\%$ after 100 cycles. Two voltage plateaus at 2.35 and 2.16 V were well defined upon discharging, which were in line with their CV profiles (Figure XVII.7.4b). Reduced polarization of SPC-2 was also found according to the CV analysis compared with that of SPAN baseline, demonstrating the enhanced kinetics of our synthesized SPC-2 cathodes.

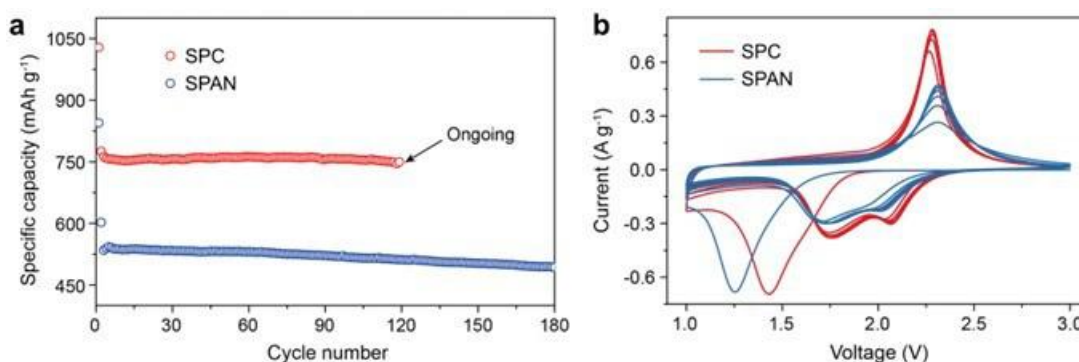


Figure XVII.7.4 (a) Cycling performances of optimized SPC and SPAN cathodes in carbonate electrolyte at current density of 100 mA/g. The SPC cathodes with show much improved specific capacity (initial specific capacity $> 1000 \text{ mAh/g}$ based on SPC weight, or $> 800 \text{ mAh/g}$ based on cathode weight) than that of routine SPAN cathode. (b) CV curves of SPC and SPAN cathode-based batteries at scan rate of 0.1 mV/s .

The optimized SPC-2 cathode material is durable upon enlarged cutoff window from 0.5 to 3.0 V, demonstrating its electrochemical stability (Figure XVII.7.5a). Batteries based on optimized SPC cathode demonstrated initial specific capacity over 750 mAh/g (based on the total weight of cathode) at cutoff window of 0.5 to 3.0 V (Figure XVII.7.5b). Such initial discharge capacity meets the target for this reporting period. This high specific capacity could also be well maintained upon cycling in carbonate electrolyte as shown in Figure XVII.7.5b.

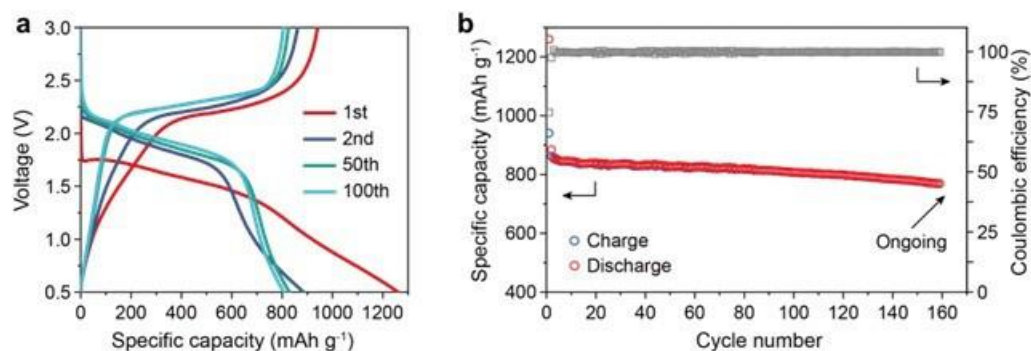


Figure XVII.7.5 (a) Charge-discharge curves of optimized SPC-2 cathode-based battery at current density of 100 mA/g in carbonate electrolyte. (b) Cycling performance and CE evolution of optimized SPC-2 cathode-based battery at current density of 100 mA/g in carbonate electrolyte.

Conclusions

In conclusions, we have accomplished our goals and Go/no Go target for the budget period 1. In specific, we have developed a series of SPC materials and accordingly synthesized polysulfide-free sulfur cathodes with significantly enhanced specific capacity for Li-S batteries using carbonate electrolytes. We were also working on the evaluation of the electrochemical performances, in-depth characterization, and computational simulation on our materials and systems.

References

1. P. G. Bruce, S. A. Freunberger, L. J. Hardwick, J. M. Tarascon, *Nature Materials* 2012, 11, 19.
2. A. Manthiram, Y. Fu, S. H. Chung, C. Zu, Y. S. Su, *Chemical Reviews* 2014, 114, 11751; Z. W. Seh, Y. Sun, Q. Zhang, Y. Cui, *Chemical Society Reviews* 2016, 45, 5605.
3. X. Ji, K. T. Lee, L. F. Nazar, *Nature Materials* 2009, 8, 500.
4. M. R. Busche, P. Adelhelm, H. Sommer, H. Schneider, K. Leitner, J. Janek, *Journal of Power Sources* 2014, 259, 289.
5. L. Qie, C. Zu, A. Manthiram, *Advanced Energy Materials* 2016, 6, 1502459.

Acknowledgements

The work was supported by the Department of Energy, under Award Number DE-EE0009650. We appreciate the support from Colleen Butcher and Coriana Fitz at National Energy Technology Laboratory and Patricia Smith from DOE.

XVII.8 Nanostructured Design of Sulfur Cathodes for High Energy Lithium-Sulfur Batteries (Stanford University)

Yi Cui, Principal Investigator

Stanford University

Department of Materials Science and Engineering, Stanford University
Stanford, CA 94305

E-mail: yicui@stanford.edu

Tien Duong, DOE Technology Development Manager

U.S. Department of Energy

E-mail: Tien.Duong@ee.doe.gov

Start Date: October 1, 2017

End Date: September 30, 2023

Project Funding (FY22): \$500,000

DOE share: \$500,000

Non-DOE share: \$0

Project Introduction

Lithium-sulfur (Li-S) batteries are regarded as next-generation high-energy storage devices for portable electronics, electric vehicles, and grid-scale storage due to their high theoretical energy density (2500 Wh kg⁻¹). The practical applications of Li-S batteries are found to be hampered by the low electronic and lithium-ion conductivity of sulfur and lithium sulfide (Li₂S), polysulfides shuttling, and poor stability of lithium metal anodes. Recently, there is a new direction to address the problems of Li-S chemistry by replacing flammable liquid electrolytes with solid-state electrolytes for achieving high energy density and safe Li-S batteries. However, the energy density and stability achieved by polymer-based all-solid-state Li-S batteries (ASSLSBs) to date have been far below expected due to uncontrolled active materials dissolution (lithium polysulfides, LiPSs) into solid polymer electrolytes (SPEs) and sluggish sulfur reaction kinetics. Despite some improvements in ASSLSBs, studies on improving sulfur reaction kinetics in solid-state electrolytes are still in its infancy. Redox mediators (RMs) with the function of electron shuttle are expected to promote sulfur species conversion and utilization. Furthermore, deep understanding of the redox chemistry during discharge/charge in ASSLSBs is crucial to design effective RMs. In this project, we prove the efficacy of RMs in ASSLSBs and reveal the redox chemistry for Li₂S cathodes using *operando* X-ray absorption spectroscopy (XAS) measurements. By thoroughly evaluating the redox potential, solubility of different RMs, soluble-type 1,5-bis(2-(2-(2-methoxyethoxy)ethoxy)ethoxy)anthra-9,10-quinon (AQT) shows the best redox potential and redox reversibility in SPEs. Using *operando* XAS, we revealed the redox chemistry of Li-S reaction in ASSLSBs based on Li₂S cathodes. By identifying the sulfur species using sulfur K-edge, we discovered the solid-solid Li₂S-sulfur conversion mechanism for the bare Li₂S cathode in the first charge cycle. This solid-solid conversion of the bare Li₂S cathodes results in a high energy barrier for activation (charge to ~4 V) and low sulfur utilization. Incorporating AQT, *operando* XAS demonstrates the formation of polysulfides in the first charge cycle and the solid-polysulfide-solid reaction mechanism in ASSLSBs based on Li₂S@AQT cathodes. The continuing effectiveness of the AQT RM beyond the first cycle was further confirmed with the observation of minimal polarization and improved long cycling stability and Coulombic efficiency (CE, average 98.9 % for 150 cycles).

Objectives

The charge capacity limitations of conventional transition metal oxide cathodes are overcome by designing optimized nano-architected sulfur cathodes. This study aims to enable sulfur cathodes with high capacity and long cycle life by developing sulfur cathodes from the perspective of RMs design, which will be used to combine with lithium metal anodes to generate high-energy Li-S batteries. *Operando* XAS and optical microscopy combined with ex situ analyses are used to investigate Li-S conversion kinetics and polysulfide dissolution behavior in SPEs. We propose that some of the material design improvements originally developed in liquid electrolytes can be incorporated to solid-state electrolytes with excellent outcomes. RMs, which play

a vital role in some liquid electrolyte-based electrochemical energy storage systems, will be applied in solid polymer based ASSLSBs in this study. Sulfur cathodes with RMs are designed and fabricated to overcome issues related to polysulfide dissolution and the insulating nature of sulfur in ASSLSBs. The batteries with RMs deliver better reversible capacity, faster reaction kinetics, and longer cycling life as compared to bare sulfur cathodes.

Approach

The approaches refer to three main parts: (I) advanced nanostructured sulfur cathodes design and synthesis, including (1) develop novel sulfur nanostructures with multi-functional coatings for the confinement of sulfur/lithium polysulfides to address the issues of active materials loss and low conductivity; (2) develop/discover optimal nanostructured materials/RMs that can capture the polysulfide dissolved and enhance the Li-S conversion kinetics in the electrolyte; (3) develop space efficiently packed nanostructured sulfur cathode to increase the volumetric energy density and rate capability; (4) identify the interaction mechanism between sulfur species and different types of oxides/sulfides/RMs, and find the optimal material to improve the capacity and cycling of sulfur cathode. (II) Structure and property characterization, including (1) ex situ scanning electron microscopy; (2) in situ optical microscopy; (3) in situ optical XAS. (III) Electrochemical testing including (1) coin cells; (2) A set of electrochemical techniques.

Results

The reaction mechanism of RMs in ASSLSBs is shown in Figure XVII.8.1a, which is considered as a two-step process involving electrochemical and chemical reactions. During charging, oxidized RMs (RM_{ox}) chemically oxidizes Li_2S to LiPSs while RM_{ox} is reduced to reduced RMs (RM_{red}) (step A, chemical reaction). RM_{red} in turn is electrochemically oxidized to the initial state of RM_{ox} by giving electrons to current collectors (step B). RMs shuttle electrons between the current collectors and isolated Li_2S which would have otherwise remained inactive. The charging voltage of the cell is determined by the electrochemical step (step B). Therefore, we propose that the reduced charge polarization and improved sulfur utilization for ASSLSBs can be realized by choosing an appropriate RM, as shown in Figure XVII.8.1b. Two criteria are paramount for effective RMs: 1) They should be soluble in SPEs; 2) They should have a redox potential slightly higher than that of Li_2S . We select three typical RMs originally developed in liquid electrolytes to examine their electrochemical properties in SPEs, including 1,5-bis(2-(2-(2-methoxyethoxy)ethoxy)ethoxy) anthra-9,10-quinone (AQT), anthraquinone-2-carboxylic acid (AQC), and lithium iodide (LiI). RMs are first mixed with polyethylene oxide (PEO)/lithium bis(trifluoromethanesulfonyl)imide (LiTFSI) electrolytes in acetonitrile solution, and then dropcasted on the carbon paper as the electrodes. Figure XVII.8.1c-e shows cyclic voltammogram (CV) curves of the RM electrodes versus lithium metal in PEO/LiTFSI SPEs. Compared with LiI and AQC, AQT showed the most favorable redox potentials, matching that of Li_2S oxidation and best redox reversibility.

To understand the roles of effective RMs, we perform the *operando* XAS measurements for Li_2S electrodes in polymer-based ASSLSBs. Figure XVII.8.2a shows the *operando* XAS results on a Li_2S -lithium (Li) cell during the first galvanostatic electrochemical cycle. At the open-circuit voltage, the XAS spectrum for Li_2S cathodes shows a feature at 2473.5 eV, indicating pure Li_2S at the pristine state. As the charging process proceeds, an additional peak at 2472.7 eV, assigned to the sulfur (S) 1s to 3p transition of elemental S, appears and gradually becomes stronger with continued delithiation. Meanwhile, no extra pre-edge feature corresponding to the terminal S of lithium polysulfides (LiPSs) at 2470.7 eV are observed, indicating no detectable LiPSs formation. To further quantify the content change of Li_2S and S during the first charging process, the two-phase fitting for the *operando* XAS spectra was conducted. As shown in Figure XVII.8.2b, the content of Li_2S decreases monotonously as the charging proceeds while that of S is increased. At the end of the first charging process, all Li_2S disappears and only the S phase exists. Therefore, we propose that Li_2S is gradually consumed and directly converted to S through a solid-solid reaction in the first charging process (Figure XVII.8.2c), showing the sluggish Li_2S oxidation in ASSLSBs.

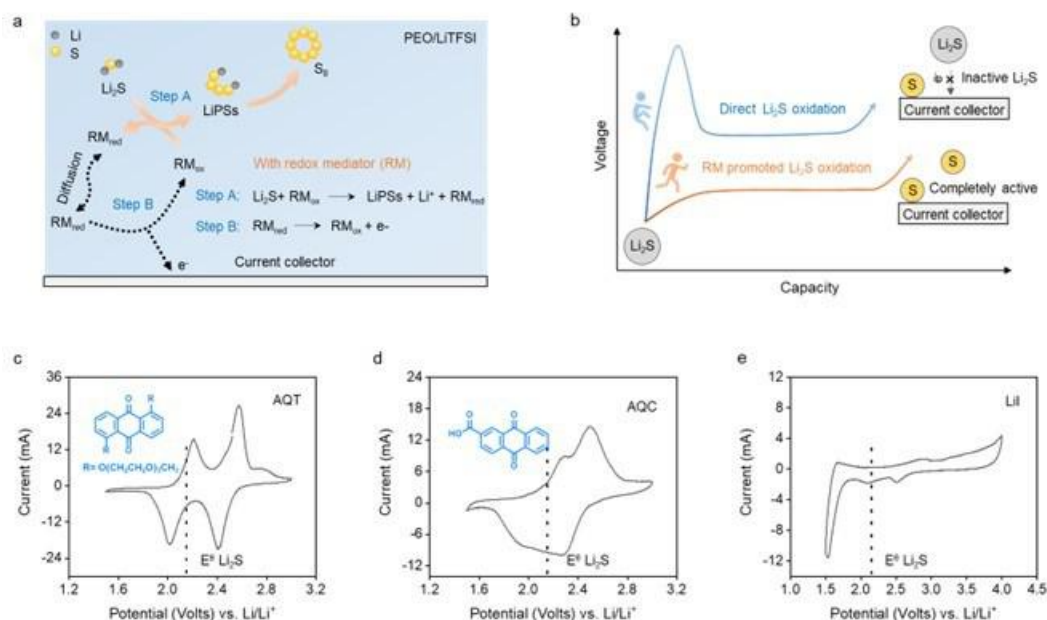


Figure XVII.8.1 Designing redox mediators (RMs) for all-solid-state lithium-sulfur batteries (ASSLSBs). (a) The proposed reaction scheme of the RMs for ASSLSBs. Effective RMs solubilized in the solid polymer electrolytes (SPEs) shuttle electrons between current collectors and the surfaces of isolated Li_2S particles. During the charging process, RM_{ox} chemically oxidizes Li_2S to polysulfides while RM_{ox} is reduced to RM_{red} (step A, chemical reaction). RM_{red} diffuses toward the current collector and is oxidized to the initial state of RM_{ox} near the current collector surface (step B, electrochemical reaction). The light blue color indicates the SPEs. (b) Schematic first charge profiles of ASSLSBs with (orange line) and without RM (blue line). A high charging voltage (~ 4 V versus Li^+/Li) is necessary to activate Li_2S in the first charge process. Li_2S is directly converted to elemental sulfur through a two-phase transformation. Grey: Li_2S particles; yellow: sulfur. (c-e) Cyclic voltammograms (CV) curves and chemical structure of (c) AQT, (d) AQC, and (e) Lil in PEO/LiTFSI solid polymer electrolytes (SPEs) at a scan rate of 0.1 mV s^{-1} . The dotted line is the equilibrium potential of Li_2S (~ 2.15 V versus Li^+/Li).

To further understand the redox chemistry after incorporating AQT RM, we conduct *operando* S K-edge XAS measurements for $\text{Li}_2\text{S}@ \text{AQT}$ electrodes. The feature of elemental S at 2472.7 eV shows a gradual increase, indicating the transformation from Li_2S to S during the charging process. Particularly, typical features of LiPSs are observed from the XAS spectra in the red rectangle in Figure XVII.8.2d, while that are not observed for bare Li_2S cathodes during the whole first charge process. We further calculate the average chain length of LiPSs at different charge stages based on the area ratio of main-edge peaks to pre-edge peaks. Figure XVII.8.2e shows the average chain length of LiPSs (n) as a function of the state of charge. At the beginning of charging, the value of n is around 4 and then significantly increases to 8 as the electrochemical reaction proceeds. At the end of the charge process, the pre-edge feature of LiPSs disappears while the main-edge feature of the elemental S (2472.7 eV) becomes more prominent. These results indicate Li_2S cathodes with AQT undergo a different Li-S reaction mechanism with bare Li_2S for the activation cycle, as proposed in Figure XVII.8.2c and Figure XVII.8.2f.

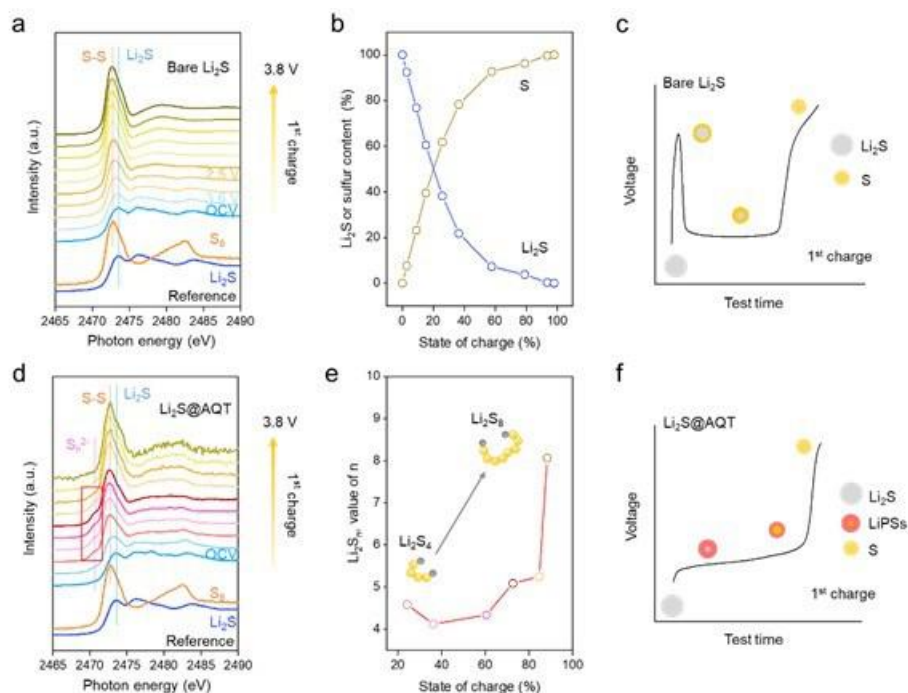


Figure XVII.8.2 Operando XAS to understand RM chemistry in ASSLSBs. Operando S K-edge XAS spectra of (a) bare Li_2S cathodes and (d) $\text{Li}_2\text{S}@AQT$ cathodes in polymer-based ASSLSBs for the first charge process. XAS spectra of Li_2S (2473.5 eV) and S (2472.7 eV) shown in the bottom are used as references. The pre-edge feature at 2470.7 eV is identified as the fingerprint of LiPSs from the terminal S. (b) Contents of Li_2S and S calculated from two-phase fitting of the XAS spectra in (a) as a function of test time. The corresponding charge curve shows a high energy barrier around 4 V for Li_2S activation. Schematics for proposed Li-S reaction mechanism in ASSLSBs, using Li_2S cathodes (c) without/(f) with AQT RM. (e) The average chain length of LiPSs as a function of the state of charge for $\text{Li}_2\text{S}@AQT$ cathodes during the first charging.

We further prove the efficacy of AQT beyond the first activation cycle in ASSLSBs by testing the cycling performance of Li_2S cathodes without/with AQT in lithium metal batteries (type 2032) with SPEs. As-assembled cells are first charged to 3.8 V for Li_2S activation and then constructed for galvanostatic cycling tests from 1.6 to 2.8 V. Figure XVII.8.3a and Figure XVII.8.3b show that adding AQT significantly enhances the cycling stability of ASSLSBs. For the bare Li_2S cathode, significant capacity fading (from 579 mAh g^{-1} to 384 mAh g^{-1}) is observed within 20 cycles at 0.1 C with a lower average Coulombic efficiency of 85%. In contrast, the $\text{Li}_2\text{S}@AQT$ cell shows a stabilized capacity, retained at 997 mAh g^{-1} after 20 cycles.

The enhanced cycling performance of $\text{Li}_2\text{S}@AQT$ cathodes is attributed to eliminating the cumulative growth of a thick insulating sulfur/ Li_2S film and decreasing the amount of soluble sulfur species in the SPEs, which are further confirmed by *in situ* impedance study. Before cycling, the impedance spectrum of the as-assembled bare Li_2S cells showed a larger semicircle than $\text{Li}_2\text{S}@AQT$ cells in the high-frequency region, which indicates higher charge-transfer resistance in the former case (Figure XVII.8.3c and Figure XVII.8.3d). After cycling, the impedance of the $\text{Li}_2\text{S}@AQT$ cell remains low and stable over 10 cycles, in contrast to the high and increased impedance in the bare Li_2S cell. It is noted that the decreased impedance after the first cycle for bare Li_2S cathodes results from the enhanced contact between cathodes and SPEs.

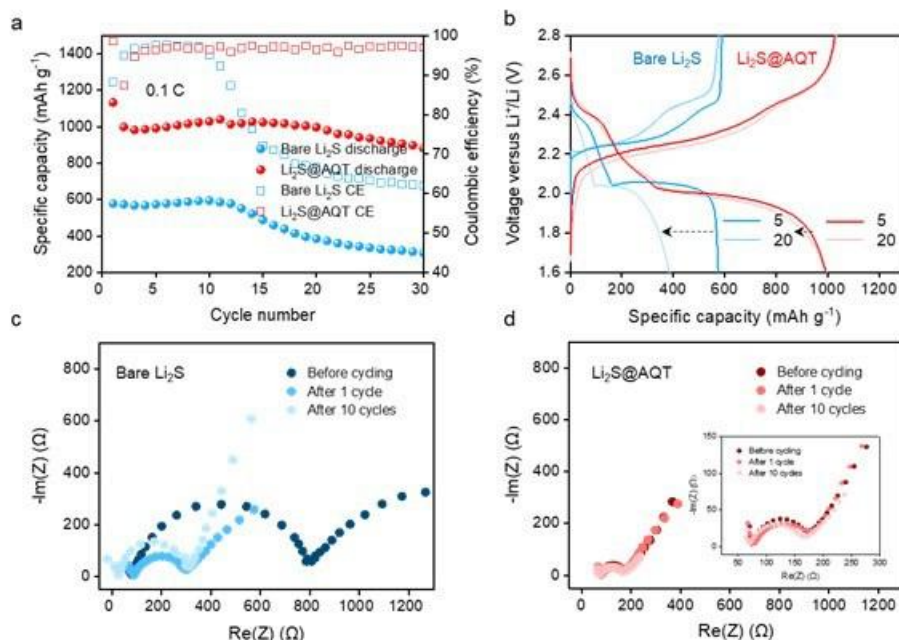


Figure XVII.8.3 Electrochemical performance of Li₂S cathodes without/with AQT redox mediator (RM) in ASSLSBs. (a) Cycling performance and Coulombic efficiency of Li₂S cathodes without/with AQT at 0.1 C for 30 cycles. (b) Typical charge-discharge voltage profiles of Li₂S cathodes without/with AQT at the 5th cycle and the 20th cycle at 0.1 C. Nyquist plots of (c) the Li₂S-Li cell and (d) the Li₂S@AQT-Li cell before and after different cycles. Inset in the first figure shows the zoom-in Nyquist plot for the Li₂S@AQT-Li cell.

After incorporating AQT, lithium polysulfides prefer to stay on the cathode side, and are rapidly oxidized/reduced during charging/discharging. We further fabricated the high mass-loading Li₂S cathodes with AQT (Li₂S@AQT) and tested their cycling performance in the Li-S batteries (type 2032) with SPEs. The Li₂S@AQT cell obtained an areal capacity of 2.3 mAh cm⁻² with a high mass-loading of Li₂S (3.7 mg cm⁻²) at 60°C (Figure XVII.8.4a), which corresponds to a high cell-level energy density of 416 Wh kg⁻¹. The energy density is calculated from the average discharge voltage (2.1 V), cell capacity (2.3 mAh cm⁻²), and total mass of the cathode (6.1 mg cm⁻², excluding current collector), the solid electrolyte with redox mediators (RMs) (2.9 mg cm⁻²), and the anode (2.6 mg cm⁻²). Figure XVII.8.4b displays the cycling performance of the high-loading Li-S battery at a current density of 0.25 mA cm⁻². The cycling shows a slight capacity decay for the initial equilibrium cycles and remains stable with a discharge capacity of 640 mA h g⁻¹ after 15 cycles.

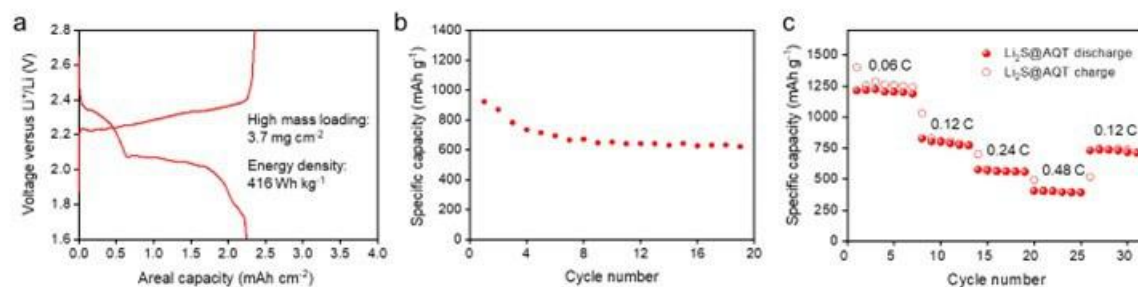


Figure XVII.8.4 Electrochemical performance of Li₂S cathodes with AQT RM in ASSLSBs. (a) Voltage profile at the 2nd cycle of the Li₂S@AQT cell with a high mass-loading (3.7 mg cm⁻²) at a current density of 0.25 mA cm⁻². (b) Cycling performance of the high loading cell. (c) Specific capacity of Li₂S@AQT cathodes cycled from 0.06 to 0.48 C. All cells are operated at 60°C.

Finally, the rate performance of as-prepared cathodes is investigated by cycling cells at different C-rates (Figure XVII.8.4c). The Li₂S@AQT cell, benefiting from the effective AQT enhanced Li-S reaction kinetics, shows a good rate capability, achieving a discharge capacity of 1214 mAh g⁻¹, 827 mAh g⁻¹, 577 mAh g⁻¹,

and 406 mAh g_s⁻¹ based on commercial Li₂S at 0.06 C, 0.12 C, 0.24, and 0.48 C, respectively. All the above results show that AQT enables promoted both reaction kinetics and stability to achieve high-performance ASSLSBs.

Conclusions

In all, in the past one year, we have made great progress in developing high energy density all-solid-state Li-S batteries. We have successfully proved that RMs are effective in all-solid-state batteries. An anthraquinone based redox center with the desired redox potential, high stability, and sufficient solubility in the SPEs was rationally designed to facilitate Li₂S oxidation. Using operando sulfur K-edge X-ray absorption near edge spectroscopy, we directly tracked the sulfur speciation and revealed the redox chemistry for Li₂S cathodes in ASSLSBs for the first time. Li₂S cathodes with AQT RMs delivers a discharge capacity as high as 1133 mAh g_s⁻¹. The Li₂S@AQT cell demonstrates superior cycling stability (average Coulombic efficiency 98.9% for 150 cycles) and rate capability owing to the effective AQT enhanced Li-S reaction kinetics. This work opens a new avenue for designing RMs in the solid-state system sheds light on developing next-generation batteries with high efficiency, long cycle life, and high safety.

Key Publications

1. Xin Gao, Xueli Zheng, Yuchi Tsao, Pu Zhang, Xin Xiao, Yusheng Ye, Jun Li, Yufei Yang, Rong Xu, Zhenan Bao, and Yi Cui* All-Solid-State Lithium-Sulfur Batteries Enhanced by Redox Mediators. *J. Am. Chem. Soc.* 2021, 143, 43, 18188-18195.

XVIII Beyond Li-ion R&D: Lithium-Air Batteries

A lithium-air cell benefits from using oxygen molecules at the positive electrode. Oxygen reacts with positively charged lithium ions to form lithium peroxide. Electrons are drawn out of the electrode until no more lithium peroxide can be formed. For the rechargeable Li-air battery, the practical energy density could be ~800 Wh/kg. An advantage of such batteries is their open structure; that is, they can absorb the active cathode material (oxygen) from the surrounding environment instead of having to carry it within. However, their open structure also leads to several challenges. Although significant progresses have been made in recent years on the fundamental properties of lithium-air batteries, many barriers still need to be addressed before their practical application in EVs.

The rest of this chapter contains detailed reports on the status of the following individual projects.

- Lithium-Air Batteries (ANL)
- Lithium Oxygen Battery Design and Predictions (ANL)
- Development of a High-Rate Lithium-Air Battery Using a Gaseous CO₂ Reactant (UIC).

XVIII.1 Lithium-Air Batteries (ANL)

Khalil Amine, Principal Investigator

Argonne National Laboratory
9700 South Cass Avenue
Lemont, IL 60439
E-mail: amine@anl.gov

Larry Curtiss, Co-Principal Investigator

Argonne National Laboratory
9700 South Cass Avenue
Lemont, IL 60439
E-mail: curtiss@anl.gov

Tien Duong, DOE Technology Development Manager

U.S. Department of Energy
E-mail: Tien.Duong@ee.doe.gov

Start Date: October 1, 2018

End Date: September 30, 2025

Project Funding (FY22): \$480,000

DOE share: \$480,000

Non-DOE share: \$0

Project Introduction

Lithium-oxygen batteries are of much interest because they offer, in principle, ten times the energy density of conventional lithium-ion systems. The inherent energy potential of lithium metal approaches that of gasoline, but there are challenges that remain to be able to unlock this potential. While today's lithium-ion batteries may provide acceptable power for hybrid electric vehicles and all-electric vehicles, they do not yet provide sufficient energy for the long distance driving desired by consumers. A breakthrough in Li-oxygen battery technology would significantly increase the possibility of extending the electric range of these vehicles with the added advantages of reducing battery cost and weight.

The successful implementation of non-aqueous Li-air cells has been hampered because of severe materials problems that have limited electrochemical performance. These include (1) the non-aqueous electrolytes can be unstable under both the charge and discharge conditions, thereby seriously limiting cycle life; (2) during discharge, the solid and insoluble Li_2O_2 and/or other lithium oxide products are deposited on the surface or within the pores of the carbon cathode, thereby passivating the surface as well as clogging the pores and restricting oxygen flow; (3) degradation of the lithium anode due to oxygen crossover destroys the integrity and functioning of the cell; and (4) commonly used transition metal cathode catalysts, do not access the full capacity of the oxygen electrode or enable sufficiently high rates.

The team led by Dr. Khalil Amine at Argonne National Laboratory is working on problems that limit the electrochemical performance of the Li-oxygen battery, including the stability of the organic electrolytes, development of new cathode catalysts, and new electrolytes. This effort will lead to the development of a reversible lithium oxygen battery that provides much higher energy density than state-of-the-art lithium-ion batteries for electric vehicles

Objectives

This project will develop new cathode materials and electrolytes for Li-air batteries for long cycle life, high capacity, and high efficiency. The goal is to obtain critical insight that will provide information on the charge and discharge processes in Li-air batteries to enable new advances to be made in their performance. This will be done using state-of-the-art characterization techniques combined with state-of-the-art computational methodologies to understand and design new materials and electrolytes for Li-air batteries.

Approach

The project is using a joint theoretical/experimental approach for design and discovery of new cathode and electrolyte materials that act synergistically to reduce charge overpotentials and increase cycle life. Synthesis methods, in combination with design principles developed from computations, are used to make new cathode architectures. Computational studies are used to help understand decomposition mechanisms of electrolytes and how to design electrolytes with improved stability. The new cathodes and electrolytes are tested in Li-O₂ cells. Characterization, along with theory, is used to understand the performance of materials used in the cell and to make improved materials.

Results

Functioning mechanism of metal-free catalyst platforms

We have been exploring new metal-free catalyst platforms for enabling low overpotential charge of Li-O₂ batteries across various current densities and types of carbon-based substrate materials. This platform is based on what is traditionally called a solid-electrolyte interphase (SEI), which is an organic/inorganic interphase that is formed by the reduction of electrolyte components. We specifically studied the functioning mechanism of the SEI layer and its role as a cathode for a Li-O₂ battery.

We discovered profound properties in the ether-based SEI layer when exposed to O₂ gas. Shown in Figure XVIII.1.1A, the open-circuit potential is measured while the SEI is exposed to and allowed to rest in an O₂ atmosphere over 6 hours. It was apparent that the potential of the SEI changed drastically during this process (stabilizing after ~4 hours). A constant current charge revealed (Figure XVIII.1.1B) a multi-plateau voltage profile followed by an almost no capacity contribution from continued cycling after the first charge. This eliminates the possibility that the SEI layer can contribute significantly to charge/discharge capacity after the 1st charge cycle. A similar conclusion was found in the 1st and 4th cycle of cyclic voltammetry (Figure XVIII.1.1C-D), respectively) where the large initial irreversible peak at ~3.75 V decreased drastically from the 1st to 4th cycle. However, a small peak at ~3.0 V remained, indicating that there are reversible electrochemical processes derived from the SEI layer, which likely contributes to its catalytic function.

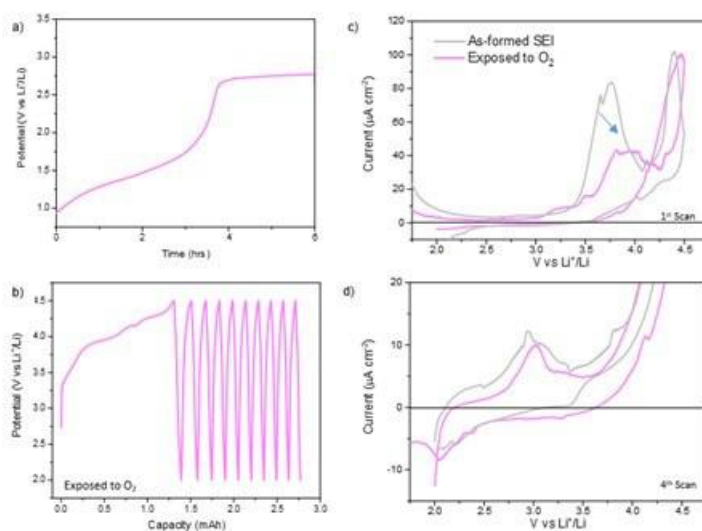


Figure XVIII.1.1 A) Open circuit potential of SEI vs Li metal (reference electrode) when exposed to O₂ gas. B) Cycling profile of the SEI vs Li metal cell in Ar atmosphere *after* forming exposing the SEI to O₂. Cyclic voltammograms of the pristine SEI and SEI exposed to O₂ gas C) 1st scan and D) 2nd scan, indicating the relatively reversible CV current peak at ~3.0 V vs Li⁺/Li.

To determine if the charging benefit of using the SEI is derived from a direct SEI-Li₂O₂ contact mechanism or a solution mechanism between SEI-derived soluble species, we designed what we called an interlayer cell. The main feature of this cell is that the interlayer is not electronically connected to the circuit of the battery (Figure XVIII.1.2A). We pre-deposited Li₂O₂ onto a carbon paper (Figure XVIII.1.2C-D) and used it as the interlayer.

With the a O₂-exposed SEI as the cathode, we charged the cell (voltage profile shown in Figure XVIII.1.2B), and found that the Li₂O₂ content decreased substantially (Figure XVIII.1.2E-F). This is strong evidence that the functioning mechanism of the SEI layer is based on a the formation of soluble species that can diffuse to and oxidize the Li₂O₂, i.e. a soluble catalyst. Future studies will dive deeper into which species are present and also the the role of the SEI layer on the deposition kinetics and mechanism of Li₂O₂.

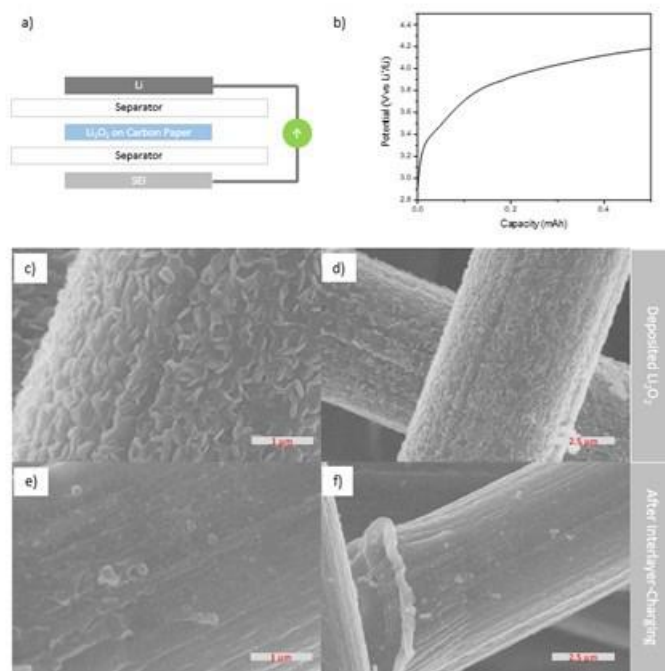


Figure XVIII.1.2 A) Schematic of interlayer-based electrochemical cell we developed for studying the catalyst B) Constant current charging profile of the bare SEI-based cathode. Deposited Li₂O₂ over the surface on a carbon paper gas diffusion layer (GDL), C) high and D) low magnification. SEM of the carbon paper GDL after charging in an interlayer position (no electrical contact to circuit at E) high and F) low magnification.

Identification of functional groups in metal-free catalyst platforms

We have specifically investigated the functional groups that are present in the platforms. To study the chemistry of the SEI layer at various stages of its processing and application, we employed attenuated total reflectance-Fourier transform infrared spectroscopy (ATR-FTIR). We first sampled the SEI right after formation (Figure XVIII.1.3A), which revealed a relatively featureless spectrum in comparison to when the SEI is exposed to O₂ (Figure XVIII.1.3B). After exposure to O₂, peaks at around 1621 and 1670 cm⁻¹ increased, suggesting that lithium carboxylate and lithium oxalate groups appeared. Interesting after Li₂O₂ deposition, the peaks disappeared indicating either some elimination of the carboxylate species or a coverage of these species (Figure XVIII.1.3C). After oxidation/delithiation, the peaks reappeared, suggesting that the process is quite reversible. Importantly, the separator present in the cell used for oxidizing the Li₂O₂-SEI cathode, also exhibited some peaks at ~1620 cm⁻¹. In alignment with the previous quarter's report, we confirm again that the species the SEI is generating is soluble in the electrolyte.

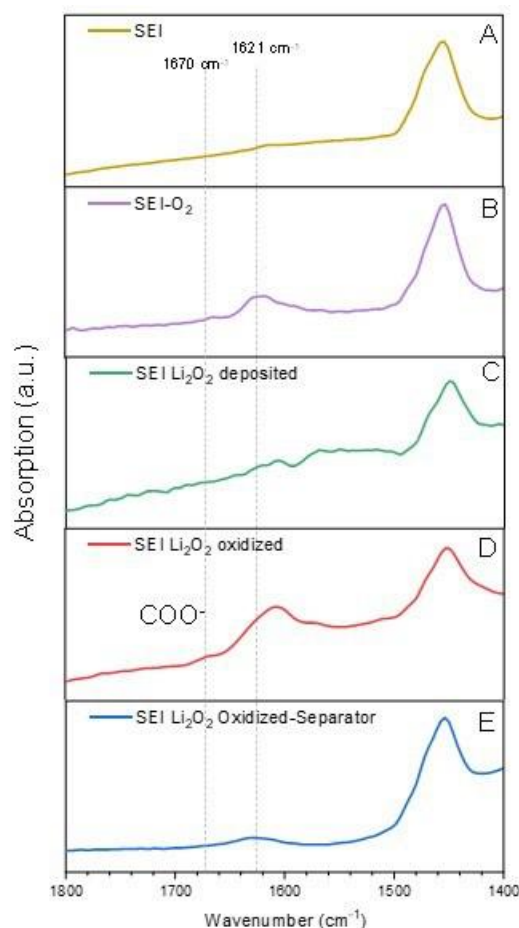


Figure XVIII.1.3 Attenuated total reflectance-Fourier transform infrared spectroscopy of A) as formed solid electrolyte interphase (SEI) catalytic layer, B) SEI exposed to oxygen for 6 hours, C) SEI deposited with Li_2O_2 , D) SEI with Li_2O_2 delithiated, and E) the separator used in the cell in D.

X-ray photoelectron spectroscopy was also used to investigate how the SEI reacts to O_2 exposure. Figure XVIII.1.4 shows the C1s spectrum for the pristine SEI and after exposure to oxygen. Reaction of the SEI to O_2 seems to decrease the proportion of $\text{C}=\text{O}$ and increase the proportion of $\text{O}-\text{C}=\text{O}$, which aligns well with the ATR-FTIR analysis. Furthermore the O 1s analysis revealed that the $\text{R}-\text{C}=\text{O}$ groups appeared to have increased while the $\text{R}-\text{C}-\text{O}$ decreased. It is, therefore clear that the functioning mechanism of the SEI entails first the deposition of a non-toroidal like Li_2O_2 with a weaker structure that can be more easily delithiated. The benefit of the morphology of the Li_2O_2 is further compounded by the generation of some soluble catalyst that can diffuse and assist in the oxidation of Li_2O_2 .

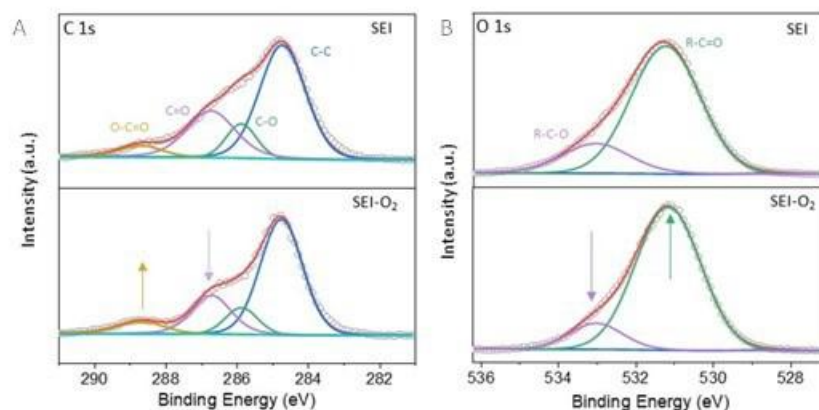


Figure XVIII.1.4 X-ray photoelectron spectroscopy of the SEI-coated cathode before and after exposure to O₂ at A) C 1s and B) O 1s.

Role of functional groups in metal-free catalyst platforms

We determined that there are likely carboxyl groups formed after exposure to pure O₂, possibly creating carboxylate and oxalate groups. After cycling, these same groups were found on the separator of the cell indicating these functional groups also exist as soluble species. Accordingly we suspect that these groups have a potential role in catalyzing the oxidation of lithium peroxide *via* a solution-phase mechanism.

Up to this point it is clear that the benefit of the SEI coating is at least in its ability to charge Li₂O₂ in an efficient manner. We have investigated its advantage in regard to its participation in discharge or Li₂O₂ deposition. Figure XVIII.1.5A displays the deep discharge of our SEI-coated layer in comparison to a baseline carbon paper cell. It is apparent that with the SEI-coating, the discharge capacity significantly increased (>3 mAh cm⁻² vs 1 mAh cm⁻² of carbon paper). This is a somewhat odd finding as the deposition of the SEI layer does not to any significant degree change the morphology of the carbon paper. To investigate the mechanism, we employed reduction-chronoamperometry. In alignment with our constant current discharges, the capacity of the SEI-coated carbon paper has a much higher capacity (Figure XVIII.1.5B). Figure XVIII.1.5C-D shows that the carbon paper possesses a very strong current peak, which according to the Avrami equation indicates a very fast kinetic growth constant. This appears to result in poor performance. The SEI does not have such a large sharp peak but has a broad peak. To corroborate this result, we performed SEM (Figure XVIII.1.6A-B) on the discharge product and found almost no large deposits of Li₂O₂ in comparison to the pristine carbon paper samples (Figure XVIII.1.6C-D). Moreover, cryogenic TEM (Figure XVIII.1.5E) and SAED (Figure XVIII.1.6F) further indicates that the location of the Li₂O₂ growth is on top of the SEI and not within nor underneath the SEI. These results appear to have conflicting conclusions. Specifically, why does smaller size Li₂O₂ passivate the surface of the carbon paper less quickly than the larger sized Li₂O₂ (from the pristine carbon paper). We are working on an explanation for this process, which could change how we understand the Li₂O₂ deposition.

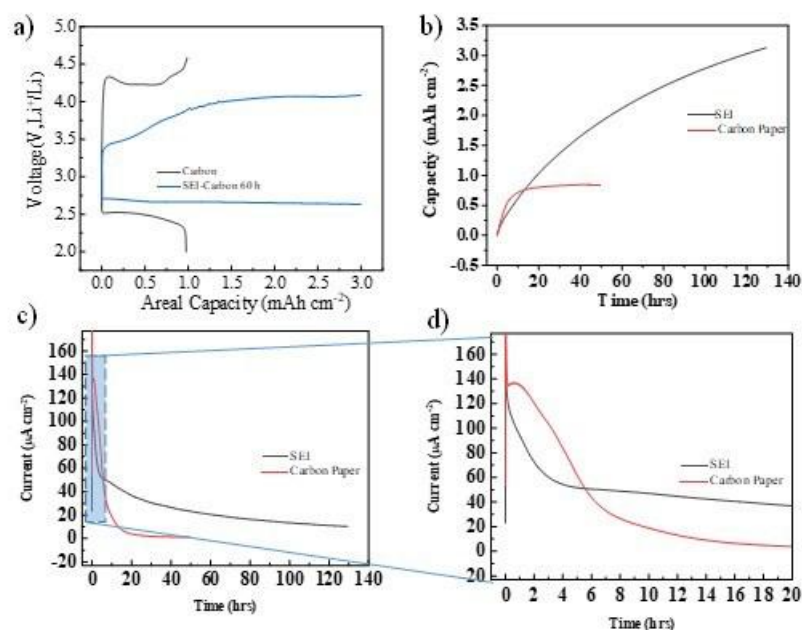


Figure XVIII.1.5 A) Deep discharge of Li-O₂ using carbon paper and using SEI-coated carbon paper at 50 $\mu\text{A cm}^{-2}$ until 3 mAh cm^{-2} or until voltage cutoff of 2 V vs Li⁺/Li is reached. Potentiostatic hold of Li-O₂ battery at 2.5 V vs Li⁺/Li. B) The cumulative capacity by integrating the current response. C) The current response of the carbon paper and the SEI-coated carbon paper. D) Expanded view of the current response showing details of the current peak, indicating passivation.

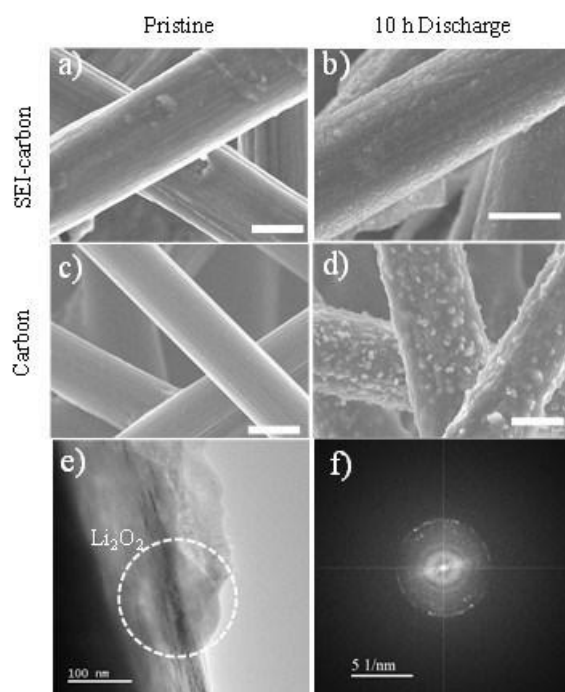


Figure XVIII.1.6 Microscopy of discharge product. SEM of SEI-carbon paper A) before and B) after discharge. SEM of carbon paper C) before and D) after discharge. E) Cryogenic TEM of discharge product clearly indicating the Li₂O₂ spatially sits over the SEI-layer rather than inside. F) SAED of the discharge product indicating it is mostly Li₂O₂

An Ir₃Li cathode for a lithium superoxide-based Li-O₂ battery

One of the major challenges for Li-oxygen batteries is the high charge overpotential, which results in a low energy efficiency. It has recently been shown that lithium superoxide, which is a good electronic conductor and has a low charge overpotential, can be formed in a Li-O₂ battery using iridium as a catalyst. It was speculated that an Ir₃Li alloy forms that acts as effective template for growth of the LiO₂. In this work Ir₃Li was thermally synthesized in bulk prior to implementation on a reduced graphene oxide (rGO) cathode of a Li-O₂ cell.

Ir₃Li particles ranging from 200 nm - 5 μ m were synthesized using a thermal reaction between Ir and Li metals at 800 °C. The powder was characterized using XRD and was demonstrated to be phase pure. A comprehensive characterization of the electronic properties of Ir₃Li was conducted to determine its properties and relevance for use as a LiO₂ battery cathode. The characterization from conductive AFM, SQUID, and EPR measurements revealed that the synthesized Ir₃Li has metallic like character with an affinity to O₂ adsorption, which is needed to act as an appropriate ORR/OER catalyst. XPS analysis supported by DFT calculations indicated that the Ir is negatively charged, likely enhancing its catalytic properties for oxygen reduction and evolution (ORR/OER). Raman studies demonstrated that the Ir₃Li material was stable in air exposure up to 4 weeks. In summary, the bulk Ir₃Li was found to have comparable electrical conductivity to Ir metal, possess metal-like magnetic properties, and have an affinity towards O₂ adsorption.

An Ir₃Li and rGO 1:1 mixture was added to a GDL (gas diffusion layer) electrode using a PVDF binder to form an Ir₃Li -rGO cathode. The resulting cathode was assembled in a Swagelok type Li-O₂ cell with a Li metal anode and a 1 M Li triflate in TEGDME soaked glass fiber separator. For comparison, a similar Li-O₂ cell with a rGO/GDL cathode was also assembled. Both cells were cycled at a current density of 0.05 mA/cm² and capacity of 1000 mAh/g. The first five electrochemical discharge-charge cycles are shown in Figure XVIII.1.7A-B for the rGO/GDL and Ir₃Li-rGO/GDL cells, respectively. For the Li-O₂ cell with the rGO/GDL cathode, two charge plateaus at ~3.6-3.8 and 4.2 V were observed. For the Li-O₂ cell with the Ir₃Li-rGO/GDL cathode, the charging potential remained mostly below 3.5-3.7 V except towards the end of the first charging cycle. For detailed discharge product characterization on the Ir₃Li -rGO/GDL cathode, a different cell was discharged at 0.05 mA/cm² current density to a capacity of 1360 mAh/g. The larger capacity experiment was performed to increase the mass of the discharge product deposited on the cathode to enable Raman and titration analysis of the discharge product(s). The voltage profile during cycling of the cell is shown in Figure XVIII.1.7C

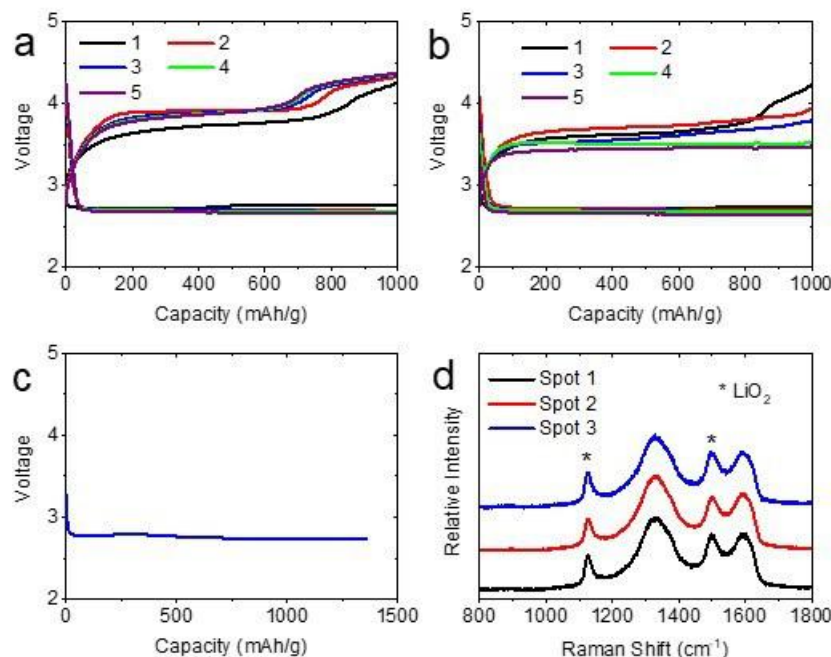


Figure XVIII.1.7 (a) The first five cycles of a Li-O₂ cell with rGO/GDL cathode with a current density 0.05 mA/cm², (b) The first five cycles of a Li-O₂ cell with Ir₃Li-rGO/GDL cathode (c) Deep discharge of Ir₃Li-rGO cathode in a Li-O₂ cell, (d) Raman spectra of deep discharged Ir₃Li-rGO cathode in a Li-O₂ cell showing strong LiO₂ peaks at different areas.

After discharge, the cell was disassembled inside an argon filled glovebox. The cathode with discharge product(s) was dried inside the glovebox, cut in half, and subjected to micro-Raman and titration analysis with Ti(IV)OSO₄ followed by UV-Vis of the titrant in order to determine the chemistry of the discharge product. The micro-Raman spectra is shown in Figure XVIII.1.7D. The titrant absorbance value indicated that the presence of Li₂O₂ was negligible on the discharged cathode. Raman spectra were collected on several different areas and demonstrated strong LiO₂ characteristic peaks at 1125 and 1505 cm⁻¹, along with the characteristic rGO/graphitic peaks at 1328 and 1596 cm⁻¹. These results indicate that LiO₂ was the dominant discharge product. TEM also confirmed the LiO₂ discharge product.

The noble metal-like properties of the Ir₃Li catalyst determined in this study, along with its crystal lattice similarities to LiO₂ demonstrated through DFT analysis, will help enable design guidelines for future catalysts to be implemented in Li-O₂ batteries.

Conclusions

During the past year we have investigated a new metal-free catalyst platform for enabling low overpotential charge of Li-O₂ batteries across various current densities and types of carbon-based substrate materials. This platform is based on what is traditionally called as solid-electrolyte interphase, which is an organic/inorganic interphase that is formed by the reduction of electrolyte components. We have investigated the properties of the interphase, the different functional groups in the interphase, and the role of these groups in the discharge and charge chemistries and how to improve the performance of Li-O₂ batteries.

It has recently been shown that lithium superoxide, which is a good electronic conductor and has a low charge overpotential, can be formed in a Li-O₂ battery using iridium as a catalyst. It was speculated that an Ir₃Li alloy forms that acts as effective template for growth of the LiO₂. During the past year, we found that the crystal lattice similarities of the synthesized Ir₃Li alloy to LiO₂ led to formation of lithium superoxide as the discharge product with a resulting lowered charge potential. This work will help enable design guidelines for future catalysts to be implemented in Li-O₂ batteries with better efficiency.

Key Publications

1. Plunkett, S. T., Kondori, A., You Chung, D., Wen, J., Wolfman, M., Lapidus, S. H., Ren, Y., Amine, R., Amine, K., Mane, A. U., Asadi, M., Al-Hallaj, S., Chaplin, B. P., Lau, K. C., Wang, H.-H., Curtiss, L. A., A New Cathode Material for a Li–O₂ Battery Based on Lithium Superoxide *ACS Energy Letters* 7 (8), 2619-2626 (2022)
2. Bi, X.; Li, J.; Dahbi, M.; Alami, J.; Amine, K.; Lu, J.; Understanding the role of Lithium iodide in Lithium oxygen batteries. *Advanced Materials* 2021, DOI: 10.1002/adma.202106148.
3. Zhao, T.; Yao, Y.; Yuan, Y.; Wang, M.; Wu, F.; Amine, K.; Lu, J. A universal method to fabricating porous carbon for Li–O₂ battery. *Nano Energy* 2021, 82, 105782.
4. Plunkett, S. T., Zhang, C., Lau, K. C., Kephart, M. R., Wen, JG, Chung, D. Y., Phelan, D., Ren, Y., Amine, K., Al-Hallaj, S., Chaplin, B. P., Wang, H.-H., Curtiss, L. A., Electronic Properties of Ir₃Li and Ultra-Nanocrystalline Lithium Superoxide Formation, *Nano Energy* 2021, 90, 106549.
5. Peng, X.; Li, T.; Zhong, L.; Lu, J. Flexible metal–air batteries: An overview. *SmartMat* 2021, 2, 123.
6. Li, J.; Bi, X.; Amine, K.; Lu, J. Understanding the Effect of Solid Electrocatalysts on Achieving Highly Energy-Efficient Lithium–Oxygen Batteries. *Adv. Energy & Sustainability Res.* 2021, 2, 2100045.
7. Bi, X; Lu, J; Amine, K. UChicago Argonne LLC, 2021. Rechargeable Lithium-Hydroxide Based Non-Aqueous Lithium Oxygen Batteries. U.S. Patent Application 16/545,127.
8. Lu, J; Amine, K; Guo, YY; Zeng, XQ; Bi, XX. UChicago Argonne LLC, 2021. Cathode for alkaline earth air batteries. US Patent App. 16/856,302.

XVIII.2 Lithium Oxygen Battery Design and Predictions (ANL)

Larry Curtiss, Principal Investigator

Argonne National Laboratory
9700 South Cass Avenue
Lemont, IL 60439
E-mail: curtiss@anl.gov

Amin Salehi, Co-Principal Investigator

University of Illinois at Chicago
Department of Mechanical and Industrial Engineering
Chicago, IL 60607
Email: salehikh@uic.edu

Ahn T. Ngo, Co-Principal Investigator

University of Illinois at Chicago
Department of Mechanical and Industrial Engineering
Chicago, IL 60607
Email: ahnngo@uic.edu

Tien Duong, DOE Technology Development Manager

U.S. Department of Energy
E-mail: Tien.Duong@ee.doe.gov

Start Date: October 1, 2019
Project Funding: \$1,800,000

End Date: September 30, 2023
DOE share: \$1,800,000

Non-DOE share: \$0

Project Introduction

Lithium (Li)-oxygen (O_2) batteries are considered as a potential alternative to Li-ion batteries for transportation applications due to their high theoretical specific energy. The high energy density of Li- O_2 batteries is made possible because of the formation of the Li_2O_2 product, which can store significantly higher amounts of energy compared to other energy storage systems because of the Li-O bonds. However, the challenge is that the decomposition of Li_2O_2 during the charge process requires charge transfer, which is difficult because of the large band gap of solid Li_2O_2 likely covering catalytic sites. This leads to a sluggish charge process requiring higher potentials for Li_2O_2 decomposition, which in turn reduces the energy efficiency of the battery and puts the electrolyte at risk of degradation. Additionally, the charge potential can depend on the morphology and size of Li_2O_2 product. The major issues with the existing Li- O_2 systems include degradation of the anode electrode, reactions with air components, clogging of the cathode, and electrolyte instability. These issues are being addressed in this project.

Objectives

The objective of this work is to develop new materials for Li- O_2 batteries that give longer cycle life, higher charge/discharge rates, and improved efficiencies in an air environment. New electrolyte blends and additives are being investigated that can reduce clogging and at the same time can promote the cathode functionality needed to reduce charge overpotentials and increase discharge/charge rates. The cathode materials are based on high to medium entropy two-dimensional transition metal dichalcogenides (TMDCs) that we have found to be among the best oxygen reduction and evolution catalysts. New high entropy alloys are being investigated. The objective is to design and predict new electrolytes that work with these catalysts to give longer cycle life, high charge rates, good efficiencies, and high capacities needed to make scale up possible for these types of batteries.

Approach

The project is using a joint theoretical/experimental approach for design and discovery of new cathode and electrolyte materials that act synergistically to reduce charge overpotentials and increase cycle life. Synthesis methods, in combination with design principles developed from computations, are used to make new cathode architectures. Computational studies are used to help understand decomposition mechanisms of electrolytes and how to design electrolytes with improved stability. The new cathodes and electrolytes are tested in Li-O₂ cells. Characterization, along with theory, is used to understand the performance of materials used in the cell and to make improved materials.

Results

Investigation of a highly active tin sulfide based catalyst for high-rate Li-O₂ battery performance

Li-air batteries necessitate discovery of novel electrocatalysis processes to significantly enhance the formation and decomposition of the discharge products upon battery cycling. We are working on a novel co-catalytic system comprised of tin sulfide (SnS) nanoflakes(NF)/ reduced graphene oxide (rGO) as a solid catalyst and a dual functional additive that provides a liquid phase catalyst as well as an anode protection. The goal this work is to develop a co-catalytic process that enables operating the battery at high current rates up to 1mA/cm². It is found that the catalytic activity of SnS NFs/rGO catalyst for both oxygen reduction and evolution reactions occurring during the discharge and charge, respectively, far exceed those of state-of-the-art catalysts from carbon, noble metal, and transition metal dichalcogenide families.

Thus far, cathode materials such as Pt, Pd, Ir, and oxides like Pb/BiRO, Cr₂O₃, MnCo₂O₄, and 2D materials such as MoS₂ have been reported to exhibit improved redox process during discharge and charge processes. However, these studies are generally limited to low current densities (e.g., <0.1 mA/cm). To operate the batteries at much high rates, in this work, we discovered that SnS (NF) catalysts embedded with reduced graphene oxide (rGO) shows an excellent catalytic activity during the discharge and charge.

To evaluate the galvanostatic cycling performance of SnS catalysts, Swagelok battery cells were assembled in an Ar-filled glovebox with both oxygen and humidity levels less than 0.1 ppm. The battery is composed of a Li metal foil anode, a porous glass-fiber separator, SnS/rGO cathode and 30 μ L of DMSO/EMIM-BF₄ (volumetric ratio of 9:1) electrolyte. Galvanostatic cycling results of the battery cells at the current density of 0.3 mA/cm² with the capacity of 3000 mAh/g (corresponding areal capacity of 0.3 mA/cm²) are shown in Figure XVIII.2.1A. Results indicate that the battery with the SnS/rGO electrode has a charge potential of ~4V at the first cycle, which remained below 4.3 V for 40 cycles. The battery operates up to 60 cycles before reaching the cut-off potential of 4.6 V. However, the battery with 2D MoS₂ catalyst can only run one cycle with the charge potential of 4.9V, shown by the black dashed line in Figure XVIII.2.1A. This is consistent with the lower catalytic activity of MoS₂ compared to SnS in Figure XVIII.2.1C,D. Results for Pt and Au activities are also given in these figures for comparison. To determine the effect of Li anode degradation on the cyclability of the SnS based system, we replaced the Li anode with a fresh one after 50 cycles and the results are shown in Figure XVIII.2.1B. It is found that the SnS catalysts are still functional for another 45 cycles at the same cut-off range confirming the stability of the catalyst and indicate the necessity of anode protection for longer battery operation.

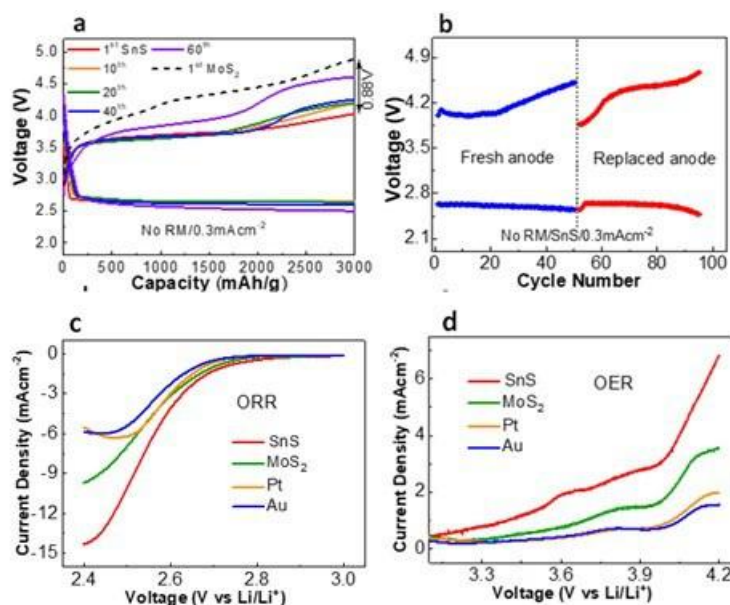


Figure XVIII.2.1 (a) Galvanostatic cycling results of Li–air cell with SnS/rGO and MoS₂ cathodes at the current density of 0.3 mA cm⁻². No redox mediator was used for both batteries. The dashed black line represents the charge potential of MoS₂ at the 1st cycle. (b) Cycle numbers vs charge/discharge potential for the fresh (blue) and replaced (red) Li anode after 50 cycles of operation of the SN catalyst. (c-d) Linear sweep voltammetry results of SnS/rGO NFs, MoS₂ NFs, Au NPs and Pt NPs electrodes under ORR and OER with a sweeping rate of 10 mV/s.

Computational studies of the active sites and electronic structure of the tin sulfide catalyst.

We have investigated using density functional calculations several aspects of the SnS catalyst. The adsorption of O₂ and formation of O₂⁻ by reduction on the catalyst surface is an important factor in determining the rate at which oxygen reduction occurs and thus the efficiency of the discharge process. We investigated six possible adsorption sites for O₂ on the SnS surface as shown in Figure XVIII.2.2. In five of the six (C1–C5) the binding energy is about 1 eV, which is large enough to support oxygen reduction. The O₂ binds to a Sn in these five cases. The O₂ binds weakly on the surface in the sixth site (C6). The result of this study is significantly different from our previous study of MoS₂ in a Li–O₂ battery where the Mo edge was found to be so reactive from DFT calculations that the O₂ dissociated on the Mo edges. This would result in driving the reaction toward full oxidation of the Mo edge and poisoning of the catalyst. To avoid this an ionic liquid was used as the electrolyte because it was hypothesized that it can effectively prevent O₂ from dissociating on the electrode. The DFT calculations showed that the strong electrostatic interaction between the ionic liquid (EMIM⁺ ions) prevents interaction with more than one Mo at a time to prevent complete O₂ dissociation on the Mo edge and leads to the formation of effective oxygen reduction site. This is unnecessary in the case of SnS as the interaction with O₂ is not nearly as strong as shown in Figure XVIII.2.2.

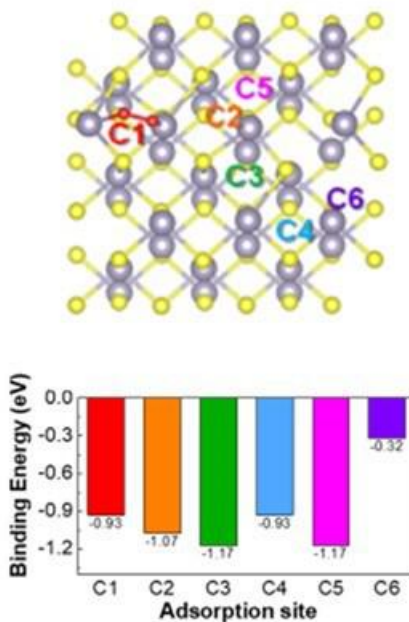


Figure XVIII.2.2 DFT calculations for (top) six O_2 adsorption on SnS considered in DFT calculations (an example of O_2 adsorption structure is given for C1) and (bottom) O_2 adsorption energies for the six sites.

In the through solution mechanism Li_2O_2 can form by disproportionation of LiO_2 either in solution or on the surface after deposition of LiO_2 on the surface, i.e. $2\text{LiO}_2 \rightarrow \text{Li}_2\text{O}_2 + \text{O}_2$. The reaction pathways for disproportionation in solution of a LiO_2 dimer was computed for the electrolyte assuming a dielectric constant of DMSO. The reaction pathway computed using the accurate G4MP2 quantum chemical method, which is shown in Figure XVIII.2.3, indicates small barrier and favorable thermodynamics for formation of Li_2O_2 in solution. Whether the disproportionation occurs in solution or on the surface, the formation mechanism will involve nucleation and growth of the discharge product on the surface of the cathode. In the case of the SnS catalyst and the DMSO based electrolyte the morphology of the Li_2O_2 is toroids, similar to what has been found in other studies.

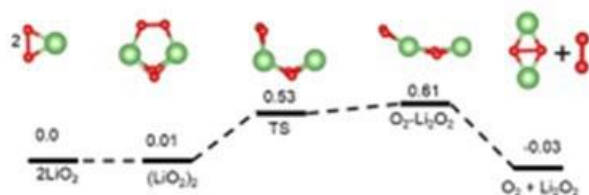


Figure XVIII.2.3 G4MP2 free energies for LiO_2 disproportionation to Li_2O_2 in DMSO solvent.

Development of new electrolyte redox mediators that work with the SnS catalyst

We have investigated using a new bifunctional additive for redox mediation and lithium anode protection for the SnS catalyst. The bifunctional additive used in the electrolyte is SnI_2 . It acted as a redox mediator (RM) to enhance the decomposition of discharge product and as a reactant to protect the Li anode. The Sn^{2+} cation enables the formation of a $\text{Sn}^{2+}/\text{Sn-Li}$ solid-electrolyte-interphase (SEI) layer, and thus protects the anode from parasitic side reactions, oxygen/superoxide crossover, and shuttle effect of redox mediators. On the other hand, the anion redox couple of I^-/I_3^- enables active mediation of Li_2O_2 during the charging process, which effectively reduces the charge potential. Thus, the SnI_2 is referred to as a bifunctional additive. At a current density of 0.3 mA/cm^2 , the discharge potential remained above 2.45 V over 100 cycles with 125mM of SnI_2 . The charge

potential for SnI_2 is as low as 3.5 V at the first cycle and is gradually increased to 4.2 V after the 120th cycle with the capacity of 3000 mAh/g.

For comparison, we performed the battery experiments with LiI as the most reported RM and SnS/rGO cathode. The battery with RM of LiI lasts for only 20 cycles before its discharge potential drops below 2.45V. Since both LiI and SnI_2 involve the I^-/I_3^- couple, it is concluded that the protective SEI layer formed from Sn^{2+} helps to achieve higher cycle life of the cell. Besides, we noticed that LiI mediated cells possess fewer life cycles than the cell without the additive. This early death of the cell may be attributed to the shuttling effect of LiI that poisons the anode with accumulated cycles. Furthermore, a battery with neither catalyst nor additive (rGO only) is only able to run for 12 cycles before reaching the discharge cut-off voltage. This is 10 times lower than the cyclability of SnI_2/SnS co-catalyst system.

The chemical composition of the protected Li anode resulting from the reaction with SnI_2 was studied using XPS. As shown in Figure XVIII.2.4A, two major Sn peaks were observed at 486.5 eV (Sn 3d5/2) and 495 eV (Sn 3d3/2), which were indexed to Sn^{2+} . Moreover, two minor peaks located at 484.3 eV (Sn 3d5/2) and 493 eV (Sn 3d3/2) correspond to the formation of metallic Sn/Li-Sn components on the SEI layer. TEM was also carried out to further study the SEI layer formed on the anode surface. Figure XVIII.2.4B shows the low-angle annular dark-field (LAADF) image and the inset figure exhibits the bright field image of the protected Li anode. EDS and EELS were performed on the selected region in Figure XVIII.2.1b to further identify the elemental composition of the protective surface (SEI layer) on the surface of the anode. As shown in Figure XVIII.2.4C, EDS mapping of a selected area reveals the existence of Sn along with oxygen (dissolved in electrolyte). Figure XVIII.2.4D shows the EELS results of Li K- and Sn K-edge taken from the top of the same flake in Figure XVIII.2.4B. The sharp Li K- and Sn K-edges in the spectra confirm the presence of these elements in the surface layer after the 5th cycling of the batteries. At the same time, neither EDS nor EELS results show substantial existence of nitrogen or iodine. These results suggest the absence of shuttling effect resulting from RMs or parasitic side products (e.g. Li_3N) during cycling, which further confirms the effectiveness and robustness of the Sn-based SEI layer under high current densities. In addition, EIS was conducted on the anode as shown in Figure XVIII.2.4E. Our results indicate a rise in the charge transfer resistance from 15 ohms to 70 ohms after 20 cycles. Furthermore, the difference between the charge transfer resistance, Z_{real} from 15th to 20th cycles is <5 ohms, implying that the SEI layer becomes stable.

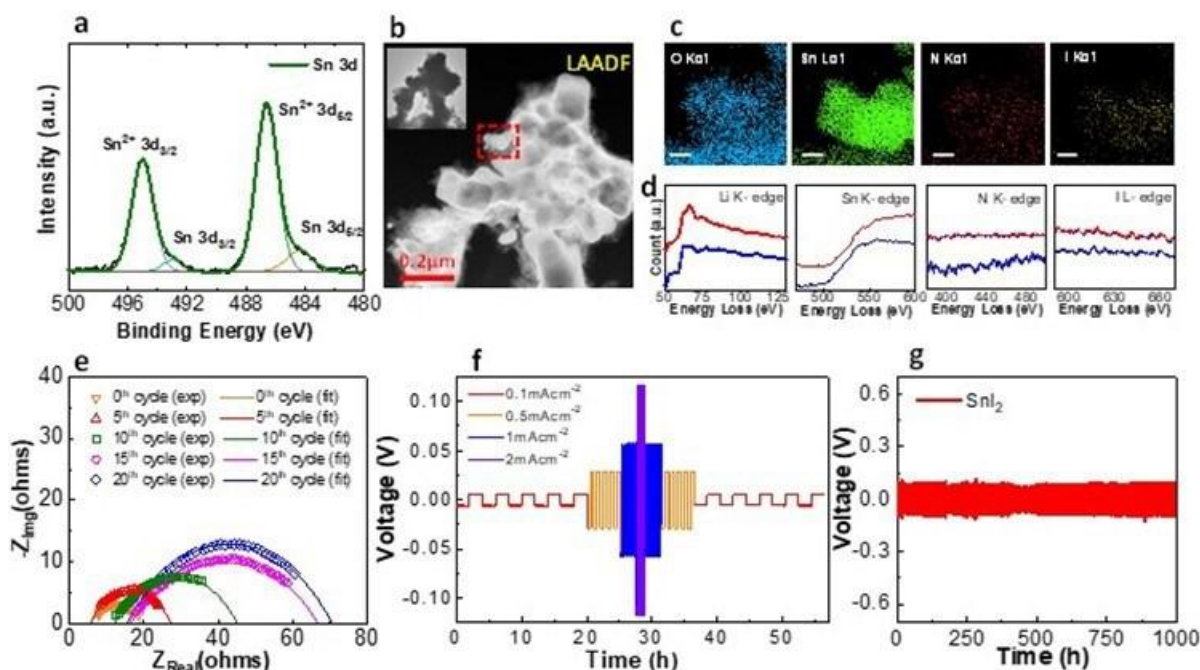


Figure XVIII.2.4 Characterization results of the anode in Li-air battery with RM of SnI_2 . The results include (a) XPS of Sn 3d region after 5 cycles. (b) HAADF and inserted bright field image of the Sn protected anode. (c) EDS mapping of the anode surface. The area taken was from the rectangular box marked in figure b. All scale bars represent a length of 100nm, (d) EELS results from the same region of the Sn protected anode surface. (e) Anode EIS results. The dots represent the experimental data, and the lines represent the fitted data. Symmetrical study of electrolyte with the cell consists of two Li metal electrodes for (f) attenuation test under different current densities and (g) long-time durability test of electrolyte at a constant current density of 0.5mAcm^{-2} .

Apart from the anode protection, it is also critical to confirm the long-term durability of the SnI_2 electrolyte. For this purpose, an attenuation test was performed on Li|Li symmetrical coin cells with a fixed capacity of 0.2mAcm^{-2} and a current density sweeping between 0.1mAcm^{-2} and 2mAcm^{-2} (shown in Figure XVIII.2.4F). We observed no loss in coulombic efficiency while the cell runs for up to 57 hours. The long-term performance of the Li anode was also studied inside Li|Li symmetrical cells with the current density of 0.5mAcm^{-2} during stripping and plating (Figure XVIII.2.4G). Results indicate that the symmetrical cell was able to cycle for more than 1000 hours while the range of the operating voltage remains almost constant (-0.09V to 0.09V). These results confirm the robustness and high ionic conductivity of the SnI_2 electrolyte, which is suitable for fast charging.

Computational investigation of a bifunctional additive

We have used computational methods to study a new bifunctional additive, SnI_2 , for redox mediation and lithium anode protection for insight into how it works in the experiments. Ab initio molecular dynamics (AIMD) density functional calculations were used to provide insight into several aspects of the new bifunctional additive for Li-air cells and how they work. First, the mechanism by which the new SnI_2 electrolyte additive can provide an anode protection layer and not affect the cathode was investigated using the AIMD) simulations. Second, the role of the SnI_2 additive in reducing the charge potential was explained.

The results from our density functional calculations on the SnI_2 additive are given in Figure XVIII.2.5. The calculations are based on AIMD simulations with an LiTFSI/DMSO/EMIM- BF_4 electrolyte and added SnI_2 molecules. The results for SnI_2 reacting on a Li metal (100) surface in at the electrolyte interface (initial and final structures) are given in Figure XVIII.2.5A. It shows that the SnI_2 dissociates with the surface and Sn migrates into the Li. This is the first step in the formation of the protective Sn film on the Li. The reaction of SnI_2 with a SnS surface was also used to investigate whether it would have any detrimental effect on the cathode surface. The result (initial and final structures) is given in Figure XVIII.2.5B showing that the SnI_2 does not dissociate on the SnS surface, unlike on the Li surface. The result for the anode surface provides an

explanation for the formation of the Sn film to protect the Li anode as found in experimental studies presented previously.

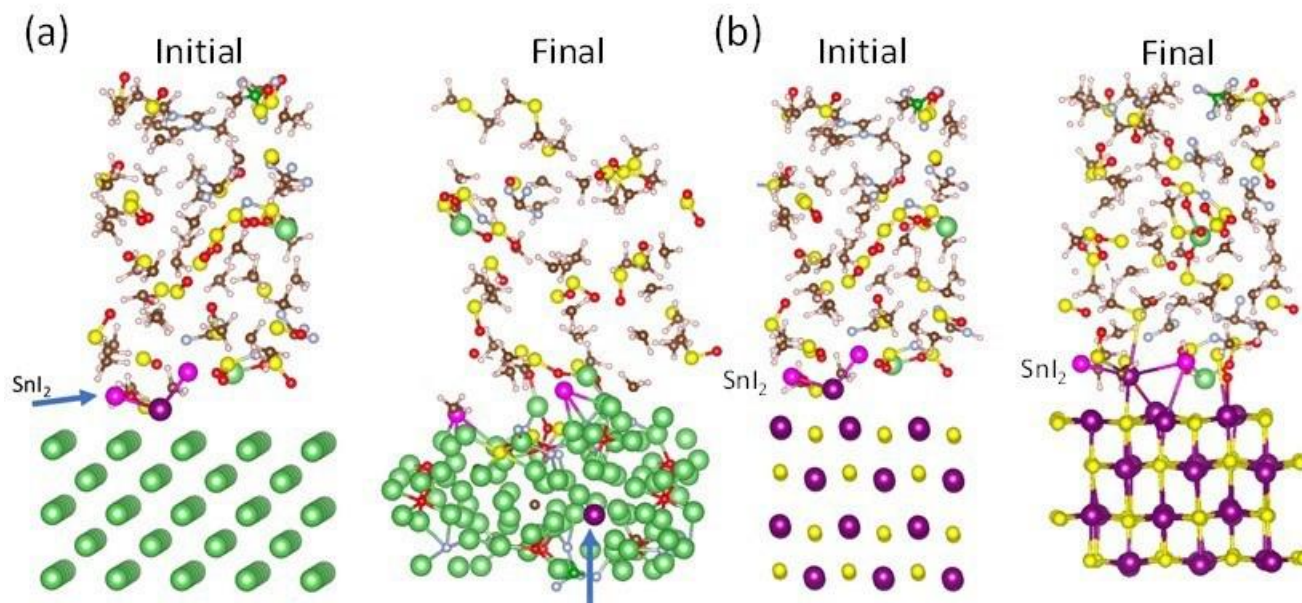


Figure XVIII.2.5 DFT calculations for (a) initial and final structure of SnI_2 reacting on a Li metal (100) surface, (b) initial and final structure of SnI_2 reacting on a SnS surface

The SnI_2 additive also has a role in reducing the charge potential. The AIMD calculations in Figure XVIII.2.5A reveal that the SnI_2 decomposition on the Li surface results in LiI formation. The LiI is known to act as an effective redox mediator to reduce the charge potential for decomposing Li_2O_2 . In a previous study, we have shown by DFT calculations how when LiI is oxidized to form LiI_3 at around 3.5 V vs Li/Li^+ , the LiI_3 can act as a catalyst with a small barrier of ~ 0.5 eV to facilitate decomposition of the Li_2O_2 . These DFT calculations explain how the SnI_2 additive can provide the LiI needed for the redox mediator to assist in the catalysis of the charge reaction. This results in a lower charge potential for the SnS based cathode compared to when the SnI_2 is not included as an additive. With inclusion of the additive the charge potential is reduced from over 4 V to about 3.5 V., a significant improvement.

Conclusions

A novel catalytic system comprised of tin sulfide (SnS) nanoflakes as a solid catalyst and tin iodide (SnI_2) as a dual-functional electrolyte additive has been studied as part of our program to find new catalysts and additives for high rate Li- O_2 batteries. This system enables operating the battery at high current rates up to 10 000 mA g^{-1} (corresponding to 1 mA cm^{-2}). The SnS catalyst shows outstanding catalytic activity for both oxygen reduction and evolution reactions compared to carbon, noble metal, and other transition metal dichalcogenides. It also exhibits good structural integrity at high rates. The computations indicate numerous possible oxygen reduction sites without oxygen dissociations on the SnS surface through solution mechanism that is likely responsible for the formation of Li_2O_2 . The calculations also indicate that the role of the SnI_2 is not only reacting with the lithium anode to provide protection but reducing the charge potential by promoting catalytic decomposition of the Li_2O_2 .

Key Publications

1. A high-rate lithium-air battery enabled by a MnO_2 based colloidal electrolyte, Sina Rastegar, Zahra Hemmat, Sachin Kumar Singh, Naveen Dandu, Chengji Zhang, Alireza Ahmadiparidari, Tomas Rojas, Leily Majidi, Shuxi Wang, Ahmad Jaradat, Rajeev Assary, Paul Redfern, Sanja Tepavcevic,

- Arunkumar Subramanian, Anh T. Ngo, Larry A. Curtiss, Amin Salehi-Khojin, ACSNano 16, 11, 18187–18199 (2022) <https://doi.org/10.1021/acsnano.2c05305>
2. “Nanostructured Conductive Metal Organic Frameworks for Sustainable Low Charge Overpotentials in Li–Air Batteries,” Leily Majidi, Alireza Ahmadiparidari, Nannan Shan, Sachin Kumar Singh, Chengji Zhang, Zhehao Huang, Sina Rastegar, Khagesh Kumar, Zahra Hemmat, Anh T. Ngo, Peter Zapol, Jordi Cabana, Arunkumar Subramanian, Larry A. Curtiss, Amin Salehi-Khojin, Small, Volume 18, 10 December 2021 <https://doi.org/10.1002/sml.202102902>
 3. “High Performance Air Breathing Flexible Lithium–Air Battery,” Ahmad Jaradat, Chengji Zhang, Sachin Kumar Singh, Junaid Ahmed, Alireza Ahmadiparidari, Leily Majidi, Sina Rastegar, Zahra Hemmat, Shuxi Wang, Anh T. Ngo, Larry A. Curtiss, Matthew Daly, Arunkumar Subramanian, Amin Salehi-Khojin, Small, 17(42) 2102072 (2021).
 4. “Lowering Charge Potentials with Negligible Capacity Loss in High Rate Lithium Oxygen Batteries,” Alireza Ahmadiparidari, Shadi Fuladi, Leily Majidi, Samuel Plunkett, Erik Sarnello, Zahra Hemmat, Sina Rastegar, Saurabh Misal, Paul C Redfern, Jianguo Wen, Tao Li, Anh Tuan Ngo, Fatemeh Khalili-Araghi, Larry A. Curtiss, Amin Salehi-Khojin, J. Power Sources, **491**, 229506 (2021).
 5. “A Lithium-Oxygen Battery that Operates in Dry Air with a Bifunctional InX₃ (X=Br,I) Electrolyte Additive,” Sina Rastegar, Zahra Hemmat, Chengji Zhang, Samuel Plunkett, J. G. Wen, Naveen Dandu, Tomas Rojas, Leily Majidi, Saurabh Misal, Anh T. Ngo, Larry A. Curtiss, Amin Salehi-Khojin, ACS Applied Materials & Interfaces **13**, 4915-4922 (2021).

XVIII.3 Development of a High-Rate Lithium-Air Battery Using a Gaseous CO₂ Reactant (UIC)

Amin Salehi, Principal Investigator

University of Illinois at Chicago
Department of Mechanical and Industrial Engineering
Chicago, IL 60607
Email: salehikh@uic.edu

Anh T. Ngo, Co-Principal Investigator

University of Illinois at Chicago
Department of Chemical Engineering
Chicago, IL 60607
Email: ahnngo@uic.edu

Vikas Berry, Co-Principal Investigator

University of Illinois at Chicago
Department of Chemical Engineering
Chicago, IL 60607
Email: vikasb@uic.edu

Haiyan Croft, DOE Technology Development Manager

U.S. Department of Energy
E-mail: Haiyan.Croft@ee.doe.gov

Start Date: October 1, 2021
Project Funding: \$1,500,000

End Date: December 31, 2022
DOE share: \$1,500,000

Non-DOE share: \$0

Project Introduction

Lithium (Li)-air batteries are considered as a potential alternative to Li-ion batteries for transportation applications due to their high theoretical specific energy. Most work in this area is focused on use of O₂ as the reactant. However, newer concepts for using gaseous reactants, such as CO₂ that have a theoretical specific energy density of 1876 Wh/kg, provide opportunities for further exploration. This project will produce a thorough understanding of key chemical and electronic parameters that govern the operation of Li-CO₂ batteries in realistic conditions. Achieving our objectives will generate a library of fundamental properties of TMDC and ionic liquid-based electrolytes with the most promise toward for the Li-CO₂ battery applications. The methodologies employed, and the insight generated will also be valuable beyond advancing the field of Li-CO₂ batteries.

Objectives

The main objective of this project is to develop a novel strategy to enable operation of Li-CO₂ batteries at high-capacity high-rate with a long-cycle-life. The experiments will be performed in both Swagelok and pouch cells. In the former case, we will use: (i) a novel co-catalyst system comprised of inexpensive and earth-abundant transition metal dichalcogenide (TMDC) materials that work in synergy with ionic liquid (IL)-based electrolytes to enhance the efficiency of reactions during discharge and charge processes, (ii) a solution-based catalyst (redox mediator (RM)) to reduce the charge overpotential and increase the energy efficiency of the battery, (iii) high porosity cathode electrodes to increase the electrodes surface area, gas permeability, stability, electrical conductivity, and lifetime of the battery operation, and (iv) a solid electrolyte interface (SEI) layer to protect the anode against oxidation without affecting the ionic transport of Li⁺ species in the system. At the pouch cell level, we will design and construct a stackable pouch cell to deliver a capacity of >200mAh.

Approach

The above targets will be achieved through an integrated approach based on materials synthesis, testing, characterization, analysis, and computation. We will synthesize catalysts and test them in cells along with developing new electrolytes and additives. These cathode materials with new electrolyte blends and additives will work in synergy to reduce charge potentials and increase stability of the battery. Density functional and ab-initio molecular dynamic simulations will be performed to understand the battery operation and make predictions of new materials for the Li-CO₂ battery.

Results

Investigation of a mid-entropy 2D catalyst for high-rate Li-CO₂ battery performance

The Li-CO₂ battery concept involves CO₂ reduction and evolution reactions during discharge and charge, respectively, on the surface of a cathode with an electrolyte based on lithium salts. Most Li-CO₂ battery studies have shown evidence for Li₂CO₃ upon discharge and for its disappearance upon charge. However, they are still far from practical applications due to low current densities (500-1000 mA/g) and low capacities (500-1000 mAh/g). Additionally, these batteries show poor reversibility of discharge products (e.g., Li₂CO₃ and carbon) during the battery cycling leading to short cycle life. It is crucial to operate Li-CO₂ batteries under a carbon neutral condition to reversibly balance the electrochemical reactions during discharge and charge.

In this project, we developed, for the first time, Li-CO₂ battery chemistry based on a novel 2D based medium-entropy cathode catalyst of (NbTa)_{0.5}BiS₃ that works in synergy with an electrolyte blend of ZnI₂, lithium bis(trifluoromethanesulfonyl)imide (LiTFSI), dimethyl sulfoxide (DMSO) and ionic liquid (IL) of 1-Ethyl-3-methylimidazolium tetrafluoroborate (EMIM-BF₄) with the volumetric ratio of 9:1.

The crystalline 2D (NbTa)_{0.5}BiS₃ was synthesized using a chemical vapor transport (CVT) method. To prepare the nanoflakes (NFs) of (NbTa)_{0.5}BiS₃, the synthesized powder was exfoliated in isopropyl alcohol (IPA) using probe sonication followed by a centrifugation process. Dynamic light scattering (DLS) measurements reveal the lateral size of the flakes with an average value of 287 nm. To identify the elemental composition of the flakes, we have carried out the scanning electron microscopy-energy dispersive spectroscopy and transmission electron microscopy (SEM-EDS, TEM-EDS) confirming the uniform distribution of constituent elements and flakes composition as (NbTa)_{0.5}BiS₃. To determine the crystallinity of Nb_{0.5}Ta_{0.5}BiS₃, XRD was performed on a sample produced after exfoliation in the liquid phase. The sharp diffraction peaks indicate a highly crystalline material. All major reflections in the XRD pattern were indexed and fit with an orthorhombic unit cell with Pmm2 space group and $a = 5.75 \text{ \AA}$, $b = 36.16 \text{ \AA}$, and $c = 22.98 \text{ \AA}$, closely related to the layered structure of NbBiS₃. The results indicate that (NbTa)_{0.5}BiS₃ is the dominant phase in the sample.

To study the catalytic activity of (NbTa)_{0.5}BiS₃ NFs for CO₂ reduction and evolution reactions (CO₂RR/CO₂ER) occurring during discharge and charge, respectively, linear sweep voltammetry (LSV) was performed within potential range of 2.4-4.5 V. We performed LSV and electrochemical impedance spectroscopy (EIS) experiments with different IL/DMSO ratios. Results indicate that the ratio of 1:9 (IL/DMSO) provides the best performance. For comparison, experiments were also performed using Pt and Au nanoparticles (NPs) under identical conditions. Figure XVIII.3.1A shows the CO₂RR results with the current density of 19.8 mA/cm² for (NbTa)_{0.5}BiS₃ NFs at 2.4 V. Both Pt NPs and Au NPs showed much lower current densities of 4.7 mA/cm² and 3.5 mA/cm², respectively. Figure XVIII.3.1B demonstrates CO₂ER results for these catalysts with the highest current density of 9.77 mA/cm² at 4.5 V for (NbTa)_{0.5}BiS₃. These values for Pt NPs and Au NPs are 2 mA/cm² and 0.8 mA/cm², respectively. Besides, we performed a LSV control experiment on (NbTa)_{0.5}BiS₃ catalyst without the ionic liquid to examine its contribution to CO₂RR/CO₂ER. As shown in Figure XVIII.3.1A-B, using pure DMSO electrolyte (without ionic liquid), the current density drops from 19.8 mA/cm² to 6.4 mA/cm² at 2.4 V during CO₂RR and from 9.8 mA/cm² to 4.4 mA/cm² at 4.5 V during CO₂ER implying that ionic liquid plays significant role in improving the electrochemical performance of these reactions (CO₂RR/ CO₂ER). This is attributed to much higher CO₂ solubility in the ionic liquid

based electrolyte compared to DMSO, which can potentially reduce mass transport limitations during CO₂RR/CO₂ER specially at high current rates. The EIS results shown in Figure XVIII.3.1C-D indicate that the charge transfer values are much lower for (NbTa)_{0.5}BiS₃ compared to other tested catalysts. These results confirm that (NbTa)_{0.5}BiS₃ has a much greater catalytic activity and lower charge transfer resistance than Pt NPs and Au NPs tested under identical experimental conditions.

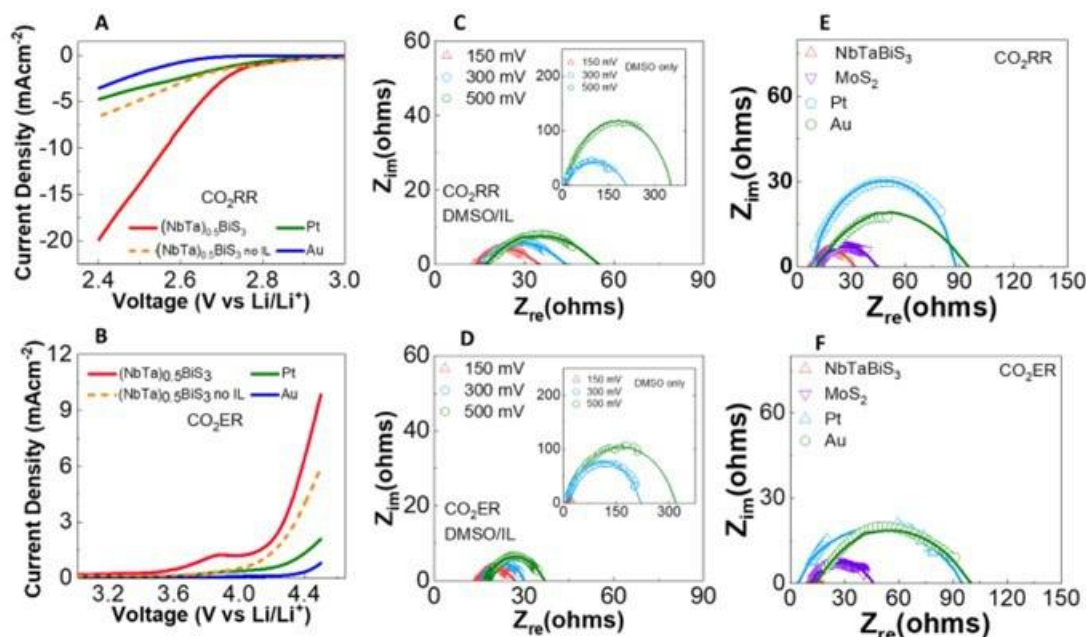


Figure XVIII.3.1 **LSV and EIS results.** (A-B) Linear sweep voltammetry results of (NbTa)_{0.5}BiS₃ NFs, Au and Pt nanoparticles (NPs) coated cathode electrodes under: (A) CO₂RR and (B) CO₂ER. (C-D) EIS measurements for (NbTa)_{0.5}BiS₃ NFs coated cathode catalyst at different applied overpotentials during: (C) CO₂RR and (D) CO₂ER. Insets show control experiments in DMSO electrolyte (without IL). (E-F) EIS measurements of different catalysts tested during: (E) CO₂RR and (F) CO₂ER with the overpotential of 150 mV.

To test the battery performance of (NbTa)_{0.5}BiS₃, galvanostatic cycling experiments were performed on the coin cell type battery inside CO₂ chamber with an electrolyte blend comprised of 1M of Lithium LiTFSI and two different concentrations of ZnI₂ additive in DMSO and EMIM-BF₄ ionic liquid with a volumetric ratio of 9 to 1, respectively. Figure XVIII.3.2A displays the charge and discharge curves at the current density of 0.5 mA/cm² with capacity of 2000 mAh/g (corresponding to 0.2 mAh/cm²). This battery with ZnI₂ performs up to 125 cycles with discharge and charge potentials of ~ 2.6 V and 4.5, respectively. The battery is also operated up to 50 cycles (Figure XVIII.3.2B) with 0.5 mA/cm² current density and capacity of 5000 mAh/g (0.5 mAh/cm²) as well as up to 100 cycles (Figure XVIII.3.2C) with 0.3 mA/cm² and capacity of 3000 mAh/g (0.3 mAh/cm²) at the cut-off potential of ~ 2.6 V and 4.5 V.

Figure XVIII.3.2D demonstrates the current attenuation (rate capability) results. The current density of the battery was increased from 0.1 mA/cm² to 0.5 mA/cm² during discharge and swept back to the original discharge value. The voltage difference between initial and final values is negligible (less than 5 mV) after 25000 mAh/g discharge capacity confirming the robustness of the cathode catalyst and electrolyte blend during discharge process.

Figure XVIII.3.2E shows the results of control battery experiments collected at the current density of 0.5 mA/cm² with the capacity of 5000 mAh/g (0.5 mAh/cm²). For the case of (NbTa)_{0.5}BiS₃ catalyst without redox mediator of ZnI₂ (RM), the battery was able to run for 30 cycles before dropping the discharge potential below 2.4 V. However, the battery can run up to 60 cycles with ZnI₂ which confirms better performance of (NbTa)_{0.5}BiS₃ with electrolyte additive (ZnI₂). On the other hand, the battery with (NbTa)_{0.5}BiS₃ and LiI RM

can only run for 25 cycles before its discharge voltage decreases to 2.4 V. We note that the polarization gap for all batteries is similar. These results suggest that ZnI_2 does not have a redox mediator role in reducing the charge potential at such a high current density and capacity. Thus, we conclude that: (i) the $(\text{NbTa})_{0.5}\text{BiS}_3$ solid catalyst is only responsible for $\text{CO}_2\text{RR}/\text{CO}_2\text{ER}$ during discharge and charge, (ii) the role of ZnI_2 is limited to the solid/electrolyte interphase (SEI) layer formation on the Li anode surface, which will be discussed later, and (iii) the SEI layer based on only Li_2CO_3 , which usually forms on the Li anode surface in presence of CO_2 species through a chemical process, is not effective in such a high current rate operation of the battery as evidenced from lower battery cycling (30 vs. 60 with ZnI_2).

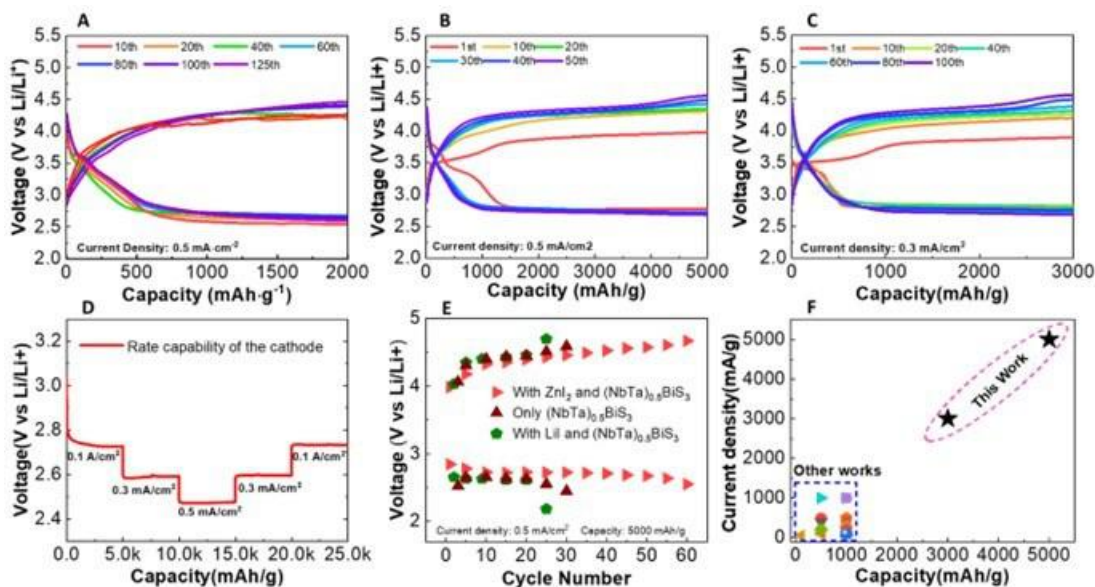


Figure XVIII.3.2 **Electrochemical performance of Li- CO_2 battery.** Discharge/charge curves at the current density and capacity of: (A) 0.5 mA/cm^2 and 0.2 mAh/cm^2 (2000 mAh/g), (B) 0.5 mA/cm^2 and 0.5 mAh/cm^2 (5000 mAh/g), and (C) 0.3 mA/cm^2 and 0.3 mAh/cm^2 (3000 mAh/g). (D) Rate capability results of $(\text{NbTa})_{0.5}\text{BiS}_3$. (E) Cycling results for $(\text{NbTa})_{0.5}\text{BiS}_3$ with ZnI_2 , only $(\text{NbTa})_{0.5}\text{BiS}_3$, $(\text{NbTa})_{0.5}\text{BiS}_3$ with LiI . (F) Comparison of gravimetric current density vs capacity of the Li- CO_2 battery for our work (black stars) with other works.

Other results (not shown here) indicate the battery with Pt NP and Au NP only operates 19 and 15 cycles, respectively, with the same electrolyte blend including ZnI_2 additive and experimental conditions. MoS_2 as one of the best 2D catalysts also fails after 20 cycles while it can operate up to 500 cycles at the low current density of 0.05 mA/cm^2 . Figure XVIII.3.2F illustrates a comparison between this work and other studies in the literature. Both the gravimetric current density and the capacity were improved significantly with an achieved current density of 5-50 times and a capacity of 5-100 times compared to other works. The areal current density and the capacity were also significantly enhanced compared to literature.

Computational results for mechanistic understanding of the battery operation

Density functional (DFT) was used to investigate the $\text{Li}_2\text{CO}_3/\text{C}$ formation on a $(\text{NbTa})_{0.5}\text{BiS}_3$ catalyst as well as the stability of the catalyst. We first investigated the energies of different $(\text{NbTa})_{0.5}\text{BiS}_3$ surfaces including 001, 010, 011, 100, 101, 110, 111. The surface energies were determined for different terminations of each facet, including Nb, Ta, S and Bi terminations using ab initio molecular dynamics. All the 21 surfaces were optimized with and without spin polarization due to the possible magnetic properties. The equation given below was used to calculate the surface energies for each Nb, Ta, S and Bi termination of the different $(\text{NbTa})_{0.5}\text{BiS}_3$ surfaces.

$$\sigma = \frac{1}{2A} (E_{\text{slab}} - n_{\text{slab}} E_{\text{bulk}})$$

where, A is the area of the surface, E_{slab} is the energy of the slab, E_{bulk} is the energy of one unit in the bulk and n_{slab} is the number of bulk units in the surface slab. Figure XVIII.3.3A shows the surface energies calculated for all the surfaces for the spin polarized case and Figure XVIII.3.3B shows results for the cases without spin. For spin polarized calculations, the Nb-terminated (110) surface has the lowest surface energy of 0.000044 eV/A², while the Nb-terminated (010) surface is the lowest surface energy of 0.0044 eV/A² for non-spin calculations. The energy difference between these two surfaces is very small, so we can assume that they are similar. We note that the high-rate capability of the new (NbTa)_{0.5}BiS₃ catalyst is consistent with the extremely small surface energies found in these DFT calculations, which suggest that by use of a multi-element alloy the catalyst can be very stable and withstand the high current density without degradation.

Based on the above calculations showing many possible facets and terminations with very low surface energies, we chose the (110) facet to investigate the reaction mechanism for C/Li₂CO₃ formation. The mechanism was evaluated on three different (110) terminated (NbTa)_{0.5}BiS₃ surfaces, i.e. Nb terminated-, Ta terminated- and Bi terminated. The structures of these surfaces are shown in Figure XVIII.3.3C. For the free energy calculations, we considered the entropy changes and zero-point energies for CO₂ adsorption step by assuming these two terms are small and neglectable for surface reactions. The potential dependence for free energies was calculated based on the computational hydrogen electrode by referencing to the Li/Li⁺ electrode.

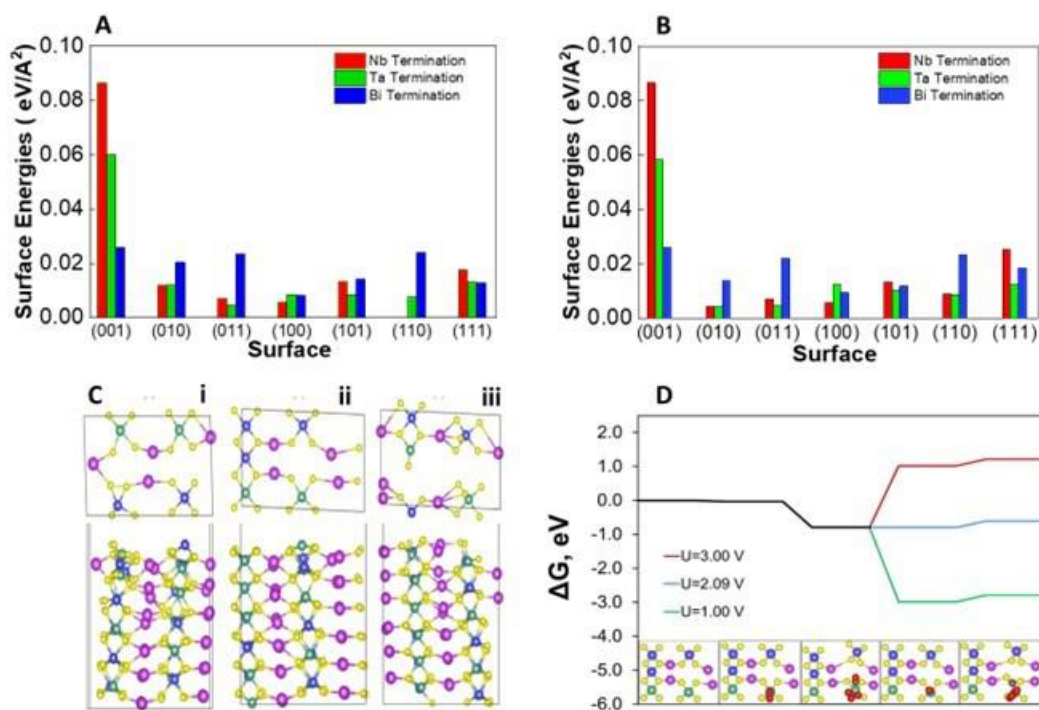


Figure XVIII.3.3 DFT calculations. (A-B) Surface energies with/without spin polarized surface. Note that due to the very small energy, the Nb terminated (110) surface energy does not show in (A). (C) The top and side views of (i) Ta-terminated, (ii) Nb-terminated, (iii) Bi-terminated (NbTa)_{0.5}BiS₃ (110) surfaces. The black lines are the periodic boundaries of the supercells. (D) The potential-dependent mechanistic analysis of Li₂CO₃ and C formations on a Nb-terminated (NbTa)_{0.5}BiS₃ (110) surface. The adsorption configurations are present in the bottom panels. The Nb, Ta, Bi, S, C and O atoms are in green, blue, purple, yellow, brown, and red, respectively.

The potential dependent reaction mechanism for Li₂CO₃ and C formation on the Nb-terminated (110) (NbTa)_{0.5}BiS₃ surface, the most stable termination from our calculations, is displayed in Figure XVIII.3.3D. The applied potentials were intended to level up the potential dependent step, i.e., CO and Li₂CO₃ formation step. The CO₂ adsorption with a Nb-O bond is slightly exergonic with a free energy of -0.01 eV. After CO₂

adsorption and dissociative adsorption of a second CO_2 , the formation of co-adsorbed CO^* and CO_3^* ($\text{CO}^*/\text{CO}_3^*$) is favorable with negative free energy of -0.77 eV. The third step involves the ($\text{Li}^+ + \text{e}^-$) pair transfer resulting Li_2CO_3 formation with CO remaining on the surface (CO^*). This step is quite downhill (-4.18 eV) and is potential dependent due to addition of electrons. This electrochemical step is favorable below about 2.09 V versus Li/Li^+ , which is approximately consistent with the experimental discharge potential considering the approximation made in the model such as the lack of explicit electrolyte molecules. The most stable adsorption geometry for the remaining CO^* is Nb site indicating it is still the active site. The process by which the amorphous carbon forms to satisfy the bulk reaction stoichiometry can be explained by a reaction of another CO_2 with CO^* , which is only slightly endothermic on this surface with a reaction energy of 0.19 eV. In this adsorption configuration, CO_3 binds on Nb site, while C binds on the 3-fold site of Nb-S-S. It is notable that Nb-terminated (110) surface is more favorable for C^*/CO_3^* formation compared with the Ta-terminated and Bi-terminated surfaces. In the medium-entropy cathode catalyst $(\text{NbTa})_{0.5}\text{BiS}_3$, based on our density functional calculations, the Nb-terminated (110) surface is more favorable for C^*/CO_3^* formation compared with the Ta-terminated and Bi-terminated surfaces. Thus, the role of the Nb is as the catalytic site for the Li- CO_2 reaction. The role of the other elements is that they provide for a multi-element material with extremely small surface energies as found in the DFT calculations. The stability of this multi-element material enables it to withstand the high current density without degradation. This is also consistent with our TEM results that confirm the excellent stability of the catalyst.

Conclusions

A new medium-entropy cathode catalyst, $(\text{NbTa})_{0.5}\text{BiS}_3$, is found to enable reversible Li/ CO_2 electrochemistry to operate at high rates. This medium-entropy cathode catalyst is combined with an ionic liquid-based electrolyte blend to give a Li- CO_2 battery that operates at a high current density of 0.5 mA/cm^2 and capacity of 0.5 mAh/cm^2 for up to 125 cycles. This far exceeds Li- CO_2 batteries previously reported in the literature. Density functional calculations of 21 surfaces of $(\text{NbTa})_{0.5}\text{BiS}_3$ revealed that many of them are exceptionally stable surfaces and is likely the reason for the capability the Li- CO_2 battery based on it to operate at such high rates. The stability is also confirmed by experimental characterization. In addition, the calculations indicate that a Nb terminated surface promotes Li- CO_2 electrochemistry resulting in Li_2CO_3 and carbon formation, consistent with the products found in the cell. These results open new direction to design and develop high performance Li- CO_2 batteries.

Key Publications

1. Jaradat, C. Zhang, S. S. Sutar, N. Shan, S. Wang, S. K. Singh, T. Yang, K. Kumar, K. Sharma, S. Namvar, A. Alireza, T. Rojas, V. Berry, J. Cabana-Jimenez, Z. Huang, A. Subramanian, A. T. Ngo, L. A. Curtiss, A. Salehi-khojin, A High-Rate Li- CO_2 Battery Enabled by Two Dimensional Medium-Entropy Catalyst, *Advanced Materials*, revision requested.

XIX Beyond Li-ion R&D: Sodium-Ion Batteries

The rechargeable sodium-ion battery uses sodium ions (Na^+) as its charge carriers, but its working principle and cell construction are analogous to those for lithium-ion batteries – the main difference is the use of sodium instead of lithium. Such batteries are of interest because unlike lithium-ion, they may be less dependent on critical materials in short supply (or materials limited to certain parts of the earth, or materials having an adverse environmental impact). A significant advantage of using sodium-ion batteries would be the abundant availability of sodium. However, they face some challenges to their large-scale commercialization in electric drive applications, including their relatively low energy density and limited cycle life.

The rest of this chapter contains detailed reports on the status of the following individual projects.

- An Exploratory Studies of Novel Sodium-Ion Battery Systems (BNL)
- Development of Advanced High-energy and Long-life Sodium-ion Battery (ANL)
- Tailoring High Capacity, Reversible Anodes for Sodium-Ion Batteries (LBNL)
- Electrolytes and Interfaces for Stable High-Energy Sodium-ion Batteries (Pacific Northwest National Laboratory).

XIX.1 An Exploratory Studies of Novel Sodium-Ion Battery Systems (BNL)

Xiao-Qing Yang, Principal Investigator

Chemistry division, Brookhaven National laboratory
Bldg. 555, Brookhaven National Lab.
Upton, NY 11973
E-mail: xyang@bnl.gov

Enyuan Hu, Co-Principal Investigator

Chemistry division, Brookhaven National laboratory
Bldg. 555, Brookhaven National Lab.
Upton, NY 11973
E-mail: enhu@bnl.gov

Tien Duong, DOE Technology Development Manager

U.S. Department of Energy
E-mail: Tien.Duong@ee.doe.gov

Start Date: October 1, 2021

End Date: September 30, 2022

Project Funding (FY22): \$380,000

DOE share: \$380,000

Non-DOE share: \$0

Project Introduction

The next generation of rechargeable battery systems with higher energy and power density, lower cost, better safety characteristics, and longer calendar and cycle life need to be developed to meet the challenges to power electrified vehicles in the future. Na-ion battery systems have attracted more and more attention due to the more abundant and less expensive nature of Na resources. However, building a sodium battery requires redesigning battery technology to accommodate the chemical reactivity and larger size of sodium cations. Since Na-ion battery research is an emerging technology, new materials to enable Na electrochemistry and the discovery of new redox couples and the related diagnostic studies of these new materials and redox couples are quite important. This project uses the synchrotron based in situ x-ray diagnostic tools developed at BNL to evaluate the new materials and redox couples, to explore in-depth fundamental understanding of the reaction mechanisms aiming to improve the performance of these materials and provide guidance for new material developments. This project also focuses on developing advanced diagnostic characterization techniques for these studies. The synchrotron based in situ X-ray techniques (x-ray diffraction, x-ray pair distribution function, or PDF, and x-ray absorption XAS) are combined with other imaging and spectroscopic tools such as transmission electron microscopy (TEM), scanning transmission electron microscopy (STEM), mass spectroscopy (MS), transmission x-ray microscopy (TXM), as well as neutron diffraction (ND) and neutron PDF (NPDF). In FY2022, this BNL team has performed several successful experimental studies at various beamlines of National Synchrotron Light Source II (NSLSII) such as x-ray Powder diffraction (XPD), and ISS beamlines. In FY2022, through collaborating with scientists at University of California at Irvine, this team also has carried out studies using the 3D TEM tomography and STEM, EELS on the new cathode materials for Na-ion batteries. Through collaboration with scientists at Oak Ridge National Lab. (ORNL), XRD, XAS and soft x-ray XAS studies on a new P2-structured $\text{Na}_{0.66}[\text{Cu}_{0.33}\text{Mn}_{0.67}]\text{O}_2$ cathode material for Na-ion batteries.

Objectives

The primary objective of this project is to develop new advanced in situ material characterization techniques and to apply these techniques to support the development of new cathode, anode, and electrolyte materials with high energy and power density, low cost, good abuse tolerance, and long calendar and cycle life for the next generation of Sodium-ion batteries (SIBs) to power plug-in hybrid electric vehicles (PHEV) and electric

vehicles (EV). The diagnostic studies have been focused on issues relating to capacity retention, thermal stability; cycle life and rate capability of advanced Na-ion and beyond Li-ion batteries

Approach

This project has used the synchrotron based in situ x-ray diagnostic tools developed at BNL to evaluate the new materials and redox couples to enable a fundamental understanding of the mechanisms governing the performance of these materials and provide guidance for new material and new technology development regarding Na-ion battery systems. These techniques include:

- Using nano-probe beamline at NSLSII to study the elemental distribution of new solid electrolyte materials for Na-ion batteries
- Using transmission x-ray microscopy (TXM) to do multi-dimensional mapping of cathode materials of Na-ion batteries
- Design and carry out three-dimensional (3D) STEM tomography experiments to study new cathode materials for Na-ion batteries at pristine state and after multiple cycling.

Results

In FY2022, advanced diagnostic techniques have been successfully applied to the studies of the new sodium cathode materials NaMnFeCoNiO_2 (NMFCN). To understand the structure evolution of NMFCN, synchrotron-based X-ray Diffraction (XRD) and high-angular dark field scanning transmission electron microscopy (HAADF-STEM) is performed. The XRD results in Figure XIX.1.1(a) shows the O3-type layer structure of NMFCN pristine material. Figure XIX.1.1(b) & Figure XIX.1.1(c) show the atomic structure of NMFCN in pristine state and after 1st charge, respectively. The contrast of HAADF-STEM images in Figure XIX.1.1(b) & Figure XIX.1.1(c) is sensitive to the atomic number of the projected underlying atomic columns. The constant intensity in Figure XIX.1.1(b) indicates that transition metals are uniformly distributed throughout the particle and the O3-structure observed by using STEM is consistent with the XRD results shown in Figure XIX.1.1(a). Interestingly, it is found that after first charge process, the atomic structure of NLNMF is partially transformed from O3-type to P3-type. As shown in Figure XIX.1.1(c), after 1st charge, there is a mixture of O3 and P3 structure in this material. Figure XIX.1.1(d) schematically shows the phase transformation from pure O3 structure to a mixture of O3-P3 structure after 1st charge.

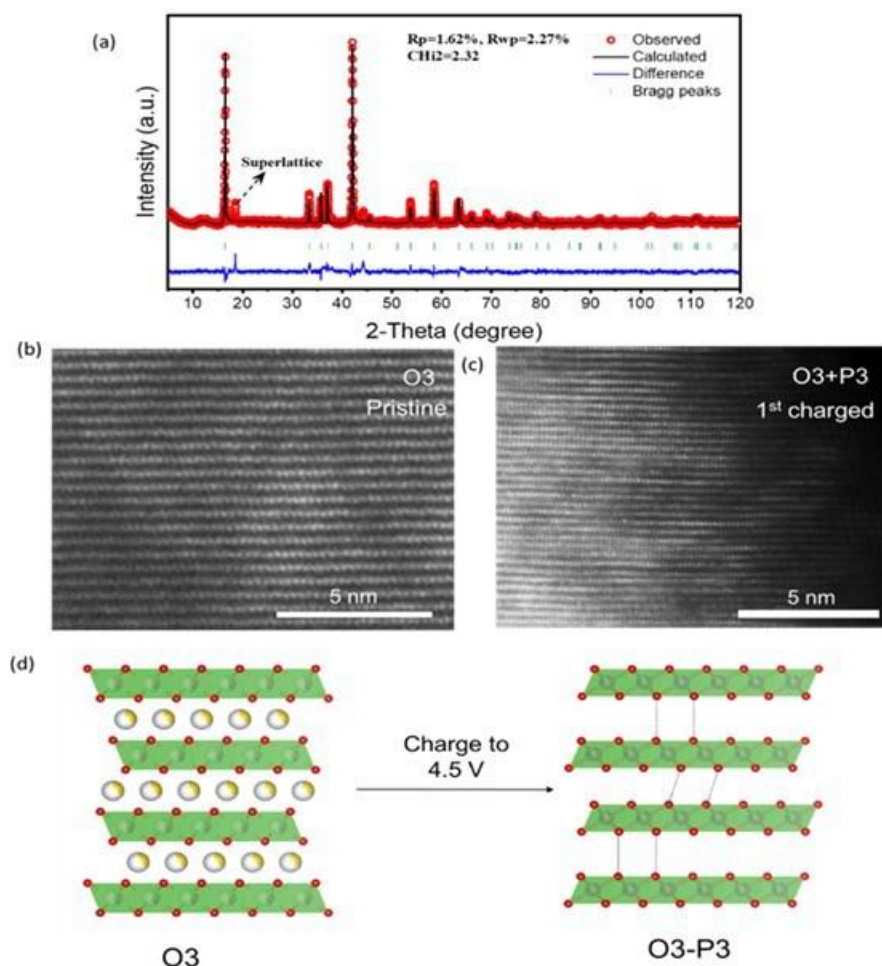


Figure XIX.1.1 Structure characterization. (a) XRD of pristine NaMnFeCoNiO₂; (b) HAAD-STEM image of pristine NaMnFeCoNiO₂; (c) HAAD-STEM image of NaMnFeCoNiO₂ after 1st charge; (d) schematic illustration of phase transformation during 1st charge.

In FY2022 at **BNL**, in collaboration with scientists at **ORNL**, Advanced diagnostic techniques have been successfully applied to the studies of the new sodium cathode materials, P3-type Na_{2/3}Cu_{1/3}Mn_{2/3}O₂. Half of the Na⁺ in this compound (corresponding to the nominal oxidation of Cu²⁺ to Cu³⁺) can be reversibly extracted/inserted at two different plateaus with minimum voltage hysteresis. Detailed structure and electronic structure investigation reveal that charge compensation at the 3.5 V plateau is mainly contributed from the oxidation of p-d hybridized states, leading to the increase of p-d hybridization. In contrast, holes are predominantly created on a state with primary oxygen 2p parentage at the 4.1 V charge plateau. The highly reversible voltage and capacity in Na_{2/3}Cu_{1/3}Mn_{2/3}O₂ highlights that oxygen 2p holes can be stabilized by forming localized bound state with singly occupied Cu dx²-y². These findings open new routes to design and explore cathode materials utilizing reversible lattice oxygen redox beyond the widely adopted A-O-A (A is an alkali metal) configuration.

High resolution in situ XRD data were collected to monitor the structural evolution during the initial charge and discharge with the up cut off voltages set to 4.1 V. During the initial charge, a two-phase reaction is identified for the 3.55 V plateau (Figure XIX.1.2). The (001) and (002) reflections (in the monoclinic setting, corresponding to the (003) and (006) reflections in the conventional P3 type structure) shift toward lower angle during charging. These Bragg peaks indicate the dimension along crystallography *c*-axis and the shifts suggest the expansion of the interlayer spacing after Na⁺ extraction. In contrast, the (10-2) and (20-2) reflections shift to higher angle during charging. The position of these peaks are determined by both *a* and *c* axes. Considering

that c expands during this process, the only possibility for peaks shifting to lower angle is that a axis shrinks. Interestingly, the (031) reflection remains almost unchanged. This peak is associated with the dimensions along both b and c axes, but the peak position is more sensitive to the former than the latter. Therefore, the behavior of (031) peak suggests that b axis is mostly unchanged during the 3.55 V plateau.

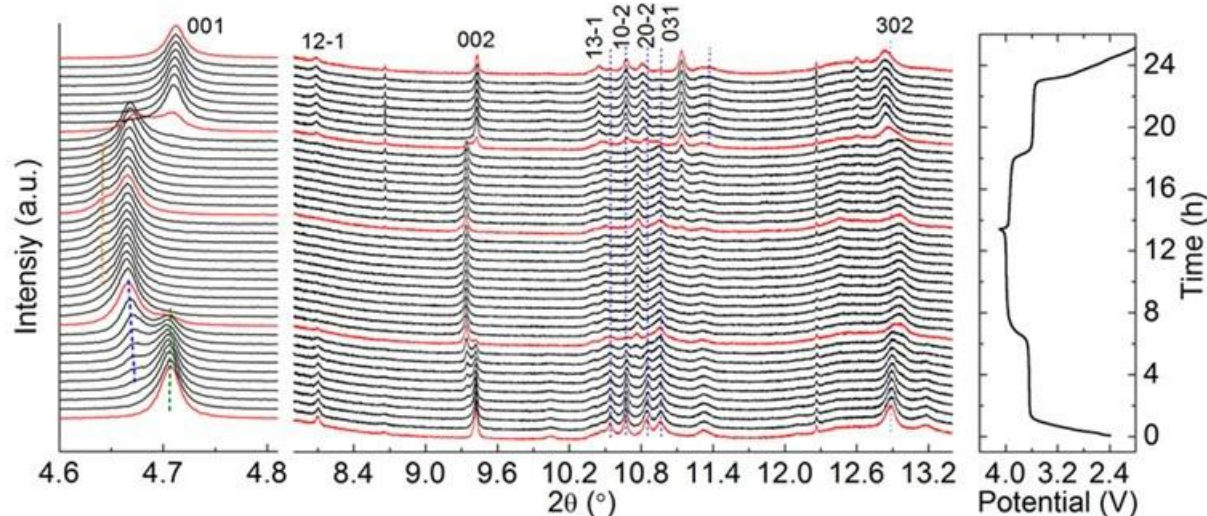


Figure XIX.1.2 In situ XRD with up cut-off voltage of 4.1 V.

In situ x-ray absorption spectroscopy (XAS) studies have been completed for P3-structured $\text{Na}_{0.66}[\text{Cu}_{0.33}\text{Mn}_{0.67}]\text{O}_2$. Figure XIX.1.3a shows the evolution of x-ray absorption near edge structure (XANES) of XAS for both copper and manganese K-edges during the 1st cycle. The edge position of copper XANES shifts to higher energies during charge and shifts back to lower energy during discharge. In contrast, the edge position of manganese XANES is mostly unchanged during the whole charge-discharge process. This clearly indicates that copper is the active element contributing to the capacity during charge-discharge while manganese is inert. To study the local structural changes around copper and manganese, the extended x-ray absorption fine structure (EXAFS) data are Fourier transformed and the results are shown in Figure XIX.1.3b. The first peak corresponds to the bond between transition metal (TM, copper or manganese) and oxygen and the second one corresponds to the TM-TM correlation. Through fitting these spectra against the model structure, detailed local structural information can be obtained. Satisfactory fitting was obtained after considering the presence of copper manganese local ordering and Jahn-Teller distortion for copper atoms. The results are shown in Figure XIX.1.3c. Jahn-Teller distortion splits the copper-oxygen bonds into short ones (changes during cycling plotted in the top panel of Figure XIX.1.3c) and long ones (the middle panel of Figure XIX.1.3c). At the beginning of charge, the short copper-oxygen bond shrinks and so does the long one with a larger value, meaning that the difference between them becomes smaller. This is likely due to the oxidation of copper cations that directly removes the 3d electrons on copper and therefore weakens the Jahn-Teller distortion. Further charging leads to shrinkage of the short bond but expansion of the long one. This could be associated with the oxygen redox process that no longer removes electrons directly from the copper 3d states but more likely from the oxygen-dominated states instead. The more complicated bond lengths evolution at the end stage of charge may be associated with the phase transition in this material. The manganese-oxygen bond length (bottom panel in Figure XIX.1.3c) is mostly unchanged during the charge-discharge process, which is expected and consistent with the XANES results shown in Figure XIX.1.3a.

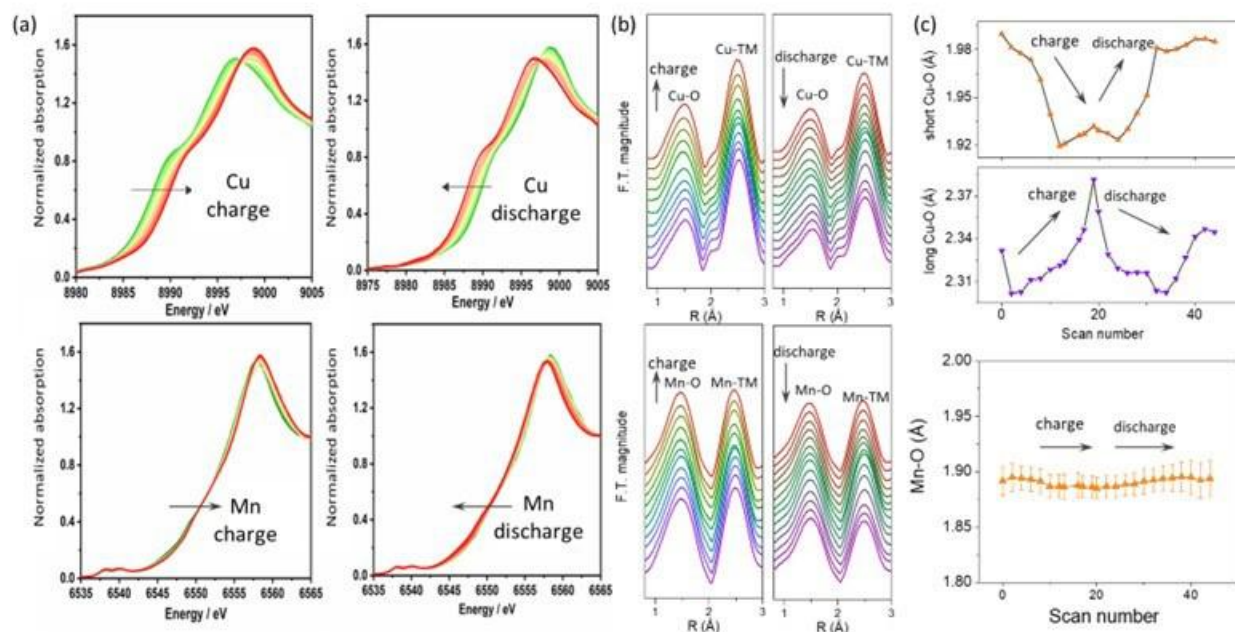


Figure XIX.1.3 (a) In situ XANES and (b) in situ Fourier transformed EXAFS for copper and manganese during the 1st charge-discharge process. (c) evolution of bond lengths for fitted short copper-oxygen (top panel), long copper-oxygen (middle panel), and manganese-oxygen (bottom panel) during charge-discharge. The error bar for copper-oxygen bond length is very small and cannot be seen in the figure.

The *ex situ* soft x-ray absorption spectroscopy (sXAS) studies have been completed for P3-structured $\text{Na}_{0.66}[\text{Cu}_{0.33}\text{Mn}_{0.67}]\text{O}_2$. At pristine state (Figure XIX.1.4), the L3-edge of Cu shows a nearly standard Cu^{2+} feature with only one sharp white line peak around 930 eV (vertical dotted line in Figure XIX.1.4a) which corresponds to the transition from d^9 ground electronic configuration to the $\bar{c}d^{10}$ (\bar{c} denotes a core hole). After charged to 3.66 V, the white line peak at ~930 eV shifts towards higher energy, indicating the oxidation of Cu^{2+} cation. Meanwhile, a new shoulder peak emerges just above 932 eV (upward arrows in Figure XIX.1.4a) which is likely related to hybridization with ligand oxygen and oxygen hole states formation. This interpretation is also supported by the O K-edge XANES data measured at the same time (Figure XIX.1.4b), where a shoulder peak (~526.5 eV, upward arrows in Figure XIX.1.4b) clearly emerges at the end of 3.66 V plateau before the main pre-edge peak (< ~528 eV, vertical dotted line in Figure XIX.1.4b) which has nearly zero shift from pristine state. The changes of Cu L3- and O K-edge XANES together suggest that, during 3.66 V plateau, Cu^{2+} is oxidized and Cu-O hybridization becomes stronger. After charged to 4.10 V (Figure XIX.1.4a), the white line peak around 930 eV of Cu L3-edge XANES surprisingly moves back to the original position of the pristine state. Though it seems that Cu gets back to +2 valence state, the shoulder peak around 932 eV preserves and becomes even stronger with only slight shift towards lower energy relative to that of the end of 3.66 V plateau, implying different electronic state from that of standard Cu^{2+} at pristine state. This new feature is closely related to ligand oxygen anions. As seen in Figure XIX.1.4b, both the main pre-edge peak ~528 eV and the shoulder peak ~526.5 eV slightly shift towards higher energy end and the shoulder peak becomes more prevalent compared to that at the end of 3.66 V plateau, which suggests more participation of O in the active redox at 4.10 V. In fact, the electronic features observed here at 4.10 V fit the profile of Zhang-Rice singlet (ZR) state that was first reported for high T_c superconducting cuprate materials. The ZR state refers to a special correlated electronic state formed between a center Cu^{2+} with one hole in its e_g orbital and a ligand O also with one hole in its p orbital ($\text{Cu}^{2+}:3d^9\text{-O}:2p^5$ or simplified as $d^9\bar{L}$ where \bar{L} denotes a ligand hole). The 930 eV white line peak and a shoulder peak around 931.5 eV~932 eV of Cu L3-edge XANES are a signature of ZR singlet state corresponding to the excitation from $d^9\bar{L}$ to $\bar{c}d^{10}\bar{L}$. Therefore, it is very likely that lattice oxygen dominates the redox reaction at 4.10 V with a new correlated electronic state formed between O hole and Cu^{2+} hole.

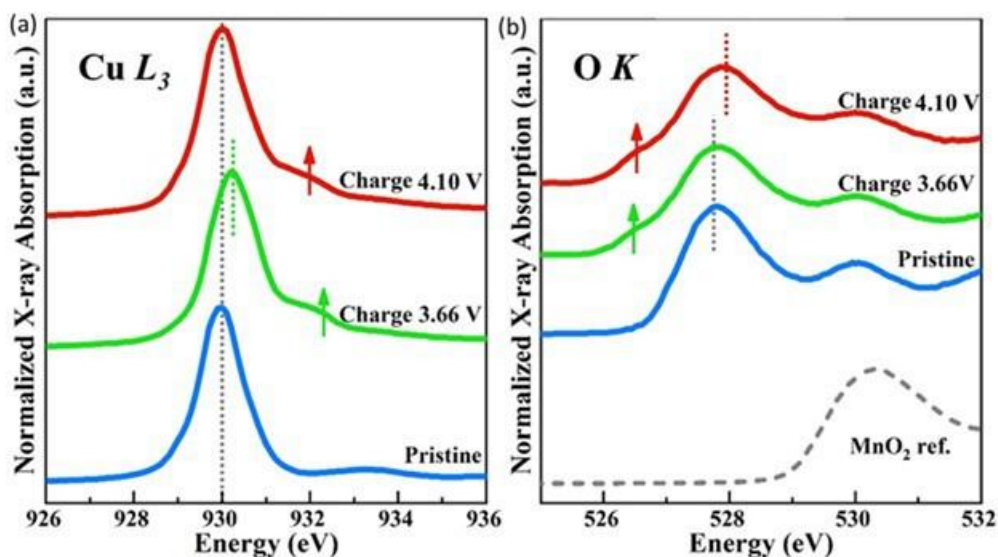


Figure XIX.1.4 Cu L_3 edge (left panel) and O K-edge (right panel) for P3-NaCuMnO at pristine state, charged to 3.66 V, and charged to 4.10 V. The vertical dotted lines indicate the position of main peak, and the upward arrows indicate the rising of shoulder peaks and their positions.

Conclusions

This project, “Exploratory Studies of Novel Sodium-Ion Battery Systems (BNL)”, has been successfully completed in FY2022. All milestones have been completed. The publication records are very good. Extensive collaboration with other national Labs, US universities and international research institutions were well established.

Key Publications

Publications

1. Ming-Hui Cao,* Ren-Yan Li, Shi-Ya Lin, Shao-Di Zheng, Lu Ma, Sha Tan, Enyuan Hu, Zulipiya Shadike,* Xiao-Qing Yang* and Zheng-Wen Fu*, “Oxygen redox chemistry in P2- $\text{Na}_{0.6}\text{Li}_{0.11}\text{Fe}_{0.27}\text{Mn}_{0.62}\text{O}_2$ Cathode for High-Energy Na-Ion Batteries”, *J. Mater. Chem. A*, 2021,9, 27651-27659, DOI: 10.1039/D1TA08471B, Publication Date: November 18, 2021
2. Ghulam Ali, Mobinul Islam, Deu S. Bhang, Young Hwa Jung, Mingyuan Ge, Yong S. Chu, Kyung-Wan Nam, Yonghua Du, Xiao-Qing Yang, Hun-Gi Jung, Seong-Min Bak*, Kyung Yoon Chung*, “Self-Standing $\text{Co}_2.4\text{Sn}_{0.6}\text{O}_4$ Nano Rods as High-Performance Anode Materials for Sodium-Ion Battery and Investigation on Its Reaction Mechanism”, *Chemical Engineering Journal*, DOI: 10.1016/j.cej.2022.135791, Publication date: March 14, 2022.
3. Libing Yao, Peichao Zou, Chunyang Wang, Jiahao Jiang, Lu Ma, Sha Tan, Kevin A Beyer, Feng Xu, Enyuan Hu*, Huolin L Xin*, “High-Entropy and Superstructure-Stabilized Layered Oxide Cathodes for Sodium-Ion Batteries”, *Advanced Energy Materials*, DOI: 10.1002/aenm.202201989. Publication date: September 08, 2022.

Presentations

1. Arthur Ronne, Jue Liu, Lu Ma, Hui Zhong, Jianming Bai, Minyuan Ge, Xianghui Xiao, Wah-Keat Lee, Steven Ehrlich, Sanjit Ghose, Xiao-Qing Yang, Yu-chen Karen Chen-Wiegart, and Enyuan Hu*, “High Capacity, High Voltage Na-ion Cathodes Enabled with Oxygen and Copper Redox”, presented at 242 ECS meeting, October 11, 2022, Atlanta, Georgia, USA.

XIX.2 Development of Advanced High-energy and Long-life Sodium-ion Battery (ANL)

Khalil Amine, Principal Investigator

Argonne National Laboratory
9700 South Cass Avenue
Lemont, IL 60439
E-mail: amine@anl.gov

Christopher S. Johnson, Co-Principal Investigator

Argonne National Laboratory
9700 South Cass Avenue
Lemont, IL 60439
E-mail: cjohnson@anl.gov

Tien Duong, DOE Technology Development Manager

U.S. Department of Energy
E-mail: Tien.Duong@ee.doe.gov

Start Date: January 1, 2019

End Date: September 30, 2022

Project Funding (FY22): \$585,000

DOE share: \$585,000

Non-DOE share: \$0

Project Introduction

Considering the natural abundance and low cost of sodium resources, sodium-ion batteries (SIBs) have received much attention for large-scale electrochemical energy storage.[1] However, the larger ionic radius of Na^+ (1.02 Å) than Li^+ (0.67 Å) brings more challenges on the development of good Na-host materials with optimal electrochemical properties. On one hand, despite most SIBs cathode materials are either imitating or duplicating from lithium analogues, there are significant differences in the intercalation chemistries between sodiation and lithiation. The layered oxides cathodes deliver very high energy density, but undergo more complex phase transition during charge/discharge, resulting in severe capacity fade during prolonged cycling. [2] On the other hand, the absence of suitable anode materials has obstructed progress in the development of SIBs. Two of the most promising anode materials, graphite and silicon have limited sodium storage capability. Hard carbon can demonstrate reversible sodiation/de-sodiation, but the capacity is lower than 300 mAh g⁻¹, significantly limited the energy density of SIBs. [3,4] Alloying anode materials such as phosphorus can deliver high capacity, but suffer from huge volume changes and severe parasitic reactions with the electrolytes, resulting in rapid capacity degradation during long-term cycling. [5]

Via advanced diagnostic tools including synchrotron X-ray probes and computational modeling, the team led by Dr. Khalil Amine and Dr. Christopher S. Johnson at Argonne National Laboratory (ANL) is focusing on the development of rational cathode materials, anode materials and electrolytes to develop long life and high energy SIBs with low cost and high safety. A major focus is on enabling Fe/Mn cathode systems, which, if possibly used, requires advanced mechanistic knowledge of the (electro)chemistry of Fe behavior in non-aqueous battery systems. For this year, our annual report feature our results on transition metal layered oxide cathodes. Previous reports have included results from anodes, such as Red Phosphorus with doped antimony, and Zintl phases of Pb and doped Pb. Herein we feature work that discusses *operando* synthesis methods of cathodes and a result which defines the importance of synthetically fabricating and producing well defined layered oxide structures. Native strain in the layered oxide was found to direct the resultant electrochemistry. In the second part of the report, we feature our findings on iron's behavior in SIBs. Fe is complicated in the cell because Fe^{4+} appears to be reactive at the electrode surface, and is also unstable to ionic movement over to the Na layer within the bulk.

Objectives

The project objective is to develop high-energy SIBs with long life, low cost and high safety. The energy density target is 200 Wh kg⁻¹ and/or 500 Wh L⁻¹, wherein the anode capacity and cathode capacity targets are 600 mAhg⁻¹ and 200 mAhg⁻¹, respectively.

Approach

In a team approach, the Na-ion battery group will create a versatile Na-ion battery chemistry with beneficial advantages such as low cost, safety, recycling, and sustainability of materials used. The team will work in a synergistic way so that the final design is the culmination of advances in phosphorus carbon composites mated with optimized lead or other highly dense metalloids, such as tin and/or antimony and derivatives thereof, for the recyclable anode. Synthesis and optimization of such blended composite anodes will be conducted in parallel to diagnostic characterization of structures, phase formation, and cycling stability. Cathode work will involve (1) gradient cathodes consisting of Fe-Mn compositions, and (2) intergrowths of layer stacking sequenced oxides. If resources allow, the team also will attempt to stabilize cathode surfaces using ALD methods, particularly for the benefit of staving off dissolution of manganese and mitigating iron/electrolyte reactivity.

Results

Part One: Native lattice strain induced structural earthquake in sodium layered oxide cathodes

The structures of cathode materials significantly affect their electrochemical performance. Unlike lithium-ion batteries cathodes that exhibit only O-type structure, the sodium layered oxide cathodes can be classed into O-type and P-type depending on the surrounding Na environment and the number of unique oxide layers. In FY21, it has been found that rapid cooling (i.e. quenching) is important to obtain pure O3 phase material, which however would induce significant lattice strain. In FY22, we have conducted a systematic study on the effect of native lattice strain on the cycling stability of O3 NaNi_{0.4}Mn_{0.4}Co_{0.2}O₂ cathode.

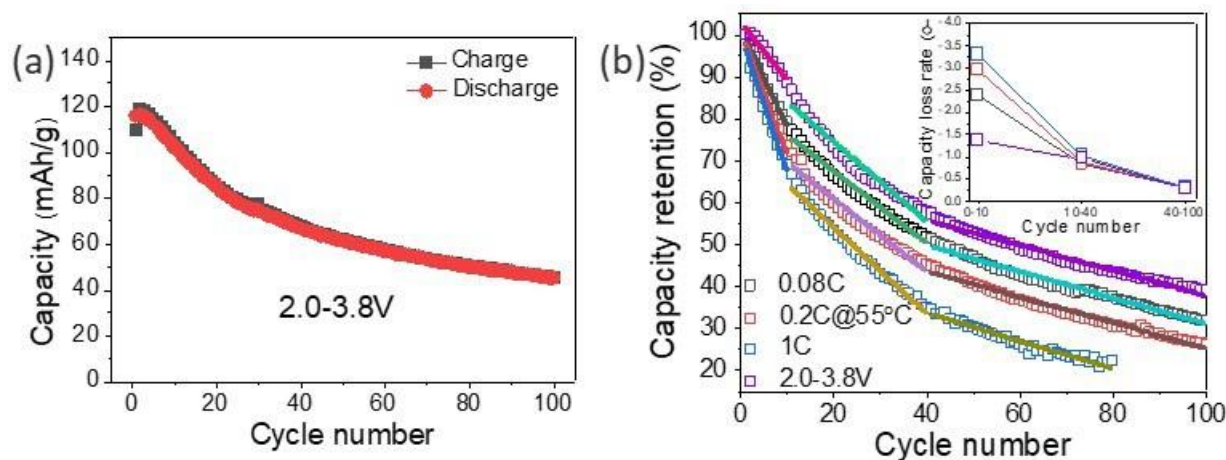


Figure XIX.2.1 (a) Cycling performance of strained O3 NaNi_{0.4}Mn_{0.4}Co_{0.2}O₂ cathode within 2.0–3.8 V (vs. Na/Na⁺) at 0.08C (1C=180 mA g⁻¹). (b) Normalized capacity retention of O3 NaNi_{0.4}Mn_{0.4}Co_{0.2}O₂ cathode at different cycling conditions. The capacity loss rate in (b) is the slope of the linear fitting curve of the capacity.

It was previously reported that the high-voltage instability of layered cathodes may come from the parasitic side reactions with the electrolytes. We therefore limited the charge cut-off voltage of the O3 cathode from 4.4 V to 3.8 V (vs. Na/Na⁺) to reduce the effect of electrolytes instability. Surprisingly, the cycle stability was not improved by lowering the charge cut-off voltage, which contradicts results in other studies of reported sodium layered oxide cathodes with narrow voltage window. A capacity retention of only 38.7% was attained after 100 cycles (Figure XIX.2.1a). Moreover, the charge/discharge test of the highly strained NaNi_{0.4}Mn_{0.4}Co_{0.2}O₂ cathode at elevated voltage or temperature demonstrated similar rapid degradation (Figure XIX.2.1b). Interestingly, the capacity fade rate (inset in Figure XIX.2.1b), which were obtained by linear fitting of the

capacity retention curve, is almost same after the first 10 cycles, regardless of voltage window, testing temperature and charge/discharge rate, whereas they exhibited significantly different results for the first 10 cycles. The results indicate that the capacity degradation of the highly strained $\text{NaNi}_{0.4}\text{Mn}_{0.4}\text{Co}_{0.2}\text{O}_2$ cathode might be controlled by a specific factor, while such factor was regulated by the operating conditions in the early stage of charge/discharge.

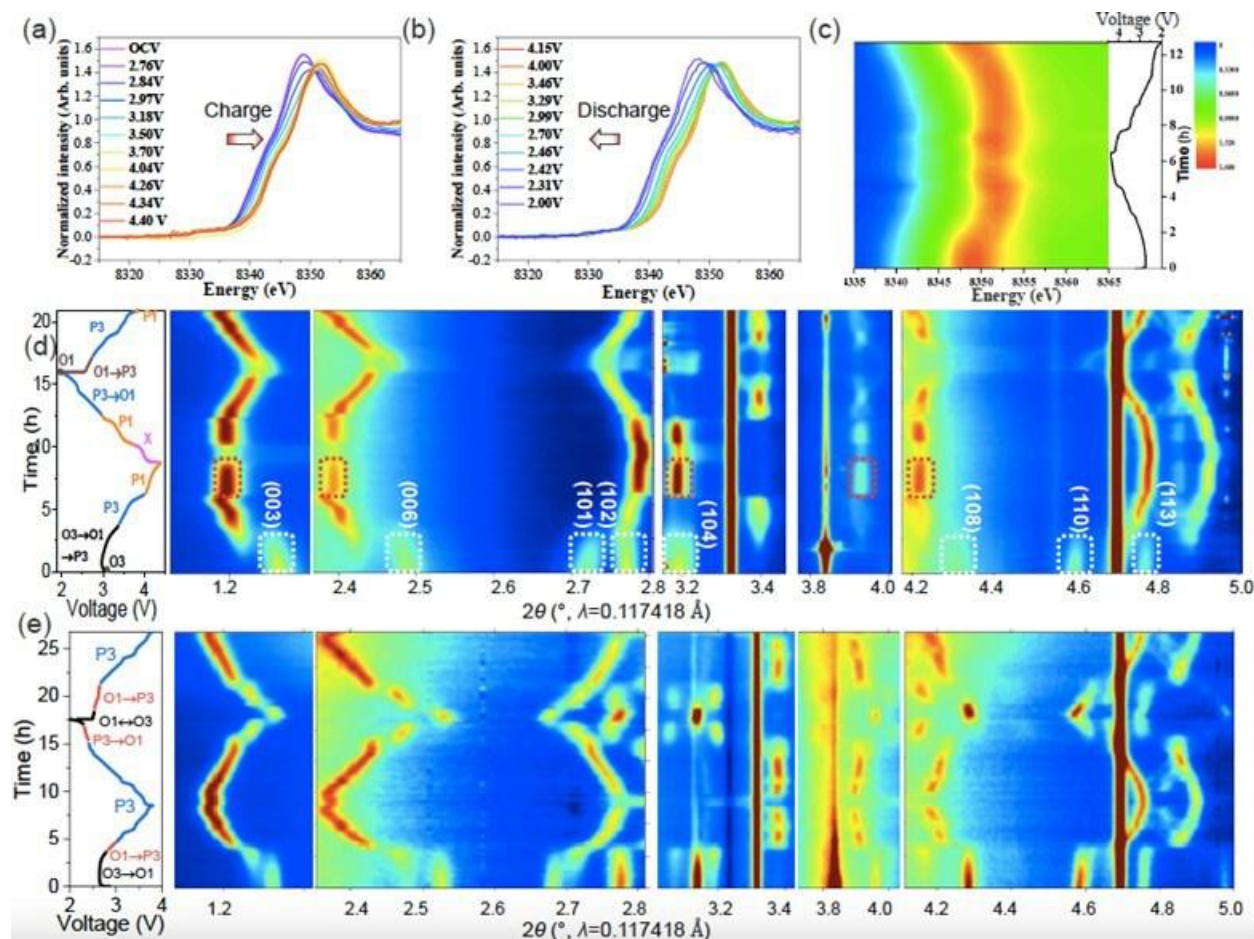


Figure XIX.2.2 In situ synchrotron characterization during charge/discharge. In situ Ni K-edge XANES of strained O3 $\text{NaNi}_{0.4}\text{Mn}_{0.4}\text{Co}_{0.2}\text{O}_2$ within 2.0-4.4V: (a) during charge, (b) during discharge and (c) 2D contour plot during charge/discharge. Voltage profiles and the corresponding 2D contour plot of in situ SXRD patterns during charge/discharge of O3 $\text{NaNi}_{0.4}\text{Mn}_{0.4}\text{Co}_{0.2}\text{O}_2$ cathode within (d) 2.0-4.4 V and (e) 2.0-3.8 V. The colour in (c-e) represent the intensity, with red for highest and blue for lowest.

To further elucidate the degradation mechanism, in situ Ni K-edge X-ray absorption near-edge spectroscopy (XANES) characterization was carried out to understand the redox couple evolution of the highly strained $\text{NaNi}_{0.4}\text{Mn}_{0.4}\text{Co}_{0.2}\text{O}_2$ cathode during charge/discharge within 2.0-4.4 V, which can provide the oxidation state changes of Ni element during battery operation. As shown in Figure XIX.2.2a and 2b, the Ni K-edge shifted to high-energy upon extraction of Na^+ due to the oxidation of Ni^{2+} to $\text{Ni}^{3+}/\text{Ni}^{4+}$ during charge, while it shifted back to lower energy during discharge due to the reduction of $\text{Ni}^{3+}/\text{Ni}^{4+}$ to Ni^{2+} . In general, as shown in the 2D contour plot of Ni K-edge XANES throughout the whole charge/discharge process (Figure XIX.2.2c), the Ni undergoes a highly reversible Ni oxidation/reduction during charge/discharge within 2.0-4.4 V. Even after cycling for 10 cycles that has triggered severe capacity degradation in the strained O3 cathode, Ni still exhibit reversible redox reactions (Figure XIX.2.3a), which cannot explain the severe capacity loss of strained $\text{NaNi}_{0.4}\text{Mn}_{0.4}\text{Co}_{0.2}\text{O}_2$ cathode reported here. The redox reaction behaviour of Co and Mn in the O3 strained $\text{NaNi}_{0.4}\text{Mn}_{0.4}\text{Co}_{0.2}\text{O}_2$ cathode were also explored and both showed reversible transformation during cycling

within 2.0–4.4 V (Figure XIX.2.3b & Figure XIX.2.3c), indicating that the observed capacity degradation is not regulated by the working voltage window.

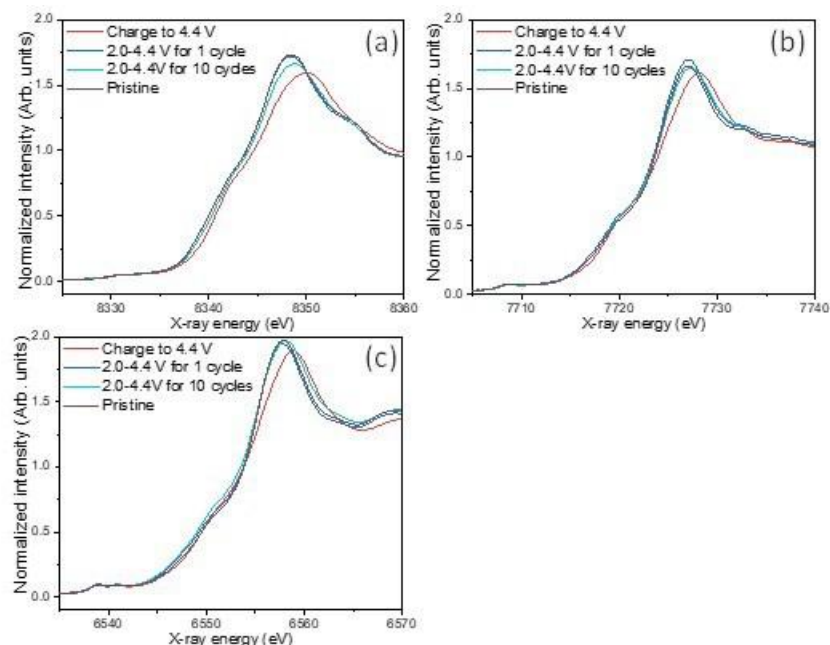


Figure XIX.2.3 (a) Ni, (b) Co and (c) Mn K-edge XANES of strained O3 $\text{NaNi}_{0.4}\text{Mn}_{0.4}\text{Co}_{0.2}\text{O}_2$ cathode at different charge/discharge states.

We further performed in situ SXR to reveal the phase transition of strained $\text{NaNi}_{0.4}\text{Mn}_{0.4}\text{Co}_{0.2}\text{O}_2$ cathode with controlled voltage window. Figure XIX.2.2d shows the 2D contour plot of in situ SXR patterns during charge/discharge within 2.0–4.4 V, in accompaniment with the corresponding voltage curve and phase transition process. As shown, the electrode before charge/discharge can be well indexed using O3 phase. Upon charge, the (003) and (006) peaks shifted toward lower angles, which indicated an expansion of the c lattice parameter due to the increased oxygen electrostatic repulsion between oxygen layers induced by the removal of Na^+ . Meanwhile, the (101), (102), (110) and (113) peaks moved towards higher angles during charge, corresponding to shrinkage of a lattice parameter due to the oxidation of TM. In addition, the intensity of O3 phase gradually decreased, while the peaks of O1 phase started to appear. Upon further charge, the O1 phase was then transformed into P3 phase starting at 3.37 V. At the long plateau beyond 4.0 V, the structure of P1 phase started to dominate the charged product. At the end of the charge process, an unknown X phase with low Na content and crystallinity was formed. Therefore, the phase transformation of strained $\text{NaNi}_{0.4}\text{Mn}_{0.4}\text{Co}_{0.2}\text{O}_2$ cathode during high-voltage charge can be described as $\text{O3} \rightarrow \text{O1} \rightarrow \text{P3} \rightarrow \text{P1} \rightarrow \text{X}$, which is similar to the previously reported O3 sodium layered cathode when charged to high voltage. During the discharge process, the phase transformation process reversed. However, at the beginning of the discharge process, the XRD intensities of (00 l) peaks are very weak and broad, indicating severe lattice strain at the c -axis direction that prevent the re-insertion of Na^+ . Moreover, as evidenced by the disappearance of O3 (003), (006), (101), (108) and (110) peaks of O3 phase, the O1 phase (rather than the original O3 phase) dominated the fully discharged electrode, indicating an irreversible phase transition during high-voltage cycling.

In sharp contrast with that charge/discharge within 2.0–4.4 V, the highly strained $\text{NaNi}_{0.4}\text{Mn}_{0.4}\text{Co}_{0.2}\text{O}_2$ cathode exhibited a highly reversible phase transformation of $\text{O3} \leftrightarrow \text{O1} \leftrightarrow \text{P3}$ with a lower charge cut-off voltage of 3.8 V. As clearly shown in Figure XIX.2.2e, the in situ SXR patterns during the whole charge/discharge process presented a highly symmetric feature, and all the peaks of O3 phase were fully recovered at the end of the discharge process. Such a reversible phase transition during charge/discharge of layered oxide cathodes are

often considered favorable for the stabilization of their cycle performance. However, we illustrate that this is not the case of the highly strained $\text{NaNi}_{0.4}\text{Mn}_{0.4}\text{Co}_{0.2}\text{O}_2$ cathode (Figure XIX.2.2e).

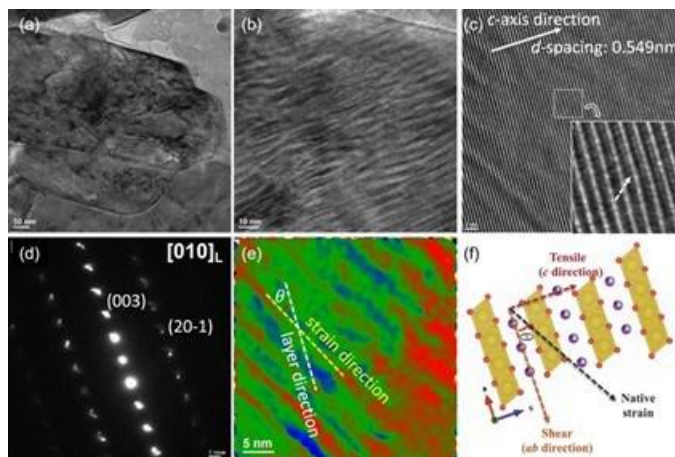


Figure XIX.2.4 (a) Low and (b) high magnification, (c) high-resolution bright-field TEM image, (d) SAED pattern, (e) GPA analysis and (f) atomic structural model of the strained O3 $\text{NaNi}_{0.4}\text{Mn}_{0.4}\text{Co}_{0.2}\text{O}_2$. Inset in (c) is the zoomed-in view of the region marked by white square. The color in (c) represent the intensity, with red for highest and blue for lowest. θ is the angle between layered direction and strain direction. The yellow, red, blue, grey and purple spheres in (f) represents Na, O, Ni, Co and Mn atoms, respectively.

The aforementioned result indicate that the capacity degradation of the strained O3 $\text{NaNi}_{0.4}\text{Mn}_{0.4}\text{Co}_{0.2}\text{O}_2$ cathode is not due to cycling-induced structural deformation, but may be related to native structural features. We will further use advanced electron microscopy to examine the native crystallographic structure and investigate how it affect the degradation during cycling. We found that quenching could induce significant native lattice strain in the layered oxide cathode, e.g., O3 $\text{NaNi}_{0.4}\text{Mn}_{0.4}\text{Co}_{0.2}\text{O}_2$ cathode. Figure XIX.2.4a and 4b shows the low and high magnification TEM image of the pristine $\text{NaNi}_{0.4}\text{Mn}_{0.4}\text{Co}_{0.2}\text{O}_2$ particle, respectively. The quenched cathode exhibited highly rough surface and fluctuated strain contours in a large area. These structural features have been mostly observed in the cycled cathodes materials, but barely in the pristine cathodes. The HRTEM image in Figure XIX.2.4c illustrates that the d -spacing along the c -axis direction is about 0.549 nm, which is stretched by about 3.58% compared to that of standard O3 phase (0.530 nm). A closer examination (inset of Figure XIX.2.4c) clearly shows the existence of severe lattice distortion along the c -axis direction, in which we can see the curved lattice fringe and overlap of TM atoms and Na atoms. Such lattice distortion might accelerate cation mixing or cation migration during cycling, leading to undesired structural evolution and hence capacity/voltage fade. The selected area electron diffraction (SAED) pattern in Figure XIX.2.4d is in good agreement with the [010] projection of layered O3 cathode but exhibits obvious spot splitting. All these structural features are due to the native high lattice strain induced during the quenching process, leading to the highly metastable nature of strained O3 cathode. The corresponding geometric phase analysis (GPA) of Figure XIX.2.4c provided the direct strain distribution of the $\text{NaNi}_{0.4}\text{Mn}_{0.4}\text{Co}_{0.2}\text{O}_2$ cathode, which showed an angle between layered direction and strain direction (Figure XIX.2.4e). Such native lattice strain can be thus separated into tensile stress along the c -axis direction that tend to stretch the lattice, and shear stress along the ab -axis direction that will compress the lattice (Figure XIX.2.4f). Upon extraction of Na^+ , such metastable structure tends to undergo spontaneous strain relaxation and cause significant structural degradation.

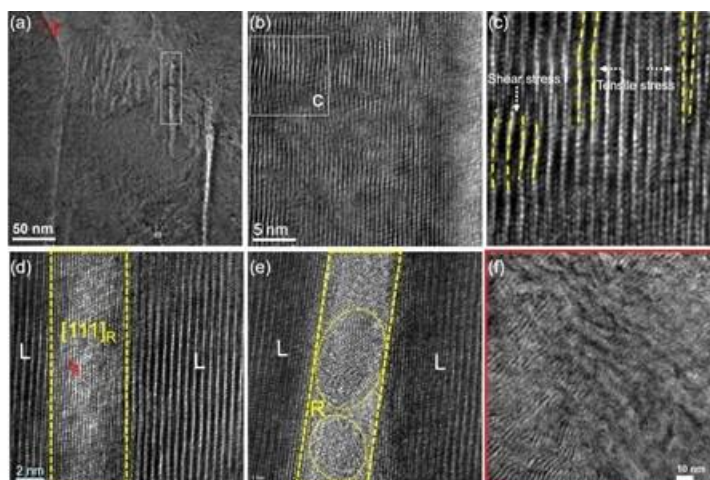


Figure XIX.2.5 TEM characterization on cycled O3 $\text{NaNi}_{0.4}\text{Mn}_{0.4}\text{Co}_{0.2}\text{O}_2$ cathode particle (2.0–4.4 V for 100 cycles). (a) Low and (b) high magnification TEM image. (c) Zoomed-in view of the dashed square area in (b). (d–e) Zoomed-in views of the dashed rectangle area in (a). (f) Zoomed-in view of dot-circle area in (a).

Figure XIX.2.5a shows the bright-field TEM image of strained $\text{NaNi}_{0.4}\text{Mn}_{0.4}\text{Co}_{0.2}\text{O}_2$ cathode after charge/discharge within 2.0–4.4 V at 0.08 C for 100 cycles. Compared to the pristine one (Figure XIX.2.4b), a large portion of native lattice strain was relaxed since the strain contours disappeared. HRTEM image (Figure XIX.2.5b) and the zoomed-in view (Figure XIX.2.5c) show that there are numerous stacking faults and dislocations as a catastrophic consequence of strain relaxation. In particular, we can clearly see the bending of lattice (yellow dashed lines in Figure XIX.2.5c) parallel to the layered direction due to the shear stress along the *ab*-axis. Moreover, the tensile stress along the *c*-axis direction led to evolution of lattice dislocations and stacking faults. As a result, it will be difficult to re-insert Na^+ into the Na layer because of the crossover of TM cations that might occupy the Na sites and damage layered structure, implied by the disappearance of (00*l*) peaks in the in situ SXRD patterns at the beginning of the discharge process. Hence, the material suffered from a dramatic capacity loss.

On the other hand, by examining the strain-relaxed region in Figure XIX.2.5a (marked by white rectangle), it was found that the observed gaps between two layered planes are not empty; they are composed by low-crystalline fragmented domains. Figure XIX.2.5d clearly showed that a layer of NiO-like rock-salt structure with (111) plane was formed at the tip of premature crack region. In general, the (111) plane of rock-salt structure is energetically and structurally favourable, and has a high tolerance against compression strain. However, the native high lattice strain in the quenched cathode significantly exceeds both tensile and compression limit of rock-salt phase, thus leading to the formation of rock-salt fragments with different orientation (Figure XIX.2.5e). In contrast, in the strain-unrelaxed region (blue circle in Figure XIX.2.5a), the curved lattice fringes were preserved, and no formation of cracks or premature cracks can be observed even at the grain boundaries that have long been considered as the preferred crack-initiating sites (Figure XIX.2.5f). The curved lattice fringes of strained layered oxide cathodes introduced by quenching during material synthesis are similar to the curved stratum of the earth during earthquake due to the stored elastic strain energy. The extraction/insertion of Na^+ plays a similar role to plate motion, which leads to the release of stored energy (native strain) in a way of cracking, displacement and dip/strike faulting that also occurred during the structural degradation of layered cathodes.

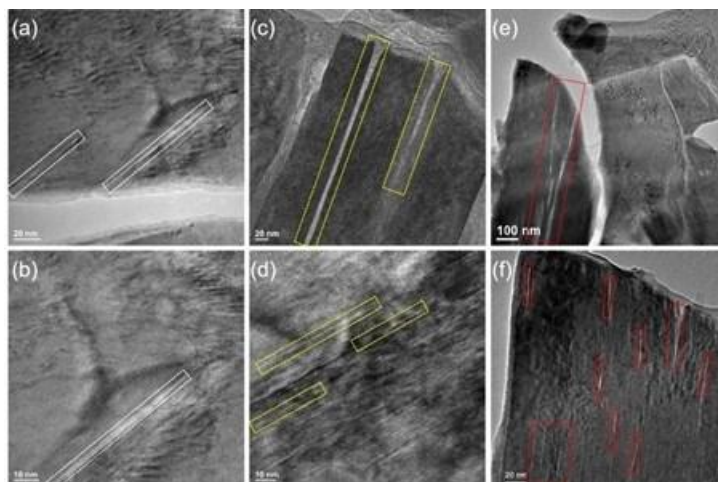


Figure XIX.2.6 Strain relaxation under different condition. Low and high magnification TEM images of O3 $\text{NaNi}_{0.4}\text{Mn}_{0.4}\text{Co}_{0.2}\text{O}_2$ cathode after 100 cycles within 2.0-4.4 V at different condition: (a-b) 0.08 C under room temperature; (c-d) 0.2 C under 55 °C, and (e-f) 1 C under room temperature.

We further investigated the influence of charge/discharge rates and temperature on the strain relaxation process. Figure XIX.2.6 compares the structures of cycled strained $\text{NaNi}_{0.4}\text{Mn}_{0.4}\text{Co}_{0.2}\text{O}_2$ cathode after 100 cycles of charge/discharge under different conditions. Under a low charge/discharge rate of 0.08 C at room temperature, the strain relaxation was relatively smooth, leading to the formation of straight incision (marked by white rectangles in Figure XIX.2.6a and Figure XIX.2.6b). This is because the extraction/insertion of Na^+ is proceeding in a very slow manner, which can thus minimize the effect of stress heterogeneity. This is similar to common phenomena, such as smooth plate motion or tearing wrinkle paper in a slow manner. Again, we can see the tip of the gap was terminated at the end of the strain-unrelaxed region. With elevated temperature, we can see the propagation and widening of gaps (marked by yellow rectangles in Figure XIX.2.6c) as well as new formation of high-density nanogaps (marked by yellow rectangles in Figure XIX.2.6d). This might be because of the increased extraction/insertion kinetic of Na^+ at high temperature. By switching to fast charging/discharging, the strain relaxation is aggressive and vigorous, thus leading to formation of both large (marked by red rectangles in Figure XIX.2.6e) and high-density nanocracks (marked by red rectangles in Figure XIX.2.6f) with curved incision.

In brief, through a combination of advanced diagnostics from material synthesis to cell failure, we have discovered the essential role of synthesis-induced native lattice strain in triggering the structure earthquake of sodium layered oxide cathodes during cycling. The spontaneous relaxation of internal strain that exceeds the threshold limit is the fundamental origin of the abrupt degradation of sodium layered oxide cathodes. Furthermore, we showed that such process is not regulated by the charge cut-off voltage, but is strongly coupling with working temperature and charging/discharging rates that can tailor the movement of Na^+ . Our work indicates an urgent need to revisit the crystallographic structure of sodium /lithium layered oxide cathodes such as strain, oxygen vacancies, nanopores, domain boundaries and other intrinsic defects, and to understand how they affect common battery phenomenon such as capacity fade and voltage decay/hysteresis. Our work also indicates that a rational strain management during cycling of sodium/lithium layered cathodes is required to maximize cycle life.

Part Two: Entropy and crystal-facet modulation of P2-type layered cathodes for long-lasting sodium-based batteries

We further developed a series of P2 type single-crystal sodium layered $\text{Na}_{0.62}\text{Mn}_{0.67}\text{Ni}_{0.23}\text{Cu}_{0.05}\text{Mg}_{0.09-2y}\text{Ti}_y\text{O}_2$ cathode by simultaneously tuning their entropy and crystal facets, and investigated their electrochemical/thermal stability. The optimized composition is $\text{Na}_{0.62}\text{Mn}_{0.67}\text{Ni}_{0.23}\text{Cu}_{0.05}\text{Mg}_{0.07}\text{Ti}_{0.01}\text{O}_2$, designated as CuMgTi-571. The CuMgTi-571 cathode could deliver an initial specific capacity of 148.2

mAh/g and a reversible capacity of ~ 133 mAh/g after 100 cycles at 12 mA/g during charge/discharge within 2.0–4.3 V, demonstrating good cycling stability.

To check the impact of entropy and crystal-facet tuning on the structural stability of the material, in situ synchrotron high energy X-ray diffraction (HEXRD) was conducted on CuMgTi-571 during charge/discharge, and the results are displayed in Figure XIX.2.7. Figure XIX.2.7a and 7b shows the waterfall and contour plot of HEXRD patterns of the CuMgTi-571 electrode charged/discharged at 0.1 C (12 mA g⁻¹) between 2.0 and 4.3 V, respectively. Upon Na⁺ extraction (charge), the (002) and (004) peaks shift toward lower $2\theta^\circ$ angle due to the increase in the repulsive electrostatic interaction between adjacent MO₂ sheets; while (010), (012), (108), and (112) peaks consecutively shift toward a higher $2\theta^\circ$ angle with the contraction of *a*-, *b*-axis. During the subsequent discharge, the XRD pattern of CuMgTi-571 exhibited an exactly opposite evolution. During the whole charge/discharge process, the well-defined peaks corresponding to the P2 phase are well maintained and returned to the initial states after one full cycle. No new peaks belong to OP4, O2 or Z phase are detected when charged to 4.3 V, and no existing peaks vanish or split, indicating that new phase formation and phase transition do not occur in this material. The changes of lattice parameter upon cycling based on the refinement results are displayed in Figure XIX.2.7c. It is clear that the lattice parameter evolution is highly reversible during the charge and discharge process. The largest changes of the *a*, *c*, and *V* in the first cycle are only 0.74%, 0.91% and 0.57%, respectively. The high reversibility of lattice parameter evolution and structural evolution upon Na⁺ (de-)intercalation manifests the unusual structure stability of entropy and crystal facet-tuned cathode.

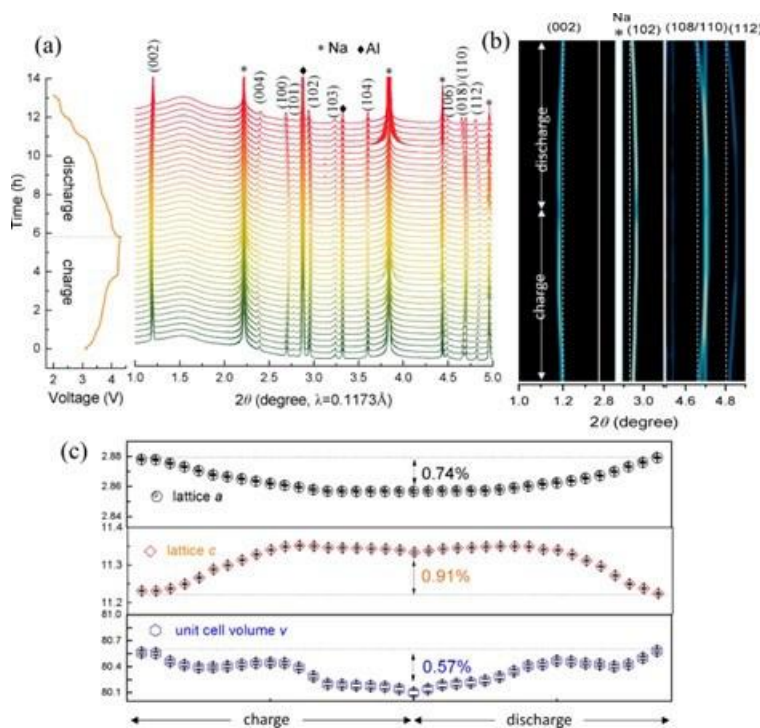


Figure XIX.2.7 In situ HEXRD characterization in coin cell configuration at 25 °C. (a) The waterfall plot and (b) contour plot of in situ HEXRD patterns for CuMgTi-571 within 2.0–4.3 V. (c) Evolution of cell parameters and cell volume during the charge/discharge process.

In situ HEXRD during heating of de-sodiated cathode powder was also performed to investigate the phase stability of entropy and crystal-facet tuned cathodes at high temperature (heating from 30°C to 450°C) to investigate their thermal tolerance (Figure XIX.2.8a and Figure XIX.2.8b). The tested CuMgTi-571 and Na_{0.62}Mn_{0.67}Ni_{0.37}O₂ (NaMNO₂) materials were scraped from 4.2 V-charged cathodes. The (002) peak, which is most sensitive to the Na content during charging/discharging, is usually used to monitor the phase transformation of P2-type layered cathodes during heating. The (002) reflection of charged CuMgTi-571

continuously moves to lower angle with increasing the temperature due to the lattice expansion caused by heating (Figure XIX.2.8a). Distinct from CuMgTi-571, the (002) reflection of charged NaMNO₂ first shifts to lower angle upon heating, and then moves to higher angle when the heating temperature reached above 222°C (Figure XIX.2.8b). Such phenomenon indicates that new phases such as spinel or rock-salt were formed in the charged NaMNO₂ during the heating. Moreover, the (002) peak fading starts at 350°C and 322°C for the CuMgTi-571 and NaMNO₂ cathodes, respectively, further confirming the inferior structural stability of the NaMNO₂. The formation of new phase and inferior structural stability would lead to irregular migration channel and hence sluggish Na⁺ diffusion.

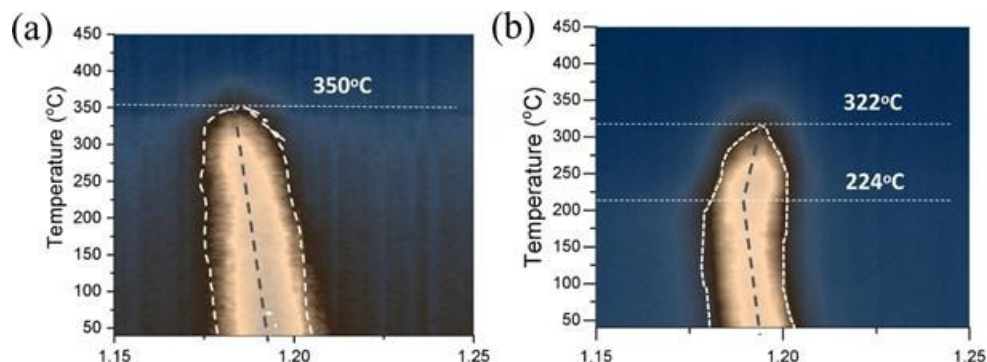


Figure XIX.2.8 The 2D contour XRD plots of de-sodiated (a) CuMgTi-571 and (b) NaMNO₂ during the heating from 30 °C to 450 °C at 5 °C min⁻¹, the tested samples during heating are de-sodiated cathode powder scraped from 4.2 V-charged cathodes.

In brief, configurational entropy could result in a thermodynamically stable structure through a local minimization of Gibbs free energy, and a high percentage of {010} facets in the layered cathodes could provide more channels for ion transport. Based on the advantages of high entropy and high active facets, a combinatorial strategy of entropy modulation and active-facet modulation will be developed to determine repetitive factors that predict structural stabilization which can lead to optimization of ion-migration pathways of P2-type layered cathodes.

Part Three: Fe behavior in layered transition metal oxide cathodes

Previous studies of layered sodium transition metal oxides have shown that Fe substitution can improve the electrochemical performance of the Co-free Na_x(Mn,Ni)O₂ cathodes, not to mention its economic advantage. Regarding the optimum Fe content, less than 50% substitution has been unequivocally suggested in the literature. The high-Fe composition tends to aggravate the cycle performance of the cathodes, even more so when a high cut-off voltage is used. Despite the growing number of works in Fe-containing layered cathodes, most of these works focus on cycling under moderate voltage ranges, such as below 4.0 V vs. Na, and the origin of the high-voltage cycling vulnerability of the Fe-rich compositions remains unclear yet. Another critical concern in layered sodium transition metal oxides (Na_xMO₂) is their poor ambient air storage stability. The hygroscopic nature of the sodium cathodes leads to hydration, Na extraction, and degradation on the air-exposed surface, which in turn cause practical process and performance issues such as gas evolution, slurry gelation, and electrolyte decomposition. These could incur additional costs for material storage, transportation, and manufacturing in the battery manufacturing.

In the last fiscal year, the team discussed the detailed mechanisms governing the surface degradation of charged cathodes, which are mainly triggered by the highly reactive Fe⁴⁺ species [6]. In this fiscal year, as part of our continued efforts towards high-performance Fe-based cathodes, we've studied the effect of Fe content on the high-voltage cycling performance and air-storage stability of the Fe-based layered Na(Ni,Mn,Fe)O₂ cathodes.

Fe migration and performance limitation

The $\text{NaNi}_{1/3}\text{Mn}_{1/3}\text{Fe}_{1/3}\text{O}_2$ (NMF111) and $\text{NaNi}_{1/4}\text{Mn}_{1/4}\text{Fe}_{1/2}\text{O}_2$ (NMF112) powder samples were synthesized by solid-state reaction of $(\text{Ni}_{0.5}\text{Mn}_{0.5})_{1-x}\text{Fe}_x(\text{OH})_2$ and NaOH precursors. The transition metal hydroxide precursors were prepared by co-precipitation method using a continuous-stir-tank-reactor (CSTR). The prepared oxide particles have spherical, secondary particle morphology (average particle size $\sim 10\ \mu\text{m}$). The Rietveld refinement analysis of the powder XRD data confirms a highly crystalline single-phase material with α - NaFeO_2 layered structure (Figure XIX.2.9a and b). The calculated lattice parameters are $a = 2.987\ \text{\AA}$ and $c = 15.972\ \text{\AA}$ for NMF111; and $a = 2.997\ \text{\AA}$ and $c = 16.009\ \text{\AA}$ for NMF112. The lattice parameters and cell volume increase with higher Fe content due to the larger ionic radii of high spin Fe^{3+} than that of $(\text{Ni}^{2+}_{0.5}\text{Mn}^{4+}_{0.5})$.

In Figure XIX.2.9c-f, both cathodes show similar reversible capacity and cycle stability when the low cut-off voltage of 3.8 V vs. Na is used. However, when a higher cut-off voltage (i.e., $> 4.0\ \text{V}$ vs. Na) is applied, NMF112 exhibits severer degradation in cycle performance than NMF111. According to our previous study on the charge compensation mechanism of NMF111, Ni redox accounts for the majority of charge compensation below $\sim 4.0\ \text{V}$, and Fe redox is only activated in the higher voltage range [7]. Interestingly, the threshold cut-off voltage above which the cycle stability significantly degrades corresponds well with the point where $\text{Ni}^{2+}/\text{Ni}^{4+}$ redox is depleted and $\text{Fe}^{3+}/\text{Fe}^{4+}$ redox kicks in. This observation suggests that the destabilization of NMF111 and NMF112 during high-voltage charging is closely associated with the activation of $\text{Fe}^{3+}/\text{Fe}^{4+}$ redox.

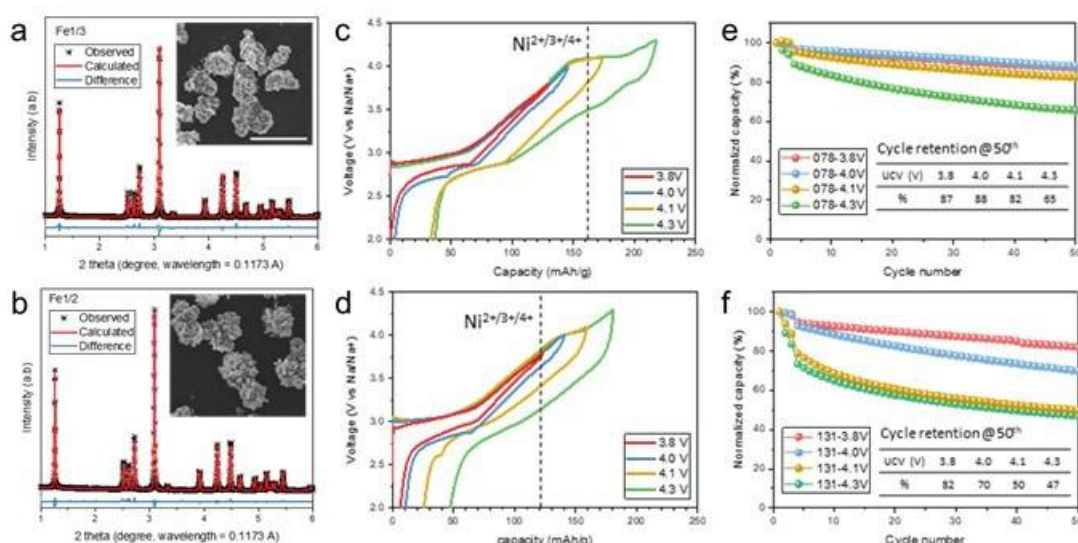


Figure XIX.2.9 XRD pattern (a, b), voltage profile (c, d), and cycle performance (e, f) of NMF111 (a, c, e) and NMF112 (b, d, f); (i = 10 mA/g for the first three cycles and 30 mA/g for the next cycles).

Figure XIX.2.10a and b show the operando synchrotron XRD data of the NMF111 and NMF112 cells collected during the initial cycle between 2 and 4.3 V vs. Na. Both cathode materials exhibit similar O3 to P3 and O'3 (monoclinically distorted O3 phase) type phase transitions overall. However, a more careful examination of the phase evolution reveals that NMF112 has an extended O3/P3 and P3/O'3 biphasic regions (Figure XIX.2.10b). This trend is even more evident when compared with the phase evolution of the Fe-free, $\text{NaNi}_{0.5}\text{Mn}_{0.5}\text{O}_2$ cathode (NM11), in which distinct single phases regions develop sequentially, along with narrower biphasic regions in between, as the phase transition proceeds. Figure XIX.2.10c-f show the synchrotron XRD patterns selected at different state-of-charges (SOCs; 3.8, 4.0, and 4.3 V vs. Na) and after discharged from those SOC. In Figure XIX.2.10c and d, the NMF112 shows severe peak broadening and a decrease in peak intensity when charged above 4.0 V vs. Na. This can be attributed to the increased structural disordering due to the migration of Fe ions from the transition metal layers to sodium layers [8,9]. The much

smaller c-axis parameter for the NMF112 at the 4.3 V SOC further suggests significant c-axis contraction due to the high concentration of the migrated Fe ions in the sodium layers. Figure XIX.2.10e and f compare the structural reversibility after the initial cycle. NMF111 recovers its pristine structure after one charge and discharge cycle up to 4.3 V. However, NMF112 indicates incomplete phase recovery after 4.3 V cycling, whereas the phase transition is relatively reversible when cycled up to a lower cut-off voltages (≤ 4.0 V vs. Na).

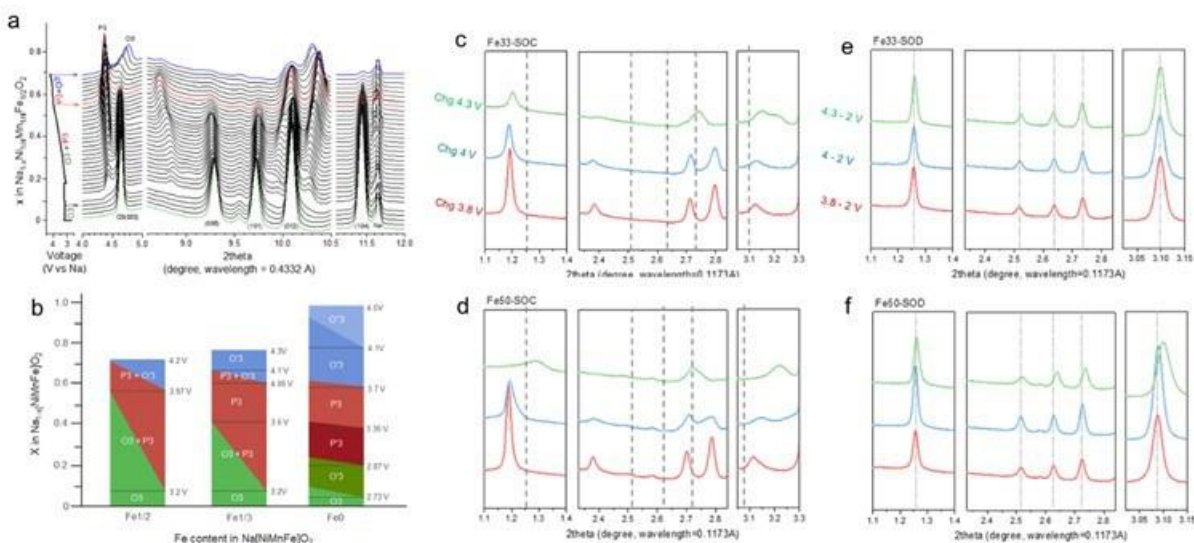


Figure XIX.2.10 XRD pattern (a, b), voltage profile (c, d), and cycle performance (e, f) of NMF111 (a, c, e) and NMF112 (b, d, f); ($i = 10$ mA/g for the first three cycles and 30 mA/g for the next cycles).

Our electrochemical performance and operant XRD data shed light on the fundamental structural origin of the poorer cycle stability of the high-Fe NMF cathodes. First, the facile layer gliding and phase transition from the pristine O3 to P3 structure are hindered by a pinning effect from the migrated Fe ions in the sodium layer. Second, the migrated Fe provides a tighter inter-slab binding in the sodium layer resulting in a higher energy barrier for the stabilization of single P3 phase, and an earlier transition to the O'3 phase at high SOC. Such an early transition to the high-SOC O'3 phase in NMF112 results in premature contraction of the c-axis, making further sodium extraction difficult. Third, the Fe migration is only partially reversible, and the high concentration of residual Fe in sodium layers after a discharge increases the impedance for sodium extraction and insertion in the following cycles. In conclusion, our work clearly indicates that the bulk structural issues associated with Fe migration, as well as the chemical instability at the particle surface, need to be addressed to enable the stable, high-capacity cycling of the high-Fe NMF cathodes. At Argonne, multi-faceted surface/bulk modification strategies are being pursued to this end.

Air-storage stability of Fe-based layered cathodes

A series of layered $\text{Na}[(\text{Ni}_{0.5}\text{Mn}_{0.5})_{1-x}\text{Fe}_x]\text{O}_2$ cathode materials was synthesized using co-precipitation and solid-state reaction method described in the previous section. The powder samples were exposed to ambient air for several days, and the degree of degradation was evaluated by X-ray diffraction (XRD) as shown in Figure XIX.2.11. The as-synthesized pristine cathodes have an O3-type layered structure with stoichiometric Na content ($\text{O3-Na}_{1.0}\text{MO}_2$). After being air-exposed, the XRD data exhibit changes in the O3 structure and the formation of degradation products. The Fe0 sample shows the most significant structural degradation among the samples (Figure XIX.2.11a). The parent O3 layered phase transformed to P3 structure, indicating a significant amount of Na extraction from the layered structure ($\text{P3-Na}_{1-y}\text{MO}_2$), and new peaks corresponding to Na_2CO_3 and NiO appeared. In striking contrast, the Fe2/3 sample preserves the O3 layered structure better; the XRD pattern shows only a slight peak shift corresponding to c-axis expansion and a-axis contraction, indicating less sodium extraction ($\text{O3-Na}_{1-y}\text{MO}_2$). In Figure XIX.2.11d, the lattice parameter changes for the

air-exposed cathodes reveal a clear trend of suppressed Na extraction and structural degradation with increasing Fe-content.

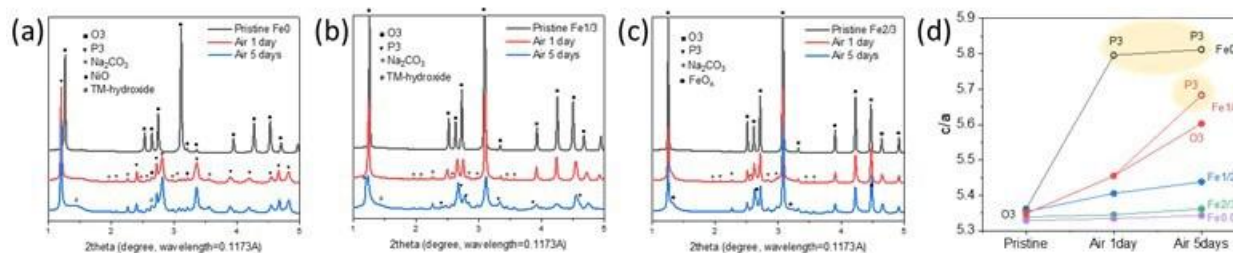


Figure XIX.2.11 (a-c) Powder XRD patterns of $\text{Na}[(\text{Ni}_{0.5}\text{Mn}_{0.5})_{1-x}\text{Fe}_x]\text{O}_2$ ($x = 0, 1/3$, and $2/3$), and (d) changes in the c/a lattice parameter ratio before and after air-exposure.

Figure XIX.2.12 compares the particle morphologies before and after the air exposure. All the pristine samples show similar secondary particle morphologies comprising aggregated plates of primary particles. After being exposed to ambient air for five days, the surface of low-Fe cathodes ($\text{Fe}0$, $\text{Fe}1/3$) is fully covered by a thick layer of residual sodium species, Na_2CO_3 . In contrast, the high-Fe cathodes ($\text{Fe}1/2$, $\text{Fe}2/3$, $\text{Fe}0.8$) better preserve the pristine surface morphology and Na_2CO_3 grows as rod-shaped crystals rather than surface covering [10]. The lower Na_2CO_3 quantity in the high-Fe cathodes was confirmed by both X-ray photoelectron spectroscopy (XPS) and thermal gravimetric analysis (TGA) data (data not shown). We presume that a slower surface degradation and sodium extraction rate of the high-Fe cathodes provide a suitable condition for the growth of rod-shaped Na_2CO_3 crystals.

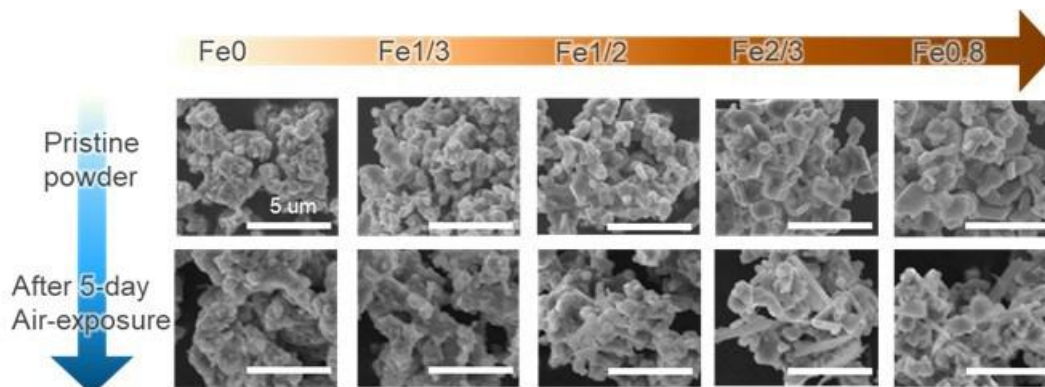


Figure XIX.2.12 SEM particle morphologies of $\text{Na}[(\text{Ni}_{0.5}\text{Mn}_{0.5})_{1-x}\text{Fe}_x]\text{O}_2$ ($x = 0, 1/3, 1/2, 2/3$, and 0.8) before and after air-exposure for five days.

It can be postulated from the above observations that the sodium extraction from the stoichiometric $\text{O}3\text{-NaMO}_2$ triggers the cathode degradation during the ambient storage. There are two possible mechanisms by which the sodium deficient layered oxide phase maintains the charge neutrality: (1) transition metal oxidation ($\text{Na}_{1-y}\text{M}^{3+,4+}\text{O}_2$) and (2) proton exchange ($\text{H}_y\text{Na}_{1-y}\text{M}^{3+}\text{O}_2$) [11]. The $\text{O}3$ to $\text{P}3$ phase transition shown in the low-Fe compounds corresponds well with the typical phase transition during the electrochemical sodium deintercalation from $\text{O}3\text{-NaMO}_2$ materials. However, phase degradation via the proton exchange mechanism cannot be completely ruled out because $\text{P}3$ -type layered structure can also be stabilized in the proton exchanged layered H_yMO_2 [12]. In order to better understand the degradation mechanism, we have examined the oxidation states of transition metals after air exposure. As shown in Figure XIX.2.13.a-c, the oxidation state of Ni increases to a higher value after air exposure, supporting the transition metal oxidation mechanism. (Note that Mn and Fe remain in their pristine oxidation states, Mn^{4+} and Fe^{3+} .) This result suggests the air stability of layered NaMO_2 cathodes is closely correlated with their oxidation potential. Figure XIX.2.13d exhibits the open-circuit voltages (OCV) for $\text{Na}_{1-y}[(\text{Ni}_{0.5}\text{Mn}_{0.5})_{1-x}\text{Fe}_x]\text{O}_2$ linearly increase with Fe content, x .

Therefore, the improved air-storage stability of the high-Fe compounds can be attributed to their higher oxidation barrier, which suppresses the sodium extraction from the lattice and the subsequent cascades of phase degradation.

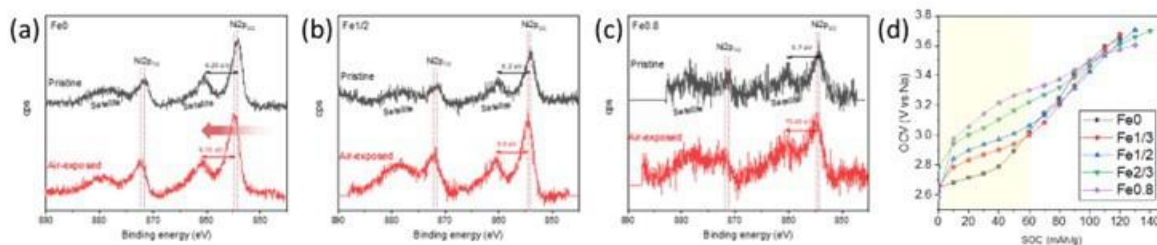


Figure XIX.2.13 X-ray photoelectron spectroscopy (XPS) Ni2p spectra of the pristine and air-exposed (a) $\text{Na}[\text{Ni}_{0.5}\text{Mn}_{0.5}]\text{O}_2$, (b) $\text{Na}[\text{Ni}_{0.25}\text{Mn}_{0.25}\text{Fe}_{0.5}]\text{O}_2$, and $\text{Na}[\text{Ni}_{0.1}\text{Mn}_{0.1}\text{Fe}_{0.8}]\text{O}_2$; (d) open-circuit voltages profiles of $\text{Na}[(\text{Ni}_{0.5}\text{Mn}_{0.5})_{1-x}\text{Fe}_x]\text{O}_2$.

Conclusions

Through a combination of synchrotron X-ray and electron microscopy characterization, we have clearly revealed the effect of synthesis-induced native lattice strain in triggering the structural earthquake during cycling of O3 type layered cathodes. We have further developed a high-performance P2 $\text{Na}_{0.62}\text{Mn}_{0.67}\text{Ni}_{0.23}\text{Cu}_{0.05}\text{Mg}_{0.07}\text{Ti}_{0.01}\text{O}_2$ layered cathode with improved (de) sodiation reversibility and thermal stability.

When we move to Fe-rich layered oxide cathodes, the instability of the materials become apparent, particularly at higher voltages above 4.0 V. This indicates instability issues with Fe when it becomes oxidized (presumably to tetravalent Fe). In addition, surface reactivity issues with the pristine material and water and, subsequently in the cell with electrolyte interactions also affects the oxidized electrode adversely. Bulk changes and layer gliding and stacking in the *c*-axis direction changes throughout the voltage profile. However, we find that a balance of 1/3 Fe in the composition is beneficial to performance in a moderate voltage window. We also surmise that if the movement of Fe can be locked within the transition metal (TM) layer upon material oxidation using pillaring cations in the Na layer and dopants in the TM layer then we can improve stability. Moreover, electrode coatings on the surface of the particle could address instabilities with the electrolyte. Electrolyte changes and additives need to be discovered and optimized.

Key Publications

Patents

1. Liu, X.; Xu, G. L.; Amine, K.; Electroactive materials for secondary batteries. United States Patent 11,394,022, granted on July 19, 2022.
2. Xu, G. L.; Zhao, C.; Liu, Y.; Amine, K.; Coatings for battery cathode materials. United States patent application, filed on September 28, 2022.

Publication

1. Liu, X.; Xu, G. L.(*); Kolluru, V. S.; Li, Q.; Zhou, X.; Liu, Y.; Yin, L.; Zhuo, Z.; Daali, A.; Fan, J.; Liu, W.; Ren, Y.; Xu, W.; Deng, J.; Hwang, I.; Ren, D.; Feng, X.; Sun, C.; Huang, L.; Zhou, T.; Du, M.; Chen, Z.; Sun, S.-G.; Chan, M.; Yang, W.(*); Ouyang, M.(*); Amine, K.(*). Origin and regulation of oxygen redox instability in high-voltage battery cathodes. *Nature Energy*, 2022, 7, 808-817. Publication date: June 02, 2022.
2. Holguin, K.; Qin, K.; Kamphaus, E. P.; Chen, F.; Cheng, L.(*); Xu, G. L.(*); Amine, K.; Luo, C(*). Establishing substitution rules of functional groups for high-capacity organic anode materials in Na-ion batteries. *J. Power Sources* 2022, 533, 231383. Publication date: June 15, 2022.
3. Daali, A.; Zhao, C.; Zhou, X.; Yang, Z.; Amine, R.; Liu, Y.; Wilkistar, O.; Xu, G. L.(*); Amine, K.(*). Tuning working potential of silicon-phosphorus anode via microstructure control for high-

energy lithium-ion batteries. *J. Solid State Electrochem.* 2022, 26, 1919-1927. Publication date: June 14, 2022.

4. Fu, F.(*); Liu, X.; Fu, X.; Chen, H.; Huang, L.; Fan, J.; Le, J.; Wang, Q.; Yang, W.; Ren, Y.; Amine, K.(*); Sun, S.-G.; Xu, G. L.(*). Entropy and crystal-facet modulation of P2-type layered cathodes for long-lasting sodium-based batteries. *Nature Communications*, 2022, 13, 2826. Publication date: May 20, 2022.
5. Xiao, B.; Liu, X.; Song, M.; Yang, X.; Omenya, F.; Feng, S.; Sprenkle, V.; Amine, K.; Xu, G.-L.; Li, X.; Reed, D. A General Strategy for Batch Development of High-Performance and Cost-Effective Sodium Layered Cathodes. *Nano Energy*, 2021, 106371. Publication date: Nov 2021.
6. Liu, X.; Zhou, X.; Liu, Q.; Diao, J.; Zhao C.; Li, L.(*); Liu, Y.(*); Xu, W.; Daali, A.; Harder, R.; Robinson, I. K.; Dhahi, M.; Alami, J.; Chen, G.; Xu, G. L.(*); Amine, K.(*). Multiscale understanding of surface structural effects on high-temperature operational resiliency of layered oxide cathodes. *Adv. Mater.* 2021, 2107326. Oct 26, 2021.
7. Xiao, B.; Liu, X.; Chen, X.; Lee, G. H.; Song, M.; Yang, X.; Omenya, F.; Reed, D.; Sprenkle, V.; Ren, Y.; Sun, C. J.; Yang, W.; Amine, K.; Li, X.(*); Xu, G. L.(*); Li, X.(*). Uncommon Behavior of Li Doping Suppresses Oxygen Redox in P2-type Manganese-Rich Sodium Cathodes. *Adv. Mater.* 2021, 2107161. Publication date: Oct 11, 2021.
8. Park, J.; Ku, K.; Son, S.-B.; Gim, J.; Kim, Y.; Lee, E.; Johnson, C., Effect of Electrolytes on the Cathode-Electrolyte Interfacial Stability of Fe-Based Layered Cathodes for Sodium-Ion Batteries. *Journal of the Electrochemical Society* 2022, 169 (3), 030536.
9. Oh, H. J.; Kang, H. K.; Ahn, H.; Park, J.; Choi, J.; Kim, H. Y.; Lee, E.; Yeo, S. Y.; Choi, Y. O.; Yeang, B. J., Layered oxide cathode-inspired secondary hard carbon microsphere anode material for high-power and long-life rechargeable batteries. *Chemical Engineering Journal* 2022, 140252.
10. Tomich, A.; Park, J.; Son, S.-B.; Kamphaus, E.; Lyu, X.; Dogan, F.; Carta, V.; Gim, J.; Li, T.; Cheng, L.; Lee, E.; Lavallo, V.; Johnson, C. S., A Carboranyl Electrolyte Enabling Highly Reversible Sodium Metal Anodes via a “Fluorine-Free” SEI. *Angewandte Chemie International Edition* 2022.

Presentations

1. Xu, G. L.; Amine, K.; Development of Layered Oxides Cathodes and N Phosphorus Anode for High-Energy and Low-Cost Sodium-Ion Batteries. 2021 Materials Research Society Fall Meeting and Exhibit (Virtual), Boston, MA US, December 6, 2021 - December 8, 2021.
2. Xu, G. L.; Amine, K.; "Beyond phase transition and parasitic reactions: native lattice strain induced structural earthquake in sodium layered oxide cathodes." Invited poster presented at the 21st International Meeting on Lithium Batteries (IMLB 2022), Sydney Australia, June 26, 2022-July 1, 2022.
3. Park, J.; Han, J.; Gim, J.; Bak, S.-M.; Ahmed, S.; Iddir, H.; Garcia, J.; Kim, Y.; Lee, E.; Johnson, C. "Insights into the Na-Alloying Mechanism and Zintl Phase Transition of Lead-Based Anodes"; 242nd Electrochemical Society Meeting, Atlanta, GA, October 9-13, 2022
4. Park, J.; Gim, J.; Son, S.-B.; Hou, D.; Jeong, H.; Chang, L.; Xiong, H.; Kim, Y.; Lee, E.; Johnson, C., A Study on Air Storage Characteristics of O3-type Na[Ni¹/2Mn¹/2]1-xFexO2 cathode materials for Sodium-ion batteries, 2022 MRS fall meeting, Boston, MA, Nov 27-Dec 2, 2022.
5. Zuo, W.; Xu, G. L.; Amine, K.; "The air stability of sodium layered oxide cathodes"; 242nd Electrochemical Society Meeting, Atlanta, GA, October 9-13, 2022

References

1. N. Yabuuchi, et al., *Chemical Reviews* 114 (2014):11636-11682.
2. M. Han, et al., *Energy & Environmental Science* 8 (2015):81-102.
3. Y. Wen, et al., *Nature Communications* 5 (2014): 4033.
4. S. Huang, et al., *Adv. Mater.* 30 (2018):1706637.
5. H. Kang, et al., *Journal of Materials Chemistry A* 3 (2015):17899-17913.
6. J. Park, K. Ku, S.-B. Son, J. Gim, Y. Kim, E. Lee, and C. Johnson, *J. Electrochem. Soc.*, 169, 30536 (2022).

7. C. Deng, E. Gabriel, P. Skinner, S. Lee, P. Barnes, C. Ma, J. Gim, M. L. Lau, E. Lee, and H. Xiong, *ACS Appl. Mater. Interfaces*, 12, 51397 (2020).
8. E. Lee, D. E. Brown, E. E. Alp, Y. Ren, J. Lu, J.-J. Woo, and C. Johnson, *Chem. Mater.*, 27, 6755 (2015).
9. E. Talaie, V. Duffort, H. L. Smith, B. Fultz, and L. Nazar, *Energy Environ. Sci.*, 8, 2512 (2015).
10. Y. Sun and Z.-F. Ma, et al., *ACS Appl. Energy Mater.* 2021, 4, 2061.
11. W. Zuo and Y. Yang, et al., *Nature Commun.* 2020, 11, 3544.
12. Robertson and P. G. Bruce, *Chem. Mater.* 2003, 15, 1984.

Acknowledgements

We would like to thank Dr. Guiliang Xu and Dr. Eungje Lee at ANL for the major contribution to this project.

XIX.3 Tailoring High Capacity, Reversible Anodes for Sodium-Ion Batteries (LBNL)

Marca M. Doeff, Principal Investigator

Lawrence Berkeley National Laboratory
1 Cyclotron Road
Berkeley, CA 94720
E-mail: mmdoeff@lbl.gov

Tien.Duong, DOE Technology Development Manager

U.S. Department of Energy
E-mail: Tien.Duong@ee.doe.gov

Start Date: October 1, 2021

End Date: September 30, 2024

Project Funding (FY22): \$300,000

DOE share: \$300,000

Non-DOE share: \$0

Project Introduction

Stepped layered titanates are promising materials for use as anodes in sodium-ion batteries, based on their earth-abundance, low cost, reasonably high density, and low sodium insertion potentials (~ 0.3 - 0.6 V vs. Na^+/Na , on average). We have identified several materials that deliver capacities in excess of 200 mAh/g and cycle reversibly in sodium half-cell configurations [1-3]. In particular, the physical and electrochemical properties of lepidocrocite-type titanates having the general formula $\text{A}_x\text{Ti}_{2-y}\text{M}_y\text{O}_4$ ($\text{A}=\text{K}^+$, Cs^+ , Rb^+ and $\text{M}=\text{metal}$ or vacancy located in the transition metal layer), can be readily tuned by exchanging the large cations, A, with Na^+ , and by varying the identity of M, as well as the overall composition (x and y). For example, additional diffusional pathways for Na^+ are present when M is a mobile cation such as Li^+ compared to the less mobile Mg^{2+} cation, resulting in higher practical capacities [4]. Based on a similar principle, capacities in excess of 220 mAh/g can be obtained when vacancies are incorporated in the transition metal layer [3]. In addition to composition, however, it is clear that the electrochemical properties of these materials are very sensitive to preparation conditions such as dehydration temperature, as well as details of the cell assembly, such as the type of electrolytic solution used [3, 5]. Furthermore, an analysis of cyclic voltammetry data on cells made with vacancy-containing lepidocrocite titanates indicated that the redox mechanism is complex, including both surface and diffusional components. In some cases, the practical capacity exceeds the theoretical (assuming reductive intercalation of sodium into available sites between titanate layers), also suggesting that surface processes may contribute to the capacity. Finally, less titanium is reduced than expected, assuming a purely diffusional redox process, as observed by Ti K-edge X-ray absorption experiments on pristine, discharged, and partially discharged electrodes. Work for this project is directed towards understanding the role that vacancies and defects play in determining the electrochemistry of stepped, layered titanates and to design materials with better electrochemical properties based on these observations. A specific goal is to improve the capacity, reversibility, and rate capability of these promising electrode materials without compromising first cycle efficiencies.

Objectives

The planned work is conceived to overcome the main obstacle to the practical realization of sodium-ion batteries; the lack of a suitable anode material. Experiments are designed to improve the practical reversible capacities and overcome the high first cycle coulombic inefficiencies of promising low voltage sodium titanates, as well as to assess the stabilities of the sodiated (partially and fully discharged) products of the electrochemical reactions. Some effort is devoted to consideration of electrolytes and understanding of the electrolyte/anode interface, which must go hand-in-hand with anode development. The ultimate goal is to produce a high capacity (200-250 mAh/g), stable, and reversible low voltage anode material suitable for use in a sodium-ion battery configuration. An ideal electrode would be able to deliver 225 mAh/g at C/3 rate, with good capacity retention (80% or better) in a full cell configuration for at least 100 cycles.

Approach

Candidate stepped layered titanates are synthesized by appropriate routes (hydrothermal, solid state methods, etc.) and ion-exchanged by soft chemical techniques if deemed necessary. Materials are then characterized physically using both laboratory techniques and synchrotron techniques, including X-ray diffraction (XRD), Fourier transform infrared spectroscopy (FTIR), Raman spectroscopy, scanning electron microscopy (SEM), transmission electron microscopy (TEM), X-ray absorption spectroscopy (XAS), X-ray photoelectron spectroscopy (XPS), etc. Structure-function relationships are built to correlate the effect of changing structure and surface characteristics on electrochemical properties. Sodium half-cells are built and cycled under a variety of conditions to understand the electrochemistry and the limitations of the materials. Techniques commonly used include galvanostatic cycling, potentiostatic or galvanostatic intermittent titration technique (PITT or GITT) and cyclic voltammetry (CV). Some attention is paid to the effect of changing electrolytic solution on properties such as first cycle coulombic efficiency. Ex situ and in situ experiments such as XPS on partially or fully discharged or cycled electrodes are used to gain understanding about redox mechanisms. The thermal behavior of candidate materials is also examined by subjecting materials to various heating regimes and examining structural changes by carrying out in situ XRD and spectroscopic analysis.

Results

Prior work from this laboratory [3] identified a promising anode material prepared by ion-exchanging the parent compound $\text{Cs}_{0.74}\text{Ti}_{1.815}\square_{0.185}\text{O}_4$ to form the sodiated analog $\text{Na}_{0.74}\text{Ti}_{1.815}\square_{0.185}\text{O}_4 \cdot 1.27\text{H}_2\text{O}$, designated NTO hereafter. After drying and at low rates, NTO can deliver nearly 230 mAh/g at an average potential of about 0.6V vs. Na^+/Na in sodium half-cell configurations. The electrochemical properties are dependent upon the history of exposure to atmosphere; NTO exposed to air for 10 minutes exhibits a somewhat different voltage profile in half-cells than that of the material kept rigorously dry. Power law analysis of CV curves for half-cells indicates that the air-exposed material exhibits more pseudo-capacitive behavior than the one not exposed to air, particularly in the high voltage region above 1.0V. A possible explanation is reaction of adventitious water with surface defects to form electroactive sites that are different from those that are present in the dry material. While the high voltage region is responsible for the majority of capacity fading seen in cells containing either material, the cycling behavior of the air-exposed NTO was somewhat better than that of the dry NTO. These intriguing observations prompted us to initiate a study on the effect of thermal annealing on the electrochemical behavior of NTO. Depending on temperature, heat-treatment may remove or modify surface defects or initiate bulk structural changes, which may affect electrochemical behavior in profound ways.

Figure XIX.3.1 shows *in situ* synchrotron XRD data on NTO heated to the indicated temperatures. The pristine material is a layered compound, space group *Immm*, which maintains its structure up to about 150°C. Above this temperature, it converts to another layered structure, space group *Cmcm*, with a considerably smaller interlayer spacing, consistent with loss of interlayer water. The main structural difference is the coordination of sodium, which is located in a rectangular prism with eight-fold coordination in the *Immm* structure, but is in a trigonal prism coordinated by six oxygen atoms in *Cmcm*. Upon further heating, NTO converts to an unknown structural intermediate, possibly a layered/tunnel intergrowth, before changing to a phase similar to the tunnel compound, $\text{Na}_2\text{Ti}_6\text{O}_{13}$, above about 700°C. The lower sodium content of $\text{Na}_2\text{Ti}_6\text{O}_{13}$ suggests that there is concomitant loss of sodium or formation of sodium oxide, hydroxide, or carbonate as well. Table XIX.3.1 gives the structural parameters of selected NTOs identified during the heating process.

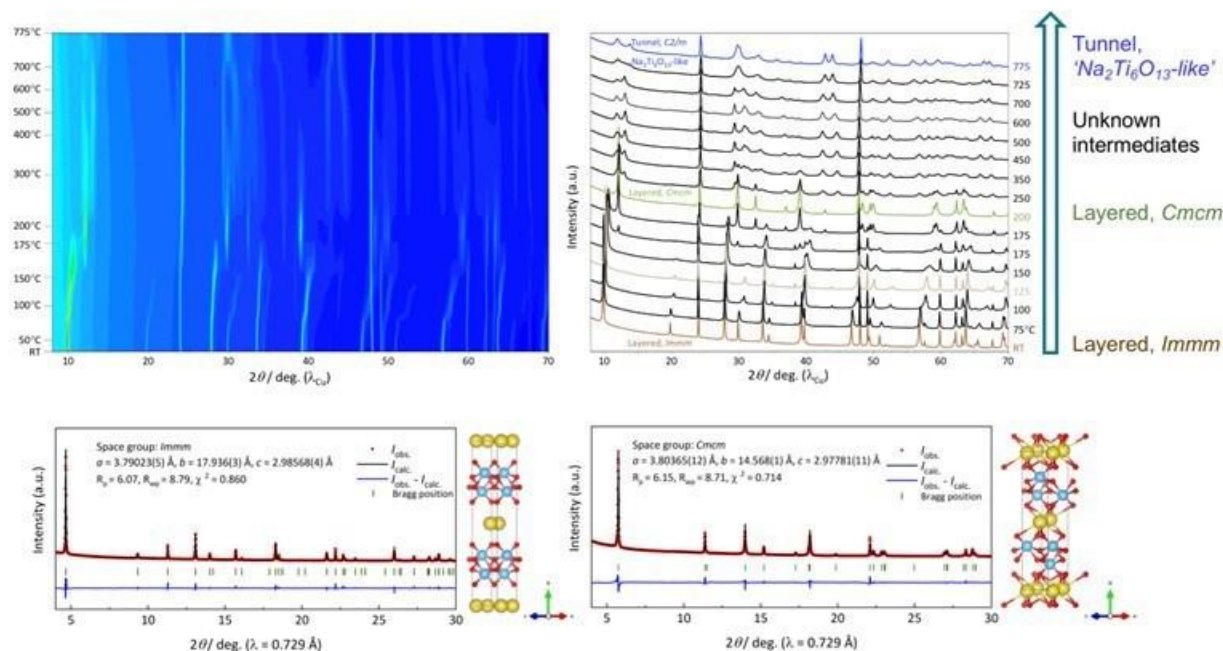


Table XIX.3.1 Structural parameters of NTOs heated to indicated temperatures during the *in situ* XRD experiment

Temperature, °C	Space group	<i>a</i> , Å	<i>b</i> , Å	<i>c</i> , Å
RT	<i>Immm</i>	3.79023(5)	17.936(3)	2.98568(4)
100	<i>Immm</i>	3.79758(11)	17.4395(11)	2.98114(10)
125	<i>Immm</i>	3.80007(8)	17.331(1)	2.98163(7)
150	<i>Immm</i>	3.80208(13)	17.0748(13)	2.98406(12)
200	<i>Cmc21</i>	3.80255(7)	14.5614(5)	2.97737(6)

Broadening of the diffraction peaks, most likely due to the structural disorder, *e.g.*, the positions of sodium ions inside the crystalline lattice, makes the profile fitting of XRD patterns collected at moderate and high temperatures difficult. However, Raman spectroscopy on *ex situ* samples lend additional insight to the structural changes (Figure XIX.3.2). The spectra for samples heated at 60°C and 100°C are typical of those of lepidocrocite-structured titanates [7]. Notably, a broad band at 796 cm⁻¹ that can be assigned to Ti–O–H vibrations [8] weakened and finally disappeared upon heating, as a result of loss of OH⁻ between TiO₆ layers caused by dehydration. As the temperature was raised, further changes were observed, with the spectra of NTO heated to 700°C or 800°C finally resembling that of the tunnel compound Na₂Ti₆O₁₃ [9]. Although bands were observed at similar positions of 167, 194, 223, 392, and 411 cm⁻¹ in the spectra of the 500 °C- and 600 °C-heated materials as in the spectrum of Na₂Ti₆O₁₃, their overall spectra are clearly different from Na₂Ti₆O₁₃. These appear to be structural intermediates between that of layered and tunnel compounds.

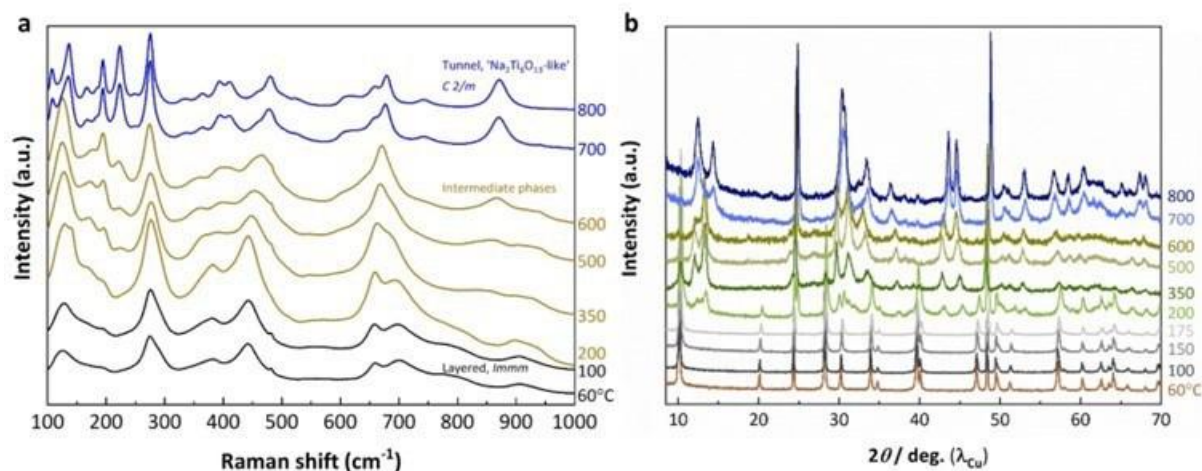


Figure XIX.3.2 (a) Raman spectra and (b) laboratory XRD patterns of NTOs heated *ex situ* in air at temperatures ranging from 60 °C to 800 °C. Taken from reference 6.

Figure XIX.3.2b shows *ex situ* laboratory XRD patterns of NTOs heated to various temperatures. While the trends above 350 °C are the same as for the *in situ* experiments, there are differences at lower temperatures. In stark contrast to the *in situ* heating experiment, a mixture of the parent layered orthorhombic *Immm* phase and the intermediate phase was obtained after *ex situ* heating at 200 °C. This could be explained by differences in the heating time and/or temperature between *in situ* and *ex situ* heating, as well as the hygroscopic nature of NTO which causes the anhydrous phase to take up water and convert back to the hydrous phase. The NTO-containing electrodes are dried under vacuum to remove water used during preparation, so the effect of vacuum-drying at a low temperature was also evaluated. The anhydrous layered *Cmcm* structure was obtained after vacuum drying at 60 °C, similar to the phase obtained after *in situ* heating at 200 °C. A mixture of the layered *Immm* phase and the intermediate phase was obtained after vacuum drying at 100 °C, which is similar to what happens after *ex situ* heating under air at 200 °C. The thermal behavior of NTO is not only sensitive to temperature, but also time and atmosphere.

Figure XIX.3.3 shows the electrochemistry of sodium half-cells containing the NTOs heated to various temperatures. The composite electrodes containing the thermally treated NTOs were vacuum-dried at 60 °C prior to incorporation into half-cells. Electrodes made with 60 °C-heated NTO that were further vacuum dried at 100 °C were also included for comparison. An electrolyte of 0.5 M sodium tetraphenylborate (NaBPh₄) in diethylene glycol dimethyl ether (DEGDME) was used. Initial capacities for cells containing NTO-350 °C and NTO-500 °C were much lower than those of NTOs prepared at lower temperatures when discharged between the standard limits of 2.0-0.1 V, but they gradually increased upon cycling (see Figure XIX.3.3a for the cell containing NTO-500 °C). When using a lower first discharge cut-off voltage of 0.05 V, the 2nd and subsequent discharge capacities using a limit of 0.1 V increased substantially (Figure XIX.3.3b). In other words, the NTOs treated at temperatures above 350 °C needed to be activated to realize their full capacity, either by repeated cycling or by an initial discharge to low potential.

Figure XIX.3.3c shows the second cycles of cells containing NTOs heated to different temperatures, including those of the activated NTOs prepared at high temperatures, and Figure XIX.3.3d shows the dQ/dV plots. It is quite clear that thermal treatment has a profound effect on the electrochemical properties. The voltage profile of the cell with NTO-800 °C shows a plateau near 0.9 V similar to that seen with Na₂Ti₆O₁₃, but the profiles of cells with NTO-350 °C and NTO-500 °C are sloping and featureless. In contrast, NTO-60 °C and NTO-100 °C show several small plateaus (evident as peaks in the dQ/dV plots), although they are more apparent for the former than the latter. The best capacity retention upon cycling was obtained for cells containing NTO-350 °C and NTO-500 °C (Figure XIX.3.3d). Na/NTO-500 °C cells cycled over 740 times at a current equivalent to 200

mA/g retained over 80% of the capacity after two initial formation cycles (not shown). A comparison of the capacity evolution in the high-voltage (1.0 – 2.0 V vs. Na⁺/Na) and low-voltage (0.1 – 1.0 V vs. Na⁺/Na) regions revealed that 500 °C-heated NTO exhibits lower capacity and more stable cycling at high voltages than the 60 °C-heated NTO, whereas less significant differences were observed in the low voltage region (Figure XIX.3.4).

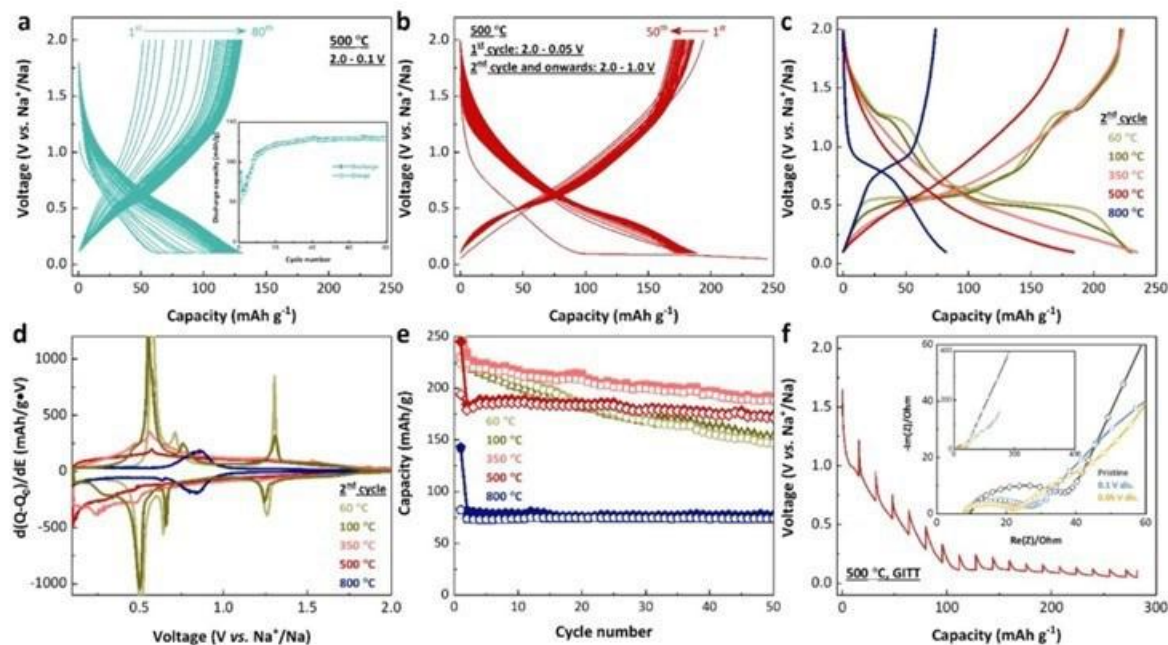


Figure XIX.3.3 Galvanostatic discharge-charge voltage profiles of sodium half cells containing 500 °C-heated NTO cycled between 0.1 and 2.0 V vs. Na⁺/Na (a) without and (b) with an initial ‘activation’ cycle between 0.05 and 2.0 V vs. Na⁺/Na. The inset in (a) shows the discharge capacity as a function of cycle number. (c) The second cycle galvanostatic discharge-charge voltage profiles between 0.1 and 2.0 V vs. Na⁺/Na of NTOs heated to the indicated temperatures (d) the corresponding dQ/dV plots, and (e) capacity retention over 50 cycles. For the initial cycle, a cycling voltage window of 0.1 – 2.0 V vs. Na⁺/Na is used for 60 °C- and 100 °C-heated NTOs, while 0.05 – 2.0 V vs. Na⁺/Na was used for 350 °C-, 500 °C-, and 800 °C heated NTOs. (f) Galvanostatic intermittent titration technique (GITT) voltage profile of 500 °C-heated NTO, the inset shows the evolution of electrochemical impedance spectroscopy (EIS) spectra as a function of discharge potentials. All the cells were cycled at a current rate of 8 mA g⁻¹ (0.008 mA cm⁻²) using a sodium metal anode and a solution of 0.5 M NaBPh₄ in DEGDME as the electrolyte. Taken from reference 6.

Galvanostatic intermittent titration technique (GITT) measurements were carried out during the first discharge to study the initial ‘activation’ process of 500 °C-heated NTO (Figure XIX.3.3e). The reduced polarization observed at the higher depth of discharge indicates improvement of electrode kinetics. This observation is consistent with the electrochemical impedance spectroscopy (EIS) results (inset).

Ex situ synchrotron XRD patterns were obtained on partially and fully discharged and recharged electrodes of NTO-60 °C and NTO-500 °C (Figure XIX.3.5). These reveal quite different structural evolutions of the two types of materials as they underwent discharge and charge. Peaks belonging to the NTO-500 °C phase nearly vanish in the partially and fully discharged electrodes, and do not reappear upon charge, indicating amorphization. *Ex situ* high resolution TEM images support this interpretation (Figure XIX.3.6). In contrast, there appears to be a reversible sodium insertion process for NTO-60 °C. The appearance and disappearance of a few new weak and broad peaks in some of the patterns suggest that the insertion process may involve formation of a new phase, although it is not possible to determine its structure from the limited data. The structural change may be responsible for some of the high voltage irreversibility observed during cycling.

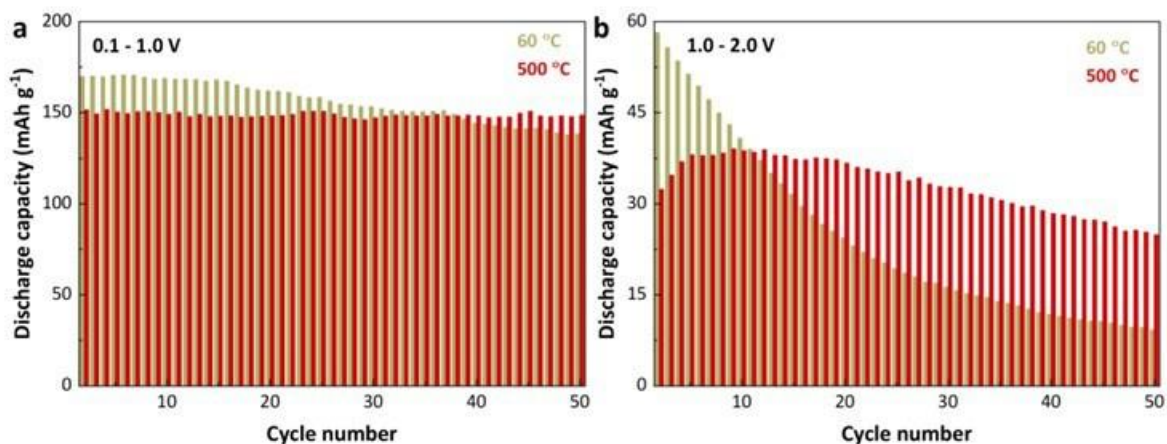


Figure XIX.3.4 Capacity retention of sodium half-cells containing NTO-60°C or NTO-500°C as a function of cycle number in the 0.1-1.0V region (left) and the 1.0-2.0V region (right). Taken from reference 6.

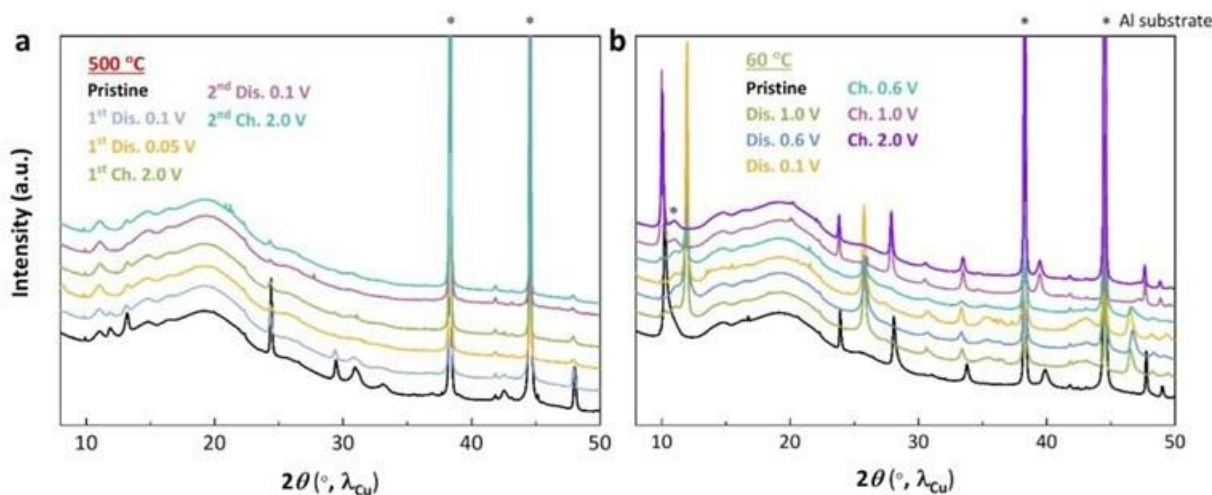


Figure XIX.3.5 *Ex situ* synchrotron XRD patterns of electrodes containing NTO-500°C (a) and NTO-60°C (b) discharged and charged to the indicated potentials. Taken from reference 6.

Ti K-edge XAS (Figure XIX.3.7) was carried out *ex situ* on pristine, discharged, and recharged NTO-60°C and NTO-500°C electrodes. Both systems show evidence of Ti reduction and changes in the pre-edge region consistent with intercalation processes. Linear combination fitting of the Ti K-edge XANES spectra using Ti₂O₃ and TiO₂ references estimated 13.1 % and 22.9 % of Ti⁴⁺ reduction to Ti³⁺ respectively for 60 °C- and 500 °C-heated NTOs. Assuming a pure reductive intercalation mechanism, 78.7 % and 63.5 % of Ti⁴⁺ should be reduced to Ti³⁺ in 60 °C- and 500 °C-heated NTOs by the end of discharge. This discrepancy suggests that a hybrid reaction mechanism involving both reductive intercalation and surface reactions is responsible for the large capacities of NTOs heated at 60 and 500 °C, in accordance with our previous findings based on electrochemical analyses.

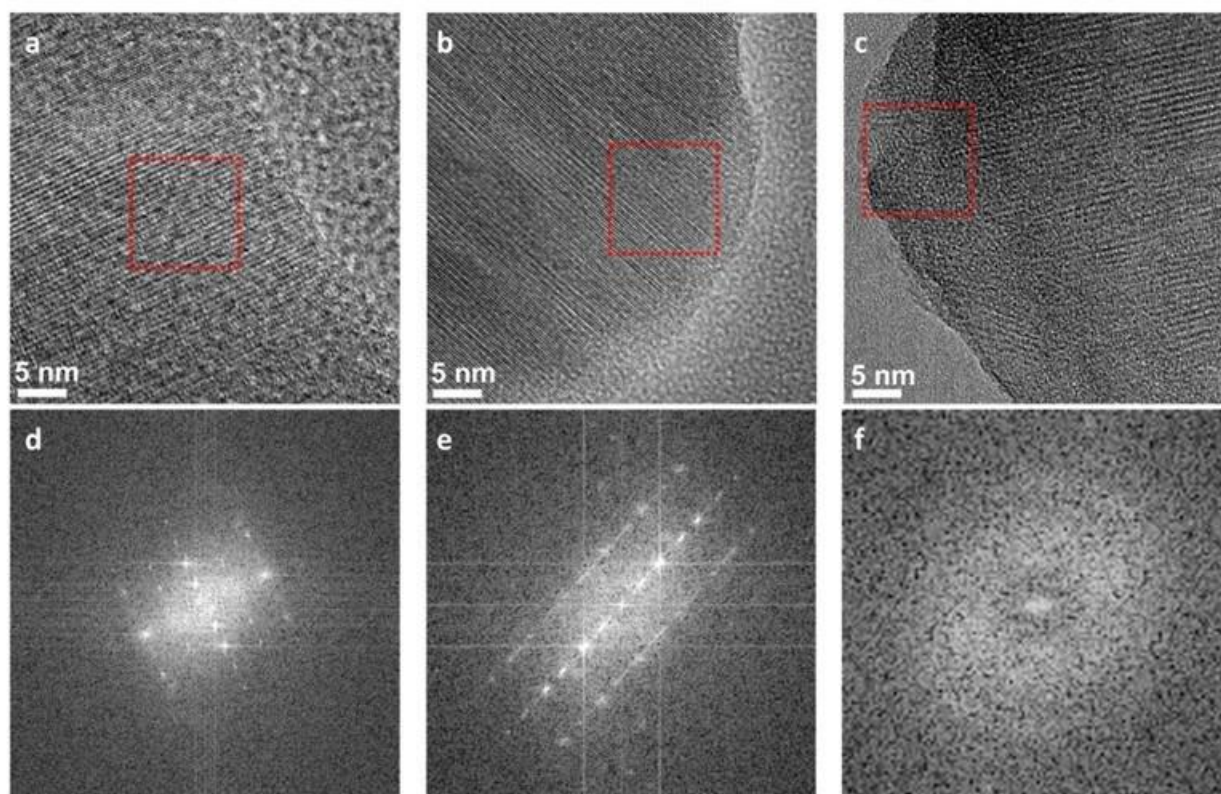


Figure XIX.3.6 *Ex situ* HRTEM images of individual 500 °C-heated NTO particles in the (a) pristine state, and after initial discharge to (b) 0.1 and (c) 0.05 V vs. Na^+/Na . Their corresponding fast Fourier transform (FFT) patterns of the local regions highlighted by the red squares are shown in (d-f). Taken from reference 6.

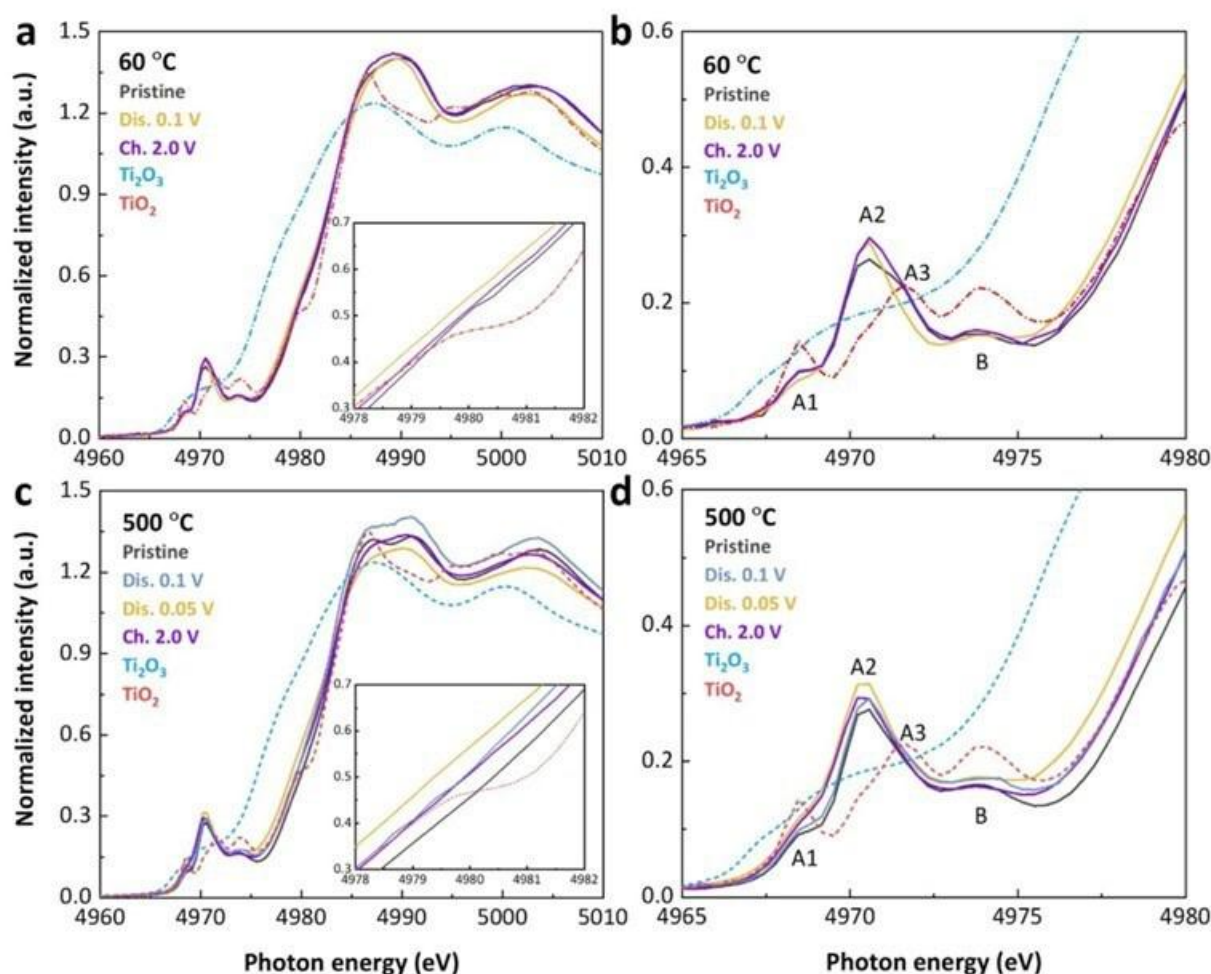


Figure XIX.3.7 *Ex situ* Ti K-edge XAS spectra of pristine, discharged and charged NTO-60°C (a) and NTO-500°C (c) electrodes. Pre-edge regions are shown in (b) and (d).

Conclusions

The structural changes and electrochemical properties of lepidocrocite-type sodium titanate $\text{Na}_{0.74}\text{Ti}_{1.815}\square_{0.185}\text{O}_4 \cdot 1.27\text{H}_2\text{O}$ (NTO) under different post-synthesis heating conditions were studied. *In situ* synchrotron high-temperature XRD and *ex situ* Raman spectroscopy showed that the layered hydrous *Immm* structure of NTO first converts to a layered anhydrous *Cmcm* structure at 200 °C, and eventually transforms to a $\text{Na}_2\text{Ti}_6\text{O}_{13}$ -like tunnel structure at 700 °C *via* an unidentified intermediate phase. Electrochemical characterization revealed that NTOs heated at lower temperatures with layered structures generally exhibit higher capacities than NTOs heated at higher temperature with tunnel structures. The voltage profiles also change as a function of heating temperature, with the materials prepared at higher temperatures exhibiting less high voltage (1.0 V - 2.0 V vs. Na^+/Na) capacities than those prepared at lower temperatures. This is significant because the high voltage processes are primarily associated with surface reactions that result in severe capacity fading. The material heated at 500 °C could retain 94.3% of its capacity of 184 mAh g^{-1} over 50 cycles at a moderate rate. This material also required an ‘activation’ process involving amorphization; either by an initial cycle to 0.05 V vs. Na^+/Na or prolonged cycling, to reach its full capacity. In contrast, NTO heated at low temperatures (*e.g.*, 60 °C) remains crystalline and undergoes reversible phase change with a large reversible capacity of 228 mAh g^{-1} but retains only 64.8 % of its capacity over 50 cycles. NTO heated at

800 °C delivers a low capacity of 82.3 mAh g⁻¹ although the capacity retention is 94.1 % over 50 cycles. Synchrotron X-ray absorption spectroscopy implied that the relatively large capacities obtained for 60 °C- and 500 °C-heated NTOs were due to both reductive intercalation and surface reactions.

Key Publications

1. Yin, W., Barim, G., Peng, X., Kedzie, E.A., Scott, M. C., McCloskey B., and Doeff M. M., “Tailoring the Structure and Electrochemical Performance of Sodium Titanate Anodes by Post-synthesis Heating”, *J. Mater. Chem. A* (2022) <https://doi.org/10.1039/D2TA07403F>

References

1. Shirpour, M., Cabana, J., and Doeff, M., “New Materials based on a Layered Sodium Titanate for Dual Electrochemical Na and Li Intercalation Systems” *Energy & Environ. Sci.*, 6, (2013): 2538-2547.
2. Shirpour, Mona, Cabana, Jordi, and Doeff, Marca “Lepidocrocite-type Layered Titanate Structures: New Lithium and Sodium Ion Intercalation Anode Materials”, *Chem. Mater.* 26, (2014): 2502-2512.
3. Yin, W., Alvarado, J., Barim, G., Scott, M.C., Peng, X. and Doeff, M., “A Layered Nonstoichiometric Lepidocrocite-type Sodium Titanate Anode Material for Sodium-Ion Batteries” *MRS Energy & Sustainability* (2021): DOI: 10.1557/s43581-021-00008-6.
4. Markus, Isaac, Engelke, Simon, Shirpour, Mona, Asta, Mark, and Doeff, Marca “Experimental and Computational Investigation of Lepidocrocite Anodes for Sodium-Ion Batteries” *Chem. Mater.* 28, (2016): 4284-4291.
5. Alvarado, J., Barim, G., Quilty C.D., Yi, E., Takeuchi K. J., Takeuchi, E.S., Marschilok, A. C., and Doeff, M. M., “Optimization of Nonatitanate Electrodes for Sodium-ion Batteries”, *J. Mater. Chem. A* 8 (2020): DOI:10.1039/D0TA07561B
6. Yin, W., Barim, G., Peng, X., Kedzie, E.A., Scott, M. C., McCloskey B., and Doeff M. M., “Tailoring the Structure and Electrochemical Performance of Sodium Titanate Anodes by Post-synthesis Heating”, *J. Mater. Chem. A* (2022) <https://doi.org/10.1039/D2TA07403F>
7. Gao, T., Fjellvag, H., and Norby, P. “Raman Scattering Properties of a Protonic Titanate H_xTi_{2-x/4}□_{x/4}O₄·H₂O (□, vacancy, x=0.7) with Lepidocrocite-type Layered Structure” *J. Phys. Chem. B* 112, (2008):9400-9405.
8. Byeon, Song-Ho, Lee, Sung-Ohk, and Kim, Hongdoo, “Structure and Raman Spectra of Layered Titanium Oxides” *J. Solid State Chem.* 130 (1997):110-116.
9. Bamberger, C.E. and Begun, G. M. “Sodium Titanates: Stoichiometry and Raman Spectra”, *J. Am. Ceram. Soc.* 20 (1987): C48-C51.

XIX.4 Electrolytes and Interfaces for Stable High-Energy Sodium-ion Batteries (Pacific Northwest National Laboratory)

Phung M. Le, Principal Investigator

Pacific Northwest National Laboratory
902 Battelle Boulevard
Richland, WA 99354
E-mail: phung.le@pnnl.gov

Tien Duong, DOE Technology Development Manager

U.S. Department of Energy
E-mail: Tien.Duong@ee.doe.gov

Start Date: October 1, 2021

End Date: September 30, 2022

Project Funding (FY22): \$500,000

DOE share: \$500,000

Non-DOE share: \$0

Project Introduction

The sodium (Na)-ion battery (NIB) is a potential alternative energy source for electric vehicles and grid applications due to the low cost and the natural abundance of sodium. The performance of NIBs largely depends on the performance of electrode materials and electrolytes, especially on the stability of high capacity and high voltage cathode materials required to realize the high energy density potential of NIBs. In recent years, a series of new cathode materials have been developed. However, stability of these cathodes at high voltage conditions is strongly limited by the electrochemical window of electrolytes. Although the capacity of these cathode increases with increasing voltage, but its cycle life decreases with increasing voltage. The unstable solid electrolyte interphase (SEI) formed on anode and cathode electrode interphase (CEI) formed on the cathode of NIBs can lead to poor utilization of electrode materials, fast capacity fading. In addition, flammability of electrolyte also leads to safety concerns. Therefore, there is an urgent need to develop more stable and safe electrolytes to enable applications of high voltage cathode. To reach this goal, a fundamental understanding on the nature of the dynamic interface between electrode and electrolyte is critical. The sluggish redox kinetics also remains to be a challenge for high power applications and need to be further improved.

Objectives

1. Develop high voltage electrolytes based on fluorinated solvent ($\geq 4.2\text{V}$) to be compatible with high-voltage cathode material, including $\text{Na}_2\text{Fe}_2(\text{CN})_6$ and $\text{NaNi}_{0.68}\text{Mn}_{0.22}\text{Co}_{0.1}\text{O}_2$ (NaNMC). High concentration electrolytes and localized high concentration electrolytes will be investigated. Fluorinated phosphate-based solvent will also be combined with carbonate solvent to optimize the ionic conductivity, viscosity and cycling performance of these electrolytes.
2. Design new electrolytes to enable extremely high coulombic efficiency ($>99.5\%$) of Na stripping/plating process on different current collectors (copper, aluminum, carbon coated copper and aluminum foil). Various localized high concentration electrolytes will be investigated in this task. The optimized electrolyte will be used with highly stable cathode ($\text{Na}_3\text{V}_2(\text{PO}_4)_3$) to evaluate the feasibility of anode-free Na batteries.
3. Investigate fundamental mechanism behind the stability of electrolytes and electrode, especially on their interphases. The anode, cathode and electrolytes obtained from cycled cells will be characterized using XPS, TEM, EIS, etc. to understand the fundamental mechanisms behind the stability of SEI and CEI layers.

Approach

- Optimize the electrolyte components and concentrations to develop innovative electrolytes and additives with improved electrochemical and physical properties. Phosphate and fluorinated phosphate-based electrolytes will be investigated to improve the cycling performance of high voltage and high

energy NIB. Ether-based electrolyte will be also optimized to stabilize the sodium metal anode and demonstrate anode-less sodium batteries

- Use in situ and ex situ spectroscopy methods to unravel the origin of the SEI/CEI layer at the dynamic interface, providing guidance for the electrolyte and interface design and enabling high capacity and long life of Na-ion batteries.

Results

Developed high voltage electrolytes based on fluorinated solvent ($\geq 4.2\text{V}$) to be compatible with high-voltage cathode material, including $\text{Na}_2\text{Fe}_2(\text{CN})_6$ and $\text{NaNi}_{0.68}\text{Mn}_{0.22}\text{Co}_{0.1}\text{O}_2$ (NaNMC)

Developing advanced sodium electrolytes are crucial to stabilize the electrode/electrolyte interfacial reactions and thus extend cycling stability for high energy density sodium batteries at high voltage conditions.

Therefore, we have been developing high voltage electrolyte based on tetraglyme and fluorinated phosphate solvents to be compatible with high-voltage cathode materials, including $\text{Na}_2\text{Fe}_2(\text{CN})_6$ and $\text{NaNi}_{0.68}\text{Mn}_{0.22}\text{Co}_{0.1}\text{O}_2$ (NaNMC). Tetraglyme-based electrolytes with 1M NaBF_4 and initial 10 % amount of the fluorinated solvent (VC, FEC, BTFE, or TTE) were studied in half-cells using NaNMC cathode. As shown in Figure XIX.4.1a, the electrolyte containing 10 %vol. of VC showed the best cycling performance compared to other co-solvents. Typically, it displays the highest initial discharge capacity of 156.7 mAh/g as well as the capacity retention of 70% for 200 cycles. Besides, the initial CE is as high as 94.5% and reaches 99.5% after few cycles. Further studies will be continued with the variation of VC content as co-solvent in tetraglyme based electrolyte to enhance the long cycling performance. Meanwhile, the rational design of mixed electrolytes between 2,2,2-trifluoroethyl phosphate and different solvent like DME, MDC, TMS and TFP at high NaFSI concentration ($>1.2\text{ M}$) were investigated for HC|| NaNMC full cells in a voltage range of 1.2-4.2 V (Figure XIX.4.1b-c). The molar ratio of electrolyte components (NaFSI: co-solvent: TFP) is fixed at 1:1.5:2 in mol. The developed electrolytes are compatible with conventional polymer separator (PP or PE).

The use of high polar co-solvents helps to saturate the unique solvation structure of electrolyte and modify the SEI/CEI composition for strongly stabilizing electrode–electrolyte interphase. Among the co-solvents, DMC and TMS exhibited the best long-cycling performance of full cell HC||NaNMC, which shows a good initial discharge capacity of 164.5 mAh/g; 160.9 mAh/g and capacity retention of 87.8%; 86.6 % after 300 cycles, respectively. In addition, these electrolytes also display a good CE of $> 99\%$ after 5 cycles. The interfacial structure and composition of SEI/CEI layers will be further investigated to understand the superior performance of full cells using these electrolytes.

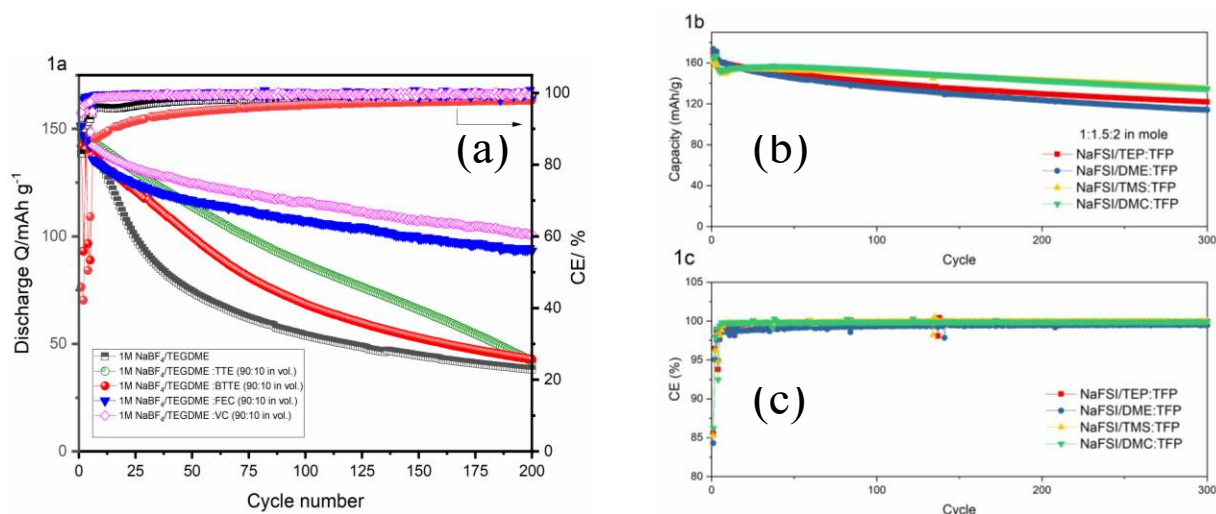


Figure XIX.4.1 (a) Cycling performance of mixed electrolytes based on tetraglyme- fluorinated solvent (VC, FEC, BTTE or TTE) in 90:10 (%vol.) with 1M NaBF₄ in Na||NaNMC half-cell at C/10 rate, mass loading: 3.0 – 4.0 mg/cm²; at voltage range of 2 – 4.2 V. (b-c) Cycling performance of rational electrolytes of NaFSI: co-solvent: TFP = 1: 1.5: 2 in mol. used for full cell of HC||NaNMC (mass loading 1.5 mAh cm⁻²), 3 formation cycles at 0.05 C and cycling at 0.2 C rate (1C = 200 mA/g), voltage range of 1.2 – 4.2 V.

Characterize CEI/SEI interphase properties in optimized electrolyte to probe the mechanism of high voltage cycling stability of NIBs

In this work, the underline mechanism of electrochemical/chemical reaction at the electrode/electrolyte interface was explored to correlate with the obtained electrochemical performance in the optimized electrolytes. Herein, we compared the electrochemical performance of HC||NaNMC full cells with three different electrolytes: NaPF₆/EC-EMC (3:7 in vol) as the baseline carbonate electrolyte (named NaPF₆/EC:EMC), 1 M sodium bis(fluorosulfonyl)imide (NaFSI)/TFP (named NaFSI/TFP), and 1.5 M NaFSI/ dimethyl carbonate (DMC):TFP (1.5:2 in mole or 1.6:8.4 in wt.) as the advanced electrolyte (named NaFSI/DMC:TFP). As shown in Figure XIX.4.2, the cell with a baseline carbonate electrolyte exhibits poor long-term cycling performance with the capacity retention is only 28.1% after 300 cycles (specific capacity of 154.3/43.4 mAh g⁻¹ for 4th/300th cycle). In contrast, the cell with NaFSI/TFP electrolyte shows better long cycling performance, with 75.8% capacity retention after 300 cycles and specific capacity of 151.6/114.9 mAh g⁻¹ at 4th/ 300th cycle, but the overpotential of the cell during long cycling still increases as shown in Figure XIX.4.2c. In contrast, the cell with optimized NaFSI/DMC:TFP electrolyte shows the best long-term cycling performance, with 94.8% capacity retention after 300 cycles (specific capacity of 153.2/145.3 mAh g⁻¹ for 4th/ 300th cycle). The initial CE is 84.49% in NaFSI/DMC:TFP electrolyte compared with 81.21% in NaPF₆/EC:EMC electrolyte, indicating less side-reactions with electrolyte during cycling.

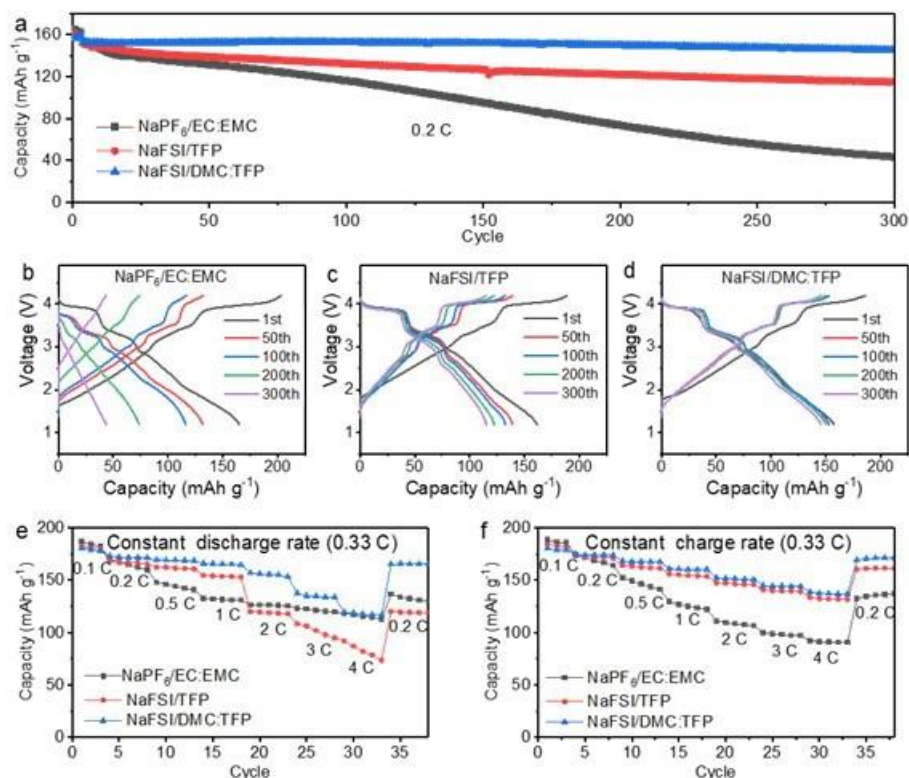


Figure XIX.4.2 Electrochemical performance of HC | NaNMC full cells. **a**, cycling performance of HC | NaNMC full cells using different electrolytes cycled at 0.2 C after three formation cycles at 0.1 C. The cathode loading is 1.5 mAh cm⁻². **b–d**, Voltage curves as a function of cycle number of HC | NaNMC full cells using NaPF₆/EC:EMC (**b**), NaFSI/TFP (**c**) and NaFSI/DMC:TFP (**d**) electrolytes. **e–f**, Rate performance of HC | NaNMC full cells at different charge C-rates with a constant discharge rate at 0.33 C (**e**) and different discharge C-rates with a constant charge rate of 0.33 C (**f**) after three formation cycles at 0.1 C.

To further explain the superior performance of NaFSI/DMC:TFP, the compositions and properties (i.e. dissolution) of the SEI layer on cycled HC electrodes surface were analyzed. In a carbonate-based electrolyte, the preferential decomposition of carbonate solvent induces an organic-rich SEI layer. In a NaFSI/TFP electrolyte, SEI layer contains more F and P- based components formed by the decomposition of TFP solvent. In a sharp contrast, both TFP solvent (strong F 1s and P 2p peaks) and significant amount of NaFSI salt (high intensity of N 1s and S 2p peaks) were decomposed in a NaFSI/DMC:TFP electrolyte and generated an inorganic-rich SEI layer. The degrees of SEI dissolution are quantified by the XPS atomic ratio change (absolute value of atomic ratio difference between cycled and cycled-solvent soaked electrodes) of the SEI (Figure XIX.4.3). The much lower atomic ratio change of SEI components after soaking in TFP solvent (Figure XIX.4.3d) than that in carbonate EC:EMC solvent (Figure XIX.4.3a) indicates excellent capability of TFP solvent to suppress the SEI dissolution due to its low dielectric constant. In the high resolution XPS spectra, there is obvious peak change of C 1s (Figure XIX.4.3b) and NaPF_x peak disappearance (Figure XIX.4.3c) after soaking in EC:EMC solvent, while only minor intensity adjustment of C 1s (Figure XIX.4.3e) and the same N 1s peak intensity (Figure XIX.4.3f) before/after soaking in TFP solvent. Furthermore, atomic ratio change of salt derived components (N/S) are significantly lower than solvent decomposition derived components (C/P) in Figure XIX.4.3d, proving the tuned SEI components from salt decomposition shows less solubility than solvent derived components, and emphasizing the necessity to tune SEI components.

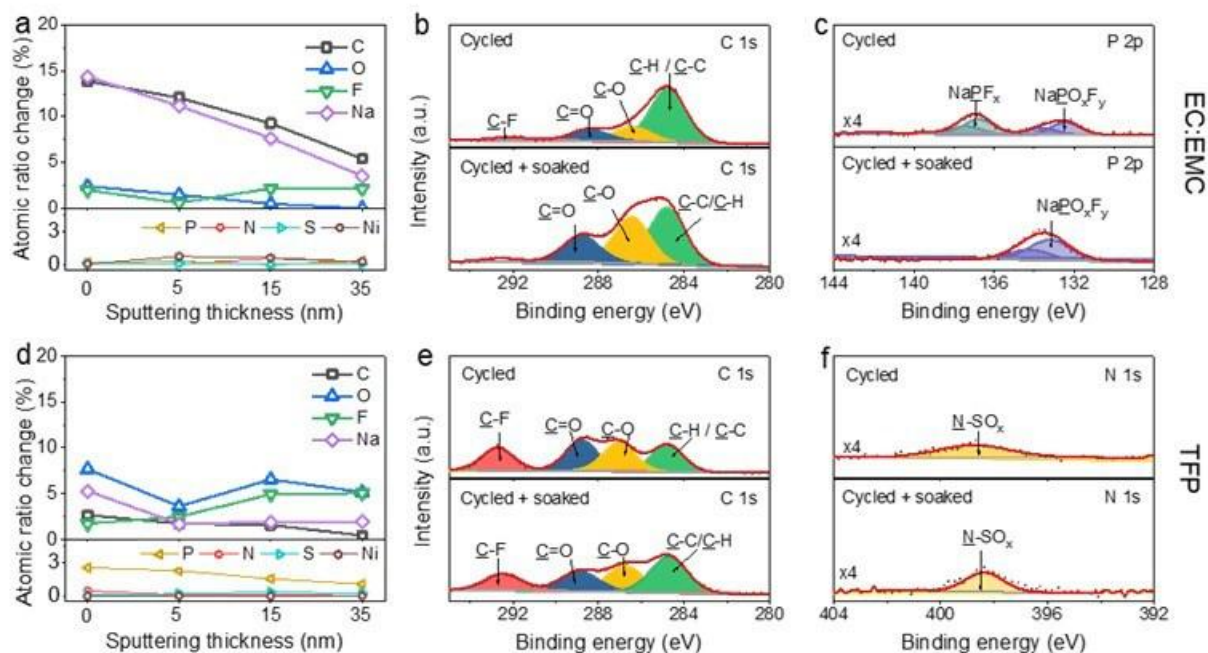


Figure XIX.4.3 XPS characterization to identity SEI dissolution. a,d: The absolute value of difference of quantified SEI atomic composition ratios between the cycled and cycled-soaked hard carbon anodes as a function of the sputtering thickness. b, c, e, f: XPS spectra of C 1s (b, e), P 2p (c), and N 1s (f) of the hard carbon anodes (signal depth = 0 nm). The cycled hard carbon anodes were cycled in NaPF₆/EC:EMC (a, upper of b and c), NaFSI/TFP (d, upper of e and f) electrolytes for 100 cycles. The cycled-soaked hard carbon anodes were soaking cycled hard carbon electrodes with EC: EMC (a, bottom of b and c) and TFP (d, bottom of e and f) solvents for 50 h.

Design new electrolytes with very high coulombic efficiency (>99.5%) for stripping/plating process of sodium metal on different current collectors

Design new electrolytes based on ether solvent (monoglyme, diglyme and tetraglyme) could enable extremely high reversible sodium stripping/plating process for developing the sodium anode-free cell or sodium metal batteries. The glymes have been recently reported to stabilize the sodium metal in plating/stripping process¹. Specifically, tetraglyme based electrolytes with 1M salt (NaPF₆, NaOTf and NaBF₄) enable extremely high CE (>99.5%) of stripping and plating process using half-cell Na||Cu (Figure XIX.4.4). The highest CE is obtained for 1M NaOTf in TEGDME solvent. Based on the good results obtained for Na||Cu half-cell using tetraglyme based electrolytes, different current collectors (Al, C coated Al and C coated Cu) were investigated for stripping/plating process (Table XIX.4.1). It can be observed that using copper foil as current collector in half-cell exhibited the highest CE in all three TEGDME and DEGDME based electrolytes (>99.5 %). However, other current collectors displayed lower CE compared to the copper foil in half-cell.

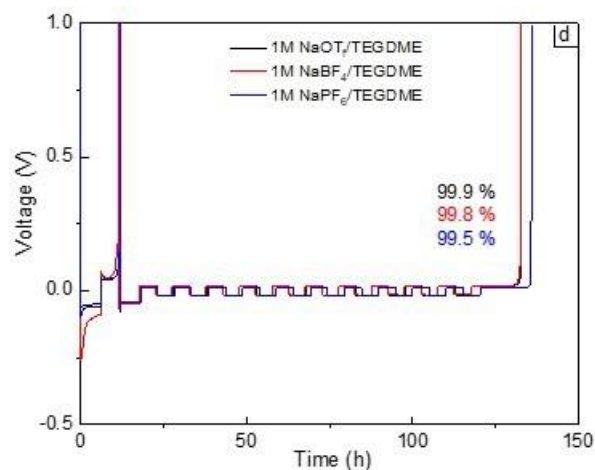


Figure XIX.4.4 Voltage vs time and CE calculated using the reported protocol of cycling in three different electrolytes.

Table XIX.4.1 Coulombic efficiency of stripping/plating process in half-cell Na || different current collectors

Electrolyte	CE of stripping/plating process			
	Na Cu	Na C coated Cu	Na Al	Na C coated Al
1M NaBF ₄ /TEGDME	99.5	98.3	97.7	99.2
1M NaPF ₆ /TEGDME	99.7	-	-	97.3
1M NaOTf/TEGDME	99.8	98.5	98.5	99.6
1M NaBF ₄ /DEGDME	95.6	-	-	-
1M NaPF ₆ /DEGDME	99.7	-	-	-
1M NaOTf/DEGDME	99.5	99.0	98.2	99.6

As the cycle life of anode-free sodium batteries depends on the CE of sodium plating/stripping process, it should use an electrolyte with the highest CE for further testing on the half-cell of Na||Na₃V₂(PO₄)₃ (NVP) cathode. Figure XIX.4.5 presents the cycling performance of Na||NVP half-cell for 100 cycles in DEGDME and TEGDME based electrolytes. The highest capacity retention was obtained for 1M NaPF₆ in TEGDME.

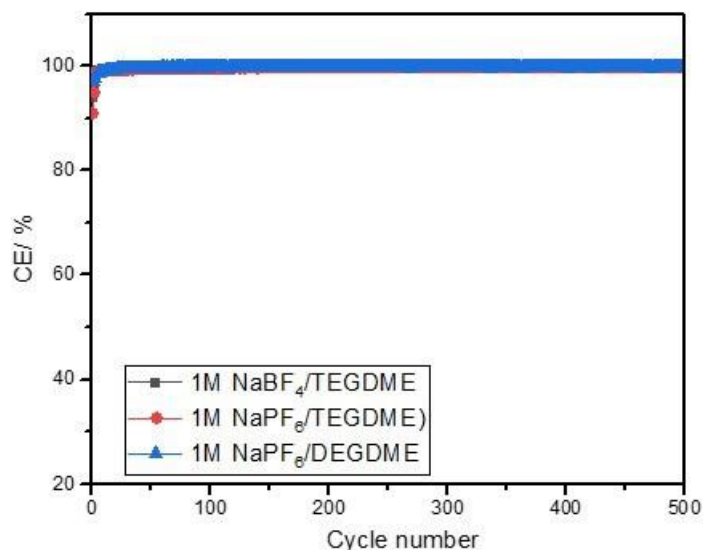


Figure XIX.4.5 Capacity retention of Na||NVP half-cell in DEGDME and TEGDME based electrolytes for 100 cycles

The feasibility of anode-free sodium batteries using the new electrolytes and $\text{Na}_3\text{V}_2(\text{PO}_4)_3$ cathode.

Several ether-based electrolytes were investigated to demonstrate the feasibility of anode-free sodium batteries with $\text{Na}_3\text{V}_2(\text{PO}_4)_3$ (NVP) cathode. Various current collectors (Al, Cu/C, Al/C, and Cu) were used as an anode to test for the feasibility of anode-less cells in baseline electrolyte 1M $\text{NaPF}_6/\text{TEGDME}$ (tetraglyme) and localized high concentration electrolyte (LHCE) with a molar ratio of $\text{NaFSI}:\text{DME}:\text{TTE}$ 1:1:2. (Figure XIX.4.6) and shows the compatibility test of electrolytes with Na anode and NVP cathode using Na||Cu and Na||NVP half-cells in the test cycle. Both baseline and LHCE are well-compatible with anode and cathode, which is demonstrated by high CE of the sodium stripping/plating process (>99.0 %) and high discharge capacity (115 and 120 mAh g^{-1} for baseline and LHCE, respectively).

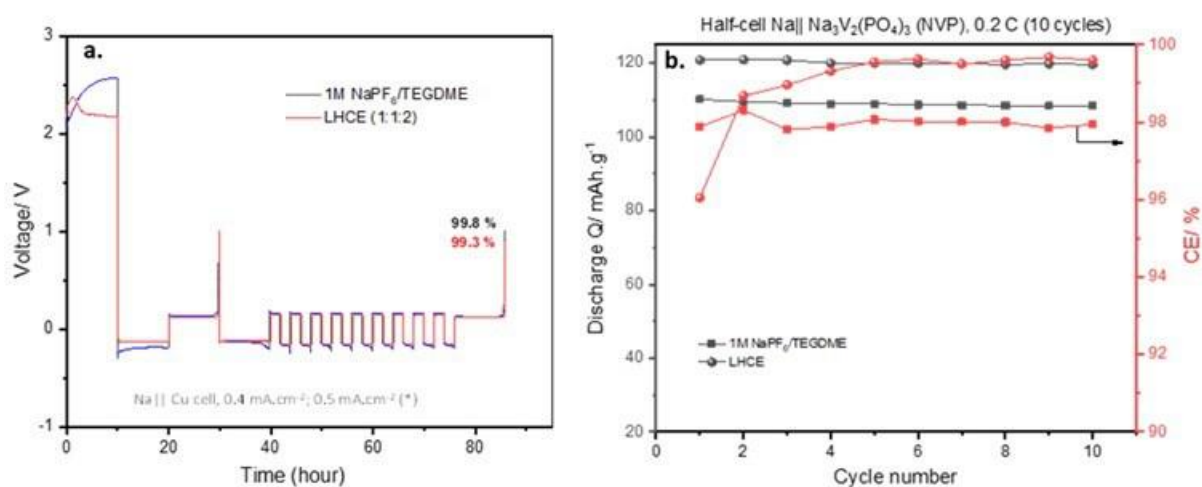


Figure XIX.4.6 (a) Sodium stripping/plating efficiency in two different electrolytes (testing condition: plating 4 mAh cm^{-2} and fully stripping to 1 V and cycling for 10 cycles at 0.5 mA cm^{-2}). (b) Cycling performance of half-cell Na||NVP cathode in 10 cycles at 0.2C.

The performances of anode-free sodium batteries is displayed in Figure XIX.4.7. To eliminate the loss of sodium-ion inventory by side reaction with anode current collector and cathode, both anode current collector and cathode were pre-cycled before matching the full-cell. As a result, the voltage profiles of anode-free

sodium cells in both electrolytes looks like the one of the Na||NVP half-cell, indicating the typical operation of the cells. The initial discharge capacity and Coulombic efficiency in baseline electrolyte are relatively lower than the values obtained for LHCE (Table XIX.4.2). The higher than 100% CE of anode-free sodium batteries in the initial cycle can be attributed to the side reactions with substrate. Large fluctuation in CE of the cell with baseline electrolyte indicates an unstable SEI layer formed in baseline electrolyte. In contrast, CE of the cell with LHCE demonstrate are much more stable during cycling, indicating a much more stable SEI formed in LHCE. The capacity fading is quickly observed in the cell with baseline electrolyte, while the cell with LHCE show much better cycling stability. The capacity retention of cell with LHCE-based electrolytes is about 65% after 50 cycles. The factors causing this fading and the strategies to extend the cycle life of anode-free sodium batteries will be further investigated.

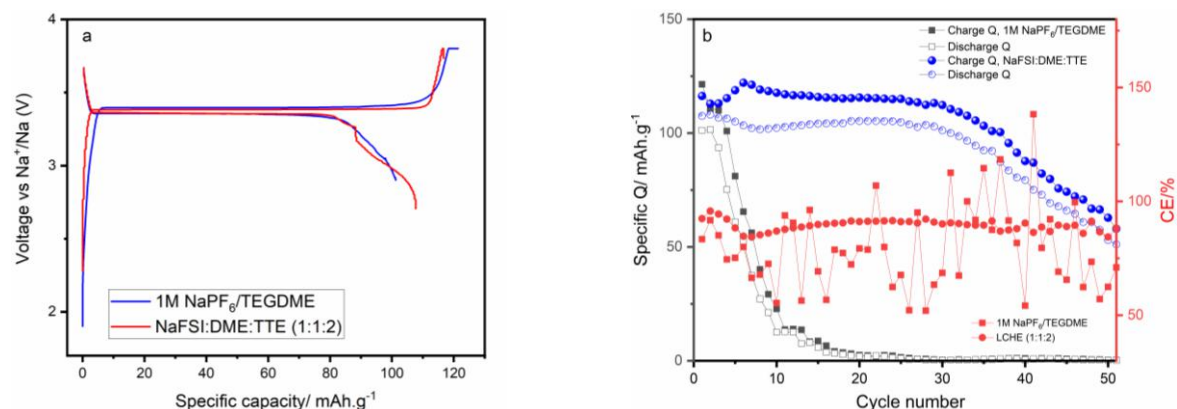


Figure XIX.4.7 (a) Initial charge-discharge profile of Cu||NVP cell in two electrolyte; (b) Cycling performance of the anode-free sodium batteries for 50 cycles (formation cycle: 1st cycle: 0.1 C, charge CV, cycling: 2nd – 7th cycle: 0.2 C, charge CV, 8th cycle: 0.3 C, discharge 0.2 C, charge CV; NVP loading mass: 3–4 mg/cm²)

Table XIX.4.2 The values indicating the performance of anode-free sodium batteries in two electrolytes

Electrolyte	1st discharge Q/ (mAh.g ⁻¹)	1st CE/ %	50th discharge Q/(mAh.g ⁻¹)	50th CE/ %	Capacity retention after 50 cycles
1M NaPF ₆ /TEGDME	101.2	83.4	0.3	62.4	-
LHCE	107.5	94.2	64.6	89.5	60.1

Conclusions

- Designed an advanced low solvation electrolyte (NaFSI/DMC:TFP) for 4.2 V high voltage sodium ion batteries. The electrolyte can stabilize 4.2 V HC||NaNMC full cells with 90% capacity retention after 300 cycles
- Novel TFP based-electrolyte is compatible with PE and effectively suppress SEI dissolution through manipulating solvation structures for less free-solvents, and tuned SEI components from the salt decomposition with the lower solubility in the electrolyte.
- Ether-based electrolyte is a good choice for highly stable operation of sodium stripping/plating process on different current collector. LHCE based on ether solvent demonstrate the feasibility of anode free-sodium batteries using Na₃V₂(PO₄)₃ and a Cu current collector.

Key Publications

- Yan Jin, Phung M. L. Le, Peiyuan Gao, Yaobin Xu, Biwei Xiao, Mark H. Engelhard, Xia Cao, Thanh D. Vo, Jiangtao Hu, Lirong Zhong, Bethany E. Matthews, Ran Yi, Chongmin Wang, Xiaolin Li, Jun Liu & Ji-Guang Zhang, “Low solvation electrolytes for high voltage sodium ion batteries”, Nature Energy, 2022.

2. Yan Jin, Yaobin Xu, Biwei Xiao, Mark H Engelhard, Ran Yi, Thanh D Vo, Bethany E Matthews, Xiaolin Li, Chongmin Wang, Phung ML Le, Ji-Guang Zhang, Stabilizing Interfacial Reactions for Stable Cycling of High-Voltage Sodium Batteries, *Advanced Functional Material*, 2022, 2204995.
3. Phung Le et al., “Tetraglyme based electrolytes enable excellent cycling performance of sodium metal batteries”, 241st ECS Meeting in Vancouver (Canada), May 29 – June 2, Poster presentation.
4. Yan Jin et al., “Low solvation electrolytes for high voltage sodium ion batteries”, IMLB2022, June 26th - July 1, Sydney (Australia), Poster presentation

References

1. Yuan Tian et al., “Recently advances and perspectives of anode-free rechargeable batteries”, *Nano Energy* 78 (2020), 105344.
2. Phung ML Le et al., *Adv. Funct. Mat.* 2020, 30, 2001151.

Acknowledgements

Key contributors include Dr. Yan Jin and Ji-Guang Zhang

XX Beyond Li-ion R&D: Battery500

The Battery500 Consortium (B500) has the goal to increase the energy density of advanced lithium (Li) batteries to beyond what can be achieved in today's Li-ion batteries. Specifically, the B500 aims to increase the specific energy (up to 500 Wh/kg) relative to today's battery technology, achieve 1,000 charge/discharge cycles, and reduce the cost of cells to significantly less than \$100 kWh⁻¹, an important U.S. Department of Energy (DOE) goal for carbon-neutral energy and electrification. The consortium objectives are to: (i) overcome the fundamental scientific barriers to extract the maximum capacity from electrode materials for next-generation Li batteries on the pouch cell level; (ii) leverage and integrate the latest advances in electrode materials and battery chemistries; (iii) optimize cell design and properties of the best electrode materials on the cell level; and (iv) validate cell performance and scale up to industry-relevant levels.

The consortium focuses on two most promising battery chemistries, Li-metal anode with high-voltage/high-capacity metal oxide cathodes like LiNi_xMn_yCo_{1-x-y}O₂ (NMC) and Li metal with sulfur (S) cathodes, to achieve the 500 Wh kg⁻¹ goal. The consortium addresses the fundamental challenges of Li dendrite formation, undesired interfacial reactions, structural degradation, poor ionic and electronic transport, and poor accessibility of active materials, as well as shuttling reaction products in high-energy batteries at the cell level. B500 will develop an integrated approach to rapidly incorporate the latest advances in materials discoveries and breakthroughs into advanced cell-level designs and fabrication, and to optimize and validate the cell properties under realistic conditions. The consortium involves three keystone projects and a cross-cutting project: (1) materials and interfaces; (2) electrode architectures; (3) cell fabrication and validation; and (4) cross-cutting research. Each keystone project and the cross-cutting task address specific scientific challenges required to deliver next-generation, high-energy, Li battery technologies to industry, including high-energy Li||NM cells, high-energy Li||S cells, and low-cost S cells.

This rest of this chapter contains a description of the current phase (Phase 2) of the efforts by the multitude of team members of the Battery500 Consortium.

XX.1 Battery 500 phase 2 (PNNL)

Jun Liu, Principal Investigator

Pacific Northwest National Laboratory
902 Battelle Boulevard
Richland, WA 99354
E-mail: jun.liu@pnnl.gov

Yi Cui, Co-Principal Investigator

Stanford University/SLAC
450 Serra Mall
Stanford, CA 94305
E-mail: yicui@stanford.edu

Tien Duong, DOE Technology Development Manager

U.S. Department of Energy
E-mail: Tien.Duong@ee.doe.gov

Start Date: October 1, 2021
Project Funding: \$15,000,000

End Date: September 30, 2022

DOE share: \$15,000,000

Non-DOE share: \$0

Project Introduction

The overall goal of the Battery500 Consortium phase 2 (B500) is to increase the energy density of advanced lithium (Li) batteries to beyond what can be achieved in today's Li-ion batteries. Specifically, the B500 aims to increase the specific energy (up to 500 Wh kg⁻¹) relative to today's battery technology, achieve 1,000 charge/discharge cycles, and reduce the cost of cells to significantly less than \$100 kWh⁻¹, an important U.S. Department of Energy (DOE) goal for carbon-neutral energy and electrification. The consortium objectives are to: (i) overcome the fundamental scientific barriers to extract the maximum capacity from electrode materials for next-generation Li batteries on the pouch cell level; (ii) leverage and integrate the latest advances in electrode materials and battery chemistries; (iii) optimize cell design and properties of the best electrode materials on the cell level; and (iv) validate cell performance and scale up to industry-relevant levels.

The consortium focuses on two most promising battery chemistries, Li-metal anode with high-voltage/high-capacity metal oxide cathodes like LiNi_xMn_yCo_{1-x-y}O₂ (NMC) and Li metal with sulfur (S) cathodes, to achieve the 500 Wh kg⁻¹ goal. The consortium addresses the fundamental challenges of Li dendrite formation, undesired interfacial reactions, structural degradation, poor ionic and electronic transport, and poor accessibility of active materials, as well as shuttling reaction products in high-energy batteries at the cell level. B500 will develop an integrated approach to rapidly incorporate the latest advances in materials discoveries and breakthroughs into advanced cell-level designs and fabrication, and to optimize and validate the cell properties under realistic conditions. The consortium involves three keystone projects and a cross-cutting project: (1) materials and interfaces; (2) electrode architectures; (3) cell fabrication and validation; and (4) cross-cutting research. Each keystone project and the cross-cutting task address specific scientific challenges required to deliver next-generation, high-energy, Li battery technologies to industry, including high-energy Li||NM cells, high-energy Li||S cells, and low-cost S cells

Objectives

The overall goal of the consortium is to increase the energy density of advanced lithium batteries to beyond what can be achieved in today's state-of-the-art Li-ion batteries. The Battery500 Consortium aims to increase the specific energy (up to 500 Wh kg⁻¹) and achieve 1,000 charge/discharge cycles, with cost reduction of the cells to significantly less than \$100 per kWh⁻¹. This goal directly addresses the U. S. Department of Energy priority to achieve a carbon-free electricity sector by 2035 and to decarbonize the transportation sector by

developing and manufacturing the next-generation, high-energy, low-cost batteries to enable a wide deployment of electric vehicles (EVs) in the marketplace.

Approach

This project focuses on the two most promising battery chemistries: Li-metal anode with high-voltage/high-capacity metal oxide cathodes like $\text{LiNi}_x\text{Mn}_y\text{Co}_{1-x-y}\text{O}_2$ (NMC), and lithium metal with sulfur cathodes. The project focus is to design novel electrode and cell architectures to meet the 500 Wh/kg goal. The consortium will work closely with battery/material manufacturers, suppliers, and end users / original equipment manufacturers in the United States to ensure the technologies being developed by this project are well aligned with industry needs, poised for transitioning to real production, and helpful in securing the supply chain in the United States.

Results

Keystone project 1: Materials and interfaces

Keystone Project 1 addresses the general approaches to attain the goal of robust 500 Wh/kg cells through materials development for cathode, anode, and electrolytes.

In FY2022, **UT Austin** synthesized a novel, cobalt- and manganese-free high-nickel cathode. To stabilize the high-nickel cathode without cobalt and manganese, abundant and low-cost metals, such as aluminum, titanium, and magnesium, were introduced to give $\text{LiNi}_{0.93}\text{Al}_{0.05}\text{Ti}_{0.01}\text{Mg}_{0.01}\text{O}_2$ (NATM). To demonstrate the improved stability of NATM relative to $\text{LiNi}_{0.94}\text{Co}_{0.06}\text{O}_2$ (NC) and $\text{LiNi}_{0.90}\text{Mn}_{0.05}\text{Co}_{0.05}\text{O}_2$ (NMC), coin cells and pouch cells were assembled. Figure XX.1.1a, b demonstrate a small reduction in capacity with NATM, which is balanced in part by an increase in the operating voltage. Meanwhile, all three materials exhibit similar rate capability (Figure XX.1.1c). Cycling performance of the cells in Figure XX.1.1d suggest substantial improvement in the stability of NATM, especially over the singly-doped NC cathode. To evaluate this stability over extended cycling and avoid any contribution to capacity fade from lithium-metal anode, pouch cells with graphite were assembled. Once again, the NATM cathode delivers the highest capacity retention, with 82% after 800 cycles compared to 60% for NMC and 52% for NC (Figure XX.1.1e). To probe the physical origins of the superior cyclability of NATM, time-of-flight secondary-ion mass spectroscopy (TOF-SIMS) analysis was performed on the cycled cathodes. Total signals of common electrolyte decomposition products such as POF_2^- and $\text{C}_2\text{H}_3\text{O}^-$ are reduced for NATM, indicating less aggressive electrolyte reaction and cathode-electrolyte interphase formation (Figure XX.1.1f). The cycled NATM cathode also displays much reduced particle cracking, further contributing to the enhanced capacity retention (Figure XX.1.1g).

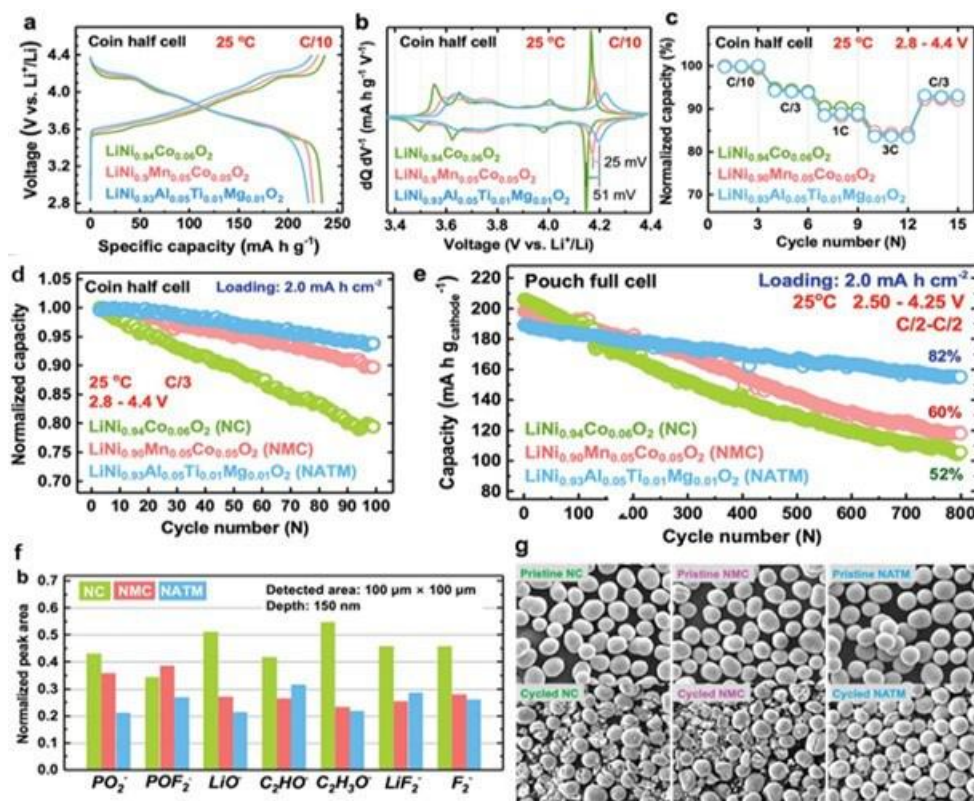


Figure XX.1.1 Electrochemical performances of NC, NMC, and NATM cathodes in coin cells with Li-metal anode and in pouch cells with graphite anode. (a) Charge and discharge curves and (b) dQ/dV curves of the 3rd C/10 formation cycle. (c) Rate performance tests with a constant C/5 charge rate. Cyclability evaluation in (d) coin cells for 100 cycles at a C/3 rate between 2.8 and 4.4 V and in (e) pouch cells for 800 cycles at a C/2 rate between 2.5 and 4.25 V. (f) Normalized peak areas of the raw TOF-SIMS data of the interphasial fragments on the cathodes after 800 cycles. Each sample is sputtered three times on three different locations to yield normalized average peak areas. (g) SEM images of pristine and cycled cathodes after 800 cycles. The scale bars in (g) are 20 μm .

UT Austin team developed a novel concept of electrolyte, namely localized saturated electrolyte (LSE), to stabilize high-Ni layered oxide cathodes. Different from the state-of-the-art localized high concentration electrolytes (LHCEs) based on LiFSI with high solubilities, the developed LSE is based on Li salts with low-to medium solubility. Specifically, the Li salts in an LSE include, but are not limited to, LiPF_6 , LiBF_4 , LiDFOB , LiBOB , LiClO_4 , LiAsF_6 , and the combination of these salts. The main solvents could be any organic solvents that have low- to medium-solubility (1 to 5 M) of these salts, and the diluents could be any organic solvents that improve the wettability to the separator, but do not break the contact ion pairs (CIPs) and aggregates (AGGs) solvation structure in the electrolytes. Figure XX.1.2a shows the schematics of the conventional LP57 electrolyte and the developed LiPF_6 -based LSE. The change in the solvation structure in the saturated electrolyte (SE) and the LSE is supported by Raman spectra (Figure XX.1.2b) and NMR spectroscopy (Figure XX.1.2c). The Li^+ solvation structure is dominated by CIPs and AGGs in the SE and the LSE, while it is mainly composed of solvent-separated ion pairs (SSIPs) in the LP57 electrolyte.

Cobalt-free LiNiO_2 was selected to examine the effectiveness of the developed LSE electrolyte. The LiNiO_2 sample has a secondary particle diameter of $\sim 12 \mu\text{m}$, which is composed of primary particles with a size on the order of 100 nm, as shown in the scanning electron microscopy (SEM) images in Figure XX.1.2d. Figure XX.1.2e shows that the LSE improves the self-discharge performance of the LiNiO_2 electrode. The cell voltage with the LP57 electrolyte decreased fast and reached 4.160 V after being stored at 45 °C for 100 h. By comparison, the cell voltage remained at 4.235 V with the LSE after the storage. A full discharge at the C/10 rate was conducted after the storage to evaluate the capacity retention. The capacity remaining was increased

from 85.0% (LP57) to 98.8% (LSE). Figure XX.1.2f further illustrates that the LSE largely improves the cycling stability of the LiNiO_2 electrode. The LiNiO_2 cell with the LSE shows an initial discharge capacity of 221 mA h g^{-1} at 1C rate and retains 80% of its initial capacity after 500 cycles. Moreover, when the EC/EMC solvent was replaced with the FEC/EMC, the cycle life was further extended to 600 cycles with 81.3% of capacity retention. These cycling performances of LiNiO_2 are better than that with LP57 electrolyte, which showed only 55% capacity retention after 200 cycles, and the state-of-the-art LHCE (M47), which maintained 84% after 200 cycles. Atomic resolution annular dark-field scanning transmission electron microscopy (ADF-STEM) images of cycled LiNiO_2 were collected to examine the phase transformation at the surface (Figure XX.1.2g,h). By selecting and masking the reflections from the layered, spinel, and rock-salt structures in the fast Fourier transformed (FFT) pattern, followed by an inverse FFT analysis, the area containing each structure can be identified, which are labeled in the figures. LiNiO_2 with the LP57 electrolyte (Figure XX.1.2g) contains the rock-salt phase (red color) with a depth of 4–5 nm and a significantly transformed area of the spinel phase (yellow). In contrast, LiNiO_2 cycled in the LSE (Figure XX.1.2h) only contains a very thin rock-salt phase of 1–2 nm, and the spinel phase is sporadically distributed in small areas. Therefore, the LSE suppresses oxygen loss and a deep reduction of nickel ions on the surface of LiNiO_2 cathode and prevents the formation of electrochemically inactive phases (spinel-like or rock-salt structure) during long-term cycling. Moreover, the Li CE of the LSE was measured in a $\text{Li}||\text{Cu}$ cell. Figure XX.1.2i shows that the Li CE reaches 98.2% after stabilization, which is lower than that of the state-of-the-art value of 99.5% for LHCE. Future work will focus on increasing the Li CE of the LSE by adding more appropriate additives.

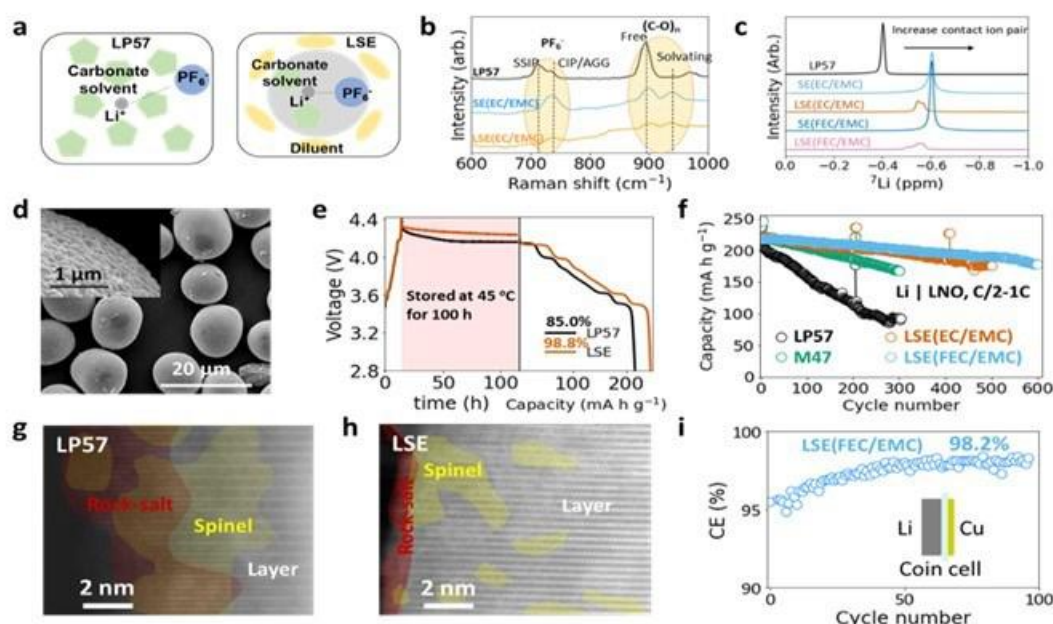


Figure XX.1.2 (a) Schematic illustrations of the LP57 electrolyte and LSE. (b) Raman spectra of the three electrolytes in the range of 600 to 1000 cm^{-1} . (c) ^7Li NMR spectra of different electrolytes to study Li^+ coordination. (d) SEM images of LiNiO_2 microspheres with an average diameter of $12 \mu\text{m}$ (secondary particles). The inset zooms into the surface of a secondary particle to show the primary particles. (e) Self-discharge performance of LiNiO_2 cathodes tested at 45°C . (f) Cycling performances of LiNiO_2 with the LP57 electrolyte (300 cycles), LiFSI-based LHCE (M47, 300 cycles), LSE(EC/EMC) (500 cycles), and LSE(FEC/EMC) (600 cycles) at room temperature with 2 mA h cm^{-2} loading. The charge rate was C/2 and the discharge rate was 1C in the voltage range of 2.8 – 4.4 V. STEM images at the surface of a cycled LiNiO_2 particle with (g) the LP57 electrolyte and (h) the LSE. (i) Coulombic efficiency (CE) of the developed LSE measured with a $\text{Li}||\text{Cu}$ coin cell. The test current and capacity were, respectively, 0.5 mA cm^{-2} and 1 mAh cm^{-2} .

Stanford University rationally designed a steric effect tuned ether molecule, 1,2-diethoxyethane (DEE, Figure XX.1.3a), as the weakly-solvating electrolyte solvent for improving Li metal battery performance. The molecular design principle is to utilize a steric hindrance effect to tune the solvation structures of Li^+ ions. They hypothesized that by substituting the methoxy groups on DME with larger-sized ethoxy groups, the

resulting DEE should have a weaker solvation ability and consequently more anion-rich inner solvation shells, both of which enhance interfacial stability at the cathode and anode (Figure XX.1.3a). Molecular dynamics simulations were performed to provide more detailed information about solvation structures (Figure XX.1.3b). Comparing the most probable solvation structures of 1 M LiFSI/DME and 1 M LiFSI/DEE, the latter must accommodate four extra carbons and eight extra hydrogens, which results in an additional energy penalty for DEE coordination. As a result, DEE has a lower average coordination number to Li⁺ due to its bulkier size. Overall, in the order of 1 M LiFSI/DME < 1 M LiFSI/DEE < 4 M LiFSI/DME < 4 M LiFSI/DEE, the anion-to-solvent ratios increase and thus the probability of multiple FSI⁻ within Li⁺ solvation shell increases (Figure XX.1.3b), both of which are consistent with the weaker solvation at higher concentration as well as the weaker solvation in DEE than in DME. The Li CE were determined by a modified Aurbach method (Figure XX.1.3c). With 1 M LiFSI, CE of DEE reaches 99.02% and outperforms that of DME at 98.16%. Such high CE even at a normal salt concentration indicates superior compatibility of DEE with Li. At higher LiFSI concentration of 4 M, both DME and DEE show improved CEs (99.04% and 99.38%, respectively). The higher CE of DEE compared to DME at 4 M further showcases the improved stability of DEE at the Li anode. Finally, under stringent full-cell conditions of 4.8 mAh cm⁻² the cell using NMC811 cathode, 50 μ m thin Li, and high cutoff voltage at 4.4 V, the best-performing electrolyte 4 M LiFSI/DEE enabled 182 cycles with 80% capacity retention while 4 M LiFSI/DME only achieved 94 cycles (Figure XX.1.3d).

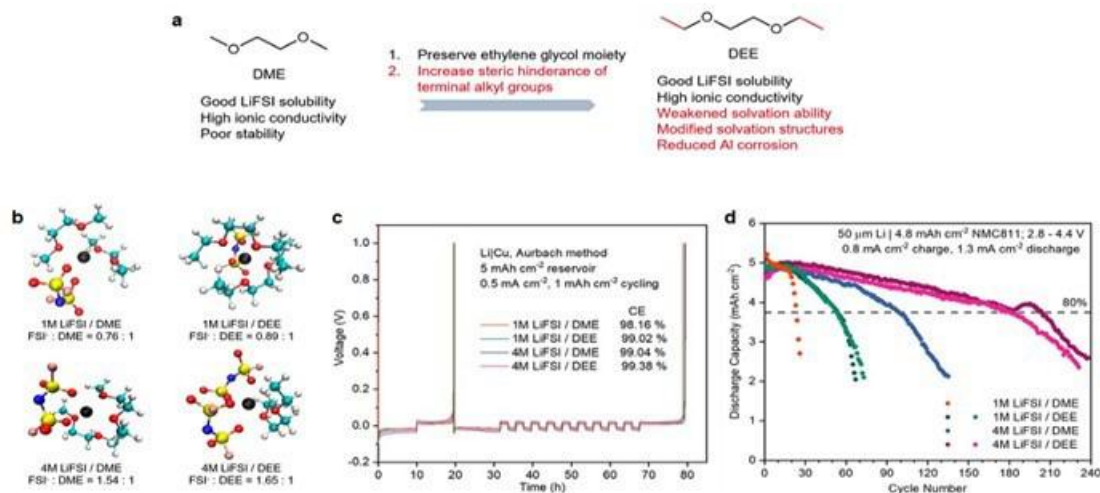


Figure XX.1.3 (a) Molecular design from DME to DEE. (b) MD simulations for 1 M LiFSI/DME, 1 M LiFSI/DEE, 4 M LiFSI/DME and 4 M LiFSI/DEE. (c) Aurbach method to determine the average Li metal CE using different electrolytes. (d) Cycling performance of thin-Li | high-loading NMC811 full cells under limited electrolyte and practical cycling conditions.

XPS is commonly used to characterize SEI and help people understand the connections between the chemical speciation of SEIs and the performance of LMBs. However, the state of the SEI might be affected by artifacts introduced during XPS experiments, resulting in erroneous extraction of chemical information. The **SLAC/Stanford** team has identified specific procedures that may introduce errors during Li SEI analysis and provided guidelines for accurate SEI characterization in future studies. Herein, four themes were identified that could contribute to erroneous extraction of chemical information from the XPS analysis of SEIs. An SEI formed on top of Li anode (2 mAh cm⁻² of Li deposited at 0.5 mA cm⁻² with L40 electrolyte) was investigated as an example. Specifically, the following avenues for errors during XPS analysis of SEIs were discovered. Effects of Sample Preparation Method: Up to 98 % variation in the ratios of chemical species in the SEI was identified through variations in sample rinsing methods (Figure XX.1.4a). Residual solvents (EC) and salts were observed to coexist with the SEI and contribute to the variations, thus the sample preparation methods should be clearly reported to ensure that SEI analysis results are consistent in the future. Spatial Location of Sampling Region: Variations in spatial location of XPS analysis on a given SEI result in up to 66 % variation

in the F/C ratio in the SEI (Figure XX.1.4b). The results show that as the XPS analysis was subject to the inhomogeneity of SEI samples. We recommend that measurements should be carried out on at least three distinct SEI spots to provide statistical confidence. Time-Dependence of SEI Species: The duration of SEI exposure under ultrahigh vacuum in the XPS chamber changed the SEI chemical markers by as much as 84 %, resulting in both changes in elemental ratios and specific chemical species in the SEI (Figure XX.1.4c). Therefore, it is important that XPS data collection, especially across different SEIs, is carried out within a short time window to ensure that SEI states are comparable. Effect of Sputtering: A mixture of Li_2CO_3 and LiF particles was studied as a model SEI. Ar^+ sputtering significantly altered the F/C and O/C ratios of the model SEI (Figure XX.1.4d). It also preferentially decomposed SEI components (e.g., Li_2CO_3) and introduced artifacts in the form of new chemical species (e.g., Li_2O) into SEI analysis. Therefore, one needs to be cautious when carrying out Ar^+ sputtering of SEI samples during XPS analysis because it could introduce artifacts into the data.

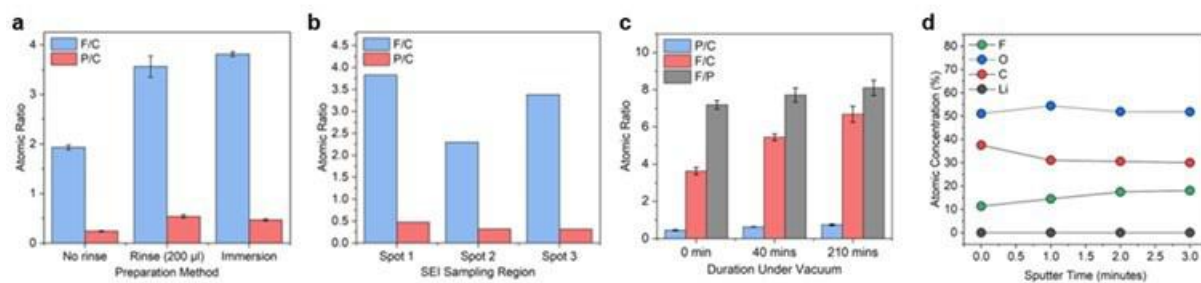


Figure XX.1.4 Chemical species changes during XPS measurement. (a) Atomic ratio as a function of three SEI preparation methods. (b) SEI atomic ratio as a function of sampling region. (c) SEI atomic ratio as a function of duration of SEI inactivity under ultrahigh vacuum. (d) Atomic concentration of model SEI ($\text{Li}_2\text{CO}_3 + \text{LiF}$ mixture) for different Ar^+ sputtering times.

In **Binghamton University**, the thermal analysis lab continues to be set-up and an overall research plan is defined. The operando DSC cell provides new capability to determine thermal events in operating coin cells. This should allow the researchers to monitor the formation of the SEI layers in the initial cycles as well as the breakdown of electrolyte under extreme conditions. This will help define the limits of operability for each electrolyte for high Nickel NMC. However, the materials that the coin cell is constructed of can also react with the electrolyte leading to heat evolution. Using this high sensitivity DSC method, such reactions can mask the reactions being studied. To measure the magnitude of these challenges faced by the coin cell corrosion, the impact of adding additional aluminum foil to the cathode current collector was determined and the results are shown in Figure XX.1.5. The upper charging voltage was capped at 4.5 V, since our previous studies showed that breakdown occurs at voltages higher than 4.5 V. The heat evolution of NMC 811 cells with no additional aluminum on the cathode are shown in Figure XX.1.5a, while the results for cell with an extra aluminum foil added are shown in Figure XX.1.5b; both current collectors were aluminum-coated. There is clearly a marked difference with the T3 and ED2 electrolytes showing essentially no heat evolution for the extra protected cathode current collector. The other electrolytes will be further studied. This study highlights the need for a close examination of all cell components.

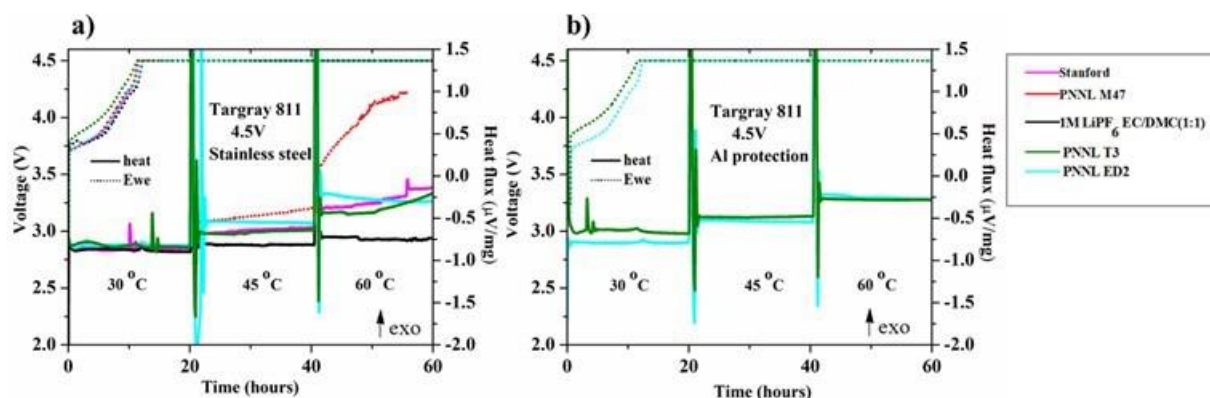


Figure XX.1.5 *Operando* DSC measurements (dotted curves for electrochemical test and solid curves for the measured heat flux) of novel ether-based M47, ED2, T3, Stanford (1M LiFSI in FDMB) electrolytes and traditional carbonate electrolyte (1M LiPF₆ in EC/DMC (1:1)) for TARGRAY NMC 811 that were charged and held at 4.5 V, while ramp heating and isothermally holding at 30 °C, 45 °C and 60 °C for 20h, **a)** Al-coated MTI coin cell parts **b)** Al-coated Hohsen coin cell with Al foil added on cathode side.

Thermal stability studies of electrolytes and solid electrolyte interphase (SEI): **Binghamton University** team studied (1) the reactivity of cell components, (2) the stability of the new ether electrolytes in contact with Li, and (3) the heat evolved during the evolution of the SEI layer. The stainless-steel components used in coin cells can react with the electrolyte even when are covered with aluminum (coated or foil). It was found that the Hohsen cell contains molybdenum in the steel (Figure XX.1.6a), which is less reactive than the MTI cells. The more reactive MTI cell results in an additional 10% heat release, beyond that due to the reactions of the active material (Figure XX.1.6b). The LiFSI-ether electrolytes were found to be stable to fresh Li during the melting process (Figure XX.1.6c, d). The electrolytes alone showed no thermal events up to 300°C; all showed the expected endothermic melting peak of Li and a subsequent exothermic reaction. In the presence of the NMC811, the expected exothermic oxygen reaction was observed, but its peak temperature was found to be dependent on the electrolyte used and in some cases higher than that of the NMC without electrolyte. This is being further investigated. Extra heat is expected to be evolved during the formation of the SEI layer, and this should decrease after the formation of the SEI. Figure XX.1.6e shows the cycling of NMC811 in several carbonate electrolytes and advanced ether electrolytes. The heat evolved for the first three cycles are given in Figure XX.1.6f. The expected decrease in heat evolution was observed for the carbonate electrolytes but was not the case for the ether-based electrolytes, even with the heat increased in some cases. This is being followed up with more measurements after the 10th cycle.

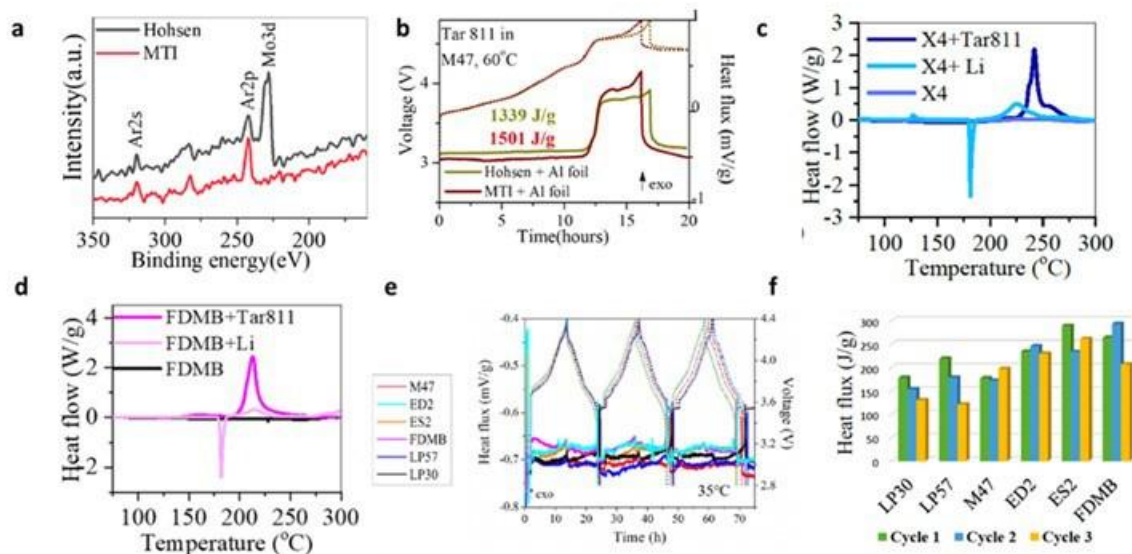


Figure XX.1.6 (a) XPS study of coin cell components. (b) Heat evolved for NMC 811 with the M47 electrolyte using the aluminum protected Hohsen and MTI cells. (c, d) Studies of X4 (PNNL) and FDMB (Stanford) electrolytes. Ex-situ DSC profiles of electrolyte alone, electrolyte + Targray NMC811 charged to 4.8 V, and electrolyte + Li metal anode after charge. (e, f) Cycling and Heat evolution of coin cells cycled between 4.4 and 2.8 V at C/10 current rate.

3D Host Li Anode – University of Washington (UW) systematically evaluated the 3D porous carbon as Li hosts for high-energy rechargeable Li metal batteries in different kinds of electrolytes. The results demonstrated that the nature of the electrolyte has the dominant effect on determining the CE and cyclability of Li metal anode. In this FY2022, we have investigated the cycle performance of the Cu foam as Li hosts with three types of electrolytes, high concentration electrolyte (HCE, LiFSI: DME=1:1.2, by mol), localized high concentrated electrolyte (LHCE, LiFSI:DME:TTE=1:1.2:3 by mol), and fluorinated-1,2-diethoxyethanes electrolyte (F5DEE, 1.2M LiFSI in F5DEE), which have been proved to show good compatibility with Li metal anode. We are trying to figure out the optimum electrolyte composition for 3D hosts so that we can study the geometrical effect (pore size and shape, tortuosity, specific surface area, etc.) in future studies.

Figure XX.1.7a shows the 10th charge/discharge curves of Li/Cu foam cells in the HCE, LHCE, and F5DEE electrolytes at 1 mA/cm². The cell with F5DEE electrolyte shows the highest Coulombic efficiency (CE) and the lowest overpotential, which can be attributed to the high ionic conductivity of the F5DEE electrolytes and the high efficiency of interfacial ion transport.[1] The cycling performance of the Li/Cu cells in the HCE, LHCE, and F5DEE electrolytes is shown in Figure XX.1.7b. The cells using HCE and LHCE electrolytes need tens of activation cycles to ramp up to 99% CE. In contrast, the cell using F5DEE electrolytes exhibits a substantial improvement, with activation periods decreasing to around 10 cycles, indicating a robust and stable SEI is formed in the F5DEE electrolytes. Therefore, the optimal electrolyte for the 3D Li host is found to be the F5DEE electrolyte and we will study the geometrical effect of the 3D host in it to realize a high energy density Li battery.

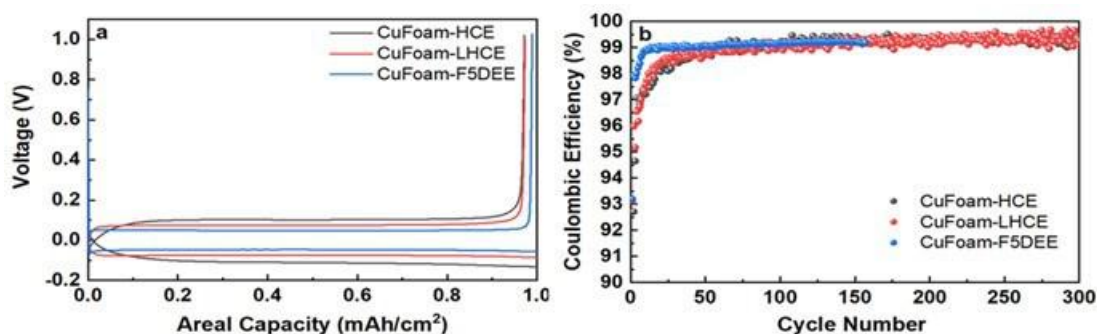


Figure XX.1.7 (a) The 10th charge/discharge curves and (b) Coulombic efficiency of Li/Cu batteries in HCE, LHCE, and F5DEE electrolytes (at 1 mA cm⁻² current density and 1 mAh cm⁻² areal capacity)

Previously, **UW** team successfully prepared the Li_{1.3}Al_{0.3}Ti_{1.7}(PO₄)₃ (LATP)-coated polyethylene (PE) separator with a thickness of coating layer of ~1.25 μm, and the Li||NMC811 batteries using ceramic coated PE separators showed higher capacity retention than those using bare PE separators. In this FY2022, **UW** used radio-frequency magnetron sputtering to directly deposit a thin layer of LATP on PE separators. The deposition was carried out for 2 h at a power density of 2.63 W cm⁻² in pure 5 mTorr Ar environment at ~40°C. The thickness of the coated LATP layer is ~40 nm measured by a Bruker DektakXT Contact Profilometer. The mass of the PE separator only increased by 4.5% after coating with LATP, which is beneficial to realizing high energy density batteries. Figure XX.1.8a shows the Nyquist plots of the SS/separator/SS cells, where SS stands for stainless steel. The ionic conductivities of the bare PE and LATP-coated PE separators infiltrated with carbonate electrolyte (1 M LiPF₆ in EC/EMC (3:7 by wt.) with 2 wt.% VC additive) at room temperature are calculated to be 0.53 and 0.71 mS cm⁻¹, respectively; based on

$$\sigma = d/(RA)$$

where d is the thickness of the separator, A is the area of the SS electrode, and R is the bulk resistance obtained from the high-frequency intercept of the Nyquist curve on the x-axis. The higher ionic conductivity of the LATP-coated PE separator as compared to the bare PE can be ascribed to better electrolyte wettability of the LATP-coated PE and can help to improve the rate performance in battery cells. The electrochemical performance of separators was evaluated by cycling the Li||NMC811 half cells (N/P ratio = 0.4) with the LHCE (LiFSI:DME:TTE=1:1.2:3 by mol.) at 25 °C. The mass loading of the NMC811 cathode is ~20 mg cm⁻². As shown in Figure XX.1.8b, the battery using LATP-coated PE separator exhibits an initial reversible capacity of 196.4 mAh g⁻¹ with a CE of 86.7% at 0.1C between 2.8 V and 4.4 V, similar to that using bare PE separator (193.5 mAh g⁻¹, 85.8%). After the formation cycles, both batteries deliver similar discharge capacities and CEs at 0.33C. These batteries are still being cycled, and the team will examine if the battery using ultrathin LATP-coated PE separator presents better cycling performance in the LHCE electrolyte.

PSU team introduced a new electrolyte formulation with all aspects of solvents, salts, and additives optimized to achieve the target Coulombic efficiency (CE) of 99.5%. The new highly wettable fluorinated electrolyte with a new solvating solvent system can stabilize the batteries under practical working conditions with retained solvation chemistry because they are high-concentration electrolytes with improved wettability on the separator and electrode's surfaces. It consists of 1 M LiPF₆ dissolved in a mixture of carbonate-based solvating system and a fluorinated ether-based diluent, which is named as fluorinated saturated electrolyte (FSE). Here, we marked E1 for conventional electrolyte 1M LiPF₆ in EC/EMC (1:1 v/v), AFSE stands for FSE with 0.1 wt.% additive. The improved wettability between electrolyte/separator/electrode interfaces ensures homogeneous Li transport, which lowers the risk of incomplete plating and stripping (that is, related to capacity loss) as well as local overcharge. In this approach, the Li₂O–LiF-rich SEI nanostructure is completely different from the conventional SEI that displays a highly crystalline and Li₂CO₃-dominant structure.

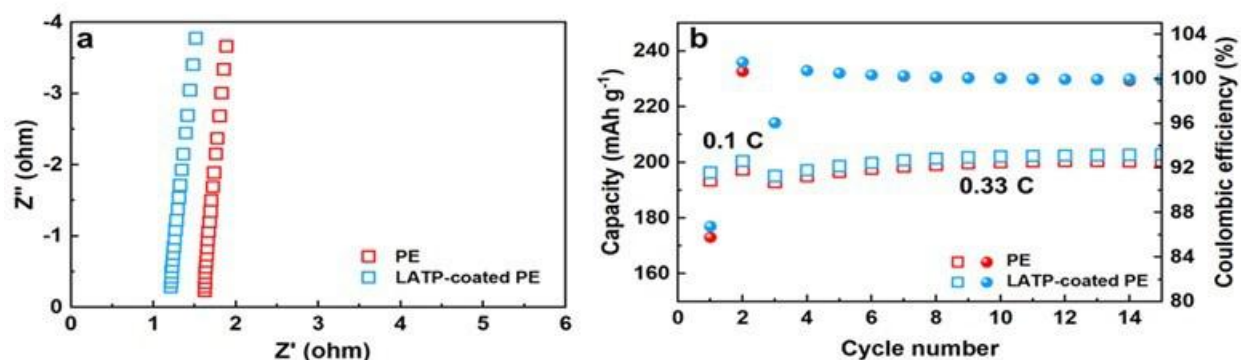


Figure XX.1.8 (a) Nyquist plots of the bare PE and LATP-coated PE separators. (b) cycling performance of the Li||NMC811 batteries with bare PE or ultra-thin LATP-coated PE separator.

The accurate CE of Li||Cu cell was determined by the Aurbach method using the simple plating and stripping process published by Pacific Northwest National Laboratory team. In this method, an excessive amount of charge is used to deposit Li onto the Cu substrate first as a Li reservoir, then a smaller portion of this charge is used to cycle Li between working and counter electrodes for 10 cycles. After 10 cycles, a final exhaustive strip of the remaining Li reservoir is performed to the cut-off voltage. The final stripping charge, corresponding to the quantity of Li remaining after cycling, is measured as shown in Figure XX.1.9. Under a current density of 0.5 mA.cm⁻² and Li deposition capacity of 1.0 mAh.cm⁻², the baseline E1 only delivered a CE of 88%; in contrast, a substantially improved CE of 99.5% was achieved in AFSE with a new solvent system and additive (Figure XX.1.9a). The wettability of the FSE electrolyte is much improved on the separator compared to the conventional E1 electrolyte with poor wetting behavior (Figure XX.1.9d). After 10h resting, the Li-metal anode after the 1st charge shows non-uniform Li plating, especially at the center, while the Li metal with FSE electrolyte shows homogeneous Li deposition. In addition, For the cell using E1 electrolyte, it could not be charged after 1 h resting (black-dash line) and 5 h resting (red-dash line). In contrast, the cell using FSE shows normal charge curves for all cases (Figure XX.1.9b). It indicated that the resting period of 1h and 5h is not enough for conventional electrolyte to wet out the surfaces of separator and electrodes to facilitate the charging process. However, with improved wettability, FSE can wet out the surfaces of separator and electrode even in only 1h resting.

Figure XX.1.9c indicates that the FSE significantly improves the cycling stability of NMC 811 with a cutoff voltage of 4.3 V. All the cycling data were collected with CR- 2016 type coin cells with a high loading cathode of 4 mAh cm⁻², a 50 μm thin Li-metal anode, and lean electrolyte amount of 5.5 μL/mAh. As shown in Figure XX.1.9c, the NMC 811 cell with the FSE shows an initial discharge capacity of 2.78 mAh at 0.5C rate and retains 80% of its initial capacity after 265 cycles. Similarly, AFSE enabled significantly improved cycling stability, delivering an 80% capacity retention of 2.66 mAh after 280 cycles. In addition, the average CE is nearly 99.9% for the cells tested with FSE and AFSE. By comparison, using the baseline electrolyte of E1, the cell decays quickly and reaches 70% of its original capacity of 2.79 mAh only after 50 cycles. The average CE is only 99.0 % in the first 50 cycles.

The Li-deposition morphology was probed on the Li-metal anode by using scanning electron microscopy (SEM). At a current density of 0.5 mA cm⁻², the Li seeds that formed in the E1 electrolyte have a needle-shaped morphology (Figure XX.1.10a) and are smaller than those formed in FSE and AFSE electrolytes. This finding implies that the growth of Li dendrites is exaggerated in the conventional electrolyte without additives and at low Li⁺ concentration. By contrast, Li seeds formed in FSE and AFSE are uniform and show an island-shaped morphology. As shown in Figure XX.1.10d, the thickness of deposited Li in the E1 electrolyte is 25 μm with loose and mossy structures, while the deposited Li in the FSE and AFSE electrolyte is only 20 μm with dense and chunky structures (Figure XX.1.10e,f). The morphological difference indicates a significantly

reduced surface area and thus restrained side reactions between Li-metal anode and electrolyte, resulting in limited SEI reformation and reduced electrolyte consumption.

In conclusion, the newly developed electrolyte AFSE can promote much more uniform Li deposition and improved CE. More importantly, AFSE demonstrates improved cycling performance with the Li||NMC811 full cells. Furthermore, SEM study reveals that the electrolyte greatly influences the SEI chemistry and compositions, generating a robust and non-dendritic Li deposition on the anode surface.

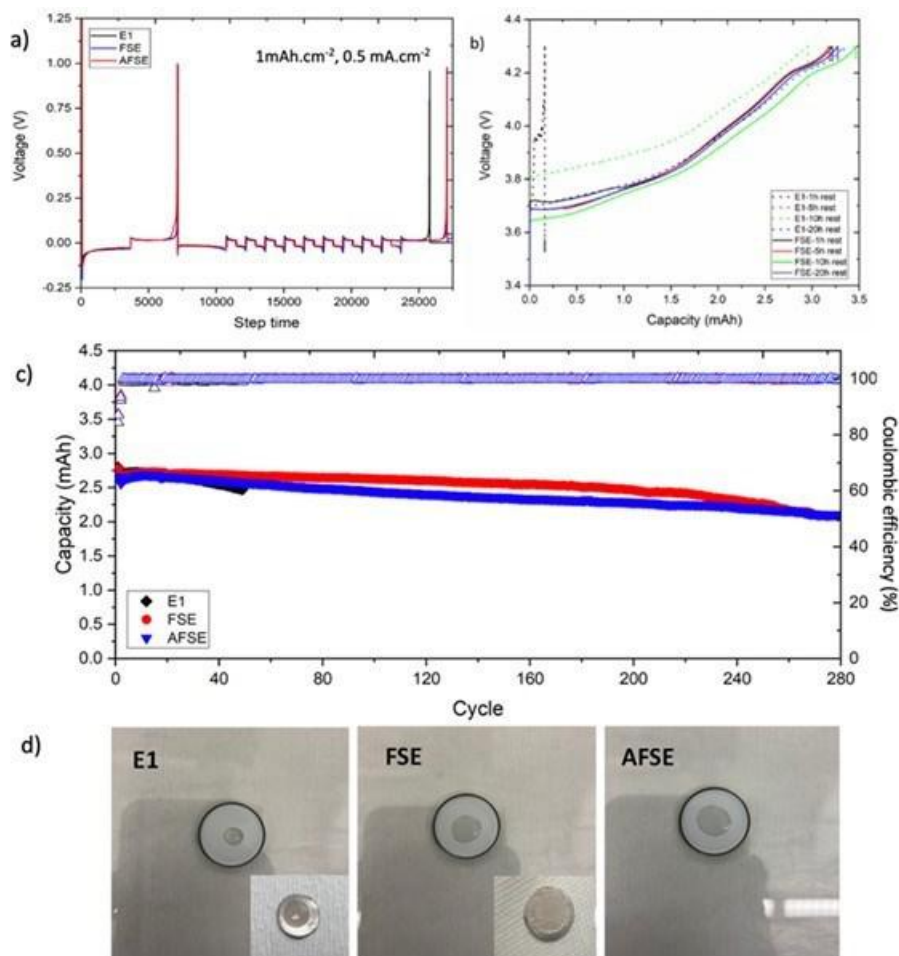


Figure XX.1.9 (a) Aurbach coulombic efficiency of Li||Cu cell in different electrolytes, (b) charge curves of different electrolytes with various resting time, (c) electrochemical performance of the NMC811||Li coin cells tested in different electrolytes, and (d) wettability of the electrolytes on Celgard separators and Li metals after 1st charge.

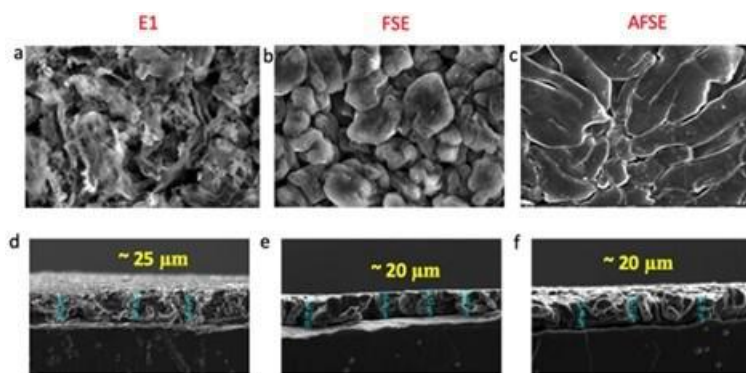


Figure XX.1.10 Morphology of Li-metal anode after 10 cycles: (a-c) top-view SEM images and (d-f) cross-view images of Li anodes in different electrolytes.

UMD team developed a new nitrate-reinforced carbonate-based electrolyte using the conventional salt concentration of around 1 M for Li-SPAN batteries. SPAN recently emerges as a promising transition-metal-free and high-energy cathode material for metal-based batteries. Compared to the conventional carbon-sulfur composite, SPAN provides better dispersion and confinement of the sulfur-based active species via means of covalent interaction. That being said, SPAN is typically preferred to contain a small amount of elemental sulfur to enhance the specific capacity. Therefore, the electrolyte needs to be accordingly designed to ensure cycling stability. It is well known that highly concentrated ether-based electrolytes can support decent SPAN cycling. However, their high cost, high viscosity as well as volatility/flammability of ethers might be of concern. UMD team developed a new nitrate-reinforced carbonate-based electrolyte using the conventional salt concentration of around 1 M. This electrolyte allows desired amount of decomposition of NO_3^- and PF_6^- anions to form inorganic-rich interphases on both Li and SPAN surfaces. The combination between low electronic conductivity of LiF and high ionic conductivity of nitrogen-contained species provides good protection against side reactions, enabling good performance for both SPAN cathode (> 200 cycles, Figure XX.1.11c) and Li metal anode (CE 99.66%, Figure XX.1.12a). The Li||SPAN full cell also showed promising cyclability (Figure XX.1.12b). In contrast, the baseline electrolyte (4 M LiFSI in DME) shorted the SPAN half cell after 130 cycles (Figure XX.1.11a). In the future, the team will continue to optimize other cell parameters towards practical conditions using the nitrate-reinforced electrolyte to achieve the goal of high-energy density Li-S batteries.

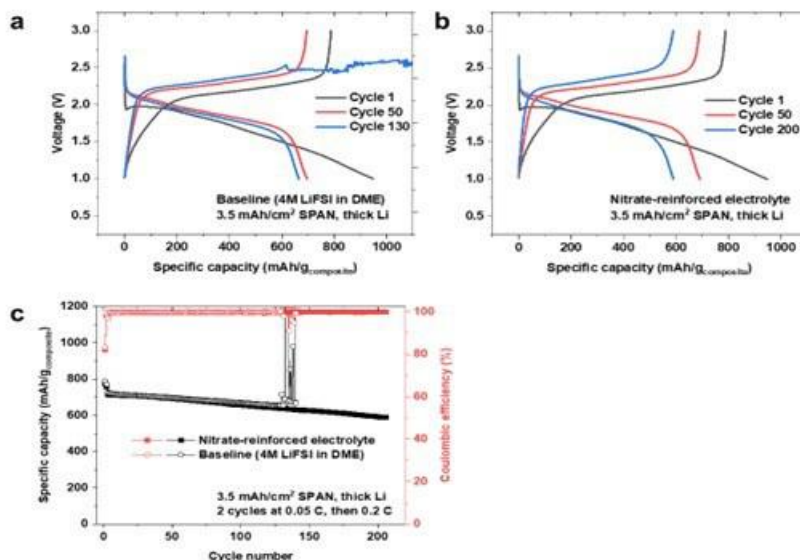


Figure XX.1.11 11 Charge-discharge curves of Li | SPAN half cells in (a) 4 M LiFSI in DME, (b) the nitrate-reinforced electrolyte; and (c) long-term cycling performance in both electrolytes

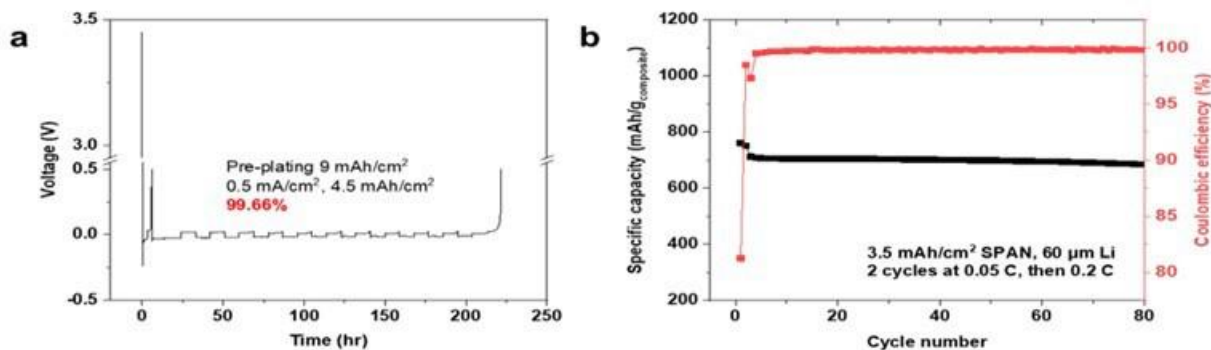


Figure XX.1.12 (a) Li plating/stripping efficiency and (b) cycling performance of Li | SPAN full cell in nitrate-reinforced electrolyte

Liu's team at UCSD studied four LHCEs with high areal loading ($> 6 \text{ mAh cm}^{-2}$) SPAN as the cathode, a material which is known to offer stable cycling with no polysulfide dissolution problem when the appropriate electrolyte is chosen. Based on the understanding of the role of transport, **UCSD** team identified a DME-based LHCE as the optimal choice to fabricate a 2 Ah pouch cell. The study demonstrates the significance of electrolyte bulk in realizing stable cycling of high-energy-density LMBs with high areal capacity cathodes. Four LHCEs were prepared using LiFSI as salt and four different ethers as main solvents due to ether's superior stability with LMA. The four ethers are dibutyl ether (DBE), diisopropyl ether (DiPE), diethyl ether (DEE), DME, and the four electrolytes are LDBE, LDiPE, LDEE, and LDME respectively. These four electrolytes were saturated with LiFSI salt and then diluted by Bis(2,2,2-trifluoroethyl) ether (BTFE) in 1:2 solvent to diluent mole ratio. Several physical properties had been tested and calculated for these four electrolytes, including the concentration, conductivity, viscosity, and transference number. The concentration follows the trend of LDME $>$ LDEE $>$ LDBE $>$ LDiPE. The ionic conductivity measured in Swagelok cells without separator shows the trend of LDME \gg LDEE $>$ LDiPE $>$ LDBE, consistent with the dielectric constants of the four primary solvents. Furthermore, the electrolyte viscosity and transference number were also measured. LDME showed the highest viscosity and lowest transference number. LDiPE is the least viscous and of the highest transference number. The viscosity trend follows the same trend as the concentration. The team also calculated the Sand's capacity and the LDME showed the highest Sand's

capacity (LDME>LDEE>LDiPE>LDBE). This implies that cells with LDME are less prone to ion depletion, which is one of the main driving forces for uncontrollable dendrite growth. **UCSD** team's previous report has shown that to deliver $> 300 \text{ Wh kg}^{-1}$ energy density at cell level, SPAN cathode with $> 6 \text{ mAh cm}^{-2}$ areal capacity is needed. Figure XX.1.13a shows the cycling performance of four electrolytes in full cell configuration, when $> 6 \text{ mAh cm}^{-2}$ SPAN cathodes were paired with Li metal. The charge and discharge current density was 1.2 mA cm^{-2} for all cells. Cells with LDBE, LDiPE, and LDEE electrolytes failed at 23rd, 27th, and 46th cycle, respectively, while the cell with LDME electrolyte lasted 130 cycles without noticeable capacity fading. The symptoms of cell failure are classic soft shorting behavior. The charging capacity exceeded the theoretical value as Li dendrites penetrated the separator and leaked electrons. The voltage fluctuated as the Li dendrites propagated to the cathode and broke after reacting with the positive electrode (Figure XX.1.13b). **UCSD** team correlated the electrolyte transport properties with the cell shorting behavior. The onset of shorting started earlier for electrolytes with lower conductivities rather than with lower CE values. Figure XX.1.13c, d illustrate the correlation between cycle number and Sand's capacity, where a clear linear relationship of cycled number with increasing Sand's capacity is observed. When considering the effect of the separator, the cells are substantially cycled longer than those without a separator as predicted by the Sand's capacity. This provides a theoretical explanation for the dendrite shorting behavior. In systems with low Sand's capacities, ion depletion can be triggered when paired with high capacity cathode, which will accelerate dendrite growth. The other electrolyte properties, including the viscosity and transference number, show no apparent correlation with the shorting behavior. LDME shows the highest viscosity and lowest transference number, but the longest cycle life among four electrolytes. The LDiPE is the least viscous and of the highest transference number but only delivered 27 cycles before shorting. Therefore, this study challenges the assumption that both great efficiency and outstanding transport properties are needed for electrolytes to enable high energy density Li||SPAN cells.

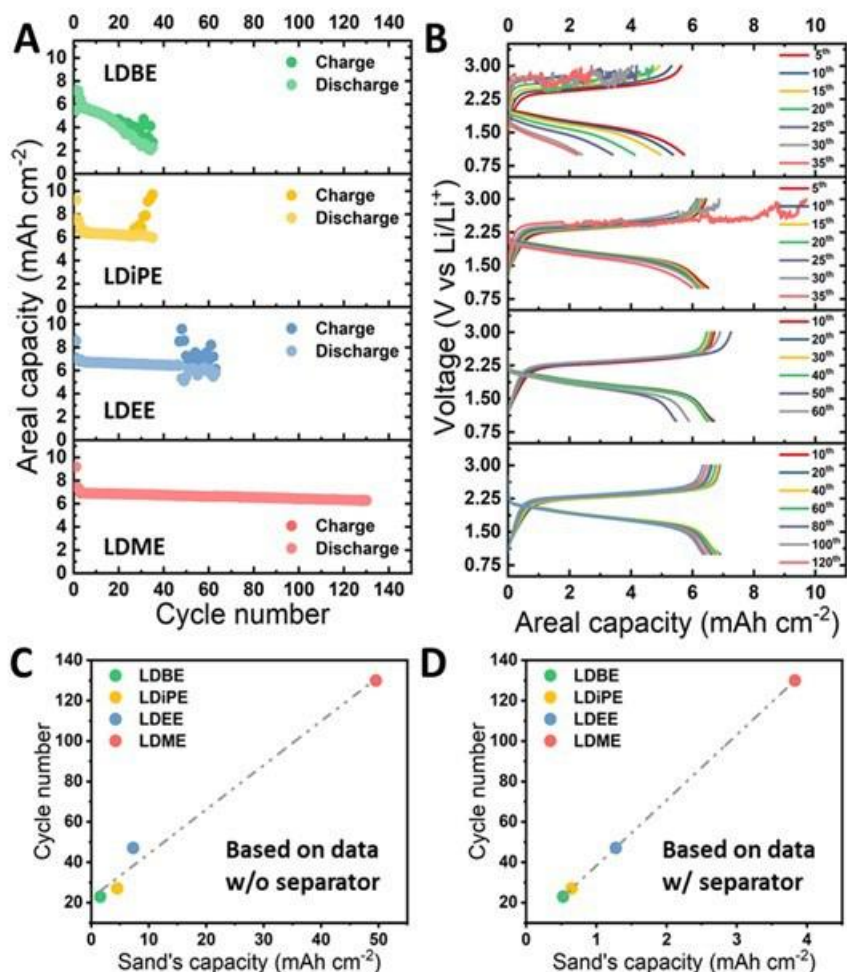


Figure XX.1.13 Capacity retentions and voltage profiles of high areal capacity ($> 6 \text{ mAh cm}^{-2}$) Li||SPAN cells in different electrolytes. (a) Charge/discharge areal capacity retention of Li||SPAN cells with different electrolytes. (b) Voltage profiles of Li||SPAN cells with different electrolytes. Cycle numbers versus Sand's capacity of cells with different electrolytes based on data measured (c) without and (d) with separator. Cells were cycled under C/20 for 2 cycles, and then followed by C/5 cycling.

Meng's team at UCSD explored the effect of porosity on the corrosion rate of Li in the last previously. It was found that the porosity of the plated Li is the major factor in determining the Li corrosion rate. The corrosion rate of Li is directly related to the porosity of the Li. In FY2022, the team further explored the effect of surface chemistry on the corrosion rate of Li. To elucidate the effects of surface chemistry on the corrosion rate of Li metal, XPS with depth profiling was performed on the freshly deposited and corroded Li metal to verify the interphases chemical information (Figure XX.1.14). Two representative electrolyte systems, 1) high concentration ether based electrolyte, Bisalt (4.7m LiFSI + 2.3m LiTFSI in DME) and 2) carbonate base electrolyte, Gen 2 (1.2M LiPF₆ in EC:EMC), were chosen for this study. Meng's team identified that the fresh SEI components in the two electrolyte systems are almost identical. In the Bisalt samples, the change of intensity of C-F peak with depth implies the presence of Li salt (LiTFSI and LiFSI) on the surface of the Li, which can be confirmed by the 533 eV peak in O 1s and peaks in C 1s spectra as well (C-F at 293 eV and C-S=O at 289 eV). Other than the Li salts, Li-F, Li₂O and typical organic species such as C-O/C=O/ROLi can be recognized. Figure XX.1.14b demonstrates the results from Gen 2 sample, which is quite like the Bisalt samples considering the major components include Li-F, Li₂O and typical organic species in the freshly deposited samples. After 3 weeks of resting, in the Bisalt samples, there is an accumulation of Li salt in the surface of the Li, while other SEI components still preserve well in the surface layers. However, in the Gen 2 case, the Li₂O content mostly disappeared after 3 weeks of resting. The surface layers mainly consist of LiF after the corrosion. The results of Gen 2 samples show that the SEI layers have undergone a significant change

during the resting period (highlighted by blue and violet shades), which correspond to the corrosion trend of the Li deposited in Gen 2 where a fast corrosion rate is observed throughout the 5 weeks of resting. Based on the results so far, it can be concluded that in the case of Bisalt electrolyte, where ether-based solvents are used, the SEI components are much more stable than those of the Gen 2 electrolyte. Although XPS depth profiling can provide us valuable information about the SEI components evolution during the corrosion period, the exact SEI structure of the Li deposited from each electrolyte remains unclear. More work should be done to carefully examine the nano-structure of the Li SEI, which might be the key in determining the stability of the SEI. The importance of a stable SEI layer also reflected in the slow corrosion trend in the Bisalt samples. Therefore, we believe that the SEI layers need to be stable enough to survive the corrosion process for mitigating the continuous mass loss of Li in liquid electrolyte.

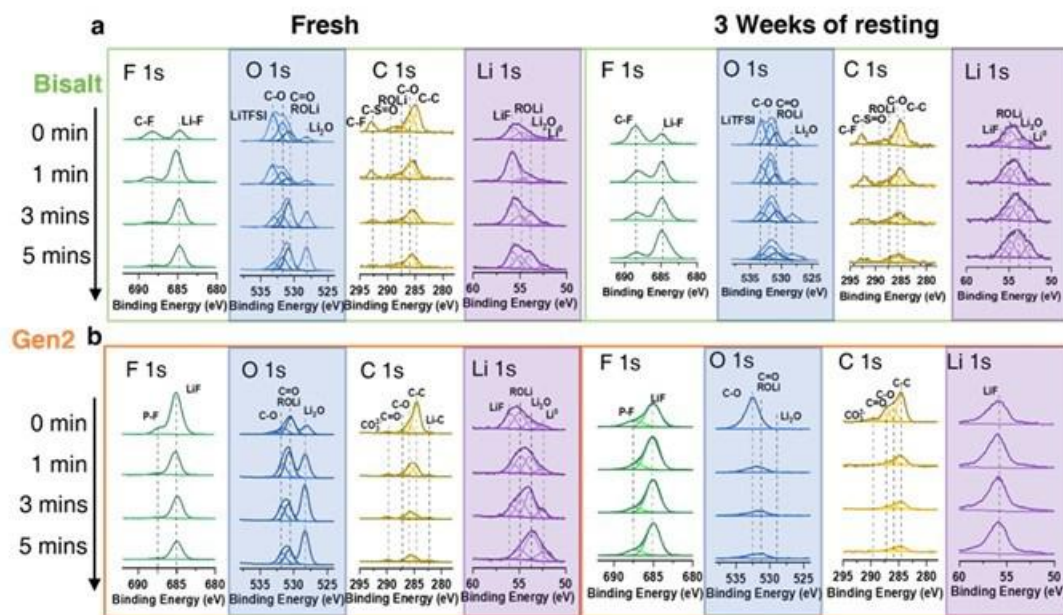


Figure XX.1.14 The XPS depth profiling of deposited Li metal. Chemical evolution of F 1s, O 1s, C 1s, and Li 1s of (a) Bisalt electrolyte and (b) Gen 2 electrolyte before and after 3 weeks of resting in its corresponding electrolyte.

Electrolyte development for SPAN cathodes: **PNNL** team has investigated several new electrolytes for Li||SPAN cells. Six solvating solvents were selected to prepare the high concentration electrolytes (HCEs) first. Among these electrolytes, SS4-HCE shows the highest average Li coulombic efficiency (CE, ~99.3%) (Figure XX.1.15a). Since HCEs have a wettability issue to the polyolefin separators and the thick electrode laminates due to their high viscosities, localized high concentration electrolytes (LHCEs) were developed by adding selected diluent in HCEs to reduce the viscosity and improve the wettability. These newly developed electrolytes are named SS4-based electrolytes. Two SS4-based LHCEs (SS4-LHCE-1 and SS4-LHCE-2) were prepared, and they demonstrate improved average Li CEs (above 99.5%) compared to SS4-HCE (97.9% to 99.1%, Figure XX.1.15b). The average Li CEs are very similar to that of the Battery500 E-baseline electrolyte (LiFSI-DME-BTTFE (0.901:1:2 by mol)) for SPAN cells. In general, the electrolyte with a higher efficiency could enhance the cycling performance of the Li||SPAN cells. To investigate the compatibility of the electrolytes with Li-metal anode, 1 mAh cm⁻² of Li was deposited on the Cu electrode at a current density of 0.5 mA cm⁻². The Li deposited with SS4-LHCEs exhibits larger particle size and denser morphologies than that deposited with E-baseline electrolyte (Figure XX.1.15c). This result indicates that SS4-LHCEs could be more compatible with Li-metal anode than E-baseline electrolyte.

For the cycle life test, the Li||SPAN cell consists of a SPAN cathode (4.5~5 mg cm⁻², from UCSD), a PE separator (20 μm thick), a Li foil (250 μm thick), and 30 μL electrolyte. Before starting the cycle life test, all cells were conditioned by two formation cycles at a current density of C/20 (where 1C = 2.7-3.0 mA cm⁻²)

under the voltage range of 1 to 3 V. In the initial charge/discharge profiles, the cells using three electrolytes show similar polarization (Figure XX.1.16a-c). The Li||SPAN cells with SS4-LHCE-1 and SS4-LHCE-2 have capacity retentions of 92.5% and 88.3%, respectively, after 150 cycles at a current density of C/5 as shown in Figure XX.1.16d. The cells using SS4-LHCE-1 show a slightly higher capacity retention (92.5%) than those using E-baseline electrolyte (~89.6%). These cells are still under testing.

It is interesting to note that even though E-baseline electrolyte has a higher ionic conductivity (Figure XX.1.17a), SS4-LHCE-1 delivers a better charge-rate capability (Figure XX.1.17b). To understand the relationship between the ionic conductivity and the charge-rate capability, the compatibility of SS4-LHCEs with the SPAN cathode will be investigated. Furthermore, post-mortem analyses will be performed to reveal the interphase properties of SS4-LHCE and electrodes.

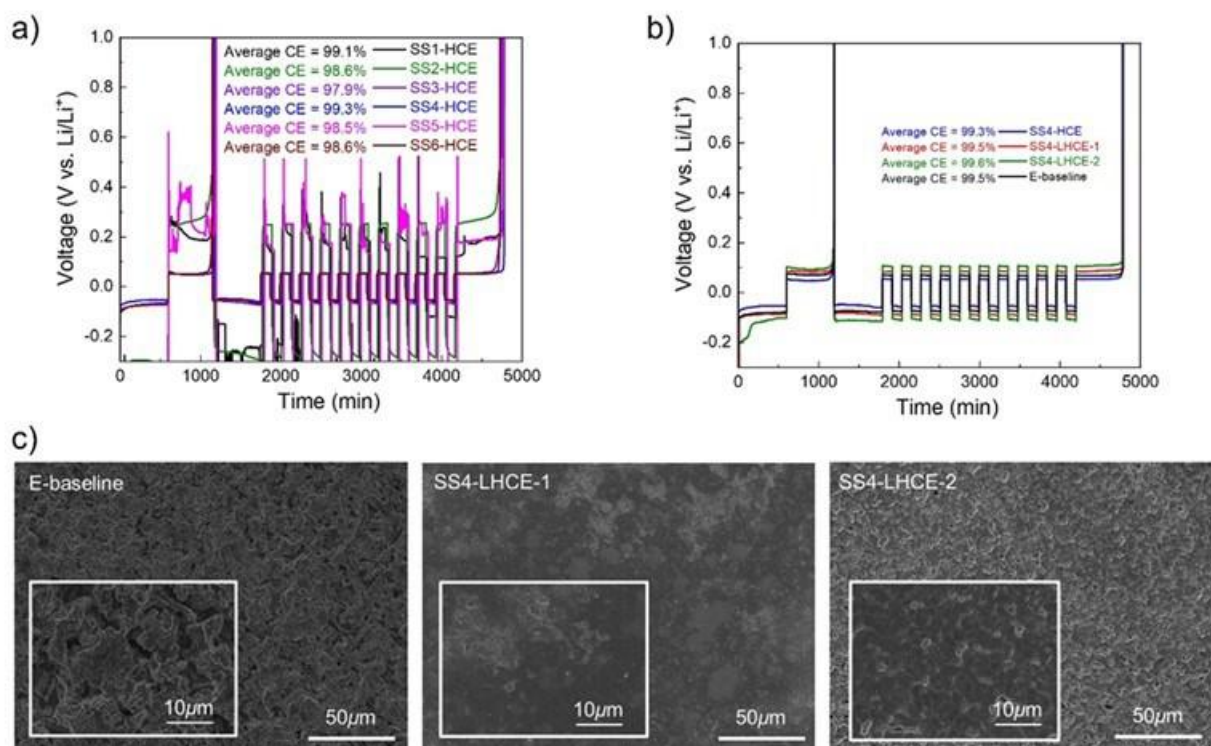


Figure XX.1.15 (a) Average CEs of Li||Cu cells with HCEs using six solvating solvents. (b) Average CEs of Li||Cu with SS4-based LHCEs and E-baseline. (c) Li deposition morphologies on Cu electrodes at a current density of 0.5 mA cm⁻² for a capacity of 1 mAh cm⁻².

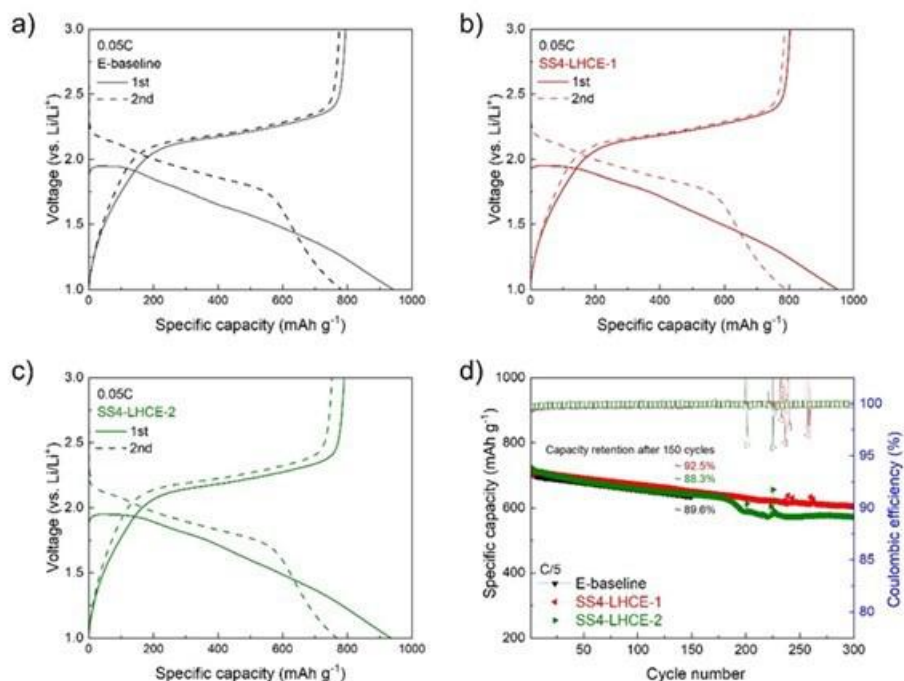


Figure XX.1.16 Charging/discharging profiles of Li|SPAN cells at a current density of C/20 with (a) E-baseline, (b) SS4-LHCE-1, and (c) SS4-LHCE-2. (d) Performances of Li|SPAN cells with studied electrolytes at a current density of C/5 in the voltage range of 1 – 3 V.

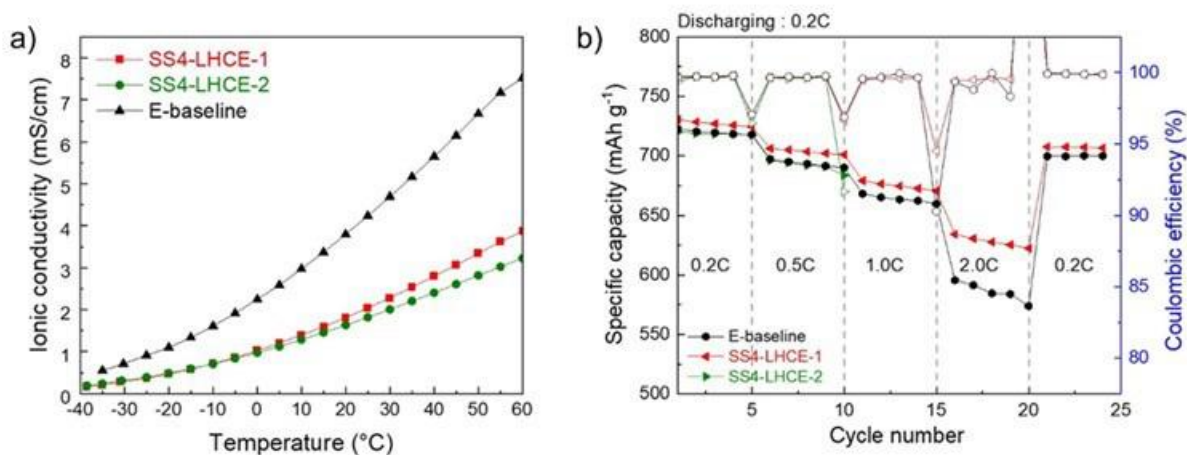


Figure XX.1.17 (a) Ionic conductivities at different temperatures. (b) Charge-rate capability of Li|SPAN cells with the studied electrolytes at a constant discharging current density of C/5 in the voltage range of 1 – 3 V.

Keystone project 2: Electrode architectures

The goal of the Keystone 2 is to design, model, fabricate and characterize the effect of electrode architecture on electrode and cell performance in support of reaching the project of 500 Wh kg⁻¹ cell specific energy. Such studies include both high-capacity cathode materials such as high Ni content NMC and sulfurized polymer cathode, as well as lithium metal anodes.

Effect of polymer precursors on sulfurized polymer performance:

UCSD studied the relationship between the molecular structure of sulfurized polymer and its performance as a cathode. More specifically, we strived to understand how the sulfur substituted at different sites on the pyridine ring influences the battery performance. The purpose for this study is to understand why SPAN has such a high reversibility in battery, and if we could design and synthesize a polymer that has even better performance than SPAN. As shown in Figure XX.1.18A, three sulfurized pyridine polymers had been selected to study the influence of sulfur substitution sites on the pyridine ring. SPAN, where the majority of the sulfur atoms are connected to the pyridine position 4 even though some sulfur groups can connect to other pyridine ring positions at the edge of its polymer chain, (labelled in red color in Figure XX.1.18A). In SP2VP, formed from P2VP as the precursor, besides the position 4 C-S bond formation, the pyridine rings' other positions can also bond with sulfur (labelled in blue color in Figure XX.1.18A). SP4VP, formed from a P4VP precursor, can be considered as the 'opposite' of SPAN - every position on pyridine can be substituted by sulfur except for position 4. All polymers were synthesized by mixing their precursors with excess amount of sulfur and heated at 450°C under inert gas protection. After the sulfurization, all these polymers (PAN, P2VP, and P4VP) turned from white to black color, suggesting the formation of large conjugated structures. All these polymers have similar functional groups. The FTIR spectra for SPAN and SP4VP are shown in Figure XX.1.18B. Both materials have similar covalent bonds, such as conjugated pyridine rings, C-S, and S-S bonds. Some slight peak shifts between the two materials, such as the C-S bond at around 940 cm^{-1} and ring bonded with sulfur at 1172 cm^{-1} suggest that the S atoms are substituted at different positions on the pyridine ring. Since the three polymers' major differences are the C-S bonding positions on the pyridine ring, their performance differences as a battery cathode are likely linked to this factor.

Figure XX.1.18C shows the 1st and 2nd charge-discharge profiles for the three materials. SPAN, the one with the highest ratio of position 4 C-S components, shows the highest discharge voltage plateau (1.6V 1st discharge, 1.8V 2nd discharge). SP2VP has fewer position 4 C-S bonds; its discharge voltage plateau is lower (1.4V 1st discharge, 1.6V 2nd discharge). The lowest voltage plateau was observed with SP4VP (1.2V 1st discharge, 1.5V 2nd discharge), which has no position 4 C-S bonds. On the other hand, all three materials have similar reversible capacity starting with the 2nd cycle when the cutoff voltages of SP2VP and SP4VP are set at 0.5 V vs the 1 V limit used for SPAN. SP4VP and SP2VP also have a very high 1st discharge capacity (>1000mAh/g) in this expanded voltage range; its irreversibility is very similar to SPAN despite the voltage window difference.

These results suggest that high capacity S-containing polymers that can cycle in carbonate electrolytes are not limited to SPAN only. Sulfurizing precursors containing already formed pyridine rings to form polymers, e.g., SP4VP and SP2VP, similar capacities as SPAN can be obtained. These findings open up the possibility of investigating other polymer precursors with related structures. The origin of the lower discharge potential requires further investigation. We hypothesized that the availability of the 4 position on pyridine ring might play an important role. This hypothesis can also explain why SPAN synthesized from high molecular weight precursor PAN can result in high capacities. Since it has less polymer edge per unit mass, the ratio of position 4 C-S will be higher. Future study will focus on how to further enhance the position 4 C-S bonding in SPAN, and examine other polymer structures that can offer higher operating voltage and capacities.

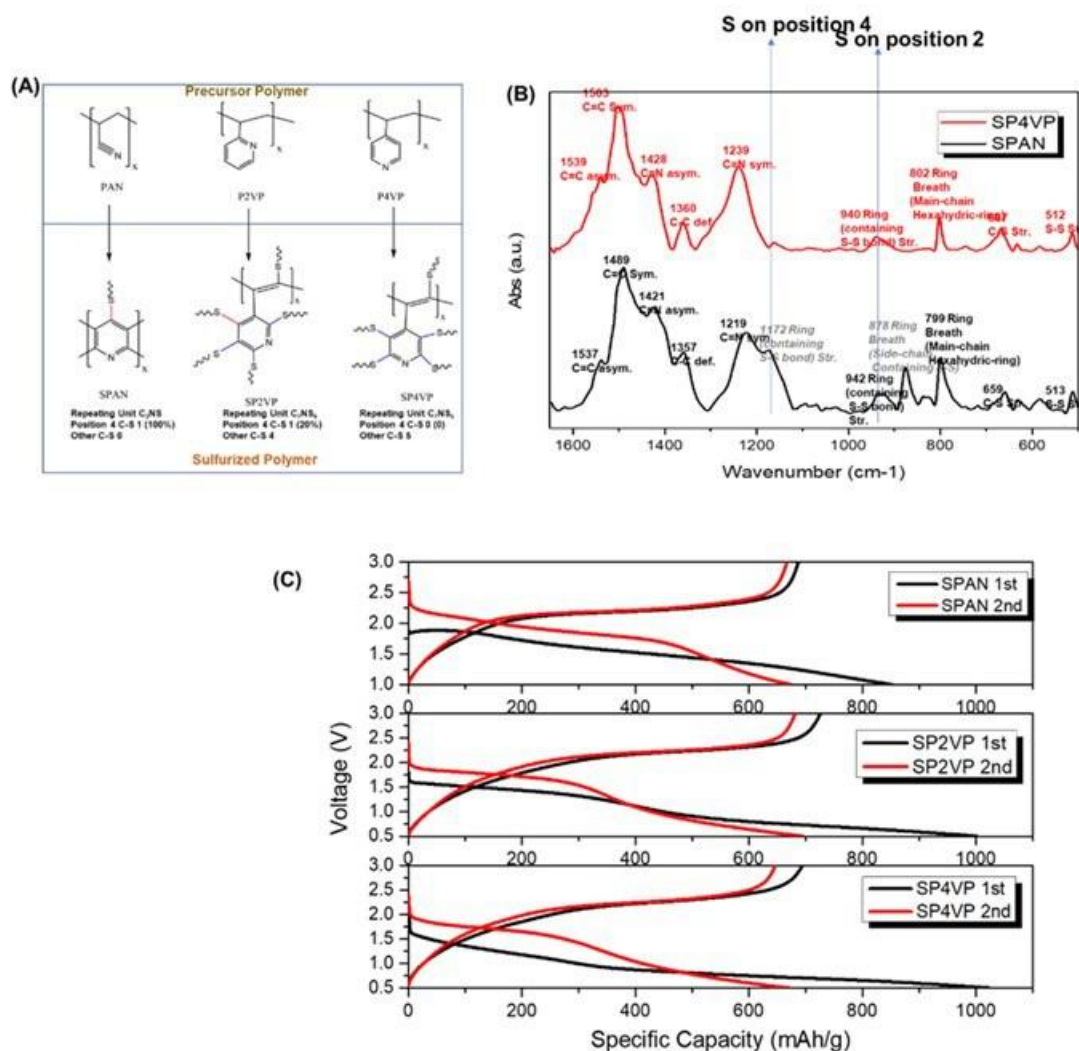


Figure XX.1.18 Sulfurized Pyridine Polymer for Battery (A) Structure of three polymers before and after sulfurization (B) IR for SPAN and SP4VP; (C) Charge/Discharge curves for SPAN, SP2VP and SP4VP in liquid battery. (Cathode Weight Ratio: Active Material: Carbon Black: Binder 8:1:1, with LFP EC/DMC Electrolyte, Charge/Discharge rate 0.2C)

The reaction mechanism of sulfurized polyacrylonitrile (SPAN):

The bonding environment of the S in the SPAN was analyzed by FTIR to probe the pristine molecular structure of SPAN synthesized at 300°C, 450°C and 550°C previously by UCSD team. It was found that there were three types of carbon (C) and sulfur (S) bonding environment. The cycling performance of the SPAN synthesized at different temperatures was further analyzed. Coin cells with SPAN electrodes were assembled with excess Li and electrolyte, and the cells were cycled at C/3 for studying the cycling stability of the SPAN electrodes. As Figure XX.1.19a shows, after the first 3 cycles, the discharge capacity of both the 450SPAN and the 550SPAN were stabilized (at around 520 mAh/g and 300 mAh/g respectively). However, the discharge capacity of 300SPAN keeps decreasing even after the first 3 formation cycles. The capacity retention results are in good agreement with the elemental analysis results reported previously. There is a decrease of S content in the SPAN synthesized at higher temperature which might largely come from the loss of the bridging S_x. As a result, the 300SPAN contains the highest amount of S in its molecule, which might form irreversible lithium polysulfides during the electrochemical cycling. Figure XX.1.19b shows the voltage profiles of the 300SPAN cell. As shown in the figure, at the beginning of 1st cycle, the discharge voltage starts at around 1.8V, which means that there is almost no elemental S left in the molecule. However, the dip at the beginning of the voltage profile, which is also presented in the elemental S voltage profiles, suggests there might be

formation of lithium polysulfide during the discharge. As the cycling continues, there is also a gradual decrease in the discharge capacity observed in the cell. The Figure XX.1.19c shows the cycling voltage profile of 450SPAN. The voltage profiles of the 450SPAN are mostly similar to that of the 300SPAN, except there is no dip at the beginning of the 1st cycle discharge voltage profile. Furthermore, there is no noticeable decrease in the discharge capacity for the first 30 cycles. The Figure XX.1.19d shows the cycling voltage profile of 550SPAN. The discharge capacity of the 550SPAN is the lowest among the three SPANs, which might be caused by the decrease of S amount in the molecules. Interestingly, the 550SPAN voltage profile shows an extra plateau in both charge and discharge voltage profile when compared to those of 300SPAN and 450SPAN. The exact reason for this extra plateau is under investigation. With the results so far, it can be concluded that the synthesis temperature of SPAN needs to be strictly controlled as it will have large impact on the molecular structure, S content and the cycling performance. More XPS and Raman analysis are being conducted to further decipher the reaction mechanism of SPAN.

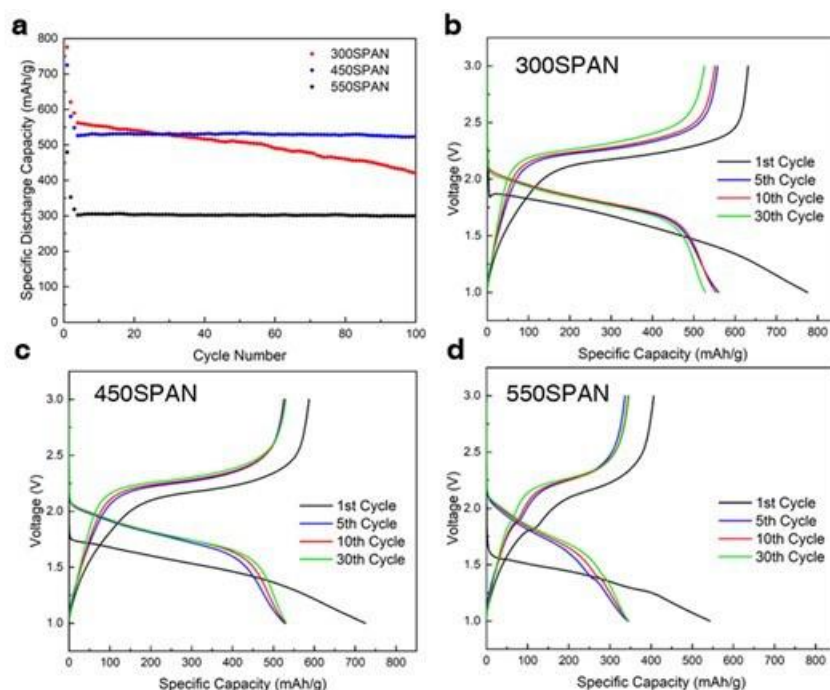


Figure XX.1.19 a) The cycling performance and the voltage profiles of SPAN synthesized at three different temperatures: b) 300°C (300SPAN), c) 450°C (450SPAN) and d) 550°C (550SPAN).

Unraveling the Working Mechanism for SPAN Cathode: In collaboration with Meng's group at UCSD, Liu's group further characterized the correlations between the structure of SPAN and synthesis temperature. Liu's group also characterized the functional groups in SPAN and their impacts on the battery performance. As shown in Figure XX.1.20, XPS and FTIR were applied for characterizing the structures of SPANs synthesized at different temperatures. In Figure XX.1.20A, the XPS N 1s peak shows that there are 3 Nitrogen components, which are pyridine-N, graphite-N, and N-H, respectively. For sulfur, in the XPS sulfur 2p spectra, C=S, C-S, and S-S are the main sulfur components in SPAN (the additional S-O is due to surface oxidation of S). In FTIR, the C-S peak can be deconvoluted into three components, indicating that the SPAN has three C-S species, which are the aromatic, non-aromatic, and bridging C-S bonds. As shown in Figure XX.1.20B, the synthesis temperature can impact the ratios of these functional groups. Figure XX.1.20C shows all of these functional groups and their molecular structures.

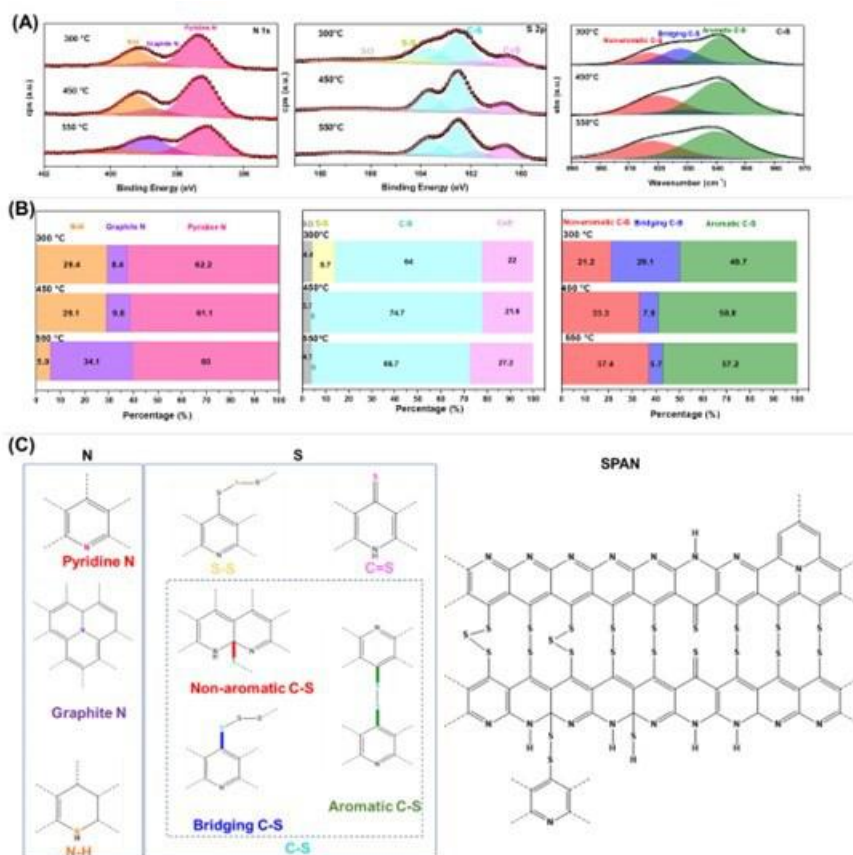


Figure XX.1.20 Functional groups and structure of SPAN. (A) XPS spectra for SPAN synthesized at different temperature; (B) Compositional ratio in SPAN derived from XPS results shown in (A); and (C) molecular structure of SPAN.

Previously, the **UCSD** team have shown the reaction mechanism of the SPAN cathode and pinpointed the root cause for the 1st cycle irreversible capacity loss. According to the proposed reaction mechanism, after the 1st cycle, the aromaticity of the SPAN molecule will be increased. The enhanced conjugation structure of SPAN can in turn increase the electronic conductivity of the polymer molecule. To prove our hypothesis, a carbon-free and additive-free thin film SPAN is made to study the electronic conductivity of SPAN before and after cycling. To synthesize the thin film SPAN, the PAN-Dimethylformamide (1M) solution is first spin-coated on a Ti substrate at 2000 r.p.m. for 30 seconds. The films are later dried at 100°C for 1 hour and then sulfurized in an Ar-flowing tube furnace at 350°C for 6 hours. As shown in Figure XX.1.21, the thin film SPAN deposited on the Ti substrate (Figure XX.1.21a) shows a thickness of only 200 nm (Figure XX.1.21b), a length scale similar to the particle size of SPAN. As shown in Figure XX.1.21c and Figure XX.1.21d, there is no morphological change from precursor PAN to product SPAN. The thin film SPAN is dense, pore-free, and smooth. In Figure XX.1.21e, the STEM-EDX mapping shows that, like the regular SPAN powders, the N, S and C elements are uniformly distributed across the thin film. FTIR (Figure XX.1.21f) shows that all functional groups of SPAN thin film are the same as those of SPAN powders. The thin film SPAN on Ti is cycled in a coin cell setup. Glass fiber is used as the separator and 1 M LiTFSI in DME/DOL (1:1) with 2 wt% LiNO₃ is used as electrolytes. Galvanostatic charge/discharge is conducted in a fixed voltage range of 1–3 V vs. Li/Li⁺ at room temperature with C/20 (1 C = 550 mAh/g) rate based on the SPAN loading. After cycling, the thin film SPAN is recovered from the coin cell and an 80 nm thick Cu is vapor deposited on the top of it in an Ar glove box (Figure XX.1.21g). According to our hypothesis, the loss/conversion of non-aromatic sulfur/nitrogen during the 1st cycle is associated with an increase in the degree of conjugation. In principle, this should lead to an increase in the electrical conductivity. This is indeed confirmed by the measurement of the pristine and the 1st charged SPAN thin films (Figure XX.1.21h). After the 1st charge, the SPAN

conductivity increases by two orders of magnitude (from 1.21×10^{-7} to $4.43 \times 10^{-5} \text{ S cm}^{-1}$). This result further proves our proposed SPAN reaction mechanism: the unwanted non-aromatic sulfur/nitrogen is lost after the 1st cycle and the increased aromaticity can improve the cycling stability of the SPAN.

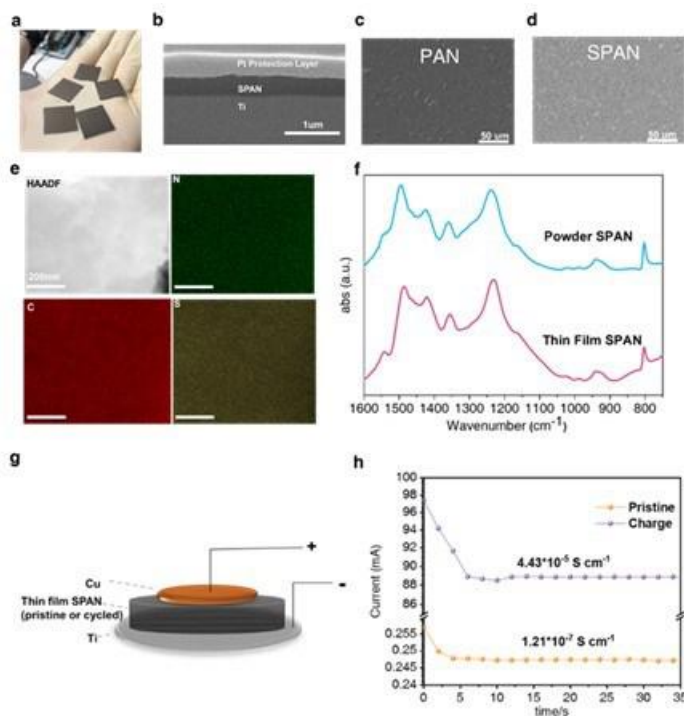


Figure XX.1.21 Characterizations of thin film SPAN. (a) photo of thin film SPAN synthesized on-top of Ti substrate. (b) FIB-SEM image of the cross-section of thin film SPAN on Ti substrate. Top-view SEM images for the (c) precursor (polyacrylonitrile) thin film and (d) SPAN thin film. (e) STEM-EDX mapping of thin film SPAN and (f) FTIR spectra of the powder and thin film SPAN. (g) Schematic and (h) results of the electrical conductivity test for SPAN thin film before and after the 1st cycle.

Controlling the Chemical Corrosions of Li Metal Anodes:

Previously, UCSD has reported the trend of Li metal corrosion rate in carbonate-based Gen2 electrolyte and a high concentration ether-based electrolyte (dual salt). It was found that the corrosion rate of the Li metal might be related to two parameters: 1) the porosity of the Li; 2) the surface chemistry of the Li. In FY2022, we studied the effect of porosity on the corrosion rate of Li in the Gen2 electrolyte. In UCSD previous work on the pressure effects on the Li metal deposition, it was shown that the stacking pressure could effectively control the porosity of deposited Li. To further investigate the effects of Li porosity on the corrosion rate, a split cell together with a pressure sensor was used for controlling the stacking pressure during Li plating (Figure XX.1.22a), which can help us to obtain deposited Li with different porosities. Similar to the previous case, 0.318 mAh of Li is plated onto Cu substrate at a rate of 0.5 mAh/cm^2 in Gen2 electrolyte. However, the electrode size is changed from 1.27 cm^2 to 0.385 cm^2 to accommodate the smaller size of the split cell. Two different stacking pressures, coin cell pressure (150 kPa) and optimized Li plating pressure (350 kPa), were applied during the Li plating process. The plated Li with the Cu substrate is recovered from the split cell and immersed in flooded electrolyte for corrosion study. Figure XX.1.22b shows the Li^0 mass retention (%) of the Li plated under two pressures. The lower porosity of the Li plated under 350 kPa showed clear evidence in suppressing the Li corrosion rate. The metallic Li^0 lost about 18% of its original mass after 20 days. In contrast, 29.2% of Li^0 was lost in the case of coin cell pressure of 150 kPa. When comparing the improved Li corrosion trend to that of Li plated in dual-salt electrolyte under coin cell pressure, it is found that the two corrosion trends are similar (Figure XX.1.22c), demonstrating that with the optimized stacking pressure applied during Li plating, the resulting low porosity Li can have a reduced corrosion rate even in conventional carbonate electrolyte comparable with the dual-salt electrolyte. The cryo-FIB/SEM images also illustrated the

morphological change of the Li plated under different pressures before and after corrosion. From the top-view and cross-sectional images of the Li plated under coin cell pressure, the resulting Li is in whisker-like morphology (Figure XX.1.22d, Figure XX.1.22h). However, just after 7 days of immersion in Gen2 electrolyte, there is a noticeable shrinkage in both the plated Li's thickness and the diameter of whiskers. In contrast, the morphology of Li plated under 350 kPa pressure did not show a significant change. The Li retained its dense morphology after 7 days of immersion, especially in the cross-section. The only noticeable changes were occurred on the top surface of the dense Li where some flower-like materials begin to form on the surface. With these results, it can be seen that the Li corrosion only takes place at the interface between Li and the electrolyte. Therefore, the porosity of the plated Li should play a major role in controlling the corrosion rate of Li. In the future, the role of surface chemistry in the corrosion of Li metal will be studied in more details.

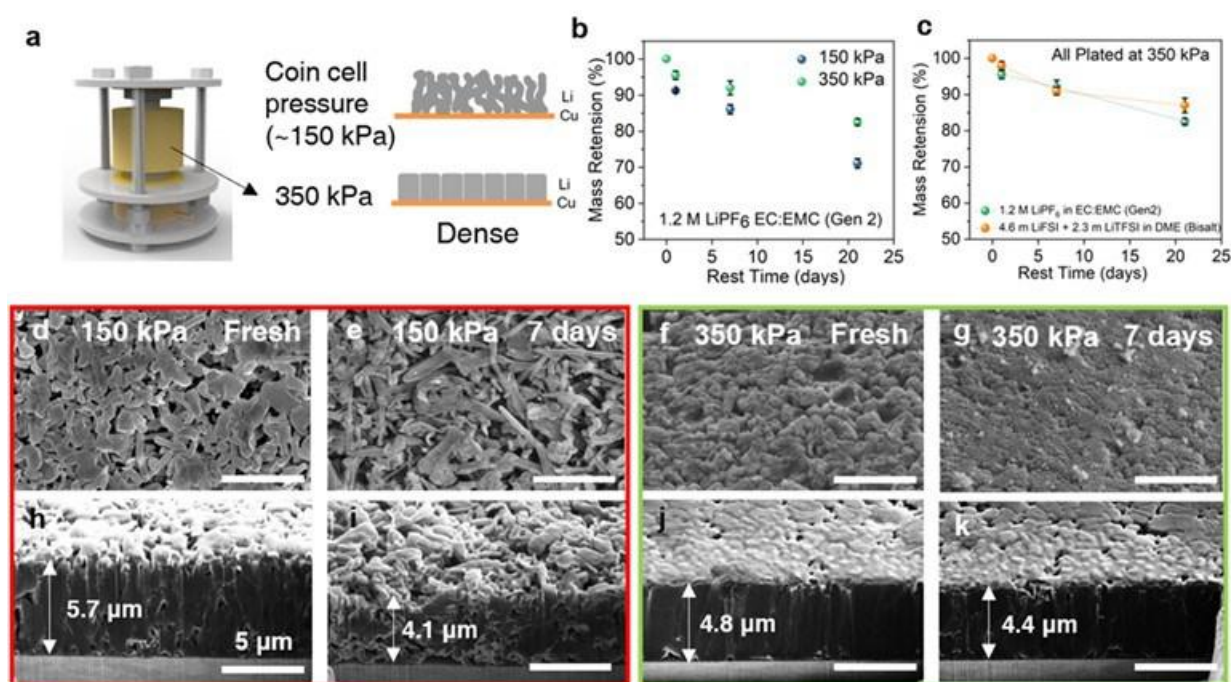


Figure XX.1.22 The effect of morphology control on limiting the corrosion of Li in liquid electrolyte. a) Schematics of stacking pressure control set up. b) Trend of Li⁰ mass retention (%) of Li plated under 2 different stacking pressure (coin cell pressure and 350 kPa pressure) in Gen 2 electrolyte. c) The comparison between Li⁰ mass retentions (%) of Li plated in Gen 2 electrolyte with 350 kPa and in Bisalt electrolyte in coin cell. d-k) The top-view and cross-sectional SEM images of the deposited Li metal in Gen 2 electrolyte: under coin cell pressure after d, h) freshly deposited, e, i) after 7 days of resting and under 350 kPa pressure after f, j) freshly deposited, g, k) after 7 days of resting.

Effect of Mg additive on Li metal plating:

Prof. Goodenough's group at UT Austin introduced one simple electrolyte additive $\text{Mg}(\text{ClO}_4)_2$ to achieve stable lithium plating/stripping and improve the cycling life of rechargeable Li-metal batteries. Li/Cu and Li/Li symmetric cells were assembled to evaluate the interfacial chemistry of the metallic lithium anode with localized high concentration electrolytes (LHCEs Figure XX.1.23). The electrolyte with $\text{Mg}(\text{ClO}_4)_2$ delivered a much higher Coulombic efficiency ($\sim 99.0\%$) than the cell with the pristine one ($\sim 96.0\%$) at 1 mA cm^{-2} during 400 cycles (Figure XX.1.23a to Figure XX.1.23c). The good stability with the metallic lithium anode for the LHCE with the additive is observed at 1 and 2 mAh cm^{-2} in the symmetric Li/Li cells (Figure XX.1.23d to 2-6e); no apparent voltage polarization increase was seen. Figure XX.1.23f to 2-6i compare the Li-metal surface after cycling with different electrolytes. After being cycled in LHCE with $\text{Mg}(\text{ClO}_4)_2$ additive, the Li metal showed a more compact and smoother surface. Large Li particles with over $5 \mu\text{m}$ and

low tortuosity are packed closely. The deposited Li ($\sim 40\ \mu\text{m}$ thick, Figure XX.1.23i) is much thinner than that formed in the pristine LHCE; the compact Li deposition with a low surface area can significantly mitigate the parasitic reaction between the electrolyte and the metallic lithium anode.

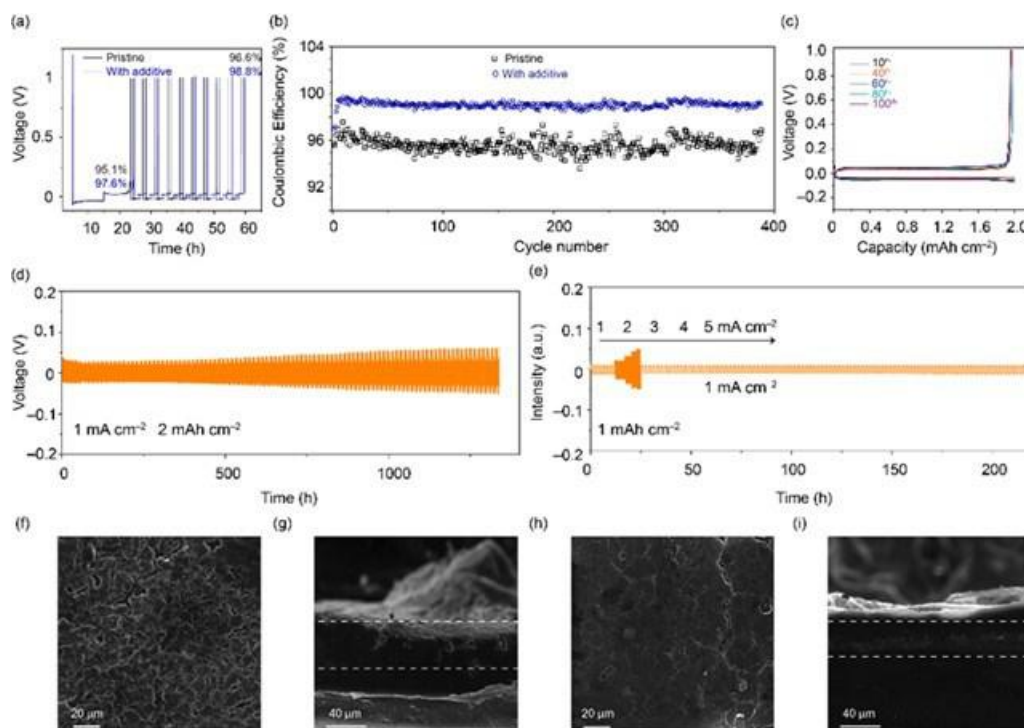


Figure XX.1.23 (a) Electrochemical performance of Li/Cu cells at $1\ \text{mA cm}^{-2}$. (b) Coulombic efficiency of Li/Cu cells at $1\ \text{mA cm}^{-2}$ and $1\ \text{mAh cm}^{-2}$ for 400 cycles. (c) Galvanostatic Li plating/stripping profile of Li/Cu cells at $1\ \text{mA cm}^{-2}$ and $2\ \text{mAh cm}^{-2}$. (d) Long-term cycling of Li/Li symmetrical cell with the additive $\text{Mg}(\text{ClO}_4)_2$. (e) Rate performance of symmetrical cell. SEM top-view/cross-section images of cycled Li-metal anodes (100 cycles) obtained from LHCE (f, g) without and (h, i) with the additive.

Influence of electrolyte additive on the performance of high Ni content, NMC 811 cathode:

UT Austin introduced a simple additive $\text{Mg}(\text{ClO}_4)_2$ into the localized high concentration electrolyte (LHCE) to reduce electrolyte-Li reaction, protect Li surface, and stabilize the anode architecture for long-term cycling. As shown in Figure XX.1.24, cells assembled using LHCE with the additive demonstrates a superior capacity retention of 96.3% at C/10 rate after 100 cycles compared with a capacity retention of 93.0% for cells using pristine LHCE without the additive. The additive also helps improve the rate capability and coulombic efficiency (Figure XX.1.24B and Figure XX.1.24C). The discharge capacities with pristine LHCE are 219, 212, and 197 mAh g^{-1} at, respectively, C/10, C/3, and 1C rates. When the rate is increased to 2C, a fast capacity decay is evident, and a capacity of 174 and 170 mAh g^{-1} is seen at, respectively, 3C and 5C rates. The cell capacity returned back to 210 mAh g^{-1} when the rate was reduced back to C/3, which may have been caused by the damage to Li anode at high current densities during fast charge. In contrast, the cell with LHCE with $\text{Mg}(\text{ClO}_4)_2$ additive performs significantly better at high charge rates, showing stable specific discharge capacities of ~ 186 , 184, and 178 mAh g^{-1} at, respectively, 2C, 3C, and 5C rates. The specific capacity then recovers back to 214 mAh g^{-1} after the charge rate was back to C/3. These results clearly show that the LHCE with additive reduces the damage to the integrity of SEI and enables high current density cycling. The additive also enhances the coulombic efficiency as seen in Figure XX.1.24C.

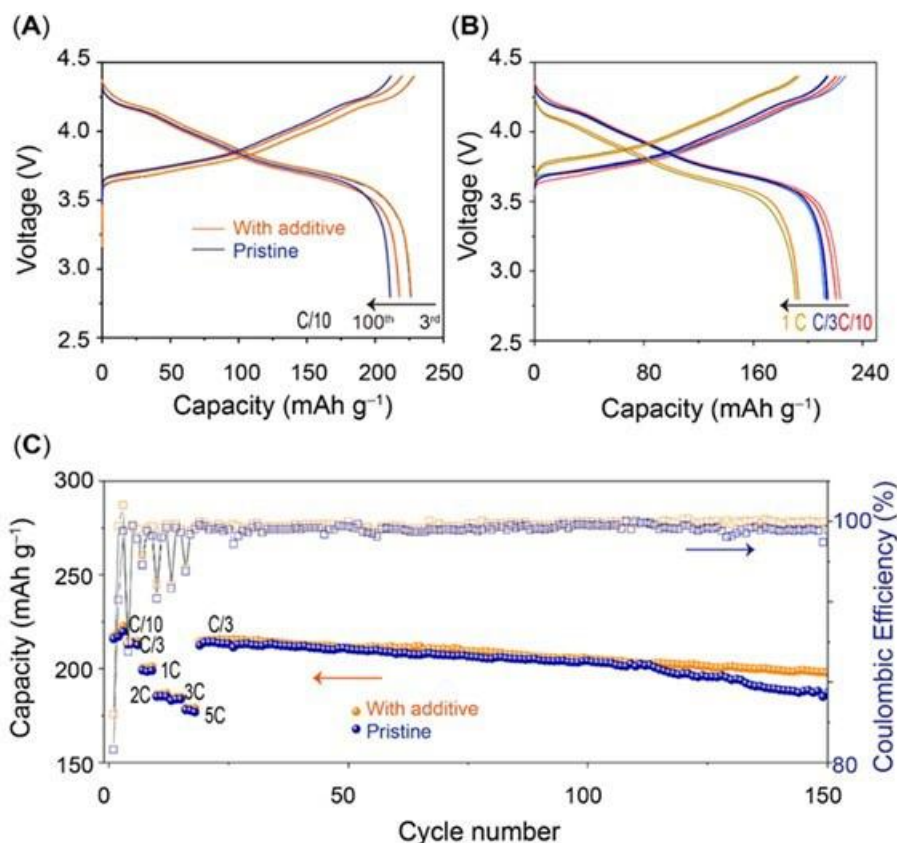


Figure XX.1.24 Electrochemical characterizations of the Li/NCM811 cells. (A) Charge and discharge curves of Li/NCM811 cells with LHCE with and without $\text{Mg}(\text{ClO}_4)_2$ additive at C/10 rate for 100 cycles. (B) Charge and discharge profiles of LHCE with additive under various rates. (C) Rate performance, long term cycling performance, and Coulombic efficiency of the Li/NCM811 cells with LHCE with and without $\text{Mg}(\text{ClO}_4)_2$ additive

Separator Coating

University of Washington made progress about the $\text{Li}_4\text{Ti}_5\text{O}_{12}$ (LTO) coating on the anode side of the separator to improve the electrochemical performances of Li-metal batteries. Previously, we demonstrated that $\text{Li}_{1.3}\text{Al}_{0.3}\text{Ti}_{1.7}(\text{PO}_4)_3$ (LTAP) coating on the anode side of the separator has a beneficial impact on Li-metal anode cycling since the decomposition products at the Li|LTAP interface are electronically insulative while ionically conductive. Compared to LTAP, the spinel structured LTO has a stable structure and high ionic conductivity, as well as good compatibility with electrolytes, indicating its potential to homogenize lithium ions flux and stabilize the interface of the Li metal anode. Here, we report the preparation of an LTO (~10 μm thickness) coated Polyethylene (LTO@PE) separator via doctor blading and employed it in Li-metal batteries. In the Li||Cu half-cell, the Coulombic efficiency (CE) is up to 99.4%, which is similar to our previous data using the PE separator, but the overpotential decreased. Furthermore, using LTO@PE in Li-metal full cell (50 μm Li||NCM622) exhibits capacity retention of 94.4% after 130 cycles, which presents much higher cycle stability than that of using uncoated PE separator full cell. In the first experiment of this study, the nano-sized (20 nm) LTO: Poly(vinylidene fluoride) (PVDF) with a ratio of 9:1 dissolved in 1-Methyl-2-pyrrolidinone (NMP) solvent to make a slurry. The slurry was coated on one side of the PE separator via doctor blading. The thickness was controlled at around 10 μm . Then, the LTO@PE was dried under 60 °C in a vacuum oven for 12 h. Following, it was pouched in a diameter of 20 mm. The CE, cycle stability, and polarization voltage were evaluated in Li||Cu coin cell. The selected galvanotactic charge and discharge curves and CE versus cycle number are shown in Figure XX.1.25a and Figure XX.1.25b. During the initial discharge process, there is a voltage plateau at ~1.45 V vs. Li/Li^+ , corresponding to Li ions insertion into LTO frameworks. The initial CE was 67% and quick jumped to 99% after about 20 cycles. The average CE was 99.4%.

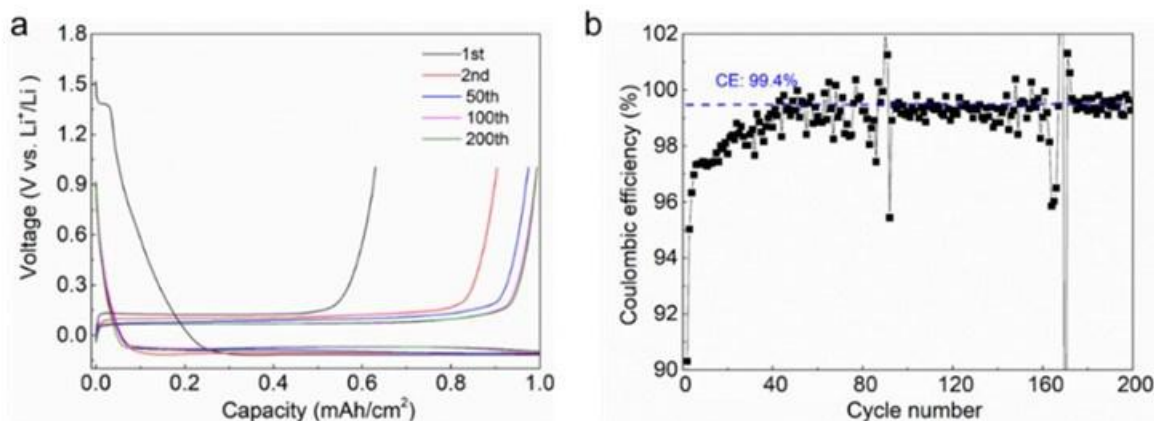


Figure XX.1.25 (a, b) Selected galvanotactic charge and discharge curves and CE versus cycle number of Li||Cu coin cell using LTO@PE separator. The electrolyte is the 1.49 M lithium bis(fluorosulfonyl)imide (LiFSI) in a mixture of DME and 1,1,2,2-tetrafluoroethyl-2,2,3,3-tetrafluoropropyl ether (TTE), with DME and TTE a molar ratio of 1.2:3. The deposition capacity is 1 mAh cm⁻² at a current density of 1 mA cm⁻² with a volume of 60 μ L for each coin cell. In this testing procedure, a given amount of Li metal is plated on a Cu foil and then stripped off with a cutoff voltage of 1 V vs Li/Li⁺.

The electrochemical performance of 50 μ m Li||NMC622 (4 mAh cm⁻²) full cells using the uncoated PE and LTO@PE separators is shown in Figure XX.1.26. The selected galvanotactic charge and discharge curves using the PE separator shown in Figure XX.1.26a indicate that the capacity is maintained at 4.7 mAh after 30 cycles at the rate of C/3 charge and C/3 discharge (the cell is still cycling).). Panel b in Figure XX.1.26b shows selected galvanotactic charge and discharge curves of the full cell using the LTO@PE separator under the same conditions. The capacity is maintained at 4.7 mAh after 130 cycles, corresponding to a 94.4% capacity retention rate (the cell is still cycling). The capacity versus cycle number graph shown in Figure XX.1.26c confirmed the high stability of the full cell using the LTO@PE separator compared to the uncoated PE separator.

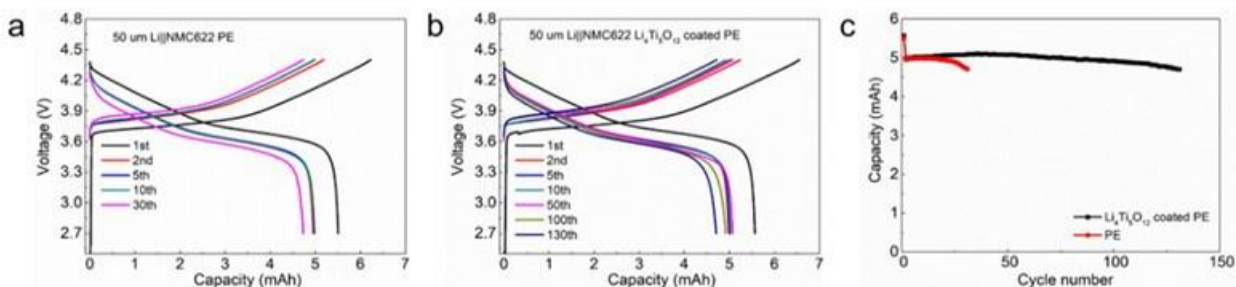


Figure XX.1.26 (a, b) Selected galvanotactic charge and discharge curves of 50 μ m Li||NMC622 (4 mAh cm⁻²) full cell using PE and LTO@PE separators. (c) Capacity versus cycle number of 50 μ m Li||NMC622 full cell. All cells were charged and discharged at C/10 for the first formation cycle and then cycled at a C/3 charge and discharge in the voltage window of 2.7–4.4 V. The electrolyte was LHCE, with a volume of 60 μ L for each coin cell.

Oxide Cathode Thickness Optimization:

UW team studied the optimization of cathode thickness. Thicker electrodes allow for a de facto increase in energy density since the weight percentage of electrochemically inactive current collectors is reduced in the stack. However, thicker cathodes can also run into diffusion limits at higher current densities leading to underutilization of the active material. The optimization of an ideal cathode thickness is non-trivial and requires greater scientific understanding. Coin cells were cycled with high-Ni NMC cathodes of thicknesses 50–200 μ m, against Li-foil anodes, at a series of C-rates. The results showed a sharp capacity drop at high current densities, a hallmark of reaching the diffusion limit. However, the diffusion limit showed no thickness dependence (see Figure XX.1.27). This runs counter to the models in literature describing the diffusion limit,

which predict a gravimetric capacity drop with increasing cathode thickness. This discrepancy appears in some published data as well, where the authors have only looked at the capacity drop with C-rate, rather than looking at the capacity drop with current density and cathode thickness side-by-side. In the literature data, this discrepancy only appears for NMC cathodes, not LFP cathodes.

To study this discrepancy, further studies are planned: a series of NMC622, LCO, and LFP cathodes with different thicknesses will be cycled at different current densities, to determine if there is a thickness dependence. For each cathode batch, EIS will be used to measure the effective diffusion coefficient to verify the difference in morphology among different dried cathode strips. To test whether the lack of a thickness dependence in NMC cathodes is due to the absence of a diffusion limit, further tests will be conducted by varying the salt concentration in the electrolyte to reduce the ionic conductivity. Limiting the electrolyte concentration should, at some point, induce a diffusion limit if there isn't one already.

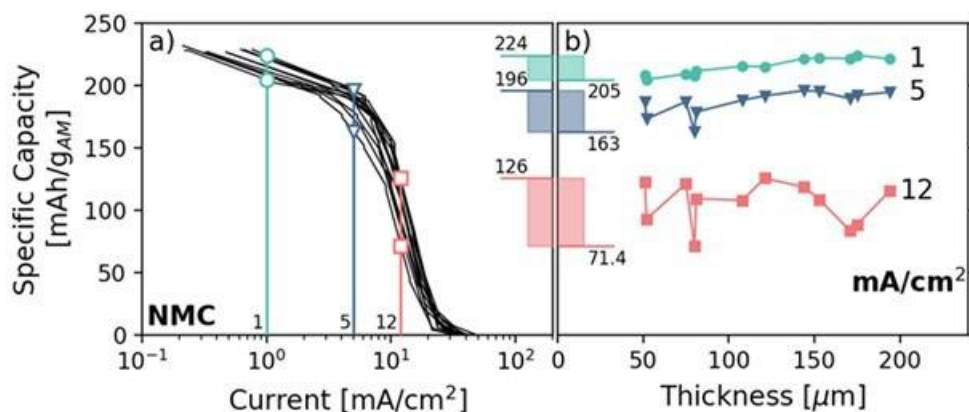


Figure XX.1.27 Initial data showing no significant impact to the specific capacity as a function of cathode thickness.

Lithium metal deposition behavior on copper foam was studied by SEM after a capacity of 10mAh/cm² of Li metal was deposited (see Figure XX.1.28). Top view of Cu foam shows porous structure of deposited Li metal in LHCE-M47. The cross-sectional view shows the same porous deposited Li metal on the right side which is towards separator. However, Li metal was only deposited on the top surface of copper foam, instead of the bottom of it due to the limitation of lithium-ion diffusion in electrolyte and lithiophilicity of 3D host surface. The surface modification to enhance lithiophilicity needs to be studied further.

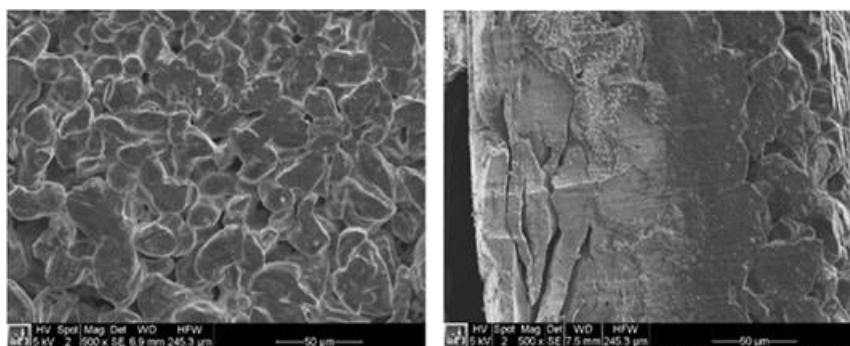


Figure XX.1.28 Top-view (left) and cross-sectional view (right) of electrochemically deposited Li metal on Cu foam in LHCE.

The PNNL team continued the study of root causes for the CEI formation and evolution on SPAN cathode surface in Li||SPAN cells with two electrolytes, LFSI-ether (an LHCE of LiFSI-1.2DME-3TTE, by mol.) and LPF-carbonate (a baseline electrolyte of 1 M LiPF₆ in EC-EMC (3:7 by vol.) + 2 wt.% VC), through experimental investigation and computational simulations. The surfaces of SPAN cathodes were examined

through ex situ XPS characterization at different discharge states (Points I, II and III in Figure XX.1.29a, corresponding to discharge specific capacities of ~ 40 , ~ 1060 and ~ 1770 mAh g $^{-1}$, respectively) and after the first cycle (Point IV in Figure XX.1.29a) in both LPF-carbonate and LFSI-ether, as well as after 5 cycles in LFSI-ether. Li₂S₂ is revealed to be the main active product of lithiation in SPAN and the Li⁺ trapped by Li-S, Li-N and Li-C bonds are the main contribution of irreversible capacity loss in the first cycle for Li||SPAN batteries, regardless of the electrolyte system. In addition, the reactions between Li₂S₂ and C-O/C=O in LPF-carbonate or C-F of TTE and N-S of LiFSI in LSI-ether initiate the growth of a CEI layer. In LPF-carbonate, the solvent dominated decomposition process in the initial cycle leads to the formation of CEI on the inner and outer layers of the SPAN surface. In contrast, for LFSI-ether, the DME decomposition is suppressed and the decomposition process is dominated by LiFSI salt, resulted in less organic species which have large molecule size. Thus, the CEI formed in LFSI-ether can fill into the SPAN bulk and strengthen SPAN like pinning layer. Furthermore, the CEI layer formed in LFSI-ether is demonstrated to be more conductive, robust, and thin, leading to long-term cycling stability with high S loading under both room and high temperatures, fast discharge capability and superior Low temperature performance.

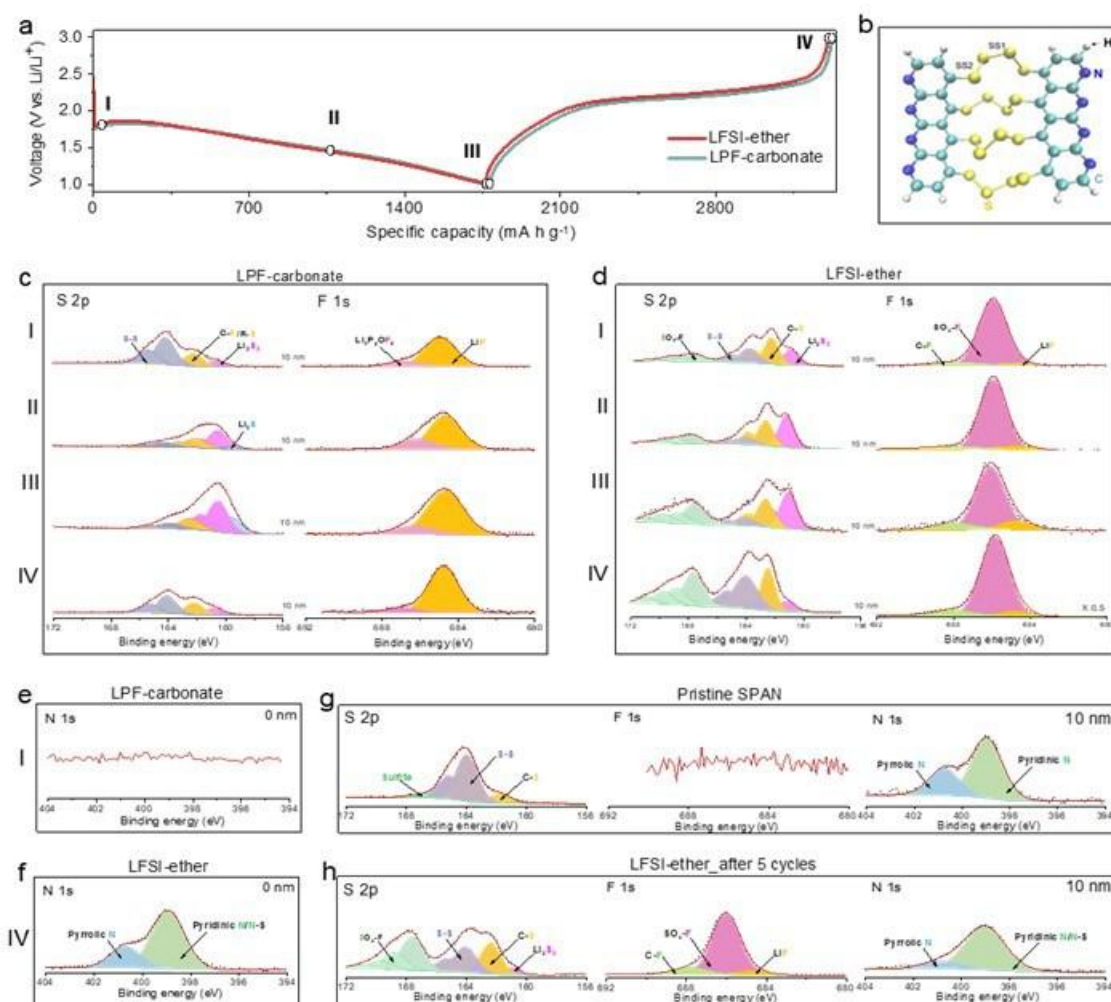


Figure XX.1.29 (a) The initial discharge/charge profiles of Li || SPAN cells with different electrolytes at C/10 rate. Sampling points (I, II, III and IV) for XPS characterizations are marked with dots and numbers. (b) One SPAN structure used in AIMD simulation. (c, d) S 2p and F 1s XPS spectra collected on the surfaces of SPAN cathodes at different discharge states (points I, II and III) and charge state (point IV) in (c) LPF-carbonate and (d) LFSI-ether electrolytes, respectively. (e, f) N 1s XPS spectra at signal depth of 0 nm for SPAN (e) at point I in LPF-carbonate and (f) at point IV in LFSI-ether. (g, h) S 2p, F 1s and N 1s XPS spectra collected on the surfaces of (g) pristine SPAN and (h) SPAN after 5 cycles in LFSI-ether. (Signal depth = 10 nm).

Computational identification of Functional electrocatalysts for Li_2S_2 to Li_2S conversion:

University of Pittsburgh (U-Pitt) conducted theoretical modeling to probe the kinetic barriers related to the conversion of Li_2S_2 , the intermediate polysulfide phase, to Li_2S , the final phase, with the main goal being to identify functional electrocatalysts.

One computational task conducted in FY2022 at **U-Pitt** is identification of effective Li-ion conductors (LIC) needed for encapsulation of S nanoparticles to prevent the dissolution of polysulfide species (PSs) and the corresponding shuttling effect. For these purposes several materials belonging to the stoichiometric formula, $\text{Li}_7(\text{TM})\text{N}_4$, TM = transition metals, collected in Table XX.1.1 have been chosen as potential LICs for the computational evaluations of the Li-ion conductivity/mobility as well as structural and electrochemical stability in the presence of an electric field during electrochemical cycling of the battery. The nudged elastic band method has been used as the main computational approach for calculating the potential energy profiles of the Li-ion paths through the different types of channels present in the considered LIC materials.

The crystal structures of many of the $\text{Li}_7(\text{TM})\text{N}_4$ type compounds are very similar and demonstrate open Li-channels which do not contain transition metal atoms as shown in Figure XX.1.30. Thus, the transition metals, TMs do not affect noticeably the Li-ion conductivity through these channels and the computational estimation of the Li-ion mobility for these systems could be executed only for one typical compound in this materials family, such as Li_7NbN_4 belonging to the cubic space group #205 (Pa-3).

It can be observed that the structure in the [110] direction contains channels representing rows of quite large interstitial sites. These channels may serve as efficient pathways for Li-ion mobility during electrochemical cycling. In this case the Li pathway would have a Zig-Zag shape as shown in Figure XX.1.30 with the green arrows.

Furthermore, a computational study was conducted to compare the Li-mobility/diffusivity in these two directions. This involved estimation of the activation barriers of the Li-ion diffusion pathways and thus, in turn, identification of crystallographic directions in which the Li-ions can move the most effectively with minimal resistance from the other atoms in the lattice.

Table XX.1.1 Cohesive energies and band gaps of the considered LIC systems

LIC	E_{coh} (eV/at)	E_{BG} (eV)
Li_7NbN_4	-4.06	3.35
Li_7VN_4	-3.95	3.01
Li_7NiN_4	-3.14	0
Li_7MnN_4	-3.56	0

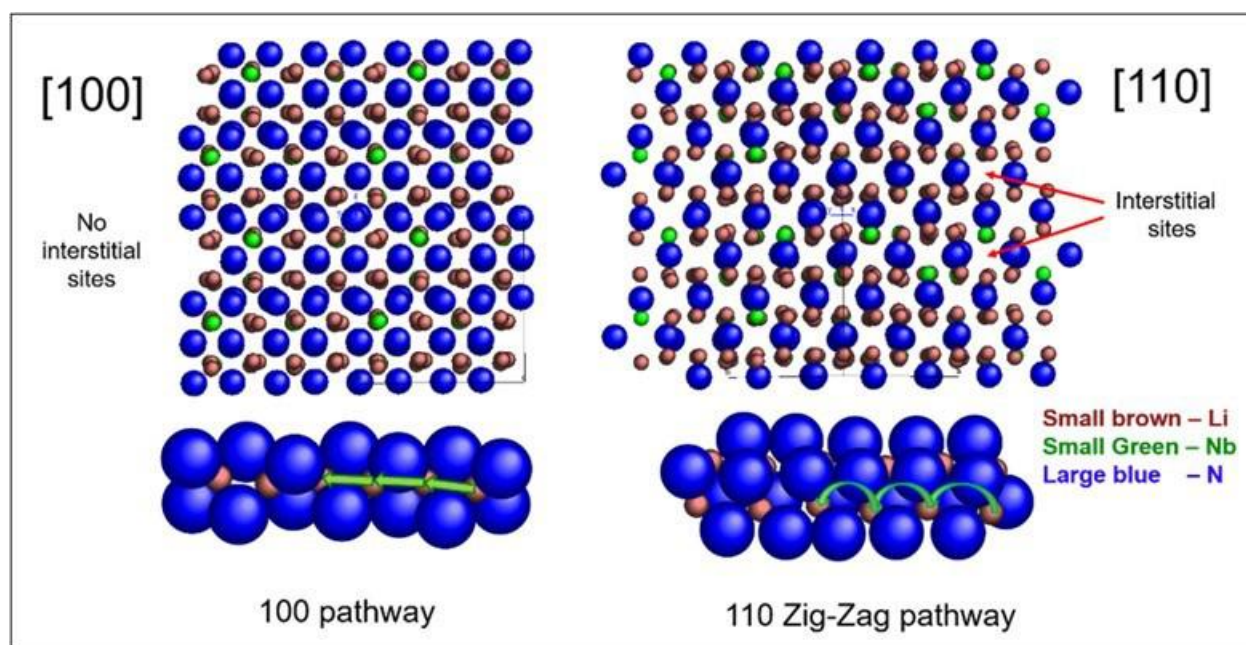


Figure XX.1.30 Crystal structure of Li_7NbN_4 as the typical LIC with Li-ion channels in $[100]$ and $[110]$ directions. Green arrows denote the hopping of Li-ions/vacancies for the different Li-hopping pathways.

Here again, the climbing image nudged elastic band (CNEB) approach was used to calculate the activation barriers of the Li-ion diffusivity in the $[100]$ and $[110]$ directions. For estimation of the activation barriers across these two directions 7 different intermediate points were chosen for performing the calculations of the potential energy profile between the initial and final positions of the Li-ion for the selected pathways in these two directions (totally 9 points). Both energy profiles for these two directions are shown in Figure XX.1.31. It can be construed that the Li-ion mobility profile in the $[100]$ direction demonstrates higher activation barrier than that in the $[110]$ direction (0.284 eV vs. 0.223 eV) which indicates that the $[110]$ direction is noticeably preferable for facilitating and channeling the Li-ion mobility contrasted with the $[100]$ direction. This result also proves the notion regarding efficiency of Li-ion mobility through the large interstitial channels presented in the crystal structure. Finally, for assessing the structural and electrochemical stability of the LICs in the presence of the electric field, a very approximate rudimentary evaluation can be presented by comparison of cohesive energies, E_{coh} and the band gaps, E_{BG} obtained from the electronic structure calculations. The higher the E_{coh} and the E_{BG} , the material system can be perceived to be likely more stable in the harsh electrochemical conditions. Thus, from the values of E_{coh} and band gaps, E_{BG} listed in Table XX.1.1, it can be deciphered that Li_7NbN_4 and Li_7VN_4 could be such prospective LIC candidates for promoting facile transport of Li-ions and thus serving as effective additives in the sulfur cathode configuration for use in the Li-S batteries.

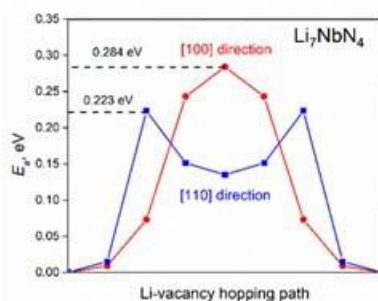


Figure XX.1.31 Potential energy profiles for Li-mobility in $[100]$ (red) and $[110]$ (blue) directions.

Keystone project 3: Cell fabrication, testing and diagnosis

The goal of Keystone Project 3 is to focus on pouch cell design, integration, fabrication, and testing using new materials and cell components provided across different teams in the consortium. The project team will focus on addressing the science and engineering challenges at pouch cell levels, while the other two keystone projects will support this effort by scaling up new materials and identifying feasible solutions for electrode coating using nano or nanostructure materials at scales that can be adopted for fabricating practical cells.

In FY2022, INL studied the effects of formation cycling temperature on the cycle life of Li metal batteries. For Li-ion cells it is known that early cycling and formation play a distinct role in cell performance and eventual cycle life. While extensive effort has been placed on advancing formation for Li-ion cells there is a lack of good understanding how different early life protocols impact Li metal batteries (LMBs). The advancement of electrolytes such as localized high concentration electrolyte (LHCE) developed by the Battery500 team and high concentration electrolytes (HCE) which rely on unique ion solvation. To more directly understand the role of early cycling on life and formation of a stable SEI studies were performed to study how the interface and performance evolved when early cycling was performed at different temperatures. It was found that cycle life was optimized when early cycling was at 25°C.

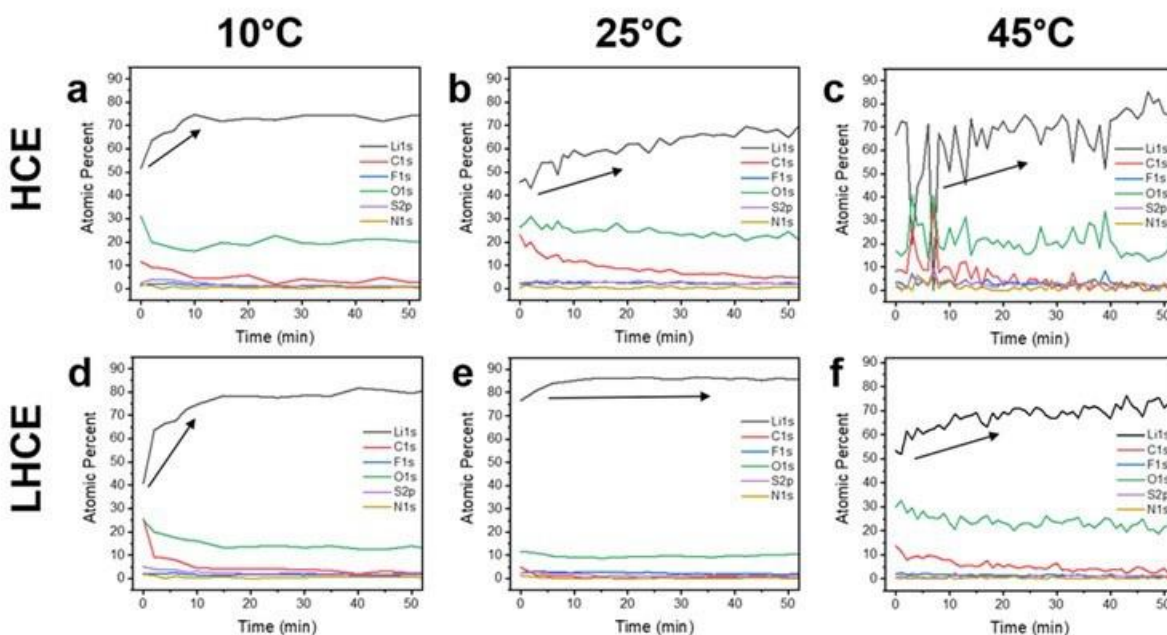


Figure XX.1.32 XPS depth profiles for (top) HCE and (bottom) LHCE electrolyte cells at (a, d) 10 °C, (b, e) 25 °C, and (c, f) 45 °C during formation cycles.

To understand this performance X-ray photoelectron spectroscopy (XPS) with depth profiling was utilized to observe SEI composition after 2 formation cycles (C/20) at the end of discharge in HCE and LHCE electrolytes at various temperatures (Figure XX.1.32). General trends in atomic percent of lithium tells the story of SEI thickness, where a high amount (>70 at. %) suggests a presence of lithium metal. Trends in other atomic concentrations as a function of depth (measured in minutes of sputtering) are also observable with depth profiling. In HCE, the higher temperatures have linear trends in elemental concentration over time of sputtering, revealing thicker SEIs. At 10°C, HCE has a relatively thin SEI, where an initial transition in elemental make-up is observed, until after ~10 minutes of sputtering the elemental variation is consistent and greater than 70 at. % Li. Further, intermittent presence of enriched lithium was observed early-on in the depth profile for HCE at 45°C, which could imply an existence of “dead” Li. Though isolated from the active lithium foil, dead Li exists in a lithium-metal state, which could result in the intermittent increases in lithium

concentration in the depth profile. For LHCE, a thin SEI structure is seen for 10°C and a linear trend (i.e., thicker SEI) is seen for 45°C. At 25°C, there is more than 80 at% Li present that remains relatively uniform for the entirety of the sputtering; therefore, the SEI is very thin for LHCE at 25°C after formation cycles.

Table XX.1.2 XPS depth profile atomic ratios of fluorine, sulfur, and nitrogen to carbon, average over the range of the SEI for each electrolyte and temperature (a cut-off of 20 minutes sputtering was used for depth profiles with linear trends)

	HCE			LHCE		
	10 °C	25 °C	45 °C	10 °C	25 °C	45 °C
F:C Ratio	0.25	0.20	0.21	0.25	1.07	0.24
S:C Ratio	0.45	0.23	0.16	0.45	1.86	0.097
N:C Ratio	0.089	0.038	0.24	0.074	1.63	0.086

Looking more closely at the lower concentrated elements (Table XX.1.2), an increase in FSI⁻ anion, inorganic-rich byproducts (fluorine, sulfur, and nitrogen) relative to carbon is observed for LHCE at 25°C, while others have relatively lower sulfur, nitrogen, and fluorine content in ratio to carbon. Carbon is the prominent product of DME reaction with lithium, seen during the charge desolvation process of SSIPs (i.e., high Li⁺-DME interaction structures). Oxygen was excluded due to its role in both FSI⁻ and DME reactions to form SEI; the distinction of oxygen products will be discussed later with XPS peak deconvolution. Others have noted that the amount of fluorine (such as LiF) present in the SEI is paramount for improved cyclability. This work presents the same idea from a different angle, where a decreased amount of organics (deemed bad actors) in the SEI also leads to improved cyclability, even though relative fluorine concentration is not a massive contributor to the SEI composition. Therefore, methods of producing a more ideal SEI can operate in promoting supportive products (e.g., LiF and other inorganics) and/or demoting inferior products (e.g., carbon-based organics).

In other work efforts, INL focused on the development of approaches for analyzing degradation, safety, and failure of high-Ni NMC-based high-energy cell design and evaluation, Idaho National Laboratory (INL) has developed an electrochemical analytic diagnosis (eCAD) approach to evaluate “battery electrode formulation and cell performance” correlation with the capability of quantitative analyses to provide detailed information for improvements. Currently, two cathode materials, NMC 622 and NMC 811 from multiple sources, are being used as the model materials for cell design improvements and evaluation. Here, a theoretical framework revealed by the eCAD analyses is used for the comparison of the different cell designs and materials to provide more insight about what aspect is critical for performance improvement. An example of the analysis is shown in Figure XX.1.33.

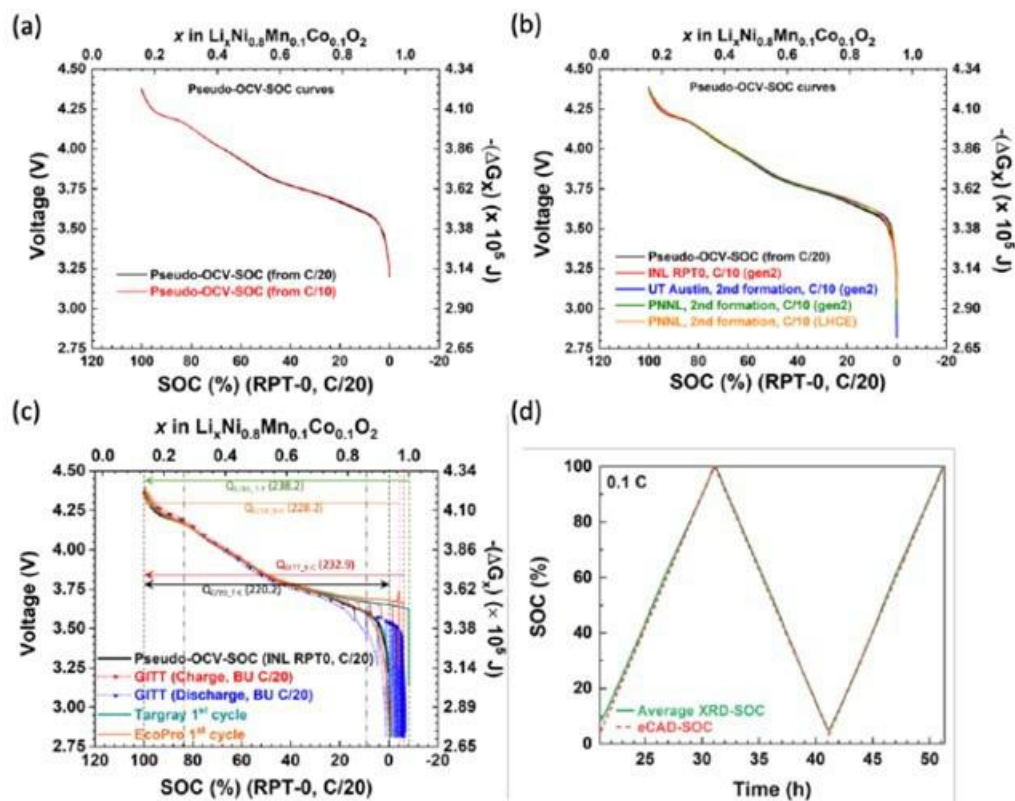


Figure XX.1.33 Comparison of different results developed using the eCAD method. A) using coin cell data at C/20 and C/10, b) with different cathode formulations, cell configurations and electrolytes, c) comparison to galvanostatic intermittent titration (GITT) results and d) comparison of eCAD derived state-of-charge (SOC) and XRD determined SOC.

To ensure the flexibility of the analysis, the results from two different material manufacturers and cells prepared at 4 different institutions were analyzed. The results were also directly compared with XRD data captured as a function of state-of-charge. Aspects of the analysis are also able to evaluate how the utilization of the cathode materials changes over time. These results can directly show how one electrode or processing condition can impact cell energy. If used across the course of cycling it can also suggest how slight changes in utilization lead to enhanced life or more rapid cell failure. Combined the methods provide a means to compare across results more directly across samples and provide a more common ‘baseline’ for comparison.

A concept of “cycle life projection” (CLP) of rechargeable Li metal cells has been reported by INL as part of the cross-platform comparison approach to evaluate cell performance reported by the Battery500 consortium. This CLP approach can provide a verifiable and quantitative validation of the cycle life results from different team members in the consortium consistently and help establishing a useful basis of comparison against the goal of achieving 1,000 cycles in a cell formulation and design with an “early prediction and assessment” capability. The principle and application of electrochemical analytic diagnosis (eCAD) for battery performance evaluation and failure analysis have been reported in the literature [1-3] and illustrated in previous quarterly reports. Besides the unique capability for capacity fade analysis, recently we also applied the eCAD technique to track Li inventory as a new capability to quantify and qualify battery cell performance and efficiency. This approach requires a proper alignment of typical charge discharge voltage profiles with the Li content in the cathode active material (CAM) and uses the well-defined “equilibrium open circuit voltage (OCV or V_{eq}) versus Li content in CAM” relationship to evaluate the charge retention and Li inventory changes during the charge discharge processes in the test.

Another important aspect of the eCAD approach is the ability to utilize a theoretical framework in the cross-platform comparisons. This aspect is somehow overlooked in the battery evaluation in the past. Thus, a proper

introduction of this framework deems necessary. The theoretical capacity (Q_{Th}) of the NMC composition can be calculated based on the Li content in CAM. For NMC622-based cells, $Q_{Th} = 276.5$ Ah/kg (or mAh/g) is obtained from the theoretical calculation based on the removal of one Li from a fully lithiated NMC622 stoichiometry. In general, Q_{Th} is rather constant across the entire $LiNi_xMn_yCo_zO_2$ composition, where $x+y+z=1$, e.g., from $Q_{Th} = 277.9$ Ah/kg for NMC333 to $Q_{Th} = 275.5$ Ah/kg for NMC811. Thus, using Q_{Th} as the basis for the cross-platform comparison is quite useful, as this method provides a reliable framework for performance evaluation, and this approach is insensitive to the formulations of CAM, electrode, cell, or the configuration of the cell.

Figure XX.1.34 shows the data transformation process of the eCAD approach. Here, the formation cycle of a Li-NMC622 coin cell is used as an example. The cell was charged and discharged between $V_{min} = 2.5$ V and $V_{max} = 4.5$ V at C/10 in the formation cycle. Figure XX.1.34(a) shows the charge-discharge voltage profiles, and with a proper determination of the IR potential of the cell, the corresponding IR-free voltage ($V_{IR-free}$) profiles in the formation cycle. The utilization of the NMC622 capacity differs between the charge ($Q_{ch} = 198.1$ mAh/g) and the discharge segment ($Q_{dis} = 178.7$ mAh/g) with a Coulombic efficiency of 90.2% and a first cycle capacity loss of 19.4 mAh/g in the formation cycle. Also presented in the figure is the pseudo-open circuit voltage (pseudo-OCV) vs. state-of-charge (SOC) profile determined from another Li-NMC622 cell by averaging the charge and discharge voltage profiles at C/20 rate in the initial reference performance test (RPT 0) that has been validated in another experiment. The pseudo-OCV vs. SOC curve has been demonstrated as a reliable and universal profile to align the $V_{IR-free}$ voltage profiles with the Li content in the CAM consistently [1]. Based on the RPT 0 results and the pseudo-OCV vs. SOC curve, the capacity measured between 2.5 V and 4.5 V is $Q_{pseudo-OCV(2.5-4.5V)} = 204.0$ mAh/g for NMC622 cells. To understand the differences in the capacity utilization and the CAM utilization, the charge and discharge profiles are further analyzed by eCAD using the pseudo-OCV vs. SOC curve, which has close agreement with the Li content in the CAM. Comparing $Q_{ch} = 198.1$ mAh/g and $Q_{pseudo-OCV(2.5-4.5V)} = 204.0$ mAh/g, hypothesizing that the difference is due to the CAM utilization, the charge profile could be corrected with the CAM utilization coefficient, which is considered as the ratio of $Q_{ch} / Q_{pseudo-OCV(2.5-4.5V)}$, the resulting charge $V_{IR-free}$ profile is shown in Figure XX.1.34(b). The same procedure was used for the discharge segment and the discharge $V_{IR-free}$ profile is also shown in Figure XX.1.34(b). The excellent agreement among the charge, discharge $V_{IR-free}$ profiles and the pseudo-OCV vs. SOC curve in Figure XX.1.34(b) indicates the voltage profiles all aligned with the Li content in CAM consistently. Once the Li content alignment was achieved, the capacity utilization of CAM in each polarization regime is clearly quantified in correspondence with the Li content change in the CAM composition. In other words, the correspondence between the capacity utilization and the CAM utilization is clearly validated as shown in Figure XX.1.34(b). From this example, the CAM utilization coefficient can be expressed in a general term as

$$\text{CAM Utilization Coefficient} = Q_{measured} / Q_{pseudo-OCV(V_{min}-V_{max})} \quad (1)$$

which is defined by the rate of the polarization and V_{min} and V_{max} in the test protocol.

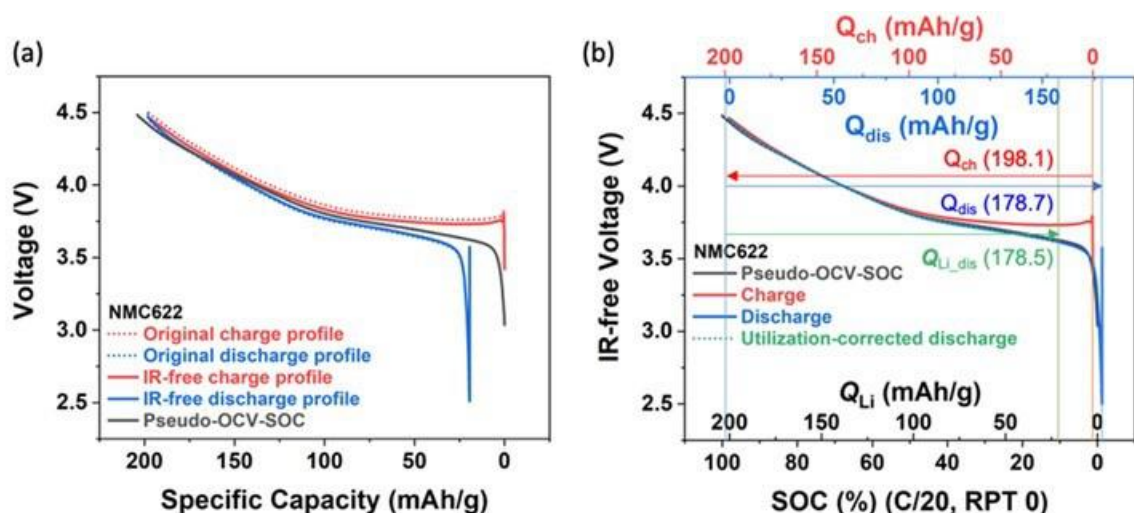


Figure XX.1.34 Analysis of the formation cycle of a Li-NMC622 cell using the eCAD technique. (a) The charge and discharge voltage profiles and the associated IR-free voltage ($V_{IR-free}$) profiles. Also presented is the pseudo-OCV vs. SOC curve, which is obtained from a validated Li-NMC622 cell during an initial RPT at C/20. (b) The reconciled charge and discharge $V_{IR-free}$ vs. SOC profiles in correspondence with the Li content in NMC622.

Figure XX.1.35 shows the results of the cycle aging test on the Li-NMC622 cell. The specific capacity of the cell from reference performance test (RPT) 0 to RPT 2 are shown as a function of cycle number in Figure XX.1.35(a). Based on the charge capacity retention over cycles, the useful cycle life (>80% initial capacity) under cycle aging can be projected as shown in Figure XX.1.35(b). Depending on the cycling rate, the capacity retention could exhibit different fade rate, so the useful life projections could be rate dependent as shown. The useful life projection based on the early fade rate is about 212 cycles for C/20, 209 cycles for C/10, 87 cycles for C/3, and 124 cycles for C/3 which was measured immediately after the C/20 charge discharge cycles in three RPTs. The C/3 cycles that came after RPTs represent scenarios of a long rest period for the cell to recuperate during the C/20 cycling in PRT. Using the eCAD analysis, the useful life projections are shown in Figure XX.1.35(c) based on the CAM utilization. Based on the same cutoff criterion for the end-of-life condition, the useful life projection for each rate is extended to a higher cycle number: 213 cycles for C/3, 259 cycles for C/10, and 371 cycles for C/20 in terms of the CAM utilization coefficient. It is quite well studied and accepted in the literature that the Li diffusion and transport limitation in the NMC cathodes is the dominant factor that determines the capacity [4-9]. This cause also explains the origin of the CAM utilization fade even at the slow rate of C/20 if an insufficient rest period prevents CAM from fully recovery of the Li content in equilibrium because the Li concentration gradient still exists or the inhomogeneous distribution of the Li content in the bulk persists. If this hypothesis pertains to the observation, the useful life projection at C/20 by CAM utilization implies that the useful life will still suffer from this cause. As the rate increases, the severity of the useful life reduction from the same cause will amplify for C/10 and C/3.

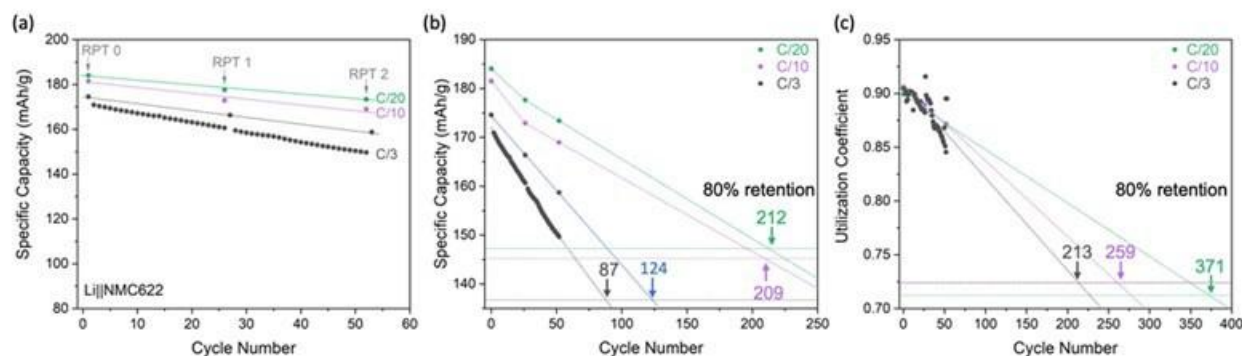


Figure XX.1.35 (a) Charge capacity retention curve of the Li-NMC622 cell in the cycle aging test. (b) Projections of useful life based on charge capacity retention as a function of cycle number. (c) Projections of useful life based on the Li inventory retention and CAM utilization as a function of cycling rate

INL team has completed scaling up of SPAN at a 10 g per batch. SPAN as a promising cathode candidate has attracted more attention due to less shuttling problem compared with traditional Li-S batteries using elemental sulfur cathode. For practical application, scaling up high-quality and reproducible SPAN materials is highly required. INL team is responsible for providing high-quality SPAN powders and electrodes to the Batt500 Li-S teams. In this scale up work, 5 g polyacrylonitrile (PAN) with 20 g of sulfur was sealed and vulcanized at 450 °C for 6 hours and then heated at 300°C to remove remaining elemental sulfur with flowing Ar gas in a tube furnace. Pure SPAN powders >10 g per batch was successfully synthesized (Figure XX.1.36a and Figure XX.1.36b). The sulfur content in SPAN was found to be largely affected by the sealing state during vulcanization process. The improved seal can enhance the sulfur content of SPAN from 42% to 50 wt.% based on the elemental analysis.

The SPAN electrodes with SPAN mass loading of ~6 g/cm² and ~9 g/cm² as well as porosity of ~60% were prepared and tested in Li|SPAN coin cells. High concentration electrolyte (4M LiFSI in DME) was used. The coin cell assembly and testing follow the standard protocols made by Batt500 team. The enhanced sulfur content in SPAN due to improved seal during vulcanization process resulted in specific capacity in terms of SPAN to be increased from 583 mAh/g to 727 mAh/g (Figure XX.1.36c) after 2 formation cycles at a charge/discharge rate of C/20 (1C=600 mA/g). Additionally, as can be seen in Figure XX.1.36d, the two electrodes with different SPAN mass loadings show good cycling performances at a charge/discharge rate of C/10. The cells are still running, and the cell performance will be used as a baseline for future development of new materials (e.g., electrolytes) used in Li-SPAN batteries. Over 5 batches of SPAN powders (>10 g per batch) have been synthesized with the same approach. The SPAN electrodes prepared with the obtained SPAN powders from different batches all showed high specific capacity of over 700 mAh/g. Therefore, the improved seal during synthesis process can not only increase SPAN quality with improved sulfur content but also improve the reproducibility. However, current synthesis process requires excess sulfur. To increase the yield per batch, the removal of the large amount of elemental sulfur might cause safety issue due to solid sulfur stuck at the outlet of the tube furnace. Thus, new improved synthesis approach needs to be developed in the future.

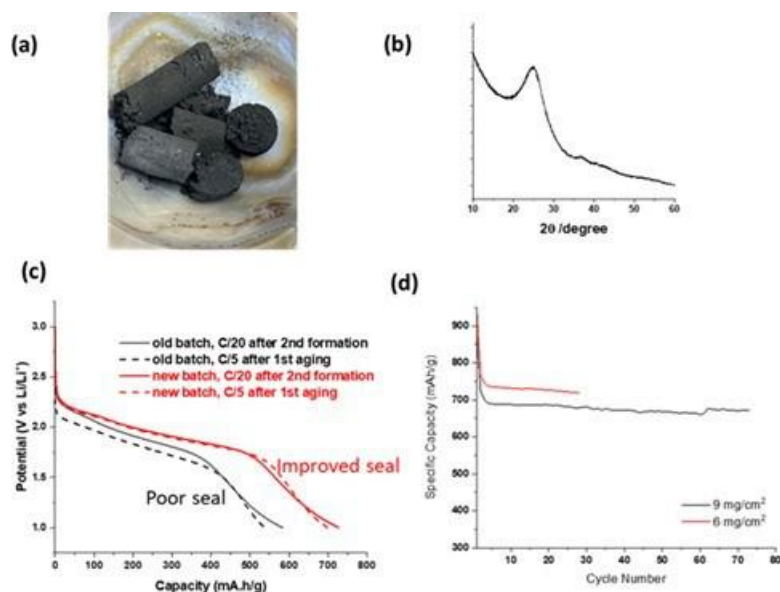


Figure XX.1.36 a) SPAN powders with over 10 g per batch. b) XRD pattern of SPAN powders after vulcanization and removal of elemental sulfur. c) Discharge curves of SPAN prepared at different sealing states. d) Cycling performances of Li-SPAN cells with different SPAN mass loadings.

In order to accelerate the development of new materials (e.g. electrolytes) used in Li-SPAN batteries, INL team is responsible for preparing reliable high-mass loading SPAN electrodes and providing them to Battery500 team members for coin-cell level study. The slurries for doctor-blade casting SPAN electrodes need to be optimized. The slurry recipe (Gen 1) results from UCSD (Prof. Ping Liu's group, Figure XX.1.37 (a)) had been used to prepare high-mass loading SPAN electrodes. However, the reproducibility when using this recipe is not good enough and cracking on the edges of the electrodes after drying were frequently observed. Therefore, based on this recipe, INL's team optimized the slurry formula through the following aspects:

1. Carboxymethyl Cellulose (CMC) binder is not very soluble in water. Therefore, 2 wt% of CMC aqueous solutions were added to slurries instead of the 5 wt% used in the original recipe to enable binders to be distributed uniformly in the slurries.
2. The total solid contents, including SPAN, Super P and CMC binders, were reduced from 25 wt% to 16.25 wt% to improve the uniformity of solids distribution in the slurries.
3. 10 wt% of Isopropyl alcohol (IPA) was added into slurries to further reduce the cracks or wrinkles.

Therefore, INL team developed reliable Gen 2 slurry recipe (Figure XX.1.37(a)) and reproduced at least 6 pieces of electrodes without any cracks and wrinkles. The areal mass loading of SPAN and electrode porosity are around 6 mg/cm^2 and 60%, respectively. The electrochemical performances of the 6 batches of SPAN electrodes were evaluated with 4M LiFSI in DME electrolytes in the coin cells. It can be seen from Figure XX.1.37(b-c), the reproducibility of the electrodes is very good in terms of electrochemical performances. Each SPAN electrode delivers the specific discharge capacity of over 650 mAh/g during aging cycles (at C/10). Those reliable and high-quality SPAN electrodes have been shipped to our Battery500 team members (e.g. GM, UM, PSU, SLAC and PNNL) for developing new materials.

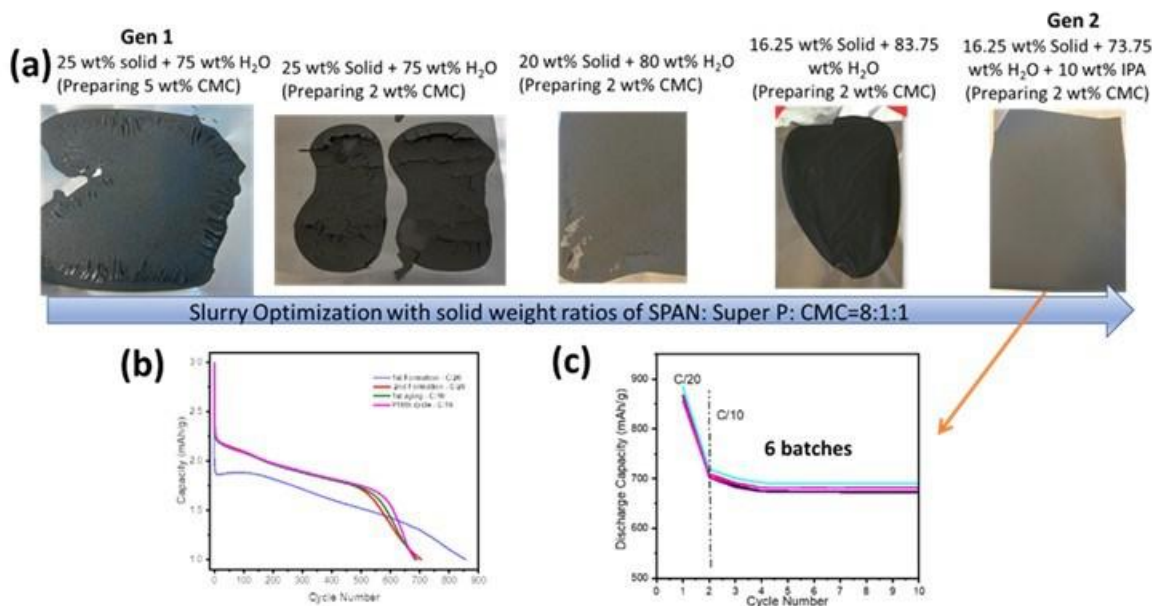


Figure XX.1.37 (a) Optimization of slurries for doctor-blade casting reproducible and high-quality SPAN electrodes. (b) Discharge curves of a typical SPAN electrode and (c) discharge capacities vs. cycling number for 6 batches SPAN electrodes based on Gen 2 recipe.

The **GM** team led the Li-S pouch cell sub-team including 6 university/national lab research teams. Since January 2022, a bi-weekly meeting is scheduled for technical update of the sub-team. To help drive data consistency, the GM team provided S/C cathode to all sub-team institutions to serve as the baseline electrode for comparison with advances developed across each team's development purpose. To complement the baseline electrodes a corresponding testing protocol including component specification and testing condition/setup was also discussed, agreed upon and adopted for utilization across the sub-team.

At **GM**, non-destructive CT and ultrasonic transmission mapping equipment were installed, and an overall research plan was defined. These capabilities will allow the researchers to monitor lithium plating morphology and study the root causes of electrolyte degradation without tearing down the cells. At the same time, C/S cathode formulation was optimized, and roll-to-roll coater parameter continues to be calibrated to improve the continuous double-sided coating uniformity and quality. GM was able to confirm larger batch coating quality of sulfur cathode electrodes using the roll-to-roll coater, as demonstrated in Figure XX.1.38, which shows the good electrochemical performance of cathodes with areal sulfur loading of 3.75 mgS/cm² and 5.2 mgS/cm². In addition, GM prepared a new batch coating for baseline samples and shipped out to all Li-S teams for performance verifications.

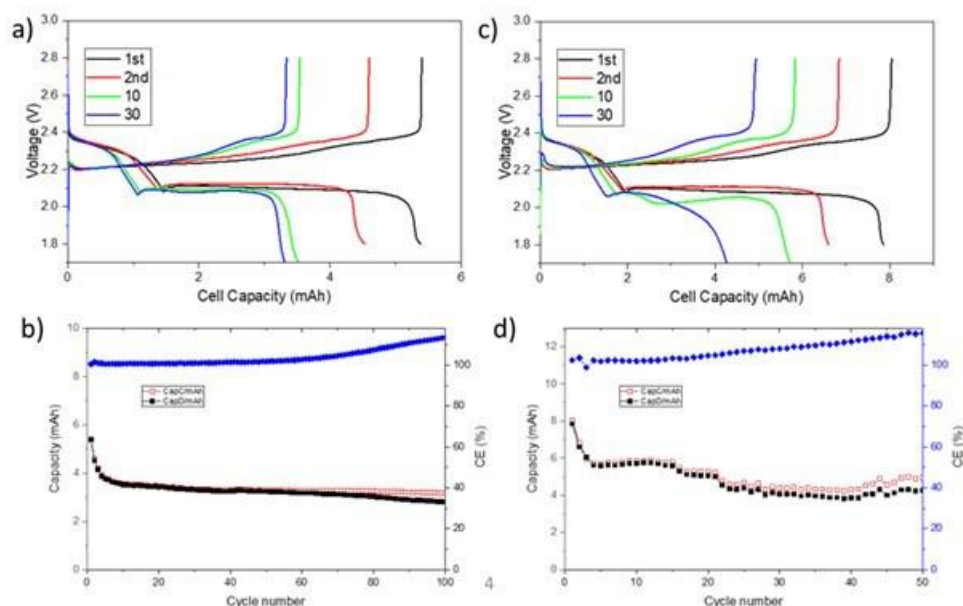


Figure XX.1.38 Electrochemical performance of sulfur cathodes with areal sulfur loading of (a,b) 3.75 mgS/cm² and (c,d) 5.2 mgS/cm²

GM team completed installation and system calibration of the ultrasonic scanning system. Some initial trials using the commercial Li-ion batteries were proceeded to check the system. Figure XX.1.39 shows the cell which was soaked in the silicon oil bath and hooked up with the cycler during the scan. Figure XX.1.39 shows the transmission image obtained by the ultrasonic scanning system with both fresh and end of life cells. The electrode wetted by electrolyte has higher ultrasonic transmissivity than the dry electrodes. In the mapping plot, the transmission intensity is correlated to the electrolyte distribution in the cell. Further testing and system calibration is on the way to get better resolution and intensity correlation.

For the cathode fabrication, GM started larger batch mixing trial with new mixer targeting longer coating per batch. Initial coating test and validation was completed for double-sided coating with the previous selected loading. The loading variation between two sides can be controlled within 10% difference under continuous coating condition. In addition to the double-sided coating, GM kept on with single-sided coating with “standard” loading for baseline purpose. During FY202, GM have sent out single-sided coated baseline electrode to all other Li-S teams for evaluation. GM also provided some single layer pouch format cell using the same batch of the electrode to BNL for studies using synchrotron beamlines. (See Figure XX.1.40.)

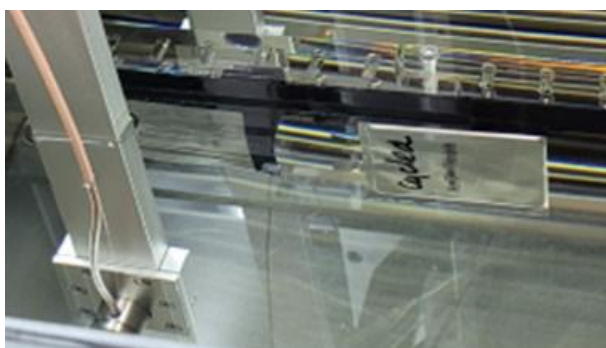


Figure XX.1.39 Photo of Testing cell within oil bath during testing

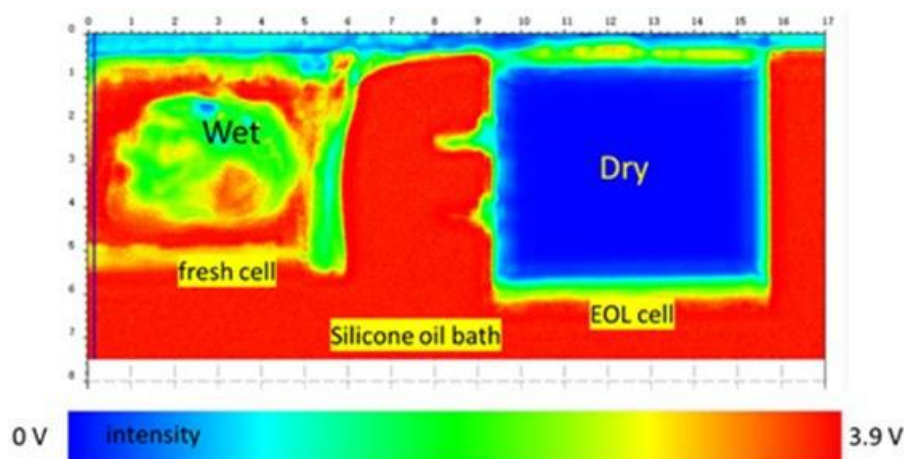


Figure XX.1.40 Ultrasonic transmission image of the fresh cell and end of life (EOL) cell

Keystone project 4: Cross-Cutting Research

The goal of the Cross-cutting team is to develop & deploy advanced characterization tools in support of the three Keystone efforts, with a focus on probing specific materials and interfaces for Keystone 1, probing individual electrodes for Keystone 2, and probing the whole cell for Keystone 3.

Nucleation of Li metal anode during Li plating:

The **SLAC/Stanford** team (Chueh and Cui) has developed the *operando* electrochemical atomic force microscopy (EC-AFM) to study lithium plating. This capability is now available to the Battery500 consortium to carry out *operando* study of microstructural evolution during lithium plating in various electrolyte systems. Briefly *operando* EC-AFM is used to investigate lithium plating at approximately 1 nm spatial resolution (x, y and z). The microstructure of initial SEI formation on copper, the nucleation events during the early stage of lithium plating, and the growth morphology during later stage in lithium plating are captured dynamically at a time resolution of several seconds per μm^2 . This technique is complementary to *ex-situ* cryo-EM studies, providing dynamics information to complement the high spatial and chemical resolution of cryo-EM. Similarly, *operando* AFM is also complementary to *operando* XRD studies by providing local nanostructure information. For our technique development, three stages of lithium plating were investigated: (1) SEI growth on copper, (2) lithium nucleation, and (3) lithium growth. We have deployed an Asylum Cypher environmental EC-AFM inside a temperature-controlled Ar-filled glovebox. A pressure-free liquid cell, consisting of a large, ring electrode (lithium metal) serves as a quasi-reference electrode; a copper foil serves as the working electrode. To eliminate mass transport effects (migration of lithium ions from the center of the cell to the ring counter electrode at the edge of the cell), the copper foil is masked such that approximately 1 mm disc is available to deposit lithium. This configuration eliminates a distribution of resistances and overpotential during lithium plating, thereby assuring uniformity. We have successfully conducted *operando* AFM for over 100 hours in a single experimental run, demonstrating the robustness of the measurement setup. For development purposes and to simplify the experiment, we selected the Gen2 electrolyte (1M LiPF₆ in EC:EMC). Work is ongoing to investigate other electrolytes being studied by Battery500. Figure XX.1.41a shows the initial SEI growth on copper at the potential of 30 mV vs. Li/Li⁺ over 25 hours recorded by *operando* AFM. This potential was chosen so that we can monitor the pre-plating SEI growth. Two morphologies are clearly observed in the SEI: sub-50-nm "grains" and > 200-nm "particles". Over the measurement period, both types of microstructures grew in size. The large SEI particle eventually grew to be approximately 250-nm wide and 80-nm tall. Figure XX.1.41b shows the subsequent Li nucleation at 1 $\mu\text{Ah cm}^{-2}$ of charge passed. Immediately evident is the wide distribution of nucleus size, which subsequently grew at different rates. Finally, Figure XX.1.41c shows the later-stage lithium growth at 0.5 mAh cm^{-2} of charge passed. There, nanoscale faceting and roughening (feature size ~ 50 nm) of large lithium particles (~ 500 nm) were observed. The recorded lithium plating dynamics, from the pre-plating SEI growth stage to the Li nucleation stage to the later Li

particle growth stage provides quantitative information on the microstructure evolution, which directly impacts the coulombic efficiency and reversibility of Li plating/stripping.

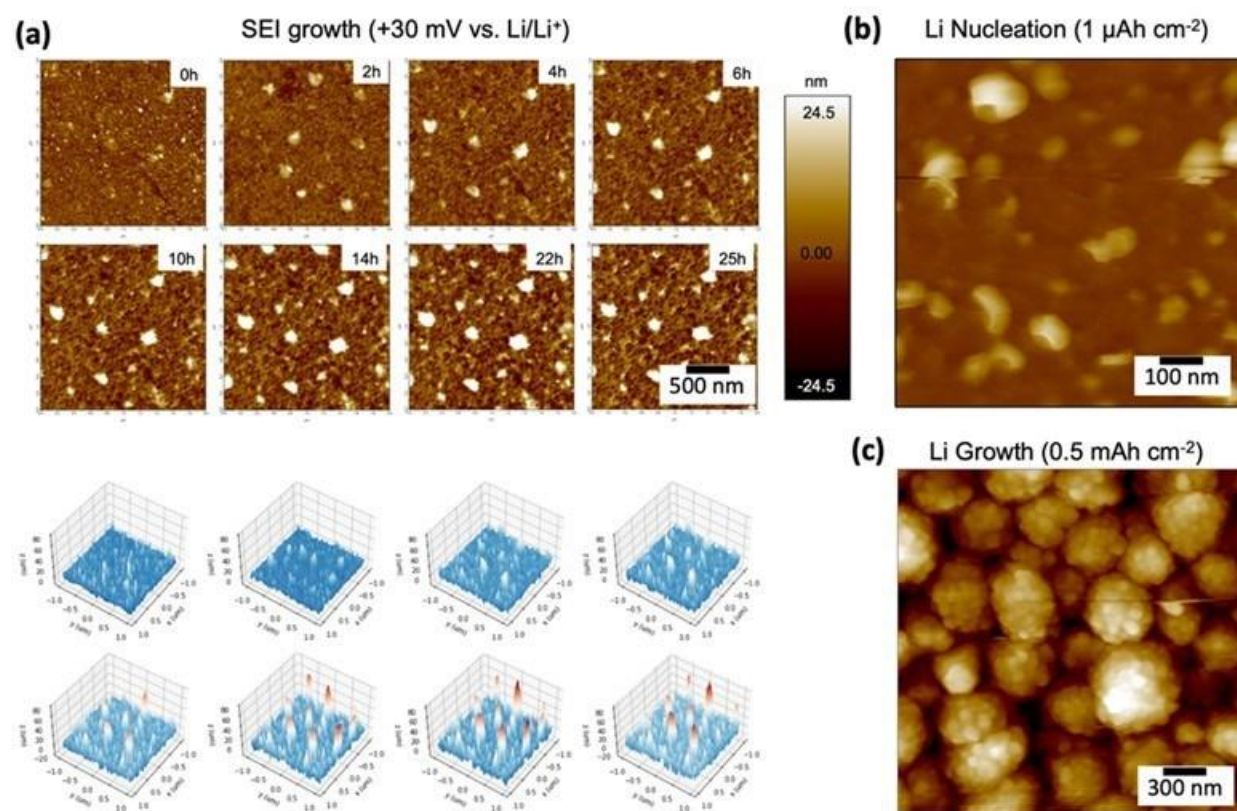


Figure XX.1.41 Operando atomic force microscopy of lithium plating in three stages. (a) SEI growth on copper at +30 mV vs. Li/Li⁺ potential prior to the lithium plating. Measurement over 25 hours reveals dual microstructure (grain + particles) which roughens with time. (b) Lithium nucleation showing a broad distribution of nuclei sizes. (c) Later-stage lithium growth showing faceted grain structure. The amount of charge passed is indicated in the figure.

Operando EC-AFM imaging of lithium plating and SEI growth:

SLAC/Stanford team (Chueh and Cui), building on the momentum from this operando electrochemical atomic force microscopy (EC-AFM) imaging of lithium plating and SEI growth, further investigated lithium metal SEI growth dynamics in a localized high concentration electrolyte (LHCE) LiFSI-1.2DME-3TTE (in collaboration with **Bao** at **SLAC/Stanford**). Using this unique experimental capability, we probed the passivation behavior of lithium metal and assess the SEI growth kinetics, a contributor to Coulombic efficiency. This method complements other Battery500 SEI characterization capabilities such as cryo-EM as it measures the growth dynamics in-situ, thereby removing the possibility of SEI damage and un-swelling during sample preparation. We developed a method to quantify the SEI growth kinetics on lithium metal. To establish a reference height, we first grow a substantially thick SEI on plated lithium on copper (growth time > 25 hours) (Figure XX.1.42a). Then, using the EC-AFM tip, we selectively remove the SEI and reveal unpassivated lithium metal “pit” (Figure XX.1.42b). By assuming that well-passivated region exhibits negligible further growth, it serves as a reference height against which the SEI thickness is measured. The exposed lithium metal pit increases in thickness with time, which is plotted in Figure XX.1.42c. Over 5 hours, the SEI grows by 14 nm and follows a power law of 0.47 with respect to time, suggesting a diffusion-limited behavior. This result contrasts sharply with our previous observation on Battery500 Gen2 electrolyte (1M LiPF₆ in EC:EMC) where we observed two regimes: rapid SEI growth (linear/super-linear with time) and

diffusive SEI growth. It appears that LiFSI-1.2DME-3TTE LHCE immediately passivates with no rapid SEI growth regime, pointing towards the benefit of this electrolyte in passivating lithium metal.

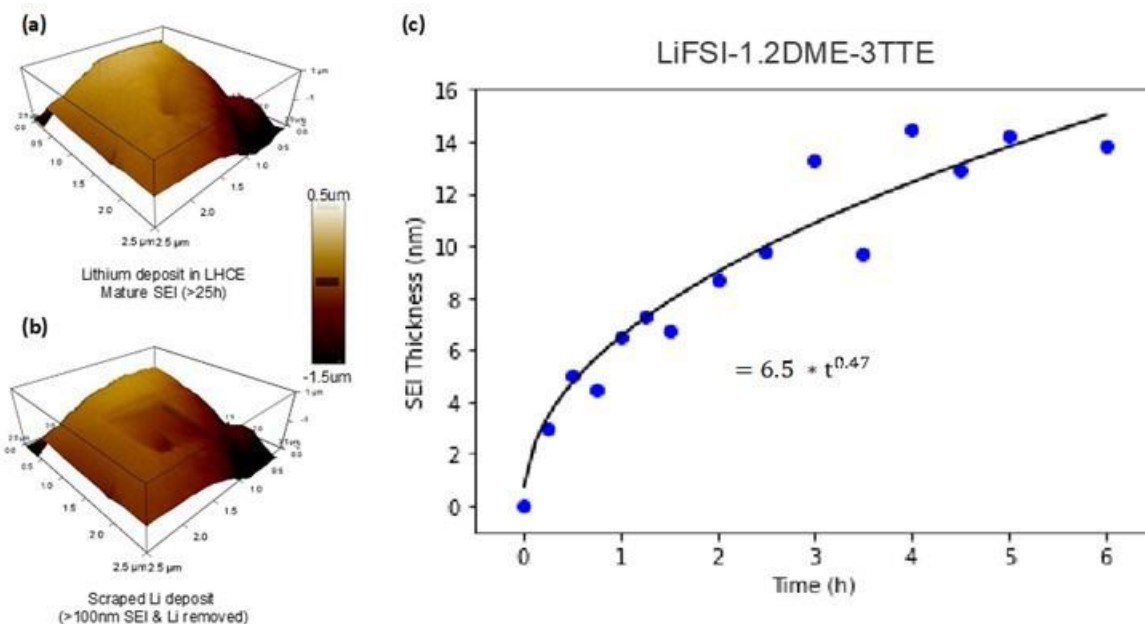


Figure XX.1.42 Operando electrochemical atomic force microscope images of lithium metal deposited in LiFSI-1.2DME-3TTE electrolyte: (a) before indentation and (b) after indentation to measure the soft SEI thickness (c) over 6 hours.

Spectroscopic mapping of the heterogeneous SOC of NMC811 cathodes:

The SLAC team led by Johanna Nelson Weker is systematically investigating the calendar aging of single-layer Li-metal pouch cells with NMC811 cathodes using the synchrotron measurement techniques of micro X-ray fluorescence (μ -XRF) and micro X-ray absorption near edge structure (μ -XANES). Specifically, μ -XRF provides elemental maps of the different transition metals in the batteries, while μ -XANES quantifies the oxidation states of the transition metals and thus can be used to distinguish differences in state-of-charge (SOC) in regions of interest (ROIs) within the cathode. These studies are being carried out as part of a comprehensive B500 team effort starting with INL (fabrication and electrochemical testing of cells under different aging protocols) and BNL (non-destructive X-ray diffraction mapping to identify ROIs), and finishing with SLAC (synchrotron μ -XRF and μ -XANES studies) and INL (laboratory characterization using XPS and other standard techniques). In preparation for these systematic long-term aging studies, preliminary proof-of-principle measurements were carried out on one single pouch cell to validate and optimize measurement and analysis procedures.

Using SSRL beamline 2-3, preliminary *in situ* and *ex situ* measurements were performed to collect data from both an aged pouch cell after 600 cycles and a pristine cathode sheet. The two samples were mapped using X-ray micro fluorescence (μ -XRF) on an instrument with an adjustable X-ray beam size of 1-5 μ m. Figure XX.1.43 shows elemental maps corresponding to the response of Ni, Mn and Co taken simultaneously from the pristine NMC811 electrode with 1 μ m focusing optics. From these maps the distributions of each transition metal element in individual cathode particles of the NMC811 cathode are clearly visible in a small ROI.

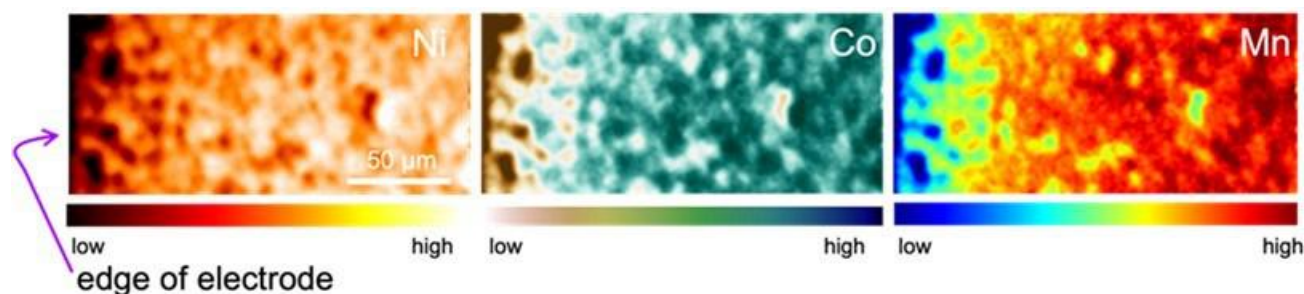


Figure XX.1.43 μ -XRF maps for Ni, Co, and Mn of a pristine NMC811 electrode using 1 μ m focusing optics.

Baseline operando diffraction studies of inhomogeneity in Li-S pouch cells:

The BNL team worked together with INL and GM to apply synchrotron diffraction methods to investigate the speciation and inhomogeneity in Li-S pouch cell batteries. In the first set of beamline experiments, it was observed that the capacity and rate capabilities of Li-S cells used for *operando* cycling experiments had severely degraded relative to the performance measured at INL for equivalent cells that were not shipped to the beamline. Despite the poor cycling behavior of cells during our first *operando* diffraction experiments, the diffraction data suggested that *operando* diffraction studies would have sufficient sensitivity to track many important changes that occur during cycling. Through the partnership with the industrial labs at GM, a set of three very high quality Li-S cells was obtained for the next synchrotron experiments (Figure XX.1.44a). Two of these had the same relatively high sulfur loading of 6 mg/cm², with one cell (GM-1) subjected to an additional 2 weeks of aging relative to the other cell (GM-2). The third cell (GM-3) was prepared with half the sulfur loading. By comparing the data from the cells, it is possible to test both the effects of calendar life and sulfur loading on the speciation and inhomogeneity of Li-S cells. From the electrochemical data collected during the operando diffraction studies (Figure XX.1.44b), it could be seen that the highest specific capacity during the first discharge was obtained for the low-loading sulfur cell (GM-3, 1200 mAh/g S), while the capacity of the high-loading cell was slightly lower (GM-2, 1100 mAh/g S) and that of the cell with both high-loading and a longer calendar life was substantially lower (GM-1, 900 mAh/g S). However, all three capacities remained comparable to typical literature values for high quality Li-S cells (~1000 mAh/g S).

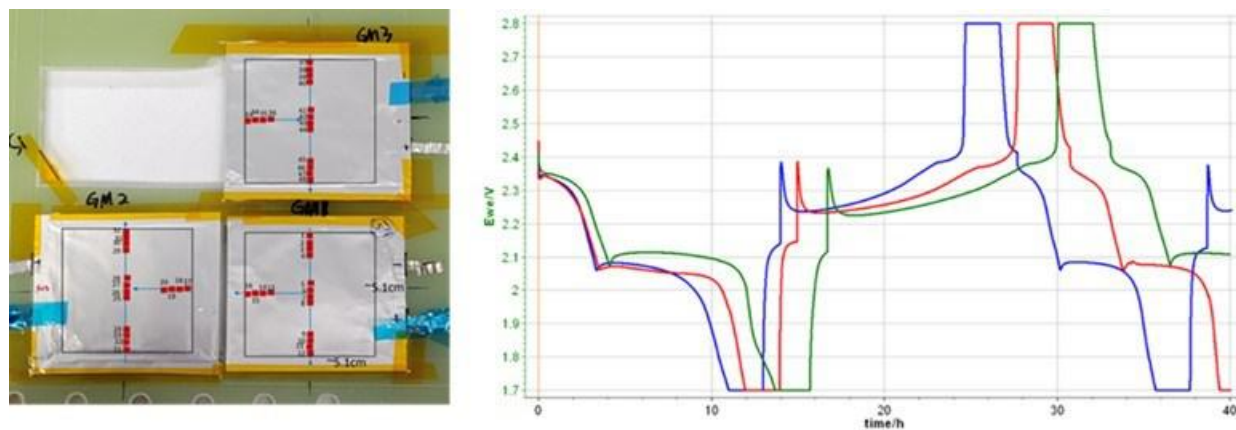


Figure XX.1.44 (a) Photograph of the three Li-S pouch cells used in operando synchrotron diffraction experiments with points being probed marked with red squares. (b) Voltage profile for the three cells. Blue: GM-1 (high loading, longest calendar aging). Red: GM-2 (high loading). Green: GM-3 (low loading). Cells were evaluated with a CC-CV-rest protocol.

During operando diffraction testing, each of the three cells was monitored at 16 different points, 4 points near the center of the cell and 4 points near each of 3 different edges of the cell. Most points in all three cells showed a similar sequence of phases during cycling (Figure XX.1.45a), with the a-S₈ that was initially present disappearing over the first few hours of discharge, and Li₂S appearing and growing in intensity as the

discharge continued. During the subsequent charge process, the Li_2S was gradually eliminated, followed by the subsequent appearance of S_8 in the form of $\beta\text{-S}_8$ – behavior which was consistent with prior literature. Although this type of behavior was observed for many of the studied points, it was not universal. This can be seen for the points at the bottom of cell GM-2 (Figure XX.1.45b). They had substantially worse behavior, which can be seen both in the persistence of $\alpha\text{-S}_8$ to much later times during the first discharge and in the lack of formation of Li_2S at all during the first discharge. This inhomogeneity was greatly mitigated in the low-loading cell, which highlights the extra challenges of meeting the Battery500 goal of realizing long lifetimes in high-energy density cells which necessarily having high loadings. Our initial results here provide the groundwork for continuing studies which probe the effect of the environment (*e.g.*, applied pressure, temperature), cycling conditions (*e.g.*, C rate), and cell aging on the inhomogeneity in the cell, all of which may be playing an important role in controlling the accessible capacity of the sulfur cathodes.

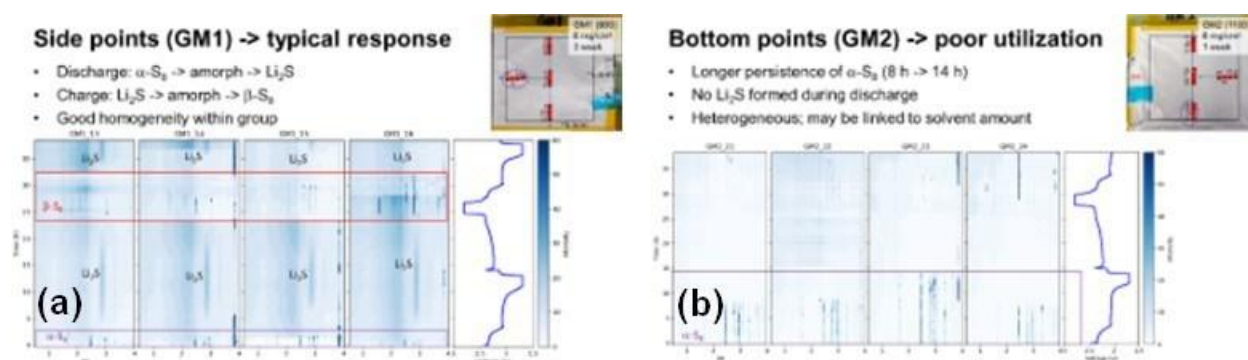


Figure XX.1.45 (a) Points exhibiting a typical response during cycling. (b) Points with low activity.

The **BNL** team applied synchrotron-based x-ray pair distribution function (PDF) together with molecular dynamic (MD) simulation to understand the role of Li^+ solvation structure in determining SEI chemistry. This work was done in collaboration with Keystone 1 researchers in the **PNNL** team of Battery500, as well as with external collaborators at the Army Research Laboratory (ARL) for molecular dynamic (MD) simulations. In this work, comparative studies were done for low concentration electrolytes (LCE) with a 1M salt concentration and high concentration electrolytes (HCE) with a 5 M salt concentration. Three common battery solvents were investigated: 1,2-dimethoxyethane (DME), dimethyl carbonate (DMC), and propylene carbonate (PC), with the same LiFSI salt used for all of them. The PDF results obtained from the Fourier transform of x-ray scattering data collected out to high Q values are plotted in the form of $G(r)$ for all six liquid samples in Figure XX.1.46a, with the molecular structure of the key components given in Figure XX.1.46b. In all cases, the first PDF peak which is centered around 1.5 Å is found to be significantly broader than for the analogous peaks observed previously for solid SEI samples obtained using the same electrolyte formulations. This first peak includes the contributions from directly bonded atom pairs, including the C=O (1.28 Å), C-O (1.36 Å), and C-C (1.54 Å) bonds of solvents as well as the S-N (1.56 Å), S=O (1.43 Å), and S-F (1.54 Å) bonds of the FSI⁻ anion, where the typical bond distances are indicated in parentheses. This contrasts with the case of the solid SEI, which was either dominated by solvent-derived molecular species LCE SEI samples were studied or was dominated by FSI reduction products when HCE SEI samples were studied. The next most clearly resolved PDF peak is at 2.5 Å and corresponds to the next-nearest neighbor interactions as the bond angles remain well defined. However, peaks at larger distances correspond to more distant atoms whose relative positions depend on torsion angles that are quite variable in liquid samples. This leads to a loss of coherence, broadening of PDF peaks, and the absence of features attributable to specific bonding interactions beyond ~5 Å. When the PDF patterns of the LCE and HCE electrolytes are compared, it can be seen that the 1.5 Å and 2.5 Å peaks of the HCE samples are higher in intensity, and that this extra intensity present at longer distances (larger r) than for the LCE samples. This is a consequence of the sulfur atoms in the FSI anion, which scatter x-rays more strongly than the C atoms in the solvent and which have ligand distances that are about 0.2 Å longer than for C atoms. Due to the low atomic number of Li, it is extremely challenging to extract information

about atomic pairs involving Li from experimental x-ray PDF measurements. Therefore, molecular dynamic (MD) simulations were carried out to better understand the Li ion coordination in the electrolyte. The electrolyte solvation structure obtained from MD simulations closely matches the experimentally measured PDF patterns for both LCE and HCE samples (Figure XX.1.46c), suggesting that the MD simulations are able to reproduce the real physical behavior of samples. In order to investigate the effect of the electrolyte concentration on the Li environment in the electrolyte, the partial PDFs for just the Li-O_{anion} (blue) and Li-O_{solvent} (orange) atoms were calculated using the MD simulation results (Figure XX.1.46d). It is found that in LCEs, the Li coordination is dominated by solvent molecules, while in HCEs, a large number of FSI anions become a part of the Li coordination environment. The decomposition of the HCE at the interphase can therefore lead to the formation of SEI with large amount of solid nanocrystalline LiF. This type of SEI has better Li⁺ transport, anode protection properties, and electrochemical performance than the SEI formed from LCEs. These results demonstrated that synchrotron-based PDF is a powerful tool to study the Li solvation structure in electrolytes and can provide direct insights into the origin of the improved SEI and Li metal anode protection that occurs for certain electrolyte formulations.

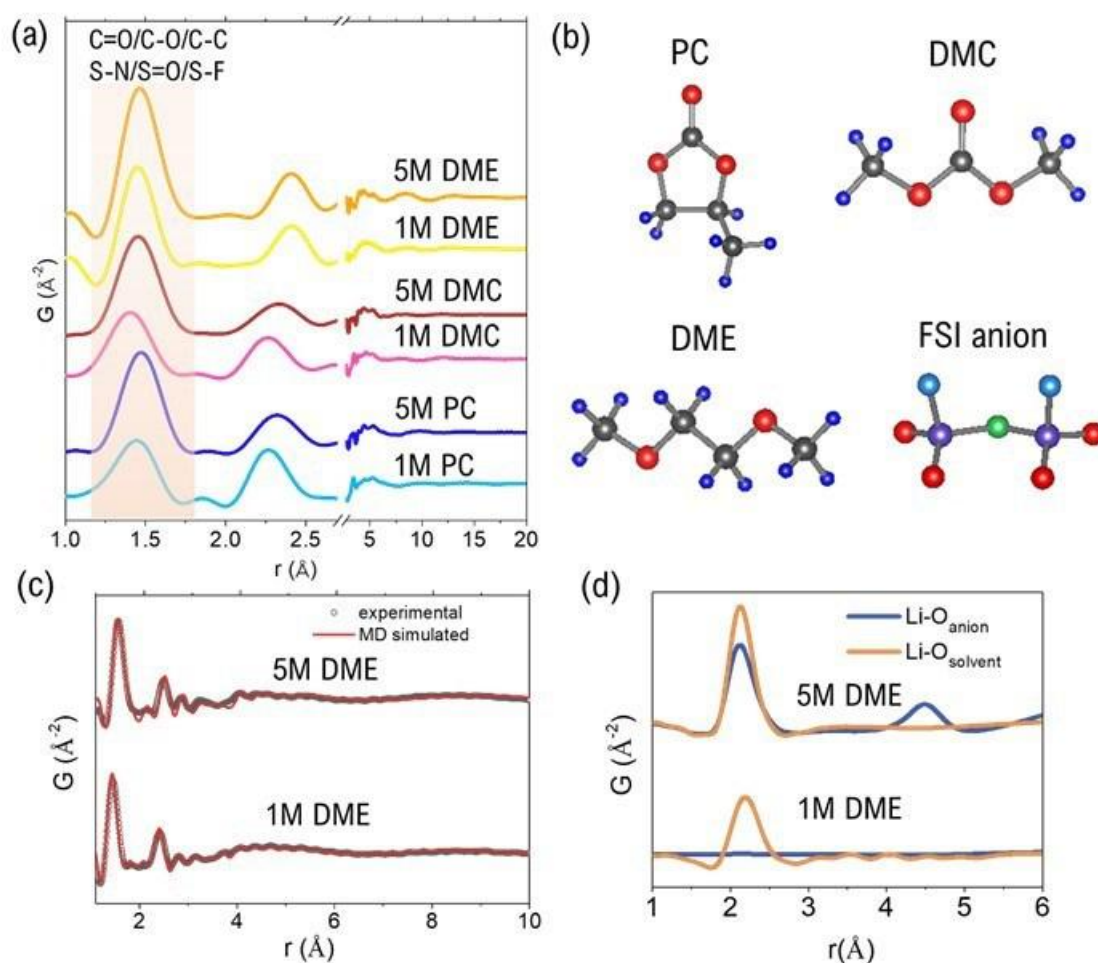


Figure XX.1.46 Characterization of the electrolyte structure. (a) X-ray PDF data for low (1M) and high (5M) concentration LiFSI electrolytes with PC, DMC, or DME as the solvent. (b) Molecular structure of the three solvents and the FSI anion. Carbon atoms are shown in black, hydrogen in dark blue, oxygen in red, nitrogen in green, and sulfur in purple. (c) Comparison of measured and calculated (using the electrolyte structure determined by MD simulation) PDF patterns for HCE and LCE DME electrolytes, and of (d) partial PDFs calculated from MD simulations for pairs of Li-anion oxygen (blue) and Li-solvent oxygen (orange).

The **BNL** team (in close collaboration with **UCSD**) applied synchrotron-based x-ray pair distribution function (PDF) characterization techniques to study the bulk structure changes of sulfurized polyacrylonitrile (SPAN)

cathodes in Li-S batteries during cycling in different electrolytes. Synchrotron x-ray pair distribution function (PDF) methods were used by **BNL** team to study the structure changes of SPAN in different electrolytes, since it is an ideal tool for studying atomic pairs in non-crystalline solids and liquid. PDF is basically a histogram of all the atomic pairs whose corresponding peak intensity is weighted by the abundance of the pairs and the X-ray scattering power of involved atoms. In this manner, it was possible to directly monitor the evolution of bonds and interactions of interested atom pairs during electrochemical cycling in different electrolytes. Figure XX.1.47 shows the PDF data of pristine SPAN and SPAN after the 1st discharge, 1st charge, 2nd charge, and 50th charge, with an arrow indicating the peak corresponding to the C-S bond. The C-S peak shifted to larger r values after the 1st discharge (lithiation), which is likely caused by the C-S-Li interactions. These changes were reversible, with a return to the pristine distance after completion of the 1st charge. After 50 cycles, the C-S length for SPAN cycled in DOL/DME baseline electrolyte was slightly longer than after the 2nd cycle, while that for cycled in UCSD electrolyte was almost the same as after the 2nd cycle, indicating the better reversibility of SPAN cycled in UCSD electrolyte.

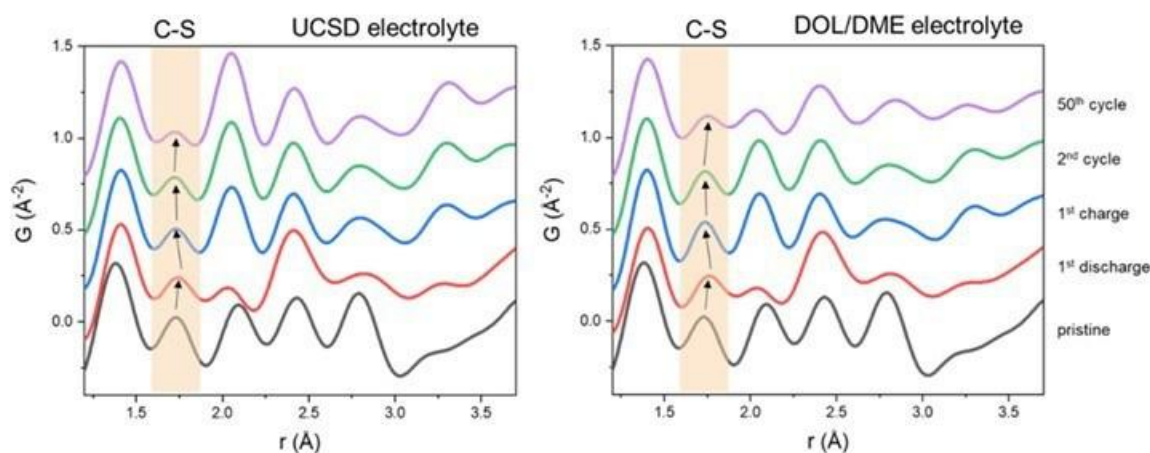


Figure XX.1.47 PDF results comparing SPAN structural changes during cycling in the UCSD electrolyte (left) and the DOL/DME electrolyte (right), with the peak corresponding to the C-S bond distance highlighted.

The reasons for the capacity decay at high voltage could be the impedance hike due to incessant electrolyte decomposition, the unstable solid-electrolyte interphase, the formation of rock-salt species on cathode surface, and the combination of them. When charging voltage is increased to 4.8V, only 77.27% discharge capacity left after 200 cycles for the baseline electrolyte. In contrast, cells using electrolyte with 1% additive of LiDFP demonstrate much more stable capacity retention during long-term high voltage cycling with 97.64% original capacity retention even after 200 cycles (Figure XX.1.48a). To evaluate the impedance resulting from different electrolytes at high voltage, electrochemical impedance spectroscopy (EIS) was performed, which indeed reveals the impedance buildup from the initial cycle to the 10th cycle. The effect of electrolyte on impedance becomes more pronounced after 200 cycles, while the LiDFP additive is able to effectively suppress the impedance growth (Figure XX.1.48b). Quantitative analysis by fitting the equivalent circuit model (Figure XX.1.48c) yields the contact resistance (R_b), surface film resistance (R_{sf}), and charge transfer resistance (R_{ct}), which are summarized in Figure XX.1.48d. For electrolyte using 1% LiDFP, the extremely small R_{ct} indicates the formation of highly conductive interphase, enabling facile charge transfer reactions on the interphase even after long-term cycling. When the additive amount is increased to 2%, both R_{sf} and R_{ct} are increased, but the bulk resistance (R_b) is mostly the same, suggesting the worse performance in excessive additive at 2% is caused by interphasial resistance. The origin of this optimum LiDFP amount (1%) might stem from the fact that the decomposition of LiDFP produces both LiF and HF simultaneously. While LiF is generally regarded as a desired interphase component, excessive LiF makes interphase more resistive. On the other hand, HF is known to be detrimental as it can attack the cathode surface and damage the interphase.

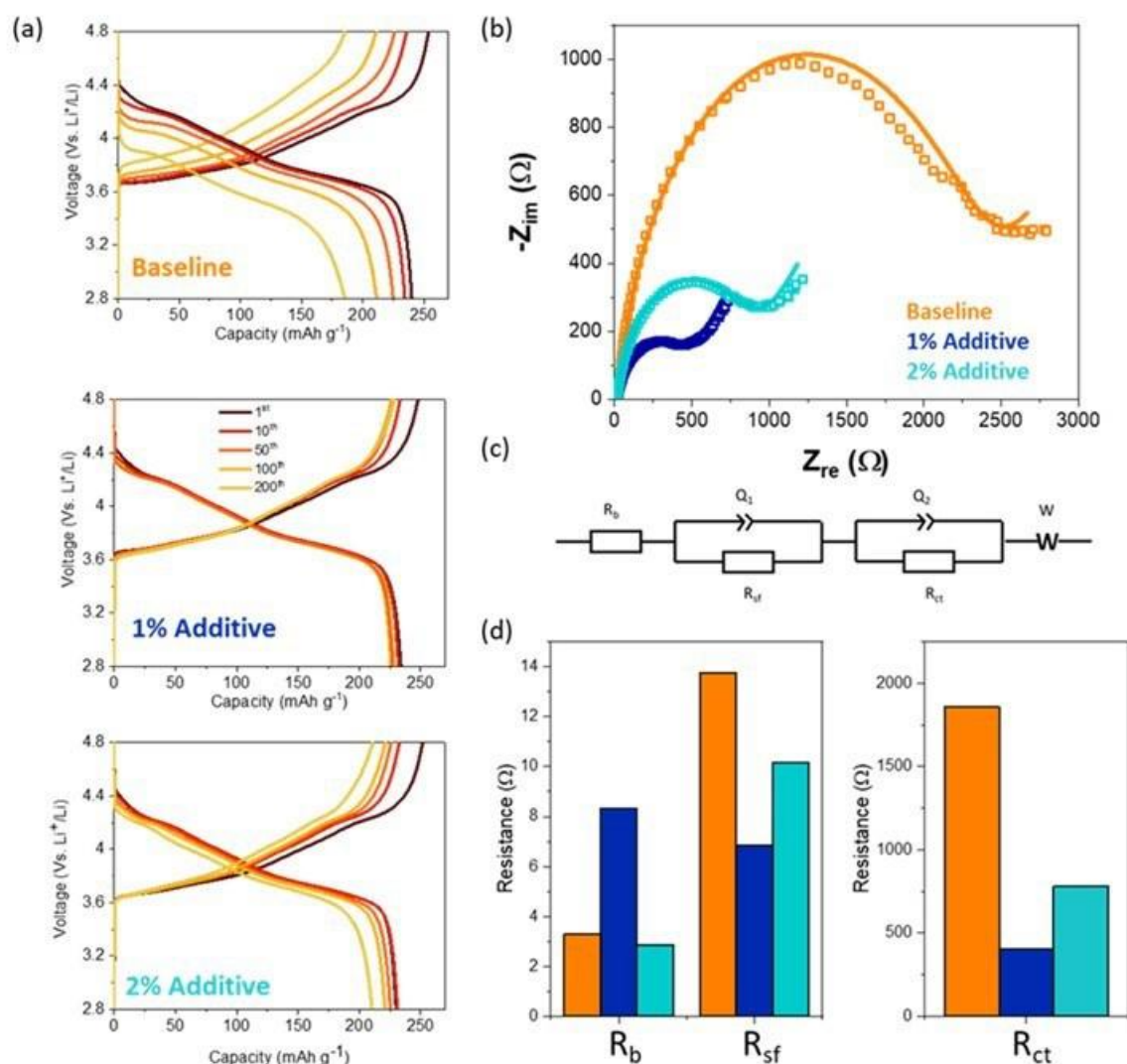


Figure XX.1.48 Electrochemical performance of Li | NMC76 cells using different electrolytes. Charge-discharge profiles from selected cycles within 2.8V-4.8V. The baseline electrolyte is 1M LiPF₆ in EC | EMC (3:7) and the 'with additive' electrolyte is the baseline electrolyte with 1% LiDFP (by weight) or 2% LiDFP (by weight) added. (b) Electrochemical impedance spectroscopy (EIS) results of Li | NMC76 after 200 cycles using different electrolytes. (c) Equivalent circuit for EIS modeling (R_b : contact resistance, R_{sf} : surface film resistance, R_{ct} : charge transfer resistance). (d) EIS fitting results for Li | NMC76 cells after 200 cycles with different electrolytes.

Quantification of Li and S inventory loss in Li-S Batteries: Previously, the UCSD group of Meng developed an analytical method based on titration gas chromatography to quantify inactive (dead) Li⁰ in Li metal batteries and to correlate Li inventory losses with Coulombic efficiency (CE). It has been observed in Li-S batteries that drastic decay in specific capacity during cycling occurs along with the formation of soluble and insoluble polysulfides, but it has been hard to correlate their formation with the cycling CE. It is therefore crucial to quantify both the S and Li inventory losses during cycling and find key reasons for the capacity decay in the Li-S batteries. High performance liquid chromatography (HPLC) was used to differentiate and quantify each individual polysulfide species in the electrolyte, building on prior work by Prof. Deyang Qu in an Advanced Battery Material Research (BMR) project. HPLC is an analytical technique widely used to quantify individual species in mixtures by separating them based on their polarity using a gradient of mobile phases. Through HPLC-UV, it is possible to quantify dissolved elemental S and also to probe the distribution of derivatized

polysulfides qualitatively. Additionally, it is possible to quantify the relative distribution of derivatized polysulfides using HPLC-MS. To quantify dissolved S concentration in the electrolyte, HPLC-UV ($\lambda = 210$ nm) was first used to establish a calibration curve of elemental S in DME (Figure XX.1.49a, Figure XX.1.49b), which exhibited good linearity ($R^2 = 0.9998$). In-house standards consisting of elemental S dissolved in DME were used for this purpose. Separate peaks for DME and sulfur could be observed when using pure methanol as the mobile phase.

Polysulfides are harder to analyze due to their metastable and dynamic nature. One approach is to use a derivatizing agent which does not change the distribution of these polysulfide species significantly but can instead stabilize them in the solution so that individual derivatized species can be quantitatively probed. In-house mixtures of polysulfides were made by mixing elemental S and Li_2S in DME. Methyl triflate was then used to derivatize a small amount of the diluted polysulfide mixture. These species were later analyzed using HPLC-UV at $\lambda = 230$ nm (Figure XX.1.49c) and peak assignments were made based on prior literature. We used a gradient of water and methanol for better separation of derivatized polysulfides. It was found that the retention time of different derivatized polysulfides had a nearly logarithmic dependence on the number of S atoms in the chain (Figure XX.1.49d). These results demonstrate that the separation of polysulfides in the mixed solution through HPLC-UV is possible. In the future, these methodologies will be further developed to quantify the concentration of each individual polysulfide species in the mixed solution.

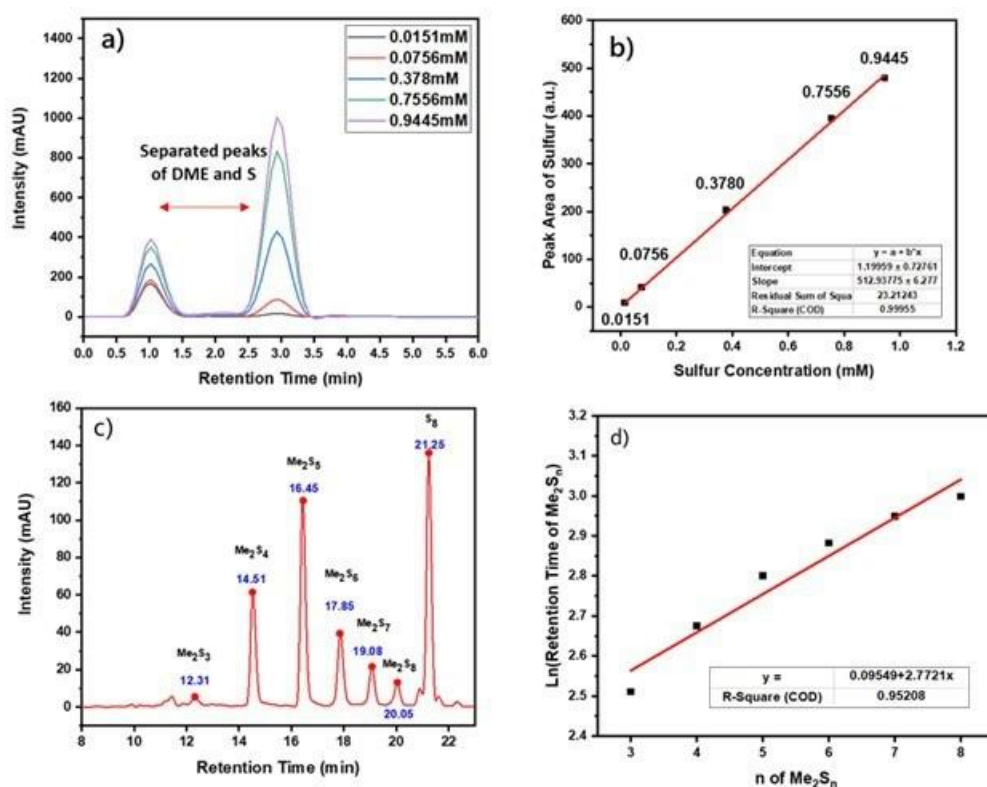


Figure XX.1.49 (a) HPLC-UV chromatograms of five different standards of elemental S in DME: 0.0151mM, 0.0756mM, 0.378 mM, 0.7556mM and 0.9445mM. (b) Calibration curve obtained by plotting the area under the S peak in HPL-UV chromatogram against the S concentration. (c) HPLC-UV chromatogram of derivatized polysulfides using methyl triflate as a derivatization agent. (d) Plot of logarithm of retention time of a particular derivatized polysulfide against the number of S atoms in it

The UCSD group of Meng found that the porosity of plated Li plays a major role in controlling the corrosion rate of Li in liquid electrolytes. When optimized stack pressure is applied during Li plating process, nearly 100% dense Li is achieved even with Gen 2 electrolyte (1M LiPF_6 in EC:EMC). The dense Li exhibited slower corrosion than porous Li when resting in electrolyte. The effect of porosity on the corrosion rate of Li was

further explored. To test if the Li electrode porosity is the dominating factor of corrosion rate, we selectively deposited Li in Gen 2 electrolyte under a range of stack pressures, allowing the controlled deposition of Li with systematically varying porosities. Pressure control was accomplished using a split cell together with a pressure sensor. Cryo-FIB/SEM was used to obtain a 3D reconstruction of the plated Li and to determine its porosity (Figure XX.1.50). With an optimized stack pressure of 350 kPa, the deposited Li has a porosity of only 0.68%. On decreasing the stack pressure to 250 kPa, 150 kPa and 50 kPa, the resulting Li has porosities of 8.6%, 37% and 44%, respectively. After measuring the porosity of the different Li samples, the as-plated Li was then immersed into the Gen 2 electrolyte for three weeks. The Li^0 mass loss was used to calculate the corrosion rate of the Li using the equation $R = \Delta m / (A_s T)$, where Δm is the change in mass, A_s is the electrode area, and T is the corrosion time. As shown in Figure XX.1.50e, the Li corrosion rate directly correlates with the porosity of the plated Li. These results further validated our hypothesis that the porosity of the plated Li is the major factor in determining the Li corrosion rate. It can be concluded that the Li corrosion only takes place at the interface between Li and the electrolyte. If the porosity of the Li can be strictly controlled, the corrosion of Li should also be largely mitigated. In the future, the role of surface chemistry in the corrosion of Li metal will be studied in detail.

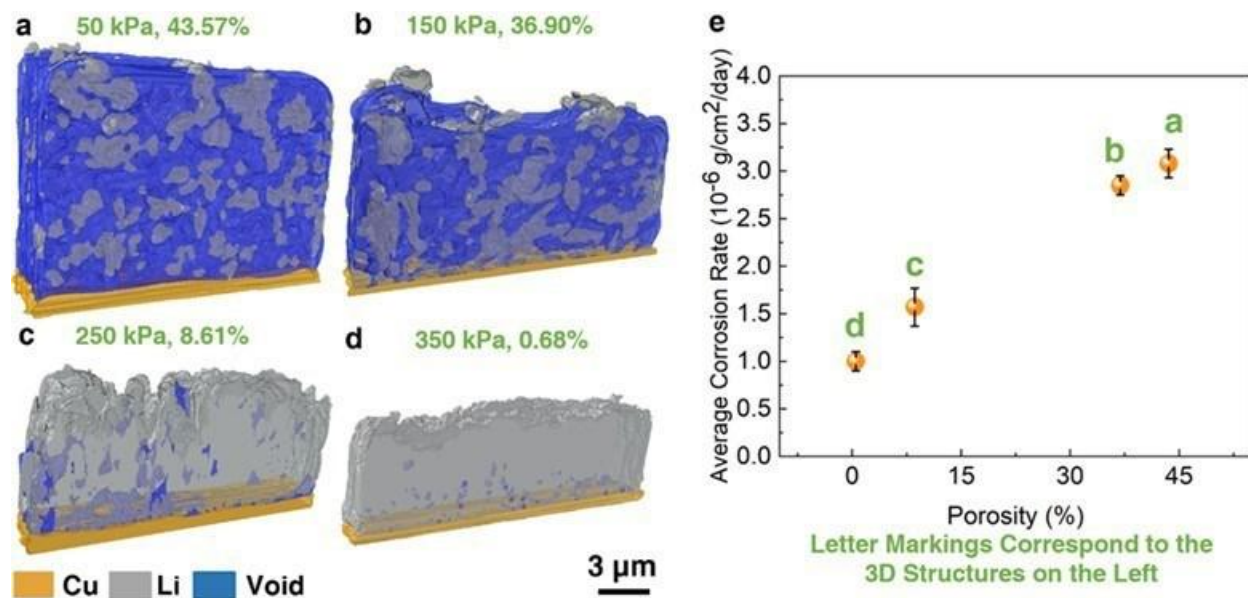


Figure XX.1.50 3D reconstruction of deposited Li metal plated under different stacking pressures resulting in different Li porosities: (a) 50 kPa and 43.57% porosity; (b) 150 kPa and 36.90% porosity; (c) 250 kPa and 8.61% porosity and (d) 350 kPa and 0.51% porosity. (e) Li metal corrosion rate and its correlation with the porosity of the freshly deposited Li. All Li is plated in Gen 2 electrolyte. A total amount of 0.318 mAh of Li is plated at a rate of 0.5 mA/cm² for each sample.

Meng's team at UCSD carried out studies on quantification of sulfur inventory loss in Li-S batteries. Lithium-Sulfur batteries consist of Sulfur (S) on the cathode side and Lithium (Li) metal on the anode side. Polysulfides have been identified as the necessary evil in Li-S batteries that start to form during the first discharge cycle. However, very few efforts have been put into quantifying or understanding the effect of polysulfides on cell performance. Previously many qualitative ex-situ High Performance Liquid Chromatography (HPLC) studies have been done by derivatizing the polysulfides into stable methylated species to differentiate different polysulfides solved in the electrolyte. These studies proved its applicability in this system, and identifying the species based on their chain lengths became possible. However, due to the lack of absorptivity data for the derivatized polysulfides or lack of standards for longer chain polysulfides, quantitative interpretation has not been yet possible. Also, the analysis was limited to qualitatively identifying elemental S₈ and polysulfides. It did not include a consolidated picture of potential losses in the form of dead Li from Li metal anode and other insoluble polysulfides on the cathode side. A comprehensive methodology needs to be developed to track both

the Li and S inventory evolution in the cell at different stages of cycling. UCSD team proposed to utilize a series of characterization tools to decipher the key bottleneck that limits the cycle life of Li-S systems (Figure XX.1.51). On the S cathode side, insoluble species such as S_8 and Li_2S that remained in the cathode after cycling will be quantified by Thermogravimetric analysis (TGA). Titration Gas Chromatography (TGC) have already been established in our previous work and will be used to track Li inventory losses. The soluble polysulfide species in the electrolyte will be quantified by HPLC. In the end, a correlation between the Li and S inventory loss with the overall cell capacity evolution will be obtained.

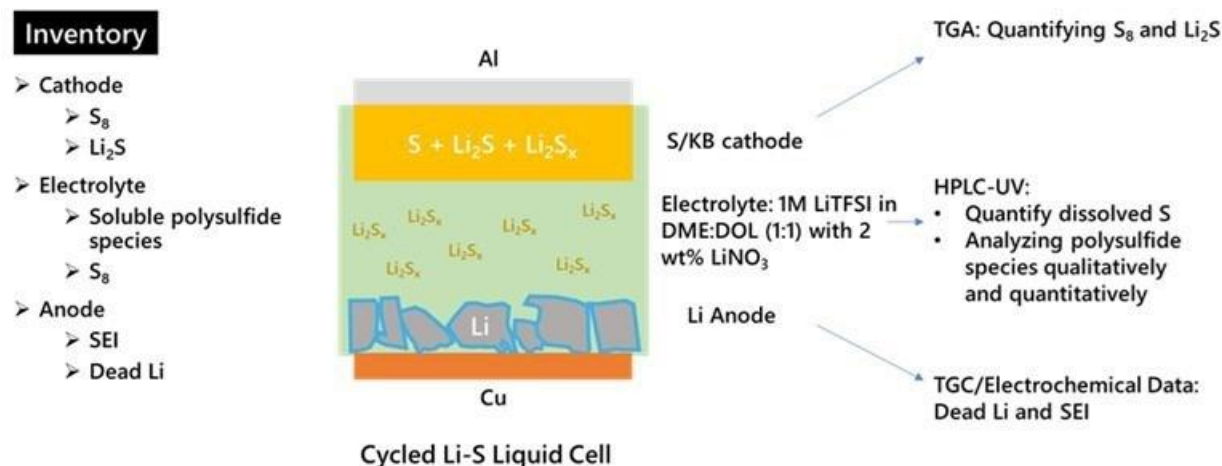


Figure XX.1.51 Schematic of methodology to quantify and track inventory losses in Li-S battery

Quantification of Lithium and Sulfur inventory loss in Li-S Batteries using HPLC-UV: Previously, Meng's group at UCSD has shown the separation and identification of each polysulfide species in Dimethoxyethane (DME) solution using HPLC-UV. Meng group has further established the calibration curve of S_8 in DME. To do that, 6.045 mg of S_8 was first dissolved in 5mL of DME to get 4.722 mM S_8 which was further diluted to 0.9445mM, 0.7556mM, 0.378mM, 0.0756mM and 0.0151mM of S_8 . S_8 quantification was achieved by getting the calibration curve for the elemental S_8 by calculating the area under the intensity v/s retention time data and the concentration (Figure XX.1.52a and Figure XX.1.52b). A linear relation with $R^2=0.99999$ was achieved. For these measurements, five different concentrations of S_8 dissolved in DME were loaded in the autosampler, and UV measurements were done at 210nm, 230 nm, 300nm and 800nm. S_8 had maximum absorbance at 210nm and was chosen for all sulfur quantification measurements. These results demonstrated that the calibration curve of S_8 in DME through HPLC-UV is successfully established. In the future, Meng group will continue to develop calibration curves for each individual polysulfide species in order to quantify the concentration of each one of them in a mixed solution.

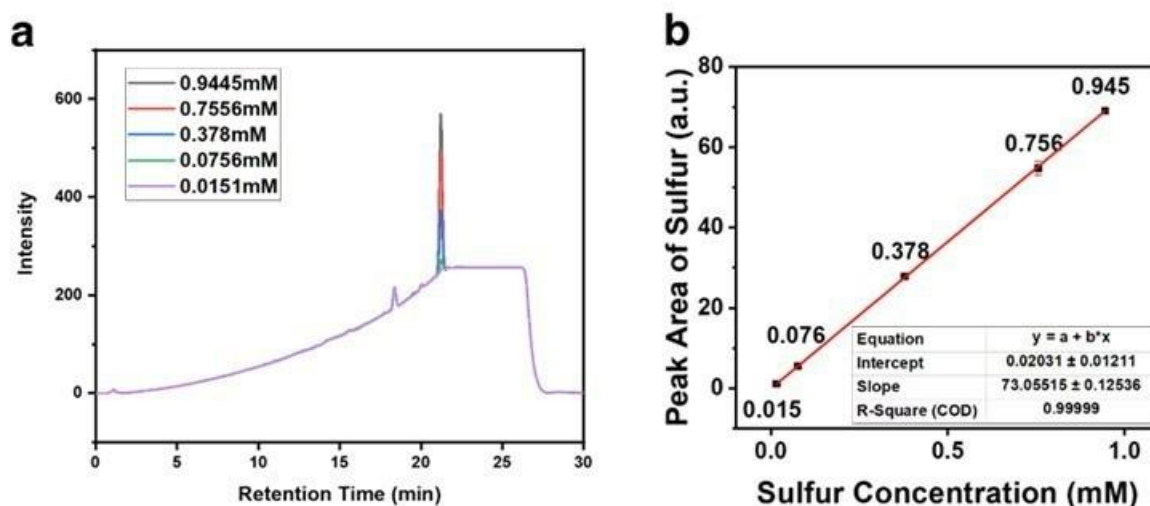


Figure XX.1.52 (a) Chromatograms of different Elemental Sulfur Concentrations, and (b) the calibration curve for Elemental Sulfur

Computational work was done by the team at **Texas A&M** to directly understand the electrolyte structure and transport properties. Specifically, density functional theory (DFT) was used with a thermodynamic integration method implemented in constrained-*ab initio* molecular dynamics (c-AIMD) to calculate the free energy profile for different pathways transporting the Li cation pathway toward the anode. The trajectory and evolution of the solvation complex surrounding the Li cation along with the effect of salt concentration and diluent presence were studied in three different liquids: low concentration electrolyte (LCE), high concentration electrolyte (HCE), and localized high concentrated electrolyte (LHCE). The thermodynamic integration method allowed us to identify energy barriers and their correlation with changes in Li-ion solvation. In dilute electrolytes (1.21M LiFSI in DMC), the energy barriers during the diffusion are relatively low (< 0.2 eV) and the cation deposition on the surface is guided by the anion and solvent reduction. In HCE (5.49 M LiFSI in DMC), the high connectivity between the primary solvation complex with the rest of the electrolyte leads to a significant increase in the energy barriers (> 3 eV) for diffusion and the ion complexes can get trapped in the electrolyte, slowing down their surface deposition and enabling a thick and compact SEI to be built through anion decomposition. In LHCE (1.27 M LiFSI in DMC/BTFE) the BTFE diluent helps reduce the barriers (most of them in the order of 0.3 eV) present in HCE and breaking up the high cation-solvation complex connectivity, thereby facilitating cation diffusion and simultaneous SEI formation processes. Figure XX.1.53 illustrates some of the events captured during the dynamic evolution of the systems. The rate of cation deposition near the surface is clearly impacted by the rate of the electrolyte decomposition reactions. Once the SEI starts to be formed, the cation gets trapped within charged fragments and radical species. The nature and chemistry of the electrolyte defines the SEI rate of nucleation and morphology, and both are crucial to facilitate or impede ionic diffusion. In Figure XX.1.53, three carbonate molecules and an anion solvate the cation in LCE. Near the surface, the higher reduction potential of the anion determines its rotation toward the surface dragging the rest of the solvation complex, whereas Li^+ cannot escape the anion network in HCE. In contrast, similar environments in LHCE can be overcome because of the weakly interacting diluent molecule that breaks the strong cation-anion interaction

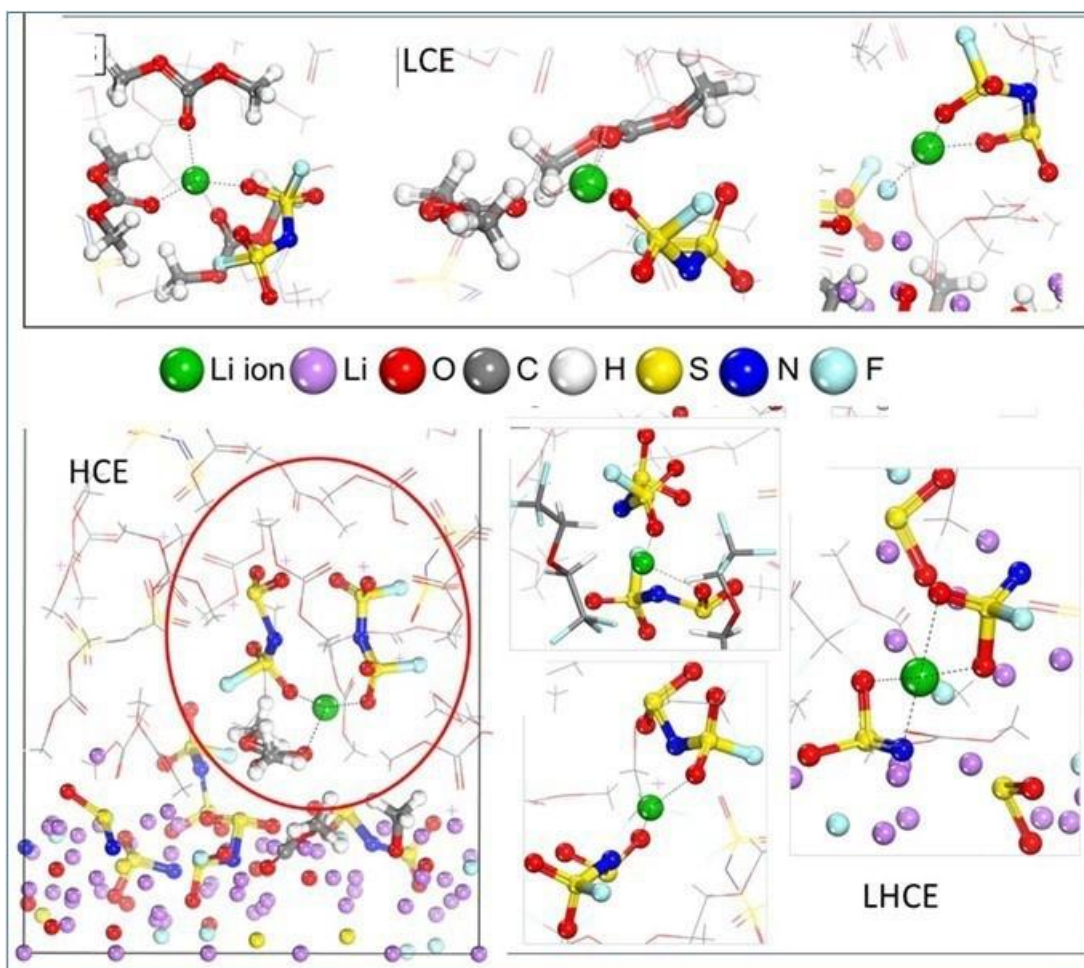


Figure XX.1.53 Near the anode surface, solvated Li^+ in LCE electrolyte complex (top) diffuses through the electrolyte guided by the anion high electron affinity. In HCE (bottom left) Li^+ gets trapped in a thick 3D network that is broken only through anion reduction and thick SEI formation. In LHCE, the presence of the diluent in the 2nd solvation shell disrupts the strong cation-anion interaction and allows Li^+ migration with barriers comparable to LCE.

The **Texas A&M** team has implemented a simulation method that combines classical molecular dynamics and *ab initio* molecular dynamics (AIMD) to follow the evolution of the solid-electrolyte interphase (SEI) in timeframes that go well beyond the AIMD capabilities while keeping the AIMD accuracy. In the new simulation scheme, AIMD is used to describe the localized electrochemical reactions, while classical MD addresses the longer-range and longer-time chemical reactions in the electrolyte along with the mass transfer. In this way, the team has demonstrated the SEI morphology evolution as a function of salt concentration for LiFSI in DMC. One of the findings is the formation of a stratified morphology with well-defined regions of amorphous LiO_x (predominantly), LiF_x , and LiS_xN_y . Figure XX.1.54 illustrates the amorphous LiO_x SEI morphology found in a 5M LiFSI in DMC electrolyte. The effects of electrolyte/anode ratio and solvent chemistry on the SEI morphology and properties have been identified. It was found that the compactness of the amorphous Li oxide phase has a maximum as a function of the electrolyte/anode ratio. The nature of the solvent also affects the SEI density due to the formation of wet or dry regions. We expect these properties to affect Li ion transport through the SEI. In a parallel study, we are investigating ion transport through a Li_2S film on Li metal. We have detected ion and charge transport mechanisms occurring when reactions are taking place on the surface of the film-covered Li surface. The main findings include spontaneous ion hopping mechanisms driven by electron transfer from the Li anode through the Li_2S SEI. Current work investigates the link between SEI morphology and chemistry with Li ion transport mechanisms.

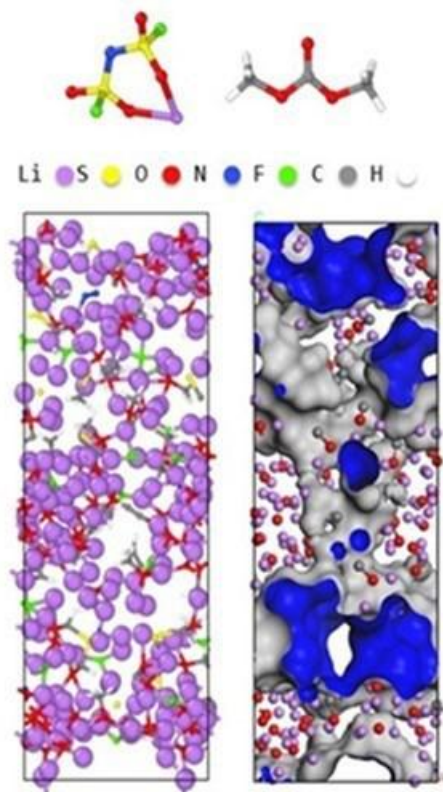


Figure XX.1.54 Evolution of SEI morphology at the Li metal surface in a 5M LiFSI in DMC solution from AIMD/classical MD simulations. Left: Well defined regions of amorphous Li oxide connected by less dense regions of LiF_x and LiS_xN_y structures. Right: Blue and gray are outer and inner surfaces enclosing Li oxide volumes.

Conclusions

This project has been successfully completed in FY2022. All milestones have been completed. The publication records are very good: **2 US patent applications** were filed by the Battery500 team member institutions. **49 peer reviewed papers** were published, and more than **80 invited presentations** were delivered in FY2022. Extensive collaboration within the consortium, between the consortiums and seedling teams, as well as with other national Labs and US universities has been well established and achieved very fruitful results.

Key Publications

Patents

1. Zhenan Bao, Yi Cui, Zhiao Yu, Yangju Lin, Tuning Fluorination Degree of Ether and Carbonate Based Electrolyte Solvents for Lithium and Lithium Metal Batteries, US Provisional Patent Application No. 63/283,828, Filed date: 11/29/2021.
2. Zhenan Bao, Yi Cui, Yuelang Chen, Zhiao Yu, Yangju Lin, Molecular Design Strategies to Achieve Favorable Ion Solvation Structures for Stable Operation of Lithium Metal Batteries, US Provisional Patent Application No. 63/270,506, Filed date: 10/21/2021.

Publications

1. Yuelang Chen,[†] Zhiao Yu,[†] Paul E. Rudnicki, Huaxin Gong, Zhuojun Huang, Sang Cheol Kim, Jian-Cheng Lai, Xian Kong, Jian Qin, Yi Cui, Zhenan Bao, “Steric Effect Tuned Ion Solvation Enabling Stable Cycling of High-Voltage Lithium Metal Battery”, *Journal of the American Chemical Society* 2021, DOI: 10.1021/jacs.1c09006. Publication date: October 28, 2021.
2. Xin Gao, Xueli Zheng, Yuchi Tsao, Pu Zhang, Xin Xiao, Yusheng Ye, Jun Li, Yufei Yang, Rong Xu, Zhenan Bao, Yi Cui, “All-Solid-State Lithium-Sulfur Batteries Enhanced by Redox Mediators”,

- Journal of the American Chemical Society* 2021, DOI: 10.1021/jacs.1c07754. Publication date: October 22, 2021.
3. Zehao Cui, Qiang Xie, Arumugam Manthiram, "A Cobalt- and Manganese-Free High-Nickel Layered Oxide Cathode for Long-Life, Safer Lithium-Ion Batteries", *Advanced Energy Materials* 2021, DOI: 10.1002/aenm.202102421. Publication date: October 04, 2021.
 4. Y. Ren, Z. Cui, A. Bhargav, J. He, A. Manthiram, "A Self-healable Sulfide/Polymer Composite Electrolyte for Long-life, Low-lithium-excess Lithium-metal Batteries," *Advanced Functional Materials*, 2021. DOI: <https://doi.org/10.1002/adfm.202106680>. Publication date (web): October 03, 2021.
 5. J. Langdon, Z. Cui, and A. Manthiram, "Role of Electrolyte in Overcoming the Challenges of LiNiO₂ Cathode in Lithium Batteries," *ACS Energy Letters* 6, 3809-3816 (2021). DOI: <https://doi.org/10.1021/acsenenergylett.1c01714>. Publication date (web): October 07, 2021.
 6. Zulipiya Shadike*, Sha Tana, Ruqian Lin, Xia Cao, Enyuan Hu* and Xiao-Qing Yang*, "Engineering and characterization of interphases for Lithium metal anode", *Chemical Sciences*, DOI: 10.1039/D1SC06181J, Publication date: December 8, 2021.
 7. Chinnam, Parameswara R., Leidong Xu, Lu Cai, Nikolaus L. Cordes, Sangwook Kim, Corey M. Efaw, Daniel J. Murray, Eric J. Dufek, Hongyi Xu, and Bin Li. "Unlocking Failure Mechanisms and Improvement of Practical Li-S Pouch Cells through In Operando Pressure Study." *Advanced Energy Materials* (2021): 2103048. DOI: 10.1002/aenm.202103048. Publication date: December 7, 2021.
 8. Zhaohui Wu, Haodong Liu, Sicen Yu, Ping Liu, "Binder effects on cycling performance of high areal capacity SPAN electrode", *Journal of The Electrochemical Society*, (2021), **168**, 110504. DOI: 10.1149/1945-7111/ac315b, Publication date: November 02, 2021
 9. C. Fang, B. Lu, G. Pawar, M. Zhang, D. Cheng, S. Chen, M. Ceja, J.-M. Doud, M. Cai, B. Liaw, Y. S. Meng, "Pressure-tailored highly-reversible lithium metal electrode for rechargeable lithium batteries." *Nature Energy* 6 (2021) 987–994. DOI: 10.1038/s41560-021-00917-3, Publication date: October 18, 2021.
 10. S. Angarita-Gomez and P. B. Balbuena, "Understanding Solid Electrolyte Interphase Nucleation and Growth on Lithium Metal Surfaces," *Batteries*, 7, 73, (2021), DOI: 10.3390/batteries7040073, Publication date: November 2, 2021 (web).
 11. L. Su, H. Charalambous, Z. Cui, and A. Manthiram, "High-efficiency, Anode-free Lithium-metal Batteries with a Close-packed Homogeneous Lithium Morphology," *Energy & Environmental Science* 2022. DOI: <https://doi.org/10.1039/D1EE03103A>. Publication date (web): January 6, 2022.
 12. W. Shin and A. Manthiram, "A Facile Potential Hold Method for Fostering Inorganic-rich Solid-electrolyte Interphase for Anode-free Lithium-metal Batteries," *Angewandte Chemie* 2022. DOI: <https://doi.org/10.1002/anie.202115909>. Publication date (web): January 18, 2022.
 13. Y. Ren, W. Shin, and A. Manthiram, "Operating High-energy Lithium-metal Pouch Cells with Reduced Stack Pressure Through a Rational Lithium-host Design," *Advanced Energy Materials* 2022. DOI: <https://doi.org/10.1002/aenm.202200190>. Publication date (web): March 25, 2022.
 14. Diego E. Galvez-Aranda and Jorge M. Seminario, "Li-Metal Anode in a Conventional Li-Ion Battery Electrolyte: Solid Electrolyte Interphase Formation using Ab Initio Molecular Dynamics," *J. Electrochem. Soc.*, 169, 030502, (2022). DOI: 10.1149/1945-7111/ac55c8 Published March 3, 2022
 15. Kang Xu*, Wu Xu*, and Sheng S. Zhang*, "Austen Angell's Legacy in Electrolyte Research", *Journal of Non-crystalline Solids*: X, 2022, 14, 100088, DOI: 10.1016/j.nocx.2022.100088. Publication date: March 8, 2022
 16. Sha Tan, Haodong Liu, Zhaohui Wu, Conan Weiland, Seong-Min Bak, Arthur Ronne, Ping Liu, M. Stanley Whittingham, Zulipiya Shadike*, Enyuan Hu*, Xiao-Qing Yang*, "Isoxazole-based Electrolytes for Lithium Metal Protection and Lithium-Sulfurized Polyacrylonitrile (SPAN) Battery Operating at Low Temperature", *Journal of the Electrochemical Society*, DOI: 10.1149/1945-7111/ac58c5, Publication date: February 25, 2022.
 17. Cosby, Monty R., Gia M. Carignan, Zhuo Li, Corey M. Efaw, Charles C. Dickerson, Liang Yin, Yang Ren, Bin Li, Eric J. Dufek, Peter G. Khalifah. "Operando Synchrotron Studies of Inhomogeneity

- during Anode-free Plating of Li Metal in Pouch Cell Batteries." *Journal of the Electrochemical Society* (2022) 169 (2): 020571, DOI:10.1149/1945-7111/ac5345. Publication date: February 28, 2022.
18. Yu, Sicen, Zhaohui Wu, John Holoubek, Haodong Liu, Emma Hopkins, Yuxuan Xiao, Xing Xing, Myeong Hwan Lee, and Ping Liu. "A Fiber - Based 3D Lithium Host for Lean Electrolyte Lithium Metal Batteries." *Advanced Science* (2022): 2104829. DOI: 10.1002/advs.202104829. Publication date: February 01, 2022.
 19. Holoubek, John, Qizhang Yan, Haodong Liu, Emma J. Hopkins, Zhaohui Wu, Sicen Yu, Jian Luo, Tod A. Pascal, Zheng Chen, and Ping Liu. "Oxidative Stabilization of Dilute Ether Electrolytes via Anion Modification." *ACS Energy Letters* 7 (2022): 675-682. DOI: 10.1021/acsenenergylett.1c02723. Publication date: January 18, 2022.
 20. Holoubek, John, Kangwoon Kim, Yijie Yin, Zhaohui Wu, Haodong Liu, Mingqian Li, Amanda Chen et al. "Electrolyte design implications of ion-pairing in low-temperature Li metal batteries." *Energy & Environmental Science* (2022). DOI: 10.1039/D1EE03422G. Publication date: March 7, 2022.
 21. Z. Yu, P.E. Rudnicki, Z. Zhang, Z. Huang, H. Celik, S.T. Oyakhire, Y. Chen, X. Kong, S. Kim, X. Xiao, H. Wang, Y. Zheng, G.A. Kamat, M. Kim, S.F. Bent, J. Qin, Y. Cui, Z. Bao, "Rational solvent molecule tuning for high-performance lithium metal battery electrolytes". *Nature Energy* 7, 94–106, 2022. DOI: 10.1038/s41560-021-00962-y. Publication date: January 13, 2022.
 22. M.S. Kim, Z. Zhang, P.E. Rudnicki, Z. Yu, J. Wang, H. Wang, S.T. Oyakhire, Y. Chen, S.C. Kim, W. Zhang, D.T. Boyle, X. Kong, R. Xu, Z. Huang, W. Huang, S.F. Bent, L. Wang, J. Qin, Z. Bao, Y. Cui, "Suspension electrolyte with modified Li⁺ solvation environment for lithium metal batteries". *Nature Materials*. 21, 445-454, 2022. DOI: 10.1038/s41563-021-01172-3. Publication date: January 17, 2022.
 23. H. Wang, Z. Yu, X. Kong, S. Kim, D.T. Boyle, J. Qin, Z. Bao, Y. Cui, Y., "Liquid electrolyte: The nexus of practical lithium metal batteries", *Joule*, 6, 588-616, 2022. DOI: 10.1016/j.joule.2021.12.018. Publication date: January 20, 2022
 24. Z. Zhang, Y. Li, R. Xu, W. Zhou, Y. Li, S.T. Oyakhire, Y. Wu, J. Xu, H. Wang, Z. Yu, D.T. Boyle, W. Huang, Y. Ye, H. Chen, J. Wan, Z. Bao, W. Chiu, Y. Cui, "Capturing the swelling of solid-electrolyte interphase in lithium metal batteries". *Science*, 375, 66-70, 2022. DOI: 10.1126/science.abi8703. Publication date: January 6, 2022.
 25. J. Xiao, C. Anderson, X. Cao, H.-J. Chang, R. Feng, Q. Huang, Y. Jin, H. Job, J.-M. Kim, P. M. L. Le, D. Liu, L. Seymour, N. Shamim, L. Shi, B. Sivakumar, "Electrochemistry in Understanding and Designing Electrochemical Energy Storage Systems" (invited for Women in Electrochemistry Special issue), *Journal of The Electrochemical Society*, 2022, 169, 010524. DOI: : 10.1149/1945-7111/ac4a55. Publication date: January 19, 2022.
 26. Stefany Angarita-Gomez and Perla B. Balbuena, "Ion Motion and Charge Transfer Through a Solid-electrolyte Interphase: An Atomistic View," *Journal of Solid State Electrochemistry* 2022. DOI: <https://doi.org/10.1007/s10008-022-05227-6>. Publication date (web): June 23, 2022.
 27. Stefany Angarita-Gomez and Perla B. Balbuena, "Ion Mobility and Solvation Complexes at Liquid-solid Interfaces in Dilute, High Concentrated, and Localized High Concentrated Electrolytes," *Material Advances* 2022. DOI: <https://doi.org/10.1039/d2ma00541g>. Publication date (web): June 30, 2022.
 28. Zhiao Yu, Weilai Yu, Yuelang Chen, Luca Mondonico, Xin Xiao, Yu Zheng, Fang Liu, Samantha T. Hung, Yi Cui and Zhenan Bao, "Tuning Fluorination of Linear Carbonate for Lithium-ion Batteries," *Journal of the Electrochemical. Society* 2022. DOI: <https://doi.org/10.1149/1945-7111/ac67f5>. Publication date (web): April 27, 2022.
 29. W. Shin and A. Manthiram, "Fast and Simple Ag/Cu Ion Exchange on Cu Foil for Anode-free Lithium-metal Batteries," *ACS Applied Materials & Interfaces* 2022. DOI: <https://doi.org/10.1021/acsami.2c01980>. Publication date (web): April 6, 2022.
 30. L. Su, E. Jo, and A. Manthiram, "Protection of Cobalt-free LiNiO₂ from Degradation with Localized Saturated Electrolytes in Lithium-metal Batteries," *ACS Energy Letters* 2022. DOI: <https://doi.org/10.1021/acsenenergylett.2c01081>. Publication date (web): June 1st, 2022.

31. L. Shi, C.S. Anderson, L. Mishra, H. Qiao, N.L. Canfield, Y. Xu, C. Wang, T. Jang, Z. Yu, S. Feng, P.M. Le, V.R. Subramanian, C. Wang, J. Liu, J. Xiao, and D. Lu*, “Early Failure of Lithium–sulfur Batteries at Practical Conditions: Crosstalk between Sulfur Cathode and Lithium Anode,” *Advanced Science* 2022. DOI: <https://doi.org/10.1002/advs.202201640>. Publication date (web): May 7, 2022.
32. Moni K. Datta, Ramalinga Kuruba, T. Prasada Rao, Oleg I. Velikokhatnyi, and Prashant N. Kumta, “Chapter 11 - New approaches to high-energy density cathode and anode architectures for lithium-sulfur batteries”, *Lithium-Sulfur Batteries, Advances in High-Energy Density Batteries*, 2022, 354 – 439, DOI: 10.1016/B978-0-12-819676-2.00014-1. Publication date: June 17, 2022.
33. *Lithium-Sulfur Batteries, Advances in High-Energy Density Batteries*, Edited by Prashant N. Kumta, Aloysius F. Hepp, Moni K. Datta and Oleg I. Velikokhatnyi, Elsevier Book Publications, 2022, DOI: 10.1016/C2018-0-04066-9. Publication date: (available online) 1st Edition – June 12, 2022. ISBN: 978-0-1-819676-2.
34. Sha Tan, Zulipiya Shadike, Jizhou Li, Xuelong Wang, Yang Yang, Ruoqian Lin, Arthur Cresce, Jiangtao Hu, Adrian Hunt, Iradwikanari Waluyo, Lu Ma, Federico Monaco, Peter Cloetens, Jie Xiao, Yijin Liu*, Xiao-Qing Yang*, Kang Xu*, and Enyuan Hu*, “Additive engineering for robust interphases to stabilize high-Ni layered structures at ultra-high voltage of 4.8 V”, *Nature Energy*, VOL 7, June 2022 484–494 DOI: 10.1038/s41560-022-01020-x. Publication date: May 9, 2022.
35. J. Kim, M.H. Engelhard, B. Lu, Y. Xu, S. Tan, B.E. Matthews, S. Tripathi, X. Cao, C. Niu, E. Hu, S.-M. Bak, C. Wang, Y. S. Meng, J.-G. Zhang*, W. Xu*, “Fast-charging Lithium Metal Batteries Enabled by Double-layer Protected Lithium Metal Anode,” *Advanced Functional Materials* 2022. DOI: <https://doi.org/10.1002/adfm.202207172>. Publication date (web): September 23, 2022.
36. Fengxia Xin, Anshika Goel, Xiaobo Chen, Hui Zhou, Jianming Bai, Sizhan Liu, Feng Wang, Guangwen Zhou, and M Stanley Whittingham, “Electrochemical Characterization and Microstructure Evolution of Ni-rich Layered Cathode Materials by Niobium Coating/Substitution,” *Chemistry of Materials* 2022. DOI: <https://doi.org/10.1021/acs.chemmater.2c01461>. Publication date (web): August 16, 2022.
37. Oyakhire ST, Gong H, Cui Y, Bao Z, Bent SF, “An X-ray Photoelectron Spectroscopy Primer for Solid Electrolyte Interphase Characterization in Lithium Metal Anodes,” *ACS Energy Letters* 2022. DOI: <https://doi.org/10.1021/acsenergylett.2c01227>. Publication date (web): July 12, 2022.
38. Yu, W, Yu, Z, Cui, Y, Bao, Z, “Degradation and Speciation of Li Salts during XPS Analysis for Battery Research,” *ACS Energy Letters* 2022. DOI: <https://doi.org/10.1021/acsenergylett.2c01587>. Publication date (web): September 6, 2022.
39. Boyle, D. T, Li, Y, Pei, A, Vilá, R. A, Zhang, Z, Sayavong, P, Kim, M. S, Huang, W, Wang, H, Liu, Y, Xu, R, Sinclair, R, Qin, J, Bao, Z, Cui, Y, “Resolving Current-dependent Regimes of Electroplating Mechanisms for Fast Charging Lithium Metal Anodes,” *Nano Letters* 2022. DOI: <https://doi.org/10.1021/acs.nanolett.2c02792>. Publication date (web): October 10, 2022.
40. Kim, S. C, Wang, J, Xu, R, Zhang, P, Chen, Y, Huang, Z, Yang, Y, Yu, Z, Oyakhire, S, Zhang, W, Kim, M. S, Boyle, D, Sayavong, P, Qin, J, Bao, Z, Cui, Y, “High Entropy Electrolytes for Practical Lithium Metal Batteries,” *ChemRxiv* (preprint) 2022. DOI: <https://doi.org/10.26434/chemrxiv-2022-j40p4>. Publication date (web): September 13, 2022.
41. Zhaohui Wu, Haodong Liu, John Holoubek, Cassidy Anderson, Lili Shi, Hridayanand Khemchandani, Dongping Lu, Dianying Liu, Chaojiang Niu, Jie Xiao, and Ping Liu, “The Role of Ion Transport in the Failure of High Areal Capacity Li Metal Batteries,” *ACS Energy Letters* 2022. DOI: <https://doi.org/10.1021/acsenergylett.2c01114>. Publication date (web): July 25, 2022.
42. Bingyu Lu, Weikang Li, Diyi Cheng, Miguel Ceja, Wurigumula Bao, Chengcheng Fang, Ying Shirley Meng, “Suppressing Chemical Corrosions of Lithium Metal Anodes,” *Advanced Energy Materials* 2022. DOI: <https://doi.org/10.1002/aenm.202202012>. Publication date (web): October 28, 2022.
43. Bingyu Lu, Wurigumula Bao, Weiliang Yao, Jean-Marie Doux, Chengcheng Fang, Ying Shirley Meng, “Methods — Pressure Control Apparatus for Lithium Metal Battery,” *Journal of The Electrochemical Society* 2022. DOI: <https://doi.org/10.1149/1945-7111/ac834c>. Publication date (web): July 29, 2022.

44. Yuxun Ren, Amruth Bhargav, Woonchul Shin, Hyunki Sul, Arumugam Manthiram, “Anode-free Lithium–Sulfur Cells Enabled by Rationally Tuning Lithium Polysulfide Molecules,” *Angewandte Chemie* 2022. DOI: <https://doi.org/10.1002/anie.202207907>. Publication date (web): July 7, 2022.
45. Jayse Langdon, Richard Sim, Arumugam Manthiram, “Gas Generation in Lithium Cells with High-Nickel Cathodes and Localized High-concentration Electrolytes,” *ACS Energy Letters* 2022. DOI: <https://doi.org/10.1021/acsenergylett.2c01444>. Publication date (web): July 19, 2022.
46. Laisuo Su, Xunhua Zhao, Michael Yi, Harry Charalambous, Hugo Celio, Yuanyue Liu, Arumugam Manthiram, “Uncovering the Solvation Structure of LiPF₆-based Localized Saturated Electrolytes and Their Effect on LiNiO₂-based Lithium-metal Batteries,” *Advanced Energy Materials* 2022. DOI: <https://doi.org/10.1002/aenm.202201911>. Publication date (web): August 2, 2022.
47. Jayse Langdon, Arumugam Manthiram, “Crossover Effects in Lithium-metal Batteries with a Localized High Concentration Electrolyte and High-Nickel Cathodes,” *Advanced Materials* 2022. DOI: <https://doi.org/10.1002/adma.202205188>. Publication date (web): August 19, 2022.
48. Laisuo Su, Arumugam Manthiram, “Lithium-metal Batteries via Suppressing Li Dendrite Growth and Improving Coulombic Efficiency,” *Small Structures* 2022. DOI: <https://doi.org/10.1002/ssstr.202200114>. Publication date (web): September 8, 2022.
49. Liu, J. Xia, W. Zhang, H. Wan, J. Zhang, J. Xu, J. Rao, T. Deng, S. Hou, B. Nan, C. Wang, “Salt-in-Salt Reinforced Carbonate Electrolyte for Li Metal Batteries,” *Angewandte Chemie* 2022. DOI: <https://doi.org/10.1002/anie.202210522>. Publication date (web): August 30, 2022.

Presentations (invited)

1. M. Stanley Whittingham, “Li-Ion Batteries: Pushing the Limits for Electrifying the Transportation Sector”, CBMM Niobium Webinar, October 5th, 2021.
2. M. Stanley Whittingham, Van Vlack Lecture, “The Lithium Battery, from a Dream to Readiness to Take on Climate Change – Materials Opportunities and Challenges”, Materials Science & Engineering, U. Michigan, October 8th, 2021.
3. M. Stanley Whittingham, MLH Green Lecture, “The Lithium Battery, from a Dream to Readiness to Take on Climate Change – Opportunities and Challenges”, October 11th, 2021. Chemistry Department, Oxford University, October 11th, 2021.
4. M. Stanley Whittingham, “Lithium Batteries: From a Dream to Enabling a Clean Fossil-Free World”, Africa MRS, November 9th, 2021.
5. M. Stanley Whittingham, “Energy Storage is Key to Attainment of Fossil-free Energy”, Faraday Institution, UK, November 17th, 2021.
6. M. Stanley Whittingham, Symposium X “The Lithium Battery: From a Dream to Readiness to Take-On Climate Change – Materials Challenges” Materials Research Society, Boston, MA, November 30th, 2021.
7. Manthiram, “A Path Toward Sustainable Battery Technologies,” 240th Electrochemical Society Meeting, Orlando, FL, October 10 – 14, 2021 (invited talk).
8. Manthiram, “A Solid-state Chemistry Perspective of Layered Oxide Cathodes for Lithium-ion Batteries,” 240th Electrochemical Society Meeting, Orlando, FL, October 10 – 14, 2021 (invited talk).
9. Manthiram, “Sustainable Next-generation Battery Chemistries,” UT Austin Portugal 2021 Annual Conference, Virtual, October 20 – 21, 2021 (invited talk).
10. Manthiram, “Sustainable Battery Chemistries for Electrical Energy Storage,” Materials Research Society-Taiwan International Conference (2021 MRSTIC), Taipei, Taiwan, MA, November 13 – 17, 2021 (invited plenary talk).
11. Manthiram, “Delineating and Controlling the Electrode-Electrolyte Interfacial Reactions in High Energy Density Batteries,” American Institute of Chemical Engineers Annual Meeting Meeting, Boston, MA, November 14 – 19, 2021 (invited talk).
12. Manthiram, “Sustainable Battery Technologies for Vehicle Electrification,” 3rd IEEE Bombay Section Signature Conference (IBSSC-2021), Bombay, India, November 18 – 20, 2021 (invited talk).

13. Manthiram, "Sustainable Battery Technologies for Clean Energy and Environment," Third Indian Materials Conclave and 32nd Annual General Meeting of the Materials Research Society of India, Bangalore, India, December 20 – 23, 2021 (invited talk).
14. Ji-Guang Zhang, "Lithium Metal Anodes with Nonaqueous Electrolytes," Storage X Symposium, Oct. 8, 2021.
15. Ji-Guang Zhang, "Stability of Li Metal Anode and Calendar Life of Lithium Metal Batteries," 240th ECS meeting, Oct. 10, 2021.
16. J. Xiao, "Materials Chemistry in Electrochemical Energy Storage," Chemistry Department Seminar (virtual), Binghamton University, November 5th, 2021.
17. J. Xiao, "From Materials Science to Prototype Batteries and Cell Manufacturing," International Battery Materials Association (virtual), October 24, 2021.
18. Ping Liu, "Li-S batteries with pyrolyzed polymer sulfur cathodes," International Battery Association Meeting, October 2021.
19. Ping Liu, "Design of Stable Cathodes for Solid State Li-S Batteries," Materials Research Society Meeting, December 2021.
20. Shirley Meng, Keynote Talk, "Advanced characterization for Li metal and solid state batteries", 2021 MRS, Boston, Nov. 29th 2021.
21. Perla B. Balbuena, "Electron and Ion Transport in Li-metal Batteries: Role of the Electrolyte," Invited Seminar to Texas Tech University, October 8, 2021.
22. Perla B. Balbuena, "Interrogating Electrochemical Interfaces at the Atomistic Level: Links to Macroscopic Behavior," Invited Seminar to University of Colorado, Boulder, November 18, 2021
23. Manthiram, "Sustainable Next-generation Battery Technologies," International Conference on Energy Materials and Devices, Banarus Hindu University, Varanasi, India, January 11 – 12, 2022 (plenary talk).
24. Manthiram, "Sustainable Battery Chemistries for Electrical Energy Storage," University of Utah, Denver, CO, January 26, 2022.
25. Manthiram, "Sustainable Battery Chemistries for Electrical Energy Storage," Gyeongsang National University, Jinju, South Korea, February 7, 2022 (invited).
26. Manthiram, "Sustainable Battery Chemistries for a Cleaner Environment" International Virtual Conference on Advanced Materials for Sustainable Energy and Environment, Coimbatore, India, February 16, 2022 (Inaugural Address).
27. Manthiram, "A Path Forward for Sustainable Battery Chemistries," Spotlights in Advanced Science/Small Science: Advances in Smart Materials and Energy Research Webinar, Wiley Publisher, Weinheim, Germany, March 15 – 16, 2022 (invited talk).
28. Manthiram, "Towards Practically Viable Lithium–sulfur Batteries," Battery Conference, Korea Battery Industry Association, Seoul, South Korea, March 17 – 19, 2022 (invited talk).
29. M. Stanley Whittingham, "Energy Storage is Key to Attainment of Fossil-free Energy", The 2022 International Conference on Hierarchical Green Energy", Taiwan, January 15th, 2022.
30. M. Stanley Whittingham, "The Critical Role of Storage for Renewable Energy and Climate Change", Global Young Scientists Meeting, Singapore January 17th, 2022.
31. M. Stanley Whittingham, "The Challenges Facing Lithium Batteries as they Address Climate Change", Arkema, February 3rd, 2022.
32. J. Xiao, "Electrochemical Energy Storage: An Integration of Materials Science, Electrochemistry and Engineering", Seminar at Dalhousie University, March 24th, 2022.
33. J. Xiao, "Single Crystal Ni-Rich Cathode Materials for Advanced Li-ion Batteries", ACS Spring Meeting, March 21, 2022.
34. J. Xiao, "Battery500 Consortium Overview", Lithium Metal Battery Symposium, MPSC Symposium Series (virtual), March 3rd, 2022.
35. J. Xiao, "Battery500 Consortium Overview", US – UK Battery Technology Research and Innovation Online Summit (virtual), February 1st, 2022

36. Perla B. Balbuena, “Interfacial Phenomena in Batteries: What Can We Learn From Theory?,” Seminar to Université de Sherbrooke, Sherbrooke, Canada, April 7, 2022.
37. Perla B. Balbuena, “Theory/Computation Role in Tuning Surface/Electrolyte Interfaces for Enhancing Catalytic Performance,” Texas A&M Research Computing Symposium (RCS), Texas A&M University, College Station, TX, May 23, 2022.
38. Jorge M. Seminario, “Beyond Graphite for Li-ion Batteries: Searching for Lithium Metal Alternatives using Quantum Mechanical Methods,” Texas A&M Research Computing Symposium (RCS), Texas A&M University, College Station, TX, May 23, 2022.
39. W. Xu, “Development of Electrolytes for Lithium Batteries,” Saft America, Cockeysville, MD, June 24, 2022.
40. W. Xu, “Electrolytes for Lithium-ion Batteries,” Lecture at 2022 University of Washington Battery Class, University of Washington, Seattle, April 11, 2022.
41. Ji-Guang Zhang, “Challenges for Li Metal and Si Anodes,” University of Washington, Seattle, WA, April 18, 2022.
42. Manthiram, “Clean Energy Technologies,” My Introduction to Engineering (MITE) Summer Enrichment Camp, Equal Opportunity in Engineering Program, University of Texas at Austin, Austin, TX, June 6, 2022
43. Manthiram, “Battery Chemistries for Relieving Supply Chain Issues of Today, Tomorrow, and Day-after-tomorrow,” 2022 Spring Biannual Meeting: Science and Technology Enablers of a Domestic Extreme Battery Supply Chain, University of Maryland, College Park, MD, June 10, 2022
44. Manthiram, “Sustainable Battery Technologies for Relieving Supply Chain Issues,” Automotive Electrification Tech Forum Speaker Series, 3M, Minneapolis, MN, June 15, 2022
45. Manthiram, “Delineating the Intricacies of High-Nickel Cathodes for Lithium-ion Batteries,” 21st International Meeting on Lithium Batteries, Sydney, Australia, June 26 – July 1st, 2022
46. Prashant N. Kumta, “Perspectives on Materials for Energy Applications”, Lehigh University, Bethlehem, PA, April 19, 2022.
47. Y.S. Meng, Keynote Talk - "Advanced Characterization and Metrology Development for Lithium Metal Batteries" International Meeting on Lithium Batteries IMLB 2022, Sydney, Australia June 29, 2022
48. Y.S. Meng, Invited Talk - "Rechargeable Lithium Metal Batteries", E02 Symposium, Electrochemical Society ECS, Vancouver, Canada, June 1, 2022.
49. Y.S. Meng, Invited Talk - "Cryo-EM for Battery Materials", Gordon Research Conference GRC Battery, June 6, 2022.
50. M. Stanley Whittingham, Ta-You-Wu Lecture, “The Lithium Battery: From a Dream to Readiness to Take-On Climate Change”, University of Buffalo, April 28th, 2022.
51. M. Stanley Whittingham, Derby Lecture, “The Lithium Ion Battery, from a Dream to Domination of Energy Storage – Future Chemistry and Materials Challenges”, University of Kentucky, Louisville, KY. May 5th, 2022.
52. M. Stanley Whittingham, “The Challenges Facing Lithium Batteries as they Address Climate Change”, Clariant, Louisville, KY, May 6th, 2022.
53. M. Stanley Whittingham, Derby Public Lecture, “The Electric Economy and Climate Change: The Critical Role of Energy Storage”, University of Kentucky, Louisville, KY. May 6th, 2022.
54. M. Stanley Whittingham, “The Pros and Cons of Solid vs Liquid Electrolytes in Lithium Batteries”, Materials Research Society, Honolulu, Hawaii, May 9th, 2022.
55. M. Stanley Whittingham, “The Electric Economy and Climate Change: The Critical Role of Energy Storage”, Vestal High School, Vestal, NY, May 19th, 2022.
56. M. Stanley Whittingham, Van Vlack Public Lecture, “Overcoming Climate Change: The Critical Role and Challenges of Energy Storage”, University of Michigan, Ann Arbor, MI, May 23rd, 2022.
57. M. Stanley Whittingham, Ben Pei, Isiksu Buyker, Krystal Lee, Fengxia Xin and Hui Zhou, “Pushing the Limits of NMC Cathodes”, 241st Electrochemical Society Meeting, Vancouver, BC, Canada, May 31st, 2022.

58. M. Stanley Whittingham, Opening Plenary, “Pushing the Limits of Lithium Batteries”, IMLB-2022, Sydney, Australia, June 27th, 2022. M. Stanley Whittingham
59. W. Xu, J. Kim, X. Cao, and J. Zhang, “Enabling Lithium Metal Anode by Advancing Electrolytes and Lithium Protection,” American Chemical Society (ACS) Fall 2022, Chicago, IL, August 22, 2022.
60. M. Stanley Whittingham, “Pushing the Limits of Li-ion Batteries at their 50 Year Anniversary,” 1st Distinguished Engineering Lecture Series, University of New South Wales, Sydney, Australia, July 1st, 2022.
61. M. Stanley Whittingham, “The Key Role of Solid State Ionics in the Development of Lithium-ion Batteries,” Solid State Ionics, Boston, MA, July 19, 2022.
62. M. Stanley Whittingham, “Lithium-based Batteries: 1970 – Today,” John B. Goodenough 100th Birthday, Austin, TX, July 22, 2022.
63. M. Stanley Whittingham, Hui Zhou, Fengxia Xin, Ben Pei, Isiksu Buyuker, Krystal Lee and Jie Xiao and the Battery500 team, “Pushing the Limits of Lithium Batteries,” International Society of Electrochemistry (ISE) Meeting, Online, September 12, 2022.
64. M. Stanley Whittingham, Fengxia Xin and the Battery500 team, “Role of Nb in Nickel-rich Layered Oxide Cathodes for Lithium-ion Batteries,” 2022 International Conference on Niobium Based Batteries, Online, September 14, 2022.
65. Z Huang, Y Cui, Z Bao, “Solving a Metal Issue with Organic (Macro)Molecules,” ACS Fall 2022, Chicago, IL, August 21 – 25, 2022.
66. Z Huang, Y Cui, Z Bao, “Advanced Polymer Coatings for Li Metal Anodes,” ACS Fall 2022, Chicago, IL, August 21 – 25, 2022.
67. Z Huang, Y Cui, Z Bao, “Improving the Lithium Metal Battery Performance with a Polymer Layer,” ACS Fall 2022, Chicago, IL, August 21 – 25, 2022.
68. Y. Lin, Z. Bao, “Dynamic Enamine-one Bonds Enabled Sustainable Polymeric Materials,” ACS Fall 2022, Chicago, IL, August 21 – 25, 2022.
69. Ping Liu, “Approaches to Mitigating Internal Shorting of Lithium Batteries,” ACS Fall 2022, Chicago, IL, August 21, 2022.
70. Shirley Meng, “Designing Better Materials for Future Batteries,” International Conference on Materials for Humanity 2022 (MH 22), Singapore, September 21, 2022.
71. Prashant N. Kumta, “From Lithiated Transition Metal Oxides to Silicon to Lithium-Sulfur: Evolution of Electrochemically Active Materials,” Symposium A02: Research and Development of Primary and Secondary Batteries, 242nd Electrochemical Society Meeting, Atlanta, GA, October 9 – 13, 2022.
72. Manthiram, “Delineating the Intricacies of High-Nickel Cathodes for Lithium-ion Batteries,” 21st International Meeting on Lithium Batteries, Sydney, Australia, June 26 – July 1, 2022.
73. Manthiram, “Battery Chemistries for a Sustainable Future,” Workshop on Electrochemical Energy Storage and Conversion Towards Carbon Neutrality, Hong Kong Polytechnic University, Hong Kong, July 4 – 5, 2022.
74. Manthiram, “Delineating the Intricacies of the Interfacial Chemistry of High-Nickel Cathodes in Lithium-based Batteries,” PlugVolt Battery Seminar, Plymouth, MI, July 12 – 14, 2022.
75. Manthiram, “Delineating the Intricacies of the Interfacial Chemistry of High-Nickel Cathodes in Lithium-based Batteries,” 23rd International Conference on Solid State Ionics (SSI23), Boston, MA, July 17 – 22, 2022.
76. Manthiram, “A Path Toward Sustainable Energy Storage,” John Goodenough Energy Storage Lecture Series, The University of Texas at Austin, Austin, TX, September 8, 2022.
77. Manthiram, “Sustainable Battery Chemistries for a Cleaner Planet,” University of Michigan, Ann Arbor, MI, September 16, 2022.
78. Manthiram, “Electrical Energy Storage: Near-term and Long-term Perspectives,” University of Louisiana, Lafayette, LA, September 23, 2022.
79. J. Xiao, “PNNL R&D in Primary and Secondary Lithium Metal Batteries,” 242nd Electrochemical Society Meeting, Atlanta, GA, October 12, 2022.

80. J. Xiao, “An Integrated Science and Engineering Approach for Next-generation Battery Materials and Technology,” ORCAS 2022: International Conference on Energy Conversion and Storage, San Juan, WA, September 8, 2022.

(This page intentionally left blank)

